Report from Working Group 3: Beyond the Standard Model physics at the HL-LHC and HE-LHC Physics of the HL-LHC, and Perspectives at the HE-LHC

Baker, Michael J ; Ježo, Tomáš ; Matorras Cuevas, P ; Takahashi, Yuta

Abstract: This is the third out of five chapters of the final report [1] of the Workshop on Physics at HL-LHC, and perspectives on HE-LHC [2]. It is devoted to the study of the potential, in the search for Beyond the Standard Model (BSM) physics, of the High Luminosity (HL) phase of the LHC, defined as 3 ab^{-1} of data taken at a centre-of-mass energy of 14 TeV, and of a possible future upgrade, the High Energy (HE) LHC, defined as 15 ab^{-1} of data at a centre-of-mass energy of 27 TeV. We consider a large variety of new physics models, both in a simplified model fashion and in a more model-dependent one. A long list of contributions from the theory and experimental (ATLAS, CMS, LHCb) communities have been collected and merged together to give a complete, wide, and consistent view of future prospects for BSM physics at the considered colliders. On top of the usual standard candles, such as supersymmetric simplified models and resonances, considered for the evaluation of future collider potentials, this report contains results on dark matter and dark sectors, long lived particles, leptoquarks, sterile neutrinos, axion-like particles, heavy scalars, vector-like quarks, and more. Particular attention is placed, especially in the study of the HL-LHC prospects, to the detector upgrades, the assessment of the future systematic uncertainties, and new experimental techniques. The general conclusion is that the HL-LHC, on top of allowing to extend the present LHC mass and coupling reach by $20 - 50$

DOI: https://doi.org/10.23731/CYRM-2019-007.585

CERN Yellow Reports: Monographs CERN-2019-007

Report on the Physics at the HL-LHC, and Perspectives for the HE-LHC

Editors:

Andrea Dainese

Michelangelo Mangano

Andreas B. Meyer

Aleandro Nisati

Gavin Salam

Mika Anton Vesterinen

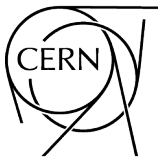

CERN Yellow Reports: Monographs
Published by CERN, CH-1211 Geneva 23, Switzerland

ISBN 978-92-9083-549-3 (PDF)
ISSN 2519-8076 (Online)
DOI https://doi.org/10.23731/CYRM-2019-007

Accepted for publication by the CERN Report Editorial Board (CREB) on 2 December 2019
Available online at http://publishing.cern.ch/ and http://cds.cern.ch/

This volume is indexed in: CERN Document Server (CDS) and INSPIRE

This volume should be cited as:
Physics of the HL-LHC, and Perspectives at the HE-LHC, CERN Yellow Reports: Monographs, CERN-2019-007 (CERN, Geneva, 2019), https://doi.org/10.23731/CYRM-2019-007

Abstract

This report comprises the outcome of five working groups that have studied the physics potential of the high-luminosity phase of the LHC (HL-LHC) and the perspectives for a possible future high-energy LHC (HE-LHC). The working groups covered a broad range of topics: Standard Model measurements, studies of the properties of the Higgs boson, searches for phenomena beyond the Standard Model, flavor physics of heavy quarks and leptons and studies of QCD matter at high density and temperature.

The work is prepared as an input to the ongoing process of updating the European Strategy for Particle Physics, a process that will be concluded in May 2020.

Preface

The high-luminosity phase of the LHC (HL-LHC) will extend the LHC programme to the second half of the 2030's, with a major increase in the statistics relative to what has been collected so far. As approved, the HL-LHC project will deliver (a) pp collisions at 14 TeV with an integrated luminosity of 3 ab^{-1} each for ATLAS and CMS and 50 fb^{-1} for LHCb, and (b) PbPb and pPb collisions with integrated luminosities of 13 nb^{-1} and 50 nb^{-1}, respectively. With the newly proposed upgrades of the detector, the LHCb experiment could increase its target luminosity to 300 fb^{-1}, and an extension of the heavy ion programme could lead to 1.2 pb^{-1} of integrated luminosity for pPb collisions, with the addition of collisions of other nuclear species.

A large effort has taken place over the last few years, to define the detector upgrades required to sustain the HL-LHC event rates while maintaining, and often significantly improving, the detectors' physics performance. This work, accompanied by the experience gained with the data analyses so far, has made it possible to explore the HL-LHC physics potential in a realistic, concrete and reliable way. Building on this groundwork, and on the theoretical progress stimulated by the interpretation of the data from the first two runs of the LHC, the Workshop documented in this Yellow Report carried out an extensive review of the HL-LHC prospects. Five working groups covered a broad range of topics:

1. Standard Model measurements
2. Studies of the properties of the Higgs boson
3. Searches for phenomena beyond the Standard Model
4. Flavor physics of heavy quarks and leptons
5. Studies of QCD matter at high density and temperature.

This Report has a companion Volume, collecting the ATLAS and CMS notes that provide additional details on all reported analyses.

A rich picture has emerged, defining new ambitious targets for critical measurements ranging from the Higgs couplings and self-coupling, to the W mass, flavor properties, and more. New opportunities have been considered in the search of new physics, with emphasis on the class of models that lead to the most challenging and elusive signatures, and which could have evaded detection so far. The goals of precise Quark-Gluon Plasma studies and the new questions raised by current LHC data have led to the confirmation of the programme of runs with Pb nuclei and a proposal to collide lighter nuclei in Run 5.

The workshop has made it clear that physics at the HL-LHC will not be just a bare rerun of previous analysis strategies and techniques. The immense statistics will open the way to new ideas, stimulating creativity and original thinking, leading to better ways to control the experimental and theoretical systematics, and ultimately to improve the precision of the measurements and the sensitivity to new physics. It will be the task of the coming generations of young physicists to uncover and fully exploit the fantastic opportunities created by the HL-LHC!

The possibility of increasing the LHC energy to 27 TeV, by using the 16 T dipoles under development in the context of the Future Circular Collider project, expanded the scope of the Workshop. Each working group analyzed the reach of this possible future project (the high-energy LHC, HE-LHC), documenting its findings in parallel with the presentation of the HL-LHC results.

The HL-LHC projections presented in this Report set a new and very challenging reference benchmark to assess the added value, and required performance, of future colliders. This was stressed on several occasions

during the 2019 CERN Council Open Symposium on the update of the European Strategy for Particle Physics, in Granada. We therefore trust that these HL-LHC projections, together with the studies of the HE-LHC physics potential, will be useful to the ongoing strategy update process.

The Workshop engaged the LHC experimental and theoretical communities, through a year-long world-wide effort. We are deeply grateful to the working group conveners for successfully leading this big effort, and to all participants, for their commitment and substantial contributions. We also thank Angela Ricci, who provided administrative support and assistance.

The workshop steering committee has been constituted by:

A. Dainese, M. Mangano, A. B. Meyer, A. Nisati, G. Salam and M. Vesterinen

The working groups were convened by:

P. Azzi, S. Farry, P. Nason, A. Tricoli and D. Zeppenfeld
WG1: Standard Model physics at the HL-LHC and HE-LHC
Corresponding convener: Stephen.Farry@cern.ch

M. Cepeda, S. Gori, P. Ilten, M. Kado and F. Riva
WG2: Higgs physics at the HL-LHC and HE-LHC
Corresponding convener: Kado@lal.in2p3.fr

X. Cid Vidal, M. D'Onofrio, P. J. Fox, R. Torre and K. A. Ulmer
WG3: Beyond the Standard Model physics at the HL-LHC and HE-LHC
Corresponding convener: Riccardo.Torre@cern.ch

A. Cerri, V. V. Gligorov, S. Malvezzi, J. Martin Camalich and J. Zupan
WG4: Opportunities in flavour physics at the HL-LHC and HE-LHC
Corresponding convener: Jure.Zupan@gmail.com

Z. Citron, A. Dainese, J. F. Grosse-Oetringhaus, J. M. Jowett, Y.-J. Lee, U. A. Wiedemann and M. Winn
WG5: Future physics opportunities for high-density QCD at the LHC with heavy-ion and proton beams
Corresponding convener: Jan.Fiete.Grosse-Oetringhaus@cern.ch

Contents

Standard Model physics at the HL-LHC and HE-LHC
Report from Working Group 1 1

Higgs physics at the HL-LHC and HE-LHC
Report from Working Group 2 221

Beyond the Standard Model physics at the HL-LHC and HE-LHC
Report from Working Group 3 585

Opportunities in flavour physics at the HL-LHC and HE-LHC
Report from Working Group 4 867

Future physics opportunities for high-density QCD at the LHC with heavy-ion and proton beams
Report from Working Group 5 1159

Report from Working Group 1: Standard Model physics at the HL-LHC and HE-LHC

Physics of the HL-LHC, and Perspectives at the HE-LHC

Conveners:
P. Azzi[1], *S. Farry*[2], *P. Nason*[3,4], *A. Tricoli*[5], *D. Zeppenfeld*[6]

Contributors:
R. Abdul Khalek[7,8], *J. Alimena*[9], *N. Andari*[10], *L. Aperio Bella*[11], *A.J. Armbruster*[11], *J. Baglio*[12], *S. Bailey*[13], *E. Bakos*[14], *A. Bakshi*[15], *C. Baldenegro*[16], *F. Balli*[10], *A. Barker*[15], *W. Barter*[17], *J. de Blas*[18,1], *F. Blekman*[19], *D. Bloch*[20], *A. Bodek*[21], *M. Boonekamp*[10], *E. Boos*[22], *J.D. Bossio Sola*[23], *L. Cadamuro*[24], *S. Camarda*[11], *F. Campanario*[25], *M. Campanelli*[26], *J.M. Campbell*[27], *Q.-H. Cao*[28,29,30], *V. Cavaliere*[5], *A. Cerri*[31], *G.S. Chahal*[17,32], *B. Chargeishvili*[33], *C. Charlot*[34], *S.-L. Chen*[35], *T. Chen*[36], *L. Cieri*[3], *M. Ciuchini*[37], *G. Corcella*[38], *S. Cotogno*[34], *R. Covarelli*[39,40], *J.M. Cruz-Martinez*[41], *M. Czakon*[42], *A. Dainese*[1], *N.P. Dang*[43], *L. Darmé*[44], *S. Dawson*[5], *H. De la Torre*[45], *M. Deile*[11], *F. Deliot*[10], *S. Demers*[46], *A. Denner*[47], *F. Derue*[48], *L. Di Ciaccio*[49], *W.K. Di Clemente*[50], *D. Dominguez Damiani*[51], *L. Dudko*[22], *A. Durglishvili*[33], *M. Dünser*[11], *J. Ebadi*[52], *R.B. Ferreira De Faria*[53], *G. Ferrera*[41,54], *A. Ferroglia*[55], *T.M. Figy*[36], *K.D. Finelli*[56], *M.C.N. Fiolhais*[57,53], *E. Franco*[58], *R. Frederix*[59], *B. Fuks*[60,61], *B. Galhardo*[53,62], *J. Gao*[63], *J.R. Gaunt*[11], *T. Gehrmann*[64], *A. Gehrmann-De Ridder*[65], *D. Giljanovic*[66,34], *F. Giuli*[67], *E.W.N. Glover*[32], *M.D. Goodsell*[68], *E. Gouveia*[53], *P. Govoni*[3,4], *C. Goy*[49], *M. Grazzini*[64], *A. Grohsjean*[51], *J.F. Grosse-Oetringhaus*[11], *P. Gunnellini*[69], *C. Gwenlan*[70], *L.A. Harland-Lang*[13], *P.F. Harrison*[71], *G. Heinrich*[72], *C. Helsens*[11], *M. Herndon*[73], *O. Hindrichs*[21], *V. Hirschi*[65], *A. Hoang*[74], *K. Hoepfner*[42], *J.M. Hogan*[75,76], *A. Huss*[11], *S. Jahn*[72], *Sa. Jain*[77], *S.P. Jones*[11], *A.W. Jung*[15], *H. Jung*[51], *S. Kallweit*[4], *D. Kar*[78], *A. Karlberg*[64], *T. Kasemets*[79], *M. Kerner*[64], *M.K. Khandoga*[10], *H. Khanpour*[80], *S. Khatibi*[81], *A. Khukhunaishvili*[82], *J. Kieseler*[11], *J. Kretzschmar*[2], *J. Kroll*[50], *E. Kryshen*[83], *V.S. Lang*[51], *L. Lechner*[84], *C.A. Lee*[5], *M. Leigh*[85], *D. Lelas*[58], *R. Les*[86], *I.M. Lewis*[16], *B. Li*[87], *Q. Li*[28], *Y. Li*[88], *J. Lidrych*[51], *Z. Ligeti*[89], *J.M. Lindert*[90,32], *Y. Liu*[91], *K. Lohwasser*[92], *K. Long*[73], *D. Lontkovskyi*[19], *G. Majumder*[77], *M. Mancini*[19], *P. Mandrik*[93], *M.L. Mangano*[11], *I. Marchesini*[19], *C. Mayer*[94], *K. Mazumdar*[77], *J.A. McFayden*[11], *P.M. Mendes Amaral Torres Lagarelhos*[53], *A.B. Meyer*[51], *S. Mikhalcov*[95], *S. Mishima*[96], *A. Mitov*[97], *M. Mohammadi Najafabadi*[52], *M. Moreno Llácer*[11], *M. Mulders*[11], *M. Myska*[98], *M. Narain*[76], *A. Nisati*[58,99], *T. Nitta*[100], *A. Onofre*[101], *S. Pagan Griso*[89,102], *D. Pagani*[59], *E. Palencia Cortezon*[103], *A. Papanastasiou*[97], *K. Pedro*[27], *M. Pellen*[97], *M. Perfilov*[22], *L. Perrozzi*[65], *B.A. Petersen*[11], *M. Pierini*[11], *J. Pires*[104], *M.-A. Pleier*[5], *S. Plätzer*[74], *K. Potamianos*[88], *S. Pozzorini*[64], *A.C. Price*[90], *M. Rauch*[6], *E. Re*[11,105], *L. Reina*[106], *J. Reuter*[51], *T. Robens*[107], *J. Rojo*[8], *C. Royon*[16], *S. Saito*[77], *A. Savin*[73], *S. Sawant*[77], *B. Schneider*[27], *R. Schoefbeck*[84], *M. Schoenherr*[32,11], *H. Schäfer-Siebert*[6], *M. Seidel*[11], *M. Selvaggi*[11], *T. Shears*[2], *L. Silvestrini*[58,11], *M. Sjodahl*[108], *K. Skovpen*[19], *N. Smith*[27], *D. Spitzbart*[84], *P. Starovoitov*[109], *C.J.E. Suster*[110], *P. Tan*[27], *R. Taus*[21], *D. Teague*[73], *K. Terashi*[111], *J. Terron*[112], *S. Uplap*[77], *F. Veloso*[53], *M. Verzetti*[64], *M.A. Vesterinen*[71], *V.E. Vladimirov*[71], *P. Volkov*[22], *G. Vorotnikov*[22], *M. Vranjes Milosavljevic*[14], *N. Vranjes*[14], *E. Vryonidou*[11], *D. Walker*[90], *M. Wiesemann*[11], *Y. Wu*[113], *T. Xu*[10], *S. Yacoob*[85], *E. Yazgan*[114], *J. Zahreddine*[48], *G. Zanderighi*[11,72], *M. Zaro*[8], *O. Zenaiev*[51], *G. Zevi Della Porta*[115], *C. Zhang*[114], *W. Zhang*[76], *H.L. Zhu*[113,5], *R. Zlebcik*[51], *F.N. Zubair*[11]

[1] INFN Sezione di Padova, Padova, Italy
[2] Oliver Lodge Laboratory, University of Liverpool, Liverpool, United Kingdom
[3] INFN Sezione di Milano-Bicocca, Milano, Italy

https://doi.org/10.23731/CYRM-2019-007.1

[4] Università degli Studi di Milano-Bicocca, Dipartimento di Fisica "G.Occhialini", Piazza della Scienza 3, 20126 Milan, Italy
[5] Brookhaven National Laboratory (BNL), USA
[6] Karlsruher Institut für Technologie (KIT), Institut für Theoretische Physik (TP), Wolfgang-Gaede-Str. 1, 76131 Karlsruhe, Germany
[7] Department of Physics and Astronomy, VU University, NL-1081 HV Amsterdam, Netherlands
[8] Nikhef National Institute for Subatomic Physics, Amsterdam, Netherlands
[9] The Ohio State University, Columbus, USA
[10] IRFU, CEA, Université Paris-Saclay, France
[11] European Laboratory for Particle Physics, CERN, Geneva, Switzerland
[12] Institut for Theoretical Physics, Eberhard Karls University Tübingen, Auf der Morgenstelle 14, D-72076 Tübingen, Germany
[13] Rudolf Peierls Centre, Beecroft Building, Parks Road, Oxford, OX1 3PU, United Kingdom
[14] Institute of Physics, University of Belgrade, Belgrade, Serbia
[15] Purdue University, West Lafayette, USA
[16] The University of Kansas, Lawrence, USA
[17] Imperial College, London, United Kingdom
[18] Università di Padova, Padova, Italy
[19] Vrije Universiteit Brussel, Brussel, Belgium
[20] Université de Strasbourg, CNRS, IPHC UMR 7178, Strasbourg, France
[21] University of Rochester, Rochester, NY, USA
[22] Skobeltsyn Institute of Nuclear Physics, Lomonosov Moscow State University, Moscow, Russia
[23] Universidad de Buenos Aires, Buenos Aires, Argentina
[24] University of Florida, Gainesville, USA
[25] Theory Division, IFIC, University of Valencia-CSIC, E-46980 Paterna, Valencia, Spain
[26] Department of Physics and Astronomy, University College London, London, United Kingdom
[27] Fermi National Accelerator Laboratory, P.O. Box 500 Batavia, 60510 USA
[28] Department of Physics and State Key Laboratory of Nuclear Physics and Technology, Peking University, Beijing 100871, China
[29] Collaborative Innovation Center of Quantum Matter, Beijing 100871, China
[30] Center for High Energy Physics, Peking University, Beijing 100871, China
[31] Department of Physics and Astronomy, University of Sussex, Brighton, United Kingdom
[32] Institute for Particle Physics Phenomenology, University of Durham, Durham, UK
[33] High Energy Physics Institute of Tbilisi State University, Tbilisi, Georgia
[34] LLR, Ecole polytechnique, CNRS/IN2P3, Université Paris-Saclay, Palaiseau, France
[35] Key Laboratory of Quark and Lepton Physics (MoE) and Institute of Particle Physics, Central China Normal University, China
[36] Department of Mathematics, Statistics, and Physics, Wichita State University, Wichita KS, USA
[37] INFN Sezione di Roma Tre, Via della Vasca Navale 84, I-00146 Roma, Italy
[38] INFN, Laboratori Nazionali di Frascati, Frascati, Italy
[39] Istituto Nazionale di Fisica Nucleare (INFN) Sezione di Torino , Italy
[40] Università di Torino, Torino, Italy
[41] Universita' di Milano, Dipartimento di Fisica, Milano, Italy
[42] RWTH Aachen University, III. Physikalisches Institut A, Aachen, Germany
[43] University of Louisville, Louisville, Kentucky, USA
[44] Narodowe Centrum Badań Jądrowych (NCBJ), Hoża 69, 00-681 Warszawa, Poland
[45] Department of Physics and Astronomy, Michigan State University, East Lansing, Michigan, USA
[46] Department of Physics, Yale University, New Haven CT, USA
[47] Universität Würzburg, Institut für Theoretische Physik und Astrophysik, Emil-Hilb-Weg 22, 97074

Würzburg, Germany
[48] Laboratoire de Physique Nucléaire et de Hautes Energies (LPNHE), Sorbonne Université, Paris-Diderot Sorbonne Paris Cité, CNRS/IN2P3, France
[49] LAPP, Univ. Grenoble Alpes, Univ. Savoie Mont Blanc, CNRS/IN2P3, Annecy, France
[50] Department of Physics and Astronomy, University of Pennsylvania, Philadelphia, Pennsylvania, USA
[51] Deutsches Elektronen-Synchrotron, Hamburg, Germany
[52] School of Physics, Institute for Research in Fundamental Sciences (IPM), P.O. Box 19395-5531, Tehran, Iran
[53] Laboratório de Instrumentação e Física Experimental de Partículas - LIP, Lisboa, Portugal
[54] INFN, Sezione di Milano, Via Celoria 16, I-20133 Milan, Italy
[55] Physics Department, New York City College of Technology, CUNY, 300 Jay Street, Brooklyn, NY 11201 USA
[56] Boston University, Department of Physics, Boston, Massachusetts, USA
[57] Science Department, Borough of Manhattan Community College, New York, NY 10007, USA
[58] INFN, Sezione Roma I, Roma, Italy
[59] Technische Universität München, München, Germany
[60] Laboratoire de Physique Théorique et Hautes Énergies (LPTHE), Boite 126, T13-14 4ème étage, 4 place Jussieu, F-75252 Paris CEDEX 05, France
[61] Institut Universitaire de France, 103 boulevard Saint-Michel, 75005 Paris, France
[62] Laboratório de Instrumentação e Física Experimental de Partículas - LIP, Coimbria, Portugal
[63] School of Physics and Astronomy, Shanghai Jiao Tong University, Shanghai, China
[64] Physik-Institut, Universitaet Zurich, 8057 Zurich, Switzerland
[65] Department of Physics, ETH Zurich, CH-8093 Zurich, Switzerland
[66] University of Split, Split, Croatia
[67] Università di Roma Tor Vergata, Dipartimento di Fisica, Roma, Italy
[68] Laboratoire de Physique Theorique et Hautes Energies, UMR 7589, Sorbonne Université et CNRS, Boîte 126, T13-14 4ème étage, 4 place Jussieu, F-75252 Paris CEDEX 05, France
[69] University of Hamburg, Hamburg, Germany
[70] Denys Wilkinson Building, University of Oxford, Oxford, OX1 3RH, United Kingdom
[71] Department of Physics, University of Warwick, Coventry, United Kingdom
[72] Max Planck Institute for Physics, Foehringer Ring 6, 80805 Munich, Germany
[73] University of Wisconsin - Madison, Madison, USA
[74] University of Vienna, Vienna, Austria
[75] Bethel University, St. Paul, USA
[76] Brown University, Providence, USA
[77] Tata Institute of Fundamental Research, Mumbai, India
[78] School of Physics, University of the Witwatersrand, South Africa
[79] PRISMA Cluster of Excellence and Institute for Physics (THEP), Johannes Gutenberg University Mainz, D-55099 Mainz, Germany
[80] Department of Physics, University of Science and Technology of Mazandaran, P.O.Box 48518-78195, Behshahr, Iran
[81] Department of Physics, University of Tehran, North Karegar Ave., Tehran 14395-547, Iran
[82] Cornell University, Physics Department, Ithaca, NY, USA
[83] Petersburg Nuclear Physics Institute (PNPI), Gatchina, Russia
[84] Institut für Hochenergiephysik, Wien, Austria
[85] University of Cape Town, South Africa
[86] Department of Physics, University of Toronto, Toronto, Canada
[87] Department of Physics, University of Michigan, Ann Arbor, Michigan, USA

[88] DESY, Hamburg and Zeuthen, Germany
[89] Lawrence Berkeley National Laboratory, 1 Cyclotron Road, Berkeley CA 94720 USA
[90] Durham University, Institute for Particle Physics Phenomenology, Ogden Centre for Fundamental Physics, South Road, Durham DH1 3LE, United Kingdom
[91] College of Nuclear Science and Technology,Beijing Normal University,100875 Beijing, China, Beijing Radiation Center, Beijing 100875, China
[92] University of Sheffield, Sheffield, United Kingdom
[93] Institute for High Energy Physics of National Research Centre 'Kurchatov Institute', Protvino, Russia
[94] Henryk Niewodniczanski Institute of Nuclear Physics Polish Academy of Sciences, Kraków, Poland
[95] Research Institute for Nuclear Problems of Byelorussian State University, Minsk, Belarus
[96] Institute of Particle and Nuclear Studies, High Energy Accelerator Research Organization (KEK), Tsukuba 305-0801, Japan
[97] Cavendish Laboratory, University of Cambridge, Cambridge, United Kingdom
[98] Czech Technical University in Prague, Prague, Czech Republic
[99] Sapienza Universita' di Roma, Dipartimento di Fisica
[100] Waseda University, Waseda Research Institute for Science and engineering (WISE), Tokyo, Japan
[101] Physics Department, University of Minho, 4710 - 057, Braga, Portugal
[102] University of California, Berkeley, California, USA
[103] Universidad de Oviedo, Oviedo, Spain
[104] CFTP, Instituto Superior Técnico, Universidade de Lisboa, Avenida Rovisco Pais 1, 1049 Lisboa, Portugal
[105] LAPTh, 9 Chemin de Bellevue, F-74941 Annecy Cedex, France
[106] Physics Department, Florida State University, Tallahassee, Florida, USA
[107] Rudjer Boskovic Institute, Bijenicka cesta 54, P.O. Box 180, 10002 Zagreb, Croatia
[108] Department of Astronomy and Theoretical Physics, Lund University, Lund, Sweden
[109] Kirchhoff-Institut für Physik, Heidelberg, Germany
[110] University of Sydney, Sydney, Australia
[111] International Center for Elementary Particle Physics and Department of Physics, The University of Tokyo, Japan
[112] Physics Department, Universidad Autonoma de Madrid, Spain
[113] University of Science and Technology of China, Hefei, China
[114] Institute of High Energy Physics, Chinese Academy of Sciences, Beijing, China
[115] University of California, San Diego, La Jolla, USA

Abstract

The successful operation of the Large Hadron Collider (LHC) and the excellent performance of the ATLAS, CMS, LHCb and ALICE detectors in Run-1 and Run-2 with pp collisions at center-of-mass energies of 7, 8 and 13 TeV as well as the giant leap in precision calculations and modeling of fundamental interactions at hadron colliders have allowed an extraordinary breadth of physics studies including precision measurements of a variety physics processes. The LHC results have so far confirmed the validity of the Standard Model of particle physics up to unprecedented energy scales and with great precision in the sectors of strong and electroweak interactions as well as flavour physics, for instance in top quark physics. The upgrade of the LHC to a High Luminosity phase (HL-LHC) at 14 TeV center-of-mass energy with 3 ab^{-1} of integrated luminosity will probe the Standard Model with even greater precision and will extend the sensitivity to possible anomalies in the Standard Model, thanks to a ten-fold larger data set, upgraded detectors and expected improvements in the theoretical understanding. This document summarises the physics reach of the HL-LHC in the realm of strong and electroweak interactions and top quark physics, and provides a glimpse of the potential of a possible further upgrade of the LHC to a 27 TeV pp collider, the High-Energy LHC (HE-LHC), assumed to accumulate an integrated luminosity of 15 ab^{-1}.

Contents

1 Introduction . . . 8
2 Theoretical tools . . . 9
2.1 High Order QCD calculations . . . 9
2.2 Electroweak corrections . . . 11
2.3 Monte Carlo generators . . . 13
2.4 PDF calculations and tools . . . 16
2.5 Effective Field Theory calculations and tools . . . 20
3 Experimental environment at HL-LHC . . . 22
3.1 Analysis methods, particle reconstruction and identification . . . 22
3.1.1 ATLAS and CMS performance . . . 22
3.1.2 LHCb performance . . . 23
3.2 Treatment of systematic uncertainties . . . 24
3.3 Precision Luminosity . . . 24
4 Electroweak processes . . . 28
4.1 Vector boson fusion . . . 28
4.2 Vector boson scattering processes . . . 38
4.2.1 Measurements of $W^{\pm}W^{\pm}$ scattering and extraction of the longitudinal scattering component . . . 38
4.2.2 High Order corrections in VBS $W^{\pm}W^{\pm}$ production . . . 42
4.2.3 Measurements of WZ scattering at the HL-HLC . . . 46
4.2.4 Prospects for quartic gauge coupling measurements in VBS . . . 51
4.2.5 Measurements of ZZ scattering . . . 53
4.2.6 The production of WW / WZ via vector boson scattering with semi-leptonic final states 59
4.3 Tri-boson production . . . 63
4.4 Precision electroweak measurements . . . 67
4.4.1 NNLO predictions for Z-boson pair production . . . 67
4.4.2 Gauge-boson pair production with MATRIX . . . 69
4.4.3 Projections for measurements of anomalous 3-gauge boson couplings . . . 76
4.4.4 Prospects for the measurement of the W-boson mass . . . 77
4.4.5 Prospects for the measurement of the effective weak mixing angle . . . 80
4.4.6 The global EW fit . . . 86
5 Strong interactions . . . 93
5.1 Jet and photon production . . . 93
5.1.1 Inclusive jet production . . . 93
5.1.2 High–p_{T} light– and heavy–flavour jet measurements at the HL–LHC . . . 97
5.1.3 Inclusive photon production . . . 99
5.1.4 Diphoton production . . . 102
5.2 Ultimate Parton Densities . . . 104
5.2.1 HL-LHC measurements for PDF studies . . . 104

5.2.2 Ultimate PDFs from HL-LHC data . . . 109
5.3 Underlying Event and Multiple Parton Interactions . . . 114
5.3.1 Underlying Event at 27 TeV . . . 114
5.3.2 Double Parton Scattering . . . 115
6 Top quark physics . . . 120
6.1 Top quark cross section . . . 120
6.1.1 The $t\bar{t}$ production cross section: theoretical results . . . 120
6.1.2 Prospects in the measurement of differential $t\bar{t}$ cross sections . . . 122
6.1.3 PDF constraints from double-differential $t\bar{t}$ cross sections . . . 122
6.1.4 Forward top quark physics . . . 123
6.1.5 Single top cross section: theoretical results . . . 126
6.2 Four top production at the HL/HE-LHC . . . 131
6.2.1 The complete NLO corrections to four-top production . . . 131
6.2.2 Prospect for experimental measurements . . . 132
6.3 Four top quarks as a probe of new physics . . . 134
6.3.1 Limits on pseudoscalar colour-octets . . . 134
6.3.2 Limits on top-Higgs interaction from multi-top final state . . . 136
6.3.3 Constraining four-fermion operators in the EFT . . . 137
6.3.4 Top quark dipole moment in multi-top production . . . 138
6.4 The $t\bar{t}V$ production at the HL/HE-LHC . . . 140
6.4.1 The $t\bar{t}Z$ cross sections at NLO QCD and EW . . . 140
6.4.2 The complete-NLO corrections to $t\bar{t}W$ . . . 141
6.5 Top mass . . . 141
6.5.1 Theoretical issues . . . 141
6.5.2 Experimental projections . . . 145
6.6 Top quark properties and couplings . . . 148
6.6.1 Top quark charge asymmetries at LHCb . . . 148
6.6.2 A method to determine $|V_{cb}|$ at the weak scale in top quark decays . . . 150
6.7 Flavour changing neutral current . . . 152
6.8 Effective coupling interpretations for top quark cross sections and properties . . . 156
6.8.1 The top quark couplings to the W boson . . . 157
6.8.2 The $t\bar{t}\gamma$ production . . . 158
6.8.3 The $t\bar{t}Z$ production . . . 158
7 Forward physics . . . 161
7.1 Photon-induced collisions at the HL–LHC . . . 161
7.1.1 Anomalous quartic gauge couplings with proton tagging at the HL–LHC . . . 161
7.2 Central exclusive production: QCD prospects . . . 164
7.3 Tagged proton at the HL–LHC: experimental prospects . . . 165
7.4 Low-mass central exclusive production . . . 172

1 Introduction

The Large Hadron Collider (LHC) is one of largest scientific instruments ever built. To extend its discovery potential, the LHC will undergo a major upgrade in the 2020s, the High-Luminosity LHC (HL-LHC). The HL-LHC will collide protons against protons at 14 TeV centre-of-mass energy with an instantaneous luminosity a factor of five greater than the LHC and will accumulate ten times more data, resulting in an integrated luminosity of 3 ab^{-1}.

The LHC results have so far confirmed the validity of the Standard Model of particle physics up to unprecedented energy scales and with great precision in the sectors of strong and electroweak interactions, Higgs boson as well as flavour physics including top quark properties. The HL-LHC program, thanks to a ten-fold larger data set, upgraded detectors and expected improvements in the theoretical understanding, will extend the sensitivity to new physics in direct and indirect searches for processes with low production cross sections and harder signatures. In addition, a considerable improvement is expected in precise measurements of properties of the Higgs boson, e.g. couplings measurements at the percent level, and of Standard Model (SM) production processes. Several of these measurements will be limited by the uncertainties on the knowledge of the partonic inner structure of the proton, i.e. Parton Denstity Functions (PDFs). Global PDF fits of several HL-LHC measurements will allow a significant improvement in PDF uncertainties and, in turn, in measurements of SM parameters, e.g. the weak mixing angle and the W boson mass. Anomalies in precision measurements in the SM sector can become significant when experimental measurements and theoretical predictions reach the percent level of precision, and when probing unprecedented energy scales in the multi-TeV regime. These anomalies could give insights to new physics effects from higher energy scales.

Additional studies on the potential of a possible further upgrade of the LHC to a 27 TeV pp collider, the High-Energy LHC (HE-LHC), assumed to accumulate an integrated luminosity of 15 ab^{-1}, have also been carried out.

A year long Workshop organized at CERN in 2017-2018 brought together experimentalists from the ATLAS, CMS, LHCb, and ALICE Collaborations and theorists to study the expected physics reach of the HL-LHC project and its possible upgrade to the HE-LHC. Studies of the Workshop in the sectors of electroweak and strong interactions as well as top physics were carried out within the Working Group 1 (WG1) and the results are summarized in this report that constitutes a chapter of the HL/HE-LHC Yellow Report volume to be submitted to the European Strategy Group.

The report first introduces the theoretical tools used for the following theoretical projections and their expected future improvements as well as the experimental performance assumed in the following experimental analyses. Dedicated sections summarize the results of the studies in the areas of electroweak processes, strong interactions, top physics including effective coupling interpretations, and proposes studies of forward physics that are possible with new forward detectors. The sections focus on physics projections for the HL-LHC and the expected improvements in measurement precision or kinematic reach compared to LHC. In some cases the studies are extended to HE-LHC highlighting the larger statistics and energy reach of HE-LHC compared to HL-LHC. In the following sections the authors of the theoretical contributions are listed in footnotes to the section titles. Where the authors are not explicitly indicated, they are the experimental LHC Collaborations.

2 Theoretical tools

2.1 High Order QCD calculations[1]

In order to exploit the full potential of the High-Luminosity LHC physics program, the high precision of experimental data must be compared to theoretical predictions that have the same accuracy. Precision calculations in QCD are typically classified into fixed-order expansions in the coupling constant α_s, and into predictions that resum large logarithms to all orders in α_s. The latter are usually also subdivided into numerical parton-shower approaches and analytic resummed calculations. In recent years, a lot of work has been devoted also to matching and merging fixed-order and resummed calculations, so as to have an improved accuracy in all regions of phase space.

The technical ingredients required for a fixed-order calculation to higher orders are the computation of real, virtual or, from two loop on, mixed real-virtual amplitudes, the calculations of the required master integrals and a procedure to regularize intermediate soft and collinear divergences. The first non-trivial contribution is of next-to-leading order (NLO). Here, the basis of master integrals required to compute any process at one-loop in QCD had been known for a long time, and is now available in public codes [1, 2]. In addition, two general subtraction methods (FKS [3] and CS [4]), well suited for automation, were developed. The tensor reduction of virtual amplitudes (i.e. the reduction of virtual amplitude into a combination of master integrals) proved to be the most difficult problem, since the most straightforward approaches yielded too complex results for generic processes. Around ten to fifteen years ago, a number of breakthrough ideas [5–10] led to algorithms for tensor reduction that can be automatized efficiently. With all ingredients in place, a number of tools to compute NLO cross sections for generic LHC processes in an automated way were developed. These tools are today heavily used at the LHC and will be indispensable for future phenomenology. The most widely used tools include GOSAM [11], MADLOOP [12], or OPENLOOPS [10]. It is interesting to note that, in the early days of NLO calculations, also slicing approaches were suggested to handle intermediate divergences (see e.g. [13]). They were however soon abandoned in favour of subtraction approaches.

While NLO tools are certainly more appropriate then leading-order (LO) generators to accurately predict LHC distributions, already with Run-2 data it is clear that an even better perturbative accuracy is required to match the precision of data. One of the first explicit demonstrations of this fact was given by the WW cross section [14–16], that raised interest because of discrepancies in the extrapolated total cross section between theory and data both at 7 TeV and 8 TeV, and both at ATLAS and CMS. The discrepancy could be resolved thanks to the inclusion of next-to-next-to-leading (NNLO) corrections and thanks to the observation that the extrapolation from the fiducial to the inclusive cross section had a larger uncertainty than the estimated one. This example highlights the importance of quoting also fiducial cross sections, prior to any Monte Carlo based extrapolation, and of including NNLO corrections when comparing to high-precision data.

Current years are seeing an incredibly fast progress in the calculation of NNLO cross sections (for recent short reviews see e.g. Ref. [17, 18]). The current status is that all non-loop induced $2 \to 2$ SM processes are known at NNLO, including dijet production [19] that has the most complicated subprocess and singularity structure. This breakthrough was possible thanks to the development of new methods to compute two-loop integrals. One idea that was exploited to a great extent is the fact that polylogarithmic integrals can be calculated by means of differential equations [20–23]. Currently, the processes that are more difficult to compute are those that involve internal masses, since they lead not only to polylogarithms but also to elliptic integrals. Examples include loop-induced processes like gluon-fusion Higgs or di-Higgs production with full top-mass dependence, or gluon induced di-boson production.

With the High-Luminosity run of the LHC, it will be possible to explore the Higgs transverse

[1] Contributed by G. Zanderighi.

momentum spectrum up to almost 1 TeV, where the large-m_t approximation is well-known to fail. Recently, two-loop NLO results for the Higgs transverse momentum spectrum became available [24,25], but genuine NNLO predictions for these loop-induced processes are still out of reach.

The calculations of multi-scale two-loop amplitudes with massive internal particles relevant for Higgs-, top- and vector-boson production, and in particular the mathematical structures beyond multiple polylogarithms that appear in these amplitudes, is a very active area of research today [26–39]. The developments of yet new ideas and computational methods are eagerly needed. Approaches for the full numerical calculation of master integrals also exist (see e.g. Ref. [40–43] and references therein), requiring however considerable computing power as the complexity increases.

As far as the problem of canceling divergences, quite a number of different approaches are being pursued now. They can be broadly divided into subtractions methods (antenna subtraction [44], sector-improved residue subtraction [45–48], nested subtraction [49], colourful subtraction [50], projection to Born [51]) or slicing methods (q_T-subtraction [52], N-jettiness [53,54]). These methods are being scrutinized, compared, and refined, and while it is not clear yet which method will prevail, it seems realistic to assume that, by the beginning of the High-Luminosity phase, the issue of handling intermediate divergences in NNLO calculations will be considered solved. An ambitious goal is in fact to have $2 \to 3$ NNLO results by the beginning of the High-Luminosity phase. A milestone would be certainly to have NNLO prediction for ttH production. Motivated by the success at one-loop, a lot of effort is devoted to extending generalized unitarity and the OPP methods beyond one loop (see e.g. Ref. [55]). Currently, $2 \to 3$ processes are a very active subject of study, with initial results of 3-jet amplitudes starting to appear [56–62].

Beyond NNLO, two calculations of LHC processes exist today at N^{3}LO for inclusive Higgs production in the large m_t approximation [63, 64] and for vector-boson-fusion (VBF) Higgs production in the structure function approximation [65]. The complexity of these calculations suggest that it will be very hard to extend this level of accuracy to more complicated processes, since the technology they use explicitly exploits the simplicity of these two processes, and cannot be easily extended to more complex ones.

Besides fixed-order, also resummed calculations have seen a leap in recent years. The accuracy with which particular observables can be resummed analytically reaches N^{3}LL (see e.g. Ref, [66–68]), which means three towers of logarithmic terms down compared to the leading logarithms that arise when only soft and collinear gluons are correctly accounted for. These results are properly matched to fixed order NNLO calculations.

Resummed calculations rely either on methods based upon coherent branching [69, 70] or upon Soft Collinear Effective Theory (SCET) [71]. So far, the two approaches have also been considered as complementary, in fact both methods proceed by performing a systematic expansion of the contributions to the cross section. Recent work highlights the connection between the two methods [72].

While the logarithmic accuracy of resummed calculations is impressive, the formal accuracy of parton showers is much less advanced. Unlike resummed calculations, that are targeted to a well defined cross section or distribution, Monte Carlo generators make predictions for several kind of observables at the same time, and, at present, a rigorous way to qualify their accuracy is missing. First studies in this direction can be found in [73]. Nevertheless, attempts to improve some aspects of the shower algorithms are the focus of recent work. Different approaches are taken: one can incorporate the spin-color interference into showers [74], include higher-order splitting functions and $1 \to 3$ splitting kernels into showers [75, 76] or consider different shower evolution variables [77, 78]. It seems likely that by the start of the High-Luminosity program we will have a much better theoretical control on the parton shower evolution and the uncertainty associated to it.

In the same way as the progress in NLO went hand in hand with the development of matching

procedures of NLO and parton shower, a number of approaches have been suggested recently to match NNLO calculations and parton showers [79–81]. The bottleneck in these approaches is currently the fact that they rely on a reweighing procedure that is differential in the Born phase space. Such a reweighing is possible for relatively simple processes but becomes numerically unfeasible for more complicated ones. It seems reasonable to expect that in the next years better NNLOPS approaches will be developed that do not rely on any reweighing to the NNLO. This would make it possible to have NNLO predictions matched to parton shower (PS), also called NNLOPS, to more generic processes for which an NNLO calculation is available, as is currently the case at NLO.

2.2 Electroweak corrections[2]

Existing tools

In the last few years, the automation of electroweak (EW) NLO corrections has witnessed an impressive progress, for what concerns both one-loop and real-emission contributions (and their combination), by collaborations such as RECOLA [82, 83] with SHERPA [84, 85], OPENLOOPS [10] with SHERPA, GOSAM [11, 86] with either MADDIPOLE [87, 88] or SHERPA, and MadGraph5_aMC@NLO [12, 89]. For most of these codes tuned comparisons have also been published [90, 91], displaying excellent agreement among them. Although the capabilities and reach in process complexity can differ from one computer program to another, recent results obtained with these tools [92–117] clearly demonstrate how automation has made it possible to tackle problems whose complexity is too great to justify their solutions through traditional approaches.

Stemming from these advances, newer applications have become possible, one of these is the computation of the so-called "complete-NLO" corrections. In general, a given scattering processes can proceed through n different coupling combinations at LO (for example, $t\bar{t}$ or dijet production receives contributions at order α_s^2, $\alpha_s\alpha$ and α^2); typically only the term with the largest power of α_s is retained, owing to the fact that $\alpha_s \gg \alpha$. This structure generates a similar one at N^{p}LO, with $n+p$ contributions, and the term "complete-NLO" means the (simultaneous) computation of all the terms entering at LO and NLO. Among the computer programs cited above, some have been employed for the computation of the complete-NLO corrections. In most of the cases the impact of the various contributions closely follows the pattern one would expect from the coupling powers, as it is the case for dijet production [106], top-pair [113] possibly with one extra jet [116]. However, there exist processes for which the coupling hierarchy is violated, or even flipped. Examples are same-sign W production with two jets [111], top-pair production in association with a W boson and four-top production [115].

Corrections beyond NLO

Similarly to the NLO case, also NNLO corrections can be organized in powers of α and α_s. At the moment, $\mathcal{O}(\alpha_s^2)$ NNLO QCD calculations have been performed for many production processes at the LHC. Conversely, complete NNLO mixed QCD-EW calculations of $\mathcal{O}(\alpha_s\alpha)$ have not been performed for any process yet. These calculations are essential in order to pin down the theoretical uncertainties for processes that at the HL- and HE-LHC will be measured with very high precision. For this reason a great effort has been already invested for achieving this result and great progress can be expected in the next years. We recall the calculations that have been performed for Drell-Yan production [118, 119] in the resonance region via the pole approximation. For this kind of calculations two-loop amplitudes [120–124] as well as regularized double-real emissions [125] are necessary ingredients. Similarly, NNLO mixed QCD-EW corrections to gluon-gluon-fusion (ggF) Higgs production, which are induced by three-loop diagrams, have been estimated in ref. [126]. Further recent calculations [127, 128] support those

[2] Contributed by D. Pagani, M. Zaro and M. Schönherr.

results and, in particular, support the fact that they can be correctly approximated via the so-called multiplicative approach. In short: NNLO mixed QCD-EW $\sim$ NLO QCD $\times$ NLO EW.

The aforementioned multiplicative approach is in general a very good approximation when the bulk of QCD and EW corrections at NLO is dominated by soft effects and Sudakov logarithms, respectively. Given the current lack of exact NNLO mixed QCD-EW calculations, this approximation is already being used for estimating these corrections and/or missing higher orders uncertainties of different processes. First (N)NNLO QCD calculations including NLO EW corrections via the multiplicative approach have already appeared [63, 113, 129] and are already necessary for a correct interpretation of current data; this level of accuracy will be mandatory for more processes at HL and HE-LHC.

Besides NNLO mixed QCD-EW corrections of $\mathcal{O}(\alpha_s\alpha)$, non-negligible contributions can emerge also from large $\mathcal{O}(\alpha^n)$ corrections with $n > 1$. These typically involve final-state radiation (FSR) from massless/light particles and Sudakov logarithms. Both effects can be resummed, (at LL) via shower simulations (see the following sections on matching with QED showers and with EW showers), or analytically. In the case of Sudakov logarithms, general methods for their calculation [130, 131] and techniques for resumming them [132, 133] are already known since quite some time. Based on the study already performed for 100 TeV proton–proton collisions [134], at the HE-LHC, the resummation of Sudakov effects may be relevant in the tail of distributions.

Matching with QED shower

Fixed order computations need to be matched to parton showers, which compute a fully differential numerical resummation and implement the evolution of both QCD and EW particles from the hard scale to low scales, connecting it to the non-perturbative hadronization stage to arrive at fully differential particle level that can be subjected to detector level data. This matching has been fully automated for NLO QCD calculations. At NLO EW accuracy only selected process specific solutions exist [135–139]. As all parton showers incorporate a joint QCD+QED parton evolution, general matching procedures, which are still lacking at the moment, will become available in the near future. This will enable precise particle level predictions that can be subjected to detector simulations for highly realistic and detailed studies.

Additionally, first solutions exist to incorporate approximate electroweak corrections in multijet merged calculations [98, 116, 140]. In these approximations, the universal nature of EW corrections in the high energy limit, where they are dominated by Sudakov-type logarithms of virtual origin, is exploited. Thus, these methods will form the cornerstone of precise particle-level predictions at large transverse momenta, which are at the basis of the increased reach of both the HL– and HE–LHC new physics search program.

Weak showers

All parton showers publicly available in the major Monte-Carlo event generators HERWIG, PYTHIA and SHERPA contain both QCD and QED splitting functions to numerically resum the respective logarithms at (N)LL accuracy. First steps towards parton showers incorporating also weak effects in their splitting functions have been taken recently [141, 142]. The now complete electroweak splitting functions suffer from their strong dependence on the helicity of the propagating parton. These parton showers, however, operate in the spin-averaged approximation, neglecting all spin-correlations. The current effort to understand the full spin dependence of the electroweak part of the evolution of partons [143, 144] in analytic resummations is complemented by efforts to keep the full colour and spin structure, including non-diagonal parts of the (now matrix-valued) evolution equations, in the parton shower community. In time for the High Luminosity Upgrade fully spin-dependent parton evolution will then be incorporated in fully differential parton shower resummations that can then produce accurate predictions for the

emission probabilities of secondary weakly interacting particles and gauge bosons.

2.3 Monte Carlo generators[3]

The complexity of the final states, together with the complexity of the detectors that analyse them, are such that a full simulation of an event, yielding a realistic multi-particle final state distribution, is an indispensable theoretical tool for the physics of high-energy hadron colliders. Driven by the needs of the Tevatron and LHC, the physics of Monte Carlo (MC) generators has seen steady progress from its inception to the present, and is, at the moment, a field in active development. The current LHC physics program, as well as the requirements for its HL-LHC and eventually its HE-LHC phases, has evidenced several areas of development that need to be addressed by theorists. These are mainly driven by the quest for higher precision and accuracy, but also by practical issues, such as the need for generating very large samples for the most abundant LHC processes, and for the efficient handling of the variations of the input parameters needed in order to study uncertainties.

Much progress in this field takes place within the main collaborations that maintain the widely used general purpose Monte Carlo generators, i.e. HERWIG [145–147], PYTHIA [148,149] and SHERPA [84] but there is also a large theoretical community that works on more specialised aspects of Monte Carlo generators, such as formal/theoretical advances to improve the resummation accuracy, and to improve the fixed-order accuracy in the generation of the primary event and of the hardest radiations accompanying it.

In spite of the several challenges ahead of us, considering the evolution of the field in the last twenty years, it can be anticipated that considerable progress will be made from now up to the beginning (around 2025) and in the following ten-fifteen years of the high luminosity program. This progress will take place in particularly favourable conditions, as the running of the LHC and the data accumulated will provide continuous feedback to the theoretical work in the field.

It can be can anticipated major developments in the following directions: precision for inclusive observables, logarithmic accuracy, technical improvements for fast and efficient generation of events, and improvements in the modeling of hadronization and underlying event.

Precision for inclusive observables

In this context, let us generically refer to “precision" as a measure of the accuracy of the result as well as of the size of the left-over uncertainties that can be achieved in the computation of inclusive quantities, i.e. those that can be computed directly in fixed-order calculations. Fixed-order calculation have always been, and are now, ahead of the precision that Monte Carlo generators can provide for inclusive observables. Since their wide use started, and up to about twenty years ago, shower MC’s had typically leading order precision for inclusive observables, while the state of the art for fixed order computations was at the Next-to-Leading-Order (NLO) level. Thanks to the introduction of general methods for interfacing shower Monte Carlo to fixed-order NLO calculations, like AMC@NLO [150], POWHEG [151], and more recently the KRK-NLO method [152], the state of the art for shower MC’s precision has reached the NLO level. On the other hand, progress in fixed-order computations, including the evaluation of two-loop amplitudes and the development of several subtraction methods, allowed NNLO calculations to become available for a rather large set of processes. It is therefore natural to wonder whether *general methods for interfacing Shower generators to NNLO calculation will be available at the start of the High Luminosity program.* NNLO-PS methods have already appeared for relatively simple processes, typically in the production of massive colourless final states [79, 80, 153–155]. However, the methods used so far do not seem to have the generality needed to handle processes of increasing complexity, and it is very likely that new theoretical breakthroughs will be needed.

[3] Contributed by F. Maltoni, M. Schönherr and P. Nason.

Achieving NNLO accuracy for a given final state, for example for Higgs production, implies also the NLO accuracy for the the same final state in association with a jet, i.e. the HJ process in the Higgs example. In practical applications, the less ambitious goal of having NLO accuracy for inclusive result, and also achieve NLO accuracy for the final states that also include associated production of jets, thus achieving an extension of the CKKW [156] method to NLO order, can be extremely useful.

The availability of automated NLO corrections for arbitrary processes including a relatively large number of associated jets has paved the way to important developments in this direction. Several proposals to merge samples with different jet multiplicity computed at the NLO, usually called "NLO-PS matrix-element merging", have been put forward. These are the FXFX method [157], implemented in the AMC@NLO framework; the UNLOPS method [158], implemented in PYTHIA and the MEPSNLO method [159], implemented in SHERPA. All methods introduce a separation scale that defines the jet multiplicity for a given event, and allows to generate inclusive samples out of non-overlapping samples with different jet multiplicity. Whether these procedures really achieve NLO accuracy for observables involving different jet multiplicity also when generic (i.e. different from those used at the generation level) separation scales are chosen, is a delicate question, which is still a matter of debate. Alternative merging procedures, that consider more carefully the problems that may arise at the boundary of the merging regions and also aim at improving the resummation accuracy , have been proposed in the GENEVA approach [160], and presently applied to Drell-Yan production [155,161]. The goal of achieving NLO accuracy for different jet multiplicity has also been achieved without the use of merging with the so called MINLO procedure [162, 163].

While NLO-PS generators for standard QCD processes can be obtained with a fairly high level of automation, there are processes that require particular attention, typically the loop induced ones. An example of one such process is Higgs-pair production, that has been implemented first in AMC@NLO [164] using an approximation for the yet unknown two-loop contributions and then in POWHEG and AMC@NLO as soon as the results of the two-loop computation has become available. [166, 167]. There are several other gg loop-induced processes for which a full NLO+PS implementation is still missing which, thanks to the quick developments in computation of two-loop amplitudes, are expected to become available in the coming years.

Another important direction where there has been considerable progress recently is the automation of the computation of EW corrections [83, 85, 89, 95] to the point that fixed-order NLO QCD and EW corrections are readily available for virtually all processes of interest. Details can be found in Section 2.2. An general interface of these calculations to shower generators that correctly account for QED radiation for these computations, however, is not yet available. The problem in this case is the consistent handling of photon radiation, that can arise both from the shower and from the fixed-order calculation. These pose new problems compared to the production of coloured partons, where the presence of individual partons cannot be required in the final state, and thus showers develop inclusively generating jets from partons. Photons, on the other hand, can be explicitly detected in the final state, and an NLO+PS scheme should take care of handling both shower generated photons and those originating in the NLO calculation in a consistent way, in order to give a reliable description of both collinear photons embedded in jets and highly energetic isolated ones. A scheme for achieving this in the Drell-Yan case has been presented in Ref. [136, 137] in the context of the POWHEG method. A scheme using fragmentation functions has been introduced in Ref. [89].

Finally, it is to be noted that the progress achieved recently to account for intermediate resonant states in the NLO+PS context [168–170] will likely be essential in the framework of electro-weak corrections. In this case, weak vector bosons are part of the electroweak corrections and their presence entail a correct handling of their decays also in presence of extra QED radiation. It is expected that interfacing complete NLO EW-QCD calculations with a shower approach (QED+QCD) will become standard procedure by the beginning of HL-LHC.

Accuracy in resummation

As current state of the art, shower generators rely upon the first order Altarelli-Parisi splitting kernels, together with some appropriate scheme to handle soft emissions, either by angular ordering in parton shower cascades or using dipole shower algorithms. Several studies have appeared recently aiming at improving parton showers by increasing the accuracy of specific ingredients, either by developing novel shower schemes that remain within the standard parton or dipole branching, such as DIRE [77] and Vincia [78, 171]; by going beyond the typical probabilistic cascade of the shower algorithms and handling directly the quantum density matrix [172]; and by incorporating higher order splitting functions [76, 152, 173–175].

While fixed order improvements in shower MC generators have the clear goal of reaching the same fixed order accuracy as the corresponding computations for inclusive observables, it is less straightforward to quantify how improvements in the shower algorithms impact the precision of the description of observables that require resummation. In a recent study [73], some criteria were proposed in order to address this problem. In particular, two criteria were examined: the first refers to the ability of a shower algorithm to correctly reproduce the singularity structure of n-parton matrix elements, while the second measures the level of accuracy of a shower algorithm in the computation of a general class of observables that require resummation. It was found that there are regions where commonly used shower algorithms fail to reproduce the correct singularity structure of the matrix elements, and that this affects the logarithmic resummation accuracy of the shower already in the leading term, yet at subleading number of colours, and in the next-to-leading term at leading colour.

Thus, the current trend of research moves along parallel directions, not only by seeking improvements in the shower algorithms in particular areas, but also by critical examination of the shower formalism in an attempt to qualify their accuracy in a more solid way.

Technical improvements

The pressing requirements of the LHC physics program have already had an impact in driving technical improvements in Monte Carlo generators. In particular, the need to study uncertainties, corresponding to a large set of combination of parameter variations when generating a sample, often leading to several hundreds variations, has led to the development of procedures to implement the variation of parameters by reweighting the same event, rather than generating independent samples. Besides the obvious simplification of having to deal with a single event sample, this has also the advantage that the effects of variations of the input parameters are affected by smaller theoretical errors, since they all apply to the same generated event. A method for reweigthing the full shower development was presented in Ref. [176] and implemented in HERWIG in Ref. [177]. A similar method was presented in [178] for PYTHIA, and in Ref. [179] for SHERPA. Reweighting techniques to evaluate uncertainties as well as for other applications are available in MADGRAPH5_AMC@NLO [12, 180] and in POWHEG.

For certain common Standard Model processes, a large statistics is often required, and is especially needed to populate the kinematic tails at large transverse momenta. The most advanced generators usually suffer from poor performance, especially in such areas of the phase space, and thus the need for more accurate tools must be balanced with the practical needs for large samples. These problems will need to be addressed on a case by case basis, depending upon the process that is been considered, and the specific purpose that a generator for that process should serve. The presence of negative weights, for example, should be minimised for generators that must produce large samples to be fed through detector simulators. The sampling of suppressed tails of phase space, on the other hand, may be easily increased by suitable bias functions. It is also apparent that attention should be given to whether new computer architectures may be advantageously explored for Monte Carlo generators, such as MPIs and GPU architectures, and that new software techniques making use of Boosted Decision Trees or Deep Neural Networks may provide advantages over traditional techniques of Monte Carlo integration and

phase space generation [181].

Hadronization and underlying event

A recent fascinating direction in parton shower MC's is towards establishing a unified picture in the description of multi-parton dynamics in pp, pA, and AA collisions [182]. Traditionally, pp collisions have been described through the picture of double-, single- and non-diffractive interactions of partons in a vacuum in pp collisions. AA collisions, on the other hand, are typically described in terms of the dynamics of a quark gluon plasma, with a formalism more related to hydrodynamics than particle physics. A series of observations in high-multiplicity pp events at the LHC, however, have exposed remarkable similarities and features in common with those observed in pA and AA collisions, at least with respect to flavour composition and flow. The question therefore arises whether a new state of matter, the quark gluon plasma, is actually formed in high-multiplicity pp events and how this could be tested quantitatively. Efforts and new ideas have recently emerged towards having a unified MC description of such events. This has started with a simple stacking of (soft and hard) pp events [183]. A recent proposal, Angantyr [184], has been inspired by the old Fritiof model [185] and the notion of wounded nucleons. While more elaborated than a stacking approach, it does not yet feature a description of collective effects. In the coming years, progress will be achieved by first identifying the experimental features that are genuine signatures of the formation of a quark gluon plasma, and those which could be associated to other effects. Alternative explanations would likely also be of a collective character, yet without requiring a phase transition.

The intense ongoing theoretical and experimental work in this framework is likely to lead to new breakthrough in the modeling of the hadronization phase and the underlying event before the beginning of the HL-LHC running.

In the description of the underlying event in pp collisions, a key role is played by multi-parton interactions (MPI, see Sec. 5.3). There has been recent progress in the theoretical understanding of double parton scattering that has been summarised in Sec. 5.3.2. There it is also shown that at the HL-LHC it may be possible to find evidence of correlations in double parton interactions. This opens the possibility of constructing improved models of MPI in MC generators, to be eventually refined in the first few years of running of the HL-LHC.

2.4 PDF calculations and tools[4]

At the HL-LHC, a precise knowledge of the quark and gluon structure of the proton will be essential for many analyses. These include the profiling of the Higgs boson sector [186], direct searches for new heavy BSM states [187], indirect BSM searches by e.g. means of the SMEFT [188], and the measurement of fundamental SM parameters such as the W boson mass [189], the Weinberg mixing angle [190] or the strong coupling constant [191] and its running.

This section gives a brief review the PDF tools that will be used in this Report for the studies of the SM chapter. Those aspects of modern PDF fits that are more relevant for studies at the HL-LHC will be also highlighted. The end of this section will provide some perspectives about the role of PDFs at the HE-LHC. It must be stressed that this document is not intended to be a review of recent developments on PDFs, and the reader is referred to [192–194] and reference therein, for further details in this sense.

The studies presented in this Report will be based mostly on the PDF4LHC15 set [195], constructed from the statistical combination and subsequent reduction [196–198] of the CT14 [199], MMHT14 [2 and NNPDF3.0 [201] global analyses. The PDF4LHC15 set is interfaced to matrix-elements calculators and Monte Carlo shower programs by means of the LHAPDF6 package [202].

[4] Contributed by L. Harland-Lang, J. Gao and J. Rojo.

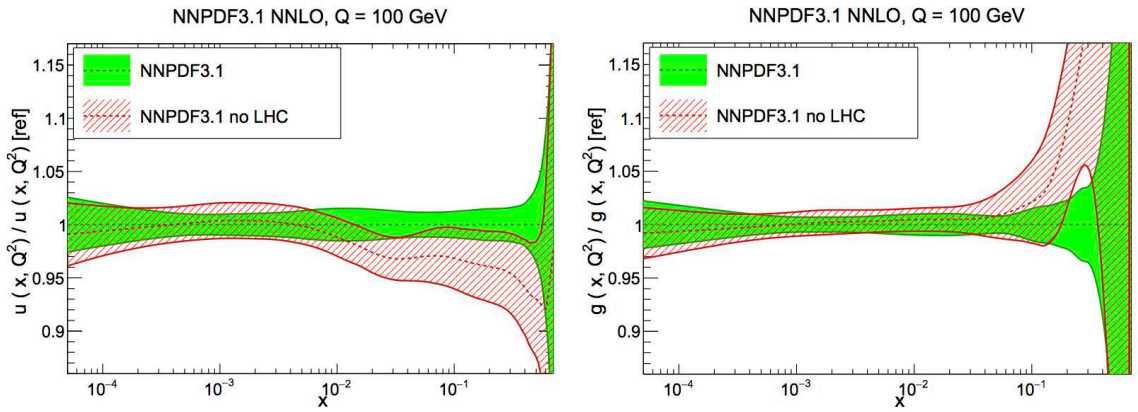

Fig. 1: Comparison of the NNPDF3.1NNLO fits with and without LHC data, normalized to the central value of the former at $Q = 100$ GeV. The up quark (left) and the gluon (right plot) are shown. The bands indicate the 68% confidence level PDF uncertainty.

Quantifying the impact of LHC measurements.

In recent years, one of the main developments in global PDF fits has been the increasingly significant role played by LHC processes in providing stringent PDF constraints. The combination of high precision LHC data with state-of-the art NNLO theory calculations for such hadronic processes as top-quark pair production [203], the transverse momentum spectrum of Z bosons [204], direct photon production [205], and inclusive jet production [206] is having an important impact on precision PDF fits. To illustrate this, Fig. 1 compares the recent NNPDF3.1 fit [207] with and without the LHC data at $Q = 100$ GeV for the up quark and gluon PDFs. The marked impact of the LHC data for $x \gtrsim 0.005$ can be observed both for central values and for the PDF uncertainties. It is of particular note that only Run-1 data has been included in these fits. Thus, it is clear that the addition of data from Run-2 and -3 first and then from the HL-LHC, for which the precision and reach will be greatly increased, should lead to further improvements in the determination of the proton structure. A subsequent section of this report will quantify the impact of HL-LHC measurements, demonstrating that a significant reduction can be expected and providing a public PDF set including the expected constraints from the final HL-LHC dataset.

Fast interfaces to (N)NLO calculations

To avoid the direct evaluation of the lengthy (N)NLO hadronic cross sections during the fit itself, a method of fast interfaces is generally applied, whereby the CPU time intensive part of the higher–order calculation is pre–computed once using a complete interpolation basis for the input PDFs. For a number of years, the APPLGRID [208] and FASTNLO [209] tools have been available for a range of NLO processes. The former is interfaced to the MCFM [210] and NLOJET++ [211] programs. More recently, the AMCFAST interface [212] to MADGRAPH5_AMC@NLO [12] has also been developed. Results within the FASTNLO framework for differential top quark production at NNLO are already available [213, 214], while work is ongoing within the APPLFAST project to extend the FASTNLO and APPLGRID technology to NNLO. This will be interfaced by default to the NNLOJET program [206], but will be reusable for other theory codes. Thus, for future PDF fits, relevant to HL and HE-LHC running, fast interface implementations of NNLO theory calculations are expected to be the standard.

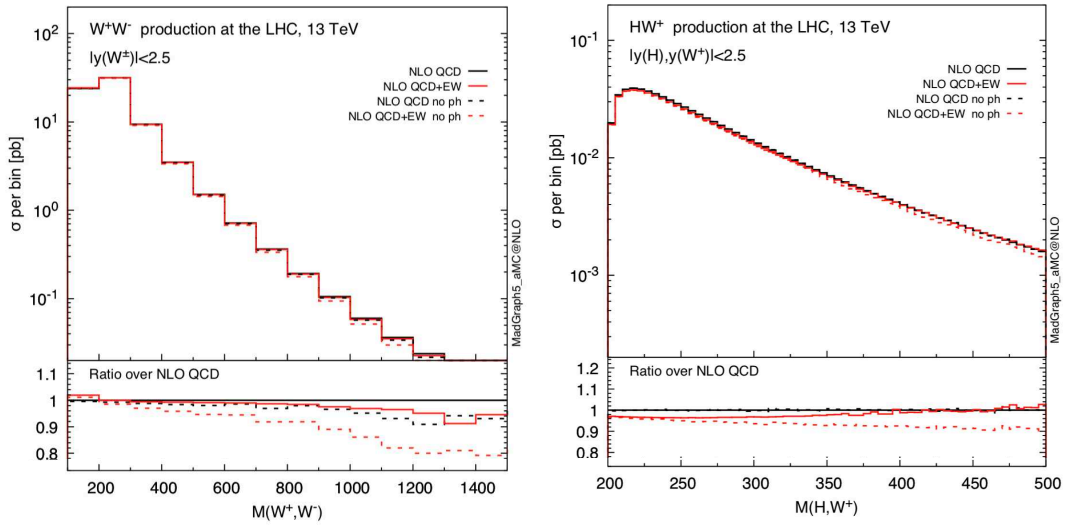

Fig. 2: Photon-initiated contributions partially cancel the NLO EW corrections in the TeV region, as shown for the case of W^+W^- production (left) and hW^+ production (right plot) at 13 TeV.

Theoretical uncertainties

Given the high precision expected for HL-LHC data, it will be crucial to include all sources of experimental, methodological, and theoretical uncertainties associated with PDFs in order to ensure robust predictions. An important issue in this context is to estimate the theoretical uncertainties in PDFs due to missing higher orders (MHOU) in the perturbative expansion for the theory prediction [215], which are so far ignored in all global fits. There is by now some evidence that MHOUs can be comparable, if not larger, than the nominal PDF uncertainties based on the propagation of experimental and methodological uncertainties. In this context, HL-LHC projections should ideally be based on PDFs that consistently account for MHOUs in addition to other sources of uncertainties.

To keep such uncertainties to a minimum, global PDF fits will need to include higher-order perturbative corrections either at fixed-order or at all-orders using some form of resummation. In the former case, encouraging recent progress with N^{3}LO splitting functions [216] suggest that an (approximate) N^{3}LO fit might be within the reach of the HL-LHC era, to match the precision of partonic cross-sections for processes such as Higgs production in gluon fusion [63, 217]. In the latter case, one can use threshold (BFKL) resummation [218, 219] to reduce theoretical uncertainties at the large-x (small-x) kinematic regions. Indeed, several state-of-the-art predictions for LHC processes include threshold resummation, such as for example top quark pair production [220].

Electroweak effects and photon-initiated contributions

The enhanced coverage of the TeV region at the HL-LHC requires not only higher-order QCD corrections to be accounted for, but also electroweak ones, which can be enhanced due to Sudakov logarithms [221]. In the context of PDF studies, there are two main considerations to take into account. First of all, exploiting the constraints from the HL-LHC measurements for PDF fits will require systematically accounting for NLO EW corrections. Secondly, PDFs with QED effects and thus with photon-initiated contributions should become the baseline. It has now been demonstrated [222, 223] (see Ref. [224] for a recent implementation within a global fit) that the photon PDF can be determined with percent–level uncertainties and carry up to $\simeq 0.5\%$ of the proton's momentum. For certain processes, in the TeV region the photon-initiated contributions can have a comparable size but opposite sign to the NLO virtual

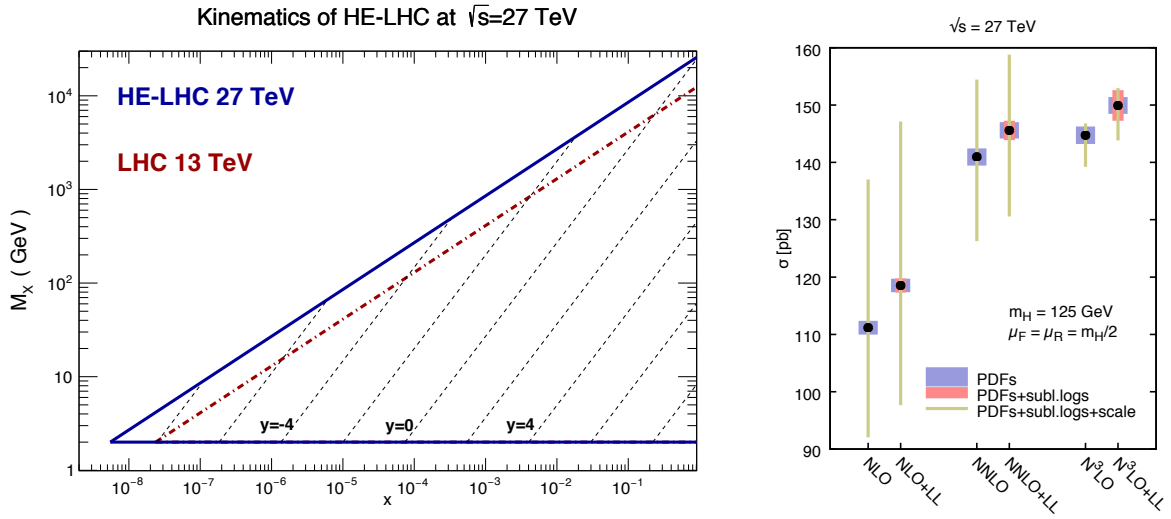

Fig. 3: Left: kinematic coverage of the HE-LHC at $\sqrt{s} = 27$ TeV compared to 13 TeV. Right: the Higgs cross section at the HE-LHC, for different orders and with/without (LL) low–x resummation, and with uncertainty bands from PDF, subleading logarithms, and scale variations [226].

EW corrections, and therefore it is crucial to include both consistently. This is illustrated in Fig. 2 in the specific cases of W^+W^- and hW^+ production at 13 TeV. A more detailed discussion of EW corrections for HL-LHC studies is presented later in the report.

Perspectives at the High Energy LHC

At a centre-of-mass energy of $\sqrt{s} = 27$ GeV, a number of novel phenomena are expected to arise, due to the increased phase space available. Much of this has already been discussed in the context of the Future Circular Collider (FCC) studies at $\sqrt{s} = 100$ TeV [134,225]. To begin with, as illustrated in Fig. 3, when going to higher energies one becomes more sensitive to the small-x region, even for electroweak-scale observables, implying that BFKL resummation effects could become relevant.

Indeed, for $M_X \simeq 100$ GeV the NNPDF3.1sx results [219] at NNLO and at NNLO+NLLx for the gg luminosities are found to differ at the $\simeq 5\%$ level at the HE–LHC. In Ref. [226] a detailed study of SM Higgs boson production via gluon fusion has been performed, consistently including BFKL resummation in the PDFs (see Ref. [219]) and coefficient functions. The role of the former is found to be dominant, and while the impact is mild at the LHC, for the HE–LHC a larger increase is seen relative to the N^{3}LO result with fixed–order NNLO PDFs, that lies outside the fixed–order PDF uncertainty bands, see Fig. 3 (right). This highlights the important role such effects will play at high energies and precision.

Another effect that might become relevant at the HE-LHC are the electroweak PDFs [143, 227] from the resummation of large collinear logarithms of the masses of the W and Z bosons, which become effectively massless at high energies. Related to this is the top quark PDF, which can be (and is) straightforwardly generated within the standard PDF framework. When included with a suitably matched flavour scheme, this may provide a more accurate description of processes involving top quarks [228,229]. In addition, at $\sqrt{s} = 27$ TeV, knowledge of the small-x PDFs will be also required for the modeling of soft and semi-hard QCD dynamics in Monte Carlo event generators [134, 230]. In turn, an improved understanding of the PDFs in the ultra-low-x regime will have implications in high-energy astrophysics, for processes such as cosmic ray detection and for signal and background event rates in neutrino telescopes [231].

2.5 Effective Field Theory calculations and tools[5]

State of the art

The success of the Standard Model Effective Theory (SMEFT) programme at the LHC relies on the availability of public tools for calculations in this framework. Among the most important of these are Monte Carlo (MC) tools for providing realistic predictions for collider processes both for phenomenological studies and experimental analyses. In this respect, significant efforts are being made to implement the effects of dimension-6 operators in MC event generators. Concerning Leading Order (LO) predictions, recent progress includes SMEFTSIM, a complete implementation of the dimension-6 operators in the Warsaw basis [232], an alternative implementation of the Warsaw basis in the R_ξ gauge [233], DIM6TOP, an implementation of top quark operators under various flavour assumptions [234] and the Higgs Effective Lagrangian (HEL) [235] implementation of SILH basis operators. Complementary to SMEFT implementations, there also exist several models of anomalous couplings such as the Higgs Characterisation [236–238] and BSM Characterisation models [239]. These models are all made available in the Universal FEYNRULES Output (UFO) format that can be imported into general purpose Monte Carlo tools, such as MADGRAPH5_AMC@NLO or SHERPA, to generate events and interface them to parton shower generators (PS). A powerful aspect of this workflow is that, once implemented, the model is generic enough to enable event generation for any desired process.

Implementations of particular processes in the presence of dimension-6 operators exist also in other frameworks. An example is the weak production of Higgs in association with a vector boson in POWHEG based on the NLO computation of [240], the implementation of Higgs pair production in the EFT in HPAIR (including approximate NLO corrections) [241] and in HERWIG [147, 242]. Two well-known tools for calculating cross sections for Higgs production via gluon fusion including higher order QCD corrections, HIGLU [243, 244] and SUSHI [245], can also include the effects of modified top and bottom quark Yukawas and the dimension-5 Higgs-gluon-gluon operator. The latter code also permits event generation at NLOQCD+PS accuracy via AMCSUSHI [246] including modified top and bottom quark Yukawa couplings. For a variety of processes with electroweak and Higgs bosons in the final state (VBF H, W and Z production, weak boson pair production, vector-boson-scattering processes, triboson production) the VBFNLO program [247, 248] provides NLO QCD corrections together with implementations of dimension-6 operators and, in the case of VBS and triboson production, dimension-8 operators.

There are also EFT-specific tools providing a number of useful interfaces and calculations. EHDECAY [249, 250] is a package for the calculation of Higgs boson branching fractions including SMEFT effects parametrised by SILH basis operators. The freedom of basis choice in the SMEFT implies that arbitrarily many equivalent descriptions of the model can be formulated. This has important consequences for the development of EFT tools given that any numerical implementation of EFT effects requires choosing a specific basis. A SMEFT basis translation tool, ROSETTA [239], can be used to numerically transform points in parameter space from one basis to another. It adopts the SLHA convention for model parameter specification and provides an interface to Monte Carlo event generation tools through the aforementioned BSMC model. Furthermore, additional interfaces exist to other programs such as EHDECAY, internal routines testing compatibility of Higgs signal-strength and EW precision measurements as well as providing predictions for di-Higgs production cross sections in the SMEFT. Rosetta provides SMEFT basis-independent access to these functionalities. A related tool is DEFT [251], a python code that can check if a set of operators forms a basis, generate a basis and change between bases. A similar implementation based on FEYNRULES is ALLYOURBASES, that performs the reduction of an arbitrary dimension-6 operator into the Warsaw basis operator set. Efforts are also underway to establish a common format for the Wilson coefficients [252], which will allow interfacing various programs computing the matching and running of the operators such as DIM6TOOLS [253] and

[5] Contributed by E. Vryonidou.

WILSON [254]. A public fitting framework that can be used to obtain constraints on the EFT is HEPFIT, which is based on the Bayesian Analysis Toolkit, and includes Higgs and electroweak precision observables.

Future Developments

There is significant progress in computing NLO QCD corrections for the EFT, in both the top and Higgs sector [240, 255–262]. This progress, now on a process-by-process basis, will eventually lead to a full automation of QCD corrections for the SMEFT. As experimental measurements become increasingly systematics dominated, the importance of higher order calculations grows. The complete implementation of dimension-6 operators at NLO, including some flavour symmetry assumptions, is in preparation. This implementation will enable the computation of NLO-QCD corrections to any tree-level process, bringing the Monte Carlo automation to the same level as the Standard Model.

Another direction in which progress is expected over the coming years is the computation of weak corrections in the SMEFT. A small sample of computations has been done, e.g. weak corrections to Higgs production and decay due to top quark loops [263] and due to modified trilinear Higgs coupling [264–266] as well as Higgs and Z-boson decays [267–272]. Due to the behaviour of the Sudakov logarithms, weak corrections are typically important for high transverse momentum regions. Therefore at HE/HL-LHC their impact is expected to be enhanced. It can be expected that the recent progress on a process-by-process basis will eventually lead to the automation of the computation of weak loops in the EFT, as in the Standard Model.

Finally progress is expected in linking tools which compute the running and mixing of the operators with Monte Carlo tools. This will allow the automatic computation of cross-sections and differential distributions taking into account the mixing and running of the operator coefficients.

3 Experimental environment at HL-LHC

3.1 Analysis methods, particle reconstruction and identification

Different approaches have been used by the experiments and in theoretical prospect studies, hereafter named projections, to assess the sensitivity in searching for new physics at the HL-LHC and HE-LHC. For some of the projections, a mix of the approaches described below is used, in order to deliver the most realistic result. The total integrated luminosity for the HL-LHC dataset is assumed to be 3000 fb^{-1} at a centre-of-mass energy of 14 TeV. For HE-LHC studies the dataset is assumed to be 15 ab^{-1} at a centre-of-mass of 27 TeV. The effect of systematic uncertainties is taken into account based on the studies performed for the existing analyses and using common guidelines for projecting the expected improvements that are foreseen thanks to the large dataset and upgraded detectors, as described in Section 3.2.

Detailed-simulations are used to assess the performance of reconstructed objects in the upgraded detectors and HL-LHC conditions, as described in Sections 3.1.1,3.1.2. For some of the projections, such simulations are directly interfaced to different event generators, parton showering (PS) and hadronisation generators. Monte Carlo (MC) generated events are used for Standard Model (SM) and beyond-the-Standard-Model (BSM) processes, and are employed in the various projections to estimate the expected contributions of each process.

Extrapolations of existing results rely on the existent statistical frameworks to estimate the expected sensitivity for the HL-LHC dataset. The increased centre-of-mass energy and the performance of the upgraded detectors are taken into account for most of the extrapolations using scale factors on the individual processes contributing to the signal regions. Such scale factors are derived from the expected cross sections and from detailed simulation studies.

Fast-simulations are employed for some of the projections in order to produce a large number of Monte Carlo events and estimate their reconstruction efficiency for the upgraded detectors. The upgraded CMS detector performance is taken into account encoding the expected performance of the upgraded detector in DELPHES [273], including the effects of pile-up interactions. Theoretical contributions use DELPHES [273] with the commonly accepted HL-LHC card corresponding to the upgraded ATLAS and CMS detectors.

Parametric-simulations are used for some of the projections to allow a full re-optimization of the analysis selections that profit from the larger available datasets. Particle-level definitions are used for electrons, photons, muons, taus, jets and missing transverse momentum. These are constructed from stable particles of the MC event record with a lifetime larger than 0.3×10^{-10} s within the observable pseudorapidity range. Jets are reconstructed using the anti-k_{T} algorithm [274] implemented in the Fastjet [275] library, with a radius parameter of 0.4. All stable final-state particles are used to reconstruct the jets, except the neutrinos, leptons and photons associated to W or Z boson or τ lepton decays. The effects of an upgraded ATLAS detector are taken into account by applying energy smearing, efficiencies and fake rates to generator level quantities, following parameterisations based on detector performance studies with the detailed simulations. The effect of the high pileup at the HL-LHC is incorporated by overlaying pileup jets onto the hard-scatter events. Jets from pileup are randomly selected as jets to be considered for analysis with $\sim 2\%$ efficiency, based on studies of pile-up jet rejection and current experience.

3.1.1 ATLAS and CMS performance

The expected performance of the upgraded ATLAS and CMS detectors has been studied in detail in the context of the Technical Design Reports and subsequent studies; the assumptions used for this report and a more detailed description are available in Ref. [276, 277]. For CMS, the object performance in the central region assumes a barrel calorimeter aging corresponding to an integrated luminosity of

1000 fb^{-1}.

The triggering system for both experiments will be replaced and its impact on the triggering abilities of each experiment assessed; new capabilities will be added, and, despite the more challenging conditions, most of the trigger thresholds for common objects are expected to either remain similar to the current ones or to even decrease [278, 279].

The inner detector is expected to be completely replaced by both experiments, notably extending its coverage to $|\eta| < 4.0$. The performance for reconstructing charged particles has been studied in detail in Ref. [280–282].

Electrons and photons are reconstructed from energy deposits in the electromagnetic calorimeter and information from the inner tracker [283–286]. Several identification working points have been studied and are employed by the projection studies as most appropriate.

Muons are reconstructed combining muon spectrometer and inner tracker information [287, 288].

Jets are reconstructed by clustering energy deposits in the electromagnetic and hadronic calorimeters [283, 284, 289] using the anti-k_{T} algorithm [274]. B-jets are identified via b-tagging algorithms. B-tagging is performed if the jet is within the tracker acceptance ($|\eta| < 4.0$). Multivariate techniques are employed in order to identify $b-$jets and $c-$jets, and were fully re-optimized for the upgraded detectors [280, 282]. An 70% $b-$jet efficiency working point is used, unless otherwise noted.

High p_{T} boosted jets are reconstructed using large-radius anti-k_{T} jets with a distance parameter of 0.8. Various jet substructure variables are employed to identify boosted W/Z/Higgs boson and top quark jets with good discrimination against generic QCD jets.

Missing transverse energy is reconstructed following similar algorithms as employed in the current data taking. Its performance has been evaluated for standard processes, such as top pair production [280, 290].

The addition of new precise-timing detectors and its effect on object reconstruction has also been studied in Ref. [286, 291], although its results are only taken into account in a small subset of the projections in this report.

3.1.2 LHCb performance

The LHCb upgrades are shifted with respect to those of ATLAS and CMS. A first upgrade will happen at the end of Run-2 of the LHC, to run at a luminosity five times larger (2×10^{33}cm^{-2}s^{-1}) in LHC Run-3 compared to those in Runs-1 and-2, while maintaining or improving the current detector performance. This first upgrade (named Upgrade I) will be followed by by the so-called Upgrade II (planned at the end of Run-4) to run at a luminosity of $\sim 2 \times 10^{34}$cm^{-2}s^{-1}.

The LHCb MC simulation used in this document mainly relies on the PYTHIA 8 generator [292] with a specific LHCb configuration [293], using the CTEQ6 leading-order set of parton density functions [294]. The interaction of the generated particles with the detector, and its response, are implemented using the GEANT toolkit [295, 296], as described in Ref. [297].

The reconstruction of jets is done using a particle flow algorithm, with the output of this clustered using the anti-k_{T} algorithm as implemented in FASTJET, with a distance parameter of 0.5. Requirements are placed on the candidate jet in order to reduce the background formed by particles which are either incorrectly reconstructed or produced in additional pp interactions in the same event.

Concerning the increased pile-up, different assumptions are made, but in general the effect is assumed to be similar to the one in Run-2.

3.2 Treatment of systematic uncertainties

It is a significant challenge to predict the expected systematic uncertainties of physics results at the end of HL-LHC running. It is reasonable to anticipate improvements to techniques of determining systematic uncertainties over an additional decade of data-taking. To estimate the expected performance, experts in the various physics objects and detector systems from ATLAS and CMS have looked at current limitations to systematic uncertainties in detail to determine which contributions are limited by statistics and where there are more fundamental limitations. Predictions were made taking into account the increased integrated luminosity and expected potential gains in technique. These recommendations were then harmonized between the experiments to take advantage of a wider array of expert opinions and to allow the experiments to make sensitivity predictions on equal footing [276, 277]. For theorists' contributions, a simplified approach is often adopted, loosely inspired by the improvements predicted by experiments.

General guide-lining principles were defined in assessing the expected systematic uncertainties. Theoretical uncertainties are assumed to be reduced by a factor of two with respect to the current knowledge, thanks to both higher-order calculation as well as reduced PDF uncertainties [298]. All the uncertainties related to the limited number of simulated events are neglected, under the assumption that sufficiently large simulation samples will be available by the time the HL-LHC becomes operational. For all scenarios, the intrinsic statistical uncertainty in the measurement is reduced by a factor $1/\sqrt{\mathrm{L}}$, where L is the projection integrated luminosity divided by that of the reference Run-2 analysis. Systematics driven by intrinsic detector limitations are left unchanged, or revised according to detailed simulation studies of the upgraded detector. Uncertainties on methods are kept at the same value as in the latest public results available, assuming that the harsher HL-LHC conditions will be compensated by method improvements.

The uncertainty in the integrated luminosity of the data sample is expected to be reduced down to 1% by a better understanding of the calibration methods and their stability employed in its determination, and making use of the new capabilities of the upgraded detectors.

In addition to the above scenario (often referred to as "YR18 systematics uncertainties" scenario), results are often compared to the case where the current level of understanding of systematic uncertainties is assumed ("Run-2 systematic uncertainties") or to the case of statistical-only uncertainties.

3.3 Precision Luminosity

Motivation

Measurements of production cross sections provide fundamental tests of theoretical predictions. Ultimate precision both of the experimental measurements and the theoretical predictions is required in order to determine fundamental parameters of the Standard Model and to constrain or discover beyond-the-Standard-Model phenomena. At the LHC, the precision of cross section measurements is limited by the uncertainty of the integrated luminosity, currently about 2%. The impact of all other experimental uncertainties combined is smaller than $\sim$ 1% (2–3%) for Drell-Yan ($t\bar{t}$) cross section measurements, respectively [299, 300]. For the HL-LHC [301], significant improvements of the luminosity measurement are being planned. A target uncertainty of 1% has been set, and this is also assumed for many of the results presented in this report. Such improvement is expected to be achieved by combination of improved luminosity detector instrumentation, currently in the design phase, and refined analysis techniques, rapidly developing during the analysis of Run-2 data. In the following, we provide a short description of the general plan towards the 1% target for the integrated luminosity at the HL-LHC.

Van der Meer Scans

At hadron colliders, the precision of theoretical predictions for inclusive cross sections, e.g. for Z/γ^* production, is limited by the knowledge of the parton density functions (PDFs) in the proton, and the

uncertainty is of the order of 3–5% [302]. A more precise, and purely experimental method to determine the luminosity is based on the Van der Meer (VdM) scan technique [303]. In VdM scans, beam axes are moved in the transverse planes, x and y, across each other such that the beam overlap integral can be determined. From the measured overlap integral, and the beam currents, the instantaneous luminosity during the VdM scan is determined [304].

In practice, VdM scan data are typically recorded with a small number of low pile-up bunches well separated in time, with special interaction-region optics optimised for the measurement of the luminous-region parameters [304–306], and with the bunch intensity lowered to about 3/4 of that during physics runs so as to reduce beam-beam biases while retaining adequate statistics in the luminometers. To transfer the luminosity information from VdM scans to high pileup operation, rate measurements are performed during the VdM scan, in several detectors. The absolute scale, i.e. the relation between the measured rate in a given detector and the luminosity measurement is a detector-specific calibration constant, usually referred to as visible cross section σ_{vis}, relating the measured event rate $\mathrm{d}N/\mathrm{d}t$ to the instantaneous luminosity through the relation $\mathrm{d}N/\mathrm{d}t = L \cdot \sigma_{\text{vis}}$. The integrated luminosity for a complete data taking period, e.g. a full year of data taking is then obtained by continuous rate measurements throughout the year. The integrated normalized rate measurement then corresponds to the integrated luminosity.

Systematic Uncertainties

The uncertainty in the integrated luminosity consists of three components [306, 307]: the absolute-scale uncertainty, i.e. that on the measured visible cross-sections extracted from the VdM-scan analysis; the calibration-transfer uncertainty, which affects the extrapolation of the visible cross-section from the low pile-up, low luminosity VdM regime to the high pile-up, high luminosity physics regime; and the stability uncertainty, that arises from possible time-dependencies and degradations of the detector response affecting the rate measurement over time. Improved analysis techniques, better detectors and extended data takings dedicated to precision luminosity measurements are required to reduce the current uncertainty towards the 1% goal.

Absolute Scale Uncertainty

Dominant uncertainties in the luminosity scale arise from the modeling of, and the potential non-linear correlations between, the horizontal and vertical beam profiles; from inconsistencies between equivalent visible cross-section measurements carried out during the same calibration session or using different luminometers; from the absolute displacement scale of the beams during the scans; and from beam-orbit stability. In Run-2, these and other uncertainties have been reduced using refined methods and dedicated additional data have been recorded for such specific purposes. Improvements of the uncertainty can be achieved by combination of different complementary approaches, of results obtained using different detectors, and of datasets obtained from different VdM scans.

An alternative technique, complementary to VdM scans, was established by the LHCb experiment [308]. The shape of a single beam is measured as the distribution of beam-gas interactions. For this purpose a gas is injected into the interaction region during the VdM fill. The combination of VdM-scan and beam-gas imaging measurements leads to further reduction of the uncertainty, at least for LHCb, thanks to the exquisite performance of the VELO vertex detector.

Calibration-transfer Uncertainty

In the HL-LHC area, the VdM calibration will typically be carried out under similar conditions as in Run-2, i.e. at a pile-up level of about 0.5 interactions per bunch crossing, and with a luminosity of a few Hz/μbarn. In contrast, the physics running during the HL-LHC, will be characterized by pile-up

parameters of up to 200 interactions per bunch crossing, and by average instantaneous luminosities of 50 Hz/nb, two to three times the peak instantaneous luminosity achieved so far. This will lead to an increase of the uncertainties associated with non-linearities in luminometer response. Most luminosity detectors for HL-LHC are still being designed. Drawing on Run-1 and Run-2 experience with precision luminosity measurements, the design of the future detectors aims to reduce the associated systematic uncertainties. HL-LHC detectors are required to behave linearly over several orders of magnitude in their track, energy or hit rate measurements, with residual non-linearities that are reproducible and monitorable. Special runs with scans at intermediate instantaneous luminosity can be used to pin down nonlinear behaviour further.

Long-term stability and consistency of luminosity measurements

In the past, one obvious way to determine stability and linearity effects has been to devise and compare the luminosity measurements by several detectors, using different technologies, with uncorrelated systematics. Since 2016, experiments started to exploit so-called emittance scans. These are short VdM scans (duration of minutes) performed at standard physics optics and currents, regularly at the beginning and at the end of fills [309–312]. While the emittance scans are not primarily designed for the precision determination of σ_{vis}, trends over time, or as a function of instantaneous luminosity, can be used to determine stability effects, such as aging, independently for each given detector. The combination of emittance scans and of rate comparisons between redundant and independent detector systems has been successfully used to discover and control drifts and trends throughout Run-2, the longest LHC data-taking period so far, during which 150 fb^{-1} worth of data were recorded. As a result, the uncertainty in the integrated luminosity in recent years remained at around 2-2.5% even though the pile-up extrapolation range and the duration of the integration periods increased significantly.

Recent Ideas

Additional methods are being discussed among luminosity experts of the LHC experiments and machine. One method recently developed is to use the rate measurement of $Z \to \mu\mu$ production [313]. This is a high-rate physics process with in-situ calibration capabilities. Luminosity and Z boson rate are experimentally related through the following formula: $\sigma_Z = N_Z/(L \times \epsilon_{Z\to\mu\mu})$ where N_Z is the number of reconstructed Z bosons, L the integrated luminosity, and $\epsilon_{Z\to\mu\mu}$ the $Z \to \mu\mu$ event reconstruction efficiency. If $\epsilon_{Z\to\mu\mu}$ and L are known, then the fiducial Z boson production cross section σ_Z can directly be determined from the measured event rate. To minimize the uncertainties associated with luminometer non-linearities and long-term stability, the fiducial Z boson cross section is measured from data recorded during an extended proton–proton production run at low pileup. This run should be close in time to one or two extended VdM scans. The efficiency $\epsilon_{Z\to\mu\mu}$ can be determined in situ, using the tag-and-probe method on the same event sample [313]. Once the cross section is measured at sub-percent level precision, the continuous rate measurement can be used to transfer the calibration to the high pileup dataset. The integrated luminosity will be given by the total number of produced Z bosons, corrected by the time-integrated muon identification efficiency with an uncertainty consisting of the absolute scale uncertainty from the VdM scan (or, in LHCb, beam-gas imaging scan), and a remaining uncertainty in the pileup dependency of the muon identification efficiency.

Conclusions Towards HL-LHC

The aim for HL-LHC is to measure luminosity with substantially improved precision. This aim can be achieved by combination of three ingredients:

1. High precision luminosity detectors are needed to provide high-granularity bunch-by-bunch luminosity measurements, with very good linearity and stability.

2. Advanced, multiple and redundant VdM scans and refined VdM analysis techniques can lead to substantial improvements.

3. Novel techniques, such as the measurement of fiducial Z boson production rates exploiting in-situ efficiency determination, provide handles for advancement of the integrated luminosity uncertainty towards the 1% target.

In order to achieve these goals during HL-LHC, a suite of tests and proof-of-concept measurements is being developed which should be carried out already during Run-3.

4 Electroweak processes

The study of electroweak processes is a central topic of SM tests. Given the small electroweak couplings, high luminosity provides a crucial handle for gaining precision in these measurements, in particular for complex final states with relatively small cross sections. Prospects for those measurements and for their theoretical description are considered in the following for vector boson fusion (VBF) and vector boson scattering (VBS) processes, for di-boson and tri-boson production, and for single weak boson production processes, which promise unprecedented precision on W-mass and weak mixing angle measurements.

4.1 Vector boson fusion[6]

This sub-section discusses the prospects for vector boson fusion Higgs production at the HL-LHC and the HE-LHC, respectively. A particular focus is to investigate how hard and how forward the two tag jets are expected to be at 27 TeV. The efficiency of VBF cuts will be discussed, and fiducial cross sections and differential distributions for a set of typical analysis cuts will be determined. Finally, the quality of the VBF approximation will be considered, in particular when extra jet activity in addition to the two tag jets is required.

The relevant parameters used for the calculations in this chapter are reported here. More details can be found in LHC Higgs Cross Section Working Group report [186]. The gauge boson masses and widths are set to

$$m_W = 80.385 \text{ GeV}, \qquad \Gamma_W = 2.085\text{GeV}. \tag{1}$$

$$m_Z = 91.1876 \text{ GeV}, \qquad \Gamma_Z = 2.4952 \text{ GeV}. \tag{2}$$

and the Fermi constant is

$$G_F = 1.16637 \cdot 10^{-5} \text{ GeV}^{-2}. \tag{3}$$

The Higgs is described in the narrow width approximation with mass $m_H = 125$ GeV. The parton distribution function PDF4LHC15_nnlo_100_pdfas is used and the central renormalization and factorization scale is set to $\mu_0 = m_W$, unless otherwise specified.

Detector requirements

VBF production is characterized by two hard and forward jets accompanying the two bosons. The requirement of two such jets can significantly reduce the QCD induced background along with the electroweak production stemming from s-channel processes. The transverse hardness of the VBF jets is fundamentally set by the mass scale of the virtual vector bosons. It is therefore expected that the jet spectrum is not very sensitive to the collider centre-of-mass energy, and in particular that the jets do not get appreciably harder when increasing the energy.

Figure 4 shows the fraction of total VBF cross sections that survives the cut on the transverse momentum of the two tag jets for the three collider energies 14, 27, and 100 TeV. As can be seen, the cross section drops rapidly as the p_{T}-cut is increased. In particular, at 27 TeV, roughly 60% survive for $p_{\mathrm{T,tag}} > 30$ GeV, which diminishes to 30% of the total VBF cross section for $p_{\mathrm{T,tag}} > 50$ GeV. It will therefore be of great importance to the VBF program to be able to keep the jet definition not too hard.

Given that the two tag jets tend to be forward in the detector volume, it is of interest to study how many jets are lost above a certain rapidity threshold. Figure 5 shows the fraction of events with $\max\left(\left|y_{j_1}\right|, \left|y_{j_2}\right|\right)$ above some threshold at $\sqrt{s} = 27$ TeV for various jet p_{T} definitions. As can be seen

[6] Contribution by F. Campanario, T. Chen, J. M. Cruz-Martinez, T. Figy, A. Karlberg, S. Plätzer and M. Sjödahl.

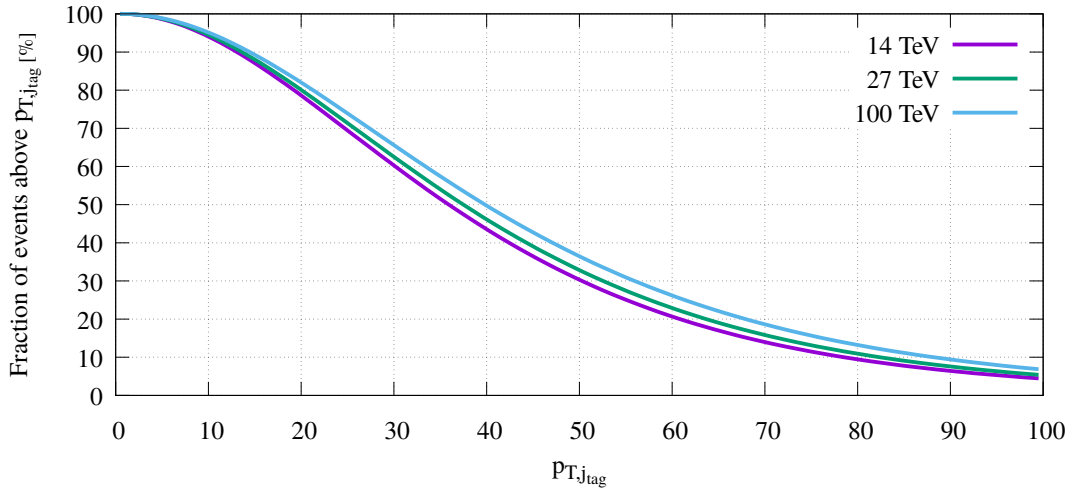

Fig. 4: Fraction of the total VBF cross section surviving a p_{T} cut on the two hardest jets of $p_{\mathrm{T,j_{tag}}}$ for three different collider energies. The results shown here are computed at LO.

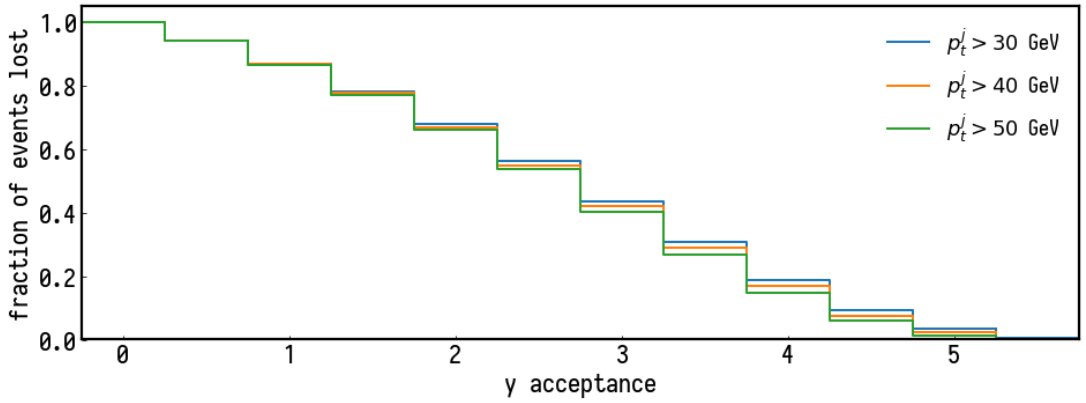

Fig. 5: Fraction of events lost as a function of the rapidity acceptance of the detector at a collider energy of $\sqrt{s} = 27$ TeV. Results shown for three different tag jet transverse momentum cuts. The results shown here are computed at LO.

from the plot, about 20% of the cross section has $\max\left|y_{j_1}\right|, \left|y_{j_2}\right| > 4$. For comparison, this number is $\sim 5\%$ at 14 TeV. Additionally one finds that these losses increase to $\sim 30\%$ when imposing the dedicated VBF cuts for 27 TeV defined below. Hence, in order to maximize the potential of VBF analyses at the HE-LHC it will be highly desirable that the detectors have a rapidity reach beyond 4.0.

HL-LHC

For VBF production with a centre of mass energy of $\sqrt{s} = 14$ TeV, VBF cuts as in Ref. [186] are used, with two anti-k_{T} jets with $R = 0.4$ and

$$p_{\mathrm{T}}^j > 20 \text{ GeV}, \qquad |y_j| < 5.0, \qquad |y_{j_1} - y_{j_2}| > 3.0, \qquad M_{jj} > 130 \text{ GeV}. \tag{4}$$

The requirement on the rapidity separation and invariant mass significantly reduces background contributions to the process $pp \to Hjj$.

Table 1 reports the fiducial VBF cross section under the above cuts. The cross section includes

Table 1: Fiducial VBF cross sections including QCD and EW corrections and their uncertainties for collider energy $\sqrt{s} = 14$ TeV and for a Higgs-boson mass $m_H = 125$ GeV. The QCD corrections have been updated compared to those reported in Ref. [186].

σ^{VBF}[fb]	Δ_{scale}[%]	$\Delta_{\text{PDF}\oplus\alpha_s}$[%]	$\sigma^{\text{DIS}}_{\text{NNLOQCD}}$[fb]	δ_{EW}[%]	σ_γ[fb]	$\sigma_{s\text{-channel}}$[fb]
2259	$^{+1.5}_{-1.3}$	$\pm 2.1/\pm 0.4/\pm 2.1$	2401	-6.9	23.6	32.9

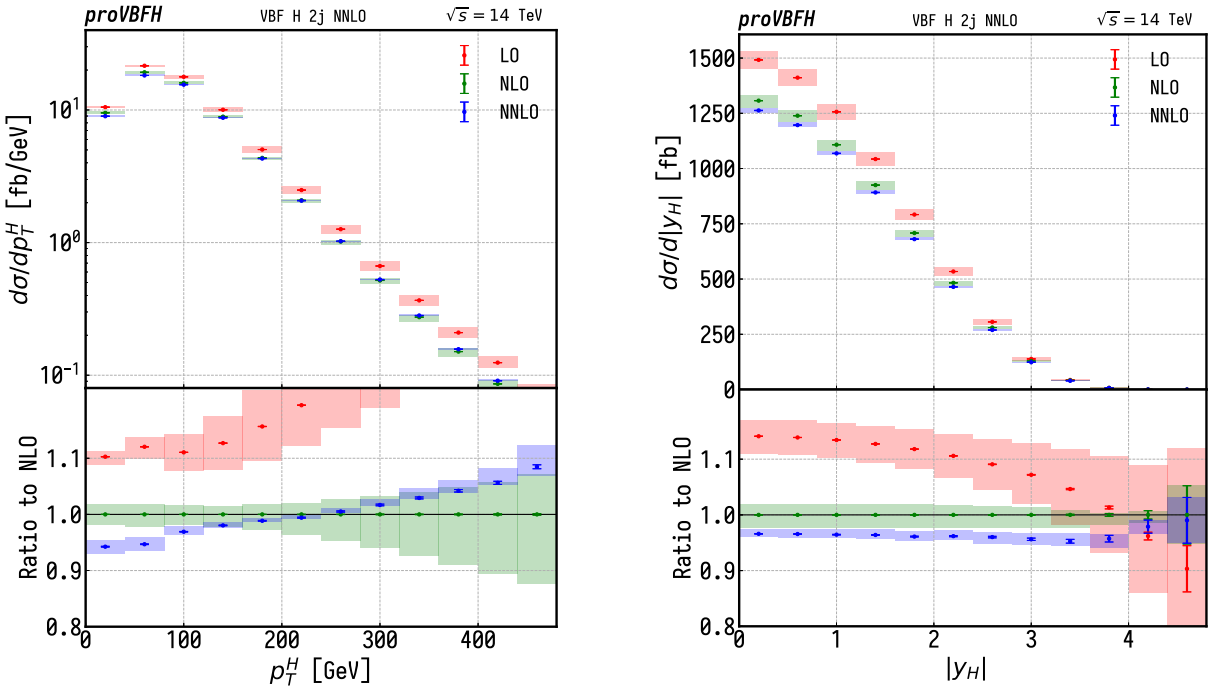

Fig. 6: Transverse momentum and rapidity of the Higgs boson after the cuts of eq. (4) and at a collider energy $\sqrt{s} = 14$ TeV.

NNLO-QCD corrections in the DIS approximation and NLO-EW corrections including photon induced contributions. Shown separately is the s-channel contribution which is not included in the total number. The NNLO-QCD corrections have been computed with PROVBFH-1.1.0 [51, 65, 314–316] and the electroweak contributions with HAWK-2.0 [317–320].

HE-LHC

For fiducial cross sections at a centre-of-mass energy of $\sqrt{s} = 27$ TeV, all physical parameters are kept unchanged with respect to the previous sections. The contributions of the gluon fusion (ggF) and VBF channels to Hjj production are compared, and results are presented for the effects of the NLO and NNLO QCD corrections to VBF Hjj production as computed in NNLOJET [321] with a redefined set of VBF cuts for the new energy choice.

For the comparison of VBF to the ggF background, any kind of VBF cut is omitted, requiring only two jets with

$$p_{\text{T}}^j > 30\,\text{GeV}, \qquad |y_j| < 5.0, \tag{5}$$

defined using the anti-k_{T} algorithm [322] with $R = 0.4$. The total cross section for ggF and VBF is shown in Table 2. Both the ggF and VBF contributions are computed with the parton-level Monte Carlo

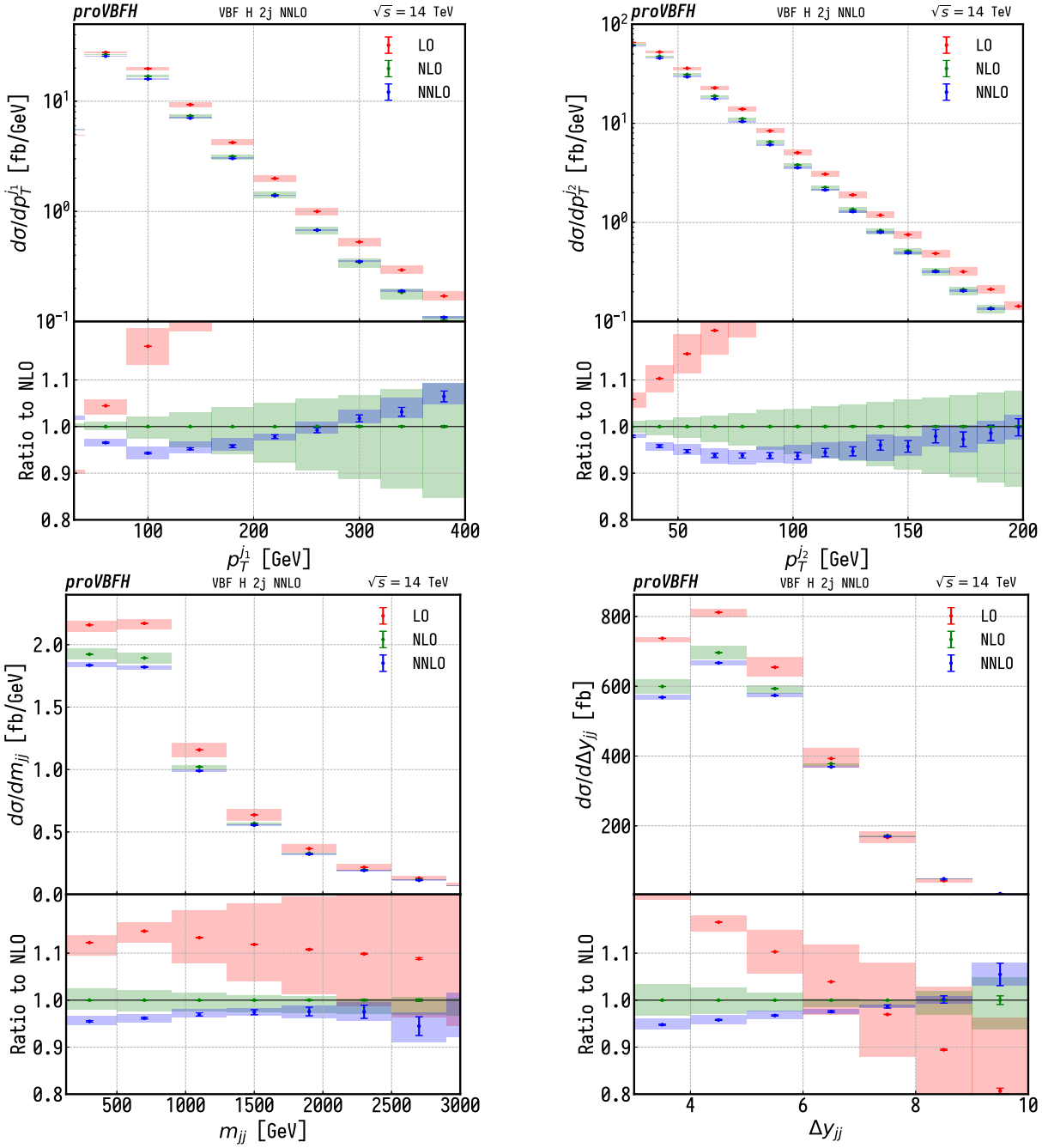

Fig. 7: In the top row the transverse momentum the two hardest jet after the cuts of eq. (4) and at collider energy $\sqrt{s} = 14$ TeV. In the bottom row the invariant mass and absolute rapidity gap between the two hardest jets.

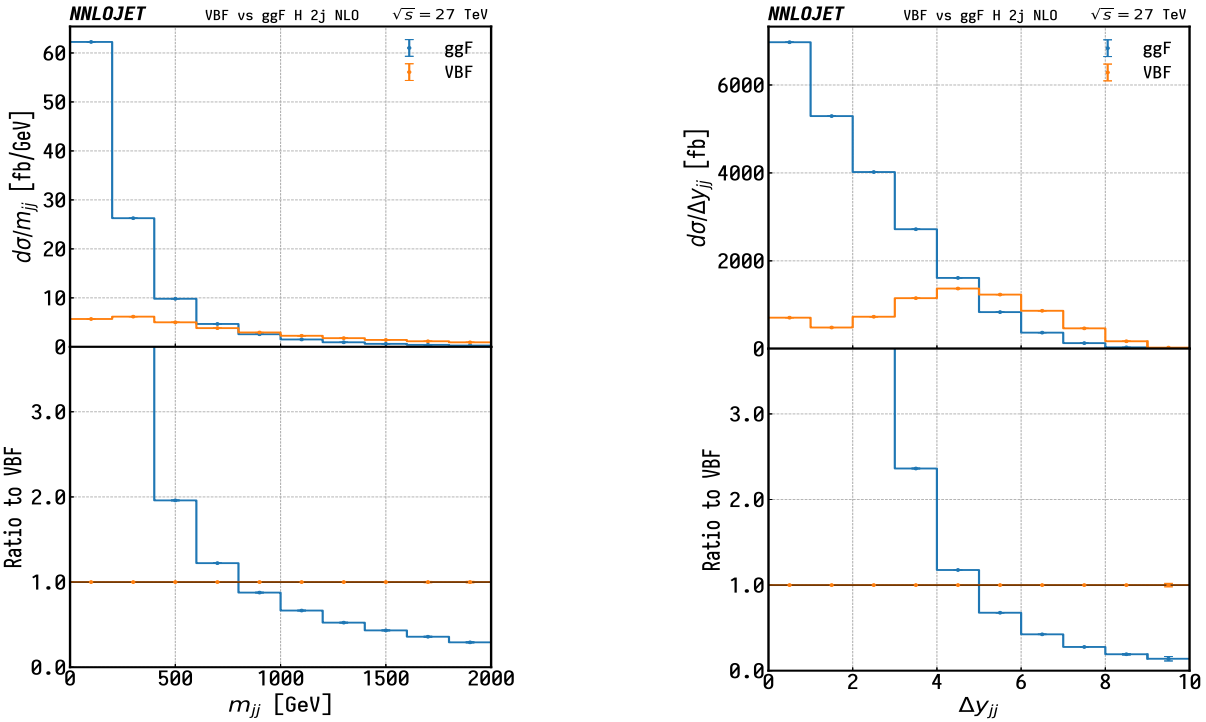

Fig. 8: Differential distributions for the invariant mass (left) and spatial distribution (right) of the dijet system. At lower values of m_{jj} and Δy_{jj} one observes a strong dominance of the ggF channel. For larger values of both observables, however, the VBF channel gains importance.

NNLOJET which includes ggF Higgs production in the heavy top limit (HTL) [67,68,323–325] among other processes [19, 206, 326–332]. The comparison of Table 2 is done at NLO QCD since Higgs plus two jets in gluon fusion is only available at this accuracy level.

In order to define a set of cuts which enhance the VBF contribution, the invariant mass (m_{jj}) and the spacial distribution (through the rapidity gap between both jets, Δy_{jj}) of the dijet system formed by the two leading jets is considered. The VBF production mode dominates over ggF in the large rapidity separation region ($\Delta y_{jj} > 4.5$) as well as for moderate and high values of the dijet invariant mass ($m_{jj} > 700$ GeV).

Table 2: Comparison between Higgs production by gluon fusion and vector boson fusion for a centre-of-mass energy $\sqrt{s} = 27$ TeV, at NLO QCD. Errors correspond to Monte Carlo statistics.

Production mode	Total cross section (fb)	% of Total
ggF (HTL)	21984 ± 10	75.32 ± 0.04
VBF	7203 ± 2	24.68 ± 0.01

Fiducial cross sections for VBF at $\sqrt{s} = 27$ TeV are defined with a set of tight VBF cuts,

$$\Delta y_{jj} > 4.5, \qquad m_{jj} > 600 \text{ GeV}, \tag{6}$$

requiring the two leading jets to be found in opposite rapidity hemispheres with a maximum rapidity of $|y_j| < 5.0$. In Table 3 the fiducial cross section is computed for three choices of the cut on the transverse momentum of the two leading jets: $p_{\mathrm{T}}^j > \{30, 40, 50\}$ GeV while differential distributions for $p_{\mathrm{T}}^j > 30$ GeV are shown in Figs. 9 and 10. The Hjj contribution in the VBF approximation as well as plots in this section are calculated at NNLO QCD accuracy with NNLOJET, electroweak corrections

Table 3: Fiducial VBF cross sections including QCD and EW corrections and their uncertainties for collider energy $\sqrt{s} = 27$ TeV ($m_H = 125$ GeV). For completeness the s-channel contribution (corresponding to $pp \to HV \to q\bar{q}$) is also included.

σ^{VBF}[fb]	Δ_{scale}[%]	$\sigma^{\text{DIS}}_{\text{NNLOQCD}}$[fb]	δ_{EW}[%]	σ_γ[fb]	$\sigma_{s\text{-channel}}$[fb]	p_{T}^j cut [GeV]
2805	$^{+1.05}_{-0.02}$	3059	−9.6	39.8	5.9	30
2087	$^{+1.13}_{-1.05}$	2283	−10.0	32.3	4.4	40
1442	$^{+1.43}_{-1.61}$	1586	−10.5	22.3	3.0	50

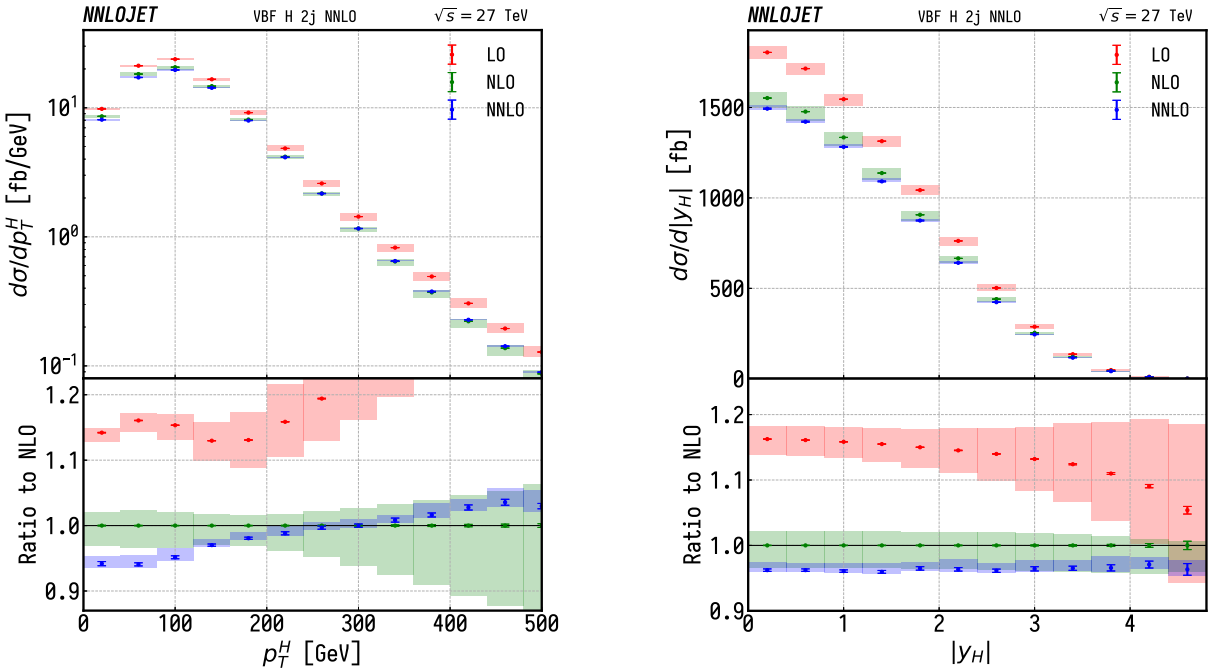

Fig. 9: Kinematical variables for the Higgs boson at $\sqrt{s} = 27$ TeV for tight VBF cuts. The NLO corrections are of more than -10 % across the whole considered range. The NNLO corrections, much smaller than NLO, show good convergence of the perturbative series. The NNLO corrections changes sign for high transverse momentum (left). For the rapidity distribution (right) they remain stable across the entire range of the observable.

and the s-channel contribution shown in Table 3 are again computed with HAWK-2.0. Shaded boxes in all plots represent scale variations with $\mu_R = \mu_F = \{0.5, 2\}\mu_0$ with the central scale $\mu_0 = m_W$ and error bars represent statistical uncertainties from the Monte Carlo integration. In Fig. 9 the transverse momentum and rapidity distribution of the Higgs boson is shown. The kinematical variables for the system formed by the two leading jets are shown in Fig. 10.

Comparison of* HJETS++ *and* VBFNLO *for Higgs boson production

The HJETS++ 1.1 module implements [333–336] electroweak Higgs boson plus two and three jet production. The one-loop integrals are computed using the techniques discussed in Ref. [337] and the colour algebra is performed using COLORFULL [338]. For the VBF approximation, the matrix elements encoded in VBFNLO version 3.0 beta 5 [247, 248, 339, 340] are used, with HERWIG 7 as the event generator [146, 147, 341, 342]. Jet reconstruction is performed on final state partons using the

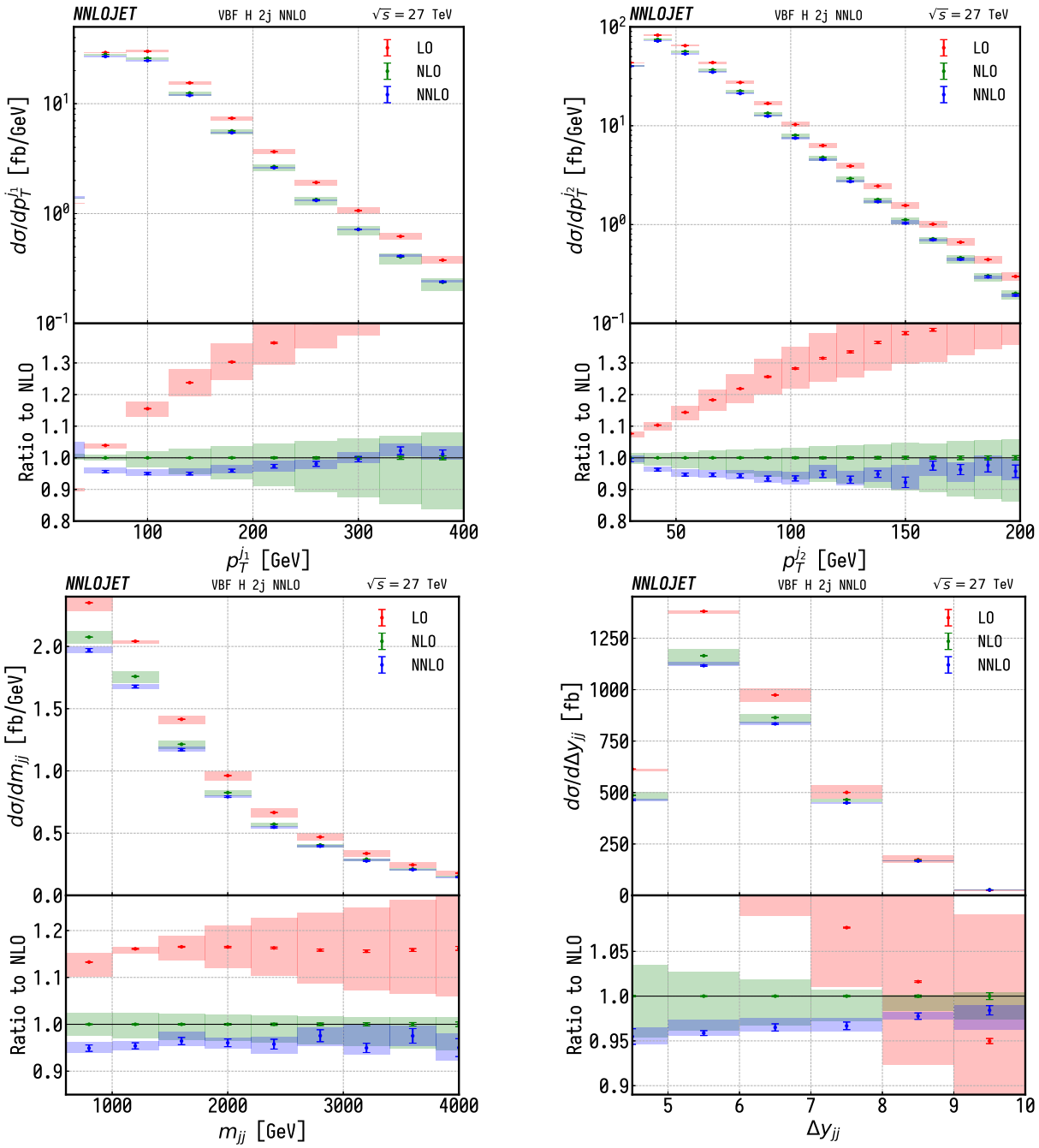

Fig. 10: The top row shows the transverse momentum of the two leading jets ordered in rapidity at $\sqrt{s} = 27$ TeV for tight VBF cuts. The bottom row depicts the kinematical variables for the dijet system they form. Note that NNLO corrections noticeably reduce the scale uncertainties for both observables over the entire range considered. NLO corrections are big for moderate and high transverse momentum with a scale uncertainty that grows with the transverse momentum. This behaviours is softened by the NNLO corrections.

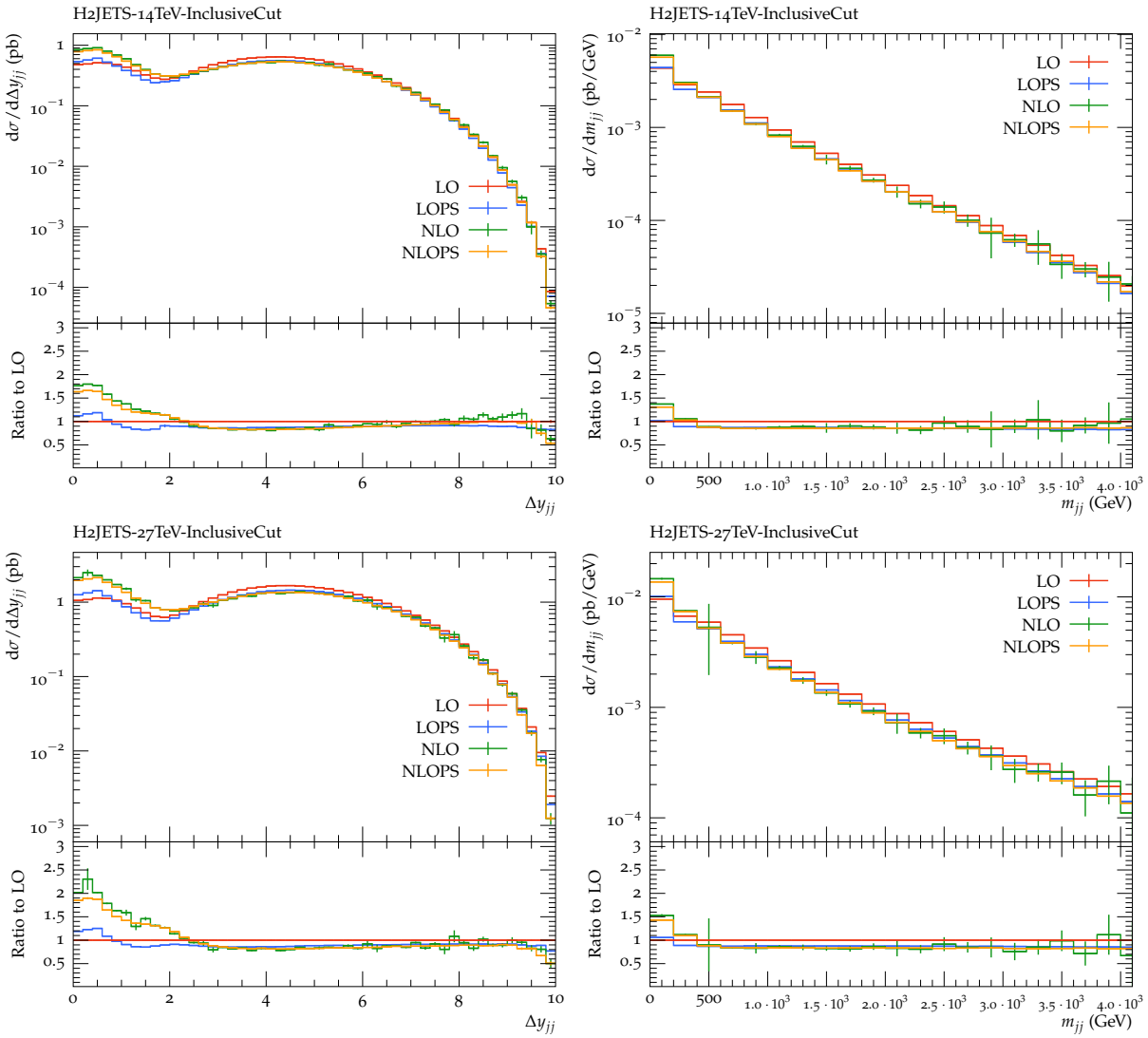

Fig. 11: Differential distributions of Δy_{jj} and m_{jj} at $\sqrt{s} = 14$ TeV (top row) and $\sqrt{s} = 27$ TeV (bottom row). HJETS++ matrix elements and inclusive cuts are used in the $H + 2$ jets calculations.

anti-k_T algorithm [322] in the FASTJET library [343]. Simulated events are analyzed via RIVET [344].

For comparison plots of Higgs plus two jet calculations, collider energies of $\sqrt{s} = 14$ TeV and $\sqrt{s} = 27$ TeV are considered. Two kinematic variables, namely the invariant mass, m_{jj}, and the spatial distribution, Δy_{jj}, of the two tag jets are chosen to present their differential distributions. Parton distribution functions PDF4_LHC15_nlo_100 are used, while all other input parameters are the same as given at the beginning of Section 4.1. Differential distributions for leading order, leading order plus parton shower, next-to-leading order, and next-to-leading order plus parton shower are shown in Fig. 11, with the inclusive cuts defined in eq. (5). Comparison plots between two different matrix elements, HJETS++ and VBFNLO are shown in Fig. 12. VBFNLO uses the VBF approximation throughout, i.e. s-channel contributions such as $pp \to VH \to jjH$ production need to be added as separate processes. The comparison between HJETS++ and VBFNLO thus also serves to highlight the phase space regions where the VBF approximation is warranted.

The tight VBF cuts applied for $\sqrt{s} = 14$ TeV are defined as

$$p_T^j > 30 \text{ GeV}, \qquad |y_j| < 5.0, \qquad |y_{j_1} - y_{j_2}| > 3.0, \qquad M_{jj} > 130 \text{ GeV}. \tag{7}$$

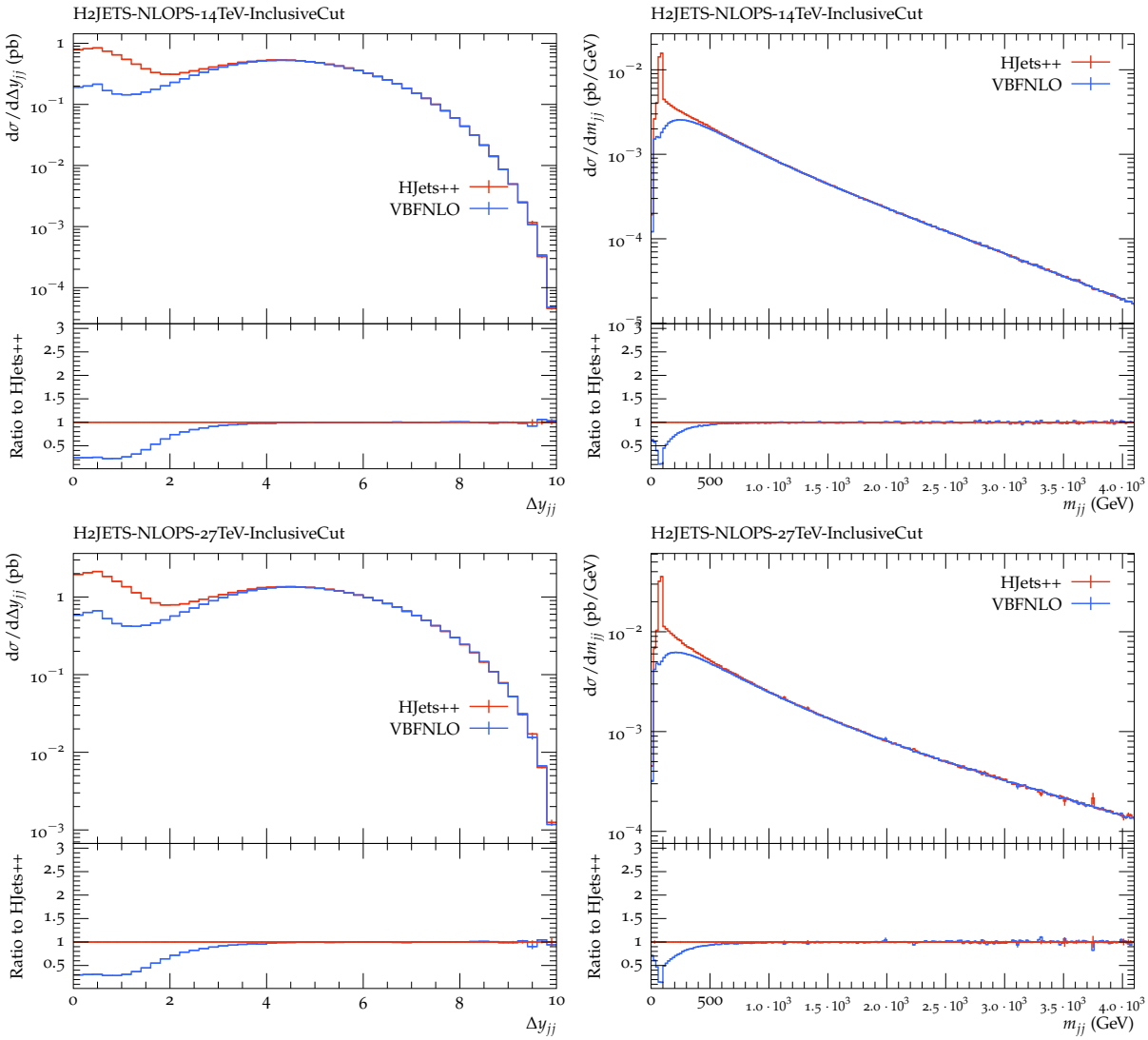

Fig. 12: The distributions of kinematic variables in $H + 2$ jets at $\sqrt{s} = 14$ TeV (top row) and $\sqrt{s} = 27$ TeV (bottom row). Comparisons are between the HJETS++ matrix elements and the VBFNLO matrix elements at NLO plus parton shower. Plots indicate that both HJETS++ and VBFNLO calculations agree once the tight VBF cuts are applied.

For $\sqrt{s} = 27$ TeV comparison plots, the tight VBF cuts defined in eq. (6) are used. The VBFNLO calculation is consistent with the HJETS++ calculation after applying the tight VBF cut.

Fig. 13 shows differential distributions of kinematics variables for the NLO full and approximate results at $\sqrt{s} = 14$ TeV and $\sqrt{s} = 27$ TeV. The comparison of the full and approximate calculations are shown in the second and third rows of Fig. 13 for tight VBF cuts for the transverse momentum of the third jet $p_{\mathrm{T}}^{j_3}$ and the centrality of the third jet $y^{\star}_{j_3} = (y_{j_3} - \frac{1}{2}(y_{j_1} + y_{j_2}))/|y_{j_1} - y_{j_2}|$. For the $\sqrt{s} = 27$ TeV tight VBF cuts ($\Delta y_{jj} > 4.5$, $m_{jj} > 600$ GeV, and $y_{j_1} \cdot y_{j_2} < 0$), one observes excellent agreement between the full and approximate calculation. For the $\sqrt{s} = 14$ TeV tight VBF cuts ($\Delta y_{jj} > 3.0$, $m_{jj} > 130$ GeV, and $y_{j_1} \cdot y_{j_2} < 0$), the full and approximate calculations still do not converge. However, for $\Delta y_{jj} > 4.0$ or $m_{jj} > 600$ GeV the full and approximate calculations would compare quite well.

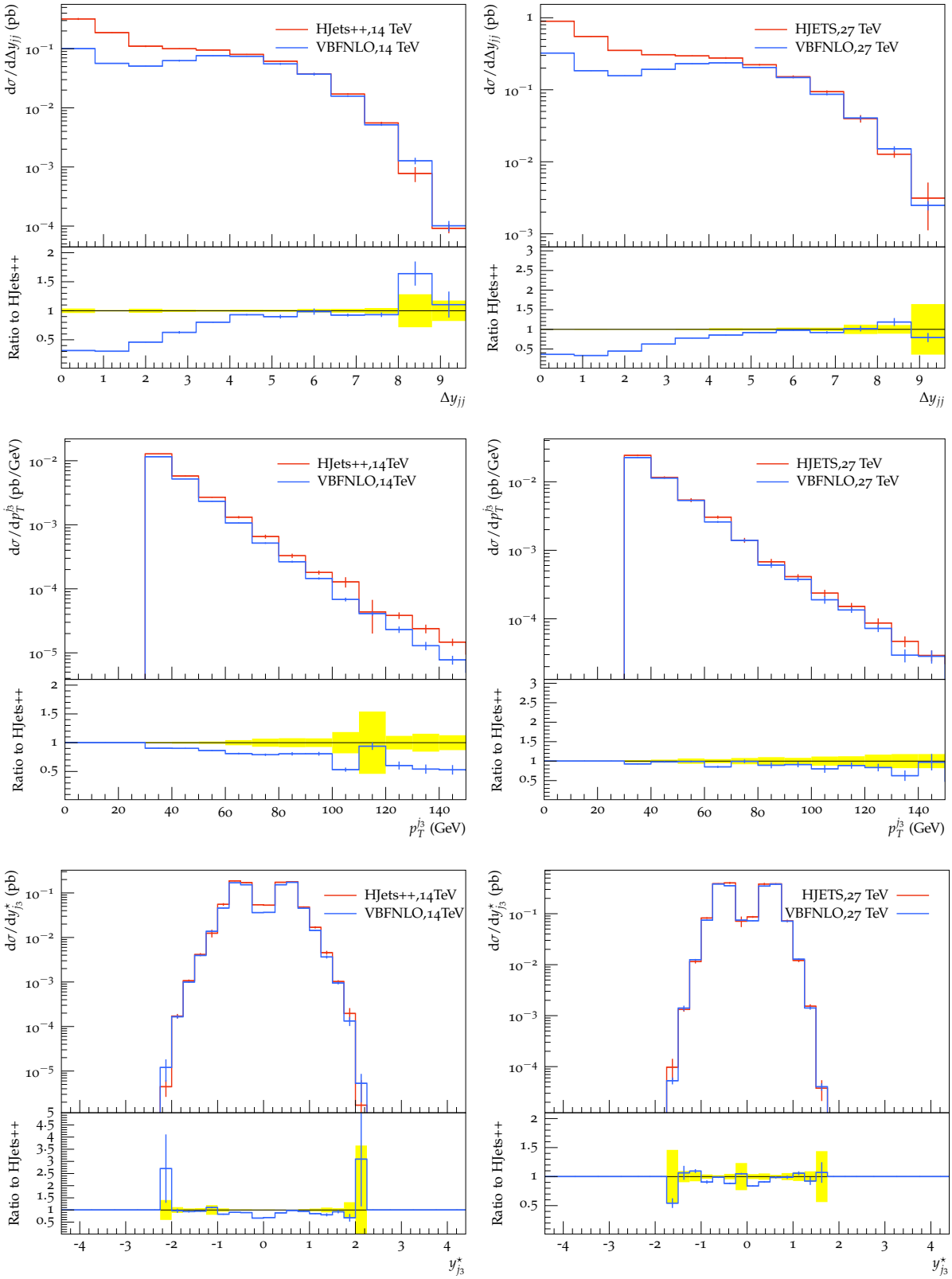

Fig. 13: Kinematics distributions for $H + 3$ jet production at NLO for the full result (HJETS++) and the approximate result (VBFNLO) for $\sqrt{s} = 14$ TeV (first column) and $\sqrt{s} = 27$ TeV (second column). The kinematic distribution Δy_{jj} (top row) is shown for inclusive selection cuts. The kinematic distributions for $p_{\mathrm{T}}^{j_3}$ and $y^\star_{j_3}$ are shown for VBF tight selection cuts.

4.2 Vector boson scattering processes

The study of the scattering of two massive vector bosons $V = W, Z$ (vector boson scattering, VBS) provides a key opportunity to probe the nature of the electroweak symmetry breaking (EWSB) mechanism as well as physics beyond the Standard Model (SM) [345, 346]. It is still unknown whether the discovered Higgs boson [347] preserves unitarity of the longitudinal VV scattering amplitude at all energies, or if other new physics processes are involved [348–352]. In the VBS topology, two incoming quarks radiate bosons which interact, yielding a final state of two jets from the outgoing quarks, and two massive bosons which decay into fermions. This final state can be the result of $VVjj$ electroweak (EW) production with and without a scattering topology, or of processes involving the strong interaction.

4.2.1 Measurements of $W^{\pm}W^{\pm}$ scattering and extraction of the longitudinal scattering component

With the largest cross section ratio of electroweak to strong production [353, 354], events with $W^{\pm}W^{\pm}$ plus two jets ($W^{\pm}W^{\pm}jj$) provide one of the best opportunities to study the scattering of two vector bosons. ATLAS and CMS have both observed the EW process at 13 TeV with significances of 6.9 σ and 5.5 σ, respectively [355, 356].

This section describes the prospects for the study of $W^{\pm}W^{\pm}jj$ at $\sqrt{s} = 14$ TeV at the HL-LHC, with the HL-LHC upgraded ATLAS and CMS detectors [357, 358]. Results are presented for a range of integrated luminosities $\mathcal{L}$, from 300 fb^{-1}through 8000 fb^{-1}, where the first value corresponds to one year of data taking, and the latter to 10 years of combined data sets collected by the ATLAS and CMS experiments in the most optimistic scenario.

In both ATLAS and CMS analyses, the signal (VBS and non-VBS EW) and background (QCD) $W^{\pm}W^{\pm}jj$ events are simulated at leading order using MADGRAPH5_AMC@NLO [12, 150] with the NNPDF3.0 set [201, 359], interfaced with PYTHIA V8 [149] for parton showering, hadronization and underlying event modelling. The information about the polarization of the individual W bosons in the signal process is extracted by generating a separate set of events using the DECAY package of MADGRAPH(v1.5.14). The other backgrounds – top ($t\bar{t}$ + jets, single-top), Drell-Yan, diboson ($W\gamma$, $W^{\pm}W^{\pm}$ and WZ) and triboson ($WW\gamma$, $WZ\gamma$, WWW, WWZ, WZZ, ZZZ) – are generated with either MADGRAPH5_AMC@NLO POWHEG [360], or PYTHIA V8. The analyses use generated events obtained either using a fully simulated description of the HL-LHC CMS detector, implemented using the GEANT4 package [296] (CMS) or using a parameterised description of the detector response [276] (ATLAS). Additional details for each analysis are provided in the relevant reports from CMS [358] and ATLAS [357].

The experimental signature of the $W^{\pm}W^{\pm}jj$ scattering process consists of exactly two isolated leptons (electrons or muons) with the same electric charge, two jets well-separated in rapidity, and moderate E_{T}^{miss}. The event selection requirements for the two experiments are listed in Table 4. A minimum requirement on the dilepton mass reduces the contamination from low-mass Drell-Yan processes, with an additional restriction excluding the Z mass in the dielectron channel where the likelihood of charge misidentification is higher. A requirement on E_{T}^{miss}further reduces the background from charge misidentified events, and events containing any b-tagged jets[7] are vetoed to suppress background contribution from $t\bar{t}$ production. A veto on additional preselected leptons significantly reduces background from WZ events. The two leading jets are required to have a large invariant mass, and large angular separation, to satisfy the expected VBS topology. Since leptons in the EW $W^{\pm}W^{\pm}jj$ process are expected to be located in the central region defined by the forward-backward jets, non-VBS background can be suppressed with a requirement on the centrality of the two leptons. CMS uses the Zeppenfeld variable

[7] The b-tagging of jets in CMS is performed with the Deep Combined Secondary Vertex discriminator based on a deep neural network [363].

Table 4: ATLAS and CMS event selection criteria for $W^{\pm}W^{\pm}jj$ candidate events, with $\ell = e, \mu$ and j as the leading(sub-leading) lepton or jet.

Selection requirement	ATLAS Selection	CMS Selection
Signal lepton p_{T}	p_{T}> 28(25) GeV	p_{T}> 20 GeV
Signal lepton η	$\lvert\eta\rvert \leq 4.0$	$\lvert\eta\rvert \leq 3.0$
Tag jet p_{T}	p_{T}> 90(45) GeV	p_{T}> 50 GeV
Tag jet η	$\lvert\eta\rvert \leq 4.5$	$\lvert\eta\rvert \leq 4.7$
Dilepton mass	$m_{\ell\ell} > 28$ GeV	$m_{\ell\ell} > 20$ GeV
Z_{ee} veto	$\lvert m_{ee} - m_Z\rvert > 10$ GeV	$\lvert m_{ee} - m_Z\rvert > 15$ GeV
E_{T}^{miss}	E_{T}^{miss}> 40 GeV	E_{T}^{miss}> 40 GeV
Number of b-tagged jets	0	0
Jet selection	Anti-k_{T} [361] jets with $\Delta R_{\ell,j} > 0.3$	Anti-k_{T} PUPPI [362] jets with $\Delta R_{\ell,j} >$
Preselected lepton veto	p_{T}> 7(6) GeV	p_{T}> 10 GeV
Dijet rapidity separation	$\Delta\eta_{j,j} > 2.5$	$\Delta\eta_{j,j} > 2.5$
Dijet mass	$m_{jj} > 520$ GeV	$m_{jj} > 500$ GeV
Lepton centrality	ζ > -0.5	Z_{MAX} < 0.75

[364], defined for a given lepton with pseudorapidity η_ℓ as

$$Z_\ell = \frac{[\eta_\ell - 0.5(\eta_1 + \eta_2)]}{|(\eta_1 - \eta_2)|},$$

where η_1, η_2 refer to the pseudorapidities of the leading and subleading jets. The maximum value of this variable, Z_{MAX}, for any of the leptons is required to be less than 0.75. ATLAS uses a requirement on the function ζ, where $\zeta = \min[\min(\eta_{\ell 1}, \eta_{\ell 2}) - \min(\eta_{j1}, \eta_{j2}), \max(\eta_{j1}, \eta_{j2}) - \max(\eta_{\ell 1}, \eta_{\ell 2})]$

The event selections are optimized to maximize signal acceptance (CMS) or minimize fake background (ATLAS). ATLAS uses tight electron requirements, which have a lower efficiency (around 50% [276]).

The expected event yields are summarized in Table 5 for CMS, and Table 6 for ATLAS. The m_{jj} distributions after the full event selection for $\mathcal{L} = 3000\,\mathrm{fb}^{-1}$ are presented in Fig. 14 . The main background contributions in the final signal region are due to inclusive $t\bar{t}$ and WZ productions, where the third lepton in the event was not reconstructed within the detector acceptance. ATLAS explicitly models the background contributions from jets faking electrons and lepton charge misidentification, which also contribute significantly in the signal region, while CMS includes the fake contribution under $t\bar{t}$ and does not consider the charge-misidentified or triboson backgrounds in this study, since their contributions were found to be negligible. The integrated number of signal and background events as a function of the dilepton invariant mass is shown in Figure 16 for the ATLAS selection.

The uncertainty of the expected cross section measurement as a function of integrated luminosity is measured by fitting the m_{jj} distribution, using a binned maximum likelihood approach with all systematic uncertainties in the form of nuisance parameters with log- normal distributions. The correlations among different sources of uncertainties are taken into account while different final states are considered as independent channels in the fit. CMS considers three channels categorised by lepton flavour (ee, eμ

Table 5: CMS expected yields for signal and background contributions for $\mathcal{L} = 3000\,\text{fb}^{-1}$.

Process	Expected yield, $\mathcal{L} = 3000\,\text{fb}^{-1}$
$W^{\pm}W^{\pm}$ (QCD)	196
$t\bar{t}$	5515
WZ	1421
$W\gamma$	406
Total Background	7538
Signal $W^{\pm}W^{\pm}$ (EW)	5368

Table 6: The ATLAS expected signal and background event yields after the optimised full event selection for a corresponding integrated luminosity of $\mathcal{L}$=3000 fb^{-1}. Events tagged as either "charge misidentification" or "jets faking leptons" are summed for all background samples and combined into a single entry each in the table. Remaining events are listed separately per process. Both QCD and EW production of WZ processes are included in the diboson background.

Process	All channels	$\mu^{\pm}\mu^{\pm}$	$e^{\pm}e^{\pm}$	$\mu^{\pm}e^{\pm}$	$e^{\pm}\mu^{\pm}$
$W^{\pm}W^{\pm}jj$(QCD)	168.7	74.6	19.7	32.2	42.2
Charge Misidentification	200	0.0	11	30	160
Jets faking electrons	460	0.0	130	260	70
$WZ + ZZ$	1286	322	289	271	404
Tribosons	76	30.1	9.6	15.1	21.6
Other non-prompt	120	29	16.6	50	19
Total Background	2310	455	480	660	710
Signal $W^{\pm}W^{\pm}jj$(EW)	2958	1228	380	589	761

and $\mu\mu$), while ATLAS uses eight channels by lepton flavour and charge (e^+e^+, e^-e^-, $e^+\mu^+$, $e^-\mu^-$, μ^+e^+, μ^-e^-, $\mu^+\mu^+$, $\mu^-\mu^-$).

The experimental uncertainties, statistical and systematic, in the CMS analysis contribute to a total uncertainty on the signal strength of 3.2% for 3000 fb^{-1}. Including a theoretical uncertainty of 3% and an uncertainty on the luminosity of 1%, the total uncertainty reaches a value of 4.5% for 3000 fb^{-1}. For the ATLAS analysis experimental systematics on the trigger, leptons, jets, and flavour tagging are taken from the 13 TeV analysis unchanged, while for the baseline estimation, rate uncertainties on the backgrounds are halved. An "optimistic" set of uncertainties is also presented, where the uncertainties on the non-data-driven backgrounds are aggressively reduced. The total uncertainty is presented in Fig. 15 as a function of the integrated luminosity. The values of $\mathcal{L}$ exceeding 3000 fb^{-1} are an estimation of a combination of the measurements from CMS and ATLAS, effectively doubling the total integrated luminosity.

The total $W^{\pm}W^{\pm}jj$ VBS cross section can be decomposed into the polarized components based on the decays of the individual W bosons. Either or both can be longitudinally (L) or transversely (T) polarized, giving rise to final states of LL, TT as well as the mixed state LT (with TL combination implied). The LL component, $W^{\pm}_{\text{L}}W^{\pm}_{\text{L}}jj$, is expected to be only about 6-7% of the total VBS cross

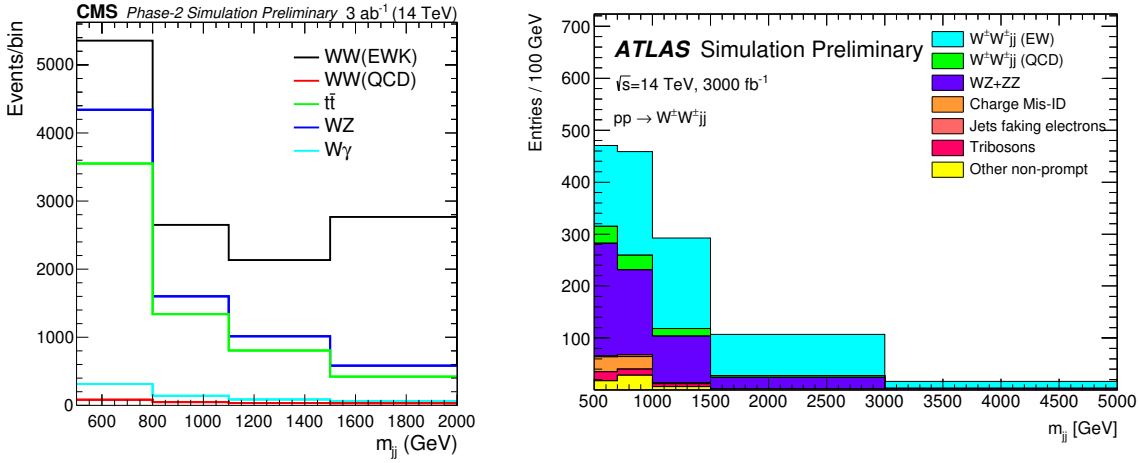

Fig. 14: The distribution of the invariant mass of the two leading jets after the selection requirements for an integrated luminosity of 3000 fb^{-1}, for CMS (left) and ATLAS (right).

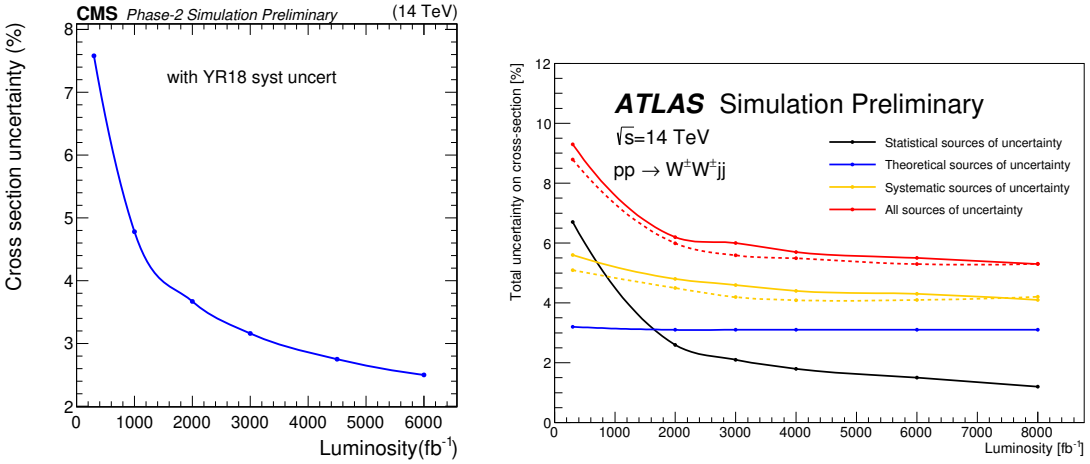

Fig. 15: The estimated uncertainty of the EW $W^{\pm}W^{\pm}$ cross section measurement as a function of the integrated luminosity, for CMS (left), only statistical and experimental systematic uncertainties are considered, and ATLAS (right).

section for jet $p_{\mathrm{T}} > 50$ GeV. The difference in azimuthal angle between the two leading jets, $\Delta\phi_{jj}$, has the potential for discriminating the LL component of the VBS scattering from TT and LT contributions. Since the signal-to-background separation for the EW $W^{\pm}W^{\pm}jj$ process improves with increasing m_{jj} as shown in Fig. 14 (left), the $\Delta\phi_{jj}$ distributions are studied in two ranges of m_{jj}: for 500-1100 GeV and above 1100 GeV. Figure 17 shows the combination of signal and background yields as a function of $\Delta\phi_{jj}$ for high m_{jj} regions. Using a simultaneous fit to two mass regions[8], the significance for the observation of the LL process is estimated as a function of integrated luminosity. The significance is found to be up to 2.7 standard deviations for $\mathcal{L} = 3000\,\mathrm{fb}^{-1}$. The gradual improvement of signal significance as a function of integrated luminosity is shown in Fig. 18 right. A combination of ATLAS and CMS results, using fully simulated ATLAS events and improved electron efficiency, is expected to reach an expected significance of 3 standard deviations with 2000 fb^{-1} per experiment. In addition,

[8]The low m_{jj} region serves to constrain the $t\bar{t}$/fake background.

recent studies [365] have shown that advances in machine learning can also improve the prospects for the measurement of the $W_{\mathrm{L}}^{\pm}W_{\mathrm{L}}^{\pm}jj$ process.

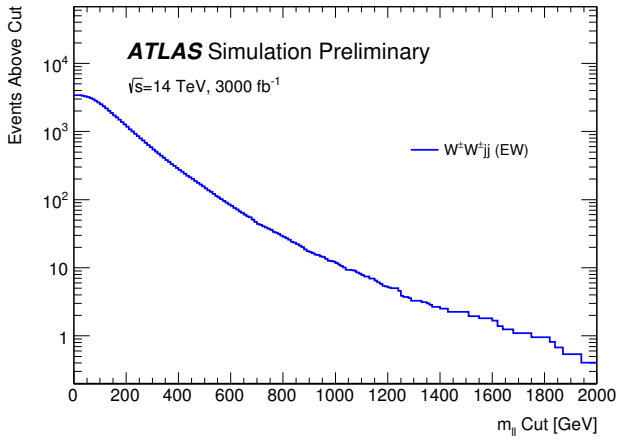

Fig. 16: Integrated number of events as a function of dilepton invariant mass for events passing all selection criteria of the ATLAS signal region.

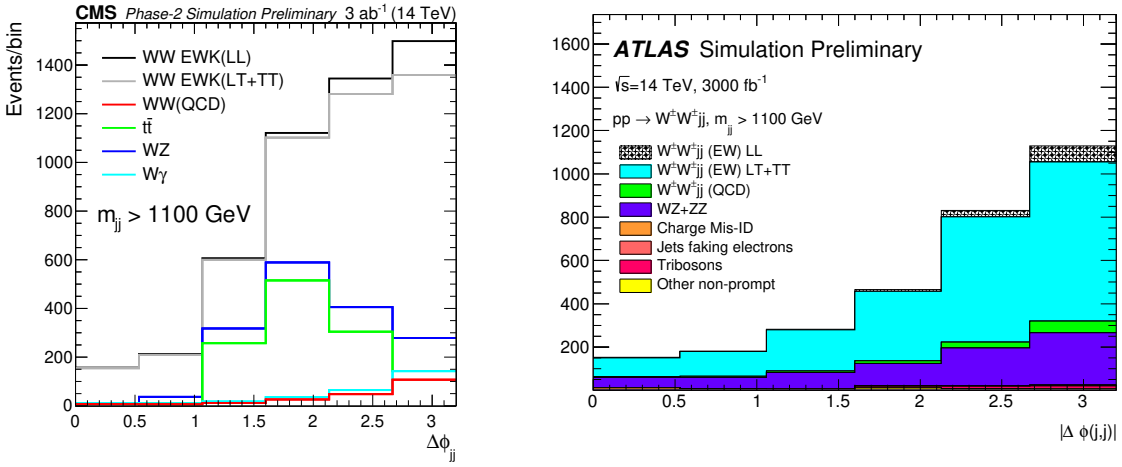

Fig. 17: Distribution of the azimuthal angle difference between two leading jets for dijet invariant mass above 1100 GeV.

4.2.2 High Order corrections in VBS $W^{\pm}W^{\pm}$ production[9]

The expected experimental precision in the measurement of VBS processes offers great opportunities to probe the electroweak (EW) sector and its associated symmetry breaking mechanism (see Refs. [134, 366, 367] for 100 TeV-collider studies). Therefore, it is of prime importance to make precise theoretical predictions available for the future operation of the LHC. In this contribution, predictions for NLO EW corrections are provided for the LHC running in its high-luminosity and high-energy configurations. The HL set-up corresponds to a centre-of-mass energy of 14 TeV while the HE one refers to 27 TeV.

[9] Contribution by A. Denner and M. Pellen.

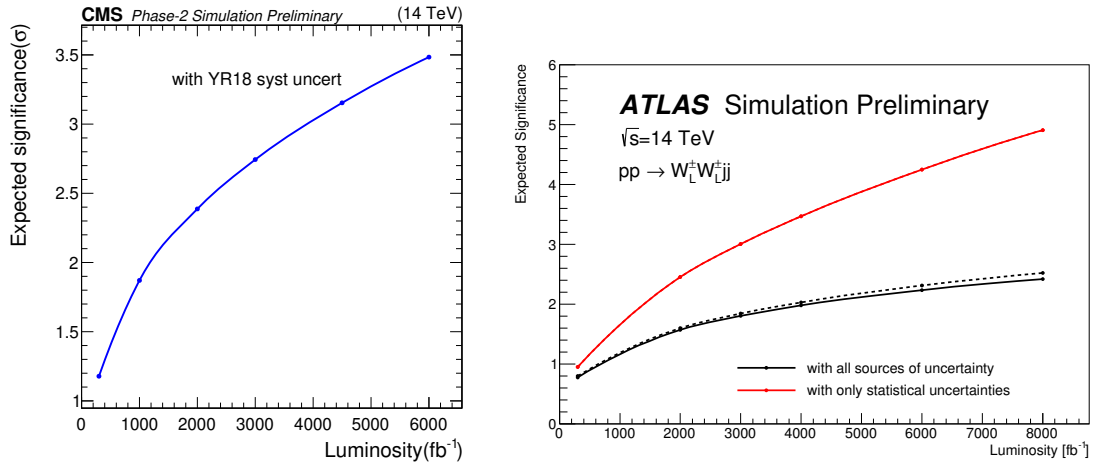

Fig. 18: Significance of the observation of the scattering of a pair of longitudinally polarized W bosons as a function of the integrated luminosity at CMS (left) and ATLAS (right).

For both centre-of-mass energies the same type of event selections has been used. These predictions represent important benchmarks as they indicate the expected rates when accounting for NLO EW corrections. The NLO EW corrections have been shown to be very large for VBS processes [103] and even the dominating NLO contribution for same-sign WW scattering [111]. Nonetheless, the inclusion of NLO QCD corrections is necessary as they can significantly distort the shape of jet-related observables [111,368–376]. In addition, they drastically reduce theoretical uncertainties. The QCD corrections for all VBS signatures can be obtained from public programs such as MADGRAPH5_AMC@NLO [12], POWHEG [151,314,377], SHERPA [84,378], or VBFNLO [247,248,339].

In this study, the NLO EW corrections have been obtained from MOCANLO+RECOLA [82,82,91] based on a full NLO computation [111] for the same-sign WW signature. While the exact value of the corrections is expected to be different for other signatures, their magnitudes and nature should be similar.

The hadronic scattering processes are simulated at the LHC with a centre-of-mass energies $\sqrt{s} = 14\,\text{TeV}$ and $\sqrt{s} = 27\,\text{TeV}$. The NNNPDF 3.1 LUXQED parton distribution functions (PDFs) [224] with five massless flavours,[10] NLO-QCD evolution, and a strong coupling constant $\alpha_s(M_Z) = 0.118$ are employed.[11] Initial-state collinear singularities are factorised according to the $\overline{\text{MS}}$ scheme, consistently with the conventions in the NNPDF set.

The other input parameters have been chosen as in Ref. [375]. For the massive particles, the following masses and decay widths are used:

$$\begin{aligned} m_t &= 173.21\,\text{GeV}, & \Gamma_t &= 0\,\text{GeV}, \\ M_Z^{\text{OS}} &= 91.1876\,\text{GeV}, & \Gamma_Z^{\text{OS}} &= 2.4952\,\text{GeV}, \\ M_W^{\text{OS}} &= 80.385\,\text{GeV}, & \Gamma_W^{\text{OS}} &= 2.085\,\text{GeV}, \\ M_H &= 125.0\,\text{GeV}, & \Gamma_H &= 4.07 \times 10^{-3}\,\text{GeV}. \end{aligned} \tag{8}$$

The measured on-shell (OS) values for the masses and widths of the W and Z bosons are converted into

[10] For the process considered, no bottom (anti-)quarks appear in the initial or final state at LO and NLO, as they would lead to top quarks rather than light jets in the final state.

[11] The corresponding identifier `lhaid` in the program LHAPDF6 [202] is 324900.

pole values for the gauge bosons ($V = W, Z$) according to Ref. [379],

$$\begin{aligned} M_V &= M_V^{\text{OS}} / \sqrt{1 + (\Gamma_V^{\text{OS}} / M_V^{\text{OS}})^2}\,, \\ \Gamma_V &= \Gamma_V^{\text{OS}} / \sqrt{1 + (\Gamma_V^{\text{OS}} / M_V^{\text{OS}})^2}. \end{aligned} \tag{9}$$

The EW coupling is fixed in the G_μ scheme [380] according to

$$\alpha = \frac{\sqrt{2}}{\pi} G_\mu M_{\text{W}}^2 \left(1 - \frac{M_{\text{W}}^2}{M_{\text{Z}}^2}\right), \tag{10}$$

with

$$G_\mu = 1.16637 \times 10^{-5}\,\text{GeV}^{-2}, \tag{11}$$

and M_V^2 corresponds to the real part of the squared pole mass. The complex-mass scheme [381–383] is used throughout to treat unstable intermediate particles in a gauge-invariant manner.

The central value of the renormalisation and factorisation scales is set to

$$\mu_{\text{R}} = \mu_{\text{F}} = \sqrt{p_{\text{T,j}_1}\, p_{\text{T,j}_2}}. \tag{12}$$

The transverse momenta are those of the two hardest jets. This choice of scale has been shown to provide stable NLO-QCD predictions [373].

Following experimental measurements [354, 384–386] and prospect studies [387], the event selection used in the present study is:

– The two same-sign charged leptons are required to fulfill cuts on transverse momentum, rapidity, separation in the rapidity–azimuthal-angle, and the lepton-pair invariant mass,

$$p_{\text{T},\ell} > 20\,\text{GeV}, \qquad |y_\ell| < 4.0, \qquad \Delta R_{\ell\ell} > 0.3, \qquad m_{\ell\ell} > 20\,\text{GeV}. \tag{13}$$

– The total missing transverse momentum, computed from the vectorial sum of the transverse momenta of the two neutrinos, is required to be

$$p_{\text{T,miss}} > 40\,\text{GeV}\,. \tag{14}$$

– QCD partons (light quarks and gluons) are clustered using the anti-k_{T} algorithm [274] with jet-resolution parameter $R = 0.4$. Cuts on the jets' transverse momenta and rapidities are imposed,

$$p_{\text{T},j} > 30\,\text{GeV}, \qquad |y_j| < 4.0. \tag{15}$$

VBS cuts are applied to the two jets with largest transverse momentum, specifically on the invariant mass of the di-jet system, as well as on the rapidity separation of the two jets and their separation from leptons,

$$m_{jj} > 500\,\text{GeV}, \qquad |\Delta y_{jj}| > 2.5, \qquad \Delta R_{j\ell} > 0.3. \tag{16}$$

– Finally, the centrality of the leptons is enforced according to Ref. [387]:

$$\zeta = \min\left[\min\left(y_{\ell_1}, y_{\ell_2}\right) - \min\left(y_{j_1}, y_{j_2}\right), \max\left(y_{j_1}, y_{j_2}\right) - \max\left(y_{\ell_1}, y_{\ell_2}\right)\right] > 0. \tag{17}$$

– For EW corrections, real photons and charged fermions are clustered using the anti-k_{T} algorithm with radius parameter $R = 0.1$. In this case, leptons and quarks are understood as *dressed fermions*.

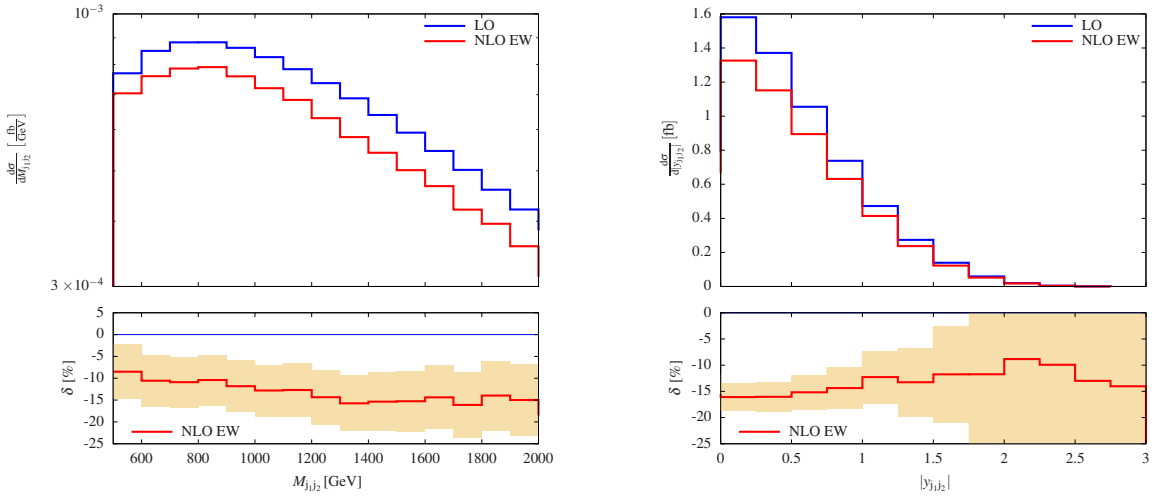

Fig. 19: Differential distributions in the invariant mass of the two jets (left) and their rapidity (right) in $pp \to \mu^+\nu_\mu e^+\nu_e jj$ at 14 TeV including NLO EW corrections (upper panel) and relative NLO EW corrections (lower panel). The yellow band describes the expected statistical uncertainty for a high-luminosity LHC collecting 3000 fb^{-1} and represents a relative variation of $\pm 1/\sqrt{N_{\text{obs}}}$ where N_{obs} is the number of observed events in each bin.

In the following discussion of SM predictions for the HL- and HE-LHC both QCD and EW corrections have been combined. For VBS processes EW corrections are particularly large and therefore of prime importance. The leading contributions originate from the exchange of massive gauge bosons in the virtual corrections. They tend to grow large and negative in the high-energy limit owing to so-called Sudakov double logarithms. As shown in Ref. [103], large EW corrections are an intrinsic feature of VBS at the LHC. While this study is based on the same-sign W channel, it has been further confirmed recently by the computation of large EW corrections to the WZ channel [388, 389].

Given their size and the foreseen experimental precision, these corrections are actually measurable. Because they involve interactions of the EW sector, their measurement would constitute a further test of the SM. On the left hand-side of Fig. 19, the distribution in the invariant mass of the two leading jets is shown at LO and NLO EW for the process $pp \to \mu^+\nu_\mu e^+\nu_e jj$ at 14 TeV. The yellow band describes the expected statistical uncertainty for a HL LHC collecting 3000 fb^{-1}. On the right hand-side for Fig. 19, a similar plot for the absolute rapidity of the jet pair is shown. It is thus clear that with the expected luminosity, one is not only sensitive to the VBS process but also to its EW corrections.

In Fig. 20, the distributions in the invariant mass of the visible system ($e^+\mu^+jj$) at both 14 TeV (left) and 27 TeV (right) are shown. As expected, the corrections are larger for higher centre-of-mass energy due to the higher representative scale of the process. In the tail of the distribution where new physics could play an important role, the corrections are particularly large and reach about 25% for the 27 TeV set-up. Note that in the present predictions, the real radiation of massive gauge bosons is not taken into account. This effect has been estimated to be of the order of few percent for the HL set-up when considering the total cross section. While this effect is for now negligible, for the HL and HE mode of the LHC, it will become relevant in the same way as the use of VBS approximations in theoretical predictions [375]. These observations are further confirmed via the cross sections for the two centre-of-mass energies at LO (using full matrix element) and NLO EW given in Table 7. At 27 TeV the EW corrections are a few percent larger than at 14 TeV (-18.9% against -15.1%, respectively). Note that the jump in energy from 14 TeV to 27 TeV is accompanied by an increase by more than a factor 3 in

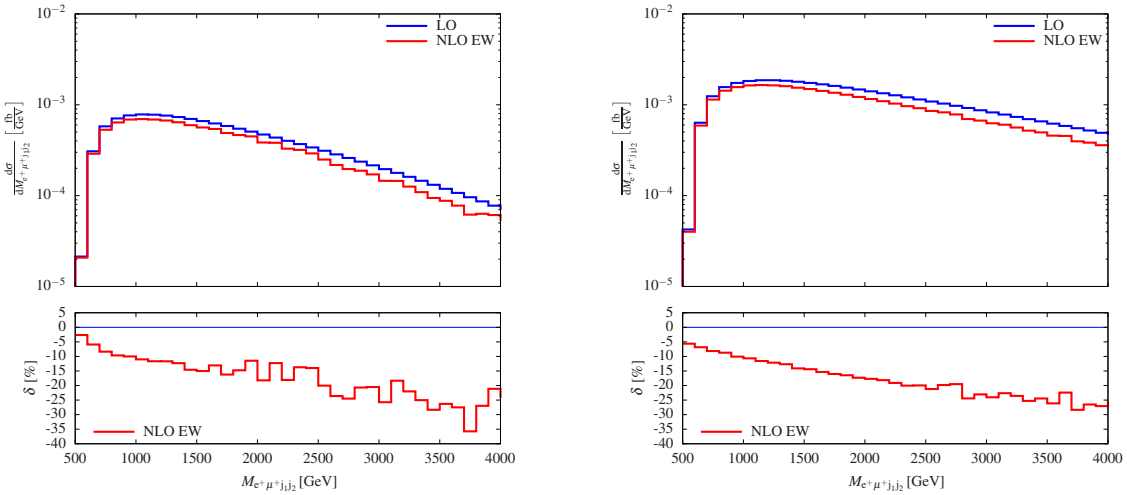

Fig. 20: Differential distribution in the invariant mass of the visible system ($e^+\mu^+jj$) in $pp \to \mu^+\nu_\mu e^+\nu_e jj$ at 14 TeV (left) and 27 TeV (right) including NLO EW corrections (upper panel) and relative NLO EW corrections (lower panel).

Table 7: Cross sections at LO ($\mathcal{O}\left(\alpha^6\right)$) and NLO EW ($\mathcal{O}\left(\alpha^7\right)$) for $pp \to \mu^+\nu_\mu e^+\nu_e jj$ at both 14 TeV and 27 TeV at the LHC. The relative EW corrections are given in percent, and the digits in parentheses indicate the integration error.

	σ^{LO} [fb]	$\sigma^{\text{NLO}}_{\text{EW}}$ [fb]	δ_{EW} [%]
14 TeV	1.4282(2)	1.213(5)	−15.1
27 TeV	4.7848(5)	3.881(7)	−18.9

the cross section at LO.

4.2.3 Measurements of WZ scattering at the HL-HLC

Prospects are presented for measuring the WZ electroweak production in fully leptonic final state at the HL-LHC. This work includes studies of the polarised WZ production: measurements of the vector bosons in longitudinally polarized states are of particular importance, since they give direct access to the nature of the electroweak symmetry breaking via the exchange of a Higgs bosons in the t-channel as shown in Fig. 21. Another relevant aspect of WZ production lies in the probe of the non-abelian structure of the Standard Model via sensitive tests to triple and quartic gauge couplings, a topic which is partially addressed in the next subsection. Measurements of the electroweak production using 36 $\text{fb}^{-1}$of the proton-proton collisions at 13 TeV were reported by both the ATLAS [390] and CMS [391] collaborations. The existing results are strongly limited by the statistical uncertainties of the data samples, therefore the integrated luminosity expected at the end of the HL-LHC operation is mandatory to fully exploit the physics behind VBS in WZ production via measurement of differential distributions and the polarization of the final state bosons.

In proton-proton collisions, the VBS process results from the interaction of two bosons radiated by the initial quarks leading to a final state with two centrally produced bosons and two forward jets. The main irreducible background is represented by events in which the same final state is mediated by strong interactions (QCD−WZ) and where the two bosons are not the direct result of a scattering

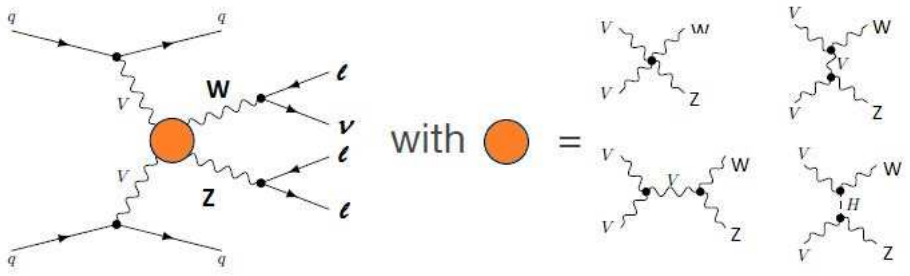

Fig. 21: Feymann diagrams contributing to VBS WZ production.

process. Other backgrounds consist of different di-boson final states (ZZ, $Z\gamma$), tri-bosons and tV or $t\bar{t}V$ production, where V is a Z or a W boson. The amount of the non-prompt backgrounds, where one or more lepton candidates are coming from jets misidentified as leptons, ultimately depends on the detector geometry, reconstruction technique and event selection requirements.

The signal selection requires events with three isolated leptons with $\mathrm{p_T}$ > 15 GeV with $|\eta| < 4$ for ATLAS and $|\eta| < 2.8$ (3.0) for muons (electrons) for CMS. In addition, at least one lepton should pass the single lepton trigger (ATLAS). In order to suppress the background from ZZ processes, events containing four or more lepton candidates are discarded. At least one of the three lepton candidates is required to have $\mathrm{p_T}$ > 25 GeV. The event must have at least one pair of leptons of the same flavor and opposite charge, with an invariant mass that is consistent with the nominal Z boson mass at $M_Z = 91.188$ GeV within 10 GeV for ATLAS and 15 GeV for CMS. This pair is considered as a Z boson candidate. The third lepton is assigned to the W boson and its $\mathrm{p_T}$ is required to be greater than 20 GeV. Finally, E_T^{miss} (CMS) or the transverse mass of the W candidate computed using E_T^{miss} and the $\mathrm{p_T}$ of the third lepton (ATLAS) is required to be above 30 GeV. The VBS signature is characterized by the presence of two forward jets. Jets are reconstructed with the anti-k_T algorithm with distance parameter 0.4. For ATLAS, the event is selected if it contains two jets in opposite hemispheres with $\mathrm{p_T^{jet}}$ greater than 30 GeV and $|\eta^{\mathrm{jet}}|$ < 3.8. For CMS, the event is selected if it contains two jets with $\mathrm{p_T^{jet}}$ > 50 GeV and $|\eta^{\mathrm{jet}}|$ < 4.7. In addition, the pseudorapidity separation between jets, $\Delta\eta_{jj}$, is requested to be greater than 2.5. Finally, the dijet mass m_{jj} is required to be greater than 500 GeV. The full list of selection requirements is summarized in Table 8.

Distinct approaches are used by ATLAS and CMS, respectively based on simulation at 14 TeV and on extrapolation from Run-2 results. ATLAS uses Monte Carlo samples generated with a fast simulation based on the parameteriation of the performance of the HL-LHC detector and where jets from pileup (PU) interactions corresponding to <μ> = 200 are added to the event record; a loose event selection and a conservative background hypothesis is used. The signal events are generated at LO with SHERPA 2.2.2 [84] and the QCD$-WZ$ background is simulated at NLO with SHERPA 2.2.0: in Ref. [390], it was shown that the QCD$-WZ$ background predictions might be overestimated by 40% in certain regions of the phase-space. And with a $\mathrm{p_T^{jet}}$cut as low as 30 GeV, an $|\eta^{jet}|$ cut less than 3.8, corresponding to the HL-LHC tracker acceptance, was found necessary to maintain the contamination of PU jets in signal (resp. QCD$-WZ$) events from 18% (resp. 69%) to 2% (resp. 11%).

The CMS projection is based on MC samples with full simulation of the CMS detector at 13 TeV and data driven background estimates, see Ref. [392]. The cross sections of samples are scaled for this projection from 13 to 14 TeV using SM predictions, for the data-driven backgrounds the scaling is done using appropriate mixture of simulated events. The performance of the CMS detector at the HL-LHC at pileup 200 is simulated using DELPHES. It is proven that lepton and PUPPI [362] jet reconstruction allow to keep the same or better level of reconstruction efficiency and background rejection as in existing data; no additional corrections are applied in the projection. An additional scaling factor is applied to

Table 8: Summary of event selection requirements.

Variables	ATLAS	CMS
$p_T(\ell)$ [GeV]	> 15	> 15
$p_T(\ell_{lead})$	> 25	–
$p_T(\ell_{Z,1})$, $p_T(\ell_{Z,2})$ [GeV]		$> 25, > 15$
$p_T(\ell_W)$ [GeV]	> 20	> 20
$\lvert\eta(\mu)\rvert$	< 4.0	< 2.8
$\lvert\eta(e)\rvert$	< 4.0	< 3.0
$\lvert m_Z - m_Z^{PDG}\rvert$ [GeV]	< 10	< 15
$m_{3\ell}$ [GeV]	–	> 100
$m_{\ell\ell}$ [GeV]	–	> 4
E_T^{miss} [GeV]	–	> 30
M_T^W [GeV]	> 30	–
n_j	≥ 2	≥ 2
$\lvert\eta(j)\rvert$	< 3.8	< 4.7
p_T^{jet} [GeV]	> 30	> 50
$\Delta R(j, \ell)$	–	> 0.4
$p_T(b)$ [GeV]	–	> 30
n_{b-jet}	–	$= 0$
m_{jj}	> 500	> 500
$\Delta\eta_{jj}$	Opp. hemis.	> 2.5
$\lvert\eta_{3\ell} - \frac{1}{2}(\eta_{j_1} + \eta_{j_2})\rvert$	–	< 2.5

Table 9: Expected signal and background yields corresponding to the event selection listed in Table 8 for 3000 fb^{-1}. Background contributions are grouped differently for ATLAS and CMS.

Process	ATLAS	CMS
EW$-WZjj$	3889	2757
QCD$-WZ$	29754	3486
$t\bar{t}V$	3145	–
tZ	2221	–
tV/VVV	–	1374
Non prompt	–	1192
ZZ	1970	–
VV	–	398
Zγ	–	296

account for the increased pseudorapidity coverage of the HL-LHC CMS detector. The ATLAS and CMS signal and background yields are summarized in Table 9 for the total integrated luminosity of 3000 fb^{-1}.

To extract the electroweak signal, ATLAS uses nominally a final m_{jj} cut optimised at 600 GeV or a multivariate analysis (BDT) based on 25 variables that are shown to best separate the signal and background events. The shape of the BDT output is shown in Fig. 22 left. In the CMS case, a 2D distribution of dijet invariant mass in bins of dijet angular separation is used, as shown in Fig. 22 right. The measurement of the EW$-WZjj$ production cross section results from a maximum likelihood fit of this distribution performed simultaneously for four different lepton combinations in the final states,

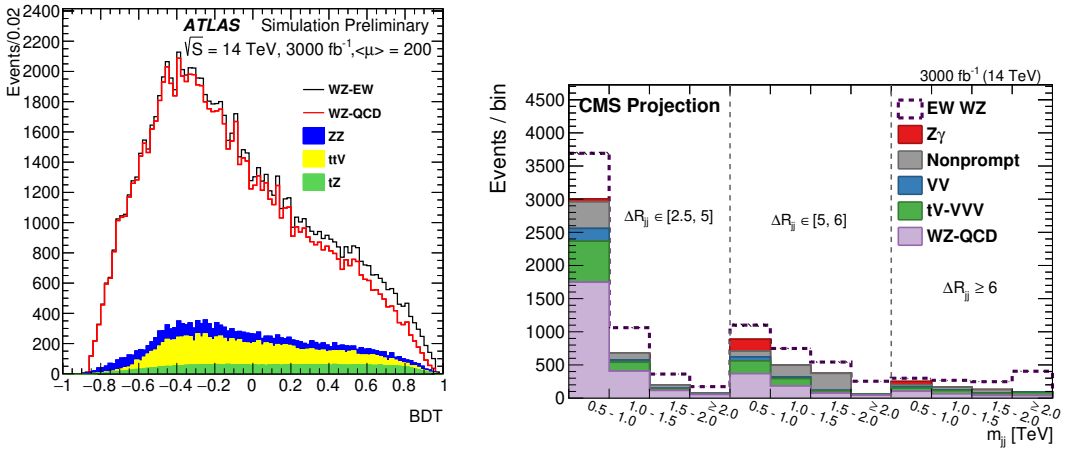

Fig. 22: Example of BDT distribution for 3000 fb^{-1}(left). The m_{jj} distributions in bins of ΔR_{jj} for 3000 fb^{-1}(right).

each combination being considered as independent decay channel. The systematic uncertainties are represented by nuisance parameters in the fit and are allowed to vary according to their probability density functions. The correlations across bins, between different sources of uncertainty and decay channels are taken into account. The background contributions are allowed to vary within the estimated uncertainties.

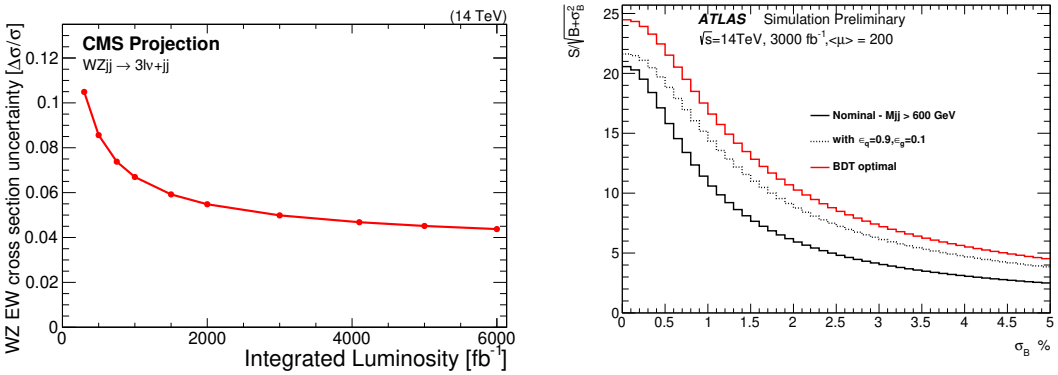

Fig. 23: Expected uncertainty on the cross section measurement as a function of the integrated luminosity for the CMS projection (left). Signal significance versus the total background uncertainty for the ATLAS simulation (right), presented for the nominal selection, along with two alternative selections meant to mitigate the QCD$-WZ$ background.

The experimental systematic error will be dominated by the jet energy related uncertainties, and amounts to a maximum of 5%. The non-prompt background uncertainty may also be significant depending on the final state. Depending on the level of QCD$-WZ$ background, the theoretical error affecting its modeling will eventually dominate. However it is expected that the impact of these uncertainties can be controlled to less that 5% using refined and diverse control regions allowed by the large statistics at HL-LHC. The total uncertainty of the electroweak cross section measurement as a function of luminosity is shown in Fig. 23 left for the CMS projection, while the signal significance as a function of the projected total uncertainty on background is presented in Fig. 23 right for the ATLAS simulation as it is

arguable whether the theoretical uncertainty can be precisely predicted at this stage.

The polarisation of the final state bosons can be measured inclusively for each boson in two different final state configurations, ZW^+ and ZW^- or combined in a doubly longitudinally polarised final state. The $\cos\theta^*_Z$ ($\cos\theta^*_W$), where θ^*_Z represents the angle of the lepton with the Z (W) direction in the WZ rest frame, is the most sensitive differential distribution to the polarisation of the Z (W) boson. An example of the $\cos\theta^*_Z$ distribution is shown in Fig. 24 left for the EW$-WZjj$ signal and the sum of backgrounds for $Z(W^+)$ final state; the distribution is fitted with three parameters: the longitudinal polarised fraction F0, the left-handed minus right-handed contributions and the number of EW$-WZjj$ events using three polarisation templates plus the two background contributions. The result of the fit is shown in Fig. 24 left, where the fraction of EW$-WZjj$ events where the Z-boson is longitudinally, left or right polarised are represented, while the log-likelihood profile corresponding to F0 is presented in Fig. 24 right. The significance to measure F0, computed as $\sqrt{-2log(\lambda(F0=0))}$, is estimated to be between 1.5 and 2.5 σ for $Z(W^+)$ and 0.7 and 1.5 σ for W^- depending on the final selection that affects the signal purity, and systematic assumptions on the total background normalisation.

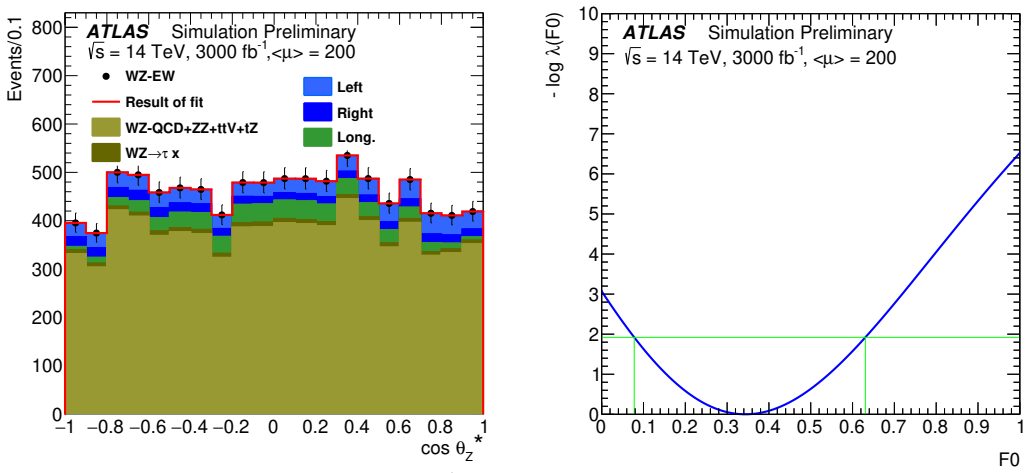

Fig. 24: Distribution of $\cos\theta^*_Z$ for 3000 fb^{-1}and result of the fit of the long, polarised contribution (F0), left- and right-handed contributions on top of the sum of backgrounds and of the $WZ \to x\tau$ background, both contributions taken into account with a normalisation error of 2.5% (left). Shape of the log-likelihood profile for the F0 parameter around its minimum (right) .

To measure the doubly longitudinal (LL) process, an approach based on the jets kinematics similar to this for the total EW$-WZjj$ cross section is used by CMS. The LL fraction is expected to be of the order of 5% of the total EW$-WZjj$ production ([393]) and its unrolled 2D distribution is shown in Fig. 25 left for 3000 fb^{-1}. It can be observed that the LL contribution is increasing from 2-3% to 7-8% for high angular separation between jets and for high invariant mass of the dijet system. In the fit, the LL fraction is considered as signal, while the rest of the EW$-WZjj$ process is considered as an additional background. The systematic uncertainties of the LL and non-LL fractions are considered as fully correlated within the total electroweak cross section. The significance of the LL observation as a function of integrated luminosity is shown in Fig. 25 right: the red curve presents the significance if only statistical uncertainties of the measurement are taken into account and the black line presents the results including the systematics as discussed above.

The results presented in this section confirm that the EW$-WZjj$ cross section can be measured with accuracy at the HL-LHC if the jets from pileup collisions in the events are well separated from the jets produced in the hard interactions. Increased pseudorapidity coverage of the detectors should

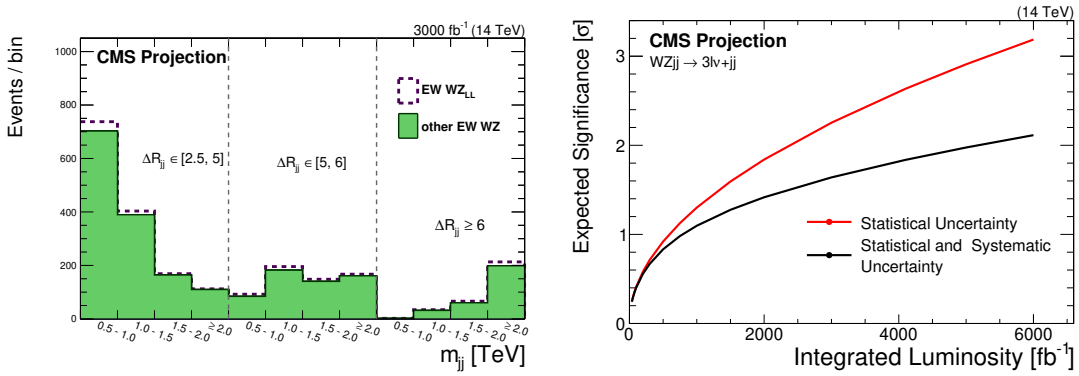

Fig. 25: Unrolled 2D $(\Delta R_{jj}; m_{jj})$ LL and non-LL distribution for 3000 fb^{-1}(left). Significance of the LL observation with and without systematic error (right).

improve precision of such measurement. The single polarized cross sections can also be measured and the double polarized measurement requires more sophisticated methods, including development of multivariate discriminants for better separation of the signal from background. Systematic uncertainties also start to play a significant role at the HL-LHC, in particular those affecting the theoretical prediction.

4.2.4 Prospects for quartic gauge coupling measurements in VBS[12]

Due to the strong gauge theory cancellations between the different Feynman graphs present in VBS (Fig. 21) the various VBS processes provide excellent probes for the structure of gauge boson interactions, in particular for the quartic gauge couplings. Deviations from SM predictions can conveniently be parameterised by an effective Lagrangian, $\mathcal{L}_{\text{EFT}} = \sum_i f_i/\Lambda^{d_i-4}\,\mathcal{O}_i^{(d_i)}$, where the operators $\mathcal{O}_i^{(d_i)}$ of energy dimension d_i are built with the covariant derivative of the SM Higgs doublet field, $D_\mu\Phi$, and the $SU(2)_L$ and $U(1)_Y$ field strength tensors $\widehat{W}_{\mu\nu}$ and $\widehat{B}_{\mu\nu}$ (normalized according to $[D_\mu, D_\nu] = \widehat{W}_{\mu\nu} + \widehat{B}_{\mu\nu}$). At the dimension six level, all allowed operators in $\mathcal{L}_{\text{EFT}}$ also contribute to trilinear couplings of electroweak gauge bosons or to hVV couplings, which are better measured in $q\bar{q} \to VV$ processes or in Higgs boson decay. Thus, operators of energy dimension eight, which do not give rise to anomalous trilinear couplings, are used for a parameterisation of anomalous quartic gauge couplings (aQGC), which is sufficiently general for the present purpose. In the following, the operator basis of Ref. [394, 395] with VBFNLO normalization [374, 396, 397] is used to assess the sensitivity of VBS $W^\pm W^\pm jj$ and $WZjj$ production to aQGC, with the subset of operators

$$\mathcal{O}_{S_0} = \left[\left(D_\mu\Phi\right)^\dagger D_\nu\Phi\right] \times \left[\left(D^\mu\Phi\right)^\dagger D^\nu\Phi\right], \tag{18a}$$

$$\mathcal{O}_{S_1} = \left[\left(D_\mu\Phi\right)^\dagger D^\mu\Phi\right] \times \left[\left(D_\nu\Phi\right)^\dagger D^\nu\Phi\right] \tag{18b}$$

$$\mathcal{O}_{T_0} = \text{Tr}\left[\widehat{W}_{\mu\nu}\widehat{W}^{\mu\nu}\right] \times \text{Tr}\left[\widehat{W}_{\alpha\beta}\widehat{W}^{\alpha\beta}\right], \tag{18c}$$

$$\mathcal{O}_{T_1} = \text{Tr}\left[\widehat{W}_{\alpha\nu}\widehat{W}^{\mu\beta}\right] \times \text{Tr}\left[\widehat{W}_{\mu\beta}\widehat{W}^{\alpha\nu}\right] \tag{18d}$$

$$\mathcal{O}_{M_0} = \text{Tr}\left[\widehat{W}_{\mu\nu}\widehat{W}^{\mu\nu}\right] \times \left[\left(D_\beta\Phi\right)^\dagger D^\beta\Phi\right], \tag{18e}$$

$$\mathcal{O}_{M_1} = \text{Tr}\left[\widehat{W}_{\mu\nu}\widehat{W}^{\nu\beta}\right] \times \left[\left(D_\beta\Phi\right)^\dagger D^\mu\Phi\right]. \tag{18f}$$

in $\mathcal{L}_{\text{EFT}} = \sum_i \frac{f_i}{\Lambda^4}\mathcal{O}_i$. At high invariant masses, $\sqrt{s}$, of the $VV \to VV$ subprocess, the tree level insertions of the dimension eight operators lead to matrix elements which grow like s^2 and violate

[12] Contribution by H. Schäfer-Siebert and D. Zeppenfeld.

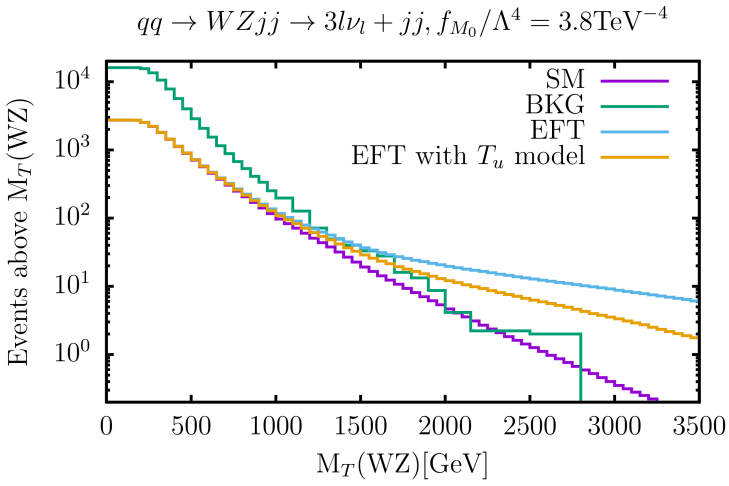

Fig. 26: Integrated WZ transverse mass distribution for $f_{M_0}/\Lambda^4 = 3.8$ TeV^{-4} within the pure EFT, the unitarization of the T_u-model as well as the SM VBS signal and the background predictions based on the ATLAS $WZjj$ analysis.

unitarity within the accessible energy range of the LHC. This unphysical behaviour is avoided below by using the unitarization scheme of Ref. [397], dubbed T_u-model, which is a variant of K-matrix unitarization, producing close to maximal absolute values of the partial wave amplitudes at high energies.

In the presence of aQGC which signify strong interactions in the bosonic sector, VBS cross sections are enhanced at high VV invariant masses, which feeds into observables correlated to m_{VV} such as the integrated dilepton invariant mass distribution for $W^\pm W^\pm jj$ events shown in Fig. 16 or the integrated WZ transverse mass distribution shown in Fig. 26. The $m_{\mathrm{T}}(WZ)$-distribution is obtained from the ATLAS $WZjj$ analysis (see Table 8) with the additional cuts $m_{jj} > 600$ GeV, $\Delta\eta_{jj} > 3.0$ on the invariant mass and the rapidity separation of the tagging jets, and $|\eta_\mu| < 2.7$ on muon rapidity. Also shown in Fig. 26 are $m_{\mathrm{T}}(WZ)$-distributions for $f_{M_0}/\Lambda^4 = 3.8$ TeV^{-4} within the pure EFT and including the unitarization of the T_u-model for the VBS $WZjj$ signal. Detector effects are included by assuming the same efficiencies in each $m_{\mathrm{T}}(WZ)$ bin as for the SM EW signal. The processes contributing to the background distribution in Fig. 26 are listed in Table 9. The aQGC leads to an excess of events at very high $m_{\mathrm{T}}(WZ)$. Assuming that no significant excess is observed in the high energy tail, one finds the expected 95% CL bounds on aQGC listed in Table 10. Also shown in the Table are bounds expected from $W^\pm W^\pm jj$ production, based on the dilepton invariant mass distribution of Fig. 16. The expected bounds for the HE-LHC are obtained in a similar fashion, assuming the same signal to background ratio as at 14 TeV for the SM case, and generating VBS $W^\pm W^\pm jj$ and $WZjj$ events with VBFNLO at LO QCD.

The above procedure provides conservative estimates for the sensitivity to aQGC in VBS: The experimental VBS analyses focused on the significance of the various SM VBS signals and did not try to optimize sensitivity to deviations at highest VV invariant masses, as would be favorable for aQGC measurements. Taking into account weak boson rapidity and transverse momentum distributions and correlations, the sensitivity to aQGC could be improved somewhat. On the other hand, dedicated analyses including Sudakov suppression at high invariant mass, as discussed in Section 4.2.2, which is expected to slightly decrease sensitivity to aQGC, have not been performed yet in the above setting.

Table 10: Expected bounds (in TeV^{-4}) on the coefficients of dimension-8 operators, assuming no significant excess in the integrated $m_{\mathrm{T}}(WZ)$ ($WZjj$) or m_{ll} ($W^{\pm}W^{\pm}jj$) distributions at high mass.

	14 TeV		27 TeV	
	$WZjj$	$W^{\pm}W^{\pm}jj$	$WZjj$	$W^{\pm}W^{\pm}jj$
f_{S_0}/Λ^4	[-8,8]	[-6,6]	[-1.5,1.5]	[-1.5,1.5]
f_{S_1}/Λ^4	[-18,18]	[-16,16]	[-3,3]	[-2.5,2.5]
f_{T_0}/Λ^4	[-0.76,0.76]	[-0.6,0.6]	[-0.04,0.04]	[-0.027,0.027]
f_{T_1}/Λ^4	[-0.50,0.50]	[-0.4,0.4]	[-0.03,0.03]	[-0.016,0.016]
f_{M_0}/Λ^4	[-3.8,3.8]	[-4.0,4.0]	[-0.5,0.5]	[-0.28,0.28]
f_{M_1}/Λ^4	[-5.0,5.0]	[-12,12]	[-0.8,0.8]	[-0.90,0.90]

4.2.5 Measurements of ZZ scattering

This section presents the studies performed for VBS in the ZZ fully leptonic decay channel for HL-LHC and HE-LHC. Despite the very low cross section times branching fraction, the reconstruction of all final state leptons allows to precisely measure the angular distributions of the Z decays to optimally separate the longitudinal from the dominating transverse polarizations. In addition, a precise measurement of the hard scattering centre-of-mass energy is possible from the reconstructed four-leptons invariant mass. Last but not least, the reducible background in this channel is very small, making it an ideal case for high statistics measurement since the impact of associated experimental systematics uncertainties is expected to be very small.

The ATLAS analysis is performed with simulated events at generator level at 14 TeV, where the detector effects of lepton and jet reconstruction and identification were estimated by corrections, assuming a mean number of interactions per bunch crossing of 200. The CMS analysis is based on the experimental investigation of VBS in the ZZ channel using 36 fb^{-1} of data collected in 2016 [398] which showed an observed significance of 2.7 standard deviations. This analysis is projected to HL-LHC conditions [399] by scaling the expected yields for the signal and background processes, taking into account the increase in luminosity and scattering energy as well as the changes in acceptance and selection efficiencies between the LHC Phase-1 (13 TeV) and the HL-LHC (14 TeV) configurations. The DELPHES simulation [273] is then used to assess the sensitivity to VBS $Z_{\mathrm{L}}Z_{\mathrm{L}}$. The HL-LHC result is further projected to the HE-LHC configuration.

Several Monte Carlo event generators were used to simulate the signal and background contributions. In the ATLAS analysis, both the EW-$ZZjj$ and QCD-$ZZjj$ processes with the $ZZ \to 4\ell$ decays are modeled using SHERPA v2.2.2 [84] with the NNPDF3.0NNLO [400] parton distribution functions (PDFs) set. The signal sample is generated with two jets at Matrix Element (ME) level. The background process is modeled with next-to-leading order (NLO) QCD accuracy for events with up to one outgoing parton and with leading order (LO) accuracy for the case with two and three partons, in a phase space of $m_{\ell\ell} > 4$ GeV and at least two leptons with $p_{\mathrm{T}} > 5$ GeV. Other backgrounds have minor contributions to the 4ℓ channel and therefore are not included. The CMS analysis uses MADGRAPH5_AMC@NLO v2.3.3 [401] to simulate the EW-$ZZjj$ signal and QCD-$ZZjj$ background samples with zero, one, and two outgoing partons at Born level at NLO. The different jet multiplicities are merged using the FxFx scheme [157] with a merging scale of 30 GeV, and leptonic Z boson decays were simulated using MADSPIN [402]. The gluon loop-induced production of two Z bosons ($ggZZ$) is simulated at LO with MCFM v.7.0.1 [403], and checked with a dedicated simulation of the loop-induced $\mathrm{gg} \to ZZjj$ process using MADGRAPH5_AMC@NLO. The NNPDF3.0 PDF set is also used. The interference between EW-$ZZjj$ and QCD-$ZZjj$ processes is found to be small and is neglected in both analyses. Simulated samples with polarization information on the outgoing Z bosons

are generated using MADGRAPH5_AMC@NLO v1.5.14 and the DECAY package from this version.

The selections are based on Run-2 analyses and have been modified according to the expected changes for the detectors at HL-LHC. The foreseen forward lepton coverage is up to $|\eta| = 4.0$ for both electrons and muons in ATLAS, while it is is up to $|\eta| = 3.0(2.8)$ for electrons (muons) in the CMS upgrade, with an option for an extension of up to $|\eta| = 4.0$ for electrons. Candidate events should contain two pairs of oppositely charged isolated leptons (electrons or muons), consistent with the decays of two on-shell Z bosons. The VBS topology is ensured by requiring at least two jets with large invariant mass and η separation in the cut based analysis, whereas an inclusive selection is used when the signal extraction is performed with a multivariate discriminant (BDT). Table 11 summarizes the details of the selection criteria used by the ATLAS and CMS collaborations.

Table 11: Event selections used in ATLAS and CMS analyses. For the leptons η and p_{T} in CMS the first number refers to electrons and the second, in parenthesis, to muons.

	ATLAS	CMS
lepton η	$\|\eta\| < 4.0$	$\|\eta\| < 3.0(2.8)$ ($\|\eta\| < 4.0(2.8)$, extended optio
lepton p_{T}	$p_{\mathrm{T}} > 20, 20, 10, 7$ GeV	$p_{\mathrm{T}} > 20, 12(10), 10, 7(5)$ GeV
N leptons	exactly 4	≥ 4
Z mass	$60 < m_{ll} < 120$ GeV	$60 < m_{ll} < 120$ GeV
Z_1 definition	m_{ll} closest to PDG [404] value	p_{T}-leading Z
jet η	$\|\eta\| < 4.5$	$\|\eta\| < 4.7$
jet p_{T}	$p_{\mathrm{T}} > 30(70)$ GeV for $\|\eta\| < 3.8(> 3.8)$	$p_{\mathrm{T}} > 30$ GeV
N jets	≥ 2, with $\eta^{j_1} \times \eta^{j_2} < 0$	≥ 2
VBS cuts	$m_{jj} > 600$ GeV and $\|\Delta\eta_{jj}\| > 2$	$m_{jj} > 100$ GeV, signal extraction from BDT

The distributions of the ZZ invariant mass (m_{ZZ}) and the azimuthal angular difference between the two Z bosons ($|\Delta\phi(ZZ)|$) are shown in Fig. 27, after the ATLAS event selection. The numbers of selected signal and background events are quoted in Table 12, normalized to 3000 fb^{-1} of integrated luminosity. In addition to the baseline selection, two alternative selections are also studied to compare different detector scenarios at the HL-LHC. Uncertainties in the table refer to expected data statistical

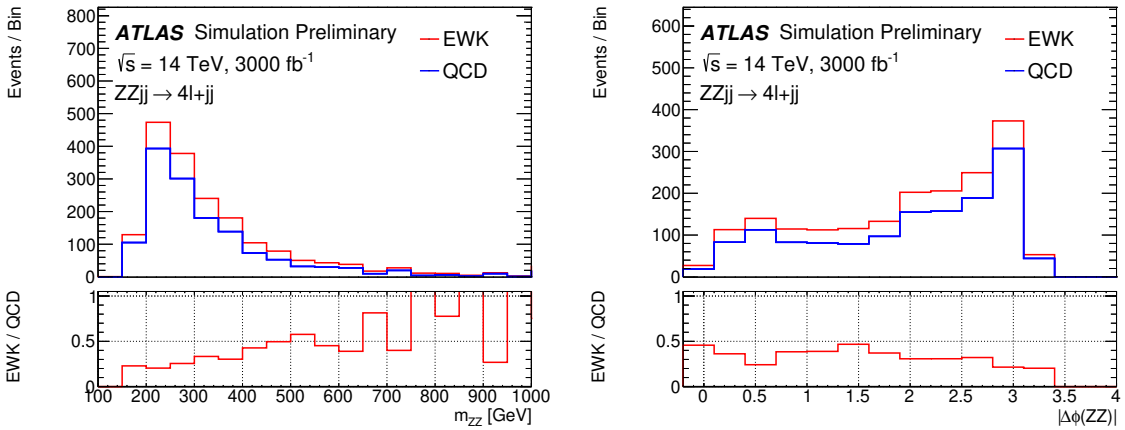

Fig. 27: Detector level distributions of m_{ZZ} and $|\Delta\phi(ZZ)|$ for the EW and QCD $ZZjj$ processes after the cut-based event selection, normalized to 3000 fb^{-1}.

uncertainty at 14 TeV with 3000 fb^{-1}. The benefit of the extension for the rejection of PU jets is

Table 12: Comparison of event yields for the signal ($N_{\mathrm{EW}-ZZjj}$) and background ($N_{\mathrm{QCD}-ZZjj}$) processes, and expected significance of EW-$ZZjj$ processes, normalized to 3000 fb^{-1} data at 14 TeV, for baseline and alternative selections.

Selection	$N_{\mathrm{EW}-ZZjj}$	$N_{\mathrm{QCD}-ZZjj}$	$N_{\mathrm{EW}-ZZjj}$ / $\sqrt{N_{\mathrm{QCD}-ZZjj}}$
Baseline	432 ± 21	1402 ± 37	11.5 ± 0.6
Leptons with $\|\eta\| < 2.7$	373 ± 19	1058 ± 33	11.5 ± 0.6
PU jet suppression only in $\|\eta\| < 2.4$	536 ± 23	15470 ± 124	4.3 ± 0.2

clear. The extended tracking coverage improves the lepton detection efficiency and increases the number of signal events, providing larger event yield for differential cross section measurements and for the longitudinal scattering. However, the overall significance of observing the EW-$ZZjj$ process does not improve as much, due to larger increase of the QCD-$ZZjj$ background contribution. This is due to the ZZ system being more centrally produced in EW processes than in QCD processes. These results, however, do not include the gluon-induced contribution, for which the ZZ system is found to be more centrally produced than for the leading quark-induced contribution. Moreover, in the case of the longitudinal scattering, the η distribution of longitudinally polarized Z bosons is peaked in the forward region, therefore extended coverage is beneficial in this case as will be shown in the following.

The dominant systematics for 4ℓ channel are from theoretical modeling of the QCD-$ZZjj$ background processes. The ATLAS analysis considers different sizes of systematic uncertainty in the background modeling of 5, 10 and 30%. The 30% uncertainty is a conservative estimation from direct calculation by comparing different choices of PDF sets and QCD renormalization and factorization scales, following recommendation from PDF4LHC [195]. The 5% one is an optimistic estimation where enough data events from QCD enriched control region at the HL-LHC could be used to provide constraints on the theoretical modeling of QCD-$ZZjj$ processes. For the experimental sources, the jet uncertainties have been checked following the studies in Ref. [405] and the effect is within fluctuation of the simulated events, which is at the 5% level. Thus a 5% uncertainty is used as a conservative estimate of the experimental uncertainties. In this analysis these uncertainties are treated as uncorrelated and summed up quadratically. The CMS analysis considers two scenarios for the systematic uncertainties. The first scenario ('Run-2 scenario') consists in using the same systematic uncertainties as those used for the Run-2 analysis, apart from the uncertainty in the gluon-induced background contribution for which a 10% uncertainty is considered. In the second scenario ('YR18 scenario'), improved systematic uncertainties are assumed to be obtained from the more data and better understanding of the detector. In this scenario, the theory systematic uncertainties (PDF and QCD scales) are halved with respect to the Run-2 scenario. In this analysis the systematic uncertainties are considered as nuisances in the fit and profiled.

Figure 28 (left) shows the result of a scan over different m_{jj} cuts in addition to the ATLAS baseline selection, for an integrated luminosity of 3000 fb^{-1}. The expected significance of EW-$ZZjj$ production processes is calculated as $\mathrm{Significance} = S/\sqrt{\sigma(B)^2_{stat.} + \sigma(B)^2_{syst.}}$, where S denotes the number of signal events after the selection, and $\sigma(B)_{stat.}$ and $\sigma(B)_{syst.}$ refer to the statistical and systematic uncertainties in background yield. The statistical uncertainty is estimated from expected data yield at 14 TeV with 3000 fb^{-1}.

The CMS analysis employs a multivariate discriminant based on a boosted decision tree (BDT) to extract the EW-$ZZjj$ signal from the QCD-$ZZjj$ background processes. Seven observables are used in the BDT, including m_{jj}, $|\Delta\eta_{\mathrm{jj}}|$, m_{ZZ}, as well as the Zeppenfeld variables [364] $\eta^*_{Z_{1,2}} = \eta_{Z_{1,2}} - (\eta_{\mathrm{jet}_1} + \eta_{\mathrm{jet}_2})/2$ of the two Z bosons, and the ratio between the p_{T} of the tagging jet system and the scalar sum

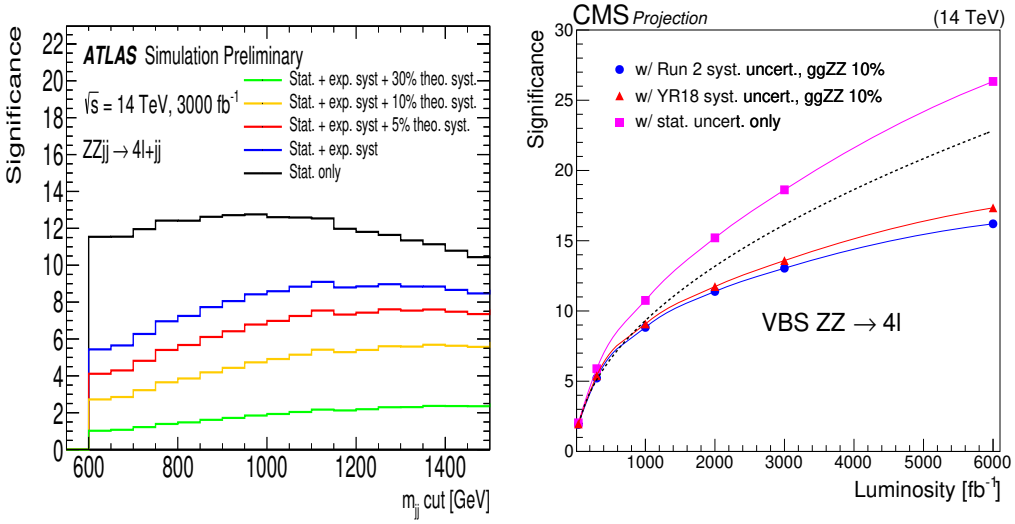

Fig. 28: Expected significance of EW-$ZZjj$ processes as a function of different m_{jj} cuts for 3000 fb^{-1}, for different sizes of theoretical uncertainties in the QCD-$ZZjj$ background modeling (left). Projected significance in the multivariate analysis as a function of the integrated luminosity for the two considered scenario and a 10% uncertainty in the loop-induced $ggZZ$ background yield, as well as with only the statistical uncertainties included (right).

of p_{T} of the tagging jets ($R(p_{\mathrm{T}})^{\mathrm{jets}}$). The BDT also exploits the event balance $R(p_{\mathrm{T}})^{\mathrm{hard}}$, defined as the transverse component of the vector sum of the Z bosons and tagging jets momenta, normalized to the scalar p_{T} sum of the same objects [406]. The modeling of all these observables was checked with Run-2 data in a background-enriched region [398]. A maximum likelihood fit of the BDT distributions for signal and backgrounds is used to extract the signal strength. The shape and normalization of each distribution are allowed to vary within their respective uncertainties. Figure 28 (right) shows the projected significance for a 10% uncertainty in the loop-induced $ggZZ$ background yield, as a function of the integrated luminosity and for the two scenarios described above, as well as for a scenario with only the statistical uncertainty included. The dashed line shows the projected significance as obtained scaling the 2016 result with statistical uncertainty only by the luminosity ratio. The impact of a multivariate analysis is clear for such small signal. The expected significance is 13.0σ (13.6σ) for the Run-2 (YR18) systematic scenario, with a 10% uncertainty in the loop-induced $ggZZ$ background yield and an integrated luminosity of 3000 fb^{-1}.

A fiducial phase space is defined at generator level with the same kinematic selections as listed in Table 11, and is used to study the expected precision of the cross section measurements. Table 13 shows the expected cross section measurement in this phase space for 3000 fb^{-1}, with the statistical only case, and the cases with different sizes of theoretical uncertainties. The statistical uncertainty is at 10% level and the integrated cross section measurement becomes dominated by experimental and modeling uncertainty in the QCD-$ZZjj$ background. For the possible extension of the HL-LHC run to 4000 fb^{-1}, the statistical uncertainty will be further reduced to 8% level.

Table 13: Summary of expected cross section measurements for different theoretical uncertainties. The statistical uncertainty is estimated from expected data yield at 14 TeV with 3000 fb^{-1}. Different uncertainties are summed up quadratically.

	Cross section [fb]	Stat. only	Plus exp.	Plus 5% theo.	Plus 10% theo.	Plus 30% theo.
EW-$ZZjj$	0.21	$\pm$0.02	$\pm$0.04	$\pm$0.05	$\pm$0.08	$\pm$0.21

The projected measurement uncertainty from the CMS analysis is 9.8% (8.8%) for the Run-2 (YR18) scenario and for a 10% uncertainty in the loop-induced $ggZZ$ background yield, for an integrated luminosity of 3000 fb^{-1}and a coverage of up to $|\eta| = 3$ for electrons. Extending the coverage up to $|\eta| = 4$ for electrons, the expected measurement uncertainty becomes 9.5% and 8.5%, respectively. In these estimates it is assumed that a fiducial cross section close to the detector volume is used, such that the measurement is to first order insensitive to theoretical uncertainties in the signal cross section.

In addition, the expected differential cross section measurements of the EW-$ZZjj$ processes at 14 TeV have been studied in the defined phase space, as a function of m_{jj}, and m_{ZZ}, as shown in Fig. 29. The expected differential cross section measurements are calculated bin by bin as

$$\sigma = \frac{N_{\mathrm{pseudo-data}} - N_{\mathrm{QCD}-ZZjj}}{L * C_{\mathrm{EW}-ZZjj}},\ C_{\mathrm{EW}-ZZjj} = \frac{N^{det.}_{\mathrm{EW}-ZZjj}}{N^{part.}_{\mathrm{EW}-ZZjj}}, \tag{19}$$

where $N_{\mathrm{pseudo-data}}$ is the expected number of data events with 3000 fb^{-1} luminosity, and $N_{\mathrm{QCD}-ZZjj}$ and $N_{\mathrm{EW}-ZZjj}$ are the number of predicted events from QCD-$ZZjj$ and EW-$ZZjj$ processes, respectively. The $C_{\mathrm{EW}-ZZjj}$ factor refers to the detector efficiency for EW-$ZZjj$ processes, calculated as number of selected signal events at detector level ($N^{det.}_{\mathrm{EW}-ZZjj}$), divided by number of selected events at particle level in the fiducial phase space ($N^{part.}_{\mathrm{EW}-ZZjj}$). Both the statistical only case (statistical uncertainty is estimated from expected data yield at 14 TeV with 3000 fb^{-1}) and the ones with different sizes of theoretical uncertainties on the background modeling are shown in Fig. 29.

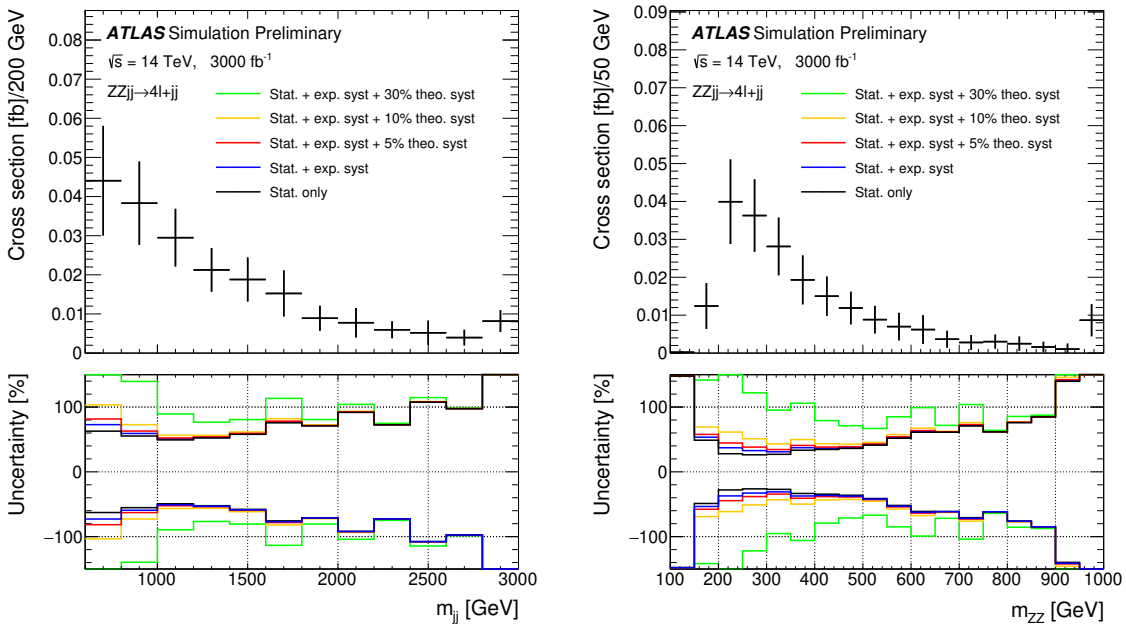

Fig. 29: Expected differential cross sections at 14 TeV for the EW-$ZZjj$ processes as a function of m_{jj}(left) and m_{ZZ} (right). Results are shown with different sizes of systematic uncertainties.

The decay angle $\cos\theta^*$ of the lepton direction in the Z decay rest frame with respect to the Z momentum direction in the laboratory frame is the most distinctive feature of longitudinal Z bosons (Z_{L}). The Z boson p_{T} and η distributions also carry information on $Z_{\mathrm{L}}Z_{\mathrm{L}}$ production, in particular longitudinal Z bosons are produced with a lower p_{T} and more forward, compared to transverse polarizations (Z_{T}). The distributions of $\cos\theta^*$, p_{T} and η of both Z bosons, together with the distributions of all observables used to separate VBS processes from QCD backgrounds and described above are employed as input to a BDT to separate the VBS $Z_{\mathrm{L}}Z_{\mathrm{L}}$ signal from all backgrounds. The BDT is trained separately

to discriminate the VBS $Z_{\mathrm{L}}Z_{\mathrm{L}}$ signal from the QCD backgrounds (QCD BDT) and to discriminate the VBS $Z_{\mathrm{L}}Z_{\mathrm{L}}$ signal from the VBS background (VBS BDT). Cut values are defined on the QCD BDT and on the VBS BDT output values, which maximizes the overall significance estimator $S/\sqrt{B}$ for the selected events. The corresponding signal efficiency is 14.1% and the VBS, leading QCD-$ZZjj$ and loop-induced $ggZZ$ background efficiencies are 1.6%, 0.03% and 0.05%, respectively. It is assumed that the VBS $Z_{\mathrm{L}}Z_{\mathrm{L}}$ fraction, defined as VBS $Z_{\mathrm{L}}Z_{\mathrm{L}}$ / VBS $(Z_{\mathrm{L}}Z_{\mathrm{L}} + Z_{\mathrm{L}}Z_{\mathrm{T}} + Z_{\mathrm{T}}Z_{\mathrm{T}})$ will be measured, rather than the absolute VBS Z_{L} Z_{L} cross section. In such ratio measurement, the systematic uncertainties from luminosity, and selection efficiency, as well as theoretical uncertainties on the VBS and VBS background cross section cancel out, such that only the uncertainties in the QCD backgrounds yields are considered.

Figure 30 shows the expected significance for the VBS $Z_{\mathrm{L}}Z_{\mathrm{L}}$ fraction as a function of the integrated luminosity and for the two scenarios described above and a 10% uncertainty in the loop-induced $ggZZ$ background yield, as well as for a scenario with only the statistical uncertainty included. A significance of 1.4σ is reached for 3000 fb^{-1}. As expected from the ratio measurement, the effect of systematic uncertainties is very small. Results are also shown for an integrated luminosity of 6000 fb^{-1}, which would approximately correspond to combining ATLAS and CMS after 3000 fb^{-1}. Table 14

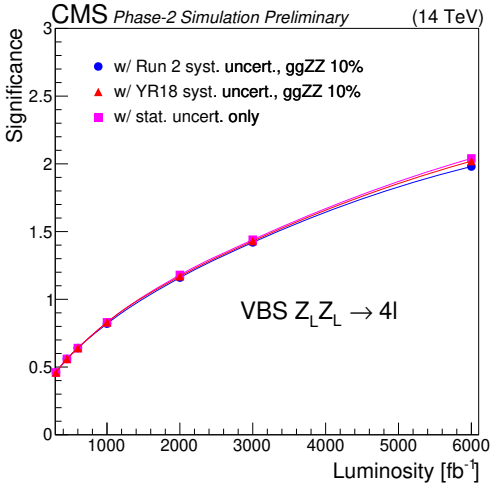

Fig. 30: Expected significance for the VBS $Z_{\mathrm{L}}Z_{\mathrm{L}}$ fraction as a function of the integrated luminosity and for systematic uncertainties according to the Run-2 and YR18 scenario, as well as with only the statistical uncertainties included.

presents the expected significance and relative uncertainty in the VBS $Z_{\mathrm{L}}Z_{\mathrm{L}}$ fraction for various η coverage configurations. The foreseen coverage extension of up to $|\eta| = 3\ (2.8)$ for electrons (muons) leads to a $\sim 13\%$ improvement for the significance and precision on the VBS $Z_{\mathrm{L}}Z_{\mathrm{L}}$ fraction. An extension of up to $|\eta| = 4$ for electrons would allow to further improve by $\sim 4\%$ both significance and cross section measurement uncertainty.

Finally, a simple scaling of the signal and background cross sections is performed to assess the sensitivity to the VBS $Z_{\mathrm{L}}Z_{\mathrm{L}}$ fraction at HE-LHC. An integrated luminosity of 15 ab^{-1} is considered, together with a c.o.m energy of 27 TeV. The cross section ratios $\sigma_{27\,\mathrm{TeV}}$ / $\sigma_{14\,\mathrm{TeV}}$ are evaluated at LO with MADGRAPH(v5.4.2) [393] for the EW signal and the leading QCD-$ZZjj$ background, and with MCFM(v.7.0.1) [403] for the $ggZZ$ loop-induced background. Table 15 shows the expected significance and relative uncertainty for the VBS $Z_{\mathrm{L}}Z_{\mathrm{L}}$ fraction at HE-LHC, compared to HL-LHC. The HE-LHC machine would allow to bring the sensitivity (uncertainty) for the measurement of the VBS $Z_{\mathrm{L}}Z_{\mathrm{L}}$ frac-

Table 14: Significance and measurement uncertainty for the VBS $Z_{\mathrm{L}}Z_{\mathrm{L}}$ fraction for different acceptance configurations at HL-LHC. In the quoted η coverages, the first number corresponds to electrons while the number in parentheses corresponds to muons.

η coverage	significance	VBS $Z_{\mathrm{L}}Z_{\mathrm{L}}$ fraction uncertainty (%)
$\lvert\eta\rvert < 2.5$ (2.4)	1.22σ	88
$\lvert\eta\rvert < 3.0$ (2.8)	1.38σ	78
$\lvert\eta\rvert < 4.0$ (2.8)	1.43σ	75

tion to the level of $\sim 5\sigma$ ($\sim 20\%$).

Table 15: Expected significance and measurement uncertainty for the VBS $Z_{\mathrm{L}}Z_{\mathrm{L}}$ fraction at HL-LHC and HE-LHC with and without systematic uncertainties included.

	significance		precision (%)	
	w/ syst. uncert.	w/o syst. uncert.	w/ syst. uncert.	w/o syst. uncert.)
HL-LHC	1.4σ	1.4σ	75%	75%
HE-LHC	5.2σ	5.7σ	20%	19%

4.2.6 The production of WW / WZ via vector boson scattering with semi-leptonic final states

The existing Run-2 VBS measurements and the above analyses have focused on channels involving the fully leptonic boson decays, or decay modes involving photons. The semileptonic channels can however offer some interesting advantages: the $V \to q\bar{q}$ branching fractions are much larger than the leptonic ones and the use of jet substructure techniques with large-radius jet reconstruction allows to reconstruct and identify the V-boson produced in the high-p_{T} region, which is the most sensitive to new physics effects. This section presents the sensitivity of the ATLAS experiment to VBS in the $V(qq)W(\ell\nu)$ final state, assuming an integrated luminosity of 300 or 3000 fb^{-1} of pp collisions at $\sqrt{s}$= 14 TeV.

This analyses uses generator-level samples of the main signal and background processes, combined with the parameterisations of the detector performance (muon and jet reconstruction and selection efficiencies and momentum resolutions) expected at the HL-LHC from fully simulated samples. The parametrized detector resolutions are used to smear the generator-level particle transverse momenta, while the parametrized efficiencies are used to reweigh the selected events. All generated samples were produced at $\sqrt{s}$= 14 TeV and normalized to luminosities of 300 or 3000 fb^{-1} when the results are presented.

The electroweak (EW) $VVjj$ production is modeled using MADGRAPH5_AMC@NLO v2.3.3 [12], plus PYTHIA8 [292] for fragmentation. The main background sources are W bosons produced in association with jets (W+jets), with significant contributions from top-quark production (both $t\bar{t}$ pair and single-top), non-resonant vector-boson pair production (ZZ, WZ and WW) and Z bosons produced in association with jets (Z+jets). Background originating from multi-jet processes are expected to be negligible due to the event selection requirements. Details about the samples generation can be found in Ref. [407].

To increase the purity of considered events, several requirements are placed on the constituents of an event. Events are required to have exactly one lepton. Generator-level electrons or muons are required to be isolated and pass the tight identification criteria [405] and to have $p_{\mathrm{T}} > 27$ GeV. Events are required to contain a hadronically-decaying W/Z candidate, reconstructed either from two small-R

jets, defined as the resolved channel, or from one large-R jet, designated the boosted channel. Small-R jets are defined using the anti-k_{T} algorithm [408] with a radius parameter of R = 0.4. The identification of jets originating from b-quarks is done by finding jets with generator-level b-hadron within a cone of $\Delta R < 0.4$ around the jet direction. Similarly, the anti-k_{T} algorithm with a radius parameter of R = 1.0 is used to reconstruct large-R jets. The large-R jets are trimmed using the standard ATLAS trimming parameters [409]. It is assumed that the performance of a future W/Z-boson tagger at the HL-LHC conditions will have similar, if not better, performance as existing boson taggers. To simulate the effect of Run-2 W/Z-boson tagging performance [410, 411] events which contain a large-R jet are scaled by the expected boson tagging efficiency for the $V \rightarrow qq$ with kinematics corresponding to the large-R jet, calculated from fully-simulated 13 TeV Monte-Carlo (MC) samples. The missing transverse energy E_{T}^{miss} is required to be greater than 60 GeV, which suppresses the expected multijet background to a negligible level. By constraining the E_{T}^{miss} + lepton system to be consistent with the W mass, the z component of the neutrino (ν) momentum can be reconstructed by solving a quadratic equation.

Experimentally, VBS is characterized by the presence of a pair of vector bosons and two forward jets with a large separation in pseudorapidity and a large dijet invariant mass. Therefore the VBS search is required to have 2 additional forward VBS-topology tagging jets in the event in addition to jets associated with the boson decay, similar to the resonant VBF search. The VBS tagging jets are required to be non-b-tagged, be in the opposite hemispheres, $\eta(j_1^{\mathrm{tag}}) \cdot \eta(j_2^{\mathrm{tag}}) < 0$, and to have the highest dijet invariant mass among all pairs of jets remaining in the event after the $V \rightarrow jj$ jet selection. After the tagging jet pair are selected, it is required that both tagging jets should have p_{T} >30 GeV, and that the invariant mass of the two tagging jets system is greater than 400 GeV . In the merged selection, events are required to have at least one large-R jet with $p_{\mathrm{T}}(J) > 200$ GeV and $|\eta(J)| < 2$. From those candidate large-R jets, the one with the smallest $|m(J) - m(W/Z)|$ is selected as the signal large-R jet. Mass window cuts and boson tagging efficiencies are applied as described above. To suppress backgrounds with top quarks, an event is rejected if any of the reconstructed jets outside the large R jet, is identified as containing a b-quark. If events fail the merged VBS selection, the resolved selection is then applied. Signal jets are chosen as the pair with $m(jj)$ closest to the W/Z mass. The signal jet pairs are then required to have $|m(jj) - m(W/Z)| < 15$ GeV. To suppress backgrounds with top quarks, an event is rejected if any of the reconstructed jets is identified as containing a b-quark.

To optimize the signal sensitivity, Boosted Decision Trees (BDT) for the resolved and merged searches were trained on the background and signal MC samples in the respective regions. Four variables are included in the merged BDT: the invariant mass of the $l\nu J$ system, the lepton η, the second tag jet p_{T} and the boson centrality ζ_V. The boson centrality is defined as $\zeta_V = min(\Delta\eta_+, \Delta\eta_-)$ where $\Delta\eta_+ = max(\eta(j_1^{\mathrm{tag}}), \eta(j_2^{\mathrm{tag}})) - max(\eta(\ell\nu), \eta(J))$ and $\Delta\eta_- = min(\eta(\ell\nu), \eta(J)) - min(\eta(j_1^{\mathrm{tag}}), \eta(j_2^{\mathrm{tag}}))$. In the resolved BDT, eight variables were used: the invariant mass of the $WVjj$ system , the lepton η, the p_{T} of both VBS-tagging jets and sub-leading signal jet, the boson centrality defined similarly to above, the $\Delta\eta$ between signal jets, and the ΔR between the lepton and neutrino candidate. These variables were chosen as they are the minimal subset of variables with the greatest separation between the signal and background, that provide significant improvement when added during the training. The BDT were trained using a gradient descent BDT algorithm, maximizing the Gini index, in the TMVA package [412]. The BDT are chosen as the discriminants and their distributions are used in the final fit for the VBS search shown in Figure 31.

If an event fails either a mass-window cut or a b-veto but passes all other events then the event is categorized as a W or top control region. These regions are used to constrain the normalization and shape systematics of the background.

The results are extracted by performing a simultaneous binned maximum-likelihood fit to the BDT distributions in the signal regions and the W+jets and $t\bar{t}$ control regions. A test statistic based on the profile likelihood ratio [413] is used to test hypothesized values of the signal cross section. The

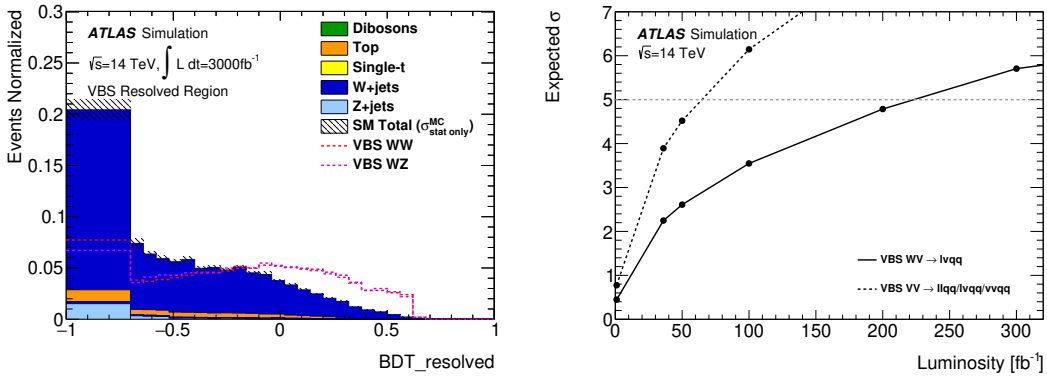

Fig. 31: Final signal and background distributions for the VBS search in the respective resolved signal region for the normalized BDT response. Background distributions are separated into production type. VBS signals in WW and WZ mode are overlaid as dashed curves where appropriate. Both background and signal BDT distributions are normalized to unity (left). Expected signal significance as a function of integrated luminosity up to 300 fb^{-1}. The solid black curve is the significance from the $\ell\nu qq$channel, while the black dashed curve shows the expected significance from all semi-leptonic channels assuming equal sensitivity (right).

likelihood is defined as the product of the Poisson likelihoods for all signal and control regions for a given production mechanism category and channel. Systematic uncertainties are taken into account as constrained nuisance parameters with Gaussian or log-normal distributions. The main background modelling systematics, namely the W+jets and $t\bar{t}$ shape uncertainties, are constrained by the corresponding control regions and are treated as uncorrelated among the resolved and merged signal regions.

The expected significance for the SM VBS process is 5.7σ at 300 fb^{-1} as shown in Fig. 31. The expected cross section uncertainties are 18% at 300 fb^{-1} and 6.5% at 3000 fb^{-1}. The effects of unfolding were not considered for the cross section estimates. If control regions are not used to constrain the systematics the expected significance is reduced to 3.6σ at 300 fb^{-1}. Likewise the cross section uncertainty are increased to 28% at 300 fb^{-1} and 10% at 3000 fb^{-1} when control regions are ignored.

4.2.6.1 Electroweak WW / WZ production analysis at HE-LHC

The prospect analysis at HE-LHC [414] mimics the analysis at HL-LHC but the DELPHES simulation is used [415]. VBS signal samples are produced in the same manner as the HL-LHC analysis. The major backgrounds W+jets and $t\bar{t}$ production are simulated with MADGRAPH and aMC@NLO respectively, interfaced with PYTHIA. Z+jets, single top and diboson contribution are not simulated and are expected to contribute at most 10% to the total background.

The unprecedented energy of pp collisions at the HE-LHC will significantly improve sensitivity to new multi-TeV particles over LHC and HL-LHC. However, the experimental environment is expected to be challenging at the HE-LHC, primarily due to a significant increase of the number of pp collisions in a same and nearby bunch crossings (pile-up). The HE-LHC is planned to be operated at a centre-of-mass energy of 27 TeV with 800 pile-up collisions at the peak luminosity. Such extreme pile-up conditions are expected to be particularly challenging for identifying hadronically decaying W/Z boson as the extra contribution of particles produced from pile-up collisions into jets could degrade the performance of W/Z boson tagger significantly. It is therefore important to assess the performance of pile-up mitigation technique at the HE-LHC in order to have a reliable estimate of the search sensitivity.

The study presented here focuses on the performance of pile-up mitigation techniques and W/Z

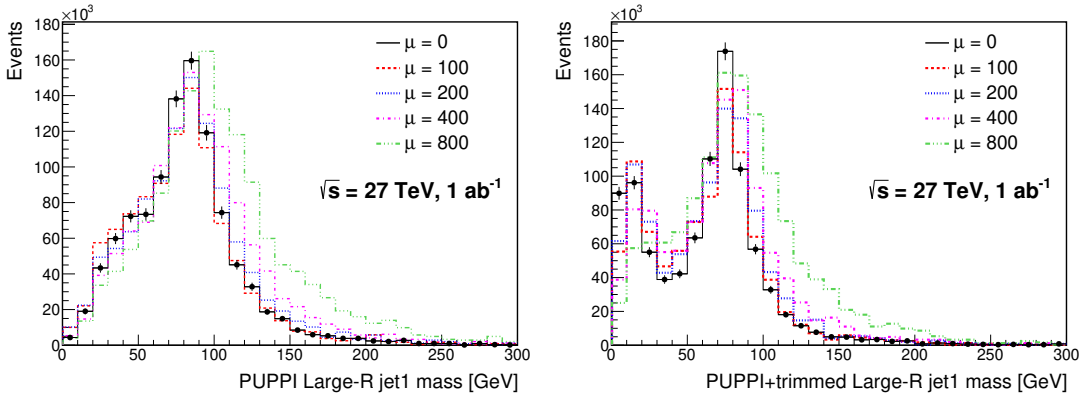

Fig. 32: Leading large-R jet mass (left) after applying the PUPPI algorithm at an integrated luminosity of 1 ab^{-1} at $\sqrt{s}$ = 27 TeV with five different pile-up overlay conditions of μ_{pileup} = 0, 100, 200, 400 and 800. The right plots shows the same distribution but after additionally requiring that the jets are trimmed with the conditions described in the text.

boson tagging. The VBS signal events are produced with the overlay of minimum-bias pp interactions generated using PYTHIA 8. The minimum-bias interactions are overlaid onto hard scattering event using Poisson probability distribution with the mean number of interactions (μ_{pileup}) varied from 0 to 100, 200, 400 and 800. Furthermore, the minimum-bias interactions are distributed randomly in z and timing using Gaussian profiles of $\sigma_z = 5.3$ cm and $\sigma_t = 160$ ps, respectively (z=0 at the detector centre and t=0 for hard scattering event). The overlaid VBS signal events are processed through DELPHES with two pile-up mitigation techniques: the Pile-up Per Particle Identification (PUPPI) algorithm [362] used in CMS and the trimming procedure used in ATLAS. The trimming parameters of the p_{T} fraction cut and the sub-jet reclustering radius are chosen to be the same as those used in ATLAS. For the PUPPI algorithm the standard DELPHES implementation is used.

Figure 32 shows the leading large-R jet mass (m_J) for the PUPPI-only jets and the PUPPI+trimmed jets, both required to have $p_{\text{T}} > 200$ GeV. The m_J distribution get shifted towards lower values with the trimming applied, enhancing the peak around m_W . The residual pile-up effect is still visible as a shift towards larger values with increasing μ_{pileup}, but the overall signal yield after the mass-window and D_2 requirements (e.g, $D_2 < 1.5$) is largely stable. This indicates that an impact to the W/Z-boson tagging performance from expected pile-up collisions at the HE-LHC can be mitigated to the level where the tagging performance is similar to what is expected at Run-2 or the HL-LHC. Therefore, the study presented in the rest of this note is based on the W/Z-boson tagging performance at Run-2.

The sensitivity to the VBS signal at 27 TeV is extracted in the same manner as the HL-LHC analysis. The event selection is similar and a BDT is built using the same variables both in the resolved and boosted channel. For more details about the BDT and the setup used please refer to citation. Figure 33 shows the expected cross section uncertainty as function of integrated luminosity at 27 TeV compared to the one obtained at 14 TeV. The results are very consistent and show that given the same luminosity the same uncertainty can be reached at 27 TeV. Prospects are also presented for the extraction of the longitudinal component of the WW scattering. For the extraction of the longitudinal component in VBS processes, the electroweak $WWjj$ samples are generated with the DECAY program to identify the polarization state of the produced V bosons. The generated events are then classified according to the polarization state: both V bosons are longitudinally (LL) or transversely (TT) polarized, or in the mixed state (LT). Each event is showered using PYTHIA and then processed through the DELPHES simulation.

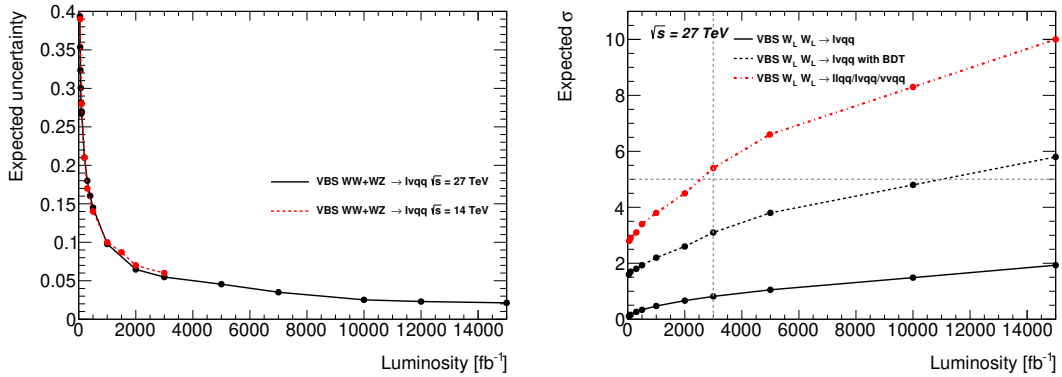

Fig. 33: The expected cross section uncertainty as function of integrated luminosity at 27 TeV compared to the one obtained at 14 TeV (left). Right: Observed significance as a function of the luminosity and expected uncertainty for the EW W_LW_L signal assuming a 10% fraction predicted by MADGRAPH (right). One line shows the results obtained by fitting a single variable, the total invariant mass of the system and the other one shows the expected significance using the BDT. The third line shows the expected significance assuming the combination of all three semi-leptonic channels with the same sensitivity.

In this case a BDT is built training the signal samples ($WW\ LL$) against the sum of the backgrounds which include the TT and LT component of the electroweak $WWjj$ samples. The observed significance expected with this simple setup is shown in the right figure of Fig. 33. One line shows the results obtained by fitting a single variable, the total invariant mass of the system and the other one shows the expected significance using the BDT. The third line shows the expected significance assuming the combination of all three semi-leptonic channels with the same sensitivity. It is expected to reach 5σ sensitivities with 3000 fb^{-1} combining all the semileptonic channels.

4.3 Tri-boson production

The production of multiple heavy gauge bosons V (= $W^{\pm}, Z$) opens up a multitude of potential decay channels categorised according to the number of charged leptons in the final state. The sensitivity prospect studies have been performed related to the production of $W^{\pm}W^{\pm}W^{\mp}$, $W^{\pm}W^{\mp}Z$ or $W^{\pm}ZZ$ followed by the fully leptonic or semi-hadronic[13] decays: $W^{\pm}W^{\pm}W^{\mp} \to \ell^{\pm}\nu\ell^{\pm}\nu\ell^{\mp}\nu$, $W^{\pm}W^{\pm}W^{\mp} \to \ell^{\pm}\nu\ell^{\pm}\nu jj$, $W^{\pm}W^{\mp}Z \to \ell^{\pm}\nu\ell^{\pm}\nu\ell^{+}\ell^{-}$, $W^{\pm}W^{\mp}Z \to \ell^{\pm}\nu jj\ell^{+}\ell^{-}$, $W^{\pm}ZZ \to \ell^{\pm}\nu\ell^{+}\ell^{-}\ell^{+}\ell^{-}$, $W^{\pm}ZZ \to \ell^{\pm}\nu\ell^{+}\ell^{-}\nu\nu$, $W^{\pm}ZZ \to jj\ell^{+}\ell^{-}\ell^{+}\ell^{-}$ and $W^{\pm}ZZ \to \ell^{\pm}\nu\ell^{+}\ell^{-}jj$, with $\ell = e$ or μ. Prospect studies have been performed, using a cut-based analysis, corresponding to an integrated luminosity of 3000 fb^{-1} and 4000 fb^{-1} of proton–proton collisions at a centre-of-mass energy of $\sqrt{s}$ = 14 TeV, expected to be collected by the ATLAS detector at the HL-LHC [301]. In this section we summarize only results that are expected to provide the best sensitivity according to the full prospect studies documented in [416].

Monte Carlo (MC) simulated event samples are used to predict the background from SM processes and to model the multi-boson signal production. The effects of an upgraded ATLAS detector are taken into account by applying energy smearing, efficiencies and fake rates to generator level quantities, following parameterisations based on detector performance studies with full simulation and HL-LHC conditions. The most relevant MC samples have equivalent luminosities (at 14 TeV) of at least 3000 fb^{-1}. Several MC generators are used to model the production of signal and dominant SM background

[13] In case of semi-hadronic channels we assume that one of the vector bosons decays hadronically while the other two decay leptonically.

processes relevant for the analysis.

For the generation of triboson signal events, matrix elements for all combinations of $pp \to VV$ ($V = W^{\pm}, Z$) have been generated using SHERPA v2.2.2 [84] with up to two additional partons in the final state, including full next-to-leading-order calculations (NLO) [417–419] accuracy for the inclusive process. All diagrams with three electroweak couplings are taken into account, including diagrams involving Higgs propagators. However, since these samples use factorised decays with on-shell vector bosons, the resonant contribution from those diagrams can not be reached from the 125 GeV Higgs. In order to account for the contribution coming from these diagrams the corresponding production of VH ($V = W, Z$) bosons is added to the signal. Electroweak NLO corrections to the signal production cross sections are not considered in this analysis. The diboson processes are generated with SHERPA event generator following the approach described in [420]. For the simulation of the top quark pair and the production of VH ($V = W, Z$) bosons POWHEG [151, 314, 377]+PYTHIA [148] was used as described in [421], while for the $t\bar{t}$ + V ($V = W, Z, H$) MADGRAPH5_aMC@NLO [12] interfaced to PYTHIA was used as in [422].

The expected multi-boson yields are normalised to the SHERPA predictions, while the $t\bar{t}$ + V ($V = W, Z, H$) yields are normalized to NLO. The top quark pair-production contribution is normalised to approximate NNLO+NNLL accuracy [41, 423].

Experimental signatures

The experimental signature of the triboson processes considered in these studies consists of at least three charged leptons, moderate $E_{\mathrm{T}}^{\mathrm{miss}}$ originating from the leptonic decay of W bosons, and jets in case one of the vector bosons decays hadronically. The event selection starts from the one used in the published analysis in Ref. [424], but considers tighter selection criteria in terms of transverse momentum of the selected objects and missing transverse momentum of the event, in order to suppress higher pile-up contributions expected at the HL-LHC. The selection requirements used to define the signal regions are obtained from an optimization to maximize the sensitivity to $W^{\pm}W^{\pm}W^{\mp}$, $W^{\pm}W^{\mp}Z$ and $W^{\pm}ZZ$ processes and to reduce the contributions from SM background processes. In the case of $W^{\pm}W^{\pm}W^{\mp} \to \ell^{\pm}\nu\ell^{\pm}\nu\ell^{\mp}\nu$ channel, three separate signal regions are defined based on the number of same-flavour opposite-sign (SFOS) lepton pairs in the event: 0SFOS ($e^{\pm}e^{\pm}\mu^{\mp}$, $\mu^{\pm}\mu^{\pm}e^{\mp}$), 1SFOS ($e^{\pm}e^{\mp}\mu^{\pm}$, $e^{\pm}e^{\mp}\mu^{\mp}$, $\mu^{\pm}\mu^{\mp}e^{\pm}$, $\mu^{\pm}\mu^{\mp}e^{\mp}$) and 2SFOS ($e^{\pm}e^{\pm}e^{\mp}$, $\mu^{\pm}\mu^{\pm}\mu^{\mp}$). Similarly, in $W^{\pm}W^{\mp}Z \to \ell^{\pm}\nu\ell^{\pm}\nu\ell^{+}\ell^{-}$ channel, two signal regions are defined based on the selection of SFOS or different-flavour opposite-sign (DFOS) lepton-pair events: SFOS ($e^{\pm}e^{\mp}\mu^{\mp}\mu^{\pm}$, $e^{\pm}e^{\mp}e^{\pm}e^{\mp}$, $\mu^{\mp}\mu^{\pm}\mu^{\mp}\mu^{\pm}$) and DFOS ($e^{\pm}e^{\mp}\mu^{\mp}e^{\pm}$, $\mu^{\mp}\mu^{\pm}\mu^{\mp}e^{\pm}$). To select $W^{\pm}W^{\pm}W^{\mp} \to \ell^{\pm}\nu\ell^{\pm}\nu jj$ candidates, events are required to have exactly two leptons with the same electric charge, and at least two jets. Three different final states are considered based on the lepton flavour, namely $e^{\pm}e^{\pm}$, $e^{\pm}\mu^{\pm}$ and $\mu^{\pm}\mu^{\pm}$. In the case of $W^{\pm}ZZ$ process, separate set of selection criteria are defined in order to select events in which vector bosons undergo either fully leptonic of semi-hadronic decay. In all channels, events are rejected if they have identified b-jets. This selection requirement suppresses background involving top quarks, with marginal impact on the signal efficiency. Full description to the optimized selection criteria, estimated systematic uncertainties and expected signal and background event yields for all channels considered in the study are available in Ref. [416]. Three channels, 0SFOS $W^{\pm}W^{\pm}W^{\mp} \to 3\ell\,3\nu$, DFOS $W^{\pm}W^{\mp}Z \to 4\ell\,2\nu$ and $W^{\pm}ZZ \to 5\ell\,1\nu$, for which we give details in the following, are estimated to provide best sensitivities. Tables 16 to 18 show the kinematic selection criteria used to select signal events in these channels.

Results

The SM processes that mimic the multi-boson signal signatures by producing at least three prompt leptons or two prompt leptons with the same electric charge, can be grouped into the following categories:

Table 16: Event selection criteria for $W^{\pm}W^{\pm}W^{\mp} \to 3\ell\ 3\nu$ candidate events.

$W^{\pm}W^{\pm}W^{\mp} \to \ell^{\pm}\nu\ell^{\pm}\nu\ell^{\mp}\nu$	0SFOS events: $e^{\pm}e^{\pm}\mu^{\mp}$, $\mu^{\pm}\mu^{\pm}e^{\mp}$
Preselection	Exactly 3 charged *tight* leptons with $p_{\mathrm{T}} > 30$ GeV and $\lvert\eta\rvert < 4$
SFOS dilepton mass	$m_{\ell\ell}^{\mathrm{SFOS}} > 20$ GeV
Angle between the trilepton system and $\vec{E}_{\mathrm{T}}^{miss}$	$\lvert\varphi^{3\ell} - \varphi^{\vec{E}_{\mathrm{T}}^{miss}}\rvert > 2.5$
Z boson veto	$\lvert m_{\mathrm{ee}} - m_{\mathrm{Z}}\rvert > 15$ GeV
Jet veto	At most one jet with $p_{\mathrm{T}} > 30$ GeV and $\lvert\eta\rvert < 2.5$
b-jet veto	No identified b-jets with $p_{\mathrm{T}} > 30$ GeV

Table 17: Event selection criteria for $W^{\pm}W^{\mp}Z \to 4\ell\ 2\nu$ candidate events. The four-lepton mass $m_{4\ell}$ is calculated as invariant mass of the four-lepton system.

$W^{\pm}W^{\mp}Z \to \ell^{\pm}\nu\ell^{\pm}\nu\ell^{+}\ell^{-}$	DFOS events: $e^{\pm}e^{\mp}\mu^{\mp}e^{\pm}$, $\mu^{\mp}\mu^{\pm}\mu^{\mp}e^{\pm}$
Preselection	Exactly 4 charged *loose* (3^{rd} and 4^{th} *tight*) leptons with $p_{\mathrm{T}}(1,2) > 30$ GeV, $p_{\mathrm{T}}(3,4) > 25$ GeV and $\lvert\eta\rvert < 4$
SFOS dilepton mass	$\lvert m_{\ell\ell}^{\mathrm{SFOS}} - 91\ \mathrm{GeV}\rvert < 15$ GeV
DFOS dilepton mass	$m_{\ell\ell}^{\mathrm{DFOS}} > 40$ GeV
Four-lepton mass	$m_{4\ell} > 250$ GeV
b-jet veto	No identified b-jets with $p_{\mathrm{T}} > 30$ GeV

Table 18: Event selection criteria for $W^{\pm}ZZ \to 5\ell\ 1\nu$ candidate events. Two-lepton pairs of the same flavour and opposite charge have to satisfy same-flavour dilepton mass selection requirement. The transverse mass is calculated from the $E_{\mathrm{T}}^{\mathrm{miss}}$ and the lepton that does not pass dilepton mass requirement.

$W^{\pm}ZZ \to \ell^{\pm}\nu\ell^{+}\ell^{-}\ell^{+}\ell^{-}$	$5\ell 1\nu$
Preselection	Exactly 5 charged *loose* (4^{rd} and 5^{th} *tight*) leptons with $p_{\mathrm{T}}(1,2,3) > 30$ GeV, $p_{\mathrm{T}}(4,5) > 25$ GeV and $\lvert\eta\rvert < 4$
SFOS dilepton mass	$\lvert m_{\ell\ell}^{\mathrm{SFOS}} - 91\ \mathrm{GeV}\rvert < 15$ GeV
Transverse mass	$m_{\mathrm{T}} > 40$ GeV
b-jet veto	No identified b-jets with $p_{\mathrm{T}} > 30$ GeV

– The WZ and ZZ processes, referred to as "diboson background";
– The WWW, WWZ, WZZ, ZZZ processes, excluding the signal process under study, referred to as "triboson background";
– The VH and $t\bar{t}H$ processes, excluding the processes which are added to the signal, referred to as "Higgs+X background";
– The production of four top quarks, top quark associated with WZ bosons or $t\bar{t}$ associated with W, Z, WZ or $W^{\pm}W^{\mp}$ bosons, referred to as "top background";
– Processes that have non-prompt leptons (electrons) originating from misidentified jets (referred to as "fake-lepton background");
– Processes that produce prompt charged leptons, but the charge of one lepton is misidentified (referred to as "charge-flip background").

The contributions from the WW and $t\bar{t}$ processes are accounted for in the fake-lepton and charge-flip backgrounds. The diboson, triboson, Higgs+X and top background sources are estimated using simulated events, with the dominant irreducible background in most of the channels originating from the diboson processes. In some channels the contribution of the fake-lepton background, which is derived by applying the pre-defined (p_{T}, η)-dependent likelihood as described in Section 3, becomes significant.

The charge-flip background has been investigated and found to be negligible in all considered processes.

In $W^{\pm}W^{\pm}W^{\mp} \to 3\ell\ 3\nu$ channel, the background is dominated by the irreducible diboson background and fake-lepton contribution. The contribution of signal events containing Higgs decays are at the level of 40%. In $W^{\pm}W^{\mp}Z \to 4\ell\ 2\nu$ channel with two leptons being of different flavour, this requirement suppresses a large fraction of the diboson background. Contribution of Higgs decays is quite smaller with respect to the one in $W^{\pm}W^{\pm}W^{\mp} \to 3\ell\ 3\nu$ due to smaller lepton p_{T} and invariant mass requirement $m_{\ell\ell}^{\mathrm{DFOS}} > 40$ GeV. In the $W^{\pm}ZZ$ channel, the most promising signal region is the one with five charged leptons. In this case, the fake-lepton contribution becomes significant. The background is dominated by rare top production of $t\bar{t}ZW$.

Figure 34 shows relevant distributions in the three channels: the $m_{\mathrm{T}}^{3\ell}$ distribution for the $W^{\pm}W^{\pm}W^{\mp}$ - $3\ell\ 3\nu$ channel, the distribution of transverse momenta of the two-lepton system $p_{\mathrm{T}}^{\ell\ell}$ in $W^{\pm}W^{\mp}Z \to 4\ell\ 2\nu$ channel and the distribution of two lepton invariant mass $p_{\mathrm{T}}^{\ell\ell}$ selected to give the mass closest to the mass of the Z boson in $W^{\pm}ZZ \to 5\ell\ 1\nu$ channel.

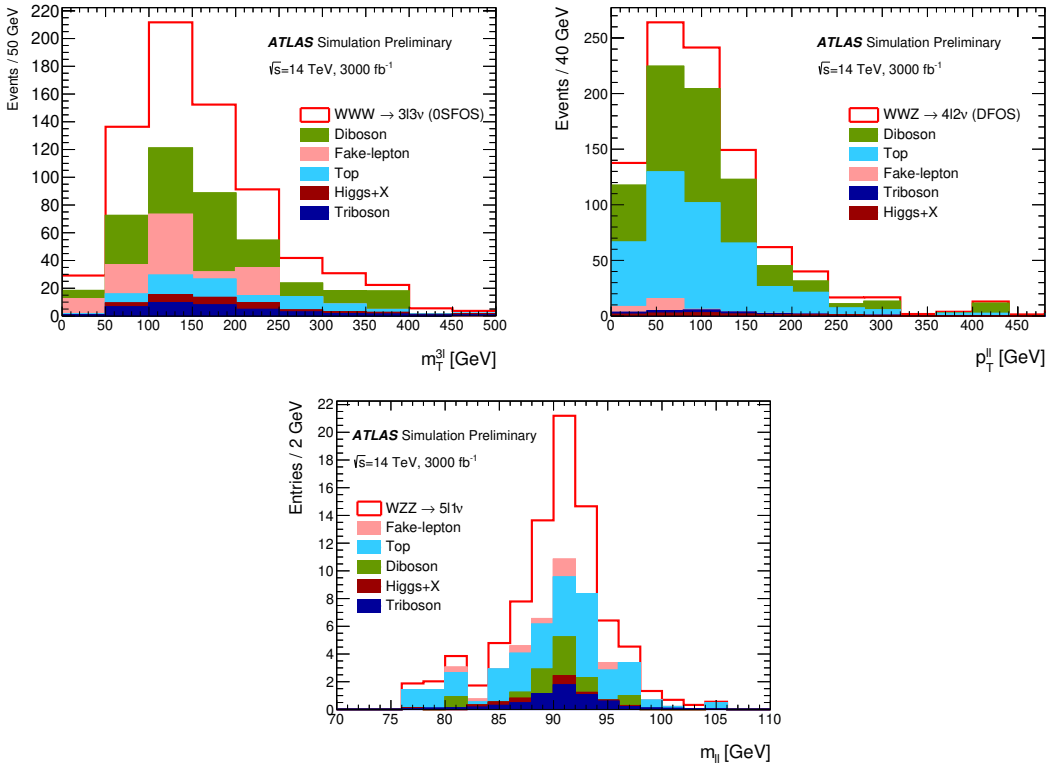

Fig. 34: The distribution of $m_{\mathrm{T}}^{3\ell}$ for the $W^{\pm}W^{\pm}W^{\mp} \to 3\ell\ 3\nu$ channel (top left), the distribution of transverse momenta of the two-lepton system $p_{\mathrm{T}}^{\ell\ell}$ in $W^{\pm}W^{\mp}Z \to 4\ell\ 2\nu$ channel (top right) and the distribution of two lepton invariant mass $p_{\mathrm{T}}^{\ell\ell}$ selected to give the mass closest to the mass of the Z boson in $W^{\pm}ZZ \to 5\ell\ 1\nu$ channel (bottom) as expected from the signal and background processes at 3000 fb^{-1} after applying the selection criteria from Tables 16 to 18.

Systematic uncertainties in the signal and background predictions arise from the uncertainties in the measurement of the integrated luminosity, from the experimental modelling of the signal acceptance and detection efficiency, and from the background normalisation. With the much larger integrated luminosity and a sophisticated understanding of the detector performance and backgrounds at the HL-LHC, we expect experimental uncertainties related to the lepton reconstruction and identification efficiencies as well as lepton energy/momentum resolution and scale modelling of 1%, to the $E_{\mathrm{T}}^{\mathrm{miss}}$ modelling of

1%, to the jet energy scale and resolution of 1.5% and 5% in the fully leptonic and leptons+jets channels, respectively, to the luminosity measurement of 1% and to the expected pileup of 1% [276]. Based on the extrapolations of current ATLAS measurements and assuming a reduction of the uncertainty at the level of 15–80%, depending on the process and the origin of the systematics, the following systematic uncertainties on the cross section normalisation for each of the background processes are assumed: 4% on σ_{diboson}, 30% on σ_{triboson}, 3% on $\sigma_{t\bar{t}}$, 20% on $\sigma_{t\bar{t}H}$, 6% on $\sigma_{t\bar{t}Z}$, and 11% on $\sigma_{t\bar{t}W}$. The uncertainty on the level of the fake-lepton background is estimated to be 10%. Taking these assumptions into account, we estimate the total systematic uncertainty on the background of 9% for $W^{\pm}W^{\pm}W^{\mp} \to 3\ell 3\nu$ and $W^{\pm}ZZ \to 5\ell 1\nu$ channels and 6% in $W^{\pm}W^{\mp}Z \to 4\ell 2\nu$ channel. Assuming that the number of signal events follows a Poissonian distribution and taking into account an estimated systematic uncertainty on the background, the signal significance Z_{σ} and the estimated precision on the signal strength measurement, $\frac{\Delta\mu}{\mu}$ are calculated using the asymptotic formula from Ref. [413]. Only experimental uncertainties are taken into account for the signal. Uncertainties related to the limited number of MC events are neglected. The total number of signal and background events expected after applying the full set of selection requirements from Tables 16 to 18 in three selected channels, the corresponding signal significance and the expected precision on the signal strength measurement, for an integrated luminosity of 3000 fb^{-1} are shown in Table 19.

Table 19: Expected number of signal and background events, the expected signal significance Z_{σ} and the estimated precision on the signal strength measurement, $\frac{\Delta\mu}{\mu}$ in $W^{\pm}W^{\pm}W^{\mp} \to 3\ell 3\nu$, $W^{\pm}W^{\mp}Z \to 4\ell 2\nu$ and $W^{\pm}ZZ \to 5\ell 1\nu$ channels after applying the selection criteria from Tables 16 to 18.

	$W^{\pm}W^{\pm}W^{\mp} \to 3\ell 3\nu$	$W^{\pm}W^{\mp}Z \to 4\ell 2\nu$	$W^{\pm}ZZ \to 5\ell 1\nu$
Signal	312	168	19
Diboson	208	357	4.0
Triboson	37	11	3.0
Higgs+X	25	10	0.3
Top	60	390	15
fake-lepton	97	16	3.0
Total:	427	784	25
Significance Z_{σ}	6.7	3.0	3.0
Significance Z_{σ} (4000 fb^{-1})	7.0	3.1	3.4
Precision $\frac{\Delta\mu}{\mu}$	11%	27%	36%
Precision $\frac{\Delta\mu}{\mu}$ (4000 fb^{-1})	10%	25%	31%

The HL-LHC offers a large improvement to multi-boson production, where this simple cut-and-count approach provides sensitivities larger than 3σ in the three channels considered in this analysis. It should be noted that more mature analysis techniques such as MVA, would likely improve these results further. However, high level of background control, mainly diboson background as well as instrumental background arising from fake-leptons, will be needed in order to maintain desired level of precision.

4.4 Precision electroweak measurements

4.4.1 NNLO predictions for Z-boson pair production[14]

The results presented in this section are produced using the program described in Ref. [425] with the NNPDF3.0 [201] set of parton distribution functions. The parton densities and α_s are evaluated at each corresponding order (i.e. $(n{+}1)$-loop α_s is used at N^{n}LO, with $n = 0, 1, 2$) and $N_f = 5$ massless quark flavours are considered. For the renormalisation (μ_R) and factorisation (μ_F) scales two choices are investigated: $\mu_R = \mu_F = m_Z$ and the dynamic scale $\mu_R = \mu_F = m_{ZZ}/2$. The G_{μ} EW scheme is

[14] Contribution by G. Heinrich, S. Jahn, S. Jones, M. Kerner and J. Pires.

used where the EW input parameters have been set to $G_F = 1.16639 \times 10^{-5}$, $m_W = 80.399$ GeV and $m_Z = 91.1876$ GeV. The top quark and Higgs boson masses that are included in the real-virtual one-loop contributions and in the loop-induced gg channel have been set to $m_t = 173.2$ GeV and $m_H = 125$ GeV, respectively. The one-loop contributions are calculated with the program GoSam [11, 86]. For the NNLO real radiation the N-jettiness subtraction scheme [53, 54, 426, 427] is employed. The process dependent hard function has been extracted from the two-loop amplitude computed in Ref. [428] and cross-checked with an in-house calculation. The top quark contributions in the double virtual two-loop diagrams are not included in the results below. Table 20 shows cross section results for the central scale $\mu_R = \mu_F = m_Z$, including 7-point scale variations. In Table 21 results for the dynamic scale $\mu_R = \mu_F = m_{ZZ}/2$ are given.

Table 20: Inclusive cross section for ZZ production at the LHC for $\sqrt{s}$ =14 TeV and $\sqrt{s}$ =27 TeV at LO, NLO and NNLO with $\mu_R = \mu_F = m_Z$. The uncertainties are obtained by varying the renormalisation and factorisation scales in the range $m_Z/2 < \mu_R, \mu_F < 2m_Z$ with the constraint $0.5 < \mu_F/\mu_R < 2$.

	σ_{LO} [pb]	σ_{NLO} [pb]	σ_{NNLO} [pb]	$gg \to ZZ$ [pb]
14 TeV	$10.80^{+5.7\%}_{-6.7\%}$	$15.55^{+3.0\%}_{-2.4\%}$	$18.50^{+3.0\%}_{-3.2\%}$	$1.56^{+25\%}_{-18\%}$
27 TeV	$23.59^{+10.0\%}_{-10.9\%}$	$35.59^{+3.2\%}_{-4.2\%}$	$44.52^{+3.7\%}_{-4.1\%}$	$4.81^{+25\%}_{-18\%}$

Table 21: Inclusive cross section for ZZ production at the LHC for $\sqrt{s}$ =14 TeV and $\sqrt{s}$ =27 TeV at LO, NLO and NNLO with the dynamic scale choice $\mu_R = \mu_F = m_{ZZ}/2$. The uncertainties are obtained by varying the renormalisation and factorisation scales in the range $m_{ZZ}/4 < \mu_R, \mu_F < m_{ZZ}$ with the constraint $0.5 < \mu_F/\mu_R < 2$.

	σ_{LO} [pb]	σ_{NLO} [pb]	σ_{NNLO} [pb]	$gg \to ZZ$ [pb]
14 TeV	$11.03^{+5.2\%}_{-6.1\%}$	$15.38^{+2.5\%}_{-2.0\%}$	$18.20^{+3.3\%}_{-2.3\%}$	$1.41^{+23\%}_{-18\%}$
27 TeV	$24.68^{+9.0\%}_{-9.8\%}$	$35.43^{+2.6\%}_{-3.7\%}$	$43.71^{+3.3\%}_{-3.2\%}$	$4.41^{+23\%}_{-17\%}$

Figures 35 and 36 show largely non-overlapping scale uncertainty bands between NLO and NNLO, both for a fixed central scale choice $\mu = m_Z$ as well as for a dynamic central scale choice $\mu = m_{ZZ}/2$. This demonstrates that for this process, the scale variations are insufficient to estimate missing higher order terms in the perturbative expansion. This is mostly due to the fact that at NNLO, the loop-induced gluon fusion channel $gg \to ZZ$ opens up, and due to the large gluon flux it represents a numerically significant contribution, about 8% at $\sqrt{s} = 14$ TeV and 11% at $\sqrt{s} = 27$ TeV of the total NNLO cross section, for both central scale choices. Further studies of the gluon channel can be seen in Refs. [429,430]. Since this new channel contributes for the first time at NNLO its contribution cannot be captured by the scale variations of the NLO cross section. Therefore, with increasing perturbative order, a systematic reduction of the factorisation scale dependence of the cross section is observed (indicated by the thickness of the scale uncertainty band), while there is no significant reduction of the renormalisation scale dependence. To show that this effect can be attributed to the gluon fusion channel opening up at NNLO, the NNLO result excluding this channel is also shown in Figs. 35 and 36.

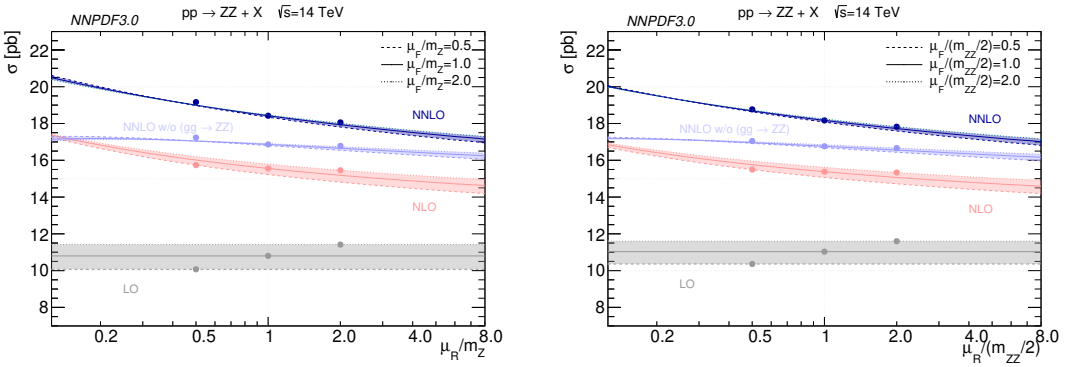

Fig. 35: Renormalisation and factorisation scale dependence of the ZZ cross section for $\sqrt{s} = 14\,\text{TeV}$ at LO, NLO and NNLO for the fixed central scale choice $\mu_R = \mu_F = m_Z$ (left) and for the dynamic central scale choice $\mu_R = \mu_F = m_{ZZ}/2$ (right). The NNLO result without the gluon fusion contributions is shown in light blue. The thickness of the bands show the variation with the factorisation scale, while the slope shows the renormalisation scale dependence. The scale uncertainties are the envelope of scale variations by a factor of two up and down with the constraint $0.5 < \mu_F/\mu_R < 2$, i.e. 7-point scale variations.

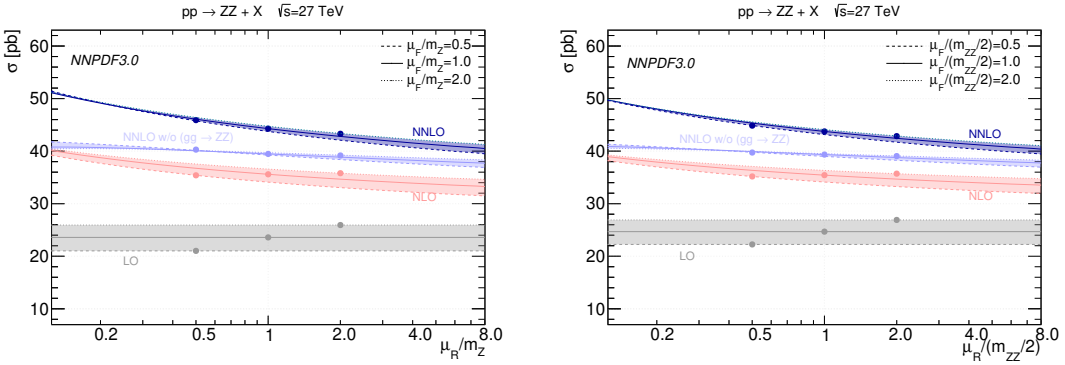

Fig. 36: Renormalisation and factorisation scale dependence of the ZZ cross section for $\sqrt{s} = 27\,\text{TeV}$ at LO, NLO and NNLO for the fixed central scale choice $\mu_R = \mu_F = m_Z$ (left) and for the dynamic central scale choice $\mu_R = \mu_F = m_{ZZ}/2$ (right). The NNLO result without the gluon fusion contributions is shown in light blue, and the bands are produced in the same way as in Fig. 35.

4.4.2 Gauge-boson pair production with MATRIX[15]

NNLO QCD predictions for W^+W^-, $W^\pm Z$ and ZZ production in proton–proton collisions are presented in this section. Two LHC upgrade scenarios are considered, namely the HL-LHC running at $\sqrt{s} = 14\,\text{TeV}$ with an assumed integrated luminosity of $3\,\text{ab}^{-1}$, and the HE-LHC at $\sqrt{s} = 27\,\text{TeV}$ with $15\ \text{ab}^{-1}$. More precisely, the following inclusive hard-scattering processes are considered

$$
\begin{aligned}
pp &\to \ell^+\nu_\ell\,\ell'^-\bar{\nu}_{\ell'} + X\,,\\
pp &\to \ell\nu_\ell\,\ell'^+\ell'^- + X\,,\\
pp &\to \ell^+\ell^-\ell'^+\ell'^- + X\,,
\end{aligned}
$$

where all off-shell effects and interference contributions are fully accounted for.

[15] Contribution by S. Kallweit, M. Grazzini and M. Wiesemann.

All results are obtained with the public parton-level NNLO framework MATRIX. This program, and earlier versions of it, have been used to compute state-of-the-art QCD predictions for gauge-boson pair production processes [431–439].[16] All tree-level and one-loop amplitudes are evaluated with OPENLOOPS[17] [10,444]. At two-loop level the $q\bar{q} \to VV'$ amplitudes of Ref. [428] are used.

The complex mass scheme [382] is applied throughout, i.e. complex W- and Z-boson masses are used and the EW mixing angle is defined as $\cos\theta_W^2 = (m_W^2 - i\Gamma_W m_W)/(m_Z^2 - i\Gamma_Z m_Z)$. For the input of the weak parameters the G_μ scheme is employed with $\alpha = \sqrt{2}\, G_\mu |(m_W^2 - i\Gamma_W m_W)\sin^2\theta_W|/\pi$. The following parameters are set, $G_F = 1.16639\times10^{-5}\,\text{GeV}^{-2}$, $m_W = 80.399\,\text{GeV}$, $\Gamma_W = 2.1054\,\text{GeV}$, $m_Z = 91.1876\,\text{GeV}$, $\Gamma_Z = 2.4952\,\text{GeV}$, $m_H = 125\,\text{GeV}$ and $\Gamma_H = 0.00407\,\text{GeV}$. Furthermore, a diagonal CKM matrix is used.

The number of light quarks is chosen differently for the processes under consideration: all W^+W^- results are obtained by applying the four-flavour scheme (4FS) with massive top and bottom quarks in order to consistently remove top-quark contamination by omitting the (separately IR finite) partonic processes with real bottom-quark emissions. In the 4FS, the on-shell bottom mass $m_b = 4.92\,\text{GeV}$ is used. For all other processes the five-flavour scheme (5FS) is applied with a vanishing bottom mass $m_b = 0$. The top quark is treated as massive and unstable throughout, and m_t is set to 173.2 GeV as well as $\Gamma_t = 1.44262\,\text{GeV}$.[18]

The MMHT2014 [200] sets of parton distribution functions (PDFs) are used with $n_f = 4$ or $n_f = 5$ active quark flavours, consistently with the flavour scheme under consideration. N^{n}LO ($n = 0, 1, 2$) predictions are obtained by using PDFs at the same perturbative order and the evolution of α_S at $(n+1)$-loop order, as provided by the corresponding PDF set. To be precise, in the 5FS MMHT2014lo68cl, MMHT2014nlo68cl, and MMHTnnlo68cl at LO, NLO, and NNLO are used. In the 4FS MSTW2008lo68cl_nf4, MMHT2014nlo68cl_nf4, and MMHT2014nnlo68cl_nf4 at LO, NLO, and NNLO are used.

The central predictions are obtained by setting the factorization and renormalization scales to $\mu_F = \mu_R = \mu_0 \equiv E_{\text{T},V_1} + E_{\text{T},V_2}$, with $E_{\text{T},V_i} = \sqrt{M_{V_i}^2 + p_{\text{T},V_i}^2}$, where M_{V_i} is the invariant mass and p_{T,V_i} the transverse momentum of the respective vector boson. Uncertainties from missing higher-order contributions are estimated in the usual way by independently varying μ_F and μ_R in the range $0.5\mu_0 < \mu_F, \mu_R < 2\mu_0$ with the constraint $0.5 < \mu_F/\mu_R < 2$.

In Table 22 cross sections are presented for W^+W^-, $W^\pm Z$ and ZZ production, inclusive over the phase space of the final-state leptons, for pp collisions at $\sqrt{s} = 14\,\text{TeV}$ and $\sqrt{s} = 27\,\text{TeV}$. Throughout, only a basic selection cut on Z bosons is applied, by requiring the invariant masses of all opposite-sign same-flavour lepton pairs to be within a Z-mass window of $66\,\text{GeV} < m_{\ell^-\ell^+} < 116\,\text{GeV}$, which is necessary to avoid divergencies induced by soft intermediate photons. The gain in the inclusive cross section at $\sqrt{s} = 27\,\text{TeV}$ is roughly a factor of 2.5 for all processes under consideration, see last column of Table 22. The importance of QCD corrections is seen: Higher-order contributions are huge, especially for $W^\pm Z$ production. The NLO corrections range from about $+36\%$ to $+82\%$ depending on process and collider energy, while NNLO QCD corrections are still sizeable and induce a further increase of the cross sections of 13% to 20%. The cross-section ratio for W^+Z/W^-Z production is about 1.55 at NNLO for $\sqrt{s} = 14\,\text{TeV}$, changes to 1.42 for $\sqrt{s} = 27\,\text{TeV}$, and is essentially independent on the perturbative order.

[16] It was also used in the NNLL+NNLO computation for W^+W^- and ZZ production of Ref. [440], and in the NNLOPS computation for W^+W^- production of Ref. [153].

[17] OPENLOOPS which relies on the fast and stable tensor reduction of COLLIER [441,442], supported by a rescue system based on quad-precision CUTTOOLS [443] with ONELOOP [2] to deal with exceptional phase-space points.

[18] Massive top-quark contributions are neglected in the virtual two-loop corrections, but are kept everywhere else in the computations.

Table 22: Inclusive cross sections for W^+W^-, $W^\pm Z$ and ZZ production where the leptonic decays of the bosons are included.

σ [fb] (correction)		LO	NLO (NLO/LO−1)	NLO′+gg (NLO′+gg/NLO−1)	NNLO (NNLO/NLO−1)	$\frac{\sigma_{\rm NNLO}(27\,\text{TeV})}{\sigma_{\rm NNLO}(14\,\text{TeV})}$
W^+W^-	$\sqrt{s} = 14\,\text{TeV}$	$897.27(9)^{+4.3\%}_{-5.3\%}$	$1303.3(1)^{+2.7\%}_{-2.2\%}$ (+45.3%)	$1386.1(2)^{+3.7\%}_{-2.9\%}$ (+6.4%)	$1485.(1)^{+2.4\%}_{-2.2\%}$ (+13.9%)	2.33
	$\sqrt{s} = 27\,\text{TeV}$	$2091.5(2)^{+7.6\%}_{-8.6\%}$	$2988.4(3)^{+2.8\%}_{-2.9\%}$ (+42.9%)	$3213.0(4)^{+4.1\%}_{-3.2\%}$ (+7.0%)	$3457.(4)^{+2.8\%}_{-2.4\%}$ (+15.6%)	
W^+Z	$\sqrt{s} = 14\,\text{TeV}$	$60.322(6)^{+3.4\%}_{-4.3\%}$	$106.15(1)^{+3.6\%}_{-3.0\%}$ (+76.0%)	—	$120.5(1)^{+2.0\%}_{-1.9\%}$ (+13.5%)	2.35
	$\sqrt{s} = 27\,\text{TeV}$	$136.66(1)^{+6.8\%}_{-7.8\%}$	$248.51(2)^{+4.0\%}_{-3.3\%}$ (+81.8%)	—	$283.4(3)^{+2.1\%}_{-2.1\%}$ (+14.0%)	
W^-Z	$\sqrt{s} = 14\,\text{TeV}$	$39.182(4)^{+3.7\%}_{-4.7\%}$	$68.430(7)^{+3.7\%}_{-3.0\%}$ (+74.6%)	—	$77.63(7)^{+1.9\%}_{-1.9\%}$ (+13.4%)	2.57
	$\sqrt{s} = 27\,\text{TeV}$	$96.70(1)^{+7.2\%}_{-8.2\%}$	$175.44(2)^{+4.0\%}_{-3.3\%}$ (+81.4%)	—	$199.7(2)^{+2.0\%}_{-2.0\%}$ (+13.8%)	
ZZ	$\sqrt{s} = 14\,\text{TeV}$	$24.500(2)^{+4.3\%}_{-5.3\%}$	$34.201(3)^{+2.0\%}_{-1.8\%}$ (+39.6%)	$37.531(4)^{+3.3\%}_{-2.6\%}$ (+9.7%)	$39.64(4)^{+2.4\%}_{-2.1\%}$ (+15.9%)	2.40
	$\sqrt{s} = 27\,\text{TeV}$	$58.622(6)^{+7.9\%}_{-8.9\%}$	$79.757(8)^{+2.2\%}_{-3.0\%}$ (+36.1%)	$89.89(1)^{+3.7\%}_{-3.0\%}$ (+12.7%)	$95.20(9)^{+2.9\%}_{-2.4\%}$ (+19.4%)	

It should be stressed that QCD radiative corrections may change quite significantly as soon as fiducial cuts on the leptonic final state are applied, or when kinematical distributions are considered. The corrections for the inclusive cross sections in Table 22 should therefore be understood as illustrative, and the use of inclusive K-factors to obtain NNLO predictions from lower order results with different sets of cuts should be avoided in general.

It is interesting to quantify the size of the loop-induced gluon fusion contribution of the charge-neutral processes, which is part of the NNLO QCD corrections. By NLO′+gg its sum is denoted with the NLO cross section computed with NNLO PDFs. The NLO′+gg result for W^+W^- production is 6.4% (7.0%) larger than the NLO result at $\sqrt{s} = 14\,(27)\,\text{TeV}$, while their difference is even 9.7% (12.7%) for ZZ production. These numbers amount to roughly half of the full NNLO correction of the W^+W^- process, and even about two-thirds for ZZ production. However, one has to bear in mind that under typical fiducial selection requirements on the leptons and missing transverse energy, the impact of the loop-induced contribution decreases significantly, especially for W^+W^- production. Furthermore, its relative contribution is strongly suppressed as far as the tails of the kinematical distributions are concerned, due to the large-x suppression of the gluon density.

To illustrate how strongly the radiative corrections may depend on the fiducial cuts, in Table 23 cross sections are shown with a minimum $p_{\text{T,min}} = 100\,\text{GeV}$ cut on the transverse momentum of the charged leptons and the missing energy. More precisely, depending on the process the following cuts have been applied, as shown in Table 24.

As can be read from Tables 22 and 23, radiative corrections at NLO can be enormous for some processes with $p_{\text{T,min}} = 100\,\text{GeV}$, ranging from +51% to even +281%. Also the NNLO corrections are significantly increased with respect to the inclusive case, and can be as large as +27%. It is also apparent that the importance of the loop-induced gluon fusion contribution is significantly reduced. For W^+W^- production, due to the applied $p_{\text{T,miss}}$ cut the NLO′+gg contribution is even smaller than the NLO cross

Table 23: Cross sections with a $p_{\mathrm{T,min}} = 100\,\mathrm{GeV}$ cut on the transverse momentum of the charged leptons and the missing energy for W^+W^-, $W^\pm Z$ and ZZ production.

σ [fb] (correction)		LO	NLO (NLO/LO−1)	NLO′+gg (NLO′+gg/NLO−1)	NNLO (NNLO/NLO−1)	$\frac{\sigma_{\mathrm{NNLO}}(27\,\mathrm{TeV})}{\sigma_{\mathrm{NNLO}}(14\,\mathrm{TeV})}$
W^+W^-	$\sqrt{s} = 14\,\mathrm{TeV}$	$0.920(1)^{+2.7\%}_{-2.7\%}$	$2.827(5)^{+9.7\%}_{-8.0\%}$ (+207.1%)	$2.793(7)^{+9.9\%}_{-8.1\%}$ (−1.2%)	$3.51(1)^{+5.2\%}_{-5.0\%}$ (+24.3%)	3.93
	$\sqrt{s} = 27\,\mathrm{TeV}$	$2.847(3)^{+0.08\%}_{-0.5\%}$	$10.83(2)^{+8.2\%}_{-6.9\%}$ (+280.5%)	$10.66(2)^{+8.4\%}_{-7.1\%}$ (−1.6%)	$13.80(4)^{+5.3\%}_{-4.8\%}$ (+27.3%)	
W^+Z	$\sqrt{s} = 14\,\mathrm{TeV}$	$0.06524(8)^{+3.3\%}_{-3.2\%}$	$0.1273(3)^{+7.1\%}_{-5.8\%}$ (+95.2%)	—	$0.1485(9)^{+3.4\%}_{-3.3\%}$ (+16.6%)	3.82
	$\sqrt{s} = 27\,\mathrm{TeV}$	$0.1919(2)^{+0.1\%}_{-0.5\%}$	$0.4642(8)^{+7.0\%}_{-5.8\%}$ (+141.9%)	—	$0.568(3)^{+3.8\%}_{-3.6\%}$ (+22.5%)	
W^-Z	$\sqrt{s} = 14\,\mathrm{TeV}$	$0.03289(4)^{+3.1\%}_{-3.1\%}$	$0.0641(2)^{+7.5\%}_{-6.0\%}$ (+94.9%)	—	$0.0767(5)^{+3.4\%}_{-3.5\%}$ (+19.7%)	4.34
	$\sqrt{s} = 27\,\mathrm{TeV}$	$0.1121(1)^{+0.\%}_{-0.3\%}$	$0.2719(5)^{+7.2\%}_{-5.9\%}$ (+142.7%)	—	$0.333(2)^{+3.7\%}_{-3.5\%}$ (+22.5%)	
ZZ	$\sqrt{s} = 14\,\mathrm{TeV}$	$0.02108(3)^{+3.1\%}_{-3.1\%}$	$0.0318(1)^{+3.8\%}_{-3.2\%}$ (+50.6%)	$0.0342(1)^{+5.4\%}_{-4.3\%}$ (+7.7%)	$0.0371(3)^{+3.6\%}_{-3.0\%}$ (+16.9%)	3.70
	$\sqrt{s} = 27\,\mathrm{TeV}$	$0.0675(1)^{+0.\%}_{-0.2\%}$	$0.1100(3)^{+3.5\%}_{-2.8\%}$ (+62.9%)	$0.1235(3)^{+5.4\%}_{-4.3\%}$ (+12.3%)	$0.1371(7)^{+4.3\%}_{-3.5\%}$ (+24.7%)	

Table 24: Selection cuts applied in the analysis for the different processes.

	W^+W^-	$W^\pm Z$	ZZ
lepton cuts	$p_{\mathrm{T},\ell_{1/2}} > p_{\mathrm{T,min}}$	$p_{\mathrm{T},\ell_{1/2/3}} > p_{\mathrm{T,min}}$	$p_{\mathrm{T},\ell_{1/2/3/4}} > p_{\mathrm{T,min}}$
neutrino cuts	$p_{\mathrm{T,miss}} > p_{\mathrm{T,min}}$	$p_{\mathrm{T,miss}} > p_{\mathrm{T,min}}$	—

section by -1.2% (-1.6%) at $\sqrt{s} = 14\,(27)\,\mathrm{TeV}$ (i.e. the positive impact of the gg channel is smaller than the negative effect from using NNLO PDFs instead of NLO PDFs in the NLO′+gg prediction). For ZZ production, it is still sizeable with 7.7% (12.3%), but its relative contribution at $\mathcal{O}(\alpha_{\mathrm{S}}^2)$ has decreased from roughly two-thirds in the inclusive case to less than half of the NNLO corrections for $p_{\mathrm{T,min}} = 100\,\mathrm{GeV}$. Furthermore, compared to the inclusive results an even more substantial increase of the cross sections is observed from $\sqrt{s} = 14\,\mathrm{TeV}$ to $\sqrt{s} = 27\,\mathrm{TeV}$ of roughly a factor of four. This can be understood by the fact, that the additional energy enlarges the available phase-space, especially at high momentum transfer.

From the results in Table 22 and 23 it is clear that the perturbative uncertainties at NLO cannot account for the additional loop-induced gluon fusion contribution that appears at NNLO. Besides that, also the genuine NNLO corrections to the quark–antiquark production mechanism cannot be anticipated from NLO scale variations, which in turn means that the NLO uncertainties are underestimated. The inclusion of NNLO corrections is therefore crucial. At this order all partonic channels are included for the first time, and scale variations can be used to obtain an estimate of the actual size of missing higher-order terms. However, the NLO corrections to the loop-induced gluon fusion contribution are relevant and should be included when possible, especially at $\sqrt{s} = 27\,\mathrm{TeV}$ where gluons with smaller x are

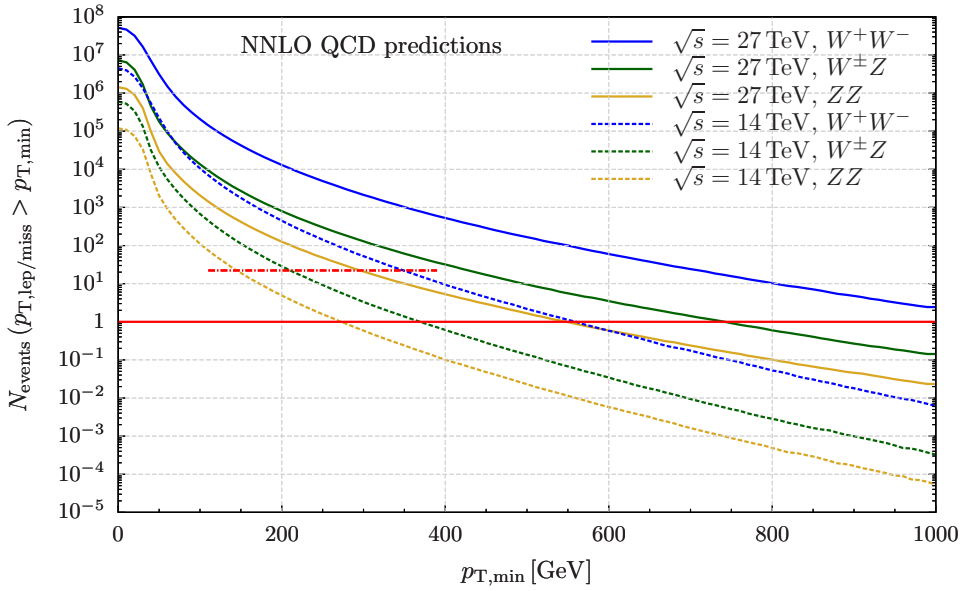

Fig. 37: Cumulative number of events as a function of $p_{\text{T,min}}$ for the following production processes: W^+W^- (blue), $W^\pm Z$ (green), and ZZ (orange); at 14 TeV (dashed) and 27 TeV (solid).

probed. In particular in tails of high-energy observables, the inclusion of NLO EW corrections and their interplay with QCD corrections will also need to be investigated. Nevertheless NNLO QCD results are presented in the following, but the above-mentioned extensions will become available well before the start of the HL-LHC.

The differential results in diboson processes in light of the HL and HE upgrades of the LHC are now discussed. Since the importance of highest-order predictions is evident from the previous discussion, only NNLO QCD accurate results are presented here. The cumulative cross section with a minimum $p_{\text{T,min}}$ cut, as introduced above is considered first. In order to analyse the number of expected events as a function of $p_{\text{T,min}}$, the cross sections have been translated into event numbers by assuming an integrated luminosity of $3\,\text{ab}^{-1}$ at 14 TeV and of $15\,\text{ab}^{-1}$ at 27 TeV.

Figure 37 shows the expected number of events as a function of $p_{\text{T,min}}$. Since the transverse momentum of all leptonic final states are restricted simultaneously, the reach in the tails may appear smaller than expected, and would be significantly larger if a cut on the transverse momentum of only the leading lepton or the missing energy were to be considered. However, the toy scenario considered is well suited to compare the three diboson production processes, and to quantify the relative gain of the additional energy and luminosity.

The curves in Fig. 37 show all production processes under consideration: W^+W^- (blue), $W^\pm Z$ (green), and ZZ (orange); at 14 TeV (dashed) and 27 TeV (solid). The horizontal red line shows the one-event threshold, below which no events are expected anymore. The following features are evident in the plot: At $\sqrt{s} = 14\,\text{TeV}$ events up to $p_{\text{T,min}}$ values of roughly 550 GeV, 370 GeV, and 270 GeV are expected for W^+W^-, $W^\pm Z$, and ZZ production, respectively. At $\sqrt{s} = 27\,\text{TeV}$ these values read >1000 GeV, 740 GeV, and 550 GeV. To put these numbers into perspective, a dash-dotted red line for the present status at the end of Run-2 is added, which represents the one-event threshold for $150\,\text{fb}^{-1}$ at 13 TeV (14 TeV $\to$ 13 TeV conversion approximated by a constant cross-section correction factor of 0.9). Its intersection points with the $\sqrt{s} = 14\,\text{TeV}$ curves indicates the current reach of the LHC, which is roughly up to 350 GeV, 210 GeV, and 140 GeV for W^+W^-, $W^\pm Z$, and ZZ production, respectively. The improved reach in the tails at 27 TeV is not only related to the larger inclusive cross section and

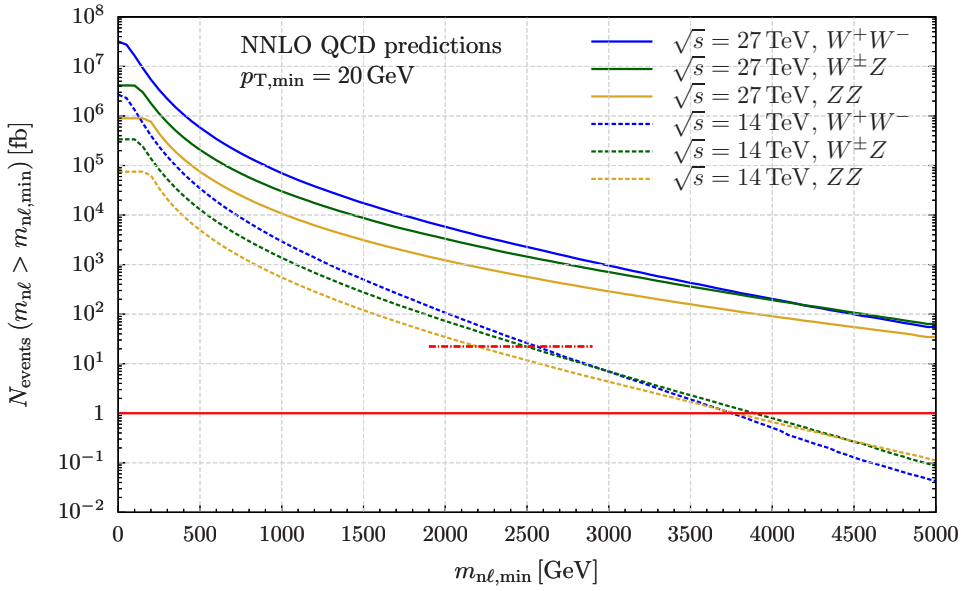

Fig. 38: Cumulative number of events as a function of $m_{n\ell,\mathrm{min}}$ for the following production processes: W^+W^- (blue), $W^\pm Z$ (green), and ZZ (orange); at 14 TeV (dashed) and 27 TeV (solid).

higher luminosity, but also the enlarged phase-space available with higher energies plays an important role: Whereas the solid curves fall only by $7-8$ orders of magnitude in the range of $0\,\mathrm{GeV} \leq p_{\mathrm{T,min}} \leq 1000\,\mathrm{GeV}$, the dashed 14 TeV curves fall by more than 9 orders of magnitude in the same region. This also explains why the 14 TeV W^+W^- result, which has a much larger inclusive cross section, crosses the red one-event line at almost the same point as the 27 TeV ZZ result.

In Fig. 38 the reach of the three vector-boson pair production processes is considered for future LHC upgrades in the invariant-mass distributions of all produced charged leptons. A scenario is chosen where $p_{\mathrm{T,min}}$, defined as before in the three processes, is 20 GeV in order to have at least a rough definition of the fiducial phase-space. The expected number of events, assuming the same integrated luminosities as stated above, is shown for $\sqrt{s} = 14\,\mathrm{TeV}$ (dashed) and $\sqrt{s} = 27\,\mathrm{TeV}$ (solid) with a lower cut $m_{n\ell} > m_{n\ell,\mathrm{min}}$, where n is the number of leptons in the respective process, i.e., for W^+W^- production it is the distribution in $m_{2\ell}$ (blue), for $W^\pm Z$ it is the one in $m_{3\ell}$ (green), and for ZZ in $m_{4\ell}$ (orange). The significant reach in energy for both the HL run of the LHC and a potential HE upgrade is evident, where “reach" refers to the point where the curves cross the red horizontal one-event threshold. A resonance in the tails of the invariant masses of two leptons (plus missing transverse momentum) or of four leptons is indeed a realistic signature predicted by many BSM theories. While with the current Run-2 data (red, dash-dotted line crossing the 14 TeV results) searches can hardly pass the two TeV frontier, future LHC upgrades will probe mass scales of a few TeV at 14 TeV with $3\,\mathrm{ab}^{-1}$, or potentially even up to ten TeV at 27 TeV with $15\,\mathrm{ab}^{-1}$. It is also apparent that despite $\sigma_{W^+W^-} \gg \sigma_{W^\pm Z} \gg \sigma_{ZZ}$ holding inclusively, the point where the three lines fall below one event is much closer. This is simply caused by the fact that the phase space of the four-lepton system in ZZ production is larger than the one of the three-lepton system in $W^\pm Z$ production, where some energy is taken by the additional neutrino. An analogous interpretation applies to W^+W^- production. Furthermore, also here the significantly enlarged phase space induced by the increase in energy at 27 TeV is evident: The 27 TeV results drop by roughly $4-5$ orders of magnitude in the displayed range, while the 14 TeV ones drop by more than 6 orders.

The study is continued by analysing the importance of the additional fiducial phase space that

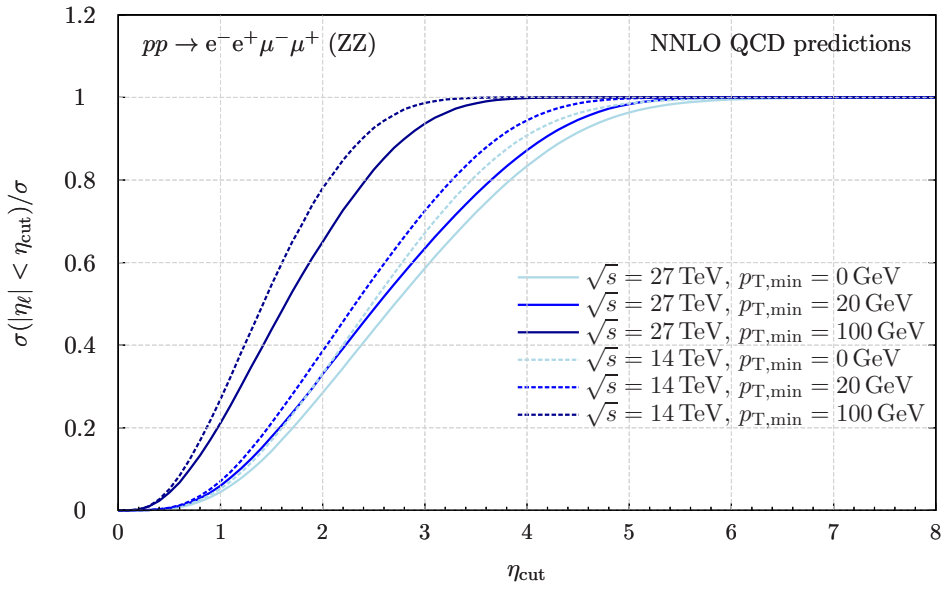

Fig. 39: Rapidity efficiency of the charged leptons.

becomes available with detector upgrades to enlarge the accessible rapidity range of charged leptons. Since very similar results were found for W^+W^-, $W^\pm Z$ and ZZ production in that respect, in Fig. 39 the rapidity efficiency of the four-lepton signature for ZZ production only is shown. The rapidity efficiency is defined as the ratio of the cross section with an absolute-rapidity cut η_{cut} on all four charged leptons, divided by the inclusive cross section. As for $\eta_{\text{cut}} \to \infty$ no cut is applied, the ratio tends to unity for large η_{cut} values. The efficiency as a function of η_{cut} is studied for three $p_{T,\text{min}}$ scenarios: inclusive (light blue), $p_{T,\text{min}} = 20\,\text{GeV}$ (blue), and $p_{T,\text{min}} = 100\,\text{GeV}$ (dark blue); at 14 TeV (dashed) and 27 TeV (solid). It is directly observed that the efficiency decreases with the machine energy. In other words, a small rapidity threshold at 27 TeV results in a much larger (relative) reduction of the cross section than at 14 TeV. This is because the additional energy induces more forward (and boosted) leptons, and it shows that detector upgrades that enlarge the measurable rapidity range become even more important at the HE LHC. Requiring minimum transverse-momentum cuts, on the other hand, has the effect of increasing the rapidity efficiency, which is particularly striking for $p_{T,\text{min}} = 100\,\text{GeV}$. The reason for this is simple: Leptons with high transverse momentum are predominantly produced at central rapidities.

The scenario with $p_{T,\text{min}} = 20\,\text{GeV}$ provides the most realistic fiducial setup, which is actually not much different from the fully inclusive case, and is discussed here. Typical rapidity cuts on charged leptons with the current LHC detectors are of the order of $\eta_\ell = 2.5$. Future detector upgrades for the HL phase of the LHC can be expected to reach rapidities at the level of $\eta_\ell = 4$. At 14 (27) TeV this would allow us to improve measurements of fiducial cross from a $<60\%$ ($\sim 50\%$) efficiency for $\eta_{\text{cut}} = 2.5$ to a $>90\%$ ($\lesssim 90\%$) efficiency for $\eta_{\text{cut}} = 4$. This implies that the available inclusive cross section will be hardly reduced by fiducial rapidity requirements anymore once the detectors have been upgraded. This statement holds even more when considering scenarios with boosted leptons: For $p_{T,\text{min}} = 100\,\text{GeV}$ the efficiency is practically 100% for $\eta_{\text{cut}} = 4$.

4.4.3 *Projections for measurements of anomalous 3-gauge boson couplings*[19]

The sensitivity of the production of W^+W^- pairs to anomalous gauge boson and anomalous fermion couplings at future LHC upgrades is now discussed. The $SU(2) \times U(1)$ structure of the electroweak sector of the Standard Model determines the W^+W^-V interactions ($V = \gamma, Z$). The amplitudes for the production of W^+W^- pairs involve subtle cancellations between contributions that grow with energy, so the pair production of gauge bosons is extremely sensitive to new physics interactions. Assuming C and P conservation, the most general Lorentz invariant $3-$gauge boson couplings can be written as in Ref. [445, 446]

$$\begin{aligned}\mathcal{L}_V &= -ig_{WWV}\Big\{(1+\delta g_1^V)\left(W^+_{\mu\nu}W^{-\mu}V^{\nu} - W^-_{\mu\nu}W^{+\mu}V^{\nu}\right) + (1+\delta\kappa^V)W^+_{\mu}W^-_{\nu}V^{\mu\nu}) \\ &\quad + \frac{\lambda^V}{M_W^2}W^+_{\rho\mu}W^{-\mu}{}_{\nu}V^{\nu\rho}\Big\}, \end{aligned} \tag{20}$$

where $V = \gamma, Z$, $g_{WW\gamma} = e$, $g_{WWZ} = g\cos\theta_W$, $s_W \equiv \sin\theta_W$, $c_W \equiv \cos\theta_W$, and in the SM, $\delta g_1^V = \delta\kappa^V = \lambda^V = 0$. Because of gauge invariance, this form can be translated into the language of effective field theory, where δg_1^V, $\delta\kappa^V$, $\lambda^V \sim \frac{v^2}{\Lambda^2}$, with Λ the scale of BSM physics, $\Lambda \gg v$.

The effective couplings of fermions to gauge fields are parameterised as,

$$\begin{aligned}\mathcal{L} &= \frac{g}{c_W}Z_\mu\left[g_L^{Zq} + \delta g_L^{Zq}\right]\bar{q}_L\gamma_\mu q_L + g_Z Z_\mu\left[g_R^{Zq} + \delta g_R^{Zq}\right]\bar{q}_R\gamma_\mu q_R \\ &\quad + \frac{g}{\sqrt{2}}\left\{W_\mu\left[(1+\delta g_L^W)\bar{q}_L\gamma_\mu q'_L + \delta g_R^W\bar{q}_R\gamma_\mu q'_R\right] + h.c.\right\}, \end{aligned} \tag{21}$$

where Q_q is the electric charge of the quarks, and q denotes up-type or down-type quarks. The anomalous fermion couplings also scale as $\delta g_{L,R}^{Zq}, \delta g_{L,R}^W \sim \frac{v^2}{\Lambda^2}$. The SM quark couplings are $g_R^{Zq} = -s_W^2 Q_q$ and $g_L^{Zq} = T_3^q - s_W^2 Q_q$ with $T_3^q = \pm\frac{1}{2}$. $SU(2)$ invariance relates the coefficients, $\delta g_L^W = \delta g_L^{Zf} - \delta g_L^{Zf'}$, $\delta g_1^Z = \delta\kappa^Z + \frac{s_W^2}{c_W^2}\delta\kappa^\gamma$ and $\lambda^\gamma = \lambda^Z$, where f denotes up-type quarks and f' down-type quarks.

The anomalous 3-gauge boson and fermion couplings have been implemented into the POWHEG BOX framework [447–449] for W^+W^- production and samples of events are generated with $pp \to W^+W^- \to \mu^\pm e^\mp \nu\nu$. Fits to 8 TeV data [450, 451] illustrate the importance of including both anomalous fermion and 3-gauge boson couplings. The sensitivity to anomalous couplings results almost entirely from contributions quadratic in the anomalous couplings and the effects of anomalous 3-gauge boson and fermion couplings are numerically similar.

To probe the sensitivity to anomalous couplings, events are generated using the cuts

$$p_{\rm T}^l > 30\ {\rm GeV},\ |\ \eta^l\ | < 2.5,\ m_{ll} > 10\ {\rm GeV}, E_{\rm T}^{\rm miss} > 20\ {\rm GeV}\,. \tag{22}$$

These cuts are similar to those applied in the ATLAS [452] and CMS [453] extractions of anomalous coupling limits using the 8 TeV data. A hypothetical future systematic uncertainty of $\delta_{sys} = 16\%$ is postulated and a cut on the $p_{\rm T}$ of the leading lepton applied such that the systematic error is smaller than the statistical error, $\delta_{stat} = \frac{1}{\sqrt{L\sigma(p_{l,T}^{lead} > p_{\rm T}^{cut})}} > \delta_{sys}$,where L is the integrated luminosity. The integrated cross section above a $p_{\rm T}^{cut}$ is evaluated, assuming a 50 % efficiency and the cuts set as

$$27\ {\rm TeV\ with}\ 15\,{\rm ab}^{-1}:\ \ p_{\rm T}^{cut} = 750\ {\rm GeV}, \qquad 14\ {\rm TeV\ with}\ 3\,{\rm ab}^{-1}: p_{\rm T}^{cut} = 1350\ {\rm GeV}\,. \tag{23}$$

[19] Contribution by J. Baglio, S. Dawson and I. M. Lewis.

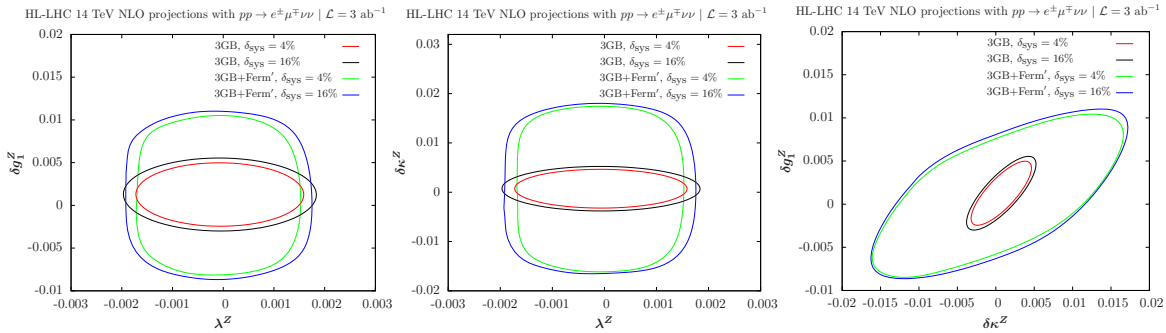

Fig. 40: Projections for 14 TeV with 3 ab^{-1}. $p_{\mathrm{T},cut} = 750$ GeV, corresponding to $\delta_{stat} = 16\%$ with $\delta_{sys} = 4\%$ and $\delta_{sys} = 16\%$. The curves labelled 3GB have SM Z-fermion couplings, while the curves labelled 3GB +Ferm' allow the Z-fermion couplings to vary around a central value of 0.

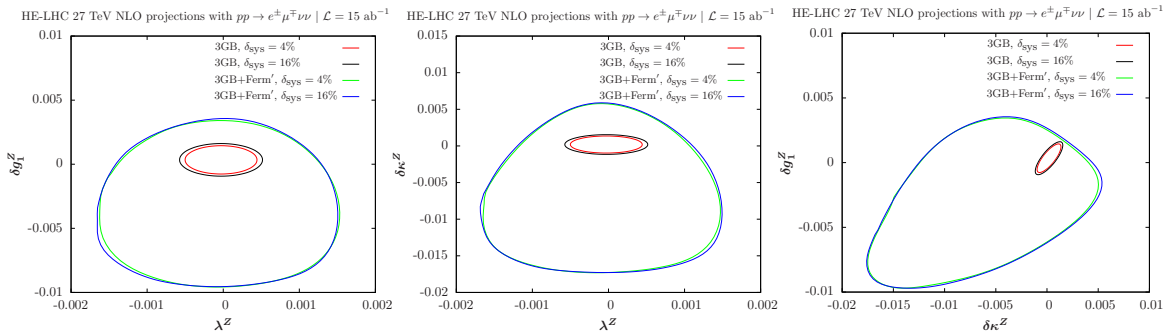

Fig. 41: Projections for 27 TeV with 15 ab^{-1}. $p_{\mathrm{T},cut} = 1350$ GeV, corresponding to $\delta_{stat} = 16\%$ with $\delta_{sys} = 4\%$ and $\delta_{sys} = 16\%$. The curves labelled 3GB have SM Z-fermion couplings, while the curves labelled 3GB +Ferm' allow the Z-fermion couplings to vary around a central value of 0.

The calculations are performed at NLO QCD, using CT14qed-inc-proton PDFs, and the renormalisation/factorisation scales are taken to be to be $M_{WW}/2$. It is assumed the $Wl\nu$ couplings in the decays are SM-like.

The results of the scans are shown in Figs. 40 and 41; the allowed regions are within the ellipses. A significant improvement going from 14 TeV to 27 TeV is seen, while the improvement from reducing the systematic error, $\delta_{sys} = 0.16 \to 0.04$, is marginal. The fermion couplings are allowed to vary around 0, assuming the 2σ errors from fits to LEP data. As can be seen, by including the anomalous fermion couplings, the sensitivity of the scan is significantly reduced [449, 450, 454]. This effect is quite pronounced at 27 TeV and implies that global fits to both anomalous fermion and 3 gauge boson couplings are necessary.

4.4.4 Prospects for the measurement of the W-boson mass

Special low pile-up proton-proton collision data at the HL-LHC (and HE-LHC) will be of large interest for W boson physics. At $\sqrt{s} = 14$ TeV and for an instantaneous luminosity of $\mathcal{L} \sim 5 \times 10^{32}$ cm^{-2}s^{-1}, corresponding to two collisions per bunch crossing on average, about $2{\times}10^6$ W boson events can be collected in one week. Such a sample provides a statistical sensitivity at the permille level for cross section measurements, at the percent level for measurements of the W boson transverse momentum distribution, and of about 10 MeV for a measurement of m_W. The increased acceptance provided by the new inner detector in ATLAS, the ITk [281], extends the coverage in pseudorapidity from $|\eta| < 2.5$ to

$|\eta| < 4$ and allows further constraints on the parton density functions (PDFs) from cross section measurements, reducing the corresponding uncertainties in the measurement of m_W. An energy increase at the HE-LHC to $\sqrt{s} = 27$ TeV [455] could play a similar role. A first quantitative study of the potential improvement in the W-boson mass using low pile-up data at the HL-LHC and HE-LHC is discussed in [456] considering only statistical and PDF uncertainties. Experimental systematic uncertainties can be maintained at a level similar to the statistical uncertainty, since they are largely dominated by the statistics of the low pile-up samples. Other theoretical uncertainties in the modelling of the W-boson production, like the description of the boson transverse momentum distribution, will also be constrained by measurements using these data.

Leptonic W boson decays are characterised by an energetic, isolated electron or muon, and significant missing transverse momentum reflecting the decay neutrino. The hadronic recoil, u_{T}, is defined from the vector sum of the transverse momenta of all reconstructed particles in the event excluding the charged lepton, and provides a measure of the W boson transverse momentum. The lepton transverse momentum, p_{T}^{ℓ}, the missing transverse momentum, $E_{\mathrm{T}}^{\mathrm{miss}}$, and the hadronic recoil are related through $\vec{E}_{\mathrm{T}}^{\mathrm{miss}} = -(\vec{p}_{\mathrm{T}}^{\ell} + \vec{u}_{\mathrm{T}})$. The p_{T}^{ℓ} and $E_{\mathrm{T}}^{\mathrm{miss}}$ distributions have sharp peaks at $p_{\mathrm{T}}^{\ell} \sim E_{\mathrm{T}}^{\mathrm{miss}} \sim m_W/2$. The transverse mass m_{T}, defined as $m_{\mathrm{T}} = \sqrt{2p_{\mathrm{T}}^{\ell}E_{\mathrm{T}}^{\mathrm{miss}}\cos(\phi_{\ell} - \phi_{\mathrm{miss}})}$, peaks at $m_{\mathrm{T}} \sim m_W$.

Events are generated at $\sqrt{s} = 14$ and 27 TeV using the W_EW_BMNNP process [136] of the POWHEG v1 event generator [314], with electroweak corrections switched off. The CT10 PDF set [457] is used, and parton shower effects are included using the PYTHIA v8 event generator [149] with parameters set according to the AZNLO tune [458]. Final-state QED corrections are applied using PHOTOS [459]. The energy resolutions of the lepton and hadronic recoil are parameterised as a function of the truth-related observables in order to emulate detector effects. These parameterised resolutions are checked against simulated distributions at the reconstructed level, and they agree at the level of a few percent.

Events are selected by applying the following cuts to the object kinematics, after resolution corrections: $p_{\mathrm{T}}^{\ell} > 25$ GeV, $E_{\mathrm{T}}^{\mathrm{miss}} > 25$ GeV, $m_{\mathrm{T}} > 50$ GeV and $u_{\mathrm{T}} < 15$ GeV; $|\eta_{\ell}| < 2.4$ or $2.4 < |\eta_{\ell}| < 4$. The first set of cuts selects the range of the kinematic peaks of the W boson decay products, restricting to the region of small p_{T}^{W} to maximise the sensitivity of the distributions to m_W. Two pseudorapidity ranges are considered, corresponding to the central region accessible with the current ATLAS detector, and to the forward region accessible in the electron channel with the ITk.

The Monte Carlo samples are produced using the CT10 PDF set, $m_W^{\mathrm{ref}} = 80.399$ GeV, and the corresponding Standard Model prediction for Γ_W. Kinematic distributions for the different values of m_W are obtained by applying an event weight to the reference samples based on the ratio of the Breit–Wigner densities corresponding to m_W and m_W^{ref}, for a given value of the final state invariant mass. A similar event weight, calculated internally by POWHEG and corresponding to the ratio of the event cross sections predicted by CT10 and several alternate PDFs, is used to obtain final state distributions corresponding to the CT14 [199], MMHT2014 [200], HL-LHC [298] and LHeC [460] PDF sets and their associated uncertainties. Compared to current sets such as CT14 and MMHT2014, the HL-LHC set incorporates the expected constraints from present and future LHC data; it starts from the PDF4LHC convention [195] and comes in three scenarios corresponding to more or less optimistic projections of the experimental uncertainties. The LHeC PDF set represents the impact of a proposed future high-energy, high-luminosity ep scattering experiment [461] on the uncertainties in the proton structure, using the theoretically best understood process for this purpose.

The shift in the measured value of m_W resulting from a change in the assumed PDF set is estimated as follows. Considering a set of template distributions obtained for different values of m_W and a given reference PDF set, and "pseudo-data" distributions obtained for $m_W = m_W^{\mathrm{ref}}$ and an alternate set i (representing, for example, uncertainty variations with respect to the reference set), the preferred value

of m_W for this set is determined by minimising the χ^2 between the pseudo-data and the templates. The preferred value is denoted m_W^i, and the corresponding variation is defined as $\delta m_W^i = m_W^i - m_W^{\text{ref}}$. The statistical uncertainty on the measurement is estimated from the half width of the χ^2 function one unit above the minimum.

The present study considers measurements of m_W in separate categories, corresponding to W^+ and W^- events; five pseudorapidity bins, $|\eta_\ell| < 0.6$, $0.6 < |\eta_\ell| < 1.2$, $1.2 < |\eta_\ell| < 1.8$, $1.8 < |\eta_\ell| < 2.4$, and $2.4 < |\eta_\ell| < 4$; p_{T}^ℓ and m_{T} distribution fits; and two centre-of-mass energies ($\sqrt{s} = 14$ and 27 TeV). For each category α and for the PDF sets considered here, the Hessian uncertainty corresponding to a given set is estimated as $\delta m_{W\alpha}^+ = \left[\sum_i \left(\delta m_{W\alpha}^i\right)^2\right]^{1/2}$, if $\delta m_{W\alpha}^i > 0$, and as $\delta m_{W\alpha}^- = \left[\sum_i \left(\delta m_{W\alpha}^i\right)^2\right]^{1/2}$, if $\delta m_{W\alpha}^i < 0$, where i runs over the uncertainty sets, and $\delta m_{W\alpha}^i$ is calculated with respect to the reference PDF set. For CT10 and CT14, the uncertainties are divided by a factor 1.645 to match the 68% CL. Only symmetrised uncertainties, $\delta m_{W\alpha} = (\delta m_{W\alpha}^+ + \delta m_{W\alpha}^-)/2$, are considered for simplicity. The correlation of PDF uncertainties between different measurement categories is calculated as $\rho_{\alpha\beta} = \frac{\sum_i \delta m_{W\alpha}^i \delta m_{W\beta}^i}{\delta m_{W\alpha} \delta m_{W\beta}}$.

PDF variations generate correlated variations in the p_{T}^W and p_{T}^Z distributions, while the latter are strongly constrained by experimental data [458, 462]. These constraints were used in the ATLAS measurement of m_W [189], bringing significant reduction in the PDF uncertainties. The uncertainties estimated here are thus conservative from this perspective, and partly account for uncertainties in the p_{T}^W distribution.

The overall measurement precision is evaluated by combining the results obtained in the different categories using the BLUE prescription [463]. Only statistical and PDF uncertainties are considered. The former are assigned assuming an integrated luminosity of 200 pb^{-1}, and normalising the samples to the expected cross-sections. The expected measurement uncertainties, together with their statistical and PDF components, are summarised in Fig. 42 (a) for CT10. The numbers quoted for $0 < |\eta_\ell| < 2.4$ correspond to the combination of the four pseudorapidity bins in this range. Moderate or negative PDF uncertainty correlations, leading to reduced combined uncertainties, are observed between categories of different W-boson charges, and between central and forward pseudorapidities, at given $\sqrt{s}$. On the other hand, PDF uncertainty correlations tend to be large and positive between $\sqrt{s} = 14$ and 27 TeV, for a given boson charge and lepton pseudorapidity range. With 200 pb^{-1} of data collected at each energy, a total uncertainty of about 10 MeV is obtained.

Table 25 and Fig. 42 (b) compare the uncertainties obtained for different PDF sets. The CT10 and CT14 sets display similar uncertainty correlations, leading to similar improvements under combination of categories, and yielding comparable final PDF uncertainties. The MMHT2014 uncertainties are about 30% lower. The three projected HL-LHC PDF sets give very similar uncertainties; the most conservative one is shown here. Compared to CT10 and CT14, a reduction in PDF uncertainty of about a factor of two is obtained. The LHeC projection results from a QCD fit to 1 ab^{-1} of ep scattering pseudodata, with $E_e = 60$ GeV and $E_p = 7$ TeV. Such a sample could be collected in about five years, synchronously with the HL-LHC operation. In this configuration, the neutral- and charged-current DIS samples are sufficient to disentangle the first and second generation parton densities without ambiguity, and reduce the PDF uncertainty below 2 MeV, a factor 5–6 compared to present knowledge. Also in this case the m_W measurement will benefit from the large W boson samples collected at the LHC, and from the anti-correlation between central and forward categories. In this context, PDF uncertainties would still be sub-leading with 1 fb^{-1} of low pile-up data.

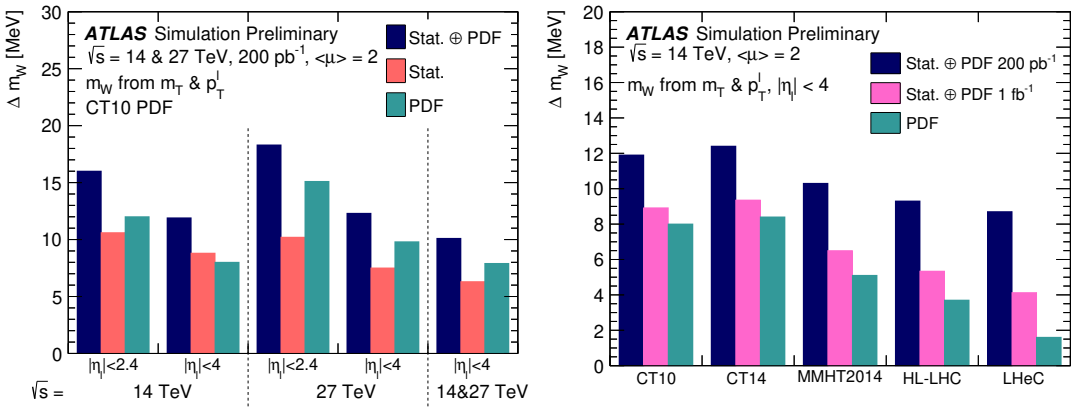

(a) (b)

Fig. 42: Measurement uncertainty for combined fits to the p_{T}^{ℓ} and m_{T} distributions (a) in different lepton acceptance regions and for different centre-of-mass energies, using the CT10 PDF set and for 200 pb^{-1}collected at each energy and (b) for different PDF sets in $|\eta_{\ell}| < 4$, for 200 pb^{-1}and 1 fb^{-1}collected at $\sqrt{s} = 14$ TeV. The numbers quoted for $0 < |\eta_{\ell}| < 2.4$ correspond to the combination of the four pseudorapidity bins in this range.

Table 25: Measurement uncertainty for different lepton acceptance regions, centre-of-mass energies and PDF sets, combined fits to the p_{T}^{ℓ} and m_{T} distributions, and for 200 pb^{-1}collected at each energy. The numbers quoted for $0 < |\eta_{\ell}| < 2.4$ correspond to the combination of the four pseudorapidity bins in this range. In each case, the first number corresponds to the sum of statistical and PDF uncertainties, and the numbers between parentheses are the statistical and PDF components, respectively.

$\sqrt{s}$ [TeV]	Lepton acceptance	Uncertainty in m_W [MeV]		
		CT10	CT14	MMHT2014
14	$\|\eta_{\ell}\| < 2.4$	16.0 (10.6 $\oplus$ 12.0)	17.3 (11.4 $\oplus$ 13.0)	15.4 (10.7 $\oplus$ 11.1)
14	$\|\eta_{\ell}\| < 4$	11.9 (8.8 $\oplus$ 8.0)	12.4 (9.2 $\oplus$ 8.4)	10.3 (9.0 $\oplus$ 5.1)
27	$\|\eta_{\ell}\| < 2.4$	18.3 (10.2 $\oplus$ 15.1)	18.8 (10.5 $\oplus$ 15.5)	16.5 (9.4 $\oplus$ 13.5)
27	$\|\eta_{\ell}\| < 4$	12.3 (7.5 $\oplus$ 9.8)	12.7 (8.2 $\oplus$ 9.7)	11.4 (7.9 $\oplus$ 8.3)
14+27	$\|\eta_{\ell}\| < 4$	10.1 (6.3 $\oplus$ 7.9)	10.1 (6.9 $\oplus$ 7.4)	8.6 (6.5 $\oplus$ 5.5)

$\sqrt{s}$ [TeV]	Lepton acceptance	Uncertainty in m_W [MeV]	
		HL-LHC	LHeC
14	$\|\eta_{\ell}\| < 2.4$	11.5 (10.0 $\oplus$ 5.8)	10.2 (9.9 $\oplus$ 2.2)
14	$\|\eta_{\ell}\| < 4$	9.3 (8.6 $\oplus$ 3.7)	8.7 (8.5 $\oplus$ 1.6)

4.4.5 Prospects for the measurement of the effective weak mixing angle

At leading order dilepton pairs are produced through the annihilation of a quark and antiquark via the exchange of a Z boson or a virtual photon: $q\bar{q} \rightarrow Z/\gamma^{*} \rightarrow \ell^{+}\ell^{-}$. The definition of the forward-backward asymmetry, $\mathrm{A_{FB}}$, is based on the angle θ^{*} of the lepton (ℓ^{-}) in the Collins-Soper [464, 465] frame of the dilepton system:

$$\mathrm{A_{FB}} = \frac{\sigma_{\mathrm{F}} - \sigma_{\mathrm{B}}}{\sigma_{\mathrm{F}} + \sigma_{\mathrm{B}}}, \tag{24}$$

where σ_{F} and σ_{B} are the cross sections in the forward ($\cos\theta^* > 0$) and backward ($\cos\theta^* < 0$) hemispheres, respectively. In this frame the θ^* is the angle of the ℓ^- direction with respect to the axis that bisects the angle between the direction of the quark and opposite direction of the anti-quark. In pp collisions the direction of the quark is assumed to be in the boost direction of the dilepton pair. Here, $\cos\theta^*$ is calculated using laboratory-frame quantities as follows:

$$\cos\theta^* = \frac{2(p_1^+ p_2^- - p_1^- p_2^+)}{\sqrt{M^2(M^2+P_{\mathrm{T}}^2)}} \times \frac{P_{\mathrm{z}}}{|P_{\mathrm{z}}|}, \tag{25}$$

where M, P_{T}, and P_{z} are the mass, transverse momentum, and longitudinal momentum, respectively, of the dilepton system, and $p_1(p_2)$ are defined in terms of energy, $e_1(e_2)$, and longitudinal momentum, $p_{\mathrm{z},1}(p_{\mathrm{z},2})$, of the negatively (positively) charged lepton as $p_{\mathrm{i}}^{\pm} = (e_i \pm p_{\mathrm{z},i})/\sqrt{2}$ [464].

A non-zero $\mathrm{A_{FB}}$ in dilepton events arises from the vector and axial-vector couplings of electroweak bosons to fermions. At tree level, the vector v_{f} and axial-vector a_{f} couplings of Z bosons to fermions (f) are:

$$v_{\mathrm{f}} = T_3^{\mathrm{f}} - 2Q_{\mathrm{f}} \sin^2\theta_{\mathrm{W}}, \tag{26}$$

$$a_{\mathrm{f}} = T_3^{\mathrm{f}}, \tag{27}$$

where T_3^{f} and Q_{f} are the third component of the weak isospin and the charge of the fermion, respectively, and $\sin^2\theta_{\mathrm{W}}$ is the weak mixing angle, which is related to the masses of the W and Z bosons by the relation $\sin^2\theta_{\mathrm{W}} = 1 - M_{\mathrm{W}}^2/M_{\mathrm{Z}}^2$. Electroweak radiative corrections affect these leading-order relations. An effective weak mixing angle, $\sin^2\theta_{\mathrm{eff}}^{\mathrm{f}}$, is defined based on the relation between these couplings: $v_{\mathrm{f}}/a_{\mathrm{f}} = 1 - 4|Q_{\mathrm{f}}|\sin^2\theta_{\mathrm{eff}}^{\mathrm{f}}$, with $\sin^2\theta_{\mathrm{eff}}^{\mathrm{f}} = \kappa_{\mathrm{f}}\sin^2\theta_{\mathrm{W}}$, where flavour-dependent κ_{f} is determined by electroweak corrections. Consequently, precise measurements of $\mathrm{A_{FB}}$ can be used to extract the effective leptonic weak mixing angle ($\sin^2\theta_{\mathrm{eff}}^{\mathrm{lept}}$).

The most precise previous measurements of $\sin^2\theta_{\mathrm{eff}}^{\mathrm{lept}}$ were performed by the LEP and SLD experiments [466]. There is, however, a known tension of about 3 standard deviations between the two most precise measurements. Measurements of $\sin^2\theta_{\mathrm{eff}}^{\mathrm{lept}}$ have also been performed by the LHC and Tevatron experiments [467–472].

In measurements of $\mathrm{A_{FB}}$ (or associated angular variables) in leptonic decays of Z bosons at a pp collider, the assignment of the z-axis is crucial. At low rapidities, there is a two-fold ambiguity in the direction of the initial state quark and anti-quark; the colliding quark is equally likely to be in either proton and the parton level asymmetry is diluted. However, at higher rapidities, the Z boson tends to be produced in the direction of travel of the quark, since the (valence) quark tends to be at higher Bjorken-x than the anti-quark. This means that the dilution between parton level and proton level quantities is significantly smaller at larger rapidities, illustrated in Fig. 43, and a larger forward-backward asymmetry is induced. Consequently, the forward acceptance of LHCb, in addition to the increased forward coverage of the ATLAS and CMS detectors, will be crucial to achieving the most precise measurement of $\sin^2\theta_{\mathrm{eff}}^{\mathrm{lept}}$ possible at the HL-LHC.

The uncertainties on the parton distribution functions translate into sizeable variations in the observed $\mathrm{A_{FB}}$ values, which have limited the precision of current measurements of $\sin^2\theta_{\mathrm{eff}}^{\mathrm{lept}}$ at the LHC. However, the changes in PDFs affect the $\mathrm{A_{FB}}(M_{\ell\ell}, Y_{\ell\ell})$ distribution in a different way from changes in $\sin^2\theta_{\mathrm{eff}}^{\mathrm{lept}}$. Because of this behaviour, the distribution of $\mathrm{A_{FB}}$ can itself be used to constrain the PDF uncertainties on the extraction of $\sin^2\theta_{\mathrm{eff}}^{\mathrm{lept}}$ using either a Bayesian χ^2 reweighting method [473–475] (in the case of PDFs with Monte Carlo replicas) or through a profiling procedure [476] (in the case of PDFs with Hessian error sets).

Prospects for the measurement of the effective weak mixing angle using the forward-backward asymmetry, $\mathrm{A_{FB}}$, in Drell-Yan di-lepton events at the HL-LHC at ATLAS [477], CMS [478] and LHCb [479]

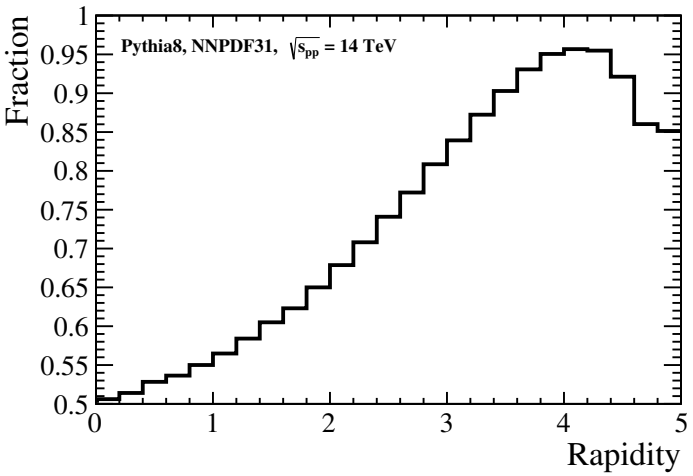

Fig. 43: The fraction of events where the Z boson travels in the same direction along the z-axis as the colliding quark, in proton-proton collisions with $\sqrt{s} = 14$ TeV. This increases as the event becomes more forward, reaching a maximum in the region probed by LHCb. The decrease once the rapidity is greater than 4 is because the fraction of collisions involving valence quarks decreases (the Bjorken-x value of the high momentum quark in these collisions is typically greater than 0.3). No detector effects are simulated for this figure.

have been performed and are reported here. The leptonic effective weak mixing angle is extracted from measurements of $\mathrm{A_{FB}}$ in dilepton events by minimising the χ^2 value between the simulated data and template $\mathrm{A_{FB}}$ distributions representing different $\sin^2\theta^{\mathrm{lept}}_{\mathrm{eff}}$ values and PDF variations. The LHCb and CMS analyses consider the dimuon final state, while the ATLAS analysis considers the dielectron final state. For CMS and LHCb the samples and different $\sin^2\theta^{\mathrm{lept}}_{\mathrm{eff}}$ templates are generated at next-to-leading order using the POWHEG event generator [480–483], where the NNPDF3.0 [484] PDF set is used in the case of the CMS analysis, and the NNPDF3.1 PDF set [207] for LHCb. For CMS, the analysis is performed at generator level without the effect of smearing due to detector effects[20] while for LHCb, a smearing is performed where the momentum resolution and reconstruction efficiency is assumed to be similar to the performance of the current detector [485]. In the case of ATLAS, events are generated with POWHEG and overlaid with additional inelastic pp collisions per bunch-crossing simulated with PYTHIA. Parameterisations of the expected ATLAS detector performances during the HL-LHC runs [486] are then applied on particle-level objects to emulate the detector response. Lepton trigger and identification efficiencies are derived as a function of η and p_{T} and used to estimate the likelihood of a given lepton to fulfil either the trigger or identification requirements, which have been optimised for the level of pile-up expected at the HL-LHC [405]. The $\mathrm{A_{FB}}$ distributions are generated, at leading order (LO) in QCD, with DYTURBO, an optimised version of DYRES/DYNNLO [487] with NNLO CT14 PDF and the world average value for $\sin^2\theta^{\mathrm{lept}}_{\mathrm{eff}} = 0.23153$.

The HL-LHC CMS detector will extend the pseudorapidity, η, coverage of the muon reconstruction from the current configuration of 2.4 to 2.8. In the CMS analysis an event is selected if there are at least two muons with $|\eta| < 2.8$ and with the leading p_{T} muon $p_{\mathrm{T}} > 25$ GeV and the second leading muon $p_{\mathrm{T}} > 15$ GeV. Figure 44 shows the $\mathrm{A_{FB}}$ distributions in bins of dimuon mass and rapidity for different energies and pseudorapidity acceptances. As expected, at higher centre-of-mass energies the observed $\mathrm{A_{FB}}$ is smaller because the interacting partons have smaller x-values which results in a smaller fraction of dimuon events produced by the valence quarks, which also means more dilution. The samples are normalised to the integrated luminosities of 19 fb^{-1} for $\sqrt{s} = 8$ TeV and to 10 – 3000 fb^{-1}

[20] A comparison of 8 TeV predictions and measured values suggests the effect is not significant.

for $\sqrt{s} = 14$ TeV samples and the simulated data are shown for $\sqrt{s} = 8$ TeV and $\sqrt{s} = 14$ TeV for two different selection requirements, $|\eta| < 2.4$ and 2.8. Extending the pseudorapidity acceptance significantly increases the coverage for larger x-values in the production and reduces both the statistical and PDF uncertainties, as shown below.

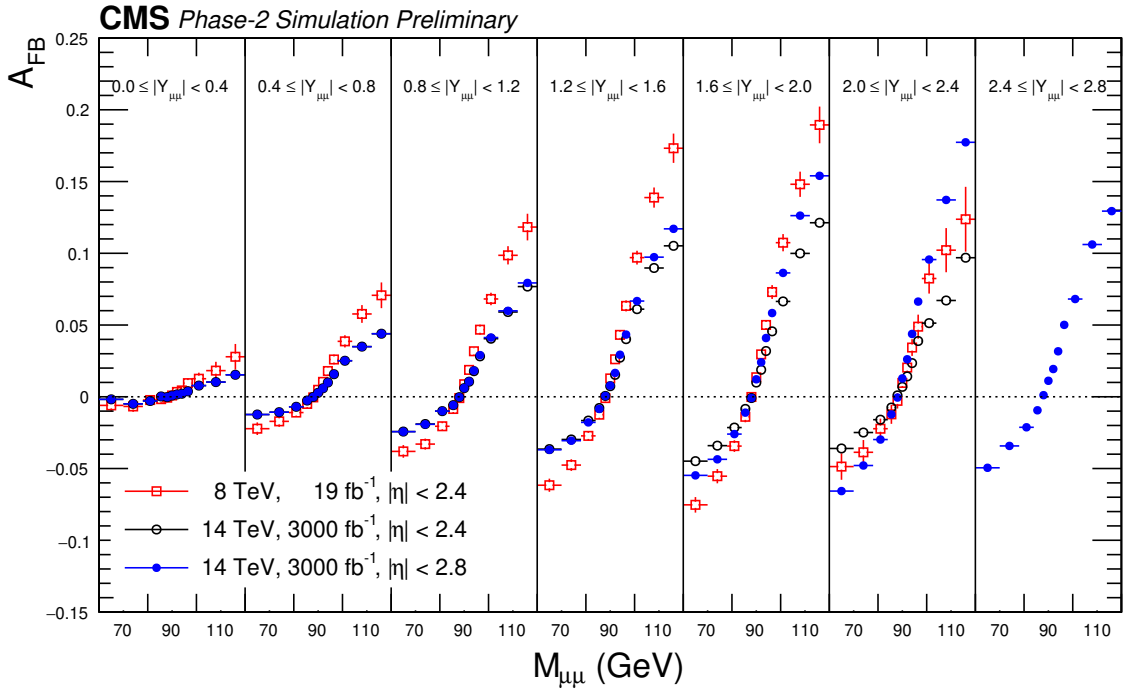

Fig. 44: Forward-backward asymmetry distribution, $\mathrm{A_{FB}}(M_{\mu\mu}, Y_{\mu\mu})$, in dimuon events at $\sqrt{s} = 8$ TeV and 14 TeV. The distributions are made with POWHEG event generator using NNPDF3.0 PDFs and interfaced with PYTHIA v8 for parton-showering, QED final-state radiation (FSR) and hadronization. Following acceptance selections are applied to the generated muons after FSR: $|\eta| < 2.4$ (or $|\eta| < 2.8$), $p_{\mathrm{T}}^{\mathrm{lead}} > 25$ GeV, $p_{\mathrm{T}}^{\mathrm{trail}} > 15$ GeV. The error bars represent the statistical uncertainties for the integrated luminosities corresponding to 19 fb^{-1} at $\sqrt{s} = 8$ TeV and 3000 fb^{-1} at $\sqrt{s} = 14$ TeV.

In the case of the 14 TeV analysis with a large number of events (> 200 fb^{-1}), the pseudo-data are too precise to estimate the PDF uncertainties with the Bayesian reweighting approach because the replica distributions are too sparse compared to the statistical uncertainties. Therefore, the PDF uncertainties after the Bayesian reweighting are estimated by extrapolating from the lower values of integrated luminosities.

The corresponding values for various luminosities at CMS are summarized in Table 26. One can see from the table that with the extended pseudorapidity coverage of $|\eta| < 2.8$, the statistical uncertainties are reduced by about 30% and the PDF uncertainties are reduced by about 20%, compared to $|\eta| < 2.4$ regardless of the target integrated luminosity and for both nominal and constrained PDF uncertainties.

The LHCb detector has coverage in the pseudorapidity range $2 < \eta < 5$ and expects to install its 'Upgrade II' in Long Shutdown 4. Following this upgrade, LHCb will collect at least 300 fb^{-1} of data, allowing high precision measurements. The forward acceptance of LHCb brings a number of benefits in measurements of $\sin^2\theta_{\mathrm{eff}}^{\mathrm{lept}}$ at the LHC. The lower level of dilution in the forward region results in a larger sensitivity to $\sin^2\theta_{\mathrm{eff}}^{\mathrm{lept}}$ and the PDF effects are (in relative terms) smaller, providing both statistical precision in measurements of the weak mixing angle and a reduction in PDF uncertainties. In addition, LHCb does not simply probe forward rapidities of the Z boson: the leptons themselves are located over

Table 26: Statistical, nominal NNPDF3.0, and constrained NNPDF3.0 uncertainties of the extracted $\sin^2\theta^{\text{lept}}_{\text{eff}}$ value at CMS at 14 TeV for muon acceptances of $|\eta| < 2.4$ and $|\eta| < 2.8$ and for different values of integrated luminosity. For comparison, results of the 8 TeV estimate of this analysis are compared to the results obtained from 8 TeV measurement [488].

L_{int}	$\delta_{\text{stat}}[10^{-5}]$		$\delta^{\text{nominal}}_{\text{nnpdf3.0}}[10^{-5}]$		$\delta^{\text{constrained}}_{\text{nnpdf3.0}}[10^{-5}]$	
(fb^{-1})	$\|\eta\| < 2.4$	$\|\eta\| < 2.8$	$\|\eta\| < 2.4$	$\|\eta\| < 2.8$	$\|\eta\| < 2.4$	$\|\eta\| < 2.8$
10	76	51	75	57	39	29
100	24	16	75	57	27	20
500	11	7	75	57	20	16
1000	8	5	75	57	18	14
3000	4	3	75	57	15	12
19	43		49		27	
19 (from [488])	44		54		32	

a significant range of rapidities, allowing extremal values of $\cos\theta^*$ to be probed, increasing sensitivity to the weak mixing angle. Finally, LHCb has the ability to select events at low momentum using a flexible full software trigger and real time analysis scheme (from Run-3 onwards). It is therefore foreseen that the LHCb Upgrade II will be able to select Z boson decays where one lepton has transverse momentum above 20 GeV, while the other lepton has a transverse momentum above 5 GeV. Such low thresholds again increase the sensitivity to asymmetric events at high $|\cos\theta^*|$. In addition to the advantages of the extended forward acceptance for such measurements, as part of Upgrade II LHCb is expected to undergo a significant calorimeter upgrade[21] allowing similar precision to be achieved in both the dielectron and dimuon final states.

LHCb has performed a study of projected sensitivities, considering the dimuon final state. The experiment is assumed to have coverage in the region $2.0 < \eta < 5$. Toy measurements of the forward-backward asymmetry are used to determine the sensitivity of measurements at LHCb Upgrade II to the weak mixing angle. Only statistical uncertainties are considered alongside the effects of knowledge of PDFs. The statistical uncertainty on $\sin^2\theta^{\text{lept}}_{\text{eff}}$ is expected to be below 5×10^{-5} with 300 fb^{-1} of data. The expected PDF uncertainty from current PDF knowledge is $\sim 20 \times 10^{-5}$, but with Bayesian reweighting this can be reduced to the level of about 10×10^{-5} (with analysis of a dataset corresponding to an integrated luminosity of 300 fb^{-1}). This reduction assumes systematic effects are negligible in comparison to statistical uncertainties, though the current knowledge of PDFs means that any measurement in the forward region is expected to offer a smaller PDF uncertainty than the total uncertainties in the previous best measurements of the weak mixing angle. The main challenge of such measurements at LHCb Upgrade II will therefore be to control systematic uncertainties in order to ensure the overall measurement also achieves high precision; however, the large dataset of J/ψ and Υ mesons to be recorded is expected to aid the understanding of effects such as the momentum scale (which introduced the largest systematic uncertainty in the Run-1 analysis at LHCb). This should enable a measurement at LHCb Upgrade II with a precision similar to or better than that achieved in the combination of measurements at LEP and SLD.

In the ATLAS analysis di-electron candidates are selected where each electron has p_{T} in excess of 25 GeV and the combined invariant mass is in the region of the Z pole. A new inner tracking system (ITk) will extend the tracking coverage of the ATLAS detector from $|\eta| \leq 2.5$ up to $|\eta| \leq 4.0$ at the HL-LHC, providing the ability to reconstruct forward charged particle tracks, which can be matched to calorimeter clusters for forward electron reconstruction. The selected data sample is split into three

[21] This upgrade will offer an extended dynamic range within the ECAL, offering improved electron momentum resolution.

channels, where both electrons are in the central region, satisfying $|\eta| < 2.47$ (the CC channel), where one electron is central and the other is forward, satisfying $2.5 < \eta < 4.2$ (the CF channel), and finally where both electrons are forward (the FF channel). Events are selected by requiring at least one electron firing the single electron trigger, except in the FF channel, where a dielectron trigger is required.

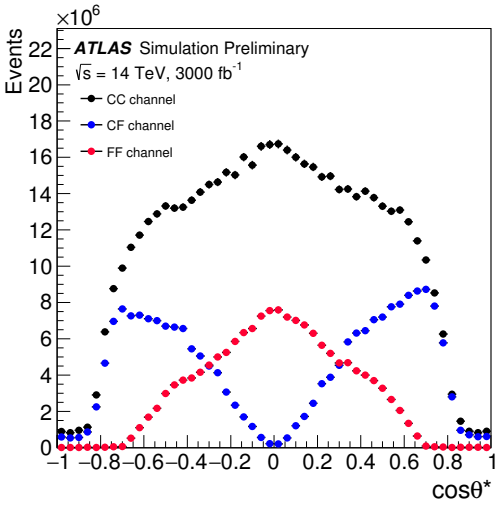

Fig. 45: The $\cos\theta^*$ distribution for CC, CF and FF channels for selected Drell-Yan di-electron events expected for 3000 fb^{-1} of data at $\sqrt{s} = 14$ TeV.

As Fig. 45 shows, the CF channel selects events at high $\cos\theta^*$ values where the forward-backward asymmetry is more pronounced, and consequently the sensitivity to $\sin^2\theta^{\text{lept}}_{\text{eff}}$ is higher in this channel. While the LHCb and CMS analyses consider only uncertainties due to statistics and PDFs, the ATLAS analysis considers also various sources of experimental uncertainty which affect the precision of the extraction of A_{FB}. The main contributions arise from the limited knowledge of the momentum scale and resolution of the electrons, and the background contributions, which are mostly relevant in the CF and FF channels.

The extraction of $\sin^2\theta^{\text{lept}}_{\text{eff}}$ is performed by minimising the χ^2 value comparing particle-level A_{FB} distributions with different weak mixing angle hypotheses in invariant mass and rapidity bins combining the CC, CF and FF channels. A global fit is performed where $\sin^2\theta^{\text{lept}}_{\text{eff}}$ is extracted while constraining the PDF uncertainties using a profiling procedure following that used in a previous ATLAS publication [489] and implemented in the xFitter package [490].

With this analysis, a significant reduction of the light quark uncertainties at low x is seen and combining the three channels together, the measurement reaches a precision of $18{\cdot}10^{-5}$ ($\pm 16{\cdot}10^{-5}$ (PDF) $\pm 9{\cdot}10^{-5}$ (exp.)). The uncertainty of the results remains dominated by the limited knowledge of the PDFs.

In the context of the Yellow Report for the HL-LHC, prospect PDF fits including HL-LHC pseudo-data of future PDF-sensitive measurements from ATLAS, CMS and LHCb were performed (see Sec. 5.2). Three prospect PDF scenarios were considered and compared with the reference PDF set PDF4LHC15 [195]. The expected sensitivity of the $\sin^2\theta^{\text{lept}}_{\text{eff}}$ measurements with 3000 fb^{-1} at $\sqrt{s} = 14$ TeV is improved by 10-25% depending on the prospect PDFs scenario considered. In Table 27 the precision on $\sin^2\theta^{\text{lept}}_{\text{eff}}$ obtained with the "ultimate" HL-LHC PDF set is compared with the with the one obtained with CT14NNLO PDF set.

The sensitivity of the analysis to the $\sin^2\theta^{\text{lept}}_{\text{eff}}$ extraction is also estimated with a prospect PDF set including expected data from the LHeC collider [460]. In this case the PDF uncertainty is reduced by an additional factor of 5 with respect to the one obtained with the HL-LHC prospect PDFs.

Table 27: The value of $\sin^2\theta^{\text{lept}}_{\text{eff}}$ with the breakdown of uncertainties from the ATLAS preliminary results at $\sqrt{s} = 8$ TeV with $20\,\text{fb}^{-1}$ [491] is compared to the projected $\sin^2\theta^{\text{lept}}_{\text{eff}}$ measurements with $3000\,\text{fb}^{-1}$ of data at $\sqrt{s} = 14$ TeV for two PDF sets considered in this note. All the numbers values are given in units of 10^{-5}. Note that other sources of systematic uncertainties, such as the impact of the MC statistical uncertainty, evaluated in Ref. [491] are not considered in this prospect analysis. For the HL-LHC prospect PDFs the "ultimate" scenario is chosen.

	ATLAS $\sqrt{s} = 8$ TeV	ATLAS $\sqrt{s} = 14$ TeV	ATLAS $\sqrt{s} = 14$ TeV
$\mathcal{L}$ [fb^{-1}]	20	3000	3000
PDF set	MMHT14	CT14	PDF4LHC15$_{HL-LHC}$
$\sin^2\theta^{\text{lept}}_{\text{eff}}$ [$\times 10^{-5}$]	23140	23153	23153
Stat.	$\pm$ 21	$\pm$ 4	$\pm$ 4
PDFs	$\pm$ 24	$\pm$ 16	$\pm$ 13
Experimental Syst.	$\pm$ 9	$\pm$ 8	$\pm$ 6
Other Syst.	$\pm$ 13	-	-
Total	$\pm$ 36	$\pm$ 18	$\pm$ 15

To conclude, the accuracy of measurements of the weak mixing angle obtained with an analysis of A_{FB} in Z events at $\sqrt{s} = 14$ TeV with $3000\,\text{fb}^{-1}$ at ATLAS and CMS and $300\,\text{fb}^{-1}$ at LHCb at the HL-LHC exceed the precision achieved in all previous single-experiment results to date and the measurements are dominated by PDF uncertainties. To explore the full potential of the HL-LHC data it will be therefore essential to reduce PDF uncertainties. A significant improvement of the sensitivity of the measurement is observed in the ATLAS analysis when using prospect PDF sets including ancillary Drell-Yan measurements performed with the data collected during the high luminosity phase of the LHC and at the LHeC collider.

4.4.6 The global EW fit[22]

The measurement of the Higgs Boson mass (M_H) at the Large Hadron Collider (LHC) has provided the last input to the global fit of electroweak (EW) precision observables (EWPO), which can now be used to effectively constrain new physics. Moreover, the measurement of Higgs-boson production and decay rates that is at the core of the physics program of the LHC Run-2 will further constrain those interactions that directly affect Higgs-boson physics.

The HL-LHC will have the potential to provide more constraining bounds on new physics via the global fit to EWPO and Higgs data, thanks to the higher precision it will reach both in the measurement of some of the crucial input parameters of global EW fits (e.g. M_W, m_t, M_H, and $\sin^2\theta^{\text{lept}}_{\text{eff}}$), and in the measurement of Higgs-boson total and differential rates. In this study the reach of the HL-LHC in constraining new physics is explored via a global fit to EWPO. Earlier studies on the prospects for the LHC were performed in [492, 493].

In the following, details are provided first on the parameters and procedure of the global EW fit. Next the results are interpreted within the Standard Model (SM). Finally, the EW fit is used to constrain new physics beyond the SM. The results are presented for both the current data and the projections in the HL-LHC scenario.

The global fit of EWPO is performed using the HEPFIT package [494], a general tool to combine direct and indirect constraints on the SM and its extensions in any statistical framework. The default fit proce-

[22] Contribution by J. de Blas, M. Ciuchini, E. Franco, S. Mishima, M. Pierini, L. Reina, and L. Silvestrini.

dure, used here, follows a Bayesian statistical approach and uses BAT (Bayesian Analysis Toolkit) [495]. Flat priors are used for all input parameters, and the likelihoods are built assuming Gaussian distributions for all experimental measurements. The output of the fit is therefore given as the posterior distributions for each input parameters and observables, calculated using a Markov Chain Monte Carlo method.

All EWPO are calculated as a SM core plus corrections. The SM core includes all available higher-order corrections, including the latest theoretical developments in the calculation of radiative corrections to the EWPO of [496, 497].[23] New physics corrections are computed at the leading order. The HEPFIT code allows for the implementation of different models of new physics. In particular, as explained below, the study is specialised in the general framework of the so called SM effective field theory (SMEFT), where the SM Lagrangian is extended by the addition of operators of canonical mass dimension higher than four (limited to the basis of operators of canonical dimension six in this study).

As far as EWPO are concerned, this study updates the EWPO fit of Refs. [493, 498, 499], including recent updates on the theory calculations [497] and experimental measurements [190, 491, 500–506]. The uncertainties on some input parameters that have been obtained by including hadron collider data are further reduced, in order to account for the level of accuracy expected for the HL-LHC. In all these projections it is assumed that the central values for the HL-LHC measurements will not change with respect to current data. In particular the following assumptions are made:

1. The W mass, whose uncertainty obtained by combining ATLAS and Tevatron+LEP2 measurements is currently around 12 MeV [189, 507–509] could be measured at the HL-LHC with a precision of 7 MeV. This number is derived from the current estimate of the statistical plus PDF uncertainty using 1 fb^{-1} of data reported in Sec. 4.4.4, and assuming systematic errors to be of similar size to the statistical ones. In this fit a measurement of $M_W = 80.379 \pm 0.007$ GeV is therefore added to the current combination.

2. An aggressive estimate of the current uncertainty on the top-quark mass, obtained by combining current Tevatron and LHC measurements, puts the uncertainty on m_t at the level of 0.4 GeV. It will be difficult to further reduce this number at the HL-LHC, since the remaining uncertainty is mainly of systematic and theoretical origin. In the current fit $m_t = 172.8 \pm 0.4$ GeV is used.

3. The measurements of the effective angle $\sin^2\theta^{\rm lept}_{\rm eff}$ can also be improved at the HL-LHC. Currently, a combination of the latest LHC and Tevatron results returns a precision for this observable of $\sim 0.00022 - 0.00027$, depending on the assumptions made in combining common uncertainties. For the HL-LHC fit, the combination is repeated using the ATLAS projections outlined in Sec. 4.4.5 where the HL-LHC PDF set is used, corresponding to the value $\sin^2\theta^{\rm lept}_{\rm eff} = 0.23143 \pm 0.00015$.

4. The error on the Higgs-boson mass, currently around 0.20 GeV, can be reduced to 0.05 GeV [510, 511].

5. The HL-LHC should also be able to improve the current knowledge on the W width, whose precision of 42 MeV is currently given by the combination of LEP2 and Tevatron measurements. This uncertainty is dominated by the hadron collider measurement. While there is no available information about a possible determination of this quantity at the (HL-)LHC, the conservative assumption that the HL-LHC can achieve a precision on Γ_W at least as good as the one on the current average is used. An independent HL-LHC measurement of $\Gamma_W = 2.085 \pm 0.042$ GeV is therefore added. This gives a 30 MeV uncertainty when combined with the current average.

[23] The uncertainties associated to missing higher-order corrections to the SM predictions for the EWPO are also taken into account in the fits, via nuisance parameters with Gaussian priors.

Finally, apart from the improved precision of the HL-LHC measurements, the assumption is made that, by the end of the HL-LHC run, better measurements of some of the SM input parameters are possible from other experiments. In particular, following Ref. [493, 498], it is assumed that: 1) the uncertainty on $\Delta\alpha^{(5)}_{\rm had}(M_Z)$ can be reduced to $\pm 5 \times 10^{-5}$ by using data from currently ongoing and future experiments that measure the cross section for $e^+e^- \to$ hadrons, and 2) future lattice QCD measurements will provide a determination of the strong coupling constant with accuracy $\delta\alpha_S(M_Z) = \pm 0.0002$. The measurements of all other EWPO and input parameters have been kept to their currently available values. The current values of all EWPO measurements, as well as the corresponding HL-LHC projected uncertainties, are listed in the second and third columns of Table 28, respectively.

Table 28: Current experimental measurement, HL-LHC projected uncertainty, posterior, and pull for the five input parameters ($\alpha_s(M_Z)$, $\Delta\alpha^{(5)}_{\rm had}(M_Z)$, M_Z, m_t, M_H), and for the main EWPO considered in the SM fit. The pulls in the last column are obtained comparing the experimental measurements with the predictions from a fit *removing* the corresponding observable(s) (See for e.g. Ref. [493] for details.).

	Measurement	HL-LHC uncertainty	Posterior		Pull
			Current	HL-LHC	Current/HL-LHC
$\alpha_s(M_Z)$	0.1180 ± 0.0010	± 0.0002	0.1180 ± 0.0009	0.1180 ± 0.0002	$0/0.5$
$\Delta\alpha^{(5)}_{\rm had}(M_Z)$	0.027611 ± 0.000111	± 0.00005	0.02758 ± 0.00011	0.02759 ± 0.00005	$1.1/2.1$
M_Z [GeV]	91.1875 ± 0.0021		91.1880 ± 0.0020	91.1890 ± 0.0020	$-1.3/-2.6$
m_t [GeV]	172.8 ± 0.7	± 0.4	173.2 ± 0.66	173.1 ± 0.38	$-1.7/-2.9$
M_H [GeV]	125.13 ± 0.17	± 0.05	125.13 ± 0.17	125.13 ± 0.05	$1.4/3$
M_W [GeV]	80.379 ± 0.012	± 0.007	80.362 ± 0.006	80.367 ± 0.004	$1.6/2.7$
Γ_W [GeV]	2.085 ± 0.042	± 0.042	2.0885 ± 0.0006	2.0889 ± 0.0003	-0.1
$\mathrm{BR}_{W\to\ell\nu}$	0.1086 ± 0.0009		0.10838 ± 0.00002	0.10838 ± 0.000005	0.2
$\mathrm{BR}_{W\to\mathrm{had}}$	0.6741 ± 0.0027		0.67486 ± 0.00007	0.67486 ± 0.00001	-0.3
$\sin^2\theta^{\rm lept}_{\rm eff}(Q^{\rm had}_{\rm FB})$	0.2324 ± 0.0012		0.23151 ± 0.00006	0.23150 ± 0.00005	0.7
$P^{\rm pol}_\tau = A_\ell$	0.1465 ± 0.0033		0.14711 ± 0.0005	0.14713 ± 0.0004	-0.2
Γ_Z [GeV]	2.4952 ± 0.0023		2.4946 ± 0.0007	2.4947 ± 0.0005	0.3
σ^0_h [nb]	41.540 ± 0.037		41.492 ± 0.008	41.491 ± 0.006	1.3
R^0_ℓ	20.767 ± 0.025		20.749 ± 0.008	20.749 ± 0.006	0.7
$A^{0,\ell}_{\rm FB}$	0.0171 ± 0.0010		0.01623 ± 0.0001	0.016247 ± 0.00008	0.9
A_ℓ (SLD)	0.1513 ± 0.0021		0.14711 ± 0.0005	0.14718 ± 0.0004	1.9
R^0_b	0.21629 ± 0.00066		0.21586 ± 0.0001	0.21586 ± 0.0001	$0.7/0.6$
R^0_c	0.1721 ± 0.0030		0.17221 ± 0.00005	0.17221 ± 0.00005	0
$A^{0,b}_{\rm FB}$	0.0992 ± 0.0016		0.10313 ± 0.00032	0.10319 ± 0.00026	$-2.4/-2.5$
$A^{0,c}_{\rm FB}$	0.0707 ± 0.0035		0.07369 ± 0.00024	0.07373 ± 0.0002	-0.9
A_b	0.923 ± 0.020		0.93475 ± 0.00004	0.93476 ± 0.00004	-0.6
A_c	0.670 ± 0.027		0.66792 ± 0.0002	0.66794 ± 0.0002	0.1
$\sin^2\theta^{\rm lept}_{\rm eff(Had.coll.)}$	0.23143 ± 0.00027	± 0.00015	0.23151 ± 0.00006	0.23150 ± 0.00005	$-0.5/-0.9$

The results of the SM global fit to EWPO for both the present (LHC) and future (HL-LHC) scenarios are collected in Table 28. These are given in the form of the mean and standard deviation for each of the observables, as derived from the posterior of the fits. For each EWPO the "pull" is also computed, defined as the difference between the experimental value and the SM prediction computed by removing each observable from the fit (not shown in the table), normalized to the total uncertainty. As it is apparent, the differences in the posteriors between both fits are quite small. However, looking at the pulls one can see that, should the central values of the SM input parameters remain the same, the expected improvements in their experimental uncertainties, combined with the more precise measurements of some EWPO at the HL-LHC, would significantly increase the tension between the indirect determinations of M_Z, m_t, and M_H from the EW fit and the corresponding experimental measurements, pushing them to the 3σ

level. The improvement in the precision on m_t would also reduce the parametric uncertainty on some observables, e.g. the W mass, bringing the total residual error very close to the intrinsic uncertainty associated to missing higher-order corrections in the calculation of M_W. As in the case of some of the SM inputs, the expected improvement on the experimental precision of M_W, without a significant deviation on the central value, would add some tension between theory and experiment, pushing the pull for this observable well beyond the 2σ level. The impact of the HL-LHC measurements on the EW fit is well illustrated in Fig. 46 where one can see the comparison between direct (i.e. experimental) and indirect constraints on the fit input parameters given for both the current and HL-LHC scenarios in the M_W vs. m_t and the M_W vs. $\sin^2\theta^{\rm lept}_{\rm eff}$ planes respectively.

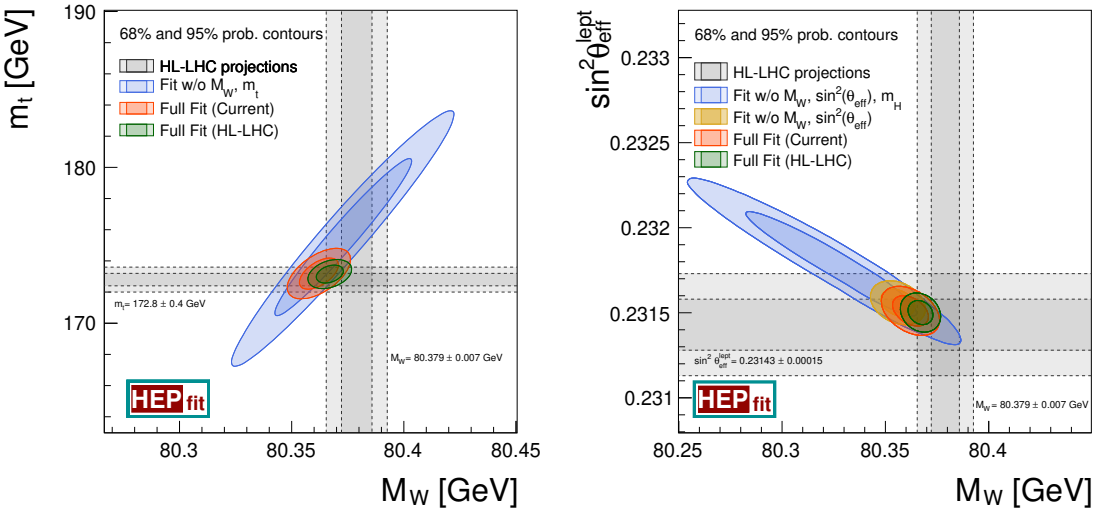

Fig. 46: Comparison of the indirect constraints on M_W and m_t with the current experimental measurements and the expected improvements at the HL-LHC (left). The same in the M_W-$\sin^2\theta^{\rm lept}_{\rm eff}$ plane (right).

The EWPO, being measured in processes mediated by the exchange of a Z or W boson, are extremely sensitive to any new physics that modifies the propagation of such particles. This results in a universal modification of the interactions between the EW gauge bosons and the SM fermions, which, from the point of view of EWPO, can be described in terms of only three parameters: the well-known S, T, and U oblique parameters [512]. The study of the constraints on the S, T, and U parameters is one of the classical benchmarks in the study of EW precision constraints on new physics, and it is well motivated from a theory point of view, within the context of universal theories. The results of the fit to the S, T, and U parameters are given in Table 29. The results are presents in terms of the full (S,T,U) fit and also assuming $U = 0$, which is motivated in theories where EW symmetry breaking is realised linearly, since in that case $U \ll S, T$. In both cases the current constraints are compared with the expected precision at the HL-LHC, which, in some cases, could improve the sensitivity to such new physics effects by up to $\sim 30\%$. The results for the ST fit ($U = 0$) are shown in Fig. 47, illustrating also the constraints imposed by the different EWPO.

As stressed above, the STU parameterisation only describes universal deformations with respect to the SM predictions. In order to systematically explore the impact of global EW precision fits on new physics, the framework of the SMEFT is adopted in what follows. In this formalism, the SM Lagrangian is extended via operators of dimension five and higher, i.e.

$$\mathcal{L}_{\rm eff} = \mathcal{L}_{\rm SM} + \sum_{d>4} \frac{1}{\Lambda^{d-4}} \mathcal{L}_d, \quad \text{with} \quad \mathcal{L}_d = \sum_i C_i \mathcal{O}_i^{(d)}, \quad \left[\mathcal{O}_i^{(d)}\right] = d\,, \tag{28}$$

Table 29: Results of the fit for the oblique parameters S, T, U; and S, T ($U = 0$). Projections for the uncertainties at the HL-LHC are given in the last column.

	Result	Correlation Matrix			Precision at HL-LHC
S	0.04 ± 0.10	1.00			0.09
T	0.08 ± 0.12	0.90	1.00		0.12
U	0.00 ± 0.09	-0.62	-0.84	1.00	0.08
S	0.04 ± 0.08	1.00			0.06
T	0.08 ± 0.06	0.90	1.00		0.05
($U = 0$)					

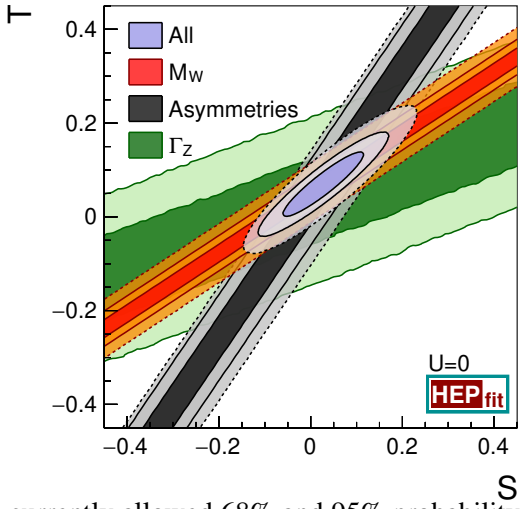

Fig. 47: Comparison of the currently allowed 68% and 95% probability regions in the S, T fit ($U = 0$) (dashed contours) with the HL-LHC projections (solid contours). The different bands illustrate the bounds from the different EWPO included in the fit and the projected improvements at the HL-LHC.

where Λ denotes the cut-off scale of the SMEFT. This new physics scale introduces a first hierarchical ordering between contributions of operators of lower versus higher dimension, where higher-dimension operators are suppressed by inverse powers of Λ. Each term in $\mathcal{L}_d$ is a linear combination of d-dimensional operators $O_i^{(d)}$ built in terms of SM fields, with Wilson coefficients C_i that can depend on both SM masses and couplings, as well as new physics parameters. For the analysis of EWPO the leading new physics corrections come from dimension-six operators ($\mathcal{L}_6$). The study is limited to this order in the effective theory expansion. Using the complete basis of dimension-six interactions presented in Ref. [513], the Z-pole and W observables in Table 28 are corrected at the leading order by 10 different operators. The bosonic operators

$$\mathcal{O}_{\phi D} = |\phi^\dagger D^\mu \phi|^2 \quad \text{and} \quad \mathcal{O}_{\phi WB} = (\phi^\dagger \sigma_a \phi) W^a_{\mu\nu} B^{\mu\nu},$$

modify the gauge-boson propagators in a way similar to the T and S parameters, respectively. Among the remaining operators,

$$\mathcal{O}^{(1)}_{\phi\psi} = (\phi^\dagger \overleftrightarrow{D^\mu} \phi)(\overline{\psi}\gamma_\mu \psi) \quad \text{and} \quad \mathcal{O}^{(3)}_{\phi F} = (\phi^\dagger \sigma_a \overleftrightarrow{D^\mu} \phi)(\overline{F}\gamma_\mu \sigma_a F),$$

with $\psi = l,\ e,\ q,\ u\ , d$ and $F = l, q$ (where l and q denote the SM left-handed fermion doublets, e, u, d the SM right-handed fermion singlets, and flavour universality is assumed), correct, upon EW symmetry

breaking, the EW couplings of the Z and W bosons to quarks and leptons. Finally, the four-lepton operator $\mathcal{O}_{ll} = (\bar{l}\gamma_\mu l)\,(\bar{l}\gamma^\mu l)$ modifies the muon decay amplitude and, by affecting the extraction of the Fermi constant, propagates its effect to all the different observables considered in the EW global fit.

The aim of a global fit to EWPO data is to constrain the corresponding Wilson coefficients. Of the ten operators considered, only eight combinations can be constrained using EW precision data in the case of flavour universal couplings. This means that in the basis of [513] there are two flat directions which, for simplicity are lifted by performing a field redefinition to exchange $C_{\phi D}$ and $C_{\phi WB}$ with two interactions that do not enter in EWPO. The results of the fit to EWPO using the projected HL-LHC data are shown in Fig. 48, both for the case in which the eight remaining coefficients are active and fitted simultaneously and for the case in which only one coefficient at a time is active and independently fitted. The results of both fits are also summarised in Table 30 where the HL-LHC bounds are additionally compared to current bounds. It can be seen that the HL-LHC could improve the current bounds on some of the considered Wilson coefficients by up to a 10-30%, although for most coefficients the effect is much milder both when different effective interactions are fitted simultaneously and individually.

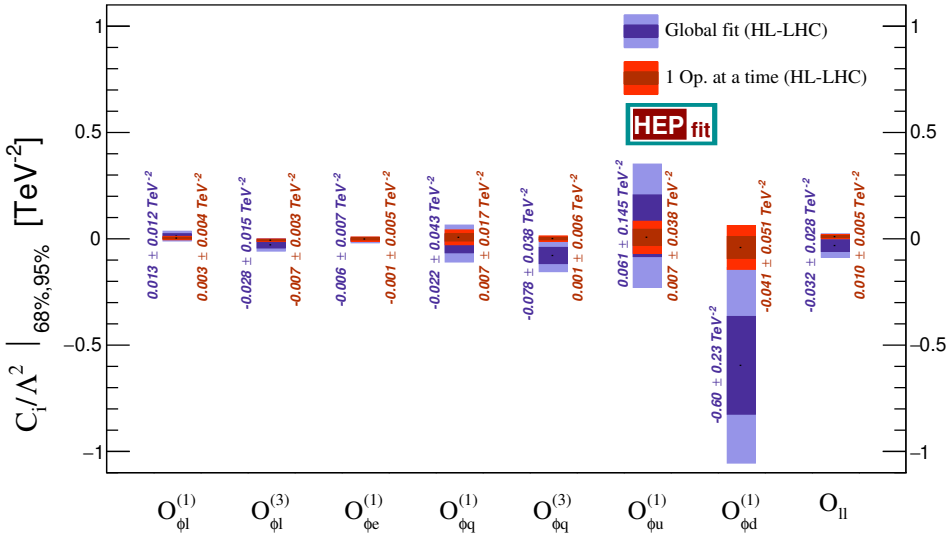

Fig. 48: 68% and 95% probability limits on the dimension-six operator coefficients C_i/Λ^2 [TeV^{-2}] from the global fit to EWPO at HL-LHC including all operators (in blue), compared with the limits obtained assuming only one operator at a time (in red). See Table 30 for the comparison with current uncertainties.

Table 30: Results of the fit to the coefficients of the SMEFT dimension-six Lagrangian. The uncertainties shown refer to the fit performed assuming the presence of only one effective operator at a time and to the case when all (eight) operators are active at the same time (global fit). Projections for the uncertainties at the HL-LHC are given in the last two columns. Result shown for the ratios $\overline{C}_i \equiv C_i/\Lambda^2$. See text for details.

	Current uncertainty [TeV^{-2}]		Precision at HL-LHC [TeV^{-2}]	
Operator Coefficient	1 op. at a time	Global fit	1 op. at a time	Global fit
$\overline{C}_{\phi l}^{(1)}$	0.004	0.012	0.004	0.012
$\overline{C}_{\phi q}^{(1)}$	0.018	0.044	0.017	0.043
$\overline{C}_{\phi e}$	0.005	0.009	0.005	0.007
$\overline{C}_{\phi u}$	0.040	0.146	0.038	0.145
$\overline{C}_{\phi d}$	0.054	0.237	0.051	0.230
$\overline{C}_{\phi l}^{(3)}$	0.004	0.017	0.003	0.015
$\overline{C}_{\phi q}^{(3)}$	0.007	0.040	0.006	0.038
$\overline{C}_{ll}$	0.007	0.028	0.005	0.028
$\overline{C}_{\phi WB}$	0.003	–	0.002	–
$\overline{C}_{\phi D}$	0.007	–	0.005	–

5 Strong interactions

This section presents studies at the HL-LHC and HE-LHC conditions for jet and photon production, parton density functions, underlying event and multi/double-parton interactions. Thanks to the larger integrated luminosity at the HL-LHC and HE-LHC and the jump in centre-of-mass energy at the HE-LHC, an increase in the kinematic reach is expected for light- and heavy-flavour jet production as well as photon production. An improvement is also expected in the experimental systematic uncertainty on the jet calibration. The measurements of jet and photon production cross sections in addition to other processes, e.g. Drell-Yan and top quark, at the HL-LHC will help improve the understanding of the parton density functions. The level of the underlying event activity is not expected to change significantly at the HL-LHC given the small increase in centre-of-mass energy from $\sqrt{s} = 13$ TeV at the LHC Run-2 to $\sqrt{s} = 14$ TeV at the HL-LHC, however a significant increase is expected at the HE-LHC energy of $\sqrt{s} = 27$ TeV. Multi-parton interactions are expected to play a more significant role at higher energies and, thanks to the large statistics available at both the HL- and HE-LHC, new measurements can be carried out to test more precisely the current theoretical models.

5.1 Jet and photon production [24]

This section presents phenomenological studies of inclusive jet, dijet, heavy-flavour jet production as well as inclusive photon, diphoton, and associated photon and jet production at future upgrades at the HL and HE stages of the LHC. In particular the reach in yields for these processes is investigated. A comparison between the results expected at the future design centre-of-mass energies of $\sqrt{s} = 14$ TeV and $\sqrt{s} = 27$ TeV is presented.

5.1.1 Inclusive jet production

Jets are reconstructed using the anti-k_{T} algorithm [274] with distance parameter R=0.4 as implemented in the FastJet software package [343], and calibrated following the procedure described in [514]. The total jet energy scale (JES) uncertainty in ATLAS Run-2 measurements comprises of 88 sources, and all need to be propagated through the analysis in order to correctly account for uncertainty correlations in the jet calibration in the final result. Here follows a summary of the analysis detailed in Ref. [515].

A reduced set of uncertainty components (nuisance parameters) is derived from eigenvectors and eigenvalues of the diagonalised total JES covariance matrix on the jet level. The globally reduced configuration with 19 nuisance parameters (NPs) is used in this study. Eight NPs coming from the in situ techniques are related to the detector description, physics modelling and measurements of the Z/γ energies in the ATLAS calorimeters. Three describe the physics modelling, the statistics of the dijet MC sample and the non-closure of the method used to derive the η-intercalibration [514]. Single-hadron response studies [516] are used to describe the JES uncertainty in the high-p_{T} jet regions, where the in situ studies have limited statistics. Four NPs are due to the pile-up corrections of the jet kinematics that take into account mis-modelling of N_{PV} and $\langle\mu\rangle$ distributions, the average energy density ρ, and the residual p_{T} dependence. Finally, two uncertainty components take into account the difference in the calorimeter response to the quark- and gluon-initiated jets (flavour response) and the jet flavour composition, and one uncertainty estimates the correction for the energy leakage beyond the calorimeter, the "punch-through" effect.

In order to estimate the precision in the jet cross section measurements at the HL-LHC, three scenarios of possible uncertainties in the jet energy scale calibration are defined.

In all three scenarios, the high-p_{T} uncertainty, the punch-through uncertainty and the flavour composition uncertainty are considered to be negligible. The JES uncertainty in the high-p_{T} range will be accessed using the multi-jet balance (MJB) method, rather than single hadron response measurements,

[24] Contributed by the experimental collaborations, and by L. Cieri, G. Ferrera, A. Huss, and J. Pires.

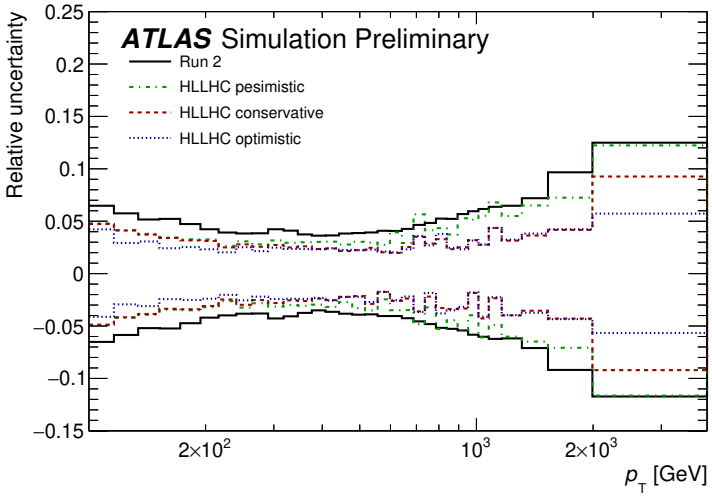

Fig. 49: Relative uncertainties in the inclusive jet cross section measurements at the HL-LHC due the JES uncertainties. Three HL-LHC scenarios are compared to the Run-2 performance. Black line corresponds to the Run-2 performance. Green, red and blue lines represent pessimistic, conservative and optimistic scenarios, respectively.

since the high statistics at the HL-LHC will allow precision JES measurements in the high-p_{T} region. Flavour composition and flavour response uncertainties are derived from the MC generators. With the advances in the MC modelling and development of tunes, these uncertainties could be significantly reduced. The flavour composition uncertainties are set to zero to highlight the maximal impact of possible future improvements in the understanding of parton shower and hadronisation modeling on the precision of the jet energy measurements. The flavour response uncertainties are kept the same as in Run-2 or reduced by a factor of two in conservative and optimistic scenarios, respectively.

The pile-up uncertainties, except the ρ topology uncertainty, are considered to be negligible. Current small uncertainties in the JES due to mis-modelling of N_{PV} and $\langle\mu\rangle$ distributions and the residual p_{T} dependence lead to a very small uncertainties at the HL-LHC conditions. With the advances of new pile-up rejection techniques, the ρ topology uncertainty could be maintained at a level comparable to the one in Run-2 or reduced by a factor of two. This is addressed in conservative and optimistic scenarios.

Since the Run-2 jet energy resolution (JER) uncertainty estimation is conservative, the final Run-2 JER uncertainty is expected (based on Run-1 experience) to be about twice as small as the current one. Therefore, the JER uncertainty is estimated to be half of that in Run-2.

The remaining uncertainty sources are fixed in different scenarios as follows:

- Conservative scenario:
  - All in situ components are kept the same as in Run-2, except the uncertainties related to the photon energy measurement in the high-E_{T} range and the MJB method uncertainties whose uncertainties are reduced by a factor of two, since those are expected to be improved at the HL-LHC;
  - The MC modelling uncertainty in the η-intercalibration is reduced by a factor of two while the other two are neglected. Currently, the MC modelling uncertainty is derived through a comparison of leading-order (LO) pQCD generators. With future advances in next-to-leading-order MC generators this uncertainty is expected to improve;
  - The flavour response uncertainty is set to the Run-2 value;

  - The ρ-topology uncertainty is unchanged compared to Run-2 results;
- Optimistic scenario:
  - All in situ components are treated identically to the conservative scenario;
  - All three uncertainty sources in the η-intercalibration method are set to zero;
  - The flavour response uncertainty is reduced by a factor of two compared to Run-2 results;
  - ρ-topology uncertainty is two times smaller as in Run-2;
- Pessimistic scenario:
  - Same as the optimistic scenario, but all uncertainty sources of in situ methods are retained from Run-2.

All components of the JES uncertainty are propagated from the jet-level to the cross section level as follows. The jet p_{T} is scaled up and down by one standard deviation of each source of uncertainty. The difference between the nominal detector-level spectrum and the systematically shifted one is taken as a systematic uncertainty. All JES uncertainties are treated as bin-to-bin correlated and independent from each other in this procedure. The unfolding of the detector-level distributions to the particle-level spectrum is not performed is this study. A possible modification of the shapes of uncertainty components during the unfolding procedure is expected to be small and neglected in this study.

The inclusive jet cross-sections are studied as a function of the jet transverse momentum for jets with $p_{\mathrm{T}} > 100$ GeV and within $|y| < 3$. The total JES uncertainty in the inclusive jet cross section measurement for the three HL-LHC scenarios is depicted in Fig. 49 and is compared to the total JES uncertainty estimate for the Run-2 jet cross section measurements. The total JES uncertainty in the low p_{T} range is the same as in Run-2 and is about 2% better in the high-p_{T} region. In the conservative and pessimistic scenarios the JES uncertainties in the cross section are very similar in the intermediate and high-p_{T} range, while the JES uncertainty is about 1% better in the low-p_{T} range for the optimistic scenario.

The predicted number of events estimated using the program NNLOJET [326], which includes next-to-next-to-leading order QCD calculations for both single jet inclusive [206] and dijet inclusive [19] production, is shown in Fig. 50 (left and right respectively). In the dijet analysis, a second jet with $p_{\mathrm{T}} > 75$ GeV is required in the event. The lower panels show the ratios of events yields at 27 TeV and 14 TeV. This plot shows an enhancement of the cross section growing with the jet p_{T} (left) and dijet mass (right). In summary, assuming $\mathcal{L}_{int} = 3\ \mathrm{ab}^{-1}$ of pp collision data at $\sqrt{s} = 14$ TeV the p_{T} reach of the measurement is 5 TeV with the observation of dijet events of mass up to 9 TeV. At the HE-LHC upgrade, an increase in cross section by a factor between 10^3 and 10^6 in the tails of the distributions extends the p_{T} range of the measurement by a factor of 2 up to 9 TeV, allowing the observation of dijet events of mass up to 16 TeV.

The increase in cross section in these scenarios will allow for a very precise multi-differential measurement of inclusive jet production. Working at a fixed centre-of-mass energy, the high-p_{T} the high-x and the large Q^2 region are probed and the sensitivity to higher order QCD/EW effects and BSM signals is increased. On the other hand, at fixed-p_{T}, an increase in the collider energy and the inclusion of the forward detector regions increase the coverage to the low-x regime, which is highly sensitive to small-x resummation effects. For these reasons, it will be necessary to have accurate jet predictions covering both regions.

To this end Fig. 51 presents the double-differential k-factors at $\sqrt{s} = 14$ TeV (left) and $\sqrt{s} = 27$ TeV (right) for the inclusive jet p_{T} (top), differentially in p_{T} and rapidity $|y|$ and dijet mass (bottom) differentially in dijet mass m_{jj} and rapidity difference $y^* = 1/2\ |y_{j1} - y_{j2}|$. The shaded bands assess the scale uncertainty at different perturbative orders, LO, NLO and NNLO. As for the value of the renormalization (μ_R) and factorization (μ_F) scales $\mu = \hat{H}_T$ is used, i.e. the scalar sum of the p_{T} of all

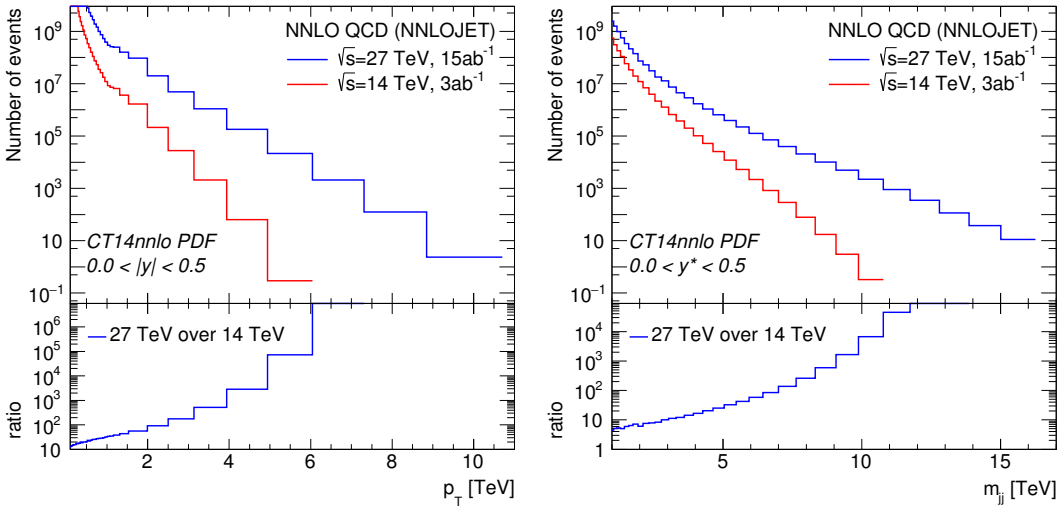

(a) (b)

Fig. 50: Predicted number of inclusive jet events as a function of the jet p_{T} (left) and dijet events as a function of dijet mass m_{jj} (right) at NNLO, assuming an integrated luminosity of 3 ab^{-1} (15 ab^{-1}) of pp collision data at $\sqrt{s}$=14 TeV ($\sqrt{s}$=27 TeV).

partons in the event, as recommended in [332] for the inclusive jet p_{T}, and the dijet mass $\mu = m_{jj}$ for the dijet mass distribution, as recommended in [19].

For the inclusive jet p_{T} large NLO effects at high-p_{T} and central rapidity of approximately 90% (14 TeV) and 50% (27 TeV) are observed with large NLO scale uncertainties of $\mathcal{O}(20-30\%)$. At NNLO moderate corrections across the entire p_{T} and rapidity range are observed, except at high-p_{T} in the central rapidity slices where the NNLO effects can reach between 10 to 30%. An excellent convergence of the perturbative result is observed as well as a significant reduction in the scale uncertainty of the cross section when going from NLO to NNLO. The NNLO scale uncertainties are estimated at the $< 5\%$ level. Similarly to the inclusive jet p_{T} case, an excellent convergence of the perturbative result for the dijet mass is observed. The NNLO/NLO k-factors are typically $< 10\%$ and alter the shape of the prediction at low m_{jj} and low y^*. A large reduction is observed in the scale variation and NNLO scale uncertainties are estimated to be below the 5% level, even at large m_{jj}. Scale uncertainties at this level are well below the PDF uncertainty, highlighting the huge potential to constrain PDFs with inclusive jet data.

Measurements of weak bosons [517], top quarks [518], photon and jet production [519] (and many others) performed by the LHC Collaborations have been already used by the global PDF groups [199, 200, 207, 520] in the determination of the proton structure. Comparisons of inclusive jet and dijet production cross sections using different PDF sets at $\sqrt{s} = 14$ and 27 TeV, show 5–10% differences respectively between central values in the low and intermediate p_{T} and m_{jj} regions, consistent with current PDF uncertainties. Larger differences between the predictions of the various PDF sets in the high-p_{T} and m_{jj} range highlight the expected constraining power of future measurements at the HL-LHC and HE-LHC.

A study to estimate the impact of future PDF-sensitive measurements at the HL-LHC on PDFs determination was performed in [298] and reported in Sec. 5.2. Three possible scenarios for the experimental systematic uncertainties were considered. This study concluded that HL-LHC measurements will further reduce the PDF uncertainties, and published dedicated PDF sets, PDF4LHC HL-LHC, with

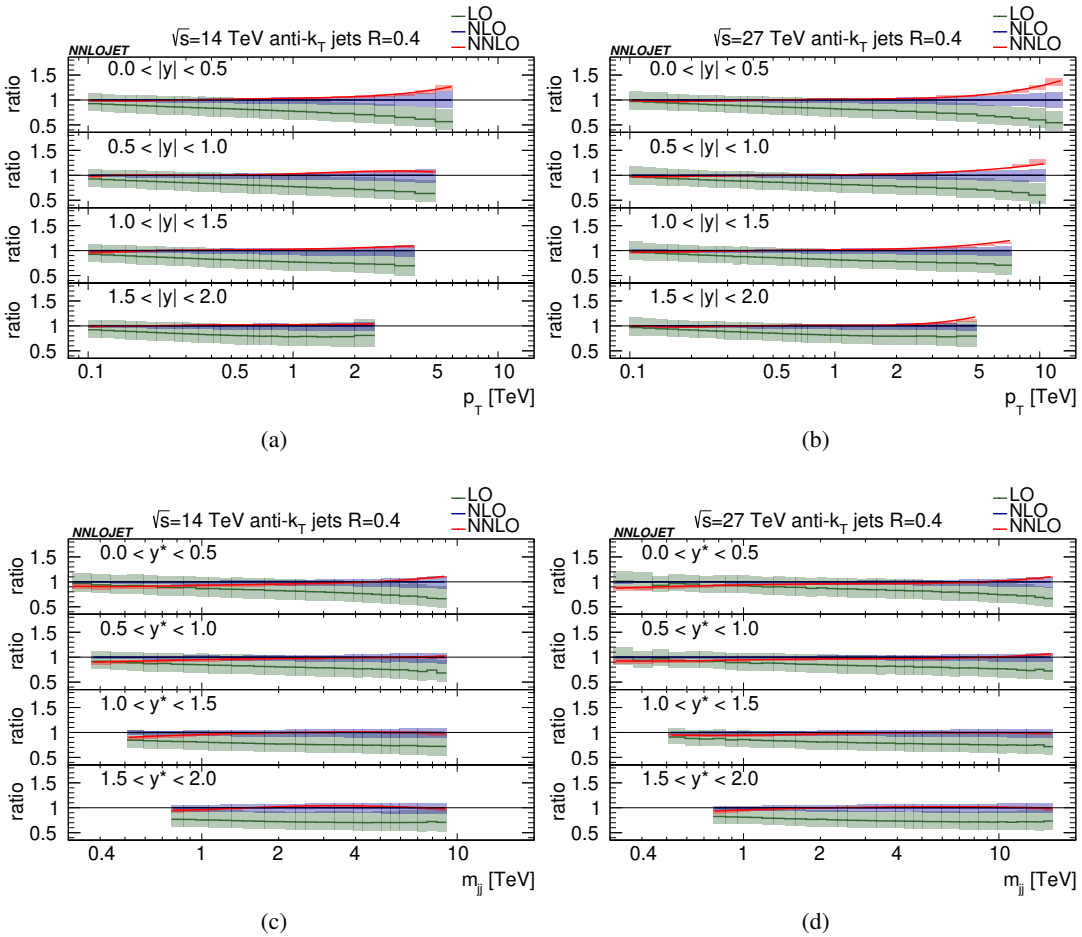

Fig. 51: Predictions for the inclusive jet p_{T} (top) and dijet mass m_{jj} (bottom) at LO (green), NLO (blue) and NNLO (red) at (a and c) $\sqrt{s} = 14$ TeV and (b and d) $\sqrt{s} = 27$ TeV normalised to the NLO result.

the inclusion of HL-LHC pseudo-data in the fits. Figure 52 depicts the comparison of PDF uncertainties in the inclusive jet and dijet production cross sections for CT14 and PDF4LHC HL-LHC (conservative scenario) in pp collisions at $\sqrt{s} = 14$ and 27 TeV. A significant reduction in the PDF uncertainty is expected with the inclusion of PDF-sensitive measurements in HL-LHC PDF fits.

5.1.2 High–p_{T} light– and heavy–flavour jet measurements at the HL–LHC

The program of jet physics will substantially profit from the HL-LHC data since higher scales can be reached and the region of very low partonic momentum fractions x can be accessed, where the parton density becomes large. Measurements of jets originating from b quarks are important to investigate the heavy-flavor contribution to the total jet cross section and to study the agreement of the measurement with available theoretical predictions. In particular, inclusive b-jet production is very sensitive to higher-order corrections and to parton showers. In top quark production processes, top jets can be defined when the top quark decays hadronically and all decay products can be clustered into a single jet. The production of W bosons is studied in the high-p_{T} region, where the W bosons decay hadronically and are reconstructed as jets. Jet substructure techniques are applied to discriminate the jets originating from top quarks and W bosons from the QCD background.

Higher order QCD radiation affects the distribution of the angular correlation, and the region

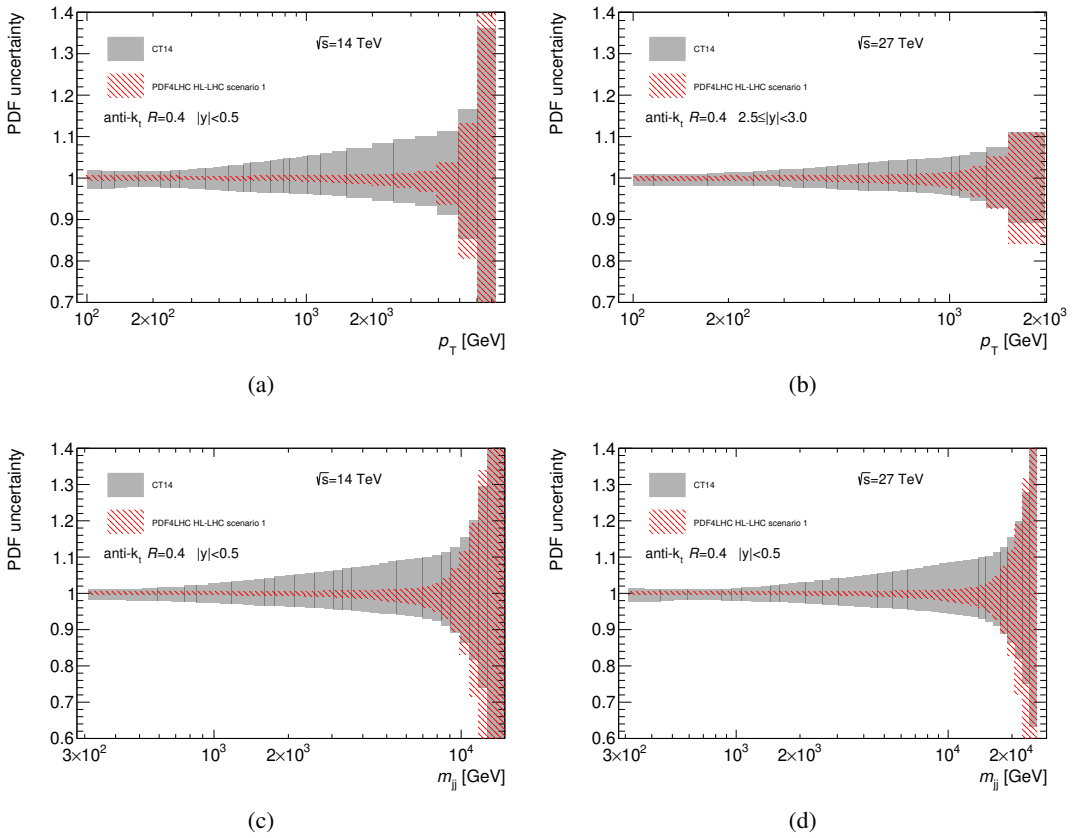

Fig. 52: Comparison of PDF uncertainty in the inclusive jet (a,b) and dijet (c,d) cross sections calculated using the CT14 PDF set and the conservative PDF4LHC HL-LHC scenario 1 (i.e. scenario C in Sec. 5.2) [298] set at $\sqrt{s} = 14$ TeV (left) and $\sqrt{s} = 27$ TeV (right).

where the jets are back-to-back in the transverse plane is particularly sensitive to multiple "soft" gluon contributions, treated by all-order resummation and parton showers. This region is of particular interest since soft-gluon interference effects between the initial and final state can be significant [521, 522]. The azimuthal correlations $\Delta\phi = |\phi_2 - \phi_1|$ between the two leading p_{T} jets and their dependency on the production process is of particular interest because of color interference effects [523, 524].

Compared to Run-2 measurements at $\sqrt{s} = 13$ TeV the increase of the centre-of-mass energy leads to about twice larger cross section at highest p_{T}. Taking into account the much higher luminosity and the higher cross section, the statistical uncertainty is expected to be around six times smaller, compared to the analysis of the Run-2 data [525].

Measurements of high-p_{T} jets originated from b-quarks are sensitive to the higher-order corrections, parton shower modeling and the parton densities of the proton. In Fig. 53 (left), the inclusive b-jet cross section differential in p_{T} is shown for centre-of-mass energy of 13 and 14 TeV and rapidity $|y| < 0.5$. The depicted statistical uncertainties correspond to the luminosity $300\,\mathrm{fb}^{-1}$ (13 TeV) and $3\,\mathrm{ab}^{-1}$ (14 TeV). The systematic uncertainty of the measurement is dominated by the jet energy scale uncertainty, which is of similar size as for inclusive jets, and the b-tagging uncertainty, which is expected to play a role mainly at higher p_{T} where it is about 10%. It can be seen that the p_{T} reach at HL-LHC for the inclusive b-jets is about 3 TeV, where about 30 events with $p_{\mathrm{T}} > 3\,\mathrm{TeV}$ are expected.

It is worth noticing that at high-p_{T} the mass of the b-quark is nearly negligible with respect to

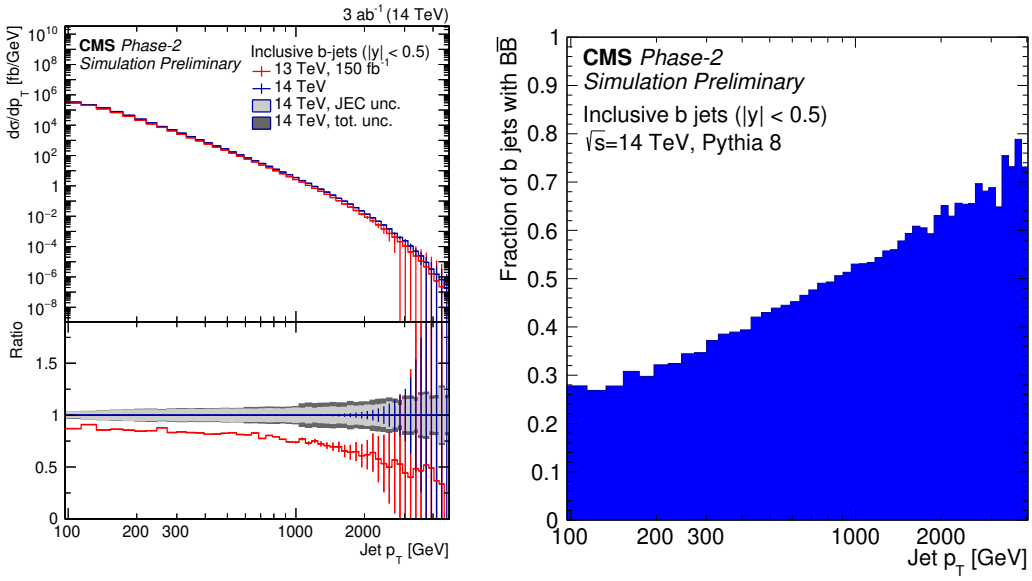

Fig. 53: The inclusive b-jet cross section differential in the p_{T} (left). The error bars show the statistical uncertainty corresponding to the given luminosity, while the gray band represent the systematic uncertainty from the jet-energy-scale and the total systematic uncertainty. The fraction of b-jets containing both B and $\bar{B}$ hadrons as a function of p_{T} (right).

the jet momentum. This leads to the high probability that the b-quark is not produced in the hard subprocess, but in the parton shower. As the mass of the b-quark becomes negligible, the probability of gluon splitting into $b\bar{b}$-pairs is similar to any other flavour (excluding top). In this case, the pair of the B-hadrons is expected to be found inside the b-jet, where one consists of a b-quark, the second a $\bar{b}$-quark. The fraction of such jets as a function of p_{T} as predicted by PYTHIA v8 MC is shown on Fig. 53 (right). In the future, it will be crucial to disentangle between b-jets with b-quarks produced in the shower, and b-jets with b-quarks produced in the hard sub-process.

Figure 54 shows a comparison of the jet cross sections as a function of p_{T} and as a function of $\Delta\phi$ for the different processes applying the anti-k_{T} clustering algorithm [526] with $R = 0.8$. In Fig. 54 (left) the inclusive b-jet cross section is shown (for comparison with the inclusive jet cross section), while in Fig. 54 (right) the two-b-jet cross section is shown. Except for the cross section for W production, the statistical uncertainties shown correspond to an integrated luminosity of 3 ab^{-1} including efficiencies due to b-tagging and selection at the detector level, estimated using the DELPHES simulation. Details of the studies can be found in Ref. [525].

It can be seen that the shapes of the p_{T} spectra are comparable but the top-jet cross section is about ten thousand times smaller than the inclusive jet cross section. The ratio to the inclusive dijet cross section as a function of $\Delta\phi$ illustrates the differences in shape of the $\Delta\phi$ distribution of the different processes (all processes are normalized at $\Delta\phi = \pi$), which depend on the partonic configuration of the initial state.

5.1.3 Inclusive photon production

Here follows a summary of the studies detailed in Ref. [515] of inclusive isolated photon production and photon production in association with at least one jet. In both analyses the photon is required to have a transverse energy in excess of 400 GeV and the pseudorapidity to lie in the range $|\eta^{\gamma}| < 2.37$ excluding the region $1.37 < |\eta^{\gamma}| < 1.56$. The photon is required to be isolated by imposing an upper limit on

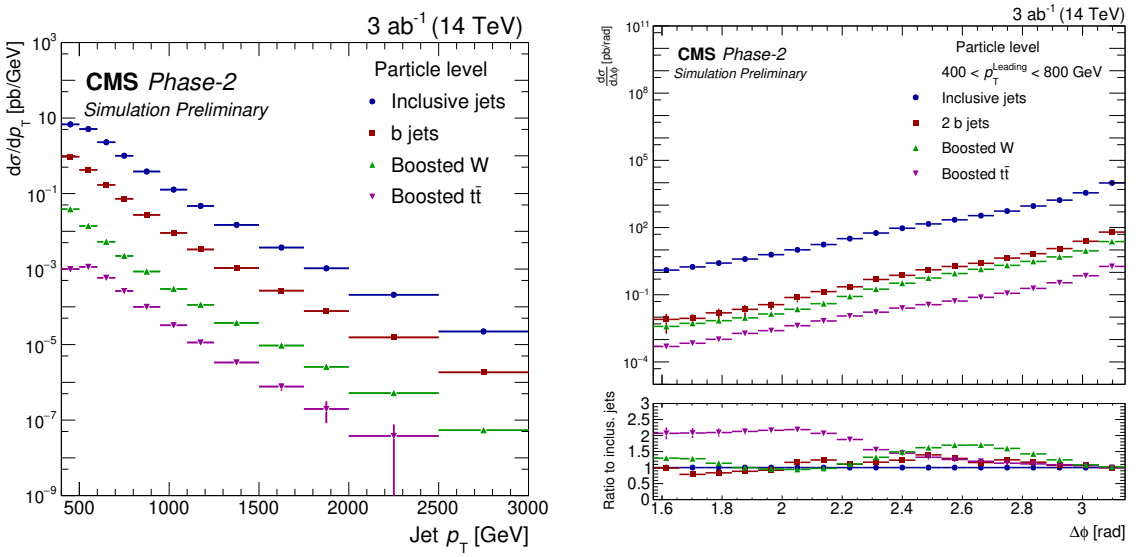

Fig. 54: The particle-level differential jet cross sections (with anti-k_{T} $R = 0.8$) as a function of the jet p_{T} (left) and dijet $\Delta\phi$ (right) for various processes. In the left plot the inclusive b jet cross section is shown (for comparison with the inclusive jet cross section), while for $\Delta\phi$ the two-b-jet cross section is shown. For the ratio the normalization is fixed arbitrarily at $\Delta\phi = \pi$. The cross section of W production does not include statistical uncertainties corrected for efficiencies and background subtraction.

the amount of transverse energy inside a cone of size $\Delta R = 0.4$ in the η–ϕ plane around the photon, excluding the photon itself: $E_{\mathrm{T}}^{\mathrm{iso}} < E_{\mathrm{T,max}}^{\mathrm{iso}}$.

In the inclusive photon analysis, the goal is the measurement of the differential cross section as a function of E_{T}^{γ} in four regions of the photon pseudorapidity: $|\eta^{\gamma}| < 0.6$, $0.6 < |\eta^{\gamma}| < 1.37$, $1.56 < |\eta^{\gamma}| < 1.81$ and $1.81 < |\eta^{\gamma}| < 2.37$. Photon isolation is enforced by requiring $E_{\mathrm{T}}^{\mathrm{iso}} < 4.2 \cdot 10^{-3} \cdot E_{\mathrm{T}}^{\gamma} + 4.8$ GeV.

In the photon+jet analysis, jets are reconstructed using the anti-k_{T} algorithm [274] with a radius parameter $R = 0.4$. Jets overlapping with the photon are not considered if the jet axis lies within a cone of size $\Delta R = 0.8$. The leading jet is required to have transverse momentum above 300 GeV and rapidity in the range $|y^{\mathrm{jet}}| < 2.37$. No additional condition is used for the differential cross section as a function of $p_{\mathrm{T}}^{\mathrm{jet}}$. For the differential cross section as a function of the invariant mass of the photon+jet system additional constraints are imposed: $m^{\gamma-\mathrm{jet}} > 1.45$ TeV, $|\cos\theta^{*}| < 0.83$ and $|\eta^{\gamma} \pm y^{\mathrm{jet}}| < 2.37$. These additional constraints are imposed to remove the bias due to the rapidity and transverse-momentum requirements on the photon and the leading jet [527, 528]. Photon isolation is enforced by requiring $E_{\mathrm{T}}^{\mathrm{iso}} < 4.2 \cdot 10^{-3} \cdot E_{\mathrm{T}}^{\gamma} + 10$ GeV.

The yields of inclusive isolated photons and of photon+jet events are estimated using the program JETPHOX 1.3.1_2 [529, 530]. This program includes a full next-to-leading-order QCD calculation of both the direct-photon and fragmentation contributions to the cross sections for the $pp \to \gamma + \mathrm{X}$ and $pp \to \gamma + \mathrm{jet} + \mathrm{X}$ reactions. The number of massless quark flavours is set to five. The renormalisation (μ_{R}), factorisation (μ_{F}) and fragmentation (μ_{f}) scales are chosen to be $\mu_{\mathrm{R}} = \mu_{\mathrm{F}} = \mu_{\mathrm{f}} = E_{\mathrm{T}}^{\gamma}$. The calculations are performed using the MMHT2014 [531] parameterisations of the proton parton distribution functions (PDFs) and the BGF set II of parton-to-photon fragmentation functions at NLO [532]. The strong coupling constant $\alpha_{\mathrm{s}}(m_{\mathrm{Z}})$ is set to the value assumed in the fit to determine the PDFs. The reliability of the estimated yields using the program JETPHOX is supported by the high purity of the signal photons, the mild unfolding corrections and the fact that the NLO QCD predictions describe adequately

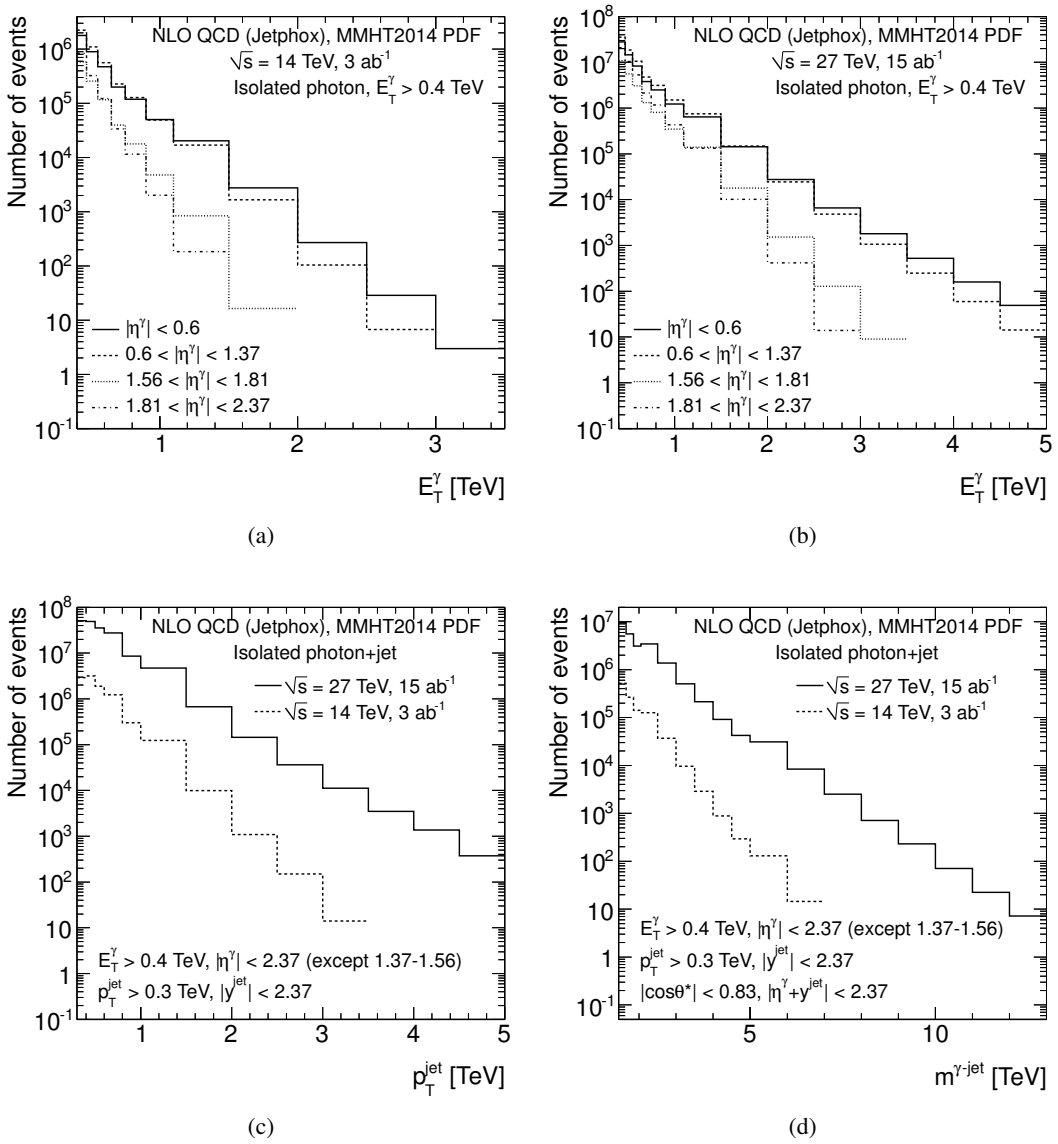

Fig. 55: (a,b) Predicted number of inclusive isolated photon events as a function of E_{T}^{γ} assuming an integrated luminosity of 3 ab^{-1} (15 ab^{-1}) of pp collision data at $\sqrt{s} = 14$ TeV (27 TeV) in different ranges of photon pseudorapidity: $|\eta^{\gamma}| < 0.6$ (solid histogram), $0.6 < |\eta^{\gamma}| < 1.37$ (dashed histogram), $1.56 < |\eta^{\gamma}| < 1.81$ (dotted histogram) and $1.81 < |\eta^{\gamma}| < 2.37$ (dot-dashed histogram). (c,d) Predicted number of photon+jet events assuming an integrated luminosity of 3 ab^{-1} (15 ab^{-1}) of pp collision data at $\sqrt{s} = 14$ TeV (27 TeV) as a function of (c) $p_{\mathrm{T}}^{\mathrm{jet}}$ and (d) $m^{\gamma-\mathrm{jet}}$.

the measurements of these processes using pp collisions at $\sqrt{s} = 13$ TeV [533, 534].

The predicted number of inclusive isolated photon events as a function of E_{T}^{γ} in the different ranges of $|\eta^{\gamma}|$ assuming an integrated luminosity of 3 ab^{-1} (15 ab^{-1}) of pp collision data at $\sqrt{s} = 14$ TeV (27 TeV) is shown in Figure 55(a) and 55(b). For the HL-LHC (HE-LHC), the reach in E_{T}^{γ} is (a) 3–3.5 (5) TeV for $|\eta^{\gamma}| < 0.6$, (b) 2.5–3 (5) TeV for $0.6 < |\eta^{\gamma}| < 1.37$, (c) 1.5–2 (3–3.5) TeV for $1.56 < |\eta^{\gamma}| < 1.81$ and (d) 1–1.5 (2.5–3) TeV for $1.81 < |\eta^{\gamma}| < 2.37$. This represents a significant extension of the region measured so far with pp collisions at $\sqrt{s} = 13$ TeV [533]; as an example, at the

HL-LHC (HE-LHC) the $E_{\rm T}^{\gamma}$ reach is extended from 1.5 TeV to 3–3.5 (5) TeV for $|\eta^{\gamma}| < 0.6$.

The predicted number of photon+jet events as a function of $p_{\rm T}^{\rm jet}$ and $m^{\gamma-{\rm jet}}$ assuming an integrated luminosity of 3 ab^{-1} (15 ab^{-1}) of pp collision data at $\sqrt{s} = 14$ TeV (27 TeV) is shown in Figs. 55(c) and 55(d). In comparison with the latest measurements at $\sqrt{s} = 13$ TeV [534], the expectations obtained at the HL-LHC (HE-LHC) extend significantly the reach in $p_{\rm T}^{\rm jet}$ from 1.5 TeV to 3.5 (5) TeV and $m^{\gamma-{\rm jet}}$ from 3.3 TeV to 7 (12) TeV.

5.1.4 Diphoton production

The production of photon pairs (diphotons) with high invariant mass is a very important process for physics studies at high-energy hadron colliders. Photons are very clean final states and photon energies and momenta can be measured with high precision in modern electromagnetic calorimeters. Therefore *prompt* photons represent ideal probes to test the properties of the Standard Model (SM) [535]– [536] and they are also important in searches for new-physics signals (see, e.g., Refs. [537]– [538]). Owing to the above reasons, it is important to provide accurate theoretical predictions for diphoton production at LHC energies. This task requires in particular, the calculation of QCD and EW radiative corrections at high perturbative orders.

This contribution considers diphoton production in pp collisions at the $\sqrt{s} = 14$ GeV and $\sqrt{s} = 27$ GeV energies, and presents perturbative QCD results up to the NNLO by using the smooth cone isolation criterion [25]. Within the smooth cone isolation criterion [539] (see also Refs. [540,541]) photons are selected by fixing the size R of the isolation cone and imposing a maximal amount of hadronic energy ($E_{\rm T}^{had}(r)$) allowed inside the cone

$$E_{\rm T}^{had}(r) \leq E_{\rm T\,max}\,\chi(r;R)\,, \quad \text{in } \textit{all} \text{ cones with } r \leq R\,, \tag{29}$$

with a suitable choice of the r dependence of the isolation function $\chi(r;R)$. The smooth isolation function $\chi(r;R)$ used is [26]

$$\chi(r;R) = \left(\frac{1-\cos(r)}{1-\cos(R)}\right)^{n}\,, \tag{30}$$

and the value of the power n is set to the $n = 1$. This value of n avoids the sensitivity of the cross section to soft (collinear) photons for large (small) value of n [544]. The radius of the photon isolation cone is set at the value $R = 0.4$ and $E_{\rm T\,max} = 10$ GeV. Detailed comparisons between standard and smooth cone isolation criteria have been presented in Refs. [90, 544–546].

The following kinematic cuts are applied:

$$p_{\rm T}^{\gamma;\,hard} > 40\ GeV, \qquad p_{\rm T}^{\gamma;\,soft} > 30\ GeV, \qquad |y_{\gamma}| < 2.8\,, \tag{31}$$

where $p_{\rm T}^{\gamma;\,hard}$ and $p_{\rm T}^{\gamma;\,soft}$ are respectively the transverse momenta of the harder and softer photon and $|y_{\gamma}|$ is the photon rapidity. The minimum angular distance between the two photons is $R_{\gamma\gamma}^{\rm min} = 0.4$.

A lower limit $r_{\rm cut}$ is implemented on the ratio $p_{{\rm T}\gamma\gamma}/M_{\gamma\gamma}$ ($p_{{\rm T}\gamma\gamma} > r_{\rm cut} M_{\gamma\gamma}$) [547], and values in the range $r_{\rm cut} = 0.08\%$–0.15% are used. The perturbative uncertainty is computed as the envelope of three-point scale variation by considering the two asymmetric scale configurations with $\{\mu_R = \mu_0/2,\ \mu_F = 2\mu_0\}$ and $\{\mu_R = 2\mu_0\,,\ \mu_F = \mu_0/2\}$ and the central scale $\{\mu_R = \mu_F = \mu_0\}$.

This study begins by considering the invariant mass ($M_{\gamma\gamma}$) distribution up to value of 2 TeV. The LO, NLO and NNLO QCD results for a centre–of–mass energy of $\sqrt{s} = 14$ TeV are presented in Fig.56 (left). It is first observed the presence of a LO threshold at an invariant mass $M^{LO} = 2p_{\rm T}^{\gamma;\,hard}$. The

[25] The NNLO QCD calculation within the standard cone isolation criterion has not been performed yet.

[26] The same form of the isolation function is used in the NNLO predictions reported in Refs. [536, 542, 543].

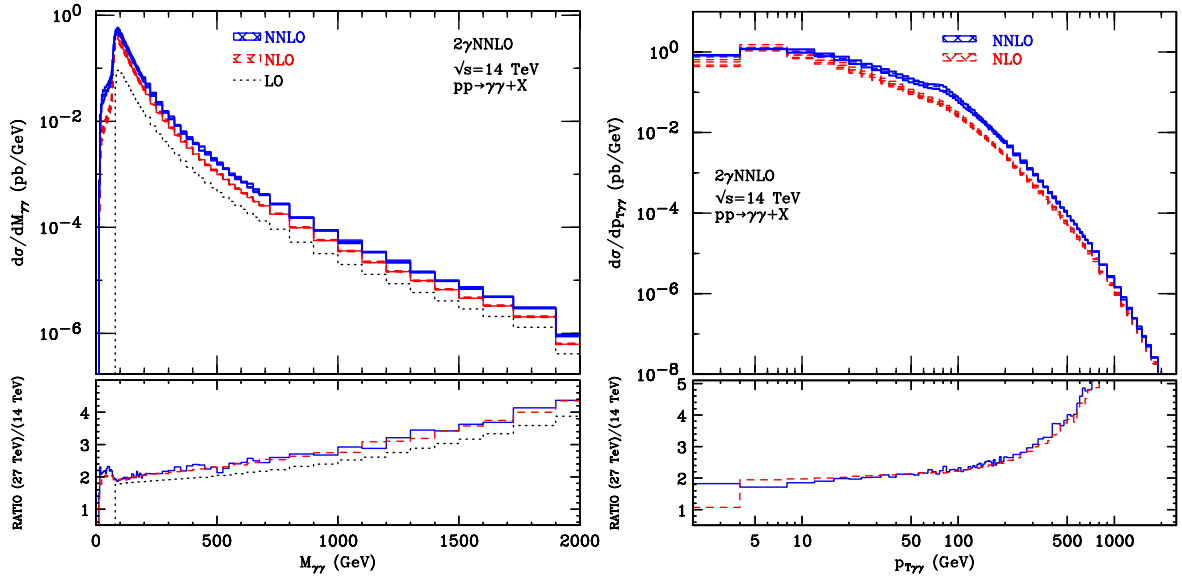

Fig. 56: The differential cross sections $d\sigma/dM_{\gamma\gamma}$ (left) and $d\sigma/dp_{\mathrm{T}\gamma\gamma}$ (right) at $\sqrt{s} = 14$ TeV are shown in the upper panel at LO (black dotted), NLO (red dashed) and NNLO (blue solid). The NLO and NNLO scale variation bands are obtained as detailed in the text. In the lower subpanels the ratio between cross sections at two different centre–of–mass energies ($\sqrt{s} = 27$ TeV and $\sqrt{s} = 14$ TeV) is also shown. The selection cuts are described in the text.

bulk of the cross section is concentrated in the region around M^{LO} while for large values of $M_{\gamma\gamma}$ the distribution rapidly decreases. At high invariant mass, $M_{\gamma\gamma} > 1$ TeV, the cross section is dominated by the quark annihilation ($q\bar{q}$) partonic subprocess (the other partonic subprocesses are suppressed by one order of magnitude or more). The NNLO K factor, $K^{NNLO} = \sigma^{NNLO}/\sigma^{NLO}$, is flat at large values of $M_{\gamma\gamma}$ and it is roughly equal to the NNLO K factor of the $q\bar{q}$ channel. The lower subpanel of Figure 56 (left) presents results for the ratio (R) between the invariant mass distribution at $\sqrt{s} = 27$ TeV and $\sqrt{s} = 14$ TeV. At LO the dynamic enhancement of the ratio can be described roughly as $\mathcal{G}(M^2_{\gamma\gamma}/27^2\ \mathrm{TeV}^2)/\mathcal{G}(M^2_{\gamma\gamma}/(14^2\ \mathrm{TeV}^2)$, where $\mathcal{G}(\tau) = \log(\tau) \times \mathcal{L}_{q\bar{q}}(\tau, \mu_f)$ and $\mathcal{L}$ are the integrated parton luminosities. The ratio at NLO and NNLO is numerically similar to the corresponding LO one. The enhancement of the ratio R at large values of invariant mass is directly related to the increasing the centre–of–mass energy and it reaches the value $R \sim 4$ at $M_{\gamma\gamma} \simeq 1$ TeV.

Finally theoretical results are presented for the transverse momentum ($p_{\mathrm{T}\gamma\gamma}$) distribution. The NLO and NNLO predictions with a centre–of–mass energy of $\sqrt{s} = 14$ TeV are shown in the upper panel of Figure 56 (right). Given the LO kinematical constraint $p_{\mathrm{T}\gamma\gamma} = 0$, the (N)NLO correction represent *effectively* an (N)LO prediction. Moreover, in the small $p_{\mathrm{T}\gamma\gamma}$ region, the convergence of the fixed order expansion is spoiled by the presence of large logarithmic corrections. Reliable perturbative results require an all order resummation of these enhanced logarithmic contributions.

The lower subpanel of Figure 56 (right) presents results for the ratio (R) between the transverse momentum distribution at $\sqrt{s} = 27$ TeV and $\sqrt{s} = 14$ TeV. The ratio increases at large value of $p_{\mathrm{T}\gamma\gamma}$, reaching $R \sim 4$ for $p_{\mathrm{T}\gamma\gamma} \simeq 1$ TeV.

It is observed that the uncertainty bands for the NLO and NNLO results fail to overlap in most of the kinematical regions. This suggests that the computed scale dependence at NNLO cannot be considered a reliable estimate of the true perturbative uncertainty. As an alternative approach the perturbative uncertainty of the NNLO result can be estimated by considering half of the difference between the NNLO and NLO results at central values of the scales [544].

It is finally observed that the photon fragmentation component (which is absent in the case of smooth cone isolation) mainly affects the the low invariant mass region, where the cross section is strongly suppressed. Conversely, the intermediate and high invariant mass region, the transverse momentum distribution and the value of total cross section, are less sensitive to photon fragmentation effects. In particular, for isolation parameters commonly used in the experimental analysis at the LHC, the quantitative differences between smooth and standard isolation predictions are much smaller than the corresponding perturbative uncertainties. This observation justifies the use of the smooth cone criterion in the theoretical calculations.

5.2 Ultimate Parton Densities[27]

The goal of this study is to quantify the precision that can be expected in the determination of the parton distribution functions (PDFs) of the proton in the HL-LHC era. Such "ultimate PDFs" will provide an important ingredient for the physics projections at the HL-LHC with a robust estimate of theoretical uncertainties, including some of those presented in other chapters of this Yellow Report. With this motivation, HL-LHC pseudo-data have been generated for a number of PDF-sensitive measurements such as top-quark, Drell-Yan, isolated photon, and W+charm production, and then studied the constraints that these pseudo-data impose on the global PDF analysis by means of the Hessian profiling method. While such studies have been performed in the context of future lepton-hadron colliders, see e.g. [461, 548] for the LHeC, this is the first time that such a systematic effort has been directed to the projections for a future hadron collider. The study below is described in further detail in [549].

5.2.1 HL-LHC measurements for PDF studies

The PDF-sensitive processes that will be considered in this study are listed here first. In all cases, pseudo-data is generated for a centre-of-mass energy of $\sqrt{s} = 14$ TeV assuming a total integrated luminosity of $\mathcal{L} = 3$ ab^{-1} for the CMS and ATLAS experiments, and of $\mathcal{L} = 0.3$ ab^{-1} for the LHCb experiment. With these settings, HL-LHC pseudo-data has been generated for the following processes:

- High-mass Drell-Yan, specifically the dilepton invariant mass differential distributions $d\sigma(pp \to ll)/dm_{ll}$ for $m_{ll} \gtrsim 110$ GeV for a central rapidity acceptance, $|\eta^l| \leq 2.4$. This process is particularly useful for quark flavour separation, in particular of the poorly known large-x sea quarks.
- Differential distributions in top-quark pair production, providing direct information on the large x gluon [203]. Specifically, pseudo-data has been generated for the top-quark transverse momentum $p_{\rm T}^t$ and rapidity y_t as well as for the top-quark pair rapidity $y_{t\bar{t}}$ and invariant mass $m_{t\bar{t}}$.
- The transverse momentum distribution of the Z bosons in the large $p_{\rm T}^Z$ region for central rapidity $|y_Z| \leq 2.4$ and different bins of the dilepton invariant mass m_{ll}. This process is relevant to constrain the gluon and the antiquarks at intermediate values of x [204].
- The production of W bosons in association with charm quarks (both in the central and forward region). This process provides a sensitive handle to the strangeness content of the proton [550, 551]. The pseudo-data for this process has been generated as function of the pseudorapidity η_l of the charged lepton from the W boson decay.
- Prompt isolated photon production, which represents a complementary probe of the gluon PDF at intermediate values of x [205, 552]. Here the pseudo-data have been generated as differential distributions in the photon transverse momentum $p_{\rm T}^\gamma$ for different bins in the photon pseudorapidity η^γ.
- Differential distributions for on-peak W and Z boson production in the forward region, $2.0 \leq \eta_l \leq 4.5$, covered by detectors with large acceptance, including forward rapidity. These measure-

[27] Contribution by R. Abdul Khalek, S. Bailey, J. Gao, L. Harland-Lang and J. Rojo.

ments constrain quark flavour separation, including the strange and charm content of the proton, in the large and small x region [553].

– The inclusive production of jets in different bins of rapidity (both in the central and forward region) as a function of $p_{\rm T}^{\rm jet}$. Jets have been reconstructed using the anti–k_t algorithm [274] with $R = 0.4$, and provide information on the large-x gluon and valence quarks [554].

In all cases, the binning and kinematic cuts from the most recent $\sqrt{s} = 13$ TeV analyses or the corresponding 8 TeV analyses if the former are not available, are taken as the baseline. The binning has been suitably extended to account for the extended kinematic coverage achieved with $\mathcal{L} = 3$ (0.3) ab^{-1}. The statistical uncertainties are computed from the number of events per bin, while systematic errors are rescaled as compared to the 13 (or 8) TeV baseline analysis, see below. Various scenarios for the reduction of systematic errors are considered, from a more conservative one to a more optimistic one. The overall acceptance of the selection cuts (which affects the final event yield per bin) is estimated globally again based on the reference experimental analysis.

As mentioned above, this list of processes is not exhaustive: several other important processes will provide useful information on the parton distributions in the HL-LHC era, from inclusive dijet production [19] to single top quark [555] and D meson production [231], see also [193]. In addition, progress may be expected from both the experimental and theory sides leading to novel processes, not considered so far, being added to the PDF fitting toolbox. Even with these caveats, the list above is extensive enough to provide a reasonable snapshot of the PDF-constraining potential of the HL-LHC.

It is worth emphasising that the projections are based on pseudo-data which have been generated specifically for this study. They are thus not endorsed by the LHC experiments, although the feedback received from the ATLAS, CMS, and LHCb contact persons have been taken into account.

Generation of HL-LHC pseudo-data and fitting procedure

For each of the HL-LHC processes listed above, theoretical predictions have been generated at next-to-leading order (NLO) using MCFM [210] interfaced to APPLGRID [208] to produce the corresponding fast grids. The central value of the pseudo-data is first produced according the central prediction of the PDF4LHC15 NNLO set [195], and then fluctuations as expected by the corresponding experimental uncertainties are included. Since the present study is based on pseudo-data, it does not account for higher-order QCD effects or electroweak corrections. As in the case of PDF closure tests [201], here only the relative reduction of PDF uncertainties once the HL-LHC data are added are of interest, while by construction the central value will be mostly unaffected.

To be more specific, if $\sigma_i^{\rm th}$ is the theoretical cross-section for bin i of a given process, computed with PDF4LHC15 NNLO, then the central value of the HL-LHC pseudo-data $\sigma_i^{\rm exp}$ is constructed by means of

$$\sigma_i^{\rm exp} = \sigma_i^{\rm th} \times \left(1 + r_i \cdot \delta_{{\rm tot},i}^{\rm exp} + \lambda \cdot \delta_{\mathcal{L}}^{\rm exp}\right) \, , \tag{32}$$

where r_i, λ are univariate Gaussian random numbers, $\delta_{{\rm tot},i}^{\rm exp}$ is the total (relative) experimental uncertainty corresponding to this specific bin, and $\delta_{\mathcal{L}}^{\rm exp}$ is the luminosity uncertainty related to the experiment. The latter are taken to be 1.5% for each of the CMS, ATLAS, and LHCb experiments. The motivation for adding the fluctuations on top of the central theoretical predictions is to simulate the statistical and systematic uncertainties of an actual experimental measurement. In eq. (32) the total experimental error is defined as

$$\delta_{{\rm tot},i}^{\rm exp} \equiv \left(\left(\delta_{{\rm stat},i}^{\rm exp}\right)^2 + \left(f_{\rm corr} \times f_{\rm red} \times \delta_{{\rm sys},i}^{\rm exp}\right)^2 \right)^{1/2} \, . \tag{33}$$

In this expression, the relative statistical error $\delta_{{\rm stat},i}^{\rm exp}$ is computed as

$$\delta_{{\rm stat},i}^{\rm exp} = \left(f_{\rm acc} \times N_{{\rm ev},i}\right)^{-1/2} \, , \tag{34}$$

where $N_{\mathrm{ev},i} = \sigma_i^{\mathrm{th}} \times \mathcal{L}$ is the expected number of events in bin i at the HL-LHC with $\mathcal{L} = 3\ (0.3)\ \mathrm{ab}^{-1}$, and $f_{\mathrm{acc}} \leq 1$ is an acceptance correction which accounts for the fact that, for some of the processes considered, such as top quark pair production, there is a finite experimental acceptance and/or one needs to include the effects of branching fractions. The value of f_{acc} is then determined by extrapolation using the reference dataset. The one exception to this is the case of forward W+charm production, for which no baseline measurement has so far been performed by LHCb; here the acceptance is set to $f_{\mathrm{acc}} = 0.3$ to account for the anticipated c–jet tagging efficiency. In eq. (33), $\delta_{\mathrm{sys},i}^{\mathrm{exp}}$ indicates the total systematic error of bin i taken from the reference LHC measurement at either 8 TeV or 13 TeV. The correction factor $f_{\mathrm{red}} \leq 1$ accounts for the expected improvement in the average systematic uncertainties at the HL-LHC in comparison to Run-2, due to both detector improvements and the enlarged dataset for calibration.

With the exception of the luminosity in eq. (33) the systematic uncertainties have simply been added in quadrature with the statistical ones. That is, correlations between systematic errors are not taken into account. The full inclusion of such correlations goes beyond the scope of the closure tests being pursued in this exercise, which aim simply to provide a reasonable extrapolation of the expected PDF reach at the HL-LHC. In particular, the expected improvements in the overall size of the systematic uncertainties can only be based on the estimates and expectations provided by the LHC collaborations, and cannot be predicted with absolute certainty. The situation is certainly even more challenging in the case of the specific mutual correlations of the systematic uncertainties, which will be sensitive to the precise experimental setup in the future. However, simply excluding the effects of correlations would artificially reduce the impact of the pseudo-data into the fit.

For this reason, an effective correction factor f_{corr} is introduced to accounts for the fact that data with correlated systematic uncertainties is more constraining than the same data where all errors are added in quadrature. The value of f_{corr} has been checked against the available $\sqrt{s} = 8$ TeV top quark [556,557] and the 13 TeV W+charm [558] differential distributions, that is f_{corr} is varied until the PDF impact is in line with the result including full experimental correlations. This turns out to have a value of between $f_{\mathrm{corr}} \simeq 1.0$ and 0.3 depending on the data set and observable. A factor of $f_{\mathrm{corr}} = 0.5$ is taken in what follows.

In Table 31 a summary of the features of the HL-LHC pseudo-data generated for the present study is collected. For each process, the kinematic coverage, the number of pseudo-data points used N_{dat}, the values of the correction factors f_{acc}, f_{corr}, and f_{red}; and finally the reference from the 8 TeV or 13 TeV measurement used as baseline to define the binning and the systematic uncertainties of the HL-LHC pseudo-data are indicated. A total of $N_{\mathrm{dat}} = 768$ pseudo-data points are then used in the PDF profiling. The values of the reduction factor for the systematic errors f_{red} are varied between 1 (0.5) and 0.4 (0.2) in the conservative and optimistic scenarios for a 8 TeV (13 TeV) baseline measurement. This choice is motivated because available 13 TeV measurements are based on a relatively small $\mathcal{L}$ and therefore cannot be taken as representative of the systematic errors expected at the HL-LHC, even in the most conservative scenario.

Hessian profiling

There exist a number of techniques that can be used to quantify the impact on PDFs of the pseudo-data listed in Table 31. In the case of Monte Carlo sets such as NNPDF, the Bayesian reweighting method [564,565] reproduces the result of a direct fit, but it is restricted by the fact that information loss limits its reliability when the measurements provide significant new information. For Hessian sets such as PDF4LHC15_100 instead, the profiling technique [476] is more suitable to achieve the same purpose.

Table 31: Summary of the features of the HL-LHC pseudo-data generated for the present study. For each process the kinematic coverage, the number of pseudo-data points used $N_{\rm dat}$ across all detectors, the values of the correction factors $f_{\rm corr}$ and $f_{\rm red}$; and finally the reference from the 8 TeV or 13 TeV measurement used as baseline to define the binning and the systematic uncertainties of the HL-LHC pseudo-data, as discussed in the text, are indicated.

Process	Kinematics	$N_{\rm dat}$	$f_{\rm corr}$	$f_{\rm red}$	Baseline
Z $p_{\rm T}$	$20\,{\rm GeV} \leq p_{\rm T}^{ll} \leq 3.5$ TeV $12\,{\rm GeV} \leq m_{ll} \leq 150\,{\rm GeV}$ $\lvert y_{ll}\rvert \leq 2.4$	338	0.5	$(0.4, 1)$	[559] (8 TeV)
high-mass Drell-Yan	$p_{\rm T}^{l1(2)} \geq 40(30)\,{\rm GeV}$ $\lvert\eta^l\rvert \leq 2.5, m_{ll} \geq 116\,{\rm GeV}$	32	0.5	$(0.4, 1)$	[560] (8 TeV)
top quark pair	$\lvert y_t\rvert \leq 2.4$	110	0.5	$(0.4, 1)$	[557] (8 TeV)
W+charm (central)	$p_{\rm T}^{\mu} \geq 26\,{\rm GeV}, p_{\rm T}^{c} \geq 5\,{\rm GeV}$ $\lvert\eta^{\mu}\rvert \leq 2.4$	12	0.5	$(0.2, 0.5)$	[558] (13 TeV)
W+charm (forward)	$p_{\rm T}^{\mu} \geq 20\,{\rm GeV}, p_{\rm T}^{c} \geq 20\,{\rm GeV}$ $p_{\rm T}^{\mu+c} \geq 20\,{\rm GeV}$ $2 \leq \eta^{\mu} \leq 5, 2.2 \leq \eta^{c} \leq 4.2$	10	0.5	$(0.4, 1)$	LHCb projection
Direct photon	$E_{\rm T}^{\gamma} \lesssim 3$ TeV, $\lvert\eta_{\gamma}\rvert \leq 2.5$	118	0.5	$(0.2, 0.5)$	[561] (13 TeV)
Forward W, Z	$p_{\rm T}^{l} \geq 20\,{\rm GeV}, 2.0 \leq \eta^{l} \leq 4.5$ $2.0 \leq y_{ll} \leq 4.5$ $60 \leq m_{ll} \leq 120\,{\rm GeV}$	90	0.5	$(0.4, 1)$	[562] (8 TeV)
Inclusive jets	$\lvert y\rvert \leq 3, R = 0.4$	58	0.5	$(0.2, 0.5)$	[563] (13 TeV)
Total		712			

This Hessian profiling is based on the minimization of

$$\chi^2\left(\beta_{\rm exp}, \beta_{\rm th}\right) = \sum_{i=1}^{N_{\rm dat}} \frac{1}{\left(\delta_{{\rm tot},i}^{\rm exp}\sigma_i^{\rm th}\right)^2}\left(\sigma_i^{\rm exp} + \sum_j \Gamma_{ij}^{\rm exp}\beta_{j,{\rm exp}} - \sigma_i^{\rm th} + \sum_k \Gamma_{ik}^{\rm th}\,\beta_{k,{\rm th}}\right)^2 + \sum_j \beta_{j,{\rm exp}}^2 + T^2\sum_k \beta_{k,{\rm th}}^2\,, \tag{35}$$

with $\sigma_i^{\rm exp}$ ($\sigma_i^{\rm th}$) are the central values of a given experimental measurement (theory prediction), $\beta_{j,{\rm exp}}$ are the nuisance parameters corresponding to the set of fully correlated experimental systematic uncertainties, $\beta_{k,{\rm th}}$ are the nuisance parameters corresponding to the PDF Hessian eigenvectors, $N_{\rm dat}$ is the number of data points and T is the tolerance factor. The matrices $\Gamma_{ij}^{\rm exp}$ and $\Gamma_{ik}^{\rm th}$ encode the effects of the corresponding nuisance parameters on the experimental data and on the theory predictions, respectively.

As mentioned above, in this study the statistical and experimental uncertainties are added in quadrature excluding the luminosity, and then the effects of the missing correlations are accounted for

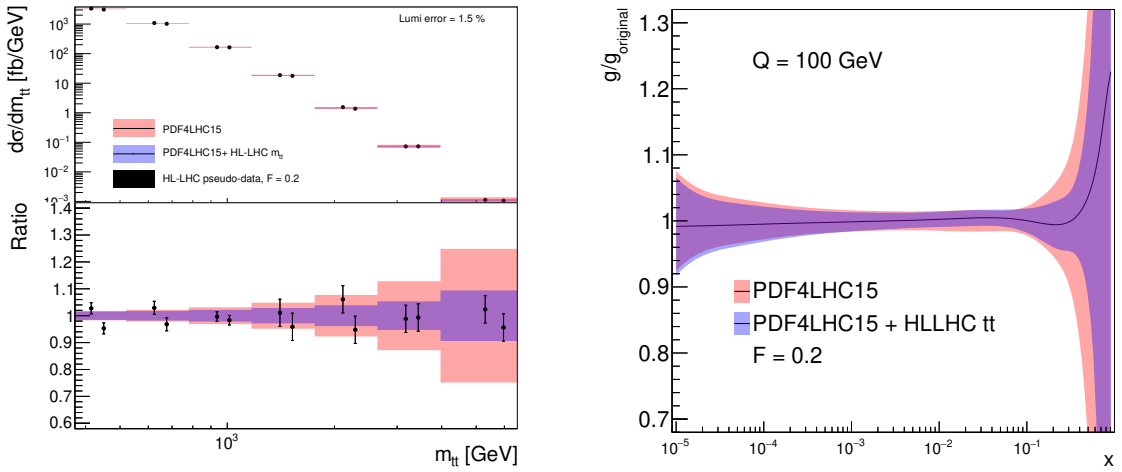

Fig. 57: Comparison of the predictions for the $m_{t\bar{t}}$ distribution in top-quark pair production at the HL-LHC using PDF4LHC15 with the associated pseudo-data and with the profiled results with $F \equiv f_{\rm corr} \cdot f_{\rm red} = 0.2$ (left). The corresponding differences at the level of the gluon PDF at $Q = 100$ GeV before and after profiling all top-quark pair production observables (right).

by means of the factor $f_{\rm corr}$. For this reason there are only nuisance parameters for the luminosity errors, and for an overall normalization uncertainty of 5% in forward W+charm production due to charm-jet tagging. If eq. (35) is minimised with respect to these nuisance parameters, this gives:

$$\chi^2\left(\beta_{\rm th}\right) = \sum_{i,j=1}^{N_{\rm dat}} \left(\sigma_i^{\rm exp} - \sigma_i^{\rm th} + \sum_k \Gamma_{ik}^{\rm th}\,\beta_{k,\rm th}\right) \left(\rm cov\right)_{ij}^{-1} \left(\sigma_j^{\rm exp} - \sigma_j^{\rm th} + \sum_m \Gamma_{jm}^{\rm th}\,\beta_{m,\rm th}\right) + T^2 \sum_k \beta_{k,\rm th}^2\,, \tag{36}$$

where:

$$\left(\rm cov\right)_{ij} = \delta_{ij}\left(\delta_{{\rm tot},i}^{\rm exp}\sigma_i^{\rm th}\right)^2 + \sum \Gamma_{i,\rm lumi/norm}^{\rm exp}\Gamma_{j,\rm lumi/norm}^{\rm exp}. \tag{37}$$

eq. (36) is then minimised with respect to the Hessian PDF nuisance parameters $\beta_{k,\rm th}$, which can be interpreted as leading to PDFs that have been optimised to describe this new dataset. The resulting Hessian matrix on $\beta_{k,\rm th}$ at the minimum can be diagonalised to construct the new eigenvector directions. Finally, the PDF uncertainties are determined from the $\Delta\chi^2 = T^2$ criteria. In the studies presented here, a global $T = 3$ is used which approximately corresponds to the average tolerance determined dynamically in the CT14 and MMHT14 analyses.

Results for individual processes

The results of the Hessian profiling of PDF4LHC15 from individual processes are now presented, and subsequently the corresponding results from the combination of all the HL-LHC processes are considered in different scenarios. First, the top-quark pair production case listed in Table 31 is considered. In Fig. 57 the comparison of the predictions for the $m_{t\bar{t}}$ distribution in top-quark pair production at the HL-LHC using PDF4LHC15 is shown with the associated pseudo-data for ATLAS and CMS experiments, and with the profiled results with $F \equiv f_{\rm corr} \cdot f_{\rm red} = 0.2$. The corresponding impact at the level of the gluon PDF at $Q = 100$ GeV is also presented before and after profiling with all $t\bar{t}$ data in Table 31. It is clear that the HL-LHC pseudo-data in this scenario will have much smaller uncertainties than the PDF uncertainties, so there is a marked reduction on the PDF errors on the gluon at large-x. Note that the two points in each of the bins in Fig. 57 (left) correspond to the ATLAS and CMS pseudo-data.

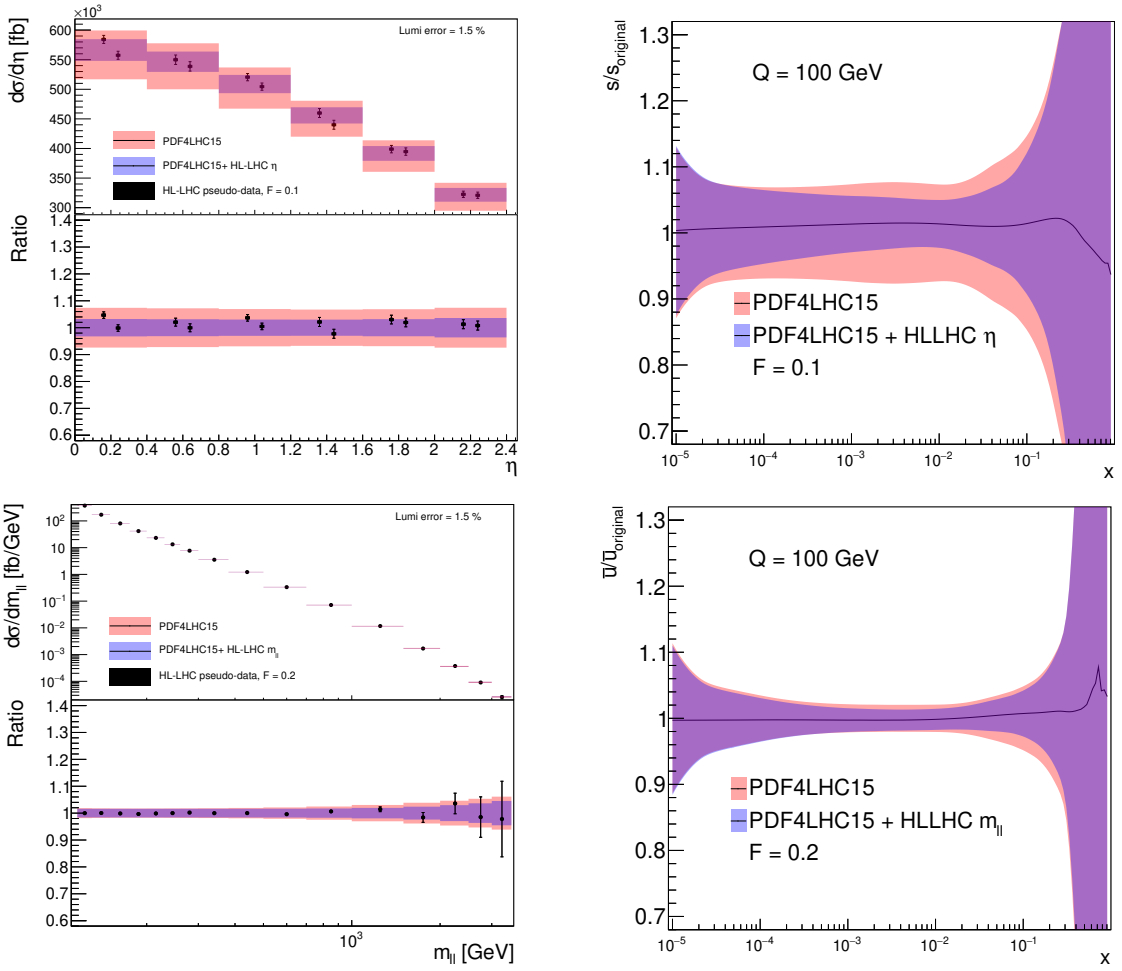

Fig. 58: Same as Fig. 57 for W+charm quark production with impact on strange quark PDF (upper) and the high-mass Drell-Yan process with impact on $\bar{u}$ PDF (lower).

Two other representative processes are considered next: W+charm quark production in central rapidity region and the high-mass Drell-Yan process. In Fig. 58 the same comparison is shown as in Fig. 57 for these two processes. In the case of the W+charm quark production, a clear reduction of PDF errors is observed in the strangeness, $s+\bar{s}$, at intermediate values of x, highlighting the sensitivity of this measurement to the strange content of the proton. For the case of high-mass Drell-Yan, the uncertainties on the $\bar{u}$ quark PDF are reduced at large x region. Here the impact is rather moderate, as experimental and PDF errors are comparable even in the high m_{ll} region.

5.2.2 Ultimate PDFs from HL-LHC data

The final profiled PDF sets are based on the combined datasets listed in Table 31; these provide an estimate of the impact of future HL-LHC measurements into our knowledge of the quark and gluon structure of the proton. In Table 32 the three scenarios for the systematic uncertainties of the HL-LHC pseudo-data assumed in the present exercise are listed. These scenarios, ranging from more conservative to more optimistic, differ among them in the reduction factor $f_{\rm red}$, eq. (33), applied to the systematic errors of the reference 8 TeV or 13 TeV measurements. In particular, in the optimistic scenario a reduction of the systematic errors by a factor 2.5 compared to the reference 8 TeV measurements is assumed. A

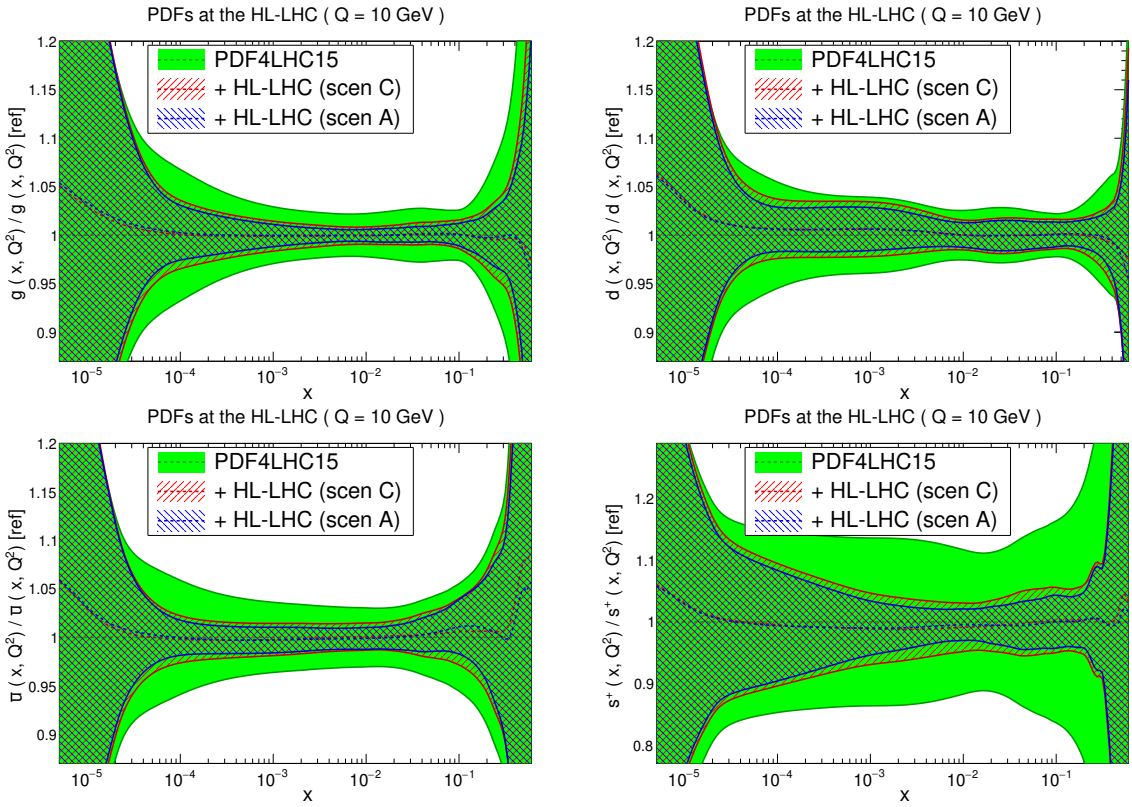

Fig. 59: Comparison of PDF4LHC15 with the profiled sets with HL-LHC data in scenarios A and C (see text). The gluon, down quark, up anti-quark, and total strangeness at $Q = 10$ GeV are shown, normalized to the central value of the baseline.

large factor of 5 for the 13 TeV measurements is assumed, correcting for the fact that these are based in the initial datasets which generally have larger systematic errors in comparison to the 8 TeV case. The name of the corresponding `LHAPDF` grid is also indicated in each case.

Table 32: The three scenarios for the systematic uncertainties of the HL-LHC pseudo-data assumed in the present exercise. These scenarios, ranging from conservative to optimistic, differ among them in the reduction factor $f_{\rm red}$, eq. (33), applied to the systematic errors of the reference 8 TeV or 13 TeV measurements. The name of the corresponding `LHAPDF` grid is also indicated in each case.

Scenario	$f_{\rm red}$ (8 TeV)	$f_{\rm red}$ (13 TeV)	`LHAPDF` set	Comments
A	0.4	0.2	`PDF4LHC_nnlo_hllhc_scen3`	Optimistic
B	0.7	0.36	`PDF4LHC_nnlo_hllhc_scen2`	Intermediate
C	1	0.5	`PDF4LHC_nnlo_hllhc_scen1`	Conservative

Then in Fig. 59 a comparison of the baseline PDF4LHC15 set is presented with the profiled sets based on HL-LHC pseudo-data from scenarios A and C in Table 32. Specifically, the gluon, down quark, up anti-quark, and total strangeness at $Q = 10$ GeV are shown, normalized to the central value of the baseline. The predictions of scenarios A and C (optimistic and conservative respectively) are observed to be reasonably similar. This demonstrates that the results are relatively robust against the projections of how experimental errors will be reduced in HL-LHC measurements. A marked reduction of PDF

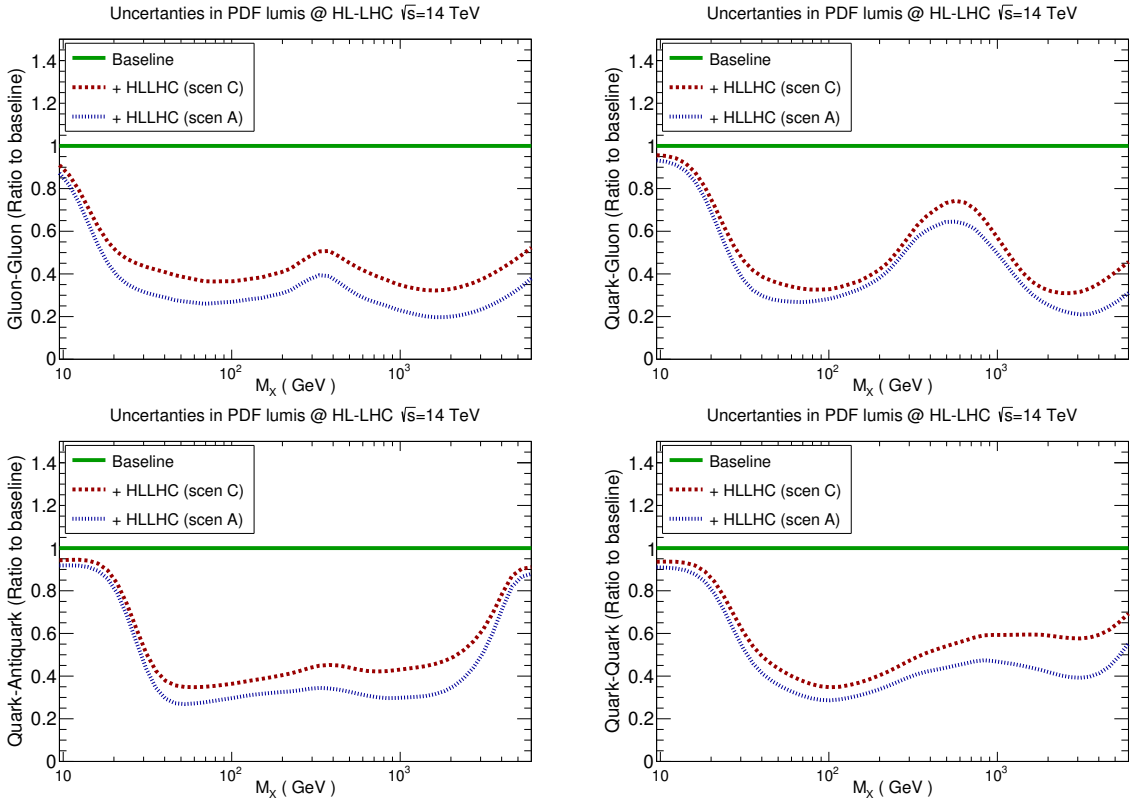

Fig. 60: The reduction of PDF uncertainties in the gg, qg, $q\bar{q}$, and qq luminosities at $\sqrt{s} = 14$ TeV due to the HL-LHC pseudo-data (in scenarios A and C) with respect to the PDF4HC15 baseline.

uncertainties is visible in all cases, and is particularly significant for the gluon and the sea quarks, which are worse known than the valence quarks.

Next, the partonic luminosities are investigated, in particular by quantifying the improvement in the PDF uncertainties in different initial-state partonic combinations from the HL-LHC pseudo-data. In Fig. 60 the reduction of PDF uncertainties are shown in the gg, qg, $q\bar{q}$, and qq luminosities at $\sqrt{s} = 14$ TeV due to the HL-LHC pseudo-data (in scenarios A and C) with respect to the PDF4HC15 baseline. The average values of this PDF error reduction for three different invariant mass bins (low, medium, and high values of M_X) is shown in the table in Fig. 61.[28] The value outside (inside) brackets correspond to scenario C (A). Note that in this table the us luminosity is also listed, which contributes to processes such as inclusive W^+ production.

From the comparisons in Fig. 60 and in Fig. 61 it is observed the overall error reduction is not too sensitive to the specific projections assumed for the experimental systematic uncertainties. In the intermediate mass bin, $40 \text{ GeV} \leq M_X \leq 1 \text{ TeV}$, the reduction of PDF uncertainties ranges roughly between a factor of 2-4, depending on the partonic channel and the scenario for the systematic errors. For example, for the gg luminosity in the range relevant for Higgs production, a reduction by a factor $\simeq 3$ in scenario A is found. A similar improvement is found in the high mass region, $M_X \geq 1$ TeV, directly relevant for beyond-SM (BSM) searches. In the optimistic scenario, the PDF error reduction at high masses ranges between a factor 4 for the gg luminosity to around a factor 2 for the qq and $q\bar{q}$ ones. On the other hand, the PDF error reduction is more moderate in the low mass region, $M_X \lesssim 20$ GeV, since none of the processes in Table 31 is directly sensitive to it.

[28] The average is computed from 10 points per mass bin, log-spaced in M_X.

PDF uncertainties HLLHC / Current	10 GeV < M_X < 40 GeV	40 GeV < M_X < 1 TeV	1 TeV < M_X < 6 TeV
g-g luminosity	0.58 (0.49)	0.41 (0.29)	0.38 (0.24)
q-g luminosity	0.71 (0.65)	0.49 (0.42)	0.39 (0.29)
quark-quark luminosity	0.78 (0.73)	0.46 (0.37)	0.60 (0.45)
quark-antiquark luminosity	0.73 (0.70)	0.40 (0.30)	0.61 (0.50)
up-strange luminosity	0.73 (0.67)	0.38 (0.27)	0.42 (0.38)

Fig. 61: The uncertainties associated to different PDF luminosities, normalised to the uncertainties of the current baseline (PDF4LHC15). The average for three different invariant mass M_X bins is computed. The numbers outside (inside) brackets correspond to the conservative (optimistic) scenario.

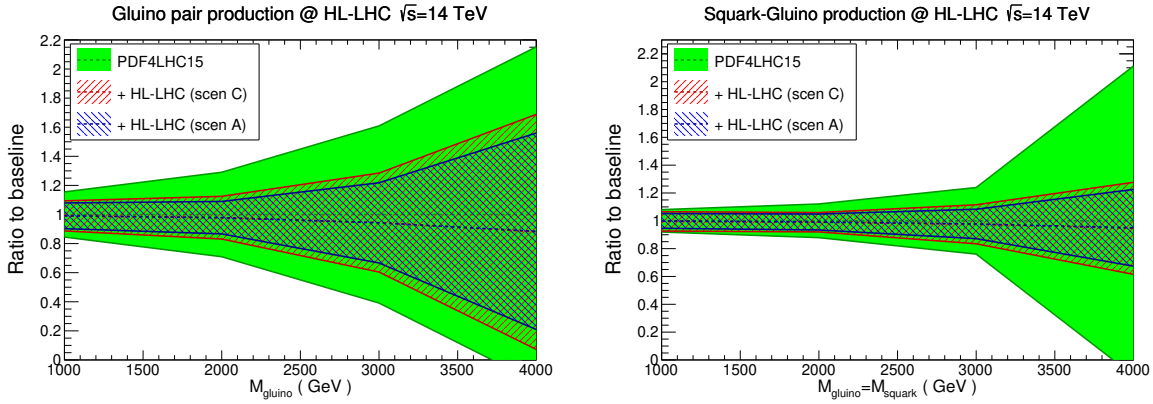

Fig. 62: Comparison between the baseline PDF4LHC15 predictions for high-mass supersymmetric particle production at the HL-LHC with the corresponding HL-LHC projections corresponding to scenarios C and A, normalised to the central value of the baseline. The results for gluino-gluino and squark-gluino production cross-sections are shown at $\sqrt{s} = 14$ TeV.

Implications for LHC phenomenology

Now some selected phenomenological implications of these "ultimate" PDFs at the HL-LHC are presented for a variety of processes, both within the SM and beyond. First high-mass supersymmetric (SUSY) particle production at the HL-LHC is considered, where sparticles masses up to $\simeq 3$ TeV can be searched for. While this SUSY scenario is considered for concreteness, similar results will hold for the production of new BSM states within other models. In Fig. 62 the comparison between the baseline PDF4LHC15 predictions with the corresponding HL-LHC results is shown corresponding to scenarios C and A (conservative and optimistic respectively), normalised to the central value of the former. Specifically, the cross-sections for gluino-gluino and squark-gluino are shown at $\sqrt{s} = 14$ TeV. Theoretical predictions have been computed at leading order (LO) using PYTHIA8.235 [292] with the SLHA2 benchmark point [566] for a range of sparticle masses. For simplicity, underlying event and multiple interactions have been ignored.

From the comparisons in Fig. 62, the constraints on the PDFs from the HL-LHC pseudo-data

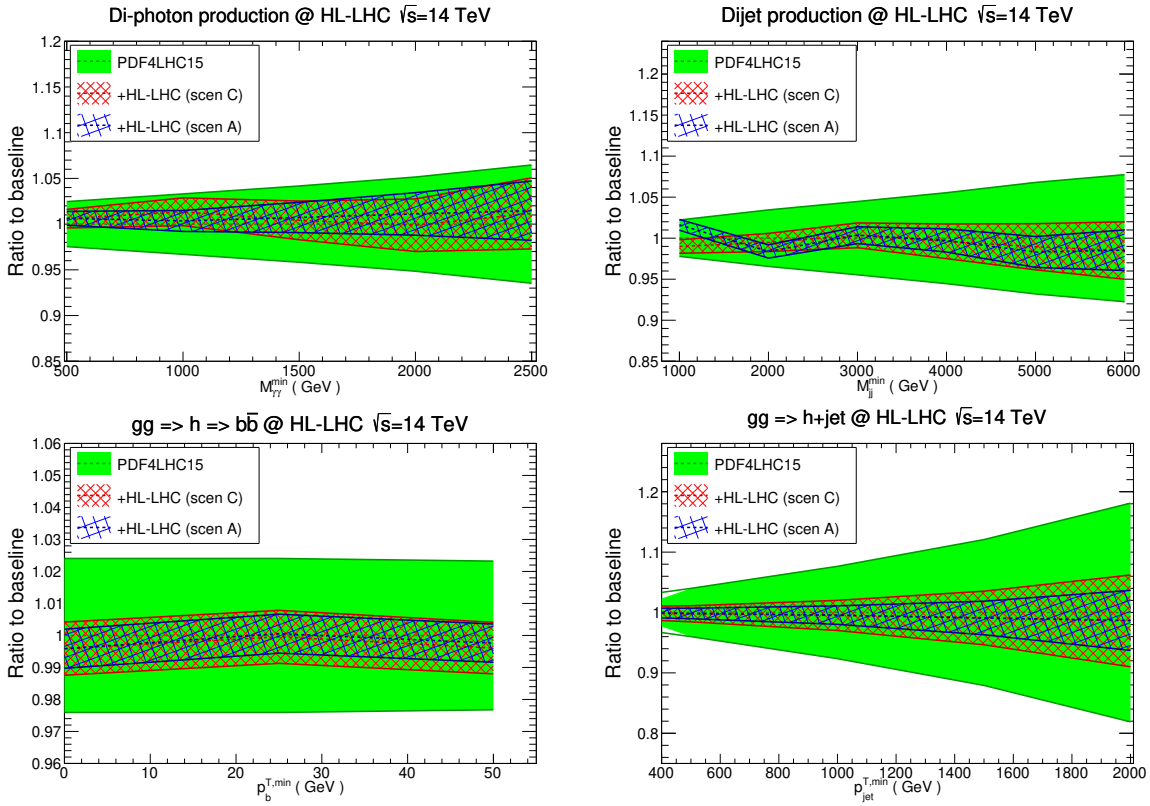

Fig. 63: Same as Fig. 62 for Standard Model processes. The upper plots show diphoton (dijet) production as a function of the minimum invariant mass $M_{\gamma\gamma}^{\rm min}$ ($M_{jj}^{\rm min}$). The bottom plots show Higgs boson production in gluon fusion, first inclusive and decaying into $b\bar{b}$ as a function of $p_b^{\rm T,min}$, and then in association with a hard jet as a function of $p_{\rm jet}^{\rm T,min}$.

lead to a marked reduction to the uncertainties in the high-mass SUSY cross-sections, consistent with the corresponding reduction at the level of luminosities reported in Fig. 60. For instance, for gluino pair-production with $M_{\tilde{g}} = 3$ TeV, the PDF uncertainties are reduced from $\simeq 60\%$ to $\simeq 25\%$ in the optimistic scenario. An even more marked reduction is found for the squark-gluino cross-section, specially at large sparticle masses. More moderate improvements are found in the case of squark-antisquark production, due to the limited constraints that the HL-LHC provides on the large-x antiquarks, at least for the processes considered here. In this case, an error reduction of a factor of $\simeq 25\%$ is found for $M_{\tilde{q}} = 3$ TeV.

Next, in Fig. 63 a similar comparison is presented as that of Fig. 62, now for various SM processes. The upper plots display diphoton (dijet) production as a function of the minimum invariant mass $M_{\gamma\gamma}^{\rm min}$ ($M_{jj}^{\rm min}$). The bottom plots show Higgs boson production in gluon fusion, first inclusive and decaying into $b\bar{b}$ as a function of $p_b^{\rm T,min}$, and then in association with a hard jet as a function of $p_{\rm jet}^{\rm T,min}$. These cross-sections have been computed at LO with `MCFMv8.2` [210] with the basic ATLAS and CMS acceptance cuts. The use of leading-order theory is justified as only the relative impact of the PDF error reduction is of interest, rather than providing state-of-the-art predictions for the rates.

From the comparisons in Fig. 63, the two scenarios, A and C, give similar results. In the case of dijet production, which at large masses is dominated by the qq and qg luminosities, PDF errors are expected to reduce down to $\simeq$2% even for invariant masses as large as $M_{jj} = 6$ TeV. A similar conclusion can be drawn for diphoton production, also sensitive to the qq partonic initial state. Concerning

Higgs boson production in gluon fusion, in the inclusive case the HL-LHC constraints should lead to PDF errors below the percent level. For Higgs boson production in association with a hard jet, a marked error reduction is found, suggesting that PDF uncertainties in the $p_{\rm T}^h$ distribution should be down to at most the $\simeq$2% level at the HL-LHC in the entire relevant kinematical range.

Summary and outlook

In this study, the constraints that HL-LHC measurements are expected to impose on the quark and gluon structure of the proton have been quantified. The impact of a range of physical processes have been assessed, from weak gauge boson and jet production to top quark and photon production, and the robustness of the results has been studied with respect to different projections for the experimental systematic uncertainties. It is found that, in the invariant mass region $M_X \gtrsim 100$ GeV, the HL-LHC measurements can be expected to reduce the PDF uncertainties in processes such as Higgs boson or SUSY particle production by a factor between 2 and 4, depending on the dominant partonic luminosity and on the scenario for the systematic errors. Therefore, the exploitation of the HL-LHC constraints on PDFs will feed into improved theoretical predictions for a range of phenomenologically relevant processes both within and beyond the SM.

Two caveats are relevant at this point. First, only a non–exhaustive subset of all possible measurements of relevance for PDF fits has been considered. Other processes not considered here, due to currently anticipated measurements and those not foreseen but which may well added to the PDF toolbox in the future, will certainly increase the PDF impact in some regions. Second, any possible issues such as data incompatibility, theoretical limitations, or issues with the data correlation models, which may limit the PDF impact in some cases have been ignored. All these issues can only be tackled once the actual measurements are presented.

The results of this study are made publicly available in the `LHAPDF6` format [202], with the grid names listed in Table 32. This way, the "ultimate" PDFs produced here can be straightforwardly applied to related physics projections of HL-LHC processes taking into account our improved knowledge of the partonic structure of the proton which is expected by then.

5.3 Underlying Event and Multiple Parton Interactions

Underlying event (UE), defined as a accompanying activity to hard proton-proton scattering process, is an unavoidable background to collider observables for most measurements and searches. The UE activity is not constant on an event-by-event basis, so the contribution from UE cannot be subtracted. However by using measurements sensitive to UE activity, the modelling of it in Monte Carlo (MC) event generators is *tuned*.

Multiple parton interactions (MPI) are one of the most important contributors to UE. The dependence of MPI on the centre-of-mass energy ($\sqrt{s}$) cannot be derived from first principles, rather modelled by looking at data at different centrer-of-mass energies, from Tevatron to LHC. At the start of the LHC, it was found that the this energy extrapolation of MPI based in Tevatron Run-1 and -2 data (at $\sqrt{s} = 1.8$ TeV and $\sqrt{s} = 1.96$ TeV) did not describe the LHC data at $\sqrt{s} = 900$ GeV and at $\sqrt{s} = 7$ TeV [567], and predictions of different MC generators varied significantly. These generators were then tuned using LHC Run-1 and Run-2 ($\sqrt{s} = 13$ TeV) data.

5.3.1 Underlying Event at 27 TeV[29]

The level of UE activity at the HL-LHC centre-of-mass energy of $\sqrt{s} = 14$ TeV is expected to be very similar to the one measured at $\sqrt{s} = 13$ TeV in Run-2. Given such a small increment in centre-of-mass

[29] Contribution by D. Kar.

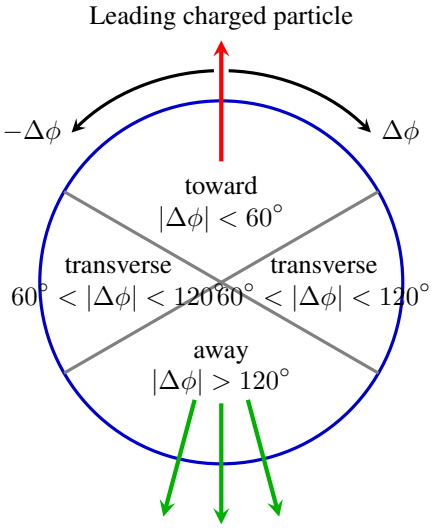

Fig. 64: Definition of UE regions in the azimuthal angle with respect to the leading charged particle

energy, it is expected that the current MC tunes will be generally valid at HL-LHC too. On the other hand, to get a sense of the UE activity at HE-LHC, two state-of-the-art MC generators, PYTHIA8 [292] (v235) with Monash tune [230] and HERWIG7 [146, 147] (v713) with default tune were used. As the first measurements at a new centre-of-mass energy data are easiest to perform in inclusive (i.e minimum-bias) events, 5 million such events were generated in each case. The UE activity is measured using the leading charged particle as the reference object, and defining the usual UE regions with respect to it, as shown in Fig. 64.

In Fig. 65, the scalar sum (density in per unit η-ϕ area) of charged particles and charged particle multiplicity (density) as a function of leading charged particle p_{T} are shown. The data is from the ATLAS measurement at $\sqrt{s} = 13$ TeV [568], while MC predictions both at $\sqrt{s} = 13$ TeV and $\sqrt{s} = 27$ TeV are shown. A few conclusions can be drawn. The activity increases by about 25 - 30% by roughly doubling the centre-of-mass energy, and the predictions by both generators are extremely consistent. The typical plateau-like behaviour of the activity with increasing leading charged particle p_{T} can be seen at $\sqrt{s} = 27$ TeV as well.

The similarity in predictions by two different generators is a welcoming sign, and perhaps indicates that the modelling of MPI evolution with centre-of-mass energy is mature enough. Of course at $\sqrt{s} = 27$ TeV, the events will be very active, and disentangling the effect of MPI in even typical UE observables will be a challenge, and innovative topologies and observables will be have to be devised in order perform UE measurements.

The analysis and plots are done using the Rivet [344] analysis framework.

5.3.2 Double Parton Scattering[30]

An instance of MPI is the double parton scattering (DPS) that occurs when one has two distinct hard parton-parton collisions in a single proton-proton interaction. In terms of the total cross section to produce a final state AB that may be divided into two subsets A and B, DPS is formally power suppressed by $\sim \Lambda^2_{QCD}/\min(Q^2_A, Q^2_B)$ compared to the more-familiar single parton scattering (SPS) mechanism. However, in practice there are various processes and kinematic regions where DPS contributes at a similar (or greater) level than SPS. Processes include those in which the SPS is suppressed by small/multiple

[30] Contribution by S. Cotogno, M. Dunser, J. R. Gaunt, T. Kasemets, and M. Myska.

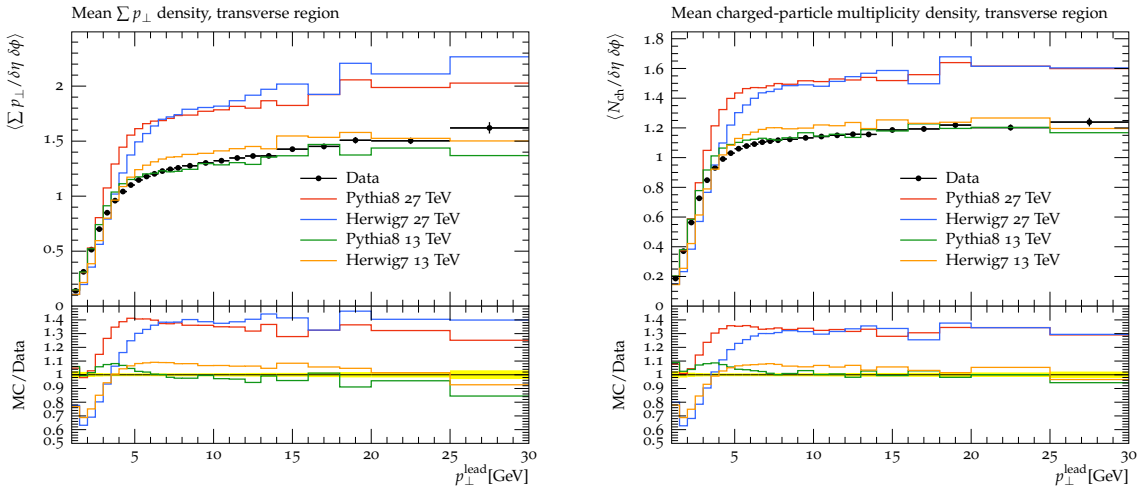

Fig. 65: Comparison of the UE activities in different centre-of-mass energies.

coupling constants, such as same-sign WW production, and processes where at least one part of the final state can be produced via a comparatively low scale scattering – e.g. those involving a charm/bottom quark pair.

The full theoretical description of DPS in QCD is rather complex, and many of the steps towards its formulation were achieved only recently [569–574]. As a result, many past studies of DPS have taken a strongly simplified approach in which it is assumed that the two colliding partons from each proton are entirely uncorrelated with one another, and that the (single) parton density in momentum fraction x and impact parameter $\mathbf{b}$ may be factorised into the PDF and a transverse profile depending only on $\mathbf{b}$. In this case the DPS cross section simplifies into the so-called 'pocket formula':

$$\sigma_{\text{DPS}}^{AB} \simeq \frac{\sigma_{\text{SPS}}^{A}\sigma_{\text{SPS}}^{B}}{\sigma_{\text{eff}}} \tag{38}$$

The quantity σ_{eff} is a geometrical factor of order of the proton radius squared. The modelling of more general multiple parton interactions (MPI) in Monte Carlo event generators such as HERWIG and PYTHIA is based on similar approximations.

The eq. (38) does not take into account the possibility that the two partons from either or both protons may have arisen as the result of a perturbative $1 \to 2$ splitting of a single parton into two. It also does not take into account a multitude of possible correlations between two partons in a proton, in spin, colour, and momentum fraction x_i, correlations between x_i and the transverse separation between partons $\mathbf{y}$, as well as potential interference contributions in parton type. These correlations and QCD effects can result in a DPS cross section differing from the prediction of eq. (38), both in terms of overall rate and also, crucially, in distributions.

Studies of DPS at the LHC and earlier colliders have essentially been restricted to extractions of a single number, the DPS rate, for several processes. From these early studies, in which the error bars are large and multiple factors change between measurements (x values, parton channels, scales...), nothing conclusive can be determined thus far concerning correlations. However, the increased luminosity of the HL-LHC will provide the statistics needed to study differential distributions with sufficiently small uncertainties that it will be possible to probe quantum correlations between partons in the proton and the dynamics of the $1 \to 2$ splitting for the first time. The results of these studies can be fed back and used to improve the theoretical modelling of DPS (and more general MPI), yielding improved DPS signal or background predictions.

As can be inferred from eq. (38), DPS roughly scales as the fourth power of a parton distribution, whilst SPS only scales as the second power. This means that for given hard scales Q_A, Q_B, the DPS cross section grows faster than the SPS one as the collider energy increases (and decrease x), meaning that at a HE-LHC DPS will be more prominent and easily measurable than at the LHC. At the same time, at the lower x values involved the effects of the correlations and $1 \to 2$ splittings will be different - a combination of measurements of different processes at both the HL-LHC and HE-LHC should help us to separate out the effects of the different correlations.

Let us illustrate the general points above using a concrete process – namely same-sign WW production, where both Ws decay leptonically into e or μ. A simple correlation-sensitive observable for this process is the asymmetry a_{η_l}:

$$a_{\eta_l} = \frac{\sigma(\eta_1 \cdot \eta_2 < 0) - \sigma(\eta_1 \cdot \eta_2 > 0)}{\sigma(\eta_1 \cdot \eta_2 < 0) + \sigma(\eta_1 \cdot \eta_2 > 0)}, \tag{39}$$

where $\eta_{1,2}$ are the rapidities of the two leptons. This quantity measures the discrepancy between the number of times the produced leptons emerge into opposite hemispheres of the detector and the number of times they emerge into the same hemisphere, normalised by the total number of lepton pairs produced. In the absence of parton correlations, it is found that $a_{\eta_l} = 0$; any departure from this value indicates the presence of correlations. A more differential version of this asymmetry is the cross section differential in the product $\eta_1 \cdot \eta_2$. Here an absence of correlations yields a symmetric distribution under $\eta_1 \cdot \eta_2 \leftrightarrow -\eta_1 \cdot \eta_2$, and an asymmetric distribution indicates correlations. In the below studies a cut of $|\eta_i| < 2.4$ is always applied.

One type of correlation that will clearly affect these observables are correlations in momentum fraction x between the partons. This type of effect was investigated in [575]. Here, the double parton distributions (DPDs) were calculated at an input scale of $Q_0^2 = 0.26\,\text{GeV}^2$ from a constituent quark model calculation where the proton is taken as being composed only from the three quarks uud. At this scale there are necessarily strong correlations in x space from the fact that there are only three quarks and due to the constraint $\sum_i x_i = 1$. These inputs were then evolved up to the W mass scale via the double DGLAP equations, with effects of $1 \to 2$ splittings being ignored. In Fig. 66, the green band represents their result at $\sqrt{s} = 14$ TeV for a quantity equal to $\sigma(\eta_1 \cdot \eta_2 < 0)/\sigma(\eta_1 \cdot \eta_2 > 0)$ – their result corresponds to $a_{\eta_l} \sim 0.05$. On the same plot is given the anticipated sensitivity of the CMS experiment at the HL-LHC (3 ab^{-1}) [576] and the lowest values of this ratio that would allow one to reject the hypothesis of eq. (38) at the 95% confidence level. These results indicate good prospects of the HL-LHC measuring a_{η_l} values on the few per cent level for this process.

One simple feature that must necessarily be present in the true DPDs, and is taken into account by the DPDs of [575] but not by eq. (38), is the fact that removing one valence u quark from the proton halves the probability to find another, and there is no chance to find two valence d quarks (this requirement is formally expressed in the number sum rules of [577]). This effect is highly relevant to a_{η_l} as it results in a reduction of cross section for large $\eta_1 \cdot \eta_2$ (which probes the 'double valence' region in one DPD) whilst leaving the cross section elsewhere unchanged. To investigate the size of a_{η_l} resulting from this effect only, DPD inputs are constructed at $Q_0 = 1$ GeV based on a factorised ansatz of a product of MSTW2008LO PDFs times a transverse factor, except that in the uu and dd cases the PDF part is given by $D^u(x_1)D^u(x_2) - \frac{1}{2}D^{u_v}(x_1)D^{u_v}(x_2)$ and $D^d(x_1)D^d(x_2) - D^{d_v}(x_1)D^{d_v}(x_2)$ respectively. Evolving these inputs and using them to calculate the W^+W^+ cross section at $\sqrt{s} = 13$ TeV, an asymmetry of ~ 0.017 is observed, indicating that these simple 'valence number effects' are at least one important driving force in the asymmetry of [575].

Correlations in (longitudinal) spin can affect the rapidity distributions of the produced leptons [578] and result in a nonzero a_{η_l}. The potential size of effects from spin correlations was investigated recently in [579]. In this study the unpolarised double parton distributions were constructed according to

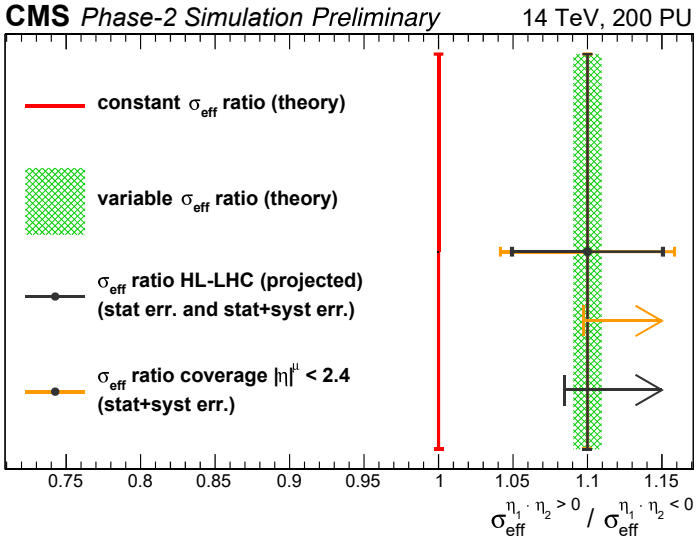

Fig. 66: Ratio of σ_{eff} for $\eta_1 \cdot \eta_2 > 0$ and $\eta_1 \cdot \eta_2 < 0$, which is equal to the inverse ratio for σ_{DPS}. The value of this in the absence of parton correlations is 1 (red line), whilst the prediction of [575] is given by the green band. The black error bars indicate systematic uncertainty attainable by the CMS experiment at 3 ab^{-1}, the orange bars include systematic uncertainties assuming a conservative correlation of 0.8 between them for $\eta_1 \cdot \eta_2 > 0$ and $\eta_1 \cdot \eta_2 < 0$. The vertical line on the arrows indicates the lowest measured value of the ratio that would allow the exclusion of the uncorrelated parton hypothesis (i.e. eq. (38) with constant σ_{eff}) at 95% CL. The black arrow corresponds to muon rapidity coverage $|\eta| < 2.8$, and the orange arrow $|\eta| < 2.4$.

an uncorrelated ansatz at an initial scale of 1 GeV. The polarised double parton distributions, encoding parton spin correlations, were chosen at the initial scale to correspond to the maximal possible spin correlations (technically, saturate the positivity bounds [580]), in such a way that the effects on the cross section would be maximal. These distributions were evolved to the W mass and used to compute polarised and unpolarised W^+W^+ cross sections at $\sqrt{s} = 13$ TeV. The resulting $\eta_1 \cdot \eta_2$ distribution is shown in Fig. 67(a) – the corresponding value of a_{η_l} is 0.07, which is even larger than that resulting from x correlations. One should, however, bear in mind that this is a maximal value, and that there are possibilities for the polarised distributions at the input scale, compatible with the positivity bounds, that also ultimately yield negative values for a_{η_l} [581]. Figure 67(b) shows the expected significance of a measured non-zero asymmetry as a function of luminosity L, using a rapidity cut $|\eta_i| > 0.6$ imposed such that the asymmetry a_{η_l} rises to 0.11 (but overall W^+W^+ cross section reduces from 0.51 fb to 0.29 fb). The blue band shows the sensitivity achievable using the $\mu^+\mu^+$ channel only, whilst the red band shows the sensitivity attainable using $\mu^+\mu^+$, μ^+e^+, and e^+e^+ assuming a similar sensitivity can be achieved for electrons as for muons. This plot reinforces the notion that a few per cent level asymmetry can be measured at the HL-LHC.

To investigate how $1 \to 2$ splittings may affect the asymmetry a_{η_l}, the code discussed in section 9 of [571] was upgraded to include charm and bottom quarks above the appropriate mass thresholds (chosen here to be equal to the MSTW 2008 values of 1.40 GeV and 4.75 GeV respectively). The 'intrinsic' and 'splitting' part of the DPDs were initialised as in [571] – in particular, the intrinsic part was initialised according to an uncorrelated ansatz, up to a suppression factor near the phase space boundary $x_1 + x_2 = 1$, that does not have a strong impact on a_{η_l}. Then, any nonzero value of a_{η_l} will be almost entirely due to $1 \to 2$ splitting effects. Computing W^+W^+ cross sections at $\sqrt{s} = 13$ TeV it

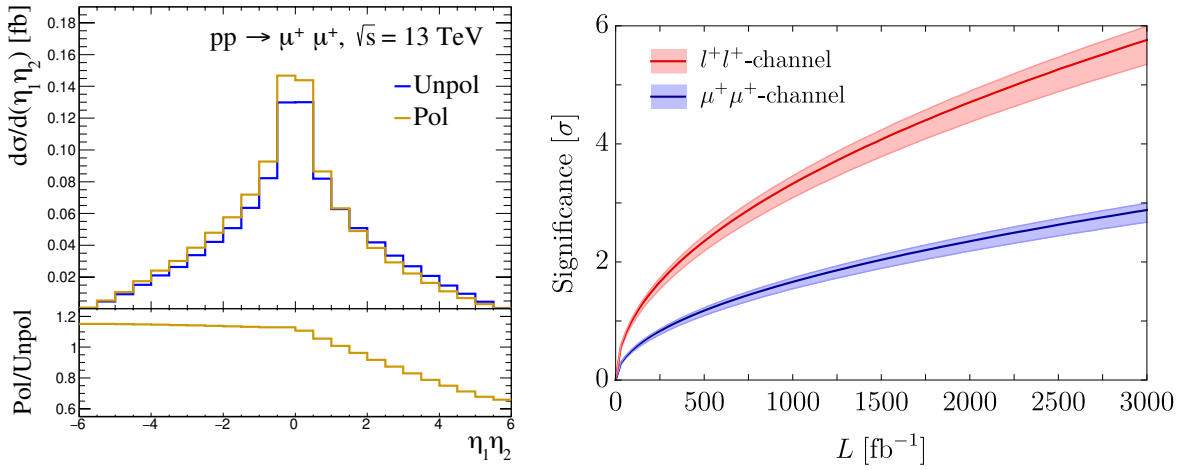

Fig. 67: Distribution in product of rapidities for two positively charged muons arising from W^+W^+ DPS. The blue plot includes only the unpolarised contribution, whilst the yellow also includes longitudinally polarised contributions (left). Estimated significance of a nonzero asymmetry as the distance in standard deviations of a measured asymmetry from zero, when the W^+W^+ cross section is 0.29 fb and asymmetry is 0.11 (right). This corresponds to the calculation of [579] with polarised contributions, and a cut on muon $|\eta| > 0.6$. The uncertainty bands indicate dependence of the sensitivity on assumptions regarding the subtraction of SPS backgrounds. More details regarding the set-up for both panels may be found in [579].

is found that $a_{\eta_l} \sim 0.028$, which is of similar size to the asymmetry arising from other sources.

Note that the asymmetries from x correlations, valence number effects and $1 \to 2$ splitting are in the same direction (favouring $\eta_1 \cdot \eta_2 < 0$ over $\eta_1 \cdot \eta_2 > 0$), whilst polarisation effects can potentially either favour a positive or negative asymmetry.

At the HE-LHC, the asymmetry should be smaller for the same cuts on $|\eta_i|$ – as x is lowered, we move away from the 'double valence' region where valence number effects are important, and the ratio of polarised to unpolarised quark distributions reduces (see Fig. 6 of [582]). Repeating the study above where a minimal modification of the uncorrelated ansatz at the input scale is made to take account of number effects, but at $\sqrt{s} = 27$ TeV, it is found that $a_{\eta_l} \sim 0.008$. Including instead the effects of the $1 \to 2$ splittings yields $a_{\eta_l} \sim 0.013$ at $\sqrt{s} = 27$ TeV. At the HE-LHC (and the HL-LHC) it could be interesting to compare same-sign WW, which is comparatively weakly affected by $1 \to 2$ parton splitting (due to the fact there is no direct LO splitting yielding, for example uu), with processes that should receive stronger contributions from parton splitting, such as low mass Drell-Yan or $b\bar{b}b\bar{b}$ production, to probe in detail the effects of the $1 \to 2$ parton splitting and compare to theoretical predictions. More detailed studies in this direction are needed.

In conclusion, the HL-LHC offers the opportunity to measure the effects of correlations between partons, via measurements of DPS processes, for the first time. In same-sign WW production a good observable to probe correlations is the lepton pseudorapidity asymmetry a_{η_l}, which can only be nonzero in the presence of correlations – theoretical calculations indicate values of a_{η_l} at LHC energies on the order of a few per cent, which should be measurable at the HL-LHC. By combining measurements of various processes sensitive to DPS at the HL-LHC, and later and the HE-LHC, it will be ultimately possible to build up a picture of the various correlatons existing between partons in the proton.

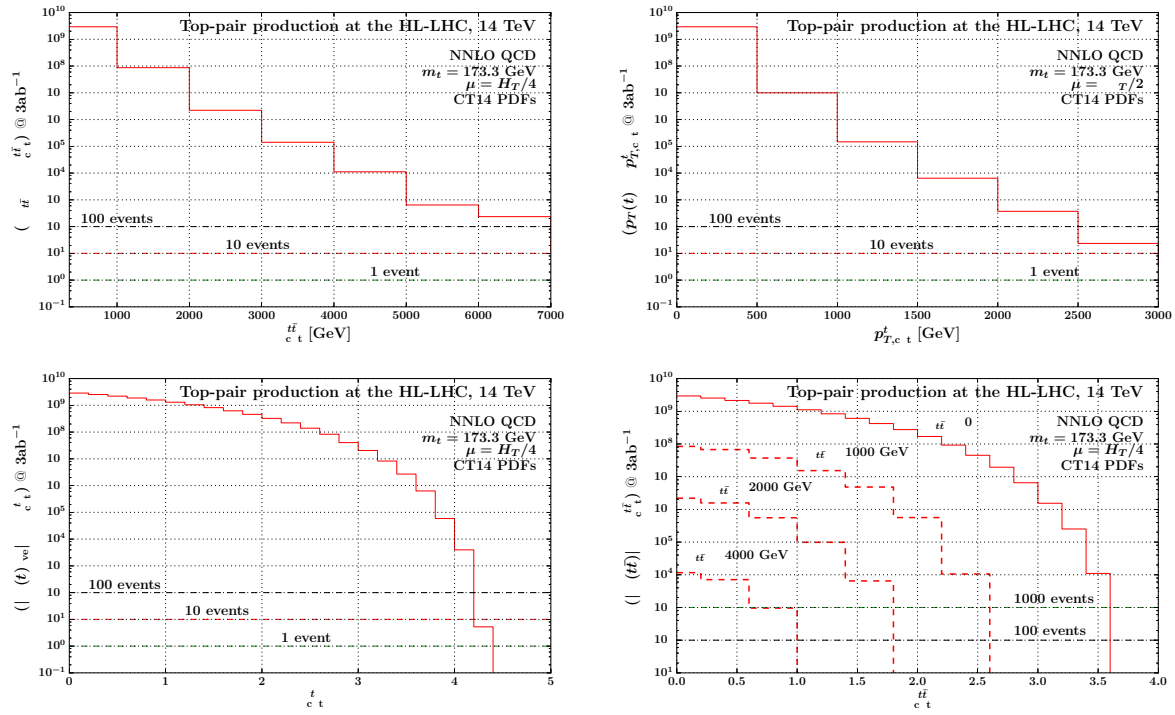

Fig. 68: Cumulative differential distributions for HL-LHC at 14 TeV.

6 Top quark physics

Precision measurements of top quark properties present an important test of the SM. As the heaviest particle in the SM, the top quark plays an important role for the electroweak symmetry breaking and becomes a sensitive probe for physics beyond the SM.

6.1 Top quark cross section

6.1.1 The $t\bar{t}$ production cross section: theoretical results[31]

This sub-section provides a quick reference for the kinematic reach of the main $t\bar{t}$ differential distributions for both HL and HE-LHC. Figures 68 and 69 are given in terms of expected events for the proposed ultimate luminosities for both colliders: 3 ab^{-1} for the HL-LHC running at 14 TeV and 15 ab^{-1} for the 27 TeV HE-LHC. The results are presented as plots of cumulative differential distributions and should be interpreted as follows: the histograms show the numbers of expected events (for the luminosities given above) above a given cut in any one of the four kinematic variables: $m_{t\bar{t}}, p_{\mathrm{T,avt}}, y_{\mathrm{avt}}$ and $y_{t\bar{t}}$. Note that the cut corresponds to the left edge of a bin. The predictions are based on the CT14 parton distributions [199] with value of the top quark mass $m_t = 173.3$ GeV which is close to the current world average. The calculation is based on Ref. [583] and uses the dynamical scales of Ref. [213].

Figure 68 presents predictions for the four cumulative distributions specified above in the case of the $t\bar{t}$ production at the HL-LHC (14 TeV), computed in NNLO QCD. In conclusion the HL-LHC allows detailed studies of top quark pair production with $m_{t\bar{t}}$ of up to about 7 TeV. Events with even larger values of $m_{t\bar{t}}$ are kinematically accessible and one expects about 10 events with $m_{t\bar{t}} > 7$ TeV. Therefore, the region $m_{t\bar{t}} > 7$ TeV provides a low SM background for, for example, searches for decays of BSM heavy particles to $t\bar{t}$ pairs. A detailed understanding of the SM background - at the level of one expected event - will require a dedicated future effort due to the significant MC error in that region.

[31] Contributed by M. Czakon, A. Mitov, and A. Papanastasiou.

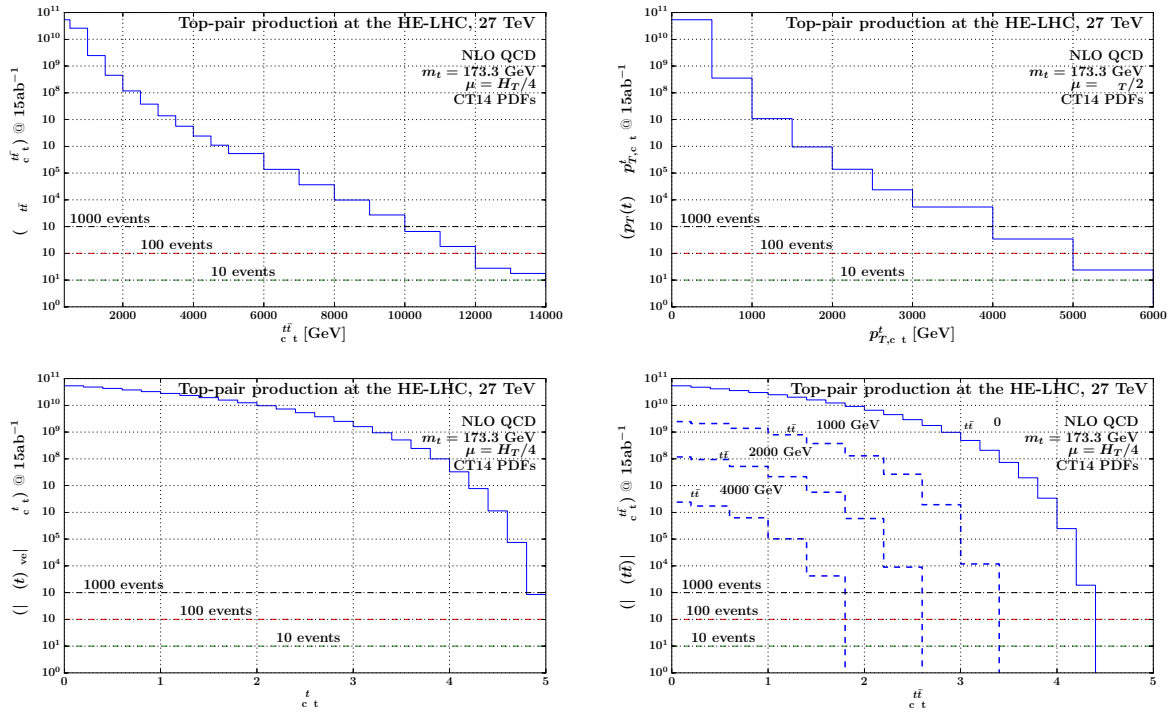

Fig. 69: Cumulative differential distributions for HE-LHC at 27 TeV.

The top quark $p_{\rm T}$ distribution can probe $p_{\rm T}$ values as high as 2.5 TeV, with a total of about 30 events expected beyond that value.

The HL-LHC offers the possibility to access top production at high rapidity which might provide a link between top measurements at LHCb on one hand and ATLAS and CMS on the other. Indeed, in Fig. 68 it can be observed that top quarks with rapidity $y_{\rm avt}$ as large as 4 will be copiously produced. The cross-section is a steeply falling function at large rapidity with a maximum attainable value of around 4.2 or so. Similarly, the rapidity of top quark pairs can be measured in detail up to values exceeding 3.4 with the maximum reach at about $y_{t\bar{t}} \sim 3.6$. In Fig. 68 it is shown the $y_{t\bar{t}}$ distribution for a set of cuts on the top pair invariant mass. One should bear in mind that the NNLO $y_{t\bar{t}}$ calculation has significant MC error in the bins with 10 events or less.

Figure 69 presents the predictions for the same four cumulative distributions but in NLO QCD for the case of $t\bar{t}$ production at the HE-LHC (27 TeV). From this figure one can easily conclude that the increase in the kinematic reach over the HL-LHC is very substantial. There will be few hundred events with $m_{t\bar{t}}$ above 11 TeV and a similar number of events can be measured with $p_{\rm T}$ above 4 TeV. For the reliable description of such kinematics the inclusion of EW corrections as well as yet higher order soft and or collinear radiation will be essential; see Ref. [113, 220].

Very large rapidities can be attained at the HE-LHC. In particular, the top quark rapidity $y_{\rm avt}$ distribution can be measured to values as high as 4.8 with excellent statistics. Indeed, about 1000 events are expected above $y_{\rm avt} = 4.8$. The top pair rapidity can reach values as high as 4.4 and, if no additional cuts are applied, few thousand events will be produced with $y_{t\bar{t}} > 4.2$. As for the case of 14 TeV it is also show in Fig. 69 the expected number of events as a function of $y_{t\bar{t}}$ for several cuts in $m_{t\bar{t}}$.

6.1.2 *Prospects in the measurement of differential $t\bar{t}$ cross sections*

A study is presented for the resolved reconstruction of top quark pairs in the e/μ+jets channels and a projection of differential $t\bar{t}$ cross sections measurements with an integrated luminosity of 3 ab^{-1} at 14 TeV [584]. The analysis techniques are based on previous measurements of differential $t\bar{t}$ cross sections at 13 TeV [585, 586]. It is shown that such a measurement is feasible at the HL-LHC despite the expected large number of pileup interactions. The precision of the differential cross section can profit from the enormous amount of data and the extended η-range of the HL-LHC CMS detector. The results are used to estimate the improvement of measurements of parton distribution functions.

This study is based on a DELPHES simulation of the HL-LHC CMS detector [587–590] using the Monte Carlo program POWHEG [151, 314, 360, 377] (v2,hvq) in combination with PYTHIA [148, 292] (v8.219) for the generation of $t\bar{t}$ events at NLO accuracy. Events with a single isolated electron or muon with $p_{\mathrm{T}} > 30$ GeV and $|\eta| < 2.8$ are selected. Events with additional isolated electrons or muons with $p_{\mathrm{T}} > 15$ GeV and $|\eta| < 2.8$ are rejected. At least 4 jets with $p_{\mathrm{T}} > 30$ GeV and $|\eta| < 4.0$ are required, where at least 2 of the jets have to be identified as b jets. It is essential that the PUPPI algorithm [591] is used for the mitigation of pileup contribution when the jets are clustered and the $\vec{p}_{\mathrm{T}}^{\,\mathrm{miss}}$ is calculated.

A detailed description of the $t\bar{t}$ reconstruction is presented in [585,586]. For the reconstruction all possible permutations of assigning detector-level jets to the corresponding $t\bar{t}$ decay products are tested and a likelihood that a certain permutation is correct is evaluated. In each event, the permutation with the highest likelihood is selected. The likelihood is constructed from the 2 dimensional m_t–m_{W} distribution of correctly assigned jets for the hadronically decaying top quark and the distribution of $D_{\nu,\mathrm{min}}$ obtained when calculating the neutrino momentum [592] for the leptonically decaying top quark. A comparison of the expected event yields and the migration matrices together with their properties are shown in Fig. 70 for the HL-LHC expectation. Despite the high pileup a performance of the $t\bar{t}$ reconstruction similar to the one in 2016 [586] can be reached, while the portion of the direct measurable phase space is increased due to the extended η-range.

The following experimental uncertainties are estimated based on the expected performance of the HL-LHC CMS detector [277]: electron and muon identification, b-tagging efficiencies, jet energy and $\vec{p}_{\mathrm{T}}^{\,\mathrm{miss}}$ calibration, and luminosity. All theoretical and modelling uncertainties have been reduced by a factor two.

The unfolded results of the differential $t\bar{t}$ cross section measurements as a function of p_{T} and rapidity y of the hadronically decaying top quark ($\mathrm{t_h}$) are shown in Fig. 71. In Fig. 72 the normalized double-differential cross section as a function of $M(t\bar{t})$ vs $|y(t\bar{t})|$ is shown. The strong impact of these measurement on PDF constraints is studied in Section 6.1.3. The high amount of data and the extended η-range of the HL-LHC detector allow for fine-binned measurements in phase-space regions — especially at high rapidity — that are not accessible in current measurements. The most significant reduction of uncertainty is expected due to an improved jet energy calibration.

6.1.3 *PDF constraints from double-differential $t\bar{t}$ cross sections*

The impact of differential $t\bar{t}$ cross section measurements at the HL-LHC on the proton PDFs is quantitatively estimated using a profiling technique [476], which is based on minimizing χ^2 function between data and theoretical predictions taking into account both experimental and theoretical uncertainties arising from PDF variations. The analysis is performed using the XFITTER program [490], with the theoretical predictions for the $t\bar{t}$ cross sections calculated at NLO QCD using the MG5_AMC@NLO [12] framework, interfaced with the APPLGRID [208] and AMCFAST [593] programs. Three NLO PDF sets were chosen for this study: ABMP16 [594], CT14 [199], and NNPDF3.1 [207]. The normalized double-differential $t\bar{t}$ production cross sections as a function of $M(t\bar{t})$ vs $|y(t\bar{t})|$ are used which are expected to impose stringent constraints on the gluon distribution [595]. The χ^2 value is calculated using

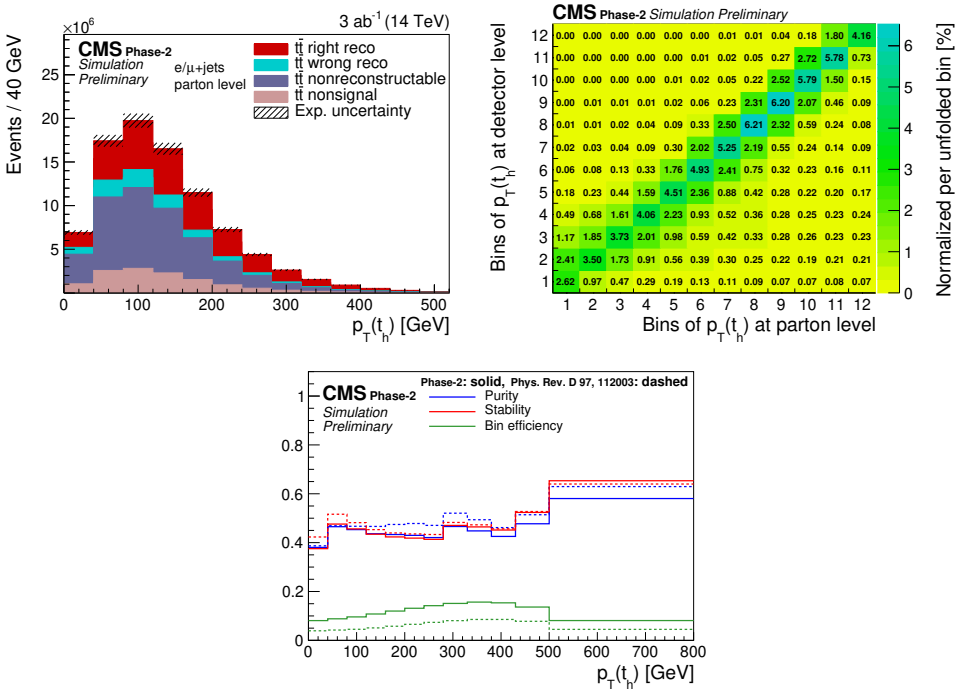

Fig. 70: Expected signal yields (top-left), migration matrices (top-right), and its properties (bottom) for measurements of $p_{\mathrm{T}}(\mathrm{t_h})$ for the HL-LHC (Phase-2) simulation. The purity is defined as the fraction of parton-level top quarks in the same bin at the detector level, the stability as the fraction of detector-level top quarks in the same bin at the parton level, and the bin efficiency as the ratio of the number of events found in a certain bin at detector level and the number of events found at parton-level in the same bin.

the full covariance matrix representing the statistical and systematic uncertainties of the data, while the PDF uncertainties are treated through nuisance parameters. The values of these nuisance parameters at the minimum are interpreted as optimized or profiled PDFs, while their uncertainties determined using the tolerance criterion of $\Delta\chi^2 = 1$ correspond to the new PDF uncertainties. The profiling approach assumes that the new data are compatible with theoretical predictions using the existing PDFs, such that no modification of the PDF fitting procedure is needed. Under this assumption, the central values of the measured cross sections are set to the central values of the theoretical predictions. The original and profiled ABMP16, CT14, and NNPDF3.1 uncertainties of the gluon distribution at the scale $\mu_{\mathrm{f}}^2 = 30\,000\,GeV^2 \simeq m_{\mathrm{t}}^2$ are shown in Fig. 73. A consistent impact of the $t\bar{t}$ data on the PDFs is observed for the three PDF sets. The uncertainties of the gluon distribution are drastically reduced once the $t\bar{t}$ data are included in the fit.

6.1.4 Forward top quark physics

Three measurements of top production have been performed by LHCb during Run-1 and -2 of the LHC with a precision of (20-40)%, limited by the available data samples. As LHCb collects data at a lower rate than ATLAS and CMS, and has a limited acceptance, the measurements have focused on a partial reconstruction of the $t\bar{t}$ final state in order to make optimal use of statistics. Additionally, as no estimate of missing energy is available, the measurements are performed at the level of the lepton and jets only, with no full top quark reconstruction performed. The first observation in the forward region was made in the μb final state, where the top quark is identified by the presence of a muon and a b-jet [596]. This final state has the highest signal yield, but suffers from the largest backgrounds, in particular from W boson production in association with a b-jet. It also cannot separate single top and top pair production,

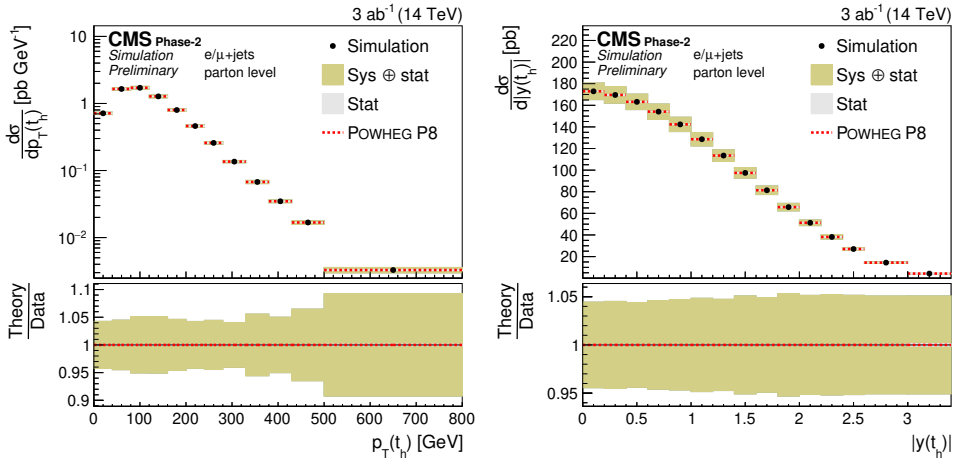

Fig. 71: Projections of the differential cross sections as a function of $p_{\mathrm{T}}(\mathrm{t_h})$ (right) and $|y(\mathrm{t_h})|$ (left).

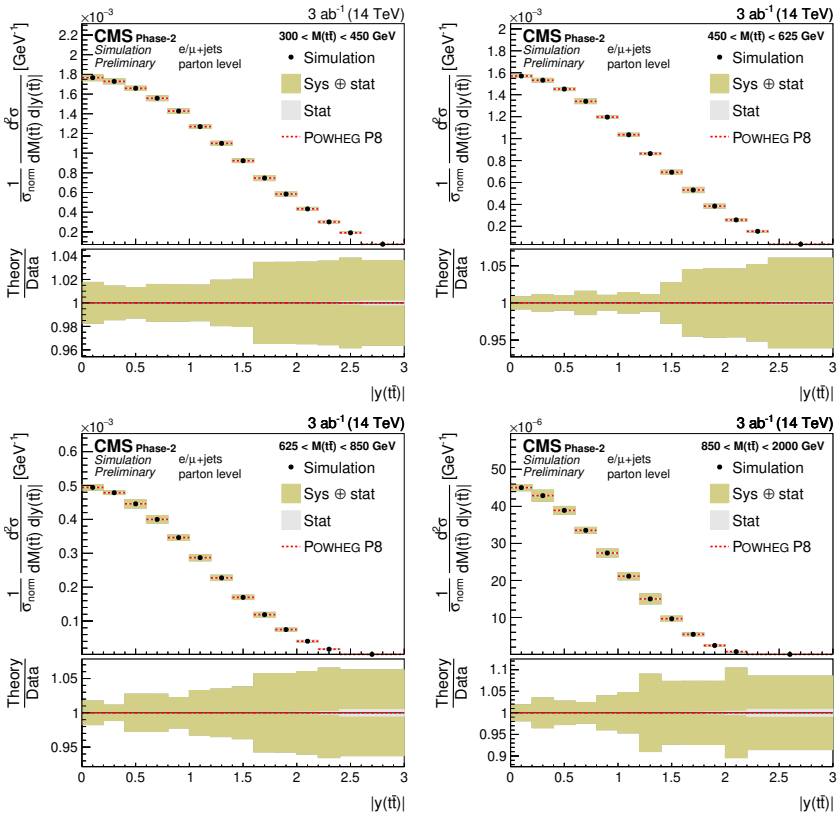

Fig. 72: Projections of the double-differential cross section as a function of $|y(t\bar{t})|$.

which both contribute to the final state. Measurements were also performed in the ℓbb final state [597] and μeb final state [598], which suffer from lower statistics but select the signal with a higher purity.

While current measurements in the top sector at LHCb have been statistically limited, the available dataset at the HL-LHC, where LHCb is expected to collect 300 fb^{-1}, will permit precision measurements of the top quark pair production cross-section in the forward region, providing complementary information to ATLAS and CMS. The expected number of top pair events to be reconstructed at LHCb are given in Table 33, where the yields are obtained using next-to-leading predictions from the AMC@NLO gen-

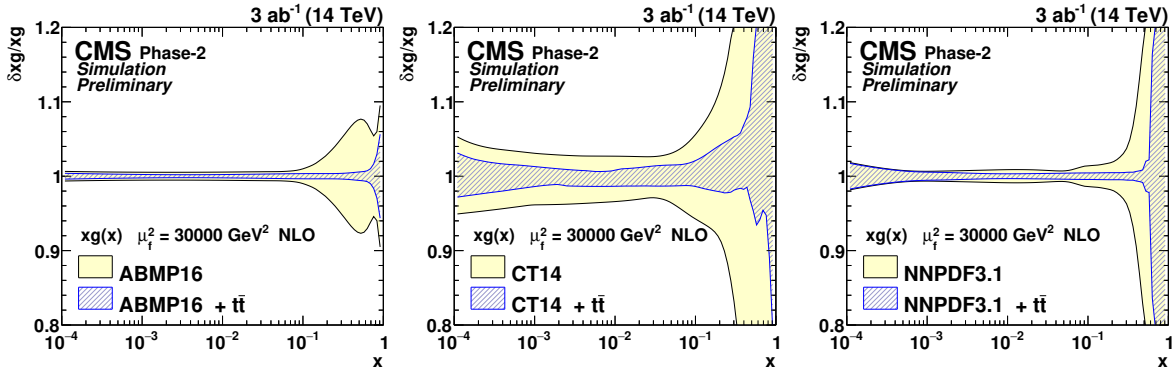

Fig. 73: The relative gluon PDF uncertainties of the original and profiled ABMP16 (left), CT14 (middle) and NNPDF3.1 (right) sets.

Table 33: The number of $t\bar{t}$ events expected to be reconstructed at LHCb per final state using a dataset corresponding to an integrated luminosity of 300 fb^{-1}. The mean value of Bjorken-x of the most energetic initiating parton is also shown for each final state.

Final state	300 fb^{-1}	$< x >$
ℓb	830k	0.295
$\ell b\bar{b}$	130k	0.368
μeb	12k	0.348
$\mu eb\bar{b}$	1.5k	0.415

erator interfaced with PYTHIA v8, with electroweak corrections approximated as described in Ref. [599]. Leptons are required to satisfy $2.0 < \eta < 4.5$ and $p_{\mathrm{T}} > 20$ GeV, while jets are required to satisfy $2.2 < \eta < 4.2$ and $p_{\mathrm{T}} > 20$ GeV in all final states except the ℓb final state, where the p_{T} threshold is raised to 60 GeV to combat the increased background. The detector efficiency is extrapolated from current measurements, where increases of between 10 and 50% are expected due to to improvements in the b-tagging algorithm and analysis techniques. Both muons and electrons are assumed to be employed for all analyses with similar efficiencies due to anticipated improvements in electron performance at LHCb during the HL-LHC. Measurements are expected to be made at sub-percent statistical precision in the ℓb final state, and at the percent level in the μeb and μebb final states. The dominant systematic uncertainties are expected to arise from the purity determination, particularly for the single lepton final states, and the knowledge of the b-tagging efficiency, which are both expected to be at the level of a few percent.

As $t\bar{t}$ production in the LHCb acceptance probes very large values of Bjorken-x, it has the potential to provide significant constraints on the gluon PDF in this region. The potential of the μeb final state was evaluated in Ref. [600], where reductions of 20% were found for a cross-section measurement with a precision of 4%. Even more stringent constraints can be obtained through precise differential cross-section measurements, and measurements in the μebb final state, both of which will only be possible with the data available at the HL-LHC.

6.1.5 *Single top cross section: theoretical results*[32]

Although top quarks are predominantly produced in $t\bar{t}$ pairs through strong interactions, a substantial fraction of them is also produced through the exchange of electroweak bosons. In the latter case, only a single (anti-)top is produced per collision, hence one refers to these processes as "single-top" production. Despite their smaller rates with respect to pair production, single-top processes offer unique opportunities to study the electroweak structure of top interactions.

The purpose of this section is to summarize the state-of-the-art for the computation of single-top production cross sections, and highlight what type of studies could be performed with an HL/HE-LHC upgrade.

It is customary to categorize single-top production in the SM according to the virtuality of the W-boson involved in the leading-order $2 \to 2$ partonic process: the s-channel processes ($q\bar{q}' \to t\bar{b}$) involve the exchange of a time-like W boson, the t-channel processes $bq \to tq'$ involve the exchange of a space-like W, while associated Wt-production ($bg \to tW^-$) involves the production of a top quark in association with a W boson.

Although convenient, the above characterization suffers two theoretical issues:

- a classification in terms of underlying $2 \to 2$ processes implicitly assumes that the b-quark is treated as massless, i.e. the computations are performed in the so-called five-flavour number scheme (5FNS). This framework effectively resums large logarithms of the form $\ln m_b/Q$, where Q is a typical transverse scale of the process and as such it is particularly appropriate for observables that are only sensitive to large $p_{\rm T} \gg m_b$ scales, like for example total cross sections. However, especially in the t-channel case, there are important observables which are sensitive to small transverse scales $p_{\rm T} \sim m_b$ (e.g. the kinematics of the "spectator" b-jet which originates from initial state $g \to b\bar{b}$ splitting, particularly at small $p_{\rm T}$). In this case, the 5FNS is not appropriate and it is important to treat the b-quark as massive, i.e. to work in four-flavour mass scheme (4FNS). In this scheme, the t-channel LO process becomes $2 \to 3$: $gq \to t\bar{b}q'$. The 4FNS and 5FNS are formally equivalent, but differences can arise when the perturbative expansion is truncated, and in practice these effects might be relevant for some observables [601–603]. Within this context, the advantages of a HL/HE upgrade is twofold. On the one hand, the larger dataset and increased energy would allow for more harsh selection cuts that would effectively remove regions of the phase space sensitive to small transverse scales. This would allow for a clean theoretical description using the 5FNS, which does not suffer from large logarithmic contaminations. On the other hand, it would allow one to explore with high accuracy the transition region between the range of validity of the 4FNS and 5FNS, thus providing important information on their interplay.
- once higher-order corrections are included, the distinction between s and t channels does not hold, due to interference effects. These interference effects first appear at order $\mathcal{O}(\alpha_s^2\alpha^2)$, i.e. at NNLO in the 5FNS, or at NLO in the 4FNS, and are color and (typically) kinematic suppressed. Given the large hierarchy and small kinematic overlap between t- and s- channels, interference effects are typically very small in pp collisions, but may in principle play a role if very high accuracy is required for specific observables. Moreover, once the W and top decay products are included, interferences arise also between $t\bar{t}$, single-top (with Wt-production, as well as t-channel in the 4FNS) and $WWb\bar{b}$ production, unless the narrow-width limit $\Gamma_t \to 0$ is taken. These effects can play a role for high precision studies, see e.g. [169, 604].

In spite of the above issues, as long as only NLO QCD corrections are considered, it is possible to compute well-defined cross-sections for s and t-channel in the 5FNS, and, by imposing a jet-veto on b-jets, to suppress the contamination of $t\bar{t}$ to the Wt process, thereby allowing for a sensible definition

[32] Contributed by F. Caola and E. Re.

of the cross section for the latter channel as well. In Table 34 the NLO cross sections are reported for the 3 channels at the LHC, for centre-of-mass energies of 14 and 27 TeV. Scale and PDF uncertainties are also reported. At both energies, the t-channel is the dominant production mechanism. The relative importance of the s-channel decreases with the collider energy, while it increases for Wt associated production.

Table 34: Single-top inclusive cross sections at NLO for the LHC at 14 and 27 TeV, in the 5FNS. All results were obtained using PDF4LHC15_nlo_mc, the central value for the renormalization and factorizations scales (μ_R, μ_F) have been set equal to $m_t = 173.2$ GeV and varied by a factor of two, with the constraint $1/2 \leq \mu_R/\mu_F \leq 2$. For these predictions, V_{tb} has been set to one. For Wt-channel only, a jet-veto on b-jets has been used ($p_{\mathrm{T,b_j}} < 50$ GeV), and the central value for μ_R and μ_F has been set to 50 GeV too.

	14 TeV			27 TeV		
	σ [pb]	Δ_{μ_R,μ_F}	Δ_{PDF}	σ [pb]	Δ_{μ_R,μ_F}	Δ_{PDF}
t-channel (t)	156	$^{+3\%}_{-2.2\%}$	$\pm$ 2.3 %	447	$^{+3\%}_{-2.6\%}$	$\pm$ 2%
t-channel ($\bar{t}$)	94	$^{+3.1\%}_{-2.1\%}$	$\pm$ 3.1%	299	$^{+3.1\%}_{-2.5\%}$	$\pm$ 2.6%
s-channel (t)	6.8	$^{+2.7\%}_{-2.2\%}$	$\pm$ 1.7%	14.8	$^{+2.7\%}_{-3.2\%}$	$\pm$ 1.8%
s-channel ($\bar{t}$)	4.3	$^{+2.7\%}_{-2.2\%}$	$\pm$ 1.8%	10.4	$^{+2.7\%}_{-3.3\%}$	$\pm$ 1.8%
Wt-channel (t or $\bar{t}$)	36	$^{+2.9\%}_{-4.4\%}$	$\pm$ 5%	137	$^{+3.8\%}_{-6.1\%}$	$\pm$ 4%

Figure 74 also shows, for the t-channel case, the cumulative cross section with a minimum $p_{\mathrm{T,min}}$ cut on the top, or antitop, transverse momentum, obtained at NLO in the 5FNS. The two horizontal bars

Fig. 74: Cumulative cross section for t-channel single-(anti)top production in the 5FNS at 14 and 27 TeV as a function of $p_{\mathrm{T,min}}$. The same settings used to obtain results in Table 34 were used here.

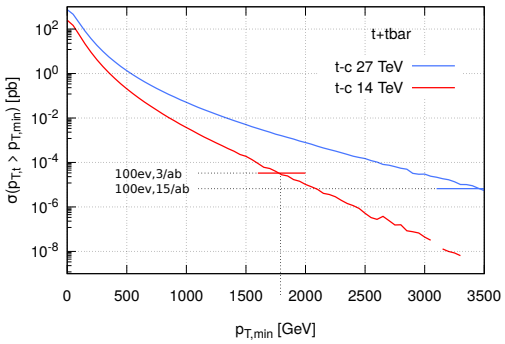

in the plot correspond to the cross sections for which one has 100 events, by assuming an integrated luminosity of 3 ab^{-1} at 14 TeV (red) and of 15 ab^{-1} at 27 TeV (blue).

For t-channel production, NNLO QCD corrections have also been computed in Refs. [555, 605, 606].[33] These corrections have been obtained in the structure function approximations, where higher-order corrections to the light and heavy-quark lines ($q \to q'W$ and $b \to tW$, respectively) are computed separately. Within this approximation, the terms which are not included at NNLO are color suppressed

[33] NNLO QCD results were also obtained for s-channel, see Ref. [607].

($1/N_c^2$), and hence estimated to be negligible for phenomenology, given the moderate size of NNLO effects. Moreover, when working in these approximations, interference effects between s and t-channel are also absent. The results obtained in Refs [605, 606] indicate that NNLO QCD corrections are small: the total cross sections at NNLO increase by at most 2% with respect to the NLO result (when the latter is obtained with NLO PDFs), whereas the relative scale uncertainty is reduced by at least $\sim 50\%$. Moreover, the NNLO result is contained within the NLO uncertainty band, showing extremely good convergence for the perturbative expansion.[34] Despite the fact that the total cross section shows excellent perturbative stability, more sizeable effects can be noticed in some differential distributions, where NNLO/NLO corrections can reach $\mathcal{O}(10\%)$ in certain regions of the transverse momentum distributions of the top (anti-)quark and the pseudo-rapidity distributions of the leading jet. In these cases, scale variation may underestimate the actual theoretical uncertainty.

NNLO corrections to the top quark decay are also known [608, 609], and they can be combined with the NNLO corrections to production using the "on-shell top-quark approximation" where the top width Γ_t is kept finite, but tree-level interference effects between the single top production and decay stage are neglected, as well as loop diagrams with a virtual gluon connecting the production and decay stages. This is an excellent approximation for inclusive-enough quantities, since omitted corrections are suppressed by a factor $\Gamma_t/m_t < 1\%$ [35]. More details can be found in Ref. [555].

In presence of fiducial cuts, it is important to stress that QCD corrections are more pronounced, with NNLO effects amounting about 5% on total rates as well as differential distributions. In this case, corrections from pure decay are typically half of those from pure production. Finally, it should be noted that NLO EW corrections to on-shell single top production are small, $\sim$ few permille, see e.g. [89]. The EW effect can become more relevant in tails of distributions, or for observables highly sensitive to off-shell effects.

Single-top can also be produced in association with a Z boson (tZq). Although the cross section is smaller than in the aforementioned channels, a HL/HE upgrade at the LHC will allow one to measure well this production process too. QCD NLO corrections to tZq-production are known [611]. Table 35 reports the total cross sections at NLO in the SM, for centre-of-mass energies of 14 and 27 TeV.

Table 35: Single-top production cross section in association with a Z boson, at NLO for the LHC at 14 and 27 TeV, in the 5FNS. All results were obtained using PDF4LHC15_nlo_mc, the renormalization and factorizations scales have been set equal to $m_t = 173.2$ GeV.

	σ [fb] @14 TeV	σ [fb] @27 TeV
tZq-channel (t)	639	2536
tZq-channel ($\bar{t}$)	350	1543

As far as phenomenology is concerned, single-top offers the possibility to perform several studies within and beyond the SM. Within the "SM only" hypothesis, one can use it to extract information about the SM V_{tb} matrix element, as discussed for instance in Ref. [612]. Setting constraints on the b-quark PDF might also be possible, by looking at charge ratios, i.e. ratios of $t/\bar{t}$ cross sections. These ratios depend in general upon the PDFs used, and notably, in the t-channel case, on the b-quark PDF. Moreover, they can be predicted quite accurately, as most of the theoretical uncertainties cancel out in the ratio, leaving a residual theoretical uncertainty from scale variation (at NNLO) of few percent for each PDF set, as shown for instance in Fig. 29 of Ref. [555]. Although the charge ratio for total

[34] When NLO corrections are computed with NNLO PDFs, the NNLO/NLO ratio is instead slightly smaller than one, but the conclusions remain the same.

[35] This is not the case for exclusive observables, which are sensitive to off-shell effects in the reconstructed top mass M_{Wb}, and beyond kinematic edges, see Ref. [610] for a thorough analysis.

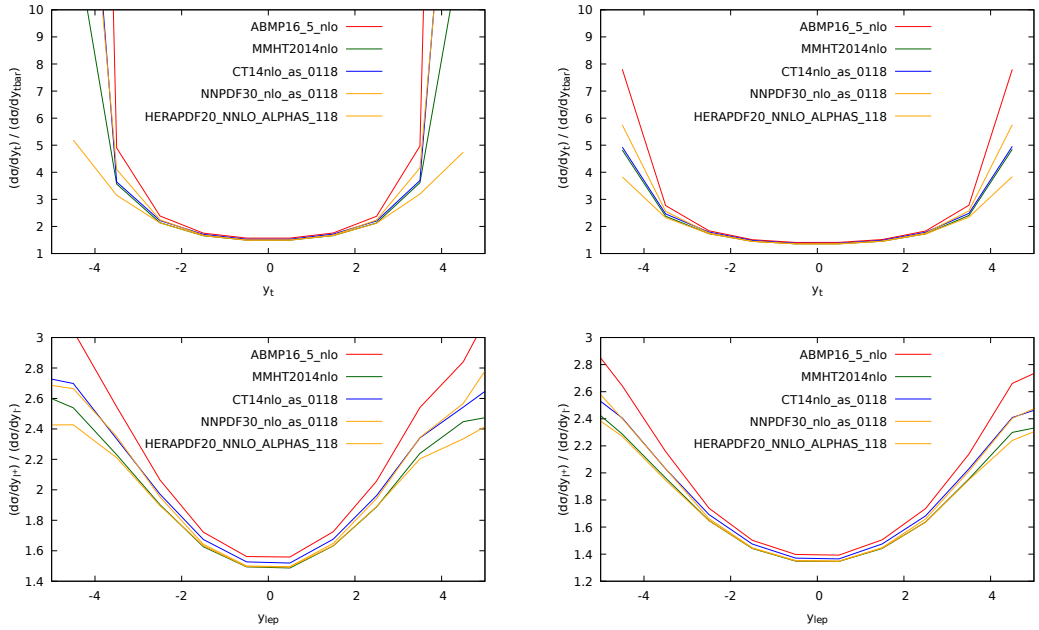

Fig. 75: Differential charge ratios $\mathcal{O}_t/\mathcal{O}_{\bar{t}}$ at 14 (left panels) and 27 (right panels) TeV for the top quark and charged lepton rapidities, in t-channel single-top production.

cross sections $\sigma_t/\sigma_{\bar{t}}$ exhibits a dependence upon the PDF set [613, 614], slightly more pronounced sensitivity might be obtained by looking at differential distributions, such as $(d\sigma/dy_t)/(d\sigma/dy_{\bar{t}})$ and $(d\sigma/dy_{\ell^+})/(d\sigma/dy_{\ell^-})$, which also allow one to constrain the u/d ratio in the proton. In Fig. 75 such a comparison among different PDF sets is shown, for LHC collisions at 14 and 27 TeV: differences among different PDF sets can be observed, especially at large rapidities. It is clear that a HL upgrade will allow one to reduce the statistical uncertainty at large rapidities, giving the chance to discriminate among different PDF sets. As the available phase space opens up, further sensitivity might be expected at 27 TeV.

Single-top processes offer also several opportunities to probe some new-physics scenarios[36]. In order to systematically interpret potential deviations from the SM, it is particularly convenient to work in the SM Effective Field Theory (SMEFT) [615, 616], where the SM is augmented by a set of higher-dimension operators. If the discussion is limited to dimension-6 operators, the SMEFT Lagrangian has the form

$$\mathcal{L}_{\rm SMEFT} = \mathcal{L}_{\rm SM} + \sum_i \frac{C_i}{\Lambda^2}\mathcal{O}_i + \mathcal{O}(\Lambda^{-4}). \tag{40}$$

where the sum runs over all the dimension-6 operators that maintain the SM symmetries. The remarkable virtue of t-channel single-top production is that its cross section only depends upon a limited number of dimension-6 operators, thereby allowing to set bounds on them relatively easily. At LO and in the 5FNS only three operators contribute:

$$\mathcal{O}_{tW} = i\big(\bar{Q}\sigma^{\mu\nu}\,\tau_I\,t\big)\,\tilde{\phi}\,W^I_{\mu\nu} + \text{h.c.}\,, \tag{41}$$

$$\mathcal{O}^{(3)}_{\phi q} = i\big(\phi^\dagger \overleftrightarrow{D}_\mu\,\tau_I\phi\big)\big(\bar{q}_i\,\gamma^\mu\,\tau^I\,q_i\big) + \text{h.c.}\,, \tag{42}$$

$$\mathcal{O}^{(3,1)}_{Qq} = \big(\bar{q}_i\,\gamma_\mu\,\tau_I q_i\big)\big(\bar{Q}\,\gamma^\mu\,\tau^I Q\big)\,, \tag{43}$$

[36] In the following the discussion is limited to the t-channel case, and the production in association with a Z boson.

in agreement with the notation of [234]. The operators of eq. (41)-eq. (42) modify the Wtb interaction in the following way

$$\begin{aligned}\mathcal{L}_{Wtb}^{\dim-6} &= -\frac{g}{\sqrt{2}}\bar{b}(x)\gamma^{\mu}P_L t(x)\,W_{\mu}(x)\left(1+\frac{C_{\varphi Q}^{(3)}v^2}{\Lambda^2}\right)\\ &+ \frac{2\,v\,C_{tW}}{\Lambda^2}\bar{b}(x)\sigma^{\mu\nu}P_R t(x)\,\partial_{\nu}W_{\mu}(x) + \text{h. c.}\,, \end{aligned} \tag{44}$$

where $v = 246$ GeV is the Higgs doublet vacuum expectation value, and y_t the top quark Yukawa coupling. Here and below it is assumed $V_{tb} = 1$. Note that the four-fermion operator of eq. (43) introduces a contact $udtb$ interaction. From eq. (44) it is clear that setting bounds on the SMEFT using single-top measurements allows to probe in detail the structure of the Wtb coupling. A comprehensive discussion can be found in Ref. [262], where a NLO study of the effect of these operators on total and differential distributions in single top production and decay is performed.

In the SMEFT, the single top cross section can be parameterised as

$$\sigma = \sigma_{SM} + \sum_i \frac{1\text{TeV}^2}{\Lambda^2}C_i\sigma_i + \sum_{i\leq j}\frac{1\text{TeV}^4}{\Lambda^4}C_iC_j\sigma_{ij}. \tag{45}$$

To establish the impact of the operators on single top production at HL/HE-LHC, Table 36 shows the ratio $r_i = \sigma_i/\sigma_{SM}$ for 14 TeV and 27 TeV both for the inclusive cross section and the high transverse momentum region. Results are obtained in the 5FNS with NNPDF3.0 LO PDFs [201]. Central scales for μ_R, μ_F are chosen as m_t. It is found that the impact of the operator in eq. (42) remains unchanged when going from 14 to 27 TeV, as its effect is to only rescale the SM coupling. The impact of the dipole operator in eq. (41) is only mildly affected by going to the HE-LHC, whereas the sensitivity to the four-fermion operator is the one which benefits most by probing the high p_{T} tail and by the HE-LHC.

Table 36: Comparison among the LO sensitivities of $t-$ channel single-top to the three operators described in eq. (41)-(43), for the inclusive cross-section and with a cut $p_{\text{T}}^t > 350$ GeV, at 14 and 27 TeV. Results are obtained in the 5FNS with NNPDF3.0 LO PDFs [201], the renormalization and factorizations scales have been set equal to $m_t = 173.2$ GeV. The interference term $r_i = \sigma_i/\sigma_{SM}$ (when non-zero) and the square $r_{i,i} = \sigma_{i,i}/\sigma_{SM}$ are given for each operator. σ_i and $\sigma_{i,i}$ are defined in eq. (45).

	t-channel 14 TeV	($p_{\text{T}}^t > 350$ GeV)	t-channel 27 TeV	($p_{\text{T}}^t > 350$ GeV)
σ_{SM}	225 pb	0.746 pb	640 pb	3.40 pb
r_{tW}	0.025	0.052	0.022	0.040
$r_{tW,tW}$	0.014	0.31	0.016	0.34
$r_{\phi Q^{(3)}}$	0.12	0.12	0.12	0.12
$r_{\phi Q^{(3)},\phi Q^{(3)}}$	0.0037	0.0037	0.0037	0.0037
$r_{Qq^{(3,1)}}$	-0.36	-6.45	-0.39	-6.79
$r_{Qq^{(3,1)},Qq^{(3,1)}}$	0.135	18.8	0.222	26.8

Production in association with a Z boson is also important in the BSM context. A complete study of its sensitivity to BSM effects was performed in Ref. [261], where the interplay with t-channel single-top, as well as single-top production in association with a Higgs boson, is discussed thoroughly, and at NLO. Table 6 of [261] reports a comparison among the sensitivity of these processes to various

operators. Current limits from other processes, as well as current and future projections for bounds that can be achieved looking into tZj production are also discussed (e.g. in Fig. 6 of Ref. [261]). For some operators, notably $\mathcal{O}_{tW}$ and $\mathcal{O}_{\phi q}^{(3)}$, the improvement due to considering tZj measurements at HL are remarkable, especially when tails of distributions are considered. It is likely that even more promising results could be obtained at HE.

Another goal of a HL/HE upgrade is to extract bounds on (or find evidence of) WWZ anomalous gauge couplings, or FCNC. In this context, tZq is quite important both because it is sensitive to these effects, as well as because it's an irreducible background, as its production rate is competitive with $t\bar{t}Z$ production, where these effects are typically looked for.

6.2 Four top production at the HL/HE-LHC

The production of four top quarks is one of the rare processes in top quark physics that has large sensitivity to variety of new physics effects (including effective field theory sensitivity and sensitivity to anomalous top-Higgs couplings), while at the same time it is interesting in the Standard Model context as a complex QCD process. The cross section at 13 TeV is about fifty times smaller than $t\bar{t}$H production, with multiple precision calculations predicting values of $\sigma_{t\bar{t}t\bar{t}} = 9.2^{+2.9}_{-2.4}$fb (NLO) and $\sigma_{t\bar{t}t\bar{t}} = 11.97^{+2.15}_{-2.51}$fb (NLO+EW) [12, 115, 617].

ATLAS and CMS have published multiple papers where limits on $t\bar{t}t\bar{t}$ production were presented as SM-oriented searches [618–620] and/or derived as a side product of searches for new physics, typically coming from searches for vector-like quarks or MSSM SUSY signatures [621–625].

The production of $t\bar{t}t\bar{t}$ is a rare SM process that is expected to be discovered by future LHC runs, including HL-LHC and HE-LHC. The increase in collision energy is important for $t\bar{t}t\bar{t}$ production because the cross section is largely induced by gluons in the initial state, leading to a substantial improvement in the signal-to-background ratio when the collision energy of the LHC is increased. Analyses looking for the production of $t\bar{t}t\bar{t}$ also are well-suited for interpretation in SMEFT [234].

The $t\bar{t}t\bar{t}$ process has not yet been observed at the LHC. Once closer to observation, and considering the sensitivity of $t\bar{t}t\bar{t}$ production to new physics scenarios in the top quark and scalar section, it is prudent to instead consider how accurately the cross section can be measured. Of course in the future analysis techniques are also expected to improve, and dedicated analyses will surely improve this sensitivity, but this is beyond the scope of this study. It is however important to keep in mind that such a study is less sensitive to systematic uncertainties on the background determination, while being more sensitive to the signal modelling uncertainties and overall branching fraction and acceptance of the selection.

6.2.1 The complete NLO corrections to four-top production[37]

In this section the so-called "complete"-NLO corrections to four-top production at the HE and HL-LHC is computed. Four-top production can proceed through different terms of order $\alpha_s^p \alpha^q$ with $p+q = 4,\ 5$ at LO and at NLO respectively. The term complete-NLO refers to computation of all terms with $p+q \leq 5$, which has been performed for the first time in Ref. [115] by employing the newly-released version of MG5_AMC@NLO [12] capable of computing mixed QCD and electroweak corrections [89]. Among the various contributions, the NLO QCD corrections ($p = 5$, $q = 0$) are also included, which have been known for some years [617, 626]. Despite that power-counting arguments suggest that the larger q the more suppressed a contribution is, it has been shown in Ref. [115] that this is not the case for $t\bar{t}t\bar{t}$ production. In fact, terms with up to two powers of α still contribute to several 10%s with respect to the $\mathcal{O}(\alpha_s^4)$ LO contribution. One of the reasons why this happens is because of the large Higgs-top Yukawa coupling; furthermore, important cancellations appear among these terms, which may be spoiled by non-SM effects.

[37] Contributed by R. Frederix, D. Pagani and M. Zaro.

This short paragraph reports inclusive predictions for the HL and HE-LHC, with a centre-of-mass energy of respectively 14 TeV and 27 TeV. For differential distributions, the qualitative and quantitative behaviour is very similar to the predictions at 13 TeV reported in Ref. [115]. The same setup and notation of Ref. [115], is used, where the interested reader can find more details as well as predictions for 13 and 100 TeV.

Table 37: Cross section for four-top production at the HL and HE-LHC, in various approximations, for $\mu = H_{\rm T}/4$. See Ref. [115] for details.

σ[fb]	LO_{QCD}	$\text{LO}_{\text{QCD}} + \text{NLO}_{\text{QCD}}$	LO	LO + NLO	$\frac{\text{LO(+NLO)}}{\text{LO}_{\text{QCD}}\text{(+NLO}_{\text{QCD}})}$
14 TeV	$9.04^{+69\%}_{-38\%}$	$14.72^{+19\%}_{-23\%}$	$10.04^{+63\%}_{-35\%}$	$15.83^{+18\%}_{-21\%}$	1.11 (1.08)
27 TeV	$81.87^{+62\%}_{-36\%}$	$135.19^{+19\%}_{-21\%}$	$91.10^{+56\%}_{-33\%}$	$143.93^{+17\%}_{-20\%}$	1.11 (1.06)

Table 37 reports the total-cross section for $t\bar{t}t\bar{t}$ production in different approximations, and Table 38 the breakdown of the different orders contributing at LO and NLO, as fraction of the $\mathcal{O}(\alpha_s^4)$ LO contribution, LO_1. It is observed that the pattern of relative corrections is rather similar between 14 and 27 TeV. In particular, besides NLO_1 which is entirely of QCD origin, and thus displays a strong dependence on the renormalisation and factorisation scales, such a feature is present also for NLO_2 and NLO_3, which witnesses the fact that they receive an important contribution through QCD corrections from LO_2 and LO_3 respectively, on top of the electroweak corrections from LO_1 and LO_2. Furthermore, NLO_2 and NLO_3 tend to cancel each other almost exactly, leading to a complete-NLO prediction well within the uncertainty band of the one at NLO QCD accuracy. Such a feature may be spoiled by effects beyond the Standard Model, such as anomalous Higgs-top couplings. Thus, NLO corrections cannot be neglected when similar studies are performed, such as those presented in Sec. 6.3.2.

6.2.2 Prospect for experimental measurements

ATLAS has studied the potential to measure the Standard Model $t\bar{t}t\bar{t}$ cross section using 3000 fb^{-1} of HL-LHC data in the channel with several leptons [627]. Events are selected if they contain at least two isolated leptons with the same charge or at least three isolated leptons. At least six jets among which at least three are b-tagged are required. In addition the scalar sum of the $p_{\rm T}$ of all selected jets and leptons ($H_{\rm T}$) is requested to be $H_{\rm T} > 500$ GeV and the missing transverse momentum $E_{\rm T}^{miss} > 40$ GeV. In order to extract the measured $t\bar{t}t\bar{t}$ cross section a fit is performed to the $H_{\rm T}$ distributions in several signal regions according to the jets and b-jets multiplicities: at least 6 jets and exactly 3 b-jets, or at least 6 jets and at least 4 b jets. These regions are further split in events with two same-charge leptons or with at least three leptons leading to 4 signal regions.

The background arises from $t\bar{t}V$ process, multiboson and $t\bar{t}H$ events as well as events with fake, non prompt or charge mis-identified leptons. The rate of this difficult instrumental background is computed from the ATLAS 36 fb^{-1} analysis [625] in the relevant regions with different lepton and b-tagged jet multiplicities. The number of events selected in the different signal regions are shown in Fig. 76.

The main sources of systematic uncertainties taken into account come from uncertainties on the fake lepton background and on the SM background and signal normalisations. A maximum-likelihood fit is performed simultaneously in the four signal regions to extract the $t\bar{t}t\bar{t}$ signal cross section normalised to the prediction from the SM. The impact of systematic uncertainties on the background expectations is described by nuisance parameters. As a result of the fit, the expected uncertainty on the measured $t\bar{t}t\bar{t}$ cross section is found to be 11%. The systematic uncertainty that impacts the precision the most is uncertainty in the normalisation of the $t\bar{t}V$ and instrumental background in the region with at least 6 jets

Table 38: $t\bar{t}t\bar{t}$: $\sigma_{(\mathrm{N})\mathrm{LO}_i}/\sigma_{\mathrm{LO}_{\mathrm{QCD}}}$ ratios at 14 and 27 TeV, for different values of $\mu = \mu_R = \mu_F$. See Ref. [115] for details.

$\delta[\%]$	14 TeV			27 TeV		
	$\mu = H_{\mathrm{T}}/8$	$\mu = H_{\mathrm{T}}/4$	$\mu = H_{\mathrm{T}}/2$	$\mu = H_{\mathrm{T}}/8$	$\mu = H_{\mathrm{T}}/4$	$\mu = H_{\mathrm{T}}/2$
LO_2	-25.8	-28.1	-30.4	-23.6	-25.9	-28.2
LO_3	32.5	38.9	45.8	30.7	37.0	43.8
LO_4	0.2	0.3	0.4	0.1	0.2	0.2
LO_5	0.0	0.0	0.1	0.0	0.0	0.1
NLO_1	14.7	62.9	103.3	21.7	65.1	101.9
NLO_2	8.1	-3.5	-15.1	5.0	-4.4	-13.9
NLO_3	-10.0	1.8	15.8	-7.8	1.6	13.2
NLO_4	2.2	2.7	3.4	1.6	2.0	2.4
NLO_5	0.1	0.2	0.2	0.1	0.2	0.2
NLO_6	< 0.1	< 0.1	< 0.1	< 0.1	< 0.1	< 0.1
$\mathrm{NLO}_2 + \mathrm{NLO}_3$	-1.9	-1.7	0.7	-2.8	-2.8	-0.7

and exactly 3 b-jets. Overall the impact of the systematic uncertainties remain limited as a fit without systematic uncertainties leads to a precision of 9% on the extracted $t\bar{t}t\bar{t}$ cross section.

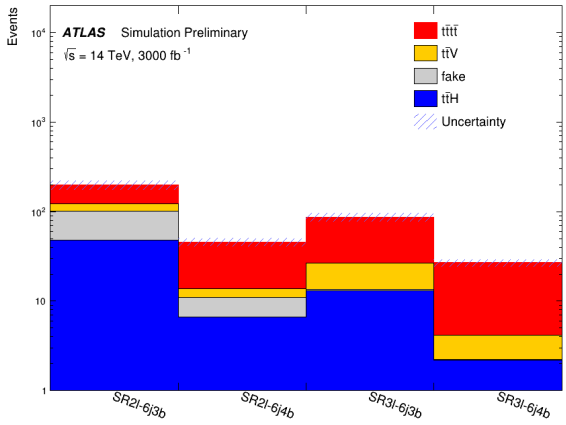

Fig. 76: Event yields of signal and background processes in the different signal regions used to extract the $t\bar{t}t\bar{t}$ cross section for an integrated luminosity of 3000 fb^{-1} [627].

The most sensitive result of the CMS collaboration on the Standard Model $t\bar{t}t\bar{t}$ process [618] is based on an integrated luminosity of 35.9 fb^{-1}and a centre-of-mass energy of 13 TeV, and relies on events with 2 same-sign leptons or 3 or more leptons. This Run-2 analysis sets an expected 95% CL upper limit on the $t\bar{t}t\bar{t}$ production cross section of $20.8^{+11.2}_{-6.9}$ fb, and an expected significance (based on a cross section of 9.2 fb) of 1.0 standard deviations above the background-only hypothesis.

The result of Ref. [618] is used to derive extrapolations for HL and HE-LHC, which are described in Ref. [628] and summarized below. The extrapolations rely on a simple rescaling of the signal and background cross sections, and make different assumptions on the systematic uncertainties. First, the statistical uncertainties are considered, then the same systematic uncertainties as the Run-2 published result are used, and finally these systematics are progressively reduced as a function of the integrated luminosity.

The expected sensitivity on the $t\bar{t}t\bar{t}$ cross section for different HL and HE-LHC scenarios is listed in Table 39. Based on these results, evidence for $t\bar{t}t\bar{t}$ production will become possible with around 300 fb^{-1} of HL-LHC data at $\sqrt{s} = 14$ TeV, at which point the statistical uncertainty on the measured cross section will be of the order of 30% and the measurement will have a total uncertainty of around 33-43%, depending on the systematic uncertainty scenario considered. For larger datasets at HL-LHC, all scenarios considered become dominated by systematic uncertainties. With 3 ab^{-1} the cross section can be constrained to 9% statistical uncertainty, and the total uncertainty of a measurement ranges between 18% and 28% depending on the considered systematic uncertainties. At HE-LHC the $t\bar{t}t\bar{t}$ cross section is expected to be constrained to within a 1-2% statistical uncertainty, and the systematic uncertainties also decrease due to the improved signal to background ratio at $\sqrt{s} = 27$ TeV. Future changes to the analysis strategy might allow improvements based on optimizing the interplay between statistical and systematic uncertainties.

The $t\bar{t}t\bar{t}$ cross section measurements can also be used to constrain the Wilson coefficients of the $\mathcal{O}_R$, $\mathcal{O}_L^{(1)}$, $\mathcal{O}_B^{(1)}$ and $\mathcal{O}_B^{(8)}$ dimension-6 operators of the Effective-Field-Theory (EFT) Lagrangian. These constraints are included in Ref. [628] for both HL-LHC and HE-LHC scenarios.

Table 39: Expected sensitivity for the production cross section of $t\bar{t}t\bar{t}$ production, in percent, at 68% confidence level. The fractional uncertainty on the cross section signal strength is given for various LHC upgrade scenarios. Cross sections are corrected for the changes expected by $\sqrt{s}$. For the 15 ab^{-1} 27 TeV scenario, the systematic uncertainty extrapolation is no longer valid, so only the statistical uncertainty is provided.

Int. Luminosity	$\sqrt{s}$	*Stat. only* (%)	*Run-2* (%)	*YR18* (%)	*YR18+* (%)
300 fb^{-1}	14 TeV	$+30, -28$	$+43, -39$	$+36, -34$	$+36, -33$
3 ab^{-1}	14 TeV	± 9	$+28, -24$	$+20, -19$	± 18
3 ab^{-1}	27 TeV	± 2	$+15, -12$	$+9, -8$	$+8, -7$
15 ab^{-1}	27 TeV	± 1			

6.3 Four top quarks as a probe of new physics

Heavy coloured resonances decaying into a pair of top quarks are present in many new physics theories [629–633]. Such particles are typically pair-produced at large rate and their decay then leads to a substantial enhancement of four-top production. Current bounds on such a setup are driven by a recent CMS analysis of four-top events [618], using 35.9 fb^{-1} of LHC collisions at a centre-of-mass energy of 13 TeV. Those bounds however are expected to strongly improve in the upcoming years, as illustrated in following contributions, with the example of a scalar colour-octet field O, traditionally dubbed a sgluon.

6.3.1 Limits on pseudoscalar colour-octets[38]

The effective Lagrangian describing the couplings of such a sgluon to the Standard Model is given by [634]

$$\mathcal{L} \supset g_8 d_{abc} O^a G^b_{\mu\nu} G^{\mu\nu c} + \tilde{g}_8 d_{abc} O^a G^b_{\mu\nu} \tilde{G}^{\mu\nu c} + \left\{ \bar{q} \left[\mathbf{y_8^L} P_L + \mathbf{y_8^R} P_R \right] O^a T_a q + \text{h.c.} \right\} , \qquad (46)$$

where T^a and d_{abc} are respectively the fundamental representation matrices and symmetric structure constants of $SU(3)$. Moreover, flavour and fundamental colour indices are understood for simplicity and the gluon field strength (dual field strength) tensor is denoted by $G^a_{\mu\nu}$ ($\tilde{G}^a_{\mu\nu}$). The focus here is on the case of a pseudoscalar sgluon with $g_8 = 0$ and purely imaginary $\mathbf{y_8}$ matrices, and it is additionally enforced

[38] Contributed by B. Fuks, L. Darmé and M.D. Goodsell.

$\tilde{g}_8 = 0$ as in Dirac gaugino supersymmetric scenarios. A non-vanishing $\tilde{g}_8$ coupling would however weaken the bounds by reducing the sgluon branching ratio into top quarks. In order to assess the impact of future search on the potential discovery of a sgluon, recasting strategy is followed here, as detailed in Ref. [635]. An NLO UFO module [636] is generated through FEYNRULES [637], NLOCT [638] and FEYNARTS [639] and it is used to generate events within the MG5_AMC@NLO framework [12], the hard-scattering matrix elements being convolved with the NNPDF3.0 NLO set of parton densities [201] and the sgluon decays being achieved with MADSPIN [402] and MADWIDTH [640]. Parton showering and hadronisation are performed by PYTHIA 8 [149] and the response of the CMS detector is simulated with DELPHES 3 [273] and FASTJET [343]. Finally, the four-top selection strategy of CMS [618] is mimicked by using the MADANALYSIS 5 [641–643] framework.

The best signal region (SR6) from Ref. [618], in terms of constraints, focuses on a topology featuring one pair of same-sign leptons, at least 4 b-jets and at least 5 hard jets. It is shown the observed and expected limits on the pseudoscalar octet cross section times the corresponding branching ration into four top quarks in Fig. 77 (left). While the analysis of Ref. [618] targeted a Standard Model four-top signal, future studies adopting a new physics signal selection strategy relying on the large differences in the final-state kinematics could be more adapted and lead to sizeable improvement in the reach [635].

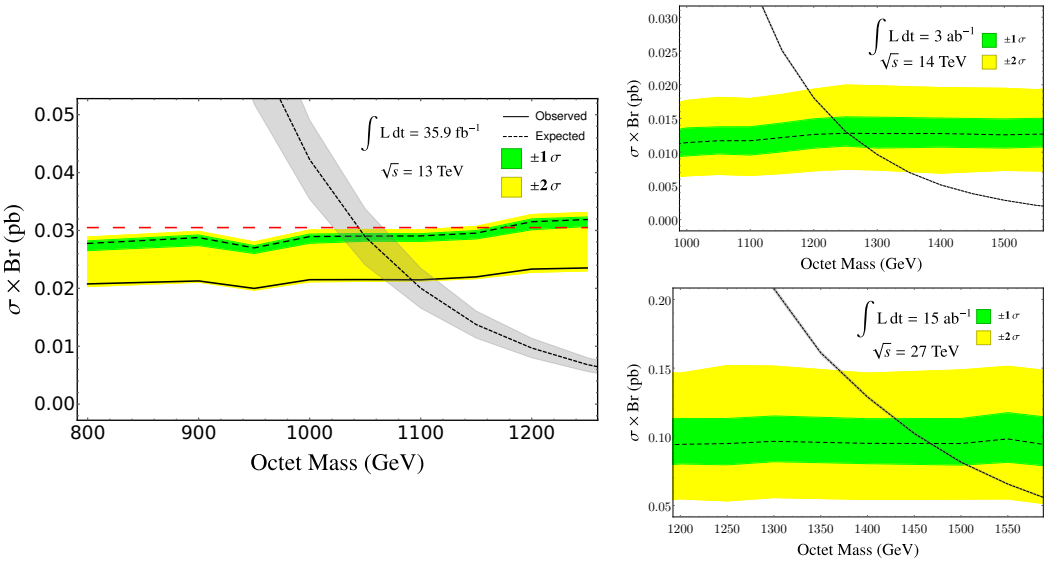

Fig. 77: Left: Expected (dashed) and observed (solid) pseudoscalar sgluon pair-production cross section excluded at the 95% confidence level when making use of the results associated with the SR6 region of the four-top CMS analysis of Ref. [618]. Theoretical predictions for the signal rate are indicated by the grey band. Right: expected limits for proton-proton collisions at centre-of-mass energies of 14 (top) and 27 (bottom) TeV, with the sgluon cross-section as the fine dotted line.

To calculate the projected sensitivity of the HL/HE-LHC, it is assumed that the current selection efficiencies at 13 TeV are similar to the future ones, and moreover rescale the four-top and other SM backgrounds by the appropriate partonic luminosities relative to those at 13 TeV. The rescaling factor for the non-four-top SM background is taken to be the largest ratio of the ttZ and ttW background component, using the projected cross-sections reported in Sec. 6.8. Factors of 1.3 and 12 are obtained for the 14 and 27 TeV cases, respectively. According to Sec. 6.2.1, the four-top cross section is then set to 15.83 fb and 144 fb at 14 and 27 TeV, respectively, recalling that the 13 TeV cross section is of 11.97 fb. The results for the projected mass limits are then given in the following Table 40, together with the 13 TeV value for reference.

Table 40: Results for the projected mass limits on pseudo-scalar color octets.

	$35.9\,\text{fb}^{-1}$, 13 TeV	$3\,\text{ab}^{-1}$, 14 TeV	$15\,\text{ab}^{-1}$, 27 TeV
Octet mass (GeV)	1060	1260	1470

6.3.2 Limits on top-Higgs interaction from multi-top final state[39]

Four top-quark ($t\bar{t}t\bar{t}$) production provides a powerful tool to probe the Top-quark Yukawa coupling (y_t) [644]. In the SM the $t\bar{t}t\bar{t}$ production can be induced either by the pure gauge interaction (involving the gluon, Z-boson or photon in the intermediate state) [645] or by the Higgs boson mediation [644]. Defining the general top-Higgs coupling as $y_t \equiv \kappa_t y_t^{\rm SM}$ with $y_t^{\rm SM}$ the top-Yukawa coupling in the SM, the leading-order cross section of $t\bar{t}t\bar{t}$ production can be parameterised as

$$\sigma(t\bar{t}t\bar{t}) = \sigma(t\bar{t}t\bar{t})^{\rm SM}_{g/Z/\gamma} + \kappa_t^2\sigma(t\bar{t}t\bar{t})^{\rm SM}_{\rm int} + \kappa_t^4\sigma(t\bar{t}t\bar{t})^{\rm SM}_{H}, \tag{47}$$

where $\sigma(t\bar{t}t\bar{t})^{\rm SM}_{g/Z,\gamma,\ H,\ \rm int}$ denotes the cross section induced by the pure gauge interaction, Higgs-boson mediation and the interfere effect, respectively. Note that $\sigma^{\rm SM}_{H,\rm int}$ is comparable to $\sigma(t\bar{t}t\bar{t})^{\rm SM}_{g/Z,\gamma}$ as $y_t^{\rm SM} \sim 1$ in the SM. For example, the leading order calculation with the renormalization/factorization scale (μ) fixed to the dynamics scale [12] yields

$$\begin{aligned}
&\text{HL}-\text{LHC}\ (\sqrt{s}=14\ \text{TeV}) \quad : \quad \sigma(t\bar{t}t\bar{t}) = \ 13.14 - \ \ 2.01\kappa_t^2 + \ 1.52\kappa_t^4 \ \ [\text{fb}] \\
&\text{HE}-\text{LHC}\ (\sqrt{s}=27\ \text{TeV}) \quad : \quad \sigma(t\bar{t}t\bar{t}) = 115.10 - 15.57\kappa_t^2 + 11.73\kappa_t^4 \ \ [\text{fb}]
\end{aligned} \tag{48}$$

Clearly, $\sigma(t\bar{t}t\bar{t})$ depends only on κ_t such that it directly probes y_t without any assumption on Higgs boson. The above values suffer from a large μ dependence; when varying the scale by a factor 2, the cross section varies by about 50%. It is crucial to take the full next-to-leading order corrections [115,617] into account to get a realistic simulation. Here, the tree level events are generated and the cross section rescaled to the NLO.

A special signature of the $t\bar{t}t\bar{t}$ events is the same-sign charged leptons (SSL) from the two same-sign top quarks. The other two top quarks are demanded to decay hadronically to maximize the event rate. Therefore, the topology of the signal event consists of two same-sign charged leptons, four b-quarks, four light-flavor quarks, and two invisible neutrinos. In practice it is challenging to identify four b-jets. Instead, it is required for at least 5 (6) jets to be tagged and three of them to be identified as b-jets at the HL(HE)-LHC, respectively. The two invisible neutrinos appear as a missing transverse momentum $E_{\rm T}^{miss}$ in the detector. The SM backgrounds contain $t\bar{t}+X$, $W^\pm W^\pm jj$ and $W^\pm W^\pm jj$ processes. See Ref. [644] for the details of those kinematic cuts used to disentangle the $t\bar{t}t\bar{t}$ signal from the huge backgrounds. It is demanded that $E_{\rm T}^{miss} > 100$ GeV at the HL-LHC and $E_{\rm T}^{miss} > 150$ GeV at the HE-LHC. Table 41 displays the numbers of signal and background events after applying the kinematics cuts listed in each row sequentially. In Table 41, at the HL-LHC the $t\bar{t}t\bar{t}$ production cross section is multiplied by a constant K-factor of 1.27 with uncertainty 27% (see Ref. [617]), while at the HE-LHC the cross section is rescaled to NLO order of $143.93^{+17\%}_{-20\%}$ fb (see Table 37 in Sec. 6.2.1).

The MC simulation shows that the $t\bar{t}t\bar{t}$ production ($\kappa_t = 1$) can be discovery at a 5σ confidence level with an integrated luminosity of 2075 fb^{-1} at the HL-LHC and 146 fb^{-1} at the HE-LHC, respectively. The event rate is not enough for measuring y_t precisely at the HL/HE-LHC but it is good for bounding y_t; for example, a direct bound $\kappa_t \leq 1.41\ [1.37, 1.47]$ is obtained at the HL-LHC and $\kappa_t \leq 1.15\ [1.12, 1.17]$ $(1.12\ [1.10, 1.13],\ 1.10\ [1.08, 1.12])$ with an luminosity of 10 $(20,\ 30)$ ab^{-1} at the HE-LHC, respectively.

[39] Contributed by Qing-Hong Cao, Shao-Long Chen and Yandong Liu.

A few words of care on the interpretation of results from this study are however necessary: as it has been discussed in Sec. 6.2.1, the complete-NLO corrections to $t\bar{t}t\bar{t}$ are large and can involve terms proportional to y_t^3, y_t^5 and y_t^6 (on top of y_t^2 and y_t^4 already present at LO). However, since in such corrections y_t is renormalised, an extension of our study will not be immediately possible at NLO.

Table 41: The numbers of signal and background events at the HL-LHC with an integrated luminosity of 300 fb^{-1} (left) and at the HE-LHC with an integrated luminosity of 1 ab^{-1}. The cuts listed in the row are applied sequentially [644].

HL-LHC	Basic	SSL	Jets	$\not{E}_T$	m_T	H_T
$t\bar{t}t\bar{t}_H$	577.22	9.82	4.68	2.43	1.33	1.21
$t\bar{t}t\bar{t}_{g/Z/\gamma}$	5006.34	78.15	37.02	19.25	11.09	10.16
$t\bar{t}t\bar{t}_{\text{int}}$	-764.67	-12.79	-6.19	-3.23	-1.93	-1.77
$t\bar{t}$	2.5×10^8	28802.4	44.1	18.9	0	0
$t\bar{t}W^+$	32670	2359.5	36.9	17.7	12.3	8.7
$t\bar{t}W^-$	16758	1397.1	49.5	9.9	4.5	4.5
$t\bar{t}Z$	24516	2309.4	20.1	10.8	10.8	9.3
$W^\pm W^\pm jj$	4187.7	1147.5	0.11	0	0	0

HE-LHC	Basic	SSL	Jets	$\not{E}_T$	m_T	H_T
$t\bar{t}t\bar{t}_H$	15174.4	260.09	84.61	27.92	15.42	15.17
$t\bar{t}t\bar{t}_{g/Z/\gamma}$	148898.	2421.08	814.77	268.02	168.55	166.77
$t\bar{t}t\bar{t}_{\text{int}}$	-20141.9	-347.81	-117.95	-36.17	-20.14	-19.66
$t\bar{t}$	3.3×10^7	130207	291.9	0	0	0
$t\bar{t}W^+$	1.3×10^6	11488.5	171.0	39.6	27.1	27.1
$t\bar{t}W^-$	7.6×10^5	7387.1	99.5	19.9	9.9	9.9
$t\bar{t}Z$	3.9×10^6	20748.7	507.2	129.7	70.8	70.8
$W^\pm W^\pm jj$	888700	7947.0	4.7	3.5	0	0

6.3.3 Constraining four-fermion operators in the EFT[40]

The four-top total cross section measurement can be interpreted within the SMEFT framework [646][41]. Following the notation in Refs. [646] and [234], the relevant operators consist of four independent four-top-quark operator coefficients, $\tilde{C}_{\text{tt}}$, $\tilde{C}^{(+)}_{\text{QQ}}$, $\tilde{C}^{(1)}_{\text{Qt}}$, $\tilde{C}^{(8)}_{\text{Qt}}$, and fourteen independent two-light-two-top-quark ($qqtt$) operator coefficients, $\tilde{C}^{(8)}_{\text{td}}$, $\tilde{C}^{(1)}_{\text{td}}$, $\tilde{C}^{(8)}_{\text{Qd}}$, $\tilde{C}^{(1)}_{\text{Qd}}$, $\tilde{C}^{(8)}_{\text{tu}}$, $\tilde{C}^{(1)}_{\text{tu}}$, $\tilde{C}^{(8)}_{\text{Qu}}$, $\tilde{C}^{(1)}_{\text{Qu}}$, $\tilde{C}^{(8,1)}_{\text{Qq}}$, $\tilde{C}^{(1,1)}_{\text{Qq}}$, $\tilde{C}^{(8,3)}_{\text{Qq}}$, $\tilde{C}^{(1,3)}_{\text{Qq}}$, $\tilde{C}^{(8)}_{\text{tq}}$, $\tilde{C}^{(1)}_{\text{tq}}$. Here $\tilde{C}_i \equiv C_i/\Lambda^2$. O_{tG} is relevant but better constrained by other processes.

To estimate the projected limits on these coefficients, a few simple assumptions are made: 1) the effective operators do not significantly change the distribution of events, so the sensitivity mainly comes from inclusive measurements; 2) a kinematic cut M_{cut} of a few TeV can be applied to the total mass of the four tops to make sure the SMEFT can be matched to BSM models with scales larger than this energy (i.e. following Ref. [647]); and 3) M_{cut} does not significantly change the projected sensitivity on cross section measurements. By combining the expected experimental sensitivity discussed in Sec. 6.2.2 and the theoretical predictions presented in Sec. 6.2.1 it is estimated that the total cross section can be

[40] Contributed by Cen Zhang.

[41] This interpretation is also present in Ref. [628].

determined with an uncertainty of 102%, 58%, and 40%, at 95% CL level, for the 13, 14 and 27 TeV runs respectively. The corresponding integrated luminosities are 300 fb^{-1}, 3 ab^{-1} and 15 ab^{-1}.

For illustration, Fig. 78 shows the signal strength dependence on two operator coefficients: one four-top coefficient (left) and one $qqtt$ coefficient (right), assuming a 3 TeV M_{cut}. The cross section becomes more sensitive to the four-top operator coefficient at larger energies. Together with smaller uncertainties, the limit on this coefficient is significantly improved with the 27 TeV run. On the other hand, the cross section becomes less sensitive to the $qqtt$ operator coefficient as the energy increases. The limits are thus not very much affected by energy. Table 42 presents individual limits on all 18 operator coefficients, assuming $M_{cut} = 3$ TeV.

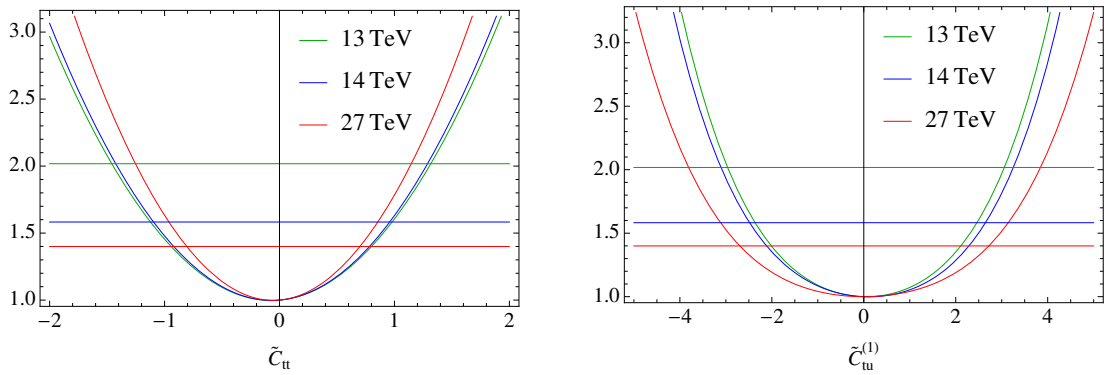

Fig. 78: Four-top signal strength as a function of operator coefficients, $\tilde{C}_{tt}$ (left) and $\tilde{C}_{tu}^{(1)}$ (right). Horizontal lines represent the expected measurements at each energy. $M_{cut} = 3$ TeV is applied.

6.3.4 Top quark dipole moment in multi-top production[42]

This paragraph presents the study of the sensitivity of the four top quark production on the strong dipole moments of the top quark [648]. Within the SM framework, the top quark dipole moments are zero at tree level, however, higher-order corrections could generate non-zero strong dipole moments for the top quark. The top quark strong dipole moments have very small values in the SM, so that they would not be observable at the LHC experiments. However, there are extensions of the SM in which sizable contributions to these dipole moments arise, making them accessible by the experiments at the LHC [649, 650]. As a result, observation of any significant deviation of dipole moments from zero would point to beyond the SM physics. The most general effective Lagrangian describing the $gt\bar{t}$ coupling considering dimension-6 operators can be parametrized as [651]:

$$\mathcal{L}_{gt\bar{t}} = -g_s\bar{t}\frac{\lambda^a}{2}\gamma^\mu t G^a_\mu - g_s\bar{t}\lambda^a\frac{i\sigma^{\mu\nu}q_\nu}{m_t}(d^g_V + id^g_A\gamma_5)tG^a_\mu,$$

where the chromomagnetic and chromoelectric dipole moments of the top quark are denoted by d^g_V and d^g_A (both are zero in the SM at leading order). Direct bounds on both d^g_V and d^g_A were obtained from the top quark pair cross section measurements at the LHC and the Tevatron. The bounds on the dipole moments using the $t\bar{t}$ cross section at the LHC and Tevatron were found to be: $-0.012 \leq d^g_V \leq 0.023$, $|d^g_A| \leq 0.087$ [652]. Four-top quark production is also affected by the $gt\bar{t}$ effective coupling and provides a powerful way to probe the chromomagnetic and chromoelectric dipole moments of the top quark. The representative Feynman diagrams with the effective $gt\bar{t}$ coupling denoted by filled red circles are shown in Fig. 79. The contribution of the top quark dipole moments to the $t\bar{t}t\bar{t}$ production cross section is determined with the MG5_aMC@NLO package [12]. By taking into account at most

[42] Contributed by J. Ebadi, H. Khanpour, S. Khatibi and M. Mohammadi Najafabadi.

Table 42: Limits on 14 $qqtt$ operator coefficients and 4 four-top operator coefficients, expected at the 13, 14 and 27 TeV scenarios, at the 95% CL level.

	13 TeV	14 TeV	27 TeV
$\tilde{C}_{\rm td}^{(8)}$	[-9.8, 6.4]	[-8.8, 5.4]	[-6.6, 5.4]
$\tilde{C}_{\rm td}^{(1)}$	[-3.9, 4.1]	[-3.3, 3.4]	[-3.3, 3.3]
$\tilde{C}_{\rm Qd}^{(8)}$	[-9.6, 6.2]	[-8.8, 5.2]	[-7.6, 5.2]
$\tilde{C}_{\rm Qd}^{(1)}$	[-4., 4.]	[-3.3, 3.3]	[-3.4, 3.3]
$\tilde{C}_{\rm tu}^{(8)}$	[-8.2, 4.8]	[-6.4, 4.3]	[-9.6, 4.5]
$\tilde{C}_{\rm tu}^{(1)}$	[-3., 3.1]	[-2.5, 2.6]	[-2.7, 2.7]
$\tilde{C}_{\rm Qu}^{(8)}$	[-7.8, 4.6]	[-7.8, 4.]	[-5.8, 4.2]
$\tilde{C}_{\rm Qu}^{(1)}$	[-3., 3.]	[-2.6, 2.6]	[-2.7, 2.7]
$\tilde{C}_{\rm Qq}^{(8,1)}$	[-7.5, 4.2]	[-6., 3.6]	[-6.5, 3.7]
$\tilde{C}_{\rm Qq}^{(1,1)}$	[-2.5, 2.7]	[-2.1, 2.3]	[-2.2, 2.3]
$\tilde{C}_{\rm Qq}^{(8,3)}$	[-5.8, 4.8]	[-4.7, 4.2]	[-5.4, 4.]
$\tilde{C}_{\rm Qq}^{(1,3)}$	[-2.6, 2.6]	[-2.1, 2.2]	[-2.2, 2.2]
$\tilde{C}_{\rm tq}^{(8)}$	[-7.1, 3.9]	[-6.9, 3.3]	[-5.1, 3.4]
$\tilde{C}_{\rm tq}^{(1)}$	[-2.6, 2.6]	[-2.2, 2.2]	[-2.3, 2.2]
$\tilde{C}_{\rm tt}$	[-1.5, 1.3]	[-1.1, 0.96]	[-0.81, 0.7]
$\tilde{C}_{\rm QQ}^{(+)}$	[-1.5, 1.3]	[-1.1, 0.96]	[-0.81, 0.7]
$\tilde{C}_{\rm Qt}^{(1)}$	[-2.4, 2.4]	[-1.8, 1.8]	[-1.3, 1.3]
$\tilde{C}_{\rm Qt}^{(8)}$	[-5.3, 4.4]	[-4.1, 3.1]	[-3., 2.3]

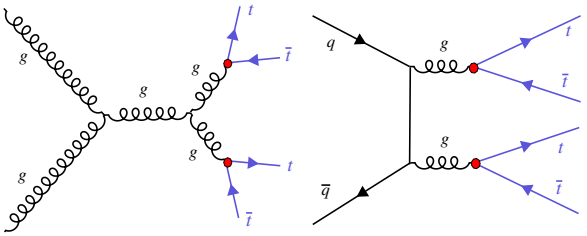

Fig. 79: Representative Feynman diagrams for the $t\bar{t}t\bar{t}$ production where the effects of the strong dipole moments are shown as filled red circles.

an effective vertex in each diagram, the total four top cross section at $\sqrt{s} = 14$ TeV has the following form:

$$\begin{aligned} \sigma(pp \to t\bar{t}t\bar{t})(\text{fb}) &= \sigma_{\rm SM} + 154.8 \times d_V^g + 3404.4 \times (d_V^g)^2, \\ \sigma(pp \to t\bar{t}t\bar{t})(\text{fb}) &= \sigma_{\rm SM} + 2731.3 \times (d_A^g)^2, \end{aligned} \tag{49}$$

where the SM four top quark cross section is denoted by $\sigma_{\rm SM}$. The linear terms are due to the interference between the new physics and SM with the contribution of the order of Λ^{-2}. The quadratic terms suppressed by Λ^{-4} power are the pure contributions of the strong dipole moments. To estimate the sensitivity of the four top process to dipole moments, the same-sign dilepton channel is the focus here due to its clean signature and very low background contribution. The main background contributions

Table 43: Limits at 95% CL on the chromoelectric and chromomagnetic dipole moments $d_V^{g,Z}$ at 95% CL for the HL-LHC and HE-LHC.

Coupling	HL-LHC, 14 TeV, 3 ab^{-1}	HE-LHC, 27 TeV, 15 ab^{-1}
d_V^g	[-0.084, 0.009]	[-0.063, 0.001]
d_A^g	[-0.030, 0.030]	[-0.011, 0.011]

come from the $t\bar{t}W$ and $t\bar{t}Z$ processes. Signal and the background processes are generated with the MG5_aMC@NLO package at leading order. PYTHIA v6 [653] is used for hadronization, showering and decay of unstable particles. Jets are reconstructed using the anti-k_{T} algorithm [274]. Signal events are selected by requiring exactly two same-sign charged leptons with $p_{\mathrm{T}}^{\ell} > 25$ GeV and $|\eta^{\ell}| < 2.5$. The missing transverse energy has to be larger than 30 GeV. Each event is required to have at least eight jets with $p_{\mathrm{T}} > 30$ GeV and $|\eta| < 2.5$ from which at least three should be b-tagged jets. All objects in the final state are required to be well isolated objects by requiring $\Delta R(i,j) > 0.4$. Table 43 presents limits at 95% CL on the chromoelectric (d_A^g) and chromomagnetic (d_V^g) dipole moments for the HL-LHC and HE-LHC. The HE-LHC improves the HL-LHC bound on d_A^g by about a factor of three and the upper bound on d_V^g by one order of magnitude. The four top-quark production at the HE-LHC would be able to tighten the upper limit on d_A^g (d_V^g) by a factor of two (eight) with respect to the top pair production at the HL-LHC [652].

6.4 The $t\bar{t}V$ production at the HL/HE-LHC

6.4.1 $t\bar{t}Z$ cross sections at NLO QCD and EW[43]

This section provides the cross section for $t\bar{t}Z$ production at the HL and HE-LHC. The results are accurate up to NLO QCD and NLO EW accuracy [99]. NLO QCD and EW corrections are computed simultaneously with MG5_aMC@NLO [12], more specifically by using the recently-released version capable of mixed-coupling expansions [89]. The same setup as in Ref. [186] is used (see in particular Sec. 1.6.7.a), except for the PDF set, for which the PDF4LHC15_nlo_30_pdfas set [195] is employed. In fact, at variance with the predictions in Ref. [186], photon-initiated contributions are not included, since recent studies on the photon distribution became available [222, 223], and the corresponding photon density gives negligible contributions for $t\bar{t}Z$. The quoted EW corrections include the LO term at $\mathcal{O}(\alpha^2\alpha_s)$ and the NLO one at $\mathcal{O}(\alpha^2\alpha_s^2)$. At variance with $t\bar{t}W$ production, for which other contributions, subleading in the couplings, turn instead to be relevant (see Sec. 6.4.2), it has been shown in Ref. [89] that such contributions can be safely neglected for $t\bar{t}Z$.

Cross-sections for $t\bar{t}Z$ are quoted in Table 44, together with the NLO/LO QCD K-factor, the relative impact of EW corrections, and the theory uncertainties. For the latter, the uncertainty coming from scale variations, the PDF uncertainty and the α_s one are quoted separately.

Table 44: Cross section, in pb, for $t\bar{t}Z$ production at the HL and HE-LHC. Uncertainties on the cross sections are at the per-mil level.

$\sqrt{s}$	$\sigma_{\mathrm{QCD}}^{\mathrm{NLO}}$	$\sigma_{\mathrm{QCD+EW}}^{\mathrm{NLO}}$	K_{QCD}	δ_{EW} [%]	scale [%]		PDF [%]	α_s [%]
14 TeV	1.018	1.015	1.40	-0.3	+9.6	-11.2	±2.7	± 2.8
27 TeV	4.90	4.81	1.45	-2.0	+9.9	-10.4	±2.0	± 2.0

[43] Contributed by R. Frederix, D. Pagani and M. Zaro.

6.4.2 The complete-NLO corrections to $t\bar{t}W$[44]

This section presents the so-called "complete"-NLO corrections to $t\bar{t}W^{\pm}$ production. This process can proceed through different terms of order $\alpha_s^p \alpha^{q+1}$ with $p+q = 2,\ 3$ at LO and at NLO respectively. The term complete-NLO refers to computation of all terms with $p+q \leq 3$, which has been performed for the first time in Ref. [115] by employing the newly-released version of MG5_aMC@NLO [12] capable of computing mixed QCD and electroweak corrections [89]. Among the various contributions, the complete-NLO corrections include the NLO QCD ones ($p = 3$, $q = 0$) [418, 419, 654, 655], and the NLO EW corrections ($p = 2$, $q = 2$) [99]. This short paragraph reports inclusive predictions for the HL and HE-LHC, with a centre-of-mass energy of respectively 14 TeV and 27 TeV. The same setup and notation of Ref. [115] is used, where the interested reader can find more details as well as predictions for 13 and 100 TeV.

Table 45: Cross section for $t\bar{t}W^{\pm}$ production at the HL and HE-LHC, in various approximations, for $\mu = H_{\rm T}/2$. Number in parentheses are computed with a jet veto. See Ref. [115] for details.

σ[fb]	LO_{QCD}	$\text{LO}_{\text{QCD}} + \text{NLO}_{\text{QCD}}$	LO	LO + NLO	$\frac{\text{LO}(+\text{NLO})}{\text{LO}_{\text{QCD}}(+\text{NLO}_{\text{QCD}})}$
14 TeV	$414^{+23\%}_{-18\%}$	$628^{+11\%}_{-11\%}$ $(521^{+5\%}_{-7\%})$	$418^{+23\%}_{-17\%}$	$670^{+12\%}_{-11\%}$ $(548^{+6\%}_{-7\%})$	1.07 (1.05)
27 TeV	$1182^{+21\%}_{-16\%}$	$2066^{+14\%}_{-11\%}$ $(1561^{+7\%}_{-7\%})$	$1194^{+21\%}_{-16\%}$	$2329^{+14\%}_{-11\%}$ $(1750^{+7\%}_{-7\%})$	1.13 (1.12)

Table 45 reports the total-cross section for $t\bar{t}W^{\pm}$ production in different approximations, and Table 46 the breakdown of the different orders contributing at LO and NLO, as fraction of the $\mathcal{O}(\alpha_s^2\alpha)$ LO contribution, LO_1. Number in parentheses are computed by vetoing hard central jets, with $p_{\rm T} > 100\,\text{GeV}$ and $\eta < 2.5$. As it can be gathered from the tables, the jet veto is beneficial in order to reduce the NLO QCD corrections, in particular the large contribution coming from hard real emissions with a soft or collinear W boson. It can be appreciated how the NLO_3 contribution is actually larger than the NLO_2 (the EW corrections) despite the extra power of α, and how such a contribution grows with the collider energy. As explained in Ref. [115], this is due to the $t-W$ scattering process [656]. Since the size of NLO_3 is not much affected by the jet veto, a measurement of the $t-W$ scattering from the $t\bar{t}W$ cross section should be possible.

6.5 Top mass

6.5.1 Theoretical issues[45]

The currently most precise methods for top mass measurements at the LHC are the so called "direct measurements" which are obtained exploiting information from the kinematic reconstruction of the measured top quark decay products, and their corresponding combinations. The typical errors currently quoted for the direct LHC top mass measurements are of the order of 500-600 MeV, and with the prospect of the high luminosity operations, as can be seen from Fig. 80 of the following section, the projected future experimental uncertainty is around 200 MeV. Such a high precision entails also a high level of scrutiny concerning the extracted top mass value. In direct measurements, the measured top mass is the value of the top mass parameter in the Monte Carlo generator that is used to fit top-mass sensitive distributions, because the complexity of the measurement is such that the extraction of these distributions corrected for detector effects, to be compared with analytic calculations, is not feasible. In this respect, the scrutiny must also regard theoretical aspects dealing with how the Monte Carlo models

[44] Contributed by R. Frederix, D. Pagani and M. Zaro.

[45] Contribution by G. Corcella, P. Nason, A. Hoang and H. Yokoya.

Table 46: $t\bar{t}W$: $\sigma_{(\mathrm{N})\mathrm{LO}_i}/\sigma_{\mathrm{LO}_{\mathrm{QCD}}}$ ratios at 14 and 27 TeV, for different values of $\mu = \mu_r = \mu_f$. LO_2 is identically zero and is not quoted in the table. Number in parentheses are computed with a jet veto. See Ref. [115] for details.

$\delta[\%]$	14 TeV			27 TeV		
	$\mu = H_{\mathrm{T}}/4$	$\mu = H_{\mathrm{T}}/2$	$\mu = H_T$	$\mu = H_{\mathrm{T}}/4$	$\mu = H_{\mathrm{T}}/2$	$\mu = H_{\mathrm{T}}$
LO_3	0.8	1.0	1.1	0.9	1.0	1.2
NLO_1	37.4 (7.7)	51.8 (25.9)	64.7 (41.9)	67.4 (18.4)	74.8 (32.0)	82.0 (44.3)
NLO_2	−4.5 (−4.7)	−4.3 (−4.5)	−4.1 (−4.3)	−5.1 (−5.4)	−5.0 (−5.2)	−4.8 (−5.1)
NLO_3	13.0 (9.7)	13.3 (9.9)	13.6 (10.1)	25.5 (19.8)	26.1 (20.2)	26.6 (20.6)
NLO_4	0.02 (−0.00)	0.03 (0.00)	0.05 (0.01)	0.06 (0.01)	0.08 (0.02)	0.10 (0.03)

the relevant mass sensitive distributions, keeping in mind that all effects that can lead to variations of the result in the 100 MeV range should be considered.

The top mass parameter, as all coupling constants characterizing the underlying field theory, requires renormalization, and its precise value depends upon the adopted renormalization scheme. The differences in the top mass in different renormalization prescriptions used in the theoretical community are parametrically of order $R\,\alpha_s(R)$, with R between about 1 GeV and m_t, and thus can amount from a few hundred MeV to several GeV. It is thus clear that an experimental result, in order to be of any use, must specify to which scheme the measured value corresponds to.

At present, the experimental collaborations have renounced to qualify direct mass measurements by also specifying a renormalization scheme. This is a consequence of the fact that no full agreement has been reached among theorists on this issue. Some authors have argued that, in view of the inherent leading-order nature of the Monte Carlo generators, no scheme can be specified for the mass measured in direct measurements, since at leading order all schemes are equivalent. This argument was also used as part of the motivation in favour of alternative measurements where the mass-sensitive observable is directly computed in perturbation theory at NLO or NNLO accuracy, and is compared to experimental distributions already corrected for detector effects [657, 658]. For example, the total cross section for $t\bar{t}$ production is sensitive to the top mass, it has been computed up to the NNLO order in QCD [41], and can be used to extract a top mass value [659–661]. Similarly, in Ref. [657, 658], shape observables constructed out of the $t\bar{t}+\mathrm{jet}$ kinematics are used.

Several theoretical works have appeared proposing alternative techniques to measure the top mass, partly to provide predictions with at least NLO precision to allow for a mass determination in a well-defined mass scheme, and partly to circumvent other aspects of direct measurements that may be considered problematic. The authors of Ref. [662] presented a method, based upon the charged-lepton energy spectrum, that is not sensitive to top production kinematics, but only to top decay, and does not make use of jets. Since top decays have been computed at NNLO accuracy [608, 609], they argue that a very accurate measurement may be achieved in this way. Other authors have advocated using the invariant mass of boosted top jets supplemented by light grooming (see Ref. [663] and references therein). In Ref. [664], the b-jet energy peak position is proposed as mass-sensitive observable, that is claimed to have a reduced sensitivity to production dynamics. In Ref. [665], the use of lowest Mellin moments of lepton kinematic distributions is discussed. In the leptonic channel, it is also possible to use distributions based on the "transverse" mass variable [666], which generalizes the concept of transverse mass for a system with two identical decay branches [667, 668]. Some of these methods have been effectively exploited by the experimental collaborations [666, 669–672] to yield alternative determinations of m_t. They are consistent within errors with direct measurements, and thus provide valuable checks. It turns out, however, that at the moment their errors are not competitive with direct measurements, mostly be-

cause the (less direct) observables of the alternative methods do not have the top mass discriminating power of the direct method. Furthermore, in view of the larger errors, the assessment of their eventual theoretical uncertainties is a less demanding task in comparison to the case of direct measurements.

The notion that the Monte Carlo mass parameter cannot be qualified as a field theoretical mass has extensively permeated the discussions regarding the interpretation of top mass measurements. This notion, however, oversimplifies the situation, because more precise statements on the Monte Carlo mass parameter can be made. In reality, the accuracy of Shower Monte Carlo's depends upon the observables one considers. As a trivial example, the total cross section for the production of top quarks is predicted at leading order by standard Shower Monte Carlo's, so that the value of the top mass extracted by fitting it to the measured total production cross section would indeed carry a scheme ambiguity of order $m_t\alpha_s$, because the pole or the $\overline{\rm MS}$ schemes can be used for computing the total cross section at higher orders. Such measurement cannot be qualified by specifying any particular scheme.[46] This is not the case if one considers as an observable the mass of the top decay products. In Ref. [673], for example, it is pointed out that, in the narrow width limit, a perturbative calculation of the mass of the top decay products performed in the pole mass scheme yields the pole mass at any perturbative order. Since Monte Carlo generators, when performing heavy particle decay, strictly conserve the mass of the decaying particle, it can be inferred that the Monte Carlo mass parameter should be identified with the pole mass up to non-perturbative effects[47] as far as the mass of the decay products is concerned. From a different point of view, in Ref. [674] it is argued that since the top-quark decay is treated with a Breit-Wigner form in the Monte Carlo generators, and due to the infrared shower cutoff $Q_0 \approx 1\,\text{GeV}$, the top mass parameter should be close to top mass schemes that are compatible with the Breit-Wigner form. In turn, these schemes yield mass values that differ from the pole mass by terms of order $\alpha_s(R)R$, with $R \approx \Gamma_t \approx Q_0$. In a subsequent work [675], it is argued that, in the narrow width limit, one can relate the Monte Carlo mass parameter to a running mass (such as the MSR mass [676]) evaluated at the scale of the Monte Carlo shower cutoff Q_0, as long as $Q_0 \gtrsim 1\,\text{GeV}$. These arguments entail that the Monte Carlo mass parameter differs from the top pole mass by several hundred MeV. It must also be noted that theoretical papers that make use of the direct top mass (noticeably those on electroweak precision fits [404, 492], and calculations inherent to the issue of the SM vacuum stability [677–679]) interpret the direct measurement results as being close to the pole mass, up to a theoretical error of few hundred MeV.

A problem that has received much attention is the presence of an infrared renormalon in the pole mass definition. The QCD perturbative series for the difference of the pole mass and the $\overline{\rm MS}$ mass has factorially divergent coefficients [680, 681]. This is related to an ambiguity of the order of a typical hadronic scale in the pole mass. Estimates of this inherent ambiguity vary from 110 to 250 MeV [682–685]. It should be stressed, however, that the finite width of the top screens the effects of soft radiation, so that this ambiguity *does not affect the physics* of top production and decay. This mean that the pole mass ambiguity does not represent in principle a limitation on the precision of top quark mass measurements, since short-distance mass schemes that are free of the pole mass ambiguity can be adopted. So in view of the considerable time to the start of the LHC HL program, the pole mass ambiguity, if it becomes a limiting factor, can be easily avoided, and is thus not discussed further here.

Accepting the fact that the difference between the top mass in direct measurements and the top pole mass is of the order of few hundred MeV, and in view of the current and projected accuracy of the direct measurements, several works have appeared in the literature to better quantify the difference. In [686] numerical relations between the Monte Carlo mass parameter and the pole mass as well as the

[46] In fact, at the moment, Monte Carlo generators that achieve NLO accuracy for sufficiently inclusive cross section are routinely used in top mass studies.

[47] In the narrow width limit the top can propagate a long time before decay, and long-distance non-perturbative effects can manifest themselves there, and affect the mass by a few hundred MeV.

MSR mass [676] were determined from comparing hadron level resummed analytic NNLL calculations performed in SCET factorization and Monte Carlo output (using PYTHIA v8.2) for the 2-Jettiness distribution at the top mass resonance for boosted top jets in e^+e^- annihilation.[48] In the work of Ref. [675], exploiting the fact that soft emission effects both in shower Monte Carlo and in full QCD can be computed as long as the shower cut Q_0 is a perturbative scale, the analytic structure of angular ordered shower algorithms was examined in detail and compared to the one of resummed calculations in SCET factorization for hemisphere masses for boosted top jets in e^+e^- annihilation. From the analysis an analytic relation at $\mathcal{O}(\alpha_s)$ between the shower mass parameter and the pole mass was calculated which is proportional to $Q_0\,\alpha_s(Q_0)$.

The results of Ref. [675, 686] are obtained in the context of global event-shape-type top jets observables in e^+e^- annihilation, which are different from observables involving jets of the top decay product that enter the direct measurements. Furthermore, the findings of Ref. [675] represent parton level results and refer exclusively to angular ordered parton showers. Future work should be aimed to lift these limitations and to extend studies of this sort to observables that enter the direct measurements at the LHC. Such studies are also valuable to expose effects that should be included to eventually match the experimental accuracy.

Direct measurements are not the only context where theoretical effects in the top mass that are linear in the strong interaction scale, i.e. of the order of few hundred MeV, do arise. In Ref. [688], the production and decay of a top quark is considered in a very simplified context, and in a particular approximation, such that non-perturbative corrections can be examined in relation to the factorial growth of the coefficients of the perturbative expansions. Linear power corrections are found to affect all observables that make use of jets. But it was also found that typical leptonic observables are also affected by linear power corrections. Notice that this implies that the total cross section is also affected by linear power corrections, as soon as selection cuts are imposed. These kind of studies can also be extended to more complex measurement procedures, eventually making use of jet calibration, in order to understand to what extent these theoretical limitations to the precision can be removed.

The discussion carried out so far has highlighted theoretical issues that should be studied in more depth in order to advance our understanding of the theoretical precision of the measurements. In essence these issues are related to the physics of different stages of soft emission, where a deeper insight would allow to draw conclusions motivated by perturbation theory, that may be extrapolated to low scales. There are also aspects of the event simulations that on the one hand only have to do with relatively hard scales, and can be reliably computed, and on the other hand are more related to the modeling of hadronization effects that currently cannot be computed from first principles. There is a current research effort, aimed at improving the simulation of top production and decay, in both these directions. It includes both the improvement of perturbative accuracy, and the improvement in the overall shower-hadronization aspects. Regarding the perturbative accuracy, recent progress has been achieved in the Monte Carlo implementation of finite width and off-resonance effects [169], whose impact has also been investigated in Ref. [689]. Regarding the hadronization aspects, the importance of the colour reconnection models has been recognized and investigated in Ref. [690,691]. Furthermore, studies of the sensitivity of top-mass sensitive observables to the perturbative accuracy, to the shower implementation and to the hadronization model, are being carried out. In one such study [692], significant differences were found when comparing HERWIG v7 and PYTHIA v8, where the former adopts an angular ordered shower, and the latter has a dipole shower, in the description of top-mass sensitive observables. In general, there is a range of equally plausible simulation models than can be used to describe heavy quark

[48] This procedure is often quoted as a form of calibration of the Monte Carlo top mass parameter. It must be noted that the same terminology has also been used in a different context in Ref. [687], where it is suggested that the Monte Carlo mass parameter can be constrained by fitting it from kinematic normalized distributions predicted from the Monte Carlo generator, simultaneously with an inclusive cross section measurement, that is then compared to a fixed order calculation.

production and decay, that will include different Monte Carlo generators, different Monte Carlo tunes in a given generator, and different implementations of some component of a generator, like for example the colour reconnection model. As more work is done by exploring different options for simulation models, the range of models may enlarge, and potentially also the error in mass measurement may increase. This increase in the error should be contrasted by limiting the range of models, typically by requiring that some key observables are in reasonable agreement with data, or by scrutiny concerning the models themselves. An example of a study in this direction is given in Ref. [693], where the sensitivity of the top-mass error upon the uncertainties in key Monte Carlo tuning parameters is studied, and a set of calibration observables strongly sensitive to the Monte Carlo parameters, but with very mild sensitivity to the top mass, is considered in order to reduce the parametric uncertainties.

A complementary way of reducing the error is to find variants of measurement methods that reduce the dependence of the extracted mass from the range of models. In situ jet calibration is routinely used by the experimental collaborations in top mass measurement. This procedure not only reduces the experimental error associated with the jet energy scale, but it may also reduces the theoretical error, by reducing the sensitivity of the measurements from features of jet simulations in the generators. More specific proposals in this direction have appeared in Ref. [694], where the impact of adopting jet grooming techniques to the jets in direct top mass measurements is examined.

As mentioned earlier, alternative techniques for mass measurements are currently explored, and will become more precise at the HL-LHC. As shown in Fig. 80 in the following subsection, the mass measurement from single top production will acquire a precision similar to the one available today from direct measurements. The end-point measurement using the J/Ψ will also reach a precision near 600 MeV. Thus, at the HL-LHC there will likely be one highly precise measurement technique, plus a number of independent methods supporting its results. It should not be forgotten however, that high luminosity and/or high energy may also offer opportunities for new techniques. In Ref. [663], the use of grooming techniques applied to boosted top jets is studied, with the goal of directly extracting a short distance mass. To what extent the high luminosity phase can make this technique feasible is a matter for future studies. Another example is given in the work of Ref. [695], where it is argued that a glitch in the dilepton spectrum should be visible for a dilepton invariant mass near twice the top mass. This effect is due to the diphoton production subprocess $gg \to \gamma\gamma$ mediated by a top loop. The projected statistical error for the mass determination using this method is of 2-3 GeV for the High Luminosity LHC, and 0.3-0.6 GeV for the 27 TeV High Energy option. A 1 GeV error systematic from the EM calorimeter calibration should also accounted for. Furthermore, a complete study of the projected theoretical error is not yet available. It is nevertheless interesting to remember that "out of the box" thinking may lead to progress in this area.

In summary, from a theoretical point of view, much work is still needed to put the top mass measurements at the HL-LHC on a solid ground. Such work should comprise more thorough experimental work aimed at understanding and reduce the sources of errors; theoretical work in the framework of Monte Carlo studies and simulation; and formal theoretical work aimed at understanding conceptual aspects. Such work is already under way, and it is expected that much more will be understood by the time the High Luminosity program starts. Thus, in spite of the many challenges, one can expect that a theoretical precision matching the foreseeable experimental errors for top mass measurements at the HL-HLC can be achieved.

6.5.2 Experimental projections

The input material for the experimental summary is collected in Ref [696, 697]. The measurement of the top quark mass $m_t$with high precision is a crucial task for the expected 3000 fb^{-1}of pp collision data expected in HL-LHC. The top quark mass is one of the free parameters within the Standard Model and its Yukawa coupling is predicted to be close to unity. Therefore it may play a special role in the electroweak

symmetry breaking. The top quark mass dominantly contributes to the quantum corrections of the Higgs field, which become important for any extrapolation of the Standard Model to extremely high energies, from a few hundred GeV and above. At these high energies some of the fundamental deficiencies of the Standard Model can be further investigated, such as the stability of the electroweak vacuum state in the Higgs potential. Thus, precise measurements of the top quark mass allow for consistency tests of the Standard Model and to look for signs of new physics beyond.

The top quark mass is measured using various techniques and in different decays channels by the ATLAS and CMS experiments following two different approaches. Firstly, direct $m_t$measurements are obtained exploiting information from the kinematic reconstruction of the measured top quark decay products, and their corresponding combinations. This information is obtained from Monte Carlo (MC) simulated events using different assumed values for the top quark mass parameter in the program. Therefore, such results relate to measurements of the input parameter of MC event generators, and differences between different MC are covered by a specific systematic uncertainty. The relation between the measured Monte-Carlo top quark mass parameter and theoretical mass schemes such as the pole mass is discussed in detail in Section 6.5.1. Secondly, indirect determinations of m_t are obtained based on the comparison of inclusive or differential $t\bar{t}$ production cross-section to the corresponding theory calculations, thus sensitive to m_t^{pole}.

The methods exploited for the measurement of m_t directly using the kinematic properties of the $t\bar{t}$ (or single-top quark) decay products are the template, the matrix element and the ideogram methods. In the template method, based on a full ($t\bar{t}$ $\rightarrow$lepton+jets, $t\bar{t}$ $\rightarrow$all-jets) or partial ($t\bar{t}$ $\rightarrow$dilepton and single-top quark) reconstruction of the kinematics underlying the top-quark(s) decay, probability density functions (templates) for observables sensitive to the underlying m_t, and to additional parameters, are constructed based on MC simulation. These templates are fitted to functions interpolating between the different input values of m_t, fixing all other parameters of the functions. Finally, an unbinned likelihood fit to the observed data distribution of the observable is used to obtain the value of m_t describing the data best. Typically, for single top and dilepton events the $m(lb)$ variable is used, whereas for the lepton+jets events the m_t^{reco} obtained from a kinematic fit is more appropriate. The ideogram method can be considered as a computational effective approximation of a matrix element method. After a kinematic fit of the decay products to a $t\bar{t}$ hypothesis, MC-based likelihood functions are exploited for each event (ideograms) that depend only on the parameters to be determined from the data. The ideograms reflect the compatibility of the kinematics of the event with a given decay hypothesis. As in the case of the template method, ideograms can be generalised in multiple dimensions depending on the number of input observables used.

The latest ATLAS combination of direct m_t measurements leads to of top quark mass value of $m_t = 172.69 \pm 0.48$ TeV with a total precision of $\sim 0.28\%$ [698]. The latest CMS combination of direct m_t measurements leads to of top quark mass value of $m_t = 172.44 \pm 0.48$ TeV with a total precision of $\sim 0.28\%$ [arXiv:1509.04044]. The precision in each of these analyses is primarily limited by systematic effects, in particular by the modelling of top quark production and decay and by the jet energy scale. Analysis techniques have been developed to use in-situ constraints from the data on a global jet energy scale factor or light jet and b-jet energy scale (3D fits) [698], which still suffer from statistical uncertainties, which will be reduced strongly at the HL-LHC. The total amount of 3000 fb^{-1}of 14 TeV data would clearly decrease the statistical uncertainty in these analyses. Therefore, the statistical precision in each analysis should be traded in various ways for a reduced total systematic uncertainty by cutting into phase space regions where the systematic uncertainties are high.

A variety of alternative methods are exploited to supplement the top quark mass measurements from direct mass reconstruction based on jet observables. One source of alternative observables is the usage of the b-jet information in the $t\bar{t}$ decay, e.g. via final states featuring J/ψ produced in the b-hadron decays or secondary vertices in b-jets. With the alternative approaches, a large variety of other

m_t^{MC} measurements can be done, which have different sensitivities to the top quark production and decay mechanisms and making therefore different contributions to the systematic uncertainties. Compared to the template method with the standard final states, the sensitivity to the light-jet and b-jet energy scale (respectively JES and b-JES) is expected to be reduced. One of the limiting factors of this approach is the small branching fraction, $\mathcal{B}(t\bar{t} \to (W^+b)(W^-b) \to (\ell\nu_\ell J/\psi(\to \mu^+\mu^-)X)(qq'b) \sim 4.1 \times 10^{-4}$, where $\ell = e, \mu$. On the other hand the modelling of b-fragmentation and b-decay are expected to be among the dominating sources of systematic uncertainties of these two analyses and need to be studied extensively in a dedicated study to reduce the signal modelling uncertainties. Both measurements can contribute in different ways to the final combination to improve the precision measurement of m_t. Individual m_t results resting on various techniques and $t\bar{t}$ (or single-top quark) decay channels, have different sensitivities to statistical and systematic effects, and to the details of the MC simulation. To exploit the full physics potential of the available measurements, and to profit from their diversity and complementarity, they are combined, thereby further increasing our knowledge on m_t.

In some alternative techniques the top quark mass is extracted by comparing cross sections or distributions that can be calculated directly in QCD at either NLO or NNLO, to corresponding distributions extracted from data. The mass parameter used in the NLO or NNLO calculation (either the $\overline{\mathrm{MS}}$ or the Pole top mass) is obtained by fitting the theoretical cross-section or distribution to the measured one. In this framework, mass measurements have been performed using as observables the inclusive $t\bar{t}$ cross-section, the differential decay rate in $t\bar{t}$+1 jet events, lepton and dilepton differential cross-sections.

Due to the changes of the detector performance for the HL-LHC, it is difficult to estimate precisely the effects of systematic uncertainties. The sources of uncertainty are assumed to be the same as the current ones. The estimated Run-2 uncertainties are scaled to align with HL-LHC extrapolations developed by the ATLAS and CMS Collaborations and documented in Ref. [699]. The impact of the experimental systematic uncertainties will likely be reduced relative to their effect on the Run-2 analysis given the large datasets available, allowing precise performance studies to be conducted. The jet reconstruction uncertainties on m_t are expected to be divided by a factor up to two, while uncertainties related to the reconstruction of electrons and muons remain the same as in Run-2. The theory modelling uncertainties are expected to be divided by a factor two compared to existing values. The larger HL-LHC dataset will allow for dedicated tuning and good understanding of NLO MC generators matched to parton showers, as already started with Run-2 data [421]. Another large contribution to the uncertainties stems from the modelling of QCD interactions, which can be investigated and constrained using differential measurements of the mass parameter itself or other ancillary measurements in parts of the phase space not yet accessible. These measurements are partially already being performed [700–702], but will benefit from more statistics, therefore strong constraints from the high statistics at the HL-LHC are expected.

For this report, ATLAS Collaboration presents projections for the top quark mass measurement accuracy using $t\bar{t} \to$ lepton+jets events with $J/\psi \to \mu^+\mu^-$ in the final state [697]. Samples of simulated events for signal and background processes are produced at 14 TeV centre-of-mass energy. They include the production of $t\bar{t}$ pairs, single-top quarks and W/Z bosons in association with jets. After the event generation step, a fast simulation of the trigger and detector effects is added with the dedicated ATLAS software framework. The event selection follows the analysis done at 8 TeV [703]. Events are required to have at least one charged isolated lepton with $p_{\mathrm{T}} > 25$ GeV and $|\eta| < 4$ and at least 4 jets with $p_{\mathrm{T}} > 25$ GeV and $|\eta| < 4.5$. No requirement is applied on the number of b-tagged jets. J/ψ candidates are reconstructed using all pairs of opposite charge sign soft muons with $p_{\mathrm{T}} > 4$ GeVand $|\eta| < 4.5$ The top quark mass is obtained from a template method with unbinned likelihood maximisation approach. A statistical uncertainty of 0.14 GeVis expected, with a systematic uncertainty of 0.48 GeV.

This paragraph discusses the potential of selected top quark mass measurements at the HL-LHC done by the CMS Collaboration, as described in detail in Ref [696]. The extrapolations are based on measurements performed at 7 and 8 TeV centre-of-mass energy using 5 fb^{-1}and 19.7 fb^{-1}, respectively.

The numbers presented here do not include the possible ambiguity in the interpretation of the measured value with respect to a well defined renormalisation scheme. However, also the measurement of the pole mass from the inclusive $\mathrm{t\bar{t}}$ cross-section cross section is extrapolated to HL-LHC conditions.

Typically, the jet energy scale uncertainties play a dominant role for top quark mass measurements. The contribution from background processes, important only for the measurement using single top events, is expected to be well under control. For the extrapolation of the extraction of m_t from the total cross-section, the cross-section measurement is assumed to be ultimately limited by the luminosity uncertainty, here assumed to be 1.5%. For the prediction, no predictions beyond NNLO are assumed, such that the uncertainty due to scale variations is constant.

The resulting extrapolated uncertainties on the top quark mass measurements are summarised in Fig. 80. The measurement using J/ψ mesons and using in general secondary vertices benefit the most from higher statistics. But also the other measurements improve significantly, mostly from more precise understanding of systematic uncertainties, as discussed above, such that ultimately, the precision will range between 0.1% (which is of the order of Λ_{QCD}) and 0.7%.

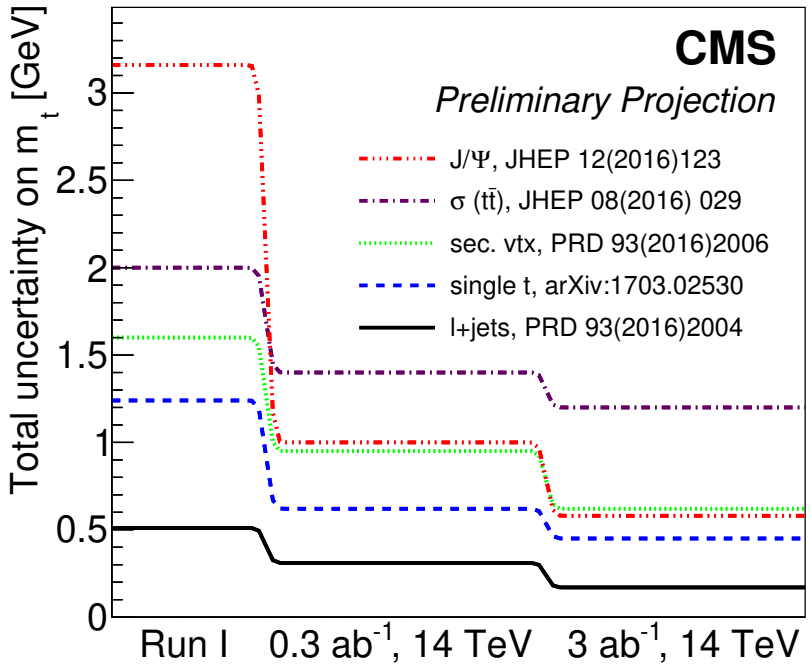

Fig. 80: The top mass measurement uncertainty for different methods as a function of integrated luminosity as obtained by CMS.

6.6 Top quark properties and couplings

6.6.1 Top quark charge asymmetries at LHCb

The top quark charge asymmetry present in quark-initiated production is diluted by the presence of gluon-gluon fusion and the increased quark content in the proton at forward rapidities gives LHCb additional sensitivity to this observable. As LHCb takes data at a lower rate than ATLAS and CMS, and has a limited acceptance, a partial reconstruction of the $t\bar{t}$ final state is anticipated in order to make

Table 47: Projected total uncertainties on the top quark mass for 3 ab^{-1} and $\sqrt{s}$=14 TeV obtained with different methods as obtained by CMS.

Method	Statistical	Systematic	Total (GeV)
$t\bar{t}$ lepton+jets	0.17	0.02	0.17
single-t t-channel	0.45	0.06	0.45
$m_{sv\ell}$	0.62	0.02	0.62
J/ψ	0.24	0.53	0.58
$\sigma_{t\bar{t}}$	0.4% (exp)	0.4% (theory)	1.2

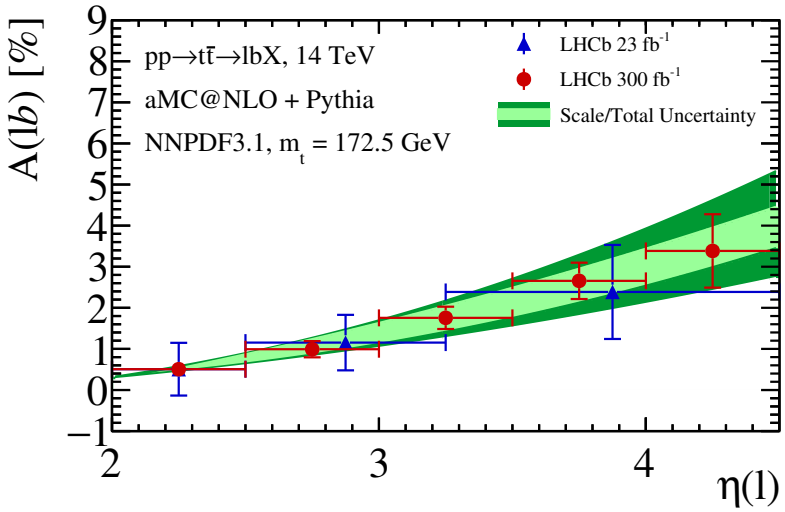

Fig. 81: The predicted SM asymmetry at LHCb as a function of lepton pseudorapidity in the ℓb final state at 14 TeV. The bands show the uncertainty on the theoretical predictions due to scale variations (light green) and due to combined scale, PDF and α_s variations (dark green). The expected statistical precision on measurements performed by LHCb using 23 and 300 fb^{-1} of data is indicated by the error bars on the points.

optimal use of statistics, as described in Sec. 6.1.4. The expected differential single lepton asymmetry at LHCb, inferred from the rate of $\ell^+ b$ and $\ell^- b$ production as a function of lepton pseudorapidity, is shown in Fig. 81 [704]. The expected statistical precision of a dataset corresponding to 300 fb^{-1} of integrated luminosity, the total expected at LHCb during the HL-LHC, is shown, along with the theoretical uncertainties due to scale, α_s and PDF uncertainties. The projection indicates that LHCb will have sufficient statistics to make a non-zero observation of the $t\bar{t}$ charge asymmetry at the HL-LHC. The dominant systematic uncertainty on the measurement is expected to come from the knowledge of the background contributions, particularly from W production in association with b-jets. Other final states, where an additional b-jet or lepton are required to be present will provide additional information as, despite the lower statistical precision, they probe larger values of Bjorken-x and select the data sample with a higher purity.

6.6.2 *A method to determine $|V_{cb}|$ at the weak scale in top quark decays*

In a recent paper [705], a new method was proposed to measure the $|V_{cb}|$ element of the Cabibbo Kobayashi Maskawa (CKM) quark mixing matrix at the scale $q \simeq m_W$, using top decays at the LHC. To date, $|V_{cb}|$ has always been measured in B decays, i.e. at an energy scale $q \simeq \frac{m_b}{2}$, far below the weak scale, and it is currently known to an uncertainty of about 2% [509]:

$$|V_{cb}| = (42.2 \pm 0.8) \times 10^{-3}. \tag{50}$$

In the proposed measurement at the LHC, $|V_{cb}|$ will be measured at the scale $q \simeq m_W$, more representative of the weak scale. The motivation for such a measurement is that the traditional extraction of $|V_{cb}|$ in B decays relies heavily on the operator product expansion, and its sensitivity is significantly affected by theoretical uncertainties [509]. In contrast, in dealing with decays of on-shell Ws, as here, the theoretical situation is likely to be much cleaner and the systematic uncertainties will be very different. Moreover, there could be significant evolution of $|V_{cb}|$ between $q \simeq \frac{m_b}{2}$ and $q \simeq m_W$ due to radiative corrections: e.g. the application (somewhat inappropriately) of the Standard Model (SM) six-quark evolution equations [706] at two-loop order [707] to the CKM matrix between $q \simeq \frac{m_b}{2}$ and $q \simeq m_W$ yields a fractional increase in $|V_{cb}|$ of $\simeq 5\%$, see Fig. 82. While the correct treatment for SM evolution at such

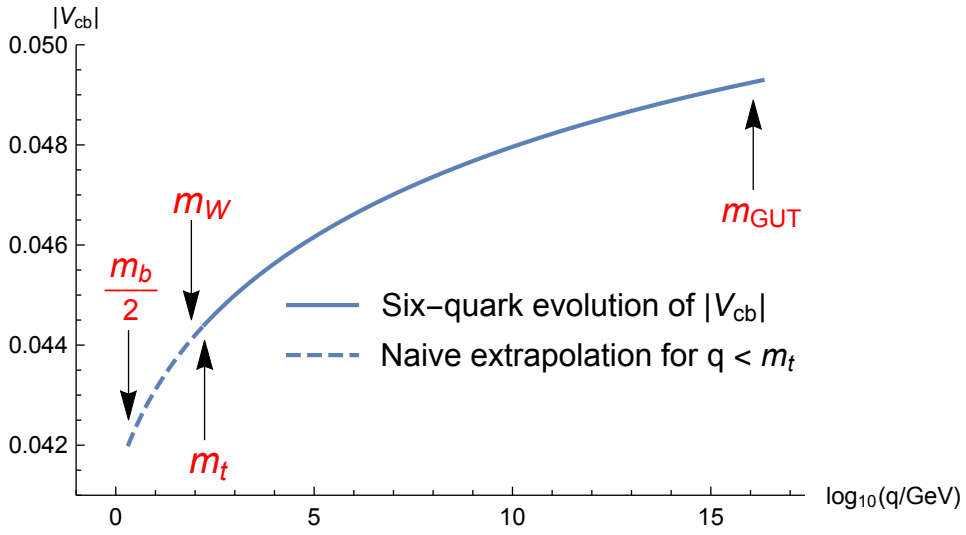

Fig. 82: Renomalisation Group evolution of $|V_{cb}|$ using the six-quark running scheme [706–708] between m_{GUT} and $\frac{m_b}{2}$. Previous publications stop at m_t, while a correct procedure would use a five-quark scheme for $q \lesssim m_t$. This naive procedure at least suggests the possibility of significant low-energy evolution of $|V_{cb}|$.

low energies is rather to use an effective field theory, integrating out the top quark below $q \sim m_t$ [708], such a calculation of the $|V_{cb}|$ running has not yet appeared in the literature. Thus the low-energy evolution of $|V_{cb}|$ is currently completely uncertain, while the naive calculation outlined above at least opens the possibility that its running might be observable, if $|V_{cb}|$ can be measured at or above the weak scale.

The proposed method uses the decays of tagged $t\bar{t}$ pairs with one semileptonic top decay, (the tag), $\bar{t} \to \bar{b}W^- \to \bar{b}\ell^-\bar{\nu}_\ell$, and the other a hadronic decay, $t \to bW \to b\bar{q}c$, where $\bar{q}$ is a charge $\frac{1}{3}$ antiquark (charge-conjugate decays will be assumed everywhere unless otherwise stated). The fraction of these in which $\bar{q} = \bar{b}$ is (up to negligible phase-space factors), exactly $|V_{cb}|^2$. Using this ratio, otherwise leading experimental uncertainties in most of the tagging efficiencies are cancelled. Thus the required signal will contain three tagged b-jets and a tagged c-jet, in addition to a charged lepton and missing transverse momentum.

Taking as a starting point, efficiencies from existing ATLAS and CMS $t\bar{t}$ cross-section analyses, already-achieved experimental tagging performances [709–714], and reasonable assumptions about backgrounds, it is estimated [705], that the fractional uncertainty on $|V_{cb}|$ which can be obtained at a single experiment using the Run-2 dataset is:

$$\frac{\Delta|V_{cb}|}{|V_{cb}|} \sim 0.07, \tag{51}$$

which is statistics-limited. Averaging the two experiments would give a fractional error of $\sim 5\%$.

Since the values of the systematic uncertainties on the tagging performances used to calculate eq. (51) were based roughly on their present determinations, the result is generalised in Fig. 83, to show

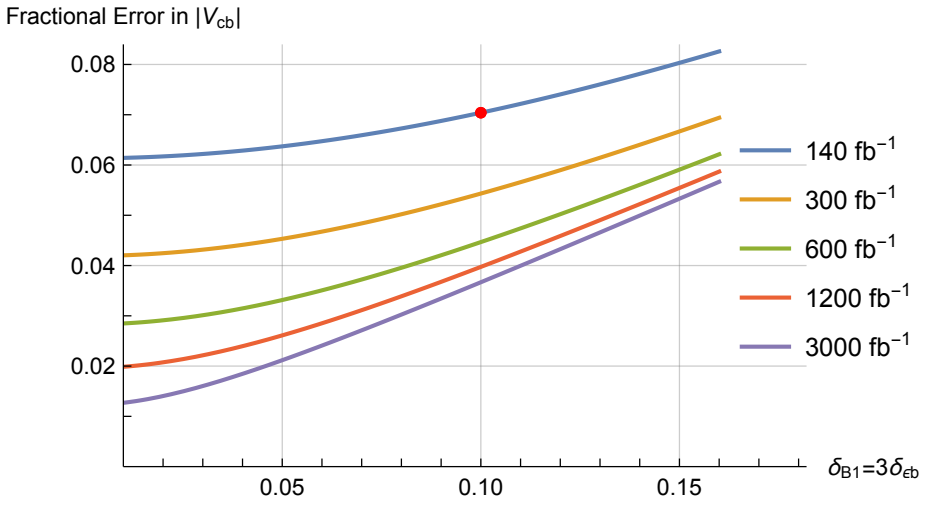

Fig. 83: Estimated fractional error in $|V_{cb}|^2$ as a function of the systematic uncertainties δ_{ϵ_b} in the b-jet tagging efficiency and $\delta_{\mathcal{B}_1}$ in the light-to-b jet flavour mis-tag probability, and integrated luminosity. For ease of presentation, we assume $\delta_{\mathcal{B}_1} \simeq 3\delta_{\epsilon_b}$ as it is at the time of writing. The top curve represents the Run-2 statistics and the red point on it indicates the illustrative values used to obtain eq. (51). The second curve corresponds to luminosity projections for Run-3, while the bottom curve is for the projected integrated luminosity for HL-LHC. We have allowed for a 15% increase in the $t\bar{t}$ cross section in the lower three curves, corresponding to an increase in beam collision energy to 14 TeV.

the dependence of the obtained fractional error on the systematic uncertainties as they vary. Also shown in Fig. 83 are the results using larger datasets, corresponding to various future LHC luminosity scenarios. The systematics-limited regime is represented by the linear-sloping region towards the bottom-right part of the figure, while the statistics-limited regime lies close to the y-axis, where the benefit of more statistics is most marked. The figure shows that making the measurement with future LHC data promises further improvements from both increased statistics and if tagging performance uncertainties can be reduced. E.g. if $\delta_{\mathcal{B}_1} = 3\delta_{\epsilon_b}$ can be reduced to $\simeq 0.05$, then at the end of Run-3, the uncertainty on $|V_{cb}|$ per experiment using this method could be as low as 4.5%, giving a fractional uncertainty on the average of the two $|V_{cb}|$ measurements of $\sim 3\%$. HL-LHC would then deliver a further reduction in the measurement uncertainty of better than a factor of 2. Either of these higher statistics measurements could give sensitivity for the first time to the renormalisation group running of $|V_{cb}|$.

6.7 Flavour changing neutral current

Processes with flavour-changing neutral currents (FCNC) are forbidden at tree level and are strongly suppressed in higher orders by the Glashow-Iliopoulos-Maiani (GIM) mechanism [715]. The SM predicts the branching fractions for top quark FCNC decays of $\mathcal{O}(10^{-12}$–$10^{-16})$ [716–718]. However, various extensions of the SM allow a significant enhancement of the FCNC top quark decay rates arising from possible contributions of new particles [718–720]. Any deviations from heavily suppressed top FCNC rates would be a clear sign of new physics. The FCNC interactions of the top quark with the SM gauge and Higgs bosons can be described through the following anomalous coupling Lagrangian:

$$\begin{aligned}\mathcal{L} = \sum_{q=u,c} [\sqrt{2} g_s \frac{\kappa_{gqt}}{\Lambda} \bar{t}\sigma^{\mu\nu} T_a (f_{Gq}^L P_L + f_{Gq}^R P_R) q G_{\mu\nu}^a + \\ + \frac{g}{\sqrt{2} c_W} \frac{\kappa_{zqt}}{\Lambda} \bar{t}\sigma^{\mu\nu} (f_{Zq}^L P_L + f_{Zq}^R P_R) q Z_{\mu\nu} + \frac{g}{4 c_W} \zeta_{zqt} \bar{t}\gamma^{\mu} (f_{Zq}^L P_L + f_{Zq}^R P_R) q Z_{\mu} - \\ - e \frac{\kappa_{\gamma qt}}{\Lambda} \bar{t}\sigma^{\mu\nu} (f_{\gamma q}^L P_L + f_{\gamma q}^R P_R) q A_{\mu\nu} + \\ + \frac{g}{\sqrt{2}} \bar{t} \kappa_{Hqt} (f_{Hq}^L P_L + f_{Hq}^R P_R) q H] + h.c., \end{aligned} \tag{52}$$

where P_L and P_R are chiral projection operators in spin space, κ_{Xqt} is the anomalous coupling for tXq vertex ($X = g, Z, \gamma, H$), ζ_{Zqt} is the additional anomalous coupling for tZq vertex, f_{Xq}^L and f_{Xq}^R are the left and right-handed complex chiral parameters with an unitarity constraint of $|f_{Xq}^L|^2 + |f_{Xq}^R|^2 = 1$. Each of the anomalous couplings can be probed in events with the top quark pair production where one of the top quark decays via FCNC interaction, as well as in events with the associated production of the single top quark with a gluon, Z boson, γ, or Higgs boson.

Top-gluon

The gqt FCNC process was studied by CMS [721] in single top quark events. The event signature includes the requirement of one isolated lepton and exactly one b and one non-b jet to be present in the final state with the dominant background arising from the $t\bar{t}$+jets and W+jets production. The signal events are simulated in the SINGLETOP Monte-Carlo (MC) generator [722] based on the COMPHEP v4.5.2 package [723]. The backgrounds processes are estimated with the MG5_AMC@NLO v2.5.2 [393] package, showered and hadronized with PYTHIA v8.230 [149]. The full detector simulation has been performed for the signal and background events. A Bayesian neural network technique is used to separate signal from background events. The shape of the neural networks discriminants are used in the statistical analysis to estimate the expected sensitivity to the contribution from FCNC. Bayesian inference is used to obtain the posterior probabilities based on an Asimov data set of the background-only model. We assume the same systematic scenario as in Ref. [724]. To obtain the individual exclusion limits on $|\kappa_{tug}|/\Lambda$ and $|\kappa_{tcg}|/\Lambda$ we assume the presence of only one corresponding FCNC parameter in the FCNC signal Monte Carlo model. These individual limits can be used to calculate the upper limits on the branching fractions $\mathcal{B}(t \to ug)$ and $\mathcal{B}(t \to cg)$ [725]. The expected exclusion limits at 95% C.L. on the FCNC couplings and the corresponding branching fractions are given in Table 48. In addition the two-dimensional contours that reflect the possible simultaneous presence of both FCNC parameters are shown in Fig. 84. In this case both FCNC couplings are implemented in the FCNC signal Monte Carlo model. The expected limits can be compared with the recent CMS results [726] for the upper limits on the branching fractions of 2.0×10^{-5} and 4.1×10^{-4} for the decays $t \to ug$ and $t \to cg$, respectively.

Table 48: The expected exclusion 1D limits at 95% C.L. on the FCNC couplings and the corresponding branching fractions for an integrated luminosity of 300 fb^{-1} and 3000 fb^{-1}. In addition, a comparison with statistic-only uncertainties is shown.

Integrated luminosity	$\mathcal{B}(t \to ug)$	$\lvert\kappa_{tug}\rvert/\Lambda$	$\mathcal{B}(t \to cg)$	$\lvert\kappa_{tcg}\rvert/\Lambda$
300 fb^{-1}	$9.8 \cdot 10^{-6}$	0.0029 TeV^{-1}	$99 \cdot 10^{-6}$	0.0091 TeV^{-1}
3000 fb^{-1}	$3.8 \cdot 10^{-6}$	0.0018 TeV^{-1}	$32 \cdot 10^{-6}$	0.0052 TeV^{-1}
3000 fb^{-1} Stat. only	$1.0 \cdot 10^{-6}$	0.0009 TeV^{-1}	$4.9 \cdot 10^{-6}$	0.0020 TeV^{-1}

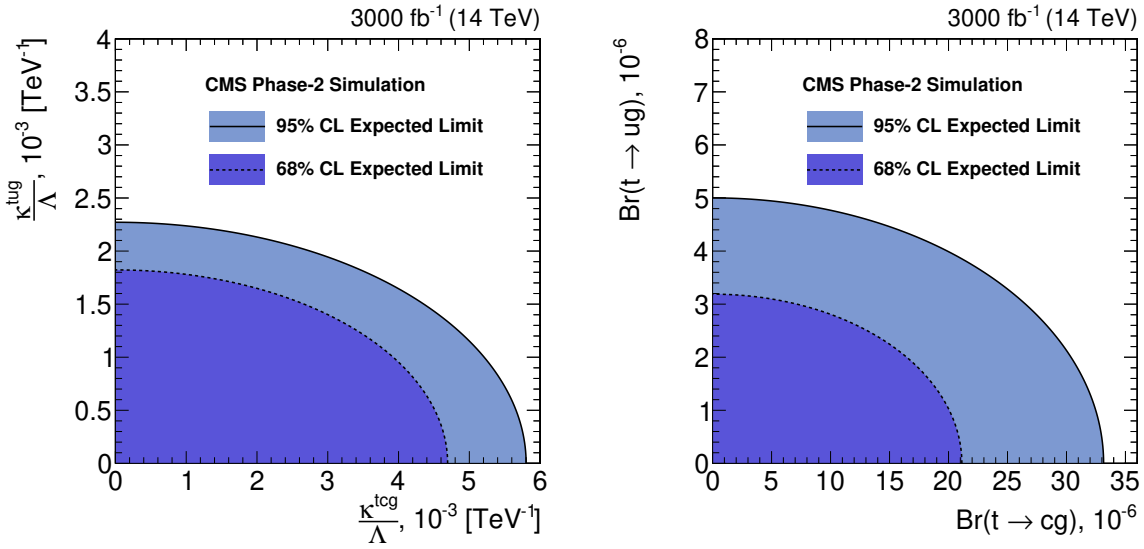

Fig. 84: Two-dimensional expected limits on the FCNC couplings and the corresponding branching fractions at 68% and 95% C.L. for an integrated luminosity of 3000 fb^{-1}.

Top-Z

The ATLAS Collaboration studied the sensitivity to the tqZ interaction, by performing an analysis, detailed in Ref. [727], based on simulated samples and following the strategy detailed in Ref [728] for the analysis of Run-2 data at 13 TeV centre-of-mass energy and the general recommendations for HL-LHC studies for this report. The study is performed in the three charged lepton final state of $t\bar{t}$ events, in which one of the top quarks decays to qZ, $(q = u, c)$ and the other one decays to bW ($t\bar{t} \to bWqZ \to b\ell\nu q\ell\ell$). The kinematics of the events are reconstructed through a χ^2 minimisation and dedicated control regions are used to normalize the main backgrounds and constrain systematic uncertainties. The main uncertainties, in both the background and signal estimations, are expected to come from theoretical normalization uncertainties and uncertainties in the modeling of background processes in the simulation. Different scenarios for the systematic uncertainties are considered, ranging from the conservative estimations obtained with the 13 TeV data analysis, to those that assume a factor two improvement due to expected advances in theoretical predictions. Figure 85 shows the χ^2 distribution for the events reconstructed in the signal region, after the combined fit of signal and control regions under the background-only hypothesis. A binned likelihood function $L(\mu, \theta)$ is used to extract the signal normalisation. An improvement by a factor of five is expected with respect to the current 13 TeV data analysis results. The limits on the branching ratio are at the level of 4 to 5 $\times 10^{-5}$ depending on the considered scenarios assumed for the systematic uncertainties.

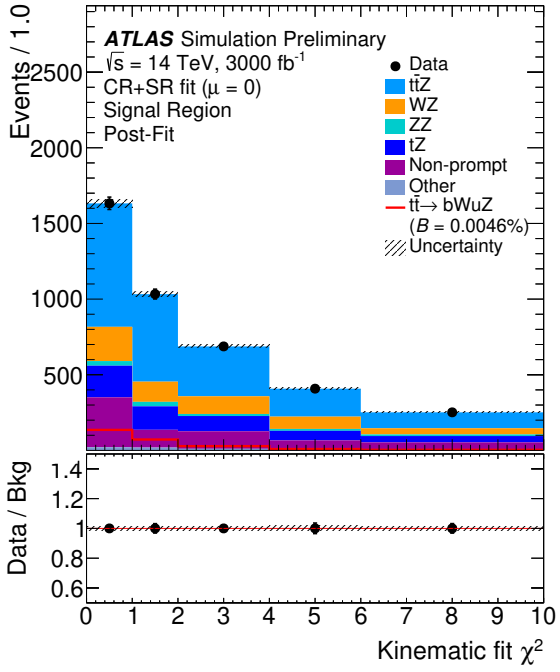

Fig. 85: The distributions for the χ^2 for events reconstructed in the signal region, after the combined fit of signal and control regions under the background-only hypothesis. The data points are from the "Asimov dataset", defined as a total expected pre-fit background. The number of signal events is normalized to the expected branching ratio limit of $B(t \to uZ) = 4.6 \cdot 10^{-5}$. The dashed area represents the systematic uncertainty on the background prediction.

Top-γ

The $t\gamma q$ anomalous interactions have been probed by CMS at 8 TeV in events with single top quarks produced in association with a photon [729] and the resulting exclusion limits are $\mathcal{B}(t \to \gamma u) < 1.3\ (1.9) \times 10^{-4}$ and $\mathcal{B}(t \to \gamma c) < 2.0\ (1.7) \times 10^{-3}$.

In this section, the sensitivity of the upgraded CMS detector to $tq\gamma$ FCNC transitions is estimated for integrated luminosities of 300 and 3000 fb^{-1} using single top quark production via $q \to q\gamma$, with q being a u or a charm quark [724]. This analysis focuses on subsequent SM decays of the top quark in a W boson and bottom quark, with the W boson decays leptonically to a muon or electron and a neutrino. The finale state signature is the presence of a single muon or electron, large missing transverse momentum, a b-jet, and an isolated high energy photon, with a broad η spectrum. The photon properties themselves provide good separation with respect to the dominant background processes from W+jets, and single top or top quark pair production in association with photons. For the discrimination of signal and background events, and to set the limits on the FCNC couplings, the events are split into two categories depending on the pseudo-rapidity of the photon (central region with $|\eta_\gamma| < 1.4$ and forward region with $1.6 < |\eta_\gamma| < 2.8$). In the central (forward) region the photon p_{T} (energy) is used as a discriminating distribution: the low p_{T} (energy) is background dominated, while the high p_{T} (energy) region is populated by signal events. The distributions are shown in Fig. 86.

The limits on the cross section for the single top quark production via $tq\gamma$ are obtained considering systematic uncertainties from variations of the renormalization and factorization scale, b-tagging and jet energy scale corrections and their effects as propagated to missing transverse energy, lepton efficiency

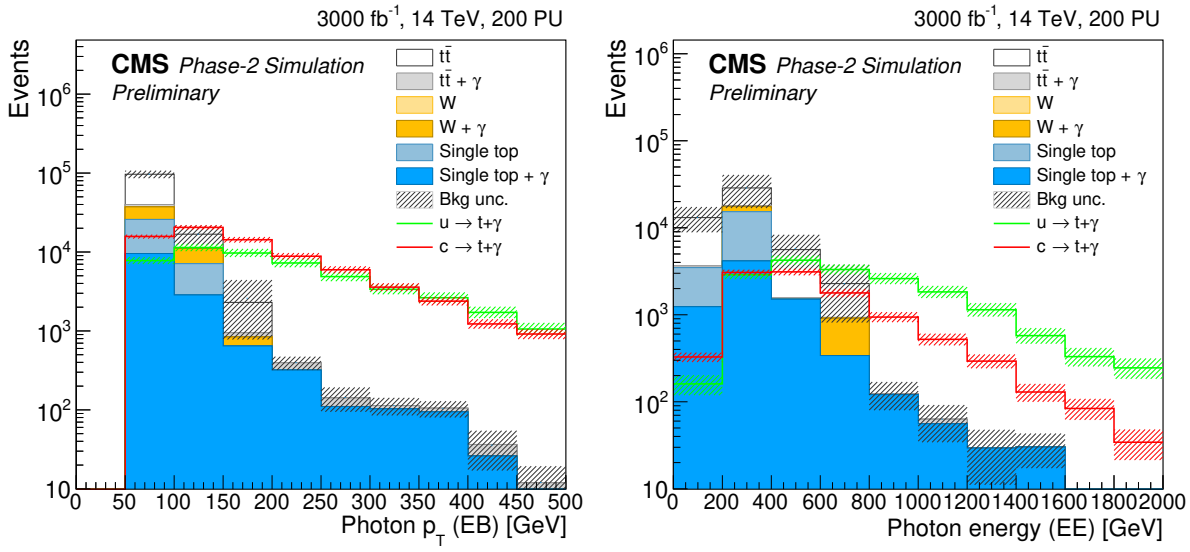

Fig. 86: Transverse momentum of photon candidates for the central η region (left) and energy of photon candidates in the forward region (right).

and luminosity.

These studies yield the following upper limite on the branching ratios at 95%C.L.: $\mathcal{B}(t \to \gamma u) < 8.6 \times 10^{-6}$, $\mathcal{B}(t \to \gamma c) < 7.4 \times 10^{-5}$.

Top-Higgs

The tHq interactions are studied by ATLAS in top quark pair events with $t \to qH, H \to \gamma\gamma$ [730] and $H \to WW$ [731] at 13 TeV. The former analysis explores the final state with two isolated photons. For leptonic top quark decays the selection criteria includes the requirement of one isolated lepton, exactly one b jet, and at least one non-b jet. In case of hadronic top quark decays the analysis selects events with no isolated leptons, at least one b jet, and at least three additional non-b jets. The dominant background processes are associated with the production of non-resonant $\gamma\gamma$+jets, $t\bar{t}$+jets and W+$\gamma\gamma$ events. The resultant limits are $\mathcal{B}(t \to Hu) < 2.4\ (1.7) \times 10^{-3}$ and $\mathcal{B}(t \to Hc) < 2.2\ (1.6) \times 10^{-3}$. The search for FCNC in $H \to WW$ includes the analysis of multilepton final states with either two same-sign or three leptons. The dominant backgrounds arising from the ttW, ttZ and non-prompt lepton production are suppressed with a BDT. The obtained limits are $\mathcal{B}(t \to Hu) < 1.9\ (1.5) \times 10^{-3}$ and $\mathcal{B}(t \to Hc) < 1.6\ (1.5) \times 10^{-3}$. The tHq anomalous couplings are probed by CMS in $H \to b\bar{b}$ channel in top quark pair events, as well as in single top associated production with a Higgs boson, at 13 TeV [732]. The event selection includes the requirement of one isolated lepton, at least two b jets, and at least one additional non-b jet. The dominant $t\bar{t}$ background is suppressed with a BDT discriminant to set the exclusion limits of $\mathcal{B}(t \to Hu) < 4.7\ (3.4) \times 10^{-3}$ and $\mathcal{B}(t \to Hc) < 4.7\ (4.4) \times 10^{-3}$. Preliminary projections suggest $\mathcal{B}(t \to Hq) < \mathcal{O}(10^{-4})$ [733, 734].

Table 49: Summary of the projected reach for the 95% C.L. limits on the branching ratio for anomalous flavor changing top couplings.

$\mathcal{B}$ limit at 95%C.L.	3 ab^{-1}, 14 TeV	15ab^{-1}, 27 TeV	Ref.
$t \to gu$	3.8×10^{-6}	5.6×10^{-7}	[721]
$t \to gc$	32.1×10^{-6}	19.1×10^{-7}	[721]
$t \to Zq$	$2.4 - 5.8 \times 10^{-5}$		[733]
$t \to \gamma u$	8.6×10^{-6}		[724]
$t \to \gamma c$	7.4×10^{-5}		[724]
$t \to Hq$	10^{-4}		[733]

6.8 Effective coupling interpretations for top quark cross sections and properties[49]

Effective Field Theory (SMEFT) [615, 616], where the SM is augmented by a set of higher-dimension operators

$$\mathcal{L}_{\text{SMEFT}} = \mathcal{L}_{\text{SM}} + \sum_i \frac{C_i}{\Lambda^2}\mathcal{O}_i + \mathcal{O}(\Lambda^{-4}). \tag{53}$$

As an example the relevant operators for the tWb vertex are:

$$\mathcal{O}_{tW} = i\left(\bar{Q}\sigma^{\mu\nu}\,\tau_I\,t\right)\tilde{\phi}\,W^I_{\mu\nu} + \text{h.c.} \tag{54}$$

$$\mathcal{O}^{(3)}_{\phi q} = i\left(\phi^\dagger \overleftrightarrow{D}_\mu\,\tau_I\phi\right)\left(\bar{q}_i\,\gamma^\mu\,\tau^I q_i\right) + \text{h.c.} \tag{55}$$

in agreement with the notation of [234].

The operators of eq. (54)-(55) modify the Wtb interaction in the following way

$$\begin{aligned}\mathcal{L}^{\text{dim}-6}_{Wtb} &= -\frac{g}{\sqrt{2}}\bar{b}(x)\gamma^\mu P_L t(x)\,W_\mu(x)\left(1 + \frac{C^{(3)}_{\varphi Q}v^2}{\Lambda^2}\right)\\ &+ \frac{2\,v\,C_{tW}}{\Lambda^2}\bar{b}(x)\sigma^{\mu\nu}P_R t(x)\,\partial_\nu W_\mu(x) + \text{h. c.}\,,\end{aligned} \tag{56}$$

where $v = 246$ GeV is the Higgs doublet vacuum expectation value, and y_t the top quark Yukawa coupling. Here and below it is assumed $V_{tb} = 1$. It must be noted that a slightly different approach [735–739], not using operators but anomalous couplings, has also been used in the literature. It is straightforward to connect the operator coefficients with the anomalous couplings description. The connection between the operator coefficients to the anomalous couplings is discussed in Ref. [651]. The Wtb vertex can be probed in single top production ($t-, Wt, s-$channel top production), W helicity fractions and forward-backward asymmetries.

Similarly the coupling of the top to the Z and photon can be parameterised by the dimension-6 operators as discussed in Ref. [234], where the relevant degrees of freedom are discussed. The relevant degrees of freedom for the top-Z interaction $c^-_{\phi Q}, c^3_{\phi Q}, c_{\phi t}, c^{[I]}_{tZ}$ whilst the photon-top interaction depends on $c^{[I]}_{tA}$ as defined in Ref. [234]. Phenomenological studies of top production in association with a vector boson or a photon exist in the literature [258, 259, 740, 741] including NLO QCD corrections.

This section examines the prospects of probing top charged and neutral couplings at the HL-LHC.

[49] Contributed by L. Lechner, D. Spitzbart, R. Schöfbeck, D. Azevedo,F. Déliot, A. Ferroglia, M. C. N. Fiolhais, E. Gouveia, A. Onofre, E. Vryonidou, and M. Moreno Llacer.

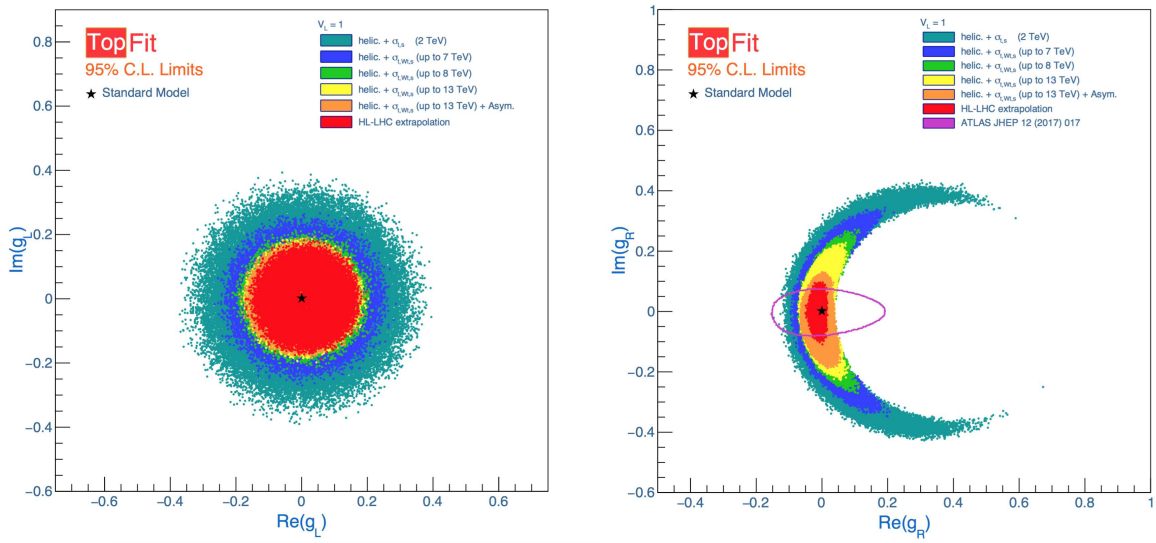

Fig. 87: Limits at 95% CL on the allowed regions for anomalous couplings [752]. The two-dimensional distributions of the Re versus the Im components of $g_{\rm L}$ (left) and $g_{\rm R}$ (right), are shown.

6.8.1 The top quark couplings to the W boson

The latest and most precise measurements on single top quark production cross sections ($t-, Wt-$ and $s-$channels) [614, 742–748], W boson helicity fractions (F_0,$F_{\rm L}$ and $F_{\rm R}$) [749, 750] and forward-backward asymmetries (A_{FB}^{ℓ},A_{FB}^{N},A_{FB}^{T}) [751], measured at different centre-of-mass energies i.e., 2 TeV at Tevatron and 7, 8 and 13 TeV at the LHC, were used to set stringent 95% CL limits on possible new physics that affect the Wtb vertex structure. The results were extrapolated to the HL-LHC phase of the LHC, by assuming the full expected luminosity (3000 fb^{-1}) and scaling the uncertainties obtained at the LHC for $\sqrt{s} = 13$ TeV (the central value of the observables were assumed to be the Standard Model prediction at 14 TeV). The statistical and simulation related uncertainties were scaled according to the total integrated luminosity at the HL-LHC. All generator and signal modelling related systematic uncertainties of these observables were extrapolated to be half of their current value, in accordance with the recent ATLAS and CMS official recommendations for the High-Luminosity studies. All experimental performance related uncertainties (leptons and jets, efficiencies, energy resolutions, etc.) were considered to maintain the current value at 13 TeV, at the exception of the efficiency of tagging jets from the hadronization of $b-$quarks (b-tagging), which is expected to be reduced by half. These extrapolated measurements were included in the global fit, in combination with the current measurements, in order to estimate expected limits on the real and imaginary components of the top quark couplings. The allowed regions of the new couplings are presented in Figure 87 and Table 50. Figure 87 allows also for a comparison between current LHC results and the HL-LHC projections.

Table 50: Allowed regions for anomalous couplings.

HL-LHC	$g_{\rm R}$	$g_{\rm L}$	$V_{\rm R}$
Allowed Region (Re)	[-0.05 , 0.02]	[-0.17 , 0.19]	[-0.28 , 0.32]
Allowed Region (Im)	[-0.11 , 0.10]	[-0.19 , 0.18]	[-0.30 , 0.30]

6.8.2 The $t\bar{t}\gamma$ production

Measurements of $t\bar{t}\gamma$ production at the HL-LHC are studied by ATLAS in terms of the expected precision for the measurements of fiducial and differential cross sections in leptonic final states and the expected limits that can be imposed on the Wilson coefficients of operators relevant to $t\bar{t}\gamma$ production [753]. These operators are the O_{tB}, O_{tG}, and O_{tW} in Ref. [234]. The analysis is performed in the same way as the 13 TeV $t\bar{t}\gamma$ analysis [754], by selecting leptonic decay final states of the $t\bar{t}$ pair with an isolated high-p_{T} photon. Compared to the 13 TeV analysis, data statistical uncertainty is scaled down according to the integrated luminosity at the HL-LHC. Monte Carlo (MC) statistical uncertainty is ignored as it is expected to have enough MC events generated. Theoretical uncertainties are reduced by a factor of two due to the expected improvement in the theoretical tools and background estimation and experimental uncertainties are in general kept the same, with respect to the uncertainties in the 13 TeV analysis. The fiducial cross-section measurement can reach an uncertainty as low as 3% (8%) in the channel with two (one) leptons and requiring a photon candidate with p_{T} larger than 20 (500) GeV. The expected uncertainties of differential cross-section measurements, normalised to unity, for several typical observables like the photon p_{T} and η, are found to be in general below 5%. The expected uncertainty of the absolute differential cross-section as a function of the photon p_{T} is interpreted as 95% CL limits for the relevant EFT operators, as shown in Table 51 for single-lepton and dilepton final states.

Table 51: Expected 95 % CL intervals for the three Wilson coefficients relevant to $t\bar{t}\gamma$ production.

Operator	$\mathcal{O}_{tB}$	$\mathcal{O}_{tG}$	$\mathcal{O}_{tW}$
Single lepton	[-0.5,0.3]	[-0.1,0.1]	[-0.3,0.5]
Dilepton	[-0.6,0.4]	[-0.1,0.1]	[-0.4,0.3]

6.8.3 The $t\bar{t}Z$ production

Many beyond the Standard Model (BSM) predictions include anomalous couplings of the top quark to the electroweak gauge bosons [649, 755–760]. While this study is restricted to the $t\bar{t}Z$ channel and the CMS HL-LHC detector with a luminosity scenario of 3 ab^{-1}, it goes beyond earlier work [741] and studies the sensitivity of the $t\bar{t}Z$ process using differential cross section data [761]. The results are interpreted in terms of the SM effective field theory [234] and limits are set on the relevant Wilson coefficients of the Warsaw basis [513] C_{tZ}, $C_{tZ}^{[\mathrm{Im}]}$, $C_{\phi t}$ and $C_{\phi Q}$ [762, 763].

Events are generated at the parton level at LO using MG5_aMC@NLO v2.3.3 [12], and decay them using MadSpin [402, 764]. Parton showering and hadronization are done using Pythia v8.2 [149, 292]. Fast detector simulation was performed using Delphes [273], with the CMS reconstruction efficiency parameterisation for the HL-LHC upgrade. The mean number of interactions per bunch crossing (pileup, PU) is varied from 0 to 200. Jets are reconstructed with the FastJet package [343] and using the anti-k_{T} algorithm [274] with a cone size $R = 0.4$. Besides the signals, the main backgrounds are also generated in the leptonic final states in order to achieve a realistic background prediction. The WZ, tZq, tWZ, $t\bar{t}\gamma$ and $t\bar{t}Z$ processes are normalized to cross sections calculated up to next-to-leading order (NLO) in perturbative QCD.

The results on the inclusive $t\bar{t}Z$ cross section from ATLAS [765, 766] and CMS [767–770] show that the three lepton channel, where the Z and one of the W bosons originating from a top quark decay leptonically is the most sensitive. Thus, it is required to have three reconstructed leptons (e or μ) with $\mathrm{p_T}(l)$ thresholds of 10, 20, and 40 GeV, respectively, and $|\eta(l)| < 3.0$. It is furthermore required that there is among them a pair of opposite-sign same-flavor leptons consistent with the Z boson by requiring $|m(ll) - m_{\mathrm{Z}}| < 10$ GeV. Reconstructed leptons are removed within a cone of $\Delta R < 0.3$

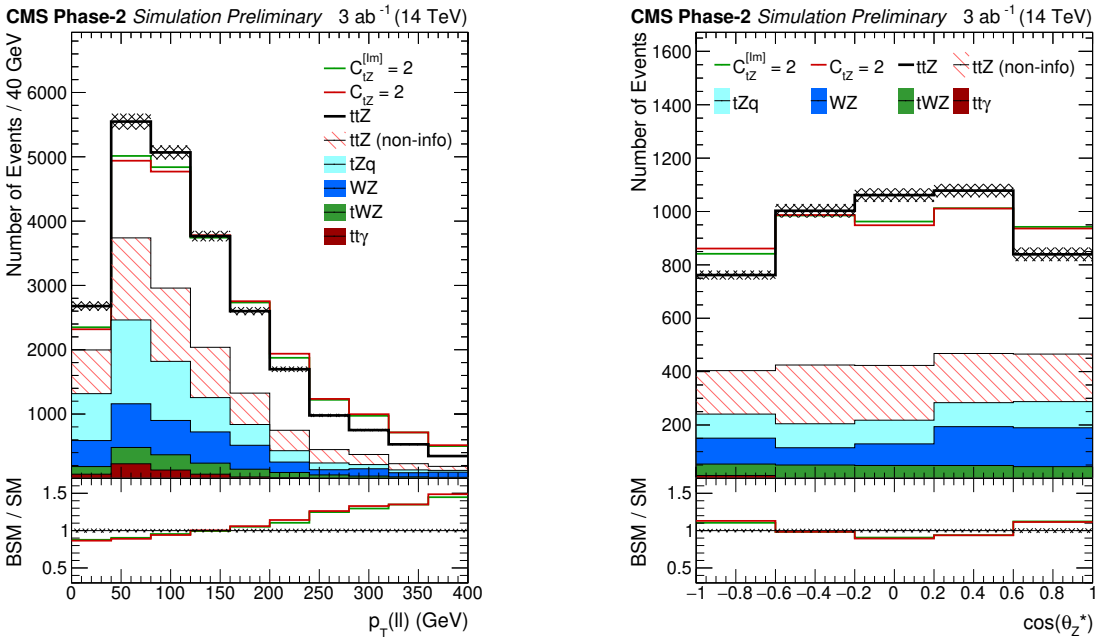

Fig. 88: Differential cross sections of $p_T(Z)$ (left) and $\cos\theta^*_Z$ (right) for the in the text mentioned selection and the HL-LHC scenario. For $\cos\theta^*_Z$, additionally $p_T(Z) > 200$ GeV is applied.

to any reconstructed jet satisfying $p_T(j) > 30$ GeV. Furthermore, at least 3 jets are required with $p_T(j) > 30$ GeV and $|\eta(j)| < 4.0$, where one of the jets has been identified as a b-tag jet according to the DELPHES specification.

The distributions of the above-mentioned observables are considered in equally sized bins of the transverse Z boson momenta $p_T(Z)$ [740] and $\cos\theta^*_Z$, the relative angle of the negatively charged lepton to the Z boson direction of flight in the rest frame of the boson. The differential cross sections for the SM (black) and BSM (colored lines) interpretations in $t\bar{t}Z$ with respect to $p_T(Z)$ and $\cos\theta^*_Z$ are shown in Fig. 88 for $C_{tZ} = 2$ $(\Lambda/\text{TeV})^2$ and $C_{tZ}^{[\text{Im}]} = 2$ $(\Lambda/\text{TeV})^2$. The BSM distributions are normalized to the SM yield in the plots to visualize the discriminating features of the parameters. The part of the signal which does not contain information on the Wilson coefficients is shown hatched, backgrounds are shown in solid colors.

The predicted yields are estimated for the 3 ab^{-1} HL-LHC scenario at $\sqrt{s} = 13$ TeV and scaled to 14 TeV, where an additional small background from non-prompt leptons is taken from Ref. [770] and scaled to 3 ab^{-1}. A profiled maximum likelihood fit of the binned likelihood function $L(\theta)$ is performed and it is considered $q(r) = -2\log(L(\hat{\theta})/L(\hat{\theta}_{\text{SM}}))$, where $\hat{\theta}$ and $\hat{\theta}_{\text{SM}}$ are the set of nuisance parameters maximizing $L(\theta)$ at the BSM and SM point, respectively. Experimental uncertainties are estimated based on the expected performance of the HL-LHC CMS detector. In Table 52, the 68% and 95% CL intervals of the likelihood scan for the $t\bar{t}Z$ process are shown, where one non-zero Wilson coefficient is considered at a time, and all others are set to zero.

Table 53 shows the 68% and 95% CL intervals of the likelihood ratios for two pairs of Wilson coefficients corresponding to modified neutral current interactions ($C_{\phi t}$ and $C_{\phi Q}$) and dipole moment interactions (C_{tZ} and $C_{tZ}^{[\text{Im}]}$). The corresponding second Wilson coefficient is included in the profiling of nuisance parameters.

In Fig. 89, the log-likelihood scan for the $t\bar{t}Z$ process is shown in the $C_{\phi Q}/C_{\phi t}$ parameter plane (left) and the dipole moment parameter plane $C_{tZ}/C_{tZ}^{[\text{Im}]}$ (right). The green (red) lines show the 68% (95%) CL contour line and the SM parameter point corresponds to $C_{\phi t} = C_{\phi Q} = 0$ and $C_{tZ} = C_{tZ}^{[\text{Im}]} = 0$.

Table 52: Expected 68 % and 95 % CL intervals, where one Wilson coefficient at a time is considered non-zero.

Wilson coefficient	68 % CL $(\Lambda/\text{TeV})^2$	95 % CL $(\Lambda/\text{TeV})^2$
$C_{\phi t}$	[-0.47, 0.47]	[-0.89, 0.89]
$C_{\phi Q}$	[-0.38, 0.38]	[-0.75, 0.73]
C_{tZ}	[-0.37, 0.36]	[-0.52, 0.51]
$C_{tZ}^{[\text{Im}]}$	[-0.38, 0.36]	[-0.54, 0.51]

Table 53: Expected 68 % and 95 % CL intervals for the selected Wilson coefficients in a profiled scan over the 2D parameter planes $C_{\phi Q}/C_{\phi t}$ and $C_{tZ}/C_{tZ}^{[\text{Im}]}$. The respective second parameter of the scan is left free.

Wilson coefficient	68 % CL $(\Lambda/\text{TeV})^2$	95 % CL $(\Lambda/\text{TeV})^2$
$C_{\phi t}$	[-1.65, 3.37]	[-2.89, 6.76]
$C_{\phi Q}$	[-1.35, 2.92]	[-2.33, 6.69]
C_{tZ}	[-0.37, 0.36]	[-0.52, 0.51]
$C_{tZ}^{[\text{Im}]}$	[-0.38, 0.36]	[-0.54, 0.51]

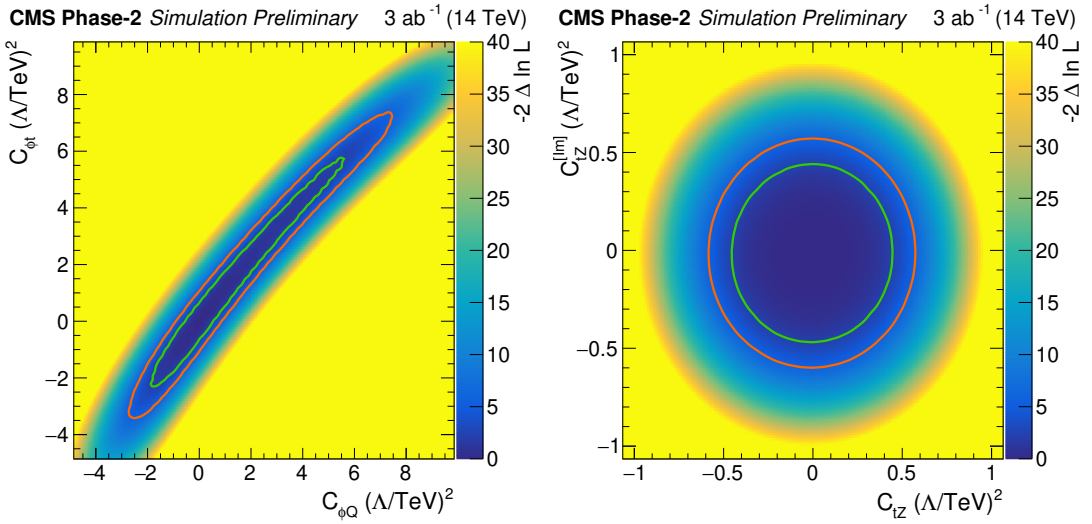

Fig. 89: Scan of the negative likelihood in the $C_{\phi Q}/C_{\phi t}$ (left) and $C_{tZ}/C_{tZ}^{[\text{Im}]}$ parameter planes (right) for the $t\bar{t}Z$ process under the SM hypothesis. The 68% (95%) CL contour lines are given in green (red).

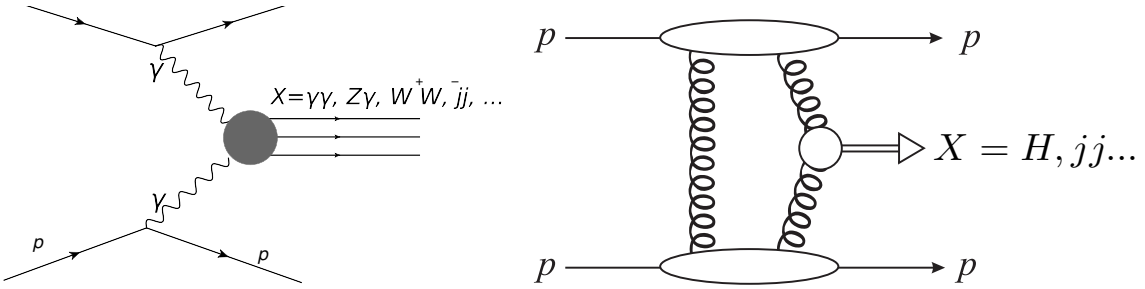

Fig. 90: Schematic diagram of the production of a system X in (left) two–photon (right) QCD–initiated central exclusive production.

7 Forward physics

7.1 Photon-induced collisions at the HL–LHC[50]

Central exclusive production (CEP) corresponds to the production of a central system X, and nothing else, with two outgoing intact protons:

$$pp \to p \; + \; X \; + \; p \; . \tag{57}$$

Such a process may be mediated by photon exchange, with the elastic photon emission vertex leaving the protons intact, see Fig. 90 (left). A range of SM (e.g. $X = \gamma\gamma$, $Z\gamma$, ZZ, $\ell\bar{\ell}$) and BSM states (e.g. $X =$ axion–like particles, monopoles, SUSY particles) may be produced in this way. These have the benefit of:

- The theoretical framework to model the underlying production mechanism, based on the equivalent photon approximation [771], is very well understood. Moreover, due to the peripheral nature of the interaction the possibility for additional inelastic proton–proton interactions (in other words of multiple–particle interactions) is very low.
- As the mass of the central system increases, the relative size of any contribution from QCD–initiated production, see section 7.2, becomes increasingly small [772], due to the strong Sudakov suppression in vetoing on additional QCD radiation.

CEP therefore offers a unique opportunity at the LHC to observe the purely photon–initiated production of electromagnetically charged objects at the LHC in a clean and well understood environment; in this context the LHC is effectively used as a photon–photon collider. The cross sections for such processes can be relatively small, in particular at higher mass, and therefore to select such events it is essential to run during nominal LHC running with tagged protons. The increased statistics available during the HL–LHC stage will allow these studies to push to higher masses and lower cross sections, increasing the discovery potential. A detailed study for the example case of anomalous quartic gauge couplings is discussed below.

7.1.1 Anomalous quartic gauge couplings with proton tagging at the HL–LHC[51]

This section discusses the discovery potential of anomalous quartic gauge interactions at the LHC via the measurement of central exclusive production (see Refs. [773–780]). The central system X is reconstructed in the central detector (CMS, ATLAS) while the outgoing protons, which remain intact due to

[50] Section edited by L. Harland-Lang.
[51] Contribution by C. Baldenegro and C. Royon.

the coherent photon exchange, can be reconstructed with dedicated tracking detectors located in the very forward region at about $\pm$ 210 m (220 m) with respect to the interaction point of the CMS (ATLAS) experiment. The fractional momentum loss of the outgoing protons $\xi = \Delta p/p$ is reconstructed offline. Central exclusive production processes satisfy $m_X = m_X^{\text{fwd}} = \sqrt{\xi_1 \xi_2 s}$ and $y_X = y_X^{\text{fwd}} = \frac{1}{2}\log\left(\frac{\xi_1}{\xi_2}\right)$, where m_X and y_X are the mass and rapidity of the system X reconstructed with the central detector, m_X^{fwd} and y_X^{fwd} are the mass and rapidity of the system X reconstructed with the forward detectors and $\sqrt{s}$ is the proton-proton centre-of-mass energy. This relationship sets a powerful offline selection tool for background suppression, since non-exclusive events are not correlated to the forward protons.

In these projections, it is assumed that a similar set-up as with the CT-PPS and AFP detectors is possible at the HL-LHC. An overview of the physics case for light-by-light scattering is given as the prototype example, and the quartic $\gamma\gamma\gamma Z$ coupling is given as an instance of other gauge couplings that could be studied at the HL-LHC. These projections consider also the impact of the difference of the measured time-of-flight for the intact protons with various timing precisions (on the order of 10 ps), which can be used to determine the longitudinal coordinate of the event vertex down to $\sim$ 2 mm. Time-of-flight measurements can help further reduce the background, especially at the HL-LHC where the number of interactions per bunch crossing will range from 140-200.

Scattering of light-by-light in p-p collisions

Under the assumption that there exists a New Physics energy scale Λ much heavier than the experimentally accessible energy E, new physics manifestations can be described using an effective Lagrangian valid for $\Lambda \gg E$. Among these operators, the pure photon dimension-eight operators $\mathcal{L}_{4\gamma} = \zeta_1^{4\gamma} F_{\mu\nu}F^{\mu\nu}F_{\rho\sigma}F^{\rho\sigma} + \zeta_2^{4\gamma} F_{\mu\nu}F^{\nu\rho}F_{\rho\lambda}F^{\lambda\mu}$ induce the $\gamma\gamma\gamma\gamma$ interaction. This coupling can be probed in $pp \to p(\gamma\gamma \to \gamma\gamma)p$ reactions. This sub-process and the SM light-by-light scattering one are implemented in the Forward Physics Monte Carlo (FPMC) [781] event generator. The Equivalent Photon Approximation is used to calculate the emitted coherent photon flux off the protons.

With proton tagging, one can probe $\gamma\gamma \to \gamma\gamma$ collisions from about 300 GeV to 2 TeV. The mass acceptance on the photon pair is limited mainly by the acceptance of ξ of the proton taggers ($0.015 \leq \xi \leq 0.15$). The background is dominated by non-exclusive diphoton production events overlapped with uncorrelated events with intact protons coming from the secondary collisions occurring in the same bunch crossing. This background can be suppressed by looking at the central and forward systems kinematic correlations (the aforementioned mass and rapidity matching). The irreducible background coming from the SM exclusive diphoton production is negligible at large invariant masses. The background can be further suppressed if the time-of-flight difference of each of the scattered protons is measured. The precision of the event vertex longitudinal position determined with the time-of-flight measurement is given by $\delta z = c\,\delta t/\sqrt{2}$, where c is the speed of light and δt is the timing precision. In these projections, the average pileup of 200 collisions per bunch crossing was considered.

The expected bounds on the anomalous couplings $\zeta_{1,2}^{4\gamma}$ at 95% CL are calculated based on the total expected background rate and can be seen in Fig. 91. The reach on the quartic couplings $\zeta_{1,2}^{4\gamma}$ down

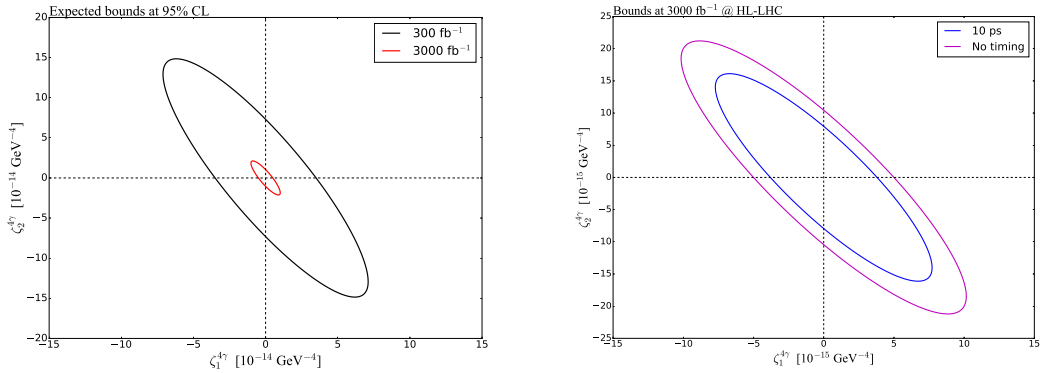

Fig. 91: Expected bounds at 95% CL on the anomalous quartic coupling for 300 fb^{-1} and at the HL-LHC with 3000 fb^{-1} (no time-of-flight measurement) (left). Expected bounds at 95% CL on the anomalous couplings at the HL-LHC with time-of-flight measurement with precision of 10 ps and without time-of-flight measurement (right).

to $5 \cdot 10^{-14}$ GeV^{-4} with 300 fb^{-1} at 14 TeV, and down to $1 \cdot 10^{-14}$ GeV^{-4} at the HL-LHC with a luminosity of 3000 fb^{-1} without using time-of-flight information. The last bound can be improved by a factor of ~ 1.2 if the timing precision is of 10 ps.

Constraining $\gamma\gamma\gamma Z$ coupling via $pp \to p(\gamma\gamma \to \gamma Z)p$

The $\gamma\gamma\gamma Z$ interaction is induced at one-loop level in the SM via loops of fermions and $W^{\pm}$ bosons. Loops of heavy particles charged under $\mathrm{SU}(2)_L \times \mathrm{U}(1)_Y$ contribute to the $\gamma\gamma\gamma Z$ couplings. The dimension-eight effective operators are $\mathcal{L}_{\gamma\gamma\gamma Z} = \zeta_1^{3\gamma Z} F^{\mu\nu} F_{\mu\nu} F^{\rho\sigma} Z_{\rho\sigma} + \zeta_2^{3\gamma Z} F^{\mu\nu} \tilde{F}_{\mu\nu} F^{\rho\sigma} \tilde{Z}_{\rho\sigma}$, which induce the $\gamma\gamma\gamma Z$ interaction. This induces the anomalous $\gamma\gamma \to \gamma Z$ scattering and generates the rare SM decay $Z \to \gamma\gamma\gamma$. This coupling can be probed in $pp \to p(\gamma\gamma \to \gamma Z)p$ reactions. The sub-process was implemented in the FPMC event generator as well.

Since the exclusive channel is very clean, it allows the possibility of studying exclusive $Z\gamma$ production with the Z boson decaying into a charged lepton pair or to hadrons (dijet or large radius jet signature). The signature $(Z \to \ell\bar{\ell}) + \gamma$ is much cleaner, but has vastly fewer events than $(Z \to \text{hadrons}) + \gamma$ final states. A similar event selection is applied on the exclusive $Z\gamma$ production as in the exclusive $\gamma\gamma$ case. The sensitivity on the anomalous coupling at 95% CL combining both channels at 14 TeV with 300 fb^{-1} of data is on the order of $1 \cdot 10^{-13}$ GeV $^{-4}$ (see Fig. 92). For the HL-LHC with 3000 fb^{-1} it scales down to $1 \cdot 10^{-14}$ GeV^{-4} when combining both channels. The time-of-flight measurement can improve the expected bounds by a factor of ~ 2 .

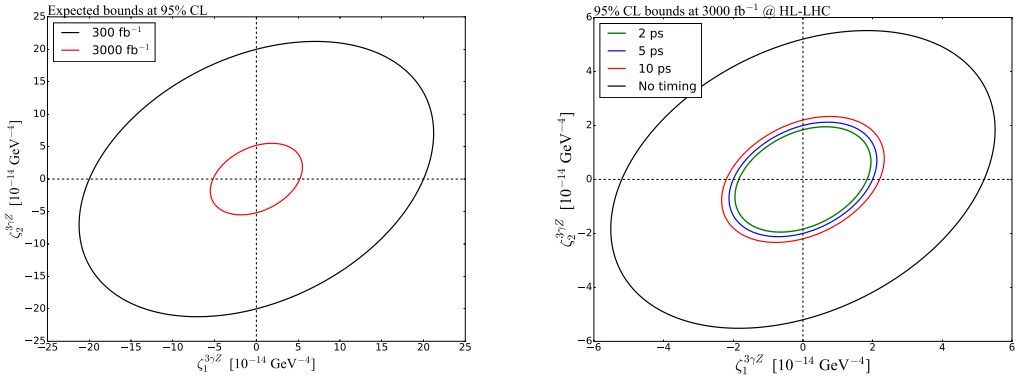

Fig. 92: Expected bounds on the anomalous couplings at 95% CL with 300 fb^{-1} and 3000 fb^{-1} at the HL-LHC (no time-of-flight measurement) (left). Expected bounds at 95%CL for timing precisions of $\delta t = 2,\ 5,\ 10$ ps at the HL-LHC (right).

7.2 Central exclusive production: QCD prospects[52]

The CEP process may be mediated purely by the strong interaction, and in such a case if the mass of the central system is large enough a perturbative approach may be applied, via the diagram shown in Fig. 90 (right), see [782, 783] for reviews. As well as probing QCD in a novel regime, the exclusive nature of this process has the benefit that the produced object obeys a quantum number selection rule. Namely the object must be C even, while the production of P even states with $J_z = 0$ angular momentum projection on the beam axis is strongly dominant. From the point of view of the production of new BSM states or the understanding of existing QCD bound states (e.g. exotic quarkonia) this therefore has the benefit of identifying the produced object quantum numbers. The $J_z = 0$ selection implies that only certain helicity configurations in the underlying $gg \to X$ production process contribute, which also leads to unique phenomenological consequences. A detailed discussion of this selection rule can be found in [783] and the references therein. Two example processes, namely exclusive jet and Higgs boson production, are discussed briefly below. These represent higher mass test cases relevant to HL–LHC running with tagged protons at ATLAS or CMS. The possibilities for the observation of lower mass objects with the ALICE detector will be addressed in section 7.4.

The exclusive production of jets provides a new and unexplored area of QCD phenomenology. This process has been first observed at the Tevatron [784, 785]. The quantum number selection rule discussed above has a number of consequences that are quite distinct from the standard inclusive channels. In particular, the production of purely gluonic dijets is predicted to be strongly dominant, allowing a study of purely gg jets from a colour–singlet initial state. In the three–jet case the presence of 'radiation zeros' [786], that is a complete vanishing in the leading order amplitudes for certain kinematic configurations, is expected. This phenomena is well known in electroweak processes, but this is the only known example of a purely QCD process where this occurs. Some representative predictions for the HL–LHC are shown in Table 54. These are calculated using the SUPERCHIC 2.5 MC generator [787], which provides the most up to date predictions for CEP processes. The cross sections are suppressed

[52] Contribution by L. Harland-Lang.

Table 54: Parton–level predictions for exclusive two and three jet production cross sections (in pb) at the LHC for different cuts on the minimum central system invariant mass M_X at $\sqrt{s} = 14$ TeV. The jets are required to have transverse momentum $p_{\mathrm{T}} > 20$ GeV for $M_X(\mathrm{min}) = 75, 150$ GeV and $p_{\mathrm{T}} > 40$ GeV for $M_X(\mathrm{min}) = 250$ GeV and pseudorapidity $|\eta| < 2.5$. The anti-k_{T} algorithm with jet radius $R = 0.6$ is used in the three jet case and the $q\bar{q}$ cross sections correspond to one massless quark flavour.

$M_X(\mathrm{min})$	gg	$q\bar{q}$	$b\bar{b}$	ggg	$gq\bar{q}$
75	130	0.032	0.082	5.0	0.11
150	4.5	6.1×10^{-4}	1.1×10^{-3}	0.70	0.019
250	0.15	2.2×10^{-5}	2.7×10^{-5}	0.016	4.3×10^{-4}

relative to the inclusive case, but are nonetheless relatively large. On the other hand, in the three jet case, in particular in the invariant mass region that may be relevant for the acceptance of proton tagging detectors, the cross sections are lower and would clearly benefit from as large a data sample as possible for studies of novel features, such as radiation zeros and other jet shape variables.

The production of the Higgs boson through exclusive gg fusion would represent a completely new observation channel. As discussed in more detail in [783], this has the potential to shed light on the CP properties of the state, as well as its coupling to b quarks in a distinct way to inclusive channels. The cross section for a SM Higgs, as predicted by SUPERCHIC 2.5 [787], is $\sigma(|y_H| < 2.5) = (1 \overset{\times}{\div} 2)$ fb, where the dominant uncertainties are due to PDFs and modelling of the soft gap survival probability. The predicted rate is therefore relatively small, and would again benefit both from the increased statistics available in HL running, and even more crucially from the potential installation of new tagging detectors at a larger distance from the ATLAS or CMS interaction points (IPs), see section 7.3, which would extend the existing mass acceptance into the Higgs region.

7.3 Tagged proton at the HL–LHC: experimental prospects

This section discusses possible locations for movable near-beam detectors along the outgoing beam lines near IP5, designed for detecting the leading protons from central production processes (Fig. 90, eq. (57)). While the results which follow consider the possibilities for detectors in association with the CMS experiment, similar qualitative prospects are expected in the case of the ATLAS detector, although this is not discussed explicitly here. After identifying the best-suited positions, the proton detection acceptance and hence the central-mass tagging reach is calculated for each of these positions as a function of beam parameters and based on present-day assumptions on optics, collimation scheme and near-beam-detector insertion rules from machine protection arguments. Given that at the time of this report the crossing-angle plane in IP5 (horizontal as until LS3, or vertical) has not yet been decided, both options have been investigated. It has to be pointed out that the crossing planes of IP1 and IP5 have to be different: one will be horizontal, the other vertical.

While in the CT-PPS (later PPS) project [788] in Run-2 the near-beam detectors were Roman Pots inherited from the TOTEM experiment [789, 790] and upgraded for high-luminosity operation [791], no technological assumptions are made at this early stage of preparation for HL-LHC. The highly demanding engineering and detector physics challenges are not addressed here.

The search for suitable detector locations around IP5 is driven by the goal to cover the widest possible range of central masses M to be measured via the fractional momentum losses

$$\xi_{1/2} = \frac{\Delta p_{1/2}}{p} \tag{58}$$

of the two surviving protons using the relation

$$M^2 = \xi_1 \, \xi_2 \, s \, , \tag{59}$$

where $\sqrt{s} = 14\,\text{TeV}$ is the centre-of-mass energy.

The minimum accessible ξ of leading protons at a location z [53] along the beam line is given by

$$\xi_{\text{min}}(\alpha, \beta^*, z) = \frac{[n_{\text{TCT}}(\beta^*) + \Delta n]\sigma_{\text{XRP}}(\beta^*, z) + \Delta d + \delta}{D_{x,\text{XRP}}(\alpha, \xi_{\text{min}}, z)} \, , \tag{60}$$

where σ_x is the horizontal beam width depending on the optics (characterised by β^*), D_x is the horizontal dispersion depending on the crossing-angle α, n_{TCT} is the half-gap of the tertiary collimators (TCT) as defined by the collimation scheme, $\Delta n = 3$ is the retraction of the near-beam detector housings (e.g. Roman Pots) relative to the TCT position in terms of σ_x, $\Delta d = 0.3\,\text{mm}$ is an additional safety retraction to allow for beam orbit fluctuations, and the constant δ, typically 0.5 mm, accounts for any distance between the outer housing surface closest to the beam and the sensitive detector. The dependence of the dispersion on ξ implies that eq. (60) has to be resolved for ξ_{min} after parameterising $D_x(\xi)$.

The first step of the study is to plot the z-dependent quantities, σ_x and D_x, along the outgoing beam line for one typical HL-LHC optics configuration (Fig. 93, left). The resulting ξ_{min} is shown in Fig. 93 (right). Note that for vertical crossing smaller values are reached. The locations most suitable for the measurement of small $|\xi|$ values are marked in red. Closer layout inspection of the region around the minimum at 232 m (inside the quadrupole Q6) indicated two promising locations: at 220 m (just before the collimator TCL6) and at 234 m (after the exit of Q6). Even smaller momentum losses can be reached at 420 m (the "missing magnet" region already studied previously by the FP420 project [792]).

The apparent sign change of ξ_{min} at $z \approx 270\,\text{m}$ reflects the sign change of the dispersion at that location (as seen in the left panel of the figure). It means that the diffractive proton trajectories transition from $x > 0$ to $x < 0$. The implication for the potential detector location at 420 m is that detectors need to be placed in the confined space between the incoming and the outgoing beam pipes, excluding conventional Roman Pot technology. A further complication is that in this location the beam pipes are in a cryostat, necessitating more involved engineering changes.

A region of interest for the detection of higher masses lies at 196 m just upstream of the collimator TCL5 that intercepts protons with large $|\xi|$ (section 7.3). Locations even further upstream, before TCLX4, would give an even higher upper mass cut but are excluded due to the prohibitively high low-mass limit leaving no acceptance interval.

In summary, for the more detailed discussions in the following sections, four detector locations have been retained: 196 m, 220 m, 234 m, 420 m.

[53] In this article the variable z is used for the longitudinal coordinate instead of s to avoid confusion with the Mandelstam s.

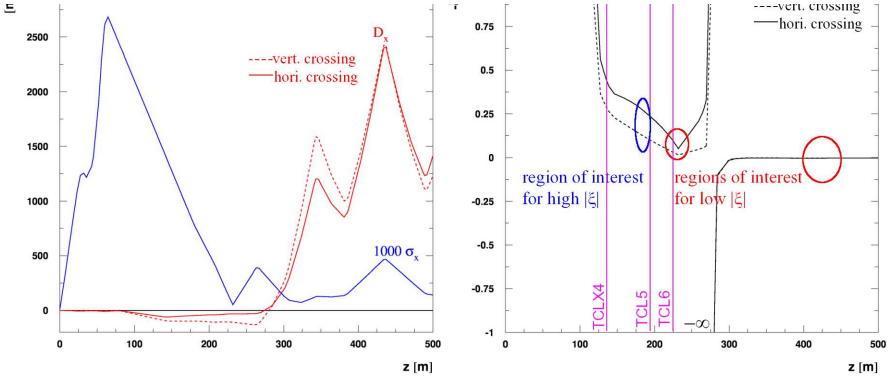

Fig. 93: Horizontal dispersion and beam width (scaled by 1000) as a function of the distance s from IP5 for Beam 1, i.e. in LHC Sector 5-6 (left). Minimum accepted ξ as a function of z according to eq. (60) for $(\alpha/2, \beta^*) = (250\,\mu\text{rad}, 15\,\text{cm})$ and $n_{\text{TCT}} = 12.9$ (right). The TCL collimator positions are indicated. In both pictures the continuous and dashed lines represent horizontal and vertical crossing in IP5, respectively.

Crossing-Angle and Optics Dependence of the Mass Acceptance Limits

In the previous section, only one specific combination of crossing-angle α and beam optics (β^*) was considered. However, at HL-LHC luminosity levelling will be performed in all fills by changing α and β^* in a pre-defined sequence. For the present study the $(\alpha/2,\, \beta^*)$ trajectories envisaged in [793] were used.

Minimum Mass

The minimum mass accepted at a location z for given α and β^* can be calculated using eq. (59) and (60). For simplicity, symmetric optics in the two beams, i.e. equal ξ_{min}, are assumed:

$$M_{\text{min}} = |\xi_{\text{min}}|\,\sqrt{s}\,. \tag{61}$$

The α and ξ dependencies of D_x can be parameterised based on simulations with MAD-X [794]. The α dependence is linear, and the ξ-dependence can be linearly approximated within the ξ-ranges relevant in practice.

The β^* dependence of σ_{XRP} was calculated analytically, profiting from invariance properties of the presently planned family of ATS optics. This is likely to change in the future and will need to be adapted.

The β^* dependence of n_{TCT} follows the presently foreseen collimation strategy [795] of keeping the TCT gap constant at $d_{\text{TCT}} = 12.9\,\sigma_{\text{TCT}}(\beta^* = 15\,\text{cm})$ (for nominal emittance $\varepsilon_n = 2.5\,\mu\text{m rad}$), implying $n_{\text{TCT}}(\beta^*) = \frac{d_{\text{TCT}}}{\sigma_{\text{TCT}}(\beta^*)}$, where an analytical expression for $\sigma_{\text{TCT}}(\beta^*)$ can be derived.

The result of this calculation, contour lines of M_{min} in the beam parameter space $(\alpha/2, \beta^*)$, is shown in Fig. 94 for the four detector locations chosen in the previous section. Some possible luminosity-levelling trajectories are drawn, too. The start point at the beginning of the fill is always at the maximum β^* value.

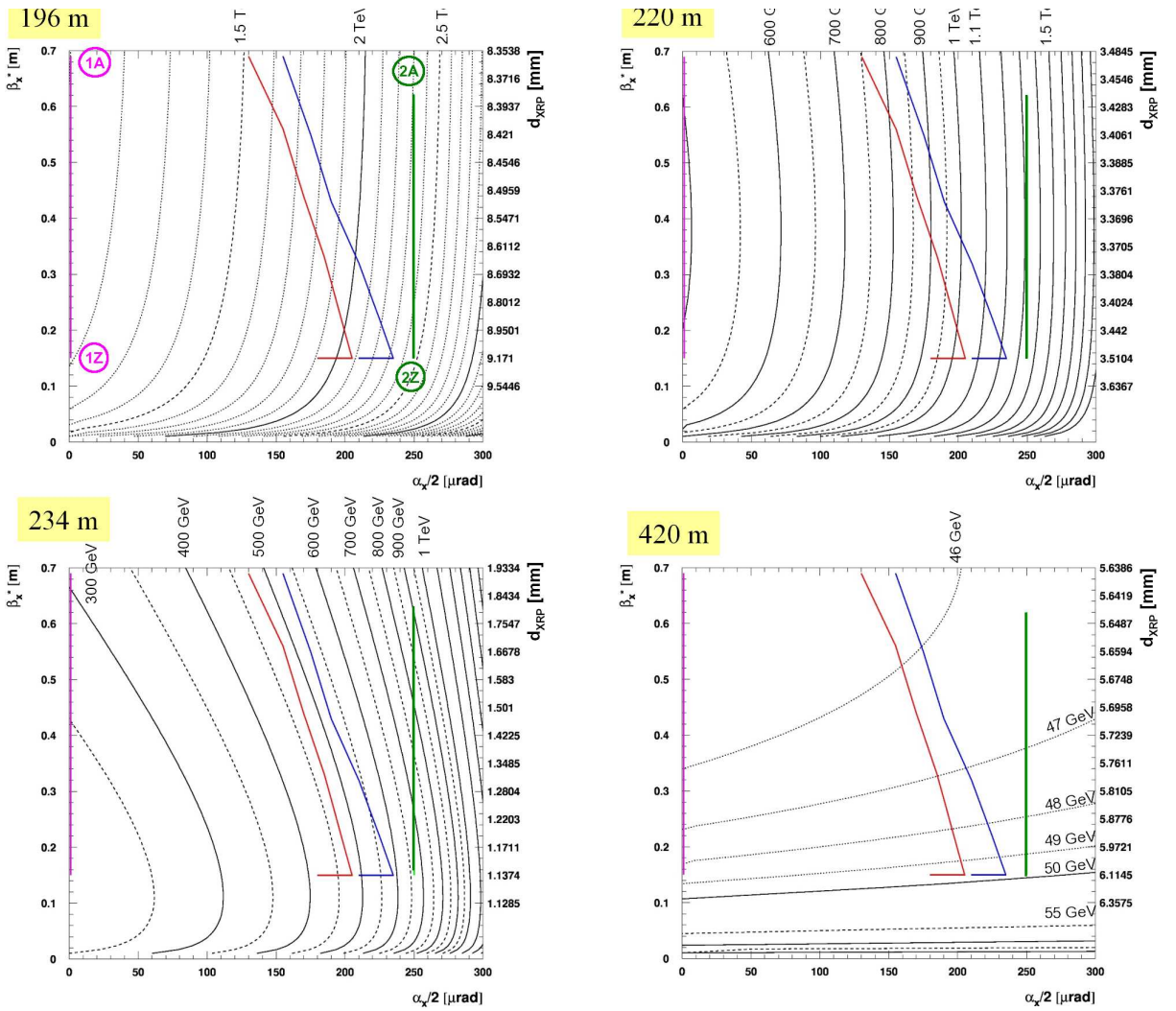

Fig. 94: Contour lines for the minimum accepted mass $M_{\min} = |\xi|_{\min}\sqrt{s}$ in the crossing-angle/optics parameter space $(\alpha/2, \beta^*)$. On the right-hand ordinate the XRP approach distance is calculated from β^*. The coloured lines represent possible luminosity-levelling trajectories [793]. For horizontal crossing: green corresponds to "baseline", blue to "relaxed adaptive", red to "aggressive adaptive"; for vertical crossing: violet corresponds to any trajectory. The labels (1A) – (2Z) in the first panel define the trajectory start and end points used in Figs. 96 and 97.

From these graphs the following conclusions are drawn:

- The main driving factor for the minimum mass is the dispersion which in turn is fully determined by the crossing-angle. The optics (via β^*) plays a minor role.
- If the 420 m location can be instrumented, the minimum mass is about 50 GeV with only a very weak dependence on the optics, the crossing-angle and its plane (horizontal or vertical).
- Without the 420 m location, the vertical crossing gives a much better low-mass acceptance (210 GeV)

Maximum Mass

The maximum mass accepted at a location z is determined by the tightest aperture restriction d_A upstream of z and the dispersion there:

$$M_{\text{max}} = |\xi_{\text{max}}| \sqrt{s} = \frac{d_A}{D_A(\alpha, \xi_{\text{max}})} \,. \tag{62}$$

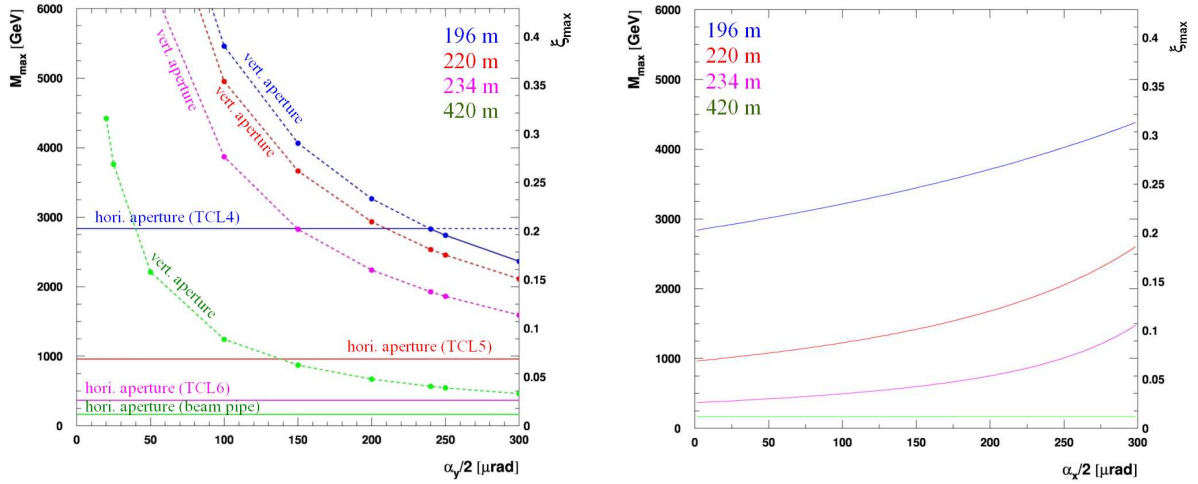

Fig. 95: Maximum accepted diffractive mass for each detector location as a function of the crossing-angle. Vertical crossing (left): both horizontal and vertical apertures contribute to the mass limits. The continuous lines denote the most restrictive, i.e. dominant, limitations. Horizontal crossing (right): only the horizontal apertures contribute.

In the case of the vertical beam crossing in IP5, both the horizontal and vertical apertures may impose limitations, whereas in the case of the horizontal crossing there is no substantial vertical dispersion and hence no acceptance loss from the vertical aperture. Figure 95 shows the results of a complete aperture study. It was concluded that even for vertical crossing most limitations come from the horizontal aperture and that for all locations, except 420 m, this horizontal aperture is limited by the TCL collimators. At 420 m, on the other hand, the beam-pipe absorbs diffractive protons with $|\xi| > 0.012$. The highest masses are accepted by the unit at 196 m: up to 2.7 TeV for vertical crossing and up to 4 TeV for horizontal crossing.

Mass-Rapidity Acceptance

The CEP acceptance for a given point in the beam parameter space (α, β^*) can be visualised by drawing for every instrumented detector location the $|\xi|$-acceptance bands – whose limits are calculated according to the previous section – in the mass-rapidity plane

$$\left(\ln \frac{M}{\sqrt{s}}, y\right) = \left(\frac{1}{2}(\ln \xi_1 + \ln \xi_2), \frac{1}{2}(\ln \xi_1 - \ln \xi_2)\right) \,. \tag{63}$$

cases defined in Fig. 94: points (1A) and (1Z) for any trajectory with vertical crossing in IP5, points (2A) and (2Z) for the "Baseline" trajectory with horizontal crossing. The projections on the mass axis, under the approximation of flat rapidity distributions, are given in Fig. 97.

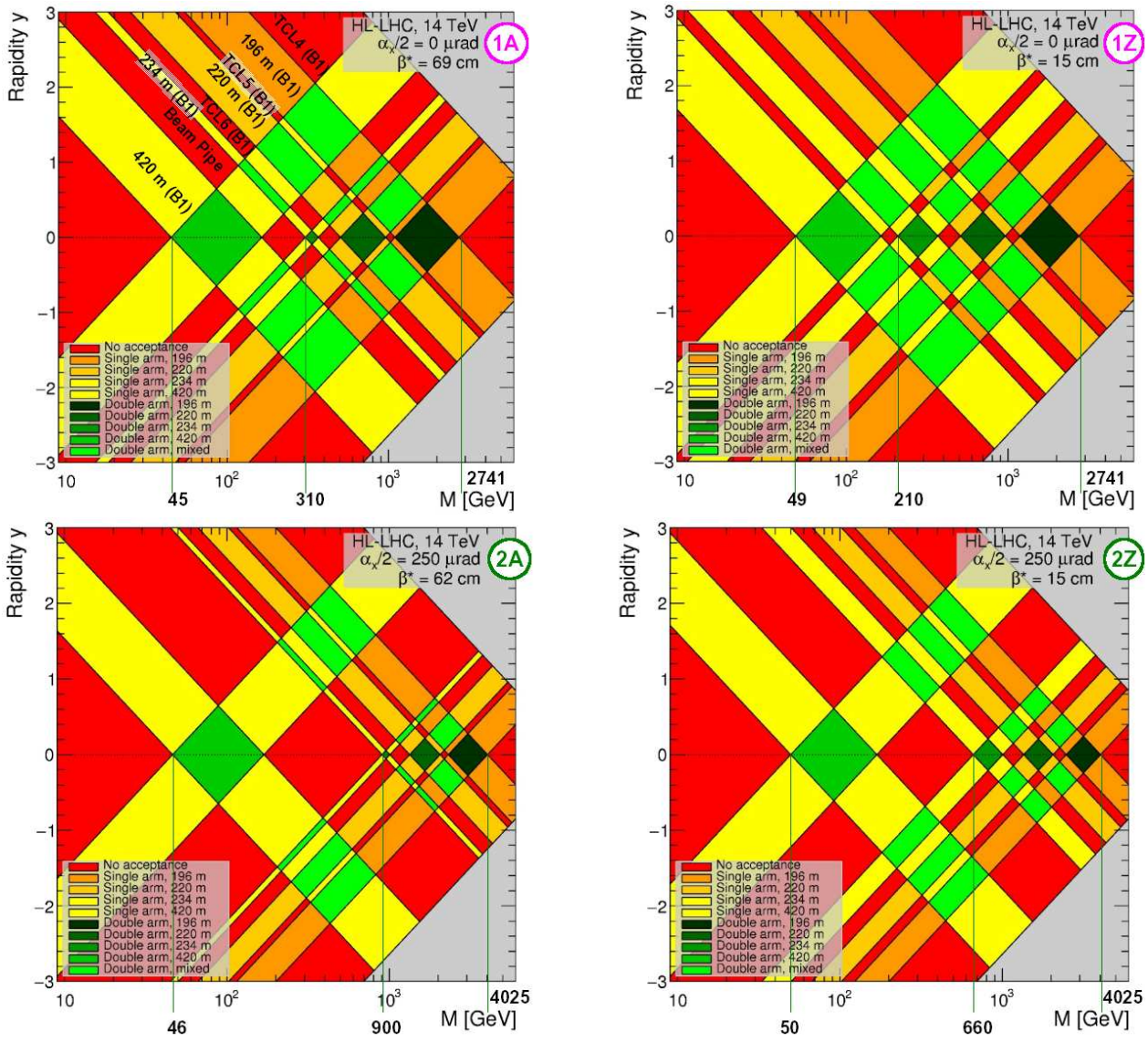

Fig. 96: Acceptance for the protons from central diffraction in the mass-rapidity plane. The yellow/orange colour tones mark single-arm proton acceptance, the green tones mark double-arm acceptance. Top: start and end point of any levelling trajectory for vertical crossing, bottom: start and end point of the baseline levelling trajectory for horizontal crossing.

The following observations are made:

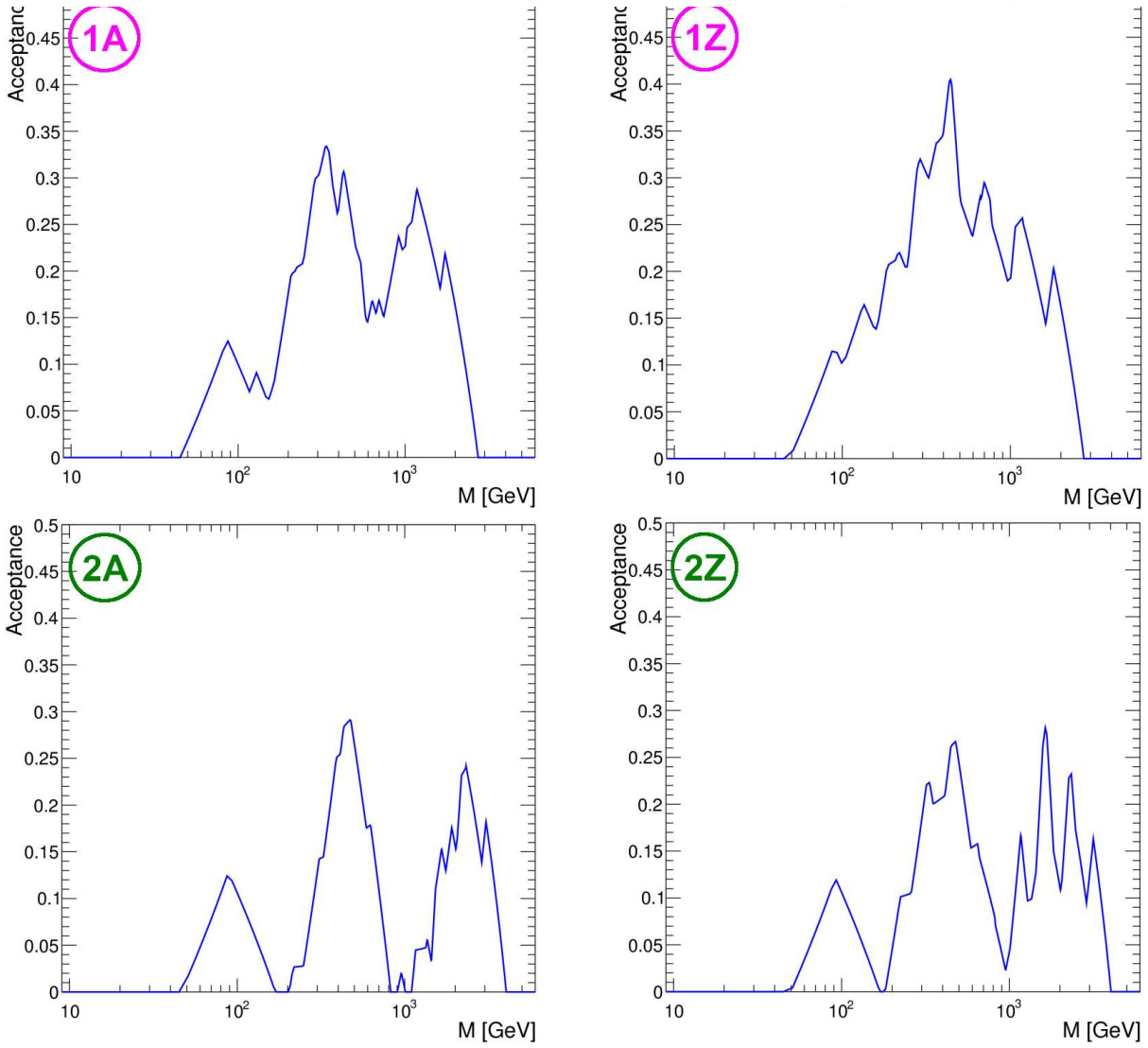

Fig. 97: Projection of the (M, y) acceptance on the mass axis, adding up all the double-arm areas of Fig. 96 for the same points in the (α, β^*) beam parameter space.

– The acceptance zones of the four detector locations are non-overlapping and separated by gaps. For horizontal crossing the gaps are wider than for vertical crossing.
– Although the double-arm acceptance has mass gaps at central rapidities, the mixed acceptance zones combining different detector units in the two arms of the experiment (e.g. 420 m left + 234 m right) fill some of these mass gaps by providing acceptance at forward rapidities.
– The gaps between the acceptances of 196 m, 220 m and 234 m can potentially be closed by opening TCL5 and TCL6 a little further if allowable from machine protection arguments. On the other

aperture. It could only be closed by adding a detector unit near 300 m.

7.4 Low-mass central exclusive production

Central exclusive production of low-mass diffractive states in pp collisions at the LHC may serve as a valuable source of information on the non-perturbative aspects of strong interaction. At low masses, CEP is usually described in terms of a double pomeron exchange (DPE) mechanism. DPE is expected to be an ideal process for the investigation of meson resonances with $I^G(J^{PC}) = 0^+(0^{++}, 2^{++}, \ldots)$ quantum numbers and gluonic bound states. Glueball searches in CEP are of particular interest because lattice QCD calculations predict the lightest glueballs to have masses $M_G(0^{++}) = 1710$ MeV and $M_G(2^{++}) = 2390$ MeV [796]. Pure glueballs are predicted to decay equally well into pair of pions, kaons or η mesons with suppressed two photon decays. However this simple signature is spoiled by the fact that glueballs are expected to mix with nearby $q\bar{q}$ states.

Central-exclusive production of low-mass resonances in $\pi\pi$ and KK channels has been extensively studied in fixed target experiments at CERN and Fermilab (see review in [782]) and recent collider experiments at RHIC [797], Tevatron [798] and the LHC [799]. The partial-wave analysis (PWA) has been performed in several experiments to investigate the spin-parity nature of the centrally produced system [800–802]. There is a clear evidence of supernumerous light scalar meson states, not fitting well into the conventional groundstate $q\bar{q}$ nonet and suggesting that some of these states have significant gluonic component. The $f_0(1370)$, $f_0(1500)$ and $f_0(1710)$ mesons are considered as most promising glueball-meson mixing state candidates but the nature of all these states is still open for discussion [803]. In the tensor sector, the lightest isoscalar $q\bar{q}$ states $f_2(1270)$ and $f_2'(1525)$ are well established however there are at least four additional reported tensor resonances requiring confirmation.

CEP can be also used to investigate the spin structure of the Pomeron and its coupling to hadrons. Historically, the Pomeron was considered as effective spin 1 quasiparticle supported by successful fits of total and differential pp cross sections [804]. Recently, an alternative approach based on the tensorial Pomeron has been developed [805] providing definitive predictions and restrictions of spin-parity, polarization and rapidity of the produced diffractive system in CEP at the LHC [806–808].

Multidifferential measurements and PWA of $\pi\pi$, KK and $p\bar{p}$ final states in a wide range of invariant masses in CEP at the LHC would also allow one to constrain poorly known Pomeron-meson couplings and form-factors in various phenomenological models [806, 809] and also build a transition to perturbative QCD models of hadron pair production in CEP [810] valid at high invariant masses and transverse momenta of the produced pair. Another important outcome of CEP measurements would be a determination of the absorptive corrections, the probability that the rapidity gaps would be filled with particles from accompanying initial- or final-state interactions. The central exclusive production of meson pairs therefore represents a process of much phenomenological interest, which can shed light on both perturbative and non-perturbative aspects of QCD.

Perturbative aspects of QCD can be also investigated in CEP of heavy quarkonium states [783]. Detailed studies of χ_c resonances in CEP at the LHC would provide a valuable input to test the ideas and methods of the QCD physics of bound states. Measurements of the outgoing proton momentum distributions, cross sections and relative abundances of χ_{c0}, χ_{c1} and χ_{c2} states would be important for the test of the overall theoretical formalism.

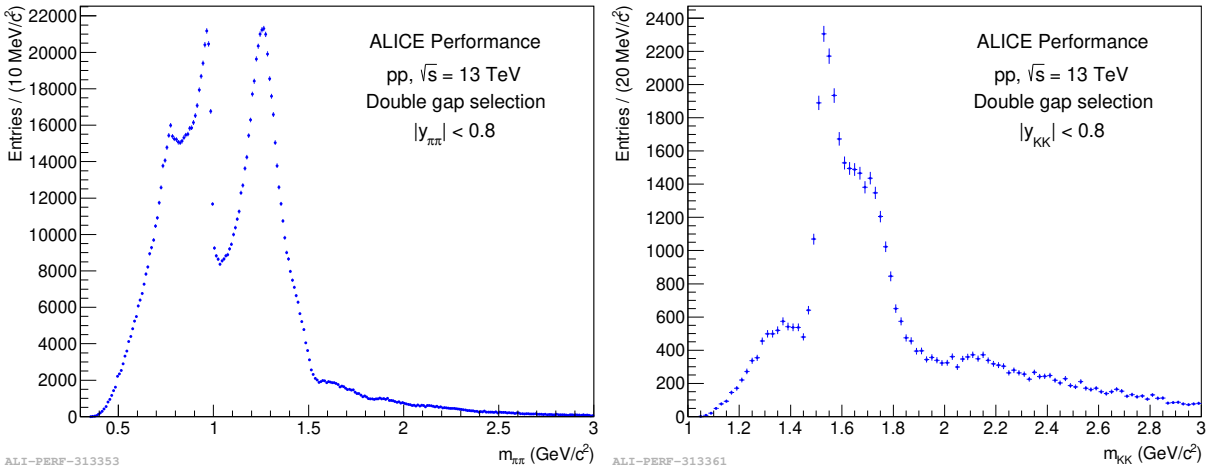

Fig. 98: Raw invariant mass spectra of $\pi^+\pi^-$ (left) and K^+K^- (right) pairs in CEP events collected by ALICE in proton-proton collisions at $\sqrt{s} = 13$ TeV.

Measurements of CEP processes rely on the selection of events with only few tracks in an otherwise empty detector, therefore large pseudorapidity coverage and low pileup conditions are essential to guarantee the event emptiness. The ALICE detector nicely matches these requirements. Low material budget, access to low transverse momenta and excellent particle identification capabilities in ALICE serve as additional advantages. First CEP measurements have been already performed by ALICE in the LHC Run-1 and -2. Figure 98 illustrates raw invariant mass spectra of $\pi^+\pi^-$ and K^+K^- pairs in CEP events collected by ALICE in proton-proton collisions at $\sqrt{s} = 13$ TeV, where one can easily identify several resonance structures. ALICE is going to collect a much larger sample of central exclusive events and significantly extend the scope of the CEP program in proton-proton collisions in LHC Run-3 with expected integrated luminosity of about 200 pb^{-1} at $\sqrt{s} = 14$ TeV and 6 pb^{-1} at $\sqrt{s} = 5.5$ TeV profiting from much better efficiency in the continuous readout mode. The CEP program includes glueball searches and precision hadron spectroscopy in $\pi^+\pi^-$, K^+K^-, $p\bar{p}$, $2\pi2K$, 4π and other channels. The expected high integrated luminosity will also allow ALICE to measure the spectrum of heavy quarkonium states in various decay channels, e.g. a yield of at least 50,000 $\chi_{c0} \to \pi^+\pi^-$ decays is expected in CEP events by the end of Run-3 based on cross section estimates from SUPERCHIC generator [811].

The LHCb experiment can extend the CEP program to forward rapidities. High luminosity at moderate pileup and good hadron PID capabilities would be particularly useful for the studies of heavy quarkonium states in central exclusive events. Measurements of low-mass central exclusive production processes with proton tagging might be also possible with the ATLAS and CMS detectors during low pile-up runs at high β^*.

Acknowledgements

We would like to thank the LHC experimental Collaborations and the WLCG for their essential support. We are especially grateful for the efforts by the computing, generator and validation groups who were instrumental for the creation of large simulation samples. We thank the detector upgrade groups as well as the physics and performance groups for their input. Not least, we thank the many colleagues who have provided useful comments on the analyses.

References

[1] R. K. Ellis and G. Zanderighi, *Scalar one-loop integrals for QCD*, JHEP **02** (2008) 002, arXiv:0712.1851 [hep-ph].

[2] A. van Hameren, *OneLOop: For the evaluation of one-loop scalar functions*, Comput. Phys. Commun. **182** (2011) 2427–2438, arXiv:1007.4716 [hep-ph].

[3] S. Frixione, Z. Kunszt, and A. Signer, *Three jet cross-sections to next-to-leading order*, Nucl. Phys. **B467** (1996) 399–442, arXiv:hep-ph/9512328 [hep-ph].

[4] S. Catani and M. H. Seymour, *A General algorithm for calculating jet cross-sections in NLO QCD*, Nucl. Phys. **B485** (1997) 291–419, arXiv:hep-ph/9605323 [hep-ph]. [Erratum: Nucl. Phys.B510,503(1998)].

[5] R. Britto, F. Cachazo, and B. Feng, *Generalized unitarity and one-loop amplitudes in N=4 super-Yang-Mills*, Nucl. Phys. **B725** (2005) 275–305, arXiv:hep-th/0412103 [hep-th].

[6] G. Ossola, C. G. Papadopoulos, and R. Pittau, *Reducing full one-loop amplitudes to scalar integrals at the integrand level*, Nucl. Phys. **B763** (2007) 147–169, arXiv:hep-ph/0609007 [hep-ph].

[7] R. K. Ellis, W. T. Giele, Z. Kunszt, and K. Melnikov, *Masses, fermions and generalized D-dimensional unitarity*, Nucl. Phys. **B822** (2009) 270–282, arXiv:0806.3467 [hep-ph].

[8] W. T. Giele, Z. Kunszt, and K. Melnikov, *Full one-loop amplitudes from tree amplitudes*, JHEP **04** (2008) 049, arXiv:0801.2237 [hep-ph].

[9] R. K. Ellis, Z. Kunszt, K. Melnikov, and G. Zanderighi, *One-loop calculations in quantum field theory: from Feynman diagrams to unitarity cuts*, Phys. Rept. **518** (2012) 141–250, arXiv:1105.4319 [hep-ph].

[10] F. Cascioli, P. Maierhofer, and S. Pozzorini, *Scattering Amplitudes with Open Loops*, Phys. Rev. Lett. **108** (2012) 111601, arXiv:1111.5206 [hep-ph].

[11] G. Cullen et al., *GOSAM-2.0: a tool for automated one-loop calculations within the Standard Model and beyond*, Eur. Phys. J. **C74** (2014) no. 8, 3001, arXiv:1404.7096 [hep-ph].

[12] J. Alwall, R. Frederix, S. Frixione, V. Hirschi, F. Maltoni, O. Mattelaer, H. S. Shao, T. Stelzer, P. Torrielli, and M. Zaro, *The automated computation of tree-level and next-to-leading order differential cross sections, and their matching to parton shower simulations*, JHEP **07** (2014) 079, arXiv:1405.0301 [hep-ph].

[13] T. O. Eynck, E. Laenen, L. Phaf, and S. Weinzierl, *Comparison of phase space slicing and dipole subtraction methods for gamma* —> anti-Q*, Eur. Phys. J. **C23** (2002) 259–266, arXiv:hep-ph/0109246 [hep-ph].

[14] ATLAS Collaboration, G. Aad et al., *Measurement of W^+W^- production in pp collisions at $\sqrt{s} = 7$ TeV with the ATLAS detector and limits on anomalous WWZ and WWγ couplings*, Phys. Rev. **D87** (2013) no. 11, 112001, arXiv:1210.2979 [hep-ex]. [Erratum: Phys. Rev.D88,no.7,079906(2013)].

[15] CMS Collaboration, S. Chatrchyan et al., *Measurement of the W^+W^- Cross section in pp Collisions at $\sqrt{s} = 7$ TeV and Limits on Anomalous $WW\gamma$ and WWZ couplings*, Eur. Phys. J. **C73** (2013) no. 10, 2610, arXiv:1306.1126 [hep-ex].

[16] CMS Collaboration, S. Chatrchyan et al., *Measurement of W+W- and ZZ production cross sections in pp collisions at sqrt(s) = 8 TeV*, Phys. Lett. **B721** (2013) 190–211, arXiv:1301.4698 [hep-ex].

[17] G. Heinrich, *QCD calculations for the LHC: status and prospects*, in *5th Large Hadron Collider Physics Conference (LHCP 2017) Shanghai, China, May 15-20, 2017*. 2017. arXiv:1710.04998 [hep-ph].

[18] S. Dittmaier, *Standard Model Theory*, in *Proceedings, 2017 European Physical Society Conference on High Energy Physics (EPS-HEP 2017): Venice, Italy, July 5-12, 2017*. 2017. arXiv:1709.08564 [hep-ph]. https://pos.sissa.it/314/581/pdf.

[19] J. Currie, A. Gehrmann-De Ridder, T. Gehrmann, E. W. N. Glover, A. Huss, and J. Pires, *Precise predictions for dijet production at the LHC*, Phys. Rev. Lett. **119** (2017) no. 15, 152001, arXiv:1705.10271 [hep-ph].

[20] A. V. Kotikov, *Differential equations method: The Calculation of vertex type Feynman diagrams*, Phys. Lett. **B259** (1991) 314–322.

[21] A. V. Kotikov, *Differential equation method: The Calculation of N point Feynman diagrams*, Phys. Lett. **B267** (1991) 123–127. [Erratum: Phys. Lett.B295,409(1992)].

[22] J. M. Henn, *Multiloop integrals in dimensional regularization made simple*, Phys. Rev. Lett. **110** (2013) 251601, arXiv:1304.1806 [hep-th].

[23] C. G. Papadopoulos, *Simplified differential equations approach for Master Integrals*, JHEP **07** (2014) 088, arXiv:1401.6057 [hep-ph].

[24] S. P. Jones, M. Kerner, and G. Luisoni, *Next-to-Leading-Order QCD Corrections to Higgs Boson Plus Jet Production with Full Top-Quark Mass Dependence*, Phys. Rev. Lett. **120** (2018) no. 16, 162001, arXiv:1802.00349 [hep-ph].

[25] J. M. Lindert, K. Kudashkin, K. Melnikov, and C. Wever, *Higgs bosons with large transverse momentum at the LHC*, Phys. Lett. **B782** (2018) 210–214, arXiv:1801.08226 [hep-ph].

[26] L. Adams, C. Bogner, and S. Weinzierl, *The two-loop sunrise graph in two space-time dimensions with arbitrary masses in terms of elliptic dilogarithms*, J. Math. Phys. **55** (2014) no. 10, 102301, arXiv:1405.5640 [hep-ph].

[27] J. M. Henn, K. Melnikov, and V. A. Smirnov, *Two-loop planar master integrals for the production of off-shell vector bosons in hadron collisions*, JHEP **05** (2014) 090, arXiv:1402.7078 [hep-ph].

[28] F. Caola, J. M. Henn, K. Melnikov, and V. A. Smirnov, *Non-planar master integrals for the production of two off-shell vector bosons in collisions of massless partons*, JHEP **09** (2014) 043, arXiv:1404.5590 [hep-ph].

[29] T. Gehrmann, A. von Manteuffel, L. Tancredi, and E. Weihs, *The two-loop master integrals for* $q\bar{q} \to VV$, JHEP **06** (2014) 032, arXiv:1404.4853 [hep-ph].

[30] C. G. Papadopoulos, D. Tommasini, and C. Wever, *Two-loop Master Integrals with the Simplified Differential Equations approach*, JHEP **01** (2015) 072, arXiv:1409.6114 [hep-ph].

[31] C. G. Papadopoulos, D. Tommasini, and C. Wever, *The Pentabox Master Integrals with the Simplified Differential Equations approach*, JHEP **04** (2016) 078, arXiv:1511.09404 [hep-ph].

[32] E. Remiddi and L. Tancredi, *An Elliptic Generalization of Multiple Polylogarithms*, Nucl. Phys. **B925** (2017) 212–251, arXiv:1709.03622 [hep-ph].

[33] R. Bonciani, V. Del Duca, H. Frellesvig, J. M. Henn, F. Moriello, and V. A. Smirnov, *Two-loop planar master integrals for Higgs→ 3 partons with full heavy-quark mass dependence*, JHEP **12** (2016) 096, arXiv:1609.06685 [hep-ph].

[34] L. Adams, E. Chaubey, and S. Weinzierl, *Analytic results for the planar double box integral relevant to top-pair production with a closed top loop*, JHEP **10** (2018) 206, arXiv:1806.04981 [hep-ph].

[35] L. Adams, E. Chaubey, and S. Weinzierl, *Simplifying Differential Equations for Multiscale Feynman Integrals beyond Multiple Polylogarithms*, Phys. Rev. Lett. **118** (2017) no. 14, 141602, arXiv:1702.04279 [hep-ph].

[36] L. Adams, C. Bogner, A. Schweitzer, and S. Weinzierl, *The kite integral to all orders in terms of elliptic polylogarithms*, J. Math. Phys. **57** (2016) no. 12, 122302, arXiv:1607.01571 [hep-ph].

[37] J. Ablinger, J. Blümlein, A. De Freitas, M. van Hoeij, E. Imamoglu, C. G. Raab, C. S. Radu, and C. Schneider, *Iterated Elliptic and Hypergeometric Integrals for Feynman Diagrams*, J. Math. Phys. **59** (2018) no. 6, 062305, arXiv:1706.01299 [hep-th].

[38] A. von Manteuffel and L. Tancredi, *A non-planar two-loop three-point function beyond multiple polylogarithms*, JHEP **06** (2017) 127, arXiv:1701.05905 [hep-ph].

[39] J. Broedel, C. Duhr, F. Dulat, B. Penante, and L. Tancredi, *Elliptic symbol calculus: from elliptic polylogarithms to iterated integrals of Eisenstein series*, JHEP **08** (2018) 014, arXiv:1803.10256 [hep-th].

[40] S. Becker and S. Weinzierl, *Direct numerical integration for multi-loop integrals*, Eur. Phys. J. **C73** (2013) no. 2, 2321, arXiv:1211.0509 [hep-ph].

[41] M. Czakon, P. Fiedler, and A. Mitov, *Total Top-Quark Pair-Production Cross Section at Hadron Colliders Through $O(\alpha_S^4)$*, Phys. Rev. Lett. **110** (2013) 252004, arXiv:1303.6254 [hep-ph].

[42] C. Bogner, A. Schweitzer, and S. Weinzierl, *Analytic continuation and numerical evaluation of the kite integral and the equal mass sunrise integral*, Nucl. Phys. **B922** (2017) 528–550, arXiv:1705.08952 [hep-ph].

[43] S. Borowka, G. Heinrich, S. Jahn, S. P. Jones, M. Kerner, J. Schlenk, and T. Zirke, *pySecDec: a toolbox for the numerical evaluation of multi-scale integrals*, Comput. Phys. Commun. **222** (2018) 313–326, arXiv:1703.09692 [hep-ph].

[44] A. Gehrmann-De Ridder, T. Gehrmann, and E. W. N. Glover, *Antenna subtraction at NNLO*, JHEP **09** (2005) 056, arXiv:hep-ph/0505111 [hep-ph].

[45] G. Heinrich, *A numerical method for NNLO calculations*, Nucl. Phys. Proc. Suppl. **116** (2003) 368–372, arXiv:hep-ph/0211144 [hep-ph]. [,368(2002)].

[46] M. Czakon, *A novel subtraction scheme for double-real radiation at NNLO*, Phys. Lett. **B693** (2010) 259–268, arXiv:1005.0274 [hep-ph].

[47] R. Boughezal, K. Melnikov, and F. Petriello, *A subtraction scheme for NNLO computations*, Phys. Rev. **D85** (2012) 034025, arXiv:1111.7041 [hep-ph].

[48] M. Czakon and D. Heymes, *Four-dimensional formulation of the sector-improved residue subtraction scheme*, Nucl. Phys. **B890** (2014) 152–227, arXiv:1408.2500 [hep-ph].

[49] F. Caola, K. Melnikov, and R. Röntsch, *Nested soft-collinear subtractions in NNLO QCD computations*, Eur. Phys. J. **C77** (2017) no. 4, 248, arXiv:1702.01352 [hep-ph].

[50] V. Del Duca, C. Duhr, A. Kardos, G. Somogyi, and Z. Trócsányi, *Three-Jet Production in Electron-Positron Collisions at Next-to-Next-to-Leading Order Accuracy*, Phys. Rev. Lett. **117** (2016) no. 15, 152004, arXiv:1603.08927 [hep-ph].

[51] M. Cacciari, F. A. Dreyer, A. Karlberg, G. P. Salam, and G. Zanderighi, *Fully Differential Vector-Boson-Fusion Higgs Production at Next-to-Next-to-Leading Order*, Phys. Rev. Lett. **115** (2015) no. 8, 082002, arXiv:1506.02660 [hep-ph]. [Erratum: Phys. Rev. Lett.120,no.13,139901(2018)].

[52] S. Catani, L. Cieri, G. Ferrera, D. de Florian, and M. Grazzini, *Vector boson production at hadron colliders: a fully exclusive QCD calculation at NNLO*, Phys. Rev. Lett. **103** (2009) 082001, arXiv:0903.2120 [hep-ph].

[53] R. Boughezal, C. Focke, X. Liu, and F. Petriello, *W-boson production in association with a jet at next-to-next-to-leading order in perturbative QCD*, Phys. Rev. Lett. **115** (2015) no. 6, 062002, arXiv:1504.02131 [hep-ph].

[54] J. Gaunt, M. Stahlhofen, F. J. Tackmann, and J. R. Walsh, *N-jettiness Subtractions for NNLO QCD Calculations*, JHEP **09** (2015) 058, arXiv:1505.04794 [hep-ph].

[55] S. Badger, H. Frellesvig, and Y. Zhang, *Hepta-Cuts of Two-Loop Scattering Amplitudes*, JHEP **04** (2012) 055, arXiv:1202.2019 [hep-ph].

[56] S. Badger, H. Frellesvig, and Y. Zhang, *A Two-Loop Five-Gluon Helicity Amplitude in QCD*, JHEP **12** (2013) 045, arXiv:1310.1051 [hep-ph].

[57] S. Badger, G. Mogull, A. Ochirov, and D. O'Connell, *A Complete Two-Loop, Five-Gluon Helicity Amplitude in Yang-Mills Theory*, JHEP **10** (2015) 064, arXiv:1507.08797 [hep-ph].

[58] T. Gehrmann, J. M. Henn, and N. A. Lo Presti, *Analytic form of the two-loop planar five-gluon all-plus-helicity amplitude in QCD*, Phys. Rev. Lett. **116** (2016) no. 6, 062001, arXiv:1511.05409 [hep-ph]. [Erratum: Phys. Rev. Lett.116,no.18,189903(2016)].

[59] S. Badger, G. Mogull, and T. Peraro, *Local integrands for two-loop all-plus Yang-Mills amplitudes*, JHEP **08** (2016) 063, arXiv:1606.02244 [hep-ph].

[60] D. C. Dunbar, G. R. Jehu, and W. B. Perkins, *Two-loop six gluon all plus helicity amplitude*, Phys. Rev. Lett. **117** (2016) no. 6, 061602, arXiv:1605.06351 [hep-th].

[61] S. Badger, C. Brønnum-Hansen, H. B. Hartanto, and T. Peraro, *First look at two-loop five-gluon scattering in QCD*, Phys. Rev. Lett. **120** (2018) no. 9, 092001, arXiv:1712.02229 [hep-ph].

[62] S. Abreu, F. Febres Cordero, H. Ita, B. Page, and M. Zeng, *Planar Two-Loop Five-Gluon Amplitudes from Numerical Unitarity*, Phys. Rev. **D97** (2018) no. 11, 116014, arXiv:1712.03946 [hep-ph].

[63] C. Anastasiou, C. Duhr, F. Dulat, E. Furlan, T. Gehrmann, F. Herzog, A. Lazopoulos, and B. Mistlberger, *High precision determination of the gluon fusion Higgs boson cross-section at the LHC*, JHEP **05** (2016) 058, arXiv:1602.00695 [hep-ph].

[64] B. Mistlberger, *Higgs boson production at hadron colliders at N^3LO in QCD*, JHEP **05** (2018) 028, arXiv:1802.00833 [hep-ph].

[65] F. A. Dreyer and A. Karlberg, *Vector-Boson Fusion Higgs Production at Three Loops in QCD*, Phys. Rev. Lett. **117** (2016) no. 7, 072001, arXiv:1606.00840 [hep-ph].

[66] W. Bizon, P. F. Monni, E. Re, L. Rottoli, and P. Torrielli, *Momentum-space resummation for transverse observables and the Higgs $p_\perp$ at N^3LL+NNLO*, JHEP **02** (2018) 108, arXiv:1705.09127 [hep-ph].

[67] X. Chen, T. Gehrmann, E. W. N. Glover, A. Huss, Y. Li, D. Neill, M. Schulze, I. W. Stewart, and H. X. Zhu, *Precise QCD Description of the Higgs Boson Transverse Momentum Spectrum*, Phys. Lett. **B788** (2019) 425–430, arXiv:1805.00736 [hep-ph].

[68] W. Bizoń, X. Chen, A. Gehrmann-De Ridder, T. Gehrmann, N. Glover, A. Huss, P. F. Monni, E. Re, L. Rottoli, and P. Torrielli, *Fiducial distributions in Higgs and Drell-Yan production at N^3LL+NNLO*, JHEP **12** (2018) 132, arXiv:1805.05916 [hep-ph].

[69] J. C. Collins, D. E. Soper, and G. F. Sterman, *Transverse Momentum Distribution in Drell-Yan Pair and W and Z Boson Production*, Nucl. Phys. **B250** (1985) 199–224.

[70] S. Catani, L. Trentadue, G. Turnock, and B. R. Webber, *Resummation of large logarithms in e+ e- event shape distributions*, Nucl. Phys. **B407** (1993) 3–42.

[71] C. W. Bauer, D. Pirjol, and I. W. Stewart, *Soft collinear factorization in effective field theory*, Phys. Rev. **D65** (2002) 054022, arXiv:hep-ph/0109045 [hep-ph].

[72] C. W. Bauer and P. F. Monni, *A numerical formulation of resummation in effective field theory*, arXiv:1803.07079 [hep-ph].

[73] M. Dasgupta, F. A. Dreyer, K. Hamilton, P. F. Monni, and G. P. Salam, *Logarithmic accuracy of parton showers: a fixed-order study*, JHEP **09** (2018) 033, arXiv:1805.09327 [hep-ph].

[74] Z. Nagy and D. E. Soper, *Effects of subleading color in a parton shower*, JHEP **07** (2015) 119, arXiv:1501.00778 [hep-ph].

[75] S. Jadach, A. Kusina, W. Placzek, and M. Skrzypek, *On the dependence of QCD splitting functions on the choice of the evolution variable*, JHEP **08** (2016) 092, arXiv:1606.01238 [hep-ph].

[76] S. Höche and S. Prestel, *Triple collinear emissions in parton showers*, Phys. Rev. **D96** (2017) no. 7, 074017, arXiv:1705.00742 [hep-ph].

[77] S. Höche and S. Prestel, *The midpoint between dipole and parton showers*, Eur. Phys. J. **C75** (2015) no. 9, 461, arXiv:1506.05057 [hep-ph].

[78] N. Fischer, S. Prestel, M. Ritzmann, and P. Skands, *Vincia for Hadron Colliders*, Eur. Phys. J. **C76** (2016) no. 11, 589, arXiv:1605.06142 [hep-ph].

[79] S. Alioli, C. W. Bauer, C. Berggren, F. J. Tackmann, J. R. Walsh, and S. Zuberi, *Matching Fully Differential NNLO Calculations and Parton Showers*, JHEP **06** (2014) 089, arXiv:1311.0286 [hep-ph].

[80] K. Hamilton, P. Nason, E. Re, and G. Zanderighi, *NNLOPS simulation of Higgs boson production*, JHEP **10** (2013) 222, arXiv:1309.0017 [hep-ph].

[81] S. Höche, Y. Li, and S. Prestel, *Drell-Yan lepton pair production at NNLO QCD with parton showers*, Phys. Rev. **D91** (2015) no. 7, 074015, arXiv:1405.3607 [hep-ph].

[82] S. Actis, A. Denner, L. Hofer, J.-N. Lang, A. Scharf, and S. Uccirati, *RECOLA: REcursive Computation of One-Loop Amplitudes*, Comput. Phys. Commun. **214** (2017) 140–173, arXiv:1605.01090 [hep-ph].

[83] S. Actis, A. Denner, L. Hofer, A. Scharf, and S. Uccirati, *Recursive generation of one-loop amplitudes in the Standard Model*, JHEP **04** (2013) 037, arXiv:1211.6316 [hep-ph].

[84] T. Gleisberg, S. Hoeche, F. Krauss, M. Schonherr, S. Schumann, F. Siegert, and J. Winter, *Event generation with SHERPA 1.1*, JHEP **02** (2009) 007, arXiv:0811.4622 [hep-ph].

[85] M. Schönherr, *An automated subtraction of NLO EW infrared divergences*, Eur. Phys. J. **C78** (2018) no. 2, 119, arXiv:1712.07975 [hep-ph].

[86] G. Cullen, N. Greiner, G. Heinrich, G. Luisoni, P. Mastrolia, G. Ossola, T. Reiter, and F. Tramontano, *Automated One-Loop Calculations with GoSam*, Eur. Phys. J. **C72** (2012) 1889, arXiv:1111.2034 [hep-ph].

[87] R. Frederix, T. Gehrmann, and N. Greiner, *Automation of the Dipole Subtraction Method in MadGraph/MadEvent*, JHEP **09** (2008) 122, arXiv:0808.2128 [hep-ph].

[88] T. Gehrmann and N. Greiner, *Photon Radiation with MadDipole*, JHEP **12** (2010) 050, arXiv:1011.0321 [hep-ph].

[89] R. Frederix, S. Frixione, V. Hirschi, D. Pagani, H. S. Shao, and M. Zaro, *The automation of next-to-leading order electroweak calculations*, JHEP **07** (2018) 185, arXiv:1804.10017 [hep-ph].

[90] J. R. Andersen et al., *Les Houches 2015: Physics at TeV Colliders Standard Model Working Group Report*, in *9th Les Houches Workshop on Physics at TeV Colliders (PhysTeV 2015) Les Houches, France, June 1-19, 2015*. 2016. arXiv:1605.04692 [hep-ph]. http://lss.fnal.gov/archive/2016/conf/fermilab-conf-16-175-ppd-t.pdf.

[91] J. R. Andersen et al., *Les Houches 2017: Physics at TeV Colliders Standard Model Working Group Report*, in *10th Les Houches Workshop on Physics at TeV Colliders (PhysTeV 2017) Les Houches, France, June 5-23, 2017*. 2018. arXiv:1803.07977 [hep-ph]. http://lss.fnal.gov/archive/2018/conf/fermilab-conf-18-122-cd-t.pdf.

[92] A. Denner, L. Hofer, A. Scharf, and S. Uccirati, *Electroweak corrections to lepton pair production in association with two hard jets at the LHC*, JHEP **01** (2015) 094, arXiv:1411.0916 [hep-ph].

[93] A. Denner, R. Feger, and A. Scharf, *Irreducible background and interference effects for Higgs-boson production in association with a top-quark pair*, JHEP **04** (2015) 008, arXiv:1412.5290 [hep-ph].

[94] A. Denner and R. Feger, *NLO QCD corrections to off-shell top-antitop production with leptonic decays in association with a Higgs boson at the LHC*, JHEP **11** (2015) 209, arXiv:1506.07448 [hep-ph].

[95] S. Kallweit, J. M. Lindert, P. Maierhöfer, S. Pozzorini, and M. Schönherr, *NLO electroweak automation and precise predictions for W+multijet production at the LHC*, JHEP **04** (2015) 012, arXiv:1412.5157 [hep-ph].

[96] S. Frixione, V. Hirschi, D. Pagani, H. S. Shao, and M. Zaro, *Weak corrections to Higgs hadroproduction in association with a top-quark pair*, JHEP **09** (2014) 065, arXiv:1407.0823 [hep-ph].

[97] M. Chiesa, N. Greiner, and F. Tramontano, *Automation of electroweak corrections for LHC processes*, J. Phys. **G43** (2016) no. 1, 013002, arXiv:1507.08579 [hep-ph].

[98] S. Kallweit, J. M. Lindert, P. Maierhofer, S. Pozzorini, and M. Schönherr, *NLO QCD+EW predictions for V + jets including off-shell vector-boson decays and multijet merging*, JHEP **04** (2016) 021, arXiv:1511.08692 [hep-ph].

[99] S. Frixione, V. Hirschi, D. Pagani, H. S. Shao, and M. Zaro, *Electroweak and QCD corrections to top-pair hadroproduction in association with heavy bosons*, JHEP **06** (2015) 184, arXiv:1504.03446 [hep-ph].

[100] B. Biedermann, M. Billoni, A. Denner, S. Dittmaier, L. Hofer, B. Jäger, and L. Salfelder, *Next-to-leading-order electroweak corrections to $pp \to W^+W^- \to 4$ leptons at the LHC*, JHEP **06** (2016) 065, arXiv:1605.03419 [hep-ph].

[101] B. Biedermann, A. Denner, S. Dittmaier, L. Hofer, and B. Jäger, *Electroweak corrections to $pp \to \mu^+\mu^- e^+ e^- + X$ at the LHC: a Higgs background study*, Phys. Rev. Lett. **116** (2016) no. 16, 161803, arXiv:1601.07787 [hep-ph].

[102] A. Denner and M. Pellen, *NLO electroweak corrections to off-shell top-antitop production with leptonic decays at the LHC*, JHEP **08** (2016) 155, arXiv:1607.05571 [hep-ph].

[103] B. Biedermann, A. Denner, and M. Pellen, *Large electroweak corrections to vector-boson scattering at the Large Hadron Collider*, Phys. Rev. Lett. **118** (2017) no. 26, 261801, arXiv:1611.02951 [hep-ph].

[104] B. Biedermann, A. Denner, S. Dittmaier, L. Hofer, and B. Jager, *Next-to-leading-order electroweak corrections to the production of four charged leptons at the LHC*, JHEP **01** (2017) 033, arXiv:1611.05338 [hep-ph].

[105] A. Denner, J.-N. Lang, M. Pellen, and S. Uccirati, *Higgs production in association with off-shell top-antitop pairs at NLO EW and QCD at the LHC*, JHEP **02** (2017) 053, arXiv:1612.07138 [hep-ph].

[106] R. Frederix, S. Frixione, V. Hirschi, D. Pagani, H.-S. Shao, and M. Zaro, *The complete NLO corrections to dijet hadroproduction*, JHEP **04** (2017) 076, arXiv:1612.06548 [hep-ph].

[107] D. Pagani, I. Tsinikos, and M. Zaro, *The impact of the photon PDF and electroweak corrections on $t\bar{t}$ distributions*, Eur. Phys. J. **C76** (2016) no. 9, 479, arXiv:1606.01915 [hep-ph].

[108] B. Biedermann, S. Bräuer, A. Denner, M. Pellen, S. Schumann, and J. M. Thompson, *Automation of NLO QCD and EW corrections with Sherpa and Recola*, Eur. Phys. J. **C77** (2017) 492, arXiv:1704.05783 [hep-ph].

[109] S. Kallweit, J. M. Lindert, S. Pozzorini, and M. Schönherr, *NLO QCD+EW predictions for $2\ell 2\nu$ diboson signatures at the LHC*, JHEP **11** (2017) 120, arXiv:1705.00598 [hep-ph].

[110] M. Chiesa, N. Greiner, M. Schönherr, and F. Tramontano, *Electroweak corrections to diphoton plus jets*, JHEP **10** (2017) 181, arXiv:1706.09022 [hep-ph].

[111] B. Biedermann, A. Denner, and M. Pellen, *Complete NLO corrections to W^+W^+ scattering and its irreducible background at the LHC*, JHEP **10** (2017) 124, arXiv:1708.00268 [hep-ph].

[112] B. Biedermann, A. Denner, and L. Hofer, *Next-to-leading-order electroweak corrections to the production of three charged leptons plus missing energy at the LHC*, JHEP **10** (2017) 043, arXiv:1708.06938 [hep-ph].

[113] M. Czakon, D. Heymes, A. Mitov, D. Pagani, I. Tsinikos, and M. Zaro, *Top-pair production at the LHC through NNLO QCD and NLO EW*, JHEP **10** (2017) 186, arXiv:1705.04105 [hep-ph].

[114] N. Greiner and M. Schönherr, *NLO QCD+EW corrections to diphoton production in association with a vector boson*, JHEP **01** (2018) 079, arXiv:1710.11514 [hep-ph].

[115] R. Frederix, D. Pagani, and M. Zaro, *Large NLO corrections in $t\bar{t}W^{\pm}$ and $t\bar{t}t\bar{t}$ hadroproduction from supposedly subleading EW contributions*, JHEP **02** (2018) 031, arXiv:1711.02116 [hep-ph].

[116] C. Gütschow, J. M. Lindert, and M. Schönherr, *Multi-jet merged top-pair production including electroweak corrections*, Eur. Phys. J. **C78** (2018) no. 4, 317, arXiv:1803.00950 [hep-ph].

[117] M. Schönherr, *Next-to-leading order electroweak corrections to off-shell WWW production at the LHC*, JHEP **07** (2018) 076, arXiv:1806.00307 [hep-ph].

[118] S. Dittmaier, A. Huss, and C. Schwinn, *Mixed QCD-electroweak $O(\alpha_s\alpha)$ corrections to Drell-Yan processes in the resonance region: pole approximation and non-factorizable corrections*, Nucl. Phys. **B885** (2014) 318–372, arXiv:1403.3216 [hep-ph].

[119] S. Dittmaier, A. Huss, and C. Schwinn, *Dominant mixed QCD-electroweak $O(\alpha_s\alpha)$ corrections to Drell–Yan processes in the resonance region*, Nucl. Phys. **B904** (2016) 216–252, arXiv:1511.08016 [hep-ph].

[120] A. Kotikov, J. H. Kuhn, and O. Veretin, *Two-Loop Formfactors in Theories with Mass Gap and Z-Boson Production*, Nucl. Phys. **B788** (2008) 47–62, arXiv:hep-ph/0703013 [HEP-PH].

[121] W. B. Kilgore and C. Sturm, *Two-Loop Virtual Corrections to Drell-Yan Production at order $\alpha_s\alpha^3$*, Phys. Rev. **D85** (2012) 033005, arXiv:1107.4798 [hep-ph].

[122] R. Bonciani, *Two-loop mixed QCD-EW virtual corrections to the Drell-Yan production of Z and W bosons*, PoS **EPS-HEP2011** (2011) 365.

[123] R. Bonciani, S. Di Vita, P. Mastrolia, and U. Schubert, *Two-Loop Master Integrals for the mixed EW-QCD virtual corrections to Drell-Yan scattering*, JHEP **09** (2016) 091, arXiv:1604.08581 [hep-ph].

[124] A. von Manteuffel and R. M. Schabinger, *Numerical Multi-Loop Calculations via Finite Integrals and One-Mass EW-QCD Drell-Yan Master Integrals*, JHEP **04** (2017) 129, arXiv:1701.06583 [hep-ph].

[125] R. Bonciani, F. Buccioni, R. Mondini, and A. Vicini, *Double-real corrections at $\mathcal{O}(\alpha\alpha_s)$ to single gauge boson production*, Eur. Phys. J. **C77** (2017) no. 3, 187, arXiv:1611.00645 [hep-ph].

[126] C. Anastasiou, R. Boughezal, and F. Petriello, *Mixed QCD-electroweak corrections to Higgs boson production in gluon fusion*, JHEP **04** (2009) 003, arXiv:0811.3458 [hep-ph].

[127] M. Bonetti, K. Melnikov, and L. Tancredi, *Higher order corrections to mixed QCD-EW contributions to Higgs boson production in gluon fusion*, Phys. Rev. **D97** (2018) no. 5, 056017, arXiv:1801.10403 [hep-ph]. [Erratum: Phys. Rev.D97,no.9,099906(2018)].

[128] C. Anastasiou, V. Del Duca, E. Furlan, B. Mistlberger, F. Moriello, A. Schweitzer, and C. Specchia, *Mixed QCD-electroweak corrections to Higgs production via gluon fusion in the small mass approximation*, arXiv:1811.11211 [hep-ph].

[129] J. M. Lindert et al., *Precise predictions for $V+$ jets dark matter backgrounds*, Eur. Phys. J. **C77** (2017) no. 12, 829, arXiv:1705.04664 [hep-ph].

[130] A. Denner and S. Pozzorini, *One loop leading logarithms in electroweak radiative corrections. 1. Results*, Eur. Phys. J. **C18** (2001) 461–480, arXiv:hep-ph/0010201 [hep-ph].

[131] A. Denner and S. Pozzorini, *One loop leading logarithms in electroweak radiative corrections. 2. Factorization of collinear singularities*, Eur. Phys. J. **C21** (2001) 63–79, arXiv:hep-ph/0104127 [hep-ph].

[132] J.-y. Chiu, F. Golf, R. Kelley, and A. V. Manohar, *Electroweak Sudakov corrections using effective field theory*, Phys. Rev. Lett. **100** (2008) 021802, arXiv:0709.2377 [hep-ph].

[133] J.-y. Chiu, R. Kelley, and A. V. Manohar, *Electroweak Corrections using Effective Field Theory: Applications to the LHC*, Phys. Rev. **D78** (2008) 073006, arXiv:0806.1240 [hep-ph].

[134] M. L. Mangano et al., *Physics at a 100 TeV pp Collider: Standard Model Processes*, CERN Yellow Report (2017) no. 3, 1–254, arXiv:1607.01831 [hep-ph].

[135] C. Bernaciak and D. Wackeroth, *Combining NLO QCD and Electroweak Radiative Corrections to W boson Production at Hadron Colliders in the POWHEG Framework*, Phys. Rev. **D85** (2012) 093003, arXiv:1201.4804 [hep-ph].

[136] L. Barze, G. Montagna, P. Nason, O. Nicrosini, and F. Piccinini, *Implementation of electroweak corrections in the POWHEG BOX: single W production*, JHEP **04** (2012) 037, arXiv:1202.0465 [hep-ph].

[137] L. Barze, G. Montagna, P. Nason, O. Nicrosini, F. Piccinini, and A. Vicini, *Neutral current Drell-Yan with combined QCD and electroweak corrections in the POWHEG BOX*, Eur. Phys. J. **C73** (2013) no. 6, 2474, arXiv:1302.4606 [hep-ph].

[138] A. Mück and L. Oymanns, *Resonace-improved parton-shower matching for the Drell-Yan process including electroweak corrections*, JHEP **05** (2017) 090, arXiv:1612.04292 [hep-ph].

[139] F. Granata, J. M. Lindert, C. Oleari, and S. Pozzorini, *NLO QCD+EW predictions for HV and HV +jet production including parton-shower effects*, JHEP **09** (2017) 012, arXiv:1706.03522 [hep-ph].

[140] M. Chiesa, G. Montagna, L. Barze, M. Moretti, O. Nicrosini, F. Piccinini, and F. Tramontano, *Electroweak Sudakov Corrections to New Physics Searches at the LHC*, Phys. Rev. Lett. **111** (2013) no. 12, 121801, arXiv:1305.6837 [hep-ph].

[141] J. R. Christiansen and T. Sjöstrand, *Weak Gauge Boson Radiation in Parton Showers*, JHEP **04** (2014) 115, arXiv:1401.5238 [hep-ph].

[142] F. Krauss, P. Petrov, M. Schoenherr, and M. Spannowsky, *Measuring collinear W emissions inside jets*, Phys. Rev. **D89** (2014) no. 11, 114006, arXiv:1403.4788 [hep-ph].

[143] C. W. Bauer, N. Ferland, and B. R. Webber, *Standard Model Parton Distributions at Very High Energies*, JHEP **08** (2017) 036.

[144] J. Chen, T. Han, and B. Tweedie, *Electroweak Splitting Functions and High Energy Showering*, JHEP **11** (2017) 093, arXiv:1611.00788 [hep-ph].

[145] G. Corcella, I. G. Knowles, G. Marchesini, S. Moretti, K. Odagiri, P. Richardson, M. H. Seymour, and B. R. Webber, *HERWIG 6: An Event generator for hadron emission reactions with interfering gluons (including supersymmetric processes)*, JHEP **01** (2001) 010, arXiv:hep-ph/0011363 [hep-ph].

[146] M. Bahr et al., *Herwig++ Physics and Manual*, Eur. Phys. J. **C58** (2008) 639–707, arXiv:0803.0883 [hep-ph].

[147] J. Bellm et al., *Herwig 7.0/Herwig++ 3.0 release note*, Eur. Phys. J. **C76** (2016) no. 4, 196, arXiv:1512.01178 [hep-ph].

[148] T. Sjostrand, S. Mrenna, and P. Z. Skands, *PYTHIA 6.4 Physics and Manual*, JHEP **05** (2006) 026, arXiv:0603175 [hep-ph].

[149] T. Sjöstrand, S. Ask, J. R. Christiansen, R. Corke, N. Desai, P. Ilten, S. Mrenna, S. Prestel, C. O. Rasmussen, and P. Z. Skands, *An Introduction to PYTHIA 8.2*, Comput. Phys. Commun. **191** (2015) 159–177, arXiv:1410.3012 [hep-ph].

[150] S. Frixione and B. R. Webber, *Matching NLO QCD computations and parton shower simulations*, JHEP **06** (2002) 029, arXiv:hep-ph/0204244 [hep-ph].

[151] P. Nason, *A New Method for Combining NLO QCD with Shower Monte Carlo Algorithms*, JHEP **11** (2004) 040, arXiv:0409146 [hep-ph].

[152] S. Jadach, W. Płaczek, S. Sapeta, A. Siódmok, and M. Skrzypek, *Matching NLO QCD with parton shower in Monte Carlo scheme — the KrkNLO method*, JHEP **10** (2015) 052, arXiv:1503.06849 [hep-ph].

[153] E. Re, M. Wiesemann, and G. Zanderighi, *NNLOPS accurate predictions for W^+W^- production*, JHEP **12** (2018) 121, arXiv:1805.09857 [hep-ph].

[154] S. Höche, Y. Li, and S. Prestel, *Higgs-boson production through gluon fusion at NNLO QCD with parton showers*, Phys. Rev. **D90** (2014) no. 5, 054011, arXiv:1407.3773 [hep-ph].

[155] S. Alioli, C. W. Bauer, C. Berggren, F. J. Tackmann, and J. R. Walsh, *Drell-Yan production at NNLL'+NNLO matched to parton showers*, Phys. Rev. **D92** (2015) no. 9, 094020, arXiv:1508.01475 [hep-ph].

[156] S. Catani, F. Krauss, R. Kuhn, and B. R. Webber, *QCD matrix elements + parton showers*, JHEP **11** (2001) 063, arXiv:hep-ph/0109231 [hep-ph].

[157] R. Frederix and S. Frixione, *Merging meets matching in MC@NLO*, JHEP **12** (2012) 061, arXiv:1209.6215 [hep-ph].

[158] L. Lönnblad and S. Prestel, *Merging Multi-leg NLO Matrix Elements with Parton Showers*, JHEP **03** (2013) 166, arXiv:1211.7278 [hep-ph].

[159] S. Hoeche, F. Krauss, M. Schonherr, and F. Siegert, *QCD matrix elements + parton showers: The NLO case*, JHEP **04** (2013) 027, arXiv:1207.5030 [hep-ph].

[160] S. Alioli, C. W. Bauer, C. J. Berggren, A. Hornig, F. J. Tackmann, C. K. Vermilion, J. R. Walsh, and S. Zuberi, *Combining Higher-Order Resummation with Multiple NLO Calculations and Parton Showers in GENEVA*, JHEP **09** (2013) 120, arXiv:1211.7049 [hep-ph].

[161] S. Alioli, C. W. Bauer, S. Guns, and F. J. Tackmann, *Underlying event sensitive observables in Drell-Yan production using GENEVA*, Eur. Phys. J. **C76** (2016) no. 11, 614, arXiv:1605.07192 [hep-ph].

[162] K. Hamilton, P. Nason, C. Oleari, and G. Zanderighi, *Merging H/W/Z + 0 and 1 jet at NLO with no merging scale: a path to parton shower + NNLO matching*, JHEP **05** (2013) 082, arXiv:1212.4504 [hep-ph].

[163] R. Frederix and K. Hamilton, *Extending the MINLO method*, JHEP **05** (2016) 042, arXiv:1512.02663 [hep-ph].

[164] F. Maltoni, E. Vryonidou, and M. Zaro, *Top-quark mass effects in double and triple Higgs production in gluon-gluon fusion at NLO*, JHEP **11** (2014) 079, arXiv:1408.6542 [hep-ph].

[165] G. Heinrich, S. P. Jones, M. Kerner, G. Luisoni, and E. Vryonidou, *NLO predictions for Higgs boson pair production with full top quark mass dependence matched to parton showers*, JHEP **08** (2017) 088, arXiv:1703.09252 [hep-ph].

[166] S. Borowka, N. Greiner, G. Heinrich, S. Jones, M. Kerner, J. Schlenk, U. Schubert, and T. Zirke, *Higgs Boson Pair Production in Gluon Fusion at Next-to-Leading Order with Full Top-Quark Mass Dependence*, Phys. Rev. Lett. **117** (2016) no. 1, 012001, arXiv:1604.06447 [hep-ph]. [Erratum: Phys. Rev. Lett.117,no.7,079901(2016)].

[167] S. Borowka, N. Greiner, G. Heinrich, S. P. Jones, M. Kerner, J. Schlenk, and T. Zirke, *Full top quark mass dependence in Higgs boson pair production at NLO*, JHEP **10** (2016) 107, arXiv:1608.04798 [hep-ph].

[168] T. Ježo and P. Nason, *On the Treatment of Resonances in Next-to-Leading Order Calculations Matched to a Parton Shower*, JHEP **12** (2015) 065, arXiv:1509.09071 [hep-ph].

[169] T. Ježo, J. M. Lindert, P. Nason, C. Oleari, and S. Pozzorini, *An NLO+PS generator for $t\bar{t}$ and Wt production and decay including non-resonant and interference effects*, Eur. Phys. J. **C76** (2016) no. 12, 691, arXiv:1607.04538 [hep-ph].

[170] R. Frederix, S. Frixione, A. S. Papanastasiou, S. Prestel, and P. Torrielli, *Off-shell single-top production at NLO matched to parton showers*, JHEP **06** (2016) 027, arXiv:1603.01178 [hep-ph].

[171] W. T. Giele, D. A. Kosower, and P. Z. Skands, *A simple shower and matching algorithm*, Phys. Rev. **D78** (2008) 014026, arXiv:0707.3652 [hep-ph].

[172] Z. Nagy and D. E. Soper, *Jets and threshold summation in Deductor*, Phys. Rev. **D98** (2018) no. 1, 014035, arXiv:1711.02369 [hep-ph].

[173] S. Jadach, A. Kusina, M. Skrzypek, and M. Slawinska, *Monte Carlo modelling of NLO DGLAP QCD evolution in the fully unintegrated form*, Nucl. Phys. Proc. Suppl. **205-206** (2010) 295–300, arXiv:1007.2437 [hep-ph].

[174] S. Höche, F. Krauss, and S. Prestel, *Implementing NLO DGLAP evolution in Parton Showers*, JHEP **10** (2017) 093, arXiv:1705.00982 [hep-ph].

[175] F. Dulat, S. Höche, and S. Prestel, *Leading-Color Fully Differential Two-Loop Soft Corrections to QCD Dipole Showers*, Phys. Rev. **D98** (2018) no. 7, 074013, arXiv:1805.03757 [hep-ph].

[176] J. Bellm, S. Plätzer, P. Richardson, A. Siódmok, and S. Webster, *Reweighting Parton Showers*, Phys. Rev. **D94** (2016) no. 3, 034028, arXiv:1605.08256 [hep-ph].

[177] J. Bellm, G. Nail, S. Plätzer, P. Schichtel, and A. Siódmok, *Parton Shower Uncertainties with Herwig 7: Benchmarks at Leading Order*, Eur. Phys. J. **C76** (2016) no. 12, 665, arXiv:1605.01338 [hep-ph].

[178] S. Mrenna and P. Skands, *Automated Parton-Shower Variations in Pythia 8*, Phys. Rev. **D94** (2016) no. 7, 074005, arXiv:1605.08352 [hep-ph].

[179] E. Bothmann, M. Schönherr, and S. Schumann, *Reweighting QCD matrix-element and parton-shower calculations*, Eur. Phys. J. **C76** (2016) no. 11, 590, arXiv:1606.08753 [hep-ph].

[180] O. Mattelaer, *On the maximal use of Monte Carlo samples: re-weighting events at NLO accuracy*, Eur. Phys. J. **C76** (2016) no. 12, 674, arXiv:1607.00763 [hep-ph].

[181] J. Bendavid, *Efficient Monte Carlo Integration Using Boosted Decision Trees and Generative Deep Neural Networks*, arXiv:1707.00028 [hep-ph].

[182] T. Sjöstrand, *Collective Effects: the viewpoint of HEP MC codes*, Nucl. Phys. **A982** (2019) 43–49, arXiv:1808.03117 [hep-ph].

[183] J. Bellm and C. Bierlich, *PISTA: Posterior Ion STAcking*, arXiv:1807.01291 [hep-ph].

[184] C. Bierlich, G. Gustafson, L. Lönnblad, and H. Shah, *The Angantyr model for Heavy-Ion Collisions in PYTHIA8*, JHEP **10** (2018) 134, arXiv:1806.10820 [hep-ph]. [JHEP18,134(2020)].

[185] B. Andersson, G. Gustafson, and B. Nilsson-Almqvist, *A Model for Low p(t) Hadronic Reactions, with Generalizations to Hadron - Nucleus and Nucleus-Nucleus Collisions*, Nucl. Phys. **B281** (1987) 289–309.

[186] LHC Higgs Cross Section Working Group Collaboration, D. de Florian et al., *Handbook of LHC Higgs Cross Sections: 4. Deciphering the Nature of the Higgs Sector*, arXiv:1610.07922 [hep-ph].

[187] W. Beenakker, C. Borschensky, M. Kramer, A. Kulesza, E. Laenen, S. Marzani, and J. Rojo, *NLO+NLL squark and gluino production cross-sections with threshold-improved parton distributions*, Eur. Phys. J. **C76** (2016) no. 2, 53.

[188] S. Alioli, M. Farina, D. Pappadopulo, and J. T. Ruderman, *Precision Probes of QCD at High Energies*, JHEP **07** (2017) 097.

[189] ATLAS Collaboration, M. Aaboud et al., *Measurement of the W-boson mass in pp collisions at $\sqrt{s} = 7$ TeV with the ATLAS detector*, Eur. Phys. J. **C78** (2018) no. 2, 110, arXiv:1701.07240 [hep-ex]. [Erratum: Eur. Phys. J.C78,no.11,898(2018)].

[190] CDF, D0 Collaboration, T. A. Aaltonen et al., *Tevatron Run II combination of the effective leptonic electroweak mixing angle*, Phys. Rev. **D97** (2018) no. 11, 112007, arXiv:1801.06283 [hep-ex].

[191] R. D. Ball, S. Carrazza, L. Del Debbio, S. Forte, Z. Kassabov, J. Rojo, E. Slade, and M. Ubiali, *Precision determination of the strong coupling constant within a global PDF analysis*, Eur. Phys. J. **C78** (2018) no. 5, 408.

[192] J. Gao, L. Harland-Lang, and J. Rojo, *The Structure of the Proton in the LHC Precision Era*, Phys. Rept. **742** (2018) 1–121.

[193] J. Rojo et al., *The PDF4LHC report on PDFs and LHC data: Results from Run I and preparation for Run II*, J. Phys. **G42** (2015) 103103.

[194] S. Forte and G. Watt, *Progress in the Determination of the Partonic Structure of the Proton*, Ann. Rev. Nucl. Part. Sci. **63** (2013) 291–328, arXiv:1301.6754 [hep-ph].

[195] J. Butterworth et al., *PDF4LHC recommendations for LHC Run II*, J. Phys. **G43** (2016) 023001, arXiv:1510.03865 [hep-ph].

[196] J. Gao and P. Nadolsky, *A meta-analysis of parton distribution functions*, JHEP **1407** (2014) 035.

[197] S. Carrazza, J. I. Latorre, J. Rojo, and G. Watt, *A compression algorithm for the combination of PDF sets*, Eur. Phys. J. **C75** (2015) 474.

[198] S. Carrazza, S. Forte, Z. Kassabov, J. I. Latorre, and J. Rojo, *An Unbiased Hessian Representation for Monte Carlo PDFs*, Eur. Phys. J. **C75** (2015) no. 8, 369.

[199] S. Dulat, T.-J. Hou, J. Gao, M. Guzzi, J. Huston, P. Nadolsky, J. Pumplin, C. Schmidt, D. Stump, and C. P. Yuan, *New parton distribution functions from a global analysis of quantum chromodynamics*, Phys. Rev. D **93** (2016) no. 3, 033006, arXiv:1506.07443 [hep-ph].

[200] L. A. Harland-Lang, A. D. Martin, P. Motylinski, and R. S. Thorne, *Parton distributions in the LHC era: MMHT 2014 PDFs*, Eur. Phys. J. C **75** (2015) no. 5, 204, arXiv:1412.3989 [hep-ph].

[201] NNPDF Collaboration, R. D. Ball et al., *Parton distributions for the LHC Run II*, JHEP **04** (2015) 040, arXiv:1410.8849 [hep-ph].

[202] A. Buckley, J. Ferrando, S. Lloyd, K. Nordström, B. Page, M. Rüfenacht, M. Schönherr, and G. Watt, *LHAPDF6: parton density access in the LHC precision era*, Eur. Phys. J. **C75** (2015) 132, arXiv:1412.7420 [hep-ph].

[203] M. Czakon, N. P. Hartland, A. Mitov, E. R. Nocera, and J. Rojo, *Pinning down the large-x gluon with NNLO top-quark pair differential distributions*, JHEP **04** (2017) 044.

[204] R. Boughezal, A. Guffanti, F. Petriello, and M. Ubiali, *The impact of the LHC Z-boson transverse momentum data on PDF determinations*, JHEP **07** (2017) 130.

[205] J. M. Campbell, J. Rojo, E. Slade, and C. Williams, *Direct photon production and PDF fits reloaded*, Eur. Phys. J. **C78** (2018) no. 6, 470.

[206] J. Currie, E. W. N. Glover, and J. Pires, *Next-to-Next-to Leading Order QCD Predictions for Single Jet Inclusive Production at the LHC*, Phys. Rev. Lett. **118** (2017) no. 7, 072002, arXiv:1611.01460 [hep-ph].

[207] NNPDF Collaboration, R. D. Ball et al., *Parton distributions from high-precision collider data*, Eur. Phys. J. C **77** (2017) 663, arXiv:1706.00428 [hep-ph].

[208] T. Carli, D. Clements, A. Cooper-Sarkar, C. Gwenlan, G. P. Salam, F. Siegert, P. Starovoitov, and M. Sutton, *A posteriori inclusion of parton density functions in NLO QCD final-state calculations at hadron colliders: The* APPLGRID *project*, Eur. Phys. J. C **66** (2010) 503, arXiv:0911.2985 [hep-ph].

[209] fastNLO Collaboration, M. Wobisch, D. Britzger, T. Kluge, K. Rabbertz, and F. Stober, *Theory-Data Comparisons for Jet Measurements in Hadron-Induced Processes*, arXiv:1109.1310 [hep-ph].

[210] R. Boughezal, J. M. Campbell, R. K. Ellis, C. Focke, W. Giele, X. Liu, F. Petriello, and C. Williams, *Color singlet production at NNLO in MCFM*, Eur. Phys. J. **C77** (2017) no. 1, 7.

[211] Z. Nagy, *Three jet cross-sections in hadron hadron collisions at next-to-leading order*, Phys. Rev. Lett. **88** (2002) 122003, arXiv:hep-ph/0110315 [hep-ph].

[212] V. Bertone, R. Frederix, S. Frixione, J. Rojo, and M. Sutton, *aMCfast: automation of fast NLO computations for PDF fits*, JHEP **1408** (2014) 166.

[213] M. Czakon, D. Heymes, and A. Mitov, *Dynamical scales for multi-TeV top-pair production at the LHC*, JHEP **04** (2017) 071, arXiv:1606.03350 [hep-ph].

[214] M. Czakon, D. Heymes, and A. Mitov, *fastNLO tables for NNLO top-quark pair differential distributions*, arXiv:1704.08551 [hep-ph].

[215] E. Bagnaschi, M. Cacciari, A. Guffanti, and L. Jenniches, *An extensive survey of the estimation of uncertainties from missing higher orders in perturbative calculations*, JHEP **02** (2015) 133.

[216] S. Moch, B. Ruijl, T. Ueda, J. A. M. Vermaseren, and A. Vogt, *Four-Loop Non-Singlet Splitting Functions in the Planar Limit and Beyond*, JHEP **10** (2017) 041.

[217] F. Dulat, B. Mistlberger, and A. Pelloni, *Differential Higgs production at N^3LO beyond threshold*, JHEP **01** (2018) 145.

[218] M. Bonvini, S. Marzani, J. Rojo, L. Rottoli, M. Ubiali, R. D. Ball, V. Bertone, S. Carrazza, and N. P. Hartland, *Parton distributions with threshold resummation*, JHEP **09** (2015) 191.

[219] R. D. Ball, V. Bertone, M. Bonvini, S. Marzani, J. Rojo, and L. Rottoli, *Parton distributions with small-x resummation: evidence for BFKL dynamics in HERA data*, Eur. Phys. J. **C78** (2018) no. 4, 321.

[220] M. Czakon, A. Ferroglia, D. Heymes, A. Mitov, B. D. Pecjak, D. J. Scott, X. Wang, and L. L. Yang, *Resummation for (boosted) top-quark pair production at NNLO+NNLL' in QCD*, JHEP **05** (2018) 149, arXiv:1803.07623 [hep-ph].

[221] K. Mishra et al., *Electroweak Corrections at High Energies*, in *Proceedings, 2013 Community Summer Study on the Future of U.S. Particle Physics: Snowmass on the Mississippi (CSS2013): Minneapolis, MN, USA, July 29-August 6, 2013*. 2013. arXiv:1308.1430 [hep-ph]. http://lss.fnal.gov/archive/2013/conf/fermilab-conf-13-514-cms.pdf.

[222] A. Manohar, P. Nason, G. P. Salam, and G. Zanderighi, *How bright is the proton? A precise determination of the photon parton distribution function*, Phys. Rev. Lett. **117** (2016) no. 24, 242002, arXiv:1607.04266 [hep-ph].

[223] A. V. Manohar, P. Nason, G. P. Salam, and G. Zanderighi, *The Photon Content of the Proton*, JHEP **12** (2017) 046, arXiv:1708.01256 [hep-ph].

[224] NNPDF Collaboration, V. Bertone, S. Carrazza, N. P. Hartland, and J. Rojo, *Illuminating the photon content of the proton within a global PDF analysis*, SciPost Phys. **5** (2018) no. 1, 008, arXiv:1712.07053 [hep-ph].

[225] J. Rojo, *Parton Distributions at a 100 TeV Hadron Collider*, PoS **DIS2016** (2016) 275, arXiv:1605.08302 [hep-ph].

[226] M. Bonvini, *Small-x phenomenology at the LHC and beyond: HELL 3.0 and the case of the Higgs cross section*, Eur. Phys. J. **C78** (2018) no. 10, 834, arXiv:1805.08785 [hep-ph].

[227] B. Fornal, A. V. Manohar, and W. J. Waalewijn, *Electroweak Gauge Boson Parton Distribution Functions*, JHEP **05** (2018) 106.

[228] T. Han, J. Sayre, and S. Westhoff, *Top-Quark Initiated Processes at High-Energy Hadron Colliders*, JHEP **04** (2015) 145.

[229] V. Bertone, A. Glazov, A. Mitov, A. Papanastasiou, and M. Ubiali, *Heavy-flavor parton distributions without heavy-flavor matching prescriptions*, JHEP **04** (2018) 046.

[230] P. Skands, S. Carrazza, and J. Rojo, *Tuning PYTHIA 8.1: the Monash 2013 Tune*, European Physical Journal C **74** (2014) 3024, arXiv:1404.5630 [hep-ph].

[231] R. Gauld and J. Rojo, *Precision determination of the small-x gluon from charm production at LHCb*, Phys. Rev. Lett. **118** (2017) no. 7, 072001, arXiv:1610.09373 [hep-ph].

[232] I. Brivio, Y. Jiang, and M. Trott, *The SMEFTsim package, theory and tools*, JHEP **12** (2017) 070, arXiv:1709.06492 [hep-ph].

[233] A. Dedes, W. Materkowska, M. Paraskevas, J. Rosiek, and K. Suxho, *Feynman rules for the Standard Model Effective Field Theory in R_x -gauges*, JHEP **06** (2017) 143, arXiv:1704.03888 [hep-ph].

[234] D. Barducci et al., *Interpreting top-quark LHC measurements in the standard-model effective field theory*, arXiv:1802.07237 [hep-ph].

[235] A. Alloul, B. Fuks, and V. Sanz, *Phenomenology of the Higgs Effective Lagrangian via FEYNRULES*, JHEP **04** (2014) 110, arXiv:1310.5150.

[236] F. Maltoni, K. Mawatari, and M. Zaro, *Higgs characterisation via vector-boson fusion and associated production: NLO and parton-shower effects*, Eur. Phys. J. **C74** (2014) no. 1, 2710, arXiv:1311.1829 [hep-ph].

[237] F. Demartin, F. Maltoni, K. Mawatari, B. Page, and M. Zaro, *Higgs characterisation at NLO in QCD: CP properties of the top-quark Yukawa interaction*, Eur. Phys. J. **C74** (2014) no. 9, 3065, arXiv:1407.5089 [hep-ph].

[238] F. Demartin, F. Maltoni, K. Mawatari, and M. Zaro, *Higgs production in association with a single top quark at the LHC*, Eur. Phys. J. **C75** (2015) no. 6, 267, arXiv:1504.00611 [hep-ph].

[239] A. Falkowski, B. Fuks, K. Mawatari, K. Mimasu, F. Riva, and V. Sanz, *Rosetta: an operator basis translator for Standard Model effective field theory*, Eur. Phys. J. **C75** (2015) no. 12, 583, arXiv:1508.05895 [hep-ph].

[240] K. Mimasu, V. Sanz, and C. Williams, *Higher Order QCD predictions for Associated Higgs production with anomalous couplings to gauge bosons*, JHEP **08** (2016) 039, arXiv:1512.02572 [hep-ph].

[241] R. Grober, M. Muhlleitner, and M. Spira, *Higgs Pair Production at NLO QCD for CP-violating Higgs Sectors*, Nucl. Phys. **B925** (2017) 1–27, arXiv:1705.05314 [hep-ph].

[242] F. Goertz, A. Papaefstathiou, L. L. Yang, and J. Zurita, *Higgs boson pair production in the D=6 extension of the SM*, JHEP **04** (2015) 167, arXiv:1410.3471 [hep-ph].

[243] M. Spira, *HIGLU: A program for the calculation of the total Higgs production cross-section at hadron colliders via gluon fusion including QCD corrections*, arXiv:hep-ph/9510347 [hep-ph].

[244] M. Spira, *HIGLU and HDECAY: Programs for Higgs boson production at the LHC and Higgs boson decay widths*, Nucl. Instrum. Meth. **A389** (1997) 357–360, arXiv:hep-ph/9610350 [hep-ph].

[245] R. V. Harlander, S. Liebler, and H. Mantler, *SusHi Bento: Beyond NNLO and the heavy-top limit*, Comput. Phys. Commun. **212** (2017) 239–257, arXiv:1605.03190 [hep-ph].

[246] H. Mantler and M. Wiesemann, *Hadronic Higgs production through NLO + PS in the SM, the 2HDM and the MSSM*, Eur. Phys. J. **C75** (2015) no. 6, 257, arXiv:1504.06625 [hep-ph].

[247] K. Arnold et al., *VBFNLO: A Parton level Monte Carlo for processes with electroweak bosons*, Comput. Phys. Commun. **180** (2009) 1661–1670, arXiv:0811.4559 [hep-ph].

[248] K. Arnold et al., *VBFNLO: A Parton Level Monte Carlo for Processes with Electroweak Bosons – Manual for Version 2.5.0*, arXiv:1107.4038 [hep-ph].

[249] A. Djouadi, J. Kalinowski, and M. Spira, *HDECAY: A Program for Higgs boson decays in the standard model and its supersymmetric extension*, Comput. Phys. Commun. **108** (1998) 56–74, arXiv:hep-ph/9704448 [hep-ph].

[250] R. Contino, M. Ghezzi, C. Grojean, M. Mühlleitner, and M. Spira, *eHDECAY: an Implementation of the Higgs Effective Lagrangian into HDECAY*, Comput. Phys. Commun. **185** (2014) 3412–3423, arXiv:1403.3381 [hep-ph].

[251] B. Gripaios and D. Sutherland, *DEFT: A program for operators in EFT*, arXiv:1807.07546 [hep-ph].

[252] J. Aebischer et al., *WCxf: an exchange format for Wilson coefficients beyond the Standard Model*, Comput. Phys. Commun. **232** (2018) 71–83, arXiv:1712.05298 [hep-ph].

[253] A. Celis, J. Fuentes-Martin, A. Vicente, and J. Virto, *DsixTools: The Standard Model Effective Field Theory Toolkit*, Eur. Phys. J. **C77** (2017) no. 6, 405, arXiv:1704.04504 [hep-ph].

[254] J. Aebischer, J. Kumar, and D. M. Straub, *Wilson: a Python package for the running and matching of Wilson coefficients above and below the electroweak scale*, Eur. Phys. J. **C78** (2018) no. 12, 1026, arXiv:1804.05033 [hep-ph].

[255] C. Degrande, B. Fuks, K. Mawatari, K. Mimasu, and V. Sanz, *Electroweak Higgs boson production in the standard model effective field theory beyond leading order in QCD*, Eur. Phys. J. **C77** (2017) no. 4, 262, arXiv:1609.04833 [hep-ph].

[256] S. Alioli, W. Dekens, M. Girard, and E. Mereghetti, *NLO QCD corrections to SM-EFT dilepton and electroweak Higgs boson production, matched to parton shower in POWHEG*, JHEP **08** (2018) 205, arXiv:1804.07407 [hep-ph].

[257] D. Buarque Franzosi and C. Zhang, *Probing the top-quark chromomagnetic dipole moment at next-to-leading order in QCD*, Phys. Rev. **D91** (2015) no. 11, 114010, arXiv:1503.08841 [hep-ph].

[258] C. Zhang, *Single Top Production at Next-to-Leading Order in the Standard Model Effective Field Theory*, Phys. Rev. Lett. **116** (2016) no. 16, 162002, arXiv:1601.06163 [hep-ph].

[259] O. Bessidskaia Bylund, F. Maltoni, I. Tsinikos, E. Vryonidou, and C. Zhang, *Probing top quark neutral couplings in the Standard Model Effective Field Theory at NLO in QCD*, JHEP **05** (2016) 052, arXiv:1601.08193 [hep-ph].

[260] F. Maltoni, E. Vryonidou, and C. Zhang, *Higgs production in association with a top-antitop pair in the Standard Model Effective Field Theory at NLO in QCD*, JHEP **10** (2016) 123, arXiv:1607.05330 [hep-ph].

[261] C. Degrande, F. Maltoni, K. Mimasu, E. Vryonidou, and C. Zhang, *Single-top associated production with a Z or H boson at the LHC: the SMEFT interpretation*, JHEP **10** (2018) 005, arXiv:1804.07773 [hep-ph].

[262] M. de Beurs, E. Laenen, M. Vreeswijk, and E. Vryonidou, *Effective operators in t-channel single top production and decay*, Eur. Phys. J. **C78** (2018) no. 11, 919, arXiv:1807.03576 [hep-ph].

[263] E. Vryonidou and C. Zhang, *Dimension-six electroweak top-loop effects in Higgs production and decay*, JHEP **08** (2018) 036, arXiv:1804.09766 [hep-ph].

[264] G. Degrassi, P. P. Giardino, F. Maltoni, and D. Pagani, *Probing the Higgs self coupling via single Higgs production at the LHC*, JHEP **12** (2016) 080, arXiv:1607.04251 [hep-ph].

[265] W. Bizon, M. Gorbahn, U. Haisch, and G. Zanderighi, *Constraints on the trilinear Higgs coupling from vector boson fusion and associated Higgs production at the LHC*, JHEP **07** (2017) 083, arXiv:1610.05771 [hep-ph].

[266] S. Di Vita, C. Grojean, G. Panico, M. Riembau, and T. Vantalon, *A global view on the Higgs self-coupling*, JHEP **09** (2017) 069, arXiv:1704.01953 [hep-ph].

[267] C. Hartmann and M. Trott, *Higgs Decay to Two Photons at One Loop in the Standard Model Effective Field Theory*, Phys. Rev. Lett. **115** (2015) no. 19, 191801, arXiv:1507.03568 [hep-ph].

[268] C. Hartmann and M. Trott, *On one-loop corrections in the standard model effective field theory; the $\Gamma(h \to \gamma\gamma)$ case*, JHEP **07** (2015) 151, arXiv:1505.02646 [hep-ph].

[269] C. Hartmann, W. Shepherd, and M. Trott, *The Z decay width in the SMEFT: y_t and λ corrections at one loop*, JHEP **03** (2017) 060, arXiv:1611.09879 [hep-ph].

[270] S. Dawson and P. P. Giardino, *Higgs decays to ZZ and $Z\gamma$ in the standard model effective field theory: An NLO analysis*, Phys. Rev. **D97** (2018) no. 9, 093003, arXiv:1801.01136 [hep-ph].

[271] A. Dedes, M. Paraskevas, J. Rosiek, K. Suxho, and L. Trifyllis, *The decay $h \to \gamma\gamma$ in the Standard-Model Effective Field Theory*, JHEP **08** (2018) 103, arXiv:1805.00302 [hep-ph].

[272] S. Dawson and P. P. Giardino, *Electroweak corrections to Higgs boson decays to $\gamma\gamma$ and W^+W^- in standard model EFT*, Phys. Rev. **D98** (2018) no. 9, 095005, arXiv:1807.11504 [hep-ph].

[273] DELPHES 3 Collaboration, J. de Favereau, C. Delaere, P. Demin, A. Giammanco, V. Lemaître, A. Mertens, and M. Selvaggi, *DELPHES 3, A modular framework for fast simulation of a generic collider experiment*, JHEP **02** (2014) 057, arXiv:1307.6346 [hep-ex].

[274] M. Cacciari, G. P. Salam, and G. Soyez, *The Anti-k_t Jet Clustering Algorithm*, JHEP **04** (2008) 063, arXiv:0802.1189 [hep-ph].

[275] M. Cacciari, G. P. Salam, and G. Soyez, *FastJet User Manual*, Eur. Phys. J. **C72** (2012) 1896, arXiv:1111.6097 [hep-ph].

[276] ATLAS Collaboration, *Expected performance of the ATLAS detector at the High-Luminosity LHC*, ATL-PHYS-PUB-2019-005, CERN, Geneva, Jan, 2019. http://cds.cern.ch/record/2655304.

[277] CMS Collaboration, *Expected performance of the physics objects with the upgraded CMS detector at the HL-LHC*, CERN-CMS-NOTE-2018-006, CERN, Geneva, Dec, 2018. https://cds.cern.ch/record/2650976.

[278] ATLAS Collaboration, *Technical Design Report for the Phase-II Upgrade of the ATLAS TDAQ System*, CERN-LHCC-2017-020. ATLAS-TDR-029, CERN, Geneva, Sep, 2017. http://cds.cern.ch/record/2285584.

[279] CMS Collaboration, *The Phase-2 Upgrade of the CMS L1 Trigger Interim Technical Design Report*, CERN-LHCC-2017-013. CMS-TDR-017, CERN, Geneva, Sep, 2017. https://cds.cern.ch/record/2283192. This is the CMS Interim TDR devoted to the upgrade of the CMS L1 trigger in view of the HL-LHC running, as approved by the LHCC.

[280] ATLAS Collaboration, *Technical Design Report for the ATLAS Inner Tracker Pixel Detector*, CERN-LHCC-2017-021. ATLAS-TDR-030, CERN, Geneva, Sep, 2017. http://cds.cern.ch/record/2285585.

[281] ATLAS Collaboration, *Technical Design Report for the ATLAS Inner Tracker Strip Detector*, CERN-LHCC-2017-005. ATLAS-TDR-025, CERN, Geneva, Apr, 2017. http://cds.cern.ch/record/2257755.

[282] CMS Collaboration, *The Phase-2 Upgrade of the CMS Tracker*, CERN-LHCC-2017-009. CMS-TDR-014, CERN, 2017. https://cds.cern.ch/record/2272264.

[283] ATLAS Collaboration, *Technical Design Report for the Phase-II Upgrade of the ATLAS LAr Calorimeter*, CERN-LHCC-2017-018. ATLAS-TDR-027, CERN, Geneva, Sep, 2017. http://cds.cern.ch/record/2285582.

[284] CMS Collaboration, *The Phase-2 Upgrade of the CMS Barrel Calorimeters Technical Design Report*, CERN-LHCC-2017-011. CMS-TDR-015, CERN, 2017. https://cds.cern.ch/record/2283187.

[285] CMS Collaboration, *The Phase-2 Upgrade of the CMS Endcap Calorimeter*, CERN-LHCC-2017-023. CMS-TDR-019, 2017. https://cds.cern.ch/record/2293646.

[286] CMS Collaboration, *Technical Proposal for a MIP Timing Detector in the CMS Experiment Phase-2 Upgrade*, CERN-LHCC-2017-027. LHCC-P-009, 2017. https://cds.cern.ch/record/2296612.

[287] ATLAS Collaboration, *Technical Design Report for the Phase-II Upgrade of the ATLAS Muon Spectrometer*, CERN-LHCC-2017-017. ATLAS-TDR-026, CERN, Geneva, Sep, 2017. http://cds.cern.ch/record/2285580.

[288] CMS Collaboration, *The Phase-2 Upgrade of the CMS Muon Detectors*, CERN-LHCC-2017-012. CMS-TDR-016, 2017. https://cds.cern.ch/record/2283189.

[289] ATLAS Collaboration, *Technical Design Report for the Phase-II Upgrade of the ATLAS Tile Calorimeter*, CERN-LHCC-2017-019. ATLAS-TDR-028, CERN, Geneva, Sep, 2017. http://cds.cern.ch/record/2285583.

[290] CMS Collaboration, *Technical Proposal for the Phase-II Upgrade of the CMS Detector*, Cern-lhcc-2015-010, Geneva, Jun, 2015. https://cds.cern.ch/record/2020886.

[291] ATLAS Collaboration, *Technical Proposal: A High-Granularity Timing Detector for the ATLAS Phase-II Upgrade*, CERN-LHCC-2018-023. LHCC-P-012, CERN, Geneva, Jun, 2018. http://cds.cern.ch/record/2623663.

[292] T. Sjostrand, S. Mrenna, and P. Z. Skands, *A Brief Introduction to PYTHIA 8.1*, Comput. Phys. Commun. **178** (2008) 852–867, arXiv:0710.3820 [hep-ph].

[293] I. Belyaev et al., *Handling of the generation of primary events in Gauss, the LHCb simulation framework*, J. Phys. Conf. Ser. **331** (2011) 032047.

[294] J. Pumplin, D. Stump, J. Huston, H. Lai, P. M. Nadolsky, et al., *New generation of parton distributions with uncertainties from global QCD analysis*, JHEP **07** (2002) 012, arXiv:hep-ph/0201195 [hep-ph].

[295] J. Allison et al., *Geant4 developments and applications*, IEEE Trans. Nucl. Sci. **53** (2006) 270. SLAC-PUB-11870.

[296] S. Agostinelli et al., *GEANT4: A Simulation Toolkit*, Nucl. Instrum. Meth. **A 506** (2003) 250. SLAC-PUB-9350.

[297] M. Clemencic et al., *The LHCb simulation application, Gauss: Design, evolution and experience*, J. Phys. Conf. Ser. **331** (2011) 032023.

[298] R. Abdul Khalek, S. Bailey, J. Gao, L. Harland-Lang, and J. Rojo, *Towards Ultimate Parton Distributions at the High-Luminosity LHC*, Eur. Phys. J. **C78** (2018) no. 11, 962, arXiv:1810.03639 [hep-ph].

[299] ATLAS Collaboration, G. Aad et al., *Measurement of $W^{\pm}$ and Z-boson production cross sections in pp collisions at $\sqrt{s} = 13$ TeV with the ATLAS detector*, Phys. Lett. **B759** (2016) 601–621, arXiv:1603.09222 [hep-ex].

[300] CMS Collaboration, A. M. Sirunyan et al., *Measurement of the $t\bar{t}$ production cross section using events with one lepton and at least one jet in pp collisions at $\sqrt{s}$ = 13 TeV*, JHEP **09** (2017) 051, arXiv:1701.06228 [hep-ex].

[301] G. Apollinari, I. Béjar Alonso, O. Brüning, P. Fessia, M. Lamont, L. Rossi, and L. Tavian, *High-Luminosity Large Hadron Collider (HL-LHC): Technical Design Report V. 0.1*. CERN Yellow Reports: Monographs. CERN, Geneva, 2017. https://cds.cern.ch/record/2284929.

[302] H. Ogul and K. Dilsiz, *Cross Section Prediction for Inclusive Production of Z Boson in pp Collisions at $\sqrt{s} = 14$ TeV: A Study of Systematic Uncertainty Due to Scale Dependence*, Adv. High Energy Phys. **2017** (2017) 8262018, arXiv:1702.07206 [hep-ph].

[303] S. van der Meer, *Calibration of the effective beam height in the ISR*, CERN-ISR-PO-68-31. ISR-PO-68-31, CERN, Geneva, 1968. https://cds.cern.ch/record/296752.

[304] P. Grafström and W. Kozanecki, *Luminosity determination at proton colliders*, Prog. Part. Nucl. Phys. **81** (2015) 97–148.

[305] H. Bartosik and G. Rumolo, *Production of single Gaussian bunches for Van der Meer scans in the LHC injector chain*, CERN-ACC-NOTE-2013-0008, 2013. https://cds.cern.ch/record/1590405.

[306] CMS Collaboration, *CMS luminosity measurement for the 2017 data-taking period at* $\sqrt{s} = 13$ TeV, CMS-PAS-LUM-17-004, CERN, Geneva, 2018. https://cds.cern.ch/record/2621960.

[307] ATLAS Collaboration, M. Aaboud et al., *Luminosity determination in pp collisions at* $\sqrt{s}$ *= 8 TeV using the ATLAS detector at the LHC*, Eur. Phys. J. **C76** (2016) no. 12, 653, arXiv:1608.03953 [hep-ex].

[308] LHCb Collaboration, R. Aaij et al., *Precision luminosity measurements at LHCb*, JINST **9** (2014) no. 12, P12005, arXiv:1410.0149 [hep-ex].

[309] M. Hostettler and G. Papotti, *Beam Size Estimation from Luminosity Scans at the LHC During 2015 Proton Physics Operation*, in *Proceedings, 7th International Particle Accelerator Conference (IPAC 2016): Busan, Korea, May 8-13, 2016*, p. MOPMR025. 2016.

[310] O. Karacheban and T. Peter, *CMS emittance scans for luminosity calibration in 2017*, AYSS-2018: XXII International Scientific Conference of Young Scientists and Specialists , https://indico.jinr.ru/contributionDisplay.py?contribId=348&confId=436.

[311] M. Hostettler, K. Fuchsberger, G. Papotti, Y. Papaphilippou, and T. Pieloni, *Luminosity Scans for Beam Diagnostics*, Phys. Rev. Accel. Beams **21** (2018) no. 10, 102801, arXiv:1804.10099 [physics.acc-ph].

[312] CMS Collaboration, O. Karacheban, *CMS emittance scans for luminosity calibration in 2017*, CMS-CR-2018-062, CERN, Geneva, Jun, 2018. https://cds.cern.ch/record/2630628.

[313] J. Salfeld-Nebgen and D. Marlow, *Data-Driven Precision Luminosity Measurements with Z Bosons at the LHC and HL-LHC*, JINST **13** (2018) no. 12, P12016, arXiv:1806.02184 [hep-ex].

[314] S. Alioli, P. Nason, C. Oleari, and E. Re, *A General Framework for Implementing NLO Calculations in Shower Monte Carlo Programs: the POWHEG BOX*, JHEP **06** (2010) 043, arXiv:1002.2581 [hep-ph].

[315] P. Nason and C. Oleari, *NLO Higgs boson production via vector-boson fusion matched with shower in POWHEG*, JHEP **02** (2010) 037, arXiv:0911.5299 [hep-ph].

[316] B. Jager, F. Schissler, and D. Zeppenfeld, *Parton-shower effects on Higgs boson production via vector-boson fusion in association with three jets*, JHEP **07** (2014) 125, arXiv:1405.6950 [hep-ph].

[317] M. Ciccolini, A. Denner, and S. Dittmaier, *Electroweak and QCD corrections to Higgs production via vector-boson fusion at the LHC*, Phys. Rev. **D77** (2008) 013002, arXiv:0710.4749 [hep-ph].

[318] M. Ciccolini, A. Denner, and S. Dittmaier, *Strong and electroweak corrections to the production of Higgs + 2jets via weak interactions at the LHC*, Phys. Rev. Lett. **99** (2007) 161803, arXiv:0707.0381 [hep-ph].

[319] A. Denner, S. Dittmaier, S. Kallweit, and A. Muck, *Electroweak corrections to Higgs-strahlung off W/Z bosons at the Tevatron and the LHC with HAWK*, JHEP **03** (2012) 075, arXiv:1112.5142 [hep-ph].

[320] Denner, Ansgar and Dittmaier, Stefan and Kallweit, Stefan and Mück, Alexander, *HAWK 2.0: A Monte Carlo program for Higgs production in vector-boson fusion and Higgs strahlung at hadron colliders*, Comput. Phys. Commun. **195** (2015) 161–171, arXiv:1412.5390 [hep-ph].

[321] J. Cruz-Martinez, T. Gehrmann, E. Glover, and A. Huss, *Second-order QCD effects in Higgs boson production through vector boson fusion*, Physics Letters B **781** (2018) 672 – 677.

[322] M. Cacciari and G. P. Salam, *Dispelling the* N^3 *Myth for the* k_t *Jet-Finder*, Phys. Lett. **B 641** (2006) 57, arXiv:0512210 [hep-ph].

[323] X. Chen, T. Gehrmann, E. W. N. Glover, and M. Jaquier, *Precise QCD predictions for the production of Higgs + jet final states*, Phys. Lett. **B740** (2015) 147–150, arXiv:1408.5325 [hep-ph].

[324] X. Chen, J. Cruz-Martinez, T. Gehrmann, E. W. N. Glover, and M. Jaquier, *NNLO QCD corrections to Higgs boson production at large transverse momentum*, JHEP **10** (2016) 066, arXiv:1607.08817 [hep-ph].

[325] L. Cieri, X. Chen, T. Gehrmann, E. W. N. Glover, and A. Huss, *Higgs boson production at the LHC using the q_T subtraction formalism at N^3LO QCD*, JHEP **02** (2019) 096, arXiv:1807.11501 [hep-ph].

[326] T. Gehrmann et al., *Jet cross sections and transverse momentum distributions with NNLOJET*, in *13th International Symposium on Radiative Corrections: Application of Quantum Field Theory to Phenomenology (RADCOR 2017) St. Gilgen, Austria, September 24-29, 2017*. 2018. arXiv:1801.06415 [hep-ph].

[327] A. Gehrmann-De Ridder, T. Gehrmann, E. W. N. Glover, A. Huss, and T. A. Morgan, *Precise QCD predictions for the production of a Z boson in association with a hadronic jet*, Phys. Rev. Lett. **117** (2016) no. 2, 022001, arXiv:1507.02850 [hep-ph].

[328] J. Currie, T. Gehrmann, and J. Niehues, *Precise QCD predictions for the production of dijet final states in deep inelastic scattering*, Phys. Rev. Lett. **117** (2016) no. 4, 042001, arXiv:1606.03991 [hep-ph].

[329] A. Gehrmann-De Ridder, T. Gehrmann, E. W. N. Glover, A. Huss, and D. M. Walker, *Next-to-Next-to-Leading-Order QCD Corrections to the Transverse Momentum Distribution of Weak Gauge Bosons*, Phys. Rev. Lett. **120** (2018) no. 12, 122001, arXiv:1712.07543 [hep-ph].

[330] J. Currie, T. Gehrmann, E. W. N. Glover, A. Huss, J. Niehues, and A. Vogt, *N^3LO corrections to jet production in deep inelastic scattering using the Projection-to-Born method*, JHEP **05** (2018) 209, arXiv:1803.09973 [hep-ph].

[331] J. Niehues and D. Walker, *NNLO QCD corrections to jet production in charged current deep inelastic scattering*, Physics Letters B **788** (2019) 243 – 248.

[332] J. Currie, A. Gehrmann-De Ridder, T. Gehrmann, E. W. N. Glover, A. Huss, and J. Pires, *Infrared sensitivity of single jet inclusive production at hadron colliders*, JHEP **10** (2018) 155, arXiv:1807.03692 [hep-ph].

[333] F. Campanario, T. M. Figy, S. Plätzer, and M. Sjodahl, *Electroweak Higgs Boson Plus Three Jet Production at Next-to-Leading-Order QCD*, Phys. Rev. Lett. **111** (2013) no. 21, 211802, arXiv:1308.2932 [hep-ph].

[334] F. Campanario, T. M. Figy, S. Plätzer, and M. Sjodahl, *NLO QCD Corrections to Electroweak Higgs Boson Plus Three Jet Production at the LHC*, PoS **RADCOR2013** (2013) 042, arXiv:1311.5455 [hep-ph].

[335] F. Campanario, T. M. Figy, S. Plätzer, and M. Sjodahl, *Beyond the t-channel Approximation: Next-to-Leading Order QCD Corrections to Electroweak Higgs Boson Production Plus Three Jets Production at the LHC*, PoS **LL2014** (2014) 025, arXiv:1407.5050 [hep-ph].

[336] F. Campanario, T. M. Figy, S. Plätzer, M. Rauch, P. Schichtel, and M. Sjödahl, *Stress testing the vector-boson-fusion approximation in multijet final states*, Phys. Rev. D **98** (Aug, 2018) 033003.

[337] F. Campanario, *Towards pp -> VVjj at NLO QCD: Bosonic contributions to triple vector boson production plus jet*, JHEP **10** (2011) 070, arXiv:1105.0920 [hep-ph].

[338] M. Sjodahl, *ColorFull – a C++ library for calculations in SU(Nc) color space*, Eur. Phys. J. **C75** (2015) no. 5, 236, arXiv:1412.3967 [hep-ph].

[339] J. Baglio et al., *Release Note - VBFNLO 2.7.0*, arXiv:1404.3940 [hep-ph].

[340] T. Figy, V. Hankele, and D. Zeppenfeld, *Next-to-leading order QCD corrections to Higgs plus three jet production in vector-boson fusion*, JHEP **02** (2008) 076, arXiv:0710.5621 [hep-ph].

[341] S. Platzer and S. Gieseke, *Dipole Showers and Automated NLO Matching in Herwig++*, Eur. Phys. J. **C72** (2012) 2187, arXiv:1109.6256 [hep-ph].

[342] J. Bellm et al., *Herwig 7.1 Release Note*, arXiv:1705.06919 [hep-ph].

[343] M. Cacciari, G. P. Salam, and G. Soyez, *FastJet User Manual*, Eur. Phys. J. **C72** (2012) 1896, arXiv:1111.6097 [hep-ph].

[344] A. Buckley, J. Butterworth, L. Lonnblad, D. Grellscheid, H. Hoeth, J. Monk, H. Schulz, and F. Siegert, *Rivet user manual*, Comput. Phys. Commun. **184** (2013) 2803–2819, arXiv:1003.0694 [hep-ph].

[345] J. Bagger, V. D. Barger, K.-m. Cheung, J. F. Gunion, T. Han, G. A. Ladinsky, R. Rosenfeld, and C. P. Yuan, *The Strongly interacting WW system: Gold plated modes*, Phys. Rev. D **49** (1994) 1246–1264, arXiv:hep-ph/9306256.

[346] J. Bagger, V. D. Barger, K.-m. Cheung, J. F. Gunion, T. Han, G. A. Ladinsky, R. Rosenfeld, and C. P. Yuan, *CERN LHC analysis of the strongly interacting WW system: Gold plated modes*, Phys. Rev. D **52** (1995) 3878–3889, arXiv:hep-ph/9504426.

[347] CMS Collaboration, *Observation of a new boson at a mass of 125 GeV with the CMS experiment at the LHC*, Phys. Lett. B **716** (2012) 30–61, arXiv:1207.7235 [hep-ex].

[348] M. J. G. Veltman, *Second Threshold in Weak Interactions*, Acta Phys. Polon. B **8** (1977) 475. Print-77-0040 (UTRECHT).

[349] B. W. Lee, C. Quigg, and H. B. Thacker, *The Strength of Weak Interactions at Very High-Energies and the Higgs Boson Mass*, Phys. Rev. Lett. **38** (1977) 883–885. FERMILAB-PUB-77-022-THY.

[350] B. W. Lee, C. Quigg, and H. B. Thacker, *Weak Interactions at Very High-Energies: The Role of the Higgs Boson Mass*, Phys. Rev. D **16** (1977) 1519. FERMILAB-PUB-77-030-THY.

[351] HEPAP Subcommittee Collaboration, HEPAP Subcommittee Collaboration, *Building for Discovery: Strategic Plan for U.S. Particle Physics in the Global Context*, . https://inspirehep.net/record/1299183/files/FINAL_P5_Report_053014.pdf.

[352] R. Aleksan et al., *Physics Briefing Book: Input for the Strategy Group to draft the update of the European Strategy for Particle Physics*, . https://cds.cern.ch/record/1628377. Open Symposium held in Cracow from 10th to 12th of September 2012.

[353] E. Accomando, A. Ballestrero, S. Bolognesi, E. Maina, and C. Mariotti, *Boson-boson scattering and Higgs production at the LHC from a six fermion point of view: Four jets + l nu processes at* $\mathcal{O}(\alpha_{em}^6)$, JHEP **03** (2006) 093, arXiv:hep-ph/0512219.

[354] B. Zhu, P. Govoni, Y. Mao, C. Mariotti, and W. Wu, *Same Sign WW Scattering Process as a Probe of Higgs Boson in pp Collision at* $\sqrt{s} = 10$ *TeV*, Eur. Phys. J. C **71** (2011) 1514, arXiv:1010.5848 [hep-ex].

[355] ATLAS Collaboration, *Observation of electroweak production of a same-sign* W *boson pair in association with two jets in pp collisions at* $\sqrt{s} = 13$ *TeV with the ATLAS detector*, ATLAS-CONF-2018-030, CERN, Geneva, Jul, 2018. https://cds.cern.ch/record/2629411.

[356] CMS Collaboration, A. M. Sirunyan et al., *Observation of electroweak production of same-sign W boson pairs in the two jet and two same-sign lepton final state in proton-proton collisions at* $\sqrt{s} = 13$ *TeV*, Phys. Rev. Lett. **120** (2018) no. 8, 081801, arXiv:1709.05822 [hep-ex].

[357] ATLAS Collaboration, *Prospects for the measurement of the $W^{\pm}W^{\pm}$ scattering cross section and extraction of the longitudinal scattering component in pp collisions at the High-Luminosity LHC with the ATLAS experiment*, ATL-PHYS-PUB-2018-052, CERN, Geneva, 2018. https://cds.cern.ch/record/2652447.

[358] CMS Collaboration, *Study of $W^{\pm}W^{\pm}$ production via vector boson scattering at the HL-LHC with the upgraded CMS detector*, CMS-PAS-FTR-18-005, CERN, Geneva, 2018. https://cds.cern.ch/record/2646870.

[359] R. D. Ball et al., *Parton distributions with LHC data*, Nucl. Phys. B **867** (2013) 244, arXiv:1207.1303 [hep-ph].

[360] J. M. Campbell, R. K. Ellis, P. Nason, and E. Re, *Top-Pair Production and Decay at NLO Matched with Parton Showers*, JHEP **04** (2015) 114, arXiv:1412.1828 [hep-ph].

[361] M. Cacciari, G. P. Salam, G. Soyez, *The anti-k_t jet clustering algorithm*, JHEP **04** (2008) 063, arXiv:0802.1189 [hep-ph].

[362] D. Bertolini, P. Harris, M. Low, and N. Tran, *Pileup Per Particle Identification*, JHEP **10** (2014) 059, arXiv:1407.6013 [hep-ph].

[363] D. Guest, J. Collado, P. Baldi, S.-C. Hsu, G. Urban, and D. Whiteson, *Jet flavor classification in high-energy physics with deep neural networks*, Phys. Rev. D **94** (Dec, 2016) 112002. https://link.aps.org/doi/10.1103/PhysRevD.94.112002.

[364] D. L. Rainwater, R. Szalapski, and D. Zeppenfeld, *Probing color singlet exchange in Z + two jet events at the CERN LHC*, Phys. Rev. **D54** (1996) 6680–6689, arXiv:hep-ph/9605444 [hep-ph].

[365] J. Searcy, L. Huang, M.-A. Pleier, and J. Zhu, *Determination of the WW polarization fractions in $pp \to W^{\pm}W^{\pm}jj$ using a deep machine learning technique*, Phys. Rev. D **93** (2016) no. 9, 094033, arXiv:1510.01691 [hep-ph].

[366] D. Gonçalves, T. Plehn, and J. M. Thompson, *Weak boson fusion at 100 TeV*, Phys. Rev. **D95** (2017) no. 9, 095011, arXiv:1702.05098 [hep-ph].

[367] B. Jäger, L. Salfelder, M. Worek, and D. Zeppenfeld, *Physics opportunities for vector-boson scattering at a future 100 TeV hadron collider*, Phys. Rev. **D96** (2017) no. 7, 073008, arXiv:1704.04911 [hep-ph].

[368] B. Jäger, C. Oleari, and D. Zeppenfeld, *Next-to-leading order QCD corrections to W^+W^- production via vector-boson fusion*, JHEP **07** (2006) 015, arXiv:hep-ph/0603177 [hep-ph].

[369] B. Jäger, C. Oleari, and D. Zeppenfeld, *Next-to-leading order QCD corrections to Z boson pair production via vector-boson fusion*, Phys. Rev. **D73** (2006) 113006, arXiv:hep-ph/0604200 [hep-ph].

[370] G. Bozzi, B. Jäger, C. Oleari, and D. Zeppenfeld, *Next-to-leading order QCD corrections to W^+Z and W^-Z production via vector-boson fusion*, Phys. Rev. **D75** (2007) 073004, arXiv:hep-ph/0701105 [hep-ph].

[371] B. Jäger, C. Oleari, and D. Zeppenfeld, *Next-to-leading order QCD corrections to W^+W^+jj and W^-W^-jj production via weak-boson fusion*, Phys. Rev. **D80** (2009) 034022, arXiv:0907.0580 [hep-ph].

[372] B. Jäger and G. Zanderighi, *NLO corrections to electroweak and QCD production of W^+W^+ plus two jets in the POWHEGBOX*, JHEP **11** (2011) 055, arXiv:1108.0864 [hep-ph].

[373] A. Denner, L. Hošeková, and S. Kallweit, *NLO QCD corrections to W^+W^+jj production in vector-boson fusion at the LHC*, Phys. Rev. **D86** (2012) 114014, arXiv:1209.2389 [hep-ph].

[374] M. Rauch, *Vector-Boson Fusion and Vector-Boson Scattering*, arXiv:1610.08420 [hep-ph].

[375] A. Ballestrero et al., *Precise predictions for same-sign W-boson scattering at the LHC*, Eur. Phys. J. **C78** (2018) no. 8, 671, arXiv:1803.07943 [hep-ph].

[376] B. Jager, A. Karlberg, and J. Scheller, *Parton-shower effects in electroweak $WZjj$ production at the next-to-leading order of QCD*, Eur. Phys. J. **C79** (2019) no. 3, 226, arXiv:1812.05118 [hep-ph].

[377] S. Frixione, P. Nason, and C. Oleari, *Matching NLO QCD Computations with Parton Shower Simulations: the POWHEG Method*, JHEP **11** (2007) 070, arXiv:0709.2092 [hep-ph].

[378] T. Gleisberg, S. Höche, F. Krauss, A. Schälicke, S. Schumann, and J.-C. Winter, *SHERPA 1.α: A Proof of concept version*, JHEP **02** (2004) 056, arXiv:hep-ph/0311263 [hep-ph].

[379] D. Yu. Bardin, A. Leike, T. Riemann, and M. Sachwitz, *Energy-dependent width effects in e^+e^--annihilation near the Z-boson pole*, Phys. Lett. **B206** (1988) 539–542.

[380] A. Denner, S. Dittmaier, M. Roth, and D. Wackeroth, *Electroweak radiative corrections to $e^+e^- \to WW \to 4$ fermions in double-pole approximation: The RACOONWW approach*, Nucl. Phys. **B587** (2000) 67–117, arXiv:hep-ph/0006307 [hep-ph].

[381] A. Denner et al., *Predictions for all processes $e^+e^- \to 4$fermions $+\gamma$*, Nucl. Phys. **B560** (1999) 33–65, arXiv:hep-ph/9904472.

[382] A. Denner et al., *Electroweak corrections to charged-current $e^+e^- \to 4$ fermion processes: Technical details and further results*, Nucl. Phys. **B724** (2005) 247–294, arXiv:hep-ph/0505042.

[383] A. Denner and S. Dittmaier, *The complex-mass scheme for perturbative calculations with unstable particles*, Nucl. Phys. Proc. Suppl. **160** (2006) 22–26, arXiv:hep-ph/0605312 [hep-ph]. [,22(2006)].

[384] ATLAS Collaboration, G. Aad et al., *Evidence for Electroweak Production of $W^\pm W^\pm jj$ in pp Collisions at $\sqrt{s} = 8$ TeV with the ATLAS Detector*, Phys. Rev. Lett. **113** (2014) no. 14, 141803, arXiv:1405.6241 [hep-ex].

[385] ATLAS Collaboration, M. Aaboud et al., *Measurement of $W^\pm W^\pm$ vector-boson scattering and limits on anomalous quartic gauge couplings with the ATLAS detector*, Phys. Rev. **D96** (2017) 012007, arXiv:1611.02428 [hep-ex].

[386] CMS Collaboration, V. Khachatryan et al., *Study of vector boson scattering and search for new physics in events with two same-sign leptons and two jets*, Phys. Rev. Lett. **114** (2015) no. 5, 051801, arXiv:1410.6315 [hep-ex].

[387] ATLAS Collaboration, *Studies on the impact of an extended Inner Detector tracker and a forward muon tagger on $W^\pm W^\pm$ scattering in pp collisions at the High-Luminosity LHC with the ATLAS experiment*, . https://cds.cern.ch/record/2298958.

[388] C. Schwan, *NLO EW corrections for W and Z scattering at the LHC*, 2018. https://indico.cern.ch/event/702614/.

[389] A. Denner, S. Dittmaier, P. Maierhöfer, M. Pellen, and C. Schwan, *QCD and electroweak corrections to WZ scattering at the LHC*, arXiv:1904.00882 [hep-ph].

[390] ATLAS Collaboration, *Observation of electroweak $W^\pm Z$ boson pair production in association with two jets in pp collisions at $\sqrt{s} = 13$ TeV with the ATLAS detector*, Submitted to: Phys. Lett. (2018) , arXiv:1812.09740 [hep-ex].

[391] CMS Collaboration, *Measurement of electroweak WZ production and search for new physics in pp collisions at sqrt(s) = 13 TeV*, CMS-PAS-SMP-18-001, CERN, Geneva, 2018. https://cds.cern.ch/record/2629457.

[392] CMS Collaboration, *Prospects for the measurement of electroweak and polarized WZ to 3lv production cross sections at the High-Luminosity LHC* , CMS-PAS-FTR-18-038, CERN, Geneva, 2018. https://cds.cern.ch/record/2650774.

[393] J. Alwall, M. Herquet, F. Maltoni, O. Mattelaer, and T. Stelzer, *MadGraph 5: going beyond*, JHEP **06** (2011) 128, arXiv:1106.0522 [hep-ph].

[394] O. J. P. Éboli, M. C. Gonzalez-Garcia, and J. K. Mizukoshi, $pp \to jje^{\pm}\mu^{\pm}\nu\nu$ *and* $jje^{\pm}\mu^{\mp}\nu\nu$ *at* $\mathcal{O}(\alpha_{\rm em}^6)$ *and* $\mathcal{O}(\alpha_{\rm em}^4\alpha_s^2)$ *for the study of the quartic electroweak gauge boson vertex at CERN LHC*, Phys. Rev. D **74** (Oct, 2006) 073005. https://link.aps.org/doi/10.1103/PhysRevD.74.073005.

[395] O. J. P. Éboli and M. C. Gonzalez–Garcia, *Classifying the bosonic quartic couplings*, Phys. Rev. **D93** (2016) no. 9, 093013, arXiv:1604.03555 [hep-ph].

[396] M. Baak et al., *Working Group Report: Precision Study of Electroweak Interactions*, in *Proceedings, Community Summer Study 2013: Snowmass on the Mississippi (CSS2013): Minneapolis, MN, USA, July 29-August 6, 2013*. 2013. arXiv:1310.6708 [hep-ph].

[397] G. Perez, M. Sekulla, and D. Zeppenfeld, *Anomalous quartic gauge couplings and unitarization for the vector boson scattering process* $pp \to W^+W^+jjX \to \ell^+\nu_\ell\ell^+\nu_\ell jjX$, Eur. Phys. J. **C78** (2018) no. 9, 759, arXiv:1807.02707 [hep-ph].

[398] CMS Collaboration, T. Sirunyan et al., *Measurement of vector boson scattering and constraints on anomalous quartic couplings from events with four leptons and two jets in proton-proton collisions at sqrt(s) = 13 TeV.*, Phys. Lett. B **774** (Aug, 2017) 682–705. 24 p, arXiv:1708.02812.

[399] CMS Collaboration, *Vector Boson Scattering prospective studies in the ZZ fully leptonic decay channel for the High-Luminosity and High-Energy LHC upgrades*, CMS-PAS-FTR-18-014, CERN, Geneva, 2018. https://cds.cern.ch/record/2650915.

[400] NNPDF Collaboration, R. D. Ball et al., *Parton distributions for the LHC Run II*, JHEP **04** (2015) 040, arXiv:1410.8849 [hep-ph].

[401] J. Alwall, R. Frederix, S. Frixione, V. Hirschi, F. Maltoni, O. Mattelaer, H.-S. Shao, T. Stelzer, P. Torielli, and M. Zaro, *The automated computation of tree-level and next-to-leading order differential cross sections, and their matching to parton shower simulations*, JHEP **07** (2014) 079, arXiv:1405.0301 [hep-ph].

[402] P. Artoisenet, R. Frederix, O. Mattelaer, and R. Rietkerk, *Automatic spin-entangled decays of heavy resonances in Monte Carlo simulations*, JHEP **03** (2013) 015, arXiv:1212.3460 [hep-ph].

[403] J. M. Campbell and R. K. Ellis, *MCFM for the Tevatron and the LHC*, Nucl. Phys. B Proc. Suppl. **205-206** (2010) 10, arXiv:1007.3492 [hep-ph].

[404] Particle Data Group Collaboration, C. Patrignani et al., *Review of Particle Physics*, Chin. Phys. **C40** (2016) no. 10, 100001.

[405] ATLAS Collaboration, *Expected performance for an upgraded ATLAS detector at High-Luminosity LHC*, ATL-PHYS-PUB-2016-026, CERN, Geneva, Oct, 2016. https://cds.cern.ch/record/2223839.

[406] CMS Collaboration, V. Khachatryan et al., *Measurement of electroweak production of two jets in association with a Z boson in proton–proton collisions at* $\sqrt{s} = 8$ *TeV*, Eur. Phys. J. C **75** (2015) 66, arXiv:1410.3153 [hep-ex].

[407] ATLAS Collaboration, *HL-LHC prospects for diboson resonance searches and electroweak vector boson scattering in the* $WW/WZ \to \ell\nu qq$ *final state*, ATL-PHYS-PUB-2018-022, CERN, Geneva, Oct, 2018. https://cds.cern.ch/record/2645269.

[408] M. Cacciari, C. P. Salam and G. Soyez, *The anti-k_t jet clustering algorithm*, JHEP **04** (2008) 063.

[409] D. Krohn, J. Thaler, and L.-T. Wang, *Jet Trimming*, JHEP **02** (2010) 084, arXiv:0912.1342 [hep-ph].

[410] ATLAS Collaboration, G. Aad et al., *Identification of boosted, hadronically decaying W bosons and comparisons with ATLAS data taken at $\sqrt{s} = 8$ TeV*, Eur. Phys. J. **C76** (2016) no. 3, 154, arXiv:1510.05821 [hep-ex].

[411] ATLAS Collaboration, *Identification of boosted, hadronically-decaying W and Z bosons in $\sqrt{s} = 13$ TeV Monte Carlo Simulations for ATLAS*, ATL-PHYS-PUB-2015-033, CERN, Geneva, Aug, 2015. https://cds.cern.ch/record/2041461.

[412] A. Hocker et al., *TMVA - Toolkit for Multivariate Data Analysis*, arXiv:physics/0703039 [physics.data-an].

[413] G. Cowan, K. Cranmer, E. Gross, and O. Vitells, *Asymptotic formulae for likelihood-based tests of new physics*, Eur. Phys. J. **C71** (2011) 1554, arXiv:1007.1727 [physics.data-an]. [Erratum: Eur. Phys. J.C73,2501(2013)].

[414] V. Cavaliere, R. Les, T. Nitta, and K. Terashi, *HE-LHC prospects for diboson resonance searches and electroweak WW/WZ production via vector boson scattering in the semi-leptonic final states*, arXiv:1812.00841 [hep-ex].

[415] The DELPHES 3 Collaboration, de Favereau, J., Delaere, C. *et al.*, *DELPHES 3: a modular framework for fast simulation of a generic collider experiment*, JHEP **02** (2014) 057, arXiv:1307.6346 [hep-ex].

[416] ATLAS Collaboration, *Prospect studies for the production of three massive vector bosons with the ATLAS detector at the High-Luminosity LHC*, ATL-PHYS-PUB-2018-030, CERN, Geneva, Nov, 2018. https://cds.cern.ch/record/2647220.

[417] A. Lazopoulos, T. McElmurry, K. Melnikov, and F. Petriello, *Next-to-Leading Order QCD Corrections to $t\bar{t}Z$ Production at the LHC*, Phys. Lett. **B 666** (2008) 62, arXiv:0804.2220 [hep-ph].

[418] M. Garzelli, A. Kardos, C. Papadopoulos, and Z. Trocsanyi, *$t\bar{t}W^{\pm}$ and $t\bar{t}Z$ Hadroproduction at NLO Accuracy in QCD with Parton Shower and Hadronization Effects*, JHEP **11** (2012) 056, arXiv:1208.2665 [hep-ph].

[419] J. M. Campbell and R. K. Ellis, *$t\bar{t}W^{\pm}$ Production and Decay at NLO*, JHEP **07** (2012) 052, arXiv:1204.5678 [hep-ph].

[420] ATLAS Collaboration, *Multi-Boson Simulation for 13 TeV ATLAS Analyses*, ATL-PHYS-PUB-2017-005, 2017. https://cds.cern.ch/record/2261933.

[421] ATLAS Collaboration, *Improvements in $t\bar{t}$ modelling using NLO+PS Monte Carlo generators for Run 2*, ATL-PHYS-PUB-2018-009, 2018. https://cds.cern.ch/record/2630327.

[422] ATLAS Collaboration, *Modelling of the $t\bar{t}H$ and $t\bar{t}V(V = W, Z)$ processes for $\sqrt{s} = 13$ TeV ATLAS analyses*, ATL-PHYS-PUB-2016-005, 2016. https://cds.cern.ch/record/2120826.

[423] M. Czakon and A. Mitov, *Top++: A Program for the Calculation of the Top-Pair Cross-Section at Hadron Colliders*, Comput. Phys. Commun. **185** (2014) 2930, arXiv:1112.5675 [hep-ph].

[424] ATLAS Collaboration, M. Aaboud et al., *Search for triboson $W^{\pm}W^{\pm}W^{\mp}$ production in pp collisions at $\sqrt{s} = 8$ TeV with the ATLAS detector*, Eur. Phys. J. **C77** (2017) no. 3, 141, arXiv:1610.05088 [hep-ex].

[425] G. Heinrich, S. Jahn, S. P. Jones, M. Kerner, and J. Pires, *NNLO predictions for Z-boson pair production at the LHC*, JHEP **03** (2018) 142, arXiv:1710.06294 [hep-ph].

[426] I. W. Stewart, F. J. Tackmann, and W. J. Waalewijn, *Factorization at the LHC: From PDFs to Initial State Jets*, Phys. Rev. **D81** (2010) 094035, arXiv:0910.0467 [hep-ph].

[427] R. Boughezal, C. Focke, W. Giele, X. Liu, and F. Petriello, *Higgs boson production in association with a jet at NNLO using jettiness subtraction*, Phys. Lett. **B748** (2015) 5–8, arXiv:1505.03893 [hep-ph].

[428] T. Gehrmann, A. von Manteuffel, and L. Tancredi, *The two-loop helicity amplitudes for $q\bar{q}' \to V_1 V_2 \to 4$ leptons*, JHEP **09** (2015) 128, arXiv:1503.04812 [hep-ph].

[429] S. Alioli, F. Caola, G. Luisoni, and R. Röntsch, *ZZ production in gluon fusion at NLO matched to parton-shower*, Phys. Rev. **D95** (2017) no. 3, 034042, arXiv:1609.09719 [hep-ph].

[430] M. Grazzini, S. Kallweit, M. Wiesemann, and J. Y. Yook, *ZZ production at the LHC: NLO QCD corrections to the loop-induced gluon fusion channel*, JHEP **03** (2019) 070, arXiv:1811.09593 [hep-ph].

[431] M. Grazzini, S. Kallweit, D. Rathlev, and A. Torre, *$Z\gamma$ production at hadron colliders in NNLO QCD*, Phys. Lett. **B731** (2014) 204–207, arXiv:1309.7000 [hep-ph].

[432] M. Grazzini, S. Kallweit, and D. Rathlev, *$W\gamma$ and $Z\gamma$ production at the LHC in NNLO QCD*, JHEP **07** (2015) 085, arXiv:1504.01330 [hep-ph].

[433] F. Cascioli, T. Gehrmann, M. Grazzini, S. Kallweit, P. Maierhöfer, A. von Manteuffel, S. Pozzorini, D. Rathlev, L. Tancredi, and E. Weihs, *ZZ production at hadron colliders in NNLO QCD*, Phys. Lett. **B735** (2014) 311–313, arXiv:1405.2219 [hep-ph].

[434] M. Grazzini, S. Kallweit, and D. Rathlev, *ZZ production at the LHC: fiducial cross sections and distributions in NNLO QCD*, Phys. Lett. **B750** (2015) 407–410, arXiv:1507.06257 [hep-ph].

[435] T. Gehrmann, M. Grazzini, S. Kallweit, P. Maierhöfer, A. von Manteuffel, S. Pozzorini, D. Rathlev, and L. Tancredi, *W^+W^- Production at Hadron Colliders in Next to Next to Leading Order QCD*, Phys. Rev. Lett. **113** (2014) no. 21, 212001, arXiv:1408.5243 [hep-ph].

[436] M. Grazzini, S. Kallweit, S. Pozzorini, D. Rathlev, and M. Wiesemann, *W^+W^- production at the LHC: fiducial cross sections and distributions in NNLO QCD*, JHEP **08** (2016) 140, arXiv:1605.02716 [hep-ph].

[437] M. Grazzini, S. Kallweit, D. Rathlev, and M. Wiesemann, *$W^\pm Z$ production at hadron colliders in NNLO QCD*, Phys. Lett. **B761** (2016) 179–183, arXiv:1604.08576 [hep-ph].

[438] M. Grazzini, S. Kallweit, D. Rathlev, and M. Wiesemann, *$W^\pm Z$ production at the LHC: fiducial cross sections and distributions in NNLO QCD*, JHEP **05** (2017) 139, arXiv:1703.09065 [hep-ph].

[439] S. Kallweit and M. Wiesemann, *ZZ production at the LHC: NNLO predictions for $2\ell 2\nu$ and 4ℓ signatures*, Phys. Lett. **B786** (2018) 382–389, arXiv:1806.05941 [hep-ph].

[440] M. Grazzini, S. Kallweit, D. Rathlev, and M. Wiesemann, *Transverse-momentum resummation for vector-boson pair production at NNLL+NNLO*, JHEP **08** (2015) 154, arXiv:1507.02565 [hep-ph].

[441] A. Denner, S. Dittmaier, and L. Hofer, *COLLIER - A fortran-library for one-loop integrals*, PoS **LL2014** (2014) 071, arXiv:1407.0087 [hep-ph].

[442] A. Denner, S. Dittmaier, and L. Hofer, COLLIER*: a fortran-based Complex One-Loop LIbrary in Extended Regularizations*, Comput. Phys. Commun. **212** (2017) 220–238, arXiv:1604.06792 [hep-ph].

[443] G. Ossola, C. G. Papadopoulos, and R. Pittau, *CutTools: A Program implementing the OPP reduction method to compute one-loop amplitudes*, JHEP **03** (2008) 042, arXiv:0711.3596 [hep-ph].

[444] F. Buccioni, S. Pozzorini, and M. Zoller, *On-the-fly reduction of open loops*, Eur. Phys. J. **C78** (2018) no. 1, 70, arXiv:1710.11452 [hep-ph].

[445] K. J. F. Gaemers and G. J. Gounaris, *Polarization Amplitudes for e+ e- —> W+ W- and e+ e- —> Z Z*, Z. Phys. **C1** (1979) 259. CERN-TH-2548.

[446] K. Hagiwara, R. D. Peccei, D. Zeppenfeld, and K. Hikasa, *Probing the Weak Boson Sector in e+ e- —> W+ W-*, Nucl. Phys. **B282** (1987) 253–307. DESY-86-058.

[447] T. Melia et al., *W^+W^-, WZ and ZZ production in the POWHEG BOX*, JHEP **11** (2011) 078, arXiv:1107.5051 [hep-ph].

[448] P. Nason and G. Zanderighi, *W^+W^- , WZ and ZZ production in the POWHEG-BOX-V2*, Eur. Phys. J. **C74** (2014) no. 1, 2702, arXiv:1311.1365 [hep-ph].

[449] J. Baglio, S. Dawson, and I. M. Lewis, *NLO effects in EFT fits to W^+W^- production at the LHC*, Phys. Rev. **D99** (2019) no. 3, 035029, arXiv:1812.00214 [hep-ph].

[450] J. Baglio, S. Dawson, and I. M. Lewis, *An NLO QCD effective field theory analysis of W^+W^- production at the LHC including fermionic operators*, Phys. Rev. **D96** (2017) no. 7, 073003, arXiv:1708.03332 [hep-ph].

[451] A. Alves, N. Rosa-Agostinho, O. J. P. Éboli, and M. C. Gonzalez-Garcia, *Effect of Fermionic Operators on the Gauge Legacy of the LHC Run I*, Phys. Rev. **D98** (2018) no. 1, 013006, arXiv:1805.11108 [hep-ph].

[452] ATLAS Collaboration, G. Aad et al., *Measurement of total and differential W^+W^- production cross sections in proton-proton collisions at $\sqrt{s} = 8$ TeV with the ATLAS detector and limits on anomalous triple-gauge-boson couplings*, JHEP **09** (2016) 029, arXiv:1603.01702 [hep-ex].

[453] CMS Collaboration, V. Khachatryan et al., *Measurement of the $\mathrm{W^+W^-}$ cross section in pp collisions at $\sqrt{s} = 8$ TeV and limits on anomalous gauge couplings*, Eur. Phys. J. **C76** (2016) no. 7, 401, arXiv:1507.03268 [hep-ex].

[454] C. Grojean, M. Montull, and M. Riembau, *Diboson at the LHC vs LEP*, JHEP **03** (2019) 020, arXiv:1810.05149 [hep-ph].

[455] F. Zimmermann, *HE-LHC Overview, Parameters and Challenges*, ICFA Beam Dyn. Newslett. **72** (2017) 138–141. http://inspirehep.net/record/1647471/files/9999999_138-141.pdf.

[456] ATLAS Collaboration, *Prospects for the measurement of the W-boson mass at the HL- and HE-LHC*, . https://cds.cern.ch/record/2645431. ATL-PHYS-PUB-2018-026.

[457] H.-L. Lai, M. Guzzi, J. Huston, Z. Li, P. M. Nadolsky, et al., *New parton distributions for collider physics*, Phys. Rev. D **82** (2010) 074024, arXiv:1007.2241 [hep-ph].

[458] ATLAS Collaboration, *Measurement of the Z/γ^* boson transverse momentum distribution in pp collisions at $\sqrt{s} = 7$ TeV with the ATLAS detector*, JHEP **09** (2014) 145, arXiv:1406.3660 [hep-ex].

[459] N. Davidson, T. Przedzinski, and Z. Was, *PHOTOS interface in C++: Technical and Physics Documentation*, Comput. Phys. Commun. **199** (2016) 86–101, arXiv:1011.0937 [hep-ph].

[460] M. Klein and V. Radescu, *Partons from the LHeC*, . https://cds.cern.ch/record/1564929.

[461] LHeC Study Group Collaboration, J. L. Abelleira Fernandez et al., *A Large Hadron Electron Collider at CERN: Report on the Physics and Design Concepts for Machine and Detector*, J. Phys. **G39** (2012) 075001, arXiv:1206.2913 [physics.acc-ph].

[462] ATLAS Collaboration, *Measurement of the transverse momentum and ϕ^*_η distributions of Drell-Yan lepton pairs in proton–proton collisions at $\sqrt{s} = 8$ TeV with the ATLAS detector*, Eur. Phys. J. C **76** (2016) 291, arXiv:1512.02192 [hep-ex].

[463] A. Valassi, *Combining correlated measurements of several different physical quantities*, Nucl. Instrum. Meth. A **500** (2003) 391–405.

[464] J. C. Collins and D. E. Soper, *Angular Distribution of Dileptons in High-Energy Hadron Collisions*, Phys. Rev. **D16** (1977) 2219.

[465] M. Chaichian, M. Hayashi, and K. Yamagishi, *Angular Distributions of High Mass Dileptons With Finite Transverse Momentum in High-energy Hadronic Collisions*, Phys. Rev. **D25** (1982) 130. [Erratum: Phys. Rev.D26,2534(1982)], HU-TFT-81-13.

[466] SLD Electroweak Group, DELPHI, ALEPH, SLD, SLD Heavy Flavour Group, OPAL, LEP Electroweak Working Group, L3 Collaboration, S. Schael et al., *Precision electroweak measurements on the Z resonance*, Phys. Rept. **427** (2006) 257, arXiv:hep-ex/0509008 [hep-ex].

[467] CMS Collaboration, S. Chatrchyan et al., *Measurement of the weak mixing angle with the Drell-Yan process in proton-proton collisions at the LHC*, Phys. Rev. D **84** (2011) 112002, arXiv:1110.2682 [hep-ex].

[468] ATLAS Collaboration, G. Aad et al., *Measurement of the forward-backward asymmetry of electron and muon pair-production in pp collisions at $\sqrt{s}$ = 7 TeV with the ATLAS detector*, JHEP **09** (2015) 049, arXiv:1503.03709 [hep-ex].

[469] LHCb Collaboration, R. Aaij et al., *Measurement of the forward-backward asymmetry in $Z/\gamma^* \to \mu^+\mu^-$ decays and determination of the effective weak mixing angle*, JHEP **11** (2015) 190, arXiv:1509.07645 [hep-ex].

[470] CDF Collaboration, T. A. Aaltonen et al., *Indirect measurement of $\sin^2\theta_W$ (or M_W) using $\mu^+\mu^-$ pairs from γ^*/Z bosons produced in $p\bar{p}$ collisions at a center-of-momentum energy of 1.96 TeV*, Phys. Rev. D **89** (2014) 072005, arXiv:1402.2239 [hep-ex].

[471] CDF Collaboration, T. A. Aaltonen et al., *Measurement of $\sin^2\theta^{\rm lept}_{\rm eff}$ using e^+e^- pairs from γ^*/Z bosons produced in $p\bar{p}$ collisions at a center-of-momentum energy of 1.96 TeV*, Phys. Rev. D **93** (2016) 112016, arXiv:1605.02719 [hep-ex].

[472] D0 Collaboration, V. M. Abazov et al., *Measurement of the effective weak mixing angle in $p\bar{p} \to Z/\gamma^* \to e^+e^-$ events*, Phys. Rev. Lett. **115** (2015) 041801, arXiv:1408.5016 [hep-ex].

[473] W. T. Giele and S. Keller, *Implications of hadron collider observables on parton distribution function uncertainties*, Phys. Rev. D **58** (1998) 094023, arXiv:hep-ph/9803393 [hep-ph].

[474] N. Sato, J. F. Owens, and H. Prosper, *Bayesian Reweighting for Global Fits*, Phys. Rev. D **89** (2014) 114020, arXiv:1310.1089 [hep-ph].

[475] A. Bodek, J. Han, A. Khukhunaishvili, and W. Sakumoto, *Using Drell-Yan forward-backward asymmetry to reduce PDF uncertainties in the measurement of electroweak parameters*, Eur. Phys. J. C **76** (2016) 115, arXiv:1507.02470 [hep-ex].

[476] H. Paukkunen and P. Zurita, *PDF reweighting in the Hessian matrix approach*, JHEP **12** (2014) 100, arXiv:1402.6623 [hep-ph].

[477] ATLAS Collaboration, *Prospect for a measurement of the Weak Mixing Angle in $pp \to Z/\gamma^* \to e^+e^-$ ATLAS detector at the High Luminosity Large Hadron Collider*, ATL-PHYS-PUB-2018-037, CERN, Geneva, Nov, 2018. https://cds.cern.ch/record/2649330.

[478] CMS Collaboration, *A proposal for the measurement of the weak mixing angle at the HL-LHC*, CMS-PAS-FTR-17-001, CERN, Geneva, 2017. https://cds.cern.ch/record/2294888.

[479] W. J. Barter, *Prospects for measurement of the weak mixing angle at LHCb*, LHCb-PUB-2018-013. CERN-LHCb-PUB-2018-013, CERN, Geneva, Nov, 2018. https://cds.cern.ch/record/2647836.

[480] S. Alioli, P. Nason, C. Oleari, and E. Re, *NLO vector-boson production matched with shower in POWHEG*, JHEP **07** (2008) 060, arXiv:0805.4802 [hep-ph].

[481] P. Nason, *A new method for combining NLO QCD with shower Monte Carlo algorithms*, JHEP **11** (2004) 040, arXiv:hep-ph/0409146 [hep-ph].

[482] S. Frixione, P. Nason, and C. Oleari, *Matching NLO QCD computations with parton shower simulations: the POWHEG method*, JHEP **11** (2007) 070, arXiv:0709.2092 [hep-ph].

[483] S. Alioli, P. Nason, C. Oleari, and E. Re, *A general framework for implementing NLO calculations in shower Monte Carlo programs: the POWHEG BOX*, JHEP **06** (2010) 043, arXiv:1002.2581 [hep-ph].

[484] NNPDF Collaboration, R. D. Ball et al., *Parton distributions for the LHC Run II*, JHEP **04** (2015) 040, arXiv:1410.8849 [hep-ph].

[485] LHCb Collaboration, R. Aaij et al., *LHCb Detector Performance*, Int. J. Mod. Phys. **A30** (2015) no. 07, 1530022, arXiv:1412.6352 [hep-ex].

[486] ATLAS Collaboration, *ATLAS Phase-II Upgrade Scoping Document*, CERN-LHCC-2015-020, Geneva, Sep, 2015. http://cds.cern.ch/record/2055248.

[487] S. Catani, L. Cieri, G. Ferrera, D. de Florian, and M. Grazzini, *Vector Boson Production at Hadron Colliders: A Fully Exclusive QCD Calculation at Next-to-Next-to-Leading Order*, Phys. Rev. Lett. **103** (Aug, 2009) 082001. https://link.aps.org/doi/10.1103/PhysRevLett.103.082001.

[488] CMS Collaboration, *Measurement of the weak mixing angle with the forward-backward asymmetry of Drell-Yan events at 8 TeV*, CMS-PAS-SMP-16-007, CERN, Geneva, 2017. http://cds.cern.ch/record/2273392.

[489] ATLAS Collaboration, M. Aaboud et al., *Measurement of the Drell-Yan triple-differential cross section in pp collisions at* $\sqrt{s} = 8$ *TeV*, JHEP **12** (2017) 059, arXiv:1710.05167 [hep-ex].

[490] S. Alekhin et al., *HERAFitter*, Eur. Phys. J. **C75** (2015) no. 7, 304, arXiv:1410.4412 [hep-ph].

[491] ATLAS Collaboration, *Measurement of the effective leptonic weak mixing angle using electron and muon pairs from* Z*-boson decay in the ATLAS experiment at* $\sqrt{s} = 8$ *TeV*, ATLAS-CONF-2018-037, CERN, Geneva, Jul, 2018. https://cds.cern.ch/record/2630340.

[492] Gfitter Group Collaboration, M. Baak, J. Cúth, J. Haller, A. Hoecker, R. Kogler, K. Mönig, M. Schott, and J. Stelzer, *The global electroweak fit at NNLO and prospects for the LHC and ILC*, Eur. Phys. J. **C74** (2014) 3046, arXiv:1407.3792 [hep-ph].

[493] J. de Blas, M. Ciuchini, E. Franco, S. Mishima, M. Pierini, L. Reina, and L. Silvestrini, *Electroweak precision observables and Higgs-boson signal strengths in the Standard Model and beyond: present and future*, JHEP **12** (2016) 135, arXiv:1608.01509 [hep-ph].

[494] HEPfit *Collaboration*, https://web.archive.org/web/20181110113242/http://hepfit.roma1.infn.it, Archived 10 November 2018.

[495] A. Caldwell, D. Kollar, and K. Kroninger, *BAT: The Bayesian Analysis Toolkit*, Comput. Phys. Commun. **180** (2009) 2197–2209, arXiv:0808.2552 [physics.data-an].

[496] I. Dubovyk, A. Freitas, J. Gluza, T. Riemann, and J. Usovitsch, *The two-loop electroweak bosonic corrections to* $\sin^2\theta^b_{eff}$, Phys. Lett. **B762** (2016) 184–189, arXiv:1607.08375 [hep-ph].

[497] I. Dubovyk, A. Freitas, J. Gluza, T. Riemann, and J. Usovitsch, *Complete electroweak two-loop corrections to Z boson production and decay*, Phys. Lett. **B783** (2018) 86–94, arXiv:1804.10236 [hep-ph].

[498] J. de Blas, M. Ciuchini, E. Franco, S. Mishima, M. Pierini, L. Reina, and L. Silvestrini, *Electroweak precision constraints at present and future colliders*, PoS **ICHEP2016** (2017) 690, arXiv:1611.05354 [hep-ph].

[499] J. de Blas, M. Ciuchini, E. Franco, S. Mishima, M. Pierini, L. Reina, and L. Silvestrini, *The Global Electroweak and Higgs Fits in the LHC era*, PoS **EPS-HEP2017** (2017) 467, arXiv:1710.05402 [hep-ph].

[500] A. Keshavarzi, D. Nomura, and T. Teubner, *Muon* $g-2$ *and* $\alpha(M_Z^2)$*: a new data-based analysis*, Phys. Rev. **D97** (2018) no. 11, 114025, arXiv:1802.02995 [hep-ph].

[501] CMS Collaboration, A. M. Sirunyan et al., *Measurement of the top quark mass using single top quark events in proton-proton collisions at* $\sqrt{s} = 8$ *TeV*, Eur. Phys. J. **C77** (2017) no. 5, 354, arXiv:1703.02530 [hep-ex].

[502] ATLAS Collaboration, *Measurement of the top quark mass in the* $t\bar{t}$ *lepton+jets channel from* $\sqrt{s}$*=8 TeV ATLAS data*, ATLAS-CONF-2017-071, CERN, Geneva, 2017.

[503] CMS Collaboration, A. M. Sirunyan et al., *Measurement of the top quark mass with lepton+jets final states using* p p *collisions at* $\sqrt{s} = 13$ *TeV*, Eur. Phys. J. **C78** (2018) no. 11, 891, arXiv:1805.01428 [hep-ex].

[504] CMS Collaboration, A. M. Sirunyan et al., *Measurements of properties of the Higgs boson decaying into the four-lepton final state in pp collisions at* $\sqrt{s} = 13$ *TeV*, JHEP **11** (2017) 047, arXiv:1706.09936 [hep-ex].

[505] ATLAS Collaboration, M. Aaboud et al., *Measurement of the Higgs boson mass in the* $H \to ZZ^* \to 4\ell$ *and* $H \to \gamma\gamma$ *channels with* $\sqrt{s} = 13$ *TeV pp collisions using the ATLAS detector*, Phys. Lett. **B784** (2018) 345–366, arXiv:1806.00242 [hep-ex].

[506] CMS Collaboration, *Measurement of the weak mixing angle using the forward-backward asymmetry of Drell-Yan events in pp collisions at 8 TeV*, Eur. Phys. J. **C78** (2018) 701, arXiv:1806.00863 [hep-ex].

[507] ALEPH, DELPHI, L3, OPAL, LEP Electroweak Collaboration, S. Schael et al., *Electroweak Measurements in Electron-Positron Collisions at W-Boson-Pair Energies at LEP*, Phys. Rept. **532** (2013) 119–244, arXiv:1302.3415 [hep-ex].

[508] CDF Collaboration, T. A. Aaltonen et al., *Precise measurement of the W -boson mass with the Collider Detector at Fermilab*, Phys. Rev. **D89** (2014) no. 7, 072003, arXiv:1311.0894 [hep-ex].

[509] Particle Data Group Collaboration, M. Tanabashi et al., *Review of Particle Physics*, Phys. Rev. **D98** (2018) no. 3, 030001.

[510] S. Dawson et al., *Working Group Report: Higgs Boson*, in *Proceedings, 2013 Community Summer Study on the Future of U.S. Particle Physics: Snowmass on the Mississippi (CSS2013): Minneapolis, MN, USA, July 29-August 6, 2013*. 2013. arXiv:1310.8361 [hep-ex]. http://www.slac.stanford.edu/econf/C1307292/docs/EnergyFrontier/Higgs-18.pdf.

[511] M. Cepeda et al., *Higgs Physics at the HL-LHC and HE-LHC*, arXiv:1902.00134 [hep-ph].

[512] M. E. Peskin and T. Takeuchi, *Estimation of oblique electroweak corrections*, Phys. Rev. **D46** (1992) 381–409. SLAC-PUB-5618.

[513] B. Grzadkowski, M. Iskrzynski, M. Misiak, and J. Rosiek, *Dimension-Six Terms in the Standard Model Lagrangian*, JHEP **10** (2010) 085, arXiv:1008.4884 [hep-ph].

[514] ATLAS Collaboration, *Jet energy scale measurements and their systematic uncertainties in proton–proton collisions at $\sqrt{s}$=13 TeV with the ATLAS detector*, Phys. Rev. D **96** (2017) 072002, arXiv:1703.09665 [hep-ex].

[515] ATLAS Collaboration, *Prospects for jet and photon physics at the HL-LHC and HE-LHC*, ATL-PHYS-PUB-2018-051, CERN, Geneva, Dec, 2018. http://cds.cern.ch/record/2652285.

[516] ATLAS Collaboration, *A measurement of the calorimeter response to single hadrons and determination of the jet energy scale uncertainty using LHC Run-1 pp-collision data with the ATLAS detector*, Eur. Phys. J. C **77** (2017) 26, arXiv:1607.08842 [hep-ex].

[517] ATLAS Collaboration, *Measurement of the inclusive $W^{\pm}$ and Z/gamma cross sections in the electron and muon decay channels in pp collisions at $\sqrt{s} = 7$ TeV with the ATLAS detector*, Phys. Rev. **D85** (2012) 072004, arXiv:1109.5141 [hep-ex].

[518] ATLAS Collaboration, *Measurement of the cross section for top-quark pair production in pp collisions at $\sqrt{s} = 7$ TeV with the ATLAS detector using final states with two high-pt leptons*, JHEP **05** (2012) 059, arXiv:1202.4892 [hep-ex].

[519] ATLAS Collaboration, *Measurement of inclusive jet and dijet production in pp collisions at $\sqrt{s} = 7$ TeV using the ATLAS detector*, Phys. Rev. **D86** (2012) 014022, arXiv:1112.6297 [hep-ex].

[520] S. Alekhin, J. Blümlein, S. Moch, and R. Placakyte, *Parton distribution functions, α_s, and heavy-quark masses for LHC Run II*, Phys. Rev. **D96** (2017) no. 1, 014011, arXiv:1701.05838 [hep-ph].

[521] P. Sun, C. P. Yuan, and F. Yuan, *Transverse Momentum Resummation for Dijet Correlation in Hadronic Collisions*, Phys. Rev. **D92** (2015) no. 9, 094007, arXiv:1506.06170 [hep-ph].

[522] J. Collins and J.-W. Qiu, *k_T factorization is violated in production of high-transverse-momentum particles in hadron-hadron collisions*, Phys. Rev. D **75** (2007) 114014, arXiv:0705.2141 [hep-ph].

[523] S. Catani, M. Grazzini, and H. Sargsyan, *Transverse-momentum resummation for top-quark pair production at the LHC*, JHEP **11** (2018) 061, arXiv:1806.01601 [hep-ph].

[524] S. Catani, M. Grazzini, and A. Torre, *Transverse-momentum resummation for heavy-quark hadroproduction*, Nucl.Phys. B **890** (2015) 518–538, arXiv:1408.4564 [hep-ph].

[525] CMS Collaboration, *High-p_{T} jet measurements at HL-LHC*, CMS Physics Analysis Summary CMS-PAS-FTR-18-032, 2018. http://cds.cern.ch/record/2651219.

[526] M. Cacciari, G. P. Salam, and G. Soyez, *The anti-k_{t} jet clustering algorithm*, JHEP **04** (2008) 063, 0802.1189.

[527] ATLAS Collaboration, *Dynamics of isolated-photon plus jet production in pp collisions at $\sqrt{s} = 7$ TeV with the ATLAS detector*, Nucl. Phys. B **875** (2013) 483, arXiv:1307.6795 [hep-ex].

[528] ATLAS Collaboration, *High-E_T isolated-photon plus jets production in pp collisions at $\sqrt{s} = 8$ TeV with the ATLAS detector*, Nucl. Phys. B **918** (2017) 257, arXiv:1611.06586 [hep-ex].

[529] S. Catani, M. Fontannaz, J. Ph. Guillet and E. Pilon, *Cross section of isolated prompt photons in hadron-hadron collisions*, JHEP **0205** (2002) 028, arXiv:hep-ph/0204023 [hep-ph].

[530] P. Aurenche, M. Fontannaz, J. Ph. Guillet, E. Pilon and M. Werlen, *A new critical study of photon production in hadronic collisions*, Phys. Rev. D **73** (2006) 094007, arXiv:hep-ph/0602133 [hep-ph].

[531] L.A. Harland-Lang, A.D. Martin, P. Motylinski and R.S. Thorne, *Parton distributions in the LHC era: MMHT 2014 PDFs*, Eur. Phys. J. **C 75** (2015) 204, arXiv:1412.3989 [hep-ph].

[532] L. Bourhis, M. Fontannaz and J.Ph. Guillet, *Quark and gluon fragmentation functions into photons*, Eur. Phys. J. C **2** (1998) 529, arXiv:hep-ph/9704447 [hep-ph].

[533] ATLAS Collaboration, *Measurement of the cross section for inclusive isolated-photon production in pp collisions at $\sqrt{s}$=13 TeV using the ATLAS detector*, Phys. Lett. B **770** (2017) 473, arXiv:1701.06882 [hep-ex].

[534] ATLAS Collaboration, *Measurement of the cross section for isolated-photon plus jet production in pp collisions at $\sqrt{s}$=13 TeV using the ATLAS detector*, Phys. Lett. B **780** (2018) 578, arXiv:1801.00112 [hep-ex].

[535] CDF Collaboration, T. Aaltonen et al., *Measurement of the Cross Section for Prompt Isolated Diphoton Production in $p\bar{p}$ Collisions at $\sqrt{s} = 1.96$ TeV*, Phys. Rev. **D84** (2011) 052006, arXiv:1106.5131 [hep-ex].

[536] ATLAS Collaboration, M. Aaboud et al., *Measurements of integrated and differential cross sections for isolated photon pair production in pp collisions at $\sqrt{s} = 8$ TeV with the ATLAS detector*, Phys. Rev. **D95** (2017) no. 11, 112005, arXiv:1704.03839 [hep-ex].

[537] ATLAS Collaboration, G. Aad et al., *Search for diphoton events with large missing transverse momentum in 7 TeV proton-proton collision data with the ATLAS detector*, Phys. Lett. **B718** (2012) 411–430, arXiv:1209.0753 [hep-ex].

[538] CMS Collaboration, V. Khachatryan et al., *Search for diphoton resonances in the mass range from 150 to 850 GeV in pp collisions at $\sqrt{s} = 8$ TeV*, Phys. Lett. **B750** (2015) 494–519, arXiv:1506.02301 [hep-ex].

[539] S. Frixione, *Isolated photons in perturbative QCD*, Phys. Lett. **B429** (1998) 369–374, arXiv:hep-ph/9801442 [hep-ph].

[540] S. Frixione and W. Vogelsang, *Isolated photon production in polarized pp collisions*, Nucl. Phys. **B568** (2000) 60–92, arXiv:hep-ph/9908387 [hep-ph].

[541] S. Catani et al., *QCD*, in *1999 CERN Workshop on standard model physics (and more) at the LHC, CERN, Geneva, Switzerland, 25-26 May: Proceedings*. 2000. arXiv:hep-ph/0005025 [hep-ph]. http://weblib.cern.ch/abstract?CERN-TH-2000-131.

[542] ATLAS Collaboration, G. Aad et al., *Measurement of isolated-photon pair production in pp collisions at $\sqrt{s} = 7$ TeV with the ATLAS detector*, JHEP **01** (2013) 086, arXiv:1211.1913 [hep-ex].

[543] CMS Collaboration, S. Chatrchyan et al., *Measurement of differential cross sections for the production of a pair of isolated photons in pp collisions at $\sqrt{s} = 7$ TeV*, Eur. Phys. J. **C74** (2014) no. 11, 3129, arXiv:1405.7225 [hep-ex].

[544] S. Catani, L. Cieri, D. de Florian, G. Ferrera, and M. Grazzini, *Diphoton production at the LHC: a QCD study up to NNLO*, JHEP **04** (2018) 142, arXiv:1802.02095 [hep-ph].

[545] L. Cieri, *Diphoton isolation studies*, Nucl. Part. Phys. Proc. **273-275** (2016) 2033–2039, arXiv:1510.06873 [hep-ph].

[546] J. R. Andersen et al., *Les Houches 2013: Physics at TeV Colliders: Standard Model Working Group Report*, arXiv:1405.1067 [hep-ph].

[547] M. Grazzini, S. Kallweit, and M. Wiesemann, *Fully differential NNLO computations with MATRIX*, Eur. Phys. J. **C78** (2018) no. 7, 537, arXiv:1711.06631 [hep-ph].

[548] LHeC Study Group Collaboration, J. L. Abelleira Fernandez et al., *On the Relation of the LHeC and the LHC*, arXiv:1211.5102 [hep-ex].

[549] L. A. Harland-Lang, V. A. Khoze, and M. G. Ryskin, *Exclusive LHC physics with heavy ions: SuperChic 3*, Eur. Phys. J. **C79** (2019) no. 1, 39, arXiv:1810.06567 [hep-ph].

[550] W. J. Stirling and E. Vryonidou, *Charm production in association with an electroweak gauge boson at the LHC*, Phys. Rev. Lett. **109** (2012) 082002, arXiv:1203.6781 [hep-ph].

[551] CMS Collaboration, *Measurement of the muon charge asymmetry in inclusive pp to WX production at $\sqrt{s}$ = 7 TeV and an improved determination of light parton distribution functions*, Phys.Rev. **D90** (2014) 032004.

[552] D. d'Enterria and J. Rojo, *Quantitative constraints on the gluon distribution function in the proton from collider isolated-photon data*, Nucl. Phys. **B860** (2012) 311–338, arXiv:1202.1762 [hep-ph].

[553] NNPDF Collaboration, J. Rojo, *Improving quark flavor separation with forward W and Z production at LHCb*, PoS **DIS2017** (2018) 198, arXiv:1705.04468 [hep-ph].

[554] J. Rojo, *Constraints on parton distributions and the strong coupling from LHC jet data*, Int. J. Mod. Phys. **A30** (2015) 1546005, arXiv:1410.7728 [hep-ph].

[555] E. L. Berger, J. Gao, and H. X. Zhu, *Differential Distributions for t-channel Single Top-Quark Production and Decay at Next-to-Next-to-Leading Order in QCD*, JHEP **11** (2017) 158, arXiv:1708.09405 [hep-ph].

[556] CMS Collaboration, *Measurement of the differential cross section for top quark pair production in pp collisions at $\sqrt{s} = 8$ TeV*, Eur. Phys. J. **C75** (2015) no. 11, 542.

[557] ATLAS Collaboration, *Measurements of top-quark pair differential cross-sections in the lepton+jets channel in pp collisions at $\sqrt{s} = 8$ TeV using the ATLAS detector*, Eur. Phys. J. **C76** (2016) no. 10, 538.

[558] CMS Collaboration, *Measurement of associated production of W bosons with charm quarks in proton-proton collisions at $\sqrt{s} = 13$ TeV with the CMS experiment at the LHC*, CMS-PAS-SMP-17-014, CERN, Geneva, 2018. https://cds.cern.ch/record/2314570.

[559] ATLAS Collaboration, *Measurement of the transverse momentum and ϕ^*_η distributions of Drell-Yan lepton pairs in proton-proton collisions at $\sqrt{s} = 8$ TeV with the ATLAS detector*, Eur. Phys. J. **C76** (2016) no. 5, 291.

[560] ATLAS Collaboration, *Measurement of the double-differential high-mass Drell-Yan cross section in pp collisions at $\sqrt{s} = 8$ TeV with the ATLAS detector*, JHEP **08** (2016) 009.

[561] ATLAS Collaboration, *Measurement of the cross section for inclusive isolated-photon production in pp collisions at $\sqrt{s} = 13$ TeV using the ATLAS detector*, Phys. Lett. **B770** (2017) 473–493.

[562] LHCb Collaboration, *Measurement of forward W and Z boson production in pp collisions at $\sqrt{s} = 8$ TeV*, JHEP **01** (2016) 155.

[563] CMS Collaboration, V. Khachatryan et al., *Measurement of the double-differential inclusive jet cross section in proton–proton collisions at $\sqrt{s} = 13$ TeV*, Eur. Phys. J. **C76** (2016) no. 8, 451, arXiv:1605.04436 [hep-ex].

[564] R. D. Ball, V. Bertone, F. Cerutti, L. Del Debbio, S. Forte, et al., *Reweighting and Unweighting of Parton Distributions and the LHC W lepton asymmetry data*, Nucl.Phys. **B855** (2012) 608–638.

[565] NNPDF Collaboration, R. D. Ball, V. Bertone, F. Cerutti, L. Del Debbio, S. Forte, A. Guffanti, J. I. Latorre, J. Rojo, and M. Ubiali, *Reweighting NNPDFs: the W lepton asymmetry*, Nucl. Phys. B **849** (2011) 112–143, arXiv:1012.0836 [hep-ph]. [Erratum: Nucl. Phys.B855,927(2012)].

[566] B. C. Allanach et al., *SUSY Les Houches Accord 2*, Comput. Phys. Commun. **180** (2009) 8–25, arXiv:0801.0045 [hep-ph].

[567] ATLAS Collaboration, *Measurement of underlying event characteristics using charged particles in pp collisions at $\sqrt{s} = 900GeV$ and 7 TeV with the ATLAS detector*, Phys. Rev. **D83** (2011) 112001, arXiv:1012.0791 [hep-ex].

[568] ATLAS Collaboration, *Measurement of charged-particle distributions sensitive to the underlying event in $\sqrt{s} = 13$ TeV proton-proton collisions with the ATLAS detector at the LHC*, JHEP **03** (2017) 157, arXiv:1701.05390 [hep-ex].

[569] M. Diehl, D. Ostermeier, and A. Schafer, *Elements of a theory for multiparton interactions in QCD*, JHEP **03** (2012) 089, arXiv:1111.0910 [hep-ph]. [Erratum: JHEP03,001(2016)].

[570] M. Diehl, J. R. Gaunt, D. Ostermeier, P. Plößl, and A. Schäfer, *Cancellation of Glauber gluon exchange in the double Drell-Yan process*, JHEP **01** (2016) 076, arXiv:1510.08696 [hep-ph].

[571] M. Diehl, J. R. Gaunt, and K. Schönwald, *Double hard scattering without double counting*, JHEP **06** (2017) 083, arXiv:1702.06486 [hep-ph].

[572] M. G. A. Buffing, M. Diehl, and T. Kasemets, *Transverse momentum in double parton scattering: factorisation, evolution and matching*, JHEP **01** (2018) 044, arXiv:1708.03528 [hep-ph].

[573] B. Blok, Yu. Dokshitser, L. Frankfurt, and M. Strikman, *pQCD physics of multiparton interactions*, Eur. Phys. J. **C72** (2012) 1963, arXiv:1106.5533 [hep-ph].

[574] A. V. Manohar and W. J. Waalewijn, *A QCD Analysis of Double Parton Scattering: Color Correlations, Interference Effects and Evolution*, Phys. Rev. **D85** (2012) 114009, arXiv:1202.3794 [hep-ph].

[575] F. A. Ceccopieri, M. Rinaldi, and S. Scopetta, *Parton correlations in same-sign W pair production via double parton scattering at the LHC*, Phys. Rev. **D95** (2017) no. 11, 114030, arXiv:1702.05363 [hep-ph].

[576] CMS Collaboration, *The Phase-2 Upgrade of the CMS Muon Detectors*, CERN-LHCC-2017-012. CMS-TDR-016, CERN, Geneva, Sep, 2017. https://cds.cern.ch/record/2283189.

[577] J. R. Gaunt and W. J. Stirling, *Double Parton Distributions Incorporating Perturbative QCD Evolution and Momentum and Quark Number Sum Rules*, JHEP **03** (2010) 005, arXiv:0910.4347 [hep-ph].

[578] T. Kasemets and M. Diehl, *Angular correlations in the double Drell-Yan process*, JHEP **01** (2013) 121, arXiv:1210.5434 [hep-ph].

[579] S. Cotogno, T. Kasemets, and M. Myska, *A spin on same-sign W-boson pair production*, arXiv:1809.09024 [hep-ph].

[580] M. Diehl and T. Kasemets, *Positivity bounds on double parton distributions*, JHEP **05** (2013) 150, arXiv:1303.0842 [hep-ph].

[581] S. Cotogno, *Polarized partons in hadrons at high energy - The structure of hadrons from single and double parton interactions*. PhD thesis, Vrije U., Amsterdam, 2018-09. http://inspirehep.net/record/1725056/.

[582] M. Diehl, T. Kasemets, and S. Keane, *Correlations in double parton distributions: effects of evolution*, JHEP **05** (2014) 118, arXiv:1401.1233 [hep-ph].

[583] M. Czakon, D. Heymes, and A. Mitov, *High-precision differential predictions for top-quark pairs at the LHC*, Phys. Rev. Lett. **116** (2016) no. 8, 082003, arXiv:1511.00549 [hep-ph].

[584] CMS Collaboration, *Projection of measurements of differential ttbar production cross sections in the e/u+jets channels in pp collisions at the HL-LHC*, CMS-PAS-FTR-18-015, CERN, Geneva, 2018. https://cds.cern.ch/record/2651195.

[585] CMS Collaboration, V. Khachatryan et al., *Measurement of differential cross sections for top quark pair production using the lepton+jets final state in proton-proton collisions at 13 TeV*, Phys. Rev. D **95** (2017) 092001, arXiv:1610.04191 [hep-ex].

[586] CMS Collaboration, A. M. Sirunyan et al., *Measurement of differential cross sections for the production of top quark pairs and of additional jets in lepton+jets events from pp collisions at* $\sqrt{s} = 13$ *TeV*, Phys. Rev. D **97** (2018) 112003, arXiv:1803.08856 [hep-ex].

[587] CMS Collaboration, *The Phase-2 Upgrade of the CMS Tracker*, Technical Report CERN-LHCC-2017-009, 2017. https://cds.cern.ch/record/2272264.

[588] CMS Collaboration, *The Phase-2 Upgrade of the CMS Barrel Calorimeters Technical Design Report*, Technical Report CERN-LHCC-2017-011, 2017. https://cds.cern.ch/record/2283187.

[589] CMS Collaboration, *The Phase-2 Upgrade of the CMS Endcap Calorimeter*, Technical Report CERN-LHCC-2017-023, 2017. https://cds.cern.ch/record/2293646.

[590] CMS Collaboration, *The Phase-2 Upgrade of the CMS Muon Detectors*, Technical Report CERN-LHCC-2017-012, 2017. https://cds.cern.ch/record/2283189.

[591] D. Bertolini, P. Harris, M. Low, and N. Tran, *Pileup Per Particle Identification*, JHEP (2014) 059, arXiv:1407.6013 [hep-ph].

[592] B. A. Betchart, R. Demina, and A. Harel, *Analytic solutions for neutrino momenta in decay of top quarks*, Nucl. Instrum. Meth. **A736** (2014) 169–178, arXiv:1305.1878 [hep-ph].

[593] V. Bertone, R. Frederix, S. Frixione, J. Rojo, and M. Sutton, *aMCfast: automation of fast NLO computations for PDF fits*, JHEP **08** (2014) 166, arXiv:1406.7693 [hep-ph].

[594] S. Alekhin, J. Blümlein, and S. Moch, *NLO PDFs from the ABMP16 fit*, Eur. Phys. J. **C78** (2018) no. 6, 477, arXiv:1803.07537 [hep-ph].

[595] CMS Collaboration, A. M. Sirunyan et al., *Measurement of double-differential cross sections for top quark pair production in pp collisions at* $\sqrt{s} = 8$ *TeV and impact on parton distribution functions*, Eur. Phys. J. **C77** (2017) no. 7, 459, arXiv:1703.01630 [hep-ex].

[596] LHCb collaboration, R. Aaij et al., *First observation of top quark production in the forward region*, Phys. Rev. Lett. **115** (2015) 112001 LHCb-PAPER-2015-022, CERN-PH-EP-2015-132, arXiv:1506.00903 [hep-ex].

[597] LHCb collaboration, R. Aaij et al., *Measurement of the* $t\bar{t}$*,* $W + b\bar{b}$ *and* $W + c\bar{c}$ *production cross sections in pp collisions at* $\sqrt{s} = 8$ *TeV*, Phys. Lett. **B767** (2017) 110 LHCb-PAPER-2016-038, CERN-EP-2016-232, arXiv:1610.08142 [hep-ex].

[598] LHCb collaboration, R. Aaij et al., *Measurement of forward top pair production in the dilepton channel in pp collisions at* $\sqrt{s} = 13$ *TeV*, LHCb-PAPER-2017-050, CERN-EP-2018-022, arXiv:1803.05188 [hep-ex]. submitted to JHEP.

[599] R. Gauld, *Leptonic top-quark asymmetry predictions at LHCb*, Phys. Rev. **D91** (2015) 054029, arXiv:1409.8631 [hep-ph].

[600] R. Gauld, *Feasibility of top quark measurements at LHCb and constraints on the large-*x *gluon PDF*, JHEP **02** (2014) 126, arXiv:1311.1810 [hep-ph].

[601] J. M. Campbell, R. Frederix, F. Maltoni, and F. Tramontano, *NLO predictions for t-channel production of single top and fourth generation quarks at hadron colliders*, JHEP **10** (2009) 042, arXiv:0907.3933 [hep-ph].

[602] J. M. Campbell, R. Frederix, F. Maltoni, and F. Tramontano, *Next-to-Leading-Order Predictions for t-Channel Single-Top Production at Hadron Colliders*, Phys. Rev. Lett. **102** (2009) 182003, arXiv:0903.0005 [hep-ph].

[603] R. Frederix, E. Re, and P. Torrielli, *Single-top t-channel hadroproduction in the four-flavour scheme with POWHEG and aMC@NLO*, JHEP **09** (2012) 130, arXiv:1207.5391 [hep-ph].

[604] F. Cascioli, S. Kallweit, P. Maierhöfer, and S. Pozzorini, *A unified NLO description of top-pair and associated Wt production*, PoS **LL2014** (2014) 026.

[605] M. Brucherseifer, F. Caola, and K. Melnikov, *On the NNLO QCD corrections to single-top production at the LHC*, Phys. Lett. **B736** (2014) 58–63, arXiv:1404.7116 [hep-ph].

[606] E. L. Berger, J. Gao, C. P. Yuan, and H. X. Zhu, *NNLO QCD Corrections to t-channel Single Top-Quark Production and Decay*, Phys. Rev. **D94** (2016) no. 7, 071501, arXiv:1606.08463 [hep-ph].

[607] Z. L. Liu and J. Gao, *s -channel single top quark production and decay at next-to-next-to-leading-order in QCD*, Phys. Rev. **D98** (2018) no. 7, 071501, arXiv:1807.03835 [hep-ph].

[608] J. Gao, C. S. Li, and H. X. Zhu, *Top Quark Decay at Next-to-Next-to Leading Order in QCD*, Phys. Rev. Lett. **110** (2013) no. 4, 042001, arXiv:1210.2808 [hep-ph].

[609] M. Brucherseifer, F. Caola, and K. Melnikov, *$\mathcal{O}(\alpha_s^2)$ corrections to fully-differential top quark decays*, JHEP **04** (2013) 059, arXiv:1301.7133 [hep-ph].

[610] A. S. Papanastasiou, R. Frederix, S. Frixione, V. Hirschi, and F. Maltoni, *Single-top t-channel production with off-shell and non-resonant effects*, Phys. Lett. **B726** (2013) 223–227, arXiv:1305.7088 [hep-ph].

[611] J. Campbell, R. K. Ellis, and R. Röntsch, *Single top production in association with a Z boson at the LHC*, Phys. Rev. **D87** (2013) 114006, arXiv:1302.3856 [hep-ph].

[612] J. Alwall, R. Frederix, J. M. Gerard, A. Giammanco, M. Herquet, S. Kalinin, E. Kou, V. Lemaitre, and F. Maltoni, *Is $V_{(tb)} \simeq 1$?*, Eur. Phys. J. **C49** (2007) 791–801, arXiv:hep-ph/0607115 [hep-ph].

[613] ATLAS Collaboration, M. Aaboud et al., *Measurement of the inclusive cross-sections of single top-quark and top-antiquark t-channel production in pp collisions at $\sqrt{s}$ = 13 TeV with the ATLAS detector*, JHEP **04** (2017) 086, arXiv:1609.03920 [hep-ex].

[614] CMS Collaboration, A. M. Sirunyan et al., *Cross section measurement of t-channel single top quark production in pp collisions at $\sqrt{s} = 13$ TeV*, Phys. Lett. **B772** (2017) 752–776, arXiv:1610.00678 [hep-ex].

[615] S. Weinberg, *Phenomenological Lagrangians*, Physica **A96** (1979) no. 1-2, 327–340.

[616] W. Buchmuller and D. Wyler, *Effective Lagrangian Analysis of New Interactions and Flavor Conservation*, Nucl. Phys. **B268** (1986) 621–653. CERN-TH-4254/85.

[617] G. Bevilacqua and M. Worek, *Constraining BSM Physics at the LHC: Four top final states with NLO accuracy in perturbative QCD*, JHEP **07** (2012) 111, arXiv:1206.3064 [hep-ph].

[618] CMS Collaboration, A. M. Sirunyan et al., *Search for standard model production of four top quarks with same-sign and multilepton final states in proton–proton collisions at $\sqrt{s} = 13$ TeV*, Eur. Phys. J. **C78** (2018) no. 2, 140, arXiv:1710.10614 [hep-ex].

[619] CMS Collaboration, A. M. Sirunyan et al., *Search for standard model production of four top quarks in proton-proton collisions at $\sqrt{s}$ = 13 TeV*, Phys. Lett. **B772** (2017) 336–358, arXiv:1702.06164 [hep-ex].

[620] CMS Collaboration, V. Khachatryan et al., *Search for Standard Model Production of Four Top Quarks in the Lepton + Jets Channel in pp Collisions at $\sqrt{s}$ = 8 TeV*, JHEP **11** (2014) 154, arXiv:1409.7339 [hep-ex].

[621] CMS Collaboration, V. Khachatryan et al., *Search for new physics in same-sign dilepton events in proton–proton collisions at $\sqrt{s} = 13$ TeV*, Eur. Phys. J. **C76** (2016) no. 8, 439, arXiv:1605.03171 [hep-ex].

[622] ATLAS Collaboration, G. Aad et al., *Search for supersymmetry at $\sqrt{s}$=8 TeV in final states with jets and two same-sign leptons or three leptons with the ATLAS detector*, JHEP **06** (2014) 035, arXiv:1404.2500 [hep-ex].

[623] ATLAS Collaboration, G. Aad et al., *Search for production of vector-like quark pairs and of four top quarks in the lepton-plus-jets final state in pp collisions at $\sqrt{s} = 8$ TeV with the ATLAS detector*, JHEP **08** (2015) 105, arXiv:1505.04306 [hep-ex].

[624] ATLAS Collaboration, M. Aaboud et al., *Search for pair production of up-type vector-like quarks and for four-top-quark events in final states with multiple b-jets with the ATLAS detector*, JHEP **07** (2018) 089, arXiv:1803.09678 [hep-ex].

[625] ATLAS Collaboration, M. Aaboud et al., *Search for new phenomena in events with same-charge leptons and b-jets in pp collisions at $\sqrt{s} = 13$ TeV with the ATLAS detector*, JHEP **12** (2018) 039, arXiv:1807.11883 [hep-ex].

[626] F. Maltoni, D. Pagani, and I. Tsinikos, *Associated production of a top-quark pair with vector bosons at NLO in QCD: impact on $\mathrm{t\bar{t}H}$ searches at the LHC*, JHEP **02** (2016) 113, arXiv:1507.05640 [hep-ph].

[627] ATLAS Collaboration, *HL-LHC prospects for the measurement of the Standard Model four-top-quark production cross-section*, ATL-PHYS-PUB-2018-047, 2018. https://cds.cern.ch/record/2651870.

[628] CMS Collaboration, *Projections of sensitivities for tttt production at HL-LHC and HE-LHC*, CMS-PAS-FTR-18-031, CERN, Geneva, 2018. http://cds.cern.ch/record/2650211.

[629] P. J. Fox, A. E. Nelson, and N. Weiner, *Dirac gaugino masses and supersoft supersymmetry breaking*, JHEP **08** (2002) 035, arXiv:hep-ph/0206096 [hep-ph].

[630] G. Burdman, B. A. Dobrescu, and E. Ponton, *Resonances from two universal extra dimensions*, Phys. Rev. **D74** (2006) 075008, arXiv:hep-ph/0601186 [hep-ph].

[631] G. D. Kribs, E. Poppitz, and N. Weiner, *Flavor in supersymmetry with an extended R-symmetry*, Phys. Rev. **D78** (2008) 055010, arXiv:0712.2039 [hep-ph].

[632] K. Benakli and M. D. Goodsell, *Dirac Gauginos in General Gauge Mediation*, Nucl. Phys. **B816** (2009) 185–203, arXiv:0811.4409 [hep-ph].

[633] C. Kilic, T. Okui, and R. Sundrum, *Vectorlike Confinement at the LHC*, JHEP **02** (2010) 018, arXiv:0906.0577 [hep-ph].

[634] S. Calvet, B. Fuks, P. Gris, and L. Valery, *Searching for sgluons in multitop events at a center-of-mass energy of 8 TeV*, JHEP **04** (2013) 043, arXiv:1212.3360 [hep-ph].

[635] L. Darmé, B. Fuks, and M. Goodsell, *Cornering sgluons with four-top-quark events*, Phys. Lett. **B784** (2018) 223–228, arXiv:1805.10835 [hep-ph].

[636] C. Degrande, C. Duhr, B. Fuks, D. Grellscheid, O. Mattelaer, and T. Reiter, *UFO - The Universal FeynRules Output*, Comput. Phys. Commun. **183** (2012) 1201–1214, arXiv:1108.2040 [hep-ph].

[637] A. Alloul, N. D. Christensen, C. Degrande, C. Duhr, and B. Fuks, *FeynRules 2.0 - A complete toolbox for tree-level phenomenology*, Comput. Phys. Commun. **185** (2014) 2250–2300, arXiv:1310.1921 [hep-ph].

[638] C. Degrande, *Automatic evaluation of UV and R2 terms for beyond the Standard Model Lagrangians: a proof-of-principle*, Comput. Phys. Commun. **197** (2015) 239–262, arXiv:1406.3030 [hep-ph].

[639] T. Hahn, *Generating Feynman diagrams and amplitudes with FeynArts 3*, Comput. Phys. Commun. **140** (2001) 418–431, arXiv:hep-ph/0012260 [hep-ph].

[640] J. Alwall, C. Duhr, B. Fuks, O. Mattelaer, D. G. Öztürk, and C.-H. Shen, *Computing decay rates for new physics theories with FeynRules and MadGraph5_aMC@NLO*, Comput. Phys. Commun. **197** (2015) 312–323, arXiv:1402.1178 [hep-ph].

[641] E. Conte, B. Fuks, and G. Serret, *MadAnalysis 5, A User-Friendly Framework for Collider Phenomenology*, Comput. Phys. Commun. **184** (2013) 222–256, arXiv:1206.1599 [hep-ph].

[642] E. Conte, B. Dumont, B. Fuks, and C. Wymant, *Designing and recasting LHC analyses with MadAnalysis 5*, Eur. Phys. J. **C74** (2014) no. 10, 3103, arXiv:1405.3982 [hep-ph].

[643] B. Dumont, B. Fuks, S. Kraml, S. Bein, G. Chalons, E. Conte, S. Kulkarni, D. Sengupta, and C. Wymant, *Toward a public analysis database for LHC new physics searches using MADANALYSIS 5*, Eur. Phys. J. **C75** (2015) no. 2, 56, arXiv:1407.3278 [hep-ph].

[644] Q.-H. Cao, S.-L. Chen, and Y. Liu, *Probing Higgs Width and Top Quark Yukawa Coupling from $t\bar{t}H$ and $t\bar{t}t\bar{t}$ Productions*, Phys. Rev. **D95** (2017) no. 5, 053004, arXiv:1602.01934 [hep-ph].

[645] V. D. Barger, A. L. Stange, and R. J. N. Phillips, *Four heavy quark hadroproduction*, Phys. Rev. **D44** (1991) 1987–1996.

[646] C. Zhang, *Constraining $qqtt$ operators from four-top production: a case for enhanced EFT sensitivity*, Chin. Phys. **C42** (2018) no. 2, 023104, arXiv:1708.05928 [hep-ph].

[647] R. Contino, A. Falkowski, F. Goertz, C. Grojean, and F. Riva, *On the Validity of the Effective Field Theory Approach to SM Precision Tests*, JHEP **07** (2016) 144, arXiv:1604.06444 [hep-ph].

[648] M. Malekhosseini, M. Ghominejad, H. Khanpour, and M. Mohammadi Najafabadi, *Constraining top quark flavor violation and dipole moments through three and four-top quark productions at the LHC*, Phys. Rev. **D98** (2018) no. 9, 095001, arXiv:1804.05598 [hep-ph].

[649] T. Ibrahim and P. Nath, *The Top quark electric dipole moment in an MSSM extension with vector like multiplets*, Phys. Rev. **D82** (2010) 055001, arXiv:1007.0432 [hep-ph].

[650] B. Yang, J. Han, and X. Zhang, *Production of $Zt\bar{t}$ and $Zt\bar{T}$ in the littlest Higgs model with T-parity at High Energy Colliders*, Eur. Phys. J. **C73** (2013) no. 12, 2639.

[651] J. A. Aguilar-Saavedra, *A Minimal set of top anomalous couplings*, Nucl. Phys. **B812** (2009) 181–204, arXiv:0811.3842 [hep-ph].

[652] J. A. Aguilar-Saavedra, B. Fuks, and M. L. Mangano, *Pinning down top dipole moments with ultra-boosted tops*, Phys. Rev. **D91** (2015) 094021, arXiv:1412.6654 [hep-ph].

[653] T. Sjostrand, L. Lonnblad, S. Mrenna, and P. Z. Skands, *Pythia 6.3 physics and manual*, arXiv:hep-ph/0308153 [hep-ph].

[654] V. Hirschi, R. Frederix, S. Frixione, M. V. Garzelli, F. Maltoni, and R. Pittau, *Automation of one-loop QCD corrections*, JHEP **05** (2011) 044, arXiv:1103.0621 [hep-ph].

[655] F. Maltoni, M. L. Mangano, I. Tsinikos, and M. Zaro, *Top-quark charge asymmetry and polarization in $t\bar{t}W^{\pm}$ production at the LHC*, Phys. Lett. **B736** (2014) 252–260, arXiv:1406.3262 [hep-ph].

[656] J. A. Dror, M. Farina, E. Salvioni, and J. Serra, *Strong tW Scattering at the LHC*, JHEP **01** (2016) 071, arXiv:1511.03674 [hep-ph].

[657] S. Alioli, P. Fernandez, J. Fuster, A. Irles, S.-O. Moch, P. Uwer, and M. Vos, *A new observable to measure the top-quark mass at hadron colliders*, Eur. Phys. J. **C73** (2013) 2438, arXiv:1303.6415 [hep-ph].

[658] G. Bevilacqua, H. B. Hartanto, M. Kraus, M. Schulze, and M. Worek, *Top quark mass studies with $t\bar{t}j$ at the LHC*, JHEP **03** (2018) 169, arXiv:1710.07515 [hep-ph].

[659] CMS Collaboration, V. Khachatryan et al., *Measurement of the t-tbar production cross section in the e-mu channel in proton-proton collisions at sqrt(s) = 7 and 8 TeV*, JHEP **08** (2016) 029, arXiv:1603.02303 [hep-ex].

[660] ATLAS Collaboration, G. Aad et al., *Measurement of the $t\bar{t}$ production cross-section using $e\mu$ events with b-tagged jets in pp collisions at $\sqrt{s}$ = 7 and 8* TeV *with the ATLAS detector*, Eur. Phys. J. **C74** (2014) no. 10, 3109, arXiv:1406.5375 [hep-ex]. [Addendum: Eur. Phys. J.C76,no.11,642(2016)].

[661] U. Langenfeld, S. Moch, and P. Uwer, *Measuring the running top-quark mass*, Phys. Rev. **D80** (2009) 054009, arXiv:0906.5273 [hep-ph].

[662] S. Kawabata, Y. Shimizu, Y. Sumino, and H. Yokoya, *Weight function method for precise determination of top quark mass at Large Hadron Collider*, Phys. Lett. **B741** (2015) 232–238, arXiv:1405.2395 [hep-ph].

[663] A. H. Hoang, S. Mantry, A. Pathak, and I. W. Stewart, *Extracting a Short Distance Top Mass with Light Grooming*, arXiv:1708.02586 [hep-ph].

[664] K. Agashe, R. Franceschini, D. Kim, and M. Schulze, *Top quark mass determination from the energy peaks of b-jets and B-hadrons at NLO QCD*, Eur. Phys. J. **C76** (2016) no. 11, 636, arXiv:1603.03445 [hep-ph].

[665] S. Frixione and A. Mitov, *Determination of the top quark mass from leptonic observables*, JHEP **09** (2014) 012, arXiv:1407.2763 [hep-ph].

[666] CMS Collaboration, A. M. Sirunyan et al., *Measurement of the top quark mass in the dileptonic $t\bar{t}$ decay channel using the mass observables $M_{b\ell}$, M_{T2}, and $M_{b\ell\nu}$ in pp collisions at $\sqrt{s} = 8$ TeV*, Phys. Rev. **D96** (2017) no. 3, 032002, arXiv:1704.06142 [hep-ex].

[667] C. G. Lester and D. J. Summers, *Measuring masses of semiinvisibly decaying particles pair produced at hadron colliders*, Phys. Lett. **B463** (1999) 99–103, arXiv:hep-ph/9906349 [hep-ph].

[668] A. J. Barr, B. Gripaios, and C. G. Lester, *Transverse masses and kinematic constraints: from the boundary to the crease*, JHEP **11** (2009) 096, arXiv:0908.3779 [hep-ph].

[669] CMS Collaboration, *Determination of the normalised invariant mass distribution of $\mathrm{t\bar{t}}$+jet and extraction of the top quark mass*, CMS-PAS-TOP-13-006, CERN, Geneva, 2016. https://cds.cern.ch/record/2153653.

[670] CMS Collaboration, *Measurement of the top-quark mass from the b jet energy spectrum*, CMS-PAS-TOP-15-002, CERN, Geneva, 2015. https://cds.cern.ch/record/2053086.

[671] ATLAS Collaboration, G. Aad et al., *Determination of the top-quark pole mass using $t\bar{t}$ + 1-jet events collected with the ATLAS experiment in 7 TeV pp collisions*, JHEP **10** (2015) 121, arXiv:1507.01769 [hep-ex].

[672] ATLAS Collaboration, M. Aaboud et al., *Measurement of lepton differential distributions and the top quark mass in $t\bar{t}$ production in pp collisions at $\sqrt{s} = 8$ TeV with the ATLAS detector*, Eur. Phys. J. **C77** (2017) no. 11, 804, arXiv:1709.09407 [hep-ex].

[673] P. Nason, *The Top Mass in Hadronic Collisions*, in *From My Vast Repertoire ...: Guido Altarelli's Legacy*, A. Levy, S. Forte, and G. Ridolfi, eds., pp. 123–151. 2019. arXiv:1712.02796 [hep-ph].

[674] A. H. Hoang and I. W. Stewart, *Top Mass Measurements from Jets and the Tevatron Top-Quark Mass*, Nucl. Phys. Proc. Suppl. **185** (2008) 220–226, arXiv:0808.0222 [hep-ph].

[675] A. H. Hoang, S. Plätzer, and D. Samitz, *On the Cutoff Dependence of the Quark Mass Parameter in Angular Ordered Parton Showers*, JHEP **10** (2018) 200, arXiv:1807.06617 [hep-ph].

[676] A. H. Hoang, A. Jain, C. Lepenik, V. Mateu, M. Preisser, I. Scimemi, and I. W. Stewart, *The MSR mass and the $\mathcal{O}\left(\Lambda_{\rm QCD}\right)$ renormalon sum rule*, JHEP **04** (2018) 003, arXiv:1704.01580 [hep-ph].

[677] G. Degrassi, S. Di Vita, J. Elias-Miro, J. R. Espinosa, G. F. Giudice, G. Isidori, and A. Strumia, *Higgs mass and vacuum stability in the Standard Model at NNLO*, JHEP **08** (2012) 098, arXiv:1205.6497 [hep-ph].

[678] D. Buttazzo, G. Degrassi, P. P. Giardino, G. F. Giudice, F. Sala, A. Salvio, and A. Strumia, *Investigating the near-criticality of the Higgs boson*, JHEP **12** (2013) 089, arXiv:1307.3536 [hep-ph].

[679] A. Andreassen, W. Frost, and M. D. Schwartz, *Scale Invariant Instantons and the Complete Lifetime of the Standard Model*, Phys. Rev. **D97** (2018) no. 5, 056006, arXiv:1707.08124 [hep-ph].

[680] I. I. Y. Bigi, M. A. Shifman, N. G. Uraltsev, and A. I. Vainshtein, *The Pole mass of the heavy quark. Perturbation theory and beyond*, Phys. Rev. **D50** (1994) 2234–2246, arXiv:hep-ph/9402360 [hep-ph].

[681] M. Beneke and V. M. Braun, *Heavy quark effective theory beyond perturbation theory: Renormalons, the pole mass and the residual mass term*, Nucl. Phys. **B426** (1994) 301–343, arXiv:hep-ph/9402364 [hep-ph].

[682] M. Beneke, P. Marquard, P. Nason, and M. Steinhauser, *On the ultimate uncertainty of the top quark pole mass*, Phys. Lett. **B775** (2017) 63–70, arXiv:1605.03609 [hep-ph].

[683] A. H. Hoang, C. Lepenik, and M. Preisser, *On the Light Massive Flavor Dependence of the Large Order Asymptotic Behavior and the Ambiguity of the Pole Mass*, JHEP **09** (2017) 099, arXiv:1706.08526 [hep-ph].

[684] A. Pineda, *Determination of the bottom quark mass from the Upsilon(1S) system*, JHEP **06** (2001) 022, arXiv:hep-ph/0105008 [hep-ph].

[685] G. S. Bali, C. Bauer, A. Pineda, and C. Torrero, *Perturbative expansion of the energy of static sources at large orders in four-dimensional SU(3) gauge theory*, Phys. Rev. **D87** (2013) 094517, arXiv:1303.3279 [hep-lat].

[686] M. Butenschoen, B. Dehnadi, A. H. Hoang, V. Mateu, M. Preisser, and I. W. Stewart, *Top Quark Mass Calibration for Monte Carlo Event Generators*, Phys. Rev. Lett. **117** (2016) no. 23, 232001, arXiv:1608.01318 [hep-ph].

[687] J. Kieseler, K. Lipka, and S.-O. Moch, *Calibration of the Top-Quark Monte Carlo Mass*, Phys. Rev. Lett. **116** (2016) no. 16, 162001, arXiv:1511.00841 [hep-ph].

[688] S. Ferrario Ravasio, P. Nason, and C. Oleari, *All-orders behaviour and renormalons in top-mass observables*, JHEP **01** (2019) 203, arXiv:1810.10931 [hep-ph].

[689] G. Heinrich, A. Maier, R. Nisius, J. Schlenk, M. Schulze, L. Scyboz, and J. Winter, *NLO and off-shell effects in top quark mass determinations*, JHEP **07** (2018) 129, arXiv:1709.08615 [hep-ph].

[690] S. Argyropoulos and T. Sjöstrand, *Effects of color reconnection on $t\bar{t}$ final states at the LHC*, JHEP **11** (2014) 043, arXiv:1407.6653 [hep-ph].

[691] J. R. Christiansen and P. Z. Skands, *String Formation Beyond Leading Colour*, JHEP **08** (2015) 003, arXiv:1505.01681 [hep-ph].

[692] S. Ferrario Ravasio, T. Ježo, P. Nason, and C. Oleari, *A theoretical study of top-mass measurements at the LHC using NLO+PS generators of increasing accuracy*, Eur. Phys. J. **C78** (2018) no. 6, 458, arXiv:1801.03944 [hep-ph].

[693] G. Corcella, R. Franceschini, and D. Kim, *Fragmentation Uncertainties in Hadronic Observables for Top-quark Mass Measurements*, Nucl. Phys. **B929** (2018) 485–526, arXiv:1712.05801 [hep-ph].

[694] A. Andreassen and M. D. Schwartz, *Reducing the Top Quark Mass Uncertainty with Jet Grooming*, JHEP **10** (2017) 151, arXiv:1705.07135 [hep-ph].

[695] S. Kawabata and H. Yokoya, *Top-quark mass from the diphoton mass spectrum*, Eur. Phys. J. **C77** (2017) no. 5, 323, arXiv:1607.00990 [hep-ph].

[696] CMS Collaboration, *ECFA 2016: Prospects for selected standard model measurements with the CMS experiment at the High-Luminosity LHC*, CMS PAS-FTR-16-006, 2017. https://cds.cern.ch/record/2262606.

[697] ATLAS Collaboration, *Projection of the top quark mass measurement accuracy using $J/\psi \to \mu^+\mu^-$ in $t\bar{t}$ events in proton-proton collisions with 3000 fb^{-1} at the HL-LHC*, ATL-PHYS-PUB-2018-042, 2018. http://cdsweb.cern.ch/record/2649882.

[698] ATLAS Collaboration, *Measurement of the top quark mass in the $t\bar{t} \to$lepton+jets channel from $\sqrt{s} = 8$TeV ATLAS data and combination with previous results*, subm. Eur. Phys. J. C , arXiv:1810.01772 [hep-ex].

[699] *Recommendations on systematic uncertainties for HL-LHC*, https://web.archive.org/https://twiki.cern.ch/twiki/bin/view/LHCPhysics/HLHELHCCommonSystematics.

[700] CMS Collaboration, *Study of the underlying event, b-quark fragmentation and hadronization properties in tbart events*, CMS-PAS-TOP-13-007, CERN, Geneva, 2013. https://cds.cern.ch/record/1600599.

[701] CMS Collaboration, *Measurement of the top quark mass using the B-hadron lifetime technique*, CMS-PAS-TOP-12-030, CERN, Geneva, 2013. https://cds.cern.ch/record/1563140.

[702] CMS Collaboration, *Underlying event measurement with ttbar+X events with p-p collision data at sqrt(s)=13 TeV*, CMS-PAS-TOP-15-017, CERN, Geneva, 2015. https://cds.cern.ch/record/2114809.

[703] ATLAS Collaboration, *Reconstruction of J/ψ mesons in $t\bar{t}$ final states in proton–proton collisions at $\sqrt{s} = 8$ TeV with the ATLAS detector*, ATLAS-CONF-2015-040, 2015. https://cds.cern.ch/record/2046216.

[704] LHCb collaboration, *Physics case for an LHCb Upgrade II — Opportunities in flavour physics, and beyond, in the HL-LHC era*, CERN-LHCC-2018-027 LHCb-PUB-2018-009, CERN, Geneva, 2018. arXiv:1808.08865 [hep-ex].

[705] P. F. Harrison and V. E. Vladimirov, *A Method to Determine $|V_{cb}|$ at the Weak Scale in Top Decays at the LHC*, JHEP **01** (2019) 191, arXiv:1810.09424 [hep-ph].

[706] T. P. Cheng, E. Eichten, and L.-F. Li, *Higgs Phenomena in Asymptotically Free Gauge Theories*, Phys. Rev. **D9** (1974) 2259. SLAC-PUB-1340.

[707] M. E. Machacek and M. T. Vaughn, *Two Loop Renormalization Group Equations in a General Quantum Field Theory. 2. Yukawa Couplings*, Nucl. Phys. **B236** (1984) 221–232. NUB-2611.

[708] C. Balzereit, T. Mannel, and B. Plumper, *The Renormalization group evolution of the CKM matrix*, Eur. Phys. J. **C9** (1999) 197–211, arXiv:hep-ph/9810350 [hep-ph].

[709] ATLAS Collaboration, *Optimisation of the ATLAS b-tagging performance for the 2016 LHC Run*, ATL-PHYS-PUB-2016-012, CERN, Geneva, Jun, 2016. https://cds.cern.ch/record/2160731.

[710] ATLAS Collaboration, M. Aaboud et al., *Measurements of b-jet tagging efficiency with the ATLAS detector using $t\bar{t}$ events at $\sqrt{s} = 13$ TeV*, JHEP **08** (2018) 089, arXiv:1805.01845 [hep-ex].

[711] ATLAS Collaboration, *Measurement of b-tagging Efficiency of c-jets in $t\bar{t}$ Events Using a Likelihood Approach with the ATLAS Detector*, ATLAS-CONF-2018-001, CERN, Geneva, Mar, 2018. https://cds.cern.ch/record/2306649.

[712] ATLAS Collaboration, *Calibration of light-flavour jet b-tagging rates on ATLAS proton-proton collision data at $\sqrt{s} = 13$ TeV*, ATLAS-CONF-2018-006, CERN, Geneva, Apr, 2018. https://cds.cern.ch/record/2314418.

[713] ATLAS Collaboration, M. Aaboud et al., *Search for the Decay of the Higgs Boson to Charm Quarks with the ATLAS Experiment*, Phys. Rev. Lett. **120** (2018) no. 21, 211802, arXiv:1802.04329 [hep-ex].

[714] CMS Collaboration, A. M. Sirunyan et al., *Identification of heavy-flavour jets with the CMS detector in pp collisions at 13 TeV*, JINST **13** (2018) no. 05, P05011, arXiv:1712.07158 [physics.ins-det].

[715] S. L. Glashow, J. Iliopoulos, and L. Maiani, *Weak Interactions with Lepton-Hadron Symmetry*, Phys. Rev. D **2** (Oct, 1970) 1285–1292.

[716] G. Eilam, J. L. Hewett, and A. Soni, *Rare decays of the top quark in the standard and two-Higgs-doublet models*, Phys. Rev. D **44** (Sep, 1991) 1473–1484.

[717] B. Mele, S. Petrarca, and A. Soddu, *A New evaluation of the $t \to cH$ decay width in the standard model*, Phys. Lett. **B435** (1998) 401–406, arXiv:hep-ph/9805498 [hep-ph].

[718] J. A. Aguilar-Saavedra, *Top flavor-changing neutral interactions: Theoretical expectations and experimental detection*, Acta Phys. Polon. **B35** (2004) 2695–2710, arXiv:hep-ph/0409342 [hep-ph].

[719] F. Larios, R. Martinez, and M. A. Perez, *New physics effects in the flavor-changing neutral couplings of the top quark*, Int. J. Mod. Phys. **A21** (2006) 3473–3494, arXiv:hep-ph/0605003 [hep-ph].

[720] Top Quark Working Group Collaboration, K. Agashe et al., *Working Group Report: Top Quark*, in *Proceedings, 2013 Community Summer Study on the Future of U.S. Particle Physics: Snowmass on the Mississippi (CSS2013): Minneapolis, MN, USA, July 29-August 6, 2013*. 2013. arXiv:1311.2028 [hep-ph]. http://www.slac.stanford.edu/econf/C1307292/docs/Top-21.pdf.

[721] CMS Collaboration, *Prospects for the search for gluon-mediated FCNC in top quark production with the CMS Phase-2 detector at the HL-LHC*, CMS-PAS-FTR-18-004, CERN, Geneva, 2018. https://cds.cern.ch/record/2638815.

[722] E. E. Boos, V. E. Bunichev, L. V. Dudko, V. I. Savrin, and A. V. Sherstnev, *Method for simulating electroweak top-quark production events in the NLO approximation: SingleTop event generator*, Phys. Atom. Nucl. **69** (2006) 1317.

[723] CompHEP Collaboration, E. Boos, V. Bunichev, M. Dubinin, L. Dudko, V. Ilyin, A. Kryukov, V. Edneral, V. Savrin, A. Semenov, and A. Sherstnev, *CompHEP 4.4: Automatic computations from Lagrangians to events*, Nucl. Instrum. Meth. **A534** (2004) 250–259, arXiv:hep-ph/0403113 [hep-ph].

[724] CMS Collaboration, *The Phase-2 Upgrade of the CMS Endcap Calorimeter*, CERN-LHCC-2017-023. CMS-TDR-019, CERN, Geneva, Nov, 2017. https://cds.cern.ch/record/2293646.

[725] J. J. Zhang, C. S. Li, J. Gao, H. Zhang, Z. Li, et al., *Next-to-leading order QCD corrections to the top quark decay via model-independent FCNC couplings*, Phys. Rev. Lett. **102** (2009) 072001, arXiv:0810.3889 [hep-ph].

[726] CMS Collaboration, V. Khachatryan et al., *Search for anomalous Wtb couplings and flavour-changing neutral currents in t-channel single top quark production in pp collisions at $\sqrt{s} = 7$ and 8 TeV*, JHEP **02** (2017) 028, arXiv:1610.03545 [hep-ex].

[727] ATLAS Collaboration, *Sensitivity of searches for the flavour-changing neutral current decay $t \to qZ$ using the upgraded ATLAS experiment at the High Luminosity LHC*, ATL-PHYS-PUB-2019-001, 2019. https://cds.cern.ch/record/2653389.

[728] ATLAS Collaboration, M. Aaboud et al., *Search for flavour-changing neutral current top-quark decays $t \to qZ$ in proton-proton collisions at $\sqrt{s} = 13$ TeV with the ATLAS detector*, JHEP **07** (2018) 176, arXiv:1803.09923 [hep-ex].

[729] CMS Collaboration, V. Khachatryan et al., *Search for Anomalous Single Top Quark Production in Association with a Photon in pp Collisions at $\sqrt{s} = 8$ TeV*, JHEP **04** (2016) 035, arXiv:1511.03951 [hep-ex].

[730] ATLAS Collaboration, M. Aaboud et al., *Search for top quark decays $t \to qH$, with $H \to \gamma\gamma$, in $\sqrt{s} = 13$ TeV pp collisions using the ATLAS detector*, JHEP **10** (2017) 129, arXiv:1707.01404 [hep-ex].

[731] ATLAS Collaboration, M. Aaboud et al., *Search for flavor-changing neutral currents in top quark decays $t \to Hc$ and $t \to Hu$ in multilepton final states in proton-proton collisions at $\sqrt{s} = 13$ TeV with the ATLAS detector*, Phys. Rev. **D98** (2018) no. 3, 032002, arXiv:1805.03483 [hep-ex].

[732] CMS Collaboration, A. M. Sirunyan et al., *Search for the flavor-changing neutral current interactions of the top quark and the Higgs boson which decays into a pair of b quarks at $\sqrt{s} =$ 13 TeV*, JHEP **06** (2018) 102, arXiv:1712.02399 [hep-ex].

[733] ATLAS Collaboration, *Expected sensitivity of ATLAS to FCNC top quark decays $t \to Zu$ and $t \to Hq$ at the High Luminosity LHC*, ATL-PHYS-PUB-2016-019, CERN, Geneva, Aug, 2016. https://cds.cern.ch/record/2209126.

[734] ATLAS Collaboration, *Sensitivity of ATLAS at HL-LHC to flavour changing neutral currents in top quark decays $t \to cH$, with $H \to \gamma\gamma$*, ATL-PHYS-PUB-2013-012, CERN, Geneva, Sep, 2013. http://cds.cern.ch/record/1604506.

[735] J. A. Aguilar-Saavedra, J. Carvalho, N. F. Castro, F. Veloso, and A. Onofre, *Probing anomalous Wtb couplings in top pair decays*, Eur. Phys. J. **C50** (2007) 519–533, arXiv:hep-ph/0605190 [hep-ph].

[736] J. A. Aguilar-Saavedra, *Single top quark production at LHC with anomalous Wtb couplings*, Nucl. Phys. **B804** (2008) 160–192, arXiv:0803.3810 [hep-ph].

[737] J. A. Aguilar-Saavedra and S. Amor Dos Santos, *New directions for top quark polarization in the t-channel process*, Phys. Rev. **D89** (2014) no. 11, 114009, arXiv:1404.1585 [hep-ph].

[738] A. Prasath V, R. M. Godbole, and S. D. Rindani, *Longitudinal top polarisation measurement and anomalous Wtb coupling*, Eur. Phys. J. **C75** (2015) no. 9, 402, arXiv:1405.1264 [hep-ph].

[739] A. Jueid, *Probing anomalous Wtb couplings at the LHC in single t-channel top quark production*, Phys. Rev. **D98** (2018) no. 5, 053006, arXiv:1805.07763 [hep-ph].

[740] R. Röntsch and M. Schulze, *Constraining couplings of top quarks to the Z boson in $t\bar{t}$ + Z production at the LHC*, JHEP **07** (2014) 091, arXiv:1404.1005 [hep-ph]. [Erratum: JHEP09,132(2015)].

[741] R. Röntsch and M. Schulze, *Probing top-Z dipole moments at the LHC and ILC*, JHEP **08** (2015) 044, arXiv:1501.05939 [hep-ph].

[742] CDF, D0 Collaboration, T. A. Aaltonen et al., *Tevatron Combination of Single-Top-Quark Cross Sections and Determination of the Magnitude of the Cabibbo-Kobayashi-Maskawa Matrix Element $\mathbf{V_{tb}}$*, Phys. Rev. Lett. **115** (2015) no. 15, 152003, arXiv:1503.05027 [hep-ex].

[743] CDF, D0 Collaboration, T. A. Aaltonen et al., *Observation of s-channel production of single top quarks at the Tevatron*, Phys. Rev. Lett. **112** (2014) 231803, arXiv:1402.5126 [hep-ex].

[744] ATLAS Collaboration, M. Aaboud et al., *Fiducial, total and differential cross-section measurements of t-channel single top-quark production in pp collisions at 8 TeV using data collected by the ATLAS detector*, Eur. Phys. J. **C77** (2017) no. 8, 531, arXiv:1702.02859 [hep-ex].

[745] ATLAS Collaboration, G. Aad et al., *Evidence for single top-quark production in the s-channel in proton-proton collisions at $\sqrt{s}$ =8 TeV with the ATLAS detector using the Matrix Element Method*, Phys. Lett. **B756** (2016) 228–246, arXiv:1511.05980 [hep-ex].

[746] CMS Collaboration, S. Chatrchyan et al., *Measurement of the single-top-quark t-channel cross section in pp collisions at $\sqrt{s} = 7$ TeV*, JHEP **12** (2012) 035, arXiv:1209.4533 [hep-ex].

[747] CMS Collaboration, S. Chatrchyan et al., *Evidence for associated production of a single top quark and W boson in pp collisions at $\sqrt{s}$ = 7 TeV*, Phys. Rev. Lett. **110** (2013) 022003, arXiv:1209.3489 [hep-ex].

[748] CMS Collaboration, V. Khachatryan et al., *Search for s channel single top quark production in pp collisions at $\sqrt{s} = 7$ and 8 TeV*, JHEP **09** (2016) 027, arXiv:1603.02555 [hep-ex].

[749] CDF, D0 Collaboration, T. Aaltonen et al., *Combination of CDF and D0 measurements of the W boson helicity in top quark decays*, Phys. Rev. **D85** (2012) 071106, arXiv:1202.5272 [hep-ex].

[750] ATLAS Collaboration, M. Aaboud et al., *Measurement of the W boson polarisation in $t\bar{t}$ events from pp collisions at $\sqrt{s}$ = 8 TeV in the lepton + jets channel with ATLAS*, Eur. Phys. J. **C77** (2017) no. 4, 264, arXiv:1612.02577 [hep-ex].

[751] ATLAS Collaboration, M. Aaboud et al., *Analysis of the Wtb vertex from the measurement of triple-differential angular decay rates of single top quarks produced in the t-channel at $\sqrt{s}$ = 8 TeV with the ATLAS detector*, JHEP **12** (2017) 017, arXiv:1707.05393 [hep-ex].

[752] F. Déliot, M. C. N. Fiolhais, and A. Onofre, *Top Quark Anomalous Couplings at the High-Luminosity Phase of the LHC*, Mod. Phys. Lett. **A34** (2019) 1950142, arXiv:1811.02492 [hep-ph].

[753] ATLAS Collaboration, *Prospects for the measurement of $t\bar{t}\gamma$ with the upgraded ATLAS detector at the High-Luminosity LHC*, ATL-PHYS-PUB-2018-049, 2018. http://cdsweb.cern.ch/record/2652168.

[754] ATLAS Collaboration, M. Aaboud et al., *Measurements of inclusive and differential fiducial cross-sections of $t\bar{t}\gamma$ production in leptonic final states at $\sqrt{s}$ = 13 TeV in ATLAS*, arXiv:1812.01697 [hep-ex].

[755] W. Hollik, J. I. Illana, S. Rigolin, C. Schappacher, and D. Stockinger, *Top dipole form-factors and loop induced CP violation in supersymmetry*, Nucl. Phys. **B551** (1999) 3–40, arXiv:hep-ph/9812298 [hep-ph]. [Erratum: Nucl. Phys.B557,407(1999)].

[756] K. Agashe, G. Perez, and A. Soni, *Collider Signals of Top Quark Flavor Violation from a Warped Extra Dimension*, Phys. Rev. **D75** (2007) 015002, arXiv:hep-ph/0606293 [hep-ph].

[757] A. L. Kagan, G. Perez, T. Volansky, and J. Zupan, *General Minimal Flavor Violation*, Phys. Rev. **D80** (2009) 076002, arXiv:0903.1794 [hep-ph].

[758] T. Ibrahim and P. Nath, *The Chromoelectric Dipole Moment of the Top Quark in Models with Vector Like Multiplets*, Phys. Rev. **D84** (2011) 015003, arXiv:1104.3851 [hep-ph].

[759] C. Grojean, O. Matsedonskyi, and G. Panico, *Light top partners and precision physics*, JHEP **10** (2013) 160, arXiv:1306.4655 [hep-ph].

[760] F. Richard, *Can LHC observe an anomaly in $t\bar{t}Z$ production?*, arXiv:1304.3594 [hep-ph].

[761] CMS Collaboration, *Anomalous couplings in the tt+Z final state at the HL-LHC*, CMS-PAS-FTR-18-036, CERN, Geneva, 2018. https://cds.cern.ch/record/2652018.

[762] J. Brehmer, K. Cranmer, F. Kling, and T. Plehn, *Better Higgs boson measurements through information geometry*, Phys. Rev. **D95** (2017) no. 7, 073002, arXiv:1612.05261 [hep-ph].

[763] J. Brehmer, *New Ideas for Effective Higgs Measurements*. PhD thesis, U. Heidelberg (main), 2017. http://inspirehep.net/record/1624219.

[764] S. Frixione, E. Laenen, P. Motylinski, and B. R. Webber, *Angular correlations of lepton pairs from vector boson and top quark decays in Monte Carlo simulations*, JHEP **04** (2007) 081, arXiv:hep-ph/0702198 [HEP-PH].

[765] ATLAS Collaboration, G. Aad et al., *Measurement of the $t\bar{t}W$ and $t\bar{t}Z$ production cross sections in pp collisions at $\sqrt{s} = 8$ TeV with the ATLAS detector*, JHEP **11** (2015) 172, arXiv:1509.05276 [hep-ex].

[766] ATLAS Collaboration, *Measurement of the $t\bar{t}Z$ and $t\bar{t}W$ production cross sections in multilepton final states using 3.2 fb^{-1} of pp collisions at $\sqrt{s} = 13$ TeV with the ATLAS detector*, Eur. Phys. J. C **77** (2017) 40, arXiv:1609.01599 [hep-ex].

[767] CMS Collaboration, S. Chatrchyan et al., *Measurement of associated production of vector bosons and ttbar in pp collisions at $\sqrt{s} = 7TeV$*, Phys. Rev. Lett. **110** (2013) 172002, 1303.3239.

[768] CMS Collaboration, V. Khachatryan et al., *Measurement of top quark-antiquark pair production in association with a W or Z boson in pp collisions at $\sqrt{s} = 8$ TeV*, Eur. Phys. J. C **74** (2014) 3060, arXiv:1406.7830 [hep-ex].

[769] CMS Collaboration, V. Khachatryan et al., *Observation of top quark pairs produced in association with a vector boson in pp collisions at $\sqrt{s} = 8$ TeV*, JHEP **01** (2016) 096, arXiv:1510.01131 [hep-ex].

[770] CMS Collaboration, A. M. Sirunyan et al., *Measurement of the cross section for top quark pair production in association with a W or Z boson in proton-proton collisions at $\sqrt{s} = 13$ TeV*, JHEP **08** (2018) 011, arXiv:1711.02547 [hep-ex].

[771] V. M. Budnev, I. F. Ginzburg, G. V. Meledin, and V. G. Serbo, *The Two photon particle production mechanism. Physical problems. Applications. Equivalent photon approximation*, Phys. Rept. **15** (1975) 181–281.

[772] V. A. Khoze, A. D. Martin, and M. G. Ryskin, *Prospects for new physics observations in diffractive processes at the LHC and Tevatron*, Eur.Phys.J. **C23** (2002) 311–327, arXiv:hep-ph/0111078 [hep-ph].

[773] C. Baldenegro, S. Fichet, G. von Gersdorff, and C. Royon, *Searching for axion-like particles with proton tagging at the LHC*, JHEP **06** (2018) 131, arXiv:1803.10835 [hep-ph].

[774] C. Baldenegro, S. Fichet, G. von Gersdorff, and C. Royon, *Probing the anomalous $\gamma\gamma\gamma Z$ coupling at the LHC with proton tagging*, JHEP **06** (2017) 142, arXiv:1703.10600 [hep-ph].

[775] S. Fichet, G. von Gersdorff, and C. Royon, *Measuring the Diphoton Coupling of a 750 GeV Resonance*, Phys. Rev. Lett. **116** (2016) no. 23, 231801, arXiv:1601.01712 [hep-ph].

[776] S. Fichet, G. von Gersdorff, and C. Royon, *Scattering light by light at 750 GeV at the LHC*, Phys. Rev. **D93** (2016) no. 7, 075031, arXiv:1512.05751 [hep-ph].

[777] S. Fichet, G. von Gersdorff, B. Lenzi, C. Royon, and M. Saimpert, *Light-by-light scattering with intact protons at the LHC: from Standard Model to New Physics*, JHEP **02** (2015) 165, arXiv:1411.6629 [hep-ph].

[778] S. Fichet, G. von Gersdorff, O. Kepka, B. Lenzi, C. Royon, and M. Saimpert, *Probing new physics in diphoton production with proton tagging at the Large Hadron Collider*, Phys. Rev. **D89** (2014) 114004, arXiv:1312.5153 [hep-ph].

[779] E. Chapon, C. Royon, and O. Kepka, *Anomalous quartic W W gamma gamma, Z Z gamma gamma, and trilinear WW gamma couplings in two-photon processes at high luminosity at the LHC*, Phys. Rev. **D81** (2010) 074003, arXiv:0912.5161 [hep-ph].

[780] O. Kepka and C. Royon, *Anomalous $WW\gamma$ coupling in photon-induced processes using forward detectors at the LHC*, Phys. Rev. **D78** (2008) 073005, arXiv:0808.0322 [hep-ph].

[781] M. Boonekamp, A. Dechambre, V. Juranek, O. Kepka, M. Rangel, C. Royon, and R. Staszewski, *FPMC: A Generator for forward physics*, arXiv:1102.2531 [hep-ph].

[782] M. G. Albrow, T. D. Coughlin, and J. R. Forshaw, *Central Exclusive Particle Production at High Energy Hadron Colliders*, Prog.Part.Nucl.Phys. **65** (2010) 149–184, arXiv:1006.1289 [hep-ph].

[783] L. A. Harland-Lang, V. A. Khoze, M. G. Ryskin, and W. Stirling, *Central exclusive production within the Durham model: a review*, Int.J.Mod.Phys. **A29** (2014) 1430031, arXiv:1405.0018 [hep-ph].

[784] CDF Collaboration, T. Aaltonen et al., *Observation of Exclusive Dijet Production at the Fermilab Tevatron $p^{-}\bar{p}$ Collider*, Phys. Rev. **D77** (2008) 052004, arXiv:0712.0604 [hep-ex].

[785] D0 Collaboration, V. M. Abazov et al., *High mass exclusive diffractive dijet production in $\mathrm{p\bar{p}}$ collisions at $\sqrt{\mathrm{s}}$ = 1.96 TeV*, Phys.Lett. **B705** (2011) 193–199, arXiv:1009.2444 [hep-ex].

[786] L. A. Harland-Lang, *Planar radiation zeros in five-parton QCD amplitudes*, JHEP **1505** (2015) 146, arXiv:1503.06798 [hep-ph].

[787] L. A. Harland-Lang, V. A. Khoze, and M. G. Ryskin, *Exclusive physics at the LHC with SuperChic 2*, Eur. Phys. J. **C76** (2016) no. 1, 9, arXiv:1508.02718 [hep-ph].

[788] The CMS and TOTEM Collaborations, *CMS-TOTEM Precision Proton Spectrometer Technical Design Report*, CERN-LHCC-2014-021. https://cds.cern.ch/record/1753795.

[789] TOTEM Collaboration, *Technical Design Report*, CERN-LHCC-2004-002; addendum CERN-LHCC-2004-020. http://cds.cern.ch/record/704349.

[790] TOTEM Collaboration, G. Anelli et al., *The TOTEM experiment at the CERN Large Hadron Collider*, JINST **3** (2008) S08007.

[791] TOTEM Collaboration, *TOTEM Upgrade Proposal*, CERN-LHCC-2013-009. https://cds.cern.ch/record/1554299.

[792] FP420 R, D Collaboration, M. G. Albrow et al., *The FP420 & Project: Higgs and New Physics with forward protons at the LHC*, JINST **4** (2009) T10001, arXiv:0806.0302 [hep-ex].

[793] N. Karastathis et al., *Field quality to achieve the required lifetime goals (with beam-beam)*, 7th HL-LHC Collaboration Meeting, 15.11.2017, https://indico.cern.ch/event/647714/contributions/2646093.

[794] CERN, *The MAD-X Program*. https://web.archive.org/web/https://www.cern.ch/madx/, accessed April 2019.

[795] D. Mirarchi et al., *TCL/TCTs setting scenarios for HL-LHC*, Collimation Upgrade Specification Meeting #83, 24.02.2017, https://indico.cern.ch/event/614887/.

[796] C. J. Morningstar and M. J. Peardon, *The Glueball spectrum from an anisotropic lattice study*, Phys. Rev. **D60** (1999) 034509, arXiv:hep-lat/9901004 [hep-lat].

[797] STAR Collaboration, R. Sikora, *Recent results on Central Exclusive Production with the STAR detector at RHIC*, in *Diffraction and Low-x 2018 (Difflowx2018) Reggio Calabria, Italy, August 26-September 1, 2018*. 2018. arXiv:1811.03315 [hep-ex].

[798] CDF Collaboration, T. A. Aaltonen et al., *Measurement of central exclusive $\pi^+\pi^-$ production in $p\bar{p}$ collisions at $\sqrt{s} = 0.9$ and 1.96 TeV at CDF*, Phys. Rev. **D91** (2015) no. 9, 091101, arXiv:1502.01391 [hep-ex].

[799] CMS Collaboration, V. Khachatryan et al., *Exclusive and semi-exclusive pi+pi- production in proton-proton collisions at sqrt(s) = 7 TeV*, arXiv:1706.08310 [hep-ex].

[800] E690 Collaboration, M. A. Reyes et al., *Partial wave analysis of the centrally produced K(s) K(s) system at 800-GeV/c*, Phys. Rev. Lett. **81** (1998) 4079–4082. FERMILAB-PUB-97-223-E.

[801] WA102 Collaboration, D. Barberis et al., *A Partial wave analysis of the centrally produced K+ K- and K0(S) K0(S) systems in p p interactions at 450-GeV/c and new information on the spin of the f(J)(1710)*, Phys. Lett. **B453** (1999) 305–315, arXiv:hep-ex/9903042 [hep-ex].

[802] WA102 Collaboration, D. Barberis et al., *A Partial wave analysis of the centrally produced pi0 pi0 system in p p interactions at 450-GeV/c*, Phys. Lett. **B453** (1999) 325–332, arXiv:hep-ex/9903044 [hep-ex].

[803] V. Crede and C. A. Meyer, *The Experimental Status of Glueballs*, Prog. Part. Nucl. Phys. **63** (2009) 74–116, arXiv:0812.0600 [hep-ex].

[804] F. E. Close and G. A. Schuler, *Evidence that the pomeron transforms as a nonconserved vector current*, Phys. Lett. **B464** (1999) 279–285, arXiv:hep-ph/9905305 [hep-ph].

[805] P. Lebiedowicz, O. Nachtmann, and A. Szczurek, *Exclusive central diffractive production of scalar and pseudoscalar mesons tensorial vs. vectorial pomeron*, Annals Phys. **344** (2014) 301–339, arXiv:1309.3913 [hep-ph].

[806] P. Lebiedowicz, O. Nachtmann, and A. Szczurek, *Central exclusive diffractive production of $\pi^+\pi^-$ continuum, scalar and tensor resonances in pp and $p\bar{p}$ scattering within tensor pomeron approach*, Phys. Rev. **D93** (2016) no. 5, 054015, arXiv:1601.04537 [hep-ph].

[807] P. Lebiedowicz, O. Nachtmann, and A. Szczurek, *Towards a complete study of central exclusive production of K^+K^- pairs in proton-proton collisions within the tensor Pomeron approach*, Phys. Rev. **D98** (2018) 014001, arXiv:1804.04706 [hep-ph].

[808] P. Lebiedowicz, O. Nachtmann, and A. Szczurek, *Central exclusive diffractive production of $p\bar{p}$ pairs in proton-proton collisions at high energies*, Phys. Rev. **D97** (2018) no. 9, 094027, arXiv:1801.03902 [hep-ph].

[809] L. A. Harland-Lang, V. A. Khoze, and M. G. Ryskin, *Modelling exclusive meson pair production at hadron colliders*, Eur. Phys. J. **C74** (2014) 2848, arXiv:1312.4553 [hep-ph].

[810] L. A. Harland-Lang, V. A. Khoze, M. G. Ryskin, and W. J. Stirling, *Central exclusive meson pair production in the perturbative regime at hadron colliders*, Eur. Phys. J. **C71** (2011) 1714, arXiv:1105.1626 [hep-ph].

[811] L. A. Harland-Lang, V. A. Khoze, and M. G. Ryskin, SuperChic2*: a New Monte Carlo for Central Exclusive Production*, Acta Phys. Polon. Supp. **8** (2015) 751–756.

Report from Working Group 2: Higgs physics at the HL-LHC and HE-LHC

Physics of the HL-LHC, and Perspectives at the HE-LHC

Conveners:
M. Cepeda[1,2], S. Gori[3], P. Ilten[4], M. Kado[5,6,7], F. Riva[8]

Contributors:
R. Abdul Khalek[9,10], A. Aboubrahim[11], J. Alimena[12], S. Alioli[13,13], A. Alves[14], C. Asawatangtrakuldee[15], A. Azatov[16,17], P. Azzi[18], S. Bailey[19], S. Banerjee[20], E.L. Barberio[21], D. Barducci[16], G. Barone[22], M. Bauer[20], C. Bautista[23], P. Bechtle[24], K. Becker[25], A. Benaglia[26], M. Bengala[27], N. Berger[28], C. Bertella[29], A. Bethani[30], A. Betti[24], A. Biekotter[31], F. Bishara[15], D. Bloch[32], P. Bokan[33], O. Bondu[34], M. Bonvini[6], L. Borgonovi[35,36], M. Borsato[37], S. Boselli[38], S. Braibant-Giacomelli[35,36], G. Buchalla[39], L. Cadamuro[40], C. Caillol[41], A. Calandri[42,43], A. Calderon Tazon[44], J.M. Campbell[45], F. Caola[20], M. Capozi[46], M. Carena[45,47], C.M. Carloni Calame[48], A. Carmona[49], E. Carquin[50], A. Carvalho Antunes De Oliveira[51], A. Castaneda Hernandez[52], O. Cata[53], A. Celis[54], A. Cerri[55], F. Cerutti[56,57], G.S. Chahal[58,20], A. Chakraborty[59], G. Chaudhary[60], X. Chen[61], A.S. Chisholm[1,4], R. Contino[62], A.J. Costa[27], R. Covarelli[63,64], N. Craig[65], D. Curtin[66], L. D'Eramo[67], N.P. Dang[68], P. Das[69], S. Dawson[22], O.A. De Aguiar Francisco[1], J. de Blas[70,18], S. De Curtis[71], N. De Filippis[72,73], H. De la Torre[74], L. de Lima[75], A. De Wit[15], C. Delaere[34], M. Delcourt[34], M. Delmastro[28], S. Demers[76], N. Dev[77], R. Di Nardo[78], S. Di Vita[79], S. Dildick[80], L.A.F. do Prado[81,23], M. Donadelli[82], D. Du[83], G. Durieux[84,15], M. Dührssen[1], O. Eberhardt[85], K. El Morabit[86], J. Elias-Miro[1], J. Ellis[87,51,1], C. Englert[88], R. Essig[89], S. Falke[28], M. Farina[89], A. Ferrari[90], A. Ferroglia[91], M.C.N. Fiolhais[92], M. Flechl[93], S. Folgueras[94], E. Fontanesi[35,36], P. Francavilla[67,95], R. Franceschini[96,97], R. Frederix[98], S. Frixione[99], G. Gómez-Ceballos[100], A. Gabrielli[56,57], S. Gadatsch[1], M. Gallinaro[27], A. Gandrakota[101], J. Gao[102], F.M. Garay Walls[103], T. Gehrmann[61], Y. Gershtein[101], T. Ghosh[104], A. Gilbert[1], R. Glein[105], E.W.N. Glover[20], R. Gomez-Ambrosio[20], R. Gonçalo[27], D. Gonçalves[106], M. Gorbahn[107], E. Gouveia[27], M. Gouzevitch[108], P. Govoni[26,13], M. Grazzini[61], B. Greenberg[101], K. Grimm[109], A.V. Gritsan[110], A. Grohsjean[15], C. Grojean[15], J. Gu[111], R. Gugel[25], R.S. Gupta[20], C.B. Gwilliam[112], S. Höche[113], M. Haacke[103], Y. Haddad[58], U. Haisch[46], G.N. Hamity[114], T. Han[106], L.A. Harland-Lang[19], R. Harnik[45], S. Heinemeyer[44,115], G. Heinrich[46], B. Henning[8], V. Hirschi[43], K. Hoepfner[116], J.M. Hogan[117,118], S. Homiller[119,22], Y. Huang[120], A. Huss[1], S. Jézéquel[28], Sa. Jain[69], S.P. Jones[1], K. Köneke[25], J. Kalinowski[121], J.F. Kamenik[122,123], M. Kaplan[100], A. Karlberg[61], M. Kaur[60], P. Keicher[86], M. Kerner[61], A. Khanov[124], J. Kieseler[1], J.H. Kim[125], M. Kim[126], T. Klijnsma[43], F. Kling[127], M. Klute[100], J.R. Komaragiri[128], K. Kong[125], J. Kozaczuk[129], P Kozow[121], C. Krause[45], S. Lai[33], J. Langford[58], B. Le[21], L. Lechner[93], W.A. Leight[130], K.J.C. Leney[131], T. Lenz[24], C-Q. Li[132], H. Li[83], Q. Li[133], S. Liebler[134], J. Lindert[20], D. Liu[135], J. Liu[136], Y. Liu[137], Z. Liu[138,45], D. Lombardo[8], A. Long[139], K. Long[41], I. Low[140,135], G. Luisoni[46], L.L. Ma[83], A.-M. Magnan[58], D. Majumder[125], A. Malinauskas[19], F. Maltoni[141], M.L. Mangano[1], G. Marchiori[67,67], A.C. Marini[100], A. Martin[77], S. Marzani[142,99], A. Massironi[1], K.T. Matchev[40,143], R.D. Matheus[23], K. Mazumdar[69], J. Mazzitelli[61], A.E. Mcdougall[21], P. Meade[119], P. Meridiani[6], A.B. Meyer[15], E. Michielin[18], P. Milenovic[1,144], V. Milosevic[58], K. Mimasu[141], B. Mistlberger[145], M. Mlynarikova[146], M. Mondragon[147], P.F. Monni[1], G. Montagna[148,48], F. Monti[26,13], M. Moreno Llacer[1], A. Mueck[149], P.C. Muiño[27], C. Murphy[150], W.J. Murray[151], P. Musella[43], M. Narain[118], R.F. Naranjo Garcia[130], P. Nath[11], M. Neubert[152], O. Nicrosini[48], K. Nikolopoulos[4], A. Nisati[6,7], J.M. No[115], M.L. Ojeda[153], S.A. Olivares Pino[103], A. Onofre[154], G. Ortona[155], S. Pagan Griso[56,57], D. Pagani[98], E. Palencia Cortezon[94], C. Palmer[156], C. Pandini[1], G. Panico[157,71], L. Panwar[128], D. Pappadopulo[158], M. Park[159], R. Patel[105], F. Paucar-Velasquez[101], K. Pedro[45], L. Pernie[80], L. Perrozzi[43], B.A. Petersen[1], E. Petit[160], G. Petrucciani[1], G. Piacquadio[161], F. Piccinini[48], M. Pieri[162], T. Plehn[37], S. Pokorski[121], A. Pomarol[163],

https://doi.org/10.23731/CYRM-2019-007.221

E. Ponton[23,164], *S. Pozzorini*[61], *S. Prestel*[45], *K. Prokofiev*[165], *M. Ramsey-Musolf*[166], *E. Re*[1,167], *N.P. Readioff*[160], *D. Redigolo*[168,169], *L. Reina*[170], *E. Reynolds*[4,4], *M. Riembau*[8], *F. Rikkert*[98], *T. Robens*[171], *R. Roentsch*[172,1], *J. Rojo*[10], *N. Rompotis*[112], *J. Rorie*[139], *J. Rosiek*[121], *J. Roskes*[110], *J.T. Ruderman*[158], *N. Sahoo*[69], *S. Saito*[69], *R. Salerno*[155], *P.H. Sales De Bruin*[173], *A. Salvucci*[174], *K. Sandeep*[60], *J. Santiago*[175], *R. Santo*[27], *V. Sanz*[55], *U. Sarica*[110], *A. Savin*[41], *A. Savoy-Navarro*[81,176], *S. Sawant*[69], *A.C. Schaffer*[5], *M. Schlaffer*[177], *A. Schmidt*[116], *B. Schneider*[45], *R. Schoefbeck*[93], *M. Schröder*[86], *M. Scodeggio*[130], *E. Scott*[58], *L. Scyboz*[46], *M. Selvaggi*[1], *L. Sestini*[18], *H.-S. Shao*[178], *A. Shivaji*[141,179], *L. Silvestrini*[6,1], *L. Simon*[149], *K. Sinha*[180], *Y. Soreq*[1,84], *M. Spannowsky*[181], *M. Spira*[182], *D. Spitzbart*[93], *E. Stamou*[47], *J. Stark*[160], *T. Stefaniak*[15], *B. Stieger*[183,184], *G. Strong*[27], *M. Szleper*[185], *K. Tackmann*[130], *M. Takeuchi*[186], *S. Taroni*[77], *M. Testa*[187], *A. Thamm*[1], *V. Theeuwes*[188,189], *L.A. Thomsen*[76], *S. Tkaczyk*[45], *R. Torre*[99,1], *F. Tramontano*[190,191], *K.A. Ulmer*[105], *T. Vantalon*[15], *L. Vecchi*[192], *R. Vega-Morales*[175], *E. Venturini*[16], *M. Verducci*[97,96], *C. Vernieri*[113], *T. Vickey*[114], *M. Vidal Marono*[34], *P. Vischia*[94], *E. Vryonidou*[1], *P. Wagner*[24], *V.M. Walbrecht*[46], *L.-T. Wang*[136], *N. Wardle*[58], *D.R. Wardrope*[193], *G. Weiglein*[15], *S. Wertz*[34], *M. Wielers*[194], *J.M. Williams*[100], *R. Wolf*[86], *A. Wulzer*[1], *M. Xiao*[110], *H.T. Yang*[56,57], *E. Yazgan*[120], *Z. Yin*, *T. You*[195,38], *F. Yu*[49,196], *G. Zanderighi*[1,46], *D. Zanzi*[1], *M. Zaro*[10,10], *S.C. Zenz*[58,197], *D. Zerwas*[5], *M. Zgubič*[198], *J. Zhang*[83], *L. Zhang*[137], *W. Zhang*[118], *X. Zhao*[34,22], *Y.-M. Zhong*[199]

[1]CERN, Geneva; [2]CIEMAT, Madrid; [3]UC, Santa Cruz, SCIPP; [4]U. Birmingham, Sch. Phys. Astron.; [5]LAL, Orsay; [6]INFN, Rome 1; [7]U. Rome 1, La Sapienza, Dept. Phys.; [8]U. Geneva, Dept. Theor. Phys.; [9]Vrije U., Amsterdam, Dept. Phys. Astron.; [10]Nikhef, Amsterdam; [11]Northeastern U.; [12]Ohio State U., Columbus; [13]U. Milan Bicocca, Dept. Phys.; [14]Diadema, Sao Paulo Fed. U.; [15]DESY, Hamburg; [16]SISSA, Trieste; [17]INFN, Trieste; [18]INFN, Padua; [19]U. Oxford, Ctr. Theor. Phys.; [20]Durham U., IPPP; [21]ARC, CoEPP, Melbourne; [22]Brookhaven Natl. Lab., Dept. Phys.; [23]UNESP Sao Paulo, IFT; [24]U. Bonn, Phys. Inst.; [25]U. Freiburg, Inst. Phys.; [26]INFN, Milan Bicocca; [27]LIP, Lisbon; [28]LAPP, Annecy; [29]CAS, Beijing; [30]U. Manchester, Sch. Phys. Astron.; [31]U. Heidelberg, ITP; [32]IPHC, Strasbourg; [33]U. Gottingen, II. Phys. Inst.; [34]Cathol. U. Louvain, CP3; [35]INFN, Bologna; [36]U. Bologna, Dept. Phys.; [37]U. Heidelberg, Phys.Inst.; [38]U. Cambridge; [39]LMU Munich; [40]U. Florida, Gainesville, Dept. Phys.; [41]U. Wisconsin, Madison, Dept. Phys.; [42]CPPM, Marseille; [43]ETH, Zurich, Dept. Phys.; [44]IFCA, Santander; [45]Fermilab; [46]MPI Phys., Munich; [47]U. Chicago; [48]INFN, Pavia; [49]U. Mainz, PRISMA; [50]U. Tech. Federico Santa Maria, Valparaiso; [51]NICPB, Tallinn; [52]Sonora U.; [53]U. Siegen, Dept. Phys.; [54]LMU Munich, Dept. Phys.; [55]U. Sussex, Brighton, Dept. Phys. Astron.; [56]LBNL, Berkeley, Div. Phys.; [57]UC, Berkeley, Dept. Phys.; [58]Imperial Coll., London, Dept. Phys.; [59]KEK, Tsukuba; [60]Panjab U., Chandigarh; [61]U. Zurich, Phys. Inst.; [62]Scuola Normale Superiore, Pisa; [63]INFN, Turin; [64]U. Turin, Dept. Exp. Phys.; [65]UC, Santa Barbara, Dept. Phys.; [66]U. Toronto; [67]LPNHE, Paris; [68]U. Louisville, Dept. Phys.; [69]TIFR, Mumbai, DHEP; [70]U. Padua, Dept. Phys.; [71]INFN, Florence; [72]INFN, Bari; [73]Polytech. Bari; [74]Michigan State U., East Lansing, Dept. Phys. Astron.; [75]Federal da Fronteira Sul U.; [76]Yale U., Dept. Phys.; [77]U. Notre Dame, Dept. Phys.; [78]UMass, Amherst, Dept. Phys.; [79]INFN, Italy; [80]TAMU, College Station; [81]IRFU, Saclay, DPP; [82]U. Sao Paulo, Inst. Phys.; [83]Shandong U., Jinan; [84]Technion, IIT, Dept. Phys.; [85]IFIC, Valencia; [86]KIT, Karlsruhe, ETP; [87]King's Coll. London; [88]U. Glasgow, Sch. Phys. Astron.; [89]Stony Brook U.; [90]Uppsala U., Dept. Phys. Astron.; [91]CUNY, City Tech.; [92]CUNY, BMCC; [93]OEAW, Vienna; [94]U. Oviedo, Dept. Phys.; [95]INFN, Pisa; [96]U. Rome 3, Dept. Math. Phys.; [97]INFN, Rome 3; [98]Tech. U., Munich, Dept. Phys.; [99]INFN, Genoa; [100]MIT, Cambridge; [101]Rutgers U., Piscataway, Dept. Phys. Astron.; [102]SJTU, Sch. Phys. Astron., Shanghai; [103]Pontificia U. Catol. Chile, Santiago, Dept. Phys.; [104]U. Hawaii; [105]U. Colorado, Boulder, Dept. Phys.; [106]U. Pittsburgh; [107]U. Liverpool; [108]IPNL, Lyon; [109]Cal State, East Bay; [110]Johns Hopkins U.; [111]UC, Davis; [112]U. Liverpool, Dept. Phys.; [113]SLAC; [114]U. Sheffield, Dept. Phys. Astron.; [115]IFT, Madrid; [116]RWTH Aachen; [117]Bethel Coll.; [118]Brown U., Dept. Phys.; [119]Stony Brook U., YITP; [120]CAS, IHEP, Beijing; [121]U. Warsaw, Fac. Phys.; [122]J. Stefan Inst., Ljubljana; [123]U. Ljubljana, Fac. Math. Phys.; [124]OKState, Stillwater, Dept. Phys.; [125]U. Kansas, Lawrence, Dept. Phys. Astron.; [126]POSTECH, Pohang; [127]UC, Irvine, Dept. Phys. Astron.; [128]Indian Inst. Sci., Bangalore; [129]U. Illinois, Urbana-Champaign; [130]DESY, Zeuthen;

[131]Southern Methodist U., Dept. Phys.; [132]USTC, Hefei, DMP; [133]Peking U., Beijing, Sch. Phys.; [134]KIT, Karlsruhe, TP; [135]Argonne Natl. Lab., HEP Div.; [136]Chicago U., EFI; [137]Nanjing U., Dept. Phys.; [138]U. Maryland, College Park, Dept. Phys.; [139]Rice U., Dept. Phys. Astron.; [140]Northwestern U., Dept. Phys. Astron.; [141]Cathol. U. Louvain; [142]U. Genoa, Dept. Phys.; [143]U. Florida, Gainesville; [144]U. Belgrade; [145]MIT, Cambridge, CTP; [146]Charles U., Prague, Inst. Part. Nucl. Phys.; [147]UNAM, Mexico, IFUNAM; [148]U. Pavia, Dept. Nucl. Theor. Phys.; [149]RWTH, Aachen, Phys. Inst.; [150]Brookhaven Natl. Lab.; [151]U. Warwick, Dept. Phys.; [152]U. Mainz; [153]U. Toronto, Dept. Phys.; [154]U. Minho, Dept. Math.; [155]LLR, Palaiseau; [156]Princeton U.; [157]U. Florence, Dept. Phys. Astron.; [158]New York U.; [159]Seoultech, Seoul; [160]LPSC, Grenoble; [161]Stony Brook U., Dept. Phys. Astron.; [162]UC, San Diego, Dept. Phys.; [163]U. Barcelona, IFAE; [164]ICTP-SAIFR, Sao Paulo; [165]HKUST, Hong Kong; [166]UMass, Amherst; [167]LAPTH, Annecy; [168]Tel-Aviv U., Dept. Part. Phys.; [169]IAS, Princeton; [170]Florida State U., Tallahassee, Dept. Phys.; [171]RBT, Zagreb; [172]KIT, Karlsruhe, Dept. Phys.; [173]U. Washington, Seattle, Dept. Phys.; [174]Chinese U. Hong Kong; [175]U. Granada, CAFPE; [176]APC, Paris; [177]Weizmann Inst. Sci., Rehovot, Fac. Phys.; [178]LPTHE, Paris; [179]IISER, Mohali; [180]U. Oklahoma, Norman; [181]Durham U., Dept. Phys.; [182]PSI, Villigen; [183]U. Nebraska, Lincoln; [184]U. Nebraska, Lincoln, Dept. Phys. Astron.; [185]NCBJ, Warsaw; [186]U. Tokyo; [187]INFN, LNF, Frascati; [188]U. Gottingen, Inst. Theor. Phys.; [189]IPhT, Saclay; [190]U. Naples, Dept. Phys. Sci.; [191]INFN, Naples; [192]EPFL, Lausanne, LPTP; [193]U. Coll. London, Dept. Phys. Astron.; [194]RAL, Didcot; [195]U. Cambridge, Cavendish Lab.; [196]U. Mainz, Inst. Phys.; [197]Queen Mary U. London, Sch. Phys. Astron.; [198]U. Oxford, Part. Phys. Dept.; [199]Boston U.

Abstract

The discovery of the Higgs boson in 2012, by the ATLAS and CMS experiments, was a success achieved with only a percent of the entire dataset foreseen for the LHC. It opened a landscape of possibilities in the study of Higgs boson properties, Electroweak Symmetry breaking and the Standard Model in general, as well as new avenues in probing new physics beyond the Standard Model. Six years after the discovery, with a conspicuously larger dataset collected during LHC Run 2 at a 13 TeV centre-of-mass energy, the theory and experimental particle physics communities have started a meticulous exploration of the potential for precision measurements of its properties. This includes studies of Higgs boson production and decays processes, the search for rare decays and production modes, high energy observables, and searches for an extended electroweak symmetry breaking sector. This report summarises the potential reach and opportunities in Higgs physics during the High Luminosity phase of the LHC, with an expected dataset of pp collisions at 14 TeV, corresponding to an integrated luminosity of 3 ab^{-1}. These studies are performed in light of the most recent analyses from LHC collaborations and the latest theoretical developments. The potential of an LHC upgrade, colliding protons at a centre-of-mass energy of 27 TeV and producing a dataset corresponding to an integrated luminosity of 15 ab^{-1}, is also discussed.

Contents

1 Introduction . . . 229
1.1 Experimental analysis methods and objects definitions . . . 230
1.1.1 ATLAS and CMS performance . . . 231
1.1.2 LHCb . . . 231
1.1.3 Treatment of systematic uncertainties . . . 232
1.2 Implications for beyond the Standard Model theories . . . 232
1.2.1 Heavy new physics: precision tests and effective field theories . . . 232
1.2.2 Light new physics: rare processes and new degrees of freedom . . . 234
2 Higgs boson precision measurements . . . 236
2.1 Introduction . . . 236
2.2 Theoretical predictions for the Higgs boson production . . . 236
2.2.1 Cross sections for 13, 14 and 27 TeV HE-LHC . . . 236
2.2.2 Projections of uncertainty reductions for the HL-LHC . . . 245
2.2.3 Predictions for boosted Higgs production . . . 247
2.2.4 Dependence of gluon-fusion cross section at 14 and 27 TeV on m_H . . . 249
2.2.5 PDF uncertainty expectations at the HE/HL-LHC . . . 249
2.3 Overview of experimental analysis for the Higgs boson measurement channels . . . 255
2.3.1 Extrapolation assumptions . . . 255
2.3.2 $H \to \gamma\gamma$ . . . 256
2.3.3 $H \to Z\gamma \to \ell\ell\,\gamma$ . . . 257
2.3.4 $H \to ZZ^* \to 4\ell$ . . . 258
2.3.5 $H \to WW^* \to \ell\nu\,\ell\nu$ . . . 258
2.3.6 $H \to \tau^+\tau^-$ . . . 259
2.3.7 $H \to b\bar{b}$ . . . 261
2.3.8 $H \to \mu^+\mu^-$ . . . 263
2.4 Fiducial and differential cross-section measurements . . . 265
2.4.1 Measurements using $H \to \gamma\gamma$, $H \to ZZ^* \to 4\ell$, (boosted) H $\to$ b$\bar{\text{b}}$ decay channels . . . 265
2.4.2 Measurement of $p_T(H)$ spectrum in t$\bar{\text{t}}$H production mode . . . 266
2.5 Direct and indirect probing of top Yukawa coupling . . . 270
2.5.1 Measurements in t$\bar{\text{t}}$H and tH production modes . . . 270
2.5.2 Constraints from differential measurements . . . 275
2.6 Combination of Higgs boson measurement projections . . . 276
2.6.1 Production mode cross-sections in different decay channels . . . 279
2.6.2 Cross sections per-production mode . . . 279
2.6.3 Branching ratios per-decay mode . . . 279
2.7 Kappa interpretation of the combined Higgs boson measurement projections . . . 284
2.7.1 Interpretations and results for HL-LHC . . . 284
2.7.2 Higgs boson coupling measurements projections estimates for HE-LHC . . . 286
2.8 Higgs couplings precision overview in the Kappa-framework and the nonlinear EFT . . . 287
2.9 Interpretation of the Higgs couplings in terms of Composite Higgs models . . . 294

2.10 Probing of anomalous HVV interactions . . . 300
2.10.1 Probes using differential distributions of CP sensitive observables . . . 300
2.10.2 Experimental constraints on anomalous HVV couplings . . . 305
3 Di-Higgs production and Higgs self couplings . . . 309
3.1 Higgs boson pair production cross section . . . 309
3.1.1 SM Calculation . . . 309
3.1.2 Di-Higgs production in the non-linear EFT with full m_t-dependence at NLO QCD . . . 312
3.2 Double Higgs measurements and trilinear coupling: experimental prospects . . . 318
3.2.1 Measurements with the ATLAS experiment . . . 319
3.2.2 Measurements with the CMS experiment . . . 324
3.2.3 Combination of measurements . . . 330
3.3 Double Higgs measurements and trilinear coupling: alternative methods . . . 332
3.3.1 Prospects for $hh \to (b\bar{b})(WW^*) \to (b\bar{b})(\ell^+\ell^-\nu_\ell\bar{\nu}_\ell)$ . . . 332
3.3.2 Prospects for $bb\gamma\gamma$: Bayesian optimisation and BDT . . . 335
3.4 HE-LHC prospects . . . 339
3.4.1 Theoretical prospects: from kinematics to dynamics . . . 339
3.4.2 Theoretical prospects: importance of the gluon fusion single Higgs background. . . . 343
3.4.3 Experimental prospects with the ATLAS detector . . . 346
3.4.4 Comparison of results . . . 347
3.5 Indirect probes . . . 347
3.5.1 Indirect probes through single Higgs boson production . . . 348
3.5.2 Indirect probes of the trilinear coupling through differential distributions measurements with the CMS detector . . . 352
3.5.3 Global fit . . . 353
3.6 Implications of the HH measurements . . . 356
3.6.1 Implications for flavor models . . . 356
3.6.2 Implications for theories of electroweak phase transition . . . 358
3.7 Summary . . . 362
4 High Energy Probes . . . 365
4.1 Electroweak Precision Tests in High-Energy Di-boson Processes . . . 365
4.2 WH/ZH at high energy/luminosity . . . 369
4.3 Novel measurements of anomalous triple gauge couplings . . . 373
4.4 Electroweak Precision Tests in High-Energy Drell-Yan Processes . . . 376
4.5 Testing the universal Higgs non-linearity . . . 377
4.6 Higgs pair production in vector-boson fusion at the HL-LHC . . . 380
4.7 Higgs Couplings in High-Energy Multi-boson Processes . . . 384
4.8 Dimension-6 EFT effects on Vector Boson Scattering at high energies . . . 387
4.9 Same-sign WW scattering and EFT applicability . . . 390
5 Higgs boson mass and width . . . 394
5.1 Theory review . . . 394
5.2 Measurement of the Higgs boson mass . . . 397

5.3 Constraints from off-shell Higgs boson production . . . 398
5.4 Width from the di-photon interference rate . . . 400
5.5 Mass shift from the di-photon interference . . . 403
6 Invisible decays of the Higgs boson . . . 406
6.1 Main channels for direct searches . . . 407
6.2 Interpretation and combination with precision Higgs boson measurements . . . 410
6.2.1 Experimental input . . . 410
6.2.2 Effective description of Higgs portal models . . . 411
6.3 Higgs portal interpretations . . . 413
6.3.1 Minimal Higgs Portal . . . 413
6.3.2 Scalar singlet portal . . . 414
6.4 Conclusions . . . 418
7 Higgs flavor and rare decays . . . 419
7.1 Introduction . . . 419
7.2 New Physics benchmarks for modified Higgs couplings . . . 421
7.3 Inclusive Search with Flavor tagging (charm and strange) . . . 427
7.3.1 Charm quark tagging . . . 427
7.3.2 Strange quark tagging . . . 431
7.4 Exclusive Higgs decays . . . 432
7.5 Lepton flavor violating decays of the Higgs . . . 434
7.6 Yukawa constraints from Higgs distributions . . . 435
7.6.1 Determinations of Higgs boson coupling modifiers using differential distributions . . . 435
7.6.2 $W^{\pm}h$ charge asymmetry . . . 437
7.7 CP Violation . . . 440
7.7.1 $t\bar{t}h$ . . . 440
7.7.2 $\tau\bar{\tau}h$ . . . 441
8 Global effective field theory fits . . . 443
8.1 Prospective SMEFT Constraints from HL- and HE-LHC Data . . . 443
8.2 Global constraints on universal new physics at the HL/HE-LHC . . . 446
8.3 Global analysis including the Higgs self-coupling . . . 454
9 Searches for beyond the standard model Higgs physics . . . 457
9.1 Exotic decays of the 125 GeV Higgs boson . . . 457
9.1.1 First Level Track Jet Trigger for Displaced Jets at High Luminosity LHC . . . 457
9.1.2 Higgs exotic decays into long-lived particles . . . 464
9.1.3 Projection of CMS search for exotic H $\rightarrow aa \rightarrow 2b2\tau$ . . . 468
9.1.4 Projection of CMS search for exotic H $\rightarrow aa \rightarrow 2\mu2\tau$ . . . 470
9.1.5 Exotic decays of the Higgs to $2b2\mu$ . . . 472
9.1.6 Exotic Higgs Decays to dark photons . . . 474
9.1.7 Exotic Higgs decays to axion-like particles: $h \rightarrow Za$ and $h \rightarrow aa$ . . . 478
9.2 LHC searches for additional heavy neutral Higgs bosons in fermionic final states . . . 482
9.2.1 Projection of Run-2 ATLAS searches for MSSM heavy neutral Higgs bosons . . . 482

9.2.2 Projection of Run-2 CMS searches for MSSM heavy neutral Higgs bosons 487
9.3 LHC searches for additional heavy neutral Higgs bosons in bosonic final states 493
9.3.1 Projection of Run-2 CMS searches for a new scalar resonance decaying to a pair of Z bosons 493
9.4 Additional channels for heavy Higgs bosons 494
9.4.1 Sensitivity to heavy Higgs bosons from the 2HDM in "Higgs-to-Higgs" decays 494
9.4.2 Interference effects in heavy Higgs searches 497
9.4.3 MSSM charged Higgs bosons 503
9.5 Direct and indirect sensitivity to heavy Higgs bosons using MSSM benchmark scenarios 505
9.6 Direct and indirect sensitivity to heavy Twin Higgs bosons 507
9.6.1 The simplified model with a long lived singlet scalar 508
9.6.2 A specific realisation: the Twin Higgs model 511
9.7 Production of $t\bar{t}h$ and $t\bar{t}hh$ at the LHC in Composite Higgs models 512
9.8 New Higgs bosons below the 125 GeV Higgs mass 518
9.8.1 Searches for low mass Higgs bosons (below 120 GeV) 518
9.8.2 HL-LHC projections of LHCb searches for 2HDM+S light pseudoscalars 522
10 Conclusions and Outlook 525
10.1 Higgs properties and EW phenomena at the HL-LHC 525
10.2 Potential of the HE-LHC 527

References **530**

1 Introduction

One of the main goals of the physics program at the Large Hadron Collider is to elucidate the origin of electroweak symmetry breaking.

Relativistic quantum field and gauge theories have been remarkably successful to describe fundamental particles and their interactions. In this context, the seminal work of Brout, Englert [1], Higgs [2, 3, 4] and Guralnik, Hagen and Kibble [5, 6], has provided a consistent mechanism for the generation of gauge boson masses. The Glashow-Weinberg-Salam theory extended this mechanism proposing a theory of the electroweak interactions [7, 8, 9], introducing a doublet of complex scalar fields, which couples also to fermions, providing them with a mass which would otherwise be absent. This is now known as the Standard Model (SM) of particle physics. A complete and detailed description of the Higgs mechanism can be found at [10]. A salient prediction of the theory is the presence of a Higgs boson. The discovery of the Higgs boson with a mass of 125 GeV, during the first run of the LHC at reduced centre-of-mass energies of 7 TeV and 8 TeV, is a landmark result that has reshaped the landscape of High Energy physics [11, 12]. The mass of the Higgs boson is particularly favourable as it allows to measure directly a large number of its couplings. It has also important consequences in terms of probing the self-consistency of the Standard Model both through the global fit of precision observables and through its interpretation as a measure of the Higgs boson self coupling, allowing to extrapolate the SM at higher energies and verify the stability of the vacuum.

The existence of the Higgs boson as a light scalar leads to the hierarchy or naturalness problem, as its mass at the weak scale happens to be particularly sensitive to general larger scales beyond the SM (BSM), therefore apparently requiring a large fine tuning of fundamental parameters. Addressing the naturalness problem is and has been for decades one of the main guiding principles for the development of theories beyond the Standard Model. There are two main classes of theories attempting to address the naturalness problem: the first are weakly coupled theories, where the Higgs boson remains an elementary scalar and its mass is protected by additional symmetries, as in Supersymmetric theories. The second are strongly coupled solutions, which involve new strong interactions at approximately the TeV scale and deliver naturally light composite scalars as Pseudo Nambu-Goldstone bosons. Both approaches can have large effects on the phenomenology of the Higgs particle and in some cases predict new states that could be observed at the LHC.

Other questions of fundamental importance can affect the phenomenology of the Higgs boson. The question of the nature of the Electroweak Phase transition is strongly intertwined with Higgs physics where, in many scenarios, a detailed study of the Higgs pair production can reveal the strength of the transition. Similarly, certain models of Dark Matter involve potentially large effects on the phenomenology of the Higgs particle. These fundamental questions, and many more, can be addressed by the study of the Higgs boson at the LHC and its high luminosity (HL) and high energy (HE) upgrades.

Since the discovery, a large campaign of measurements of the properties of the Higgs boson has started, including exclusive production modes and differential cross sections. Many new ideas have emerged during the completion of this program. This chapter presents a reappraised estimate of the potential of the HL-LHC and the HE-LHC projects to measure the properties of the Higgs boson, highlighting the opportunities for measurements of fundamental importance.

Section 2 presents the foreseen program for precision measurements of the Higgs boson coupling properties through exclusive production modes and differential cross sections. Section 3 presents the potential to measure double Higgs production and to constrain the Higgs trilinear coupling, both through the double Higgs production and indirect probes from single Higgs boson production. Section 4 is devoted to a new class of measurements unique to the HL-HE program: high-energy probes. These include Higgs processes like associated production of a Higgs and a W or Z boson, or vector boson fusion (VBF), for which the centre-of-mass energy is not limited to the Higgs mass, and it extends to Drell Yan, di-boson processes and vector boson scattering, which provide a context in which high-energy

measurements can be associated with precision observables. Section 5 focuses on measurements of the Higgs mass and opportunities for the measurement of the Higgs boson width. Section 6 describes the constraints on the invisible decays of the Higgs boson and the indirect constraints on the couplings of the Higgs boson to undetected particles from the measurement of the Higgs boson couplings, in particular in the framework of Higgs portal and dark matter models. Section 7 will discuss approaches to constrain light and non diagonal Higgs Yukawa couplings directly and indirectly. Section 8 is devoted to a global interpretation of the measurements in the framework of the Standard Model Effective Field Theory. Section 9 is devoted to the discussion of the prospects for probing additional Higgs bosons both with a mass above or below 125 GeV, and for discovering a wide range of exotic Higgs boson decays.

1.1 Experimental analysis methods and objects definitions

Different approaches have been used by the experiments and in theoretical prospect studies, hereafter named projections, to assess the sensitivity in searching for new physics at the HL-LHC and HE-LHC. For some of the projections, a mix of the approaches described below is used, in order to deliver the most realistic result. The total integrated luminosity for the HL-LHC dataset is assumed to be 3000 fb^{-1} at a centre-of-mass energy of 14 TeV. For HE-LHC studies the dataset is assumed to be 15 ab^{-1} at a centre-of-mass of 27 TeV. The effect of systematic uncertainties is taken into account based on the studies performed for the existing analyses and using common guidelines for projecting the expected improvements that are foreseen thanks to the large dataset and upgraded detectors, as described in Section 1.1.3.

Detailed-simulations are used to assess the performance of reconstructed objects in the upgraded detectors and HL-LHC conditions, as described in Sections 1.1.1,1.1.2. For some of the projections, such simulations are directly interfaced to different event generators, parton showering (PS) and hadronisation generators. Monte Carlo (MC) generated events are used for SM and BSM processes, and are employed in the various projections to estimate the expected contributions of each process.

Extrapolations of existing results rely on the existent statistical frameworks to estimate the expected sensitivity for the HL-LHC dataset. The increased centre-of-mass energy and the performance of the upgraded detectors are taken into account for most of the extrapolations using scale factors on the individual processes contributing to the signal regions. Such scale factors are derived from the expected cross sections and from detailed simulation studies.

Fast-simulations are employed for some of the projections in order to produce a large number of Monte Carlo events and estimate their reconstruction efficiency for the upgraded detectors. The upgraded CMS detector performance is taken into account encoding the expected performance of the upgraded detector in DELPHES [13], including the effects of pile-up interactions. Theoretical contributions use DELPHES with the commonly accepted HL-LHC card corresponding to the upgraded ATLAS and CMS detectors.

Parametric-simulations are used for some of the projections to allow a full re-optimisation of the analysis selections that profit from the larger available datasets. Particle-level definitions are used for electrons, photons, muons, taus, jets and missing transverse momentum. These are constructed from stable particles of the MC event record with a lifetime larger than 0.3×10^{-10} s within the observable pseudorapidity range. Jets are reconstructed using the anti-k_t algorithm [14] implemented in the FastJet [15] library, with a radius parameter of 0.4. All stable final-state particles are used to reconstruct the jets, except the neutrinos, leptons and photons associated to W or Z boson or τ lepton decays. The effects of an upgraded ATLAS detector are taken into account by applying energy smearing, efficiencies and fake rates to generator level quantities, following parametrisations based on detector performance studies with the detailed simulations. The effect of the high pileup at the HL-LHC is incorporated by overlaying pileup jets onto the hard-scatter events. Jets from pileup are randomly selected as jets to be considered for analysis with $\sim 2\%$ efficiency, based on studies of pile-up jet rejection and current experience.

1.1.1 ATLAS and CMS performance

The expected performance of the upgraded ATLAS and CMS detectors has been studied in detail in the context of the Technical Design Reports and subsequent studies; the assumptions used for this report and a more detailed description are available in Ref. [16, 17]. For CMS, the object performance in the central region assumes a barrel calorimeter ageing corresponding to an integrated luminosity of $1000\ \text{fb}^{-1}$.

The triggering system for both experiments will be replaced and its impact on the triggering abilities of each experiment assessed; new capabilities will be added, and, despite the more challenging conditions, most of the trigger thresholds for common objects are expected to either remain similar to the current ones or to even decrease [18, 19].

The inner detector is expected to be completely replaced by both experiments, notably extending its coverage to $|\eta| < 4.0$. The performance for reconstructing charged particles has been studied in detail in Ref. [20, 21, 22].

Electrons and photons are reconstructed from energy deposits in the electromagnetic calorimeter and information from the inner tracker [23, 24, 25, 26]. Several identification working points have been studied and are employed by the projection studies as most appropriate.

Muons are reconstructed combining muon spectrometer and inner tracker information [27, 28].

Jets are reconstructed by clustering energy deposits in the electromagnetic and hadronic calorimeters [29, 23, 24] using the anti-k_T algorithm [14]. B-jets are identified via b-tagging algorithms. B-tagging is performed if the jet is within the tracker acceptance ($|\eta| < 4.0$). Multivariate techniques are employed in order to identify $b-$jets and $c-$jets, and were fully re-optimised for the upgraded detectors [20, 22]. An 70% $b-$jet efficiency working point is used, unless otherwise noted.

High p_T boosted jets are reconstructed using large-radius anti-k_T jets with a distance parameter of 0.8. Various jet substructure variables are employed to identify boosted W/Z/Higgs boson and top quark jets with good discrimination against generic QCD jets.

Missing transverse energy is reconstructed following similar algorithms as employed in the current data taking. Its performance has been evaluated for standard processes, such as top pair production [20, 30].

The addition of new precise-timing detectors and its effect on object reconstruction has also been studied in Ref. [31, 26], although its results are only taken into account in a small subset of the projections in this report.

1.1.2 LHCb

The LHCb upgrades are shifted with respect to those of ATLAS and CMS. A first upgrade will happen at the end of Run 2 of the LHC, to run at a luminosity five times larger ($2 \times 10^{33}\text{cm}^{-2}\text{s}^{-1}$) in LHC Run 3 compared to those in Runs 1 and 2, while maintaining or improving the current detector performance. This first upgrade phase (named Upgrade I) will be followed by by the so-called Upgrade II phase (planned at the end of Run 4) to run at an even more challenging luminosity of $\sim 2\times10^{34}\text{cm}^{-2}\text{s}^{-1}$.

The LHCb MC simulation used in this document mainly relies on the PYTHIA 8 generator [32] with a specific LHCb configuration [33], using the CTEQ6 leading-order set of parton density functions [34]. The interaction of the generated particles with the detector, and its response, are implemented using the GEANT toolkit [35, 36], as described in Ref. [37].

The reconstruction of jets is done using a particle flow algorithm, with the output of this clustered using the anti-kT algorithm as implemented in FastJet, with a distance parameter of 0.5. Requirements are placed on the candidate jet in order to reduce the background formed by particles which are either incorrectly reconstructed or produced in additional pp interactions in the same event.

Concerning the increased pile-up, different assumptions are made, but in general the effect is assumed to be similar to the one in Run 2.

1.1.3 Treatment of systematic uncertainties

It is a significant challenge to predict the expected systematic uncertainties of physics results at the end of HL-LHC running. It is reasonable to anticipate improvements to techniques of determining systematic uncertainties over an additional decade of data-taking. To estimate the expected performance, experts in the various physics objects and detector systems from ATLAS and CMS have looked at current limitations to systematic uncertainties in detail to determine which contributions are limited by statistics and where there are more fundamental limitations. Predictions were made taking into account the increased integrated luminosity and expected potential gains in technique. These recommendations were then harmonised between the experiments to take advantage of a wider array of expert opinions and to allow the experiments to make sensitivity predictions on equal footing [16, 17]. For theorists' contributions, a simplified approach is often adopted, loosely inspired by the improvements predicted by experiments.

General guide-lining principles were defined in assessing the expected systematic uncertainties. Theoretical uncertainties are assumed to be reduced by a factor of two with respect to the current knowledge, thanks to both higher-order calculation as well as reduced parton distribution functions (PDF) uncertainties [38]. All the uncertainties related to the limited number of simulated events are neglected, under the assumption that sufficiently large simulation samples will be available by the time the HL-LHC becomes operational. For all scenarios, the intrinsic statistical uncertainty in the measurement is reduced by a factor $1/\sqrt{\mathrm{L}}$, where L is the projection integrated luminosity divided by that of the reference Run 2 analysis. Systematics driven by intrinsic detector limitations are left unchanged, or revised according to detailed simulation studies of the upgraded detector. Uncertainties on methods are kept at the same value as in the latest public results available, assuming that the harsher HL-LHC conditions will be compensated by method improvements.

The uncertainty in the integrated luminosity of the data sample is expected to be reduced down to 1% by a better understanding of the calibration methods and their stability employed in its determination, and making use of the new capabilities of the upgraded detectors.

In addition to the above scenario (often referred to as "YR18 systematics uncertainties" scenario), results are often compared to the case where the current level of understanding of systematic uncertainties is assumed ("Run 2 systematic uncertainties") or to the case of statistical-only uncertainties.

1.2 Implications for beyond the Standard Model theories

1.2.1 Heavy new physics: precision tests and effective field theories

Precision measurements provide an important tool to search for heavy BSM dynamics, associated with mass scales beyond the LHC direct energy reach, exploiting the fact that such dynamics can still have an impact on processes at smaller energy, via virtual effects. In this context the well-established framework of effective field theories (EFTs) allows to systematically parametrise BSM effects and how they modify SM processes. Assuming lepton and baryon number conservation, the leading such effects can be captured by dimension-6 operators,

$$\mathcal{L}_{\text{eff}} = \mathcal{L}_{\text{SM}} + \frac{1}{\Lambda^2}\sum_i c_i \mathcal{O}_i + \cdots \tag{1}$$

for dimensionless coefficients c_i and, for simplicity, a common suppression scale Λ. Table 1 proposes a set of operators considered in this report. This set is *redundant*, in the sense that different combinations of operators might lead to the same physical effect; moreover this set is *not complete*, in the sense that there are more operators at dimension-6 level. In practical applications we will always be interested in identifying *minimal* (non-redundant) subsets of operators that contribute to a given process; we will also be interested that these operators be complete, at least under some well motivated assumption. For instance, the assumption that new physics only couples to the SM bosons, leads to the *universal* set of operators, from the second panel in table 1. Alternatively, the minimal flavour violation assumption [39] provides

a well-motivated framework to focus on operators with a certain, family-universal, flavour structure; operators with a richer flavour structure will be studied in a dedicated section 7.

Table 1: A list of dimension-6 SMEFT operators used in this chapter, defined for one family only; operators suppressed in the minimal flavour violation assumption [39], have been neglected (in particular dipole-type operators). Some combinations are redundant and can be eliminated as described in the text.

Higgs-Only Operators		
$\mathcal{O}_H = \frac{1}{2}(\partial^\mu \lvert H\rvert^2)^2$	$\mathcal{O}_6 = \lambda \lvert H\rvert^6$	
$\mathcal{O}_{y_u} = y_u \lvert H\rvert^2 \bar{Q}\widetilde{H}u$	$\mathcal{O}_{y_d} = y_d \lvert H\rvert^2 \bar{Q}Hd$	$\mathcal{O}_{y_e} = y_e \lvert H\rvert^2 \bar{L}He$
$\mathcal{O}_{BB} = g'^2 \lvert H\rvert^2 B_{\mu\nu}B^{\mu\nu}$	$\mathcal{O}_{GG} = g_s^2 \lvert H\rvert^2 G^A_{\mu\nu}G^{A\mu\nu}$	$\mathcal{O}_{WW} = g^2 \lvert H\rvert^2 W^I_{\mu\nu}W^{I\mu\nu}$
Universal Operators		
$\mathcal{O}_T = \frac{1}{2}(H^\dagger \overleftrightarrow{D_\mu} H)^2$	$\mathcal{O}_{HD} = (H^\dagger D^\mu H)^*(H^\dagger D_\mu H)$	$\mathcal{O}_{3G} = \frac{1}{3!}g_s f_{abc} G^{a\,\nu}_\mu G^b_{\nu\rho} G^{c\,\rho\mu}$
$\mathcal{O}_W = \frac{ig}{2}(H^\dagger \sigma^a \overleftrightarrow{D^\mu} H)D^\nu W^a_{\mu\nu}$	$\mathcal{O}_B = \frac{ig'}{2}(H^\dagger \overleftrightarrow{D^\mu} H)\partial^\nu B_{\mu\nu}$	$\mathcal{O}_{WB} = gg'(H^\dagger \sigma^I H)W^I_{\mu\nu}B^{\mu\nu}$
$\mathcal{O}_{HW} = ig(D^\mu H)^\dagger \sigma^a (D^\nu H)W^a_{\mu\nu}$	$\mathcal{O}_{HB} = ig'(D^\mu H)^\dagger (D^\nu H)B_{\mu\nu}$	$\mathcal{O}_{3W} = \frac{1}{3!}g\epsilon_{abc} W^{a\,\nu}_\mu W^b_{\nu\rho} W^{c\,\rho\mu}$
$\mathcal{O}_{2G} = \frac{1}{2}\left(D^\nu G^a_{\mu\nu}\right)^2$	$\mathcal{O}_{2B} = \frac{1}{2}\left(\partial^\rho B_{\mu\nu}\right)^2$	$\mathcal{O}_{2W} = \frac{1}{2}\left(D^\rho W^a_{\mu\nu}\right)^2$
and $\mathcal{O}_H, \mathcal{O}_6, \mathcal{O}_{BB}, \mathcal{O}_{WW}, \mathcal{O}_{GG}, \mathcal{O}_y = \sum_\psi \mathcal{O}_{y_\psi}$		
Non-Universal Operators that modify Z/W couplings to fermions		
$\mathcal{O}_{HL} = (iH^\dagger \overleftrightarrow{D_\mu} H)(\bar{L}\gamma^\mu L)$	$\mathcal{O}^{(3)}_{HL} = (iH^\dagger \sigma^a \overleftrightarrow{D_\mu} H)(\bar{L}\sigma^a\gamma^\mu L)$	$\mathcal{O}_{He} = (iH^\dagger \overleftrightarrow{D_\mu} H)(\bar{e}\gamma^\mu e)$
$\mathcal{O}_{HQ} = (iH^\dagger \overleftrightarrow{D_\mu} H)(\bar{Q}\gamma^\mu Q)$	$\mathcal{O}^{(3)}_{HQ} = (iH^\dagger \sigma^a \overleftrightarrow{D_\mu} H)(\bar{Q}\sigma^a\gamma^\mu Q)$	
$\mathcal{O}_{Hu} = (iH^\dagger \overleftrightarrow{D_\mu} H)(\bar{u}\gamma^\mu u)$	$\mathcal{O}_{Hd} = (iH^\dagger \overleftrightarrow{D_\mu} H)(\bar{d}\gamma^\mu d)$	
CP-odd operators		
$\mathcal{O}_{H\widetilde{W}} = (H^\dagger H)\widetilde{W}^I_{\mu\nu}W^{I\mu\nu}$	$\mathcal{O}_{H\widetilde{B}} = (H^\dagger H)\widetilde{B}_{\mu\nu}B^{\mu\nu}$	$\mathcal{O}_{\widetilde{W}B} = (H^\dagger \sigma^I H)\widetilde{W}^I_{\mu\nu}B^{\mu\nu}$
	$\mathcal{O}_{3\widetilde{W}} = \frac{1}{3!}g\epsilon_{abc} W^{a\,\nu}_\mu W^b_{\nu\rho}\widetilde{W}^{c\,\rho\mu}$	

Reduction to a minimal basis is achieved via integration by parts and field re-definitions, equivalent in practice to removing combinations proportional to the equations of motion. These imply relations between the operators of table 1; the most important ones being (Y denotes here hyper-charge)

$$\mathcal{O}_{HB} = \mathcal{O}_B - \frac{1}{4}\mathcal{O}_{BB} - \frac{1}{4}\mathcal{O}_{WB}\,, \qquad \mathcal{O}_{HW} = \mathcal{O}_W - \frac{1}{4}\mathcal{O}_{WW} - \frac{1}{4}\mathcal{O}_{WB} \tag{2}$$

$$\mathcal{O}_B = \frac{g'^2}{2}\sum_\psi Y_\psi \mathcal{O}_{H\psi} - \frac{g'^2}{2}\mathcal{O}_T\,, \qquad \mathcal{O}_T = \mathcal{O}_H - 2\mathcal{O}_{HD} \tag{3}$$

$$\mathcal{O}_W = \frac{g^2}{2}\Big[\left(\mathcal{O}_{y_u} + \mathcal{O}_{y_d} + \mathcal{O}_{y_e} + \text{h.c.}\right) - 3\mathcal{O}_H + 4\mathcal{O}_6 + \frac{1}{2}\sum_{\psi_L}\mathcal{O}^{(3)}_{H\psi_L}\Big]\,, \tag{4}$$

and similar expressions for $\mathcal{O}_{2W}$ and $\mathcal{O}_{2B}$ in terms of the products of $SU(2)$ and $U(1)$ SM currents. Eqs. (2-4) can be used to define minimal, non-redundant operator bases; for instance, in the context of Higgs physics, the operators $\mathcal{O}_H, \mathcal{O}_W, \mathcal{O}_B, \mathcal{O}_{HW}, \mathcal{O}_{HB}$ are retained at the expense of $\mathcal{O}_{HD}$, $\mathcal{O}_{WW}$, $\mathcal{O}_{WB}$, $\mathcal{O}^{(3)}_{HL}$, $\mathcal{O}_{HL}$ in what is known as the SILH basis [40], while in the opposite case we refer to the Warsaw basis [41].[1]

[1] In addition, the SILH basis gives preference to the operators $\mathcal{O}_{2W}$ and $\mathcal{O}_{2B}$, which are more easily found in universal BSM theories, while the Warsaw basis swaps them in terms of four-fermions operators.

These operators induce two types of effects: some that are proportional to the SM amplitudes and some that produce genuinely new amplitudes. The former are better accessed by high-luminosity experiments in kinematic regions where the SM is the largest. The most interesting example of this class for the LHC are Higgs couplings measurements in single-Higgs processes. The operators in the top panel of table 1 have the form $|H|^2 \times \mathcal{L}_{\rm SM}$, with $\mathcal{L}_{\rm SM}$ denoting operators in the SM Lagrangian, and imply small modifications $\propto v^2/\Lambda^2$ of the Higgs couplings to other SM fields, with respect to the SM value. These are often parametrised as rescalings of the SM rates, $\kappa_i^2 = \Gamma_i/\Gamma_i^{\rm SM}$ ($\Gamma^{\rm SM}$ the Higgs partial width into channel i) *assuming* the same Lorentz structure as that of the SM, i.e. providing an overall energy-independent factor. This is known as the kappa framework [42]. We discuss Higgs couplings in detail in sections 2 and 4 .

Among effects associated with new amplitudes, that cannot be put in correspondence with the κs, particularly interesting are BSM energy-growing effects. At dimension-6 level we find effects that grow at most quadratically with the energy. This implies a quadratic enhancement of the sensitivity to these effects, as we consider bins at higher and higher energy. This can be contrasted with high-intensity effects, whose sensitivity increases only with the square root of the integrated luminosity, and eventually saturates as systematics become comparable. High-energy effects are the ideal target of the HL and HE LHC programs, as we discuss in section 4. In section 8, we combine the results from the various EFT analyses and provide a global perspective on the HL and HE LHC sensitivity to EFT effects.

Ultimately, the goal of these global fits is to provide a model-independent framework to which large classes of specific models can be matched an analysed. We provide some example in section 8.

1.2.2 Light new physics: rare processes and new degrees of freedom

A complementary way to unveil BSM physics affecting the Higgs sector of Nature is the search for very rare processes involving the 125 GeV Higgs boson and for extended Higgs sectors.

The SM predicts several processes involving the Higgs boson to be very rare. Notable examples are the di-Higgs production, as well as the Higgs decays to first and second generation quarks and leptons. The search for these rare processes can unveil the presence of new degrees of freedom. Particularly, measurements of the di-Higgs production cross section (Sec. 3) will give constraints on the Higgs trilinear interaction, therefore providing information on electroweak symmetry breaking and allowing to set constraints on e.g. the nature of the phase transition between the trivial Higgs vacuum and the vacuum we observe at present (Sec. 3.6.2) and on the presence of extended Higgs sectors. The HL and HE stages of the LHC will be crucial to achieve this goal thanks to the relatively sizeable di-Higgs samples that will be produced: $\mathcal{O}(100\ \mathrm{K})$ at HL-LHC and $\mathcal{O}(2\ \mathrm{millions})$ at HE-LHC (compared to the $\mathcal{O}(6\ \mathrm{K})$ di-Higgs produced at Run 1 and 2 LHC). Furthermore, the branching ratios of SM rare Higgs decay modes such as $h \to \mu^+\mu^-$, $h \to Z\gamma$, and $h \to cc$ have been only mildly upper bounded by present LHC searches due in part to the low statistics ($h \to \mu^+\mu^-$, $h \to Z\gamma$) and, in part, to the background limited analyses ($h \to cc$). An important progress on these rare decay modes is expected at the HL and HE-LHC. For example, the HL-LHC will be able to discover and have a $(10-13)\%$ accuracy measurement of the di-muon decay mode (Sec. 2.3.8). Knowing the Higgs couplings to light quark and lepton generations will shed light on BSM flavor models and possibly on the SM flavor puzzle (Sec. 7).

Beyond rare SM Higgs processes, BSM models that contain new light degrees of freedom, X_i, generically predict rare exotic Higgs, decays $h \to X_i X_j$ or $h \to X_i\ \mathrm{SM}_j$ where SM_j is a SM particle (Secs. 6 and 9.1. For a review see e.g. [43]). A typical example is the Higgs decaying to light dark matter particles. Thanks to the tiny Higgs width (~ 4 MeV), even very feebly coupled new light particles can lead to relatively sizeable Higgs branching ratios that can be probed by the LHC in the future. On the one hand, the HL and HE-LHC will produce huge samples of Higgs bosons from its main production mode, gluon fusion ($\mathcal{O}(10^8)$ and $\mathcal{O}(10^9)$, respectively). This can allow the search for super rare and low background signatures. On the other hand, the sample of Higgs bosons produced from sub-leading production modes in association with other SM particles (e.g. tth) will be sizeable, increasing the discovery

prospects for rare and more background limited Higgs decay signatures. Therefore, the HL/HE-LHC Higgs exotic decay program can be uniquely sensitive to the existence of a broad range of new light weakly coupled particles (on condition that trigger and analysis thresholds will be kept relatively low, to allow capturing this set of soft signatures).

In many BSM theories, electroweak symmetry is broken not only by one Higgs boson, but by several degrees of freedom. Examples are supersymmetric theories, composite Higgs theories, as well as theories of neutral naturalness. Overall, extended Higgs sectors can lead to new interesting signatures that are not contained in the SM. The search for additional Higgs bosons is a high priority for current and future colliders. The ATLAS and CMS collaborations have performed several searches for heavy neutral and charged Higgs bosons during the first two runs of the LHC. At the same time, the LHCb collaboration (as well as ATLAS and CMS) has pursued several searches for new Higgs bosons with a mass below 125 GeV. The reach of all these searches will expand considerably in the future and, especially, at the HL and HE-LHC. In Secs. 9.2-9.4 and 9.8 of this report, we study the prospects for testing some of the most promising signatures. Most of the BSM models that predict the existence of an extended Higgs sector, also predict a 125 GeV Higgs with the interactions which are generically different from the SM predictions. As we will show in Secs. 9.5-9.7, the study of the interplay between new Higgs searches and Higgs coupling measurements will be a powerful tool to probe vast regions of parameter space of BSM theories with an extended electroweak symmetry breaking sector.

2 Higgs boson precision measurements[2]

2.1 Introduction

The large number of events expected in almost all Higgs boson measurement channels for the HL-LHC and HE-LHC will allow very precise measurements of the Higgs boson production cross sections and its couplings to gauge bosons and fermions. In many measurement channels, the expected overall statistical, experimental and theoretical uncertainties will be comparable in size. Therefore, a close interaction between the communities of the experimental and theoretical particle physicists will be needed in order to reach the best possible measurements of the Higgs boson properties.

Experimental sensitivity for the Higgs boson properties measurements is estimated by extrapolating the performance of the existing measurements to the HL-LHC data set, assuming the experiments will have a similar level of detector and triggering performance. Results are presented for two assumptions on the size of the experimental and theoretical systematic uncertainties that will be achievable by the time of HL-LHC (so called conservative and optimistic scenarios). Details on the extrapolation methodology and scenarios will be presented in Section 2.3.

Section 2.2 provides an overview of theoretical predictions for the Higgs boson production at 14 and 27 TeV and of the uncertainties that are expected to be reached by the time of the final HL-LHC and HE-LHC measurements. These predictions are used as input to sensitivity studies of the ATLAS and CMS Higgs boson cross section and coupling measurements in individual channels that are summarised in Section 2.3 and for the expectations for differential cross section measurements presented in Section 2.4. Section 2.5 puts emphasis on all measurements related to the top Yukawa coupling, as this is the largest Yukawa coupling in the Standard Model with a value close to unity and, hence, of special interest in understanding the Higgs mechanism and its relation to fermions. The combination of the expected measurements in ATLAS and CMS are presented in Section 2.6 together with an interpretation in the kappa-model [44, 42] in Section 2.7.

The kappa-framework is closely related to a non-linear EFT, and projections of measurements of EFT coefficients in a non-linear EFT are presented in Section 2.8 together with a translation of these results in terms of composite Higgs scenarios in section 2.9. Finally, probes of anomalous HVV interactions are discussed in Section 2.10.

2.2 Theoretical predictions for the Higgs boson production[3]

Cross-section predictions for the high-energy (HE) LHC, and their associated theoretical uncertainties, are discussed and shown in Section 2.2.1. Predictions are computed for a proton-proton collider with a pp centre-of-mass energy $\sqrt{s} = 27$ TeV and use a Higgs boson mass of $m_H = 125.09 \pm 0.5$ GeV. All other parameters are taken from YR4 [45], with exceptions noted where they are important. Projections of progress towards a reduction in theoretical uncertainties, on the timescale of the high-luminosity (HL) LHC (3 ab^{-1} of pp collisions at $\sqrt{s} = 14$ TeV), are discussed in Section 2.2.2. Tables summarising a detailed study of the dependence of the gluon-fusion cross section on the mass of the Higgs boson are presented in Section 2.2.4.

2.2.1 Cross sections for 13, 14 and 27 TeV HE-LHC

This section provides updated cross-sections for the LHC operating at energies of 13, 14 and 27 TeV. All predictions [46] include the latest theoretical input and supersede the older results in YR4 [45].

[2] Contact Editors: S. Alioli, M. Dührssen, P. Milenovic

[3] Contacts: K. Becker, C. Bertella, M. Bonvini, A. Calderon Tazon, J. Campbell, F. Caola, X. Chen, P. Francavilla, S. Frixione, R. Frederix, T. Gehrmann, N. Glover, Y. Haddad, V. Hirschi, A. Huss, S. Jones, A. Karlberg, M. Kerner, J. Lindert, G. Luisoni, G. Marchiori, S. Marzani, A. Massironi, B. Mistlberger, P. Monni, M. Moreno Llacer, A. Mück, D. Pagani, C. Palmer, C. Pandini, L. Perrozzi, S. Pozzorini, E. Re, L. Reina, H.S. Shao, L. Simon, B. Stieger, V. Theeuwes, F. Tramontano, M. Zaro

2.2.1.1 *Gluon fusion*

In this section we document cross section predictions for a standard model Higgs boson produced through gluon fusion in 27 TeV pp collisions. To derive predictions we include contributions based on perturbative computations of scattering cross sections as studied in Ref. [47]. We include perturbative QCD corrections through next-to-next-to-next-to-leading order (N^3LO), electroweak (EW) and approximated mixed QCD-electroweak corrections as well as effects of finite quark masses. The only modification with respect to YR4 [45] is that we now include the exact N^3LO heavy top effective theory cross section of Ref. [48] instead of its previous approximation. The result of this modification is only a small change in the central values and uncertainties. To derive theoretical uncertainties we follow the prescriptions outlined in Ref. [47]. We use the following inputs:

E_{CM}	27 TeV
$m_t(m_t)$	162.7 GeV
$m_b(m_b)$	4.18 GeV
$m_c(3\ \text{GeV})$	0.986 GeV
$\alpha_S(m_Z)$	0.118
PDF	PDF4LHC15_nnlo_100 [49]

(5)

All quark masses are treated in the $\overline{\text{MS}}$ scheme. To derive numerical predictions we use the program `iHixs` [50].

Sources of uncertainty for the inclusive Higgs boson production cross section have been assessed recently in refs. [47, 51, 52, 45]. Several sources of theoretical uncertainties were identified.

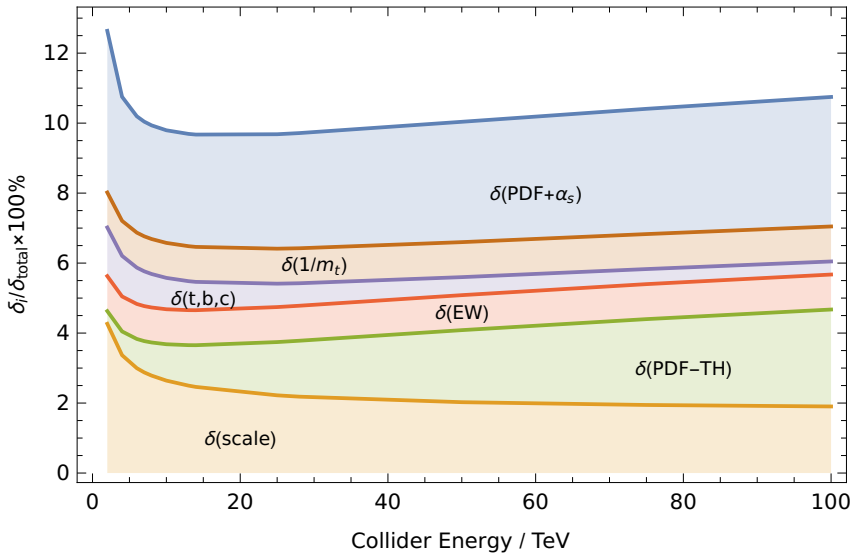

Fig. 1: The figure shows the linear sum of the different sources of relative uncertainties as a function of the collider energy. Each coloured band represents the size of one particular source of uncertainty as described in the text. The component $\delta(\text{PDF}+\alpha_S)$ corresponds to the uncertainties due to our imprecise knowledge of the strong coupling constant and of parton distribution functions combined in quadrature.

– Missing higher-order effects of QCD corrections beyond N^3LO (δ(scale)).
– Missing higher-order effects of electroweak and mixed QCD-electroweak corrections at and beyond $\mathcal{O}(\alpha_S\alpha)$ (δ(EW)).
– Effects due to finite quark masses neglected in QCD corrections beyond NLO (δ(t,b,c) and $\delta(1/m_t)$)

– Mismatch in the perturbative order of the parton distribution functions (PDF) evaluated at NNLO and the perturbative QCD cross sections evaluated at N^{3}LO (δ(PDF-TH)).

In the tables the linear sum of the effect of those uncertainties is referred to as δ(theory). In addition, the imprecise knowledge of the parton distribution functions and of the strong coupling constant play a dominant role. The individual size of these contributions can be seen in fig. 1 as a function of the collider energy [50]. As can be easily inferred the relative importance of the different sources of uncertainty is impacted only mildly by changing the centre of mass energy from 13 TeV to 27 TeV. Inclusive cross sections for $m_H = 125.09$ GeV are given in Table 2. As noted above, the exact treatment of N^{3}LO QCD corrections results in a small shift in the cross-section at 13 TeV, relative to the YR4 result, and a slight reduction in the overall theoretical uncertainty.

Table 2: Gluon fusion Higgs boson production cross sections and uncertainties as a function of the pp collider energy.

$\sqrt{s}$	σ	δ(theory)	δ(PDF)	$\delta(\alpha_s)$
13 TeV	48.61 pb	$^{+2.08\text{pb}}_{-3.15\text{pb}}$ $\binom{+4.27\%}{-6.49\%}$	± 0.89 pb ($\pm 1.85\%$)	$^{+1.24\text{pb}}_{-1.26\text{pb}}$ $\binom{+2.59\%}{-2.62\%}$
14 TeV	54.72 pb	$^{+2.35\text{pb}}_{-3.54\text{pb}}$ $\binom{+4.28\%}{-6.46\%}$	± 1.00 pb ($\pm 1.85\%$)	$^{+1.40\text{pb}}_{-1.41\text{pb}}$ $\binom{+2.60\%}{-2.62\%}$
27 TeV	146.65 pb	$^{+6.65\text{pb}}_{-9.44\text{pb}}$ $\binom{+4.53\%}{-6.43\%}$	± 2.81 pb ($\pm 1.95\%$)	$^{+3.88\text{pb}}_{-3.82\text{pb}}$ $\binom{+2.69\%}{-2.64\%}$

The dependence of the inclusive gluon-fusion cross-section on the Higgs boson mass at $\sqrt{s} = 14$ and 27 TeV is detailed at the end of this note in Section 2.2.4.

Impact of threshold and high-energy corrections

Recently, Ref. [53] has performed a study of the effects of simultaneous threshold and high-energy (small Bjorken x) resummations on the inclusive Higgs boson production cross section. In this brief section we summarise the main conclusions, while the numerical results will be discussed in the following section. For more details we refer the reader to Ref. [53]:

1. At different collider energies, it was found that the impact of threshold resummation amounts to about $+1\%$ on top of the N^{3}LO cross section [52]. The size of this effect is compatible with other estimates of the size of missing higher-order corrections.
2. Conversely, the inclusion of small-x resummation was found to increase the cross section by about one percent at 13 TeV, and by about $3\% - 4\%$ at 27 TeV, with respect to the N^{3}LO prediction. The correction grows even larger at higher energies, reaching about $+10\%$ for a 100 TeV pp collider. The inclusion of high-energy resummation affects differently the perturbative coefficient functions and the parton densities.
   – The effect on the coefficient functions is very moderate, and remains below the 1% level for different collider energies. This indicates that the production of a Higgs boson at present and future colliders does not probe very small values of the momentum fraction at which the coefficient functions are evaluated. In turn, this implies that currently and at future colliders PDFs are probed at intermediate values of x.
   – The parton densities receive a large correction from small-x resummation. Its effect is twofold: on one hand, the *evolution* of the gluon density is modified by the inclusion of small-x effects, and at average values of x probed in Higgs production this leads to a moderate effect on the parton densities at m_H (cf. Fig. 2.2 of Ref. [54]). On the other hand, the PDFs used in the double-resummed prediction of Ref. [53] (`NNPDF31sx_nnlonllx_as`

_0118 [54]) include small-x data from HERA, which Ref. [54] observes to require high-energy resummation for the fit to be robust. The fixed-order prediction of Ref. [53] instead uses a PDF set which fits the small-x HERA data without including high-energy resummation (NNPDF31sx_nnlo_as_0118 [54]). This results in sizeable differences in the parton distribution functions and drives the large correction to the N^{3}LO total cross section observed in Ref. [53].

Summarising, the sizeable corrections to the N^{3}LO prediction due to high-energy resummation observed in Ref. [53] are, to a large extent, due to the need for high-energy resummation in the PDF fit which are necessary to get a reliable description of small-x HERA data. Performing a fit without high energy resummation results in considerable tension with respect to low Q^2 HERA data. In order to corroborate these findings, and assess precisely the effect of high-energy resummation on parton distribution fits, it is important to make progresses in the theoretical knowledge of small-x dynamics. Furthermore, it would be desirable to include additional small-x collider data in the fits of parton distributions. We would like to encourage the PDF and theory community to further investigate these effects in view of future high energy colliders.

Predictions for double-resummed cross section

The setup is the same of the YR4 ($m_H = 125$ GeV, $m_t = 172.5$ GeV, $m_b = 4.92$ GeV, $m_c = 1.51$ GeV, $\alpha_s(m_Z^2) = 0.118$, $\mu_f = \mu_r = m_H/2$), with the only difference being that we do not use PDF4LHC but the NNPDF31sx_nnlonllx_as_0118 set of Ref. [54]. Since these resummed PDFs are available for a single value of α_s, we could not compute the α_s uncertainty in our result. The results are collected in Tab. 3.

For each value of the collider energy, we give the full N^{3}LO+N^{3}LL+LLx cross section which includes top, bottom and charm contributions (as discussed in Ref. [55]) and EW corrections included in the complete factorisation approach, i.e. as a $+5\%$ contribution. The breakdown of the individual terms contributing to the cross section (the main contribution assuming only top runs in the loop, the bottom+charm correction, and the EW correction) is presented in the third column. In the next columns, we present various sources of uncertainties, following Ref. [53]:

- Missing higher-order uncertainty (scale uncertainty) $\delta_{\rm scale}^{\rm 42var}$. It is the envelope of standard 7-point scale variations for each of the sub-leading variations of threshold resummed contributions, resulting in a total of 42 variation.
- PDF uncertainty $\delta_{\rm PDFs}$. This is the standard NNPDF Monte Carlo replica uncertainty, but it does not contain the α_s uncertainty, as previously discussed.
- Sub-leading small-x logarithms uncertainty $\delta_{\rm subl.logs}$. This uncertainty is computed as described in Refs. [53, 55], and it likely overestimates the effect of sub-leading contributions in the coefficient functions. However, as argued in Refs. [53, 55], this uncertainty can be considered as an estimate of the uncertainty from sub-leading contributions in the PDFs. In this respect, this provides an alternative to the uncertainty from missing higher-order PDFs adopted in YR4, which should thus not be included.

Additional uncertainties from missing $1/m_t^2$ effects, missing bottom+charm effects and sub-leading EW effects should be included according to the YR4 prescription. Since the N^{3}LO heavy-top result is matched to the exact small-x according to the construction of Ref. [55], the "truncation of the soft expansion" uncertainty discussed in YR4 should not be considered.

Finally, in the last column of the table we present the ratio of our resummed result with a purely fixed-order N^{3}LO cross section obtained with the same settings but using the NNLO parton distribution functions NNPDF31sx_nnlo_as_0118 of Ref. [54]. This is useful to understand how large the effect of resummation(s) in our prediction is. We see in particular that the effect (of small-x resummation) grows

Table 3: Values of the N^{3}LO+N^{3}LL+LLx gluon-fusion cross section for selected values of the pp collision energy and for a Higgs boson mass $m_H = 125$ GeV. We use the NNPDF31sx PDFs with $\alpha_s(m_Z^2) = 0.118$, $m_t = 173$ GeV, $m_b = 4.92$ GeV and $m_c = 1.51$ GeV.

$\sqrt{s}$	$\sigma_{\text{N}^3\text{LO+N}^3\text{LL+LL}x}$	$= \sigma_t + \Delta\sigma_{bc} + \Delta\sigma_{\text{EW}}$	$\delta^{42\text{var}}_{\text{scale}}$	δ_{PDFs}	$\delta_{\text{subl.logs}}$	$\frac{\sigma_{\text{N}^3\text{LO+N}^3\text{LL+LL}x}}{\sigma_{\text{N}^3\text{LO}}}$
13 TeV	48.93 pb	$(49.26 - 2.66 + 2.33)$ pb	$^{+4.0}_{-3.8}\%$	$\pm 1.2\%$	$\pm 1.8\%$	1.020
14 TeV	55.22 pb	$(55.56 - 2.96 + 2.63)$ pb	$^{+4.0}_{-3.8}\%$	$\pm 1.1\%$	$\pm 1.9\%$	1.023
27 TeV	151.6 pb	$(151.6 - 7.2 + 7.2)$ pb	$^{+4.0}_{-4.0}\%$	$\pm 1.0\%$	$\pm 2.3\%$	1.046

Table 4: VBF Higgs boson production cross-sections in pp collisions for centre-of-mass energies up to 27 TeV and a Higgs boson mass $m_H = 125.09$ GeV. The s-channel cross-section is the contribution from Higgs-strahlung diagrams with hadronic weak-boson decay [45].

$\sqrt{s}$ [TeV]	σ^{VBF} [fb]	Δ_{scale} [%]	$\Delta_{\text{PDF}\oplus\alpha_s}$ [%]	$\sigma^{\text{DIS}}_{\text{NNLO}}$ [fb]	δ_{ELWK} [%]	σ_γ [fb]	$\sigma_{s\text{-ch}}$ [fb]
13	3766	$^{+0.43}_{-0.33}$	± 2.1	3939	-5.3	35.3	1412
14	4260	$^{+0.45}_{-0.34}$	± 2.1	4460	-5.4	40.7	1555
27	11838	$^{+0.66}_{-0.36}$	± 2.1	12483	-6.2	129	3495

with the collider energy, reaching 4.6% at the HE-LHC. For any of the scales, approximately $+1\%$ of the effect of resummations is due to threshold resummation (in the coefficient functions), while the rest of the effect is due to small-x resummation, which mostly comes from the PDFs (see Ref. [53]) as discussed in the previous subsection.

2.2.1.2 Vector boson fusion

The vector-boson fusion (VBF) cross sections are computed with the same settings as in YR4 and reported in Tab. 4. The description of the setup can be found in the YR4 itself. The EW and photon cross sections have been computed using the `LUXqed_plus_PDF4LHC_nnlo_100` [56, 57] PDF set and hence the 13 and 14 TeV cross sections differ slightly from those reported in the YR4, where `NNPDF23_nlo_as_0118_qed` [58] was used instead. The QCD cross section was computed at NNLO with proVBFH [59, 60], while the EW and photon contributions have been computed at NLO with HAWK [61, 62, 63].

We note that the photon induced contribution is more reliably predicted here than was the case in the YR4 due to the LUXqed method. In particular the photon PDF should no longer be considered as a source of uncertainty as in eq. (I.5.7) in the YR4, as it is now constrained at the percent level. Quantitatively the photon induced contributions are reduced by about 30% compared to in the YR4.

The s-channel contributions at 13 and 14 TeV have on the other hand increased compared to the YR4 results. This is due to the updated set of parton distribution functions used for this prediction, i.e. `LUXqed_plus_PDF4LHC_nnlo_100` instead of `NNPDF23_nlo_as_0118_qed`. We also note that the relative size of the s-channel decreases as the collider energy increases - from 47% at 7 TeV to 30% at 27 TeV.

2.2.1.3 VH production

In Tabs. 5–14 we report the inclusive cross sections for associated production of a Higgs boson and a weak gauge boson $V = W, Z$, for pp collisions at 13, 14 and 27 TeV. The results have been obtained using HAWK, combining NNLO QCD and NLO EW corrections [64, 63, 65, 66, 67, 68, 69], by means of a multiplicative scheme, as described in the YR4 studies (eq. I.5.15 and I.5.16 of Ref. [45]). For

Table 5: Cross-section for the process $pp \to WH$. Both W^+ and W^- contributions are included. The photon contribution is not included. Results are given for a Higgs boson mass $m_H = 125.09$ GeV.

$\sqrt{s}$ [TeV]	$\sigma_{\text{NNLO QCD}\otimes\text{NLO EW}}$ [pb]	Δ_{scale} [%]	$\Delta_{\text{PDF}\oplus\alpha_s}$ [%]
13	1.358	$^{+0.51}_{-0.51}$	1.35
14	1.498	$^{+0.51}_{-0.51}$	1.35
27	3.397	$^{+0.29}_{-0.72}$	1.37

Table 6: Cross-section for the process $pp \to W^+H$. The photon contribution is not included. Results are given for a Higgs boson mass $m_H = 125.09$ GeV.

$\sqrt{s}$ [TeV]	$\sigma_{\text{NNLO QCD}\otimes\text{NLO EW}}$ [pb]	Δ_{scale} [%]	$\Delta_{\text{PDF}\oplus\alpha_s}$ [%]
13	0.831	$^{+0.74}_{-0.73}$	1.79
14	0.913	$^{+0.64}_{-0.76}$	1.78
27	1.995	$^{+0.43}_{-1.04}$	1.84

Table 7: Cross-section for the process $pp \to W^-H$. The photon contribution is not included. Results are given for a Higgs boson mass $m_H = 125.09$ GeV.

$\sqrt{s}$ [TeV]	$\sigma_{\text{NNLO QCD}\otimes\text{NLO EW}}$ [pb]	Δ_{scale} [%]	$\Delta_{\text{PDF}\oplus\alpha_s}$ [%]
13	0.527	$^{+0.59}_{-0.63}$	2.03
14	0.585	$^{+0.55}_{-0.68}$	1.98
27	1.402	$^{+0.36}_{-0.93}$	2.03

Table 8: Cross-section for the process $pp \to l^+\nu H$. The photon contribution is included, and also reported separately in the last column. Results are given for a Higgs boson mass $m_H = 125.09$ GeV.

$\sqrt{s}$ [TeV]	$\sigma_{\text{NNLO QCD}\otimes\text{NLO EW}}$ [pb]	Δ_{scale} [%]	$\Delta_{\text{PDF}\oplus\alpha_s}$ [%]	σ_γ
13	0.094	$^{+0.71}_{-0.70}$	1.72	$4.1\ 10^{-3}$
14	0.104	$^{+0.61}_{-0.73}$	1.70	$4.7\ 10^{-3}$
27	0.232	$^{+0.40}_{-0.97}$	1.72	$1.5\ 10^{-2}$

Table 9: Cross-section for the process $pp \to l^-\bar{\nu}H$. The photon contribution is included, and also reported separately in the last column. Results are given for a Higgs boson mass $m_H = 125.09$ GeV.

$\sqrt{s}$ [TeV]	$\sigma_{\text{NNLO QCD}\otimes\text{NLO EW}}$ [pb]	Δ_{scale} [%]	$\Delta_{\text{PDF}\oplus\alpha_s}$ [%]	σ_γ
13	0.0598	$^{+0.57}_{-0.60}$	1.94	$2.6\ 10^{-3}$
14	0.0666	$^{+0.52}_{-0.64}$	1.89	$3.1\ 10^{-3}$
27	0.1628	$^{+0.34}_{-0.87}$	1.90	$1.1\ 10^{-2}$

Table 10: Cross-section for the process $pp \to ZH$. The predictions for the $gg \to ZH$ channel are computed at LO, rescaled by the NLO K-factor in the $m_t \to \infty$ limit, and supplemented by the NLL_{soft} resummation. The photon contribution is omitted. Results are given for a Higgs boson mass $m_H = 125.09$ GeV.

$\sqrt{s}$ [TeV]	$\sigma_{\text{NNLO QCD}\otimes\text{NLO EW}}$ [pb]	Δ_{scale} [%]	$\Delta_{\text{PDF}\oplus\alpha_s}$ [%]
13	0.880	$^{+3.50}_{-2.68}$	1.65
14	0.981	$^{+3.61}_{-2.94}$	1.90
27	2.463	$^{+5.42}_{-4.00}$	2.24

Table 11: Cross-section for the process $pp \to ZH$. The photon and $gg \to ZH$ contributions are omitted. Results are given for a Higgs boson mass $m_H = 125.09$ GeV.

$\sqrt{s}$ [TeV]	$\sigma_{\text{NNLO QCD}\otimes\text{NLO EW}}$ [pb]	Δ_{scale} [%]	$\Delta_{\text{PDF}\oplus\alpha_s}$ [%]
13	0.758	$^{+0.49}_{-0.61}$	1.78
14	0.836	$^{+0.51}_{-0.62}$	1.82
27	1.937	$^{+0.56}_{-0.74}$	2.37

Table 12: Cross-section for the process $gg \to ZH$. Predictions are computed at LO, rescaled by the NLO K-factor in the $m_t \to \infty$ limit, and supplemented by the NLL_{soft} resummation. Results are given for a Higgs boson mass $m_H = 125.09$ GeV.

$\sqrt{s}$ [TeV]	$\sigma_{\text{NNLO QCD}\otimes\text{NLO EW}}$ [pb]	Δ_{scale} [%]	$\Delta_{\text{PDF}\oplus\alpha_s}$ [%]
13	0.123	$^{+24.9}_{-18.8}$	4.37
14	0.145	$^{+24.3}_{-19.6}$	7.47
27	0.526	$^{+25.3}_{-18.5}$	5.85

Table 13: Cross-section for the process $pp \to l\bar{l}H$. The photon contribution is included, and reported separately in the last column. Results are given for a Higgs boson mass $m_H = 125.09$ GeV.

$\sqrt{s}$ [TeV]	$\sigma_{\text{NNLO QCD}\otimes\text{NLO EW}}$ [pb]	Δ_{scale} [%]	$\Delta_{\text{PDF}\oplus\alpha_s}$ [%]	σ_γ
13	$2.97\ 10^{-2}$	$^{+3.49}_{-2.67}$	1.64	$1.4\ 10^{-4}$
14	$3.31\ 10^{-2}$	$^{+3.59}_{-2.92}$	1.89	$1.6\ 10^{-4}$
27	$8.32\ 10^{-2}$	$^{+5.39}_{-3.97}$	1.85	$5.4\ 10^{-4}$

Table 14: Cross-section for the process $pp \to \nu\bar{\nu}H$. Results are given for a Higgs boson mass $m_H = 125.09$ GeV.

$\sqrt{s}$ [TeV]	$\sigma_{\text{NNLO QCD}\otimes\text{NLO EW}}$ [pb]	Δ_{scale} [%]	$\Delta_{\text{PDF}\oplus\alpha_s}$ [%]
13	0.177	$^{+3.50}_{-2.68}$	1.65
14	0.197	$^{+3.59}_{-2.92}$	1.89
27	0.496	$^{+5.41}_{-3.99}$	2.24

ZH production, the loop-induced $gg \to ZH$ channel has been computed at NLO+NLL, using a Born-improved Higgs effective field theory (HEFT) approach, and added linearly.

The contribution from photon-induced channels depends on the specific decay mode of the vector boson, and thus it has been removed from the total cross-sections, while it is instead included in the total result for the dedicated cross-sections where decay products are specified. In the latter cases, the individual photon-induced cross section is also separately reported.

The results at 27 and 14 TeV show a similar pattern of good perturbative convergence. There are two points that deserve some specific comment:

1. As can be evinced from the above tables, photon-induced contributions are relatively important in the $pp \to l^{\pm}\nu H$ case (where they amount to $\sim 4-7\%$ of the total cross section). For the $pp \to l\bar{l}H$ case instead, they contribute to only $\sim 4-7$ permille.
   We also notice that the relative weight of the photon-induced channel is computed more reliably than in the results previously obtained for the YR4 study: the changes in the values of σ_γ from the YR4 results (which also had large uncertainties) to those presented here are indeed non-negligible, and they are due to the fact that the photon PDF is now constrained significantly better, thanks to the LUXqed approach [56, 57]. We refer the reader to paragraph I.5.2.c of the YR4 for details on how this channel was treated previously. For the numbers in the new tables, the cross section for σ_γ was computed using the LUXqed_plus_PDF4LHC15_nnlo PDF set. For completeness, we also included an update for the 13 TeV cross sections using this PDF set.
2. As far as the loop-induced $gg \to ZH$ process is concerned, we remind that this channel starts contributing only at order α_S^2, hence it is part of the NNLO corrections to the $pp \to ZH$ cross section. Nevertheless, due to the gluon luminosity, its relative size is important, especially at large centre-of-mass energies. Due to the fact that it is a loop-induced channel, this contribution is known exactly (i.e. retaining finite values for the top mass) only at LO. However, because of its numerical size, and due to the fact that it contributes to the total cross section with a leading-order-like scale uncertainty, it is important to compute it at higher order. Exact NLO corrections to $gg \to ZH$ are not yet available. The numbers in the tables are obtained using a Born-improved HEFT approach, which essentially consists in computing the process at LO exactly, and rescaling it with the NLO/LO K-factor obtained in the $m_t \to \infty$ limit. NLL threshold effects have also been included. At order α_S^3 there are however many other gluon-gluon initiated sub-processes that are not yet calculated. It is reasonable to expect that for VH the correction to the loop induced process will be the first at order α_S^3 to be evaluated in the near future, so that this contribution can provide an order of magnitude estimate of the remaining perturbative uncertainty coming from the missing higher orders.

2.2.1.4 $t\bar{t}H$ and tH

Cross sections for $t\bar{t}H$ and $tH + \bar{t}H$ production at $\sqrt{s} = 14$ and 27 TeV are presented in Tables 15-17 and Tables 18-20 respectively. Results have been obtained using the same setup as in YR4, and considering three values for M_H, namely $M_H = 125.09 \pm 0.5$ GeV. The theoretical uncertainties from renormalisation and factorisation scale dependence, PDF, and α_s are calculated as explained in Sec. I.6.2 of YR4 [45], to which we refer for full details. $t\bar{t}H$ predictions include NLO QCD [70, 71, 72, 73, 74, 75, 76] and NLO QCD+EW corrections [75, 77, 76], while $tH + \bar{t}H$ predictions are accurate at NLO QCD only [78]. In both cases, `MadGraph5_aMC@NLO` [79, 80] has been employed for the computation of the cross sections. As expected, going to higher energies greatly enhances both $t\bar{t}H$ and $tH + \bar{t}H$ cross sections.

Table 15: NLO QCD+EW cross sections for $t\bar{t}H$ production at the 13 TeV LHC, taken from Ref. [45].

m_{H} [GeV]	$\sigma^{\mathrm{NLO}}_{\mathrm{QCD+EW}}$ [fb]	Scale [%]	α_s [%]	PDF [%]	PDF+α_s [%]
124.59	512.2	$^{+5.8}_{-9.2}$	2.0	3.0	3.6
125.09	506.5	$^{+5.8}_{-9.2}$	2.0	3.0	3.6
125.59	500.7	$^{+5.8}_{-9.2}$	2.0	3.0	3.6

Table 16: NLO QCD+EW cross sections for $t\bar{t}H$ production at the 14 TeV LHC.

m_{H} [GeV]	$\sigma^{\mathrm{NLO}}_{\mathrm{QCD+EW}}$ [fb]	Scale [%]	α_s [%]	PDF [%]	PDF+α_s [%]
124.59	619.3	$^{+6.1}_{-9.2}$	1.9	2.9	3.5
125.09	612.8	$^{+6.0}_{-9.2}$	1.9	2.9	3.5
125.59	605.6	$^{+6.1}_{-9.2}$	1.9	2.9	3.5

Table 17: NLO QCD+EW cross sections for $t\bar{t}H$ production at a 27 TeV proton–proton collider.

m_{H} [GeV]	$\sigma^{\mathrm{NLO}}_{\mathrm{QCD+EW}}$ [pb]	Scale [%]	α_s [%]	PDF [%]	PDF+α_s [%]
124.59	2.90	$^{+7.9}_{-9.0}$	1.8	2.1	2.8
125.09	2.86	$^{+7.8}_{-9.0}$	1.8	2.1	2.8
125.59	2.84	$^{+7.9}_{-9.0}$	1.8	2.1	2.8

Table 18: NLO QCD cross sections for the $t-$channel tH and $\bar{t}H$ production at the 13 TeV LHC, taken from Ref. [45].

m_{H} [GeV]	$\sigma_{t\mathrm{H}+\bar{t}\mathrm{H}}$ [fb]	Scale+FS [%]	α_s [%]	PDF [%]	PDF+α_s [%]	$\sigma_{t\mathrm{H}}$ [fb]	$\sigma_{\bar{t}\mathrm{H}}$ [fb]
124.59	74.52	$^{+6.6}_{-14.7}$	1.2	3.5	3.7	49.04	25.49
125.09	74.26	$^{+6.5}_{-14.7}$	1.2	3.5	3.7	48.89	25.40
125.59	74.09	$^{+6.5}_{-15.2}$	1.2	3.6	3.7	48.75	25.32

Table 19: NLO QCD cross sections for the $t-$channel tH and $\bar{t}H$ production at the 14 TeV LHC.

m_{H} [GeV]	$\sigma_{t\mathrm{H}+\bar{t}\mathrm{H}}$ [fb]	Scale+FS [%]	α_s [%]	PDF [%]	PDF+α_s [%]	$\sigma_{t\mathrm{H}}$ [fb]	$\sigma_{\bar{t}\mathrm{H}}$ [fb]
124.59	90.35	$^{+6.4}_{-14.6}$	1.2	3.4	3.6	59.15	31.21
125.09	90.12	$^{+6.4}_{-14.7}$	1.2	3.4	3.6	58.96	31.11
125.59	89.72	$^{+6.4}_{-14.8}$	1.2	3.4	3.6	58.70	31.02

Table 20: NLO QCD cross sections for the $t-$channel tH and $\bar{t}H$ production at a 27 TeV proton–proton collider.

m_{H} [GeV]	$\sigma_{t\mathrm{H}+\bar{t}\mathrm{H}}$ [fb]	Scale+FS [%]	α_s [%]	PDF [%]	PDF+α_s [%]	$\sigma_{t\mathrm{H}}$ [fb]	$\sigma_{\bar{t}\mathrm{H}}$ [fb]
124.59	419.0	$^{+5.0}_{-12.3}$	1.3	2.6	2.9	263.3	155.7
125.09	417.9	$^{+5.0}_{-12.5}$	1.3	2.6	2.9	262.8	155.1
125.59	416.4	$^{+5.0}_{-12.6}$	1.3	2.6	2.9	261.8	154.7

2.2.2 Projections of uncertainty reductions for the HL-LHC

This section discusses improvements to the theoretical predictions that may be possible on the timescale of the HL-LHC. Estimates of potential reductions in current theoretical uncertainties are made where possible and potential limiting factors identified.

2.2.2.1 Gluon fusion

Improving substantially on any of the current sources of uncertainty represents a major theoretical challenge that should be met in accordance with our ability to utilise said precision and with experimental capabilities. The computation of sub-leading mass and EW corrections is currently being addressed by several groups, and therefore it is likely to be achieved in the next decade. Although such computations will allow for a better control over some sources of uncertainty, their final impact on the full theoretical error is likely to be moderate as current estimates indicate. Another source of error that might improve in the forthcoming years is that related to the parton densities. In particular, the extraction of N^3LO PDFs would lead to the disappearance of the PDF-TH uncertainty. Similar considerations apply to the error on the strong coupling constant, that will be reduced due to more accurate extractions. Overall, the above progress would ultimately lead to a notable reduction of the uncertainties of Figure 1.

It is obvious that the future precision of experimental measurement of Higgs boson properties will challenge the theoretical community. Achieving a significant improvement of our current theoretical understanding of the Higgs boson and its interactions will inspire us to push the boundaries of our capabilities to predict and extract information. New ways of utilising quantum field theory in our endeavours have to be explored and our perturbative and non-perturbative understanding of hadron scattering processes has to evolve substantially. It is clear that this exciting task can only be mastered by a strong and active collider phenomenology community.

Impact of future precision of parton distribution function

It is a tantalising question to ask by how much one of the largest sources of uncertainty - the imprecise knowledge of PDFs - would be reduced if already all future LHC data were available. To this end a study was performed in ref. [38] (see also Section 2.2.5) that uses simulated future data with accordingly shrunken statistical uncertainties to constrain parton distribution functions. The authors used pseudo data corresponding to measurements of ATLAS, CMS and LHCb for key precision processes after $3ab^{-1}$ of integrated luminosity were collected at the High-Luminosity LHC at 14 TeV. They then performed a new fit according to the PDF4LHC15 framework [49] and studied the implications of their analysis. The resulting PDFs are readily available and can be used in order to estimate the impact of this future data on specific observables. Three scenarios were considered in this study that assume that experimental systematic uncertainties will shrink at different levels relative to the 8 TeV run of the LHC. Scenario 1, scenario 2 and scenario 3 assume that the future systematic uncertainty will be equal, shrunk by a factor 0.7 or a factor of 0.4 w.r.t to the 8 TeV run respectively.

Evaluating the inclusive Higgs boson production cross section with this simulated PDFs results in the PDF uncertainties summarised in Tab. 21. Note, that the central values stay unchanged and all other uncertainties are not afflicted by the change of PDFs. Even the most pessimistic scenario leads to a reduction of the PDF uncertainty by factor of two. However, this projections should be viewed only as a first estimate for the determination of PDFs from future measurements. Predicting the future development and correlation of systematic experimental uncertainties is non trivial and may differ strongly from observable to observable. PDF uncertainties may in the future also be adversely impacted by a more accurate treatment of theoretical uncertainties in the predictions of cross sections that serve as input for PDF extraction. Data incompatibilities may occur for various reasons. It is clear that an understanding of the structure of the proton at percent level accuracy is clearly a formidable task and rightly deserves significant research in the future.

Table 21: Uncertainty due to imprecise knowledge of PDFs estimated with current and simulated future PDFs for different scenarios and at different collider energies.

E_{CM}	Current	Scenario 1	Scenario 2	Scenario 3
13 TeV	$\pm 1.85\%$	$\pm 0.78\%$	$\pm 0.69\%$	$\pm 0.59\%$
14 TeV	$\pm 1.85\%$	$\pm 0.78\%$	$\pm 0.68\%$	$\pm 0.58\%$
27 TeV	$\pm 1.95\%$	$\pm 0.81\%$	$\pm 0.72\%$	$\pm 0.61\%$

2.2.2.2 *Vector boson fusion*

VBF Higgs boson production is currently known at a very high theoretical accuracy. In the structure-function approximation, the cross section has been computed fully inclusively at N^{3}LO accuracy in QCD. Fiducial calculations in the same approximation exist at NNLO accuracy in QCD. The only contribution which is currently unknown is the contribution from two-loop diagrams with gluon exchange between the two VBF quark lines. The conceptual difficulty is that it is a $2 \to 3$ process and that currently there are no methods available for evaluating two-loop diagrams with more than four external legs. It is realistic that such methods will become available before the HE-LHC is in operation. Beyond the VBF approximation, the full NLO corrections in both the strong and electroweak coupling have been computed. The electroweak contributions are of the same order as, or in certain phase space regions even larger than, the NNLO QCD corrections. Taking all of this into account, it has been estimated that the VBF cross section under typical VBF cuts has an accuracy at the 1% level. In order to connect these calculations to experimental measurements one would ideally need merged 2- and 3-jet NLO samples matched with the parton shower [81, 82] (NLOPS level) or even better a fully exclusive generator for VBF matched with the parton shower at NNLO (NNLOPS) . It is realistic that this will become available within the next few years and certainly before the HL-/HE-LHC phases.

2.2.2.3 *VH production*

The Higgs couplings to W and Z bosons are related by $SU(2)_L$ gauge invariance. As such, the measurement of the Higgs associated production with a W or a Z is complementary to the vector boson fusion process, as first considered in e^+e^- colliders in Ref. [83]. At the time of writing, the numbers shown in Section 2.2.1.3 are the best estimates available for the $pp \to VH$ contribution. As far as the ZH final state is concerned, due to the progress made in the last couple of years for the computation of top-mass effects at NLO in Higgs-boson pair production, it is foreseeable that, in the forthcoming years (definitely in the timescale of HL/HE LHC), an exact NLO result (including finite-m_t effects) will be available also for $gg \to ZH$. If one assumes that a pattern similar to what was found for di-higgs production [84] also holds for $gg \to ZH$, one can expect that the total NLO/LO K-factor will be slightly smaller than in the HEFT limit (from 1.9–2.0 to $\sim$1.6) and the final scale uncertainty for the $gg \to ZH$ cross section will decrease from 18–25% to about 15%.[4]

All the above results have been obtained for a stable Higgs boson. For the Higgs boson decay to bottom quarks, it is known that higher-order corrections to the m_{bb} line-shape are relevant, as shown in Ref. [85] and also recently confirmed in Ref. [86]. Although explicit studies are not available, one can expect that effects similar to those observed at 13–14 TeV in the region $m_{bb} < m_H$ will persist also at higher energies.

The matching of fixed-order corrections to parton showers (PS) is available for the $pp \to VH$ signal processes, at NLO as well as at NNLO [87, 88]. As for Higgs decays to bottom quarks, a fixed-order

[4] We stress that these numbers have been obtained as a back-of-the-envelope estimate through a comparison with di-higgs production.

study [86] suggests that higher-order corrections to the m_{bb} shape are not always very well modelled by a LO + parton shower treatment of the $H \to b\bar{b}$ decay. Event generators as the one developed in Ref. [88], and improvements thereof for the treatment of radiation off b-quarks [89], will allow one to assess this issue in the forthcoming years. A solid prediction of the $H \to b\bar{b}$ decay, also matched to parton-showers, can definitely be expected in the timescale of HL/HE LHC.

Furthermore, once the exact $gg \to ZH$ computation at NLO will be completed, a NLO matching to parton-shower will be straightforward to achieve, thereby improving on the currently available more advanced treatments, where a LO-merging of the exact matrix elements for $gg \to ZH$ and $gg \to ZH$+1-jet is performed.

Finally, as for the VH and VHJ event generators, recently there has been also the completion of the NLO EW corrections matched to the parton shower [90] showing once again the relevance of the EW corrections for the distributions for both the fixed order and the matched predictions.

2.2.2.4 $t\bar{t}H$ and tH

The cross sections for $t\bar{t}H$ and tH production are known at NLO accuracy in QCD [70, 72, 91] and, in the case of $t\bar{t}H$, NLO EW corrections have also been calculated [75, 77]. The corresponding theoretical uncertainty is of the order of 10–15% and is mainly induced by the residual scale dependence and, to a lesser extent, by PDF uncertainties. A drastic improvement can only come from the calculation of the NNLO QCD corrections. Given the ongoing rapid progress in cross section calculations with NNLO accuracy in QCD, it is foreseeable that NNLO QCD corrections to $t\bar{t}H$ and tH will become available in the next decade. In this scenario it is reasonable to expect a factor-two improvement of the theoretical accuracy.

On the other hand, the extraction of the $t\bar{t}H$ signal is at the moment mainly limited by the theoretical uncertainties in the modelling of the background, mainly $t\bar{t}b\bar{b}$ and $t\bar{t}W$+jets, via Monte Carlo generators. The reliable assessment of the related uncertainties and their further reduction are the main goals of an ongoing campaign of theoretical studies within the HXSWG. On a time scale of 5–10 years such background uncertainties may be reduced by a factor two to three.

2.2.3 Predictions for boosted Higgs production

The HL and HE LHC upgrades would allow for in-depth analyses of high-p_t tail of the Higgs transverse momentum distribution. This region is particularly interesting as it is very sensitive to BSM physics in the Higgs sector. For example, measures in the boosted region would allow one to lift the degeneracy between ggH and ttH couplings, and more in general to probe the internal structure of the ggH interaction. In this section, we report theoretical predictions for boosted Higgs production.

We first present results for the 13-TeV LHC. In Fig. 2(left) we show the cumulative Higgs transverse momentum distribution, defined as

$$\Sigma(p_t^H) = \int_{p_t^H}^{\infty} \frac{d\sigma}{dp_t},$$

for the main production channels. The ggF prediction is obtained by rescaling the exact NLO with the NNLO $K-$factor in the $m_t \to \infty$ approximation, and it does not contain EW corrections. The VBF and VH predictions include NNLO QCD and NLO EW corrections, while the $t\bar{t}H$ prediction includes NLO QCD and EW corrections. In Fig. 2(right), we show the relative importance of the different production mechanisms.[5] As it is well known, at high p_t the ggF channel becomes somewhat less dominant. Still,

[5] The small feature around $p_t \sim 750$ GeV in the ggF channel is due to lack of statistics in the theoretical simulation and it is not a genuine physical feature.

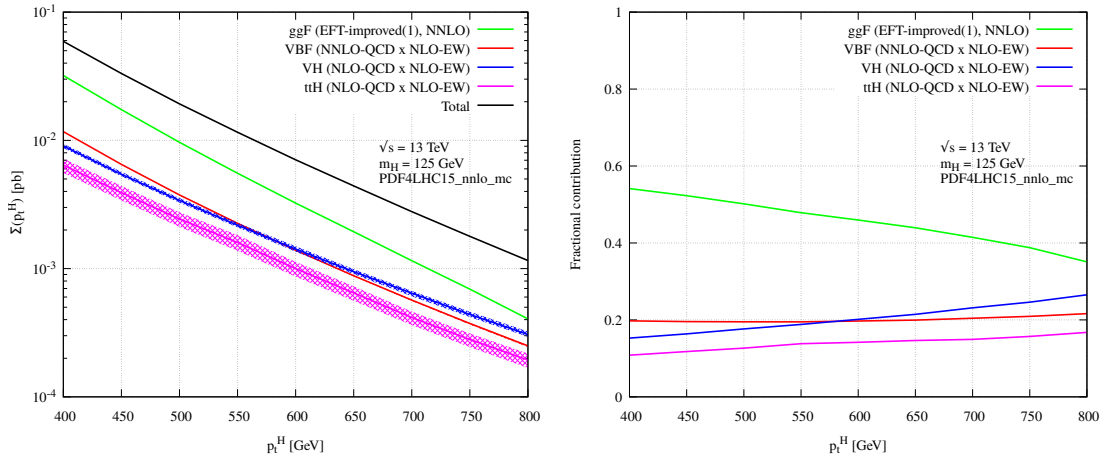

Fig. 2: Boosted Higgs prediction at the 13-TeV LHC. Left: cumulative transverse momentum distribution. Right: relative importance of different production mechanisms. See text for details.

radiative corrections strongly enhance this channel, which remains the dominant one in the TeV region. A very similar picture is expected for the HL-LHC.

Figs. 3 and 4 show similar predictions for the HE-LHC. In Fig. 3, all predictions are LO. At high

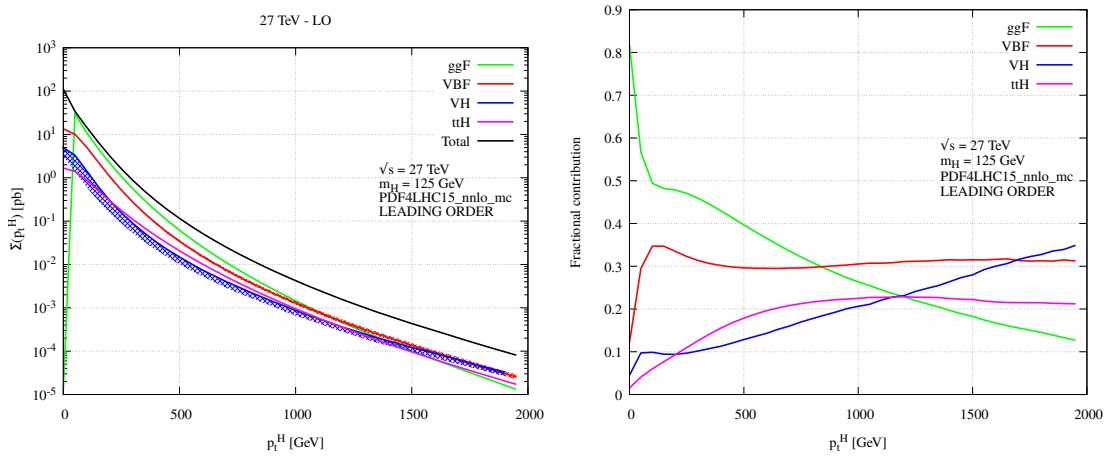

Fig. 3: LO boosted Higgs prediction at the 27-TeV LHC. Left: cumulative transverse momentum distribution. Right: relative importance of different production mechanisms. See text for details.

p_t, the ggF channel become sub-dominant compared to the other ones. VBF becomes the dominant channel around $p_t \sim 1$ TeV, and VH around $p_t \sim 2$ TeV. In the TeV region, the $t\bar{t}H$ channel becomes larger than ggF.

This picture is however significantly altered by radiative correction, whose size and impact is very different for different channels. This is shown in Fig. 4, where predictions include radiative corrections. More precisely, the VBF, VH and $t\bar{t}H$ predictions have the same accuracy as the ones in Fig. 2. The ggF prediction contains exact LO mass effects rescaled by the NLO $K-$factor in the m_t approximation. This is expected to provide an excellent approximation of the exact NLO result. Radiative corrections enhance the relative importance of the ggF and $t\bar{t}H$ channels, which still dominate over VBF well into

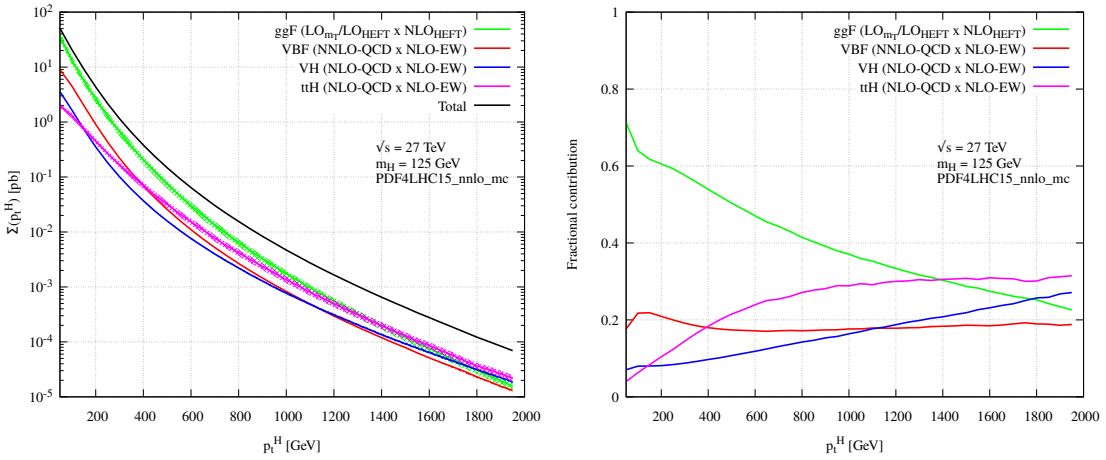

Fig. 4: Boosted Higgs prediction at the 27-TeV LHC, including radiative corrections. Left: cumulative transverse momentum distribution. Right: relative importance of different production mechanisms. See text for details.

the multi-TeV region. At large $p_t \sim 1.5$ TeV, the $t\bar{t}H$ channel becomes the dominant one.

Obtaining accurate and precise theoretical predictions in the boosted region is very challenging. Nevertheless, it is natural to expect progress in the timescale for the HL and HE LHC upgrades. This would allow for a proper scrutiny of the structure of Higgs interactions in the multi-TeV regime.

2.2.4 *Dependence of gluon-fusion cross section at* 14 *and* 27 *TeV on* m_H

The dependence of the inclusive gluon-fusion cross-section on the Higgs boson mass is shown in Tables 22 and 23, for pp collisions at $\sqrt{s} = 14$ and 27 TeV, respectively.

2.2.5 *PDF uncertainty expectations at the HE/HL-LHC*[6]

PDFs in the HL-LHC era. The detailed understanding of the quark and gluon structure of the proton, quantified by the parton distribution functions (PDFs) [92, 93, 94], is an essential ingredient for the theoretical predictions at hadron colliders. PDF uncertainties represent one of the dominant theoretical systematic errors both for direct searches of new physics beyond the Standard Model (BSM) [95] as well as in the profiling of the Higgs boson sector [45]. Therefore, improving our knowledge of the proton structure is an essential task for the high-precision physics program to be carried out at future runs of the LHC, including the HL-LHC era.

Modern global PDF fits [96, 97, 98, 99] include a wide range of LHC measurements in processes such as the production of jets, weak gauge bosons, and top quark pairs, among others. Recent breakthroughs in the calculation of NNLO QCD and NLO QED and electroweak corrections to most PDF-sensitive processes have been instrumental in allowing for the full exploitation of the information provided by the LHC measurements. The impact of high-precision LHC data combined with state-of-the art perturbative calculations has been quantified for many of the processes of interest, such as top-quark pair production [100, 101], the transverse momentum spectrum of Z bosons [102], direct photon production [103, 104], D meson production in the forward region [105, 106, 107], W production in association with charm quarks [108, 109], and inclusive jet production [110, 111].

From the point of view of PDF determinations, the availability of the immense data samples at the

[6] Contacts: R. Abdul Khalek, S. Bailey, J. Gao, L. Harland-Lang, J. Rojo

Table 22: The gluon-fusion cross-section in pp collisions at $\sqrt{s} = 14$ TeV, for different values of the Higgs boson mass m_H.

m_H [GeV]	Cross Section [pb]	+ δTh. [%]	- δTh. [%]	$\pm\delta$(PDF+α_S) [%]	$\pm\delta\alpha_S$ [%]	$\pm\delta$ PDF [%]
125.09	54.72	4.29	−6.46	3.20	2.61	1.85
124.59	55.10	4.29	−6.48	3.20	2.61	1.86
125.59	54.34	4.28	−6.45	3.20	2.61	1.85
120.00	58.85	4.37	−6.61	3.23	2.63	1.87
120.50	58.42	4.37	−6.60	3.22	2.63	1.87
121.00	58.00	4.36	−6.58	3.22	2.63	1.87
121.50	57.56	4.35	−6.57	3.22	2.62	1.86
122.00	57.15	4.34	−6.55	3.22	2.62	1.86
122.50	56.75	4.33	−6.54	3.21	2.62	1.86
123.00	56.35	4.32	−6.52	3.21	2.62	1.86
123.50	55.95	4.31	−6.51	3.21	2.61	1.86
124.00	55.56	4.30	−6.49	3.21	2.61	1.86
124.10	55.48	4.30	−6.49	3.20	2.61	1.86
124.20	55.41	4.30	−6.49	3.20	2.61	1.86
124.30	55.33	4.30	−6.49	3.20	2.61	1.86
124.40	55.25	4.30	−6.48	3.20	2.61	1.86
124.50	55.17	4.30	−6.48	3.20	2.61	1.86
124.60	55.10	4.29	−6.48	3.20	2.61	1.86
124.70	55.02	4.29	−6.47	3.20	2.61	1.86
124.80	54.94	4.29	−6.47	3.20	2.61	1.86
124.90	54.86	4.29	−6.47	3.20	2.61	1.86
125.00	54.79	4.29	−6.47	3.20	2.61	1.86
125.10	54.71	4.29	−6.46	3.20	2.61	1.85
125.20	54.64	4.28	−6.46	3.20	2.61	1.85
125.30	54.56	4.28	−6.46	3.20	2.61	1.85
125.40	54.48	4.28	−6.45	3.20	2.61	1.85
125.50	54.41	4.28	−6.45	3.20	2.61	1.85
125.60	54.33	4.28	−6.45	3.20	2.61	1.85
125.70	54.26	4.28	−6.44	3.20	2.61	1.85
125.80	54.18	4.27	−6.44	3.20	2.60	1.85
125.90	54.11	4.27	−6.44	3.20	2.60	1.85
126.00	54.03	4.27	−6.44	3.20	2.60	1.85
126.50	53.66	4.26	−6.42	3.19	2.60	1.85
127.00	53.29	4.25	−6.41	3.19	2.60	1.85
127.50	52.92	4.25	−6.40	3.19	2.60	1.85
128.00	52.56	4.24	−6.38	3.19	2.60	1.85
128.50	52.20	4.23	−6.37	3.18	2.59	1.85
129.00	51.85	4.22	−6.35	3.18	2.59	1.85
129.50	51.50	4.21	−6.34	3.18	2.59	1.84
130.00	51.15	4.20	−6.33	3.18	2.59	1.84

HL-LHC will permit a significant extension of the kinematic coverage of PDF-sensitive measurements as well as a marked improvement in their statistical and systematic uncertainties. In this contribution, we

Table 23: The gluon-fusion cross-section in pp collisions at $\sqrt{s} = 27$ TeV, for different values of the Higgs boson mass m_H.

m_H [GeV]	Cross Section [pb]	+ δTh. [%]	- δTh. [%]	$\pm\delta$(PDF+α_S) [%]	$\pm\delta\alpha_S$ [%]	$\pm\delta$ PDF
125.09	146.65	4.53	−6.43	3.30	2.66	1.95
124.59	147.55	4.55	−6.45	3.30	2.67	1.95
125.59	145.75	4.52	−6.42	3.30	2.66	1.95
120.00	156.35	4.64	−6.60	3.33	2.69	1.97
120.50	155.36	4.63	−6.58	3.33	2.69	1.97
121.00	154.36	4.62	−6.56	3.33	2.69	1.97
121.50	153.38	4.61	−6.55	3.32	2.68	1.96
122.00	152.41	4.60	−6.54	3.32	2.68	1.96
122.50	151.45	4.59	−6.52	3.32	2.68	1.96
123.00	150.50	4.58	−6.50	3.31	2.68	1.96
123.50	149.56	4.57	−6.49	3.31	2.67	1.96
124.00	148.64	4.56	−6.47	3.31	2.67	1.95
124.10	148.45	4.56	−6.47	3.31	2.67	1.95
124.20	148.27	4.56	−6.46	3.31	2.67	1.95
124.30	148.08	4.55	−6.46	3.31	2.67	1.95
124.40	147.90	4.55	−6.46	3.31	2.67	1.95
124.50	147.72	4.55	−6.46	3.31	2.67	1.95
124.60	147.53	4.55	−6.45	3.30	2.67	1.95
124.70	147.35	4.54	−6.45	3.30	2.67	1.95
124.80	147.17	4.54	−6.44	3.30	2.67	1.95
124.90	146.99	4.54	−6.44	3.30	2.67	1.95
125.00	146.81	4.54	−6.44	3.30	2.67	1.95
125.10	146.63	4.53	−6.43	3.30	2.66	1.95
125.20	146.45	4.53	−6.43	3.30	2.66	1.95
125.30	146.27	4.53	−6.43	3.30	2.66	1.95
125.40	146.09	4.53	−6.42	3.30	2.66	1.95
125.50	145.91	4.52	−6.42	3.30	2.66	1.95
125.60	145.73	4.52	−6.42	3.30	2.66	1.95
125.70	145.55	4.52	−6.41	3.30	2.66	1.95
125.80	145.37	4.52	−6.41	3.30	2.66	1.95
125.90	145.20	4.52	−6.41	3.30	2.66	1.95
126.00	145.02	4.51	−6.40	3.30	2.66	1.95
126.50	144.14	4.50	−6.39	3.29	2.66	1.94
127.00	143.26	4.49	−6.37	3.29	2.66	1.94
127.50	142.40	4.48	−6.36	3.29	2.65	1.94
128.00	141.54	4.48	−6.34	3.28	2.65	1.94
128.50	140.69	4.47	−6.33	3.28	2.65	1.94
129.00	139.84	4.46	−6.31	3.28	2.65	1.93
129.50	139.00	4.46	−6.30	3.27	2.64	1.93
130.00	138.18	4.45	−6.29	3.27	2.64	1.93

summarise the main results of our PDF projections for the HL-LHC era presented in [38]. The main idea is to quantify the impact of the future HL–LHC measurements on the proton PDFs and their uncertainties,

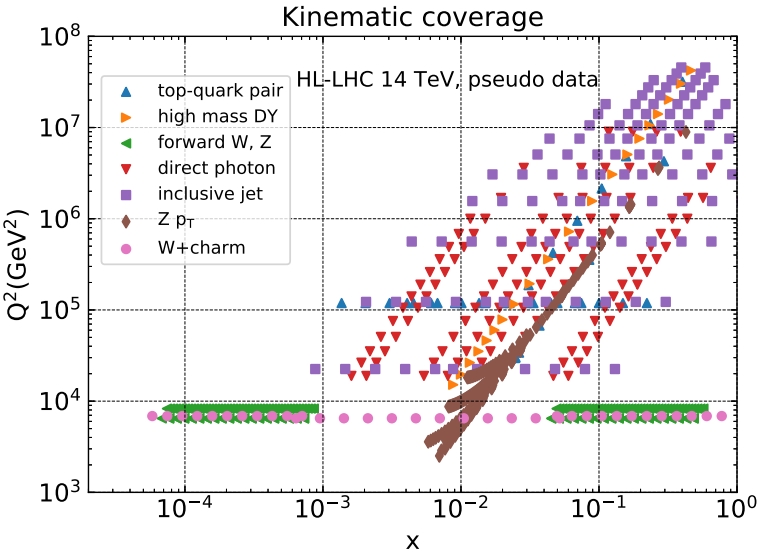

Fig. 5: The kinematic coverage in the (x, Q^2) plane of the HL–LHC pseudo-data.

with emphasis on their implications for Higgs physics. Specifically, we quantify the constraints of the HL–LHC pseudo-data on the PDF4LHC15 set [112, 113, 114, 115] by means of the Hessian Profiling method [116] (see also [117]). We choose the PDF4LHC15 set since it broadly represents the state-of-the-art understanding of the proton structure.

In Fig. 5 we show the kinematic coverage in the (x, Q^2) plane of the HL–LHC pseudo-data included in this analysis. As indicated there, we have simulated pseudo-data for the following processes: top quark pair production, high-mass and forward Drell-Yan W, Z production, direct photon and inclusive jet production, the transverse momentum of Z bosons, and the production of W bosons in association with charm quarks. The HL–LHC pseudo-data therefore spans a wide region in the kinematic plane, namely $6 \times 10^{-5} < x < 0.7$ and 40 GeV $< Q < 7$ TeV. In particular, one sees that the HL-LHC coverage of the large-x region, where current PDF fits exhibit large uncertainties, is markedly improved as compared to available LHC measurements.

Results. As an illustration of the impact of individual sets of HL-LHC pseudo-data, in Fig. 6 we show the comparison between the HL–LHC projected measurements and the theoretical predictions for the lepton rapidity distribution in forward W+charm production and for the invariant mass $m_{t\bar{t}}$ distribution in top-quark pair production. These two particular datasets probe the poorly-known strange quark and the gluon at large-x, respectively. The theory calculations are shown both before (PDF4LHC15) and after profiling. In the bottom panel, we show the same results normalised to the central value of the original theory calculation. In both cases we see that the expected precision of the HL-LHC measurements is rather higher than the current PDF uncertainties, and therefore we observe a marked improvement once they are included in PDF4LHC15 via the Hessian profiling.

In this study we have considered three different scenarios for the experimental systematic uncertainties of the HL–LHC pseudo-data. These scenarios, ranging from more conservative to more optimistic, differ among them in the reduction factor applied to the systematic errors of the reference 8 TeV or 13 TeV measurements, see [38] for more details. In particular, in the optimistic scenario we assume a reduction of the systematic errors by a factor 2.5 (5) as compared to the reference 8 TeV (13 TeV) measurements, while for the conservative scenario we assume no reduction in systematic errors with respect to the 8 TeV reference. Reassuringly, we obtain that the main results of our study depend only mildly in the specific assumption for the values of this reduction factor.

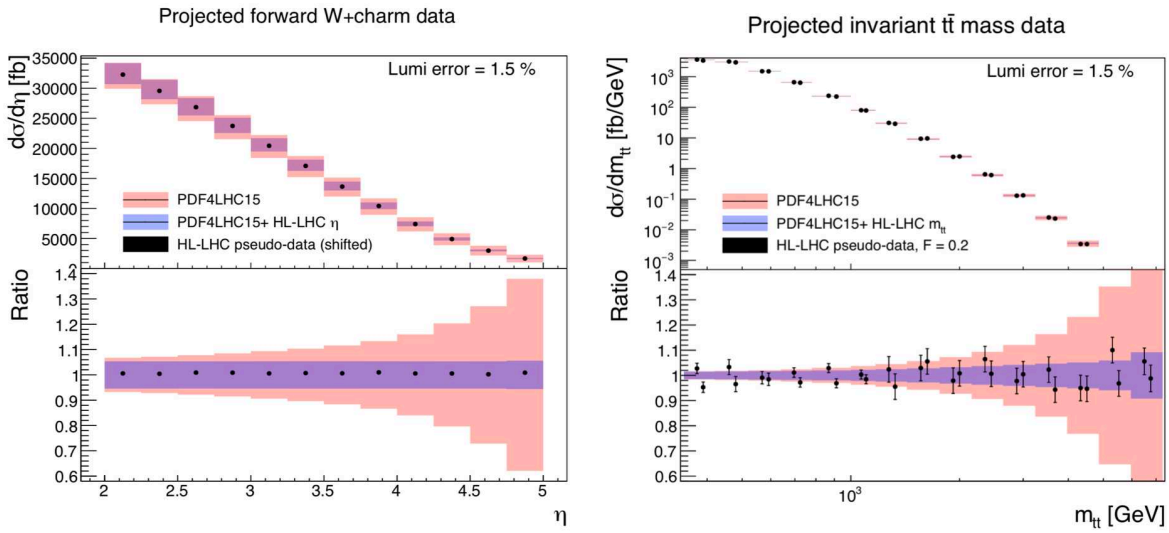

Fig. 6: Comparison between the HL–LHC pseudo-data and the theoretical predictions for forward $W+$charm production (left) and for the invariant mass $m_{t\bar{t}}$ distribution in top-quark pair production (right). The theory calculations are shown both before (PDF4LHC15) and after profiling.

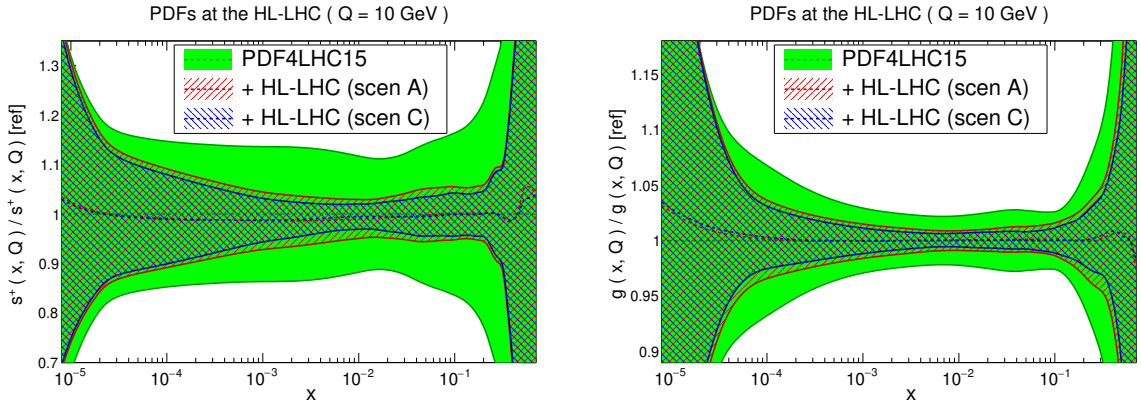

Fig. 7: Comparison of the PDF4LHC15 set with the profiled sets with HL–LHC pseudo-data. We show the strange (left) and gluon (right) PDFs normalised to the central value of the baseline.

In Fig. 7 we compare the PDF4LHC15 set with the strange quark and gluon PDFs obtained once the entire set of HL-LHC pseudo-data summarised in Fig. 5 has been included via profiling. We show results both in the conservative (A) and optimistic (C) scenarios for the projections of the experimental systematic uncertainties. We observe that the impact of the HL–LHC pseudo-data is reasonably similar in both scenarios. This is due to the fact that we have chosen those processes which will benefit from a significant improvement in statistics, independent of the specific assumption about the systematic errors. These then tend to lie in kinematic regions where the PDFs themselves are generally less well determined. We also observe a marked reduction of the PDF uncertainties in all cases. In the case of the gluon PDF, there is an improvement of uncertainties in the complete relevant range of momentum fraction x. This is a direct consequence of the fact that we have included several HL–LHC processes that have direct sensitivity to the gluon content of the proton, including jet, direct photon, and top quark pair production, as well as the transverse momentum of Z bosons. As we discuss next, this has direct implications for the phenomenology of Higgs boson production.

Table 24: The reduction of the PDF uncertainties as compared to the PDF4LHC15 baseline for different initial partonic combinations in the optimistic (conservative) scenario.

Ratio to baseline	$10\text{ GeV} \leq M_X \leq 40\text{ GeV}$	$40\text{ GeV} \leq M_X \leq 1\text{ TeV}$	$1\text{ TeV} \leq M_X \leq 6\text{ TeV}$
gluon-gluon	0.50 (0.60)	0.28 (0.40)	0.22 (0.34)
quark-quark	0.74 (0.79)	0.37 (0.46)	0.43 (0.59)
quark-antiquark	0.71 (0.76)	0.31 (0.40)	0.50 (0.60)

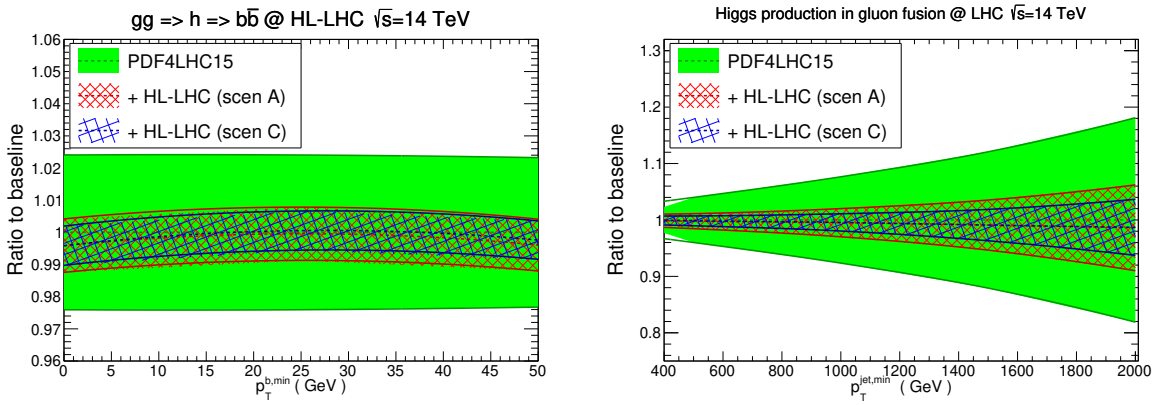

Fig. 8: Comparison of the predictions for SM Higgs production cross-sections at $\sqrt{s} = 14$ TeV between the PDF4LHC15 baseline and the profiled PDF sets with HL–LHC pseudo–data.

Implications for Higgs physics. In Table 24 we indicate the reduction of the PDF uncertainties in comparison to the PDF4LHC15 baseline for different initial partonic combinations (that is, a value of 1 corresponds to no improvement). Results are presented for three different bins of the invariant mass M_X of the produced system for the three initial states relevant for Higgs production: gluon-gluon (for $gg \to h$ and $t\bar{t}h$), quark-quark (for vector boson fusion) and quark-antiquark (for associated Wh and Zh production). The values shown outside (inside) the brackets correspond to the optimistic (conservative) scenario. We can see that for the M_X region relevant for the SM Higgs boson production, as well as for related BSM Higgs-like scalars, namely $40\text{ GeV} \leq M_X \leq 1\text{ TeV}$, the HL-LHC pseudo-data leads to a reduction by almost a factor four in the optimistic scenario in the gg channel, and around a factor three in the $q\bar{q}$ and qq channels. This implies that precision calculations of Higgs production at the HL-LHC should be possible with significantly reduced PDF uncertainties compared to current state-of-the-art predictions.

To illustrate this improvement, in Fig. 8 we present the comparison of the predictions for SM Higgs production at $\sqrt{s} = 14$ TeV between the PDF4LHC15 baseline and the profiled PDF sets. Specifically, we show Higgs boson production in gluon fusion with heavy top quark effective theory, both inclusive and decaying into $b\bar{b}$ as a function of $p_T^{b,\min}$ (left), and then in association with a hard jet as a function of its transverse momentum $p_{\rm T}^{\rm jet,min}$ (right). The calculations have been performed using `MCFM8.2` with leading-order matrix elements. The marked reduction of PDF uncertainties is consistent with the values reported in Table 24.

Finally, there are two caveats to be added concerning this study. First we have only considered a subset of all possible measurements of relevance for PDF fits at HL–LHC. Second, possible data

incompatibility has not been accounted for fully. These may strengthen and weaken, respectively, the constraining powers of future LHC data on PDFs.

The results of this study are made publicly available in the LHAPDF6 format [118], for the three scenarios that have been considered, and can be downloaded from:

```
https://data.nnpdf.science/HLLHC_YR/PDF4LHC15_nnlo_hllhc_scen1.tgz
https://data.nnpdf.science/HLLHC_YR/PDF4LHC15_nnlo_hllhc_scen2.tgz
https://data.nnpdf.science/HLLHC_YR/PDF4LHC15_nnlo_hllhc_scen3.tgz
```

2.3 Overview of experimental analysis for the Higgs boson measurement channels[7]

2.3.1 Extrapolation assumptions

The results presented in this Section are based on the extrapolation to an expected integrated luminosity of 3000 fb^{-1} of the corresponding ATLAS and CMS Run-2 results. For some of the Higgs decay final states (ATLAS: WW^*, $Z\gamma$, $t\bar{t}H$, $\tau\tau$; CMS: WW^*, $Z\gamma$, $\gamma\gamma$, ZZ^*, $t\bar{t}H$, $\tau\tau$, $b\bar{b}$ and $\mu\mu$) the extrapolation is performed from results obtained with the 2015-2016 36 fb^{-1} datasets; the remaining final state analyses (ATLAS: $\gamma\gamma$, ZZ^*, $b\bar{b}$ and $\mu\mu$) use the results based on the 2015+2016+2017 80 fb^{-1} data samples. The starting points of the extrapolated results are measurements based on datasets of size $\mathcal{O}(1\%)$ of the expected HL-LHC integrated luminosity. The extrapolations are in this regard very limited with respect to the potential reach of the real HL-LHC analyses, which large statistics will allow to probe corners of the phase space inaccessible at the LHC Run-2.

In addition to the increase in integrated luminosity, the ATLAS extrapolations also account for the increase of signal and background cross-sections from $\sqrt{s}$ = 13 TeV to 14 TeV. In those cases, the signal yields have been scaled according to the Higgs boson production cross sections values at 13 and 14 TeV, as reported in Ref. [45]. Similarly, the background yields have been scaled according to the parton luminosity ratio between 13 and 14 TeV, as reported in Ref. [42], by taking into account whether the background process is predominantly quark pair or gluon pair initiated.

Object reconstruction efficiencies, resolutions and fake rates are assumed to be similar in the Run-2 and HL-LHC environments, based on the assumption that the planned upgrades of the ATLAS and CMS detectors will compensate for the effects of the increase of instantaneous luminosity and higher pile-up environment at HL-LHC. For the systematic uncertainties which include experimental, signal and background components, two scenarios have been considered. The first scenario (S1) assumes the same values as those used in the published Run-2 analyses. The second scenario (S2) implements a reduction of the systematic uncertainties according to the improvements expected to be reached at the end of HL-LHC program in twenty years from now: the correction factors follow the recommendations from Ref. [119]. In certain analyses some of the systematic uncertainties are treated in a specific way, and this is discussed explicitly in each corresponding section. In all analyses, the theory uncertainties for signal and background are generally halved, except where more precise extrapolated values have been provided. Details on the projections of theoretical uncertainties are given in Section 2.2.2. The reduction of the theory uncertainties in gluon-fusion Higgs production is for instance associated to a better understanding of the correlation of their components, leading to their sum in quadrature in scenario S2, instead of the linear sum used in S1 (see Section 2.2.2.1 for details). The uncertainties related to missing higher orders in theory calculations are in particular discussed in Section 2.2.5: these uncertainties are halved in all analyses extrapolation in scenario S2, even though larger improvements are expected in some cases (e.g. gluon-fusion Higgs production). The uncertainty on the luminosity is set to 1%. The uncertainty related to Monte Carlo samples statistics is assumed to be negligible.

The extrapolated results are generally limited by systematic uncertainties. It is worth noting that, despite all efforts to design proper projections, the values of the systematic uncertainties of the Run-

[7] Contacts: M. Delmastro, N. De Filippis, P. Francavilla, A. Gilbert, S. Jezequel, P. Milenovic, M. Testa

2 analyses cannot fully account neither for the HL-LHC data-taking conditions, nor for the level of understanding of the various sources of systematic uncertainties that will be achieved by fully exploiting the large HL-LHC statistic. The systematic models in current Run-2 analyses are in fact designed for the needs of Run-2, and hence lack flexibility and details needed to account for full-fledged HL-LHC analyses. In this sense, these extrapolated uncertainties are to be considered an approximation: future analyses will exploit and gain sensitivity from phase space regions that are not accessible yet, or use analysis techniques that reduce the impact of systematic uncertainties. In many cases one can as well expect that several uncertainties will be be highly constrained with very large luminosity, and therefor updated uncertainty models with greater flexibility will be needed to properly fit the data.

In the following, all analyses segment the selected events according to the objects produced in association with the Higgs boson decay products and their topology, in order to maximise the sensitivity to the main Higgs production modes ($ggF+b\bar{b}H$, VBF, $VH = qqZH+ggZH+WH$ and top = $t\bar{t}H+tH$) and to reduce the uncertainties on the respective cross sections. Details on how this segmentation is performed, and on the event selection and categorisation in the various analyses, are found in the Run-2 analysis references quoted in each section.

2.3.2 $H \to \gamma\gamma$[8]

The measurement of the Higgs boson properties in the $H \to \gamma\gamma$ channel is performed using the events that contain two isolated photon candidates passing good quality requirements in the precision regions of the detectors. Events are further segmented according to the objects accompanying the di-photon system, in order to maximise the sensitivity to the main Higgs production modes and to reduce the uncertainties on the respective cross sections, as well as to the Simplified Template Cross Section (STXS, first introduced in Refs. [45, 120]) in the merged version of Stage-1. The Higgs production cross sections are measured for a Higgs boson absolute rapidity $|y_H|$ smaller than 2.5, and with further requirements on the objects accompanying the di-photon system (e.g. jet p_{T}). The $H \to \gamma\gamma$ signal is extracted by means of a combined signal-plus-background fit of the di-photon invariant mass spectra in the various event categories, where both the continuous background and the signal resonance are parametrised by analytic functions. The shape properties of the signal PDF are obtained by Monte Carlo (MC) simulation, and constrained by performance studies of the photon energy scale and resolution. The background PDF is completely determined by the fit on data, with systematic uncertainties attributed to the specific choice of functional form following the procedure described in Ref. [11] or using the discrete profiling method [121]. More details on the analyses methods can be found in most recent measurements in the $H \to \gamma\gamma$ channel published by ATLAS [122] and CMS [123].

The performance of the measurement of the Higgs boson properties in the $H \to \gamma\gamma$ channel at HL-LHC is extrapolated from the most recent measurements by ATLAS with $80\,\mathrm{fb}^{-1}$ [122] and by CMS with $36\,\mathrm{fb}^{-1}$ [123]. The main systematic uncertainties affecting the results are the background modelling uncertainty, missing higher order uncertainties causing event migrations between the bins, photon isolation efficiencies and jet uncertainties. On top of the common assumptions mentioned in Section 2.3.1, the results of the studies performed by ATLAS include a 10% increase of the background modelling systematic uncertainties, to account for the potentially worst knowledge of the background composition in each analysis category at HL-LHC: this assumption has anyway negligible impact. In the Run-2 analyses, a conservative 100% uncertainty on the heavy flavour resonant background in top-sensitive categories is applied. Measurements by ATLAS and CMS of the heavy flavour content, or the b-jet multiplicity, are expected to better constrain these contributions: for the S2 scenario extrapolation, this uncertainty is therefore halved.

Figure 9 shows the ratio of the extrapolated $H \to \gamma\gamma$ ATLAS measurements of the cross sections times branching fraction of the main Higgs production modes to their respective theoretical SM predic-

[8] Contact: S. Falke

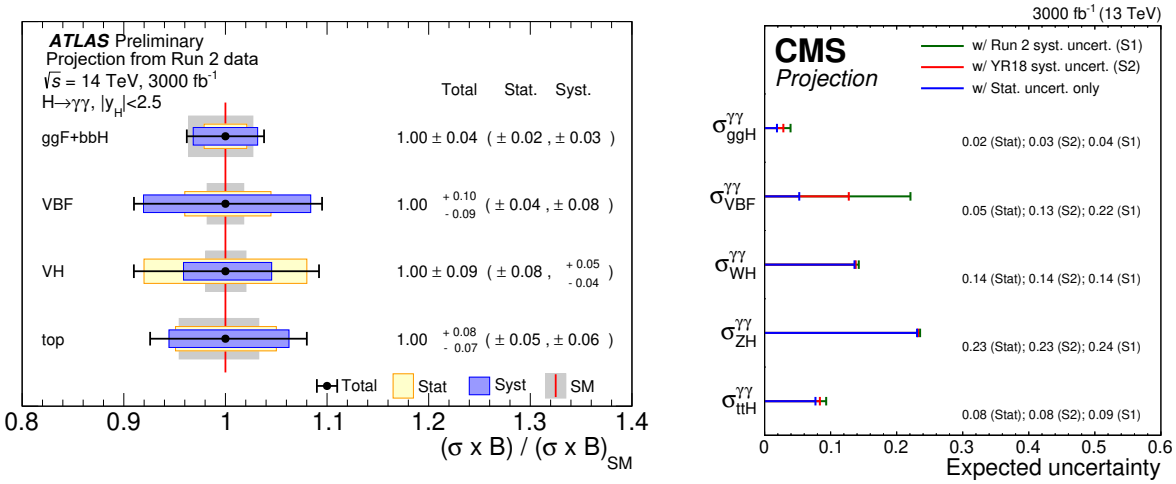

Fig. 9: Cross-section times branching fraction measurements of the main Higgs production modes in the $H \to \gamma\gamma$ decay channel, as extrapolated at the HL-LHC. In case of ATLAS results (left) the ratios of cross sections to their respective theoretical SM predictions are shown for scenario S2, while in case of CMS results (right) the uncertainties on these measurements are shown for S1, S2, and Stat-only scenarios..

tions (left), and uncertainties on these measurements for S1, S2, and stat-only scenarios as extrapolated using the $H \to \gamma\gamma$ CMS measurements (right). CMS extrapolation is obtained from the simultaneous fit in all production and decay modes, as described in Section 2.6.1. The reduction of the total uncertainty with respect to the $80\,\text{fb}^{-1}$ results ranges from a factor of about 2 (3) for the S1 (S2) scenario for the $ggH + b\bar{b}H$, VBF, top cross sections, to a factor of about 5(6) for the VH cross section, that remains dominated by the statistical uncertainty.

2.3.3 $H \to Z\gamma \to \ell\ell\,\gamma$[9]

Due to the small branching fraction in the SM, the $H \to Z\gamma$ decay has not yet been observed at the LHC. The experimental observed limits at the 95% confidence level are currently 6.6 times the SM prediction for a Higgs boson mass of 125.09 GeV by ATLAS and 3.9 times the SM prediction for a Higgs boson mass of 125 GeV by CMS, based on the analyses of $36\,\text{fb}^{-1}$ of pp collision at $\sqrt{s} = 13$ TeV described in Ref. [124, 125].

The analyses select events with an isolated photon candidate passing good quality requirements in the precision regions of the detectors, and a di-lepton system with properties compatible with that of the decay of a Z boson. Events are separated according to lepton flavour, the event kinematic properties, and the presence of jets compatible with the VBF production of the Higgs boson, in order to maximise the signal sensitivity. The signal is sought for by means of a combined signal-plus-background fit of the photon-di-lepton invariant mass spectra in various event categories, where both the continuous background and the signal resonance are parametrised by analytic functions. The Run-2 analyses are strongly driven by statistical uncertainty, and the main systematic uncertainties are from the bias associated to the background modelling, based on the MC simulation of some background processes, and on low-statistics data control regions for others.

The extrapolations to HL-LHC are performed with a simple scaling approach, assuming the same signal and background modelling used in the Run-2 analyses. All experimental and systematic uncertainties are considered to remain the same (S1), except the uncertainty associated to the background modelling, which is taken to be negligible. The latter assumption is based on the idea that, thanks to

[9] Contact: Y. Huang

the large HL-LHC statistics and the use of modern functional modelling techniques, the background shape could be constrained exclusively using data with great accuracy, thus dramatically reducing the modelling uncertainty.

The ATLAS expected significance to the SM Higgs boson decaying in $Z\gamma$ is 4.9 σ with 3000 fb^{-1}. Assuming the SM Higgs production cross section and decay branching ratios, the signal strength is expected to be measured with a ± 0.24 uncertainty. The cross section times branching ratio for the $pp \to H \to Z\gamma$ process is projected to be measured as 1.00 ± 0.23 times the SM prediction. Even at the HL-LHC scenario S1, the analysis sensitivity to $H \to Z\gamma$ will remain driven by the statistical uncertainty. The dominant source of systematic uncertainty in the extrapolation is that associated to the missing higher order uncertainties [126].

2.3.4 $H \to ZZ^* \to 4\ell$[10]

The measurement of the Higgs boson properties in the $H \to ZZ^* \to 4\ell$ channel is performed using the events that contain at least two same-flavour opposite-sign di-lepton pairs, chosen from isolated electrons and muons candidates passing good quality requirements in the precision regions of the detectors. Additional constraints on the kinematic properties of the lepton pair associated with the decay of the on-shell Z boson, and on the global topology of the event, helps to improve the signal to background ratio. The four-lepton invariant mass resolution is improved by correcting for the emission of final-state radiation photons by the leptons. The $H \to ZZ^* \to 4\ell$ signal is extracted from the four-lepton invariant mass spectra in the different event categories, after having evaluated the background components using simulations to constrain their shapes, and data control regions to extrapolate their normalisation in the signal regions. Signal to background sensitivity is in general enhanced using the multivariate and/or matrix-element based techniques. More details on the analyses methods can be found in most recent measurements in the $H \to ZZ^* \to 4\ell$ channel published by ATLAS [127] and CMS [128].

The performance of the measurement of the Higgs boson properties in the $H \to ZZ^* \to 4\ell$ at HL-LHC is extrapolated from the most recent measurements by ATLAS with 80 fb^{-1} [127], and by CMS with 36 fb^{-1} [128]. CMS extrapolation is obtained from the simultaneous fit in all production and decay modes, as described in Section 2.6.1. The dominant systematic uncertainties affecting the extrapolation of the ggH cross section measurement are the lepton reconstruction and identification efficiencies, and pile-up modelling uncertainties. The VBF and VH cross-sections are primarily affected by the uncertainty on the jet energy scale and resolution, and by the missing higher order uncertainties. These and the parton shower modelling primarily affects the extrapolated top cross section.

The VBF, VH and especially top measurements in the $H \to ZZ^* \to 4\ell$ decay channel remain largely dominated by statistical uncertainty when extrapolated to 3000 fb^{-1} while the $ggH + b\bar{b}H$ cross section is dominated by systematic uncertainties both in scenario S1 and S2. Figure 10 shows the ratio of the extrapolated $H \to ZZ^* \to 4\ell$ ATLAS measurements of the main Higgs boson production modes to their respective theoretical SM predictions in the scenario S2 (left), and uncertainties on these measurements for S1, S2, and stat-only scenarios as extrapolated using the $H \to ZZ^* \to 4\ell$ CMS measurements (right). The ggF and top $H \to ZZ^* \to 4\ell$ measurements at HL-LHC are expected to reach a level of precision comparable to the projected uncertainty on the corresponding theory predictions.

2.3.5 $H \to WW^* \to \ell\nu\,\ell\nu$[11]

The measurement of the Higgs boson properties in the $H \to WW^* \to e\nu\mu\nu$ channel is performed using the events that contain two opposite-charged isolated leptons passing good quality requirements in the precision region of the detectors and missing transverse momentum. Additional requirements on the event kinematic properties are applied to reduce the various background components (e.g. requirements

[10] Contacts: A. Gabrielli, A. Schaffer, V. Walbrecht
[11] Contacts: R. Gugel, K. Koeneke

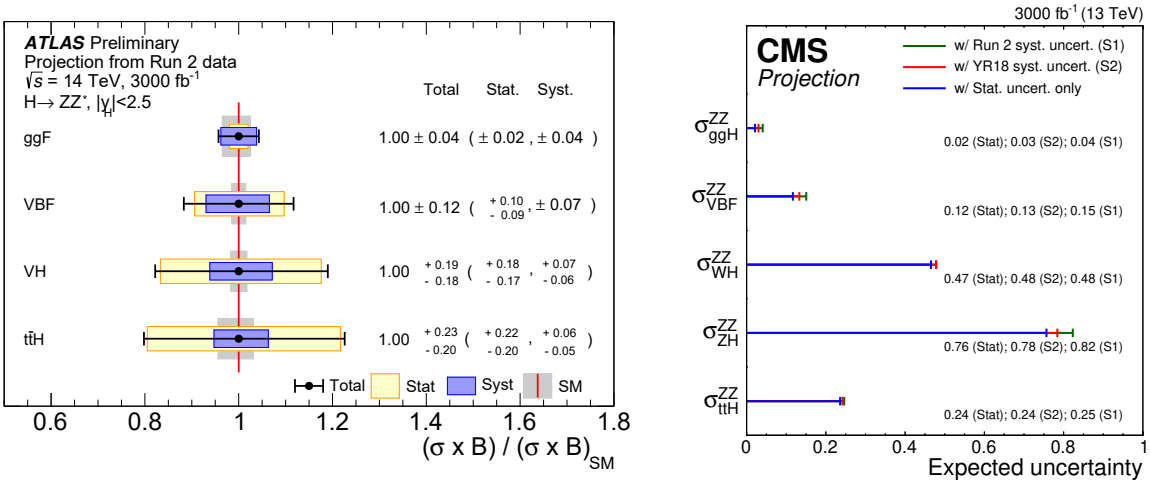

Fig. 10: Cross-section times branching fraction measurements of the main Higgs boson production modes in the $H \to ZZ^* \to 4\ell$ decay channel, as extrapolated at the HL-LHC. In case of ATLAS results (left) the ratios of cross sections to their respective theoretical SM predictions are shown for scenario S2, while in case of CMS results (right) the uncertainties on these measurements are shown for S1, S2, and Stat-only scenarios.

on the di-lepton invariant mass, transverse mass of the di-lepton + missing-transverse-energy (MET) system). Events are categorised as a function of the jet multiplicity in order to exploit the different background composition in different categories, and to help extracting the Higgs ggH and VBF production cross sections. The normalisations of the top ($t\bar{t}$ and $W+t$), and $Z \to \tau\tau$ backgrounds are set using dedicated control regions of the same jet multiplicity as the signal category to which the normalisation is transferred. In case of the (non-resonant) WW background, its normalisation is either determined using dedicated control regions (ATLAS approach) or by using theoretical prediction with corresponding uncertainty on it (CMS approach). More details on the analyses methods can be found in most recent measurements in the $H \to WW^* \to e\nu\mu\nu$ channel published by ATLAS [129] and CMS [130].

The performance of the measurements of Higgs boson properties in the $H \to WW^* \to e\nu\mu\nu$ channel at HL-LHC is extrapolated from the most recent measurements in this channel performed by ATLAS with 80 fb^{-1} [129] and by CMS with 36 fb^{-1} [130]. These measurements are completely dominated by systematic uncertainties, and their extrapolation to the S2 scenario shows the expected reduction by a factor two. The measurement of the ggH cross section by branching fraction is dominated by theoretical PDF uncertainty, followed by experimental uncertainties affecting the signal acceptance, including uncertainties on the jet energy scale and flavour composition, and lepton mis-identification; the VBF result suffers from similar dominant uncertainties. Figure 11 shows the ratio of the extrapolated $H \to WW^* \to e\nu\mu\nu$ ATLAS measurements of the main Higgs production modes to their respective theoretical SM predictions in scenario S2 (left), and uncertainties on these measurements for S1, S2, and Stat-only scenarios as extrapolated using the $H \to WW^* \to e\nu\mu\nu$ CMS measurements (right). CMS extrapolation is obtained from the simultaneous fit in all production and decay modes, as described in Section 2.6.1.

2.3.6 $H \to \tau^+\tau^-$ [12]

The measurement of the Higgs boson in the $H \to \tau^+\tau^-$ channel considers the leptonic (τ_{lep}) and the hadronic (τ_{had}) decays of the τ lepton. Three subs-channels ($\tau_{lep}\tau_{lep}$, $\tau_{lep}\tau_{had}$ and $\tau_{had}\tau_{had}$) are defined by requirements on the number of hadronically decaying τ-leptons candidates and leptons (electrons or

[12] Contacts: M. Mlynarikova, L. Thomsen

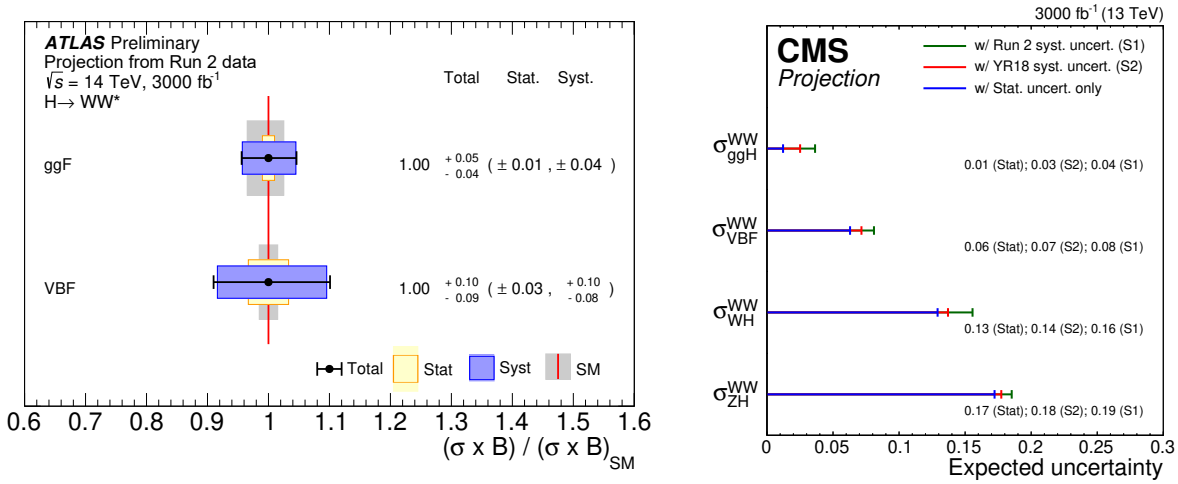

Fig. 11: Cross-section times branching fraction measurements of the main Higgs production modes in the $H \to WW^* \to e\nu\mu\nu$ decay channel, as extrapolated at the HL-LHC. In case of ATLAS results (left) the ratios of cross sections to their respective theoretical SM predictions are shown for scenario S2, while in case of CMS results (right) the uncertainties on these measurements are shown for S1, S2, and Stat-only scenarios.

muons) in the event. Candidate events are divided into categories using kinematic properties to target cases in which the Higgs boson is produced with a boost ($p_{\mathrm{T}} > 100$ GeV), primarily from gluon fusion, and cases primarily produced from vector boson fusion, in which the Higgs boson is produced with two jets separated in pseudo-rapidity. Additional requirements are employed to discriminate signal from background. One of the most important variables is the mass of the $\tau\tau$ system, calculated in ATLAS with the Missing Mass Calculator [131], and in CMS with a dynamical likelihood technique named SVFit [132]. The normalisation of the dominant backgrounds ($Z \to \ell^+\ell^-$, $t\bar{t}$, Fake-τ_{had}) is determined using dedicated control regions, or extracted directly in each signal region ($Z \to \tau^+\tau^-$, the dominant and irreducible background). More details on the analysis methods can be found in the most recent measurements in the $H \to \tau^+\tau^-$ channels published by ATLAS [133] and CMS [134].

The performance of the measurements of Higgs boson properties in the $H \to \tau^+\tau^-$ channel at HL-LHC is extrapolated from the recent measurements in this channel performed by ATLAS [135] and by CMS [134] with $36\,\mathrm{fb}^{-1}$. The measurements of the cross sections for the gluon fusion and vector boson fusion production modes are dominated by systematic uncertainties, as can be seen in Table 25, which lists the total expected uncertainties on the cross sections normalised to their SM values as well as the different contributions from different types of uncertainties. The dominant contributions, the experimental and background modelling errors, are due to uncertainties on jet calibration and resolution, on the reconstruction of the E_T^{miss}, and on the determination of the background normalisation from signal and control regions.

Figure 12 shows the ratio of the extrapolated $H \to \tau^+\tau^-$ ATLAS measurements of the main Higgs production modes to their respective theoretical SM predictions in scenario S2 (left), and uncertainties on these measurements for S1, S2, and Stat-only scenarios as extrapolated using the $H \to \tau^+\tau^-$ CMS measurements (right). In case of the ATLAS extrapolation, the SM uncertainties are divided by two compared to their current values, which approximately corresponds to the scaling expected from S2 scenario. The figure shows that at the HL-LHC the measurement will reach a level of precision which is similar to the theory predictions. These systematic uncertainties are dominated by the theoretical errors on the signal acceptance for the gluon fusion measurement both for S1 and S2. In the measurement of the vector boson fusion cross section, the effects of the experimental errors and uncertainties on the background modelling become more relevant, particularly in S2.

Table 25: Expected results for the production mode cross-section measurement in the $H \to \tau^+\tau^-$ channel with 36 fb^{-1} of Run 2 data and at the HL-LHC. Uncertainties are reported relative to the SM cross section at the corresponding centre-of-mass energy. Both scenarios have been considered for the systematic uncertainties in the HL-LHC extrapolation.

Experiment, Process	ATLAS, ggF		ATLAS, VBF	
Scenario	S1	S2	S1	S2
Total uncertainty	$^{+23.1\%}_{-18.5\%}$	$^{+12.3\%}_{-10.8\%}$	$^{+9.3\%}_{-9.3\%}$	$^{+8.0\%}_{-7.6\%}$
Statistical uncert.	$^{+3.1\%}_{-3.1\%}$	$^{+3.1\%}_{-3.1\%}$	$^{+3.4\%}_{-3.4\%}$	$^{+3.4\%}_{-3.4\%}$
Experimental uncert.	$^{+6.0\%}_{-6.2\%}$	$^{+4.1\%}_{-3.9\%}$	$^{+5.2\%}_{-5.6\%}$	$^{+4.9\%}_{-4.5\%}$
Signal theory uncer.	$^{+20.3\%}_{-16.0\%}$	$^{+10.4\%}_{-9.0\%}$	$^{+6.3\%}_{-5.3\%}$	$^{+2.7\%}_{-3.3\%}$
Background theory uncer.	$^{+8.0\%}_{-5.5\%}$	$^{+3.1\%}_{-2.4\%}$	$^{+3.4\%}_{-3.4\%}$	$^{+3.8\%}_{-3.8\%}$

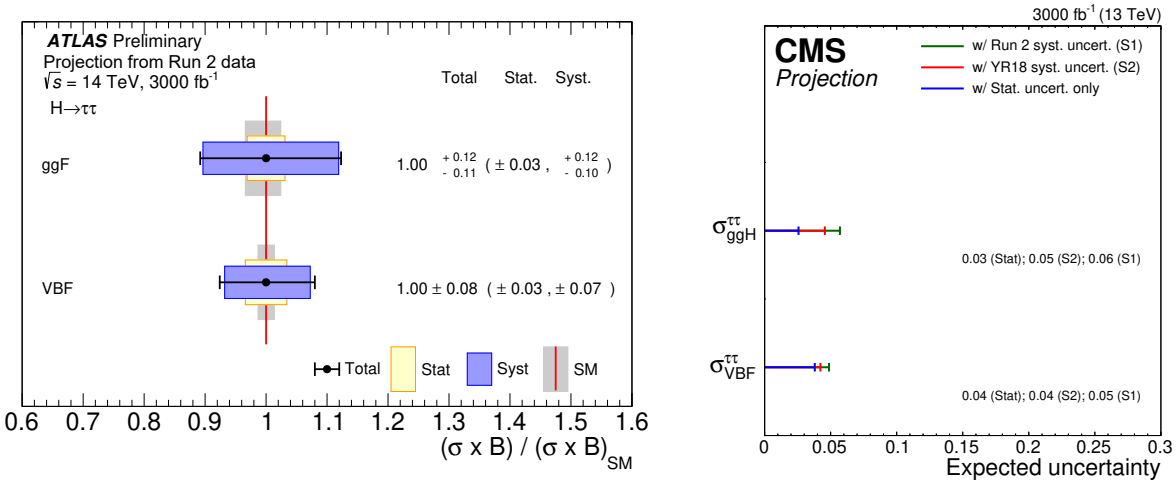

Fig. 12: (Right) ATLAS comparison, for $H \to \tau^+\tau^+$ final state applying scenario S2, between the expected precision on production-mode cross section times branching ratio normalised to their SM expectation at HL-LHC and the theoretical uncertainty on the SM prediction. (Left) CMS expected precision on production-mode cross section times branching ratio for $H \to \tau^+\tau^+$ final state in case of S1, S2, and stat-only scenarios.

2.3.7 $H \to b\bar{b}$[13]

The measurement of the Higgs boson in the $H \to b\bar{b}$ channel presented here considers the Higgs boson production in association with a vector boson ($V = W/Z$). Searches for $H \to b\bar{b}$ in association with a vector boson drove the recent observation of this decay mode reported by the ATLAS and CMS Collaborations [136, 137]. The analyses make use of leptonic decays of the vector boson for triggering and to reduce the multi-jet background: the final states of the VH system covered in the analyses always contain two b-jets and either zero, one or two electrons or muons. Both leptons are required to have the same flavour in the two lepton selection. Major backgrounds arising from SM production of vector boson plus heavy- or light-flavour jets, in addition to $t\bar{t}$ production, are controlled and constrained via dedi-

[13] Contacts: L. D'eramo, C. Li, G. Marchiori, A. de Wit

cated control regions. The b-jet energy resolution is improved by using multivariate energy regression techniques (CMS), or sequential corrections (ATLAS), and a boosted decision tree is used to improve the discrimination between signal and background. The distribution of this multivariate discriminator is used as the discriminating variable in the signal extraction fit.

The ATLAS and CMS Collaborations have both recently reported the observation of the $H \to b\bar{b}$ decay [136, 137]. The studies presented here are performed by extrapolating this most recent ATLAS $H \to b\bar{b}$ measurements using a dataset corresponding to an integrated luminosity of 78.9 fb^{-1}, and by extrapolating a previous analysis by the CMS Collaboration. In this previous analysis evidence for the $H \to b\bar{b}$ decay in the VH production mode was reported using a dataset corresponding to an integrated luminosity of 35.9 fb^{-1} [138].

Figure 13 shows the extrapolation of the signal strength uncertainty per-channel (CMS) and per-production mode (ATLAS). The details of the contributions of different sources of uncertainty in scenarios S1 and S2 for the projection of the ATLAS and CMS analyses are shown in Table 26. The large improvement, by a factor 2.5–3, in the uncertainty of the measurement for the WH (1-lepton channel) compared to the Run-2 results (around 45%) is caused by the integrated luminosity scaling of the uncertainty in the modelling of the W boson p_{T} distribution for both the collaborations, being the dominant uncertainty in scenario S1.

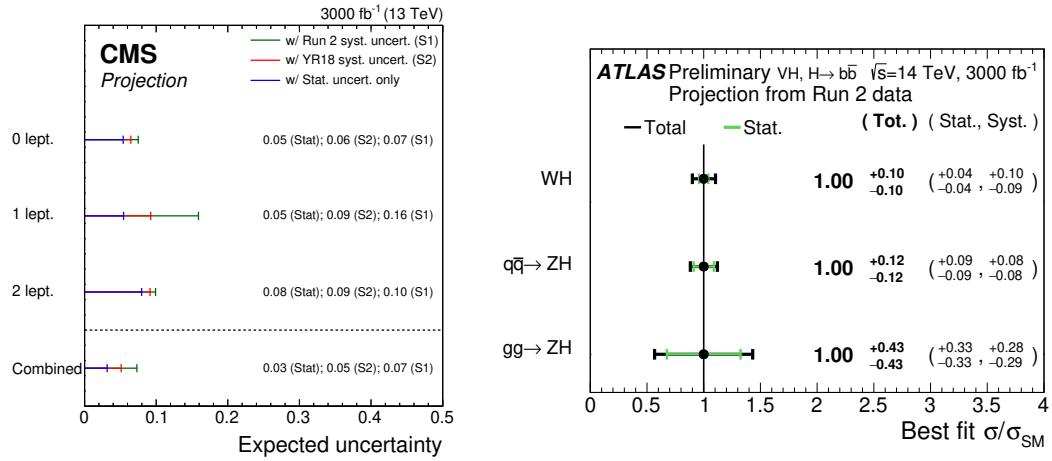

Fig. 13: Extrapolation of the uncertainties estimated by the CMS collaboration (left) and by the ATLAS collaboration (right) for the $H \to b\bar{b}$ channel. The figure gives the uncertainties per-channel and on the combined signal strengths on the left, and per-production mode on the right. Values are given for the S1 (with Run 2 systematic uncertainties [138]) and S2 (with YR18 systematic uncertainties) scenarios, as well as a scenario in which all systematic uncertainties are removed. Only the S2 scenario is presented in the plot by the ATLAS collaboration (S1 is presented in Table 26).

Both in scenario S1 and S2 the largest component of the systematic uncertainty is theoretical. This arises from the uncertainty in the gluon-induced ZH ($gg \to ZH$) production cross section due to QCD scale variations. The $gg \to ZH$ process contributes a small fraction of the total ZH process. Despite this, the uncertainty in the production cross section for this process due to QCD scale variations becomes dominant because it is very large: 25% for the $gg \to ZH$ process, compared to approximately 0.7% for the $qq \to ZH$ process [45]. The theoretical uncertainties on the $gg \to ZH$ production are reduced to 15% in the S2. An important contribution to the uncertainty is due to category-acceptance uncertainties in the dominant $Z+bb$ and $W+bb$ backgrounds due to QCD scale variations, as well as the uncertainty in the $qq \to ZH$ and WH production cross section due to QCD scale variations. To improve the precision of the measurement it is therefore important to improve these theoretical uncertainties.

Table 26: Contributions of particular groups of uncertainties, expressed as percentages, in S1 (with Run 2 systematic uncertainties [138]) and S2 (with YR18 systematic uncertainties) for the CMS and ATLAS analyses of the $H \to b\bar{b}$ channel. The total uncertainty is decomposed into four components: signal theory, background theory, experimental and statistical. In the CMS results, the signal theory uncertainty is further split into inclusive and acceptance parts, and the contributions of the b-tagging and JES/JER uncertainties to the experimental component are also given. In the ATLAS results, the contributions of the four groups of uncertainties are presented for $pp \to WH$, $qq \to ZH$ and $gg \to ZH$ separately.

Experiment	CMS	
Process	$pp \to VH$	
Scenario	S1	S2
Total uncertainty	7.3%	5.1%
Statistical uncert.	3.2%	3.2%
Experimental uncert.	2.6%	2.2%
b-tagging	2.2%	2.0%
JES and JER	0.7%	0.6%
Signal theory uncer.	5.4%	2.6%
Inclusive	4.6%	2.2%
Acceptance	2.7%	1.3%
Background uncert.	2.8%	2.3%

Experiment	ATLAS					
Process	$pp \to WH$		$qq \to ZH$		$gg \to ZH$	
Scenario	S1	S2	S1	S2	S1	S2
Total uncertainty	$^{+14.9\%}_{-13.8\%}$	$^{+10.4\%}_{-10.0\%}$	$^{+13.8\%}_{-13.2\%}$	$^{+12.1\%}_{-11.8\%}$	$^{+49.8\%}_{-49.0\%}$	$^{+43.2\%}_{-43.3\%}$
Statistical uncert.	$^{+4.1\%}_{-4.1\%}$	$^{+4.1\%}_{-4.1\%}$	$^{+9.0\%}_{-8.9\%}$	$^{+9.0\%}_{-8.9\%}$	$^{+33.3\%}_{-33.3\%}$	$^{+33.3\%}_{-33.3\%}$
Experimental uncert.	$^{+4.8\%}_{-4.7\%}$	$^{+4.4\%}_{-4.3\%}$	$^{+6.5\%}_{-6.3\%}$	$^{+5.7\%}_{-5.5\%}$	$^{+24.9\%}_{-25.0\%}$	$^{+20.8\%}_{-20.4\%}$
Signal theory uncer.	$^{+8.0\%}_{-7.0\%}$	$^{+4.6\%}_{-4.1\%}$	$^{+6.1\%}_{-5.5\%}$	$^{+3.1\%}_{-2.8\%}$	$^{+18.1\%}_{-14.0\%}$	$^{+9.6\%}_{-8.0\%}$
Background uncert.	$^{+10.8\%}_{-10.0\%}$	$^{+7.2\%}_{-6.9\%}$	$^{+5.4\%}_{-4.8\%}$	$^{+4.8\%}_{-4.6\%}$	$^{+20.7\%}_{-21.8\%}$	$^{+17.7\%}_{-18.1\%}$

In the future, and at the HL-LHC in particular, the b-tagging efficiency may change. The conditions could worsen the efficiency, but at the same time new detectors and new techniques could also lead to an improvement in the b-tagging efficiency. The effect of changes in b-tagging efficiency on the overall signal strength uncertainty has been evaluated by the CMS collaboration, showing that an improvement of 10% in the b-tagging efficiency leads to a relative improvement in the signal strength uncertainty of up to 6% [139].

2.3.8 $H \to \mu^+\mu^-$ [14]

The $H \to \mu^+\mu^-$ analyses play a crucial role in the determination of the couplings to the second fermion generation. The analyses search for a narrow peak in the di-muon invariant mass over a smoothly falling background, dominated by Drell–Yan and top-pair productions. Events are selected requiring two op-

[14] Contacts: M. Klute, H. Li, G. Marchiori, A.Marini, M. Verducci, M. Zgubic, J. Zhang

positely charged muons passing loose quality criteria to retain as much signal as possible. The overall sensitivity to this decay mode benefits from multivariate or sequential categorisation techniques that allow separating the two dominant production modes, the vector boson fusion (with the typical presence of a forward-backward jet pair) and the gluon fusion. Additional enhancements in the sensitivity are achieved by a further sub-categorisation based on the muon momentum resolution. More details on the analysis methods can be found in the most recent searches of the $H \to \mu^+\mu^-$ channels published by ATLAS [140] and CMS [141].

The extrapolation studies presented here by ATLAS Collaboration are based on a previous analysis performed by that collaboration using the 2015–2017 proton-proton collision dataset collected at $\sqrt{s} = 13\,\text{TeV}$, which corresponds to an integrated luminosity of $79.8\,\text{fb}^{-1}$ [140]. In addition to the standard extrapolation procedure, the di-muon signal widths are reduced by 15-30% thanks to the improvements expected from the performance of the ATLAS upgrade Inner Tracker (ITk) [20]. In this analysis, the $Z \to \mu^+\mu^-$ background is fully determined by data, and it is modelled by fitting the di-muon invariant mass $m_{\mu\mu}$ distribution in each category using a Breit–Wigner function convoluted with a Gaussian summed to a smooth function.

Similar studies have been carried out by the CMS Collaboration, based on the analysed data collected during 2016 and corresponding to an integrated luminosity of $36\,\text{fb}^{-1}$ [142]. The analysis was optimised to have the overall best sensitivity to a standard model Higgs boson inclusively with respect to the production modes with the data collected in 2016. In addition to the extrapolation procedure based on the increased luminosity, the di-muon invariant mass width is reduced in order to match the expected increase in performances due to the upgrade in the tracking system [22] and displayed in Fig. 14. The di-muon mass resolution plays a crucial role in the analysis performances and in the systematic uncertainty induced by the choice of the background function. The CMS experiment [143] benefits from the large $4\,\text{T}$ solenoidal fields that allowed it to achieve down to 1.1% di-muon mass resolution in 2016 and, with the upgrade projects, the CMS detector will be able to reach in the best category a di-muon mass resolution of 0.65% [22].

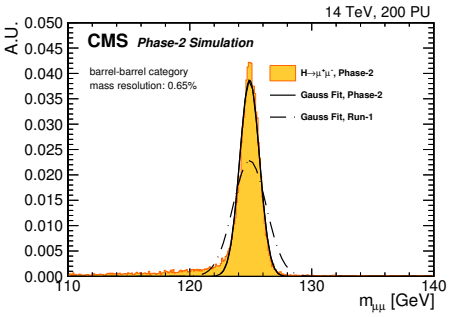

Fig. 14: The di-muon invariant mass distribution for $H \to \mu^+\mu^-$ decays for muons in the central region, simulated with the Phase-2 detector. [22].

Table 27 shows the expected precision on the signal strength (ATLAS) and branching fraction (CMS) measurement with $3000\,\text{fb}^{-1}$ of HL-LHC data in the scenarios S1 and S2. In both scenarios, the analysis is limited by the statistical uncertainty, while the leading systematic uncertainty is the bias introduced by the choice of the function describing the background (spurious signal uncertainty), and the uncertainties on the modelling of the signal (their reduction in S2 contributes to an overall improvement of 10% on the precision of the measurement). Expected uncertainties on signal strength vary from 15 to 13% (ATLAS) and on the branching fraction vary from 13 to 10% (CMS), accordingly to the projection scenario. CMS extrapolation is obtained from the simultaneous fit in all production and decay modes, as described in Section 2.6.1.

Table 27: Expected precision on the signal strength measurement in the $H \to \mu^+\mu^-$ channels with 3000 fb^{-1} of HL-LHC data with the two systematic uncertainties scenarios. For the HL-LHC extrapolation, the improved ITk resolution has been emulated.

Experiment	ATLAS	
Process	Combination	
Scenario	S1	S2
Total uncertainty	$^{+15\%}_{-14\%}$	$^{+13\%}_{-13\%}$
Statistical uncert.	$^{+12\%}_{-13\%}$	$^{+12\%}_{-13\%}$
Experimental uncert.	$^{+3\%}_{-3\%}$	$^{+2\%}_{-2\%}$
Theory uncer.	$^{+8\%}_{-5\%}$	$^{+5\%}_{-4\%}$

Experiment	CMS	
Process	Combination	
Scenario	S1	S2
Total uncertainty	13%	10%
Statistical uncert.	9%	9%
Experimental uncert.	8%	2%
Theory uncer.	5%	3%

2.4 Fiducial and differential cross-section measurements[15]

2.4.1 Measurements using $H \to \gamma\gamma$, $H \to ZZ^* \to 4\ell$, (boosted) $H \to b\bar{b}$ decay channels[16]

In the context of Higgs boson property measurements, one of the main goals of HL-LHC, differential measurements provide a probe of various Higgs boson properties by looking at distortions of differential distributions. The $p_{\mathrm{T}}^{\mathrm{H}}$ distribution is of particular interest, as potential new physics may reside in the tails of the distribution, which cannot be measured in inclusive measurements [144, 145, 146]. Differential Higgs boson production cross section measurements are available for a range of observables from both the ATLAS [147, 148, 149, 150, 151, 152] and CMS [153, 154, 155, 156, 128, 157] Collaborations at $\sqrt{s}$ = 8 and 13 TeV.

The most recent $p_{\mathrm{T}}^{\mathrm{H}}$ spectra at $\sqrt{s}$ = 13 TeV from both the ATLAS [152] and CMS [157] Collaborations are projected to an integrated luminosity of 3000 fb^{-1} [139, 158]. The projection of the $p_{\mathrm{T}}^{\mathrm{H}}$ differential cross section measurement by the CMS Collaboration is shown in Fig. 15, for both scenarios S1 and S2. The corresponding total uncertainties are respectively given in Tables 28 and 29. With respect to the uncertainties affecting the measurement based on an integrated luminosity of 35.9 fb^{-1}, the uncertainties at 3000 fb^{-1} in the higher $p_{\mathrm{T}}^{\mathrm{H}}$ region are about a factor of ten smaller. This is expected, as the uncertainties in this region remain statistically dominated. The uncertainties in the lower $p_{\mathrm{T}}^{\mathrm{H}}$ region are however no longer statistically dominated, as can been seen by comparing Table 28 with Table 29,

[15] Contacts: M. Delmastro, A. Gilbert, T. Klijnsma, J. Langford, W. Leight, R. Naranjo Garcia, A. Salvucci, M. Scodeggio, K. Tackmann, N. Wardle, C. Vernieri

[16] Contacts: M. Delmastro, T. Klijnsma

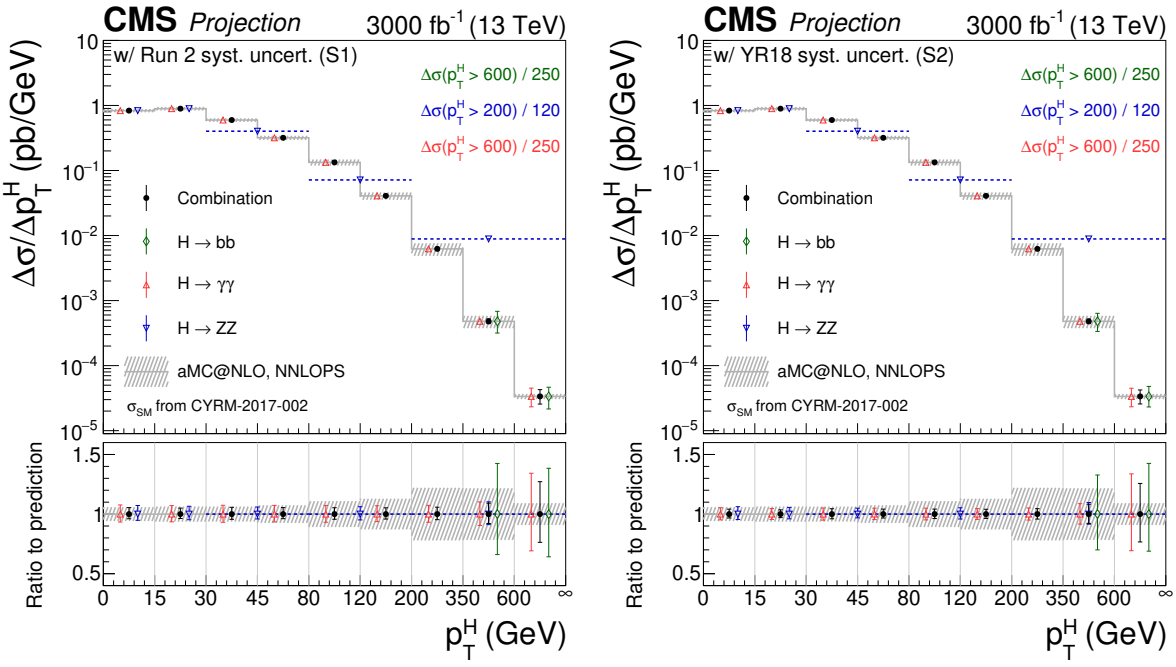

Fig. 15: Projected differential cross section for $p_{\mathrm{T}}{}^{\mathrm{H}}$ at an integrated luminosity of 3000 fb^{-1} [157], under S1 (upper, with Run 2 systematic uncertainties [159]) and S2 (lower, with YR18 systematic uncertainties).

where the reduced systematic uncertainties in S2 yield a reduction in the total uncertainty of up to 25% compared to S1.

Figure 16 shows the ATLAS projections to 3000 fb^{-1} of the differential measurements of $p_{\mathrm{T}}{}^{\mathrm{H}}$, the Higgs rapidity $|y_H|$, the jet multiplicity N_{jets} of jets with $p_{\mathrm{T}} > 30$ GeV and the transverse momentum of the leading jet accompanying the Higgs boson p_{H}^{j1}, as obtained by combining the measurement in the $H \to \gamma\gamma$ and $H \to ZZ^* \to 4\ell$ channels, in scenarios S1 and S2. The relative uncertainties affecting the $p_{\mathrm{T}}{}^{\mathrm{H}}$ measurement are given in Tables 28 and 29. The ATLAS combined $p_{\mathrm{T}}{}^{\mathrm{H}}$ measurement extrapolation exhibits relative uncertainties ranging from about 5% in the lower $p_{\mathrm{T}}{}^{\mathrm{H}}$ bins to about 9% in the highest $p_{\mathrm{T}}{}^{\mathrm{H}}$ bin in scenario S1, reducing to uncertainties ranging from $\sim 4\%$ to $\sim 8\%$ in scenario S2.

Due to a different choice of $p_{\mathrm{T}}{}^{\mathrm{H}}$ binning by ATLAS and CMS, and the lack of a more sophisticated study of the correlation of systematic uncertainties, it was chosen not to combine the projected spectra presented above. Instead, the projections from CMS are scaled to an integrated luminosity of 6000 fb^{-1}, providing a proxy estimate of the overall sensitivity of an eventual combination of measurements by the two experiments. Figure 17 shows the CMS projection at 6000 fb^{-1}, with the same systematic scaling as for the projection at 3000 fb^{-1}. As expected at very high integrated luminosity, the systematic uncertainties dominate the statistical ones.

2.4.2 *Measurement of $p_T(H)$ spectrum in $t\bar{t}H$ production mode*[17]

This section describes the strategy for measuring the differential p_T cross section for Higgs boson production in association with at least one top quark, and decaying to photons ($\mathrm{t\bar{t}H}$ + tH, $\mathrm{H} \to \gamma\gamma$), at the High-Luminosity LHC with the CMS Phase-2 detector. The $\mathrm{H} \to \gamma\gamma$ decay mode provides a final state in which the decay of the Higgs boson can be fully reconstructed, and a direct measurement of the p_T differential cross-section can be made.

[17] Contacts: N. Wardle, J. Langford

Table 28: Relative uncertainties on the projected $p_{\mathrm{T}}{}^{\mathrm{H}}$ spectrum measurements by ATLAS and CMS under S1 at 3000 fb^{-1}. The relative uncertainty of the CMS projection is also given at 6000 fb^{-1} to represent the sensitivity achievable by an eventual ATLAS and CMS combination.

3000 fb^{-1} ATLAS											
$p_{\mathrm{T}}{}^{\mathrm{H}}$ [GeV]	0-10	10-15	15-20	20-30	30-45	45-60	60-80	80-120	120-200	200-350	350-1000
H $\rightarrow \gamma\gamma$	6.5%	5.9%		6.2%	6.0%	6.5%	6.7%	6.0%	5.4%	6.3%	9.5%
H $\rightarrow$ ZZ	9.0%	8.1%	8.9%	6.9%	6.3%	6.8%	6.8%	6.2%	6.7%	13.2%	24.3
Combination	5.5%	4.8%		5.0%	4.7%	5.0%	5.1%	4.6%	4.4%	5.4%	8.7%

3000 fb^{-1} CMS									
$p_{\mathrm{T}}{}^{\mathrm{H}}$ [GeV]	0-15	15-30	30-45	45-80	80-120	120-200	200-350	350-600	600-∞
H $\rightarrow \gamma\gamma$	5.1%	6.8%	7.1%	6.9%	7.1%	6.7%	7.1%	9.9%	32.5%
H $\rightarrow$ ZZ	5.4%	5.7%	5.0%		5.5%		9.6%		
H $\rightarrow$ bb	none							38.2%	37.1%
Combination	4.7%	4.4%	5.0%	4.7%	4.8%	4.7%	5.2%	8.5%	25.4%
6000 fb^{-1}									
Combination	4.0%	3.7%	4.0%	3.9%	4.0%	4.0%	4.3%	6.3%	18.3%

Table 29: Relative uncertainties on the projected $p_{\mathrm{T}}{}^{\mathrm{H}}$ spectrum measurements by ATLAS and CMS under S2 at 3000 fb^{-1}. The relative uncertainty of the CMS projection is also given at 6000 fb^{-1} to represent the sensitivity achievable by an eventual ATLAS and CMS combination.

3000 fb^{-1} ATLAS											
$p_{\mathrm{T}}{}^{\mathrm{H}}$ [GeV]	0-10	10-15	15-20	20-30	30-45	45-60	60-80	80-120	120-200	200-350	350-1000
H $\rightarrow \gamma\gamma$	5.3%	4.6%		4.9%	4.7%	5.4%	5.7%	4.9%	4.2%	5.1%	8.7%
H $\rightarrow$ ZZ	8.3%	7.6%	8.3%	6.3%	5.7%	6.2%	6.3%	5.7%	6.4%	13.1%	23.2%
Combination	4.5%	3.8%		3.9%	3.6%	4.1%	4.2%	3.7%	3.5%	4.5%	8.2%

3000 fb^{-1} CMS									
$p_{\mathrm{T}}{}^{\mathrm{H}}$ [GeV]	0-15	15-30	30-45	45-80	80-120	120-200	200-350	350-600	600-∞
H $\rightarrow \gamma\gamma$	5.1%	4.6%	5.1%	4.8%	4.9%	4.5%	5.1%	8.6%	32.2%
H $\rightarrow$ ZZ	5.4%	4.8%	4.1%		4.7%		9.1%		
H $\rightarrow$ bb	none							31.4%	36.8%
Combination	3.7%	3.3%	4.2%	3.7%	4.0%	3.8%	4.4%	8.0%	24.5%
6000 fb^{-1}									
Combination	2.9%	2.6%	3.2%	2.9%	3.0%	2.9%	3.2%	5.8%	17.9%

The expected precision of the analysis is determined based on simulated proton-proton (pp) events, at a centre of mass energy of 14 TeV. Simulated signal and background events are generated using a combination of POWHEG v2.0 [160, 81], MADGRAPH5_AMC@NLO v2.2.2 [79], SHERPA v2.2.5 [161], and interfaced with PYTHIA v8.205 [32]. The signal and background events are processed with DELPHES [13], using the CMS Phase-2 card, to simulate the response of the upgraded CMS detector to showered particles. Full details of the analysis can be found in Ref. [162].

2.4.2.1 Analysis strategy

An event selection is applied to the simulated background and signal events following a similar strategy to the CMS Run 2 H $\rightarrow \gamma\gamma$ strategy [123]. The events are required to contain two photons, with $|\eta^{\gamma}| < 2.4$ excluding the region $1.44 < |\eta^{\gamma}| < 1.57$, with an invariant mass satisfying $100 < m_{\gamma\gamma} < 180$ GeV, where the leading-p_T (sub-leading-p_T) photon satisfies $\mathrm{p}_T^{\gamma}/m_{\gamma\gamma} > 1/3$ (1/4). The two photons are also required to be separated by $\Delta R_{\gamma\gamma} > 0.4$. The photons must also be isolated, which is achieved by requiring that the sum of charged transverse momentum in a cone of radius $\Delta R_{\gamma} = 0.4$, centred on the photon direction, is less than $0.3\,\mathrm{p}_T^{\gamma}$. For events where more than one photon pair passes the selection, then the pair with $m_{\gamma\gamma}$ closest to the Higgs boson mass is chosen.

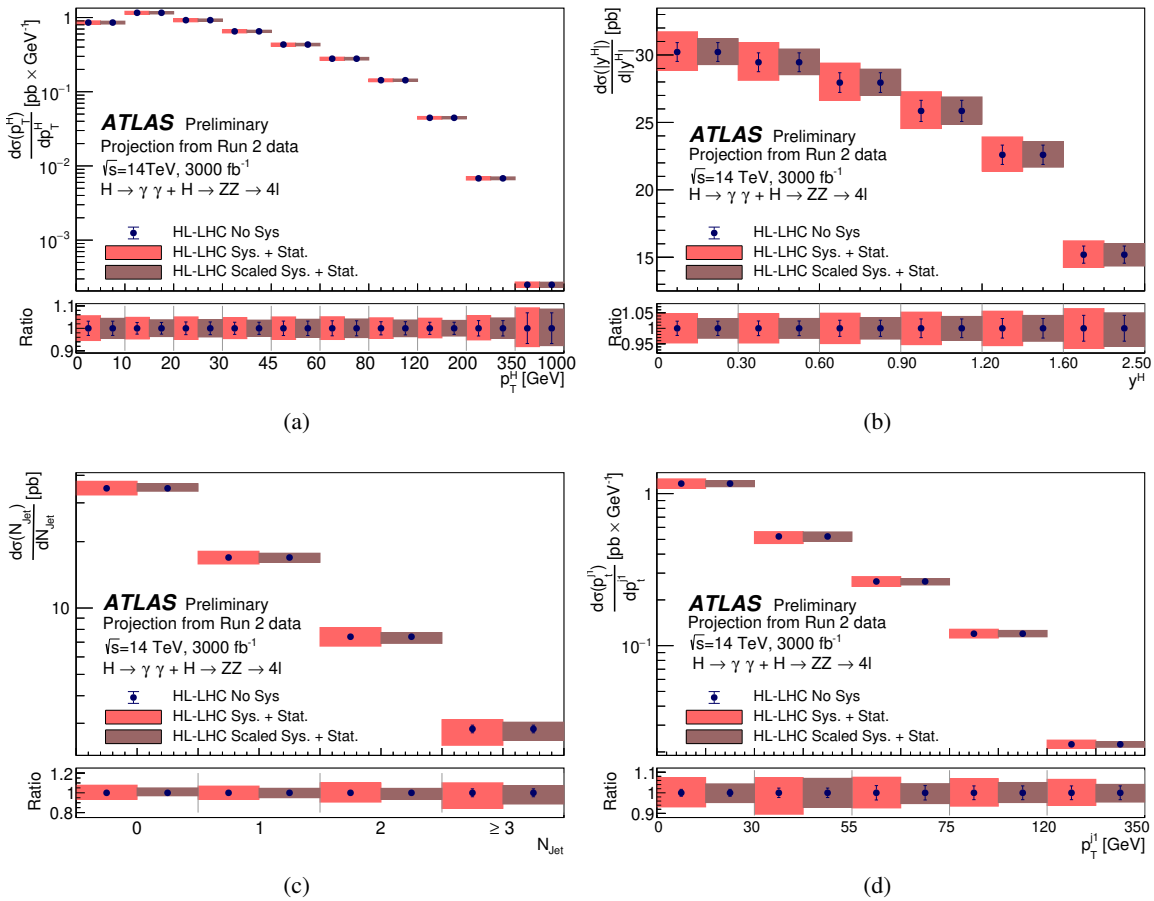

Fig. 16: Differential cross sections measured by ATLAS in the full phase space, extrapolated to the full HL-LHC luminosity for the combination of the $H \to \gamma\gamma$ and $H \to ZZ^* \to 4\ell$ decay channels for (a) Higgs boson transverse momentum $p_{\mathrm{T}}{}^{\mathrm{H}}$, (b) Higgs boson rapidity $|y_H|$, (c) number of jets N_{jets} with $p_{\mathrm{T}} > 30$ GeV, and (d) the transverse momentum of the leading p_{H}^{j1}. For each point both the statistical (error bar) and total (shaded area) uncertainties are shown. Two scenarios are shown: one with the current Run2 systematic uncertainty (S1) and one with scaled systematic uncertainties (S2).

In order to isolate the production of the Higgs boson in association with top quarks, the selection requires all events to have at least one $b-$tagged jet. Such events are separated into two orthogonal categories based on the decay products of the top quark, a hadronic category and a leptonic category. In the hadronic category, events must contain at least 3 jets, clustered using the anti-k_T algorithm with a cone size of 0.4, separated by $\Delta R > 0.4$ with respect to both photon candidates. The jets are required to have $\mathrm{p}_T > 25$ GeV and $|\eta| < 4$. In the leptonic category, only 2 jets are required, however, in addition, the events must contain at least one isolated muon or electron. The muons or electrons must satisfy $\mathrm{p}_T > 20$ GeV and $|\eta| < 2.4$, excluding the region $1.44 < |\eta^{\gamma}| < 1.57$ for electrons. The muons must satisfy an isolation requirement that the sum of all reconstructed particles p_T, inside a cone of radius $\Delta R = 0.4$, excluding the muon itself, is less than 0.25 times the transverse momentum of the muon. In addition, for electrons, the invariant mass of pairs formed from the electron and either selected photon, $m_{e\gamma}$, is required to be greater than 95 GeV to reduce contamination from $Z \to e^+e^-$ decays. Events passing the leptonic category selection are excluded from the hadronic selection to maintain orthogonality of the two categories. For the signal extraction, boosted decision tree (BDT) classifiers are trained independently in each channel, which distinguish between signal-like and background-like events, using input variables related to the kinematics of the events, such as the lepton and jet momenta

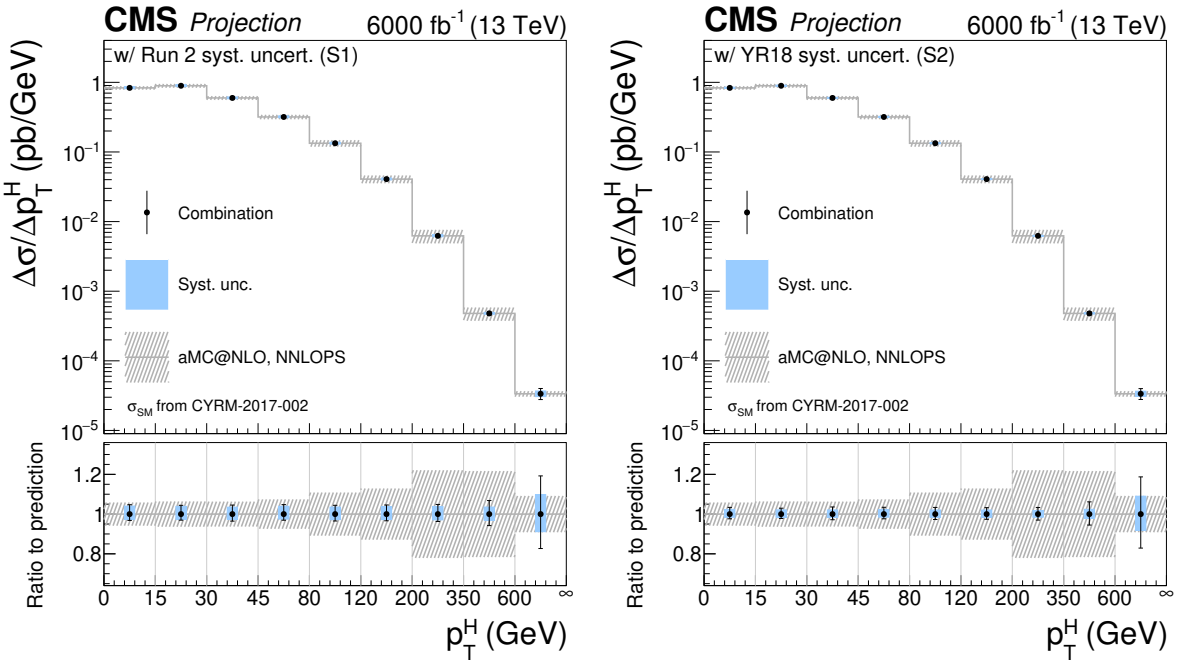

Fig. 17: Projected differential cross section for $p_{\mathrm{T}}{}^{\mathrm{H}}$ at an integrated luminosity of 6000 fb^{-1} (representing the sensitivity achievable by an eventual ATLAS and CMS combination), under scenarios S1 and S2.

and pseudo-rapidities, and the scalar sum of transverse momentum of all final state objects in the event. Events are required to have output BDT values greater than fixed thresholds, which are tuned to provide the best sensitivity to κ_λ. The hadronic category is further split into two different regions of BDT output, for events with di-photon transverse momentum ($\mathrm{p}_T^{\gamma\gamma}$) less than 350 GeV, to reduce the contamination of gluon fusion Higgs boson production.

Finally, the events are further divided into six bins of $\mathrm{p}_T^{\gamma\gamma}$, given in Tab. 30, making a total of 17 categories.

Table 30: bin boundaries which define the $p_{\mathrm{T}}{}^{\mathrm{H}}$ regions for which the differential cross sections are measured. These also correspond to the bins in which the hadronic and leptonic event categories are sub-divided.

p_T^H or $\mathrm{p}_T^{\gamma\gamma}$ bin boundaries (GeV)						
0	45	80	120	200	350	∞

Experimental systematic uncertainties are included in the signal model, which can cause migration both between the different categories and in and out of the fiducial region. The dominant uncertainties are related to the reconstruction and identification efficiencies for photons and b jets as well as the energy scale and resolution of reconstructed jets. Furthermore, theoretical uncertainties are included on the rates of ggH and VH contamination, which modify both the overall normalisation and the relative contamination between the different categories for these processes. The background estimation follows the same strategy as in the CMS Run 2 H $\rightarrow \gamma\gamma$ analysis [123], in that the parameters of the background functions are free to float in the fit, and constrained directly from the data. Therefore the uncertainties on the background will be statistical in nature. However, the impact of increasing the rate of fake photons in the background component has been studied and was found to reduce the sensitivity to κ_λ by roughly 10% in the worst case scenario [162].

2.4.2.2 *Differential cross-section results*

In order to account for resolution effects, the signal events are separated based on the p_T^H at generator level. Signal and background models are constructed using the simulated events in each category. The signal model accounts for the relative populations of events from the different production processes as well as from different p_T^H bins, and the di-photon mass resolution expected from events in each category. The background model is constructed from a fit of smoothly falling functions to the weighted sum of simulated background samples, accounting for the different fake photon rates for each source of background and normalised to the total background yield expected in 3000 fb$^-$1 of High-Luminosity LHC data. The differential cross-section is determined from a simultaneous maximum likelihood fit to an Asimov data set [163] corresponding to 3 ab^{-1}, and assuming SM Higgs boson production in each category. Systematic uncertainties are accounted for through the introduction of constrained nuisance parameters in the log-likelihood, which are profiled.

The results of this fit are given in figure 18. The results shown are unfolded back to a fiducial region which is common to both the hadronic and leptonic selections, and shown using only the hadronic or leptonic categories, and their combination. The theoretical uncertainties displayed on the predicted $t\bar{t}H + tH$ cross section are calculated by modifying the renormalisation and factorisation scales up and down by a factor of 2.

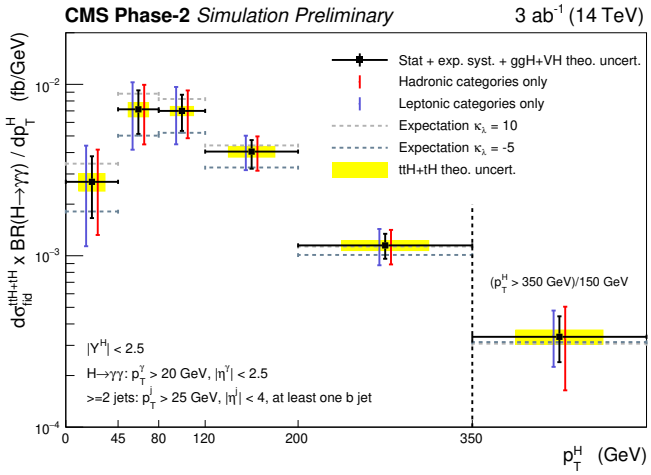

Fig. 18: The expected p_T^H differential $t\bar{t}H$ + tH cross sections times branching ratio, along with their uncertainties [162]. The error bars on the black points include the statistical uncertainty, the experimental systematic uncertainties and the theoretical uncertainties related to the ggH and VH contamination, which is subtracted in the fit. The cross section for $p_T^H > 350$ GeV is scaled by the width of the previous bin. The expected $t\bar{t}H$ + tH cross sections for anomalous values of the Higgs boson self-coupling (κ_λ = 10 and κ_λ = -5) are shown by the horizontal dashed lines.

2.5 Direct and indirect probing of top Yukawa coupling[18]

2.5.1 *Measurements in $t\bar{t}H$ and tH production modes*[19]

One of the main targets of the High-Luminosity LHC upgrade is to achieve precision measurements of the Higgs boson properties. The Yukawa coupling of the Higgs boson to the top quark is expected to be of the order of unity and could be partially sensitive to effects beyond the Standard Model. Therefore, a direct measurement of the coupling of the Higgs boson to top quarks is extremely important to access possible

[18] Contacts: A. Calandri, P. Das, K. El Morabit, S. Folgueras, S. Gadatsch, A. Gilbert, P. Keicher, T. Klijnsma, K. Mazumdar, M. Schröder

[19] Contacts: A. Calandri, M. Schröder

deviations in the top quark's Yukawa couplings due to couplings to new particles. Such a measurement can be performed by measuring the rate of the process where the Higgs boson is produced in association with a pair of top quarks ($t\bar{t}H$) or a single top quark (tH). Even though the $t\bar{t}H$ process is characterised by a small cross section compared to the dominant gluon fusion Higgs boson production (approximately two orders of magnitude smaller), the signature with top quarks in the final state can be exploited to reconstruct the event and gives access to many Higgs boson decay modes. The SM tH production cross-section is yet smaller by a factor five, but due to interference effects between diagrams with top-Higgs and W-boson-Higgs couplings, the process allows access to the sign of the top-Higgs Yukawa coupling. The ATLAS and CMS Collaborations have searched for the $t\bar{t}H$ and tH production with LHC Run 2 data of 2015, 2016, and 2017, and observed the Higgs boson production in association with a top-quark pair [164, 165]. The analyses are sensitive to a large variety of final-state event topologies, $H\rightarrow WW^*$, $H\rightarrow ZZ^*$, $H\rightarrow \tau^+\tau^-$, $H \rightarrow b\bar{b}$ and $H\rightarrow \gamma\gamma$. Dedicated multivariate analysis techniques, including boosted decision trees and deep neural networks, that combine the information of several discriminating variables, as well as classifiers based on a matrix element method are utilised to identify the signal against the background.

In this Section, projections based on dedicated analyses with $36\,\text{fb}^{-1}$ of Run-II data of 2016 are presented, which target the $t\bar{t}H$, $H \rightarrow b\bar{b}$ channel with leptonic decays of the $t\bar{t}$ system [166, 167] and the $t\bar{t}H$ multi-lepton final state [168], where the Higgs boson decays into a pair of Z and W vector bosons or into τ leptons. Furthermore, results are presented for the projection of a search for tH production that considers all of the above decay channels [169].

2.5.1.1 Sensitivity to $t\bar{t}H$ production in the $b\bar{b}$ and multi-lepton final states

The $t\bar{t}H$ analyses in the $H \rightarrow b\bar{b}$ final state benefit from the large branching ratio. At the same time, the relatively poor b jet energy resolution, the large jet combinatorics, and the sizeable background of SM processes with large modelling uncertainties, in particular $t\bar{t}$ +heavy-flavour jet ($t\bar{t}+\text{HF}$) production, pose major challenges. The expected relative precision of the $t\bar{t}H$, $H \rightarrow b\bar{b}$ cross-section measurement reaches the level of 20%-14% for the ATLAS analysis and 15%-11% for the CMS analysis [170, 139] corresponding to 7%-11% relative uncertainty on the signal strength (μ), depending on the scenario and the assumptions of the $t\bar{t}+\text{HF}$ background modelling, as detailed below.

Table 31 shows a breakdown of the contributing sources of uncertainty in the CMS analysis; their evolution with integrated luminosity is depicted in Fig. 19. Compared to the result at $35.9\,\text{fb}^{-1}$, the relative contribution of the experimental uncertainties, such as the b-tagging uncertainty, remains approximately the same, while the signal-theory uncertainty component increases and becomes the major uncertainty component, mostly driven by the inclusive cross-section uncertainty on the SM prediction entering μ. The statistical uncertainty becomes small compared to the systematic components. A similar behaviour is observed in the ATLAS analysis.

In both analyses, a rather sizeable reduction of the uncertainties related to the modelling of the $t\bar{t}+\text{HF}$ background, which relies on MC simulation, is observed. Relevant nuisance parameters are constrained to a few percent, such as the nuisance parameters describing the difference between four and five-flavour scheme calculations which is treated as a 2-point systematic uncertainty in the ATLAS analysis (Fig. 20) or the nuisance parameters describing the additional $t\bar{t}+\text{HF}$ cross-section uncertainties in the CMS analysis (Table 31 and Fig. 19). This is attributed to the increasing power of the profile likelihood fit to constrain the uncertainties.

The results illustrate that the background modelling, which has been designed to work well with $35.9\,\text{fb}^{-1}$ of data, will need to be refined at $3000\,\text{fb}^{-1}$, requiring improved simulations or in-situ measurements of the $t\bar{t}+\text{HF}$ processes themselves. The observed constraints on the $t\bar{t}+\text{HF}$ background model systematics uncertainties shown in Fig. 20 demonstrate that there will be enough data at the HL-LHC to obtain further information about the background beyond the current modelling. The level at which the nuisance parameters are constrained at $3000\,\text{fb}^{-1}$, corresponding to a few percent cross-section uncer-

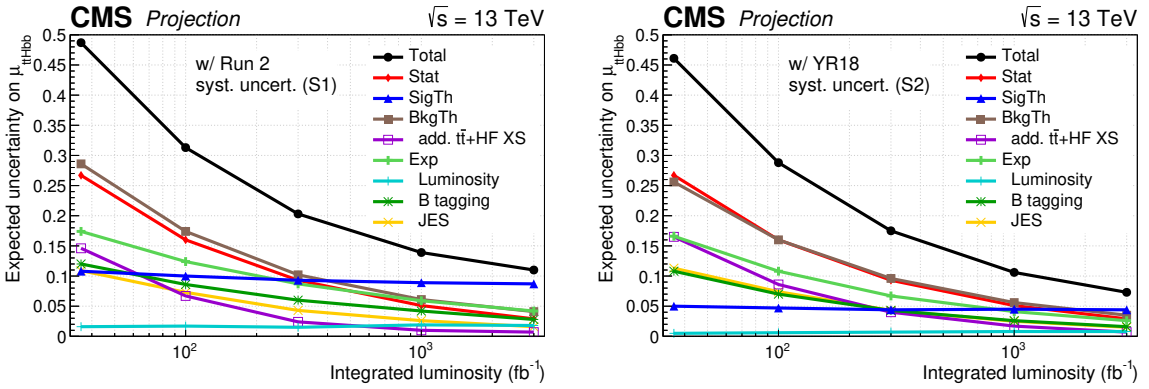

Fig. 19: Expected uncertainties on the $t\bar{t}H$ signal strength in the $H \to b\bar{b}$ channel as a function of the integrated luminosity under the S1 (left) and S2 (right) scenarios at CMS. Shown are the total uncertainty (black) and contributions of different groups of uncertainties. Results with $35.9\,\text{fb}^{-1}$ are intended for comparison with the projections to higher luminosities and differ in parts from [167] for consistency with the projected results: uncertainties due to the limited number of MC events have been omitted and the assumptions in S1/S2 on the theory uncertainties are applied.

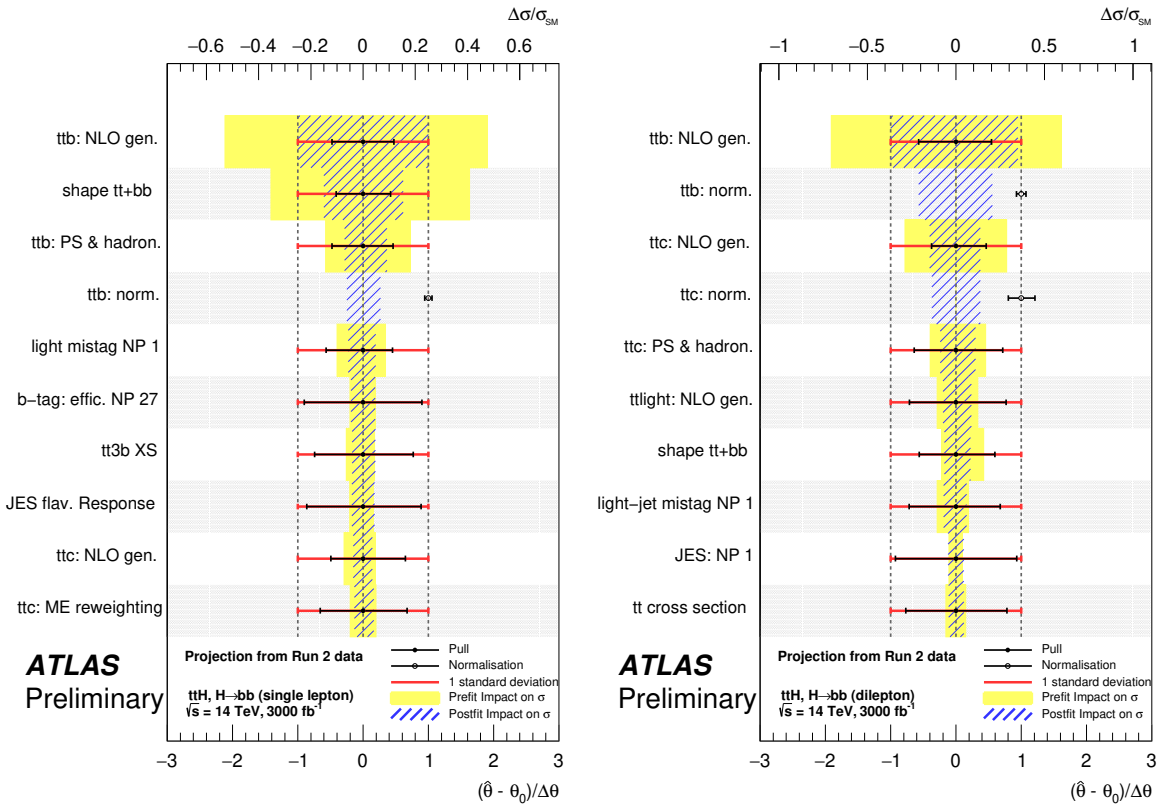

Fig. 20: Ranking of the ten most significant systematics uncertainties under S2 in the single lepton (a) and di-lepton (b) final states at ATLAS listed in accordance to their post-fit impact on the $t\bar{t}H$ cross section.

Table 31: Breakdown of the contributions to the expected uncertainties on the $t\bar{t}H$ signal-strength μ in the $H \to b\bar{b}$ channel at different luminosities for the scenarios S1 and S2 at CMS. The uncertainties are given in percent relative to $\mu = 1$. Results with 35.9 fb^{-1} are intended for comparison with the projections to higher luminosities and differ in parts from [167] for consistency with the projected results: uncertainties due to the limited number of Monte Carlo statistics have been omitted and the assumptions in S1/S2 on the theory uncertainties are applied.

	S1		S2	
Source	35.9 fb^{-1}	3000 fb^{-1}	35.9 fb^{-1}	3000 fb^{-1}
Total	48.7	11.1	46.1	7.3
Stat	26.7	2.9	26.7	2.9
SigTh	10.8	8.7	5.0	4.4
BkgTh	28.6	4.1	25.6	3.5
$t\bar{t}$ + HF XS	14.6	0.8	16.5	0.7
Exp	17.4	4.2	16.6	2.6
Luminosity	1.6	1.8	0.5	0.8
B tagging	12.0	2.8	10.8	1.6
JES	10.9	1.6	11.3	1.6

Table 32: Breakdown of the contributions to the expected uncertainties on the $t\bar{t}H$ cross section in the $H \to b\bar{b}$ channel at different luminosities for the scenarios S1 and S2 at ATLAS. As discussed in the text, the extrapolation assumes the limitations on the reduction of the $t\bar{t}$ + HF modelling to a factor 2 and a factor 3 of the Run 2 prior uncertainties (Section 2.2.2.4). Therefore, the additional modelling uncertainty used for the extrapolation is 23% in S1 and 15% in S2. Uncertainties due to the limited number of Monte Carlo statistics have been omitted and the assumptions in S1/S2 on the theory uncertainties are applied.

Final state	Scenario	Δ_{tot}/σ_{SM}	$\Delta_{stat}/\sigma_{SM}$	Δ_{exp}/σ_{SM}	Δ_{sig}/σ_{SM}	Δ_{bkg}/σ_{SM}	$\Delta\mu_{sig}$
$t\bar{t}H, H \to b\bar{b}$	Run 2, 36 fb^{-1}	$^{+0.61}_{-0.61}$	$^{+0.22}_{-0.22}$	$^{+0.27}_{-0.28}$	$^{+0.10}_{-0.09}$	$^{+0.47}_{-0.47}$	$^{+0.15}_{-0.15}$
(single lepton)	HL-LHC S1	$^{+0.25}_{-0.20}$	$^{+0.02}_{-0.02}$	$^{+0.10}_{-0.10}$	$^{+0.08}_{-0.06}$	$^{+0.22}_{-0.17}$	$^{+0.10}_{-0.11}$
	HL-LHC S2	$^{+0.18}_{-0.15}$	$^{+0.02}_{-0.02}$	$^{+0.09}_{-0.09}$	$^{+0.06}_{-0.05}$	$^{+0.14}_{-0.11}$	$^{+0.08}_{-0.07}$
$t\bar{t}H, H \to b\bar{b}$	Run 2, 36 fb^{-1}	$^{+1.06}_{-1.08}$	$^{+0.51}_{-0.51}$	$^{+0.32}_{-0.31}$	$^{+0.11}_{-0.12}$	$^{+0.90}_{-0.92}$	$^{+0.14}_{-0.14}$
(di-lepton)	HL-LHC S1	$^{+0.32}_{-0.26}$	$^{+0.06}_{-0.06}$	$^{+0.13}_{-0.13}$	$^{+0.08}_{-0.07}$	$^{+0.27}_{-0.21}$	$^{+0.11}_{-0.09}$
	HL-LHC S2	$^{+0.23}_{-0.20}$	$^{+0.06}_{-0.06}$	$^{+0.11}_{-0.11}$	$^{+0.06}_{-0.06}$	$^{+0.17}_{-0.15}$	$^{+0.08}_{-0.08}$

tainty, demonstrate the level of sensitivity at which the data will be able to distinguish different models and sets a benchmark for the required precision. Monte Carlo prediction will thus need to improve sufficiently to match the data within the uncertainties expected at 3000 fb^{-1}.

Following the expected improvement by a factor two to three in the theoretical uncertainties on the $t\bar{t}$ + HF cross-section calculation described in Section 2.2.2.4, ATLAS and CMS have also performed the $t\bar{t}H$, $H \to b\bar{b}$ extrapolation assuming that the reduction of the $t\bar{t}$ + HF modelling uncertainties is limited to factors of two (in scenario S1) and three (in scenario S2) relative to the uncertainty at 35.9 fb^{-1}. In this case, the obtained relative $t\bar{t}$+HF modelling uncertainties are approximately 23% (S1) and 15% (S2) in the ATLAS analysis as reported in Table 32 and approximately 15% (S1) and 10% (S2) in the CMS analysis. These results enter the combined coupling measurement presented in Sections 2.6 and 2.7. The impact of limiting the constraints of the $t\bar{t}$ + HF uncertainties on the total uncertainties on the extracted parameters is relatively small, e.g. the uncertainty on κ_t increases by approximately 10% and 15% in CMS and ATLAS, respectively.

Studies in the channel of the boosted regime using substructure techniques, where the Higgs boson has significant transverse momentum, have been carried out and reported in [171]. The main background

Table 33: Breakdown of the contributions to the expected uncertainties on the $t\bar{t}H$ cross section in the multi-lepton channel at different luminosities for the scenarios S1 and S2 at ATLAS. Uncertainties due to the limited number of Monte Carlo statistics have been omitted and the assumptions in S1/S2 on the theory uncertainties are applied.

Final state	Scenario	Δ_{tot}/σ_{SM}	$\Delta_{stat}/\sigma_{SM}$	Δ_{exp}/σ_{SM}	Δ_{sig}/σ_{SM}	Δ_{bkg}/σ_{SM}	$\Delta\mu_{sig}$
$t\bar{t}H, H \to$ ML (no τ)	Run 2, 36 fb^{-1}	$^{+0.40}_{-0.40}$	$^{+0.33}_{-0.34}$	$^{+0.15}_{-0.15}$	$^{+0.10}_{-0.10}$	$^{+0.13}_{-0.13}$	$^{+0.13}_{-0.13}$
	HL-LHC S1	$^{+0.18}_{-0.18}$	$^{+0.04}_{-0.04}$	$^{+0.13}_{-0.14}$	$^{+0.08}_{-0.08}$	$^{+0.12}_{-0.12}$	$^{+0.11}_{-0.11}$
	HL-LHC S2	$^{+0.17}_{-0.17}$	$^{+0.04}_{-0.04}$	$^{+0.12}_{-0.13}$	$^{+0.05}_{-0.05}$	$^{+0.09}_{-0.09}$	$^{+0.07}_{-0.07}$
$t\bar{t}H, H \to$ ML (with τ)	Run 2, 36 fb^{-1}	$^{+0.64}_{-0.64}$	$^{+0.54}_{-0.54}$	$^{+0.29}_{-0.29}$	$^{+0.10}_{-0.09}$	$^{+0.14}_{-0.13}$	$^{+0.13}_{-0.13}$
	HL-LHC S1	$^{+0.27}_{-0.28}$	$^{+0.07}_{-0.07}$	$^{+0.23}_{-0.23}$	$^{+0.09}_{-0.08}$	$^{+0.12}_{-0.12}$	$^{+0.11}_{-0.11}$
	HL-LHC S2	$^{+0.25}_{-0.25}$	$^{+0.07}_{-0.07}$	$^{+0.22}_{-0.22}$	$^{+0.05}_{-0.05}$	$^{+0.07}_{-0.07}$	$^{+0.07}_{-0.07}$

remains the top pair production in association with additional heavy flavour quarks, however the boosted regime allows to reduce the combinatorial background and therefore the use of side-bands in the invariant mass distribution. This study confirms the statistical power of the analysis and the side-bands, but would require a more detailed study of the background systematic uncertainties to be fully compared with the current projected results based on the LHC Run 2 analysis.

In conclusion, $t\bar{t}H$ production in the $H \to b\bar{b}$ final state will provide a powerful channel to probe the top-Higgs Yukawa coupling at the HL-LHC. The control of the $t\bar{t}$ + HF background is crucial, and it is expected to benefit from measuring relevant quantities from data, thus mitigating the impact of theoretical uncertainties.

ATLAS performs the extrapolation to HL-LHC also for the ttH multi-lepton (ML) final state [170] where the Higgs boson decays into a pair of Z and W vector bosons or into a pair of τ leptons. Table 33 shows the results on the extrapolation to 3000 fb^{-1} under S1 and S2. As shown in the ranking plot in Figure 21, in the τ final state, the dominant uncertainty pertains to the object reconstruction for such a channel. It is also worth noting that the main theoretical systematic uncertainties concerns the modelling of the tt+V background. Finally, fake lepton uncertainties are moderately constrained as well: this is due to the absence of a reduction factor of prior uncertainties for such a source of systematic uncertainties under S1 and S2.

2.5.1.2 Sensitivity to tH production[20]

The sensitivity to the tH process at the HL-LHC is determined by extrapolating a combination of Run 2 analyses based on 35.9 fb^{-1} of data at $\sqrt{s} = 13$TeV [169]. Two of these analyses are dedicated searches for tHq: one targets a multi-lepton final state in which the Higgs boson decays to WW, ZZ or $\tau\tau$ pairs, and the other targets the $H \to bb$ decay. In both analyses the presence of at least one central b tagged jet and an isolated lepton from the top quark decay is required. Furthermore, the presence of a light quark jet at high pseudorapidity, a unique feature of the tHq production mode, is exploited. Both analyses also rely heavily on multivariate techniques to discriminate the signal against the large tt+jets background. The $\gamma\gamma$ final state is also utilised, via a reinterpretation of the inclusive $H \to \gamma\gamma$ analysis [123]. In this analysis the tHq and tHW processes primarily contribute to the"$t\bar{t}H$ leptonic" and "$t\bar{t}H$ hadronic" event categories, and these are included in the combination.

In Figure 22 the variation of the expected upper limits on μ_{tH} is shown as a function of the integrated luminosity for the S1 and S2 scenarios. The limits are determined assuming a background-only hypothesis in which the ttH process is considered as following the SM expectation ($\mu_{ttH} = 1$). In order to minimise further assumptions on the rate of ttH production, μ_{ttH} is treated as a free parameter in the

[20] Contacts: K. Mazumdar, P. Das

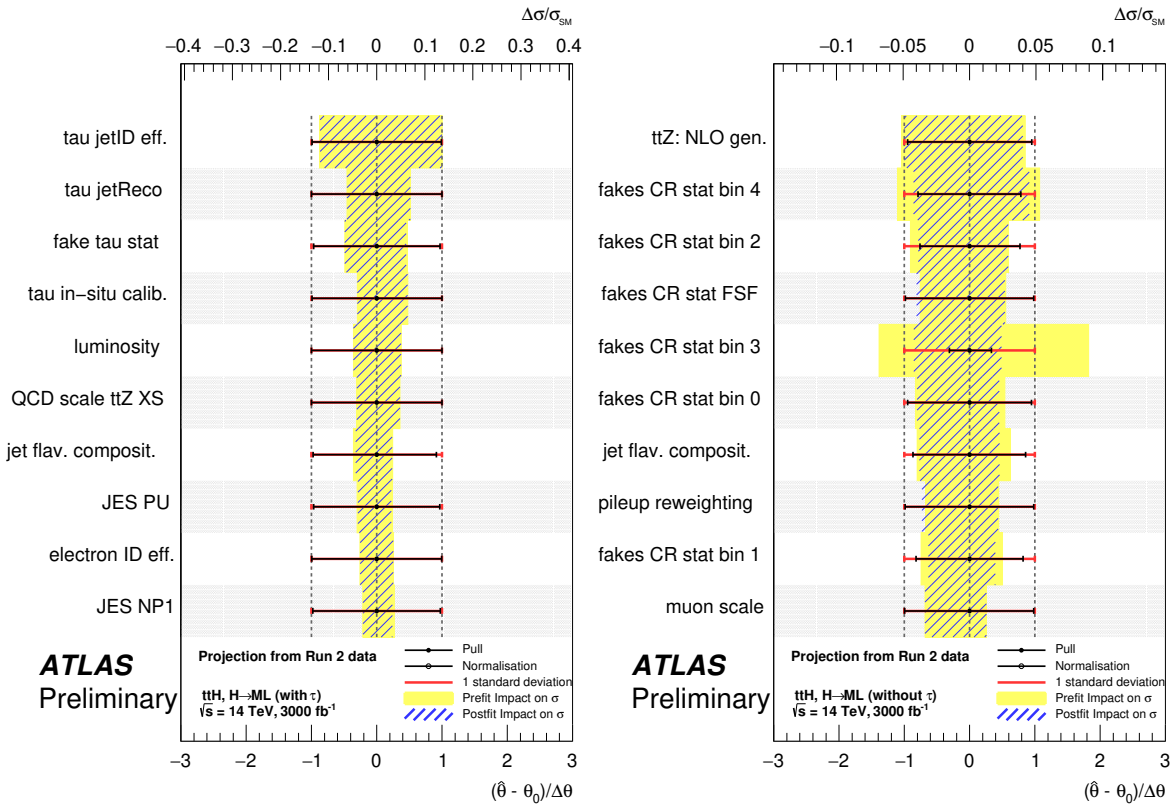

Fig. 21: Ranking of the ten most significant systematic uncertainties under S2 in the $t\bar{t}H$ multi-lepton (ML) final state with (a) and without (b) τ leptons in the ATLAS analysis listed in accordance to their post-fit impact on the $t\bar{t}H$ cross section.

fit. In the S1 scenario the expected median upper limit on μ_{tH} at 3000 fb^{-1} is determined to be 2.35. The corresponding value in S2 is 1.51. With the 3000 fb^{-1} dataset and foreseen reduction in systematic uncertainties in S2, the expected upper limit on μ_{tH} improves by about a factor of eight with respect to the current exclusion.

The evolution of the expected uncertainty on the measurement of μ_{tH}, assuming the SM rate, is given in Table 34. Values are given for two cases of background: one in which μ_{ttH} is unconstrained in the fit, and one in which it is fixed to the SM value of 1. In the latter case the uncertainties are reduced by around 10% at 3000 fb^{-1}, indicating that a precise simultaneous measurement of the ttH signal strength will be needed to obtain the optimal sensitivity to the tH channel. In both cases it is found that the reduced systematic uncertainties in S2 improve the precision by up to 30%.

2.5.2 *Constraints from differential measurements*[21]

Higgs boson couplings can be constrained by fitting theoretical predictions for p_T^H [173, 174, 175] to data, exploiting not only the overall normalisation (as is done in inclusive measurements [144, 145, 146]), but also the shape of the distribution. One of the first constraints on Higgs boson couplings using differential Higgs boson production cross sections was made in Ref. [173]. The limits $\kappa_c \in [-16, 18]$ at 95% CL were found, using data collected by the ATLAS Collaboration at $\sqrt{s} = 8$TeV [176], corresponding to an integrated luminosity of 20.3 fb^{-1}. More recently, the CMS Collaboration performed a similar fit using data [159] collected at $\sqrt{s} = 13$TeV, corresponding to an integrated luminosity of

[21] Contact: T. Klijnsma

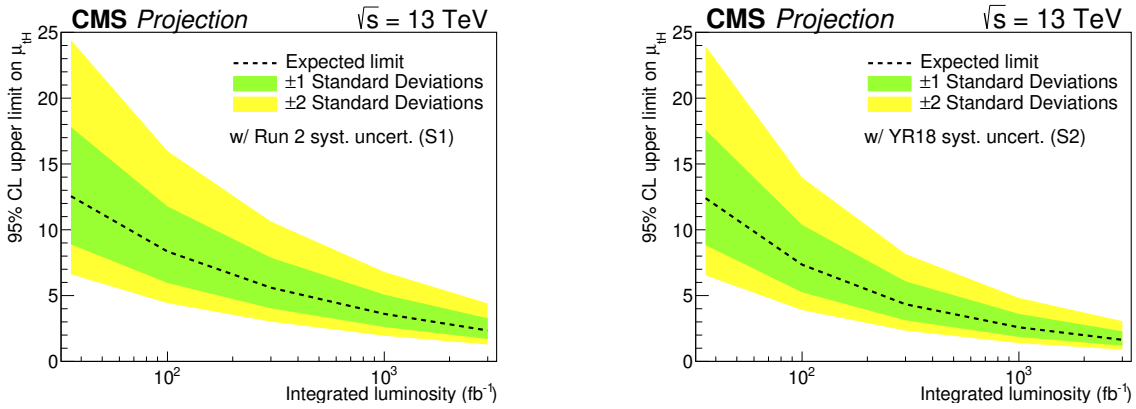

Fig. 22: The variation of expected upper limit on μ_{tH} with integrated luminosity for two projection scenarios S1 (with Run 2 systematic uncertainties [172]) and S2 (with YR18 systematic uncertainties).

Table 34: The $\pm1\sigma$ uncertainties on expected μ_{tH}=1 for scenarios S1 (with Run 2 systematic uncertainties [172]) and S2 (with YR18 systematic uncertainties) at all three luminosities, considering also the case when $\mu_{\mathrm{t\bar{t}H}}$ is fixed at the SM value 1.

		μ_{ttH} floating	μ_{ttH} fixed
S1	35.9 fb^{-1}	$^{+6.2}_{-5.8}$	$^{+5.8}_{-5.4}$
	300 fb^{-1}	$^{+2.9}_{-2.8}$	$^{+2.5}_{-2.4}$
	3000 fb^{-1}	$^{+1.2}_{-1.2}$	$^{+1.1}_{-1.0}$
S2	35.9 fb^{-1}	$^{+6.2}_{-5.8}$	$^{+5.8}_{-5.3}$
	300 fb^{-1}	$^{+2.2}_{-2.2}$	$^{+2.0}_{-2.0}$
	3000 fb^{-1}	$^{+0.9}_{-0.9}$	$^{+0.8}_{-0.8}$

36.1 fb^{-1}. The limits on κ_{b} and κ_{c} are discussed in Section 7.6, whereas the interpretation in terms of κ_{t} and c_{ggh}, the anomalous direct coupling to the gluon field, is discussed here. The projected simultaneous limits on κ_{t} and c_{ggh} at 3000 fb^{-1} are shown in Fig. 23, assuming branching fractions that scale according to SM predictions. It is expected to observe the loop in the gluon-fusion production process, which is clear from the fact that heavy top mass limit, given by the point $(\kappa_{\mathrm{t}} = 0, c_{ggh} =\sim 1/12)$, is excluded.

In order to determine solely the constraint obtained from the distribution (and not the overall normalisation), the fit is repeated with the branching fractions implemented as nuisance parameters with no prior constraint, effectively profiling the overall normalisation. With this parametrisation, the sensitivity to the sign of κ_{t} coming from the H $\rightarrow \gamma\gamma$ branching fraction is lost. The fits obtained this way are shown in Fig. 24; although less significantly, the loop is still distinguished from the point-like coupling to the gluon field, using only the information in the shape of the distribution.

2.6 Combination of Higgs boson measurement projections[22]

The projections documented in this section [139, 126] are based on the extrapolation of the following analyses:

– H $\rightarrow \gamma\gamma$, with ggH, VBF, VH and ttH production [123, 122, 164],

[22] Contacts: R. Di Nardo, A. Gilbert, H. Yang, N. Berger, D. Du, M. Dührssen, A. Gilbert, R. Gugel, L. Ma, B. Murray, P. Milenovic

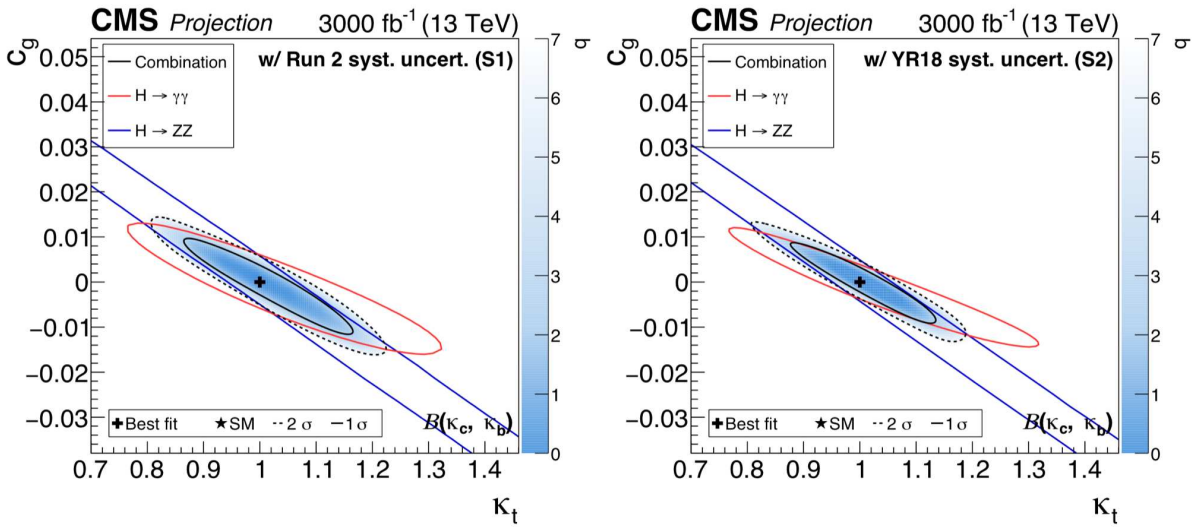

Fig. 23: Projected simultaneous fit for κ_t and c_{ggh}, assuming a coupling dependence of the branching fractions for Scenario 1 (left) and Scenario 2 (right). The one standard deviation contour is drawn for the combination ($H \to \gamma\gamma$, $H \to ZZ$, and $H \to bb$), the $H \to \gamma\gamma$ channel, and the $H \to ZZ$ channel in black, red, and blue, respectively. For the combination the two standard deviation contour is drawn as a black dashed line, and the shading indicates the negative log-likelihood, with the scale shown on the right hand side of the plots.

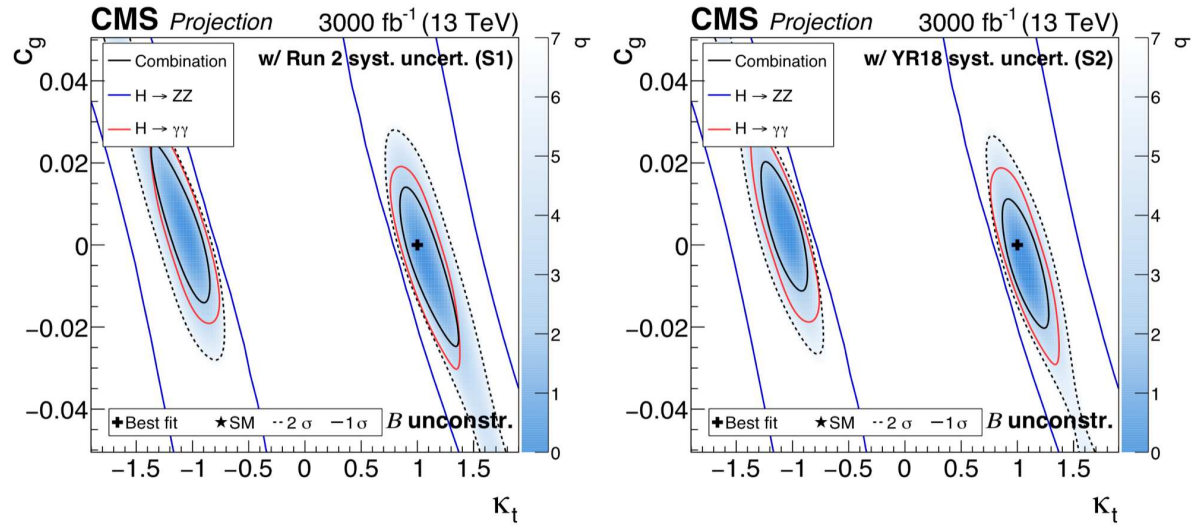

Fig. 24: Projected simultaneous fit for κ_t and c_{ggh} with the branching fractions implemented as nuisance parameters with no prior constraint for Scenario 1 (left) and Scenario 2 (right). The one standard deviation contour is drawn for the combination ($H \to \gamma\gamma$, $H \to ZZ$, and $H \to bb$), the $H \to \gamma\gamma$ channel, and the $H \to ZZ$ channel in black, red, and blue, respectively. For the combination the two standard deviation contour is drawn as a black dashed line, and the shading indicates the negative log-likelihood, with the scale shown on the right hand side of the plots.

- $H \to ZZ^{(*)} \to 4\ell$, with ggH, VBF, VH and ttH production [128, 127],
- $H \to WW^{(*)} \to \ell\nu\ell\nu$, with ggH, VBF and VH production [177, 129],
- $H \to \tau\tau$, with ggH and VBF production [134, 135],
- VH production with $H \to bb$ decay [138, 136],
- Boosted H production with $H \to bb$ decay [178],
- ttH production with $H \to$ leptons [179, 168],
- ttH production with $H \to bb$ [167, 180, 166],
- $H \to \mu\mu$, with ggH and VBF production [142, 181],
- $H \to Z\gamma$, with ggH and VBF production [124].

The projected results given in this section are based on the combined measurement of these channels [182, 183]. In the following results, the signal model in the $H \to \mu\mu$ channel is modified to account for the improved di-muon mass resolution in the Phase-2 ATLAS and CMS tracker upgrades [22, 20]. In CMS, it is estimated that the reduced material budget and improved spatial resolution of the upgraded tracker will yield a 40% improvement in the di-muon mass resolution, for example a reduction from 1.1% to 0.65% for muons in the barrel region. In ATLAS, instead, the reduction of the di-muon invariant mass resolution is estimated to be between 15% and 30% depending on the analysis categories (forward/central).

In the ATLAS projection the expected signal and background yields in all channels are scaled to account for the increasing cross sections going from $\sqrt{s} = 13\,\text{TeV}$ to $\sqrt{s} = 14\,\text{TeV}$, while no scaling is performed in the CMS projection. The impact of this scaling on the projected sensitivity is found to be small.

Projections are given for three different sets of measurements:

- **Higgs boson production cross sections in different decay channels**: the parameters of interest are the cross sections times branching fractions for ggH, VBF, WH, ZH and ttH production in each relevant decay mode, normalised to their SM predictions.
- **Higgs boson production cross sections**: the parameters of interest are the production cross sections normalised to the corresponding SM predictions $\sigma_i/\sigma_i^{\text{SM}}$ where $i =$ ggH, VBF, WH, ZH and ttH, assuming the SM values for the branching fractions. The small contribution from bbH is grouped with ggH while the ZH process includes ZH production with the gluon-gluon initial state. The overall theoretical uncertainties on the inclusive SM cross section predictions are not included, while the uncertainties on the branching ratios are included as the values are assumed to be given by the SM.
- **Higgs boson branching fractions**: the parameters of interest are the branching fractions normalised to the corresponding SM values $\text{BR}_f/\text{BR}_f^{\text{SM}}$, where $f = ZZ, WW, \gamma\gamma, \tau\tau, bb, \mu\mu, Z\gamma$ assuming the SM cross sections for the production modes. In this case the uncertainties on the decay branching ratios are not included, while the overall QCD scales and PDF+α_S uncertainties on the inclusive production cross sections are included.

For each projected measurement the uncertainty is decomposed into four components: statistical, experimental, background theory and signal theory. The combination is based on the assumption that these components are independent within each experiment. Among them, the statistical and experimental uncertainties are treated as fully uncorrelated between the two experiments, while the signal and background theory uncertainties are assumed to be fully correlated. The combination is performed for each parameter individually using the the BLUE methodology as described in Ref. [184]. This procedure does not take into account correlations that may exist between parameters. These arise when analysis channels are sensitive to more than one production or decay mode and the chosen fit observables do not fully distinguish between these, as well as when the same systematic uncertainties apply to multiple

production or decay modes. The effect of including these correlations via a simultaneous combination of all parameters has been verified, utilising the same BLUE methodology and including the complete covariance matrices for both experiments, and is found to have a minor effect on the projection results. Specifically, the effect on the combined statistical and experimental uncertainties is negligible given the reported precision. For the theory uncertainties this procedure can lead to smaller values than in the case where these correlations are neglected. This is a feature of the methodology of Ref. [184], due to the different approaches concerning the theoretical uncertainties used in the extrapolations by the two experiments, which leads to differences in some of the correlation values. However, it is expected that by the time of the HL-LHC both experiments will employ a more consistent treatment of the theoretical uncertainties, making this reduction largely artificial. This motivates the choice to combine measurement projections independently and neglect such correlations in the following results.

2.6.1 Production mode cross-sections in different decay channels

The expected $\pm 1\sigma$ uncertainties on the production mode cross sections in the different decay channels in S2 are summarised in Figure 25 for ggH and VBF, in Figure 26 for WH and ZH, in Figure 27. These are shown for ATLAS, CMS and their combination. Additionally, the numerical values for the ATLAS-CMS combination in scenario S2 are also reported in the figures, with the uncertainty decomposed in three components: statistical, experimental and theory. There are few cases where the extrapolation is currently available only for one experiment (e.g. only $gg \to H \to bb$ in CMS, and only H $\to$ Zγ in ATLAS). In these cases, the combined result is obtained by using the same available extrapolation for both experiments. The correlations between the different production mode cross-sections in different decay channels are in general small, with the exception of the ZH and WH measurements in the H $\to$ ZZ decay (for this reason the VH cross-section is also reported) and the ggH and VBF production mode cross sections in the H $\to \mu\mu$ decay.

The numerical values of the expected $\pm 1\sigma$ uncertainties on the per-production-mode cross sections in the different decay channels for the ATLAS and CMS projections are given in Table 35. The table gives the breakdown of the uncertainty into four components: statistical, signal theory, background theory and experimental for both scenarios S1 and S2.

2.6.2 Cross sections per-production mode

The expected $\pm 1\sigma$ relative uncertainties on the per-production-mode cross sections parameters in S2 for ATLAS, CMS and their combination are summarised in Figure 28. Additionally, the numerical values for the ATLAS-CMS combination are also given, with the uncertainty decomposed in three components: statistical, experimental and theory. In scenario S2 the contribution from the statistical, experimental and theoretical uncertainties to the total error for the combined ggH and VBF cross section measurements is similar. For WH and ZH production cross section measurements, the statistical and theoretical uncertainty are the dominant one. Finally, the total uncertainty on the ttH production cross section measurement is dominated by the theoretical uncertainty, which is almost a factor two larger with respect to the other components. The numerical values of the expected $\pm 1\sigma$ uncertainties on the per-production-mode cross sections for the ATLAS and CMS projections are given in Table 36. The table gives the breakdown of the uncertainty into four components: statistical, signal theory, background theory and experimental for both scenarios S1 and S2.

2.6.3 Branching ratios per-decay mode

The expected $\pm 1\sigma$ uncertainties on the per-decay-mode branching ratios normalised to the SM expectations in S2 for ATLAS, CMS and their combination are summarised in Figure 29. Additionally, the numerical values for the ATLAS-CMS combination are also reported in the figure, with the uncertainty decomposed in three components: statistical, experimental and theory. The S2 uncertainties for the com-

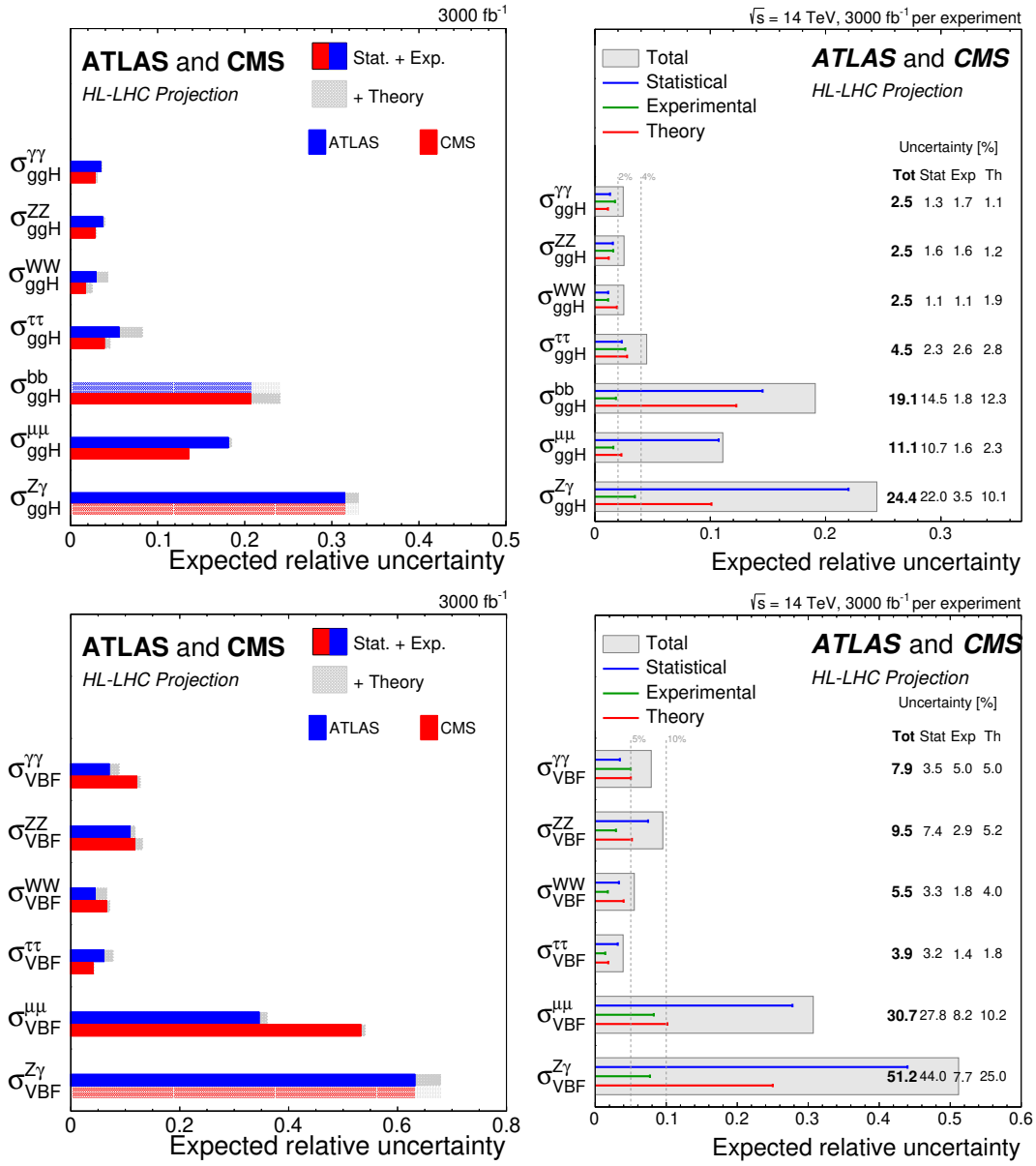

Fig. 25: (left) Summary plot showing the total expected $\pm 1\sigma$ uncertainties in S2 (with YR18 systematic uncertainties) on the ggH (top) and VBF (bottom) production cross sections in the different decay modes normalised to the SM predictions for ATLAS(blue) and CMS (red). The filled coloured box corresponds to the statistical and experimental systematic uncertainties, while the hatched grey area represent the additional contribution to the total uncertainty due to theoretical systematic uncertainties. In the cases where the extrapolation is performed only by one experiment, same performances are assumed for the other experiment and this is indicated by a hatched bar. (right) Summary plot showing the total expected $\pm 1\sigma$ uncertainties in S2 (with YR18 systematic uncertainties) on the ggH (top) and VBF (bottom) production cross sections in the different decay modes normalised to the SM predictions for the combination of ATLAS and CMS extrapolations. For each measurement, the total uncertainty is indicated by a grey box while the statistical, experimental and theory uncertainties are indicated by a blue, green and red line respectively. In addition, the numerical values are also reported.

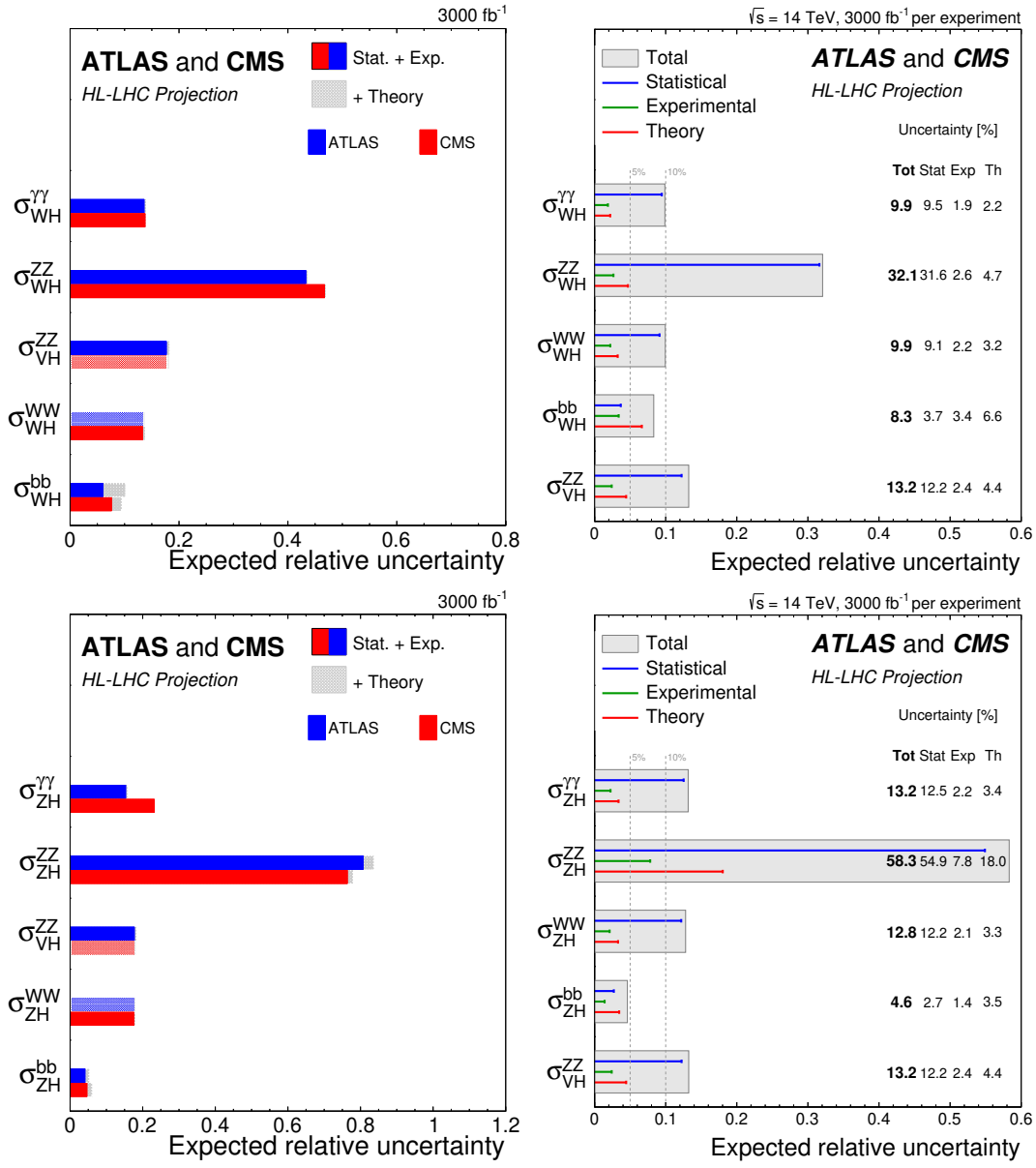

Fig. 26: (left) Summary plot showing the total expected $\pm 1\sigma$ uncertainties in S2 (with YR18 systematic uncertainties) on the WH (top) and ZH (bottom) production cross sections in the different decay modes normalised to the SM predictions for ATLAS(blue) and CMS (red). The filled coloured box corresponds to the statistical and experimental systematic uncertainties, while the hatched grey area represent the additional contribution to the total uncertainty due to theoretical systematic uncertainties. In the cases where the extrapolation is performed only by one experiment, same performances are assumed for the other experiment and this is indicated by a hatched bar. (right) Summary plot showing the total expected $\pm 1\sigma$ uncertainties in S2 (with YR18 systematic uncertainties) on the WH (top) and ZH (bottom) production cross sections in the different decay modes normalised to the SM predictions for the combination of ATLAS and CMS extrapolations. For each measurement, the total uncertainty is indicated by a grey box while the statistical, experimental and theory uncertainties are indicated by a blue, green and red line respectively. In addition, the numerical values are also reported.

Table 35: The expected $\pm 1\sigma$ uncertainties, expressed as percentages, on the per-production-mode cross sections in the different decay modes for ATLAS (left) and CMS (right). Values are given for both S1 (with Run 2 systematic uncertainties [182]) and S2 (with YR18 systematic uncertainties). The total uncertainty is decomposed into four components: statistical (Stat), signal theory (SigTh), background theory (BkgTh) and experimental (Exp).

ATLAS						
		3000 fb^{-1} uncertainty [%]				
		Total	Stat	Exp	SigAcc	BkgTh
$\sigma^{\gamma\gamma}_{ggH}$	S1	5.2	1.7	4.7	1.1	1.2
	S2	3.6	1.7	3.0	0.9	0.5
σ^{ZZ}_{ggH}	S1	4.9	2.0	3.7	1.8	1.9
	S2	3.9	2.0	3.0	1.0	1.0
σ^{WW}_{ggH}	S1	6.0	1.2	3.2	3.7	3.4
	S2	4.3	1.2	2.7	2.1	2.4
$\sigma^{\tau\tau}_{ggH}$	S1	10.6	3.3	5.0	7.5	4.4
	S2	8.2	3.3	4.4	5.4	2.7
$\sigma^{\mu\mu}_{ggH}$	S1	19.9	17.9	2.8	8.0	0.1
	S2	18.5	17.9	2.7	3.8	0.1
$\sigma^{Z\gamma}_{ggH}$	S1	33.3	31.1	4.9	10.1	0.3
	S2	33.3	31.1	4.9	10.1	0.3
$\sigma^{\gamma\gamma}_{VBF}$	S1	12.0	4.4	7.3	8.2	2.1
	S2	8.9	4.4	5.5	5.4	0.9
σ^{ZZ}_{VBF}	S1	13.0	9.6	5.1	6.8	2.1
	S2	11.8	9.6	5.1	4.5	1.2
σ^{WW}_{VBF}	S1	10.3	3.3	3.9	7.7	4.5
	S2	6.6	3.3	2.9	4.0	2.8
$\sigma^{\tau\tau}_{VBF}$	S1	8.7	3.7	4.1	5.5	3.8
	S2	7.8	3.7	4.8	3.2	3.6
$\sigma^{\mu\mu}_{VBF}$	S1	38.7	32.5	11.7	17.1	0.2
	S2	36.1	32.5	11.7	10.4	0.3
$\sigma^{Z\gamma}_{VBF}$	S1	68.2	62.2	10.9	25.0	0.5
	S2	68.2	62.2	10.9	25.0	0.5
$\sigma^{\gamma\gamma}_{WH}$	S1	14.8	13.1	5.2	4.0	1.3
	S2	13.8	13.1	3.3	2.8	0.7
σ^{ZZ}_{VH}	S1	18.7	17.3	4.2	5.4	2.2
	S2	18.1	17.3	3.4	4.1	1.7
σ^{bb}_{WH}	S1	14.1	4.3	4.9	7.3	10.1
	S2	10.1	4.4	4.1	4.2	6.9
$\sigma^{\gamma\gamma}_{ZH}$	S1	17.0	14.9	5.1	6.3	1.3
	S2	15.7	14.9	3.2	3.7	0.6
σ^{bb}_{ZH}	S1	7.0	3.5	2.7	4.0	3.6
	S2	5.2	3.5	2.0	2.1	2.4
$\sigma^{\gamma\gamma}_{ttH}$	S1	10.0	4.6	5.9	6.4	1.5
	S2	7.4	4.6	4.1	3.9	0.5
σ^{ZZ}_{ttH}	S1	20.5	18.6	4.1	7.3	1.7
	S2	19.3	18.6	3.1	3.8	0.9
$\sigma^{WW\tau\tau}_{ttH}$	S1	22.1	6.3	18.2	7.0	8.1
	S2	20.2	6.3	17.9	4.3	5.1
σ^{bb}_{ttH}	S1	19.9	3.2	4.2	7.4	17.8
	S2	14.2	3.2	3.4	4.4	12.7

CMS						
		3000 fb^{-1} uncertainty [%]				
		Total	Stat	Exp	SigAcc	BkgTh
$\sigma^{\gamma\gamma}_{ggH}$	S1	3.9	1.9	3.3	0.7	1.0
	S2	2.8	1.9	2.1	0.8	0.9
σ^{ZZ}_{ggH}	S1	4.1	2.1	2.7	1.2	1.7
	S2	3.0	2.1	1.8	0.8	0.7
σ^{WW}_{ggH}	S1	3.6	1.2	1.5	2.9	1.0
	S2	2.5	1.2	1.2	1.6	0.9
$\sigma^{\tau\tau}_{ggH}$	S1	5.7	2.6	3.5	3.3	1.7
	S2	4.6	2.6	2.9	2.3	0.7
σ^{bb}_{ggH}	S1	34.3	20.6	10.0	23.7	3.2
	S2	24.7	20.6	2.6	12.2	1.5
$\sigma^{\mu\mu}_{ggH}$	S1	15.9	13.4	8.0	2.6	1.9
	S2	13.5	13.4	2.0	1.4	0.6
$\sigma^{\gamma\gamma}_{VBF}$	S1	22.1	5.2	19.9	7.9	1.3
	S2	12.7	5.2	10.9	4.0	0.3
σ^{ZZ}_{VBF}	S1	15.1	11.7	1.8	8.8	2.4
	S2	13.3	11.7	1.3	5.9	0.8
σ^{WW}_{VBF}	S1	8.1	6.3	2.0	4.4	1.8
	S2	7.2	6.3	1.6	2.8	1.1
$\sigma^{\tau\tau}_{VBF}$	S1	4.9	3.8	2.0	2.8	1.5
	S2	4.2	3.8	1.3	1.2	0.4
$\sigma^{\mu\mu}_{VBF}$	S1	57.3	53.2	11.3	18.0	4.5
	S2	54.0	53.2	2.6	9.5	1.0
$\sigma^{\gamma\gamma}_{WH}$	S1	14.3	13.6	3.7	2.0	1.4
	S2	13.8	13.6	1.7	1.5	0.2
σ^{ZZ}_{WH}	S1	47.9	46.5	7.8	11.2	2.8
	S2	47.8	46.5	3.8	4.0	0.8
σ^{WW}_{WH}	S1	15.6	12.9	6.5	5.3	2.2
	S2	13.7	12.9	3.1	2.9	1.5
σ^{bb}_{WH}	S1	16.0	5.6	9.8	5.3	10.8
	S2	9.4	5.6	5.1	2.2	5.1
$\sigma^{\gamma\gamma}_{ZH}$	S1	23.5	23.1	2.9	3.1	1.5
	S2	23.2	23.1	1.2	2.4	0.4
σ^{ZZ}_{ZH}	S1	82.3	75.7	16.4	26.3	7.6
	S2	78.4	75.7	9.9	15.1	1.3
σ^{WW}_{ZH}	S1	18.5	17.2	3.5	5.3	2.4
	S2	17.7	17.2	3.0	2.8	1.7
σ^{bb}_{ZH}	S1	7.9	4.2	2.3	5.6	3.1
	S2	6.0	4.2	1.9	2.9	2.6
$\sigma^{\gamma\gamma}_{ttH}$	S1	9.3	7.7	3.9	3.5	1.0
	S2	8.4	7.7	2.7	1.9	0.2
σ^{ZZ}_{ttH}	S1	24.6	23.6	4.2	4.9	2.5
	S2	24.2	23.6	3.1	2.6	1.8
σ^{WW}_{ttH}	S1	11.2	4.2	9.1	1.8	4.5
	S2	8.7	4.2	6.9	1.1	3.0
σ^{bb}_{ttH}	S1	15.9	2.8	3.9	0.0	15.2
	S2	10.8	2.8	2.7	0.1	10.0
$\sigma^{\tau\tau}_{ttH}$	S1	16.5	8.7	13.1	3.4	3.5
	S2	14.2	8.7	10.9	1.6	2.1

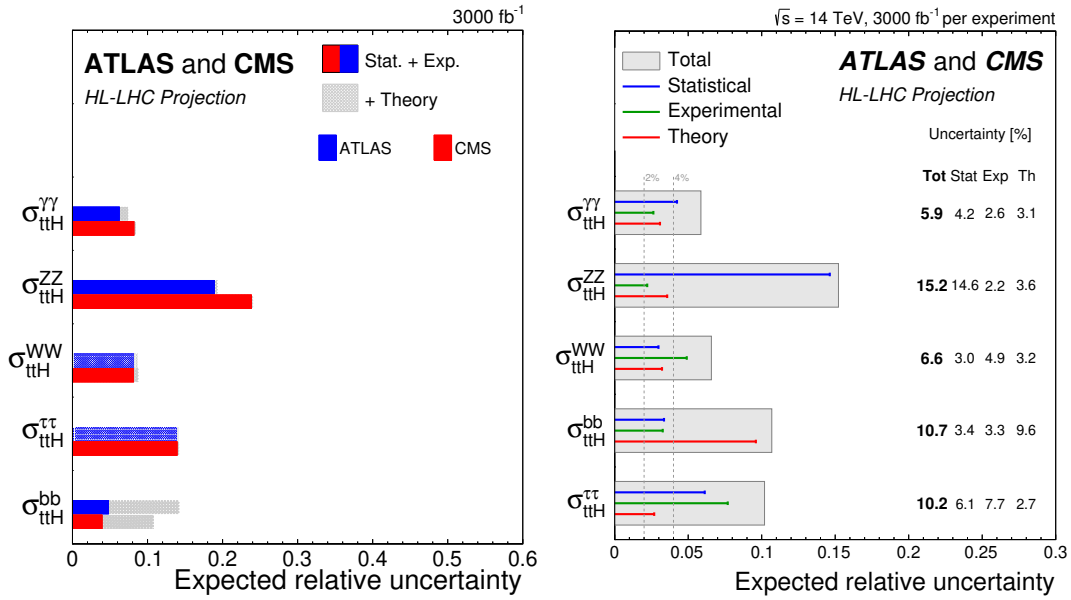

Fig. 27: (left) Summary plot showing the total expected $\pm 1\sigma$ uncertainties in S2 (with YR18 systematic uncertainties) on the ttH production cross section in the different decay modes normalised to the SM predictions for ATLAS (blue) and CMS (red). The filled coloured box corresponds to the statistical and experimental systematic uncertainties, while the hatched grey area represent the additional contribution to the total uncertainty due to theoretical systematic uncertainties. In the cases where the extrapolation is performed only by one experiment, same performances are assumed for the other experiment and this is indicated by a hatched bar. (right) Summary plot showing the total expected $\pm 1\sigma$ uncertainties in S2 (with YR18 systematic uncertainties) on the ttH production cross sections in the different decay modes normalised to the SM predictions for the combination of ATLAS and CMS extrapolations. For each measurement, the total uncertainty is indicated by a grey box while the statistical, experimental and theory uncertainties are indicated by a blue, green and red line respectively. In addition, the numerical values are also reported.

Table 36: The expected $\pm 1\sigma$ uncertainties, expressed as percentages, on the per-production-mode cross sections normalised to the SM values for ATLAS (left) and CMS (right). Values are given for both S1 (with Run 2 systematic uncertainties [182]) and S2 (with YR18 systematic uncertainties). The total uncertainty is decomposed into four components: statistical (Stat), signal theory (SigTh), background theory (BkgTh) and experimental (Exp).

ATLAS						
		3000 fb^{-1} uncertainty [%]				
		Total	Stat	Exp	SigTh	BkgTh
σ_{ggH}	S1	3.5	0.8	2.1	2.1	1.6
	S2	2.4	0.8	1.7	1.2	1.0
σ_{VBF}	S1	5.5	2.0	2.7	3.7	2.1
	S2	4.2	2.0	2.3	2.2	1.7
σ_{WH}	S1	9.3	4.0	4.0	5.1	5.4
	S2	7.7	4.0	3.4	3.3	4.5
σ_{ZH}	S1	6.2	3.4	2.4	3.4	3.0
	S2	4.8	3.4	1.8	2.0	2.1
σ_{ttH}	S1	6.7	1.9	3.1	3.7	4.3
	S2	5.3	1.9	2.8	2.4	3.3

CMS						
		3000 fb^{-1} uncertainty [%]				
		Total	Stat	Exp	SigTh	BkgTh
σ_{ggH}	S1	2.4	0.8	1.2	1.6	0.9
	S2	1.7	0.8	0.9	0.9	0.6
σ_{VBF}	S1	4.1	2.6	2.1	2.0	1.3
	S2	3.5	2.6	1.6	1.8	0.3
σ_{WH}	S1	8.1	4.6	5.2	2.6	3.3
	S2	6.4	4.6	3.2	1.5	2.7
σ_{ZH}	S1	6.7	3.9	2.1	4.3	2.5
	S2	5.4	3.9	1.7	2.4	2.3
σ_{ttH}	S1	5.8	1.8	3.1	1.9	4.1
	S2	4.6	1.8	2.4	1.1	3.4

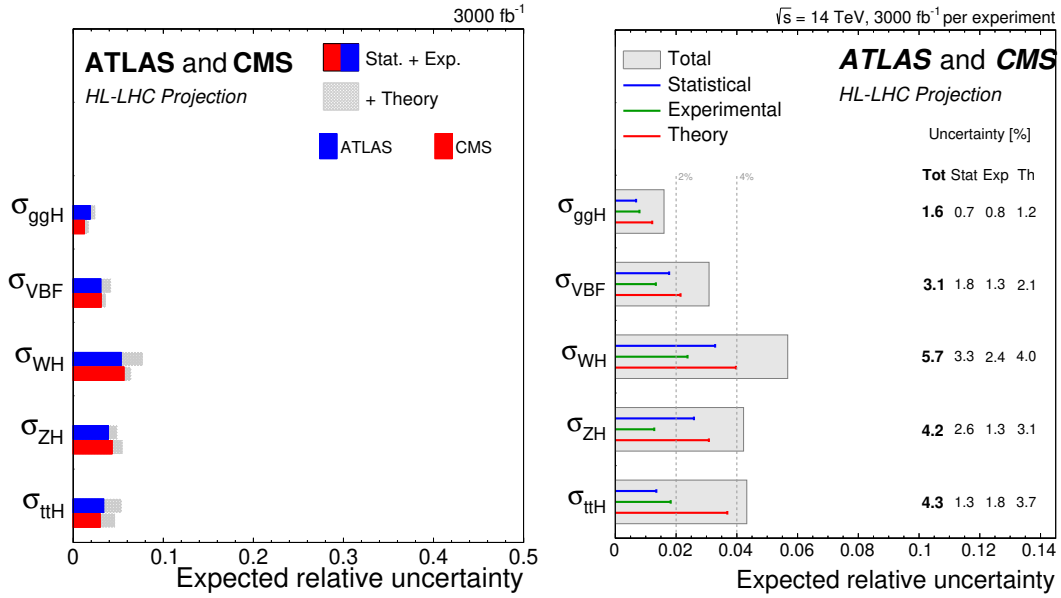

Fig. 28: (left) Summary plot showing the total expected $\pm 1\sigma$ uncertainties in S2 (with YR18 systematic uncertainties) on the per-production-mode cross sections normalised to the SM predictions for ATLAS (blue) and CMS (red). The filled coloured box corresponds to the statistical and experimental systematic uncertainties, while the hatched grey area represent the additional contribution to the total uncertainty due to theoretical systematic uncertainties. (right) Summary plot showing the total expected $\pm 1\sigma$ uncertainties in S2 (with YR18 systematic uncertainties) on the per-production-mode cross sections normalised to the SM predictions for the combination of ATLAS and CMS extrapolations. For each measurement, the total uncertainty is indicated by a grey box while the statistical, experimental and theory uncertainties are indicated by a blue, green and red line respectively. In addition, the numerical values are also reported.

bined ATLAS-CMS extrapolation range from $2-4\%$, with the exception of that on $B^{\mu\mu}$ at 8% and on $B^{Z\gamma}$ at 19%. The numerical values in both S1 and S2 for ATLAS and CMS are given in Table 37 where the the breakdown of the uncertainty into four components is provided. In projections of both experiments, the S1 uncertainties are up to a factor of 1.5 larger than those in S2, reflecting the larger systematic component. The systematic uncertainties generally dominate in both S1 and S2. In S2 the signal theory uncertainty is the largest, or joint-largest, component for all parameters except $BR^{\mu\mu}$ and $B^{Z\gamma}$, which remain limited by statistics due to the small branching fractions.

The correlations range up to 40%, and are largest between modes where the sensitivity is dominated by gluon-fusion production. This reflects the impact of the theory uncertainties affecting the SM prediction of the gluon-fusion production rate.

2.7 Kappa interpretation of the combined Higgs boson measurement projections[23]

2.7.1 Interpretations and results for HL-LHC

In this section combination results are given for a parametrisation based on the coupling modifier, or κ-framework [42]. A set of coupling modifiers, $\vec{\kappa}$, is introduced to parametrise potential deviations from the SM predictions of the Higgs boson couplings to SM bosons and fermions. For a given production process or decay mode j, a coupling modifier κ_j is defined such that,

$$\kappa_j^2 = \sigma_j/\sigma_j^{\rm SM} \quad \text{or} \quad \kappa_j^2 = \Gamma^j/\Gamma^j_{\rm SM}. \tag{6}$$

[23] Contacts: R. Di Nardo, A. Gilbert, H. Yang, N. Berger, D. Du, M. Dührssen, A. Gilbert, R. Gugel, L. Ma B. Murray, P. Milenovic

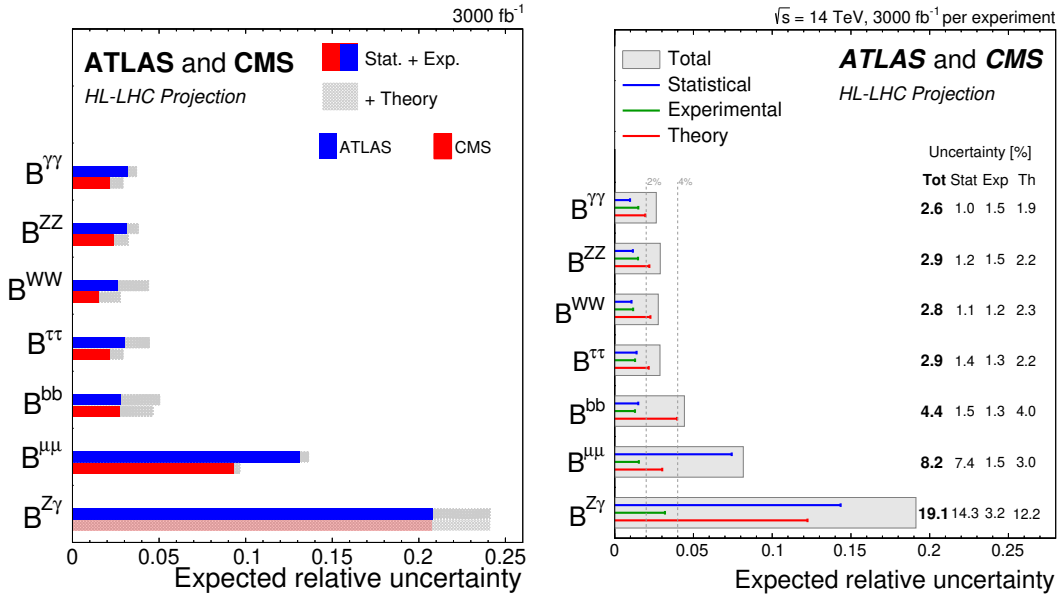

Fig. 29: (left) Summary plot showing the total expected $\pm 1\sigma$ uncertainties in S2 (with YR18 systematic uncertainties) on the per-decay-mode branching ratios normalised to the SM predictions for ATLAS (blue) and CMS (red). The filled coloured box corresponds to the statistical and experimental systematic uncertainties, while the hatched grey area represent the additional contribution to the total uncertainty due to theoretical systematic uncertainties. (right) Summary plot showing the total expected $\pm 1\sigma$ uncertainties in S2 (with YR18 systematic uncertainties) on the per-decay-mode branching ratios normalised to the SM predictions for the combination of ATLAS and CMS extrapolations. For each measurement, the total uncertainty is indicated by a grey box while the statistical, experimental and theory uncertainties are indicated by a blue, green and red line respectively. In addition, the numerical values are also reported.

In the SM, all κ_j values are positive and equal to unity. Six coupling modifiers corresponding to the tree-level Higgs boson couplings are defined: κ_{W}, κ_{Z}, κ_{t}, κ_{b}, κ_{τ} and κ_{μ}. In addition, the effective coupling modifiers κ_{g}, κ_{γ} and $\kappa_{\mathrm{Z}\gamma}$ are introduced to describe ggH production, $\mathrm{H} \to \gamma\gamma$ decay and $\mathrm{H} \to \mathrm{Z}\gamma$ decay loop processes. The total width of the Higgs boson, relative to the SM prediction, varies with the coupling modifiers as $\Gamma_{\mathrm{H}}/\Gamma_{\mathrm{H}}^{\mathrm{SM}} = \sum_j \mathrm{B}_{\mathrm{SM}}^{j}\kappa_j^2/(1-\mathrm{B}_{\mathrm{BSM}})$, where $\mathrm{B}_{\mathrm{SM}}^{j}$ is the SM branching fraction for the $\mathrm{H} \to jj$ channel and $\mathrm{B}_{\mathrm{BSM}}$ is the Higgs boson branching fraction to BSM final states. In the results for the κ_j parameters presented here $\mathrm{B}_{\mathrm{BSM}}$ is fixed to zero and only decays to SM particles are allowed. Projections are also given for the upper limit on $\mathrm{B}_{\mathrm{BSM}}$ when this restriction is relaxed, in which an additional constraint that $|\kappa_{\mathrm{V}}| < 1$ is imposed. A constraint on $\Gamma_{\mathrm{H}}/\Gamma_{\mathrm{H}}^{\mathrm{SM}}$ is also obtained in this model by treating it as a free parameter in place of one of the other κ parameters.

The expected uncertainties for the coupling modifier parametrisation for ATLAS, CMS [126, 139] and their combination for scenario S2 are summarised in Figure 30. The numerical values in both S1 and S2 for ATLAS and CMS are provided in Table 38. For the combined measurement in S2, the uncertainty components contribute at a similar level for κ_{γ}, κ_{W}, κ_{Z} and κ_{τ}. The signal theory remains the main component for κ_{t} and κ_{g}, while κ_{μ} and $\kappa_{\mathrm{Z}\gamma}$ are limited by statistics.

The expected 1σ uncertainty on $\mathrm{B}_{\mathrm{BSM}}$, for the parametrisation with $\mathrm{B}_{\mathrm{BSM}} \geq 0$ and $|\kappa_{\mathrm{V}}| \leq 1$, is 0.033 (0.049) in S1 and 0.027 (0.032) in S2 for CMS (ATLAS), where in the latter case the statistical uncertainty is the largest component. The expected uncertainty for the ATLAS-CMS combination on $\mathrm{B}_{\mathrm{BSM}}$ is 0.025 in S2. The uncertainty on $\Gamma_{\mathrm{H}}/\Gamma_{\mathrm{H}}^{\mathrm{SM}}$, determined for CMS only, is 0.05 (0.04) in S1 (S2).

The correlation coefficients between the coupling modifiers are in general larger compared to the

Table 37: The expected $\pm 1\sigma$ relative uncertainties, expressed as percentages, on the Higgs boson branching ratios normalised by the SM expectations for ATLAS (left) and CMS (right). Values are given for both S1 (with Run 2 systematic uncertainties [182]) and S2 (with YR18 systematic uncertainties). The total uncertainty is decomposed into four components: statistical (Stat), signal theory (SigTh), background theory (BkgTh) and experimental (Exp).

ATLAS						
		3000 fb^{-1} relative uncertainty [%]				
		Total	Stat	Exp	SigTh	BkgTh
$B^{\gamma\gamma}$	S1	6.0	1.2	4.7	3.3	1.4
	S2	3.7	1.2	2.9	1.8	0.6
B^{WW}	S1	5.8	1.0	2.8	4.3	2.6
	S2	4.4	1.0	2.4	3.2	1.6
B^{ZZ}	S1	5.3	1.6	3.0	3.7	1.7
	S2	3.8	1.6	2.7	1.9	1.0
B^{bb}	S1	7.6	2.0	2.4	5.0	4.7
	S2	5.0	2.0	1.9	2.8	3.2
$B^{\tau\tau}$	S1	6.0	1.7	2.7	4.4	2.4
	S2	4.4	1.7	2.5	2.8	1.7
$B^{\mu\mu}$	S1	14.9	12.7	3.2	6.8	0.3
	S2	13.7	12.7	3.2	3.7	0.3
$B^{Z\gamma}$	S1	24.2	20.3	4.5	12.2	0.0
	S2	24.2	20.3	4.5	12.2	0.0

CMS						
		3000 fb^{-1} relative uncertainty [%]				
		Total	Stat	Exp	SigTh	BkgTh
$B^{\gamma\gamma}$	S1	4.4	1.3	2.6	3.3	0.3
	S2	3.0	1.3	1.7	1.9	0.3
B^{WW}	S1	4.0	1.0	1.4	3.5	1.0
	S2	2.8	1.0	1.1	2.2	0.9
B^{ZZ}	S1	5.0	1.6	2.5	3.5	1.9
	S2	3.2	1.6	1.7	2.1	0.7
B^{bb}	S1	7.0	2.1	2.3	5.2	3.6
	S2	4.7	2.1	1.7	2.4	2.9
$B^{\tau\tau}$	S1	3.9	1.6	1.9	2.6	1.5
	S2	2.9	1.6	1.4	1.9	0.6
$B^{\mu\mu}$	S1	12.8	9.1	7.6	4.7	0.8
	S2	9.6	9.1	1.7	2.6	0.8

one related to the signal strength (up to $+75\%$). One reason for this is that the normalisation of any signal process depends on the total width of the Higgs boson, which in turn depends on the values of the other coupling modifiers. The largest correlations involve κ_b, as this gives the largest contribution to the total width in the SM. Therefore improving the measurement of the $H \to bb$ process will improve the sensitivity of many of the other coupling modifiers at the HL-LHC.

Projections have also been determined for a parametrisation based on ratios of the coupling modifiers ($\lambda_{ij} = \kappa_i/\kappa_j$) together with a reference ratio of coupling modifiers $\kappa_{gZ} = \kappa_g\kappa_Z/\kappa_H$. This parametrisation requires no assumption on the total width of the Higgs boson, as its effective modifier κ_H has been absorbed into the ratio κ_{gZ}. The results of this projection for ATLAS, CMS and their combination in S2 are given in Fig 31. The numerical values in both S1 and S2 for ATLAS and CMS are given in Table 39.

2.7.2 Higgs boson coupling measurements projections estimates for HE-LHC

As discussed above, except for the κ_μ and $\kappa_{Z\gamma}$ coupling modifiers measured directly through the rare decay channels $H \to \mu^+\mu^-$ and $H \to (Z \to \ell^+\ell^-)\gamma$, the precision of the measurement of the Higgs boson couplings at HL-LHC are limited by systematic uncertainties and in particular those related to the theoretical predictions and the modelling of the signal and the backgrounds.

Detailed studies on how the main systematic uncertainties will be reduced with foreseeable theoretical developments and the input of the large amount of data from the HL-LHC have not been carried out so far, except for PDF uncertainties. A very approximate estimate can however be given from the studies made for the projected sensitivities at HL-LHC, where HE-LHC sensitivities are derived neglecting the statistical uncertainty taking into account the increase in centre-of-mass energy of 27 TeV and the much larger dataset of 15 ab^{-1} for all measurements, except $H \to \mu\mu$ and $H \to Z\gamma$ channel where

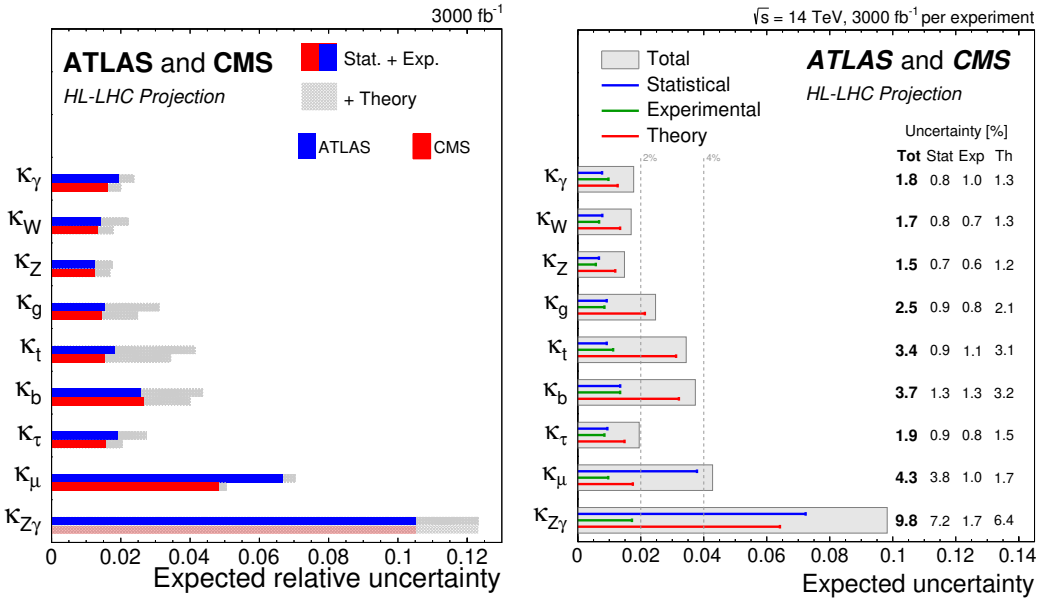

Fig. 30: (left) Summary plot showing the total expected $\pm 1\sigma$ uncertainties in S2 (with YR18 systematic uncertainties) on the coupling modifier parameters for ATLAS (blue) and CMS (red). The filled coloured box corresponds to the statistical and experimental systematic uncertainties, while the hatched grey area represent the additional contribution to the total uncertainty due to theoretical systematic uncertainties. (right) Summary plot showing the total expected $\pm 1\sigma$ uncertainties in S2 (with YR18 systematic uncertainties) on the coupling modifier parameters for the combination of ATLAS and CMS extrapolations. For each measurement, the total uncertainty is indicated by a grey box while the statistical, experimental and theory uncertainties are indicated by a blue, green and red line respectively.

a simple scaling of the cross sections and luminosities is applied, which is a fair assessment with the current systematic uncertainties and assuming that the experimental performance and systematic uncertainties are unchanged with respect to the current LHC experiments. Two scenarios are then assumed for the theoretical and modelling systematic uncertainties on the signal and backgrounds. The first (S2) is the foreseen baseline scenario at HL-LHC, and the second (S2′) is a scenario where theoretical and modelling systematic uncertainties are halved, which in many cases would correspond to uncertainties roughly four times smaller than for current Run 2 analyses. It should be noted that HL-LHC measurements, whose precision is limited by systematic uncertainties, would also improve for S2'. The results of these projections are reported in Table 40.

2.8 Higgs couplings precision overview in the Kappa-framework and the nonlinear EFT[24]

After the discovery of the Higgs boson at the LHC, the first exploration of the couplings of the new particle at Run I and Run II has achieved an overall precision at the level of ten percent. One of the main goals of Higgs studies at the HL-LHC or HE-LHC will be to push the sensitivity to deviations in the Higgs couplings close to the percent level.

In this section we study the projected precision that would be possible at such high luminosity and high energy extensions of the LHC from a global fit to modifications of the different single-Higgs couplings. Other important goals of the Higgs physics program at the HL/HE-LHC, such as extending/complementing the studies of the total rates with the information from differential distributions, or getting access to the Higgs trilinear coupling, will be covered in other parts of this document.

In order to study single-Higgs couplings, we introduce a parametrisation, the nonlinear EFT, that

[24] Contacts: J. de Blas, O. Catà, O. Eberhardt, C. Krause

Table 38: The expected $\pm 1\sigma$ uncertainties, expressed as percentages, on the coupling modifier parameters.Values are given for both S1 (with Run 2 systematic uncertainties [182]) and S2 (with YR18 systematic uncertainties). The total uncertainty is decomposed into four components: statistical (Stat), signal theory (SigTh), background theory (BkgTh) and experimental (Exp).

ATLAS						
		3000 fb^{-1} uncertainty [%]				
		Total	Stat	SigTh	BkgTh	Exp
κ_γ	S1	3.7	0.9	2.2	1.4	2.5
	S2	2.4	0.9	1.1	0.9	1.7
κ_W	S1	3.1	0.8	1.9	1.9	1.3
	S2	2.2	0.8	1.2	1.3	1.2
κ_Z	S1	2.6	0.8	1.8	1.2	1.1
	S2	1.8	0.8	1.0	0.8	0.9
κ_g	S1	4.2	1.0	3.2	2.2	1.4
	S2	3.1	1.0	2.2	1.6	1.2
κ_t	S1	6.3	1.1	4.9	3.4	1.6
	S2	4.2	1.1	2.6	2.7	1.4
κ_b	S1	6.2	1.6	3.7	4.1	2.3
	S2	4.4	1.6	2.1	2.8	2.0
κ_τ	S1	3.7	1.1	2.6	1.8	1.7
	S2	2.7	1.1	1.5	1.2	1.6
κ_μ	S1	7.7	6.4	3.6	1.4	1.9
	S2	7.0	6.4	2.0	0.9	1.8
$\kappa_{Z\gamma}$	S1	12.7	10.2	6.9	1.4	2.5
	S2	12.4	10.2	6.4	0.9	2.4

CMS						
		3000 fb^{-1} uncertainty [%]				
		Total	Stat	SigTh	BkgTh	Exp
κ_γ	S1	2.9	1.1	1.8	1.0	1.7
	S2	2.0	1.1	0.9	0.8	1.2
κ_W	S1	2.6	1.0	1.7	1.1	1.1
	S2	1.8	1.0	0.9	0.8	0.8
κ_Z	S1	2.4	1.0	1.7	0.9	0.9
	S2	1.7	1.0	0.9	0.7	0.7
κ_g	S1	4.0	1.1	3.4	1.3	1.2
	S2	2.5	1.1	1.7	1.1	1.0
κ_t	S1	5.5	1.0	4.4	2.7	1.6
	S2	3.5	1.0	2.2	2.1	1.2
κ_b	S1	6.0	2.0	4.3	2.9	2.3
	S2	4.0	2.0	2.0	2.2	1.8
κ_τ	S1	2.8	1.2	1.8	1.1	1.4
	S2	2.0	1.2	1.0	0.9	1.0
κ_μ	S1	6.7	4.7	2.5	1.0	3.9
	S2	5.0	4.7	1.3	0.8	1.1

transparently connects with the κ-formalism, but is based on the language of effective field theories (EFTs). We then present a fit to the projected HL/HE-LHC uncertainties both in the κ-formalism and in the more general nonlinear EFT, discussing the expected sensitivities to deviations on the Higgs couplings at the HL/HE-LHC, and compare with the recent results obtained using current data from [185]. The translation of these results in terms of composite Higgs scenarios will be discussed in section 2.9.

The κ-formalism was introduced in [44, 42] as an interim framework to report on the measurements of the Higgs-boson couplings and characterise the nature of the Higgs boson. The κ_i are defined as ratios of measured cross sections and decay widths with respect to their SM expectation, *i.e.*

$$\kappa_X^2 = \frac{\sigma(X_i \to h + X_f)}{\sigma(X_i \to h + X_f)_{\rm SM}}, \qquad \kappa_Y^2 = \frac{\Gamma(h \to Y)}{\Gamma(h \to Y)_{\rm SM}}, \tag{7}$$

so that the SM is recovered for $\kappa_i = 1$. This framework, defined at the level of signal strengths, was appropriate for the observables under study at Run I, which tested deviations in event rates. For Run II and the analyses required at the HL/HE-LHC, differential information is needed and the formalism defined by eq. (7) has to be extended. In practice it then becomes more efficient to work directly at the level of Lagrangians. Here we will discuss the interpretation of the κ factors within the electroweak chiral Lagrangian (EWChL or HEFT). Within this EFT, the contributions to processes with a single Higgs, in

Table 39: The expected $\pm 1\sigma$ uncertainties, expressed as percentages, on the ratios of coupling modifier parameters for ATLAS and CMS [126, 139]. Values are given for both S1 (with Run 2 systematic uncertainties [182]) and S2 (with YR18 systematic uncertainties). The total uncertainty is decomposed into four components: statistical (Stat), signal theory (SigTh), background theory (BkgTh) and experimental (Exp).

ATLAS						
		3000 fb^{-1} uncertainty [%]				
		Total	Stat	SigTh	BkgTh	Exp
κ_{gZ}	S1	3.4	0.8	2.8	0.9	1.5
	S2	2.2	0.8	1.5	0.5	1.3
$\lambda_{\gamma Z}$	S1	3.1	1.0	1.5	0.6	2.4
	S2	2.2	1.0	0.7	0.5	1.7
λ_{WZ}	S1	2.7	0.9	1.5	1.3	1.5
	S2	2.2	0.9	1.0	1.0	1.4
λ_{Zg}	S1	4.5	1.3	3.7	1.6	1.6
	S2	3.4	1.3	2.4	1.3	1.4
λ_{tg}	S1	6.1	1.3	5.4	1.8	1.8
	S2	3.9	1.3	3.0	1.3	1.7
λ_{bZ}	S1	5.3	1.6	3.1	3.3	2.2
	S2	3.9	1.6	1.8	2.3	2.0
$\lambda_{\tau Z}$	S1	3.4	1.2	2.3	1.4	1.8
	S2	2.6	1.2	1.3	1.0	1.7
$\lambda_{\mu Z}$	S1	7.7	6.4	3.6	0.9	2.1
	S2	7.0	6.4	1.9	0.5	1.9
$\lambda_{Z\gamma Z}$	S1	12.7	10.2	6.9	1.0	2.6
	S2	12.3	10.2	6.3	0.5	2.5

CMS						
		3000 fb^{-1} uncertainty [%]				
		Total	Stat	SigTh	BkgTh	Exp
κ_{gZ}	S1	3.2	0.8	2.7	0.9	1.2
	S2	1.9	0.8	1.4	0.4	0.8
$\lambda_{\gamma Z}$	S1	2.6	1.0	1.1	1.0	1.8
	S2	1.8	1.0	0.7	0.2	1.2
λ_{WZ}	S1	2.3	0.9	1.4	1.0	1.3
	S2	1.6	0.9	0.8	0.5	0.9
λ_{Zg}	S1	3.9	1.4	3.2	1.1	1.4
	S2	2.6	1.4	1.8	0.7	1.1
λ_{tg}	S1	5.8	1.2	5.0	1.8	1.9
	S2	3.5	1.2	2.5	1.3	1.6
λ_{bZ}	S1	5.2	1.7	3.4	2.6	2.3
	S2	3.4	1.7	1.7	1.7	1.7
$\lambda_{\tau Z}$	S1	2.6	1.2	1.2	1.2	1.6
	S2	1.9	1.2	0.9	0.4	1.2
$\lambda_{\mu Z}$	S1	6.6	4.7	2.2	1.1	4.0
	S2	5.0	4.7	1.1	0.4	1.2

Table 40: Projected sensitivities of the measurements of Higgs boson couplings at HE-LHC.

Coupling	S2	S2′
k_γ	1.6	1.2
k_W	1.5	1.0
k_Z	1.3	0.8
k_g	2.2	1.3
k_t	3.2	1.9
k_b	3.5	2.1
k_τ	1.7	1.1
k_μ	2.2	1.7
$k_{Z\gamma}$	6.9	4.1

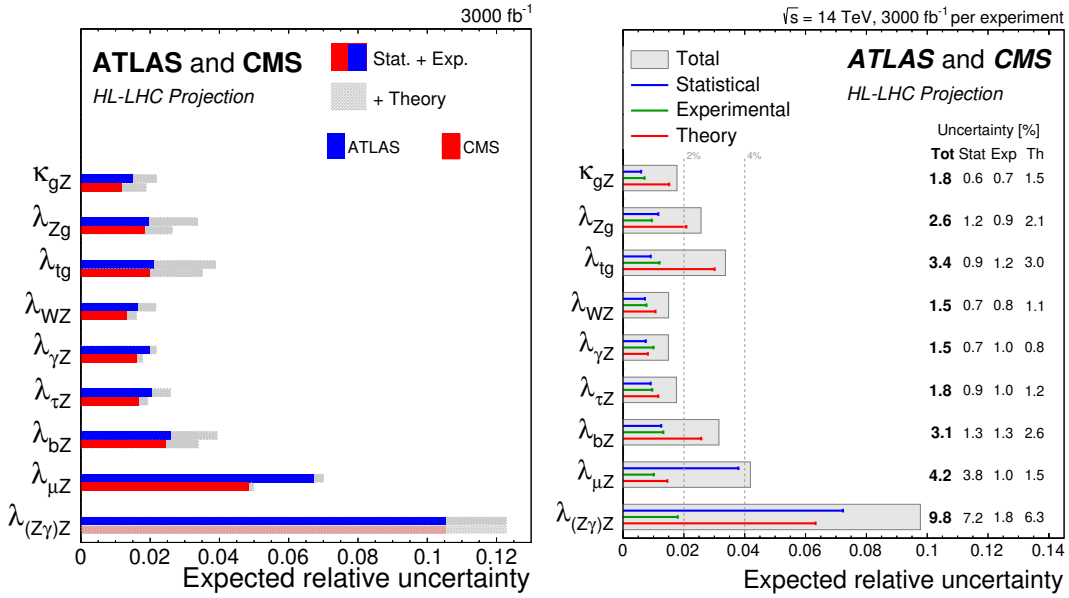

Fig. 31: (left) Summary plot showing the total expected $\pm 1\sigma$ uncertainties in S2 (with YR18 systematic uncertainties) on the ratios of coupling modifier parameters for ATLAS (blue) [126] and CMS (red) [139]. The filled coloured box corresponds to the statistical and experimental systematic uncertainties, while the hatched grey area represent the additional contribution to the total uncertainty due to theoretical systematic uncertainties. (right) Summary plot showing the total expected $\pm 1\sigma$ uncertainties in S2 (with YR18 systematic uncertainties) on the ratios of coupling modifier parameters for the combination of ATLAS and CMS extrapolations. For each measurement, the total uncertainty is indicated by a grey box while the statistical, experimental and theory uncertainties are indicated by a blue, green and red line respectively.

the unitary gauge, are [186, 187, 185]

$$\begin{aligned}\mathcal{L}_{\text{fit}} = 2c_V\left(m_W^2 W_\mu^+ W^{-\mu} + \tfrac{1}{2}m_Z^2 Z_\mu Z^\mu\right)\frac{h}{v} - \sum_\psi c_\psi m_\psi \bar{\psi}\psi\frac{h}{v} \\ + \frac{e^2}{16\pi^2}c_\gamma F_{\mu\nu}F^{\mu\nu}\frac{h}{v} + \frac{e^2}{16\pi^2}c_{Z\gamma}Z_{\mu\nu}F^{\mu\nu}\frac{h}{v} + \frac{g_s^2}{16\pi^2}c_g \text{tr}\left[G_{\mu\nu}G^{\mu\nu}\right]\frac{h}{v},\end{aligned} \tag{8}$$

where m_i is the mass of particle i, $\psi \in \{t, b, c, \tau, \mu\}$, and the c_i describe the modifications of the Higgs couplings. The previous Lagrangian differs from a naive rescaling of Higgs couplings, even though superficially it might seem to be equivalent. In particular, the Standard Model is consistently recovered in eq. (8) for

$$c_i^{\text{SM}} = \begin{cases} 1 & \text{for } i = V, t, b, c, \tau, \mu \\ 0 & \text{for } i = g, \gamma, Z\gamma. \end{cases} \tag{9}$$

This Lagrangian, taken in isolation, leads to a theory with a parametrically low cutoff: it has therefore to be thought as part of a bigger EFT: the EWChL [188, 189, 190, 191, 192, 193, 194, 195, 196, 197, 198, 199, 200, 201, 202, 203, 204, 205]. This is a bottom-up EFT, constructed with the particle content and symmetries of the SM. These are the same requirements adopted in the construction of the SMEFT. The main difference between both EFTs concerns the Higgs field. In the EWChL, the Higgs boson, h, is included as a scalar singlet, with couplings unrelated to the ones of the Goldstone bosons of electroweak symmetry breaking (EWSB). Therefore, h is not necessarily part of an SU(2) doublet and consequently (contrary to the SMEFT) the leading-order Lagrangian is already an EFT, leading potentially to $O(1)$

effects in the κs and to a potentially low cutoff. Further details and explanations are discussed in [206, 207, 208, 204, 205, 187, 209].

Focusing on the leading effects in single-Higgs processes only, the full EWChL reduces to eq. (8) which, if needed, can be extended to describe other processes: double-Higgs production from gluon fusion, for instance, would require three more operators, corresponding to the interactions $h^3, \bar{t}th^2, ggh^2$ [21 45, 211, 212] (see section 3.1.2.1). Since the observed processes are mediated by both tree level and one-loop amplitudes at the first non-vanishing order, operators of leading order in the EFT (first line of eq. (8)) and next-to-leading order in the EFT (second line of eq. (8)) have to be included [187]. Corrections beyond the leading ones, both strong and electroweak, can also be incorporated to arbitrary order in the description of Higgs processes. These corrections involve additional operators, not present in eq. (8), but contained in the EWChL.

As stated above, the couplings in eq. (8) can receive a priori large contributions and have to be considered as $\mathcal{O}(1)$ numbers. This is the expectation if new physics contains strongly-coupled new interactions at the electroweak scale. In other scenarios of compositeness, new-physics interactions can be associated with a larger scale f and progressively decoupled from the SM: it is therefore useful to understand the Wilson coefficients in eq. (8) as functions of the parameter $\xi = v^2/f^2$. The scale f could correspond, for example, to the scale of global symmetry breaking in composite Higgs models (see the discussion in sec. 2.9). The SM is then recovered for $\xi = 0$. For $\xi \ll 1$, one can perform an expansion in ξ on top of the loop expansion in the EWChL. This yields a double expansion in ξ and $1/16\pi^2$ [213], in the spirit of the strongly-interacting light Higgs (SILH) [40]. The expected size of the Wilson coefficients is then

$$c_i = c_i^{\text{SM}} + \mathcal{O}(\xi). \tag{10}$$

The mapping of the Wilson coefficients c_i to the κ_i parameters is done using the relations of the signal strengths computed from the Lagrangian in eq. (8). The necessary formulas can be found in [186, 185]. These relations can be written as

$$\kappa_i = |f_i(c_j)| \equiv \frac{|\mathcal{A}_i(c_j)|}{|\mathcal{A}_i(c_j^{\text{SM}})|}, \tag{11}$$

where $\mathcal{A}$ is the corresponding transition amplitude of each process (the absolute value on the right hand side is necessary, as the loop functions of the light fermions $(b, \tau, \mu, \dots)$ for the κ_γ, κ_g and $\kappa_{Z\gamma}$ are complex). We can obtain an approximate inverse of eq. (11), to connect both formalisms in the opposite direction, by assuming that all the imaginary parts are negligible.[25] With the assumption of vanishing imaginary parts, eq. (11) becomes

$$\begin{pmatrix} \kappa_V \\ \kappa_t \\ \kappa_b \\ \kappa_\ell \\ \kappa_g \\ \kappa_\gamma \\ \kappa_{Z\gamma} \end{pmatrix} = \begin{pmatrix} 1 & 0 & 0 & 0 & 0 & 0 & 0 \\ 0 & 1 & 0 & 0 & 0 & 0 & 0 \\ 0 & 0 & 1 & 0 & 0 & 0 & 0 \\ 0 & 0 & 0 & 1 & 0 & 0 & 0 \\ 0 & 1.055 & -0.055 & 0 & 1.389 & 0 & 0 \\ 1.261 & -0.268 & 0.004 & 0.004 & 0 & -0.304 & 0 \\ 1.059 & -0.060 & 0.001 & 6 \cdot 10^{-5} & 0 & 0 & -0.083 \end{pmatrix} \cdot \begin{pmatrix} c_V \\ c_t \\ c_b \\ c_\tau \\ c_g \\ c_\gamma \\ c_{Z\gamma} \end{pmatrix}. \tag{12}$$

These numbers also include the leading QCD corrections of the $h \to \gamma\gamma$ and $gg \to h$ amplitude. An explicit comparison of this approximation and the full formulas shows only negligible numerical

[25] This is a good approximation for some of the coefficients in $f_i(c_j)$, for example for the coefficient of c_t, or as long as the Wilson coefficients stay relatively close to the SM value. This is not the case for the coefficients of the light fermion loops, where real and imaginary parts are of similar size.

differences. The inverse of eq. (12) is

$$\begin{pmatrix} c_V \\ c_t \\ c_b \\ c_\tau \\ c_g \\ c_\gamma \\ c_{Z\gamma} \end{pmatrix} = \begin{pmatrix} 1 & 0 & 0 & 0 & 0 & 0 & 0 \\ 0 & 1 & 0 & 0 & 0 & 0 & 0 \\ 0 & 0 & 1 & 0 & 0 & 0 & 0 \\ 0 & 0 & 0 & 1 & 0 & 0 & 0 \\ 0 & -0.759 & 0.040 & 0 & 0.720 & 0 & 0 \\ 4.149 & -0.883 & 0.012 & 0.012 & 0 & -3.290 & 0 \\ 12.736 & -0.722 & 0.015 & 0.001 & 0 & 0 & -12.029 \end{pmatrix} \cdot \begin{pmatrix} \kappa_V \\ \kappa_t \\ \kappa_b \\ \kappa_\ell \\ \kappa_g \\ \kappa_\gamma \\ \kappa_{Z\gamma} \end{pmatrix} . \tag{13}$$

With these relations one can translate the results of a κ_i fit into the EWChL formalism and vice-versa.

Fit to HL/HE-LHC Higgs precision data. The fits presented in what follows have been performed using the `HEPfit` package [214, 215], and following a Bayesian statistical approach. The prior for the different model parameters both in the EFT and in the κ framework are taken as flat, centred around the SM solution, and restricting the ranges to avoid other solutions present due to the parametrisation invariances of the different formalisms. Since no direct sensitivity to the $H \to c\bar{c}$ channel is available in the HL/HE-LHC inputs used for the fits, we fix the corresponding parameters controlling the $Hc\bar{c}$ interactions to their SM values ($c_c, \kappa_c = 1$). [26]

To assess the sensitivity to deviations from the SM, we assume the future measurements are SM-like and include them in the likelihood of the fit assuming Gaussian distributions with standard deviations given by the corresponding projections for the experimental uncertainties.

The analysis of current constraints has been taken directly from [185], which is based on the experimental data from [216, 217, 218, 219, 220, 221, 222, 223, 224, 225, 226, 227, 228, 229, 230, 231, 232, 233, 234, 144, 168, 140, 166, 124, 235, 236, 237, 238, 142, 138, 128, 134, 150, 239, 130, 167, 179, 180]. For the HL-LHC fits we use the corresponding ATLAS and CMS projections presented in this document in sections 2.3 and 2.6. Since CMS does not currently have any projections for the $H \to Z\gamma$ channel, we assume measurements with the same precision as ATLAS. For the systematics and theory uncertainties we use the 2 scenarios presented in section 2.3.1: S1, for which the systematics are kept as in current values, and S2, where experimental systematics are reduced with the luminosity and theory errors are reduced. The correlations between the ATLAS and CMS sets of inputs were not available for these fits and are therefore ignored. We note that the absence of that information can result, in some cases, in somewhat optimistic bounds. This is particularly the case for those couplings whose uncertainty is dominated by theoretical errors (e.g. κ_t).

Finally, we follow the ATLAS and CMS guidelines to estimate the HE-LHC uncertainties for the different signal strengths. Starting from the HL-LHC S2 projections we define the *Base* HE-LHC scenario by scaling the statistical uncertainties according to the changes in the production cross section going from 14 TeV to 27 TeV, as well as the different luminosities (3 ab^{-1} for the HL-LHC and 15 ab^{-1} in the HE-LHC):

$$\delta_{\text{stat}}\mu_{\text{HE-LHC}} = \sqrt{\frac{\sigma^{14\text{TeV}}_{pp\to H} \times 3\,\text{ab}^{-1}}{\sigma^{27\text{TeV}}_{pp\to H} \times 15\,\text{ab}^{-1}}}\,\delta_{\text{stat}}\mu_{\text{HL-LHC}}. \tag{14}$$

Other experimental and theory uncertainties are kept as in the HL-LHC S2 case. To compare the results with those that would be possible in a scenario where better understanding of theory errors or systematics is achieved, it was suggested to use a more optimistic scenario where such uncertainties are further reduced by a factor of 2. We also include this optimistic scenario in our fits, and we denote it by *"Opt."*. One should note, however, that such a scenario does not come from a systematic extrapolation of the possible reduction of uncertainties. It is only an educated guess for illustration purposes.

[26] See [185] for a discussion of the multiplicities of the different solutions in the fit as well as the effect of letting the charm coupling float in the fits in absence of a significant direct constraint.

In Table 41 we show the results of the fit for the different scenarios discussed above for the EWChL. The numbers for the HL-LHC and the HE-LHC are reported independently (i.e. the HE-LHC does not includes the HL-LHC results on the Higgs couplings). These results are also shown in Figure 32. The analogous results for the fit using the κ formalism are presented in Table 42 and Figure 33. In order to put both approaches on an equal theoretical footing, in the κ fit we assumed custodial symmetry as well as the absence of extra exotic decays of the Higgs. As expected from the discussion above, the results show an excellent agreement between the c_i and κ_i fits for most of the parameters. The exceptions are the parameters entering in loop-induced processes, $c_{g,\gamma,Z\gamma}$ and $\kappa_{g,\gamma,Z\gamma}$, whose interpretation differs in the two formalisms. In particular, the interplay between $c_{\gamma,Z\gamma}$ and the couplings modifying the SM loops results in a significant difference between the $c_{\gamma,Z\gamma}$ results and the ones for $\kappa_{\gamma,Z\gamma}$.

Focusing our attention on the HL-LHC results, we observe that, even in the conservative S1 scenario, the knowledge of the different EFT parameters, c_i, and Higgs-couplings modifiers, κ_i, will improve by at least a factor of 2-3 with respect to current experimental limits. The improvement is more marked for channels that benefit from very high statistics, such as $H \to \mu^+\mu^-$, with a precision ~ 7 times better than in the current fit, and $H \to Z\gamma$ where current data does not allow to set any meaningful bound on $c_{Z\gamma}$, $\kappa_{Z\gamma}$. Further progress is expected at the HE-LHC where, for instance, we foresee 1% level determinations for the Higgs couplings to vector bosons and τ leptons. As one can see by comparing the HL-LHC S2 and HE-LHC Base scenarios, the precision of the interactions associated with the main Higgs couplings will be controlled, to a large extent, by systematic and theory errors.

One must be careful with the interpretation of these results, though. These projections implicitly assume that departures from the SM appear only as modifications in the Higgs couplings or, in other words, that any other interaction entering the relevant Higgs processes is exactly SM-like. However, at the level of precision we observe in the results, close to the 1%, this may not be a justified assumption given current bounds on other electroweak interactions that could modify, e.g. VBF or VH associated production. This comment applies even more to the HE-LHC uncertainties obtained assuming the reduced theory and systematic uncertainties which, in particular, predict a sub-percent precision for the Higgs coupling to vector bosons. We believe this to be too aggressive. A more realistic assessment of the HE-LHC uncertainties would require an equally realistic study of the experimental precision at that machine, as well as the results of a full global fit combining Higgs data with other relevant observables of the EW sector. We refer to section 8 for more details in this regard (in the context of the SMEFT).

Table 41: Comparison of the current and HL/HE-LHC 68% probability sensitivities to the c_i coefficients, as shown in Figure 32.

	Current limits [185]	HL-LHC S1	HL-LHC S2	HE-LHC (Base)	HE-LHC (Opt.)
c_V	1.01 ± 0.06	± 0.017	± 0.011	± 0.009	± 0.005
c_t	$1.04^{+0.09}_{-0.1}$	± 0.040	± 0.025	± 0.020	± 0.010
c_b	0.95 ± 0.13	± 0.042	± 0.028	± 0.023	± 0.012
c_τ	1.02 ± 0.1	± 0.023	± 0.017	± 0.012	± 0.007
c_μ	$0.58^{+0.4}_{-0.38}$	± 0.053	± 0.042	± 0.019	± 0.013
c_g	$-0.01^{+0.08}_{-0.07}$	± 0.032	± 0.020	± 0.016	± 0.008
c_γ	0.05 ± 0.2	± 0.066	± 0.045	± 0.033	± 0.019
$c_{Z\gamma}$	–	± 1.061	± 1.048	± 0.45	± 0.314

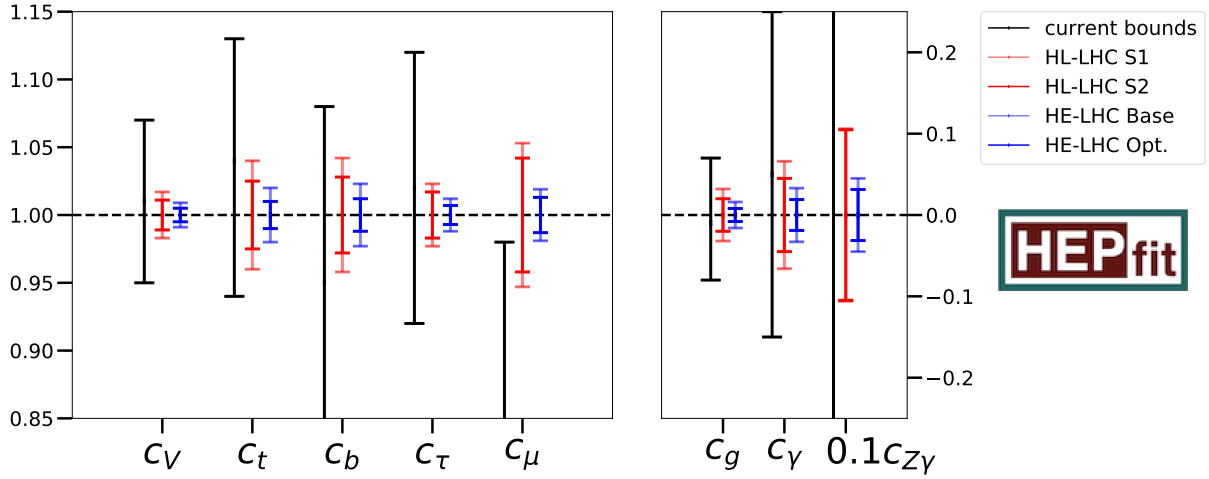

Fig. 32: Current and HL/HE-LHC constraints on c_i. The left line of each coupling is the current bound, from Ref. [185]. The central line is the projection to the HL-LHC, with the S1 scenario in light red and S2 in dark red. The right line is the projection to HE-LHC, with the base scenario in light blue and the optimistic one in dark blue.

Table 42: Comparison of the current and HL/HE-LHC 68% probability sensitivities to the SM Higgs-coupling modifiers κ_i, as shown in Figure 33.

	Current limits [185]	HL-LHC S1	HL-LHC S2	HE-LHC (Base)	HE-LHC (Opt.)
κ_V	1.01 ± 0.06	± 0.017	± 0.011	± 0.009	± 0.005
κ_t	$1.04^{+0.09}_{-0.1}$	± 0.040	± 0.025	± 0.020	± 0.010
κ_b	0.94 ± 0.13	± 0.042	± 0.028	± 0.023	± 0.012
κ_τ	1.0 ± 0.1	± 0.023	± 0.017	± 0.012	± 0.007
κ_μ	$0.58^{+0.4}_{-0.38}$	± 0.053	± 0.042	± 0.019	± 0.013
κ_g	$1.02^{+0.08}_{-0.07}$	± 0.027	± 0.018	± 0.015	± 0.008
κ_γ	0.97 ± 0.07	± 0.023	± 0.016	± 0.012	± 0.007
$\kappa_{Z\gamma}$	–	± 0.094	± 0.093	± 0.040	± 0.028

2.9 Interpretation of the Higgs couplings in terms of Composite Higgs models[27]

Composite Higgs (CH) models postulate that the Standard SM Higgs sector is UV-completed by a strongly-coupled dynamics characterised by some scale m_*, not too far above the TeV. Since, by analogy with QCD, m_* can naturally be small compared to any existing microscopic scale, this framework provides an attractive solution to the hierarchy problem.

Historically, precision *indirect* tests, mainly from EW data, have resulted in important constraints on strongly-coupled extensions of the SM. The discovery of the Higgs boson has removed the uncertainty associated to the value of m_h but otherwise has not improved those bounds qualitatively. On the other hand, *direct* access to the Higgs boson properties has had a qualitative impact on CH scenarios: we now know that viable realizations must contain a light scalar resonance h with properties that mimic those of the SM Higgs boson. This observation excludes Higgless solutions to the hierarchy problem (like old-fashioned technicolor), but leaves open a number of options, a representative set of which will be discussed here. Overall, CH scenarios with a Higgs-like resonance continue to offer a very compelling explanation of the weak scale.

[27] Contact: L. Vecchi

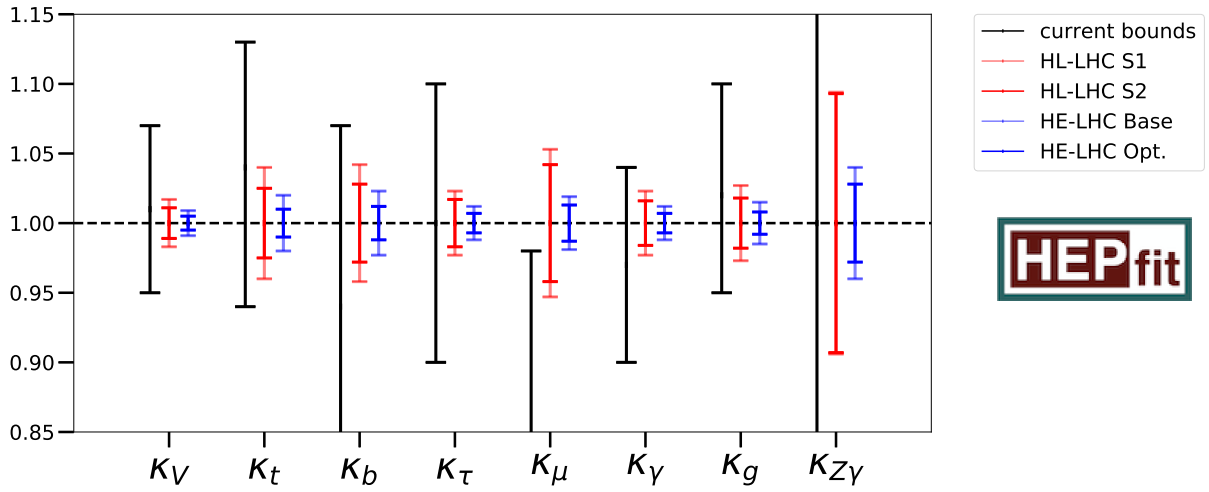

Fig. 33: Current and future constraints on κ_i. The left line of each κ is the current bound, from Ref. [185]. The central line is the projection to the HL-LHC, with the S1 scenario in light red and S2 in dark red. The right line is the projection to HE-LHC, with the base scenario in light blue and the optimistic one in dark blue.

In this section we will focus on two representative classes of CH scenarios that predict a light scalar with SM-like couplings:

1) the Strongly-Interacting Light Higgs (SILH). In this class the exotic strong dynamics generates a light scalar doublet H with the same $SU(2)_w \times U(1)_Y$ charges of the SM Higgs, and it is the latter which spontaneously breaks the EW symmetry [240, 241]. The doublet H may be part of a Nambu-Goldstone multiplet, or simply be an accidentally light scalar. The physical Higgs boson h belonging to the composite doublet behaves as the SM Higgs boson up to corrections induced by higher-dimensional operators suppressed by the strong coupling scale m_*.
2) the Strongly-Interacting Light Dilaton (SILD). In this class of theories the strong dynamics is assumed to feature the spontaneous breaking of an approximate scale invariance at a scale f_D. In such a framework the low energy EFT possesses an approximate Nambu-Goldstone mode, the dilaton, which automatically has couplings aligned along the direction of those of the SM Higgs [242]. The key difference compared to the SILH is that this is a non-decoupling scenario, in which the new physics threshold is controlled by the EW scale. We interpret the SILD as a representative of CH scenarios based on the EW chiral Lagrangian, in which the EW symmetry is non-linearly realised and the Higgs-like particle h is not embedded in an EW doublet H.

The main goal of this section is to review what we can learn about the CH picture from the investigation of the Higgs properties at the HL and HE-LHC. We will focus on modifications of the on-shell couplings, as opposed to off-shell rates like double-Higgs production or $VV \to VV$ scattering. Of course, more direct ways to test the CH hypothesis include the observation of new resonances. Here we however assume that the new resonances are too heavy to be directly accessible and focus on the low energy EFT for the light state h.

The SILH

The operators that dominantly impact on-shell processes involving h are collected in table 43 under the assumption that H is an EW doublet. We do not include operators of higher dimension and those that are severely constrained by precision data, which for this reason are expected to lead to negligible corrections

Table 43: List of the dimension-6 operators relevant to our study of modified Higgs couplings in the SILH class. We use the basis of [40]. Here y_ψ are the SM Yukawa couplings and $V = Z, W$.

Operator name	Operator definition	Main on-shell process
$\mathcal{O}_H$	$\frac{1}{2}\,\partial_\mu(H^\dagger H)\partial^\mu(H^\dagger H)$	$h \to \psi\bar{\psi}, VV^*$
$\mathcal{O}_6$	$\lambda_h(H^\dagger H)^3$	$h^* \leftrightarrow hh$
$\mathcal{O}_y$	$\sum_{\psi=u,d,e} y_\psi\ \bar{\psi}_L H\psi_R(H^\dagger H)$	$h \to \psi\bar{\psi}$
$\mathcal{O}_{HW}$	$ig(D^\mu H)^\dagger\sigma^i(D^\nu H)W^i_{\mu\nu}$	$h \to VV^*, \gamma Z$
$\mathcal{O}_{HB}$	$ig'(D^\mu H)^\dagger(D^\nu H)B_{\mu\nu}$	$h \to ZZ^*, \gamma Z$
$\mathcal{O}_g$	$g_s^2 H^\dagger H G^a_{\mu\nu}G^{a\mu\nu}$	$h \to gg$
$\mathcal{O}_\gamma$	$g'^2 H^\dagger H B_{\mu\nu}B^{\mu\nu}$	$h \to \gamma\gamma, \gamma Z, ZZ$

to the rates induced by those in the table. [28] In particular, in realistic SILH scenarios the Higgs coupling to fermions must be aligned to the SM Yukawas. For illustrative purposes, here we further simplify our discussion specialising on realisations in which the SM fermions are all coupled analogously to the strong sector, such that a universal fermionic operator $\mathcal{O}_y$ is sufficient. (We will comment below on more general scenarios.)

The observables that are mostly affected by the new interactions are shown in the third column of table 43. An estimate of the various Wilson coefficients in concrete CH models reveals that corrections to $h \to WW^*, ZZ, \psi\bar{\psi}$ are typically dominated by $\mathcal{O}_{H,y}$ [40]. Those to the radiative processes $h \to gg, \gamma\gamma$ are controlled by 1-loop diagrams with an insertion of $\mathcal{O}_{H,y}$ if the doublet H is a Nambu-Goldstone mode of the strong dynamics, but may also receive important contributions from $\mathcal{O}_{g,\gamma}$ if H is an accidentally light resonance. For what concerns $h \to \gamma Z$ we find that $\mathcal{O}_{H,y}$ give contributions parametrically comparable to $\mathcal{O}_{HW,HB}$. The same is true for $\mathcal{O}_\gamma$, but only when H is not a Nambu-Goldstone mode. Because the sensitivity on $h \to \gamma Z$ is appreciably weaker than $h \to \gamma\gamma$, it makes sense to simplify our discussion by neglecting the impact of $\mathcal{O}_{HW,HB}$ in our fit. Similarly, we will ignore $\mathcal{O}_6$ since this operator only controls the very poorly known Higgs self-couplings.

From these considerations follows that the leading on-shell signatures of the Higgs-like state h in SILH scenarios can be characterised by the reduced set of operators

$$\delta\mathcal{L}_{\rm SILH} = \frac{g_*^2}{m_*^2}\bar{c}_H\mathcal{O}_H + \frac{g_*^2}{m_*^2}\bar{c}_y\mathcal{O}_y + \frac{g_*^2}{16\pi^2 m_*^2}\bar{c}_g\mathcal{O}_g + \frac{g_*^2}{16\pi^2 m_*^2}\bar{c}_\gamma\mathcal{O}_\gamma, \tag{15}$$

where $\bar{c}_{H,y,g,\gamma}$ are expected to be of order unity and g_*, m_* are the typical couplings and mass scale of the new physics. We included a factor of $g_*^2/16\pi^2$ in front of the last two operators in order to emphasise their radiative nature [40]. We further assumed CP is approximately satisfied by the strong sector.

We can now match the Wilson coefficients appearing in (15) onto the phenomenological Lagrangian (8) for the light boson h, up to additional interactions that are irrelevant to the present analysis. The resulting modified Higgs couplings are collected here:

$$c_V = 1 - \frac{\bar{c}_H}{2}\xi, \quad c_y = 1 - \left(\frac{\bar{c}_H}{2} + \bar{c}_y\right)\xi, \quad c_g = 2\bar{c}_g\xi, \quad c_\gamma = \bar{c}_\gamma\xi \tag{16}$$

[28] These include $\mathcal{O}_T = (H^\dagger \overleftrightarrow{D_\mu} H)(H^\dagger \overleftrightarrow{D^\mu} H)/2$, $\mathcal{O}_W = ig(H^\dagger\sigma^i \overleftrightarrow{D_\mu} H)(D_\nu W^{\mu\nu})^i/2$, $\mathcal{O}_B = ig'(H^\dagger \overleftrightarrow{D_\mu} H)(\partial_\nu B^{\mu\nu})/2$, current-current interactions $H^\dagger \overleftrightarrow{D_\mu} H\bar{\psi}\gamma^\mu\psi$ and $H^\dagger\tau^a \overleftrightarrow{D_\mu} H\bar{\psi}\gamma^\mu\tau^a\psi$ containing non-universal couplings to the SM fermions ψ, and dipole operators. The operator $\mathcal{O}_T$ is constrained by the EW ρ parameter; whereas $\mathcal{O}_W + \mathcal{O}_B$ by the EW S parameter. Current-current operators are constrained by LEP and the non-observation of rare flavor-violating processes. Dipole operators are severely constrained by measurements of electric and magnetic moments. See, e.g., [243] for more details.

Table 44: Projected HL/HE sensitivity (95% CL) on the SILH parameter $\xi = v^2/f^2$ (and on f in TeV) in our benchmark scenarios. Systematic uncertainties are treated according to the conservative scenario S1.

	$\bar{c}_H$	$\bar{c}_y$	$\lvert\bar{c}_g\rvert$	$\lvert\bar{c}_\gamma\rvert$	expected LHC14		HL-LHC		HE-LHC	
					ξ	f [TeV]	ξ	f [TeV]	ξ	f [TeV]
SILH1a	1	0	0	0	0.094	0.80	0.045	1.2	0.022	1.7
SILH1b	1	1	0	0	0.064	0.97	0.021	1.7	0.011	2.3
SILH2a	1	0	1	1	0.019	1.8	0.012	2.3	0.0062	3.1
SILH2b	1	1	1	1	0.018	1.8	0.0096	2.5	0.0050	3.5

where we defined

$$\xi \equiv \frac{g_*^2 v^2}{m_*^2} \equiv \frac{v^2}{f^2}, \tag{17}$$

with $v = 246$ GeV. Note that our assumption of SM fermion-universality implies that c_y is a single real number (independent of $\psi = u, d, e$). This leaves us with a total of 4 independent parameters (16). Our truncation of the EFT to dimension 6 operators is crucially associated to the working hypothesis $\xi \ll 1$: operators of higher dimension are suppressed by larger powers of ξ.

2.9.0.1 Analysis

The expected reach of the HL (3 ab^{-1}) and HE (15 ab^{-1}) LHC on the modified Higgs couplings has been presented in Section 2.8. Here we specialise to scenarios defined by the 4 couplings $c_{V,y,g,\gamma}$.

To better quantify the sensitivity of the future LHC upgrades on CH models we identify the benchmark scenarios shown in table 44. SILH1 is intended to capture the low energy physics of CH models with a Nambu-Goldstone boson H, where couplings to the massless gauge bosons are suppressed [40]. SILH2 is expected to mimic scenarios with an accidentally light CH doublet, since in that case one typically expects $|\bar{c}_{g,\gamma}|$ of order unity. To assess the impact of the fermionic coupling $\bar{c}_y$ we distinguished between scenarios with $\bar{c}_y = 0$ (a) and $\bar{c}_y = 1$ (b); models in which the SM fermions have different couplings for the various SM representations $\psi = u, d, e$ should lie somewhat in between these two.

In table 44 we present, for each benchmark model, the expected HL/HE sensitivity. We treat the systematic uncertainties using the conservative hypothesis S1. Note the significant impact of a non-vanishing $\bar{c}_{g,\gamma}$ — especially the coupling to gluons; of the four options with $\bar{c}_{g,\gamma} = \pm 1$ we quote only the most stringent bound for brevity. Making a fair comparison between present LHC data and our projections is not possible because current data slightly favours values $\bar{c}_{V,y} > 1$, a fact that in some benchmark models results in stronger constraints than our projections (even when restricting our fit to the domain $0 < \xi < 1$). Perhaps a more significant measure of the improvement of the HL/HE-LHC can be obtained if we artificially assume the currently preferred central values are $c_V = c_y = 1, c_g = c_\gamma = 0$, as in our projections. This way we obtain the 95% CL *expected limits* shown in table 44.

Recalling our definition (17) we can translate the results of table 44 into a lower bound on the new physics scale m_* as a function of the size of the typical coupling g_* of the exotic sector. The result is shown in Fig 34. For presentation purposes, in the figure we only show the reach of the HL-LHC and HE-LHC on the benchmark models SILH1b (black) and SILH2b (red). The constrained region lies on the left of each line. The bounds tend to push the CH scenario towards the SM limit $\xi \to 0$, obtained decoupling the new physics scale. We see that in the case the exotic dynamics is maximally strongly coupled ($g_* \sim 4\pi$) the LHC will be able to indirectly access mass scales of order $20 - 30$ TeV.

In Fig 34 we also include (blue dashed and dot-dashed lines) the current 95% CL limits derived

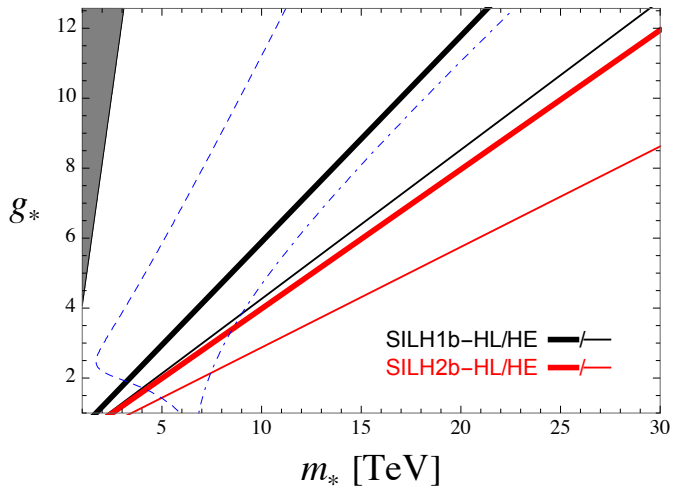

Fig. 34: The constraints of table 44 are interpreted as lower bounds on the new physics scale m_* for a given coupling g_* of the strong dynamics, see (17). The blue lines define lower bounds on m_* from current EW precision tests for two different assumptions on the UV dynamics (see text). The grey region identifies the unphysical regime $\xi > 1$.

from precision EW data [244] and encoded in the oblique parameters (with $U = 0$)

$$\widehat{S} = (1 - c_V^2)\frac{g^2}{96\pi^2}\ln\frac{m_*}{m_Z} + \widehat{S}_{\rm UV} \qquad (18)$$
$$\widehat{T} = -(1 - c_V^2)\frac{3g'^2}{32\pi^2}\ln\frac{m_*}{m_Z} + \widehat{T}_{\rm UV}.$$

Note that these include 1-loop effects within (8) as well as contributions from heavy particles of mass $\sim m_*$ that we parametrised via $\widehat{S}_{\rm UV} = m_W^2/m_*^2$ and $\widehat{T}_{\rm UV}$. The blue dot-dashed line refers to scenarios in which additional violations of custodial symmetry are negligible, $\widehat{T}_{\rm UV} = 0$, whereas the blue dashed line to the more natural expectation $\widehat{T}_{\rm UV} = \xi 3y_t^2/(16\pi^2)$. Precision EW data already exclude a sizeable portion of parameter space. However, as our plot clearly illustrates, these *indirect* bounds significantly depend on unknown physics at the cutoff scale m_*. Hence, a *direct* probe of the Higgs couplings provides a more robust and model-independent assessment of a given CH scenario.

The SILD

The dominant interactions of the dilaton (still denoted by h) to the SM are derived from an EFT with non-linearly realised EW symmetry, where the Nambu-Goldstone bosons eaten by the $W^\pm, Z^0$ are encapsulated into the unitary matrix Σ, which transforms as $\Sigma \to U_w \Sigma U_Y^\dagger$ under $SU(2)_w \times U(1)_Y$. The powers of the singlet h are fully determined by the approximate conformal symmetry. Neglecting possible (small) sources of custodial symmetry breaking, one identifies the dominant interactions: [242]

$$\begin{aligned}\mathcal{L}_{\rm SILD} &= \frac{v^2}{4}{\rm tr}[D_\mu\Sigma^\dagger D^\mu\Sigma]\left(1+\frac{h}{f_D}\right)^2 - \sum_{\psi=u,d,l} m_\psi \bar\psi_L \Sigma \psi_R \left(1+\frac{h}{f_D}\right)^{1+\gamma_\psi} \qquad (19)\\ &+ \frac{g_s^2}{16\pi^2}\delta_s G^a_{\mu\nu}G^{a\mu\nu}\frac{h}{f_D} + \frac{e^2}{16\pi^2}\delta_e\gamma_{\mu\nu}\gamma^{\mu\nu}\frac{h}{f_D}\\ &+ \cdots,\end{aligned}$$

where the dots refer to operators that impact negligibly our analysis. In the unitary gauge, the first operator in (19) describes the main coupling between h and the EW vector bosons. The couplings to

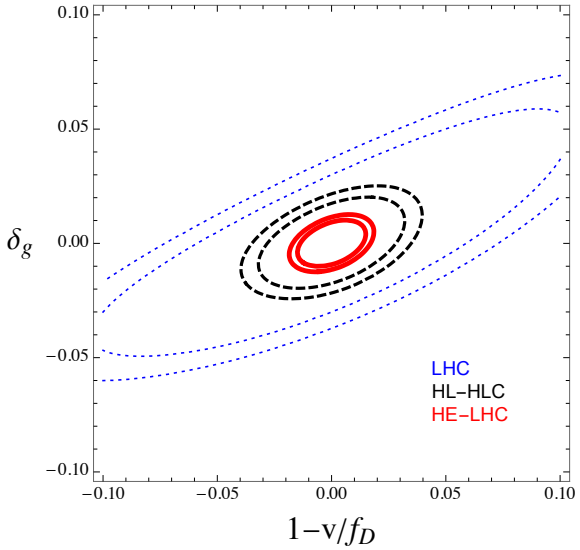

Fig. 35: Expected sensitivity at the $95\%, 99\%$ CL of the LHC (blue dotted), HL-LHC (black dashed) and HE-LHC (red solid) on SILD scenarios. For definiteness we set $\delta_\gamma = \gamma_y = 0$.

fermions depend on how the latter interact with the underlying (approximately) conformal dynamics and are therefore model-dependent. A family-universal interaction in (19) is expected in any UV theory that does not suffer from sizeable flavor-changing effects, which would otherwise be in tension with precision flavor observables. Interactions with the unbroken gauge bosons in the second line of (19) also depend on the details of the UV dynamics. We do not make any restrictive assumption here (besides an approximate CP symmetry) and instead allow the parameters $\delta_{g,\gamma}$ to acquire any real value. We however included a loop factor to emphasise we expect them to arise at the loop level. Similarly to what we have already stressed above (15), novel corrections to γZ are not important to our analysis and can be ignored in a first assessment: the Lagrangian (19) is enough to capture the dominant on-shell signatures of the SILD scenario as well. From (35) one obtains a Lagrangian like (8) with

$$c_V = \frac{v}{f_D}, \quad c_y = (1+\gamma_y)\frac{v}{f_D}, \quad c_g = 2\delta_g \frac{v}{f_D}, \quad c_\gamma = \delta_\gamma \frac{v}{f_D}. \tag{20}$$

Under the simplifying assumption of flavor universality ($\gamma_{u,d,e} = \gamma_y$) our EFT contains only 4 independent real parameters.

We are now able to draw a few conclusions. First, as anticipated, experimental constraints on c_V force $f_D \simeq v$, see Fig. 35. Therefore the SILD, as any other framework based on the non-linear chiral Lagrangian (i.e. where h is not part of a Higgs doublet), implies the characteristic mass of the new physics lies at the relatively low scale $g_* v \lesssim 4\pi v \sim 3$ TeV. On the one hand this is an exciting possibility because it suggests its UV completion is more likely to be accessible at the LHC. On the other hand, a strong dynamics at such low scales contributing to EW symmetry breaking is in serious tension with EW precision data (e.g. $\widehat{S}_{\rm UV} \sim m_W^2/m_*^2 \sim g^2/(16\pi^2)$ is typically too large as in technicolor). One can only hope the UV theory somehow cures this problem, though no concrete mechanism to achieve this is known.

Secondly, explicit realisations of the SILD are characterised by sizeable couplings to the massless gauge bosons, $|\delta_{g,\gamma}| = \mathcal{O}(1)$, and this appears to be in conflict with data. For example, the prototypical SILD scenario — in which the entire SM is part of the conformal sector — has $\delta_g = +46/3, \delta_\gamma = -34/9$ [242] and is already excluded with large confidence. Scenarios with partially composite SM, $|\delta_{g,\gamma}| \sim 0.1$, will be subject to the significant constraints from the HL and HE upgrades, see Fig. 35. Unfortunately, even in this case there is no known symmetry argument that may be invoked to ensure

$|\delta_{g,\gamma}| \ll 1$. The only way to accommodate such a constraint within explicit strongly-coupled models seems to be via fine tuning.

Overall, the SILD scenario — and all scenarios based on a non-linear realisation of the EW symmetry — suffers from a major drawback compared to the SILH: the SM is recovered by *tuning* several (often uncorrelated) parameters. This is because the former do not possess a simple decoupling mechanism (analogous to the $\xi \to 0$ limit in the SILH) that switches off the new physics corrections to precision data as well as $c_{V,y,g,\gamma}$. The *simultaneous* non-observation of new physics at the TeV scale and of deviations from the SM in the future LHC upgrades would then unambiguously prove that the Higgs boson must be the missing component of the doublet responsible for EW symmetry breaking. In such a situation the only compelling realisation of the CH paradigm is represented by the SILH class.

2.10 Probing of anomalous HVV interactions

2.10.1 Probes using differential distributions of CP sensitive observables[29]

We present prospects for studies on *CP*-odd couplings in the interactions of the Higgs boson with the electroweak gauge bosons as well as in the Yukawa couplings of the Higgs boson with fermions, in particular with $\tau^+\tau^-$ pairs.

2.10.1.1 CP-odd VVH couplings

While a large number of studies assessing the impact of *CP*-even effective operators on Higgs physics is available in the literature (see for instance our analysis in Ref. [245] and the references therein), the present analysis is focused on the impact of *CP*-odd effective operators on the interactions among the Higgs boson and the electroweak bosons. In the Higgs basis, the CP-violating (CPV) sector of the BSM Lagrangian affecting VVH couplings is given by,

$$\mathcal{L}_{\rm CPV} = \frac{H}{v}\left[\tilde{c}_{\gamma\gamma}\frac{e^2}{4}A_{\mu\nu}\tilde{A}^{\mu\nu} + \tilde{c}_{Z\gamma}\frac{e\sqrt{g_1^2+g_2^2}}{2}Z_{\mu\nu}\tilde{A}^{\mu\nu} + \tilde{c}_{ZZ}\frac{g_1^2+g_2^2}{4}Z_{\mu\nu}\tilde{Z}^{\mu\nu} + \tilde{c}_{WW}\frac{g_2^2}{2}W^+_{\mu\nu}\tilde{W}^{-\mu\nu}\right] \quad (21)$$

where, g_1 and g_2 are the $U(1)_Y$ and $SU(2)_L$ gauge coupling constants. Out of the above four parameters, only three are independent. In particular,

$$\tilde{c}_{WW} = \tilde{c}_{ZZ} + 2s^2_\theta\tilde{c}_{Z\gamma} + s^4_\theta\tilde{c}_{\gamma\gamma}. \quad (22)$$

The processes which are sensitive to CP-odd operators are the Higgstrahlung processes (WH and ZH), the vector boson fusion (VBF) and the Higgs decay into four charged leptons ($H \to 4\ell$). Here we focus on angular observables which are sensitive to CPV effects. Indeed, since the total cross-section is a CP-even quantity, the $1/\Lambda^2$ effects of CPV operators can affect the shape of some specific kinematic distributions only.

2.10.1.2 Global Fit

To study the sensitivity on CP-violating parameters $\tilde{c}_{Z\gamma}$ and $\tilde{c}_{ZZ}$ at HL and HE-LHC, we perform a χ^2 fit using, as observable, the signal strength ($\mu_{i,f}$) in the Higgs production channel (i) and Higgs decay channel (f). We can build a χ^2 as follows:

$$\chi^2(\tilde{c}_{Z\gamma}, \tilde{c}_{ZZ}) = \sum_{i,f}\frac{(\mu_{i,f} - \mu^{\rm obs.}_{i,f})^2}{\Delta^2_{i,f}} \quad (23)$$

[29] Contacts: S. Boselli, C. M. Carloni Calame, G. Montagna, O. Nicrosini, F. Piccinini, A. Shivaji, F. Yu, M. M. Llacer

Table 45: Estimated uncertainties [%] on the determination of single-Higgs production channels in $H \to 4\ell$ decay mode. These are CMS projections for high-luminosity LHC (14 TeV centre of mass energy and 3 ab^{-1} integrated luminosity) in scenario S1 (systematic uncertainties are kept constant with luminosity) taken from Ref. [139].

Process		Combination	Statistical	Theory (Sig.)	Theory (Bkg.)	Experimental
$H \to ZZ$	ggF	6.6	2.1	5.4	1.7	2.7
	VBF	15.2	11.7	9.1	2.4	1.8
	WH	48.0	46.5	6.2	2.8	7.8
	ZH	82.5	75.7	27.0	7.6	16.4
	$t\bar{t}H$	26.9	23.6	10.9	2.5	4.2

The signal strength, $\mu_{i,f}$ is a function of the BSM parameters and it is defined as,

$$\mu_{i,f} = \mu_i \times \mu_f \tag{24}$$

$$= \frac{\sigma_i^{\rm BSM}}{\sigma_i^{\rm SM}} \times \frac{{\rm BR}_f^{\rm BSM}}{{\rm BR}_f^{\rm SM}}. \tag{25}$$

The total uncertainty, $\Delta^2_{i,f}$ includes theoretical, experimental systematic and statistical uncertainties, which are added in quadrature. The one-sigma uncertainties for the high-luminosity (14 TeV centre of mass energy and 3 ab^{-1} integrated luminosity) are given in table 45. Assuming the same acceptance efficiency, we scale the statistical uncertainties at 14 TeV and 3 ab^{-1} luminosity appropriately to obtain the statistical uncertainties at 27 TeV and 15 ab^{-1} luminosity. The theoretical and experimental systematic uncertainties are kept unchanged.

When considering kinematic distributions in the fit, we estimate the statistical uncertainty in each bin by scaling the overall statistical uncertainty by the fraction of number of events in each bin. On the other hand, the theoretical and systematic uncertainties are assumed to be the same in all the bins implying a very conservative scenario.

Since we are interested in the sensitivity on the CPV parameters that can be reached at HL and HE LHC, due to the present lack of experimental data, we take $\mu_{i,f}^{\rm obs.} = 1$, implying that the future data would be consistent with the SM hypothesis. In the current analysis, we consider all the single Higgs production channels and Higgs decaying to four charged-leptons, *i.e* $i = {\rm ggF}, {\rm VBF}, ZH, WH, t\bar{t}H$ and $f = 4\ell(2e2\mu, 4e, 4\mu)$. The projected uncertainties in these channels for HL-LHC are given in table 45. All the results in the following sections are presented taking M_H =125 GeV.

Production signal strengths : Inclusive

The first step is to calculate the signal strengths for the relevant production channels in presence of the CP-violating parameters $\tilde{c}_{Z\gamma}$ and $\tilde{c}_{ZZ}$. We use `Madgraph5_aMC@NLO` [79] to obtain the inclusive cross sections in presence of these parameters. We have generated the required UFO model file for `Madgraph` using the `FeynRules` package [246, 247]. At 14 TeV, the production signal strengths are given by,

$$\mu_{ZH}^{\rm 14TeV} = 1.00 + 0.54\,\tilde{c}_{Z\gamma}^2 + 2.80\,\tilde{c}_{ZZ}^2 + 0.95\,\tilde{c}_{Z\gamma}\tilde{c}_{ZZ} \tag{26}$$

$$\mu_{WH}^{\rm 14TeV} = 1.00 + 0.84\,\tilde{c}_{Z\gamma}^2 + 3.87\,\tilde{c}_{ZZ}^2 + 3.63\,\tilde{c}_{Z\gamma}\tilde{c}_{ZZ} \tag{27}$$

$$\mu_{\rm VBF}^{\rm 14TeV} = 1.00 + 0.25\,\tilde{c}_{Z\gamma}^2 + 0.45\,\tilde{c}_{ZZ}^2 + 0.45\,\tilde{c}_{Z\gamma}\tilde{c}_{ZZ} \tag{28}$$

At 27 TeV, the corresponding signal strengths are given by,

$$\mu_{ZH}^{27\text{TeV}} = 1.00 + 0.63\,\tilde{c}_{Z\gamma}^2 + 3.26\,\tilde{c}_{ZZ}^2 + 1.11\,\tilde{c}_{Z\gamma}\tilde{c}_{ZZ} \quad (29)$$

$$\mu_{WH}^{27\text{TeV}} = 1.00 + 0.98\,\tilde{c}_{Z\gamma}^2 + 4.48\,\tilde{c}_{ZZ}^2 + 4.16\,\tilde{c}_{Z\gamma}\tilde{c}_{ZZ} \quad (30)$$

$$\mu_{\text{VBF}}^{27\text{TeV}} = 1.00 + 0.32\,\tilde{c}_{Z\gamma}^2 + 0.67\,\tilde{c}_{ZZ}^2 + 0.65\,\tilde{c}_{Z\gamma}\tilde{c}_{ZZ} \quad (31)$$

The BSM predictions for VBF are derived using following cuts,

$$p_T(j) > 20\text{ GeV}, |\eta(j)| < 5, \Delta\eta_{jj} > 3, m_{jj} > 130\text{ GeV}.$$

We find that the VH production modes are more sensitive to $\tilde{c}_{ZZ}$ parameters. The ggF and $t\bar{t}H$ production channels are unaffected in presence of CP-violating VVH couplings. Therefore,

$$\mu_{\text{ggF}}^{14\text{TeV}} = \mu_{\text{ggF}}^{27\text{TeV}} = 1.00 \quad (32)$$

$$\mu_{t\bar{t}H}^{14\text{TeV}} = \mu_{t\bar{t}H}^{27\text{TeV}} = 1.00. \quad (33)$$

In the present analysis we consider only kinematic distributions of the Higgs decay products, in the Higgs rest frame.

Decay signal strength : Inclusive

Now we turn to the calculation of the signal strength for the decay channel $H \to 4\ell$. This decay channel receives contributions from $2e^+2e^-$ $(4e)$, $2\mu^+2\mu^-$ (4μ) and $e^+e^-\mu^+\mu^-$ $(2e2\mu)$ final states. We use the latest version of the `Hto4l` event generator [245] to obtain the partial decay widths in these channels in presence of $\tilde{c}_{Z\gamma}$ and $\tilde{c}_{ZZ}$. Both the e and μ are treated as massless. The ratio of the partial decay widths in BSM and in SM (R_Γ) for different channels are given by,

$$R_\Gamma(H \to 2e2\mu) = 1 + 1.174\,\tilde{c}_{Z\gamma}^2 + 0.00291\,\tilde{c}_{ZZ}^2 + (-0.00762)\,\tilde{c}_{Z\gamma}\tilde{c}_{ZZ} \quad (34)$$

$$R_\Gamma(H \to 4e) = R_\Gamma(H \to 4\mu) = 1 + 1.106\,\tilde{c}_{Z\gamma}^2 + 0.00241\,\tilde{c}_{ZZ}^2 + (-0.00595)\,\tilde{c}_{Z\gamma}\tilde{c}_{ZZ}. \quad (35)$$

The above expression for Higgs decay into $2e2\mu$ and $4e$ are obtained after applying a selection cut of 4 GeV on the leading and sub-leading lepton pairs of opposite sign.

In the present analysis, we also assume that the total Higgs decay width remains unchanged in presence of BSM. In this case, the signal strength for decay is just the ratio of decay widths in BSM and in SM, that is,

$$\mu_{4\ell} = \frac{\Gamma_{4\ell}^{\text{BSM}}}{\Gamma_{4\ell}^{\text{SM}}} = 1 + 1.138\,\tilde{c}_{Z\gamma}^2 + 0.00265\,\tilde{c}_{ZZ}^2 + (-0.00674)\,\tilde{c}_{Z\gamma}\tilde{c}_{ZZ} \quad (36)$$

We note that, the dependence of the 4ℓ decay signal strength on the parameter $\tilde{c}_{ZZ}$ is very weak.

Decay signal strength : Differential

We now turn to assessing the role of kinematic distributions in $H \to 4\ell$ decay channel, which are affected by CP-violating VVH couplings, in improving the sensitivity on $\tilde{c}_{Z\gamma}$ and $\tilde{c}_{ZZ}$ at the HL and

HE-LHC. The Higgs rest frame angle ϕ between the decay planes of the two intermediate gauge bosons is very sensitive to the CP-Violating VVH couplings [248, 249, 250, 251]. We have considered 50 bins of ϕ-distribution to perform the fit at differential level. For each bin, we calculate the signal strength ($\mu_{4\ell,j}; j = 1 \to 50$) corresponding to Eq. 36. Unlike $\mu_{4\ell}$ in Eq. 36, $\mu_{4\ell,j}$ is also sensitive to linear terms in $\tilde{c}_{Z\gamma}$ and $\tilde{c}_{ZZ}$.

2.10.1.3 **Result: HL and HE-LHC Analyses**

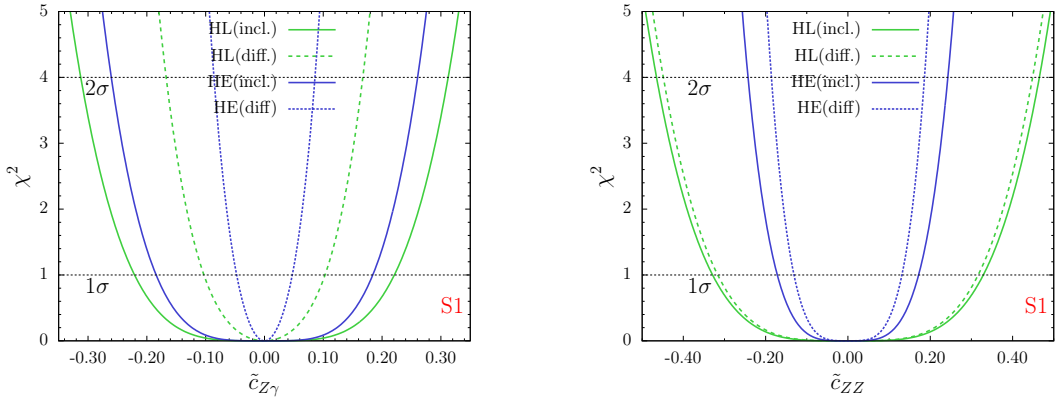

Fig. 36: χ^2 dependence on CP-violating parameters taking one parameter non-zero at a time at HL-LHC (3 ab^{-1}, green) and HE-LHC (15 ab^{-1}, blue) for uncertainty scenario S1. The solid lines refer to the fit performed using $H \to 4\ell$ decay width at inclusive level (1 bin) while, the dashed lines refer to the fit obtained using $H \to 4\ell$ decay width at differential level (ϕ-distribution with 50 bins).

The results of the χ^2 fit for CP-violating parameters $\tilde{c}_{Z\gamma}$ and $\tilde{c}_{ZZ}$ are displayed in Fig. 36 and Fig. 37. In these results, *incl.* refers to the fit obtained using the partial decay width information in the $H \to 4\ell$ channel, while *diff.* refers to the fit obtained using ϕ-distribution in $H \to 4\ell$ decay. In Fig. 36, we show 1σ and 2σ bounds on $\tilde{c}_{Z\gamma}$ and $\tilde{c}_{ZZ}$ in a one parameter (1P) analysis. We find that at HL-LHC we are more sensitive to $\tilde{c}_{Z\gamma}$ than to $\tilde{c}_{ZZ}$. At the inclusive level we gain better sensitivity on $\tilde{c}_{ZZ}$ than on $\tilde{c}_{Z\gamma}$ when going from HL-LHC to HE-LHC. This is mainly due to a stronger dependence of the production signal strength on parameter $\tilde{c}_{ZZ}$. However, due to a stronger dependence of $\mu_{4\ell}$ on $\tilde{c}_{Z\gamma}$ the effect of using ϕ-distribution in the fit is larger for $\tilde{c}_{Z\gamma}$ than for $\tilde{c}_{ZZ}$.

In Fig. 37, we provide 1σ contour lines in the $\tilde{c}_{Z\gamma} - \tilde{c}_{ZZ}$ plane. We can see that the parameters $\tilde{c}_{Z\gamma}$ and $\tilde{c}_{ZZ}$ are weekly correlated. Once again we find that using ϕ-distribution in the fit improves our sensitivity on CP-violating parameters significantly. The parameter $\tilde{c}_{ZZ}$ is mainly constrained by the production channels VH and VBF. We have given a summary of 1σ bounds on $\tilde{c}_{Z\gamma}$ and $\tilde{c}_{ZZ}$ obtained from our analyses for HL and HE-LHC in Table 46.

2.10.1.4 $h \to \tau^+\tau^-$

The most promising direct probe of CP violation in fermionic Higgs decays is the $\tau^+\tau^-$ decay channel, which benefits from a relatively large τ Yukawa giving a SM branching fraction of 6.3%. Measuring the CP violating phase in the tau Yukawa requires a measurement of the linear polarisations of both τ leptons and the azimuthal angle between them. This can be done by analysing tau substructure, namely the angular distribution of the various components of the tau decay products.

The main τ decay modes studied include $\tau^\pm \to \rho^\pm(770)\nu$, $\rho^\pm \to \pi^\pm\pi^0$ [252, 253, 254, 255, 256, 257] and $\tau^\pm \to \pi^\pm\nu$ [258, 259, 260]. Assuming CPT symmetry, collider observables for CP violation must be built from differential distributions based on triple products of three-vectors. In the first case, $h \to \pi^\pm\pi^0\pi^\mp\pi^0\nu\nu$, angular distributions built only from the outgoing charged and neutral pions are

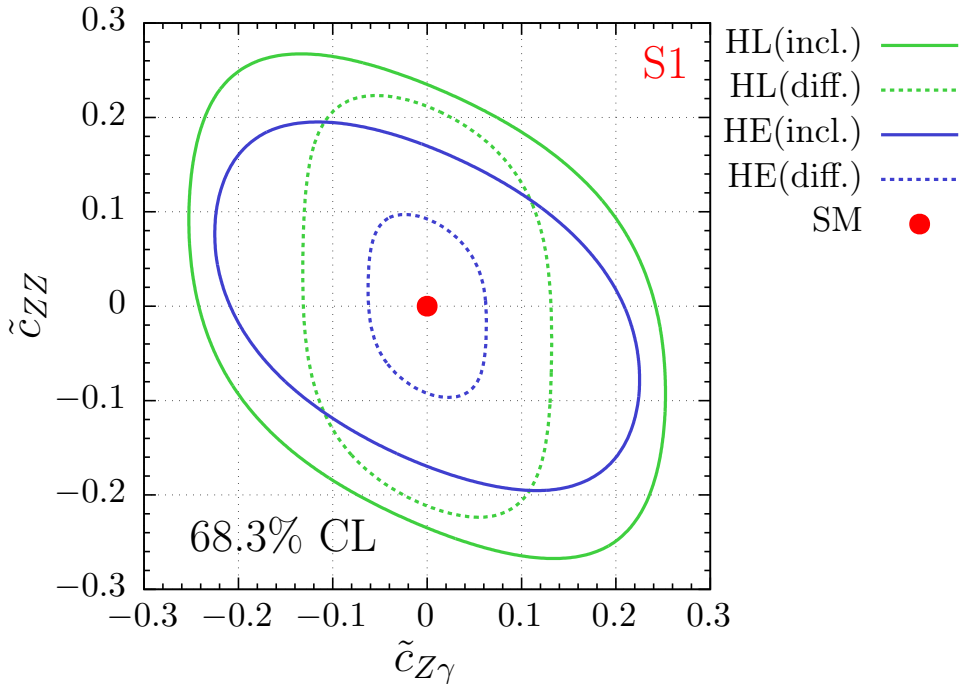

Fig. 37: 1σ reach on $\tilde{c}_{Z\gamma}$ and $\tilde{c}_{ZZ}$ at HL-LHC (3 ab^{-1}, green) and HE-LHC (15 ab^{-1}, blue) for uncertainty scenario S1. The solid lines refer to the fit performed using $H \to 4\ell$ decay width at inclusive level (1 bin) while, the dashed lines refer to the fit obtained using $H \to 4\ell$ decay width at differential level (ϕ-distribution with 50 bins).

Table 46: Summary of 1σ bounds on $\tilde{c}_{Z\gamma}$ and $\tilde{c}_{ZZ}$ from various analyses considered in our study for uncertainty scenario S1. 1P refers to the case where only one parameter is non-zero while 1P$_{marg.}$ refers to the case in which the effect of one of the two parameters is marginalised.

Analysis \ Parameter	$\tilde{c}_{Z\gamma}$	$\tilde{c}_{ZZ}$	Case
HL-LHC (4ℓ, incl.)	[-0.22,0.22]	[-0.33,0.33]	1P
	[-0.25,0.25]	[-0.27,0.27]	1P$_{marg.}$
HL-LHC (4ℓ, diff.)	[-0.10,0.10]	[-0.31,0.31]	1P
	[-0.13,0.13]	[-0.22,0.22]	1P$_{marg.}$
HE-LHC (4ℓ, incl.)	[-0.18,0.18]	[-0.17,0.17]	1P
	[-0.23,0.23]	[-0.20,0.20]	1P$_{marg.}$
HE-LHC (4ℓ, diff.)	[-0.05,0.05]	[-0.13,0.13]	1P
	[-0.06,0.06]	[-0.10,0.10]	1P$_{marg.}$

used to determine the CP properties of the initial τ Yukawa coupling. In the second case, $h \to \pi^{\pm}\pi^{\mp}\nu\nu$, there are not enough reconstructible independent momenta to construct an observable sensitive to CP violation, requiring additional kinematic information such as the τ decay impact parameter.

In the kinematic limit when each outgoing neutrino is taken to be collinear with its corresponding reconstructed $\rho^{\pm}$ meson, the acoplanarity angle, denoted Φ, between the two decay planes spanned by the $\rho^{\pm} \to \pi^{\pm}\pi^{0}$ decay products is exactly analogous to the familiar acoplanarity angle from $h \to 4\ell$ CP-property studies [261, 262]. Hence, by measuring the τ decay products in the single-prong final state, suppressing the irreducible $Z \to \tau^{+}\tau^{-}$ and reducible QCD backgrounds, and reconstructing the acoplanarity angle of ρ^{+} vs. ρ^{-}, the differential distribution in Φ gives a sinusoidal shape whose maxima and minima correspond to the CP-phase in the τ Yukawa coupling. We can parametrise the τ Yukawa

coupling to include CP violation using the Lagrangian term $\frac{y_\tau}{\sqrt{2}} h\bar{\tau}(\cos\Delta + i\sin\Delta\gamma^5)\tau$, where y_τ is the magnitude of the tau Yukawa coupling and remains fixed to the SM value for this study.

An optimal observable using the collinear approximation was derived in [255]. Assuming 70% efficiency for tagging hadronic τ final states, and neglecting detector effects, the estimated sensitivity for the CP-violating phase Δ of the τ Yukawa coupling using 3 ab^{-1} at the HL-LHC is 8.0°. A more sophisticated analysis [256] found that detector resolution effects on the missing transverse energy distribution degrade the expected sensitivity considerably, and as such, about 1 ab^{-1} is required to distinguish a pure scalar coupling (CP phase is zero) from a pure pseudoscalar coupling (CP phase is 90°).

At the HE-LHC, the increased signal cross section for Higgs production is counterbalanced by the increased background rates, and so the main expectation is that improvements in sensitivity will be driven by the increased luminosity and more optimised experimental methodology. Rescaling with the appropriate luminosity factors, the optimistic sensitivity to the τ Yukawa phase from acoplanarity studies is 4-5°, while the more conservative estimate is roughly an order of magnitude bigger.

2.10.1.5 $t\bar{t}h$

CP violation in the top quark-Higgs coupling is strongly constrained by EDM measurements and Higgs rate measurements [263]. However, these constraints assume that the light quark Yukawa couplings and hWW couplings are set to their SM values. If this is not the case, the constraints on the phase of the top Yukawa coupling are less stringent.

Assuming the EDM and Higgs rate constraints can be avoided, the CP structure of the top quark Yukawa can be probed directly in $pp \to t\bar{t}h$. Many simple observables, such as $m_{t\bar{t}h}$ and $p_{T,h}$ are sensitive to the CP structure, but require reconstructing the top quarks and Higgs.

Some $t\bar{t}h$ observables have been proposed recently that access the CP structure without requiring full event reconstruction. These include the azimuthal angle between the two leptons in a fully leptonic $t/bart$ decay with the additional requirement that the $p_{T,h} > 200\,\text{GeV}$ [264], and the angle between the leptons (again in a fully leptonic $t/\bar{t}$ system) projected onto the plane perpendicular to the h momentum [265]. These observables only require that the Higgs is reconstructed and are inspired by the sensitivity of $\Delta\phi_{\ell^+\ell^-}$ to top/anti-top spin correlations in $pp \to t\bar{t}$ [266]. The sensitivity of both of these observables improves at higher Higgs boost (and therefore higher energy), making them promising targets for the HE-LHC, though no dedicated studies have been carried out to date.

2.10.2 Experimental constraints on anomalous HVV couplings[30]

2.10.2.1 Experimental constraints from $H \to ZZ^{(*)} \to 4\ell$ decays

The projections for anomalous coupling measurements from H $\to$ ZZ$^{(*)}$ $\to 4\ell$ decays at the HL-LHC were studied within the context of the last ECFA HL-LHC Experiments Workshops in 2013 and 2014 [267]. The obtained limits are quantified in terms of the effective couplings g_i introduced in the invariant amplitude describing the interaction of a spin-0 particle and and two spin-one gauge bosons introduced in Refs. [268] and [42]. The couplings g_1, g_2 and g_3 correspond to the interaction with the CP-even and g_4 to the interaction with the CP-odd boson, respectively. The direct measurement of couplings is free of assumptions on the size of the interference effects and its results can be expressed in terms of the (f_{g_i}, ϕ_i) parametrisation:

$$f_{g_i} = \frac{|g_i|^2\sigma_i^2}{|g_1|^2\sigma_1^2 + |g_2|^2\sigma_2^2 + |g_4|^2\sigma_4^2}; \quad \phi_{g_i} = \arg\left(\frac{g_i}{g_1}\right).$$

In this analysis g_2 and g_4 are measured separately, assuming the simultaneous presence of only g_1 and of the coupling under study, this corresponds to set $g_2 = 0$ ($g_4 = 0$) in the expression of f_{g_4} (f_{g_2}) above.

[30] Contacts: K. Prokofiev, A. Gritsan, P. Milenovic, H. Roskes, U. Sarica

The analysis was performed by fitting the observables based on the analytic calculation of Leading Order Matrix Element describing $H \to ZZ^{(*)} \to 4\ell$ decays in the presence of anomalous couplings. The final fit is based on Monte Carlo modelling of the expected signal at each bin of the $(\Re(g_i)/g_1; \Im(g_i)/g_1)$ plane, where g_i represents g_2 or g_4. The irreducible ZZ background was suppressed by using a dedicated Boosted Decision Tree discriminant.

Following the event selection and applying the fit methodology described above, the expected exclusion of the non-Standard Model contributions given the Standard Model data is evaluated for 300 and 3000 fb^{-1}. Examples of the corresponding exclusion plots are given in Figure 38. With a conservative analysis limits of $f_{g_4} < 0.037$ at 95% CL and $f_{g_2} < 0.12$ at 95% CL for 3000 fb^{-1} are obtained. This allows a sensitive test of the tensor structure of the H $\to$ ZZ couplings at the HL-LHC.

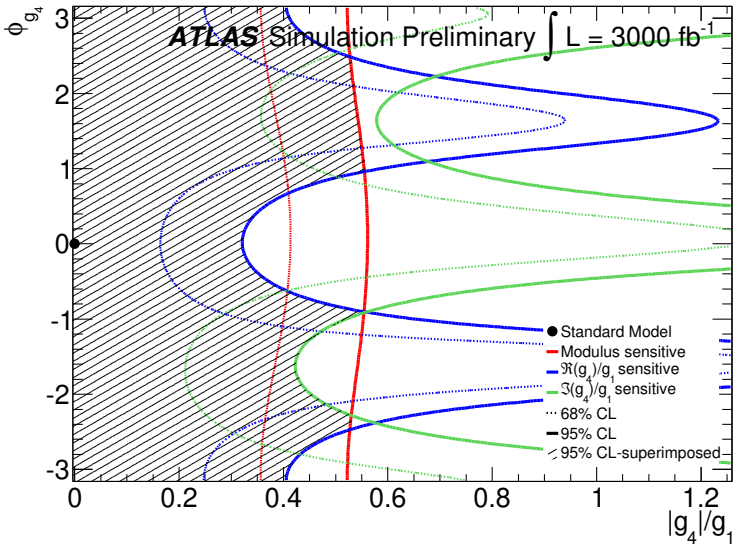

Fig. 38: Results of the g_4-sensitive fits projected onto the $(|g_4|/g_1, \phi_{g_4})$ plane for 3000 fb^{-1}. The shaded area corresponds to the most restrictive exclusion of the three observables.

2.10.2.2 Experimental constraints from production and decay in $H \to ZZ^{(*)} \to 4\ell$ channel

Anomalous contributions in the spin-0 tensor structure of HVV interactions can be characterised by coefficients a_2, a_3, Λ_1, and Λ_Q defined in Refs. [269, 270]. The a_2 and a_3 coefficients have one-to-one correspondence with the g_2 and g_4 coefficients mentioned in Section 2.10.2.1. The contribution to the

total cross section from these coefficients is parametrised in terms of their fractional contribution to on-shell $H \to 2e2\mu$ decays via the fractions f_{ai} and phases ϕ_{ai} [269, 270]. Constraints on these anomalous contributions can further be improved by including off-shell Higgs boson production. An enhancement of signal events is expected in the presence of either anomalous HVV couplings or large Higgs boson total width, Γ_H [270, 45, 271].

In the study from Ref. [139], only the tensor structure proportional to a_3 is considered using either the combination of on-shell and off-shell events or with only on-shell events with 4ℓ decay, following the techniques described in Refs. [269, 45, 271]. Constraints are placed in terms of $f_{ai}\cos(\phi_{ai})$ with the assumptions $\phi_{ai} = 0$ or π, $a_i^{ZZ} = a_i^{WW}$, and $\Gamma_H = \Gamma_H^{SM}$ in the case of limits from the combined on-shell and off-shell likelihood parametrisation.

The projections are shown in Fig. 39 and summarised in Table 47. Systematic uncertainties are found to have a negligible effect on the results for $f_{a3}\cos(\phi_{a3})$ using either on-shell and off-shell events combined or only on-shell events, so only the case when systematic uncertainties are as in Run 2 [271], is shown.

Table 47: Summary of the 95% C.L.intervals for $f_{a3}\cos(\phi_{a3})$, under the assumption $\Gamma_H = \Gamma_H^{SM}$ for projections at 3000 fb^{-1} [139]. The constraints are multiplied by 10^4, and the values are given only for the case when systematic uncertainties are as in Run 2 [271].

Parameter	Scenario	Projected 95% CL interval
$f_{a3}\cos(\phi_{a3})$	Only on-shell	$[-1.8, 1.8] \times 10^{-4}$
$f_{a3}\cos(\phi_{a3})$	On-shell and off-shell	$[-1.6, 1.6] \times 10^{-4}$

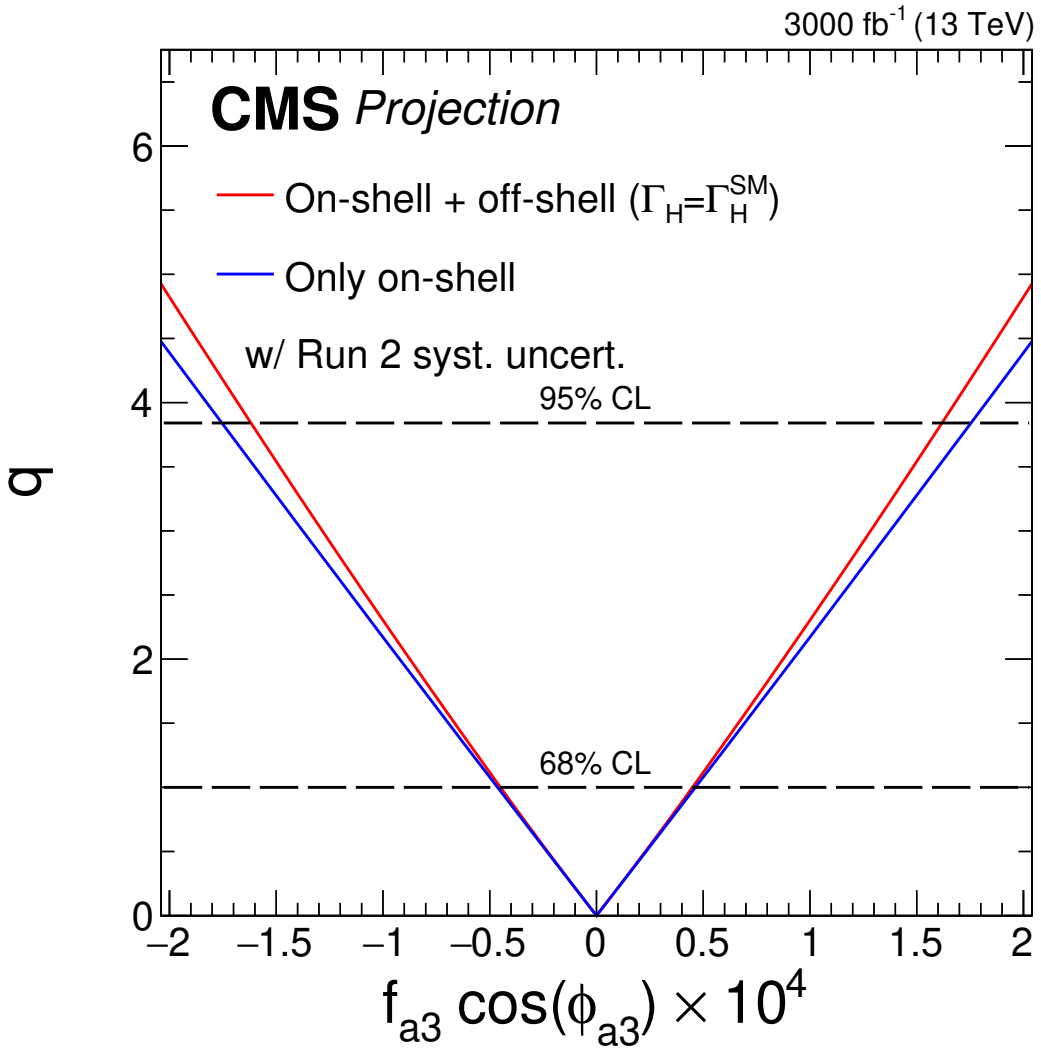

Fig. 39: Likelihood scans for projections on $f_{a3}\cos(\phi_{a3})$ at 3000 fb^{-1} [139]. The scans are shown using either the combination of on-shell and off-shell events (red) or only on-shell events (blue). The dashed lines represent the effect of removing all systematic uncertainties. The dashed horizontal lines indicate the 68% and 95% CLs, and the $f_{a3}\cos(\phi_{a3})$ scans assume $\Gamma_{\mathrm{H}} = \Gamma_{\mathrm{H}}^{\mathrm{SM}}$.

3 Di-Higgs production and Higgs self couplings[31]

The HL-LHC is expected to be a Higgs boson factory, and the study of the double-Higgs (HH) production is one of the key goal of this high-luminosity program. Despite the small production cross-section compared to the single-Higgs boson production, more than 100000 HH pairs should be produced by the HL-LHC per experiment. The trilinear self-interaction of the Higgs boson is described by the coupling strength $\lambda_{HHH} = \frac{m_H^2}{2v}$, where m_H is the Higgs boson mass, and v the electroweak symmetry breaking vacuum expectation value. Measurements of the Higgs trilinear interaction would provide constraints on the shape of the Higgs potential close to the minimum and would allow to verify the electroweak symmetry breaking mechanism of the SM. The existence of an extended scalar sector or the presence of new dynamics at higher scales could modify the Higgs boson self-couplings. In the following the trilinear self-coupling strength, measured relative to the SM expectation is denoted by $\kappa_\lambda = c_{hh} = \lambda = \lambda_{HHH}/\lambda_{HHH}^{SM}$.

This section describes the prospects for studies of the Higgs boson pair production at the HL-LHC and HE-LHC and is organised as follows: the state-of-the-art NLO computations of the Higgs boson pair production cross sections is shown in Section 3.1. Section 3.2 describes the prospect experimental analyses with the ATLAS and CMS experiments with realistic conditions, while Section 3.3 concentrates on alternative methods with phenomenology studies. Studies at the HE-LHC are shown in Section 3.4 with both phenomenological and experimental perspectives. Indirect probes of the trilinear couplings are described in Section 3.5, using differential cross-section measurements or global fits. Finally Section 3.6 shows the implications of the trilinear coupling measurements on b-physics and the electroweak phase transition.

3.1 Higgs boson pair production cross section

3.1.1 SM Calculation

3.1.1.1 HH production via gluon fusion at NNLO[32]

The fusion of gluons via a heavy-quark (mainly top-quark) loop is the most important production mechanism of Higgs boson pairs at hadron colliders within the SM. The NLO QCD corrections for this process have been known in the large-m_t limit for some time [272], and the NNLO cross section has also been computed within this approximation [273]. The NLO corrections retaining the full dependence on the top-quark mass have been obtained for the first time in Refs. [274, 84], and have been recently confirmed by an independent calculation [275]. On top of this, an improved NNLO prediction –labelled NNLO$_{\rm FTa}$ for full-theory approximation– was presented in Ref. [276]. This approximation is obtained by combining one-loop double-real corrections with full m_t dependence with suitably reweighted real-virtual and double-virtual contributions evaluated in the large-m_t limit. Furthermore, the stability of the QCD perturbative expansion at this order has been confirmed by consistently matching the NNLO$_{\rm FTa}$ prediction with the next-to-next-to-leading logarithmic terms coming from threshold resummation [277].

More details on the NLO results with full-m_t dependence (including the effect coming from variations in the Higgs self-coupling and the contributions arising from BSM EFT operators) are provided in the following sections, therefore we focus here on the state-of-the-art NNLO prediction, i.e., the NNLO$_{\rm FTa}$ result from Ref. [276].

Before focusing on the numerical results, it is worth to stress out that the NNLO cross sections presented here, as well as the NLO predictions for gluon fusion present in the following sections, are computed using the on-shell scheme for the top-quark mass renormalisation . Some partial results on the uncertainties related to the m_t scheme and scale choice have been presented in Ref. [275] at NLO, and further studies to gauge the size of their effect on the total cross section and distributions are in progress.

[31] Contact Editors: L. Cadamuro, E. Petit, M. Riembau
[32] Contact: J. Mazzitelli

Table 48: Inclusive cross sections for Higgs boson pair production at NNLO_{FTa} for centre-of-mass energies of 14 TeV and 27 TeV. Scale uncertainties are reported as superscript/subscript. The estimated uncertainty of the approximation due to finite top-quark mass effects is also presented, as well as the PDF and α_S uncertainties.

$\sqrt{s}$ [TeV]	NNLO_{FTa} [fb]	m_t unc.	PDF unc.	α_S unc.	PDF+α_S unc.
14	$36.69^{+2.1\%}_{-4.9\%}$	$\pm 2.7\%$	$\pm 2.1\%$	$\pm 2.1\%$	$\pm 3.0\%$
27	$139.9^{+1.3\%}_{-3.9\%}$	$\pm 3.4\%$	$\pm 1.7\%$	$\pm 1.8\%$	$\pm 2.5\%$

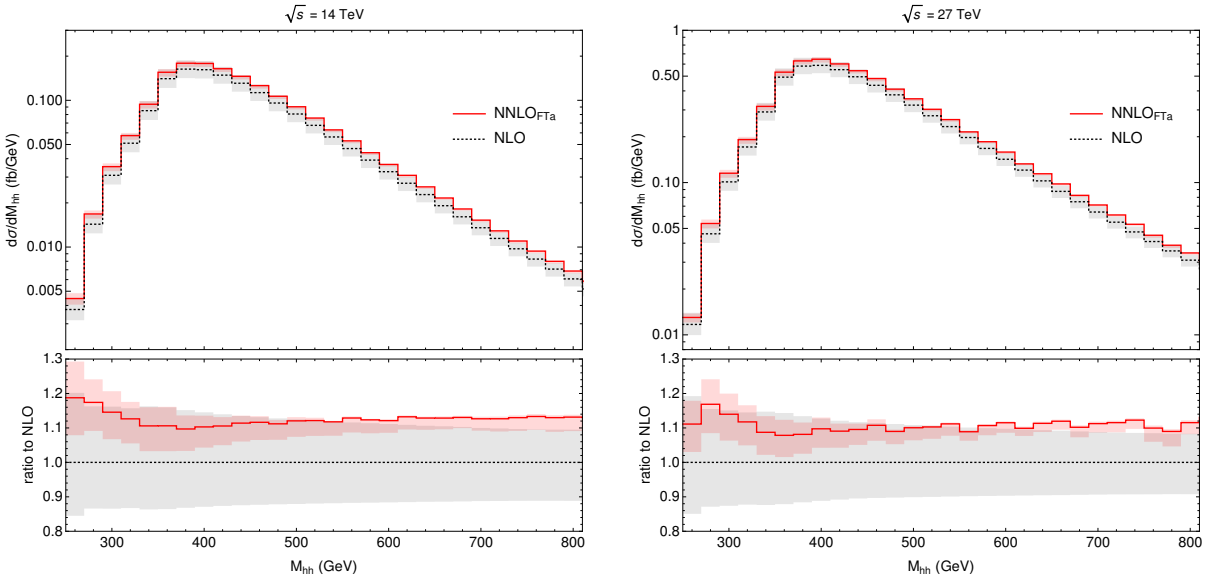

Fig. 40: Higgs boson pair invariant mass distribution at NNLO_{FTa}, together with the NLO prediction, at 14 TeV (left) and 27 TeV (right). The lower panels show the ratio with respect to the NLO prediction, and the filled areas indicate the scale uncertainties.

This source of uncertainty is for the moment not considered in the NLO and NNLO predictions.

In Table 48 we present results for the total cross section at $\sqrt{s} = 14$ TeV and 27 TeV. We use the values $m_h = 125$ GeV for the Higgs boson mass and $m_t = 173$ GeV for the on-shell top quark mass. The NNLO PDF4LHC15 sets of parton distribution functions are used, and PDF and α_S uncertainties are also provided. An estimation of the systematic uncertainty of the approximation due to missing finite-m_t effects is also presented, and it is found to be at the few percent level. For the renormalisation and factorisation scales we use the central value $\mu_0 = M_{hh}/2$, which has been shown to provide a better convergence for the fixed order prediction [277]. We obtain the scale uncertainties via the usual 7-point scale variation.

The NNLO_{FTa} predictions from Ref. [276] are also fully differential in the Higgs boson pair and the associated jet activity. As an example, we present the Higgs pair invariant mass distribution at 14 TeV and 27 TeV in Figure 40, together with the corresponding NLO prediction. We can observe the strong reduction in the size of the scale uncertainties when including the NNLO_{FTa} corrections, and the sizeable overlap with the NLO uncertainty band (not present between the LO and NLO predictions), suggesting a significant improvement in the perturbative convergence as we move from NLO to NNLO.

3.1.1.2 *HH production in sub-dominant channels*[33]

Table 49: Signal cross section (in fb) for HH production at NLO QCD.

$\sqrt{s}$ (TeV)	ZHH	WHH	VBF HH	$ttHH$	$tjHH$
14	$0.359^{+1.9\%}_{-1.3\%} \pm 1.7\%$	$0.573^{+2.0\%}_{-1.4\%} \pm 1.9\%$	$1.95^{+1.1\%}_{-1.5\%} \pm 2.0\%$	$0.948^{+3.9\%}_{-13.5\%} \pm 3.2\%$	$0.0383^{+5.2\%}_{-3.3\%} \pm 4.7\%$
27	$0.963^{+2.1\%}_{-2.3\%} \pm 1.5\%$	$1.48^{+2.3\%}_{-2.5\%} \pm 1.7\%$	$8.21^{+1.1\%}_{-0.7\%} \pm 1.8\%$	$5.27^{+2.0\%}_{-3.7\%} \pm 2.5\%$	$0.254^{+3.8\%}_{-2.8\%} \pm 3.6\%$

Results shown in Table 49 have been obtained within the MADGRAPH5_AMC@NLO [79] framework, as in Ref. [278]. The renormalisation and factorisation scale was set to $m_{HH}/2$ and varied up and down by a factor of two to obtain the scale uncertainties. The 5-flavour PDF4LHC NLO Monte Carlo PDF set was used to obtain the results (LHAPDF set number 90500, *PDF4LHC15_nlo_mc*). The WHH results are the sum of the W^+ and W^- cross-sections. Similarly $tjHH$ involves both top and anti-top production.

3.1.1.3 *Probing the Higgs boson self-coupling in di-Higgs production with full m_t-dependence at NLO QCD*[34]

In this section we consider the impact of varying the Higgs self-coupling λ on the NLO computations of the HH production cross section. In particular, we announce a version of the ggHH code [84, 279, 274] implemented in the POWHEG-BOX-V2 [160] where variations of λ are accessible to the user in a parton shower Monte Carlo program at full NLO.

3.1.1.4 *Total cross sections at different values of the trilinear coupling*

In Table 50 we list total cross sections at 14 TeV and 27 TeV for various values of the trilinear Higgs coupling λ.

Table 50: Total cross sections for Higgs boson pair production at full NLO. The given uncertainties are scale uncertainties.

$\lambda_{\rm BSM}/\lambda_{\rm SM}$	$\sigma_{\rm NLO}$@14TeV [fb]	$\sigma_{\rm NLO}$@27TeV [fb]	K-fac.@14TeV	K-fac.@27TeV
1	$32.88^{+13.5\%}_{-12.5\%}$	$127.7^{+11.5\%}_{-10.4\%}$	1.66	1.62
2	14.91	59.10	1.58	1.52
2.4	13.81	53.67	1.65	1.60
3	19.82	69.84	1.97	1.89
5	98.42	330.61	2.21	2.18
0	73.84	275.29	1.79	1.78
-1	137.69	504.9	1.87	1.83

The results have been obtained using the parton distribution functions PDF4LHC15_nlo_100_pdfas 97, 98, 280], along with the corresponding value for α_s for both the NLO and the LO calculation. The masses have been set to $m_h = 125\,\text{GeV}$, $m_t = 173\,\text{GeV}$, and the top quark width has been set to zero. The scale uncertainties are the result of a 7-point scale variation around the central scale $\mu_0 = m_{hh}/2$,

[33] Contact: E. Vryonidou
[34] Contacts: G. Heinrich, S. Jones, M. Kerner, G. Luisoni, L. Scyboz

with $\mu_{R,F} = c_{R,F}\,\mu_0$, where $c_R, c_F \in \{2, 1, 0.5\}$, except that the extreme variations $(c_R, c_F) = (2, 0.5)$ and $(c_R, c_F) = (0.5, 2)$ are omitted.

Table 50 also shows that the K-factors do vary substantially as functions of the trilinear coupling. This fact is illustrated in Fig. 41, where it is demonstrated that the K-factor takes values between 1.57 and 2.16.

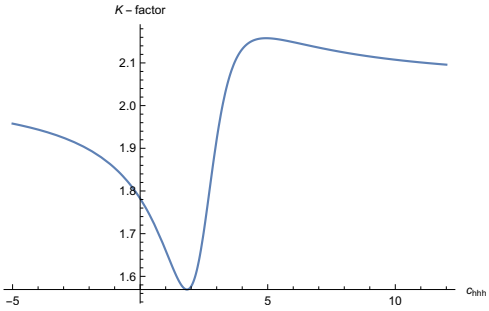

Fig. 41: Variation of the NLO K-factor with the trilinear coupling, $\sqrt{s} = 14\,\text{TeV}$.

3.1.1.5 Differential cross sections at 14 TeV and 27 TeV

In Figs. 42 and 43 we show the m_{hh} distribution for various values of $\lambda = \lambda_{\text{BSM}}/\lambda_{\text{SM}}$ at 14 TeV. Figs. 44 and 45 show results for the m_{hh} distribution at 27 TeV. The scale variation band for $\lambda = 1$ is also included. Note that $\lambda = 2.4$ is the value where the cross section as a function of λ goes through a minimum, due to maximal destructive interference between diagrams containing the trilinear coupling and diagrams which do not contain Higgs boson self-couplings.

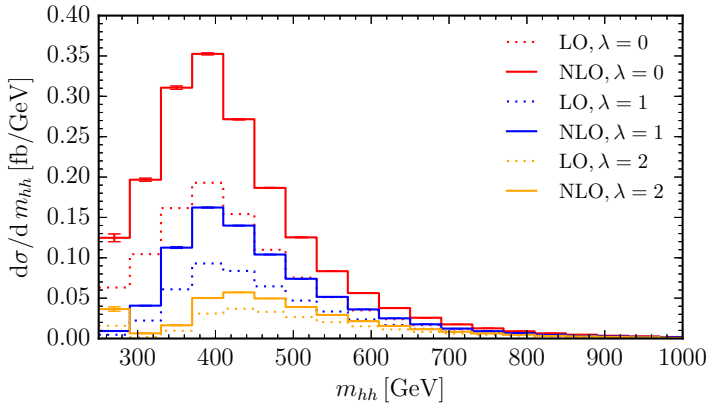

(a)

Fig. 42: Higgs boson pair invariant mass distributions for various values of λ (relative to λ_{SM}) at 14 TeV.

Fig. 46 shows the Higgs boson pair invariant mass distributions at NLO as a function of $\lambda = c_{hhh}$ as a 3-dimensional heat map. The dip in the distribution around $c_{hhh} = 2.4$ is clearly visible.

3.1.2 Di-Higgs production in the non-linear EFT with full m_t-dependence at NLO QCD[35]

3.1.2.1 The Higgs sector in the non-linear EFT framework

Below we will describe the potential impact of physics beyond the Standard Model through a non-linear Effective Field Theory, also called the electroweak chiral Lagrangian including a light Higgs boson [204,

[35] Contacts: G. Buchalla, A. Celis, M. Capozi, G. Heinrich, L. Scyboz

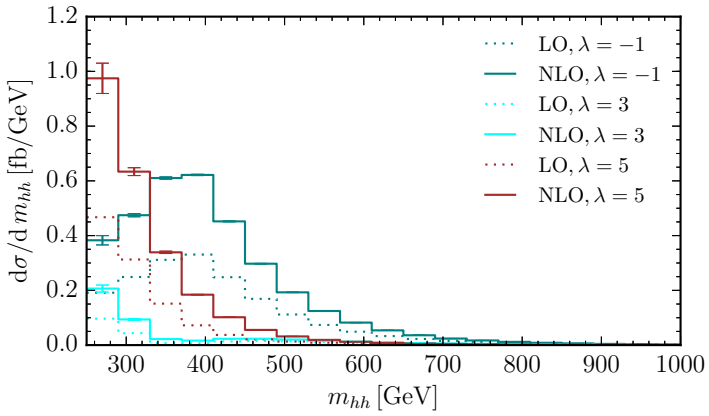

Fig. 43: Higgs boson pair invariant mass distributions for $\lambda = \lambda_{\rm BSM}/\lambda_{\rm SM} = -1, 3, 5$ at 14 TeV.

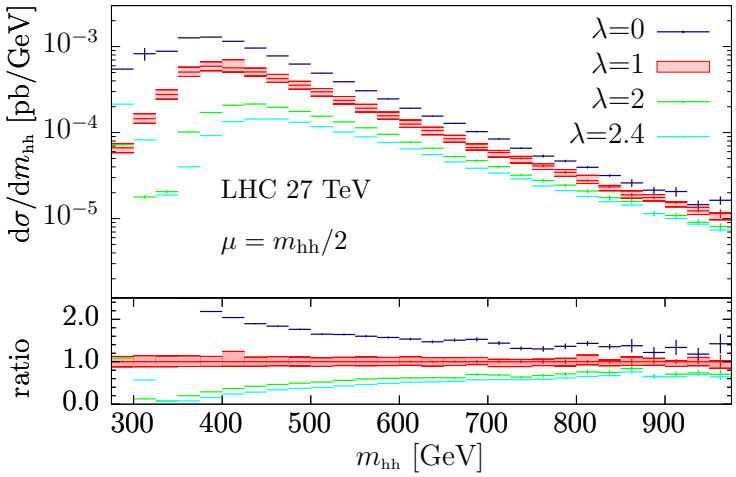

Fig. 44: Higgs boson pair invariant mass distributions for $\lambda = \lambda_{\rm BSM}/\lambda_{\rm SM} = 0, 1, 2, 2.4$ at 27 TeV. The scale uncertainties for the SM value of c_{hhh} are shown as a red band.

205, 207]. This framework provides us with a consistent EFT for New Physics in the Higgs sector, where the Higgs field is an electroweak singlet h, independent of the Goldstone matrix $U = \exp(2i\varphi^a T^a/v)$. The latter transforms as $U \to g_L U g_Y^\dagger$ under the SM gauge group. The symmetry is non-linearly realised on the Goldstone fields φ^a, therefore the name non-linear EFT. More details about this framework already have been given in Section 2.8. Therefore we restrict ourselves to stating the part of the Lagrangian relevant for our study of anomalous Higgs couplings:

$$\mathcal{L} \supset -m_t \left(c_t \frac{h}{v} + c_{tt} \frac{h^2}{v^2} \right) \bar{t}\, t - c_{hhh} \frac{m_h^2}{2v} h^3 + \frac{\alpha_s}{8\pi} \left(c_{ggh} \frac{h}{v} + c_{gghh} \frac{h^2}{v^2} \right) G^a_{\mu\nu} G^{a,\mu\nu} \,. \tag{37}$$

To lowest order in the SM $c_t = c_{hhh} = 1$ and $c_{tt} = c_{ggh} = c_{gghh} = 0$. In general, all couplings may have arbitrary values of $\mathcal{O}(1)$. Note that we have extracted a loop factor from the definition of the Higgs-gluon couplings.

The leading-order diagrams are shown in Fig. 47. Examples for virtual diagrams at NLO are shown in Fig. 48. For further details we refer to Ref. [212].

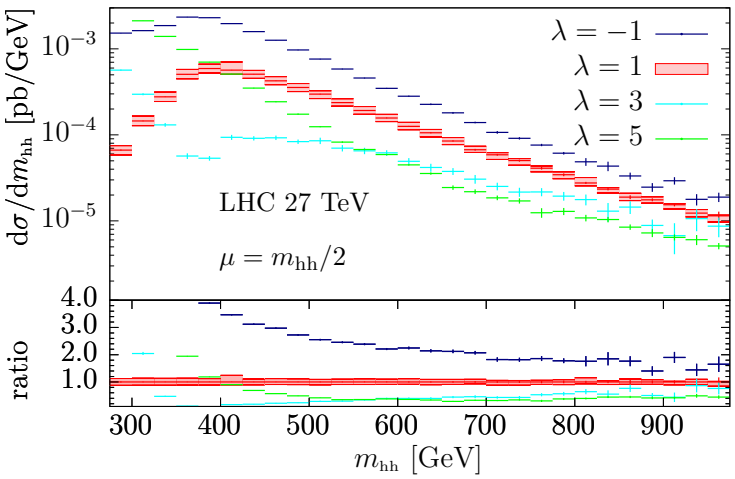

Fig. 45: Higgs boson pair invariant mass distributions for $\lambda = \lambda_{\rm BSM}/\lambda_{\rm SM} = -1, 1, 3, 5$ at 27 TeV. The scale uncertainties for the SM value of λ are shown as a red band.

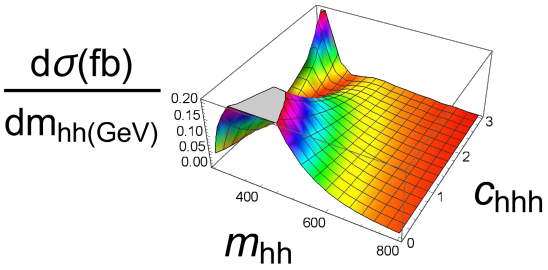

Fig. 46: 3-dimensional visualisation of the m_{hh} distribution at 14 TeV, as a function λ.

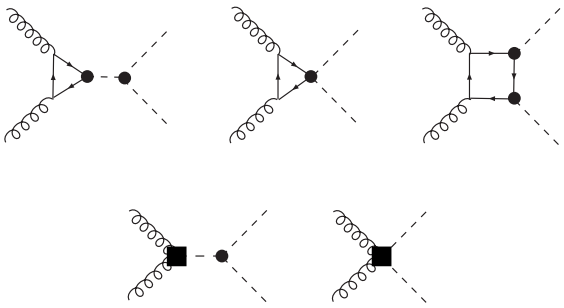

Fig. 47: Higgs-pair production in gluon fusion at leading order in the non-linear EFT Lagrangian.

3.1.2.2 Total cross sections for 14 and 27 TeV at some benchmark points

In the following we will show results for some benchmark points, specified in Table 51, some of them having been first defined in Refs. [281]. The results at 14 TeV and 27 TeV are given in Table 52. Note that our conventions for c_{ggh} and c_{gghh} differ from the ones in Ref. [281, 282], the relations are $c_{ggh} = \frac{2}{3}c_g$ and $c_{gghh} = -\frac{1}{3}c_{2g}$, where c_g, c_{2g} are the couplings defined in Refs. [281, 282]. We also take into account recent constraints on c_{ggh} from Refs. [182, 185] and the limits on the Higgs boson pair production cross section from Refs [283, 284]. This is why we do not show results for the original benchmark point 5 anymore, as its value for c_{ggh} is outside the 2-sigma band of a combined fit of c_{ggh}, c_t from single Higgs production data [182, 185]. Benchmark point 6 is interesting because its value for c_{hhh} is near the point where maximal destructive interference takes place between triangle-type and box-type contributions if

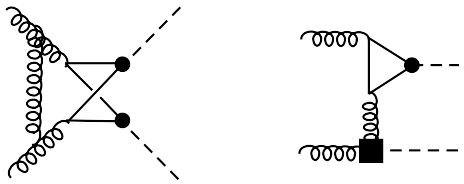

Fig. 48: Examples of virtual diagrams contributing at NLO QCD.

the other couplings are SM-like, leading to a total cross section which is below the SM value.

Table 51: Benchmark points used for the distributions shown below.

Benchmark	c_{hhh}	c_t	c_{tt}	c_{ggh}	c_{gghh}
5a	1	1	0	$2/15$	$4/15$
6	2.4	1	0	$2/15$	$1/15$
7	5	1	0	$2/15$	$1/15$
8a	1	1	1/2	$4/15$	0
SM	1	1	0	0	0

Table 52: Total cross sections at 14 and 27 TeV at NLO (2nd column), K-factor σ_{NLO}/σ_{LO} (3rd column), scale uncertainty (4th column), statistical uncertainty (5th column) and the ratio to the SM total cross section at NLO (6th column).

Benchmark	σ_{NLO} [fb]	K-factor	scale uncert. [%]	stat. uncert. [%]	$\frac{\sigma_{NLO}}{\sigma_{NLO,SM}}$
B_{5a} [14 TeV]	38.64	1.78	$+4,\ -12$	0.24	1.17
B_{5a} [27 TeV]	198.64	1.75	$+2,\ -10$	0.43	1.56
B_6 [14 TeV]	24.69	1.89	$+2,\ -11$	2.1	0.75
B_6 [27 TeV]	97.25	1.58	$+1,\ -6$	1.6	0.76
B_7 [14 TeV]	169.41	2.07	$+9,\ -12$	2.2	5.14
B_7 [27 TeV]	598.20	2.11	$+8,\ -10$	2.0	4.68
B_{8a} [14 TeV]	41.70	2.34	$+6,\ -9$	0.63	1.27
B_{8a} [27 TeV]	179.52	2.33	$+4,\ -7$	0.49	1.40
SM [14 TeV]	32.95	1.66	$+14,\ -13$	0.1	1
SM [27 TeV]	127.7	1.62	$+12,\ -10$	0.1	1

Table 52 shows that the total cross sections increase by a factor of 3.5-5 when increasing the centre-of-mass energy from 14 TeV to 27 TeV. The increase for B_{5a} is largest because of the large value of c_{gghh}, which yields a contribution growing linearly with energy.

3.1.2.3 HH invariant mass distributions at 14 and 27 TeV at some benchmark points

In Figs. 49 and 50 we show Higgs boson pair invariant mass distributions for the benchmark points 7 and 8a. For both of them the shape of the distribution is very different from the SM one, and the K-factor is non-homogeneous over the whole m_{hh}-range. Benchmark point 7 is characterised by a large enhancement of the low m_{hh} region, induced by the large value of c_{hhh}. The lower ratio plot shows the ratio of the two approximations "Born-improved HEFT" and "$\text{FT}_{\text{approx}}$" to the full NLO, where the

former denotes the $m_t \to \infty$ limit rescaled by the m_t-dependent LO, while $\text{FT}_{\text{approx}}$ includes the Born-improved $m_t \to \infty$ limit for the virtual part and the full m_t-dependence for the real radiation part. One can see from Fig. 49 that these approximations are off by about 20% even below the $2m_t$ threshold. Therefore one cannot claim that the $m_t \to \infty$ limit works well in the region below $\sim 400\,\text{GeV}$. As the triangle-type contributions are dominating for $c_{hhh} = 5$, their full m_t-dependence plays a significant role.

Benchmark point 8a shows a characteristic dip near $m_{hh} = 2\,m_t$ and an enhancement in the tail compared to the SM. As the total cross section for B_{8a} is very similar to the SM one, both at 14 TeV and at 27 TeV, this is an example where the discriminating power of differential information is very important.

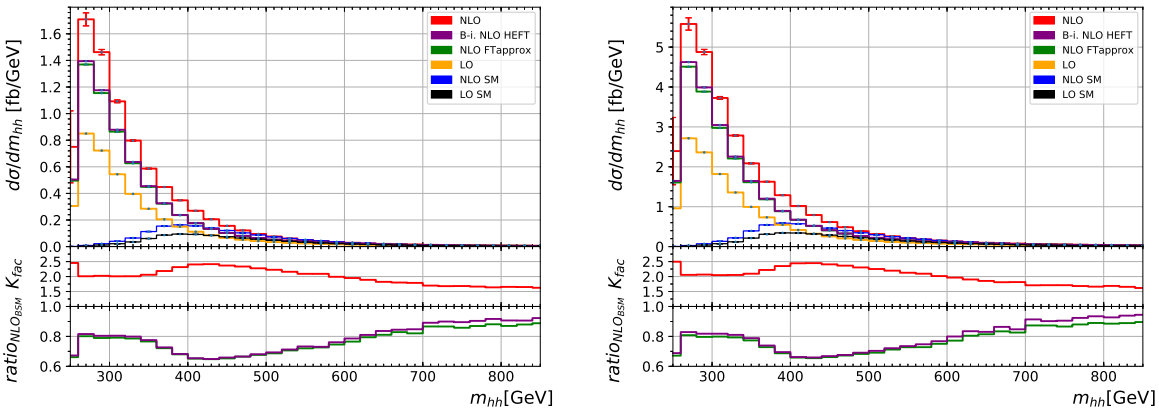

Fig. 49: Higgs boson pair invariant mass distributions for benchmark point 7, $c_{hhh} = 5, c_t = 1, c_{tt} = 0, c_{ggh} = 2/15, c_{gghh} = 1/15$, at 14 TeV (left) and 27 TeV (right).

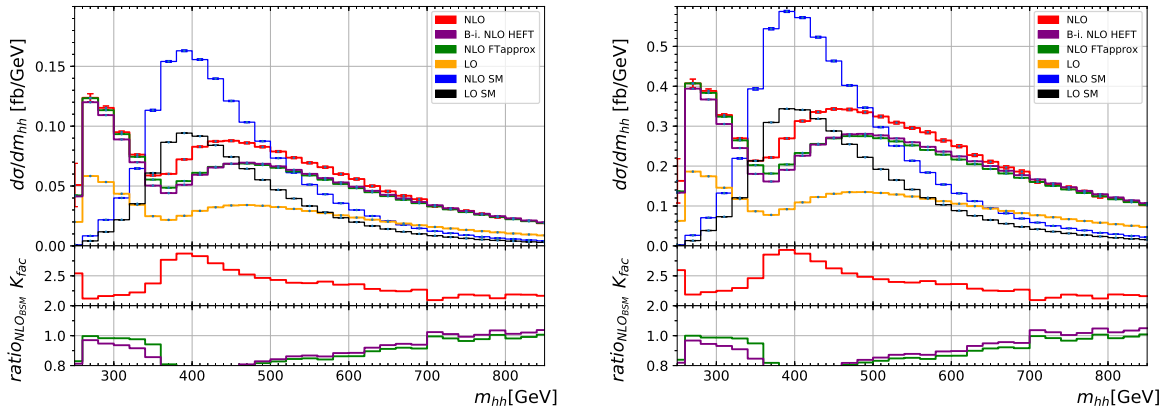

Fig. 50: Higgs boson pair invariant mass distributions for benchmark point 8a, $c_{hhh} = 1, c_t = 1, c_{tt} = 0.5, c_{ggh} = 4/15, c_{gghh} = 0$, at 14 TeV (left) and 27 TeV (right).

3.1.2.4 Characterising the BSM parameter space

The total cross section can be written in terms of the 15 coefficients $A_1, \ldots, A_{15}$, at LO [281, 285] and in terms of 23 coefficients at NLO [212].

$$\sigma^{\text{NLO}}/\sigma^{\text{NLO}}_{SM} = A_1\, c_t^4 + A_2\, c_{tt}^2 + A_3\, c_t^2 c_{hhh}^2 + A_4\, c_{ggh}^2 c_{hhh}^2 + A_5\, c_{gghh}^2 + A_6\, c_{tt} c_t^2 + A_7\, c_t^3 c_{hhh}$$

$$
\begin{aligned}
&+ A_8\, c_{tt} c_t\, c_{hhh} + A_9\, c_{tt} c_{ggh} c_{hhh} + A_{10}\, c_{tt} c_{gghh} + A_{11}\, c_t^2 c_{ggh} c_{hhh} + A_{12}\, c_t^2 c_{gghh} \\
&+ A_{13}\, c_t c_{hhh}^2 c_{ggh} + A_{14}\, c_t c_{hhh} c_{gghh} + A_{15}\, c_{ggh} c_{hhh} c_{gghh} \\
&+ A_{16}\, c_t^3 c_{ggh} + A_{17}\, c_t c_{tt} c_{ggh} + A_{18}\, c_t c_{ggh}^2 c_{hhh} + A_{19}\, c_t c_{ggh} c_{gghh} \\
&+ A_{20}\, c_t^2 c_{ggh}^2 + A_{21}\, c_{tt} c_{ggh}^2 + A_{22}\, c_{ggh}^3 c_{hhh} + A_{23}\, c_{ggh}^2 c_{gghh}\,. \qquad (38)
\end{aligned}
$$

Based on our results for $A_1, \ldots, A_{23}$, we produce heat maps for the ratio σ/σ_{SM}, varying two of the five parameters, while for the fixed parameters the SM values are used, along with $\sigma_{SM}^{\rm LO}[14\,\text{TeV}] = 19.85\,\text{fb}$, $\sigma_{SM}^{\rm NLO}[14\,\text{TeV}] = 32.95\,\text{fb}$. The couplings are varied in a range which seems reasonable when taking into account the current constraints on the Higgs coupling measurements as well as recent limits on the di-Higgs production cross section [283, 284].

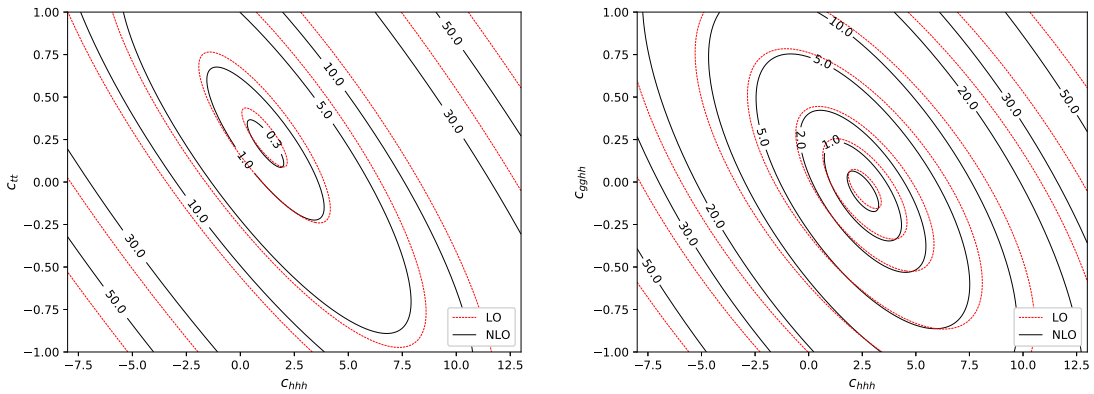

Fig. 51: Iso-contours of σ/σ_{SM}: (a) c_{hhh} versus c_{tt} and (b) c_{hhh} versus c_{gghh} at $\sqrt{s} = 14\,\text{TeV}$.

Fig. 51 shows variations of the triple Higgs coupling c_{hhh} in combination with c_{tt} and c_{gghh} at $\sqrt{s} = 14\,\text{TeV}$. We observe that the deviations from the SM cross section can be substantial. In Fig. 52

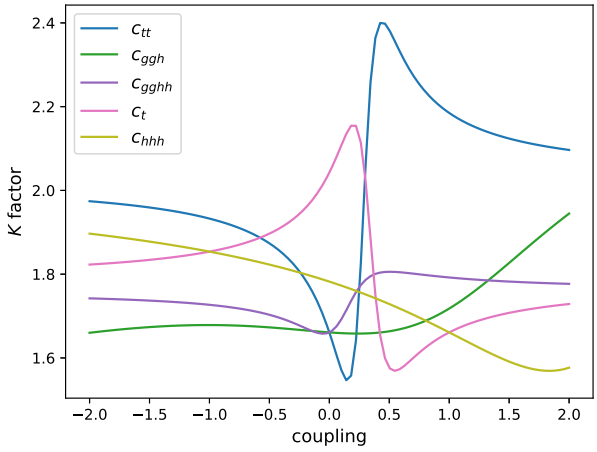

Fig. 52: K-factors for the total cross section at $\sqrt{s} = 14\,\text{TeV}$ as a function of the different couplings.

we show the K-factors as a function of the coupling parameters, with the others fixed to their SM values. It shows that the K-factors exhibit a much stronger dependence on the coupling parameters once the full top quark mass dependence is taken into account when compared to the results in the $m_t \to \infty$ limit [210, 286].

Fig. 53 shows the Higgs boson pair invariant mass distributions as a function of (a) c_{tt} and (b) c_{gghh} as 3-dimensional heat maps. In case (a) the other couplings are fixed to their SM values. We can see that large values of $|c_{tt}|$ lead to a substantial increase of the cross section, in particular at low m_{hh} values. In case (b) the other couplings are fixed to their SM values except for c_{hhh}, which is fixed to

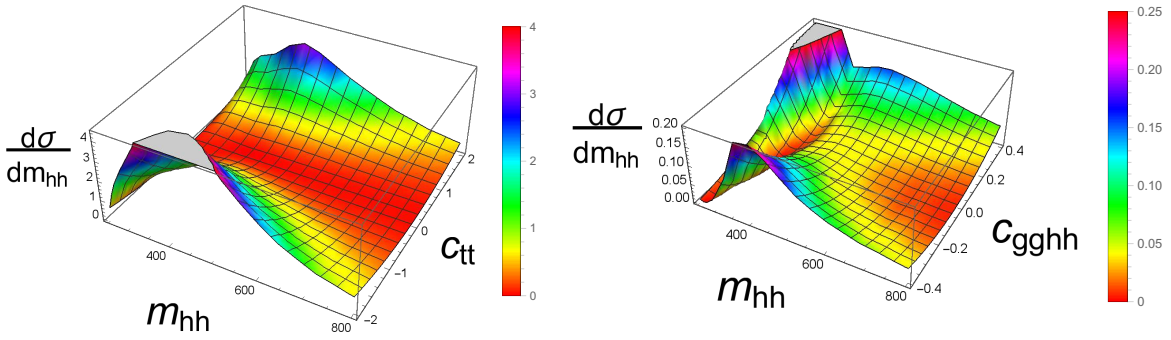

Fig. 53: 3-dimensional visualisation of the m_{hh} distribution (in units of fb/GeV) at 14 TeV as a function of (a) c_{tt} and (b) c_{gghh}. In case (a) all other couplings are fixed to their SM values, in case (b) $c_{hhh} = 2.4$.

$c_{hhh} = 2.4$ in order to demonstrate the following point: varying only c_{hhh}, the m_{hh} distribution shows a dip in the differential cross section just below $m_{hh} \sim 2m_t$ for $c_{hhh} \sim 2.4$, while the low m_{hh} region gets enhanced for larger values of c_{hhh}, see Section 3.1.1.3. However, this pattern can get destroyed by non-zero Higgs-gluon contact interactions. While c_{ggh} is increasingly well constrained meanwhile, c_{gghh} still could be relatively large. We can see from Fig. 53(b) that the dip is not present for very low (negative) c_{gghh} values and also gets very shallow for values of $c_{gghh} \sim 0.4$. Therefore it would be premature to conclude that a dip in the m_{hh} distribution points to a value of c_{hhh} close to 2.4.

We also point out that the LO and NLO A_i coefficients for both the total cross section and the m_{hh} distributions at both 14 TeV and 27 TeV are available as ancillary files coming with Ref. [212]. These data files allow to reconstruct the full NLO result for any point in the 5-dimensional parameter space.

3.2 Double Higgs measurements and trilinear coupling: experimental prospects

The current Run 2 measurements of the Higgs-boson-pair production are performed with approximately 36 fb^{-1} of collision data at a centre-of-mass energy of 13 TeV, combining different decay channels [284, 283]. The ATLAS collaboration reports the combined observed (expected) limit on the non-resonant Higgs-boson-pair production cross-section of 6.7 (10.4) times the SM expectation. The ratio of the Higgs boson self-coupling to its SM expectation is observed (expected) to be constrained at 95% CL to $-5.0 < \kappa_\lambda < 12.1$ ($-5.8 < \kappa_\lambda < 12.0$). The reported combined observed (expected) limit on the non-resonant Higgs-boson-pair production cross-section by the CMS collaboration is 22.2 (12.8) times the predicted Standard Model cross-section. The ratio of the Higgs boson self-coupling to its SM expectation is observed (expected) to be constrained at 95% CL to $-11.8 < \kappa_\lambda < 18.8$ ($-7.1 < \kappa_\lambda < 13.6$).

Only the production of HH pairs through gluon-gluon fusion is considered (the other production mechanisms being more than an order magnitude smaller), with an expected cross-section of $36.69^{+2.1\%}_{-4.9\%}$ fb at 14 TeV as described in Section 3.1.1.1. The state of the art NNLO/NNLL calculation with finite top mass effects included at NLO in QCD is used, for a Higgs boson mass of 125 GeV. Scale uncertainties are reported as superscript/subscript. The estimated top quark mass uncertainty of the NNLOFTapprox predictions is also computed, together with PDF and α_S uncertainties. PDF uncertainties are estimated within the Born-improved approximation. The calculation is performed in the on-shell top quark mass scheme. The Feynman diagram which exhibits a λ_{HHH} dependence interferes destructively with the box diagram that is independent of λ_{HHH}, thus a small increase in the value of λ_{HHH}decreases the expected

HH production cross section, and modifies the distributions of event kinematics.

3.2.1 Measurements with the ATLAS experiment[36]

A direct measurement of the Higgs boson trilinear self-coupling λ_{HHH} can be made via the study of Higgs boson pair production.

The small SM non-resonant HH production cross section means that it is necessary to consider final states where at least one of the two Higgs bosons decays into a final state with a large branching ratio, ie $H \to b\bar{b}$. The most promising decays channels are $HH \to b\bar{b}b\bar{b}$, $HH \to b\bar{b}\tau\tau$ and $HH \to b\bar{b}\gamma\gamma$ with branching ratios of 33.9, 7.3 and 0.26% respectively.

The expected performance for the $b\bar{b}b\bar{b}$ and $b\bar{b}\tau\tau$ channels is assessed through extrapolation of measurements performed by the ATLAS detector using 24.3 fb^{-1} and 36.1 fb^{-1} of data, respectively, obtained at $\sqrt{s} = 13$ TeV during Run 2. The expected performance for the $b\bar{b}\gamma\gamma$ channel is assessed through the use of truth-level Monte Carlo samples. These MC samples have been adjusted with parametrised functions to estimate the response of the upgraded ATLAS detector at the HL-LHC, assuming a mean pile-up rate $<\mu>$ = 200. An 8% improvement in b-tagging efficiency is expected for all channels as a result of improvements to the inner tracker [20]. This improvement is factored into the $b\bar{b}b\bar{b}$ and $b\bar{b}\tau\tau$ extrapolations, and it is included in the smearing functions used in the $b\bar{b}\gamma\gamma$ analysis.

A short description of the analysis strategy and of the results is given here, and further details can be found in Ref. [287]. The systematic uncertainties used follow the common recommendations for HL-LHC studies [16].

3.2.1.1 The $HH \to b\bar{b}b\bar{b}$ channel

Projections for this channel were made by extrapolating from the ATLAS Run 2 analysis of 24.3 fb^{-1} of 13 TeV data, described in Ref. [20]. This extrapolation assumes similar detector performance to Run 2. Four central jets with transverse momentum higher than 40 GeV are paired to construct the Higgs boson candidates. Additional requirements are made on Higgs boson mass and transverse momentum, and the pseudorapidity between the two Higgs boson candidates. The acceptance times efficiency of the full event selection for the SM signal is of 1.6%, and around 95% of the background consists of multi-jet events. This dominant background is assessed using data-driven techniques.

The largest source of systematic uncertainty comes from the ability to model the QCD multi-jet background using control regions in data. A conservative assumption in the extrapolation is made that the systematic uncertainties related to this background are left unchanged. Figure 54a shows the impact of this uncertainty on the results.

The final analysis discriminant, m_{HH}, showed in Figure 54b, is the invariant mass of the selected four-jet system, after a correction based on the known Higgs boson mass. The significance neglecting the systematic uncertainties is 1.4 standard deviations, while it is 0.61 standard deviations when the current systematic uncertainties are included. The high number of pile-up events at the HL-LHC cause difficulties in maintaining high acceptance when triggering on multi-jet final states. Ref. [18] proposes a trigger menu which thresholds corresponding to asking for jets with a transverse energy higher than 75 GeV. In the scenario without systematic uncertainties this would degrades the sensitivity by 50% relative to the threshold used by default in this extrapolation.

[36] Contacts: A. Bethani, A. Betti, P. Bokan, E. Carquin, M. Donadelli, A. Ferrari, K. Grimm, C. Gwilliam, M. Haacke, S. Lai, K. Leney, T. Lenz, S. Olivares Pino, E. Petit, N. Readioff, P. Sales De Bruin, J. Stark, F. Garay Walls, D. Wardrope, M. Wielers

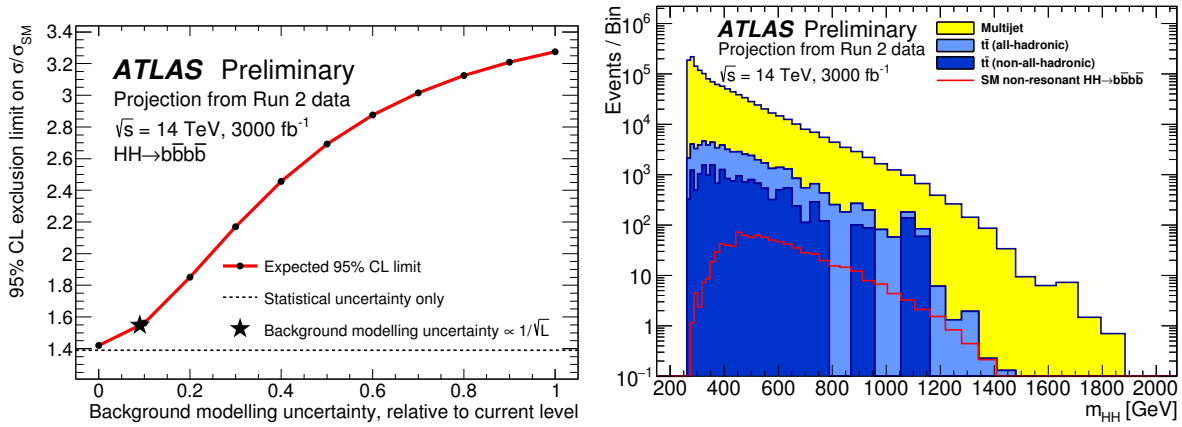

(a) (b)

Fig. 54: (a) Expected 95% CL upper limit on $\sigma_{HH}/\sigma_{HH}^{SM}$, as a function of the pre-fit background modelling uncertainties, which are each scaled by a common, constant factor relative to the corresponding uncertainty in the Run 2 analysis (i.e. the uncertainties of the analysis of the 2016 dataset correspond to 1 here). The limit achievable assuming that the overall uncertainty scales with luminosity as $1/\sqrt{L}$ is shown by the star point. The limit obtained when considering only statistical uncertainties is shown as the dashed line. The extrapolated sensitivities are calculated assuming a jet p_T threshold of 40 GeV. (b) Stacked m_{HH} histograms of the $t\bar{t}$ and multi-jet backgrounds extrapolated from 24.3 fb^{-1} (the 2016 dataset) to 3000 fb^{-1}. The predicted SM non-resonant Higgs boson pair production signal is shown as the red line.

3.2.1.2 The $HH \to b\bar{b}\tau\tau$ channel

Results [287] for this channel are computed by extrapolating from the Run 2 analysis of 36.1 fb^{-1} of 13 TeV data [288], which currently sets the world's strongest limit by a single channel on the di-Higgs production. The leptonic/hadronic and hadronic/hadronic decay modes of the τ-lepton are considered, the first one being separated in two categories, depending on the trigger used. A multivariate analysis with a Boosted Decision Tree is performed to separate the signal from the background processes. The Run 2 BDT distributions are scaled to the integrated luminosity of 3000 fb^{-1}, taking into account the change of cross-section with the increased centre-of-mass energy. The binning of those BDT distributions is also redefined to take into account the increased number of events. A profile-likelihood fit is applied to the BDT score distributions shown in Figures 55a to 55c.

In the Run 2 analysis one of the dominant systematic uncertainty is the one coming from the limited statistics of the MC samples used to estimate the background. In the baseline scenario, following the prescriptions of Ref. [16], this uncertainty is neglected. Different scenarios are considered: the one in which the systematic uncertainties remain the same as for the Run 2 analysis (scenario S1 described in Section 2.3.1); the scenario with the current systematic uncertainties but neglected MC statistical uncertainties and the baseline scenario for systematic uncertainties (scenario S2 described in Section 2.3.1). The effect on those various scenarios is shown in Figure 55d.

The expected significance without systematic uncertainties is of 2.5 standard deviations, while it is 2.1 standard deviations when the baseline scenario for the systematic uncertainties is considered.

For the measurement of κ_λ the output score of a BDT trained on the $\kappa_\lambda = 20$ signal is used as the final discriminant. This was shown to provide similar performance with BDTs trained specifically for every κ_λ value, as $\kappa_\lambda = 20$ corresponds to a softer m_{HH} spectrum, which is where the nominal BDT is less sensitive. The minimum negative-log-likelihood for a SM signal hypothesis is shown in Figure 55d.

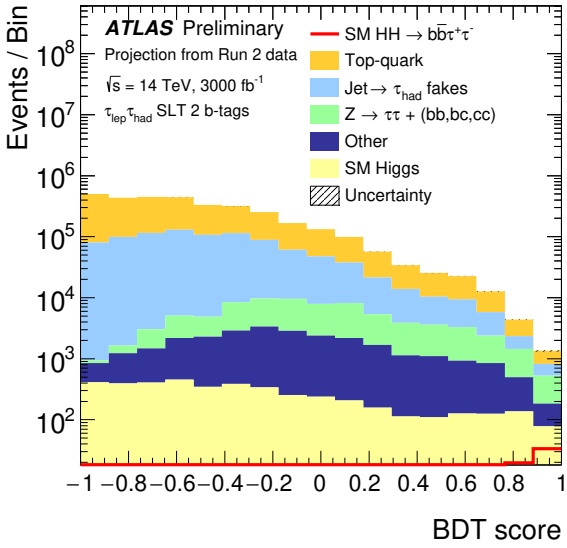

(a) $\tau_{lep}\tau_{had}$ channel passing a single-lepton trigger (SLT)

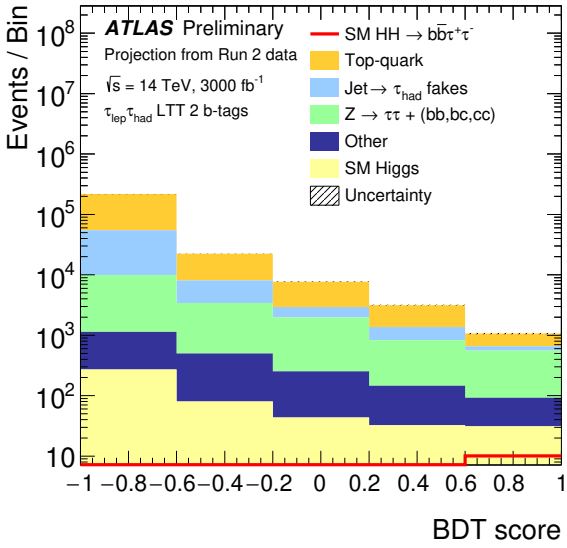

(b) $\tau_{lep}\tau_{had}$ channel passing a lepton-plus-τ_{had} trigger (LTT)

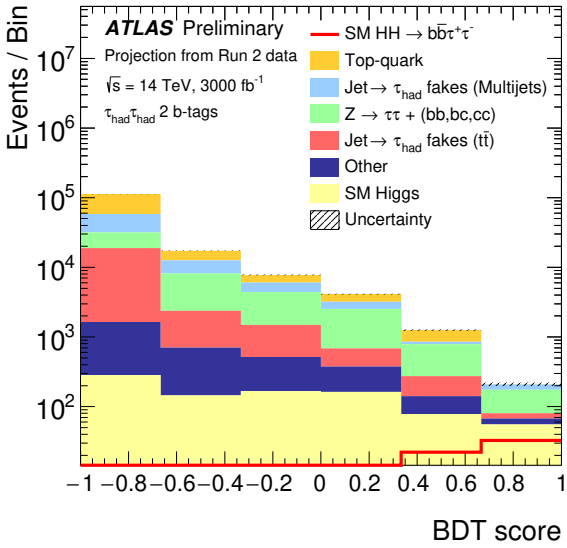

(c) $\tau_{had}\tau_{had}$ channel

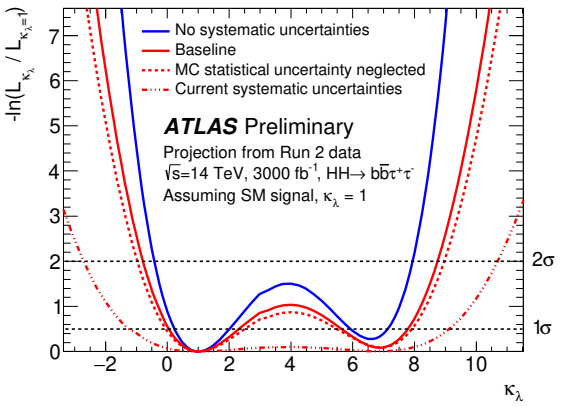

(d)

Fig. 55: (a), (b), (c) Distributions of the BDT score for the three categories of the analysis, extrapolated to 3000 fb^{-1} of data. The background distributions are shown after the fit based on a background-only Asimov dataset and the signal is scaled to the SM prediction. The hatched bands represent the combined statistical and systematic uncertainty for the baseline scenario. These uncertainty bands are included in the plots for completeness but are very small. (d) Negative natural logarithm of the ratio of the maximum likelihood for κ_λ to the maximum likelihood for $\kappa_\lambda = 1$, obtained from fits to the Asimov dataset that contains the $\kappa_\lambda = 1$ signal. Four different scenarios are considered for the systematic uncertainties.

3.2.1.3 The $HH \to b\bar{b}\gamma\gamma$ channel

The analysis [287] is based on truth level particles convoluted with the detector resolution, efficiencies and fake rates computed for $\mu = 200$ which were extracted from fully simulated samples using the detector layout described in Ref. [20]. The selection is made using a multivariate analysis with a BDT using

the full kinematic information of the event, in particular to reject the continuum and $t\bar{t}H$ backgrounds. The di-photon invariant mass distribution, $m_{\gamma\gamma}$, is shown in Figure 56a. The number of signal, single Higgs and continuum background in a 123-127 GeV window is 6.5, 3.2 and 3.7 respectively.

The systematic uncertainties follow the prescriptions of Ref. [16]. Their effect is very small since this channel will still be dominated by statistical uncertainties at the end of the HL-LHC programme.

The sensitivity of the analysis to κ_λ is assessed by using the m_{hh} distribution for events in a 123 $< m_{\gamma\gamma} <$ 127 GeV. This distribution is shown in Figure 56b for different values of κ_λ and split into eight categories. It should be noted that the BDT was trained on the SM signal only, so the constraints on κ_λ are pessimistic. Using separate BDTs trained on specific values of κ_λ would bring negligible improvements at negative values of κ_λ, but up to 1σ reduction in the expected limit at high positive values of κ_λ. The expected significance was evaluated to be 2.1 and 2.0 standard deviations with and without systematic uncertainties included.

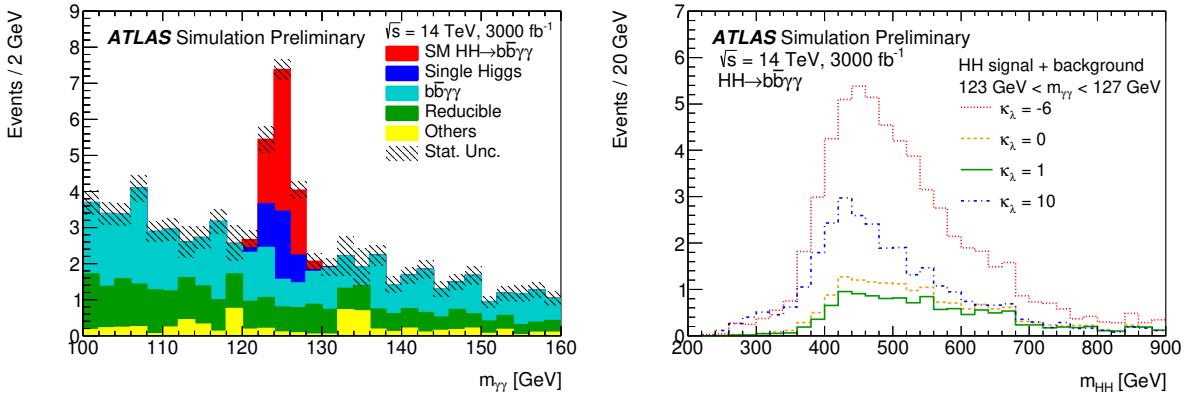

(a) (b)

Fig. 56: (a) Distribution of $m_{\gamma\gamma}$ following the BDT response cut. The reducible background processes consist of $c\bar{c}\gamma\gamma$, $jj\gamma\gamma$, $b\bar{b}j\gamma$, $c\bar{c}j\gamma$, and $b\bar{b}jj$ events. Other background processes come from $Z(b\bar{b})\gamma\gamma$, $t\bar{t}$ and $t\bar{t}\gamma$. (b) Distributions of $m_{b\bar{b}\gamma\gamma}$ for combined signal and background events passing the BDT selection and the requirement 123 GeV $< m_{\gamma\gamma} <$ 127 GeV, for various values of κ_λ.

3.2.1.4 Combined results

The combination of various channels is realised by constructing a combined likelihood function that takes into account data, models and correlated systematic uncertainties from all channels.

Setting appropriate nuisance parameters (NP) to be correlated with one another induced a negligible change in the combination results compared to assuming all nuisance parameters are uncorrelated. No strong correlation between any of the NP are found by the fits, with the exception of some correlation between the background models of the $b\bar{b}b\bar{b}$ and $b\bar{b}\tau\tau$ channels. Theoretical uncertainties on the cross-sections have negligible impact on the combined results.

The combined significance is 3.5 and 3.0 standard deviations with and without systematic uncertainties included. Table 53 shows the signal strength measured in the individual channels, as well as the combination, when the SM HH signal is injected.

The combined sensitivity of the three channels to κ_λ is assessed by generating an Asimov dataset containing the background plus SM signal. The ratio of the negative-log-likelihood of the maximum likelihood fit for κ_λ was calculated and shown in Figure 57. A morphing technique [289] is used to generate signal distributions of m_{HH} for any arbitrary value of κ_λ.

The 68% Confidence Intervals for κ_λ, from the likelihood ratio test performed on the Asimov

Table 53: Signal strength measured in the individual channels and their combination using an Asimov dataset with SM HH signal injected.

Measured μ	**Statistical-only**	**Statistical + Systematic**
$HH \to b\bar{b}b\bar{b}$	1.0 ± 0.6	1.0 ± 1.6
$HH \to b\bar{b}\tau\tau$	1.0 ± 0.4	1.0 ± 0.5
$HH \to b\bar{b}\gamma\gamma$	1.0 ± 0.6	1.0 ± 0.6
Combined	1.00 ± 0.31	1.0 ± 0.4

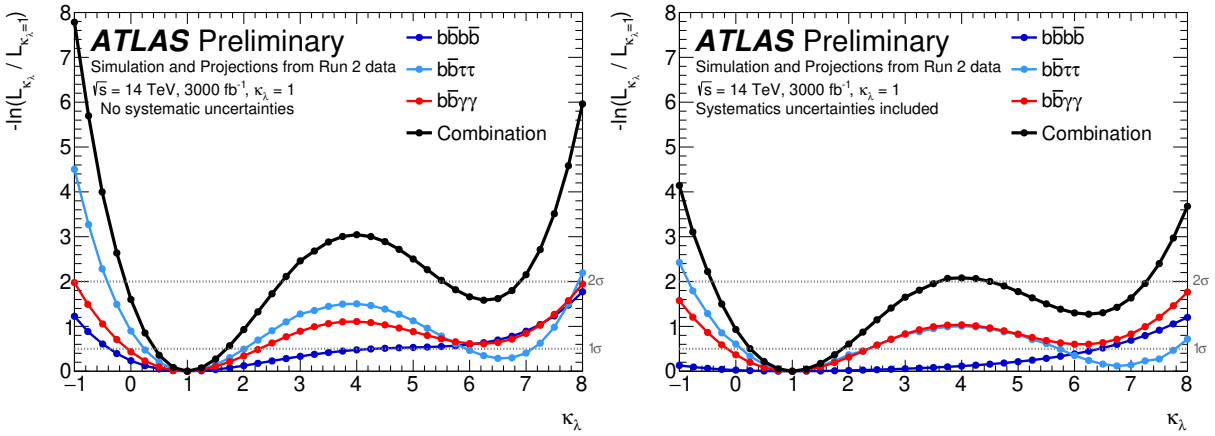

(a) Statistical uncertainties only

(b) Statistical + systematic uncertainties

Fig. 57: Maximum likelihood for κ_λ divided by the maximum likelihood for κ_λ = 1 for (a) the fits with only statistical uncertainties and (b) the fits with all systematic uncertainties as nuisance parameters. The black circles show the results for the combination, while the coloured markers show the values coming from the individual channels. The dashed lines at $-\ln\left(L_{\kappa_\lambda}/L_{\kappa_\lambda=1}\right) = 0.5$ and 2.0 indicate the values corresponding to the 1σ and 2σ Confidence Intervals (CI), respectively (assuming an asymptotic χ^2 distribution of the test statistic).

dataset created from the backgrounds and the SM HH signal are $0.4 \leq \kappa_\lambda \leq 1.7$ and $0.25 \leq \kappa_\lambda \leq 1.9$ with and without systematic uncertainties respectively. The Confidence Intervals per channel are summarised in Table 54. The Higgs boson self-coupling is constrained at 95% confidence level (CL) to $-0.4 \leq \kappa_\lambda \leq 7.3$ ($-0.1 \leq \kappa_\lambda \leq 2.7 \cup 5.5 \leq \kappa_\lambda \leq 6.9$), with (without) systematic uncertainties.

Table 54: 68% Confidence Intervals for κ_λ, estimated for an Asimov dataset containing the backgrounds plus SM signal.

	Statistical-only	**Statistical + Systematic**
$HH \to b\bar{b}b\bar{b}$	$-0.4 \leq \kappa_\lambda \leq 4.3$	$-2.3 \leq \kappa_\lambda \leq 6.4$
$HH \to b\bar{b}\tau\tau$	$0.2 \leq \kappa_\lambda \leq 2.0 \cup 5.9 \leq \kappa_\lambda \leq 7.2$	$0.1 \leq \kappa_\lambda \leq 2.3 \cup 5.7 \leq \kappa_\lambda \leq 7.8$
$HH \to b\bar{b}\gamma\gamma$	$-0.1 \leq \kappa_\lambda \leq 2.4$	$-0.2 \leq \kappa_\lambda \leq 2.5$
combined	$0.4 \leq \kappa_\lambda \leq 1.7$	$0.25 \leq \kappa_\lambda \leq 1.9$

Assuming the SM HH signal the expected exclusion significance for the κ_λ = 0 hypothesis, i.e. no Higgs self-coupling, is 1.4 and 1.8 standard deviations with and without systematic uncertainties respectively.

3.2.2 *Measurements with the CMS experiment*[37]

The work described in this section studies the prospects for HH production at the HL-LHC with the CMS experiment. The five decay channels bbbb, bb$\tau\tau$, bbWW (WW $\to \ell\nu\ell'\nu'$ with $\ell, \ell' = \mathrm{e}, \mu$), bb$\gamma\gamma$, and bbZZ (ZZ $\to \ell\ell\ell'\ell'$ with $\ell, \ell' = \mathrm{e}, \mu$) are explored. The corresponding branching fractions and the total number of HH events expected to be produced at the HL-LHC assuming $\sqrt{s} = 14\,\mathrm{TeV}$ and an integrated luminosity of $3000\,\mathrm{fb}^{-1}$ are reported in Table 55.

A short description of the analysis strategy and of the results is given here, and further details can be found in Ref. [290].

Table 55: Branching fraction of the five decay channels considered in the CMS HH prospects, and corresponding number of events produced at the end of HL-LHC operations assuming $\sqrt{s} = 14\,\mathrm{TeV}$ and an integrated luminosity of $3000\,\mathrm{fb}^{-1}$. The symbol ℓ denotes either a muon or an electron. In the bbWW decay channel, ℓ from the intermediate production of a τ lepton are also considered in the branching fraction.

Channel	bbbb	bb$\tau\tau$	bbWW($\ell\nu\ell\nu$)	bb$\gamma\gamma$	bbZZ($\ell\ell\ell\ell$)
$\mathcal{B}$ [%]	33.9	7.3	1.7	0.26	0.015
Number of events	37000	8000	1830	290	17

A parametric simulation based on the DELPHES [13] software is used to model the CMS detector response in the HL-LHC conditions. The DELPHES simulation accounts for the effects of multiple hadron interactions ("pileup") by overlaying simulated minimum-bias events with on average 200 interactions per bunch crossing. The performance of reconstruction and identification algorithms for electrons, muons, tau decays to hadrons (τ_{h}) and a neutrino, photons, jets (including the identification of those containing heavy flavour particles), and the missing transverse momentum vector $\vec{p}_{\mathrm{T}}^{\,\mathrm{miss}}$ is parametrised based on the results obtained with a full simulation of the CMS detector and dedicated reconstruction algorithms.

3.2.2.1 *The $HH \to bbbb$ channel*

While characterised by the largest branching fraction among the HH final states, the bbbb decay channel suffers from a large contamination from the multi-jet background that makes it experimentally challenging. Two complementary strategies are explored here to identify the signal contribution. For those events where the four jets from the HH $\to$ bbbb decay can all be reconstructed separately, also referred to as the "resolved" topology, the usage of multivariate methods is explored to efficiently identify the signal contribution in the overwhelming background. In cases where the invariant mass of the HH system, m_{HH}, is large, the high Lorentz boost of both Higgs bosons may results in a so-called "boosted" event topology where the two jets from a H $\to$ b$\bar{\mathrm{b}}$ decay overlap and are reconstructed as a single, large-area jet. Resolved topologies correspond to the large majority of SM HH events, giving the largest sensitivity on this signal. Boosted topologies help to suppress the multi-jet background and provide sensitivity to BSM scenarios where the differential HH production cross section is enhanced at high m_{HH} by the presence of ggHH and ttHH effective contact interactions.

In the resolved topology, events are pre-selected by requiring four jets with $\mathrm{p}_T > 45$ GeV and $|\eta| < 3.5$ that satisfy the medium b-tagging working point, corresponding to a b jet identification efficiency of approximately 70% for a light flavour and gluon jet mis-identification rate of 1%. Triggers are assumed to be fully efficient in the phase space defined by this selection. In scenarios where the minimal

[37] Contacts: A. Benaglia, M. Bengala, O. Bondu, L. Borgonovi, S. Braibant, L. Cadamuro, A. Carvalho, C. Delaere, M. Delcourt, N. de Filippis, E. Fontanesi, M. Gallinaro, M. Gouzevitch, J. R. Komaragiri, D. Majumder, K. Mazumdar, F. Monti, G. Ortona, L. Panwar, N. Sahoo, R. Santo, G. Strong, M. Vidal, S. Wertz

jet trigger $p_T$threshold is increased the loss in sensitivity to the SM signal amounts to approximately 10% and 25% for a 10 and 30 GeV increase, respectively.

The four selected b tagged jets are combined into the two Higgs boson candidates H_1 and H_2, choosing the pairs of jets with the minimal invariant mass difference. The invariant mass of the two Higgs candidates is required to satisfy the relation:

$$\sqrt{\left(m_{H_1} - 120\,\text{GeV}\right)^2 + \left(m_{H_2} - 120\,\text{GeV}\right)^2} < 40\,\text{GeV} \tag{39}$$

i.e. a circular selection where the centre and radius are chosen based on the expected response and resolution of the CMS detector, accounting for the energy loss from undetected neutrinos from B hadron decays.

Because of the very large QCD multi-jet background, a multivariate discriminant, in the form of a boosted decision tree, is trained to identify the HH signal contribution and used as the discriminant variable. Other background processes considered are $t\bar{t}$ and single Higgs boson production. The output of the BDT discriminant is shown in Fig. 58.

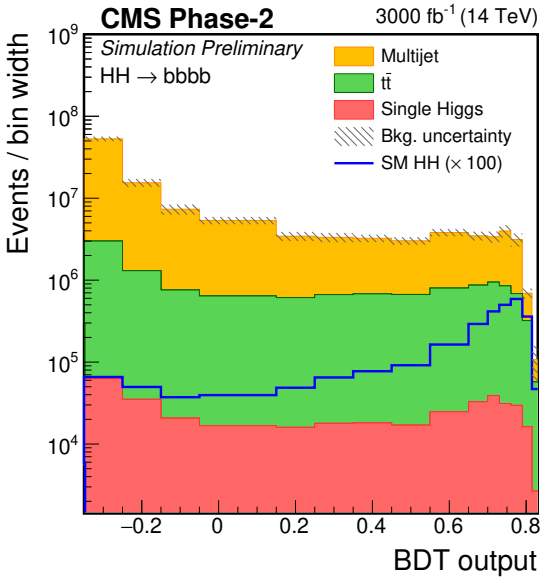

Fig. 58: BDT output distribution for the signal and background processes considered in the bbbb resolved search.

The boosted topology offers a good handle to investigate effective Higgs boson contact interactions predicted in BSM scenarios that enhance the HH production cross section at high m_{HH} values. For that reason, the prospects in this channels focus on anomalous couplings and make use of the shape benchmarks signals described in Ref. [281]. Large radius jets, clustered with the anti-k_{T} algorithm with a cone radius of 0.8 (AK8 jets), are used to identify the overlapping b jets. The event is required to contain at least two AK8 jets with $p_T > 300\,\text{GeV}$ and $|\eta| < 3$. The two highest p_T jets are chosen in case multiple candidates satisfy such requirements. The soft drop [291, 292] jet grooming algorithm is used to remove soft and collinear components of the jet and retain the two sub-jets associated with the showering and hadronisation of the two b quarks from the $H \to b\bar{b}$ decay. A selection is applied on the N-sub-jettiness variable [293] to reduce the background contamination, mostly represented by di-jet production from QCD interactions. Algorithms for the b jet identification are applied on the sub-jets with a working point corresponding to an efficiency of about 49% for genuine b jets for a mis-identification rate of light flavour and gluon jets of about 1%. Events are divided in two categories if they contain exactly three (3b category) or exactly four (4b category) b-tagged sub-jets.

The invariant mass of the two selected AK8 , M_{JJ}, is used to look for the presence of a signal. Its distribution is shown in Fig. 59 for the two event categories.

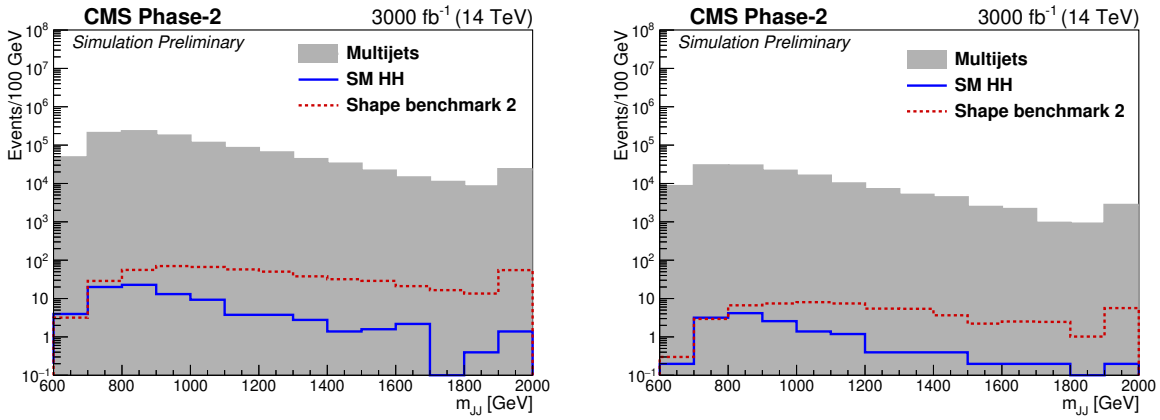

Fig. 59: Invariant mass of the two selected AK8 jets in the boosted bbbb HH search for the multi-jet background and the SM (blue) and shape benchmark 2 (red) signals. The distributions on the left are for the 3b and those on the right are for the 4b sub-jet b-tagged categories. Both signals are normalised to the SM HH production cross section for visualisation.

3.2.2.2 The $HH \to bb\tau\tau$ channel

The bb$\tau\tau$ decay channel is experimentally favourable thanks to its sizeable branching fraction of 7.3% and the moderate background contamination. Out of the six possible decay channels of the $\tau\tau$ system, the $\mu\tau_{\mathrm{h}}$, eτ_{h}, and $\tau_{\mathrm{h}}\tau_{\mathrm{h}}$ final states are considered here, corresponding together to about 88% of the total branching ratio. Events in the three channels are selected requiring the presence of a τ_{h}candidate in association to an isolated muon, electron, or another τ_{h} depending on the final state considered. Events in all the three categories above are then required to contain at least two b-tagged jets with $\mathrm{p}_T > 30$ GeV and $|\eta| < 2.4$.

The main backgrounds are $\mathrm{t\bar{t}}$ and Drell-Yan production of τ pairs. Their separation is experimentally challenging because of the incomplete reconstruction of the event due to the presence of neutrinos from τ decays that escape detection.

A multivariate analysis method is thus used to identify the signal contribution and separate if from the large background. The usage of state-of-the-art machine learning techniques is studied in this work. The discriminant consists of a pair of ensembles of ten fully connected deep neural networks (DNN), each with three hidden layers of 100 neurons, trained to separate the HH signal from the background processes using a wide set of kinematic variables, a few of which are shown for illustration in Fig. 60. Each network is trained using events from all three $\tau\tau$ decay channels, and advanced optimisation techniques are explored and applied to maximise the expected sensitivity.

3.2.2.3 The $HH \to b\bar{b}\gamma\gamma$ channel

Despite its low branching fraction, the bb$\gamma\gamma$ decay channel is one of the most sensitive to HH production. It benefits of an excellent di-photon invariant mass ($m_{\gamma\gamma}$) resolution and on the possibility to fully reconstruct all final state objects. The analysis strategy combines these two aspects and uses a multivariate kinematic discriminant to suppress the background contributions, and the $m_{\gamma\gamma}$ signature to look for the presence of a signal.

The H $\to \gamma\gamma$ candidate is built from two photons in the collision event that satisfy identification, isolation, and quality criteria. Only events where the two photons satisfy $|\eta| < 2.5$ and $100 < m_{\gamma\gamma} <$

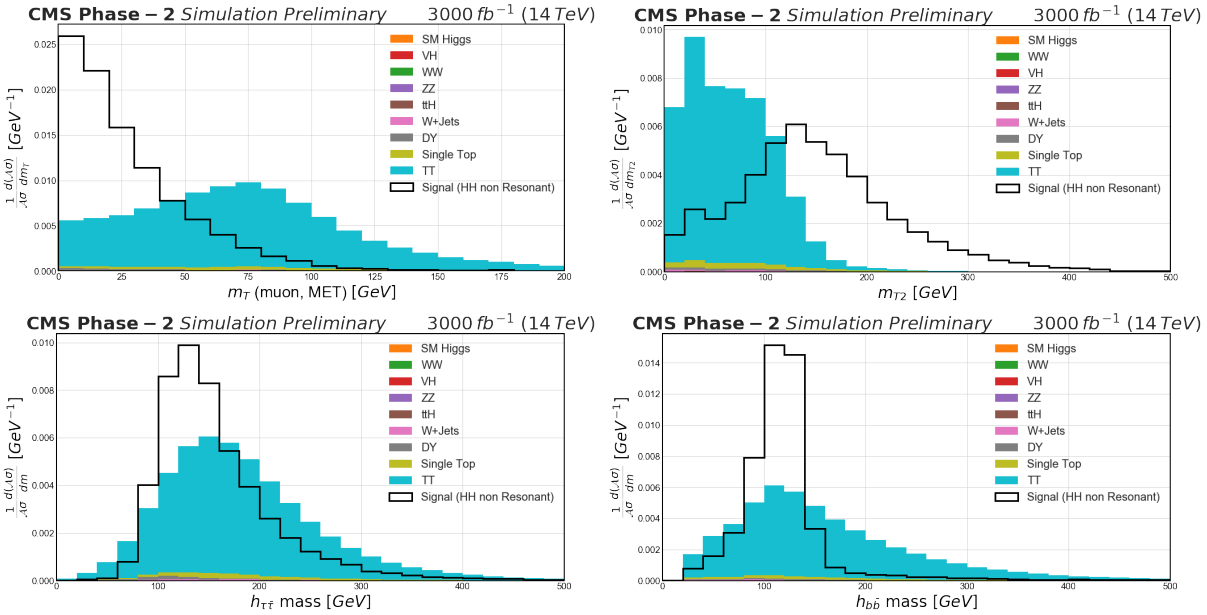

Fig. 60: Example distributions for some of the discriminant variables used as input of the bb$\tau\tau$ deep neural network: muon transverse mass (top left), system transverse mass m_{T2} (top right), and invariant mass of the $\tau\tau$ (bottom left) and bb (bottom right) systems.

150 are considered. The H $\rightarrow$ bb candidate is built from the two jets with the highest b tag discriminant value that satisfy $\mathrm{p}_T > 25$ GeV and $|\eta| < 2.5$. The background from light flavour jets is suppressed by requiring both jets to satisfy a loose working point of the b tagging algorithm, corresponding to a 90% efficiency for a genuine b-jet and 10% mis-identification rate. The di-jet invariant mass is required to be between 80 and 190 GeV.

The backgrounds mainly consist of non-resonant $\gamma\gamma$ production in association with heavy flavour jets, with a smaller contribution from $\gamma\gamma$ plus light flavour jets, and single Higgs boson production in association with top quark (ttH, with H $\rightarrow \gamma\gamma$).

A multivariate discriminant in the form of a BDT is used to suppress the ttH background. The BDT is trained to identify the presence of decay products from W bosons originating from top quark decays, and combines the information on the presence and properties of leptons, additional jets, and helicity angles of the HH system and its decay products. A selection on the discriminant is applied, rejecting approximately 75% of the ttH events for a 90% signal efficiency.

A second BDT classifier is trained to separate the HH signal from the non-resonant di-photon background. Several variables related to the kinematic properties of the event and to the quality of the selected objects are combined, and background-like events with a low BDT scores are rejected.

Events thus selected are simultaneously classified based on the value of the BDT discriminant described above and on the reduced mass of the four objects selected, defined as:

$$M_{\mathrm{X}} = m_{\gamma\gamma\mathrm{jj}} - m_{\gamma\gamma} - m_{\mathrm{jj}} + 250\,\mathrm{GeV}, \tag{40}$$

where $m_{\gamma\gamma\mathrm{jj}}$, $m_{\gamma\gamma}$, and m_{jj} refer respectively to the four body, di-photon, and di-jet invariant masses. The definition of M_{X} mitigates resolution effects by using the expected Higgs boson mass. Two intervals of the BDT scores are used to define medium and high purity categories (MP and HP), and events in each category are further divided in a low, medium, and high mass category if $250 < M_{\mathrm{X}} < 350$ GeV, $350 < M_{\mathrm{X}} < 380$ GeV, or $480 < M_{\mathrm{X}}$ GeV, respectively. While the high mass category is the most sensitive to SM HH production, low mass categories are important to constrain anomalous values of the Higgs boson self-coupling, that enhance the cross section at the m_{HH} threshold.

The signal is extracted from a simultaneous fit in each of the 3×2 categories defined above. A parametric maximum likelihood fit of the signal and background in the $(m_{\gamma\gamma}, m_{\mathrm{jj}})$ is used. An example of the expected event distributions in the high mass and high purity category for the two variables is shown in Fig. 61.

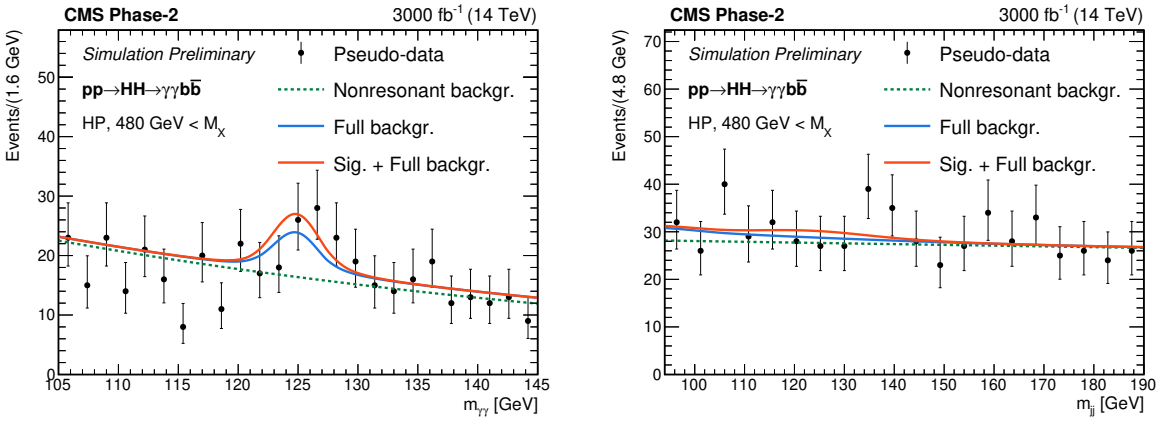

Fig. 61: Expected distribution of events in the photon (left column) and jet (right column) pair invariant mass for the high mass and high purity event category. The full circles denote pseudo-data obtained from the expected events yields for the sum of the signal and background processes for $3000\,\mathrm{fb}^{-1}$.

3.2.2.4 The $HH \to b\,b\,W\,W \to b\,b\ell\nu\ell\nu$ channel

We consider here HH final states containing two b jets and two neutrinos and two leptons, either electrons or muons. The decay channels involved are thus $\mathrm{H} \to \mathrm{bb}$ in association with either a $\mathrm{H} \to \mathrm{Z}(\ell\ell)\mathrm{Z}(\nu\nu)$ or a $\mathrm{H} \to \mathrm{W}(\ell\nu)\mathrm{W}(\ell\nu)$ decay. While the analysis described in the following is optimised for $\mathrm{HH} \to \mathrm{bbWW}$ decays, that provide the largest branching fraction, the contribution of Higgs boson decays to both WW and ZZ, globally denoted as VV, is considered. Decays of the VV system to tau leptons subsequently decaying to electrons or muons with the associated neutrinos are also considered in the simulated signal samples. The corresponding branching fraction for the $\mathrm{VV} \to \ell\nu_\ell\ell\nu_\ell$ decay is 1.73 %.

The dominant and sub-dominant background processes are the $\mathrm{t\bar{t}}$ production in its fully leptonic decay mode, and Drell-Yan production of lepton pairs in association with jets. As both are irreducible background processes, i.e., they result in the same final state as the signal, the kinematic properties of the signal and background events are used and combined in an artificial Neural Network (NN) discriminant to enhance the sensitivity.

Events are required to contain two isolated leptons of opposite electric charge, with an invariant mass $m_{\ell\ell} > 12\mathrm{GeV}$ to suppress leptonia resonances and $m_{\mathrm{Z}} - m_{\ell\ell} > 15\,\mathrm{GeV}$ to suppress Drell-Yan lepton pair production. The $\mathrm{H} \to \mathrm{bb}$ decay is reconstructed by requiring the presence of two b-tagged jets in the event with $\mathrm{p}_T > 20$ GeV and $|\eta| < 2.8$, separated from the selected leptons by a distance of $\Delta\mathrm{R} = \sqrt{\Delta\phi^2 + \Delta\eta^2} > 0.3$.

The NN discriminant utilises information related to object kinematics. The variables provided as input to the NN exploit the presence of two Higgs bosons decaying into two b-jets on the one hand, and two leptons and two neutrinos on the other hand, which results in different kinematics for the di-lepton and di-jet systems between signal and background processes. The set of variables used as input is:$m_{\ell\ell}$, m_{jj}, $\Delta R_{\ell\ell}$, ΔR_{jj}, $\Delta\phi_{\ell\ell,\mathrm{jj}}$, defined as the $\Delta\phi$ between the di-jet and the di-lepton systems, $\mathrm{p}_T^{\ell\ell}$, $\mathrm{p}_T^{\mathrm{jj}}$, $\min(\Delta R_{\mathrm{j},\ell})$, and $\mathrm{M_T}$, defined as $\mathrm{M_T} = \sqrt{2\mathrm{p}_T^{\ell\ell}\mathrm{p}_T^{\mathrm{miss}}(1 - \cos(\Delta\phi(\ell\ell, \mathrm{p}_T^{\mathrm{miss}})))}$.

The output of the NN is used as the discriminant variable in the three decay channels studied, and its distribution is reported in Fig. 62.

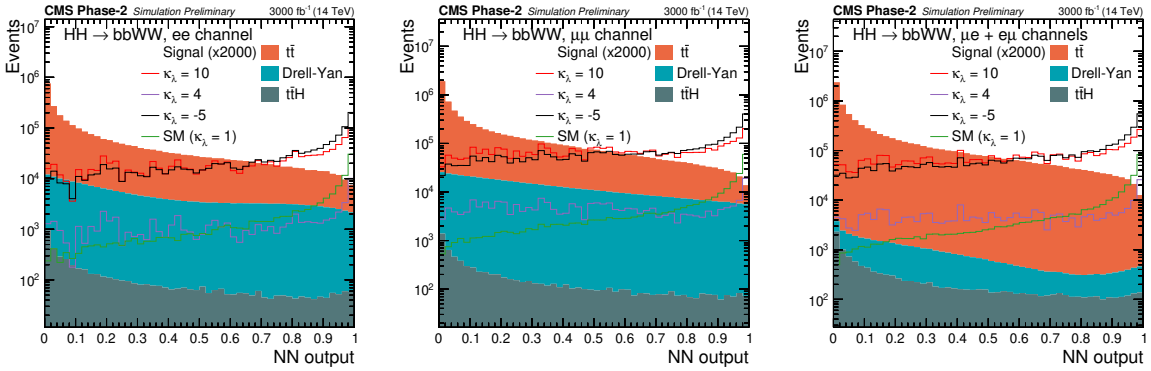

Fig. 62: The output of the bbWW NN after the selections, evaluated in the e^+e^- (left) , $\mu^+\mu^-$ (middle), $e^\pm\mu^\mp$ (right) channels.

3.2.2.5 The $HH \to bbZZ \to bb4\ell$ channel

The HH searches at the LHC have so far focused on final states with a sizeable branching ratio because of the small cross section of this process. The HL-LHC will open the possibility to study rare but clean decay channels thanks to the large dataset available. The bbZZ(4ℓ) channel, that is investigated in this work, benefits from the clean four lepton signature to clearly identify signal events in the busy pileup environment of the HL-LHC.

Events are required to have at least four identified and isolated (isolation < 0.7) muons (electrons) with $p_T > 5(7)$ GeV and $|\eta| < 2.8$. The two Z boson candidates are formed from pairs of opposite-charge leptons The Z candidate with the invariant mass closest to the nominal Z mass is denoted as Z_1, while the other one is labelled as Z_2. Z candidates are required to have an invariant mass in the range [40, 120] GeV (Z_1) and [12, 120] GeV (Z_2), respectively. The four leptons invariant mass is requested to be in the range [120,130] GeV. At least two (but not more than three) b-tagged jets are also required to be present and have an invariant mass. The jet pair is required to have an invariant mass in the range [80, 160] GeV and an angular distance between the 2 jets between 0.5 and 2.3. The number of events thus selected are used to look for the presence of a signal on top of the background processes, mostly constituted of single Higgs boson production in the 4ℓ final state. The distribution of the four lepton invariant mass is shown in Fig, 63.

3.2.2.6 Combined results

The five decay channels are combined statistically assuming the SM Higgs boson branching fractions. Assuming the presence of a signal with the properties predicted by the SM, its total expected significance is 2.6σ. If instead the background only hypothesis is assumed, an expected upper limit on the SM HH signal cross section can be set to 0.77 times the SM prediction. The contributions from the five decay channels and the combined expected sensitivities are reported in Tab. 56.

Prospects for the measurement of the Higgs boson self coupling are also studied. Under the assumption that no HH signal exists, 95% CL upper limits on the SM HH production cross section are derived as a function $\kappa_\lambda = \lambda_{\rm HHH}/\lambda^{\rm SM}_{\rm HHH}$, where $\lambda^{\rm SM}_{\rm HHH}$ denotes the SM prediction. The result is illustrated in Fig. 64. A variation of the excluded cross section, directly related to changes in the HH kinematic properties, can be observed as a function of κ_λ.

Assuming instead that a HH signal exists with the properties predicted by the SM, prospects for the measurement of the $\lambda_{\rm HHH}$ are derived. The scan of the likelihood as a function of the κ_λ coupling is shown in Fig. 64. The projected confidence interval on this coupling corresponds to $[0.35, 1.9]$ at the 68% CL and to $[-0.18, 3.6]$ at the 95% CL. The peculiar likelihood function structure, characterised by

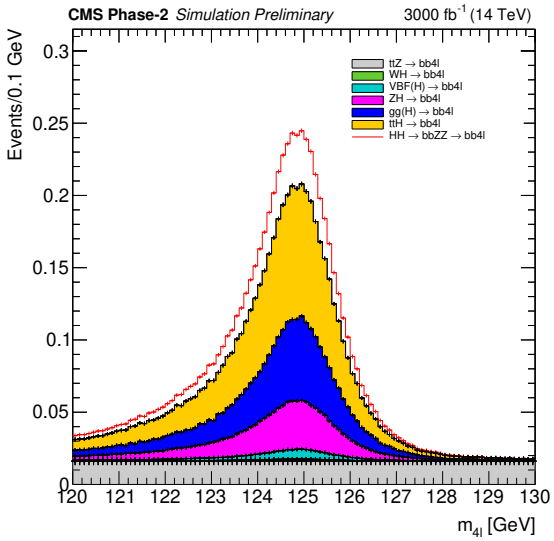

Fig. 63: Invariant mass distribution of the four leptons selected at the end of the analysis for the bb4ℓ final state.

Table 56: Significance, upper limit at the 95% confidence level, and uncertainty on the signal strength μ of the SM HH signal for the five channels studied and their combination. Numbers are reported both considering statistical and systematic uncertainties (Stat. + syst.), and neglecting the latter (Stat. only).

Channel	Significance		95% CL limit on $\sigma_{\mathrm{HH}}/\sigma_{\mathrm{HH}}^{\mathrm{SM}}$		Measured signal strength μ	
	Stat. + syst.	Stat. only	Stat. + syst.	Stat. only	Stat. + syst.	Stat. only
bbbb	0.95	1.2	2.1	1.6	$1.00^{+1.08}_{-1.04}$	$1.00^{+0.84}_{-0.83}$
bb$\tau\tau$	1.4	1.6	1.4	1.3	$1.00^{+0.73}_{-0.71}$	$1.00^{+0.65}_{-0.64}$
bbWW($\ell\nu\ell\nu$)	0.56	0.59	3.5	3.3	$1.00^{+1.8}_{-1.8}$	$1.00^{+1.7}_{-1.7}$
bb$\gamma\gamma$	1.8	1.8	1.1	1.1	$1.00^{+0.61}_{-0.56}$	$1.00^{+0.56}_{-0.53}$
bbZZ($\ell\ell\ell\ell$)	0.37	0.37	6.6	6.5	$1.0\ ^{+3.2}_{-2.5}$	$1.0\ ^{+3.2}_{-2.5}$
Combination	2.6	2.8	0.77	0.71	$1.00^{+0.41}_{-0.39}$	$1.00^{+0.36}_{-0.36}$

two local minimums, is related to the dependence of the total cross section and HH kinematic properties on κ_λ, while the relative height of the two minimums depends to the capability of the analyses to access differential m_{HH} information. The degeneracy of the second minimum is largely removed thanks to the bb$\gamma\gamma$ analysis and its m_{HH} categorisation.

3.2.3 Combination of measurements[38]

A simple combination is performed of the measurements from the ATLAS and CMS collaborations described in Sections 3.2.1 and 3.2.2. The channels are treated as uncorrelated, in particular because the systematic uncertainties that we could expect to be correlated between the experiments, such as the theory uncertainties and the luminosity uncertainty, have little impact on the individual results. Since the measurements in the $HH \to b\bar{b}VV(ll\nu\nu)$ and $HH \to b\bar{b}ZZ(4l)$ are only performed by the CMS

[38] Contacts: L. Cadamuro, E. Petit, D. Wardrope

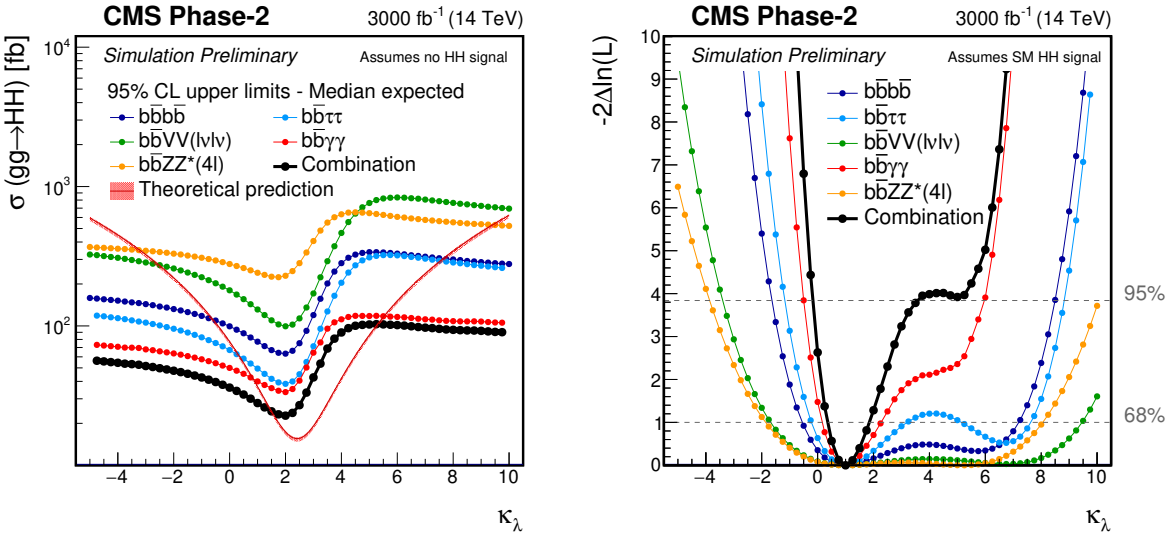

Fig. 64: Left: upper limit at the 95% CL on the HH production cross section as a function of $\kappa_\lambda = \lambda_{\mathrm{HHH}}/\lambda^{\mathrm{SM}}_{\mathrm{HHH}}$. The red band indicated the theoretical production cross section. Right: expected likelihood scan as a function of $\kappa_\lambda = \lambda_{\mathrm{HHH}}/\lambda^{\mathrm{SM}}_{\mathrm{HHH}}$. In both figures the results are shown separately for the five decay channels studied and for their combination.

experiment, the likelihoods for those two channels are scaled to 6000fb^{-1} in the combination. The significances are added in quadrature and the negative-log-likelihood are simply added together. A summary of the different expected significances, as well as the combination, are shown in Table 57. A combined significance of 4 standard deviation can be achieved with all systematic uncertainties included.

Table 57: Significance in standard deviations of the individual channels as well as their combination.

	Statistical-only		**Statistical + Systematic**	
	ATLAS	CMS	ATLAS	CMS
$HH \to b\bar{b}b\bar{b}$	1.4	1.2	0.61	0.95
$HH \to b\bar{b}\tau\tau$	2.5	1.6	2.1	1.4
$HH \to b\bar{b}\gamma\gamma$	2.1	1.8	2.0	1.8
$HH \to b\bar{b}VV(ll\nu\nu)$	-	0.59	-	0.56
$HH \to b\bar{b}ZZ(4l)$	-	0.37	-	0.37
combined	3.5	2.8	3.0	2.6
	Combined		Combined	
	4.5		4.0	

Comparisons of the minimum negative-log-likelihoods for ATLAS and CMS are shown in Figure 65. In those plots the likelihoods for the $HH \to b\bar{b}VV(ll\nu\nu)$ and $HH \to b\bar{b}ZZ(4l)$ channels are not scaled to 6000fb^{-1}. A difference of shape between the two experiments can be seen around the second minimum. This difference comes mainly from the $HH \to b\bar{b}\gamma\gamma$ channel as illustrated in Figure 65b. In this channel both experiment use categories of the m_{HH} distributions. But for ATLAS the analysis was optimised to increase the significance of the SM signal so the low values of the m_{HH} distribution are cut by the selection cuts, while for CMS a category of events with low values of m_{HH} is very powerful to remove the second minimum, while having no effect on the SM signal. The lower precision on κ_λ is slightly better for CMS thanks to the contribution of the $HH \to b\bar{b}b\bar{b}$ channel, as well as the $HH \to b\bar{b}VV(ll\nu\nu)$ and $HH \to b\bar{b}ZZ(4l)$ ones, while the higher precision on κ_λ is similar

between the two experiments.

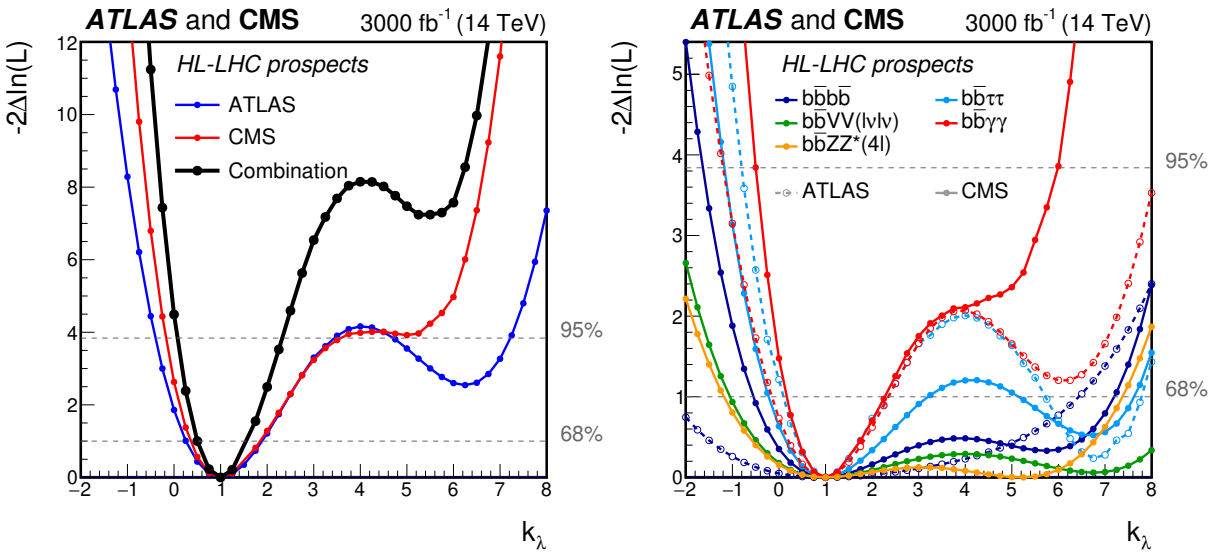

(a) (b)

Fig. 65: (a) Minimum negative-log-likelihood as a function of κ_λ, calculated by performing a conditional signal+background fit to the background and SM signal. (a) The black line corresponds to the combined ATLAS and CMS results, while the blue and red lines correspond to the ATLAS and CMS standalone results respectively. (b) The different colours correspond to the different channels, the plain lines correspond to the CMS results while the dashed lines correspond to the ATLAS results.

The combined minimum negative-log-likelihoods are shown in Figure 66. The 68% Confidence Intervals for κ_λ are $0.52 \leq \kappa_\lambda \leq 1.5$ and $0.57 \leq \kappa_\lambda \leq 1.5$ with and without systematic uncertainties respectively. The second minimum of the likelihood is excluded at 99.4% CL. A summary of the 68% CI for each channel in each experiment, as well as the combination are shown in Figure 66b.

3.3 Double Higgs measurements and trilinear coupling: alternative methods

3.3.1 *Prospects for $hh \to (b\bar{b})(WW^*) \to (b\bar{b})(\ell^+\ell^-\nu_\ell\bar{\nu}_\ell)$*[39]

In this section, we discuss the discovery prospects for double Higgs production in the $hh \to (b\bar{b})(WW^*)$ channel. In order to increase sensitivity in the di-lepton channel [294, 295, 296], we propose a novel kinematic method, which relies on two new kinematic functions, *Topness* and *Higgsness* [297]. They characterise features of the major $(t\bar{t})$ background and of hh events, respectively. The method also utilises two less commonly used variables, the subsystem M_{T2} (or subsystem M_2) [298, 299, 300] for $t\bar{t}$ and the subsystem $\sqrt{\hat{s}}_{min}$ (or subsystem M_1) [301, 302, 300] for hh production. For any given event, Topness [303, 297] quantifies the degree of consistency to di-lepton $t\bar{t}$ production, where there are 6 unknowns (the three-momenta of the two neutrinos, $\vec{p}_\nu$ and $\vec{p}_{\bar{\nu}}$) and four on-shell constraints, for m_t, $m_{\bar{t}}$, m_{W^+} and m_{W^-}, respectively. The neutrino momenta can be fixed by minimising the quantity

$$\chi^2_{ij} \equiv \min_{\not{p}_T=\vec{p}_{\nu T}+\vec{p}_{\bar{\nu}T}} \left[\frac{\left(m^2_{b_i\ell^+\nu} - m^2_t\right)^2}{\sigma^4_t} + \frac{\left(m^2_{\ell^+\nu} - m^2_W\right)^2}{\sigma^4_W} + \frac{\left(m^2_{b_j\ell^-\bar{\nu}} - m^2_t\right)^2}{\sigma^4_t} + \frac{\left(m^2_{\ell^-\bar{\nu}} - m^2_W\right)^2}{\sigma^4_W} \right], \quad (41)$$

[39] Contacts: J. Han Kim, M. Kim, K. Kong, K.T. Matchev, M. Park

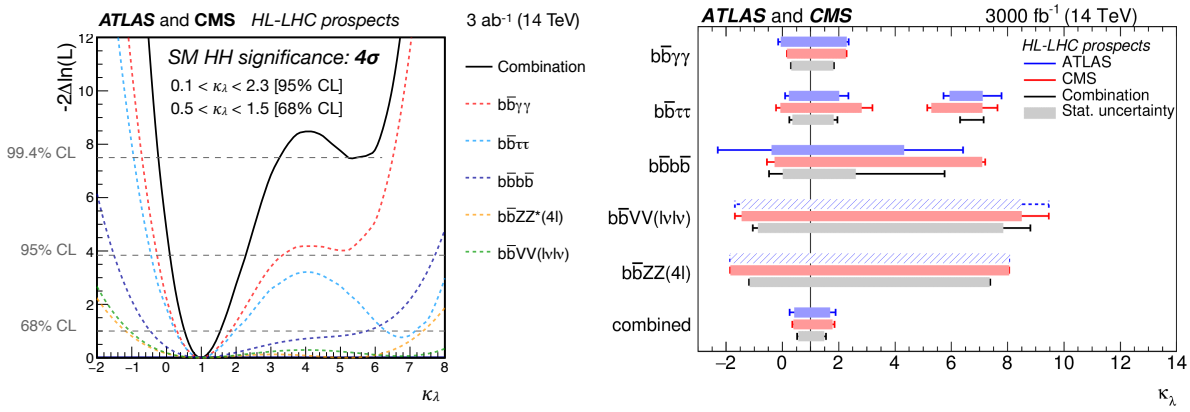

(a) (b)

Fig. 66: (a) Minimum negative-log-likelihood as a function of κ_λ, calculated by performing a conditional signal+background fit to the background and SM signal. The coloured dashed lines correspond to the combined ATLAS and CMS results by channel, and the black line to their combination. The likelihoods for the $HH \to b\bar{b}VV(ll\nu\nu)$ and $HH \to b\bar{b}ZZ(4l)$ channels are scaled to 6000 fb^{-1}.(b) Expected measured values of κ_λ for the different channels for the ATLAS in blue and the CMS experiment in red, as well as the combined measurement. The lines with error bars show the total uncertainty on each measurement while the boxes correspond to the statistical uncertainties. In the cases where the extrapolation is performed only by one experiment, same performances are assumed for the other experiment and this is indicated by a hatched bar.

subject to the missing transverse momentum constraint, $\vec{\not{p}}_T = \vec{p}_{\nu T} + \vec{p}_{\bar{\nu} T}$. Since there is a twofold ambiguity in the paring of a b-quark and a lepton, we define *Topness* as the smaller of the two χ^2s,

$$T \equiv \min\left(\chi^2_{12}, \chi^2_{21}\right). \tag{42}$$

In double Higgs production, the two b-quarks arise from a Higgs decay ($h \to b\bar{b}$), and therefore their invariant mass m_{bb} can be used as a first cut to enhance the signal sensitivity. For the decay of the other Higgs boson, $h \to WW^* \to \ell^+\ell^-\nu\bar{\nu}$, we define *Higgsness* [297] as follows:

$$H \equiv \min\left[\frac{\left(m^2_{\ell^+\ell^-\nu\bar{\nu}} - m_h^2\right)^2}{\sigma^4_{h_\ell}} + \frac{\left(m^2_{\nu\bar{\nu}} - m^2_{\nu\bar{\nu},peak}\right)^2}{\sigma^4_\nu} + \min\left(\frac{\left(m^2_{\ell^+\nu} - m_W^2\right)^2}{\sigma^4_W} + \frac{\left(m^2_{\ell^-\bar{\nu}} - m^2_{W^*,peak}\right)^2}{\sigma^4_{W^*}}, \frac{\left(m^2_{\ell^-\bar{\nu}} - m_W^2\right)^2}{\sigma^4_W} + \frac{\left(m^2_{\ell^+\nu} - m^2_{W^*,peak}\right)^2}{\sigma^4_{W^*}}\right)\right] \tag{43}$$

where m_{W^*} is the invariant mass of the lepton-neutrino pair which resulted from the off-shell W. It satisfies $0 \le m_{W^*} \le m_h - m_W$ and $m^{peak}_{W^*} = \frac{1}{\sqrt{3}}\sqrt{2\left(m_h^2 + m_W^2\right) - \sqrt{m_h^4 + 14 m_h^2 m_W^2 + m_W^4}}$ is the peak in the m_{W^*} distribution. $m^{peak}_{\nu\bar{\nu}} = m^{peak}_{\ell\ell} \approx 30$ GeV is the location of the peak in the $\frac{d\sigma}{dm_{\nu\bar{\nu}}}$ or $\frac{d\sigma}{dm_{\ell\ell}}$ distribution [297, 304].

The σ values in Eqs. (41) and (43) result from the experimental uncertainties and intrinsic particle widths. In principle, they can be treated as free parameters and tuned using a neutral network (NN), a boosted decision tree (BDT), etc. In our numerical study, we use $\sigma_t = 5$ GeV, $\sigma_W = 5$ GeV, $\sigma_{W^*} = 5$ GeV, $\sigma_{h_\ell} = 2$ GeV, and $\sigma_\nu = 10$ GeV. The main contribution in Eq. (43) comes from the on-shell

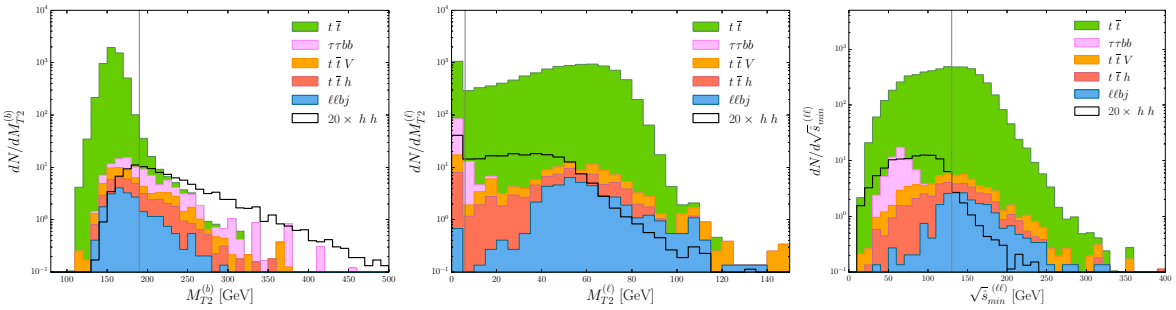

Fig. 67: Distributions for signal (hh) and all backgrounds ($t\bar{t}$, $t\bar{t}h$, $t\bar{t}V$, $\ell\ell bj$ and $\tau\tau bb$) for $M_{T2}^{(b)}$, $M_{T2}^{(\ell)}$ and $\sqrt{\hat{s}_{min}^{(\ell\ell)}}$ after loose baseline selection cuts defined in Ref. [297]. The vertical lines at $M_{T2}^{(b)} = 190$ GeV, $M_{T2}^{(\ell)} = 6$ GeV and $\sqrt{\hat{s}_{min}^{(\ell\ell)}} = 130$ GeV mark the optimised cuts.

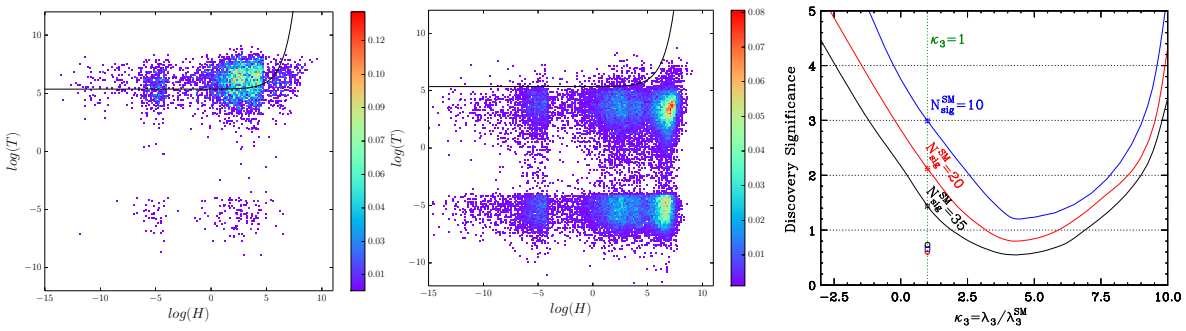

Fig. 68: Scatter distribution of ($\log H$, $\log T$) for signal (hh in the left) and backgrounds ($t\bar{t}$, $t\bar{t}h$, $t\bar{t}V$, $\ell\ell bj$ and $\tau\tau bb$ in the middle) after loose baseline selection cuts. The right panel shows the expected discovery significance at the 14 TeV LHC with 3 ab^{-1} as a function of the triple Higgs coupling κ_3. We obtain each curve by applying the same set of cuts optimised for the SM point ($\kappa_3 = 1$) to non-SM points ($\kappa_3 \neq 1$) for $\mathrm{N}_{\mathrm{sig}}^{\mathrm{SM}} = 35$ in black, $\mathrm{N}_{\mathrm{sig}}^{\mathrm{SM}} = 20$ in red and $\mathrm{N}_{\mathrm{sig}}^{\mathrm{SM}} = 10$ in blue. The curves in the left and middle panel are the optimised cuts for the $\mathrm{N}_{\mathrm{sig}}^{\mathrm{SM}} = 20$ case. The three symbols ◊, ◯ and □ display the signal significance using CMS-NN [294], CMS-BDT [295] and BDT [296], respectively.

conditions for the Higgs and the W, while the effects of the invariant mass of the two neutrinos and the off-shell W are minor.

Along with Higgsness and Topness, we adopt the subsystem $\hat{s}_{min}^{(\ell\ell)}$ for $h \to W^{\pm}W^{*\mp} \to \ell^+\ell^-\nu\bar{\nu}$ [301, 302] and the subsystem M_{T2} for the $b\bar{b}$ system ($M_{T2}^{(b)}$) and the lepton system ($M_{T2}^{(\ell)}$) [299]. The variable $\hat{s}_{min}^{(\mathrm{v})}$ is defined as $\hat{s}_{min}^{(\mathrm{v})} = m_{\mathrm{v}}^2 + 2\left(\sqrt{|\vec{P}_T^{\,\mathrm{v}}|^2 + m_{\mathrm{v}}^2}|\not{p}_T| - \vec{P}_T^{\,\mathrm{v}} \cdot \not{p}_T\right)$ [301, 302, 300], where (v) represents a set of visible particles under consideration, while m_{v} and $\vec{P}_T^{\,\mathrm{v}}$ are their invariant mass and transverse momentum, respectively. It provides the minimum value of the Mandelstam invariant mass $\hat{s}$ which is consistent with the observed visible 4-momentum vector. The M_{T2} is defined as $M_{T2}(\tilde{m}) \equiv \min\left\{\max\left[M_{TP_1}(\vec{p}_{\nu T}, \tilde{m}),\ M_{TP_2}(\vec{p}_{\bar{\nu}T}, \tilde{m})\right]\right\}$ where $\tilde{m}$ is the test mass for the daughter particle and the minimisation over the transverse masses of the parent particles M_{TP_i} ($i = 1, 2$) is performed over the transverse neutrino momenta $\vec{p}_{\nu T}$ and $\vec{p}_{\bar{\nu}T}$ subject to the $\not{p}_T$ constraint [298, 299, 300, 305, 306, 307, 308].

Events for the signal and all relevant background processes were simulated as described in Ref. [297]. After basic selection cuts, we use the kinematic information discussed above for further background suppression. Distributions of $M_{T2}^{(b)}$, $M_{T2}^{(\ell)}$ and $\sqrt{\hat{s}_{min}^{(\ell\ell)}}$ are shown in Fig. 67, while scatter distributions of

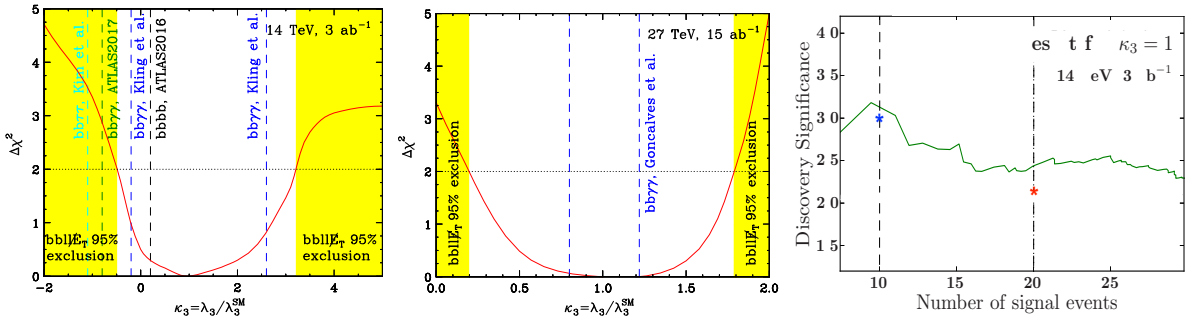

Fig. 69: Significance for observing an anomalous Higgs self-coupling at the 14 TeV LHC with an integrated luminosity of 3 ab^{-1} (left) and at 27 TeV with 15 ab^{-1} (middle). Right: the effect of using a Deep Learning algorithm to improve the discovery significance for $\kappa_3 = 1$ shown in the right panel of Fig. 68.

Topness and Higgsness are displayed in Fig. 68. The right panel in Fig. 68 shows the expected signal significance at the HL-LHC as a function of the triple Higgs coupling κ_3. We obtain each curve by applying the same set of cuts optimised for the SM point ($\kappa_3 = 1$) to non-SM points ($\kappa_3 \neq 1$) for $N_{sig}^{SM} = 35$ in black, $N_{sig}^{SM} = 20$ in red and $N_{sig}^{SM} = 10$ in blue. The three symbols $\diamondsuit$, $\bigcirc$ and $\square$ show the signal significance using CMS-NN [294], CMS-BDT [295] and BDT [296], respectively.

Finally Fig. 69 shows the significance for observing an anomalous Higgs self-coupling at the 14 TeV LHC with an integrated luminosity of 3 ab^{-1} and at 27 TeV with 15 ab^{-1}, respectively. For the HL-LHC, we follow the analysis presented in Ref. [297]. The red solid curves are obtained with nominal efficiencies for b (mis-)tagging ($\epsilon_{b\to b} = 0.7$, $\epsilon_{c\to b} = 0.2$ and $\epsilon_{j\to b} = 0.01$) [309]. The HL-LHC will rule out the Higgs self-coupling outside the range $(-0.5, 3.2)$. The four vertical dashed lines in the left panel represent the expected 95% CL exclusion of κ_3 in the $bbbb$ channel (black, from Ref. [310]), in the $bb\gamma\gamma$ channel (blue, from Ref. [311] and green from Ref. [312]) and in the $bb\tau\tau$ channel (cyan, from Ref. [211]). We notice that the sensitivity in the $bbWW^*$ channel is comparable to the sensitivity in those other channels. For the 27 TeV study, we normalise our signal cross section to 139.9 fb [276], and use K factors of $K = 1.56$ for $t\bar{t}$ production [313], $K = 1.28$ for $t\bar{t}h$ [314], $K = 1.54$ for $t\bar{t}V$ and a conservative $K = 2$ for $\ell\ell b\bar{b}$ and $\tau\tau b\bar{b}$ [297]. Our result shows that the 27 TeV collider could observe double Higgs production at 5σ for a wide range of values for κ_3 and would be able to exclude κ_3 outside the range $(0.2, 1.8)$ (for a comparative study in the $bb\gamma\gamma$ channel, see Ref. [315] (vertical, dashed lines in the middle panel)).

In summary, we obtained a significant increase in the signal sensitivity for hh production in the di-lepton channel compared to previous analyses [294, 295, 296]. The method can be easily incorporated into more advanced algorithms for further improvement. For example, using deep learning (convolutionary neutral network) slightly improves the discovery significance, see the right panel of Fig. 69. The discussed method is very general and can be easily applied to other processes such as the semi-leptonic final state, resonant hh production, non-resonant production with more than one Higgs boson, etc. It is straightforward to generalise the idea to different topologies in searches for other BSM particles as well.

3.3.2 *Prospects for $bb\gamma\gamma$: Bayesian optimisation and BDT*[40]

Searches for double Higgs pair production in the $b\bar{b}\gamma\gamma$ channel are an important target for the future. In this section, we study this problem at the 14 TeV LHC in two steps, following [316]:

(i) We first propose a Bayesian optimisation approach to select cuts on kinematic variables and study its performance compared to manual and random cuts, taking into account systematic uncertainties.

[40] Contacts: A. Alves, T. Ghosh, and K. Sinha

We demonstrate our results with the Python algorithm `Hyperopt` .

(ii) We next perform a joint optimisation of kinematic cuts and boosted decision trees (BDT) hyper-parameters to further discriminate signal and background events. For our calculations, we use the `XGBoost` implementation of BDTs for Python.

3.3.2.1 Signal and Backgrounds

For the simulation of the signal, we use `MadGraph5_aMC@NLO_v2.3.3` [317], to generate $pp \to hh$ process exclusively at the leading order (LO). The simulation of our signal include both the triangle and box diagrams. We scale our LO cross-section by the partial NNLO K-factor of 2.27 [318], calculated in the large quark mass limit and use the resulting production cross section of 36.8 fb.

The following backgrounds were taken into account in our study: (i) $b\bar{b}\gamma\gamma$; (ii) Zh with $Z \to b\bar{b}$ and $h \to \gamma\gamma$; (iii) $b\bar{b}h$ with $h \to \gamma\gamma$; (iv) $t\bar{t}h \to b\bar{b} + \gamma\gamma + X$; (v) $jj\gamma\gamma$ where the light-jets jj are mistaken for a b-jet pair in the detector; (vi) $b\bar{b}jj$, where the light-jets jj are mistaken for a photon pair; (vii) $c\bar{c}\gamma\gamma$, where a c-jet is mis-tagged as a b-jet; $(viii)$ $b\bar{b}\gamma j$, where one light-jet is mistaken for a photon; (ix) $c\bar{c}\gamma j$ where the c-jets are mis-tagged as bottom jets and the light-jet as a photon. We note that the $b\bar{b}\gamma j$, $c\bar{c}\gamma\gamma$, and $c\bar{c}\gamma j$ backgrounds were neglected in several early studies.

The cross section normalisations for the backgrounds from (i) - (v) are taken from ref. [285], which we consider reliable. In order to obtain the distributions of the kinematic variables of interest, we pass our simulated events to `PYTHIA_v6.4` [319] for showering, hadronisation and underlying event and finally to `DELPHES_v3.3` [13] for detector simulation. For all further details of our signal and background simulation, we refer to our paper [316].

The following basic cuts were applied on both signal and background:

$$\begin{aligned} & p_T(j) > 20 \text{ GeV}, \; p_T(\gamma) > 20 \text{ GeV}, \; |\eta(j)| < 2.5, \; |\eta(\gamma)| < 2.5 \\ & 100 \text{ GeV} < |M_{jj}| < 150 \text{ GeV}, \; 100 \text{ GeV} < |M_{\gamma\gamma}| < 150 \text{ GeV} \; . \end{aligned} \tag{44}$$

The number of backgrounds events after imposing the basic cuts for 3 ab^{-1} of integrated luminosity is shown in Table 58.

Table 58: The number of signal and the various types of backgrounds considered in this work after imposing the basic cuts of eq. (44) for 3 ab^{-1} of data. We found $b\bar{b}jj$ negligible after cuts and after estimating the probability of the jet pair faking a photon pair.

signal	$b\bar{b}\gamma\gamma$	$c\bar{c}\gamma\gamma$	$jj\gamma\gamma$	$b\bar{b}\gamma j$	$t\bar{t}h$	$c\bar{c}\gamma j$	$b\bar{b}h$	Zh	total backgrounds
42.6	1594.5	447.7	160.3	137	101.1	38.2	2.4	1.8	2483

3.3.2.2 Bayesian Optimisation

The $b\bar{b}\gamma\gamma$ channel has been studied by several groups using cut and count strategies. Once signal and background cross sections are normalised to the proper values, one finds that the analysis of any particular group does not radically outperform that of any other. For a detailed comparison, we refer to Table 2 of [316].

Bayesian optimisation offers a systematic way to obtain the most optimal cuts on a set of kinematic variables. The algorithm we utilise is implemented in the Python library `HyperOpt` , based on the so-called sequential model-based optimisation (SMBO) technique [320, 321, 322].

The kinematic variables used in our study are: (i) transverse momentum of b-jets and photons: $p_T(b)$ and $p_T(\gamma)$; (ii) $b\bar{b}$ and $\gamma\gamma$ invariant masses: M_{bb} and $M_{\gamma\gamma}$, where signal events exhibit resonance peaks at m_h; (iii) transverse momentum of $b\bar{b}$ and $\gamma\gamma$: $p_T(bb)$ and $p_T(\gamma\gamma)$; (iv) invariant mass of two

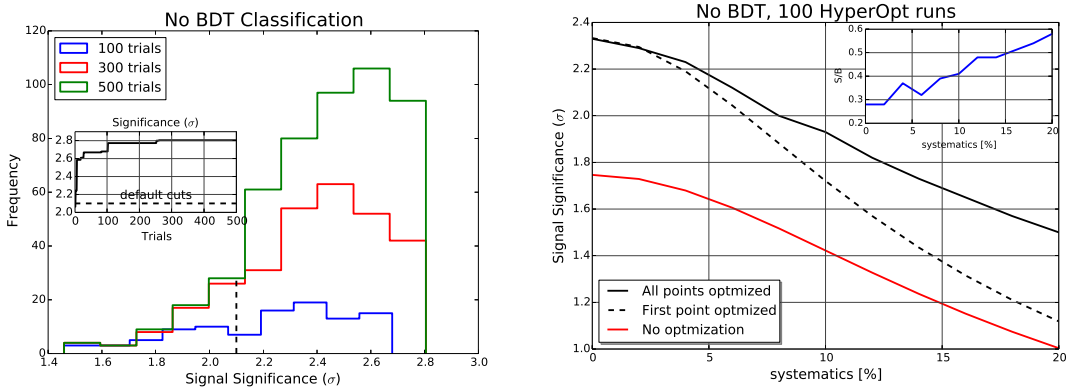

Fig. 70: **Left panel:** The left panel shows the optimised search with the TPE algorithm in `HyperOpt` with no systematic errors. The inset frame in the left plot shows the significance as a function of the number of trials. $S/\sqrt{B}$ is used to compute the signal significance. The black dashed line represents the results obtained with the cuts of Azatov *et. al.*, ref. [285]. **Right panel:** The $S/\sqrt{B+(\varepsilon_B B)^2}$ significance metric as a function of ε_B, the systematic uncertainty in the total background rate. The red line represents the default cuts of Azatov *et. al.*, the black dashed assumes an optimised strategy just for the 0% systematics point, while for the solid upper line, the algorithm was solicited to learn the best cuts for each systematics level from 0 to 20%. In the inner plot we show the S/B ratio for the point-to-point optimisation case.

b-jets and two photons: $M_{bb\gamma\gamma}$; (v) distance between pairs of b-jets and photons: $\Delta R(bb)$, $\Delta R(\gamma\gamma)$ and $\Delta R(b\gamma)$, where $\Delta R = \sqrt{(\Delta\eta)^2 + (\Delta\phi)^2}$ in the pseudo-rapidity and azimuthal angle plane (η, ϕ); (vi) the fraction $E_T/M_{\gamma\gamma}$ for the two hardest photons in the event; these are variables used in experimental searches as in Ref. [323, 143].

In Figure 70, we display the results obtained from the Bayesian optimisation of cuts on the above kinematic variables. We see that after 100-200 trials, the signal significance does not change much and the optimised cuts achieved a significance of 2.81σ against 2.1σ of the manual search of ref. [285], a 34% improvement. If $b\bar{b}\gamma j$, $c\bar{c}\gamma\gamma$, and $c\bar{c}\gamma j$ backgrounds are incorporated, the Bayesian search reached 2.48σ against 1.85σ of the cuts of ref. [285], again roughly the same improvement. The performance of the Bayesian algorithm is also displayed in Figure 70.

3.3.2.3 BDT Analysis

We now turn to a discussion of the BDT analysis, for which we utilise the `XGBoost` implementation of BDTs for Python. `XGBoost` is chosen for its good discrimination performance, speed and capacity of parallelisation. For our analysis we simulated $\sim$ 880000; depending on the cuts, however, the total number of events usually drops to around 100000–300000 events which also turned out to be a sufficient number of samples to keep over-fitting under control.

Using `HyperOpt`, we perform a joint optimisation of the kinematic variables introduced previously in conjunction with the following BDT hyper-parameters: the `number of boosted trees`, the `learning rate`, the `maximum depth of the trees`, and the minimum sum of instance weight needed in a child to continue the splitting process of the tress, `min_child_weight`. All the BDT results were obtained from a 5-fold cross validation by randomly splitting training and testing samples at the proportion of 2/3 and 1/3 of the total sample, respectively. We allowed for 300 trials in `HyperOpt`.

Hyper-parameters like the `number of boosted trees`, `maximum depth of the trees` and the `min_child_weight` are directly related to the complexity of the algorithm by controlling the num-

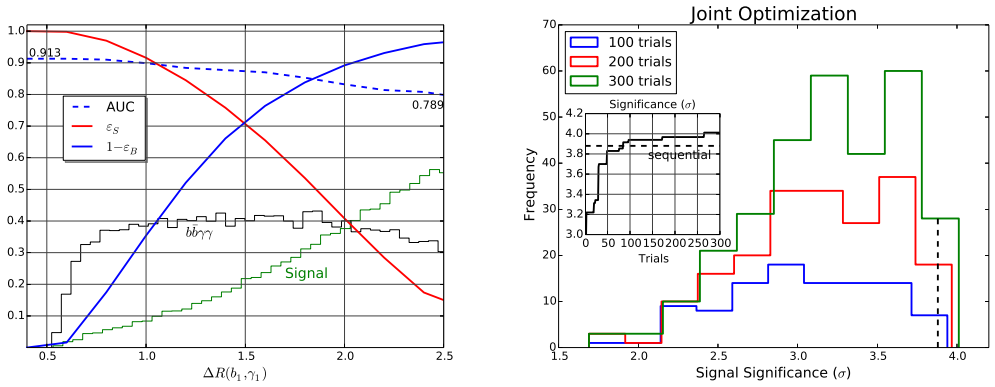

Fig. 71: **Left panel:** We show the results of the effects of imposing hard cuts on $\Delta R_{b_1\gamma_1}$ for the BDT performance, see [316] for further details. **Right panel:** The histogram of number of cut strategies producing a given significance interval in a BDT-aided classification analysis. The inset plot shows the significance as a function of the number of `HyperOpt` trials. No systematics are assumed, the backgrounds are those of ref. [285] and the $S/\sqrt{B}$ used to compute the signal significances. The black dashed line represents the results obtained with the default cuts of Azatov *et. al.*, ref. [285].

ber, size and configuration of the trees. The `learning rate`, also known as `shrinkage` in this context, is a parameter that controls the weight new trees have to further model the data. A large value permits a larger effect from new added trees and might lead to more severe over-fitting. There are other parameters which can be eventually used to prevent over-fitting and loss of generalisation power, but we found that tuning these parameters was sufficient to achieve a good performance.

A comparative result of a simple cut and count analysis and a sequential optimisation of cuts and BDT hyper-parameters are presented Table 59. We note that BDT outperforms simple cut and count, even when cutting is performed using Bayesian optimisation. This is due to the better discrimination between the signal and background classes achieved by the machine learning algorithms as they find more profound correlations among the kinematic features and those classes. These correlations cannot be fully explored in simple/manual rectangular cut-and-count analyses.

Table 59: Signal significances for cut-and-count and BDT for 0, 10 and 20% systematics. We took all backgrounds into account for the computation of the AMS with optimised cuts and an integrated luminosity of 3 ab^{-1} at the 14 TeV LHC. The bold-face numbers represent the significances expected with the level of systematics anticipated by the experimental collaborations in refs. [312, 143]. The numbers inside brackets are the significances computed with the default cuts of Azatov *et. al.*, ref. [285], which we took as baseline results.

systematics (%)	Cut-and-count	BDT
0	2.34[1.76]	3.88
10	**1.93**[1.43]	**3.57**
20	1.51[1.0]	3.10

However, there is a trade-off between the efficiency of the cuts and the ML performance which is usually neglected in phenomenological works where these tools are employed. The reasoning is simple: cutting harder cleans up more backgrounds but weakens the correlations between the kinematic variables and the event classes, thereby decreasing the ML performance. On the other hand, relaxing the cuts makes the correlations stronger helping to boost ML but the discrimination power gained might not be enough to get a good significance with a large number of surviving back- ground events. Hence, a joint optimisation of cuts and BDT hyper-parameters improve the performance of our analysis further.

The maximum AMS significance is 4.0σ for a joint optimisation analysis of cuts and BDT hyper-parameters. The final selections of the kinematic variables and BDT hyper-parameters are the following $p_T(1) > 72$ GeV, $p_T(2) > 20$ GeV; $\Delta R_{ij} > 0.15$, $\Delta R_{ii} < 3.6$; $M_{b\bar{b}\gamma\gamma} > 370$ GeV, $p_{T_{ii}} > 145$ GeV, $M_{b_1\gamma_1} > 100$ GeV; $|M_{bb} - m_h| < 27$ GeV, $|M_{\gamma\gamma} - m_h| < 11$ GeV; `number of trees` $= 157$; `learning rate` $= 0.101$; `maximum tree depth` $= 14$; `min_child_weight` $= 5$. We have denoted $p_T(1)$ as the leading b-jet or photon, and $p_T(2)$ as the next-to-leading b-jet or photon.

The results are shown in Figure 71. The left panel shows the normalised $\Delta R_{b_1\gamma_1}$ histograms for the signal and the $b\bar{b}\gamma\gamma$ continuum background, the signal efficiency (background rejection) is the red (blue) line, and the area under the Receiver-Operator curve (ROC), AUC, is the dashed line. The bigger the AUC, the better the performance of a cut-and-count analysis based on that distribution. On the right panel, we show the histogram of number of cut strategies producing a given significance interval in a BDT-aided joint optimisation analysis. Finding this optimal performance from the competition between hard cuts and an ML algorithm is the core of the method presented in the section.

3.4 HE-LHC prospects

This section shows prospective results that could be obtained with 15 ab^{-1} of data at a centre-of-mass energy of 27 TeV at the HE-LHC.

3.4.1 Theoretical prospects: from kinematics to dynamics[41]

sHiggs pair production $pp \to hh$ offers a direct path to pin down the Higgs self-coupling λ at a hadron collider [324, 325, 326, 327, 328, 329]. Theoretical studies as well as current analyses point to the $b\bar{b}\gamma\gamma$ decay as the most promising signature at the LHC [330, 331]. For the high-luminosity LHC (HL-LHC), ATLAS and CMS projections indicate a very modest sensitivity to the Higgs self-coupling [312, 295]. In the optimistic scenario that we can neglect systematic uncertainties, those studies indicate that the LHC will probe the coupling at 95% confidence level $-0.8 < \kappa_\lambda < 7.7$, where the SM value is $\kappa_\lambda = \lambda/\lambda_{SM} = 1$, falling short in precision in comparison to other Higgs property measurements at the LHC, and far from satisfactory in probing the Higgs potential. For example, $\mathcal{O}(1)$ determination of κ_λ would be required to test some of the EW Baryogenesis models [332, 333, 334, 335, 336, 337, 338, 339].

Because of the rapidly growing gluon luminosity at higher energies, the hh production cross section increases by about a factor of 4 (40) at 27 (100) TeV. This means that at the HE-LHC with the anticipated integrated luminosity of 15 ab^{-1} the number of events in the $b\bar{b}$ $\gamma\gamma$ channel increases by a factor $4 \times 5 = 20$ to around 5k events. A 100 TeV hadron collider with a projected integrated luminosity of 30 ab^{-1} features another increase by a factor $10 \times 2 = 20$, to around 100k expected Higgs pair events in the Standard Model. This estimate shows how the combination of increased energy and increased luminosity slowly turns Higgs pair production into a valid channel for precision measurements [315].

3.4.1.1 Information in Distributions

Previous studies have shown that multivariate analysis, taking into account kinematic distributions, gives a substantially better reach on the Higgs self coupling over the purely rate-based analysis [315, 311, 340, 341]. In the following, we therefore summarise which kinematic features include information about the Higgs self-coupling.

At leading order, Higgs pair production receives contributions both from a triangular loop diagram sensitive to the Higgs-self coupling and from a box or continuum diagram. The box contribution completely dominates the total rate over most of the phase space, making the Higgs coupling measurements a challenge. While we can define a number of kinematic observables describing the continuum backgrounds, the measurement of the Higgs self-coupling relies on a simple $2 \to 2$ process with two

[41] Contacts: D. Gonçalves, T. Han, F. Kling, T. Plehn, M. Takeuchi

independent kinematic variables.

Three distinct phase space regions provide valuable information on a modified Higgs self-coupling, all from a large destructive interference between the triangle and box contributions. First, there is the threshold [327, 328, 329, 342, 343, 344] in the partonic centre of mass energy $m_{hh} \approx 2m_h$. Based on the effective Higgs-gluon Lagrangian [345, 346, 347] we can therefore write the corresponding amplitude for Higgs pair production as

$$\frac{\alpha_s}{12\pi v}\left(\frac{\kappa_\lambda \lambda_{\text{SM}}}{s-m_h^2}-\frac{1}{v}\right) \to \frac{\alpha_s}{12\pi v^2}\left(\kappa_\lambda - 1\right) \overset{\text{SM}}{=} 0\,. \tag{45}$$

While the heavy-top approximation is known to give a poor description of the signal kinematics as a whole, it does describe the threshold dependence correctly [342, 343, 344]. This indicates that we can search for a deviation of the Higgs self-coupling by looking for an enhancement of the rate at threshold. Second, an enhanced sensitivity to the self-coupling appears as top mass effect. For large positive values of λ absorptive imaginary parts lead to a significant dip in the combined rate at the threshold $m_{hh} \approx 2m_t$ [348, 349, 311]. The sharpest interference dip takes place near $\kappa_\lambda \approx 2$ while for negative values of κ_λ the interference becomes constructive. Finally, the triangular and box amplitudes have a generally different scaling in the limit $m_{hh} \gg m_h, m_t$ [327, 328, 329, 348, 349]. While the triangle amplitude features an explicit suppression of either m_h^2/m_{hh}^2 or m_t^2/m_{hh}^2 at high invariant mass, the box diagrams drops more slowly towards the high-energy regime. This explains why a rate based analysis focusing on the high di-Higgs mass region only has limited sensitivity. The impact of all three kinematic features can be quantified statistically and indicate that essentially the full information on the Higgs self-coupling can be extracted through a shape analysis of the m_{hh} distribution [341].

In Fig. 72 we present the signal and background distributions for three relevant kinematic variables: m_{hh}, $p_{T,h}$ and $\Delta R_{\gamma\gamma}$. Using the MADMAX approach [350, 351], based on the Neyman Pearson Lemma we also estimate the maximum significance with which any multi-variate analysis will be able to extract an anomalous self-coupling $\kappa_\lambda \neq 1$. The corresponding differential distribution of maximum significance are shown as solid lines in Fig. 72. In addition to the signal features, the significance is limited by the rapidly dropping backgrounds, covering both of the above-mentioned regions with an enhanced dependence on the triangle diagram. In the absence of background, the significance indeed peaks between the production threshold and the top-mass threshold [311]. The drop towards large values of m_{hh} is a combination of the dominance of the box diagram in the signal and the limited number of expected signal events. The significance with which we can extract modified self-couplings either smaller ($\kappa_\lambda = 0$) or larger ($\kappa_\lambda = 2$) than in the Standard Model shows a similar phase space dependence. The only difference is a slightly harder significance distributions for $\kappa_\lambda = 2$, an effect of the dip at $m_{hh} \approx 2m_t$.

3.4.1.2 Detector-Level Analysis

Based on our findings above, we now design a detailed analysis strategy to extract the Higgs self-coupling with a focus on the shape of the m_{hh} distribution [315]. Our signal is $pp \to hh + X \to b\bar{b}\,\gamma\gamma + X$. The signal and background samples are generated with MADGRAPH5+PYTHIA8 [317, 79, 32], including one extra jet using the MLM scheme [352].

In the final state we demand two b-tagged jets and two isolated photons with the minimal acceptance and trigger cuts

$$p_{T,j} > 30 \text{ GeV}, \quad |\eta_j| < 2.5, \quad p_{T,\gamma} > 30 \text{ GeV}, \quad |\eta_\gamma| < 2.5, \quad \Delta R_{\gamma\gamma,\gamma j,jj} > 0.4\,. \tag{46}$$

The background to our $b\bar{b}\,\gamma\gamma$ signal consists of other Higgs production modes ($t\bar{t}h, Zh$) with $h \to \gamma\gamma$, continuum $b\bar{b}\gamma\gamma$ production, and of multi-jet events with light-flavor jets faking either photons or b-jets ($jj\gamma\gamma, b\bar{b}\gamma j$) [353].

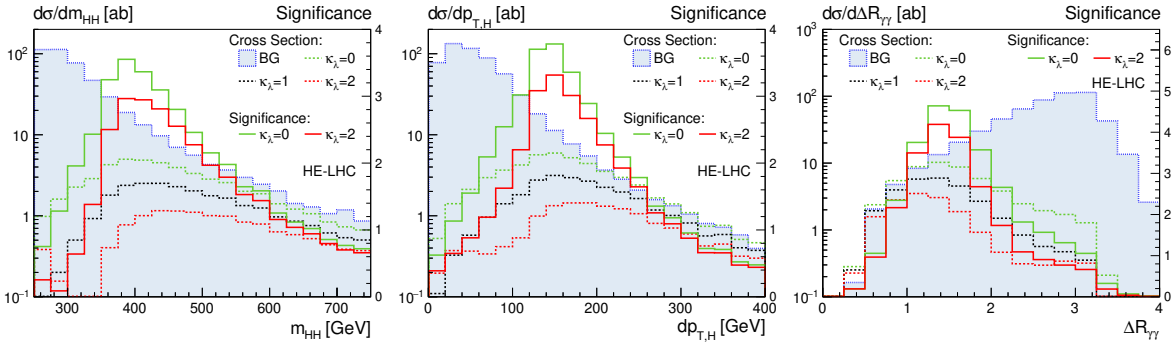

Fig. 72: Kinematic distributions (dashed lines with left vertical axes) and significance distribution (solid lines with right vertical axes) assuming a Higgs self-coupling with $\kappa_\lambda = 0, 1, 2$ for the HE-LHC. The significance describes the discrimination of an anomalous self-coupling $\kappa_\lambda \neq 1$ from the SM hypothesis $\kappa_\lambda = 1$.

The proper simulation of efficiencies and fake rates are a key ingredient for a realistic background estimate in this analysis. For the HE-LHC and the future 100 TeV collider we follow the ATLAS projections [354]. The efficiency for a tight photon identification can be well parametrised by

$$\epsilon_{\gamma\to\gamma} = 0.863 - 1.07 \cdot e^{-p_{T,\gamma}/34.8\ \text{GeV}}\ , \tag{47}$$

and a jet-to-photon mis-identification rate by

$$\epsilon_{j\to\gamma} = \begin{cases} 5.30\cdot 10^{-4}\ \exp\left(-6.5\left(p_{T,j}/(60.4\ \text{GeV})-1\right)^2\right) & \text{for } p_{T,j} < 65\ \text{GeV}\ , \\ 0.88\cdot 10^{-4}\ \left[\exp\left(-(p_{T,j}/(943\ \text{GeV})\right) + 248\ \text{GeV}/p_{T,j}\right] & \text{for } p_{T,j} > 65\ \text{GeV}\ . \end{cases} \tag{48}$$

This leads to a photon efficiency of about 40% at $p_{T,\gamma} = 30$ GeV, saturating around 85% for $p_{T,\gamma} > 150$ GeV. Note that the Higgs decay products tend to be soft, $p_{T,\gamma} \sim m_h/2$. For b-tagging, we adopt an efficiency with $\epsilon_b = 0.7$ associated with mis-tag rates of 15% for charm quarks and 0.3% for light flavors. These flat rates present a conservative estimate from the two dimensional distribution on (p_{Tj}, η_j) shown in the HL-LHC projections [311]. Encouragingly, the small light flavor fake rate projections result in a strong suppression for the initially dominant $jj\gamma\gamma$ background.

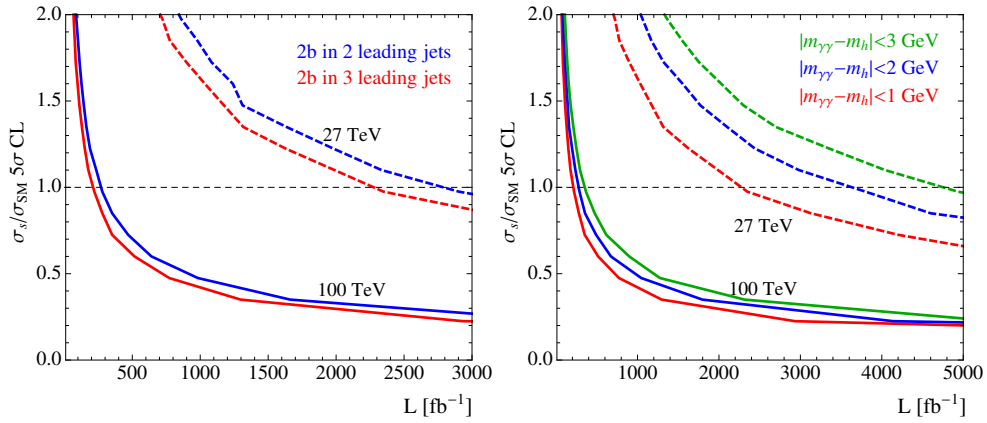

Fig. 73: Luminosity required for a 5σ discover of Higgs pair production for the HE-LHC (dashed) and a 100 TeV collider (full). Left: sensitivity in terms of the total rate, demanding two b-tags among the two or three leading jets and assuming $|m_{\gamma\gamma} - m_h| < 1$ GeV. Right: sensitivity for three mass windows $|m_{\gamma\gamma} - m_h| < 1, 2, 3$ GeV. We assume the SM hypothesis with $\kappa_\lambda = 1$ and use a binned log-likelihood analysis of the m_{hh} distribution.

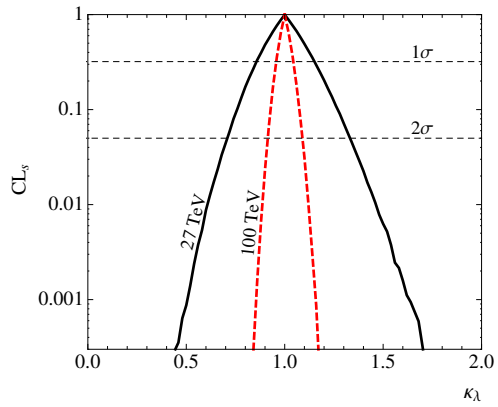

Fig. 74: Confidence level for separating an anomalous Higgs self-coupling hypothesis from the Standard Model $\kappa_\lambda = 1$.

To control the continuum backgrounds, we require two Higgs mass windows,

$$|m_{bb} - m_h| < 25 \text{ GeV}, \quad |m_{\gamma\gamma} - m_h| < 1 \text{ GeV}. \tag{49}$$

An obvious way to enhance the Higgs pair signal is to improve the resolution on the reconstructed photons and b-jets from the Higgs decays. We adopt the rather conservative resolution for m_{bb} as in Eq. (49). Any improvement on it in experiments would be greatly helpful for the signal identification and background separation.

To take the information in the the differential distribution m_{hh} into account, we employ a binned log-likelihood analysis based on the CL$_s$ method, using the full m_{hh} distribution to extract κ_λ [355]. As a starting point, we show the 5σ determination on the Higgs pair signal strength for the SM hypothesis $\kappa_\lambda = 1$ as a function of the luminosity in the left panel of Fig. 73. Here we require two b-tagged jets among the two or three leading jets. We decompose the latter case in two sub-samples (bb, bbj) and (jbb, bjb). We see how exploring the extra-jet emission significantly improves the significance as compared to the standard procedure adopted in the literature. The 5σ measurement for HE-LHC is pushed from 2.8 ab^{-1} to below 2.3 ab^{-1}.

In the right panel of Fig. 73 we show the discovery reach for the Higgs pair signal at HE-LHC and a 100 TeV collider for three di-photon invariant mass resolutions described by a Gaussian width of $0.75, 1.5, 2.25$ GeV and corresponding Higgs mass windows $|m_{\gamma\gamma} - m_h| < 1, 2, 3$ GeV. As resolution of 1.5 GeV has already been achieved at the LHC [356]. Higgs pair production will be discovered at the HE-LHC with approximately 2.5 ... 5 ab^{-1} and at the 100 TeV collider with 0.2 ... 0.3 ab^{-1} of data, in both cases well below the design luminosity.

As commented in the introduction, there exist physics scenarios in which the Higgs self-coupling could be modified at the level of order one deviation from the SM value. The accurate measurement of the Higgs self-coupling via Higgs pair production at future colliders has the best promise to uncover the new physics associated with the Higgs sector. In Fig. 74, we show the accuracy on this measurement. We find that the Higgs self-coupling can be measured with a precision

$$\begin{aligned} &\kappa_\lambda \approx 1 \pm 15\% \text{ at } 68\% \text{ CL} \quad \text{and} \quad \kappa_\lambda \approx 1 \pm 30\% \text{ at } 95\% \text{ CL} \qquad (\text{HE-LHC, 27 TeV, } 15\ ab^{-1}), \\ &\kappa_\lambda \approx 1 \pm 5\% \quad \text{at } 68\% \text{ CL} \quad \text{and} \quad \kappa_\lambda \approx 1 \pm 10\% \text{ at } 95\% \text{ CL} \qquad (\text{100 TeV, } 30\ ab^{-1}). \end{aligned} \tag{50}$$

While our conclusions on the determination of Higgs-self-interaction at future hadron colliders are robust and important, there is still room to improve. Although the final state $b\bar{b}\ \gamma\gamma$ is believed to be the most sensitive channel because of the background suppression and signal reconstruction, there

exist complementary channels such as $gg \to hh \to b\bar{b}\,\tau^+\tau^-$, $b\bar{b}\,W^+W^-$, $b\bar{b}\,b\bar{b}$, etc. The kinematics-based measurement and the all features related to QCD radiation at higher energies should be equally applicable to all of them.

3.4.2 Theoretical prospects: importance of the gluon fusion single Higgs background.[42]

The Higgs self-coupling plays a central role in the spontaneous breaking of electroweak symmetry, and governs a pure elementary scalar interaction – one that has never been observed in nature. Unfortunately, due to the small rate of hh production, measuring the Higgs self-coupling at a 14 TeV appears exceedingly difficult unless it deviates substantially from the Standard Model value [357, 312]. A precision measurement of the Higgs self-coupling is thus one of the primary goals of any higher energy collider. In this section we use the convention

$$V_{\text{int}} = \lambda_3 \frac{m_h^2}{2v} h^3 + \lambda_4 \frac{m_h^2}{8v^2} h^4 \tag{51}$$

such that in the SM $\lambda_3 = 1$.

While the prospects of a 100 TeV collider in measuring the self-coupling have been well studied [358], relatively less attention has been paid to intermediate energy colliders such as HE-LHC. Previous studies indicate that the $hh \to b\bar{b}\gamma\gamma$ channel has the most promising signature at hadron colliders, and this is expected to be true at 27 TeV as well. However, the $b\bar{b}\gamma\gamma$ channel still suffers from significant backgrounds from particle mis-identification in the detector, making a dedicated detector study including these effects essential. Finally, as discussed below, single-Higgs production – including through gluon-fusion – is a significant background that must be properly understood to accurately project the capabilities of HE-LHC. In what follows, we present a projection of the capabilities of a HE-LHC to measure the self-coupling with these intricacies carefully considered.

3.4.2.1 Signal and Background Simulations

The signal and background samples generated for this study are summarised in Table 60. We also show the cross sections of 14 TeV samples generated for validation with previous projections.

The details of the signal and background simulations mimic those in Ref. [359]. The $pp \to hh \to b\bar{b}\gamma\gamma$ signal is simulated at leading order using MADGRAPH5_AMC@NLO [79, 360] using the NNPDF2.3LO PDF set [280] including all finite top mass effects. The MADSPIN package [361] was used for the Higgs boson decays and PYTHIA 8 [319] for the showering and hadronisation of events. The LO signal is normalised to match the state of the art NNLO/NNLL calculation with finite top mass effects included at NLO in QCD [276]. Additional samples with the self-coupling modified to values between -1 and 10 times the SM value were also generated. Representative kinematic distributions of the signal at parton level are shown in Fig. 75.

Backgrounds to the $b\bar{b}\gamma\gamma$ decay channel include single Higgs production modes, non-resonant QCD backgrounds, as well as $Z(b\bar{b})\gamma\gamma$ and $t\bar{t}(+\gamma)$ production. We include all backgrounds where up to two additional photons or b-jets can arise from either misidentified light jets or electrons misidentified as photons.

The background from single Higgs production via gluon fusion ($ggF(\gamma\gamma)$) was generated in MADGRAPH with up to two extra partons allowed in the matrix element, with no additional k-factor due to the already present real emissions. Events from other single Higgs production modes were generated directly in PYTHIA 8 at LO and normalised based on the recommendations in Ref. [45]. The remaining backgrounds were generated in MADGRAPH interfaced with PYTHIA 8 for showering and hadronisation, with one additional jet allowed in the matrix element with MLM matching [362, 363] to the parton shower.

[42] Contacts: S. Homiller, P. Meade

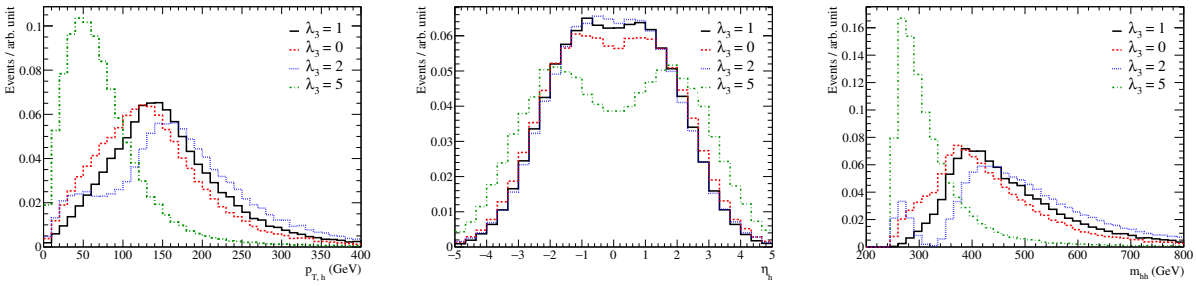

Fig. 75: (Left:) The transverse-momentum distribution of the true Higgs bosons generated in our 27 TeV samples, prior to showering and detector smearing, for several different values of λ_3. (Centre:) The same, but for the Higgs pseudorapidity. Right: The same, but for the distribution of the true Higgs pair invariant mass.

Table 60: List of signal and background processes, the event generator used to simulate the matrix element and parton shower, and the cross section of each process along with the corresponding order in QCD at which the cross section is normalised. In the right-most column we show the expected number of events after all the event selection criteria have been applied.

Process	Generator	$\sigma \cdot BR$ [fb]		Order QCD	Expected Events
		14 TeV	27 TeV		(27 TeV, 15 ab^{-1})
$h(b\bar{b})h(\gamma\gamma)$	MADGRAPH/PYTHIA 8	0.11	0.41	NNLO/NNLL	209.6 ± 0.2
$tth(\gamma\gamma)$	PYTHIA 8	1.40	6.54	NLO	286.8 ± 1.6
$Zh(\gamma\gamma)$	PYTHIA 8	2.24	5.58	NLO	67.1 ± 0.7
$ggF(\gamma\gamma)$	MADGRAPH/PYTHIA 8	83.2	335.1	N^{3}LO	349.7 ± 9.5
$b\bar{b}\gamma\gamma$	MADGRAPH/PYTHIA 8	3.4×10^2	9.5×10^2	LO	414.6 ± 10.3
$c\bar{c}\gamma\gamma$	MADGRAPH/PYTHIA 8	4.4×10^2	1.5×10^3	LO	185.7 ± 4.2
$jj\gamma\gamma$	MADGRAPH/PYTHIA 8	5.9×10^3	1.4×10^4	LO	63.3 ± 3.8
$b\bar{b}j\gamma$	MADGRAPH/PYTHIA 8	1.1×10^6	3.4×10^6	LO	199.6 ± 9.4
$c\bar{c}j\gamma$	MADGRAPH/PYTHIA 8	4.8×10^5	1.6×10^6	LO	25.3 ± 3.0
$b\bar{b}jj$	MADGRAPH/PYTHIA 8	3.7×10^8	1.5×10^9	LO	155.4 ± 8.2
$Z(b\bar{b})\gamma\gamma$	MADGRAPH/PYTHIA 8	2.61	5.23	LO	21.5 ± 0.4
$t\bar{t}$	MADGRAPH/PYTHIA 8	6.7×10^5	2.9×10^6	NNLO	11.6 ± 3.3
$t\bar{t}\gamma$	MADGRAPH/PYTHIA 8	1.7×10^3	7.9×10^3	NLO	145.0 ± 10.3
Total Background					1925.8 ± 22.7
Significance ($S/\sqrt{B}$)					4.77 ± 0.14

3.4.2.2 Detector Simulation

To approximate the effects of detector resolution and reconstruction efficiencies, we use DELPHES 3 with a dedicated card developed to approximate the performance of ATLAS and CMS at HL-LHC. We take this as a reasonable benchmark for the expected performance after the HE-LHC upgrade.

With respect to the DELPHES setup used in [359], the card here has an improved E-Cal resolution and assumes a higher photon identification efficiency, but a somewhat degraded di-jet mass resolution. Aside from resolution and efficiency effects, particle mis-identification in the detector is also an important source of backgrounds to $hh \to b\bar{b}\gamma\gamma$. To avoid issues with MC statistics, we implement b-tagging and jet mis-tagging rates at analysis level using a reweighting scheme, with probabilities taken as functions of the jet p_T as in Ref. [359]. These probabilities correspond to roughly $p_{b\to b} \approx 70\%$, $p_{c\to b} \approx 20\%$ and $p_{j\to b} \lesssim 1\%$. The probability for a light jet to fake a photon in the detector is also included via reweighting at analysis level as a function of p_T (see [359]) which peaks at 5×10^{-4} for $p_{T,j} \sim 60\,\text{GeV}$ before falling exponentially to $\sim 1 \times 10^{-4}$.

3.4.2.3 *Results and Limits on the Self-Coupling*

To isolate the $hh \to b\bar{b}\gamma\gamma$ signal, we implement selection cuts as follows:

- At least 2 isolated photons and b-tagged jets with leading $p_T > 60\,\text{GeV}$ and sub-leading $p_T > 35\,\text{GeV}$, all with $|\eta_{\gamma,b}| < 2.5$.
- $p_{T,\gamma\gamma}, p_{T,b\bar{b}} > 125\,\text{GeV}$.
- $\Delta R_{b\bar{b}}, \Delta R_{\gamma\gamma} < 3.5$.
- $|m_{\gamma\gamma} - 125.0\,\text{GeV}| < 4.0\,\text{GeV}$.
- $|m_{b\bar{b}} - 125.0\,\text{GeV}| < 25\,\text{GeV}$.
- $n_{\text{jets}} < 6$ for jets with $p_T > 30\,\text{GeV}$, $|\eta| < 2.5$.
- No isolated leptons with $p_T > 25\,\text{GeV}$.
- $|\cos\theta_{hh}| < 0.8$.

where $\cos\theta_{hh}$ is the decay angle of the Higgs boson pair evaluated in the lab frame (see Fig. 76).

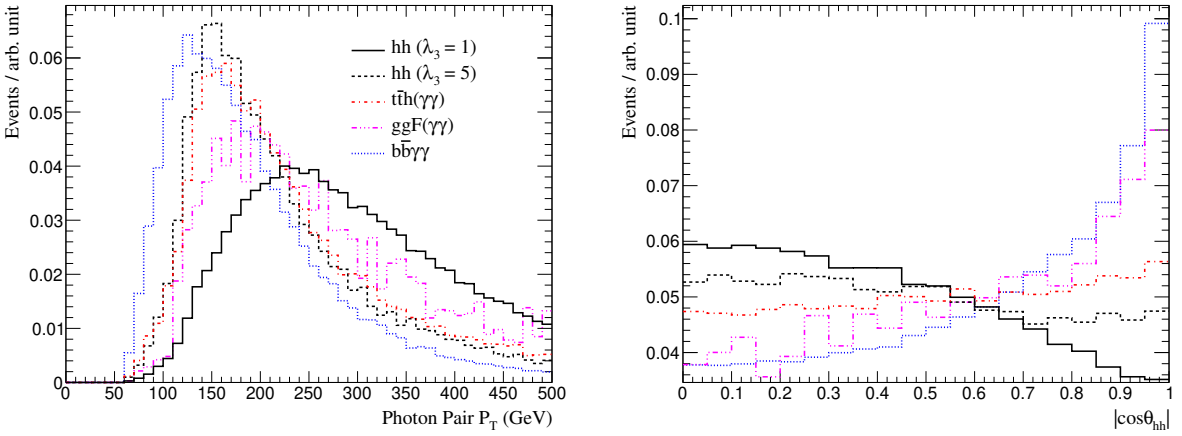

Fig. 76: Normalised distributions of (Left:) the p_T of the reconstructed $h \to \gamma\gamma$ and (Right:) the magnitude of $\cos\theta_{hh}$, the Higgs decay angle defined in the text. We show the distributions for the signal with $\lambda_3 = 1$ and 5 as well as several representative backgrounds.

Note that cuts on the p_T and Δ_R of the $\gamma\gamma$ and $b\bar{b}$ pair are tightly correlated with the invariant mass of the hh system. As seen in Fig. 76 the photon pair p_T has strong discriminating power for the SM hh signal, but for non-SM values of λ_3, the signal and background become more degenerate.

The final selection efficiency is 3.4%, and the expected number of events from each signal/backgrou channel after applying all the cuts and detector effects is given in Table 60 assuming 15 ab^{-1} integrated luminosity at HE-LHC. The uncertainty for each sample is estimated by partitioning the full event sample in to sub-samples and computing the standard deviation of the results from each sub-sample.

The largest backgrounds are from continuum $bb\gamma\gamma$ and single Higgs production and decay to $\gamma\gamma$. Particularly, we see that the ggF induced mode contributes an $\mathcal{O}(1)$ background, despite being neglected in previous studies. The accurate modelling of the extra jets that arise in the hadron collision is a necessity for properly understanding this contribution. Other large backgrounds arise from processes where a jet is reconstructed as a photon – even when two fake photons are needed. Finally, we see that $t\bar{t}$ and $t\bar{t}\gamma$ are not insignificant backgrounds with the set of cuts we've applied. Several of these backgrounds might be mitigated by exploring the additional kinematic information in events with multiple jets, but the single-Higgs production backgrounds are difficult to reduce in light of the true $h \to \gamma\gamma$ present.

To understand the attainable precision on λ_3, we assume a hypothetical observation of $S+B$ events after all selection cuts with S and B as in Table 60. This allows us to derive 68 and 95% confidence intervals on the expected number of signal events using a likelihood scan, including only the MC and statistical uncertainties. The expected number of signal events with 15 ab^{-1} integrated luminosity is plotted in Fig. 77 along with the 1σ (2σ) regions in green (yellow).

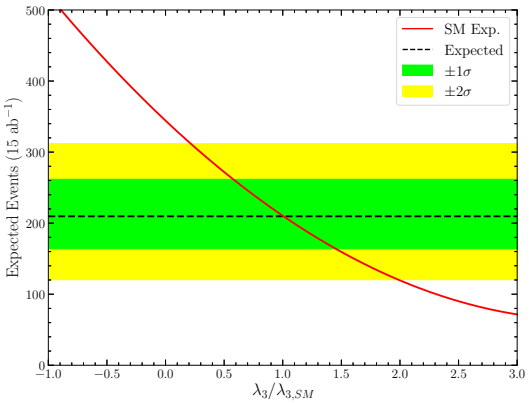

Fig. 77: The expected number of signal events in a hypothetical experiment assuming the signal and background rates computed in Table 60 at $L = 15$ ab^{-1} for HE-LHC with the regular detector performance assumption. The black dashed line indicates the expected number of events from signal while the green (yellow) regions show the 1σ (2σ) uncertainty regions arising from a likelihood scan with the statistical and MC uncertainties on the signal and background counts. The red curve shows the expected number of events from signal in a background free measurement as a function of λ_3, accounting for the changes in the signal acceptance due to kinematic differences at different λ_3

We can also compute the expected number of events at 15 ab^{-1} as a function of λ_3, taking into account both the varying σ_{hh} cross section and the modified acceptance due to changes in the signal kinematics. The resulting curve is shown in red in Fig. 77. The intersection of this curve with the 1 and 2σ regions indicate the expected precision on λ_3 in the absence of systematic uncertainties. We find

$$\lambda_3 \in [0.58, 1.45] \quad \text{at } 68\% \text{ C.L.} \tag{52}$$

Note that, as a result of the destructive interference between the triangle and box diagrams leading to hh production, there is a degeneracy in the expected number of events around $\lambda_3 \sim 5$. However, the kinematic structure of the hh signal is very different at large values of λ_3, and such values could be easily rejected using differential measurements (e.g, with $m_{hh} = m_{b\bar{b}\gamma\gamma}$ or $p_{T,hh}$), so the degeneracy can be safely ignored for the purposes of this work.

In conclusion, we find that with a full account of the detector effects and backgrounds to $hh \to b\bar{b}\gamma\gamma$, a cut based analysis leads to an expected significance of $4.77 \pm 0.14\sigma$, corresponding to a 45% measurement of the Higgs self-coupling at 27 TeV with 15 ab^{-1}. Future improvements can be made both by considering other decay channels (e.g., $hh \to b\bar{b}b\bar{b}, b\bar{b}\tau\tau$, and $b\bar{b}WW$) and by exploiting the additional information present in the hh invariant mass distribution, as discussed elsewhere in this report.

3.4.3 Experimental prospects with the ATLAS detector[43]

The results presented in Section 3.2.1 were extended to provide estimates of the prospects at the HE-LHC, assuming a centre of mass collision energy of 27 TeV and 15 ab^{-1} of data.

The assumption is made that the detector performance will be the one of the HL-LHC ATLAS detector. Comparisons between simulation at centre of mass energy of 14 and 27 TeV show that the kinematic of the Higgs boson decay particles, as well as the m_{HH} distribution are similar. However the pseudorapidity of the particle tends to point more frequently in the forward region, which would decrease

[43] Contacts: P. Bokan, E. Petit, N. Readioff, M. Wielers

the acceptance by around 10%. This effect is not taken into account and the impact is expected to be small.

The event yields for the various background processes are scaled by the luminosity increase and the cross-section ratio between the two centre of mass energies. For the signal the cross-section of 139.9 fb is used, as described in Section 3.1.1.1.

Without including systematic uncertainties a significance of 7.1 and 10.7 standard deviations is expected for the $b\bar{b}\gamma\gamma$ and $b\bar{b}\tau\tau$ channels respectively. The hypothesis of no Higgs self-coupling can be excluded with a significance of 2.3 and 5.8 standard deviations respectively. Finally the κ_λ parameter is expected to be measured with a 68% CI precision of 40% and 20% for the two channels respectively. With the $b\bar{b}\gamma\gamma$ channel, if the HL-LHC systematic uncertainties were considered this precision would be 50%, dominated by the uncertainty on the photon energy resolution. If this uncertainty were divided by a factor 2 then the precision would be 45%.

3.4.4 Comparison of results

The results presented in Sections 3.4.1 and 3.4.3 appear to be quite different, with the κ_λ parameter being measured with a precision of 15% and 40% respectively at 68% CL. Thorough studies were performed to understand the difference. The result from the ATLAS experiment is an extrapolation of the HL-LHC results (which consider a mean pile-up rate of 200) which were optimised to increase the sensitivity to the SM signal, but could be improved for a precise measurement of κ_λ. In particular low values of the di-Higgs invariant mass below 400 GeV are suppressed where most of the sensitivity lies. When a selection similar to the one in Section 3.4.1 is applied to ATLAS simulated samples, 40% more background events are found. Half of it comes from missing background processes, while the other half comes from differences in the selection because of the effect of pile-up in the ATLAS simulation. There is also a categorisation based on the p_{T}-ordering of the jets and b-jets which improves the results as shown in Figure 73 but is hard to reproduce when large pile-up is considered.

In order to get an estimate of the best sensitivity achievable with HE-LHC data, a simple combination of the results of the $b\bar{b}\gamma\gamma$ channel presented in Section 3.4.1 and the results presented with the $b\bar{b}\tau\tau$ presented in Section 3.4.3 is performed. No correlations are taken into account in this combination, and no systematic uncertainties are considered. A precision of around 10% could be then achieved. The $b\bar{b}\tau\tau$ measurement alone is used as an upper value of this precision, so at this point we can consider that the κ_λ parameter could be measured with a precision of 10 to 20%, as illustrated in Figure 78. It should also be noted that the second minimum of the likelihood would be unambiguously excluded at the HE-LHC.

It should be emphasised that these results rely on assumptions of experimental performance in very high pile up environment O(800-100) that would require further validation with more detailed studies, and that no systematic uncertainties are considered at this point. On the other hand these studies do not include the additional decay channels that have already been studied for HL-LHC, and of others that could become relevant at the HE-LHC. Exclusive production modes are also very interesting to take into consideration for this measurement. The potential improvements from these have not yet been assessed yet.

3.5 Indirect probes

In this section we discuss the possibility of indirectly extract information on the trilinear self interaction of the Higgs boson via precise measurements of single-Higgs production [364, 365, 366, 367, 368, 369, 370, 371, 372] at the HL-LHC and HE-LHC. This strategy is complementary to the direct measurement via double-Higgs production, which already at leading order, i.e. at one loop in the case of $gg \to HH$, depends on the trilinear Higgs self interaction. In the case of single-Higgs production, on the contrary, the Higgs self interactions enter only via one-loop corrections, i.e., at the two-loop level for the gluon-fusion (ggF) production mode. The effects of modified Higgs self interactions are therefore generically much

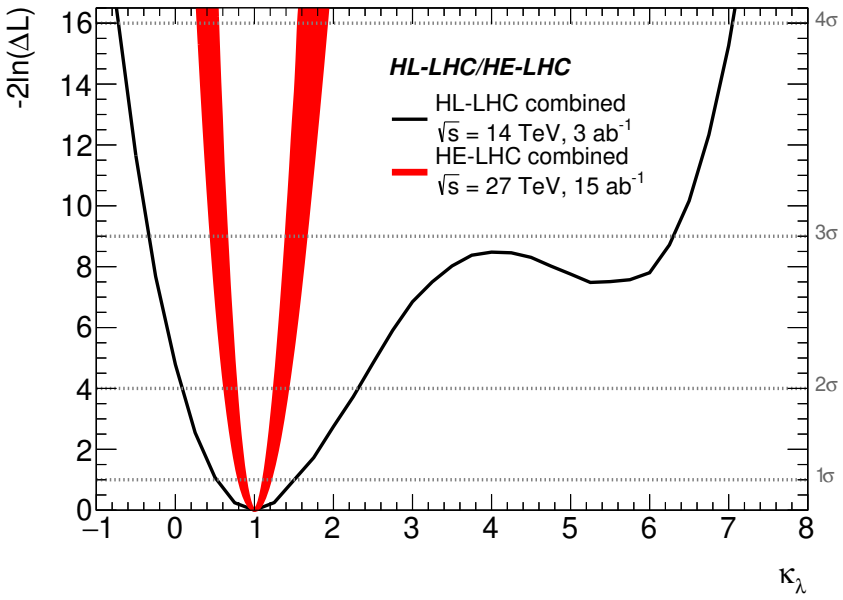

Fig. 78: Expected sensitivity for the measurement of the Higgs trilinear coupling through the measurement of direct HH production at HE-LHC. The black line corresponds to the combination of ATLAS and CMS measurements with HL-LHC data presented in Section 3.2.3, with systematic uncertainties considered. The red band corresponds to an estimate of the sensitivity using a combination of the $b\bar{b}\gamma\gamma$ and $b\bar{b}\tau\tau$ channels, without systematic uncertainties considered.

smaller, but for single-Higgs production processes the precision of the experimental measurements is and will be much better than for double-Higgs production. This, and the fact that for single-Higgs production many different final states and both inclusive as well as differential measurements are possible will lead to competitive indirect determinations of the trilinear Higgs self coupling. In [373, 374] also electroweak precision observables have been considered to this purpose.

3.5.1 Indirect probes through single Higgs boson production[44]

In the following subsection, we will briefly recall the calculation framework introduced in [365, 366]. We also provide numerical results for the effects due to a modified trilinear Higgs coupling in the most important inclusive and differential single-Higgs production cross sections as well as the Higgs branching ratios. Based on these results, we will analyse the sensitivity of the HL-LHC and HE-LHC in constraining the trilinear Higgs self interactions.

3.5.1.1 Theoretical framework

The effects of anomalous Higgs interactions can be extracted from experimental data via the signal strength parameters μ_i^f, which are defined for any specific combination of production and decay channel $i \to H \to f$ as follows

$$\mu_i^f \equiv \mu_i \times \mu^f = \frac{\sigma(i)}{\sigma^{\rm SM}(i)} \times \frac{\rm BR(f)}{\rm BR^{SM}(f)} \,. \tag{53}$$

Here the quantities μ_i and μ^f are the production cross sections $\sigma(i)$ ($i = gg$F, VBF, WH, ZH, $t\bar{t}H$, tHj) and the branching ratios $\rm BR(f)$ ($f = \gamma\gamma, ZZ, WW, b\bar{b}, \tau\tau, \mu\mu$) normalised to their SM values,

[44] Contacts: W. Bizon, M. Gorbahn, U. Haisch, F. Maltoni, D. Pagani, A. Shivaji, G. Zanderighi, X. Zhao

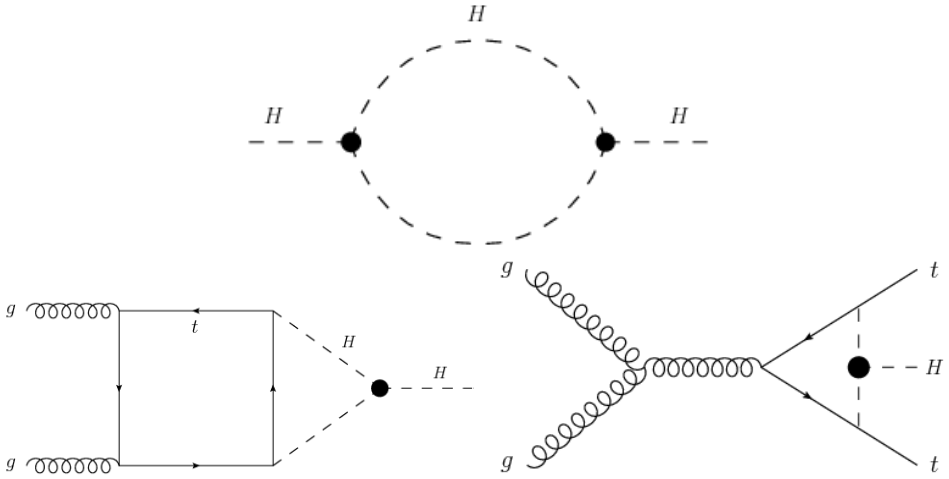

Fig. 79: Examples of NLO contribution of the Higgs self-coupling to single Higgs observables. Top: Contribution to the Higgs self-coupling, which generates a global correction to all amplitudes. Bottom: Examples of diagrams contributing to the ggF (left) and $t\bar{t}H$ (right) production modes.

respectively. Assuming on-shell production, the product $\mu_i \times \mu^f$ therefore corresponds to the rate for the $i \to H \to f$ process normalised to the corresponding SM prediction.

The quantities μ_i and μ^f that enter the definition of μ_i^f in (53) can be expressed as

$$\mu_i = 1 + \delta\sigma_{\lambda_3}(i)\,, \qquad \mu^f = 1 + \delta\mathrm{BR}_{\lambda_3}(f)\,, \tag{54}$$

where $\delta\sigma_{\lambda_3}(i)$ and $\delta\mathrm{BR}_{\lambda_3}(f)$ are the deviations induced by an anomalous trilinear Higgs self interaction to the production cross sections and branching ratios, respectively. This definition can be straightforwardly extended to the differential level and one has $\mu_i^f = \mu_i = \mu^f = 1$ in the SM.

In single-Higgs production, the trilinear Higgs self interactions start to enter only at the one-loop level in the case of VBF, WH, ZH, $t\bar{t}H$, tHj production, while in the case of ggF production and the decays $H \to gg, \gamma\gamma$ one has to calculate two-loop EW corrections. The appearance of the quadrilinear Higgs self coupling in single-Higgs processes is further delayed by one loop order.

For the strategy discussed here, the anomalous trilinear Higgs self interactions can be equivalently parametrised either via an anomalous trilinear coupling

$$\lambda_3 \equiv \kappa_3 \lambda_3^{\mathrm{SM}} \tag{55}$$

where $\lambda_3^{\mathrm{SM}} = m_H^2/(2v^2)$ with $v = (\sqrt{2}G_F)^{-1/2} \simeq 246\,\mathrm{GeV}$ the EW vacuum expectation value, or via the corresponding dimension-six operator

$$\mathcal{O}_6 = -\frac{\lambda_3^{\mathrm{SM}} c_6}{v^2}\,|\Phi|^6\,, \tag{56}$$

with Φ denoting the usual SM Higgs doublet. In the normalisation adopted in (56), the simple relation

$$\kappa_3 = 1 + c_6\,, \tag{57}$$

is obtained and allows to translate constraints on the coupling modifier κ_3 into bounds on the Wilson coefficient c_6 and vice versa.

In the presence of modified trilinear Higgs self interactions, all single-Higgs production and decay channels receive two types of contributions [365, 366], as shown in Fig 79: firstly, a process and

Table 61: C_1^σ coefficients for inclusive single-Higgs production cross sections at different CM energies.

C_1^σ [%]	ggF	VBF	WH	ZH	ttH	tHj
13 TeV	0.66	0.64	1.03	1.19	3.51	0.91
14 TeV	0.66	0.64	1.03	1.18	3.47	0.89
27 TeV	0.66	0.62	1.01	1.16	3.20	0.79

Table 62: C_1^σ coefficients for single-Higgs production processes at 13 TeV in different $p_T(H)$ bins.

$p_T(H)$ [GeV]	$[0, 25]$	$[25, 50]$	$[50, 100]$	$[100, 200]$	$[200, 500]$	> 500
VBF	0.97	0.88	0.73	0.58	0.45	0.29
ZH	2.00	1.75	1.21	0.51	0.01	-0.10
WH	1.70	1.49	1.04	0.44	0.01	-0.09
$t\bar{t}H$	5.31	5.07	4.38	3.00	1.27	0.17
tHj	1.23	1.18	1.02	0.74	0.33	-0.06

kinematic dependent one, denoted as C_1 hereafter, which is linear in c_6 or κ_3 and second, a universal one proportional to the Higgs wave function renormalisation constant Z_H, which is proportional to κ_3^2 and therefore contains both a linear and quadratic piece in c_6. The quantity $\delta\sigma_{\lambda_3}(i)$ introduced in (54) as well as any differential distribution related to it can thus be written as[45]

$$\delta\sigma_{\lambda_3}(i) = (\kappa_3 - 1)\, C_1^\sigma + \left(\kappa_3^2 - 1\right) \delta Z_H = c_6 C_1^\sigma + \left(2c_6 + c_6^2\right) \delta Z_H \,, \tag{58}$$

where δZ_H denotes the one-loop correction to the Higgs wave function renormalisation constant associated to modifications of the trilinear Higgs self coupling. In the case of the decays, the effects due to Higgs wave function renormalisation cancel in the branching ratios, and as a result the quantities $\delta\mathrm{BR}_{\lambda_3}(f)$ defined in (54) take the following form

$$\delta\mathrm{BR}_{\lambda_3}(f) = (\kappa_3 - 1)\, \left(C_1^\Gamma - C_1^{\Gamma_{\mathrm{tot}}}\right) = c_6 \left(C_1^\Gamma - C_1^{\Gamma_{\mathrm{tot}}}\right) . \tag{59}$$

Here $C_1^{\Gamma_{\mathrm{tot}}}$ is an effective term that describes the process dependent corrections to the total decay width of the Higgs boson.

In the following we provide the values of the C_1 coefficients that are used in the numerical analyses presented in section 4. The given values correspond to the input

$$\begin{aligned} G_F &= 1.1663787 \times 10^{-5}\,\mathrm{GeV}^{-2} \,, \qquad m_W = 80.385\,\mathrm{GeV} \,, \\ m_Z &= 91.1876\,\mathrm{GeV} \,, \qquad m_H = 125\,\mathrm{GeV} \,, \qquad m_t = 172.5\,\mathrm{GeV} \,. \end{aligned} \tag{60}$$

For these parameters one finds numerically [366]

$$\delta Z_H = -1.536 \times 10^{-3} \,, \qquad C_1^{\Gamma_{\mathrm{tot}}} = 2.3 \times 10^{-3} \,. \tag{61}$$

In the calculations of production cross sections and distributions, the renormalisation and factorisation scales are taken to be $\mu_R = \mu_F = \frac{1}{2}\sum_f m_f$ with m_f the masses of the particles in the final state and `PDF4LHC2015` [112] parton distribution functions are used. On the other hand, the dependence of the C_1 coefficients on μ_R, μ_F and the PDF set is negligible.

[45] This equation is in reality a linearised version of the complete formula that is used for extracting the results in Section ... and involves the Higgs wave function resummation [366, 370]. Also (59) is a linear expansion.

Table 63: Same as table 62 but for a CM energy of 27 TeV.

$p_T(H)$ [GeV]	$[0,25]$	$[25,50]$	$[50,100]$	$[100,200]$	$[200,500]$	>500
VBF	0.65	0.65	0.65	0.62	0.52	0.29
ZH	2.00	1.74	1.21	0.50	0.00	-0.10
WH	1.70	1.49	1.04	0.44	0.01	-0.09
$t\bar{t}H$	5.00	4.78	4.14	2.86	1.23	0.22
tHj	1.06	1.03	0.91	0.69	0.33	0.02

Table 64: C_1^Γ coefficients for the phenomenologically relevant decay modes of the Higgs boson.

C_1^Γ [%]	$\gamma\gamma$	ZZ	WW	gg
on-shell H	0.49	0.83	0.73	0.66

In table 61 we list the values of C_1^σ for the various production modes at different centre of mass (CM) energies. One first notices that WH, ZH and especially ttH production depend stronger on the anomalous trilinear Higgs self coupling than the ggF, the VBF and the tHj channel. Furthermore, in the case of WH, ZH and ttH production the loop corrections contributing to C_1^σ feature a Sommerfeld enhancement, which results in an increased sensitivity to anomalous trilinear Higgs self interactions at low energies [366, 367, 370]. This feature is illustrated in tables 62 and 63 where we give the values of C_1^σ in bins of the Higgs transverse momentum $p_T(H)$ for pp collisions at 13 TeV and 27 TeV, respectively.[46] Table 64 finally provides the values of the C_1^Γ coefficients for the decay modes of the Higgs boson that are relevant in our numerical study.

Notice that all the formulas and numbers presented in this subsection take into account only effects associated to an anomalous trilinear Higgs self coupling. The extension to more general and physically motivated scenarios that include also other new-physics effects is simple and has been worked out in [368, 370]. It consists in adding to (58) and (59) the effects of other anomalous interactions such as a modified top Yukawa coupling or altered/new gauge-Higgs vertices. In the next subsection, we perform a global analyses of the constraints on λ_3 that the HL-LHC and the HE-LHC should be able to set. We thereby follow the lines of the study [368], using the results for the coefficients C_1 provided above.

As discussed in refs. [370, 368], the constraints that can be set on c_6 critically depend on the interplay between the following aspects:

- The number of additional parameters related other anomalous interactions.
- The number of independent measurements considered in the analysis.
- The inclusion of differential information.
- The assumptions on the theoretical and experimental (statistical and systematic) errors.

In the section 3.5.3 we explore this interplay for the cases of the HL- and HE-LHC following the lines of the study presented in refs. [368] augmented with the new results provided in this section. Independent analyses performed by the ATLAS and CMS collaborations with a full-fledged treatment of all the correlations among experimental uncertainties are desirable, and the first steps towards this are being presented in the next section 3.5.2. It is worth noting that, when other anomalous interactions are also considered, the effects of $Z_H^{\rm BSM}$ are degenerate with those in general affecting the Higgs wave-function normalisation, typically parametrised via the Wilson coefficient $\mathcal{C}_H$. Thus, the coefficients C_1^σ and therefore the differential distributions have a primary role in the extraction of the information on κ_3 from measurements of single Higgs production.

[46] Results for a different binning or different observables can be easily obtained with the code presented in [370].

Table 65: Process dependant C_1 values for each bin of $p_{\mathrm{T}}^{\mathrm{H}}$.

$p_T(H)$ [GeV]	$[0, 45]$	$[45, 80]$	$[80, 120]$	$[120, 200]$	$[200, 350]$	> 350
ttH	5.31	4.73	3.92	2.79	1.42	0.42
tH	1.32	1.19	1.00	0.75	0.40	0.06
VH	1.66	1.23	0.77	0.35	0.02	-0.09

We also recall that limits on κ_3 or equivalently c_6 obtained with this strategy are sensible only when $|\kappa_3| < 20$; as discussed in refs. [366] this limit guarantees that the perturbative loop expansion is converging and that the leading missing higher orders depending on $\kappa_3 - 1 = c_6$ are below 10% level. On the contrary, as discussed in refs. [375, 372], when the information from double Higgs production is considered a more cautious limit $|\kappa_3| < 6$ should be adopted in order to achieve both perturbative unitarity and the convergence of the loop expansion.

3.5.2 *Indirect probes of the trilinear coupling through differential distributions measurements with the CMS detector*[47]

As detailed in the previous section, an alternative approach to probing the Higgs boson self-coupling is to measure deviations of the inclusive and differential Higgs boson production rates. Contributions to single Higgs boson production from the Higgs boson self-coupling are sizeable for production in association with a pair of top quarks ($\mathrm{t\bar{t}H}$) or a single top-quark (tH). The contributions are greatest in these production modes due to the large mass of the top quark. Differential cross section measurements, in particular as a function of the Higgs boson transverse momentum p_{T}^{H}, allow one to disentangle the effects of modified Higgs boson self-coupling values from other effects such as the presence of anomalous top–Higgs couplings.

The differential cross-section measurements, described in section 2.4.2, are used to extract a constraint on the Higgs boson self-coupling (λ_3), by parametrising deviations from SM predictions as described in the previous section. The kinematic dependence of these deviations are determined by reweighting signal events, on an event by event basis, using the tool described in Ref. [376], which calculates λ_3-dependent corrections to the tree level cross-sections as a function of the kinematic properties of the event, and is encapsulated as a varying C_1 coefficient. The value of C_1 depends on both the Higgs boson production mode and the kinematic properties of the event. Table 65 shows the values of C_1 calculated in the fiducial region for $\mathrm{t\bar{t}H}$ and tH production, in each bin of $p_{\mathrm{T}}^{\mathrm{H}}$.

In addition, the contribution from VH production is included by similarly calculating the C_1 values for VH, $\mathrm{H} \to \gamma\gamma$ events. For the contribution of $\gamma\gamma \to \mathrm{H}$ and to account for modifications of the $\mathrm{H} \to \gamma\gamma$ decay width, the parametrisations which have been calculated for inclusive events provided in Ref. [366] are used directly.

Figure 80 shows a scan of the profile log-likelihood as a function of κ_λ. In the scan, all other Higgs boson couplings are assumed to attain their SM values. For the purposes of constraining κ_λ, theoretical uncertainties in the differential $\mathrm{t\bar{t}H}$ + tH cross section, as described in section 2.4.2, are included in the signal model. The results when only including the hadronic or leptonic categories are shown in addition to the result obtained from their combination.

The profiled log-likelihood in the region around $5 < \kappa_\lambda < 15$ results from the behaviour of the parametrisations which modify the predicted cross sections. For the $\mathrm{t\bar{t}H}$ production mode, the derivative of the predicted cross section with respect to κ_λ changes sign in this region, such that the predicted cross section is relatively stable for different values of κ_λ. This degeneracy is however somewhat resolved by the other production modes for which the change in sign occurs at different values of κ_λ. With $3\,\mathrm{ab}^{-1}$

[47] Contacts: N. Wardle, J. Langford

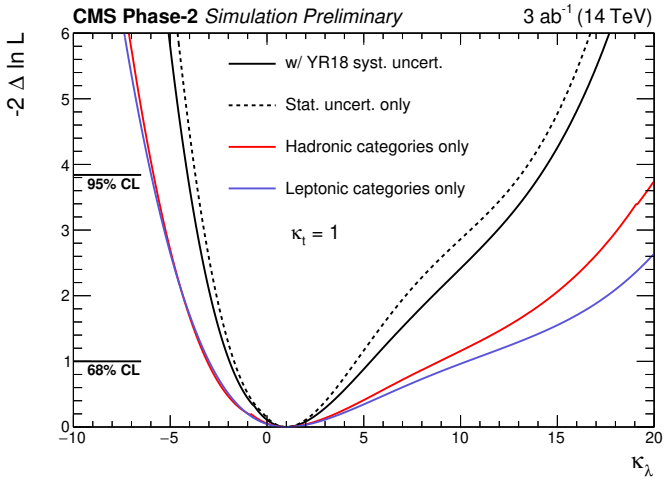

Fig. 80: Profile log-likelihood scan as a function of κ_λ. The individual contributions of the statistical and systematic uncertainties are separated by performing a likelihood scan with all systematics removed. Additionally, the contributions from the hadronic and leptonic channels have been separated, shown in red and purple, respectively.

of data collected by CMS at the HL-LHC, this result shows that a constraint of $-4.1 < \kappa_\lambda < 14.1$ at the 95% confidence level (CL) is achievable from the differential cross-section measurement of a single Higgs boson decay channel produced in association with tops, using data from only one of the two general purpose detectors at the HL-LHC.

The $t\bar{t}H$ + tH differential cross section measurements are also sensitive to other potential BSM effects, such as those which give rise to anomalous top–Higgs couplings. A two-dimensional profile log-likelihood scan is shown in Fig. 81 as a function of κ_λ and μ_H. The parameter μ_H is a multiplicative scaling factor which is common to all Higgs boson production modes and all ${p_\mathrm{T}}^\mathrm{H}$ bins. Even with this additional parameter, constraints on κ_λ are still achievable, owing to the information retained in the shape of the ${p_\mathrm{T}}^\mathrm{H}$ distribution. The constraint on κ_λ is $-7.1 < \kappa_\lambda < 14.1$ at the 95% CL, when the log-likelihood is also profiled with respect to μ_H.

3.5.3 Global fit[48]

Assuming that the trilinear coupling is the only coupling deviating from its SM value, single Higgs observables can give competitive bounds with double Higgs production, see Refs. [365, 366, 367, 373, 370] [49]. Nevertheless, departures of the Higgs self-coupling from its SM prediction signal the existence of new dynamics that, in general, would leave an imprint on other Higgs couplings as well which have a strong impact on the bound as shown by Ref. [368]. The importance of a global fit is therefore two-fold, namely to assess the robustness of the studies that take into account deformations exclusively in the Higgs trilinear coupling, and to single out the sensitivity on the single-Higgs couplings that is required to minimise the impact of the possible correlations.

To include the effect of the different deformations away from the SM, we use the EFT framework described in Ref. [368], where 9 parameters describe the deviations of the single-Higgs couplings. In particular, we consider three[50] parameters for the Yukawa interactions (δy_t, δy_b, δy_τ,), two for the contact interactions with gluons and photons (c_{gg} , $c_{\gamma\gamma}$), rescalings of the SM hZZ and hWW interac-

[48] Contacts: S. Di Vita, G. Durieux, C. Grojean, J. Gu, Z. Liu, G. Panico, M. Riembau, T. Vantalon

[49] Electroweak processes where the Higgs trilinear coupling enter at the two loop level have also been studied in [374].

[50] If other fermionic decay channels can be observed, further parameters can be included, with no effect on the number of degrees of freedom.

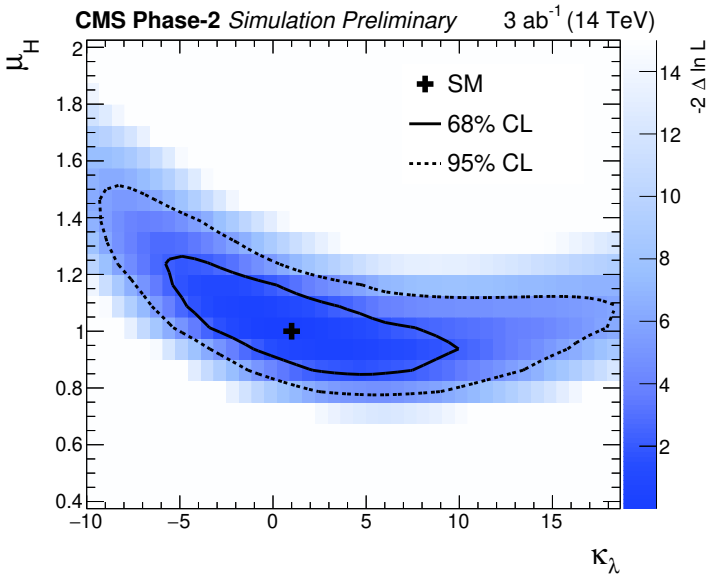

Fig. 81: Results of the two-dimensional likelihood scan in κ_λ-vs-μ_H, where μ_H allows all Higgs boson production modes to scale relative to the SM prediction. The 68% and 95% confidence level contours are shown by the solid and dashed lines respectively. The SM expectation is shown by the black cross.

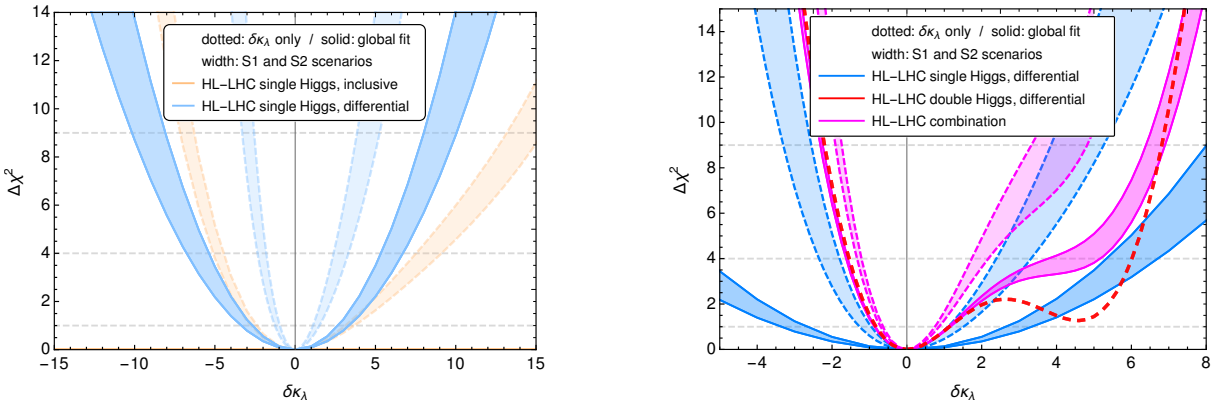

Fig. 82: χ^2 analysis of the Higgs self-coupling $\delta\kappa_\lambda$ using single- and double-Higgs processes for the HL-LHC at 13 TeV and 3 ab^{-1}. The widths of the lines correspond to the differences between the scenarios S1 and S2. **Left:** Comparison of the constraints obtained using inclusive single-Higgs processes (orange), with the ones using differential observables (blue). Dashed is an exclusive fit while solid is the result of a global fit. **Right:** Comparison of the constraints from differential single Higgs (blue), with those from differential double-Higgs data (dashed red) and its combination (pink).

tions (parametrised by one coefficient, δc_z, if custodial symmetry is unbroken), and three coefficients ($c_{zz}, c_{z\Box}, c_{z\gamma}$) parametrising interactions of the Higgs with the electroweak bosons that have non-SM tensor structures. Note that two combinations of the last three parameters are constrained by di-boson data, showing an interesting interplay between the gauge and the Higgs sectors. A global fit on the Higgs self-coupling, parametrised by $\delta\kappa_\lambda$ (which is zero in the SM) using only inclusive single Higgs observables, and taking into account the additional 9 EFT deviations described above, suffers from a flat direction. To lift it, it is necessary to include data from differential measurements of those processes, since the single-Higgs deformations and $\delta\kappa_\lambda$ tend to affect the distributions in complementary ways.

As input for the uncertainties we consider the S1 and S2 scenarios, corresponding to the projected

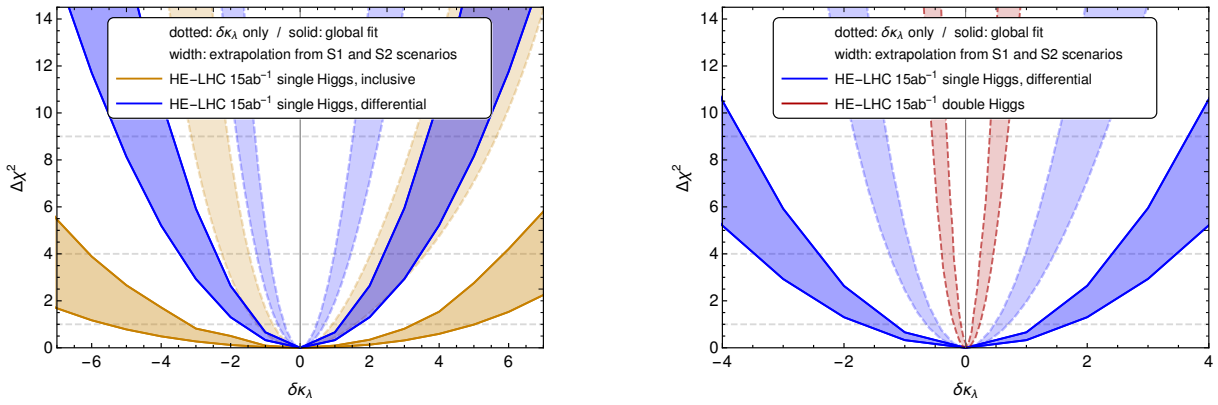

Fig. 83: χ^2 analysis of the Higgs self-coupling $\delta\kappa_\lambda$ using single- and double-Higgs processes for the HE-LHC at 27 TeV and 15 ab^{-1}. The widths of the lines correspond to the differences between the projected uncertainties from the scenarios S1 and S2. **Left:** Comparison of the constraints obtained using inclusive single-Higgs processes (orange), with the ones using differential observables (blue). Dashed is an exclusive fit while solid is the result of a global fit. **Right:** Comparison of the constraints from differential single Higgs (blue), with those from differential double-Higgs data (dashed red).

uncertainties on the inclusive signal strengths of the different production and branching ratio modes of the Higgs, recommended by ATLAS and CMS. The projections of the differential uncertainties are estimated by first rescaling the statistical uncertainty on each bin. This gives an overestimation of the actual reach since it assumes a flat background distribution while it tends to peak at lower invariant masses. We use therefore the CMS analysis on $h \to \gamma\gamma$ in $t\bar{t}h$ production as a template for the tilt of the background. With this we get a good agreement with the CMS fit on the trilinear coupling using this channel only, and we use it as a simple guess for the rest of the uncertainties.

The global fit for the HL-LHC is summarised in Fig. 82. In the left plot, we show in green the $\Delta\chi^2$ including only single-Higgs data, both in an exclusive study (dotted, pale colour), and after profiling over all the other parameters (solid, strong colour). The width of the lines correspond to the difference between the scenarios S1 and S2. The fact that the lines are not very separated means that the constraints are mostly statistics dominated. In orange, we consider only inclusive measurements, while in blue we include the differential information. We can see that, in a global fit, the constraint on the trilinear coupling is worsened due to correlations (mainly with the top Yukawa δy_t and the contact interaction with gluons c_{gg}, and, to a lesser degree, between δy_b and δc_z. The inclusion of the differential information allows to partially remove the flat directions. In the right plot we compare the constraints using differential observables with the ones obtained from double Higgs production, taken from the study in Ref. [285], in dashed red. We include the combination in pink. While double-Higgs is clearly driving the bound, differential single-Higgs data is nonetheless relevant as it can help lift the degenerate minima around $\delta\kappa_\lambda \sim 5$.

We now discuss projections for the HE-LHC at 27 TeV with 15 ab^{-1} of integrated luminosity. For the uncertainties we perform a simple extrapolation where the theory and systematic uncertainties are kept the same as in the HL-LHC projections, while the statistical uncertainty is rescaled accordingly [315]. We show the results in Fig. 83. In the left plot, in brown, we present the χ^2 analysis using the projections for the single-Higgs channels at HE-LHC at the inclusive level. Inclusive measurements are able to lift the flat direction due to the measurement of the $th + j$ production and the $z\gamma$ decay. In blue we present the results using differential observables. We note that the with of the line indicates that, contrary to the HL-LHC case, the constraint is limited by systematics, as expected. In the right plot we compare the constraints with the projections coming from double Higgs production measurement.

3.6 Implications of the HH measurements

3.6.1 Implications for flavor models[51]

In the Two-Higgs-Doublet Model (2HDM), the term $H_1 H_2 \equiv H_1^T (i\sigma_2) H_2$ is a SM singlet which can however be charged under an additional $U(1)$ flavor symmetry. This is an interesting possibility that allows to generate the different fermion masses with a Froggatt-Nielsen (FN) mechanism where the flavon is replaced by the $H_1 H_2$ operator. In this way, the new physics scale Λ where the higher dimensional FN operators are generated is tied to the electroweak scale, leading to much stronger phenomenological consequences. Let us assume for concreteness a type-I like 2DHM with the following Yukawa Lagrangian

$$\mathcal{L}_Y \supset y^u_{ij} \left(\frac{H_1 H_2}{\Lambda^2}\right)^{n_{u_{ij}}} \bar{q}^i_L H_1 u^j_R + y^d_{ij} \left(\frac{H_1^\dagger H_2^\dagger}{\Lambda^2}\right)^{n_{d_{ij}}} \bar{q}^i_L \tilde{H}_1 d^j_R + y^\ell_{ij} \left(\frac{H_1^\dagger H_2^\dagger}{\Lambda^2}\right)^{n_{e_{ij}}} \bar{\ell}^i_L \tilde{H}_1 e^j_R + \text{h.c.}\,, \tag{62}$$

where $\tilde{H}_1 \equiv i\sigma_2 H_1^*$ as usual and the charges $n_{u,d,e}$ are a combination of the $U(1)$ charges of H_1, $(H_1 H_2)$ and the different SM fermion fields. For simplicity, we set the flavor charges of $(H_1 H_2)$ and H_2 to 0 and 1, respectively, such that

$$n_{u_{ij}} = a_{q_i} - a_{u_j}, \quad n_{d_{ij}} = -a_{q_i} + a_{d_j}, \quad n_{e_{ij}} = -a_{\ell_i} + a_{e_j}, \tag{63}$$

if we denote by $a_{q_i}, a_{u_i}, \ldots$, the $U(1)$ charges of the SM fermions. In general, the fermion masses are given by

$$m_\psi = y_\psi \varepsilon^{n_\psi} \frac{v}{\sqrt{2}}, \quad \varepsilon = \frac{v_1 v_2}{2\Lambda^2} = \frac{t_\beta}{1+t_\beta^2} \frac{v^2}{2\Lambda^2}, \tag{64}$$

with the vacuum expectation values $\langle H_{1,2} \rangle = v_{1,2}$ and $t_\beta \equiv v_1/v_2$. Besides being able to accommodate the observed hierarchy of SM fermion masses and mixing angles for the right assignment of flavor charges [377, 378], this framework can lead to enhanced diagonal Yukawa couplings between the Higgs and the SM fermions while having suppressed flavour changing neutral currents (FCNCs). If we denote by h and H the two neutral scalar mass eigen-states, with h being the observed 125 GeV Higgs, the couplings between the scalars $\varphi = h, H$ and SM fermions $\psi_{L_i,R_i} = P_{L,R}\psi_i$ in the mass eigen-basis read

$$\mathcal{L} = g_{\varphi \psi_{L_i} \psi_{R_j}}\, \varphi\, \bar{\psi}_{L_i} \psi_{R_j} + \text{h.c.} \tag{65}$$

with i, such that $u_i = u, c, t,\ d_i = d, s, b$ and $e_i = e, \mu, \tau$. This induces flavor-diagonal couplings

$$g_{\varphi \psi_{L_i} \psi_{R_i}} = \kappa^\varphi_{\psi_i} \frac{m_{\psi_i}}{v} = \left(g^\varphi_{\psi_i}(\alpha,\beta) + n_{\psi_i}\, f^\varphi(\alpha,\beta)\right) \frac{m_{\psi_i}}{v}, \tag{66}$$

as well as flavor off-diagonal couplings

$$g_{\varphi \psi_{L_i} \psi_{R_j}} = f^\varphi(\alpha,\beta) \left(\mathcal{A}_{ij} \frac{m_{\psi_j}}{v} - \frac{m_{\psi_i}}{v} \mathcal{B}_{ij}\right). \tag{67}$$

The flavor universal functions in (66) and (67) read

$$g^h_{\psi_i} = \frac{c_{\beta-\alpha}}{t_\beta} + s_{\beta-\alpha}\,, \qquad g^H_{\psi_i} = c_{\beta-\alpha} - \frac{s_{\beta-\alpha}}{t_\beta}\,, \tag{68}$$

and

$$f^h(\alpha,\beta) = c_{\beta-\alpha}\left(\frac{1}{t_\beta} - t_\beta\right) + 2 s_{\beta-\alpha}\,, \quad f^H(\alpha,\beta) = -s_{\beta-\alpha}\left(\frac{1}{t_\beta} - t_\beta\right) + 2 c_{\beta-\alpha}\,, \tag{69}$$

[51] Contacts: M. Bauer, M. Carena, A. Carmona

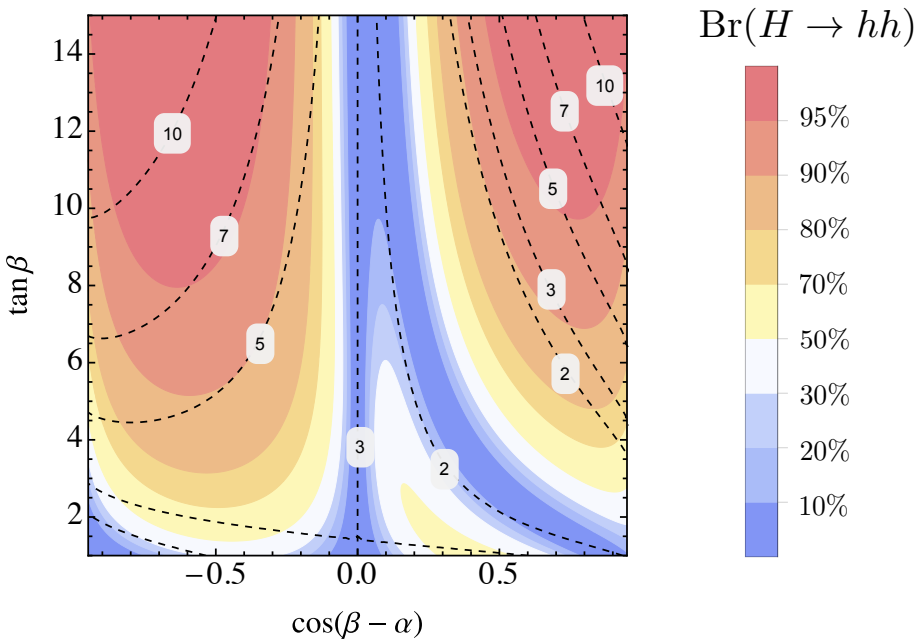

Fig. 84: Br($H \to hh$) as a function of $\cos(\beta-\alpha)$ and $\tan\beta$ for $M_H = M_{H^\pm} = 550$ GeV and $M_A = 450$ GeV. The dashed contours correspond to constant values $|\kappa^h_\psi|$ for $n_\psi = 1$.

where $c_x \equiv \cos x$, $s_x \equiv \sin x$. One can see that, unless all flavor charges for a given type of fermions are equal, the off-diagonal elements in matrices $\mathcal{A}$ and $\mathcal{B}$ lead to FCNCs which are chirally suppressed by powers of the ratio ε, see [341] for more details.

The scalar couplings to the different gauge bosons are the same as in a normal type-I 2HDM while the scalar coupling between the heavy Higgs H and two SM Higgs scalars h, as well as the triple Higgs coupling can be expressed as [379, 380]

$$g_{Hhh} = \frac{c_{\beta-\alpha}}{v}\Big[\big(1-f^h(\alpha,\beta)s_{\beta-\alpha}\big)\big(3M_A^2-2m_h^2-M_H^2\big)-M_A^2\Big]\,, \tag{70}$$

$$g_{hhh} = -\frac{3}{v}\Big[f^h(\alpha,\beta)c^2_{\beta-\alpha}(m_h^2-M_A^2)+m_h^2 s_{\beta-\alpha}\Big]\,, \tag{71}$$

where M_A is the pseudoscalar mass. The $U(1)$ flavor symmetry restricts the number of allowed terms in the scalar potential forbidding e.g. terms proportional to H_1H_2. The interesting feature is that one can rewrite such self scalar interactions with the help of the function $f^h(\alpha,\beta)$, since it is somehow related to the combination $H_1H_2^\dagger$ appearing in both the scalar potential and the higher dimensional operators generating the different Yukawa couplings. Therefore, the parameter space for which $f^h(\alpha,\beta) \gg 1$ and $c_{\beta-\alpha} \neq 0$ leads to maximally enhanced diagonal couplings of the SM Higgs to fermions (66) as well as to an enhancement of the trilinear couplings (70) and (71). For maximally enhanced Yukawa couplings, the mass of the heavy Higgs H cannot be taken arbitrarily large and resonant Higgs pair production has to be present. This correlation between the enhancement of the Higgs Yukawa couplings κ^h_ψ and Br($H \to hh$) is illustrated for $M_H = M_A = M_{H^\pm} = 500$ GeV in Fig. 84 where we plot the dependence of Br($H \to hh$) on $c_{\beta-\alpha}$ and t_β. The dashed contours correspond to constant values of $|\kappa^h_\psi|$ for $n_\psi = 1$. This correlation does not dependent of the factor n_ψ, although $n_\psi > 1$ leads to a larger enhancement. The two exceptions for which this correlation breaks down are the limits $c_{\beta-\alpha} \approx 0$ and $c_{\beta-\alpha} \approx \pm 1$. Whereas the second case is strongly disfavoured by SM Higgs couplings strength measurements, the first one (which corresponds to the decoupling limit) is at odds with the flavor model, for it requires large values of the spurion $\mu_3 \propto M_A$ which softly breaks the $U(1)$ flavor symmetry.

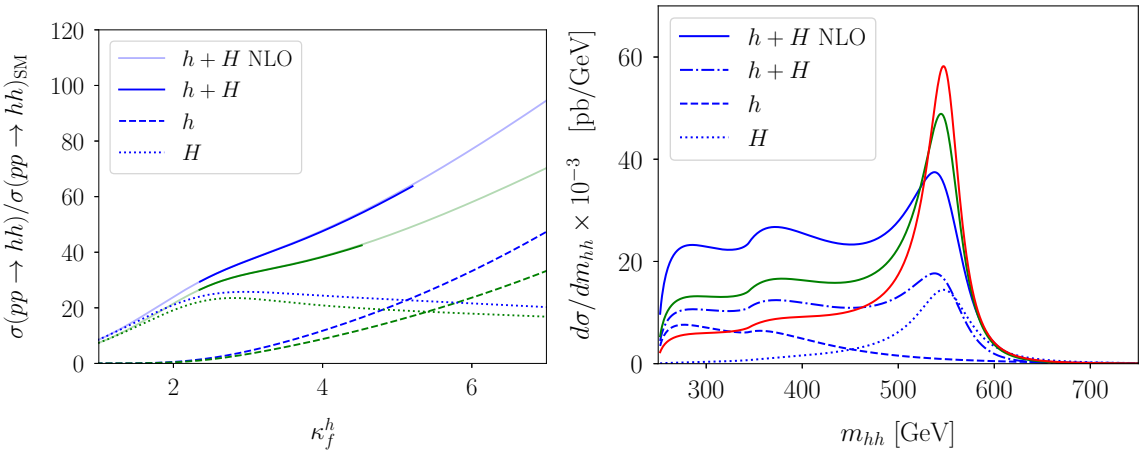

Fig. 85: Left: Cross section for Higgs pair production in units of the SM prediction as a function of κ_ψ^h for $c_{\beta-\alpha} = -0.45$ (-0.4) and $M_A = 450$ GeV, $M_H = M_{H^\pm} = 550$ GeV in blue (green) at $\sqrt{s} = 27$ TeV. Right: Invariant mass distribution for the different contributions to the signal with $c_{\beta-\alpha} = -0.45$ and $\kappa_\psi^h = 5$ (blue), $\kappa_\psi^h = 4$ (green) and $\kappa_\psi^h = 3$ (red) at $\sqrt{s} = 27$ TeV, respectively.

The enhancement in Br$(H \to hh)$ shown in Figure 84 is partially cancelled in the production cross section $\sigma(gg \to H)$ for large values of t_β due to the fact that $\sigma(gg \to H) \propto 1 + 1/t_\beta^2 - (\kappa_t^h)^2$, with $\kappa_t^h \approx 1$. However, the cross-section $\sigma(gg \to h \to hh)$ is not suppressed for such values of t_β and the combination of both contributions leads to a continuous enhancement in the di-Higgs cross-section. There is therefore a non-trivial interplay between resonant and non-resonant contributions, which we illustrate in the left panel of Fig. 85, where we plot both contributions assuming as a function of κ_ψ^h for fixed values of $c_{\beta-\alpha}$ (which is a monotonic function of t_β). We assume a centre-of-mass energy of $\sqrt{s} = 27$ TeV and set $M_A = 450$ GeV and $M_H = M_{H^\pm} = 550$ GeV, while choosing two different values of $c_{\beta-\alpha} = -0.45$ and -0.4. Dashed (dotted) lines correspond to the non-resonant (resonant) contributions, whereas the solid lines represent the full $\sigma(gg \to hh)$ in the 2HDM in units of the SM prediction, both at LO and NLO. Solid lines show the NLO results, while the solid shaded lines mark the values of κ_ψ excluded by perturbativity and unitarity constraints [381]. More details about the calculation of the signal and plots for $\sqrt{s} = 13$ TeV can be found in Ref. [341]. The values of κ_ψ^h in Fig. 85 correspond to $n_\psi = 1$ but values of $\mathcal{O}(10)$ and larger are obtained for $n_\psi > 1$. We also show in the right panel of Fig. 85 the invariant mass distribution for the different contributions to the di-Higgs signal for $c_{\beta-\alpha} = -0.45$ and three different values of $\kappa_\psi^h = 3, 4$ and 5. The interesting feature is that, when the enhancement in the Higgs Yukawa couplings is large enough, the interference between both non-resonant and resonant contributions turns the broad peak into a shoulder in the $d\sigma/dm_{hh}$ distribution for the total cross section, as shown for the case $\kappa_\psi^h = 5$ by the blue line in the right panel of Fig. 85. Resolving such shape in the invariant mass distribution can be quite challenging. We encourage a dedicated analysis considering the corresponding $d\sigma/dm_{hh}$ templates to maximise the sensitivity to features in the di-Higgs invariant mass distribution from the simultaneous enhancement of g_{hhh}, g_{Hhh} and κ_ψ^h.

3.6.2 Implications for theories of electroweak phase transition[52]

Introduction. Explaining the origin of the cosmic matter-antimatter asymmetry is a key open problem at the interface of high energy physics and cosmology. A number of scenarios have been proposed, ranging in energy scales from $\sim 10^{12}$ and above to below the electroweak scale and corresponding to different

[52] Contacts: J. Kozaczuk, A.J. Long, J.M. No, M.J. Ramsey-Musolf

eras in cosmic history. One of the most compelling – electroweak baryogenesis – ties the generation of the asymmetry to electroweak symmetry breaking (for a review, see Ref. [382]). In this scenario, the universe must have undergone a first order phase from the electroweak symmetric to broken phase at a temperature $T_{\rm EW} \sim 100$ GeV. If such a transition occurred, then there must have also existed sufficiently active CP-violating interactions to produce the observed asymmetry. Neither requirement is satisfied by the Standard Model. The symmetry-breaking transition for a 125 GeV Higgs boson is known to be of a crossover type, and the CP-violating interactions encoded in the Cabibbo-Kobayashi-Maskawa matrix are too feeble to have produced the observed asymmetry. Thus, viable electroweak baryogenesis (EWBG) requires physics beyond the standard model that couples to the Higgs boson.

The HE LHC would provide new opportunities to search for this BSM physics. Studies of di-Higgs production, measurements of the Higgs triple self-coupling, and precision tests of other Higgs couplings are particularly interesting as probes of the new interactions needed for a first order electroweak phase transition (EWPT). For the first order phase transition to be sufficiently strong, so as to provide the needed conditions for EWBG, the new interactions must be mediated by particles with masses below roughly one TeV, making them accessible to pp collisions at $\sqrt{s} = 27$ TeV. While a definitive program of searching for these interactions would likely require higher centre of mass energy, the HE LHC would significantly extend the discovery reach over what is accessible at the HL LHC. Below, we provide a few key examples that illustrate this possibility.

Higgs Potential at Finite Temperature. The nature of the EWSB transition is governed by the temperature-dependent Higgs potential, $V_{\rm EFF}(\varphi, T)$. In the regime where $T \gg M_W$, this potential takes the simple form

$$V_{\rm EFF}(\varphi, T) = D(T^2 - T_0^2)\varphi^2 - (ET + e)\varphi^3 + \bar{\lambda}\varphi^4 + \cdots \quad . \tag{72}$$

In the SM one has $e = 0$, while D, T_0, E and $\bar{\lambda}$ are all non-vanishing functions of the zero temperature parameters of the theory (e.g., gauge, Yukawa, and Higgs self-couplings). At any temperature, the minimum of energy is obtained when φ equals its vacuum expectation value $v(T)$, with $v(0) = 246$ GeV. The Higgs boson field is just the difference $h = \varphi - v(0)$.

At sufficiently high temperatures, the minimum of the potential resides at the origin, *i.e.*, $v(T) = 0$. As the universe cools, however, the minimum eventually moves away from the origin, corresponding to the onset of EWSB. The details of this evolution, and the nature of the transition (first order, second order, or crossover) depends on the values of the couplings in Eq. (72). Since the latter are determined by the $T = 0$ interactions, measurements of Higgs boson properties allow one to infer the thermal history of electroweak symmetry breaking.

Assuming the SM form of the $T = 0$ Higgs potential and Higgs couplings to other SM particles, lattice studies imply that for a 125 GeV Higgs boson, the symmetry-breaking transition is of a cross over type [383, 384, 385, 386]. Thus, one of the three "Sakharov conditions" for successful baryogenesis [387] – out of equilibrium dynamics – would not have been satisfied, thereby precluding EWBG. However, the presence of additional bosons that interact with the Higgs boson could yield a first order EWPT even for a 125 GeV Higgs boson (see e.g., [382, 388]). A sufficiently strong first order EWPT may arise if these interactions induce changes in the zero-temperature vacuum structure of the scalar potential and/or generate finite-temperature quantum corrections that modify the parameters in Eq. ((72)). In addition, the presence new neutral scalars that may also obtain vacuum expectation values may allow for a richer thermal history than in the SM universe, including the presence of new symmetry-breaking phases that preceded the presence of the "Higgs phase" [389, 390, 391, 392].

Collider Probes. Existing searches for new scalars at the LHC, together with present measurements of Higgs boson properties, generally rule out a strong first order transition if the new scalars are charged under $\mathrm{S}(3)_C$ [393, 394]. In contrast, interactions involving scalars that carry only EW quantum numbers (EW multiplets) or no SM quantum numbers at all (singlets) are considerably less constrained. Cross sections for directly producing these scalars can be as small as a few fb when model parameters are consistent with a strong first order EWPT. If one of these scenarios is realised in nature, then one may

or may not be able to discover it at the HL LHC. The higher energy and integrated luminosity of the HE LHC would significantly expand this discovery potential.

Perhaps, the simplest illustration of this potential is the extension of the SM scalar sector with a single real singlet scalar [395, 396, 397, 398, 399, 400, 401, 402, 403, 404, 405, 333, 406], the "xSM" [407] (for analogous studies with a complex singlet, see [408, 409]). The xSM contains two Higgs-like scalars, h_1 and h_2 that are admixtures of the neutral component of the SM Higgs doublet and the singlet. For a wide range or model parameters, the interactions in the xSM scalar potential can lead to a strong first order EWPT when the SM-like state h_1 has a mass of 125 GeV. The associated collider signatures direct and indirect effects: direct production of scalar pairs; include modifications of the Higgs self-coupling, which may be as as large as $\mathcal{O}(1)$ or small as a few percent; and a shift in the associated production (Zh_1) cross section.

We consider first scalar pair production. In pp collisions, a pair of SM-like scalars h_1 can be produced through an on-shell h_2, corresponding to the so-called "resonant di-Higgs production". Each h_1 then decays to the conventional Higgs boson decay products, yielding various combinations. The possibilities for discovery through the "resonant di-Higgs production" process are illustrated in Fig. 86, where the results are obtained by combining the 4τ and $\mathrm{b\bar{b}}\gamma\gamma$ final states [403] (for early studies of resonant di-Higgs production, see, *e.g.*. Ref. [353]). Each coloured band gives the projected significance N_σ of observation as a function of the h_2 mass, with the N_σ range obtained by varying over all other model parameters consistent with a strong first order EWPT, constraints from EW precision observables, and present LHC Higgs signal strength determinations. The maximum h_2 mass consistent with a strong first order EWPT is just below 900 GeV. Results are shown for different prospective centre of mass energies.

At the time this work was completed, no analysis had been performed for $\sqrt{s} = 27$ TeV and 15 ab^{-1} integrated luminosity. Consequently, we show in the left panel the reach for the LHC and a 100 TeV pp collider and in the right panel the corresponding reach for $\sqrt{s} = 50$, 100, and 200 TeV with 30 ab^{-1}. As one can see, the HL-LHC discovery potential is limited to a relatively modest portion of the light h_2 parameter space, whereas the FCC-hh with 30 ab^{-1} would enable discovery over the entire first order EWPT-viable parameter space in this model. Interpolating by eye, one can anticipate that the reach for the HE LHC will lie somewhere between that of the LHC and the 50 TeV band in the right panel.

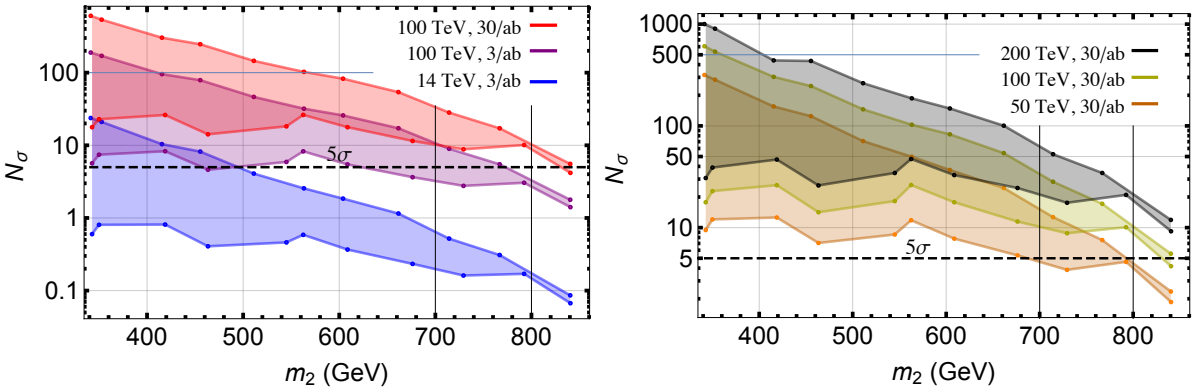

Fig. 86: Discovery potential for the singlet-induced strong first order EWPT using resonant di-Higgs production combining 4τ and $\mathrm{b\bar{b}}\gamma\gamma$ final states [403]. Vertical axis gives significance as a function of the singlet-like scalar mass m_2. Left panel gives comparison of the reach for the HL-LHC (blue band) and the FCC-hh with 3 ab^{-1} and 30 ab^{-1} (purple and red bands, respectively). Right panel shows the prospective reach for different centre of mass energies, assuming 30 ab^{-1}.

It is worth noting that the foregoing analyses are based on the assumption that the di-Higgs pro-

duction process is dominated by the resonant amplitude. As discussed in Section 9.6.2, inclusion of interference with non-resonant amplitudes may lead to an enhanced sensitivity, particularly at higher values of the singlet-like mass m_2. The corresponding gain in going to the HE-LHC may be as much as a 40-50% increase in mass reach compared to that of the HL-LHC, depending on the choice of other model parameters.

Another class of signatures providing important information about the couplings in the Higgs potential in singlet-extended Higgs sectors involves pair production of the new scalar itself. These processes can complement resonant di-Higgs production in their coverage of the parameter space. For example, the process $pp \to h_2 h_2 \to 3\ell 3\nu jj$ was analysed in Ref. [333] and shown to provide good sensitivity to the first-order EWPT-compatible parameter space at both the high luminosity LHC and a future 100 TeV collider for masses below the di-Higgs threshold. While the analogous study has not been performed for the 27 TeV HE-LHC, $h_2 h_2$ production should still provide sensitivity to the couplings in the potential responsible for strengthening the EWPT, improving over the reach of the HL-LHC. In models in which a new $\mathbb{Z}_2$ symmetry is imposed on the singlet scalar, the VBF-like topology $pp \to jjh_2 h_2$ can be used to access the relevant Higgs portal coupling. In this case, h_2 is stable and escapes the detector as missing energy. Ref. [402] showed that this process at 100 TeV can probe first-order EWPTs for relatively low scalar masses. The analogous studies for the 14 TeV HL-LHC and 27 TeV HE-LHC remain to be done.

Beyond direct production, the HE LHC will provide opportunities to observe indirect signatures of a strong first order EWPT through modifications of Higgs couplings. Considering first the xSM, the mixing between the doublet and singlet states will lead to modifications of the Higgs triple self coupling. This possibility is indicated in Fig. 87, where we show he correlation between the critical temperature for the first order EWPT and the triple self coupling. The vertical axis gives the ratio of the xSM triple self-coupling of Higgs-like state h_1 to its Standard Model value, corresponding to the quantity κ_λ introduced earlier in this chapter. According to the analysis presented in the first part of Section 3.4.1, a 15% determination of κ_λ may be possible using the $bb\gamma\gamma$ channel (however, see a parallel analysis later in that section for a less optimistic projection). This sensitivity corresponds roughly to the width of the green band in Fig. 87. One can see that there exists a wide range of xSM parameter choices that would lead to an observable deviation of κ_λ with the HE LHC.

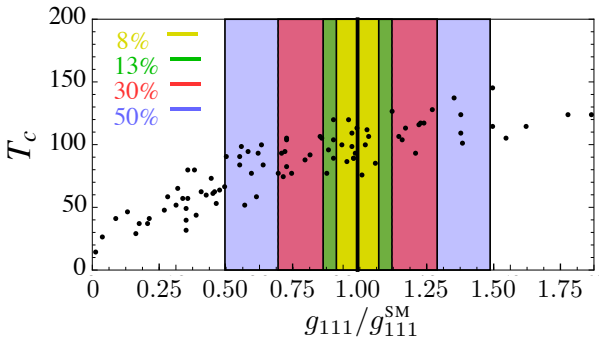

Fig. 87: Parameter space scan for a singlet model extension of the Standard Model. The points indicate a first order phase transition. These points lead to signals observable at future colliders. Shown is the correlation between critical temperature T_c (vertical axis) and the triple Higgs ($h_1 h_1 h_1$) coupling scaled to its SM value (horizontal axis). SM prediction for the latter is indicated as $g_{111}/g_{111}^{\rm SM} = 1$. Adapted from Ref. [410]

Going beyond the SM, one may also anticipate a strong first order EWPT in scalar sector extensions carrying electroweak charge. Among the most widely studied ones, such scenario is the 2HDM. The authors of Refs. [412, 413] have shown that the strong phase transition would be correlated with the presence of the $A^0 \to ZH^0$ decay and that a nearly definitive probe of this possibility could be achieved

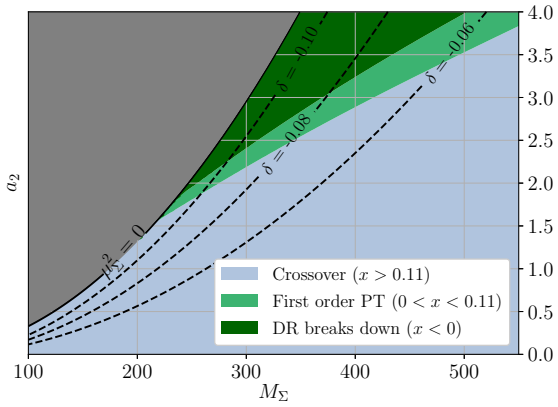

Fig. 88: EW phase diagram for the real triplet extension of the SM scalar sector. Horizontal axis gives the triplet mass and vertical axis indicates the triplet-Higgs coupling. Light blue and green regions correspond to cross-over and first order transitions. Dark green ("DR breaks down") and grey regions indicate parameter choices for which the present non-perturbative computations are not applicable. Dashed lines indicate relative shift δ in the Higgs di-photon decay rate compared to its Standard Model value. From Ref. [411].

with the LHC. An interesting alternative is a scalar EW triplet with vanishing hyper-charge.Interactions between the latter and the Standard Model doublet could lead to breaking of electroweak symmetry through either a single transition to the Higgs phase or through a succession of transitions [389]. Recently, the latter possibility has been explored in Ref. [411] using non-perturbative methods. In this work, it is shown how a precise measurement of the Higgs di-photon decay rate could probe the nature of the transition in this scenario. Fig. 88 illustrates this possibility. The horizontal and vertical axes give the triplet mass and coupling to the Higgs boson, respectively. The light blue and green regions correspond to a cross-over transition and first order phase transition, respectively. The dashed lines indicate the relative reduction in the Higgs di-photon decay rate relative to the prediction for the Standard Model. When combined with knowledge of the triplet mass, a precise measurement of the di-photon decay rate would indicate whether the transition is first order or crossover. As shown in Fig. 30, one expects to achieve a 1.8% (1σ) determination of the Higgs-di-photon coupling parameter κ_γ with the HL-LHC.

3.7 Summary

A measurement of the Higgs self-coupling is not only one of the last corners of the SM to be experimentally tested, but also a particularly interesting one due to its important implications on our knowledge of the Higgs potential, and the direct implications on the nature of electroweak symmetry breaking, the stability of our universe's vacuum and the matter-antimatter asymmetry. In this chapter we presented a study on the capabilities of the HL-LHC and HE-LHC programs to elucidate on these fundamental questions.

The Higgs self-coupling appears at tree level in the production of Higgs boson pairs. The SM cross section for $pp \to$ HH computed at full NLO precision is $32.88^{13.5\%}_{-12.5\%}$ fb at $\sqrt{s} = 14$ TeV and $127.7^{11.5\%}_{-10.4\%}$ fb at $\sqrt{s} = 27$ TeV, a factor 4 increase between the two centre of mass energies. The full NLO dependence on the trilinear coupling has been computed and illustrated in Table 50 for selected coupling strength values. The NLO cross section has been computed for a set of benchmark points in the nonlinear EFT formalism as reported in Table 52.

The ATLAS projections at HL-LHC for the $b\bar{b}b\bar{b}$, $b\bar{b}\tau\bar{\tau}$ and $b\bar{b}\gamma\gamma$ decay modes are summarised in

Fig. 57. Considering the systematic uncertainties, the $b\bar{b}b\bar{b}$ channel gives the constraints $-2.3 \leq \kappa_\lambda \leq 6.4$ at 68% CL; the $b\bar{b}\tau\bar{\tau}$ allows to resolve the region between the two minima giving $0.1 \leq \kappa_\lambda \leq 2.3 \cup 5.7 \leq \kappa_\lambda \leq 7.8$; and the $b\bar{b}\gamma\gamma$ gives the best precision with the interval $-0.2 \leq \kappa_\lambda \leq 2.5$.

The CMS projections include, on top of the channels studied by ATLAS, the decays $b\bar{b}\ell\nu\ell\nu$ and $b\bar{b}\ell\ell\ell\ell$, with projected constraints $-1.7 \leq \kappa_\lambda \leq 9.6$ and $-1.8 \leq \kappa_\lambda \leq 8.1$ respectively. For the other channels, the projected reach is $-0.6 \leq \kappa_\lambda \leq 7.2$ for $b\bar{b}b\bar{b}$, $-0.2 \leq \kappa_\lambda \leq 3.2 \cup 5.2 \leq \kappa_\lambda \leq 7.7$ for $b\bar{b}\tau\bar{\tau}$ and $0.3 \leq \kappa_\lambda \leq 2.3$ for $b\bar{b}\gamma\gamma$.

Experiments provide a combination of the projections, summarised in Fig 65 and Fig. 66. A combined significance of 4σ for the SM HH signal is predicted. The 68% CL intervals are $0.52 \leq \kappa_\lambda \leq 1.5$ and $0.57 \leq \kappa_\lambda \leq 1.5$ with and without systematic uncertainties respectively. The second minimum is excluded at 99.4% CL, and the hypothesis corresponding to the absence of self-coupling ($\kappa_\lambda = 0$) is excluded at the 95% CL.

Further improvements in the analysis are proposed. The Topness and Higgsness variables can further increase the signal sensitivity for HH production, and improved multivariate methods are proposed to improve the background discrimination in the $b\bar{b}\gamma\gamma$ channel.

For the future HE-LHC upgrade, ATLAS presented projections for the $b\bar{b}b\bar{b}$ and $b\bar{b}\tau\bar{\tau}$ channels, with an expected sensitivity of around 10%-20% on κ_λ.

A complementary strategy to extract the trilinear from the LHC data consists in considering NLO corrections to single Higgs observables that depend on the self-coupling. This dependence has been computed and is presented in Tables 61,62,63,64. The CMS experiment has provided a first analysis based on this strategy using $t\bar{t}$H production with the decay H $\rightarrow \gamma\gamma$, with a resulting constraint of $-2 \leq \kappa_\lambda \leq 5.5$, see Fig. 80. Considering that other parameters may affect single Higgs process, this has been studied under the perspective of a global fit, presented in Fig. 82 estimating a $-3 \leq \kappa_\lambda \leq 3$ reach at 68% CL, complementing the constraints from double Higgs boson production. At HE-LHC, the projections are presented in Fig. 83.

Implications of the HH measurements involve a wide variety of models. We present the interpretation within a flavour model which implies large Yukawa couplings for the light quarks, modifying the di-Higgs invariant mass distribution non-trivially, see Fig. 85. Also, Higgs boson pair production plays a crucial role on understanding the nature of the electroweak symmetry breaking phase transition, which might imply potentially observable effects if there are new states modifying the potential so that the matter-antimatter asymmetry can be explained via electroweak baryogenesis.

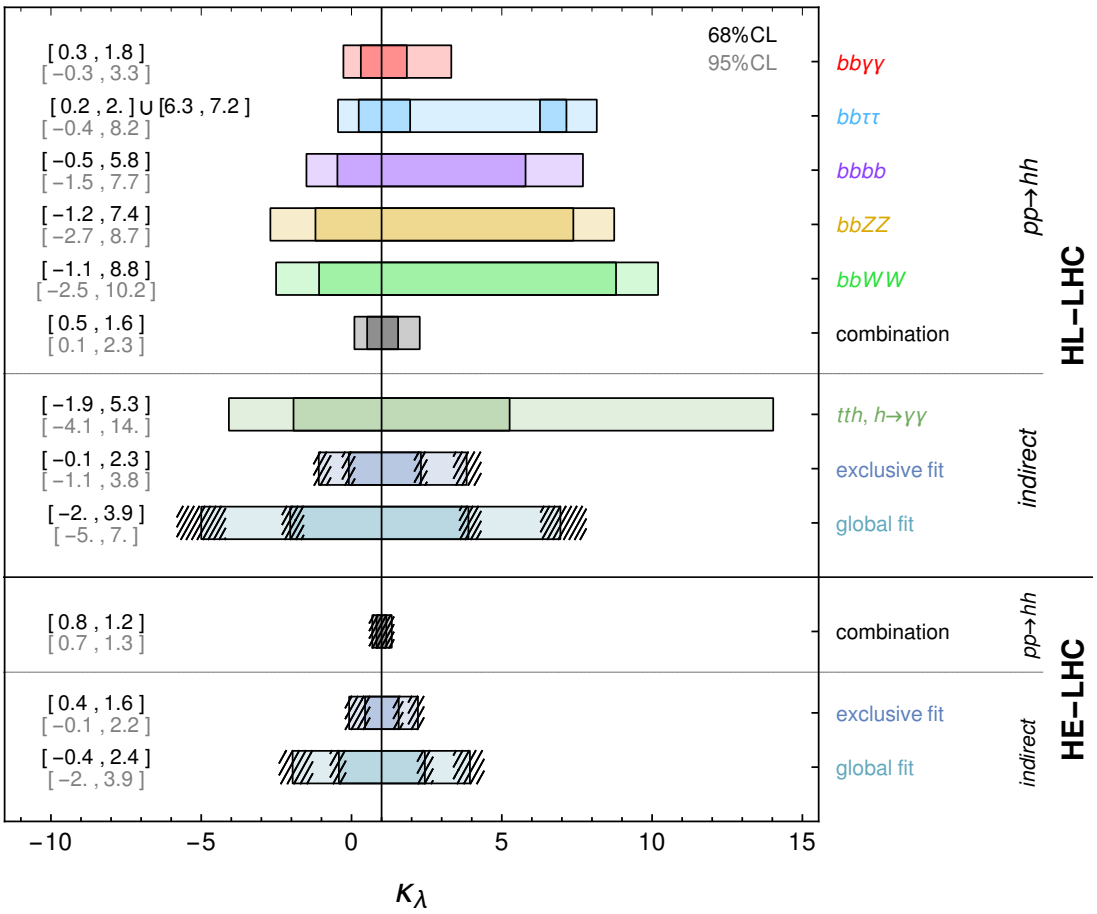

Fig. 89: Summary plot for the different expected constraints on the Higgs boson self-coupling κ_λ at HL-LHC and at HE-LHC. The dashed lines correspond to uncertainties on the values, when any.

4 High Energy Probes[53]

An important aspect of both the HL and HE programs, is their enhanced sensitivity to the high-energy tails of kinematic distributions. These constitute genuinely *new* observables with which we can realistically conceive *high-energy precision tests* that have been impossible at previous experimental facilities. There are two reasons that make this precision program appealing. The first is that we can *define* the high-energy region as that in which statistical uncertainty becomes comparable to systematic uncertainty: in this way, high-energy precision probes are, by construction, expected to deliver the fastest relative improvement with accumulated luminosity, contrary to other observables which are, sooner or later, saturated by systematics.

The second reason why these tests are particular interesting is that the very framework in which precision tests are conceived, that of Effective Field Theories (EFTs) - see section 1.2.1 - implies effects that grow with the energy E. In particular, at the dimension-6 level, the expected growth is $\propto E^2$, implying a quadratic enhancement of the signal. As an order of magnitude estimate, an LHC $O(10\%)$ measurement at 1 TeV, is equivalent in precision to a $O(0.1\%)$ measurement at LEP (where at the Z-pole $E \approx 100$ GeV). For this reason, the HL-LHC (and even more so its HE upgrade) constitute an important continuation of the precision program.

In this chapter, we provide a perspective on the importance of these high-energy probes, and collect a number of contributions that target energy-growing effects in the EFT framework. Our focus is of course Higgs-physics; yet, in the high-energy limit $E \gg m_W$, the longitudinal polarisations of gauge bosons are also associated with the scalar sector, as can be understood by the Equivalence Theorem [414, 415], where external longitudinally-polarised vector states are represented in Feynman diagrams as the corresponding scalar Goldstone bosons, up to corrections of order m_W/E from diagrams with gauge external lines. This brings us to study, in wider generality, processes involving gauge and Higgs bosons.

Sections 4.1 and 4.2 discuss the reach to modified Higgs sectors from WZ, WH and ZH high-p_T distributions, while section 4.3 focuses on an additional class of effects, associated with new physics in the transverse polarisations of vectors, that also modifies WZ processes. Drell-Yann processes also constitute a very clean and powerful probe for new physics coupling to the electroweak bosons, as we discuss in section 4.4. In sections 4.5 and 4.6 we motivate and study modifications of the $hhWW$ coupling, that can be tested in VBF processes and in section 4.7 we provide a generic perspective on the effects associated with Higgs couplings modifications at high-energy. Finally, a more complete EFT discussion of the VBF topology appears in section 4.8 and in section 4.9 for the same-sign case.

4.1 Electroweak Precision Tests in High-Energy Di-boson Processes[54]

In this section we classify the leading new-physics effects that can be tested in di-boson channels, showing that they can be encapsulated in four real "high-energy primary" (HEP) parameters [416] . We also assess the reach on these parameters at the HL-LHC and at future hadronic colliders, focusing in particular on the fully leptonic WZ channel that appears particularly promising.

We are interested in processes which fulfil two conditions. First, their amplitudes must receive BSM contributions that grow with E^2 at the leading order (i.e., $d = 6$) in the EFT operator expansion. Second, the SM amplitudes must be constant and sizeable at high energy, in such a way that, at the linear order in the EFT Wilson coefficient, the E^2-growth of the BSM amplitudes results into a E^2-growth of the differential cross-sections thanks to the SM-BSM interference. As explained in detail in Ref. [416], only $pp \to V_L V_L$ and $pp \to V_L h$ (see section 4.2) production processes enjoy quadratic energy growth at the interference level; we thus focus on these in the rest of the section.[55]

[53] Contact Editor: F. Riva

[54] Contacts: R. Franceschini, G. Panico, A. Pomarol, F. Riva, A. Wulzer

[55] Notice however that promising strategies to circumvent the non-interference problem have been recently proposed [417, 418], which allow for instance to "resurrect" interference effects in transverse vector bosons production, see also section 4.3.

Table 66: Parameter combinations (in the high- and in the low-energy primary bases) that control E^2-enhanced effects in each polarised longitudinal di-boson production process. Here, $T_Z^f = T_3^f - Q_f s^2_{\theta_W}$ and Y_{L,f_R} is the hyper-charge of the left-handed and right-handed quark (e.g., $Y_L = 1/6$).

Amplitude	High-energy primaries	Low-energy primaries
$\bar{u}_L d_L \to W_L Z_L, W_L h$	$\sqrt{2} a_q^{(3)}$	$\sqrt{2}\frac{g^2}{m_W^2}\left[c_{\theta_W}(\delta g^Z_{uL} - \delta g^Z_{dL})/g - c^2_{\theta_W}\delta g_1^Z\right]$
$\bar{u}_L u_L \to W_L W_L$ $\bar{d}_L d_L \to Z_L h$	$a_q^{(1)} + a_q^{(3)}$	$-\frac{2g^2}{m_W^2}\left[Y_L t^2_{\theta_W}\delta\kappa_\gamma + T_Z^{u_L}\delta g_1^Z + c_{\theta_W}\delta g^Z_{dL}/g\right]$
$\bar{d}_L d_L \to W_L W_L$ $\bar{u}_L u_L \to Z_L h$	$a_q^{(1)} - a_q^{(3)}$	$-\frac{2g^2}{m_W^2}\left[Y_L t^2_{\theta_W}\delta\kappa_\gamma + T_Z^{d_L}\delta g_1^Z + c_{\theta_W}\delta g^Z_{uL}/g\right]$
$\bar{f}_R f_R \to W_L W_L, Z_L h$	a_f	$-\frac{2g^2}{m_W^2}\left[Y_{f_R} t^2_{\theta_W}\delta\kappa_\gamma + T_Z^{f_R}\delta g_1^Z + c_{\theta_W}\delta g^Z_{fR}/g\right]$

In order to assess the leading energy behaviour, it is sufficient to study the amplitude in the unbroken phase, where the EW bosons are massless and the $G_{\rm SM} = {\rm SU}(2)_L \times {\rm U}(1)_Y$ symmetry is exact. Given that the Goldstone bosons live in the Higgs doublet H, together with the Higgs particle, $G_{\rm SM}$ implies that the high-energy behaviour of the former ones are connected with the latter. This is the reason why $V_L V_L$ and $V_L h$ production processes, collectively denoted as $\Phi\Phi'$ in what follows, should be considered together.

Focusing our interest to the production of $\Phi\Phi'$ out of a quark q' with helicity λ' and an anti-quark $\bar{q}$ with helicity λ we can restrict the form of the BSM amplitudes that interfere with SM one. At order E^2/M^2 in the EFT expansion the relevant BSM effects can be parametrised as corrections to the $J = 1$ partial wave amplitudes [416], namely

$$\delta\mathcal{A}\left(q'_\pm \bar{q}_\mp \to \Phi\Phi'\right) = f^{\Phi\Phi'}_{q'_\pm\bar{q}_\mp}(s)\sin\theta = \frac{1}{4}A^{\Phi\Phi'}_{q'_\pm\bar{q}_\mp} E^2 \sin\theta^* \,, \tag{73}$$

where θ^* is the scattering angle in the $\Phi\Phi'$ centre of mass, and $E = \sqrt{s}$ is the centre of mass energy.

Eq. (73) shows that at the leading order in the SM EFT expansion each di-boson process is sensitive at high energy to a single constant new-physics parameter $A^{\Phi\Phi'}_{q'_\pm\bar{q}_\mp}$ for every combination of initial or final states. This can be taken real since its imaginary part does not interfere with the SM. In addition, the SM symmetry group, which is restored in the high-energy limit, as previously explained, implies several relations among these parameters [416]. As a consequence, only 4 HEP parameters are enough to parametrise the BSM effects we are interested in. This is very non-trivial from an EFT perspective, since a total of 6 anomalous couplings coming from $d = 6$ effective operators contribute to longitudinal di-boson processes. These couplings can be identified as δg^Z_{uL}, δg^Z_{uR}, δg^Z_{dL}, δg^Z_{dR}, δg_1^Z and $\delta\kappa_\gamma$ in the notation of Ref. [419]. The relations between the HEP parameters and the 4 combinations of the low-energy primaries that produce growing-with-energy effects are reported in the third column of table 66, while the relations between the HEP and the Wilson coefficients in the SILH basis [40], see table 1, are given by

$$a_q^{(3)} = \frac{g^2}{M^2}(c_W + c_{HW} - c_{2W}) \,, \quad a_q^{(1)} = \frac{g'^2}{3M^2}(c_B + c_{HB} - c_{2B}) \,, \tag{74}$$

and

$$a_u = -2a_d = 4a_q^{(1)} \,. \tag{75}$$

These relations can also be written using the $\hat{S}$, $\hat{T}$, W and Y parameters (we follow the notation of

Table 67: List of acceptance and analysis cuts.

acceptance cuts	$p_{T,\ell} > 30\text{GeV}\,, \quad |\eta_\ell| < 2.4$
analysis cuts	$p_{T,VV}/p_{T,V} < 0.5$ $\lvert\cos\theta^*\rvert \leq 0.5$

Ref. [420]) in addition to the two anomalous triple gauge couplings (aTGC), δg_1^Z and $\delta\kappa_\gamma$. We have

$$a_q^{(3)} = -\frac{g^2}{m_W^2}\left(c_{\theta_W}^2\,\delta g_1^Z + W\right)\,, \quad a_q^{(1)} = \frac{g'^2}{3m_W^2}\left(\hat{S} - \delta\kappa_\gamma + c_{\theta_W}^2\,\delta g_1^Z - Y\right)\,, \tag{76}$$

which can be useful in order to compare HEP analyses from LHC with other experiments, such as LEP.

In the Warsaw basis [41], the HEP are transparently identified with contact interactions between quarks and scalars [56], see Table 1

$$a_u = 4\frac{c_R^u}{M^2}\,, \quad a_d = 4\frac{c_R^d}{M^2}\,, \quad a_q^{(1)} = 4\frac{c_L^{(1)}}{M^2}\,, \quad a_q^{(3)} = 4\frac{c_L^{(3)}}{M^2}\,. \tag{77}$$

To illustrate the HL/HE-LHC reach on the high-energy primaries we focus on WZ production. This channel gives access to the $a_q^{(3)}$ primary and has a very high sensitivity to new physics [416]. We consider the fully leptonic final state

$$pp \to W^\pm Z + \text{jets} \to \ell\nu\ell'\bar{\ell}' + \text{jets}\,, \quad \text{with } \; l, l' = e, \mu\,,$$

which is likely to be measured with good accuracy and can benefit from a straightforward reconstruction of the final-state leptons and a very low reducible background [421]. At the experimental level the situation might not be too much different from the neutral Drell-Yan process, in which a measurement with 2% relative systematic uncertainty of the differential cross-section was performed, with run-1 LHC data, up to TeV energies [422]. A systematic uncertainty of 5% might be considered as a realistic goal for the differential cross-section measurement in the leptonic WZ channel.

The main obstacle to obtain sensitivity to new physics is the potentially large contribution of the other polarisations, which for our purposes constitute a background, since they are insensitive to the new physics parameter $a_q^{(3)}$. Due to the symmetry structure, the emission of transversely polarised W and Z bosons in the central rapidity region is disfavoured [416]. No suppression is instead expected for longitudinally polarised gauge bosons, therefore it is advantageous to concentrate our analysis on central scattering region, $|\cos\theta^*| \sim 0$, or, equivalently, at large $p_{T,V}$ ($p_{T,V} > 1$ TeV). We stress that other di-boson processes, e.g. $pp \to WW$, do not enjoy this suppression of transverse vector boson emission, therefore are expected to be less sensitive probes of the high energy primaries.

We now estimate the reach on $a_q^{(3)}$ based on a full NLO simulation of the $pp \to 3\ell\nu$ process, see Ref. [416]. We consider generation-level leptons momenta, but we include an overall detector efficiency for reconstructing the three leptons that we estimate around 50% [423]. We furthermore apply standard acceptance cuts on the leptons (see Table 67). The same-flavor and opposite-charge lepton pair with invariant mass closer to the Z boson mass is taken as the Z candidate and the remaining lepton is taken to be the decay product of the W boson. The missing transverse energy vector of the event ($\not{E}_T$) is estimated from the generation-level transverse neutrino momentum, to which we apply a Gaussian smearing with standard deviation $\sigma^2_{\not{E}_{T_i}} = (0.5)^2 \cdot \sum_f |p_i| \cdot \text{GeV}$.

In order to highlight the production of longitudinally polarised vector bosons in the central rapidity region, it is useful to eliminate events with hard real radiation, which tend to be more abundant for

[56] These relations, as well as those in eq. (74), are obtained by computing the di-boson helicity amplitudes in the presence of the EFT operators, and matching with the results of the low energy primaries. See Ref. [416] for details.

our background of transverse polarised gauge bosons. To tame real radiation events in a controlled way we employ a selection on the transverse momentum of the WZ system, denoted by $p_{T,VV} = |\vec{p}_{T,W} + \vec{p}_{T,Z}|$.[57] We require $p_{T,VV}$ to be smaller than 50% of the transverse momentum of the gauge bosons in the event, $p_{T,V} = \min(p_{T,W}, p_{T,Z})$. We also impose a cut on the scattering angle in the WZ centre of mass frame $|\cos\theta^*| \leq 0.5$. The cuts are summarised in Table 67.

The kinematic variables described so far allow us to determine $p_{T,Z}$ and $p_{T,W}$, and in turn $p_{T,V}$ and $p_{T,VV}$, used to construct the binned distribution and for the selection cuts. In order to extract $|\cos\theta^*|$ the neutrino rapidity is reconstructed by the standard technique of imposing the invariant mass of the neutrino plus lepton system to be as close as possible to the physical W boson mass. A twofold ambiguity in the reconstruction is resolved by imposing the $|\cos\theta^*|$ cut on both solutions, i.e. by retaining for the analysis only events such that both the possible neutrino configurations satisfy the selection criteria.

We study the 3 collider energy options that correspond to the LHC (14 TeV), to the High-Energy LHC (HE-LHC, 27 TeV) and to the FCC-hh (100 TeV). In each case we consider suitably designed $p_{T,V}$ bins, namely

$$\begin{aligned} \text{LHC:} \quad & p_{T,V} \in \{100, 150, 220, 300, 500, 750, 1200\}\,, \\ \text{HE-LHC:} \quad & p_{T,V} \in \{150, 220, 300, 500, 750, 1200, 1800\}\,, \\ \text{FCC:} \quad & p_{T,V} \in \{220, 300, 500, 750, 1200, 1800, 2400\}\,. \end{aligned} \tag{78}$$

The binning is chosen such as to cover the kinematic regime that is accessible at each collider and it is taken as fine as possible in order to maximise the BSM sensitivity. On the other hand, a minimum bins size $\Delta p_{T,V}/p_{T,V} \gtrsim 30\%$ is required in order to avoid a degradation of the accuracy due to the $p_{T,V}$ resolution.

The predicted cross-sections are used to construct the χ^2, under the assumption that observations agree with the SM, and are eventually used to derive 95% CL bounds on $a_q^{(3)}$. The uncertainties in each bin are the sum in quadrature of the statistical error, obtained from the SM expected events yield, and of a systematical component (uncorrelated across bins) which we take as a fixed fraction (δ_{syst}) of the SM expectations. With this procedure we obtain, for different collider energies and luminosities and for $\delta_{\text{syst}} = 5\%$

$$\begin{aligned} \text{HL-LHC, } 3\,\text{ab}^{-1}\text{:} \quad & a_q^{(3)} \in [-4.9, 3.9]\,10^{-2}\,\text{TeV}^{-2} \\ \text{HE-LHC, } 10\,\text{ab}^{-1}\text{:} \quad & a_q^{(3)} \in [-1.6, 1.3]\,10^{-2}\,\text{TeV}^{-2} \\ \text{FCC-hh, } 20\,\text{ab}^{-1}\text{:} \quad & a_q^{(3)} \in [-7.3, 5.7]\,10^{-3}\,\text{TeV}^{-2} \end{aligned} \tag{79}$$

We see that the HE-LHC will improve the HL-LHC reach by a factor of 3, while a gain of nearly one order of magnitude would be possible with the FCC-hh collider. The FCC-hh reach is comparable with the one of CLIC, as extracted from the analysis in Ref. [425].

The results of eq. (79) rely on BSM cross-section predictions obtained by integrating up to very high centre of mass energies, formally up to the collider threshold. Therefore these limits assume that the description of the underlying BSM model offered by the EFT is trustable in the whole relevant kinematic regime, i.e. that the cutoff M of the BSM EFT is high enough. We quantify how large M concretely needs to be for our results to hold by studying [426, 427, 428] how the limit deteriorates if only events with low WZ invariant mass, $m_{\text{WZ}} < m_{\text{WZ}}^{\text{max}}$ are employed. This obviously ensures that the limit is consistently set within the range of validity of the EFT provided the EFT cutoff M is below $m_{\text{WZ}}^{\text{max}}$. The results are reported in figure 90. Since the 95% CL interval is nearly symmetric around the origin only the upper limit is reported in the figure for shortness.

[57] Alternatively, a jet veto might be considered, which however could lead to lower accuracy because of the experimental and theoretical uncertainties in jets reconstruction. See also Ref. [424] for a different approach.

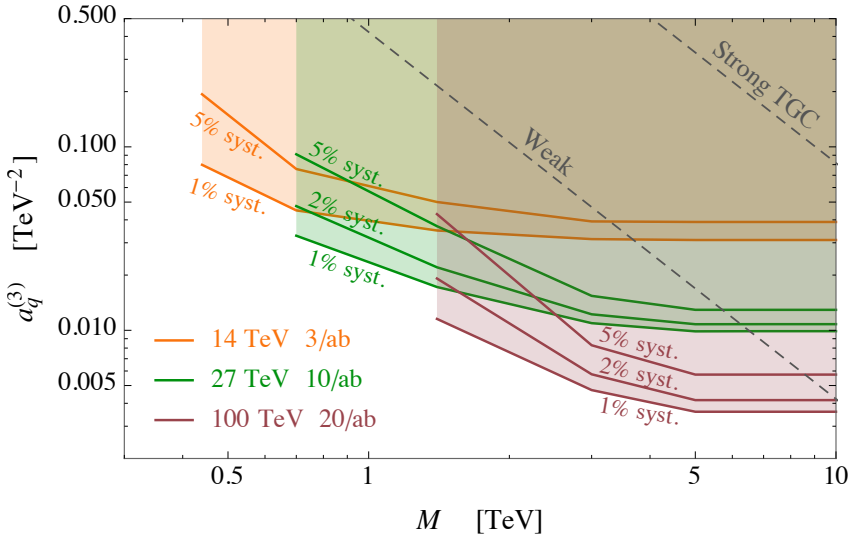

Fig. 90: Expected 95% CL bounds from fully leptonic WZ on the high-energy primary parameter $a_q^{(3)}$ as a function of the new physics scale M. The plots reports the results for the HL-LHC (orange lines), HE-LHC (green lines) and FCC-hh (brown lines) for different values of the systematic uncertainties.

Several conclusions can be drawn from figure 90. First of all we see that the reach saturates for $m_{\rm WZ}^{\rm max}$ below around 1.5 TeV at the HL-LHC if the systematic uncertainties are low, meaning that the limits obtained without $m_{\rm WZ}$ cut apply to theories with cutoff M above that threshold. The threshold grows to around 3 and 4 TeV at the HE-LHC and at the FCC-hh, respectively. The figures show that $\delta_{\rm syst} = 5\%$ is sufficient to probe "Weak" theories in all cases, but it also shows that the impact of larger or smaller uncertainties on the reach can be significant. Systematic errors at the $\delta_{\rm syst} = 5\%$ level already make an appreciable difference with respect to $\delta_{\rm syst} = 1\%$. This is due to the fact that the low-$p_{T,V}$ bins have small statistical error and the reach in those bins benefits from lower systematics. The effect is even more pronounced at the HE-LHC and at the FCC-hh, where even with $\delta_{\rm syst} = 2\%$ the reach deteriorates significantly with respect the ideal case $\delta_{\rm syst} = 1\%$. The fact that more accurate measurements would improve the reach of future colliders is an element that should be taken into account in the design of the corresponding detectors.

4.2 WH/ZH at high energy/luminosity[58]

In this section we perform a collider study of the Higgs-strahlung process, $pp \to Z(\ell^+\ell^-)h(b\bar{b})$ in the Standard Model Effective Field Theory (SMEFT) framework. We will see that the leading high energy contribution to the $pp \to Zh$ process comes from the four contact interactions $hZ_\mu \bar{u}_{L,R}\gamma^\mu u_{L,R}$ and $hZ_\mu \bar{d}_{L,R}\gamma^\mu d_{L,R}$ that appear in the dimension-6 Lagrangian. These are the same four EFT directions, the so called "high energy primaries" that control high energy Wh, WW and WZ production (see Ref. [416]). The (pseudo-)observables involved in these di-boson processes (anomalous TGCs and Z-pole observables) have already been constrained at LEP. We show in this note that because of the higher energies accessible at the LHC one can obtain bounds on these observables that are at least an order of magnitude stronger than those obtained at LEP.

The vertices in the dimension 6 Lagrangian that contribute to the $ff \to Vh$ (where $V = W, Z$) process in unitary gauge are as follows,

$$\Delta\mathcal{L}_6 \supset \sum_f \delta g_f^Z Z_\mu \bar{f}\gamma^\mu f + \delta g_{ud}^W (W_\mu^+ \bar{u}_L \gamma^\mu d_L + h.c.) + g_{VV}^h\, h \left[W^{+\mu} W_\mu^- + \frac{1}{2c_{\theta_W}^2} Z^\mu Z_\mu \right]$$

[58] Contacts: S. Banerjee, R.S. Gupta, C. Englert, M. Spannowsky

$$+\delta g^h_{ZZ}\, h\frac{Z^\mu Z_\mu}{2c^2_{\theta_W}} + \sum_f g^h_{Zf}\,\frac{h}{v}Z_\mu \bar{f}\gamma^\mu f + g^h_{Wud}\,\frac{h}{v}(W^+_\mu \bar{u}_L\gamma^\mu d_L + h.c.) + \kappa_{Z\gamma}\frac{h}{v}A^{\mu\nu}Z_{\mu\nu}$$
$$+\kappa_{WW}\,\frac{h}{v}W^{+\,\mu\nu}W^-_{\mu\nu} + \kappa_{ZZ}\,\frac{h}{2v}Z^{\mu\nu}Z_{\mu\nu}\,. \tag{80}$$

Here we have used the Lagrangian presented in Ref. [419, 429], where α_{em}, m_Z and m_W have been used as input parameters and any corrections to the SM vector boson propagators have been traded in favour of the vertex corrections. After summing over all V-polarisations, the leading piece in the high energy cross-section deviation for $ff \to Vh$, is proportional to the four contact interactions: g^h_{Zf}, with $f = u_L, u_R, d_L$ and d_R.[59] Table 68, shows the linear combinations of Wilson coefficients contributing to the four g^h_{Zf} couplings in different EFT bases. The aforementioned directions are shown in the BSM Primary basis of Ref. [419], where the Wilson coefficients are already constrained pseudo-observables. In this basis we see that these can be written in terms of already constrained LEP (pseudo)observables.

Given the inability to control the polarisation of the initial state partons in a hadron collider, the process, in reality, only probes two of the above four directions. Taking only the interference term, we find these directions to be

$$g^Z_{\mathbf{u}} = g^h_{Zu_L} + \frac{g^Z_{u_R}}{g^Z_{u_L}} g^h_{Zu_R},\; g^Z_{\mathbf{d}} = g^h_{Zd_L} + \frac{g^Z_{d_R}}{g^Z_{d_L}} g^h_{Zd_R}\,. \tag{81}$$

At a given energy, a linear combination of the up-type and down-type coupling deviations, enters the interference term for the $pp \to Zh$ process, $g^Z_{\mathbf{p}} = g^Z_{\mathbf{u}} + \frac{\mathcal{L}_d(\hat{s})}{\mathcal{L}_u(\hat{s})} g^Z_{\mathbf{d}}$, where $\mathcal{L}_{u,d}$ is the $u\bar{u}$, $d\bar{d}$ luminosity at a given partonic centre of mass energy. The luminosity ratio changes very little with energy: between 0.65 and 0.59 as $\sqrt{\hat{s}}$ is varied from 1 to 2 TeV. Thus, to a good approximation, $pp \to Zh$ probes the single direction,

$$g^Z_{\mathbf{p}} = g^h_{Zu_L} - 0.76\; g^h_{Zd_L} - 0.45\; g^h_{Zu_R} + 0.14\; g^h_{Zd_R}\,. \tag{82}$$

using $\hat{s} = (1.5\text{ TeV})^2$. Using Tab. 68, one can now write this in terms of the LEP-constrained pseudo-observables,

$$\begin{aligned} g^h_{Z\mathbf{p}} &= 2\,\delta g^h_{Zu_L} - 1.52\,\delta g^h_{Zd_L} - 0.90\,\delta g^h_{Zu_R} + 0.28\,\delta g^h_{Zd_R} \\ &\quad -0.14\,\delta\kappa_\gamma - 0.89\,\delta g^Z_1 \\ g^h_{Z\mathbf{p}} &= -0.14\,(\delta\kappa_\gamma - \hat{S} + Y) - 0.89\,\delta g^Z_1 - 1.3\,W \end{aligned} \tag{83}$$

where the first and second lines apply respectively to the general and universal case (third and fourth row of Table 68).

To estimate the cut-off for our EFT, note that the g^h_{Vf} couplings arise from current-current operators that can be generated, for instance, by integrating out at tree-level a heavy $SU(2)_L$ triplet (singlet) vector W'^a (Z') that couples to SM fermion currents, $\bar{f}\sigma^a\gamma_\mu f$ ($\bar{f}\gamma_\mu f$) with a coupling g_f and to the Higgs current $iH^\dagger\sigma^a \overleftrightarrow{D}_\mu H$ ($iH^\dagger \overleftrightarrow{D}_\mu H$) with a coupling g_H. This gives $g^h_{Zf} \sim g_H g g_f v^2/\Lambda^2$, where Λ is the mass of the massive vector and thus the cut-off for our EFT description. A universal coupling to the SM fermions can arise via kinetic mixing of the heavy vector with the SM gauge bosons; this would give $g_f = g/2$ ($g_f = g' Y$), such that,

$$g^h_{Zu_L,d_L} \sim \frac{g_H g^2 v^2}{2\Lambda^2},\; g^h_{Zu_R,d_R} \sim \frac{g_H g g' Y_{u_R,d_R} v^2}{\Lambda^2}. \tag{84}$$

For a given set of couplings $\{g^h_{Zu_L}, g^h_{Zd_L}, g^h_{Zu_R}, g^h_{Zd_R}\}$, the cut-off is evaluated using Eq. 84 with $g_H = 1$ (note that this is somewhat larger than the value corresponding to the SM hZZ coupling) and taking the

[59] There exists a basis independent constraint at the dimension-6 level, $\sqrt{2}\; g^h_{Wud} = (g^h_{Zd_L} - g^h_{Zu_L})$.

Table 68: The linear combinations of Wilson coefficients contributing to the contact interaction couplings $g^h_{Zf}$where $f = u_L, d_L, u_R, d_R$. the direction for a given f can be read off from this table by substituting the corresponding value of the $SU(2)_L$ and $U(1)_Y$ quantum numbers T^f_3 and Y_f. Here $\hat{c}_W = c_W + c_{HW} - c_{2W}$ and $\hat{c}_B = c_B + c_{HB} - c_{2B}$. For the nomenclature of the operators, their corresponding Wilson coefficients and observables see for eg. Ref. [416].

	EFT directions probed by high energy $ff \to Vh$ production
Warsaw Basis [41]	$-\frac{2g}{c_{\theta_W}}\frac{v^2}{\Lambda^2}(\lvert T^f_3\rvert c^1_L - T^f_3 c^3_L + (1/2 - \lvert T^f_3\rvert)c_f)$
BSM Primaries [419]	$\frac{2g}{c_{\theta_W}} Y_f t^2_{\theta_W}\delta\kappa_\gamma + 2\delta g^Z_f - \frac{2g}{c_{\theta_W}}(T^f_3 c^2_{\theta_W} + Y_f s^2_{\theta_W})\delta g^Z_1$
SILH Lagrangian [40]	$\frac{g}{c_{\theta_W}}\frac{m^2_W}{\Lambda^2}(2\lvert T^f_3\rvert\hat{c}_W - 2t^2_{\theta_W} Y_f \hat{c}_B)$
Universal observables	$\frac{2g}{c_{\theta_W}} Y_f t^2_{\theta_W}(\delta\kappa_\gamma - \hat{S} + Y) - \frac{2g}{c_{\theta_W}}(T^f_3 c^2_{\theta_W} + Y_f s^2_{\theta_W})\delta g^Z_1 - \frac{2g}{c_{\theta_W}} T^f_3 W$
High Energy Primaries [416]	$-\frac{2m^2_W}{g c_{\theta_W}}(\lvert T^f_3\rvert a^{(1)}_q - T^f_3 a^{(3)}_q + (1/2 - \lvert T^f_3\rvert)a_f)$

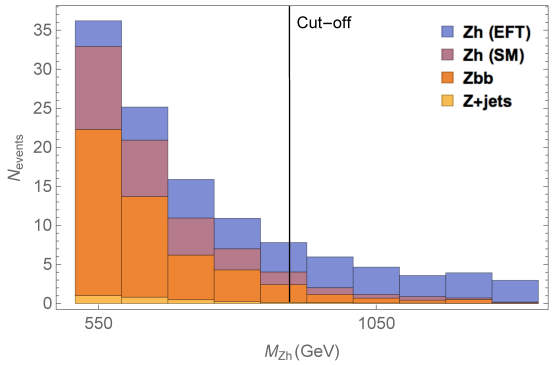

Fig. 91: The differential distribution of events at an integrated luminosity of 300 fb^{-1} with respect to M_{Zh} for the EFT signal as well as the different backgrounds. The EFT signal corresponds to the point $\{g^h_{Zu_L}, g^h_{Zd_L}, g^h_{Zu_R}, g^h_{Zd_R}\} = \{-0.005, 0.0001, -0.010, 0.005\}$ which is allowed by LEP bounds. The vertical line shows the cut-off evaluated using Eq. 84.

smallest of the four values.

For our collider analysis, we consider $Z(\ell^+\ell^-)h$ production from a pair of quarks as well as from a pair of gluons. For the decay of the Higgs boson, we find that at an integrated luminosity of 300 fb^{-1}, the di-photon mode is not feasible as it yields less than 5 events at high energies ($p_{T,Z} > 150$ GeV). We thus focus on the decay $h \to b\bar{b}$ to obtain large statistics. The dominant backgrounds are then $Zb\bar{b}$ and the irreducible Zh production in SM. Reducible contributions also arise from $Z+$ jets production (where we include c-quarks but do not require that they are explicitly tagged). We employ the BDRS approach [430] and demand a fat jet with a cone radius of $R = 1.2$. More details of the Monte-Carlo analysis, the QCD corrections, the detailed cut-based and multivariate analyses (MVA) can be found in Ref. [431]. Finally, we find a cut-based (MVA) SM Zh to $Zb\bar{b}$ ratio of ~ 0.26 (0.50).

To discriminate between the EFT signal and the irreducible SM $Zh(b\bar{b})$ background we study the growth of the EFT cross-section at high energies. This can be seen in Fig. 91 where we show the differential distribution with respect to M_{Zh}, the invariant mass of the leptons and the fat jet, for the EFT signal as well as for the different backgrounds. The EFT signal corresponds to a point that can be excluded in our analysis but is allowed by the LEP constraint. To fully utilise the shape deviation of the EFT signal with respect to the background, we perform a binned log likelihood analysis assuming a 5% systematic

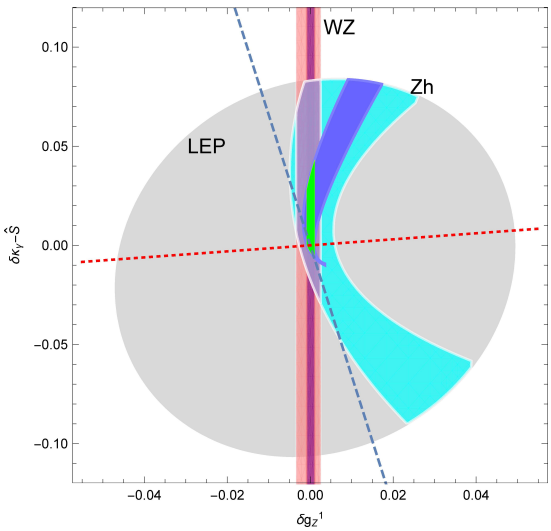

Fig. 92: The light blue (dark blue) region above shows the projection for the allowed region with 300 fb^{-1} (3 ab^{-1}) data from the $pp \to Zh$ process in the $\delta\kappa_\gamma - \hat{S}$ vs δg_1^Z plane for universal models. We show in grey the allowed region after LEP bounds (taking the TGC $\lambda_\gamma = 0$, a conservative choice) are imposed. In pink (dark pink) we show the region that corresponds to the projection from the WZ process with 300 fb^{-1} (3 ab^{-1}) data derived in Ref. [416] and the purple (green) region shows the region that survives from a combination of the Zh and WZ projections with 300 fb^{-1} (3 ab^{-1}) data.

error taking only events below the cut-off (evaluated as explained below Eq. 84). To obtain the 95% CL exclusion curve, we assume that the observed number of events would agree with the SM.

Taking into account only the SM-BSM interference term, we find the following per-mille level bounds for 300 (3000) fb^{-1},

$$g^h_{Z\mathbf{p}} \in [-0.004, 0.004] \;\; ([-0.001, 0.001]) \tag{85}$$

The above bounds translate to a lower bound on the scale of new physics given by 2.4 TeV (4.4 TeV) at 300 fb^{-1} (3000 fb^{-1}) using Eq. 84. To compare the above projections with existing LEP bounds, one can now extract bounds on the LEP observables contributing to $g^h_{Z\mathbf{p}}$ in Eq. 83 by turning them on one by one. We show the results in Tab. 69. For the TGCs δg_1^Z and $\delta\kappa_\gamma$, our projections are much stronger than the LEP bounds and in the case of the Z-pole observables δg_f^Z, that parametrise the deviations of the Z coupling to quarks, they are comparable.

For the universal case, we perform a more detailed analysis. The results are shown in the $\delta\kappa_\gamma - \hat{S}$ vs. δg_1^Z plane in Fig. 92 for the interesting class of models where $W = Y = 0$ [416]. The direction related to the $pp \to Zh$ interference term, *i.e.*, $g^h_{Z\mathbf{p}} = 0$ (see Eq. 82 and the second line of Eq. 83) is shown by the dashed blue line, whereas the direction orthogonal to it is shown by the dotted red line. Once the LEP II bounds [432] from the $e^+e^- \to W^+W^-$ process are imposed, the allowed region that remains is shown by the grey shaded area. We show the results of this work in blue (light (dark) blue for results at 300 (3000) fb^{-1}). The shape of the allowed region arises due to the fact that the interference term vanishes along the dashed blue line and the squared term increases in magnitude as we move away from the origin. This curves the allowed region away from the dashed line as we move away from the origin. The accidental cancellation of the interference term means that our bounds are susceptible to dimension-8 effects along this direction. On the other hand our bounds are more robust and not susceptible to such effects in the orthogonal direction shown by the red dotted line.

Table 69: Comparison of the bounds obtained in this work with existing LEP bounds obtained by turning on the LEP observables in Eq. 83 one by one and using Eq. 85. The LEP bounds on the Z coupling to quarks has been obtained from Ref. [433], the bound on the TGCs from Ref. [432], the bound on $\hat{S}$ from Ref. [434] and finally the bounds on W, Y have been obtained from Ref. [420]. Except for the case of the bounds on δg_f^Z, all of the bounds in the last column were derived by turning on only the given parameter and putting all other parameters to zero. The numbers outside (inside) brackets, in the second column, denote our bounds with $\mathcal{L} = 300\ (3000)$ fb^{-1}.

	Our Projection	LEP Bound
$\delta g^Z_{u_L}$	$\pm 0.002\ (\pm 0.0007)$	-0.0026 ± 0.0016
$\delta g^Z_{d_L}$	$\pm 0.003\ (\pm 0.001)$	0.0023 ± 0.001
$\delta g^Z_{u_R}$	$\pm 0.005\ (\pm 0.001)$	-0.0036 ± 0.0035
$\delta g^Z_{d_R}$	$\pm 0.016\ (\pm 0.005)$	0.0016 ± 0.0052
δg^Z_1	$\pm 0.005\ (\pm 0.001)$	$0.009^{+0.043}_{-0.042}$
$\delta \kappa_\gamma$	$\pm 0.032\ (\pm 0.009)$	$0.016^{+0.085}_{-0.096}$
$\hat{S}$	$\pm 0.032\ (\pm 0.009)$	0.0004 ± 0.0007
W	$\pm 0.003\ (\pm 0.001)$	0.0000 ± 0.0006
Y	$\pm 0.032\ (\pm 0.009)$	0.0003 ± 0.0006

As VV production constrains the same set of operators as the Vh production in Fig. 92, we also show the projected bound from the WZ process at 300 fb^{-1} obtained in Ref. [416] (see section 4.1). Only the purple region remains when both these bounds are combined at 300 fb^{-1}. This shrinks further to the green region at 3000 fb^{-1}. A drastic reduction in the allowed LEP region is thus possible by considering the $pp \to Zh$ at high energies.

4.3 Novel measurements of anomalous triple gauge couplings[60]

In this work we are interested in the measurement of the Standard Model (SM) Triple Gauge Couplings (TGCs). This is a classic test of the SM and a possible measurement of deviations from its expectations would signify an invaluable piece of information for the theory beyond the SM. A consistent way to parametrise such possible deviations is through the SM Effective Field Theory (EFT) approach. We are going to consider the SM EFT as defined in [418, 435], in particular we are going to focus on the measurement of the EFT operator $\mathcal{O}_{3W}$, see Table 1, which is associated to the the anomalous triple gauge coupling (aTGC) λ_z.

A precise determination of the TGC stems from the measurement of the $2 \to 2$ cross section $\sigma(q\bar{q} \to VV)$ [436, 421]. Naive dimensional analysis and standard EFT reasoning predicts that the energy scaling of such cross-section is given by

$$\sigma(q\bar{q} \to VV) \sim \frac{g_{\rm SM}^4}{E^2}\left[1 + \overbrace{c_i \frac{E^2}{\Lambda^2}}^{\rm BSM_6 \times SM} + \overbrace{c_i^2 \frac{E^4}{\Lambda^4}}^{{\rm BSM_6}^2} + \dots\right], \tag{86}$$

where the first factor $g_{\rm SM}^4/E^2$ accounts for the energy flux of the initial quarks, c_i are the relevant Wilson coefficients, and we have omitted numerical factors. In (86) we have explicitly indicated dimension six squared (${\rm BSM_6}^2$) and SM-dimension six interference terms (${\rm BSM_6} \times$ SM).[61] The ellipses in (86) are due

[60] Contacts: A. Azatov, D. Barducci, J. Elias-Miró, E. Venturini

[61] Note that operators of dimension 7 necessarily violate either baryon or lepton number. We assume the scale of such symmetry violation to be very large and therefore irrelevant for di-boson physics at the LHC.

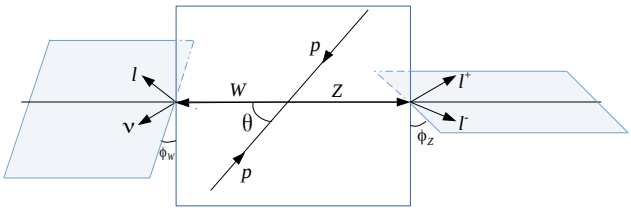

Fig. 93: Angles for $2 \to 4$ scattering.

to corrections from operators of dimension ≥ 8, which we will neglect. The leading such term is an interference term of the type $\text{BSM}_8 \times \text{SM}$ and it is of order $O(E^4/\Lambda^4)$.

A closer inspection however reveals that the $2 \to 2$ di-boson production through the dimension six operator $\mathcal{O}_{3W}$ has an interference piece with a suppressed energy scaling. Indeed, the energy scaling of such process is

$$\sigma(q\bar{q} \to VV) \sim \frac{g_{\text{SM}}^4}{E^2}\left[1 + C_{3W}\frac{m_V^2}{\Lambda^2} + C_{3W}^2\frac{E^4}{\Lambda^4} + O(E^4/\Lambda^4)\right]. \tag{87}$$

This is a consequence of the helicity selection rules, see [437, 438, 418, 417]. The suppressed energy scaling can be problematic for the correct EFT interpretation of the $\sigma(q\bar{q} \to VV)$ measurement. Namely, in view of (87), the sensitivity on C_{3W} is largely dominated by the quadratic piece BSM_6^2, which is $O(E^4/\Lambda^4)$. Furthermore, in this case, the measurements become insensitive to the sign of the Wilson coefficient. The main objective of the present work is to improve the sensitivity to the linear piece $\text{BSM}_6 \times \text{SM}$. We will present two classes of solutions to achieve this goal. Firstly, in section 4.3 we will show that the differential angular cross-section of the process $q\bar{q} \to VV \to 4\psi$ has a large sensitivity on $\text{BSM}_6 \times \text{SM}$ compared to the inclusive cross-section. Secondly, in section 4.3 we will show that accounting for extra radiation $q\bar{q} \to VV + j$ also results in an improved sensitivity on the leading piece $\text{BSM}_6 \times \text{SM}$. These measurements are specially interesting in a HL/HE phase of the LHC, for which we show the prospects below.

Next we will present two ways to improve the sensitivity to the aTGC λ_z by restoring the energy growth $g_{\text{SM}}^4/E^2\left[1 + c_i E^2/\Lambda^2 + \dots\right]$ of the interference piece $\text{BSM}_6 \times \text{SM}$ of the $\mathcal{O}_{3W}$ operator.

Interference resurrection via angular distributions

The first way of enhancing the interference term is by noting that in a collider experiment instead of the $2 \to 2$ process we actually measure a $2 \to 4$ scattering, i.e. vector bosons decay into fermions $q\bar{q} \to V_1V_2 \to 4\psi$. Let us start by considering the differential cross section for the production of the polarised particles $W_{T+}Z_T \to W_{T+}l_+\bar{l}_-$[62]

$$\frac{d\sigma(q\bar{q} \to W_{T_+}l_-\bar{l}_+)}{d\text{LIPS}} = \frac{1}{2s}\frac{\left|\sum_i(\mathcal{M}^{\text{SM}}_{q\bar{q}\to W_{T_+}Z_i} + \mathcal{M}^{\text{BSM}}_{q\bar{q}\to W_{T_+}Z_i})\mathcal{M}_{Z_i\to l_-\bar{l}_+}\right|^2}{\left(k_Z^2 - m_Z^2\right)^2 + m_Z^2\Gamma_Z^2}, \tag{88}$$

where sum runs over intermediate Z polarisations and $d\text{LIPS} \equiv (2\pi)^4\delta^4(\sum p_i - p_f)\prod_i d^3p_i/\left(2E_i(2\pi)^3\right)$ is the Lorentz Invariant differential Phase Space. Then in the narrow width approximation the leading contribution to the interference, i.e. the cross term SM $\times$ BSM_6 in 88, is given by $d\sigma_{\text{int}}(q\bar{q} \to W_{T_+}l_-\bar{l}_+)/d\phi_Z \propto E^2/\Lambda^2\cos(2\phi_Z)$, where ϕ_Z is the azimuthal angle between the plane defined by the decaying leptons and the plane defined by the collision and WZ momenta, see Fig. 93. Note that $d\sigma_{\text{int}}(q\bar{q} \to W_{T_+}l_-\bar{l}_+)/d\phi_Z$ has the energy growth expected from naive dimensional analysis, see Eq. 86.

[62] We ignore the longitudinal Z polarisation which is sub-dominant at the LHC [439].

An analogous derivation goes through if we also consider the decay of the W gauge boson. The differential interference term for the process $q\bar{q} \to$WZ$\to 4\psi$ is unsuppressed and modulated as

$$\frac{d\sigma_{\rm int}(q\bar{q} \to WZ \to 4\psi)}{d\phi_Z\, d\phi_W} \propto \frac{E^2}{\Lambda^2}\left(\cos(2\phi_Z) + \cos(2\phi_W)\right), \tag{89}$$

where $\phi_{W,Z}$ are the corresponding azimuthal angles. Integrating 89 over the fermion phase space the interference term vanishes as expected from the discussion above. Since the dependence on the two azimuthal angles is additive, integrating over ϕ_W leads to a differential cross-section that is modulated by $\cos(2\phi_Z)$ and that features E^2/Λ^2 energy growth. We will use the result in Eq. 89 to prove the aTGC λ_Z, with an increased overall sensitivity to both the magnitude and sign of the Wilson coefficient.

Following Ref. [417], we make a few remarks on the experimental measurement of $\phi_{Z,W}$ in Eq. 89. The angle ϕ_Z can be determined up to an ambiguity $\phi_Z \leftrightarrow \phi_Z \pm \pi$, since experimentally we can only measure the charges but not the helicities of the leptons from Z decay. The reconstruction of the W azimuthal angle ϕ_W in the $l\nu$ final state suffers from an ambiguity $\phi_W \leftrightarrow \pi - \phi_W$ due to the twofold ambiguity in the determination of the neutrino momentum. Interestingly, none of these ambiguities affects Eq. 89.

Interference resurrection via jet emission

A second way to resurrect the expected energy growth of the interference term is based on the observation that the helicity selection rule holds only at leading-order [418]. So the next-to-leading-order (NLO) effects will necessarily lead to the enhancement of the interference. Virtual effects are expected to be suppressed by a factor $\mathcal{O}(\alpha_s/4\pi)$ with respect to the contributions coming from azimuthal modulation discussed in the previous section. A complete study at NLO accuracy for the operator $\mathcal{O}_{3W}$ together with its CP-odd counterpart can be found in [435]. Alternatively we will consider processes with an extra hard jet emission, which will improve on the signal over the background ratio. In this case, since we are dealing with the hard $2 \to 3$ process, the same polarisation configuration $q\bar{q} \to V_\pm V_\pm g_\mp$ is allowed both in SM and in the BSM five point amplitude with the $\mathcal{O}_{3W}$ insertion. Therefore the interference is not suppressed and the leading quadratic energy scaling is restored by requiring an extra (hard) QCD radiation.

Results

HL-LHC. In order to test the sensitivity of the High-Luminosity (HL) phase of the LHC on the $\mathcal{O}_{3W}$ with the proposed solution to the non-interference behaviour we proceed in the following way. We generate with `MadGraph5 aMC@NLO` [79] parton level events for $pp \to W^\pm Z$ decaying into a four leptons (electron and muon) final state together with events for the same process where we allow for a jet emission in the initial state. We perform two different analyses (see [418] for more details): an inclusive one where we restrict to events up to $p_T^j < 100$ GeV and do not bin on the ϕ_Z variable and an exclusive one where we bin both on the jet transverse momentum and on ϕ_Z, where for the latter we define two bins with the threshold $|\cos(\phi_Z)| = 1/\sqrt{2}$. All together the results for the bound on the C_{3W} Wilson coefficient are reported in Fig. 94 as a function of the maximum transverse mass of the WZ system, which allows to have an estimate of the validity of the EFT computation, see again [418] for a detailed discussion [63].

One might wonder if a simulation beyond the parton level accuracy might spoil these results. To this end we have performed a more detailed simulation by showering the events through `PYTHIA 8` [79] and simulating the detector response via `Delphes 3` [13]. By analysing the density of events in the two azimuthal bins we found that with respect to the parton level case the relative difference is of at most a few %, thus making our parton level analysis solid.

HE-LHC. We now estimate the reach of a future HE phase of the LHC with $\sqrt{s} = 27$ TeV. For these preliminary results we adopt the same binning, both in ϕ_Z and in jet transverse momentum, of the

[63] These results are obtained by keeping both the linear and the quadratic terms in the cross section determination.

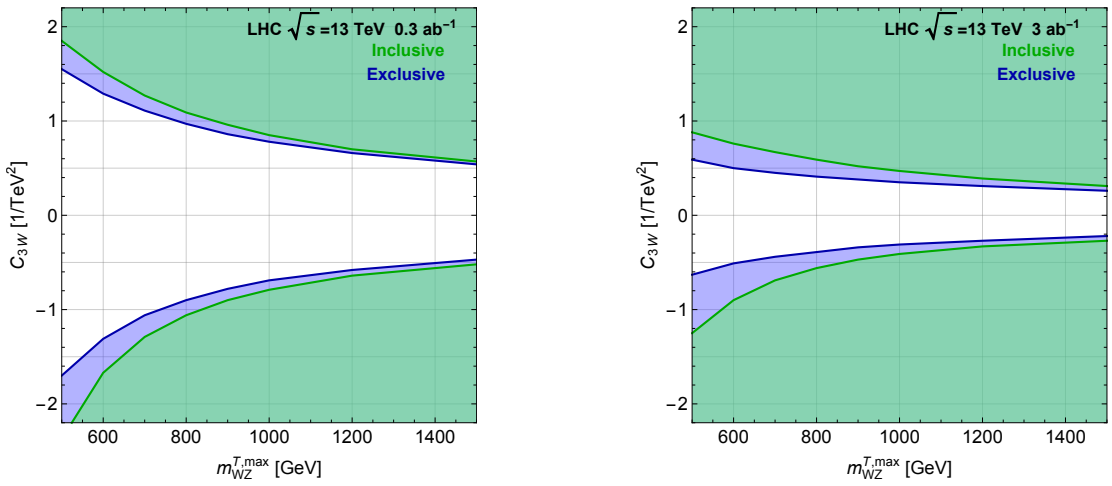

Fig. 94: Bounds on the C_{3W} Wilson coefficient for the inclusive and exclusive categories at the LHC 13 for 300 fb^{-1} (left) and 3000 fb^{-1} (right) of integrated luminosity.

previous section. We show the results in Fig. 95. We found a slight increase of order 30% on the reach on C_{3W}. We expect that a dedicated HE analysis will lead to a further improvement of these bounds; this can be done by exploiting in a more efficient way the high energy tails of the differential distributions. In [435] we also present a complete NLO study for the HE-LHC stage.

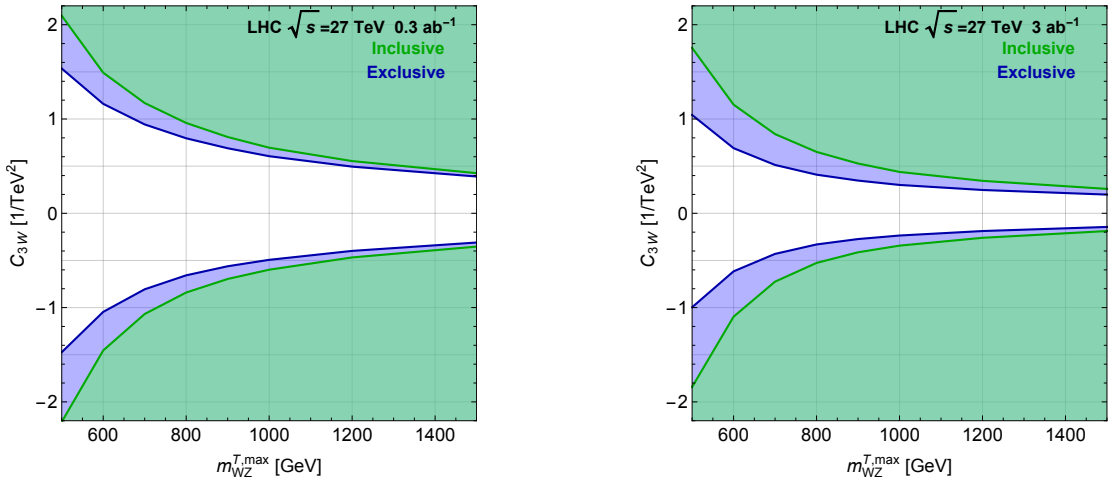

Fig. 95: Bounds on the C_{3W} Wilson coefficient for the inclusive and exclusive categories at the LHC 27 for 300 fb^{-1} (left) and 3000 fb^{-1} (right) of integrated luminosity.

4.4 Electroweak Precision Tests in High-Energy Drell-Yan Processes[64]

The simplest process allowing to set constraints on EFT operators is Drell-Yan di-lepton and lepton-neutrino production at high invariant mass, for concreteness we focus on oblique corrections only, generalisations being rather obvious. These corrections can be parametrised in the electroweak sector by the four oblique parameters S, T, W and Y. These correspond to four operators that modify the propagators of the W and Z bosons both on the pole (S and T) and off the pole, i.e. on the tails (W and Y). Hadron

[64] Contacts: S. Alioli, M. Farina, G. Panico, D. Pappadopulo, J.T. Ruderman, R. Torre, A. Wulzer

colliders can hardly compete with lepton colliders for pole observable. However, due to the enhancement of the kinematic distributions with respect to the corresponding SM ones at high energy, hadron colliders are particularly suited to study off-pole observables like W and Y. Deviations from the SM proportional to W and Y can be parametrised through the two operators from table 1,

$$-\frac{W}{2m_W^2}\mathcal{O}_{2W}\,, \quad -\frac{Y}{2m_W^2}\mathcal{O}_{2W} \tag{90}$$

They modify the neutral and charged gauge boson propagators as

$$P_N = \begin{bmatrix} \frac{1}{q^2} - \frac{t^2\mathrm{W}+\mathrm{Y}}{m_Z^2} & \frac{t\left(\left(\mathrm{Y}+\hat{\mathrm{T}}\right)c^2+s^2\mathrm{W}-\hat{\mathrm{S}}\right)}{\left(c^2-s^2\right)\left(q^2-m_Z^2\right)} + \frac{t(\mathrm{Y}-\mathrm{W})}{m_Z^2} \\ \star & \frac{1+\hat{\mathrm{T}}-\mathrm{W}-t^2\mathrm{Y}}{q^2-m_Z^2} - \frac{t^2\mathrm{Y}+\mathrm{W}}{m_Z^2} \end{bmatrix} \tag{91}$$
$$P_C = \frac{1+\left(\left(\hat{\mathrm{T}}-\mathrm{W}-t^2\mathrm{Y}\right)-2t^2\left(\hat{\mathrm{S}}-\mathrm{W}-\mathrm{Y}\right)\right)/(1-t^2)}{(q^2-m_W^2)} - \frac{\mathrm{W}}{m_W^2}\,,$$

Studying the tails of the invariant mass distribution of two leptons and of the transverse mass of lepton-neutrino, one can set constraints on these observables. For details on the procedure see ref. [440], also extended to di-jet and multi-jet analyses in ref.s [441, 442]. The prospect results for the HL-LHC and HE-LHC are shown in fig. 96

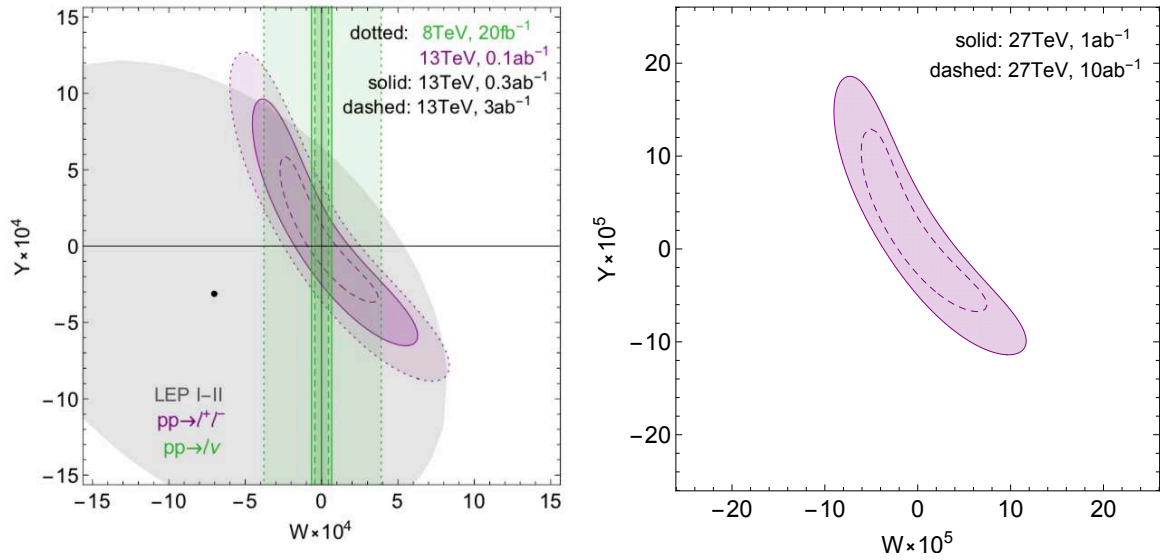

Fig. 96: Left: LHC and HL-LHC. Right: HE-LHC

4.5 Testing the universal Higgs non-linearity[65]

In this section we motivate precision measurements on the tensor structures of one Higgs couplings with two electroweak gauge bosons (HVV) and two Higgses couplings with two electroweak gauge bosons (HHVV) in HE/HL LHC. There exist special relations between HVV and HHVV couplings in composite Higgs models that are universal, independent of the symmetry breaking pattern invoked in a particular model. These "universal relations" are controlled by a single input parameter, the decay constant f of the pseudo-Nambu-Goldstone Higgs boson. Testing the universal relations requires measuring the tensor structures of HVV and HHVV couplings to high precision. In particular, HHVV interactions

[65] Contacts: D. Liu, I. Low, Z. Yin

Table 70: Single Higgs coupling coefficients C_i^h for the non-linearity case (NL) and the purely dimension-6 contributions (D6) in SMEFT. Here c_w, t_w and c_θ denote $\cos\theta_W, \tan\theta_W$ and $\cos\theta$, respectively, where θ_W is the weak mixing angle. $\mathcal{D}^{\mu\nu}$ denotes $\partial^\mu\partial^\nu - \eta^{\mu\nu}\partial^2$. Hermitian conjugate of an operator is implied when necessary.

$\mathcal{I}_i^h$	C_i^h (NL)	C_i^h (D6)
(1) $\frac{h}{v}Z_\mu\mathcal{D}^{\mu\nu}Z_\nu$	$\frac{4c_{2w}}{c_w^2}(-2c_3+c_4^-)+\frac{4}{c_w^2}c_4^+c_\theta$	$2(c_W+c_{HW})+2t_w^2(c_B+c_{HB})$
(2) $\frac{h}{v}Z_{\mu\nu}Z^{\mu\nu}$	$-\frac{2c_{2w}}{c_w^2}(c_4^-+2c_5^-)-\frac{2}{c_w^2}(c_4^+-2c_5^+)c_\theta$	$-(c_{HW}+t_w^2c_{HB})$
(3) $\frac{h}{v}Z_\mu\mathcal{D}^{\mu\nu}A_\nu$	$8(-2c_3+c_4^-)t_w$	$2t_w(c_W+c_{HW}-c_B-c_{HB})$
(4) $\frac{h}{v}Z_{\mu\nu}A^{\mu\nu}$	$-4(c_4^-+2c_5^-)t_w$	$-t_w(c_{HW}-c_{HB})$
(5) $\frac{h}{v}W_\mu^+\mathcal{D}^{\mu\nu}W_\nu^-$	$4(-2c_3+c_4^-)+4c_4^+c_\theta$	$2(c_W+c_{HW})$
(6) $\frac{h}{v}W_{\mu\nu}^+W^{-\mu\nu}$	$-4(c_4^-+2c_5^-)-4(c_4^+-2c_5^+)c_\theta$	$-2c_{HW}$

remains as one of the few untested predictions of the Standard Model Higgs boson, which can be probed through the double Higgs production in the vector boson fusion (VBF) channel at the LHC. Below we summarise the main results. The phenomenological details and theoretical foundation can be found in Refs. [443, 444, 445, 446]

At the leading two-derivative order, the HVV and HHVV couplings in composite Higgs models in the unitary gauge is given by the following simple expression:

$$\mathcal{L}^{(2)} = \frac{1}{2}\partial_\mu h\partial^\mu h + \frac{g^2f^2}{4}\sin^2(\theta+h/f)\left(W_\mu^+W^{-\mu}+\frac{1}{2\cos^2\theta_W}Z_\mu Z^\mu\right), \tag{92}$$

where $v = 246$ GeV, f is the decay constant of the composite Higgs boson and $\sin\theta = v/f$. This result is independent of the symmetry breaking pattern of the strong composite sector in the UV, apart from the overall normalisation of f, which does depend on the UV model.

At the four-derivative level, we parametrise the HVV and HHVV couplings as follows:

$$\mathcal{L}^{(4)} = \sum_i \frac{m_W^2}{m_\rho^2}\left(C_i^h\mathcal{I}_i^h + C_i^{2h}\mathcal{I}_i^{2h}\right), \tag{93}$$

where the definition of the operators $\mathcal{I}_i^h$ and $\mathcal{I}_i^{2h}$ are presented in Table 70 and Table 71. On the other hand, C_i^h and C_i^{2h} are Wilson coefficients which depend on six unknowns $(\theta, c_3, c_4^\pm, c_5^\pm)$ in composite Higgs models and on four unknowns $(c_W, c_B, c_{HW}, c_{HB})$ in the Standard Model Effective Field Theory (SMEFT). In the above $m_\rho = g_\rho f$ is the typical mass scale of the new composite resonances. The different Lorentz structures lead to different angular distributions in the decay products and, therefore, can be measured accordingly. At the LHC Run 1, testing the tensor structure of HVV couplings was among the top priorities and gave confidence to the Higgs nature of the 125 GeV resonance. (See, for example, Ref. [447].) A similar program for HHVV coupling is currently lacking and should be pursued at HE/HL LHC.

In general, we have two different Lorentz structure in the HVV couplings:

$$\frac{h}{v}V_{1\,\mu}\mathcal{D}^{\mu\nu}V_{2\,\nu}\,, \qquad \frac{h}{v}V_{1\,\mu\nu}V_2^{\mu\nu}\,, \tag{94}$$

where $\mathcal{D}^{\mu\nu} = \partial^\mu\partial^\nu - \eta^{\mu\nu}\partial^2$ and $V_{1,2} \in \{W, Z, \gamma\}$ with electric charge conservation implicitly indicated. For HHVV couplings we have:

$$\frac{h^2}{v^2}V_{1\,\mu}\mathcal{D}^{\mu\nu}V_{2\,\nu}\,, \quad \frac{h^2}{v^2}V_{1\,\mu\nu}V_2^{\mu\nu}\,, \quad \frac{\partial_\mu h\partial_\nu h}{v^2}V_1^\mu V_2^\nu\,, \quad \frac{\partial_\mu h\partial^\mu h}{v^2}V_1^\mu V_{2\mu}\,. \tag{95}$$

Table 71: The coupling coefficients C_i^{2h} involve two Higgs bosons for universal non-linearity case (NL) and the dimension-six case in SMEFT (D6). A cross ($\times$) means there is no contribution at the order we considered. Notice $C_i^{2h} = C_i^h/2$ for SMEFT at the dimension-6 level. $c_{2\theta}$ and s_θ denote $\cos 2\theta$ and $\sin\theta$, respectively.

$\mathcal{I}_i^{2h}$	C_i^{2h} (NL)	C_i^{2h} (D6)
(1) $\frac{h^2}{v^2} Z_\mu \mathcal{D}^{\mu\nu} Z_\nu$	$\frac{2c_{2w}}{c_w^2}(-2c_3 + c_4^-)c_\theta + \frac{2}{c_w^2} c_4^+ c_{2\theta}$	$\frac{1}{2}C_1^h$
(2) $\frac{h^2}{v^2} Z_{\mu\nu} Z^{\mu\nu}$	$-\frac{c_{2w}}{c_w^2}(c_4^- + 2c_5^-)c_\theta - \frac{1}{c_w^2}(c_4^+ - 2c_5^+)c_{2\theta}$	$\frac{1}{2}C_2^h$
(3) $\frac{h^2}{v^2} Z_\mu \mathcal{D}^{\mu\nu} A_\nu$	$4t_w(-2c_3 + c_4^-)c_\theta$	$\frac{1}{2}C_3^h$
(4) $\frac{h^2}{v^2} Z_{\mu\nu} A^{\mu\nu}$	$-2t_w(c_4^- + 2c_5^-)c_\theta$	$\frac{1}{2}C_4^h$
(5) $\frac{h^2}{v^2} W_\mu^+ \mathcal{D}^{\mu\nu} W_\nu^-$	$2(-2c_3 + c_4^-)c_\theta + 2c_4^+ c_{2\theta}$	$\frac{1}{2}C_5^h$
(6) $\frac{h^2}{v^2} W_{\mu\nu}^+ W^{-\mu\nu}$	$-2(c_4^- + 2c_5^-)c_\theta - 2(c_4^+ - 2c_5^+)c_{2\theta}$	$\frac{1}{2}C_6^h$
(7) $\frac{(\partial_\nu h)^2}{v^2} Z_\mu Z^\mu$	$\frac{8}{c_w^2} c_1 s_\theta^2$	$\times$
(8) $\frac{\partial_\mu h \partial_\nu h}{v^2} Z^\mu Z^\nu$	$\frac{8}{c_w^2} c_2 s_\theta^2$	$\times$
(9) $\frac{(\partial_\nu h)^2}{v^2} W_\mu^+ W^{-\mu}$	$16 c_1 s_\theta^2$	$\times$
(10) $\frac{\partial^\mu h \partial^\nu h}{v^2} W_\mu^+ W_\nu^-$	$16 c_2 s_\theta^2$	$\times$

The ultimate goal then will be to measure these different tensor structures at CLIC.

From Table 70 and Table 71, we can extract relations among C_i^h and C_i^{2h} that only depend on the θ. We call them "universal relations" as they represent universal predictions of a composite Higgs boson, whose nonlinear interactions are dictated by the underlying shift symmetries acting on the four components of the Higgs doublet [443, 444, 445, 446]. Some examples of universal relations involving both HVV and HHVV couplings are:

$$\frac{C_3^{2h}}{C_3^h} = \frac{C_4^{2h}}{C_4^h} = \frac{1}{2}\cos\theta\,, \tag{96}$$

$$\frac{C_5^{2h} - C_3^{2h}/2t_w}{C_5^h - C_3^h/2t_w} = \frac{C_6^{2h} - C_4^{2h}/t_w}{C_6^h - C_4^h/t_w} = \frac{\cos 2\theta}{2\cos\theta} \approx \frac{1}{2}\left(1 - \frac{3}{2}\xi\right)\,, \tag{97}$$

$$\frac{s_{2w}\, C_1^{2h} - c_{2w}\, C_3^{2h}}{s_{2w}\, C_1^h - c_{2w}\, C_3^h} = \frac{s_{2w}\, C_2^{2h} - c_{2w}\, C_4^{2h}}{s_{2w}\, C_2^h - c_{2w}\, C_4^h} = \frac{\cos 2\theta}{2\cos\theta} \approx \frac{1}{2}\left(1 - \frac{3}{2}\xi\right)\,. \tag{98}$$

These relations depend on one single parameter θ or, equivalently, $\xi = v^2/f^2$. In other words, they can be used to over-constrain the parameter f. If the 125 GeV Higgs boson indeed arises as a pseudo-Nambu-Goldstone boson, the decay constant f as measured from the different universal relations must be consistent with one another.

In order to test the universal relations, it is necessary to measure the tensor structures of HHVV couplings. This is where the HE/HL LHC could have an advantage over circular lepton colliders. At a hadron collider, C_i^h can be measured from single Higgs decays into four leptons in a fashion similar to the analysis performed in Ref. [447], while measurements on C_i^{2h} would have to rely on double Higgs production in the VBF channel and the associated production with a Z boson. The production topology is displayed in Fig. 97.

In Fig. 98 we show the double Higgs production rate in the VBF channel and the associated production channel in a hadron collider as a function of the centre-of-mass energy $\sqrt{S}$, adopting the

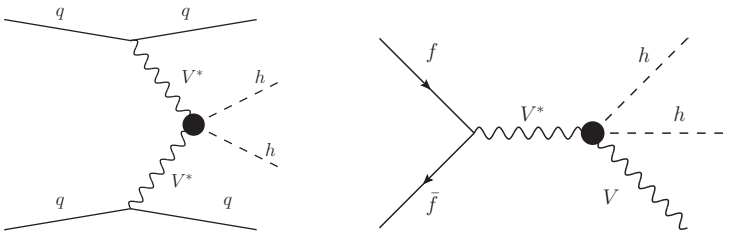

(a) Double Higgs production through vector boson fusion.

(b) Double Higgs production in association with a vector boson.

Fig. 97: Production and decay topology of venues to test the HHVV couplings at the LHC. A black dot represents contributions from various Feynman diagrams.

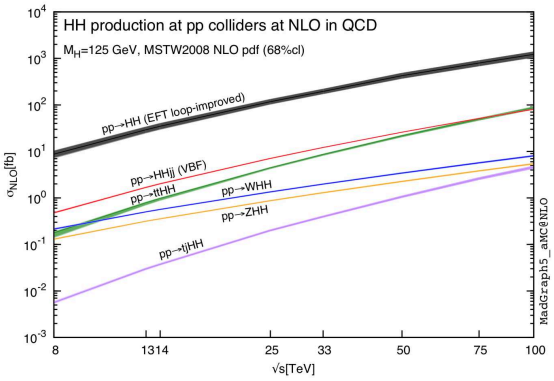

Fig. 98: Double Higgs production rates, including the VBF and associate production channels, at a hadron collider. This figure is adopted from Ref. [278].

computation done in Ref. [278]. The VBF rate at 13 TeV is less than 1 fb, while at 27 TeV the cross-section is about 3 fb, which offers the best chance to probe the HHVV couplings at the LHC.

The analysis of the HHVV coupling is further discussed in the next section 4.6.

4.6 Higgs pair production in vector-boson fusion at the HL-LHC[66]

While the dominant production channel of Higgs boson pairs at hadron colliders is the gluon-fusion mechanism, other channels are also of phenomenological relevance. In particular, Higgs pair production in weak vector-boson fusion [448] is interesting since it probes the strength of the Higgs non-linear interactions with vector bosons at high energies. This process can therefore provide unique information to test the nature of the Higgs boson, whether it is a composite or elementary state, and whether or not it emerges as a Nambu-Goldstone boson (NGB) of some new dynamics at the TeV scale [40, 449, 450].

The production of Higgs pairs in the VBF channel [40, 449, 451, 452, 453, 454] proceeds via the soft emission of two vector bosons from the incoming protons followed by the hard $VV \to hh$ scattering, with $V = W, Z$. In the SM, the VBF inclusive cross section at 14 TeV is around 2 fb (see Fig. 98), more than one order of magnitude smaller than in gluon fusion. Higher order QCD corrections are moderate ($\sim 10\%$) as expected for an electroweak process. Despite the small rate, Higgs pair production via VBF is relevant since even small modifications of the SM couplings induce a striking increase of the

[66] Contacts: F. Bishara, R. Contino, J. Rojo

cross section as a function of the di-Higgs invariant mass, for instance in models where the Higgs is a composite pseudo-NGB (pNGB) of new strong dynamics at the TeV scale [240]. In these theories, the Higgs anomalous couplings imply a growth of the $VV \to hh$ cross section with the partonic centre-of-mass energy, $\hat{\sigma} \propto \hat{s}/f^4$, where f is the pNGB decay constant [40]. This enhanced sensitivity to the underlying strength of the Higgs interactions makes double Higgs production via VBF a key process to test the nature of the electroweak symmetry breaking dynamics and to constrain the $hhVV$ quartic coupling in a model-independent way.

Here we review the feasibility of measuring and interpreting the VBF Higgs pair production at the HL-LHC in the $hh \to b\bar{b}b\bar{b}$ final state. While QCD multi-jet backgrounds are huge, this final state turns out to be within the reach of the HL-LHC thanks to the unique VBF topology, characterised by two forward jets well separated in rapidity and with a large invariant mass and a reduced hadronic activity in the central region. In addition, the di-Higgs system will acquire a substantial boost in the presence of BSM dynamics, and jet substructure techniques [455, 456, 457] make it possible to fully exploit the high-energy limit and optimise the signal significance.

To describe the deviations of the Higgs couplings with respect to their SM values we follow [449] where a general parametrisation of the couplings of a light Higgs-like scalar h to the SM vector bosons and fermions was introduced. In this formalism, assuming that the couplings of the Higgs boson to SM fermions scale with their masses and do not violate flavor, the resulting effective Lagrangian is given by

$$\begin{aligned}\mathcal{L} \supset & \frac{1}{2}(\partial_\mu h)^2 - V(h) + \frac{v^2}{4}\mathrm{Tr}\Big(D_\mu \Sigma^\dagger D^\mu \Sigma\Big)\left[1 + 2c_V\,\frac{h}{v} + c_{2V}\,\frac{h^2}{v^2} + \dots\right] \\ & - m_i\,\bar{\psi}_{Li}\,\Sigma\left(1 + c_\psi\,\frac{h}{v} + \dots\right)\psi_{Ri} \;+\; \text{h.c.}\,,\end{aligned} \tag{99}$$

where $V(h)$ denotes the Higgs potential,

$$V(h) = \frac{1}{2}m_h^2 h^2 + c_3\,\frac{1}{6}\left(\frac{3m_h^2}{v}\right)h^3 + c_4\,\frac{1}{24}\left(\frac{3m_h^2}{v^2}\right)h^4 + \dots \tag{100}$$

The parameters c_V, c_{2V}, c_ψ, c_3, and c_4 are in general arbitrary coefficients, normalised so that they equal 1 in the SM. In this contribution we focus on the determination of c_{2V} by means of di-Higgs VBF production in the $b\bar{b}b\bar{b}$ final state.

Analysis strategy

Signal and background events are simulated at leading-order (LO) by means of matrix-element generators and then processed through a parton shower (PS). The dominant background is given by QCD multi-jet production, while other backgrounds, such as top-quark pair production and Higgs pair production via gluon-fusion, turn out to much smaller. After the parton shower, events are clustered with FASTJET v3.0.1 [15] using the anti-k_t algorithm [14] with a jet radius $R = 0.4$. The resulting jets are then processed through a b-tagging algorithm, where a jet is tagged as b-jet with probability $\varepsilon(b\text{-tag}) = 0.75$ if it contains a b-quark with $p_T^b > 15\,\text{GeV}$. In order to account for b-jet mis-identification (fakes), jets which do not meet this requirement are also tagged as b-jets with probability $\varepsilon(c\text{-mistag}) = 0.1$ or $\varepsilon(q, g\text{-mistag}) = 0.01$ depending on whether they contain a c-quark or not. Only events with four or more jets, of which at least two must be b-tagged, are retained at this stage.

Subsequently to b-tagging, events are classified through a scale-invariant tagging procedure [456, 457]. This step is crucial to efficiently reconstruct the Higgs boson candidates and suppress the otherwise overwhelming QCD backgrounds while at the same time taking into account all the relevant final-state topologies. The basic idea of this method is to robustly merge three event topologies – boosted, intermediate and resolved – into a common analysis. This is particularly relevant for our study given that the degree of boost of the di-Higgs system strongly depends on the deviations of c_{2V} from its SM value.

Acceptance cuts to match detector coverage are applied to signal and background events. We require the p_T of both the light and b-tagged jets to be larger than 25 GeV, while the pseudo-rapidities of light and b-tagged jets, η_j and η_b, are limited by the coverage of the forward calorimeters and by the tracking region where b-tagging can be applied respectively. We also impose a set of selection cuts tailored to the VBF topology which is characterised by two forward and very energetic jets with little hadronic activity between them. In particular, we cut on the rapidity separation $\Delta y_{jj} \equiv |y_j^{\text{lead}} - y_j^{\text{sub-lead}}| > 5$ and the invariant mass $m_{jj} > 700$ GeV of the two VBF-tagging jets, and impose a central jet veto (CJV) on the hardest non-VBF light jet in the central region. The VBF tagging jets are defined as the pair of light jets satisfying the acceptance cuts with the largest invariant mass m_{jj}. Moreover, a CJV cut is imposed in VBF analyses to veto light jets with pseudo-rapidity η_{j_3} lying between those of the VBF-tagging jets, $\eta_j^{\text{max}} > \eta_{j_3} > \eta_j^{\text{min}}$, above a p_{T} threshold of 45 GeV.

Figure 99 (right) shows the m_{hh} distribution after all analysis cuts for both for the signal (SM and $c_{2V} = 0.8$) and the total background. For $c_{2V} = 0.8$, the crossover between the resolved and boosted categories takes place at $m_{hh} \simeq 1.5$ TeV, although this specific value depends on the choice of the jet radius R [456]. Unsurprisingly, we find that background events are always dominated by the resolved topology. The decomposition of the total background in terms of individual processes as a function of m_{hh} is shown in Fig. 99 (left), where each component is stacked on top of each other. We see how the $4b$ background dominates for large m_{hh} while the $2b2j$ one is instead the most important for small m_{hh}.

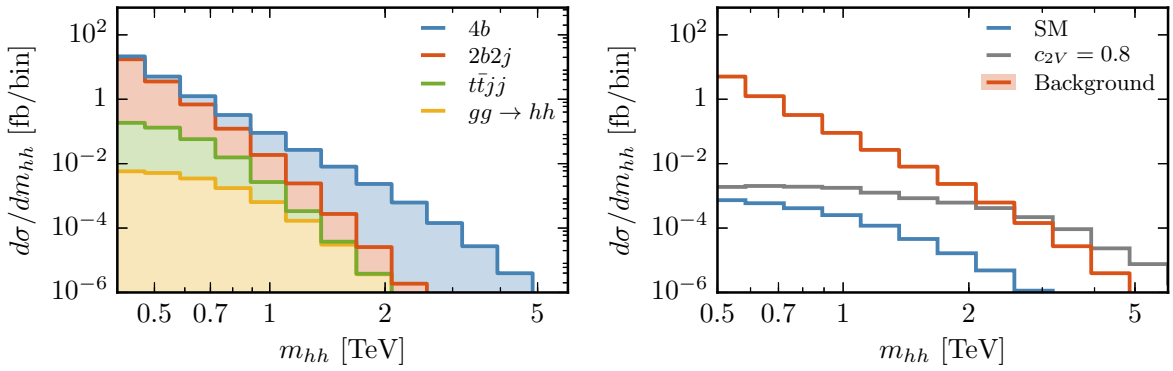

Fig. 99: Left: Decomposition of the total background into individual processes as a function of m_{hh} after all analysis cuts have been imposed. Right: the di-Higgs invariant mass distribution after all analysis cuts for the signal (SM and $c_{2V} = 0.8$) and the total background.

Table 72: Cross sections, in fb, after the successive application of the acceptance, VBF cuts, and Higgs reconstruction cuts for signal events (SM and $c_{2V} = 0.8$) and for the total background.

		Cross-sections (fb)			
		Acceptance	VBF	Higgs reco.	$m_{hh} > 500$ GeV
14 TeV	Signal SM	0.011	0.0061	0.0039	0.0020
	Signal $c_{2V} = 0.8$	0.035	0.020	0.017	0.011
	Bkgd (total)	1.3×10^5	4.9×10^3	569	47

The cross-sections after the successive application of the acceptance, VBF cuts, and Higgs reconstruction cuts for signal events (SM and $c_{2V} = 0.8$) and for the total background is shown in Tab. 72. We find that the VBF di-Higgs signal in the SM is rather small already after the basic acceptance cuts. However, the signal event yield is substantially increased for $c_{2V} \neq 1$ as illustrated by the benchmark

value of $c_{2V} = 0.8$ leading to more than a factor 3 (5) enhancement compared to the SM after the acceptance (all analysis) cuts. The fact that this cross-section enhancement for the $c_{2V} = 0.8$ scenario is more marked at the end of the analysis is not a coincidence: our selection cuts have been designed so as to improve the sensitivity to c_{2V} by increasing the signal significance in the large-m_{hh} region. Note however that even after all analysis cuts the background is still much larger than the signal (either SM or $c_{2V} = 0.8$) at the level of inclusive rates. It is only by exploiting the large-m_{hh} region that the former can be made small enough to achieve high signal significances.

Projections for the HL-LHC

Following the analysis strategy outlined in the previous section, we can now estimate the expected precision on the determination of the c_{2V} coupling at the HL-LHC. In the left panel of Fig. 100 we show the posterior probabilities for c_{2V} at 14 TeV, from where we can assess the expected precision its measurement at the HL-LHC assuming SM couplings. The corresponding 68% probability intervals for the determination of c_{2V} at the HL-LHC are are listed in Table 73 for two different scenarios for the background cross section.

Table 73: Expected precision (at 68% probability level) for the measurement of $\delta_{c_{2V}}$ at the HL-LHC for SM values of the Higgs couplings, for two scenarios for the background cross section.

	68% probability interval on $\delta_{c_{2V}}$	
	$1 \times \sigma_{\text{bkg}}$	$3 \times \sigma_{\text{bkg}}$
LHC_{14}	$[-0.37, 0.45]$	$[-0.43, 0.48]$
HL-LHC	$[-0.15, 0.19]$	$[-0.18, 0.20]$

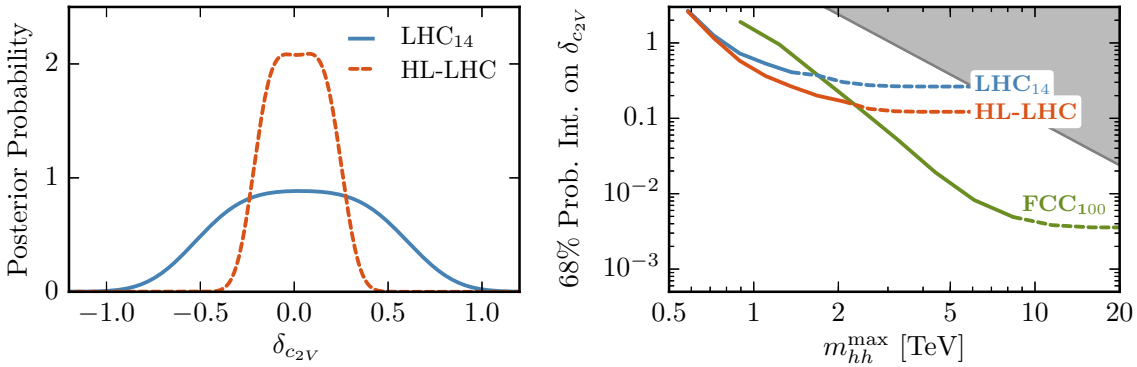

Fig. 100: Left: posterior probability densities for $\delta_{c_{2V}}$ at the HL-LHC. Right: expected precision for a measurement of $\delta_{c_{2V}}$ at the 68% CL as a function of m_{hh}^{max}, where the grey area indicates the region where $\delta_{c_{2V}} > \delta_{c_{2V}}^{\text{max}}$. The transition between solid and dashed curves occurs at the last bin wit hat least one event.

From Table 73, we find that the c_{2V} coupling, for which there are currently no direct experimental constraints, can be measured with a precision of around $^{+19\%}_{-15\%}$ at the HL-LHC. It is interesting to compare these results with the experimental precision expected on the fiducial VBF di-Higgs cross section after all analysis cuts, expressed in terms of μ, the signal strength parameter normalised to the SM result We find that the 95% CL upper limits on μ for the nominal background cross section is $\mu \leq 109$ with 300 fb^{-1}, and $\mu \leq 49$ at the HL-LHC. This result highlights that the high precision expected on c_{2V} can obtained despite the loose constraints expected on the VBF di-Higgs cross section itself.

The results of Table 73 have been obtained by making full use of the information contained on the di-Higgs invariant mass distribution m_{hh}. However, the EFT expansion might break down at large

enough values of m_{hh}, corresponding to large partonic centre-of-mass energies, and some assessment on the validity of our procedure is thus required. In particular, results can be consistently derived within the EFT framework only if the new physics scale Λ is larger than the largest value of m_{hh} included in the analysis. Constraining Λ requires making assumptions on the structure of the UV dynamics extending the SM [458]. For example, for the case where the new physics is characterised by a single coupling strength g_* and mass scale Λ [40], one expects $\delta_{c_{2V}} \approx g_*^2 v^2/\Lambda^2$, so that for maximally strongly-coupled UV completions (with $g_* \simeq 4\pi$) it is possible to derive the upper limit $\delta_{c_{2V}} < 16\pi^2 v^2/\Lambda^2$ which connects $\delta_{c_{2V}}$ with the new physics scale Λ. The validity of the EFT can thus be monitored by introducing a restriction $m_{hh} \leq m_{hh}^{\rm max}$, and then determining how the sensitivity on $\delta_{c_{2V}}$ varies as a function of $m_{hh}^{\rm max}$ [458]. The precision on $\delta_{c_{2V}}$ is shown in Fig. 100 (right) as a function of $m_{hh}^{\rm max}$, where the grey area indicates the region where $\delta_{c_{2V}} > \delta_{c_{2V}}^{\rm max} = 16\pi^2 v^2/m_{hh}^{\rm max}$. As expected, increasing $m_{hh}^{\rm max}$ leads to stronger constraints. We therefore find that in the kinematic region accessible at the HL-LHC the EFT description of the di-Higgs VBF process should be valid.

4.7 Higgs Couplings in High-Energy Multi-boson Processes[67]

In this section, based on Ref. [459], we present a novel program to test the Higgs couplings *off-shell* and at high-energy, via their contributions to the physics of longitudinally polarised gauge bosons. We will show that this program is potentially competitive with *on-shell* measurements, but it also offers endless opportunities of refinements and improvements.

Our leitmotiv is that *any* observable modification of a SM coupling will produce in *some* process a growth with energy. In some sense, this is obvious: since the SM is the only theory that can be extrapolated to arbitrarily high-energy, any departure from it can have only a finite range of validity, a fact that is made manifest by a disproportionate growth in some scattering amplitude. Theories with a finite range of validity are, by definition, EFTs; for this reason the best vehicle to communicate our message is the EFT language where deviations on Higgs couplings come from the operators $\mathcal{O}_{BB}, \mathcal{O}_{WW}, \mathcal{O}_{y_t}, \mathcal{O}_6$, etc. We stress nevertheless that at, tree level, the very same conclusions can be reached in the κ framework [42] or in the unitary-gauge framework of Ref. [45, 419].

The operators of that we will be interested on have the form $|H|^2 \times \mathcal{O}^{\rm SM}$, with $\mathcal{O}^{\rm SM}$ a dimension-4 SM operator (i.e. kinetic terms, Higgs potential, and Yukawas) times

$$|H|^2 = \frac{1}{2}\left(v^2 + 2hv + h^2 + 2\phi^+\phi^- + (\phi^0)^2\right) \tag{101}$$

where h is the physical Higgs boson and $\phi^{\pm,0}$ are the would-be longitudinal polarisations of W- and Z-bosons. In this contribution we focus on the last two terms, and study processes with longitudinal gauge bosons instead of processes with an on-shell Higgs; we dub this search strategy "Higgs without Higgs" - HwH in short [459]. For each modification of a Higgs coupling we identify a process where couplings different from the SM ones induce a high-energy growth in the amplitude with respect the SM,

$$\kappa_t : pp \to jt + V_L V_L' \tag{102}$$
$$\kappa_\lambda : pp \to jjh + V_L V_L', \quad pp \to jj + 4V_L, \tag{103}$$
$$\kappa_{\gamma\gamma, Z\gamma} : pp \to jj + V'V, \tag{104}$$
$$\kappa_V : pp \to jj + V_L V_L', \tag{105}$$
$$\kappa_g : pp \to W_L^+ W_L^-, Z_L Z_L, \tag{106}$$

where $V_L V_L' \equiv \{W_L^\pm W_L^\pm, W_L^\pm W_L^\mp, W_L^\pm Z_L, Z_L Z_L\}$ (similarly $4V_L$ a generic longitudinally polarised final state) and $V^{(\prime)}$ any (longitudinal or transverse) vector, including photons. In the following paragraphs we explore these processes in turn and provide a first estimate of the potential HwH reach at the

[67] Contacts: B. Henning, D. Lombardo, M. Riembau, F. Riva

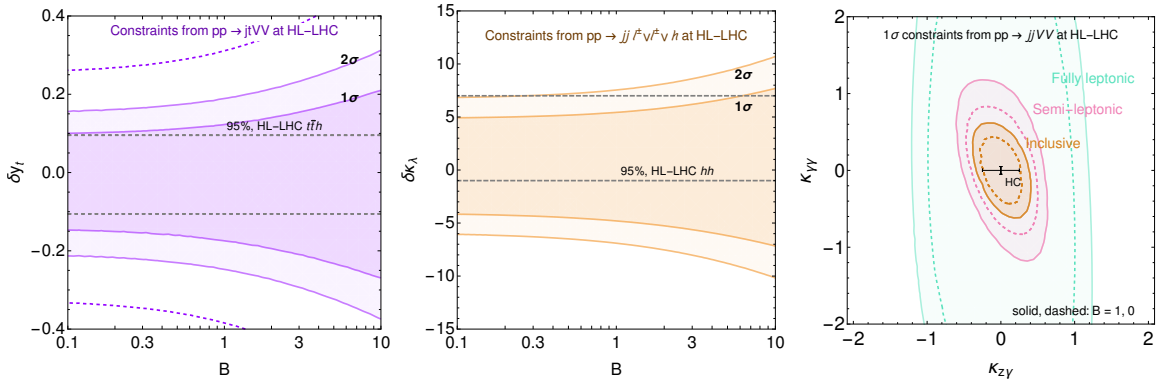

Fig. 101: *LEFT: HL-LHC (3000 fb^{-1}) sensitivity on modifications of the top quark Yukawa δy_t from the process in eq. (102) (shaded bands), and from measurements of Higgs couplings (95%C.L., dashed grey lines); B controls additional backgrounds (for $B = 1$ the analysis includes a number of background events equal to the SM signal); 1σ results without the 0ℓ and 1ℓ categories correspond to the dashed purple line. CENTRE: same but for modifications of the Higgs trilinear $\delta\kappa_\lambda$. RIGHT: 1σ reach for modification of the Higgs-$\gamma\gamma$ and $Z\gamma$ rates, using high-E measurements (green,pink,brown bands correspond to leptonic,semi-leptonic, and also hadronic final states) or Higgs couplings (black error bars).*

HL-LHC in comparison with the reach from Higgs couplings measurements. Our results are based on leading order (LO) MadGraph simulations [79], where the Higgs couplings have been modified using FeynRules [460] and checked against the model of Ref. [461].

The top Yukawa. Modifications of the Yukawa coupling of the Higgs boson to top quarks is reputedly difficult to measure on the h resonance [164]; however, an anomalous top quark Yukawa induces a quadratic energy growth in the five point amplitude involving a bottom quark, a top, and three longitudinal bosons $W_L V_L V_L$. This amplitude leads to a process with a final state consisting of a top quark, a forward jet and two longitudinally polarised vector bosons in the final state.[68]

The top carries a large transverse momentum p_T^t due to the hardness of the process, which makes it a good discriminator. We consider two categories, for $p_T^t > 250(500)$ GeV. A forward jet with $|\eta_j| > 2.5$, $p_T^j > 30$ GeV and $E_j > 300$ GeV is required. The signal is classified by counting the number of extra leptons reconstructed in the event. The following table shows the number of signal events at the 14 TeV HL-LHC with 3000 fb^{-1}, for $p_T^t > 250$ GeV/ $p_T^t > 500$ GeV,

Process	0ℓ	1ℓ	$\ell^\pm\ell^\mp$	$\ell^\pm\ell^\pm$	$3\ell(4\ell)$
$W^\pm W^\mp$	3449/567	1724/283	216/35	-	-
$W^\pm W^\pm$	2850/398	1425/199	-	178/25	-
$W^\pm Z$	3860/632	965/158	273/45	-	68/11
ZZ	2484/364	-	351/49	-	(12/2)

The categories with two or more leptons have small background. The largest source of background for the hadronic modes comes from $\bar{t}tjj \to tWbjj$ where a bj pair is taken to reconstruct a W/Z-boson. The initial $\bar{t}tjj$ cross section is approximately six orders of magnitude bigger than the ones we are interested in, but we have verified that simple cuts on the invariant mass of the bj pair, on the rapidity of the forward jet, on p_T^t, and on the separation between the W and the b, as well as vector boson tagging techniques [463], can reduce this background to a level that is comparable with the signal.

We broadly parametrise this and other backgrounds by a uniform rescaling B of the SM signal expectation in each bin (so that for $B = 1$ we add an irreducible background equal to the SM signal in

[68] See also Ref. [462] that studies tHj final states which exhibits linear E-growth with modifications of the top-Yukawa.

each channel), and show the estimated reach in the left panel of Fig. 101. The dashed grey lines compare our results with those from Higgs Couplings measurements (see section 2. For illustration we also show results that focus on channels with at least 2 leptons with a dashed purple line: here the backgrounds are much smaller. The large number of events left in the zero and one lepton categories makes it possible to extend the analysis to higher energies, where not only the effects of the energy growth will be enhanced, but also the background reduced.

The Higgs self coupling. Measurements of the Higgs self-coupling have received enormous attention in collider studies. In the di-Higgs channel at HL-LHC precision can reach $\delta\kappa_\lambda \in [-1.8, 6.7]$ at 95%C.L. [312] using the $b\bar{b}\gamma\gamma$ final state. Here we propose the processes of Eq. (103) with VBS scattering topology and a multitude of longitudinally polarised vector bosons. The modified coupling $\delta\kappa_\lambda$, or the operator $\mathcal{O}_6$, induces a linear growth with energy w.r.t. the SM in processes with $jjhV_LV_L$ final state, and a quadratic growth in processes with $jjV_LV_LV_LV_L$. For the former, the same-sign $W^\pm W^\pm hjj$ with leptonic (e, μ) decays is particularly favourable for its low background: two same-sign leptons (2ssl) and VBS topology offers a good discriminator against background, allowing for $h \to \bar{b}b$ decays. For illustration we focus on this channel in which the SM gives $N_{\rm SM} \simeq 50$ events. Backgrounds from $t\bar{t}jj$ enter with a mis-identified lepton, but it can be shown that they can be kept under control with the efficiencies reported in [464] and with VBS cuts on the forward jets. A potentially larger background is expected to come from fake leptons, but the precise estimation of it is left for future work.

The results -shown in the centre panel of Fig. 101- are very encouraging: this simple analysis can match the precision of the by-now very elaborate di-Higgs studies. There are many directions in which this approach can be further refined: *i)* including the many other final states, both for the vector decays and for the Higgs decay *ii)* including the E^2-growing $jjV_LV_LV_LV_L$ topologies, *iii)* taking into account differential information. Moreover, the process studied grows only linearly with energy w.r.t. the SM amplitude with transverse vectors in the final state, but it grows quadratically w.r.t. the SM final states, so *iv)* measurements of the polarisation fraction can improve this measurement.

Higgs to $\gamma\gamma$, $Z\gamma$. These decay rates are loop-level and small in the SM: their measurement implies therefore tight constraints on possible large (tree-level) BSM effects, which in the EFT language are captured by the operators $\mathcal{O}_{WW,BB}$.[69] These also enter in high-energy VBS eq. (104), and they represent a beautiful additional motivation (together with κ_V, see below) to study these processes, which at present are often interpreted in the context of anomalous quartic gauge couplings (QGC) [465], corresponding to dimension-8 operators.

We perform a simple analysis of vector boson scattering (VBS) with $W^\pm W^\pm, ZZ, WZ, Z\gamma$ final states. For the first three we use the usual cuts on the forward jets: $|\delta_{jj}| > 2.5$, $p_T^j > 30$ GeV and $m_{jj} > 500$ GeV [466]. A kinematic variable that captures the hardness of the $2 \to 2$ process is the scalar sum of the p_T^V of the vector bosons, and therefore we bin the distribution in bins of 250 GeV up to 2 TeV. For the $Z\gamma$ final state, we follow the analysis for aQGC of [467].

The combined results are displayed in the right panel of Fig. 101, for fully leptonic, semi-leptonic and fully hadronic decays, for backgrounds $B = 0, 1$ where, as explained above, $B = 1$ corresponds to an additional background of the same order as the SM. Note that we translated the constraints on c_{BB}, c_{WW} to the $\kappa_{\gamma\gamma}, \kappa_{z\gamma}$. We find that the $ZZ, Z\gamma$ final states provide the best reach. For comparison, the individual reach from HL-LHC measurements of HC (section 2) is shown by the black error bars. These clearly offer an unbeatable sensitivity in the $h\gamma\gamma$ direction; the $hZ\gamma$ direction is however less tested, and our simple analysis of high-energy probes shows promising results.

[69] The same operators also affect the h couplings to Z_TZ_T and W_TW_T. The same qualitative analysis can be performed with focus on the $hA_{\mu\nu}A^{\mu\nu}$ and $hA_{\mu\nu}Z^{\mu\nu}$ vertices, but we prefer to work here with the gauge invariant $\mathcal{O}_{WW,BB}$ operators.

Higgs to W^+W^-, ZZ. It is known that modifications of the tree-level hZZ and hW^+W^- SM couplings (assumed here to be controlled by a unique parameter, corresponding for instance to $\mathcal{O}_H$ in the SILH basis [40]) imply a quadratic E-growth in longitudinal VBS. This is discussed in detail in Ref. [449] (and [450] for linear colliders), where it is pointed out that, in the SM, the longitudinal component is suppressed by an accidental factor ~ 2000, which is equivalent to a very large irreducible background. This motivated studies of VBS hh pair production instead, see [448], finding at 1σ, $\delta\kappa_V \lesssim 8\%$, comparable to $\delta\kappa_V \lesssim 5\%$ from HC.[70]

Higgs to gg. This coupling modifies the main production mode at hadron colliders and is, therefore, very well measured. The most interesting high-energy process that can be associated with this coupling is $gg \to ZZ$, which has been discussed in Refs. [468, 469, 470]. Using the results from Ref. [468] we estimate HwH versus HC reach at the end of the HL-LHC, in particular we have considered a scenario with and one without the background and three different decay channels . We find that

$$\begin{aligned} &\text{HC:} && |\kappa_g| \lesssim 0.025 \\ &\text{HwH:} && |\kappa_g| \lesssim 0.24\,/\,0.06\,/\,0.01 \\ &\text{HwH} && (\text{no } \bar{q}q \to Z_T Z_T): \ |\kappa_g| \lesssim 0.09\,/\,0.02\,/\,0.005 \end{aligned} \tag{107}$$

where the numbers stand for the fully leptonic / semi-leptonic / fully hadronic channels.

The partonic $\bar{q}q \to Z_T Z_T$ process represents here the main irreducible background, as it does not interfere with our $gg \to Z_L Z_L$ amplitude with longitudinal polarisation. Its reduction would constitute an important aspect of HwH analyses. Notice that, unfortunately, in the SM the $gg \to Z_L Z_L$ process is extremely suppressed at high-E, to the benefit of the transverse TT one, see Ref. [471]. This implies that the $SM - BSM$ interference is also suppressed.

Despite these difficulties, which might be overcome in more refined analyses (along the lines of [417, 418]), the high-E results remain competitive in the semi-leptonic and fully hadronic channels, assuming that the background from $\bar{q}q \to Z_T Z_T$ can be efficiently suppressed.

In summary, the preliminary results are very positive, especially given the potential of improvements that we foresee. Simple cut-and-count analyses were shown, in some cases, to match the precision of sophisticated Higgs Coupling measurements. For instance, the $jjW^\pm W^\pm h$ channel with leptonic decays, allows a precision comparable to di-Higgs production in measuring the Higgs self-coupling. Similarly, modifications of the top Yukawa can be measured in the many $jt + V_L V_L'$ final states to a precision in the ballpark of Higgs coupling measurements. VBS processes and ZZ at high-energy offer further alternative possibilities to test the Higgs coupling to electroweak gauge bosons and to gluons, respectively.

4.8 Dimension-6 EFT effects on Vector Boson Scattering at high energies[71]

In this note we assess the sensitivity of vector boson scattering (VBS) processes to different dimension-6 ($\dim = 6$) operators. We focus here on the ZZ final state, decaying to 4 charged leptons. This experimental channel, currently statistically limited at the LHC [472], will become more interesting at the HL-LHC because of the attainable selection purity. The full reconstruction of the final states also gives access to cleaner observables with respect to final states involving W bosons, where neutrino 4-momenta

[70] The authors of [448] assume separate couplings of the vector bosons to h or h^2; when the Higgs is part of a doublet, these are proportional. Moreover, the numbers we report here are indicative: both HC measurements and the di-Higgs analysis have optimistic and pessimistic scenarios in which these numbers might differ.

[71] Contacts: R. Covarelli, R. Gomez-Ambrosio

must be inferred using approximated methods. This analysis can nevertheless be repeated analogously to other VBS final states.

In [473] we studied the purely electroweak component of the $pp \to ZZjj$ process, referred to as VBS(ZZ). Sensitivity to several $\dim = 6$ operators has been demonstrated, as well as the impact of such EFT contribution on the VBS cross-section and triple and quartic gauge couplings (TGCs and QGCs).

Here we update predictions for the HL-LHC setup and show the kinematic distributions for a handful of relevant operators. For the $\dim = 6$ parametrisations we use the *Warsaw basis* from [41], following the notation and classification from [474]. Other technical details can be found in the original publication [473].

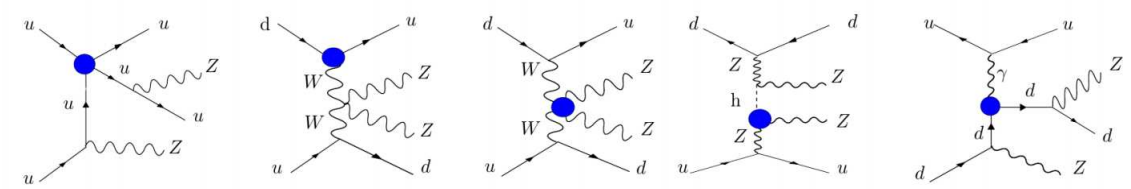

Fig. 102: Examples of some EFT diagrams for the VBS(ZZ) signal. The blobs represent $\dim = 6$ insertions.

Effective Field Theory parametrisation

We consider the standard SMEFT parametrisation of eq. (1).[72] Further, the SMEFT amplitudes and cross sections can be parametrised as

$$\mathcal{A}_{EFT} = \mathcal{A}_{SM} + \frac{g'}{\Lambda^2}\mathcal{A}_6 + \frac{g'^2}{\Lambda^4}\mathcal{A}_8 + \dots \tag{108}$$

$$\sigma_{EFT} \sim |\mathcal{A}_{SM}|^2 + 2\frac{g'}{\Lambda^2}\mathcal{A}_{SM}\mathcal{A}_6 + \frac{g'^2}{\Lambda^4}\left(2\mathcal{A}_{SM}\mathcal{A}_8 + |\mathcal{A}_6|^2\right) + \dots \tag{109}$$

Here, we assume the linear contribution (red) of the EFT effects to be leading. Analysis of the $\dim = 6$ quadratic terms and the $\dim = 8$ interference terms (both in blue) will be subject of further studies. In particular, $\dim = 8$ are commonly associated with quartic gauge couplings and such contribution, albeit sub-leading, would represent some added value to the linear $\dim = 6$ prediction.

Definition of the fiducial region

The VBS(ZZ) process has a very peculiar experimental signature, with two energetic forward jets and 4 identifiable charged leptons ($\ell, \ell' = \mu$ or e). The electroweak component of the process $pp \to ZZjj \to \ell\bar{\ell}\ell'\bar{\ell}'jj$ is defined and isolated through some experimental cuts. The ones used in the CMS analysis (in the measurement of the fiducial cross-section) can be found in [472]. Here we define a similarly VBS-enriched region, with a relaxed m_{jj} selection:

$$p_T(j) > 30\text{GeV} \quad \Delta\eta(j_1 j_2) > 2.4 \quad m_{jj} > 100\text{GeV} \quad \textit{on-shell} Z_1, Z_2 \tag{110}$$

EFT analysis

In tables 74 and 75 we show the sensitivities to different $\dim = 6$ operators of the VBS(ZZ) process, as well as of its main background at LHC: the di-boson production channel from quark-antiquark annihilation associated to gluon radiation (studied in depth by CMS for LHC runs I and II in [475], QCD(ZZ)).

[72] In particular, we assume CP symmetry, neglecting the CP-odd operators since their impact on VBS cross-sections and differential distributions is negligible. However it is well known that certain variables of these processes (namely spin correlations and polarisations) can be sensible to CP-violation.

Further, in figure 103 we show differential distributions for a subset of operators. In particular we chose the three operators that directly affect triple and quartic gauge couplings, with the following notation, which differs from that of table 1,

$$\mathcal{O}_W = \frac{3!}{g}\mathcal{O}_{3W} \quad \mathcal{O}_{HW} = \frac{1}{g^2}\mathcal{O}_{WW} \quad \mathcal{O}_{HWB} = \frac{1}{gg'}\mathcal{O}_{WB} \tag{111}$$

However, as reported in tables 74 and 75, there are other relevant operators for the VBS process, for example $\mathcal{O}_{\ell\ell}$, the 4-lepton operator that affects G_F, or $\mathcal{O}_{HB}$ that enters the Z boson propagator. More details can be found for example in [476].

Figure 103 should be interpreted as follows: we select one paradigmatic operator (for example $\mathcal{O}_W$), and see how much does its interference term affect the VBS and di-boson signals (2.5% in this case). As the VBS(ZZ) cross section is still mostly unconstrained experimentally, while the QCD(ZZ) has a 21% uncertainty in the 2-jet bin [475], we know the bounds within which we can vary this coefficient. If we assume for example a 10% positive interference with the total cross-section, we observe that such a small contribution to the total cross-section can represent a large modification in certain bins of the differential distributions. This advantage is twofold: with this procedure we can select the optimal bin(s) for the study and fit of each EFT operator; and, by applying unitarity considerations, we can constrain the values of the Wilson coefficients further. In our example, a contribution of 10% in $\mathcal{O}_W$, still allowed for the total rate, has a large impact on the high energy bins of the $p_T(Z_1)$ distribution.

Conclusions

The VBS(ZZ) and QCD(ZZ) final states, still largely unexplored at the LHC, will be an important source of constraints on $\dim = 6$ EFT operators at the HL-LHC. We have shown the impact that values of Wilson coefficients still experimentally allowed have on differential distributions that are easily accessible experimentally in this channel.

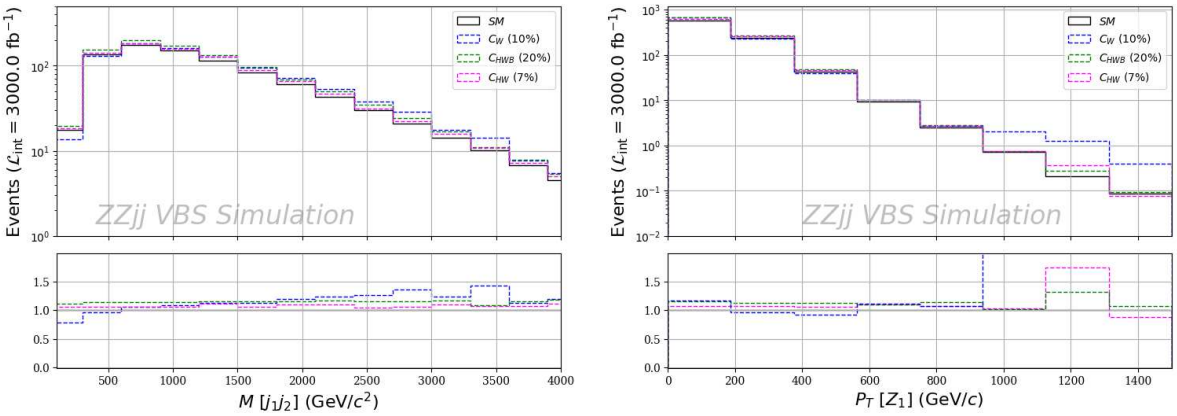

Fig. 103: Two generic simulations showing the EFT effects on key differential distributions: invariant mass of the di-jet system (left) and transverse momentum of the leading Z boson (right). We selected arbitrary values for the Wilson coefficients $\{c_W, c_{HW}, c_{HWB}\}$. Notice that the notation differs from table 1.

Table 74: Different sensitivities to each of the Warsaw basis operators. The operators that are not listed do not intervene in the process, or do it in a negligible way. Each sensitivity ϵ_i is calculated as $\epsilon_i = |\frac{\sigma_{EFT}-\sigma_{SM}}{\sigma_{SM}}|$, and they include a standard EFT pre-factor $\frac{v^2}{\Lambda^2}|_{\Lambda=1\text{TeV}}$ which needs to be taken into account if substituting values for the c_i in the table. NB: we quote the absolute value for the sensitivities ϵ. Notice that the notation differs from table 1.

VBS Signal	Signal strengths (Linear EFT)
Class 1:	$\mathcal{O}_W = c_W \cdot 2.5\%$
Class 3:	$\mathcal{O}_{HD} = c_{HD} \cdot 6.0\%$
Class 4:	$\mathcal{O}_{HW} = c_{HW} \cdot 5\%, \mathcal{O}_{CHB} = c_{HB} \cdot 0.2\%, \mathcal{O}_{HWB} = c_{HWB} \cdot 14\%$
Class 7:	$\mathcal{O}_{Hl^{(3)}} = c_{Hl^{(3)}} \cdot 48\%, \mathcal{O}_{Hq^{(1)}} = c_{Hq^{(1)}} \cdot 2\%,$ $\mathcal{O}_{Hq^{(3)}} = c_{Hq^{(3)}} \cdot 46\%, \mathcal{O}_{Hu} = c_{Hu} \cdot 0.8\%$
Class 8a: $(L\bar{L})(L\bar{L})$	$(G_F \to) \mathcal{O}_{\ell\ell} = c_{\ell\ell} \cdot 24\%$, $\mathcal{O}_{qq^{(1)}} = c_{qq^{(1)}} \cdot 12\%,$ $\mathcal{O}_{qq^{(11)}} = c_{qq^{(11)}} \cdot 14\%, \mathcal{O}_{qq^{(33)}} = c_{qq^{(33)}} \cdot 100\%, \mathcal{O}_{qq^{(31)}} = c_{qq^{(31)}} \cdot 75\%$

Table 75: Sensitivities to the different $\dim = 6$ operators in the di-boson production channel, main background for the VBS(ZZ) at LHC. A large sensitivity does not necessarily mean that a large EFT effect is expected, since the corresponding Wilson coefficient might as well be very small. Notice that the notation differs from table 1.

ZZ Di-boson	Sensitivities (Linear EFT)
Class 1:	$\mathcal{O}_G = 2.5\%, \quad \mathcal{O}_W = 2.5\%$
Class 3:	$\mathcal{O}_{HD} = 6.0\%$
Class 4:	$\mathcal{O}_{CHW} = 0.2\%, \mathcal{O}_{CHG} = 8\%, \mathcal{O}_{CHB} = 0\%, \mathcal{O}_{CHWB} = 12\%$
Class 7:	$\mathcal{O}_{Hl^{(3)}} = c_{Hl^{(3)}} \cdot 25\%$, $\mathcal{O}_{Hq^{(1)}} = c_{Hq^{(1)}} \cdot 3\%,$ $\mathcal{O}_{Hq^{(3)}} = c_{Hq^{(3)}} \cdot 31\%, \mathcal{O}_{Hu} = c_{Hu} \cdot 1.1\%$
Class 8a: $(L\bar{L})(L\bar{L})$	$(G_F \to) \mathcal{O}_{\ell\ell} = c_{\ell\ell} \cdot 12\%$, $\mathcal{O}_{qq^{(1)}} = c_{qq^{(1)}} \cdot 1.0\%,$ $\mathcal{O}_{qq^{(11)}} = c_{qq^{(11)}} \cdot 1.3\%, \mathcal{O}_{qq^{(33)}} = c_{qq^{(33)}} \cdot 8.4\%, \mathcal{O}_{qq^{(31)}} = c_{qq^{(31)}} \cdot 8.0\%$

4.9 Same-sign WW scattering and EFT applicability[73]

Although any statistically significant deviation in data from the Standard Model(SM) predictions would be a manifestation of a BSM physics, the question is what we can learn about its scale and its strength before discovering new particles. The appropriate tool for answering this question is the Effective Field Theory(EFT) approach: the information about the scale Λ and the strength C of new physics is encoded in the Wilson coefficients of the higher dimension operators, $f_i = C^m/\Lambda^n$. The usefulness of any EFT analysis of a given process relies on the assumption that only a few higher-dimension terms in the expansion $\mathcal{L} = \mathcal{L}_{SM} + \sum_i f_i^{(6)}\mathcal{O}_i^{(6)} + \sum_i f_i^{(8)}\mathcal{O}_i^{(6)} + \ldots$ provide adequate approximation to an unknown UV completion. This assumption introduces a strong model-dependent aspect and therefore it is convenient to introduce the concept of EFT “models" defined by the choice of operators and the values of their Wilson coefficients $(\mathcal{O}_i^{(d)}, f_i^{(d)})$. Our focus is on the proper use of the EFT "models" in their range of validity for the WW scattering in purely leptonic W decay channels where the WW invariant mass cannot be determined experimentally. A full explanation of the concept is to be found in [477] and here we summarise the main points..

Following a common practice we take one operator at a time setting others to zero, which effectively defines the EFT “model", and consider the process $pp \to 2jW^+W^+ \to 2jl^+\nu l'^+\nu'$. The EFT “model" can be maximally valid up to the invariant mass M of the W^+W^+ system $M < \Lambda \leq M^U$, where $M^U = M^U(f)$ is the perturbative partial wave unitarity bound in the chosen EFT "model". If the

[73] Contacts: G. Chaudhary, J. Kalinowski, M. Kaur, P. Kozów, S. Pokorski, J. Rosiek, K. Sandeep, M. Szleper, S. Tkaczyk

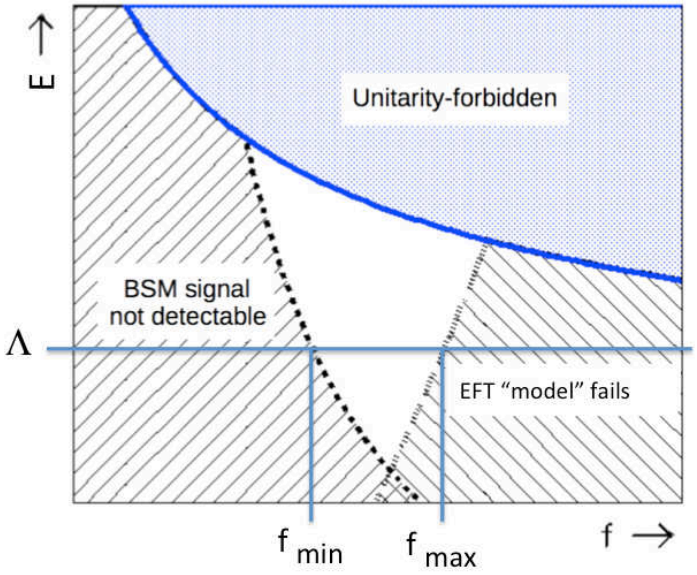

Fig. 104: Cartoon plot showing the regions in f_i and Λ in terms of BSM signal observability and applicability of the EFT "model" for the same-sign WW process with purely leptonic decays. The white triangle shows the region where the BSM physics can be studied within the chosen EFT "model".

kinematic range M_{max} at the LHC is greater than Λ, there is necessarily a contribution to observables from the region $\Lambda < M < M_{max}$. Two questions arise:1) what is the discovery region in the space (Λ, f) for the chosen EFT "model", 2) if a deviation from the SM predictions is indeed observed, how to verify the chosen EFT "model" by fitting it to a set of experimental distributions D and in what range of Λ, f_i such a fit is really meaningful?

For a given EFT "model" the unitarity bound is very different for different helicity amplitudes. As M^U we take the *lowest* value from T-matrix diagonalisation of the W^+W^+ and W^+W^-, universally for all helicity amplitudes. The BSM signal S of the EFT "model" $(\mathcal{O}_i^{(d)}, f_i^{(d)})$ can be defined as the deviation from SM predictions observed in the distribution of some observable D, $S = D^{model} - D^{SM}$. A quantitative estimate of the signal can be written as

$$D^{model} = \int_{2M_W}^{\Lambda} \frac{d\sigma}{dM}\Big|_{model} dM + \int_{\Lambda}^{M_{max}} \frac{d\sigma}{dM}\Big|_{SM} dM\,, \tag{112}$$

which comes uniquely from the operator that defines the "model" in its range of validity and assumes only the SM contribution in the region $M > \Lambda$. BSM contribution from the region above Λ may enhance the signal, but it may also preclude proper description of the data in the EFT "model", which makes sense *if and only if* this additional contribution is small enough compared to the contribution from the validity region. For a quantitative estimate of this contribution we define a second estimate in which all the helicity amplitudes above Λ are assumed to remain constant at their respective values they reach at Λ

$$D^{model} = \int_{2M_W}^{\Lambda} \frac{d\sigma}{dM}\Big|_{model} dM + \int_{\Lambda}^{M_{max}} \frac{d\sigma}{dM}\Big|_{A=const} dM. \tag{113}$$

For $\Lambda = \Lambda_{max}$ this prescription regularises the helicity amplitudes that violate unitarity at M^U. We adopt the criterion that the EFT "model" is tested for values of $(\Lambda \leq M^U, f_i)$ when the signals computed from Eq.(112) are statistically consistent within 2σ with the signals computed with Eq.(113).

The observability of the EFT "model" predictions imposes some minimum value of f_{min}, while the description within the EFT "model" imposes some maximum value of f_{max} such that signal estimates computed from Eqs.(112) and (113) remain statistically consistent. For $\Lambda = M^U$ a finite interval of f_i values is possible, while for $\Lambda < M^U$ the respective limits on f_i depend on the actual value of Λ. It is illustrated in a cartoon plot in Fig. 104, where the white "triangle" is bounded from above by the unitarity bound $M^U(f_i)$, from the left by the signal significance criterion and from the right by the consistency criterion. The EFT "model" could be the right framework to describe the BSM signal as long as the "triangle" shown in our cartoon plot is not empty.

Our preferred strategy for data analysis is as follows:
a) Measure distributions D that offer the highest sensitivity to the studied EFT "model",
b) if deviations from the SM are observed, fit the values of $(\Lambda \leq M^U, f_i)$ according to Eq.(113),
c) using the fitted values of f_i and Λ recalculate D templates according to Eq.(112),
d) check statistical consistency between estimates based on Eqs.(112) and (113).
Physics conclusions from the obtained (Λ, f_i) values can only be drawn if such a consistency is found. Stability of the result against alternative regularisation methods would provide a measure of uncertainty of the procedure - too much sensitivity to the region above Λ means the procedure is destined to fail and that data cannot be described within the chosen EFT "model".

To demonstrate our strategy we considered EFT "models" defined by one-at-a-time dimension-8 operator that affects $WWWW$ couplings. Details of the simulation of events for the process $pp \to jj\mu^+\mu^+\nu\nu$ (at 14 TeV with 3/ab integrated luminosity) and their processing according to our strategy can be found in [477]. Assuming Λ equal to the respective unitarity bounds, the lower and upper limits for the values of f for each dimension-8 operator, for positive and negative f values, as well as the applicability "triangles" in the (Λ, f_i) plane for each operator have been calculated. These limits define the (continuous) sets of testable EFT "models" based on the choice of single dimension-8 operators.

Following the above strategy we have calculated the expected reach for the dim-8 operator O_{M7} at the HE-LHC and compared it with the obtained reach for the HL-LHC (14 TeV) from Ref. [477], assuming in each case an integrated luminosity of 3/ab. Fig.105 shows the respective "EFT triangles". It is evident that increasing the proton energy allows to explore much lower values of the Wilson coefficients, with lower limits for a 5σ BSM discovery being shifted by as much as almost an order of magnitude. On the other hand, the upper limit on consistent EFT description shifts likewise by a similar amount. This is due to the fact that by increasing the collision energy more and more events come from the region, where $M > \Lambda$ and therefore shrinking the range of Wilson coefficients that satisfy our consistency criterion. Overall, the area of the actual "EFT triangle" does not get significantly larger for 27 TeV compared to 14 TeV, even when viewed in a log scale.

To summarise: we have analysed the physics potential of "EFT models" defined by the choice of single dimension-8 operators in the same-sign WW scattering process in the purely leptonic decay modes. We argue that usage of EFT "models" in the analysis of purely leptonic W decay channels requires bounding the possible contribution from the region $M_{WW} > \Lambda$, no longer described by the "model", and ensuring it does not significantly distort the measured distributions compared to what they would have looked from the region of EFT validity alone and propose a data analysis strategy to satisfy the above requirements. We find that the "triangles" turned to be rather narrow, even when going from 14 to 27 TeV of pp beam energy . This result reinforces our former conclusion that study of BSM effects by means of varying single Wilson coefficients has little physics potential and future data analysis should be rather focused on simultaneous fits of many operators to the combined data from all VBS processes. We find this conclusion to hold equally regardless of the actual beam energy.

Acknowledgements: Work partially supported by the National Science Centre (Poland) grants DEC-2015/18/M/ST2/00054, DEC-2016/23/G/ST2/04301 (SP), DEC-2015/19/B/ST2/02848 (JR) and HARMONIA project UMO-2015/18/M/ST2/00518 (JK) as well as the COST Action CA16108. ST is supported by Fermi Research Alliance, LLC under Contract No. De-AC02-07CH11359 with the US

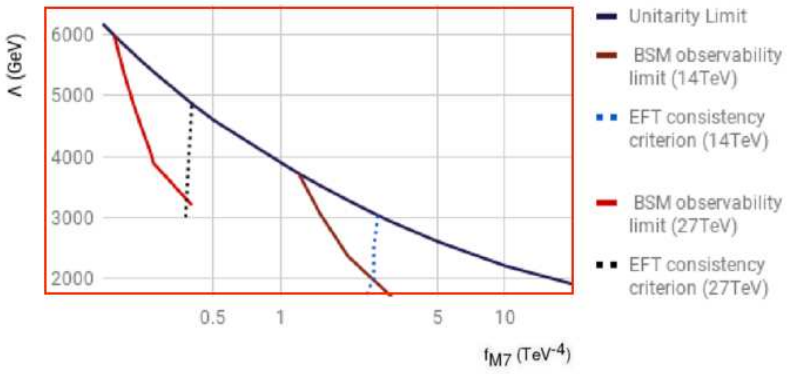

Fig. 105: Regions in f_{M7} and Λ in terms of BSM signal observability for the EFT "model" based on $\mathcal{O}_{M7}$ operator at the HL- and HE-LHC.

DoE. The work of PK has been supported by the Spanish MINECO project FPA2016-78220-C3-1- P (Fondos FEDER).

5 Higgs boson mass and width[74]

5.1 Theory review[75]

The total decay width is an important property of the Higgs boson, as it contains information about the interactions of the Higgs with all other fundamental particles, and is predictable both in the Standard Model and its extensions. Therefore, measuring this property is an important part of Higgs studies. Direct measurements of the Higgs width are very challenging at hadron colliders, as these require a scan of the invariant mass profile of the Higgs decay products. This is limited by detector resolution to roughly ~ 1 GeV, which is three orders of magnitude larger than the SM prediction of $\Gamma_H \sim 4$ MeV. Current LHC measurements have already attained this level of precision. Although no explicit projection has been made, it is expected that the direct method will only be able to constrain the Higgs width to $\mathcal{O}(100)$ times the SM value.[76]

Given this situation, there has been considerable interest in devising indirect probes of the Higgs width. In general, a standard Higgs analysis in the $H \to X$ decay channel measures the production cross section times branching ratio, $\sigma \sim \sigma_{\rm prod} \times \Gamma_{H\to X}/\Gamma_H$, and is thus only sensitive to a combination of the coupling and the width. Schematically,

$$\sigma \sim \frac{g^2_{\rm prod} \times g^2_{\rm dec}}{\Gamma_H}, \tag{114}$$

where $g_{\rm prod}$ and $g_{\rm dec}$ are the couplings that enter the Higgs production and decay channels, respectively. An independent measurement of the couplings and the decay width is therefore not possible from such analyses. The idea behind all indirect determinations of Γ_H is to find an observable whose dependence on g_i and Γ_H is different from Eq. (114), which allows one to lift the coupling/width degeneracy. Indirect determinations can be broadly separated in two classes: *on-shell* methods, which rely on interference effects on the Higgs resonant peak, and *off-shell* methods, which combine on-peak and off-peak information. In the following, we provide a quick overview of these methods, emphasising their strengths and weaknesses.

The starting point of the on-shell methods [478, 479, 480, 481] is the observation that measurements in the $H \to X$ decay channel receive a contribution both from the signal $pp \to H \to X$ process and from the continuum background $pp \to X$, and the two interfere. Schematically, the amplitude for the process can be written as

$$\mathcal{A}_{pp\to X} = \frac{S{m_H}^2}{s - {m_H}^2 + i m_H \Gamma_H} + B, \tag{115}$$

where $S \propto g_{\rm prod} \times g_{\rm dec}$ is the signal part and B is the background contribution. This leads to

$$|\mathcal{A}_{pp\to X}|^2 = \frac{{m_H}^4}{(s-{m_H}^2)^2 + {m_H}^2{\Gamma_H}^2} \times \left[|S|^2 + \frac{(s-{m_H}^2)}{{m_H}^2} 2{\rm Re}(SB^*) + \frac{\Gamma_H}{m_H} 2{\rm Im}(SB^*)\right] + |B|^2. \tag{116}$$

Here, $|S|^2 \propto g^2_{\rm prop} \times g^2_{\rm dec}$, but $SB^* \propto g_{\rm prop} \times g_{\rm dec}$, so a combined determination of the signal $|S|^2$ and interference SB^* contributions can lift the coupling/width degeneracy of Eq. (114), thus giving access to Γ_H. For this method to be effective, one needs to consider channels where the interference is large. The best candidate is the $gg \to H \to \gamma\gamma$ channel: indeed, in this case both the $gg \to H$ production and the $H \to \gamma\gamma$ are loop induced, as is the continuum contribution $gg \to \gamma\gamma$. This implies that at least naively there is a loop enhancement factor in the interference w.r.t. the pure signal, thus making the former noticeable.

[74] Contact Editors: Z. Liu, M. Xiao

[75] Contacts: F. Caola, R. Röntsch

[76] Lower bounds on the Higgs width can be obtained from lifetime measurements.

The *real part of the interference* in Eq. (116) is anti-symmetric around the Higgs peak, so it does not affect the total rate. However, it leads to a distortion in the shape of the $m_{\gamma\gamma}$ distribution around the Higgs peak, which in turns translates into a slight shift in the reconstructed Higgs mass [479]. The size of this mass shift is proportional to the interference contribution, whose dependence on couplings and width is different from Eq. (114). A measurement of the mass shift then allows for a determination of Γ_H. This can be done for example by comparing the mass extracted in the $\gamma\gamma$ channel with that determined in the $4l$ channel, where these interference effects are negligible. However, even if the $4l$ channels lead to a very good mass determination once high enough statistics have been accumulated, extracting the mass shift from a $\gamma\gamma$ vs $4l$ comparison introduces additional systematics. One way to circumvent this issue is to consider only the $\gamma\gamma$ decay mode and to compare different kinematic regions, although detailed systematic studies within this approach have not yet been done. This is possible since the interference is strongly dependent on the transverse momentum of the Higgs [480]. In particular, hard radiation tends to lessen this effect somewhat. Another candidate for a reference mass could be obtained from studying Higgs production in association with two hard jets. Indeed, in this case there are cancellations between the ggF and VBF contributions and the net result for the interference is very small [482]. Theoretical predictions for the mass shift are under good control, with the interference being known to NLO in QCD [480, 483, 484] and matched to parton shower [161, 485]. It turns out that radiative corrections deplete the interference contribution somewhat. Although it is well known that higher order corrections are important for Higgs physics, for this analysis the main limitation comes from experimental systematics, namely the detector response, which must be properly modelled to extract the interference contribution from the measured mass shift. In the SM, the mass shift at the LHC is rather small, $\Delta m_{\gamma\gamma} \sim \mathcal{O}(30)$ MeV. This implies that it will be extremely difficult for this method to access the region $\Gamma_H \lesssim 10 \times \Gamma_{H,\mathrm{SM}}$. Detailed projections at the HL-LHC can be found in Sec. 5.5.

The *imaginary part of the interference* [480, 481] in Eq. (116) is symmetric around the Higgs peak, so it leads to a change in the rate. Unfortunately, because of helicity conservation this imaginary part is highly suppressed at LO. Higher order corrections provide a new mechanism to generate an imaginary part, lifting this suppression [480]. However, because the bulk of the interference effectively enters at NLO, the anticipated loop enhancement factor in the interference relative to the pure signal (mentioned above) is not present, and the actual size of the effect is quite small. In the SM, it reduces the total rate by about 2%, which makes it challenging to observe, and the effect is further diluted by additional radiation [481]. Thus this technique requires very good control on the total rate, both experimental and theoretical. To reduce the former, it is profitable to consider cross-section ratios; for example, the $\gamma\gamma$ to $4l$ ratio is projected to be measured at the few percent level. However, this introduces additional experimental and theoretical systematics, including theoretical model dependence since one would need to make assumptions about the structure of Higgs couplings. For this reason, it may be advantageous to perform the interference effect extraction in the $\gamma\gamma$ channel alone, by considering different kinematic regions. As with the real part of the interference, this effect is also quite sensitive to the transverse momentum of the Higgs, with the bulk of the interference effect confined to the small p_t region, as shown in an NLO analysis in Ref. [481]. However, since the interference is essentially an NLO effect, as discussed above, the residual theoretical uncertainty at this order is still quite sizeable. Moreover, a fine-grained comparison of the low and high Higgs p_t regions requires very good theoretical control. For the former, this is notoriously complicated as several different effects are at play, see e.g. [486] and references therein for a recent discussion of this point. Because of this, assuming a few percent experimental accuracy, the width extraction from this method would be limited by theoretical uncertainties. Although computing higher order corrections for this effect is well beyond our current ability, it is reasonable to assume that the situation will improve on the HL/HE-LHC timescale, along the lines described in Section 2.2. Currently, it is expected that this technique will lead to bounds of the order $\Gamma_H \sim \mathcal{O}(10) \times \Gamma_{H,\mathrm{SM}}$, see section 5.4 for details.

The main advantage of the on-shell width determinations discussed above is that they require

minimal theoretical assumptions on potential BSM effects. This is because couplings are extracted at the same energy scale, ideally from the same process. However, since interference effects scale like $g_{\rm prod} \times g_{\rm dec}$ at the first power, the constraints on the width are relatively mild. Indeed, if one assumes that the on-shell rates are kept fixed, a linear dependence on the coupling translates into a square root dependence on the width.

Another option to constrain the width is off-shell methods [487, 488, 489, 490], which are based on the following observation. Schematically, the cross section can be written as

$$\sigma \sim \frac{g^2_{\rm prod} \times g^2_{\rm dec}}{(s - {m_H}^2)^2 + {m_H}^2 {\Gamma_H}^2}. \tag{117}$$

On the resonant peak, this leads to the usual relation in Eq. (114). Typically, most of the cross section is concentrated there. In the VV decay channel though there is a sizeable contribution from the off-shell $s \gg {m_H}^2$ region [487]: indeed, Higgs decay to vector bosons is strongly enhanced at high energy. In the far off-shell region, Eq. (117) reduces to $\sigma \sim (g^2_{\rm prod} \times g^2_{\rm dec})/s^4$. Assuming that the on-peak rates are kept fixed, this quadratic dependence on the couplings translates into a linear dependence on Γ_H, allowing this quantity to be constrained by a comparison of on- and off-shell rates.

However, it is important to stress that to extract Γ_H from off-shell measurements one has to assume that on-shell and off-shell couplings are the same. Since the two are evaluated at very different energy scales, this introduces a theoretical model dependence that is not present in the on-shell methods. Indeed, there are several new physics scenarios where BSM effects decorrelate on- and off- shell couplings, see e.g. [468, 491, 492, 493] and sections 4.7, 4.8 where some of these effects are discussed explicitly. These include, for example, new light degrees of freedom coupled to the Higgs, additional Higgs states, or anomalous HVV couplings. Therefore, to constrain the width using an off-shell analysis, it is important to perform complementary measurements to control potential BSM effects. This was studied in detail for the case of HVV anomalous couplings in [494]. Projections at the HL-LHC will be presented in section 5.3. In general, off-shell measurements offer the opportunity to investigate Higgs interactions at high energy scale, thus leading to interesting information that is not limited to the width extraction. For example, in combination with measurements of boosted Higgs, HH and $t\bar{t}H$, an off-shell analysis can help lifting the degeneracy between ggH and $t\bar{t}H$ couplings [468]. The off-shell program will clearly benefit from the increased statistics and energy of the HL/HE upgrade. For example, this would allow for off-shell studies in the VBF production mode [495]. Although the rate here is very small, by looking at same-sign vector boson final states one can significantly reduce backgrounds. Although it is estimated that HL-LHC measurements in this channel would lead to constraints at the same level of current ones in the ggF channel [495], the completely different production mechanism makes them complementary to the ggF constraints, thus allowing for a less model dependent interpretation. Aside from these considerations, it is interesting to study the potential of future LHC upgrades to constrain Γ_H under the assumption that no large decorrelations between on- and off-shell couplings occur. Because of the linear dependence on the width discussed above, such constraints are rather powerful. Indeed, assuming a reasonable reduction in the theoretical uncertainty in the HL-LHC timescale, it will be possible to probe values close to the SM value $\Gamma_H \sim 4$ MeV. Projections under different assumptions for the theoretical uncertainty are reported in section 5.3.

A reliable theoretical description of the off-shell region is non trivial. First, there is a large $q\bar{q} \to VV$ background, which needs to be properly subtracted to access the signal yield. More important, there is an irreducible $gg \to VV$ continuum background that interferes with the signal process $gg \to H \to VV$. The interference effect is sizeable and destructive, which is a consequence of the Higgs mechanism ensuring unitarity in the SM. Because of the large interference, it is necessary to have good theoretical control not only on the signal process but also on the continuum background amplitude. This is non trivial, since the $gg \to VV$ process is loop induced, so higher order corrections – expected to be large given the gg initial state – involve multi-loop amplitudes. Moreover, at large invariant masses,

the contribution of virtual top quarks to the amplitude becomes dominant. Its proper description would then require multi-loop amplitudes involving internal massive states, which are extremely challenging to compute. For this reason, exact predictions for the background amplitude are only known to LO in the off-shell region. NLO corrections are known below the top threshold, and only in an approximate form above [496, 497, 498, 499, 500, 501, 502]. Nevertheless, recent developments in numerical techniques [274] make NLO computations for the background feasible in the near future. One subtle point in this discussion is the role of quark-initiated reactions. On the one hand, they appear naturally in the computation of NLO corrections to $gg \to VV$ from initial state splitting. On the other hand this kind of contribution – although separately finite and gauge invariant – only forms a small subset of the whole $qg \to VVq$ process at $\mathcal{O}(\alpha_s^3)$, which are part of the genuine N^{3}LO corrections to the quark-initiated $q\bar{q} \to VV$ process. Therefore, only including the contribution coming from initial state splitting in the $gg \to VV$ process, although formally possible, may not entirely capture the correct physics. In general, this problem is not particularly relevant because the gluon channel provides the bulk of the contribution. This is however no longer the case if strong requirements on extra jet activities (typical e.g. for WW analysis) are imposed. Understanding this issue is an interesting theoretical problem, and the high statistics available at the HL/HE-LHC motivates its detailed investigation. Another issue that should be investigated is the impact of electroweak corrections, which can be sizeable at high energy. Once again, although they are currently unknown, it is natural to expect progress in this direction within the HL-LHC timescale.

The modelling of the $gg \to H \to VV$ process is under better control than the background one. Still, since in the far off-shell region the top loop cannot be approximated by a contact interaction, computations are still much harder than in the on-shell region, where such an approximation is justified. As a consequence, exact results are only known to NLO. A full computation of NNLO corrections would require significant advances on current technology, which are however likely to occur in the HL-LHC timescale. It is reasonable to expect [45] that the K-factor for the exact theory is rather similar to that obtained from calculations in which the top loop is integrated out. In the absence of an exact calculation, one can use this approximation to estimate rates at the HL/HE LHC.

The HL/HE-LHC upgrade will improve off-shell analysis in several ways. On the one hand, the larger statistics will allow for a better discrimination of the $q\bar{q} \to VV$ vs $gg \to VV$ background and – crucially – interference. Currently, this is done by using the different kinematic behaviour of these contributions. Clearly, a higher statistical sample would allow for more powerful discrimination. Furthermore, increasing the collider energy would lead to a larger fraction of gluon initiated events w.r.t. quark initiated events. For example, the $(gg \to H \to VV)/(q\bar{q} \to VV)$ ratio increases by a factor of roughly 1.5 in the off-shell region when the centre-of-mass energy is increased from 14 TeV to 27 TeV. Furthermore, the increase in the total rate at the HE-LHC will lead to a significant number of off-shell events in the few-TeV region. This would allow for precise investigations of the Higgs sector in the high-energy region, which could shed light on the unitarity structure of the SM.

5.2 Measurement of the Higgs boson mass[77]

The measurement of the Higgs boson mass by the ATLAS and CMS experiments at the LHC is [10]:

$$m_H = 125.18 \pm 0.16 \text{ GeV}$$

This precision is reached with the two high resolution Higgs boson measurement channels the $H \to ZZ^* \to 4\ell$ and $H \to \gamma\gamma$. At the LHC Run 2, the precision in the latter channel is already limited by the systematic uncertainty on the photon energy scale. The photon energy response is calibrated using both electrons from Z decays (which requires to be extrapolated from electrons to photons) and radiative Z events reconstructed with two charged leptons and a photon, which is limited by statistics in

[77] Contacts: G. Barone, A. Gabrielli

the transverse momentum range of interest. The most precise measurement is obtained in the 4μ and the $2e2\mu$ where the on-shell Z mass constraint can be applied to the $2e$ system.

Detailed studies of the calibration of the muons, electrons and photons with the very large HL-LHC sample have not been done yet, however it is plausible that the mass of the Higgs boson will be measured with a precision of 10-20 MeV, assuming that with the higher statistics the analysis will be further optimised to gain in statistical precision and that systematic uncertainties on the muon transverse momentum scale will significantly improve with the higher statistics.

5.3 Constraints from off-shell Higgs boson production[78]

Extracting the Higgs width from off-shell measurements are performed in ATLAS [503] and CMS [271] experiments using LHC Run 1 and Run2 data. The latest constraints on the Higgs width are < 14.4 MeV and < 9.2 MeV from ATLAS and CMS, respectively. Theoretical basis of the measurements is that on-shell and off-shell couplings are the same. Developed on the experimental analyses, the expected precision on the Higgs width at the luminosity of 3000 fb^{-1} is given in this section.

The CMS projection adopted the same analysis strategy as defined in the Run 2 analysis [271], where the 4ℓ final state is used. Events are selected and put into different categories that are sensitive to ggF, VBF and VH production modes. The invariant mass of the four leptons, matrix-element based discriminant separating the major signal and background events and discriminants sensitive to the width are used in each category. The ratio between off-shell and on-shell event yields and the shape of the observables are sensitive to the Higgs width. To extrapolate to 3000 fb^{-1}, event yields are scaled with luminosity. Assumptions on the uncertainties are made, and two scenarios are considered [139]:

- **"Run 2 systematic uncertainties" scenario (S1):** All systematic uncertainties are kept constant with integrated luminosity. The performance of the CMS detector is assumed to be unchanged with respect to the reference analysis;
- **"YR18 systematic uncertainties" scenario (S2):** Theoretical uncertainties are scaled down by a factor of two, while experimental systematic uncertainties are scaled down with the square root of the integrated luminosity until they reach a defined minimum value based on estimates of the achievable accuracy with the upgraded detector.

The projections are shown in Fig. 106. Limits on Γ_{H} are given for an approximate S2 in which the experimental systematics are not reduced, while the theoretical systematics are halved with respect to S1. The 10% additional uncertainty applied on the QCD NNLO K factor on the gg background process is kept the same in this approximated S2 in order to remain conservative on the understanding of these corrections on this background component. It is also noted that the uncertainties on the signal and background QCD NNLO K factors are smaller in the Run 2 analysis [271] than in previous projections using Run 1 data [504]. The expected Γ_{H} precision in S2 is $4.1^{+1.0}_{-1.1}$ MeV.

The ATLAS projection [504] is based on the ATLAS Run1 analysis [222]. $\text{H} \rightarrow \text{ZZ} \rightarrow 4\ell$ final state is used. Events are selected and put in ggF, VBF and VH categories. The invariant mass of the four leptons and a matrix-element based discriminant sensitive to both signal background separation and width variation are used. In the extrapolation to 3000 fb^{-1}, event yields are scaled with luminosity and the change in the centre mass of energy. Only theoretical uncertainties are taken into account, as the experimental ones have a negligible impact. The treatment of theoretical uncertainty is close to Run1 analysis, with more conservative ones below:

- The k-factor uncertainty for the gg initial state signal, background and their interference is taken as 30%. Based on the latest theory papers, this uncertainty is considered to be conservative, and is 10% is the CMS projection result.

[78] Contacts: M. Xiao, U. Sarica

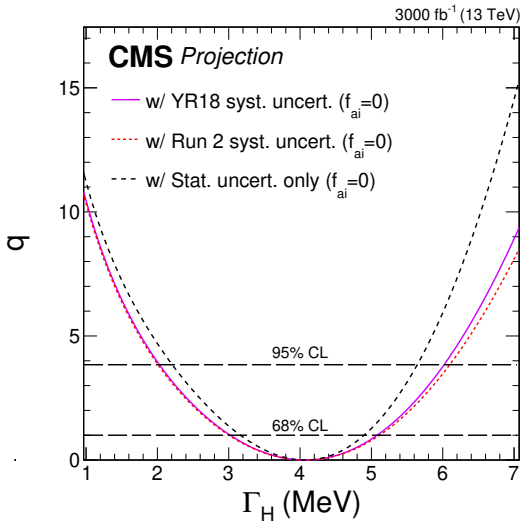

Fig. 106: Likelihood scans for projections on Γ_{H} at 3000 fb^{-1} [139]. Scenarios S2 (solid magenta) and S1 (dotted red) are compared to the case where all systematics (dashed black) are removed. The dashed horizontal lines indicate the 68% and 95% CLs.

– The background to signal k-factor ratio $R_H^B(\mathrm{mZZ})$ uncertainty, two benchmarks are considered: 10% and 30%.

The expected precision on Γ_{H} at 3000 fb^{-1} is $4.2^{+1.5}_{-2.1}$ MeV as shown in Fig. 107. It is more conservative than the CMS result, and the cause of it was discussed above.

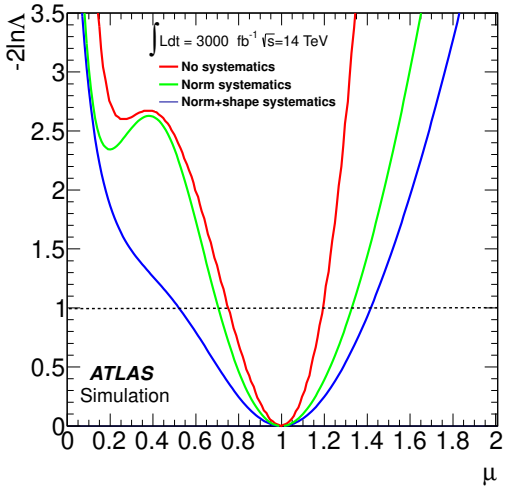

Fig. 107: Likelihood scans on $\mu_{\mathrm{off-shell}}$ with and without systematic uncertainties. The error on μ is computed at the 1σ level and the uncertainty on $R_H^B(\mathrm{mZZ})$ is set to 30%.

In conclusion, it is reasonable to believe the realistic precision from ATLAS at 3000 fb^{-1} will be better than the number above. Using the CMS numbers, we con estimate that with CMS and ATLAS measurements combined, the precision on the width can reach $4.1^{+0.7}_{-0.8}$ MeV.

5.4 Width from the di-photon interference rate[79]

The SM Higgs total decay width can be constrained from the change in on-shell Higgs rates due to interference effects between the Higgs signal and the QCD background [481]. This change in rates requires the existence of a so-called strong phase in the amplitudes, that can be present both in the Higgs signal and in the continuum background, as is the case in the SM. We shall demonstrate that, the different scaling behaviour between the strong phase induced interference and the Breit-Wigner parts of the on-shell Higgs rate may allow the placement of bounds on, or even measurements of, the Higgs boson total width. Both theoretical and experimental uncertainties are the leading limiting factors in this program. On the other hand, without the strong phase induced interference effects, fits to on-shell Higgs rates can only place bounds on the total width by making definite theoretical assumptions [505, 44, 506].

It is useful to write the amplitude for $gg \to h \to \gamma\gamma$ in a form which explicitly factors out the loop-induced couplings to gluons (F_{gg}) and photons ($F_{\gamma\gamma}$),

$$A_h \equiv A_{gg\to h\to\gamma\gamma} \propto \frac{\hat{s}}{\hat{s} - m_h^2 + i\Gamma_h m_h} F_{gg} F_{\gamma\gamma}\,. \tag{118}$$

Both the Higgs couplings F_{gg} and $F_{\gamma\gamma}$ as well as the background amplitude $A_{\rm bkg}$ receive absorptive contributions that arise from loops of particles that are sufficiently light to be on shell. The resulting induced phases are usually dubbed 'strong phases' in the flavor literature and we will adopt this terminology here.[80] In the presence of a strong phase we can write the interference term as

$$\begin{aligned} |\mathcal{M}_h|^2_{\rm int} \quad &\equiv 2\Re[A_h A^*_{\rm bkg}] = \frac{2|A_{\rm bkg}||F_{gg}||F_{\gamma\gamma}|}{(\hat{s} - m_h^2)^2 + \Gamma_h^2 m_h^2} \\ &\times\Big[(\hat{s} - m_h^2)\cos(\delta_{\rm bkg} - \delta_h) + m_h\Gamma_h \sin(\delta_{\rm bkg} - \delta_h)\Big], \end{aligned} \tag{119}$$

where we have taken $\delta_h = \arg[F_{gg}] + \arg[F_{\gamma\gamma}]$ and $\delta_{\rm bkg} = \arg[A_{\rm bkg}]$ as the signal and background strong phases, respectively. The first term in the square bracket is the contribution to the interference term that does not modify the overall rate upon integration over $\hat{s}$. The second term is the subject of this work and leads to a modified rate in the presence of a strong phase. For convenience, we define $|\mathcal{M}_h|^2_{\rm int} = \mathcal{R}_h^{\rm int} + \mathcal{I}_h^{\rm int}$ and $\delta_s = \delta_{\rm bkg} - \delta_h$ such that

$$\begin{aligned} \mathcal{R}_h^{\rm int} &\equiv \frac{2|A_{\rm bkg}||F_{gg}||F_{\gamma\gamma}|}{(\hat{s} - m_h^2)^2 + \Gamma_h^2 m_h^2}(\hat{s} - m_h^2)\cos\delta_s \\ \mathcal{I}_h^{\rm int} &\equiv \frac{2|A_{\rm bkg}||F_{gg}||F_{\gamma\gamma}|}{(\hat{s} - m_h^2)^2 + \Gamma_h^2 m_h^2} m_h\Gamma_h \sin\delta_s. \end{aligned} \tag{120}$$

In the SM the dominant contribution to $\mathcal{I}_h^{\rm int}$ comes from the phase of the background amplitude at two loops [507, 478]. The signal amplitude also contains a strong phase, mainly due to bottom quark loops. We have performed a calculation of the interference effect that accounts for absorptive effects from both signal and background. In Fig. 108 we illustrate the features of the interference effects. The line shape, the differential cross-section as a function of $\hat{s}$, is shown for the pure Breit-Wigner (only $|A_h|^2$), and for the interference contributions $\mathcal{I}_h^{\rm int}$ and $\mathcal{R}_h^{\rm int}$ as well as for the sum of both. For visualisation, the interference contribution $\mathcal{I}_h^{\rm int}$ has been magnified by a factor of 10. In this figure we show the line-shapes obtained including NLO effects with virtual corrections only. After summing over different interfering

[79] Contacts: J. Campbell, M. Carena, R. Harnik, Z. Liu. This manuscript has been authored by Fermi Research Alliance, LLC under Contract No. DE-AC02-07CH11359 with the U.S. Department of Energy, Office of Science, Office of High Energy Physics.

[80] Strong phases, which are CP even, get their name because they often arise in flavor physics from QCD dynamics. This is in contrast with CP odd weak phases, e.g., the relative size of the Higgs couplings to $F\tilde{F}$ versus FF.

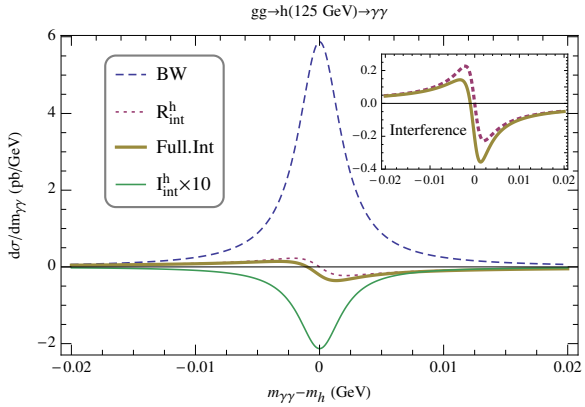

Fig. 108: The line-shape induced by various contributions to the cross-section for $gg \to h \to \gamma\gamma$ in the SM. The Breit-Wigner line-shape, with no interference, is shown in blue (dashed) while the effect of $\mathcal{R}_h^{\rm int}$ and $\mathcal{I}_h^{\rm int}$ (multiplied by a factor of 10) are shown in red (dotted) and green (solid), respectively. The overall effect of the interference in the full NLO calculation is given by the brown (solid) line. The insert in the top right is a magnification of the corresponding interference line-shapes.

helicity amplitudes, we obtain averaged strong phases $\delta_h = (\pi + 0.036)$ and $\delta_{\rm bkg} = -0.205$ for the signal and background, respectively.

As a concrete example that demonstrates the potential of this novel effect, without loss of generality we can consider excursions in the flat direction corresponding to,

$$\frac{|F_{gg}|^2|F_{\gamma\gamma}|^2}{|F_{gg}^{\rm SM}|^2|F_{\gamma\gamma}^{\rm SM}|^2} = \frac{\Gamma_h}{\Gamma_h^{\rm SM}}\,. \tag{121}$$

The total Higgs cross section can then be written as,

$$\sigma = \sigma_{\rm BW}^{\rm SM}\left(1+\frac{\sigma_{\rm int}^{\rm SM}}{\sigma_{\rm BW}^{\rm SM}}\sqrt{\frac{\Gamma_h}{\Gamma_h^{\rm SM}}}\right) \simeq \sigma_{\rm BW}^{\rm SM}\left(1-2\%\sqrt{\frac{\Gamma_h}{\Gamma_h^{\rm SM}}}\right). \tag{122}$$

The result of a full NLO calculation of the interference effect are presented in Fig. 109, that shows the relative size of the interference effect as a function of the total width, normalised to its SM value, for parameter excursions defined by Eq. (121). [81] The variation of the interference effect with the total width is shown imposing a 20 GeV p_T^h-veto, with and without LHC cuts on the final state photons. Since the interference effect is largest at small scattering angles, the photon cuts reduce the expected interference. This small consideration in the SM leads to much bigger differences for $\Gamma_h \gg \Gamma_h^{\rm SM}$. Observe that in the SM the interference contribution is destructive. However, if the sign of $F_{gg}F_{\gamma\gamma}$ were flipped, $(\delta_s \to \pi + \delta_s)$, the interference effect would lead to an enhancement of the di-photon rate rather than a suppression. The theoretical scale uncertainty is shown in the bottom panel of Fig. 109 and amounts to about $^{+50\%}_{-30\%}$. For example, the interference effect is $-(2.20^{+1.06}_{-0.55})\%$ without photon cuts for SM Higgs. Although a measurement at the 2% level may be challenging at the LHC, this shows that a precise measurement of the $gg \to h \to \gamma\gamma$ rate can place a limit on the width of the Higgs boson. In this respect a measurement of the ratio of the $\gamma\gamma$ rate to the 4ℓ rate is a promising route to reduce many of the systematic and theoretical, e.g. PDF and other parametric, uncertainties.

The best measured channels at the LHC, $gg \to h \to \gamma\gamma$ and $gg \to h \to 4\ell$, provide the most accurate cross section ratio, projected to be measurable at the 4% level [519]. In contrast to single cross section measurements, the precision on this ratio is statistically limited. Keeping the current theoretical

[81] For details of the NLO calculation , see the supplemental material with Refs [508, 509, 510, 511, 512, 483, 513, 514, 97, 515, 516, 517, 518].

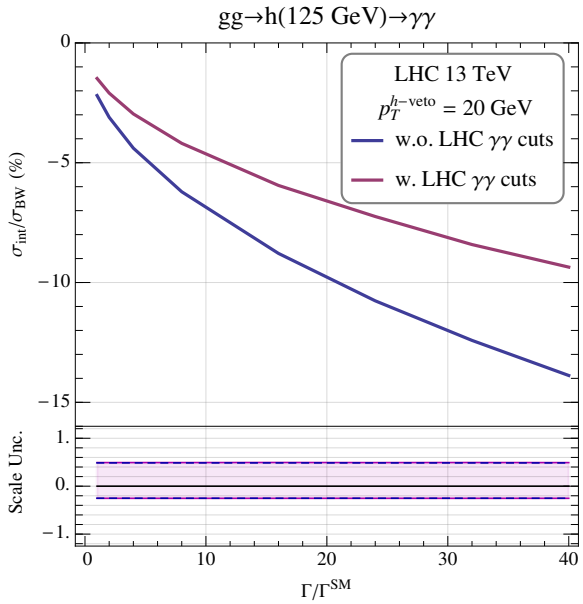

Fig. 109: The total signal rate change due to the interference effect as a function of the Higgs total width normalised to its SM value, while keeping the Breit-Wigner cross section identical to that of the SM Higgs. The magenta and blue (solid) lines represent the cases with and without LHC cuts on the final state photons, respectively. The lower panel shows the scale variation uncertainties for these interference terms as bands delimited by the blue (dashed) and magenta (solid) lines. The curves are obtained with a veto on the Higgs boson p_T at 20 GeV.

uncertainty band in mind, the projected sensitivity of 4% on the ratio of $\gamma\gamma$ to 4ℓ yields can be translated into an upper limit of 22, 14, and 8 on $\Gamma_h/\Gamma_h^{\text{SM}}$ at 1-σ level, for low, central and high theoretical expectations on this interference effect, respectively.[82] This assumes that the couplings to photons and Z bosons maintain their SM ratio and the photon and gluon couplings respect Eq. (121). The Higgs cross section precisions are anticipated to improve by a factor of three or so from statistical improvement at the HE-LHC with 27 TeV centre of mass energy and 15 fb^{-1} of integrated luminosity. This can be naively translated into lower and upper limits on the Higgs total width of $\Gamma_h/\Gamma_h^{\text{SM}} < 5$ at 1-σ level using the central value from our NLO theory calculation.

In summary, we discuss the change in the $gg \to h \to \gamma\gamma$ on-shell rate, due to interference between the Higgs signal and the QCD background amplitudes, as a way to provide a novel handle to constrain - or even measure - the Higgs boson total width. We perform a full NLO calculation at order α_s^3 of the interference effect and find that in the standard model it leads to a reduction of the on-shell rate by $\sim 2\%$. The proposed method for gaining sensitivity to the Higgs boson width is complementary to other methods that have been discussed in the literature. Altogether our study aims at motivating a more thorough examination of Higgs precision physics taking into account the strong phase induced interference effect in different Higgs boson observables.

[82] This limit is worse by one order of magnitude than the off-shell Higgs measurement that constrains the Higgs total width [487, 488, 489]. However, unlike the off-shell Higgs measurement, our effect is independent from the assumptions on the high-energy behaviour of the Higgs boson and the absence of new physics contribution in the off-shell region. For more detailed discussion, see e.g., chapter I.8 of the Higgs Yellow Report [45] and Refs. [491, 492].

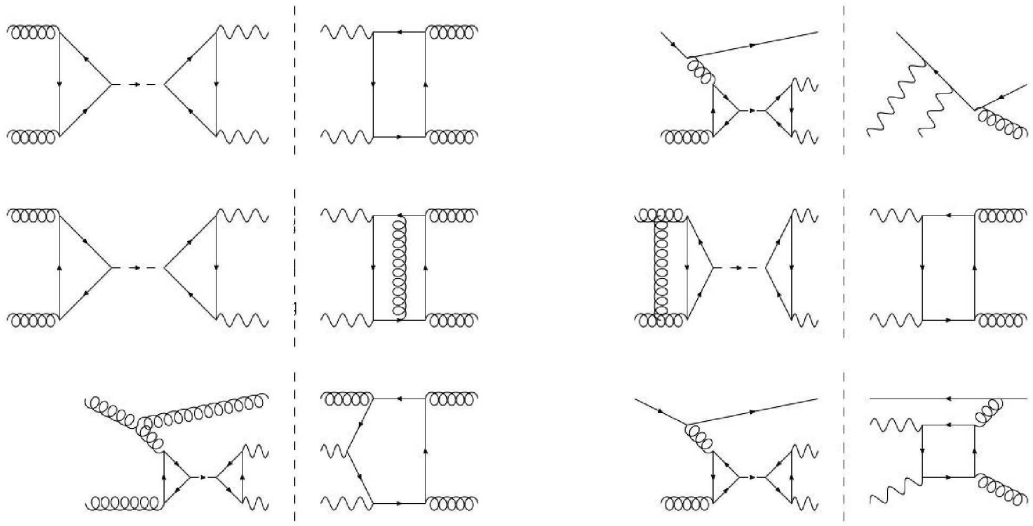

Fig. 110: Feynman diagrams describing the various processes involved in the phenomenon of interferences between $H \to \gamma\gamma$ and its background,

5.5 Mass shift from the di-photon interference[83]

A detailed study of the impact of the phenomenon of interference between the signal process $gg \to H \to \gamma\gamma$ and its irreducible background process $gg \to \gamma\gamma$ has been made in [520]. It will be summarised below.

All the results from [520] have been made with simulated data for the $\sqrt{s} = 8$ TeV dataset. A full-fledged extrapolation to higher centre of mass energies remains to be done. However, the two processes that interfere together, are induced by the same initial state and are at a similar mass scale. All the results are based on a difference between results made with simulated data where the interference have been implemented in the simulation, and simulated data where it is not. In the following, we will therefore consider that any increase of the cross-section with respect to $\sqrt{s}$ will cancel out in the difference.

The main goal of [520] was a robust estimate of the mass shift induced by the interference between $gg \to H \to \gamma\gamma$ and its irreducible background process $gg \to \gamma\gamma$ within the Standard Model (SM). This was achieved by using the Monte-Carlo generator Sherpa 2.0, that provides a specific plug-in allowing to generate datasets of weighted events, corresponding either to the the signal term ($gg \to H \to \gamma\gamma$ amplitude), the irreducible gluon-induced background term ($gg \to \gamma\gamma$ amplitude), their interference term or a any combination of these processes. The Feynman diagram describing the different processes involved are given in fig. 110.

It was the first time that Sherpa 2.0 was used in an analysis, and in particular the only time its interference module has been used. The distribution of the di-photon pair transverse momentum ($P_T^{\gamma\gamma}$) has been studied in detailed, as it is a preliminary requirement to be able to recast the mass analysis described in [521]. To get the best match of the $P_T^{\gamma\gamma}$ distribution between this simulation and the state of the art estimates, Sherpa 2.0 had to be tuned. This was done by varying the parameter $CSS\_IS\_AS\_FAC$ that controls the scale at which the parameter α_S is evaluated during parton shower evolution for the initial state. Simulated data samples were generated at several values of this parameter and compared to prediction for the Higgs boson transverse momentum from HRes2.0. The value of $CSS\_IS\_AS\_FAC$ for which both predictions were agreeing the best has been kept for the simulations used for the final result. The distributions of $P_T^{\gamma\gamma}$ obtained for a simulation of the background has been compared between ResBos and Sherpa2.0 for the best value of $CSS\_IS\_AS\_FAC$. They were found to be in reasonable agreement.

[83] Contact: C. Becot

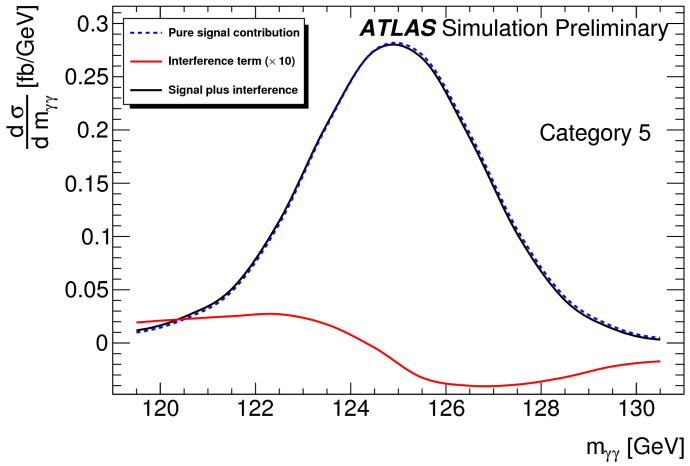

Fig. 111: Di-photon invariant mass distribution for signal and interference terms.

Then large samples of weighted signal (S) and interference (I) events were simulated. The background component was determined using a data-driven method (B). The background functions described in [521] were re-used, and they were fitted to the $\sqrt{s} = 8$ TeV dataset. This allowed to construct two varieties of simulated $m_{\gamma\gamma}$ templates, one that was made of $S + B$ and the other of $S + B + I$. These samples were then folded by the energy resolution and photon efficiencies used in [521] to mimic the detector simulation. The di-photon mass distributions induced by these different terms can be found in fig. 111. The Higgs boson mass (m_H) is measured separately on both templates, giving the values of m_H including the impact of interference (m_H^{S+B+I}), and without (m_H^{S+B}). Then the impact of the interference term itself on m_H is determined as

$$\Delta m_H = m_H^{S+B+I} - m_H^{S+B}. \tag{123}$$

Several uncertainties have been considered. First a non-closure of 3 MeV has been observed while measuring m_H^{S+B} from the S+B simulated sample, and is propagated as an experimental uncertainty. The only other experimental uncertainty stems from the choice of background function, and has been estimated at 3 MeV by trying different background functions.

For theoretical uncertainties we considered both scale variations as well as K-factor variations, as we will describe now. The renormalisation and factorisation scales were varied by a factor of 2, between $\frac{1}{2}\ m_{\gamma\gamma}$ and $2\ m_{\gamma\gamma}$ (the nominal value is $m_{\gamma\gamma}$). The resummation scale itself was varied between $\frac{1}{4}\ m_{\gamma\gamma}$ and $2\ m_{\gamma\gamma}$. Samples were re-generated at these different values of the scales for S and I, and the value of Δm_H was re-evaluated. This gave a small uncertainty of ± 4 MeV, which can be explained by the migration of events between transverse momentum categories that leads to a cancellation of these variations in the difference Δm_H.

The signal K-factor ($k_S = \dfrac{NNLO}{NLO}$) has been varied by 0.1, between $k_S = 1.35$ and $k_S = 1.55$. The background K-factor k_B is not known, and it was decided to vary it between 1 and k_S. The recipe gave an uncertainty of ± 7 MeV, which is the dominant uncertainty. Constraining k_B could lead to a huge improvement, but it requires to separate the component $gg \to \gamma\gamma$ from the inclusive $pp \to \gamma\gamma$ production. This is expected to be complicated but might be achieved by the study of angular distributions in $pp \to \gamma\gamma + jets$.

This study conducted to the following estimate of the Higgs boson mass shift induced by the interference process within the Standard Model :

$$\Delta m_H = -35 \pm 8(\text{theory}) \pm 4(\text{experimental})\text{MeV}. \tag{124}$$

The mass shift was also determined for larger widths, in the specific scenario where the width is modified but the expected number of events around the di-photon peak (S+I), is not. The mass shift was determined to be $\Delta m_H = -313 \pm 72$ MeV for $\Gamma_H = 300$ MeV and $\Delta m_H = -453 \pm 106$ MeV for $\Gamma_H = 600$ MeV. By the end of HL-LHC such deviations could be probed by comparing the mass measured in the high-precision $H \to 4l$ channel and the one measured in $H \to \gamma\gamma$. The following difference :

$$\delta m_H^{4l-\gamma\gamma} = m_H^{4l} - m_H^{\gamma\gamma} \tag{125}$$

will be largely dominated by the systematic uncertainty on $m_H^{\gamma\gamma}$. Assuming it is at the same level than the one of Run 2 [522], it would lead to an uncertainty on the measured $\delta m_H^{4l-\gamma\gamma}$ of 290 MeV, hence a shift of 580 MeV could be excluded at 95% C.L. Also assuming that $\delta m_H^{4l-\gamma\gamma}$ scales linearly with the Higgs boson width, it would allow in this naive model, to set upper limits on the Higgs boson width at $\Gamma_H < 1$ GeV at 95% C.L.

This is only using the difference between the Higgs boson mass measured in its 4 leptons decay channel and the one measured in its di-photon decay channel. Now, it is also known that the interference term will have a bigger impact in some parts of the phase space where the signal to background ratio is smaller. This is for instance the case at low $p_T^{\gamma\gamma}$, and it could be used to carry out the same inference internally in the $H \to \gamma\gamma$ channel, comparing the masses measured in two (or more) $p_T^{\gamma\gamma}$ bins. A full-fledged prospect study of this analysis remains to be done, as the only attempt carried out so far [523] suffered from large mis-modellings of the kinematic distributions and of the cross-sections. The success of such an analysis will rely on very precise predictions for the kinematic distributions, which is not yet available. This will require the development of new higher-order calculations and resummed predictions, and could be helped by the development of new Monte-Carlo tools using better showering algorithms.

6 Invisible decays of the Higgs boson[84]

Invisible decays of the 125 GeV Higgs boson are a generic prediction of new physics models that feature a light dark matter (DM) particle which couples directly or indirectly to the Standard Model Higgs field. The invisible branching ratio in the SM is very small (0.1%) so any observable rate would be evidence for physics beyond the SM. LHC searches for this signature require the Higgs boson to be produced in association with a taggable object, most importantly, a Z-boson, extra forward jets (as appearing in the vector boson fusion process), or a single high-p_T jet. Furthermore, the invisible Higgs decay to the DM particles inevitably suppresses the branching fractions for the Higgs decays to SM particles. This — along with possible model-dependent alterations of the Higgs couplings — leads to a modification of the LHC Higgs signal rates of channels with SM final states with respect to their SM expectation, which can be probed with precision Higgs measurements.

In so-called *Higgs portal* models the SM Higgs field acts as a mediator between the visible SM sector and a hidden DM sector. Commonly, an additional symmetry is introduced that prohibits interactions of single hidden sector fields with SM fields, thus allowing only pair production of hidden sector particles and rendering the lightest hidden sector particle a stable DM candidate. The *Higgs portal* and its generalisation to other non-SM Higgs bosons are found in many BSM scenarios (see e.g. Refs. [524, 525, 526, 527] and [528, 529, 530, 531, 532, 533] for models with and without supersymmetry).

The invisible decay of the Higgs is experimentally challenging because the missing transverse energy spectrum is relatively soft, where resolution and pileup effects are non-negligible. The issues associated with pileup, both from pileup jets and from pileup-induced resolution degradation, will only become more severe beyond Run 3. Significant recent advances in constituent-based pileup mitigation techniques will likely play a key role in maintaining and possibly improving the MET performance [534, 535, 536, 537, 538]. Furthermore, lepton identification and pileup jet rejection will both improve with the increased tracking acceptance planned by both ATLAS and CMS [22, 24, 28, 25, 21, 20]. Current analyses with $\sim$ 30 fb^{-1} place limits on the invisible branching ratio of the Higgs boson at about 20-25% [539, 540, 541, 542, 543, 544]. The systematic uncertainty is about the same size as the statistical uncertainty; this means that the factor of 100 increase in statistics will not necessarily translate into an improvement by a factor of 10. Early projections from ATLAS and CMS [295, 523] predict limits that are a factor of 3-5 below the current result. The main limiting systematic uncertainty is from using $W \to l\nu$ to estimate the $Z \to \nu\nu$ in the dominant VBF channel. Advances in this theory input over the next decade could significantly improve the achievable precision. Already, CMS has shown that optimistic projections with reduced systematic uncertainties are realistic - the 2016 analysis [543] follows optimistic (reduced systematic uncertainties) scaling from the 2015 projection [295].

Currently, the VBF production dominates the branching ratio limit. This is because the VBF mode has a large cross-section (about 10% of the total) and the main background $Z \to \nu\nu$ is qualitatively different (QCD production) from the same background in the VH mode (EW production). However, it is not clear which mode will dominate after Run 3, since there will be a non-trivial change in experimental conditions that will make both triggering and background rejection more difficult for both the VBF and VH modes. At the same time, there are many interesting opportunities to improve both channels from new detector capabilities (extended trackers and timing detectors) as well as new analysis techniques (e.g. quark/gluon tagging).

In this report we assess the prospects of probing *Higgs portal* models directly with future searches for invisible Higgs decays, as well as indirectly with precision Higgs rate measurements, at the LHC in the high luminosity phase with 3 ab^{-1}. Furthermore, we shall highlight the complementarity between these two probes, as well as with other constraints, e.g. with current and future limits from DM direct detection experiments and limits from LEP Higgs searches. Searches for invisible decays of the Higgs

[84] Contact Editors: A. Magnan, B. Nachman, T. Robens and T. Stefaniak

boson also have important implications for "nearly invisible" decays into neutral long-lived particles that are predicted by many models [545]. Dedicated searches set much stronger limits [546, 547, 548, 549], but the Higgs to invisible search is a model-independent constraint on all possibilities. Projections for dedicated searches as well as proposals for dedicated detectors at the LHC complex [550, 551, 552] are not discussed in this section.

This contribution is organised as follows. We briefly review in Section 6.2.1 the experimental input for the HL-LHC that we use in our study. In Section 6.2.2 we first employ an effective description of the generic phenomenological Higgs features that appear in this class of models. We then focus on two specific realisations of the Higgs portal: in Section 6.3.1 we discuss the *minimal Higgs portal*, where the SM Higgs field directly couples to an additional DM field through a quartic interaction; in Section 6.3.2 we show results for the *scalar singlet portal*, where an additional scalar singlet is acting as a mediator between the visible and hidden sector. We conclude in Section 6.4.

6.1 Main channels for direct searches

Given the VBF Higgs (VBFH) production presents the best sensitivity, this channel is chosen to investigate the sensitivity of the search with the HL-LHC [553]. The CMS phase-2 detector is simulated using Delphes [13] (fast parametrisation), with on average 200 interactions per bunch crossing. A cut-and-count approach similar to the one described in the analysis from Ref. [543] is used.

The VBFH signal samples are produced using POWHEGv2.0 [160, 81] at next-to-leading order in perturbative QCD, assuming 100% branching ratio B(H $\rightarrow$ inv.) of the Higgs boson to invisible final states, and normalised using the SM inclusive Higgs boson production cross sections provided in Ref. [45]. Full-simulation samples produced at 13 TeV are used to derive the gluon-fusion contribution, applied as a fraction of the Delphes expected VBFH yields.

The main backgrounds are processes involving vector bosons (W,Z) produced in association with jets, either through QCD or electroweak (EWK) vertices. Monte Carlo samples for these backgrounds are generated at leading order using AMC@NLOv2.2.2 [79] interfaced with PYTHIAv8.205 [319] or higher. SM processes involving top quarks also contribute to the background, and are simulated using a combination of the POWHEGand AMC@NLOgenerators. Backgrounds arising from QCD multi-jet events are simulated using AMC@NLOinterfaced with PYTHIA, imposing a minimum threshold of 1000 GeV on the di-jet mass at parton level.

The objects studied are as defined for the analysis in Ref. [543], with extended coverage in pseudorapidity η. Electrons passing loose identification criteria, with a transverse momentum $p_T > 10$ GeV, and $|\eta| < 2.8$ are vetoed. Similarly, muons passing loose identification criteria with $p_T > 20$ GeV and $|\eta| < 3.0$ are vetoed. Taus passing loose identification criteria with $p_T > 20$ GeV and $|\eta| < 2.8$ are vetoed. Jets are reconstructed using the anti-k_T algorithm [14, 15] with a parameter size of 0.4. The jets are required to have $p_T > 30$ GeV and $|\eta| < 5.0$, and are corrected for pileup effects using the "Puppi" algorithm [535].

A b-tagging algorithm is used to tag jets that originate from decays of B hadrons (b jets). The algorithm uses a combination of vertexing and timing information, and a working point with an efficiency of around 60% and a mis-tagging rate below 1% is defined to identify b jets. Events containing any identified b jets are vetoed.

The leading and sub-leading jets in the event are required to have $p_T > 80$ and 40 GeV, respectively, and be in opposite hemispheres of the detector. These two jets form the VBF di-jet pair, and further requirements are applied on the invariant mass M_{jj}, and their separations in pseudorapidity $|\Delta\eta_{jj}| > 4.0$ and azimuthal angle $|\Delta\phi_{jj}| < 1.8$.

To reject the QCD multi-jet background, for which the transverse missing energy arises from jet mis-measurements, the $\vec{\not{E}}_T$ vector is required to not be aligned with a jet using min[$\Delta\phi$(jet $\vec{p}_T$ > 30 GeV, $\vec{\not{E}}_T$)]> 0.5. The magnitude of the vector sum of the p_T of all jets with $p_T > 30$ GeV is defined as H_T^{miss}.

The analysis uses five non-overlapping event regions: the signal region (SR) where events containing charged leptons (ℓ, where ℓ = e or μ) are vetoed, and four control regions (CR) with exactly one electron or muon (W $\to$ eν CR and W $\to \mu\nu$ CR) or exactly two electrons or two muons (Z $\to$ ee CR and Z $\to \mu\mu$ CR). In the W $\to$ eν and W $\to \mu\nu$ CRs, to further reject QCD multi-jet backgrounds, the transverse mass, defined as $\sqrt{2\mathrm{p}_T^{\ell}\not{E}_T\left[1-\cos\Delta\phi(\ell,\vec{\not{E}_T})\right]}$, where p_T^{ℓ} is the transverse momentum of the lepton and $\Delta\phi(\ell,\vec{\not{E}_T})$ is the azimuthal angle between the lepton momentum and $\vec{\not{E}_T}$ vectors, is required to be less than 160 GeV. In the W$\to$eν CR a selection on $\not{E}_T > 60$ GeV is also applied due to the higher QCD multi-jet contamination than in the muon channel. In the Z $\to$ ee and Z $\to \mu\mu$ CRs, the di-lepton mass is required to be between 60 and 120 GeV. To account for the higher single-electron trigger thresholds that will be required at the HL-LHC , the leading electron p_T is required to be above 40 GeV, for both the W $\to$ eν and Z $\to$ ee CRs.

The lower threshold on the $\not{E}_T$ is varied from 130 to 400 GeV in 10 to 50 GeV steps. Likewise, the lower threshold on $\mathrm{M_{jj}}$ is varied from 1000 to 4000 GeV in 100 GeV steps. The statistical uncertainty on the MC is considered to be negligible, assuming the available MC samples will have at least 10 times the integrated luminosity available in the data. For each ($\not{E}_T$, $\mathrm{M_{jj}}$) selection, the yields are extracted in the four control regions and in the signal region, and a likelihood is constructed as the product of five Poisson terms, one per region. Upper limits on the Higgs boson production cross section times B(H $\to$ inv.) are placed at the 95% CL using the CLs criterion [355, 554, 555], with a profiled likelihood ratio as the test statistic in which systematic uncertainties are incorporated via nuisance parameters [556, 557]. Asymptotic formula are used to determine the distribution of the test statistic under signal and background hypotheses [163].

The scenario considered for the systematic uncertainties is described in table 76, together with the systematic uncertainties that were considered in Ref. [543], for comparison.

Table 76: Impact on the signal and background yields from the different sources of systematic uncertainty considered in Ref. [543] and for the HL-LHC setup considered in this analysis.

Systematic	From Ref. [543]	This analysis
e-ID	1%(reco)$\oplus$1%(idiso)	1%
μ-ID	1%(reco)$\oplus$1%(id)$\oplus$0.5%(iso)	0.5%
e-veto	0.6%(reco)$\oplus$1.5%(idiso)	1%
μ-veto on QCD V+jets	5%(reco)$\oplus$5%(id)$\oplus$2%(iso)	2%
μ-veto on EWK V+2jets	10%(reco)$\oplus$10%(id)$\oplus$6%(iso)	6%
τ-veto	1–1.5% for QCD–EWK	0.5–0.75%
b-tag-veto	0.1% (sig) 2% (top)	0.05% (sig) 1% (top)
JES	14%(sig) 2%(W/W) 1%(Z/Z)	4.5%(sig) 0.5%(W/W) 0.2%(Z/Z)
Integrated luminosity	2.5%	1%
QCD multi-jet	1.5%	1.5%
Theory on W/Z ratio	12.5%	7%
ggH normalisation	24%	20%

The analysis is expected to be systematics dominated, with the dominant systematic uncertainties due to the muon and electron efficiencies (e-ID and μ-ID in table 76), both in the control and signal regions, and the jet energy scale (JES) evaluated for the signal (sig) or on the ratios of W and Z yields in signal and control regions (W/W and Z/Z in table 76). In Ref. [543], due to the limited size of the di-lepton samples, the knowledge of the ratio of the cross sections of the W to Z boson production was used as a constraint between the two backgrounds, leading to an increased sensitivity. The theoretical uncertainty on this ratio is set at 12.5% from studies of missing higher order QCD and EWK corrections [543], for both QCD and EWK production. Once 300 fb^{-1} of data will be available, this constraint

will play a smaller role. It is expected that improvements in theoretical calculations of the ratio will lead to half the current theoretical uncertainty, namely 7%. This uncertainty is expected to have an impact of at most 3–5% for the selection with the largest expected significance and is therefore neglected in the results presented herein. However, the uncertainty will be relevant when considering very tight selection criteria on $\not{E}_T$ and M_{jj}, i.e. when the statistical uncertainty in the CRs becomes dominant.

The most stringent upper limits are achieved in the regions with lower thresholds on M_{jj} and $\not{E}_T$ of 2500 GeV and 190 GeV, respectively, for the 3000 fb^{-1} scenario. The minimum is rather flat between M_{jj} values of 2300 and 3000 GeV, and between $\not{E}_T$ values of 170 and 220 GeV, indicating limited impact from the size of the MC samples. The upper limits degrade steeply as the $\not{E}_T$ threshold increases above 250 GeV. The behaviour is similar for the 300 and 1000 fb^{-1} scenarios, with best thresholds found at lower values of $\not{E}_T$ (170 GeV) and M_{jj} (1500 and 1800 GeV respectively) due to the interplay between the size of the control regions and the systematic uncertainties.

Distributions in M_{jj} for the leading jet pair and $\not{E}_T$ in the signal region are shown in figure 112, for an integrated luminosity of 3000 fb^{-1}. The corresponding expected yields are shown in table 77. The uncertainties shown represent the statistical uncertainties due to the limited size of the Delphes samples and are not used in the calculations of the final limits.

Table 77: Number of events expected after the final selection, $M_{jj} > 2500$ GeV and $\not{E}_T > 190$ GeV, with an integrated luminosity of 3000 fb^{-1}. The uncertainties are the statistical uncertainties from the Delphes samples.

Process	SR	W $\to$ eν CR	W $\to \mu\nu$ CR	Z $\to$ ee CR	Z $\to \mu\mu$ CR
VBFH	47812 $\pm$ 584	-	-	-	-
ggH	972	-	-	-	-
Z$\to \ell\ell$ (EWK)	103 $\pm$ 8	398 $\pm$ 16	641 $\pm$ 20	1342 $\pm$ 30	1889 $\pm$ 35
Z$\to \ell\ell$ (QCD)	451 $\pm$ 90	944 $\pm$ 126	1048 $\pm$ 116	1347 $\pm$ 118	2297 $\pm$ 158
Z$\to \nu\nu$ (EWK)	15275 $\pm$ 358	-	-	-	-
Z$\to \nu\nu$ (QCD)	20968 $\pm$ 599	-	-	-	-
W$\to$ eν (EWK)	3358 $\pm$ 62	18986 $\pm$ 146	72 $\pm$ 9	33 $\pm$ 6	-
W$\to \mu\nu$ (EWK)	3426 $\pm$ 62	7 $\pm$ 3	29360 $\pm$ 181	-	17 $\pm$ 4
W$\to \tau\nu$ (EWK)	3595 $\pm$ 64	55 $\pm$ 8	87 $\pm$ 10	-	-
W$\to$ eν (QCD)	3994 $\pm$ 999	13376 $\pm$ 1656	170 $\pm$ 168	-	-
W$\to \mu\nu$ (QCD)	6891 $\pm$ 1388	-	23322 $\pm$ 2096	-	-
W$\to \tau\nu$ (QCD)	4308 $\pm$ 938	-	-	-	-
Top	2050 $\pm$ 132	2171 $\pm$ 143	3735 $\pm$ 188	107 $\pm$ 36	130 $\pm$ 39
QCD	-	-	-	-	-

The 95% CL upper limits for an integrated luminosity of 3000 fb^{-1} are shown in figure 113, left, as a function of the thresholds applied on $\not{E}_T$ assuming the MC statistical uncertainties are negligible, for the final selections described above[85] In the best case, the lowest 95% CL limit on B(H $\to$ inv.), assuming Standard Model production, is expected to be at 3.8%, for thresholds values of 2500 GeV (190 GeV) on the di-jet mass ($\not{E}_T$). If the $\not{E}_T$ resolution was to be a factor of 2 worse, the re-optimisation of the selection leads to minimum thresholds of 1800 GeV (250 GeV) on the di-jet mass ($\not{E}_T$), but a similar 95% CL limit. The limits are shown for different integrated luminosities in figure 113, right.

The performance of pileup mitigation techniques will have a significant impact on the projected sensitivity for the final VBF result. ATLAS has conducted a study to show the impact of pileup jets on the invisible Higgs branching ratio limit in the VBF channel [559] using full detector simulations based on Geant4 [36, 35] and the complete detector simulation and event reconstruction. The branching ratio limit

[85] A previous phenomenological study [558] focusing on jet tagging has found a similar behaviour for $\not{E}_T \gtrsim 250$ GeV.

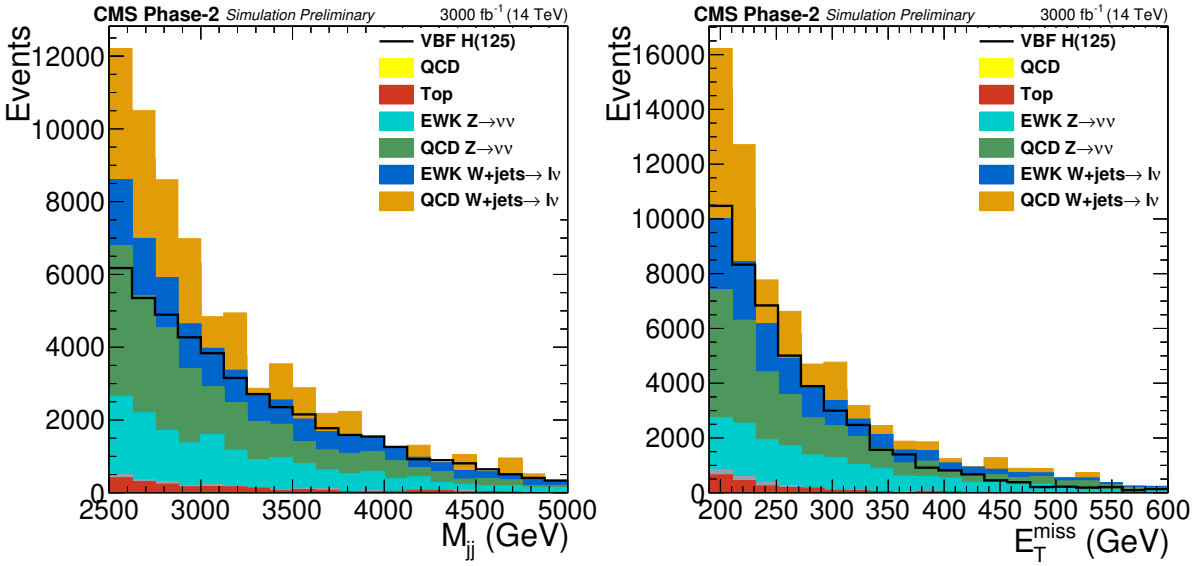

Fig. 112: Distributions of M_{jj} (left) and $\not{E}_T$ (right) in the signal region for the final selection, $M_{jj} > 2500\,\text{GeV}$ and $\not{E}_T > 190\,\text{GeV}$ [553].

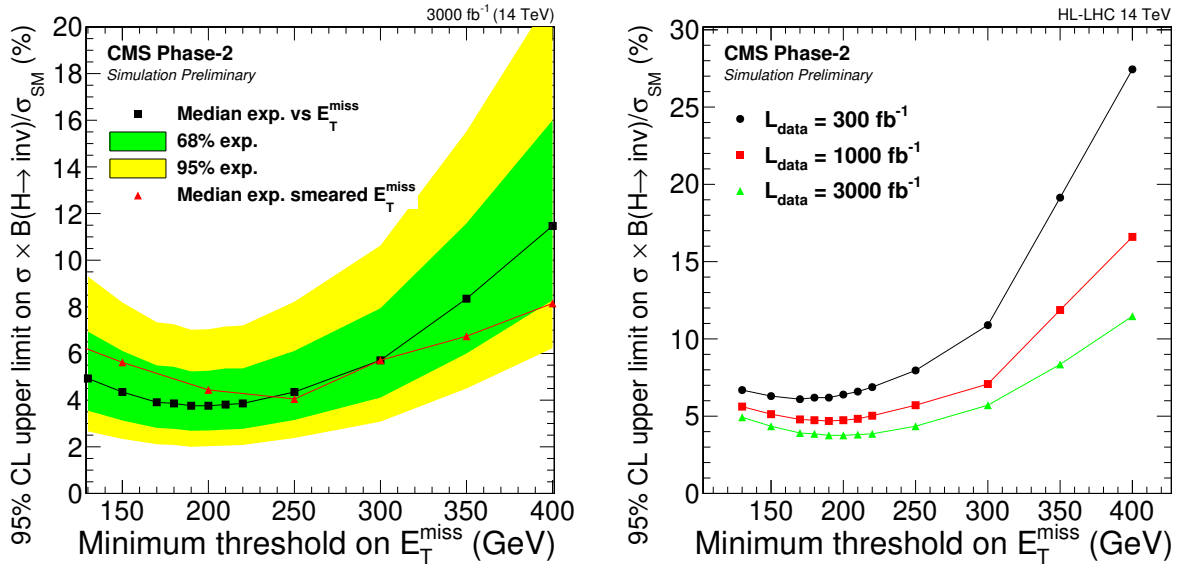

Fig. 113: Left: 95% CL limits on B(H $\rightarrow$ inv.) as a function of the minimum threshold on $\not{E}_T$, for $M_{jj} > 2500\,\text{GeV}$ and an integrated luminosity of $3000\,\text{fb}^{-1}$ [553]. Right: 95% CL limits for scenarios with different integrated luminosities.

can vary by a factor of 4 when no explicit pileup jet mitigation is used to the case when truth information is used to remove all pileup jets. Therefore, the development of improved pileup jet mitigation will be an important development to empower the invisible Higgs decay analyses in the future.

6.2 Interpretation and combination with precision Higgs boson measurements

6.2.1 Experimental input

For the VBF production channel, the projected HL-LHC limit on the invisible Higgs decay rate from the CMS experiment amounts to 4%, see Section 6.1. For the VH production channel ATLAS projected a limit of around 8% in 2013 [523]. Assuming ATLAS (CMS) performs equally well as CMS (AT-

LAS) in the VBF (VH) channel, and neglecting possible correlations of experimental and theoretical uncertainties [560], a combination of these limits results in

$$\left(\mu_{\text{VBF},VH} \cdot \text{BR}_{\text{inv}}\right)^{\text{HL-LHC}} \leq 2.5\%, \tag{126}$$

where $\mu_{\text{VBF},VH}$ is a common signal strength modifier of the VBF and VH production cross sections. In our theory interpretations below, we take Eq. (126) as a benchmark value for the prospective ATLAS and CMS combined limit on BR_{inv}.

We implemented the ATLAS and CMS HL-LHC projections for Higgs signal strength measurements for the individual production times decay modes (see Section 2.6) into the code `HiggsSignals` [561 562], including the corresponding correlation matrices. We consider the projections for both future scenarios S1 (with Run 2 systematic uncertainties) and S2 (with YR18 systematic uncertainties) [119], see Sec. 2.6.1, Tab. 35. Note that correlations of theoretical rate uncertainties between the future ATLAS and CMS measurements are taken into account in our fit via `HiggsSignals`.

We furthermore study the impact of a future electron-proton collider option (LHeC) at CERN [563, 564, 565, 566], assuming a 60 GeV electron beam, a 7 TeV proton beam and an integrated luminosity of 1 ab^{-1}. We implemented the prospective signal strength measurements at the LHeC presented in Ref. [564] into `HiggsSignals`.[86] The projected limit on the invisible Higgs decay rate is around 5% [564, 567, 568, 569, 570, 565] [87]. In combination with the above CMS and ATLAS projections, we obtain

$$\left(\mu_{\text{VBF},VH,\text{NC}} \cdot \text{BR}_{\text{inv}}\right)^{\text{HL-LHC}\oplus\text{LHeC}} \leq 2.25\%$$

as upper limit on the branching ratio of an invisible Higgs decay mode. Here, we assume the common signal strength modifier μ also applies to the neutral current (NC) Higgs production cross section at the LHeC.

6.2.2 *Effective description of Higgs portal models*

In this section we discuss the HL-LHC prospects in the context of an effective parametrisation of Higgs rate modifications that are commonly predicted by Higgs portal models, using the coupling scale factor (κ) framework [42] (see also Section 2.7). Herein, the scale factors κ_X ($X = W, Z, g, \gamma, b, \tau, \dots$) are introduced for every relevant Higgs coupling to SM particle X. The partial widths and cross sections associated with these Higgs couplings are then rescaled by κ_X^2 (see Refs. [42, 562] for more details). In addition, we treat the branching fraction for invisible Higgs decays, BR_{inv}, as free parameter.

In particular, we investigate two scenarios for the Higgs coupling modifications:

(*i*) a universal scale factor for all Higgs couplings to SM particles, $\kappa \equiv \kappa_X$ ($X = W, Z, g, \gamma, b, \tau, \dots$);

(*ii*) additional free parameters κ_g and κ_γ that rescale the loop-induced Higgs couplings to gluons and photons, respectively. The remaining (tree-level) Higgs couplings to SM particles are again rescaled universally with $\kappa \equiv \kappa_X$ ($X = W, Z, b, \tau, \dots$).

We employ the program `HiggsSignals` [561, 562] to perform a χ^2 fit to the projected HL-LHC and/or LHeC Higgs rate measurements (see Section 6.2.1) in each scenario. The resulting future 95% C.L. limit is shown in Fig. 114 as a light and dark green area for scenario (*i*) and (*ii*), respectively. The *top panels* display the HL-LHC projections for future scenarios S1 [with Run 2 systematic uncertainties] (*left*) and S2 [with YR18 systematic uncertainties] (*right*), while the *bottom panels* show the projections for LHeC (*left*) and the combination of LHeC with HL-LHC S2 measurements (*right*). In

[86] In addition to the experimental precision quoted in Ref. [564] we assume a theoretical uncertainty of 1% (1.5%) on the charged (neutral) current production cross section, as well as a 1% luminosity uncertainty.

[87] Optimisation of the signal selection, advanced background estimation techniques and details of the detector design may improve this limit down to about $(3-4)\%$ [571].

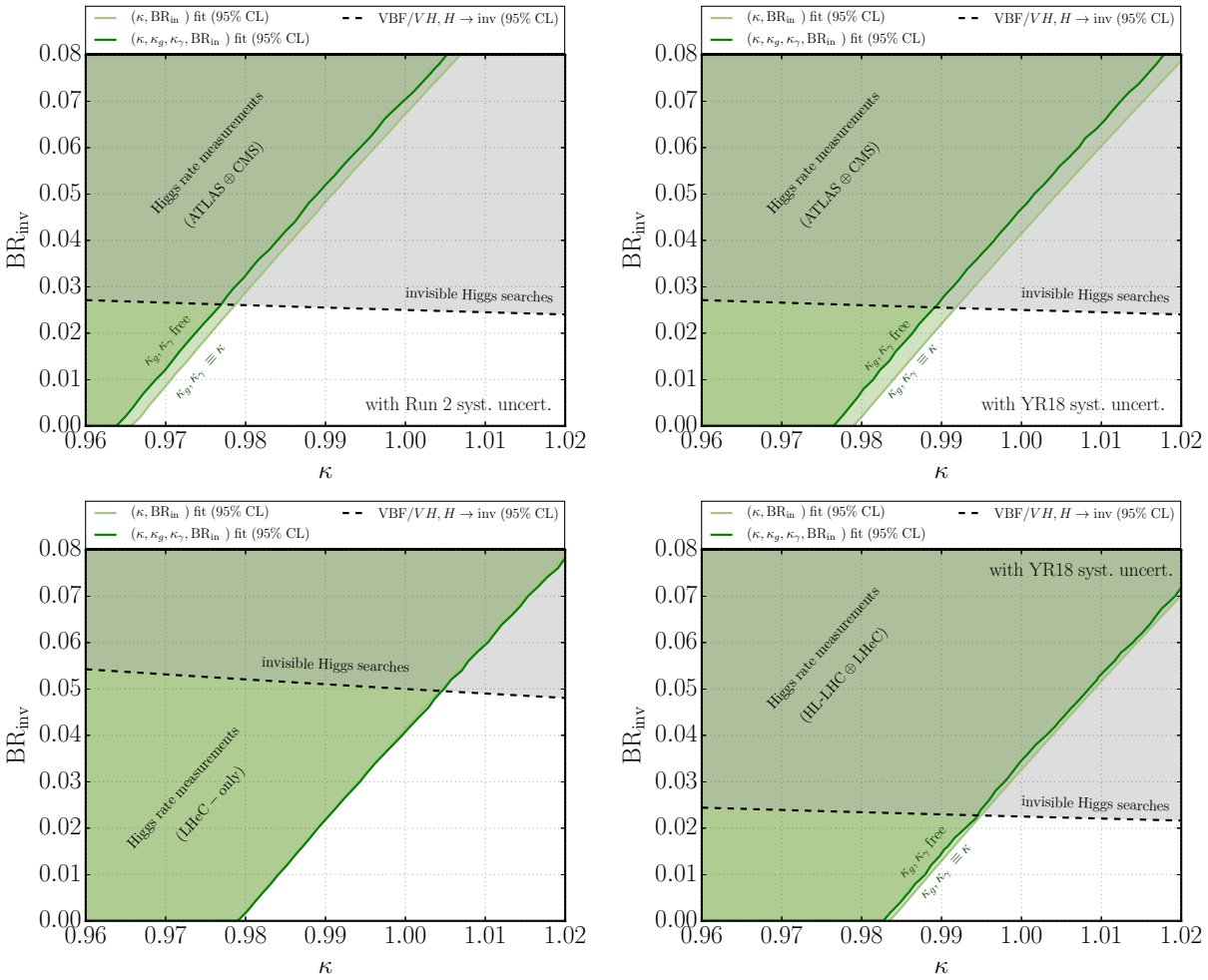

Fig. 114: Projected 95% C.L. limit in the $(\kappa, \mathrm{BR_{inv}})$ plane inferred from Higgs rate measurements (*green regions*) and direct invisible Higgs searches (*black dashed line*) at the HL-LHC and LHeC. We show results for the two future HL-LHC scenarios S1 [with Run 2 systematic uncertainties] *(top left)* and S2 [with YR18 systematic uncertainties] *(top right)* (see text for details), as well as for the LHeC *(bottom left)* and the combination of LHeC and HL-LHC [S2] *(bottom right)*. The light green area shows the limit from Higgs rates obtained by assuming no new physics contributions to the loop-induced Higgs couplings to gluons and photons, $\kappa = \kappa_g = \kappa_\gamma$, whereas for the dark green area κ_g and κ_γ are marginalised free parameters.

Tab. 78 we summarise the lower limits on the Higgs signal strength of channels with SM final states, $\kappa^2(1 - \mathrm{BR_{inv}})$, as well as the upper limits on the invisible Higgs decay rate, $\mathrm{BR_{inv}}$, assuming SM Higgs coupling strengths ($\kappa \equiv 1$), for the four future collider scenarios and for the two global fit scenarios. Note that these results do not strictly require the additional Higgs decay mode to yield an invisible final state.

These results are compared in Fig. 114 with the prospective future limits from direct searches for invisible Higgs decays (see Section 6.2.1). At the HL-LHC, assuming scenario S1 (S2), direct invisible Higgs searches are more sensitive than Higgs rates if deviations from the SM Higgs couplings are small, $\Delta\kappa \equiv 1 - \kappa \lesssim 2\ (1)\%$. For larger suppression of the Higgs couplings the Higgs rates will provide the strongest constraint. In contrast, if we allow for an enhancement of the Higgs couplings, $\kappa > 1$, the invisible Higgs searches will provide the strongest constraint (besides other bounds on the Higgs total decay width, see Sec. 5).

Table 78: Comparison of prospective 95% C.L. limits on the Higgs signal strength for SM final states, $\kappa^2(1-\mathrm{BR}_{\mathrm{inv}})$, and the invisible Higgs decay rate, $\mathrm{BR}_{\mathrm{inv}}$ (assuming SM Higgs couplings, $\kappa = 1$), for HL-LHC scenarios S1 and S2, LHeC, and the combination of LHeC and HL-LHC (assuming scenario S2). First (second) row shows the results obtained in the fit parametrisation (*i*) [(*ii*)].

fit setup	quantity	HL-LHC S1	HL-LHC S2	LHeC	LHeC $\oplus$ HL-LHC S2
$(\kappa, \mathrm{BR}_{\mathrm{inv}})$	$\kappa^2(1-\mathrm{BR}_{\mathrm{inv}})$	≥ 0.933	≥ 0.958	≥ 0.959	≥ 0.967
	$\mathrm{BR}_{\mathrm{inv}}$ $(\kappa \equiv 1)$	$\leq 6.7\%$	$\leq 4.2\%$	$\leq 4.1\%$	$\leq 3.3\%$
$(\kappa, \kappa_g, \kappa_\gamma, \mathrm{BR}_{\mathrm{inv}})$	$\kappa^2(1-\mathrm{BR}_{\mathrm{inv}})$	≥ 0.930	≥ 0.954	≥ 0.959	≥ 0.966
	$\mathrm{BR}_{\mathrm{inv}}$ $(\kappa \equiv 1)$	$\leq 7.0\%$	$\leq 4.6\%$	$\leq 4.1\%$	$\leq 3.4\%$

At the LHeC the prospective indirect Higgs rate constraints are comparable to the HL-LHC S2 prospects, reaching a precision of $\Delta\kappa \lesssim (2.1-2.3)\%$ independently of the invisible Higgs decay rate, in both fit parametrisations considered here.[88] On the other hand, the direct invisible Higgs searches at the LHeC are weaker than at the HL-LHC. In combination with the HL-LHC (assuming future scenario S2), the bounds from the Higgs rates can further be improved to coupling deviations of $\Delta\kappa \lesssim 1.7\%$.

Compared with the sensitivity of Higgs rate measurements during Run 1 of the LHC [144] to the invisible decay rate, $\mathrm{BR}_{\mathrm{inv}} \lesssim \mathcal{O}(20\%)$ (at 95% C.L.), we find that the sensitivity improves by roughly a factor of 3–5 at the HL-LHC (depending on the evolution of systematic uncertainties). In combination with LHeC results we expect the indirect limit to improve by a factor of up to 6.

6.3 Higgs portal interpretations

6.3.1 Minimal Higgs Portal

In the minimal Higgs portal model, we impose a quartic interaction of the SM Higgs doublet field H with the DM field, which could be either a scalar (S) [572], a vector (V^μ) [573] or a fermion (χ) [574] (see Refs. [575, 576] for a comprehensive overview):

$$\mathcal{L} \supset -\tfrac{1}{4}\lambda_{hSS} H^\dagger H S^2 \qquad \text{(scalar DM)} \quad \text{or} \tag{127}$$

$$\mathcal{L} \supset +\tfrac{1}{4}\lambda_{hVV} H^\dagger H V_\mu V^\mu \qquad \text{(vector DM)} \quad \text{or} \tag{128}$$

$$\mathcal{L} \supset -\tfrac{1}{4}\tfrac{\lambda_{h\chi\chi}}{\Lambda} H^\dagger H \bar{\chi}\chi \qquad \text{(fermion DM)}, \tag{129}$$

respectively. Besides these operators the Lagrangian contains an explicit mass term of the DM field, allowing us to use the mass of the DM particle, M_{DM}, as a free model parameter. In addition, the Lagrangian $\mathcal{L}$ contains DM self-interaction operators, however, these are irrelevant to our study.

If DM is light, $M_{\mathrm{DM}} < M_H/2 \simeq 62.5\mathrm{GeV}$, the above interactions lead to the invisible Higgs decay into two DM particles. An upper limit on $\mathrm{BR}_{\mathrm{inv}}$ can therefore be translated into an upper limit on the portal coupling λ of above operators, Eqs. (127)-(129), depending on M_{DM}. At the same time, the portal coupling λ governs the DM phenomenology. For DM masses $M_{\mathrm{DM}} \lesssim M_H/2$ the relic abundance of the DM particles is driven by the s-channel annihilation through the exchange of the Higgs boson.[89] As the DM–nucleon elastic scattering amplitudes are directly proportional to the portal coupling [575], it can be additionally constrained by DM direct detection experiments. These are sensitive to the elastic scattering of the DM particles with nuclei, mediated by the Higgs boson. Hence, in turn, the upper limit on λ can be translated into an upper limit on the (spin-independent) DM-nucleon scattering cross section, $\sigma_{\mathrm{DM-nucleon}}$ (see Refs. [575, 576]).

[88] The complementarity of LHeC and HL-LHC Higgs rate measurements is much stronger in more general coupling fit setups, e.g., when independent scale factors for the Higgs-W-W and Higgs-Z-Z couplings are considered [564].

[89] Assuming a standard cosmological history and thermal freeze-out dark matter, the minimal Higgs portal scenario with light DM is tightly constrained, with only a narrow mass range around $M_{\mathrm{DM}} \simeq M_H/2$ being allowed. However, this can be relaxed in alternative cosmological scenarios and DM production mechanisms, see e.g. Refs. [577, 578, 579].

In Fig. 115 we show the current [*left panel*] and prospective [*right panel*] upper limits on $\sigma_{\text{DM}-\text{nucleon}}$ inferred from a current and HL-LHC prospective upper limit on BR_{inv} of 20% and 2.5%, respectively.[90] These are shown for scalar [*blue curve*], fermion [*red curve*] and vector [*green curve*] DM. The uncertainty bands on these curves correspond to the uncertainty in the Higgs-nucleon coupling form factor, where we use the recent result from Ref. [581]. For comparison we include in Fig. 115 current limits from DM direct detection experiments XENON10 [582], XENON100 [583] and XENON1T [584], prospective limits from XENONNT [585] and SUPERCDMS at SNOLAB [586]. For completeness, we also show the favoured parameter regions from excesses seen in the DAMA/LIBRA [587], CRESST [588], CDMS II [589] and COGENT [590] experiments.[91] We furthermore indicate by the grey area in Fig. 115 the *neutrino floor*, i.e. the parameter region that is inaccessible to DM direct detection experiments due to the irreducible neutrino flux background [591][92].

Currently, the inferred limit from invisible Higgs searches yields the most sensitive constraint in the low mass region, $M_{\text{DM}} \lesssim 6, 10$ and 30GeV for scalar, fermion and vector DM, respectively, while at larger DM masses the XENON1T limit is more constraining. In particular, in the fermion and vector DM case, the BR_{inv} limit probes deep into the parameter region that is inaccessible to direct detection experiments. A future limit on the invisible Higgs decay rate from the HL-LHC will improve the limits on $\sigma_{\text{DM}-\text{nucleon}}$ by almost one order of magnitude, which pushes the limit for light scalar DM close to the neutrino floor. For fermion (vector) DM in the mass range $10\text{GeV} \lesssim M_{\text{DM}} \lesssim 20\ (60)\text{GeV}$, in case of a future excess seen in the XENONNT data, complementary measurements of an invisible Higgs decay at the HL-LHC may be possible.

6.3.2 *Scalar singlet portal*

We now turn our discussion to a model that features an additional scalar singlet in the visible sector, which provides the portal interaction to the hidden DM sector. In contrast to the minimal Higgs portal discussed in Section 6.3.1, this model allows for a modification of the 125GeV Higgs couplings, and thus for a non-trivial interplay between direct invisible Higgs searches and Higgs rate measurements at the HL-LHC. For illustration, we focus here on the case of scalar DM, the other cases (fermion and vector DM) can be treated analogously. The model is inspired by Refs. [530, 594].

The SM Higgs sector is extended by two real scalar singlet fields, S and X. Imposing a $\mathbb{Z}_2$ symmetry described by the transformation $S \to -S$, $X \to -X$, the model is characterised by the scalar potential $\mathcal{V} = \mathcal{V}_{\text{visible}} + \mathcal{V}_{\text{hidden}}$, where

$$\mathcal{V}_{\text{visible}} = \mu_\Phi^2 \Phi^\dagger \Phi + \lambda_\Phi (\Phi^\dagger \Phi)^2 + \mu_S^2 S^2 + \lambda_S S^4 + \lambda_{\Phi S} \Phi^\dagger \Phi S^2, \tag{130}$$

$$\mathcal{V}_{\text{hidden}} = \frac{1}{2}\left[\mu_X^2 X^2 + \lambda_X X^4 + \lambda_{SX} S^2 X^2 + \lambda_{\Phi X} \Phi^\dagger \Phi X^2\right]. \tag{131}$$

For the sake of simplicity we assume that the quartic interaction between the scalar doublet Φ and the DM scalar X can be neglected, $\lambda_{\Phi X} \approx 0$. After electroweak symmetry breaking the scalar $\text{SU}(2)_L$ doublet field Φ is given by $\Phi \equiv (0 \quad \phi + v)^T/\sqrt{2}$, with the vacuum expectation value (VEV) $v \approx 246\text{GeV}$. We assume the scalar field S to acquire a non-zero VEV, v_S, which softly breaks the $\mathbb{Z}_2$ symmetry, such that the singlet field S is given by $S \equiv (s + v_S)/\sqrt{2}$. Through the last term in Eq. (130) the non-zero VEVs induce a mixing of the physical degrees of freedom of these two fields, ϕ and s,

$$\begin{pmatrix} h \\ H \end{pmatrix} = \begin{pmatrix} \cos\alpha & -\sin\alpha \\ \sin\alpha & \cos\alpha \end{pmatrix} \begin{pmatrix} \phi \\ s \end{pmatrix}, \tag{132}$$

[90] For current ATLAS and CMS results for the minimal Higgs portal interpretation see Refs. [540, 539, 544, 543, 580].

[91] Note that the limits and favoured regions from DM direct detection experiments assume for the incoming flux of DM particles that the observed relic density in the Universe is fully saturated by this one DM particle species.

[92] Note that a complete study of these minimal portals would need to include further theoretical and experimental constraints on the models parameter space; see e.g. [592, 593] for recent discussions.

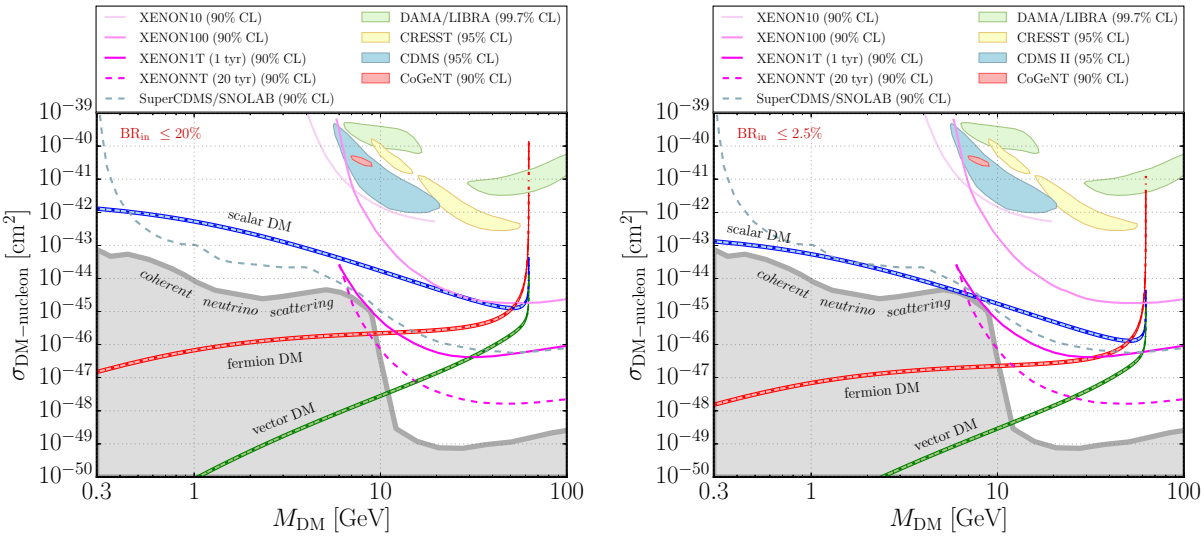

Fig. 115: Implications for the minimal Higgs portal model: Comparison of current (*left figure*) and future HL-LHC (*right figure*) limits from invisible Higgs searches with limits from DM direct detection experiments on the spin-independent DM-nucleon scattering cross section, $\sigma_{\rm DM-nucleon}$, as a function of the DM mass, $M_{\rm DM}$. The inferred limits from invisible Higgs searches are shown for scalar DM (*blue curve*), fermion DM (*red curve*) and for vector DM (*green curve*). In addition we show present limits (*solid lines*), favoured regions (*filled areas*) and future sensitivity (*dashed lines*) of the DM direct detection experiments XENON10 [582], XENON100 [583], XENON1T [584], XENONNT [585], SUPERCDMS at SNOLAB [586], DAMA/LIBRA [587], CRESST [588], CDMS II [589] and COGENT [590] (*see legend*). The grey area indicates regions inaccessible to DM direct detection experiments due to the irreducible neutrino flux background [591].

with the masses of the physical states h and H given by

$$M^2_{h/H} = \lambda_\Phi v^2 + \lambda_S v_S^2 \mp \sqrt{\left(\lambda_\Phi v^2 - \lambda_S v_S^2\right)^2 + (\lambda_{\Phi S} v v_S)^2}, \tag{133}$$

and the mixing angle $\alpha \in [-\frac{\pi}{2}, \frac{\pi}{2}]$ given by

$$\tan 2\alpha = \frac{\lambda_{\Phi S} v v_s}{\lambda_S v_S^2 - \lambda_\Phi v^2}. \tag{134}$$

In contrast, X does not acquire a VEV. As a result X is stable and thus a possible DM candidate, with a mass given by $M_X^2 = \mu_X^2 + \lambda_{SX} v_S^2/2$.

In this analysis, we assume $M_H = 125.09$GeV, and $M_h < M_H$. Furthermore, we discard the quartic interaction term $\propto \lambda_X$ in Eq. (131) as this operator is irrelevant for our study. With this, the model can then be parametrised in terms of the following input quantities:

$$M_h, \cos\alpha, v_S, M_X, \lambda_{SX}. \tag{135}$$

The couplings of the Higgs bosons h and H to SM gauge bosons and fermions are universally suppressed by the mixing,

$$g_h/g_{h,\rm SM} = \cos\alpha, \qquad g_H/g_{H,\rm SM} = \sin\alpha. \tag{136}$$

If the DM scalar X is light enough the portal coupling λ_{SX} gives rise to decays of the Higgs bosons h and H to the invisible XX final state. The partial decay widths are given by

$$\begin{aligned} \Gamma(h \to XX) &= \sin^2\alpha \cdot \Gamma_{XX}(M_h), \\ \Gamma(H \to XX) &= \cos^2\alpha \cdot \Gamma_{XX}(M_H), \end{aligned} \quad \text{with} \quad \Gamma_{XX}(M) = \frac{\lambda_{SX}^2 v_S^2}{32\pi M}\sqrt{1 - \frac{4M_X^2}{M^2}}. \tag{137}$$

Furthermore, if $M_h \leq M_H/2$, the heavier Higgs boson H can decay into hh, with the partial width given by

$$\Gamma(H \to hh) = \frac{\lambda_{Hhh}^2}{32\pi M_H}\sqrt{1-\frac{4M_h^2}{M_H^2}}, \tag{138}$$

and the effective Hhh coupling[93]

$$\begin{aligned}\lambda_{Hhh} =& -3\sin 2\alpha\,[\lambda_S v_S \sin\alpha + \lambda_\Phi v\cos\alpha] \\ & - \tan 2\alpha\left(\lambda_S v_S^2 - \lambda_\Phi v^2\right)\left[(1-3\sin^2\alpha)\frac{\cos\alpha}{v} + (1-3\cos^2\alpha)\frac{\sin\alpha}{v_S}\right].\end{aligned} \tag{139}$$

Through the successive decay of the lighter Higgs boson h into either final states with SM particles (denoted as 'SM') or the invisible XX final state, this gives rise to the following signatures[94]

$$H \to hh \to \begin{cases} (\mathrm{SM})(\mathrm{SM}), & \text{(visible)}, \\ (\mathrm{SM})(XX), & \text{(semi-invisible)}, \\ (XX)(XX), & \text{(invisible)}. \end{cases} \tag{140}$$

The branching ratio of the invisible decay of the SM-like Higgs boson H is given by

$$\mathrm{BR}_{\mathrm{inv}} = \mathrm{BR}(H \to XX) + \mathrm{BR}(H \to hh)\cdot \mathrm{BR}(h \to XX)^2. \tag{141}$$

In Fig. 116 we show the invisible Higgs decay rate $\mathrm{BR}_{\mathrm{inv}}$ in the $(M_h, \cos\alpha)$ plane, for fixed DM mass $M_X = 5$GeV, and four choices $(v_S, \lambda_{SX}) = (50\,v, 10^{-4})$ [*top left*], $(50\,v, 10^{-6})$ [*top right*], $(50\,v, 10^{-3})$ [*bottom left*] and $(5\,v, 10^{-4})$ [*bottom right*]. For better illustration, the secondary y-axis shows the deviation from the SM coupling strength, $\Delta\kappa = 1-\sin\alpha$, of the heavier Higgs boson H. The $\mathrm{BR}_{\mathrm{inv}}$ prediction is given by the black solid contours. Various constraints (at 95% C.L.) are included in the figures: future direct invisible Higgs searches (*red dashed contour/grey area*), future indirect limits from Higgs rate measurements at the HL-LHC (assuming S2) using the two parametrisations of Section 6.2.2 [cf. Fig. 114] (*solid pale/bright green contour and area*), and LEP searches for the lighter Higgs boson h (*orange contour and area*), obtained via `HiggsBounds` [595, 596, 597]. For the latter, the relevant experimental analyses are searches for $e^+e^- \to Zh$ production with h either decaying to invisible particles [598, 599, 600, 601] or to SM particles (in particular, $b\bar{b}$) [602], as well as the decay mode independent analysis by OPAL [603].

In all four panels of Fig. 116 we can identify two kinematic thresholds for the invisible H decay: at $M_h = M_H/2 \simeq 62.5$GeV, where the cascade decay $H \to hh \to (XX)(XX)$ becomes available for decreasing M_h, and at $M_h = 2M_X = 10$GeV, where the decay $h \to XX$ kinematically closes for smaller M_h, and thus the $H \to hh$ decay cannot further lead to an invisible final state. Above the first threshold, $M_h > M_H/2$, and below the second threshold, $M_h < 2M_X$, the invisible H decay is solely given by the direct decay $H \to XX$.

For the parameter choice $(v_s, \lambda_{SX}) = (50\,v, 10^{-4})$ (*top left panel*), the direct invisible Higgs searches at the HL-LHC will provide similar bounds as the indirect constraints from the Higgs rates for the mass range $M_h \in [2M_X, M_H/2]$. However, in the mass range $M_h \sim (10-40)$GeV, the LEP searches for invisible h decays will still yield the strongest exclusion. Note that the Higgs rate measurements are always constraining the sum $\mathrm{BR}(H \to \mathrm{NP}) = \mathrm{BR}(H \to XX) + \mathrm{BR}(H \to hh)$, regardless of whether the decay $H \to hh$ leads to an invisible final state. Hence, they remain to be sensitive in the low mass region $M_h < 2M_X$.

[93] Note that the relative sign between the two terms in Eq. (139) differs with respect to Eq. (13) in Ref. [530].

[94] Note that LHC searches for the semi-invisible and visible final states are highly complementary to invisible Higgs searches in this model.

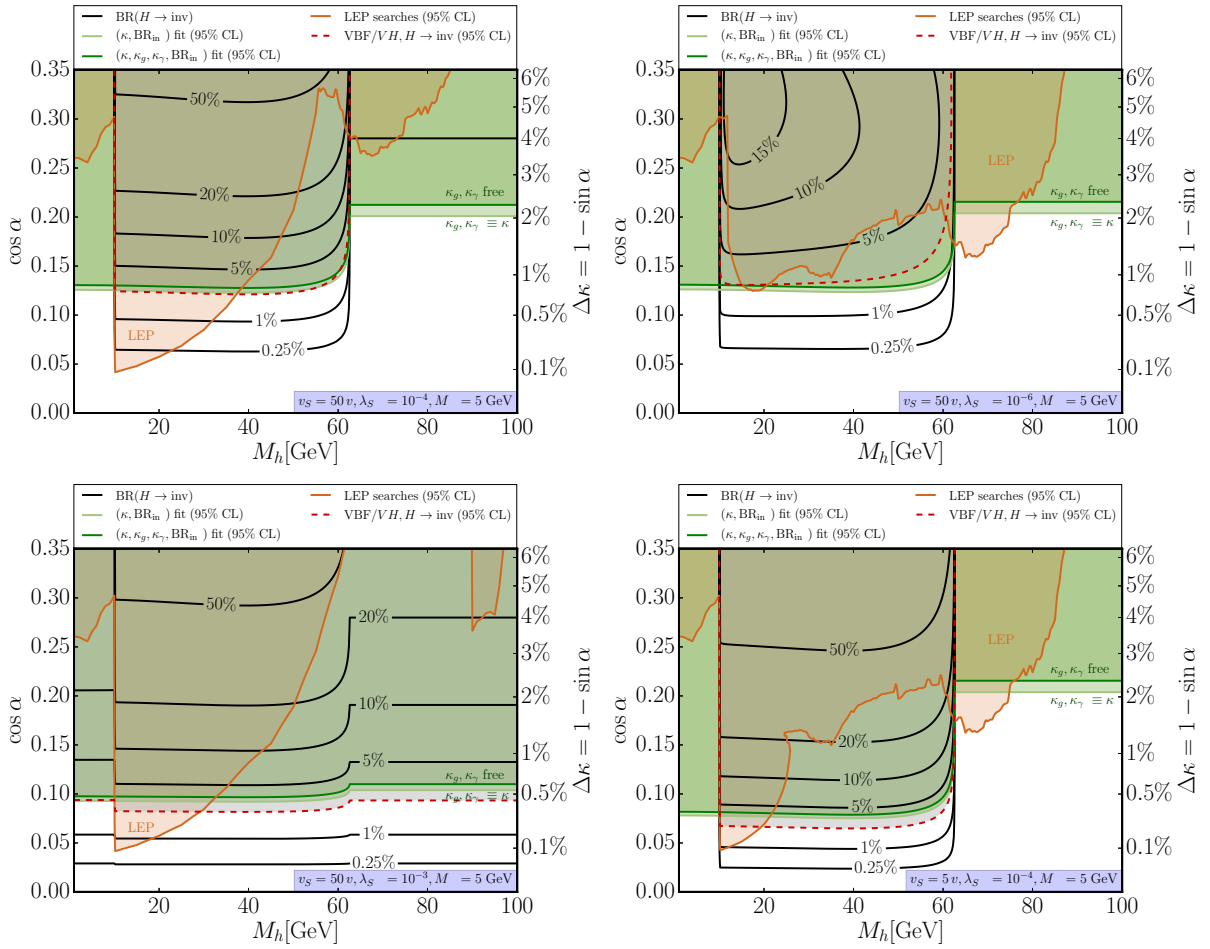

Fig. 116: Implications for the scalar singlet portal model, shown in the $(M_h, \cos\alpha)$ parameter plane for a DM mass of $M_X = 5$GeV and $(v_S, \lambda_{SX}) = (50\,v, 10^{-4})$ [*top left*], $(50\,v, 10^{-6})$ [*top right*], $(50\,v, 10^{-3})$ [*bottom left*] and $(5\,v, 10^{-4})$ [*bottom right*]. Black solid contours show the invisible Higgs decay rate, BR$(H \to \text{inv})$, the red dashed contour/grey area indicates the expected HL-LHC limit from invisible Higgs searches, pale and bright green contours/areas indicate the indirect constraints from HL-LHC Higgs rate measurements (using the two parametrisations, see Section 6.2.2), and the orange contour/area marks the excluded region from LEP searches. See text for more details.

For a larger Higgs-portal interaction, $\lambda_{SX} = 10^{-3}$ (*bottom left panel*), the direct decay $H \to XX$ becomes more prominent, leading to sizeable BR$_{\rm inv}$ even at smaller $\cos\alpha$. Here, direct invisible Higgs searches at HL-LHC will be most constraining and will supersede the LEP limits except in the mass range $M_h \sim (10 - 33)$GeV. In contrast, for very small Higgs-portal interaction, $\lambda_{SX} = 10^{-6}$ (*top right panel*) the invisible Higgs decay rates are much smaller. Nevertheless, future indirect constraints from Higgs rate measurements will supersede the LEP limits in almost the entire mass range except for M_h values between 62 to 75GeV. Note that the LEP exclusion arises from $e^+e^- \to Zh \to Z(b\bar{b})$ searches [602].

If we decrease the VEV of the singlet field, $v_s = 5\,v$ (*bottom right panel*), the effective Hhh coupling becomes larger, leading to a more pronounced $H \to hh$ decay if kinematically accessible. Hence, in the region $M_h < M_H/2$, the HL-LHC constraints both from direct invisible Higgs searches and Higgs rate measurements are very strong and supersede the LEP constraints in almost the entire mass range up to $M_h \lesssim M_H/2$. In this case, the direct invisible Higgs searches are slightly more sensitive than the Higgs rate measurements.

In summary, the example parameter choices made in Fig. 116 illustrate an interesting interplay between past LEP searches for a light Higgs boson h, future HL-LHC searches for an invisibly decaying SM-like Higgs boson H, and future HL-LHC precision Higgs rate measurements. Depending on the parameter choice, each experimental probe can be the most sensitive/constraining one, which highlights their complementarity and strongly motivates a corresponding experimental program at the HL-LHC.

6.4 Conclusions

Higgs portal models are intriguing and simple new physics scenarios that contain a dark matter candidate which can be tested at collider as well as astrophysical experiments. The HL-LHC will be able to constrain the Higgs boson–dark matter coupling constant and probe the parameter regime down to an invisible Higgs decay rate of 2%. For low dark matter masses, $M_{\mathrm{DM}} \lesssim 30$GeV, these bounds are typically more constraining than limits obtained from dark matter direct detection experiments. For a specific model with two visible scalar states and a scalar dark matter candidate, we presented scenarios for which future HL-LHC searches will supersede complementary constraints from LEP searches for a light scalar boson. In summary, the future HL-LHC measurements of the Higgs signal strength, as well as direct searches for the invisible decay of the observed Higgs boson, promise to provide important insight within the framework of Higgs portal models. The sensitivity can further be improved by the future electron-proton collider LHeC. In particular, the indirect constraints from Higgs rate measurements will improve substantially if HL-LHC and LHeC results are combined.

7 Higgs flavor and rare decays[95]

7.1 Introduction

In this section we cover the current status and future prospects for measuring the different Higgs couplings to fermions, these go under the generic name of "Higgs and Flavor". The Higgs mechanism of the SM predict that the Yukawa couplings are proportional to the fermion mass and CP conserving, or more precisely

$$y_f^{\rm SM} = \sqrt{2} m_f / v \,, \tag{142}$$

where the tree-level flavor changing couplings are zero. Currently, only the third generation Yukawa couplings were directly measured and found to be in agreement with the SM prediction, see Refs. [232, 133, 137, 136, 168, 164, 179] for recent results on $h\tau\bar{\tau}$, $hb\bar{b}$ and $h\bar{t}t$. However, for the Higgs coupling to first and second generations there are only upper bounds [604, 140, 605, 606, 607].

Below, we adapt the generalised κ framework to describe deviations of the Higgs couplings from their SM values due to new physics (NP). In particular, we define

$$\mathcal{L}_{\rm eff} = -\kappa_{f_i} \frac{m_{f_i}}{v} h \bar{f}_i f_i + i\tilde{\kappa}_{f_i} \frac{m_{f_i}}{v} h \bar{f}_i \gamma_5 f_i - \left[\left(\kappa_{f_i f_j} + i\tilde{\kappa}_{f_i f_j} \right) h \bar{f}^i_L f^j_R + \text{h.c.} \right]_{i \neq j} , \tag{143}$$

where a sum over fermion type $f = u, d, \ell$ and generations $i, j = 1, 2, 3$ is implied. The first two terms are flavour-diagonal with the first term CP-conserving and the second CP-violating. The terms in square brackets are flavour violating. The real (imaginary) part of the coefficient is CP conserving (violating). In the SM, we have $\kappa_{f_i} = 1$ while $\tilde{\kappa}_{f_i} = \kappa_{f_i f_j} = \tilde{\kappa}_{f_i f_j} = 0$.

The different Higgs Yukawa couplings can be probed by direct and indirect methods. Direct methods include $t\bar{t}h$ (for top [168, 164, 179]), $Vh, h \to b\bar{b}, c\bar{c}$ (for bottom [136, 137] and charm [604]), $h \to \ell^+\ell^-$ (for leptons [133, 140, 232]) and exclusive decays for photon and vector meson [608, 609, 610, 611] (for light quarks). In addition, the upper bound on the Higgs total width from $t \to ZZ^*$ and $h \to \gamma\gamma$ signal shapes is an unavoidable constraint on the rates to any light particles [605]. In principle, one can use the off-shell Higgs width measurement [491, 493], but it involves assumptions about the ratio between off-shell and on-shell Higgs productions. In addition, there are several indirect probes of the different Higgs Yukawa couplings, such as kinematic distributions [612, 173]. A global fit of the Higgs data also provides a bound on the different Yukawa via the bound on the non SM decays of the Higgs (up to small effects on the Higgs production, see [613, 607, 605]), however, this bound is subject to different assumptions.

The Higgs production and decay signal strengths from the CMS collaboration [182] and from ATLAS for $h \to c\bar{c}$ [604] (most recent at the time of writing) from a global fit which includes the direct observation of $t\bar{t}h$ production are

$$\begin{aligned} \mu^{ttH} &= 1.18^{+0.30}_{-0.27} \,, & \mu^{bb} &= 1.12^{+0.29}_{-0.29} \,, & \mu^{cc} &< 105 \,, \\ \mu^{\tau\tau} &= 1.20^{+0.26}_{-0.24} \,, & \mu^{\mu\mu} &= 0.68^{+1.25}_{-1.24} \,. \end{aligned} \tag{144}$$

In terms of modifications of the flavor-diagonal and CP-conserving Yukawas, the best fit values are

$$\begin{aligned} \kappa_t &= 1.11^{+0.12}_{-0.10}, & \kappa_b &= -1.10^{+0.33}_{-0.23}, \\ \kappa_\tau &= 1.01^{+0.16}_{-0.20}, & \kappa_\mu &= 0.79^{+0.58}_{-0.79}. \end{aligned} \tag{145}$$

See also [614, 182]. The light quarks u, d, and s and the charm Yukawa can be constrained from a global fit of Higgs data and precision EW measurements at LEP. Floating all couplings in the fit results in the following upper bounds [605, 607],

$$\kappa_u < 3.4 \cdot 10^3, \qquad \kappa_d < 1.7 \cdot 10^3, \qquad \kappa_s < 42, \qquad \kappa_c \lesssim 6.2.$$

[95] Contact Editors: K. Nikopoulos, A. Schmidt, L. Sestini, Y. Soreq

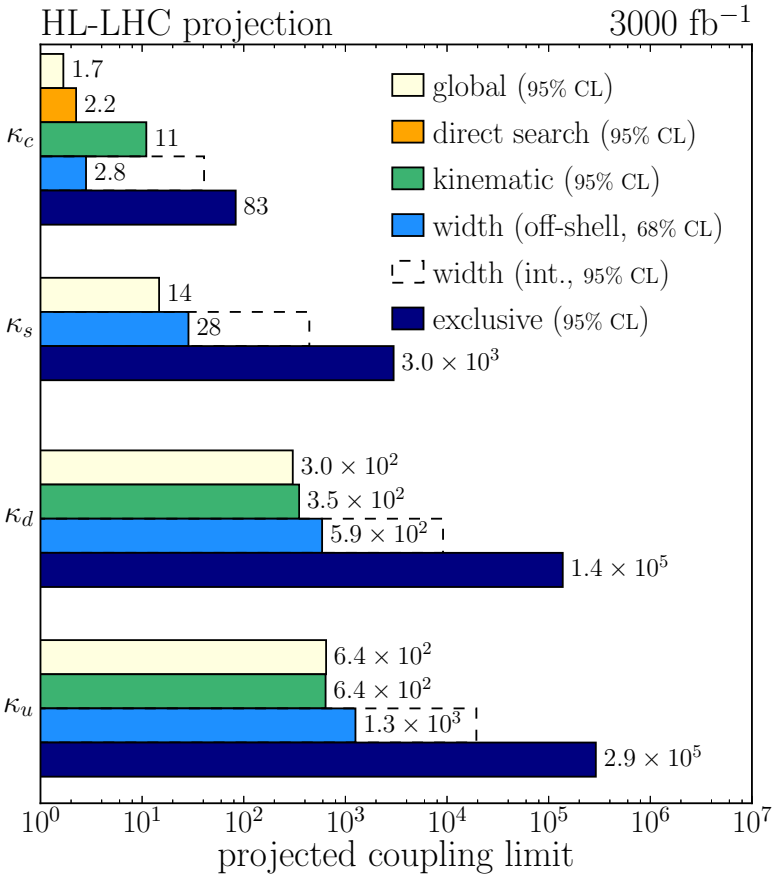

Fig. 117: Summary of the projected HL-LHC limits on the light quark Yukawa couplings, including charm.

While for the electron Yukawa, the upper bound on BR$(h \to e^+e^-)$ at the LHC translates to an upper bound, $|\kappa_e| < 611$ [615, 606]. And for future prospects, see [616, 617, 618, 608, 619, 620].

The upper bounds on $\kappa_{c,s,d,u}$ roughly correspond to the size of the SM bottom Yukawa coupling and are thus much bigger than the corresponding SM Yukawa couplings. The upper bounds can be saturated only if one allows for large cancellations between the contribution to fermion masses from the Higgs VEV and an equally large but opposite in sign contribution from NP. We will show that in models of NP motivated by the hierarchy problem, the effects of NP are generically well below these bounds. A summary of the projected limits on $\kappa_{c,s,d,u}$ is given in Fig. 117 using the methods outlined in this section: exclusive decays of the Higgs, fits of differential cross-sections, constraints from the total Higgs width assuming a value of 200 MeV, a global fit of Higgs production cross-sections, and direct searches for a $c\bar{c}$ final state.

The CP-violating flavour-diagonal Yukawa couplings, $\tilde{\kappa}_{f_i}$, are well constrained from bounds on the electric dipole moments (EDMs) [263, 621, 606, 622, 623] under the assumption of no cancellation with other contributions to EDMs beyond the Higgs contributions. For the electron Yukawa, the latest ACME measurement [624, 625] results into an upper bound of $\tilde{\kappa}_e < 1.9 \times 10^{-3}$ [606]. Whereas for the bottom and charm Yukawas, the strongest limits come from the neutron EDM [623]. Using the NLO QCD theoretical prediction, this translates into the upper bounds $\tilde{\kappa}_b < 5$ and $\tilde{\kappa}_c < 21$ when theory errors are taken into account. For the light quark CPV Yukawas, measurement of the Mercury EDM places a strong bound on the up and down Yukawas of $\tilde{\kappa}_u < 0.1$ and $\tilde{\kappa}_d < 0.05$ [626] (no theory errors) while the neutron EDM measurement gives a weaker constraint on the strange quark Yukawa of $\tilde{\kappa}_s < 3.1$ [626] (no theory errors).

Table 79: Predictions for the flavour-diagonal up-type Yukawa couplings in a sample of NP models (see text for details).

Model	κ_t	$\kappa_{c(u)}/\kappa_t$	$\tilde{\kappa}_t/\kappa_t$	$\tilde{\kappa}_{c(u)}/\kappa_t$
SM	1	1	0	0
MFV	$1+\frac{\Re(a_u v^2+2b_u m_t^2)}{\Lambda^2}$	$1-\frac{2\Re(b_u)m_t^2}{\Lambda^2}$	$\frac{\Im(a_u v^2+2b_u m_t^2)}{\Lambda^2}$	$\frac{\Im(a_u v^2)}{\Lambda^2}$
NFC	$V_{hu}\, v/v_u$	1	0	0
F2HDM	$\cos\alpha/\sin\beta$	$-\tan\alpha/\tan\beta$	$\mathcal{O}\left(\frac{m_c}{m_t}\frac{\cos(\beta-\alpha)}{\cos\alpha\cos\beta}\right)$	$\mathcal{O}\left(\frac{m_{c(u)}^2}{m_t^2}\frac{\cos(\beta-\alpha)}{\cos\alpha\cos\beta}\right)$
MSSM	$\cos\alpha/\sin\beta$	1	0	0
FN	$1+\mathcal{O}\left(\frac{v^2}{\Lambda^2}\right)$	$1+\mathcal{O}\left(\frac{v^2}{\Lambda^2}\right)$	$\mathcal{O}\left(\frac{v^2}{\Lambda^2}\right)$	$\mathcal{O}\left(\frac{v^2}{\Lambda^2}\right)$
GL2	$\cos\alpha/\sin\beta$	$\simeq 3(7)$	0	0
RS	$1-\mathcal{O}\left(\frac{v^2}{m_{KK}^2}\bar{Y}^2\right)$	$1+\mathcal{O}\left(\frac{v^2}{m_{KK}^2}\bar{Y}^2\right)$	$\mathcal{O}\left(\frac{v^2}{m_{KK}^2}\bar{Y}^2\right)$	$\mathcal{O}\left(\frac{v^2}{m_{KK}^2}\bar{Y}^2\right)$
pNGB	$1+\mathcal{O}\left(\frac{v^2}{f^2}\right)+\mathcal{O}\left(y_*^2\lambda^2\frac{v^2}{M_*^2}\right)$	$1+\mathcal{O}\left(y_*^2\lambda^2\frac{v^2}{M_*^2}\right)$	$\mathcal{O}\left(y_*^2\lambda^2\frac{v^2}{M_*^2}\right)$	$\mathcal{O}\left(y_*^2\lambda^2\frac{v^2}{M_*^2}\right)$

The flavour violating Yukawa couplings are well constrained by the low-energy flavour-changing neutral current measurements [627, 628, 629]. A notable exception are the flavour-violating couplings involving a tau lepton. The strongest constraints on $\kappa_{\tau\mu}, \kappa_{\mu\tau}, \kappa_{\tau e}, \kappa_{e\tau}$ are thus from direct searches of flavour-violating Higgs decays at the LHC [630, 631]. Finally, the LHC can also set bounds on rare FCNC top decays involving a Higgs [632, 633, 634, 635]. The strongest current bound, for example, is $\sqrt{|\kappa_{ct}|^2+|\kappa_{tc}|^2} < 0.06$ at 95%CL where the latest ATLAS bound was converted to a bound on the Yukawa modifier at leading order.

7.2 New Physics benchmarks for modified Higgs couplings[96]

Here we review the expected sizes of κ_{f_i} in popular models of weak scale NP models, some of them motivated by the hierarchy problem. Tables 79, 80, and 81, adapted from [636, 637, 638, 639, 378], summarise the predictions for the effective Yukawa couplings, κ_f, in the Standard Model, multi-Higgs-doublet models (MHDM) with natural flavour conservation (NFC) [640, 641], a "flavourful" two-Higgs-doublet model beyond NFC (F2HDM) [642, 643, 644, 645] the Minimal Supersymmetric Standard Model (MSSM) at tree level, a single Higgs doublet with a Froggat-Nielsen mechanism (FN) [646], the Giudice-Lebedev model of quark masses modified to 2HDM (GL2) [647], NP models with minimal flavour violation (MFV) [39], Randall-Sundrum models (RS) [648], and models with a composite Higgs where Higgs is a pseudo-Nambu-Goldstone boson (pNGB) [649, 650, 241, 240]. The flavour-violating couplings in the above set of NP models are collected in Tables 82 and 83. Next, we briefly discuss each of the above models, and show that the effects are either suppressed by $1/\Lambda^2$, where Λ is the NP scale, or are proportional to the mixing angles with the extra scalars.

Dimension-Six Operators with Minimal Flavor Violation (MFV). We first assume that there is a mass gap between the SM and NP. Integrating out the NP states leads to dimension six operators (after absorbing the modifications of kinetic terms using equations of motion [651]),

$$\mathcal{L}_{\rm EFT} = \frac{Y_u'}{\Lambda^2}\bar{Q}_L H^c u_R (H^\dagger H) + \frac{Y_d'}{\Lambda^2}\bar{Q}_L H d_R (H^\dagger H) + \frac{Y_\ell'}{\Lambda^2}\bar{L}_L H \ell_R (H^\dagger H) + \text{h.c.}\,, \qquad (146)$$

which correct the SM Yukawa interactions. Here Λ is the NP scale and $H^c = i\sigma_2 H^*$. The fermion mass

[96] Contact: F. Bishara

Table 80: Same as Table 79 but for down-type Yukawa couplings.

Model	κ_b	$\kappa_{s(d)}/\kappa_b$	$\tilde{\kappa}_b/\kappa_b$	$\tilde{\kappa}_{s(d)}/\kappa_b$
SM	1	1	0	0
MFV	$1+\frac{\Re(a_d v^2+2c_d m_t^2)}{\Lambda^2}$	$1-\frac{2\Re(c_d)m_t^2}{\Lambda^2}$	$\frac{\Im(a_d v^2+2c_d m_t^2)}{\Lambda^2}$	$\frac{\Im(a_d v^2+2c_d\lvert V_{ts(td)}\rvert^2 m_t^2)}{\Lambda^2}$
NFC	$V_{hd}\,v/v_d$	1	0	0
F2HDM	$\cos\alpha/\sin\beta$	$-\tan\alpha/\tan\beta$	$\mathcal{O}\left(\frac{m_s}{m_b}\frac{\cos(\beta-\alpha)}{\cos\alpha\cos\beta}\right)$	$\mathcal{O}\left(\frac{m_{s(d)}^2}{m_b^2}\frac{\cos(\beta-\alpha)}{\cos\alpha\cos\beta}\right)$
MSSM	$-\sin\alpha/\cos\beta$	1	0	0
FN	$1+\mathcal{O}\left(\frac{v^2}{\Lambda^2}\right)$	$1+\mathcal{O}\left(\frac{v^2}{\Lambda^2}\right)$	$\mathcal{O}\left(\frac{v^2}{\Lambda^2}\right)$	$\mathcal{O}\left(\frac{v^2}{\Lambda^2}\right)$
GL2	$-\sin\alpha/\cos\beta$	$\simeq 3(5)$	0	0
RS	$1-\mathcal{O}\left(\frac{v^2}{m_{KK}^2}\bar{Y}^2\right)$	$1+\mathcal{O}\left(\frac{v^2}{m_{KK}^2}\bar{Y}^2\right)$	$\mathcal{O}\left(\frac{v^2}{m_{KK}^2}\bar{Y}^2\right)$	$\mathcal{O}\left(\frac{v^2}{m_{KK}^2}\bar{Y}^2\right)$
pNGB	$1+\mathcal{O}\left(\frac{v^2}{f^2}\right)+\mathcal{O}\left(y_*^2\lambda^2\frac{v^2}{M_*^2}\right)$	$1+\mathcal{O}\left(y_*^2\lambda^2\frac{v^2}{M_*^2}\right)$	$\mathcal{O}\left(y_*^2\lambda^2\frac{v^2}{M_*^2}\right)$	$\mathcal{O}\left(y_*^2\lambda^2\frac{v^2}{M_*^2}\right)$

Table 81: Same as Table 79 but for lepton Yukawa couplings. NP effects in the pNGB model are negligible and therefore we do not report them here.

Model	κ_τ	$\kappa_{\mu(e)}/\kappa_\tau$	$\tilde{\kappa}_\tau/\kappa_\tau$	$\tilde{\kappa}_{\mu(e)}/\kappa_\tau$
SM	1	1	0	0
MFV	$1+\frac{\Re(a_\ell)v^2}{\Lambda^2}$	$1-\frac{2\Re(b_\ell)m_\tau^2}{\Lambda^2}$	$\frac{\Im(a_\ell)v^2}{\Lambda^2}$	$\frac{\Im(a_\ell)v^2}{\Lambda^2}$
NFC	$V_{h\ell}\,v/v_\ell$	1	0	0
F2HDM	$\cos\alpha/\sin\beta$	$-\tan\alpha/\tan\beta$	$\mathcal{O}\left(\frac{m_\mu}{m_\tau}\frac{\cos(\beta-\alpha)}{\cos\alpha\cos\beta}\right)$	$\mathcal{O}\left(\frac{m_{\mu(e)}^2}{m_\tau^2}\frac{\cos(\beta-\alpha)}{\cos\alpha\cos\beta}\right)$
MSSM	$-\sin\alpha/\cos\beta$	1	0	0
FN	$1+\mathcal{O}\left(\frac{v^2}{\Lambda^2}\right)$	$1+\mathcal{O}\left(\frac{v^2}{\Lambda^2}\right)$	$\mathcal{O}\left(\frac{v^2}{\Lambda^2}\right)$	$\mathcal{O}\left(\frac{v^2}{\Lambda^2}\right)$
GL2	$-\sin\alpha/\cos\beta$	$\simeq 3(5)$	0	0
RS	$1+\mathcal{O}\left(\bar{Y}^2\frac{v^2}{m_{KK}^2}\right)$	$1+\mathcal{O}\left(\bar{Y}^2\frac{v^2}{m_{KK}^2}\right)$	$\mathcal{O}\left(\bar{Y}^2\frac{v^2}{m_{KK}^2}\right)$	$\mathcal{O}\left(\bar{Y}^2\frac{v^2}{m_{KK}^2}\right)$

matrices and Yukawa couplings after EWSB are

$$M_f=\frac{v}{\sqrt{2}}\left(Y_f+Y_f'\frac{v^2}{2\Lambda^2}\right),\qquad y_f=Y_f+3Y_f'\frac{v^2}{2\Lambda^2},\qquad f=u,d,\ell\,, \tag{147}$$

Because Y_f and Y_f' appear in two different combinations in M_f and in the physical Higgs Yukawa couplings, y_f, the two, in general, cannot be made diagonal in the same basis and will lead to flavour-violating Higgs couplings.

In Tables 79-84 we show the resulting κ_f assuming MFV, i.e., that the flavour breaking in the NP sector is only due to the SM Yukawas [39, 652, 653, 654, 655, 656, 657]. This gives $Y_u'=a_uY_u+b_uY_uY_u^\dagger Y_u+c_uY_dY_d^\dagger Y_u+\cdots$, and similarly for Y_d' with $u\leftrightarrow d$, while $a_q,b_q,c_q\sim\mathcal{O}(1)$ and are in general complex. For leptons we follow [639] and assume that the SM Y_ℓ is the only flavour-breaking spurion even for the neutrino mass matrix (see also [658]). Then Y_ℓ' and Y_ℓ are diagonal in the same basis and there are no flavour-violating couplings. The flavour-diagonal κ_ℓ are given in Table 81.

Multi-Higgs-doublet model with natural flavour conservation (NFC). Natural flavour conservation in multi-Higgs-doublet models is an assumption that only one doublet, H_u, couples to the up-type quarks, only one Higgs doublet, H_d, couples to the down-type quarks, and only one doublet, H_ℓ couples to lep-

Table 82: Same as Table 79 but for flavour-violating up-type Yukawa couplings. In the SM, NFC and the tree-level MSSM the Higgs Yukawa couplings are flavour diagonal. The CP-violating $\tilde{\kappa}_{ff'}$ are obtained by replacing the real part, $\Re$, with the imaginary part, $\Im$. All the other models predict a zero contribution to these flavour changing couplings.

Model	$\kappa_{ct(tc)}/\kappa_t$	$\kappa_{ut(tu)}/\kappa_t$	$\kappa_{uc(cu)}/\kappa_t$
MFV	$\frac{\Re\left(c_u m_b^2 V_{cb}^{(*)}\right)}{\Lambda^2}\frac{\sqrt{2}m_{t(c)}}{v}$	$\frac{\Re\left(c_u m_b^2 V_{ub}^{(*)}\right)}{\Lambda^2}\frac{\sqrt{2}m_{t(u)}}{v}$	$\frac{\Re\left(c_u m_b^2 V_{ub(cb)} V_{cb(ub)}^*\right)}{\Lambda^2}\frac{\sqrt{2}m_{c(u)}}{v}$
F2HDM	$\mathcal{O}\left(\frac{m_c}{m_t}\frac{\cos(\beta-\alpha)}{\cos\alpha\cos\beta}\right)$	$\mathcal{O}\left(\frac{m_u}{m_t}\frac{\cos(\beta-\alpha)}{\cos\alpha\cos\beta}\right)$	$\mathcal{O}\left(\frac{m_c m_u}{m_t^2}\frac{\cos(\beta-\alpha)}{\cos\alpha\cos\beta}\right)$
FN	$\mathcal{O}\left(\frac{v m_{t(c)}}{\Lambda^2}\lvert V_{cb}\rvert^{\pm 1}\right)$	$\mathcal{O}\left(\frac{v m_{t(u)}}{\Lambda^2}\lvert V_{ub}\rvert^{\pm 1}\right)$	$\mathcal{O}\left(\frac{v m_{c(u)}}{\Lambda^2}\lvert V_{us}\rvert^{\pm 1}\right)$
GL2	$\epsilon(\epsilon^2)$	$\epsilon(\epsilon^2)$	ϵ^3
RS	$\sim\lambda^{(-)2}\frac{m_{t(c)}}{v}\bar{Y}^2\frac{v^2}{m_{KK}^2}$	$\sim\lambda^{(-)3}\frac{m_{t(u)}}{v}\bar{Y}^2\frac{v^2}{m_{KK}^2}$	$\sim\lambda^{(-)1}\frac{m_{c(u)}}{v}\bar{Y}^2\frac{v^2}{m_{KK}^2}$
pNGB	$\mathcal{O}(y_*^2\frac{m_t}{v}\frac{\lambda_{L(R),2}\lambda_{L(R),3}m_W^2}{M_*^2})$	$\mathcal{O}(y_*^2\frac{m_t}{v}\frac{\lambda_{L(R),1}\lambda_{L(R),3}m_W^2}{M_*^2})$	$\mathcal{O}(y_*^2\frac{m_c}{v}\frac{\lambda_{L(R),1}\lambda_{L(R),2}m_W^2}{M_*^2})$

Table 83: Same as Table 82 but for flavour-violating down-type Yukawa couplings.

Model	$\kappa_{bs(sb)}/\kappa_b$	$\kappa_{bd(db)}/\kappa_b$	$\kappa_{sd(ds)}/\kappa_b$
MFV	$\frac{\Re\left(c_d m_t^2 V_{ts}^{(*)}\right)}{\Lambda^2}\frac{\sqrt{2}m_{s(b)}}{v}$	$\frac{\Re\left(c_d m_t^2 V_{td}^{(*)}\right)}{\Lambda^2}\frac{\sqrt{2}m_{d(b)}}{v}$	$\frac{\Re\left(c_d m_t^2 V_{ts(td)}^* V_{td(ts)}\right)}{\Lambda^2}\frac{\sqrt{2}m_{s(d)}}{v}$
F2HDM	$\mathcal{O}\left(\frac{m_s}{m_b}\frac{\cos(\beta-\alpha)}{\cos\alpha\cos\beta}\right)$	$\mathcal{O}\left(\frac{m_d}{m_b}\frac{\cos(\beta-\alpha)}{\cos\alpha\cos\beta}\right)$	$\mathcal{O}\left(\frac{m_s m_d}{m_b^2}\frac{\cos(\beta-\alpha)}{\cos\alpha\cos\beta}\right)$
FN	$\mathcal{O}\left(\frac{v m_{b(s)}}{\Lambda^2}\lvert V_{cb}\rvert^{\pm 1}\right)$	$\mathcal{O}\left(\frac{v m_{b(d)}}{\Lambda^2}\lvert V_{ub}\rvert^{\pm 1}\right)$	$\mathcal{O}\left(\frac{v m_{s(d)}}{\Lambda^2}\lvert V_{us}\rvert^{\pm 1}\right)$
GL2	$\epsilon^2(\epsilon)$	ϵ	$\epsilon^2(\epsilon^3)$
RS	$\sim\lambda^{(-)2}\frac{m_{b(s)}}{v}\bar{Y}^2\frac{v^2}{m_{KK}^2}$	$\sim\lambda^{(-)3}\frac{m_{b(d)}}{v}\bar{Y}^2\frac{v^2}{m_{KK}^2}$	$\sim\lambda^{(-)1}\frac{m_{s(d)}}{v}\bar{Y}^2\frac{v^2}{m_{KK}^2}$
pNGB	$\mathcal{O}(y_*^2\frac{m_b}{v}\frac{\lambda_{L(R),2}\lambda_{L(R),3}m_W^2}{M_*^2})$	$\mathcal{O}(y_*^2\frac{m_b}{v}\frac{\lambda_{L(R),1}\lambda_{L(R),3}m_W^2}{M_*^2})$	$\mathcal{O}(y_*^2\frac{m_s}{v}\frac{\lambda_{L(R),1}\lambda_{L(R),2}m_W^2}{M_*^2})$

tons (it is possible that any of these coincide, as in the SM where $H = H_u = H_d = H_\ell$) [640, 641]. The neutral scalar components of H_i are $(v_i + h_i)/\sqrt{2}$, where $v^2 = \sum_i v_i^2$. The dynamical fields h_i are a linear combination of the neutral Higgs mass eigen-states (and include h_u and h_d). We thus have $h_i = V_{hi}h + \ldots$, where V_{hi} are elements of the unitary matrix V that diagonalises the neutral-Higgs mass terms and we only write down the contribution of the lightest Higgs, h. NFC means that there are no tree-level Flavor Changing Neutral Currents (FCNCs) and no CP violation in the Yukawa interactions $\kappa_{qq'} = \tilde{\kappa}_{qq'} = 0\,, \tilde{\kappa}_q = 0$.

There is a universal shift in all up-quark Yukawa couplings, $\kappa_u = \kappa_c = \kappa_t = V_{hu}v/v_u$. Similarly, there is a (different) universal shift in all down-quark Yukawa couplings and in all lepton Yukawa couplings, see Tables 79 - 81.

Higgs sector of the MSSM at tree level. The MSSM tree-level Higgs potential and the couplings to quarks are the same as in the type-II two-Higgs-doublet model, see, e.g., [659]. This is an example of a 2HDM with natural flavour conservation in which $v_u = \sin\beta\, v$, $v_d = \cos\beta\, v$. The mixing of $h_{u,d}$ into the Higgs mass-eigen-states h and H is given by $h_u = \cos\alpha h + \sin\alpha H$, $h_d = -\sin\alpha h + \cos\alpha H$,

Table 84: Same as Table 82 but for flavour-violating lepton Yukawa couplings.

Model	$\kappa_{\tau\mu(\mu\tau)}/\kappa_\tau$	$\kappa_{\tau e(e\tau)}/\kappa_\tau$	$\kappa_{\mu e(e\mu)}/\kappa_\tau$
F2HDM	$\mathcal{O}\left(\frac{m_\mu}{m_\tau}\frac{\cos(\beta-\alpha)}{\cos\alpha\cos\beta}\right)$	$\mathcal{O}\left(\frac{m_e}{m_\tau}\frac{\cos(\beta-\alpha)}{\cos\alpha\cos\beta}\right)$	$\mathcal{O}\left(\frac{m_\mu m_e}{m_\tau^2}\frac{\cos(\beta-\alpha)}{\cos\alpha\cos\beta}\right)$
FN	$\mathcal{O}\left(\frac{vm_{\mu(\tau)}}{\Lambda^2}\lvert U_{23}\rvert^{\mp 1}\right)$	$\mathcal{O}\left(\frac{vm_{e(\tau)}}{\Lambda^2}\lvert U_{13}\rvert^{\mp 1}\right)$	$\mathcal{O}\left(\frac{vm_{e(\mu)}}{\Lambda^2}\lvert U_{12}\rvert^{\mp 1}\right)$
GL2	$\epsilon^2(\epsilon)$	ϵ	$\epsilon^2(\epsilon^3)$
RS	$\sim\sqrt{\frac{m_{\mu(\tau)}}{m_{\tau(\mu)}}}\bar{Y}^2\frac{v^2}{m_{KK}^2}$	$\sim\sqrt{\frac{m_{e(\tau)}}{m_{\tau(e)}}}\bar{Y}^2\frac{v^2}{m_{KK}^2}$	$\sim\sqrt{\frac{m_{e(\mu)}}{m_{\mu(e)}}}\bar{Y}^2\frac{v^2}{m_{KK}^2}$

where h is the observed SM-like Higgs. The up-quark Yukawa couplings are rescaled universally, $\kappa_u = \kappa_c = \kappa_t = \cos\alpha/\sin\beta$, and similarly the down-quark Yukawas, $\kappa_d = \kappa_s = \kappa_b = -\sin\alpha/\cos\beta$. The flavour-violating and CP-violating Yukawas are zero[97]. In Tables 79-81 we limit ourselves to the tree-level expectations, which are a good approximation for a large part of the MSSM parameter space.

In the alignment limit, $\beta - \alpha = \pi/2$ [380, 661, 662, 663, 664, 665, 666], the Yukawa couplings tend toward their SM value, $\kappa_i = 1$. The global fits to Higgs data in type-II 2HDM already constrain $\beta-\alpha$ to be not to far from $\pi/2$ [667, 668, 669] so that the couplings of the light Higgs are also constrained to be close to their SM values. Note that the decoupling limit of the 2HDM, where the heavy Higgs bosons become much heavier than the SM Higgs, implies the alignment limit while the reverse is not necessarily true [661].

Flavorful two-Higgs-doublet model. In [642] a 2HDM setup was introduced in which one Higgs doublet couples only to top, bottom and tau, and a second Higgs doublet couples to the remaining fermions (see also [670, 671, 672, 673]). Such a 2HDM goes beyond NFC and therefore introduces FCNCs at tree level. However, the Yukawa couplings of the first Higgs doublet to the third generation fermions preserve a $U(2)^5$ flavour symmetry, only broken by the small couplings of the second Higgs doublet. This approximate $U(2)^5$ symmetry leads to a strong suppression of the most sensitive flavour violating transitions between the second and first generation.

The non-standard flavour structure of this "flavourful" 2HDM scenario leads to flavour non-universal modifications of all Higgs couplings. To be more precise $\kappa_t \neq \kappa_c = \kappa_u$, $\kappa_b \neq \kappa_s = \kappa_d$, and $\kappa_\tau \neq \kappa_\mu = \kappa_e$. CP violation in Higgs couplings can arise but is strongly suppressed by small fermion masses, see Tables 79 - 81. Also potentially sizeable flavour violating Higgs couplings involving the third generation fermions arise, see Tables 82 - 84. As in all 2HDMs, the Higgs couplings approach their SM values in the alignment limit, $\beta - \alpha = \pi/2$.

A single Higgs doublet with Froggatt-Nielsen mechanism (FN). The Froggatt-Nielsen [646] mechanism provides a simple explanation of the size and hierarchy of the SM Yukawa couplings. In the simplest realisation this is achieved by a $U(1)_H$ horizontal symmetry under which different generations of fermions carry different charges. The $U(1)_H$ is broken by a spurion, ϵ_H. The entries of the SM Yukawa matrix are then parametrically suppressed by powers of ϵ_H as, for example, in the lepton sector

$$\left(Y_\ell\right)_{ij} \sim \epsilon_H^{H(L_i)-H(e_j)}, \tag{148}$$

where $H(e, L)$ are the FN charges of the right- and left-handed charged lepton, respectively. The dimension 6 operators in (146) due to electroweak NP have similar flavour suppression, $\left(Y'_\ell\right)_{ij} \sim \epsilon_H^{H(e_j)-H(L_i)} v^2/\Lambda^2$ [639, 637]. After rotating to the mass eigen-basis, the lepton masses and mixing

[97] Note that beyond the tree level, in fine-tuned regions of parameter space the loops of sfermions and gauginos can lead to substantial corrections to these expressions [660].

angles are then given by [674, 675]

$$m_{\ell_i}/v \sim \epsilon_H^{|H(L_i)-H(e_i)|}, \quad |U_{ij}| \sim \epsilon_H^{|H(L_i)-H(L_j)|}, \tag{149}$$

giving the Higgs Yukawa couplings in Tables 81 and 84 in the row labelled 'FN' [637]. Similarly for the quarks, after rotating to the mass eigen-basis, the masses and the mixings are given by [674]

$$m_{u_i(d_i)}/v \sim \epsilon_H^{|H(Q_i)-H(u_i(d_i))|}, \quad |V_{ij}| \sim \epsilon_H^{|H(Q_i)-H(Q_j)|}, \tag{150}$$

where V is the Cabibbo-Kobayashi-Maskawa (CKM) mixing matrix and $H(u,d,Q)$ are the FN charges of the right-handed up and down and the left-handed quark fields, respectively.

Higgs-dependent Yukawa couplings (GL2) In the model of quark masses introduced by Giudice and Lebedev [647], the quark masses, apart from the top mass, are small because they arise from higher dimensional operators. The original GL proposal is ruled out by data, while the straightforward modification to a 2HDM (GL2) is

$$\begin{aligned}\mathcal{L}_f = c^u_{ij}\left(\frac{H_1^\dagger H_1}{M^2}\right)^{n^u_{ij}} \bar{Q}_{L,i} u_{R,j} H_1 + c^d_{ij}\left(\frac{H_1^\dagger H_1}{M^2}\right)^{n^d_{ij}} \bar{Q}_{L,i} d_{R,j} H_2 + \\ c^\ell_{ij}\left(\frac{H_1^\dagger H_1}{M^2}\right)^{n^\ell_{ij}} \bar{L}_{L,i} e_{R,j} H_2 + \text{h.c.}\,,\end{aligned} \tag{151}$$

where M is the mass scale of the mediators. In the original GL model H_2 is identified with the SM Higgs, $H_2 = H$, while $H_1 = H^c$. Taking $c^{u,d}_{ij} \sim \mathcal{O}(1)$, the ansatz $n^{u,d}_{ij} = a_i + b^{u,d}_j$ with $a = (1,1,0)$, $b^d = (2,1,1)$, and $b^u = (2,0,0)$ then reproduces the hierarchies of the observed quark masses and mixing angles for $\epsilon \equiv v^2/M^2 \approx 1/60$. The Yukawa couplings are of the form $y^{u,d}_{ij} = (2n^{u,d}_{ij}+1)(y^{u,d}_{ij})_{\rm SM}$. The SM Yukawas are diagonal in the same basis as the quark masses, while the $y^{u,d}_{ij}$ are not. Because the bottom Yukawa is largely enhanced, $\kappa_b \simeq 3$, this simplest version of the GL model is already excluded by the Higgs data. Its modification, GL2, is still viable, though [636]. For $v_1/v_2 = \tan\beta \sim 1/\epsilon$ one can use the same ansatz for $n^{u,d}_{ij}$ as before, modifying only b^d, so that $b^d = (1,0,0)$, with the results shown in Tables 79-84. For leptons we use the same scalings as for right-handed quarks. Note that the $H_1^\dagger H_1$ is both a gauge singlet and a flavour singlet. From symmetry point of view it is easier to build flavour models, if $H_1 H_2$ acts as a spurion in (151), instead of $H_1^\dagger H_1$. This possibility is severely constrained phenomenologically, though [377, 378].

Randall-Sundrum models (RS). The Randall-Sundrum warped extra-dimensional model has been proposed to address the hierarchy problem and simultaneously explain the hierarchy of the SM fermion masses [648, 676, 677, 678, 679]. Integrating out the Kaluza-Klein (KK) modes of mass m_{KK}, and working in the limit of a brane-localised Higgs, keeping only terms of leading order in v^2/m^2_{KK}, the SM quark mass matrices are given by [680] (see also [681, 682, 683, 684, 685, 686, 687, 688, 689], and Ref. [690] for a bulk Higgs scenario)

$$M^{d(u)}_{ij} = \left[F_q Y^{5D}_{1(2)} F_{d(u)}\right]_{ij} v\,. \tag{152}$$

The $F_{q,u,d}$ are 3×3 matrices of fermion wave-function overlaps with the Higgs and are diagonal and hierarchical. Assuming flavour anarchy, the 5D Yukawa matrices, $Y^{5D}_{1,2}$, are general 3×3 complex matrices with $\bar{Y} \sim \mathcal{O}(1)$ entries, but usually $\bar{Y} \lesssim 4$, see, e.g., [684]. At leading order in v^2/m^2_{KK} the Higgs Yukawas are aligned with the quark masses, i.e., $M_{u,d} = y_{u,d} v/\sqrt{2} + \mathcal{O}(v^2/m^2_{KK})$. The mis-alignments are generated by tree-level KK quark exchanges, giving

$$\left[y_{u(d)}\right]_{ij} - \frac{\sqrt{2}}{v}\left[M_{u,d}\right]_{ij} \sim -\frac{1}{3} F_{q_i} \bar{Y}^3 F_{u_j(d_j)} \frac{v^2}{m^2_{KK}}\,. \tag{153}$$

For the charged leptons, there are two choices for generating the hierarchy in the masses [680]. If left- and right-handed fermion profiles are both hierarchical (and taken to be similar) then the misalignment between the masses and Yukawas is $\sim \sqrt{m_i m_j/v^2} \times \mathcal{O}\big(\bar{Y}^2 v^2/m_{KK}^2\big)$. If only the right-handed profiles are hierarchical the misalignment is given by (see also Tables 81 and 84)

$$\big[y_\ell\big]_{ij} - \frac{\sqrt{2}}{v}\big[M_\ell\big]_{ij} \sim -\frac{1}{3}\bar{Y}^2\frac{v^2}{m_{KK}^2}\frac{m_j^\ell}{v}\,. \tag{154}$$

The Higgs mediated FCNCs are suppressed by the same zero-mode wave-function overlaps that also suppress the quark masses, (152), giving rise to the RS GIM mechanism [691, 692, 693]. Using the fact that the CKM matrix elements are given by $V_{ij} \sim F_{q_i}/F_{q_j}$ for $i < j$, Eq. (153), one can rewrite the κ_i as in Tables 79-83. The numerical analysis of Ref. [680] found that for diagonal Yukawas typically $\kappa_i < 1$, with deviations in $\kappa_{t(b)}$ up to $30\%(15\%)$, and in $\kappa_{s,c(u,d)}$ up to $\sim 5\%(1\%)$. For the charged leptons one obtains deviations in $\kappa_{\tau\mu(\mu\tau)} \sim 1(5)\times 10^{-5}$ [680]. These estimates were obtained fixing the mass of the first KK gluon excitation to 3.7 TeV, above the present ATLAS bound [694].

Composite pseudo-Goldstone Higgs (pNGB). Finally, we assume that the Higgs is a pseudo-Goldstone boson arising from the spontaneous breaking of a global symmetry in a strongly coupled sector, and couples to the composite sector with a typical coupling y_* [649, 650, 241, 240] (for a review, see [695]). Assuming partial compositeness, the SM fermions couple linearly to composite operators $O_{L,R}$, $\lambda^q_{L,i}\bar{Q}_{L,i}O^i_R + \lambda^u_{R,j}\bar{u}_{R,j}O^j_L + h.c.$, where i, j are flavour indices [696]. This is the 4D dual of fermion mass generation in 5D RS models. The SM masses and Yukawa couplings arise from expanding the two-point functions of the $O_{L,R}$ operators in powers of the Higgs field [697].

The new ingredient compared to the EFT analysis in (146) is that the shift symmetry due to the pNGB nature of the Higgs dictates the form of the higher-dimensional operators. The flavour structure and the composite Higgs coset structure completely factorise if the SM fields couple to only one composite operator. The general decomposition of Higgs couplings then becomes [697] (see also [698, 699, 700])

$$Y_u\bar{Q}_L H u_R + Y'_u\bar{Q}_L H u_R\frac{(H^\dagger H)}{\Lambda^2} + \ldots \quad\to\quad c^u_{ij}\,P(h/f)\,\bar{Q}^i_L H u^j_R\,, \tag{155}$$

and similarly for the down quarks. Here $f \gtrsim v$ is the equivalent of the pion decay constant, while $P(h/f) = a_0 + a_2(H^\dagger H/f^2) + \ldots$ is an analytic function whose form is fixed by the pattern of the spontaneous breaking and the embedding of the SM fields in the global symmetry of the strongly coupled sector. In (155) the flavour structure of Y_u and Y'_u is the same. The resulting corrections to the quark Yukawa couplings are therefore strictly diagonal,

$$\kappa_q \sim 1 + \mathcal{O}\big(v^2/f^2\big). \tag{156}$$

For example, for the models based on the breaking of $SO(5)$ to $SO(4)$, the diagonal Yukawa couplings can be written as $\kappa_q = (1 + 2m - (1 + 2m + n)(v/f)^2)/\sqrt{1-(v/f)^2}$, where n, m are positive integers [701]. The Minimal Composite Higgs Model 4 (MCHM4) corresponds to $m = n = 0$, while MCHM5 is given by $m = 0, n = 1$.

The flavour-violating contributions to the quark Yukawa couplings arise only from corrections to the quark kinetic terms [697],

$$\bar{q}_L i\not{d}_L\frac{H^\dagger H}{\Lambda^2},\ \bar{u}_R i\not{d}_R\frac{H^\dagger H}{\Lambda^2},\ldots\,, \tag{157}$$

due to the exchanges of composite vector resonances with typical mass $M_* \sim \Lambda$. After using the equations of motion these give (neglecting relative $\mathcal{O}(1)$ contributions in the sum) [697, 700, 613],

$$\kappa^u_{ij} \sim 2y_*^2\frac{v^2}{M_*^2}\Big(\lambda^q_{L,i}\lambda^q_{L,j}\frac{m_{u_j}}{v} + \lambda^u_{R,i}\lambda^u_{R,j}\frac{m_{u_i}}{v}\Big)\,, \tag{158}$$

and similarly for the down quarks. If the strong sector is CP violating, then $\tilde{\kappa}_{ij}^{u,d} \sim \kappa_{ij}^{u,d}$.

The exchange of composite vector resonances also contributes to the flavour-diagonal Yukawa couplings, shifting the estimate (156) by $\Delta\kappa_{q_i} \sim 2y_*^2 \frac{v^2}{M_*^2}\left[\left(\lambda_{L,i}^q\right)^2 + \left(\lambda_{R,i}^u\right)^2\right]$. This shift can be large for the quarks with a large composite component if the Higgs is strongly coupled to the vector resonances, $y_* \sim 4\pi$, and these resonances are relatively light, $M_* \sim 4\pi v \sim 3$ TeV. The left-handed top and bottom, as well as the right-handed top, are expected to be composite, explaining the large top mass (i.e., $\lambda_{L,3}^q \sim \lambda_{R,3}^u \sim 1$). In the anarchic flavour scenario, one expects the remaining quarks to be mostly elementary (so the remaining $\lambda_i \ll 1$). If there is some underlying flavour alignment, it is also possible that the light quarks are composite. This is most easily achieved in the right-handed sector [702, 703, 699].

In the case of the lepton sector, if we assume that there are no hierarchies in the composite sector [704] (see also [705, 706, 707, 708]), then the NP effects in the flavour diagonal and off-diagonal Yukawas are negligible. For this reason, we do not report them in Tables 81 and 84.

7.3 Inclusive Search with Flavor tagging (charm and strange)[98]

7.3.1 Charm quark tagging

In the SM, the coupling of the Higgs to bottom quarks is small, i.e., $y_b^{\rm SM} \simeq 0.016$ at $\mu = m_H$, and its coupling to charm quarks even smaller by roughly four times, i.e., $y_c^{\rm SM} \simeq 0.0036$ at $\mu = m_H$. Nevertheless, due to phase-space the process $H \to b\bar{b}$ is the dominant decay mode of the Higgs in the SM. This situation has not only made a roughly 30% precise measurement of such a small coupling possible at Run I of the LHC, but has also created opportunities to measure possible order one deviations in the coupling of the Higgs to charm quarks.

An important difference between the charm- and to some extent also the strange-quark (see section 7.3.2) with respect to up- and down-quarks is that it is possible to pursue an inclusive approach in identifying the flavour of the final state particles by c-tagging jets. The underlying geometrical/kinematic input necessary for c-tagging is similar to b-tagging with the most relevant one being the identification of displaced vertices due to the lifetime of c-hadrons. c-tagging has been used early on in Run I of the LHC by ATLAS and CMS in searches for supersymmetry, e.g., Refs. [709, 710]. Its usefulness in relations to Higgs physics was first discussed in Ref. [613] and subsequently used in Ref. [605] to recast ATLAS's and CMS's Run I analyses for $h \to b\bar{b}$ to provide the first direct LHC constraint on the charm Yukawa.

The inclusive method of probing the charm-quark Yukawa is in many ways complementary to searches for exclusive decays (see discussion of section 7.4) or searches for deviations in Higgs distributions (see section 7.6). For example, in the inclusive approach an underlying assumption is that the Higgs coupling to WW and ZZ —entering Higgs production— is SM-like, while the interpretation of Higgs distributions assumes no additional new physics contribution that affects them in a significant way. An important difference between the inclusive and the exclusive approach is that the latter relies on interference with the SM $H \to \gamma\gamma$ amplitude while the former does not. Therefore, in principle the exclusive approach may be sensitive to the sign and CP properties of the coupling to which the inclusive approach is insensitive to. At the same time, measurements of exclusive decays of the Higgs are challenging due to the small probability of fragmenting into the specific final state and large QCD backgrounds, which is why the inclusive approach appears to be the most promising one to probe deviations in the magnitude of the Higgs to charm coupling.

The most straight-forward way of inclusively probing the charm-quark Yukawa is by expanding the search for $H \to b\bar{b}$ to search for $pp \to (Z/W \to \ell\ell/\nu)(H \to c\bar{c})$ [605] (left and central panel in Fig. 118). Another possibility discussed in Ref. [617] is to search for deviations in Higgs production in association with a charm quark in which the Higgs is produced from a charm-quark in the proton parton-distribution functions (right panel in Fig. 118). We focus here on the measurement from $pp \to VH$

[98] Contacts: O.A. De Aguiar Francisco, M. Schlaffer, L. Sestini, E. Stamou

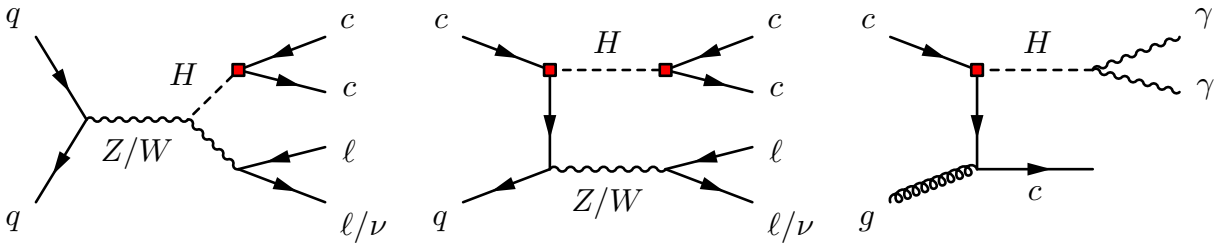

Fig. 118: Left panel, leading-order production of Higgs in association with a heavy gauge boson (Z/W) and subsequent decays. Central panel, additional production channel of Higgs in association with a heavy gauge boson that becomes relevant for large y_c [605]. Right panel, leading-order diagram to search for non-SM y_c in Higgs production in association with a charm-quark [617].

events proposed in Ref. [605] and recently performed on a 36.1 fb^{-1} sample of ZH data by ATLAS [604] at $\sqrt{s} = 13$ TeV. The following two key elements for this measurement are discussed below:

i) The experimental sensitivity in discriminating between c-jets from background b- and light-jets.

ii) Disentangling the charm-quark coupling from the bottom-quark Yukawa (breaking the degeneracy).

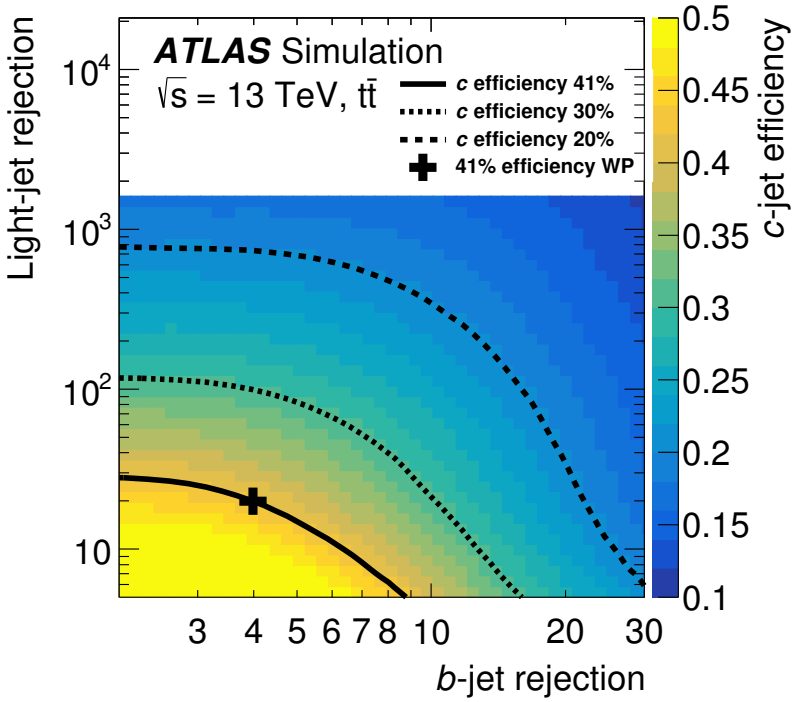

Fig. 119: Correlation of c-tagging efficiency with b- and light-quark-jet rejection in ATLAS's c-tagger employed in the analysis of Ref. [604].

Jet flavour tagging algorithms rely on Monte-Carlo simulations to assign a probability for a given jet to be produced from a specific quark-flavour. Therefore, the efficiency / confidence in associating a jet to a specific quark is correlated with the confidence to reject other hypotheses, e.g., production from light-quarks. The c-tagging tagging working point chosen in the ATLAS analysis [604] has an efficiency of approximately 41% to tag c-jets and rejection factors of roughly 4 and 20 for b- and light-quark-jets, respectively. In Figure 119 the correlation between c-tagging efficiency and rejection factors is shown.

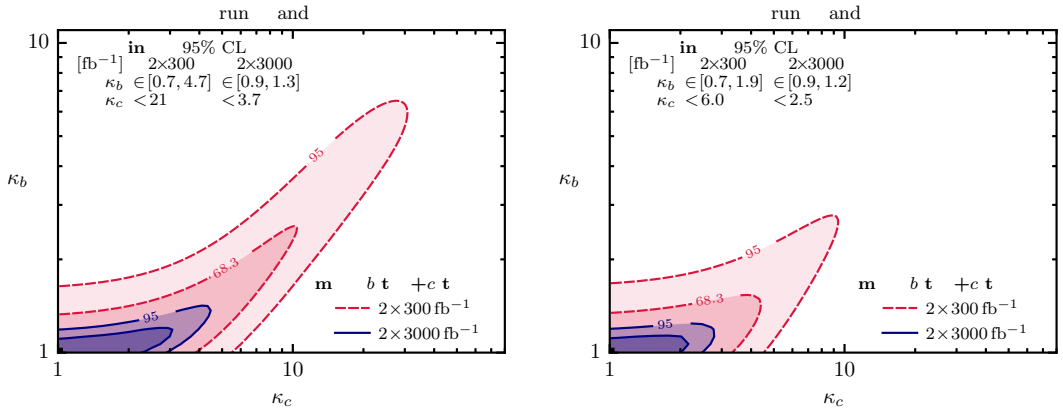

Fig. 120: Projections for measuring charm Yukawa modifications from an inclusive $H \to c\bar{c}$ search at $\sqrt{s} = 14\,\text{TeV}$ using two different c-taggers (left and right panel) [616]. In red the 95% CL region employing an integrated luminosity of $2 \times 300\,\text{fb}^{-1}$ and in blue the region employing $2 \times 3000\,\text{fb}^{-1}$.

The observed limit is $\sigma(pp \to ZH)\text{BR}(H \to c\bar{c}) < 2.7\,\text{pb}$ at 95% CL. To translate this cross-section bound to a non-trivial constraint on y_c it is essential to include the additional production channel from large charm Yukawa (central panel in Fig. 118) as demonstrated in Refs. [605]. The additional production channel is affected by the kinematics, e.g., p_T of the Z and thus depends on the details of the analysis. This "unfolding" / reinterpretation of the analysis is thus best performed by the analysis itself and cannot be avoided to obtain non-trivial constraints on the Yukawa itself. Note that at the moment the systematic uncertainties are approximately a factor of two larger than the statistical uncertainties of the $36.1\,\text{fb}^{-1}$ sample used in the analysis; the largest systematic uncertainty is associated to flavour-tagging and the tagging of c-jets in particular.

Given the rather similar lifetime of b and c hadrons, there is always a non-negligible "contamination" of the c-jet sample from jets originating from b quarks [605]. An inclusive $H \to c\bar{c}$ analysis probing y_c must thus either assume a SM value for the bottom Yukawa (as done in Ref. [604]) or allow the simultaneous variation of y_b and y_c to break the degeneracy. One possibility to achieve this is discussed in Refs. [605, 616] where more than one tagging working point with different ratios of c-tagging to b-tagging efficiency are applied.

The prospects of measuring the rate of $pp \to ZH(\to c\bar{c})$ at the HL-LHC are published in [711]. The study uses the Run II analysis [604] and rescales the results to an integrated luminosity of $3000\,\text{fb}^{-1}$. Possibilities to reduce the systematic uncertainties are discussed as well. The analysis finds that, if there is no significant NP contribution, an upper bound on the signal strength of $\mu_{ZH(c\bar{c})} < 6.3$ at 95% CL can be set. This result is to be compared with Ref. [616] in which the prospects for measuring $H \to b\bar{b}$ at $\sqrt{s} = 14\,\text{TeV}$ [712] are recast to obtain an inclusive measurement of $H \to c\bar{c}$. In the left panel of Figure 120 a c-tagging efficiency of 30% (c-tag I) is used while 50% (c-tag II) is used in the right panel. In both cases the b-jet rejection was chosen to be 5 and the light-jet rejection 200. These two tagging working points cover the currently employed tagging working point in which the c-tagging efficiency is approximately 41%. In the analysis both the charm and the bottom quark are treated as free variables; the bottom-Yukawa direction is profiled away to project the sensitivity to the charm-quark Yukawa. It was found that with $2 \times 3000\,\text{fb}^{-1}$ at $\sqrt{s} = 14\,\text{TeV}$ the high-luminosity stage of the LHC probes values of $y_c/y_c^{\text{SM}} \simeq 21(6)$ with c-tag I (c-tag II) at 95% CL, indicated by the blue regions in Figure 120.

Even though the LHCb experiment operates at lower luminosity compared to ATLAS and CMS, it has unique capabilities for discrimination between b- and c-jets thanks to its excellent vertex reconstruction system [713]. With the secondary vertex tagging (SV-tagging) LHCb achieved an identification

efficiency of 60% on b-jets, of 25% on c-jets and a light jets (light quarks or gluons) mis-identification probability of less than 0.2%. Further discrimination between light and heavy jets and between b- and c-jets is achieved by exploiting the secondary vertex kinematic properties, using Boosted Decision Tree techniques (BDTs): for instance an additional cut on the BDT that separates b- from c-jets removes 90% of $H \to b\bar{b}$ while retaining 62% of $H \to c\bar{c}$ events [714]. In the $H \to c\bar{c}$ search it is crucial to remove the $H \to b\bar{b}$ contribution since it represents an irreducible background source.

The LHCb acceptance covers $\sim$ 5% of the associated production of $W/Z + H$ at 13 TeV. Figure 121 shows the coverage of LHCb for the $b\bar{b}$ pair produced in the decay of the Higgs boson in association with a vector boson. When the two b-jets are within the acceptance, the lepton from W/Z tends to be in acceptance as well ($\sim$ 60% of times). Due to the forward geometry, Lorentz-boosted Higgs bosons are likely to be properly reconstructed.

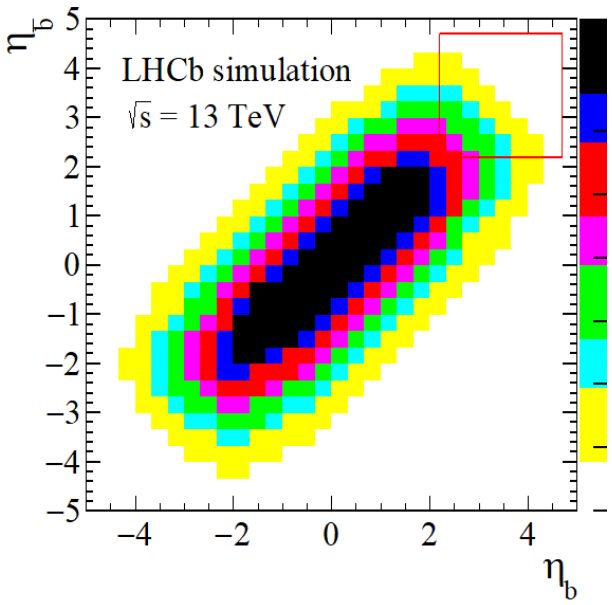

Fig. 121: 2D histogram showing the coverage of the LHCb acceptance for the $b\bar{b}$ pair produced by the Higgs decay in associated production with a W or a Z boson.

LHCb set upper limits on the $V + H(\to b\bar{b})$ and $V + H(\to c\bar{c})$ production [714] with data from LHC Run I. Without any improvements in the analysis or detector, the extrapolation of this to 300fb^{-1} at 14 TeV leads to a sensitivity of $\mu^{cc} \lesssim 50$.

Detector improvements are expected in future upgrades, in particular in impact parameter resolution which directly affects the c-tagging performance. If the detector improvement is taken into account, the c-jet tagging efficiency with the SV-tagging is expected to improve as shown in the Figure 122. A further improvement is expected from the electron reconstruction due to upgraded versions of the electromagnetic calorimeter. Electrons are used in the identification of the vector bosons associated with the Higgs. Therefore, with these improvements, the expected limit can be pushed down to $\mu^{cc} \lesssim 5 - 10$ which corresponds to a limit of 2-3 times the Standard Model prediction on the charm Yukawa coupling. This extrapolation does not include improvements in analysis techniques: for instance Deep Learning methods can be applied to exploit correlations in jets substructure properties to reduce the backgrounds.

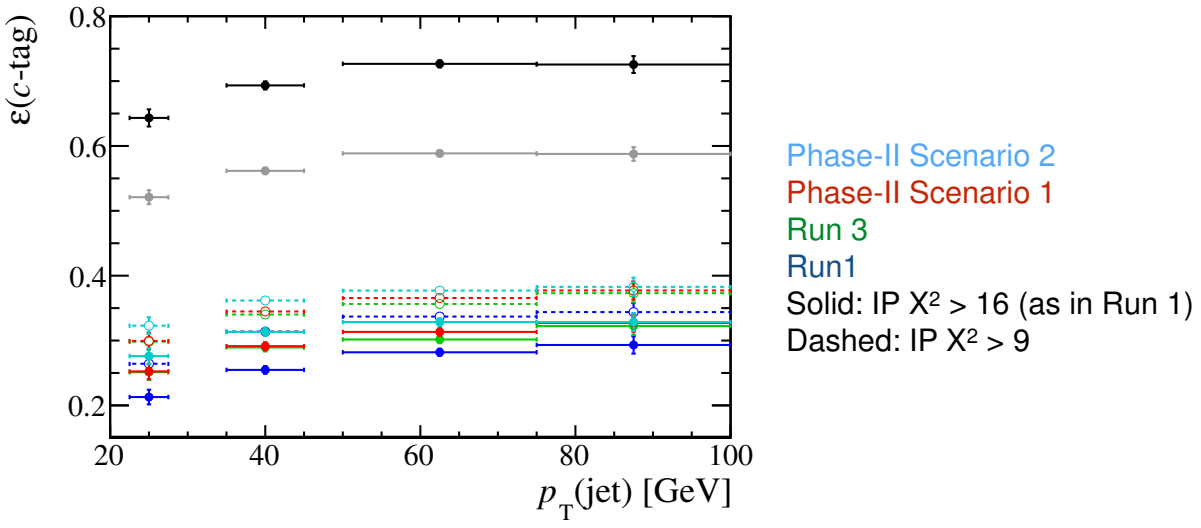

Fig. 122: LHCb c-jet SV-tagging efficiency for different scenarios in the HL-LHC conditions.

7.3.2 Strange quark tagging

Tagging strange jets from Higgs decays provides an alternative method to exclusive Higgs decays [607, 616, 618, 715, 611, 716] for constraining the Yukawa coupling of the strange quark. See Ref. [612, 717, 173, 718] for approaches using event shape and kinematic observables. The main idea behind the strange tagger described in Ref. [719] is that strange quarks—more than other partons—hadronise to prompt kaons that carry a large fraction of the jet momentum. Based on this idea a tagger is constructed to allow for an estimate of the capabilities in measurements involving strange quarks. Although the current focus at LHC is on mainly on charm and bottom tagging, recognising strange jets has been attempted before at DELPHI [720] and SLD [721], albeit in Z decays.

The shown results are based on an analysis of event samples of Higgs and W events generated with PYTHIA 8.219 [722, 319]. In each of the two hemispheres of the resonance decay, the charged pions and kaons stemming from the resonance are selected with an assumed efficiency of 95%. Similarly, K_s are identified with an efficiency of 85% if they decay within 80 cm of the interaction point into a $\pi^+\pi^-$ pair that allows to reconstruct the decaying neutral kaon. Among the two lists of Kaon candidates—one per hemisphere—one Kaon of each list is chosen for further analysis such that the scalar sum of their momenta is maximised while rejecting charged same-sign pairs. The events are separated into the categories charged-charged (CC), charged-neutral (CN) and neutral-neutral (NN) with a relative abundance of about CC:CN:NN$\approx 9:6:1$ from isospin considerations and branching ratios by the charges of the selected Kaon candidates.

All selected candidates are required to carry a large momentum $p_{||}$ along the hemisphere axis. This cut allows to reduce the background from gluon jets as gluons radiate more than quarks and therefore tend to spread their energy among more final state particles. In addition, charged Kaons need to be produced promptly, in order to reject heavy flavor jets. This latter requirement is implemented by a cut on the impact parameter d_0 after the truth value has been smeared by the detector resolution.

The efficiencies obtained in the CC and CN channel for a cut of $d_0 < 14$ μm are shown in Fig. 123. While there is clearly still ample room for improvement, this simple tagger shows already a good suppression by orders of magnitude of the bottom, charm and gluon background. Due to missing particle identification, the efficiencies for first-generation jets and strange jets are degenerate in the CC channel. However, in the CN channel, due to the required K_s, a suppression of pions is achieved that breaks this degeneracy. This is particularly interesting in light of the HL-LHC, where a large background from first generation jets is expected.

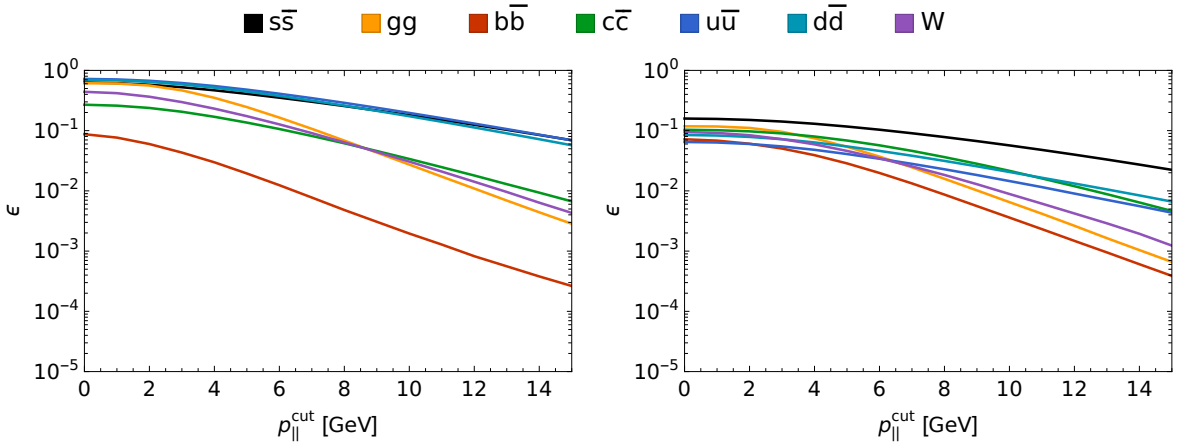

Fig. 123: Efficiencies as function of the cut on $p_{||}$ and for d_0 <14 μm to reconstruct the different Higgs decay channels and W decays as $s\bar{s}$ event by the described tagger. The left plot shows the CC channel, the right the CN channel.

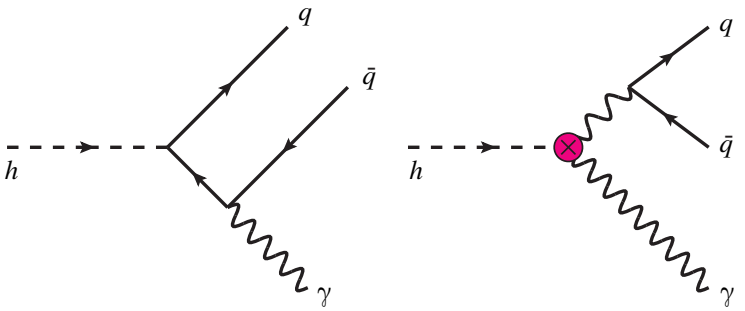

Fig. 124: The two contributions to $h \to V\gamma$ with $V = \rho, \omega, \phi, J/\psi, \Upsilon$. Left: the direct amplitude, proportional to the q-quark Yukawa; Right: indirect amplitude involve the $h\gamma\gamma$ vertex.

7.4 Exclusive Higgs decays[99]

Exclusive Higgs decays to a vector meson (V) and a photon, $h \to V\gamma$, directly probe the Higgs bottom, charm [620, 619] strange, down and up [607] quark Yukawas, as well as to the flavor violating couplings. For improved theory predictions see [618]. Within the LHC, the Higgs exclusive decays are the only direct probe of the u and d Yukawa couplings. If s-tagging will be implemented at the LHC, than the strange Yukawa will be probed both inclusive and exclusive as charm and bottom. On the experimental side, both ATLAS and CMS report first upper bounds on $h \to J/\psi\gamma$ [608, 609], $h \to \phi\gamma$ and $h \to \rho\gamma$ [715, 611]. The $h \to VZ, ZW$ modes as a probe of the Higgs electroweak coupling are discussed in [723]. Finally, Z exclusive decays are considered in [724, 725] and can be served as a test of QCD factorisation.

The Higgs exclusive decays which involve $V = \rho, \omega, \phi, J/\psi, \Upsilon$ are sensitive to the diagonal Yukawa couplings. These receive contributions from two amplitudes which are denoted as direct and indirect, see Fig. 124. The direct amplitude, first analysed in [726], involves a hard $h \to q\bar{q}\gamma$ vertex and sensitive to the q-quark Yukawa. The indirect process is mediated by $h\gamma\gamma$ vertex which is followed by a $\gamma^* \to V$ fragmentation. Since the indirect contribution is larger than the direct, the largest sensitivity to the Higgs q-quark coupling is via the interference between the two diagrams.

[99] Contact: Y. Soreq

It is beneficial to consider the ratio between $h \to V\gamma$ and $h \to \gamma\gamma$ or $h \to ZZ^* \to 4\ell$ as various of theoretical uncertainties and the dependence of the Higgs total width are cancelled [605, 618]. Moreover, since the Higgs production is inclusive for all of these modes, it cancelled in the ratio to large extension. Thus, we can write

$$\mathcal{R}_{V\gamma,f} = \frac{\mu_{V\gamma}}{\mu_f}\frac{\mathrm{BR}^{\mathrm{SM}}_{h\to V\gamma}}{\mathrm{BR}^{\mathrm{SM}}_{h\to f}} \simeq \frac{\Gamma_{h\to V\gamma}}{\Gamma_{h\to f}}\,, \tag{159}$$

where $f = ZZ^*, \gamma\gamma$, $\mu_X = \sigma_h \mathrm{BR}_X/\sigma^{\mathrm{SM}}_h \mathrm{BR}^{\mathrm{SM}}_X$, the superscript "SM" denotes the SM values and we assume a perfect cancellation of the production mechanism. For simplicity, we assume CP even Higgs coupling and find

$$\mathcal{R}_{V\gamma,f} = \alpha_{V,f}\left|1 - \left(\Delta^R_V + i\Delta^I_V\right)\frac{\bar{\kappa}_V}{\kappa^{\mathrm{eff}}_{\gamma\gamma}} + \Delta^U_V\right|^2\,, \tag{160}$$

with

$$\alpha_{V,\gamma\gamma} = 6\frac{\Gamma_{V\to e^+e^-}}{\alpha\, m_V}\left(1 - \frac{m_V^2}{m_h^2}\right)^2\,, \qquad \alpha_{V,ZZ^*} = \left|\frac{\kappa^{\mathrm{eff}}_{\gamma\gamma}}{\kappa_Z}\right|^2 \frac{\Gamma^{\mathrm{SM}}_{h\to\gamma\gamma}}{\Gamma^{\mathrm{SM}}_{h\to ZZ^*\to 4\ell}}\alpha_{V,\gamma\gamma}\,, \tag{161}$$

where κ_X is the normalised coupling with respect to its SM value. Below, we adopted the numerical values of Δ^X_V from Ref. [618]. The advantage of use $h \to \gamma\gamma$ for the normalisation is that there are only two unknown - the Higgs coupling to di-photon and the quark Yukawa. However, since $h \to ZZ^*$ is a very clean channel is serve as a good channel to use for the normalisation. Moreover, by combing the Higgs data with the electroweak precision measurements, the Higgs coupling to ZZ is known to a few percent level [668, 727], thus, there is no additional large uncertainty. We note that with the current data the bounds evaluating by using $\mathcal{R}_{V\gamma,ZZ^*}$ are slightly stronger than the ones from $\mathcal{R}_{V\gamma,\gamma\gamma}$.

For the interpretation of the experimental results in term of bounds on the different Yukawa coupling we follow Refs. [605, 616]. Denoting the 95 % CL bound on the ratio $\mathcal{R}_{V\gamma,f}$ as $\mathcal{R}^{95}_{V\gamma,f}$ we can write

$$\frac{\Delta^R_V - \sqrt{\frac{(\Delta^R_V)^2+(\Delta^I_V)^2}{\alpha_{V\gamma,f}}\mathcal{R}^{95}_{V\gamma,f} - (\Delta^I_V)^2}}{(\Delta^R_V)^2 + (\Delta^I_V)^2} < \frac{\bar{\kappa}_V}{\kappa^{\mathrm{eff}}_{\gamma\gamma}} < \frac{\Delta^R_V + \sqrt{\frac{(\Delta^R_V)^2+(\Delta^I_V)^2}{\alpha_{V\gamma,f}}\mathcal{R}^{95}_{V\gamma,f} - (\Delta^I_V)^2}}{(\Delta^R_V)^2 + (\Delta^I_V)^2}\,, \tag{162}$$

where we neglect Δ^U_V as it is a small correction. Moreover, neglecting Δ^I_V we get simplified formula, which hold to good accuracy,

$$\frac{1 - \sqrt{\mathcal{R}^{95}_{V\gamma,f}/\alpha_{V\gamma,f}}}{\Delta^R_V} < \frac{\bar{\kappa}_V}{\kappa^{\mathrm{eff}}_{\gamma\gamma}} < \frac{1 + \sqrt{\mathcal{R}^{95}_{V\gamma,f}/\alpha_{V\gamma,f}}}{\Delta^R_V}\,. \tag{163}$$

Table 85 summarises the current experimental status along with the theory interpretation in terms of light quarks Yukawa.

The prospects for probing light quark Yukawa within future LHC runs and for future colliders are estimated in Ref. [616], which we follow here. One of the important implications of the first upper bounds on the different exclusive modes is that the measurement is background dominated. Thus, even for future runs, without significant improvement of the analysis, we expect only upper bounds. Given an upper bound on $\mathcal{R}^{95}_{V\gamma,f}(E_1, \mathcal{L}_1)$, where E_1 ($\mathcal{L}_1$) stands for the collider energy (integrated luminosity), the estimated bound with E_2 and $\mathcal{L}_2$ is

$$\mathcal{R}^{95}_{V\gamma,f}(E_2, \mathcal{L}_2) = \mathcal{R}^{95}_{V\gamma,f}(E_1, \mathcal{L}_1)\sqrt{\frac{1}{R_E}\frac{\sigma^{\mathrm{SM}}_{h,E_1}\mathcal{L}_1}{\sigma^{\mathrm{SM}}_{h,E_2}\mathcal{L}_2}}\,, \tag{164}$$

Table 85: The current upper bounds, assuming SM Higgs production, on the different exclusive Higgs decays and the interpretation in terms of the Higgs Yukawa couplings. Note that $\bar{\kappa}_q = y_q/y_b^{\rm SM}$. The quoted bounds are at 95 CL.

mode	$\mathrm{BR}_{h\to V\gamma} <$	$\mathcal{R}_{V\gamma,ZZ^*} <$	Yukawa range
$J/\psi\,\gamma$	1.5×10^{-3} 8 TeV [608, 609]	9.3	$-295\kappa_Z+16\kappa_{\gamma\gamma}^{\rm eff}<\kappa_c<295\kappa_Z+16\kappa_{\gamma\gamma}^{\rm eff}$
$\phi\,\gamma$	4.8×10^{-4} 13 TeV [715, 611]	3.2	$-140\kappa_Z+10\kappa_{\gamma\gamma}^{\rm eff}<\bar{\kappa}_s<140\kappa_Z+10\kappa_{\gamma\gamma}^{\rm eff}$
$\rho\,\gamma$	8.8×10^{-4} 13 TeV [611]	5.8	$-285\kappa_Z+42\kappa_{\gamma\gamma}^{\rm eff}<2\bar{\kappa}_u+\bar{\kappa}_d<285\kappa_Z+42\kappa_{\gamma\gamma}^{\rm eff}$

Table 86: The projection for Yukawa range for future pp colliders with centre of mass energy of 14, 27 and 100 TeV. In the above table we define $L_3 \equiv (3/\mathrm{ab})/\mathcal{L}$.

mode	collider energy	$\mathcal{R}_{V\gamma,ZZ^*} <$	Yukawa range ($\kappa_V=\kappa_{\gamma\gamma}^{\rm eff}=1$)
$J/\psi\,\gamma$	14 TeV	$0.47\sqrt{L_3}$	$16-67L_3^{1/4}<\kappa_c<16+67L_3^{1/4}$
	27 TeV	$0.28\sqrt{L_3}$	$16-52L_3^{1/4}<\kappa_c<16+52L_3^{1/4}$
	100 TeV	$0.12\sqrt{L_3}$	$16-33L_3^{1/4}<\kappa_c<16+33L_3^{1/4}$
$\phi\,\gamma$	14 TeV	$0.33\sqrt{L_3}$	$11-46L_3^{1/4}<\bar{\kappa}_s<11+46L_3^{1/4}$
	27 TeV	$0.20\sqrt{L_3}$	$11-35L_3^{1/4}<\bar{\kappa}_s<11+35L_3^{1/4}$
	100 TeV	$0.083\sqrt{L_3}$	$11-23L_3^{1/4}<\bar{\kappa}_s<11+23L_3^{1/4}$
$\rho\,\gamma$	14 TeV	$0.60\sqrt{L_3}$	$44-93L_3^{1/4}<2\bar{\kappa}_u+\bar{\kappa}_d<44+93L_3^{1/4}$
	27 TeV	$0.36\sqrt{L_3}$	$44-72L_3^{1/4}<2\bar{\kappa}_u+\bar{\kappa}_d<44+72L_3^{1/4}$
	100 TeV	$0.15\sqrt{L_3}$	$44-47L_3^{1/4}<2\bar{\kappa}_u+\bar{\kappa}_d<44+47L_3^{1/4}$

where $\sigma_{h,E_{1,2}}^{\rm SM}$ is the SM Higgs production cross section, $R_E=(S_{E_1}^{\rm SM}/B_{E_1})/(S_{E_2}^{\rm SM}/B_{E_2})$ with $S(B)$ the number of signal (background) events, which encoded the difference in the analysis details and assumed to be 1 here. In Table 86,we combine Eqs. (163) and (164) along with the current bounds to estimate the future projections of probing the different light quark Yukawa. We note that the estimation in Table 86 is in agreement with the ATLAS projection of $h\to J/\psi\gamma$ [728], which quote $\mathcal{R}_{J/\psi\gamma,ZZ^*}<0.34^{+0.14}_{-0.1}$

In addition to the Higgs diagonal Yukawa, in principle, Higgs exclusive decays can probe off-diagonal couplings by measuring modes such as $h\to B_s^*\gamma$ [607]. These processes receive contribution only from the direct amplitude and there is not enhancement from interference with the relative large indirect amplitude. Moreover, the Higgs flavor violating couplings are strongly constrained by meson mixing [628, 627]. Thus, the expected rates are too small to be observe. For a detailed discussion on the $h\to VZ, VW$ channels see [716].

7.5 Lepton flavor violating decays of the Higgs[100]

The flavour violating Yukawa couplings are well constrained by the low-energy flavour-changing neutral current measurements [627, 628, 629]. A notable exception are the flavour-violating couplings involving a tau lepton. The strongest constraints on $\kappa_{\tau\mu},\kappa_{\mu\tau},\kappa_{\tau e},\kappa_{e\tau}$ are thus from direct searches of flavour-violating Higgs decays at the LHC [630, 631]. Currently, the CMS 13 TeV with 35.9 fb^{-1} [630] is the strongest constrain

$$\sqrt{y_{\mu\tau}^2+y_{\tau\mu}^2}<1.43\times10^{-3}\,,\qquad \sqrt{y_{e\tau}^2+y_{\tau e}^2}<2.26\times10^{-3}\,, \tag{165}$$

[100] Contact: Y. Soreq

which corresponds to upper 95 % CL on the branching ratio of 0.25 % and 0.61 % for $\mu\tau$ and $e\tau$, respectively. In addition, we note that once can directly measure the difference between the branching ratios of $h \to \tau e$ and $h \to \tau\mu$ as proposed in [729]. Naively, assuming that both systematics and statistical error scale with square root of the luminosity, one can expect that the sensitivity of the HL-LHC with 3000 fb^{-1} will be around the half per-mil level for the branching ratio of $h \to e\tau$ or $\to \mu\tau$.

The LHC can also set bounds on rare FCNC top decays involving a Higgs [632, 633, 634, 635]. The strongest current bound, for example, is $\sqrt{|\kappa_{ct}|^2 + |\kappa_{tc}|^2} < 0.06$ at 95 % CL.

7.6 Yukawa constraints from Higgs distributions[101]

7.6.1 Determinations of Higgs boson coupling modifiers using differential distributions

The distribution of the transverse momentum p_T of the Higgs boson has been considered before as a probe of high scale new physics running in the ggh loop [730, 731, 732, 733, 734, 735, 736, 737, 738, 739, 740, 741]. In addition, the soft spectrum is an indirect probe of the Higgs coupling to light quarks [612, 173]. Higgs production modes due to quark fusion, which are negligible in the SM, have two effects on the distributions of kinematic variables. First, the Sudakov peak will be at lower p_T around 5 GeV vs 10 GeV for gluon fusion, see [742]. This is because the effective radiation strength of gluons is several times larger than that of quarks, $\alpha_s N_c$ vs. $\alpha_s(N_c^2 - 1)/(2N_c)$, with $N_c = 3$. This leads to harder p_T spectra for gluon fusion compared to quark scattering. Therefore, the $u\bar{u}$ or $d\bar{d}$ scattering leads to a much sharper peak at lower p_T compared to gg scattering [612]. Second, in the SM, the Higgs production is dominated by gluon fusion, where the two gluons carry similar partonic x. This leads to a peak at zero Higgs rapidity. However, for $u\bar{u}$ or $d\bar{d}$ fusion, the valance quark will carry larger partonic x than the sea anti-quark. This leads to a peak in the forward direction. In case of enhanced s or c Yukawa couplings, the dominant effect is the one loop of the quarks in the $gg \to hj$ process, which has double logarithms behaviour and peaks towards lower p_T of the Higgs boson [743]. This will also result in a softer Higgs p_T spectrum [173], which can be used to constrain the charm and strange Yukawa. The impact of effect on various kinematic distributions is shown in Fig. 125. Many theoretical and experimental uncertainties are cancelled in the normalised kinematic distributions, $(1/\sigma)d\sigma/dX$ with $X = p_T, y_h$, see for example [612]. Thus, the use of them will result in a better sensitivity for probing the light quark Yukawa.

In Ref. [612], the 8 TeV ATLAS results [176] have been used to evaluate a first bound on the u and d Yukawa from kinematic distributions. The resulting 95 % CL regions obtained from the p_T distribution are

$$\bar{\kappa}_u = y_u/y_b^{\rm SM} < 0.46\,, \qquad \bar{\kappa}_d = y_d/y_b^{\rm SM} < 0.54\,, \tag{166}$$

which are stronger than the fits to the inclusive Higgs production cross sections. These upper bounds are found to be stronger than the expected due to an under-fluctuation of the data in the first p_T bin. The bounds from the rapidity distribution are found to be weaker. The sensitivities expected for Run II are shown in Fig. 126.

CMS interpreted the 13 TeV Higgs p_T spectrum with luminosity of 35.9 fb^{-1} to obtain bounds on the c and b Yukawa couplings [157]. The resulting 95 % CL intervals are

$$-4.9 < \kappa_c < 4.8\,, \qquad -1.1 < \kappa_b < 1.1\,, \tag{167}$$

if the branching fractions depend on κ_b and κ_c. In case the branching fractions are allowed to float freely the results are

$$-33 < \kappa_c < 38\,, \qquad -8.5 < \kappa_b < 18\,. \tag{168}$$

[101] Contacts: F. Yu, A. Schmidt, T. Klijnsma, Y. Soreq

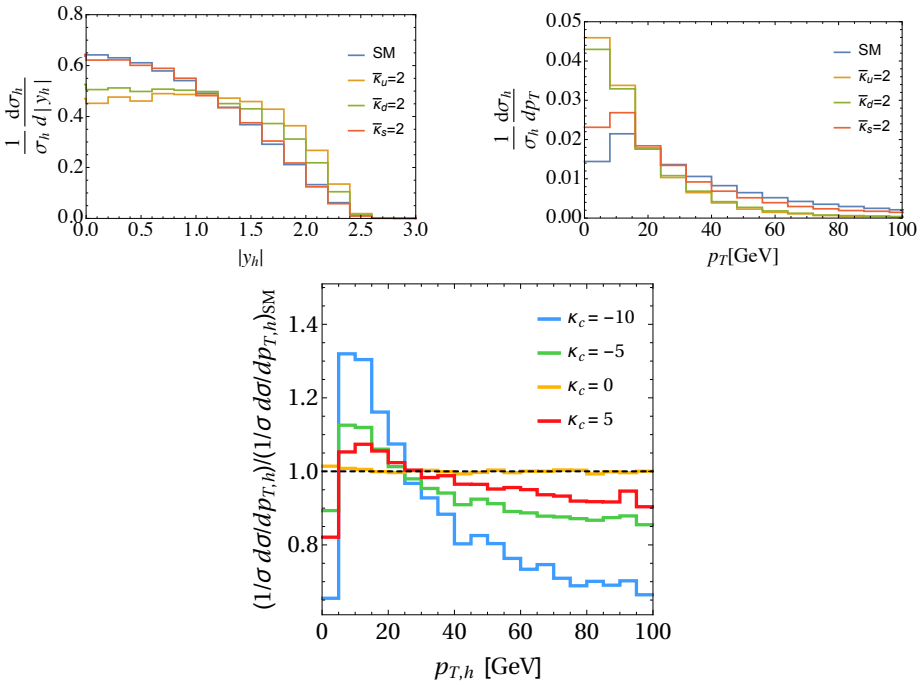

Fig. 125: Normalised distributions of kinematic variables of the Higgs boson. Left-top (Right-top) : y_h (p_T) distribution for enhanced u, d and s Yukawa compared to the SM [612]; Bottom: p_T distribution for enhanced c Yukawa [173].

The former bound on the c Yukawa is stronger than the bound from the global fit of the 8 TeV Higgs data along with the electroweak precision data, allowing all Higgs couplings to float [605]. However, it relies on strong assumptions that the Higgs couplings (besides c or b) are SM like, and it is mostly sensitive to the cross section and not to the angular shape as the latter bound.

These bounds on the c Yukawa are weaker (stronger) then the bounds from the global fit of the 8 TeV Higgs data along with the electroweak precision data allowing all Higgs coupling to float [605]

In the following these constraints on Higgs boson couplings obtained in Ref. [157] are projected to an integrated luminosity of 3000fb^{-1}, using the expected differential distributions at 3000fb^{1} presented in Sec. 2.4.1 and detailed in Ref. [139].

The Higgs boson coupling fits are based on a combination of p_T distributions from the H $\rightarrow$ $\gamma\gamma$ [156] decay channels obtained at $\sqrt{s} = 13$ TeV. Furthermore, a search for the Higgs boson produced with large $p_T$and decaying to a bottom quark-antiquark (bb) pair, which enhances the sensitivity at high $p_T{}^{H}$, is included in the κ_t/c_{ggh} fit. The Higgs boson coupling fits are performed using an simultaneous extended maximum likelihood fit to the di-photon mass, four-lepton mass, and soft-drop mass m_{SD} [291, 292] spectra in all the analysis categories of the H $\rightarrow$ $\gamma\gamma$, H $\rightarrow$ ZZ, and H $\rightarrow$ bb channels, respectively. For more details on the treatment of the input measurements, see Ref. [156].

The treatment of the decay of the Higgs boson affects the Higgs boson coupling fits. Assuming full knowledge of how the Higgs decays, i.e., assuming no beyond-the-SM contributions, the inclusive Higgs production cross section adds a strong constraint on the Higgs boson couplings in the fit. This result is obtained by parametrising the branching fractions as functions of the Higgs boson couplings. Likewise, the constraints on the Higgs boson couplings excluding the information from the inclusive cross section are of interest in order to evaluate the discriminating power of the differential distributions. This result is implemented by letting the branching fractions be determined in the fit without any prior constraint.

The expected one and two standard deviation contours of the κ_c/κ_b fit with the branching frac-

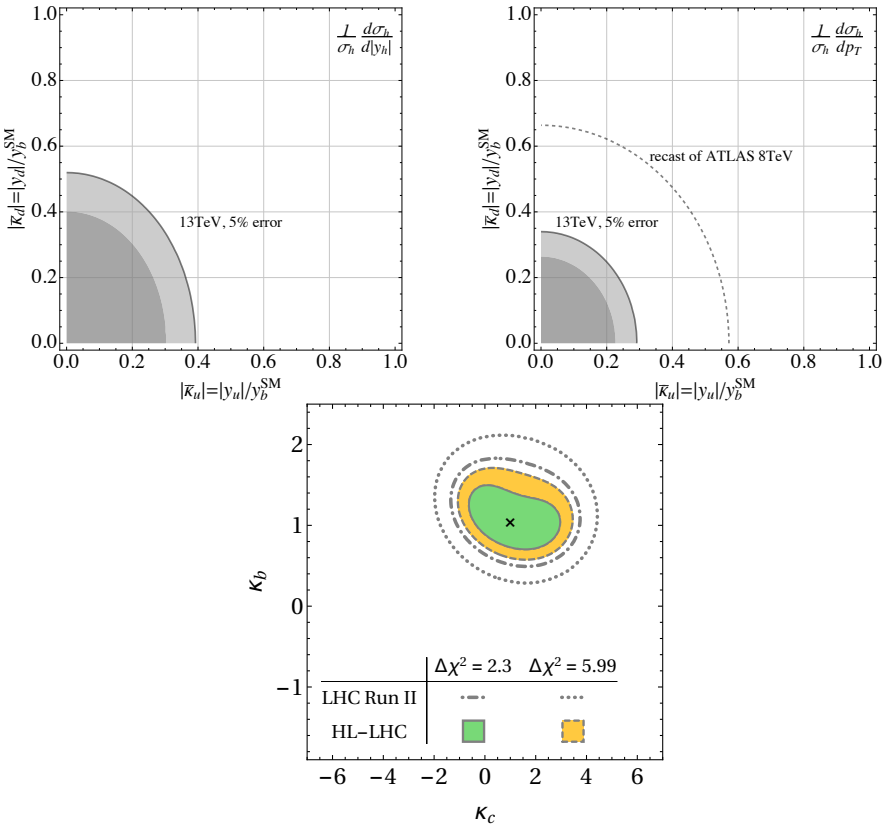

Fig. 126: The sensitivity of different angular distributions probing the light quark Yukawa couplings at 13 TeV. Left-top: u and d quark Yukawa from y_h distribution [612]; Right-top: u and d quark Yukawa from p_T distribution [612]; Bottom: b and c quark Yukawa from p_T distribution [173].

tions as functions of the Higgs boson couplings at a projected integrated luminosity of $3000\,\text{fb}^{-1}$ is shown in Fig. 127, for both scenarios of systematic uncertainty. For the $\text{H} \to \gamma\gamma$ channel the systematic uncertainties dominate if kept at the current level (i.e., in Scenario 1), but when scaled down according to the Scenario 2 prescription the systematic uncertainties are within the same order of magnitude as the statistical ones.

The same fits, but now with the branching fractions implemented as nuisance parameters with no prior constraint, are shown in 128. As this fit is dominated by statistical uncertainties even at very high integrated luminosities, the smaller systematic uncertainties in Scenario 2 have only a minor impact.

7.6.2 $W^{\pm}h$ charge asymmetry

The $W^{\pm}h$ charge asymmetry, introduced in [717], is a new, production-based probe for constraining the light quark Yukawa couplings. In contrast to decay-based probes, which rely on rare or sub-dominant Higgs decay modes, production-based probes can take advantage of the dominant Higgs decays with high signal-to-background ratios.

The main observable is the charge asymmetry between W^+h and W^- production,

$$A = \frac{\sigma(W^+h) - \sigma(W^-h)}{\sigma(W^+h) + \sigma(W^-h)}\,, \tag{169}$$

In the SM, the inclusive HE-LHC charge asymmetry is expected to be 17.3%, while the HL-LHC charge asymmetry is expected to be 21.6%. In either case, the charge asymmetry is driven by the proton PDFs

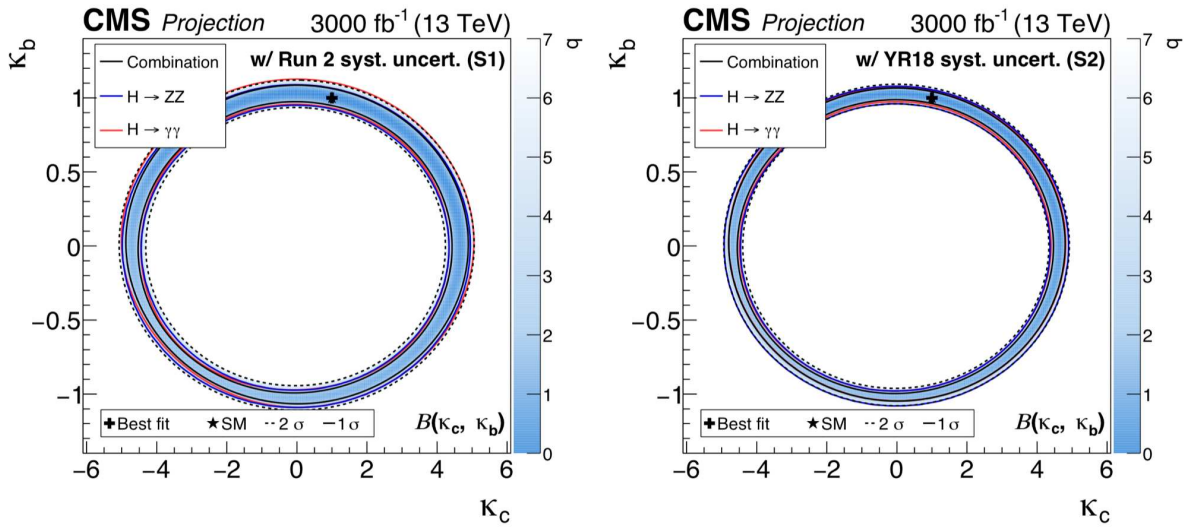

Fig. 127: Simultaneous fit to data for κ_b and κ_c, assuming a coupling dependence of the branching fractions for Scenario 1 (upper) and Scenario 2 (lower). The one standard deviation contour is drawn for the combination (H $\rightarrow \gamma\gamma$ and H $\rightarrow$ ZZ), the H $\rightarrow \gamma\gamma$ channel, and the H $\rightarrow$ ZZ channel in black, red, and blue, respectively. For the combination the two standard deviation contour is drawn as a black dashed line, and the negative log-likelihood value on the coloured axis.

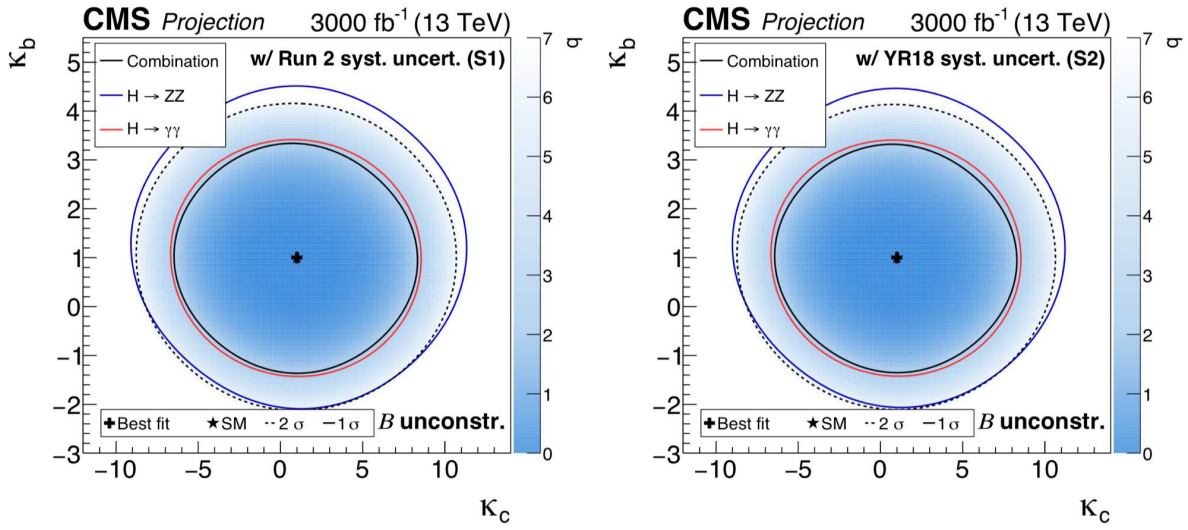

Fig. 128: As Fig. 127, but with the branching fractions implemented as nuisance parameters with no prior constraint.

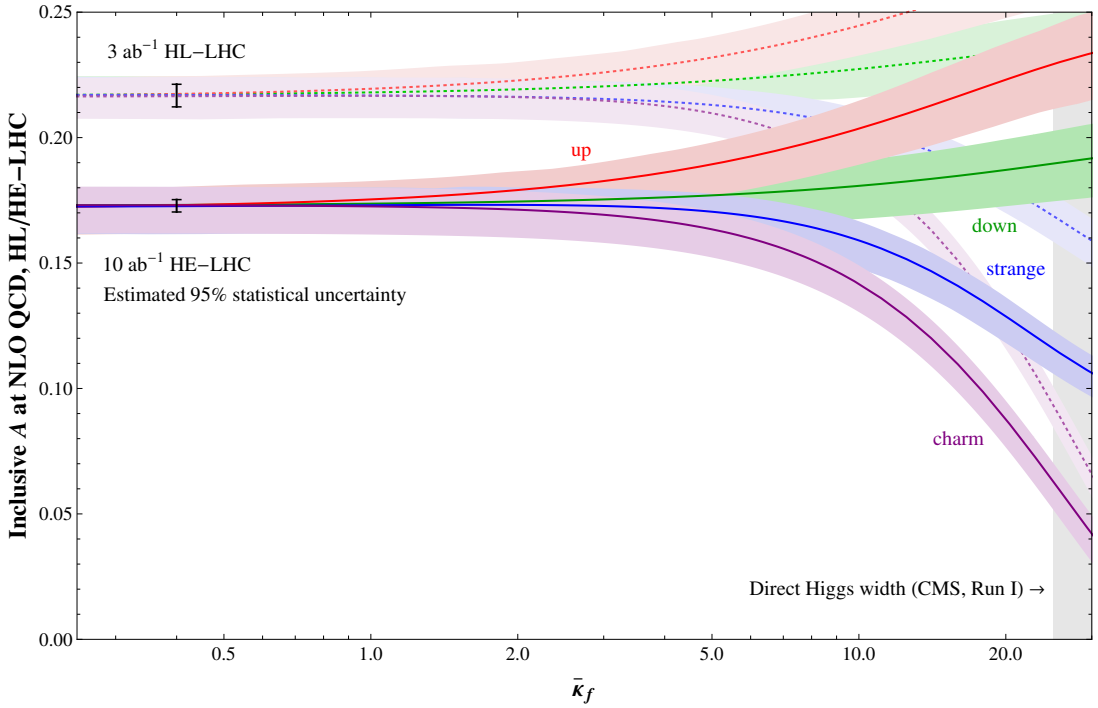

Fig. 129: Inclusive charge asymmetry for $W^{\pm}h$ production at the 27 TeV HE-LHC (solid coloured bands), and 14 TeV HL-LHC (dotted coloured bands), calculated at NLO QCD from MadGraph_aMC@NLO using NNPDF 2.3 as a function of individual Yukawa rescaling factors $\bar{\kappa}_f$ for $f = u$ (red), d (green), s (blue), and c (purple). Shaded bands correspond to scale uncertainties at 1σ from individual $\sigma(W^+h)$ and $\sigma(W^-h)$ production, which are conservatively taken to be fully uncorrelated. The expected statistical errors from this measurement using 10 ab^{-1} of HE-LHC data and 3 ab^{-1} of HL-LHC data are also shown.

and the fact that the dominant $W^{\pm}h$ production mode stems from Higgs bosons radiating from $W^{\pm}$ intermediate lines, where the Yukawa-mediated diagrams are negligible. If the quark Yukawas are not SM-like, however, the charge asymmetry can either increase or decrease, depending on the overall weight of the relevant PDFs. In particular, the charge asymmetry will increase if the down or up quark Yukawa couplings are large, reflecting the increased asymmetry of $u\bar{d}$ vs. $\bar{u}d$ PDFs; the charge asymmetry will decrease if the strange or charm Yukawa couplings are large, reflecting the symmetric nature of $c\bar{s}$ vs. $\bar{c}s$ PDFs. The sub-leading correction from the Cabibbo angle-suppressed PDF contributions determines the asymptotic behaviour for extremely large Yukawa enhancements.

The effect of individual d, u, s, or c quark Yukawa enhancements on the inclusive charge asymmetry is shown in Figure 129, in units of $\bar{\kappa}_f = y_f/y_{\mathrm{SM,\,b}}$, evaluated at the Higgs mass scale. Since $W^{\pm}h$ production probes lower Bjorken-x at the HE-LHC compared to the HL-LHC, the expected SM charge asymmetry is lower at the higher energy collider. In Figure 129, we also display the expected 0.45% statistical sensitivity to the charge asymmetry coming from an HL-LHC simulation study [717] in the $W^{\pm}h \to \ell^{\pm}\ell^{\pm}jj\nu\nu$ final state. To estimate the HE-LHC sensitivity, we simply rescale by the appropriate luminosity ratio, giving 0.25%, since we expect that the increase in both signal and background electroweak rates to largely cancel. We also indicate the constraint from the direct Higgs width constraint using Run I data from CMS [717]. The bands denote the change in the charge asymmetry from the varying the renormalisation and factorisation scales within a factor of 2.

We see that the expected statistical sensitivity supersedes the combined theoretical uncertainty

in the PDF evaluation. Hence, in addition to being an important consistency check of the SM regarding enhanced light quark Yukawa couplings, the charge asymmetry measurement in different Higgs channels can be used to help determine PDFs at the HE-LHC, assuming light quark Yukawa couplings are SM-like. Separately, enhanced light quark Yukawa couplings would also generally be expected to decrease the Higgs signal strengths, necessitating the introduction of other new physics to be consistent with current Higgs measurements [717]. If the signal strengths are fixed to SM expectation and the central prediction is used, the HE-LHC charge asymmetry measurement could constrain $\bar{\kappa}_f \lesssim 2-3$ for up and charm quarks, and $\bar{\kappa}_f \lesssim 7$ for down or strange quarks.

7.7 CP Violation[102]

The CP-violating flavor conserving Yukawa couplings, $\tilde{\kappa}_{f_i}$, can be directly probed at the HL-LHC. Here we focus on the τ and top phases, assuming that the low energy constrained can be avoided. At low energy, the different flavor diagonal CP violating coupling are bounded by EDMs [263, 621, 606, 622, 623]. For the electron Yukawa, the latest ACME measurement [624, 625] results into an upper bound of $\tilde{\kappa}_e < 1.9 \times 10^{-3}$ [606]. Whereas for the bottom and charm Yukawas, the strongest limits come from the neutron EDM [623]. Using the NLO QCD theoretical prediction, this translates into the upper bounds $\tilde{\kappa}_b < 5$ and $\tilde{\kappa}_c < 21$ when theory errors are taken into account. For the light quark CPV Yukawas, measurement of the Mercury EDM places a strong bound on the up and down Yukawas of $\tilde{\kappa}_u < 0.1$ and $\tilde{\kappa}_d < 0.05$ [626] (no theory errors) while the neutron EDM measurement gives a weaker constraint on the strange quark Yukawa of $\tilde{\kappa}_s < 3.1$ [626] (no theory errors).

7.7.1 $t\bar{t}h$

CP violation in the top quark-Higgs coupling is strongly constrained by EDM measurements and Higgs rate measurements [263]. However, these constraints assume that the light quark Yukawa couplings and hWW couplings have their SM values. If this is not the case, the constraints the phase of the top Yukawa coupling relax.

Assuming the EDM and Higgs rate constraints can be avoided, the CP structure of the top quark Yukawa can be probed directly in $pp \to t\bar{t}h$. Many simple observables, such as $m_{t\bar{t}h}$ and $p_{T,h}$ are sensitive to the CP structure, but require reconstructing the top quarks and Higgs.

Some $t\bar{t}h$ observables have been proposed recently that access the CP structure without requiring full event reconstruction. These include the azimuthal angle between the two leptons in a fully leptonic $t\bar{t}$ decay with the additional requirement that the $p_{T,h} > 200\,\text{GeV}$ [264], and the angle between the leptons (again in a fully leptonic $t/\bar{t}$ system) projected onto the plane perpendicular to the h momentum [265]. These observables only require that the Higgs is reconstructed and are inspired by the sensitivity of $\Delta\phi_{\ell^+\ell^-}$ to top/anti-top spin correlations in $pp \to t\bar{t}$ [266]. The sensitivity of both of these observables improves at higher Higgs boost (and therefore higher energy), making them promising targets for the HE-LHC, though no dedicated studies have been carried out to date.

Departures from the SM top quark Yukawa interactions with the Higgs boson can be considered by including a CP-odd component in the effective Lagrangian, i.e., $\mathcal{L}_{tth} = y_t \bar{t}(\cos\alpha + i\gamma_5 \sin\alpha)th$. The pure CP-even (CP-odd) coupling can be recovered by setting $\cos\alpha = 1$ ($\cos\alpha = 0$). Samples of $t\bar{t}h(h \to b\bar{b})$ events were generated at the LHC for $\sqrt{s} = 13$ TeV, with MADGRAPH5_AMC@NLO [79], for several mixing angles, using the `HC_NLO_X0` model [744]. All relevant SM background processes were also generated using MADGRAPH5_AMC@NLO. The analyses of the $t\bar{t}h$ ($h \to b\bar{b}$) events were carried out in the di-leptonic and semi-leptonic decay channels of the $t\bar{t}$ system. Delphes [13] was used for a parametrised detector simulation and both analyses used kinematic fits to fully reconstruct the $t\bar{t}h$

[102] Contacts: E. Gouevia, R. Harnik, B. Le, L. Lechner, Y. Li, A. Martin, A. Onofre, R. Schoefbeck, D. Spitzbart, E. Vryonidou, D. Zanzi

system. The results were extrapolated, as a function of luminosity, up to the full luminosity expected at the HL-LHC (3000 fb^{-1}).

Figure 130 (131) shows the expected CL, assuming the SM, for exclusion of the pure CP-odd scenario, as a function of the integrated luminosity, using the di-leptonic (semi-leptonic) analysis only. The CL were obtained using a di-leptonic (semi-leptonic) signal-enriched region containing events with at least 4 jets and 3 b-tagged jets (with 6 to 8 jets and 3 or 4 b-tagged jets) in which a likelihood ratio was computed from binned distributions of various discriminant observables [745, 746, 314]. Only statistical uncertainties were considered. Figure 132 shows CL obtained from the combination of different observables in each channel i.e., $\Delta\eta(\ell^+,\ell^-)$, $\Delta\phi(t,\bar{t})$ and $\sin(\theta_t^{t\bar{t}H})\sin(\theta_{W^+}^{H})$ in the di-leptonic channel and, b_4 and $\sin(\theta_t^{t\bar{t}H})\sin(\theta_{b_H}^{H})$ in the semi-leptonic channel. The combination of the two channels is also shown for comparison. The observables were treated as uncorrelated. Figure 133 shows a comparison between the CL obtained in the di-leptonic analysis alone, for the exclusion of several values of $\cos\alpha$ (between 0 and 1), taking $\Delta\eta(\ell^+,\ell^-)$ as discriminant variable.

The main conclusions of these studies can be summarised in what follows: i) many angular observables (Fig. 130 and Fig. 131) are available with the potential of discriminating between different mixing-angles ($\cos\alpha$) in the top quark Yukawa coupling; ii) the sensitivity of the semi-leptonic final state of $t\bar{t}h$ ($h\to b\bar{b}$) is higher than the di-leptonic channel alone, which requires roughly five times more luminosity for the same confidence level (Fig. 132); iii) the combination of the semi-leptonic and di-leptonic channels improves visibly the sensitivity with respect to the di-leptonic channel, providing a powerful test of the top quark-Higgs interactions in the fermionic sector.

7.7.2 $\tau\bar{\tau}h$

The most promising direct probe of CP violation in fermionic Higgs decays is the $\tau^+\tau^-$ decay channel, which benefits from a relatively large τ Yukawa giving a SM branching fraction of 6.3%. Measuring the CP violating phase in the tau Yukawa requires a measurement of the linear polarisations of both τ leptons and and the azimuthal angle between them. This can be done by analysing tau substructure, namely the angular distribution of the various components of the tau decay products.

The main τ decay modes studied include $\tau^\pm\to\rho^\pm(770)\nu$, $\rho^\pm\to\pi^\pm\pi^0$ [252, 253, 254, 255, 256, 257] and $\tau^\pm\to\pi^\pm\nu$ [258, 259, 260]. Assuming CPT symmetry, collider observables for CP violation must be built from differential distributions based on triple products of three-vectors. In the first case, $h\to\pi^\pm\pi^0\pi^\mp\pi^0\nu\nu$, angular distributions built only from the outgoing charged and neutral pions are used to determine the CP properties of the initial τ Yukawa coupling. In the second case, $h\to\pi^\pm\pi^\mp\nu\nu$, there are not enough reconstructible independent momenta to construct an observable sensitive to CP violation, requiring additional kinematic information such as the τ decay impact parameter.

In the kinematic limit when each outgoing neutrino is taken to be collinear with its corresponding reconstructed $\rho^\pm$ meson, the acoplanarity angle, denoted Φ, between the two decay planes spanned by the $\rho^\pm\to\pi^\pm\pi^0$ decay products is exactly analogous to the familiar acoplanarity angle from $h\to 4\ell$ CP-property studies. Hence, by measuring the τ decay products in the single-prong final state, suppressing the irreudicible $Z\to\tau^+\tau^-$ and reducible QCD backgrounds, and reconstructing the acoplanarity angle of ρ^+ vs. ρ^-, the differential distribution in Φ gives a sinusoidal shape whose maxima and minima correspond to the CP-phase in the τ Yukawa coupling.

An optimal observable using the collinear approximation was derived in [255]. Assuming 70% efficiency for tagging hadronic τ final states, and neglecting detector effects, the estimated sensitivity for the CP-violating phase of the τ Yukawa coupling using 3 ab^{-1} at the HL-LHC is 8.0°. A more sophisticated analysis [256] found that detector resolution effects on the missing transverse energy distribution degrade the expected sensitivity considerably, and as such, about 1 ab^{-1} is required to distinguish a pure scalar coupling (CP phase is zero) from a pure pseudoscalar coupling (CP phase is $\pi/2$).

A study on the prospect for the measurement of the $\mathcal{CP}$ state of the Higgs boson in its couplings to

τ leptons has been conducted considering 3000 fb^{-1} of pp collision data at $\sqrt{s} = 14$ TeV collected with the ATLAS detector at the HL-LHC [747]. This study investigates the sensitivity for such measurement utilising the $H \to \tau\tau$ decays where both τ leptons decay via $\tau^{\pm} \to \rho^{\pm}\nu\tau \to \pi^{\pm}\pi^{0}\nu_{\tau}$. These decays have a large branching ratio (25%) and offer a simple way to construct an observable that is sensitive to the $\mathcal{CP}$-violating phase ϕ_{τ}. Such observable is the acoplanarity angle $\varphi^{*}_{\mathcal{CP}}$ [254], that is the angle between the τ decay planes that are spanned by each pion pair in the frame where the vectorial sum of the pion momenta is vanishing. The distribution of $\varphi^{*}_{\mathcal{CP}}$ is expected to have sinusoidal shape with a phase that varies linearly with ϕ_{τ}. However, in order to observe such modulation, events need to be categorised based on the sign of the product of the asymmetries $y_{\pm} = (E_{\pm} - E_0)/(E_{\pm} + E_0)$ of the energies of the pions from each τ decay. In fact, events with opposite $y_{+}y_{-}$ have modulations shifted by π in phase.

This study is based on the measurement of the $H\tau\tau$ coupling with 36.1 fb^{-1} of $\sqrt{s} = 13$ TeV data [133] and on an extrapolation of this measurement to the HL-LHC scenario [126]. The same selections on the hadronically decaying τ leptons and on the di-τ events are applied as in the 13 TeV measurement. This assumes that at the HL-LHC the online and offline selections on the hadronically decaying τ leptons will be similar to those applied during the LHC Run-2 [18]. Optimisations of the event selection for the higher centre-of-mass energy, the exclusive τ decay of interest, and the detector effects impacting on the resolution of the observable $\varphi^{*}_{\mathcal{CP}}$ have not been investigated, but are expected to improve the sensitivity.

The performance of the upgraded ATLAS detector [20] has been evaluated with Gaussian smearings of the particle momenta simulated at particle level. The precision in measuring the direction of the π^{0} four-vector is taken to be the same as in Ref. [748]. HL-LHC simulation studies show that the π^{0} p_T and directional resolutions in correctly reconstructed decays, do not degrade in pileup of $< \mu > \sim 200$ by more than a few percent compared to Run-1. However, scenarios with worse resolutions are also considered, since this resolution is expected to have a leading effect on the precision of the $\varphi^{*}_{\mathcal{CP}}$ reconstruction. The uncertainties include only the statistical uncertainties of the expected data sample.

This study shows that even with π^{0} resolutions 1.5 times as large as in the LHC Run-2, the pseudoscalar hypothesis could be excluded at 2σ analysing only the $H \to \tau\tau$ decays where both τ leptons decay via $\tau^{\pm} \to \rho^{\pm}\nu\tau \to \pi^{\pm}\pi^{0}\nu_{\tau}$ (about 6% of the $H \to \tau\tau$ events). The $\mathcal{CP}$-violating phase could be measured at 68.3% confidence level within $\pm 18^{\circ}$ and $\pm 33^{\circ}$ assuming the nominal or a twice as large π^{0} resolution, respectively. Higher sensitivities are expected when more τ decays are included.

At the HE-LHC, the increased signal cross section for Higgs production is counterbalanced by the increased background rates, and so the main expectation is that improvements in sensitivity will be driven by the increased luminosity and more optimised experimental methodology. Rescaling with the appropriate luminosity factors, the optimistic sensitivity to the τ Yukawa phase from acoplanarity studies is 4-5°, while the more conservative estimate is roughly an order of magnitude worse.

8 Global effective field theory fits

The absence to date of conclusive signals of physics beyond the Standard Model (SM) at the Large Hadron Collider (LHC) suggests that there might be a separation of scales between the SM, and whatever may lie beyond it at some higher energy. This motivates using the Standard Model Effective Field Theory (SMEFT) as a tool to search indirectly for new physics in LHC data, given its (near) model-independence, capacity for systematic improvement, and ability to exploit simultaneously multiple datasets. For more motivation and details, see section 1.2.1. Beside the high-energy effects discussed in section 4, the HL and HE-LHC have a great potential in this context via the global fit to electroweak precision (EWPO) and Higgs data, thanks to the higher precision they will reach both in the measurement of some of the crucial input parameters of global EW fits (e.g. M_W, m_t, M_H, and $\sin^2\theta^{\rm lept}_{\rm eff}$) and the measurement of Higgs-boson total rates.

This section focuses on new physics effects, parametrised by extending the SM Lagrangian via gauge-invariant dimension-six operators in eq. (1) and estimates the reach on the Wilson coefficients provided by a global analysis, that is, an analysis with multiple observables and coefficients. A global analysis of constraints on the Wilson coefficients of the SMEFT is of critical importance when more than a few coefficients are allowed to be non-zero, since many SMEFT operators contribute to multiple observables, so that different classes of measurement should not be analysed in isolation. The importance of this feature increases as measurements from the LHC compete in precision with previous generation precision experiments.

Section 8.1 proposes a global fit based on the ATLAS and CMS signal strength extrapolations from section 2.6 and on the use of Simplified Template Cross Sections (STXS) and estimates of the WW production rate. Section 8.2 focuses on universal theories and exploits, instead of STXS, the information obtained in the analysis of high-energy observables in section 4; moreover it includes projections of electroweak precision observables in the context of HL and HE LHC. Finally section 8.3 puts emphasis on the impact of a global fit on measurements of the Higgs cubic self-coupling at the HE LHC.

8.1 Prospective SMEFT Constraints from HL- and HE-LHC Data[103]

In this note, after reviewing the SMEFT framework and our previous results [749, 750, 751, 752], we present projections for the prospective sensitivities of measurements with the approved High-Luminosity LHC (HL-LHC) project and the proposed High-Energy LHC (HE-LHC) project to Wilson coefficients. Our projections are based on ATLAS and CMS estimates of the accuracies with which they could measure Higgs production rates together with our estimates of the possible accuracies of STXS measurements, assuming plausible future reductions in theoretical and systematic errors.

We focus on dimension-6 operators, and work to linear order in the Warsaw basis [41], so as to make a consistent EFT expansion to order $\mathcal{O}(\Lambda^{-2})$. We choose α, G_F, and M_Z as input parameters for our computations, though we note that the choice of input scheme does not have much impact on the results of a fit to Wilson coefficients if a sufficiently global analysis is performed [753]. There are 2499 baryon-number-preserving dimension-6 Wilson coefficients in the SMEFT [754]. Here we assume a $U(3)^5$ flavor symmetry between the operator coefficients for the five lighter SM fermion fields, which reduces the number of (real) coefficients to 76. However only 20 of those parameters are relevant for the di-boson, electroweak precision and Higgs observables that we consider here.

In the Warsaw basis, the 11 operators from table 1 relevant for di-boson measurements and electroweak precision observables, whether through direct contributions or shifts in input parameters, can be

[103] Contacts: J. Ellis, C.W. Murphy, V. Sanz, T. You

written as [104]

$$\begin{aligned}\mathcal{L}^{\text{Warsaw}}_{\text{SMEFT}} \supset\ & \frac{C^{(3)}_{HL}}{\Lambda^2}(H^\dagger i\overleftrightarrow{D}^I_\mu H)(\bar\ell\tau^I\gamma^\mu\ell) + \frac{C_{HL}}{\Lambda^2}(H^\dagger i\overleftrightarrow{D}_\mu H)(\bar\ell\gamma^\mu\ell) + \frac{C_{LL}}{\Lambda^2}(\bar\ell\gamma_\mu\ell)(\bar\ell\gamma^\mu\ell)\\ &+ \frac{C_{HD}}{\Lambda^2}\left|H^\dagger D_\mu H\right|^2 + \frac{C_{WB}}{\Lambda^2}gg' H^\dagger\tau^I H\, W^I_{\mu\nu}B^{\mu\nu}\\ &+ \frac{C_{He}}{\Lambda^2}(H^\dagger i\overleftrightarrow{D}_\mu H)(\bar e\gamma^\mu e) + \frac{C_{Hu}}{\Lambda^2}(H^\dagger i\overleftrightarrow{D}_\mu H)(\bar u\gamma^\mu u) + \frac{C_{Hd}}{\Lambda^2}(H^\dagger i\overleftrightarrow{D}_\mu H)(\bar d\gamma^\mu d)\\ &+ \frac{C^{(3)}_{HQ}}{\Lambda^2}(H^\dagger i\overleftrightarrow{D}^I_\mu H)(\bar q\tau^I\gamma^\mu q) + \frac{C_{HQ}}{\Lambda^2}(H^\dagger i\overleftrightarrow{D}_\mu H)(\bar q\gamma^\mu q) + \frac{C_{3W}}{\Lambda^2}\frac{g}{3!}\epsilon^{IJK}W^{I\nu}_\mu W^{J\rho}_\nu W^{K\mu}_\rho\,, \end{aligned} \tag{170}$$

where Hermitian conjugate operators are implicit. The flavor indices are trivial, except for the four-lepton operator, $C_{LL} = C_{\substack{LL\\ e\mu\mu e}} = C_{\substack{LL\\ \mu ee\mu}}$ [755], and are also left implicit. There are an additional nine operators that contribute to Higgs measurements,

$$\begin{aligned}\mathcal{L}^{\text{Warsaw}}_{\text{SMEFT}} \supset\ & \frac{C_{y_e}}{\Lambda^2}y_e(H^\dagger H)(\bar\ell eH) + \frac{C_{y_d}}{\Lambda^2}y_d(H^\dagger H)(\bar q dH) + \frac{C_{y_u}}{\Lambda^2}y_u(H^\dagger H)(\bar q u\widetilde{H})\\ &+ \frac{C_{3G}}{\Lambda^2}\frac{g_s}{3!}f^{ABC}G^{A\nu}_\mu G^{B\rho}_\nu G^{C\mu}_\rho + \frac{C_H}{\Lambda^2}\frac{1}{2}\left(\partial^\mu|H|^2\right)^2 + \frac{C_{uG}}{\Lambda^2}y_u(\bar q\sigma^{\mu\nu}T^A u)\widetilde{H}\,G^A_{\mu\nu}\\ &+ \frac{C_{WW}}{\Lambda^2}g^2 H^\dagger H\, W^I_{\mu\nu}W^{I\mu\nu} + \frac{C_{BB}}{\Lambda^2}g'^2 H^\dagger H\, B_{\mu\nu}B^{\mu\nu} + \frac{C_{GG}}{\Lambda^2}g_s^2 H^\dagger H\, G^A_{\mu\nu}G^{A\mu\nu}\,. \end{aligned} \tag{171}$$

The explicit appearance of the Yukawa matrices in Eq. (171) is necessary to preserve formally the $U(3)^5$ flavor symmetry. We neglect here $\mathcal{O}_6$ which is discussed in detail in sections 3 and 8.3. All of the operators in Eq. (170) except $\mathcal{O}_{3W}$ affect Higgs measurements at leading order, and $\mathcal{O}_{3W}$ contributes to Higgs processes at next-to-leading order [754, 756, 757, 758, 759]. We note also that Higgs production in association with a top-quark pair probes additional terms in the SMEFT [760, 761, 749] that do not contribute to the other observables we consider. The only one we consider explicitly is C_{uG}, which makes the largest contribution to $t\bar t h$ production [749] [105].

In our global fit to the current data we have used the predictions for electroweak precision observables and WW scattering at LEP 2 in the Warsaw basis from Refs. [762, 763], and predictions for LHC observables are made using `SMEFTsim` [764]. The following data are used in our global fit:

- *Pre-LHC data*: We use 11 Z-pole observables from LEP 1 and one from SLC, as given in Ref. [765], as well as the W mass measurement from the Tevatron [766]. In addition, we use all the LEP 2 data for the processes $e^+e^- \to W^+W^- \to 4f$, as compiled in Ref. [762], the original experimental papers being Refs. [767, 768, 769, 770]. These measurements probe eleven directions in the SMEFT, which can be mapped to the operators in Eq. (170).
- *LHC Run 1 data*: We use all the 20 Higgs signal strengths from Table 8 of Ref. [144]. We also use the ATLAS and CMS combination for the $h \to \mu^+\mu^-$ signal strength [144], and the ATLAS $h \to Z\gamma$ signal strength [229]. We also include the W mass measurement from ATLAS [771].

[104] The operator definitions and normalisations used here differ slightly from those used in the Warsaw basis in Ref. [749]. For convenience we list here the relations between the Wilson coefficients in the two notations:

$$\begin{aligned}&\bar C_H = \frac{v^2}{\Lambda^2}C_6\,,\ \bar C^{(3)}_{H\ell} = \frac{v^2}{\Lambda^2}C^{(3)}_{HL}\,,\ \bar C^{(1)}_{H\ell} = \frac{v^2}{\Lambda^2}C_{HL}\,,\ \bar C_{\ell\ell} = \frac{v^2}{\Lambda^2}C_{LL}\,,\ \bar C_{HD} = \frac{v^2}{\Lambda^2}C_{HD}\,,\\ &\bar C_{HWB} = \frac{v^2}{\Lambda^2}gg'C_{WB}\,,\ \bar C_{He,Hu,Hd} = \frac{v^2}{\Lambda^2}C_{He,Hu,Hd}\,,\ \bar C^{(3)}_{Hq} = \frac{v^2}{\Lambda^2}C^{(3)}_{HQ}\,,\ \bar C^{(1)}_{Hq} = \frac{v^2}{\Lambda^2}C_{HQ}\,,\\ &\bar C_W = \frac{v^2}{\Lambda^2}\frac{g}{3!}C_{3W}\,,\ \bar C_{eH,dH,uH} = \frac{v^2}{\Lambda^2}C_{ye,yd,yu}\,,\ \bar C_{H\Box} = \frac{v^2}{\Lambda^2}\frac{1}{2}C_H\,,\ \bar C_{HW} = \frac{v^2}{\Lambda^2}g^2C_{WW}\,,\\ &\bar C_{HB} = \frac{v^2}{\Lambda^2}g'^2C_{BB}\,,\ \bar C_{HG} = \frac{v^2}{\Lambda^2}g_s^2C_{GG}\,,\ \bar C_G = \frac{v^2}{\Lambda^2}\frac{g_s}{3!}C_{3G}\,.\end{aligned}$$

[105] For an alternative analysis including all the operators, see [752].

– *LHC Run 2 data*: We use 25 measurements from CMS [178, 138, 167, 179, 177, 123, 128, 134], and 23 measurements from ATLAS [140, 236, 166, 168, 239, 772, 233], including experimental correlations whenever possible. In addition, we include one ATLAS measurement at 13 TeV of the differential cross section for $pp \to W^+W^- \to e^\pm\nu\mu^\mp\nu$ that requires $p_T > 120$ GeV for the leading lepton [773].

Selection of Current Results. In this Section we summarise the main result of the global fit to current data in Ref. [749]. Fig. 134 summarises the sensitivities to operator coefficients in the Warsaw basis. It shows the 95% CL bounds in TeV on the Wilson coefficients, as obtained in [749] from marginalised (orange) and individual (green) fits to the 20 dimension-6 operators entering in electroweak precision tests, di-boson and Higgs measurements at LEP, SLC, Tevatron, and LHC Runs 1 and 2. Also shown, in blue, are the analogous results of the individual fits of the HEPfit Collaboration [774, 727] [106]. We note that the degree of agreement in the individual operator fits is generally good.

Table 87 gives the Fisher information contained in a given dataset per number of measurements in that dataset, for each coefficient in the case where one operator is switched on at a time. The datasets are categorised as in Ref. [749], where a cross indicates no (current) sensitivity. This Table is the per-measurement analogue of Table 5 of Ref. [749], and shows that LHC di-boson measurements are more powerful than LEP 2 di-boson measurements for constraining triple gauge couplings (TGCs). In the Warsaw basis the three TGCs correspond to C_{WB}, C_{3W}, and a linear combination of C_{HD}, $C_{HL}^{(3)}$, C_{WB}, and C_{LL}. We note, however, that Z-pole and Higgs-pole measurements are more constraining for all but C_{3W}.

Future Projections. We use the same framework as described in Ref. [749] to project how the sensitivities to the Wilson coefficients of the SMEFT will change at HL- and HE-LHC. Our projection strategy is as follows: we leave all pre-LHC, and LHC Run-1 measurements unchanged; we adopt the CMS and ATLAS WG2 recommendations for the HL- and HE-LHC sensitivities, using the HL-LHC S2 scenario for the experimental projections on the signal strength uncertainties and their associated correlation matrix (provided separately by ATLAS and CMS); and the remaining statistical uncertainties at HL- and HE-LHC are assumed to scale naively with the integrated luminosities and cross sections:

$$\frac{\delta\mathcal{O}_{\text{HL},i}}{\delta\mathcal{O}_{\text{today},i}} = \sqrt{\frac{L_{\text{today},i}}{L_{\text{HL}}}}\,, \quad \frac{\delta\mathcal{O}_{\text{HE},i}}{\delta\mathcal{O}_{\text{today},i}} = \sqrt{\frac{\sigma_{13,i}}{\sigma_{27,i}}\frac{L_{\text{today},i}}{L_{\text{HE}}}}\,.$$

For almost all the measurements by ATLAS(CMS) $L_{\text{today},i} = 36.1(35.9)$ fb^{-1}, and we use the benchmark luminosities $L_{\text{HL}} = 3$ ab^{-1} and $L_{\text{HE}} = 15$ ab^{-1} for all the measurements in the respective HL- and HE-LHC extrapolations. The cross sections $\sigma_{13,i}$ and $\sigma_{27,i}$ refer to the SM cross sections in the signal region for a given measurement i at 13 and 27 TeV, respectively. At HE-LHC the S2 systematics are reduced by half. For the STXS and WW measurements used in Ref. [749], since no official projections have been made yet, we extrapolate the statistical part as described above and treat the systematics as unchanged for HL-LHC and halve them for HE-LHC. The correlations between experimental measurements are assumed to be unchanged.

We stress that both our projection scenarios are pessimistic in the sense that they do not take into account the additional channels [778], finer binning [45, 779, 772] and extension of the STXS method to larger kinematic regions that will become available as more data are collected. Furthermore, as suggested by Table 87, our projections under-utilise LHC di-boson scattering measurements [418, 416, 780].

[106] See also [775, 776]. For a recent fit in another basis see Ref. [777], and for a recent fit in the nonlinear Effective Theory see Ref. [185].

Table 87: *Impacts of different sets of measurements on the fit to individual Wilson coefficients in the Warsaw basis as measured by the Fisher information contained in a given dataset per number of measurements in that dataset for each coefficient. A cross indicates no (current) sensitivity.*

Coefficient	Z-pole + m_W	WW at LEP2	Higgs Run1	Higgs Run2	LHC WW high-p_T
C_{yd}	$\times$	$\times$	10	8.1	$\times$
C_{ye}	$\times$	$\times$	2.9	1.3	$\times$
C_{3G}	$\times$	$\times$	0.5	9.1	$\times$
C_{BB}	$\times$	$\times$	$9.9 \cdot 10^5$	$2.0 \cdot 10^6$	$\times$
C_H	$\times$	$\times$	8.1	15	0.1
C_{Hd}	$7.4 \cdot 10^3$	$\times$	2.0	1.5	9.8
C_{HD}	$4.3 \cdot 10^5$	51	4.6	4.5	$5.5 \cdot 10^2$
C_{He}	$6.5 \cdot 10^5$	14	$1.1 \cdot 10^{-2}$	$3.7 \cdot 10^{-2}$	$\times$
C_{GG}	$\times$	$\times$	$9.8 \cdot 10^5$	$8.6 \cdot 10^5$	$1.5 \cdot 10^4$
C_{HL}	$1.1 \cdot 10^6$	51	$1.1 \cdot 10^{-2}$	$3.6 \cdot 10^{-2}$	$4.6 \cdot 10^{-3}$
$C_{HL}^{(3)}$	$1.7 \cdot 10^6$	$1.3 \cdot 10^3$	51	49	$3.5 \cdot 10^3$
C_{HQ}	$6.4 \cdot 10^4$	$\times$	2.3	1.0	37
$C_{HQ}^{(3)}$	$4.9 \cdot 10^5$	$9.1 \cdot 10^2$	$5.9 \cdot 10^2$	$3.3 \cdot 10^2$	$5.0 \cdot 10^3$
C_{Hu}	$1.4 \cdot 10^4$	$\times$	18	12	83
C_{WW}	$\times$	$\times$	$9.1 \cdot 10^4$	$1.8 \cdot 10^5$	$7.0 \cdot 10^{-3}$
C_{WB}	$3.3 \cdot 10^6$	$1.9 \cdot 10^2$	$3.0 \cdot 10^5$	$5.7 \cdot 10^5$	$2.2 \cdot 10^3$
C_{LL}	$5.5 \cdot 10^5$	$3.3 \cdot 10^2$	16	21	$6.0 \cdot 10^2$
C_{uG}	$\times$	$\times$	18	97	$\times$
C_{yu}	$\times$	$\times$	0.4	1.8	$\times$
C_{3W}	$\times$	6.7	$\times$	$\times$	19

The results of our projections are shown in Figures 135 and 136 for individual and marginalised 95% CL sensitivities respectively. The vertical axis is the operator scale in units of TeV divided by the square root of the dimensionless Wilson coefficient. Increasingly darker shades for the four bars represent the sensitivities of the LHC up to now, HL-LHC with 3 ab^{-1}, HE-LHC with 15 ab^{-1}, and combining HL- and HE-LHC results (neglecting any correlations between the two). We see that in the individual bounds the sensitivity for each operator increases correspondingly, except for those that are only constrained by electroweak precision tests, which remain unchanged from their current LEP limits. In the marginalised case even the latter operators benefit from an improvement in the limits on other operators. We note that in going from HL- to HE-LHC there is a decrease in the marginalised sensitivity for C_{GG}, C_{uG}, and C_{yu}, despite improvements in their individual bounds. This is because C_{uG} and C_{yu} enter only in tth production, and the relative increase in their contribution with respect to C_{GG} in going from 13 to 27 TeV opens up a relatively flat direction in the parameter space, reducing the sensitivity to all three coefficients. This degeneracy can be broken by measurements at different energies, as shown in the combined HL/HE-LHC fit, or by including measurements involving top quarks.

In general, we see that data from HL- and/or HE-LHC would extend the sensitivity to new physics into the multi-TeV range for most operator coefficients, extending to tens of TeV for C_{GG}.

8.2 Global constraints on universal new physics at the HL/HE-LHC[107]

To systematically study the effects of new physics on EWPO and Higgs-boson observables we consider a SM effective field theory that adds to the Lagrangian of the SM new effective interactions of the SM

[107] Contacts: J. de Blas, M. Ciuchini, E. Franco, S. Mishima, M. Pierini, L. Reina, L. Silvestrini

fields in the form of higher-dimension ($d > 4$) local operators that preserve the SM gauge symmetry, eq. (1). While using, e.g., the complete basis of dimension-six interactions presented in Ref. [41] one can test new physics effects in a more general way (provided one has enough experimental inputs), for the purpose of the fit presented in this Section we are interested only in those new physics effects that arise in the context of the so-called *universal theories* [420, 781]. In the EFT framework universal theories can be defined such that, via field re-definitions, all new physics effects can be captured by operators involving SM bosons only. Note that this includes not only theories where the new particles couple to the SM bosonic sector, but also scenarios where the interactions occur via the SM fermionic currents. Therefore, this class of theories automatically satisfy minimal flavour violation, so the results of the global fit to Higgs and electroweak data are not affected by the strong constraints set by flavour measurements. Furthermore, we will assume only CP-preserving interactions. In particular, we will focus on the following non-redundant set of operators, among those defined in Table 1[108]:

$$\{\mathcal{O}_H, \mathcal{O}_{HD}, \mathcal{O}_6, \mathcal{O}_{GG}, \mathcal{O}_{BB}, \mathcal{O}_{WW}, \mathcal{O}_{WB}, \mathcal{O}_{HB}, \mathcal{O}_{HW}, \mathcal{O}_{2B}, \mathcal{O}_{2W}, \mathcal{O}_{3W}, \mathcal{O}_y\}. \tag{172}$$

Of course, we note that the HL-LHC data allows to constrain EFT effects beyond the context of this class of universal new physics, e.g. constraining independently Higgs couplings to different types of fermions, or operators modifying the EW interactions in a non-universal way. Therefore, the results presented in this section are to be understood not as an exhaustive exploration of the HL/HE-LHC capabilities, but as the interpretation within a particularly broad and well-motivated class of scenarios of physic beyond the SM.

The global fit of EWPO and Higgs data is performed using the `HEPfit` package [215], a general tool to combine direct and indirect constraints on the SM and its extensions in any statistical framework. The default fit procedure, which we use here, follows a Bayesian statistical approach and uses BAT (Bayesian Analysis Toolkit) [782]. We use flat priors for all input parameters, and build the likelihood assuming Gaussian distributions for all experimental measurements. The output of the fit is therefore given as the posterior distributions for each input parameter and observable, calculated using a Markov Chain Monte Carlo method.

For the results in this section we use the SMEFT class in `HEPfit` for the calculation of the dimension-6 effects in EWPO and Higgs signal strengths. The EFT expressions for these physical observables are truncated consistently with the dimension-6 expansion of the SMEFT Lagrangian, retaining only terms of order $1/\Lambda^2$, i.e.

$$O = O_{\rm SM} + \sum_i a_i \frac{C_i}{\Lambda^2}\,. \tag{173}$$

For the SM prediction of all EWPO we include all available higher-order corrections, including the latest theoretical developments in the calculation of radiative corrections to the EWPO of [783, 784]. On the other hand, for the SM predictions of Higgs production cross sections and decay rates we use the results quoted in [45] and in the current report. The new physics corrections to most Higgs production cross sections are obtained using `Madgraph`, with our own implementation of the dimension-6 SMEFT Lagrangian in a `FeynRules` UFO model, except for the corrections to the gluon-gluon fusion production cross section that is computed analytically. The corrections to Higgs decay rates are also computed using `Madgraph`, or analytically following the calculations presented in the `eHdecay` code.

One of the advantages of `HEPfit` is its modularity, allowing for an easy implementation of new physics models or additional observables. Taking advantage of this, we have extended the fits to EWPO plus Higgs signal strengths to include several of the studies presented in this report, and in particular those presented in the di-Higgs or the High Energy probes sections. We provide details of the observables in the fits for the HL-LHC or HE-LHC scenarios in what follows, before presenting our results.

[108] In principle, the physics at hadron colliders also allows to test the universal interactions $\mathcal{O}_{2G}$ and $\mathcal{O}_{3G}$. Due to the absence of HL-LHC projections for the relevant processes that can be used to constrain such operators, we do not include them in the global fits presented here.

HL-LHC inputs for the fit

We include both the projected improvements in the Higgs signal strength measurements from ATLAS and CMS in the HL-LHC scenario, as well as also the corresponding projections for the measurements of EWPO. For the details of the EWPO analysis we refer to the corresponding HL-LHC study presented in the report of the activities of the WG1 of this workshop [785]. The HL-LHC Higgs signal strength projections are implemented directly from the values provided by ATLAS and CMS in the two scenarios for systematic and theory uncertainties denoted as S1 — which assumes the same uncertainties as in current data— and S2 —where systematics are improved with the luminosity and theory uncertainties are reduced. The correlations between the ATLAS and CMS sets of inputs were not available at the time these fits were performed, and therefore we combined them in an uncorrelated manner. One must take into account that such correlations, especially between theory uncertainties, can be sizeable. Therefore, the results of this uncorrelated combination can be somewhat optimistic. Finally, estimates for the $H \to Z\gamma$ channel are not available within the set of CMS projections, so we assume measurements with the same precision as ATLAS.

These results have been further combined with several of the studies presented in this report. For the HL-LHC studies we include:

1. The differential distribution in M_{HH} in the $HH \to b\bar{b}\gamma\gamma$ channel presented in Section 3.5.3. This was available only for the HL-LHC scenario. No difference in term of the assumption for systematics is applied between the S1 and S2 scenarios.
2. The results from the study of the invariant mass distribution, M_{ZH} in the $ZH, H \to b\bar{b}$ channel in the boosted regime from Section 4.2. Results for S1 scenario assume 5% systematics while a systematic uncertainty of only 1% is applied in the S2 case.

Furthermore, we combine these results with those obtained from the high-energy measurements in the di-boson channel presented in:

3. Section 4.3: We include the bounds on the operator $\mathcal{O}_{3W}$ from the exclusive analysis. As in the ZH case, we assume a systematic uncertainty of 5% (1%) for the S1 (S2) scenario.
4. The invariant $p_{T,V}$ distributions in $pp \to WZ$ production from the analysis in Section 4.1. The systematics are applied as in the previous observables.

Finally, as we assume in our fit that the new physics only affects "low-energy" observables in a universal way, we also include:

5. The sensitivity study to the W and Y parameters —which one can map into C_{2W} and C_{2B}, respectively— in Drell-Yan production from Section 4.4. Systematics uncertainties are fixed in this case, with no difference between the S1 and S2 fits.

HE-LHC inputs for the fit

The same observables included in the HL-LHC study are also used in the HE-LHC scenario. For the case of the Higgs signal strengths, we follow the agreed ATLAS and CMS guidelines for the calculation of the HE-LHC projections. Starting from the precisions given in the HL-LHC S2 signal strengths, we scale the statistical uncertainties of the projections according to the cross section and luminosities of the HE-LHC scenario, i.e.

$$\delta_{\text{stat}}\mu_{\text{HE-LHC}} = \sqrt{\frac{\sigma^{14\text{TeV}}_{pp\to H} \times 3\text{ab}^{-1}}{\sigma^{27\text{TeV}}_{pp\to H} \times 15\text{ab}^{-1}}}\delta_{\text{stat}}\mu_{\text{HL-LHC}}. \tag{174}$$

We consider this as the *"Base"* HE-LHC scenario. A more optimistic scenario was also suggested, reducing the systematics and theory uncertainties by a factor of 2. While we also include this scenario in

our fits —we denote it by *"Opt."*— we must note that it does not come from a thoughtful extrapolation of the possible reduction of uncertainties but, instead, should be consider only as an hypothesis.

The study of EWPO observables is kept as in the HL-LHC scenario. Similarly, the studies of the M_{HH} and M_{ZH} differential distributions presented in the corresponding sections of this report where available only for $\sqrt{s} = 14$ TeV. For the HE-LHC fit we use, instead of the M_{HH} distribution, the results on the Higgs self-coupling from Section 3.4.1. For the M_{ZH} distribution we include the same result as for HL-LHC. All the other analyses are available for the HE-LHC scenario.[109] Whenever possible, the sensitivities have been scaled to the expected luminosity of 15 ab^{-1}.

The Global EFT fit for Universal new physics

The main results of the fits to universal new physics in the HL-LHC and HE-LHC are illustrated in Figures 137 and 138, respectively. The results are shown as the 95% probability limits on the *new physics interaction scale*, $\Lambda/\sqrt{|C_i|}$, associated to each operator $\mathcal{O}_i$. (We also show, in the right axis, the value translated into the sensitivities to the ratios $|C_i|/\Lambda^2$, which give the linear new physics correction to each observable.) The limits are compared with those obtained from current data from LEP/SLD, the LHC Runs 1 and 2 [727, 786, 787, 788], and the LHC sensitivity for W and Y from Ref. [440]. We also indicate, with dashed lines, the *exclusive* bounds obtained assuming that the new physics only generates one operator at a time. The difference between the global and exclusive limits indicates the presence of large correlations between the dimension-six interactions in the global fit.

As it is apparent, there is a significant improvement in the sensitivity to new physics for many types of interactions. This is particularly evident for those operators entering in the high-energy probes. For instance, the sensitivity to $\mathcal{O}_{3W}$ effects is largely improved with respect to the bounds obtained from LEP 2 $e^+e^- \to W^+W^-$ data. The operators $\mathcal{O}_{HW,HB}$ also induce effects that grow with the energy in $pp \to ZH$ or $pp \to WZ$ (for $\mathcal{O}_{HW}$), thus leading to more stringent bounds compared to the fit using current data, which does not include the effect of high-energy observables in those channels. The operators $\mathcal{O}_{2W,2B}$ are mainly constrained from their effects in Drell-Yan. The improvement in the limits on these operators is more visible in the exclusive bounds, because of the absence of HE-LHC estimates for the Drell-Yan analysis in the charged-current channel (See Section 4.4).

Finally, it is worth noticing the improvements on some of the operators whose effects in the observables we consider are constant with the energy. Such improvement is therefore the result of a pure increase in the experimental precision in the measurements of the corresponding observables. This is the case for the interactions $\mathcal{O}_{GG,WW,BB}$. Their main effect is to generate tree-level contributions to loop-induced Higgs boson observables, e.g. $gg \to H$ or $H \to \gamma\gamma, Z\gamma$, whose precision, especially for the rare decay channels, will be largely increased with more luminosity.

[109] The analysis of the Drell-Yan constraints on WY only contains projections at 27 TeV for the neutral channel $pp \to \ell^+\ell^-$. For the charged current $pp \to \ell\nu$ we use same constraints on the W parameter given at 14 TeV.

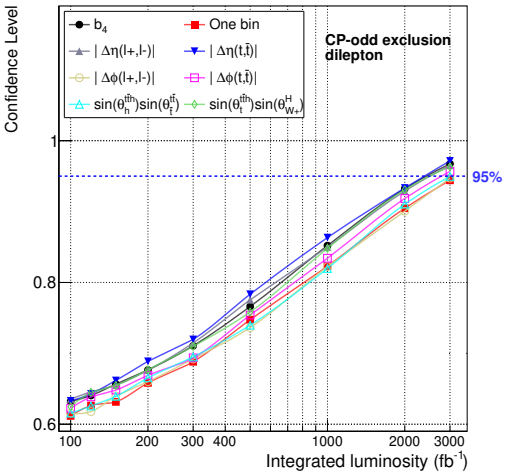

Fig. 130: Expected CL, assuming the SM, for exclusion of the pure CP-odd scenario, as a function of the integrated luminosity, using the $t\bar{t}h$ ($h \to b\bar{b}$) di-leptonic analysis only. A likelihood ratio computed from the binned distribution of the corresponding discriminant observable was used as test statistic.

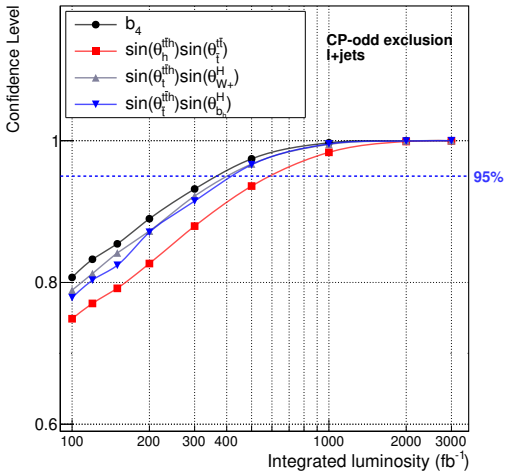

Fig. 131: Expected CL, assuming the SM, for exclusion of the pure CP-odd scenario, as a function of the integrated luminosity, using the $t\bar{t}h$ ($h \to b\bar{b}$) semi-leptonic analysis only. A likelihood ratio computed from the binned distribution of the corresponding discriminant observable was used as test statistic.

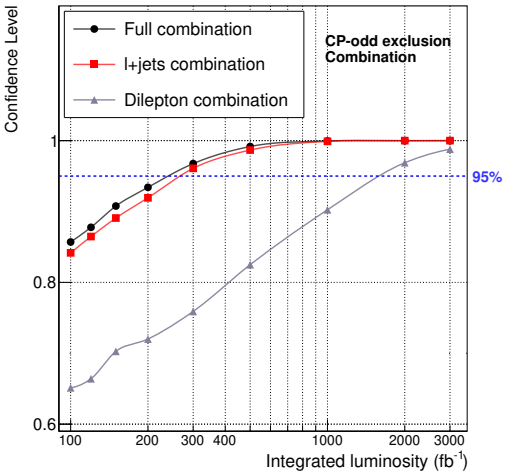

Fig. 132: Expected CL, assuming the SM, for exclusion of the pure CP-odd scenario, as a function of the integrated luminosity, combining observables in each individual channel and combining both channels. The observables were treated as uncorrelated.

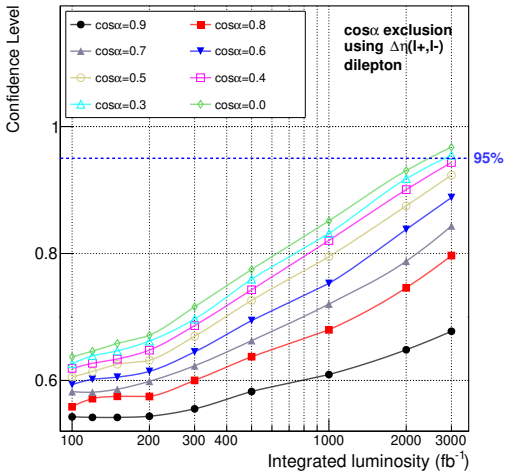

Fig. 133: Expected CL, assuming the SM, in the $t\bar{t}h$ ($h \to b\bar{b}$) di-leptonic analysis alone, for the exclusion of various $\cos\alpha$ values between 0 and 1, as a function of the integrated luminosity. The results shown used the $\Delta\eta(\ell^+, \ell^-)$ as discriminant variable.

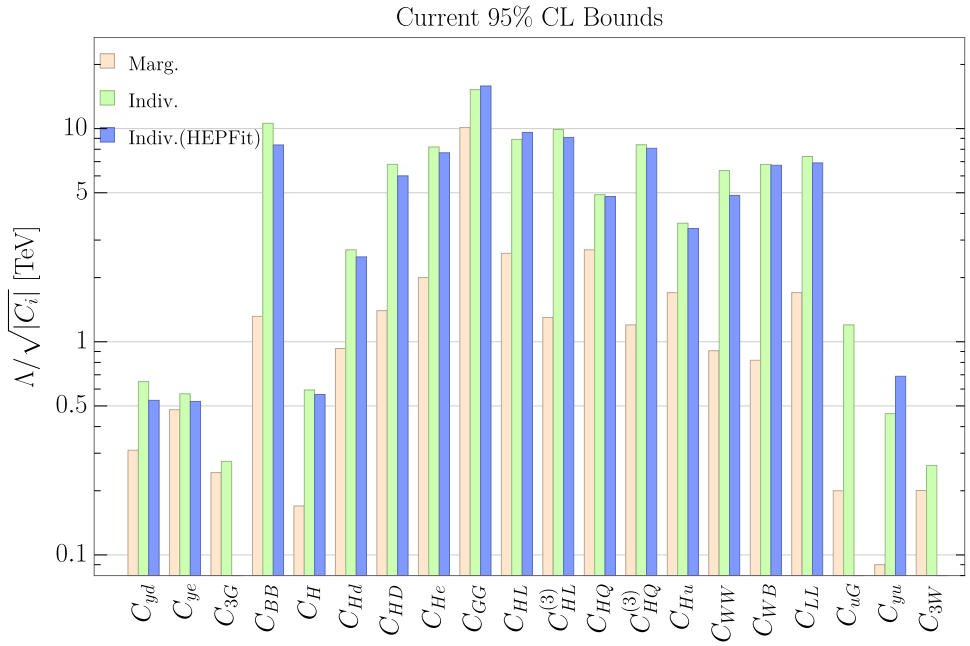

Fig. 134: *Current constraints on dimension-6 operators. The orange and green bars are the marginalised and individual limits from Ref. [749], respectively. The analogous results of the HEPfit Collaboration [774, 727] for the case where only one operator is switched on at a time are shown in blue.*

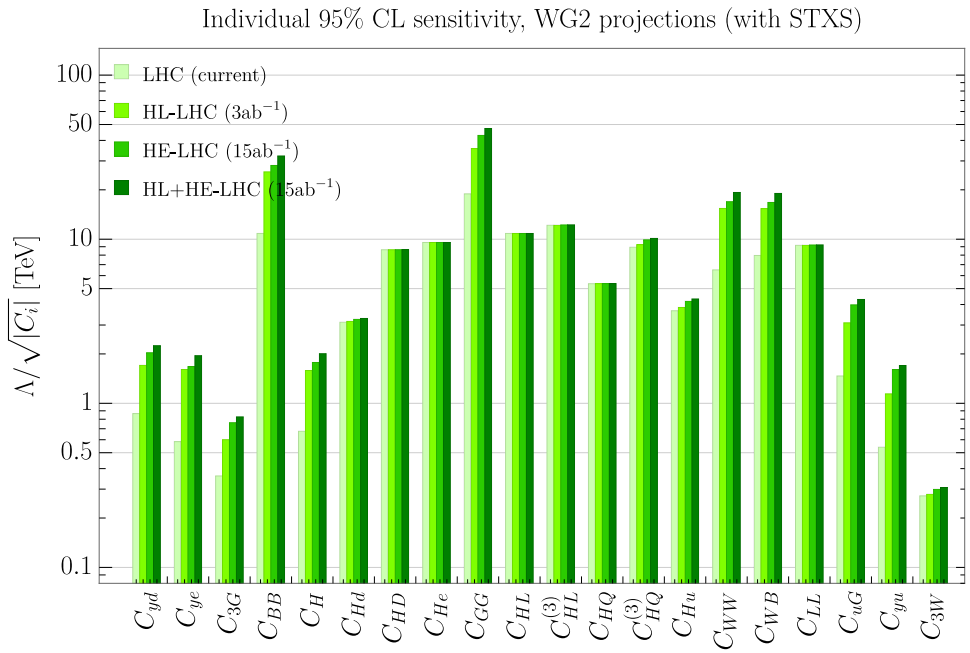

Fig. 135: *Individual 95% CL projected sensitivities for LHC, HL-LHC, HE-LHC, and combined HL/HE-LHC in increasingly darker shades of green. The vertical axis gives the reach to the scale of new physics divided by the dimensionless Wilson coefficient, in units of TeV.*

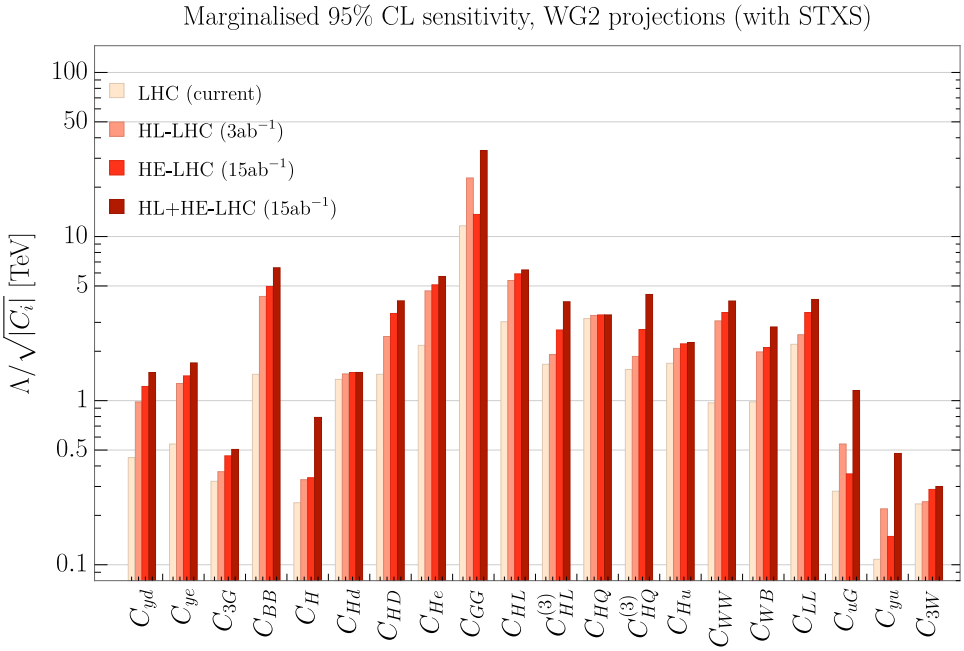

Fig. 136: *Marginalised 95% CL projected sensitivities for LHC, HL-LHC, HE-LHC, and combined HL/HE-LHC in increasingly darker shades of red. The vertical axis gives the reach to the scale of new physics divided by the dimensionless Wilson coefficient, in units of TeV.*

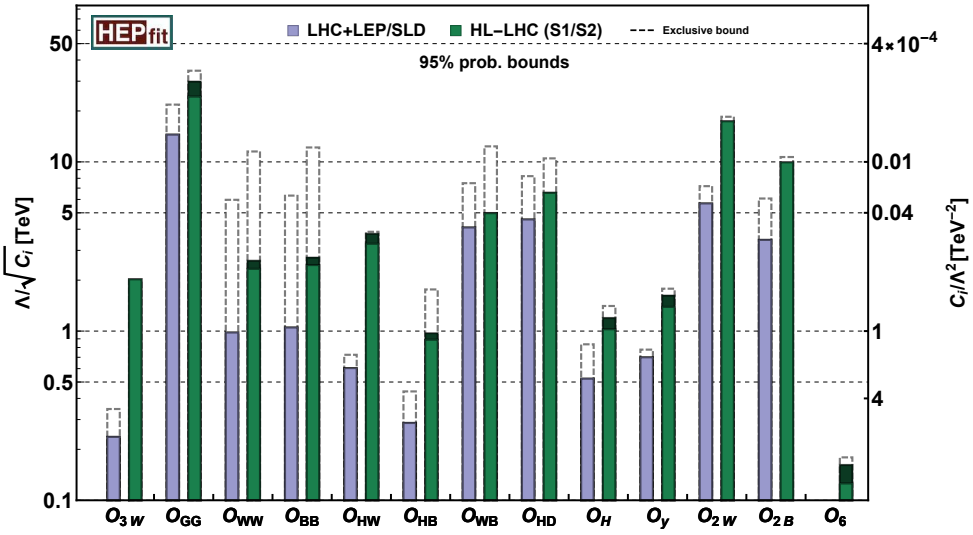

Fig. 137: 95% probability limits on the new physics interaction scale $\Lambda/\sqrt{|C_i|}$ [TeV] (left axis) and coefficients $|C_i|/\Lambda^2$ [TeV $^{-2}$] (right axis) associated to each dimension-six operator from the global fit to universal new physics at the HL-LHC (green bars, light and dark shades indicate the S1 and S2 assumptions for systematics, respectively). The limits are compared with the ones from current data (in blue), as well as those obtained assuming only one operator at a time (dashed lines).

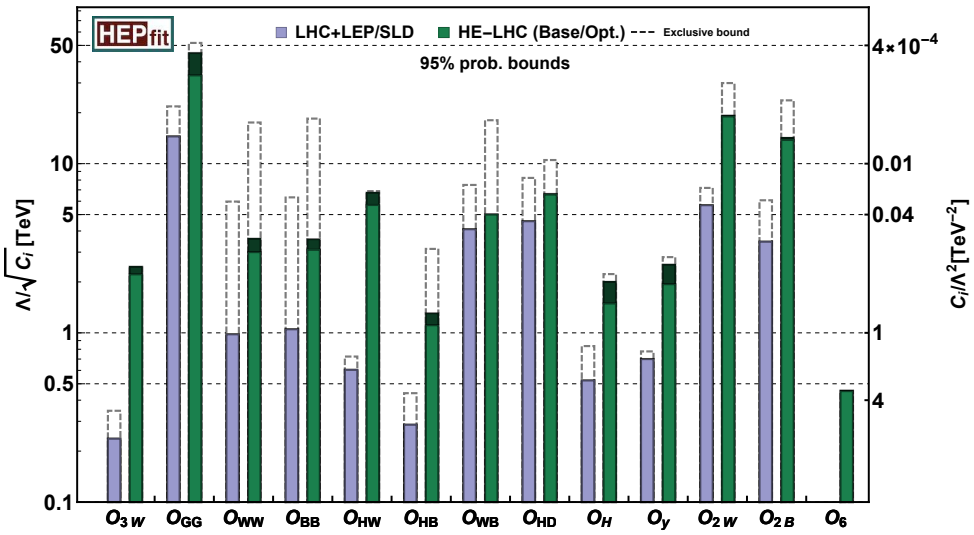

Fig. 138: 95% probability limits on the new physics interaction scale $\Lambda/\sqrt{|C_i|}$ [TeV] (left axis) and coefficients $|C_i|/\Lambda^2$ [TeV $^{-2}$] (right axis) associated to each dimension-six operator from the global fit to universal new physics at the HE-LHC (green bars, light and dark shades indicate the *Base* and *optimistic* assumptions for systematics, respectively). The limits are compared with the ones from current data (in blue), as well as those obtained assuming only one operator at a time (dashed lines).

8.3 Global analysis including the Higgs self-coupling[110]

In record time Higgs physics has moved from a spectacular discovery of a new particle to a systematic and comprehensive study of its properties [780]. One of the main goals of the physics program of a 27 TeV hadron collider is the measurement of the Higgs self-coupling in Higgs pair production [353, 311, 315, 359, 789, 790], testing for example a possible first-order electroweak phase transition as an ingredient to baryogenesis. We show that a 27 TeV hadron collider will for the first time deliver a meaningful measurement of this fundamental physics parameter [791].

We perform a global study of Higgs physics at a 27 TeV hadron collider using the effective dimension-6 Lagrangian [763]

$$\begin{aligned}\mathcal{L}_{\text{eff}} = &-\frac{\alpha_s}{8\pi}\frac{f_{GG}}{\Lambda^2}\mathcal{O}_{GG} + \frac{f_{BB}}{\Lambda^2}\mathcal{O}_{BB} + \frac{f_{WW}}{\Lambda^2}\mathcal{O}_{WW} + \frac{f_B}{\Lambda^2}\mathcal{O}_B + \frac{f_W}{\Lambda^2}\mathcal{O}_W + \frac{f_{WWW}}{\Lambda^2}\mathcal{O}_{WWW} \\ &+ \frac{f_{\phi 2}}{\Lambda^2}\mathcal{O}_{\phi 2} + \frac{f_{\phi 3}}{\Lambda^2}\mathcal{O}_{\phi 3} + \frac{f_\tau m_\tau}{v\Lambda^2}\mathcal{O}_{e\phi,33} + \frac{f_b m_b}{v\Lambda^2}\mathcal{O}_{d\phi,33} + \frac{f_t m_t}{v\Lambda^2}\mathcal{O}_{u\phi,33} \\ &+ \text{invisible decays} \,. \end{aligned} \tag{175}$$

with the operators defined in Ref. [792], and specifically

$$\mathcal{O}_{\phi 2} = \frac{1}{2}\,\partial^\mu(\phi^\dagger\phi)\partial_\mu(\phi^\dagger\phi) \qquad\qquad \mathcal{O}_{\phi 3} = -\frac{1}{3}\,(\phi^\dagger\phi)^3 \,, \tag{176}$$

describing a modified Higgs potential. In addition, we include invisible Higgs decays as an additional contribution to the total width or, equivalently, the invisible branching ratio.

The self-coupling with its unique relation to the Higgs potential is not yet included in most global analyses of SM-like Higgs couplings [749, 777, 793] because of the modest reach of the LHC Run II. However, for a 27 TeV collider with an integrated luminosity of 15 ab^{-1} we quote the expected reach [315]

$$\frac{\lambda_{3H}}{\lambda_{3H}^{(\text{SM})}} = \begin{cases} 1 \pm 15\% & 68\%\ \text{C.L.} \\ 1 \pm 30\% & 95\%\ \text{C.L.} \end{cases} \tag{177}$$

We can translate this range into the conventions of Eq.(175) assuming that the underlying new physics only affects $\mathcal{O}_{\phi 3}$,

$$V = \mu^2\,\frac{(v+H)^2}{2} + \lambda\,\frac{(v+H)^4}{4} + \frac{f_{\phi 3}}{3\Lambda^2}\,\frac{(v+H)^6}{8} \,. \tag{178}$$

The reach of the dedicated one-parameter self-coupling analysis becomes

$$\lambda_{3H} = \lambda_{3H}^{(\text{SM})}\left(1 + \frac{2v^2}{3m_H^2}\,\frac{f_{\phi 3}v^2}{\Lambda^2}\right) \qquad \text{and} \qquad \left|\frac{\Lambda}{\sqrt{f_{\phi 3}}}\right| \gtrsim \begin{cases} 1\ \text{TeV} & 68\%\ \text{C.L.} \\ 700\ \text{GeV} & 95\%\ \text{C.L.} \end{cases} \tag{179}$$

Our global analysis containing all operators in Eq.(175) is based on a re-scaling of the number of signal and background events in the 8 TeV analysis [794] to 27 TeV, assuming two experiments. For the invisible Higgs searches we use an in-house extrapolation of the WBF analysis [795] from Ref. [558] to 27 TeV. Because the effective Lagrangian of Eq.(175) includes new Lorentz structures, especially valuable information comes from the kinematic distributions [796, 794] listed in Tab. 88. They are particularly relevant for our analysis of the Higgs self-coupling, where the full kinematic information from Higgs pair production encoded in the m_{HH} distribution allows us to separate the effects of $\mathcal{O}_{\phi 2}$ and $\mathcal{O}_{\phi 3}$ [311, 315]. Following Refs. [367, 370, 368] we neglect the loop effects of $\mathcal{O}_{\phi 3}$ on single Higgs production, because they will hardly affect a global Higgs analysis.

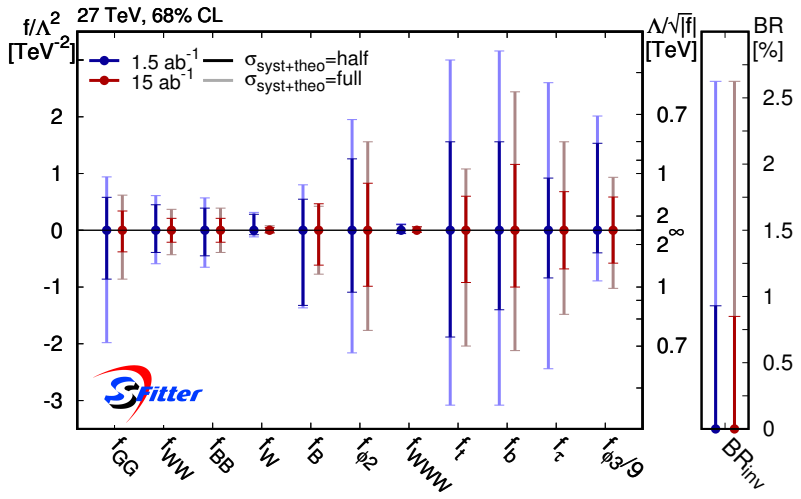

Fig. 139: Result from the global Higgs analysis in terms of dimension-6 operators. All limits are shown as profiled over all other Wilson coefficients. Figure from Ref. [791].

Table 88: Distributions included in the analysis. The number of bins includes an overflow bin for all channels. Table from Ref. [791].

channel	observable	# bins	range [GeV]
$WW \to (\ell\nu)(\ell\nu)$	$m_{\ell\ell'}$	10	$0 - 4500$
$WW \to (\ell\nu)(\ell\nu)$	$p_T^{\ell_1}$	8	$0 - 1750$
$WZ \to (\ell\nu)(\ell\ell)$	m_T^{WZ}	11	$0 - 5000$
$WZ \to (\ell\nu)(\ell\ell)$	$p_T^{\ell\ell}$ (p_T^Z)	9	$0 - 2400$
WBF, $H \to \gamma\gamma$	$p_T^{\ell_1}$	9	$0 - 2400$
$VH \to (0\ell)(b\bar{b})$	p_T^V	7	$150 - 750$
$VH \to (1\ell)(b\bar{b})$	p_T^V	7	$150 - 750$
$VH \to (2\ell)(b\bar{b})$	p_T^V	7	$150 - 750$
$HH \to (b\bar{b})(\gamma\gamma), 2j$	m_{HH}	9	$200 - 1000$
$HH \to (b\bar{b})(\gamma\gamma), 3j$	m_{HH}	9	$200 - 1000$

In Fig. 139 we show the expected reach for the global Higgs analysis in terms of dimension-6 operators for a 27 TeV LHC upgrade. For all measurements we assume the SM predictions, which means that our best-fit points will always be the SM values. To illustrate the importance of precision predictions we will show results with the current theory uncertainties as well as an assumed improvement of theory and systematics by a factor two. Asymmetric uncertainty bands arise because of correlations, but also reflect numerical uncertainties. Different colours correspond to assumed integrated luminosities of 1.5 ab^{-1} and 15 ab^{-1}. Most of the effective operators benefit from an increased statistics, because larger luminosity extends the reach of kinematic distributions, which in their tails are always statistically limited. In contrast, the Yukawa couplings $f_{b,\tau}$, which do not change the Lorentz structure, are mostly limited by the assumed systematic and theory uncertainties. Consequently, the reach for operators which modify the Lorentz structure of some Higgs interaction exceeds the reach for the Yukawa-like operators or the reach for the operator $\mathcal{O}_{\phi 2}$, which introduces a wave function renormalisation for the Higgs field and only changes the kinematics of Higgs pair production.

For the operator $\mathcal{O}_{\phi 3}$, which modifies the Higgs potential as part of a global analysis, we find the

[110] Contacts: A. Biekötter, D. Gonçalves, T. Plehn, M. Takeuchi, D. Zerwas

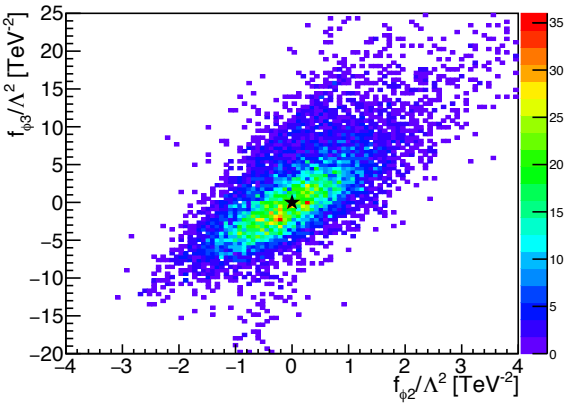

Fig. 140: Correlations between the leading operators describing Higgs pair production. Figure from Ref. [791].

limits

$$\frac{\Lambda}{\sqrt{|f_{\phi 3}|}} > 430 \text{ GeV} \qquad 68\% \text{ C.L.}$$

$$\frac{\Lambda}{\sqrt{|f_{\phi 3}|}} > 245 \text{ GeV} \quad (f_{\phi 3} > 0) \quad \text{and} \quad \frac{\Lambda}{\sqrt{|f_{\phi 3}|}} > 300 \text{ GeV} \quad (f_{\phi 3} < 0) \qquad 95\% \text{ C.L.} \tag{180}$$

These limits are diluted from the one-parameter analysis quoted in Eq.(179), largely because of the combination with $\mathcal{O}_{\phi 2}$. We can directly compare the effects from $\mathcal{O}_{\phi 2}$ and $\mathcal{O}_{\phi 3}$ for similar values of f/Λ^2 as a function of the momentum flowing through the triple-Higgs vertex or m_{HH}. In that case we find that the momentum dependence in $\mathcal{O}_{\phi 2}$ matches the effects from $\mathcal{O}_{\phi 3}$ for $m_{HH} \gtrsim 1$ TeV, with either relative sign. In Fig. 140 we show the correlation between $\mathcal{O}_{\phi 2}$ and $\mathcal{O}_{\phi 3}$ which is not accounted for in the usual Higgs pair analyses. The global analysis obviously reduces the reach for the Higgs self-coupling modification compared to a one-parameter analysis, but still indicates that a 27 TeV hadron collider will for the first time deliver a meaningful measurement of this fundamental physics parameter.

9 Searches for beyond the standard model Higgs physics[111]

HL and HE-LHC will have an unprecedented opportunity to explore not only the Higgs sector of the SM, but also extended Higgs sectors, as well as rare BSM processes involving the 125 GeV Higgs boson.

In this section, we first discuss the prospects for detecting 125 GeV Higgs exotic decays, i.e. decays to light NP particles that eventually decay back to SM particles (Sec. 9.1). Higgs exotic decays to collider stable particles (Higgs invisible decays) are already discussed in Sec. 6. Here we report the study of a large array of (semi-) visible decays as $h \to \phi\phi$, where ϕ is either a long lived scalar (Secs. 9.1.1, 9.1.2) or it promptly decays back to two SM fermions (Secs. 9.1.3-9.1.7). So far, the LHC has produced $\mathcal{O}(10)$ million Higgs bosons at its Run 1 and Run 2. This is only $\mathcal{O}(5\%)$ ($\mathcal{O}(5‰)$) the amount of Higgs bosons that will be produced by the HL (HE)-LHC. The huge Higgs statistics that will be collected at the HL/HE-LHC will be a key ingredient for the success of a Higgs exotic decay program.

In Secs. 9.2, 9.3, we then present the ATLAS and CMS prospects for searching for new heavy Higgs bosons, either in fermionic final states ($H \to \tau\tau$, as particularly motivated in Supersymmetric theories), or in bosonic final states ($H \to ZZ$, as motivated in theories that deviate from the alignment limit). These two sections are followed by a phenomenological section (Sec. 9.4) that discusses the reach of possible additional searches for neutral and charged Higgs bosons and the role of interference effects in heavy Higgs searches. The interplay of the 125 Higgs coupling measurements and searches for new degrees of freedom is discussed in Secs. 9.5-9.7 for several BSM models (the Minimal Supersymmetric SM, Twin Higgs models and composite Higgs models).

Several well motivated BSM models can also predict new Higgs bosons with a mass below 125 GeV. The prospects to probe these light Higgs bosons and the corresponding models are discussed in Sec. 9.8. Particularly, light Higgs bosons could be uniquely probed at the HL-stage of the LHCb experiment.

9.1 Exotic decays of the 125 GeV Higgs boson

9.1.1 First Level Track Jet Trigger for Displaced Jets at High Luminosity LHC[112]

The high luminosity LHC program offers many exciting opportunities to search for rare processes. It is expected that the LHC will accumulate 3 ab^{-1} of proton-proton collisions at 14TeV. The CMS detector will undergo major upgrades to all subsystems, including the tracker [22], the barrel [24] and end-cap [25] calorimeters, the muon system [28], and the trigger [19].

The bandwidth limitations of the first level (L1) trigger are one of the main problems facing current searches for exotic Higgs boson decays, as well as many other signals beyond the standard model. The process where the Higgs boson decays to two new light scalars that in turn decay to jets, H $\to \phi\phi$, is an important example. If the scalar ϕ has a macroscopic decay length, the offline analysis has no background from SM processes, but the majority of the signal events do not get recorded because they fail to be selected by the L1 trigger. The main obstacle is the high rate for low transverse momentum jets, which is made worse by additional extraneous pp collisions in the high luminosity environment.

In this note [797], we investigate the capabilities of L1 track finding [22] to increase the L1 trigger efficiency for such signals. We focus on small or moderate decay lengths of the new particles, 1–50mm, and assume, as is demonstrated by many analyses [798, 799, 800], that the offline selection can remove all SM backgrounds with only a moderate loss of efficiency.

The investigation has two major thrusts. First, we propose a jet clustering algorithm that uses the L1 tracks found with a primary vertex constraint. Second, we consider the extension of the L1 track finder to off-pointing tracks, and develop a jet lifetime tag for tracks with $|\eta| < 1.0$. Future work will include: expanding the off-pointing track finding at L1 to the full acceptance of the outer tracker; matching the

[111] Contact Editors: M. Borsato, M. Flechl, S. Gori, L. Zhang

[112] Contacts: A. Gandrakota, Y. Gershtein, R. Glein, B. Greenberg, F. Paucar-Velasquez, R. Patel, K. Ulmer

track jets with high transverse energy (E_{T}) deposits in the electromagnetic calorimeter; and finding new ways to evaluate track quality to suppress "fake" tracks that result from finding the wrong combination of track hits.

While in this study we focus on the specific Higgs boson decay to light scalars (see Ref. [43] for extensive review of physics motivations for such decays), the results and the proposed triggers are relevant for a broad spectrum of new physics searches, with or without macroscopic decay lengths.

9.1.1.1 Signal and background simulation

In these studies, the Phase-2 CMS detector is simulated using GEANT 4 [36]. Event samples corresponding to 200 collisions per bunch crossing (pileup) [19] are used for the evaluation of trigger rates.

The following signal samples are considered:

1. Displaced single muons, generated with a uniform distribution of transverse momentum (p_T) between 2 and 8GeV, uniform in η between -1 and 1, and with impact parameter d_0 distributed as a Gaussian with width $\sigma = 2$cm.
2. The decay of the SM Higgs boson $\mathrm{H}(125) \to \phi\phi \to \mathrm{b\bar{b}b\bar{b}}$, with ϕ masses of 15, 30, and 60GeV, and $c\tau$ of 0, 1, and 5cm. The production of the Higgs boson via gluon fusion is simulated by POWHEGv2.0 [801], while the hadronisation and decay is performed by PYTHIAv8.205 [319].
3. The decay of a heavy SM-like Higgs boson with mass 250GeV, $\mathrm{H}(250) \to \phi\phi \to \mathrm{b\bar{b}b\bar{b}}$, with ϕ masses of 15, 30, and 60GeV, and $c\tau$ of 0, 1, and 5cm. The production of the heavy SM-like Higgs boson via gluon fusion, its decay, and its hadronisation are all simulated with PYTHIA8 [319].

9.1.1.2 Track jets

The tracker is the most granular detector participating in the L1 decision, and therefore the most resilient to pileup. Track finding at L1 relies on selection at the front end of tracker hits that originated from high transverse momentum particles. This is achieved through use of the so-called p_T-modules consisting of two sensors separated by a few mm [22]. A particle crossing a tracker module produces a pair of hits in the two sensors. Such pairs form a "stub" if the azimuthal difference between the hits in the two sensors of a module is consistent with a prompt track with $\mathrm{p}_T \gtrsim 2$GeV.

In this section, we describe a simple jet clustering algorithm implementable in firmware, and compare it with anti-k_t jets [14] with a size parameter of $R = 0.3$, as produced by FASTJET [15].

A simplified algorithm for L1 track jets is used to facilitate the firmware implementation for the L1 trigger applications. L1 track jets are found by grouping tracks in bins of z_o, the point of closest approach to the z-axis, for the tracks. The bins are overlapping, staggered by half a bin, so that each track ends up in two bins, eliminating inefficiencies at bin edges. In each z_o bin, the $\mathrm{p}_T$of the tracks are summed in bins of η and azimuthal angle ϕ with bin size 0.2×0.23. A simplified nearest-neighbour clustering is performed, and the total $H_{\mathrm{T}} = \sum \mathrm{p}_T^{\mathrm{trk}}$ in the z_o bin is calculated. The z_o bin with the highest H_{T} is chosen. Jets obtained through this algorithm are referred to as "TwoLayer Jets." For the studies below, z_o bins with size 6 cm are used. Jets with $E_{\mathrm{T}} > 50\,(100)$GeV are required to have at least two (three) tracks.

The track purity depends on the number of stubs in the track and the χ^2 of the track fit. High-$\mathrm{p}_T$tracks are much less pure than low-$\mathrm{p}_T$tracks, with fake tracks distributed approximately uniformly in $1/\mathrm{p}_T$ while real tracks are mostly low-p_T. To mitigate the effect of high-$\mathrm{p}_T$fake tracks, any track with a reconstructed $\mathrm{p}_T$above 200GeV is assigned a $\mathrm{p}_T$of 200GeV. The track quality selection used in this analysis is summarised in Table 89.

We have verified that the TwoLayer trigger algorithm gives similar performance to a full jet clustering using the anti-k_t algorithm with a size parameter $R = 0.3$, as implemented in FASTJET. Figure 141

Table 89: Track selection for jet finding. The χ^2 selections are per degree of freedom for a 4-parameter track fit.

track p_T	4 stubs	5 stubs	6 stubs
2–10GeV	$\chi^2 < 15$	$\chi^2 < 15$	accept
10–50GeV	reject	$\chi^2 < 10$	accept
>50GeV	reject	$\chi^2 < 5$	$\chi^2 < 5$

shows the efficiency to reconstruct a track jet as function of the generator-level jet p_T. Figure 142 shows the calculated L1 trigger rates for an H_T trigger (scalar sum of $p_T$of all jets above threshold) and a quad-jet trigger (at least four jets above threshold) as a function of the threshold. H_T is computed from track jets with $p_T > 5$GeV.

The rates are computed based on a fixed number of colliding bunches. The trigger rate is computed as

$$\text{Rate} = \epsilon_{\text{LT}} N_{\text{bunches}} f_{\text{LHC}},$$

where $N_{\text{bunches}} = 2750$ bunches for 25nsbunch spacing operation, $f_{\text{LHC}} = 11246$Hz, and ϵ_{LT} is the efficiency to pass a given L1 threshold as determined in simulation. For both the L1 trigger efficiency and rate, the performance of the TwoLayer hardware algorithm is compatible with the performance from the more sophisticated algorithm from FASTJET.

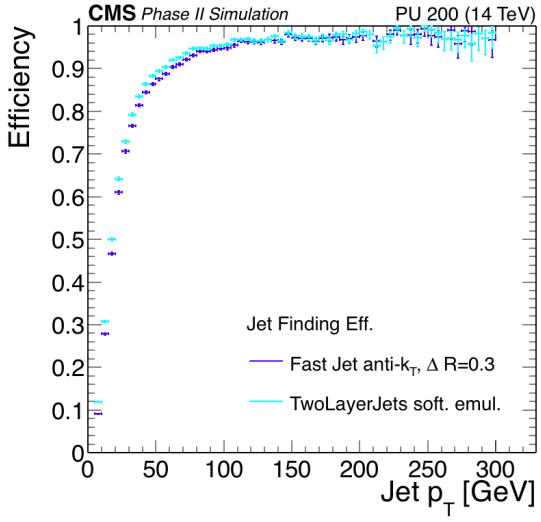

Fig. 141: The efficiency for a jet to give rise to a L1 track jet as a function of the generator-level $p_T$of the jet. The light and dark blue lines correspond to the trigger clustering (TwoLayer Jets) and anti-k_t with $R = 0.3$ (FASTJET), respectively.

9.1.1.3 Displaced track finding

In this section, we briefly describe the performance of an algorithm for reconstruction of tracks with non-zero impact parameter. This approach extends the baseline L1 Track Trigger design to handle tracks with non-zero impact parameter and to include the impact parameter in the track fit. This enhanced design is feasible without greatly altering the track finding approach, but will require more computational power than the current proposal, which considers only prompt tracks. Tracks passing the selection are clustered using the same algorithm as described in Section 9.1.1.2, and clusters containing tracks with high impact parameters are flagged as displaced jets. Though the baseline design of the L1 Track Trigger currently is optimised to find prompt tracks, these studies show that an enhanced L1 Track Trigger can extend the

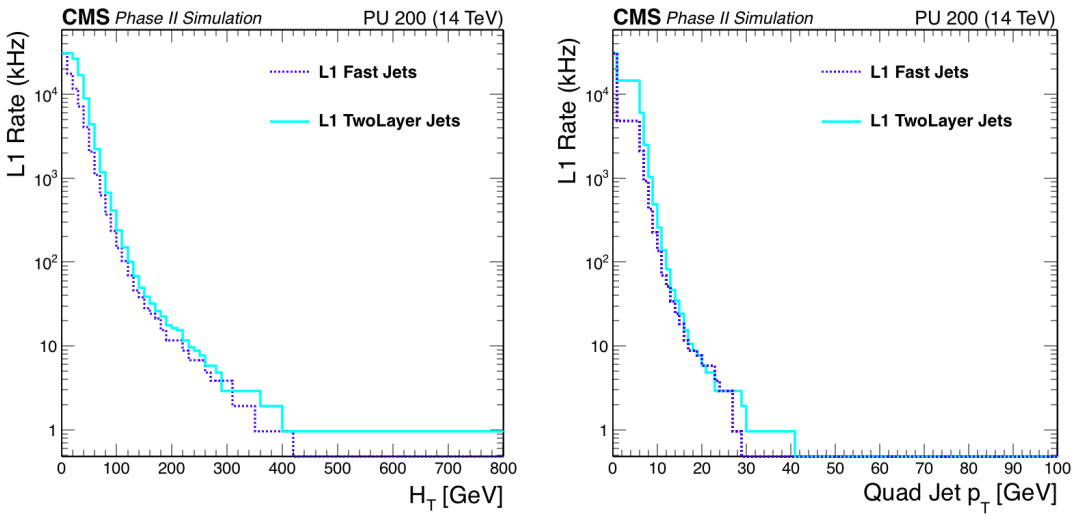

Fig. 142: Calculated L1 trigger rates for track jet based H_{T} (left) and quad-jet (right) triggers. The light and dark blue lines correspond to the trigger clustering (TwoLayer Jets) and anti-k_t with $R = 0.3$ (FASTJET), respectively.

L1 trigger acceptance to include new BSM physics signals.

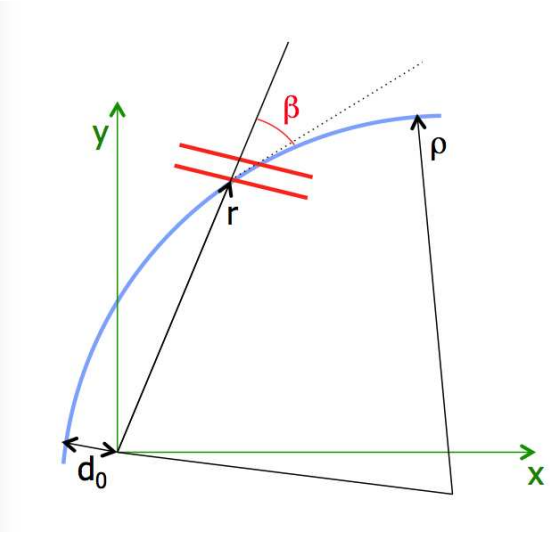

Fig. 143: A sketch of a track crossing a p_T-module.

A track with a sufficiently small impact parameter can produce a stub. For tracks with large p_T(i.e. large curvature radius ρ) and small d_0, the bending angle β between the track and the prompt infinite momentum track, as shown in Fig. 143, is

$$\beta \approx \frac{r}{2\rho} - \frac{d_0}{r}.$$

Therefore, for a given d_0, one expects the stubs to be formed more efficiently as the radius of the module r increases. Fig. 144 shows the efficiency for a displaced muon to produce a stub as a function of the signed transverse momentum and the impact parameter of the muon, as measured in the full GEANT 4-based simulation of the Phase-2 detector.

A special version of the tracklet algorithm [22] has been developed that is capable of reconstructing

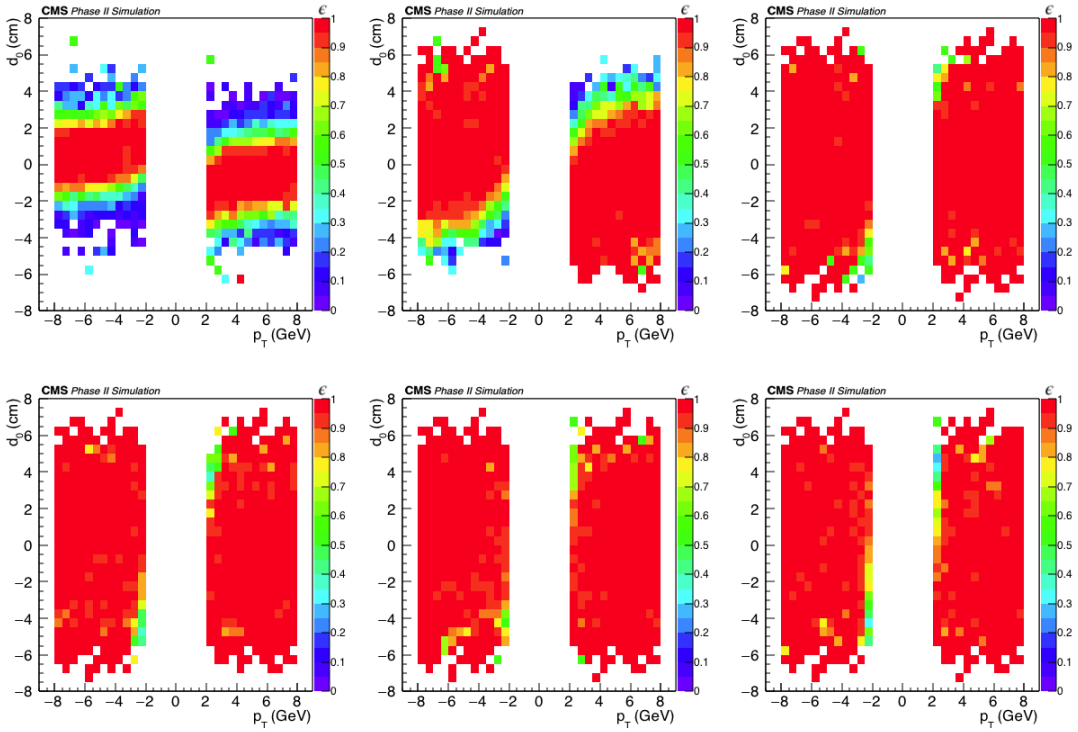

Fig. 144: The efficiency for a displaced muon to form stubs in the six barrel layers of the Phase-2 tracker, as a function of the signed muon $p_T$and impact parameter. The top row shows, from left to right, layers 1, 2, and 3; the bottom row shows layers 4, 5, and 6. The sample is comprised of 2000 muons generated with uniformly distributed transverse momentum between 2 and 8GeV and pseudorapidity $|\eta| < 1$, and with the impact parameter d_0 distributed as a Gaussian with width of 2cm.

tracks with impact parameters of a few cm. For now, the reconstruction is limited to the barrel region ($|\eta| < 1.0$). Preliminary feasibility studies show that the algorithm will have similar performance in the entire outer tracker coverage.

Fig. 145 shows the track reconstruction efficiency requiring at least four and at least five stubs on the track. As expected, allowing only four stubs on a track gives a higher efficiency for high impact parameter tracks.

For the extended track finding algorithm, two track fits are performed: a 3-parameter $r\phi$ fit yielding $1/\rho$, ϕ_0, and d_0, and a 2-parameter rz fit yielding t and z_o. The bend consistency variable is defined as

$$\text{consistency} = \frac{1}{N_{\text{stubs}}} \sum_{i=1}^{N_{\text{stubs}}} \left(\frac{\beta_i - \beta_i^{\text{exp}}}{\sigma_i} \right)^2 ,$$

where N_{stubs} is the total number of stubs comprising the track, β_i and β_i^{exp} are the measured and expected bend angles for stub i, and σ_i is the expected bend angle resolution.

Two track categories are defined, loose and tight. The selection is summarised in Table 90.

A jet is required to have at least two tracks passing the tight selection. If two or more tight tracks in a jet have $|d_0| > 0.1$cm, the jet is tagged as a displaced jet.

9.1.1.4 Results

Figure 146 shows the rate of the track jet H_{T} trigger as a function of the efficiency of the heavy SM-like Higgs boson signal. While for prompt ϕ decays one can realistically achieve 20% efficiency at an

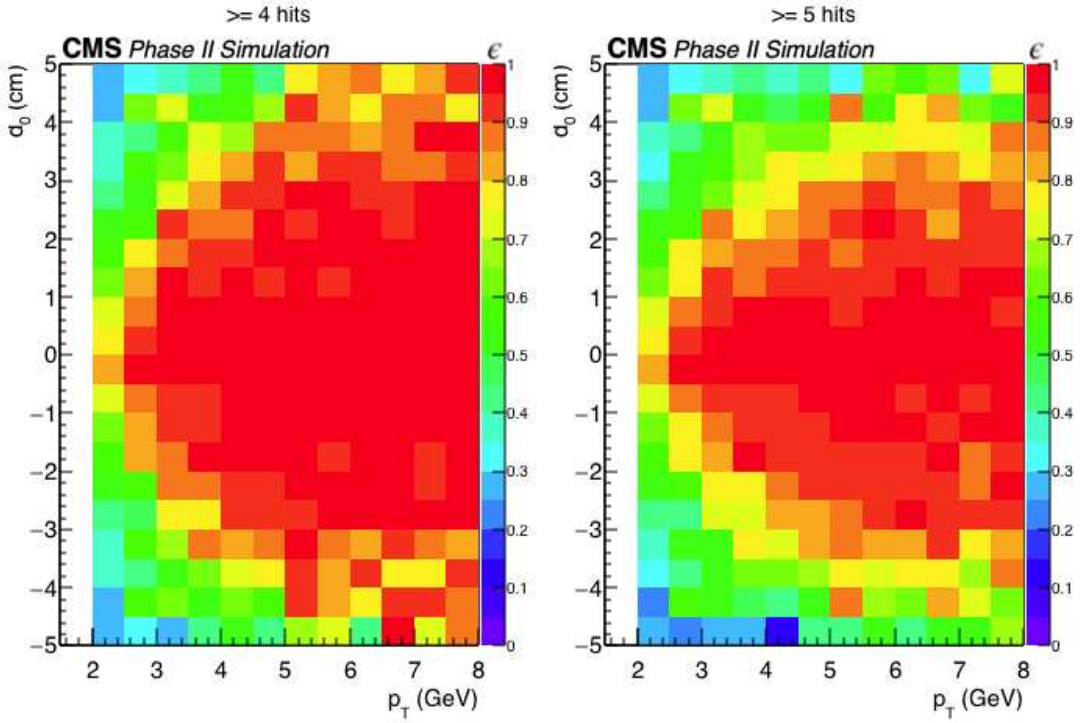

Fig. 145: The efficiency for a displaced muon to be reconstructed as a track with at least four stubs (left) and at least five stubs (right).

Table 90: Track selection criteria for jet finding with extended L1 track finding.

	Loose			Tight		
N_{stubs}	$\chi^2_{r\phi}$	χ^2_{rz}	consistency	$\chi^2_{r\phi}$	χ^2_{rz}	consistency
4	<0.5	<0.5	<1.25	reject		
≥ 5	<5.0	<2.5	<5.0	<3.5	<2.0	<4.0

L1 rate of 25kHz, the efficiency quickly drops with the decay length, since the displaced tracks are not reconstructed for d_0 values above a few mm.

The rate for the H_{T} trigger using the extended track finding is shown in Fig. 147, with and without a requirement of at least one jet with a displaced tag. The displaced tag requirement suppresses the rate by more than an order of magnitude. The displaced tracking and the trigger that requires a jet with a displaced tag make the signals with low H_{T} accessible for displaced jets.

In order to compare the results with prompt and extended track reconstruction, one needs to make a correction for the rapidity coverage: prompt tracks are found in $|\eta| < 2.4$, while the extended track algorithm currently only reconstructs tracks in $|\eta| < 1.0$. For the feasible thresholds, the rate for $|\eta| < 0.8$ and $|\eta| < 2.4$ differ by a factor of five. To scale the efficiency for finding track jets to the full $|\eta| < 2.4$ range, we derive a scale factor (SF) based on efficiency in the full η range and the central η range. The signal efficiency SFs range from 4–6, which is comparable to the increase in the L1 rate. We have confirmed that such extrapolation works for the track jets clustered with prompt tracks. Figure 148 shows the expected trigger rate as a function of efficiency for the SM and the heavy SM-like Higgs bosons.

The available bandwidth for the triggers described above, if implemented, will be decided as a part of the full trigger menu optimisation. Here, we consider two cases, 5 and 25kHz. The expected event yield for triggers using extended and prompt tracking are shown in Fig. 149, assuming branching

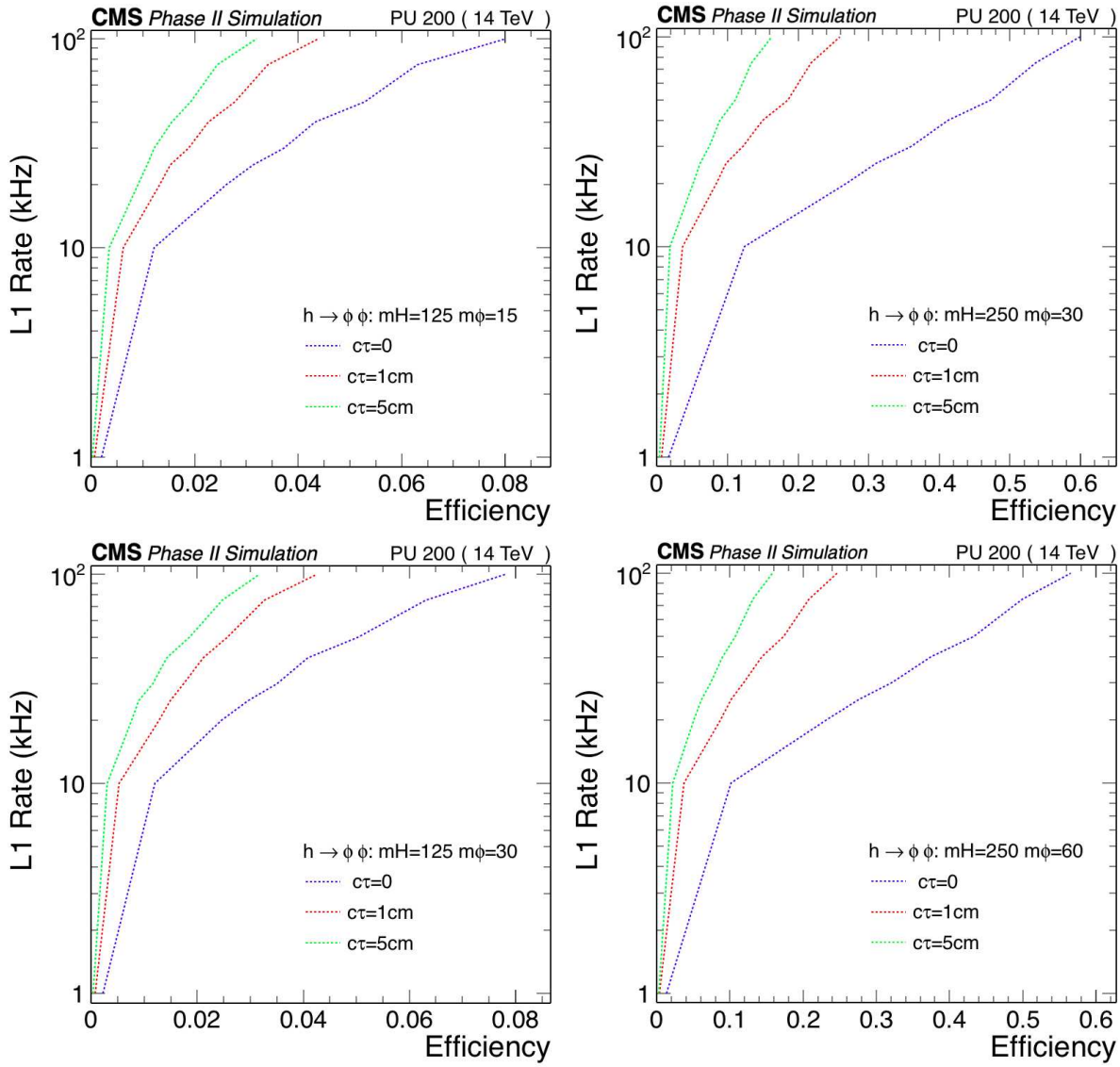

Fig. 146: The rate of the track jet H_{T} trigger as a function of signal efficiency for the SM Higgs boson (left) and the heavy SM-like Higgs boson (right) using prompt track finding.

fraction $\mathcal{B}[\mathrm{H} \to \phi\phi] = 10^{-5}$ for the SM Higgs boson. For the heavy Higgs boson, the expected number of produced signal events is set to be the same as for the SM Higgs by requiring $\sigma_{\mathrm{pp}\to\mathrm{H}(250)}\mathcal{B}[\Phi \to \phi\phi] = 10^{-5}\sigma_{\mathrm{pp}\to\mathrm{H}(125)}$.

9.1.1.5 Conclusion

We have studied the upgraded CMS detector's ability to trigger on events with long lived particles decaying into jets. Currently, such events pass the L1 trigger only if the total transverse energy in the event is above a few hundred GeV. This is an important blind spot for searches, especially for the rare exotic Higgs boson decays like $\mathrm{H} \to \phi\phi$.

In this note, a new L1 trigger strategy based on the Phase-2 CMS detector's ability to find tracks at L1 is explored. Using L1 tracks for jet reconstruction significantly suppresses pile-up and allows to accept events with lower H_{T}. For the exotic Higgs decays considered, given the total Phase-2 dataset of $3\,\mathrm{ab}^{-1}$ and branching fraction of 10^{-5}, CMS would collect $\mathcal{O}(10)$ events, which should be sufficient for

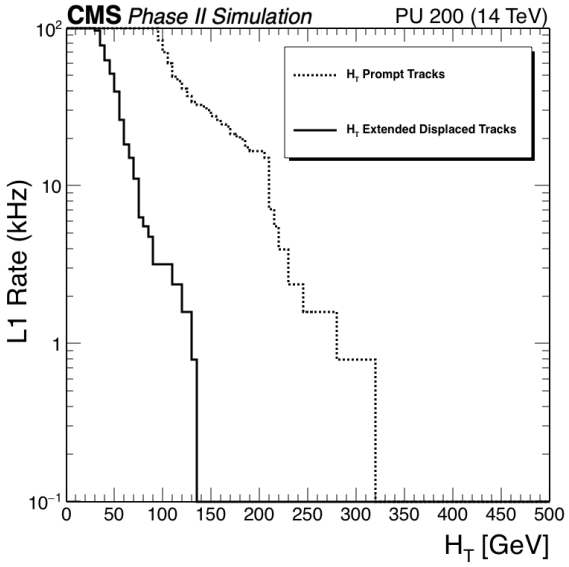

Fig. 147: The rate of the track jet H_{T} trigger using extended track finding with (solid line) and without (dashed line) a requirement of at least one jet with a displaced tag.

discovery. We also considered a plausible extension of the L1 track finder to consider tracks with impact parameters of a few cm. That approach improves the yield by more than an order of magnitude. The gains for the extended L1 track finding are even larger for the events with larger H_{T}, as demonstrated by the simulations of heavy Higgs boson decays.

9.1.2 Higgs exotic decays into long-lived particles[113]

The Higgs boson is a well-motivated portal to new physics sectors, introducing a vast variety of exotic decays [43]. The presence of long-lived particles (LLP) can be a striking feature of many new physics models [802, 803, 804, 805, 806, 807, 808, 809, 810, 811, 812, 813]. At the same time, vast swaths of the possible parameter space of the LLP remain unexplored by LHC searches. LHC general purpose detectors, ATLAS and CMS, provide full angular coverage and sizeable volume, making them ideal for LLP searches. However, searches for LLPs that decay within a few centimetre of the interaction point suffer from large SM backgrounds. LLPs produced at the LHC generically travel slower than the SM background and decay at macroscopic distances away from the interaction point. Hence, they arrive at outer particle detectors with a sizeable time delay.

Recently, precision timing upgrades with a timing resolution of 30 picoseconds have been proposed to reduce pile-up for the upcoming runs with higher luminosity, including MIP Timing Detector (MTD) [26] by the CMS collaboration for the barrel and end-cap region in front of the electromagnetic calorimeter, the High Granularity Timing Detector [814] by the ATLAS collaboration in end-cap and forward region, and similarly multiple precision timing upgrades [815] by the LHCb collaboration. As a strategy applicable to a broad range of models, we propose the use of a generic Initial State Radiation (ISR) jet to time-stamp the hard collision and require only a single LLP decay inside the detector with significant time delay. Such a strategy can greatly suppress the SM background and reach a sensitivity two orders of magnitude or more better than traditional searches in a very larger parameter space [546, 816, 817, 808]. With a general triggering and search strategy that can capture most LLP decays, we show a striking improvement in sensitivity and coverage for LLPs. In addition to the MTD at CMS, we also consider a hypothetical timing layer on the outside of the ATLAS Muon Spectrometer

[113] Contacts: J. Liu, Z. Liu, L.T. Wang

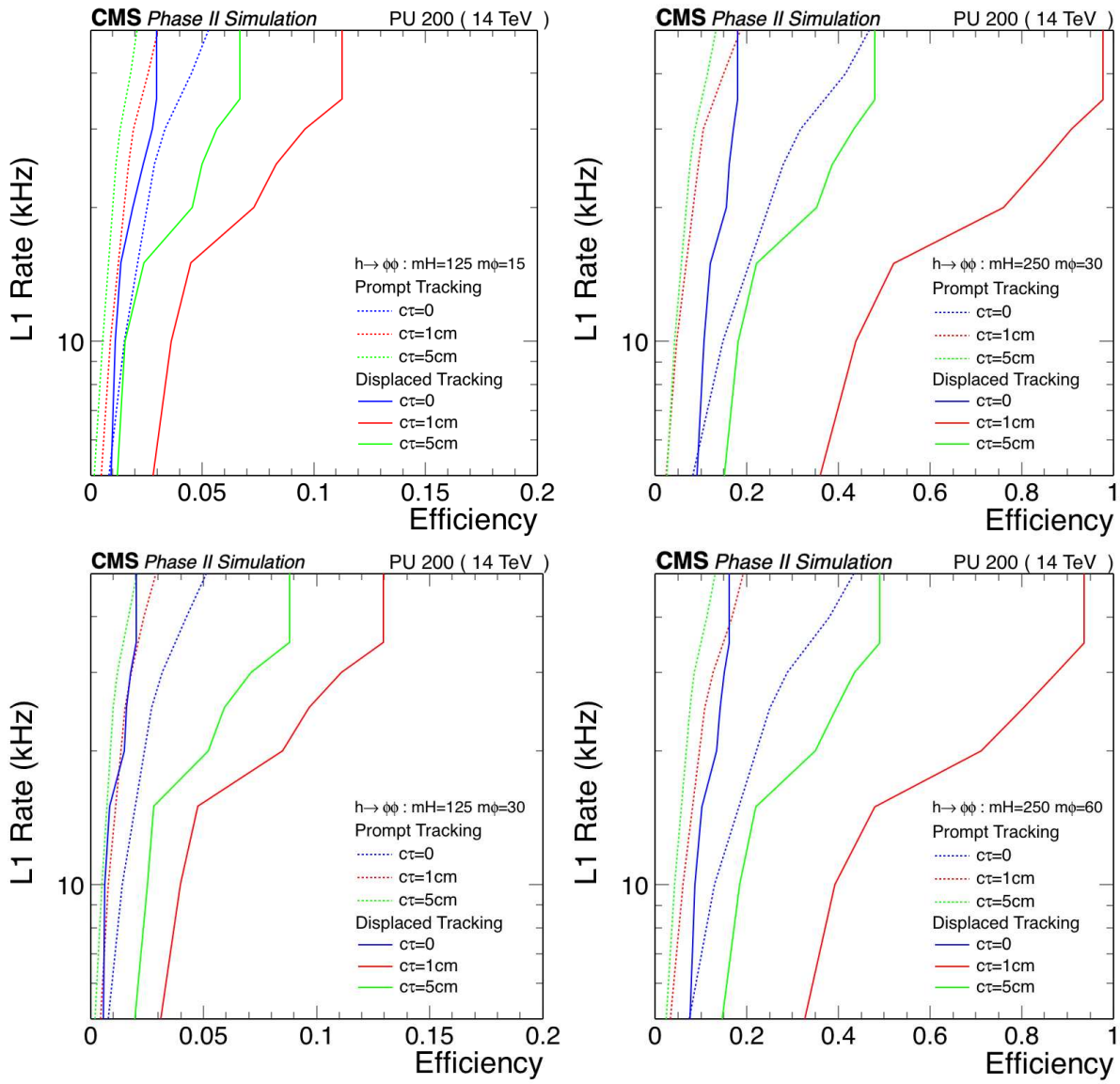

Fig. 148: The rate of the track jet H_{T} trigger as a function of signal efficiency using extended track finding for the SM Higgs (left) and the heavy SM-like Higgs (right). The extended track finding performance is extrapolated to the full outer tracker acceptance as described in text.

(MS) as an estimate of the best achievable reach of our proposal for LLPs with long lifetimes.

Higgs decaying to glueballs with subsequent decays into SM jet pairs is our benchmark model here. This occurs in model [812] where the Higgs is the portal to a dark QCD sector whose lightest states are the long-lived glueballs. Typical energy of the glueball is set by the Higgs mass, and the time delay depends on glueball mass. Time-stamping the hard collision is achieved by using an ISR jet:

$$pp \to h + j \quad , \; h \to X + X, \; X \to \mathrm{SM}, \tag{181}$$

where X represents the LLP.

While particle identification and kinematic reconstruction are highly developed, usage of timing information has so far been limited since prompt signatures are often assumed. Such an assumption could miss a crucial potential signature of an LLP, a significant time delay. Here we outline a general

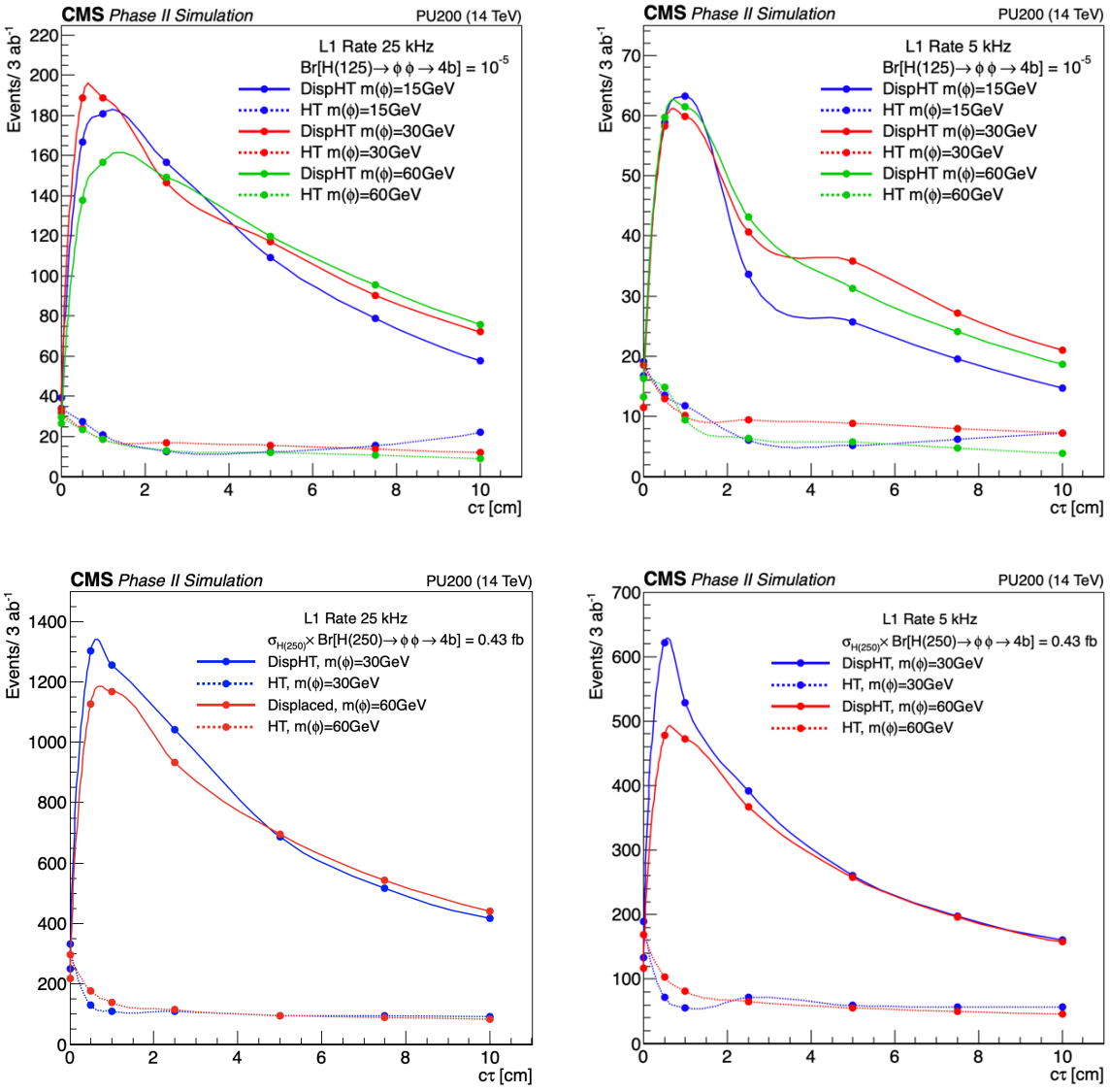

Fig. 149: This plot shows the number of triggered Higgs events (assuming $\mathcal{B}[\mathrm{H} \to \phi\phi] = 10^{-5}$, corresponding to 1700 events) as a function of $c\tau$ for two choices for the trigger rates: 25kHz(left), 5kHz(right). Two triggers are compared: one based on prompt track finding (dotted lines) and another that is based on extended track finding with a displaced jet tag (solid lines).

BSM signal search strategy that uses the timing information and the corresponding background consideration. A typical signal event of LLP is shown in the left panel of Fig. 150. The LLP, X, travels a distance ℓ_X into a detector volume and decays into two light SM particles a and b, which then reach timing detector at a transverse distance L_{T_2} away from the beam axis. Typically, the SM particles travel at velocities close to the speed of light. For simplicity, we consider neutral LLP signals where background from charged particles can be vetoed using particle identification and isolation. The decay products of X arrive at the timing layer with a time delay $\Delta t^i_{\mathrm{delay}} = \frac{\ell_X}{\beta_X} + \frac{\ell_i}{\beta_i} - \frac{\ell_{\mathrm{SM}}}{\beta_{\mathrm{SM}}}$ for ith decay products from X and $\beta_i \simeq \beta_{\mathrm{SM}} \simeq 1$. It is necessary to have prompt particles from production or decay, or ISR, which arrives at timing layer with the speed of light, to derive the time of the hard collision at the primary vertex (to "time-stamp" the hard collision).

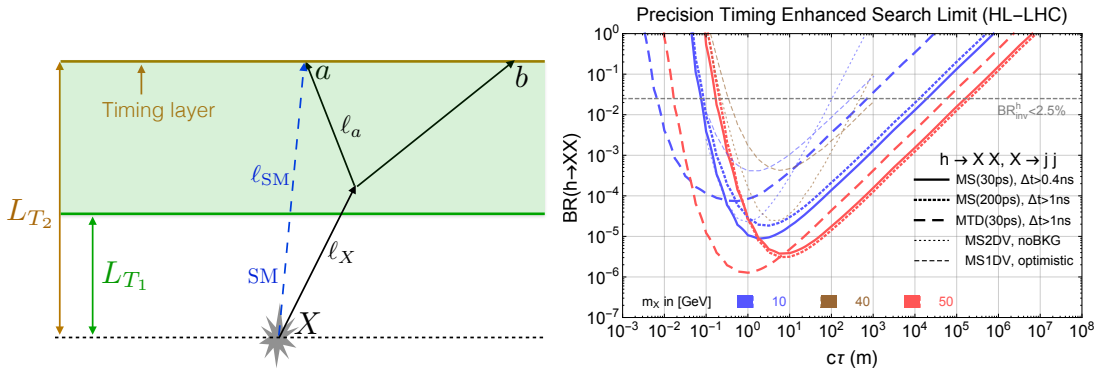

Fig. 150: Left Panel: An event topology with an LLP X decaying into two light SM particles a and b. A timing layer, at a transverse distance L_{T_2} away from the beam axis (horizontal grey dotted line), is placed at the end of the detector volume (shaded region). The trajectory of a reference SM background particle is also shown (blue dashed line). The grey polygon indicates the primary vertex. Right Panel: the 95% C.L. limit on BR$(h \to XX)$ for signal process $pp \to jh$ with subsequent decay $h \to XX$ and $X \to jj$. Different colours indicate different masses of the particle X. The thick solid and dotted (thick long-dashed) lines indicate MS (MTD) searches with different timing cuts. The numbers in parentheses are the assumed timing resolutions. Other 13 TeV LHC projections [817, 818] are plotted in thin lines. Figures are taken from Ref. [802].

We consider events with at least one ISR jet to time-stamp the primary vertex (PV) and one delayed SM object coming from the LLP decay. We propose two searches using the time delay information:

	L_{T_2}	L_{T_1}	Trigger	$\epsilon_{\rm trig}$	$\epsilon_{\rm sig}$	$\epsilon^{j}_{\rm fake}$	Ref.
MTD	1.17 m	0.2 m	DelayJet	0.5	0.5	10^{-3}	[26]
MS	10.6 m	4.2 m	MS RoI	0.25, 0.5	0.25	5.2×10^{-9}	[546]

The size of the detector volume is described by transverse distance to the beam pipe from L_{T_1} to L_{T_2}, where the timing layer is located. For both searches, we assume a similar timing resolution of 30 ps. For the MS search, because of the larger time delay and much less background due to "shielding" by inner detectors, a time resolution of 0.2 - 2 ns could achieve a similar physics reach. The $\epsilon_{\rm trig}$, $\epsilon_{\rm sig}$ and $\epsilon^{j}_{\rm fake}$ are the efficiencies for trigger, signal selection and a QCD jet faking the delayed jet signal with $p_T > 30$ GeV in MTD and MS searches, respectively.

For the MTD search, we assume a new trigger strategy of a delayed jet using the CMS MTD. This can be realised by putting a minimal time delay cut when comparing the prompt time-stamping jet with $p_T > 30$ GeV with the arrival time of another jet at the timing layer. The MTD signal, after requiring minimal decay transverse distance of 0.2 m (L_{T_1}), will not have good tracks associated with it. Hence, the major SM background is from trackless jets. The jet fake rate of $\epsilon^{\rm j,MTD}_{\rm fake} = 10^{-3}$ is estimated using `Pythia` [32] by simulating the jets with minimal p_T of 30 GeV and studying the anti-kt jets with $R = 0.4$, where all charged constituent hadrons are too soft ($p_T < 1$ GeV). For the MS search, we use the MS Region of Interest (MS RoI) trigger from a very similar search [819] as a reference, with an efficiency of $\epsilon_{\rm trig} = 0.25$ and 0.5 for the two benchmark BSM signals, and a signal selection efficiency of $\epsilon_{\rm sig} = 0.25$. The backgrounds are mainly from the punch-through jets, and the fake efficiency can be inferred to be $\epsilon^{\rm j,MS}_{\rm fake} = 5.2 \times 10^{-9}$, normalised to 1300 fake MS barrel events at 8 TeV [819]. For detailed discussion on the background estimation, see Ref. [802].

To emphasise the power of timing, we rely mostly on the timing information to suppress background and make only minimal cuts. We only require one low p_T ISR jet, with $p^{j}_{T} > 30$ GeV and

$|\eta_j| < 2.5$. In both signal benchmarks, we require that at least one LLP decays inside the detector. We generate signal events using `MadGraph5` [79] at parton level. After detailed simulations of the delayed arrival time, we derive the projected sensitivity using the cross-sections obtained in Ref. [820]. The 95% C.L. sensitivity is shown in Fig. 150. We assume X decays to SM jet pairs with 100% branching fraction. The MTD and MS searches, with 30 ps timing resolution, are plotted in thick dashed and solid lines, respectively. For MS, the best reach of BR$(h \to XX)$ is about a few times 10^{-6} for $c\tau \sim 10$ m. The reach is relatively insensitive to the mass of X when $m_X > 10$ GeV because X are moving slowly enough to pass the timing cut. For the MS search, a less precise timing resolution (200 ps) has also been considered with cut $\Delta t > 1$ ns. After the cut, the backgrounds from same-vertex hard collision (SV) and pile-up (PU) for MS search are 0.11 and 7.0×10^{-3} respectively, and the SV background dominates. The reach for heavy X is almost not affected, while reduced by a factor of around two for light X.

In the right panel of Fig. 150, we compare MTD and MS (thick lines) with 13 TeV HL-LHC (with 3 ab^{-1} integrated luminosity) projections, two displaced vertex (DV) at MS using zero background assumption (thin dotted) and one DV at MS using a data-driven method with optimistic background estimation (thin dashed) from [817]. The projected limits from invisible Higgs decay at the 14 TeV HL-LHC (see Sec. 6.2.1 of this report) is also shown in the right panel of Fig. 150.

Exploiting timing information can significantly enhance the sensitivities of LLP searches at the HL-LHC. To emphasise the advantage of timing, we made minimal requirements on the signal, with one ISR jet and a delayed signal. The temporal behaviour of the SM and detector background are not yet well understood. This novel investigation [802] requires further studies on the background behaviour at the HL- and HE-LHC to further realise the proposed trigger and analysis. Further optimisation can be developed for more dedicated searches. The time-stamping ISR jet can be replaced by other objects, such as leptons or photons. Depending on the underlying signal and model parameters, one can also use prompt objects from signal production and decay. In addition, for specific searches, one could also optimise the selection of the signal based on the decay products of LLPs. Finally, we emphasise that the current LLP searches are complimentary to the timing based searches discussed here. Once combined, the current searches should in general gain better sensitivity for heavy LLP. These future perspectives can be further extended and realised at the HE-LHC with more advanced phenomenological studies with detector, trigger and analysis, as well as higher statistics on the Higgs bosons.

9.1.3 Projection of CMS search for exotic $H \to aa \to 2b2\tau$[114]

This analysis looks for decays of the Higgs boson to pairs of pseudoscalar bosons in the final state of two τ leptons and two b quarks [821]. The $\tau\tau$ pair is reconstructed as $e\mu$, $\mu\tau_h$, or $e\tau_h$, depending on the decay modes of the τ leptons. The symbol τ_h denotes a τ lepton decaying hadronically. Only one b jet with $p_T > 20$ GeV is required to be reconstructed and tagged as originating from a b quark because the b jets originating from the pseudoscalar boson are typically soft. An improved signal sensitivity is obtained by dividing the events in four different categories depending on the visible invariant mass of the b jet and the τ candidates, denoted $m_{b\tau\tau}$. The thresholds that define the categories depend on the final state. The categories with low $m_{b\tau\tau}$ are enriched in signal events, while the categories with large $m_{b\tau\tau}$ help to constrain the backgrounds. The results are extracted with a maximum likelihood fit of the visible $\tau\tau$ mass spectrum. The dominant backgrounds at low m_A are $\mathrm{t\bar{t}}$ production as well as events with jets misidentified as τ candidates, whereas the Drell–Yan background starts to contribute for $m_a > 45$ GeV values. This analysis is only sensitive to pseudoscalar masses above 15 GeV. The sensitivity of the analysis mostly comes from the low $m_{b\tau\tau}$ category, which is statistically limited, and the statistical uncertainty strongly dominates the results.

The extrapolations summarised in Ref. [822], and presented in this section and the next two as-

[114] Contact: C. Caillol

sume that the CMS experiment will have a similar level of detector and triggering performance during the HL-LHC operation as it provided during the LHC Run 2 period [30, 22, 24, 25, 28]. The results of extrapolations, hereafter named projections, are presented for different assumptions on the size of systematic uncertainties that will be achievable by the time of HL-LHC:

- **"Run 2 systematic uncertainties" scenario:** This scenario assumes that performance of the experimental methods at the HL-LHC will be unchanged with respect to the LHC Run 2 period, and there will be no significant improvement in the theoretical descriptions of relevant physics effects. All experimental and theoretical systematic uncertainties are assumed to be unchanged with respect to the ones in the reference Run 2 analyses, and kept constant with integrated luminosity.
- **"YR18 systematics uncertainties" scenario:** This scenario assumes that there will be further advances in both experimental methods and theoretical descriptions of relevant physics effects. Theoretical uncertainties are assumed to be reduced by a factor two with respect to the ones in the reference Run 2 analyses. For experimental systematic uncertainties, it is assumed that those will be reduced by the square root of the integrated luminosity until they reach a defined lower limit based on estimates of the achievable accuracy with the upgraded detector.

In these scenarios, all the uncertainties related to the limited number of simulated events are neglected, under the assumption that sufficiently large simulation samples will be available by the time the HL-LHC becomes operational.

For all scenarios, the intrinsic statistical uncertainty in the measurement is reduced by a factor $1/\sqrt{\mathrm{R_L}}$, where $\mathrm{R_L}$ is the projection integrated luminosity divided by that of the reference Run 2 analysis.

Table 91 summarises the Run 2 uncertainties for which a lower limit value is set in the "YR18 systematics uncertainties" scenario. Systematic uncertainties in the identification and isolation efficiencies for electrons and muons are expected to be reduced to around 0.5%. The hadronic τ lepton (τ_{h}) performance is assumed to remain similar to the current level and therefore the associated uncertainties are not reduced in this scenario. The uncertainty in the overall jet energy scale (JES) is expected to reach around 1% precision for jets with $\mathrm{p}_T > 30$ GeV, driven primarily by improvements for the absolute scale and jet flavour calibrations. The missing transverse momentum uncertainty is obtained by propagating the JES uncertainties in its computation, yielding a reduction by up to a half of the Run 2 uncertainty. For the identification of b-tagged jets, the uncertainty in the selection efficiency of b (c) quarks, and in misidentifying a light jet is expected to remain similar to the current level, with only the statistical component reducing with increasing integrated luminosity. The uncertainty in the integrated luminosity of the data sample could be reduced down to 1% by a better understanding of the calibration and fit models employed in its determination, and making use of the finer granularity and improved electronics of the upgraded detectors.

Upper limits at 95% CL on $(\sigma(h)/\sigma_{\mathrm{SM}})\mathcal{B}(h \to aa \to 2b2\tau)$ are shown in Fig. 151 for different integrated luminosities and systematic uncertainty scenarios. In this expression, σ_{SM} denotes the SM production cross section of the Higgs boson, whereas $\sigma(\mathrm{h})$ is the h production cross section. The limits improve proportionally to the square root of the integrated luminosity, as the analysis is statistically limited. For an integrated luminosity of 3000 fb^{-1}, the difference between the limits in the systematic scenarios of Run 2 and YR18 is of the order of 5%, and the limits become another 5% better if all systematic uncertainties are neglected.

The limits of the $h \to aa$ analyses can be converted to limits on $\mathcal{B}(h \to aa)$ in two-Higgs-doublet models extended with a scalar singlet (2HDM+S) [43], for a given type of model, m_a, and $\tan\beta$. The limits in the four types of 2HDM+S are shown in Fig. 152, assuming 3000 fb^{-1} of data with YR18 systematic uncertainties. The colour scale indicates the upper limits on $(\sigma(h)/\sigma_{\mathrm{SM}})\mathcal{B}(h \to aa)$ that can be set assuming some values for m_a and $\tan\beta$.

Table 91: The sources of systematic uncertainty for which limiting values are applied in "YR18 systematics uncertainties" scenario.

Source	Component	Run 2 unc.	Projection minimum unc.
Muon ID		1–2%	0.5%
Electron ID		1–2%	0.5%
Photon ID		0.5–2%	0.25–1%
Hadronic τ ID		6%	Same as Run 2
Jet energy scale	Absolute	0.5%	0.1–0.2%
	Relative	0.1–3%	0.1–0.5%
	Pileup	0–2%	Same as Run 2
	Method and sample	0.5–5%	No limit
	Jet flavour	1.5%	0.75%
	Time stability	0.2%	No limit
Jet energy res.		Varies with p_T and η	Half of Run 2
$\vec{p}_T^{miss}$ scale		Varies with analysis selection	Half of Run 2
b-Tagging	b-/c-jets (syst.)	Varies with p_T and η	Same as Run 2
	light mis-tag (syst.)	Varies with p_T and η	Same as Run 2
	b-/c-jets (stat.)	Varies with p_T and η	No limit
	light mis-tag (stat.)	Varies with p_T and η	No limit
Integrated lumi.		2.5%	1%

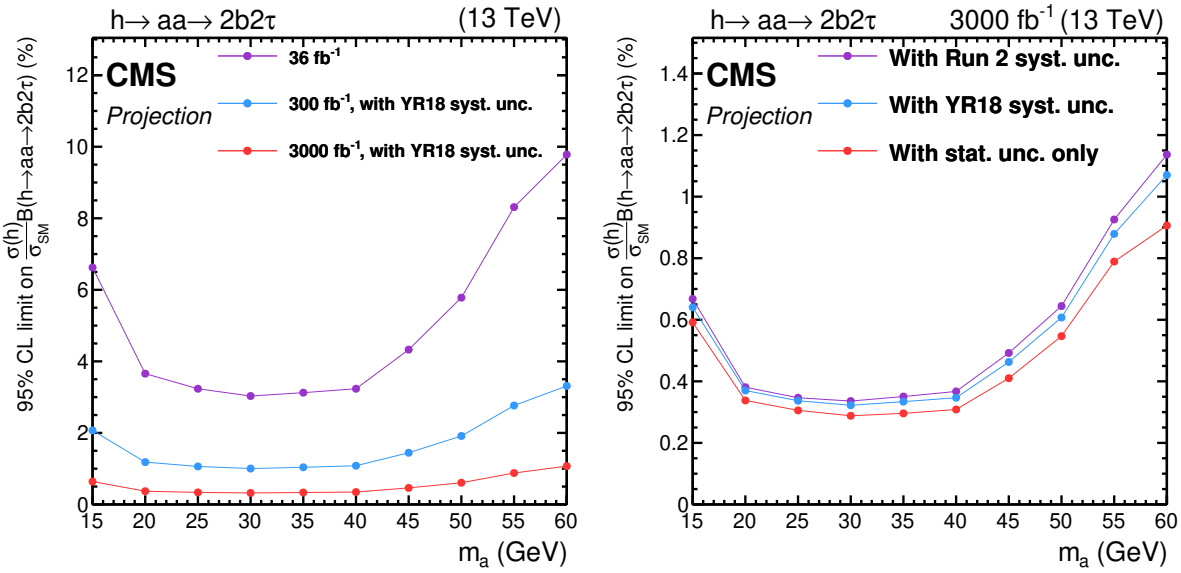

Fig. 151: Left: Projected expected limits on $(\sigma(h)/\sigma_{\text{SM}})$ times the branching fraction for $h \to aa \to 2b2\tau$, for 36, 300, and 3000 fb^{-1}. Right: Projected expected limits $(\sigma(h)/\sigma_{\text{SM}})\mathcal{B}(h \to aa \to 2b2\tau)$, comparing different scenarios for systematic uncertainties for an integrated luminosity of 3000 fb^{-1}.

9.1.4 *Projection of CMS search for exotic $H \to aa \to 2\mu 2\tau$*[115]

This analysis searches for the exotic decay of the Higgs boson to a pair of light pseudoscalars, in the final state of two muons and two τ leptons [823]. Pseudoscalar masses between 15 and 62 GeV are investigated; in this mass range the decay products from the pseudoscalars are not collimated. Several $\tau\tau$ pair possibilities are studied in this analysis: $e\mu$, $e\tau_h$, $\mu\tau_h$, and $\tau_h\tau_h$. In the case where there are 3 muons, the highest-p_t one is paired with the opposite-sign muon that has the highest-p_T among the other two, while the last muon is considered as originating from a τ lepton decay. To reduce the backgrounds from Z Z, Z+jets, and W Z +jets productions, the invariant mass of the muon pair is required to be above

[115] Contact: C. Caillol

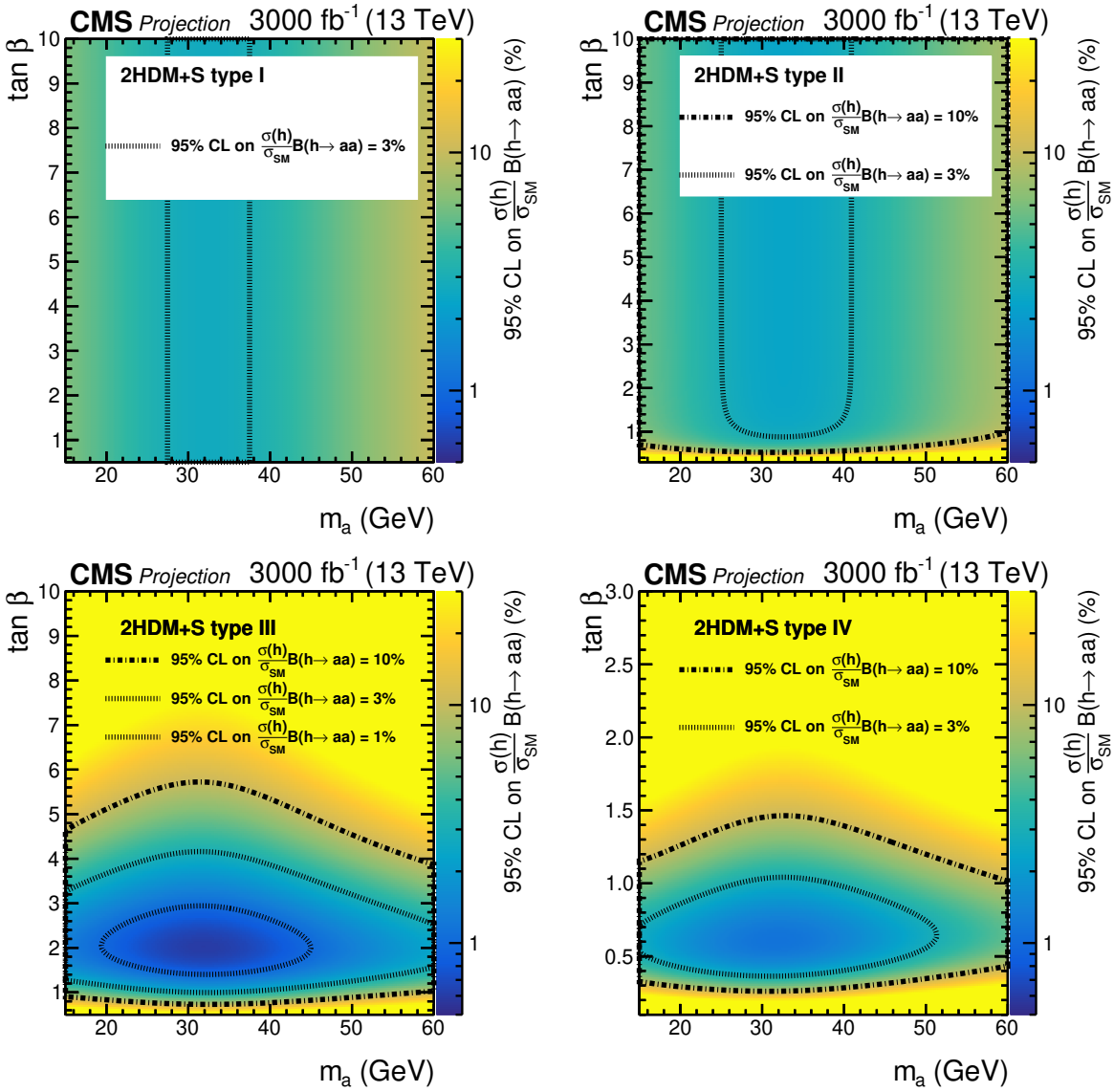

Fig. 152: Expected upper limits on $(\sigma(h)/\sigma_{\mathrm{SM}})\mathcal{B}(h \to aa)$ for 3000 fb^{-1} of data with YR18 systematic uncertainties for the $2b2\tau$ final state in 2HDM+S type-1 (top left), type-2 (top right), type-3 (bottom left), and type-4 (bottom right).

the visible invariant mass of the $\tau\tau$ pair, and the visible invariant mass of the four objects is required to be less than 110–130 GeV depending on the final state. The limits are extracted with an unbinned maximum likelihood fit of the di-muon mass spectrum. The backgrounds are characterised by a rather flat di-muon mass spectrum, while the signal $h \to aa \to 2\mu 2\tau$ forms a narrow peak in the di-muon mass spectrum. The number of expected background events below the signal peak is almost zero, especially at low di-muon mass, and the analysis is strongly statistically dominated.

In the "YR18 systematics uncertainties" scenario, in addition to the limiting values detailed in Table 91, the uncertainty in the normalisation of the reducible background is not allowed to go lower than 20% of the value used in Run-2. The corresponding limits for the $h \to aa \to 2\mu 2\tau$ search are shown in Fig. 153. They scale approximately inversely with the integrated luminosity at low m_a because the analysis is close to background-free, while they tend to scale inversely with the square root of the integrated luminosity at higher m_a, where the background is more important. This leads

to the large improvement at low m_a for 3000 fb^{-1} of collected data shown in Fig. 153. The analysis is statistically limited, even with 3000 fb^{-1} of data. The difference between the Run 2 and YR18 systematic uncertainties in terms of upper limits is up to 5%, and is the largest at high m_a.

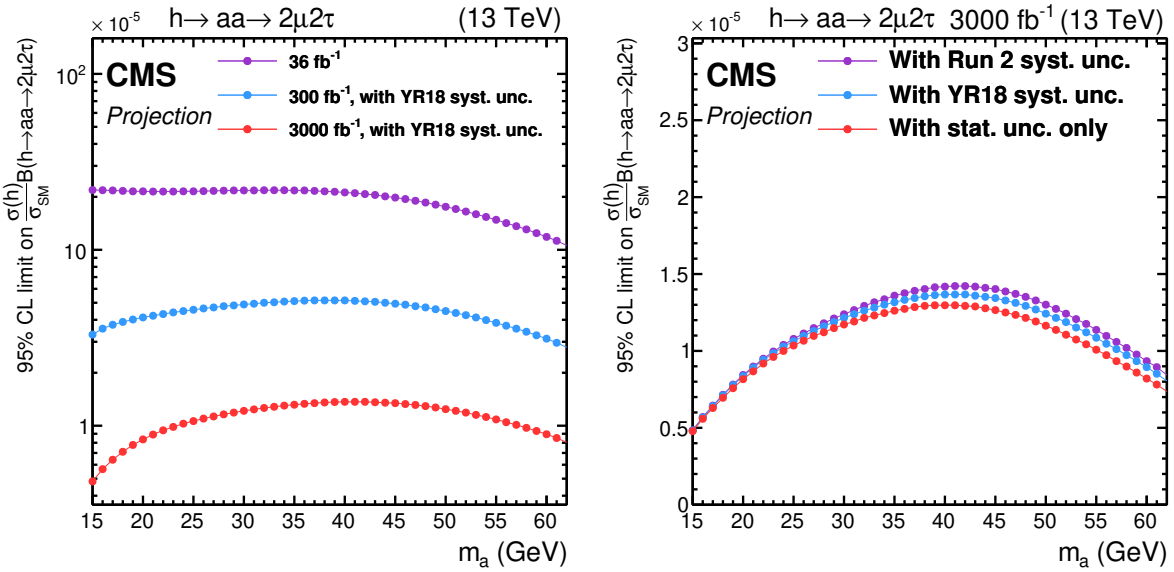

Fig. 153: Left: Projected expected limits on $(\sigma(h)/\sigma_{\text{SM}})\mathcal{B}(h \to aa \to 2\mu 2\tau)$, for 36, 300, and 3000 fb^{-1}. Right: Projected expected limits on $(\sigma(h)/\sigma_{\text{SM}})\mathcal{B}(h \to aa \to 2\mu 2\tau)$, comparing different scenarios for systematic uncertainties for an integrated luminosity of 3000 fb^{-1}.

The limits in the four types of 2HDM+S are shown in Fig 154 for the $2\mu 2\tau$ analysis, assuming 3000 fb^{-1} of data in the "YR18 systematics uncertainties" scenario.

9.1.5 *Exotic decays of the Higgs to 2b2μ*[116]

We assess the potential of an exotic Higgs decay search for $h \to 2X \to b\bar{b}\mu^+\mu^-$ to constrain theories with light CP-even ($X = s$) and CP-odd ($X = a$) singlet scalars at the HL-LHC. This contribution is based on [824]. The decay channel $h \to 2X \to b\bar{b}\mu^+\mu^-$ may represent the best discovery avenue for many models, such as the 2HDM model with an additional complex scalar singlet. It has competitive reach, and is less reliant on low-p_{T} $b-$ and $\tau-$reconstruction compared to other channels like $4b$, 4τ, and $2\tau 2\mu$.

To estimate the reach of $h \to 2X \to b\bar{b}\mu^+\mu^-$ search at the 14 TeV LHC, we take $X = a$ for simplicity. (The results for a scalar, $X = s$, will be similar.) The dominant backgrounds are Drell-Yan (DY) production with associated jets, i.e., $Z/\gamma^* + 2b/2c/2j$, where Z/γ^* produces a muon pair. A secondary background arises from $t\bar{t}$ production. Backgrounds from di-boson production (ZZ, WW, WZ) have small enough cross sections so that we can neglect them. It is also possible for QCD multi-jet events, with two jets being mis-identified as muons, to contribute to the background. We find this can be neglect for analysis with b-tags. Signal, as well as DY and $t\bar{t}$ backgrounds, are simulated at LO by `Sherpa 2.1.1` [161] for $\sqrt{s} = 14$ TeV with the CT10 PDF, and matched up to three jets. The Higgs production cross section for the signal is normalised to the cross section presented in Sec. 2.2 of this report, $\sigma_{ggF} \simeq 54.72$ pb.

Two types of analyses have been included. A conventional analysis that uses standard anti-k_t jets with a jet radius of $R \sim 0.4$. Two b-tags at 70% b-tagging efficiency working point [825] are imposed to the final states. A missing transverse energy cut of $\not{E}_T < 30$GeV suppresses the $t\bar{t}$ background. In

[116] Contact: Y.M. Zhong

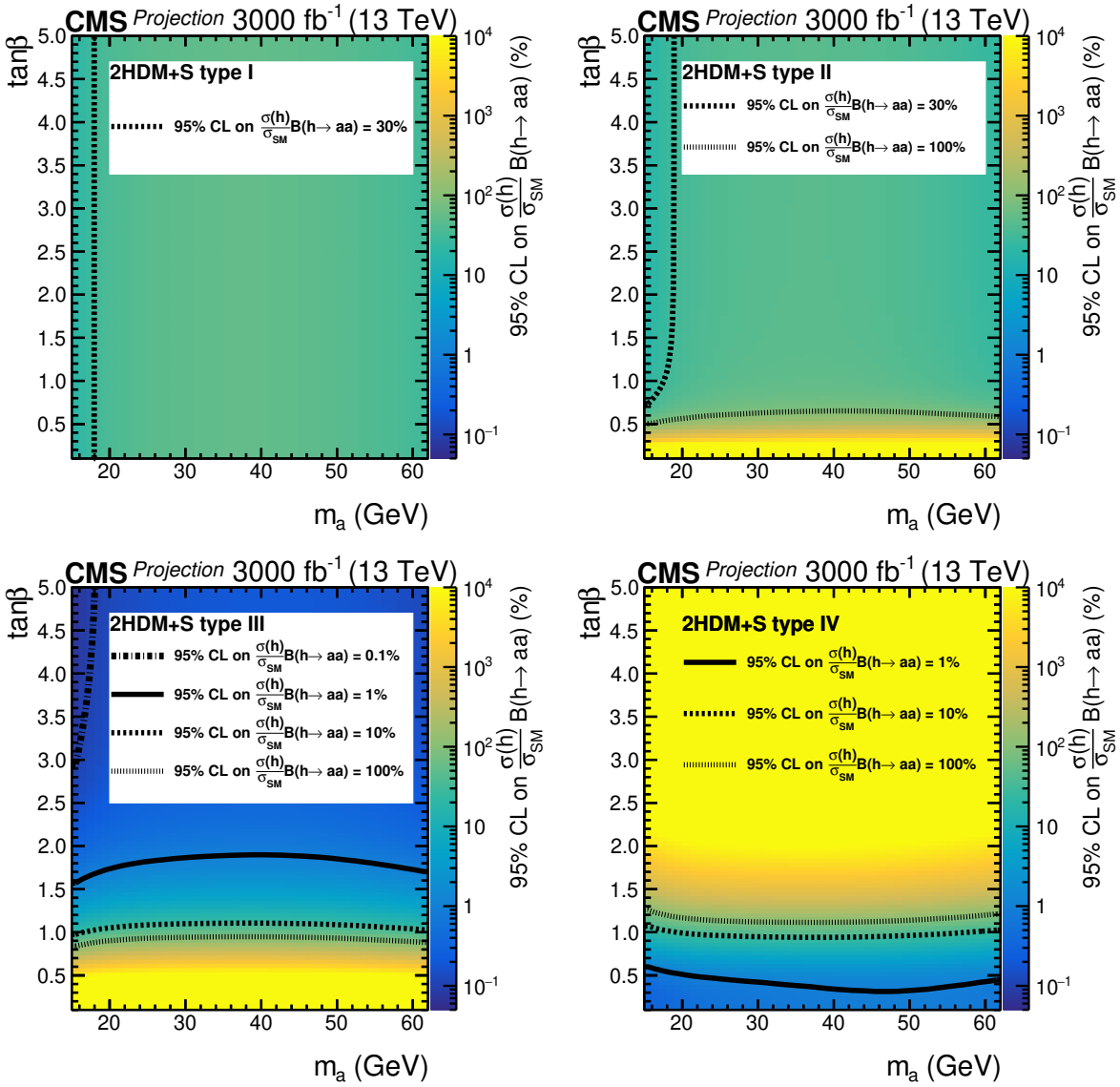

Fig. 154: Expected upper limits on $(\sigma(h)/\sigma_{\rm SM})\mathcal{B}(h \to aa)$ for 3000 fb^{-1} of data with YR18 systematic uncertainties for the $2\mu 2\tau$ final state in 2HDM+S type-1 (top left), type-2 (top right), type-3 (bottom left), and type-4 (bottom right).

addition we make use of the double-resonance structure of the signal by imposing invariant mass cuts

$$|m_{b_1 b_2 \mu_1 \mu_2} - m_h| < 15\text{GeV}, \quad |m_{b_1 b_2} - m_a| < 15\text{GeV}, \quad |m_{\mu_1 \mu_2} - m_a| < 1\text{GeV}, \tag{182}$$

separately for each m_a. After imposing the above cuts, we then perform a simple counting experiment to estimate the reach. The expected bounds are approximately independent of scalar mass for $m_a \geq 30$GeV. For $m_a < 20$GeV, the signal efficiency drops dramatically because the two b's from the a-decay become collimated. The second analysis is based on the mass drop tagger (MDT) [826], a jet substructure technique, to improve the search sensitivity for the low -m_a region. After clustering a b-tagged Cambridge/Aachen (C/A) jet with a jet radius of $R = 0.8$, we resolve its hardest sub-jets that satisfy the MDT criteria ($\mu < 0.67$, $y > 0.09$) by undoing the last step of the C/A clustering. We then apply the same missing energy and invariant mass cuts to the sub-jets as the conventional analysis.

The results of the combined substructure and conventional analyses are shown in Fig. 155. The figure shows a fairly flat sensitivity of $\text{Br}(h \to 2a \to 2b2\mu) \lesssim \text{few} \times 10^{-4}$ for 14 TeV LHC with 30 fb^{-1}

data in the range $15\text{GeV} \leq m_a \leq 60\text{GeV}$. With either 300 or 3000 fb^{-1} of data, the projected sensitivity increases to 10^{-4}, and few $\times\, 10^{-5}$, respectively. For HE-LHC (27 TeV with $15\,\text{ab}^{-1}$), we expected the number of signal and DY background events to be respectively increased by a factor of ~ 15 and ~ 12 in comparison with those of the HL-LHC. This leads to a HE-LHC reach at around $\lesssim 10^{-5}$, i.e., a factor of $15/\sqrt{12} \approx 4$ better than those of the HL-LHC. In the figure, we also show the 95% CL bounds from the 13 TeV ATLAS analysis with 36.1 fb^{-1} data [827] for this Higgs decay mode (grey shaded region). For a range of m_a values, the ATLAS bounds are better than our projections by a factor of ~ 2. This may due to more dedicated analysis techniques such as kinematic-likelihood fit [827], which improve the invariant mass resolutions. Based on the above comparison, we expect the real HL-LHC and HE-LHC reach could be better than our conservative projections.

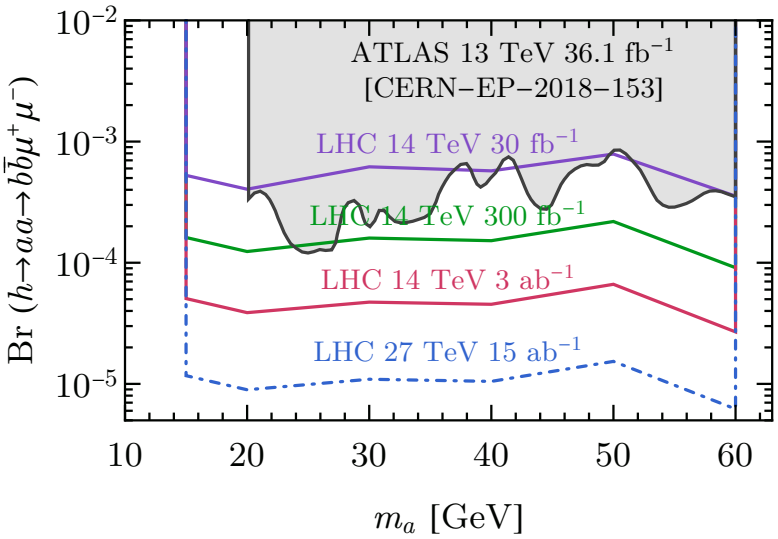

Fig. 155: Combined 95% CL projected reaches on $\text{Br}(h \to aa \to b\bar{b}\mu^+\mu^-)$ for 30 (purple), 300 (green), and 3000 (red) fb^{-1} at 14 TeV [824] and 15 ab^{-1} at 27 TeV (dash-dotted blue). The 95% CL upper limits from the 13 TeV ATLAS search with 36.1 fb^{-1} data [827] is shown as the grey shaded region.

9.1.6 Exotic Higgs Decays to dark photons[117]

Dark photons, or simply a broken or unbroken Abelian gauge interaction, are natural ingredients of hidden sectors. (See e.g. [828, 829, 830, 831, 832] for recent reviews.) Its ubiquity in such theories is particularly important because it can connect the hidden sector to the SM via two portals: the *photon portal* (strictly speaking hyper-charge portal) and the *Higgs portal*. The former refers to a renormalisable kinetic mixing between the dark photon [833, 834, 835] and the SM hyper-charge gauge boson, while the latter refers to the mixing between the SM Higgs and a "dark Higgs", S, that may be responsible for generating a nonzero dark photon mass. The most general minimal Abelian dark photon model, with no other hidden sector matter but with a dark Higgs, was studied in detail in [836]. It was found that exotic Higgs decays are an important probe of such scenarios, and a Madgraph [317] model, the Hidden Abelian Higgs Model, was supplied to conduct the necessary Monte Carlo studies. In this section, we briefly summarise the main results, include constraints from recent searches, and obtain new sensitivity projections for the HE-LHC.

There are two relevant groups of terms in the model Lagrangian. One is responsible for kinetic

[117] Contact: D. Curtin

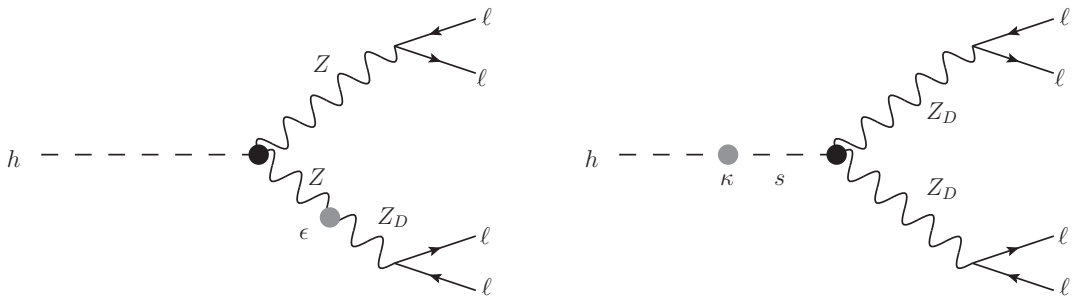

Fig. 156: Exotic Higgs decays to four leptons induced by intermediate dark photons in the Higgsed dark $U(1)_D$ model. *Left:* $h \to Z_D Z^{(*)} \to 4\ell$ via the photon portal. *Right:* $h \to Z_D Z_D \to 4\ell$ via the Higgs portal.

mixing between SM hyper-charge, $U(1)_Y$, and the broken dark Abelian gauge symmetry, $U(1)_D$:

$$\mathcal{L} \subset -\frac{1}{4}\hat{B}_{\mu\nu}\hat{B}^{\mu\nu} - \frac{1}{4}\hat{Z}_{D\mu\nu}\hat{Z}_D^{\mu\nu} + \frac{1}{2}\frac{\epsilon}{\cos\theta}\hat{Z}_{D\mu\nu}\hat{B}^{\mu\nu} + \frac{1}{2}m_{D,0}^2\hat{Z}_D^{\mu}\hat{Z}_{D\mu}\,. \tag{183}$$

The hatted fields indicate the original fields with non-canonical kinetic terms, before any field re-definition The $U(1)_Y$ and $U(1)_D$ field strengths are respectively $\hat{B}_{\mu\nu} = \partial_\mu\hat{B}_\nu - \partial_\nu\hat{B}_\mu$ and $\hat{Z}_{D\mu\nu} = \partial_\mu\hat{Z}_{D\nu} - \partial_\nu\hat{Z}_{D\mu}$, θ is the Weinberg mixing angle, and ϵ is the kinetic mixing parameter. The most general renormalisable potential for the SM and dark Higgs fields is

$$V_0(H,S) = -\mu^2|H|^2 + \lambda|H|^4 - \mu_S^2|S|^2 + \lambda_S|S|^4 + \kappa|S|^2|H|^2\,. \tag{184}$$

Here H is the SM Higgs doublet, while S is the SM-singlet 'dark Higgs' with $U(1)_D$ charge q_S. The Higgs portal coupling, κ, which links the dark and SM Higgs fields is again a renormalisable parameter that controls the mixing between the SM Higgs boson, h, and the uneaten component of the dark Higgs, s.

This simplified model gives rise to two kinds of exotic Higgs decays, shown in Fig. 156. The first is the decay through the *photon portal*: kinetic mixing between Z and Z_D allows for $h \to Z_D Z^{(\star)}$, with $\mathrm{Br} \propto \epsilon^2$. The second is the decay through the *Higgs portal*: mixing between h and s allows for $h \to Z_D Z_D$ with $\mathrm{Br} \propto \kappa^2$. We discuss these decays in more detail below, but we note that dark photon models can give rise to other signals as well. Kinetic mixing gives rise to DY-like production of dark photons and a resulting di-lepton resonance via $pp \to Z_D \to \ell^+\ell^-$. This probes the same coupling as $h \to Z_D Z^{(\star)}$ and, as we discuss below, tends to have greater sensitivity. If the dark Higgs and dark photon masses are in a suitable range, the so-called "platinum channel" becomes available [837], where $h \to 2s \to 4Z_D \to 8\ell$ with $\mathrm{Br} \propto \kappa^2$. We do not discuss this channel in detail here, but this final state, if kinematically available, is extremely conspicuous, and the corresponding low-background search could have significantly greater sensitivity to exotic Higgs decay branching ratios than the example of $h \to Z_D Z_D$ we study in this section. The mass spectrum could also allow for exotic Z-decays [838] via an intermediate dark Higgs, $Z \to Z_D s \to Z_D Z_D Z_D$. Finally, all these signatures could be dressed up or augmented by signatures of a non-minimal hidden sector, where the dark photon/Higgs could decay into invisible stable particles and/or LLPs (see e.g. [831, 545]). The space of possible signatures is clearly very rich. Even so, the simple benchmark decays we examine here give a feeling for the physics reach of the HL- and HE-LHC in probing these kinds of theories.

9.1.6.1 Decays through the photon portal

Kinetic mixing of the dark photon can allow the Higgs to undergo the decay $h \to Z_D Z^\star$ shown in the left panel of Fig. 156. A search for the four-lepton (e or μ) final state has the best sensitivity, making use

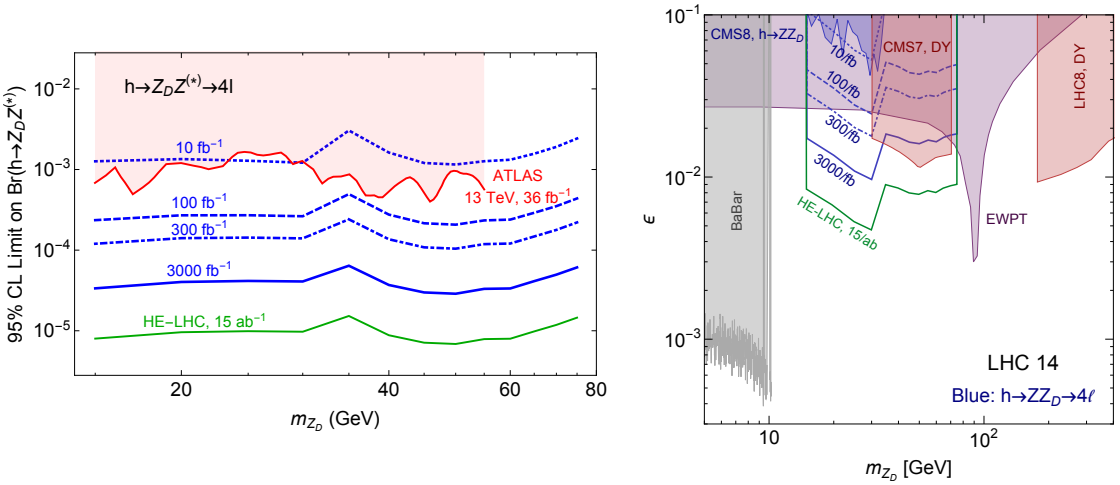

Fig. 157: Sensitivity of the (HL-)LHC and HE-LHC to $h \to Z_D Z^\star \to 4\ell$ decays, as a function of dark photon mass and exotic Higgs decay branching ratio (left) or dark photon kinetic mixing parameter ϵ (right). Figures taken from [836] with the addition of the HE-LHC projection and the recent experimental limit from [839]. Blue contours, taken from [836], correspond to the reach of 14 TeV pp collisions with the HL-LHC sensitivity indicated by a solid blue curve. The green contour corresponds to the HE-LHC at $\sqrt{s} = 27$ TeV with 15 ab^{-1} of luminosity, and is derived by rescaling the 14 TeV projections for 27 TeV signal and background cross sections, see text for details. The red shaded region on the right shows the exclusions from the recent ATLAS search at 13 TeV with 36 fb^{-1} [839].

of the known invariant mass of the Higgs and the assumed mass peak in the invariant mass of one of the lepton pairs. The HL-LHC sensitivity of such a search was estimated in [836] and is shown in Fig. 157. Exotic Higgs branching ratios of few$\times 10^{-5}$ can be probed at the HL-LHC. The projected limits of [836] can be approximately rescaled for the HE-LHC if the increase in signal and background cross section (as a function of m_{Z_D}) are known. The signal increases simply in accordance with the greater Higgs production cross section at 27 TeV compared to 14 TeV. The increase in background generally depends on m_{Z_D}, since this determines the applied invariant mass cuts. To estimate this background increase, we simulate the two main backgrounds to the four-lepton final state, di-Z/γ and $h \to ZZ^*$ production, in Madgraph at parton level for 14 and 27 TeV and apply the analysis cuts of [836]. The resulting increase in background rate is quite m_{Z_D}-independent, since the background is dominated by SM Higgs decays. We therefore adopt a uniform factor of 4.2 for the HE-LHC branching ratio sensitivity increase compared to the HL-LHC, and the resulting projection is shown as the green contour in Fig. 157. We also show the recent exclusions obtained by the ATLAS 13 TeV search for this decay with 36 fb^{-1} [839], which agrees roughly with our projections for LHC reach.

The reach in exotic Higgs branching ratio is impressive, below the 10^{-5} level at the HE-LHC. This allows exotic Higgs decay sensitivities on the kinetic mixing parameter better than 10^{-2}, surpassing, therefore, the model independent bound from electroweak precision measurements, see Fig. 157 (right). Even so, exotic Higgs decays do not lead to the most stringent probe of ϵ in this model. Instead, simple DY production of Z_D and search for the resulting di-lepton resonance on top of the Z^* background still has the greatest reach in ϵ, see Fig. 158 from [836]. For this figure, HE-LHC constraints are also derived from the 14 TeV projections by rescaling the signal and background cross sections as a function of $m_{\ell\ell} \approx m_{Z_D}$. Here, the HE-LHC could reach sensitivities better than $\epsilon \sim 10^{-3}$.

It is important to point out that while exotic Higgs decays may not be the most sensitive probe of kinetic mixing in this scenario, they nevertheless serve an important function in diagnosing the dark sector. Discovery of a resonance in the DY spectrum could indicate a conventionally coupled Z' or a

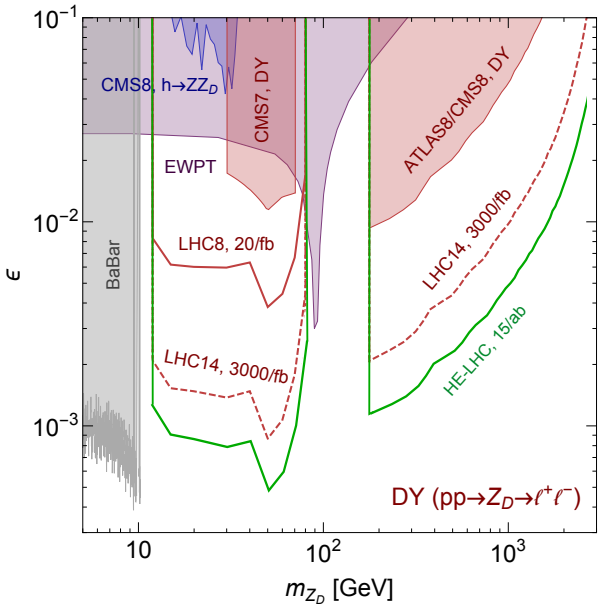

Fig. 158: Sensitivity of the (HL-)LHC and HE-LHC to DY production of Z_D and decay to two leptons, as a function of dark photon mass and kinetic mixing parameter ϵ. Figure taken from [836], indicating the sensitivity of searches at 14 TeV (red contours) with the HL-LHC sensitivity indicated by the red dashed curve. The added green contour corresponds to the HE-LHC at $\sqrt{s} = 27\,\text{TeV}$ with 15 ab^{-1} of luminosity, and is derived by rescaling the 14 TeV projections for 27 TeV signal and background cross sections, see text for details.

kinetically mixed dark photon. However, a discovery of the corresponding exotic Higgs decay would strongly suggest the latter scenario.

9.1.6.2 Decays through the Higgs portal

If the dark photon obtains its mass from a dark Higgs mechanism, one would generally expect there to be nonzero mixing with the SM Higgs. This can lead to exotic Higgs decays to dark photons, as shown in the right panel of Fig. 156.

The signal is independent of ϵ as long as ϵ is large enough for Z_D to decay promptly. Again, the four-lepton final state is the best search target, and the requirement of two di-lepton invariant masses coincident at m_{Z_D} and $m_{4\ell} \approx m_h$ is a very stringent signal requirement that greatly suppresses backgrounds. The sensitivity projections for the HL-LHC are shown in Fig. 159, with exotic Higgs branching ratios as small as $\times 10^{-6}$ being observable. We rescale these limits for the HE-LHC in an identical manner to the previous two analyses, with the resulting projection shown as the green contour. The low background of the search means sensitivity increases almost proportional to the increased signal rate at higher energy and luminosity, allowing branching ratios for $h \to Z_D Z_D$ below 10^{-7} (and, therefore, branching ratios for $h \to Z_D Z_D \to 4\ell$ below 10^{-8}) to be probed. This corresponds to tiny Higgs portal couplings of $\kappa \sim 10^{-5}$ (see right panel of the figure).

For very small ϵ, the Z_D decay is displaced, becoming a long-lived particle. In this case, exotic Higgs decays play a uniquely important role in probing the dark sector, since the photon portal could be far too small to serve as a production mechanism, while the Higgs portal could be wide open. This was analysed in [836, 545] and can lead to ϵ as small as few$\times 10^{-9}$ to be probed in Higgs exotic decays at the HL-LHC.

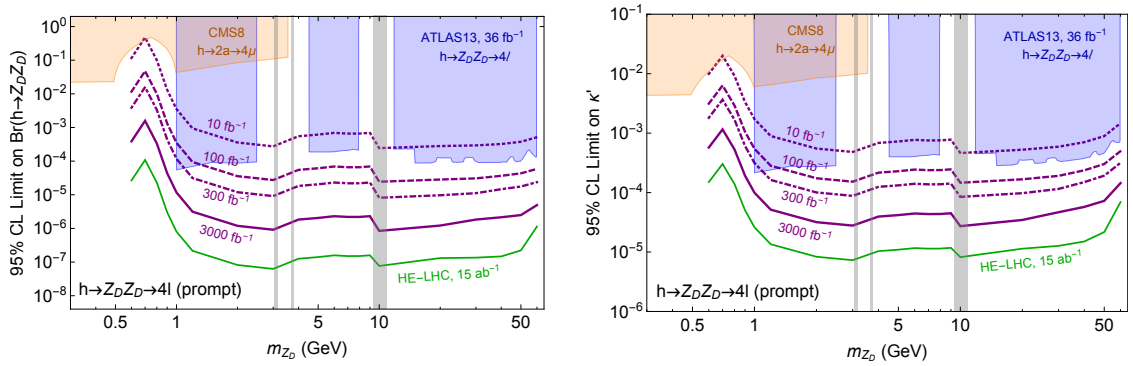

Fig. 159: Sensitivity of the (HL-)LHC and HE-LHC to $h \to Z_D Z_D$ decays, where each Z_D decays to ee or $\mu\mu$ promptly. Limits are shown as a function of dark photon mass and exotic Higgs decay branching ratio (left) or Higgs mixing parameter κ (right). Figures taken from [836] with the addition of the HE-LHC projection and the recent experimental limit from [839]. Purple contours, taken from [836], correspond to the reach of 14 TeV pp collisions with the HL-LHC sensitivity indicated by a solid purple curve. The green contour corresponds to the HE-LHC at $\sqrt{s} = 27$ TeV with 15 ab^{-1} of luminosity, and is derived by rescaling the 14 TeV projections for 27 TeV signal and background cross sections, see text for details. The blue shaded regions show the exclusions from the recent ATLAS search at 13 TeV with 36 fb^{-1} [839].

9.1.7 *Exotic Higgs decays to axion-like particles: $h \to Za$ and $h \to aa$*[118]

In this section, we discuss the exotic Higgs decays $h \to aa$ and $h \to Za$, where a is a light pseudoscalar particle often called an axion-like particle (ALP). Its interactions with SM particles are described by dimension-5 operators or higher when assuming that the ALP respects a shift symmetry apart from a soft breaking through an explicit mass term [840]

$$\begin{aligned}\mathcal{L}_{\text{eff}}^{D\leq 5} = &\frac{1}{2}\left(\partial_\mu a\right)\left(\partial^\mu a\right) - \frac{m_{a,0}^2}{2}\,a^2 + \sum_f \frac{c_{ff}}{2}\,\frac{\partial^\mu a}{\Lambda}\,\bar{f}\gamma_\mu\gamma_5 f + g_s^2\,C_{GG}\,\frac{a}{\Lambda}\,G^A_{\mu\nu}\,\tilde{G}^{\mu\nu,A} \\ &+ e^2\,C_{\gamma\gamma}\,\frac{a}{\Lambda}\,F_{\mu\nu}\,\tilde{F}^{\mu\nu} + \frac{2e^2}{s_w c_w}\,C_{\gamma Z}\,\frac{a}{\Lambda}\,F_{\mu\nu}\,\tilde{Z}^{\mu\nu} + \frac{e^2}{s_w^2 c_w^2}\,C_{ZZ}\,\frac{a}{\Lambda}\,Z_{\mu\nu}\,\tilde{Z}^{\mu\nu}\,,\end{aligned} \tag{185}$$

where $m_{a,0}$ is the explicit symmetry breaking mass term, s_w and c_w are the sine and cosine of the weak mixing angle, respectively, and Λ sets the new physics scale and is related to the ALP decay constant by $\Lambda/|C_{GG}| = 32\pi^2 f_a$. Note that an exotic Z-decay $Z \to \gamma a$ proceeds through the $C_{\gamma Z}$ operator. Interactions with the Higgs boson, ϕ, are described by the dimension-6 and 7 operators

$$\mathcal{L}_{\text{eff}}^{D\geq 6} = \frac{C_{ah}}{\Lambda^2}\left(\partial_\mu a\right)\left(\partial^\mu a\right)\phi^\dagger\phi + \frac{C_{Zh}}{\Lambda^3}\left(\partial^\mu a\right)\left(\phi^\dagger\, iD_\mu\,\phi + \text{h.c.}\right)\phi^\dagger\phi + \ldots\,, \tag{186}$$

where the first operator mediates the decay $h \to aa$, while the second one is responsible for $h \to Za$. Note that a possible dimension-5 operator coupling the ALP to the Higgs current is redundant unless it is introduced by integrating out a heavy new particle which acquires most of its mass through electroweak symmetry breaking [841, 842, 843, 844]. The exotic Higgs decay rates into ALPs are given by

$$\Gamma(h \to Za) = \frac{m_h^3}{16\pi\,\Lambda^2}|C_{Zh}^{\text{eff}}|^2\lambda^{3/2}\left(\frac{m_Z^2}{m_h^2}, \frac{m_a^2}{m_h^2}\right), \tag{187}$$

$$\Gamma(h \to aa) = \frac{m_h^3\,v^2}{32\pi\,\Lambda^4}|C_{ah}^{\text{eff}}|^2\left(1 - \frac{2m_a^2}{m_h^2}\right)^2\sqrt{1 - \frac{4m_a^2}{m_h^2}}\,, \tag{188}$$

[118] Contacts: M. Bauer, M. Neubert, A. Thamm

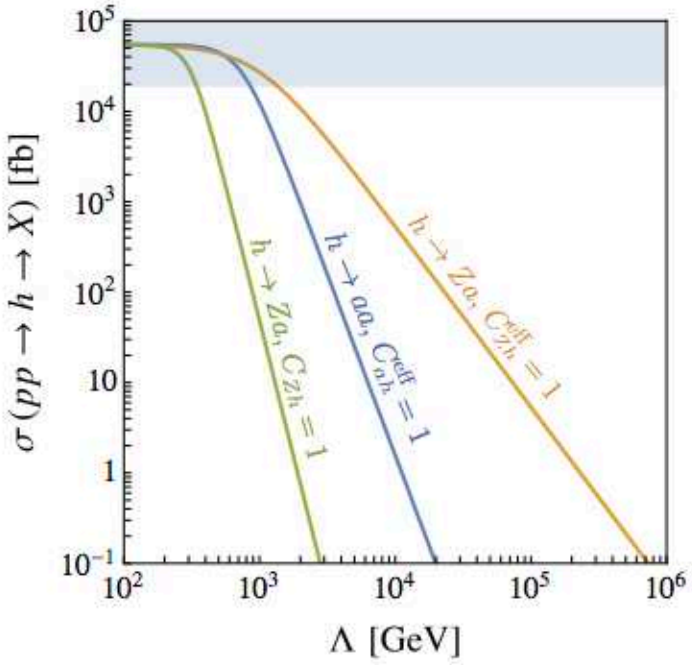

Fig. 160: Production cross sections of ALPs produced in Higgs decays at the LHC ($\sqrt{s} = 14\,\text{TeV}$) versus the new-physics scale Λ. We set $m_a = 0$ and fix the relevant Wilson coefficients to 1. For the green contour we fix $C_{Zh}^{(5)} = 0$ and only consider the dimension-7 coupling in (186). The grey regions are excluded by Higgs coupling measurements (BR$(h \to \text{BSM} < 0.34)$) [144].

where $\lambda(x,y) = (1-x-y)^2 - 4xy$ and we define $C_{Zh}^{\rm eff} = C_{Zh}^{(5)} + C_{Zh} v^2/2\Lambda^2$ to take into account possible contributions from a dimension-5 operator which originates from integrating out chiral heavy new physics. The relevant partial widths for this study are the decay of the ALP into photons and leptons. For the derivation and one-loop contributions we refer the reader to [844]

$$\Gamma(a \to \gamma\gamma) = \frac{4\pi\alpha^2 m_a^3}{\Lambda^2} \left|C_{\gamma\gamma}^{\rm eff}\right|^2, \tag{189}$$

$$\Gamma(a \to \ell^+\ell^-) = \frac{m_a m_\ell^2}{8\pi\Lambda^2} \left|c_{\ell\ell}^{\rm eff}\right|^2 \sqrt{1 - \frac{4m_\ell^2}{m_a^2}}\,. \tag{190}$$

Future hadron colliders can significantly surpass the reach of the LHC in searches for ALPs. In particular, searches for ALPs produced in exotic Higgs and Z decays profit from the higher centre-of-mass energies and luminosities of the proposed high-energy LHC (HE-LHC), planned to replace the LHC in the LEP tunnel with $\sqrt{s} = 27\,\text{TeV}$, and the ambitious plans for a new generation of hadron colliders with $\sqrt{s} = 100\,\text{TeV}$ at CERN (FCC-hh) and in China (SPPC). As benchmark scenarios we assume integrated luminosities of $3\,\text{ab}^{-1}$ at the LHC, $15\,\text{ab}^{-1}$ at the HE-LHC and $20\,\text{ab}^{-1}$ at the FCC-hh. At hadron colliders, ALP production in association with electroweak bosons suffers from large backgrounds. Previous studies of these processes have therefore focused on invisibly decaying (or stable) ALPs, taking advantage of the missing-energy signature [845, 846]. In contrast, here we focus on ALPs produced in the decays of a Higgs boson, $h \to Za$ and $h \to aa$ (for more details see [847]).

Exotic decays are particularly interesting, because even small couplings can lead to appreciable branching ratios and be as large as several percent [843, 844]. This allows us to probe large new-physics

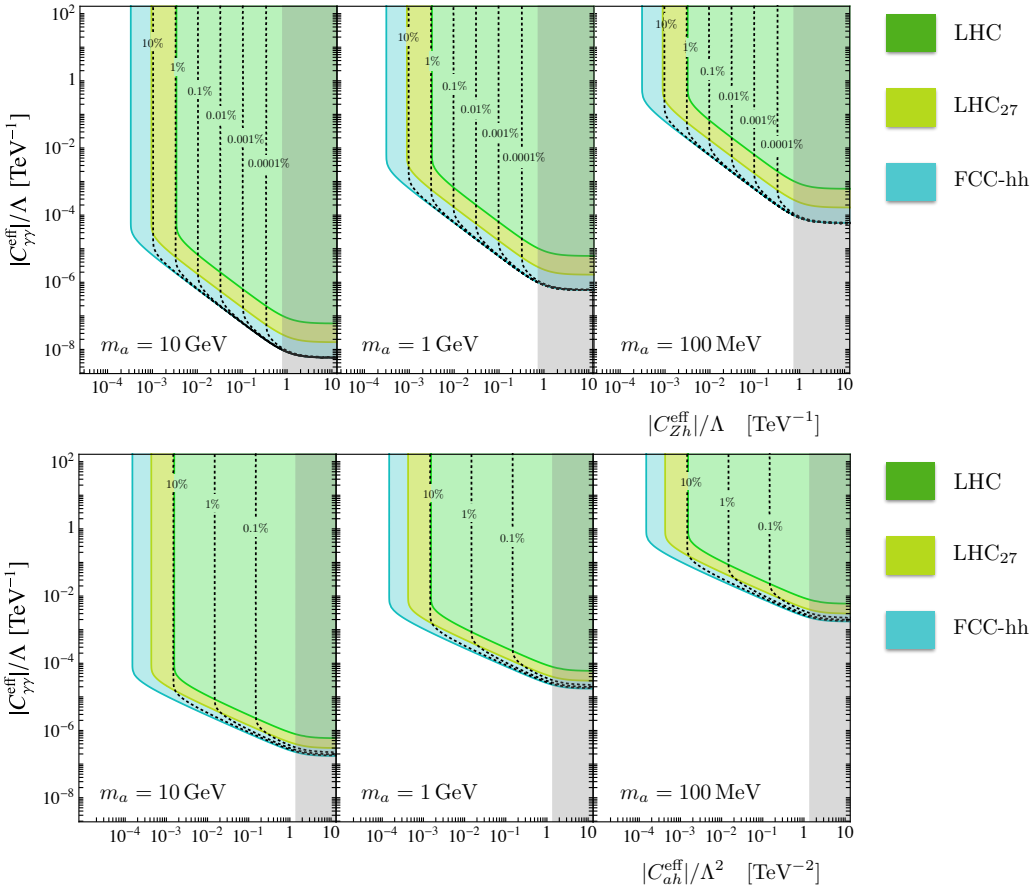

Fig. 161: Projected reach in searches for $h \to Za \to \ell^+\ell^- + 2\gamma$ and $h \to aa \to 4\gamma$ decays with the LHC with $3\,\text{ab}^{-1}$ (green), HE-LHC with $15\,\text{ab}^{-1}$ (light green) and a 100 TeV collider with $20\,\text{ab}^{-1}$ (blue). The parameter region with the solid contours correspond to a branching ratio of $\text{Br}(a \to \gamma\gamma) = 1$, and the contours showing the reach for smaller branching ratios are dotted. The grey areas indicate the regions excluded by the present upper bound on the BSM Higgs width coming from Higgs coupling fits ($\text{BR}(h \to \text{BSM} < 0.34)$) [144].

scales Λ, as illustrated in Figure 160, where we show the cross sections of the processes $pp \to h \to Za$ and $pp \to h \to aa$ at the LHC with $\sqrt{s} = 14\,\text{TeV}$. The figure nicely reflects the different scalings of the dimension-5, 6, and 7 operators in the effective ALP Lagrangian. The shaded region is excluded by the present Higgs coupling measurements constraining general beyond the SM decays of the Higgs boson, $\text{Br}(h \to \text{BSM}) < 0.34$ [144]. This leads to constraints on the coefficients $|C_{Zh}^{\text{eff}}| < 0.72\,(\Lambda/\text{TeV})$ and $|C_{ah}^{\text{eff}}| < 1.34\,(\Lambda/\text{TeV})^2$.

Light or weakly coupled ALPs can be long-lived, and thus only a fraction of them decay inside the detector and can be reconstructed. The average ALP decay length perpendicular to the beam axis is given by

$$L_a^{\perp}(\theta) = \frac{\sqrt{\gamma_a^2 - 1}}{\Gamma_a} \sin\theta\,, \tag{191}$$

where Γ_a denotes the total width of the ALP, θ is the scattering angle (in the centre-of-mass frame) and γ_a specifies the relativistic boost factor. Using the fact that most Higgs bosons are produced in the forward direction at the LHC and approximating the ATLAS and CMS detectors (as well as future detectors) by infinitely long cylindrical tubes, we first perform a Lorentz boost to the rest frame of the decaying boson.

In this frame the relevant boost factors for the Higgs decay into ALPs are given by

$$\gamma_a = \begin{cases} \dfrac{m_h^2 - m_Z^2 + m_a^2}{2 m_a m_h}\,, & \text{for } h \to Za\,, \\ \dfrac{m_h}{2 m_a}\,, & \text{for } h \to aa\,. \end{cases} \tag{192}$$

We can compute the fraction of ALPs decaying before they have travelled a certain distance $L_{\rm det}$ from the beam axis, finding

$$\begin{aligned} f^a_{\rm dec} &= \int_0^{\pi/2} d\theta\, \sin\theta \left(1 - e^{-L_{\rm det}/L_a^\perp(\theta)}\right), \\ f^{aa}_{\rm dec} &= \int_0^{\pi/2} d\theta\, \sin\theta \left(1 - e^{-L_{\rm det}/L_a^\perp(\theta)}\right)^2, \end{aligned} \tag{193}$$

where $f^a_{\rm dec}$ is relevant for $h \to Za$ decays and $f^{aa}_{\rm dec}$ applies to $h \to aa$ decays.

For prompt ALP decays, we demand all final state particles to be detected in order to reconstruct the decaying SM particle. For the decay into photons we require the ALP to decay before the electromagnetic calorimeter which, at ATLAS and CMS, is situated approximately 1.5 m from the interaction point, and we thus take $L_{\rm det} = 1.5\,$m. Analogously, the ALP should decay before the inner tracker, $L_{\rm det} = 2\,$cm, for an e^+e^- final state to be detected. We also require $L_{\rm det} = 2\,$cm for muon and tau final states in order to take full advantage of the tracker information in reconstructing these events. We define the effective branching ratios

$$\text{Br}(h \to Za \to Y\bar{Y} + X\bar{X})\big|_{\rm eff} = \text{Br}(h \to Za)\,\text{Br}(a \to X\bar{X}) f^a_{\rm dec}\,\text{Br}(Z \to Y\bar{Y})\,, \tag{194}$$

$$\text{Br}(h \to aa \to X\bar{X} + X\bar{X})\big|_{\rm eff} = \text{Br}(h \to aa)\,\text{Br}(a \to X\bar{X})^2 f^{aa}_{\rm dec}\,, \tag{195}$$

where $X = \gamma, e, \mu, \tau$ and $Y = \ell, \text{hadrons}$. Multiplying the effective branching ratios by the appropriate Higgs production cross section and luminosity allows us to derive results for a specific collider. The Higgs production cross section at 14 TeV is given by $\sigma(pp \to h) = 54.72\,$pb (see Sec. 2.2 of this report). We use the reference cross section $\sigma(gg \to h) = 146.65\,$pb at $\sqrt{s} = 27\,$TeV. At $\sqrt{s} = 100\,$TeV, the relevant cross section is $\sigma(gg \to h) = 802\,$pb [848]. We require 100 signal events, since this is what is typically needed to suppress backgrounds in new-physics searches with prompt Higgs decays [144, 219, 849] (see also [844] for further discussion). We do not take advantage of the additional background reduction obtained by cutting on a secondary vertex in the case where the ALP lifetime becomes appreciable. A dedicated analysis by the experimental collaborations including detailed simulations of the backgrounds is required to improve on our projections.

In Figure 161, we display the reach for observing 100 events at the HL-LHC, HE-LHC and FCC-hh (in green, light green and blue respectively) in searches for $pp \to h \to Za \to \ell^+\ell^-\gamma\gamma$ (upper panels) and $pp \to h \to aa \to 4\gamma$ (lower panels) for $m_a = 10\,$GeV, 1 GeV and 100 MeV (left, middle, right panel) in the $|C^{\rm eff}_{Zh}|/\Lambda - |C^{\rm eff}_{\gamma\gamma}|/\Lambda$ and $|C^{\rm eff}_{ah}|/\Lambda^2 - |C^{\rm eff}_{\gamma\gamma}|/\Lambda$ planes respectively. We assume $\text{Br}(a \to \gamma\gamma) = 1$ and indicate the reach of the FCC-hh obtained in the case that $\text{Br}(a \to \gamma\gamma) < 1$ by the black dotted lines. In $h \to Za$ searches, the HL-LHC can reach values of $|C^{\rm eff}_{Zh}|/\Lambda$ down to $3 \times 10^{-3}(\Lambda/\text{TeV})$ for all ALP masses. The HE-LHC improves this reach by a factor of 3 to $1 \times 10^{-3}(\Lambda/\text{TeV})$, while the FCC-hh increases the reach by an order of magnitude to values as small as $3 \times 10^{-4}(\Lambda/\text{TeV})$. In $|C^{\rm eff}_{\gamma\gamma}|/\Lambda$, the HL-LHC is sensitive to values larger than $10^{-7}, 10^{-5}$ and $10^{-3}(\Lambda/\text{TeV})$ for $m_a = 10\,$GeV, 1 GeV and 100 MeV, respectively, and the largest allowed value of $|C^{\rm eff}_{Zh}|/\Lambda = 0.72\,(\Lambda/\text{TeV})$. The sensitivity of the HE-LHC (FCC-hh) increases by a factor 3 (10).

The process $h \to aa$ can access $|C^{\rm eff}_{ah}|/\Lambda^2 = 1.5, 0.4, 0.15 \times 10^{-3}(\Lambda/\text{TeV})^2$ at the HL-LHC, HE-LHC and FCC-hh, respectively. In $|C^{\rm eff}_{\gamma\gamma}|/\Lambda$, the HL-LHC is sensitive to values larger than $8 \times 10^{-7}, 8 \times 10^{-5}$ and $8 \times 10^{-3}(\Lambda/\text{TeV})$ for $m_a = 10\,$GeV, 1 GeV and 100 MeV, respectively, for the

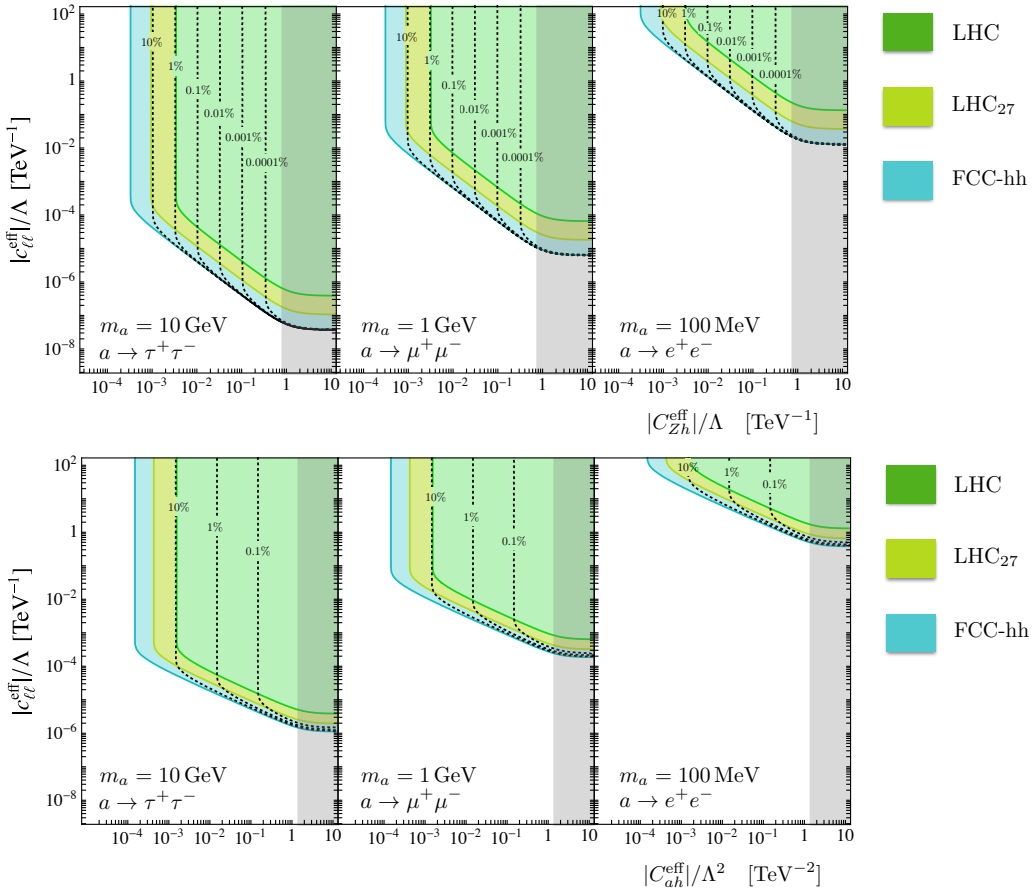

Fig. 162: Projected reach in searches for $h \to Za \to \ell^+\ell^- + \ell^+\ell^-$ and $h \to aa \to 4\ell$ decays with the LHC with $3\,\text{ab}^{-1}$ (green), HE-LHC with $15\,\text{ab}^{-1}$ (light green) and a 100 TeV collider with $20\,\text{ab}^{-1}$ (blue). The parameter region with the solid contours correspond to a branching ratio of $\text{Br}(a \to \ell^+\ell^-) = 1$, and the contours showing the reach for smaller branching ratios are dotted. The grey areas indicate the regions excluded by the present upper bound on the BSM Higgs width coming from Higgs coupling fits.

largest allowed value of $|C_{ah}^{\text{eff}}|/\Lambda$. Both the HE-LHC as well as the FCC-hh improve this reach by a factor 2 each. For all considered ALP masses, the $h \to Za$ decay could be observed at a 100 TeV collider for $\text{Br}(a \to \gamma\gamma) \gtrsim 10^{-6}$ and the $h \to aa$ decay could be fully reconstructed for $\text{Br}(a \to \gamma\gamma) \gtrsim 0.01$.

The results are similar for leptonic ALP decays. In Figure 162 we show the reach in the $|c_{\ell\ell}^{\text{eff}}|/\Lambda - |C_{Zh}^{\text{eff}}|/\Lambda$ plane (upper row) and $|c_{\ell\ell}^{\text{eff}}|/\Lambda - |C_{ah}^{\text{eff}}|/\Lambda^2$ plane (lower row) for ALP decays into taus (left), muons (middle) and electrons (right). In $|C_{Zh}^{\text{eff}}|/\Lambda$ the reach coincides with the one of the same process with ALP decays into photons. For $h \to Za$ the HL-LHC can probe values $|c_{\ell\ell}^{\text{eff}}|/\Lambda = 6\times10^{-7}, 10^{-4}, 2\times 10^{-1}$ (Λ/TeV) for $m_a = 10\,\text{GeV}$, 1 GeV and 100 MeV, respectively. The HE-LHC (FCC-hh) increases this reach by a factor 3 (10). Similarly for $h \to aa$ the HL-LHC is sensitive to values $|c_{\ell\ell}^{\text{eff}}|/\Lambda = 6 \times 10^{-6}, 10^{-3}, 2\,(\Lambda/\text{TeV})$ which the HE-LHC and FCC-hh can increase by a factor 2 each.

9.2 LHC searches for additional heavy neutral Higgs bosons in fermionic final states

9.2.1 Projection of Run-2 ATLAS searches for MSSM heavy neutral Higgs bosons[119]

The studies presented in this section have also been published in [850].

[119] Contacts: L. Zhang, Y. Liu

9.2.1.1 *Introduction*

The discovery of a Standard Model-like Higgs boson [11, 12] at the Large Hadron Collider [851] has provided important insight into the mechanism of electroweak symmetry breaking. However, it remains possible that the discovered particle is part of an extended scalar sector, a scenario that is favoured by a number of theoretical arguments [852, 853]. Searching for additional Higgs bosons is among the main goals of the High-Luminosity LHC programme [854]. The Minimal Supersymmetric Standard Model [852, 855, 856] is one of the well motivated extensions of the SM. Besides the SM-like Higgs boson, the MSSM requires two additional neutral Higgs bosons: one CP-odd (A) and one CP-even (H), which in the following are generically called ϕ. At tree level, the MSSM Higgs sector depends on only two non-SM parameters, which can be chosen to be the mass of the CP-odd Higgs boson, m_A, and the ratio of the vacuum expectation values of the two Higgs doublets, $\tan\beta$. Beyond tree level, a number of additional parameters affect the Higgs sector, the choice of which defines various MSSM benchmark scenarios, such as $m_{\mathrm{h}}^{\mathrm{mod+}}$ and hMSSM. The couplings of the additional MSSM Higgs bosons to down-type fermions are enhanced with respect to the SM Higgs boson for large $\tan\beta$ values, resulting in increased branching fractions to τ-leptons and b-quarks, as well as a higher cross section for Higgs boson production in association with b-quarks.

The projections presented in this section are extrapolations of the recent results obtained by ATLAS using the 36.1 fb^{-1} Run 2 dataset [857]. The MSSM Higgs boson with masses of 0.2–2.25 TeV and $\tan\beta$ of 1–58 is searched for in the $\tau_{\mathrm{lep}}\tau_{\mathrm{had}}$ and $\tau_{\mathrm{had}}\tau_{\mathrm{had}}$ decay modes, where τ_{lep} represents the leptonic decay of a τ-lepton, whereas τ_{h}represents the hadronic decay. The main production modes are gluon–gluon fusion and in association with b-quarks. To exploit the different production modes, events containing at least one b-tagged jet enter the b-tag category, while events containing no b-tagged jets enter the b-veto category. The total transverse mass ($m_{\mathrm{T}}^{\mathrm{tot}}$), as defined in Ref. [857], is used as the final discriminant between the signal and the background.

In making these extrapolations, the assumption is made that the planned upgrades to the ATLAS detector and improvements to reconstruction algorithms will mitigate the effects of the higher pileup which can reach up to 200 in-time pileup interactions, leading to the overall reconstruction performance matching that of the current detector. Furthermore, the assumption is made that the analysis will be unchanged in terms of selection and statistical analysis technique, though the current analysis has not been re-optimised for the HL-LHC datasets.

9.2.1.2 *Extrapolation method*

To account for the integrated luminosity increase at HL-LHC, signal and background distributions are scaled by a factor of $3000/36.1$. Furthermore, to account for the increase in collision energy from 13 TeV to 14 TeV, the background distributions are further scaled by a factor 1.18 which assumes the same parton-luminosity increase for quarks as that for gluons. The cross section of signals in various scenarios at 14 TeV are given in Ref. [45]. Possible effects on the kinematics and the $m_{\mathrm{T}}^{\mathrm{tot}}$ shape due to the collision energy increase are neglected for this study. The scaled $m_{\mathrm{T}}^{\mathrm{tot}}$ distributions for the four signal categories and one for the top control region are shown in Figures 163 and 164. These distributions are used in the statistical analysis.

The larger dataset at HL-LHC will give the opportunity to reduce the systematic uncertainties. The "Baseline" scenario for the systematic uncertainty reduction compared to current Run 2 values follows the recommendation of Ref. [16], according to which the systematic uncertainties associated with b-tagging, τ_{h} (hadronic τ decay) and theoretical uncertainties due to the missing higher order, the PDF uncertainty, etc., are reduced. The systematic uncertainties associated with the reconstruction and identification of the high-p_T τ_{h} is reduced by a factor of 2 and becomes the leading systematic uncertainty for a heavy Higgs boson with mass $m_\phi > 1$ TeV. The systematic uncertainty associated with the modelling of the jet to τ_{h} fake background is assumed to be the same as in the current analysis. For the jet to τ_{h} fake background from multi-jet in $\tau_{\mathrm{had}}\tau_{\mathrm{had}}$ channel, the modelling uncertainty is mainly due to the limited

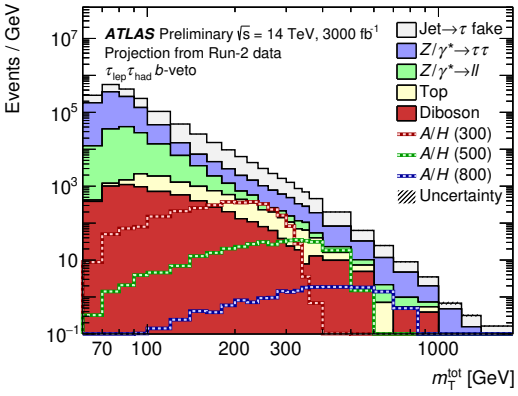

(a) $\tau_{\mathrm{lep}}\tau_{\mathrm{had}}$ b-veto category

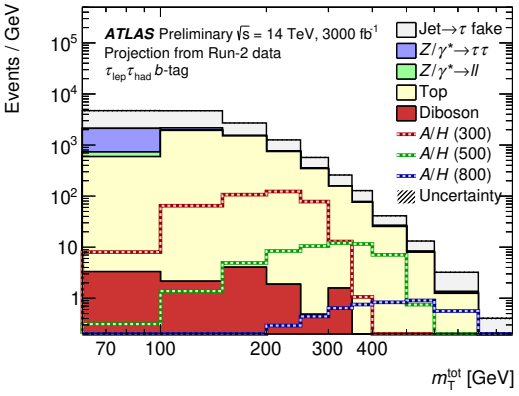

(b) $\tau_{\mathrm{lep}}\tau_{\mathrm{had}}$ b-tag category

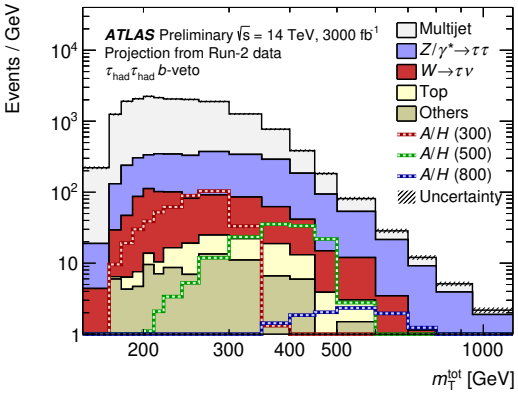

(c) $\tau_{\mathrm{had}}\tau_{\mathrm{had}}$ b-veto category

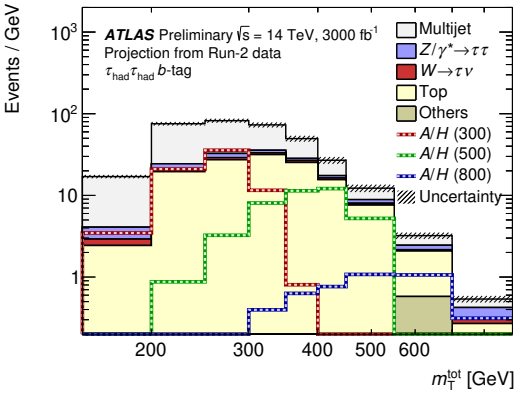

(d) $\tau_{\mathrm{had}}\tau_{\mathrm{had}}$ b-tag category

Fig. 163: Distributions of $m_{\mathrm{T}}^{\mathrm{tot}}$ for each signal category. The predictions and uncertainties (including both statistical and systematic components) for the background processes are obtained from the fit under the hypothesis of no signal. The combined prediction for A and H bosons with masses of 300, 500 and 800 GeV and $\tan\beta = 10$ in the hMSSM scenario are superimposed.

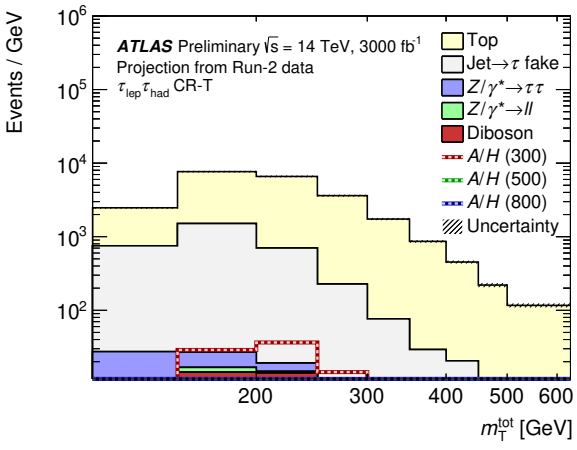

Fig. 164: Distribution of $m_{\mathrm{T}}^{\mathrm{tot}}$ distributions in in the top quark enriched control region of the $\tau_{\mathrm{lep}}\tau_{\mathrm{had}}$ channel.

data size in the control region and is reduced by a factor of 2. The statistical uncertainties on the predicted signal and background distributions, defined as the "template stat. uncertainty", is determined by the size of the MC samples and of the data sample in the control region where the τ_{h} fake factor is applied. The impact of the template stat. uncertainty is negligible in the Run 2 analysis. Assuming large enough MC samples will be generated for HL-LHC and sufficient data will be collected at HL-LHC, the uncertainties due to the sample size is ignored in this extrapolation study. To quantify the importance of the reduction of systematic uncertainties compared to current Run 2 values, results (labelled as "Unreduced") will also be given with current Run 2 values except for ignoring the template stat. uncertainty.

9.2.1.3 Results

The $m_{\mathrm{T}}^{\mathrm{tot}}$ distributions from the $\tau_{\mathrm{lep}}\tau_{\mathrm{had}}$ (separately in the electron and muon channels) and $\tau_{\mathrm{had}}\tau_{\mathrm{had}}$ signal regions, as well as the top control region, are used in the final combined fit to extract the signal. The statistical framework used to produce the Run 2 results is documented in Ref. [857] and is adapted for this HL-LHC projection study. The results are given in terms of exclusion limits [355], as well as the 5 σ discovery reach for gluon–gluon fusion and b-quarks association production modes.

9.2.1.4 Impact of systematic uncertainties

The impact of systematic uncertainties on the upper limit of the cross section times branching ratio ($\sigma \times BR(\phi \to \tau\tau)$) in the Baseline scenario are calculated by comparing the expected 95% CL upper limit in case of no systematic uncertainties, μ^{95}_{stat}, with a limit calculated by introducing a group of systematic uncertainties, μ^{95}_{i}, as described in Ref. [857]. The systematic uncertainty impacts are shown in Figure 165a for gluon–gluon fusion production and Figure 165b for b-quarks association production as a function of the scalar boson mass. The major uncertainties are grouped according to their origin, while minor ones are collected as "Others" as detailed in Ref. [857].

The impact of systematic uncertainties is significant, as they degrade the expected limits by about 10–150 percent. In the low mass range, the leading uncertainties arise from the estimation of the dominant jet to τ_{h} fake background. At high masses, the leading uncertainty is from the reconstruction and identification of high-p_T τ_{h}. Because the μ^{95}_{stat} is mainly determined by the data statistical uncertainty, regions with low statistics are dominated by this uncertainty. In Figure 165a the impact of the τ_{h} related systematic uncertainties decreases after 1 TeV due to the fact that the results at the higher mass regime are more limited by the data statistical uncertainty, while in Figure 165b the data statistical uncertainty in the b-tag category dominates in the high mass regime which leads the high-p_T τ_{h} systematic uncertainty less outstanding.

9.2.1.5 Cross section limits and discovery reach

Figure 166 shows the upper limits on the gluon–gluon fusion and b-quark associated production cross section times the branching fraction for $\phi \to \tau\tau$. To demonstrate the impact of systematic uncertainties, the expected exclusion limits with different systematic uncertainty scenarios are shown, as well as the Run 2 expected results [857]. The peaking structure around $m_\phi = 1$ TeV in figure 166a is due to the impact of the high-p_T τ_{h} systematic uncertainty. The 5 σ sensitivity line in the same figure illustrates the smallest values of the cross section times the branching fraction for which discovery level can be reached at HL-LHC: as clearly shown, the region where discovery is expected at HL-LHC extends significantly below the currently expected Run 2 exclusion region.

9.2.1.6 MSSM interpretation

Results are interpreted in terms of the MSSM. The cross section calculations follow the exact procedure used in Ref. [857], apart from the centre of mass energy is switched to 14 TeV. Figure 167 shows regions in the m_A–$\tan\beta$ plane excluded at 95% CL or discovered with 5 σ significance in the hMSSM and

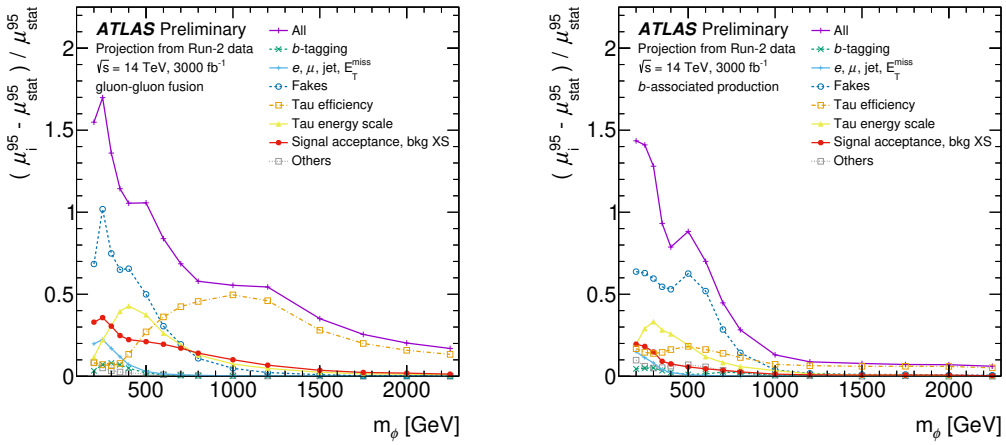

(a) gluon–gluon fusion production (b) b-associated production

Fig. 165: Impact of major groups of systematic uncertainties (Baseline) on the $\phi \to \tau\tau$ 95% CL cross section upper limits as a function of the scalar boson mass, separately for the (a) gluon–gluon fusion and (b) b-associated production mechanisms.

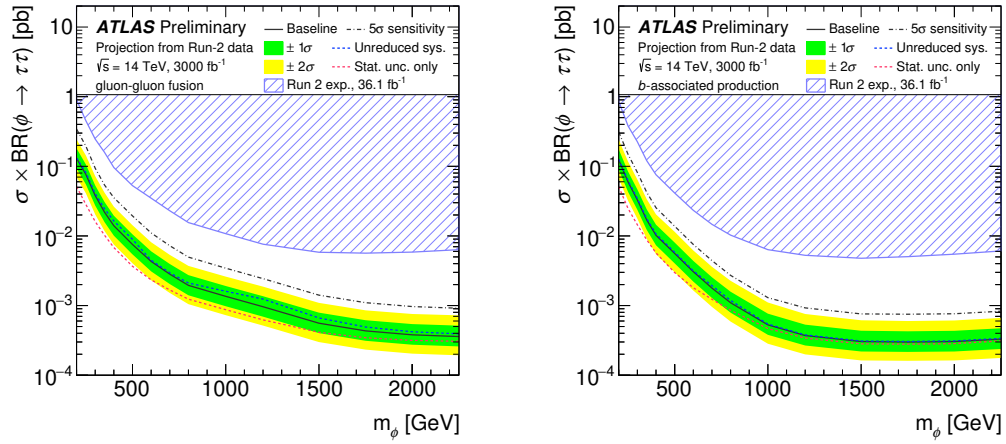

(a) gluon–gluon fusion production (b) b-associated production

Fig. 166: Projected 95% CL upper limits on the production cross section times the $\phi \to \tau\tau$ branching fraction for a scalar boson ϕ produced via (a) gluon–gluon fusion and (b) b-associated production, as a function of scalar boson mass. The limits are calculated from a statistical combination of the $\tau_e\tau_{\mathrm{had}}$, $\tau_\mu\tau_{\mathrm{had}}$ and $\tau_{\mathrm{had}}\tau_{\mathrm{had}}$ channels. "Baseline" uses the reduced systematic uncertainties scenario described in the text. "Unreduced sys." uses the same systematic uncertainties as the Run 2 analysis while ignoring the template stat. uncertainty. "Stat. unc. only" represents the expected limit without considering any systematic uncertainty. "5 σ sensitivity" shows the region with the potential of 5 σ significance in the Baseline scenario.

$m_{\mathrm{h}}^{\mathrm{mod+}}$ scenarios. In the hMSSM scenario, $\tan\beta > 1.0$ for 250 GeV $< m_A <$ 350 GeV and $\tan\beta > 10$ for $m_A = 1.5$ TeV could be excluded at 95% CL. When m_A is above the $A/H \to \mathrm{t\bar{t}}$ threshold, this additional decay mode reduces the sensitivity of the $A/H \to \tau\tau$ search for low $\tan\beta$. In the MSSM $m_{\mathrm{h}}^{\mathrm{mod+}}$ scenario, the expected 95% CL upper limits exclude $\tan\beta > 2$ for 250 GeV $< m_A <$ 350 GeV and $\tan\beta > 20$ for $m_A = 1.5$ TeV.

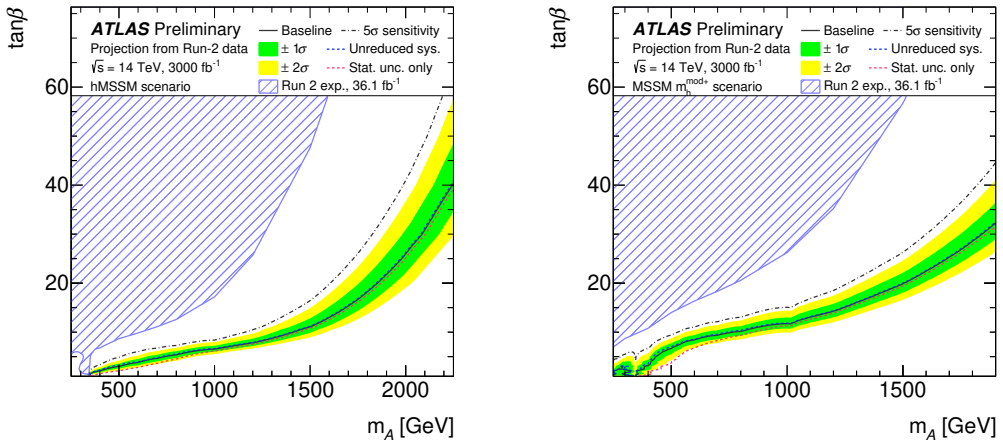

(a) hMSSM scenario

(b) $m_{\mathrm{h}}^{\mathrm{mod+}}$ scenario

Fig. 167: Projected 95% CL limits on $\tan\beta$ as a function of m_ϕ in the MSSM (a) hMSSM and (b) $m_{\mathrm{h}}^{\mathrm{mod+}}$ scenarios. The limits are calculated from a statistical combination of the $\tau_e\tau_{\mathrm{had}}$, $\tau_\mu\tau_{\mathrm{had}}$ and $\tau_{\mathrm{had}}\tau_{\mathrm{had}}$ channels. "Baseline" uses the reduced systematic uncertainties scenario described in the text. "Unreduced sys." uses the same systematic uncertainties as the Run 2 analysis while ignoring the template stat. uncertainty. "Stat. unc. only" represents the expected limit without considering any systematic uncertainty. "5 σ sensitivity" shows the region with the potential of 5 σ significance in the Baseline scenario.

9.2.1.7 Conclusion

The $H/A \to \tau\tau$ analysis documented in [857] has been extrapolated to estimate the sensitivity with 3000 fb^{-1} of the HL-LHC dataset. The expected upper limits at 95% CL or, in alternative, the 5 σ discovery reach in terms of cross section for the production of scalar bosons times the branching fraction to di-tau final states have been estimated. The region with 5 σ discovery potential at HL-LHC extends significantly below the currently expected Run 2 exclusion region. The expected limits are in the range 130–0.4 fb (130–0.3 fb) for gluon–gluon fusion (b-associated) production of scalar bosons with masses of 0.2–2.25 TeV. A factor of 6 to 18 increase in the sensitivity compared to the searches with the 36.1 fb^{-1} Run 2 data [857] is projected. In the context of the hMSSM scenario, in the absence of a signal, the most stringent limits expected for the combined search exclude $\tan\beta > 1.0$ for 250 GeV $< m_A <$ 350 GeV and $\tan\beta > 10$ for $m_A = 1.5$ TeV at 95% CL. The systematic uncertainties degrade the exclusion limit on $\sigma \times BR(\phi \to \tau\tau)$ by more than a factor of 2 for $m_\phi < 500$ GeV and about 10%–20% for $m_\phi = 2$ TeV. While the uncertainty on the estimate of fake τ_{h} dominates at low m_ϕ, the uncertainty on high-p$_T$ τ_{h} reconstruction and identification is the leading systematic uncertainty at $m_\phi > 1.0$ TeV.

9.2.2 Projection of Run-2 CMS searches for MSSM heavy neutral Higgs bosons[120]

Searches for Minimal Supersymmetric Standard Model Higgs bosons have been performed by CMS using the 2016 data from the LHC Run 2 [858, 859, 860]. So far, no significant evidence for physics beyond the SM has been found. However, the LHC to date has delivered only a small fraction of the integrated luminosity expected over its lifetime. Searches that are currently limited by statistical precision will see significant extensions in their reach as larger data sets are collected. Among the searches that will benefit are those for MSSM Higgs bosons.

[120] Contact: M. Flechl

In this section, projections are presented for the reach that can be expected at higher luminosities in searches for heavy neutral Higgs bosons that decay to a pair of tau leptons [861]. The projections are based on the most recent CMS publication for this search [860], performed using 35.9 fb^{-1} of data collected during 2016 at a centre-of-mass energy of 13 TeV. All the details of the analysis, including the simulated event samples, background estimation methods, systematic uncertainties, and different interpretations are described in Ref. [860]. Only details of direct relevance to the projection are presented here.

The analysis is a direct search for a neutral resonance decaying to two tau leptons. The following tau lepton decay mode combinations are considered: $\mu\tau_{\text{h}}$, $\text{e}\tau_{\text{h}}$, $\tau\tau$, and $\text{e}\mu$, where τ_{h} denotes a hadronically decaying tau lepton. In all these channels, events are separated into those that contain at least one b-tagged jet and those that do not contain any b-tagged jet. The goal of this categorisation is to increase sensitivity to the dominant MSSM production modes: gluon fusion (ggF) and production in association with b quarks (bbH). The final discriminant is the total transverse mass, defined in Ref. [860]. The signal hypotheses considered consist of additional Higgs bosons in the mass range from 90 GeV to 3.2 TeV. The projection of the limits is performed by scaling all the signal and background processes to integrated luminosities of 300 and 3000 fb^{-1}, where the latter integrated luminosity corresponds to the total that is expected for the High-Luminosity LHC.

A previous CMS projection of the sensitivity for MSSM Higgs boson decays to a pair of tau leptons at the HL-LHC is reported in Ref. [295]. The results are presented in terms of model independent limits on a heavy resonance (either H or A, generically referred to as H below) decaying to two tau leptons, and are also interpreted in the context of MSSM benchmark scenarios.

9.2.2.1 Projection methodology

Three scenarios are considered for the projection of the size of systematic uncertainties to the HL-LHC:

- statistical uncertainties only: all systematic uncertainties are neglected;
- Run 2 systematic uncertainties: all systematic uncertainties are held constant with respect to luminosity, i.e., they are assumed to be the same as for the 2016 analysis;
- YR18 systematic uncertainties: systematic uncertainties are assumed to decrease with integrated luminosity following a set of assumptions described below.

In the YR18 scenario, selected systematic uncertainties decrease as a function of luminosity until they reach a certain minimum value. Specifically, all pre-fit uncertainties of an experimental nature (including statistical uncertainties in control regions and in simulated event samples) are scaled proportionally to the square root of the integrated luminosity. The following minimum values are assumed:

- muon efficiency: 25% of the 2016 value, corresponding to an average absolute uncertainty of about 0.5%;
- electron, τ_{h}, and b-tagging efficiencies: 50% of the 2016 values, corresponding to average absolute uncertainties of about 0.5%, 2.5%, and 1.0%, respectively;
- jet energy scale: 1% precision for jets with $\text{p}_T > 30$ GeV;
- estimate of the background due to jets mis-reconstruction as τ_{h} [862], for the components that are not statistical in nature: 50% of the 2016 values;
- luminosity uncertainty: 1%;
- theory uncertainties: 50% of the 2016 values, independent of the luminosity for all projections.

Note that for limits in which the Higgs boson mass is larger than about 1 TeV, the statistical uncertainties dominate and the difference between the systematic uncertainties found from the different methods has a negligible impact on the results.

The lightest Higgs boson, h, is excluded from the SM versus MSSM hypothesis test for the following reason: With increasing luminosity, the search will become sensitive to this boson. However, the current benchmark scenarios do not incorporate the properties of the h boson with the accuracy required at the time of the HL-LHC. Certainly the benchmark scenarios will evolve with time in this respect. Therefore the signal hypothesis includes only the heavy A and H bosons, to demonstrate the search potential only for these.

9.2.2.2 *Model-independent limits*

The model independent 95% C.L.upper limit on the cross sections for the ggH and bbH production modes, with the subsequent decays H $\to \tau\tau$, are shown in Figs. 168 and 169 for integrated luminosities of 300, 3000 and 6000 fb^{-1}. For the limit on one process, e.g., gluon fusion, the normalisation for the other process, e.g. b-associated production, is treated as a freely varying parameter in the fit performed prior to the limit calculation. The 6000 fb^{-1} limit is an approximation of the sensitivity with the complete HL-LHC dataset to be collected by the ATLAS and CMS experiments, corresponding to an integrated luminosity of 3000 fb^{-1} each. The approximation assumes that the results of the two experiments are uncorrelated and that their sensitivity is similar. The first assumption is fulfilled to a high degree because the results are statistically limited; the validity of the second assumption is evident by comparing previous limits and projections.

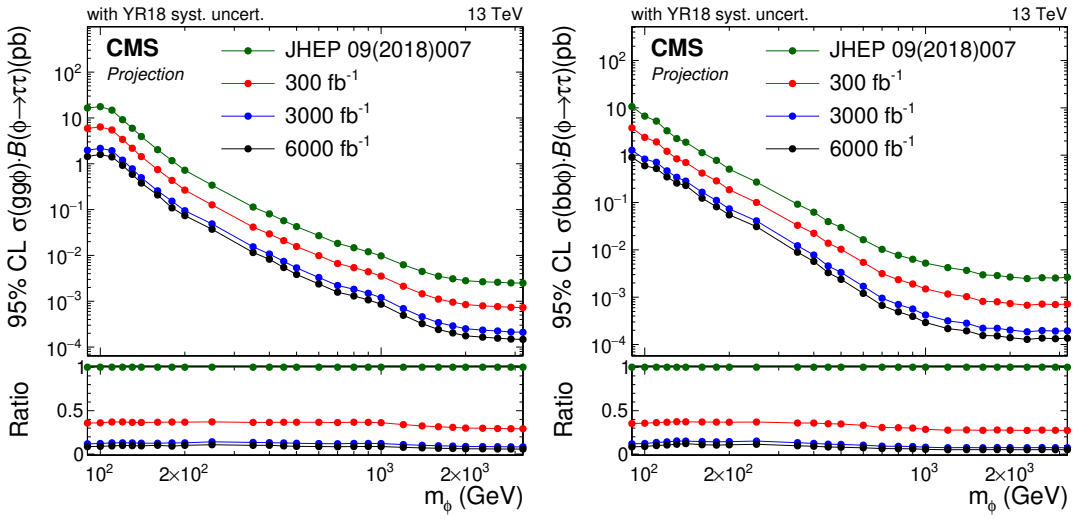

(a) ggH (b) bbH

Fig. 168: Projection of expected model independent 95% CL upper limits based on 2016 CMS data [860] for ggH and bbH production with subsequent H $\to \tau\tau$ decays, with YR18 systematic uncertainties [861]. The limit shown for 6000 fb^{-1} is an approximation of the sensitivity with the complete HL-LHC dataset to be collected by the ATLAS and CMS experiments, corresponding to an integrated luminosity of 3000 fb^{-1} each. The limits are compared to the CMS result using 2016 data [860].

For both production modes, the improvement in the limits at high mass values scales similarly to the square root of the integrated luminosity, as expected from the increase in statistical precision. The improvement at very low mass is almost entirely a consequence of reduced systematic uncertainties and not the additional data in the signal region. The difference between the Run 2 and YR18 scenarios results mostly from of the treatment of two kinds of systematic uncertainty of a statistical nature: the uncertainty related to the number of simulated events and that related to the number of events in the data control regions.

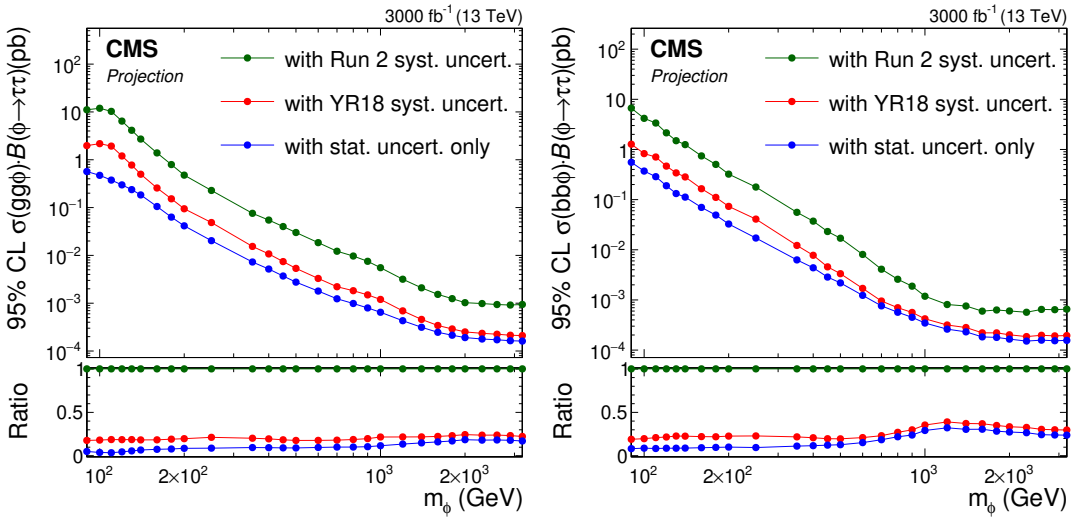

(a) ggH (b) bbH

Fig. 169: Projection of expected model-independent limits based on 2016 CMS data [860] for ggH and bbH production with subsequent H $\rightarrow \tau\tau$ decays, comparing different scenarios for systematic uncertainties for an integrated luminosity of 3000 fb^{-1}.

Figure 170 shows the exclusion contours corresponding to 68% and 95% CL for a scan of the likelihood as a function of both the gluon fusion and the b-associated cross section, for a few representative mass points.

9.2.2.3 *Model-dependent limits*

At the tree level, the Higgs sector of the MSSM can be specified by suitable choices for two variables, often chosen to be the mass m_{A} of the pseudoscalar Higgs boson and $\tan\beta$, the ratio of the vacuum expectation values of the two Higgs doublets. The typically large radiative corrections are fixed based on experimentally and phenomenologically sensible choices for the supersymmetric parameters, each choice defining a particular benchmark scenario. Generally, MSSM scenarios assume that the 125 GeV Higgs boson is the lighter scalar h, an assumption that is compatible with the current experimental constraints for at least a significant portion of the m_{A}–$\tan\beta$ parameter space. The di-tau lepton final state provides the most sensitive direct search for additional Higgs bosons predicted by the MSSM for intermediate and high values of tanβ, because of the enhanced coupling to down-type fermions.

The analysis results are interpreted in terms of these benchmark scenarios based on the profile likelihood ratio of the background-only and the tested signal-plus-background hypotheses. For this purpose, the predictions from both production modes and both heavy neutral Higgs bosons are combined. Figure 171 shows the results [860] for three different benchmark scenarios: the $m_{\mathrm{h}}^{\mathrm{mod+}}$ and tau-phobic scenarios [863] and the hMSSM [864, 865]. The sensitivity reaches up to Higgs boson masses of 2 TeV for values of $\tan\beta$ of 36, 26, and 28 for the $m_{\mathrm{h}}^{\mathrm{mod+}}$, the hMSSM, and the tau-phobic scenarios, respectively. Even at low mass, improvements are expected but in this case they are mostly a consequence of reduced systematic uncertainties and not the additional data in the signal region.

9.2.2.4 *Conclusions*

The HL-LHC projections of the most recent results on searches for neutral MSSM Higgs bosons decaying to τ leptons have been shown, based on a data set of proton-proton collisions at $\sqrt{s} = 13$ TeV collected in

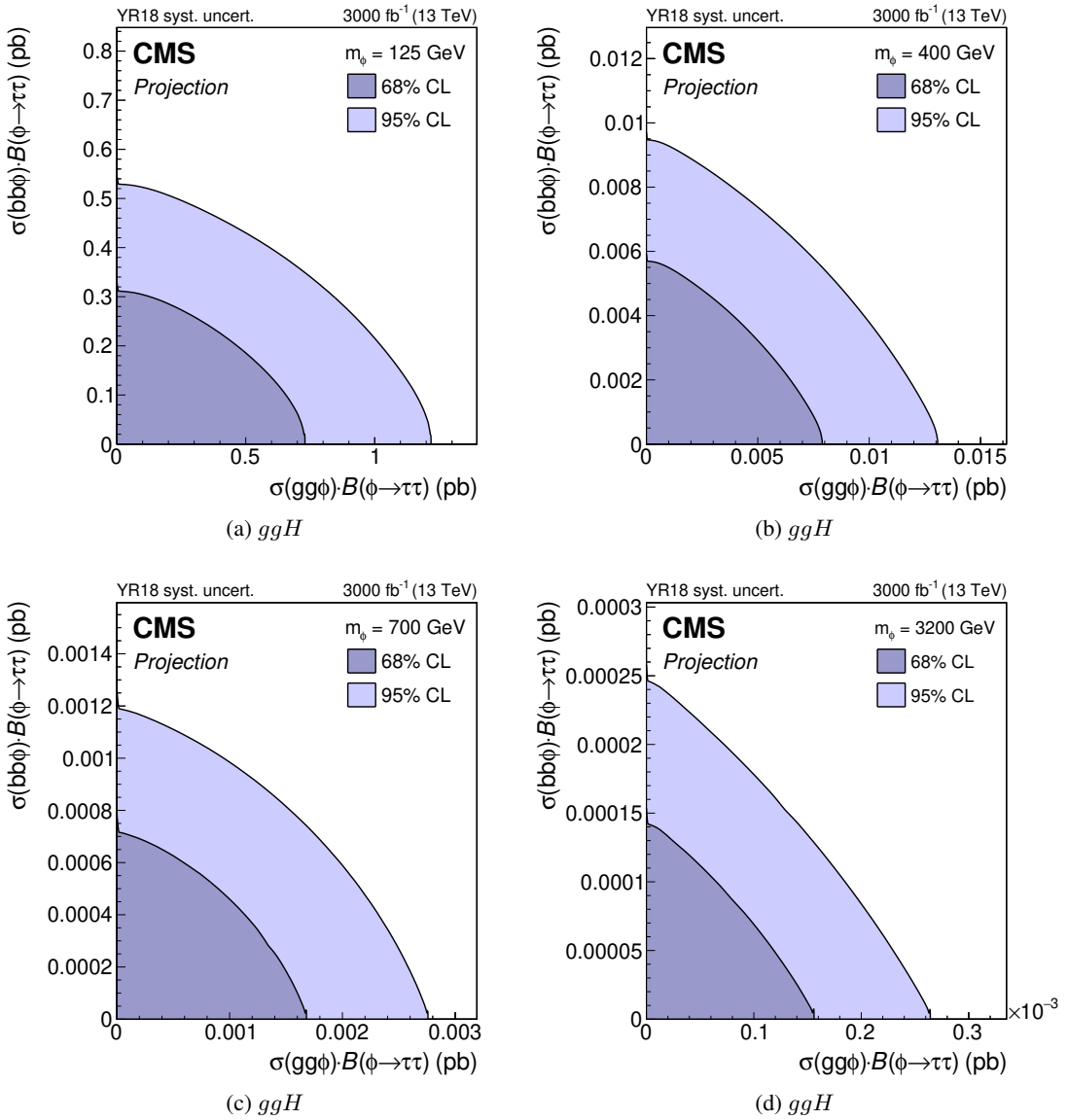

(a) ggH (b) ggH

(c) ggH (d) ggH

Fig. 170: Projection of expected model-independent limits based on 2016 CMS data [860] for a scan of the likelihood for the ggH and bbH production cross sections with subsequent H $\rightarrow \tau\tau$ decays, for an integrated luminosity of 3000 fb^{-1} and with YR18 systematic uncertainties.

2016, corresponding to a total integrated luminosity of 35.9 fb^{-1}. The assumed integrated luminosity for the HL-LHC is 3000 fb^{-1}. In terms of cross section, an order-of-magnitude improvement in sensitivity is expected for neutral Higgs boson masses above 1 TeV since here the current analysis is statistically limited by the available integrated luminosity. For lower masses, an improvement of approximately a factor of five is expected for realistic assumptions on the evolution of the systematic uncertainties. For the MSSM benchmarks, the sensitivity will reach up to Higgs boson masses of 2 TeV for values of $\tan\beta$ of 36, 26, and 28 for the $m_{\mathrm{h}}^{\mathrm{mod+}}$, the hMSSM, and the tau-phobic scenarios, respectively.

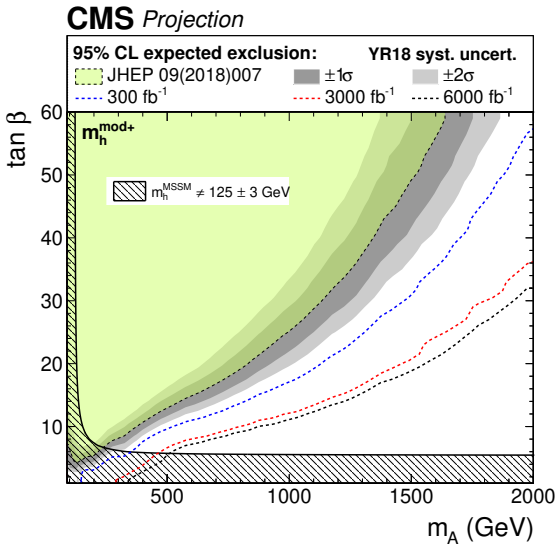

(a) $m_{\mathrm{h}}^{\mathrm{mod+}}$

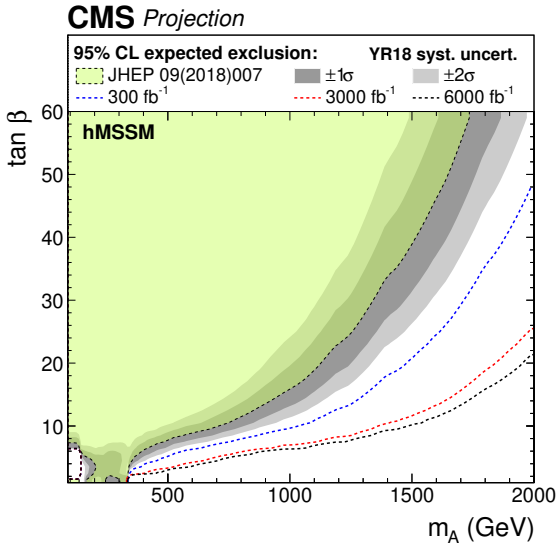

(b) hMSSM

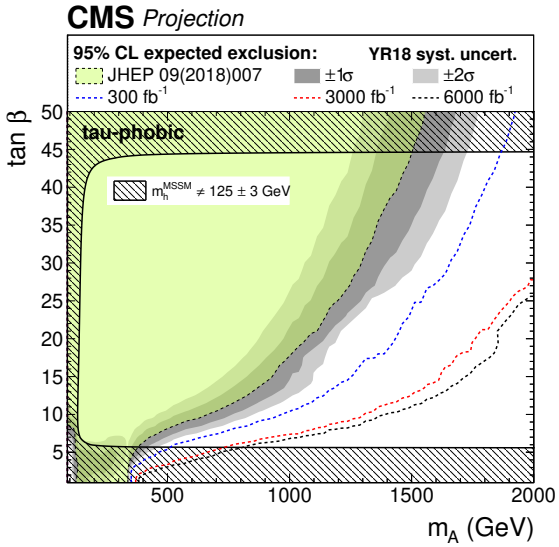

(c) tau-phobic

Fig. 171: Projection of expected MSSM H $\to \tau\tau$ 95% CL upper limits based on 2016 data [860] for different benchmark scenarios, with YR18 systematic uncertainties [861]. The limit shown for 6000 fb^{-1} is an approximation of the sensitivity with the complete HL-LHC dataset to be collected by the ATLAS and CMS experiments, corresponding to an integrated luminosity of 3000 fb^{-1} each. The limits are compared to the CMS result using 2016 data [860]; for the tau-phobic scenario, it is a new interpretation of the information given in this reference.

9.3 LHC searches for additional heavy neutral Higgs bosons in bosonic final states

9.3.1 Projection of Run-2 CMS searches for a new scalar resonance decaying to a pair of Z bosons[121]

9.3.1.1 Introduction

CMS and ATLAS collaborations have performed searches for a heavy scalar partner of the SM Higgs boson decaying into a pair of Z bosons [866, 867]. The CMS search for a heavy scalar partner of the SM Higgs boson using 35.9fb^{-1} of pp collision data [867] will be referred to as HIG-17-012 throughout this section. In HIG-17-012, the search for a scalar resonance X decaying to ZZ is performed over the mass range $130\text{GeV} < m_{\text{X}} < 3\text{TeV}$, where three final states based on leptonic or hadronic decays of Z boson, $\text{X} \to \text{ZZ} \to 4\ell$, $2\ell 2q$, and $2\ell 2\nu$ are combined. Because of the different resolutions, efficiencies, and branching fractions, each final state contributes differently depending on the signal mass hypothesis. The most sensitive final state for the mass range of 130–500GeV is 4ℓ due to its best mass resolution, whereas, for the intermediate region of 500–700GeV, $2\ell 2\nu$ is most sensitive. For masses above 700GeV the $2\ell 2q$ provides the best sensitivity. In this paper, we are particularly interested in the sensitivity in the high mass region, thus only $2\ell 2q$ is used.

In the $2\ell 2q$ final state, events are selected by combining leptonically and hadronically decaying Z candidates. The lepton pairs (electron or muon) of opposite sign and same flavor with invariant mass between 60 and 120 GeV are constructed. Hadronically decaying Z boson candidates are reconstructed using two distinct techniques, which are referred to as "resolved" and "merged". In the resolved case, the two quarks from the Z boson decay form two distinguishable narrow jets, while in the merged case a single wide jet with a large p_T is taken as a hadronically decaying Z candidate.

The two dominant production mechanisms of a scalar boson are gluon fusion (ggF) and EW production, the latter dominated by vector boson fusion (VBF) with a small contribution of production in association with an EW boson ZH or WH (VH). We define the parameter f_{VBF} as the fraction of the EW production cross section with respect to the total cross section. The results are given in two scenarios: f_{VBF} floated, and $f_{VBF} = 1$. In the expected result, the two scenarios correspond to ggF and VBF production modes, respectively. To increase the sensitivity to the different production modes, events are categorised into VBF and inclusive types. Furthermore, since a large fraction of signal events is enriched with b quark jets due to the presence of $\text{Z} \to \text{b}\overline{\text{b}}$ decays, a dedicated category is defined.

The invariant mass of ZZ and a dedicated discriminant separating signal and background distributions are compared between observation and expected background to set limits on the production cross section.

Further details of the HIG-17-012 analysis, including simulation samples, event categorisation, background estimation methods, systematic uncertainties, and different interpretations are described in Ref [867]. Only details of direct relevance to the projection of the HIG-17-012 are documented in Ref. [868] and in the following.

9.3.1.2 Extrapolation procedure

A projection of this analysis is carried out by scaling all the signal and background processes to an integrated luminosity of 3000fb^{-1}, expected to be collected at the high-luminosity LHC. This projection assumes that the CMS experiment will have a similar level of detector and triggering performance during the HL-LHC operation as it provided during the LHC Run 2 period. It does not take into account the small cross section change due to the small change in the centre of mass energy from 13 TeV to 14 TeV. The results of projection are presented for different assumptions based on the size of systematic uncertainties that is estimated for HL-LHC.

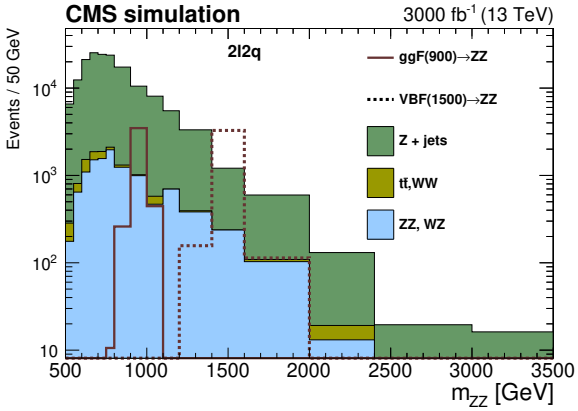

Fig. 172: The m_{ZZ} distribution of the merged category events expected at 3000fb^{-1}. Examples of a 900 GeV ggF signal and a 1500 GeV VBF signal are given. the cross section corresponds to 10 times the excluded limit.

9.3.1.3 Results

The m_{ZZ} distribution of the merged category events expected at 3000 fb^{-1} is shown in Figure 172. Figure 173 shows upper limits at the 95% confidence level on the pp $\rightarrow$ X $\rightarrow$ ZZ cross section $\sigma_X \mathcal{B}_{X\rightarrow ZZ}$ as a function of m_X for a narrow resonance whose Γ_X is much smaller than experimental resolution.

In the mass range between 550–3000 GeV, the excluded cross section of the scalar decaying to a pair of Z bosons is 0.7–5 fb for the VBF production mode and 0.8–9 fb for the ggF production mode. This represents a factor of 10 improvement with respect to the results obtained using Run 2 data. The differences between the two scenarios are minor and mostly present in the low mass region. It is because the search will still be limited by statistical uncertainties. Among all the systematic uncertainties, the theoretical uncertainty from higher order QCD corrections on the $gg \rightarrow ZZ$ background and the signal is the most dominant for the ggF search. The next important ones are the shape and yield uncertainties of the Z+jets background. They are determined from a data control region and are scaled with $1/\sqrt{L}$ in YR18 scenario. It is expected that at HL-LHC, the Z+jets background will have huge statistics, and the understanding of it will be at percent level. The effect of systematics in this search has mild effect, if no $1/\sqrt{L}$ scaling is applied, the difference in the limit is 10% at low mass and almost none in the high mass region. In the HIG-17-012 analysis, Z+jets fake rates are derived from LO MC samples, and differences with respect to NLO samples are assigned as systematic uncertainty. This major source is treated as a theoretical uncertainty and is scaled by 0.5 in the YR18 scenario. The results for wide resonances are not given in this note for simplicity. The Run-2 result has shown that the excluded cross section for a 30% width resonance will be 40% higher at 1 TeV, compared to a narrow resonance assumption.

9.4 Additional channels for heavy Higgs bosons

9.4.1 Sensitivity to heavy Higgs bosons from the 2HDM in "Higgs-to-Higgs" decays[122]

Searches for heavy scalars are highly complementary to coupling measurements of the 125 GeV Higgs h as probes of extended Higgs sectors. Di-boson search channels $H \rightarrow WW, ZZ$ probe the parameter space for which the 125 GeV Higgs is not SM-like, together with Higgs coupling measurements. Both suffer a significant loss in sensitivity to new physics scenarios in the limit of a SM-like 125 GeV Higgs, as the couplings g_{HVV} ($V = W^{\pm}, Z$) vanish in such case. For two-Higgs-doublet-model scenarios, this corresponds to the so-called alignment limit [380], where searches for heavy scalars through non-

[121] Contact: M. Xiao
[122] Contacts: K. Mimasu, J.M. No

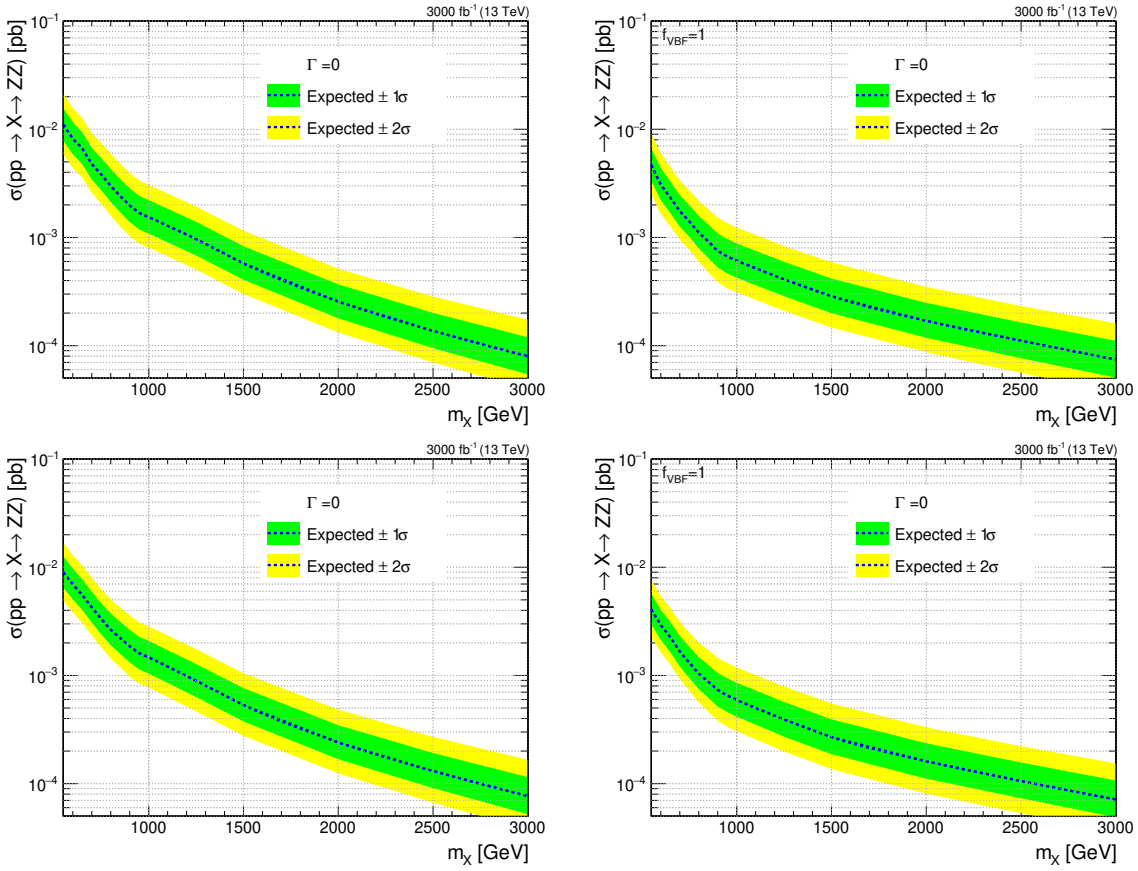

Fig. 173: Expected upper limits at the 95% CL on the pp $\to$ X $\to$ ZZ cross section as a function of m_{X}, with f_{VBF} as a free parameter (left) and fixed to 1 (right). Scenario 1 (top) and scenario 2 (bottom) are shown. The scalar particle X is assumed to have a more narrow decay width than the detector resolution. The results are shown for the $2\ell 2q$ channel.

standard "Higgs-to-Higgs" decay channels [869, 413, 870, 871, 872] as well as through fermionic decay channels [873, 874] become the key avenue to find these new states, and are crucial to cover the parameter space of 2HDMs.

In this section, we focus on HL-LHC and HE-LHC probes of 2HDM neutral scalars via "Higgs-to-Higgs" decays, and briefly discuss also their interplay with direct searches of such states in fermionic decay channels. Specifically, we consider a general scalar potential for two Higgs doublets with a softly broken $\mathbb{Z}_2$ symmetry[123] (and no CP violation), given by

$$\begin{aligned} V(H_1,H_2) &= \mu_1^2 |H_1|^2 + \mu_2^2 |H_2|^2 - \mu^2 \left[H_1^\dagger H_2 + \text{h.c.}\right] + \frac{\lambda_1}{2} |H_1|^4 + \frac{\lambda_2}{2} |H_2|^4 \\ &+ \lambda_3 |H_1|^2 |H_2|^2 + \lambda_4 \left|H_1^\dagger H_2\right|^2 + \frac{\lambda_5}{2}\left[\left(H_1^\dagger H_2\right)^2 + \text{h.c.}\right] . \end{aligned} \tag{196}$$

Regarding the couplings of the two doublets $H_{1,2}$ to fermions, we consider a Type-I and a Type-II 2HDM scenarios, with the parameters $t_\beta \equiv \tan\beta$ and $c_{\beta-\alpha} \equiv \cos(\beta-\alpha)$ controlling the coupling strength of the various 2HDM scalars to fermions and gauge bosons, respectively (see e.g. [853] for a review).

Apart from the 125 GeV Higgs h, the 2HDM scalar sector includes two neutral states H and A,

[123] In specific BSM scenarios featuring two Higgs doublets, it is possible that $\lambda_6 |H_1|^2 (H_1^\dagger H_2 + \text{h.c.})$ and $\lambda_7 |H_2|^2 (H_1^\dagger H_2 + \text{h.c.})$ terms, which explicitly break the $\mathbb{Z}_2$ symmetry, get generated radiatively even if absent at tree-level (e.g. in the MSSM). Being suppressed by $1/(4\pi)^2$, their impact on the present analysis should nevertheless be mild.

respectively CP-even and CP-odd, as well as a charged scalar $H^{\pm}$. Focusing on the neutral scalars, the decay $A \to ZH$ ($H \to ZA$) yields a powerful probe of the parameter space region with a sizeable mass splitting $m_A > m_H + m_Z$ ($m_H > m_A + m_Z$) [869, 413]. We first obtain the present 13 TeV LHC limits on the 2HDM parameter space from the search $A \to ZH$ ($Z \to \ell\ell$, $H \to b\bar{b}$) by ATLAS with 36.1 fb^{-1} [875] (see also [876, 877] for corresponding searches by CMS), considering in particular the alignment limit $c_{\beta-\alpha} = 0$. Our signal cross sections and branching fractions are obtained respectively with SUSHI [878] and 2HDMC [381], and we use the publicly available observed 95% C.L. signal cross section limits in the (m_A, m_H) plane from [875]. In order to derive a sensitivity projection of this search to HL-LHC and HE-LHC with 3000 fb^{-1} of integrated luminosity, we first perform a luminosity rescaling of the present ATLAS expected sensitivity, assuming that the background uncertainties are statistically dominated (*i.e.* we rescale the present expected sensitivity by $\sqrt{\mathcal{L}_2/\mathcal{L}_1} = \sqrt{3000/36.1}$). We then perform a further rescaling of the sensitivity from $\sqrt{s} = 13$ TeV to $\sqrt{s} = 14$ TeV (HL-LHC) and $\sqrt{s} = 27$ TeV (HE-LHC) under the assumption that the ratio of acceptance times cross section ($\mathcal{A} \times \sigma$) for the SM background for 27 TeV and 14 TeV w.r.t. 13 TeV are the same as the ratio of A production cross section[124]. The present LHC bounds and projected sensitivities for $pp \to A \to ZH$ ($Z \to \ell\ell$, $H \to b\bar{b}$) are shown in Figure 174 in the $(m_A, \tan\beta)$ plane for Type II (left) and Type I (right) 2HDM, considering respectively $m_A = m_H + 100$ GeV (top) and $m_A = m_H + 200$ GeV (bottom). We note that, since the limits from [875] neither extend above $m_A = 800$ GeV nor go below $m_H = 130$ GeV, our corresponding projections based on those limits cannot extend beyond those parameter regions either.

We then study the interplay of the $pp \to A \to ZH \to \ell\ell b\bar{b}$ search with searches for heavy scalars in fermionic decay modes, e.g. $H/A \to \tau\tau$. For this purpose, we consider the above benchmarks $m_A = m_H + 100$ GeV and $m_A = m_H + 200$ GeV for Type II 2HDM, and translate the present ATLAS $H \to \tau\tau$ limits with 36.1 fb^{-1} [857] and the 14 TeV HL-LHC sensitivity projections for $H \to \tau\tau$ from Section 9.2 to the $(m_A, \tan\beta)$ plane using SUSHI and 2HDMC, assuming $\cos(\beta - \alpha) = 0$. The results are shown in Figure 175 together with the combined HL-LHC sensitivity of $A \to ZH$ from gluon fusion and bb-associated production, highlighting the complementary between "Higgs-to-Higgs" decays and direct searches in fermionic final states. We also note that a limiting factor of the latter (as currently searched for by the experimental collaborations) for low $\tan\beta$ and $m_H > 340$ GeV is the small branching fraction $H \to \tau\bar{\tau}$ due to the opening of the $H \to t\bar{t}$ decay. This region of parameter space would therefore be efficiently explored via a search for $pp \to A \to ZH$ ($Z \to \ell\ell$, $H \to t\bar{t}$) (see e.g. [872, 879]).

In addition, we analyse the prospects for probing "Higgs-to-Higgs" decay channels within the 2HDM, when one of the scalars involved in the decay is the SM-like 125 GeV Higgs. We focus here on the decay $A \to Zh$, which vanishes in the alignment limit $\cos(\beta - \alpha) = 0$, but may yield the dominant decay mode of A even close to alignment. Following a similar procedure to the one discussed above, in Figure 176 we show the present 95% C.L. signal cross section limits in the $(m_A, \tan\beta)$ plane for 2HDM Type I, fixing $m_A = m_H = m_{H^{\pm}}$ and $\cos(\beta - \alpha) = 0.1$ (for $\tan\beta > 1$, this value of $\cos(\beta - \alpha)$ is barely within the reach of Higgs coupling measurements at HL-LHC, see e.g. [880]), from the LHC 13 TeV ATLAS search for $pp \to A \to Zh \to \ell\ell b\bar{b}$ with 36.1 fb^{-1} [881]. We also show the projected 14 TeV HL-LHC 95% C.L. sensitivity with 3 ab^{-1}, as well as the 27 TeV HE-LHC sensitivity by a rescaling of the HL-LHC limits, under the assumption that the ratio of ($\mathcal{A} \times \sigma$) for the SM background from 14 TeV to 27 TeV is the same as the ratio of signal production cross section. As Figure 176 highlights, the search for $pp \to A \to Zh \to \ell\ell b\bar{b}$ yields a powerful probe of the 2HDM parameter away for the alignment limit, probing up to $\tan\beta \sim 60$ at HE-LHC.

[124] That is, we assume signal and background increase by the same amount in going from 13 TeV to 14 TeV, or 13 TeV to 27 TeV. This is a conservative assumption particularly for high masses m_A.

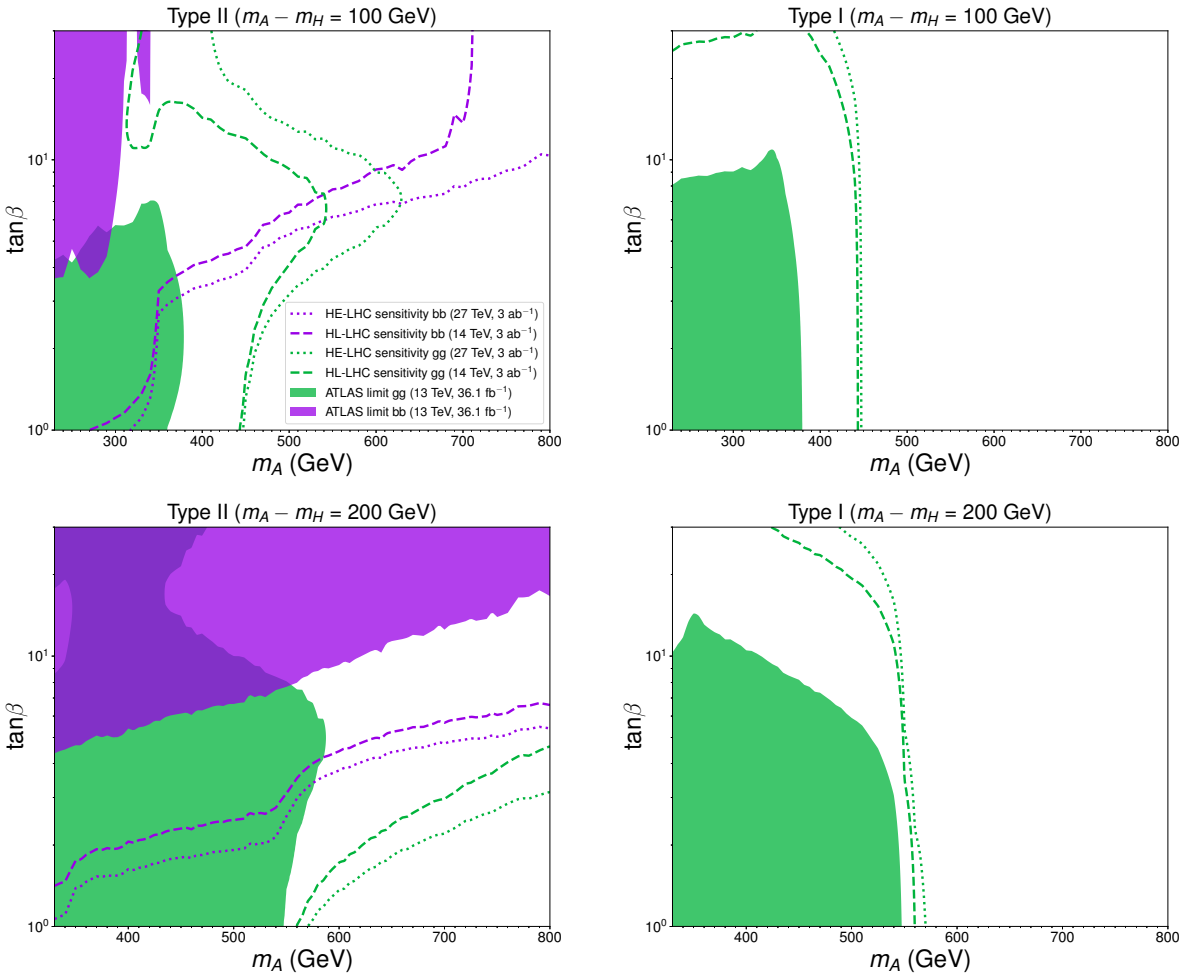

Fig. 174: 95% C.L. exclusion sensitivity for $pp \to A \to ZH \to \ell\ell b\bar{b}$ in the (m_A, tanβ) plane for 2HDM Type II (left) and Type I (right), for $m_A = m_H + 100$ GeV (top) and $m_A = m_H + 200$ GeV (bottom). The present bounds [875] are shown as solid regions, while 3000 fb^{-1} projections for 14 TeV HL-LHC and 27 TeV HE-LHC are respectively shown as dashed and dotted lines. Limits from gluon fusion are shown in green, and limits from bb-associated production (for Type II 2HDM) are shown in purple.

9.4.2 Interference effects in heavy Higgs searches[125]

The singlet SM extension serves as the simplest, yet elusive benchmark to test a sufficiently strong first-order phase transition (EWPT) compatible with the Higgs boson mass measurements at the LHC. The singlet without Z_2 protection could mix with the SM Higgs and (in most cases) a promptly decaying scalar particle would provide a rich phenomenology at colliders. The singlet scalar could be produced resonantly and decay back to pairs of SM particles, dominantly into WW, ZZ, HH and $t\bar{t}$. The signal of a singlet scalar resonance decaying into HH is a smoking-gun for singlet enhanced EWPT [398, 882, 883, 403, 333, 406, 884, 885, 886, 887, 45] (see also the discussion in Section 3.6.2).

Searches for resonant di-Higgs production have received much attention by both the ATLAS and CMS collaborations [888, 331, 889, 890, 891, 892]. In the case of a singlet resonance, constraints from SM precision measurements render these searches more challenging. From one side precision measure-

[125] Contacts: M. Carena, Z. Liu, M. Riembau. This manuscript has been authored by Fermi Research Alliance, LLC under Contract No. DE-AC02-07CH11359 with the U.S. Department of Energy, Office of Science, Office of High Energy Physics. ZL is also supported by the NSF under Grant No. PHY1620074 and by the Maryland Center for Fundamental Physics (MCFP).

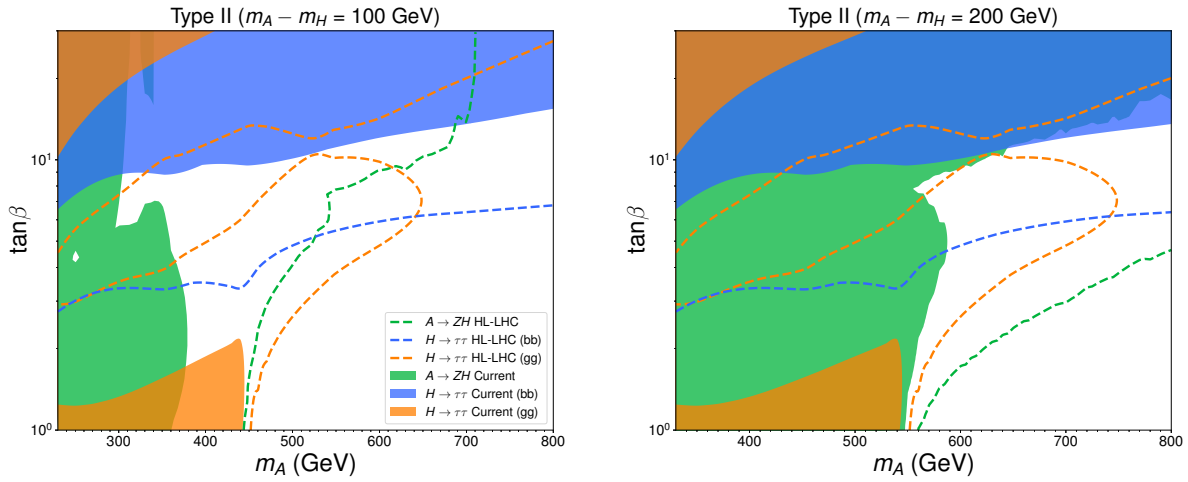

Fig. 175: 2HDM Type II 95% C.L. exclusion sensitivity for $pp \to A \to ZH \to \ell\ell b\bar{b}$ (green) in the (m_A, tanβ) plane for $m_A = m_H + 100$ GeV (left) and $m_A = m_H + 200$ GeV (right), combining gluon fusion and bb-associated production (see Figure 174). We show for comparison the 95% C.L. exclusion sensitivity for $pp \to H \to \tau\tau$ in gluon fusion (orange) and bb-associated production (blue). Present bounds are shown as solid regions, while 3000 fb^{-1} projections for 14 TeV HL-LHC are shown as dashed lines.

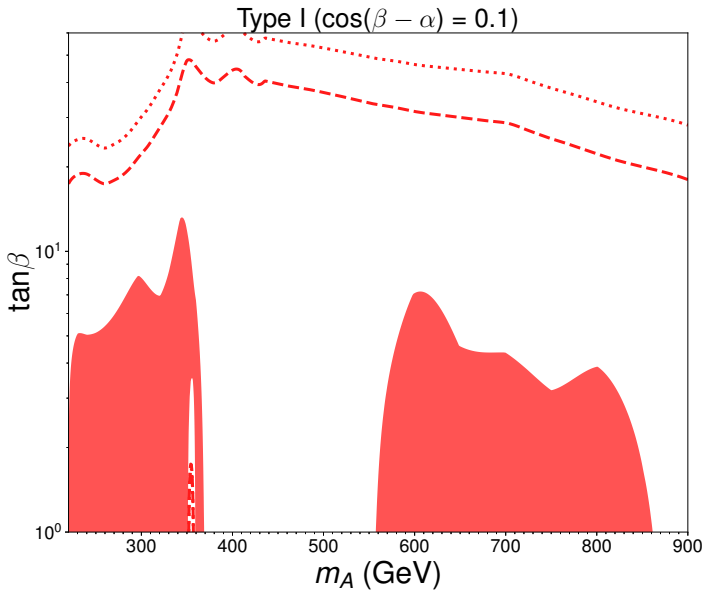

Fig. 176: 2HDM Type I 95% C.L. exclusion sensitivity for $pp \to A \to Zh \to \ell\ell b\bar{b}$ in the (m_A, tanβ) plane, for $\cos(\beta - \alpha) = 0.1$. Present bounds are shown as solid regions, while 3000 fb^{-1} projections for 14 TeV HL-LHC and 27 TeV HE-LHC are shown as dashed and dotted lines, respectively.

ments imply that the singlet-doublet mixing parameter is constrained to be small over a large region of parameter space. On the other side, the singlet only couples to SM particles through mixing with the SM Higgs doublet. This results in a reduced di-Higgs production via singlet resonance decays. In particular, the singlet resonance amplitude becomes of the same order as the SM triangle and box diagram amplitudes. Most important, in this work we shall show that a large relative phase between the SM box diagram and the singlet triangle diagram becomes important. This special on-shell interference effect

has been commonly overlooked in the literature and turns out to have important phenomenological implications. We shall choose the spontaneous Z_2 breaking scenario of the SM plus singlet to demonstrate the importance of the novel on-shell interference effect for the resonant singlet scalar searches in the di-Higgs production mode.

9.4.2.1 *Model framework*

We will consider the simplest extension of the SM that can assist the scalar potential to induce a strongly first-order electroweak phase transition, consisting of an additional real scalar singlet with a Z_2 symmetry. The scalar potential of the model can be written as

$$V(s,\phi) = -\mu^2\phi^\dagger\phi - \frac{1}{2}\mu_s^2 s^2 + \lambda(\phi^\dagger\phi)^2 + \frac{\lambda_s}{4}s^4 + \frac{\lambda_{s\phi}}{2}s^2\phi^\dagger\phi, \tag{197}$$

where ϕ is the SM doublet [126] and s represents the new real singlet field. In the above, we adopt the conventional normalisation for the couplings of the SM doublets and match the other couplings with the singlet with identical normalisation. We allow for spontaneous Z_2 breaking with the singlet s acquiring a vacuum expectation value v_s, since this case allows for interesting collider phenomenology of interference effects. As we shall show later, the (on-shell) interference effects commonly exist for loop-induced processes in BSM phenomenology and it is the focus of this paper. The CP even neutral component h of the Higgs doublet field ϕ mixes with the real singlet scalar s, defining the new mass eigen-states H and S

$$\begin{pmatrix} h \\ s \end{pmatrix} = \begin{pmatrix} \cos\theta & \sin\theta \\ -\sin\theta & \cos\theta \end{pmatrix} \begin{pmatrix} H \\ S \end{pmatrix}, \tag{198}$$

where θ is the mixing angle between these fields. The five free parameters in Eq. (197) can be traded by the two boundary conditions

$$m_H = 125\ \text{GeV}, \quad v = 246\ \text{GeV} \tag{199}$$

and the three "physical" parameters,

$$m_S, \quad \tan\beta(\equiv \frac{v_s}{v}), \text{ and } \sin\theta, \tag{200}$$

where $\tan\beta$ characterises the ratio between the VEVs of the doublet and the singlet scalar fields, respectively. Detailed relations between the bare parameters and physical parameters can be found in Ref. [339].

9.4.2.2 *Enhancing the di-Higgs signal via interference effects*

The on-shell interference effect may enhance or suppress the conventional Breit-Wigner resonance production. Examples in Higgs physics known in the literature, such as $gg \to h \to \gamma\gamma$ [481] and $gg \to H \to t\bar{t}$ [893, 894, 874, 873, 895], are both destructive. We discuss in detail in this section the on-shell interference effect between the resonant singlet amplitude and the SM di-Higgs box diagram. We shall show that in the singlet extension of the SM considered in this paper, the on-shell interference effect is generically constructive and could be large in magnitude, thus enhances the signal production rate.

The interference effect between two generic amplitudes can be denoted as non-resonant amplitude A_{nr} and resonant amplitude A_{res}. The resonant amplitude A_{res}, defined as

$$A_{res} = a_{res}\frac{\hat{s}}{\hat{s} - m^2 + i\Gamma m}, \tag{201}$$

[126] $\phi^T = (G^+, \frac{1}{\sqrt{2}}(h + iG^0 + v))$, where $G^{\pm,0}$ are the Goldstone modes.

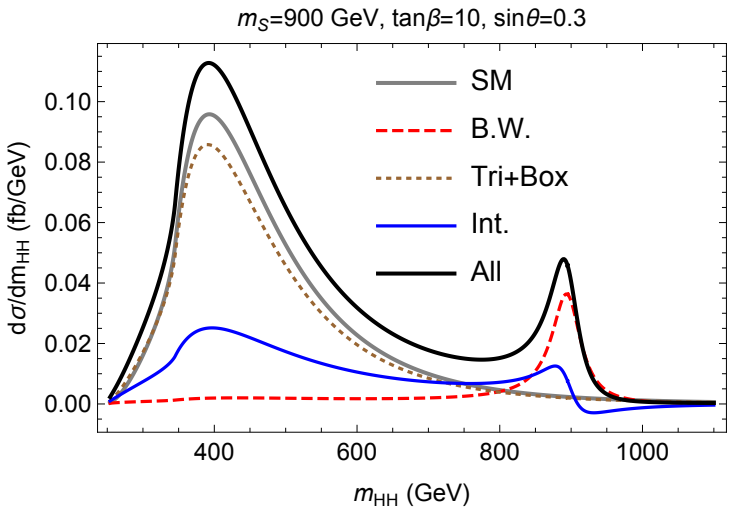

Fig. 177: The differential di-Higgs distribution for a benchmark point of the singlet extension of the SM shown in linear scale and over a broad range of the di-Higgs invariant mass. The full results for the SM and the singlet SM extension are shown by the grey and black curves, respectively. In the singlet extension of the SM, the contributions from the resonant singlet diagram, the non-resonant diagram and the interference between them are shown in red (dashed), brown (dotted) and blue curves, respectively.

has a pole in the region of interest and we parametrise it as the product of a fast varying piece containing its propagator and a slowly varying piece a_{res} that generically is a product of couplings and loop-functions. The general interference effect can then be parametrised as [894, 481],

$$\begin{aligned} |\mathcal{M}|^2_{int} &= 2\Re(A_{res} \times A^*_{nr}) = 2\,(\mathcal{I}_{int} + \mathcal{R}_{int})\,, \\ \mathcal{R}_{int} &\equiv |A_{nr}||a_{res}| \frac{\hat{s}(\hat{s}-m^2)}{(\hat{s}-m^2)^2+\Gamma^2 m^2} \cos(\delta_{res}-\delta_{nr}) \\ \mathcal{I}_{int} &\equiv |A_{nr}||a_{res}| \frac{\hat{s}\Gamma m}{(\hat{s}-m^2)^2+\Gamma^2 m^2} \sin(\delta_{res}-\delta_{nr}), \end{aligned} \tag{202}$$

where δ_{res} and δ_{nr} denote the complex phases of a_{res} and A_{nr}, respectively.

The special interference effect $\mathcal{I}_{int}$ only appears between the singlet resonant diagram and the SM box diagram. This interference effect is proportional to the relative phase between the loop functions $\sin(\delta_{\triangleright} - \delta_{\square})$ and the imaginary part of the scalar propagator which is sizeable near the scalar mass pole.

9.4.2.3 Differential distribution

We present in this section our analysis of the differential distribution of the Higgs pair invariant mass to estimate the relevance of the interference effects discussed in the previous section. We choose one of the best channels, $pp \to HH \to b\bar{b}\gamma\gamma$, as the benchmark channel to present the details of our analysis. Furthermore, we discuss another phenomenologically relevant piece of interference in the far off-shell region of the singlet scalar. We display the discovery and exclusion reach for both HL-LHC and HE-LHC for various values of $\tan\beta$ in the m_S-$\sin\theta$ plane.

In Fig. 177 we display the differential cross section as a function of the Higgs pair invariant mass for a benchmark point with a heavy scalar mass of 900 GeV, mixing angle $\sin\theta = 0.3$ and $\tan\beta = 10$. The differential cross section is shown in linear scale for a broad range of di-Higgs invariant masses, including the low invariant mass regime favoured by parton distribution functions at hadron colliders.

We choose this benchmark to show well the separation of the scalar resonance peak and the threshold enhancement peak above the $t\bar{t}$-threshold. The SM Higgs pair invariant mass distribution is given

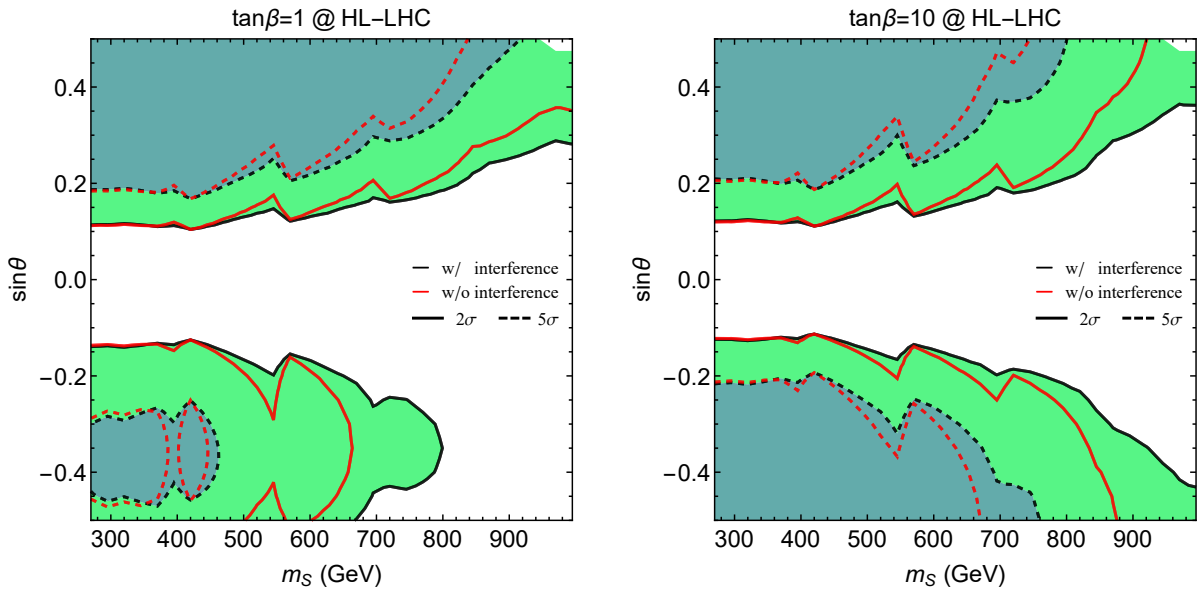

Fig. 178: Projected exclusion and discovery limits at HL-LHC in the m_S-$\sin\theta$ plane with the line-shape analysis detailed in the text for $\tan\beta = 1$ (left panel) and $\tan\beta = 10$ (right panel). The shaded regions bounded by dashed/solid curves are within the discovery/exclusion reach of the HL-LHC. The black and red lines represent the projection with and without the inclusion of the interference effects between the singlet resonance diagram and the SM Higgs pair diagram, respectively.

by the grey curve while the black curve depicts the di-Higgs invariant mass distribution from the singlet extension of the SM. It is informative to present all three pieces that contribute to the full result of the di-Higgs production, namely, the resonance contribution (red, dashed curve), the SM non-resonance contribution (box and triangle diagrams given by the brown, dotted curve), and the interference between them (blue curve). Note that the small difference between the "Tri+Box" and the "SM" line shapes is caused by the doublet-singlet scalar mixing, which leads to a $\cos\theta$ suppression of the SM-like Higgs coupling to top quarks as well as a modified SM-like Higgs trilinear coupling λ_{HHH}. We observe that the full results show an important enhancement in the di-Higgs production across a large range of invariant masses. This behaviour is anticipated from the decomposition analysis in the previous section. There is a clear net effect from the interference curve shown in blue. Close to the the scalar mass pole at 900 GeV, the on-shell interference effect enhances the Breit-Wigner resonances peak (red, dashed curve) by about 25%. Off-the resonance peak, and especially at the threshold peak, the interference term (blue curve) enhances the cross section quite sizeably as well. Hence, a combined differential analysis in the Higgs pair invariant mass is crucial in probing the singlet extension of the SM.

9.4.2.4 Discovery and exclusion reach at the HL- and HE-LHC

Using the analysis detailed in Ref. [339] through the $pp \to HH \to \gamma\gamma b\bar{b}$ channel, we obtain the discovery and exclusion projections for the HL-LHC and HE-LHC. In Fig. 178 we show the projected 2-σ exclusion and 5-σ discovery reach for the HL-LHC in the m_S-$\sin\theta$ plane for $\tan\beta = 1$ (left panel) and $\tan\beta = 10$ (right panel) in solid and dashed curves, respectively. The shaded regions are within the reach of the HL-LHC for discovery and exclusion projections. To demonstrate the relevance of the interference effects discussed in the previous sections, we show both the results obtained with and without the inclusion of the interference effects in black and red contours, respectively.

We observe in Fig. 178 that the inclusion of the interference effects extend the projections in

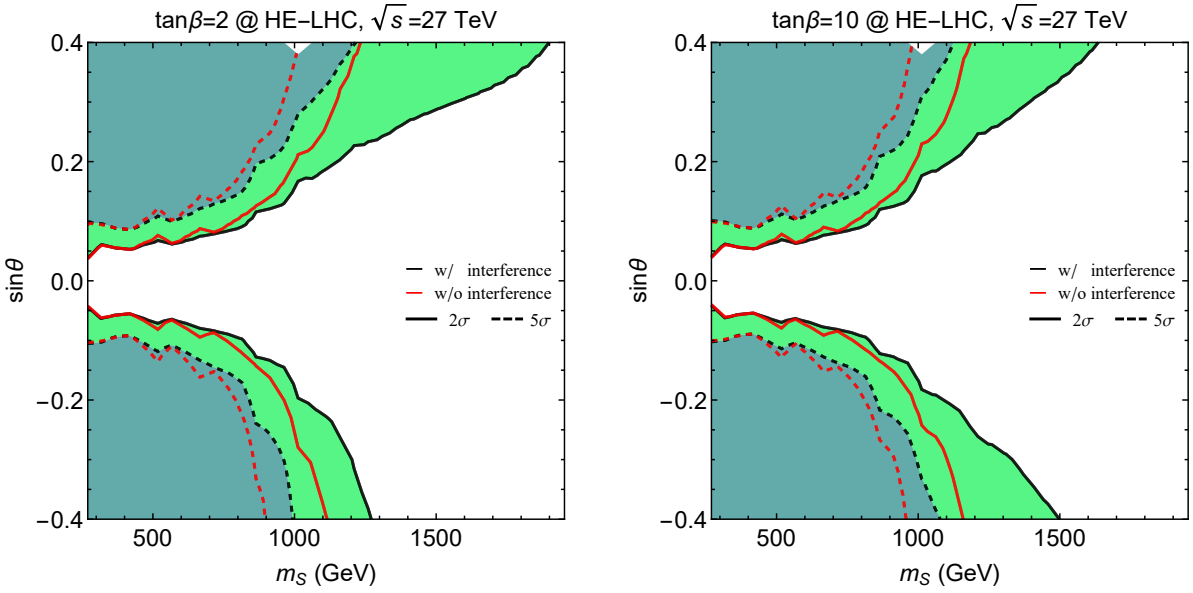

Fig. 179: Similar to Fig. 178, projected exclusion and discovery limits at HE-LHC with 27 TeV centre of mass energy and an integrated luminosity of 10 ab^{-1} for $\tan\beta = 2$ (left panel) and $\tan\beta = 10$ (right panel).

a relevant way. For example, considering the $\tan\beta = 10$ case in the right panel for $\sin\theta \simeq 0.35$ the interference effect increase the exclusion limit on m_S from 850 GeV to 1000 GeV. Note that the on-shell interference effect is larger for heavier scalar mass m_S.

In Fig. 179 we show the projections for the HE-LHC in a analogous fashion as in Fig. 178. The discovery and exclusion reach for heavy scalars can be significantly extended by the HE-LHC operating at 27 TeV centre of mass energy with 10 ab^{-1} of integrated luminosity. We show the results for $\tan\beta = 2$ (left panel) and $\tan\beta = 10$ (right panel). For example, considering the $\tan\beta = 2$ case in the right panel of Fig. 179, for $\sin\theta \simeq 0.35$ the exclusion reach increases from 1200 to 1800 GeV, once more showing the importance of including the on-shell interference effects.

9.4.2.5 Summary and outlook

In this study, we analyse the interference effects in the $gg \to HH$ process in the presence of a heavy scalar resonance. We focus on the novel effect of the on-shell interference contribution and discuss it in detail considering the framework of the singlet extension of the SM with spontaneous Z_2 breaking. The interference pattern between the resonant heavy scalar contribution and the SM non-resonant triangle and box contributions show interesting features. We highlight the constructive on-shell interference effect that uniquely arises between the heavy scalar resonance diagram and the SM box diagram, due to a large relative phase between the loop functions involved. We observe that the on-shell interference effect can be as large as 40% of the Breit-Wigner resonance contribution and enhances notably the total signal strength, making it necessary taking into account in heavy singlet searches.

To better evaluate the phenomenological implications of the interference effects in the di-Higgs searches, we carried out a line-shape analysis in the $gg \to HH \to \gamma\gamma b\bar{b}$ channel, taking into account both the on-shell and off-shell interference contributions. We find that both for the HL-LHC and HE-LHC, the proper inclusion of the interference effects increases the discovery and exclusion reach significantly.

9.4.3 *MSSM charged Higgs bosons*[127]

In this section, we discuss the potential of HL-LHC and HE-LHC for discovering a heavy charged Higgs boson [896] ($m_{H^\pm} > m_t$) in a class of high scale models, specifically SUGRA models [897, 898, 899] (for a review see [900]) consistent with the experimental constraints on the light Higgs mass at ~ 125 GeV and dark matter relic density (for a recent related work see [901]). We will focus on models where the radiative electroweak symmetry breaking is likely realised on the hyperbolic branch [902] and where the Higgs mixing parameter μ can be relatively small. Specifically we consider supergravity models with non-universalities in the Higgs sector and in the gaugino sector so that the extended parameter space of the models we consider is given by $m_0,\ A_0,\ m_1,\ m_2,\ m_3,\ m^0_{H_u},\ m^0_{H_d},\ \tan\beta,\ \mathrm{sgn}(\mu)$. Here m_0 is the universal scalar mass, A_0 is the universal trilinear coupling, m_1, m_2, m_3 are the masses of the $U(1)$, $SU(2)$, and $SU(3)_C$ gauginos, and $m^0_{H_u}$ and $m^0_{H_d}$ are the masses of the up and down Higgs bosons all at the GUT scale. To satisfy the relic density constraint in these models often one needs co-annihilation (see, e.g., [903, 904] and the references therein).

The largest production mode of the charged Higgs at hadron colliders is the one that proceeds in association with a top quark (and a low transverse momentum b-quark), $pp \to t[b]H^\pm + X$. This production mode can be realised in two schemes, namely, the four and five flavour schemes (4FS and 5FS, respectively), where in the former, the b-quark is produced in the final state and in the latter it is considered as part of the proton's sea of quarks and folded into the parton distribution functions. The cross-sections of the two production modes $q\bar{q}, gg \to tbH^\pm$ (4FS) and $gb \to tH^\pm$ (5FS), are evaluated at next-to-leading order (NLO) in QCD with `MadGraph_aMC@NLO-2.6.3` [79] using `FeynRules` [247] UFO files [246, 905] for the Type-II 2HDM. The simulation is done at fixed order, i.e., no matching with parton shower. The couplings of the 2HDM are the same as in the MSSM, but when calculating production cross-sections in the MSSM, one should take into account the SUSY-QCD effects. In our case, gluinos and stops are rather heavy and thus their loop contributions to the cross-section are very minimal. In this case, the 2HDM is the decoupling limit of the MSSM and this justifies using the 2HDM code to calculate cross-sections. For the 5FS, the bottom Yukawa coupling is assumed to be non-zero and normalised to the on-shell running b-quark mass. In the 5FS, the process is initiated via gluon-b-quark fusion while in the 4FS it proceeds through either quark-antiquark annihilation (small contribution) or gluon-gluon fusion. At finite order in perturbation theory, the cross-sections of the two schemes do not match due to the way the perturbative expansion is handled but one expects to get the same results for 4FS and 5FS when taking into account all orders in the perturbation. In order to combine both estimates of the cross-section, we use the Santander matching criterion [906] whereby

$$\sigma^{\mathrm{matched}} = (\sigma^{4\mathrm{FS}} + \alpha\sigma^{5\mathrm{FS}})/1 + \alpha, \tag{203}$$

with $\alpha = \ln\left(\frac{m_{H^\pm}}{\bar{m}_b}\right) - 2$. The uncertainties are combined as $\delta\sigma^{\mathrm{matched}} = \frac{\delta\sigma^{4\mathrm{FS}} + \alpha\delta\sigma^{5\mathrm{FS}}}{1+\alpha}$. The results are shown in Table 92.

For the parameter points considered, the $H^\pm \to \tau\nu$ channel has the smallest branching ratio but it is of interest since jets can be tau-tagged and the tau has leptonic and hadronic decay signatures. For the considered signal final states (fully hadronic), the SM backgrounds are mainly $t\bar{t}$, t+jets, $W/Z/\gamma^*$+jets, di-boson production and QCD multi-jet events which can fake the hadronic tau decays. The simulation of the charged Higgs associated production, $t[b]H^\pm$, is done at fixed order in NLO while the SM backgrounds are done at LO (which are then normalised to their NLO values) using `MadGraph` interfaced with LHAPDF [118] and `PYTHIA8` [319] which handles the showering and hadronisation of the samples. For the SM backgrounds a five-flavor MLM matching [362] is performed on the samples. Detector simulation and event reconstruction is performed by `DELPHES-3.4.2` [13] using the beta card for HL-LHC and HE-LHC studies.

The selection criteria depends on the flavour scheme under consideration. For the 4FS (5FS) we

[127] Contacts: A. Aboubrahim, P. Nath

Table 92: The NLO production cross-sections, in fb, of the charged Higgs in association with a top (and bottom) quark in the five (and four) flavour schemes along with the matched values at $\sqrt{s} = 14$ TeV and $\sqrt{s} = 27$ TeV for the ten benchmark points in [896]. The running b-quark mass, $\bar{m}_b$, is also shown evaluated at the factorisation and normalisation scales, $\mu_F = \mu_R = \frac{1}{3}(m_t + \bar{m}_b + m_{H^\pm})$.

Model	$\sigma^{\rm 4FS}_{\rm NLO}(pp \to tbH^\pm)$		$\sigma^{\rm 5FS}_{\rm NLO}(pp \to tH^\pm)$		$\sigma^{\rm matched}_{\rm NLO}$		$\mu_F = \mu_R$	$\bar{m}_b$
	14 TeV	27 TeV	14 TeV	27 TeV	14 TeV	27 TeV	(GeV)	
(a)	$49.0^{+12.6\%}_{-13.1\%}$	$272.8^{+9.2\%}_{-10.3\%}$	$71.8^{+6.6\%}_{-5.7\%}$	$397.1^{+7.0\%}_{-6.6\%}$	$65.9^{+8.1\%}_{-7.6\%}$	$365.4^{+7.6\%}_{-7.5\%}$	183.6	2.72
(b)	$34.5^{+10.6\%}_{-12.1\%}$	$204.6^{+8.1\%}_{-9.6\%}$	$58.3^{+7.0\%}_{-5.9\%}$	$336.1^{+6.9\%}_{-6.5\%}$	$52.4^{+7.9\%}_{-7.4\%}$	$303.5^{+7.2\%}_{-7.3\%}$	197.9	2.70
(c)	$29.1^{+11.1\%}_{-12.3\%}$	$175.9^{+8.2\%}_{-9.7\%}$	$48.8^{+6.7\%}_{-5.7\%}$	$285.9^{+6.4\%}_{-6.0\%}$	$43.9^{+7.8\%}_{-7.3\%}$	$259.0^{+6.8\%}_{-6.9\%}$	205.6	2.69
(d)	$24.8^{+10.9\%}_{-12.3\%}$	$149.9^{+7.1\%}_{-9.1\%}$	$42.6^{+6.3\%}_{-5.3\%}$	$264.8^{+6.8\%}_{-6.2\%}$	$38.3^{+7.4\%}_{-6.9\%}$	$237.2^{+6.8\%}_{-6.9\%}$	215.9	2.68
(e)	$18.4^{+11.2\%}_{-12.4\%}$	$120.1^{+8.3\%}_{-9.8\%}$	$32.3^{+5.9\%}_{-4.9\%}$	$206.7^{+6.4\%}_{-6.0\%}$	$29.0^{+7.1\%}_{-6.7\%}$	$186.3^{+6.8\%}_{-6.9\%}$	229.6	2.67
(f)	$13.6^{+11.3\%}_{-12.5\%}$	$93.2^{+7.8\%}_{-9.5\%}$	$25.1^{+6.1\%}_{-5.2\%}$	$169.6^{+6.7\%}_{-6.0\%}$	$22.4^{+7.3\%}_{-6.9\%}$	$152.1^{+7.0\%}_{-6.8\%}$	248.2	2.65
(g)	$13.1^{+10.5\%}_{-12\%}$	$95.8^{+7.6\%}_{-9.5\%}$	$26.0^{+6.2\%}_{-5.6\%}$	$185.1^{+6.7\%}_{-6.0\%}$	$23.1^{+7.2\%}_{-7.0\%}$	$165.0^{+6.8\%}_{-6.8\%}$	264.6	2.64
(h)	$11.2^{+10.3\%}_{-12.0\%}$	$85.1^{+7.5\%}_{-9.4\%}$	$22.7^{+6.1\%}_{-5.8\%}$	$168.3^{+6.8\%}_{-5.9\%}$	$20.2^{+7.0\%}_{-7.2\%}$	$149.9^{+6.9\%}_{-6.7\%}$	278.2	2.63
(i)	$7.8^{+11.7\%}_{-12.6\%}$	$61.1^{+8.1\%}_{-9.8\%}$	$15.8^{+6.0\%}_{-6.0\%}$	$121.0^{+6.9\%}_{-6.0\%}$	$14.0^{+7.2\%}_{-7.4\%}$	$107.9^{+7.2\%}_{-6.8\%}$	292.9	2.62
(j)	$5.5^{+12.6\%}_{-13.0\%}$	$48.9^{+9.1\%}_{-10.3\%}$	$11.6^{+6.7\%}_{-6.5\%}$	$99.4^{+6.4\%}_{-5.5\%}$	$10.3^{+7.9\%}_{-7.8\%}$	$88.7^{+6.9\%}_{-6.5\%}$	329.9	2.60

apply a lepton veto and at least five (four) jets, two (one) of which are (is) b-tagged and one is tau-tagged. To discriminate the signal from background we use gradient boosted decision trees, `GradientBoost`, which proves to be more powerful than the conventional cut-based analysis. A large set of variables have been tried in the BDT training and the ones which produced the best results were kept. The kinematic variables entering into the training of the BDTs are:

$$\begin{aligned} &E_T^{\rm miss}, \quad E_T^{\rm miss}/\sqrt{H_T}, \quad m_{T2}^{\rm jets}, \quad m_T^\tau, \quad p_T^\tau, \quad E_T^{\rm miss}/m_{\rm eff}, \\ &m_T^{\rm min}(j_{1-2}, E_T^{\rm miss}), \quad \Delta\phi(p_T^\tau, E_T^{\rm miss}), \quad N^\tau_{\rm tracks}, \quad \sum_{\rm tracks} p_T\,. \end{aligned} \tag{204}$$

The training and testing of the samples is carried out using `ROOT`'s [907] own TMVA (Toolkit for Multivariate Analysis) framework [908]. After the training and testing phase, the variable "BDT score" is created. We apply the selection criteria (as given in [896]) along with a BDT score cut > 0.95 on the SM background and on each of the 4FS and 5FS signal samples to obtain the remaining cross-sections. The signal cross-sections are combined using Eq. (203) in order to evaluate the required minimum integrated luminosity for a $\frac{S}{\sqrt{S+B}}$ discovery at the 5σ level. The results for both the 14 and 27 TeV cases are shown in Fig. 180.

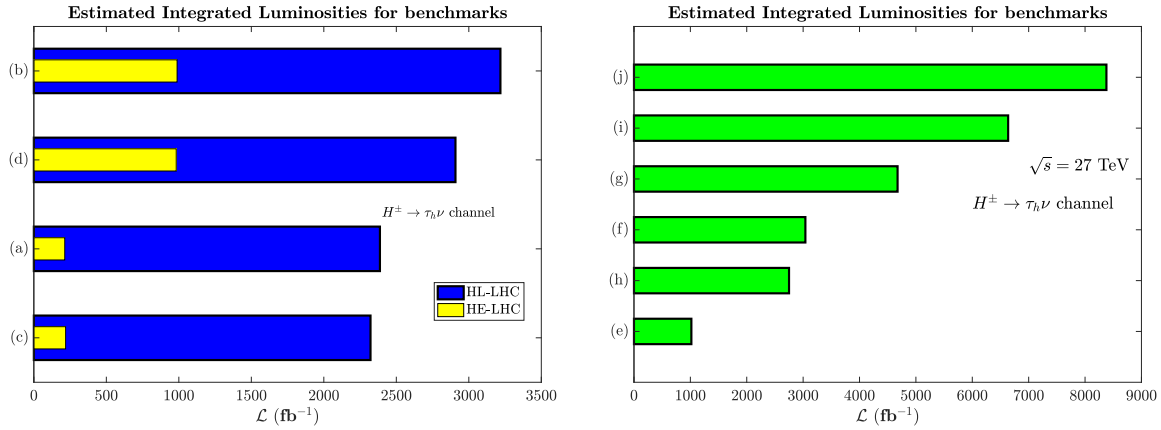

Fig. 180: The evaluated integrated luminosities, $\mathcal{L}$ (fb^{-1}), for ten benchmark points. Left plot: calculated $\mathcal{L}$ for points discoverable at both HL-LHC and HE-LHC. Right plot: calculated $\mathcal{L}$ for points discoverable only at HE-LHC.

One can see from Fig. 180 that four of the ten points may be discoverable at the HL-LHC as it nears the end of its run where a maximum integrated luminosity of 3000fb^{-1} will be collected. Given the rate at which the HL-LHC will be collecting data, points (a)-(d) will require $\sim$ 7 years of running time. On the other hand, the results from the 27 TeV collider show that all points may be discoverable for integrated luminosities much less than $15ab^{-1}$.

Acknowledgements: This research was supported in part by the NSF Grant PHY-1620575.

9.5 Direct and indirect sensitivity to heavy Higgs bosons using MSSM benchmark scenarios[128]

The LHC keeps measuring the properties of the discovered Higgs boson with increasing precision. So far the measured properties are, within current experimental and theoretical uncertainties, in agreement with the SM predictions [144]. The MSSM [909, 659, 910] is one of the best studied models with an extended Higgs sector. It predicts two scalar partners for all SM fermions as well as fermionic partners to all SM bosons. Contrary to the case of the SM, the MSSM contains two Higgs doublets. This results in five physical Higgs bosons instead of the single Higgs boson in the SM. In the absence of $\mathcal{CP}$-violating phases, these are the light and heavy $\mathcal{CP}$-even Higgs bosons, h and H, the $\mathcal{CP}$-odd Higgs boson, A, and the charged Higgs bosons, $H^\pm$.

In order to facilitate collider searches for the additional MSSM Higgs bosons, a set of new benchmark scenarios for MSSM Higgs boson searches at the LHC have been proposed recently [911]. The scenarios are compatible – at least over wide portions of their parameter space – with the most recent LHC results for the Higgs-boson properties and the bounds on masses and couplings of new particles. Each scenario contains one $\mathcal{CP}$-even scalar with mass around 125 GeV and SM-like couplings. However, the scenarios differ importantly in the phenomenology of the additional, so far undetected Higgs bosons.

The search for the additional Higgs bosons will continue at the LHC Run 3 and subsequently at the HL-LHC. These benchmark scenarios, due to their distinct phenomenology of the additional Higgs bosons, serve well to assess the reach of current and future colliders. The reach can either be direct, via the search for new Higgs bosons, or indirect, via the precise measurements of the properties of the Higgs boson at $\sim$ 125 GeV.

[128] Contacts: P. Bechtle, S. Heinemeyer, S. Liebler, T. Stefaniak, G. Weiglein

Experimental and theoretical input

In order to analyse the potential of the HL-LHC in the exploration of the MSSM Higgs sector we evaluate the direct and indirect physics reach in two of the benchmark scenarios proposed in Ref. [911]. The first scenario is the M_h^{125}: it is characterised by relatively heavy superparticles, such that the Higgs phenomenology at the LHC resembles that of a Two-Higgs-Doublet-Model with MSSM-inspired Higgs couplings. The second scenario is the $M_h^{125}(\tilde{\chi})$. It is characterised by light electroweakinos (EWinos), resulting in large decay rates of the heavy Higgs bosons H and A into charginos and neutralinos, thus diminishing the event yield of the $\tau^+\tau^-$ final state signatures that are used to search for the additional Higgs bosons at the LHC. In addition, the branching ratios of the Higgs boson at 125 GeV into a pair of photons is enhanced for small values of $\tan\beta$ due to the EWinos present in the loop.

We assess the reach of direct LHC searches in the $\tau^+\tau^-$ final state by applying the model-independent 95% CL limit projections for 6 ab^{-1} from the CMS experiment, see Sec. 9.2.2.2, Fig. 168.[129] We implemented these limits — presented as one-dimensional (marginalised) cross section limits on either the gluon fusion or $b\bar{b}$-associated production mode — in the program `HiggsBounds` [595, 596, 597, 912] to obtain the projected 95% CL exclusion in our scenarios.

We estimate the indirect reach through Higgs rate measurements by using detailed HL-LHC signal strength projections for the individual Higgs production times decay modes, including the corresponding correlation matrix, as evaluated by the ATLAS and CMS experiment assuming YR18 systematic uncertainties (S2), see Sec. 2.6.1, Tab. 35. We furthermore take cross-correlations of theoretical rate uncertainties between future ATLAS and CMS measurements into account. All this is done with the use of the program `HiggsSignals` [561].

The theory predictions are obtained from `FeynHiggs` [913, 914, 915, 916, 917, 918, 919, 920], as well as from `SusHi` [878, 51, 921, 922, 923, 924, 925, 47, 926, 927, 928, 929] for gluon fusion and matched predictions for bottom-quark annihilation [930, 931, 932, 933]. We determine the theoretical uncertainties on the Higgs production cross sections as in Ref. [911]. For the light Higgs rate measurements we use the SM uncertainties following Ref. [45].

Projected HL-LHC reach

Our projections in the M_h^{125} and the $M_h^{125}(\tilde{\chi})$ scenario in the $(M_A, \tan\beta)$ plane are presented in the left and right panel of Fig. 181, respectively. We furthermore include the current limit (magenta dotted line) for the indirect reach of the LHC in the two benchmark scenarios, as evaluated in Ref. [911], as well as the expected limit from current direct BSM Higgs searches by ATLAS [857] (red dashed line) and CMS [860] (green dashed line) in the $\tau^+\tau^-$ final state, using ~ 36 fb^{-1} of data from Run II at 13 TeV.

Within the M_h^{125} scenario the reach via measurements of the Higgs signal strengths extends to M_A values of around 900 GeV. The horizontal contour excluding $\tan\beta$ values less than 6 is due to the light Higgs mass being below 122 GeV, where the interpretation of the observed Higgs signal in terms of the light $\mathcal{CP}$-even MSSM Higgs boson h becomes invalid. The direct heavy Higgs searches in the $\tau^+\tau^-$ final state will probe the parameter space up to $M_A \leq 2550$ GeV for $\tan\beta = 50$, and up to $M_A \leq 2000$ GeV at $\tan\beta = 20$.

The picture is somewhat different in the $M_h^{125}(\tilde{\chi})$ scenario. Here the large branching ratio of the heavy neutral Higgs boson decaying to charginos and neutralinos leads to a strongly reduced direct reach of heavy Higgs to $\tau^+\tau^-$ searches. While at large values of $\tan\beta \sim 50$ the reach is only slightly weaker than in the M_h^{125} scenario, at $\tan\beta = 20$ it is significantly reduced to $M_A \leq 1700$ GeV. In order to overcome this, dedicated searches for the decays of H and A to charginos and neutralinos will have to be devised. On the other hand, Higgs rate measurements are an important complementary probe. They exclude $M_A \leq 950$ GeV and $\tan\beta \leq 12.5$. While the bound in M_A is induced through Higgs coupling modifications arising from non-decoupling, values of $\tan\beta \leq 12.5$ feature a too-large enhancement

[129] We thank Martin Flechl for helpful discussions.

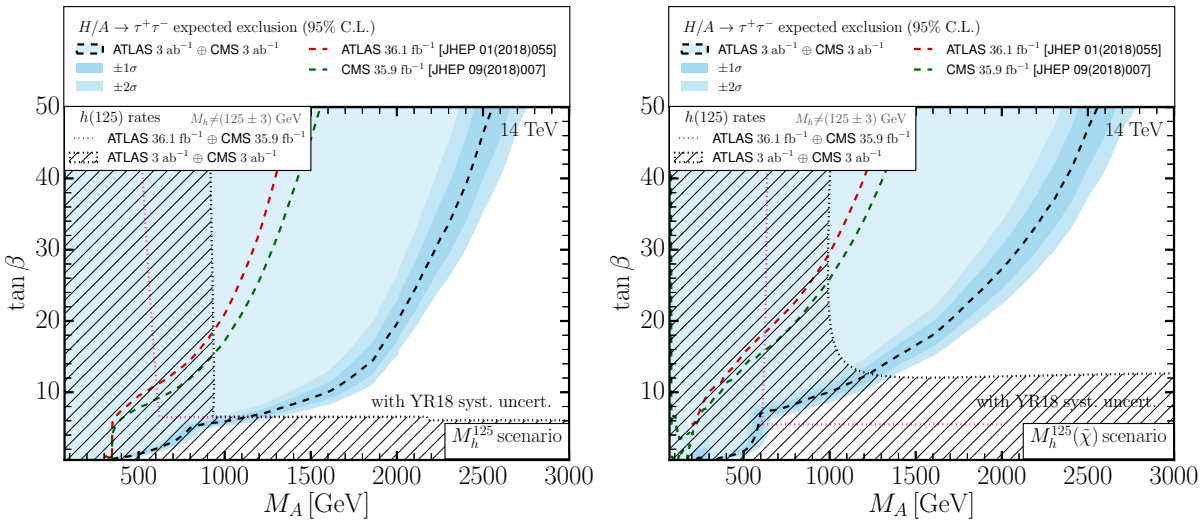

Fig. 181: HL-LHC projections in the M_h^{125} (*left*) and $M_h^{125}(\tilde{\chi})$ (*right*) scenario, assuming YR18 systematic uncertainties (S2). The dashed black curve and blue filled region indicate the HL-LHC reach via direct heavy Higgs searches in the $\tau^+\tau^-$ channel with 6 ab^{-1} of data (with the dark blue regions indicating the 1 and 2σ uncertainty), whereas the red and green dashed lines show the expected limit from current searches in this channel by ATLAS [857] and CMS [860], respectively. The current and future HL-LHC sensitivity via combined ATLAS and CMS Higgs rate measurements is shown as magenta and black dotted contours, respectively (the latter being accompanied with a hatching of the prospectively excluded region).

of the $h \to \gamma\gamma$ partial width. The combination of direct and indirect bounds yields a lower limit of $M_A \geq 1250\,\text{GeV}$ in the $M_h^{125}(\tilde{\chi})$ scenario.

In summary, the HL-LHC has the potential, using the combined direct and indirect reach, to probe the MSSM Higgs sector up to $M_A \sim$ 900-1000 GeV and possibly beyond, depending on the details of the MSSM scenario. Values larger than that, as predicted, e.g., by GUT based models [934, 935, 936, 937, 938, 939] or Finite Unified Theories [940, 941, 942], or allowed by global fits of the phenomenological MSSM [943, 944] would remain uncovered. To explore these regions an energy upgrade and/or refined Higgs signal strength measurements (e.g. at an e^+e^- collider [945]) will be necessary.

9.6 Direct and indirect sensitivity to heavy Twin Higgs bosons[130]

The existence of additional Higgs bosons is motivated by many approaches to physics beyond the Standard Model. Here we focus on the simple case of a second Higgs which is a singlet of the SM gauge group. This is motivated in many BSM constructions addressing the naturalness problem of the electroweak scale like Supersymmetry or Compositeness. Independently on naturalness, an extra singlet arises in minimal scenarios to get a first-order EW phase transition which is necessary for EW baryogenesis.

There is now an extensive suite of LHC searches for additional Higgs bosons decaying promptly into SM final states. Among these, di-boson searches are particularly promising to hunt for an additional Higgs singlets (see Refs. [867, 946, 947, 948]). A first important question for HL-LHC is to understand how these direct searches correlate with Higgs coupling deviations. This question has already been addressed for the singlet Higgs at HL-LHC in Ref. [949] (see also Sec. 6.1.4 in the WG3 physics report [950] and Sec. 6.3.2 of this report) and we summarise it here for completeness. In short, one can prove

[130] Contact: D. Redigolo

that there is limited room for discovery of the second Higgs singlet in direct production unless deviations in the SM Higgs coupling bigger than 5% will be found at HL-LHC. This is a great motivation for future machines exploring the high energy frontier in SM visible decays of the second Higgs (see for example Ref. [951] for an assessment of the reach of high-energy lepton colliders).

Here we show that the situation is radically different if the second Higgs singlet has exotic displaced decays following Ref. [952]. We focus on the case of a singlet Higgs decaying into a pair of long-lived particles (LLPs), whose decays within the detector volume set them qualitatively apart from promptly-decaying or detector-stable particles. These type of displaced decays are often present in extensions of the Higgs sector which entail rich hidden sectors coupled primarily through the Higgs portal to additional Higgs-like scalars (see Ref. [545] for a recent summary of the theory motivations).

On the experimental side, the signatures of displaced LLP's pairs produced from the decay of a heavy singlet Higgs are sufficiently distinctive that they may be identified by analyses with little or no Standard Model backgrounds even at HL-LHC, making them a promising channel for discovering additional Higgs bosons. By recasting present LHC searches for a pair of displaced tracks with different displacements [546, 816, 953, 798], we show that the discovery potential of exotic decays of the second Higgs singlet exceeds the asymptotic reach of SM Higgs coupling deviations and provides a natural avenue for the further development of searches for additional Higgs bosons. This is a promising next step to complete the experimental coverage of extended Higgs sectors at the LHC, especially because analogous decays of the 125 GeV Higgs to LLPs may be challenging to discover at the LHC due to trigger thresholds (see Ref. [43] for a summary and Refs. [954, 955, 956, 957] for collider studies of displaced signal from SM Higgs decays).

On the theory side many models addressing dark matter, baryogenesis and the hierarchy problem can be mapped to the singlet simplified model we discuss here as long as the interactions of the heavy Higgs are controlled primarily by the Higgs portal. As an example, we present the concrete case of the Twin Higgs (TH) construction, quantifying the asymptotic reach of LHC searches for a Twin Higgs decaying into a pure glue hidden valley as originally proposed in Ref. [812].

Regarding the physics opportunities of HE-LHC, we refer to [950] for a discussion of the visible decays of the singlet Higgs. A reliable assessment of the reach in exotic displaced decays strongly depends on the details of the trigger opportunities of HE-LHC and it is left for the future.

9.6.1 The simplified model with a long lived singlet scalar

We introduce the effective Lagrangian of a CP-even scalar up to dimension four:

$$\mathcal{L}_{\text{visible}} = \frac{1}{2}(\partial_\mu S) - \frac{1}{2}m_S^2 S^2 - a_{HS} S|H|^2 - \frac{\lambda_{HS}}{2} S^2|H|^2 - \frac{a_S}{3}S^3 - \frac{\lambda_S}{4}S^4 \,. \tag{205}$$

After electroweak symmetry breaking, the singlet mixes with the uneaten CP-even component of the Higgs doublet and we can write the mixing angle γ as

$$\gamma \simeq \frac{v(a_{HS} + \lambda_{HS} f)}{m_\phi^2} \quad , \quad H = \begin{pmatrix} \pi^+ \\ \frac{v+h}{\sqrt{2}} \end{pmatrix} \quad , \quad S = f + \phi \,, \tag{206}$$

where m_ϕ is the mass of the singlet in the mass basis, $v = 246$ GeV is the electroweak vacuum expectation value and f is the VEV of the singlet S. The formula shows how the mixing between the singlet and the SM Higgs is controlled by the spontaneous and/or explicit breaking of a discrete $\mathbb{Z}_2$ symmetry under which the singlet is odd ($S \to -S$) and the SM Higgs even ($H \to H$). In what follows, we focus mainly on the scenario where the singlet takes a VEV at the minimum of a $\mathbb{Z}_2$-invariant potential. Then the $\mathbb{Z}_2$-breaking is spontaneous and we have

$$\gamma \simeq \frac{\lambda_{HS}}{\lambda_S} \cdot \frac{v}{f} \quad , \quad m_\phi^2 \simeq \lambda_S f^2 \,. \tag{207}$$

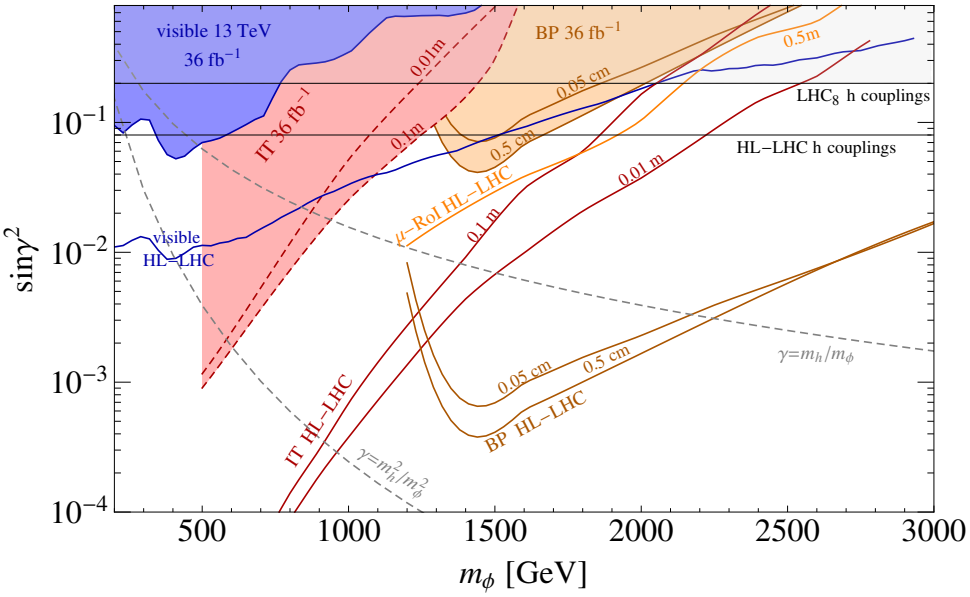

Fig. 182: Parameter space of the singlet Higgs as a function of m_ϕ and $\sin^2\gamma$. See text for details.

This is explicitly realised in Twin Higgs scenarios where $\lambda_S \simeq \lambda_{HS}$ and $\gamma \sim \frac{v}{f}$ (see Refs [809, 958]). The phenomenology of the singlet and the SM-like Higgs can be summarised as follows:

$$\frac{g_{hVV,f\bar{f}}}{g^{SM}_{hVV,f\bar{f}}} = \cos^2\gamma\,, \tag{208}$$

$$\sigma_\phi = \sin^2\gamma \cdot \sigma_h(m_\phi)\,, \tag{209}$$

$$\text{BR}_{\phi\to f\bar{f},VV} = \text{BR}_{h\to f\bar{f},VV}(1-\text{BR}_{\phi\to hh})\,, \tag{210}$$

where g_{hVV}/g^{SM}_{hVV} and $g_{hf\bar{f}}/g^{SM}_{hf\bar{f}}$ refer to the couplings of the SM-like Higgs to SM vectors and fermions, respectively, normalised to the SM prediction. The couplings of the SM-like Higgs in Eq. (208) are reduced by an overall factor, leading to a reduced production cross section in every channel but unchanged branching ratios. The production cross section of the heavy singlet σ_ϕ in Eq. (209) is the one of the SM Higgs boson at mass m_ϕ rescaled by the mixing angle. The branching ratios of the singlet into SM gauge bosons in Eq. (210) are rescaled by a common factor depending on the branching ratio into hh. The latter is model dependent but in the limit $m_\phi \gg m_W$ an approximate $SO(4)$ symmetry dictates $\text{BR}_{\phi\to hh} \simeq \text{BR}_{\phi\to ZZ} \simeq \text{BR}_{\phi\to WW}/2$.

We summarise in Fig. 182 the relative strength of existing and future di-boson and di-Higgs searches at the LHC [867, 946, 947, 948], as well as constraints coming from the precision measurement of Higgs couplings (taking for definiteness the values in [959]).

We now want to add to the setup in Eq. (205) the reach of present and future displaced searches. We consider the singlet S to be a portal to a generic dark sector. In this case the singlet S can decay abundantly to a pair of approximately long lived dark states without suppressing the signal rate. A simple example motivated by Twin Higgs constructions [812] and Hidden Valley models [960, 961]) is

$$\mathcal{L}_{\text{displaced}} = -\frac{a_{SX}}{2}SX^2 - \frac{b_{SX}}{2}S^2X - \frac{\lambda_{SX}}{4}S^2X^2 - \frac{\lambda_{SX}}{4}|H|^2X^2 - \frac{m_X^2}{2}X^2\,, \tag{211}$$

where the extra dark singlet scalar daughter X is odd under an approximate $\mathbb{Z}_2$-symmetry like S and $a_{SX} \simeq b_{SX} \simeq 0$. For $m_S > 2m_X$ the singlet S will decay into pairs of scalar daughters with a width $\Gamma_{\text{displaced}} = \frac{\lambda_{SX}^2 f^2}{8\pi m_S}$ which is now independent of the mixing in Eq. (207). The width of X into SM

states is proportional to the $\mathbb{Z}_2$-breaking operators and can be arbitrarily suppressed. In next section we show how the Twin Higgs gives an explicit realisation of this simplified model where the singlet X is identified with the lightest glueball. The mass of the glueball is naturally light because of dimensional transmutation in the dark sector, and the decay of the singlet S into dark states unsuppressed because of the rich structure of the hidden sector where heavier states shower down to the lightest glueball.

We consider the present bound and future projections at HL-LHC of the following searches [131]:

- The **muon region of interest trigger (μ-RoI)** analysis of ATLAS at 13 TeV [953] is tailored to tag displaced decays with decay length $0.5\text{ m} \lesssim c\tau \lesssim 20\text{ m}$. The 13 TeV search is an update of a previous 8 TeV analysis [546] which remains background-free with trigger performance comparable to the old search. The 95% C.L. exclusion limit is given by
$$\sigma_\phi^{13\text{ TeV}} \cdot \text{BR} = 0.083\text{ fb} \cdot \frac{L}{36.1\text{ fb}^{-1}} \cdot \frac{1}{\epsilon(m_\phi, m_X, c\tau_X)} \,. \tag{212}$$
- The **displaced di-jet pairs in the inner tracker (IT)** analysis of CMS at 8 TeV [816] is mostly sensitive to displacement with decay length $5\text{ mm} \lesssim c\tau \lesssim 1\text{ m}$. The 95% C.L. exclusion limit is given by
$$\sigma_\phi^{8\text{ TeV}} \cdot \text{BR} = 0.23\text{ fb} \cdot \frac{L}{18.5\text{ fb}^{-1}} \cdot \frac{1}{\epsilon(m_\phi, m_X, c\tau_X)} \,. \tag{213}$$
provided that m_X is not so much smaller than m_ϕ that the average boost of X collimates its decay products.
- The search based on **two displaced vertices in the beampipe (BP)** at CMS 13 beam-pipe [798] is dedicated to very small displacements $c\tau \lesssim 1\text{ mm}$. The 95% C.L. exclusion limit is given by
$$\sigma_\phi^{13\text{ beam-pipe}} \cdot \text{BR} = 0.078\text{ fb} \cdot \frac{L}{38.5\text{ fb}^{-1}} \cdot \frac{1}{\epsilon(m_\phi, m_X, c\tau_X)} \tag{214}$$
This analysis is only effective for $m_\phi \gtrsim 1$ beam-pipe due to the substantial H_T requirement, and is correspondingly only sensitive to larger values of m_X.

The above searches provide a quite extensive coverage in the X lifetime. We refer to Ref. [952] for a careful explanation and validation of the recasting. For the projection at HL-LHC we follow the procedure of Ref. [962, 949] for visible searches. As far as displaced searches are concerned we rescale the bounds linearly with the luminosity, assuming their background to remain constant at higher luminosity. This extrapolation is probably optimistic, however the new challenges to control the backgrounds for LLP searches at high luminosity could be compensated by future hardware and trigger improvements as proposed for example in [963, 802].

In principle there are three branching ratios that determine the relative contribution of displaced searches: the branching ratio into prompt or "visible" final states, $\text{BR}_{\text{visible}}$; the branching ratio into long-lived or "displaced" final states, $\text{BR}_{\text{displaced}}$, and an additional branching ratio into detector-stable or "invisible" final states, $\text{BR}_{\text{invisible}}$. In Fig. 182 we fix a representative values of LLP mass m_X and of the proper lifetime τ_X (indicated in the plot) and we assumed $\text{BR}_{\text{displaced}} \simeq \text{BR}_{\phi\to ZZ}$ and $\text{BR}_{\text{invisible}} = 0$.

From Fig. 182 we see that in the absence of singlet Higgs decays into LLPs, the sensitivity of direct searches at the HL-LHC is unlikely to surpass limits from Higgs coupling measurements for $m_\phi \gtrsim 1.5$ beam-pipe. However, for singlet Higgses decaying partly into LLPs, the potentially considerable reach of searches for displaced decays makes a direct search program competitive with Higgs coupling measurement to much higher values of m_ϕ. The primary weakness of the displaced searches is at high m_ϕ, low m_X, and large $c\tau$, where the muon RoI search loses sensitivity. Optimal coverage of this region could in principle be provided by MATHUSLA [545].

[131] The several ϵ in the equations below account for the detector acceptance and efficiency for the signal.

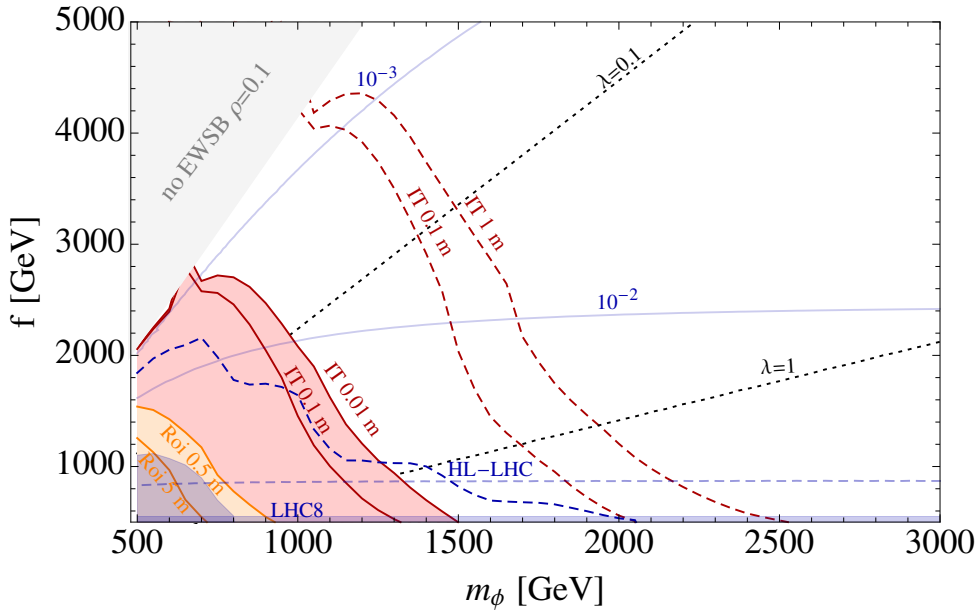

Fig. 183: Parameter space of the Fraternal Twin Higgs model as a function of the Twin Higgs mass, m_ϕ, and f overlaid with current and projected constraints from direct searches. See text for details.

9.6.2 A specific realisation: the Twin Higgs model

In all the Twin Higgs models the SM Higgs sector is extended by adding the twin Higgs H_B which is a doublet under a mirror EW gauge group $SU(2)_B$ and a singlet under the SM gauge group. The most general renormalisable potential reads

$$V = \lambda\left(|H_A|^2+|H_B|^2\right)^2 - m^2\left(|H_A|^2+|H_B|^2\right)+\kappa\left(|H_A|^4+|H_B|^4\right)+\tilde{\mu}^2|H_A|^2+\rho|H_A|^4, \quad (215)$$

where λ and $m^2(>0)$ are the $SU(4)$ preserving terms, κ preserves the $\mathbb{Z}_2$ mirror symmetry that exchanges $A \leftrightarrow B$, but breaks $SU(4)$, and $\tilde{\mu}$ and ρ are the $\mathbb{Z}_2$ breaking terms.

The requirement to reproduce the EW scale v and the Higgs mass m_h fixes 2 out of the 5 free parameters in Eq. (215). We choose the three remaining free parameters as the spontaneous breaking scale f, the physical singlet mass $m_\phi = 4\lambda f$, and the Z_2-breaking quartic ρ.

In TH models the fine-tuning is parametrically reduced with respect to the ones of regular SUSY or Composite Higgs scenarios by $\lambda_{\rm SM}/\lambda$, where $\lambda_{\rm SM} \simeq 0.13$, see e.g. Ref. [964, 965]. In models where the Z_2-breaking is mostly achieved by the quartic $\rho_{\rm hard}$ the additional gain in fine-tuning is given by $\lambda_H/|\lambda_H-\rho|$, which is maximised for ρ as close as possible to the SM quartic. This gain is however limited by the irreducible IR contributions to κ, as discussed in Ref. [964]. In Fig. 183, we show the status of a representative slicing of parameter space of the Fraternal Twin Higgs model. We refer the reader to Ref. [952] for details on the calculation of the Twin Higgs rates into visible and displaced final states. As a simplifying assumption the glueball final states are estimated by the LLP pair-production simplified model for the purposes of illustrating the potential reach of LLP searches. For each point in the figure, the mass of the lightest glueball is fixed to 50 GeV and a specific values of $c\tau$ is assumed to highlight the sensitivity of the different LLP searches. Very much in the spirit of the Fraternal Twin Higgs [812] a fixed glueball and $c\tau$ can be obtained by varying the value of the dark QCD coupling and the the one of the dark bottom Yukawa affecting quite mildly the fine-tuning of the Twin Higgs construction. The quartic $\rho = 0.1$ is chosen here because it leads to a broader parameter space with successful EWSB for a light twin Higgs mass compared to $\rho = 0$. For positive ρ the rate for $\phi \to hh$ is enhanced compared to the case of $\rho = 0$, so that limits from prompt decays in current data and HL-LHC projections (in blue) are driven by $\phi \to hh \to 4b$.

The 13 beam-pipe ATLAS muon RoI search and our extrapolation to 13 beam-pipe, 36 fb^{-1} of the 8 beam-pipe CMS inner tracker search [816] suggest that LLP searches with current 13 beam-pipe LHC data have the potential to provide broad coverage of the parameter space for Twin Higgs masses up to ~ 1.5 beam-pipe. Suitable searches at the HL-LHC could potentially extend coverage to masses of order ~ 2.5 beam-pipe, significantly exceeding the reach of searches for prompt decay products of the Twin Higgs and the sensitivity of Higgs coupling deviations. Of course the coverage of direct and displaced searches is quite sensitive to varying the lightest glueball mass and lifetime and more work is required to map out this parameter space completely.

9.7 Production of $t\bar{t}h$ and $t\bar{t}hh$ at the LHC in Composite Higgs models[132]

With the discovery of the Higgs boson [11, 12] the question of whether this resonance is a composite state has gained new prominence. We consider the effects of Higgs compositeness [240, 241, 650, 966, 649] on the $t\bar{t}h$ and $t\bar{t}hh$ processes. The first process has already been observed [164, 165], and is consistent with the SM expectation, although with large uncertainties of order 20%. The second process is of particular interest, due to the contribution of charge 2/3 vector-like "top partners" decaying in the tH channel. Searches focusing on this channel have been presented in [967], and combined ones that consider the bW, tZ and tH channels already put strong constraints on such vector-like resonances [968, 969].

In this work, we point out the non-resonant $t\bar{t}hh$ process is of considerable interest, since in light of these strong bounds it will very often account for a large fraction of the total $t\bar{t}hh$ cross-section. Furthermore, it carries information about the compositeness nature of the Higgs boson that is distinct and complimentary to the effect of the heavy fermion resonances. We also point out that the non-resonant $t\bar{t}hh$ process is closely connected to $\bar{t}th$, but would be expected to display larger deviations from the SM prediction. We present here a first step in the analysis of such processes in the context of the HL-LHC and HE-LHC for the "Minimal Composite Higgs Models" (MCHM) [970], in which the Higgs doublet is identified with the pseudo-Nambu-Goldstone bosons originating from the breaking $SO(5) \to SO(4)$ by new strong dynamics, with $SO(4)$ weakly gauged by the SM gauge group. We refer the reader to the full review in [695] for complete details on Composite Higgs. Further details on our work can be found in the companion paper [971].

Theoretical Framework

In composite Higgs models, physical states are linear superpositions of the strong sector composite resonances and the SM-like "elementary" states with the same quantum numbers, realising the paradigm of partial compositeness [972]. We focus on the top sector, which is the most relevant to the processes we study. (See Section 4.5 for a complementary study on Higgs coupling to gauge bosons). Here we present only the essential features of the analysis, referring the reader to the companion work [971] for further details. Two concrete realisations of the fermionic sector are adopted. Both share an elementary sector denoted by q_L and t_R, transforming as $(3, 2, 1/6)$ and $(3, 1, 2/3)$ under the SM gauge group.

The MCHM$_5$

In this "minimal" extension, one considers fermion resonances in a **5** of $SO(5)$, which splits into a $SO(4)$ 4-plet, Ψ_4, with mass M_4, and a $SO(4)$ singlet, Ψ_1, with mass M_1.

$$\Psi_4 \sim (X_{5/3}, X_{2/3}, T, B) \; ; \; \Psi_1 \sim \tilde{T} \, . \tag{216}$$

The states $(X_{5/3}, X_{2/3})$ transform as a $SU(2)_L$ doublet with $Y = 7/6$, while (T, B) and $\tilde{T}$ transform like q_L and t_R, respectively. These are not mass eigen-states due to the mixing with elementary

[132] Contacts: C. Bautista, L. de Lima, R.D. Matheus, E. Pontón, L.A.F. do Prado, A. Savoy-Navarro

states, described here by [133]

$$\mathcal{L}^{\mathbf{5}}_{\rm mix} \;=\; y_L f\, \bar{q}^{\mathbf{5}}_L U\,[\Psi_{\mathbf{4}}+\Psi_{\mathbf{1}}] + y_R f\, \bar{t}^{\mathbf{5}}_R U\,[\Psi_{\mathbf{4}}+\Psi_{\mathbf{1}}] + \text{h.c.} \tag{217}$$

where U parametrises the Higgs field and f is the "Higgs decay constant". All the features required for our analysis follow from diagonalisation of the charge 2/3 fermion mass matrix, which is given in Ref. [971], while the remaining resonances have masses $M_{X_{5/3}} = M_4$ and $M_B = \sqrt{M_4^2 + y_L^2 f^2}$. Deviations from a SM Higgs due to compositeness are characterised by the parameter $\xi = v^2/f^2$ (here $v = 246$ GeV). Consistency with current Higgs measurements results in $\xi \lesssim 0.1$, or $f \gtrsim 800$ GeV [668, 973, 213, 974, 975, 976, 185].

The MCHM$_{\mathbf{14}}$

In the second scenario, the composite states span a **14** of $SO(5)$ [701, 977, 978, 973, 979, 980, 981, 975]. Under $SO(4)$, in addition to a 4-plet and a singlet, as in Eq. (216), we have an additional $SO(4)$ nonet:

$$\Psi_{\mathbf{9}} \;\sim\; (U_{8/3}, U_{5/3}, U_{2/3}, Y_{5/3}, Y_{2/3}, Y_{-1/3}, Z_{2/3}, Z_{-1/3}, Z_{-4/3})\,. \tag{218}$$

The U's, Y's and Z's transform as $SU(2)_L$ triplets, with hyper-charges $Y = 5/3$, $2/3$ and $-1/3$, respectively. The Lagrangian of the MCHM$_5$ is supplemented by terms involving Ψ_9, whose mass is denoted M_9, and which mixes with the elementary states in an analogous manner to Ψ_1 and Ψ_4. We give the full charge $2/3$ and $-1/3$ mass matrices as well as the complete Lagrangian in Ref. [971]. The remaining states have masses $M_{X_{5/3}} = M_4$, $M_{U_{8/3}} = M_{U_{5/3}} = M_{Y_{5/3}} = M_{Z_{-4/3}} = M_9$.

An important distinction between the two scenarios is that when the mixing is dominated by the nonet, the leading order operator coupling the top quark to the Higgs doublet is the non-renormalisable operator $\bar{q}_L \tilde{H} t_R H^\dagger H$. In contrast, mixing through a 4-plet or singlet lead to the SM operator $\bar{q}_L \tilde{H} t_R$ (plus corrections that are higher order in v/f). In the former case the ratio of the top Yukawa coupling to the top mass is three times larger than in the second case. Cases where the nonet plays a comparable role to the 4-plet or singlet can then lead to interesting enhancements in the top Yukawa coupling, which are not present in the MCHM$_5$.

The scenarios under consideration can also affect the Higgs decays. Once the light fermion representations are chosen, and assuming their mixing angles are small, one can express the partial widths as a rescaling of the corresponding SM widths. For further details, we refer to [971].

Parameter Space and Results

Taking all parameters to be real for simplicity, the free parameters can be taken to be f, $|M_1|$, $|M_4|$, $\text{sign}(M_1)$, y_L and y_R, common for both models, plus $|M_9|$ and $\text{sign}(M_4)$ for the MCHM$_{14}$. Out of these, we choose to fix y_R to reproduce the top mass. Running of this mass from the scale of the resonances, typically around $2-3$ TeV to the relevant scales for $t\bar{t}hh$ of the order of a couple hundred GeV is taken into account to a first approximation by using a running top mass of $\bar{m}_t = 150$ GeV for the diagonalisation of the mass matrix, and of $m_t = 173$ GeV, for the kinematic quantities. We take the Higgs mass as an independent parameter, referring the reader to [971] for further discussion on this point.

We consider the following ranges for the parameters (those common to both models take the same range):

$$|M_1| \in [800, 3000]\ \text{GeV}\,, \qquad |M_4| \in [1200, 3000]\ \text{GeV}\,, \qquad M_9 \in [1300, 4000]\ \text{GeV}\,,$$

[133] In principle, one can choose different Yukawa couplings for the terms involving the **4**-plet, Ψ_4, and the singlet, Ψ_1. See [971].

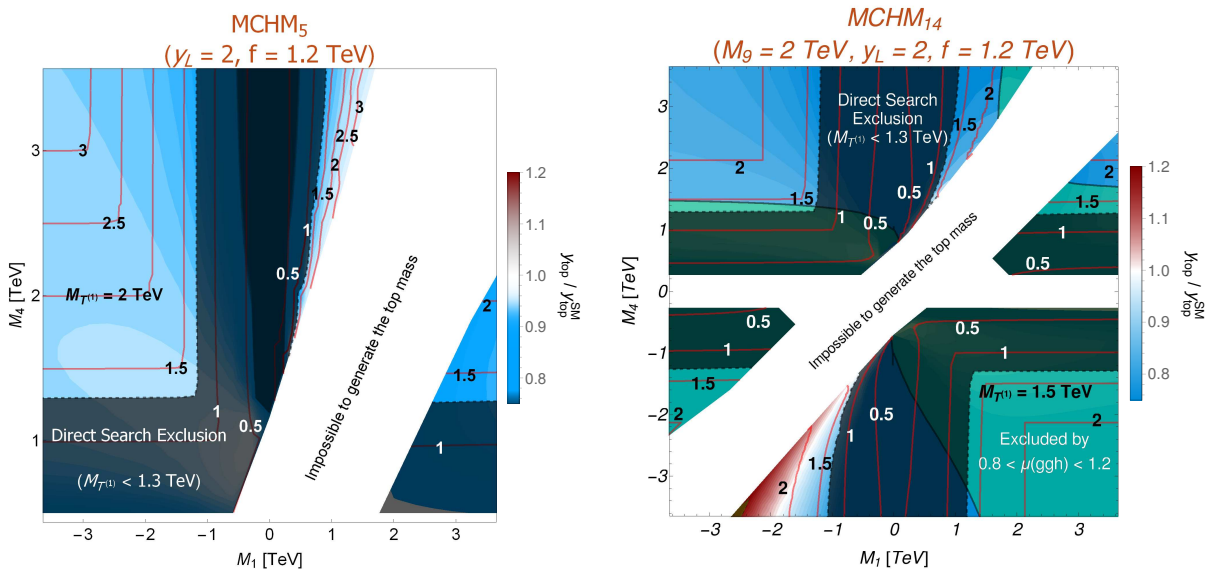

Fig. 184: Display of the values of the normalised top Yukawa coupling, $y_{\rm top}/y_{\rm top}^{\rm SM}$, in the M_1-M_4 plane. Blue colours indicate a suppression and red colours an enhancement. Also shown the curves of constant $M_{T^{(1)}}$, the mass of the lightest $Q = 2/3$ vector-like resonance. The darker bands indicate the approximate current direct exclusion of top partner VLQ resonances, assuming decays into bW, tZ and tH [968, 969].

$$f \in [800, 2000]\ \text{GeV}\ , \qquad y_L \in [0.5, 3]\ .$$

We take $y_L < 3$ and check that $y_R < 4$, in order to remain in the (semi-) perturbative regime. In Fig. 184 we show the normalised top Yukawa coupling, $y_{\rm top}/y_{\rm top}^{\rm SM}$, in the M_1-M_4 plane for both the MCHM$_5$ and MCHM$_{14}$ scenarios. We fix $y_L = 2$ and $f = 1200$ GeV, and $M_9 = 2$ TeV for the MCHM$_{14}$. In the MCHM$_5$, the scaling with f is, to first approximation, given by the function $(1-2\xi)/\sqrt{1-\xi}$, while for the MCHM$_{14}$ it is intertwined with the other parameters in a more complicated way. We see that the MCHM$_5$ always displays a suppression of the top Yukawa coupling compared to the SM limit, while the MCHM$_{14}$ can display an enhancement in certain regions of parameter space, as pointed out in [975]. We also show in the figure, curves of constant $M_{T^{(1)}}$ (red lines) and the approximate direct exclusion region (dark bands). The white area corresponds to the region in parameter space where it is not possible to reproduce the top quark mass. We also show the region where the ggh coupling deviates by more than 20% from unity, as this region is expected to be in tension with the current constraints on Higgs couplings [144].

The $t\bar{t}h$ Process

To an excellent approximation, the $t\bar{t}h$ process in the MCHM is related to the corresponding SM process by a simple rescaling of $\sigma_{\rm MCHM}(t\bar{t}h) = \left(y_t/y_t^{\rm SM}\right)^2 \sigma_{\rm SM}(t\bar{t}h)$. All the modifications due to Higgs compositeness, or mixing with vector-like fermions, enter only through the top Yukawa coupling. Therefore, only a modification in the total rate is expected, but not in kinematic distributions.

The $t\bar{t}hh$ Process

For the $t\bar{t}hh$ process there are two qualitatively different contributions:

1. Resonant processes, involving the production and decay (in the th channel) of heavy vector-like states of charge 2/3 (top partners).

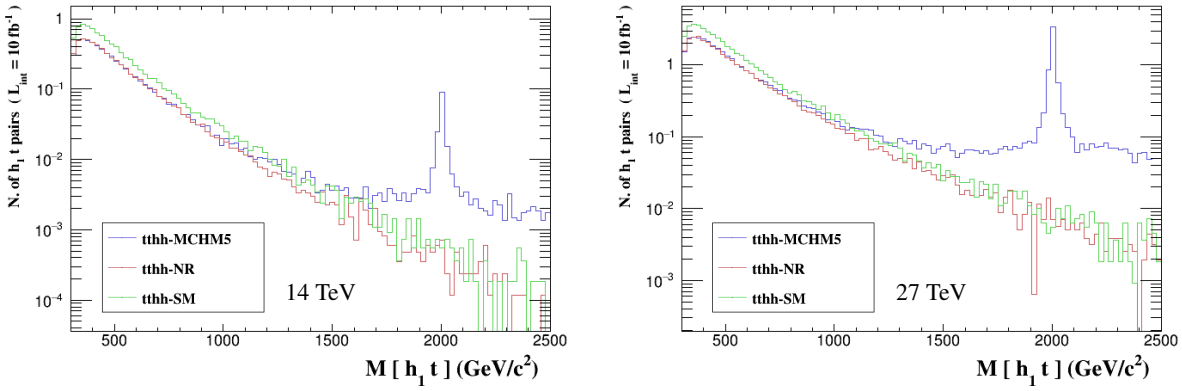

Fig. 185: Distribution of the invariant mass of the top quark and the hardest Higgs boson in the MCHM_5 ($M_1 = -2500$ TeV, $M_4 = 2$ TeV, $f = 1.8$ TeV, $y_L = 1$). The blue histogram shows the distribution of the full $t\bar{t}hh$ process in the MCHM_5, while the NR-$tthh$ cross-section is shown in red. For comparison, we also show in green the SM $t\bar{t}hh$ distribution. Plots generated with MadAnalysis 5 [982].

2. Non-resonant processes: these are defined by the diagrams that do not involve the production of the vector-like resonances.

These contributions may be used to define corresponding “non-resonant" (NR-$tthh$), and “resonant" cross sections. The later can lead to important enhancements depending on the masses, while the former carries distinct information. We find that, to an excellent approximation, the total $t\bar{t}hh$ cross-section is given by the sum of these two cross-sections.

In Fig. 185 we show the ht invariant mass distribution for the resonant and non-resonant processes for a particular point in the MCHM_5. For comparison, we also show the SM $t\bar{t}hh$ cross-section. We see that the NR-$tthh$ follows the SM cross-section, but displays a suppression. We also see that the relative importance of the resonant process w.r.t. the non-resonant one increases with larger c.m. energies. The cross-section for both processes also increases significantly with the c.m. energy (by a factor of 7 in the total $t\bar{t}hh$ cross-section when going from 14 to 27 TeV, and by a factor of 5 when restricted to NR-$tthh$).

The Non-Resonant $t\bar{t}hh$ Process

The diagrams in the MCHM scenarios contributing to the NR-$tthh$ process fall into three categories:

1. Those that involve only the ttH vertex.
2. Those that involve the trilinear Higgs self-interaction (Section 3): $\lambda = \left[(1-2\xi)/\sqrt{1-\xi}\right] \lambda_{\text{SM}}$.
3. Those that involve the $ttHH$ vertex (“double Higgs" Yukawa vertex).

The first two categories correspond to sets of *diagrams* that are identical to those in the SM. The third type involves diagrams that have no counterpart in the SM [983]. The latter is closely connected to the Higgs compositeness aspect of the MCHM scenarios, and it would therefore be extremely interesting if one could get information about such effects experimentally.

By turning off in turn the double Higgs and the trilinear coupling, we find that the effects of the former are typically at the couple to few percent level in MCHM_5 and MCHM_{14} if the $t\bar{t}h$ signal strength, $\mu(t\bar{t}h) \equiv \sigma(t\bar{t}h)/\sigma(t\bar{t}h)_{SM} < 1$, and at most 2% in MCHM_{14} if $\mu(t\bar{t}h) > 1$, with a mild dependence on the c.m. energy (at 14 and 27 TeV) in all cases, while the later contributes around 15% in MCHM_5 and MCHM_{14} if $\mu(t\bar{t}h) < 1$, and 10% in MCHM_{14} if $\mu(t\bar{t}h) > 1$ at a c.m. energy of 14 TeV, decreasing to a few percent at higher c.m. energies in all cases. For comparison, the trilinear coupling in the SM $t\bar{t}hh$ cross-section contributes about 20%, with a very mild c.m. energy dependence. Thus, the NR-$tthh$

Table 93: Sample points for MCHM$_5$ with M_1 M_4 same sign and opposite sign and for MCHM$_{14}$ with M_1 and M_4 both < 0 and $\mu(\mathrm{ttH}) > 1$.

		MCHM$_5$					MCHM$_{14}$			
		Point 1	Point 2	Point 3	Point 4	Point 5	Point 1	Point 2	Point 3	Point 4
Parameters	M_1 (GeV)	-1317	800	-960	-3350	914	-1173	-1054	-1084	-1579
	M_4 (GeV)	1580	2311	1400	3000	2632	-1823	-1826	-1767	-2512
	M_9 (GeV)	-	-	-	-	-	1382	1448	2036	2714
	f (GeV)	969	896	1186	2450	1573	882	1032	1078	1298
	y_L	1.66	1.80	0.88	1.00	2.36	1.98	1.93	2.95	2.71
	y_R	0.62	1.95	0.87	0.85	2.41	3.90	2.78	2.67	2.46
μ(tth) (All Energies)		0.83	0.85	0.92	0.975	0.95	1.40	1.14	1.15	1.11
μ(tthh) (14 TeV)		1.13	0.57	2.96	0.68	0.65	3.31	2.14	1.19	0.92
μ(tthh) (27 TeV)		2.95	0.87	8.17	0.74	0.73	7.87	5.42	2.17	1.05
NR-tthh/tthh (14 TeV)		0.44	0.90	0.20	1.00	1.00	0.44	0.45	0.81	0.99
NR-tthh/tthh (27 TeV)		0.18	0.64	0.08	0.99	0.95	0.19	0.18	0.46	0.90
$M_{T^{(1)}}$ (TeV)		1.44	1.83	1.34	3.00	2.61	1.38	1.45	1.72	2.46
$M_{T^{(2)}}$ (TeV)		1.59	2.37	1.45	3.82	3.91	1.38	1.45	2.01	2.70
$M_{T^{(3)}}$ (TeV)		2.25	2.83	1.76	3.99	4.56	1.41	1.46	2.04	2.71
$M_{B^{(1)}}$ (TeV)		2.25	2.82	1.75	3.87	4.56	1.38	1.45	2.02	2.70
$M_{X_{5/3}}$ (TeV)		1.58	2.31	1.40	3.06	2.63	1.82	1.83	1.77	2.51
BR($T^{(1)}$→t h)		0.32	0.30	0.58	0.30	0.35	0.35	0.26	0.45	0.38
BR($T^{(1)}$→W^+ b)		0.46	0.46	0.09	0.01	0.10	0.40	0.50	0.10	0.10
BR($T^{(1)}$→t Z)		0.23	0.21	0.26	0.29	0.28	0.16	0.13	0.32	0.28
BR($T^{(1)}$ →W^+ W^- t)		0	0.05	0.07	0.38	0.26	0.09	0.10	0.13	0.24

is largely determined by the top Yukawa, being related to the SM process, to a first approximation, by a scaling factor $(y_t/y_t^{\mathrm{SM}})^4$. This explains the result seen in Fig. 185, with the suppression arising from the suppression of the top Yukawa coupling in the MCHM$_5$.

The previous observation also leads to a strong correlation between the $t\bar{t}h$ and the NR-$tthh$ processes, as shown in Fig. 186. Due to the different scaling with the top Yukawa coupling, the deviations from the SM in the NR-$tthh$ process are larger than those in $t\bar{t}h$.

Set of Example Points

We show in Table 93 a number of points selected as examples that illustrate, in more detail, the properties of the MCHM$_5$ and MCHM$_{14}$. These properties are reflected in Figs. 186, 187 and 188, where these points are indicated. The MCHM$_5$ points are labelled as P$_i$, i=1 to 5, and MCHM$_{14}$ points as P'$_j$, with j=1 to 4. The points for the MCHM$_5$ exhibit a suppression in $\mu(t\bar{t}h)$ that ranges from about 15% (roughly at the current 95% C.L. limit [164, 165]) to a few percent, a sensitivity that might be achievable by the end of the HL phase of the LHC run, with smaller deviations from the SM for larger values of f (Fig 187,a). The Table 93 and Fig 188 show that the $t\bar{t}hh$ process can exhibit an enhancement for light enough resonances, increasing with higher c.m. energy, as expected. For points 2, 4 and 5 in the MCHM$_5$, the resonant production is not enough to produce an enhancement in $t\bar{t}hh$ compared to the SM, although these points correspond to two different cases; the resonances for Point 2 are slightly beyond the current direct limit whereas, on the contrary, much beyond that limit for points 4 and 5. In this case, the $t\bar{t}hh$ process is easily dominated by the NR-$tthh$ process, as defined above.

The set of example points for MCHM$_{14}$ in Table 93 exhibits an enhancement of the top Yukawa coupling, due to the effect described above and reflected in Fig 187,b. These enhancements can easily be of the order of 10-20%. Interestingly, Point 1 shows that the enhancement can be as large as 40% (while being consistent with a sufficiently small deviation in the ggh vertex [971]). The four points display as

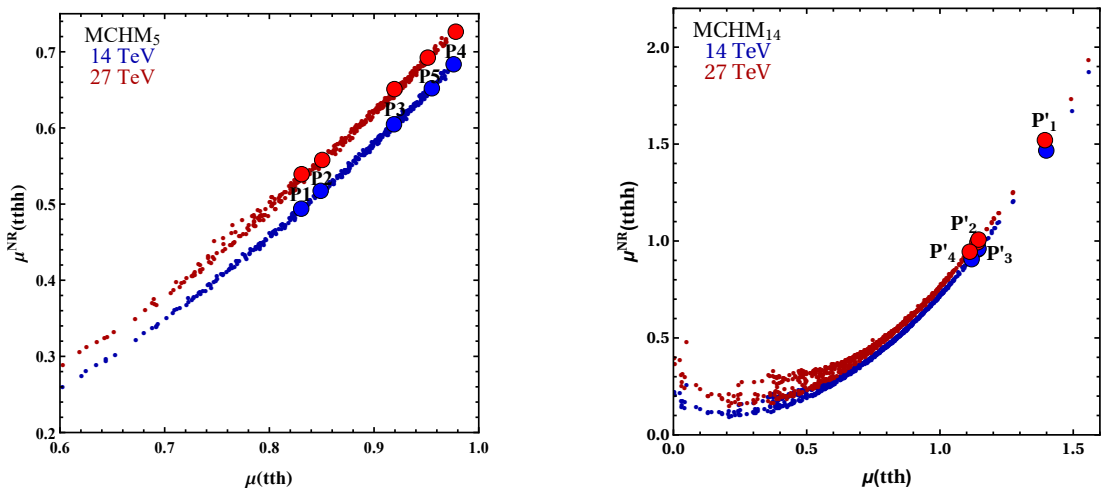

Fig. 186: Correlation between the $t\bar{t}h$ and non-resonant $t\bar{t}hh$ signal strengths (μ), for 14 and 27 TeV c.m. energies. The left (right) plots correspond to the MCHM$_5$ (MCHM$_{14}$)

well, an enhancement in the $t\bar{t}hh$ process. While about half of the rate is due to resonant production in Points 1 and 2, for points 3 and 4 the enhancement arises dominantly from the non-resonant process, reflecting the enhancement in the top Yukawa coupling. All the selected points for MCHM$_{14}$ lie in the $M_1 < 0$, $M_4 < 0$ quadrant of the right panel of Fig. 184. The properties of the other quadrants are qualitatively rather similar to those of the MCHM$_5$ (see [971]).

For completeness, Table 93 includes the spectrum of the 5 resonances in the MCHM$_5$, and of the 3 lightest 2/3 resonances, the lightest B resonance and the lightest 5/3 resonance out of the total of 14 resonances of the MCHM$_{14}$, as well as the BRs for the lightest $Q = 2/3$ one. It decays mostly into the standard th, Wb and tZ channels (with BRs that are model dependent), but in some cases it has non-negligible non-standard BRs, such as into the W^+W^-t channel.

Experimental perspectives

A deviation from the SM in the $t\bar{t}h$ production is an essential measurement for MCHM. An increase will reject the MCHM$_5$ scenario and greatly refine the areas of the parameter space where MCHM$_{14}$ would be valid. A deficit instead, would make MCHM$_5$ and MCHM$_{14}$ both possible. The measurement of this observable is expected to be achieved within 5% accuracy at the HL-LHC (Sections 2.5,2.6,2.7) and thus with very high accuracy at HE-LHC. The $t\bar{t}hh$ production process plays a major role in MCHM searches. Deviations from the SM expectation (deficit or increase) can be significant in both MCHM scenarios. The $t\bar{t}hh$ production cross-section is around 1 fb (Section 3.1) at tree level whereas $t\bar{t}h$ is about 500 times larger (Section 2.2). Therefore the aim at HL-LHC will be to evidence this process and discover if a strong deviation from SM. Higher energy together with higher luminosity (HE-LHC) will further explore MCHM.

Acknowledgements: This work was supported by the São Paulo Research Foundation (FAPESP) under Grants No. 2016/01343-7, No. 2013/01907-0, No. 2015/26624-6 and No. 2018/11505-0 and by Science Without Borders/CAPES for UNESP-SPRACE under the Grant No. 88887.116917/2016-00.

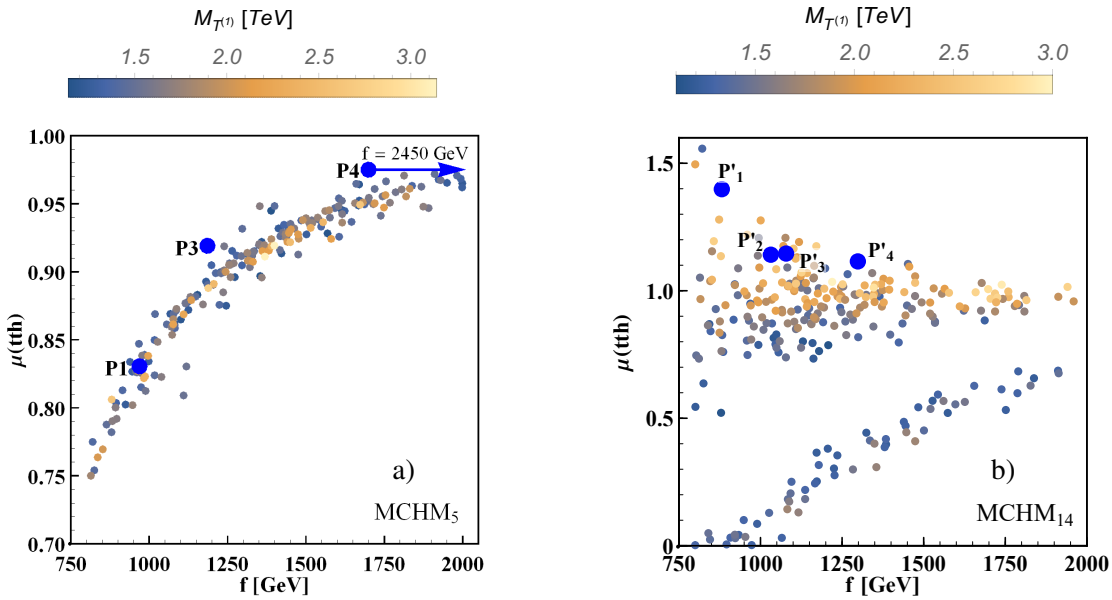

Fig. 187: The $t\bar{t}h$ signal strength as a function of the f-scale, for 14 and 27 TeV c.m. energies, with colour coded the lightest vector-like mass. The left (right) plots correspond to Q2 of MCHM$_5$ (Q3 of MCHM$_{14}$). The blue arrow indicates that the point P4 is outside the horizontal range of the plot with f=2450 GeV.

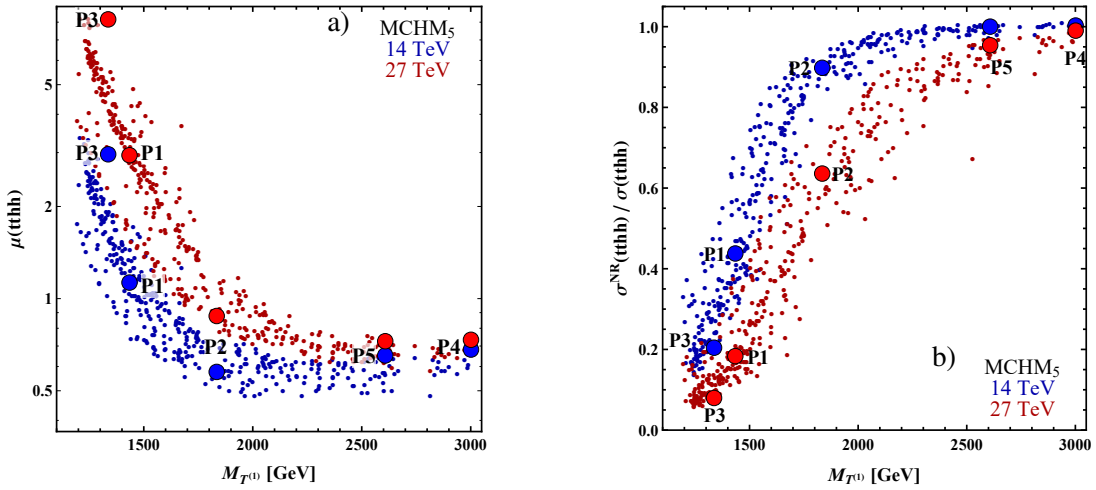

Fig. 188: The left plot shows the $t\bar{t}hh$ signal strength as a function of the lightest $Q = 2/3$ vector-like mass, T$^{(1)}$ for 14 and 27 TeV c.m. energies for the MCHM$_5$. The right plot shows the ratio between the non-resonant $t\bar{t}hh$ cross section and the total $t\bar{t}hh$ cross section as a function of T$^{(1)}$ for 14 and 27 TeV c.m. energies for the MCHM$_5$.

9.8 New Higgs bosons below the 125 GeV Higgs mass

9.8.1 Searches for low mass Higgs bosons (below 120 GeV)[134]

9.8.1.1 Introduction

Many extensions of the Standard Model Higgs sector allow for new charged and neutral Higgs bosons that can be lighter than the Higgs boson discovered [11, 12] at $\approx$ 125 GeV. However, as the observed

[134] Contacts: S. Heinemeyer, J. Santiago, R. Vega-Morales

(heavier) Higgs boson shows itself to be increasingly SM-like [668] in its couplings to WW and ZZ pairs [269, 144, 128, 447, 151, 668], as well as to fermions [136, 984], we are in general pushed into an 'alignment without decoupling' limit [380, 661], which has been examined in a number of recent studies [985, 663, 666, 986, 987, 943, 988, 911]. In this limit, the 125 GeV Higgs boson has SM like couplings without having to decouple the other Higgs bosons which might be present allowing them to be lighter than 125 GeV. In what follows we work in the alignment without decoupling limit focusing on new Higgs bosons in the mass range $65 - 120$ GeV, between the SM-like Higgs mass and its two body decay threshold.

In 2HDMs alignment occurs when one of the neutral CP-even Higgs mass eigen-states is approximately aligned in field space with the direction of the vacuum expectation value [661, 986]. For non-doublet electroweak multiplets (as well as singlets [594]), one obtains an 'aligned' SM-like Higgs when the non-doublet [989, 990] Higgs *VEV* is small, which typically also suppresses the Higgs mixing angle [991, 992]. Furthermore, in the singlet and non-doublet multiplet cases, the new Higgs bosons are (at least approximately) fermiophobic, making them generically harder to detect [993, 994, 995, 996] either directly or indirectly as we discuss more below.

In this section we summarise the relevant experimental constraints on light Higgs bosons in the mass range $65 - 120$ GeV. We also discuss models which can realise light Higgs bosons and highlight promising search signals at the LHC. This includes searching for deviations in Higgs couplings since, as emphasised in [986], even in the deep alignment regime where one might naively expect everything to be very SM-like, precise measurements of the 125 GeV Higgs boson signal strengths could uncover the existence of an extended Higgs sector. Some projections for the HL and HE LHC are also made. The aim is to encourage new experimental analysis, targeting specifically searches for light Higgs bosons at the HL/HE-LHC.

9.8.1.2 Experimental constraints on light Higgs bosons

In the mass range and alignment limit we consider, the most relevant constraints for the *anti*-aligned neutral Higgs bosons but with significant couplings to SM fermions, come from CMS $b\bar{b}X$ with $X \to \tau\bar{\tau}$ searches [997] as well as ATLAS [998] and CMS [999] searches for $X \to \tau\bar{\tau}$ decays in both the $gg \to X$ and $b\bar{b}X$ production modes. Similarly, the searches in the di-photon channel place important bounds [1000, 1001].[135] A recent CMS search [1002] for new resonances decaying to a Z boson and a light resonance, followed by $Z \to \ell\bar{\ell}$ and the light resonance decaying to $b\bar{b}$ or $\tau\bar{\tau}$ pairs, has also been shown to impose severe constraints [986] on light CP-even neutral Higgs bosons. Direct searches at LEP for light neutral Higgs states produced in pairs or in association with a Z boson are also relevant [1003, 1004, 602], setting relevant limits on the couplings of the light Higgs to SM gauge bosons. For the charged Higgs bosons, LEP searches [1005] and B-physics constraints from R_b, ϵ_K, Δm_B, $B \to X_s\gamma$, and $B \to \tau\nu$ [1006, 1007, 1008, 1009, 1010] measurements impose the most stringent constraints. These limits apply to all 2HDMs and impose particularly severe constraints on *non*-type-I 2HDMs [986] in which there is no fermiophobic limit.

As emphasised in numerous studies [1011, 1012, 995, 1013, 996], the above limits are less stringent (most limits can be rescaled) when the Higgs bosons have highly suppressed couplings to SM fermions as can happen in the type-I 2HDM [991] in the large $\tan\beta$ limit [994]. For non-doublet extended Higgs sectors one automatically has suppressed couplings to SM fermions when the non-doublet *VEV* is small (or mixing angle in the case of singlets) since they only enter (if at all) through mixing with the SM-like Higgs boson [990]. In the case of fermiophobia, the most robust probes of neutral Higgs bosons are inclusive di-photon [995, 1013, 996] and multi-photon searches [1014, 1015, 1016] which utilise the Drell-Yan pair production channel of a charged and neutral Higgs boson. Constraints from EW precision data [1017, 1018] also apply with the primary effect being that the neutral and charged

[135] It is interesting to note that the CMS search in the di-photon channel [1000] shows an excess of events at ~ 96 GeV, in the same mass range where the LEP searches in the $b\bar{b}$ final state observed a $2\,\sigma$ excess [602].

Higgs bosons are constrained to be not too different in mass.

9.8.1.3 *Models with light Higgs bosons*

A number of recent studies of the alignment without decoupling limit in 2HDMs have been performed which consider the case where the SM-like Higgs boson is not the lightest scalar. As shown in [1011, 986, 1012, 1019, 1020, 1021, 1022, 988, 1023], for type-I 2HDMs there are regions of parameter space where, along with the light CP-even scalar, both the charged and neutral CP-odd Higgs bosons can be below the SM-like Higgs mass while satisfying the constraints discussed above. This is in contrast to type-II 2HDM, where combined constraints from B meson decays [1010] and EW precision constraints [1024] require the charged and CP-odd neutral Higgs bosons to be much heavier than the mass range we consider here. Within the MSSM however, the additional particle content results in substantially weaker limits from B meson decays and EW data. In general the allowed regions of parameter space in the type-I 2HDM is much larger than in other 2HDMs [986, 988], again due to the presence of a fermiophobic limit at large $\tan\beta$ which opens up more regions of parameter space.

In the MSSM which is a type-II 2HDM, the alignment without decoupling limit [661] requires accidental cancellations between tree level and radiative corrections in the Higgs mass matrix [943, 988]. It was shown that a tuning of $\sim 10\%$ is sufficient to find agreement with the Higgs-boson rate measurements [943]. Depending on the level of alignment required, this can lead to a highly constrained parameter space, especially in the case where the SM-like Higgs is the heavier of the CP-even neutral scalars. In particular, after accounting for all relevant experimental constraints (as well as theoretical uncertainties) recent studies [911] of the alignment without decoupling limit of the MSSM [661] defined a benchmark plane of allowed parameter space with $\tan\beta \sim 5-6$ (and very large values of μ) in which the light CP-even Higgs can be between $\sim 60-100$ GeV if the charged Higgs mass is between $\sim 170-185$ GeV and the neutral CP-odd Higgs is $\sim 130-140$ GeV. Still larger allowed regions are expected in a global scan, as performed in [943]. Recent studies of the NMSSM [666, 1025] and $\mu\nu$SSM [1026] have also examined the alignment without decoupling limit finding a larger allowed parameter space than in the MSSM due to an additional gauge singlet Higgs (or right handed scalar neutrino).

For models with non-doublet multiplets the most well known are those involving electroweak triplets. In particular, Higgs triplet models with custodial symmetry [1027], as in the famous Georgi-Machacek (GM) model [989, 1028, 1029, 1030, 992] or its supersymmetric incarnations [1031, 1032, 1033], have been well studied due to their ability to easily satisfy constraints from electroweak precision data. Recent studies [1034, 1033, 996] have shown that GM-like models can allow for light neutral and charged scalars below the SM-like Higgs boson mass. In the alignment limit implied by Higgs coupling measurements, the triplet Higgs *VEV* is constrained to be small though it can still much larger than non-custodial cases [10, 1035] which are constrained by measurements of the ρ parameter. Custodial symmetry also ensures that the neutral and charged components of the Higgs multiplet have (at least approximately) degenerate masses, making them more difficult to detect due to soft decay products [1036, 1037]. For these anti-aligned and fermiophobic Higgs bosons, recent studies have emphasised di- and multi-photon searches [1016, 995, 1038, 996] as robust probes of this scenario.

9.8.1.4 *Phenomenology of light anti-aligned Higgs bosons*

In the alignment limit, single electroweak production mechanisms for the additional 'anti-aligned' neutral Higgs bosons (or small *VEV* and Higgs mixing for non-doublets), such as VBF or associated vector boson production, necessarily become suppressed. Thus the dominant production mechanisms become gluon fusion or associated $b\bar{b}$ production when there is a significant coupling to SM quarks. However, these production mechanisms become suppressed when the couplings to fermions are negligible [136], as

[136] Of course if they couple to some not too heavy coloured BSM particles, the gluon fusion cross section can be increased.

can happen in type-I 2HDM in the large $\tan\beta$ limit [1039] or non-doublet electroweak sectors which are generically fermiophobic. The same is true for the light charged Higgs bosons production channels $t \to H^{\pm} b$ and $pp \to H^{\pm} tb$ which are also obsolete in the fermiophobic limit. Note that for charged scalars coming from larger than doublet representations we can also have $W^{\pm}Z \to H^{\pm}$ VBF production, but this is again suppressed in the small non-doublet *VEV* and Higgs mixing limit.

Pair Production as a discovery channel

A different option that offers new experimental opportunities is the Drell-Yan Higgs pair production mechanism. Any extension of the SM Higgs sector by electroweak charged scalars will possess the pair production channels mediated by W and Z bosons and which are not present in the SM. Furthermore, as emphasised in [1039, 1040, 1041, 1011, 995, 996], even in the alignment and fermiophobic limits, this production mechanism is not suppressed and can be as large as $\sim 10\,pb$ at 13 TeV and $\sim 50\,pb$ and 27 TeV in the mass range we consider (see Sec. 2.2). Thus, Drell-Yan Higgs pair production can be as large or even dominate over single production mechanisms, for both charged and neutral Higgs bosons. Despite this, the Drell-Yan Higgs pair production mechanism has been largely overlooked in experimental searches with the lone exception being a recent CDF analysis of Tevatron four photon data [1016] searching for fermiophobic Higgs bosons.

The Drell-Yan pair production mechanism is mediated by the vector-Higgs-Higgs coupling. In the alignment limit, this will have vertices that are maximised in this limit and depend only on electroweak couplings and quantum numbers, while some vertices will go to zero depending on which Higgs pairs are being produced [1039, 1040, 1041, 1011, 995, 996]. Thus for the non-zero cases the coupling can be written schematically as,

$$g_{WH_M^{\pm}H_N^0} \equiv ig\, C_N (p_1 - p_2)^{\mu}, \;\; g_{ZH_M^0 H_N^0} \equiv i\frac{g}{c_W}\, C_N (p_1 - p_2)^{\mu}, \tag{219}$$

where C_N is fixed by the $SU(2)_L \times U(1)_Y$ representation [989, 1039, 1042, 1031, 992] and p_1, p_2 are the four momenta of the incoming and outgoing scalar momenta. Here H_N^0 stands for any neutral Higgs boson and can include CP-even or CP-odd neutral Higgs bosons, as well as $H_M^{\pm}$ charged Higgs bosons. There is also a photon mediated channel when both Higgs bosons are charged, but we focus on cases where at least one is neutral. In Fig. 189 we show the leading order $q\bar{q} \to V \to H_M^{\pm,0} H_N^0$ (including *PDFs*) cross section $\times\, C_N^{-2}$ for the W mediated (blue solid) and Z mediated (black dashed) channels at the LHC with $\sqrt{s} = 13$ TeV (left) and $\sqrt{s} = 27$ TeV (right) in the mass range $60 - 125$ GeV. They are computed with Madgraph [79] using a modified version of the GM model implementation of [1043] and rescaling appropriately. There are also NLO contributions which may generate $\gtrsim \mathcal{O}(1)$ K-factors for Higgs pair production [1044, 272, 1045]. These are not included in our analysis. We show four cases for mass splittings of $\Delta M \equiv M_{H_M^{\pm,0}} - M_{H_N^0} = 0, 100, 200, 300$ GeV as labelled in plot.

The dominant decay modes of the neutral Higgs bosons will be to $b\bar{b}$ and $\tau\bar{\tau}$ when there is a significant coupling to SM fermions. In the fermiophobic case, the Higgs bosons can have large branching ratios into EW gauge bosons and in particular photons at low masses. The less emphasised $Z\gamma$ channel may also offer promising opportunities [1013]. Inclusive searches for resonances can then be combined with the Drell-Yan production channel to put relatively robust bounds on branching ratios in extended Higgs sectors as done in [995, 996] for the case of decays into di-photons. For the charged Higgs bosons combing Drell-Yan pair production with decays into $W\gamma$ [1011, 1013] or four photon signals [1016] offer promising search channels.

Suggestions for searches at the HL/HE-LHC

We briefly summarise search strategies for (anti)-aligned light Higgs bosons at the (HL/HE) LHC to be added to the current searches in the mass range we consider, including $\tau\tau$, $\gamma\gamma$, $b\bar{b}$ searches based on gluon fusion and $\tau\tau$ searches based on associated $b\bar{b}$ production [998, 999, 997] as well as recent CMS searches [1002] for $A \to Zh$ with $Z \to \ell\bar{\ell}$ and $h \to \tau\tau, bb$.

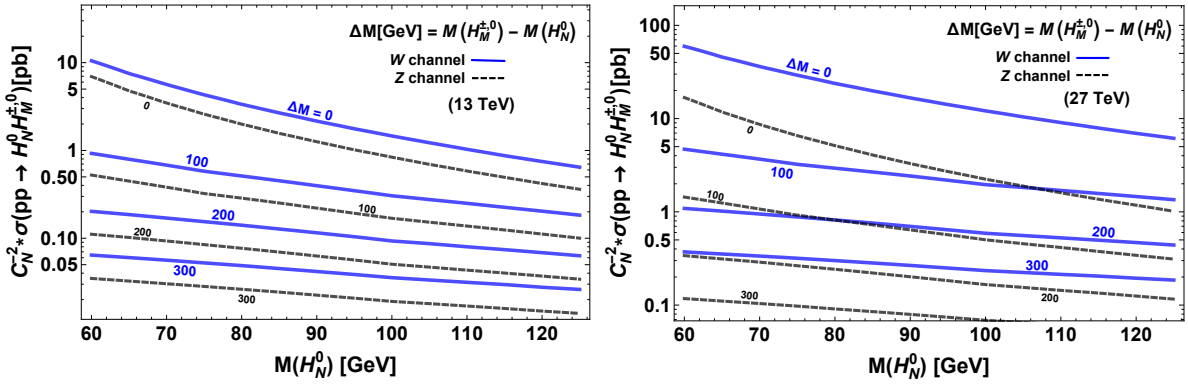

Fig. 189: Leading order cross sections (with *PDFs*) for the $q\bar{q} \to V \to H_M^{\pm,0} H_N^0$ Higgs pair production mechanism mediated by W (blue solid) and Z (black dashed) bosons at the LHC for $\sqrt{s} = 13$ TeV (left) and $\sqrt{s} = 27$ TeV (right) in the mass range $60 - 125$ GeV. We show three cases for mass splittings $\Delta M \equiv M_{H_M^{\pm,0}} - M_{H_N^0} = 0, 100, 200, 300$ GeV as labelled in plot and have factored out an overall group theory factor C_N (see Eq. (219)). The curves for a particular model can be obtained by rescaling with $(C_N)^2$ which is fixed by the $SU(2)_L \times U(1)_Y$ representation.

– Push current conventional Higgs searches in WW and ZZ, which currently [1046, 867] do not go below ~ 130 GeV, to as low a mass as possible, ideally down to ~ 65 GeV. As emphasised in [995, 996], this can help to rule out cases of a fermiophobic Higgs boson with suppressed couplings to photons, which could otherwise escape detection. Similarly, heavier Higgs bosons with the "remaining" coupling to SM gauge bosons could be detected.
– Combine *inclusive* searches for resonances with the 'universal' Drell-Yan Higgs pair production channel to put robust bounds on allowed branching ratios to $\tau\tau$, $b\bar{b}$, $Z\gamma$ and $\gamma\gamma$ final states. In the alignment limit, these bounds depend only on electroweak couplings and can be applied to any extended Higgs boson sector (with appropriate rescaling), in some cases providing the strongest limits [995, 996].
– Utilising the Drell-Yan Higgs pair production mechanism, dedicated LHC searches for more optimised, but model dependent signals such as $4\gamma + V^*$ [1039, 1016, 1019], $4\gamma + V^*V^*$ [1039], $3\gamma + V^*$ where in the last case dedicated phenomenological studies are lacking.
– Search for $\tau\tau$, $b\bar{b}$, or $\gamma\gamma$ plus missing energy as well as mono photon or mono lepton plus missing energy final states to cover cases where neutral Higgs may have an invisible decay. In particular the $\gamma\gamma$ channel appears to be very promising (especially in view of a potential signal at ~ 96 GeV [1000]).

9.8.2 *HL-LHC projections of LHCb searches for 2HDM+S light pseudoscalars*[137]

Several well-motivated extensions of the SM include a new pseudoscalar a with mass below the electroweak scale. A well-known example in the context of supersymmetry is the next-to-minimal supersymmetric SM, where this state can arise as a result of an approximate global $U(1)_R$ symmetry [1047]. Non-supersymmetric extensions featuring a light pseudoscalar include Little Higgs models, hidden valley scenarios (see [43], and references therein for details), and simplified models where a complex singlet scalar is coupled to the Higgs potential of the SM or the 2HDM. Light pseudoscalars have been searched via various collider signatures such as exotic decays of the 125 GeV scalar h discovered at the LHC (both $h \to aa$ and $h \to aZ$), radiative decays of bottomonium $\Upsilon \to a\gamma$, direct production from pp collisions

[137] Contacts: M. Borsato, U. Haisch, J.F. Kamenik, A. Malinauskas, M. Spira

in association with b-jets and also inclusively in $pp \to a + X$, where the main production mode is usually gluon-gluon fusion. The interplay of searches for exotic h decays and direct searches in pp collisions within 2HDM+S models depend on the 2HDM parameters α, β, on the mixing angle θ, on the physical spin-0 masses, and on the form of the scalar potential (see for instance [1048] for further explanations).

Despite the significantly lower luminosity collected with respect to ATLAS and CMS, LHCb has proven to be capable of placing world-best limits for low-mass pseudoscalars produced in gluon-gluon fusion [1049, 1048], by searching simply for resonant pairs of opposite-sign muons [1050, 1051]. Indeed, a large fraction of these light pseudoscalars are produced with large boosts at the LHC and end up in the LHCb acceptance. On top of that, the LHCb detector is capable of triggering on muons with transverse momenta as low as 1.8 GeV (0.5 GeV) with the current (upgraded) trigger, greatly enhancing its acceptance to $a \to \mu^+\mu^-$ with respect to ATLAS and CMS. A key ingredient of this trigger, is the LHCb capability to efficiently reject the large background due to pion mis-identification thanks to online availability of offline-quality particle identification based on information from all sub-detectors [1052, 1053]. On top of that, the large boost of the pseudoscalar a in the forward region allows to separate muons coming from semi-leptonic B decays due to their displacement with respect to the pp collision vertex.

The HL-LHC sensitivity to prompt di-muon resonances in the context of dark photon searches at LHCb can be found in [815]. The kinematic selection used for the projection is inspired by [1054] and rely on the improved performance expected after the upgrade of the LHCb trigger that will be implemented for LHC Run-3. Maintaining this exceptional performance in the HL-LHC era (i.e., with 10 times larger instantaneous luminosity) will require a redesign of the muon detector and is briefly discussed in [815].

In Figure 190, the limits on the dark photon parameter space presented in [815] are reinterpreted in the context of the 2HDM+S, following the analysis strategy detailed in [1048]. The production cross section of the pseudoscalar a and its decay rate to muons depend on the mixing angle θ, on the parameter $\tan\beta$ and on the type of the Yukawa sector of the considered 2HDM. Fixing $\tan\beta$ and the type of the 2HDM, upper limits are placed on $|\sin\theta|$ as a function of the pseudoscalar mass m_a. In all considered cases, LHCb searches in the HL-LHC era (blue contours) are found to be sensitive to values of $|\sin\theta|$ well below 1 for a large range of m_a values between 5 GeV and 70 GeV. This represents a significant improvement over the LHC Run-2 results (yellow curves), where only in the 2HDM+S scenario of type IV with $\tan\beta = 0.5$ it was possible to set physical meaningful bounds on the sine of the mixing angle θ, i.e., $|\sin\theta| < 1$, in the entire range of considered pseudoscalar masses. Notice that spin-0 states with masses around 10 GeV can be probed by searches for di-muon resonances in Υ production [1049, 1051].

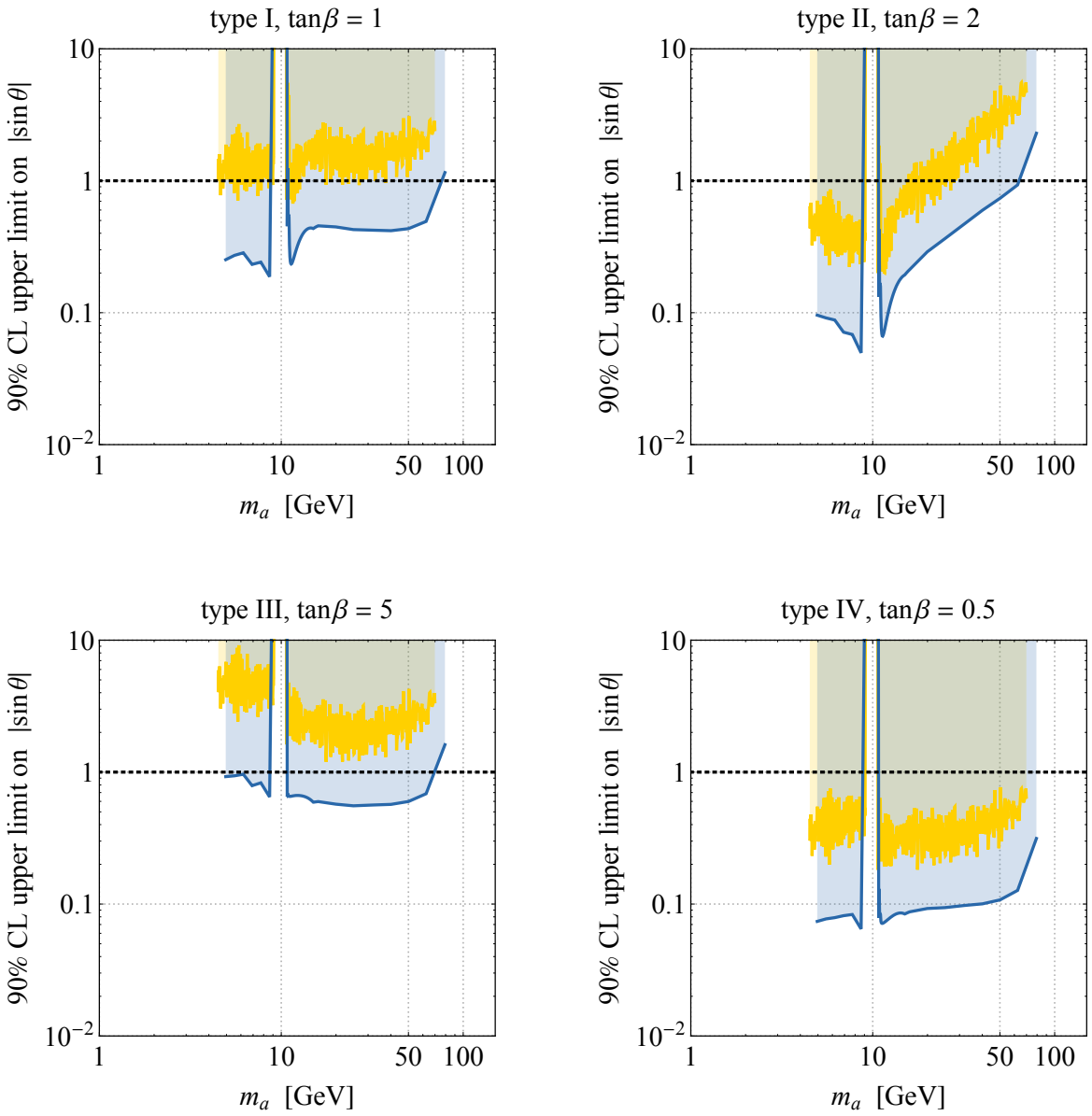

Fig. 190: Upper 90% CL limits on $|\sin\theta|$ in the 2HDM+S of type I with $\tan\beta = 1$ (top left), type II with $\tan\beta = 2$ (top right), type III with $\tan\beta = 5$ (bottom left) and type IV with $\tan\beta = 0.5$ (bottom right). The yellow curves illustrate the results of a recast [1048] of the LHCb search [1050] performed with a data set corresponding to $1.6\,\text{fb}^{-1}$ of 13 TeV pp collisions, while the blue contours are our projections to $300\,\text{fb}^{-1}$ of 14 TeV pp collision data using the expected HL-LHC dark photon limits presented in [815].

10 Conclusions and Outlook

10.1 Higgs properties and EW phenomena at the HL-LHC

The determination of Higgs boson properties, and their connection to electroweak symmetry breaking (EWSB), is a primary target of the HL-LHC physics programme. Since 2012, the Higgs physics programme has rapidly expanded, with new ideas, more precise predictions and improved analyses, into a major program of precision measurements, as well as searches for rare production and decay processes. Outstanding opportunities have emerged for measurements of fundamental importance, such as the first direct constraints on the Higgs trilinear self-coupling and the natural width. The HL-LHC programme covers also searches for additional Higgs bosons in EWSB scenarios motivated by theories beyond the SM (BSM). Finally, a rigorous effective field theory (EFT) framework allows one to parametrise in a model independent way all EW and Higgs results. The studies presented in this report update the key expectations for HL-LHC, and summarise the interpretation of the future constraints on new physics in terms of EFT couplings. This reappraisal of the future sensitivities relies on the Run 2 analyses improvements and assumes the detector performance targets established in the experiments' upgrade TDRs. Further improvements should be possible with analyses optimised for the HL-LHC data sets.

The main Higgs boson measurement channels correspond to five production modes (the gluon fusion ggF, the vector boson fusion VBF, the associated production with a vector boson WH and ZH, and the associated production with a pair of top quarks ttH) and seven decay modes: $H \to \gamma\gamma$, ZZ^*, WW^*, $\tau^+\tau^-$, $b\bar{b}$, $\mu^+\mu^-$ and $Z\gamma$. The latter two decay channels, as yet unobserved, should become visible during the next two LHC runs. The rate measurements in the aforementioned production and decay channels yield measurements of the Higgs couplings in the so-called "κ-framework". This introduces a set of κ_i factors that linearly modify the coupling of the Higgs boson to SM elementary particles, i, including the effective couplings to gluons and photons, and assuming no additional BSM contribution to the Higgs total width, Γ_H. The projected uncertainties, combining ATLAS and CMS, are summarised in Fig. 30 of Section 2. They include today's theory uncertainties reduced by a factor of two, which is close to the uncertainty that would result from using the improved HL-LHC parton distribution functions (PDFs, see Section 2.2.5) and considering signal theory uncertainties as uncorrelated. Except for rare decays, the overall uncertainties will be dominated by the theoretical systematics, with a precision close to percent level.

The main Higgs boson couplings will be measured at HL-LHC with a precision at the percent level. Large statistics will particularly help the study of complex final states, such as those arising from ttH production. The constraining power of the current ttH analyses has been limited to plausible improvements in the theory predictions, in particular in the $H \to b\bar{b}$ channel. The 3.4% precision on κ_t thus obtained is mostly due to the other direct ttH measurement channels.

These coupling measurements assume the absence of sizeable additional contributions to Γ_H. As recently suggested, the patterns of quantum interference between background and Higgs-mediated production of photon pairs or four leptons are sensitive to Γ_H. Measuring the off-shell four-fermion final states, and assuming the Higgs couplings to gluons and ZZ evolve off-shell as in the SM, the HL-LHC will extract Γ_H with a 20% precision at 68% CL. Furthermore, combining all Higgs channels, and with the assumption that the couplings to vector bosons are not larger than the SM ones ($\kappa_V \leq 1$), will constrain Γ_H with a 5% precision at 95% CL. Invisible Higgs boson decays will be searched for at HL-LHC in all production channels, VBF being the most sensitive. The combination of ATLAS and CMS Higgs boson coupling measurements will set an upper limit on the Higgs invisible branching ratio of 2.5%, at the 95% CL. The precision reach in the measurements of ratios will be at the percent level, with particularly interesting measurements of κ_γ/κ_Z, which serves as a probe of new physics entering the $H \to \gamma\gamma$ loop, can be measured with an uncertainty of 1.4%, and κ_t/κ_g, which serves as probe of new physics entering the $gg \to H$ loop, with a precision of 3.4%.

A summary of the limits obtained on first and second generation quarks from a variety of observ-

ables is given in Fig. 117 of section 7. It includes: (i) HL-LHC projections for *exclusive* decays of the Higgs into quarkonia; (ii) constraints from fits to differential cross sections of *kinematic* observables (in particular p_{T}); (iii) constraints on the total *width*, Γ_H, relying on different assumptions (the examples given in Fig. 117 correspond to a projected limit of 200 MeV on the total width from the mass shift from the interference in the di-photon channel between signal and continuous background and the constraint at 68% CL on the total width from off-shell couplings measurements of 20%); (iv) a *global* fit of Higgs production cross sections (yielding the constraint of 5% on the width mentioned herein); and (v) the *direct search* for Higgs decays to $c\bar{c}$ using inclusive charm tagging techniques. Assuming SM couplings, the latter is expected to lead to the most stringent upper limit of $\kappa_c \lessapprox 2$. A combination of ATLAS, CMS and LHCb results would further improve this constraint to $\kappa_c \lessapprox 1$.

Precision measurements provide an important tool to search for BSM physics associated to mass scales beyond the LHC direct reach. The EFT framework, where the SM Lagrangian is supplemented with dimension-6 operators $\sum_i c_i \mathcal{O}_i^{(6)}/\Lambda^2$, allows one to systematically parametrise BSM effects and how they modify SM processes. Figure 137 of section 8 shows the results of a global fit to observables in Higgs physics, as well as di-boson and Drell-Yan processes at high energy. The fit includes all operators generated by new physics that only couples to SM bosons. These operators can either modify SM amplitudes, or generate new amplitudes. In the former case, the best LHC probes are, for example, precision measurements of Higgs branching ratios. In the case of the operator $\mathcal{O}_H$, for example, the constraints in Fig. 137 translate into a sensitivity to the Higgs compositeness scale $f > 1.6$ TeV, corresponding to a new physics mass scale of 20 TeV for an underlying strongly coupled theory. The effects associated with some new amplitudes grow quadratically with the energy. For example, Drell-Yan production at large mass can access, via the operators $\mathcal{O}_{2W,2B}$, energy scales of order 12 TeV (Fig. 137).

The Run 2 experience in searches for Higgs pair production led to a reappraisal of the HL-LHC sensitivity, including several channels, some of which were not considered in previous projections: 2b2γ, 2b2τ, 4b, 2bWW, 2bZZ. Assuming the SM Higgs self-coupling λ, ATLAS and CMS project a sensitivity to the HH signal of approximately 3 σ. per experiment, leading to a combined observation sensitivity of 4 σ. These analyses, which make use also of the HH mass spectrum shape, result in the likelihood profile as a function of κ_λ shown in Fig. 66 of section 3.2.3. An important feature of these analyses is the presence of the secondary minimum in the likelihood line-shape, due to the degeneracy in the total number of HH signal events for different κ_λ values. We note that at the HL-LHC the secondary minimum can be excluded at 99.4% CL, with a constraint on the Higgs self-coupling of $0.5 < \kappa_\lambda < 1.5$ at the 68% CL. The results on HH production studies are statistics limited, therefore a dataset of at least $6\,ab^{-1}$ (ATLAS and CMS combined) is essential to achieve this objective.

Higgs studies at HL-LHC will enhance the sensitivity to BSM physics, exploiting indirect probes via precision measurements, and a multitude of direct search targets, ranging from exotic decays of the 125 GeV Higgs boson (e.g. decays including promptly decaying light scalars, light dark photons or axion-like particles, and decays involving long-lived BSM particles) to the production of new Higgs bosons, neutral and charged, at masses above or below 125 GeV. The HL-LHC will be able to probe very rare exotic decay modes of the 125 GeV Higgs boson thanks to the huge Higgs data set that will be produced (branching ratios as small as $\mathcal{O}(10^{-6})$ could be probed for sufficiently clean decay modes). Furthermore, the mass reach for new heavy Higgs bosons can be pushed to few TeV. As an example, Fig. 181 in section 9.5, shows a summary of the Minimal Supersymmetric SM regions of parameter space that will be probed by ATLAS and CMS either via direct searches of new Higgs bosons decaying to tau lepton pairs, or via indirect 125 GeV Higgs coupling measurements. The HL-LHC will have access to new Higgs bosons as heavy as 2.5 TeV at large $\tan\beta$ ($\tan\beta > 50$). Complementarily, the interpretation of Higgs precision coupling measurements will exclude Higgs bosons with masses lower than approximately 1 TeV over a large range of $\tan\beta$.

10.2 Potential of the HE-LHC

With the increase in centre-of-mass energy and luminosity, the Higgs physics programme at HE-LHC will considerably extend the reach of the entire HL-LHC program. Measurements of the Higgs boson trilinear self-coupling, of elusive decay modes (e.g. H→cc̄), of rare (e.g. H→Zγ), invisible or exotic decays will become accessible. At the same time, Higgs boson production can be explored at very large transverse momenta. Projections presented in this section are exploratory and provide qualitative results, due to the absence of clearly defined reference detectors, and in view of the highly challenging pile-up environment. Several approaches have been followed to address this issue, typically assuming experimental performances similar to those currently achieved by LHC detectors. Other studies focused on Higgs bosons produced at finite transverse momentum ($p_T > 50$ GeV), to reduce the impact of pile-up. The selection of fiducial regions in p_T and rapidity, furthermore, allows measurements of the ratios of rates for different final states, free of uncertainties related to the production dynamics and to luminosity.

Table 94: Higgs production event rates for selected processes at 27 TeV (N_{27}) and statistical increase with respect to the statistics of the HL-LHC ($N_{27} = \sigma_{27\text{ TeV}} \times 15\ ab^{-1}$, $N_{14} = \sigma_{14\text{ TeV}} \times 3\ ab^{-1}$).

	$gg \to H$	VBF	WH	ZH	$t\bar{t}H$	HH
N_{27}	2.2×10^9	1.8×10^8	5.4×10^7	3.7×10^7	4×10^7	2.1×10^6
N_{27}/N_{14}	13	14	12	13	23	19

The statistics expected for some reference production processes, and the increase with respect to the HL-LHC, are shown in Table 94. The Higgs samples will typically increase by a factor between 10 and 25, in part as a result of the 5 times larger luminosity, leading to a potential reduction in the statistical uncertainties by factors of 3 to 5. The biggest improvements arise for the channels favoured by the higher energy, such as ttH and HH.

The potential for the measurement of the Higgs boson trilinear coupling at the HE-LHC has been estimated with methods and in channels similar to those used at the HL-LHC. Extrapolation studies from the current experiments and from phenomenological studies have been carried out in the two most sensitive HH channels at the HL-LHC ($b\bar{b}\gamma\gamma$ and $b\bar{b}\tau^+\tau^-$). Several studies were made under different experimental performance and systematic uncertainty assumptions (in some cases neglecting systematic uncertainties), yielding results covering the wide range of precision estimates presented here. At the HE-LHC the HH signal would be observed unambiguously and the combined sensitivity on the trilinear coupling, κ_λ (assuming the SM value), is expected to reach a precision of 10% to 20% from the combination of these two channels alone. A comparison of the HE-LHC sensitivity to that of the HL-LHC is displayed in Fig. 78 of section 3.4, showing that the secondary minimum still visible in the HL-LHC study is unambiguously excluded at HE-LHC. These studies do not include the additional decay channels that have already been studied for HL-LHC, and of others that could become relevant at the HE-LHC. Exclusive production modes are also very interesting to take into consideration for this measurement. The potential improvements from these have not been assessed yet.

The measurement of the couplings of the Higgs boson at HL-LHC relies either on the assumption that no additional undetected contribution to the Higgs boson width is present, or that the couplings of the Higgs boson to vector bosons do not exceed those expected in the SM. In both cases, the foreseen precision in the measurements of most Higgs boson couplings at the HL-LHC is currently limited by the theoretical uncertainty on the signal predictions. The significantly larger dataset and the increase in centre-of-mass energy at HE-LHC would reduce the statistical uncertainty of these measurements to being negligible. To match the overall precision of the experimental measurements, the extraction of the couplings of the Higgs boson to photons, gluons, W, Z, taus, and b quarks will require significant theoretical improvements in the precision of the theoretical predictions for the signals.

For rare decay processes such as the di-muon channel, from an extrapolation of the HL-LHC projections, a precision of approximately 2% on the coupling modifier should be achievable. With the

current theoretical systematic uncertainties on the signal and the backgrounds, the direct measurement of the Higgs coupling modifier to top quarks is expected to reach a precision of approximately 3%. While the substantial additional amount of data at various centre-of-mass energies will undoubtedly be useful to further constrain the systematic modelling uncertainties and further progress in theoretical predictions will be achieved, the potential improvements have not been quantified. Assuming an improvement of the theoretical uncertainties of a factor of 2, the precision on the ttH coupling would reach approximately 2% (the experimental systematic uncertainty alone is approximately 1%, assuming performances similar to current LHC experiments). The significant gain in precision will be obtained mostly through ratios of couplings. Studies have shown that the ratio of the $t\bar{t}H$ to $t\bar{t}Z$ ratio could be measured at close to the percent level.

At HE-LHC energies, the $H \to c\bar{c}$ production increases relative to backgrounds, and may be observable with inclusive searches by ATLAS, CMS, and LHCb, depending on c-tagging systematic uncertainties. Unfortunately, at the HE-LHC, exclusive searches, kinematic limits, and global fits are not expected to reach the SM level for the u, d, s, and c Yukawas.

Precision measurements provide an important tool to search for BSM physics associated to mass scales beyond the LHC direct reach. The EFT framework, where the SM Lagrangian is supplemented with higher dimension operators allows one to systematically parametrise BSM effects and how they modify SM processes. These operators can either modify SM amplitudes, or generate new amplitudes. In the former case, the best LHC probes are, for example, precision measurements of Higgs branching ratios. In the case of the operator $\mathcal{O}_H$, for example, the constraints in Fig. 138 of Section 8, translate into a sensitivity to the Higgs compositeness scale $f > 2$ TeV, corresponding to a new physics mass scale of 25 TeV for an underlying strongly coupled theory.

Effects associated with new amplitudes grow quadratically (for dimension-6 operators) with the energy. The higher centre-of-mass energy and larger dataset of HE-LHC make it possible to greatly extend the measurable range in the Higgs transverse momenta, providing new opportunities: a 10% measurement at 1 TeV energy corresponds roughly to a per-mille precision measurement at the Higgs mass energy. In the context of EW physics this will allow to test, via Drell-Yan processes and the operators $\mathcal{O}_{2W,2B}$, energy scales of order 25 TeV; or, via WZ di-boson processes, mass scales of roughly 6 (100) TeV if the underlying new physics is weakly (strongly) coupled. Figure 138 shows the results of a global fit to observables in Higgs physics, as well as di-boson and Drell-Yan processes at high energy.

Another important high-energy measurement concerns the scattering of longitudinally polarised vector bosons: departures from its SM value could betray a composite nature of the Higgs. The decomposition of measurements of VBS cross-sections into the polarised components based on the decays of the individual vector bosons is experimentally challenging. Preliminary studies show that, thanks to pile-up mitigation techniques that retain Run-2 performance of hadronically decaying W/Z-boson tagging, the precision on the VBS cross section measurement in the semi-leptonic WV + jj $\to \ell\nu$ + jjjj channel can be reduced from 6.5 % (HL-LHC) to about 2 % at HE-LHC. From this measurement and from the measurement of the EW production of a Z boson pair, the purely longitudinal final state of the WW and ZZ scattering processes can be extracted with a significance of 5σ or more. Similarly, the reach for vector-boson-scattering will be extended by roughly a factor of two in the energy scale of BSM physics, i.e. the sensitivity of the HE-LHC to Wilson coefficients, f/Λ^4, of dimension eight operators, which describe anomalous quartic gauge couplings, improves by a factor 10-20.

Complementarily, the HE-LHC will offer unprecedented opportunities to directly test light TeV-scale new degrees of freedom associated to the Higgs boson and generically arising in models for electroweak symmetry breaking. Particularly, due to the large increase in the Higgs data set (see table 94), very rare exotic Higgs decays could be discovered. For example, multi-lepton signatures could be produced from Higgs decays to light BSM particles (X) as dark photons, or axion-like particles: $h \to XX \to b\bar{b}\mu\mu,\ 4\ell$. The projected HE-LHC reach on the branching ratios of these two decay modes is estimated to be $\sim 10^{-5}$ and $\sim 10^{-8}$, respectively, extending the HL-LHC reach by a factor of ~ 5 and

~ 10, respectively (see Secs. 9.1.5, 9.1.6). As shown by these numbers, the reach of particularly clean decay modes will see a major gain at the HE-LHC mainly due to the increase in Higgs statistics (from gluon fusion production). At the same time, the sample of Higgs bosons produced from sub-leading production modes in association with other SM particles (e.g. $t\bar{t}h$) will be sizeable, increasing the discovery prospects for rare and more background limited Higgs decay signatures. Therefore, the HL/HE-LHC Higgs exotic decay program can be uniquely sensitive to the existence of a broad range of new light weakly coupled particles.

The increase in energy will also open up many opportunities for the direct search of new TeV-scale degrees of freedom associated to electroweak symmetry breaking, as new heavy Higgs bosons. In this report, we have studied, for example, the reach for $pp \to S \to hh$, with h the 125 GeV Higgs boson and S a new Higgs boson, and we have shown that the HE-LHC can extend the reach to S masses that are 1.5-2 times heavier than the masses probed by the HL-LHC (see Sec. 9.4.2). Many more studies will be needed to assess the full discovery potential of the HE-LHC to extended Higgs sectors, as arising in many well motivated BSM theories.

Acknowledgements

We would like to thank the LHC experimental Collaborations and the WLCG for their essential support. We are especially grateful for the efforts by the computing, generator and validation groups who were instrumental for the creation of large simulation samples. We thank the detector upgrade groups as well as the physics and performance groups for their input. Not least, we thank the many colleagues who have provided useful comments on the analyses.

References

[1] F. Englert and R. Brout, *Broken Symmetry and the Mass of Gauge Vector Mesons*, Phys. Rev. Lett. **13** (1964) 321–323.

[2] P. W. Higgs, *Broken symmetries, massless particles and gauge fields*, Phys. Lett. **12** (1964) 132–133.

[3] P. W. Higgs, *Broken Symmetries and the Masses of Gauge Bosons*, Phys. Rev. Lett. **13** (1964) 508–509.

[4] P. W. Higgs, *Spontaneous Symmetry Breakdown without Massless Bosons*, Phys. Rev. **145** (1966) 1156–1163.

[5] G. S. Guralnik, C. R. Hagen, and T. W. B. Kibble, *Global Conservation Laws and Massless Particles*, Phys. Rev. Lett. **13** (1964) 585–587.

[6] T. W. B. Kibble, *Symmetry breaking in nonAbelian gauge theories*, Phys. Rev. **155** (1967) 1554–1561.

[7] S. L. Glashow, *Partial Symmetries of Weak Interactions*, Nucl. Phys. **22** (1961) 579–588.

[8] A. Salam, *Weak and electromagnetic interactions - in Elementary particle theory: relativistic groups and analyticity*, Weak and electromagnetic interactions - in Elementary particle theory: relativistic groups and analyticity, **ed p. 367. Almqvist and Wiksell** (1968) Proceedings of the eighth Nobel symposium.

[9] S. Weinberg, *A Model of Leptons*, Phys. Rev. Lett. **19** (1967) 1264–1266.

[10] Particle Data Group Collaboration, M. Tanabashi et al., *Review of Particle Physics*, Phys. Rev. **D98** (2018) no. 3, 030001.

[11] ATLAS Collaboration, G. Aad et al., *Observation of a new particle in the search for the Standard Model Higgs boson with the ATLAS detector at the LHC*, Phys. Lett. **B716** (2012) 1–29, arXiv:1207.7214 [hep-ex].

[12] CMS Collaboration, *Observation of a new boson at a mass of 125 GeV with the CMS experiment at the LHC*, Phys. Lett. **B716** (2012) no. CERN-PH-EP-2012-220, CMS-HIG-12-028, 30–61, arXiv:1207.7235 [hep-ex].

[13] DELPHES 3 Collaboration, J. de Favereau, C. Delaere, P. Demin, A. Giammanco, V. Lemaitre, A. Mertens, and M. Selvaggi, *DELPHES 3, A modular framework for fast simulation of a generic collider experiment*, JHEP **02** (2014) 057, arXiv:1307.6346 [hep-ex].

[14] M. Cacciari, G. P. Salam, and G. Soyez, *The anti-k_t jet clustering algorithm*, JHEP **04** (2008) 063, arXiv:0802.1189 [hep-ph].

[15] M. Cacciari, G. P. Salam, and G. Soyez, *FastJet user manual*, Eur. Phys. J. C **72** (2012) 1896, arXiv:1111.6097 [hep-ph].

[16] ATLAS Collaboration, *Expected performance of the ATLAS detector at HL-LHC*, in progress, 2018.

[17] CMS Collaboration, *Expected performance of the physics objects with the upgraded CMS detector at the HL-LHC*, CMS-NOTE-2018-006, 2018.

[18] ATLAS Collaboration, *Technical Design Report for the Phase-II Upgrade of the ATLAS TDAQ System*, ATLAS-TDR-029, CERN-LHCC-2017-020, 2017.

[19] CMS Collaboration, *The Phase-2 Upgrade of the CMS L1 Trigger Interim Technical Design Report*, CERN-LHCC-2017-013, CMS-TDR-017, 2017.

[20] ATLAS Collaboration, *Technical Design Report for the ATLAS Inner Tracker Pixel Detector*, ATLAS-TDR-030, CERN-LHCC-2017-021, 2017.

[21] ATLAS Collaboration, *Technical Design Report for the ATLAS Inner Tracker Strip Detector*, ATLAS-TDR-025, CERN-LHCC-2017-005, 2017.

[22] CMS Collaboration, *The Phase-2 Upgrade of the CMS Tracker*, CERN-LHCC-2017-009, CMS-TDR-014, 2017.

[23] ATLAS Collaboration, *Technical Design Report for the Phase-II Upgrade of the ATLAS LAr Calorimeter*, ATLAS-TDR-027, CERN-LHCC-2017-018, 2017.

[24] CMS Collaboration, *The Phase-2 Upgrade of the CMS Barrel Calorimeter*, CERN-LHCC-2017-011, CMS-TDR-015, 2017.

[25] CMS Collaboration, *The Phase-2 Upgrade of the CMS Endcap Calorimeter*, CERN-LHCC-2017-023, CMS-TDR-019, 2017.

[26] CMS Collaboration, *Technical Proposal for a MIP Timing Detector in the CMS Experiment Phase-2 Upgrade*, CERN-LHCC-2017-027, LHCC-P-009, 2017.

[27] ATLAS Collaboration, *Technical Design Report for the Phase-II Upgrade of the ATLAS Muon Spectrometer*, ATLAS-TDR-026, CERN-LHCC-2017-017, 2017.

[28] CMS Collaboration, *The Phase-2 Upgrade of the CMS Muon Detectors*, CERN-LHCC-2017-012, CMS-TDR-016, 2017.

[29] ATLAS Collaboration, *Technical Design Report for the Phase-II Upgrade of the ATLAS Tile Calorimeter*, ATLAS-TDR-028, CERN-LHCC-2017-019, 2017.

[30] CMS Collaboration, *Technical Proposal for the Phase-II Upgrade of the CMS Detector*, CERN-LHCC-2015-010, CMS-TDR-15-02, LHCC-P-008, 2015.

[31] ATLAS Collaboration, *Technical Proposal: A High-Granularity Timing Detector for the ATLAS Phase-II Upgrade*, CERN-LHCC-2018-023, LHCC-P-012, 2018.

[32] T. Sjostrand, S. Mrenna, and P. Z. Skands, *A Brief Introduction to PYTHIA 8.1*, Comput. Phys. Commun. **178** (2008) 852–867, arXiv:0710.3820 [hep-ph].

[33] I. Belyaev et al., *Handling of the generation of primary events in Gauss, the LHCb simulation framework*, J. Phys. Conf. Ser. **331** (2011) 032047.

[34] J. Pumplin, D. Stump, J. Huston, H. Lai, P. M. Nadolsky, et al., *New generation of parton distributions with uncertainties from global QCD analysis*, JHEP **07** (2002) 012, arXiv:hep-ph/0201195 [hep-ph].

[35] J. Allison et al., *Geant4 developments and applications*, IEEE Trans. Nucl. Sci. **53** (2006) 270.

[36] GEANT4 Collaboration, S. Agostinelli et al., *GEANT4: A Simulation toolkit*, Nucl. Instrum. Meth. **A 506** (2003) 250.

[37] M. Clemencic et al., *The LHCb simulation application, Gauss: Design, evolution and experience*, J. Phys. Conf. Ser. **331** (2011) 032023.

[38] R. A. Khalek, S. Bailey, J. Gao, L. Harland-Lang, and J. Rojo, *Towards Ultimate Parton Distributions at the High-Luminosity LHC*, Eur. Phys. J. **C78** (2018) no. 11, 962, arXiv:1810.03639 [hep-ph].

[39] G. D'Ambrosio, G. F. Giudice, G. Isidori, and A. Strumia, *Minimal flavor violation: An Effective field theory approach*, Nucl. Phys. **B645** (2002) 155–187, arXiv:hep-ph/0207036 [hep-ph].

[40] G. F. Giudice, C. Grojean, A. Pomarol, and R. Rattazzi, *The Strongly-Interacting Light Higgs*, JHEP **06** (2007) 045, arXiv:hep-ph/0703164 [hep-ph].

[41] B. Grzadkowski, M. Iskrzynski, M. Misiak, and J. Rosiek, *Dimension-Six Terms in the Standard*

Model Lagrangian, JHEP **10** (2010) 085, arXiv:1008.4884 [hep-ph].

[42] LHC Higgs Cross Section Working Group Collaboration, J. R. Andersen et al., *Handbook of LHC Higgs Cross Sections: 3. Higgs Properties*, arXiv:1307.1347 [hep-ph].

[43] D. Curtin et al., *Exotic decays of the 125 GeV Higgs boson*, Phys. Rev. **D90** (2014) no. 7, 075004, arXiv:1312.4992 [hep-ph].

[44] LHC Higgs Cross Section Working Group Collaboration, A. David, A. Denner, M. Duehrssen, M. Grazzini, C. Grojean, G. Passarino, M. Schumacher, M. Spira, G. Weiglein, and M. Zanetti, *LHC HXSWG interim recommendations to explore the coupling structure of a Higgs-like particle*, arXiv:1209.0040 [hep-ph].

[45] LHC Higgs Cross Section Working Group Collaboration, D. de Florian et al., *Handbook of LHC Higgs Cross Sections: 4. Deciphering the Nature of the Higgs Sector*, arXiv:1610.07922 [hep-ph].

[46] *https://twiki.cern.ch/twiki/bin/view/LHCPhysics/LHCHXSWG*, .

[47] C. Anastasiou, C. Duhr, F. Dulat, E. Furlan, T. Gehrmann, F. Herzog, A. Lazopoulos, and B. Mistlberger, *High precision determination of the gluon fusion Higgs boson cross-section at the LHC*, JHEP **05** (2016) 058, arXiv:1602.00695 [hep-ph].

[48] B. Mistlberger, *Higgs boson production at hadron colliders at N^3LO in QCD*, JHEP **05** (2018) 028, arXiv:1802.00833 [hep-ph].

[49] M. Botje et al., *The PDF4LHC Working Group Interim Recommendations*, arXiv:1101.0538 [hep-ph].

[50] F. Dulat, A. Lazopoulos, and B. Mistlberger, *iHixs 2 — Inclusive Higgs cross sections*, Comput. Phys. Commun. **233** (2018) 243–260, arXiv:1802.00827 [hep-ph].

[51] R. V. Harlander, S. Liebler, and H. Mantler, *SusHi Bento: Beyond NNLO and the heavy-top limit*, Comput. Phys. Commun. **212** (2017) 239–257, arXiv:1605.03190 [hep-ph].

[52] M. Bonvini, S. Marzani, C. Muselli, and L. Rottoli, *On the Higgs cross section at N^3LO+N^3LL and its uncertainty*, JHEP **08** (2016) 105, arXiv:1603.08000 [hep-ph].

[53] M. Bonvini and S. Marzani, *Double resummation for Higgs production*, Phys. Rev. Lett. **120** (2018) no. 20, 202003, arXiv:1802.07758 [hep-ph].

[54] R. D. Ball, V. Bertone, M. Bonvini, S. Marzani, J. Rojo, and L. Rottoli, *Parton distributions with small-x resummation: evidence for BFKL dynamics in HERA data*, Eur. Phys. J. **C78** (2018) no. 4, 321, arXiv:1710.05935 [hep-ph].

[55] M. Bonvini, *Small-x phenomenology at the LHC and beyond: HELL 3.0 and the case of the Higgs cross section*, Eur. Phys. J. **C78** (2018) no. 10, 834, arXiv:1805.08785 [hep-ph].

[56] A. Manohar, P. Nason, G. P. Salam, and G. Zanderighi, *How bright is the proton? A precise determination of the photon parton distribution function*, Phys. Rev. Lett. **117** (2016) no. 24, 242002, arXiv:1607.04266 [hep-ph].

[57] A. V. Manohar, P. Nason, G. P. Salam, and G. Zanderighi, *The Photon Content of the Proton*, JHEP **12** (2017) 046, arXiv:1708.01256 [hep-ph].

[58] NNPDF Collaboration, R. D. Ball, V. Bertone, S. Carrazza, L. Del Debbio, S. Forte, A. Guffanti, N. P. Hartland, and J. Rojo, *Parton distributions with QED corrections*, Nucl. Phys. **B877** (2013) 290–320, arXiv:1308.0598 [hep-ph].

[59] M. Cacciari, F. A. Dreyer, A. Karlberg, G. P. Salam, and G. Zanderighi, *Fully Differential Vector-Boson-Fusion Higgs Production at Next-to-Next-to-Leading Order*, Phys. Rev. Lett. **115** (2015) no. 8, 082002, arXiv:1506.02660 [hep-ph].

[60] F. A. Dreyer and A. Karlberg, *Vector-Boson Fusion Higgs Production at Three Loops in QCD*, Phys. Rev. Lett. **117** (2016) no. 7, 072001, arXiv:1606.00840 [hep-ph].

[61] M. Ciccolini, A. Denner, and S. Dittmaier, *Strong and electroweak corrections to the production*

of Higgs + 2jets via weak interactions at the LHC, Phys. Rev. Lett. **99** (2007) 161803, arXiv:0707.0381 [hep-ph].

[62] M. Ciccolini, A. Denner, and S. Dittmaier, *Electroweak and QCD corrections to Higgs production via vector-boson fusion at the LHC*, Phys. Rev. **D77** (2008) 013002, arXiv:0710.4749 [hep-ph].

[63] A. Denner, S. Dittmaier, S. Kallweit, and A. Mück, *HAWK 2.0: A Monte Carlo program for Higgs production in vector-boson fusion and Higgs strahlung at hadron colliders*, Comput. Phys. Commun. **195** (2015) 161–171, arXiv:1412.5390 [hep-ph].

[64] R. V. Harlander, J. Klappert, S. Liebler, and L. Simon, *vh@nnlo-v2: New physics in Higgs Strahlung*, JHEP **05** (2018) 089, arXiv:1802.04817 [hep-ph].

[65] R. V. Harlander, A. Kulesza, V. Theeuwes, and T. Zirke, *Soft gluon resummation for gluon-induced Higgs Strahlung*, JHEP **11** (2014) 082, arXiv:1410.0217 [hep-ph].

[66] L. Altenkamp, S. Dittmaier, R. V. Harlander, H. Rzehak, and T. J. E. Zirke, *Gluon-induced Higgs-strahlung at next-to-leading order QCD*, JHEP **02** (2013) 078, arXiv:1211.5015 [hep-ph].

[67] A. Denner, S. Dittmaier, S. Kallweit, and A. Muck, *Electroweak corrections to Higgs-strahlung off W/Z bosons at the Tevatron and the LHC with HAWK*, JHEP **03** (2012) 075, arXiv:1112.5142 [hep-ph].

[68] O. Brein, A. Djouadi, and R. Harlander, *NNLO QCD corrections to the Higgs-strahlung processes at hadron colliders*, Phys. Lett. **B579** (2004) 149–156, arXiv:hep-ph/0307206 [hep-ph].

[69] M. L. Ciccolini, S. Dittmaier, and M. Kramer, *Electroweak radiative corrections to associated WH and ZH production at hadron colliders*, Phys. Rev. **D68** (2003) 073003, arXiv:hep-ph/0306234 [hep-ph].

[70] W. Beenakker, S. Dittmaier, M. Kramer, B. Plumper, M. Spira, and P. M. Zerwas, *Higgs radiation off top quarks at the Tevatron and the LHC*, Phys. Rev. Lett. **87** (2001) 201805, arXiv:hep-ph/0107081 [hep-ph].

[71] W. Beenakker, S. Dittmaier, M. Kramer, B. Plumper, M. Spira, and P. M. Zerwas, *NLO QCD corrections to t anti-t H production in hadron collisions*, Nucl. Phys. **B653** (2003) 151–203, arXiv:hep-ph/0211352 [hep-ph].

[72] L. Reina and S. Dawson, *Next-to-leading order results for t anti-t h production at the Tevatron*, Phys. Rev. Lett. **87** (2001) 201804, arXiv:hep-ph/0107101 [hep-ph].

[73] S. Dawson, L. H. Orr, L. Reina, and D. Wackeroth, *Associated top quark Higgs boson production at the LHC*, Phys. Rev. **D67** (2003) 071503, arXiv:hep-ph/0211438 [hep-ph].

[74] S. Dawson, C. Jackson, L. H. Orr, L. Reina, and D. Wackeroth, *Associated Higgs production with top quarks at the large hadron collider: NLO QCD corrections*, Phys. Rev. **D68** (2003) 034022, arXiv:hep-ph/0305087 [hep-ph].

[75] Y. Zhang, W.-G. Ma, R.-Y. Zhang, C. Chen, and L. Guo, *QCD NLO and EW NLO corrections to $t\bar{t}H$ production with top quark decays at hadron collider*, Phys. Lett. **B738** (2014) 1–5, arXiv:1407.1110 [hep-ph].

[76] S. Frixione, V. Hirschi, D. Pagani, H. S. Shao, and M. Zaro, *Electroweak and QCD corrections to top-pair hadroproduction in association with heavy bosons*, JHEP **06** (2015) 184, arXiv:1504.03446 [hep-ph].

[77] S. Frixione, V. Hirschi, D. Pagani, H. S. Shao, and M. Zaro, *Weak corrections to Higgs hadroproduction in association with a top-quark pair*, JHEP **09** (2014) 065, arXiv:1407.0823 [hep-ph].

[78] F. Demartin, F. Maltoni, K. Mawatari, and M. Zaro, *Higgs production in association with a*

single top quark at the LHC, Eur. Phys. J. **C75** (2015) no. 6, 267, arXiv:1504.00611 [hep-ph].

[79] J. Alwall, R. Frederix, S. Frixione, V. Hirschi, F. Maltoni, O. Mattelaer, H. S. Shao, T. Stelzer, P. Torrielli, and M. Zaro, *The automated computation of tree-level and next-to-leading order differential cross sections, and their matching to parton shower simulations*, JHEP **07** (2014) 079, arXiv:1405.0301 [hep-ph].

[80] R. Frederix, S. Frixione, V. Hirschi, D. Pagani, H. S. Shao, and M. Zaro, *The automation of next-to-leading order electroweak calculations*, JHEP **07** (2018) 185, arXiv:1804.10017 [hep-ph].

[81] P. Nason and C. Oleari, *NLO Higgs boson production via vector-boson fusion matched with shower in POWHEG*, JHEP **02** (2010) 037, arXiv:0911.5299 [hep-ph].

[82] B. Jäger, F. Schissler, and D. Zeppenfeld, *Parton-shower effects on Higgs boson production via vector-boson fusion in association with three jets*, JHEP **07** (2014) 125, arXiv:1405.6950 [hep-ph].

[83] D. R. T. Jones and S. T. Petcov, *Heavy Higgs Bosons at LEP*, Phys. Lett. **84B** (1979) 440–444.

[84] S. Borowka, N. Greiner, G. Heinrich, S. P. Jones, M. Kerner, J. Schlenk, and T. Zirke, *Full top quark mass dependence in Higgs boson pair production at NLO*, JHEP **10** (2016) 107, arXiv:1608.04798 [hep-ph].

[85] G. Ferrera, G. Somogyi, and F. Tramontano, *Associated production of a Higgs boson decaying into bottom quarks at the LHC in full NNLO QCD*, Phys. Lett. **B780** (2018) 346–351, arXiv:1705.10304 [hep-ph].

[86] F. Caola, G. Luisoni, K. Melnikov, and R. Röntsch, *NNLO QCD corrections to associated WH production and $H \to b\bar{b}$ decay*, Phys. Rev. **D97** (2018) no. 7, 074022, arXiv:1712.06954 [hep-ph].

[87] W. Astill, W. Bizon, E. Re, and G. Zanderighi, *NNLOPS accurate associated HW production*, JHEP **06** (2016) 154, arXiv:1603.01620 [hep-ph].

[88] W. Astill, W. Bizoń, E. Re, and G. Zanderighi, *NNLOPS accurate associated HZ production with NLO decay* $\mathrm{H} \to b\bar{b}$, Submitted to: JHEP (2018) , arXiv:1804.08141 [hep-ph].

[89] L. Buonocore, P. Nason, and F. Tramontano, *Heavy quark radiation in NLO+PS POWHEG generators*, Eur. Phys. J. **C78** (2018) no. 2, 151, arXiv:1711.06281 [hep-ph].

[90] F. Granata, J. M. Lindert, C. Oleari, and S. Pozzorini, *NLO QCD+EW predictions for HV and HV +jet production including parton-shower effects*, JHEP **09** (2017) 012, arXiv:1706.03522 [hep-ph].

[91] S. Biswas, E. Gabrielli, and B. Mele, *Single top and Higgs associated production as a probe of the Htt coupling sign at the LHC*, JHEP **01** (2013) 088, arXiv:1211.0499 [hep-ph].

[92] J. Gao, L. Harland-Lang, and J. Rojo, *The Structure of the Proton in the LHC Precision Era*, Phys. Rept. **742** (2018) 1–121, arXiv:1709.04922 [hep-ph].

[93] J. Rojo et al., *The PDF4LHC report on PDFs and LHC data: Results from Run I and preparation for Run II*, J. Phys. **G42** (2015) 103103, arXiv:1507.00556 [hep-ph].

[94] S. Forte and G. Watt, *Progress in the Determination of the Partonic Structure of the Proton*, Ann. Rev. Nucl. Part. Sci. **63** (2013) 291–328, arXiv:1301.6754 [hep-ph].

[95] W. Beenakker, C. Borschensky, M. Kramer, A. Kulesza, E. Laenen, S. Marzani, and J. Rojo, *NLO+NLL squark and gluino production cross-sections with threshold-improved parton distributions*, Eur. Phys. J. **C76** (2016) no. 2, 53, arXiv:1510.00375 [hep-ph].

[96] NNPDF Collaboration, R. D. Ball et al., *Parton distributions from high-precision collider data*, Eur. Phys. J. **C77** (2017) no. 10, 663, arXiv:1706.00428 [hep-ph].

[97] S. Dulat, T.-J. Hou, J. Gao, M. Guzzi, J. Huston, P. Nadolsky, J. Pumplin, C. Schmidt,

D. Stump, and C. P. Yuan, *New parton distribution functions from a global analysis of quantum chromodynamics*, Phys. Rev. **D93** (2016) no. 3, 033006, arXiv:1506.07443 [hep-ph].

[98] L. A. Harland-Lang, A. D. Martin, P. Motylinski, and R. S. Thorne, *Parton distributions in the LHC era: MMHT 2014 PDFs*, Eur. Phys. J. **C75** (2015) no. 5, 204, arXiv:1412.3989 [hep-ph].

[99] S. Alekhin, J. Blümlein, S. Moch, and R. Placakyte, *Parton distribution functions, α_s, and heavy-quark masses for LHC Run II*, Phys. Rev. **D96** (2017) no. 1, 014011, arXiv:1701.05838 [hep-ph].

[100] M. Czakon, N. P. Hartland, A. Mitov, E. R. Nocera, and J. Rojo, *Pinning down the large-x gluon with NNLO top-quark pair differential distributions*, JHEP **04** (2017) 044, arXiv:1611.08609 [hep-ph].

[101] M. Guzzi, K. Lipka, and S.-O. Moch, *Top-quark pair production at hadron colliders: differential cross section and phenomenological applications with DiffTop*, JHEP **01** (2015) 082, arXiv:1406.0386 [hep-ph].

[102] R. Boughezal, A. Guffanti, F. Petriello, and M. Ubiali, *The impact of the LHC Z-boson transverse momentum data on PDF determinations*, JHEP **07** (2017) 130, arXiv:1705.00343 [hep-ph].

[103] D. d'Enterria and J. Rojo, *Quantitative constraints on the gluon distribution function in the proton from collider isolated-photon data*, Nucl. Phys. **B860** (2012) 311–338, arXiv:1202.1762 [hep-ph].

[104] J. M. Campbell, J. Rojo, E. Slade, and C. Williams, *Direct photon production and PDF fits reloaded*, Eur. Phys. J. **C78** (2018) no. 6, 470, arXiv:1802.03021 [hep-ph].

[105] R. Gauld, J. Rojo, L. Rottoli, and J. Talbert, *Charm production in the forward region: constraints on the small-x gluon and backgrounds for neutrino astronomy*, JHEP **11** (2015) 009, arXiv:1506.08025 [hep-ph].

[106] PROSA Collaboration, O. Zenaiev et al., *Impact of heavy-flavour production cross sections measured by the LHCb experiment on parton distribution functions at low x*, Eur. Phys. J. **C75** (2015) no. 8, 396, arXiv:1503.04581 [hep-ph].

[107] R. Gauld and J. Rojo, *Precision determination of the small-x gluon from charm production at LHCb*, Phys. Rev. Lett. **118** (2017) no. 7, 072001, arXiv:1610.09373 [hep-ph].

[108] ATLAS Collaboration, G. Aad et al., *Measurement of the production of a W boson in association with a charm quark in pp collisions at $\sqrt{s}$ = 7 TeV with the ATLAS detector*, JHEP **05** (2014) 068, arXiv:1402.6263 [hep-ex].

[109] CMS Collaboration, *Measurement of the muon charge asymmetry in inclusive $pp \to W + X$ production at $\sqrt{s} = 7$ TeV and an improved determination of light parton distribution functions*, Phys. Rev. **D90** (2014) no. CERN-PH-EP-2013-232, CMS-SMP-12-021, 032004, arXiv:1312.6283 [hep-ex].

[110] J. Currie, E. W. N. Glover, and J. Pires, *Next-to-Next-to Leading Order QCD Predictions for Single Jet Inclusive Production at the LHC*, Phys. Rev. Lett. **118** (2017) no. 7, 072002, arXiv:1611.01460 [hep-ph].

[111] J. Rojo, *Constraints on parton distributions and the strong coupling from LHC jet data*, Int. J. Mod. Phys. **A30** (2015) 1546005, arXiv:1410.7728 [hep-ph].

[112] J. Butterworth et al., *PDF4LHC recommendations for LHC Run II*, J. Phys. **G43** (2016) 023001, arXiv:1510.03865 [hep-ph].

[113] J. Gao and P. Nadolsky, *A meta-analysis of parton distribution functions*, JHEP **07** (2014) 035, arXiv:1401.0013 [hep-ph].

[114] S. Carrazza, J. I. Latorre, J. Rojo, and G. Watt, *A compression algorithm for the combination of*

PDF sets, Eur. Phys. J. **C75** (2015) 474, arXiv:1504.06469 [hep-ph].

[115] S. Carrazza, S. Forte, Z. Kassabov, J. I. Latorre, and J. Rojo, *An Unbiased Hessian Representation for Monte Carlo PDFs*, Eur. Phys. J. **C75** (2015) no. 8, 369, arXiv:1505.06736 [hep-ph].

[116] H. Paukkunen and P. Zurita, *PDF reweighting in the Hessian matrix approach*, JHEP **12** (2014) 100, arXiv:1402.6623 [hep-ph].

[117] C. Schmidt, J. Pumplin, C. P. Yuan, and P. Yuan, *Updating and Optimizing Error PDFs in the Hessian Approach*, Phys. Rev. **D98** (2018) no. 9, 094005, arXiv:1806.07950 [hep-ph].

[118] A. Buckley, J. Ferrando, S. Lloyd, K. Nordström, B. Page, M. Rüfenacht, M. Schönherr, and G. Watt, *LHAPDF6: parton density access in the LHC precision era*, Eur. Phys. J. **C75** (2015) 132, arXiv:1412.7420 [hep-ph].

[119] *https://twiki.cern.ch/twiki/bin/view/LHCPhysics/HLHELHCCommonSystematics*, .

[120] J. R. Andersen et al., *Les Houches 2015: Physics at TeV Colliders Standard Model Working Group Report*, in *9th Les Houches Workshop on Physics at TeV Colliders (PhysTeV 2015) Les Houches, France, June 1-19, 2015*. 2016. arXiv:1605.04692 [hep-ph].

[121] P. D. Dauncey, M. Kenzie, N. Wardle, and G. J. Davies, *Handling uncertainties in background shapes*, JINST **10** (2015) no. 04, P04015, arXiv:1408.6865 [physics.data-an].

[122] ATLAS Collaboration, *Measurements of Higgs boson properties in the diphoton decay channel using 80 fb^{-1} of pp collision data at $\sqrt{s}$ = 13 TeV with the ATLAS detector*, ATLAS-CONF-2018-028, 2018.

[123] CMS Collaboration, *Measurements of Higgs boson properties in the diphoton decay channel in proton-proton collisions at $\sqrt{s} = 13$ TeV*, JHEP **11** (2018) no. CERN-EP-2018-060, CMS-HIG-16-040, 185, arXiv:1804.02716 [hep-ex].

[124] ATLAS Collaboration, M. Aaboud et al., *Searches for the $Z\gamma$ decay mode of the Higgs boson and for new high-mass resonances in pp collisions at $\sqrt{s} = 13$ TeV with the ATLAS detector*, JHEP **10** (2017) 112, arXiv:1708.00212 [hep-ex].

[125] CMS Collaboration, *Search for the decay of a Higgs boson in the $\ell\ell\gamma$ channel in proton-proton collisions at $\sqrt{s} = 13$ TeV*, Submitted to: JHEP (2018) no. CERN-EP-2018-092, CMS-HIG-17-007, , arXiv:1806.05996 [hep-ex].

[126] ATLAS Collaboration, *Projections for measurements of Higgs boson cross sections, branching ratios, coupling parameters and mass with the ATLAS detector at the HL-LHC*, ATL-PHYS-PUB-2018-054, 2018.

[127] ATLAS Collaboration, *Measurements of the Higgs boson production, fiducial and differential cross sections in the 4ℓ decay channel at $\sqrt{s}$ = 13 TeV with the ATLAS detector*, ATLAS-CONF-2018-018, 2018. ATLAS-CONF-2018-018.

[128] CMS Collaboration, *Measurements of properties of the Higgs boson decaying into the four-lepton final state in pp collisions at $\sqrt{s} = 13$ TeV*, JHEP **11** (2017) no. CERN-EP-2017-123, CMS-HIG-16-041, 047, arXiv:1706.09936 [hep-ex].

[129] ATLAS Collaboration, *Measurements of gluon-gluon fusion and vector-boson fusion Higgs boson production cross-sections in the $H \to WW^* \to e\nu\mu\nu$ decay channel in pp collisions at $\sqrt{s}$ = 13 TeV with the ATLAS detector*, arXiv:1808.09054 [hep-ex].

[130] CMS Collaboration, *Measurements of properties of the Higgs boson decaying to a W boson pair in pp collisions at $\sqrt{s} = 13$ TeV*, Submitted to: Phys. Lett. (2018) no. FERMILAB-PUB-18-352-CMS, CERN-EP-2018-141, CMS-HIG-16-042, , arXiv:1806.05246 [hep-ex].

[131] A. Elagin, P. Murat, A. Pranko, and A. Safonov, *A New Mass Reconstruction Technique for Resonances Decaying to di-tau*, Nucl. Instrum. Meth. **A654** (2011) 481–489,

arXiv:1012.4686 [hep-ex].

[132] L. Bianchini, J. Conway, E. K. Friis, and C. Veelken, *Reconstruction of the Higgs mass in $H \to \tau\tau$ Events by Dynamical Likelihood techniques*, J. Phys. Conf. Ser. **513** (2014) 022035.

[133] ATLAS Collaboration, M. Aaboud et al., *Cross-section measurements of the Higgs boson decaying into a pair of τ-leptons in proton-proton collisions at $\sqrt{s} = 13$ TeV with the ATLAS detector*, Submitted to: Phys. Rev. (2018) , arXiv:1811.08856 [hep-ex].

[134] CMS Collaboration, *Observation of the Higgs boson decay to a pair of τ leptons with the CMS detector*, Phys. Lett. **B779** (2018) no. CERN-EP-2017-181, CMS-HIG-16-043, 283–316, arXiv:1708.00373 [hep-ex].

[135] ATLAS Collaboration, *Cross-section measurements of the Higgs boson decaying to a pair of tau leptons in proton–proton collisions at $\sqrt{s} = 13$ TeV with the ATLAS detector*, ATLAS-CONF-2018-021, 2018.

[136] ATLAS Collaboration, M. Aaboud et al., *Observation of $H \to b\bar{b}$ decays and VH production with the ATLAS detector*, Phys. Lett. **B786** (2018) 59–86, arXiv:1808.08238 [hep-ex].

[137] CMS Collaboration, *Observation of Higgs boson decay to bottom quarks*, Phys. Rev. Lett. **121** (2018) no. CERN-EP-2018-223, CMS-HIG-18-016, 121801, arXiv:1808.08242 [hep-ex].

[138] CMS Collaboration, *Evidence for the Higgs boson decay to a bottom quark-antiquark pair*, Phys. Lett. **B780** (2018) no. CERN-EP-2017-233, CMS-HIG-16-044, 501–532, arXiv:1709.07497 [hep-ex].

[139] CMS Collaboration, *Sensitivity projections for Higgs boson properties measurements at the HL-LHC*, CMS-PAS-FTR-18-011, 2018.

[140] ATLAS Collaboration, M. Aaboud et al., *Search for the dimuon decay of the Higgs boson in pp collisions at $\sqrt{s}$ = 13 TeV with the ATLAS detector*, Phys. Rev. Lett. **119** (2017) no. 5, 051802, arXiv:1705.04582 [hep-ex].

[141] CMS Collaboration, *Search for the Higgs boson decaying to two muons in proton-proton collisions at $\sqrt{s} = 13$ TeV*, Submitted to: Phys. Rev. Lett. (2018) no. CERN-EP-2018-165, CMS-HIG-17-019, , arXiv:1807.06325 [hep-ex].

[142] CMS Collaboration, *Search for the standard model Higgs boson decaying into two muons in pp collisions at sqrt(s)=13TeV*, CMS-PAS-HIG-17-019, 2017.

[143] CMS Collaboration, S. Chatrchyan et al., *The CMS Experiment at the CERN LHC*, JINST **3** (2008) S08004.

[144] CMS Collaboration, *Measurements of the Higgs boson production and decay rates and constraints on its couplings from a combined ATLAS and CMS analysis of the LHC pp collision data at $\sqrt{s} = 7$ and 8 TeV*, JHEP **08** (2016) no. ATLAS-HIGG-2015-07, CERN-EP-2016-100, CMS-HIG-15-002, 045, arXiv:1606.02266 [hep-ex].

[145] CMS Collaboration, *Combined Measurement of the Higgs Boson Mass in pp Collisions at $\sqrt{s} = 7$ and 8 TeV with the ATLAS and CMS Experiments*, Phys. Rev. Lett. **114** (2015) no. ATLAS-HIGG-2014-14, CERN-PH-EP-2015-075, CMS-HIG-14-042, 191803, arXiv:1503.07589 [hep-ex].

[146] CMS Collaboration, *Combined measurements of the Higgs boson's couplings at $\sqrt{s} = 13$ TeV*, CMS-PAS-HIG-17-031, 2018. CMS-PAS-HIG-17-031.

[147] ATLAS Collaboration, G. Aad et al., *Measurements of fiducial and differential cross sections for Higgs boson production in the diphoton decay channel at $\sqrt{s} = 8$ TeV with ATLAS*, JHEP **09** (2014) 112, arXiv:1407.4222 [hep-ex].

[148] ATLAS Collaboration, G. Aad et al., *Fiducial and differential cross sections of Higgs boson production measured in the four-lepton decay channel in pp collisions at $\sqrt{s}$ = 8 TeV with the ATLAS detector*, Phys. Lett. **B738** (2014) 234–253, arXiv:1408.3226 [hep-ex].

[149] ATLAS Collaboration, *Measurement of fiducial differential cross sections of gluon-fusion production of Higgs bosons decaying to $WW^* \to e\nu\mu\nu$ with the ATLAS detector at $\sqrt{s}$ = 8 TeV*, JHEP **08** (2016) 104, arXiv:1604.02997 [hep-ex].

[150] ATLAS Collaboration, M. Aaboud et al., *Measurements of Higgs boson properties in the diphoton decay channel with 36 fb^{-1} of pp collision data at $\sqrt{s} = 13$ TeV with the ATLAS detector*, Phys. Rev. **D98** (2018) 052005, arXiv:1802.04146 [hep-ex].

[151] ATLAS Collaboration, M. Aaboud et al., *Measurement of inclusive and differential cross sections in the $H \to ZZ^* \to 4\ell$ decay channel in pp collisions at $\sqrt{s} = 13$ TeV with the ATLAS detector*, JHEP **10** (2017) 132, arXiv:1708.02810 [hep-ex].

[152] ATLAS Collaboration, M. Aaboud et al., *Combined measurement of differential and total cross sections in the $H \to \gamma\gamma$ and the $H \to ZZ^* \to 4\ell$ decay channels at $\sqrt{s} = 13$ TeV with the ATLAS detector*, Phys. Lett. **B786** (2018) 114, arXiv:1805.10197 [hep-ex].

[153] CMS Collaboration, *Measurement of differential cross sections for Higgs boson production in the diphoton decay channel in pp collisions at $\sqrt{s} = 8$ TeV*, Eur. Phys. J. **C76** (2016) no. CERN-PH-EP-2015-195, CMS-HIG-14-016, 13, arXiv:1508.07819 [hep-ex].

[154] CMS Collaboration, *Measurement of differential and integrated fiducial cross sections for Higgs boson production in the four-lepton decay channel in pp collisions at $\sqrt{s} = 7$ and 8 TeV*, JHEP **04** (2016) no. CERN-PH-EP-2015-285, CMS-HIG-14-028, 005, arXiv:1512.08377 [hep-ex].

[155] CMS Collaboration, *Measurement of the transverse momentum spectrum of the Higgs boson produced in pp collisions at $\sqrt{s} = 8$ TeV using $H \to WW$ decays*, JHEP **03** (2017) no. CERN-EP-2016-125, CMS-HIG-15-010, 032, arXiv:1606.01522 [hep-ex].

[156] CMS Collaboration, *Measurement of inclusive and differential Higgs boson production cross sections in the diphoton decay channel in proton-proton collisions at $\sqrt{s} = 13$ TeV*, CERN-EP-2018-166, CMS-HIG-17-025, 2018. arXiv:1807.03825 [hep-ex].

[157] CMS Collaboration, *Measurement and interpretation of differential cross sections for Higgs boson production at $\sqrt{s} = 13$ TeV*, Submitted to: Phys. Lett. (2018) no. CERN-EP-2018-304, CMS-HIG-17-028, , arXiv:1812.06504 [hep-ex].

[158] ATLAS Collaboration, *Prospects for differential cross-section measurements of Higgs boson production measured in decays to ZZ and $\gamma\gamma$ with the ATLAS experiment at the High-Luminosity LHC*, ATL-PHYS-PUB-2018-040, 2018.

[159] CMS Collaboration, *Combined measurement and interpretation of differential Higgs boson production cross sections at $\sqrt{s}$=13 TeV*, CMS-PAS-HIG-17-028, 2018.

[160] S. Alioli, P. Nason, C. Oleari, and E. Re, *A general framework for implementing NLO calculations in shower Monte Carlo programs: the POWHEG BOX*, JHEP **06** (2010) 043, arXiv:1002.2581 [hep-ph].

[161] T. Gleisberg, S. Hoeche, F. Krauss, M. Schonherr, S. Schumann, F. Siegert, and J. Winter, *Event generation with SHERPA 1.1*, JHEP **02** (2009) 007, arXiv:0811.4622 [hep-ph].

[162] CMS Collaboration, *Constraints on the Higgs boson self-coupling from ttH+tH, H to gamma gamma differential measurements at the HL-LHC*, CMS-PAS-FTR-18-020, 2018.

[163] G. Cowan, K. Cranmer, E. Gross, and O. Vitells, *Asymptotic formulae for likelihood-based tests of new physics*, Eur. Phys. J. **C71** (2011) 1554, arXiv:1007.1727 [physics.data-an].

[164] ATLAS Collaboration, M. Aaboud et al., *Observation of Higgs boson production in association with a top quark pair at the LHC with the ATLAS detector*, Phys. Lett. **B784** (2018) 173–191, arXiv:1806.00425 [hep-ex].

[165] CMS Collaboration, *Observation of $\mathrm{t\bar{t}}H$ production*, Phys. Rev. Lett. **120** (2018) no. CERN-EP-2018-064, CMS-HIG-17-035, 231801, arXiv:1804.02610 [hep-ex].

[166] ATLAS Collaboration, M. Aaboud et al., *Search for the standard model Higgs boson produced in association with top quarks and decaying into a $b\bar{b}$ pair in pp collisions at $\sqrt{s}$ = 13 TeV with the ATLAS detector*, Phys. Rev. **D97** (2018) no. 7, 072016, arXiv:1712.08895 [hep-ex].

[167] CMS Collaboration, *Search for $t\bar{t}H$ production in the $H \to b\bar{b}$ decay channel with leptonic $t\bar{t}$ decays in proton-proton collisions at $\sqrt{s} = 13$ TeV*, Accepted by *JHEP* (2018) no. CERN-EP-2018-065, CERN-EP-2018-065, CMS-HIG-17-026, , arXiv:1804.03682 [hep-ex].

[168] ATLAS Collaboration, M. Aaboud et al., *Evidence for the associated production of the Higgs boson and a top quark pair with the ATLAS detector*, Phys. Rev. **D97** (2018) no. 7, 072003, arXiv:1712.08891 [hep-ex].

[169] CMS Collaboration, *Search for associated production of a Higgs boson and a single top quark in proton-proton collisions at $\sqrt{s} = 13$ TeV*, Submitted to Phys. Rev. D. (2018) no. CERN-EP-2018-305, CMS-HIG-18-009, , arXiv:1811.09696 [hep-ex].

[170] ATLAS Collaboration, *to be published*, ATLAS-PHYS-PUB-2018-XY, 2018.

[171] A. J. Costa, A. L. Carvalho, R. Gonçalo, P. Muiño, and A. Onofre, *Study of $t\bar{t}H$ production with $H \to b\bar{b}$ at the HL-LHC*, arXiv:1812.10700 [hep-ph].

[172] CMS Collaboration, *Search for the associated production of a Higgs boson and a single top quark in pp collisions at $\sqrt{s} = 13$ TeV*, CMS-PAS-HIG-18-009, 2018.

[173] F. Bishara, U. Haisch, P. F. Monni, and E. Re, *Constraining Light-Quark Yukawa Couplings from Higgs Distributions*, Phys. Rev. Lett. **118** (2017) no. 12, 121801, arXiv:1606.09253 [hep-ph].

[174] M. Grazzini, A. Ilnicka, M. Spira, and M. Wiesemann, *Effective Field Theory for Higgs properties parametrisation: the transverse momentum spectrum case*, in *Proceedings, 52nd Rencontres de Moriond on QCD and High Energy Interactions: La Thuile, Italy, March 25-April 1, 2017*, pp. 23–27. 2017. arXiv:1705.05143 [hep-ph].

[175] M. Grazzini, A. Ilnicka, M. Spira, and M. Wiesemann, *Modeling BSM effects on the Higgs transverse-momentum spectrum in an EFT approach*, JHEP **03** (2017) 115, arXiv:1612.00283 [hep-ph].

[176] ATLAS Collaboration, G. Aad et al., *Measurements of the Total and Differential Higgs Boson Production Cross Sections Combining the $H \to \gamma\gamma$ and $H \to ZZ^* \to 4\ell$ Decay Channels at $\sqrt{s}$ = 8 TeV with the ATLAS Detector*, Phys. Rev. Lett. **115** (2015) no. 9, 091801, arXiv:1504.05833 [hep-ex].

[177] CMS Collaboration, *Measurements of properties of the Higgs boson decaying to a W boson pair in pp collisions at $\sqrt{s} = 13$ TeV*, CMS-PAS-HIG-16-042, 2018.

[178] CMS Collaboration, *Inclusive search for a highly boosted Higgs boson decaying to a bottom quark-antiquark pair*, Phys. Rev. Lett. **120** (2018) no. CERN-EP-2017-207, CMS-HIG-17-010, 071802, arXiv:1709.05543 [hep-ex].

[179] CMS Collaboration, *Evidence for associated production of a Higgs boson with a top quark pair in final states with electrons, muons, and hadronically decaying τ leptons at $\sqrt{s} = 13$ TeV*, JHEP **08** (2018) no. CERN-EP-2018-017, CMS-HIG-17-018, 066, arXiv:1803.05485 [hep-ex].

[180] CMS Collaboration, *Search for $t\bar{t}H$ production in the all-jet final state in proton-proton collisions at $\sqrt{s} = 13$ TeV*, JHEP **06** (2018) no. CERN-EP-2018-038, CMS-HIG-17-022, 101, arXiv:1803.06986 [hep-ex].

[181] ATLAS Collaboration, *A search for the rare decay of the Standard Model Higgs boson to dimuons in pp collisions at $\sqrt{s} = 13$ TeV with the ATLAS Detector*, ATLAS-CONF-2018-026, 2018.

[182] CMS Collaboration, *Combined measurements of Higgs boson couplings in proton-proton*

collisions at $\sqrt{s} = 13$ *TeV*, Submitted to: Eur. Phys. J. (2018) no. CERN-EP-2018-263, CMS-HIG-17-031, , arXiv:1809.10733 [hep-ex].

[183] ATLAS Collaboration, *Combined measurements of Higgs boson production and decay using up to 80 fb*$^{-1}$ *of proton–proton collision data at* $\sqrt{s} = 13$ *TeV collected with the ATLAS experiment*, ATLAS-CONF-2018-031, 2018.

[184] A. Valassi, *Combining correlated measurements of several different physical quantities*, Nucl. Instrum. Meth. **A500** (2003) 391–405.

[185] J. de Blas, O. Eberhardt, and C. Krause, *Current and Future Constraints on Higgs Couplings in the Nonlinear Effective Theory*, JHEP **07** (2018) 048, arXiv:1803.00939 [hep-ph].

[186] G. Buchalla, O. Cata, A. Celis, and C. Krause, *Fitting Higgs Data with Nonlinear Effective Theory*, Eur. Phys. J. **C76** (2016) no. 5, 233, arXiv:1511.00988 [hep-ph].

[187] G. Buchalla, O. Cata, A. Celis, and C. Krause, *Note on Anomalous Higgs-Boson Couplings in Effective Field Theory*, Phys. Lett. **B750** (2015) 298–301, arXiv:1504.01707 [hep-ph].

[188] A. Dobado and M. J. Herrero, *Phenomenological Lagrangian Approach to the Symmetry Breaking Sector of the Standard Model*, Phys. Lett. **B228** (1989) 495–502.

[189] A. Dobado and M. J. Herrero, *Testing the Hypothesis of Strongly Interacting Longitudinal Weak Bosons in Electron - Positron Collisions at Tev Energies*, Phys. Lett. **B233** (1989) 505–511.

[190] A. Dobado, D. Espriu, and M. J. Herrero, *Chiral Lagrangians as a tool to probe the symmetry breaking sector of the SM at LEP*, Phys. Lett. **B255** (1991) 405–414.

[191] A. Dobado, M. J. Herrero, and J. Terron, *The Role of Chiral Lagrangians in Strongly Interacting* $W(l)\,W(l)$ *Signals at* pp *Supercolliders*, Z. Phys. **C50** (1991) 205–220.

[192] D. Espriu and M. J. Herrero, *Chiral Lagrangians and precision tests of the symmetry breaking sector of the Standard Model*, Nucl. Phys. **B373** (1992) 117–168.

[193] M. J. Herrero and E. Ruiz Morales, *The Electroweak chiral Lagrangian for the Standard Model with a heavy Higgs*, Nucl. Phys. **B418** (1994) 431–455, arXiv:hep-ph/9308276 [hep-ph].

[194] M. J. Herrero and E. Ruiz Morales, *Nondecoupling effects of the SM higgs boson to one loop*, Nucl. Phys. **B437** (1995) 319–355, arXiv:hep-ph/9411207 [hep-ph].

[195] F. Feruglio, *The Chiral approach to the electroweak interactions*, Int. J. Mod. Phys. **A8** (1993) 4937–4972, arXiv:hep-ph/9301281 [hep-ph].

[196] J. Bagger, V. D. Barger, K.-m. Cheung, J. F. Gunion, T. Han, G. A. Ladinsky, R. Rosenfeld, and C. P. Yuan, *The Strongly interacting W W system: Gold plated modes*, Phys. Rev. **D49** (1994) 1246–1264, arXiv:hep-ph/9306256 [hep-ph].

[197] V. Koulovassilopoulos and R. S. Chivukula, *The Phenomenology of a nonstandard Higgs boson in W(L) W(L) scattering*, Phys. Rev. **D50** (1994) 3218–3234, arXiv:hep-ph/9312317 [hep-ph].

[198] C. P. Burgess, J. Matias, and M. Pospelov, *A Higgs or not a Higgs? What to do if you discover a new scalar particle*, Int. J. Mod. Phys. **A17** (2002) 1841–1918, arXiv:hep-ph/9912459 [hep-ph].

[199] L.-M. Wang and Q. Wang, *Electroweak chiral Lagrangian for neutral Higgs boson*, Chin. Phys. Lett. **25** (2008) 1984, arXiv:hep-ph/0605104 [hep-ph].

[200] B. Grinstein and M. Trott, *A Higgs-Higgs bound state due to new physics at a TeV*, Phys. Rev. **D76** (2007) 073002, arXiv:0704.1505 [hep-ph].

[201] A. Azatov, R. Contino, and J. Galloway, *Model-Independent Bounds on a Light Higgs*, JHEP **04** (2012) 127, arXiv:1202.3415 [hep-ph].

[202] R. Alonso, M. B. Gavela, L. Merlo, S. Rigolin, and J. Yepes, *The Effective Chiral Lagrangian for a Light Dynamical "Higgs Particle"*, Phys. Lett. **B722** (2013) 330–335, arXiv:1212.3305 [hep-ph].

[203] G. Buchalla and O. Cata, *Effective Theory of a Dynamically Broken Electroweak Standard Model at NLO*, JHEP **07** (2012) 101, arXiv:1203.6510 [hep-ph].

[204] G. Buchalla, O. Cata, and C. Krause, *Complete Electroweak Chiral Lagrangian with a Light Higgs at NLO*, Nucl. Phys. **B880** (2014) 552–573, arXiv:1307.5017 [hep-ph].

[205] G. Buchalla, O. Cata, and C. Krause, *On the Power Counting in Effective Field Theories*, Phys. Lett. **B731** (2014) 80–86, arXiv:1312.5624 [hep-ph].

[206] F.-K. Guo, P. Ruiz-Femenía, and J. J. Sanz-Cillero, *One loop renormalization of the electroweak chiral Lagrangian with a light Higgs boson*, Phys. Rev. **D92** (2015) 074005, arXiv:1506.04204 [hep-ph].

[207] G. Buchalla, O. Cata, A. Celis, M. Knecht, and C. Krause, *Complete One-Loop Renormalization of the Higgs-Electroweak Chiral Lagrangian*, Nucl. Phys. **B928** (2018) 93–106, arXiv:1710.06412 [hep-ph].

[208] R. Alonso, K. Kanshin, and S. Saa, *Renormalization group evolution of Higgs effective field theory*, Phys. Rev. **D97** (2018) no. 3, 035010, arXiv:1710.06848 [hep-ph].

[209] G. Buchalla, O. Cata, A. Celis, and C. Krause, *Comment on "Analysis of General Power Counting Rules in Effective Field Theory"*, arXiv:1603.03062 [hep-ph].

[210] R. Gröber, M. Mühlleitner, M. Spira, and J. Streicher, *NLO QCD Corrections to Higgs Pair Production including Dimension-6 Operators*, JHEP **09** (2015) 092, arXiv:1504.06577 [hep-ph].

[211] J. H. Kim, Y. Sakaki, and M. Son, *Combined analysis of double Higgs production via gluon fusion at the HL-LHC in the effective field theory approach*, arXiv:1801.06093 [hep-ph].

[212] G. Buchalla, M. Capozi, A. Celis, G. Heinrich, and L. Scyboz, *Higgs boson pair production in non-linear Effective Field Theory with full m_t-dependence at NLO QCD*, arXiv:1806.05162 [hep-ph].

[213] G. Buchalla, O. Cata, and C. Krause, *A Systematic Approach to the SILH Lagrangian*, Nucl. Phys. **B894** (2015) 602–620, arXiv:1412.6356 [hep-ph].

[214] HEPfit Collaboration, *HEPfit: a Code for the Combination of Indirect and Direct Constraints on High Energy Physics Models*, .

[215] HEPfit Collaboration, http://hepfit.roma1.infn.it.

[216] CDF Collaboration, T. Aaltonen et al., *Combination fo Searches for the Higgs Boson Using the Full CDF Data Set*, Phys. Rev. **D88** (2013) no. 5, 052013, arXiv:1301.6668 [hep-ex].

[217] D0 Collaboration, V. M. Abazov et al., *Combined search for the Higgs boson with the D0 experiment*, Phys. Rev. **D88** (2013) no. 5, 052011, arXiv:1303.0823 [hep-ex].

[218] CMS Collaboration, *Measurement of Higgs boson production and properties in the WW decay channel with leptonic final states*, JHEP **01** (2014) no. CERN-PH-EP-2013-221, CMS-HIG-13-023, 096, arXiv:1312.1129 [hep-ex].

[219] CMS Collaboration, *Search for a Higgs boson decaying into a Z and a photon in pp collisions at $\sqrt{s} = 7$ and 8 TeV*, Phys. Lett. **B726** (2013) no. CERN-PH-EP-2013-113, CMS-HIG-13-006, 587–609, arXiv:1307.5515 [hep-ex].

[220] CMS Collaboration, *Search for the standard model Higgs boson produced in association with a W or a Z boson and decaying to bottom quarks*, Phys. Rev. **D89** (2014) no. CERN-PH-EP-2013-188, CMS-HIG-13-012, 012003, arXiv:1310.3687 [hep-ex].

[221] ATLAS Collaboration, G. Aad et al., *Measurement of Higgs boson production in the diphoton decay channel in pp collisions at center-of-mass energies of 7 and 8 TeV with the ATLAS detector*, Phys. Rev. **D90** (2014) no. 11, 112015, arXiv:1408.7084 [hep-ex].

[222] ATLAS Collaboration, G. Aad et al., *Measurements of Higgs boson production and couplings in the four-lepton channel in pp collisions at center-of-mass energies of 7 and 8 TeV with the*

ATLAS detector, Phys. Rev. **D91** (2015) no. 1, 012006, arXiv:1408.5191 [hep-ex].

[223] ATLAS Collaboration, G. Aad et al., *Search for the $b\bar{b}$ decay of the Standard Model Higgs boson in associated $(W/Z)H$ production with the ATLAS detector*, JHEP **01** (2015) 069, arXiv:1409.6212 [hep-ex].

[224] ATLAS Collaboration, G. Aad et al., *Observation and measurement of Higgs boson decays to WW^* with the ATLAS detector*, Phys. Rev. **D92** (2015) no. 1, 012006, arXiv:1412.2641 [hep-ex].

[225] CMS Collaboration, *Evidence for the 125 GeV Higgs boson decaying to a pair of τ leptons*, JHEP **05** (2014) no. CERN-PH-EP-2014-001, CMS-HIG-13-004, 104, arXiv:1401.5041 [hep-ex].

[226] CMS Collaboration, *Observation of the diphoton decay of the Higgs boson and measurement of its properties*, Eur. Phys. J. **C74** (2014) no. CERN-PH-EP-2014-117, CMS-HIG-13-001, 3076, arXiv:1407.0558 [hep-ex].

[227] CMS Collaboration, *Precise determination of the mass of the Higgs boson and tests of compatibility of its couplings with the standard model predictions using proton collisions at 7 and 8 TeV*, Eur. Phys. J. **C75** (2015) no. CERN-PH-EP-2014-288, CMS-HIG-14-009, 212, arXiv:1412.8662 [hep-ex].

[228] CMS Collaboration, *Search for the associated production of the Higgs boson with a top-quark pair*, JHEP **09** (2014) no. CERN-PH-EP-2014-189, CMS-HIG-13-029, 087, arXiv:1408.1682 [hep-ex].

[229] ATLAS Collaboration, G. Aad et al., *Measurements of the Higgs boson production and decay rates and coupling strengths using pp collision data at $\sqrt{s} = 7$ and 8 TeV in the ATLAS experiment*, Eur. Phys. J. **C76** (2016) no. 1, 6, arXiv:1507.04548 [hep-ex].

[230] ATLAS Collaboration, G. Aad et al., *Search for the Standard Model Higgs boson produced in association with top quarks and decaying into $b\bar{b}$ in pp collisions at $\sqrt{s}$ = 8 TeV with the ATLAS detector*, Eur. Phys. J. **C75** (2015) no. 7, 349, arXiv:1503.05066 [hep-ex].

[231] ATLAS Collaboration, G. Aad et al., *Study of (W/Z)H production and Higgs boson couplings using $H \to WW^*$ decays with the ATLAS detector*, JHEP **08** (2015) 137, arXiv:1506.06641 [hep-ex].

[232] ATLAS Collaboration, G. Aad et al., *Evidence for the Higgs-boson Yukawa coupling to tau leptons with the ATLAS detector*, JHEP **04** (2015) 117, arXiv:1501.04943 [hep-ex].

[233] ATLAS Collaboration, *Measurements of the Higgs boson production cross section via Vector Boson Fusion and associated WH production in the $WW^* \to \ell\nu\ell\nu$ decay mode with the ATLAS detector at $\sqrt{s}$ = 13 TeV*, ATLAS-CONF-2016-112, 2016.

[234] CMS Collaboration, *VBF H to bb using the 2015 data sample*, CMS-PAS-HIG-16-003, 2016.

[235] ATLAS Collaboration, M. Aaboud et al., *Measurement of the Higgs boson coupling properties in the $H \to ZZ^* \to 4\ell$ decay channel at $\sqrt{s}$ = 13 TeV with the ATLAS detector*, JHEP **03** (2018) 095, arXiv:1712.02304 [hep-ex].

[236] ATLAS Collaboration, M. Aaboud et al., *Evidence for the $H \to b\bar{b}$ decay with the ATLAS detector*, JHEP **12** (2017) 024, arXiv:1708.03299 [hep-ex].

[237] CMS Collaboration, *Measurements of properties of the Higgs boson in the diphoton decay channel with the full 2016 data set*, CMS-PAS-HIG-16-040, 2017.

[238] CMS Collaboration, *Search for the standard model Higgs boson in the dilepton plus photon channel in* pp *collisions at* $\sqrt{s} = 13$ TeV, CMS-PAS-HIG-17-007, 2018.

[239] ATLAS Collaboration, *Measurement of gluon fusion and vector boson fusion Higgs boson production cross-sections in the $H \to WW^* \to e\nu\mu\nu$ decay channel in pp collisions at $\sqrt{s} = 13$ TeV with the ATLAS detector*, ATLAS-CONF-2018-004, 2018.

[240] D. B. Kaplan and H. Georgi, *SU(2) x U(1) Breaking by Vacuum Misalignment*, Phys. Lett. **136B** (1984) 183–186.

[241] D. B. Kaplan, H. Georgi, and S. Dimopoulos, *Composite Higgs Scalars*, Phys. Lett. **136B** (1984) 187–190.

[242] W. D. Goldberger, B. Grinstein, and W. Skiba, *Distinguishing the Higgs boson from the dilaton at the Large Hadron Collider*, Phys. Rev. Lett. **100** (2008) 111802, arXiv:0708.1463 [hep-ph].

[243] R. Contino, M. Ghezzi, C. Grojean, M. Muhlleitner, and M. Spira, *Effective Lagrangian for a light Higgs-like scalar*, JHEP **07** (2013) 035, arXiv:1303.3876 [hep-ph].

[244] Gfitter Group Collaboration, M. Baak, J. Cúth, J. Haller, A. Hoecker, R. Kogler, K. Mönig, M. Schott, and J. Stelzer, *The global electroweak fit at NNLO and prospects for the LHC and ILC*, Eur. Phys. J. **C74** (2014) 3046, arXiv:1407.3792 [hep-ph].

[245] S. Boselli, C. M. Carloni Calame, G. Montagna, O. Nicrosini, F. Piccinini, and A. Shivaji, *Higgs decay into four charged leptons in the presence of dimension-six operators*, JHEP **01** (2018) 096, arXiv:1703.06667 [hep-ph].

[246] C. Degrande, C. Duhr, B. Fuks, D. Grellscheid, O. Mattelaer, and T. Reiter, *UFO - The Universal FeynRules Output*, Comput. Phys. Commun. **183** (2012) 1201–1214, arXiv:1108.2040 [hep-ph].

[247] A. Alloul, N. D. Christensen, C. Degrande, C. Duhr, and B. Fuks, *FeynRules 2.0 - A complete toolbox for tree-level phenomenology*, Comput. Phys. Commun. **185** (2014) 2250–2300, arXiv:1310.1921 [hep-ph].

[248] A. Soni and R. M. Xu, *Probing CP violation via Higgs decays to four leptons*, Phys. Rev. **D48** (1993) 5259–5263, arXiv:hep-ph/9301225 [hep-ph].

[249] D. Chang, W.-Y. Keung, and I. Phillips, *CP odd correlation in the decay of neutral Higgs boson into Z Z, W+ W-, or t anti-t*, Phys. Rev. **D48** (1993) 3225–3234, arXiv:hep-ph/9303226 [hep-ph].

[250] A. Skjold and P. Osland, *Angular and energy correlations in Higgs decay*, Phys. Lett. **B311** (1993) 261–265, arXiv:hep-ph/9303294 [hep-ph].

[251] ATLAS Collaboration, *Prospective analysis of spin- and CP-sensitive variables in H —> Z Z —> l(1)+ l(1)- l(2)+ l(2)- at the LHC*, Eur. Phys. J. **C32** (2004) no. FREIBURG-THEP-02-16, SN-ATLAS-2003-025, 209–219, arXiv:hep-ph/0212396 [hep-ph].

[252] G. R. Bower, T. Pierzchala, Z. Was, and M. Worek, *Measuring the Higgs boson's parity using tau —> rho nu*, Phys. Lett. **B543** (2002) 227–234, arXiv:hep-ph/0204292 [hep-ph].

[253] K. Desch, Z. Was, and M. Worek, *Measuring the Higgs boson parity at a linear collider using the tau impact parameter and tau —> rho nu decay*, Eur. Phys. J. **C29** (2003) 491–496, arXiv:hep-ph/0302046 [hep-ph].

[254] K. Desch, A. Imhof, Z. Was, and M. Worek, *Probing the CP nature of the Higgs boson at linear colliders with tau spin correlations: The Case of mixed scalar - pseudoscalar couplings*, Phys. Lett. **B579** (2004) 157–164, arXiv:hep-ph/0307331 [hep-ph].

[255] R. Harnik, A. Martin, T. Okui, R. Primulando, and F. Yu, *Measuring CP violation in $h \to \tau^+\tau^-$ at colliders*, Phys. Rev. **D88** (2013) no. 7, 076009, arXiv:1308.1094 [hep-ph].

[256] A. Askew, P. Jaiswal, T. Okui, H. B. Prosper, and N. Sato, *Prospect for measuring the CP phase in the $h\tau\tau$ coupling at the LHC*, Phys. Rev. **D91** (2015) no. 7, 075014, arXiv:1501.03156 [hep-ph].

[257] R. Józefowicz, E. Richter-Was, and Z. Was, *Potential for optimizing the Higgs boson CP measurement in $H \to \tau\tau$ decays at the LHC including machine learning techniques*, Phys. Rev. **D94** (2016) no. 9, 093001, arXiv:1608.02609 [hep-ph].

[258] S. Berge, W. Bernreuther, and J. Ziethe, *Determining the CP parity of Higgs bosons at the LHC in their tau decay channels*, Phys. Rev. Lett. **100** (2008) 171605, arXiv:0801.2297 [hep-ph].

[259] S. Berge and W. Bernreuther, *Determining the CP parity of Higgs bosons at the LHC in the tau to 1-prong decay channels*, Phys. Lett. **B671** (2009) 470–476, arXiv:0812.1910 [hep-ph].

[260] S. Berge, W. Bernreuther, B. Niepelt, and H. Spiesberger, *How to pin down the CP quantum numbers of a Higgs boson in its tau decays at the LHC*, Phys. Rev. **D84** (2011) 116003, arXiv:1108.0670 [hep-ph].

[261] CMS Collaboration, *Study of the Mass and Spin-Parity of the Higgs Boson Candidate Via Its Decays to Z Boson Pairs*, Phys. Rev. Lett. **110** (2013) no. CERN-PH-EP-2012-372, CMS-HIG-12-041, 081803, arXiv:1212.6639 [hep-ex].

[262] ATLAS Collaboration, G. Aad et al., *Evidence for the spin-0 nature of the Higgs boson using ATLAS data*, Phys. Lett. **B726** (2013) 120–144, arXiv:1307.1432 [hep-ex].

[263] J. Brod, U. Haisch, and J. Zupan, *Constraints on CP-violating Higgs couplings to the third generation*, JHEP **11** (2013) 180, arXiv:1310.1385 [hep-ph].

[264] M. R. Buckley and D. Goncalves, *Boosting the Direct CP Measurement of the Higgs-Top Coupling*, Phys. Rev. Lett. **116** (2016) no. 9, 091801, arXiv:1507.07926 [hep-ph].

[265] F. Boudjema, R. M. Godbole, D. Guadagnoli, and K. A. Mohan, *Lab-frame observables for probing the top-Higgs interaction*, Phys. Rev. **D92** (2015) no. 1, 015019, arXiv:1501.03157 [hep-ph].

[266] G. Mahlon and S. J. Parke, *Angular correlations in top quark pair production and decay at hadron colliders*, Phys. Rev. **D53** (1996) 4886–4896, arXiv:hep-ph/9512264 [hep-ph].

[267] *Prospects for measurements of tensor structure of the HZZ vertex in $H \to ZZ^* \to 4l$ decay with ATLAS detector*, ATL-PHYS-PUB-2013-013, 2013.

[268] Y. Gao, A. V. Gritsan, Z. Guo, K. Melnikov, M. Schulze, and N. V. Tran, *Spin determination of single-produced resonances at hadron colliders*, Phys. Rev. **D81** (2010) 075022, arXiv:1001.3396 [hep-ph].

[269] CMS Collaboration, *Constraints on the spin-parity and anomalous HVV couplings of the Higgs boson in proton collisions at 7 and 8 TeV*, Phys. Rev. **D92** (2015) no. CERN-PH-EP-2014-265, CMS-HIG-14-018, 012004, arXiv:1411.3441 [hep-ex].

[270] CMS Collaboration, *Limits on the Higgs boson lifetime and width from its decay to four charged leptons*, Phys. Rev. **D92** (2015) no. CERN-PH-EP-2015-159, CMS-HIG-14-036, 072010, arXiv:1507.06656 [hep-ex].

[271] CMS Collaboration, *Measurements of Higgs boson properties from on-shell and off-shell production in the four-lepton final state*, CMS-PAS-HIG-18-002, 2018.

[272] S. Dawson, S. Dittmaier, and M. Spira, *Neutral Higgs boson pair production at hadron colliders: QCD corrections*, Phys. Rev. **D58** (1998) 115012, arXiv:hep-ph/9805244 [hep-ph].

[273] D. de Florian and J. Mazzitelli, *Higgs Boson Pair Production at Next-to-Next-to-Leading Order in QCD*, Phys. Rev. Lett. **111** (2013) 201801, arXiv:1309.6594 [hep-ph].

[274] S. Borowka, N. Greiner, G. Heinrich, S. P. Jones, M. Kerner, J. Schlenk, U. Schubert, and T. Zirke, *Higgs Boson Pair Production in Gluon Fusion at Next-to-Leading Order with Full Top-Quark Mass Dependence*, Phys. Rev. Lett. **117** (2016) no. 1, 012001, arXiv:1604.06447 [hep-ph].

[275] J. Baglio, F. Campanario, S. Glaus, M. Mühlleitner, M. Spira, and J. Streicher, *Gluon fusion into Higgs pairs at NLO QCD and the top mass scheme*, arXiv:1811.05692 [hep-ph].

[276] M. Grazzini, G. Heinrich, S. Jones, S. Kallweit, M. Kerner, J. M. Lindert, and J. Mazzitelli,

Higgs boson pair production at NNLO with top quark mass effects, JHEP **05** (2018) 059, arXiv:1803.02463 [hep-ph].

[277] D. De Florian and J. Mazzitelli, *Soft gluon resummation for Higgs boson pair production including finite M_t effects*, JHEP **08** (2018) 156, arXiv:1807.03704 [hep-ph].

[278] R. Frederix, S. Frixione, V. Hirschi, F. Maltoni, O. Mattelaer, P. Torrielli, E. Vryonidou, and M. Zaro, *Higgs pair production at the LHC with NLO and parton-shower effects*, Phys. Lett. **B732** (2014) 142–149, arXiv:1401.7340 [hep-ph].

[279] G. Heinrich, S. P. Jones, M. Kerner, G. Luisoni, and E. Vryonidou, *NLO predictions for Higgs boson pair production with full top quark mass dependence matched to parton showers*, JHEP **08** (2017) 088, arXiv:1703.09252 [hep-ph].

[280] NNPDF Collaboration, R. D. Ball et al., *Parton distributions for the LHC Run II*, JHEP **04** (2015) 040, arXiv:1410.8849 [hep-ph].

[281] A. Carvalho, M. Dall'Osso, T. Dorigo, F. Goertz, C. A. Gottardo, and M. Tosi, *Higgs Pair Production: Choosing Benchmarks With Cluster Analysis*, JHEP **04** (2016) 126, arXiv:1507.02245 [hep-ph].

[282] A. Carvalho, M. Dall'Osso, P. De Castro Manzano, T. Dorigo, F. Goertz, M. Gouzevich, and M. Tosi, *Analytical parametrization and shape classification of anomalous HH production in the EFT approach*, arXiv:1608.06578 [hep-ph].

[283] CMS Collaboration, *Combination of searches for Higgs boson pair production in proton-proton collisions at $\sqrt{s} = 13$ TeV*, Submitted to: Phys. Rev. Lett. (2018) no. CERN-EP-2018-292, CMS-HIG-17-030, , arXiv:1811.09689 [hep-ex].

[284] ATLAS Collaboration, *Combination of searches for Higgs boson pairs in pp collisions at 13 TeV with the ATLAS experiment.*, ATLAS-CONF-2018-043, 2018.

[285] A. Azatov, R. Contino, G. Panico, and M. Son, *Effective field theory analysis of double Higgs boson production via gluon fusion*, Phys. Rev. **D92** (2015) no. 3, 035001, arXiv:1502.00539 [hep-ph].

[286] D. de Florian, I. Fabre, and J. Mazzitelli, *Higgs boson pair production at NNLO in QCD including dimension 6 operators*, JHEP **10** (2017) 215, arXiv:1704.05700 [hep-ph].

[287] ATLAS Collaboration, *Measurement prospects of the pair production and self-coupling of the Higgs boson with the ATLAS experiment at the HL-LHC*, ATL-PHYS-PUB-2018-053, 2018.

[288] ATLAS Collaboration, *A search for resonant and non-resonant Higgs boson pair production in the $b\bar{b}\tau^+\tau^-$ decay channel in pp collisions at $\sqrt{s} = 13$ TeV with the ATLAS detector*, Phys. Rev. Lett. **121** (2018) no. 19, 191801, arXiv:1808.00336 [hep-ex].

[289] ATLAS Collaboration, *A morphing technique for signal modelling in a multidimensional space of coupling parameters*, ATL-PHYS-PUB-2015-047, 2015.

[290] CMS Collaboration, *Prospects for HH measurements at the HL-LHC*, CMS-PAS-FTR-18-019, 2018.

[291] M. Dasgupta, A. Fregoso, S. Marzani, and G. P. Salam, *Towards an understanding of jet substructure*, JHEP **09** (2013) 029, arXiv:1307.0007 [hep-ph].

[292] A. J. Larkoski, S. Marzani, G. Soyez, and J. Thaler, *Soft Drop*, JHEP **05** (2014) 146, arXiv:1402.2657 [hep-ph].

[293] J. Thaler and K. Van Tilburg, *Maximizing boosted top identification by minimizing N-subjettiness*, JHEP **02** (2012) 093, arXiv:1108.2701 [hep-ph].

[294] CMS Collaboration, *Higgs pair production at the High Luminosity LHC*, CMS-PAS-FTR-15-002, 2015.

[295] CMS Collaboration, *Projected performance of Higgs analyses at the HL-LHC for ECFA 2016*, CMS-PAS-FTR-16-002, 2017.

[296] A. Adhikary, S. Banerjee, R. K. Barman, B. Bhattacherjee, and S. Niyogi, *Revisiting the non-resonant Higgs pair production at the HL-LHC*, Physics **2018** (2018) 116, arXiv:1712.05346 [hep-ph].

[297] J. H. Kim, K. Kong, K. T. Matchev, and M. Park, *Measuring the Triple Higgs Self-Interaction at the Large Hadron Collider*, arXiv:1807.11498 [hep-ph].

[298] C. G. Lester and D. J. Summers, *Measuring masses of semiinvisibly decaying particles pair produced at hadron colliders*, Phys. Lett. **B463** (1999) 99–103, arXiv:hep-ph/9906349 [hep-ph].

[299] M. Burns, K. Kong, K. T. Matchev, and M. Park, *Using Subsystem MT2 for Complete Mass Determinations in Decay Chains with Missing Energy at Hadron Colliders*, JHEP **03** (2009) 143, arXiv:0810.5576 [hep-ph].

[300] A. J. Barr, T. J. Khoo, P. Konar, K. Kong, C. G. Lester, K. T. Matchev, and M. Park, *Guide to transverse projections and mass-constraining variables*, Phys. Rev. **D84** (2011) 095031, arXiv:1105.2977 [hep-ph].

[301] P. Konar, K. Kong, and K. T. Matchev, $\sqrt{\hat{s}}\_min$ *: A Global inclusive variable for determining the mass scale of new physics in events with missing energy at hadron colliders*, JHEP **03** (2009) 085, arXiv:0812.1042 [hep-ph].

[302] P. Konar, K. Kong, K. T. Matchev, and M. Park, *RECO level* $\sqrt{s}\_min$ *and subsystem* $\sqrt{s}\_min$*: Improved global inclusive variables for measuring the new physics mass scale in* $\not{E}\_T$ *events at hadron colliders*, JHEP **06** (2011) 041, arXiv:1006.0653 [hep-ph].

[303] M. L. Graesser and J. Shelton, *Hunting Mixed Top Squark Decays*, Phys. Rev. Lett. **111** (2013) no. 12, 121802, arXiv:1212.4495 [hep-ph].

[304] W. S. Cho, D. Kim, K. T. Matchev, and M. Park, *Probing Resonance Decays to Two Visible and Multiple Invisible Particles*, Phys. Rev. Lett. **112** (2014) no. 21, 211801, arXiv:1206.1546 [hep-ph].

[305] D. Debnath, D. Kim, J. H. Kim, K. Kong, and K. T. Matchev, *Resolving Combinatorial Ambiguities in Dilepton* $t\bar{t}$ *Event Topologies with Constrained* M_2 *Variables*, Phys. Rev. **D96** (2017) no. 7, 076005, arXiv:1706.04995 [hep-ph].

[306] P. Konar, K. Kong, K. T. Matchev, and M. Park, *Superpartner Mass Measurement Technique using 1D Orthogonal Decompositions of the Cambridge Transverse Mass Variable* M_T2, Phys. Rev. Lett. **105** (2010) 051802, arXiv:0910.3679 [hep-ph].

[307] P. Konar, K. Kong, K. T. Matchev, and M. Park, *Dark Matter Particle Spectroscopy at the LHC: Generalizing M(T2) to Asymmetric Event Topologies*, JHEP **04** (2010) 086, arXiv:0911.4126 [hep-ph].

[308] W. S. Cho, K. Choi, Y. G. Kim, and C. B. Park, *Gluino Stransverse Mass*, Phys. Rev. Lett. **100** (2008) 171801, arXiv:0709.0288 [hep-ph].

[309] CMS Collaboration, *Identification of heavy-flavour jets with the CMS detector in pp collisions at 13 TeV*, JINST **13** (2018) no. CERN-EP-2017-326, CMS-BTV-16-002, P05011, arXiv:1712.07158 [physics.ins-det].

[310] ATLAS Collaboration, *Projected sensitivity to non-resonant Higgs boson pair production in the* $b\bar{b}b\bar{b}$ *final state using proton-proton collisions at HL-LHC with the ATLAS detector*, ATL-PHYS-PUB-2016-024, 2016.

[311] F. Kling, T. Plehn, and P. Schichtel, *Maximizing the significance in Higgs boson pair analyses*, Phys. Rev. **D95** (2017) no. 3, 035026, arXiv:1607.07441 [hep-ph].

[312] ATLAS Collaboration, *Study of the double Higgs production channel* $H(\to b\bar{b})H(\to \gamma\gamma)$ *with the ATLAS experiment at the HL-LHC*, ATL-PHYS-PUB-2017-001, 2017.

[313] A. Mitov, *Top pair production at a future 27 TeV HE-LHC*, HE/HL-LHC Workshop, CERN.

[314] F. Demartin, F. Maltoni, K. Mawatari, B. Page, and M. Zaro, *Higgs characterisation at NLO in QCD: CP properties of the top-quark Yukawa interaction*, Eur. Phys. J. **C74** (2014) no. 9, 3065, arXiv:1407.5089 [hep-ph].

[315] D. Gonalves, T. Han, F. Kling, T. Plehn, and M. Takeuchi, *Higgs boson pair production at future hadron colliders: From kinematics to dynamics*, Phys. Rev. **D97** (2018) no. 11, 113004, arXiv:1802.04319 [hep-ph].

[316] A. Alves, T. Ghosh, and K. Sinha, *Can We Discover Double Higgs Production at the LHC?*, Phys. Rev. **D96** (2017) no. 3, 035022, arXiv:1704.07395 [hep-ph].

[317] J. Alwall, M. Herquet, F. Maltoni, O. Mattelaer, and T. Stelzer, *MadGraph 5 : Going Beyond*, JHEP **06** (2011) 128, arXiv:1106.0522 [hep-ph].

[318] D. de Florian and J. Mazzitelli, *Two-loop virtual corrections to Higgs pair production*, Phys. Lett. **B724** (2013) 306–309, arXiv:1305.5206 [hep-ph].

[319] T. Sjostrand, S. Ask, J. R. Christiansen, R. Corke, N. Desai, P. Ilten, S. Mrenna, S. Prestel, C. O. Rasmussen, and P. Z. Skands, *An Introduction to PYTHIA 8.2*, Comput. Phys. Commun. **191** (2015) 159–177, arXiv:1410.3012 [hep-ph].

[320] S. Bergstra, R. Bardenet, Y. Bengio, and B. Kégl, *Algorithms for hyper-parameter optimization.*, Advances in Neural Information Processing Systems (2011) 2546.

[321] S. Bergstra, D. Yamins, and D. Cox, *Hyperopt: A Python Library for Optimizing the Hyperparameters of Machine Learning Algorithms.*, Proceedings of the 12th PYTHON in Science Conference, SciPy 2013 (2013) .

[322] *Hyperopt: Distributed Asynchronous Hyper-parameter Optimization*, https://github.com/hyperopt/hyperopt.

[323] ATLAS Collaboration, *Search For Higgs Boson Pair Production in the $\gamma\gamma b\bar{b}$ Final State using pp Collision Data at $\sqrt{s} = 8$ TeV from the ATLAS Detector*, Phys. Rev. Lett. **114** (2015) no. 8, 081802, arXiv:1406.5053 [hep-ex].

[324] O. J. P. Eboli, G. C. Marques, S. F. Novaes, and A. A. Natale, *TWIN HIGGS BOSON PRODUCTION*, Phys. Lett. **B197** (1987) 269–272.

[325] D. A. Dicus, C. Kao, and S. S. D. Willenbrock, *Higgs Boson Pair Production From Gluon Fusion*, Phys. Lett. **B203** (1988) 457–461.

[326] E. W. N. Glover and J. J. Van der Bij, *Higgs boson pair production via gluon fusion*, Nucl. Phys. B **309** (1987) 282–294. 20 p.

[327] T. Plehn, M. Spira, and P. M. Zerwas, *Pair production of neutral Higgs particles in gluon-gluon collisions*, Nucl. Phys. **B479** (1996) 46–64, arXiv:hep-ph/9603205 [hep-ph].

[328] A. Djouadi, W. Kilian, M. Muhlleitner, and P. M. Zerwas, *Production of neutral Higgs boson pairs at LHC*, Eur. Phys. J. **C10** (1999) 45–49, arXiv:hep-ph/9904287 [hep-ph].

[329] X. Li and M. B. Voloshin, *Remarks on double Higgs boson production by gluon fusion at threshold*, Phys. Rev. **D89** (2014) no. 1, 013012, arXiv:1311.5156 [hep-ph].

[330] ATLAS Collaboration, *Search for Higgs boson pair production in the $b\bar{b}\gamma\gamma$ final state using pp collision data at $\sqrt{s} = 13$ TeV with the ATLAS detector*, ATLAS-CONF-2016-004, 2016.

[331] ATLAS Collaboration, G. Aad et al., *Searches for Higgs boson pair production in the $hh \to bb\tau\tau, \gamma\gamma WW^*, \gamma\gamma bb, bbbb$ channels with the ATLAS detector*, Phys. Rev. **D92** (2015) 092004, arXiv:1509.04670 [hep-ex].

[332] A. Kobakhidze, L. Wu, and J. Yue, *Electroweak Baryogenesis with Anomalous Higgs Couplings*, JHEP **04** (2016) 011, arXiv:1512.08922 [hep-ph].

[333] C.-Y. Chen, J. Kozaczuk, and I. M. Lewis, *Non-resonant Collider Signatures of a Singlet-Driven Electroweak Phase Transition*, JHEP **08** (2017) 096, arXiv:1704.05844 [hep-ph].

[334] X. Gan, A. J. Long, and L.-T. Wang, *Electroweak sphaleron with dimension-six operators*,

Phys. Rev. **D96** (2017) no. 11, 115018, arXiv:1708.03061 [hep-ph].

[335] Q.-H. Cao, F. P. Huang, K.-P. Xie, and X. Zhang, *Testing the electroweak phase transition in scalar extension models at lepton colliders*, Chin. Phys. **C42** (2018) no. 2, 023103, arXiv:1708.04737 [hep-ph].

[336] B. Jain, S. J. Lee, and M. Son, *Validity of the effective potential and the precision of Higgs field self-couplings*, Phys. Rev. **D98** (2018) no. 7, 075002, arXiv:1709.03232 [hep-ph].

[337] J. de Vries, M. Postma, J. van de Vis, and G. White, *Electroweak Baryogenesis and the Standard Model Effective Field Theory*, JHEP **01** (2018) 089, arXiv:1710.04061 [hep-ph].

[338] M. Reichert, A. Eichhorn, H. Gies, J. M. Pawlowski, T. Plehn, and M. M. Scherer, *Probing baryogenesis through the Higgs boson self-coupling*, Phys. Rev. **D97** (2018) no. 7, 075008, arXiv:1711.00019 [hep-ph].

[339] M. Carena, Z. Liu, and M. Riembau, *Probing the electroweak phase transition via enhanced di-Higgs boson production*, Phys. Rev. **D97** (2018) no. 9, 095032, arXiv:1801.00794 [hep-ph].

[340] V. Barger, L. L. Everett, C. B. Jackson, A. D. Peterson, and G. Shaughnessy, *Measuring the two-Higgs doublet model scalar potential at LHC14*, Phys. Rev. **D90** (2014) no. 9, 095006, arXiv:1408.2525 [hep-ph].

[341] M. Bauer, M. Carena, and A. Carmona, *Higgs Pair Production as a Signal of Enhanced Yukawa Couplings*, Phys. Rev. Lett. **121** (2018) no. 2, 021801, arXiv:1801.00363 [hep-ph].

[342] U. Baur, T. Plehn, and D. L. Rainwater, *Measuring the Higgs boson self coupling at the LHC and finite top mass matrix elements*, Phys. Rev. Lett. **89** (2002) 151801, arXiv:hep-ph/0206024 [hep-ph].

[343] U. Baur, T. Plehn, and D. L. Rainwater, *Determining the Higgs Boson Selfcoupling at Hadron Colliders*, Phys. Rev. **D67** (2003) 033003, arXiv:hep-ph/0211224 [hep-ph].

[344] Q. Li, Z. Li, Q.-S. Yan, and X. Zhao, *Probe Higgs boson pair production via the 32j+ $\not{E}$ mode*, Phys. Rev. **D92** (2015) no. 1, 014015, arXiv:1503.07611 [hep-ph].

[345] M. A. Shifman, A. I. Vainshtein, M. B. Voloshin, and V. I. Zakharov, *Low-Energy Theorems for Higgs Boson Couplings to Photons*, Sov. J. Nucl. Phys. **30** (1979) 711–716.

[346] B. A. Kniehl and M. Spira, *Low-energy theorems in Higgs physics*, Z. Phys. **C69** (1995) 77–88, arXiv:hep-ph/9505225 [hep-ph].

[347] M. Spira, *Effective Multi-Higgs Couplings to Gluons*, JHEP **10** (2016) 026, arXiv:1607.05548 [hep-ph].

[348] M. J. Dolan, C. Englert, and M. Spannowsky, *Higgs self-coupling measurements at the LHC*, JHEP **10** (2012) 112, arXiv:1206.5001 [hep-ph].

[349] A. J. Barr, M. J. Dolan, C. Englert, and M. Spannowsky, *Di-Higgs final states augMT2ed – selecting hh events at the high luminosity LHC*, Phys. Lett. **B728** (2014) 308–313, arXiv:1309.6318 [hep-ph].

[350] K. Cranmer and T. Plehn, *Maximum significance at the LHC and Higgs decays to muons*, Eur. Phys. J. **C51** (2007) 415–420, arXiv:hep-ph/0605268 [hep-ph].

[351] T. Plehn, P. Schichtel, and D. Wiegand, *Where boosted significances come from*, Phys. Rev. **D89** (2014) no. 5, 054002, arXiv:1311.2591 [hep-ph].

[352] M. Mangano, *The so-called MLM prescription for ME/PS matching*, .

[353] U. Baur, T. Plehn, and D. L. Rainwater, *Probing the Higgs selfcoupling at hadron colliders using rare decays*, Phys. Rev. **D69** (2004) 053004, arXiv:hep-ph/0310056 [hep-ph].

[354] ATLAS Collaboration, *Expected performance for an upgraded ATLAS detector at High-Luminosity LHC*, ATL-PHYS-PUB-2016-026, 2016.

[355] A. L. Read, *Presentation of search results: The CL(s) technique*, J. Phys. **G28** (2002)

2693–2704.

[356] CMS Collaboration, *First results on Higgs to gammagamma at 13 TeV*, CMS-PAS-HIG-15-005, 2016.

[357] ATLAS Collaboration, *Prospects for measuring Higgs pair production in the channel $H(\to \gamma\gamma)H(\to b\bar{b})$ using the ATLAS detector at the HL-LHC*, ATL-PHYS-PUB-2014-019, 2014.

[358] R. Contino et al., *Physics at a 100 TeV pp collider: Higgs and EW symmetry breaking studies*, CERN Yellow Report (2017) no. 3, 255–440, arXiv:1606.09408 [hep-ph].

[359] S. Homiller and P. Meade, *Measurement of the Triple Higgs Coupling at a HE-LHC*, arXiv:1811.02572 [hep-ph].

[360] V. Hirschi and O. Mattelaer, *Automated event generation for loop-induced processes*, JHEP **10** (2015) 146, arXiv:1507.00020 [hep-ph].

[361] P. Artoisenet, R. Frederix, O. Mattelaer, and R. Rietkerk, *Automatic spin-entangled decays of heavy resonances in Monte Carlo simulations*, JHEP **03** (2013) 015, arXiv:1212.3460 [hep-ph].

[362] M. L. Mangano, M. Moretti, F. Piccinini, and M. Treccani, *Matching matrix elements and shower evolution for top-quark production in hadronic collisions*, JHEP **01** (2007) 013, arXiv:hep-ph/0611129 [hep-ph].

[363] J. Alwall et al., *Comparative study of various algorithms for the merging of parton showers and matrix elements in hadronic collisions*, Eur. Phys. J. **C53** (2008) 473–500, arXiv:0706.2569 [hep-ph].

[364] M. McCullough, *An Indirect Model-Dependent Probe of the Higgs Self-Coupling*, Phys. Rev. **D90** (2014) no. 1, 015001, arXiv:1312.3322 [hep-ph].

[365] M. Gorbahn and U. Haisch, *Indirect probes of the trilinear Higgs coupling: $gg \to h$ and $h \to \gamma\gamma$*, arXiv:1607.03773 [hep-ph].

[366] G. Degrassi, P. P. Giardino, F. Maltoni, and D. Pagani, *Probing the Higgs self coupling via single Higgs production at the LHC*, JHEP **12** (2016) 080, arXiv:1607.04251 [hep-ph].

[367] W. Bizon, M. Gorbahn, U. Haisch, and G. Zanderighi, *Constraints on the trilinear Higgs coupling from vector boson fusion and associated Higgs production at the LHC*, JHEP **07** (2017) 083, arXiv:1610.05771 [hep-ph].

[368] S. Di Vita, C. Grojean, G. Panico, M. Riembau, and T. Vantalon, *A global view on the Higgs self-coupling*, JHEP **09** (2017) 069, arXiv:1704.01953 [hep-ph].

[369] T. Barklow, K. Fujii, S. Jung, M. E. Peskin, and J. Tian, *Model-Independent Determination of the Triple Higgs Coupling at e+e- Colliders*, Phys. Rev. **D97** (2018) no. 5, 053004, arXiv:1708.09079 [hep-ph].

[370] F. Maltoni, D. Pagani, A. Shivaji, and X. Zhao, *Trilinear Higgs coupling determination via single-Higgs differential measurements at the LHC*, Eur. Phys. J. **C77** (2017) no. 12, 887, arXiv:1709.08649 [hep-ph].

[371] S. Di Vita, G. Durieux, C. Grojean, J. Gu, Z. Liu, G. Panico, M. Riembau, and T. Vantalon, *A global view on the Higgs self-coupling at lepton colliders*, JHEP **02** (2018) 178, arXiv:1711.03978 [hep-ph].

[372] F. Maltoni, D. Pagani, and X. Zhao, *Constraining the Higgs self-couplings at e^+e^- colliders*, JHEP **07** (2018) 087, arXiv:1802.07616 [hep-ph].

[373] G. Degrassi, M. Fedele, and P. P. Giardino, *Constraints on the trilinear Higgs self coupling from precision observables*, JHEP **04** (2017) 155, arXiv:1702.01737 [hep-ph].

[374] G. D. Kribs, A. Maier, H. Rzehak, M. Spannowsky, and P. Waite, *Electroweak oblique parameters as a probe of the trilinear Higgs boson self-interaction*, Phys. Rev. **D95** (2017)

no. 9, 093004, arXiv:1702.07678 [hep-ph].

[375] L. Di Luzio, R. Gröber, and M. Spannowsky, *Maxi-sizing the trilinear Higgs self-coupling: how large could it be?*, Eur. Phys. J. **C77** (2017) no. 11, 788, arXiv:1704.02311 [hep-ph].

[376] A. Shivaji and X. Zhao, *Higgs Trilinear self-coupling determination through one-loop effects*, https://cp3.irmp.ucl.ac.be/projects/madgraph/wiki/HiggsSelfCoupling, 2018.

[377] M. Bauer, M. Carena, and K. Gemmler, *Flavor from the Electroweak Scale*, JHEP **11** (2015) 016, arXiv:1506.01719 [hep-ph].

[378] M. Bauer, M. Carena, and K. Gemmler, *Creating the fermion mass hierarchies with multiple Higgs bosons*, Phys. Rev. **D94** (2016) no. 11, 115030, arXiv:1512.03458 [hep-ph].

[379] F. Boudjema and A. Semenov, *Measurements of the SUSY Higgs selfcouplings and the reconstruction of the Higgs potential*, Phys. Rev. **D66** (2002) 095007, arXiv:hep-ph/0201219 [hep-ph].

[380] J. F. Gunion and H. E. Haber, *The CP conserving two Higgs doublet model: The Approach to the decoupling limit*, Phys. Rev. **D67** (2003) 075019, arXiv:hep-ph/0207010 [hep-ph].

[381] D. Eriksson, J. Rathsman, and O. Stal, *2HDMC: Two-Higgs-Doublet Model Calculator Physics and Manual*, Comput. Phys. Commun. **181** (2010) 189–205, arXiv:0902.0851 [hep-ph].

[382] D. E. Morrissey and M. J. Ramsey-Musolf, *Electroweak baryogenesis*, New J. Phys. **14** (2012) 125003, arXiv:1206.2942 [hep-ph].

[383] K. Rummukainen, M. Tsypin, K. Kajantie, M. Laine, and M. E. Shaposhnikov, *The Universality class of the electroweak theory*, Nucl. Phys. **B532** (1998) 283–314, arXiv:hep-lat/9805013 [hep-lat].

[384] F. Csikor, Z. Fodor, and J. Heitger, *Endpoint of the hot electroweak phase transition*, Phys. Rev. Lett. **82** (1999) 21–24, arXiv:hep-ph/9809291 [hep-ph].

[385] M. Laine and K. Rummukainen, *What's new with the electroweak phase transition?*, Nucl. Phys. Proc. Suppl. **73** (1999) 180–185, arXiv:hep-lat/9809045 [hep-lat].

[386] M. Gurtler, E.-M. Ilgenfritz, and A. Schiller, *Where the electroweak phase transition ends*, Phys. Rev. **D56** (1997) 3888–3895, arXiv:hep-lat/9704013 [hep-lat].

[387] A. D. Sakharov, *Violation of CP Invariance, c Asymmetry, and Baryon Asymmetry of the Universe*, Pisma Zh. Eksp. Teor. Fiz. **5** (1967) 32–35.

[388] K. Assamagan et al., *The Higgs Portal and Cosmology*, 2016. arXiv:1604.05324 [hep-ph].

[389] H. H. Patel and M. J. Ramsey-Musolf, *Stepping Into Electroweak Symmetry Breaking: Phase Transitions and Higgs Phenomenology*, Phys. Rev. **D88** (2013) 035013, arXiv:1212.5652 [hep-ph].

[390] H. H. Patel, M. J. Ramsey-Musolf, and M. B. Wise, *Color Breaking in the Early Universe*, Phys. Rev. **D88** (2013) no. 1, 015003, arXiv:1303.1140 [hep-ph].

[391] N. Blinov, J. Kozaczuk, D. E. Morrissey, and C. Tamarit, *Electroweak Baryogenesis from Exotic Electroweak Symmetry Breaking*, Phys. Rev. **D92** (2015) no. 3, 035012, arXiv:1504.05195 [hep-ph].

[392] M. J. Ramsey-Musolf, P. Winslow, and G. White, *Color Breaking Baryogenesis*, Phys. Rev. **D97** (2018) no. 12, 123509, arXiv:1708.07511 [hep-ph].

[393] A. Katz and M. Perelstein, *Higgs Couplings and Electroweak Phase Transition*, JHEP **07** (2014) 108, arXiv:1401.1827 [hep-ph].

[394] A. Katz, M. Perelstein, M. J. Ramsey-Musolf, and P. Winslow, *Stop-Catalyzed Baryogenesis Beyond the MSSM*, Phys. Rev. **D92** (2015) no. 9, 095019, arXiv:1509.02934 [hep-ph].

[395] J. R. Espinosa and M. Quiros, *The Electroweak phase transition with a singlet*, Phys. Lett. **B305** (1993) 98–105, arXiv:hep-ph/9301285 [hep-ph].

[396] J. Choi and R. R. Volkas, *Real Higgs singlet and the electroweak phase transition in the*

Standard Model, Phys. Lett. **B317** (1993) 385–391, arXiv:hep-ph/9308234 [hep-ph].

[397] S. W. Ham, Y. S. Jeong, and S. K. Oh, *Electroweak phase transition in an extension of the standard model with a real Higgs singlet*, J. Phys. **G31** (2005) no. 8, 857–871, arXiv:hep-ph/0411352 [hep-ph].

[398] S. Profumo, M. J. Ramsey-Musolf, and G. Shaughnessy, *Singlet Higgs phenomenology and the electroweak phase transition*, JHEP **08** (2007) 010, arXiv:0705.2425 [hep-ph].

[399] J. M. Cline and K. Kainulainen, *Electroweak baryogenesis and dark matter from a singlet Higgs*, JCAP **1301** (2013) 012, arXiv:1210.4196 [hep-ph].

[400] J. R. Espinosa, T. Konstandin, and F. Riva, *Strong Electroweak Phase Transitions in the Standard Model with a Singlet*, Nucl. Phys. **B854** (2012) 592–630, arXiv:1107.5441 [hep-ph].

[401] J. M. No and M. Ramsey-Musolf, *Probing the Higgs Portal at the LHC Through Resonant di-Higgs Production*, Phys. Rev. **D89** (2014) no. 9, 095031, arXiv:1310.6035 [hep-ph].

[402] D. Curtin, P. Meade, and C.-T. Yu, *Testing Electroweak Baryogenesis with Future Colliders*, JHEP **11** (2014) 127, arXiv:1409.0005 [hep-ph].

[403] A. V. Kotwal, M. J. Ramsey-Musolf, J. M. No, and P. Winslow, *Singlet-catalyzed electroweak phase transitions in the 100 TeV frontier*, Phys. Rev. **D94** (2016) no. 3, 035022, arXiv:1605.06123 [hep-ph].

[404] T. Brauner, T. V. I. Tenkanen, A. Tranberg, A. Vuorinen, and D. J. Weir, *Dimensional reduction of the Standard Model coupled to a new singlet scalar field*, JHEP **03** (2017) 007, arXiv:1609.06230 [hep-ph].

[405] P. Huang, A. J. Long, and L.-T. Wang, *Probing the Electroweak Phase Transition with Higgs Factories and Gravitational Waves*, Phys. Rev. **D94** (2016) no. 7, 075008, arXiv:1608.06619 [hep-ph].

[406] T. Huang, J. M. No, L. Pernié, M. Ramsey-Musolf, A. Safonov, M. Spannowsky, and P. Winslow, *Resonant di-Higgs boson production in the $b\bar{b}WW$ channel: Probing the electroweak phase transition at the LHC*, Phys. Rev. **D96** (2017) no. 3, 035007, arXiv:1701.04442 [hep-ph].

[407] V. Barger, P. Langacker, M. McCaskey, M. J. Ramsey-Musolf, and G. Shaughnessy, *LHC Phenomenology of an Extended Standard Model with a Real Scalar Singlet*, Phys. Rev. **D77** (2008) 035005, arXiv:0706.4311 [hep-ph].

[408] M. Jiang, L. Bian, W. Huang, and J. Shu, *Impact of a complex singlet: Electroweak baryogenesis and dark matter*, Phys. Rev. **D93** (2016) no. 6, 065032, arXiv:1502.07574 [hep-ph].

[409] C.-W. Chiang, M. J. Ramsey-Musolf, and E. Senaha, *Standard Model with a Complex Scalar Singlet: Cosmological Implications and Theoretical Considerations*, Phys. Rev. **D97** (2018) no. 1, 015005, arXiv:1707.09960 [hep-ph].

[410] S. Profumo, M. J. Ramsey-Musolf, C. L. Wainwright, and P. Winslow, *Singlet-catalyzed electroweak phase transitions and precision Higgs boson studies*, Phys. Rev. **D91** (2015) no. 3, 035018, arXiv:1407.5342 [hep-ph].

[411] L. Niemi, H. H. Patel, M. J. Ramsey-Musolf, T. V. I. Tenkanen, and D. J. Weir, *Electroweak phase transition in the ΣSM - I: Dimensional reduction*, arXiv:1802.10500 [hep-ph].

[412] G. C. Dorsch, S. J. Huber, and J. M. No, *A strong electroweak phase transition in the 2HDM after LHC8*, JHEP **10** (2013) 029, arXiv:1305.6610 [hep-ph].

[413] G. C. Dorsch, S. J. Huber, K. Mimasu, and J. M. No, *Echoes of the Electroweak Phase Transition: Discovering a second Higgs doublet through $A\_0 \to ZH\_0$*, Phys. Rev. Lett. **113** (2014) no. 21, 211802, arXiv:1405.5537 [hep-ph].

[414] M. S. Chanowitz and M. K. Gaillard, *The TeV Physics of Strongly Interacting W's and Z's*, Nucl. Phys. **B261** (1985) 379–431.

[415] A. Wulzer, *An Equivalent Gauge and the Equivalence Theorem*, Nucl. Phys. **B885** (2014) 97–126, arXiv:1309.6055 [hep-ph].

[416] R. Franceschini, G. Panico, A. Pomarol, F. Riva, and A. Wulzer, *Electroweak Precision Tests in High-Energy Diboson Processes*, JHEP **02** (2018) 111, arXiv:1712.01310 [hep-ph].

[417] G. Panico, F. Riva, and A. Wulzer, *Diboson Interference Resurrection*, Phys. Lett. **B776** (2018) 473–480, arXiv:1708.07823 [hep-ph].

[418] A. Azatov, J. Elias-Miro, Y. Reyimuaji, and E. Venturini, *Novel measurements of anomalous triple gauge couplings for the LHC*, JHEP **10** (2017) 027, arXiv:1707.08060 [hep-ph].

[419] R. S. Gupta, A. Pomarol, and F. Riva, *BSM Primary Effects*, Phys. Rev. **D91** (2015) no. 3, 035001, arXiv:1405.0181 [hep-ph].

[420] R. Barbieri, A. Pomarol, R. Rattazzi, and A. Strumia, *Electroweak symmetry breaking after LEP-1 and LEP-2*, Nucl. Phys. **B703** (2004) 127–146, arXiv:hep-ph/0405040 [hep-ph].

[421] ATLAS Collaboration, G. Aad et al., *Measurements of $W^{\pm}Z$ production cross sections in pp collisions at $\sqrt{s} = 8$ TeV with the ATLAS detector and limits on anomalous gauge boson self-couplings*, Phys. Rev. **D93** (2016) no. 9, 092004, arXiv:1603.02151 [hep-ex].

[422] ATLAS Collaboration, G. Aad et al., *Measurement of the double-differential high-mass Drell-Yan cross section in pp collisions at $\sqrt{s} = 8$ TeV with the ATLAS detector*, JHEP **08** (2016) 009, arXiv:1606.01736 [hep-ex].

[423] ATLAS Collaboration, *Electron efficiency measurements with the ATLAS detector using the 2015 LHC proton-proton collision data*, ATLAS-CONF-2016-024, 2016.

[424] F. Campanario, R. Roth, and D. Zeppenfeld, *QCD radiation in WH and WZ production and anomalous coupling measurements*, Phys. Rev. **D91** (2015) 054039, arXiv:1410.4840 [hep-ph].

[425] J. Ellis, P. Roloff, V. Sanz, and T. You, *Dimension-6 Operator Analysis of the CLIC Sensitivity to New Physics*, JHEP **05** (2017) 096, arXiv:1701.04804 [hep-ph].

[426] D. Racco, A. Wulzer, and F. Zwirner, *Robust collider limits on heavy-mediator Dark Matter*, JHEP **05** (2015) 009, arXiv:1502.04701 [hep-ph].

[427] F. Pobbe, A. Wulzer, and M. Zanetti, *Setting limits on Effective Field Theories: the case of Dark Matter*, JHEP **08** (2017) 074, arXiv:1704.00736 [hep-ph].

[428] A. Biek$\surd$∂tter, A. Knochel, M. Kr$\surd$§mer, D. Liu, and F. Riva, *Vices and virtues of Higgs effective field theories at large energy*, Phys. Rev. **D91** (2015) 055029, arXiv:1406.7320 [hep-ph].

[429] A. Pomarol, *Higgs Physics*, in *Proceedings, 2014 European School of High-Energy Physics (ESHEP 2014): Garderen, The Netherlands, June 18 - July 01 2014*, pp. 59–77. 2016. arXiv:1412.4410 [hep-ph].

[430] J. M. Butterworth, A. R. Davison, M. Rubin, and G. P. Salam, *Jet substructure as a new Higgs search channel at the LHC*, Phys. Rev. Lett. **100** (2008) 242001, arXiv:0802.2470 [hep-ph].

[431] S. Banerjee, C. Englert, R. S. Gupta, and M. Spannowsky, *Probing Electroweak Precision Physics via Boosted Higgs-Strahlung at the Lhc*, Phys. Rev. **D98** (2018) no. 9, 095012, arXiv:1807.01796 [hep-ph].

[432] ALEPH Collaboration, DELPHI Collaboration, L3 Collaboration, OPAL Collaboration, LEP TGC Working Group, *A Combination of Preliminary Results on Gauge Boson Couplings Measured by the LEP experiments*, DELPHI-2003-068-PHYS-936. L3-NOTE-2826, LEPEWWG-2006-01, LEPEWWG-TGC-2003-01, OPAL-TN-739. ALEPH-2006-016-CONF-2003-012, 2003.

[433] A. Falkowski and F. Riva, *Model-independent precision constraints on dimension-6 operators*, JHEP **02** (2015) 039, arXiv:1411.0669 [hep-ph].

[434] M. Baak, M. Goebel, J. Haller, A. Hoecker, D. Kennedy, R. Kogler, K. Moenig, M. Schott, and J. Stelzer, *The Electroweak Fit of the Standard Model after the Discovery of a New Boson at the LHC*, Eur. Phys. J. **C72** (2012) 2205, arXiv:1209.2716 [hep-ph].

[435] A. Azatov, D. Barducci, and E. Venturini, *Precision diboson measurements at hadron colliders*, arXiv:1901.04821 [hep-ph].

[436] CMS Collaboration, *Search for anomalous couplings in boosted* $\mathrm{WW/WZ} \to \ell\nu\mathrm{q\bar{q}}$ *production in proton-proton collisions at* $\sqrt{s} = 8$ *TeV*, Phys. Lett. **B772** (2017) no. CERN-EP-2017-029, CMS-SMP-13-008, 21–42, arXiv:1703.06095 [hep-ex].

[437] L. J. Dixon and Y. Shadmi, *Testing gluon selfinteractions in three jet events at hadron colliders*, Nucl. Phys. **B423** (1994) 3–32, arXiv:hep-ph/9312363 [hep-ph].

[438] A. Azatov, R. Contino, C. S. Machado, and F. Riva, *Helicity selection rules and noninterference for BSM amplitudes*, Phys. Rev. **D95** (2017) no. 6, 065014, arXiv:1607.05236 [hep-ph].

[439] U. Baur, T. Han, and J. Ohnemus, *Amplitude zeros in W+- Z production*, Phys. Rev. Lett. **72** (1994) 3941–3944, arXiv:hep-ph/9403248 [hep-ph].

[440] M. Farina, G. Panico, D. Pappadopulo, J. T. Ruderman, R. Torre, and A. Wulzer, *Energy helps accuracy: electroweak precision tests at hadron colliders*, Phys. Lett. **B772** (2017) 210–215, arXiv:1609.08157 [hep-ph].

[441] S. Alioli, M. Farina, D. Pappadopulo, and J. T. Ruderman, *Catching a New Force by the Tail*, Phys. Rev. Lett. **120** (2018) no. 10, 101801, arXiv:1712.02347 [hep-ph].

[442] S. Alioli, M. Farina, D. Pappadopulo, and J. T. Ruderman, *Precision Probes of QCD at High Energies*, JHEP **07** (2017) 097, arXiv:1706.03068 [hep-ph].

[443] I. Low, *Adler$\hat{O}\phi\Omega$s zero and effective Lagrangians for nonlinearly realized symmetry*, Phys. Rev. **D91** (2015) no. 10, 105017, arXiv:1412.2145 [hep-th].

[444] I. Low, *Minimally symmetric Higgs boson*, Phys. Rev. **D91** (2015) no. 11, 116005, arXiv:1412.2146 [hep-ph].

[445] D. Liu, I. Low, and Z. Yin, *Universal Imprints of a Pseudo-Nambu-Goldstone Higgs Boson*, arXiv:1805.00489 [hep-ph].

[446] D. Liu, I. Low, and Z. Yin, *Universal Relations in Composite Higgs Models*, arXiv:1809.09126 [hep-ph].

[447] CMS Collaboration, *Constraints on anomalous Higgs boson couplings using production and decay information in the four-lepton final state*, Phys. Lett. **B775** (2017) no. CERN-EP-2017-143, CMS-HIG-17-011, 1–24, arXiv:1707.00541 [hep-ex].

[448] F. Bishara, R. Contino, and J. Rojo, *Higgs pair production in vector-boson fusion at the LHC and beyond*, Eur. Phys. J. **C77** (2017) no. 7, 481, arXiv:1611.03860 [hep-ph].

[449] R. Contino, C. Grojean, M. Moretti, F. Piccinini, and R. Rattazzi, *Strong Double Higgs Production at the Lhc*, JHEP **05** (2010) 089, arXiv:1002.1011 [hep-ph].

[450] R. Contino, C. Grojean, D. Pappadopulo, R. Rattazzi, and A. Thamm, *Strong Higgs Interactions at a Linear Collider*, JHEP **02** (2014) 006, arXiv:1309.7038 [hep-ph].

[451] M. J. Dolan, C. Englert, N. Greiner, and M. Spannowsky, *Further on up the road:* $hhjj$ *production at the LHC*, Phys. Rev. Lett. **112** (2014) 101802, arXiv:1310.1084 [hep-ph].

[452] G. Brooijmans et al., *Les Houches 2013: Physics at TeV Colliders: New Physics Working Group Report*, arXiv:1405.1617 [hep-ph].

[453] L.-S. Ling, R.-Y. Zhang, W.-G. Ma, L. Guo, W.-H. Li, and X.-Z. Li, *NNLO QCD corrections to Higgs pair production via vector boson fusion at hadron colliders*, Phys. Rev. **D89** (2014) no. 7, 073001, arXiv:1401.7754 [hep-ph].

[454] M. J. Dolan, C. Englert, N. Greiner, K. Nordstrom, and M. Spannowsky, *$hhjj$ production at the LHC*, Eur. Phys. J. **C75** (2015) no. 8, 387, arXiv:1506.08008 [hep-ph].

[455] G. P. Salam, *Towards Jetography*, Eur. Phys. J. **C67** (2010) 637–686, arXiv:0906.1833 [hep-ph].

[456] M. Gouzevitch, A. Oliveira, J. Rojo, R. Rosenfeld, G. P. Salam, and V. Sanz, *Scale-invariant resonance tagging in multijet events and new physics in Higgs pair production*, JHEP **07** (2013) 148, arXiv:1303.6636 [hep-ph].

[457] J. K. Behr, D. Bortoletto, J. A. Frost, N. P. Hartland, C. Issever, and J. Rojo, *Boosting Higgs pair production in the $b\bar{b}b\bar{b}$ final state with multivariate techniques*, Eur. Phys. J. **C76** (2016) no. 7, 386, arXiv:1512.08928 [hep-ph].

[458] R. Contino, A. Falkowski, F. Goertz, C. Grojean, and F. Riva, *On the Validity of the Effective Field Theory Approach to SM Precision Tests*, JHEP **07** (2016) 144, arXiv:1604.06444 [hep-ph].

[459] B. Henning, D. Lombardo, M. Riembau, and F. Riva, *Higgs Couplings without the Higgs*, arXiv:1812.09299 [hep-ph].

[460] N. D. Christensen and C. Duhr, *Feynrules - Feynman Rules Made Easy*, Comput. Phys. Commun. **180** (2009) 1614–1641, arXiv:0806.4194 [hep-ph].

[461] A. Falkowski, B. Fuks, K. Mawatari, K. Mimasu, F. Riva, and V. Sanz, *Rosetta: an operator basis translator for Standard Model effective field theory*, Eur. Phys. J. **C75** (2015) no. 12, 583, arXiv:1508.05895 [hep-ph].

[462] C. Degrande, F. Maltoni, K. Mimasu, E. Vryonidou, and C. Zhang, *Single-top associated production with a Z or H boson at the LHC: the SMEFT interpretation*, JHEP **10** (2018) 005, arXiv:1804.07773 [hep-ph].

[463] ATLAS Collaboration, *Search for diboson resonances in hadronic final states in 79.8 fb^{-1} of pp collisions at $\sqrt{s} = 13$ TeV with the ATLAS detector*, ATLAS-CONF-2018-016, 2018.

[464] CMS Collaboration, *Performance of Electron Reconstruction and Selection with the CMS Detector in Proton-Proton Collisions at ,àös = 8 TeV*, JINST **10** (2015) no. CERN-PH-EP-2015-004, CMS-EGM-13-001, P06005, arXiv:1502.02701 [physics.ins-det].

[465] O. J. P. Eboli, M. C. Gonzalez-Garcia, and J. K. Mizukoshi, *$pp \to jje^{\pm}\mu^{\pm}\nu\nu$ and $jje^{\pm}\mu^{\pm}\nu\nu$ at $\mathcal{O}(\alpha\_\mathrm{em}^6)$ and $\mathcal{O}(\alpha\_\mathrm{em}^4\alpha\_\mathrm{s}^2)$ for the Study of the Quartic Electroweak Gauge Boson Vertex at LHC*, Phys. Rev. **D74** (2006) 073005, arXiv:hep-ph/0606118 [hep-ph].

[466] ATLAS Collaboration, G. Aad et al., *Evidence for Electroweak Production of $W^{\pm}W^{\pm}jj$ in pp Collisions at $\sqrt{s} = 8$ TeV with the ATLAS Detector*, Phys. Rev. Lett. **113** (2014) no. 14, 141803, arXiv:1405.6241 [hep-ex].

[467] ATLAS Collaboration, M. Aaboud et al., *Studies of $Z\gamma$ production in association with a high-mass dijet system in pp collisions at $\sqrt{s} = 8$ TeV with the ATLAS detector*, JHEP **07** (2017) 107, arXiv:1705.01966 [hep-ex].

[468] A. Azatov, C. Grojean, A. Paul, and E. Salvioni, *Taming the off-shell Higgs boson*, Zh. Eksp. Teor. Fiz. **147** (2015) 410–425, arXiv:1406.6338 [hep-ph].

[469] G. Cacciapaglia, A. Deandrea, G. Drieu La Rochelle, and J.-B. Flament, *Higgs Couplings: Disentangling New Physics with Off-Shell Measurements*, Phys. Rev. Lett. **113** (2014) no. 20, 201802, arXiv:1406.1757 [hep-ph].

[470] A. Azatov, C. Grojean, A. Paul, and E. Salvioni, *Resolving Gluon Fusion Loops at Current and Future Hadron Colliders*, JHEP **09** (2016) 123, arXiv:1608.00977 [hep-ph].

[471] E. W. N. Glover and J. J. van der Bij, *Z Boson Pair Production via Gluon Fusion*, Nucl. Phys. **B321** (1989) 561–590.

[472] CMS Collaboration, *Measurement of vector boson scattering and constraints on anomalous quartic couplings from events with four leptons and two jets in proton,Äìproton collisions at* $\sqrt{s} = 13$ *TeV*, Phys. Lett. **B774** (2017) no. CERN-EP-2017-177, CMS-SMP-17-006, 682–705, arXiv:1708.02812 [hep-ex].

[473] R. Gomez-Ambrosio, *Studies of Dimension-Six EFT effects in Vector Boson Scattering*, arXiv:1809.04189 [hep-ph].

[474] E. E. Jenkins, A. V. Manohar, and M. Trott, *Renormalization Group Evolution of the Standard Model Dimension Six Operators I: Formalism and lambda Dependence*, JHEP **10** (2013) 087, arXiv:1308.2627 [hep-ph].

[475] CMS Collaboration, *Measurement of differential cross sections for Z boson pair production in association with jets at* $\sqrt{s} = 8$ *and 13 TeV*, CERN-EP-2018-161, CMS-SMP-17-005, 2018. arXiv:1806.11073 [hep-ex].

[476] M. Ghezzi, R. Gomez-Ambrosio, G. Passarino, and S. Uccirati, *NLO Higgs effective field theory and* κ*-framework*, JHEP **07** (2015) 175, arXiv:1505.03706 [hep-ph].

[477] J. Kalinowski, P. Kozow, S. Pokorski, J. Rosiek, M. Szleper, and S. Tkaczyk, *Same-sign WW scattering at the LHC: can we discover BSM effects before discovering new states?*, Eur. Phys. J. **C78** (2018) no. 5, 403, arXiv:1802.02366 [hep-ph].

[478] L. J. Dixon and M. S. Siu, *Resonance continuum interference in the diphoton Higgs signal at the LHC*, Phys. Rev. Lett. **90** (2003) 252001, arXiv:hep-ph/0302233 [hep-ph].

[479] S. P. Martin, *Shift in the LHC Higgs diphoton mass peak from interference with background*, Phys. Rev. **D86** (2012) 073016, arXiv:1208.1533 [hep-ph].

[480] L. J. Dixon and Y. Li, *Bounding the Higgs Boson Width Through Interferometry*, Phys. Rev. Lett. **111** (2013) 111802, arXiv:1305.3854 [hep-ph].

[481] J. Campbell, M. Carena, R. Harnik, and Z. Liu, *Interference in the* $gg \to h \to \gamma\gamma$ *On-Shell Rate and the Higgs Boson Total Width*, Phys. Rev. Lett. **119** (2017) no. 18, 181801, arXiv:1704.08259 [hep-ph].

[482] F. Coradeschi, D. de Florian, L. J. Dixon, N. Fidanza, S. Höche, H. Ita, Y. Li, and J. Mazzitelli, *Interference effects in the* $H(\to \gamma\gamma) + 2$ *jets channel at the LHC*, Phys. Rev. **D92** (2015) no. 1, 013004, arXiv:1504.05215 [hep-ph].

[483] D. de Florian, N. Fidanza, R. J. Hernandez-Pinto, J. Mazzitelli, Y. Rotstein Habarnau, and G. F. R. Sborlini, *A complete* $O(\alpha\_S^2)$ *calculation of the signal-background interference for the Higgs diphoton decay channel*, Eur. Phys. J. **C73** (2013) no. 4, 2387, arXiv:1303.1397 [hep-ph].

[484] S. P. Martin, *Interference of Higgs diphoton signal and background in production with a jet at the LHC*, Phys. Rev. **D88** (2013) no. 1, 013004, arXiv:1303.3342 [hep-ph].

[485] S. Hoeche and S. Prestel, *The midpoint between dipole and parton showers*, Eur. Phys. J. **C75** (2015) no. 9, 461, arXiv:1506.05057 [hep-ph].

[486] F. Caola, J. M. Lindert, K. Melnikov, P. F. Monni, L. Tancredi, and C. Wever, *Bottom-quark effects in Higgs production at intermediate transverse momentum*, JHEP **09** (2018) 035, arXiv:1804.07632 [hep-ph].

[487] N. Kauer and G. Passarino, *Inadequacy of zero-width approximation for a light Higgs boson signal*, JHEP **08** (2012) 116, arXiv:1206.4803 [hep-ph].

[488] F. Caola and K. Melnikov, *Constraining the Higgs boson width with ZZ production at the LHC*, Phys. Rev. **D88** (2013) 054024, arXiv:1307.4935 [hep-ph].

[489] J. M. Campbell, R. K. Ellis, and C. Williams, *Bounding the Higgs width at the LHC using full analytic results for* $gg - > e^- e^+ \mu^- \mu^+$, JHEP **04** (2014) 060, arXiv:1311.3589 [hep-ph].

[490] J. M. Campbell, R. K. Ellis, and C. Williams, *Bounding the Higgs width at the LHC:*

Complementary results from $H \to WW$, Phys. Rev. **D89** (2014) no. 5, 053011, arXiv:1312.1628 [hep-ph].

[491] C. Englert and M. Spannowsky, *Limitations and Opportunities of Off-Shell Coupling Measurements*, Phys. Rev. **D90** (2014) 053003, arXiv:1405.0285 [hep-ph].

[492] H. E. Logan, *Hiding a Higgs width enhancement from off-shell $gg(\to h*) \to ZZ$ measurements*, Phys. Rev. **D92** (2015) no. 7, 075038, arXiv:1412.7577 [hep-ph].

[493] C. Englert, Y. Soreq, and M. Spannowsky, *Off-Shell Higgs Coupling Measurements in BSM scenarios*, JHEP **05** (2015) 145, arXiv:1410.5440 [hep-ph].

[494] I. Anderson et al., *Constraining anomalous HVV interactions at proton and lepton colliders*, Phys. Rev. **D89** (2014) no. 3, 035007, arXiv:1309.4819 [hep-ph].

[495] J. M. Campbell and R. K. Ellis, *Higgs Constraints from Vector Boson Fusion and Scattering*, JHEP **04** (2015) 030, arXiv:1502.02990 [hep-ph].

[496] F. Caola, M. Dowling, K. Melnikov, R. Roentsch, and L. Tancredi, *QCD corrections to vector boson pair production in gluon fusion including interference effects with off-shell Higgs at the LHC*, JHEP **07** (2016) 087, arXiv:1605.04610 [hep-ph].

[497] J. M. Campbell, R. K. Ellis, M. Czakon, and S. Kirchner, *Two loop correction to interference in $gg \to ZZ$*, JHEP **08** (2016) 011, arXiv:1605.01380 [hep-ph].

[498] J. M. Campbell, R. K. Ellis, E. Furlan, and R. Roentsch, *Interference effects for Higgs boson mediated Z-pair plus jet production*, Phys. Rev. **D90** (2014) no. 9, 093008, arXiv:1409.1897 [hep-ph].

[499] F. Caola, K. Melnikov, R. Roentsch, and L. Tancredi, *QCD corrections to ZZ production in gluon fusion at the LHC*, Phys. Rev. **D92** (2015) no. 9, 094028, arXiv:1509.06734 [hep-ph].

[500] F. Caola, K. Melnikov, R. Roentsch, and L. Tancredi, *QCD corrections to W^+W^- production through gluon fusion*, Phys. Lett. **B754** (2016) 275–280, arXiv:1511.08617 [hep-ph].

[501] M. Bonvini, F. Caola, S. Forte, K. Melnikov, and G. Ridolfi, *Signal-background interference effects for $gg \to H \to W^+W^-$ beyond leading order*, Phys. Rev. **D88** (2013) no. 3, 034032, arXiv:1304.3053 [hep-ph].

[502] S. Alioli, F. Caola, G. Luisoni, and R. Roentsch, *ZZ production in gluon fusion at NLO matched to parton-shower*, Phys. Rev. **D95** (2017) no. 3, 034042, arXiv:1609.09719 [hep-ph].

[503] ATLAS Collaboration, M. Aaboud et al., *Constraints on off-shell Higgs boson production and the Higgs boson total width in $ZZ \to 4\ell$ and $ZZ \to 2\ell 2\nu$ final states with the ATLAS detector*, Phys. Lett. **B786** (2018) 223–244, arXiv:1808.01191 [hep-ex].

[504] *Off-shell Higgs signal strength measurement using high-mass H→ZZ→ 4l events at High Luminosity LHC*, ATL-PHYS-PUB-2015-024, 2015.

[505] M. Duhrssen, S. Heinemeyer, H. Logan, D. Rainwater, G. Weiglein, and D. Zeppenfeld, *Extracting Higgs boson couplings from CERN LHC data*, Phys. Rev. **D70** (2004) 113009, arXiv:hep-ph/0406323 [hep-ph].

[506] B. A. Dobrescu and J. D. Lykken, *Coupling spans of the Higgs-like boson*, JHEP **02** (2013) 073, arXiv:1210.3342 [hep-ph].

[507] D. A. Dicus and S. S. D. Willenbrock, *Photon Pair Production and the Intermediate Mass Higgs Boson*, Phys. Rev. **D37** (1988) 1801.

[508] Z. Bern and D. A. Kosower, *The Computation of loop amplitudes in gauge theories*, Nucl. Phys. **B379** (1992) 451–561.

[509] Z. Bern, A. De Freitas, and L. J. Dixon, *Two loop amplitudes for gluon fusion into two photons*, JHEP **09** (2001) 037, arXiv:hep-ph/0109078 [hep-ph].

[510] Z. Bern and A. G. Morgan, *Massive loop amplitudes from unitarity*, Nucl. Phys. **B467** (1996)

479–509, arXiv:hep-ph/9511336 [hep-ph].

[511] Z. Bern, L. J. Dixon, and D. A. Kosower, *One loop corrections to five gluon amplitudes*, Phys. Rev. Lett. **70** (1993) 2677–2680, arXiv:hep-ph/9302280 [hep-ph].

[512] Z. Bern, L. J. Dixon, and C. Schmidt, *Isolating a light Higgs boson from the diphoton background at the CERN LHC*, Phys. Rev. **D66** (2002) 074018, arXiv:hep-ph/0206194 [hep-ph].

[513] S. Catani and M. H. Seymour, *A General algorithm for calculating jet cross-sections in NLO QCD*, Nucl. Phys. **B485** (1997) 291–419, arXiv:hep-ph/9605323 [hep-ph].

[514] J. M. Campbell, R. K. Ellis, and C. Williams, *Vector boson pair production at the LHC*, JHEP **07** (2011) 018, arXiv:1105.0020 [hep-ph].

[515] A. Djouadi, P. Gambino, and B. A. Kniehl, *Two loop electroweak heavy fermion corrections to Higgs boson production and decay*, Nucl. Phys. **B523** (1998) 17–39, arXiv:hep-ph/9712330 [hep-ph].

[516] G. Degrassi and F. Maltoni, *Two-loop electroweak corrections to the Higgs-boson decay H —> gamma gamma*, Nucl. Phys. **B724** (2005) 183–196, arXiv:hep-ph/0504137 [hep-ph].

[517] G. Passarino, C. Sturm, and S. Uccirati, *Complete Two-Loop Corrections to H —> gamma gamma*, Phys. Lett. **B655** (2007) 298–306, arXiv:0707.1401 [hep-ph].

[518] LHC Higgs Cross Section Working Group Collaboration, S. Dittmaier et al., *Handbook of LHC Higgs Cross Sections: 1. Inclusive Observables*, arXiv:1101.0593 [hep-ph].

[519] *Projections for measurements of Higgs boson signal strengths and coupling parameters with the ATLAS detector at a HL-LHC*, , 2014.

[520] *Estimate of the m_H shift due to interference between signal and background processes in the $H \to \gamma\gamma$ channel, for the $\sqrt{s} = 8$ TeV dataset recorded by ATLAS*, ATL-PHYS-PUB-2016-009, 2016.

[521] ATLAS Collaboration, G. Aad et al., *Measurement of the Higgs boson mass from the $H \to \gamma\gamma$ and $H \to ZZ^* \to 4\ell$ channels with the ATLAS detector using 25 fb^{-1} of pp collision data*, Phys. Rev. **D90** (2014) no. 5, 052004, arXiv:1406.3827 [hep-ex].

[522] ATLAS Collaboration, M. Aaboud et al., *Measurement of the Higgs boson mass in the $H \to ZZ^* \to 4\ell$ and $H \to \gamma\gamma$ channels with $\sqrt{s} = 13$ TeV pp collisions using the ATLAS detector*, Phys. Lett. **B784** (2018) 345–366, arXiv:1806.00242 [hep-ex].

[523] *Projections for measurements of Higgs boson cross sections, branching ratios and coupling parameters with the ATLAS detector at a HL-LHC*, ATL-PHYS-PUB-2013-014, 2013.

[524] J. McDonald and N. Sahu, *Z(2)-Singlino Dark Matter in a Portal-Like Extension of the Minimal Supersymmetric Standard Model*, JCAP **0806** (2008) 026, arXiv:0802.3847 [hep-ph].

[525] J. McDonald and N. Sahu, *keV Warm Dark Matter via the Supersymmetric Higgs Portal*, Phys. Rev. **D79** (2009) 103523, arXiv:0809.0247 [hep-ph].

[526] N. Arkani-Hamed, A. Delgado, and G. F. Giudice, *The Well-tempered neutralino*, Nucl. Phys. **B741** (2006) 108–130, arXiv:hep-ph/0601041 [hep-ph].

[527] S. Profumo, T. Stefaniak, and L. Stephenson Haskins, *The Not-So-Well Tempered Neutralino*, Phys. Rev. **D96** (2017) no. 5, 055018, arXiv:1706.08537 [hep-ph].

[528] V. Barger, P. Langacker, M. McCaskey, M. Ramsey-Musolf, and G. Shaughnessy, *Complex Singlet Extension of the Standard Model*, Phys. Rev. **D79** (2009) 015018, arXiv:0811.0393 [hep-ph].

[529] T. Cohen, J. Kearney, A. Pierce, and D. Tucker-Smith, *Singlet-Doublet Dark Matter*, Phys. Rev. **D85** (2012) 075003, arXiv:1109.2604 [hep-ph].

[530] C. Englert, T. Plehn, D. Zerwas, and P. M. Zerwas, *Exploring the Higgs portal*, Phys. Lett. **B703** (2011) 298–305, arXiv:1106.3097 [hep-ph].

[531] A. Goudelis, B. Herrmann, and O. Stål, *Dark matter in the Inert Doublet Model after the discovery of a Higgs-like boson at the LHC*, JHEP **09** (2013) 106, arXiv:1303.3010 [hep-ph].

[532] Y. Bai, V. Barger, L. L. Everett, and G. Shaughnessy, *Two-Higgs-doublet-portal dark-matter model: LHC data and Fermi-LAT 135 GeV line*, Phys. Rev. **D88** (2013) 015008, arXiv:1212.5604 [hep-ph].

[533] A. Berlin, S. Gori, T. Lin, and L.-T. Wang, *Pseudoscalar Portal Dark Matter*, Phys. Rev. **D92** (2015) 015005, arXiv:1502.06000 [hep-ph].

[534] M. Cacciari, G. P. Salam, and G. Soyez, *SoftKiller, a particle-level pileup removal method*, Eur. Phys. J. **C75** (2015) no. 2, 59, arXiv:1407.0408 [hep-ph].

[535] D. Bertolini, P. Harris, M. Low, and N. Tran, *Pileup Per Particle Identification*, JHEP **10** (2014) 059, arXiv:1407.6013 [hep-ph].

[536] P. Berta, M. Spousta, D. W. Miller, and R. Leitner, *Particle-level pileup subtraction for jets and jet shapes*, JHEP **06** (2014) 092, arXiv:1403.3108 [hep-ex].

[537] P. T. Komiske, E. M. Metodiev, B. Nachman, and M. D. Schwartz, *Pileup Mitigation with Machine Learning (PUMML)*, JHEP **12** (2017) 051, arXiv:1707.08600 [hep-ph].

[538] J. Arjona Martínez, O. Cerri, M. Pierini, M. Spiropulu, and J.-R. Vlimant, *Pileup mitigation at the Large Hadron Collider with Graph Neural Networks*, arXiv:1810.07988 [hep-ph].

[539] CMS Collaboration, *Searches for invisible decays of the Higgs boson in pp collisions at $\sqrt{s}$ = 7, 8, and 13 TeV*, JHEP **02** (2017) no. CERN-EP-2016-240, CMS-HIG-16-016, 135, arXiv:1610.09218 [hep-ex].

[540] ATLAS Collaboration, G. Aad et al., *Constraints on new phenomena via Higgs boson couplings and invisible decays with the ATLAS detector*, JHEP **11** (2015) 206, arXiv:1509.00672 [hep-ex].

[541] ATLAS Collaboration, M. Aaboud et al., *Search for an invisibly decaying Higgs boson or dark matter candidates produced in association with a Z boson in pp collisions at $\sqrt{s} = 13$ TeV with the ATLAS detector*, Phys. Lett. **B776** (2018) 318–337, arXiv:1708.09624 [hep-ex].

[542] ATLAS Collaboration, G. Aad et al., *Search for invisible decays of a Higgs boson using vector-boson fusion in pp collisions at $\sqrt{s} = 8$ TeV with the ATLAS detector*, JHEP **01** (2016) 172, arXiv:1508.07869 [hep-ex].

[543] CMS Collaboration, *Search for invisible decays of a Higgs boson produced through vector boson fusion in proton-proton collisions at $\sqrt{s} = 13$ TeV*, Submitted to: Phys. Lett. (2018) no. CERN-EP-2018-139, CMS-HIG-17-023, , arXiv:1809.05937 [hep-ex].

[544] ATLAS Collaboration, M. Aaboud et al., *Search for invisible Higgs boson decays in vector boson fusion at $\sqrt{s} = 13$ TeV with the ATLAS detector*, Submitted to: Phys. Lett. (2018) , arXiv:1809.06682 [hep-ex].

[545] D. Curtin et al., *Long-Lived Particles at the Energy Frontier: The MATHUSLA Physics Case*, arXiv:1806.07396 [hep-ph].

[546] ATLAS Collaboration, G. Aad et al., *Search for long-lived, weakly interacting particles that decay to displaced hadronic jets in proton-proton collisions at $\sqrt{s} = 8$ TeV with the ATLAS detector*, Phys. Rev. **D92** (2015) no. 1, 012010, arXiv:1504.03634 [hep-ex].

[547] ATLAS Collaboration, *Search for long-lived neutral particles decaying into displaced lepton jets in proton–proton collisions at $\sqrt{s}$ = 13 TeV with the ATLAS detector*, ATLAS-CONF-2016-042, 2016.

[548] LHCb Collaboration, *Search for massive long-lived particles decaying semileptonically in the LHCb detector*, Eur. Phys. J. **C77** (2017) no. LHCB-PAPER-2016-047-CERN-EP-2016-283, CERN-EP-2016-283, LHCB-PAPER-2016-047, 224, arXiv:1612.00945 [hep-ex].

[549] CMS Collaboration, *Search for long-lived particles that decay into final states containing two electrons or two muons in proton-proton collisions at $\sqrt{s} = 8$ TeV*, Phys. Rev. **D91** (2015) no. CERN-PH-EP-2014-263, CMS-EXO-12-037, 052012, arXiv:1411.6977 [hep-ex].

[550] J. P. Chou, D. Curtin, and H. J. Lubatti, *New Detectors to Explore the Lifetime Frontier*, Phys. Lett. **B767** (2017) 29–36, arXiv:1606.06298 [hep-ph].

[551] V. V. Gligorov, S. Knapen, M. Papucci, and D. J. Robinson, *Searching for Long-lived Particles: A Compact Detector for Exotics at LHCb*, Phys. Rev. **D97** (2018) no. 1, 015023, arXiv:1708.09395 [hep-ph].

[552] V. V. Gligorov, S. Knapen, B. Nachman, M. Papucci, and D. J. Robinson, *Leveraging the ALICE/L3 cavern for long-lived exotics*, Phys. Rev. **D99** (2019) no. 1, 015023, arXiv:1810.03636 [hep-ph].

[553] CMS Collaboration, *Search for invisible decays of a Higgs boson produced through vector boson fusion at the High-Luminosity LHC*, CMS-PAS-FTR-18-016, 2018.

[554] T. Junk, *Confidence level computation for combining searches with small statistics*, Nucl. Instrum. Meth. **A434** (1999) 435–443, arXiv:hep-ex/9902006 [hep-ex].

[555] S. Dittmaier et al., *Handbook of LHC Higgs Cross Sections: 2. Differential Distributions*, arXiv:1201.3084 [hep-ph].

[556] CMS Collaboration, *Observation of a new boson with mass near 125 GeV in pp collisions at $\sqrt{s}$ = 7 and 8 TeV*, JHEP **06** (2013) no. CERN-PH-EP-2013-035, CMS-HIG-12-036, 081, arXiv:1303.4571 [hep-ex].

[557] CMS Collaboration, *Procedure for the LHC Higgs boson search combination in summer 2011*, ATL-PHYS-PUB-2011-011, CMS-NOTE-2011-005, 2011.

[558] A. Biekötter, F. Keilbach, R. Moutafis, T. Plehn, and J. Thompson, *Tagging Jets in Invisible Higgs Searches*, SciPost Phys. **4** (2018) no. 6, 035, arXiv:1712.03973 [hep-ph].

[559] ATLAS Collaboration, *Prospects for Dark Matter searches in mono-photon and VBF+E_T^{miss} final states in ATLAS*, ATL-PHYS-PUB-2018-038, 2018.

[560] CMS Collaboration, *Jet energy scale uncertainty correlations between ATLAS and CMS at 8 TeV*, ATL-PHYS-PUB-2015-049, CMS-PAS-JME-15-001, 2015.

[561] P. Bechtle, S. Heinemeyer, O. Stål, T. Stefaniak, and G. Weiglein, *$HiggsSignals$: Confronting arbitrary Higgs sectors with measurements at the Tevatron and the LHC*, Eur. Phys. J. **C74** (2014) no. 2, 2711, arXiv:1305.1933 [hep-ph].

[562] P. Bechtle, S. Heinemeyer, O. Stål, T. Stefaniak, and G. Weiglein, *Probing the Standard Model with Higgs signal rates from the Tevatron, the LHC and a future ILC*, JHEP **11** (2014) 039, arXiv:1403.1582 [hep-ph].

[563] LHeC Study Group Collaboration, J. L. Abelleira Fernandez et al., *A Large Hadron Electron Collider at CERN: Report on the Physics and Design Concepts for Machine and Detector*, J. Phys. **G39** (2012) 075001, arXiv:1206.2913 [physics.acc-ph].

[564] U. Klein, *Higgs physics at the LHeC and the HE-LHC/FCC-he*, Talk at the HL-LHC Meeting, June 2018 .

[565] U. Klein, *Higgs physics at LHeC*, Talk at Higgs Hunting 2018, July 2018 .

[566] F. Zimmermann, M. Benedikt, M. Capeans Garrido, F. Cerutti, B. Goddard, J. Gutleber, J. M. Jimenez, M. Mangano, V. Mertens, J. A. Osborne, T. Otto, J. Poole, W. Riegler, L. J. Tavian, and D. Tommasini, *Future Circular Collider*, CERN-ACC-2018-0059, 2018.

[567] Y.-L. Tang, C. Zhang, and S.-h. Zhu, *Invisible Higgs Decay at the LHeC*, Phys. Rev. **D94** (2016) no. 1, 011702, arXiv:1508.01095 [hep-ph].

[568] M. Kuze, *Search for Higgs decay to invisibles at the LHeC and the FCC-eh*, Talk at *Electrons for the LHC*, Orsay, 27 June 2018 .

[569] S. Kawaguchi, *Bachelor Thesis, Tokyo Institute of Technology, 2015*, 2015.

[570] T. Sekine, *Bachelor Thesis, Tokyo Institute of Technology, 2017*, 2017.

[571] U. Klein, *private communication*, .

[572] V. Silveira and A. Zee, *SCALAR PHANTOMS*, Phys. Lett. **161B** (1985) 136–140.

[573] O. Lebedev, H. M. Lee, and Y. Mambrini, *Vector Higgs-portal dark matter and the invisible Higgs*, Phys. Lett. **B707** (2012) 570–576, arXiv:1111.4482 [hep-ph].

[574] Y. G. Kim and K. Y. Lee, *The Minimal model of fermionic dark matter*, Phys. Rev. **D75** (2007) 115012, arXiv:hep-ph/0611069 [hep-ph].

[575] S. Kanemura, S. Matsumoto, T. Nabeshima, and N. Okada, *Can WIMP Dark Matter overcome the Nightmare Scenario?*, Phys. Rev. **D82** (2010) 055026, arXiv:1005.5651 [hep-ph].

[576] A. Djouadi, O. Lebedev, Y. Mambrini, and J. Quevillon, *Implications of LHC searches for Higgs–portal dark matter*, Phys. Lett. **B709** (2012) 65–69, arXiv:1112.3299 [hep-ph].

[577] E. Hardy, *Higgs portal dark matter in non-standard cosmological histories*, JHEP **06** (2018) 043, arXiv:1804.06783 [hep-ph].

[578] N. Bernal, C. Cosme, and T. Tenkanen, *Phenomenology of Self-Interacting Dark Matter in a Matter-Dominated Universe*, arXiv:1803.08064 [hep-ph].

[579] N. Bernal, C. Cosme, T. Tenkanen, and V. Vaskonen, *Scalar singlet dark matter in non-standard cosmologies*, Eur. Phys. J. **C79** (2019) no. 1, 30, arXiv:1806.11122 [hep-ph].

[580] ATLAS Collaboration, *Combination of searches for invisible Higgs boson decays with the ATLAS experiment*, ATLAS-CONF-2018-054, 2018.

[581] M. Hoferichter, P. Klos, J. Menendez, and A. Schwenk, *Improved limits for Higgs-portal dark matter from LHC searches*, Phys. Rev. Lett. **119** (2017) no. 18, 181803, arXiv:1708.02245 [hep-ph].

[582] XENON10 Collaboration, J. Angle et al., *A search for light dark matter in XENON10 data*, Phys. Rev. Lett. **107** (2011) 051301, arXiv:1104.3088 [astro-ph.CO].

[583] XENON100 Collaboration, E. Aprile et al., *Dark Matter Results from 225 Live Days of XENON100 Data*, Phys. Rev. Lett. **109** (2012) 181301, arXiv:1207.5988 [astro-ph.CO].

[584] XENON Collaboration, E. Aprile et al., *Dark Matter Search Results from a One Ton-Year Exposure of XENON1T*, Phys. Rev. Lett. **121** (2018) no. 11, 111302, arXiv:1805.12562 [astro-ph.CO].

[585] XENON Collaboration, E. Aprile et al., *Physics reach of the XENON1T dark matter experiment*, JCAP **1604** (2016) no. 04, 027, arXiv:1512.07501 [physics.ins-det].

[586] SuperCDMS Collaboration, R. Agnese et al., *Projected Sensitivity of the SuperCDMS SNOLAB experiment*, Phys. Rev. **D95** (2017) no. 8, 082002, arXiv:1610.00006 [physics.ins-det].

[587] C. Savage, G. Gelmini, P. Gondolo, and K. Freese, *Compatibility of DAMA/LIBRA dark matter detection with other searches*, JCAP **0904** (2009) 010, arXiv:0808.3607 [astro-ph].

[588] G. Angloher et al., *Results from 730 kg days of the CRESST-II Dark Matter Search*, Eur. Phys. J. **C72** (2012) 1971, arXiv:1109.0702 [astro-ph.CO].

[589] CDMS Collaboration, R. Agnese et al., *Silicon Detector Dark Matter Results from the Final Exposure of CDMS II*, Phys. Rev. Lett. **111** (2013) no. 25, 251301, arXiv:1304.4279 [hep-ex].

[590] CoGeNT Collaboration, C. E. Aalseth et al., *CoGeNT: A Search for Low-Mass Dark Matter using p-type Point Contact Germanium Detectors*, Phys. Rev. **D88** (2013) 012002, arXiv:1208.5737 [astro-ph.CO].

[591] J. Billard, L. Strigari, and E. Figueroa-Feliciano, *Implication of neutrino backgrounds on the reach of next generation dark matter direct detection experiments*, Phys. Rev. **D89** (2014) no. 2, 023524, arXiv:1307.5458 [hep-ph].

[592] GAMBIT Collaboration, P. Athron et al., *Status of the scalar singlet dark matter model*, Eur. Phys. J. **C77** (2017) no. 8, 568, arXiv:1705.07931 [hep-ph].

[593] GAMBIT Collaboration, P. Athron et al., *Global analyses of Higgs portal singlet dark matter models using GAMBIT*, Eur. Phys. J. **C79** (2019) no. 1, 38, arXiv:1808.10465 [hep-ph].

[594] T. Robens and T. Stefaniak, *Status of the Higgs Singlet Extension of the Standard Model after LHC Run 1*, Eur. Phys. J. **C75** (2015) 104, arXiv:1501.02234 [hep-ph].

[595] P. Bechtle, O. Brein, S. Heinemeyer, G. Weiglein, and K. E. Williams, *HiggsBounds: Confronting Arbitrary Higgs Sectors with Exclusion Bounds from LEP and the Tevatron*, Comput. Phys. Commun. **181** (2010) 138–167, arXiv:0811.4169 [hep-ph].

[596] P. Bechtle, O. Brein, S. Heinemeyer, G. Weiglein, and K. E. Williams, *HiggsBounds 2.0.0: Confronting Neutral and Charged Higgs Sector Predictions with Exclusion Bounds from LEP and the Tevatron*, Comput. Phys. Commun. **182** (2011) 2605–2631, arXiv:1102.1898 [hep-ph].

[597] P. Bechtle, O. Brein, S. Heinemeyer, O. Stål, T. Stefaniak, G. Weiglein, and K. E. Williams, HiggsBounds − 4*: Improved Tests of Extended Higgs Sectors against Exclusion Bounds from LEP, the Tevatron and the LHC*, Eur. Phys. J. **C74** (2014) no. 3, 2693, arXiv:1311.0055 [hep-ph].

[598] ALEPH, DELPHI, L3 and OPAL, LEP working group for Higgs boson searches Collaborations, *Searches for invisible Higgs bosons: Preliminary combined results using LEP data collected at energies up to 209-GeV*, in *Lepton and photon interactions at high energies. Proceedings, 20th International Symposium, LP 2001, Rome, Italy, July 23-28, 2001*. 2001. arXiv:hep-ex/0107032 [hep-ex].

[599] DELPHI Collaboration, J. Abdallah et al., *Searches for invisibly decaying Higgs bosons with the DELPHI detector at LEP*, Eur. Phys. J. **C32** (2004) 475–492, arXiv:hep-ex/0401022 [hep-ex].

[600] L3 Collaboration, P. Achard et al., *Search for an invisibly-decaying Higgs boson at LEP*, Phys. Lett. **B609** (2005) 35–48, arXiv:hep-ex/0501033 [hep-ex].

[601] OPAL Collaboration, G. Abbiendi et al., *Search for invisibly decaying Higgs bosons in e+ e- —> Z0 h0 production at s**(1/2) = 183-GeV - 209-GeV*, Phys. Lett. **B682** (2010) 381–390, arXiv:0707.0373 [hep-ex].

[602] DELPHI, OPAL, ALEPH, LEP Working Group for Higgs Boson Searches, L3 Collaboration, S. Schael et al., *Search for neutral MSSM Higgs bosons at LEP*, Eur. Phys. J. **C47** (2006) 547–587, arXiv:hep-ex/0602042 [hep-ex].

[603] OPAL Collaboration, G. Abbiendi et al., *Decay-mode independent searches for new scalar bosons with the OPAL detector at LEP*, Eur. Phys. J. **C27** (2003) 311–329, arXiv:hep-ex/0206022.

[604] ATLAS Collaboration, M. Aaboud et al., *Search for the Decay of the Higgs Boson to Charm Quarks with the ATLAS Experiment*, Phys. Rev. Lett. **120** (2018) no. 21, 211802, arXiv:1802.04329 [hep-ex].

[605] G. Perez, Y. Soreq, E. Stamou, and K. Tobioka, *Constraining the charm Yukawa and Higgs-quark coupling universality*, Phys. Rev. **D92** (2015) no. 3, 033016, arXiv:1503.00290 [hep-ph].

[606] W. Altmannshofer, J. Brod, and M. Schmaltz, *Experimental constraints on the coupling of the Higgs boson to electrons*, JHEP **05** (2015) 125, arXiv:1503.04830 [hep-ph].

[607] A. L. Kagan, G. Perez, F. Petriello, Y. Soreq, S. Stoynev, and J. Zupan, *Exclusive Window onto Higgs Yukawa Couplings*, Phys. Rev. Lett. **114** (2015) no. 10, 101802, arXiv:1406.1722 [hep-ph].

[608] ATLAS Collaboration, G. Aad et al., *Search for Higgs and Z Boson Decays to J/$\psi\gamma$ and*

$\Upsilon(nS)\gamma$ *with the ATLAS Detector*, Phys. Rev. Lett. **114** (2015) no. 12, 121801, arXiv:1501.03276 [hep-ex].

[609] CMS Collaboration, *Search for a Higgs boson decaying into* $\gamma^*\gamma \to \ell\ell\gamma$ *with low dilepton mass in pp collisions at* $\sqrt{s} = 8$ *TeV*, Phys. Lett. **B753** (2016) no. CERN-PH-EP-2015-137, CMS-HIG-14-003, 341–362, arXiv:1507.03031 [hep-ex].

[610] ATLAS Collaboration, M. Aaboud et al., *Searches for exclusive Higgs and Z boson decays into* $J/\psi\gamma$, $\psi(2S)\gamma$, *and* $\Upsilon(nS)\gamma$ *at* $\sqrt{s} = 13$ *TeV with the ATLAS detector*, Phys. Lett. **B786** (2018) 134–155, arXiv:1807.00802 [hep-ex].

[611] ATLAS Collaboration, M. Aaboud et al., *Search for exclusive Higgs and Z boson decays to* $\phi\gamma$ *and* $\rho\gamma$ *with the ATLAS detector*, arXiv:1712.02758 [hep-ex].

[612] Y. Soreq, H. X. Zhu, and J. Zupan, *Light quark Yukawa couplings from Higgs kinematics*, JHEP **12** (2016) 045, arXiv:1606.09621 [hep-ph].

[613] C. Delaunay, T. Golling, G. Perez, and Y. Soreq, *Enhanced Higgs boson coupling to charm pairs*, Phys. Rev. **D89** (2014) no. 3, 033014, arXiv:1310.7029 [hep-ph].

[614] CMS Collaboration, *Measurements of the Higgs boson production and decay rates and constraints on its couplings from a combined ATLAS and CMS analysis of the LHC pp collision data at sqrt s = 7 and 8 TeV*, CMS-PAS-HIG-15-002, 2015.

[615] CMS Collaboration, *Search for a standard model-like Higgs boson in the* $\mu^+\mu^-$ *and* e^+e^- *decay channels at the LHC*, Phys. Lett. **B744** (2015) no. CERN-PH-EP-2014-243, CMS-HIG-13-007, 184–207, arXiv:1410.6679 [hep-ex].

[616] G. Perez, Y. Soreq, E. Stamou, and K. Tobioka, *Prospects for measuring the Higgs boson coupling to light quarks*, Phys. Rev. **D93** (2016) no. 1, 013001, arXiv:1505.06689 [hep-ph].

[617] I. Brivio, F. Goertz, and G. Isidori, *Probing the Charm Quark Yukawa Coupling in Higgs+Charm Production*, Phys. Rev. Lett. **115** (2015) no. 21, 211801, arXiv:1507.02916 [hep-ph].

[618] M. König and M. Neubert, *Exclusive Radiative Higgs Decays as Probes of Light-Quark Yukawa Couplings*, JHEP **08** (2015) 012, arXiv:1505.03870 [hep-ph].

[619] G. T. Bodwin, H. S. Chung, J.-H. Ee, J. Lee, and F. Petriello, *Relativistic corrections to Higgs boson decays to quarkonia*, Phys. Rev. **D90** (2014) no. 11, 113010, arXiv:1407.6695 [hep-ph].

[620] G. T. Bodwin, F. Petriello, S. Stoynev, and M. Velasco, *Higgs boson decays to quarkonia and the* $H\bar{c}c$ *coupling*, Phys. Rev. **D88** (2013) no. 5, 053003, arXiv:1306.5770 [hep-ph].

[621] Y. T. Chien, V. Cirigliano, W. Dekens, J. de Vries, and E. Mereghetti, *Direct and indirect constraints on CP-violating Higgs-quark and Higgs-gluon interactions*, JHEP **02** (2016) 011, arXiv:1510.00725 [hep-ph].

[622] D. Egana-Ugrinovic and S. Thomas, *Higgs Boson Contributions to the Electron Electric Dipole Moment*, arXiv:1810.08631 [hep-ph].

[623] J. Brod and E. Stamou, *Electric dipole moment constraints on CP-violating heavy-quark Yukawas at next-to-leading order*, arXiv:1810.12303 [hep-ph].

[624] ACME Collaboration, J. Baron et al., *Order of Magnitude Smaller Limit on the Electric Dipole Moment of the Electron*, Science **343** (2014) 269–272, arXiv:1310.7534 [physics.atom-ph].

[625] ACME Collaboration, V. Andreev et al., *Improved limit on the electric dipole moment of the electron*, Nature **562** (2018) 355–360.

[626] J. Brod and D. Skodras, *Electric dipole moment constraints on CP-violating light-quark Yukawas*, arXiv:1811.05480 [hep-ph].

[627] R. Harnik, J. Kopp, and J. Zupan, *Flavor Violating Higgs Decays*, JHEP **03** (2013) 026,

arXiv:1209.1397 [hep-ph].

[628] G. Blankenburg, J. Ellis, and G. Isidori, *Flavour-Changing Decays of a 125 GeV Higgs-like Particle*, Phys. Lett. **B712** (2012) 386–390, arXiv:1202.5704 [hep-ph].

[629] M. Gorbahn and U. Haisch, *Searching for $t \to c(u)h$ with dipole moments*, JHEP **06** (2014) 033, arXiv:1404.4873 [hep-ph].

[630] CMS Collaboration, *Search for lepton flavour violating decays of the Higgs boson to $\mu\tau$ and $e\tau$ in proton-proton collisions at $\sqrt{s} = 13$ TeV*, JHEP **06** (2018) no. CERN-EP-2017-292, CMS-HIG-17-001, 001, arXiv:1712.07173 [hep-ex].

[631] ATLAS Collaboration, G. Aad et al., *Search for lepton-flavour-violating decays of the Higgs and Z bosons with the ATLAS detector*, Eur. Phys. J. **C77** (2017) no. 2, 70, arXiv:1604.07730 [hep-ex].

[632] ATLAS Collaboration, M. Aaboud et al., *Search for top quark decays $t \to qH$, with $H \to \gamma\gamma$, in $\sqrt{s} = 13$ TeV pp collisions using the ATLAS detector*, JHEP **10** (2017) 129, arXiv:1707.01404 [hep-ex].

[633] CMS Collaboration, *Search for top quark decays via Higgs-boson-mediated flavor-changing neutral currents in pp collisions at $\sqrt{s} = 8$ TeV*, JHEP **02** (2017) no. CERN-EP-2016-208, CMS-TOP-13-017, 079, arXiv:1610.04857 [hep-ex].

[634] ATLAS Collaboration, G. Aad et al., *Search for flavour-changing neutral current top quark decays $t \to Hq$ in pp collisions at $\sqrt{s} = 8$ TeV with the ATLAS detector*, JHEP **12** (2015) 061, arXiv:1509.06047 [hep-ex].

[635] ATLAS Collaboration, G. Aad et al., *Search for top quark decays $t \to qH$ with $H \to \gamma\gamma$ using the ATLAS detector*, JHEP **06** (2014) 008, arXiv:1403.6293 [hep-ex].

[636] F. Bishara, J. Brod, P. Uttayarat, and J. Zupan, *Nonstandard Yukawa Couplings and Higgs Portal Dark Matter*, JHEP **01** (2016) 010, arXiv:1504.04022 [hep-ph].

[637] A. Dery, A. Efrati, Y. Nir, Y. Soreq, and V. Susič, *Model building for flavor changing Higgs couplings*, Phys. Rev. **D90** (2014) 115022, arXiv:1408.1371 [hep-ph].

[638] A. Dery, A. Efrati, G. Hiller, Y. Hochberg, and Y. Nir, *Higgs couplings to fermions: 2HDM with MFV*, JHEP **08** (2013) 006, arXiv:1304.6727 [hep-ph].

[639] A. Dery, A. Efrati, Y. Hochberg, and Y. Nir, *What if $BR(h \to \mu\mu)/BR(h \to \tau\tau)$ does not equal m_μ^2/m_τ^2?*, JHEP **05** (2013) 039, arXiv:1302.3229 [hep-ph].

[640] S. L. Glashow and S. Weinberg, *Natural Conservation Laws for Neutral Currents*, Phys. Rev. **D15** (1977) 1958.

[641] E. A. Paschos, *Diagonal Neutral Currents*, Phys. Rev. **D15** (1977) 1966.

[642] W. Altmannshofer, S. Gori, A. L. Kagan, L. Silvestrini, and J. Zupan, *Uncovering Mass Generation Through Higgs Flavor Violation*, Phys. Rev. **D93** (2016) no. 3, 031301, arXiv:1507.07927 [hep-ph].

[643] W. Altmannshofer, J. Eby, S. Gori, M. Lotito, M. Martone, and D. Tuckler, *Collider Signatures of Flavorful Higgs Bosons*, Phys. Rev. **D94** (2016) no. 11, 115032, arXiv:1610.02398 [hep-ph].

[644] W. Altmannshofer, S. Gori, D. J. Robinson, and D. Tuckler, *The Flavor-locked Flavorful Two Higgs Doublet Model*, JHEP **03** (2018) 129, arXiv:1712.01847 [hep-ph].

[645] W. Altmannshofer and B. Maddock, *Flavorful Two Higgs Doublet Models with a Twist*, Phys. Rev. **D98** (2018) no. 7, 075005, arXiv:1805.08659 [hep-ph].

[646] C. D. Froggatt and H. B. Nielsen, *Hierarchy of Quark Masses, Cabibbo Angles and CP Violation*, Nucl. Phys. **B147** (1979) 277–298.

[647] G. F. Giudice and O. Lebedev, *Higgs-dependent Yukawa couplings*, Phys. Lett. **B665** (2008) 79–85, arXiv:0804.1753 [hep-ph].

[648] L. Randall and R. Sundrum, *A Large mass hierarchy from a small extra dimension*, Phys. Rev. Lett. **83** (1999) 3370–3373, arXiv:hep-ph/9905221 [hep-ph].

[649] M. J. Dugan, H. Georgi, and D. B. Kaplan, *Anatomy of a Composite Higgs Model*, Nucl. Phys. **B254** (1985) 299–326.

[650] H. Georgi, D. B. Kaplan, and P. Galison, *Calculation of the Composite Higgs Mass*, Phys. Lett. **143B** (1984) 152–154.

[651] J. A. Aguilar-Saavedra, *A Minimal set of top-Higgs anomalous couplings*, Nucl. Phys. **B821** (2009) 215–227, arXiv:0904.2387 [hep-ph].

[652] R. S. Chivukula and H. Georgi, *Composite Technicolor Standard Model*, Phys. Lett. **B188** (1987) 99–104.

[653] E. Gabrielli and G. F. Giudice, *Supersymmetric corrections to epsilon prime / epsilon at the leading order in QCD and QED*, Nucl. Phys. **B433** (1995) 3–25, arXiv:hep-lat/9407029 [hep-lat].

[654] A. Ali and D. London, *Profiles of the unitarity triangle and CP violating phases in the standard model and supersymmetric theories*, Eur. Phys. J. **C9** (1999) 687–703, arXiv:hep-ph/9903535 [hep-ph].

[655] A. J. Buras, P. Gambino, M. Gorbahn, S. Jager, and L. Silvestrini, *Universal unitarity triangle and physics beyond the standard model*, Phys. Lett. **B500** (2001) 161–167, arXiv:hep-ph/0007085 [hep-ph].

[656] A. J. Buras, *Minimal flavor violation*, Acta Phys. Polon. **B34** (2003) 5615–5668, arXiv:hep-ph/0310208 [hep-ph].

[657] A. L. Kagan, G. Perez, T. Volansky, and J. Zupan, *General Minimal Flavor Violation*, Phys. Rev. **D80** (2009) 076002, arXiv:0903.1794 [hep-ph].

[658] V. Cirigliano, B. Grinstein, G. Isidori, and M. B. Wise, *Minimal flavor violation in the lepton sector*, Nucl. Phys. **B728** (2005) 121–134, arXiv:hep-ph/0507001 [hep-ph].

[659] H. E. Haber and G. L. Kane, *The Search for Supersymmetry: Probing Physics Beyond the Standard Model*, Phys. Rept. **117** (1985) 75–263.

[660] D. Aloni, Y. Nir, and E. Stamou, *Large BR($h \to \tau\mu$) in the MSSM?*, JHEP **04** (2016) 162, arXiv:1511.00979 [hep-ph].

[661] M. Carena, I. Low, N. R. Shah, and C. E. M. Wagner, *Impersonating the Standard Model Higgs Boson: Alignment without Decoupling*, JHEP **04** (2014) 015, arXiv:1310.2248 [hep-ph].

[662] P. S. Bhupal Dev and A. Pilaftsis, *Maximally Symmetric Two Higgs Doublet Model with Natural Standard Model Alignment*, JHEP **12** (2014) 024, arXiv:1408.3405 [hep-ph].

[663] M. Carena, H. E. Haber, I. Low, N. R. Shah, and C. E. M. Wagner, *Complementarity between Nonstandard Higgs Boson Searches and Precision Higgs Boson Measurements in the MSSM*, Phys. Rev. **D91** (2015) no. 3, 035003, arXiv:1410.4969 [hep-ph].

[664] P. S. B. Dev and A. Pilaftsis, *Natural Standard Model Alignment in the Two Higgs Doublet Model*, J. Phys. Conf. Ser. **631** (2015) no. 1, 012030, arXiv:1503.09140 [hep-ph].

[665] H. E. Haber and O. Stål, *New LHC benchmarks for the $\mathcal{CP}$ -conserving two-Higgs-doublet model*, Eur. Phys. J. **C75** (2015) no. 10, 491, arXiv:1507.04281 [hep-ph].

[666] M. Carena, H. E. Haber, I. Low, N. R. Shah, and C. E. M. Wagner, *Alignment limit of the NMSSM Higgs sector*, Phys. Rev. **D93** (2016) no. 3, 035013, arXiv:1510.09137 [hep-ph].

[667] D. Carmi, A. Falkowski, E. Kuflik, T. Volansky, and J. Zupan, *Higgs After the Discovery: A Status Report*, JHEP **10** (2012) 196, arXiv:1207.1718 [hep-ph].

[668] A. Falkowski, F. Riva, and A. Urbano, *Higgs at last*, JHEP **11** (2013) 111, arXiv:1303.1812 [hep-ph].

[669] B. Grinstein and P. Uttayarat, *Carving Out Parameter Space in Type-II Two Higgs Doublets*

Model, JHEP **06** (2013) 094, arXiv:1304.0028 [hep-ph].

[670] F. J. Botella, G. C. Branco, M. N. Rebelo, and J. I. Silva-Marcos, *What if the masses of the first two quark families are not generated by the standard model Higgs boson?*, Phys. Rev. **D94** (2016) no. 11, 115031, arXiv:1602.08011 [hep-ph].

[671] D. Ghosh, R. S. Gupta, and G. Perez, *Is the Higgs Mechanism of Fermion Mass Generation a Fact? A Yukawa-less First-Two-Generation Model*, Phys. Lett. **B755** (2016) 504–508, arXiv:1508.01501 [hep-ph].

[672] A. K. Das and C. Kao, *A Two Higgs doublet model for the top quark*, Phys. Lett. **B372** (1996) 106–112, arXiv:hep-ph/9511329 [hep-ph].

[673] A. E. Blechman, A. A. Petrov, and G. Yeghiyan, *The Flavor puzzle in multi-Higgs models*, JHEP **11** (2010) 075, arXiv:1009.1612 [hep-ph].

[674] M. Leurer, Y. Nir, and N. Seiberg, *Mass matrix models: The Sequel*, Nucl. Phys. **B420** (1994) 468–504, arXiv:hep-ph/9310320 [hep-ph].

[675] Y. Grossman and Y. Nir, *Lepton mass matrix models*, Nucl. Phys. **B448** (1995) 30–50, arXiv:hep-ph/9502418 [hep-ph].

[676] T. Gherghetta and A. Pomarol, *Bulk fields and supersymmetry in a slice of AdS*, Nucl. Phys. **B586** (2000) 141–162, arXiv:hep-ph/0003129 [hep-ph].

[677] Y. Grossman and M. Neubert, *Neutrino masses and mixings in nonfactorizable geometry*, Phys. Lett. **B474** (2000) 361–371, arXiv:hep-ph/9912408 [hep-ph].

[678] S. J. Huber and Q. Shafi, *Fermion masses, mixings and proton decay in a Randall-Sundrum model*, Phys. Lett. **B498** (2001) 256–262, arXiv:hep-ph/0010195 [hep-ph].

[679] S. J. Huber, *Flavor violation and warped geometry*, Nucl. Phys. **B666** (2003) 269–288, arXiv:hep-ph/0303183 [hep-ph].

[680] A. Azatov, M. Toharia, and L. Zhu, *Higgs Mediated FCNC's in Warped Extra Dimensions*, Phys. Rev. **D80** (2009) 035016, arXiv:0906.1990 [hep-ph].

[681] S. Casagrande, F. Goertz, U. Haisch, M. Neubert, and T. Pfoh, *Flavor Physics in the Randall-Sundrum Model: I. Theoretical Setup and Electroweak Precision Tests*, JHEP **10** (2008) 094, arXiv:0807.4937 [hep-ph].

[682] M. Bauer, S. Casagrande, U. Haisch, and M. Neubert, *Flavor Physics in the Randall-Sundrum Model: II. Tree-Level Weak-Interaction Processes*, JHEP **09** (2010) 017, arXiv:0912.1625 [hep-ph].

[683] R. Malm, M. Neubert, K. Novotny, and C. Schmell, *5D Perspective on Higgs Production at the Boundary of a Warped Extra Dimension*, JHEP **01** (2014) 173, arXiv:1303.5702 [hep-ph].

[684] P. R. Archer, M. Carena, A. Carmona, and M. Neubert, *Higgs Production and Decay in Models of a Warped Extra Dimension with a Bulk Higgs*, JHEP **01** (2015) 060, arXiv:1408.5406 [hep-ph].

[685] M. Blanke, A. J. Buras, B. Duling, S. Gori, and A. Weiler, $\Delta F{=}2$ *Observables and Fine-Tuning in a Warped Extra Dimension with Custodial Protection*, JHEP **03** (2009) 001, arXiv:0809.1073 [hep-ph].

[686] M. Blanke, A. J. Buras, B. Duling, K. Gemmler, and S. Gori, *Rare K and B Decays in a Warped Extra Dimension with Custodial Protection*, JHEP **03** (2009) 108, arXiv:0812.3803 [hep-ph].

[687] M. E. Albrecht, M. Blanke, A. J. Buras, B. Duling, and K. Gemmler, *Electroweak and Flavour Structure of a Warped Extra Dimension with Custodial Protection*, JHEP **09** (2009) 064, arXiv:0903.2415 [hep-ph].

[688] K. Agashe, G. Perez, and A. Soni, *Collider Signals of Top Quark Flavor Violation from a Warped Extra Dimension*, Phys. Rev. **D75** (2007) 015002, arXiv:hep-ph/0606293

[hep-ph].

[689] K. Agashe, A. Azatov, Y. Cui, L. Randall, and M. Son, *Warped Dipole Completed, with a Tower of Higgs Bosons*, JHEP **06** (2015) 196, arXiv:1412.6468 [hep-ph].

[690] B. M. Dillon and S. J. Huber, *Non-Custodial Warped Extra Dimensions at the LHC?*, JHEP **06** (2015) 066, arXiv:1410.7345 [hep-ph].

[691] G. Cacciapaglia, C. Csaki, J. Galloway, G. Marandella, J. Terning, and A. Weiler, *A GIM Mechanism from Extra Dimensions*, JHEP **04** (2008) 006, arXiv:0709.1714 [hep-ph].

[692] K. Agashe, G. Perez, and A. Soni, *Flavor structure of warped extra dimension models*, Phys. Rev. **D71** (2005) 016002, arXiv:hep-ph/0408134 [hep-ph].

[693] K. Agashe, G. Perez, and A. Soni, *B-factory signals for a warped extra dimension*, Phys. Rev. Lett. **93** (2004) 201804, arXiv:hep-ph/0406101 [hep-ph].

[694] ATLAS Collaboration, *A search for $\mathbf{t\bar{t}}$ resonances using lepton plus jets events in proton-proton collisions at $\sqrt{s} = 8$ TeV with the ATLAS detector*, ATLAS-CONF-2015-009, 2015.

[695] G. Panico and A. Wulzer, *The Composite Nambu-Goldstone Higgs*, Lect. Notes Phys. **913** (2016) pp.1–316, arXiv:1506.01961 [hep-ph].

[696] D. B. Kaplan, *Flavor at SSC energies: A New mechanism for dynamically generated fermion masses*, Nucl. Phys. **B365** (1991) 259–278.

[697] K. Agashe and R. Contino, *Composite Higgs-Mediated FCNC*, Phys. Rev. **D80** (2009) 075016, arXiv:0906.1542 [hep-ph].

[698] M. Gillioz, R. Grober, C. Grojean, M. Muhlleitner, and E. Salvioni, *Higgs Low-Energy Theorem (and its corrections) in Composite Models*, JHEP **10** (2012) 004, arXiv:1206.7120 [hep-ph].

[699] C. Delaunay, C. Grojean, and G. Perez, *Modified Higgs Physics from Composite Light Flavors*, JHEP **09** (2013) 090, arXiv:1303.5701 [hep-ph].

[700] A. Azatov, G. Panico, G. Perez, and Y. Soreq, *On the Flavor Structure of Natural Composite Higgs Models and Top Flavor Violation*, JHEP **12** (2014) 082, arXiv:1408.4525 [hep-ph].

[701] A. Pomarol and F. Riva, *The Composite Higgs and Light Resonance Connection*, JHEP **08** (2012) 135, arXiv:1205.6434 [hep-ph].

[702] M. Redi and A. Weiler, *Flavor and CP Invariant Composite Higgs Models*, JHEP **11** (2011) 108, arXiv:1106.6357 [hep-ph].

[703] M. Redi, *Composite MFV and Beyond*, Eur. Phys. J. **C72** (2012) 2030, arXiv:1203.4220 [hep-ph].

[704] M. Redi, *Leptons in Composite MFV*, JHEP **09** (2013) 060, arXiv:1306.1525 [hep-ph].

[705] C. Csaki, C. Delaunay, C. Grojean, and Y. Grossman, *A Model of Lepton Masses from a Warped Extra Dimension*, JHEP **10** (2008) 055, arXiv:0806.0356 [hep-ph].

[706] F. del Aguila, A. Carmona, and J. Santiago, *Neutrino Masses from an A4 Symmetry in Holographic Composite Higgs Models*, JHEP **08** (2010) 127, arXiv:1001.5151 [hep-ph].

[707] C. Hagedorn and M. Serone, *Leptons in Holographic Composite Higgs Models with Non-Abelian Discrete Symmetries*, JHEP **10** (2011) 083, arXiv:1106.4021 [hep-ph].

[708] C. Hagedorn and M. Serone, *General Lepton Mixing in Holographic Composite Higgs Models*, JHEP **02** (2012) 077, arXiv:1110.4612 [hep-ph].

[709] ATLAS Collaboration, G. Aad et al., *Search for pair-produced third-generation squarks decaying via charm quarks or in compressed supersymmetric scenarios in pp collisions at $\sqrt{s} = 8$ TeV with the ATLAS detector*, Phys. Rev. **D90** (2014) no. 5, 052008, arXiv:1407.0608 [hep-ex].

[710] ATLAS Collaboration, G. Aad et al., *Search for Scalar Charm Quark Pair Production in pp Collisions at $\sqrt{s} = 8$ TeV with the ATLAS Detector*, Phys. Rev. Lett. **114** (2015) no. 16,

161801, arXiv:1501.01325 [hep-ex].

[711] ATLAS Collaboration, *Prospects for $H \to c\bar{c}$ using Charm Tagging with the ATLAS Experiment at the HL-LHC*, ATL-PHYS-PUB-2018-016, 2018.

[712] ATLAS Collaboration, *Physics at a High-Luminosity LHC with ATLAS*, 2012. ATL-PHYS-PUB-2012-004, ATL-COM-PHYS-2012-1455.

[713] LHCb Collaboration, *Identification of beauty and charm quark jets at LHCb*, JINST **10** (2015) no. CERN-PH-EP-2015-101, LHCB-PAPER-2015-016, P06013, arXiv:1504.07670 [hep-ex].

[714] LHCb Collaboration, *Search for $H^0 \to b\bar{b}$ or $c\bar{c}$ in association with a W or Z boson in the forward region of pp collisions*, CERN-LHCB-CONF-2016-006, LHCB-CONF-2016-006, 2016.

[715] ATLAS Collaboration, M. Aaboud et al., *Search for Higgs and Z Boson Decays to $\phi\gamma$ with the ATLAS Detector*, Phys. Rev. Lett. **117** (2016) no. 11, 111802, arXiv:1607.03400 [hep-ex].

[716] S. Alte, M. König, and M. Neubert, *Exclusive Weak Radiative Higgs Decays in the Standard Model and Beyond*, JHEP **12** (2016) 037, arXiv:1609.06310 [hep-ph].

[717] F. Yu, *Phenomenology of Enhanced Light Quark Yukawa Couplings and the $W^{\pm}h$ Charge Asymmetry*, JHEP **02** (2017) 083, arXiv:1609.06592 [hep-ph].

[718] J. Gao, *Probing light-quark Yukawa couplings via hadronic event shapes at lepton colliders*, JHEP **01** (2018) 038, arXiv:1608.01746 [hep-ph].

[719] J. Duarte-Campderros, G. Perez, M. Schlaffer, and A. Soffer, *Probing the strange Higgs coupling at lepton colliders using light-jet flavor tagging*, arXiv:1811.09636 [hep-ph].

[720] E. Boudinov, P. Kluit, F. Cossutti, K. Huet, M. Gunther, and O. Botner, *Measurement of the strange quark forward- backward asymmetry around the Z peak*, CONF, DELPHI-98-115, ICHEP'98, 1998.

[721] SLD Collaboration, M. Kalelkar et al., *Light quark fragmentation in polarized Z0 decays at SLD*, Nucl. Phys. Proc. Suppl. **96** (2001) 31–35, arXiv:hep-ex/0008032 [hep-ex].

[722] T. Sjöstrand, S. Mrenna, and P. Skands, *PYTHIA 6.4 physics and manual*, JHEP **05** (2006) 026, arXiv:hep-ph/0603175 [hep-ph].

[723] G. Isidori, A. V. Manohar, and M. Trott, *Probing the nature of the Higgs-like Boson via $h \to V\mathcal{F}$ decays*, Phys. Lett. **B728** (2014) 131–135, arXiv:1305.0663 [hep-ph].

[724] Y. Grossman, M. König, and M. Neubert, *Exclusive Radiative Decays of W and Z Bosons in QCD Factorization*, JHEP **04** (2015) 101, arXiv:1501.06569 [hep-ph].

[725] S. Alte, M. König, and M. Neubert, *Exclusive Radiative Z-Boson Decays to Mesons with Flavor-Singlet Components*, JHEP **02** (2016) 162, arXiv:1512.09135 [hep-ph].

[726] W.-Y. Keung, *THE DECAY OF THE HIGGS BOSON INTO HEAVY QUARKONIUM STATES*, Phys. Rev. **D27** (1983) 2762.

[727] J. de Blas, M. Ciuchini, E. Franco, S. Mishima, M. Pierini, L. Reina, and L. Silvestrini, *Electroweak precision observables and Higgs-boson signal strengths in the Standard Model and beyond: present and future*, JHEP **12** (2016) 135, arXiv:1608.01509 [hep-ph].

[728] *Search for the Standard Model Higgs and Z Boson decays to $J/\psi\gamma$: HL-LHC projections*, ATL-PHYS-PUB-2015-043, 2015.

[729] S. Bressler, A. Dery, and A. Efrati, *Asymmetric lepton-flavor violating Higgs boson decays*, Phys. Rev. **D90** (2014) no. 1, 015025, arXiv:1405.4545 [hep-ph].

[730] C. Arnesen, I. Z. Rothstein, and J. Zupan, *Smoking Guns for On-Shell New Physics at the LHC*, Phys. Rev. Lett. **103** (2009) 151801, arXiv:0809.1429 [hep-ph].

[731] A. Biekötter, J. Brehmer, and T. Plehn, *Extending the limits of Higgs effective theory*, Phys. Rev. **D94** (2016) no. 5, 055032, arXiv:1602.05202 [hep-ph].

[732] J. Brehmer, A. Freitas, D. Lopez-Val, and T. Plehn, *Pushing Higgs Effective Theory to its Limits*, Phys. Rev. **D93** (2016) no. 7, 075014, arXiv:1510.03443 [hep-ph].

[733] S. Dawson, I. M. Lewis, and M. Zeng, *Usefulness of effective field theory for boosted Higgs production*, Phys. Rev. **D91** (2015) 074012, arXiv:1501.04103 [hep-ph].

[734] M. Schlaffer, M. Spannowsky, M. Takeuchi, A. Weiler, and C. Wymant, *Boosted Higgs Shapes*, Eur. Phys. J. **C74** (2014) no. 10, 3120, arXiv:1405.4295 [hep-ph].

[735] C. Grojean, E. Salvioni, M. Schlaffer, and A. Weiler, *Very boosted Higgs in gluon fusion*, JHEP **05** (2014) 022, arXiv:1312.3317 [hep-ph].

[736] U. Langenegger, M. Spira, and I. Strebel, *Testing the Higgs Boson Coupling to Gluons*, arXiv:1507.01373 [hep-ph].

[737] J. Bramante, A. Delgado, L. Lehman, and A. Martin, *Boosted Higgses from chromomagnetic b's: $b\bar{b}h$ at high luminosity*, Phys. Rev. **D93** (2016) no. 5, 053001, arXiv:1410.3484 [hep-ph].

[738] M. Buschmann, C. Englert, D. Goncalves, T. Plehn, and M. Spannowsky, *Resolving the Higgs-Gluon Coupling with Jets*, Phys. Rev. **D90** (2014) no. 1, 013010, arXiv:1405.7651 [hep-ph].

[739] A. Azatov and A. Paul, *Probing Higgs couplings with high p_T Higgs production*, JHEP **01** (2014) 014, arXiv:1309.5273 [hep-ph].

[740] A. Banfi, A. Martin, and V. Sanz, *Probing top-partners in Higgs+jets*, JHEP **08** (2014) 053, arXiv:1308.4771 [hep-ph].

[741] M. Buschmann, D. Goncalves, S. Kuttimalai, M. Schonherr, F. Krauss, and T. Plehn, *Mass Effects in the Higgs-Gluon Coupling: Boosted vs Off-Shell Production*, JHEP **02** (2015) 038, arXiv:1410.5806 [hep-ph].

[742] J. C. Collins, D. E. Soper, and G. F. Sterman, *Transverse Momentum Distribution in Drell-Yan Pair and W and Z Boson Production*, Nucl. Phys. **B250** (1985) 199–224.

[743] U. Baur and E. W. N. Glover, *Higgs Boson Production at Large Transverse Momentum in Hadronic Collisions*, Nucl. Phys. **B339** (1990) 38–66.

[744] P. Artoisenet et al., *A framework for Higgs characterisation*, JHEP **11** (2013) 043, arXiv:1306.6464 [hep-ph].

[745] S. Amor Dos Santos et al., *Probing the CP nature of the Higgs coupling in $t\bar{t}h$ events at the LHC*, Phys. Rev. **D96** (2017) no. 1, 013004, arXiv:1704.03565 [hep-ph].

[746] D. Azevedo, A. Onofre, F. Filthaut, and R. Goncalo, *CP tests of Higgs couplings in $t\bar{t}h$ semileptonic events at the LHC*, Phys. Rev. **D98** (2018) no. 3, 033004, arXiv:1711.05292 [hep-ph].

[747] ATLAS Collaboration, *Probing the $\mathcal{CP}$ nature of the Higgs boson coupling to τ leptons at HL-LHC*, ATL-PHYS-PUB-2019-008, 2019.

[748] ATLAS Collaboration, G. Aad et al., *Reconstruction of hadronic decay products of tau leptons with the ATLAS experiment*, Eur. Phys. J. **C76** (2016) no. 5, 295, arXiv:1512.05955 [hep-ex].

[749] J. Ellis, C. W. Murphy, V. Sanz, and T. You, *Updated Global SMEFT Fit to Higgs, Diboson and Electroweak Data*, JHEP **06** (2018) 146, arXiv:1803.03252 [hep-ph].

[750] J. Ellis, V. Sanz, and T. You, *Complete Higgs Sector Constraints on Dimension-6 Operators*, JHEP **07** (2014) 036, arXiv:1404.3667 [hep-ph].

[751] J. Ellis, V. Sanz, and T. You, *The Effective Standard Model after LHC Run I*, JHEP **03** (2015) 157, arXiv:1410.7703 [hep-ph].

[752] C. W. Murphy, *Statistical approach to Higgs boson couplings in the standard model effective field theory*, Phys. Rev. **D97** (2018) no. 1, 015007, arXiv:1710.02008 [hep-ph].

[753] I. Brivio and M. Trott, *Scheming in the SMEFT... and a reparameterization invariance!*, JHEP **07** (2017) 148, arXiv:1701.06424 [hep-ph].

[754] R. Alonso, E. E. Jenkins, A. V. Manohar, and M. Trott, *Renormalization Group Evolution of the Standard Model Dimension Six Operators III: Gauge Coupling Dependence and Phenomenology*, JHEP **04** (2014) 159, arXiv:1312.2014 [hep-ph].

[755] V. Cirigliano, J. Jenkins, and M. Gonzalez-Alonso, *Semileptonic decays of light quarks beyond the Standard Model*, Nucl. Phys. **B830** (2010) 95–115, arXiv:0908.1754 [hep-ph].

[756] C. Hartmann and M. Trott, *On one-loop corrections in the standard model effective field theory; the $\Gamma(h \to \gamma\gamma)$ case*, JHEP **07** (2015) 151, arXiv:1505.02646 [hep-ph].

[757] C. Hartmann and M. Trott, *Higgs Decay to Two Photons at One Loop in the Standard Model Effective Field Theory*, Phys. Rev. Lett. **115** (2015) no. 19, 191801, arXiv:1507.03568 [hep-ph].

[758] A. Dedes, M. Paraskevas, J. Rosiek, K. Suxho, and L. Trifyllis, *The decay $h \to \gamma\gamma$ in the Standard-Model Effective Field Theory*, JHEP **08** (2018) 103, arXiv:1805.00302 [hep-ph].

[759] S. Dawson and P. P. Giardino, *Electroweak Corrections to Higgs to $\gamma\gamma$ and W^+W^- in the SMEFT*, arXiv:1807.11504 [hep-ph].

[760] F. Maltoni, E. Vryonidou, and C. Zhang, *Higgs production in association with a top-antitop pair in the Standard Model Effective Field Theory at NLO in QCD*, JHEP **10** (2016) 123, arXiv:1607.05330 [hep-ph].

[761] D. Barducci et al., *Interpreting top-quark LHC measurements in the standard-model effective field theory*, arXiv:1802.07237 [hep-ph].

[762] L. Berthier, M. Bjorn, and M. Trott, *Incorporating doubly resonant $W^{\pm}$ data in a global fit of SMEFT parameters to lift flat directions*, JHEP **09** (2016) 157, arXiv:1606.06693 [hep-ph].

[763] I. Brivio and M. Trott, *The Standard Model as an Effective Field Theory*, arXiv:1706.08945 [hep-ph].

[764] I. Brivio, Y. Jiang, and M. Trott, *The SMEFTsim package, theory and tools*, JHEP **12** (2017) 070, arXiv:1709.06492 [hep-ph].

[765] SLD Electroweak Group, DELPHI, ALEPH, SLD, SLD Heavy Flavour Group, OPAL, LEP Electroweak Working Group, L3 Collaboration, S. Schael et al., *Precision electroweak measurements on the Z resonance*, Phys. Rept. **427** (2006) 257–454, arXiv:hep-ex/0509008 [hep-ex].

[766] CDF, D0 Collaboration, T. A. Aaltonen et al., *Combination of CDF and D0 W-Boson Mass Measurements*, Phys. Rev. **D88** (2013) no. 5, 052018, arXiv:1307.7627 [hep-ex].

[767] ALEPH Collaboration, A. Heister et al., *Measurement of W-pair production in e+ e- collisions at centre-of-mass energies from 183-GeV to 209-GeV*, Eur. Phys. J. **C38** (2004) 147–160.

[768] L3 Collaboration, P. Achard et al., *Measurement of the cross section of W-boson pair production at LEP*, Phys. Lett. **B600** (2004) 22–40, arXiv:hep-ex/0409016 [hep-ex].

[769] OPAL Collaboration, G. Abbiendi et al., *Measurement of the e+ e- $\to$ W+ W- cross section and W decay branching fractions at LEP*, Eur. Phys. J. **C52** (2007) 767–785, arXiv:0708.1311 [hep-ex].

[770] DELPHI, OPAL, LEP Electroweak, ALEPH, L3 Collaboration, S. Schael et al., *Electroweak Measurements in Electron-Positron Collisions at W-Boson-Pair Energies at LEP*, Phys. Rept. **532** (2013) 119–244, arXiv:1302.3415 [hep-ex].

[771] ATLAS Collaboration, M. Aaboud et al., *Measurement of the W-boson mass in pp collisions at $\sqrt{s} = 7$ TeV with the ATLAS detector*, Eur. Phys. J. **C78** (2018) no. 2, 110, arXiv:1701.07240 [hep-ex].

[772] ATLAS Collaboration, *Combined measurements of Higgs boson production and decay in the*

$H \to ZZ^* \to 4\ell$ and $H \to \gamma\gamma$ channels using $\sqrt{s} = 13$ TeV pp collision data collected with the ATLAS experiment, , 2017.

[773] ATLAS Collaboration, M. Aaboud et al., *Measurement of the W^+W^- production cross section in pp collisions at a centre-of-mass energy of $\sqrt{s}$ = 13 TeV with the ATLAS experiment*, Phys. Lett. **B773** (2017) 354–374, arXiv:1702.04519 [hep-ex].

[774] M. Ciuchini, E. Franco, S. Mishima, and L. Silvestrini, *Electroweak Precision Observables, New Physics and the Nature of a 126 GeV Higgs Boson*, JHEP **08** (2013) 106, arXiv:1306.4644 [hep-ph].

[775] L. Silvestrini, *EW fits at HL-LHC*, https://indico.cern.ch/event/686494/contributions/3037290/attachments/1669241/2677174/silvestriniHL-LHC_SM.pdf.

[776] O. Eberhardt, *Global constraints on the dimension-6 Standard Model Effective Field Theory*, https://indico.cern.ch/event/686555/contributions/2970902/attachments/1681242/2701120/927_Eberhardt_Global_constraints_on_the_dim-6_SMEFT.pdf.

[777] A. Alves, N. Rosa-Agostinho, O. J. P. Éboli, and M. C. Gonzalez-Garcia, *Effect of Fermionic Operators on the Gauge Legacy of the LHC Run I*, Phys. Rev. **D98** (2018) no. 1, 013006, arXiv:1805.11108 [hep-ph].

[778] A. Gilbert, *CMS Higgs Combination Projections*, https://indico.cern.ch/event/747493/contributions/3091361/attachments/1695500/2728959/CMSProjections-Shared-v1.pdf.

[779] C. Hays, V. Sanz Gonzalez, and G. Zemaityte, *Constraining EFT parameters using simplified template cross sections*, LHCHXSWG-INT-2017-001, 2017.

[780] S. Dawson, C. Englert, and T. Plehn, *Higgs Physics: It ain't over till it's over*, arXiv:1808.01324 [hep-ph].

[781] J. D. Wells and Z. Zhang, *Effective theories of universal theories*, JHEP **01** (2016) 123, arXiv:1510.08462 [hep-ph].

[782] A. Caldwell, D. Kollar, and K. Kroninger, *BAT: The Bayesian Analysis Toolkit*, Comput. Phys. Commun. **180** (2009) 2197–2209, arXiv:0808.2552 [physics.data-an].

[783] I. Dubovyk, A. Freitas, J. Gluza, T. Riemann, and J. Usovitsch, *The two-loop electroweak bosonic corrections to $\sin^2\theta^b\_eff$* , Phys. Lett. **B762** (2016) 184–189, arXiv:1607.08375 [hep-ph].

[784] I. Dubovyk, A. Freitas, J. Gluza, T. Riemann, and J. Usovitsch, *Complete electroweak two-loop corrections to Z boson production and decay*, Phys. Lett. **B783** (2018) 86–94, arXiv:1804.10236 [hep-ph].

[785] P. Azzi, S. Farry, P. Nason, A. Tricoli, and D. Zeppenfeld, *Standard Model Physics at the HL-LHC and HE-LHC*, CERN-LPCC-2018-03, 2018.

[786] J. de Blas, M. Ciuchini, E. Franco, S. Mishima, M. Pierini, L. Reina, and L. Silvestrini, *Electroweak precision constraints at present and future colliders*, PoS **ICHEP2016** (2017) 690, arXiv:1611.05354 [hep-ph].

[787] J. de Blas, M. Ciuchini, E. Franco, S. Mishima, M. Pierini, L. Reina, and L. Silvestrini, *The Global Electroweak and Higgs Fits in the LHC era*, PoS **EPS-HEP2017** (2017) 467, arXiv:1710.05402 [hep-ph].

[788] J. de Blas, M. Ciuchini, E. Franco, S. Mishima, M. Pierini, L. Reina, and L. Silvestrini.

[789] V. Barger, L. L. Everett, C. B. Jackson, and G. Shaughnessy, *Higgs-Pair Production and Measurement of the Triscalar Coupling at LHC(8,14)*, Phys. Lett. **B728** (2014) 433–436, arXiv:1311.2931 [hep-ph].

[790] A. J. Barr, M. J. Dolan, C. Englert, D. E. Ferreira de Lima, and M. Spannowsky, *Higgs*

Self-Coupling Measurements at a 100 TeV Hadron Collider, JHEP **02** (2015) 016, arXiv:1412.7154 [hep-ph].

[791] A. Biekötter, D. Gonçalves, T. Plehn, M. Takeuchi, and D. Zerwas, *The Global Higgs Picture at 27 TeV*, arXiv:1811.08401 [hep-ph].

[792] A. Butter, O. J. P. Eboli, J. Gonzalez-Fraile, M. C. Gonzalez-Garcia, T. Plehn, and M. Rauch, *The Gauge-Higgs Legacy of the LHC Run I*, JHEP **07** (2016) 152, arXiv:1604.03105 [hep-ph].

[793] A. Biekötter, T. Corbett, and T. Plehn, *The Gauge-Higgs Legacy of the LHC Run II*, arXiv:1812.07587 [hep-ph].

[794] T. Corbett, O. J. P. Eboli, D. Goncalves, J. Gonzalez-Fraile, T. Plehn, and M. Rauch, *The Higgs Legacy of the LHC Run I*, JHEP **08** (2015) 156, arXiv:1505.05516 [hep-ph].

[795] O. J. P. Eboli and D. Zeppenfeld, *Observing an invisible Higgs boson*, Phys. Lett. **B495** (2000) 147–154, arXiv:hep-ph/0009158 [hep-ph].

[796] C. Englert, R. Kogler, H. Schulz, and M. Spannowsky, *Higgs coupling measurements at the LHC*, Eur. Phys. J. **C76** (2016) no. 7, 393, arXiv:1511.05170 [hep-ph].

[797] CMS Collaboration, *First Level Track Jet Trigger for Displaced Jets at High Luminosity LHC*, CMS-PAS-FTR-18-018, 2018.

[798] CMS Collaboration, *Search for long-lived particles with displaced vertices in multijet events in proton-proton collisions at $\sqrt{s}$ =13 TeV*, Phys. Rev. **D98** (2018) no. CERN-EP-2018-203, CMS-EXO-17-018, 092011, arXiv:1808.03078 [hep-ex].

[799] ATLAS Collaboration, M. Aaboud et al., *Search for the Higgs boson produced in association with a vector boson and decaying into two spin-zero particles in the $H \to aa \to 4b$ channel in pp collisions at $\sqrt{s} = 13$ TeV with the ATLAS detector*, JHEP **10** (2018) 031, arXiv:1806.07355 [hep-ex].

[800] CMS Collaboration, A. Sirunyan et al., *Search for new long-lived particles at $\sqrt{s} = 13$TeV*, Phys. Lett. B **780** (2017) 432.

[801] S. Alioli, P. Nason, C. Oleari, and E. Re, *NLO Higgs boson production via gluon fusion matched with shower in POWHEG*, JHEP **04** (2009) 002, arXiv:0812.0578 [hep-ph].

[802] J. Liu, Z. Liu, and L.-T. Wang, *Long-lived particles at the LHC: catching them in time*, arXiv:1805.05957 [hep-ph].

[803] R. Barbier et al., *R-parity violating supersymmetry*, Phys. Rept. **420** (2005) 1–202, arXiv:hep-ph/0406039 [hep-ph].

[804] G. F. Giudice and R. Rattazzi, *Theories with gauge mediated supersymmetry breaking*, Phys. Rept. **322** (1999) 419–499, arXiv:hep-ph/9801271 [hep-ph].

[805] P. Meade, M. Reece, and D. Shih, *Long-Lived Neutralino NLSPs*, JHEP **10** (2010) 067, arXiv:1006.4575 [hep-ph].

[806] A. Arvanitaki, N. Craig, S. Dimopoulos, and G. Villadoro, *Mini-Split*, JHEP **02** (2013) 126, arXiv:1210.0555 [hep-ph].

[807] N. Arkani-Hamed, A. Gupta, D. E. Kaplan, N. Weiner, and T. Zorawski, *Simply Unnatural Supersymmetry*, arXiv:1212.6971 [hep-ph].

[808] Z. Liu and B. Tweedie, *The Fate of Long-Lived Superparticles with Hadronic Decays after LHC Run 1*, JHEP **06** (2015) 042, arXiv:1503.05923 [hep-ph].

[809] Z. Chacko, H.-S. Goh, and R. Harnik, *The Twin Higgs: Natural electroweak breaking from mirror symmetry*, Phys. Rev. Lett. **96** (2006) 231802, arXiv:hep-ph/0506256 [hep-ph].

[810] G. Burdman, Z. Chacko, H.-S. Goh, and R. Harnik, *Folded supersymmetry and the LEP paradox*, JHEP **02** (2007) 009, arXiv:hep-ph/0609152 [hep-ph].

[811] J. Kang and M. A. Luty, *Macroscopic Strings and 'Quirks' at Colliders*, JHEP **11** (2009) 065,

arXiv:0805.4642 [hep-ph].

[812] N. Craig, A. Katz, M. Strassler, and R. Sundrum, *Naturalness in the Dark at the LHC*, JHEP **07** (2015) 105, arXiv:1501.05310 [hep-ph].

[813] A. Davoli, A. De Simone, T. Jacques, and V. Sanz, *Displaced Vertices from Pseudo-Dirac Dark Matter*, JHEP **11** (2017) 025, arXiv:1706.08985 [hep-ph].

[814] C. Allaire et al., *Beam test measurements of Low Gain Avalanche Detector single pads and arrays for the ATLAS High Granularity Timing Detector*, JINST **13** (2018) no. 06, P06017, arXiv:1804.00622 [physics.ins-det].

[815] LHCb Collaboration, *Physics case for an LHCb Upgrade II - Opportunities in flavour physics, and beyond, in the HL-LHC era*, CERN-LHCC-2018-027, LHCB-PUB-2018-009, 2018. arXiv:1808.08865.

[816] CMS Collaboration, *Search for Long-Lived Neutral Particles Decaying to Quark-Antiquark Pairs in Proton-Proton Collisions at $\sqrt{s} = 8$ TeV*, Phys. Rev. **D91** (2015) no. CERN-PH-EP-2014-256, CMS-EXO-12-038, 012007, arXiv:1411.6530 [hep-ex].

[817] A. Coccaro, D. Curtin, H. J. Lubatti, H. Russell, and J. Shelton, *Data-driven Model-independent Searches for Long-lived Particles at the LHC*, Phys. Rev. **D94** (2016) no. 11, 113003, arXiv:1605.02742 [hep-ph].

[818] C. Bernaciak, T. Plehn, P. Schichtel, and J. Tattersall, *Spying an invisible Higgs boson*, Phys. Rev. **D91** (2015) 035024, arXiv:1411.7699 [hep-ph].

[819] ATLAS Collaboration, M. Aaboud et al., *Search for long-lived, massive particles in events with displaced vertices and missing transverse momentum in $\sqrt{s}$ = 13 TeV pp collisions with the ATLAS detector*, Phys. Rev. **D97** (2018) no. 5, 052012, arXiv:1710.04901 [hep-ex].

[820] N. Greiner, S. Höche, G. Luisoni, M. Schönherr, J.-C. Winter, and V. Yundin, *Phenomenological analysis of Higgs boson production through gluon fusion in association with jets*, JHEP **01** (2016) 169, arXiv:1506.01016 [hep-ph].

[821] CMS Collaboration, *Search for an exotic decay of the Higgs boson to a pair of light pseudoscalars in the final state with two b quarks and two τ leptons in proton-proton collisions at $\sqrt{s} = 13$ TeV*, Phys. Lett. B **785** (2018) no. CERN-EP-2018-089, CMS-HIG-17-024, 462, arXiv:1805.10191 [hep-ex].

[822] CMS Collaboration, *Projection of searches for exotic Higgs boson decays to light pseudoscalars for the High-Luminosity LHC*, CMS-PAS-FTR-18-035, 2018.

[823] CMS Collaboration, *Search for an exotic decay of the Higgs boson to a pair of light pseudoscalars in the final state of two muons and two τ leptons in proton-proton collisions at $\sqrt{s} = 13$ TeV*, CERN-EP-2018-078, CMS-HIG-17-029, 2018. arXiv:1805.04865 [hep-ex].

[824] D. Curtin, R. Essig, and Y.-M. Zhong, *Uncovering light scalars with exotic Higgs decays to $b\bar{b}\mu^+\mu^-$*, JHEP **06** (2015) 025, arXiv:1412.4779 [hep-ph].

[825] ATLAS Collaboration, *Calibration of b-tagging using dileptonic top pair events in a combinatorial likelihood approach with the ATLAS experiment*, ATLAS-CONF-2014-004, ATLAS-COM-CONF-2014-003 (2014) .

[826] J. M. Butterworth, A. R. Davison, M. Rubin, and G. P. Salam, *Jet substructure as a new Higgs search channel at the LHC*, AIP Conf.Proc. **1078** (2009) 189–191, arXiv:0809.2530 [hep-ph].

[827] ATLAS Collaboration, M. Aaboud et al., *Search for Higgs boson decays into a pair of light bosons in the $bb\mu\mu$ final state in pp collision at $\sqrt{s}$ =13 TeV with the ATLAS detector*, arXiv:1807.00539 [hep-ex].

[828] J. Jaeckel and A. Ringwald, *The Low-Energy Frontier of Particle Physics*, Ann. Rev. Nucl. Part. Sci. **60** (2010) 405–437, arXiv:1002.0329 [hep-ph].

[829] *Fundamental Physics at the Intensity Frontier*. 2012. arXiv:1205.2671 [hep-ex].

[830] R. Essig et al., *Working Group Report: New Light Weakly Coupled Particles*, in *Proceedings, 2013 Community Summer Study on the Future of U.S. Particle Physics: Snowmass on the Mississippi (CSS2013): Minneapolis, MN, USA, July 29-August 6, 2013*. 2013. arXiv:1311.0029 [hep-ph].

[831] J. Alexander et al., *Dark Sectors 2016 Workshop: Community Report*, 2016. arXiv:1608.08632 [hep-ph].

[832] M. Battaglieri et al., *US Cosmic Visions: New Ideas in Dark Matter 2017: Community Report*, in *U.S. Cosmic Visions: New Ideas in Dark Matter College Park, MD, USA, March 23-25, 2017*. 2017. arXiv:1707.04591 [hep-ph].

[833] B. Holdom, *Two U(1)'s and Epsilon Charge Shifts*, Phys. Lett. **166B** (1986) 196–198.

[834] P. Galison and A. Manohar, *TWO Z's OR NOT TWO Z's?*, Phys. Lett. **136B** (1984) 279–283.

[835] K. R. Dienes, C. F. Kolda, and J. March-Russell, *Kinetic mixing and the supersymmetric gauge hierarchy*, Nucl. Phys. **B492** (1997) 104–118, arXiv:hep-ph/9610479 [hep-ph].

[836] D. Curtin, R. Essig, S. Gori, and J. Shelton, *Illuminating Dark Photons with High-Energy Colliders*, JHEP **02** (2015) 157, arXiv:1412.0018 [hep-ph].

[837] E. Izaguirre and D. Stolarski, *Searching for Higgs Decays to as Many as 8 Leptons*, Phys. Rev. Lett. **121** (2018) no. 22, 221803, arXiv:1805.12136 [hep-ph].

[838] N. Blinov, E. Izaguirre, and B. Shuve, *Rare Z Boson Decays to a Hidden Sector*, Phys. Rev. **D97** (2018) no. 1, 015009, arXiv:1710.07635 [hep-ph].

[839] ATLAS Collaboration, M. Aaboud et al., *Search for Higgs boson decays to beyond-the-Standard-Model light bosons in four-lepton events with the ATLAS detector at $\sqrt{s} = 13$ TeV*, JHEP **06** (2018) 166, arXiv:1802.03388 [hep-ex].

[840] H. Georgi, D. B. Kaplan, and L. Randall, *Manifesting the Invisible Axion at Low-energies*, Phys. Lett. **169B** (1986) 73–78.

[841] M. Bauer, M. Neubert, and A. Thamm, *The "forgotten" decay $S \to Z + h$ as a CP analyzer*, arXiv:1607.01016 [hep-ph].

[842] M. Bauer, M. Neubert, and A. Thamm, *Analyzing the CP Nature of a New Scalar Particle via $S \to Z + h$ Decay*, Phys. Rev. Lett. **117** (2016) 181801, arXiv:1610.00009 [hep-ph].

[843] M. Bauer, M. Neubert, and A. Thamm, *LHC as an Axion Factory: Probing an Axion Explanation for $(g-2)_\mu$ with Exotic Higgs Decays*, Phys. Rev. Lett. **119** (2017) no. 3, 031802, arXiv:1704.08207 [hep-ph].

[844] M. Bauer, M. Neubert, and A. Thamm, *Collider Probes of Axion-Like Particles*, JHEP **12** (2017) 044, arXiv:1708.00443 [hep-ph].

[845] K. Mimasu and V. Sanz, *ALPs at Colliders*, JHEP **06** (2015) 173, arXiv:1409.4792 [hep-ph].

[846] I. Brivio, M. B. Gavela, L. Merlo, K. Mimasu, J. M. No, R. del Rey, and V. Sanz, *ALPs Effective Field Theory and Collider Signatures*, Eur. Phys. J. **C77** (2017) no. 8, 572, arXiv:1701.05379 [hep-ph].

[847] M. Bauer, M. Heiles, M. Neubert, and A. Thamm, *Axion-Like Particles at Future Colliders*, arXiv:1808.10323 [hep-ph].

[848] M. L. Mangano et al., *Physics at a 100 TeV pp Collider: Standard Model Processes*, CERN Yellow Report (2017) no. 3, 1–254, arXiv:1607.01831 [hep-ph].

[849] ATLAS Collaboration, G. Aad et al., *Search for new phenomena in events with at least three photons collected in pp collisions at $\sqrt{s} = 8$ TeV with the ATLAS detector*, Eur. Phys. J. **C76** (2016) no. 4, 210, arXiv:1509.05051 [hep-ex].

[850] ATLAS Collaboration, *Prospects for the search for additional Higgs bosons in the ditau final*

state with the ATLAS detector at HL-LHC, ATL-PHYS-PUB-2018-050, 2018.

[851] L. Evans and P. Bryant, *LHC Machine*, JINST **3** (2008) S08001.

[852] A. Djouadi, *The Anatomy of electro-weak symmetry breaking. II. The Higgs bosons in the minimal supersymmetric model*, Phys. Rept. **459** (2008) 1, arXiv:hep-ph/0503173.

[853] G. C. Branco et al., *Theory and phenomenology of two-Higgs-doublet models*, Phys. Rept. **516** (2012) 1, arXiv:1106.0034 [hep-ph].

[854] *ECFA High Luminosity LHC Experiments Workshop: Physics and Technology Developments Summary submitted to ECFA. 96th Plenary ECFA meeting*, , 2015.

[855] P. Fayet, *Supersymmetry and Weak, Electromagnetic and Strong Interactions*, Phys. Lett. B **64** (1976) 159.

[856] P. Fayet, *Spontaneously Broken Supersymmetric Theories of Weak, Electromagnetic and Strong Interactions*, Phys. Lett. B **69** (1977) 489.

[857] ATLAS Collaboration, M. Aaboud et al., *Search for additional heavy neutral Higgs and gauge bosons in the ditau final state produced in 36 fb^{-1} of pp collisions at $\sqrt{s} = 13$ TeV with the ATLAS detector*, JHEP **01** (2018) 055, arXiv:1709.07242 [hep-ex].

[858] CMS Collaboration, *Search for charged Higgs bosons with the $H^{\pm} \to \tau^{\pm}\nu\_\tau$ decay channel in proton-proton collisions at $\sqrt{s} = 13$ TeV*, CMS-PAS-HIG-18-014, 2018.

[859] CMS Collaboration, *Search for beyond the standard model Higgs bosons decaying into a $\mathrm{b\bar{b}}$ pair in pp collisions at $\sqrt{s} = 13$ TeV*, JHEP **08** (2018) no. CERN-EP-2018-124, CMS-HIG-16-018, 113, arXiv:1805.12191 [hep-ex].

[860] CMS Collaboration, *Search for additional neutral MSSM Higgs bosons in the $\tau\tau$ final state in proton-proton collisions at $\sqrt{s} = 13$ TeV*, CERN-EP-2018-026, CMS-HIG-17-020, 2018. arXiv:1803.06553 [hep-ex].

[861] CMS Collaboration, *Projection of the Run 2 MSSM $H \to \tau\tau$ limits for the High-Luminosity LHC*, CMS-PAS-FTR-18-017, 2018.

[862] CMS Collaboration, *Measurement of the $\mathrm{Z}\gamma^* \to \tau\tau$ cross section in pp collisions at $\sqrt{s} = 13$ TeV and validation of τ lepton analysis techniques*, Eur. Phys. J. **C78** (2018) no. CERN-EP-2017-307, CMS-HIG-15-007, 708, arXiv:1801.03535 [hep-ex].

[863] M. Carena, S. Heinemeyer, O. Stål, C. E. M. Wagner, and G. Weiglein, *MSSM Higgs Boson Searches at the LHC: Benchmark Scenarios after the Discovery of a Higgs-like Particle*, Eur. Phys. J. **C73** (2013) no. 9, 2552, arXiv:1302.7033 [hep-ph].

[864] A. Djouadi, L. Maiani, G. Moreau, A. Polosa, J. Quevillon, and V. Riquer, *The post-Higgs MSSM scenario: Habemus MSSM?*, Eur. Phys. J. C **73** (2013) 2650, arXiv:1307.5205 [hep-ph].

[865] E. Bagnaschi et al., *Benchmark scenarios for low $\tan\beta$ in the MSSM*, Lhchxswg-2015-002, 2015.

[866] ATLAS Collaboration, M. Aaboud et al., *Combination of searches for heavy resonances decaying into bosonic and leptonic final states using 36 fb^{-1} of proton-proton collision data at $\sqrt{s} = 13$ TeV with the ATLAS detector*, Phys. Rev. **D 98** (2018) no. 5, 052008, arXiv:1808.02380 [hep-ex].

[867] CMS Collaboration, *Search for a new scalar resonance decaying to a pair of Z bosons in proton-proton collisions at $\sqrt{s} = 13$ TeV*, JHEP **06** (2018) no. CERN-EP-2018-009, CMS-HIG-17-012, 127, arXiv:1804.01939 [hep-ex].

[868] CMS Collaboration, *Projection of the search for a new scalar resonance decaying to a pair of Z bosons*, CMS-PAS-FTR-18-040, 2018.

[869] B. Coleppa, F. Kling, and S. Su, *Exotic Decays Of A Heavy Neutral Higgs Through HZ/AZ Channel*, JHEP **09** (2014) 161, arXiv:1404.1922 [hep-ph].

[870] T. Li and S. Su, *Exotic Higgs Decay via Charged Higgs*, JHEP **11** (2015) 068, arXiv:1504.04381 [hep-ph].

[871] F. Kling, J. M. No, and S. Su, *Anatomy of Exotic Higgs Decays in 2HDM*, JHEP **09** (2016) 093, arXiv:1604.01406 [hep-ph].

[872] G. C. Dorsch, S. J. Huber, K. Mimasu, and J. M. No, *Hierarchical versus degenerate 2HDM: The LHC run 1 legacy at the onset of run 2*, Phys. Rev. **D93** (2016) no. 11, 115033, arXiv:1601.04545 [hep-ph].

[873] N. Craig, F. D'Eramo, P. Draper, S. Thomas, and H. Zhang, *The Hunt for the Rest of the Higgs Bosons*, JHEP **06** (2015) 137, arXiv:1504.04630 [hep-ph].

[874] S. Gori, I.-W. Kim, N. R. Shah, and K. M. Zurek, *Closing the Wedge: Search Strategies for Extended Higgs Sectors with Heavy Flavor Final States*, Phys. Rev. **D93** (2016) no. 7, 075038, arXiv:1602.02782 [hep-ph].

[875] ATLAS Collaboration, M. Aaboud et al., *Search for a heavy Higgs boson decaying into a Z boson and another heavy Higgs boson in the $\ell\ell bb$ final state in pp collisions at $\sqrt{s} = 13$ TeV with the ATLAS detector*, Phys. Lett. **B783** (2018) 392–414, arXiv:1804.01126 [hep-ex].

[876] CMS Collaboration, *Search for neutral resonances decaying into a Z boson and a pair of b jets or τ leptons*, Phys. Lett. **B759** (2016) no. CERN-EP-2016-039, CMS-HIG-15-001, 369–394, arXiv:1603.02991 [hep-ex].

[877] CMS Collaboration, *Search for H to Z(ll)+A(bb) with 2015 data*, CMS-PAS-HIG-16-010, 2016.

[878] R. V. Harlander, S. Liebler, and H. Mantler, *SusHi: A program for the calculation of Higgs production in gluon fusion and bottom-quark annihilation in the Standard Model and the MSSM*, Comput. Phys. Commun. **184** (2013) 1605–1617, arXiv:1212.3249 [hep-ph].

[879] U. Haisch and G. Polesello, *Searching for heavy Higgs bosons in the $t\bar{t}Z$ and tbW final states*, JHEP **09** (2018) 151, arXiv:1807.07734 [hep-ph].

[880] *Prospects for New Physics in Higgs Couplings Studies with the ATLAS Detector at the HL-LHC*, ATL-PHYS-PUB-2014-017, 2014.

[881] ATLAS Collaboration, M. Aaboud et al., *Search for heavy resonances decaying into a W or Z boson and a Higgs boson in final states with leptons and b-jets in 36 fb^{-1} of $\sqrt{s} = 13$ TeV pp collisions with the ATLAS detector*, JHEP **03** (2018) 174, arXiv:1712.06518 [hep-ex].

[882] C.-Y. Chen, S. Dawson, and I. M. Lewis, *Exploring resonant di-Higgs boson production in the Higgs singlet model*, Phys. Rev. **D91** (2015) no. 3, 035015, arXiv:1410.5488 [hep-ph].

[883] S. Dawson and I. M. Lewis, *NLO corrections to double Higgs boson production in the Higgs singlet model*, Phys. Rev. **D92** (2015) no. 9, 094023, arXiv:1508.05397 [hep-ph].

[884] T. Robens and T. Stefaniak, *LHC Benchmark Scenarios for the Real Higgs Singlet Extension of the Standard Model*, Eur. Phys. J. **C76** (2016) no. 5, 268, arXiv:1601.07880 [hep-ph].

[885] I. M. Lewis and M. Sullivan, *Benchmarks for Double Higgs Production in the Singlet Extended Standard Model at the LHC*, Phys. Rev. **D96** (2017) no. 3, 035037, arXiv:1701.08774 [hep-ph].

[886] S. Dawson and I. M. Lewis, *Singlet Model Interference Effects with High Scale UV Physics*, Phys. Rev. **D95** (2017) no. 1, 015004, arXiv:1605.04944 [hep-ph].

[887] P. Huang, A. Joglekar, M. Li, and C. E. M. Wagner, *Corrections to Di-Higgs Production with Light Stops and Modified Higgs Couplings*, arXiv:1711.05743 [hep-ph].

[888] ATLAS Collaboration, M. Aaboud et al., *Search for pair production of Higgs bosons in the $b\bar{b}b\bar{b}$ final state using proton–proton collisions at $\sqrt{s} = 13$ TeV with the ATLAS detector*, Phys. Rev. **D94** (2016) no. 5, 052002, arXiv:1606.04782 [hep-ex].

[889] CMS Collaboration, *Search for Higgs boson pair production in events with two bottom quarks and two tau leptons in proton-proton collisions at sqrt(s) = 13 TeV*, CERN-EP-2017-126,

CMS-HIG-17-002, 2017. arXiv:1707.02909 [hep-ex].

[890] CMS Collaboration, *Search for resonant and non-resonant Higgs boson pair production in the* $\mathrm{b\bar{b}l\nu l\nu}$ *final state at* $\sqrt{s} = 13$ TeV, CMS-PAS-HIG-17-006, 2017.

[891] CMS Collaboration, *Search for Higgs boson pair production in the final state containing two photons and two bottom quarks in proton-proton collisions at* $\sqrt{s} = 13$ TeV, CMS-PAS-HIG-17-008, 2017.

[892] CMS Collaboration, *Search for resonant pair production of Higgs bosons decaying to bottom quark-antiquark pairs in proton-proton collisions at 13 TeV*, CMS-PAS-HIG-17-009, 2017.

[893] D. Dicus, A. Stange, and S. Willenbrock, *Higgs decay to top quarks at hadron colliders*, Phys. Lett. **B333** (1994) 126–131, arXiv:hep-ph/9404359 [hep-ph].

[894] M. Carena and Z. Liu, *Challenges and opportunities for heavy scalar searches in the* $t\bar{t}$ *channel at the LHC*, JHEP **11** (2016) 159, arXiv:1608.07282 [hep-ph].

[895] S. Jung, J. Song, and Y. W. Yoon, *Dip or nothingness of a Higgs resonance from the interference with a complex phase*, Phys. Rev. **D92** (2015) no. 5, 055009, arXiv:1505.00291 [hep-ph].

[896] A. Aboubrahim and P. Nath, *Naturalness, the hyperbolic branch and prospects for the observation of charged Higgs at high luminosity LHC and 27 TeV LHC*, Phys. Rev. **D98** (2018) 095024, arXiv:1810.12868 [hep-ph].

[897] A. H. Chamseddine, R. L. Arnowitt, and P. Nath, *Locally Supersymmetric Grand Unification*, Phys. Rev. Lett. **49** (1982) 970.

[898] P. Nath, R. L. Arnowitt, and A. H. Chamseddine, *Gauge Hierarchy in Supergravity Guts*, Nucl. Phys. **B227** (1983) 121–133.

[899] L. J. Hall, J. D. Lykken, and S. Weinberg, *Supergravity as the Messenger of Supersymmetry Breaking*, Phys. Rev. **D27** (1983) 2359–2378.

[900] P. Nath, *Supersymmetry, Supergravity, and Unification*. Cambridge Monographs on Mathematical Physics. Cambridge University Press, 2016.

[901] A. Aboubrahim and P. Nath, *Supersymmetry at a 28 TeV hadron collider: HE-LHC*, Phys. Rev. **D98** (2018) no. 1, 015009, arXiv:1804.08642 [hep-ph].

[902] K. L. Chan, U. Chattopadhyay, and P. Nath, *Naturalness, weak scale supersymmetry and the prospect for the observation of supersymmetry at the Tevatron and at the CERN LHC*, Phys. Rev. **D58** (1998) 096004, arXiv:hep-ph/9710473 [hep-ph].

[903] A. Aboubrahim, P. Nath, and A. B. Spisak, *Stau coannihilation, compressed spectrum, and SUSY discovery potential at the LHC*, Phys. Rev. **D95** (2017) no. 11, 115030, arXiv:1704.04669 [hep-ph].

[904] Aboubrahim, Amin and Nath, Pran, *Supergravity models with 50-100 TeV scalars, supersymmetry discovery at the LHC, and gravitino decay constraints*, Phys. Rev. **D96** (2017) no. 7, 075015, arXiv:1708.02830 [hep-ph].

[905] C. Degrande, *Automatic evaluation of UV and R2 terms for beyond the Standard Model Lagrangians: a proof-of-principle*, Comput. Phys. Commun. **197** (2015) 239–262, arXiv:1406.3030 [hep-ph].

[906] R. Harlander, M. Kramer, and M. Schumacher, *Bottom-quark associated Higgs-boson production: reconciling the four- and five-flavour scheme approach*, arXiv:1112.3478 [hep-ph].

[907] I. Antcheva et al., *ROOT: A C++ framework for petabyte data storage, statistical analysis and visualization*, Comput. Phys. Commun. **182** (2011) 1384–1385.

[908] P. Speckmayer, A. Hocker, J. Stelzer, and H. Voss, *The toolkit for multivariate data analysis, TMVA 4*, J. Phys. Conf. Ser. **219** (2010) 032057.

[909] H. P. Nilles, *Supersymmetry, Supergravity and Particle Physics*, Phys. Rept. **110** (1984) 1–162.

[910] J. F. Gunion and H. E. Haber, *Higgs Bosons in Supersymmetric Models. 1.*, Nucl. Phys. **B272** (1986) 1.

[911] H. Bahl, E. Fuchs, T. Hahn, S. Heinemeyer, S. Liebler, S. Patel, P. Slavich, T. Stefaniak, C. E. M. Wagner, and G. Weiglein, *MSSM Higgs Boson Searches at the LHC: Benchmark Scenarios for Run 2 and Beyond*, arXiv:1808.07542 [hep-ph].

[912] P. Bechtle, S. Heinemeyer, O. Stal, T. Stefaniak, and G. Weiglein, *Applying Exclusion Likelihoods from LHC Searches to Extended Higgs Sectors*, Eur. Phys. J. **C75** (2015) no. 9, 421, arXiv:1507.06706 [hep-ph].

[913] S. Heinemeyer, W. Hollik, and G. Weiglein, *FeynHiggs: A Program for the calculation of the masses of the neutral CP even Higgs bosons in the MSSM*, Comput. Phys. Commun. **124** (2000) 76–89, arXiv:hep-ph/9812320 [hep-ph].

[914] S. Heinemeyer, W. Hollik, and G. Weiglein, *The Masses of the neutral CP - even Higgs bosons in the MSSM: Accurate analysis at the two loop level*, Eur. Phys. J. **C9** (1999) 343–366, arXiv:hep-ph/9812472 [hep-ph].

[915] G. Degrassi, S. Heinemeyer, W. Hollik, P. Slavich, and G. Weiglein, *Towards high precision predictions for the MSSM Higgs sector*, Eur. Phys. J. **C28** (2003) 133–143, arXiv:hep-ph/0212020 [hep-ph].

[916] M. Frank, T. Hahn, S. Heinemeyer, W. Hollik, H. Rzehak, and G. Weiglein, *The Higgs Boson Masses and Mixings of the Complex MSSM in the Feynman-Diagrammatic Approach*, JHEP **02** (2007) 047, arXiv:hep-ph/0611326 [hep-ph].

[917] T. Hahn, S. Heinemeyer, W. Hollik, H. Rzehak, and G. Weiglein, *High-Precision Predictions for the Light CP -Even Higgs Boson Mass of the Minimal Supersymmetric Standard Model*, Phys. Rev. Lett. **112** (2014) no. 14, 141801, arXiv:1312.4937 [hep-ph].

[918] H. Bahl and W. Hollik, *Precise prediction for the light MSSM Higgs boson mass combining effective field theory and fixed-order calculations*, Eur. Phys. J. **C76** (2016) no. 9, 499, arXiv:1608.01880 [hep-ph].

[919] H. Bahl, S. Heinemeyer, W. Hollik, and G. Weiglein, *Reconciling EFT and hybrid calculations of the light MSSM Higgs-boson mass*, Eur. Phys. J. **C78** (2018) no. 1, 57, arXiv:1706.00346 [hep-ph].

[920] H. Bahl, T. Hahn, S. Heinemeyer, W. Hollik, S. Paßehr, H. Rzehak, and G. Weiglein, *Precision calculations in the MSSM Higgs-boson sector with FeynHiggs 2.14*, arXiv:1811.09073 [hep-ph].

[921] R. Harlander and P. Kant, *Higgs production and decay: Analytic results at next-to-leading order QCD*, JHEP **12** (2005) 015, arXiv:hep-ph/0509189 [hep-ph].

[922] R. V. Harlander and W. B. Kilgore, *Next-to-next-to-leading order Higgs production at hadron colliders*, Phys. Rev. Lett. **88** (2002) 201801, arXiv:hep-ph/0201206 [hep-ph].

[923] R. V. Harlander and W. B. Kilgore, *Production of a pseudoscalar Higgs boson at hadron colliders at next-to-next-to leading order*, JHEP **10** (2002) 017, arXiv:hep-ph/0208096 [hep-ph].

[924] C. Anastasiou, C. Duhr, F. Dulat, E. Furlan, T. Gehrmann, F. Herzog, and B. Mistlberger, *Higgs Boson GluonFfusion Production Beyond Threshold in N^3LO QCD*, JHEP **03** (2015) 091, arXiv:1411.3584 [hep-ph].

[925] C. Anastasiou, C. Duhr, F. Dulat, E. Furlan, F. Herzog, and B. Mistlberger, *Soft expansion of double-real-virtual corrections to Higgs production at N^3LO*, JHEP **08** (2015) 051, arXiv:1505.04110 [hep-ph].

[926] G. Degrassi and P. Slavich, *NLO QCD bottom corrections to Higgs boson production in the MSSM*, JHEP **11** (2010) 044, arXiv:1007.3465 [hep-ph].

[927] G. Degrassi, S. Di Vita, and P. Slavich, *NLO QCD corrections to pseudoscalar Higgs production in the MSSM*, JHEP **08** (2011) 128, arXiv:1107.0914 [hep-ph].

[928] G. Degrassi, S. Di Vita, and P. Slavich, *On the NLO QCD Corrections to the Production of the Heaviest Neutral Higgs Scalar in the MSSM*, Eur. Phys. J. **C72** (2012) 2032, arXiv:1204.1016 [hep-ph].

[929] S. Actis, G. Passarino, C. Sturm, and S. Uccirati, *NLO Electroweak Corrections to Higgs Boson Production at Hadron Colliders*, Phys. Lett. **B670** (2008) 12–17, arXiv:0809.1301 [hep-ph].

[930] M. Bonvini, A. S. Papanastasiou, and F. J. Tackmann, *Resummation and matching of b-quark mass effects in $b\bar{b}H$ production*, JHEP **11** (2015) 196, arXiv:1508.03288 [hep-ph].

[931] M. Bonvini, A. S. Papanastasiou, and F. J. Tackmann, *Matched predictions for the $b\bar{b}H$ cross section at the 13 TeV LHC*, JHEP **10** (2016) 053, arXiv:1605.01733 [hep-ph].

[932] S. Forte, D. Napoletano, and M. Ubiali, *Higgs production in bottom-quark fusion in a matched scheme*, Phys. Lett. **B751** (2015) 331–337, arXiv:1508.01529 [hep-ph].

[933] S. Forte, D. Napoletano, and M. Ubiali, *Higgs production in bottom-quark fusion: matching beyond leading order*, Phys. Lett. **B763** (2016) 190–196, arXiv:1607.00389 [hep-ph].

[934] O. Buchmueller et al., *The CMSSM and NUHM1 after LHC Run 1*, Eur. Phys. J. **C74** (2014) no. 6, 2922, arXiv:1312.5250 [hep-ph].

[935] CMS Collaboration, *The NUHM2 after LHC Run 1*, Eur. Phys. J. **C74** (2014) no. DESY-14-144, UMN-TH-3344-14, CERN-PH-TH-2014-145, FERMILAB-PUB-14-605-CMS, FTPI-MINN-14-39, KCL-PH-TH-2014-33, LCTS-2014-29, SLAC-PUB-16051, 3212, arXiv:1408.4060 [hep-ph].

[936] P. Bechtle et al., *Killing the cMSSM softly*, Eur. Phys. J. **C76** (2016) no. 2, 96, arXiv:1508.05951 [hep-ph].

[937] CMS Collaboration, *Likelihood Analysis of Supersymmetric SU(5) GUTs*, Eur. Phys. J. **C77** (2017) no. FERMILAB-PUB-16-453-CMS, IIFT-UAM-CSIC-16-105, IPPP-16-97, CERN-PH-TH-2016-217, CERN-TH-2016-217, DESY-16-156, FTPI-MINN-16-29, IFT-UAM-CSIC-16-105, KCL-PH-TH-2016-57, UMN-TH-3609-16, 104, arXiv:1610.10084 [hep-ph].

[938] CMS Collaboration, *Likelihood Analysis of the Minimal AMSB Model*, Eur. Phys. J. **C77** (2017) no. CERN-TH-2016-220, FTPI-MINN-16-30, DESY-16-155, FERMILAB-PUB-16-502-CMS, IFT-UAM-CSIC-16-112, IPMU16-0157, IPPP-16-104, KCL-PH-TH-2016-58, UMN-TH-3610-16, 268, arXiv:1612.05210 [hep-ph].

[939] J. C. Costa et al., *Likelihood Analysis of the Sub-GUT MSSM in Light of LHC 13-TeV Data*, Eur. Phys. J. **C78** (2018) no. 2, 158, arXiv:1711.00458 [hep-ph].

[940] S. Heinemeyer, M. Mondragón, and G. Zoupanos, *Finite Theories Before and After the Discovery of a Higgs Boson at the LHC*, Fortsch. Phys. **61** (2013) no. 11, 969–993, arXiv:1305.5073 [hep-ph].

[941] S. Heinemeyer, M. Mondragón, N. Tracas, and G. Zoupanos, *Reduction of parameters in Finite Unified Theories and the MSSM*, Nucl. Phys. **B927** (2018) 319–338.

[942] S. Heinemeyer, M. Mondragón, G. Patellis, N. Tracas, and G. Zoupanos, *The LHC Higgs Boson Discovery: Updated implications for Finite Unified Theories and the SUSY breaking scale*, Symmetry **10** (2018) no. 3, 62, arXiv:1802.04666 [hep-ph].

[943] P. Bechtle, H. E. Haber, S. Heinemeyer, O. Stål, T. Stefaniak, G. Weiglein, and L. Zeune, *The Light and Heavy Higgs Interpretation of the MSSM*, Eur. Phys. J. **C77** (2017) no. 2, 67, arXiv:1608.00638 [hep-ph].

[944] E. Bagnaschi et al., *Likelihood Analysis of the pMSSM11 in Light of LHC 13-TeV Data*, Eur.

Phys. J. **C78** (2018) no. 3, 256, arXiv:1710.11091 [hep-ph].

[945] A. Arbey et al., *Physics at the e+ e- Linear Collider*, Eur. Phys. J. **C75** (2015) no. 8, 371, arXiv:1504.01726 [hep-ph].

[946] ATLAS Collaboration, M. Aaboud et al., *Search for pair production of Higgs bosons in the $b\bar{b}b\bar{b}$ final state using proton-proton collisions at $\sqrt{s} = 13$ TeV with the ATLAS detector*, JHEP **01** (2019) 030, arXiv:1804.06174 [hep-ex].

[947] CMS Collaboration, *Search for a massive resonance decaying to a pair of Higgs bosons in the four b quark final state in proton-proton collisions at $\sqrt{s} = 13$ TeV*, Phys. Lett. **B781** (2018) no. CERN-EP-2017-238, CMS-B2G-16-026, 244–269, arXiv:1710.04960 [hep-ex].

[948] ATLAS Collaboration, *Search for heavy ZZ resonances in the $\ell^+\ell^-\ell^+\ell^-$ and $\ell^+\ell^-\nu\bar{\nu}$ final states using proton–proton collisions at $\sqrt{s} = 13$ TeV with the ATLAS detector*, ATLAS-CONF-2017-058, 2017.

[949] D. Buttazzo, F. Sala, and A. Tesi, *Singlet-like Higgs bosons at present and future colliders*, JHEP **11** (2015) 158, arXiv:1505.05488 [hep-ph].

[950] CMS Collaboration, *Beyond the Standard Model Physics at the HL-LHC and HE-LHC*, CERN-LPCC-2018-05, FERMILAB-PUB-18-694-CMS-T, 2018. arXiv:1812.07831 [hep-ph].

[951] D. Buttazzo, D. Redigolo, F. Sala, and A. Tesi, *Fusing Vectors into Scalars at High Energy Lepton Colliders*, JHEP **11** (2018) 144, arXiv:1807.04743 [hep-ph].

[952] S. Alipour-Fard, N. Craig, S. Gori, S. Koren, and D. Redigolo, *The second Higgs at the lifetime frontier*, arXiv:1812.09315 [hep-ph].

[953] ATLAS Collaboration, M. Aaboud et al., *Search for long-lived particles produced in pp collisions at $\sqrt{s} = 13$ TeV that decay into displaced hadronic jets in the ATLAS muon spectrometer*, Submitted to: Phys. Rev. (2018) , arXiv:1811.07370 [hep-ex].

[954] J. D. Clarke, *Constraining portals with displaced Higgs decay searches at the LHC*, JHEP **10** (2015) 061, arXiv:1505.00063 [hep-ph].

[955] C. Csaki, E. Kuflik, S. Lombardo, and O. Slone, *Searching for displaced Higgs boson decays*, Phys. Rev. **D92** (2015) no. 7, 073008, arXiv:1508.01522 [hep-ph].

[956] D. Curtin and C. B. Verhaaren, *Discovering Uncolored Naturalness in Exotic Higgs Decays*, JHEP **12** (2015) 072, arXiv:1506.06141 [hep-ph].

[957] A. Pierce, B. Shakya, Y. Tsai, and Y. Zhao, *Searching for confining hidden valleys at LHCb, ATLAS, and CMS*, Phys. Rev. **D97** (2018) no. 9, 095033, arXiv:1708.05389 [hep-ph].

[958] R. Barbieri, T. Gregoire, and L. J. Hall, *Mirror world at the large hadron collider*, arXiv:hep-ph/0509242 [hep-ph].

[959] S. Dawson et al., *Working Group Report: Higgs Boson*, in *Proceedings, 2013 Community Summer Study on the Future of U.S. Particle Physics: Snowmass on the Mississippi (CSS2013): Minneapolis, MN, USA, July 29-August 6, 2013*. 2013. arXiv:1310.8361 [hep-ex].

[960] M. J. Strassler and K. M. Zurek, *Discovering the Higgs through highly-displaced vertices*, Phys. Lett. **B661** (2008) 263–267, arXiv:hep-ph/0605193 [hep-ph].

[961] T. Han, Z. Si, K. M. Zurek, and M. J. Strassler, *Phenomenology of hidden valleys at hadron colliders*, JHEP **07** (2008) 008, arXiv:0712.2041 [hep-ph].

[962] A. Thamm, R. Torre, and A. Wulzer, *Future tests of Higgs compositeness: direct vs indirect*, JHEP **07** (2015) 100, arXiv:1502.01701 [hep-ph].

[963] Y. Gershtein, *CMS Hardware Track Trigger: New Opportunities for Long-Lived Particle Searches at the HL-LHC*, Phys. Rev. **D96** (2017) no. 3, 035027, arXiv:1705.04321 [hep-ph].

[964] A. Katz, A. Mariotti, S. Pokorski, D. Redigolo, and R. Ziegler, *SUSY Meets Her Twin*, JHEP **01**

(2017) 142, arXiv:1611.08615 [hep-ph].

[965] R. Contino, D. Greco, R. Mahbubani, R. Rattazzi, and R. Torre, *Precision Tests and Fine Tuning in Twin Higgs Models*, Phys. Rev. **D96** (2017) no. 9, 095036, arXiv:1702.00797 [hep-ph].

[966] H. Georgi and D. B. Kaplan, *Composite Higgs and Custodial SU(2)*, Phys. Lett. **145B** (1984) 216–220.

[967] ATLAS Collaboration, M. Aaboud et al., *Search for pair production of up-type vector-like quarks and for four-top-quark events in final states with multiple b-jets with the ATLAS detector*, JHEP **07** (2018) 089, arXiv:1803.09678 [hep-ex].

[968] ATLAS Collaboration, M. Aaboud et al., *Combination of the searches for pair-produced vector-like partners of the third-generation quarks at $\sqrt{s} = 13$ TeV with the ATLAS detector*, arXiv:1808.02343 [hep-ex].

[969] CMS Collaboration, *Search for vector-like T and B quark pairs in final states with leptons at $\sqrt{s} = 13$ TeV*, JHEP **08** (2018) no. FERMILAB-PUB-18-191-CMS, CERN-EP-2018-069, CMS-B2G-17-011, 177, arXiv:1805.04758 [hep-ex].

[970] K. Agashe, R. Contino, and A. Pomarol, *The Minimal composite Higgs model*, Nucl. Phys. **B719** (2005) 165–187, arXiv:hep-ph/0412089 [hep-ph].

[971] C. Bautista, L. de Lima, R. Matheus, E. Pontón, L. Fernandes do Prado, and A. Savoy-Navarro, *Production of $t\bar{t}H$ and $t\bar{t}HH$ at the LHC in Composite Higgs models*, to appear.

[972] D. B. Kaplan, *Flavor at SSC energies: A new mechanism for dynamically generated fermion masses*, Nuclear Physics B **365** (1991) no. 2, 259 – 278.

[973] M. Carena, L. Da Rold, and E. Pontón, *Minimal Composite Higgs Models at the LHC*, JHEP **06** (2014) 159, arXiv:1402.2987 [hep-ph].

[974] V. Sanz and J. Setford, *Composite Higgs Models after Run 2*, Adv. High Energy Phys. **2018** (2018) 7168480, arXiv:1703.10190 [hep-ph].

[975] D. Liu, I. Low, and C. E. M. Wagner, *Modification of Higgs Couplings in Minimal Composite Models*, Phys. Rev. **D96** (2017) 035013, arXiv:1703.07791 [hep-ph].

[976] A. Banerjee, G. Bhattacharyya, N. Kumar, and T. S. Ray, *Constraining Composite Higgs Models using LHC data*, JHEP **03** (2018) 062, arXiv:1712.07494 [hep-ph].

[977] G. Panico, M. Redi, A. Tesi, and A. Wulzer, *On the Tuning and the Mass of the Composite Higgs*, JHEP **03** (2013) 051, arXiv:1210.7114 [hep-ph].

[978] M. Montull, F. Riva, E. Salvioni, and R. Torre, *Higgs Couplings in Composite Models*, Phys. Rev. **D88** (2013) 095006, arXiv:1308.0559 [hep-ph].

[979] A. Carmona and F. Goertz, *A naturally light Higgs without light Top Partners*, JHEP **05** (2015) 002, arXiv:1410.8555 [hep-ph].

[980] S. Kanemura, K. Kaneta, N. Machida, S. Odori, and T. Shindou, *Single and double production of the Higgs boson at hadron and lepton colliders in minimal composite Higgs models*, Phys. Rev. **D94** (2016) no. 1, 015028, arXiv:1603.05588 [hep-ph].

[981] M. B. Gavela, K. Kanshin, P. A. N. Machado, and S. Saa, *The linear-non-linear frontier for the Goldstone Higgs*, Eur. Phys. J. **C76** (2016) no. 12, 690, arXiv:1610.08083 [hep-ph].

[982] E. Conte, B. Fuks, and G. Serret, *MadAnalysis 5, A User-Friendly Framework for Collider Phenomenology*, Comput. Phys. Commun. **184** (2013) 222–256, arXiv:1206.1599 [hep-ph].

[983] R. Contino, M. Ghezzi, M. Moretti, G. Panico, F. Piccinini, and A. Wulzer, *Anomalous Couplings in Double Higgs Production*, JHEP **08** (2012) 154, arXiv:1205.5444 [hep-ph].

[984] CMS Collaboration, *Observation of Higgs boson decay to bottom quarks*, CMS-PAS-HIG-18-016, 2018.

[985] N. Craig, J. Galloway, and S. Thomas, *Searching for Signs of the Second Higgs Doublet*,

arXiv:1305.2424 [hep-ph].

[986] J. Bernon, J. F. Gunion, H. E. Haber, Y. Jiang, and S. Kraml, *Scrutinizing the alignment limit in two-Higgs-doublet models. II. m_H=125 GeV*, Phys. Rev. **D93** (2016) no. 3, 035027, arXiv:1511.03682 [hep-ph].

[987] S. Profumo and T. Stefaniak, *Alignment without Decoupling: the Portal to Light Dark Matter in the MSSM*, Phys. Rev. **D94** (2016) no. 9, 095020, arXiv:1608.06945 [hep-ph].

[988] H. E. Haber, S. Heinemeyer, and T. Stefaniak, *The Impact of Two-Loop Effects on the Scenario of MSSM Higgs Alignment without Decoupling*, Eur. Phys. J. **C77** (2017) no. 11, 742, arXiv:1708.04416 [hep-ph].

[989] H. Georgi and M. Machacek, *DOUBLY CHARGED HIGGS BOSONS*, Nucl. Phys. **B262** (1985) 463–477.

[990] R. Killick, K. Kumar, and H. E. Logan, *Learning what the Higgs boson is mixed with*, Phys.Rev. **D88** (2013) 033015, arXiv:1305.7236 [hep-ph].

[991] H. E. Haber, G. L. Kane, and T. Sterling, *The Fermion Mass Scale and Possible Effects of Higgs Bosons on Experimental Observables*, Nucl. Phys. **B161** (1979) 493–532.

[992] K. Hartling, K. Kumar, and H. E. Logan, *The decoupling limit in the Georgi-Machacek model*, Phys. Rev. **D90** (2014) no. 1, 015007, arXiv:1404.2640 [hep-ph].

[993] A. G. Akeroyd, *Fermiophobic and other nonminimal neutral Higgs bosons at the LHC*, J. Phys. **G24** (1998) 1983–1994, arXiv:hep-ph/9803324 [hep-ph].

[994] A. G. Akeroyd, *Fermiophobic Higgs bosons at the Tevatron*, Phys. Lett. **B368** (1996) 89–95, arXiv:hep-ph/9511347 [hep-ph].

[995] A. Delgado, M. Garcia-Pepin, M. Quiros, J. Santiago, and R. Vega-Morales, *Diphoton and Diboson Probes of Fermiophobic Higgs Bosons at the LHC*, JHEP **06** (2016) 042, arXiv:1603.00962 [hep-ph].

[996] R. Vega, R. Vega-Morales, and K. Xie, *Light (and darkness) from a light hidden Higgs*, JHEP **06** (2018) 137, arXiv:1805.01970 [hep-ph].

[997] CMS Collaboration, *Search for a low-mass pseudoscalar Higgs boson produced in association with a $b\bar{b}$ pair in pp collisions at $\sqrt{s} = 8$ TeV*, Phys. Lett. **B758** (2016) no. FERMILAB-PUB-15-514-CMS, CERN-PH-EP-2015-284, CMS-HIG-14-033, 296–320, arXiv:1511.03610 [hep-ex].

[998] ATLAS Collaboration, G. Aad et al., *Search for neutral Higgs bosons of the minimal supersymmetric standard model in pp collisions at $\sqrt{s}$ = 8 TeV with the ATLAS detector*, JHEP **11** (2014) 056, arXiv:1409.6064 [hep-ex].

[999] CMS Collaboration, *Search for neutral MSSM Higgs bosons decaying to a pair of tau leptons in pp collisions*, JHEP **10** (2014) no. CERN-PH-EP-2014-192, CMS-HIG-13-021, 160, arXiv:1408.3316 [hep-ex].

[1000] CMS Collaboration, *Search for new resonances in the diphoton final state in the mass range between 70 and 110 GeV in pp collisions at $\sqrt{s} = 8$ and 13 TeV*, CMS-PAS-HIG-17-013, 2017.

[1001] ATLAS Collaboration, *Search for resonances in the 65 to 110 GeV diphoton invariant mass range using 80 fb^{-1} of pp collisions collected at $\sqrt{s} = 13$ TeV with the ATLAS detector*, ATLAS-CONF-2018-025, 2018.

[1002] CMS Collaboration, *Search for H/A decaying into Z+A/H, with Z to ll and A/H to fermion pair*, CMS-PAS-HIG-15-001, 2015.

[1003] OPAL, DELPHI, LEP Working Group for Higgs boson searches, ALEPH, L3 Collaboration, R. Barate et al., *Search for the standard model Higgs boson at LEP*, Phys. Lett. **B565** (2003) 61–75, arXiv:hep-ex/0306033 [hep-ex].

[1004] OPAL Collaboration, G. Abbiendi et al., *Flavor independent h0A0 search and two Higgs*

doublet model interpretation of neutral Higgs boson searches at LEP, Eur. Phys. J. **C40** (2005) 317–332, arXiv:hep-ex/0408097 [hep-ex].

[1005] LEP, DELPHI, OPAL, ALEPH, L3 Collaboration, G. Abbiendi et al., *Search for Charged Higgs bosons: Combined Results Using LEP Data*, Eur. Phys. J. **C73** (2013) 2463, arXiv:1301.6065 [hep-ex].

[1006] U. Haisch, $\bar{B} \to X\_s\gamma$*: Standard Model and Beyond*, arXiv:0805.2141 [hep-ph].

[1007] F. Mahmoudi and O. Stal, *Flavor constraints on the two-Higgs-doublet model with general Yukawa couplings*, Phys. Rev. **D81** (2010) 035016, arXiv:0907.1791 [hep-ph].

[1008] R. S. Gupta and J. D. Wells, *Next Generation Higgs Bosons: Theory, Constraints and Discovery Prospects at the Large Hadron Collider*, Phys. Rev. **D81** (2010) 055012, arXiv:0912.0267 [hep-ph].

[1009] M. Jung, A. Pich, and P. Tuzon, *Charged-Higgs phenomenology in the Aligned two-Higgs-doublet model*, JHEP **11** (2010) 003, arXiv:1006.0470 [hep-ph].

[1010] M. Misiak et al., *Updated NNLO QCD predictions for the weak radiative B-meson decays*, Phys. Rev. Lett. **114** (2015) no. 22, 221801, arXiv:1503.01789 [hep-ph].

[1011] V. Ilisie and A. Pich, *Low-mass fermiophobic charged Higgs phenomenology in two-Higgs-doublet models*, JHEP **09** (2014) 089, arXiv:1405.6639 [hep-ph].

[1012] R. Enberg, W. Klemm, S. Moretti, and S. Munir, *Electroweak production of light scalar/pseudoscalar pairs from extended Higgs sectors*, Phys. Lett. **B764** (2017) 121–125, arXiv:1605.02498 [hep-ph].

[1013] C. Degrande, K. Hartling, and H. E. Logan, *Scalar decays to $\gamma\gamma$, $Z\gamma$, and $W\gamma$ in the Georgi-Machacek model*, Phys. Rev. **D96** (2017) no. 7, 075013, arXiv:1708.08753 [hep-ph].

[1014] A. G. Akeroyd, A. Alves, M. A. Diaz, and O. J. P. Eboli, *Multi-photon signatures at the Fermilab Tevatron*, Eur. Phys. J. **C48** (2006) 147–157, arXiv:hep-ph/0512077 [hep-ph].

[1015] DELPHI Collaboration, J. Abdallah et al., *Search for fermiophobic Higgs bosons in final states with photons at LEP 2*, Eur. Phys. J. **C35** (2004) 313–324, arXiv:hep-ex/0406012 [hep-ex].

[1016] CDF Collaboration, T. A. Aaltonen et al., *Search for a Low-Mass Neutral Higgs Boson with Suppressed Couplings to Fermions Using Events with Multiphoton Final States*, Phys. Rev. **D93** (2016) no. 11, 112010, arXiv:1601.00401 [hep-ex].

[1017] M. Baak, M. Goebel, J. Haller, A. Hoecker, D. Ludwig, K. Moenig, M. Schott, and J. Stelzer, *Updated Status of the Global Electroweak Fit and Constraints on New Physics*, Eur. Phys. J. **C72** (2012) 2003, arXiv:1107.0975 [hep-ph].

[1018] Tevatron Electroweak Working Group, CDF, DELPHI, SLD Electroweak and Heavy Flavour Groups, ALEPH, LEP Electroweak Working Group, SLD, OPAL, D0, L3 Collaborations, L. E. W. Group, *Precision Electroweak Measurements and Constraints on the Standard Model*, arXiv:1012.2367 [hep-ex].

[1019] A. Arhrib, R. Benbrik, R. Enberg, W. Klemm, S. Moretti, and S. Munir, *Identifying a light charged Higgs boson at the LHC Run II*, Phys. Lett. **B774** (2017) 591–598, arXiv:1706.01964 [hep-ph].

[1020] A. Arbey, F. Mahmoudi, O. Stal, and T. Stefaniak, *Status of the Charged Higgs Boson in Two Higgs Doublet Models*, Eur. Phys. J. **C78** (2018) no. 3, 182, arXiv:1706.07414 [hep-ph].

[1021] D. Bhatia, U. Maitra, and S. Niyogi, *Discovery prospects of a light Higgs boson at the LHC in type-I 2HDM*, Phys. Rev. **D97** (2018) no. 5, 055027, arXiv:1704.07850 [hep-ph].

[1022] P. J. Fox and N. Weiner, *Light Signals from a Lighter Higgs*, JHEP **08** (2018) 025, arXiv:1710.07649 [hep-ph].

[1023] U. Haisch and A. Malinauskas, *Let there be light from a second light Higgs doublet*, JHEP **03** (2018) 135, arXiv:1712.06599 [hep-ph].

[1024] M. E. Peskin and T. Takeuchi, *Estimation of oblique electroweak corrections*, Phys. Rev. **D46** (1992) 381–409.

[1025] F. Domingo, S. Heinemeyer, S. Paßehr, and G. Weiglein, *Decays of the neutral Higgs bosons into SM fermions and gauge bosons in the $\mathcal{CP}$-violating NMSSM*, arXiv:1807.06322 [hep-ph].

[1026] T. Biekotter, S. Heinemeyer, and C. Munoz, *Precise prediction for the Higgs-boson masses in the $\mu\nu$ SSM*, Eur. Phys. J. **C78** (2018) no. 6, 504, arXiv:1712.07475 [hep-ph].

[1027] P. Sikivie, L. Susskind, M. B. Voloshin, and V. I. Zakharov, *Isospin Breaking in Technicolor Models*, Nucl. Phys. **B173** (1980) 189–207.

[1028] M. S. Chanowitz and M. Golden, *Higgs Boson Triplets With $M(W) = M(Z)\cos\theta\omega$*, Phys. Lett. **165B** (1985) 105–108.

[1029] J. F. Gunion, R. Vega, and J. Wudka, *Higgs triplets in the standard model*, Phys. Rev. **D42** (1990) 1673–1691.

[1030] J. F. Gunion, R. Vega, and J. Wudka, *Naturalness problems for rho = 1 and other large one loop effects for a standard model Higgs sector containing triplet fields*, Phys. Rev. **D43** (1991) 2322–2336.

[1031] L. Cort, M. Garcia, and M. Quiros, *Supersymmetric Custodial Triplets*, Phys.Rev. **D88** (2013) 075010, arXiv:1308.4025 [hep-ph].

[1032] M. Garcia-Pepin, S. Gori, M. Quiros, R. Vega, R. Vega-Morales, and T.-T. Yu, *Supersymmetric Custodial Higgs Triplets and the Breaking of Universality*, Phys. Rev. **D91** (2015) no. 1, 015016, arXiv:1409.5737 [hep-ph].

[1033] R. Vega, R. Vega-Morales, and K. Xie, *The Supersymmetric Georgi-Machacek Model*, JHEP **03** (2018) 168, arXiv:1711.05329 [hep-ph].

[1034] H. Davoudiasl, T. Han, and H. E. Logan, *Discovering an invisibly decaying Higgs at hadron colliders*, Phys. Rev. **D71** (2005) 115007, arXiv:hep-ph/0412269 [hep-ph].

[1035] H. E. Haber and H. E. Logan, *Radiative corrections to the Z b anti-b vertex and constraints on extended Higgs sectors*, Phys. Rev. **D62** (2000) 015011, arXiv:hep-ph/9909335 [hep-ph].

[1036] M. R. Buckley, L. Randall, and B. Shuve, *LHC Searches for Non-Chiral Weakly Charged Multiplets*, JHEP **05** (2011) 097, arXiv:0909.4549 [hep-ph].

[1037] A. Ismail, E. Izaguirre, and B. Shuve, *Illuminating New Electroweak States at Hadron Colliders*, Phys. Rev. **D94** (2016) no. 1, 015001, arXiv:1605.00658 [hep-ph].

[1038] G. Brooijmans et al., *Les Houches 2015: Physics at TeV colliders - new physics working group report*, in *9th Les Houches Workshop on Physics at TeV Colliders (PhysTeV 2015) Les Houches, France, June 1-19, 2015*. 2016. arXiv:1605.02684 [hep-ph].

[1039] A. G. Akeroyd and M. A. Diaz, *Searching for a light fermiophobic Higgs boson at the Tevatron*, Phys. Rev. **D67** (2003) 095007, arXiv:hep-ph/0301203 [hep-ph].

[1040] A. G. Akeroyd, M. A. Diaz, and F. J. Pacheco, *Double fermiophobic Higgs boson production at the CERN LHC and LC*, Phys. Rev. **D70** (2004) 075002, arXiv:hep-ph/0312231 [hep-ph].

[1041] A. G. Akeroyd, *Searching for a very light Higgs boson at the Tevatron*, Phys. Rev. **D68** (2003) 077701, arXiv:hep-ph/0306045 [hep-ph].

[1042] A. G. Akeroyd, M. A. Diaz, M. A. Rivera, and D. Romero, *Fermiophobia in a Higgs Triplet Model*, Phys. Rev. **D83** (2011) 095003, arXiv:1010.1160 [hep-ph].

[1043] K. Hartling, K. Kumar, and H. E. Logan, *GMCALC: a calculator for the Georgi-Machacek model*, arXiv:1412.7387 [hep-ph].

[1044] E. Eichten, I. Hinchliffe, K. D. Lane, and C. Quigg, *Super Collider Physics*, Rev. Mod. Phys. **56**

(1984) 579–707.

[1045] C. Degrande, K. Hartling, H. E. Logan, A. D. Peterson, and M. Zaro, *Automatic predictions in the Georgi-Machacek model at next-to-leading order accuracy*, Phys. Rev. **D93** (2016) no. 3, 035004, arXiv:1512.01243 [hep-ph].

[1046] CMS Collaboration, *Search for a Higgs boson in the mass range from 145 to 1000 GeV decaying to a pair of W or Z bosons*, JHEP **10** (2015) no. CERN-PH-EP-2015-074, CMS-HIG-13-031, 144, arXiv:1504.00936 [hep-ex].

[1047] B. A. Dobrescu and K. T. Matchev, *Light axion within the next-to-minimal supersymmetric standard model*, JHEP **09** (2000) 031, arXiv:hep-ph/0008192 [hep-ph].

[1048] U. Haisch, J. F. Kamenik, A. Malinauskas, and M. Spira, *Collider constraints on light pseudoscalars*, JHEP **03** (2018) 178, arXiv:1802.02156 [hep-ph].

[1049] U. Haisch and J. F. Kamenik, *Searching for new spin-0 resonances at LHCb*, Phys. Rev. **D93** (2016) no. 5, 055047, arXiv:1601.05110 [hep-ph].

[1050] LHCb Collaboration, *Search for Dark Photons Produced in 13 TeV pp Collisions*, Phys. Rev. Lett. **120** (2018) no. CERN-EP-2017-248, LHCB-PAPER-2017-038, 061801, arXiv:1710.02867 [hep-ex].

[1051] LHCb Collaboration, *Search for a dimuon resonance in the Υ mass region*, JHEP **09** (2018) no. LHCB-PAPER-2018-008, CERN-EP-2018-111, LHCB-PAPER-2018-008, 147, arXiv:1805.09820 [hep-ex].

[1052] LHCb Collaboration, *Tesla : an application for real-time data analysis in High Energy Physics*, Comput. Phys. Commun. **208** (2016) no. CERN-LHCB-DP-2016-001, 35–42, arXiv:1604.05596 [physics.ins-det].

[1053] LHCb Collaboration, *Real-time alignment and calibration of the LHCb Detector in Run II*, J. Phys. Conf. Ser. **664** (2015) no. LHCB-PROC-2015-011, 082010.

[1054] P. Ilten, Y. Soreq, J. Thaler, M. Williams, and W. Xue, *Proposed Inclusive Dark Photon Search at LHCb*, Phys. Rev. Lett. **116** (2016) no. 25, 251803, arXiv:1603.08926 [hep-ph].

Report from Working Group 3: Beyond the Standard Model physics at the HL-LHC and HE-LHC

Physics of the HL-LHC, and Perspectives at the HE-LHC

Convenors:
X. Cid Vidal[1], M. D'Onofrio[2], P. J. Fox[3], R. Torre[4,5], K. A. Ulmer[6],

Contributors:
A. Aboubrahim[7], A. Albert[8], J. Alimena[9], B. C. Allanach[10], C. Alpigiani[11], M. Altakach[12], S. Amoroso[13], J. K. Anders[14], J. Y. Araz[15], A. Arbey[16], P. Azzi[17], I. Babounikau[18], H. Baer[19], M. J. Baker[20], D. Barducci[21], V. Barger[22], O. Baron[23], L. Barranco Navarro[24], M. Battaglia[25], A. Bay[26], D. Bhatia[27], S. Biswas[28], D. Bloch[29], D. Bogavac[30], C. Borschensky[31], M. K. Bugge[32], D. Buttazzo[33], G. Cacciapaglia[16], L. Cadamuro[34], A. Calandri[35], D. A. Camargo[36], A. Canepa[3], L. Carminati[37,38], S. Carrá[37,38], C. A. Carrillo Montoya[39], A. Carvalho Antunes De Oliveira[40], F. L. Castillo[24], V. Cavaliere[41], D. Cavalli[37,38], C. Cecchi[42,43], A. Celis[44], A. Cerri[45], G. S. Chahal[46,47], A. Chakraborty[48], S. V. Chekanov[49], H. J. Cheng[50], J. T. Childers[49], M. Cirelli[51], O. Colegrove[52], G. Corcella[53], M. Corradi[54,55], M. J. Costa[24], R. Covarelli[56,57], N. P. Dang[58], A. Deandrea[59], S. De Curtis[60], H. De la Torre[61], L. Delle Rose[62], D. Del Re[54,63], A. Demela[37,38], S. Demers[64], R. Dermisek[65], A. De Santo[45], K. Deshpande[41], B. Dey[66], J. Donini[67], A. K. Duncan[68], V. Dutta[52], C. Escobar[24], L. Fanó[42,43], G. Ferretti[69], J. Fiaschi[70], O. Fischer[71], T. Flacke[72], E. D. Frangipane[73,74], M. Frank[15], G. Frattari[54,55], D. Frizzell[75], E. Fuchs[76], B. Fuks[51,77], E. Gabrielli[78], J. Gainer[79], Y. Gao[2], J. E. García Navarro[24], M. H. Genest[12], S. Giagu[54,55], G. F. Giudice[4], J. Goh[80], M. Gouzevitch[16], P. Govoni[81,82], A. Greljo[4], A. Grohsjean[18], A. Gurrola[83], G. Gustavino[75], C. Guyot[84], C. B. Gwilliam[2], S. Ha[85], U. Haisch[86], J. Haller[87], T. Han[88], D. Hayden[61], M. Heikinheimo[89], U. Heintz[90], C. Helsens[4], K. Hoepfner[8], J. M. Hogan[90,91], K. Huitu[89,92], P. Ilten[93], V. Ippolito[54,55], A. Ismail[94], A. M. Iyer[95], Sa. Jain[27], D. O. Jamin[96], L. Jeanty[97], T. Jezo[20], W. Johns[83], A. Kalogeropoulos[98], J. Karancsi[99,100], Y. Kats[101], H. Keller[8], A. Khanov[102], J. Kieseler[4], B. Kim[103], M. S. Kim[92], Y. G. Kim[104], M. Klasen[70], M. D. Klimek[105], R. Kogler[87], J. R. Komaragiri[106], M. Krämer[107], S. Kubota[108], A. K. Kulesza[70], S. Kulkarni[109], T. Lari[37,38], A. Ledovskoy[110], G. R. Lee[111], L. Lee[112], S. W. Lee[103], R. Leonardi[42,43], R. Les[113], I. M. Lewis[114], Q. Li[115], T. Li[116], I. T. Lim[10,73], S. H. Lim[48], K. Lin[61], Z. Liu[3,23], K. Long[117], M. Low[3], E. Lunghi[65], D. Madaffari[24], F. Mahmoudi[16], D. Majumder[114], S. Malvezzi[82], M. L. Mangano[4], E. Manoni[43], X. Marcano[118], A. Mariotti[119], M. Marjanovic[67], D. Marlow[98], J. Martin Camalich[120,121], P. Matorras Cuevas[20], M. McCullough[4], E. F. McDonald[122], J. Mejia Guisao[123], B. Mele[54], F. Meloni[13], I.-A. Melzer-Pellmann[18], C. Merlassino[14], A. B. Meyer[18], E. Michielin[17], A. J. Miller[108], L. Mittnacht[124], S. Mondal[89,92], S. Moretti[125,126], S. Mukhopadhyay[127], B. P. Nachman[73,128], K. Nam[129], M. Narain[90], M. Nardecchia[4], P. Nath[7], J. Navarro-González[24], A. Nisati[54,55], T. Nitta[130], D. L. Noel[131], M. M. Nojiri[48,132,133], J. P. Ochoa-Ricoux[134], H. Oide[5,135], M. L. Ojeda[113], S. Pagan Griso[73,128], E. Palencia Cortezon[136], O. Panella[42,43], P. Pani[13], L. Panizzi[137], L. Panwar[106], C. B. Park[72], J. Pazzini[17,138], K. Pedro[3], M. M. Perego[139], L. Perrozzi[140], B. A. Petersen[4], A. Pierce[141], G. Polesello[142], A. Policicchio[54,55], C. J. Potter[131], P. Pralavorio[35], M. Presilla[17,138], J. Proudfoot[49], F. S. Queiroz[143], G. Ramirez-Sanchez[123], D. Redigolo[144,145], A. Reimers[87], S. Resconi[37,38], M. Rimoldi[14], J. C. Rivera Vergara[134], T. Rizzo[146], C. Rogan[114], F. Romeo[83], R. Rosten[30], R. Ruiz[47,147], J. Ruiz-Alvarez[148], J. A. Sabater Iglesias[18], B. Safarzadeh Samani[45], S. Sagir[90,149], M. Saito[150], S. Saito[27], F. Sala[18], C. Salazar[148], A. Savin[117], R. Sawada[150], S. Sawant[27], I. Schienbein[12], M. Schlaffer[76], B. Schneider[3], S. C. Schuler[8], C. D. Sebastiani[54,55], S. Sekmen[103], M. Selvaggi[4], D. Sengupta[19], H. Serce[22], H. Serodio[151], L. Sestini[17], B. Shakya[25], B. Shams Es Haghi[94], P. Sheldon[83], S. Shin[152,153], F. Simonetto[17,138], L. Soffi[105], M. Spannowsky[154], J. Stupak[75], M. J. Sullivan[2],

https://doi.org/10.23731/CYRM-2019-007.585

M. Sunder[70], *Y. Takahashi*[20], *X. Tata*[79], *H. Teagle*[2], *K. Terashi*[150], *A. Tesi*[60], *A. Thamm*[4], *K. Tobioka*[155], *P. Tornambe*[108], *F. Trovato*[45], *D. Tsiakkouri*[156], *F. C. Ungaro*[122], *A. Urbano*[157], *E. Usai*[90], *N. Vanegas*[148], *L. Vaslin*[67], *C. Vázquez Sierra*[158], *I. Vivarelli*[45], *M. Vranjes Milosavljevic*[159], *H. Waltari*[89,92,126], *R. Wang*[49], *X. Wang*[94], *M. S. Weber*[14], *C. Weiland*[47,94], *M. Wielers*[125], *J. M. Williams*[160], *S. Willocq*[108], *D. Xu*[50], *K. Yagyu*[161], *E. Yazgan*[50], *R. Ye*[103], *H. D. Yoo*[129], *T. You*[131,162], *F. Yu*[124,163], *G. Zevi Della Porta*[164], *W. Zhang*[90], *C. Zhu*[50], *X. Zhuang*[50], *J. Zobec*[147], *J. Zupan*[165], *J. Zurita*[166]

[1] U. Santiago de Compostela, IGFAE, [2] U. Liverpool, Dept. Phys., [3] Fermilab, [4] CERN, Geneva, [5] INFN, Genoa, [6] U. Colorado, Boulder, Dept. Phys., [7] Northeastern U., [8] RWTH Aachen, [9] Ohio State U., Columbus, [10] U. Cambridge, DAMTP, [11] U. Washington, Seattle, Dept. Phys., [12] LPSC, Grenoble, [13] DESY, Zeuthen, [14] U. Bern, LHEP, [15] Concordia U., Montreal, Dept. Phys., [16] IPNL, Lyon, [17] INFN, Padua, [18] DESY, Hamburg, [19] U. Oklahoma, Norman, [20] U. Zurich, Phys. Inst., [21] SISSA, Trieste, [22] U. Wisconsin, Madison, [23] U. Maryland, College Park, Dept. Phys., [24] IFIC, Valencia, [25] UC, Santa Cruz, SCIPP, [26] EPFL, Lausanne, LPHE, [27] TIFR, Mumbai, DHEP, [28] RKMVU, West Bengal, [29] IPHC, Strasbourg, [30] U. Barcelona, IFAE, [31] U. Tubingen, Dept. Phys., [32] U. Oslo, Dept. Phys., [33] INFN, Pisa, [34] U. Florida, Gainesville, Dept. Phys., [35] CPPM, Marseille, [36] U. Fed. Rio Grande do Norte, Intl. Inst. Phys., [37] INFN, Milan, [38] U. Milan, Dept. Phys., [39] U. Andes, Bogota, Dept. Phys., [40] NICPB, Tallinn, [41] Brookhaven Natl. Lab., Dept. Phys., [42] U. Perugia, Dept. Phys., [43] INFN, Perugia, [44] LMU Munich, Dept. Phys., [45] U. Sussex, Brighton, Dept. Phys. Astron., [46] Imperial Coll., London, Dept. Phys., [47] Durham U., IPPP, [48] KEK, Tsukuba, [49] Argonne Natl. Lab., HEP Div., [50] CAS, IHEP, Beijing, [51] LPTHE, Paris, [52] UC, Santa Barbara, Dept. Phys., [53] INFN, LNF, Frascati, [54] INFN, Rome 1, [55] U. Rome 1, La Sapienza, Dept. Phys., [56] INFN, Turin, [57] U. Turin, Dept. Exp. Phys., [58] U. Louisville, Dept. Phys., [59] U. Lyon 1, [60] INFN, Florence, [61] Michigan State U., East Lansing, Dept. Phys. Astron., [62] U. Florence, Dept. Phys. Astron., [63] U. Rome 1, La Sapienza, [64] Yale U., Dept. Phys., [65] Indiana U., Bloomington, Dept. Phys., [66] CCNU, IOPP, Wuhan, [67] LPC, Clermont-Ferrand, [68] U. Glasgow, Sch. Phys. Astron., [69] Chalmers U. Technol., Gothenburg, [70] U. Munster, Inst. Theor. Phys., [71] KIT, Karlsruhe, [72] IBS, Daejeon, [73] LBNL, Berkeley, Div. Phys., [74] UCSC, Santa Cruz, Dept. Phys., [75] U. Oklahoma, Norman, Dept. Phys. Astron., [76] Weizmann Inst. Sci., Rehovot, Fac. Phys., [77] Inst. U. de France, [78] U. Trieste, Dept. Phys., [79] U. Hawaii, [80] Hanyang U., Seoul, Dept. Phys., [81] U. Milan Bicocca, Dept. Phys., [82] INFN, Milan Bicocca, [83] Vanderbilt U., Dept. Phys. Astron., [84] IRFU, Saclay, DPP, [85] Korea U., Seoul, [86] MPI Phys., Munich, [87] U. Hamburg, Inst. Exp. Phys., [88] U. Pittsburgh, [89] U. Helsinki, Dept. Phys., [90] Brown U., Dept. Phys., [91] Bethel Coll., [92] Helsinki Inst. Phys., [93] U. Birmingham, Sch. Phys. Astron., [94] U. Pittsburgh, Dept. Phys. Astron., [95] INFN, Naples, [96] Acad. Sin., Inst. Phys., Taipei, [97] U. Oregon, Eugene, Dept. Phys., [98] Princeton U., Dept. Phys., [99] Hungarian Acad. Sci., Debrecen, Inst. Nucl. Res., [100] KLTE-ATOMKI, [101] Ben-Gurion U., Beer-Sheva, Dept. Phys., [102] OKState, Stillwater, Dept. Phys., [103] Kyungpook Natl. U., Daegu, Dept. Phys., [104] Natl. U. Educ., Gwangju, [105] Cornell U., LEPP, [106] Indian Inst. Sci., Bangalore, [107] RWTH, Aachen, Phys. Inst., [108] UMass, Amherst, Dept. Phys., [109] OEAW, Vienna, [110] U. Virginia, Charlottesville, Dept. Phys., [111] U. Bergen, Dept. Phys. Technol., [112] Harvard U., [113] U. Toronto, Dept. Phys., [114] U. Kansas, Lawrence, Dept. Phys. Astron., [115] Peking U., Beijing, Sch. Phys., [116] Nankai U., Tianjin, [117] U. Wisconsin, Madison, Dept. Phys., [118] LPT, Orsay, [119] Vrije U. Brussels, Dept. Phys. Astrophys., [120] U. Laguna, Tenerife, Dept. Phys., [121] IAC, La Laguna, [122] ARC, CoEPP, Melbourne, [123] CINVESTAV, Mexico, [124] U. Mainz, PRISMA, [125] RAL, Didcot, [126] U. Southampton, Phys. Astron., [127] IACS, Kolkata, Dept. Theor. Phys., [128] UC, Berkeley, Dept. Phys., [129] Seoul Natl. U., [130] Waseda U., Tokyo, Dept. Phys., [131] U. Cambridge, Cavendish Lab., [132] U. Tokyo, KIPMU, [133] Sokendai, Tsukuba, [134] Pontificia U. Catol. Chile, Santiago, Dept. Phys., [135] U. Genoa, Dept. Phys., [136] U. Oviedo, Dept. Phys., [137] Uppsala U., Dept. Phys. Astron., [138] U. Padua, Dept. Phys., [139] LAL, Orsay, [140] ETH, Zurich, Dept. Phys., [141] U. Michigan, Ann Arbor, Dept. Phys., [142] INFN, Pavia, [143] U. Fed. Rio Grande do Norte, [144] IAS, Princeton, [145] Tel-Aviv U., Dept. Part. Phys., [146] SLAC, [147] Cathol. U. Louvain, CP3, [148] Antioquia U., [149] Karamanoglu Mehmetbey U., Karaman, [150] U. Tokyo, ICEPP, [151] Lund U., THEP, [152] Chicago U., EFI, [153] Yonsei U., Dept. Phys., [154] Durham U., Dept. Phys., [155] Florida State U., Tallahassee, Dept. Phys., [156] U. Cyprus, Nicosia, Dept. Phys., [157] INFN, Trieste, [158] Nikhef, Amsterdam, [159] Inst. Phys., Belgrade, [160] MIT, Cambridge, [161] Seikei U., [162] U. Cambridge, [163]

U. Mainz, Inst. Phys.,[164] UC, San Diego, Dept. Phys.,[165] U. Cincinnati, Dept. Phys.,[166] Karlsruhe U., TTP.

Abstract

This is the third out of five chapters of the final report [1] of the Workshop on *Physics at HL-LHC, and perspectives on HE-LHC* [2]. It is devoted to the study of the potential, in the search for Beyond the Standard Model (BSM) physics, of the High Luminosity (HL) phase of the LHC, defined as $3\ \mathrm{ab}^{-1}$ of data taken at a centre-of-mass energy of $14\ \mathrm{TeV}$, and of a possible future upgrade, the High Energy (HE) LHC, defined as $15\ \mathrm{ab}^{-1}$ of data at a centre-of-mass energy of $27\ \mathrm{TeV}$. We consider a large variety of new physics models, both in a simplified model fashion and in a more model-dependent one. A long list of contributions from the theory and experimental (ATLAS, CMS, LHCb) communities have been collected and merged together to give a complete, wide, and consistent view of future prospects for BSM physics at the considered colliders. On top of the usual *standard candles*, such as supersymmetric simplified models and resonances, considered for the evaluation of future collider potentials, this report contains results on dark matter and dark sectors, long lived particles, leptoquarks, sterile neutrinos, axion-like particles, heavy scalars, vector-like quarks, and more. Particular attention is placed, especially in the study of the HL-LHC prospects, to the detector upgrades, the assessment of the future systematic uncertainties, and new experimental techniques. The general conclusion is that the HL-LHC, on top of allowing to extend the present LHC mass and coupling reach by $20 - 50\%$ on most new physics scenarios, will also be able to constrain, and potentially discover, new physics that is presently unconstrained. Moreover, compared to the HL-LHC, the reach in most observables will generally more than double at the HE-LHC, which may represent a good candidate future facility for a final test of TeV-scale new physics.

Contents

1 Introduction and overview . . . 592
1.1 Analysis methods and objects definitions . . . 594
1.1.1 ATLAS and CMS performance . . . 595
1.1.2 LHCb performance . . . 596
1.2 Treatment of systematic uncertainties . . . 596
2 Supersymmetry . . . 598
2.1 Searches for gluinos and third generation squarks . . . 599
2.1.1 Gluino pair production at HL- and HE-LHC . . . 599
2.1.2 Third generation squarks at HL-LHC . . . 601
2.1.3 Gluinos and top squarks at HL-LHC in hadronic boosted signatures . . . 603
2.1.4 Implications of a stop sector signal at the HL-LHC . . . 606
2.2 Searches for charginos and neutralinos . . . 608
2.2.1 Chargino pair production at HL-LHC . . . 609
2.2.2 Chargino-Neutralino searches in multileptons at HL-LHC . . . 611
2.2.3 Chargino-Neutralino production in the $Wh \to \ell\nu\, b\bar{b}$ channel at HL-LHC . . . 612
2.2.4 Chargino-Neutralino searches with same-charge dilepton final states at HL-LHC . . . 614
2.2.5 Searches for SUSY models with compressed electroweakino mass spectra . . . 616
2.2.6 Multileptons from resonant electroweakinos in left-right SUSY at HL- and HE-LHC . . . 621
2.3 Searches for Sleptons: stau pair production at HE- and HL-LHC . . . 625
2.3.1 Searches for $\tilde{\tau}$ pair production in the hadronic channel ($\tau_h\tau_h$) at ATLAS at the HL-LHC 626
2.3.2 Searches for $\tilde{\tau}$ pair production in the $\tau_h\tau_h$ and $\tau_\ell\tau_h$ channels at CMS at the HL-LHC . . . 628
2.3.3 Remarks on stau pair production searches at HL-LHC . . . 630
2.3.4 Searches for $\tilde{\tau}$ pair production in the $\tau_h\tau_h$ and $\tau_\ell\tau_h$ channels at CMS at HE-LHC . . . 631
2.4 Other SUSY signatures and implications on SUSY models . . . 631
2.4.1 SUSY discovery potential at HL- and HE-LHC . . . 632
2.4.2 Natural SUSY at HL- and HE-LHC . . . 633
2.4.3 The pMSSM at HL- and HE-LHC . . . 637
2.4.4 Z' bosons in supersymmetric and leptophobic scenarios at HL- and HE-LHC . . . 639
3 Dark Matter and Dark Sectors Searches . . . 644
3.1 Dark Matter and Jets . . . 645
3.1.1 Studies on the sensitivity to Dark Matter of the monojet channel at HL-LHC . . . 645
3.1.2 Monojet Signatures from Heavy Coloured Particles at HL- and HE-LHC . . . 647
3.1.3 Searching for Electroweakinos in monojet final states at HL- and HE-LHC . . . 650
3.2 Dark Matter and Heavy Flavour . . . 651
3.2.1 Associated production of dark matter and heavy flavour quarks at HL-LHC . . . 651
3.2.2 Production of dark matter in association with top quarks at HL- and HE-LHC . . . 655
3.2.3 Dark matter production in single-top events at HL-LHC . . . 658
3.2.4 Four-top signatures at the HL-LHC . . . 660
3.3 Dark Matter and Electroweak Bosons . . . 662
3.3.1 Dark matter produced in association with a Z boson at HL-LHC . . . 662

3.3.2 Dark matter searches in mono-photon and VBF+$E_{\mathrm{T}}^{\mathrm{miss}}$ final states at HL-LHC 663
3.3.3 Search for Higgs portal dark matter models at HL- and HE-LHC 669
3.3.4 Singlet dark matter with slepton-like partners at HL- and HE-LHC 672
3.4 Dark sectors 675
3.4.1 Prospects for dark-photon at the HL-LHCb 675
3.4.2 Long-lived dark-photon decays at the HL-LHC 678
3.4.3 Searching for dark photons via Higgs-boson production at the HL- and HE-LHC . . . 685
4 Long Lived Particles 688
4.1 Disappearing Tracks 689
4.1.1 Prospects for disappearing track analysis at HL-LHC 689
4.1.2 Complementarities between LHeC and HL-LHC for disappearing track searches . . . 691
4.1.3 Searching for Electroweakinos with disappearing tracks analysis at HL- and HE-LHC . 693
4.2 Displaced Vertices 694
4.2.1 LLP decaying to a Displaced Vertex and $E_{\mathrm{T}}^{\mathrm{miss}}$ at HL-LHC 694
4.2.2 Displaced muons at HL-LHC 697
4.2.3 LLPs decaying into muons and jets at the HL-LHC 698
4.2.4 LLPs decaying into dijets at the HL-LHC 699
4.3 Heavy Stable Charged Particles at HL-LHC 701
4.3.1 Heavy stable charged particle search with time of flight measurements 701
4.3.2 Heavy stable charged particle search with energy loss 703
4.4 Additional examples of specialised techniques for LLP at HL-LHC 705
4.4.1 Fast timing signatures for long-lived particles 705
4.4.2 Jets reconstruction techniques for neutral LLPs 708
5 High-p_T signatures from flavour 711
5.1 Neutrino masses 711
5.1.1 Neutrino mass models at the HL- and HE-LHC 711
5.1.2 Like-sign dileptons with mirror type composite neutrinos at the HL-LHC 719
5.1.3 Search for heavy composite Majorana neutrinos at the HL- and the HE-LHC 722
5.2 Leptoquarks and Z' 725
5.2.1 Leptoquark searches in t+τ and t+μ decays at HL-LHC 726
5.2.2 Z' and leptoquarks for B decay anomalies at HL- and HE-LHC 728
5.2.3 Search for leptoquarks decaying to τ and b at HL-LHC 731
5.2.4 HE-LHC sensitivity study for leptoquarks decaying to $\tau + b$ 734
5.3 High p_T implications of flavour anomalies 735
5.3.1 EFT analysis 735
5.3.2 Constraints on simplified models for $b \to c\tau\nu$ 736
5.3.3 Constraints on simplified models for $b \to sll$ 738
6 Other BSM signatures 741
6.1 Spin 0 and 2 resonances 741
6.1.1 Resonant double Higgs production in the $4b$ final state at the HL-LHC 742
6.1.2 VBF production of resonances decaying to HH in the 4b final state at HL-LHC 744

6.1.3 Heavy Higgs bosons in models with vector-like fermions at the HL- and HE-LHC . . . 747
6.1.4 Heavy singlet scalars at HL- and HE-LHC . . . 753
6.1.5 Relaxion at the HL-LHC . . . 756
6.1.6 The HL-LHC and HE-LHC scope for testing compositeness of 2HDMs . . . 758
6.1.7 Axion-like particles at the HL- and HE-LHC . . . 761
6.1.8 Search for light pseudoscalar with taus at HL-LHC . . . 765
6.1.9 Colour octet scalar into gluons and photons at HL-LHC . . . 767
6.2 Spin 1 resonances . . . 769
6.2.1 Precision predictions for new dilepton and $t\bar{t}$ resonances at HL- and HE-LHC . . . 770
6.2.2 Searching for a RS gluon resonance in $t\bar{t}$ at the HL- and HE-LHC . . . 772
6.2.3 $Z' \to t\bar{t}$ searches at HL-LHC . . . 774
6.2.4 High mass dilepton ($ee, \mu\mu, \tau\tau$) searches at the HE-LHC . . . 776
6.2.5 Prospects for $Z' \to e^+e^-, \mu^+\mu^-$ searches at the HL- and HE-LHC . . . 778
6.2.6 $W' \to e\nu, \mu\nu$ or $tb, t \to b\ell\nu$ searches at HL-LHC . . . 781
6.2.7 Searches for $W' \to \tau + E_{\mathrm{T}}^{\mathrm{miss}}$ . . . 786
6.2.8 HL- and HE-LHC sensitivity to 2HDMs with $U(1)_X$ Gauge Symmetries . . . 787
6.2.9 Z' discrimination at HE-LHC in case of an evidence/discovery after the HL-LHC . . . 790
6.3 Spin $1/2$ resonances . . . 792
6.3.1 Search for excited leptons at HL-LHC . . . 792
6.3.2 VLQs at HL- and HE-LHC: discovery and characterisation . . . 795
6.4 Signature based analyses . . . 797
6.4.1 Coloured Resonance Signals at the HL- and HE-LHC . . . 797
6.4.2 Precision searches in dijets at the HL- and HE-LHC . . . 800
6.4.3 Dissecting heavy diphoton resonances at HL- and HE-LHC . . . 804
6.4.4 Prospects for diboson resonances at the HL- and HE-LHC . . . 807
6.4.5 Prospects for Boosted Object Tagging with Timing Layers at HL-LHC . . . 809
6.4.6 High mass resonance searches at HE-LHC using hadronic final states . . . 812
6.4.7 On the power (spectrum) of HL/HE-LHC . . . 814
7 Conclusions and Outlook . . . 817
8 Acknowledgements . . . 823

1 Introduction and overview

The LHC physics program represents one of the most successful experimental programs in Science, and has been rewarded as such with the discovery, in 2012, of the Higgs boson [3, 4]. However, this discovery was only one of the targets of the LHC, which aims at constraining, and possibly discovering, an incredible variety of new physics (NP) scenarios with imprints at the TeV scale. In order to fully profit from the LHC potential, an upgrade of its luminosity [5,6], together with consistent upgrades of the major experiments [7, 8], has already been approved by the CERN Council [9]. The High Luminosity LHC (HL-LHC) upgrade will eventually collect an integrated luminosity of $3\ \mathrm{ab}^{-1}$ of data in pp collisions at a centre-of-mass (c.o.m.) energy of $14\ \mathrm{TeV}$, which should maximise the LHC potential to uncover new phenomena.

The lack of indications for the presence of NP so far may imply that either NP is not where we expect it, or that it is elusive. The first case should not be seen as a negative result. Indeed the theoretical and phenomenological arguments suggesting NP close to the electroweak (EW) scale are so compelling, that a null result should be considered itself as a great discovery. This would shake our grounds, falsifying some of the paradigms that guided research in fundamental physics so far. In the second case, while these paradigms would be vindicated, Nature may have been clever in protecting its secrets. It may be hiding the NP at slightly higher masses or lower couplings than we expected or, perhaps, in more compressed spectra and involved signatures, making it extremely difficult to address experimentally. Both cases would lead to a discovery happening at the edge of the LHC potential, with little space left for identifying the new particles, or the new paradigms.

These considerations drove, in the last few years, intense activity worldwide to assess the future of collider experiments beyond the HL-LHC. Several proposals and studies have been performed, also in the view of the forthcoming update of the European Strategy for Particle Physics (ESPP), that will take place in 2019-2020. Several options for future colliders have been and are being considered, such as future lepton colliders, either linear e^+e^- machines like ILC [10–14] and CLIC [15, 16], or circular e^+e^- ones like FCC-ee/TLEP [17] and CepC [18, 19] and $\mu^+\mu^-$ accelerators like MAP [20] and LEMMA [21, 22], or hadron pp colliders such as a $27\ \mathrm{TeV}$ c.o.m. upgraded HE-LHC [23], a $50 - 100\ \mathrm{TeV}$ SppC [18, 19], and a $100\ \mathrm{TeV}$ FCC-hh [24–28]. Comparing the physics potentials, the needed technology and prospects for its availability, and the cost to benefit ratio of such machines is extremely challenging, but also very timely. The proposal for an e^-p collider, the LHeC [29], is also being considered to further upgrade the HL-LHC with a $60\ \mathrm{GeV}$ energy, high current electron beam by using novel Energy Recovery Linear Accelerator (ERL) techniques. The same facility could be hosted at the FCC [24].

A crucial ingredient to allow a comparison of proposed future machines is the assessment of our understanding of physics at the end of the HL-LHC program. Knowing which scenarios remain open at the end of the approved HL-LHC allows one to set standard benchmarks for all the interesting phenomena to study, that could be used to infer the potential of different future machines. Moreover, in the perspective of pushing the LHC program even further, one may wonder if the LHC tunnel and the whole CERN infrastructure, together with future magnet technology, could be exploited to push the energy up into an unexplored region with the HE-LHC, that could collect an integrated luminosity of $15\ \mathrm{ab}^{-1}$.

These two points are the foundations of the Workshop on *Physics at HL-LHC, and perspectives on HE-LHC* [2], that has been devoted, between 2017 and 2018, to the study of the physics potential of the HL- and HE-LHC. This document is the third out of five chapters of the final report [1] of the Workshop. In this chapter, the attention is focused on beyond the SM (BSM) phenomena, one of the key reasons to continue to pursue an hadron collider physics program.

Naturalness, also often referred to as the Hierarchy Problem (HP), is the main motivation to expect new physics close to the EW scale. This theoretical puzzle can be understood in different ways: from a more technical perspective, it refers to radiative corrections to the Higgs mass parameter, which can

receive contributions from new physics present up at ultraviolet (UV) scales. We have at least one important example: the scale at which gravity becomes strongly coupled, usually identified with the Planck scale, $M_{\rm Pl}$. From a more conceptual point of view it can be phrased as the question why is the Fermi constant $G_F \approx 1.2 \cdot 10^{-5}$ GeV^{-2} (EW scale $v = 246$ GeV) so much bigger (smaller) than the Newton constant $G_N \approx 6.7 \cdot 10^{-39}$ GeV^{-2} (Planck scale $M_{\rm Pl} = 1.22 \cdot 10^{19}$ GeV).

Despite the different ways of phrasing and understanding the HP, its importance is intimately related to our reductionist approach to physics and our understanding of effective field theory. We do not expect the infrared (IR) physics, *i.e.*, for instance, at the energies that we are able to probe at colliders, to be strongly affected by the details of the UV theory. Therefore, unless Naturalness is only an apparent problem and has an anthropic explanation, or it is just the outcome of the dynamical evolution of our universe, all of its solutions are based on mechanisms that screen the effects of UV physics from the IR, by effectively reducing the UV cut-off to the TeV scale.

Such mechanisms can be dynamical, similarly to what occurs for the QCD scale, or can instead arise from extended space-time symmetries, such as in Supersymmetry (SUSY) or in Extra Dimensions (ED). All of these solutions share the prediction of new degrees of freedom close to the EW scale. How close is determined by where we are willing to push the UV scale, still accepting IR parameters to strongly dependent on it. In other words, it depends on the level of cancellation between different UV parameters that we are willing to accept to reproduce the observed IR parameters. Nature gives few examples of such large cancellations, which could be a few percent accidents, but are never far below the percent level. The LHC is a machine designed to test such cancellations at the percent level in most of the common solutions to the HP. There are some exceptions, as for instance in models where the so-called top partners are neutral under the SM colour group, where the LHC can only probe the few-to-10% region. Obviously, tests of our understanding of Naturalness pass through three main approaches, addressed in the first four chapters of this report. The first is the precise test of the SM observables, both in the EW and QCD sectors, discussed in the first chapter [30], and in the flavour sector, discussed in the fourth chapter [31]; the second is the study of the properties of the Higgs boson, presented in the second chapter [32]; the third is the direct search for new physics, which is the topic of this chapter.

Since the top quark is the particle that contributes the most to the radiative correction to the Higgs mass, the main prediction of the majority of models addressing the HP is the existence of coloured particles "related" to the top quark, that can generally be called "top-partners". These may be scalars, like the top squarks (stops) in SUSY, or (vector-like) fermions, like in models of Higgs compositeness. These particles have to be light for Naturalness to be properly addressed and, due to their strong production cross section, they are among the primary signatures of Naturalness at hadron colliders. To address the HP other particles have to be light too, such as for instance the gluinos in SUSY, that in turn affect the stops masses, and the EW partners of the Higgs boson. However, while the gluino profits from a strong production cross section at hadron colliders, the EW sector remains much more difficult to test, due to the smaller cross sections. All these signatures, together with others, less tightly related to Naturalness, are studied in details in this report.

Dark Matter (DM) is one of the big puzzles of fundamental physics. While there is stunning evidence for its existence, in the form of non-baryonic contribution to the matter abundance in the Universe, there are no particular indications on what it actually is. This is due to the fact that, so far, we have only probed it through its gravitational interactions, which tell us about its abundance, but do not tell us anything about its form. It could be made of particles, but this is not the only option. However, if DM is made of weakly interacting massive particles (WIMPs), then the observed abundance can only be reproduced for a relatively small window in its mass/coupling parameter space, which turns out to lie roughly in the ten GeV to ten TeV range, making it relevant for collider experiments.

Several theoretical constructions addressing the HP also naturally predict a WIMP DM candidate. The most notable is SUSY, where EW neutral fermionic partners of the Higgs and the SM gauge bosons, the neutralinos, could be, in proper regions of the parameter space, good WIMPs. Another compelling

paradigm for DM that may be relevant for collider experiments is that of the so-called Minimal Dark Matter (MDM), that corresponds to neutral particles belonging to EW multiplets that remains stable due to accidental symmetries. The simplest examples are just the wino and higgsino DM candidates arising in SUSY, but larger multiplets are also allowed. In this case the DM mass required to provide the observed abundance grows with the dimension of the EW group representation (multiplet) and usually lies between one to ten TeV. Therefore, a coverage of the whole MDM window provides a good benchmark for future hadron colliders, such as the HE-LHC or the FCC-hh (see Ref. [28] for prospect studies of MDM at a 100 TeV collider).

Finally, the third big mystery of the SM is flavour. Why are there such big hierarchies among fermion masses, and how do neutrino masses arise? These are two of the most compelling questions of fundamental physics. The generation of the flavour structure of the SM (the Yukawa couplings) and of the neutrino masses may be tied to a scale much above the EW scale. Thus, precision flavour observables are the most sensitive window to high-scale UV physics. Indeed, the ability of LHC experiments, with a leading role of LHCb in this context, to observe extremely rare flavour transitions, allows one to set constraints on new physics corresponding to scales of hundreds, or even thousands of TeV, completely inaccessible to direct searches.

Flavour transitions indirectly constraining NP at the TeV scale and above, have a crucial interplay with direct searches for the particles that may induce such transitions. A clear example of this interplay is given by the recent flavour anomalies in neutral and charged current B decays (R_K-R_{K*}, R_D-R_{D*}, *etc.*, which are discussed at length in the fourth chapter of this report [31]. Due to the relevance of such anomalies at the time of writing this report, prospect studies on high transverse momentum particles, as vector resonances or lepto-quarks (LQ), that could explain them, are presented by both working groups.

Concerning neutrino masses, the seesaw mechanism predicts the existence of heavy (sterile) neutrinos that can provide, in particular regions of the parameter space, peculiar signatures with several leptons in the final state. These neutral particles, coupled to leptons, can also arise in cascade decays of heavy right-handed charged gauge bosons. Whether produced directly, or in decays, the HL- and HE-LHC will be able to significantly reduce the parameter space of models predicting heavy neutrinos.

The report is not structured based on a separation of the HL-LHC from the HE-LHC studies, since several analyses were done for both options, and showing them together allows for a clearer understanding. However, when summarising our results in Section 7, we present conclusions separately for HL- and HE-LHC. The report is organised as follows. The introductory part includes a brief discussion of the future detector performances in analysis methods and objects identification and of the projected systematic uncertainties. Section 2 is devoted to the study of SUSY prospects. Section 3 shows projections for DM and Dark Sectors. Section 4 contains studies relevant for Long Lived Particles (LLPs). Section 5 presents prospects for high-p_T signatures in the context of flavour physics. Section 6 is devoted to resonances, either singly or doubly produced, and to other BSM signatures. Finally, in Section 7 we present our conclusions, with a separate executive summary of the HL- and HE-LHC potentials.

1.1 Analysis methods and objects definitions

Different approaches have been used by the experiments and in theoretical prospect studies, hereafter named projections, to assess the sensitivity in searching for new physics at the HL-LHC and HE-LHC. For some of the projections, a mix of the approaches described below is used, in order to deliver the most realistic result. The total integrated luminosity for the HL-LHC dataset is assumed to be $3\ \mathrm{ab}^{-1}$ at a c.o.m. energy of $14\ \mathrm{TeV}$. For HE-LHC studies the dataset is assumed to be $15\ \mathrm{ab}^{-1}$ at a c.o.m. of $27\ \mathrm{TeV}$. The effect of systematic uncertainties is taken into account based on the studies performed for the existing analyses and using common guidelines for projecting the expected improvements that are foreseen thanks to the large dataset and upgraded detectors, as described in Section 1.2.

Detailed-simulations are used to assess the performance of reconstructed objects in the upgraded detectors and HL-LHC conditions, as described in Sections 1.1.1 and 1.1.2. For some of the projections, such simulations are directly interfaced to different event generators, parton showering (PS) and hadronisation generators. Monte Carlo (MC) generated events are used for SM and BSM processes, and are employed in the various projections to estimate the expected contributions of each process.

Extrapolations of existing results rely on the existent statistical frameworks to estimate the expected sensitivity for the HL-LHC dataset. The increased c.o.m. energy and the performance of the upgraded detectors are taken into account for most of the extrapolations using scale factors on the individual processes contributing to the signal regions. Such scale factors are derived from the expected cross sections and from detailed simulation studies.

Fast-simulations are employed for some of the projections in order to produce a large number of Monte Carlo events and estimate the reconstruction efficiency for the upgraded detectors. The upgraded CMS detector performance is taken into account encoding the expected performance of the upgraded detector in DELPHES3 [33], including the effects of pile-up interactions. Theoretical contributions use DELPHESwith the commonly accepted HL-LHC card corresponding to the upgraded ATLAS and CMS detectors.

Parametric-simulations are used for some of the projections to allow a full re-optimisation of the analysis selection criteria that benefit from the larger available datasets. Particle-level definitions are used for electrons, photons, muons, taus, jets and missing transverse momentum. These are constructed from stable particles from the MC event record with a lifetime larger than 0.3×10^{-10} s within the observable pseudorapidity range. Jets are reconstructed using the anti-k_t algorithm [34] implemented in the Fastjet [35] library, with a radius parameter of 0.4. All stable final-state particles are used to reconstruct the jets, except the neutrinos, leptons and photons associated to W or Z boson or τ lepton decays. The effects of an upgraded ATLAS detector are taken into account by applying energy smearing, efficiencies and fake rates to generator level quantities, following parameterisations based on detector performance studies with the detailed simulations. The effect of the high pileup at the HL-LHC is incorporated by overlaying pileup jets onto the hard-scatter events. Jets from pileup are randomly selected as jets to be considered for analysis with $\sim 2\%$ efficiency, based on studies of pile-up jet rejection and experience from Run-2 of the LHC.

1.1.1 ATLAS and CMS performance

The expected performance of the upgraded ATLAS and CMS detectors has been studied in detail in the context of the Technical Design Reports and subsequent studies; the assumptions used for this report and a more detailed description are available in Ref.s [7, 8]. For CMS, the object performance in the central region assumes a barrel calorimeter ageing conditions corresponding to an integrated luminosity of $1\ \mathrm{ab}^{-1}$.

The triggering system for both experiments will be replaced and its impact on the triggering abilities of each experiment assessed; new capabilities will be added, and, despite the more challenging conditions, most of the trigger thresholds for common objects are expected to either remain similar to the current ones or even to decrease [36, 37].

The inner detector is expected to be completely replaced by both experiments, notably extending its coverage to $|\eta| < 4.0$. The performance for reconstructing charged particles has been studied in detail in Ref.s [38–40]. Electrons and photons are reconstructed from energy deposits in the electromagnetic calorimeter and information from the inner tracker [41–44]. Several identification working points have been studied and are employed by the projection studies as most appropriate. Muons are reconstructed combining muon spectrometer and inner tracker information [45, 46].

Jets are reconstructed by clustering energy deposits in the electromagnetic and hadronic calorimeters [41,42,47] using the anti-k_T algorithm [34]. B-jets are identified via b-tagging algorithms. B-tagging

is performed if the jet is within the tracker acceptance ($|\eta| < 4.0$). Multivariate techniques are employed in order to identify $b-$jets and $c-$jets, and were fully re-optimised for the upgraded detectors [38, 40]. A working point with 70% efficiency for $b-$jet identification is used, unless otherwise noted. High p_T boosted jets are reconstructed using large-radius anti-k_T jets with a distance parameter of 0.8. Various jet substructure variables are employed to identify boosted $W/Z/H$ boson and top quark jets with good discrimination against generic QCD jets.

Missing transverse momentum (its modulus referred to as $E_{\mathrm{T}}^{\mathrm{miss}}$) is reconstructed following similar algorithms as employed in the Run-2 data taking. Its performance has been evaluated for standard processes, such as top-quark pair production [38, 48].

The addition of new precise-timing detectors and its effect on object reconstruction has also been studied in Ref.s [44, 49], although its results are only taken into account in a small subset of the projections in this report.

1.1.2 LHCb performance

The LHCb upgrades are shifted with respect to those of ATLAS and CMS. A first upgrade will happen at the end of Run-2 of the LHC, to run at a luminosity five times larger ($2 \times 10^{33}\mathrm{cm}^{-2}\mathrm{s}^{-1}$) in LHC Run-3 compared to those in Run-1 and Run-2, while maintaining or improving the current detector performance. This first upgrade (named Upgrade I) will be followed by by the so-called Upgrade II (planned at the end of Run-4) to run at a luminosity of $\sim 2 \times 10^{34}\mathrm{cm}^{-2}\mathrm{s}^{-1}$.

The LHCb MC simulation used in this document mainly relies on the PYTHIA 8 generator [50] with a specific LHCb configuration [51], using the CTEQ6 leading-order set of parton density functions [52]. The interaction of the generated particles with the detector, and its response, are implemented using the GEANT toolkit [53, 54] as described in Ref. [55].

The reconstruction of jets is done using a particle flow algorithm, with the output of this clustered using the anti-kT algorithm as implemented in FASTJET, with a distance parameter of 0.5. Requirements are placed on the candidate jet in order to reduce the background formed by particles which are either incorrectly reconstructed or produced in additional pp interactions in the same event. Different assumptions are made regarding the increased pile-up, though in general the effect is assumed to be similar to that in Run-2.

1.2 Treatment of systematic uncertainties

It is a significant challenge to predict the expected systematic uncertainties of physics results at the end of HL-LHC running. It is reasonable to anticipate improvements to techniques of determining systematic uncertainties over an additional decade of data-taking. To estimate the expected performance, experts in the various physics objects and detector systems from ATLAS and CMS have looked at current limitations to systematic uncertainties in detail to determine which contributions are limited by statistics and where there are more fundamental limitations. Predictions were made taking into account the increased integrated luminosity and expected potential gains in technique. These recommendations were then harmonised between the experiments to take advantage of a wider array of expert opinions and to allow the experiments to make sensitivity predictions on equal footing [7, 8]. For theorists' contributions, a simplified approach is often adopted, loosely inspired by the improvements predicted by experiments.

General guide-lining principles were defined in assessing the expected systematic uncertainties. Theoretical uncertainties are assumed to be reduced by a factor of two with respect to the current knowledge, thanks to both higher-order calculation as well as reduced PDF uncertainties [56]. All the uncertainties related to the limited number of simulated events are neglected, under the assumption that sufficiently large simulation samples will be available by the time the HL-LHC becomes operational. For all scenarios, the intrinsic statistical uncertainty in the measurement is reduced by a factor $1/\sqrt{\mathcal{L}}$, where $\mathcal{L}$ is the projection integrated luminosity divided by that of the reference Run-2 analysis. Systematics driven

by intrinsic detector limitations are left unchanged, or revised according to detailed simulation studies of the upgraded detector. Uncertainties on methods are kept at the same value as in the latest public results available, assuming that the harsher HL-LHC conditions will be compensated by improvements to the experimental methods.

The uncertainty in the integrated luminosity of the data sample is expected to be reduced down to 1% by better understanding of the calibration methods, improved stability in applying those methods, and making use of the new capabilities of the upgraded detectors [30].

In addition to the above scenario (often referred to as "YR18 systematics uncertainties" scenario), results are often compared to the case where the current level of understanding of systematic uncertainties is assumed ("Run-2 systematic uncertainties") or to the case of statistical-only uncertainties.

2 Supersymmetry

One of the main goal of collider physics is to uncover the nature of EW symmetry breaking (EWSB). Supersymmetry can resolve the hierarchy problem, as well as provide gauge coupling unification and a dark matter candidate. SUSY might be realised in nature in various ways and superpartners of the SM particles could be produced at colliders leading to many different possible detector signatures. Coloured superpartners such as squarks ($\tilde{q}$) and gluinos ($\tilde{g}$) are strongly produced and have the highest cross sections. Scalar partners of the left-handed and right-handed chiral components of the bottom quark ($\tilde{b}_{\mathrm{L,R}}$) or top quark ($\tilde{t}_{\mathrm{L,R}}$) mix to form mass eigenstates for which the bottom squark ($\tilde{b}_1$) and top squark ($\tilde{t}_1$) are defined as the lighter of the two. The lightest bottom and top squark mass eigenstates might be significantly lighter than the other squarks and the gluinos. As a consequence, $\tilde{b}_1$ and $\tilde{t}_1$ could be pair-produced with relatively large cross-sections at the HL- and HE-LHC. In the EW sector, SUSY partners of the Higgs, photon, Z, and W bosons are the spin-$1/2$ higgsinos, photino, zino, and winos that further mix in neutralino ($\tilde{\chi}^0_{1,2,3,4}$) and chargino ($\tilde{\chi}^{\pm}_{1,2}$) states, also called the electroweakinos. Their production rate is a few order of magnitudes lower than that of coloured superpartners. Superpartners of charged leptons, the sleptons ($\tilde{\ell}$), can also have sizeable production rates and are searched for at hadron colliders. Provided that R-parity conservation is assumed, SUSY particles typically decay to final states involving SM particles in addition to significant momentum imbalance due to a collider-stable lightest supersymmetric particle (LSP).

Searches of SUSY particles are presented in the following targeting HL- and HE-LHC, under various theoretical hypotheses such as the Minimal Supersymmetric Standard Model (MSSM) [57], phenomenological MSSM, light higgsinos models and more. R-parity conservation and prompt particle decays are generally assumed, whilst dedicated searches for long-lived particles are depicted in Section 4. Simplified models are also used to optimise the searches and interpret the results. The cross-sections used to evaluate the signal yields at 14 TeV are calculated to next-to-leading order in the strong coupling constant, adding the resummation of soft gluon emission at next-to-leading-logarithmic accuracy (NLO+NLL), see Ref. [58] for squarks and gluinos, and Ref.s [59, 60] for electroweakinos. The nominal cross sections and the uncertainties are taken from an envelope of cross section predictions using different PDF sets and factorisation and renormalisation scales. PDF uncertainties are dominant for strongly-produced particles. In particular, PDF uncertainties on gluino pair production ranges between 30% and 60% depending on the gluino mass, in a mass range between 1 and 4 TeV. Expected improvements due to precision SM measurements in the jet and top sector are expected at HL-LHC. In this report, nominal predictions are considered and, unless stated otherwise, no attempt to evaluate the impact of theoretical uncertainties on the reach of the searches is made. For 27 TeV c.o.m. energy, cross sections are also evaluated at NLO+NLL as shown in Fig. 2.1 for gluinos and top squarks pair production and for electroweakinos and sleptons pair production. For the latter, the NLO set from PDF4LHC is used and cross sections are presented for wino and higgsino hypotheses.

Prospects for exclusion and discovery of gluinos and top squarks are reported in Section 2.1. We show that HL-LHC will probe gluino masses up to 3.2 TeV, about $0.8-1$ TeV above the Run-2 $\tilde{g}$ mass reach for 80 fb^{-1}. Top squarks can be discovered (excluded) up to masses of 1.25 (1.7) TeV. This extends by about 700 GeV the reach of Run-2 for 80 fb^{-1}. Charginos and neutralinos studies are presented in Section 2.2, considering electroweakino decays via W, Z (also off-shell) and Higgs boson and various hypotheses for sparticles mass hierarchy. As an example, masses up to 850 (680) GeV can be excluded (discovered) for charginos decaying as $\tilde{\chi}^{\pm}_1 \to W^{(*)}\tilde{\chi}^0_1$: the results extend by about 500 GeV the mass reach obtained with 80 fb^{-1} of 13 TeV pp collisions, and extend beyond the LEP limit by almost an order of magnitude. HL-LHC searches for low momentum leptons will be sensitive to $\tilde{\chi}^{\pm}$ masses up to 350 GeV for $\Delta m(\tilde{\chi}^{\pm}_1, \tilde{\chi}^0_1) \approx 5$ GeV, and to mass splittings between 2 and 50 GeV, thus bringing significant new reach to Higgsino models. In Section 2.3, dedicated searches for sleptons are presented, and in particular for the *currently unconstrained* pair production of staus exploiting hadronically decaying tau leptons. Finally, identification of benchmark models and probing of various natural scenarios at HL- and

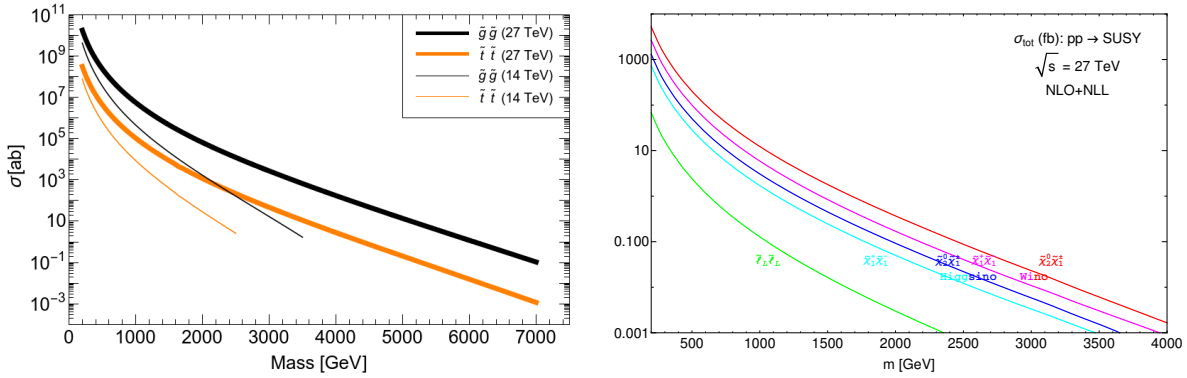

Fig. 2.1: Left: NLL+NLO predictions [58] of $\sigma(pp \to \tilde{g}\tilde{g}X)$ and $\sigma(pp \to \tilde{t}_1\tilde{t}_1^*X)$ production processes at the LHC for $\sqrt{s} = 14$ and 27 TeV c.o.m. energy (*Contribution from C. Borschensky, M. Kramer, A. Kulesza*). Right: NLO predictions [59–61] for electroweakinos and sleptons pair production for 27 TeV c.o.m. energy (*Contribution from J. Fiaschi, M. Klasen, M. Sunder*).

HE-LHC are presented in Section 2.4. For gluinos and stops HE-LHC will further increase the reach, above that of HL-LHC, by about a factor of two, and several benchmark MSSM and pMSSM models will be discoverable.

2.1 Searches for gluinos and third generation squarks

Naturalness considerations suggest that the supersymmetric partners of the third-generation SM quarks are the lightest coloured supersymmetric particles and gluinos are also within a range of few TeV. Several prospect studies have been presented by ATLAS and CMS for gluinos, bottom and top squarks (see, for example, Ref.s [62, 63]). New studies and further considerations on the HL- and HE-LHC potential for gluinos and top squarks are presented in the following sections.

2.1.1 Gluino pair production at HL- and HE-LHC

Contributors: T. Han, A. Ismail, B. Shams Es Haghi

The potential of the HL- and HE-LHC to discover supersymmetry is presented in this section focusing on searches for gluinos within MSSM scenarios. Gluino pair production has relatively large cross section and naturalness considerations indicate that gluino masses should not exceed few TeV and lie not too far above the EW scale. Hence they are certainly among the first particles that could be discovered at HL-LHC.

In the following we assume that a simplified topology dominates the gluino decay chain, culminating in jets plus missing energy in the form of a bino-like LSP $\tilde{\chi}^0$. We evaluate the sensitivity of future proton colliders to gluino pair production with gluinos decaying exclusively to $q\bar{q}\tilde{\chi}^0$ through off-shell first and second generation squarks, using a standard jets + $E_{\mathrm{T}}^{\mathrm{miss}}$ search. Currently, the reach for this simplified model with 36 fb^{-1} of 13 TeV data is roughly 2 TeV gluinos, for a massless LSP [64, 65]. A single search region requiring four jets and missing transverse momentum is optimised. In the compressed region where the gluino and LSP masses are similar, a search region with fewer jets is expected to be more effective (see, for example, Ref.s [62, 66]) but is not considered in this study.

The main SM backgrounds contributing to the final states considered are $Z(\to \nu\nu)$ + jets, $W(\to \ell\nu)$ + jets, and $t\bar{t}$ production. Other SM background sources such as dibosons and multi-jet are considered negligible. Signal and background samples are generated with MLM matching using MADGRAPH 5 [67], PYTHIA 8.2 [68]. Detector performance are simulated using DELPHES 3 [33], which employs FastJet [35] to cluster jets and uses the commonly accepted HL-LHC card corresponding to the

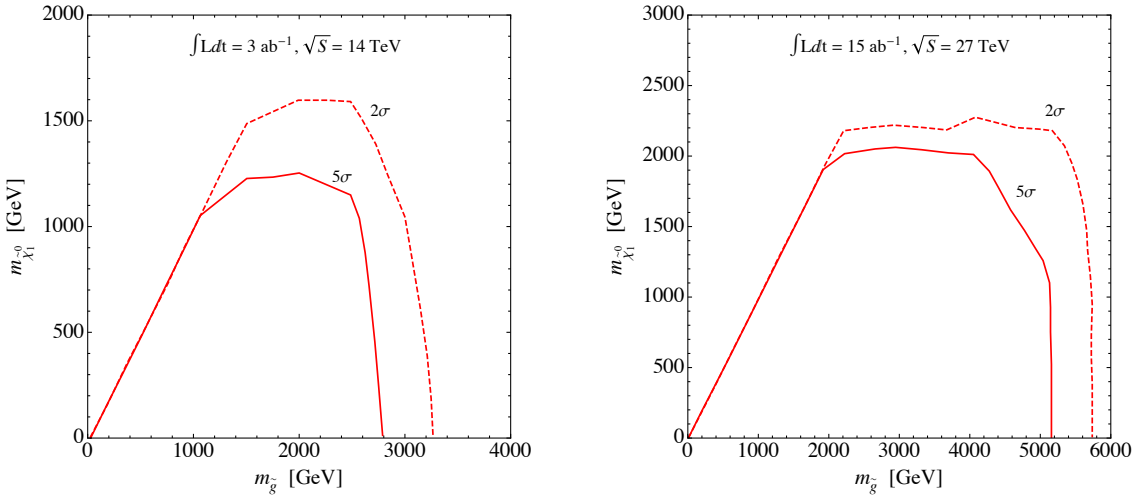

Fig. 2.1.1: Expected reach of HL- and HE-LHC in probing gluinos, in the gluino-LSP mass plane. The left (right) plots show the gluino mass reach in 14 (27) TeV pp collisions with 3 ab^{-1} (15 ab^{-1}) of data. The decay $\tilde{g} \to q\bar{q}\tilde{\chi}_1^0$ is assumed to occur with 100% branching fraction, with a bino-like LSP. Both 2σ exclusion (dashed) and 5σ discovery contours are shown.

upgraded ATLAS and CMS detectors prescribing anti-k_T jets [34] with radius 0.4. Effects due to high pile-up are not taken into account, as we expect it to have a negligible impact on our results [66]. An overall systematic uncertainty of 20% is assumed on the SM background contributions covering, among others, jet energy scale and resolution uncertainties. A generic 10% uncertainty is assumed on the signal. This does not take into account PDF-related uncertainty which might be as large as 50% for gluinos around 3 TeV, although the impact of an uncertainty of this kind is presented below for a massless LSP scenario.

Following previous works [62,66,69], we apply a set of baseline selections at both 14 and 27 TeV. We require that signal events contain no electrons (muons) with p_T above 10 (10) GeV and $|\eta|$ below 2.47 (2.4). Events are also required to contain a leading jet with $p_T > 160$ GeV and three additional jets with $p_T > 60$ GeV. In addition, a minimum missing transverse momentum of 160 GeV is required to fulfil trigger-based requirements. We reject events with $\Delta\phi(j, E_{\text{T}}^{\text{miss}}) > 0.4$ for any of the first three jets to avoid contamination from multi-jet background with mis-measured jets. To further reduce SM contributions, we demand $E_{\text{T}}^{\text{miss}}/\sqrt{H_T} > 10$ $\text{GeV}^{1/2}$ and $p_T(\text{j}_4)/H_T > 0.1$ where j_4 indicates the fourth leading jet and H_T is the sum of the transverse momentum of the jets considered in the analysis. After this baseline selection, a two dimensional optimisation over selections on $E_{\text{T}}^{\text{miss}}$ and H_T is performed to obtain the maximum significance. For the HL-LHC (HE-LHC), we vary $E_{\text{T}}^{\text{miss}}$ in steps of 0.5 (0.5) TeV from 0.5 (0.5) up to 3.0 (7.0) TeV and H_T in steps of 0.5 (0.5) TeV from 0.5 (0.5) up to 5.0 (7.0) TeV. The optimisation aims to maximise the signal significance, defined as $S/\sqrt{(B + (sysB)^2 B^2 + (sysS)^2 S^2)}$, where S indicates the number of signal events, B the total SM background events, and $sysB = 0.2$ and $sysS = 0.1$ are the systematic uncertainties on background and signal, respectively. Thanks to the optimisation procedure used in this study, the results present an improvement with respect to the existing ATLAS HL-LHC study [62], although the impact related to different assumptions on systematic uncertainties and pile-up conditions might play a non-negligible role.

Exclusion and discovery contours are shown in Fig. 2.1.1 as 2σ and 5σ contours of the significance previously defined. For a massless LSP, a gluino of approximately 3.2 TeV can be probed by the HL-LHC with 3 ab^{-1} of integrated luminosity, with a discovery potential up to 2.9 TeV. At 27 TeV with 15 $\text{ab}^{-1}$of integrated luminosity, the exclusion (discovery) reach is roughly 5.7 (5.2) TeV for massless LSP. With the signal varied within a 50% band, mimicking current PDF uncertainties for high mass gluinos, the HL-LHC (HE-LHC) exclusion reach will decrease by about 200 (400) GeV and become

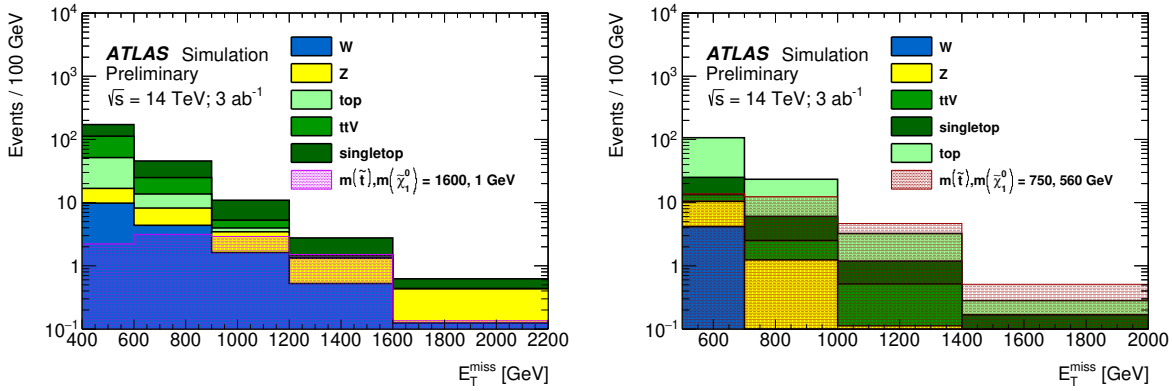

Fig. 2.1.2: $E_{\mathrm{T}}^{\mathrm{miss}}$ distribution for the $m_2^{\text{anti-}k_t^{1.2}} > 120$ GeV, $N_{b-\mathrm{jet}} \geq 2$ bin of the large Δm analysis (left) and $R_{\mathrm{ISR}} > 0.65$ bin of the diagonal analysis (right). The last bin includes overflow events.

approximately 3 (5.3) TeV.

2.1.2 Third generation squarks at HL-LHC

Contributors: I. Vivarelli, ATLAS

The expected ATLAS sensitivity to stop pair production at the HL-LHC is investigated, based upon Ref. [70]. The Run-2 analysis described in Ref. [71] is taken as reference and an event selection yielding optimal sensitivity to stop pair production with 3 $\mathrm{ab}^{-1}$of pp collisions is developed. The $\tilde{t}_1$ decaying in $t^{(*)}\tilde{\chi}_1^0$ mode is considered, where the star indicates that the top quark can possibly be off mass-shell, depending on the mass difference between the stop and the neutralino masses, $\Delta m(\tilde{t}_1, \tilde{\chi}_1^0)$. The final state analysed is that where both top quarks decay hadronically hence characterised by the presence of many jets and b-jets, and by missing transverse momentum $\mathbf{p}_{\mathrm{T}}^{\mathrm{miss}}$ (whose magnitude will be indicated by $E_{\mathrm{T}}^{\mathrm{miss}}$ in the following) stemming from the presence of the two $\tilde{\chi}_1^0$. Two kinematic regimes are considered, referred to as "large Δm" and "diagonal" in the following. The large Δm regime is where the difference between the stop and neutralino masses is large with respect to the top quark mass $\Delta m(\tilde{t}_1, \tilde{\chi}_1^0) \gg m_{\mathrm{top}}$. The top quarks emitted in the stop decay are produced on-shell, and they have a boost in the laboratory frame proportional to $\Delta m(\tilde{t}_1, \tilde{\chi}_1^0)$. The final state is hence characterised by high p_T jets and b-jets, and large $E_{\mathrm{T}}^{\mathrm{miss}}$. Typical analyses in this kinematic regimes have large acceptance, and the sensitivity is limited by the signal cross section that decreases steeply with increasing $m\left(\tilde{t}_1\right)$. If $\Delta m(\tilde{t}_1, \tilde{\chi}_1^0) \sim m_{\mathrm{top}}$, hence the diagonal regime, the extraction of the signal from the SM background stemming from mainly $t\bar{t}$ production requires a focus on events where the stop pair system recoils against substantial initial-state hadronic activity (ISR).

The analysis is performed on datasets of SM background processes and supersymmetric signals simulated through different event generators. The event selection is based on variables constructed from the kinematics of particle-level objects, selected according to reconstruction-level quantities obtained from the emulation of the detector response for HL-LHC. Particularly relevant for this analysis, jets arising from the fragmentation of b-hadrons which are tagged with a nominal efficiency of 70%, computed on a $t\bar{t}$ sample simulated assuming $\langle\mu\rangle = 200$. Reclustered jets are created by applying the anti-k_t algorithm with distance parameters $\Delta R = 0.8$ and $\Delta R = 1.2$ on signal jets, indicated in the following as anti-$k_t^{0.8}$ and anti-$k_t^{1.2}$ jet collections. A trimming procedure is applied that removes $R = 0.4$ jets from the reclustered jets if their p_T is less than 5% of the p_T of the anti-$k_t^{0.8}$ or anti-$k_t^{1.2}$ jet p_T.

Several variables are used for the event selection in the signal regions targeting the large $\Delta m(\tilde{t}_1, \tilde{\chi}_1^0)$ regime. The selection on $E_{\mathrm{T}}^{\mathrm{miss}}$ exploits the presence of the non-interacting neutralinos in the final state whilst the selections on the anti-$k_t^{1.2}$ and anti-$k_t^{0.8}$ jet masses exploit the potential presence of boosted

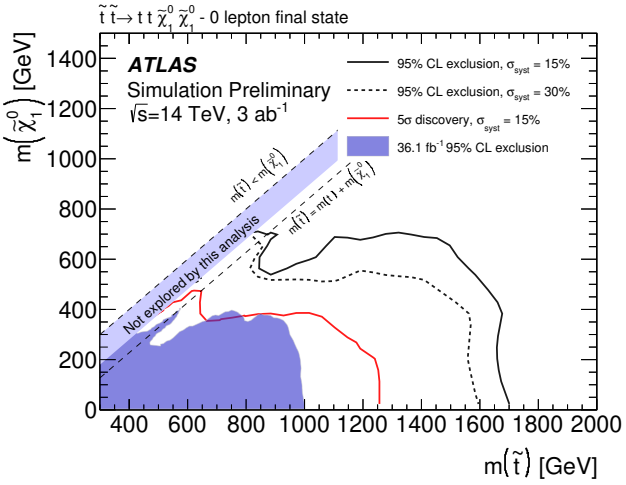

Fig. 2.1.3: Final 95% C.L. exclusion reach and 5σ discovery contour corresponding to 3 $\mathrm{ab}^{-1}$of proton-proton collisions collected by ATLAS at the HL-LHC.

top quarks and W-bosons in the final state. For the evaluation of the final exclusion sensitivity, a set of mutually exclusive signal regions is defined. The events are classified in 30 different signal regions according to the number of identified b-jets, the value of the mass of the second (ordering done in mass) reclustered jet reconstructed with distance parameter $R = 1.2$, $m_2^{\text{anti-}k_t^{1.2}}$ mass, and the value of the $E_{\mathrm{T}}^{\mathrm{miss}}$. For the evaluation of the discovery sensitivity, a set of single bin cut-and-count signal regions is defined, which apply the full preselection, and then require $N_{b-\text{jet}} \geq 2$, $m_2^{\text{anti-}k_t^{1.2}} > 120$ GeV. Four different thresholds in $E_{\mathrm{T}}^{\mathrm{miss}}$ are then defined to achieve optimal sensitivity for a 5σ discovery: $E_{\mathrm{T}}^{\mathrm{miss}} > 400, 600, 800, 1000$ GeV. For each model considered, the signal region giving the lowest p-value against the background-only hypothesis in presence of the signal is used. The basic idea of the diagonal analysis arises from the fact that, given the mass relation between the stop and the neutralino, the stop decay products (the top quark and the neutralino) are produced nearly at rest in the stop reference frame. When looked at from the lab reference frame, the transverse momentum acquired by the decay products will be proportional to their mass. If p_T^{ISR} is the transverse momentum of everything that recoils against the stop pair, it can be shown that

$$R_{\mathrm{ISR}} \equiv \frac{E_{\mathrm{T}}^{\mathrm{miss}}}{p_T^{\mathrm{ISR}}} \sim \frac{m\left(\tilde{\chi}_1^0\right)}{m\left(\tilde{t}_1\right)}. \tag{2.1.1}$$

Following this considerations, a recursive jigsaw reconstruction is performed, which makes assumptions that allow the definition of a set of variables in different reference frames. The final strategy for the assessment of exclusion sensitivity for the diagonal analysis is thus to use a set of mutually exclusive signal region defined in bins of R_{ISR} and $E_{\mathrm{T}}^{\mathrm{miss}}$. For the evaluation of the discovery sensitivity, four cut-and-count signal regions are defined, which apply the full preselection, and then require $R_{\mathrm{ISR}} > 0.7$ and $E_{\mathrm{T}}^{\mathrm{miss}} > 500, 700, 900, 1100$ GeV. For each model considered, the signal region giving the lowest p-value against the SM hypothesis in presence of signal is used.

The final $E_{\mathrm{T}}^{\mathrm{miss}}$ distribution in the bins with $m_2^{\text{anti-}k_t^{1.2}} > 120$ GeV, $N_{b-\text{jet}} \geq 2$ (for the large Δm analysis) and $R_{\mathrm{ISR}} > 0.65$ (for the diagonal analysis) are shown in Fig. 2.1.2. In all cases, the main background process is $t\bar{t}$, with significant contribution of W+jets events for the large Δm analysis. A 15% uncertainty is retained as a baseline value of the expected uncertainty for both analyses to determine both the 5σ and the 95% C.L. exclusion reach of the analysis. For the case of the estimation of the 95% C.L. exclusion sensitivity, a further scenario with doubled uncertainty (30%) is also evaluated.

The final exclusion sensitivity evaluation is done by performing a profile-likelihood fit to a set of

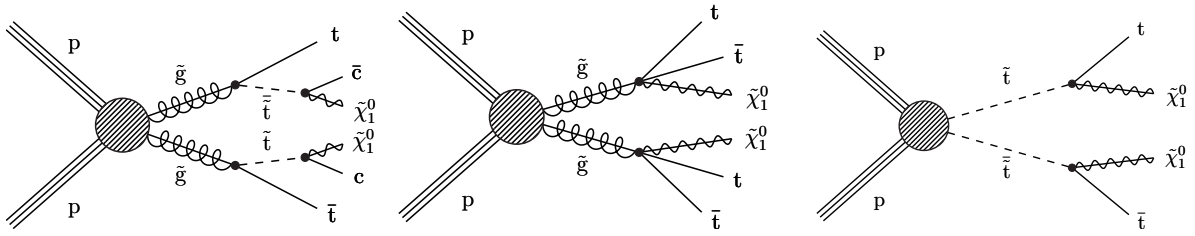

Fig. 2.1.4: Signal models considered in this analysis: T5ttcc (left), T1tttt (middle), and T2tt (right).

pseudo-data providing bin-by-bin yields corresponding to the background expectations. For each of the two analyses the likelihood is built as the product of Poissonian terms, one for each of the considered bins. Systematic uncertainties are accounted for by introducing one independent nuisance parameter for each of the bins considered. For each mass of the stop and the neutralino, the analysis yielding the smallest CLs among the large Δm and the diagonal is used. The discovery sensitivity is obtained similarly from each of the single cut-and-count regions independently. For each signal point, the profile likelihood ratio fit is performed on pseudo-data corresponding to the sum of the expected background and the signal. The discovery contour corresponds to points expected to give a 5σ p-value against the background-only hypothesis. For each signal point, the discovery signal region yielding the smallest p-value is considered. The final sensitivity of the analysis is summarised in Fig. 2.1.3 assuming a 15% uncertainty for the 5σ discovery and 95% C.L. exclusion contour, and also assuming 30% uncertainty for the 95% C.L. exclusion contour.

Top squarks can be discovered (excluded) up to masses of 1.25 (1.7) TeV for $m\left(\tilde{\chi}_1^0\right) \sim 0$ under realistic uncertainty assumptions. The reach in stop mass degrades for larger neutralino masses. If $\Delta m(\tilde{t}_1, \tilde{\chi}_1^0) \sim m_{\text{top}}$, then the discovery (exclusion) reach is 650 (850) GeV.

2.1.3 Gluinos and top squarks at HL-LHC in hadronic boosted signatures

Contributors: J. Karancsi, S. W. Lee, S. Sekmen, R. Ye, CMS

This section presents the projection of a CMS search for new physics with boosted W bosons or top quarks using the razor kinematic variables to the HL-LHC conditions. The original search performed on the Run-2 2016 dataset is part of a larger inclusive new physics search with razor variables that includes an extensive set of hadronic and leptonic search regions documented in [72].

The analysis targets final states consistent with natural SUSY. The primary model of interest is gluino-pair production, where the gluino decays to a top squark and a top quark, with a mass gap between the gluino and the top squark being large enough to give the top quark from the gluino decay a significant boost. The top squark is light, and decays to $c\tilde{\chi}_1^0$ for small mass differences with respect to the neutralino. In this simplified model, referred to as *T5ttcc* in the following, decay products of the top squark have very low transverse momentum and thus are very hard to detect. Therefore, the boosted top quark from the gluino decay is used as a handle for enhancing sensitivity. In addition, we also consider scenarios with gluinos directly decaying to $t\bar{t}\tilde{\chi}_1^0$, called *T1tttt*, and with direct production of top squark pairs, where each top squark decays to a top quark and a neutralino, referred to as *T2tt* in the following. The stop model here is equivalent to the model considered in Section 2.1.2. All models are illustrated by the diagrams in Fig. 2.1.4.

Boosted objects, which have high p_T, are characterised by merged decay products separated by $\Delta R \sim 2m/p_T$, where m is the mass of the decaying massive particle. A top quark or W boson can be identified via boosted objects within a jet of size 0.8 if it has a momentum of $\gtrsim 430$ GeV or $\gtrsim 200$ GeV, respectively. Boosted objects are more accessible at increased centre-of-mass energies, and thus will be produced more frequently at the HL-LHC and especially the HE-LHC. The search is performed in

hadronic final states with at least one boosted W-jet and one b-jet or at least one boosted top-jet, using razor kinematic variables M_R and R^2 [73], which are powerful tools that can discriminate between SM processes and production of heavy new particles decaying to massive invisible particles and massless visible particles. The analysis searches for an excess in events with high values of M_R and R^2.

The projection study, explained in detail in [74], uses the same data and MC events as in the 2016 analysis. It also follows the same object selection, event selection, background estimation, systematic uncertainty calculation, and limit setting procedures as used in the 2016 analysis. Boosted W bosons and top quarks are identified using the jet mass, the n-subjettiness variables τ_2/τ_1 and τ_3/τ_2 [75], and subjet b-tagging. Events in all signal, control, and validation regions in the analysis are required to have at least four selected anti-k_T jets with radius parameter 0.4 (AK4 jets), at least one anti-k_T jet with radius parameter 0.8 (AK8 jets) and $p_T > 200$ GeV defining the boosted phase space, and $M_R > 800$ GeV and $R^2 > 0.08$. In addition, the signal regions are required to have zero leptons and an azimuthal distance between the two megajets, two partitioned sets of jets in the event used for computing the razor variables [73], $\Delta\phi_{\text{megajets}}$, to be greater than 2.8. Three event categories are defined based on boosted object and jet multiplicities: i) W 4-5 jet: $\geq$1 reconstructed AK8 W-jet, $\geq$1 AK4 b-jet, $4 \leq n_{\text{jet}} \leq 5$; ii) W 6 jet: $\geq$1 reconstructed AK8 W-jet, $\geq$1 AK4 b jet, $n_{\text{jet}} \geq 6$; and iii) Top category: $\geq$1 reconstructed AK8 top-jet.

The dominant SM backgrounds in the signal regions originate from $t\bar{t}$+jets, single top quark production, multijet events that have jets produced through the strong interaction, and the W+jets and Z+jets processes. Data-driven methods are employed to estimate the background contributions to the signal regions. Control regions are used to isolate a process to be estimated, defined by modifying one or more signal selection criteria. After applying the signal and control region selections, resulting data and MC event distributions are scaled to the HL-LHC cross sections and integrated luminosities. For data, a procedure is designed to mimic both the statistical precision and potential modifications in shape due to different levels of cross section scaling in the various contributing processes. After scaling all distributions, background estimates in the signal regions are obtained by multiplying the observed data yields, binned in M_R and R^2, by the simulation transfer factors computed as the ratios of the yields of background MC simulation events in the signal regions to the yields in control regions. Other SM processes that contribute less significantly, such as diboson, triboson, and $\mathrm{t\bar{t}V}$, are estimated directly from the simulation. The simulated events used for obtaining both the transfer factors and the direct estimates were corrected using various data-to-simulation correction factors and event weights. The uncertainties in these correction factors and weights were taken into account as systematic uncertainties. Three different scenarios for systematic uncertainties are considered, in which the systematic uncertainties are i) taken as they are in the original analysis, (Run-2) ii) scaled down according to the expected improvements in the detector and theory calculations (YR18), and iii) neglected in order to test a case with statistical uncertainties only (stat-only). Statistical uncertainties are scaled down by $1/\sqrt{\mathcal{L}_{HL-LHC}/\mathcal{L}_{2016}}$.

The overall background estimation for the W 4-5 jet, W 6 jet, and Top categories along with distributions for several signal benchmark scenarios versus a one-dimensional representation of the bins in M_R and R^2 are shown in Figure 2.1.5, considering the YR18 systematic scenario. The most dominant systematic uncertainties on the total background estimate come from W/top tagging ($\sim 1-4\%$), b-tagging ($\sim 3\%$), jet energy scale (JES) ($\sim 3\%$), and pile-up ($\sim 1-3\%$) variations along with QCD multijet background shape uncertainties ($\sim 3-7\%$). For the simulated signal event yields, the largest contributions come from W/top tagging ($\sim 8\%$), jet energy scale (JES) ($\sim 3\%$) and b-tagging ($\sim 2\%$) variations.

The results are used to set expected upper limits on the production cross sections of various SUSY simplified models. Figure 2.1.6 shows the expected upper limits on the signal cross sections for the T5ttcc, T1tttt and T2tt simplified models for the combination of the W 4-5 jet, W 6 jet, and Top categories for the HL-LHC projection based on the YR18 scenario. Additionally, lower limits on gluino/top squark versus neutralino masses are shown for the cases of Run-2 systematic uncertainties, YR18 sys-

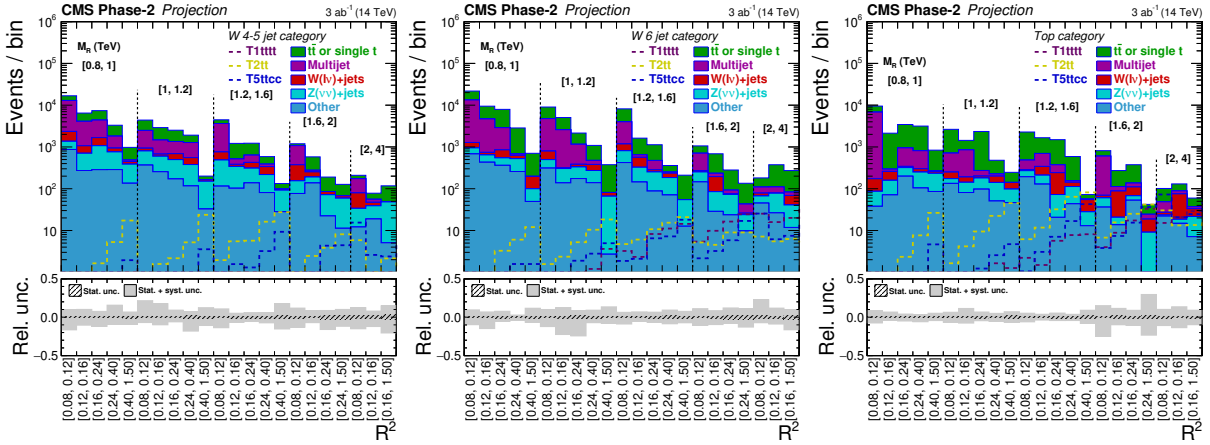

Fig. 2.1.5: M_R-R^2 distributions shown in a one-dimensional representation for background predictions obtained for the W 4-5 jet (upper left), W 6 jet (upper right), and Top (lower) categories for the HL-LHC. Statistical and systematic uncertainties for the YR18 scenario are shown with the hatched and shaded error bars, respectively. Also shown are the signal benchmark models T5ttcc with $m_{\tilde{g}} = 2$ TeV, $m_{\tilde{t}} = 320$ GeV and $m_{\tilde{\chi}^0_1} = 300$ GeV; T1tttt with $m_{\tilde{g}} = 2$ TeV and $m_{\tilde{\chi}^0_1} = 300$ GeV; and T2tt with $m_{\tilde{t}} = 1.2$ TeV and $m_{\tilde{\chi}^0_1} = 100$ GeV.

tematic uncertainties, and statistical-only scenarios for the HL-LHC case. Furthermore, projections of expected discovery sensitivity in the presence of a signal were computed. The p-values for the signal plus background and background-only hypotheses were used to obtain the expected significances in terms of number of standard deviations. Figure 2.1.7 shows the projected expected significance for the T5ttcc, T1tttt, and T2tt models based on the YR18 systematic uncertainties, along with the discovery upper bounds on the gluino/top squark versus neutralino masses for the three uncertainty scenarios for the HL-LHC.

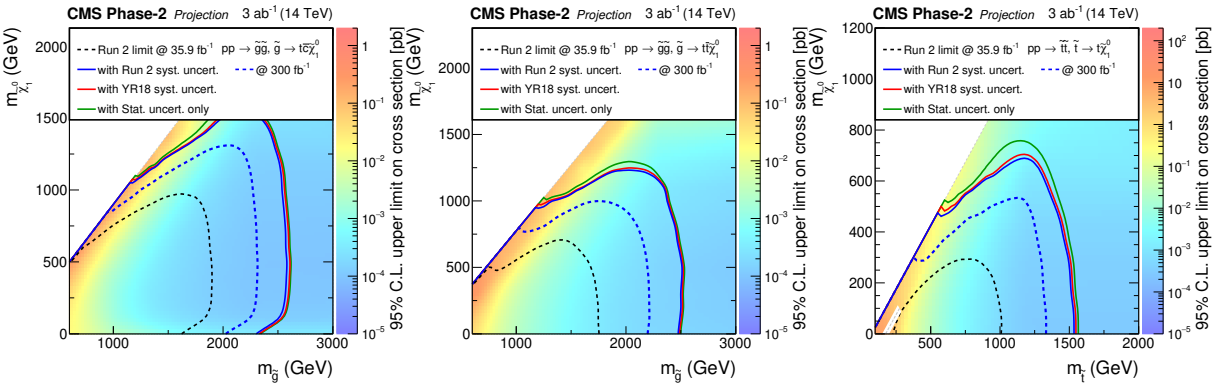

Fig. 2.1.6: Projected expected upper limits on the signal cross sections for the HL-LHC using the asymptotic CLs method versus gluino/top squark and neutralino masses for the T5ttcc (top left), T1tttt (top right), and T2tt (bottom) models for the combined W 4-5 jet, W 6 jet, and Top categories for the YR18 scenario. The contours show the expected lower limits on the gluino/top squark and neutralino masses based on the Run-2 systematic uncertainties, YR18 systematic uncertainties, and statistical-only scenarios, along with the 2016 razor boost limit and the 300 fb^{-1} limit for comparison.

The projection results show that HL-LHC would improve the gluino mass exclusion limits via top-quark by around 750 GeV, while making discovery possible for gluinos up to masses of 2.4 TeV. For top squark pair production, the discovery reach is up to 1.4 TeV, consistent with the ATLAS prospect studies in Section 2.1.2.

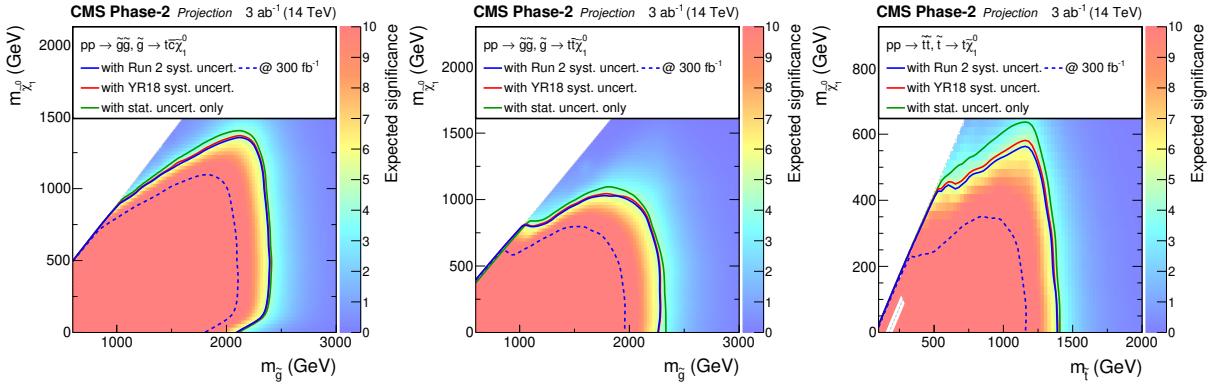

Fig. 2.1.7: Projected expected significance for the HL-LHC versus gluino/stop and neutralino masses for the T5ttcc (top left), T2tttt (top right), and T2tt (bottom) models for the combined W 4-5 jet, W 6 jet, and Top categories for the YR18 scenario. The contours show the expected discovery bounds on the gluino/top squark and neutralino masses based on the Run-2 systematic uncertainties, YR18 systematic uncertainties, and statistical-only scenarios.

2.1.4 Implications of a stop sector signal at the HL-LHC

Contributors: A. Pierce, B. Shakya

The stop sector is intricately tied to the mass of the Higgs boson. A stop sector discovery therefore provides an opportunity to test the Higgs mass relation, as well as predict subsequent signals at the LHC. This section is devoted to illustrations of such scenarios at the HL-LHC, based on the studies in Ref. [76].

The Higgs boson mass at one-loop in the MSSM is [77]

$$\begin{aligned} m_h^2 &= m_Z^2 \cos^2(2\beta) + \frac{3\sin^2\beta\, y_t^2}{4\pi^2}\Big[m_t^2 \ln\left(\frac{m_{\tilde{t}_1} m_{\tilde{t}_2}}{m_t^2}\right) + c_t^2 s_t^2 (m_{\tilde{t}_2}^2 - m_{\tilde{t}_1}^2) \ln\left(\frac{m_{\tilde{t}_2}^2}{m_{\tilde{t}_1}^2}\right) \\ &+ c_t^4 s_t^4 \left\{ (m_{\tilde{t}_2}^2 - m_{\tilde{t}_1}^2)^2 - \frac{1}{2}(m_{\tilde{t}_2}^4 - m_{\tilde{t}_1}^4) \ln\left(\frac{m_{\tilde{t}_2}^2}{m_{\tilde{t}_1}^2}\right) \right\} / m_t^2 \Big], \end{aligned} \tag{2.1.2}$$

where $\tilde{t}_1$ and $\tilde{t}_2$ are the stop mass eigenstates, θ_t is the stop mixing angle, with $\tilde{t}_1 = \cos\theta_t\, \tilde{t}_L + \sin\theta_t\, \tilde{t}_R$, $s_t(c_t) = \sin\theta_t(\cos\theta_t)$, and y_t is the top Yukawa coupling. As the mass splitting between stops increases, the latter two terms in the loop correction grow stronger; in particular, the final term switches sign and becomes negative for $m_{\tilde{t}_2} \gtrsim 2.7 m_{\tilde{t}_1}$, and can dominate for non-vanishing stop mixing and $m_{\tilde{t}_2} \gg m_{\tilde{t}_1}$. Consequently, there exists an *upper* limit on $m_{\tilde{t}_2}$ (as a function of $m_{\tilde{t}_1}$ and θ_t), beyond which it is impossible to accommodate $m_h = 125$ GeV in the MSSM. In other words, a measurement of $m_{\tilde{t}_1}$ and some knowledge of θ_t allows for an upper limit on $m_{\tilde{t}_2}$, and ruling out this window rules out the MSSM. In the following, we discuss some scenarios where such ideas can be implemented at the HL-LHC.

A Sbottom Signal in Multileptons:

Consider a spectrum such that $\tilde{b}_1 \to \tilde{t}_1 W$ (which requires both $\tilde{t}_1$ and $\tilde{b}_1$ to be somewhat left-handed) and $\tilde{t}_1 \to t\chi_0$, the mass splitting $\Delta m_{\tilde{b}_1 \tilde{t}_1}$ is sufficiently large that sbottom decays give visible multilepton signals, but direct $\tilde{t}_1$ discovery is elusive because of a squeezed spectrum. In the MSSM, $m_{\tilde{t}_2}$ is correlated with $\Delta m_{\tilde{b}_1 \tilde{t}_1}$, as shown in Fig. 2.1.8. A large splitting involves a large stop mixing angle (otherwise, $\tilde{b}_1$ is approximately degenerate with $\tilde{t}_1$); in this case, as discussed above, consistency with the Higgs mass enforces an upper limit on $m_{\tilde{t}_2}$, as seen in Fig. 2.1.8. Alternatively, the splitting can be raised by making $\tilde{t}_1$ mostly right-handed; however, in this case, $m_{\tilde{t}_2} \approx m_{\tilde{b}_1}$ and again faces an upper limit. For a sub-TeV sbottom, such limits are particularly sharp, as compatibility with the Higgs mass forces $m_{\tilde{t}_2}$ to lie within a narrow wedge shaped region, as seen in the figure.

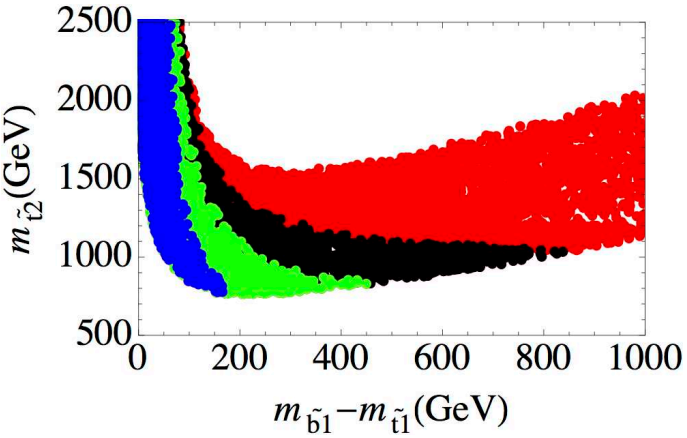

Fig. 2.1.8: $m_{\tilde{t}_2}$ as a function of the mass splitting $m_{\tilde{b}_1} - m_{\tilde{t}_1}$ for points with $120 < m_h < 130$ GeV and $m_{\tilde{t}_1} < 1$ TeV in the MSSM. Red, black, green, and blue points correspond to $m_{\tilde{b}_1} > 1000$ GeV, $750 < m_{\tilde{b}_1} < 1000$ GeV, $500 < m_{\tilde{b}_1} < 750$ GeV, and $m_{\tilde{b}_1} < 500$ GeV respectively.

Detailed analysis of the multilepton excess can shed further light on the properties of $\tilde{t}_2$: inferring $\Delta m_{\tilde{b}_1\tilde{t}_1}$ (from, *e.g.*, the lepton p_T distribution) and the sbottom mass (from, *e.g.*, the signal rate) not only narrows the allowed range of $m_{\tilde{t}_2}$ (Fig. 2.1.8) but also constrains the stop mixing angle. It is therefore possible to not only predict a relatively narrow mass window for $\tilde{t}_2$, but also get a profile of its decay channels. Such a $\tilde{t}_2$ may well be within reach of the LHC, and ruling out such a $\tilde{t}_2$ is sufficient to rule out the MSSM. This concept was implemented in Ref. [76] for a benchmark point with $m_{\tilde{t}_2} = 1022$ GeV, $m_{\tilde{b}_1} = 885$ GeV, $m_{\tilde{t}_1} = 646$ GeV, and $m_{\chi_0} = 445$ GeV. Using existing CMS search strategies for same-sign dileptons [78, 79] as well as multileptons [80, 81], it was shown that the sbottom decay signal could be identified at the HL-LHC at $3-5\sigma$ significance with $3\,\text{ab}^{-1}$of data. As discussed above, the discovery of such a sbottom signal with energetic multileptons imposes an upper limit on $m_{\tilde{t}_2}$ in the MSSM. For this benchmark point, it was also shown that modifications of the aforementioned multilepton search strategy would also allow for a $3-5\sigma$ significance discovery of the heavier stop decay $\tilde{t}_2 \to \tilde{t}_1 Z$ with $3\,\text{ab}^{-1}$of data, illustrating how using the MSSM Higgs mass relation in conjunction with a sbottom signal discovery can lead to predictions and discovery of $\tilde{t}_2$ at the HL-LHC. For details of the analysis, the interested reader is referred to [76].

Using Multiple Decay Channels for the Heavier Stop:

The HL-LHC could enable measurements in multiple channels with significant statistics. In particular, the heavier stop $\tilde{t}_2$ could be observed in multiple channels $\tilde{t}_1 Z$, $\tilde{t}_1 h$, $\tilde{b}_1 W$, and $t\chi_0$, with branching ratios (BRs) determined by the stop masses and mixing angle. We focus on the two decays $\tilde{t}_2 \to \tilde{t}_1 Z$ and $\tilde{t}_2 \to \tilde{t}_1 h$, which give rise to boosted dibosons if the mass splitting between the two stop mass eigenstates is large. In the decoupling limit in the Higgs sector, the ratio of the decay widths into these two channels is [82]:

$$R_{hZ} \equiv \frac{\Gamma(\tilde{t}_2 \to \tilde{t}_1\, h)}{\Gamma(\tilde{t}_2 \to \tilde{t}_1\, Z)} = \left[\left(1 - \frac{m^2_{\tilde{t}_1}}{m^2_{\tilde{t}_2}}\right)\cos 2\theta_{\tilde{t}} + \frac{m^2_W}{m^2_{\tilde{t}_2}}\left(1 - \frac{5}{3}\tan^2\theta_W\right)\right]^2 \approx \left(1 - \frac{m^2_{\tilde{t}_1}}{m^2_{\tilde{t}_2}}\right)^2 \cos^2 2\theta_{\tilde{t}}. \tag{2.1.3}$$

Phase space factors as well as many experimental uncertainties cancel in this ratio, offering a clean dependence on the stop mixing angle if the two stop masses are known from other measurements, enabling a check of the MSSM Higgs mass relation.

The viability of such a strategy was explored in Ref. [76] for a benchmark scenario with $m_{\tilde{t}_2} = 994$ GeV, $m_{\tilde{b}_1} = 977$ GeV, $m_{\tilde{t}_1} = 486$ GeV, and $m_{\chi_0} = 406$ GeV, with $\tilde{t}_2$ decay BRs of

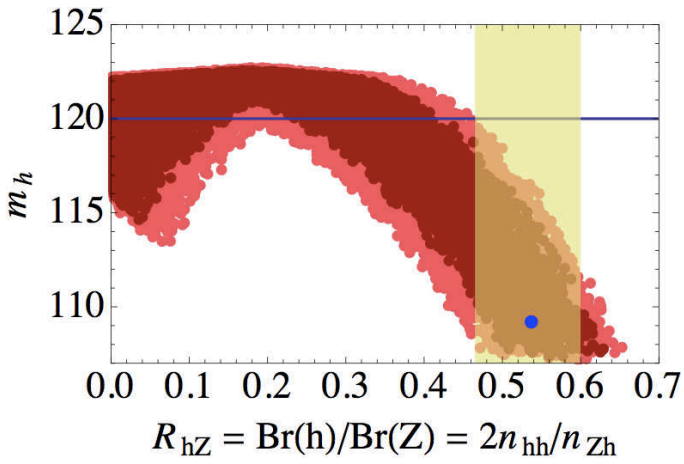

Fig. 2.1.9: MSSM Higgs mass as a function of R_{hZ}. The horizontal blue line denotes $m_h = 120$ GeV, the cutoff below which the Higgs mass is assumed to be inconsistent with the MSSM (see [76] for details). Light (dark) red bands correspond to $440 \leq m_{\tilde{t}_1} \leq 520$ GeV and $930 \leq m_{\tilde{t}_2} \leq 1030$ GeV ($450 \leq m_{\tilde{t}_1} \leq 510$ GeV and $945 \leq m_{\tilde{t}_2} \leq 1015$ GeV). The blue dot denotes the benchmark point in our analysis, which is consistent with all constraints but does not produce the correct Higgs mass in the MSSM. The golden band shows the uncertainty in the calculated value of R_{hZ} with 3 $\text{ab}^{-1}$of data at the HL-LHC.

52% and 28% into $\tilde{t}_1\, Z$ and $\tilde{t}_1\, h$ respectively, using the strategy from Ref. [83] to reconstruct boosted dibosons via fat jets. Note that measuring the ratio R_{hZ} with reasonable precision requires high statistics, motivating searches for the boosted Z and h bosons in their dominant (hadronic) decay channels rather than the cleaner decays into leptons or photons. Assuming that $m_{\tilde{t}_1}$ has been measured to lie in the range 486 ± 40 GeV from monojet or charm-tagged events, while $m_{\tilde{t}_2}$ is known to fall in the 994.2 ± 50 GeV range from various measurements (such as by combining the knowledge of $m_{\tilde{t}_1}$ with information on $p_T(Z)$ in $\tilde{t}_2 \to \tilde{t}_1 Z$ events), the MSSM Higgs mass can be calculated as a function of θ_t using Eq. (2.1.2), which can be converted to a function of the ratio R_{hZ} using Eq. (2.1.3); this relation is plotted in Fig. 2.1.9 in the broad red band for the above stop mass windows. The narrower, darker red band corresponds to narrower windows for the two stop masses, reflecting the improvement in the Higgs mass uncertainty with better knowledge of the stop masses.

The Higgs mass is small for vanishing stop mixing $\theta_t \to 0,\ \pi/2$, which corresponds to $R_{hZ} \sim \cos^2 2\theta_t$ approaching 1. On the other hand, achieving the correct Higgs mass with sub-TeV stops requires large stop mixing, which correlates with a smaller value of R_{hZ}. As seen in Fig. 2.1.9, an inferred value of R_{hZ} above some cutoff value R_0 (≈ 0.45 in this case) is incompatible with the MSSM Higgs mass relation. Such an observation would rule out the MSSM, pointing to the need for additional contributions to the Higgs mass (as is the case for the chosen benchmark point). The golden band encodes the uncertainty in the calculated value of R_{hZ} for the benchmark point that can be achieved at the HL-LHC with 3 $\text{ab}^{-1}$of data (see [76] for details). This benchmark point study illustrates that measurements of the two decay channels can be used as a consistency check of the Higgs mass and possibly rule out the MSSM at the HL-LHC.

2.2 Searches for charginos and neutralinos

The direct production of charginos and neutralinos through EW interactions may dominate the SUSY production at the LHC if the masses of the gluinos and squarks are beyond $3 - 4$ TeV. In this section, the sensitivity at the end of HL-LHC to the direct production of various SUSY partners in the EW sector under the assumption of R-parity conservation is presented. Charginos and heavier neutralinos production processes are considered, assuming they decay into the LSP via on-shell or off-shell W

and Z or Higgs bosons. Final state events characterised by the presence of charged leptons, missing transverse momentum and possibly jets and b-jets are studied and prospects are presented. Dedicated searches for higgsino-like, 'compressed' SUSY models, characterised by small mass splittings between electroweakinos, are also reported, and possible complements with new facilities are illustrated.

2.2.1 Chargino pair production at HL-LHC

Contributors: S. Carra, T. Lari, D. L. Noel, C. Potter, ATLAS

The charged wino or higgsino states might be light and decay via SM gauge bosons. In this search [84], the direct production of $\tilde{\chi}_1^+\tilde{\chi}_1^-$ is studied. The $\tilde{\chi}_1^\pm$ is assumed to be pure wino, while the $\tilde{\chi}_1^0$ is the LSP and is assumed to be pure bino and stable. The $\tilde{\chi}_1^\pm$ decays with 100% branching fraction to $W^\pm$ and $\tilde{\chi}_1^0$. Only the leptonic decays of the W are considered, resulting in final states with two opposite electric charge (OS) leptons and missing transverse energy from the two undetected $\tilde{\chi}_1^0$.

The selection closely follows the strategies adopted in the 8 TeV [85] and 13 TeV [86] searches. Events are required to contain exactly two leptons (electrons or muons) with $p_{\mathrm{T}} > 20$ GeV and $|\eta| < 2.5$ (2.47 for electrons). The lepton pair must satisfy $m_{\ell\ell} > 25$ GeV to remove contributions from low mass resonances. The two leptons must be OS, pass "tight" identification criteria, and be isolated (the scalar sum of the transverse momenta of charged particles with $p_{\mathrm{T}} > 1$ GeV within a cone of $\Delta R = 0.3$ around the lepton candidate, excluding the lepton candidate track itself, must be less than 15% of the lepton p_{T}). All leptons are required to be separated from each other and from candidate jets defined with $p_{\mathrm{T}} > 30$ GeV and $|\eta| < 2.5$. The latter requirement is imposed to suppress the background from semi-leptonic decays of heavy-flavour quarks, which is further suppressed by vetoing events having one or more jets tagged as originating from b-decays, "b-tagged jets". The chosen working point of the b-tagging algorithm correctly identifies b-quark jets in simulated $t\bar{t}$ samples with an average efficiency of 85%, with a light-flavour jet misidentification probability of a few percent (parametrised as a function of jet p_{T} and η).

The signal region is divided into two disjoint regions with a Same Flavour Opposite Sign (SFOS: e^+e^-, $\mu^+\mu^-$) or Different Flavour Opposite Sign (DFOS: $e^\pm\mu^\mp$) lepton pair to take advantage of the differing SM background composition for each flavour combination. The SFOS and DFOS regions are divided again into events with exactly zero jets or one jet, which target scenarios with large or small $\tilde{\chi}_1^\pm - \tilde{\chi}_1^0$ mass splittings, respectively. One lepton must have $p_{\mathrm{T}} > 40$ GeV to suppress the SM background, and with $p_{\mathrm{T}}^{\ell 1} > 40$ GeV and $p_{\mathrm{T}}^{\ell 2} > 20$ GeV, either the single or double lepton triggers may be used to accept the event at the HL-LHC. Events with SFOS lepton pairs with an invariant mass within 30 GeV of the Z boson mass are rejected to suppress the large $Z \to \ell\ell$ SM background. Events with $E_{\mathrm{T}}^{\mathrm{miss}}$ larger than 110 GeV and $E_{\mathrm{T}}^{\mathrm{miss}}$ significance (defined as $E_{\mathrm{T}}^{\mathrm{miss}}/\sqrt{\sum \vec{p}_{\mathrm{T}}^{\,\mathrm{leptons,\,jets}}}$) larger than $10\ \mathrm{GeV}^{1/2}$ are selected in to suppress Z+jets events with poorly measured leptons.

The stransverse mass m_{T2} is calculated using the two leptons and $E_{\mathrm{T}}^{\mathrm{miss}}$, and used as the main discriminator in the SR selection to suppress the SM background. For $t\bar{t}$ or WW decays, assuming an ideal detector with perfect momentum resolution, $m_{\mathrm{T2}}(\ell, \ell, E_{\mathrm{T}}^{\mathrm{miss}})$ has a kinematic endpoint at the mass of the W boson. Signal models with sufficient mass splittings between the $\tilde{\chi}_1^\pm$ and the $\tilde{\chi}_1^0$ feature m_{T2} distributions that extend beyond this kinematic endpoint expected for the dominant SM backgrounds. Therefore, events in this search are required to have high m_{T2} values. A set of disjoint signal regions "binned" in m_{T2} are used to maximise model-dependent exclusion sensitivity. Each SR is identified by the lepton flavour combination (SFOS or DFOS), number of jets (-0J or -1J) and the range of the m_{T2} interval. Ten high m_{T2} intervals: $[120, 140]$, $[140, 160]$, $[160, 180]$, $[180, 200]$, $[200, 250]$, $[250, 300]$, $[300, 350]$, $[350, 400]$, $[400, 500]$ and $[500, \infty]$, are used to maximise the sensitivity to $\tilde{\chi}_1^+\tilde{\chi}_1^-$ production. After the application of the full selection criteria, no Z+jets or W+jets events remain. The diboson process WW is seen to dominate the total SM background across all signal regions, due to its similarity with the SUSY signal. The stransverse mass m_{T2} of SM and SUSY events in the signal regions is shown

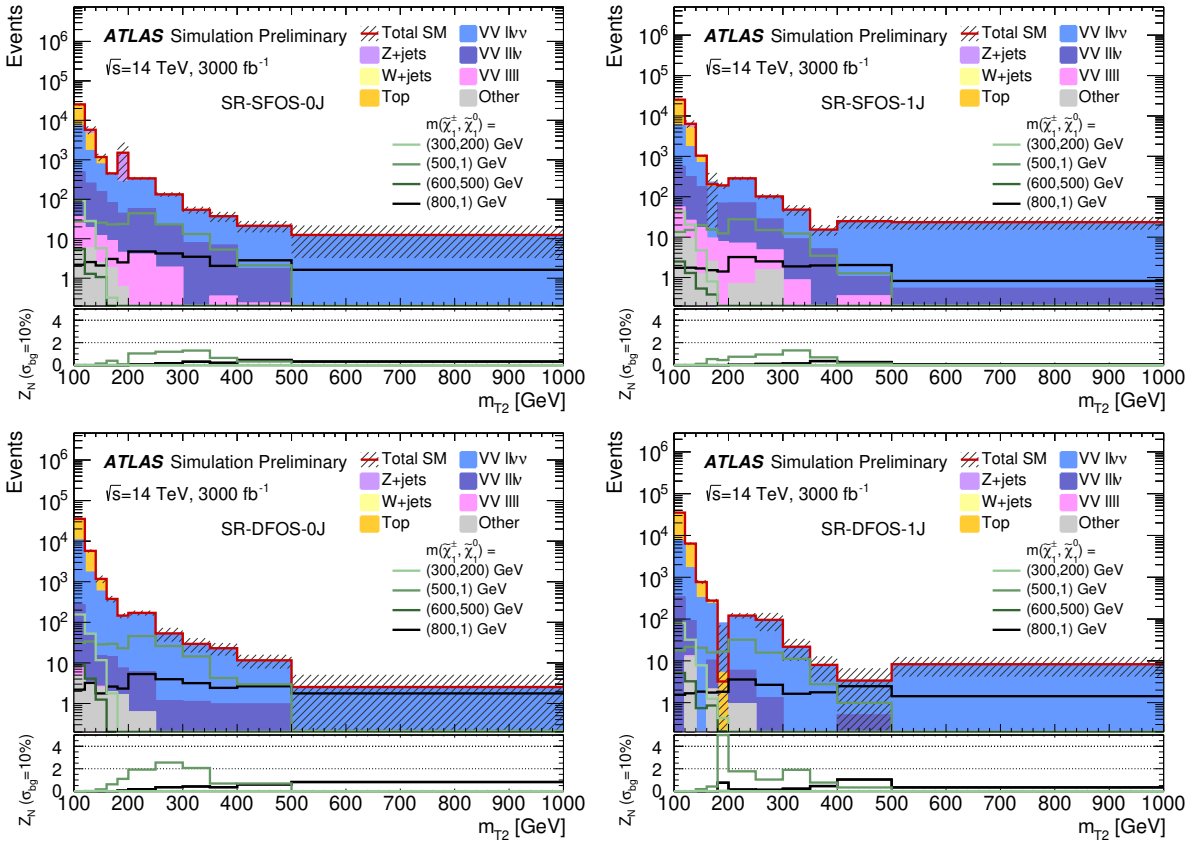

Fig. 2.2.1: Expected number of events from SM and SUSY processes in the signal regions optimised for $\tilde{\chi}_1^+\tilde{\chi}_1^-$ production, for the HL-LHC. Uncertainties shown are the MC statistical uncertainties only. The lower pad in each plot shows the significance, Z_N using a background uncertainty of 10%, for a selection of SUSY scenarios in each m_{T2} interval.

in Fig. 2.2.1, for events passing $m_{\mathrm{T2}} > 100$ GeV. The SM background drops off at lower m_{T2} values (around the W mass), while the SUSY signal is seen to have long tails to high m_{T2} values. The 2ℓ diboson SM processes show long m_{T2} tails, which is mostly from $ZZ \to \ell^+\ell^-\nu\bar{\nu}$ production; a small contribution from WW will be present due to the imperfect measurement of the leptons and $E_{\mathrm{T}}^{\mathrm{miss}}$.

To calculate the expected sensitivity to $\tilde{\chi}_1^+\tilde{\chi}_1^-$ production and decay via W bosons, the uncertainties from the normalisation of the WW background are assumed to scale inversely with the increase in luminosity, and thus decrease to $\sim 1\%$, while a better understanding of WW could halve the theoretical uncertainties to $\sim 2.5 - 5\%$. It is assumed that the experimental uncertainties will be understood to the same level, or better, than the 13 TeV analysis [86]. Two scenarios are considered for $\tilde{\chi}_1^+\tilde{\chi}_1^-$ production and decay via W bosons at the HL-LHC: the so-called Run-2 scenario, with 5% experimental uncertainty on the signal and SM background, a 10% theoretical uncertainty on the signal, and a 10% modelling uncertainty on the SM background, and the so-called baseline scenario, where the WW theoretical uncertainty can be understood to a better level and modelling uncertainty on SM background halves to 5%.

The statistical combination of all disjoint signal regions is used to set model-dependent exclusion limits. For each of the three uncertainties considered, half of the value is treated as correlated across signal regions, and the other half as uncorrelated. The exclusion potentials for $\tilde{\chi}_1^+\tilde{\chi}_1^-$ production and decay via W bosons at the HL-LHC are shown in Fig. 2.2.2 for the baseline scenario. In the absence of an excess, $\tilde{\chi}_1^+\tilde{\chi}_1^-$ production may be excluded up to 840 GeV in $\tilde{\chi}_1^\pm$ mass. For the Run-2, where the modelling uncertainty on the SM background are raised from 5% to 10%, the expected exclusion

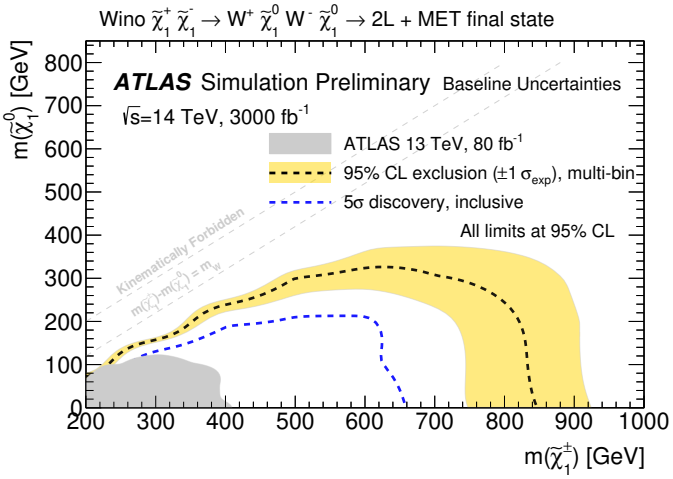

Fig. 2.2.2: The 95% C.L. exclusion and discovery potential for $\tilde{\chi}_1^+\tilde{\chi}_1^-$ production at the HL-LHC ($3\,\mathrm{ab}^{-1}$at $\sqrt{s} = 14$ TeV), assuming $\tilde{\chi}_1^\pm \rightarrow W\tilde{\chi}_1^0$ with a BR of 100%, for an uncertainty on the modelling of the SM background of 5% (baseline uncertainty). The observed limits from the analyses of 13 TeV data [86] are also shown.

Common				
lepton flavour/sign	$e^+e^-\ell^\pm$ or $\mu^+\mu^-\ell^\pm$			
	SR-0J		SR-1J	
number of jets	$= 0$		≥ 1	
Binned SR	$m_{\mathrm{T}}^{\mathrm{min}}$ [GeV]	$E_{\mathrm{T}}^{\mathrm{miss}}$ [GeV]	$m_{\mathrm{T}}^{\mathrm{min}}$ [GeV]	$E_{\mathrm{T}}^{\mathrm{miss}}$ [GeV]
	$\in [150, 250]$	$\in [200, 250]$	$\in [150, 250]$	$\in [200, 250]$
		$\in [250, 350]$		$\in [250, 350]$
		$\in [350, 450]$		$\in [350, 450]$
		$\in [450, \infty]$		$\in [450, 600]$
				$\in [600, \infty]$
	$\in [250, 400]$	$\in [150, 250]$	$\in [250, 400]$	$\in [150, 250]$
		$\in [250, 350]$		$\in [250, 350]$
		$\in [350, 500]$		$\in [350, 500]$
		$\in [500, \infty]$		$\in [500, \infty]$
	$\in [400, \infty]$	$\in [150, 350]$	$\in [400, \infty]$	$\in [150, 350]$
		$\in [350, 450]$		$\in [350, 450]$
		$\in [450, 600]$		$\in [450, 600]$
		$\in [600, \infty]$		$\in [600, \infty]$

Table 2.2.1: Signal regions for the chargino/next-to-lightest neutralino production analysis.

potential decreases by 10 GeV in $\tilde{\chi}_1^\pm$ mass and 30 GeV in $\tilde{\chi}_1^0$ mass. To calculate the discovery potential, eleven inclusive signal regions are defined with m_{T2} larger than the lower bound of each m_{T2} interval, and the inclusive signal region with the best expected sensitivity is used. At the HL-LHC, the discovery potential reaches up to 660 GeV in $\tilde{\chi}_1^\pm$ mass with the baseline scenario assumption for the background modelling uncertainty, and it decreases by 30 GeV in $\tilde{\chi}_1^\pm$ mass and 60 GeV in $\tilde{\chi}_1^0$ mass if uncertainties doubled.

2.2.2 Chargino-Neutralino searches in multileptons at HL-LHC

Contributors: A. De Santo, B. Safarzadeh Samani, F. Trovato, ATLAS

Charginos and next-to-lightest neutralinos decaying via W and Z or Higgs bosons and LSP are searched for using three-lepton signatures characterised by large missing transverse momentum [84]. A simplified model describing the direct production of $\tilde{\chi}_1^\pm\tilde{\chi}_2^0$ is studied here, where the $\tilde{\chi}_1^\pm$ and $\tilde{\chi}_2^0$ are as-

sumed to be pure wino and equal mass, while the $\tilde{\chi}_1^0$ is the LSP and is assumed to be pure bino and stable. The selection for $\tilde{\chi}_1^\pm\tilde{\chi}_2^0 \to W\tilde{\chi}_1^0 Z\tilde{\chi}_1^0$ at the HL-LHC follows the strategy used in the 13 TeV search [87]. Events are selected with exactly three leptons (electrons or muons) with $p_{\mathrm{T}} > 20$ GeV and $|\eta| < 2.5$, two of which must form an SFOS pair consistent with a Z boson decay and have $|m_{\ell\ell} - m_Z| < 10$ GeV. To resolve ambiguities when multiple SFOS pairings are present, the transverse mass m_{T} is calculated using the unpaired lepton for each possible SFOS pairing, and the combination that minimises the transverse mass, $m_{\mathrm{T}}^{\mathrm{min}}$, is chosen. The two leading leptons must have $p_{\mathrm{T}} > 25$ GeV, and $m_{\ell\ell\ell}$ must be larger than 20 GeV to reject low mass SM decays. To suppress the $t\bar{t}$ background, events are vetoed if they contain b-tagged jets with $p_{\mathrm{T}} > 30$ GeV, while the Z+jets background is suppressed by requiring $E_{\mathrm{T}}^{\mathrm{miss}} > 50$ GeV.

A set of disjoint signal regions binned in $m_{\mathrm{T}}^{\mathrm{min}}$ and $E_{\mathrm{T}}^{\mathrm{miss}}$ are used to maximise model-dependent exclusion sensitivity. Each SR is identified by the number of jets (-0J or -1J), the range of the $E_{\mathrm{T}}^{\mathrm{miss}}$ interval and the range of the $m_{\mathrm{T}}^{\mathrm{min}}$ interval, as seen in Table 2.2.1. The SRs with at least one jet are defined to extend the sensitivity for the signal benchmark points in which the mass differences between the $\tilde{\chi}_1^+$ and $\tilde{\chi}_1^0$ is small. In such scenarios higher $E_{\mathrm{T}}^{\mathrm{miss}}$in the event is expected when the $\tilde{\chi}_1^\pm\tilde{\chi}_2^0$ system recoils against the initial-state-radiation jets. The distribution of $E_{\mathrm{T}}^{\mathrm{miss}}$ and $m_{\mathrm{T}}^{\mathrm{min}}$ in the 0-jet and 1-jet categories are shown in Fig. 2.2.3 for events with $E_{\mathrm{T}}^{\mathrm{miss}} > 150$ GeV and $m_{\mathrm{T}}^{\mathrm{min}} > 150$ GeV.

To calculate the expected sensitivity to $(\tilde{\chi}_1^\pm/\tilde{\chi}_2^0)$ production, a 5% experimental uncertainty on the SM background and signal, a 10% theoretical uncertainty on the signal, and a 10% modelling uncertainty on the SM are assumed. With these uncertainty assumptions, Fig. 2.2.4 shows the expected exclusion for $\tilde{\chi}_1^\pm\tilde{\chi}_2^0 \to W\tilde{\chi}_1^0 Z\tilde{\chi}_1^0$. In the absence of an excess, chargino and neutralino masses up to 1150 GeV may be excluded. The discovery potential is also shown in Fig. 2.2.4, which reaches up to 920 GeV in chargino and neutralino masses.

2.2.3 *Chargino-Neutralino production in the $Wh \to \ell\nu\, b\bar{b}$ channel at HL-LHC*

Contributors: D. Bogavac, M. D'Onofrio, Y. Gao, M. Sullivan, H. Teagle, ATLAS

Chargino and next-to-lightest neutralinos can be searched for in one lepton plus b-jets final state events if the next-to-lightest neutralino decays into a SM-like Higgs boson and the LSP [84]. The Higgs decay mode into two b-quarks is exploited. Signal models with $\tilde{\chi}_1^\pm$ and $\tilde{\chi}_2^0$ masses up to 1.5 TeV are considered in this search. The analysis is performed separately in three signal regions targeting signal models with different values of mass difference $\Delta m = m(\tilde{\chi}_1^\pm/\tilde{\chi}_2^0) - m(\tilde{\chi}_1^0)$: low ($\Delta m < 300$ GeV), medium ($\Delta m \in [300, 600]$ GeV) and high ($\Delta m > 600$ GeV).

The expected SM background is dominated by top quark pair-production $t\bar{t}$ and single top production, with smaller contributions from vector boson production W+jets, associated production of $t\bar{t}$ and a vector boson $t\bar{t}V$ and dibosons.

The event selection follows a similar strategy as in the previous studies documented in Ref. [88]. Candidate leptons (electrons or muons) are required to have $p_{\mathrm{T}} > 25$ GeV and $|\eta| < 2.47$ (2.7), and pass "tight" and "medium" identification criteria for electrons and muons respectively. Candidate jets are reconstructed using the anti-k_t algorithm with $R = 0.4$, are required to have p_{T} greater than 25 GeV and $|\eta| < 2.5$. The jets tagged as originating from b-decays are required to pass the jet requirements described previously, and pass the MV2c10 tagging algorithm operating at 77% b-jet tagging efficiency. Candidate jets and electrons are required to satisfy $\Delta R(e, \text{jet}) > 0.2$. Any leptons within $\Delta R = 0.4$ of the remaining jet are removed. The $E_{\mathrm{T}}^{\mathrm{miss}}$ at generator level is calculated as the vectorial sum of the momenta of neutral weakly-interacting particles, in this case neutrinos and neutralinos.

Events containing exactly one lepton, and two or three jets passing the above object definitions are selected. Two of the jets are required to be b-tagged with the criteria defined above. Four key variables are further used to discriminate signal from background: the invariant mass of the two b-tagged jets, m_{bb}, the transverse momentum imbalance in the event, $E_{\mathrm{T}}^{\mathrm{miss}}$, the transverse mass constructed using the leading

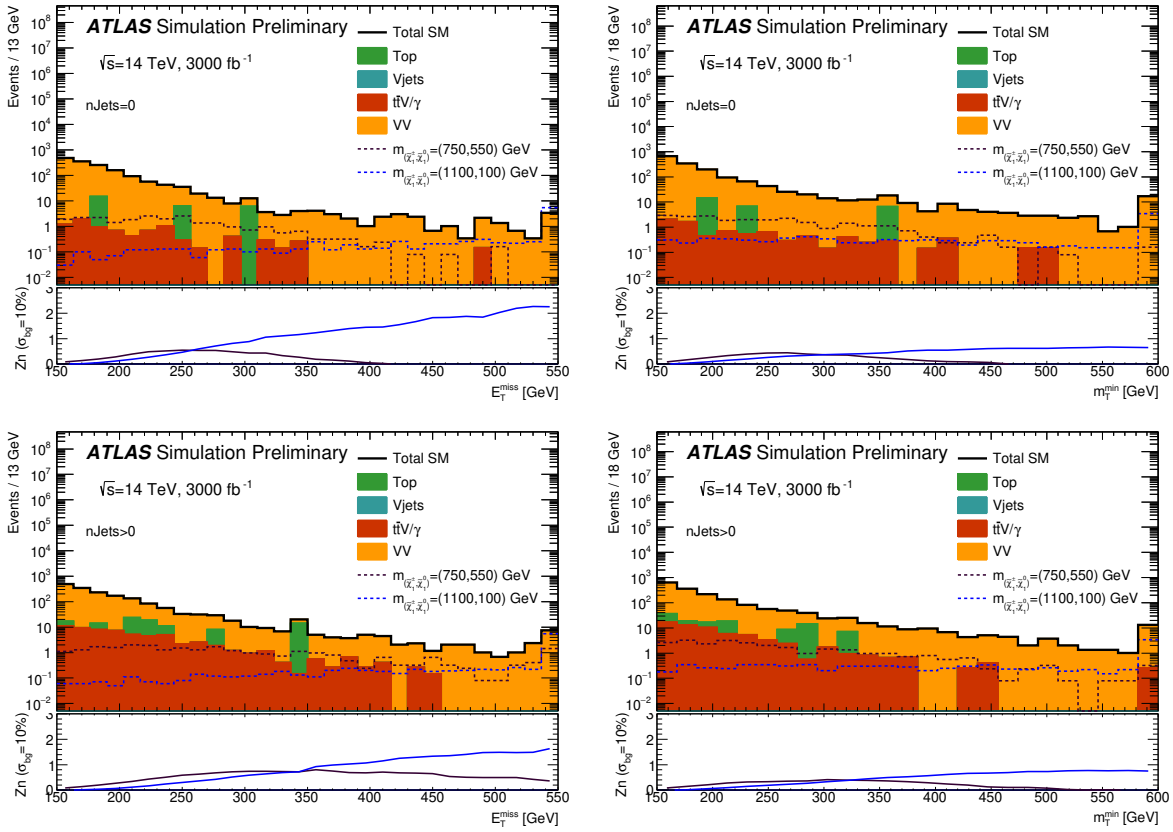

Fig. 2.2.3: Distribution of $E_{\mathrm{T}}^{\mathrm{miss}}$ and $m_{\mathrm{T}}^{\mathrm{min}}$ in the events with zero jets (top) and the events with at least one jet (bottom). All baseline requirements along with the $E_{\mathrm{T}}^{\mathrm{miss}}$ and $m_{\mathrm{T}}^{\mathrm{min}}$ selections of 150 GeV are applied. The lower pad in each plot shows the significance, Z_N using a background uncertainty of 10%, for the SUSY reference points.

lepton p_{T} and the $E_{\mathrm{T}}^{\mathrm{miss}}$, m_{T}, and the contransverse mass constructed using the two b-tagged jets, m_{CT}. The m_{bb} is used to select events which have dijet masses within a window of the Higgs boson mass. The transverse mass variable m_{T}, defined from the $E_{\mathrm{T}}^{\mathrm{miss}}$ and the leading lepton in the event, is effective at suppressing SM backgrounds containing W bosons due to the expected kinematic endpoint around the W boson mass assuming an ideal detector with perfect momentum resolution. The contransverse mass variable m_{CT} is defined for the $b\bar{b}$ system as $m_{\mathrm{CT}} = 2p_{\mathrm{T}}^{b_1}p_{\mathrm{T}}^{b_2}(1+\cos\Delta\phi_{bb})$, where $p_{\mathrm{T}}^{b_1}$ and $p_{\mathrm{T}}^{b_2}$ are transverse momenta of the two leading $b-$jets and $\Delta\phi_{bb}$ is the azimuthal angle between them. It is an effective variable to select Higgs boson decays into $b-$quarks and to suppress the $t\bar{t}$ backgrounds.

A set of common loose requirements, referred to as preselection, are applied first to suppress the fully hadronic multijet and W+jets backgrounds: $m_{\mathrm{T}} > 40$ GeV, $m_{bb} > 50$ GeV, $E_{\mathrm{T}}^{\mathrm{miss}} > 200$ GeV. A multivariate method based on boosted decision trees (BDT) is then chosen for the optimal sensitivity. In this approach, three independent BDTs (referred to as M1, M2 and M3), are trained separately in each signal region for events passing the preselection and within the m_{bb} mass window of $[105, 135]$ GeV. In all regions, the following seven variables are used as inputs: $E_{\mathrm{T}}^{\mathrm{miss}}$, m_{T}, m_{CT}, the leading lepton p_{T}, the leading and sub-leading b-jet p_{T}, as well as the angular separation of the two b-jets $\Delta R(b_1, b_2)$. The BDT output distributions are then used to optimise signal regions maximising the expected significance Z_N of the benchmark signal model. Examples of the BDT output distributions are shown in Fig. 2.2.5. The resulting signal region regions targeting models with low (SR-M1), medium (SR-M3) and high (SR-M3) Δm, are defined by requiring the BDT ranged larger than 0.25, 0.35 and 0.30, respectively.

The SM background is dominated by the top backgrounds, including both the $t\bar{t}$ and single top

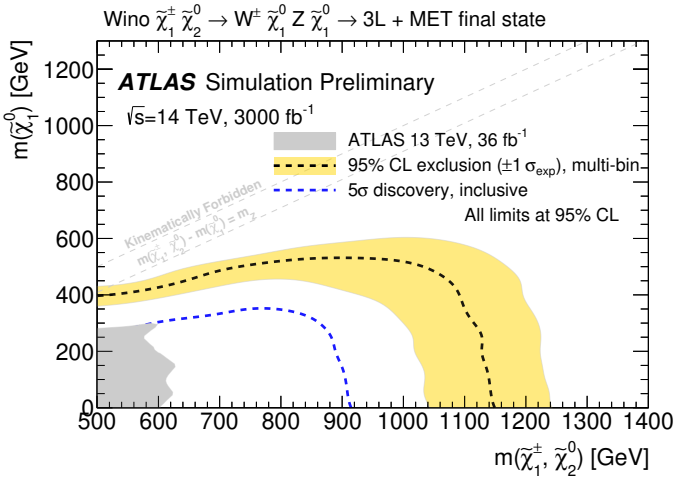

Fig. 2.2.4: Expected exclusion limit and discovery potential on SUSY simplified models for $(\tilde{\chi}_1^\pm/\tilde{\chi}_2^0)$ production with decays via W/Z bosons, assuming 15% uncertainty on the modelling of the SM backgrounds.

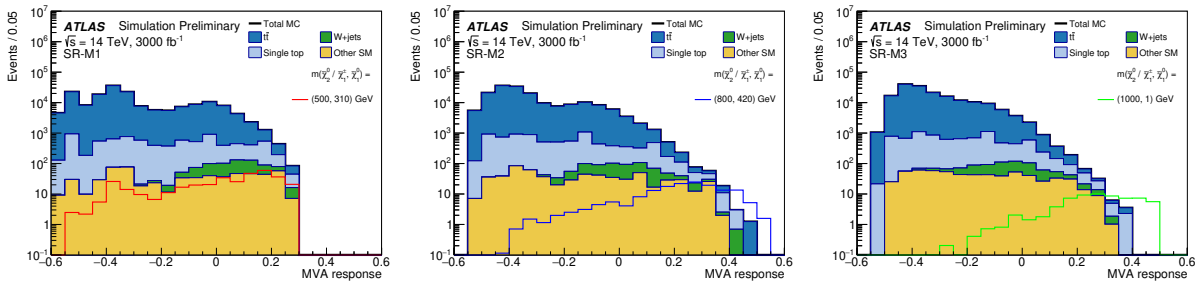

Fig. 2.2.5: Distributions of the BDT responses in the three signal regions for the events that pass the preselection and are within m_{bb} mass window of $[105, 135]$ GeV. The contributions from all SM background are shown as stacked, and the expected distribution from the benchmark signal models are overlaid.

processes. The largest systematic uncertainties arise from the theoretical modelling of the irreducible backgrounds of $t\bar{t}$ and single top, mainly from the generator difference, renormalisation and factorisation scale variations and the interference between the $t\bar{t}$ and single top background. The total theoretical uncertainty is estimated to be about 7%. Experimental uncertainties are dominated by the jet energy scale (JES) and jet energy resolution (JER), on the order of 6%. Figure 2.2.6 shows the expected 95% C.L. exclusion and 5σ discovery contours for the simplified models described earlier. In this model, masses of $\tilde{\chi}_1^\pm/\tilde{\chi}_2^0$ up to about 1280 GeV are excluded at 95% C.L. for a massless $\tilde{\chi}_1^0$. The discovery potential at 5σ can be extended up to 1080 GeV for a massless $\tilde{\chi}_1^0$.

2.2.4 Chargino-Neutralino searches with same-charge dilepton final states at HL-LHC

Contributors: G. Zevi Della Porta, A. Canepa, CMS

This section presents a search from CMS for the pair production of $\widetilde{\chi}_2^\pm$, $\widetilde{\chi}_4^0$ in the final states with two same charge leptons, large $E_{\mathrm{T}}^{\mathrm{miss}}$ and modest jet activity. The search is motivated by radiatively-driven natural supersymmetry (RNS) models, such as those presented in Section 2.4.2. In these models, the mass spectra of the supersymmetric partners of the gauge and Higgs bosons are characterised by low-mass higgsino-like $\widetilde{\chi}_1^0$, $\widetilde{\chi}_2^0$, $\widetilde{\chi}_1^\pm$, and heavier bino-like $\widetilde{\chi}_3^0$ along with mass-degenerate wino-like $\widetilde{\chi}_2^\pm$, $\widetilde{\chi}_4^0$. Two complementary analyses are designed to probe the wino and higgsino sectors of this model. The final states resulting from higgsino production, discussed in Section 2.2.5.1, are characterised by very low p_T SM particles, due to the small mass difference between the low mass states and the $\widetilde{\chi}_1^0$. The

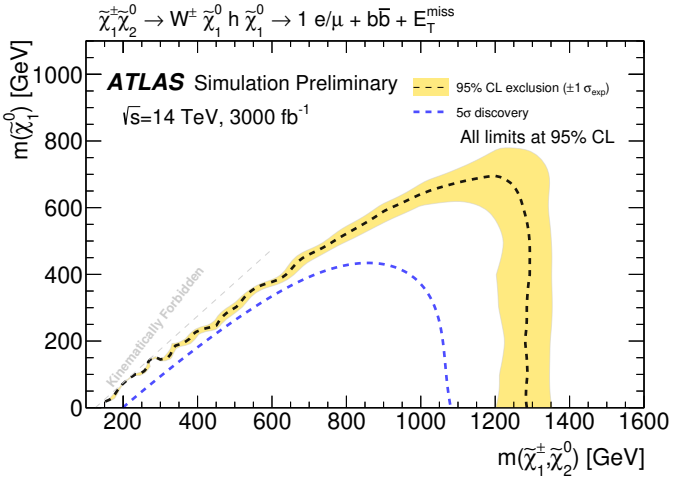

Fig. 2.2.6: Expected 95% C.L. exclusion and 5σ discovery contours in the $m(\tilde{\chi}_1^0), m(\tilde{\chi}_1^{\pm}/\tilde{\chi}_2^0)$ masses plane for the Wh-mediated simplified model.

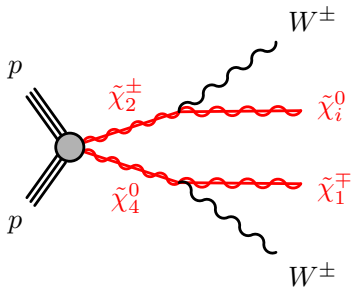

Fig. 2.2.7: Diagram for wino-like $\tilde{\chi}_2^{\pm}\tilde{\chi}_4^0$ pair-production and decay into a final state with two same charge W bosons.

final states resulting from wino production, discussed in this section, are expected to have a significant contribution of events (around 25% of the total BR) where $\tilde{\chi}_2^{\pm}\tilde{\chi}_4^0$ decay into the higgsino sector emitting same-charge W bosons as in Fig. 2.2.7 [89, 90]. This analysis is based on Ref. [91].

Estimates of signal and background yields are based on Monte Carlo samples followed by a DELPHES simulation [33] of the CMS Phase-2 detector. The signal samples are generated by MADGRAPH5_aMC@NLO (v2.3.3) [67] with up to two additional jets at leading order precision. The supersymmetric particles are then decayed by the PYTHIA 8.2 [68] package also providing showering and hadronisation. The cross-sections for SUSY production have been calculated for $\sqrt{s} = 14$ TeV at NLO-NLL using the resumming code from Ref. [59, 60] with CTEQ6.6 and MSTW2008nlo90cl PDFs. The background samples are generated with MADGRAPH 5 at LO, followed by parton showering and hadronisation with PYTHIA 6 [92]. The DELPHES-based yields of processes containing prompt leptons are corrected by the lepton reconstruction, identification and isolation efficiencies measured in Run-2 collision data. For example, the reconstruction efficiency for centrally produced electrons ranges from 60 to 86% for p_T values between 20 and 200 GeV. The DELPHES-based yields of processes containing non-prompt leptons are increased by 25%, based on Ref. [93], to account for events with misidentified leptons from light flavour quarks, which are not included by DELPHES [93].

Candidate signal events are selected if they contain two high quality and isolated leptons with $p_T \geq 20$ GeV, $|\eta| \leq 1.6$, and the same charge. Discrimination from the background processes is achieved by selecting events with no additional leptons with $p_T \geq 5$ GeV and $|\eta| \leq 4.0$ (to suppress multi-boson production), and no $p_T \geq 30$ GeV jets (to suppress events with top quarks). The remaining

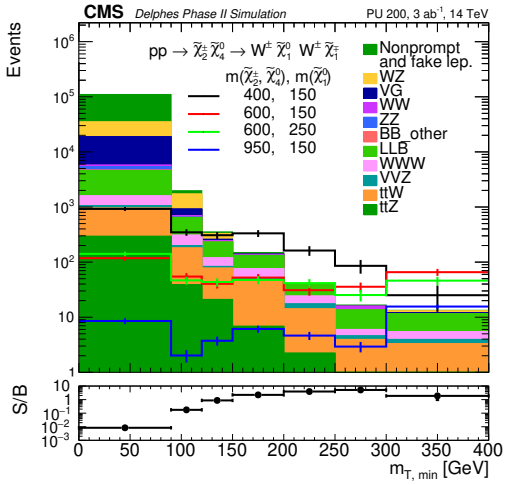

Fig. 2.2.8: Distribution of $m_{\mathrm{T,min}}$ in candidate events satisfying the signal region selection. For coloured lines displaying the signal yields, the first number in the legend refers to the $\widetilde{\chi}_2^{\pm}\widetilde{\chi}_4^0$ mass while the second number refers to the value of the $\widetilde{\chi}_1^0$ mass.

background processes include the pair production of W and Z/Z* bosons, as well as the W+jets and $t\bar{t}$ processes in association with a non-prompt or misidentified lepton. These are suppressed by imposing a tight selection on the $m_{\mathrm{T,min}}$ based on $E_{\mathrm{T}}^{\mathrm{miss}}$ and the p_T of the leptons and defined as

$$m_{T,min} = \min[m_T(p_T^{lep1}, E_{\mathrm{T}}^{\mathrm{miss}}), m_T(p_T^{lep2}, E_{\mathrm{T}}^{\mathrm{miss}})]. \tag{2.2.1}$$

Figure 2.2.8 shows the distribution of the $m_{\mathrm{T,min}}$ observable in events satisfying the signal region selection described above. To maximise the sensitivity, seven signal regions are then defined with $m_{\mathrm{T,min}}$ in the ranges $[0, 90)$, $[90, 120)$, $[120, 150)$, $[150; 200)$, $[200; 250)$, $[250; 300)$, and $[300; \infty)$ GeV.

The search sensitivity is calculated using a modified frequentist approach with the $\mathrm{CL_S}$ criterion and asymptotic results for the test statistic [94, 95]. The systematic uncertainty on the prompt (fake, signal) yields is assumed to be 20% (50%, 20%) based on the estimates computed in the corresponding search carried out in Run-2 collision data [93].

The upper limit on the production cross-section of pair produced $\widetilde{\chi}_2^{\pm}\widetilde{\chi}_4^0$ decaying into a final state with two same charge W bosons with a BR of 25% is shown in Fig. 2.2.9 for two μ scenarios (where $\mu \sim m_{\widetilde{\chi}_1^{\pm}}, m_{\widetilde{\chi}_2^0}, m_{\widetilde{\chi}_1^0}$). The value $\widetilde{\chi}_1^0 = 150$ GeV is representative of the region of parameter space outside the reach of the Run-2 search for direct production of higgsinos in the final states with two same flavour opposite sign leptons [96], while $\widetilde{\chi}_1^0 = 250$ GeV is close to the sensitivity reach of the same search when extrapolated to the HL-LHC (Section 2.2.5.1). As expected, the sensitivity depends only mildly on the value of $\widetilde{\chi}_1^0$ at large $\widetilde{\chi}_2^{\pm}\widetilde{\chi}_4^0$ mass values, while as the $\widetilde{\chi}_2^{\pm}\widetilde{\chi}_4^0$ mass approaches $\widetilde{\chi}_1^0$ the dependence is more significant. Wino-like mass degenerate $\widetilde{\chi}_2^{\pm}\widetilde{\chi}_4^0$ are excluded at 95% C.L. for masses up to 900 GeV in both the $\widetilde{\chi}_1^0 = 150$ GeV and 250 GeV scenarios. This demonstrates that the HL-LHC has the potential to probe most of the natural SUSY parameter space with EW naturalness measure $\Delta_{\mathrm{EW}} \leq 30$ [97].

2.2.5 Searches for SUSY models with compressed electroweakino mass spectra

In several SUSY scenarios, higgsinos could be light, with masses below 1 TeV, and the absolute value of the higgsino mass parameter μ is expected to be near the weak scale, while the magnitude of the bino and wino mass parameters, M_1 and M_2 can be significantly larger, *i.e.* $|\mu| \ll |M_1|, |M_2|$. This results in the three lightest electroweakino states being dominated by the higgsino component. In this scenario, their masses are separated by hundreds of MeV to tens of GeV depending on the composition of these

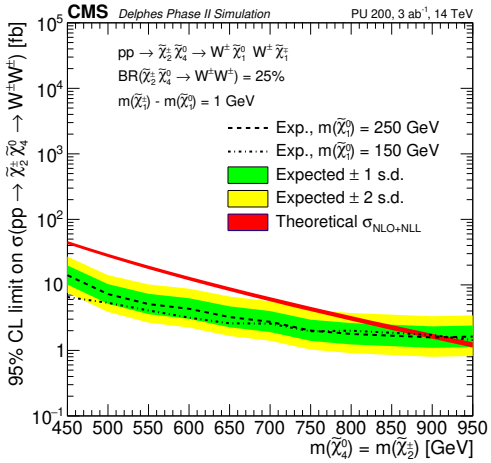

Fig. 2.2.9: Upper limit on the production cross-section of pair produced $\tilde{\chi}_2^{\pm}\tilde{\chi}_4^0$ decaying into a final state with two same charge W boson with a BR of 25% for two assumptions on the $\tilde{\chi}_1^0$ mass.

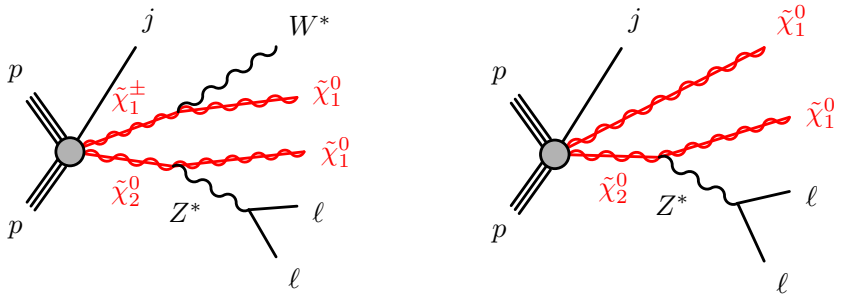

Fig. 2.2.10: Example Feynman diagrams for $\tilde{\chi}_1^{\pm}\tilde{\chi}_2^0$ (left) and $\tilde{\chi}_2^0\tilde{\chi}_1^0$ (right) s-channel pair production, followed by the leptonic decay of the $\tilde{\chi}_2^0$.

mass eigenstates, which is determined by the specific values of M_1 and M_2. Investigating either of these scenarios, with very small mass splitting between the lightest electroweakinos, is particularly challenging at hadron colliders, both due to the small cross-sections and the small transverse momenta of the final state particles. As of writing the ATLAS and CMS collaborations have searched for higgsinos in up to $36\ \mathrm{fb}^{-1}$ of proton-proton collision data [96, 98] and just started probing the parameter space beyond the LEP experiments' limits [99, 100]. By providing $3\ \mathrm{ab}^{-1}$of proton-proton collision data at a c.o.m. energy of $14\ \mathrm{TeV}$, the HL-LHC has the potential to significantly extend the sensitivity to higgsinos and thus to natural SUSY. This is depicted also in Section 2.4.2 of this report.

The model used for the development of the searches for higgsino-like $\tilde{\chi}_i^{\pm}$ and $\tilde{\chi}_j^0$ by ATLAS and CMS is a SUSY simplified model where the higgsino-like $\tilde{\chi}_1^{\pm}$ and $\tilde{\chi}_2^0$ are assumed to be quasi mass-degenerate and produced in pairs. The model contains both the $\tilde{\chi}_1^{\pm}\tilde{\chi}_2^0$ and the $\tilde{\chi}_2^0\tilde{\chi}_1^0$ production, where $\tilde{\chi}_1^{\pm}$ decays into $\mathrm{W}^*\tilde{\chi}_1^0$ and $\tilde{\chi}_2^0$ into $\mathrm{Z}^*\tilde{\chi}_1^0$, respectively, with a branching fraction of 100% (Fig. 2.2.10).

Both ATLAS and CMS analyses presented in the following exploit the presence of charged leptons with low transverse momenta arising from the off-shell W and Z bosons in the $\tilde{\chi}_1^{\pm} \rightarrow W^*\tilde{\chi}_1^0$ and $\tilde{\chi}_2^0 \rightarrow Z^*\tilde{\chi}_1^0$ decays, and large missing transverse momentum due to the presence of an ISR jet.

2.2.5.1 Higgsino search prospects at HL- and HE-LHC at CMS

Contributors: A. Canepa, J. Hogan, S. Kulkarni, B. Schneider, CMS

The results presented here are from Ref. [101] from the CMS Collaboration. If the $\tilde{\chi}_1^{\pm}$, $\tilde{\chi}_2^0$, and

Observable	Requirement
N_ℓ	$= 2$ (same flavour, opposite charge)
$\Delta R(\ell_1\ell_2)$	≤ 2.0
$N_{\text{b-jet}}$	$= 0$
N_{jet}	≤ 4
N_{ISR}	≥ 1
$\mathbf{p}_{\text{T}}^{\text{miss}}$	≥ 250 GeV
$\Delta\phi(\mathbf{p}_{\text{T}}^{\text{miss}}, p_{\text{T}}(j_{\text{ISR}}))$	≥ 2.0
m_{ℓ_1,ℓ_2}	[5,40] GeV

Table 2.2.2: Definition of the baseline signal region. In the table, N_ℓ is the number of candidate leptons; $\Delta R(\ell_1, \ell_2)$ is the angular separation between the two candidate leptons in the ϕ, η space; $N_{\text{b-jet}}$ is the number of b jets; N_{jet} is the number of candidate jets (including any ISR jet reconstructed in the event); N_{ISR} is the number of ISR jets; $\Delta\phi(\mathbf{p}_{\text{T}}^{\text{miss}}, p_{\text{T}}(j_{\text{ISR}}))$ is the azimuthal distance between the $\mathbf{p}_{\text{T}}^{\text{miss}}$ vector and the j_{ISR} p_T vector; and m_{ℓ_1,ℓ_2} is the invariant mass of the two candidate leptons.

$\widetilde{\chi}_1^0$ are higgsino-like, the mass splitting is just driven by radiative corrections and acquires values up to a few GeV. As a result, pair-produced $\widetilde{\chi}_1^\pm\widetilde{\chi}_2^0$ or pair-produced $\widetilde{\chi}_2^0\widetilde{\chi}_1^0$ can decay promptly into $\widetilde{\chi}_1^0$ only via off-shell W and Z bosons, leading to events with low transverse momentum (p_T) SM particles. In leptonic decays of the Z boson, the events will contain one same-flavour, opposite-charge lepton pair, the invariant mass of which has a kinematic endpoint at $\Delta M(\widetilde{\chi}_2^0, \widetilde{\chi}_1^0) = m(\widetilde{\chi}_2^0) - m(\widetilde{\chi}_1^0)$. Sensitivity to the signal is achieved by requiring at least one jet from initial-state radiation (ISR) that recoils against the two $\widetilde{\chi}_1^0$ and produces significant missing transverse momentum ($\mathbf{p}_{\text{T}}^{\text{miss}}$) in the event.

In the analysis muons (electrons) are selected with $5 \leq p_T \leq 30$ GeV and $|\eta| \leq 2.4\,(1.6)$. Dedicated lepton identification criteria are then applied, providing 40% to 90% efficiency for muons and 20% to 80% efficiency for electrons. Finally, identified leptons are considered candidate leptons if they are isolated. The anti-k_t algorithm with a size parameter of 0.4 is adopted to reconstruct jets. Candidate jets are reconstructed jets with $p_T > 40$ GeV and $|\eta| \leq 4.0$ and are referred to as ISR jets if $p_T > 200$ GeV and $|\eta| \leq 2.4$ (j_{ISR}). Candidate jets consistent with the decay and hadronisation of a B hadron are tagged as b jets with an efficiency of 74%. Spacial separation is imposed between each candidate lepton and jet.

To be considered for this analysis, events are requested to contain at least two low-p_T, same-flavour, opposite-charge candidate leptons, $\mathbf{p}_{\text{T}}^{\text{miss}} \geq 250$ GeV 3and at least one j_{ISR}. To further exploit the boosted topology of the signal, events are accepted only if the $\mathbf{p}_{\text{T}}^{\text{miss}}$ and the ISR candidate jet p_T satisfy $\Delta\phi(\mathbf{p}_{\text{T}}^{\text{miss}}, p_{\text{T}}(j_{\text{ISR}})) \geq 2.0$ and the angular separation between the two candidate leptons satisfies $\Delta R(\ell_1\ell_2) \leq 2.0$. Since minor hadronic activity is expected from the EW production of $\widetilde{\chi}_1^\pm$ and $\widetilde{\chi}_2^0$, an upper bound of 4 is placed on the number of candidate jets N_{jet}.

Several SM processes exhibit a signature similar to that of the signal. One background category consists of prompt processes, where both candidate leptons originate from the prompt decay of W and Z bosons. Another category is misclassified processes, where at least one of the two candidate leptons originates from a semi-leptonic decay of a B hadron, a photon conversion, a decay in flight, or a misidentified quark or gluon. The prompt background is dominated by Drell-Yan (DY), diboson, and $t\bar{t}$ production where both W bosons decay leptonically. The DY contribution is suppressed by requiring significant $\mathbf{p}_{\text{T}}^{\text{miss}}$, while rejecting events with at least one b jet reduces the $t\bar{t}$ background. The dominant misclassified processes are W and $t\bar{t}$ production where one candidate lepton originates from the W boson decay and an additional misclassified lepton is selected in the event. Rejecting events with at least one b jet reduces both contributions. Events satisfying the criteria described above, which are summarised in Table 2.2.2, form the baseline signal region for which relevant distributions are presented in Fig. 2.2.11 and 2.2.12.

The missing transverse momentum, the invariant mass of the two candidate leptons, and the sub-leading lepton $p_{\text{T}}(\ell_2)$ observables are found to provide the best discrimination between signal and

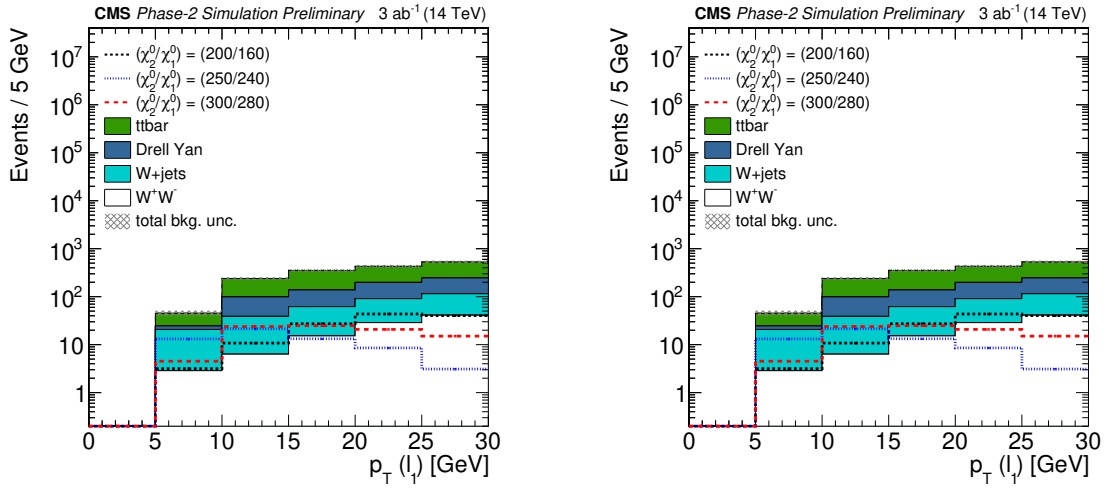

Fig. 2.2.11: Distributions of the p_T of the candidate lepton with the highest p_T (left) and the second-highest p_T (right) for background and signal events in the baseline signal region. Three selected $\widetilde{\chi}_1^{\pm}\widetilde{\chi}_2^0 + \widetilde{\chi}_2^0\widetilde{\chi}_1^0$ signal models are shown, where the first number corresponds to the mass of the $\widetilde{\chi}_2^0$ (and $\widetilde{\chi}_1^{\pm}$) and the second one to the mass of the $\widetilde{\chi}_1^0$. The uncertainty band represents systematical uncertainties.

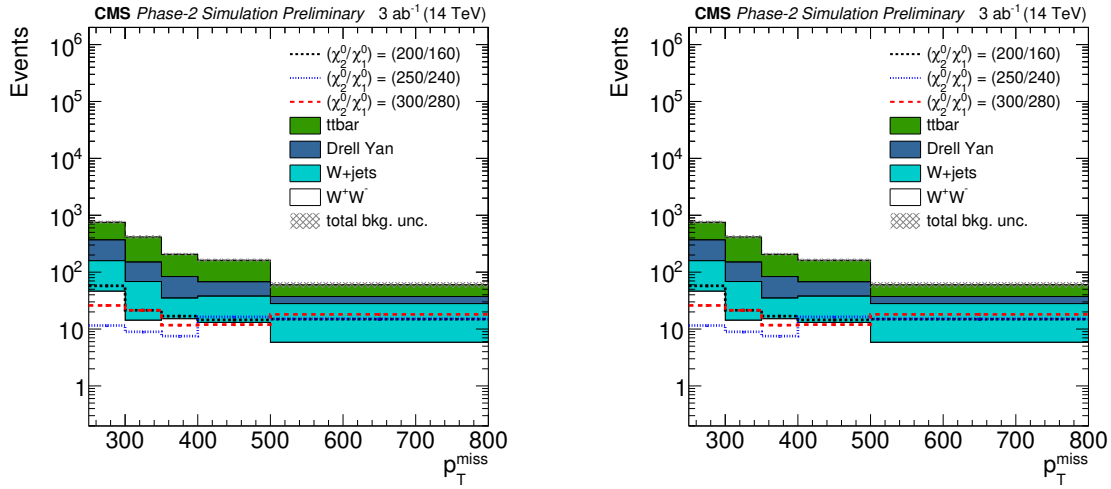

Fig. 2.2.12: Distributions of the $\mathbf{p}_{\mathrm{T}}^{\mathrm{miss}}$ (left) and m_{ℓ_1,ℓ_2} (right) for background and signal events in the baseline signal region. Three selected $\widetilde{\chi}_1^{\pm}\widetilde{\chi}_2^0 + \widetilde{\chi}_2^0\widetilde{\chi}_1^0$ signal models are shown, where the first number corresponds to the mass of $\widetilde{\chi}_2^0$ (and $\widetilde{\chi}_1^{\pm}$) and the second one to the mass of $\widetilde{\chi}_1^0$. The uncertainty band represents systematical uncertainties.

background. Events in the baseline signal region are therefore classified in 60 categories with $\mathbf{p}_{\mathrm{T}}^{\mathrm{miss}}$ values in $[250, 300, 350, 400, 500, \infty]$ GeV, m_{ℓ_1,ℓ_2} values in $[5, 10, 20, 30, 40]$ GeV, and $p_{\mathrm{T}}(\ell_2)$ in $[5, 13, 21, 30]$ GeV.

Several systematic uncertainties affect the yields of both the background and the signal processes. The dominant experimental uncertainties are those originating from the jet energy corrections ($1-2.5\%$), b-tagging efficiency (1%), lepton identification efficiency and isolation (0.5%, 2.5% for muons and electrons, respectively), and integrated luminosity (1%). An additional systematic uncertainty of 30% on the yield of the misclassified background is also assumed based on the estimate in Ref. [96]. It is assumed that the yields are not affected by the statistical uncertainty deriving from the limited number of generated events. Theoretical uncertainties in the signal cross sections and in the acceptance from the choice of parton distribution functions are considered negligible and are not included. However, a systematic

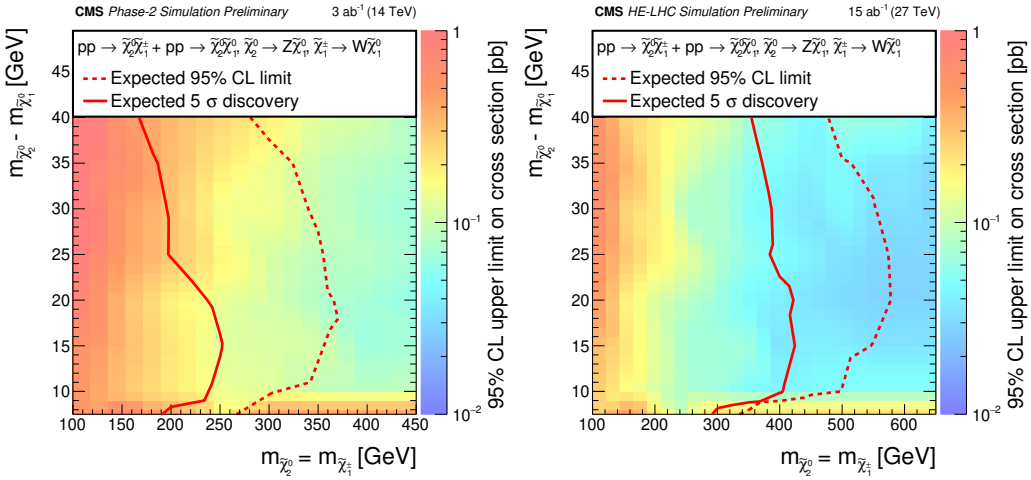

Fig. 2.2.13: 5σ discovery contours and expected 95% C.L. exclusion contours for the combined $\widetilde{\chi}_1^{\pm}\,\widetilde{\chi}_2^0$ and $\widetilde{\chi}_2^0\,\widetilde{\chi}_1^0$ production (left). Projection of the HL-LHC 5σ discovery contours and expected 95% C.L. exclusion contours for the combined $\widetilde{\chi}_1^{\pm}\,\widetilde{\chi}_2^0$ and $\widetilde{\chi}_2^0\,\widetilde{\chi}_1^0$ production for a centre-of-mass energy of 27 TeV and an integrated luminosity of 15 ab^{-1} (HE-LHC). Except for the cross sections and the integrated luminosity, the HL-LHC analysis was not modified (right). Results are presented for $\Delta M(\widetilde{\chi}_2^0, \widetilde{\chi}_1^0) > 7.5$ GeV.

uncertainty of 10% in the signal acceptance, similar to the value from Ref. [96], is included to account for the modelling of the ISR jet.

The upper limit on the cross sections is computed at 95% C.L. and shown in Fig. 2.2.13. Higgsino-like mass-degenerate $\widetilde{\chi}_1^{\pm}$ and $\widetilde{\chi}_2^0$ are excluded for masses up to 360 GeV if the mass difference with respect to the lightest neutralino $\widetilde{\chi}_1^0$ is 15 GeV, extending the sensitivity achieved in Ref. [96] by $\approx$210 GeV. Figure 2.2.13 also shows the 5σ discovery contour, computed using all signal regions without taking the look-elsewhere-effect into account. Under this assumption $\widetilde{\chi}_1^{\pm}$ and $\widetilde{\chi}_2^0$ can be discovered for masses as large as 250 GeV. These results demonstrate that the HL-LHC can significantly improve the sensitivity to natural SUSY.

Figure 2.2.13 also shows the 5σ discovery contours and expected 95% C.L. exclusion contours for the combined $\widetilde{\chi}_1^{\pm}\,\widetilde{\chi}_2^0$ and $\widetilde{\chi}_2^0\,\widetilde{\chi}_1^0$ production for the HE-LHC. The main gain in sensitivity comes from the increased luminosity, since the cross section increase for signal is the same order as that for background. Except for the cross sections and the integrated luminosity, the HL-LHC analysis was not modified for this HE-LHC projection.

2.2.5.2 *Higgsino search prospects at HL-LHC at ATLAS*

Contributors: S. Amoroso, J. K. Anders, F. Meloni, C. Merlassino, B. Petersen, J. A. Sabater Iglesias, M. Saito, R. Sawada, P. Tornambe, M. Weber, ATLAS

The presented dilepton search [102] investigates final states containing two soft muons and a large transverse momentum imbalance, which arise in scenarios where $\tilde{\chi}_2^0$ and $\tilde{\chi}_1^{\pm}$ are produced and decay via an off-shell Z and W boson, as depicted in Fig. 2.2.10. Considering the $Z \to ee$ decay is beyond the scope of this prospect study, but could further improve the sensitivity to these scenarios. Due to the very small mass splitting of the electroweakinos in this scenario, a jet arising from initial-state radiation (ISR) is required, to boost the sparticle system. First constraints surpassing the LEP limits have recently been set by the ATLAS experiment [98], excluding mass splittings down to 2.5 GeV for $m(\tilde{\chi}_1^0) = 100$ GeV.

The search targets scenarios that contain low p_T muons selected with $p_T > 3$ GeV and $|\eta| < 2.5$. Muons that originate from pile up interactions or from heavy flavour decays, referred as fake or non-prompt muons, are rejected by applying an isolation to the muon candidates. The main source of

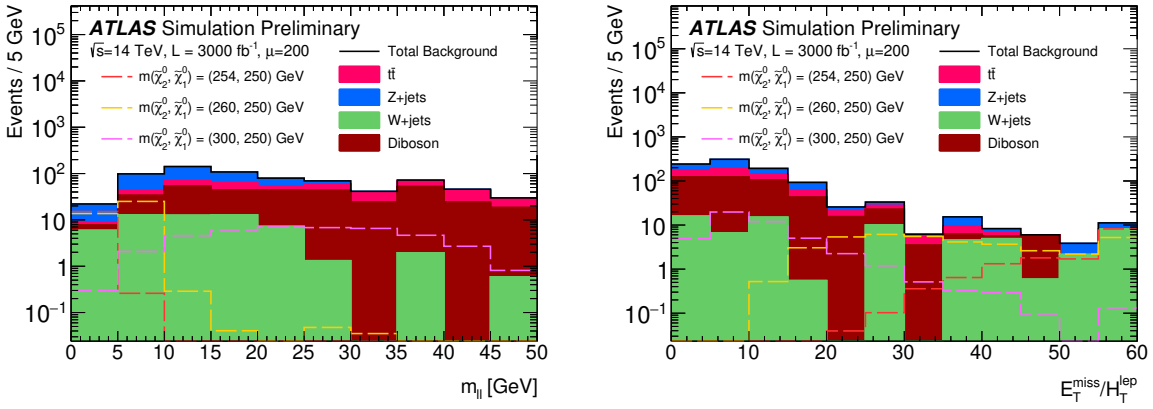

Fig. 2.2.14: Distributions of a selection of kinematic variables used for the SR optimisation in the dilepton search. The variables are presented with the full SR selections implemented aside from the selection on the variable shown. Three signal models with $m(\chi_1^0) = 250$ GeV and different mass splittings ($\Delta m(\chi_2^0, \chi_1^0) = 4,\ 10,$ and 5 GeV) are overlaid.

these fake muons are decays from heavy flavour mesons and baryons created in the quark hadronisation process. The signal region (SR) optimisation is performed by scanning a set of variables which are expected to provide discrimination between the signal scenario under consideration and the expected SM background processes. Only events with two opposite-sign muons are used in the final selection, as the muon reconstruction rate is not expected to fall dramatically and the muon fake rate is not expected to grow largely with increased pile-up. Additional requirements are applied on the leading jet of $p_T(\text{jet}_1) > 100$ GeV, and on the azimuthal separation $\Delta\phi(\text{jet}_1, E_{\text{T}}^{\text{miss}}) > 2.0$. In order to discriminate the signal from SM background processes, kinematic variables are used such as the total number of muons in the event, the total number of jets and b-jets with $p_{\text{T}} > 30$ GeV, the $E_{\text{T}}^{\text{miss}}$, the invariant mass of the dilepton system ($m_{\ell\ell}$), the angular separation between the leptons ($\Delta R(\ell, \ell)$) and more.

Figure 2.2.14 presents a selection of kinematic distributions after the full SR selection is applied, minus the selection on the variable under consideration. The final SR definitions split the $m_{\ell\ell}$ into six non-overlapping SRs, with $m_{\ell\ell}$ selections of $[1, 3]$, $[3.2, 5]$, $[5, 10]$, $[10, 20]$, $[20, 30]$ and $[30, 50]$ GeV.

The leading sources of background in the SR are from $t\bar{t}$, single-top, WW + jets, and $Z/\gamma^*(\to \tau\tau)$ + jets. The dominant source of reducible background arises from processes where one or more leptons are fake or non-prompt, such as in W+jets production. The fake/non-prompt lepton background arises from jets misidentified as leptons, photon conversions, or semileptonic decays of heavy-flavour hadrons. The total uncertainty for the dilepton search is extrapolated to be 30% and are dominated by the modelling of the fake and non-prompt lepton backgrounds, followed by the experimental uncertainties related to the jet energy scale and flavour tagging. The experimental uncertainty is assumed to be fully correlated between the background and the signal.

Figure 2.2.15 shows the 95% C.L. exclusion limits in the $m(\tilde{\chi}_2^0)$, $\Delta m(\tilde{\chi}_2^0, \tilde{\chi}_1^0)$ plane. With $3\ \text{ab}^{-1}$, $\tilde{\chi}_2^0$ masses up to 350 GeV could be excluded, as well as $\Delta m(\tilde{\chi}_2^0, \tilde{\chi}_1^0)$ between 2 and 25 GeV for $m(\tilde{\chi}_2^0) = 100$ GeV. In the figure the blue curve presents the 5σ discovery potential of the search. To calculate the discovery potential a single-bin discovery test is performed by removing the lower bound on $m_{\ell\ell}$ in the SRs previously defined.

2.2.6 Multileptons from resonant electroweakinos in left-right SUSY at HL- and HE-LHC

Contributors: M. Frank, B. Fuks, K. Huitu, S. Mondal, S. Kumar Rai, H. Waltari

Left-right supersymmetric (LRSUSY) models, based on the gauge symmetry $SU(3)_C \times SU(2)_L \times SU(2)_R \times U(1)_{\text{B-L}}$, inherit the attractive features of the left-right (LR) symmetry [103, 104], whereas

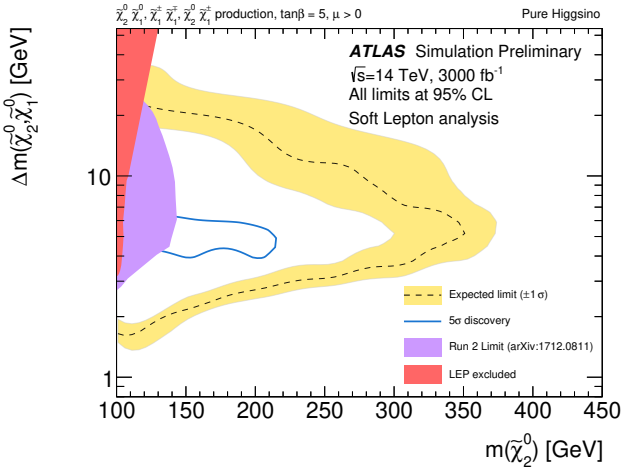

Fig. 2.2.15: Expected exclusion limit (dashed line) in the $\Delta m(\tilde{\chi}_2^0, \tilde{\chi}_1^0)$, $m(\tilde{\chi}_2^0)$ mass plane, at 95% C.L. from the dilepton analysis with 3 $\mathrm{ab}^{-1}$of 14 TeV, proton-proton collision data in the context of a pure Higgsino LSP with $\pm 1\sigma$ (yellow band) from the associated systematic uncertainties. The blue curve presents the 5σ discovery potential of the search. The purple contour is the observed exclusion limit from the Run-2 analysis. The figure also presents the limits on chargino production from LEP. The relationship between the masses of the chargino and the two lightest neutralinos in this scenario is $m(\tilde{\chi}_1^\pm) = \frac{1}{2}(m(\tilde{\chi}_1^0) + m(\tilde{\chi}_2^0))$.

they forbid any R-parity violating operators thanks to the gauged $B-L$ symmetry. To naturally describe the small magnitude of the neutrino masses and preserve R-parity, the model superfield content includes both $SU(2)_L$ and $SU(2)_R$ triplets of Higgs supermultiplets. The neutral component of the $SU(2)_R$ Higgs scalar field then acquires a large vacuum expectation value v_R, which breaks the LR symmetry and makes the $SU(2)_R$ gauge sector heavy. In order to prevent the tree-level vacuum from being a charge-breaking one, we can either rely on spontaneous R-parity violation [105], one-loop corrections [106], higher-dimensional operators [107] or additional $B-L=0$ triplets [108]. Whereas the first two options restrict v_R to be of at most about 10 TeV, the latter ones enforce v_R to lie above 10^{10} GeV. In this work, we rely on radiative corrections to stabilise the vacuum, so that the lightest supersymmetric particle (LSP) is stable and can act as a dark matter candidate.

Two viable LSP options emerge from LRSUSY, neutralinos and right sneutrinos. Out of the 12 neutralinos, gauginos and LR bidoublet, higgsinos can generally be lighter than 1 TeV. The correct relic density can be accommodated with dominantly-bino LSPs with a mass close to $m_h/2$ [109], whilst in the bidoublet higgsinos case (featuring four neutralinos and two charginos that are nearly-degenerate), co-annihilations play a crucial role and impose higgsino masses close to 700 GeV. In this setup, the rest of the spectrum is always heavier, so that SUSY could be challenging to discover. Right sneutrino LSP annihilate via the exchange of an s-channel Higgs boson through gauge interactions stemming from the D-terms [109]. Without options for co-annihilating, the LSP sneutrino mass must lie between 250 and 300 GeV. However, potential co-annihilations with neutralinos enhance the effective annihilation cross section so that the relic density constraints can be satisfied with heavier sneutrinos. The fully degenerate sneutrinos and higgsinos case impose an upper limit on the sneutrino mass of 700 GeV. Additionally, right neutrinos can also be part of the dark sector, together with the LSP [110].

Direct detection constraints imposed by the XENON1T [111] and PANDA [112] collaborations put light DM scenarios under severe scrutiny. Hence, in LRSUSY, in order to account for the relic density and direct detection constraints simultaneously, we need to focus on various co-annihilation options. In this work, we consider one right sneutrino and one higgsino LSP scenario and highlight the corresponding implications for W_R searches at the LHC. A robust signal of left-right symmetry consists in the discovery of a right gauge boson W_R, possibly together with a right neutrino N_R. Both

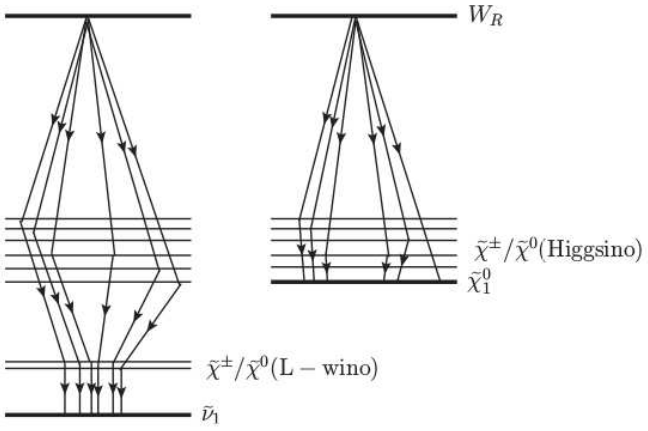

Fig. 2.2.16: The two LRSUSY spectra chosen for our study. Left: sneutrino LSP spectrum, where the W_R boson decays into multiple higgsino-like chargino-neutralino pairs, each electroweakino subsequently decaying into the sneutrino LSP either directly or through an intermediate $SU(2)_L$ wino-like chargino-neutralino pair. Right: neutralino LSP spectrum, where the W_R bosons decays into higgsino-like chargino-neutralino pairs, the electroweakinos subsequently decaying into the lightest (higgsino-like) neutralino.

the ATLAS and CMS collaborations have looked for a W_R signal in the $\ell\ell jj$ channel, excluding W_R masses up to about 4.5 TeV when at least one right-handed neutrino is lighter than the W_R-boson [113]. These exclusion limits nevertheless strongly depend on the spectrum and could be weakened or even evaded, for instance when $M_{N_R} \simeq M_{W_R}$ or for $M_{N_R} \lesssim 150$ GeV and $M_{W_R} > 3$ TeV. In addition, dijet resonance searches yield $M_{W_R} \gtrsim 3.5$ TeV [114, 115], even if these bounds can once again be relaxed by virtue of the supersymmetric W_R decay modes. On different grounds, dark matter considerations lead to favoured LRSUSY scenarios in which several neutralinos and charginos are light (so that they could co-annihilate). This motivates the investigation of a new W_R search channel where decays into pairs of electroweakinos are considered. In many LRSUSY setups, the corresponding combined BR can be as large as 25%, so that the production of multileptonic systems featuring a large amount of missing transverse momentum is enhanced. Whilst such a multilepton signal with $E_{\rm T}^{\rm miss}$ is a characteristic SUSY signal, it also provides an additional search channel for W_R-bosons at the LHC. Moreover, the resonant production mode offers the opportunity to reconstruct the W_R-boson mass through kinematic thresholds featured by various transverse observables.

In order to illustrate the above features, we perform an analysis in the context of two LRSUSY scenarios respectively featuring a sneutrino and a neutralino LSP. The results are presented for both the high c.o.m. energy ($\sqrt{s}$) and high luminosity ($\mathcal{L}$) cases, $\sqrt{s} = 14$ TeV with $\mathcal{L} = 3\,{\rm ab}^{-1}$ and $\sqrt{s} = 27$ TeV with $\mathcal{L} = 15\,{\rm ab}^{-1}$ options for the future run of the LHC. For the higgsino-like neutralino LSP case, we kept the bidoublet higgsino masses in the $700 - 750$ GeV region. In contrast, for the sneutrino DM case, the LSP mass can be much lower and has been fixed to about 400 GeV, with the second lightest superpartner being an $SU(2)_L$ wino lying about 30 GeV above and the higgsinos being again in the $700 - 750$ GeV regime. These two mass spectra are illustrated in Fig. 2.2.16. The sneutrino DM option is expected to be reachable with a lower luminosity due to the harder charged leptons arising from the cascade decays.

For our study, we followed the CMS search of multileptonic new physics signals as could emerge from electroweakino production [93]. We tested several signal regions introduced in this CMS search, all featuring different lepton multiplicities and selections on transverse kinematic variables like the missing transverse energy, the transverse momenta of various systems, the transverse mass M_T of systems made of one lepton and the missing momentum, the stransverse mass M_{T2} or the dilepton invariant mass $M_{\ell\ell}$. The two signal regions that are most suitable for the considered types of LRSUSY spectra, are listed

Signal Regions	Requirements
SRA44	$N_\ell = 3$, $N_{\rm OSSF} \geq 1$, $N_\tau = 0$, $M_T > 160$ GeV, $\not{E}_T \geq 200$ GeV, $M_{\ell\ell} \geq 105$ GeV
SRD16	$N_\ell = 2$, $N_{\rm OS} = 1$, $N_{\rm SF} = 0$, $N_\tau = 1$, $M_{T2} > 100$ GeV, $\not{E}_T \geq 200$ GeV

Table 2.2.3: The two signal regions of the analysis of Ref. [93] that are the most suitable for discovering our considered LRSUSY W_R-boson signal. Here, $N_{\rm OSSF}$ stands for the number of opposite-sign same-flavour lepton pairs, $N_{\rm OS}$ for the number of opposite-sign lepton pair and $N_{\rm SF}$ for the number of same-flavour lepton pair. Moreover, $\ell \equiv e, \mu$.

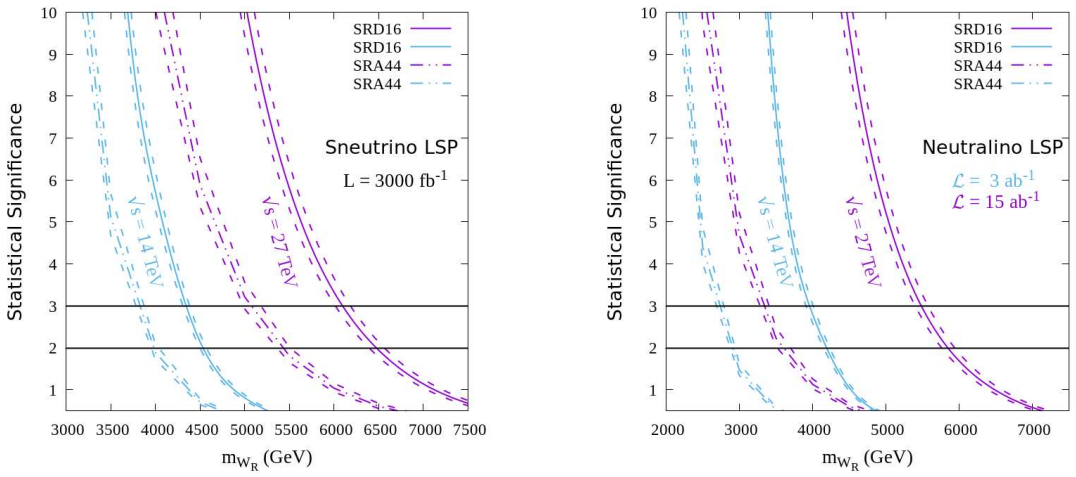

Fig. 2.2.17: Statistical significance of the two signal regions of the analysis of Ref. [93] to a LRSUSY scenarios in the case of a sneutrino (left) and a neutralino (right) LSP setup. We consider c.o.m. energies of $\sqrt{s} = 14$ and 27 TeV, and an integrated luminosities of 3 and 15 ab^{-1}.

in Table 2.2.3. In the **SRA44** region, one requires the presence of three charged leptons (electrons or muons), with at least two of them forming a pair of opposite-sign same-flavour (OSSF) leptons. One further constrains the invariant mass of this OSSF lepton system $M_{\ell\ell}$, relying on the pair that is the most compatible with a Z-boson if several combinations are possible. The transverse mass M_T of the system constructed from the third lepton and the missing momentum is finally constrained, together with the missing transverse momentum. In the **SRD16** region, one instead asks for two opposite-sign leptons (electrons and muons) and one tau-lepton. The stransverse mass M_{T2} originating from the lepton-pair is then constrained, together with the missing transverse energy.

For our simulations, we used the SARAH implementation of the LRSUSY model [116, 117] and generated the particle spectrum by means of SPHENO [118]. DM calculations were performed using MADDM [119] and LHC simulations were performed at the parton-level using MADGRAPH5 (V2.5.5) [67] with the UFO [120] model obtained from SARAH. We used the leading order set of NNPDF parton distribution functions [121]. Showering and hadronisation were performed using PYTHIA 8 [68], and we have used MADANALYSIS 5 (V1.6.40) [122–124] to handle the simulation of the response of the CMS detector (through its interface to DELPHES 3 (V3.4.1) [33] and FASTJET (V3.3.0) [35]) and to recast the CMS analysis of Ref. [93], available from the MadAnalysis 5 Public Analysis Database [125].

The results are presented in Fig. 2.2.17 for c.o.m. energies of 14 and 27 TeV. The two figures depict the reach in the W_R-boson mass M_{W_R} for the two signal regions of Table 2.2.3 for the sneutrino LSP (left) and neutralino LSP (right) scenarios. The two horizontal black lines represent the 2σ (mostly equivalent to a 95% C.L. exclusion) and 3σ statistical significance. For the $14TeV$ analysis, we considered the same SM background as in Ref. [93], appropriately scaled to the required luminosity and assuming relative errors similar to the 35.9 fb^{-1} case. For the 27 TeV analysis, we scaled all background

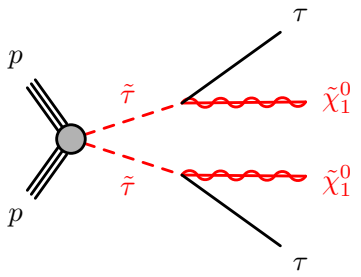

Fig. 2.3.1: Diagram for the $\tilde{\tau}$ pair-production.

contributions by a factor of 3, since the increase in the background cross-sections (for all the dominant channels) is approximately of 3 compared with $\sqrt{s} = 14$ TeV. Whilst this approximation is crude due to lack of information regarding the background contributions from non-prompt leptons and conversions at $\sqrt{s} = 27$ TeV, it allows us to get back-of-the-envelope estimations. As the targeted W_R masses are way larger than the electroweakino masses, the overall cut efficiencies do not change by more than 10%, so that uniform signal selection efficiencies could be considered throughout the entire W_R mass range of $[2, 7.5]$ TeV. We however include in our estimations the effect of a 10% variation on the background uncertainties, as depicted by the dashed lines.

The **SRD16** region proves to be the more favoured channel for both benchmark scenarios mainly because it features an almost background-free environment. It would even be more significant for a tau sneutrino LSP, as this leads to chargino decays into tau leptons. Our calculations however only consider cases where the sneutrino LSP is the electron sneutrino, so that they could be taken as conservative. The reach to sneutrino LSP scenarios is however better, as could be expected from the potentially substantial mass gap featured by the particle spectrum. Multiple hard leptons can indeed arise from the cascade decays, in contrast to the higgsino LSP scenarios where the decay products have softer momenta as the spectrum is more compressed. We observe that for sneutrino and neutralino LSP scenarios, W_R-boson masses up to respectively about 4.5 TeV and 4.2 TeV can be reached while providing enough events for electroweakinos signal sensitivity, when considering 3 ab^{-1} of proton-proton collisions at $\sqrt{s} = 14$ TeV. With $\sqrt{s} = 27$ TeV and $\mathcal{L} = 15$ ab^{-1}, the reach extends to about 6.5 TeV and 5.7 TeV respectively. All the limits are obtained from the sole **SRD16** signal region, so that the **SRA44** region could be used as a confirmatory channel if some excess would be observed.

In conclusion, within the LRSUSY framework, W_R-boson-induced neutralino and chargino production could be used as a probe for dark-matter motivated scenarios. The HL and HE phases of the LHC could hence push the limits on the sensitivity to electroweakino searches as well as on the W_R-boson mass, relying on multilepton production in association with missing transverse momentum.

2.3 Searches for Sleptons: stau pair production at HE- and HL-LHC

Slepton pair production cross sections are less than 1 fb^{-1} for sparticles above 400 GeV at 14 TeV c.o.m. energy, hence searches for these processes will benefit considerably of the large datasets to be collected at the HL-LHC. In many SUSY scenarios with large $\tan\beta$, the stau ($\tilde{\tau}$) is lighter than the selectron and smuon, resulting in tau-rich final states. Co-annihilation processes favour a light stau that has a small mass splitting with a bino LSP, as it can set the relic density to the observed value. Searches for $\tilde{\tau}$ pair production are presented in this section using final state events with at least one hadronically decaying τ lepton as performed by ATLAS and CMS.

The simplified model used for the optimisation of the searches and the interpretation of the results is shown in Fig. 2.3.1. Assumptions on the mixture of left- and right-handed τ leptons as considered by the experiments are detailed where relevant.

Selection	SR-low [GeV]	SR-med [GeV]	SR-high [GeV]	SR-exclHigh [GeV]
$p_{\mathrm{T\,jet}} >$	40	40	20	-
$p_{\mathrm{T}\tau 1} >$	150	200	200	200
$m_{\mathrm{T}\tau 1} + m_{\mathrm{T}\tau 2} >$	500	700	800	800
$m_{\mathrm{T2}}(\tau 1, \tau 2)$	$\in [80, \infty]$	$\in [130, \infty]$	$\in [130, \infty]$	$\in [80, 130]$
				$\in [130, 180]$
				$\in [180, 230]$
				$\in [230, \infty]$

Table 2.3.1: Summary of selection requirements for the direct stau signal regions.

2.3.1 Searches for $\tilde{\tau}$ pair production in the hadronic channel ($\tau_h\tau_h$) at ATLAS at the HL-LHC

Contributors: H. Cheng, D. Xu, C. Zhu, X. Zhuang, ATLAS

In the ATLAS search [84], two models describing the direct production of stau are employed: one considers stau partners of the left-handed τ lepton ($\tilde{\tau_L}$), and a second considers stau partners of the right-handed τ lepton ($\tilde{\tau_R}$). In both models, the stau decays with a branching fraction of 100% to the SM tau-lepton and the LSP. A search for stau production is presented here, which uses a final state with two hadronically decaying τ leptons, low jet activity, and large missing transverse energy ($E_{\mathrm{T}}^{\mathrm{miss}}$) from the $\tilde{\chi}_1^0$ and neutrinos. The SM background is dominated by W+jets, multi-boson production and top pair production.

The event pre-selection is based on that of the previous 8 TeV analysis [126] and 13 TeV analysis [127]. Hadronically decaying taus are selected with $p_{\mathrm{T}} > 20$ GeV and $|\eta| < 4$, while electrons and muons are selected with $p_{\mathrm{T}} > 10$ GeV and $|\eta| < 2.47$ ($|\eta| < 2.5$ for muons). Jets are reconstructed with the anti-k_t algorithm with a radius parameter of 0.4, with $p_{\mathrm{T}} > 20$ GeV and $|\eta| < 4$. To remove close-by objects from one another, an overlap removal based on ΔR is applied. In processes where jets may be misidentified as hadronically decaying taus, each jet is assigned a weight corresponding to the tau fake rate in the HL-LHC detector performance parameterisation.

Events are selected with exactly two tightly identified hadronic taus with $|\eta| < 2.5$, and the two taus must have opposite electric charge (OS). The tight tau algorithm correctly identifies one-prong (three-prong) taus with an efficiency of 60% (45%), with a light-flavour jet misidentification probability of 0.06% (0.02%). Events with electrons, muons, b-jets or forward jets ($|\eta| > 2.5$) are vetoed. The effect of a di-tau trigger is considered by requiring that the leading tau p_{T} is larger than 50 GeV and the sub-leading tau p_{T} is larger than 40 GeV, with an assumed trigger efficiency of 64%. To suppress the SM background, a loose jet veto is applied that rejects events containing jets with $|\eta| < 2.5$ and $p_{\mathrm{T}} > 100$ GeV.

Since the SUSY signal involves two undetected $\tilde{\chi}_1^0$, the resulting $E_{\mathrm{T}}^{\mathrm{miss}}$ spectrum tends to be harder than that for the the major SM backgrounds, thus $E_{\mathrm{T}}^{\mathrm{miss}} > 200$ GeV is required to reject the multi-jet background. A Z veto is imposed, where the invariant mass of the two taus, $m_{\tau\tau}$, is required to be larger than 100 GeV to suppress contributions from $Z/\gamma^* + \mathrm{jets}$ production. To suppress the top quark and multi-jet backgrounds, the sum of the two-tau transverse mass defined using the transverse momentum of the leading (next-to-leading) tau and $E_{\mathrm{T}}^{\mathrm{miss}}$, must be larger than 450 GeV. The transverse mass requirement of $m_{\mathrm{T2}} > 35$ GeV is used to to further suppress the top, W+jets and $Z/\gamma^* + \mathrm{jets}$ backgrounds.

In order to increase the discrimination power between signal and SM backgrounds several kinematic variables are further applied: the p_{T} of the next-to-leading tau, $p_{\mathrm{T}\tau 2} > 75$ GeV, and the angular separation between the leading and next-to-leading tau is required to be $\Delta\phi(\tau 1, \tau 2) > 2$ and $\Delta R(\tau 1, \tau 2) < 3$.

Following these preselection requirements, three signal regions are defined to maximise model-

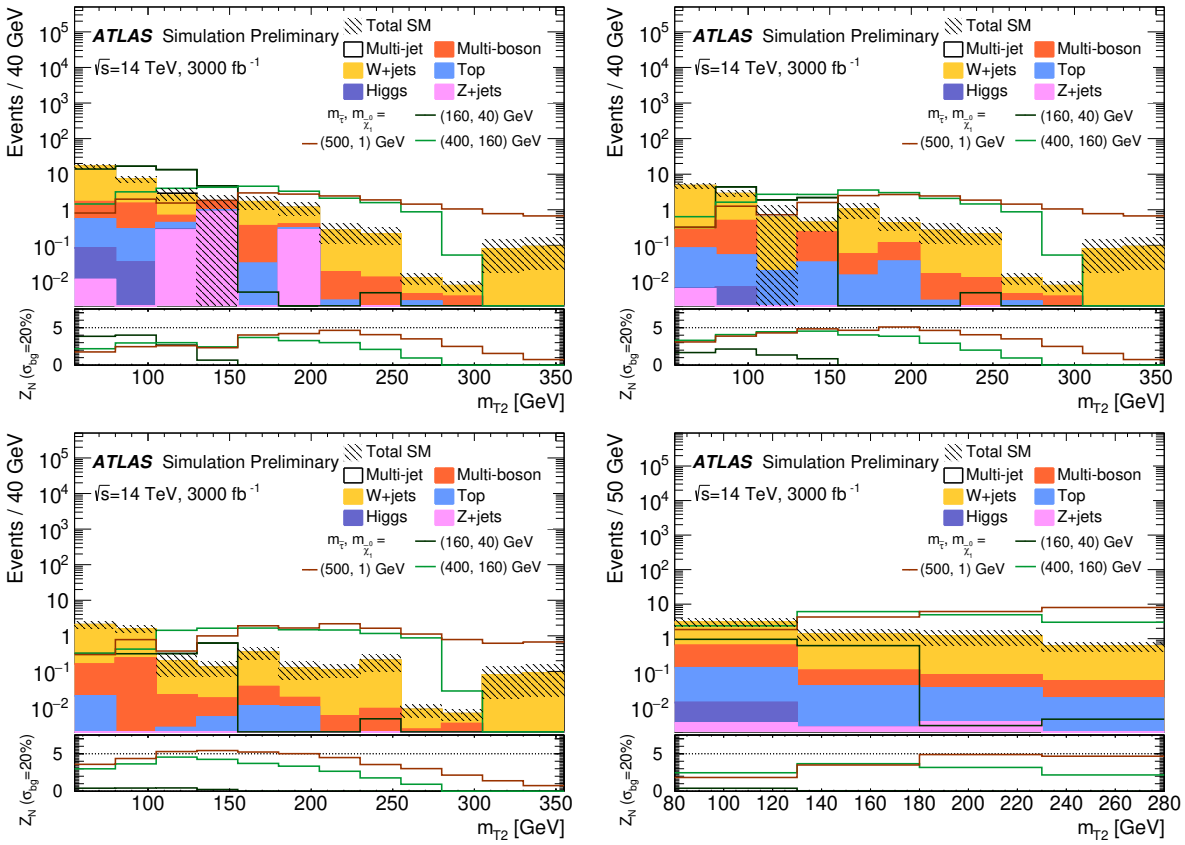

Fig. 2.3.2: Distributions of each m_{T2} variable in the SR-low, SR-med, SR-high and SR-exclHigh regions, applying all selections as Table 2.3.1 with the exception of m_{T2} itself. The stacked histograms show the expected SM backgrounds normalised to 3 ab^{-1}. The hatched bands represent the statistical uncertainties on the total SM background. For illustration, the distributions of the SUSY reference points are also shown as dashed lines. The lower pad in each plot shows the significance, Z_N using a background uncertainty of 20%, for the SUSY reference points. In the SR-exclHigh plot, the sensitivity distribution is the distribution for each m_{T2} bin.

independent discovery sensitivity targeting scenarios with low (SR-low), medium (SR-med) and high (SR-high) mass differences between the $\tilde{\tau}$ and $\tilde{\chi}_1^0$. A set of disjoint signal regions binned in m_{T2} are also defined to maximise model-dependent exclusion sensitivity based on the previous SR-high signal region with the jet veto threshold cut removed. Each SR is identified by the range of the m_{T2}. All signal regions are shown in Table 2.3.1.

Figure 2.3.2 shows the distributions of m_{T2} in these signal regions, applying all SR selections with the exception of m_{T2} itself.

The systematic uncertainties are evaluated based on the SR-high systematic uncertainty in Ref. [127]. A few of the experimental uncertainties are expected to be smaller at the HL-LHC compared to the 13 TeV studies. In particular, the tau energy scale in-situ uncertainty is scaled by a factor of 0.6 and the tau ID efficiency uncertainty is scaled by a factor of $0.45 - 0.9$. The multi-jet uncertainties scale with the increased integrated luminosity, and the background theoretical uncertainties are halved. The theoretical cross-section uncertainty for direct stau production is taken as 10%, while the MC/data related systematics are considered negligible. All other uncertainties are assumed to be the same as in the 13 TeV studies. In this assumption, the total background experimental uncertainty is $\sim 19\%$, with theoretical uncertainties on the Top, $Z/\gamma^* + \mathrm{jets}$ and Higgs backgrounds of 13%, theoretical uncertainties on the W+jets and multi-jet backgrounds of 10%, and uncertainties on the multi-boson background of 8%. This is referred to as the "Baseline uncertainty" scenario. The total uncertainty on the SUSY signal

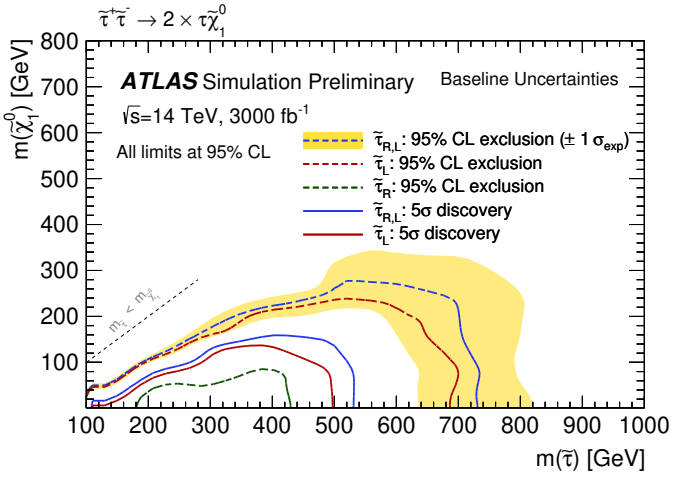

Fig. 2.3.3: 95% C.L. exclusion limits and 5σ discovery contours for 3 ab^{-1}luminosity on the pure $\tilde{\tau_L}\tilde{\tau_L}$ or $\tilde{\tau_R}\tilde{\tau_R}$ and combined $\tilde{\tau_L}\tilde{\tau_L}$, $\tilde{\tau_R}\tilde{\tau_R}$ production in HL-LHC under the baseline systematic uncertainty assumptions.

is $\sim 14\%$. Another scenario is also considered, where the expected uncertainties at the HL-LHC do not improve upon the 13 TeV studies for the SM background and signal. This results in a total background uncertainty of $\sim 38\%$ and a signal uncertainty of $\sim 21\%$ and is referred to as "Run-2 scenario".

To calculate the discovery potential, SR-low, SR-med and SR-High defined in Table 2.3.1 are used, while for the final exclusion limit, the best expected exclusion resulting from these and one additional region, SR-exclHigh, are used. The 95% C.L. exclusion limits and 5σ discovery contours on the combined $\tilde{\tau_L}\tilde{\tau_L}$ and $\tilde{\tau_R}\tilde{\tau_R}$ production, and separate $\tilde{\tau_L}\tilde{\tau_L}$ and $\tilde{\tau_R}\tilde{\tau_R}$ productions under baseline systematic uncertainty assumptions are shown in Fig. 2.3.3. The exclusion limit reaches 730 GeV in $\tilde{\tau}$ mass for the combined $\tilde{\tau_L}\tilde{\tau_L}$ and $\tilde{\tau_R}\tilde{\tau_R}$ production, and 690 GeV (430 GeV) for pure $\tilde{\tau_L}\tilde{\tau_L}$ (pure $\tilde{\tau_R}\tilde{\tau_R}$) production with a massless $\tilde{\chi}_1^0$. The discovery sensitivity reaches $110-530$ GeV ($110-500$ GeV) in $\tilde{\tau}$ mass for the combined $\tilde{\tau_L}\tilde{\tau_L}$ and $\tilde{\tau_R}\tilde{\tau_R}$ (pure $\tilde{\tau_L}\tilde{\tau_L}$) production with a massless $\tilde{\chi}_1^0$. No discovery sensitivity is found for pure $\tilde{\tau_R}\tilde{\tau_R}$ production as the production cross section is very small although a further reduction of the systematic uncertainties might open a window for discovery in the $100-200$ GeV mass range. In general, sensitivity is achieved for scenarios with large mass difference between the stau and neutralino, *i.e.* $\Delta m(\tilde{\tau}, \tilde{\chi}_1^0) > 100$ GeV.

Under the assumption where the expected uncertainties at the HL-LHC do not improve upon the 13 TeV (Run-2 scenario), the exclusion limit is reduced slightly, which down to 720 GeV in $\tilde{\tau}$ mass for the combined $\tilde{\tau_L}\tilde{\tau_L}$ and $\tilde{\tau_R}\tilde{\tau_R}$ production and 670 GeV (400 GeV) for pure $\tilde{\tau_L}\tilde{\tau_L}$ (pure $\tilde{\tau_R}\tilde{\tau_R}$) production with a massless $\tilde{\chi}_1^0$. The discovery sensitivity is also slightly reduced by about $20-50$ GeV.

2.3.2 *Searches for $\tilde{\tau}$ pair production in the $\tau_h\tau_h$ and $\tau_\ell\tau_h$ channels at CMS at the HL-LHC*

Contributors: I. Babounikau, A. Canepa, O. Colegrove, V. Dutta, I. Melzer-Pellmann, CMS

CMS investigates the expected reach for direct stau ($\tilde{\tau}$) pair production, where the $\tilde{\tau}$ decays to a τ and the lightest SUSY particle, the neutralino ($\tilde{\chi}_1^0$) [128]. Final states with either two hadronically decaying tau leptons (τ_h) or one τ_h and one electron or muon, referred to in the following as the $\tau\tau$ and $\ell\tau$ channels, respectively, are considered. In both cases we expect missing transverse momentum from the two LSPs.

The search assumes $\tilde{\tau}$ pair production in the mass-degenerate scenario. The cross-sections have been computed for $\sqrt{s} = 14$ TeV at NLO using the Prospino code [129]. Final values are calculated using the PDF4LHC recommendations for the two sets of cross sections following the prescriptions of the LHC SUSY Cross Section Working Group [61].

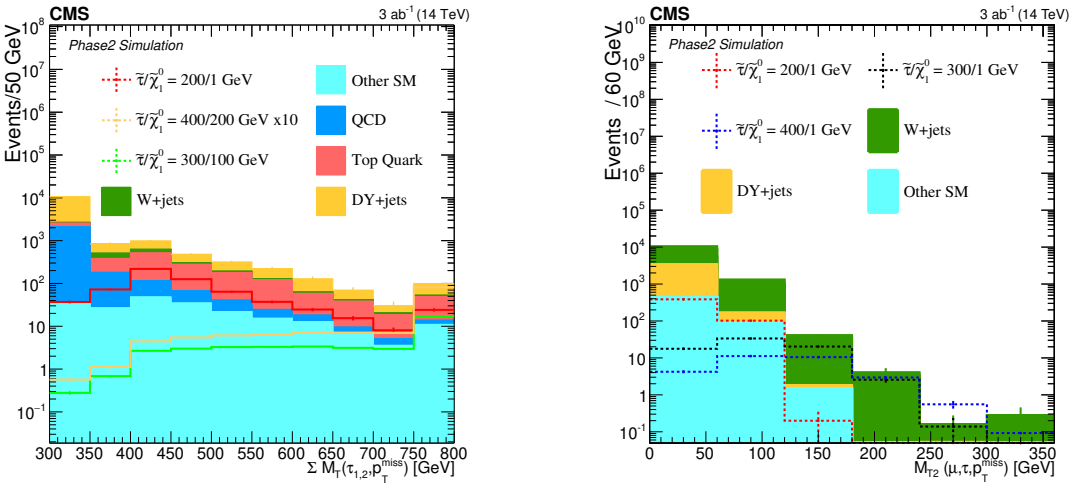

Fig. 2.3.4: Example plots for the main search variables: ΣM_T for the $\tau\tau$ analysis (left), and M_{T2} for the $\mu\tau$ analysis (right), both after the baseline selection.

The event selection for each final state requires the presence of exactly two reconstructed leptons with opposite charges, corresponding to the $\tau\tau$ or $\ell\tau$ final states. In order to pass the selection, electrons (muons) are required to have transverse momentum $p_T > 30$ GeV and pseudorapidity $|\eta| < 1.6(2.4)$ and a minimum azimuthal angle between each other of 1.5. Dedicated lepton identification criteria are applied, providing 50% to 90% efficiency for muons and 25% to 80% efficiency for electrons, depending on p_T and η. Both muons and electrons are required to be isolated.

The momentum of the τ_h candidates is required to be above 40 GeV in the $\ell\tau$ final state, while we require $p_T > 50$ GeV for the τ_h in the $\tau\tau$ final state. For both final states, the τ_h is required to be within $|\eta| < 2.3$. A tight working point is chosen for the τ_h identification in order to obtain a small rate of jets being misidentified as τ_h. The τ_h reconstruction efficiency for this working point is about 30%, with a fake rate of about 0.08% assuming an MVA optimisation. Overlaps between the two reconstructed leptons in the $\ell\tau$ final state are avoided by requiring them to have a minimum separation of $\Delta R > 0.3$.

In the $\ell\tau$ final state, all events with at least one jet are rejected. In the $\tau\tau$ channel, in order to suppress backgrounds with top quarks, we veto events containing any b-tagged jet with $p_T > 40$ GeV identified with the loose CSV working point in both final states, which corresponds to an identification efficiency of about $60 - 65\%$.

The main background for the $\tau\tau$ final state after this selection consists of quantum chromodynamics (QCD) multijet events, W+jets, DY+jets, and top quark events. Separating the background into prompt τ_h events, where both reconstructed taus are matched to a generator τ_h, and misidentified events, where one or more non-generator matched jets has been misidentified as prompt τ_h, we find that the misidentified background dominates our search regions.

In the $\ell\tau$ final state, all events with at least one jet are rejected. Due to kinematical constrains in the signal, we reduce the background from QCD multijet events by requiring a maximum separation of the two leptons in ΔR of 3.5.

In order to further improve discrimination against the SM background, we take advantage of the expected presence of two $\tilde{\chi}_1^0$ in the final state for signal events, which would lead to missing transverse momentum, $\vec{p_T}_{miss}$, defined as the projection onto the plane perpendicular to the beam axis of the negative vector sum of the momenta of all reconstructed objects in an event. Its magnitude, referred to as $\mathbf{p}_{\mathrm{T}}^{\mathrm{miss}}$, is an important discriminator between signal and SM background.

Events are then further selected using discriminating kinematic variables for each of the two final states to improve the sensitivity of the search to a range of sparticle masses, such as the trans-

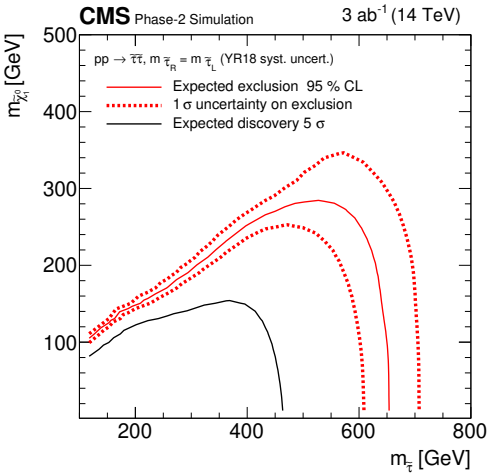

Fig. 2.3.5: Expected upper limits at the 95% C.L. (dashed line) and the 5σ discovery potential (full line) for the combination of the results of the $\tau\tau$ and $\ell\tau$ channels.

verse mass, $M_T(\ell, \vec{p_T}_m iss) \equiv \sqrt{2p_\ell \mathbf{p}_\mathrm{T}^\mathrm{miss}(1-\cos\Delta\phi(\vec{p}_\ell, \vec{p_T}_{miss}))}$, where ℓ represents the lepton. In addition, the scalar sum of the M_T calculated with the highest p_T (ℓ_1) and second highest p_T (ℓ_2) lepton and the missing transverse momentum is used to further reduce the background events: $\sum M_T = M_T(\ell_1, \vec{p_T}_{miss}) + M_T(\ell_2, \vec{p_T}_{miss})$. Finally the stransverse mass M_{T2} [130, 131] is used to discriminate the signal from the background.

The main variables that are used to define the search regions in the $\tau\tau$ final state are ΣM_T and M_{T2}, where the former is shown for the baseline selection in Fig. 2.3.4 (left). While we apply a stringent requirement of at least 400 GeV for ΣM_T, we require M_{T2} to be above 50 GeV. The $\tau\tau$ search regions are then binned in $M_{\mathrm{T2}}, \Sigma M_T$, and the number of jets n_{jet}.

In the $\ell\tau$ final state, we require $M_T(\mu, \vec{p_T}_{miss}) > 120$ GeV, which reduces the W+jets background significantly. To further suppress the SM background in the leptonic final states, $\mathbf{p}_\mathrm{T}^\mathrm{miss}$ has to be above 150 GeV, which mainly reduces QCD multijets and Drell Yan events. Additional binning in M_{T2} and the p_T of the τ_h is applied to define the search regions in the $\ell\tau$ selection. Figure 2.3.4 (right) shows the M_{T2} distribution after the baseline selection.

The dominant experimental uncertainties are those originating from jets being misidentified as τ_h (15%), τ_h identification efficiency (2.5%), the muon identification efficiency (0.5%), the electron identification efficiency (1%), the jet energy scale (1−3.5%) and resolution (3−5%), b-tagging efficiency (1%) and the integrated luminosity (1%). These systematic uncertainties are correlated between the signal and the irreducible background yields.

The expected upper limits and the discovery potential are given in Fig. 2.3.5. In mass-degenerate scenarios, degenerate production of τ sleptons are excluded up to 650 GeV with the discovery contour reaching up to 470 GeV for a massless neutralino. The $\tau\tau$ analysis has been found to drive the sensitivity, but adding the $\ell\tau$ channel enlarges the exclusion bounds by about $60 - 80$ GeV.

2.3.3 Remarks on stau pair production searches at HL-LHC

Prospects for stau pair production presented by ATLAS and CMS in the previous sections generally cover a similar region of the stau-neutralino mass plane. Stau masses up to 730 GeV are excluded by ATLAS for scenarios with large mass difference between stau and neutralino, *i.e.* $\Delta m(\tilde{\tau}, \tilde{\chi}_1^0) > 100$ GeV. CMS contours reach up to about 650 GeV covering a similar region in the parameter space. Differences in the reaches are small but noticeable, and are briefly highlighted in the following. The main difference between the ATLAS and CMS searches is the definition of the tau object. ATLAS has optimised the

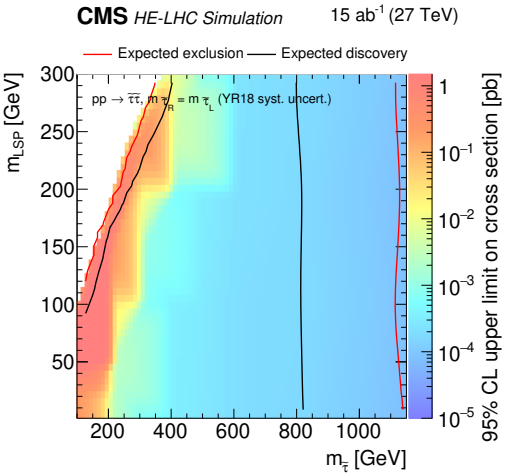

Fig. 2.3.6: Expected upper limits at the 95% C.L. (red line) and the 5σ discovery potential (black line) for the combination of the results of the $\tau\tau$ and $\ell\tau$ channels for HE-LHC.

so-called working point (WP), *i.e.* the combination of selection requirements leading to a certain level of identification efficiency and jet-rejection rate, and chosen a WP leading to 45% to 60% efficiency as a function of p_T and an average jet-rejection rate of 0.6% (0.02%) for 1-prong (3-prong) taus. The CMS analysis considers a tighter WP, resulting in an almost negligible level of misidentified taus but with lower efficiency ($\sim$ 30%). This leads to a small difference in terms of acceptance $\times$ efficiency which translates to 80 (50) GeV differences in the exclusion (discovery) contours.

Finally, we underline that the sensitivity to more compressed scenarios, as predicted in theoretically favoured co-annihilation scenarios, might be partially recovered exploiting the presence of a high p_T ISR jet, similarly to studies presented in Section 2.2.5. For this, identification of tau objects at low p_T will be crucial.

2.3.4 Searches for $\tilde{\tau}$ pair production in the $\tau_h\tau_h$ and $\tau_\ell\tau_h$ channels at CMS at HE-LHC

Contributors: I. Babounikau, A. Canepa, O. Colegrove, V. Dutta, I. Melzer-Pellmann, CMS

On top of the CMS HL-LHC analysis, we also study the influence of the increased cross section for 27 TeV and the increased luminosity of 15 ab^{-1} expected to be achieved in HE-LHC [128]. For this study the cross sections of all backgrounds and signal contributions are recalculated for $\sqrt{s} = 27$ TeV at NLO using PROSPINO. The signal region definition and kinematic distributions are the same as described in Section 2.3.2 for the HL-LHC study, but are scaled with the new cross sections and luminosity. The main gain in sensitivity comes from the increased luminosity, since the cross section increase for signal is the same order as that for background. The applied uncertainties are the same as for HL-LHC study described in Section 2.3.2.

The expected upper limits and the discovery potential are given in Fig. 2.3.6. In the mass-degenerate scenario, τ slepton production is excluded up to 1150 GeV with the discovery contour reaching up to 810 GeV for a massless neutralino. Signal events were generated up to neutralino mass of 300 GeV, at which point the discovery (exclusion) potential ranges from $400 - 800$ GeV ($350 - 1100$ GeV).

2.4 Other SUSY signatures and implications on SUSY models

Supersymmetry might manifest in different ways at hadron colliders. Simplified models help in setting the search strategy and illustrate the reach for individual processes, as shown in the prospects presented in previous sections. In this section, analyses of the discovery potential of HL- and HE-LHC are reported

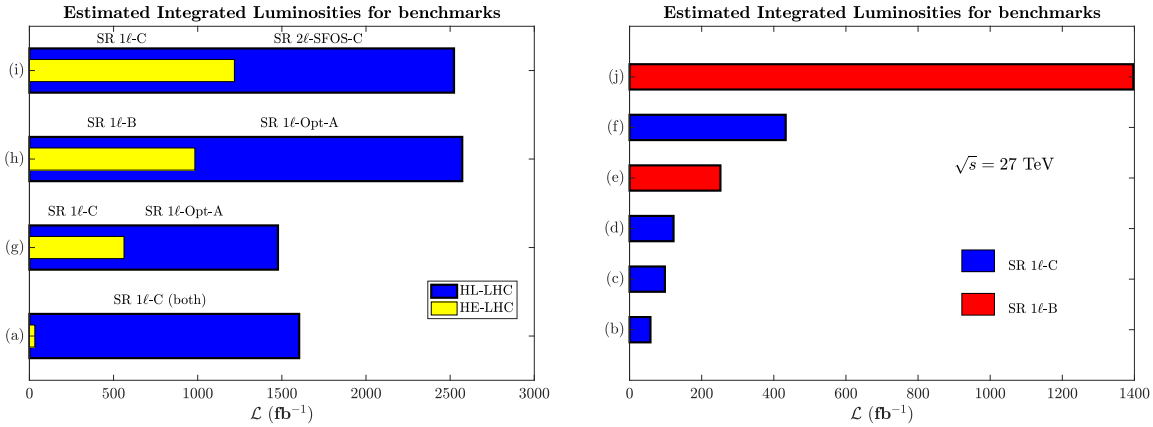

Fig. 2.4.1: Estimated integrated luminosities, $\mathcal{L}$, for a 5σ discovery of the benchmark points of Table 2.4.1. Left: comparison between $\mathcal{L}$ at HL-LHC and HE-LHC for points (a), (g), (h) and (i). Right: HE-LHC analysis for points (b), (c), (d), (e), (f) and (j). The SRs that appear in the panels are as defined in Ref. [132].

considering benchmark points in supergravity grand unified models, light higgsino scenarios, pMSSM and U(1)$'$-extended MSSM models.

2.4.1 SUSY discovery potential at HL- and HE-LHC

Contributors: A. Aboubrahim, P. Nath

We give an analysis of the discovery potential of HE-LHC with respect to the HL-LHC for supersymmetry, based on studies presented in Ref. [132]. Specifically, a set of benchmark points which are discoverable both at HE-LHC and HL-LHC are presented. In addition, we also report on a set of benchmarks which are beyond the reach of HL-LHC but are discoverable at HE-LHC. The models we consider are supergravity grand unified models [133–136] with non-universalities in the gaugino sector. Thus, the models are described by the set of parameters $m_0, m_1, m_2, m_3, A_0, \tan\beta, \mathrm{sgn}(\mu)$ where m_0 is the universal scalar mass (which can be large consistent with naturalness [137]), m_1, m_2, m_3 are the $U(1), SU(2)_L, SU(3)_C$ gaugino masses, A_0 is the universal trilinear coupling, and $\tan\beta = \langle H_2\rangle/\langle H_1\rangle$ is the ratio of the Higgs VEVS . The analysis is done under the constraints of Higgs boson mass and the relic density constraints which requires coannihilation [138–140]. The analysis uses signatures involving a single charged lepton and jets, two charged leptons and jets and three charged leptons and jets, resulting from the decay of a gluino pair (points (a)-(f) of Table 2.4.1) and the decay of $\tilde{\chi}_2^0\tilde{\chi}_1^\pm$ (points (g)-(j) of Table 2.4.1). It is found that most often the dominant signature is the single lepton and jets signature, indicated as SR-1ℓ-B or C in the figures, depending on the specific selections applied. Twelve different kinematic variables are used to discriminate the signal from the background. These consist of

$$N_{\rm jets},\ E_T^{\rm miss},\ H_T,\ m_{\rm eff},\ R,\ H_{20},\ p_T(j_n),\ m_T^\ell,\ m_T^{\rm min}(j_{1-2}, E_T^{\rm miss}) \tag{2.4.1}$$

where $N_{\rm jets}$ is the number of jets, $E_T^{\rm miss}$ is the missing transverse energy, H_T is the sum of the jets' transverse momenta, $m_{\rm eff}$ is the effective mass, $R = E_T^{\rm miss}/(E_T^{\rm miss} + p_T^\ell)$, H_{20} is the second Fox-Wolfram moment, $p_T(j_n)$ is the $n^{\rm th}$ jet transverse momentum, m_T^ℓ is the leading lepton transverse mass and $m_T^{\rm min}(j_{1-2}, E_T^{\rm miss})$ is the minimum of the transverse masses of the first and second leading jets. Finally, p_T^ℓ denotes the transverse momentum of the leading lepton.

The left panel of Fig. 2.4.1 exhibits four parameter points which are discoverable both at HE-LHC and at HL-LHC. Here one finds that the integrated luminosities needed for discovery at HL-LHC (blue bars) are 2-50 times larger than what is needed at HE-LHC (yellow bars). For these model points one finds that discovery would require an HL-LHC run between 5-8 years while the same parameter points can be discovered in a period of few weeks to ~ 1.5 yr at HE-LHC running at its optimal luminosity of

Model	h^0 [GeV]	μ [TeV]	$\tilde{\chi}_1^0$ [$\times 10^2$ GeV]	$\tilde{\chi}_1^\pm$ [$\times 10^2$ GeV]	$\tilde{t}$ [TeV]	$\tilde{g}$ [TeV]	$\Omega^{\rm th}_{\tilde{\chi}_1^0}h^2$
(a)	124	8.02	9.73	10.6	4.73	1.36	0.039
(b)	125	6.29	10.2	10.3	2.08	1.40	0.035
(c)	123	5.59	11.1	11.9	2.88	1.51	0.048
(d)	124	15.5	11.9	12.7	10.0	1.75	0.048
(e)	124	11.7	9.48	9.48	6.78	1.33	0.020
(f)	124	13.7	12.4	13.5	6.98	1.62	0.112
(g)	124	10.4	1.34	1.51	5.27	3.93	0.121
(h)	124	26.1	1.54	1.76	18.6	5.88	0.105
(i)	124	1.15	1.65	1.89	4.17	6.71	0.114
(j)	125	29.7	1.62	1.87	10.4	15.6	0.105

Table 2.4.1: The Higgs boson (h^0) mass, the μ parameter and some relevant sparticle masses, and the relic density for the benchmark points used in this analysis [132].

2.5×10^{35} cm^{-2}s^{-1}. The right panel of Fig. 2.4.1 gives a set of benchmarks which are not accessible at HL-LHC but will be visible at HE-LHC. We note that half of the benchmarks in the right panel of Fig. 2.4.1 can be discovered with less than 200 fb^{-1} of integrated luminosity at HE-LHC with few months of running at its optimal luminosity. Considering points that are just beyond the HL-LHC reach, point (j) requires a run of $\sim$ 1.6 yr while point (b) $\sim$ 3.5 weeks for discovery at the HE-LHC. In summary, the analysis above indicates that a transition from HL-LHC to HE-LHC can aid in the discovery of supersymmetry for part of the parameter space accessible to both. Further to that, HE-LHC can explore significantly beyond the realm of the parameter space accessible to HL-LHC.

2.4.2 Natural SUSY at HL- and HE-LHC

Contributors: H. Baer, V. Barger, J. Gainer, H. Serce, D. Sengupta, X. Tata

We present HL- and HE-LHC reach calculations for supersymmetry in models with light higgsinos. The light higgsino scenario is inspired by the requirement of naturalness in that if the superpotential (higgsino) mass parameter μ is much beyond the weak scale, then the weak scale soft term $m_{H_u}^2$ will have to be fine-tuned in order to maintain $m_{W,Z,h}$ at their measured mass values.

HL/HE-LHC reach for gluino pair production

In Ref. [141] we evaluated the reach of the HL-LHC for gluino pair production, assuming that $\tilde{g} \to t\tilde{t}_1$ and $\tilde{t}_1 \to b\tilde{\chi}_1^+$ or $t\tilde{\chi}_{1,2}^0$ and that the decay products of the higgsinos $\tilde{\chi}_1^\pm$ and $\tilde{\chi}_2^0$ are essentially invisible.In Ref. [142] we computed the reach of HE-LHC for both gluinos and top squarks in the light higgsino scenario (with $\sqrt{s} = 33$ TeV). These results have been updated for HE-LHC with $\sqrt{s} = 27$ TeV and 15 ab^{-1}of integrated luminosity in Ref. [143] where more details can be found. We use MADGRAPH [67] to generate gluino pair production events and SM backgrounds. We interface MADGRAPH with PYTHIA [68] for initial/final state showering, hadronisation and underlying event simulation. The DELPHES detector simulation [33] is used with specifications as listed in Ref. [142]. SM backgrounds include $t\bar{t}$, $t\bar{t}b\bar{b}$, $t\bar{t}t\bar{t}$, $t\bar{t}Z$, $t\bar{t}h$, $b\bar{b}Z$ and single top production. We require at least four high p_T jets, with two or more identified as b-jets, no isolated leptons and large $E_{\rm T}^{\rm miss}$ selections.

Results are shown in the left panel of Fig. 2.4.2 where we report the gluino pair production signal versus $m_{\tilde{g}}$ for a natural NUHM2 model line with parameter choice $m_0 = 5m_{1/2}$, $A_0 = -1.6m_0$, $m_A = m_{1/2}$, $\tan\beta = 10$ and $\mu = 150$ GeV with varying $m_{1/2}$. The results are not expected to be sensitive to this precise choice of parameters as long as first generation squarks are much heavier than

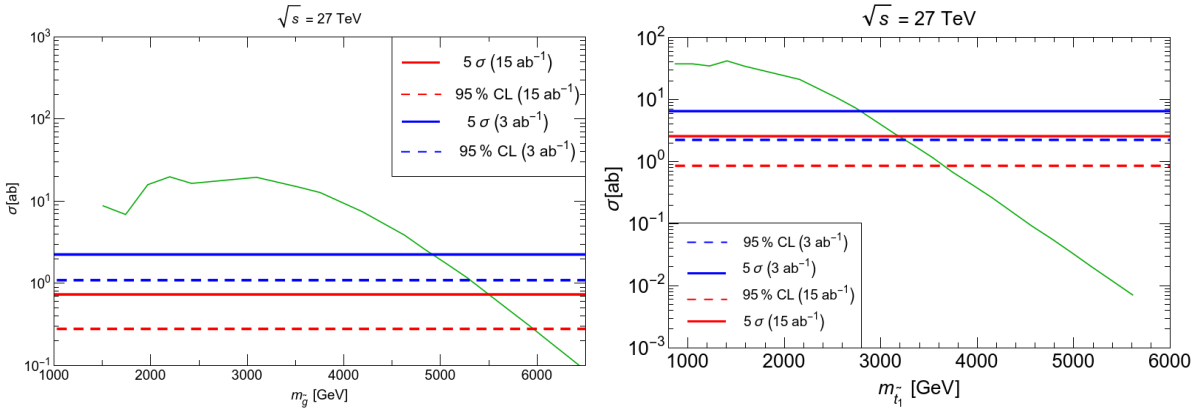

Fig. 2.4.2: Left: gluino pair production cross section vs. $m_{\tilde{g}}$ after selections at HE-LHC with $\sqrt{s} = 27$ TeV (green curve). Right: top-squark pair production cross section vs. $m_{\tilde{t}_1}$ after selections at HE-LHC with $\sqrt{s} = 27$ TeV (green curve). Both panels also show the 5σ reach and 95% C.L. exclusion lines assuming 3 and 15 ab^{-1} of integrated luminosity.

gluinos. From the figure, we see that the 5σ discovery reach of HE-LHC extends to $m_{\tilde{g}} = 4.9$ TeV for 3 ab^{-1} and to $m_{\tilde{g}} = 5.5$ TeV for 15 $\text{ab}^{-1}$of integrated luminosity. The corresponding 95% C.L. exclusion reaches extend to $m_{\tilde{g}} = 5.3$ TeV for 3 ab^{-1} and to $m_{\tilde{g}} = 5.9$ TeV for 15 $\text{ab}^{-1}$of integrated luminosity. The impact of the theoretical uncertainties related to the total production rate of gluinos is not taken into account. For comparison, the 5σ discovery reach of LHC14 is (2.4) 2.8 TeV for an integrated luminosity of (300 fb^{-1}) 3 ab^{-1} [141].

Top-squark pair production

In Ref. [142], the reach of a 33 TeV LHC upgrade for top-squark pair production was investigated. Here, we repeat the analysis but for updated LHC energy upgrade $\sqrt{s} = 27$ TeV. We use MADGRAPH [67] to generate top-squark pair production events within a simplified model where $\tilde{t}_1 \to b\widetilde{\chi}_1^{\pm}$ at 50%, and $\tilde{t}_1 \to t\widetilde{\chi}_{1,2}^0$ each at 25% branching fraction, which are typical of most SUSY models [144] with light higgsinos. The higgsino-like electroweakino masses are $m_{\widetilde{\chi}_{1,2}^0,\widetilde{\chi}_1^{\pm}} \simeq 150$ GeV. We also used MADGRAPH-PYTHIA-DELPHES for the same SM background processes as listed above for the gluino pair production case. We required at least two high p_T b-jets, no isolated leptons and large $E_{\text{T}}^{\text{miss}}$, see Ref. [143] for details.

Using these background rates for LHC at $\sqrt{s} = 27$ TeV, we compute the 5σ reach and 95% C.L. exclusion of HE-LHC for 3 and 15 ab^{-1} of integrated luminosity using Poisson statistics. Our results are shown in the right panel of Fig. 2.4.2 along with the top-squark pair production cross section after cuts versus $m_{\tilde{t}_1}$. From the figure, we see the 5σ discovery reach of HE-LHC extends to $m_{\tilde{t}_1} = 2.8$ TeV for 3 ab^{-1} and to 3.16 TeV for 15 ab^{-1}. The 95% C.L. exclusion limits extend to $m_{\tilde{t}_1} = 3.25$ TeV for 3 ab^{-1} and to $m_{\tilde{t}_1} = 3.65$ TeV for 15 ab^{-1}. We checked that S/B exceeds 0.8 whenever we deem the signal to be observable [143]. For comparison, the Atlas projected 95% C.L. LHC14 reach [145] for 3 ab^{-1} extends to $m_{\tilde{t}_1} \simeq 1.7$ TeV (see Section 2.1 for details) assuming $\tilde{t}_1 \to t\widetilde{\chi}_1^0$ decays.

Combined reach for stops and gluinos

In Fig. 2.4.3 we exhibit the gluino and top-squark reach values in the $m_{\tilde{t}_1}$ vs. $m_{\tilde{g}}$ plane. We compare the reach of HL- and HE-LHC to values of gluino and stop masses (shown by the dots) in a variety of natural SUSY models defined to have $\Delta_{\text{EW}} < 30$ [146,147], [1] including the two- and three-extra parameter non-universal Higgs models [149] (nNUHM2 and nNUHM3), natural generalised mirage mediation [150]

[1] The onset of fine-tuning for larger values of Δ_{EW} is visually displayed in Ref. [148].

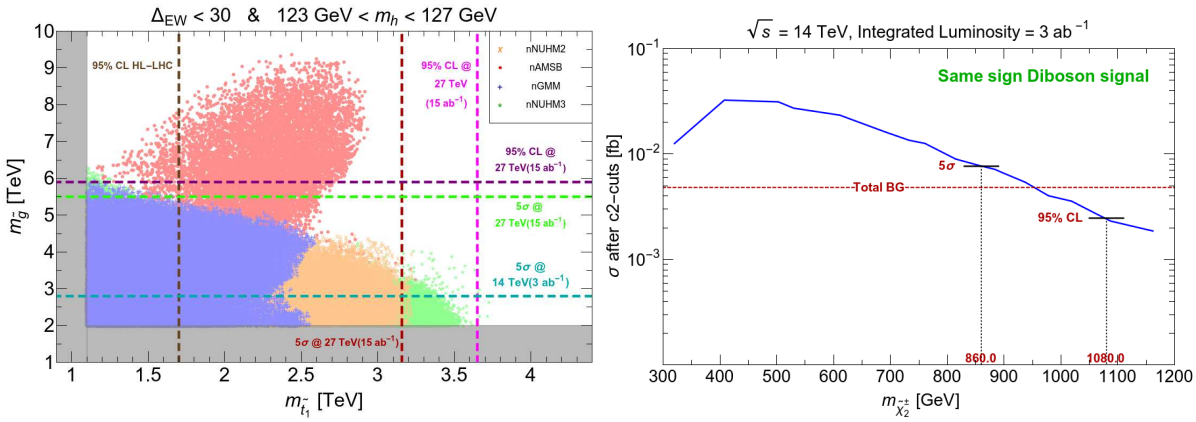

Fig. 2.4.3: Left: points in the $m_{\tilde{t}_1}$ vs. $m_{\tilde{g}}$ plane from a scan over nNUHM2, nNUHM3, nGMM and nAMSB model parameter space. We compare to recent search limits from the ATLAS/CMS experiments (shaded regions) and show the projected reach of HL- and HE-LHC. Right: cross section for SSdB production after cuts versus wino mass at the LHC with $\sqrt{s} = 14$ TeV. We show the 5σ and 95% C.L. reach assuming a HL-LHC integrated luminosity of 3 ab^{-1}.

(nGMM) and natural anomaly-mediation [151] (nAMSB). These models all allow for input of the SUSY μ parameter at values $\mu \sim 100 - 350$ GeV which is a necessary (though not sufficient) condition for naturalness in the MSSM.

The highlight of this figure is that at least one of the gluino or the stop should be discoverable at the HE-LHC. We also see that in natural SUSY models (with the exception of nAMSB), the highest values of $m_{\tilde{g}}$ coincide with the lowest values of $m_{\tilde{t}_1}$ while the highest top squark masses occur at the lowest gluino masses. Thus, a marginal signal in one channel (due to the sparticle mass being near their upper limit) should be accompanied by a robust signal in the other channel. Over most of the parameter range of weak scale natural SUSY there should be a 5σ signal in *both* the top-squark and gluino pair production channels at HE-LHC.

Same-sign diboson signature from wino pair production

The wino pair production reaction $pp \to \tilde{\chi}_2^\pm \tilde{\chi}_4^0$ can occur at observable rates for SUSY models with light higgsinos. The decays $\tilde{\chi}_2^\pm \to W^\pm \tilde{\chi}_{1,2}^0$ and $\tilde{\chi}_4^0 \to W^\pm \tilde{\chi}_1^\mp$ lead to final state dibosons which half the time give a relatively jet-free same-sign diboson signature (SSdB). This has only tiny SM backgrounds [89, 97, 152] and excellent prospects for discovery.

We have computed the reach of HL-LHC for the SSdB signature in Fig. 2.4.3 including $t\bar{t}$, WZ, $t\bar{t}W$, $t\bar{t}Z$, $t\bar{t}t\bar{t}$, WWW and $WWjj$ backgrounds. For LHC14 with 3 ab^{-1} of integrated luminosity, the 5σ reach extends to $m(\text{wino}) \sim 860$ GeV while the 95% C.L. exclusion extends to $m(\text{wino}) \sim 1080$ GeV. In models with unified gaugino masses, these would correspond to a reach in terms of $m_{\tilde{g}}$ of 2.4 (3) TeV, respectively. These values are comparable to what LHC14 can achieve via gluino pair searches with 3 ab^{-1}. The SSdB signature is distinctive for the case of SUSY models with light higgsinos.

While Fig. 2.4.3 presents the HL-LHC reach for SUSY in the SSdB channel, the corresponding reach of HE-LHC has not yet been computed. The SSdB signal arises via EW production, and the signal rates are expected to rise by a factor of a few by moving from $\sqrt{s} = 14$ TeV to $\sqrt{s} = 27$ TeV. In contrast, some of the strongly-produced SM backgrounds like $t\bar{t}$ production will rise by much larger factors. Thus, it is not yet clear whether the reach for SUSY in the SSdB channel will be increased by moving from HL-LHC to HE-LHC. We note though that other signals channels from wino decays to higgsinos plus a W, Z and Higgs boson may offer further SUSY detection possibilities.

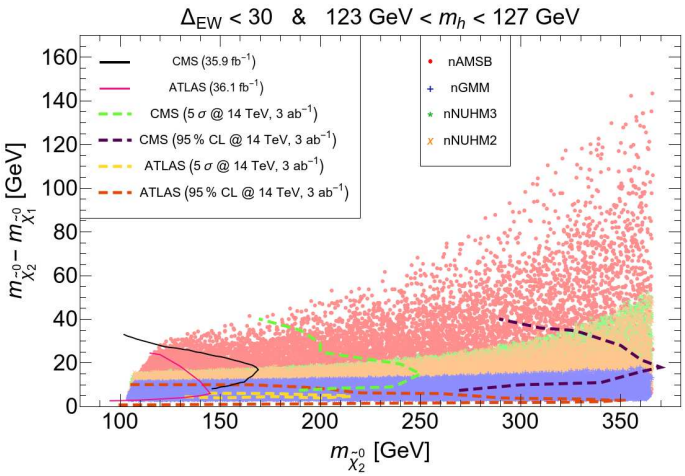

Fig. 2.4.4: Points in the $m_{\tilde{\chi}_2^0}$ vs. $m_{\tilde{\chi}_2^0} - m_{\tilde{\chi}_1^0}$ plane from a scan over nNUHM2, nNUHM3, nGMM and nAMSB model parameter space. We compare to recent search limits from the ATLAS/CMS experiments and to future reach contours for HL-LHC.

Higgsino pair production at LHC upgrades

The four higgsino-like charginos $\tilde{\chi}_1^{\pm}$ and neutralinos $\tilde{\chi}_{1,2}^0$ are the only SUSY particles required by naturalness to lie near to the weak scale at $m_{weak} \sim 100$ GeV. In spite of their lightness, they are very challenging to detect at LHC. The lightest neutralino evidently comprises just a portion of dark matter [153], and if produced at LHC via $pp \to \tilde{\chi}_1^0\tilde{\chi}_1^0$, $\tilde{\chi}_1^{\pm}\tilde{\chi}_1^{\mp}$ and $\tilde{\chi}_1^{\pm}\tilde{\chi}_{1,2}^0$ could escape detection. This is because the decay products of $\tilde{\chi}_2^0$ and $\tilde{\chi}_1^{\pm}$ are expected to be very soft, causing the signal to be well below SM processes like WW and $t\bar{t}$ production. The monojet signal arising from initial state radiation (ISR) $pp \to \tilde{\chi}_1^0\tilde{\chi}_1^0 j$, $\tilde{\chi}_1^{\pm}\tilde{\chi}_1^{\mp} j$ and $\tilde{\chi}_1^{\pm}\tilde{\chi}_{1,2}^0 j$ has been evaluated in Ref. [154] and was found to have similar shape distributions to the dominant $pp \to Zj$ background but with background levels about 100 times larger than signal. However, at HE-LHC harder monojet-like selections may be possible [155], and generic prospects studies are presented in Section 3.1 of this report.

A way forward has been proposed via the $pp \to \tilde{\chi}_1^0\tilde{\chi}_2^0 j$ channel where $\tilde{\chi}_2^0 \to \ell^+\ell^-\tilde{\chi}_1^0$: a soft opposite-sign dilepton pair recoils against a hard initial state jet radiation which serves as a trigger [156]. Experimental prospect searches presented in Section 2.2.5 by ATLAS and CMS exploit this kind of signature. The projected reach for 5σ and 95% C.L. reach at the HL-LHC with 3 ab^{-1} in $\ell^+\ell^- E_{\rm T}^{\rm miss}$ final state events are shown in the $m_{\tilde{\chi}_2^0}$ vs. $m_{\tilde{\chi}_2^0} - m_{\tilde{\chi}_1^0}$ plane in Fig. 2.4.4. The ATLAS and CMS experiments contours are shown as the yellow, green, purple and red dashed contours. We see that these contours can probe considerably more parameter space although some of natural SUSY parameter space (shown by dots for the same set of models as in Fig. 2.4.3) might lie beyond these projected reaches. So far, reach contours for HE-LHC in this search channel have not been computed but it is again anticipated that HE-LHC will not be greatly beneficial here since $pp \to \tilde{\chi}_1^0\tilde{\chi}_2^0$ is an EW production process so the signal cross section will increase only marginally while SM background processes like $t\bar{t}$ production will increase substantially.

It is imperative that future search channels try to squeeze their reach to the lowest $m_{\tilde{\chi}_2^0} - m_{\tilde{\chi}_1^0}$ mass gaps which are favoured to lie in the $3-5$ GeV region for string landscape projections [157] of SUSY mass spectra. The Atlas red-dashed contour appears to go a long way in this regard, though the corresponding 5σ reach is considerably smaller.

Summary

We have delineated the reach of the HE-LHC and compared it to the corresponding reach of the HL-LHC for SUSY models with light higgsinos, expected in a variety of natural SUSY models. While the HL-

LHC increases the SUSY search range, it appears that the HE-LHC will definitively probe natural SUSY models with $\Delta_{\rm EW} < 30$ via a 5σ discovery of at least one of the top squark or the gluino (likely even both), possibly also with signals in other channels.

2.4.3 The pMSSM at HL- and HE-LHC

Contributors: A. Arbey, M. Battaglia, F. Mahmoudi

The phenomenological MSSM (pMSSM) [158], contains 20 free parameters, and is the most general CP and R-parity conserving MSSM scenario with minimal flavour violation. It was introduced in order to reduce the theoretical prejudices of the constrained MSSM scenarios. In the following, we consider the case where the lightest neutralino is the LSP and can constitute part or all of the dark matter. Technical details concerning the pMSSM scans and software required for the presented analyses can be found in Ref. [159, 160].

SUSY and Higgs searches:

The direct SUSY searches at the LHC are extremely powerful in probing the strongly interacting sector of the MSSM. Nevertheless, scenarios with compressed spectra or with long decay chains can escape the current searches and remain challenging. In the pMSSM, such cases are not rare, and thus the complementary information from other sectors can be of interest. In particular the Higgs sector, namely the measurement of the couplings of the lightest Higgs boson as well as searches for heavier states can unveil additional MSSM phase space [32], especially during HL and HE runs of the LHC.

In the extended Higgs sector of the MSSM, the couplings of the lightest Higgs boson to up- and down-type quarks are modified by terms inversely proportional to the CP-odd A boson mass as $2M_Z^2/M_A^2 \tan^2\beta$ and $2M_Z^2/M_A^2$ respectively, providing an indirect sensitivity to the scale of M_A, if deviations in the branching fractions to up- and down-type quarks are detected, or a lower bound on M_A, if the coupling properties agree with the SM predictions. At present, the direct sensitivity to the A (and H) boson at the LHC comes mostly from the $pp \to A/H \to \tau^+\tau^-$ process. On the other hand, the bbH associate production and gluon fusion processes decrease the total cross section with $\tan\beta$ up to the point where the b-quark loops take over and the cross section increases. For $\tan\beta < 10$, the decay branching fraction is proportional to $\tan\beta$. Thus, the bounds from the $\tau\tau$ final state become particularly strong for large values of $\tan\beta$ but quite unconstrained for $\tan\beta \simeq 10$.

The modification of the Higgs couplings to fermions induced by loops of strongly interacting SUSY particles, namely the Δ_b correction in the Higgs coupling to $b\bar{b}$ is of special importance, as the SUSY contribution scales with $\mu \tan\beta M_{\tilde{g}}/M^2_{\tilde{g},\tilde{b},\tilde{t}}$. Since the value of $\mu\tan\beta$ can be much larger than the mass of the SUSY particles in the denominator, the SUSY strongly interacting sector does not decouple. Therefore, the study of the Higgs branching fractions, or the Higgs signal strengths, can unravel SUSY scenarios with strongly interacting particles at masses well beyond the kinematic reach of the LHC [161].

The sensitivity to SUSY mass scales is summarised in Fig. 2.4.5, which gives a comparison of the direct and indirect sensitivity to M_A with the mass of the gluino and squarks of the third generation, as a function of the different energies and integrated luminosities of the LHC. Direct searches are accounted for by implementing LHC Run-1 searches in jets + $E_{\rm T}^{\rm miss}$ [162, 163], jets + leptons + $E_{\rm T}^{\rm miss}$ [164–166], leptons + $E_{\rm T}^{\rm miss}$ [85, 167] and monojets [168, 169]. Signal selection cuts corresponding to each of the analyses are applied to these simulated signal events. The number of SM background events in the signal regions are taken from the estimates reported by the experiments. Results are projected to 14 TeV for 300 $\rm fb^{-1}$ and 3 $\rm ab^{-1}$ of integrated luminosity, by generating events at 14 TeV and rescaling the 8 TeV backgrounds by the corresponding increase in cross section and signal cut acceptance at the higher energy [170]. The use of 7 + 8 TeV analyses at the higher energy ensures a constant scaling for the various energy and integrated luminosity conditions considered here. In addition, the constraints from the Higgs signal strengths for the $\gamma\gamma$, WW, ZZ, $\tau\tau$ and $b\bar{b}$ channels have been added. Here we

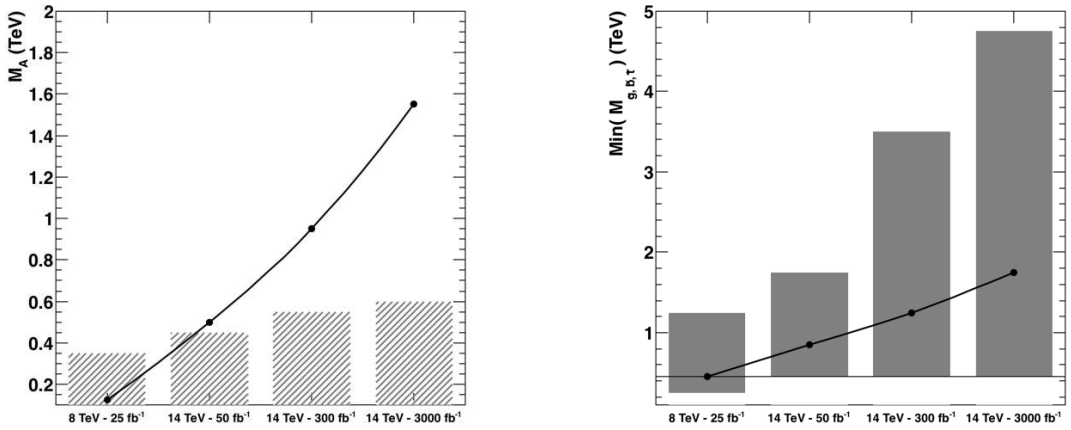

Fig. 2.4.5: Sensitivity to the mass of the CP-odd A boson (left) and the lightest state among $\tilde{g}$, $\tilde{b}$ and $\tilde{t}$ (right) as a function of the energy and luminosity of the LHC, in the pMSSM. The 95% C.L. exclusion range, when the MSSM parameters are varied, are given for the direct search by the continuous line and for the indirect constraints from the h decay properties by the filled bars (from Ref. [161]).

	LHC8 – 25 fb^{-1}	LHC14 – 50 fb^{-1}	LHC14 – 300 fb^{-1}	HL-LHC – 3 ab^{-1}
js+ℓs+MET	0.145	0.570	0.698	0.820
+h^0 μs	0.317	0.622	0.793	0.920

Table 2.4.2: Fractions of pMSSM points excluded by the combination of LHC MET searches, and the LHC Higgs data.

assume SM-like central values and evolve the statistical uncertainties according to the increase of signal events with energy and integrated luminosity [171] following the same procedures as in Ref. [161]. Table 2.4.2 summarises the fraction of pMSSM points with SUSY masses up to 5 TeV excluded by the LHC searches based on $E_{\mathrm{T}}^{\mathrm{miss}}$+jets signatures, and by the addition of the Higgs data.

Monojets

Monojet searches remain a powerful tool for discovery at pp colliders of increasing energy and luminosity and specific prospects for WIMP searches using this signature are presented in this report (Section 3). Beyond those scenarios, the monojet signature can be sensitive to specific MSSM scenarios such as decays with two gluinos or scalar tops and an ISR hard jet, when the scalar top decays are soft enough for the event to be classified as monojet-like. Expanding on the work of [172], we consider here these monojet-like signatures at $\sqrt{s}$ energies of 8, 13, 14 and 27 TeV for two different pMSSM scenarios featuring a light gluino and a light bino neutralino with a mass splitting of 10 GeV, and a light stop and bino-wino neutralino and chargino with a mass splitting slightly smaller than the top quark mass so that the stop decays into three soft jets and the lightest neutralino.

The mass splittings have been chosen to maximise the number of monojet events, and also to ensure the consistency with the dark matter relic density constraint which requires small mass splittings for co-annihilations. It is instructive to consider the scaling of the product of the monojet production cross section times efficiency with respect to the neutralino mass and the collider energy. The acceptance is defined by $\sqrt{s}$-dependent lower cuts on the jet p_T and missing energy ($E_{\mathrm{T}}^{\mathrm{miss}}$), scaled from early LHC monojet and monojet-like analyses [168,169] as discussed in details in Ref. [172]. The results are shown in Fig. 2.4.6. Although the change in cross section times efficiency from 8 to 14 TeV as a function of the mass has been relatively small, the increase in mass coverage afforded by 14 TeV is very significant. This motivates a possible further increase of the energy up to 27 TeV, and beyond.

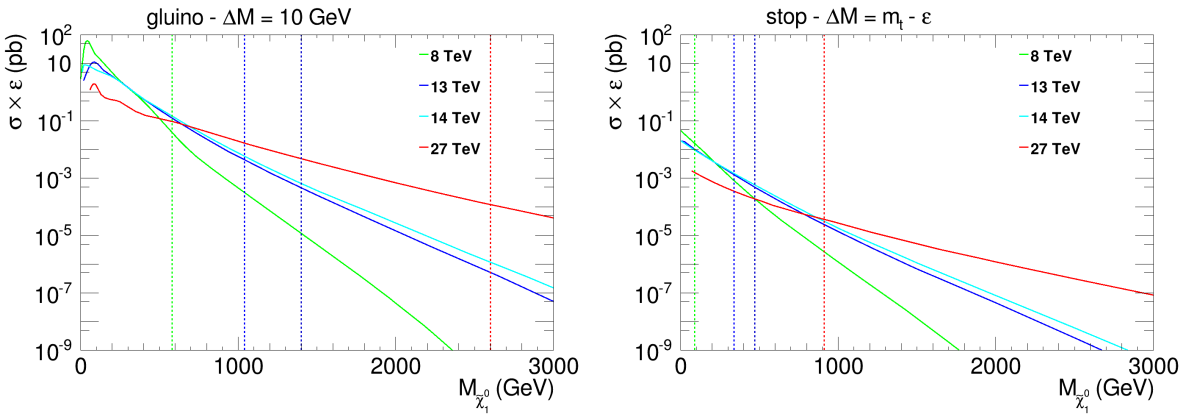

Fig. 2.4.6: Monojet production cross section times acceptance and efficiency as a function of the neutralino mass, for scenarios with a gluino (left) and a stop (right) with small mass splittings with the neutralino LSP. The different curves correspond to $\sqrt{s} = 8$, 13, 14 and 27 TeV LHC c.o.m. energies. The green vertical dashed line corresponds to an indicative exclusion limit by the LHC Run-1, the light (dark) blue line to a prospective limit for the LHC 14 TeV run with 300 fb^{-1} (3 ab^{-1}) of data, and the red line to a potential limit at 27 TeV with 15 $\text{ab}^{-1}$of data.

2.4.4 Z' bosons in supersymmetric and leptophobic scenarios at HL- and HE-LHC

Contributors: J. Y. Araz, G. Corcella, M. Frank, B. Fuks

Searching for heavy neutral vector bosons Z' is one of the challenging objectives of the LHC. Such heavy bosons are predicted by $U(1)'$ models inspired by Grand Unification Theories (GUT) as well as by the Sequential Standard Model (SSM), one of the simplest extensions of the SM wherein Z' and possible W' bosons have the same couplings as the SM Z and W. The LHC experiments have searched for Z' signals by exploring high-mass dilepton and dijet systems and have set exclusion limits of a few TeV on the Z' mass. For studies of Z'-bosons at HL/HE-LHC see Section 6.

While such analyses have assumed that the Z'-boson can only decay into SM channels, recent investigations (see, *e.g.*, Ref. [173, 174]) have considered the possibility that the Z'-boson could decay according to modes BSM, like for instance in supersymmetric final states in the so-called UMSSM framework. From the MSSM viewpoint, extending it via a $U(1)'$ group has the advantage that the extra symmetry forbids a too quick proton decay and allows to stabilise all particle masses with respect to quantum corrections. Regarding the searches, assuming BSM decays lowers the rates into lepton and quark pairs, and therefore milder exclusion limits are to be expected.

Unlike direct sparticle production in pp collisions, the Z' mass sets one further kinematic constrain on the invariant masses of the produced supersymmetric particles. Furthermore, as will be discussed in the following, there are realisations of the $U(1)'$ symmetry wherein, due to the kinetic mixing with the SM $U(1)$ group, the Z' is leptophobic. Leptonic final states can therefore occur, in the UMSSM, only through supersymmetric cascades. Such scenarios avoid the present dilepton bounds and may well be worth to be investigated, especially in the high-luminosity LHC phase.

In what follows we shall review the theoretical framework of our exploration, present some phenomenological results at the HL-LHC and then some final remarks will be given.

Grand-unified theories are based on a rank-6 group E_6, where the symmetry-breaking scheme proceeds via multiple steps:

$$E_6 \to SO(10)\otimes U(1)_\psi \to SU(5)\otimes U(1)_\chi \otimes U(1)_\psi \to SU(3)_C \otimes SU(2)_L \otimes U(1)_Y \otimes U(1)' \,. \quad (2.4.2)$$

The $U(1)'$ symmetry surviving at the EW scale can be expressed as a combination of $U(1)_\chi$ and $U(1)_\psi$, $U(1)' = U(1)_\psi \cos\theta - U(1)_\chi \sin\theta$, where θ is the E_6 mixing angle. The neutral vector bosons associated with $U(1)_\psi$ and $U(1)_\chi$ are called Z'_ψ and Z'_χ, while a generic Z' is given by their mixing.

Parameter	θ	$\tan\beta$	$\mu_{\rm eff}$ [GeV]	$M_{Z'}$ [TeV]	M_0 [TeV]	M_1 [GeV]
BM I	$-0.79\,\pi$	9.11	218.9	2.5	2.6	106.5
BM II	$0.2\,\pi$	16.08	345.3	2.5	1.9	186.7

Parameter	M_2 [GeV]	M_3 [TeV]	M_1' [GeV]	A_0 [TeV]	A_λ [TeV]	$\sin\chi$
BM I	230.0	3.6	198.9	2	5.9	-0.35
BM II	545.5	5.5	551.7	1.5	5.1	0.33

Table 2.4.3: UMSSM parameters for the reference points **BM I** and **BM II**.

We investigate possible Z' supersymmetric decays in the UMSSM. As for the particle content of the UMSSM after EWSB, one is left in the Higgs sector with two charged $H^\pm$ and four neutral scalar bosons, namely one pseudoscalar A and three neutral scalars h, H and H', where h and H are MSSM-like, with h roughly corresponding to the SM Higgs, and H' is a new singlet-like Higgs boson related to the extra $U(1)'$. In the gaugino sector, one has two extra neutralinos with respect to the MSSM, related to the supersymmetric partners of Z' and H', for a total of six $\tilde{\chi}_1^0, \ldots, \tilde{\chi}_6^0$ neutralinos. The chargino sector is unchanged, since the Z' is electrically neutral.

It was found in Ref. [175] that the very inclusion of supersymmetric modes lowers the exclusion limits on $M_{Z'}$ obtained from the analysis of the dilepton channels by about $200 - 300$ GeV, depending on the $U(1)'$ model, while searches relying on the dijet mode, which already exhibit milder limits, are basically unconstraining once BSM channels are accounted for.

In the present investigation, the mixing between the new $U(1)'$ and the SM groups plays a crucial role. First, there could be some mass mixing between the Z and Z' eigenstates parametrised by a mixing angle $\alpha_{ZZ'}$, which is nevertheless constrained by the EW precision tests (EWPT) to be very small [176]. Then, the Z and Z' can kinematically mix through an angle χ, which modifies the interaction term between the Z' and the fermions. In detail, after accounting for the kinetic mixing, the interaction of the Z' with a fermion ψ_i having charges Y_i and Q_i' under $U(1)_Y$ and $U(1)'$ is given by the Lagrangian

$$\mathcal{L}_{\rm int} = -g' \bar{\psi}_i \gamma^\mu \bar{Q}_i Z'_\mu \psi_i \,, \tag{2.4.3}$$

where $\bar{Q}_i = \frac{Q_i'}{\cos\chi} - \frac{g_1}{g'} Y_i \tan\chi$ is the modified fermion $U(1)'$ charge after kinetic mixing and g' is the $U(1)'$ coupling constant. Leptophobic scenarios can hence be obtained by requiring $\bar{Q}_i = 0$ for both left- and right-handed leptons, *i.e.*, $\bar{Q}_L = \bar{Q}_E = 0$ [177]. As discussed in Ref. [175], the leptophobic condition can be naturally achieved for the model labelled as $U(1)'_\eta$, corresponding to an E_6 mixing angle $\theta = \arccos\sqrt{5/8}$. Furthermore, using the typical GUT-inspired proportionality relation between the coupling constants of $U(1)$ and $U(1)'$ $g' = \sqrt{\frac{5}{3}}\, g_1$, the leptophobic condition is realised for $\sin\chi \approx -0.3$. As pointed out in Ref. [175], this relation can be defined either at the Z' mass scale, *i.e.* O(TeV), or at the GUT scale. Imposing unification at the Z' scale clearly yields a higher value of g' and hence a larger Z' production cross section at the LHC. In the following, we assume unification at the TeV scale.

Following [175], two UMSSM benchmark points are considered for this study, denoted by **BM I** and **BM II**, consistent with the current experimental data and featuring a leptophobic Z'. In both cases the Z' mass is set to $M_{Z'} = 2.5$ TeV. In Table 2.4.3, the relevant parameters for these reference points are reported: the particle mass spectrum can be calculated by using the SARAH code [116] and its interface with SPHENO [178]. The particle masses and the decay tables of **BMI** and **BMII** have been given in Ref. [175] and we do not quote them here for the sake of brevity. The Z' BRs into BSM final states are of about 12% for **BM I** and 15% for **BM II**. In particular, the BR of the Z' into chargino pairs

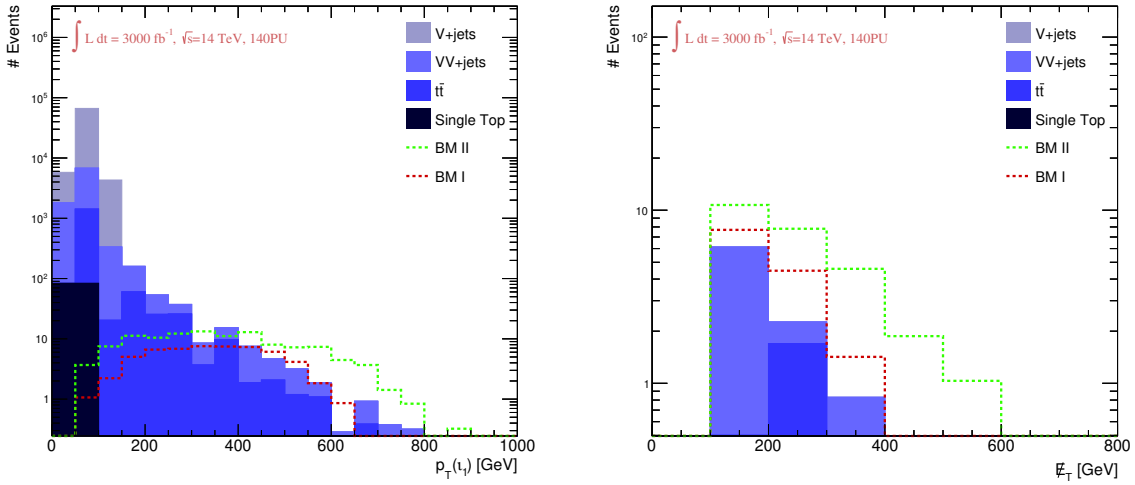

Fig. 2.4.7: Transverse momentum distribution of the leading muon l_1 after applying the first 6 cuts (left) and missing transverse-energy spectrum after all cuts (right) for both leptophobic UMSSM benchmark signals and backgrounds.

$\tilde{\chi}_1^+\tilde{\chi}_1^-$ is about 2% in **BM I** and 6% in **BM II**.

Since in **BM I** and **BM II** the mass splitting between the lightest charginos and neutralinos is larger than the W mass ($M_{\tilde{\chi}_1^\pm} \simeq 177$ GeV and $M_{\tilde{\chi}_1^0} \simeq 95$ GeV in **BM I**, $M_{\tilde{\chi}_1^\pm} \simeq 344$ GeV and $M_{\tilde{\chi}_1^0} \simeq 178$ GeV in **BM II**), then $\tilde{\chi}_1^\pm$ can undergo the transition $\tilde{\chi}^\pm \to W^\pm\tilde{\chi}_1^0$ with real W-bosons. As a case study of a leptophobic Z' in the UMSSM at the HL-LHC, we then explore the decay chain

$$pp \to Z' \to \tilde{\chi}_1^+\tilde{\chi}_1^- \to l^+l^-\not{E}_T, \tag{2.4.4}$$

where we have assumed that both W-bosons decay leptonically and $\not{E}_T$ is the missing transverse energy carried away by final-state neutrinos and neutralinos. The amplitudes of the process (2.4.4) have been computed at the NLO accuracy by means of MADGRAPH5_aMC@NLO [67], yielding a cross section of about $\sigma(pp \to Z') \simeq 120$ pb. In our phenomenological study, parton showers and hadronisation are provided by PYTHIA 8 [68], with the response of a typical LHC detector modelled according to the DELPHES 3 package [33] (version 3.3.2), the detector parameterisation being the one provided by Snowmass [179, 180]. While the default mean number of pile-up events is in this case of 140 and thus a bit low, our analysis essentially relies on very hard isolated leptons (with transverse momenta larger than 200 GeV) and a large amount of missing energy (greater than 100 GeV) which are expected to only be slightly affected by the differences. Jets are clustered following the anti-k_T algorithm [34] with a radius parameter $R = 0.6$, as implemented in the FASTJETprogram (version 3.1.3) [35].

As backgrounds to our signal, we consider single vector-boson (V) and vector-boson pair (VV) production, possibly accompanied by jets, top-quark pairs and single-top events. Our results concern pp collisions at 14 TeV and an integrated luminosity of $\mathcal{L} = 3\,\text{ab}^{-1}$, which corresponds to the HL-LHC. We require two charged muons in the final state at an invariant opening angle ΔR larger than 2.5 and take into account only isolated muons, with an activity of at most 15% of the muon transverse momentum lying in a cone of radius 0.4 centred on the muon; also, we set cuts of 300 GeV and 200 GeV on the hardest and next-to-hardest lepton and force the missing transverse momentum to be above 100 GeV. Setting such cuts, we are able to separate the signal from the background with significances s and Z_A, defined by

$$s = \frac{S}{\sqrt{B+\sigma_B^2}}, \quad Z_A = \sqrt{2\left((S+B)\ln\left[\frac{(S+B)(S+\sigma_B^2)}{B^2+(S+B)\sigma_B^2}\right] - \frac{B^2}{\sigma_B^2}\ln\left[1+\frac{\sigma_B^2 S}{B(B+\sigma_B^2)}\right]\right)}, \tag{2.4.5}$$

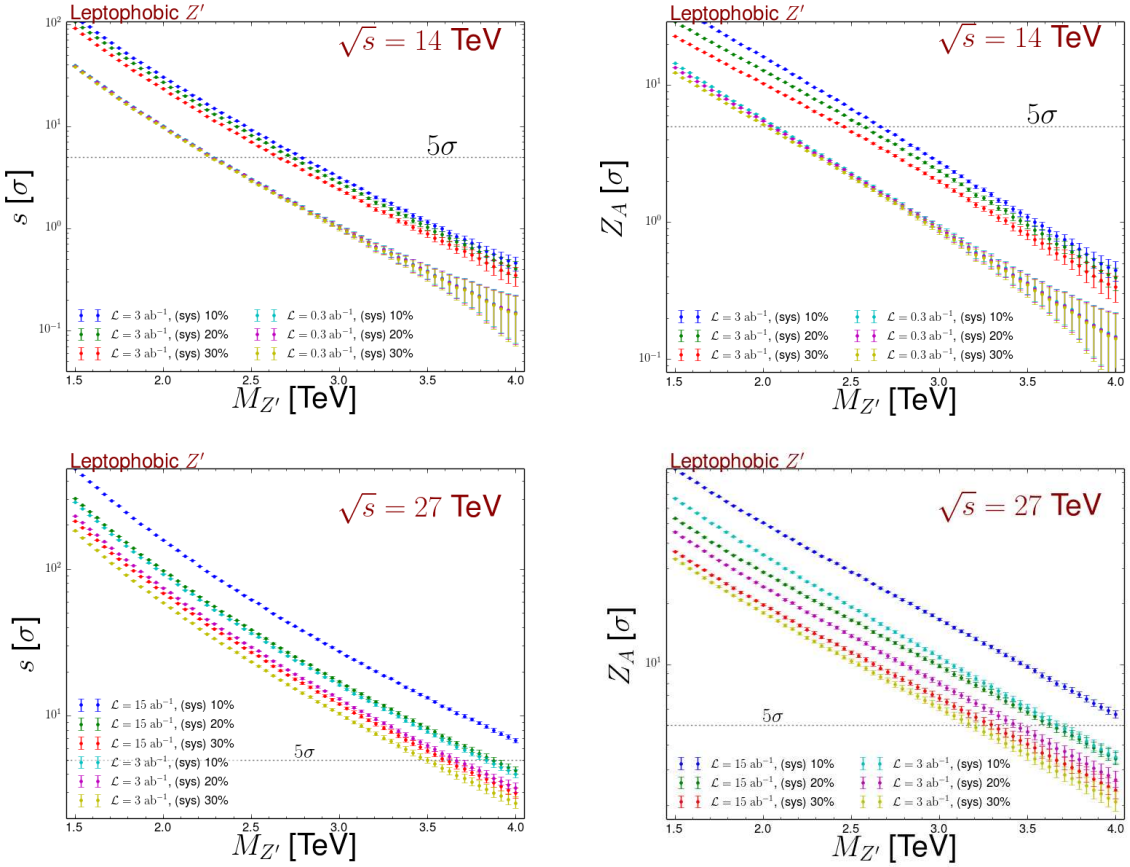

Fig. 2.4.8: Significances s (right) and Z_A (left) to discover a leptophobic Z' boson decaying into charginos as a function of its mass $M_{Z'}$, for a few values of luminosity and systematic error on the SM background. All results are obtained for a c.o.m. energy $\sqrt{s} = 14$ TeV (top) and $\sqrt{s} = 27$ TeV (bottom).

varying between 3σ and 7σ. Besides the total number of events, one can explore differential distributions, such as the leading-lepton transverse momentum or the missing transverse energy presented in Fig. 2.4.7. As for the $p_T(l_1)$ spectrum (left), all four considered backgrounds contribute at small p_T, while above 100 GeV only VV and $t\bar{t}$ events survive. The signal spectra are broad and below the backgrounds at low transverse momentum, whereas, for $p_T(l_1) > 300$ GeV, both **BM I** and **BM II** signals are competitive with the background. For even larger p_T, say $p_T(l_1) > 500$ GeV, muons coming from supersymmetric decays of a leptophobic Z' become dominant, especially for the reference point **BM II**. In Fig. 2.4.7 (right) we present the missing transverse energy, due to the lightest neutralinos $\tilde{\chi}_1^0$ in the signal and to neutrinos in the backgrounds, after all cuts are imposed. Our $\not{E}_T$ signal spectra are well above the backgrounds due to VV and $t\bar{t}$ production. The **BM II** scenario, in particular, is capable of yielding a few events up to $\not{E}_T \simeq 600$ GeV, while all backgrounds are negligible for $\not{E}_T > 400$ GeV.

We present projections for proton-proton collisions at 14 TeV and 27 TeV as functions of the luminosity, $M_{Z'}$ and different assumptions for the systematic uncertainties on the background. We consider a leptophobic Z' decaying into charginos and refer to the BM II reference point as it turns out to be the more promising setup for a possible discovery of a Z' boson in supersymmetric and leptophobic scenarios. In Fig. 2.4.8 we show the significances s (left) and Z_A (right) at 14 TeV (up) and 27 TeV (down), for a Z' mass in the 1.5 TeV $< M_{Z'} <$ 4 TeV mass window. In each figure, we consider two luminosity options chosen to be 300 fb^{-1} and 3 ab^{-1} for a collisions at a c.o.m. energy of 14 TeV, and 3 $\mathrm{ab}^{-1}$and 15 $\mathrm{ab}^{-1}$for 27 TeV collisions. We moreover allow the systematics σ_B on the SM background to vary from 10% to 30% of the background itself.

It turns out that with $300\,\mathrm{fb}^{-1}$ of 14 TeV collisions, leptophobic $Z'$with masses ranging up to 2.3 TeV could be discovered (*i.e.* $s \geq 5\sigma$) regardless of the assumption on the systematic errors (Fig. 2.4.8, top left). In the high-luminosity phase of the LHC, with a luminosity of $3\,\mathrm{ab}^{-1}$, the lower bound on the Z' mass increases to 2.6 TeV (for $\sigma_B = 0.3B$) or 2.8 TeV (for more optimistic systematics of $\sigma_B = 0.1B$). In terms of Z_A, the discovery reach is reduced to $M_{Z'} = 2$ TeV for $300\,\mathrm{fb}^{-1}$, again independently of any assumption on the background systematics σ_B, and to $2.5\,\mathrm{TeV} < M_{Z'} < 2.7\,\mathrm{TeV}$ for $3\,\mathrm{ab}^{-1}$ (Fig. 2.4.8, top right).

In the high-energy phase of the LHC at 27 TeV (Fig. 2.4.8 bottom), a visible Z'signal can be obviously obtained even for much higher masses. In detail, a significance of $s = 5\sigma$ can be reached for Z' masses ranging up to $3.8 - 4$ TeV at 27 TeV and for a luminosity of $15\,\mathrm{ab}^{-1}$. The limits are slightly worse for a reduced luminosity of $3\,\mathrm{ab}^{-1}$and then reach $3.5 - 3.7$ TeV. Using in contrast a more conservative definition of the significance Z_A, we obtain a reach of $3.7 - 4$ TeV for $15\,\mathrm{ab}^{-1}$and only of $3.2 - 3.5$ TeV for a luminosity of $3\,\mathrm{ab}^{-1}$.

We explored possible loop-holes in GUT-inspired Z' searches at the LHC by investigating supersymmetric and leptophobic models, finding that the inclusion of BSM decay modes lowers the exclusion limits on $M_{Z'}$ in dilepton final states by a few hundred GeV and that the limits from dijets can be evaded as well. In leptophobic models, only supersymmetric Z' decay chains can give rise to charged leptons. As a case study, we considered the decay of a leptophobic Z' with mass $M_{Z'} = 2.5$ TeV into charginos, leading to final states with leptons and missing energy. We chose two benchmark points in the UMSSM parameter space and found that both yield a substantial signal at LHC, which one can separate from the background with a sensitivity between 3σ and 7σ at 14 TeV and $3\,\mathrm{ab}^{-1}$. We finally investigated the reach of the high-luminosity and high-energy LHC runs in terms of the Z' mass and systematic uncertainty on the background. We found that at 14 TeV and $3\,\mathrm{ab}^{-1}$a leptophobic Z' can be discovered with a significance about 5σ for a mass $M_{Z'} < 2.8$ TeV, while at 27 TeV and $15\,\mathrm{ab}^{-1}$one can explore leptophobic and supersymmetric Z' models up to about $M_{Z'} \simeq 4$ TeV. These result make therefore the investigation of such scenarios both feasible and worthwhile at HL- and HE-LHC.

3 Dark Matter and Dark Sectors Searches

There is now overwhelming evidence for the existence of a new matter component of the universe, dark matter (DM). Precision measurements of the cosmic microwave background and gravitational lensing measurements confirm the presence of this non-luminous matter. Through its gravitational interactions we know that dark matter makes up $\sim 26\%$ of the matter-energy budget of the universe, and that the stars of the Milky Way move inside a far larger, approximately spherical, dark matter halo. However, the nature and properties of DM remain largely unknown. Searches for DM particles are performed using multiple, complementary, approaches: the measurement of elastic scattering of DM with nuclei and electrons in a detector (direct detection) [181], the detection of SM particles produced in the annihilations or decays of DM in the universe (indirect detection) [182–186], the study of the effect of DM self interactions on astrophysical systems [187], and the production of DM particles at colliders [188, 189]. The latter process is the focus of this section.

These various approaches are very complementary in nature. For instance, the first three techniques all require relic DM to interact and thus suffer from uncertainties related to our knowledge of DM's distribution whereas the production of DM at colliders does not, but is instead limited by the kinematic reach of the machine. By combining the results of all search techniques we gain a deeper understanding of the nature of dark matter.

Dark Matter production by itself does not lead to an observable signal at hadronic machines, where the total c.o.m. energy of the collision is not known. Instead if the DM system recoils against visible activity it can be searched for as missing transverse energy and momentum. We catalogue the search strategies for DM composed of a by what this visible activity is, and report on prospective DM studies in Section 3.1 to Section 3.3, while Section 3.4 is focused on searches for light vector bosons associated with forces in the dark sector. In particular, if this dark sector force is abelian then the associated "dark photon" can kinetically mix with the $U(1)$ in the SM, leading to lepton pairs, possibly with displacement, or missing energy signals.

DM production in association with a high p_T jet is presented in Section 3.1, with sensitivities depending on the careful assessment of systematics. This channel is a useful probe of DM production through the exchange of a neutral mediator that couples to the SM. It may also be produced in the decay of an exotic coloured state. Furthermore, compressed SUSY scenarios, such as higgsino or wino DM, can be probed through the monojet signature.

DM production in association with heavy flavour quarks is presented in Section 3.2. The HL-LHC will improve the sensitivity to mediator masses by a factor of 3-8 relative to the Run-2 searches with $36\ \mathrm{fb}^{-1}$, while HE-LHC will extend the coverage to otherwise inaccessible regions of the parameter space. The case of 2HDMa models is complemented by 4-top final states at HL-LHC, searched in events with two same-charge leptons, or with at least three leptons. While searches using $36\ \mathrm{fb}^{-1}$ Run-2 data have limited sensitivity considering the most favourable signal scenarios (*e.g.* $\tan\beta = 0.5$), HL-LHC will probe possible evidence of a signal with $\tan\beta = 1$, $m_H = 600$ GeV and mixing angle of $\sin\theta = 0.35$, assuming m_a masses between 400 GeV and 1 TeV, and will allow exclusion for all $200\ \mathrm{GeV} < \mathrm{m_a} < 1\ \mathrm{TeV}$.

Prospect studies where DM is produced in association with, or through interactions with, EW gauge bosons are reported in Section 3.3. Compressed SUSY scenarios, as well as other DM models, can be targeted using signatures such as mono-photon and vector-boson-fusion (VBF) production, in addition to the classic monojet channel. We show that mono-photon and VBF events allow targeting an EW fermionic triplet (minimal DM), equivalent to a wino-like signature in SUSY, for which there is no sensitivity in Run-2 searches with $36\ \mathrm{fb}^{-1}$. Masses of the $\tilde{\chi}_1^0$ up to 310 GeV (130 GeV) can be excluded by the mono-photon (VBF) channel, with improvements being possible, reducing the theoretical uncertainties. Projections for searches for a mono-Z signature with $Z \to \ell^+\ell^-$ recoiling against missing E_T, have been interpreted in terms of models with a spin-1 mediator and 2HDMa models. The exclusion is

expected for mediator masses up to 1.5 TeV, and for DM and pseudoscalar masses up to 600 GeV, a factor of ~ 3 better than the 36 fb^{-1} Run-2 constraints. The potential to target Higgs portal models and prospects for the HL- and HE-LHC to probe viable multi-TeV dark matter are also presented.

Simple DM models consist of a DM particle and a mediator that couples it to the SM. The DM may, however, sit in a larger *hidden* (or *dark*) sector with additional new states and new interactions. If these interactions include a light $U(1)$ gauge boson, A', this dark photon may mix, through the kinetic-mixing portal, with the SM photon leading to interesting collider signatures. In Section 3.4, searches for dark photons under various hypotheses of dark sectors are presented. Prospects for an inclusive search for dark photons decaying into muon or electron pairs indicate that the HL-LHC could cover a large fraction of the theoretically favoured $\epsilon - m_{A'}$ space, where ϵ is the size of the kinetic mixing between the photon and the dark photon.

3.1 Dark Matter and Jets

If DM is produced in association with QCD activity it is typically searched for in the monojet channel. The DM may be produced through a SM neutral mediator, see Section 3.1.1, or it may be produced as the decay product of a new heavy coloured state, see Section 3.1.2. Monojet-like signatures can be exploited to search for higgsinos and winos in SUSY, see Section 3.1.3. If the parent state that decays to DM is charged and relatively long lived it is more efficient to search in the disappearing track topology. Additional discussion of disappearing track analyses, in the context of long lived particle searches, can be found in Section 4.1.

3.1.1 Studies on the sensitivity to Dark Matter of the monojet channel at HL-LHC

Contributors: G. Frattari, V. Ippolito, G. Gustavino, J. Stupak, ATLAS

The goal of this study, detailed in [190], is to evaluate the impact of different assumed systematic uncertainty scenarios on the expected sensitivity to WIMP Dark Matter in the jet+$E_{\text{T}}^{\text{miss}}$ channel, based on the extrapolation to higher luminosity of the limits published by the ATLAS Collaboration with 36. fb^{-1} of pp collisions at a c.o.m. energy $\sqrt{s} = 13$ TeV [191]. The WIMPs escape the detector giving rise to large $E_{\text{T}}^{\text{miss}}$ arising if they recoil against a jet from initial state radiation (ISR) off the colliding partons, leading to the so-called monojet topology. The $E_{\text{T}}^{\text{miss}}$ in this study is calculated treating electrons and muons as invisible particles. The strategy pursued takes signal and background $E_{\text{T}}^{\text{miss}}$ distributions from the Run-2 ATLAS data analysis and scales them to 300 $\text{fb}^{-1}$and 3 ab^{-1}, exploring various scenarios for the scaling of the systematic uncertainties.

The dominant backgrounds for the 13 TeV data analysis come from W/Z+jets processes. These backgrounds are estimated using MC samples generated with SHERPA 2.2.1. MC samples are reweighted to account for higher-order QCD and EW corrections following the procedure described in Ref. [192] and are normalised in dedicated control regions (CR) described below. Sub-leading backgrounds consist of $t\bar{t}$ and single-top production, which are generated via POWHEG-BOX v2 and showered with PYTHIA 8, and diboson processes, which are taken from SHERPA. The benchmark signal process is generated for WIMP masses in the range 1 GeV $-$ 1 TeV and mediator masses in the range 10 GeV $-$ 10 TeV using POWHEG-BOX v2 with the DMV model [193], assuming mediator couplings to the quark and WIMP of $g_q = 0.25$ and $g_\chi = 1$, respectively. The small multijet and non-collision backgrounds, which are estimated from data in the 13 TeV analysis, are neglected.

The event selection follows that applied in the 13 TeV analysis and selects events with $E_{\text{T}}^{\text{miss}} > 250$ GeV in association with at least one high-p_T jet. Up to three additional jets are allowed and all jets are required to be well separated from the missing transverse momentum direction in azimuth. The signal region is required to contain no reconstructed electron or muon. Four additional CRs to isolate the dominant backgrounds are defined based on the number and type of leptons. Events with exactly one muon, no other leptons, and transverse mass in the 30–100 GeV range form the W+jets

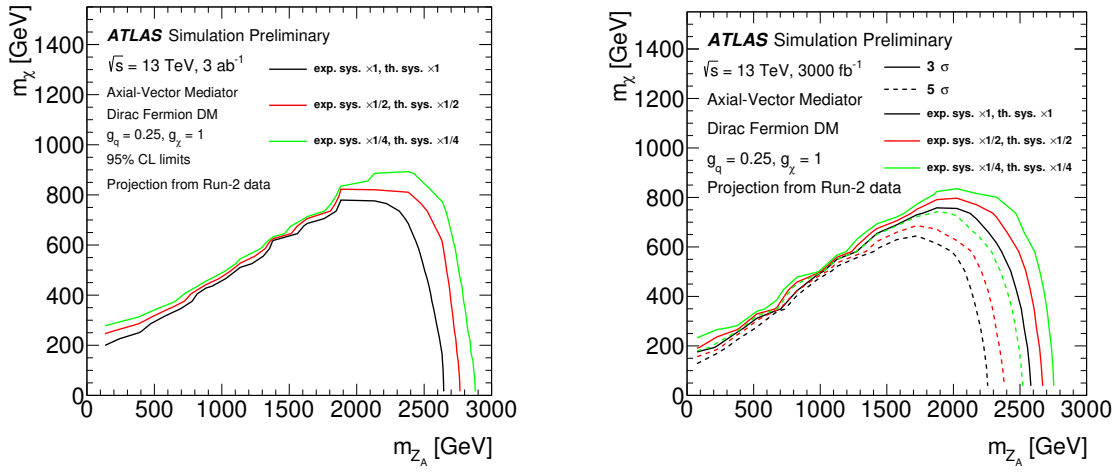

Fig. 3.1.1: Left: expected 95% C.L. excluded regions in the (m_χ, m_{Z_A}) mass plane for the axial-vector simplified model with couplings $g_q = 0.25$ and $g_\chi = 1$, for a luminosity of 3 ab^{-1}. Three contours are shown in each plot, corresponding to the three different systematic uncertainty scenarios: standard (black), reduced by a factor 2 (red) and 4 (green). Right: 3σ and 5σ discovery contours corresponding to the three different systematic uncertainty scenarios: standard (black), reduced by a factor 2 (red) and 4 (green).

($t\bar{t}$) CR if they have zero (at least one) b-tagged jet. A second W+jets CR is built by requiring exactly one electron, no other leptons, and the same transverse mass requirement. Finally, events with 2 muons with an invariant mass consistent with the Z boson form the Z+jets CR. A simultaneous, binned likelihood fit of a signal plus background model to the simulated $E_{\mathrm{T}}^{\mathrm{miss}}$ distributions of the analysis regions is performed. The signal normalisation and two additional normalisation factors, one which rescales the prediction for processes containing Z and W bosons produced in association with jets, and one for $t\bar{t}$ and single-top production, are free parameters of the fit. Nuisance parameters with Gaussian constraints are used to describe the effect of systematic uncertainties on the signal and background $E_{\mathrm{T}}^{\mathrm{miss}}$ distributions. Correlations of systematic uncertainties across $E_{\mathrm{T}}^{\mathrm{miss}}$ bins are taken into account.

The projection for high luminosity proceeds as follows:

- The $E_{\mathrm{T}}^{\mathrm{miss}}$ distributions for signal and the main backgrounds from the 13 TeV data analysis in Run-2 are scaled from 36.1 fb^{-1} to 3 ab^{-1}. The increased statistics achieved by the higher luminosity allows the discriminant to be binned more finely, increasing the number of $E_{\mathrm{T}}^{\mathrm{miss}}$ bins from 10 in the recent data analysis to 17 for the high-luminosity projection. The lower end of the last $E_{\mathrm{T}}^{\mathrm{miss}}$ bin, 1.6 TeV, is chosen in order to keep a similar level of uncertainty on signal and control region as for the Run-2 search. This turns into an improvement of about 100 GeV in the projected mediator mass reach.
- The background distributions are further scaled up by a factor of 1.27 (1.06) for Z/W+jets ($t\bar{t}$ and single top) in order to reflect the observation in the CRs of the Run-2 data analysis.
- No correction is made for the increase in the c.o.m. energy to 14 TeV at the HL-LHC since the dedicated NLO QCD and EW corrections for the main W/Z+jets background are not available. Given the signal cross-section would be expected to increase by $20-40\%$, while the dominant W/Z+jets background cross section will increase by $10-15\%$, this leads to a conservative estimate of the potential and the actual sensitivity will be slightly better than estimated here.

In Ref. [191], the main background experimental uncertainties for $E_{\mathrm{T}}^{\mathrm{miss}} > 250$ GeV (> 1 TeV) are related to the leptons (jet and $E_{\mathrm{T}}^{\mathrm{miss}}$ scales and resolution), amounting up to 1.7% (5.3%), while the main background theoretical uncertainties are related to the W/Z parton shower modelling and PDF (W/Z QCD and EW corrections), amounting to 0.8% (2%). The signal predictions are mainly affected

by jet and $E_{\mathrm{T}}^{\mathrm{miss}}$ scale and resolution uncertainties on the experimental side, and on the theory side by initial/final-state radiation and PDF uncertainties. In the high-luminosity projection, three different systematic uncertainty scenarios are tested to reflect the possible improvements in detector performance and in the theoretical modelling of signal and background processes, which could be achieved in the next years thanks to the foreseen detector upgrades and to progress in QCD and EW calculations:

- standard: same uncertainties as in Ref. [191];
- reduced by factor 2: all pre-fit signal and background uncertainties are reduced by a factor two;
- reduced by factor 4: all pre-fit signal and background uncertainties are reduced by a factor four;

The projected exclusion limits with a luminosity of 3 $\mathrm{ab}^{-1}$for these three scenarios are plotted in the (m_χ, m_{Z_A}) mass plane in Fig. 3.1.1 (left), where χ is the WIMP DM candidate and Z_A the axial-vector mediator. The 95% C.L. exclusion contour for $m_\chi = 1$ GeVcan be up to $m_{Z_A} = 2.65$ TeV, assuming the same uncertainties as in Ref. [191]. The excluded region that can be obtained by reducing by a factor two (four) all systematic uncertainties reaches, for low m_χ, mediator masses of about 2.77 (2.88) TeV. Small differences between systematic uncertainty scenarios are observed when approaching the region where the decay of the mediator in two WIMPs is off-shell ($m_{Z_A} < 2m_\chi$), due to the decrease of the signal cross-section. The discovery contours at 3 and 5σ are shown in Fig. 3.1.1 (right): for $m_\chi = 1$ GeV, a background incompatibility greater than 5σ would be reached for $m_{Z_A} = 2.25$ TeV, 2.38 TeV and 2.52 TeV assuming the same uncertainties as in Ref. [191], the scenario obtained by reducing by a factor two, and by a factor four all the systematic uncertainties, respectively. The increase in sensitivity of the scenarios with lowered systematic uncertainties was checked to be mainly driven by the reduction in the theoretical uncertainties. Among these, V+jets and diboson uncertainties, as well as theoretical uncertainties on signal processes, are similar in size and give the leading contributions.

3.1.2 Monojet Signatures from Heavy Coloured Particles at HL- and HE-LHC

Contributors: A. Chakraborty, S. Kuttimalai, S. H. Lim, M. M. Nojiri, and R. Ruiz

Search strategies for hypothetical coloured particles $\mathcal{Q}$ that can decay to dark matter candidates usually involve jets and leptons produced in association with large missing transverse energy $E_{\mathrm{T}}^{\mathrm{miss}}$. In compressed mass spectrum scenarios the visible decay products in the $\mathcal{Q} \to$DM+SM process do not have sufficient momenta to be readily distinguished from SM backgrounds and monojet-like topologies arise.

Were evidence for a new particle $\mathcal{Q}$ established at the LHC, or a successor experiment such as the HE-LHC, it would be crucial to determine the properties of $\mathcal{Q}$, especially its mass, spin, and colour representation, in order to help understand the nature of DM. Such a program would typically include investigating various collider observables that can discriminate against possible candidates for $\mathcal{Q}$, and hence requires that observables are known to sufficiently high precision. It is the case though that leading order (LO) calculations are poor approximations for QCD processes, even when using sensible scale choices. The situation, however, is more hopeful with the advent of general-purpose precision Monte Carlo event generators HERWIG [194], MADGRAPH5_AMC@NLO+PYTHIA 8 [67,68], and SHERPA [195]. With automated event generation up to NLO in QCD with parton shower (PS) matching and multijet merging, even for BSM processes [196], one can now systematically investigate the impact of crucial $\mathcal{O}(\alpha_s)$ corrections on the inclusive monojet process.

We now summarise the key findings of a recent [197] investigation into the prospect for determining the properties of a hypothetical heavy resonance $\mathcal{Q}$ associated with DM via the the monojet signature. This includes systematically quantifying theory uncertainties associated with the renormalisation, factorisation, and parton shower scales as well as those originating from distribution functions and and multijet merging using state-of-the-art technology. One finds that in aggregate, the total uncertainties are comparable to differences observed when varying $\mathcal{Q}$ itself. However, the precision achievable with

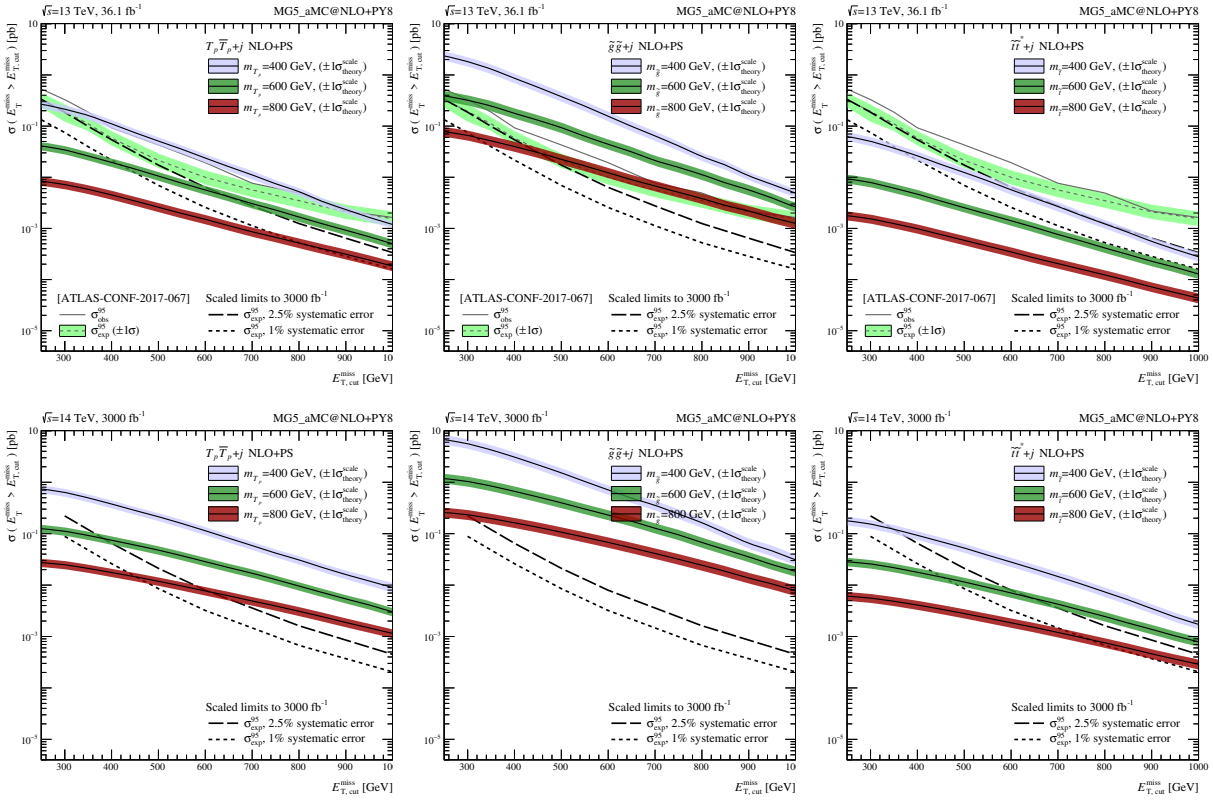

Fig. 3.1.2: Top: $pp \to \mathcal{Q}\overline{\mathcal{Q}} + j$ cross section as a function of minimum $E_{\mathrm{T}}^{\mathrm{miss}}$ after the experimental selection criteria at 13 TeV, for $\mathcal{Q} = T_p$, $\tilde{g}$, and $\tilde{t}$, with current 95% C.L. limits after $\mathcal{L} = 36.1\ \mathrm{fb}^{-1}$ of data at the 13 TeV LHC. Bottom: same plots for 14 TeV LHC. We also shown the estimated sensitivity with $\mathcal{L} = 3\ \mathrm{ab}^{-1}$, assuming $\delta_{\mathrm{Syst.}} = 2.5\%$ and 1% systematical errors.

Particle name		Colour Rep.	Lorentz Rep.	Decay	UFO Refs.
Fermionic Top partner	(T_p)	**3**	Dirac fermion	$q + X$	[200, 201]
Top squark	$(\tilde{t})$	**3**	Complex scalar	$t^* X \to bq\bar{q}' + X$	[201, 202]
Gluino	$(\tilde{g})$	**8**	Majorana fermion	$q\bar{q} + X$	[201, 202]

Table 3.1.1: Summary of signal particles, their $\mathrm{SU}(3)_c$ and Lorentz representations (Rep.), and decay mode to stable DM candidate (X).

next-to-next-to-leading order (NNLO) calculations, where available, can resolve this dilemma. In light of this, we further emphasise that the HL- and HE-LHC runs possibly resolve different candidates for the new coloured particle. For additional details beyond what is provided here, see Ref. [197].
The ATLAS and CMS collaborations have studied $\mathcal{L} = 36.1\ \mathrm{fb}^{-1}$ of $\sqrt{s} = 13$ TeV collision data using signatures with significant transverse momentum imbalance and at least one energetic jet [198, 199]. The non-observation of significant deviations from SM predictions leads to model-independent 95% C.L. upper limits on the production cross section of new particles. In Fig. 3.1.2, we show these experimental limits along with NLO+PS-accurate cross section, and associated scale uncertainty, for the $\mathcal{Q}\overline{\mathcal{Q}} + j$ process, where we include a hard jet at the matrix-element level, and for $\mathcal{Q} \in \{\tilde{t}, T_p, \tilde{g}\}$, as listed in Table 3.1.1.

We find that the lower limits on $\mathcal{Q}$ masses stand at around $m_{T_p} = 400$ GeV for the fermionic top partner and $m_{\tilde{g}} = 600$ GeV for the gluino, while no constraint on stop masses is found within the mass range under consideration. It has been observed that for high-p_T bins both the systematic and

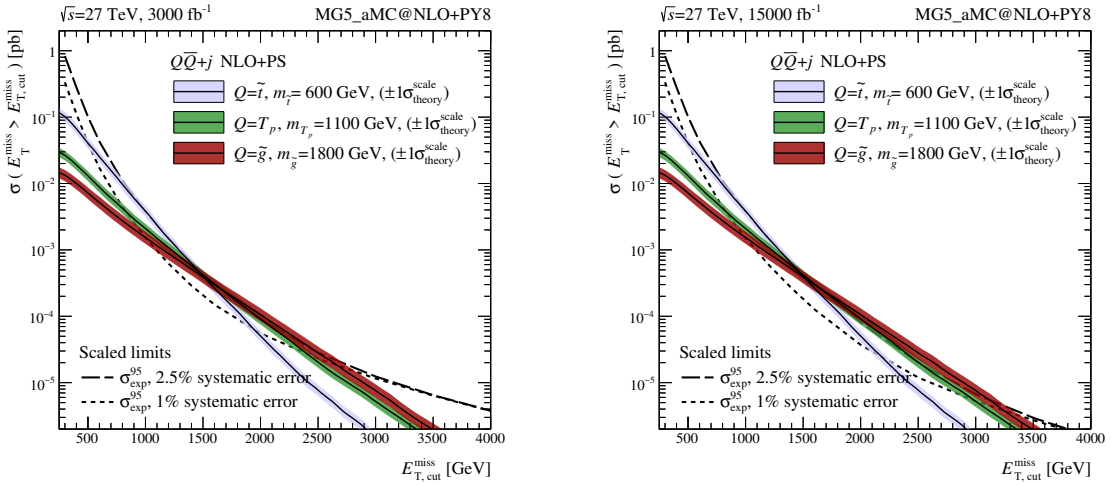

Fig. 3.1.3: Same as Fig. 3.1.2 but scaled for $\sqrt{s} = 27$ TeV assuming $\mathcal{L} = 3$ ab^{-1} (left) and 15 ab^{-1} (right).

statistical experimental uncertainties play a crucial role. Sensitivity is expected to improve at the HL-LHC due to a much larger dataset with better control on uncertainties. We calculate the expected upper limits at HL-LHC with $\mathcal{L} = 3$ ab^{-1} and $\sqrt{s} = 13$ TeV by rescaling the numbers at 13 TeV with two values of total systematic uncertainty, namely $\delta_{\text{Sys.}} = 2.5\%$ and 1%. From the scaled limits, we find that fermionic top partners with masses $m_{T_p} \lesssim 800$ GeV, gluinos with $m_{\tilde{g}} \lesssim 1000$ GeV, and stops with masses $m_{\tilde{t}} \lesssim 600$ GeV can be excluded at 13 TeV with $\mathcal{L} = 3$ ab^{-1}, using the inclusive monojet signature for a compressed mass spectrum.

Another possibility that can significantly improve the sensitivity to heavy coloured particles is increasing the beam energy of the LHC to the proposed $\sqrt{s} = 27$ TeV HE-LHC [203]. Here, we assume that the SM background is still dominated by $Z+j$ process and then scale the model-independent 95% C.L. upper limit at $\sqrt{s} = 13$ TeV according to the production cross section ratio. In Fig. 3.1.3, we estimate the expected reach at the 27 TeV LHC for $pp \to \mathcal{Q}\overline{\mathcal{Q}} + j$ process. Note, here also we assume that the detector acceptance and efficiencies are the same at 13 and 27 TeV. For comparison, we consider systematic uncertainties of 2.5% and 1%, the same considered before. We observe that with $\mathcal{L} = 3 - 15$ ab^{-1}, one can probe the compressed spectra featuring fermionic top partners with masses $m_{T_p} \lesssim 1100$ GeV, gluinos with masses $m_{\tilde{g}} \lesssim 1800$ GeV, and stops with masses $m_{\tilde{t}} \lesssim 600$ GeV.

Theoretical uncertainties associated with the monojet signal process are estimated by employing the state-of-the-art MC suites MADGRAPH5_AMC@NLO and SHERPA. A single measurement of signal cross section does not constrain the nature of $\mathcal{Q}$ uniquely as different spin and colour hypotheses can lead to identical cross sections if the mass is tuned accordingly. For example, a stop of mass 400 GeV, a fermionic top partner of mass 600 GeV, and a gluino of mass 800 GeV have practically the same $pp \to \mathcal{Q}\overline{\mathcal{Q}} + j$ cross section for $p_{T,\text{cut}}^{j_1}$ around 500 GeV at $\sqrt{s} = 14$ TeV, see Fig. 3.1.4 (left). The degeneracy, however, can be resolved through additional cross section measurements with larger $p_{T,\text{cut}}^{j_1}$. Cross section measurements at a higher c.o.m. energy can also lift this degeneracy, see Fig. 3.1.4 (right). To distinguish different new physics candidates, one, however, needs theoretical uncertainties smaller than $\mathcal{O}(30\%)$ and $\mathcal{O}(5\%/100$ GeV), respectively, on the total cross section normalisations and on the change of the cross section for $\sigma(pp \to \mathcal{Q}\overline{\mathcal{Q}} + j)$ as a function of $p_{T,\text{cut}}^{j_1}$. Alternatively, one can also consider ratios of cross sections measured at two different $p_{T,\text{cut}}^{j_1}$ and two different energies $\sqrt{s} = 14$ and 27 TeV.

We find that the monojet signal process under consideration exhibits a residual (factorisation, renormalisation, and shower) scale uncertainty around 40% at LO and 20% at NLO, and is about twice as large as the the inclusive $pp \to T_p\bar{T}_p$ cross section due to the presence of additional α_s factors. Based

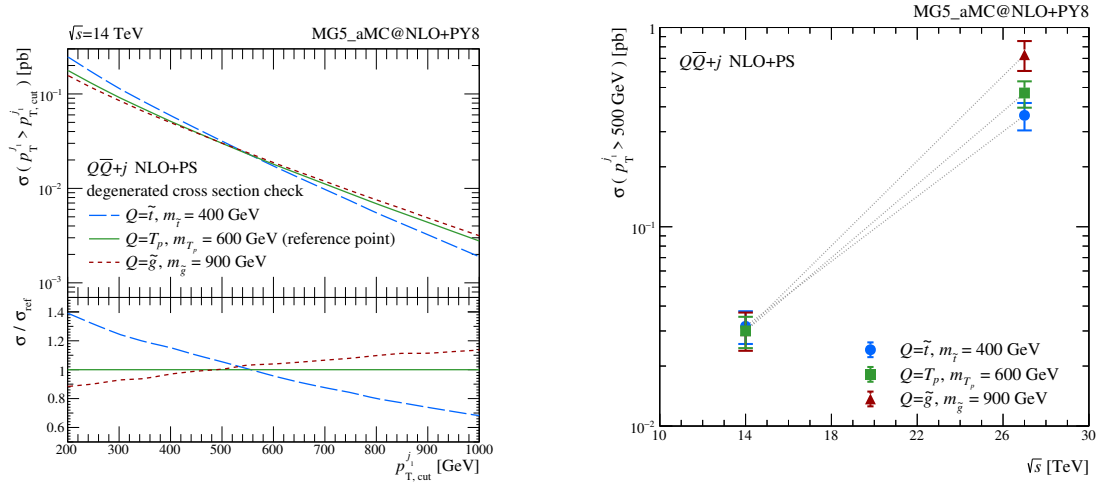

Fig. 3.1.4: Left: $pp \to \mathcal{Q}\overline{\mathcal{Q}} + j$ cross section at $\sqrt{s} = 14$ TeV as a function of jet p_T selection criterion ($p^{j_1}_{T,\mathrm{cut}}$), for representative $(\mathcal{Q}, m_{\mathcal{Q}})$ combinations. Right: $pp \to \mathcal{Q}\overline{\mathcal{Q}} + j$ cross section at $\sqrt{s} = 14$ and 27 TeV, with $p^{j_1}_{T,\mathrm{cut}} = 500$ GeV. The error bar reflects the renormalisation and factorisation scale variation.

on available NNLO calculations [204, 205], we anticipate such uncertainties can be reduced to the 10% level at NNLO. As the corrections beyond NLO mainly impact the overall normalisation, cross sections at different $p^{j_1}_{T,\mathrm{cut}}$ possess correlated uncertainties. Hence, constructing ratios and double-ratios of cross sections at different $p^{j_1}_{T,\mathrm{cut}}$, can partially cancel uncertainties and help with the identification of $\mathcal{Q}$.

3.1.3 Searching for Electroweakinos in monojet final states at HL- and HE-LHC

Contributors: T. Han, S. Mukhopadhyay, X. Wang

Among the multitude of possibilities for WIMP dark matter, particles that belong to a multiplet of the SM weak interactions are one of the best representatives. We focus on two representative scenarios for EW DM, namely a wino-like $SU(2)_L$ triplet and a Higgsino-like $SU(2)_L$ doublet. Such models are often challenging to probe in direct detection experiments due to loop-suppressed scattering cross-sections. Searches at hadron colliders are thus crucial for testing such a scenario, and depending upon the gauge representation, can be complementary to indirect detection probes in different mass windows. Moreover, since the relic abundance of EW DM is uniquely determined by its mass value, 3 TeV for wino-like triplet [206–208] and 1 TeV for Higgsino-like doublet [209], they represent a well-defined target in the collider search for DM in general. Without large additional corrections from higher-dimensional operators, the mass splitting between the charged and neutral components of the DM $\mathrm{SU(2)_L}$ multiplets is only of the order of a few hundred MeV [210, 211]. This nearly degenerate spectrum motivates two major search channels at hadron colliders for the EW DM sector, namely, the monojet with missing transverse momentum search and the disappearing charged track search. The first one is reported in this section, the second in Section 4.1.3.

We present our results [155] on the future reach of three different scenarios of collider energy and integrated luminosity: HL-LHC, HE-LHC, and FCC-hh/SppC (100 TeV, 30 ab^{-1}). We adopt as a definition of significance $S/\sqrt{B + (\Delta_B B)^2 + (\Delta_S S)^2}$ where S and B are the total number of signal and background events, and Δ_S, Δ_B refer to the corresponding percentage systematic uncertainties, respectively.

The classic monojet and missing transverse momentum search for pair production of a DM particle in association with a hadronic jet originating from initial state radiation is considered. Pair production of both the charged state $\chi^{\pm}$ and the neutral state χ^0 would contribute to the signal in the monojet search channel, since the charged pions from the charged state $\chi^{\pm}$ decay are too soft to detect at hadron

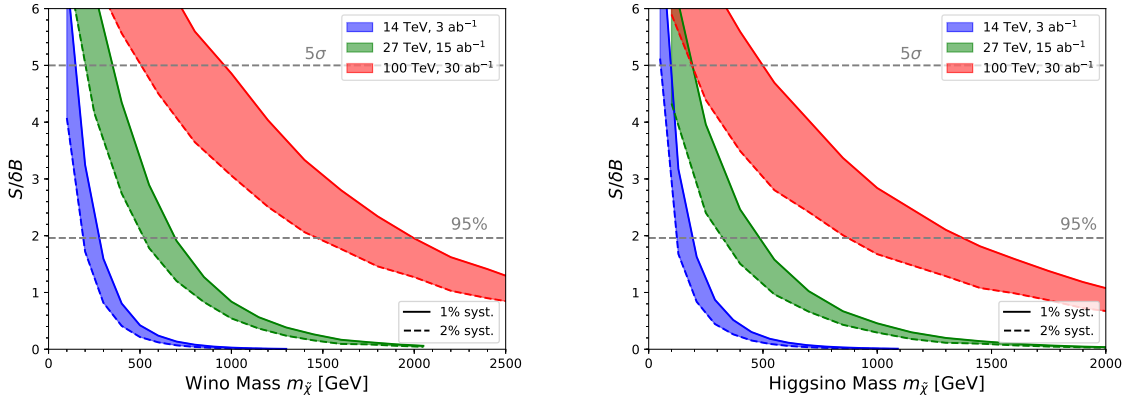

Fig. 3.1.5: Comparative reach of the HL-LHC, HE-LHC and FCC-hh/SppC options in the monojet channel for wino-like (left) and Higgsino-like (right) DM search. The solid and dashed lines correspond to optimistic values of the systematic uncertainties on the background estimate of 1% and 2% respectively, which might be achievable using data-driven methods with the accumulation of large statistics.

95% C.L.	Wino	Higgsino
14 TeV	280 GeV	200 GeV
27 TeV	700 GeV	490 GeV
100 TeV	2 TeV	1.4 TeV

Table 3.1.2: Summary of DM mass reach at 95% C.L. for an EW triplet (wino-like) and a doublet (Higgsino-like) representation, at the HL-LHC, HE-LHC and the FCC-hh/SppC colliders, in optimistic scenarios for the background systematics.

colliders. Systematic uncertainties $\Delta_B = 1-2\%$ and $\Delta_S = 10\%$ are assumed. In Fig. 3.1.5 we compare the reach of the HL-LHC, HE-LHC and FCC-hh/SppC options in the monojet channel for wino-like (left) and Higgsino-like (right) DM search. The solid and dashed lines correspond to systematic uncertainties on the background estimate of 1% and 2% respectively. Results are summarised in Table 3.1.2. In an optimistic scenario, wino-like DM mass of up to 280, 700 and 2000 GeVis expected to be probed at the 95% C.L., at the 14, 27 and 100 TeV colliders respectively. For the Higgsino-like scenario, these numbers decrease to 200, 490 and 1370 GeV, primarily due to the reduced production cross-section. Clearly, a 27 TeV collider can substantially improve the reach by a factor of two or more compared to the HL-LHC, while improvement of another factor of three can be further achieved at the 100 TeV collider.

3.2 Dark Matter and Heavy Flavour

When the mediator between the dark sector and the SM is a scalar or pseudoscalar one expects the couplings to the SM to scale with the SM fermion mass. Thus, a natural place to look for DM production is in association with pairs of top or bottom quarks, see Section 3.2.1 and Section 3.2.2. Alternatively, a neutral vector mediator with flavour-changing interactions can produce DM in association with a single top, see Section 3.2.3. Finally, scalar mediators may be searched for directly in four top final states, as shown in Section 3.2.4.

3.2.1 Associated production of dark matter and heavy flavour quarks at HL-LHC

Contributors: M. Rimoldi, E. McDonald, F. Meloni, P. Pani, F. Ungaro, ATLAS

The prospects of a search for dark matter produced in association with heavy flavour (bottom

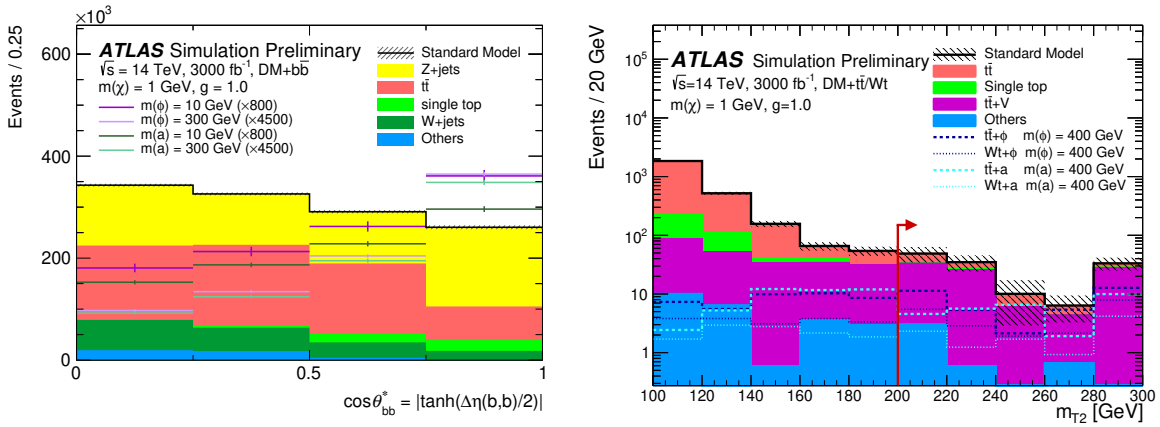

Fig. 3.2.1: Distributions of the main discriminants used for the $DM + b\bar{b}$ and $DM + t\bar{t}$ searches: $\cos\theta^*_{bb}$ (left) and m_{T2} (right). For the $\cos\theta^*_{bb}$ distribution events are required to have $E_{\mathrm{T}}^{\mathrm{miss}} > 210$ GeV, no leptons, 2 or 3 jets, and at least two b-jets. For the m_{T2} distribution events must satisfy the corresponding signal region criteria except for that on the variable shown.

or top) quarks at the HL-LHC are presented in this section [212]. The study therefore focuses on two simplified models, defined by either a scalar, ϕ, or pseudoscalar, a, mediator. In both cases, the mediating particle is taken to be colour-neutral and the dark matter candidate is assumed to be a weakly interacting Dirac fermion, χ, uncharged under the SM.

The $\chi\bar{\chi}$ production in association with top-quarks is expected to dominate at the HL-LHC. Two signatures featuring top quarks in the final state are therefore considered. The first signature, denoted $DM + t\bar{t}$, is characterised by two tops decaying di-leptonically. The second signature, $DM + W\bar{t}$, involves a single top produced in tandem with a W-boson, both of which decay leptonically. Dark matter production in association with b-quarks is also considered in this study, as it is relevant if the coupling to up-type quarks is suppressed. The $DM + b\bar{b}$ final state is equivalently well motivated as an avenue for probing the parameter space of two-Higgs doublet models. In the 2HDM+a model for example, the rate for $pp \to b\bar{b} + a$ is enhanced by the ratio of the Higgs doublet vacuum expectation values, $\tan\beta$, if a Yukawa sector of type-II is realised. A straightforward recasting of exclusion limits on the simplified pseudoscalar mediator model can then be used to extract constraints on $\tan\beta$.

A search targeting the DM+$b\bar{b}$ and DM+$t\bar{t}$ signatures was performed at the LHC using 36.1 fb^{-1} of data collected in 2015 and 2016 at a centre of mass energy of 13 TeV. This study presents the prospects for further constraining these models with HL-LHC data and is divided into two independent analyses.

Signatures with b-quarks and $E_{\mathrm{T}}^{\mathrm{miss}}$ To isolate the event topology of the $DM + b\bar{b}$ final state, events are required to have at least two b-tagged jets. The contribution from SM background processes is suppressed via the application of selection criteria based on that of the 13 TeV analysis and updated to align with HL-LHC design considerations. To reduce the contribution from leptonic and semi-leptonic $t\bar{t}$ decays and from leptonic decays of W and Z bosons, events containing at least one baseline lepton are vetoed. A further requirement of no more than 2 or 3 jets is imposed in order to control the large background from hadronic $t\bar{t}$ decays. The main background from $Z(\to \nu\bar{\nu})$+jets events is reduced by cutting on variables which exploit the difference in spin between the scalar and pseudoscalar particles and the Z boson. These variables make use of the pseudorapidity and azimuthal separations between jets, b-jets, and the missing transverse momentum. Among them, the hyperbolic tangent of the pseudo-rapidity separation between the leading and sub-leading b-jet, $\Delta\eta(b,b) = \eta(b_1) - \eta(b_2)$, is used. This variable, referred to as $\cos\theta^*_{bb}$, is expected to yield a reasonably flat distribution for b-jets produced in association with vector particles. For b-jets accompanying the production of a heavy scalar or pseudoscalar mediator however, $\cos\theta^*_{bb}$ is expected to peak around 1. Owing to this shape difference, the $\cos\theta^*_{bb}$ variable provides the best discrimination between signal and background events in the $DM + b\bar{b}$

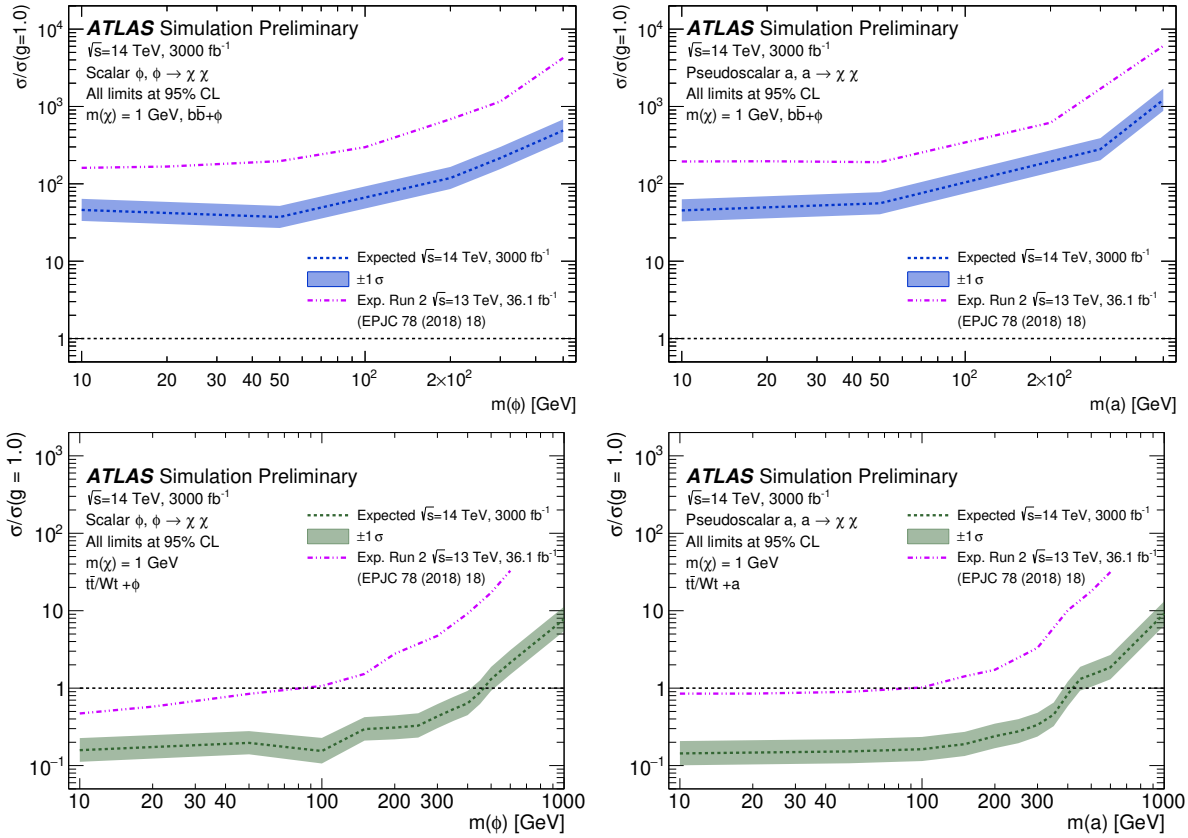

Fig. 3.2.2: Exclusion limits for the production of a colour-neutral mediator in association with bottom quarks (top) or with top quarks (bottom) in case of scalar (left) and pseudoscalar (right) mediator decaying to a pair of dark matter particles with mass 1 GeV. Also shown for comparison is the expected limit from the current analysis [213].

channel. The signal region for this search is therefore defined by four equal-width exclusive bins in $\cos\theta^*_{bb}$ as shown in Fig. 3.2.1, reflecting the configuration used in Run-2. Separate selections are derived for $m(\phi/a) < 100$ GeV and $m(\phi/a) \geq 100$ GeV to further enhance the difference in shape, which can depend strongly on the mass of the mediating particle. The resulting signal regions are denoted by $SR_{b,\text{low}}$ and $SR_{b,\text{high}}$ respectively. For more details, see Ref. [212].

Signatures with top quarks and $\boldsymbol{E}_{\mathbf{T}}^{\mathbf{miss}}$ A single signal region, denoted $SR_{2\ell}$, is used for the search targeting DM production in association with one or two top quarks. Events are required to have exactly two leptons (electrons or muons), possessing the same or different flavour and opposite electric charge. To reduce the $t\bar{t}$ background, the lepton pair must have an invariant mass larger than 100 GeV. Furthermore, candidate signal events are required to have at least one identified b-jet.

Different discriminators and kinematic variables are used to further separate the $t\bar{t} + \phi/a$ and $Wt + \phi/a$ signal from the SM background. These variables include the lepton-based transverse mass m_{T2}, the distribution for which is shown in Fig. 3.2.1 for events passing all of the SR requirements except that on m_{T2}. For the calculation of exclusion limits, the m_{T2} distribution is divided into five equal-width (20 GeV) exclusive bins.

Results For both $SR_{b,\text{low}}$ and $SR_{b,\text{high}}$, the main background consists of Z+jets events followed by hadronic decays of $t\bar{t}$. A significant contribution also comes from single top quark processes and events featuring a W-boson produced in association with jets. In $SR_{2\ell}$, the dominant background consists of di-leptonic decays of $t\bar{t}$ and $t\bar{t}Z$ with $Z \to \nu\nu$. Systematic uncertainties include theory modelling and experimental uncertainties related to, for example, the Jet Energy Scale and b-jet mis-identification. The

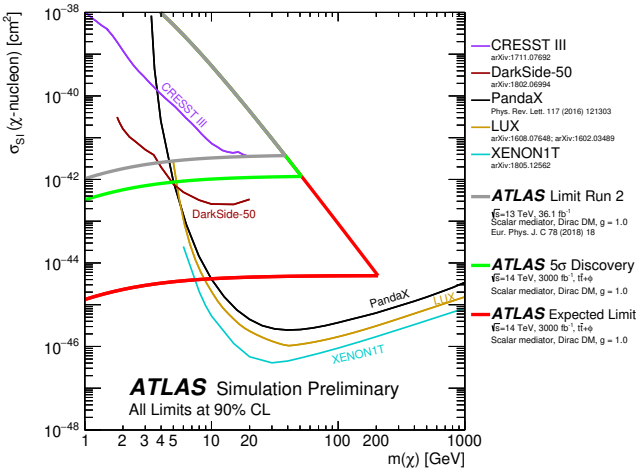

Fig. 3.2.3: Comparison of the 90% C.L. limits on the spin-independent DM-nucleon cross-section as a function of DM mass between these results and the direct-detection experiments, in the context of the colour-neutral simplified model with scalar mediator. The green contour indicates the 5σ discovery potential at HL–LHC. The lower horizontal line of the DM–nucleon scattering cross-section for the red (green) contour corresponds to value of the cross section for $m(\phi) = 430$ GeV ($m(\phi) = 105$ GeV). The grey contour indicates the exclusion derived from the observed limits for Run-2 taken from Ref. [213]. The results are compared with limits from direct detection experiments.

total systematic uncertainty on the SM background is 14% for $SR_{b,\text{low}}$/$SR_{b,\text{high}}$ and 13% for $SR_{2\ell}$.

Exclusion limits are derived at 95% C.L. for mediator masses in the range $10-500$ GeV assuming a DM mass of 1 GeV and a coupling (g) of 1.0. The limits are shown in Fig. 3.2.2 for $\phi/a \rightarrow \chi\bar{\chi}$ production in association with either bottom quarks or top quarks for $\mathcal{L} = 3$ ab^{-1} at $\sqrt{s} = 14$ TeV. Also shown for comparison are the corresponding limits at 13 TeV with 36.1 fb^{-1} taken from the previous Run-2 analysis.

For $\phi/a + b\bar{b}$, the exclusion potential at the HL-LHC is found to improve by a factor of $\sim 3-8.7$ with respect to Run-2. In the context of the 2HDM+a model with $m(A) \gg m(a)$, $\sin\theta = 0.35$ and $y_\chi = 1$, the HL-LHC limits translate to an approximate upper bound on $\tan\beta$ ranging from ~ 19 for $m(a) = 10$ GeV to ~ 100 for $m(a) = 500$ GeV, significantly extending the current phase space coverage. In final states with one or two leptonically-decaying top quarks, the mass range for which a colour-neutral scalar mediator is excluded extends from 80 GeV to 405 GeV. Similarly, exclusion of pseudoscalar masses up to 385 GeV is expected. In the case of the scalar mediator model, this represents a factor of 5 improvement with respect to the 36 fb^{-1} 13 TeV results in the same channel. An additional improvement of approximately 3 is possible when considering a statistical combination of all relevant top decay channels [214], which is not explored for the HL-LHC in this work.

For each DM and mediator mass pair, the exclusion limit on the cross-section for producing colour-neutral scalar mediator particles can be converted into a limit on the cross-section for spin-independent DM-nucleon scattering with the procedure described in Ref. [215]. Limits on the $t\bar{t} + \phi$ model at 90% C.L., corresponding to exclusion of mediator masses up to $m(\phi) = 430$ GeV, are used for this purpose. Fig. 3.2.3 shows the resulting constraints in the plane defined by the DM mass and the scattering cross-section. The maximum value of the DM-nucleon scattering cross-section depicted in the plot corresponds to the value of the cross section for a mediator mass of 10 GeV. The exclusion limits at 90% C.L. are shown in red and the 5σ discovery potential is illustrated in green. The lower horizontal line in the green (red) contour corresponds to the value of the cross section for $m(\phi) = 105$ GeV ($m(\phi) = 430$ GeV). Overlaid for comparison are the most stringent limits to date from several DM direct detection experiments.

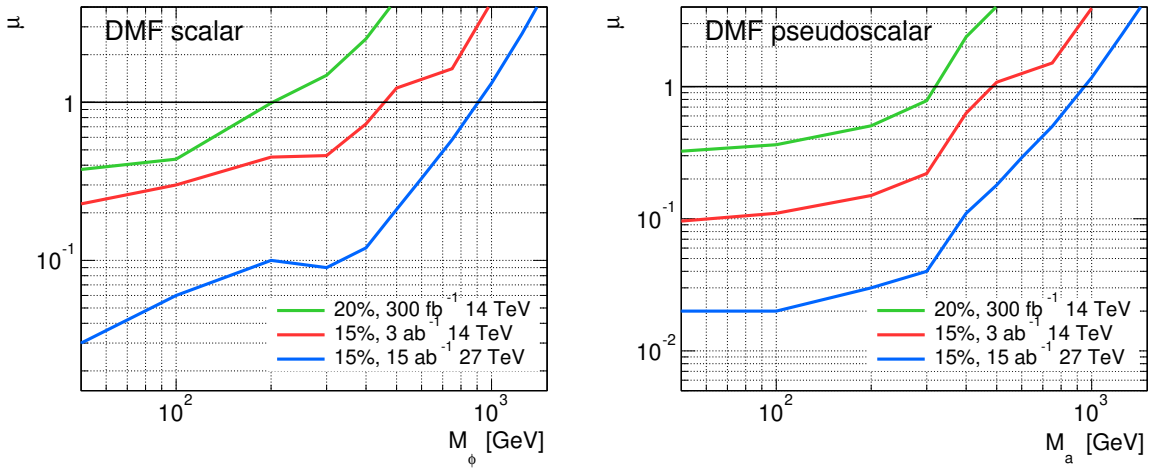

Fig. 3.2.4: Values of the signal strength μ that can be excluded at 95% C.L. as a function of the mass for DMF scalar (left) and pseudoscalar (right) mediators. The reach with 300 fb^{-1} (LHC Run-3) and 3 ab^{-1} (HL-LHC) of $\sqrt{s} = 14$ TeV data is given for a 5-bin shape fit with 20% (green curves) and 15% (red curves) errors. A hypothetical shape-fit scenario based on 15 ab^{-1} of $\sqrt{s} = 27$ TeV of data (HE-LHC) and 15% systematics is also shown (blue curves).

3.2.2 Production of dark matter in association with top quarks at HL- and HE-LHC

Contributors: U. Haisch, P. Pani, and G. Polesello

The prospects of the HL-LHC and the HE-LHC to search for DM production in association with top-quark pairs ($t\bar{t} + E_T^{\text{miss}}$) and in single-top quark events ($tX + E_T^{\text{miss}}$) are investigated. Our sensitivity studies are based on the analysis strategies presented in Ref. [216–218]. In the case of the $t\bar{t} + E_T^{\text{miss}}$ signal, the two-lepton final state is considered. Since the selections employed in Ref. [216] turn out to lead to the best performance also at the HL-LHC and the HE-LHC, the selections in our $t\bar{t} + E_T^{\text{miss}}$ sensitivity study were not changed with respect to that used in the earlier analysis. In the case of the $tX + E_T^{\text{miss}}$ signature, both the two-lepton and one-lepton final state is studied. Since modifying the selections did not notably increase the sensitivity, the selections of the dilepton search were kept identical to the ones used in Ref. [217]. The single-lepton final state selections employed in Ref. [218] were instead reoptimised in our sensitivity study to take full advantage of the increased data set expected at future high-luminosity and high-energy LHC runs.

Sensitivity study of the $t\bar{t} + E_T^{\text{miss}}$ signature: Given the presence of a sizeable irreducible background surviving all the selections, the experimental sensitivity of future $t\bar{t} + E_T^{\text{miss}}$ searches will be largely determined by the systematic uncertainty on the estimate of the SM backgrounds. This uncertainty has two main sources: first, uncertainties on the parameters of the detector performance such as the energy scale for hadronic jets and the identification efficiency for leptons, and second, uncertainties plaguing the modelling of SM processes. Depending on the process and on the kinematic selection, the total uncertainty can vary between a few percent and a few tens of percent. The present analysis does not select extreme kinematic configurations for the dominant $t\bar{t}Z$ background, and it thus should be possible to control the experimental systematics at the 10% to 30% level. In the following, we will assume a systematic error of either 20% or 15% on both background and signal, fully correlated between the two and across kinematic bins. We have checked that in the absence of an external measurement (*e.g.* a background control region) which profiles uncertainties, the use of correlated uncertainties provides the most conservative results. In addition, we consider a 5% uncertainty on the signal only to account for the theoretical uncertainty on the $t\bar{t} + E_T^{\text{miss}}$ signal.

In Fig. 3.2.4 we present sensitivity estimates at LHC Run-3, the HL-LHC and the HE-LHC for scalar (left panel) and pseudoscalar (right panel) simplified DM model mediators. The shown results

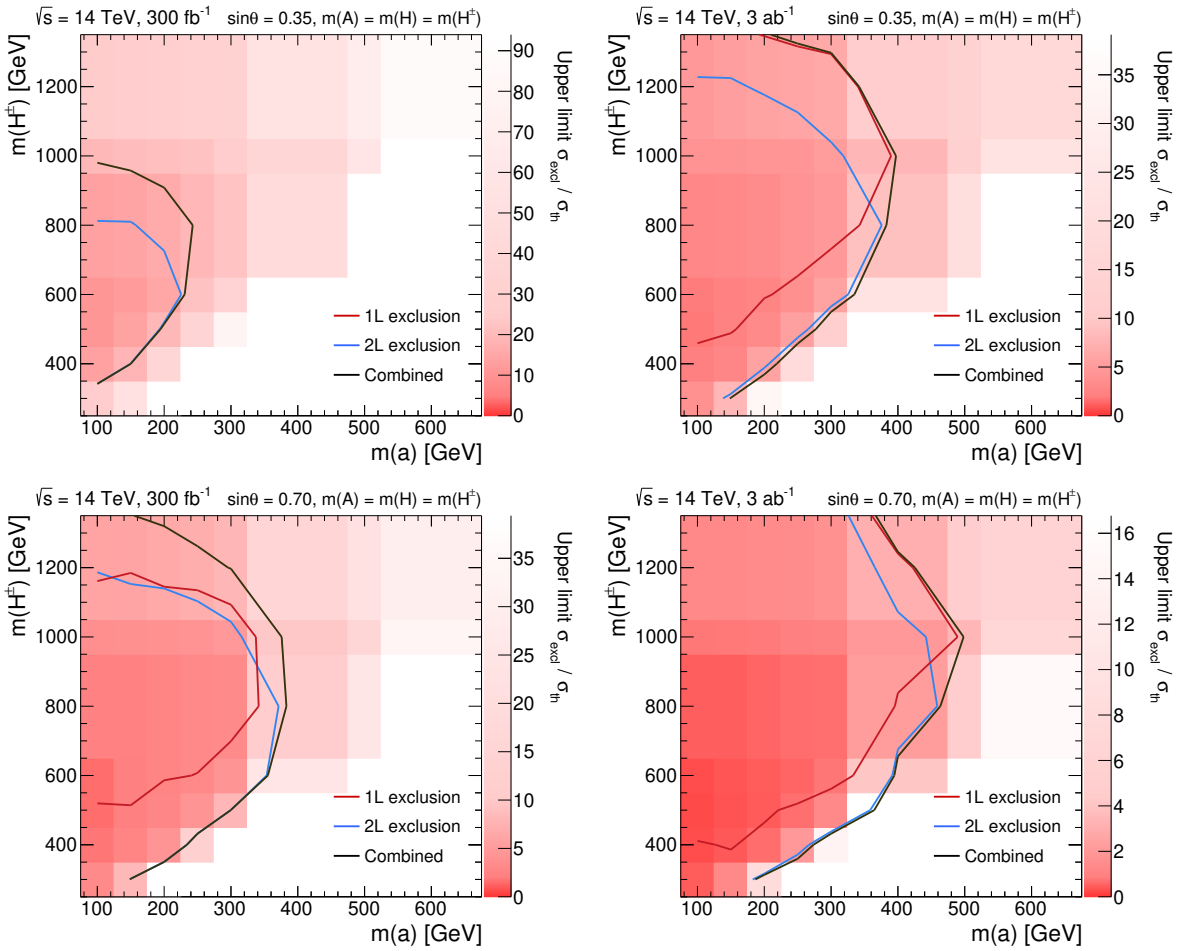

Fig. 3.2.5: 95% C.L. exclusion limits in the $m(a) - m(H^{\pm})$ plane following from our one-lepton (1L) and two-lepton (2L) analysis shown as red and blue lines. The black curves indicate the bounds obtained by a combination of the two search strategies. The used 2HDM+a parameters are indicated. The left (right) panels correspond to 300 fb^{-1} (3 ab^{-1}) of $\sqrt{s} = 14$ TeV data. Systematic uncertainties of 20% (5%) on the SM background (signal) are assumed.

correspond to a DM mass of $m_{\chi} = 1$ GeV and the coupling choices $g_q = g_{\chi} = 1$, as recommended by the ATLAS/CMS DM Forum (DMF) [219] and the LHC DM Working Group [215]. The estimated 95% C.L. exclusion limits are obtained from a 5-bin likelihood fit to the $|\cos\theta_{\ell\ell}| = \tanh(\Delta\eta_{\ell\ell}/2)$ distribution. The inclusion of shape information is motivated by the observation that the distributions of events as a function of the pseudorapidity difference $\Delta\eta_{\ell\ell}$ of the dilepton pair is different for signal and background [216]. At LHC Run-3 it should be possible to exclude DMF scalar (pseudoscalar) models that predict a signal strength of $\mu = 1$ for mediator masses up to around 200 GeV (300 GeV) using the 5-bin likelihood fit employed in our study. It should be possible to improve the maximal mass reach by roughly a factor of 2 when going from LHC Run-3 to the HL-LHC and from the HL-LHC to the HE-LHC. The corresponding 95% C.L. exclusion limits on DMF scalar (pseudoscalar) mediators are thus expected to be around 450 GeV (500 GeV) and 900 GeV (950 GeV) at the HL-LHC and the HE-LHC, respectively. Another conclusion that can be drawn from our sensitivity study is that the reach of future LHC runs depends strongly on the systematic background uncertainty, and as a result a good experimental understanding of $t\bar{t}Z$ production within the SM will be a key ingredient to a possible discovery of DM in the $t\bar{t} + E_T^{\text{miss}}$ channel.

Using the recasting procedure described in Ref. [220], the sensitivity estimates presented in Fig. 3.2.4 for the DMF spin-0 models can be translated into exclusion limits on next-generation spin-

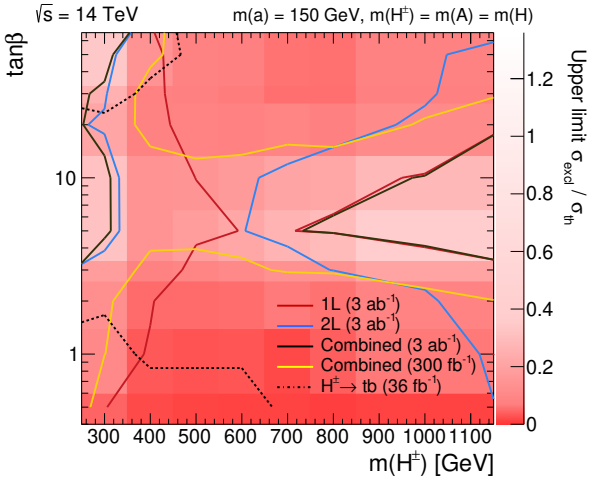

Fig. 3.2.6: Regions in the $m(H^\pm) - \tan\beta$ which can be excluded at 95% C.L. through the one-lepton (1L), two-lepton (2L) searches and their combination. The used 2HDM+a parameters are shown in the headline of the figure. The projections assume 300 fb^{-1} or 3 ab^{-1} of $\sqrt{s} = 14$ TeV data and a systematic uncertainty of 20% (5%) on the SM background (signal). The shown $H^\pm \to tb$ limits have been obtained by recasting the experimental results presented in Ref. [226].

0 DM models. In the case of the 2HDM+a model [221–225] for instance and adopting the benchmark (4.5) and (4.6) introduced in Ref. [220], one finds for $\tan\beta = 1$ the 95% C.L. bounds $m(a) \lesssim 150$ GeV (HL-LHC) and $m(a) \lesssim 350$ GeV (HE-LHC) on the mass of the 2HDM+a pseudoscalar mediator a. These numbers show again that a HE-LHC is expected to be able to significantly improve upon the HL-LHC reach, in particular for spin-0 DM model realisations that predict small $t\bar{t} + E_T^{\text{miss}}$ signal cross sections.

Sensitivity study of the $tX + E_T^{\text{miss}}$ signature: Following the analyses [217,218], we interpret our $tX + E_T^{\text{miss}}$ results in the context of the 2HDM+a model. The total background in the two-lepton selection is approximately 100 events, dominantly composed of the $t\bar{t}Z/W$ and tWZ background processes. For charged Higgs masses $m(H^\pm)$ between 300 GeV and 700 GeV, the acceptance for signal events containing at least two leptons is in the range $[0.1, 0.7]$% for $m(a) = 150$ GeV and $\tan\beta = 1$. The total background in the one-lepton selection is approximately 30 events for the leptonic-$H^\pm$ signal selection and 45 events for the hadronic-$H^\pm$ one. More than 70% of the SM background arises from $t\bar{t}Z/W$ and tZ processes in both selections and the rest is in equal parts due to the contributions of top pairs (dileptonic decays) and the single-top tW channel for the hadronic-$H^\pm$ selection, while in the case of the leptonic-$H^\pm$ selection the remaining 30% are dominated by single-top processes. For $m(H^\pm)$ in the range of 600 GeV and 1 TeV, the acceptance for signal events containing at least one lepton amounts to approximately $[0.2, 0.5]$% for $m(a) = 150$ GeV and $\tan\beta = 1$.

In Fig. 3.2.5 we present the results of our $tX + E_T^{\text{miss}}$ sensitivity study in the $m(a) - m(H^\pm)$ plane of the 2HDM+a model employing a DM mass of $m_\chi = 1$ GeV. As indicated by the headlines of the individual panels, two different values for the mixing angle in the pseudoscalar sector ($\sin\theta$) are employed. The parameters not explicitly specified have been set to the benchmark choices (4.5) made in Ref. [220]. One observes that at LHC Run-3 a combination of the one-lepton and two-lepton search should allow one to exclude masses $m(a)$ up to around 250 GeV (375 GeV) for $\sin\theta = 0.35$ ($\sin\theta = 0.7$). The corresponding HL-LHC limits instead read 400 GeV (500 GeV), implying that collecting ten times more luminosity is expected to lead to an improvement in the LHC reach by a factor of around 1.5 in the case at hand. Also notice that the one-lepton and two-lepton analyses are complementary because they have different sensitivities on $m(H^\pm)$.

One can also compare the HL-LHC reach in the $m(H^\pm) - \tan\beta$ plane to that derived in Ref. [217]

for LHC Run-3. Such a comparison is presented in Fig. 3.2.6. Numerically, we find that all values of $\tan\beta$ can be excluded for a charged Higgs mass between 300 GeV and 700 GeV, improving the LHC Run-3 forecast, which showed a coverage in $\tan\beta$ up to 3 and above 15 for the same mass range. For $m(H^{\pm}) = 1$ TeV instead, the upper limit in $\tan\beta$ is extended from 2 to 3 and the lower limit is extended from around 30 to 20. Compared to LHC Run-3 the HL-LHC is thus expected to have a significantly improved coverage in $\tan\beta$, in particular for not too heavy 2HDM spin-0 states. Limits on $m(H^{\pm})$ and $\tan\beta$ also derive from $H^{\pm}$ production followed by the decay of the charged Higgs into SM final states such as $\tau\nu$ or tb. As indicated in Fig. 3.2.6, in the 2HDM+a model the searches for $H^{\pm} \to tb$ cover an area largely complementary to the results of the $tX + E_T^{\text{miss}}$ searches.

3.2.3 Dark matter production in single-top events at HL-LHC

Contributors: L. Barranco, F. Castillo, M. J. Costa, C. Escobar, J. García-Navarro, D. Madaffari, J. Navarro, ATLAS

The expected sensitivity of a search for the non-resonant production of an exotic state decaying into a pair of invisible DM particle candidates in association with a right-handed top quark is presented [227]. Such final-state events, commonly referred to as "monotop" events, are expected to have a reasonably small background contribution from SM processes. In this analysis only the topologies where the W boson from the top quark decays into a lepton and a neutrino are considered.

The non-resonant monotop is produced via a flavour-changing neutral interaction where a top quark, a light-flavour up-type quark and an exotic massive vector-like particle V can be parametrised through a general Lagrangian [219, 228]:

$$\mathcal{L}_{\text{int}} = aV_{\mu}\bar{u}\gamma^{\mu}P_{\text{R}}t + g_{\chi}V_{\mu}\bar{\chi}\gamma^{\mu}\chi + \text{h.c.}\,, \tag{3.2.1}$$

where V is coupled to a pair of DM particles (represented by Dirac fermions $\chi\bar{\chi}$) whose strength can be controlled through a parameter g_{χ} and where P_{R} represents the right-handed chirality projector. The parameter a stands for the coupling constant between the massive invisible vector boson V, and the t- and u-quarks, and γ^{μ} are the Dirac matrices.

The experimental signature of the non-resonant monotop events with W boson decaying leptonically is one lepton from the W-boson decay, large $E_{\text{T}}^{\text{miss}}$, and one jet identified as likely to be originated from a b-quark. The signal event candidates are selected by requiring exactly one lepton with $p_{\text{T}} > 30$ GeV, exactly one jet with $p_T > 30$ GeVidentified as a b-jet and $E_{\text{T}}^{\text{miss}} > 100$ GeV. Since the considered monotop process favours final states with positive leptons, events with negative lepton charge are rejected. These criteria define the base selection.

In order to maximise the sensitivity of the study, in addition to the base selection further discrimination is achieved by applying additional criteria according to the kinematic properties of the signal while rejecting background. The transverse mass of the lepton–$E_{\text{T}}^{\text{miss}}$ system, $m_{\text{T}}(\ell, E_{\text{T}}^{\text{miss}})$, is required to be larger than 100 GeV in order to reduce the background contribution. In background events the spectrum of this quantity decreases rapidly for values higher than the W-boson mass. In signal events instead, the spectrum has a tail at higher mass values. When originating from the decay of a top quark, the lepton and the b-jet are close to each other. Therefore, events are required to have an azimuthal difference between the lepton momentum and the b-jet momentum directions ($\Delta\phi(\ell,\text{b}-jet)$) of less than 2.0, which disfavours the W+jets and diboson backgrounds.

Further selection is performed via a BDT algorithm provided by the Toolkit for Multivariate Analysis [229]. The BDT is trained to discriminate the monotop signal from the dominant $t\bar{t}$ background. For the training, since no significant difference is observed for the different mass values, the sample with $m_V = 2.5$ TeV is used. Half of the events of both signal and background samples are selected randomly and used to train the BDT. The other half is used to probe the BDT behaviour in order to avoid the presence of overtraining. The variables entering the BDT are selected from a pool of fundamental quantities,

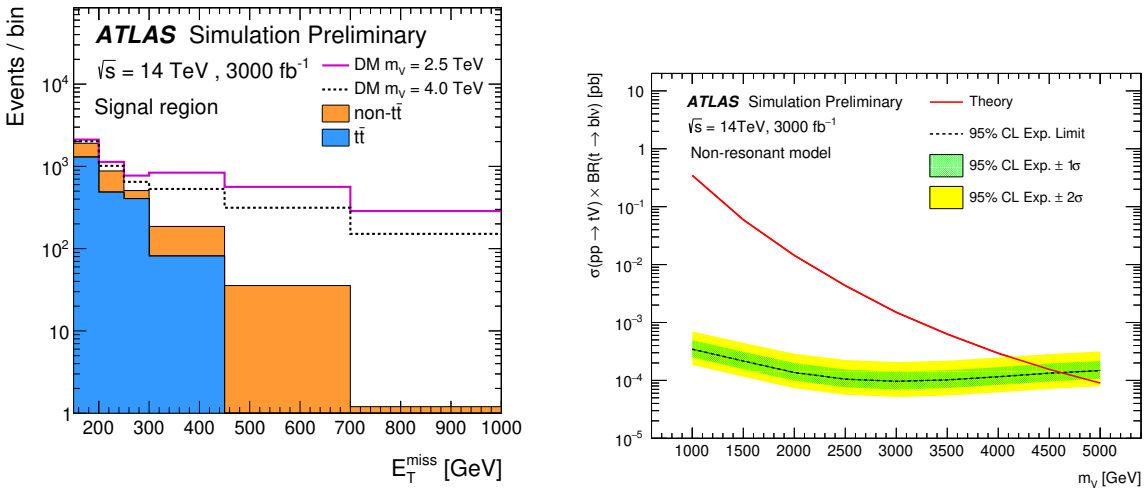

Fig. 3.2.7: Left: expected post-fit $E_{\mathrm{T}}^{\mathrm{miss}}$ distribution in the signal region. The stack distribution shows the $t\bar{t}$ and non-$t\bar{t}$ background predictions. Solid and dashed lines represent the signal corresponding to a mediator mass of 2.5 and 4.0 TeV, respectively. The signal event samples are normalised to the number of background events. The binning is the same as the optimised, non-equidistant binning used in the fit. Last bin includes overflow events. Right: expected 95% C.L. upper limits on the signal cross-section as a function of the mass of the mediator for the non-resonant model assuming $m_{\chi} = 1$ GeV, $a = 0.5$ and $g_{\chi} = 1$ using a BDT analysis. The MC statistical uncertainty is not considered but the full set of systematics, extrapolated from the 13 TeV analysis, is used.

like p_T of jets and b-jets, and angular distances. The variables selected are the ones showing the best discriminating power. In particular, $\Delta\phi(\ell, E_{\mathrm{T}}^{\mathrm{miss}})$ and $m_{\mathrm{T}}(\ell, E_{\mathrm{T}}^{\mathrm{miss}})$ are found to be the most effective variables. Only events with BDT response > 0.9 and $E_{\mathrm{T}}^{\mathrm{miss}} > 150$ GeVenter in the signal region and are used in the extraction of the result. The shape of the $E_{\mathrm{T}}^{\mathrm{miss}}$ distribution is used in the statistical analysis, as it is expected to be the most sensitive variable to the presence of new physics. The binning of this distribution is optimised for the sensitivity of the analysis in the signal region while ensuring the stability of the fit. This results in a non-equidistant binning which exhibits wider bins in regions with a large signal contribution, while preserving a sufficiently large number of background events in each bin.

Figure 3.2.7 (left) shows the post-fit $E_{\mathrm{T}}^{\mathrm{miss}}$ distribution in the signal region. The result does not include MC statistical uncertainties but incorporates effects of systematic uncertainties. The theoretical modelling of signal and background has the largest prior, 15%. The second largest source of uncertainty is the one relative to the $E_{\mathrm{T}}^{\mathrm{miss}}$ reconstruction, with 6% prior. Jet energy scale (JES) and jet energy resolution (JER) contribute with a total of 5%. The uncertainty on the requirements for pile-up jets rejection is 5%, whilst uncertainties on lepton identification, b-tagging efficiencies and luminosity are 1.2%, 2.5% and 1%, respectively.

Figure 3.2.7 (right) shows the expected 95% C.L. upper limits as a function of the mediator mass for the non-resonant model assuming $m_{\chi} = 1$ GeV, $a = 0.5$ and $g_{\chi} = 1$. After the fit, the largest impact on the result is coming from the uncertainty on the $E_{\mathrm{T}}^{\mathrm{miss}}$ reconstruction. This is expected since the $E_{\mathrm{T}}^{\mathrm{miss}}$ is the final discriminant in the analysis. The second largest contribution is coming from background and signal modelling. The other contributions are, in order of importance: pile-up jet rejection requirements, JES and JER, lepton reconstruction efficiency and b-tagging efficiency. The uncertainty on the expected luminosity is found to have the smallest effect. The expected mass limit at 95% C.L. is 4.6 TeV while the discovery reach (based on 5σ significance) is 4.0 TeV. For the current analysis the effect of possible improvements in the systematic uncertainties is estimated by reducing by half the uncertainties. This has the effect of increasing the exclusion limit (discovery reach) by 80 (50) GeV. The expectation for the equivalent of Run-3 integrated luminosity (300 fb^{-1}) is checked, obtaining an exclusion limit (discovery reach) of 3.7 TeV (3.2 TeV).

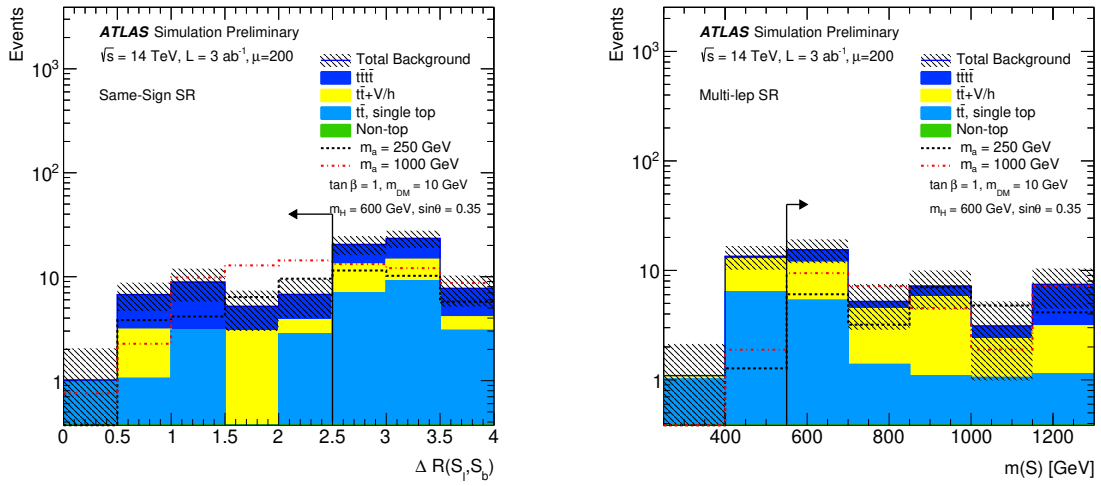

Fig. 3.2.8: Key distributions for events passing all Same-Sign (left) or Multi-lep (right) selection requirements except that on the distribution itself. The contributions from all SM backgrounds are shown, and the hashed band represents the statistical uncertainty on the total SM background prediction. The expected distributions for signal models with $m_a = 250$ GeV and $m_a = 1000$ GeV, assuming $m_H = 600$ GeV, $\sin\theta = 0.35$ are also shown as dashed lines for comparison.

3.2.4 Four-top signatures at the HL-LHC

Contributors: P. Pani, F. Meloni, ATLAS

A class of simplified models for dark matter searches at the LHC involving a two-Higgs-doublet extended sector together with an additional pseudoscalar mediator to DM, the 2HDM+a, are considered in this study [230]. The additional pseudoscalar mediator of the model, a, couples the DM particles to the SM and mixes with the pseudoscalar partner of the SM Higgs boson, A. This model is characterised by a rich phenomenology and can produce very different final states according to the production and decay modes for the various bosons composing the Higgs sector, which can decay both into dark matter or SM particles. The four-top signature is interesting if at least some of the neutral Higgs partners masses are kept above the $t\bar{t}$ threshold, since, when kinematically allowed, all four neutral bosons can contribute to this final state. The total four top-quark production cross-section is dominated by the light pseudoscalar and the heavy scalar bosons. In order to highlight this interplay, four benchmark models will be considered, assuming different choices for the mass of the light CP-odd and heavy CP-even bosons and the mixing angle between the two CP-odd weak eigenstates ($\sin\theta$).

Scenario 1 m_a sensitivity scan assuming:

a) $m_H = 600$ GeV , $\sin\theta = 0.35$.
b) $m_H = 1$ TeV , $\sin\theta = 0.7$.

Scenario 2 $\sin\theta$ sensitivity scan assuming:

a) $m_H = 600$ GeV , $m_a = 200$ GeV.
b) $m_H = 1$ TeV , $m_a = 350$ GeV.

This prospect study considers four top-quarks final states involving at least two leptons with the same electric charge or at least three or more leptons. Final states with high jet multiplicity and one lepton are also very powerful to constrain these signatures, but are not considered here. Complementary studies of the potential for the measurement of standard model production of the four top final state at CMS [231] and ATLAS [232] are also discussed in working group chapter 1 [30].

Events are accepted if they contain at least two electrons, two muons or one electron and one muon with the same electric charge or at least three leptons ($p_T > 25$ GeV). Furthermore, events are required

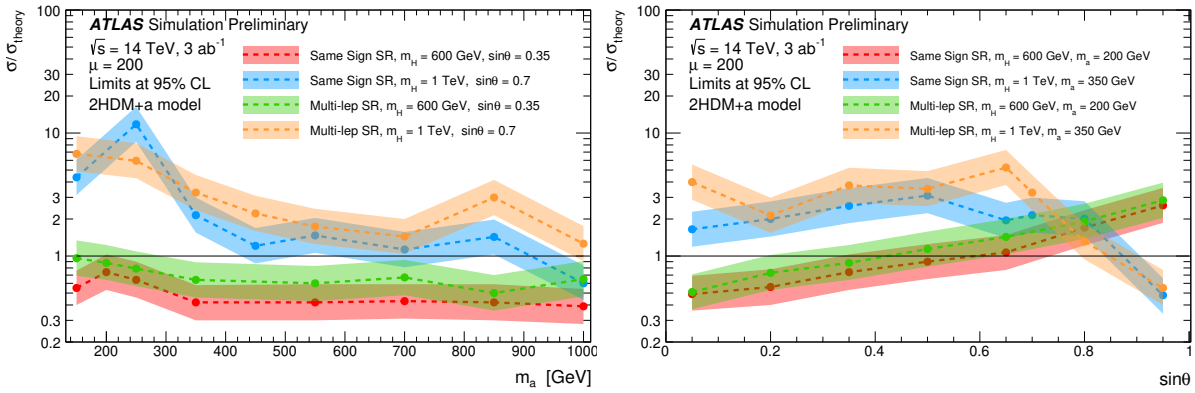

Fig. 3.2.9: Exclusion limits at 95% C.L. for Same-Sign and Multi-lep SRs in terms of excluded cross-section (σ) over the cross-section predicted by the model (σ_{theory}). Limits are derived from the analysis of 3 $\mathrm{ab}^{-1}$of 14 TeV proton-proton collision data as a function of m_a (left) or as a function of $\sin\theta$ (right) for each parameter assumptions described and indicated in the legend. The 1σ variation of the total uncertainty on the limit is indicated as a band around each exclusion line.

to contain at least three b-jets. The up to four leading leptons and up to four leading b-jets in the event are grouped respectively in two systems, called $\mathcal{S}_\ell$ and $\mathcal{S}_b$. A signal system $\mathcal{S}$ is defined by $\mathcal{S} = \mathcal{S}_\ell \cup \mathcal{S}_b$. Different discriminators and kinematic variables are used in the analysis to separate the signal from the SM background.

- $p_T(\mathcal{S}_\ell)$: the vector sum of the lepton four momenta in $\mathcal{S}_\ell$;
- $\Delta R(\mathcal{S}_\ell, \mathcal{S}_b)$: the ΔR between the vectorial sum of the leptons in $\mathcal{S}_\ell$ and the vectorial sum of the b-jets in $\mathcal{S}_b$;
- m($\mathcal{S}$): the invariant mass of the signal system $\mathcal{S}$;

A common selection is applied to all events, before further categorisations. Events are required to have at least two jets with a $p_T > 50$ GeV. In events with exactly two (anti-)electrons, the contribution of SM processes including an on-shell Z boson decaying leptonically with a lepton charge misidentification is reduced by vetoing events with 81.2 GeV $<$ m$_{\ell\ell}$ $<$ 101.2 GeV. Furthermore, low mass resonances are vetoed by requiring $m_{\ell\ell} > 15$ GeV. Two signal regions (SRs) are defined selecting events with exactly two charged leptons with the same electric charge (denoted Same-Sign) or three or more charged leptons (denoted Multi-lep). Figure 3.2.8 shows two key distributions ($\Delta R(\mathcal{S}_\ell, \mathcal{S}_b)$ and $m(\mathcal{S})$) for events passing one set of SRs requirements except for the requirement on the shown variable itself. The main backgrounds that survive the selections are the irreducible $t\bar{t}t\bar{t}$ and $t\bar{t}$+V/h channels. The dominant uncertainties are expected to be due to theoretical modelling of the irreducible backgrounds and, to a lesser extent, to the jet energy scale and resolution, and the b-tagging efficiency. Owing to the reduced statistical uncertainty and a better understanding of the physics models, it is expected that JES, JER, b-tagging efficiency and irreducible background modelling uncertainties will all be reduced. This leads to an estimate of the total background uncertainty of about 20%. The resulting experimental uncertainty is assumed to be fully correlated between the background and the signal when setting 95% C.L. exclusion limits. Furthermore, an additional systematic of 5% is considered for the signal, in order to account for the theoretical systematic uncertainty on the model.

Scans of expected exclusion limits at 95% C.L. are shown in Figures 3.2.9 as a function of m_a, for fixed m_H and $\sin\theta$ and as a function of $\sin\theta$ for fixed m_a and m_H. In all benchmarks, it is assumed that $\tan\beta = 1$ and $m_\chi = 10$ GeV. For light pseudoscalar masses above the $t\bar{t}$ decay threshold, a significance of about 3σ is expected if $m_H = 600$ GeV and $\sin\theta = 0.35$. The same benchmark is expected to be excluded for all light-pseudoscalar masses and for $\sin\theta < 0.35$ if $m_a = 200$ GeV. Mixing angles such that $\sin\theta > 0.95$ are also expected to be excluded for $m_a = 350$ GeV, $m_H = 1$ TeV and, under the

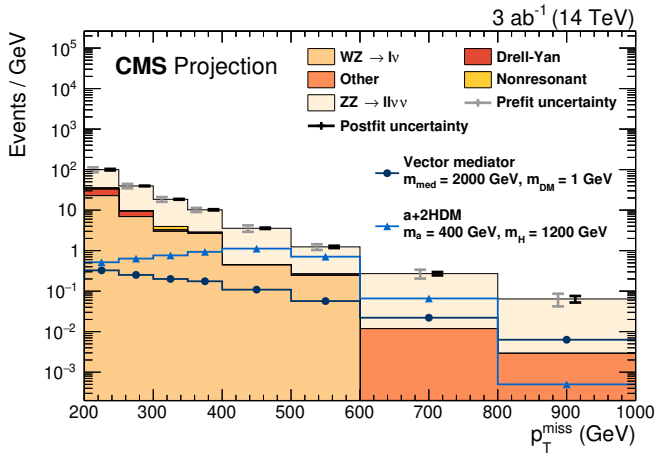

Fig. 3.3.1: Spectrum of $\mathbf{p}_{\mathrm{T}}^{\mathrm{miss}}$ in the signal region. Uncertainty bands for the background prediction are shown before and after applying a background-only maximum-likelihood fit to the Asimov dataset in signal and control regions.

same assumptions, an upper limit of about two times the theoretical cross section is set for $\sin\theta < 0.8$. Finally, $\sin\theta < 0.4$ is excluded for $m_H = 600$ GeV, $m_a = 200$ GeV. In almost all cases the Same-Sign SR yields the strongest constraints on the parameter space considered in this work. However, the Multi-lep SR offers a complementary channel whose sensitivity is of the same order of magnitude. Possibly, exploiting dedicated techniques developed to suppress or better estimate the $t\bar{t} + V$ background that affects the Multi-lep SR, this signature can achieve sensitivity comparable to the Same-Sign selection.

3.3 Dark Matter and Electroweak Bosons

DM can be produced in association with, or through interactions with, EW gauge bosons. The DM may recoil against a (leptonically decaying) Z boson that was produced as ISR or in the decay of a heavy mediator to a lighter mediator and a Z, see Section 3.3.1. It may recoil against a photon or be produced through its couplings to W, Z in VBF, as in Section 3.3.2. A standard way to couple to the dark sector is through SM "portals". UV completing the Higgs portal leads to signals only involving the mediators and not the DM, such as diHiggs or di-mediator production. Prospects are presented in Section 3.3.3. Alternatively, heavier dark sector states with couplings to the Z boson can produce DM in their decays, as shown in Section 3.3.4.

3.3.1 Dark matter produced in association with a Z boson at HL-LHC

Contributors: A. Albert, K. Hoepfner, CMS

Collider searches for DM production critically rely on a visible particle being produced in association with the sought-after invisible DM candidate. One possible choice of an accompanying SM signature is a Z boson reconstructed from an e^+e^- or $\mu^+\mu^-$ pair. In the hadronic environment of the LHC, this leptonic signature is well reconstructible and the resonant behaviour of the dilepton mass allows for efficient rejection of non-Z background processes. The presence of a signal is determined from a maximum-likelihood fit of the $\mathbf{p}_{\mathrm{T}}^{\mathrm{miss}}$ spectrum of selected events, which would be hardened by the presence of a DM signal relative to the SM backgrounds.

This study from CMS is a projection based on the results of Ref. [233]. Event-by-event weights are applied to simulated samples to account for the difference in c.o.m. energy and $\mathbf{p}_{\mathrm{T}}^{\mathrm{miss}}$ resolution between the Run-2 and HL-LHC scenarios [234]. The $\mathbf{p}_{\mathrm{T}}^{\mathrm{miss}}$ spectrum in the signal region is shown in Fig. 3.3.1.

The results are interpreted in two simplified models of DM production. In the first model, a

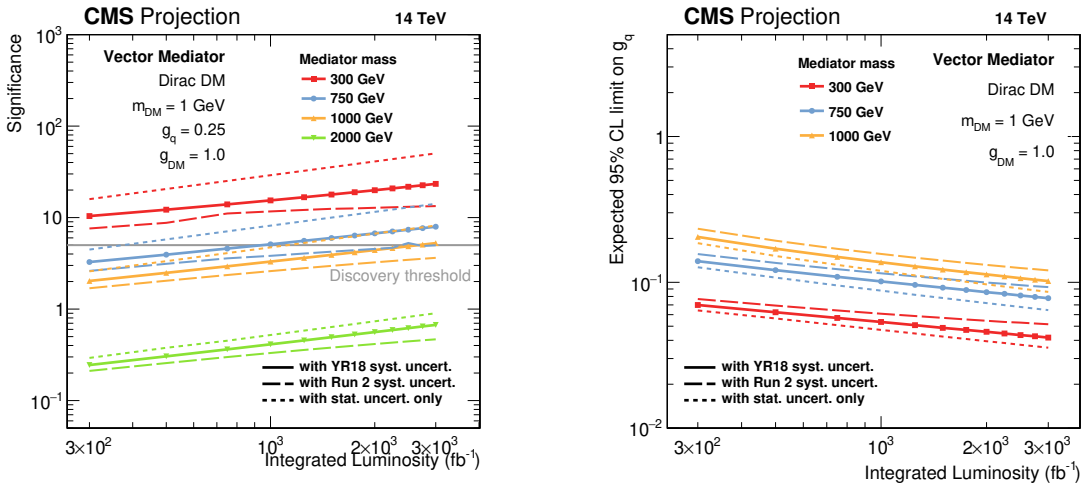

Fig. 3.3.2: Expected significance of a vector mediator signal with unity signal strength (left) and 95% C.L. exclusion limits on the coupling g_q (right). Both quantities are shown as a function of integrated luminosity for multiple choices of the mediator mass m_{med}.

minimal scenario is assumed where there is one new mediator boson and one new DM Dirac fermion χ [219]. The mediator is assumed to have vector couplings g_q and g_{DM} to quarks and DM, respectively. In the second model, referred to as "a+2HDM", the SM is extended by a second Higgs doublet as well as a light pseudoscalar DM mediator, a [224]. By allowing for the light pseudoscalar to mix with the heavier pseudoscalar state from the second Higgs doublet, the mediation mechanism can be realised without violating any of the various existing direct and indirect constraints on the scalar sector [220,224]. Importantly, this second model allows for the production of the pseudoscalar mediator and Z boson through the decay of a new heavy scalar H. This production mode provides excellent sensitivity for the $Z + \mathbf{p}_{\text{T}}^{\text{miss}}$ search compared to other searches such as jets+$\mathbf{p}_{\text{T}}^{\text{miss}}$ [220].

For the vector mediator scenario, the expected signal significance and expected exclusion limits on g_q are shown in Fig. 3.3.2. A signal with a mediator of mass $m_{\text{med}} = 750$ GeV could be discovered with $\mathcal{L}_{\text{int}} \approx 1\,\text{ab}^{-1}$, while a heavier mediator with $m_{\text{med}} = 1$ TeV would require $\mathcal{L}_{\text{int}} \approx 3\,\text{ab}^{-1}$. Especially the latter case highlights the effect of the systematic uncertainty scenarios. Improved handling of systematic uncertainties could reduce the integrated luminosity required for a discovery by a factor three, and thus advance the discovery by years. Framed as an exclusion on the mediator-quark coupling g_q, values down to 0.04 will be probed for a lighter mediator with $m_{\text{med}} = 300$ GeV, and $g_q \approx 0.1$ will be testable for $m_{\text{med}} = 1$ TeV. A heavier mediator of mass $m_{\text{med}} = 2$ TeV will remain out of reach even with the final HL-LHC dataset of $3\,\text{ab}^{-1}$. The two-dimensional exclusion as a function of the relevant particle masses for both models is shown in Fig. 3.3.3. In the case of the vector mediator, mediator masses up to ~ 1.5 TeV will be probed, assuming $m_{\text{med}}/2 > m_{\text{DM}}$. Depending on the choice of systematic uncertainty scenario, the mediator mass exclusion varies by ≈ 100 GeV. In the a+2HDM model, light pseudoscalar masses up to 600 GeV and heavy boson masses up to 1.9 TeV will be probed. Again, the choice of systematic uncertainty scenarios may influence these values by ≈ 100 GeV (m_{a}) and $100 - 150$ GeV (m_{H}). These mass exclusion ranges show an improvement of a factor ~ 2.5 in the mediator masses and up to ~ 3 for the pseudoscalar mass compared to the Run-2 result with $\mathcal{L}_{\text{int}} = 36\,\text{fb}^{-1}$ [233,235].

3.3.2 Dark matter searches in mono-photon and VBF+$E_{\text{T}}^{\text{miss}}$ final states at HL-LHC

Contributors: L. Carminati, D. Cavalli, M. Cirelli, C. Guyot, A. Demela, I. Lim, B. Nachman, M. M. Perego, S. Resconi, F. Sala, ATLAS

A prospect study for DM searches with the ATLAS detector is presented in a scenario where the

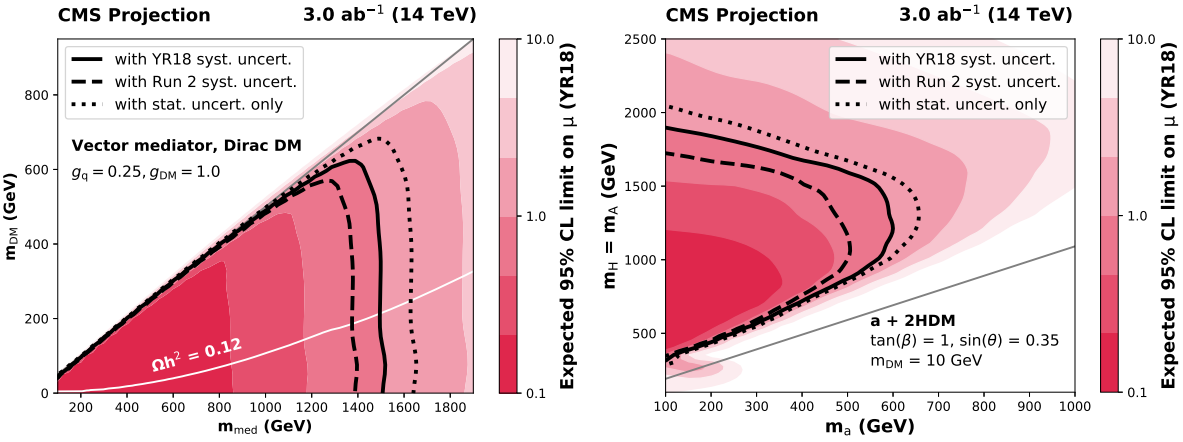

Fig. 3.3.3: Expected 95% C.L. exclusion limits on the signal strength in the vector mediator (left) and a+2HDM scenarios (right). In the vector mediator case, the exclusion is presented in the plane of the mediator and dark matter masses, while the result is shown in the plane of the pseudoscalar mediator mass m_a and the heavy boson masses $m_H = m_A$. The grey lines indicate the relevant kinematic boundaries that limit the sensitive regions: $m_{med}/2 = m_{DM}$ in the vector mediator case, and $m_H = m_a + m_Z$ in the a+2HDM case. For the vector mediator scenario, the white line indicates the parameter combinations that reproduce the observed DM relic density in the universe [236, 237].

SM is extended by the addition of an EW fermionic triplet with null hypercharge [238]. The lightest mass state of the triplet constitutes a weakly interacting massive particle DM candidate. This model is inspired by SUSY with anomaly-mediated SUSY breaking [239–241] and by models of Minimal Dark Matter (MDM) [242–244], and provides a benchmark in the spirit of simplified models [219] where the mediator is a SM particle. Projections for an integrated luminosity of 3 ab^{-1}are presented for the DM searches in the mono-photon [245] and VBF+$E_{\mathrm{T}}^{\mathrm{miss}}$ [246] final states, based on the Run-2 analyses strategy. To illustrate the experimental challenges associated to a high pile-up environment due to the high luminosity, the effect of the pile-up on the VBF invisibly decaying Higgs boson is studied as a benchmark process.

EW fermionic WIMP Dark Matter triplet

A fermionic triplet χ of the $SU(2)_L$ group with null hypercharge (Y): $\chi = \begin{pmatrix} \chi^+ \\ \chi_0 \\ \chi^- \end{pmatrix}$ is added to the SM with a Lagrangian:

$$\begin{aligned}\mathcal{L}_{MDM} &= \frac{1}{2}\bar{\chi}(i\not{D} + M)\chi \\ &= \frac{1}{2}\bar{\chi_0}(i\not{\partial} - M_{\chi^0})\chi_0 + \bar{\chi^+}(i\not{\partial} - M_{\chi^+})\chi^+ \\ &+ g(\bar{\chi^+}\gamma_\mu\chi^+(\sin\theta_W A_\mu + \cos\theta_W Z_\mu)) + \bar{\chi^+}\gamma_\mu\chi_0 W_\mu^- + \bar{\chi_0}\gamma_\mu\chi^+ W_\mu^+\end{aligned}$$

where g is the $SU(2)$ gauge coupling; M is the tree-level mass of the particle; $\sin\theta_W$ and $\cos\theta_W$ are the sine and cosine of the Weinberg angle; A_μ, Z_μ, W_μ are the SM boson fields. The lightest component of the triplet is stable if some extra symmetry is imposed, like lepton number, baryon minus lepton number or a new symmetry under which χ is charged (*e.g.* R-parity in SUSY).

At tree level all the χ components have the same mass, but a mass splitting is induced by the EW corrections given by loops of SM gauge bosons between the charged and neutral components of χ. These corrections make the charged components heavier than the neutral one (χ_0). Its mass differs by $\simeq$ 165 MeV [210] from the one of the charged components. Being neutral and stable, χ_0 constitutes a

potential DM candidate. If the thermal relic abundance is assumed, the mass of χ_0 is $M_{\chi_0} \simeq 3$ TeV. However, if χ is not the only particle composing dark matter or if it is not thermally produced [241], its mass can be $M_{\chi_0} < 3$ TeV.

This model provides a benchmark of a typical WIMP DM candidate and its phenomenology recreates the one of supersymmetric models where the Wino is the lightest SUSY particle (LSP), for this reason this triplet is referred to as *Wino-like*. As studied in Ref. [247], treating M as a free parameter, this triplet can be probed at the LHC in different ways. Once produced, the charged components of the triplet decay into the lightest neutral component χ_0 plus very soft charged pions. χ_0 is identified as $E_{\mathrm{T}}^{\mathrm{miss}}$ in the detector while the pions, because of the small mass splitting between the neutral and charged components, are so soft that they are lost and not reconstructed. Therefore, the production of χ can be searched for by in mono-X events, such as mono-jet [248] and mono-photon; in VBF +$E_{\mathrm{T}}^{\mathrm{miss}}$ events as χ can also be produced via VBF [249]; and also in events characterised by high p_T tracks (caused by $\chi^{\pm}$) which end inside the detector once they have decayed into χ_0 and soft pions, disappearing tracks [250]. The VBF production mode and the mono-photon final state, studied in this contribution, constitute a necessary complement to the mono-jet, discussed in Sections 3.1.1 and 3.1.3, and disappearing track searches, see Section 4.1.3, because of the very different dependencies on the model parameters like the EW representation and the value of the mass splitting. LEP limits exclude masses below ~ 90 GeV [99, 251, 252], therefore the focus here is on $M_{\chi_0} \geq 90$ GeV.

Signal events with a pair of χ produced in the framework of this model [247] have been generated in the $\gamma+E_{\mathrm{T}}^{\mathrm{miss}}$ and VBF+$E_{\mathrm{T}}^{\mathrm{miss}}$ final state and simulated for different values of χ_0 mass with the official ATLASFAST-II simulation of the current detector [253] at $\sqrt{s} = 13$ TeV. For the VBF+$E_{\mathrm{T}}^{\mathrm{miss}}$ analysis, diagrams not properly originating from two vector bosons (in contrast to pure VBF processes) also contribute to the signal as they produce a jets+$E_{\mathrm{T}}^{\mathrm{miss}}$ signature where the jets have large pseudorapidity separation. To consider the realistic conditions at the HL-LHC, VBF H (H$\rightarrow ZZ^* \rightarrow \nu\bar{\nu}\nu\bar{\nu}$) events have been fully simulated, using GEANT 4 [54, 254], in the upgraded ATLAS detector including the upgraded inner tracker (ITk) [255, 256], with $\langle\mu\rangle = 200$ and at $\sqrt{s} = 14$ TeV.

Mono-Photon final state

The mono-photon analysis is characterised by a relatively clean final state, containing a photon with a high transverse energy and large $E_{\mathrm{T}}^{\mathrm{miss}}$, which can be mimicked by few SM processes. The search for new phenomena performed in mono-photon events in pp collisions at $\sqrt{s} = 13$ TeV at the LHC, using data collected by the ATLAS experiment in Run-2 corresponding to an integrated luminosity of 36.1 fb^{-1} [245], has shown no deviations from the SM expectations. The Run-2 mono-photon search is reinterpreted in the context of the WIMP triplet model at HL by keeping the same strategy for background estimates and event selection to exploit the full complexity of the analysis. The dominant backgrounds consist in processes with a Z or W boson produced in association with a photon, mainly Z($\rightarrow \nu\nu$) + γ. They are estimated by rescaling the MC prediction for those backgrounds with factors obtained from a simultaneous fitting technique, based on control regions (CRs) built by reverting one or more cuts of the signal region such that one type of process becomes dominant in that region. Other backgrounds, like W/Z + jet, top and diboson, in which electrons or jets can fake photons are estimated with data-driven techniques.

Events passing the lowest unprescaled single photon trigger are selected requiring $E_{\mathrm{T}}^{\mathrm{miss}} > 150$ GeV. The leading photon has to satisfy the "tight" identification criteria and is required to have $p_{\mathrm{T}}^{\gamma} > 150$ GeV, $|\eta| < 2.37$ and to be isolated. The photon and $E_{\mathrm{T}}^{\mathrm{miss}}$ are required to be well separated, with $\Delta\phi(\gamma,\ E_{\mathrm{T}}^{\mathrm{miss}}) > 0.4$. Finally, events are required to have no electrons or muons and no more than one jet with $\Delta\phi(\mathrm{jet},\ E_{\mathrm{T}}^{\mathrm{miss}}) > 0.4$. In the Run-2 analysis the total background prediction uncertainty is dominated by the statistical uncertainty and the largest systematic uncertainties are due to the uncertainty in the rate of fake photons from jets and to the uncertainty in the jet energy scale.

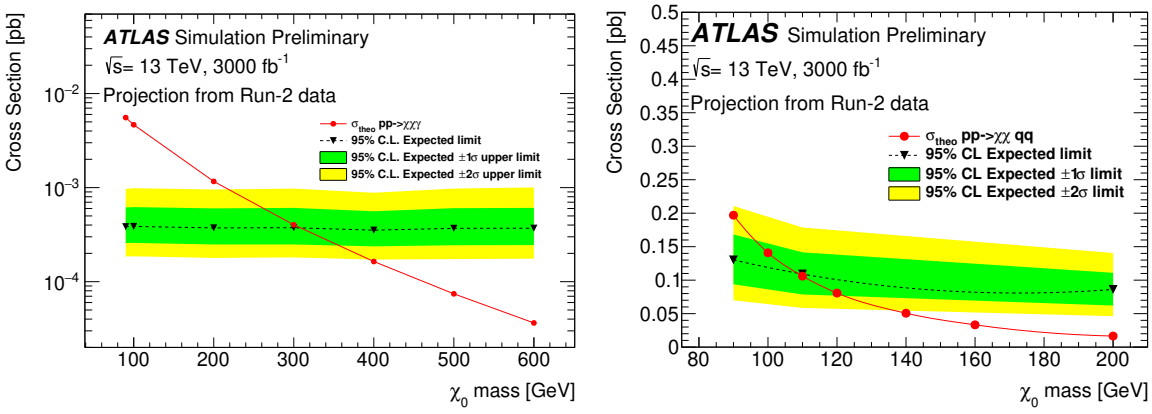

Fig. 3.3.4: Expected upper limits at 95% C.L. on the production cross section of χ as a function of χ_0 mass in (left) mono-photon final state and (right) VBF+$E_{\mathrm{T}}^{\mathrm{miss}}$ final state. Results are shown for an integrated luminosity of 3 ab^{-1}. The red line shows the theoretical cross section.

The reinterpretation of the mono-photon analysis in the WIMP triplet model uses full simulated MC signal samples and performs a simultaneous fit on the most inclusive signal region (SR), corresponding to $E_{\mathrm{T}}^{\mathrm{miss}} > 150$ GeV, that provides the best expected sensitivity. All backgrounds, including fake photons estimated with data-driven techniques, have been included in the fit rescaling the Run-2 results to the high luminosity scenario. All the systematic uncertainties on the MC background samples have been taken into account to obtain upper limits on the χ_0 production cross section. Projections of the expected upper limits on the production cross section of χ_0 at 95% C.L. for an integrated luminosity of 3 $\mathrm{ab}^{-1}$and $\sqrt{s} = 13$ TeV, are shown in Figure 3.3.4 (left). Masses of χ_0 below 310 GeV can be excluded at 95% C.L. by the analysis assuming the same systematic uncertainties adopted in Ref. [245]. The impact of the systematic uncertainty on the sensitivity of the analysis has been checked considering that the analysis will no more be limited by the statistical uncertainty at high luminosity. In a scenario in which the current systematic uncertainties are halved, an exclusion of χ_0 masses up to about 340 GeV could be reached. Thanks to the increased statistics, the analysis at high luminosity could be further optimised by performing a multiple-bin fit, thus on more bins in $E_{\mathrm{T}}^{\mathrm{miss}}$ improving the overall sensitivity of the analysis. This study is done for a c.o.m. energy of 13 TeV, a slight improvement in the signal significance is expected from the increase of the c.o.m. energy to 14 TeV foreseen for the HL-LHC.

VBF plus $E_{\mathrm{T}}^{\mathrm{miss}}$ final state

The VBF+$E_{\mathrm{T}}^{\mathrm{miss}}$ topology is characterised by two quark-initiated jets with a large separation in rapidity and $E_{\mathrm{T}}^{\mathrm{miss}}$. The sensitivity of the VBF+$E_{\mathrm{T}}^{\mathrm{miss}}$ analysis to the WIMP triplet model is presented as a reinterpretation of the Run-2 results for the high luminosity scenario foreseen for the HL-LHC. As pile-up is a key experimental challenge for event reconstruction in the VBF topology at the HL-LHC, a dedicated study of its impact is also shown using VBF $H \rightarrow$invisible as benchmark.

Projections at high luminosity for DM for EW triplet DM.
A search for an invisibly decaying Higgs boson produced via VBF has been performed by ATLAS using a dataset corresponding to an integrated luminosity of 36 fb^{-1} of pp collision at $\sqrt{s} = 13$ TeV [246]. The final state is defined by the presence of two energetic jets, largely separated in η and with $\mathcal{O}(1)$ TeV invariant mass, and large $E_{\mathrm{T}}^{\mathrm{miss}}$.

This analysis set limits on the BR $\mathcal{B}$ of the H$\rightarrow$ invisible. The main backgrounds arise from $Z \rightarrow \nu\nu$+jets and $W \rightarrow \ell\nu$+jets events. The contribution of W/Z is estimated from events in CRs enriched in $W \rightarrow \ell\nu$ (where the lepton is found) and $Z \rightarrow \ell\ell$ (with ℓ being electrons or muons) that are used to normalise the MC estimates to data through a simultaneous fitting technique and to extrapolate

the normalisation to the SR. The multijet background comes from multijet events where large $E_{\mathrm{T}}^{\mathrm{miss}}$ is generated mainly by jet mismeasurements. This is highly reduced by a tight $E_{\mathrm{T}}^{\mathrm{miss}}$ cut and is estimated via data-driven methods resulting in less than 1% of the total background.

The results are interpreted in the context of the WIMP model for an integrated luminosity of $3\ \mathrm{ab}^{-1}$. The same selections and analysis strategy are used to set limits on the cross section of the WIMP triplet produced via VBF; the only selection which has been changed is the request on the separation in pseudorapidity between the two leading jets ($\Delta\eta(j_1, j_2)$) which has been relaxed from > 4.8 to > 3.5, thus increasing the sensitivity to the model as, in addition to the pure VBF Feynman diagrams, also diagrams with strong production contribute to the signal. A SR is defined by selecting events passing the lowest unprescaled $E_{\mathrm{T}}^{\mathrm{miss}}$ trigger, containing no electron and muon, having exactly two jets with transverse momentum $p_T(j_1) > 80$ GeV and $p_T(j_2) > 50$ GeV, which are not back to back in the transverse plane ($\Delta\Phi(j_1, j_2) < 1.8$) and which are separated in pseudorapidity ($\Delta\eta(j_1, j_2) > 3.5$). Events are required to have large $E_{\mathrm{T}}^{\mathrm{miss}}$ (> 180 GeV), the two leading jets are separated from the $E_{\mathrm{T}}^{\mathrm{miss}}$ ($\Delta\Phi(j_1,\ E_{\mathrm{T}}^{\mathrm{miss}}) > 1$, $\Delta\Phi(j_2,\ E_{\mathrm{T}}^{\mathrm{miss}}) > 1$), the vectorial sum of all the jets (including the pile-up ones) is required to be $H_{\mathrm{T}}^{\mathrm{miss}} > 150$ GeV and the invariant mass of the dijet system is required to be $M(j_1, j_2) > 1$ TeV. The events in SR and in CRs are then split into three categories (*bins*) according to the invariant mass of the dijet system; the following $M(j_1, j_2)$ bins are considered: $1 - 1.5$ TeV, $1.5 - 2$ TeV and > 2 TeV.

A simultaneous fit in SR and CRs, using the three $M(j_1, j_2)$ bins to increase the signal sensitivity, is used for the $W/Z+$ jets background estimation and for the limit setting. Exclusion limits are set on the production cross section of the model using a one-sided profile likelihood ratio and the CLs technique [94, 95] with the asymptotic approximation [257]. Experimental and theoretical systematic uncertainties have been taken into account and are included in the likelihood as Gaussian-distributed nuisance parameters. The main experimental systematic uncertainties for the Run-2 VBF+$E_{\mathrm{T}}^{\mathrm{miss}}$ analysis come from JES and JER [258] and have been rescaled according to the HL expectations which are discussed in Ref. [7]. The main theoretical sources of uncertainty for the run-2 analysis come from choices on the resummation, renormalisation, factorisation and CKKW matching scale for the $W/Z+$jets backgrounds processes. A significant improvement in these systematic uncertainties is expected; therefore, the current run-2 theoretical systematic uncertainties on the $W/Z+$jets backgrounds have been rescaled down to reach the level of few $\%$ (5% of the run-2 theoretical systematic uncertainties is kept). Here is assumed that such an improvement in the theoretical systematics for VBF final state will be reached for the HL-LHC phase. The same correlation scheme that has been used in Ref. [246] is also used for the projections presented here. Uncertainties arising from the finite MC statistics of the samples used are assumed to be negligible.

The results obtained by rescaling the signals and backgrounds to an integrated luminosity of $3\ \mathrm{ab}^{-1}$ are shown in Figure 3.3.4 (right) and indicate that the lowest masses considered ($M_\chi \sim 110$ GeV) can be excluded at 95% C.L.. This study is done for a c.o.m. energy of 13 TeV, a slight improvement in the signal significance is expected from the increase of the c.o.m. energy to 14 TeV foreseen for the HL-LHC. The analysis is very sensitive to the systematic uncertainties and a further optimisation of the selection cuts on this model, together with the increase of the MC statistics in the VBF phase space, could help to achieve a better reach.

VBF analyses will probably benefit from a combination of $E_{\mathrm{T}}^{\mathrm{miss}}$ and VBF jet triggers; however, even with $E_{\mathrm{T}}^{\mathrm{miss}}$ thresholds raised by $50 - 100$ GeV with respect to the current ones, the analysis is still sensitive to this model for the masses considered.

The challenge of pile-up for VBF at HL-LHC.
In the study of the pile-up effects for VBF at the HL-LHC, jets are built from particle flow objects [259] using the anti-k_t algorithm with radius parameter $R = 0.4$ as implemented in FASTJET; they are only considered if $p_{\mathrm{T}} > 25$ GeV and $|\eta| < 4.5$. Charged particle tracks are reconstructed from hits in the Itk.

	$\frac{\mathcal{B}(H\to\text{invs.})}{\mathcal{B}_{\text{Truth, Nominal}}(H\to\text{invs.})}$	Systematic Uncertainties			
		10%	5%	5% + fixed efficiency	1%
PU jet rejec	None	–	–	0.31	0.59
	$R_{p_{\text{T}}}$	–	–	0.28	0.48
	Truth	1.0	0.48	0.07	0.10

Table 3.3.1: The limit on the $H \to$ invisible BR using the full HL-LHC dataset ($3\ \text{ab}^{-1}$) normalised to the one for the Run-2 systematic uncertainties and truth-based pile-up tagging to show the relative gains and losses possible under various scenarios. A '–' indicates a value bigger than 1.

Tracks are associated to the jets and required to have $p_{\text{T}} > 0.9$ GeV and $p_{\text{T}} < 40$ GeV (to suppress fake tracks). The difference between the primary vertex (this is the vertex with the highest $\sum p_{\text{T}}^2$) z position and the track z_0 (longitudinal impact parameter) must be less than 2σ, where σ is the sum in quadrature of the track z_0 and the vertex z uncertainties.

One of the key discriminating observables between pile-up jets and hard-scatter jets is $R_{p_{\text{T}}}$ [260], which is the sum of the p_{T} of the tracks associated to the jet normalised by the jet p_{T}. Only tracks with $\Delta R < 0.3$ are considered in the calculation of $R_{p_{\text{T}}}$. Jets are declared 'hard-scatter' if $R_{p_{\text{T}}} > 0.05$ which corresponds to 85% hard-scatter efficiency and 2% pile-up jet efficiency when $|\eta| < 1.2$ and $|z^{\text{reco}} - z^{\text{true}}| < 0.1$. $E_{\text{T}}^{\text{miss}}$ is critical to the $H \to$ invisible search; as an optimisation for the $E_{\text{T}}^{\text{miss}}$ reconstruction for the upgraded ATLAS detector is not yet available, the negative sum of the transverse momenta of all reconstructed jets ($E_{\text{T,jet}}^{\text{miss}}$) is used in this analysis.

Due to limitations of MC statistics, a simplified version of the Run-2 VBF $H \to$ invisible analysis is used. In particular, all of the angular requirements with jets are removed and there is no binning in $M(j_1, j_2)$ and $E_{\text{T,jet}}^{\text{miss}}$ is required to be > 150 GeV. For the Run-2 analysis, the event selection efficiency for $Z \to \nu\bar{\nu}$ events is about 2×10^{-6} and about 0.5% for the signal with a $\mathcal{B}(H \to \text{invisible}) = 100\%$ (which is about 85% from VBF). Contrary to the Run-2 analysis, here the ggF $H \to$ invisible contribution has been neglected. The background is nearly half QCD $Z \to \nu\bar{\nu}$ and half QCD W+jets. Since only Z+jets are used in this analysis, BR limits are computed by doubling the Z+jets background. It is likely that with the extended coverage of the ITk relative to the current tracker the lost leptons will be suppressed and thus the W+jets background will be less than the Z+jets rate so this approximation is conservative.

A simplified statistical analysis is performed to assess the impact of several scenarios on the $H \to$ invisible BR limit with the full HL-LHC dataset. A one-bin statistical test with one overall source of systematic uncertainty is performed to determine if a particular signal yield is excluded. The signal yield is scanned to determine the largest BR that would be not excluded at the 95% C.L.. Table 3.3.1 presents the limits on the $H \to$ invisible BR normalised to the one for the run-2 systematic uncertainties and truth-based pile-up tagging to show the relative gains and losses under various pile-up scenarios, corresponding to the three rows, and with different assumptions on the systematic uncertainties, corresponding to the four columns: 10% (similar to run-2), 5%, 5% assuming the same signal efficiency as in Run-2 and the background efficiency to be 10% of the signal efficiency; and finally 1%. With a realistic reduction in the systematic uncertainty and tighter selection criteria, it may be possible to significantly improve the sensitivity. The limit improves from including a simple $R_{p_{\text{T}}}$-based pile-up jet rejection, though the gap with the truth-information-based tagger indicates that there is room (and reward) for developing a more sophisticated approach.

As an overall conclusion, with a combination of pile-up robustness studies, analysis optimisation, and theory uncertainty reduction, the EW triplet DM searches at the HL-LHC, both in mono-photon and VBF+$E_{\text{T}}^{\text{miss}}$ final states, may be significantly improved.

3.3.3 *Search for Higgs portal dark matter models at HL- and HE-LHC*

Contributors: Y. G. Kim, C. B. Park, S. Shin

In a variety of BSM models, the Higgs boson is often considered as a particle mediating the interactions between the dark matter and the SM particles, dubbed as *Higgs portal*. The Higgs portal models can be categorised by the spin of DM as scalar, fermionic, or vector Higgs portal models.

The scalar Higgs portal models consider a SM singlet scalar DM (S) which has interactions with the SM Higgs doublet (H) as [261, 262] $SS^*HH^\dagger$, which is a four-dimensional operator. This type of models is often considered as a simplest reference DM model so that there exist various complementary searches combining the results from the direct detection, indirect detection, and the LHC.

The second category of Higgs portal models is the fermionic Higgs portal model considering a fermion (ψ) as DM. The interaction term between the DM (ψ) and the SM Higgs doublet can be effectively given as [263]

$$\frac{\psi\bar{\psi}HH^\dagger}{\Lambda}\,, \tag{3.3.1}$$

assuming the interaction is mediated by additional heavy particle(s) with mass scale Λ and the DM ψ is a Dirac fermion. The searches at the LHC, e.g., mono-jet with missing energy, provide constraints directly to Λ and the mass of DM. Because this is a five-dimensional operator, a renormalisable simplified model was first introduced in Ref. [264] by adding a SM real singlet scalar S which mixes between the SM Higgs doublet and the singlet scalar. Beyond the minimal set-up in Ref. [264], one can also consider the SM scalar field S a complex scalar, pseudo scalar field [265–269]. Equipped with the mixing and the existence of additional mediator (singlet-like mass eigenstate), this kind of model has been widely used in consistently explaining various experimental/observational results within the context of DM, such as possible direct detection experimental anomalies for light DM region [270], γ-ray observation from the Galactic Centre [268, 269], baryon-antibaryon asymmetry [271], and so on.

The third category of Higgs portal models is the vector DM model with interaction term between the DM (V^μ) and the SM Higgs doublet [272] $V^\mu V_\mu HH^\dagger$. The vector dark matter can be, e.g., a $U(1)$ vector field which gets a mass term though the Stueckelberg mechanism.

In this report, we focus on the Dirac fermion DM model as a benchmark model and show proper strategies searching for the signals at HL- and HE-LHC. Note that the results would apply similarly to other kind of models, *i.e.* scalar or vector DM models.

Benchmark model: As a benchmark model we choose the Singlet Fermionic Dark Matter (SFDM) model [264, 268–270, 273] because the analysis methods and results are readily applicable to other type of models. The SFDM has a dark sector composed of a SM singlet real scalar field S and a singlet Dirac fermion field ψ which is the DM candidate. The dark sector Lagrangian with most general renormalisable interactions is given by

$$\mathcal{L}^{\rm dark} = \bar{\psi}(i\not{\partial} - m_{\psi_0})\psi + \frac{1}{2}\partial_\mu S\partial^\mu S - g_S(\cos\theta\,\bar{\psi}\psi + \sin\theta\,\bar{\psi}i\gamma^5\psi)S - V_S(S,\,H), \tag{3.3.2}$$

where

$$V_S(S,\,H) = \frac{1}{2}m_0^2S^2 + \lambda_1 H^\dagger HS + \lambda_2 H^\dagger HS^2 + \frac{\lambda_3}{3!}S^3 + \frac{\lambda_4}{4!}S^4. \tag{3.3.3}$$

The interactions of the singlet sector to the SM sector arise only through the Higgs portal $H^\dagger H$ as given above. Note that the Lagrangian in Eq. (3.3.2) generally includes both scalar and pseudoscalar interaction terms in the singlet sector, in contrast to the basic model in Ref.s [263, 264, 270], following the set-up explaining the galactic γ-ray signal [268, 269]. [2]

[2] See also Ref. [266].

	$\not{E}_T^{\rm DM}$ + jet	$\not{E}_T^{\rm DM}$ + ($h_1/h_2 \to$ SM particles)	No $\not{E}_T^{\rm DM}$
Single h_1	$pp \to h_1 \to \psi\psi$	N/A	SM Higgs precision
Single h_2	$pp \to h_2 \to \psi\psi$	N/A	$pp \to h_2 \to$ SM (m_{h_2})
Double h_1h_1: c_{111}	$pp \to h_1 \to h_1h_1 \to 4\psi$	$pp \to h_1 \to h_1h_1 \to 2\psi$ + SM	$pp \to h_1 \to h_1h_1$ (double Higgs production)
Double h_1h_1, h_1h_2: c_{112}	$pp \to h_2 \to h_1h_1 \to 4\psi$ $pp \to h_1 \to h_1h_2 \to 4\psi$	$pp \to h_2 \to h_1h_1 \to 2\psi$ + SM $pp \to h_1 \to h_1h_2 \to 2\psi$ + SM (m_{h_2})	$pp \to h_2 \to h_1h_1$ (m_{h_2}) $pp \to h_1 \to h_1h_2$ (m_{h_2})
Double h_2h_2, h_1h_2: c_{122}	$pp \to h_1 \to h_2h_2 \to 4\psi$ $pp \to h_2 \to h_1h_2 \to 4\psi$	$pp \to h_1 \to h_2h_2 \to 2\psi$ + SM (m_{h_2}) $pp \to h_2 \to h_1h_2 \to 2\psi$ + SM (m_{h_2})	$pp \to h_1 \to h_2h_2$ (m_{h_2}) $pp \to h_2 \to h_1h_2$ (m_{h_2})
Double h_2h_2: c_{222}	$pp \to h_2 \to h_2h_2 \to 4\psi$	$pp \to h_2 \to h_2h_2 \to 2\psi$ + SM (m_{h_2})	$pp \to h_2 \to h_2h_2$ (m_{h_2})

Table 3.3.2: Production channels of h_1/h_2, dubbed as "h_i production", categorised by the signal types. $\not{E}_T^{\rm DM}$ is the missing transverse energy originated from the DM, "SM particles" means the SM particles produced from the decay of the Higgs bosons (h_1 and h_2), and m_{h_2} means that we can observe a h_2 resonance signal.

The SM Higgs potential is given as $V_{\rm SM} = -\mu^2 H^\dagger H + \lambda_0 (H^\dagger H)^2$ and the Higgs boson gets a VEV after electroweak symmetry breaking (EWSB), $v_h =\simeq 246$ GeV. The singlet scalar field generically develops a VEV , v_s, and hence we can expand $S = v_s + s$. There is mixing between the states $h, s$and the physical mass states are admixtures of h and s, where the mixing angle is determined by $\tan\theta_s = y/(1+\sqrt{1+y^2})$ with $y \equiv 2\mu_{hs}^2/(\mu_h^2 - \mu_s^2)$. The expressions of each matrix element in terms of the Lagrangian parameters are given in Ref. [268, 269]. Then, the tree-level Higgs boson masses are obtained as

$$m^2_{h_1,\,h_2} = \frac{1}{2}\left[(\mu_h^2 + \mu_s^2) \pm (\mu_h^2 - \mu_s^2)\sqrt{1+y^2}\right], \tag{3.3.4}$$

where we assume that h_1 corresponds to the SM-like Higgs boson.

An interesting feature of this model is that there are extra scalar self-interaction terms. The cubic self-couplings c_{ijk} for $h_ih_jh_k$ interactions, *i.e.* $c_{111}h_1^3/3! + c_{112}h_1^2h_2/2 + c_{122}h_1h_2^2/2 + c_{222}h_2^3/3!$, are functions of the scalar couplings, vacuum expectation values, and θ_s, where the exact forms are written in Ref. [268, 269]. Note that c_{112} is proportional to $\sin\theta_s$ due to the fact that $\lambda_1 + 2\lambda_2 v_s$ is also proportional to $\sin\theta_s$, while the other couplings can remain non-vanishing.

Signals at the LHC: The search strategies for SFDM at the LHC rely on the production methods of the SM-like Higgs h_1 and the singlet-like Higgs h_2. Hence, we first categorise the production channels of h_1/h_2 as following.

- Single h_1/h_2 production from the Yukawa or gauge interactions
- Double h_1/h_2 production from the scalar self-interactions

The first category implies the conventional single Higgs production mechanisms such as gluon fusion, vector boson fusion, $t\bar{t}h$, Higgsstrahlung, *etc.*. Hence, for single h_1 production, the precise measurements of the SM Higgs production mechanisms, dubbed as *Higgs precision*, would provide the indirect hints of the SFDM, unless h_1 decays to DM pair. The second category includes exotic signatures depending on the values of trilinear couplings so we further divide the production channels affected by each coupling.

As a next step, the signal type should be classified for each production channel of h_1/h_2. Here, we categorise the signal types as

- $\not{E}_T^{\rm DM}$ + jets
- $\not{E}_T^{\rm DM}$ + ($h_1/h_2 \to$ SM particles)
- No $\not{E}_T^{\rm DM}$

where $\not{E}_T^{\rm DM}$ is the missing energy from the DM production, defined to separate from the missing energy from the neutrino production in the SM, e.g., $Z \to \nu\bar{\nu}$. Such a missing energy signal from the neutrino production belongs to the last category, "No $\not{E}_T^{\rm DM}$".

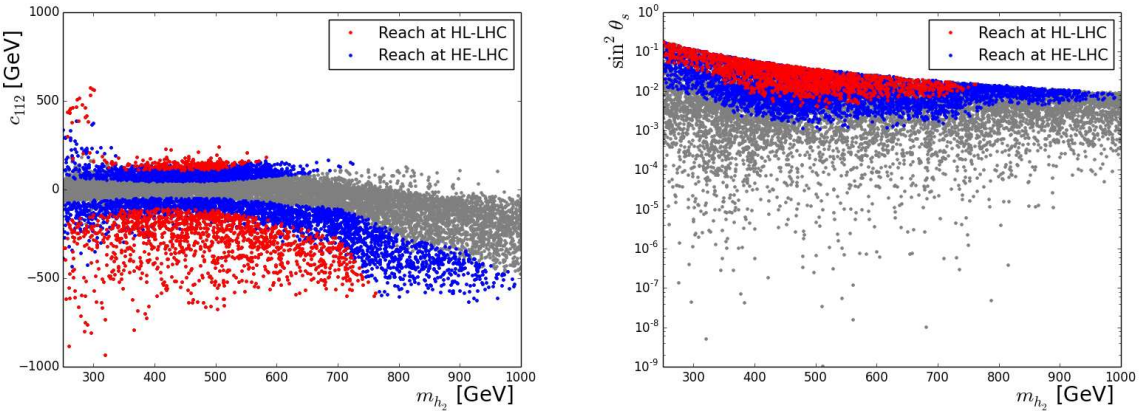

Fig. 3.3.5: Expected parameter reach by searching for on-shell $pp \to h_2 \to h_1 h_1$ at HL-LHC (HE-LHC) is shown with red (blue) scatter points in the $m_{h_2} - c_{112}$ (left) and $m_{h_2} - \sin^2\theta_s$ (right) plane. The gray scatter points are out of the reach of HE-LHC but satisfying the stability of the scalar potential $V_S(S,\, H) + V_{\rm SM}$ and the current constraints from Ref. [274].

Table 3.3.2 summarises the production channels of h_1/h_2 and the suitable signal type for each channel. As stated above, the double Higgs production channels are further classified by the trilinear coupling involved in the process. In many channels, searches for exotic resonance signals by the decay of h_2, remarked as (m_{h_2}), can be effective methods in probing the Higgs portal DM models. As long as the DM mass is larger than $m_{h_2}/2$, the BRs of $h_2 \to$ SM particles are the same as those expected for the hypothetical SM Higgs (with an arbitrary mass not restricted to ~ 125 GeV). Note that all the processes can occur altogether so one needs a combined analysis to confirm the scenario.

As preliminary but simple examples, we analyse the expected sensitivities of the on-shell processes $pp \to h_2 \to h_1 h_1$ and $pp \to h_1 \to h_2 h_2$, in the signal type "No $\not{E}_T^{\rm DM}$, assuming the Higgs bosons are produced on-shell. For the on-shell process $pp \to h_2 \to h_1 h_1$, we apply the search results for heavy scalar into $h_1 h_1 \to b\bar{b}b\bar{b}$ in ATLAS [274] with 36.1 fb^{-1} data at $\sqrt{s} = 13$ TeV. The sensitivity at HL-LHC is estimated from rescaling the upper limits in Ref. [274] by $\sqrt{36.1/3000}$ assuming the number of background events at $\sqrt{s} = 13$ TeV and $\sqrt{s} = 14$ TeV are similar. We also assume the signal significance is well approximated by signal/$\sqrt{\rm background}$ where the statistical uncertainty is dominant. On the other hand, it is non-trivial to obtain the sensitivity at HE-LHC. For simplicity, we only consider the ratio of the dominant background events (multi-jets [274]) at $\sqrt{s} = 27$ TeV and $\sqrt{s} = 13$ TeV, which is 2.9 from running MADGRAPH5NLO. In Fig. 3.3.5, we show the expected reach at HL-LHC (HE-LHC). The gray scatter points are out of the reach of HE-LHC. Note that all the scatter points satisfy the stability of the scalar potential $V_S(S,\, H) + V_{\rm SM}$ and the current constraints from Ref. [274]. From this result, we conclude that HL-LHC (HE-LHC) can constrain the parameter $|c_{112}|$ up to 100 (50), which correspond to $\sin^2\theta_s \sim 0.004$ (0.001).

For the on-shell process $pp \to h_1 \to h_2 h_2$, we apply the search results for $pp \to W h_1 \to W h_2 h_2 \to \ell\nu_\ell b\bar{b}b\bar{b}$ or $pp \to Z h_1 \to Z h_2 h_2 \to \ell\bar{\ell}b\bar{b}b\bar{b}$ in ATLAS [275] with 36.1 fb^{-1} data at $\sqrt{s} = 13$ TeV. Since the dominant background is $t\bar{t}$ + light jets, we apply the aforementioned method in obtaining the sensitivities at HL-LHC and HE-LHC for simplicity. In Fig. 3.3.6, we show the expected reach at HL-LHC (HE-LHC).The gray scatter points are out of the reach of HE-LHC but satisfying the stability of the scalar potential $V_S(S,\, H) + V_{\rm SM}$ and the current constraints from Ref. [275]. Interestingly, we estimate that HL-LHC can cover most of the parameter space unless $|c_{122}|$ is as small as ~ 5 GeV.

In summary, in this section we have explained the SFDM as a reference Higgs portal model. Since the existence of the extra scalar h_2 is a key ingredient of the model, we categorise the possible production channels of the two Higgs bosons (h_1 and h_2) and suitable signal types at the LHC. As a simple example,

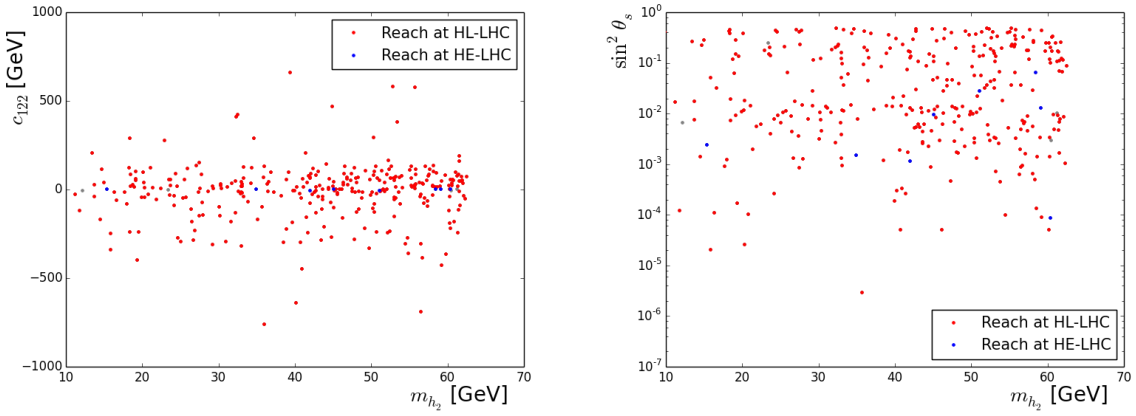

Fig. 3.3.6: Expected parameter reach by searching for on-shell $pp \to h_1 \to h_2 h_2$ (exotic Higgs decay) at HL-LHC (HE-LHC) is shown with red (blue) scatter points in the $m_{h_2} - c_{122}$ (left) and $m_{h_2} - \sin^2\theta_s$ (right) plane. The gray scatter points are out of the reach of HE-LHC but satisfying the stability of the scalar potential $V_S(S, H) + V_{\rm SM}$ and the current constraints from Ref. [275].

Field	Spin	$su(3) \times su(2)_L \times u(1)_Y$	$\mathbb{Z}_2$	Copies	DOF
χ	1/2	(1,1,0)	-1	1	4
ϕ_i	0	(1,1,-1)	-1	n	$2n$

Table 3.3.3: The new particles we introduce with their respective charges, the number of copies we consider and the number of degrees of freedom.

we estimate the experimental sensitivities of HL-LHC and HE-LHC for two simple on-shell processes $pp \to h_2 \to h_1 h_1$ and $pp \to h_1 \to h_2 h_2$ with several naive assumptions.

3.3.4 Singlet dark matter with slepton-like partners at HL- and HE-LHC

Contributors: M. J. Baker and A. Thamm

In this contribution we use a simplified model framework to explore the prospects for the HL and HE-LHC to probe viable multi-TeV dark matter. We consider a bino motivated (gauge-singlet Dirac or Majorana fermion) dark matter candidate accompanied by n dark-sector scalars with unit hypercharge, table 3.3.3. We consider the three possible Yukawa couplings with SM electrons, muons and taus individually. A pure singlet with no other nearby states cannot efficiently annihilate, resulting in overclosure of the universe. However, when dark sector scalars are included, the observed relic abundance can be recovered for a relatively wide range of masses. In Ref. [276] we determine the couplings which produce the observed abundance of dark matter and calculate the reach of a range of present and future direct detection, indirect detection and collider experiments. In this summary, we will see that there is a large region of viable parameter space for Majorana dark matter which only future colliders, such as the HL- and HE-LHC, can probe.

In addition to kinetic and mass terms, the Lagrangian only has one new interaction term (ignoring the scalar quartic, which plays no role in our phenomenology)

$$\mathcal{L} \supset \overline{\chi}(i\partial\!\!\!/ - m_\chi)\chi + \frac{1}{2}|D_\mu \phi_i|^2 - \frac{1}{2}m_\phi^2 \phi_i^2 + (y_\chi \phi_i \overline{\chi} \ell_R + h.c.)\,, \tag{3.3.5}$$

where $D_\mu = \partial_\mu - ig'YB_\mu$ and the coupling is taken to be universal, *i.e.* y_χ is the same for all ϕ_i. We consider the cases $\ell_R = e_R, \mu_R$ and τ_R, and assume that all ϕ_i have the same mass, $m_{\phi_i} = m_\phi$, and that $m_\chi < m_\phi$. We parametrise their mass splitting by $\Delta = (m_\phi - m_\chi)/m_\chi$. For illustration, we focus on $n \in \{1, 10\}$. In a supersymmetric context, the DM particle χ would correspond to a bino and

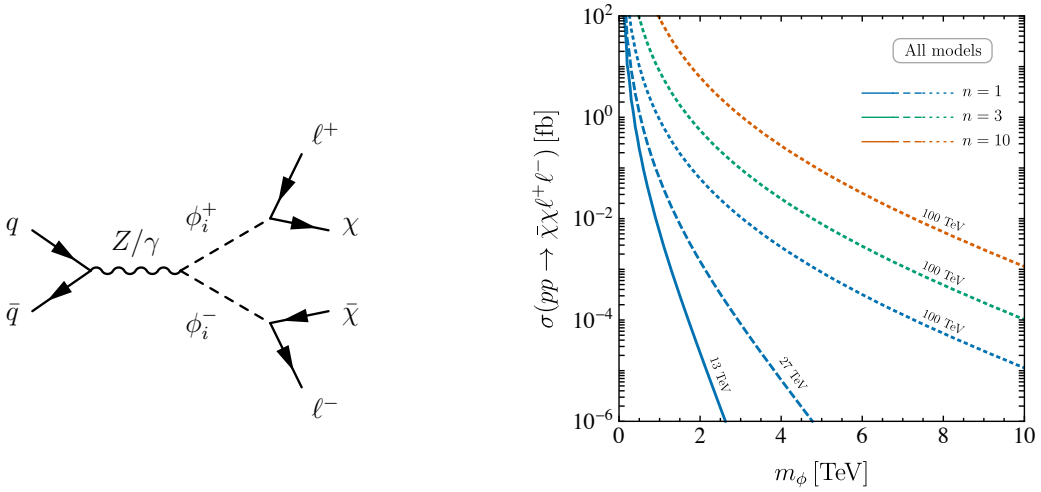

Fig. 3.3.7: Leading order partonic process contributing to $pp \to \phi^+\phi^- \to \bar{\chi}\chi\ell^+\ell^-$ (left) and its cross-section at 13 TeV, 27 TeV and 100 TeV including a K-factor of 2 (right).

the scalar ϕ_i can be identified with a right-handed slepton. In SUSY, the number of degrees of freedom of one right-handed slepton corresponds to $n = 1$, all right-handed sleptons corresponds to $n = 3$, while all right-and left-handed sleptons correspond to $n = 9$. We calculate the relic abundances in our models using MICROMEGAS V4.3.5 [277], and then restrict the new Yukawa couplings to lie on the relic surface when considering the reach of various experiments.

It is challenging to search for our dark matter models directly at a hadron collider, since the dark matter is a gauge singlet which only couples to leptons. The coannihilation partner, $\phi_i^\pm$, however is a charged scalar of similar mass. It will be pair produced in the process $pp \to \phi_i^+\phi_i^-$ with a subsequent decay to a lepton, ℓ, and χ, depicted in Fig. 3.3.7 (left), where $\mathcal{B}(\phi_i^\pm \to \chi\ell^\pm) = 1$. We focus on final states containing two opposite-sign same-flavour leptons and missing energy. As τ reconstruction at future colliders is particularly challenging to model, we do not provide collider limits for the τ models. However, it is clear that the collider reach on τ models will be somewhat worse than the limits on the models involving electrons and muons.

We present sensitivity projections for the HE-LHC with $\sqrt{s} = 27$ TeV assuming an integrated luminosity of 15 ab^{-1} [278] and for the FCC-hh with $\sqrt{s} = 100$ TeV and 20 ab^{-1} [279]. We estimate the sensitivity of future colliders to our models by adapting the analysis used in Ref. [85] to search for slepton pair production with subsequent decay to neutralinos and leptons.

The signal $pp \to \phi^+\phi^-$ is simulated using a custom SARAH V4.12.1 [280] model, we generate the signal and background parton level events using MADGRAPH5 V2.6.2 [67], simulate the showering using PYTHIA 6.4.28 [92] and perform the detector simulation with DELPHES V3.3.3 [33]. For our 27 TeV simulations, we use the default DELPHES card. For the simulations at 100 TeV we use the FCC DELPHES card implementing the configurations proposed by the FCC working group [281]. For the signal simulation, we adapt the card to treat the DM particle as missing energy. We use the LO partonic production cross-sections and multiply by a generous K-factor of 2, as we want to find the exclusion limits in the optimistic case, Fig. 3.3.7 (right). To validate our analysis, we reproduce the relevant backgrounds in Ref. [85].

The main SM backgrounds to our signal are WW, VV, WV, $t\bar{t}$, Wt and V+jets, where $V = Z, \gamma$. While only WW and VV are irreducible backgrounds, WV, $t\bar{t}$ and Wt contribute if a lepton or one or two b-jets are missed. The V+jets background is important at low values of m_{T2}, but is negligible above $m_{\text{T2}} \approx 100$ GeV. In order to isolate the signal, we impose the following cuts. Two opposite-sign same-flavour light leptons are required with $p_T > 35$ GeV and $p_T > 20$ GeV for leading and subleading

Channel	$\mu^+\mu^-\nu_{\text{all}}\bar{\nu}_{\text{all}}$		$\mu^+\mu^- l_{\text{all}}\nu$		Example Signal	
Energy [TeV]	27	100	27	100	27	100
No Cuts	2100	6900	560	1800	17	100
$p_T^{\mu_1(\mu_2)} > 35(20)$ GeV & Lepton veto	1100	620	120	160	12	14
Jet veto	690	530	45	61	3.3	9.4
$m_{\mu\mu} > 20$ GeV & $\lvert m_{\mu\mu} - m_Z\rvert > 10$ GeV	470	370	6.6	13	3.3	8.9
$m_{\text{T2}} > 200$ GeV	0.26	0.44	0.022	0.076	1.3	2.5

Table 3.3.4: Cross-sections at each stage in fb. The example signals are for the muon type model with $n = 10$ for the parameter points $m_\chi = 0.6$ TeV, $\Delta = 0.34$ (27 TeV) and $m_\chi = 0.8$ TeV, $\Delta = 0.2$ (100 TeV).

leptons, respectively. We veto events with any other leptons, which reduces the WV background. Removing events with $m_{\mu\mu} < 20$ GeV and $|m_{\mu\mu} - m_Z| < 10$ GeV significantly reduces backgrounds with a Z-boson in the final state. Finally we cut on the transverse mass [130, 131], $m_{\text{T2}} > 200$ GeV. For a process where two particles each decay to a lepton and missing energy, the m_{T2} distribution will have an end point at the mass of the heavier particle [282]. Although in Ref. [85] a cut of $m_{\text{T2}} > 90$ GeV is used, we increase this to $m_{\text{T2}} > 200$ GeV. This has a small effect on our signal efficiency, as we are mostly interested in dark matter candidates with mass larger than 200 GeV, while strongly reducing the background from $t\bar{t}$, Wt. However, even with this large cut, we find a significant background from WW, WV and VV, where at least one of the vector bosons is extremely off-shell. To include this effect in MADGRAPH we simulate $pp \to \ell^+\ell^-\nu_{\text{all}}\bar{\nu}_{\text{all}}$ and $pp \to \ell^+\ell^-\ell_{\text{all}}\nu$, where ν_{all} is ν_e, ν_μ or ν_τ and ℓ_{all} is any charged lepton. We do not find a similar large contribution from off-shell particles in the $t\bar{t}$ and Wt channels. Even though the cross-section of these gluon initiated channels grows faster than the di-boson processes as the collider energy is increased, they remain a subdominant background as the t is narrower and as this background only passes the cuts if a jet is missed, reducing the m_{T2} endpoint. Finally, we checked that the contribution from jets faking muons is negligible. In table 3.3.4 we show the cross-sections at each stage in the analysis for the background and for an example signal, $m_\chi = 0.6$ TeV, $\Delta = 0.34$ (27 TeV) and $m_\chi = 0.8$ TeV, $\Delta = 0.2$ (100 TeV), both for the $n = 10$ muon type model.

In Fig. 3.3.8 we show the differential distribution in m_{T2} for the muon-type model for the events passing all cuts, for the background and example signal. We see that $\mu^+\mu^-\nu_{\text{all}}\bar{\nu}_{\text{all}}$ is the dominant background, and $\mu^+\mu^-\ell_{\text{all}}\nu$ is around an order of magnitude smaller. This is due to both the smaller initial cross-section and the smaller efficiency. We see that both the background and the example signal falls sharply from $m_{\text{T2}} = 200$ GeV to $m_{\text{T2}} \approx 500$ GeV. However, the signal will continue to higher values of m_{T2} for other points in our parameter space. We also see that at 27 TeV, the $\mu^+\mu^-\nu_{\text{all}}\bar{\nu}_{\text{all}}$ continues out to higher values of m_{T2}, while at 100 TeV the situation is reversed.

To estimate the expected exclusion limit, we use a Poisson counting procedure for the signal and background events which pass all the cuts, based on a frequentist framework [257, 283]. In Fig. 3.3.9 we present the 90% C.L. sensitivity for the muon type models at a 27 TeV and a 100 TeV proton-proton collider. The parameter space probed is where m_χ is small and Δ is relatively large. The reach is independent of whether dark matter is Majorana or Dirac, since it depends on the ϕ-pair production cross-section and the fact that $\mathcal{B}(\phi_i^\pm \to \chi\ell^\pm) = 1$. The large m_χ region is not probed as m_ϕ increases with m_χ, and the ϕ-pair production cross-section decreases rapidly as m_ϕ increases, Fig. 3.3.7 (right). We see that in both cases the limits are strongest when there are more coannihilation partners. This is because the $pp \to \chi\bar{\chi}\ell^+\ell^-$ cross-section scales as n^2. For $n = 1$, the 27 TeV (100 TeV) machine can probe $m_\chi < 0.75$ TeV (1.2 TeV), for $n = 3$ it can probe $m_\chi < 1.3$ TeV (2.3 TeV) while for $n = 10$ the limits are $m_\chi < 2.0$ TeV (4.0 TeV). The small Δ region is not probed as in this region the momentum of the leptons is small and they are not efficiently reconstructed. This is a well known problem in the coannihilation region. The gap for lower Δ can be closed, e.g., by looking for ISR [284, 285] or for disappearing charged tracks [286–288].

We also overlay the direct and indirect detection bounds from [276], to give a summary of all the relevant current and future experimental constraints. We see that the situation is dramatically different

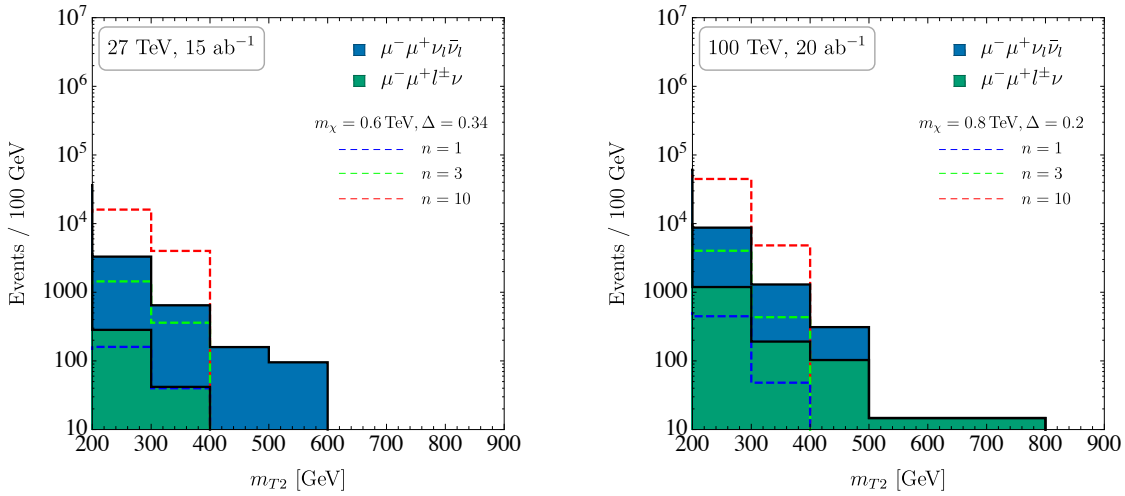

Fig. 3.3.8: m_{T2} distribution for background events passing all cuts for the muon model, and an example signal for $n = 1, 3, 10$, at 27 TeV (left) and 100 TeV (right). We do not use this information in determining the reach, but simply perform a cut-and-count analysis based on these events.

for Dirac and Majorana χ. For Dirac χ, small masses and mass splittings have already been excluded by LUX [289]. In the future, DARWIN [290] will probe the full parameter space, while colliders and indirect detection (only under the assumption of a cuspy dark matter halo profile) will be sensitive for relatively low masses and large or small Δ, respectively. We see that the challenging small Δ region at colliders is excluded by the existing bound from LUX.

For Majorana χ, on the other hand, DARWIN, with the maximum exposure, is limited to probing only small masses and small Δ, while there are no constraints from indirect detection. This is due to the velocity suppression of both the DM-nucleus and the annihilation cross-sections. The collider bounds are the same as in the Dirac case, since the mass term of χ does not enter into the production and decay of ϕ-pairs. In this case, future colliders are essential for probing the large Δ region of the parameter space.

Finally, the reach for electron final states is marginally worse than for muon final states due to the fact that the electron reconstruction efficiency is slightly worse than for muons. Again, we conclude that future colliders are essential for probing the large Δ region of the parameter space.

3.4 Dark sectors

As in our ordinary world, a dark sector could allow for long-range forces among its matter constituents. Evidence from both cosmology and astrophysics may supporting the possibility of long-range interactions among DM constituents (see, for instance, the role of massless dark photons in galaxy formation and dynamics [291–298]). In the following sections, prospect studies for searches for dark photons at HL- and HE-LHC are presented.

3.4.1 Prospects for dark-photon at the HL-LHCb

Contributors: P. Ilten, M. Williams and X. Cid Vidal, LHCb

A compelling scenario in the search for dark forces and other portals between the visible and dark sectors is that of the dark photon A'. In this case, a new $U(1)$ dark force, analogous to the electromagnetic (EM) force, can be introduced into the SM, where the dark photon is the corresponding force mediator which couples to dark matter (or matter) carrying dark charge. The A' can kinetically mix with the photon, allowing the A' to be observed in the spectra of final states produced by the EM current. This mixing can be thought of as a low-energy consequence of a loop process, potentially involving very high

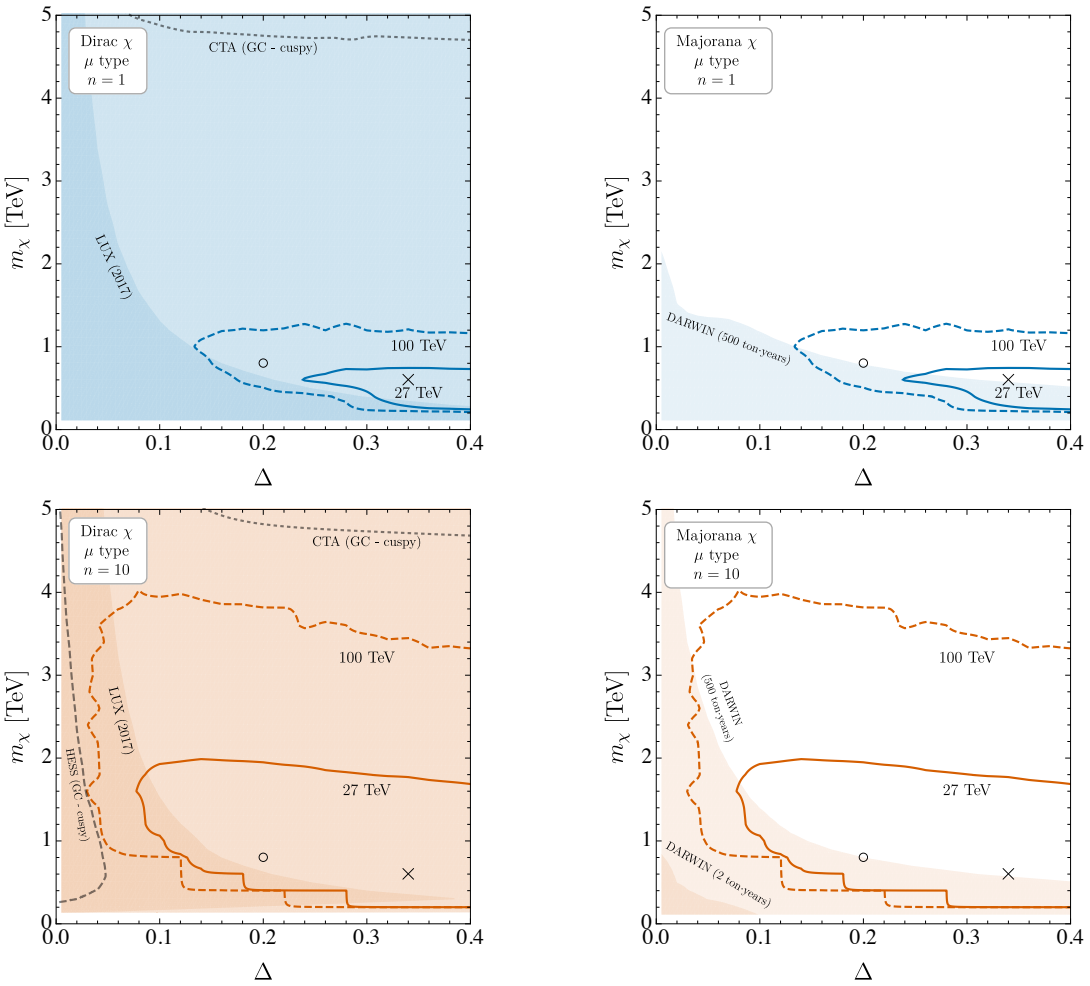

Fig. 3.3.9: Reach of future colliders at 90% C.L., current and future direct detection experiments at 90% C.L., and current and future indirect detection experiments at 95% C.L. for Dirac (left) and Majorana (right) DM interacting with a muon and one (top) and ten (bottom) coannihilation partners in the $\Delta - m_\chi$ plane. The lightly, moderately and strongly shaded regions correspond to the direct detection limits by the future DARWIN experiment with $500\,\text{ton} \cdot \text{years}$, $2\,\text{ton} \cdot \text{years}$ and the LUX limits, respectively, which are discussed in detail in Ref. [276]. The circle and cross signify our example signals shown in Fig. 3.3.8.

mass particles, that connect the visible and dark sectors.

The study of the A' model is based on two free parameters: the mixing term ε^2 and the invariant mass of the A', $m_{A'}$. The mixing term, ε^2, can be interpreted as the ratio of the dark force strength to the EM force strength. Note that for smaller values of ε^2 the dark photon can be long-lived and fly away from its production vertex. Figure 3.4.1 shows the $\varepsilon^2 - m_{A'}$ parameter space with current limits (grey fills, see Ref. [299] for details), current LHCb limits (black bands) [300], and prospects on the LHCb future reach (coloured bands). The light (dark) coloured band corresponds to discovery reach assuming 50 (300) fb^{-1} datasets. These are the expected integrated luminosities at LHCb at the end of Run-4 and Run-5 of the LHC, respectively. These discovery reaches assume increased pileup within LHCb will not have a significant effect on the dark photon reconstruction.

There are at least two complementary ways for LHCb to explore large portions of unconstrained A' parameter space. They address different regions of this space. The first involves prompt and displaced resonance searches using $D^{*0} \to D^0 e^+ e^-$ decays [301] (green bands in Fig. 3.4.1). The second is an inclusive di-muon search [302] (blue bands in Fig. 3.4.1) where the di-muon can be prompt or displaced. In both cases the lepton pair is produced from an EM current which kinetically mixes with

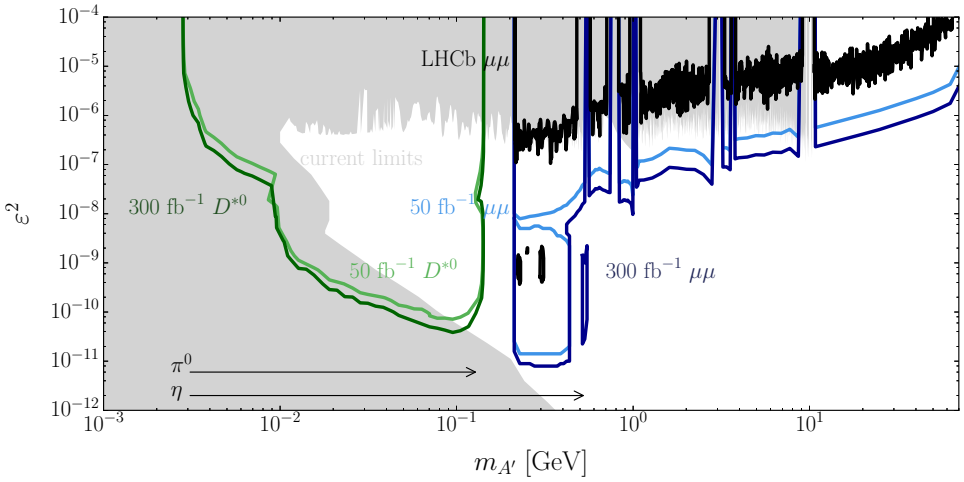

Fig. 3.4.1: Current limits (grey fills), current LHCb limits (black band), and proposed future experimental reach (coloured bands) on A' parameter space. The arrows indicate the available mass range from light meson decays into $e^+e^-\gamma$.

the A', producing a sharp resonance at the A' mass. In the first case, the A' is detected in its decay to an e^+e^- pair and in the second to a $\mu^+\mu^-$ pair. The advantage of these approaches is that they do not require the calculation of absolute efficiencies. In both cases, the signal can be normalised to the di-lepton mass sidebands near the A' resonance, where dark photon mixing with the SM virtual photon is negligible. In general, these search strategies depend on three core capabilities of LHCb: excellent secondary vertex resolution, particle identification, and real-time data-analysis. These features are also important for flavour physics, which mainly drives the design of the detector and its upgrades. In particular, the improvement in the impact parameter resolution, expected after the upgrade of the LHCb vertex locator, will be key to tackle the background produced by heavy quark decays.

For the LHCb sensitivities in Fig. 3.4.1, the sensitivity calculated using $D^{*0} \to D^0e^+e^-$ decays [301] is based on the normalisation to this channel, which at the same time is the main background for the prompt search. $D^{*0} \to D^0e^+e^-$ decays are generated using PYTHIA 8 [50], and the D^0 is reconstructed or partially reconstructed through its decay into at least two charged particles. The selection is designed to maximise the e^+e^- mass resolution and to minimise the background. The resolution and efficiencies are obtained using public LHCb information, combined with a simplified simulation of the upgraded vertex locator. For the di-muon search [302], a fiducial selection is designed so that the reconstruction efficiency is essentially flat across the dark photon parameter space, while minimising the presence of background. The relevant experimental resolutions and efficiencies, including those foreseen after subsequent detector upgrades, are taken from public LHCb documents. The normalisation channel, i.e $\mu^+\mu^-$ production originating from electromagnetic processes, and backgrounds are again studied using PYTHIA 8, corrected with experimental LHC inputs.

A first inclusive search for A' bosons decaying into muon pairs was performed by the LHCb collaboration [300] (black band in Fig. 3.4.1). This search, an implementation of the second strategy described above, used a data sample corresponding to an integrated luminosity of 1.6 fb^{-1} from pp collisions taken at $\sqrt{s} = 13$ TeV. Although the data sample used was significantly smaller than the one that will be available at the HL-LHC, this search already produced world-best upper limits in regions of $\varepsilon^2 - m_{A'}$ space. This search was limited by the presence of the LHCb hardware trigger, which severely compromised the detection efficiency of low mass dark photons at LHCb. However, this hardware level trigger will be removed from Run-3 of the LHC onwards. At the same time, this was the first simultaneous prompt and displaced A' search. With around 300 fb^{-1}, LHCb will either confirm or reject the presence of a dark photon for significant portions of the theoretically favoured parameter space. It should

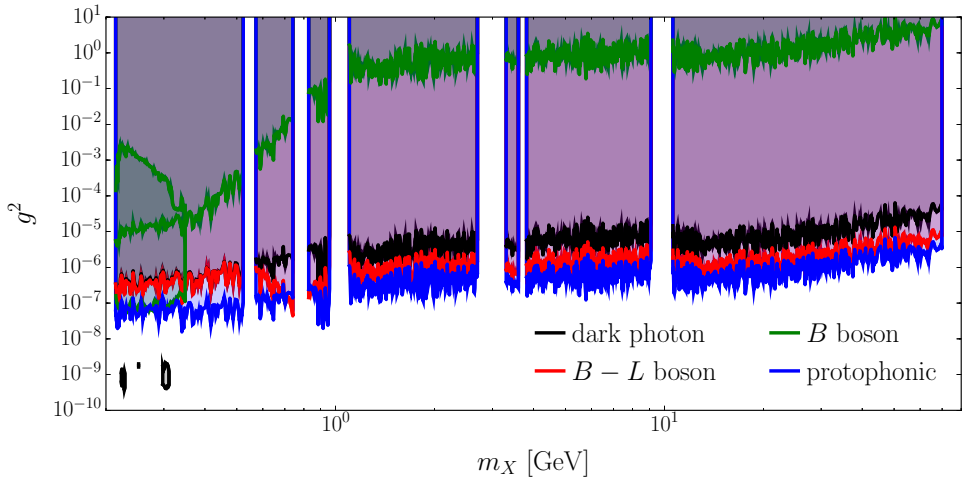

Fig. 3.4.2: Recast of the (blue) LHCb dark photon limits into the (red) B-L boson, (green) B boson, and (yellow) protophobic models using the DARKCAST tool [303].

be noted that, in non-minimal models, such as those producing dark photons through the Higgs portal, part of this parameter space can be further constrained by other experiments. Examples are given in Sections 3.4.2.1 and 3.4.3.

To cover the gap in reach between the two primary search strategies, presented above, production of A' bosons from light meson decays, $\pi^0 \to e^+e^-\gamma$ and $\eta \to e^+e^-\gamma$, is expected to be used. The parameter space coverage from light meson decays depends on the ability of the LHCb triggerless readout to quickly and efficiently reconstruct low mass and low momentum di-electron pairs. Additionally, the electron momentum resolution, degraded by incomplete bremsstrahlung recovery, dictates the di-electron mass resolution which drives parameter space coverage. More detailed studies are needed to quantify how searches for dark photons from light meson decays will help to constrain the dark photon parameter space.

One of the advantages of the dark photon model is that results can be recast into more complex vector current models, given some knowledge of the dark photon production mechanism and the detector efficiency for displaced dark photon reconstruction. Examples of these models are the $B-L$ boson which couples to the $B-L$ current, the B boson which is leptophobic and couples to baryon number, and a vector boson which mediates a protophobic force. All these models can be fully specified with two parameters: the global coupling g of the vector current for the model with the electromagnetic current, and the mass m_X of the mediating boson. For the dark photon model, this is just ε and $m_{A'}$, respectively. In Fig. 3.4.2 the initial inclusive di-muon results from LHCb [300] have been recast into these example models using the DARKCAST package [303]. Dark photon searches can also be recast to non-vector models, but such a recasting is no longer as straight forward.

3.4.2 Long-lived dark-photon decays at the HL-LHC

Among the numerous models predicting dark photons, one class of models that is particularly interesting for the LHC features the hidden sector communicating with the SM through a Higgs portal. Dark photons are produced through BSM Higgs decays. They couple to SM particles via a small kinetic mixing parameter ϵ, as described in Section 3.4.1. If ϵ is very weak, the lifetime of the dark photon can range from a few millimetres up to several meters. The lower ϵ is, the longer the dark photon lifetime will be, which then decays displaced from the primary vertex. The following searches from ATLAS and CMS target complementary scenarios and illustrate possible improvements in trigger and analysis strategies which can be used at HL-LHC.

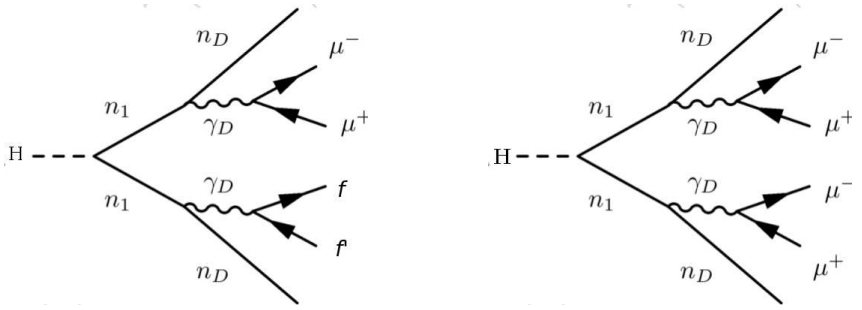

Fig. 3.4.3: Feynman diagram of the decay of SM Higgs boson to a final state containing two or more muons in Dark SUSY models. Decay chain leading to a final state containing exactly two (left) or four (right) muons.

3.4.2.1 Long-lived dark-photon decays into displaced muons at HL-LHC CMS

Contributors: K. Hoepfner, H. Keller, CMS

In the so-called Dark SUSY model [304, 305], an additional dark $U_D(1)$ symmetry is added as a supersymmetric SM extension. Breaking this symmetry gives rise to an additional massive boson, the dark photon γ_D, which couples to SM particles via a small kinetic mixing parameter ϵ. A golden channel for such searches is the decay to displaced muons.

The reconstruction of muons with large displacements is challenging both at trigger level and for the final event reconstruction, especially when the long lived particle decays outside the tracker volume and the precision of the tracker cannot be used for the analysis. To identify displacements of physical objects during reconstruction, the transverse impact parameter d_0 of the reconstructed track with respect to the primary interaction vertex is used. This analysis from CMS [306] relies on a dedicated muon reconstruction algorithm that is designed for non-prompt muons leaving hits only in the muon system. This is the displaced standalone (DSA) algorithm, using the same reconstruction techniques as prompt muons, but removing any constraint to the interaction point which is still present in the standard standalone (SA) algorithm. The DSA muon algorithm improves transverse impact parameter and transverse momentum (p_T) resolutions for displaced muons compared to the SA muon algorithm [307].

In the model studied here [306], dark photons are produced in cascade decays of the SM Higgs boson that would first decay to a pair of MSSM-like lightest neutralinos (n_1), each of which can decay further to a dark sector neutralino (n_D) and the dark photon, as shown in Fig. 3.4.3. For the branching fraction BR($H \to 2\gamma_D + \mathrm{X}$), where X denotes the particles produced in the decay of the SM Higgs boson apart from the dark photons, 20% is used. This value is in agreement with recent Run-2 studies [308] and taking into account the upper limit on invisible/non-conventional decays of the SM Higgs boson [309]. We assume neutralino masses $m(n_1) = 50$ GeV and $m(n_D) = 1$ GeV, and explore the search sensitivity for dark photon masses and lifetimes in the following ranges: $m(\gamma_D) = (1, 5, 10, 20, 30)$ GeV and $c\tau = (10, 10^2, 10^3, 5 \times 10^3, 10^4)$ mm. Final states with two and four muons are included in the analysis. In the former case, one dark photon decays to a pair of muons while the other dark photon decays to some other fermions (2-muon final state). In the latter case, both dark photons decay to muon pairs (4-muon final state). Both decay chains are shown in Fig. 3.4.3. The assumed Higgs production cross section via gluon-gluon fusion is 49.97 pb [310].

The main background for this search comes from multi-jet production (QCD), $t\bar{t}$ production, and Z/DY $\to \ell\ell$ events where large impact parameters are (mis)reconstructed. Cosmic ray muons can travel through the detector far away from the primary vertex and mimic the signature of displaced muons. However, thanks to their striking detector signature, muons from cosmic rays can be suppressed by rejecting back-to-back kinematics.

For each event, at least two DSA muons are required. If more than two exist, the ones with the highest p_T are chosen. The two muons must have opposite charge ($q_{\mu,1} \cdot q_{\mu,2} = -1$) and must be separated

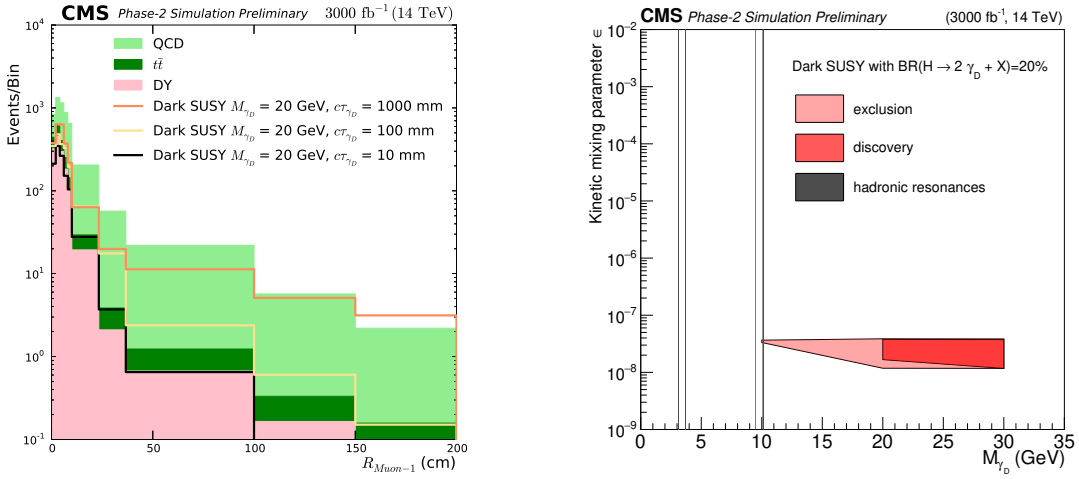

Fig. 3.4.4: Left: distance of the closest approach of the displaced muon track with maximum p_T to the primary interaction vertex, $R_{\mathrm{Muon}-1}$, for signal and background after the final event selection. Right: parameter scan in the $\epsilon - m_{\gamma_D}$ plane. The gray lines indicate the regions of narrow hadronic resonances where the analysis does not claim any sensitivity.

by $\Delta R = \sqrt{\Delta\phi^2 + \Delta\eta^2} > 0.05$. The three-dimensional angle between the two displaced muons is required to be less than $\pi - 0.05$ (not back-to-back) in order to suppress cosmic ray backgrounds. Additionally, $\mathbf{p}_{\mathrm{T}}^{\mathrm{miss}} \geq 50$ GeV is imposed to account for the dark neutralinos escaping the detector without leaving any signal.

In order to discriminate between background and signal, the three-dimensional distance from the primary vertex to the point of closest approach of the extrapolated displaced muon track, called R_{Muon}, is used. The event yield after full event selection of both selected muons as a function of $R_{\mathrm{Muon}-1}$ and $R_{\mathrm{Muon}-2}$ is used to search for the signal. Figure 3.4.4 (left) shows $R_{\mathrm{Muon}-1}$ of the first selected muon for signal and background samples.

The search is performed using a simple counting experiment approach. In the presence of the expected signal, the significance of the corresponding event excess over the expected background is assessed using the likelihood method. In order to evaluate the discovery sensitivity the same input is used as in the limit calculation, now with the assumption that one would have such a signal in the data. The discovery sensitivity is shown in the two-dimensional m_{γ_D}-$c\tau$ plane in Fig. 3.4.4 (right). This search is sensitive to large decay lengths of the dark photon.

In the absence of a signal, upper limits at 95% C.L. are obtained on a signal event yields with respect to the one expected for the considered model. A Bayesian method with a uniform prior for the signal event rate is used and the nuisance parameters associated with the systematic uncertainties are modelled with log-normal distributions. The resulting limits for the Dark SUSY models are depicted in Fig. 3.4.5. While the results shown in Fig. 3.4.5 (left) are for a dark photon with a decay length of 1 m as a function of the dark photon mass, Fig. 3.4.5 (right) shows the results for a dark photon mass of 20 GeV as a function of the decay length [306]. The relatively long lifetimes accessible in this search provide complementary sensitivity at lower values of ϵ.

3.4.2.2 Searching for dark-photons decays to displaced collimated jets of muons at HL-LHC ATLAS

Contributors: C. Sebastiani, M. Corradi, S. Giagu, A. Policicchio, ATLAS

Prospects for searches for Hidden Sectors performed by ATLAS are presented in this section [311]. The benchmark model used in this analysis is the Falkowsky-Ruderman-Volansky-Zupan (FRVZ) vector portal model. In this case, a pair of dark fermions f_{d2} is produced in the Higgs boson decay. As shown

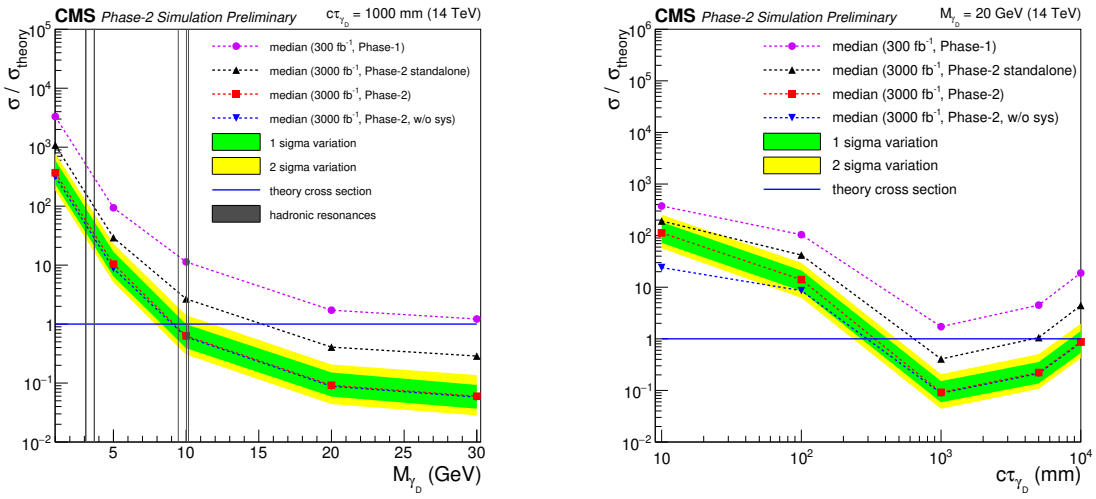

Fig. 3.4.5: 95% C.L. upper limits on production cross section $\sigma/\sigma_{\text{theory}}$ for various dark photon mass hypotheses and a fixed decay length of $c\tau = 1000$ mm (left) and a fixed mass of $M_{\gamma_D} = 20$ GeV(right). Green and yellow shaded bands show the one and two sigma range of variation of the expected 95% C.L. limits, respectively. The black dashed lines ("Phase-2 standalone") compare the expected sensitivity of the displaced muon search to the algorithm with a beamspot constraint. The gray lines indicate the regions of narrow hadronic resonances where the analysis does not claim any sensitivity.

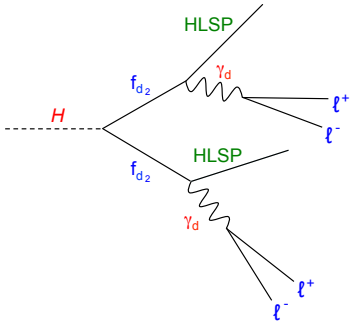

Fig. 3.4.6: The Higgs boson decay to hidden particles according to the FRVZ model.

in Fig. 3.4.6, the dark fermion decays in turn to a γ_d and a lighter dark fermion assumed to be the Hidden Lightest Stable Particle (HLSP). The dark photon, assumed as vector mediator, mixes kinetically with the SM photon and decays to leptons or light hadrons. The branching fractions depend on its mass. At the LHC, these dark photons would typically be produced with large boost, due to their small mass, resulting in collimated structures containing pairs of leptons and/or light hadrons, known as lepton-jets (LJs). If produced away from the interaction point (IP), they are referred to as "displaced LJs". The mean lifetime τ of the dark photon is a free parameter of the model, and is related to the kinetic mixing parameter ϵ by the relation:

$$\beta\gamma c\tau \propto \left(\frac{10^{-4}}{\epsilon}\right)^2 \left(\frac{100\text{ MeV}}{m_{\gamma_d}}\right)^2 \text{s}.$$

Two new muon trigger algorithms are also studied to improve the selection efficiency of displaced muon pairs. MC samples have been produced at 13 and 14 TeV c.o.m. energy for the FRVZ model assuming μ equal to 65 and 200, respectively, and various possible $c\tau$. The samples are used to assess the sensitivity of the analysis and study new triggers.

The standard ATLAS triggers are designed assuming prompt production of particles at the interaction point and therefore are very inefficient in selecting the products of displaced decays. The searches

for γ_d decays are thus based on events selected by specialised triggers dedicated to the selection of events with displaced muon pairs. However these triggers are still far from optimal. If the dark photon is highly boosted, muons are collimated and the trigger efficiency is limited by the finite granularity of the current hardware trigger level. In terms of an interval of the azimuthal angle ϕ and pseudorapidity η, the granularity is $\Delta\eta \times \Delta\phi \simeq 0.2 \times 0.2$ (Region of Interest, RoI). If the dark photon is not boosted sufficiently, the out-going muons from a displaced decay are more open and may not point to the IP. The current hardware trigger level has a tight constraint on IP pointing resulting in non-optimal selection efficiency of displaced non-pointing muon tracks.

The new ATLAS detector setup and Trigger & Data Acquisition system for the HL-LHC will offer the opportunity to develop new trigger algorithms overcoming the current limitations. Two new trigger selections have been studied in this work: one dedicated to triggering on collimated LJs in boosted scenarios, based on requiring muons in a single RoI and referred to as *L0 multi-muon scan*; a second one dedicated to triggering on non-boosted scenarios, loosening the pointing requirements applied in Run-2 and referred to as *L0 sagitta muon*. A summary of the two triggers is given below, for details see [311].

L0 multi-muon scan: this new approach allows to include in the sector logic multiple trigger candidates in the same RoI and leads to a new trigger selection with lower p_T thresholds resulting in a higher efficiency without increasing sensibly the trigger rate. The new trigger algorithm is designed to analyse hit patterns in the Muon Spectrometer. As a first step, the algorithm searches for the pattern with the highest number of hit points, called best pattern, in the MS to form the primary L0 muon candidate. Then all the other possible hit patterns, not compatible with the best pattern, are searched for in the same RoI to form the secondary L0 muon candidates. A quality cut is applied to reduce the influence of noisy hits, requiring patterns with hits on at least three different RPC layers. Patterns are requested to not share RPC hits. If at least one secondary pattern is found, an additional L0 muon is assumed to be found in the RoI. The new L0 trigger algorithm is defined by the logical OR of a single muon L0 with $p_T = 20$ GeV threshold and a multi-muon L0 with $p_T = 10$ GeV threshold. Based on signal MC samples, an overall improvement up to 7% is achieved with respect to the baseline $p_T = 20$ GeV selection, in particular for small opening angle between the two muons from the γ_d decays.

L0 sagitta muon: this approach allows to recover for loss of efficiency in case of out-going muons from non-boosted γ_d that may not be pointing to the IP. The L1 Run-2 trigger has a tight constraint on selecting only pointing muons resulting in non optimal selection of these exotic signatures. A benchmark FRVZ sample with 10 GeV γ_d mass is used to for this study. The sagitta, defined as the vertical distance from the midpoint [3] of the chord [4] to the arc [5] of the muon trajectory itself, can be used to estimate the momentum of a charged particle travelling inside a magnetic field. The sagitta of a muon track can be computed at the L0 trigger level using $\eta - \phi$ measurement points in the various RPC stations. The map between the inverse of the sagitta and the muon transverse momentum has been studied using a MC sample of single muons generated according to a uniform transverse momentum distribution. The mean value of the inverse of the sagitta for $p_T = 20$ GeV pointing truth muons is $s^{-1} = 9 \times 10^{-6}$ mm^{-1}. High transverse momentum non-pointing muons can be thus selected using a L0 muon trigger with low $p_T = 5$ GeV threshold, computing the inverse of the sagitta and requesting a cut on $s^{-1} \leq 9 \times 10^{-6}$ mm^{-1}. Overall, a $\sim 20\%$ improvement in efficiency is achieved by adding this new trigger according to MC signal studies.

Overall, with these new approaches it is possible to choose a lower single muon p_T threshold as compared to the Run-2 configuration, improving the selection efficiency of events with displaced muon pairs without increasing significantly the trigger rate, see Fig. 3.4.7.

The evaluation of the expected sensitivity of the displaced dark photon search after Run-3 and

[3] The midpoint is defined as the middle point of a segment

[4] The chord of a circle is a line segment that connects two points of the circle itself

[5] The arc is a portion of the circumference of a circle.

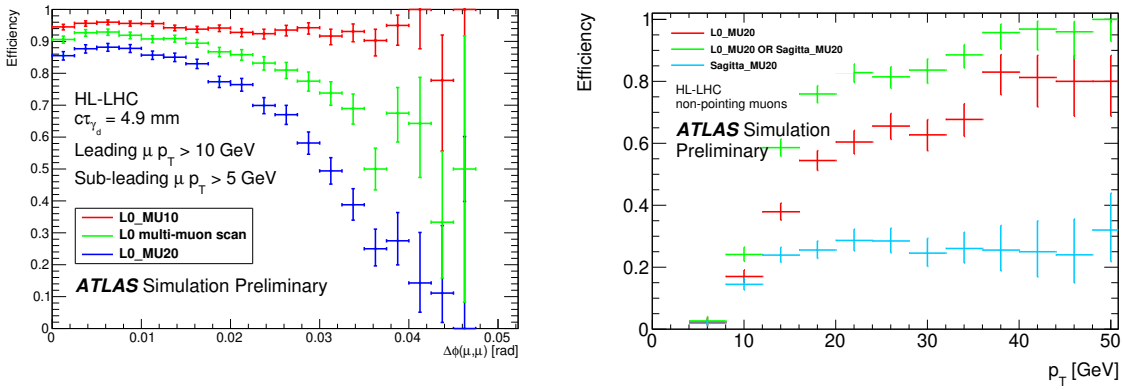

Fig. 3.4.7: Left: Efficiency for different trigger selections as a function of the opening angle of the two muons of the dark photon decay (the new L0 multi-muon scan trigger is shown in green). As a reference, two single-muon selections are shown for 10 (L1_MU10) and 20 (L1_MU20) GeV p_T threshold. Right: Trigger efficiency comparison for a FRVZ sample (the new L0 sagitta muon trigger is shown in green) as a function of the muon transverse momentum.

Excluded $c\tau$ [mm] muonic-muonic	Run-2	Run-3	HL-LHC	HL-LHC w/ L0 muon-scan
$\mathcal{B}(h \to 2\gamma_d + X) = 10\ \%$	$2.2 \leq c\tau \leq 111$	$1.15 \leq c\tau \leq 435$	$0.97 \leq c\tau \leq 553$	$0.97 \leq c\tau \leq 597$
$\mathcal{B}(h \to 2\gamma_d + X) = 1\ \%$	-	$2.76 \leq c\tau \leq 102$	$2.18 \leq c\tau \leq 142$	$2.13 \leq c\tau \leq 148$

Table 3.4.1: Ranges of γ_d $c\tau$ excluded at 95% C.L. for $h \to 2\gamma_d + X$ assuming $\mathcal{B}(h \to 2\gamma_d + X) = 10\%$ and $\mathcal{B}(h \to 2\gamma_d + X) = 1\%$ and dark photon mass of 400 MeV.

HL-LHC operations is based on the 2015+2016 Run-2 ATLAS analysis where multivariate techniques are used for signal discrimination against the backgrounds. The benchmark signal model used in the Run-2 search is a FRVZ model with 400 MeV γ_d mass and lifetime $c\tau = 49$ mm. The branching fraction of the γ_d decay to muons is 45%. Only the dominant ggF Higgs production mechanism is considered. One of the main SM backgrounds to the dark photon signal is multijet production. Samples of simulated 14 TeV multijet events are used to compute scale factors to rescale the data-driven estimates at 13 TeV c.o.m. energy to 14 TeV. These samples are also used to evaluate the systematic uncertainties. Other sources of background include cosmic rays. This is assumed to scale with duration of data taking, and the cosmic ray background from the Run 2 analysis has been scaled accordingly.

Uncertainties have been extrapolated from the Run-2 reference analysis. The statistical sources of uncertainties have been scaled with the expected integrated luminosity, for both Run-3 and HL-LHC. The systematic uncertainties for Run-3 have been assumed to be the same as in the Run-2 analysis. For the HL-LHC projection systematic uncertainties have been evaluated according to the specifications of the ATLAS collaboration for upgrade studies. Overall, the dominant uncertainties ($\sim 20\%$) are expected to be arising from pile-up.

Results for the three different scenarios (Run 3, HL-LHC and HL-LHC with trigger improvements) are presented in Table 3.4.1 for dark photons with $m_{\gamma_d} = 400$ MeV. The excluded $c\tau$ ranges assuming Higgs into dark photons branching ratio of 10% and 1% respectively are shown. The exclusion limits are re-interpreted in the context of the vector portal model. The exclusion contour plot in the plane defined by the dark photon mass and the kinetic mixing parameter ϵ is presented in Fig. 3.4.8, assuming a Higgs decay branching fraction to the hidden sector of 1% and where gaps correspond to hadronic decays not covered by this analysis.

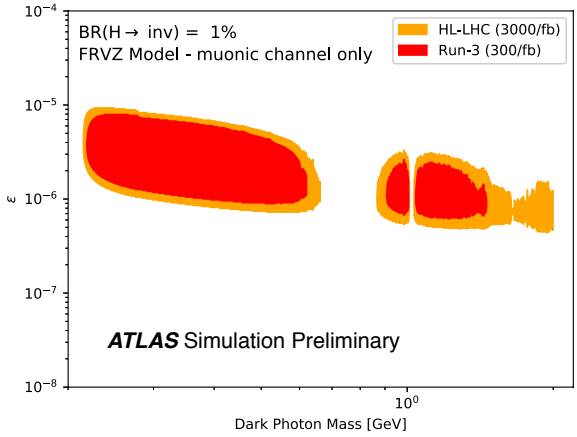

Fig. 3.4.8: Exclusion contour plot in the plane defined by the γ_d mass and the kinetic mixing parameter ϵ. Two different scenarios are shown assuming a Higgs decay branching fraction to the hidden sector of 1%: $300\ \mathrm{fb}^{-1}$ after Run-3 (red) ad $3\ \mathrm{ab}^{-1}$ after HL-LHC including multi-muon scan trigger improvement (orange).

3.4.2.3 Summary of sensitivity for dark photons from Higgs decays

The discovery reach from the ATLAS and CMS searches for dark photons can be compared to that from the generic γ_d search results shown in Fig. 3.4.1. This is reported in Fig. 3.4.9 as a function of the dark photon mass and ϵ^2: the reach of minimal models is shown together with that of models with additional assumptions on the dark photon production mechanism via Higgs decays. A 10% decay rate of the Higgs boson into dark photons is assumed for the latter. Under these assumptions, the HL-LHC ATLAS search will allow to target a crucial region with dark photon mass between 0.2 and 10 GeV and low ϵ^2, while the CMS search will cover higher γ_d masses and even lower mixing parameters. This is complementary to the LHCb and low-energy experiments reach as well as with the coverage of prompt-lepton searches at the LHC.

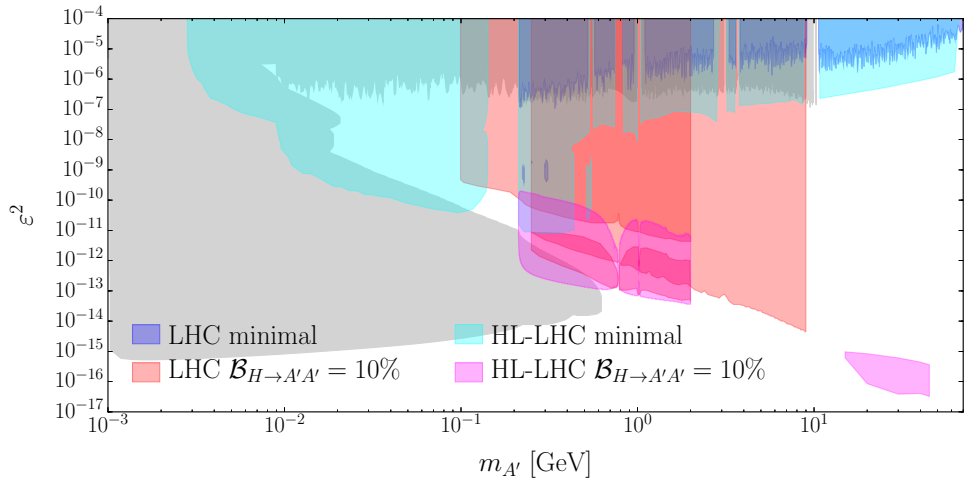

Fig. 3.4.9: Summary of the contour reach of searches for dark photons from Higgs decays. The purple, grey and blue areas are explained in Section 3.4.1, and correspond to the minimal dark photon model, with best sensitivity achieved by LHCb and low-energy experiments. The red and pink areas, explained in Section 3.4.2.2 and Section 3.4.2.1, correspond to results from ATLAS and CMS where dark photons are produced through a Higgs boson decay with a branching fraction of 10%.

3.4.3 Searching for dark photons via Higgs-boson production at the HL- and HE-LHC

Contributors: S. Biswas, E. Gabrielli, M. Heikinheimo, B. Mele

The dark-sector scenario proposed in Ref. [312, 313] is studied in this section. It aims at naturally solving the Flavour hierarchy problem, while providing suitable candidates for DM constituents. In particular, the scenario envisages the existence of stable dark-fermion fields, acting as DM particles, and heavy messenger scalar fields that communicate the interactions between the dark and the SM sectors. Both dark fermions and messenger fields are charged under an unbroken $U(1)$ interaction in the dark sector, whose non-perturbative dynamics are responsible for an exponential hierarchy in the dark fermion spectrum. Consequently, exponentially spread Yukawa couplings are radiatively generated by the dark sector, thus naturally solving the Flavour hierarchy problem.

A crucial aspect of this flavour model is that it foresees the existence of a massless dark photon. Until recently, most attention in collider physics has been given to the search for massive dark photons, whose $U(1)$ gauge field can naturally develop a *tree-level* millicharge coupling with ordinary matter fields. On the contrary, strictly massless dark photons, although very appealing from the theoretical point of view, in general lack tree-level couplings to SM fields. Indeed, the latter (even if induced, for instance, by a kinetic mixing with the ordinary photon field) can be rotated away, and reabsorbed in the gauge- and matter-field redefinition [314]. Nevertheless, thanks to the messenger fields, massless dark photons can develop higher-dimensional effective interactions with the SM fields which are suppressed by the effective scale controlling the corresponding higher-dimensional-operator coupling. Then, new dedicated search strategies for the massless dark photons are required with respect to the massive case.

The Higgs boson could play a crucial role in the discovery of massless dark photons at the LHC. As discussed in Ref. [315], by using as a benchmark the model in Ref. [312], an effective $H\gamma\bar{\gamma}$ interaction can be generated at one loop by the exchange of virtual messenger fields in the 3-point loop function. This interaction can be parametrised as $\mathcal{L}_{H\gamma\bar{\gamma}} = \frac{1}{\Lambda_{H\gamma\bar{\gamma}}} H F^{\mu\nu} \bar{F}_{\mu\nu}$, where $F^{\mu\nu}$ and $\bar{F}_{\mu\nu}$ are the field strength of the photon γ and the dark photon $\bar{\gamma}$, respectively [315]. While in general the higher-dimensional dark-photon interactions with the SM fields are suppressed, in the present case the Higgs boson can enter a nondecoupling regime in particular model parameter regions, just as happens in the SM for the Higgs couplings to two photons or gluons in the large top-quark mass limit. The effective high-energy scale $\Lambda_{H\gamma\bar{\gamma}}$ will then be proportional to the EW Higgs VEV v, rather than the characteristic new-physics mass scale. In particular, it will be given by

$$\Lambda_{H\gamma\bar{\gamma}} \;=\; \frac{6\pi v}{R\sqrt{\alpha\alpha_D}} \frac{1-\xi}{\xi^2} \tag{3.4.1}$$

where $\xi = \Delta/\bar{m}^2$ is a mixing parameter, with Δ the left-right mixing term in the messenger square-mass matrix, $\bar{m}$ is the average messenger mass, α and α_D the electromagnetic and the dark $U(1)$ fine structure couplings, respectively, while R is a product of quantum charges [316].

This regime can give rise to an exotic signature corresponding to the Higgs decay

$$H \to \gamma\bar{\gamma},$$

given by a monochromatic photon plus *massless missing momentum* (both resonating at the Higgs boson mass) with BRs $\mathcal{B}_{\gamma\bar{\gamma}}$ as large as a few percent. Below we report the results of a study of the LHC searches for this decay signature in gluon-fusion Higgs production in both the HL- and HE-LHC phases, assuming that $\mathcal{B}_{\gamma\bar{\gamma}}$ is the only parameter that affects the corresponding production mechanism.

The search strategy for the $gg \to H \to \gamma\bar{\gamma}$ process was outlined in Ref. [315] for 8 TeV and in Ref. [317] for 14 TeV, where we also discussed the vector-boson-fusion process. The final state consists of a single photon and missing transverse momentum, possibly accompanied by one or more jets arising from initial state radiation. The event selection criteria proposed in Ref. [317] were:

– one isolated ($\Delta R > 0.4$) photon with $p_T^\gamma > 50$ GeV, and $|\eta^\gamma| < 1.44$;

	$\sigma \times A$ [14 TeV]	$\sigma \times A$ [27 TeV]
$H \to \gamma\bar{\gamma}$ $(\mathcal{B}_{\gamma\bar{\gamma}} = 1\%)$	101	236
γj	202	–
$jj \to \gamma j$	432	4738
$e \to \gamma$	93	169
$W(\to \ell\nu)\gamma$	123	239
$Z(\to \nu\nu)\gamma$	283	509
total background	1133	5655

Table 3.4.2: Event yields in femtobarn for signal and backgrounds after the cuts $p_T^\gamma > 50$ GeV, $\not{E}_T > 50$ GeV, 100 GeV $< \mathrm{M}_\mathrm{T}^{\gamma\bar{\gamma}} <$ 130 GeV. The γj and jj backgrounds are obtained via the rescaling k-factors described in the text. A is the acceptance described in the text.

- missing transverse momentum satisfying $\not{E}_T > 50$ GeV;
- transverse mass in the range 100 GeV $< \mathrm{M}_\mathrm{T}^{\gamma\bar{\gamma}} <$ 130 GeV;
- no isolated leptons within $|\eta^\ell| < 2.5$,

where the transverse-mass variable is defined as $M_T^{\gamma\bar{\gamma}} = \sqrt{2p_T^\gamma \not{E}_T(1-\cos\Delta\phi)}$, and $\Delta\phi$ is the azimuthal distance between the photon transverse momentum p_T^γ, and the missing transverse momentum $\not{E}_T$.

The most important SM backgrounds are: *(i)* γj, where missing energy is created from mismeasurement of the jet energy and/or neutrinos from heavy flavour decays, and *(ii)* jj where in addition to the above, a central jet is misidentified as a photon. In our analysis we assume a probability of 0.1% for mis-tagging a jet as a photon, and a 90% reconstruction efficiency for real photons. In addition to the QCD backgrounds, we identify the following EW backgrounds: $Z\gamma$, where the Z decays into neutrinos; $W\gamma$, where the W decays leptonically (excluding taus) and the charged lepton is outside the acceptance of $|\eta^\ell| < 2.5$; and $W \to e\nu$, where the electron is misidentified as a photon. We also assume a 0.5% probability for the electron to photon mis-tagging.

We have analysed the EW backgrounds at parton level with MADGRAPH 5 V2.3.3. For the QCD backgrounds we use MADGRAPH 5 interfaced with PYTHIA, and follow the procedure outlined in Ref. [317]. In particular, we have generated event samples at 8 TeV and applied the *SUSY benchmark* event selection criteria described in the CMS analysis [318], not including the "χ^2", "$E_\mathrm{T}^\mathrm{miss}$ significance" and "α" cuts. With these omissions, the event selection criteria is very similar to our selection criteria described above. We then approximate the effect of these further, more sophisticated cuts on the QCD backgrounds, by matching our event samples with the background yield after these cuts reported in Ref. [318]. This results in a rescaling k-factor of $k = 0.11$ for the γj background, and $k = 0.058$ for the jj background at 8 TeV. Finally, we have generated the signal event samples with ALPGEN interfaced with PYTHIA, and included the gluon fusion Higgs production processes with zero to one jets.

Assuming the same rescaling factors for the QCD backgrounds at 14 and 27 TeV, we obtain the signal and background event yields reported in Table 3.4.2, clearly showing a worsening of the signal-to-background ratio at larger energies.

We then tried an alternative strategy to control the QCD background, by analysing the effect of applying a jet veto within $|\eta^j| < 4.5$, where a jet is defined as a cluster of hadrons within a cone of size $R = 0.4$ and $p_T \geq 20$ GeV, using a simple cone algorithm. In this case we no longer apply the rescaling k-factors obtained from our previous analysis, as now the cut-flow deviates from the CMS analysis presented in Ref. [318]. The resulting event yields are shown in Table 3.4.3. Based on the event yields reported in Tables 3.4.2 and 3.4.3, we estimate the reach of the HL-LHC and HE-LHC in terms of the BR of the decay mode $H \to \gamma\bar{\gamma}$ as shown in Table 3.4.4. On the basis of the present analysis, a quite good potential for HL-LHC is expected, that would allow for a (5σ) discovery reach on the corresponding

	$\sigma \times A$ [14 TeV]	$\sigma \times A$ [27 TeV]
$H \to \gamma\bar{\gamma}$ $(\mathcal{B}_{\gamma\bar{\gamma}} = 1\%)$	66.6	139.1
γj	–	–
$jj \to \gamma j$	886	31235
$e \to \gamma$	93	169
$W(\to \ell\nu)\gamma$	123	239
$Z(\to \nu\nu)\gamma$	283	509
total background	1385	32153

Table 3.4.3: Event yields in femtobarn for signal and backgrounds after the cuts $p_T^\gamma > 50$ GeV, $\not{E}_T > 50$ GeV, $100\ \text{GeV} < \text{M}_\text{T}^{\gamma\bar{\gamma}} < 130$ GeV, and jet veto within $|\eta^j| < 4.5$. A is the acceptance described in the text.

$\mathcal{B}_{\gamma\bar{\gamma}}(\%)$	$3\ \text{ab}^{-1}$@14 TeV		$15\ \text{ab}^{-1}$@27 TeV	
significance	2σ	5σ	2σ	5σ
CMS inspired	0.012	0.030	0.0052	0.013
jet veto in $\lvert\eta^j\rvert < 4.5$	0.020	0.051	0.021	0.053

Table 3.4.4: Discovery (5σ) and exclusion (2σ) reach for the $H \to \gamma\bar{\gamma}$ BR (in %) at the HL-LHC and HE-LHC.

$\mathcal{B}_{\gamma\bar{\gamma}}$ down to 3×10^{-4}, for $3\ \text{ab}^{-1}$ of integrated luminosity, provided the CMS inspired analysis of the jj background can be reliably applied in this case. Same conclusions hold for the HE-LHC project, where a 1×10^{-4} (5σ) discovery reach can be achieved, for $15\ \text{ab}^{-1}$of expected luminosity, assuming that the CMS inspired analysis of the jj background is still reliable at 27 TeV. On the other hand, if a jet veto in $|\eta^j < 4.5|$ is applied instead, lower sensitivities on $\mathcal{B}_{\gamma\bar{\gamma}}$ can be obtained, leading to discovery just for $\mathcal{B}_{\gamma\bar{\gamma}}$ down to 5×10^{-4} at both HL-LHC and HE-LHC facilities.

We nevertheless think that a more realistic detector simulation and optimisation strategy would be needed in order to make the present reach estimates more robust. In Ref. [317], one can also find a study of the vector-boson-fusion channel sensitivity to $\mathcal{B}_{\gamma\bar{\gamma}}$ at 14 TeV.

4 Long Lived Particles

There are many examples of BSM physics where new particles that can be produced at the LHC will be long lived, on collider timescales, and may travel macroscopic distances before decaying. Long lifetimes may be due to small couplings, small mass splittings, a high multiplicity of the decay final state, or a combination of these effects. Details, such as the quantum numbers of the long lived particle (LLP) and the decay products, the typical boost of the LLP and its lifetime, will determine the best search strategy. In all cases, LLPs present unique challenges for the experiments, both in terms of reconstruction/analysis and triggering, especially in the high pile up environment of the HL-LHC. A wide variety of signatures can be produced by these later decaying LLPs which depend on their charge, decay position, branching fractions, masses, and other properties, and which traditional analyses are unlikely to be sensitive to.

If the LLP is charged and decays while still in the tracker to final state particles that are either neutral or too soft to be reconstructed it will appear as a disappearing track: hits in the first few layers of the tracker with no corresponding hits in the outer layers, see Section 4.1. Such a scenario occurs in models (e.g., SUSY) with nearly degenerate charged and neutral states, where the charged pion in the decay is too soft to be seen as a track. A complementary study in the context of disappearing track searches is presented in Section 4.1.2, where the potential of LLP searches at $e^- p$ colliders is presented. We present studies for disappearing tracks searches using simplified models of $\tilde{\chi}^{\pm}$ production which lead to exclusions of chargino masses up to $m(\tilde{\chi}_1^{\pm}) = 750$ GeV (1100 GeV) for lifetimes of 1 ns for the higgsino (wino) hypothesis. When considering the lifetime predicted by theory, masses up to 300 GeV and 830 GeV can be excluded in higgsino and wino models, respectively. This improves the 36 fb^{-1} Run-2 mass reach by a factor of $2-3$.

Decays of LLPs where the decay products are not missed but instead include multiple tracks will lead to events containing at least one displaced vertex (DV). Such a signal is sensitive to both charged and neutral LLPs. If the displacement of the vertex is large, $\gamma c\tau \gtrsim 1$ m, then the only available hits are in the muon system, limiting the final states to muons as in Section 3.4.2.1 and Section 4.2.2.

If the lifetime is shorter the DV can be reconstructed in the tracker. One such analysis of gluinos decaying to a displaced jet and $E_{\text{T}}^{\text{miss}}$ is presented Section 4.2.1. Searches for long lived dark photons decaying to muons and/or jets are reported in Section 3.4.1 and Section 3.4.2. The signature of long-lived dark photons decaying to displaced muons can be reconstructed with dedicated algorithms and is sensitive to very small coupling $\epsilon^2 \sim 10^{-14}$ for masses of the dark photons between 10 and 35 GeV. Furthermore, LHCb is the only LHC experiment to be fully instrumented in the forward region $2 < \eta < 5$ and has proved to be sensitive to LLPs. This is particularly true in the low mass (few GeV) and low lifetime (few picoseconds) region of the LLPs. Prospects studies from LHCb on LLPs resulting from Higgs decays are shown in Sections 4.2.3 and 4.2.4.

For displacement of several meters LLPs will transit all of the detector before decaying. Heavy LLPs that are also charged, so called heavy stable charged particles (HSCPs), will behave in a similar fashion to a muon. However, due to their increased mass it may be possible to distinguish them from muons through their time of flight, Section 4.3.1, or anomalous energy loss, Section 4.3.2. Finally, two examples of specialised techniques for LLP with jet-like signatures are presented in Section 4.4, using timing or EM calorimeter information.

In addition to searching for LLPs in ATLAS, CMS, and LHCb there are complementary proposals to build new detectors specifically focused on LLP searches, often for light new physics produced in rare meson decays. A detailed discussion of their capabilities is beyond the scope of this work, and will be discussed elsewhere. The Beyond Collider experiments are AL3X (A Laboratory for Long-Lived eXotics) [319], CODEX-b (COmpact Detector for EXotics at LHCb) [320], FASER (ForwArd Search ExpeRiment) [321–323], milliQan [324,325], MATHUSLA (MAssive Timing Hodoscope for Ultra Stable neutraL pArticles) [326,327], and SHiP (Search for Hidden Particles) [328,329]. They use alternative search strategies and often give complementary coverage of the available parameter space. In addition

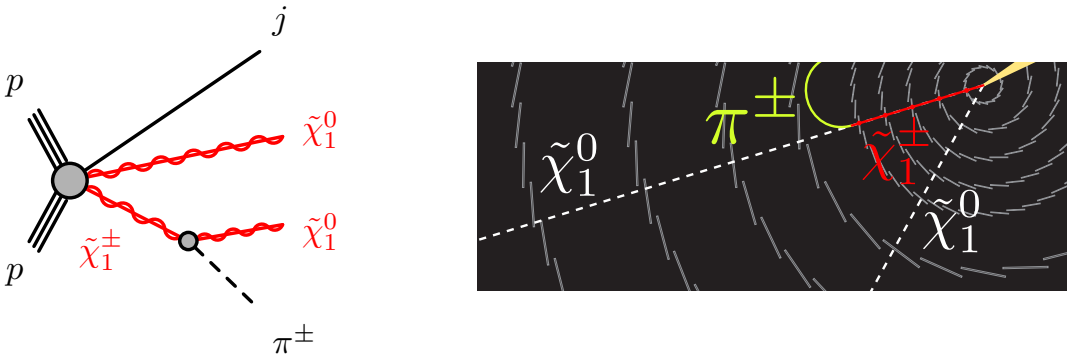

Fig. 4.1.1: Diagram depicting $\tilde{\chi}_1^\pm\tilde{\chi}_1^0$ production (left), and schematic illustration of a $pp \to \tilde{\chi}_1^\pm\tilde{\chi}_1^0 +$ jet event in the HL-LHC ATLAS detector, with a long-lived chargino (right). Particles produced in pile-up pp interactions are not shown. The $\tilde{\chi}_1^\pm$ decays into a low-momentum pion and a $\tilde{\chi}_1^0$ after leaving hits in the pixel layers.

to the afore-mentioned study on disappearing tracks, complementary studies on LLPs *e.g.* from higgs decays have been performed in the context of a future e^-p collider, resulting in good sensitivity for a wide range in $c\tau$ and mass [330].

4.1 Disappearing Tracks

A disappearing track occurs when the decay products of a charged particle, like a supersymmetric chargino, are not detected (disappear) because they either interact only weakly or have soft momenta and hence are not reconstructed. In the following, prospect studies for HL-, HE- and new proposed e^-p collider are presented, illustrating the potential of this signature as well as its experimental challenges.

4.1.1 Prospects for disappearing track analysis at HL-LHC

Contributors: S. Amoroso, J. K. Anders, F. Meloni, C. Merlassino, B. Petersen, J. A. Sabater Iglesias, M. Saito, R. Sawada, P. Tornambe, M. Weber, ATLAS

The disappearing track search [102] investigates scenarios where the $\tilde{\chi}_1^\pm$, and $\tilde{\chi}_1^0$ are almost mass degenerate, leading to a long lifetime for the $\tilde{\chi}_1^\pm$ which decays after the first few layers of the inner detector, leaving a track in the innermost layers of the detector. The chargino decays as $\tilde{\chi}_1^\pm \to \pi^\pm\tilde{\chi}_1^0$. The $\tilde{\chi}_1^0$ escapes the detector and the pion has a very low energy and is not reconstructed, leading to the disappearing track signature. Diagram and schematic illustration of production and decay process are shown in in Fig. 4.1.1. The main signature of the search is a short "tracklet" which is reconstructed in the inner layers of the detector and subsequently disappears. The tracklet reconstruction efficiency for signal charginos is estimated using fully simulated samples of $\tilde{\chi}_1^\pm$ pair production with $m(\tilde{\chi}_1^\pm) = 600$ GeV. Tracklet reconstruction is performed in two stages. Firstly "standard" tracks, hereafter referred to as tracks are reconstructed. Afterwards the track reconstruction is then rerun with looser criteria, requiring at least four pixel-detector hits. This second reconstruction uses only input hits which are not associated with tracks, referred to as "tracklets". The tracklets are then extrapolated to the strip detectors, and any compatible hits are assigned to the tracklet candidate. Tracklets are required to have $p_T > 5$ GeVand $|\eta| < 2.2$. Candidate leptons, which are used only to veto events, are selected with $p_T > 20$ GeV and $|\eta| < 2.47$ (2.7) for electrons (muons).

The signal region (SR) optimisation is performed by scanning a set of variables which are expected to provide discrimination between the signal scenario under consideration and the expected SM background processes. The final state contains zero leptons, large $E_{\mathrm{T}}^{\mathrm{miss}}$ and at least one tracklet, and events are reweighted by the expected efficiencies of tracklet reconstruction. The small mass splitting between the $\tilde{\chi}_1^\pm$ and $\tilde{\chi}_1^0$ implies they are generally produced back to back with similar transverse momentum. Hence it is necessary to select events where the system is boosted by the recoil of at least one

	SR
Total SM	4.6 ± 1.3
V+jets events	0.17 ± 0.05
$t\bar{t}$ events	0.02 ± 0.01
Fake tracklets	4.4 ± 1.3

Table 4.1.1: Yields are presented for the disappearing track SR selection with an integrated luminosity of 3 ab^{-1}at $\sqrt{s} = 14$ TeV. The errors shown are the total statistical and systematic uncertainty.

energetic ISR jet. The minimum azimuthal angular distance between the first four jets (ordered in p_{T}) and the $E_{\mathrm{T}}^{\mathrm{miss}}$ is required to be greater than 1, in order to reject events with mis-measured $E_{\mathrm{T}}^{\mathrm{miss}}$.

There are two main background contributions: SM particles that are reconstructed as tracklets, and events which contain fake tracklets. The SM particles reconstructed as tracklets are typically hadrons scattering in the detector material or electrons undergoing bremsstrahlung. The probability of an isolated electron or hadron leaving a disappearing track is calculated using samples of single electrons or pions passing through the current ATLAS detector layout, and is then scaled to take into account the ratio of material in the current ATLAS inner detector and the upgraded inner tracker. The second background contribution arises from events which contain "fake" tracklets. These events arise from $Z \to \nu\nu$ or $W \to \ell\nu$ (where the lepton is not reconstructed) and are scaled by the expected fake tracklet probability:

$$p_{\mathrm{fake,tight}}^{\mathrm{ITk}} = p_{\mathrm{fake,tight}}^{\mathrm{ATLAS}} \times \frac{R_{\mathrm{fake,loose}}^{\mathrm{ITk}}}{R_{\mathrm{fake,loose}}^{\mathrm{ATLAS}}} \times \frac{\epsilon_{z_0}^{\mathrm{ITk}}}{\epsilon_{z_0}^{\mathrm{ATLAS}}}. \tag{4.1.1}$$

In this equation, $p_{\mathrm{fake,tight}}^{\mathrm{ATLAS}}$ is the fake rate of the current Run-2 analysis [331], computed using a d_0 sideband for the track reconstruction, $R_{\mathrm{fake,loose}}^{\mathrm{ITk}}$ is the fake rate in the same d_0 sideband for ITk computed with a neutrino particle gun sample, such that all tracks are purely a result of pile-up interactions, $R_{\mathrm{fake,loose}}^{\mathrm{ATLAS}}$ is the fake rate in the d_0 sideband for ATLAS computed on data, $\epsilon_{z_0}^{\mathrm{ITk}}$ is the selection efficiency of the tracklet z_0 selection in ITk, and $\epsilon_{z_0}^{\mathrm{ATLAS}}$ is the selection efficiency of the tracklet z_0 selection in ATLAS.

Systematic uncertainty projections for both searches have been determined starting from the systematic uncertainties studied in Run-2 and evolving them to a level which the ATLAS and CMS collaborations have agreed to consider as a sensible extrapolation to HL–LHC. Hence, the theory modelling uncertainties are expected to halve while the recommendations for detector-level and experimental uncertainties are dependent upon the systematic uncertainty under consideration and are scaled appropriately from the Run-2 analysis. When setting exclusion limits, an additional systematic uncertainty of 20% is set to account for the theoretical systematic uncertainty on the models under consideration. The dominant uncertainties in the disappearing track analysis arise from the modelling of the fake tracklet component, and the total uncertainty on the background yield is extrapolated to be 30%.

Table 4.1.1 presents the expected yields in the SR for the disappearing track search for each background source, corresponding to an integrated luminosity of 3 ab^{-1}. As seen in the table the dominant background source corresponds to events with a "fake" tracklet, arising predominantly from $Z \to \nu\nu$ events with an ISR jet and high $E_{\mathrm{T}}^{\mathrm{miss}}$, which contain spurious hits that are reconstructed as a tracklet.

Limits at 95% C.L. on the chargino lifetime are shown in Fig. 4.1.2 as a function of the $\tilde{\chi}_1^{\pm}$ mass. The simplified models of chargino production considered include chargino pair production and chargino-neutralino production (both $\tilde{\chi}_1^{\pm}\tilde{\chi}_1^0$ and $\tilde{\chi}_1^{\pm}\tilde{\chi}_2^0$. The potential for the full HL-LHC dataset is expected to exclude at the 95% C.L. chargino lifetimes, assuming a wino-like (higgsino-like) LSP, of between 7 ps (10 ps) and 4 μs (1.5 μs) for light charginos with a mass of 100 GeV. Heavier wino-like (higgsino-like) charginos are excluded up to $m(\tilde{\chi}_1^{\pm}) = 1100$ GeV (750 GeV) for lifetimes of 1 ns. The discovery

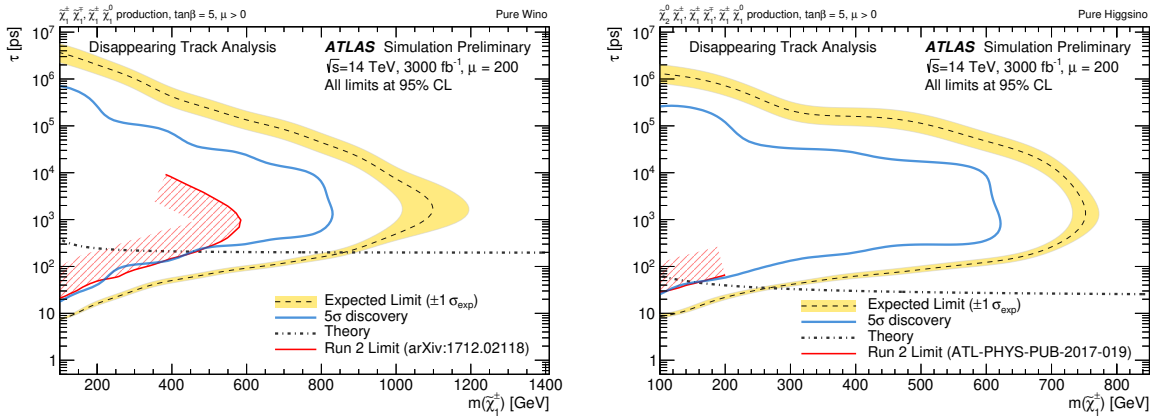

Fig. 4.1.2: Expected exclusion limits at 95% C.L. from the disappearing track search using of 3 $\mathrm{ab}^{-1}$of 14 TeV proton-proton collision data as a function of the $\tilde{\chi}_1^{\pm}$ mass and lifetime. Simplified models including both chargino pair production and associated production $\tilde{\chi}_1^{\pm}\tilde{\chi}_1^0$ are considered assuming pure-wino production cross sections (left) and pure-higgsino production cross sections (right). The yellow band shows the 1σ region of the distribution of the expected limits. The median of the expected limits is shown by a dashed line. The red line presents the current limits from the Run-2 analysis and the hashed region is used to show the direction of the exclusion. The expected limits with the upgraded ATLAS detector would extend these limits significantly. The chargino lifetime as a function of the chargino mass is shown in the almost pure wino LSP scenario (light grey) calculated at one loop level. The relationship between the masses of the chargino and the two lightest neutralinos in this scenario is $m(\tilde{\chi}_1^{\pm}) = (m(\tilde{\chi}_1^0) + m(\tilde{\chi}_2^0))/2$. The theory curve is a prediction from a pure higgsino scenario.

potential of the analysis would allow for the discovery of wino-like (higgsino-like) charginos of mass 100 GeV with lifetimes between 20 ps and 700 ns (30 ps and 250 ns), or for a lifetime of 1 ns would allow the discovery of wino-like (higgsino-like) charginos of mass up to 800 GeV (600 GeV).

Finally, Fig. 4.1.3 presents the 95% C.L. expected exclusion limits in the $\tilde{\chi}_1^0, \Delta m(\tilde{\chi}_1^{\pm}, \tilde{\chi}_1^0)$ mass plane, from both the disappearing track and dilepton searches. The yellow contour shows the expected exclusion limit from the disappearing track search, with the possibility to exclude $m(\tilde{\chi}_1^{\pm})$ up to 600 GeV for $\Delta m(\tilde{\chi}_1^{\pm}, \tilde{\chi}_1^0) < 0.2$ GeV, and could exclude up to $\Delta m(\tilde{\chi}_1^{\pm}, \tilde{\chi}_1^0) = 0.4$ GeV for $m(\tilde{\chi}_1^{\pm}) = 100$ GeV. The blue curve presents the expected exclusion limits from the dilepton search, which could exclude up to 350 GeV in $m(\tilde{\chi}_1^{\pm})$, and for a light chargino mass of 100 GeV would exclude mass differences between 2 and 15 GeV. Improvements that are expected with the upgraded detector, and search technique improvements may further enhance the sensitivity to these models. For example the sensitivity of the disappearing tracks search can be enhanced by optimising the tracking algorithms used for the upgraded ATLAS detector allowing for an increase in tracklet efficiency, the possibility of shorter tracklets produced requiring 3 or 4 hits, and further suppression of the fake tracklet component. The dilepton search sensitivity would be expected to improve by increasing the reconstruction efficiency for low p_T leptons. The addition of the electron channel would also further enhance the search sensitivity.

4.1.2 Complementarities between LHeC and HL-LHC for disappearing track searches

Contributors: K. Deshpande, O. Fischer, J. Zurita

In higgsino-like SUSY models, the Higgsinos' tiny mass splittings give rise to finite lifetimes for the charginos, which is enhanced by the significant boost of the c.o.m. system and can be used to suppress SM backgrounds [330]. The small mass splittings allow the Higgsinos to decay into $\pi^{\pm}, e^{\pm}, \mu^{\pm}$ + invisible particles, with the single visible charged particle having transverse momenta in the $\mathcal{O}(0.1)$ GeV range. In the clean environment (*i.e.* low pile up) of the e^-p collider, such single low-energy charged tracks can be reliably reconstructed, if the minimum displacement between primary and secondary vertex is at least 40 μm, and the minimum p_T of the charged SM particle is at least 100 MeV.

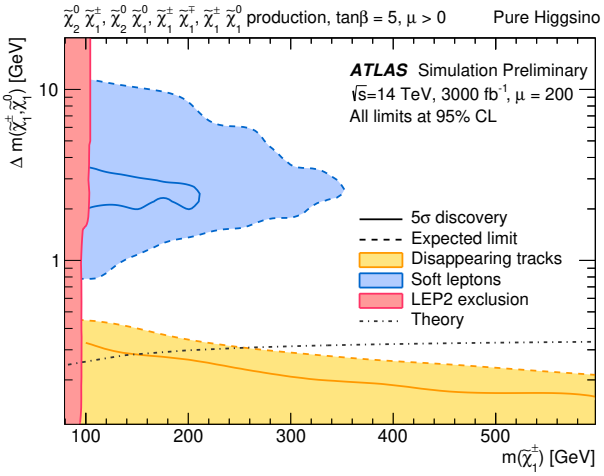

Fig. 4.1.3: Expected exclusion at the 95% C.L. from the disappearing track and dilepton searches in the $\Delta m(\tilde{\chi}_1^\pm, \tilde{\chi}_1^0)$, $m(\tilde{\chi}_1^\pm)$ mass plane. The blue curve presents the exclusion limits from the dilepton search. The yellow contour presents the exclusion limit from the disappearing track search. The figure also presents the limits on chargino production from LEP. The relationship between the masses of the chargino and the two lightest neutralinos in this scenario is $m(\tilde{\chi}_1^\pm) = \frac{1}{2}(m(\tilde{\chi}_1^0) + m(\tilde{\chi}_2^0))$. The theory curve is a prediction from a pure higgsino scenario taken from Ref. [211].

It was shown in Ref. [330] that the results do not crucially depend on the exact choice of these parameters. The associated DIS jet with $p_T > 20$ GeV ensures that the event is recorded and determines the position of the primary vertex. The charginos' decay into a neutral Higgsino and a number of SM particles with small p_T defines the secondary vertex.

Tau leptons with their proper lifetime of ~ 0.1 mm constitute an important and irreducible background. VBF can single- ($\tau^+\nu_\tau$) and pair produce taus ($\tau^+\tau^-$) together with a jet with $p_T > 20$ GeV, $|\eta| < 4.7$ at LHeC with cross sections of ~ 0.6 and ~ 0.3 pb, respectively. Kinematically, the τ decay products can be suppressed to 10^{-3} (keeping $\mathcal{O}(1)$ of the signal) by requiring $|\eta| > 1$ (in the proton beam direction), $\not{E}_T \gtrsim 30$ GeV) and the LLP final state energy to be very low ($\lesssim 1.5\Delta m$ for a given chargino lifetime). Furthermore, in the space of possible final states and decay lengths, the τ's will populate very different regions than the chargino signal, such that further suppression is possible.

The probability of detecting a chargino is computed by choosing the charged particle momentum from the appropriate phase space distribution in the chargino rest frame, then computing the minimum distance the chargino must travel for the displacement of the resulting charged track to be visible. The sensitivities of detecting at least one ($N_{1+\mathrm{LLP}}$), or two displaced vertices ($N_{2\mathrm{LLP}}$) are shown by the contours in Fig. 4.1.4 for $\mu > 0$. The darker (lighter) shading represents the contour with the lowest (highest) estimate of event yield, obtained by minimising (maximising) with respect to the two different hadronisation scenarios, and P_{jet} reconstruction assumptions. The difference between the light and dark shaded regions can be interpreted as a range of uncertainty in projected reach.

This sensitivity for Higgsinos via LHeC searches is competitive in mass reach to the monojet projections for the HL-LHC, being sensitive to masses around 200 GeV for the longest theoretically motivated lifetimes (see also Section 4.1.3). The LHeC search has the crucial advantage of actually observing the charged Higgsino parent of the invisible final state. Disappearing track searches at the HL-LHC presented in this report probe higher masses for the longest lifetimes, but lose sensitivity at shorter lifetimes. By comparison, the LHeC search is sensitive to lifetimes as short as microseconds. It is important to note how the robustness of the mass reach of e^-p colliders arise also from the fact that results are not exponentially sensitive to uncertainties in the Higgsino velocity distribution.

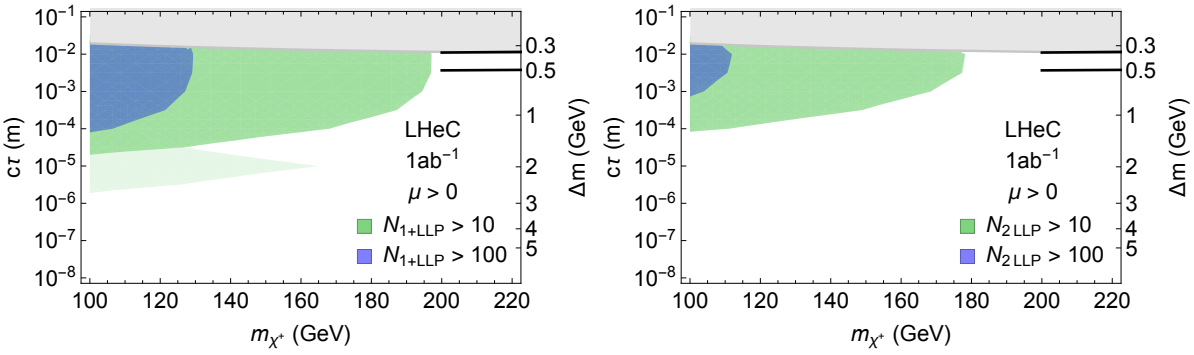

Fig. 4.1.4: Regions in the $(m_{\chi^\pm}, c\tau)$ Higgsino parameter plane where more than 10 or 100 events with at least one (left) or two (right) LLPs are observed at the LHeC. Light shading indicates the uncertainty in the predicted number of events due to different hadronisation and LLP reconstruction assumptions. Approximately 10 signal events should be discernible against the τ-background at 2σ, in particular for 2 LLPs, so the green shaded region represents an estimate of the exclusion sensitivity. For comparison, the black curves are the optimistic and pessimistic projected bounds from HL-LHC disappearing track searches from Ref. [288]. The figure is from Ref. [330].

4.1.3 Searching for Electroweakinos with disappearing tracks analysis at HL- and HE-LHC

Contributors: T. Han, S. Mukhopadhyay, X. Wang

Prospects for a disappearing charged track search are finally presented for three different scenarios of collider energy and integrated luminosity: HL-LHC, HE-LHC, and FCC-hh/SppC (100 TeV, 30 ab^{-1}). The studies are documented in Ref. [155] and are complementary to the monojet prospects reported in Section 3.1.3 for higgsino-like SUSY scenarios.

As in Section 3.1.3, the significance is defined as $S/\sqrt{B + (\Delta_B B)^2 + (\Delta_S S)^2}$ where S and B are the total number of signal and background events, and Δ_S, Δ_B refer to the corresponding percentage systematic uncertainties, respectively.

Background and signal systematic uncertainties are assumed as $\Delta_B = 20\%$ and $\Delta_S = 10\%$ respectively. In Fig. 4.1.5 we compare the reach of the HL-LHC, HE-LHC and FCC-hh/SppC options in the disappearing charged track analysis for wino-like (left) and Higgsino-like (right) DM search. The solid and dashed lines correspond to modifying the central value of the background estimate[6] by a factor of five. With the optimistic estimation of the background, wino-like DM can be probed at the 95% C.L. up to 900, 2100, and 6500 GeV, at the 14, 27, and 100 TeV colliders respectively. For the Higgsino-like scenario, these numbers are reduced to 300, 600, and 1550 GeV, primarily due to the its shorter lifetime and the reduced production rate. For the conservative estimation of the background, the mass reach for the wino-like states are modified to 500, 1500, and 4500 GeV, respectively, at the three collider energies. Similarly, for the Higgsino-like scenario, the reach becomes 200, 450, and 1070 GeV. Results for HL-LHC are also in reasonable agreement with experimental prospect studies. The signal significance in the disappearing track search is rather sensitive to the wino and Higgsino mass values (thus making the 2σ and 5σ reach very close in mass), due to the fact that the signal event rate decreases exponentially as the chargino lifetime in the lab frame becomes shorter for heavier masses.

The improvements in going from the HL-LHC to the HE-LHC, and further from the HE-LHC to the FCC-hh/SppC are very similar to those obtained for the monojet analysis, namely, around a factor of two and three, respectively. Results for both analyses are summarised in Table 4.1.2.

[6] Background is estimated by extrapolating ATLAS Run-2 analysis [332]. See [155] for details.

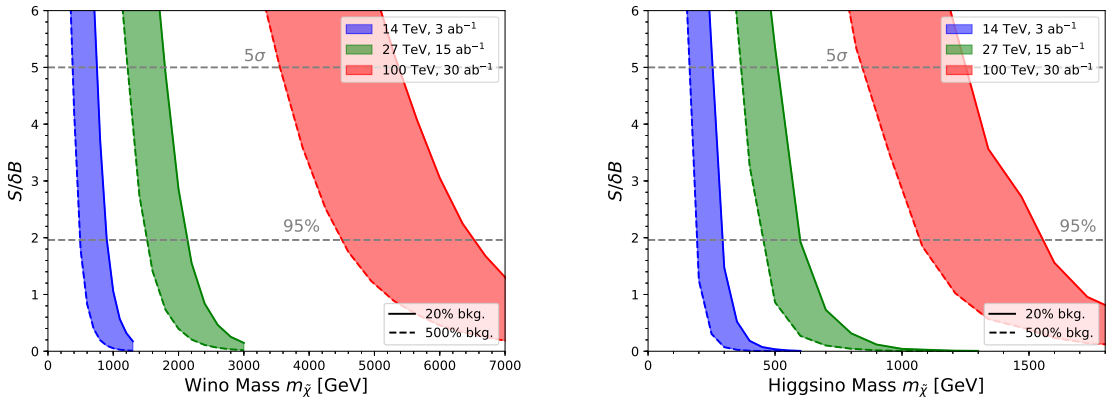

Fig. 4.1.5: Comparative reach of the HL-LHC, HE-LHC and FCC-hh/SppC options in the disappearing charged track analysis for wino-like (left) and Higgsino-like (right) DM search. The solid and dashed lines correspond to modifying the central value of the background estimate by a factor of five.

95% C.L.	Wino Monojet	Wino Disappearing Track	Higgsino Monojet	Higgsino Disappearing Track
14 TeV	280 GeV	900 GeV	200 GeV	300 GeV
27 TeV	700 GeV	2.1 TeV	490 GeV	600 GeV
100 TeV	2 TeV	6.5 TeV	1.4 TeV	1.6 TeV

Table 4.1.2: Summary of DM mass reach at 95% C.L. for an EW triplet (wino-like) and a doublet (Higgsino-like) representation, at the HL-LHC, HE-LHC and the FCC-hh/SppC colliders, in optimistic scenarios for the background systematics.

4.2 Displaced Vertices

Many models of new physics predict long-lived particles which decay within the detector but at an observable distance from the proton-proton interaction point (displaced signatures). If the decay products of the long-lived particle include multiple particles reconstructed as tracks or jets, the decay can produce a distinctive signature of an event containing at least one displaced vertex (DV). In the following sections, a number of prospects studies from ATLAS, CMS and LHCb are presented. Results are interpreted in the context of supersymmetric or higgs-portal scenarios but are applicable to any new physics model predicting one or more DVs, since the analyses are not driven by strict model assumptions.

4.2.1 LLP decaying to a Displaced Vertex and $E_{\mathrm{T}}^{\mathrm{miss}}$ at HL-LHC

Contributors: E. Frangipane, L. Jeanty, L. Lee Jr, H. Oide, S. Pagan Griso, ATLAS

There are several recent papers at the LHC which have searched for displaced vertices, including Ref.s [300, 333–335]. The projection presented here [336] requires at least one displaced vertex reconstructed within the ATLAS ITk, and events are required to have at least moderate missing transverse momentum ($E_{\mathrm{T}}^{\mathrm{miss}}$), which serves as a discriminant against background as well as an object on which to trigger. The analysis sensitivity is projected for a benchmark SUSY model of pair production of long-lived gluinos, which can naturally arise in models such as Split SUSY [337]. Each gluino hadronises into an R-hadron and decays through a heavy virtual squark into a pair of SM quarks and a stable neutralino with a mass of 100 GeV.

This study makes use of Monte Carlo simulation samples to obtain the kinematic properties of signal events, which are then used to estimate the efficiency for selecting signal events. The pair production of gluinos from proton-proton collisions at $\sqrt{s} = 13$ TeV was simulated in PYTHIA 6.428 [92] at leading order with the AUET2B [338] set of tuned parameters for the underlying event and the CTEQ6L1

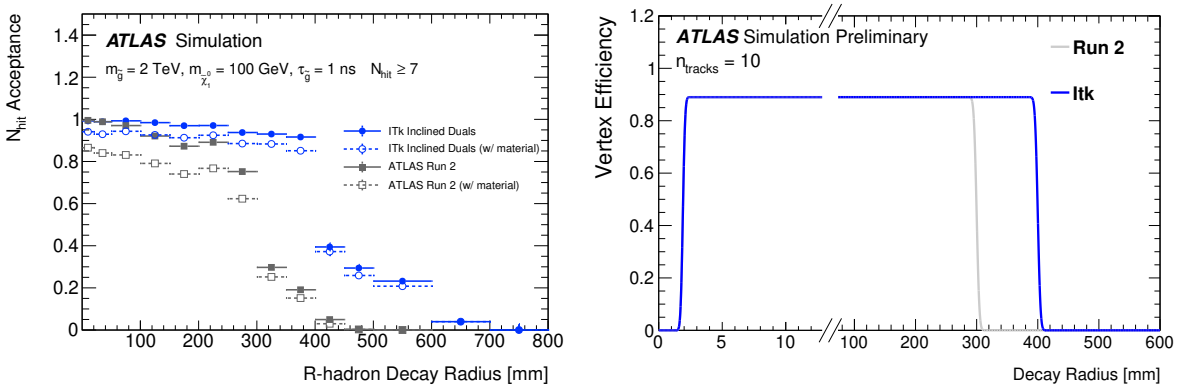

Fig. 4.2.1: Left: probability that a charged particle, with $p_T > 1$ GeVproduced in the decay of a 2.0 TeV R-hadron with a lifetime of 1 ns, passes through at least seven silicon layers, as a function of the decay radius of the R-hadron, for both the Run-2 and ITk detector layouts [256]. The probability is shown with and without the simulated effect of material producing hadronic interactions. Right: parametrised efficiency for reconstructing a displaced vertex with $n_{\text{tracks}} = 10$, as a function of the decay radius of the parent particle, as measured in Run-2 simulation and extrapolated to the ITk geometry.

parton distribution function (PDF) set [52]. After production, the gluino hadronises into an R-hadron and is propagated through the ATLAS detector by GEANT4 [54, 254] until it decays. PYTHIA 6.428 is called to decay the gluino into a pair of SM quarks and a neutralino and models the three-body decay of the gluino, fragmentation of the remnants of the light-quark system, and hadronisation of the decay products. The gluino lifetime ranges from 0.1 ns to 10 ns, and the neutralino mass is fixed to 100 GeV. To normalise the expected number of signal events in the full HL-LHC dataset, the cross-sections for pair production of gluinos are calculated at next-to-leading order at $\sqrt{s} = 14$ TeV and resummation of soft-gluon emission is taken into account at next-to-leading-logarithm accuracy (NLO+NLL) following the procedure outlined in Ref. [339].

Particle-level Monte Carlo events are used to obtain kinematic distributions for the signal. The expected track reconstruction performance is estimated by factorising it into an acceptance and an efficiency term, and assuming that the efficiency performance of the Run-2 algorithm, currently close to 100%, will be reproduced for ITk for particles which pass the acceptance. The tracking acceptance is based on the number of hits left by a charged particle traversing the silicon sensors; at least seven hits are required for both the current ID and the future ITk. To calculate the ITk acceptance for the tracks of interest, a full simulation of the ITk geometry is used. Only charged decay products with $p_T > 1$ GeV are considered and material interactions with the active and passive material of the detector are taken into account. Figure 4.2.1 (left) shows the acceptance as function of the production transverse position (radius) of the particle. The steep drop off in efficiency in the present ID at around 300 mm corresponds to the farthest radial extent of the first layer of the SCT, after which it is unlikely that a typical particle would traverse seven strip layers. In the ITk, the equivalent drop-off does not occur until after 400 mm due to the larger spacing between the silicon layers.

The current displaced vertexing performance is parametrised as a function of the transverse decay position (r_{DV}) and number of reconstructed tracks (n_{tracks}) coming from the long-lived particle decay. To extrapolate from the Run-2 efficiency to the expected performance in ITk, the same fit values are used for each bin of n_{tracks}, while the radial distance at which the vertexing efficiency starts to drop is moved from 300 mm to 400 mm to reflect the change in the location of the inner silicon strip layer, as shown for one particular example in Fig. 4.2.1 (right).

The event selection closely follows the requirements in the recent Run-2 search for a DV and MET [333]. Events are required to have at least one DV within the ITk volume and at least five tracks from the gluino decay must be reconstructed. The tracks and vertices are reconstructed with a probability

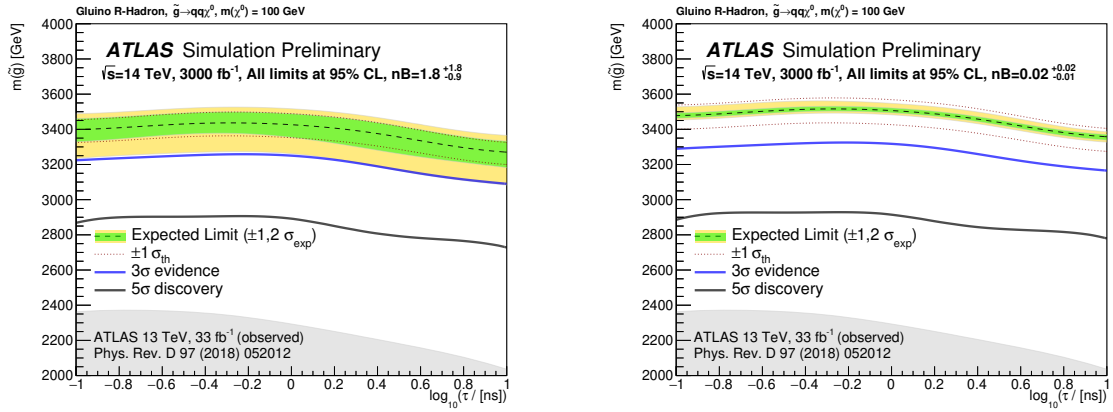

Fig. 4.2.2: Projected sensitivity for the upper limit on the mass of a gluino R-hadron that can be observed with 3σ and 5σ confidence or excluded at 95% C.L., as a function of the gluino lifetime, for a background of $1.8^{+1.8}_{-0.9}$ events (left) and a background of $0.02^{+0.02}_{-0.01}$ events (right). These results are valid for a gluino which decays to SM quarks and a stable neutralino with a mass of 100 GeV. Results assume 3 ab^{-1}of collisions at $\sqrt{s} = 14$ TeV collected with the upgraded ATLAS detector, and are compared to the observed ATLAS exclusion limits for a dataset of 33 fb^{-1} at $\sqrt{s} = 13$ TeV.

given by the procedures described above; only charged decay products with $p_T > 1$ GeV, $|\eta| < 5$, and with 6 mm $< r_{\text{prod}} < 400$ mm are considered. To exclude hadronic interactions of SM particles, the vertex must not be located within a region of the detector filled with solid materials, and the invariant mass of the reconstructed vertex must be larger than 10 GeV. The event must pass the MET trigger and offline requirements of the Run-2 search, *i.e.* MET> 250 GeV; the efficiency of passing the MET trigger and offline MET requirements is taken from the Run-2 analysis, as parametrised in Ref. [340] as a function of the generator-level MET and the R-hadron decay positions.

The background for this search is entirely instrumental in nature. For this projection, two different extrapolations of the size of current background are performed. The default extrapolation assumes that the background and its uncertainty will scale linearly with the size of the dataset, resulting in an expected background of $1.8^{+1.8}_{-0.9}$ events. However, several handles could be tightened in the analysis selection to continue to reject background without introducing appreciable signal efficiency loss. For example, additional requirements on the vertex goodness-of-fit or the compatibility of each track with the vertex could be imposed to further reduce backgrounds from low-mass vertices which are merged or crossed by an unrelated track. Therefore, a more optimistic scenario is also considered in which the total background and uncertainty are kept to the current level of $0.02^{+0.02}_{-0.01}$ events.

The signal selection uncertainties are taken to have the same relative size as in the existing Run-2 analysis. Uncertainties on the signal cross-section prediction are taken by varying the choice of PDF set and factorisation and renormalisation scales, with a reduction of 50% applied to the uncertainties to account for improvements by the time the analysis will be performed.

Using the number of expected signal and background events with their respective uncertainties, the expected exclusion limit at 95% C.L. on the gluino mass, as a function of lifetime, is calculated assuming no signal presence. In the case that signal is present, the 3σ and 5σ observation reaches are also calculated. The results are shown in Fig. 4.2.2 for both background scenarios.

The significant increase in sensitivity relative to the ATLAS result with 33 fb^{-1} at $\sqrt{s} = 13$ TeV comes in part from the increase in collision energy and integrated luminosity. For longer lifetimes, a significant gain in selection efficiency and therefore reach is also due to the larger volume of the silicon tracker, which allows displaced tracks and displaced vertices to be reconstructed at larger radii. This pushes the radius at which tracks from long-lived particles can be efficiently reconstructed from 300 to 400 mm, with corresponding gain in acceptance for lifetimes of 10 ns and greater. While the results pre-

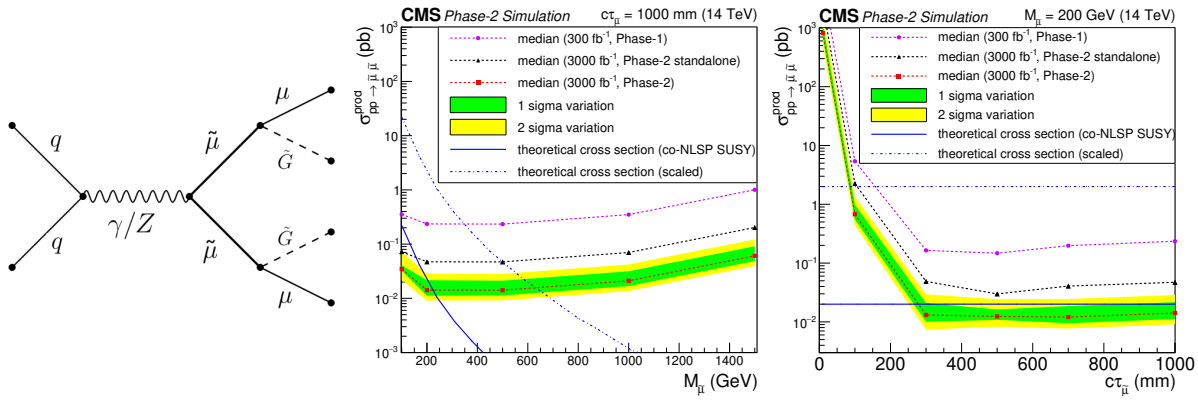

Fig. 4.2.3: Left: Feynman diagram for smuon production. Middle and right: expected 95% C.L. upper limits on long-lived smuons for various mass hypotheses and $c\tau = 1$ m. In both panels, the theoretical cross section for the specific model is represented by the blue solid line. For different SUSY breaking scales, $\tan\beta$ or otherwise modified parameters, the cross sections may be 100 times larger, reflected by the blue dash-dotted line. Green (yellow) shaded bands show the one (two) sigma range of variation of the expected 95% C.L. limits. Phase-2 results with an average 200 pileup events and an integrated luminosity of 3 $\text{ab}^{-1}$are compared to results obtained with 300 fb^{-1}. The black line shows the sensitivity without the DSA algorithm, which reduces the reconstruction efficiency by a factor three. The panel in the middle shows the limit as a function of the smuon mass and the right panel as a function of the decay length.

sented here were studied only for a fixed neutralino mass of 100 GeV, based on the results in Ref. [333], comparable sensitivity is expected over a large range of neutralino masses. As the neutralino mass increases for a fixed gluino mass, the multiplicity and momentum of the visible SM particles decreases, which in turn decreases the efficiency of the requirements on the track multiplicity, vertexing reconstruction, and vertex invariant mass as the difference between the neutralino mass and the gluino mass, m_{DV}, falls below 400 GeV.

4.2.2 Displaced muons at HL-LHC

Contributors: K. Hoepfner, H. Keller, CMS

A growing class of new physics models predict long-lived particles potentially leading to displaced signatures. In this study from CMS we discuss the potential for a SUSY GMSB model with heavy smuons decaying to a SM muon and a gravitino (yielding MET) [306, 341]. Figure 4.2.3 (left) shows the model under study. In this model the smuon is produced in pairs, and is degenerate in mass yielding long lifetimes. In such scenarios the smuon may decay after $\mathcal{O}(1\text{ m})$ or more such that the only detectable hits are in the muon system. Consequently the analysis uses a dedicated reconstruction algorithm for stand-alone muons (DSA) without a constraint on the vertex position.

It is both challenging to trigger and to reconstruct displaced muons, especially if the displacements are large. Triggers and reconstruction algorithms, generally including the primary vertex position, will not be very efficient in reconstructing tracks with large impact parameters. If the particle is sufficiently boosted, the transverse impact parameter is small(er) but the decay may occur well outside the tracker volume. In both cases, the stand-alone capabilities of the muon system constitute the only possibility for detection.

The main background for this search comes from multi-jet production (QCD), $t\bar{t}$ production, and Z/DY events if large impact parameters are (mis)reconstructed. Cosmic ray muons have been studied in Run-2 and are independent of the instantaneous luminosity. In the barrel they are efficiently rejected by the timing of the hits in the upper leg. Cosmic ray muons do not originate at the vertex and therefore pass the upper barrel sectors in reverse direction from outside in. The fraction of cosmic ray muons in the endcaps is negligible. Given the very low cross section of the signal process, it is essential to re-

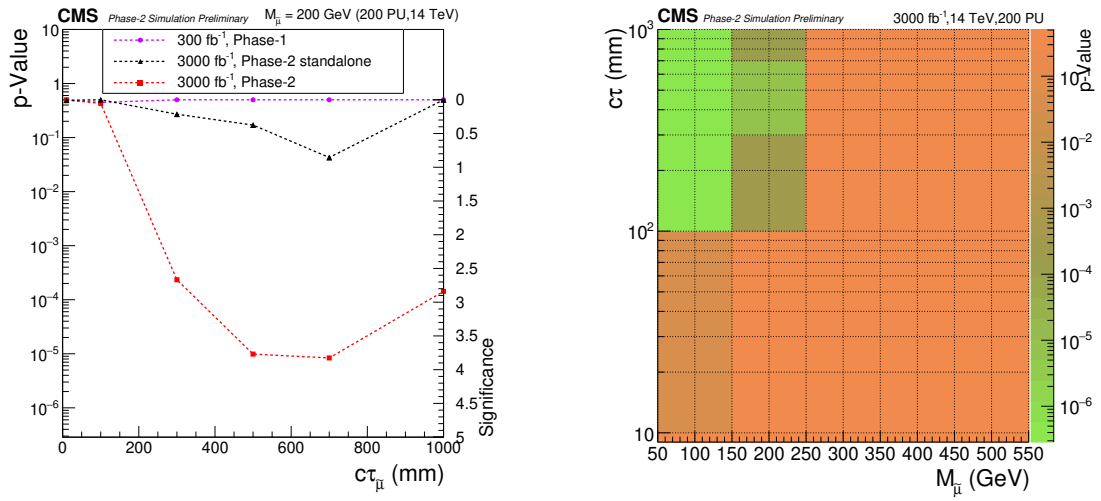

Fig. 4.2.4: Left: discovery significance and p-value for a fixed smuon mass of $M\tilde{\mu} = 200$ GeV. The displaced significance is compared to the algorithm with a beamspot constraint ("Phase-2 standalone"). Right: discovery sensitivity in the 2D parameter space of mass and decay length.

duce the background efficiently. The best background discriminator is the impact parameter significance $d_0/\sigma(d_0) \geq 10$. The muons should move in roughly opposite directions and MET should be larger than 50 GeV to account for the two gravitinos. After this selection the signal efficiency is about $4-5\%$ for $c\tau = 1000$ mm, nearly independent of the smuon mass, and $10^{-5} - 10^{-4}$ for QCD, $t\bar{t}$, and DY backgrounds.

Figure 4.2.3 shows expected exclusion limits for the gauge-mediated SUSY breaking model with the smuon being a (co-)NLSP for the predicted cross section as well as for a factor 100 larger cross section. The exclusion limits are shown as functions of smuon mass in Fig. 4.2.3 (middle) and decay length in Fig. 4.2.3 (right). The sensitivity also depends on $c\tau$ because shorter decay lengths shift the signal closer to the background. The expected exclusion limit is around 200 GeV for $c\tau = 1000$ mm with 3 ab^{-1}. For the same mass, a discovery sensitivity of 3σ significance can be reached, as shown in Fig. 4.2.4. This also illustrates the importance of the lepton trigger thresholds to be kept at a few times 10 GeV, even in the environment of 200 pileup interactions. Figure 4.2.4 also shows the discovery sensitivity in the 2-dimensional parameter space of smuon mass and decay length.

4.2.3 LLPs decaying into muons and jets at the HL-LHC

Contributors: A. Bay, X. Cid Vidal, E. Michielin, L. Sestini and C. Vázquez Sierra, LHCb

The LHCb experiment has proved to be highly competent with regard to direct searches for LLPs, being able to complement ATLAS and CMS in certain parameter space regions [342]. In this section, we provide prospects in the search for R-Parity Violating (RPV) supersymmetric neutralinos decaying semileptonically into a high-p_T muon and two jets. The results are taken from Ref. [343] which extrapolates the analysis in Ref. [344]. The neutralinos are assumed to be produced through an exotic decay of the SM Higgs boson. Prospects are shown for the expected datasets after both planned LHCb Upgrade I and Upgrade II (Run-3–Run-4 and Run-5 onwards, respectively).

The trigger efficiency for this analysis is conservatively assumed to remain unchanged with respect to the published result. However, assuming a 100% efficient first level trigger, after the removal of the hardware trigger level in Run-3, the overall trigger efficiency could improve by a factor of $2-3$. Regarding pile-up effects, a moderate penalty factor is applied to account for the increased pile-up expected in Runs 3-5 at LHCb. In order to expand the projections, the results are interpolated for different masses and lifetimes that are not considered in simulation. The interpolation is linear and two-dimensional.

$m_{\tilde{\chi}_1^0}$ (GeV/c^2)	$c\tau_{\tilde{\chi}_1^0}$ (mm)	Acceptance (%)	Total (%)	Background yield (1.7 fb^{-1})
20	**3**	28.0	0.27	2
	15	28.1	0.30	1
	30	27.8	0.24	3
30	**3**	28.7	0.78	4
	15	28.4	1.21	4
	30	28.7	0.75	2
50	**15**	31.5	2.33	2
	30	31.7	1.58	1
60	**10**	35.2	1.38	1
	50	35.5	2.84	2
	100	35.2	2.63	3

Table 4.2.1: Examples of the acceptance and total efficiencies assumed to detect a $\tilde{\chi}_1^0$ decaying semileptonically at a pp collision energy of $\sqrt{s} = 13$ TeV at the LHCb detector. Reference background yields at an integrated luminosity of 1.7 fb^{-1} are also presented. Differences in these yields are due to the effect of a multivariate classifier which is trained differently for each mass-lifetime case.

The results are obtained from a preliminary, unoptimised analysis of a subset of data collected for pp collisions at c.o.m. energy of 13 TeV. To account for a possible deterioration in the background rejection due to multiple primary interactions at high luminosity, a penalty factor of two has been applied to the background yield. The signal efficiency is obtained from the full simulation of the Higgs boson produced via gluon-gluon fusion at 13 TeV. As explained, no other change in the signal and background efficiencies due to the upgrade of the detector is considered. The difference between 13 and 14 TeV energies is assumed to be negligible. Some examples of the efficiencies and background yields assumed for these calculations can be found in Table 4.2.1.

With the updated signal and background yields, the sensitivity projections are computed. The upper limits on the branching fraction of the Higgs boson decay to a pair of neutralinos are calculated for different assumptions of neutralino masses and lifetimes and for different values of integrated luminosity. The Higgs boson production cross section is assumed to be that of the SM [345]. The actual limit is computed by comparing the 14 TeV efficiencies and background yields to Run-1, and by extrapolating the results published in Ref. [344]. The systematic uncertainties, which are sub-dominant for this result in the published analysis, are assumed to be the same as those in Run-1.

The results are shown in Fig. 4.2.5, for different integrated luminosities. These plots display the RPV neutralino mass and lifetime ranges excluded at 95% C.L.. The ranges are shown for different assumed integrated luminosities and branching fractions of the Higgs boson decay to a pair of RPV neutralinos. The region for which the mass of the neutralino is above 60 GeV is not shown in these projections, since no simulation was available. It is worth to notice that the lifetime range covered ($0.2 < c\tau < 200$mm) is constrained by the physical length of the VELO detector, since the LLP is required to decay within the VELO region in order to be able to reconstruct it. For the HL-LHC, most of the LHCb accessible neutralino phase space can be excluded for a branching fraction of the $H \to \tilde{\chi}_1^0\tilde{\chi}_1^0$ decay larger than 0.5%.

4.2.4 LLPs decaying into dijets at the HL-LHC

Contributors: X. Cid Vidal, E. Michielin, L. Sestini and C. Vázquez Sierra, LHCb

In this section, prospects are obtained for Hidden Valley (HV) [346, 347] pions (π_v) decaying hadronically into a pair of jets at LHCb. The π_v, which can be long-lived, are assumed to be produced through an exotic decay of the SM Higgs boson. The prospects in this chapter are taken from Ref. [343], whose analysis is based on a projection of the results published in Ref. [348].

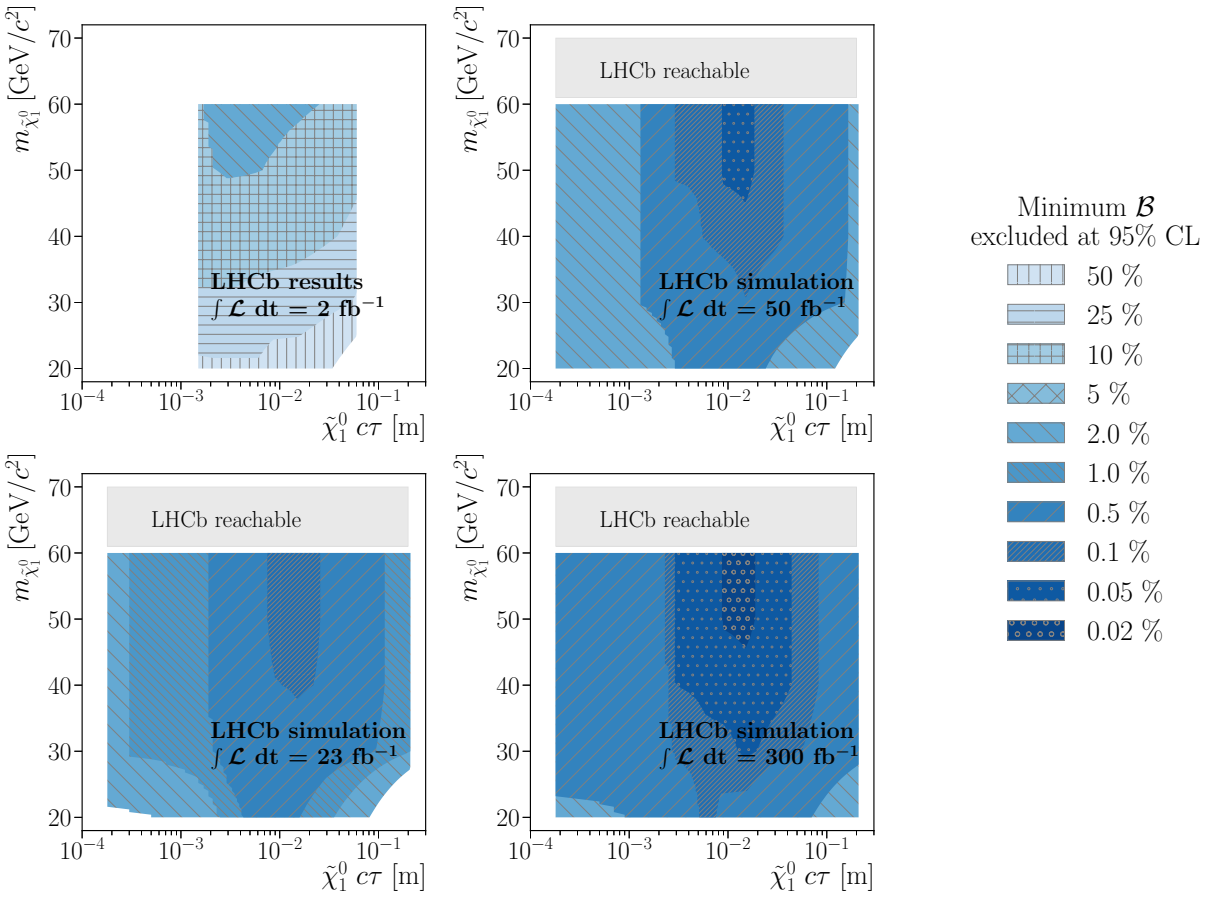

Fig. 4.2.5: Projected sensitivities of the search for RPV supersymmetric neutralinos decaying semileptonically and produced through a Higgs boson exotic decay. The results are extrapolated from Run-1 results (top left), for luminosities of 23 fb^{-1} (top right), 50 fb^{-1} (bottom left) and 300 fb^{-1} (bottom right). The results are presented in terms of the excluded parameter space of the neutralinos for different upper limits at 95% C.L. on the branching fractions of the Higgs boson decay.

The simulation of the HV pions through the Higgs portal is fully specified by the mass and the lifetime of the π_v particles, allowed to decay exclusively as $\pi_v \to \mathrm{b\bar{b}}$ since this decay mode is generally preferred in this model.

The assumptions made concerning signal efficiencies and background yields are similar to those discussed in Section 4.2.3. However, in this case, no penalty for the pile-up is applied. Signal and background yields are obtained taking into account the increase of cross sections (from $\sqrt{s} = 8$ TeV to $\sqrt{s} = 14$ TeV) and of the integrated luminosities. The scaling of the signal includes both the increase in the cross section of the Higgs boson production and that of the amount of signal falling in the acceptance of the LHCb detector. As an example, Table 4.2.2 shows some of the acceptance and total efficiencies assumed for this extrapolation for different masses and lifetimes of the HV pion. The background is scaled by a factor obtained using simulated $b\bar{b}$ events, which are expected to be the dominant contribution. The assumed yields, extrapolated from Ref. [348], can be found in Table 4.2.3 for an integrated luminosity of 23 fb^{-1}. Following the same reference, the yields are divided in bins of the radial coordinate of the HV pion decay vertex position.

With the updated backgrounds and expected signal yields, the $\mathrm{CL_S}$ method [95] is used to compute the expected upper limits for different assumptions in the integrated luminosity and of the Higgs decay branching fraction. The Higgs boson production cross section is assumed to be that of the SM [345]. The systematic uncertainties, which are not dominant for the computation of these limits in the published

$c\tau_{\pi_v}$ (mm)	Efficiency (%)	m_{π_v} GeV/c^2			
		25	**35**	**43**	**50**
3	Acceptance	26.8	21.2	17.4	14.6
	Total	0.9	1.7	1.5	1.1
30	Acceptance	16.1	15.1	13.7	12.3
	Total	0.2	0.4	0.4	0.3

Table 4.2.2: Examples of the acceptance and total efficiencies assumed to detect a π_v particle decaying to a pair of jets at a pp collision energy $\sqrt{s} = 14$ TeV at the LHCb detector. The main inefficiencies arise from the requirements to have π_v particle in the VELO and to have the decay products in the LHCb acceptance and from the reconstruction of the secondary vertex.

R_{xy} (mm)	$0.4-1$	$1-1.5$	$1.5-2$	$2-3$	$3-5$	$5-50$
Background yield (23 fb^{-1})	1.1×10^5	5.4×10^5	3.3×10^5	9.8×10^5	2.1×10^6	3.3×10^5

Table 4.2.3: Background yields assumed for the HV pion analysis at an integrated luminosity of 23 fb^{-1}. The yields are divided in bins of $R_{xy} = \sqrt{x^2+y^2}$, where x, y are the coordinates of the π_v particle decay vertex position.

analysis, are considered to be the same as in Run-1, and added as a correction factor to the limits obtained using just statistical uncertainties. With all these assumptions, the HV pion masses and lifetimes excluded at 95% C.L. are obtained. The results are shown in Fig. 4.2.6. The plots display, for different assumed integrated luminosities and branching fractions of the Higgs boson decay to a pair of HV pions, the ranges excluded at 95% C.L.. These ranges are shown as a function of the HV pion mass and lifetime. As in Section 4.2.3, the lifetime range covered is constrained by the physical length of the VELO detector. LHCb expects to exclude the existence of π_V with masses between 35 and 50 GeV/c^2 and lifetimes in the $c\tau$ range $0.1-1$ cm, pair-produced through the decay of the Higgs boson, for branching fractions of such decay above 1%. The mass region below ~ 25 GeV/c^2 is expected to be accessible studying the substructure of merged jets [349].

4.3 Heavy Stable Charged Particles at HL-LHC

Several extensions of the SM predict the existence of new heavy particles with long lifetimes. If their lifetime exceeds a few nanoseconds, such particles can travel through the majority of the detector before decaying and therefore appear as stable. In the following, two dedicated studies performed using the upgraded CMS detector at the HL-LHC are presented for particles with non-zero electric charge and for particles with anomalously high energy loss through ionisation in the silicon sensors. Emphasis is given to detector requirements necessary to perform such specialised searches.

4.3.1 Heavy stable charged particle search with time of flight measurements

Contributors: C. Carrillo, J. Goh, M. Gouzevitch, G. Ramirez-Sanchez, CMS

In this section, we consider particles with non-zero electric charge which are referred to as heavy stable charged particles (HSCPs). We concentrate on the performance in terms of specific HSCP parameters in a model-independent way rather than providing an interpretation in a dedicated model. Given the wide range of new models, it is important to stay sensitive to a wide range of unusual signatures such as very slowly moving particles. The results presented here are from the CMS Collaboration based on Ref. [341].

HSCPs will leave a direct signal in the tracker and muon systems of CMS and can be reconstructed similarly to muons. Depending on their mass, HSCPs can potentially move much more slowly than muons, which are typically travelling nearly at the speed of light ($\beta \approx 1$). Therefore, HSCPs can be identified using their time-of-flight (TOF) from the centre of CMS to the muon systems. This is

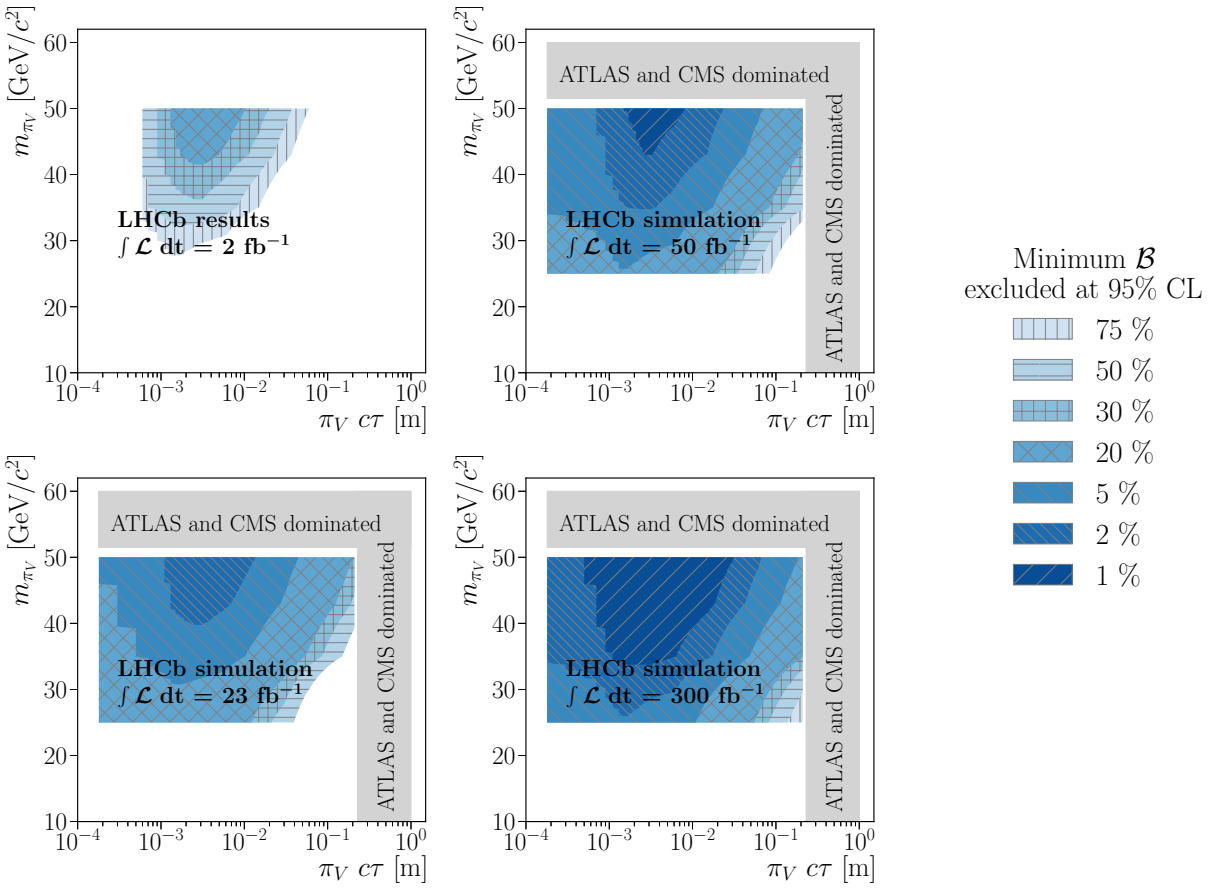

Fig. 4.2.6: Projected sensitivities of the search for HV pions decaying hadronically and produced through a Higgs boson exotic decay. The results are extrapolated from Run-1 results (top left), for luminosities of 23 fb^{-1} (top right), 50 fb^{-1} (bottom left) and 300 fb^{-1} (bottom right). The results are presented in terms of the excluded parameter space of the HV pions for different upper limits at 95% C.L. on the branching fractions of the Higgs boson decay.

illustrated in Fig. 4.3.1 for a slowly moving HSCP in comparison to relativistic muons, here from the decay of Z bosons. The latter are centred around zero time with respect to their uniquely identified bunch crossing. This study builds on the improvements from the upgrade of the RPC link boards in the CMS muon barrel and endcaps [341]. While the time resolution of the present RPC system is around 25 ns, the upgraded link board systems are expected to reach resolutions near 1 ns for the entire RPC system. This upgrade enables new analysis strategies at both the trigger and offline levels.

An HSCP trajectory is reconstructed as a slowly moving muon introducing the parameter β quantifying the (non)-relativistic velocity of the particle. The velocity may be computed by measuring the time of flight in the muon detectors at large distances from the collision point. Particles moving slowly through the muon systems leave hits with a linear pattern in hit-position versus time. The hits can be spread across several bunch crossings. Therefore, muon detectors with precise timing can provide important information for the HSCP signal searches.

Figure 4.3.2 (left) shows the achievable mass resolution for a supersymmetric $\tilde{\tau}$ lepton of 1.6 TeV mass. The resolution for the HSCP mass obtained for Phase-2 at the trigger level is comparable to that realised in Run-2 studies based on offline time-of-flight information from other muon detectors in CMS. The information provided by the RPC trigger can be used as an independent cross check of the reconstructed mass. Figure 4.3.2 (right) illustrates the expected reconstruction efficiency as a function of η and β. For $|\eta < 1.5|$, an efficiency of up to 90% can be reached for values of $\beta > 0.25$. In Run-2,

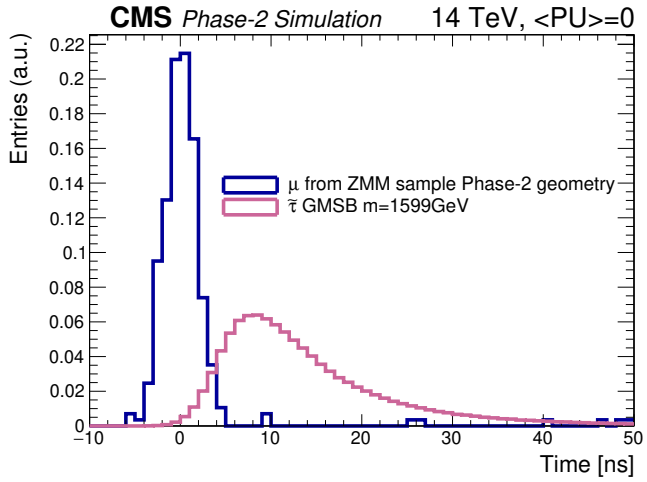

Fig. 4.3.1: Example of an RPC hit time measurement distribution for muons from the SM process $Z \to \mu\mu$ in comparison to events from semi-stable staus with a mass of about 1600 GeV, produced in $pp \to \tilde{\tau}\tilde{\tau}$ processes. The relativistic muons pass through the detector at the speed of light, hence their time of arrival is centred around zero. Decay products from the slowly moving staus arrive much later, for the given mass on average by 10 ns.

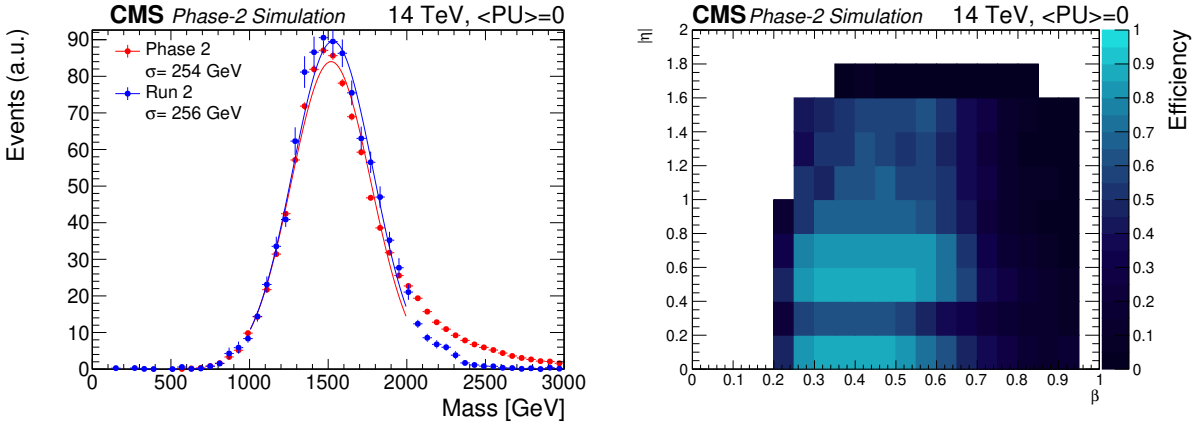

Fig. 4.3.2: Left: comparison of the mass resolution for a 1.6 TeV stau. In Run-2 the plotted resolution can only be achieved offline, while the upgraded RPC link-boards in Phase-2 provide a similar mass resolution already at the trigger level. Right: reconstruction efficiency for HSCPas a function of β and η given by the colour code of the z-axis. With the Phase-2 upgrade, events with $\beta < 0.5$ can be triggered with nearly 90% efficiency for $|\eta| < 0.8$.

the trigger is highly efficient between $0.6 < \beta < 1$, but only about 20% efficient for $\beta < 0.5$ [350, 351]. The large gain in efficiency for very slowly moving particles in Phase-2 enabled by the upgrade of the RPC trigger can be exploited in a model independent HSCP search.

4.3.2 Heavy stable charged particle search with energy loss

Contributors: J. Pazzini, J. Zobec, CMS

It may happen that the only signs of new physics are rather exotic signatures that cannot be detected with conventional analyses. An example for such a signature is the production of heavy stable charged particles with long lifetimes that move slowly through the detector, heavily ionising the sensor material as they pass through. The supersymmetric particles stau ($\tilde{\tau}$) and gluino ($\tilde{g}$) are possible examples. Often, the cross section for such processes is expected to be very small and hence the HL-LHC provides a good environment for searching for such particles. Depending on their mass and charge, we can expect anomalously high energy loss through ionisation ($\mathrm{d}E/\mathrm{d}x$) in the silicon sensors with respect

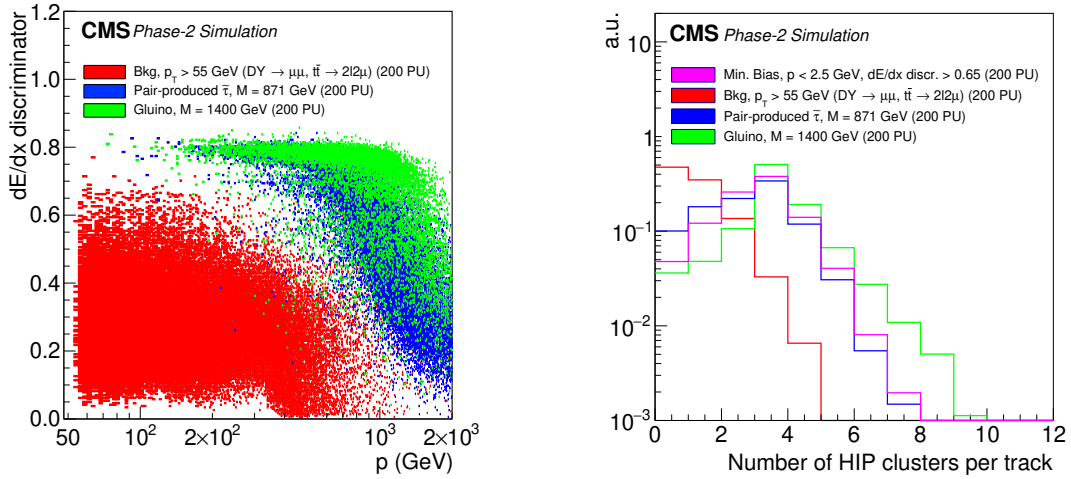

Fig. 4.3.3: Left: distribution of the $\mathrm{d}E/\mathrm{d}x$ discriminator versus track momentum (p) for tracks with high momentum ($p_T > 55$ GeV) in background events (red) and candidate signal particles. Pair produced $\tilde{\tau}$s with a mass of 871 GeV (blue), and a gluino with a mass of 1400 GeV (green), are shown. Right: the distribution of the number of high threshold clusters with HIP flag per track for the HSCP signals, gluinos (green) and $\tilde{\tau}$s (blue), highly ionising and low-momentum protons and kaons (magenta), and tracks with high momentum ($p_T > 55$ GeV) in background events (red).

to the typical energy loss for SM particles (≈ 3 MeV/cm for minimum ionising particles (MIPs) with $10 - 1000$ GeV momentum).

The present strip tracker in the CMS detector features analogue readout, and the pixel detector featured analogue readout at Phase-0 and features digital readout at Phase-1, allowing for excellent $\mathrm{d}E/\mathrm{d}x$ measurements. The Phase-2 CMS Inner Tracker will continue providing $\mathrm{d}E/\mathrm{d}x$ measurements, enabled by its Time over Threshold readout, while the Outer Tracker cannot provide such information, given that the readout is binary [352]. To increase the sensitivity for signatures with anomalously high ionisation loss, a second, programmable, threshold has been implemented in the readout electronics of some modules of the Outer Tracker, and a dedicated readout bit signals if a hit is above this second threshold [352]. Searches for heavy stable (or quasistable) charged particles (HSCPs) can thus be performed by measuring the energy loss in the Inner Tracker and by discriminating HSCPs from minimum ionising particles based on the "HIP flag" in the Outer Tracker. A threshold corresponding to the charge of 1.4 MIPs is used in the simulation, and the gain in sensitivity obtained by using the HIP flag is studied [352].

An estimator of the degree of compatibility of the track with the MIP hypothesis is defined to separate candidate HSCPs from tracks from SM background sources. The high resolution $\mathrm{d}E/\mathrm{d}x$ measurements provided by the Inner Tracker modules are used for the computation of the $\mathrm{d}E/\mathrm{d}x$ discriminator. In Fig. 4.3.3 (left) the distribution of $\mathrm{d}E/\mathrm{d}x$ versus track momentum (p) for high momentum tracks ($p_T > 55$ GeV) selected in background events and candidate signal particles is shown. Two HSCP signals, pair produced $\tilde{\tau}$s with a mass of 871 GeV and a gluino with a mass of 1400 GeV, are compared to tracks from SM processes. In Fig. 4.3.3 (right) the distribution of the number of high threshold clusters with HIP flag per track is shown for the HSCP signals (gluinos and $\tilde{\tau}$s) compared to signal-like highly ionising and low-momentum protons and kaons in simulated minimum bias samples and to tracks with high momentum ($p_T > 55$ GeV) in simulated background events. The tracks in background events have a low number of high threshold clusters with HIP flag compared to those observed for tracks in HSCP signal events and slow moving protons and kaons in minimum bias events.

Figure 4.3.4 shows the performance of the discriminator by evaluating the signal versus background efficiency curves to identify tracks from signal events and reject those originating from backgrounds. The performance curves are evaluated for two different strategies for the discriminator: the

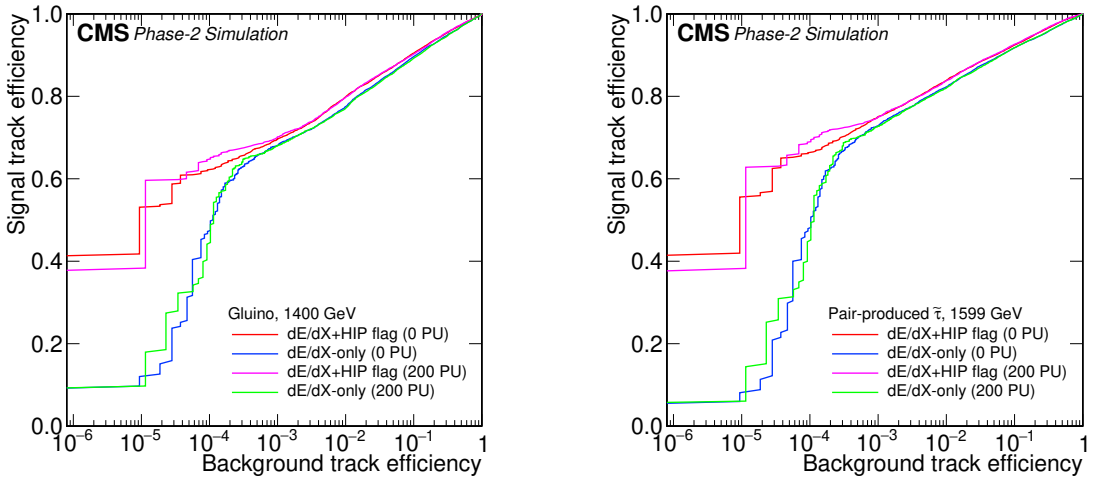

Fig. 4.3.4: Performance of the $\mathrm{d}E/\mathrm{d}x$ discriminator for selecting pair produced $\tilde{\tau}$s (left) and gluinos (right) in events with 0 PU and 200 PU. The signal versus background efficiency performance curves for a discriminator making use of both the pixel information and the Outer Tracker HIP flag (red and magenta) demonstrate a better performance compared to a discriminator trained to exploit only the $\mathrm{d}E/\mathrm{d}x$ information from the pixel modules (blue and green), for a background rejection of 10^{-6}.

original $\mathrm{d}E/\mathrm{d}x$ discriminator, which relies solely on the Inner Tracker modules ("$\mathrm{d}E/\mathrm{d}x$-only"), and a recomputed discriminator which includes the HIP flags from Outer Tracker modules ("$\mathrm{d}E/\mathrm{d}x$+HIP bit"). The signal versus background efficiency performance curves in Fig. 4.3.4 demonstrate that for a background efficiency of 10^{-6}, analogous to the Phase-1 analysis performance, the $\mathrm{d}E/\mathrm{d}x$+HIP-based discriminator leads to an expected signal efficiency of 40%, around 4 to 8 times better than the $\mathrm{d}E/\mathrm{d}x$-only discriminator. In the $\mathrm{d}E/\mathrm{d}x$-only scenario, the efficiency for the HSCP signal is about 8 times smaller than that obtained in Phase-1 [351] and about 64 times the Phase-1 luminosity would be required to reach the Phase-1 sensitivity, making this search almost untenable. The inclusion of the HIP flag for the Outer Tracker restores much of the efficiency, so that the same sensitivity as in Phase-1 will be realised with about four times the luminosity of Phase-1. The Phase-1 sensitivity will be surpassed with the full expected integrated luminosity of the HL-LHC. This study demonstrates the critical impact of the HIP flag in restoring the sensitivity of the CMS tracker for searches for highly ionising particles.

4.4 Additional examples of specialised techniques for LLP at HL-LHC

Two examples of specialised techniques relevant for LLPs are presented in this section. First, CMS illustrates the importance of precise timing detectors providing efficient measure the time of flight of LLPs between primary and secondary vertices. Second, ATLAS shows how jets arising from neutral LLPs decaying within the hadronic calorimeter can be characterised to efficiently reduce pile-up dependencies and therefore improve the sensitivity to new physics of this kind.

4.4.1 Fast timing signatures for long-lived particles

Contributors: D. del Re, A. Ledovskoy, C. Rogan, L. Soffi, CMS

A precision MIP timing detector (MTD) allows one to assign timing for each reconstructed vertex and to measure the time of flight of LLPs between primary and secondary vertices. This section presents studies from the CMS Collaboration from Ref. [353] exploring the potential of such techniques at the HL-LHC.

Using the measured displacement between primary and secondary vertices in space and time, the velocity of LLPs in the lab frame $\vec{\beta}_P^{LAB}$ (and γ_P) can be calculated. In such scenarios, the LLP can decay

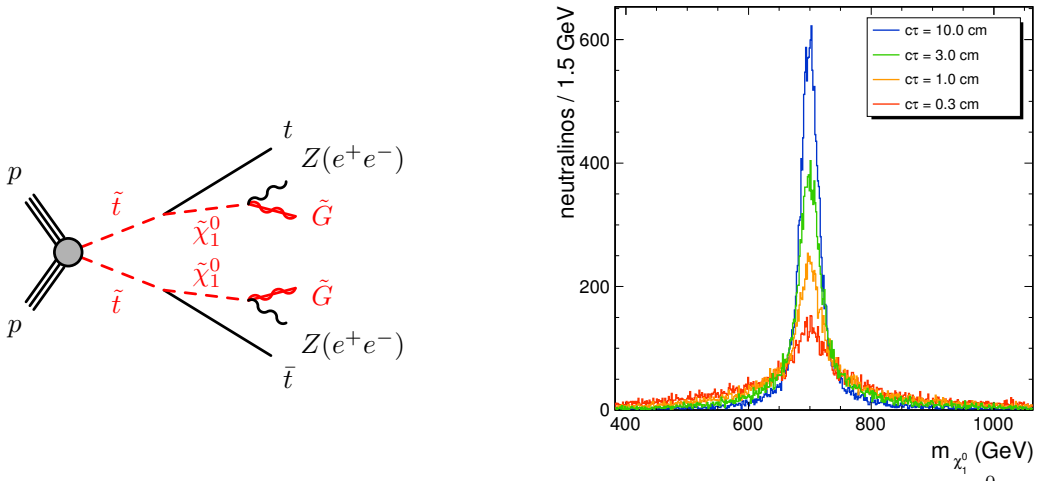

Fig. 4.4.1: Diagram for top-squark pair production and decay (left) and reconstructed mass of the $\tilde{\chi}_1^0$ (right) for decays with $M(\tilde{t}) = 1000$ GeV and $M(\tilde{\chi}_1^0) = 700$ GeV. Mass distributions are shown for various values of $c\tau$ of $\tilde{\chi}_1^0$.

to fully-visible or partially-invisible systems. Using the measured energy and momentum of the visible portion of the decay, E_P^{LAB} and $\vec{P}_P^{LAB}$, one can calculate its energy in the LLP rest frame as

$$E_V^P = \gamma_P \left(E_V^{LAB} - \vec{P}_V^{LAB} \cdot \vec{\beta}_V^{LAB} \right) = \frac{m_P^2 - m_I^2 + m_V^2}{2m_P}, \tag{4.4.1}$$

where m_P, m_V, and m_I are the masses of the LLP, the visible and the invisible systems, respectively. Assuming the mass of the invisible system is known, the subsequent mass of the LLP can be reconstructed as

$$m_P = E_V^P + \sqrt{E_V^{P\,2} + m_I^2 - m_V^2}. \tag{4.4.2}$$

The reconstruction of the decay vertex for neutral LLPs decaying to visible or partially-invisible decay products is enabled, thus offering unprecedented sensitivity in these searches at the LHC. The benefits of precision timing on such LLP searches is illustrated in two representative SUSY examples.

The first example is a gauge mediated SUSY breaking (GMSB) scenario where the $\tilde{\chi}_1^0$ couples to the gravitino $\tilde{G}$ via higher-dimension operators sensitive to the SUSY breaking scale. In such scenarios, the $\tilde{\chi}_1^0$ may have a long lifetime [354]. It is produced in top-squark pair production with $\tilde{t} \to t + \tilde{\chi}_1^0$, $\tilde{\chi}_1^0 \to Z + \tilde{G}$, and $Z \to e^+e^-$. The decay diagram is shown in Fig. 4.4.1 (left).

Events were generated with PYTHIA 8 [68]. The masses of the top-squark and neutralino were set to 1000 GeV and 700 GeV, respectively. Generator-level quantaties were smeared according to the expected experimental resolutions. A position resolution of 12 μm in each of three directions was assumed for the primary vertex [355]. The secondary vertex position for the e^+e^- pair was reconstructed assuming 30 μm track resolution in the transverse direction [355]. The momentum resolution for electrons was assumed to be 2%. And finally, the time resolution of a charged track at the vertex was assumed to be 30 ps.

The mass of the LLP was reconstructed with Eq.s (4.4.1) and (4.4.2) assuming the gravitino is massless by setting $m_I = 0$. Figure 4.4.1 (right) shows the distribution of the reconstructed mass of the neutralino for various $c\tau$ values of the LLP. The fraction of events with a separation between primary and secondary vertices of more than 3σ in both space and time as a function of MTD resolution is show in Fig. 4.4.2 (left). The mass resolution, defined as half of the shortest mass interval that contains 68% of events with 3σ displacement, as a function of MTD resolution is shown in Fig. 4.4.2 (right)

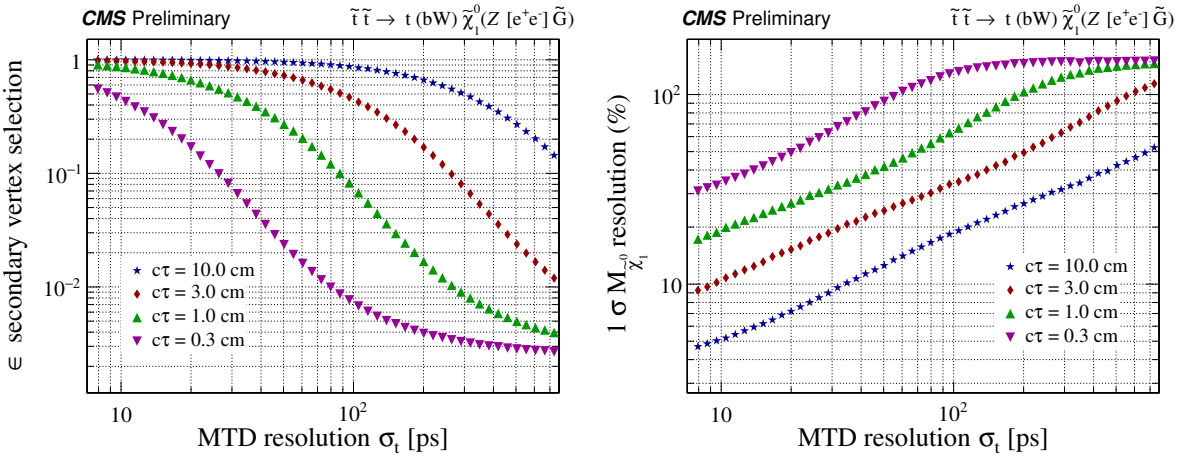

Fig. 4.4.2: Efficiency (left) and mass resolution (right) as a function of timing resolution of MTD for reconstruction of $\tilde{\chi}_1^0$ mass in SUSY GMSB example of $\tilde{\chi}_1^0 \rightarrow \tilde{G} + e^+e^-$ with $M(\tilde{\chi}_1^0) = 700$ GeV considering events with separation of primary and seconday vertices more than 3σ in both space and time.

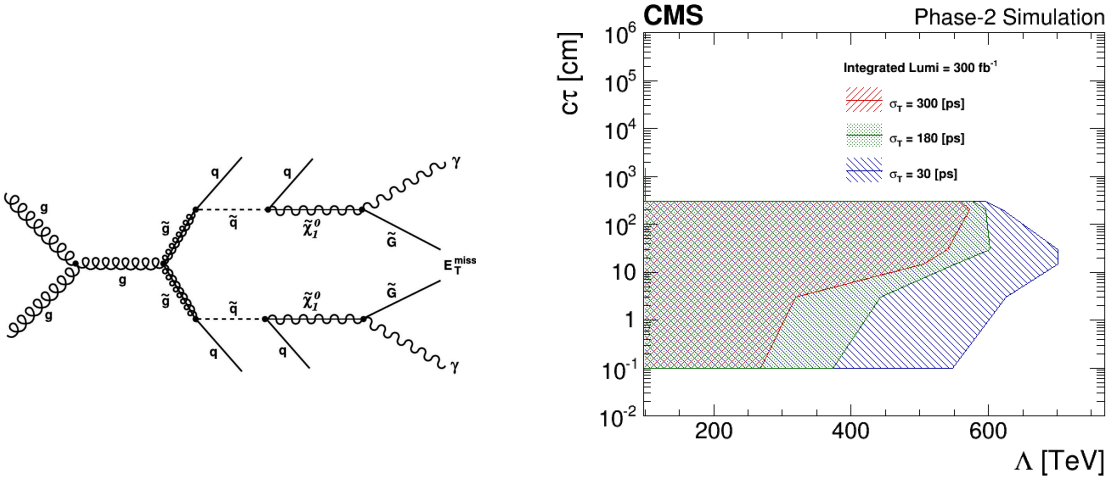

Fig. 4.4.3: Left: diagram for SUSY process that results in a diphoton final state through gluino production at the LHC. Right: sensitivity to GMSB $\tilde{\chi}_1^0 \rightarrow \tilde{G} + \gamma$ signals expressed in terms of neutralino lifetimes and masses assuming a timing detector with different values of resolution and an integrated luminosity of 300 fb^{-1}.

The second SUSY example is a GMSB benchmark scenario [346] where the lightest neutralino ($\tilde{\chi}_1^0$) is the next-to-lightest supersymmetric particle, and can be long-lived and decay to a photon and a gravitino ($\tilde{G}$), which is the LSP. Figure 4.4.3(left) shows a diagram of a possible gluino pair-production process that results in a diphoton final state.

For a long-lived neutralino, the photon from the $\tilde{\chi}_1^0 \rightarrow \tilde{G} + \gamma$ decay is produced at the $\tilde{\chi}_1^0$ decay vertex, at some distance from the beam line, and reaches the detector at a later time than the prompt, relativistic particles produced at the interaction point. The time of arrival of the photon at the detector can be used to discriminate signal from background. The time of flight of the photon inside the detector is the sum of the time of flight of the neutralino before its decay and the time of flight of the photon itself until it reaches the detector. Since the neutralino is a massive particle, the latter is clearly negligible with respect to the former. It becomes clear in this sense that in order to be sensitive to short neutralino lifetimes ($\mathcal{O}(\text{cm})$), the measurement of the photon time of flight is a crucial ingredient of the analysis. The excellent resolution of the MTD detector ($\mathcal{O}(30\ \text{ps})$) can therefore be exploited to determine with high accuracy the time of flight of the neutralino, and therefore of the photon, also in case of a short

lifetime.

A simple analysis has been performed at generator level in order to evaluate the sensitivity of a search for displaced photons at CMS in the scenario where a 30 ps timing resolution is available from the MTD. Events were generated with PYTHIA 8. The values of the Λ scale parameter were considered in the range $100 - 500$ TeV, and the neutralino lifetimes ($c\tau$) explored in the range $0.1 - 300$ cm. After requiring the neutralino decaying within the CMS ECAL acceptance and the photon energy being above a "trigger-like" threshold, the generator-level photon time of flight was smeared according to the expected experimental resolutions. A cut at photon time greater than 3σ of the considered time resolution is applied and the assumption of background being zero in this "signal region" is made. The signal efficiency of such a requirement is computed and translated, assuming the theoretical cross-sections provided in Ref. [346], in an upper limit at 95% C.L. of C.L. on the production cross-section of the $\tilde{\chi}_1^0 \to \tilde{G} + \gamma$ process.

Assuming a timing resolution of the order of 300 ps, (thus requiring photon time greater than 1 ns) close to the Run1 CMS performance [356], the analysis sensitivity in terms of neutralino mass and lifetime is computed and shown in Fig. 4.4.3 (right) for a reference luminosity of 300 fb^{-1}, along with comparisons with improved timing resolution. For the hypothesis of $\sigma_T = 180$ ps a timing cut is applied at 450 ps and for the $\sigma_T = 30$ ps the timing is required to be larger than 100 ps at selection level. As shown in the figure, the increase of the signal efficiency at small lifetime, made possible with the precise MTD, allows to extend the sensitivity region in the explored phase space of short lifetime and large masses of the neutralino.

4.4.2 Jets reconstruction techniques for neutral LLPs

Contributors: S. Pagan Griso, R. Rosten, ATLAS

Traditional methods may fail to reconstruct, or may improperly reconstruct, objects associated with LLP decays. Searches for LLPs that are neutral under the SM gauge group might be targeted exploiting hadronic calorimeters. The techniques developed are described in the following, for more details see Ref. [357].

Jets resulting from neutral LLPs decaying within the hadronic calorimeter have several properties that are uncommon in jets originating at the interaction point. Within the inner detector, they naturally lack associated tracks. They likewise lack associated energy deposits in the electromagnetic calorimeter. Furthermore, the reconstructed jets are narrower than for a similar shower originating at the interaction point (IP) due to large displacement of the decay vertex. These properties, as well as those of the jet's constituents, can be used to discriminate between jets from displaced decays and those originating from the IP. On the other hand, the reconstructed jets are similar to those associated with non-collision backgrounds (NCB). Standard jet cleaning tools tend to reject jets resembling those associated with NCB, which is a primary reason the vast majority of non-LLP-dedicated jet searches will miss this signature, while the searches for an LLP would require a dedicated jet quality selection.

The unusual signature of neutral LLP decays within the hadronic calorimeter encourages the use of dedicated triggers. At Level-1, the narrowness of the jets allows tau-candidates to be used to keep the energy threshold low while avoiding prescaling. In the higher level trigger, the low electromagnetic fraction and lack of pointing tracks can be further used to reject most jets. However, rates due to NCB, particularly beam-induced background (BIB), necessitate the use of a dedicated BIB-removal algorithm to keep rates acceptably low.

At Level-1, these dedicated triggers have benefited from the use of the Level-1 topological triggers. These have allowed for a cut on a rough estimate of the electromagnetic fraction to be applied at Level-1, allowing for the energy threshold to remain lower even as the lowest energy unprescaled Level-1 tau trigger gets pushed to higher and higher thresholds. Keeping this rate down at higher pile-up will be crucial to gathering high-statistics, high-purity samples for offline analysis. The increased longitudinal

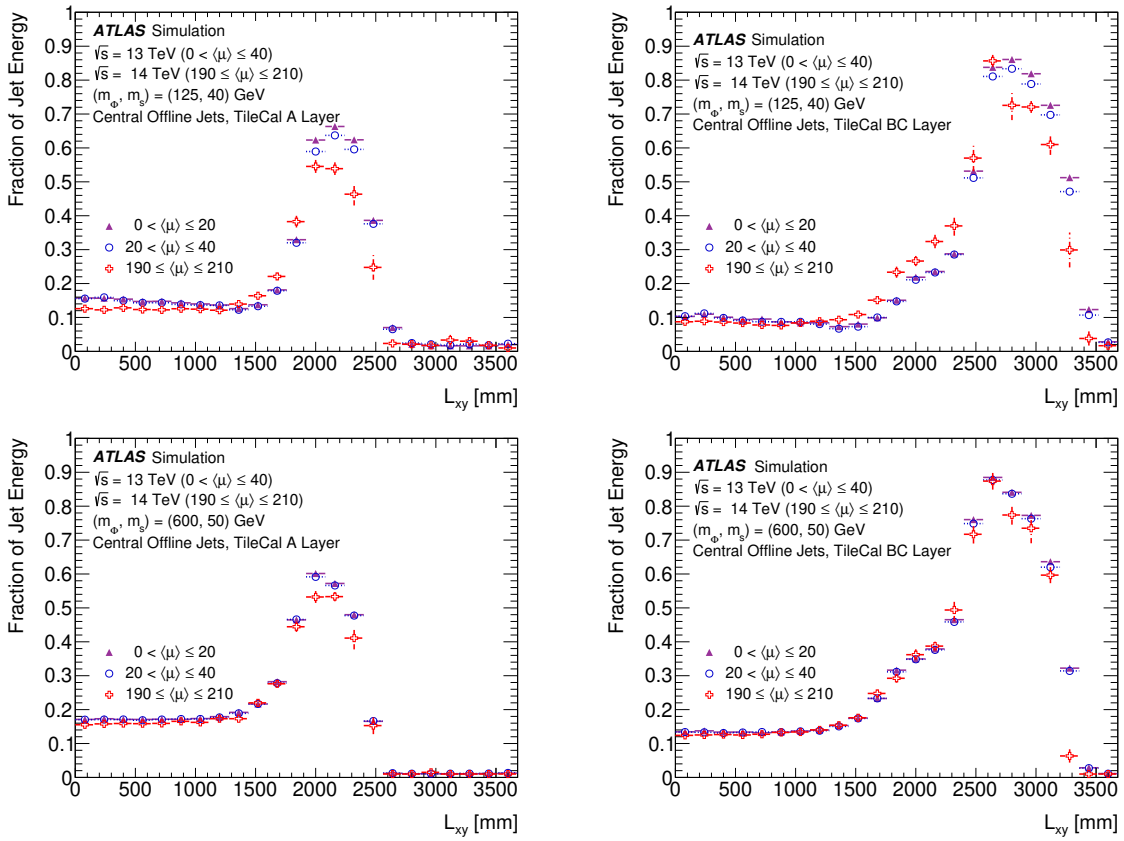

Fig. 4.4.4: Top: fraction of the jet energy deposited in A-layer (left) and BC-layer (right) of the Tile as a function of the transverse decay position of the LLP in events with a 125 GeV Higgs boson decaying to two 25 GeV LLPs. Bottom: same for events with a 600 GeV boson decaying to two 150 GeV LLPs.

Level-1 granularity in Phase-II is especially promising for such a trigger. It may allow for a quick assessment of the energy deposited per layer in a jet, which has already been found to be a good discriminator offline for LLP jets.

Pile-up presents challenges for LLP searches at the analysis level as well. Soft energy deposits in the electromagnetic calorimeter in line with energy deposits from a neutral LLP result in jets with a higher than allowed fraction of their energy in the electromagnetic calorimeter. An alternative to using this coarse fraction is to consider the energy deposited per layer.

The model used in the generation of LLP signatures is a simplified hidden-sector toy model with a sector, containing particles neutral under the SM gauge group, weakly coupled to the SM sector. Interactions between sectors may occur via a communicator particle. Due to the weak coupling between sectors, the lifetime of these particles can be long. The process here is one in which a scalar boson, ϕ, which is also the communicator, is produced during the pp collision in ATLAS and decays to a pair of hidden sector particles s. Each LLP s, in turn, decays with long lifetimes via the communicator to heavy SM states. Heavy states are preferred due to the Yukawa coupling to the ϕ boson.

Figures 4.4.4 show some examples of the fraction of total jet energy at the EM-scale deposited by the LLPs produced within the $|\eta| < 0.7$ rapidity range in the given layer for different slices of the average μ as a function of the LLP transverse decay position L_{xy}. For lighter pairs of LLPs, s and their parent particle ϕ, the effects of increasing pile-up are small, but possibly not negligible. This may motivate the introduction of multivariate analysis (MVA) technique for identifying jets consistent with displaced LLP decays. Such an MVA can be in the form of a regression that attempts to identify the decay position of the jet-initiation particle. It can be made directly pile-up-aware by including pile-up as one of its

training variables. However, as long as the MVA is given the fraction of energy in the electromagnetic calorimeter, where most of the pile-up energy will be deposited, it is expected to be able to distinguish between jets initiated by decays at the same position under different pile-up conditions.

5 High-p_T signatures from flavour

Flavour physics is often considered one of the most sensitive probes of new physics, which, depending on observable and model, can constrain new physics at scales of $1 - 10^5$ TeV. Many of the observables are associated with precision measurements at the intensity frontier. This is well documented in the flavour chapter of this report, Ref. [31]. Any small deviations in precision low energy measurements, could signal the presence of new particles in the TeV scale, whose effect, once integrated out, is to alter precision low energy observables. Thus, in tandem with low energy flavour observables, it is important to identify the high-p_T probes of flavour physics, relating direct tests with the indirect flavour probes.

Similar arguments hold for neutrino physics, where the generation of neutrino masses through the seesaw mechanism may generate a large variety of collider signatures, such as new resonances and cascade decays involving multiple leptons. In this section we first discuss the implication of neutrino mass models involving new heavy gauge bosons and sterile neutrinos, see Section 5.1. We then focus in Section 5.2 on constraints on models of Z' and leptoquarks related to B-decay flavour anomalies, and leptoquarks decaying to top and tau. Finally, in Section 5.3, we present a summary of the implications of these high-p_T prospects on the parameter space of various UV models addressing the aforementioned anomalies. Notice that part of the material included in this section is also contained in the flavour chapter of this report [31].

5.1 Neutrino masses

The potential Majorana nature of neutrinos as well as the origin of their tiny masses and large mixing angles remain some of the most pressing open issues in particle physics today. Models that address these mysteries, collective known as Seesaw models, hypothesise the presence of new particles that couple to SM fields via mixing/Yukawa couplings, SM gauge currents, and/or new gauge symmetries. The new predicted particles, often right-handed sterile neutrinos, can explain the generation of neutrino masses via a low-scale seesaw mechanism. Mixing between the active and sterile neutrinos is strongly constrained by precision measurements [358]. At the LHC, searches in purely leptonic final states have started probing masses below m_Z [359]. On the other hand, a plethora of rich physics can be studied in considerable detail at hadron colliders, and greatly complement low energy and oscillation probes of neutrinos [360,361]. Other complementary and promising searches for the low-scale seesaw neutrinos could be achievable also at future ep colliders studying lepton-flavour violating processes, *e.g.* $e^- p \to \mu^- W + j$. In this case, the leading production of heavy neutrinos depends on the mixing with the electron flavour, in contrast to production in pp collisions, where it is proportional to the total mixing. This allows us to infer the relative strength of the mixings, especially if a hierarchy is present. For more details, including comparison with ee and pp colliders, see Ref. [362].

In the following, a comprehensive summary of the discovery potential of Seesaw models at hadron colliders with collision energies of $\sqrt{s} = 14$ and 27 TeV is presented in Section 5.1.1. Heavy composite Majorana neutrinos are studied in Section 5.1.2 using same-sign leptons signatures, and using dilepton and jets signatures in Section 5.1.3.

5.1.1 Neutrino mass models at the HL- and HE-LHC

Contributors: T. Han, T. Li, X. Marcano, S. Pascoli, R. Ruiz, C. Weiland

We summarise the discovery potential of seesaw models at hadron colliders with collision energies of $\sqrt{s} = 14$ and 27 TeV. In particular, we will discuss models featuring heavy neutrinos, both pseudo-Dirac and Majorana as well as those with new gauge interaction, and models featuring scalar and fermion EW triplets. For a more comprehensive reviews on the sensitivity of colliders to neutrino mass models, see Ref.s [360, 361, 363–365] and references therein.

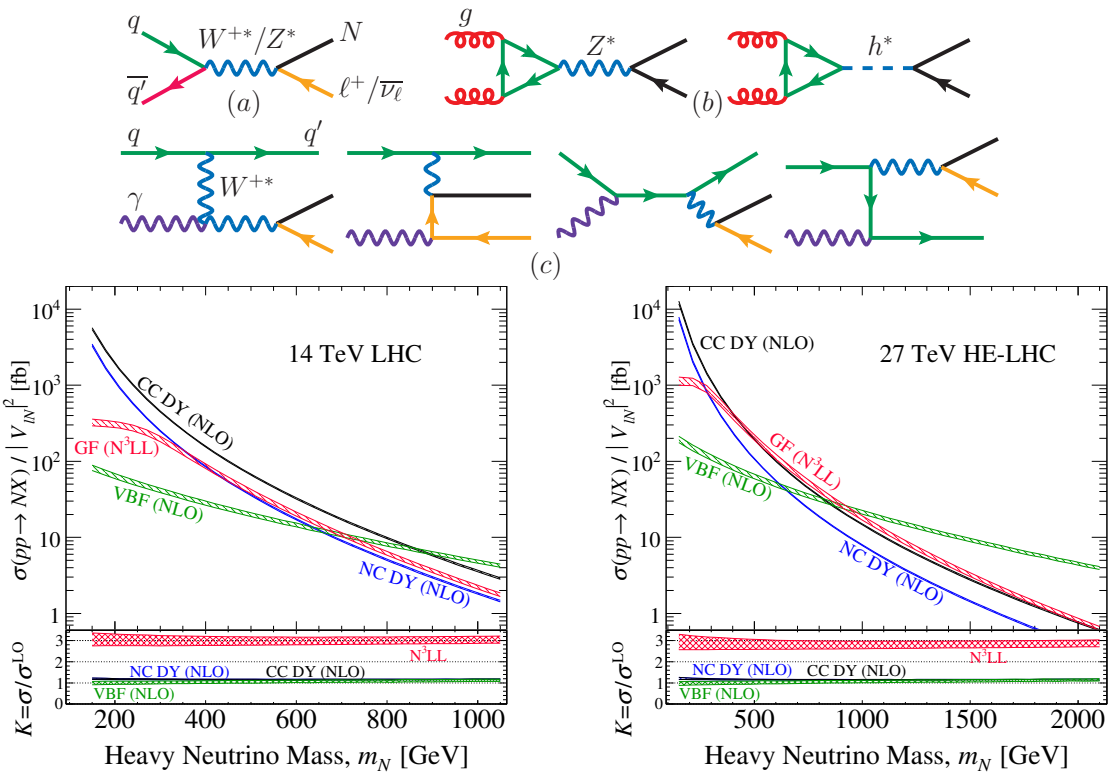

Fig. 5.1.1: Top: Born-level diagrams for heavy neutrino N production via (a) Drell-Yan, (b) gluon fusion, and (c) vector boson fusion; from Ref. [368]. Bottom: production cross sections, divided by active-heavy mixing $|V_{\ell N}|^2$, as a function of the heavy neutrino mass at $\sqrt{s} = 14$ TeV (left) and 27 TeV (right) [368, 369].

The Type I seesaw and Variants Discovery Potential at the HL- and HE-LHC

The Type I seesaw hypothesises the existence of fermionic gauge singlets with a Majorana mass term whose couplings to SM leptons generate light neutrino masses and mixing. In Ref.s [366, 367], it was proved that requiring all three light neutrinos to be massless is equivalent to the conservation of lepton number at all orders in perturbation theory. In other words, for low-scale seesaw models with only fermionic singlets, lepton number has to be nearly conserved and light neutrino masses are proportional to small lepton number violation (LNV) parameters in these models. For high-scale seesaws with only fermionic singlets, light neutrino masses are inversely proportional to large LNV mass scales, and again leads to approximate lepton number conservation at low energies. This in turn leads to the expectation that LNV processes should be suppressed in variants of the type I seesaw unless additional particles, whether they be fermions or scalars charged under the SM gauge couplings or new gauge interactions, are introduced to decouple the light neutrino mass generation from the heavy neutrino production. The updated discovery potential of heavy, SM singlet neutrinos at pp colliders is now summarised.

Heavy Neutrino Production through EW Bosons at Hadron Colliders

If kinematically accessible, heavy neutrinos N can generically be produced in hadron collisions through both neutral current and charged current processes, as shown in Fig. 5.1.1 (top). Following the prescriptions of Ref.s [368, 369], for $m_N > M_W$ and at various accuracies, the corresponding $\sqrt{s} = 14$ TeV heavy neutrino production cross sections are presented in Fig. 5.1.1 (bottom left). While the Drell-Yan (DY) process dominates at low masses, $W\gamma$ boson fusion (VBF) dominates for $m_N \gtrsim 900 - 1000$ GeV [368, 370], with gluon fusion (GF) remaining a sub-leading channel throughout [368, 371]. The situation is quite different at 27 TeV as shown in Fig. 5.1.1 (bottom right). Indeed, GF is the leading production mode for $m_N \gtrsim 450$ GeV until $m_N \approx 940$ GeV where VBF takes over.

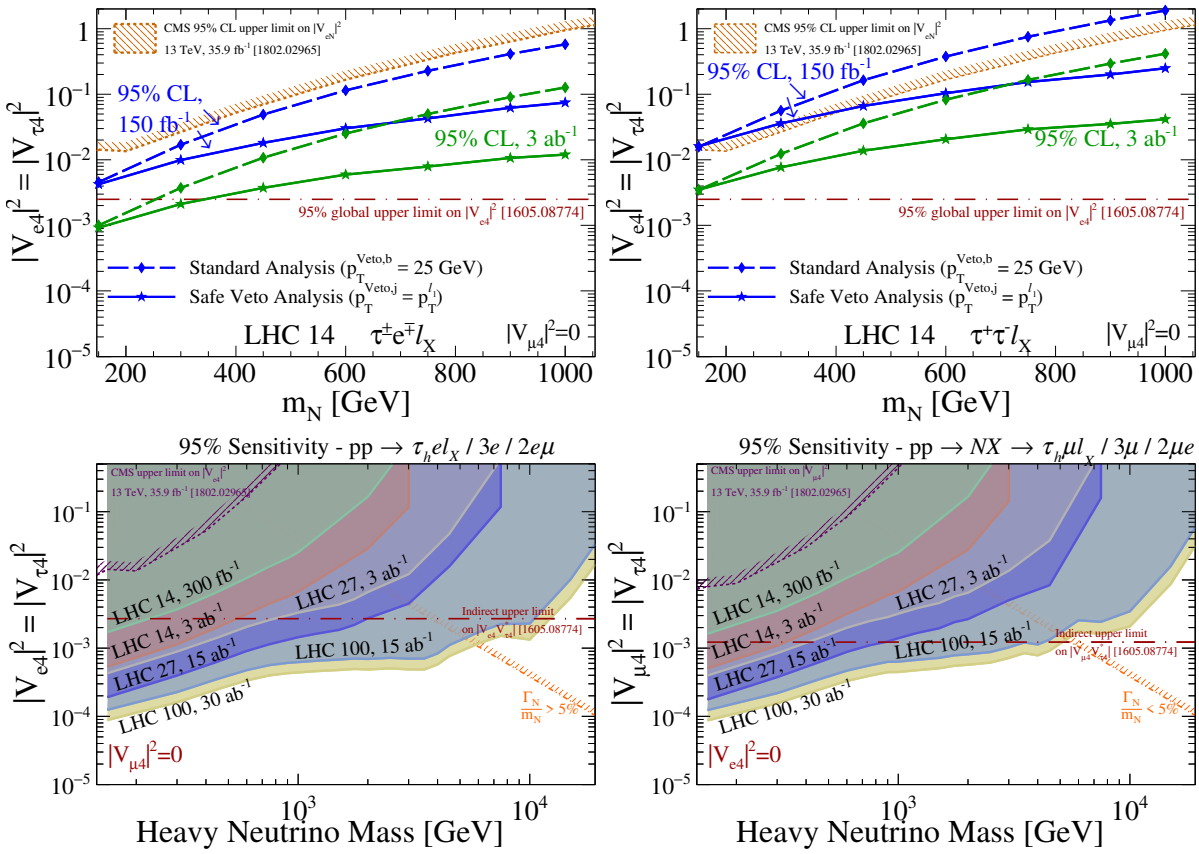

Fig. 5.1.2: Top: sensitivity to the active-heavy mixing $|V_{\ell N}|^2$ as a function of the heavy neutrino mass m_N in the trilepton final states (left) $\tau_h^\pm e^\mp \ell_X + \text{MET}$ and (right) $\tau_h^+ \tau_h^- \ell_X + \text{MET}$, assuming $|V_{e4}|^2 = |V_{\tau 4}|^2$ and $|V_{\mu 4}|^2 = 0$, at the $\sqrt{s} = 14$ TeV LHC. The dash-diamond line corresponds to the standard analysis with a b-jet veto while the solid-star line is the jet veto-based analysis [372, 373]. Bottom: for the benchmark mixing hypotheses (left) $|V_{e4}| = |V_{\tau 4}|$ with $|V_{\mu 4}| = 0$ and (right) $|V_{\mu 4}| = |V_{\tau 4}|$ with $|V_{e4}| = 0$, the projected sensitivity at $\sqrt{s} = 27$ TeV and 100 TeV using the trilepton analysis of Ref. [372].

For $m_N \approx 1$ TeV, the GF, DY, and VBF mechanisms all possess fiducial cross sections in excess of 10 fb.

Discovery Potential of Heavy Pseudo-Dirac Neutrinos in Low Scale Seesaws

The expected suppression of LNV processes in models that contain only fermionic gauge singlets motivates the study of lepton number conserving (LNC) processes. A first possibility to consider is the trilepton final state $\ell_i^\pm \ell_j^\mp \ell_k^\pm + \text{MET}$. The heavy neutrino N here is produced via both charged-current DY and VBF, and subsequently decays to only leptons, *i.e.*

$$pp \to \ell_N N + X \to \ell_N \ell_W W + X \to \ell_N \ell_W \ell_\nu \nu + X \,. \tag{5.1.1}$$

Notably, a new search strategy was recently proposed in Ref. [372, 373] based on a dynamical jet veto selection cut and found an increased sensitivity to active-heavy neutrino mixing by approximately an order of magnitude over the LHC's life. This is shown in Fig. 5.1.2 (top) specifically for the final states (L) $\tau_h^\pm e^\mp \ell_X + \text{MET}$ and (R) $\tau_h^+ \tau_h^- \ell_X + \text{MET}$, where τ_h represents a hadronically decaying τ and $\ell_X \in \{e, \mu, \tau_h\}$. With $3\,\text{ab}^{-1}$ and after taking into account global constraints on the active-heavy mixing [374] (dot-dashed line in Fig. 5.1.2 (top)), the HL-LHC is able to probe heavy neutrino masses up to 350 GeV and mixing down to $|V_{\ell N}|^2 \simeq 10^{-3}$ could be probed. For the benchmark mixing hypotheses (L) $|V_{e4}| = |V_{\tau 4}|$ with $|V_{\mu 4}| = 0$ and (R) $|V_{\mu 4}| = |V_{\tau 4}|$ with $|V_{e4}| = 0$, Fig. 5.1.2 (bottom) shows

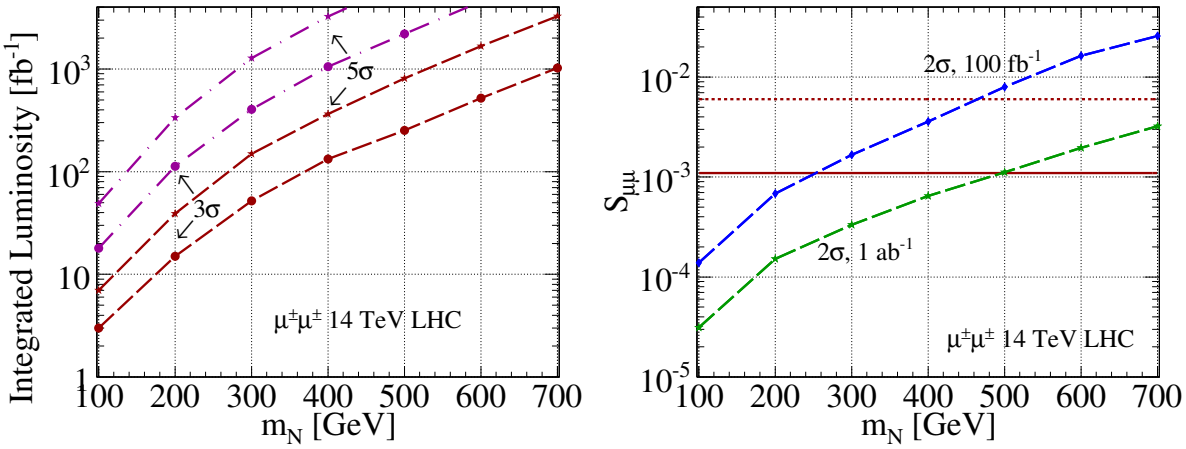

Fig. 5.1.3: Left: using the LNV final state $\mu^\pm\mu^\pm jj$, required luminosity for $3(5)\sigma$ evidence (discovery) as a function of heavy neutrino mass m_N assuming optimistic (brown) and pessimistic (purple) mixing scenarios [370]. Right: sensitivity to $N-\mu$ mixing [370] with the optimistic (pessimistic) mixing scenario is given by the horizontal dashed (full) line.

the projected sensitivity of this analysis at $\sqrt{s} = 27$ TeV and 100 TeV using the trilepton analysis of Ref. [372].

Another possibility is to search for lepton flavour violating (LFV) final states such as

$$q\,\overline{q'} \to N\,\ell_1^\pm \to \ell_1^\pm\,\ell_2^\mp\,W^\mp \to \ell_1^\pm\,\ell_2^\mp\,j\,j\,, \tag{5.1.2}$$

which was for example studied in the inverse seesaw (ISS), a low-scale variant of the type I, in Ref. [375]. Due to the strong experimental limits on $\mu \to e\gamma$ by MEG [376], the event rates involving taus are more promising than those for $e^\pm\mu^\mp jj$. Following Ref. [375], the number of $\tau^\pm\mu^\mp jj$ can be estimated using the μ_X-parametrisation [377] with the neutrino Yukawa coupling

$$Y_\nu = f \begin{pmatrix} -1 & 1 & 0 \\ 1 & 1 & 0.9 \\ 1 & 1 & 1 \end{pmatrix}. \tag{5.1.3}$$

as a representative example, and considering that only the lightest pseudo-Dirac pair is kinematically available. After $\mathcal{L} = 3(15)\ \mathrm{ab}^{-1}$, more than 100(500) LFV $\tau^\pm e^\mp jj$ events can be produced for heavy neutrino masses below 700 (1000) GeV, for pp collisions at $\sqrt{s} = 14(27)$ TeV.

Discovery Potential of Heavy Majorana Neutrinos in Phenomenological Type I Seesaw

In the presence of additional particles that can decouple the heavy neutrino production from the light neutrino mass generation, *e.g.*, new but far off-shell gauge bosons [378], the Majorana nature of the heavy neutrinos can leads to striking LNV collider signatures, such as the well-studied same-sign dilepton and jets process [379]

$$pp \to N\,\ell_1^\pm \to \ell_1^\pm\,\ell_2^\pm\,W^\mp \to \ell_1^\pm\,\ell_2^\pm + nj. \tag{5.1.4}$$

Assuming that a low-scale type I seesaw is responsible for the heavy neutrino production, Fig. 5.1.3 displays the discovery potential and active-heavy mixing sensitivity of the $\mu^\pm\mu^\pm$ channel [370]. Assuming the (pessimistic/conservative) mixing scenario of $S_{\mu\mu} = 1.1 \times 10^{-3}$ [370] the HL-LHC with $3\ \mathrm{ab}^{-1}$ is able to discover a heavy neutrino with a mass of $m_N \simeq 400$ GeV and is sensitive to masses up to 550 GeV at 3σ. Using only $1\ \mathrm{ab}^{-1}$, the HL-LHC can improve on the preexisting mixing constraints summarised in the pessimistic scenario for neutrino masses up to 500 GeV.

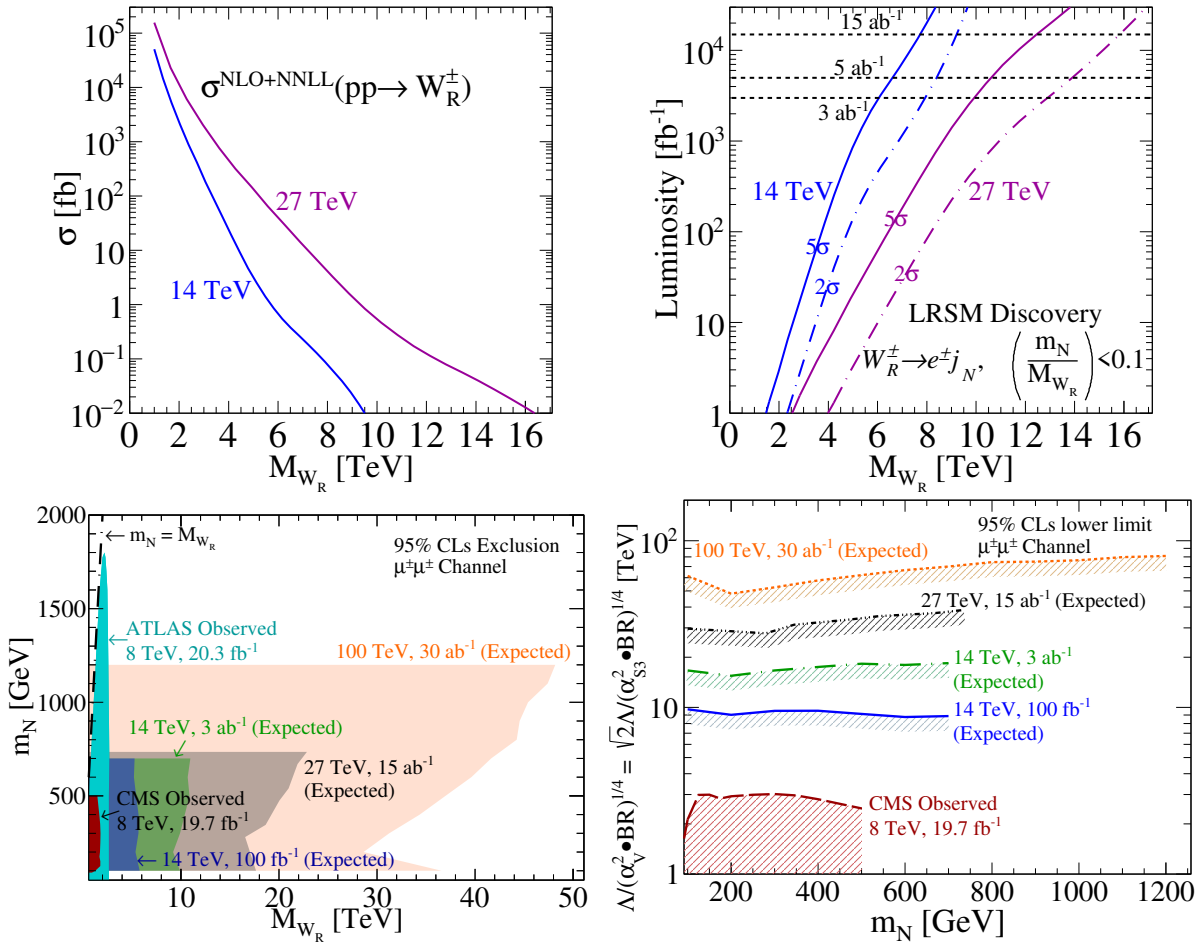

Fig. 5.1.4: Top: the total $pp \to W_R$ cross section at NLO+NNLL(Threshold) (left) and $5(2)\sigma$ discovery potential (sensitivity) via W_R decays to an electron and neutrino jet (j_N) (right), as a function of W_R mass and at $\sqrt{s} = 14$ and 27 TeV [380]. Bottom: observed and expected sensitivity to heavy Majorana neutrinos through the process $pp \to \mu^{\pm} N \to 2\mu^{\pm} + 2j$ and produced via non-resonant W_R (left) as well as dimension-six NEFT operators [378] (right).

Heavy Neutrinos and the Left-Right Symmetric Model at Colliders

The Left-Right Symmetric Model (LRSM) remains one of the best motivated high-energy completions of the SM. It addresses the origin of both tiny neutrino masses via a Type I+II seesaw hybrid mechanism as well as the SM's $V-A$ chiral structure through the spontaneous breakdown of an $SU(2)_L \otimes SU(2)_R$ symmetry, amongst other low-energy phenomena. At collider scales, the model predicts the presence of new heavy gauge bosons that are closely aligned with their gauge states $(W_R^{\pm},\ Z_R')$, heavy Majorana neutrinos (N), and a plethora of neutral and electrically charged scalars $(H_i^0,\ H_j^{\pm},\ H_k^{\pm\pm})$. Unlike $U(1)_{BL}$ neutrino mass models, the LRSM gauge couplings are fixed to the SM Weak coupling constant, up to (small) RG-running corrections. As a result, the Drell-Yan production mechanisms for W_R and Z_R result in large rates at hadron colliders. Following the procedure of Ref. [380], the $pp \to W_R^{\pm}$ cross section at NLO+NNLL(Threshold) is shown in Fig. 5.1.4 (top left) as a function of mass M_{W_R} at $\sqrt{s} = 14$ and 27 TeV. At $\sqrt{s} = 14(27)$ TeV, one sees that production cross sections for masses as large as $M_{W_R} \approx 5.5(9)$ TeV are in excess of 1 fb. For $M_{W_R} \approx 7.5(12.5)$ TeV, rates exceed 100 ab, and indicate $\mathcal{O}(10^2 - 10^3)$ events can be collected with $\mathcal{L} = 1 - 15\ \text{ab}^{-1}$ of data. Such computations up to NLO in QCD with parton shower matching, including for more generic coupling, are also publicly available following Ref.s [381, 382].

Of the many collider predictions the LRSM, one of its most promising discovery channels is

the production of heavy Majorana neutrinos from resonant W_R currents with N decaying via a lepton number-violating final state. At the partonic level, this is given by [379]

$$q_1\overline{q_2} \to W_R \to N\,\ell_i^{\pm} \to \ell_i^{\pm}\ell_j^{\pm}W_R^{\mp *} \to \ell_i^{\pm}\ell_j^{\pm}q_1'\overline{q_2'} \tag{5.1.5}$$

and has been extensively studied throughout the literature. For details; see Ref. [361] and references therein. Due to the ability to fully reconstruct Eq. (5.1.5), many properties of W_R and N can be extracted, including a complete determination of W_R chiral couplings to quarks independent of leptons [383]. Beyond the canonical $pp \to W_R \to N\ell \to 2\ell + 2j$ channel, it may be the case that the heavy neutrino is hierarchically lighter than the right-handed (RH) gauge bosons. Notably, for $(m_N/M_{W_R}) \lesssim 0.1$, N is sufficiently Lorentz boosted that its decay products, particularly the charged lepton, are too collimated to be resolved experimentally [380, 384]. Instead, one can consider the $(\ell_j^{\pm}q_1'\overline{q_2'})$-system as a single object, a *neutrino jet* [380, 381]. The hadronic process is then

$$pp \to W_R \to N\ell_i^{\pm} \to j_N\,\ell_i^{\pm}, \tag{5.1.6}$$

and inherits much of the desired properties of Eq. (5.1.5), such as the simultaneous presence of high-p_T charged leptons and lack of MET [380, 381], resulting in a very strong discovery potential. Assuming conservative detector efficiency (ε) and selection acceptance $(\mathcal{A})$ rates of $(\varepsilon, \mathcal{A}) \approx (0.33, 0.64)$ based on the realistic analysis of Ref. [380], and a branching fraction of $\mathcal{B}(W_R \to Ne \to eeq\overline{q'}) \approx 10\%$ for $(m_N/M_{W_R}) < 0.1$. Figure 5.1.4 (top right) shows the requisite integrated luminosity for $5(2)\sigma$ discovery of Eq. (5.1.6) at $\sqrt{s} = 14$ and 27 TeV. With $\mathcal{L} = 3(5)$ ab^{-1}, W_R as heavy as 6(6.5) TeV and 10(10.5) TeV, respectively, can be discovered at $\sqrt{s} = 14$ (27) TeV. With $\mathcal{L} = 15$ ab^{-1}, mass scales as heavy 16 TeV can be probed at the 2σ level at $\sqrt{s} = 27$ TeV.

For such heavy W_R and Z_R that may be kinematically outside the reach of the $\sqrt{s} = 14$ TeV LHC, one can still produce EW- and sub-TeV scale via off-shell W_R and Z_R bosons [378]. As a result, the $pp \to W_R^* \to N\ell \to 2\ell + 2j$ process occurs instead at a hard scale $Q \sim m_N$ and cannot be distinguished from the phenomenological Type I seesaw without a detailed analysis of the heavy neutrino's chiral couplings [378, 383]. However, this also means that searches for heavy N in the context of the phenomenological Type I can be recast/reinterpreted in the context of the LRSM. Subsequently, as shown in Fig. 5.1.4 (bottom left), W_R as heavy as $8-9$ TeV can be probed indirectly with $\mathcal{L} = 1$ ab^{-1} at $\sqrt{s} = 14$ TeV [378]. A similar argument can be applied to heavy neutrinos produced through dimension-six Heavy Neutrino Effective Field Theory (NEFT) operators, revealing sensitivity to mass scales up to $\Lambda \sim \mathcal{O}(10)$ TeV over the $\sqrt{s} = 14$ TeV LHC's lifetime [378], as shown in Fig. 5.1.4 (bottom right).

Type II Scalars Discovery Potential at the HL- and HE-LHC

The Type II seesaw hypothesises the existence of a new scalar $\mathrm{SU}(2)_L$ triplet that couples to SM leptons in order to reproduce the light neutrino mass spectrum and oscillation data. This is done by the spontaneous generation of a left handed Majorana mass for the light neutrinos. Moreover, the Type II scenario is notable for the absence of sterile neutrinos, demonstrating that light neutrino masses themselves do not imply the existence of additional fermions. The most appealing production mechanisms at hadron colliders of triplet Higgs bosons are the pair production of doubly charged Higgs and the associated production of doubly charged Higgs and singly charged Higgs,

$$pp \to Z^*/\gamma^* \to H^{++}H^{--}, \quad pp \to W^* \to H^{\pm\pm}H^{\mp}. \tag{5.1.7}$$

followed, in the most general situation, by lepton flavour- and lepton number-violating decays to SM charged leptons. In Fig. 5.1.5 (top left), we show the total cross section of the $pp \to H^{++}H^{--}$ and $pp \to H^{\pm\pm}H^{\mp}$ processes as a function of triplet mass (in the degenerate limit with $M_{H^{\pm}} = M_{H^{\pm\pm}}$), in collisions at $\sqrt{s} = 14$, 27, and 100 TeV.

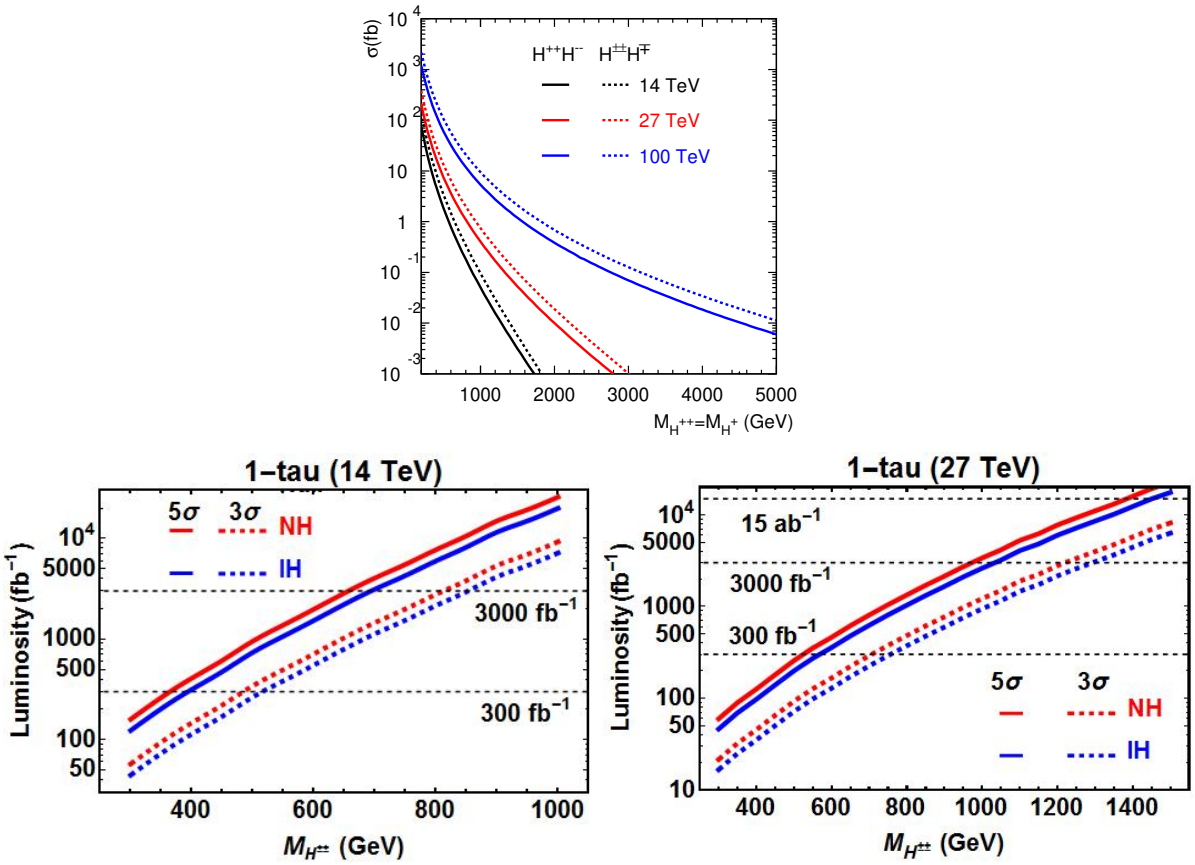

Fig. 5.1.5: Top: the total cross section for $pp \to H^{++}H^{--}$ and $H^{\pm\pm}H^{\mp}$ at $\sqrt{s} = 14$, 27, and 100 TeV. Bottom: requisite luminosity versus $M_{H^{\pm\pm}}$ for $5(3)\sigma$ discovery (evidence) for the process $pp \to H^{++}H^{--} \to \tau_h \ell^{\pm}\ell^{\mp}\ell^{\mp}$, where $\tau^{\pm} \to \pi^{\pm}\nu$, for the NH and IH at $\sqrt{s} = 14$ and 27 TeV.

In Type II scenarios, $H^{\pm\pm}$ decays to $\tau^{\pm}\tau^{\pm}$ and $\mu^{\pm}\mu^{\pm}$ pairs are comparable or greater than the $e^{\pm}e^{\pm}$ channel by two orders of magnitude. Moreover, the $\tau\mu$ channel is typically dominant in decays involving different lepton flavours [385, 386]. If such a seesaw is realised in nature, tau polarisations can help to determine the chiral property of triplet scalars: One can discriminate between different heavy scalar mediated neutrino mass mechanisms, such as those found in the Type II seesaw and Zee-Babu model, by studying the distributions of tau leptons' decay products [386, 387]. Due to the low τ_h identification efficiencies, future colliders with high energy and/or luminosity enables one to investigate and search for doubly charged Higgs decaying to τ_h pairs. Accounting for constraints from neutrino oscillation data on the doubly charged Higgs BRs, as well as tau polarisation effects [386], Fig. 5.1.5 (right) displays the 3σ and 5σ significance in the plane of integrated luminosity versus doubly charged Higgs mass for $pp \to H^{++}H^{--} \to \tau^{\pm}\ell^{\pm}\ell^{\mp}\ell^{\mp}$ at $\sqrt{s} = 14$, 27, and 100 TeV, respectively. For the one τ channel with $\tau^{\pm} \to \pi^{\pm(-)}\nu_{\tau}$, the sensitivity to doubly charged Higgs mass at HL-LHC can reach 655 GeV and 695 GeV for NH and IH respectively with a luminosity of 3 ab^{-1}. Higher masses, $1380 - 1930$ GeV for NH and $1450 - 2070$ GeV for IH, can be probed at 27 TeV with 15 $\mathrm{ab}^{-1}$and 100 TeV with 3 ab^{-1}.

Type III Leptons Discovery Potential at HL- and HE-LHC

Low-scale Type III Seesaws hypothesises the existence of heavy electrically charged $(E^{\pm})$ and neutral (N) leptons, which form a triplet under $\mathrm{SU}(2)_L$, that couple to both SM charged and neutral leptons through mixing/Yukawa couplings. Due to their gauge charges, triplet leptons also couple to EW gauge

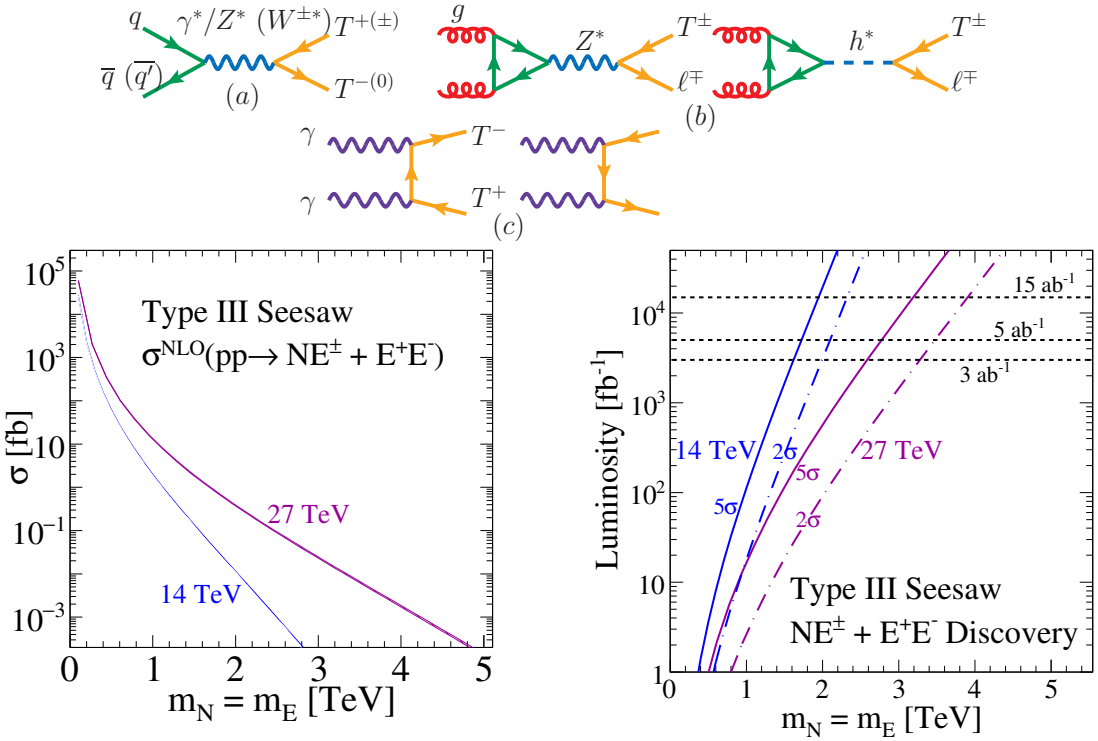

Fig. 5.1.6: Top: Born level production of Type III leptons via (a) Drell-Yan, (b) gluon fusion, and (c) photon fusion; from Ref. [361]. Bottom: at $\sqrt{s} = 14$ and 27 TeV and as a function of heavy triplet lepton mass, the summed inclusive production cross section [fb] of $pp \to NE^\pm + E^+E^-$, at NLO in QCD [388] (left), and the requisite integrated luminosity for $5(2)\sigma$ discovery (sensitivity) to $NE^\pm + E^+E^-$ based on the analyses of [389, 390] (right).

bosons appreciably and do not feature suppressed production cross section typical of seesaw scenarios with gauge singlet fermions. The presence of EW gauge couplings also implies that once a collider energy and mass are stipulated, the triplet lepton pair production cross section can be computed, up to small (and potentially negligible) mixing effects. Production mechanisms commonly found in the literature, and shown in Fig. 5.1.6 (top), include charged current and neutral current Drell-Yan, photon fusion, and gluon fusion if one considers heavy-light charged lepton associated production. A recent assessment of triplet production modes found [361] that despite the sizeable luminosities afforded to gluon fusion ($gg \to E^\pm \ell^\mp$), including its large QCD corrections [368], and photon fusion ($\gamma\gamma \to E^+E^-$), the Drell-Yan processes remain the dominant production channel of triplet leptons when kinematically accessible. In light of this, in Fig. 5.1.6 (bottom left), the summed cross sections for the Drell-Yan processes,

$$pp \to \gamma^*/Z^* \to E^+E^- \quad \text{and} \quad pp \to W^{\pm *} \to E^\pm N, \tag{5.1.8}$$

are shown at NLO in QCD, following Ref. [388], as a function of triplet masses (assuming $m_N = m_E$), at $\sqrt{s} = 14$ and 27 TeV. For $m_N, m_E \approx 1.2(1.8)$ TeV, the production rate reaches $\sigma(pp \to NE + EE) \approx 1$ fb at $\sqrt{s} = 14(27)$ TeV; and for heavier leptons with $m_N, m_E \approx 2.5(4.2)$ TeV, one sees that $\sigma(pp \to NE + EE) \approx 1$ ab.

Another consequence of the triplet leptons coupling to all EW bosons is the adherence to the Goldstone Equivalence Theorem. This implies that triplet leptons with masses well above the EW scale will preferentially decay to longitudinal polarised W and Z bosons as well as to the Higgs bosons. For decays of EW boson to jets or charged lepton pairs, triplet lepton can be full reconstructed from their final-state enabling their properties to be studied in detail. For fully reconstructible final-states,

$$NE^\pm \to \ell\ell' + WZ/Wh \quad \to \quad \ell\ell' + nj + mb, \tag{5.1.9}$$

$$E^+E^- \to \ell\ell' + ZZ/Zh/hh \quad \to \quad \ell\ell' \; + \; nj + mb, \tag{5.1.10}$$

which correspond approximately to the branching fractions $\mathcal{B}(NE) \approx 0.115$ and $\mathcal{B}(EE) \approx 0.116$, search strategies such as those considered in Ref.s [389, 390] can be enacted. Assuming a fixed detector acceptance and efficiency of $\mathcal{A} = 0.75$, which is in line to those obtained by Ref.s [389, 390], Fig. 5.1.6 (bottom right) shows as a function of triplet mass the requisite luminosity for a 5σ discovery (solid) and 2σ evidence (dash-dot) of triplet leptons at $\sqrt{s} = 14$ and 27 TeV. With $\mathcal{L} = 3 - 5$ ab^{-1}, the 14 TeV HL-LHC can discover states as heavy as $m_N, m_E = 1.6 - 1.8$ TeV. For the same amount of data, the 27 TeV HE-LHC can discover heavy leptons $m_N, m_E = 2.6 - 2.8$ TeV; with $\mathcal{L} = 15$ ab^{-1}, one can discover (probe) roughly $m_N, m_E = 3.2(3.8)$ TeV.

5.1.2 Like-sign dileptons with mirror type composite neutrinos at the HL-LHC

Contributors: M. Presilla, O. Panella, R. Leonardi

A composite scenario [391–394], where at a sufficiently high energy scale Λ (compositeness scale) the SM leptons and quarks show the effects of an internal substructure, has triggered considerable recent interest both from the theoretical [395–398] and experimental [399, 400] point of view. In particular recent studies [401] have concentrated in searching for heavy composite Majorana neutrinos at the LHC. The scenario discussed in such studies is one in which the excited neutrino (ν^*) is a Majorana particle. A recent CMS study has searched for a heavy composite Majorana neutrino (N). Using 2.6 fb^{-1} data of the 2015 Run II at $\sqrt{s} = 13$ TeV, heavy composite neutrino masses are excluded, at 95% C.L., up to $m_N = 4.35$ TeV and 4.60 (4.70) TeV for a value of $\Lambda = M_N$, from the $eeqq$ channel and the $\mu\mu qq$ channel, respectively [402, 403]. Here we focus on a mirror type assignment for the excited composite fermions. The neutrino mass term is built up from a Dirac mass, m_*, the mass of the charged lepton component of the $SU(2)$, right-handed doublet, and m_L the Majorana mass of the left-handed component (singlet) of the excited neutrino. The mass matrix is diagonalised leading to two Majorana mass eigenstates. The active neutrino field ν_R^* is thus a superposition of the two mass eigenstates with mixing coefficients which depend on the ratio m_L/m_*. We discuss the prospects of discovery of these physical states at the HL-LHC as compared with the previous searches of composite Majorana neutrinos at the LHC based on sequential type Majorana neutrinos.

We discuss a variant of the model analysed in Ref. [401, 403] taking up the scenario in which the excited fermions are organised with a mirror $SU(2)$ structure relative to the SM fermions, *i.e.* the right handed components form an $SU(2)$ doublet while the left handed components are singlets [283]. We construct a general Dirac-Majorana mass term and discuss its mass spectrum along with prospects of observing the resulting lepton number violating signatures at the HL-LHC [404].

In analogy with the usual procedure adopted in see-saw type extensions of the SM we may give a (lepton number violating) Majorana mass term to the left handed excited neutrino (ν_L^*) which is a singlet and does not actively participate to the gauge interactions in Eq. (5.1.14) –*sterile neutrino*–, while a (lepton number conserving) Dirac mass term m^* is associated to the right-handed component ν_R^* which belongs to the $SU(2)$ doublet and does participate in the gauge interactions – *active neutrino*-. We can thus write down the excited neutrino Dirac-Majorana mass term appearing in the Lagrangian density of the model as:

$$\mathcal{L}^{\text{D+M}} = -\frac{1}{2} m_L \, \bar{\nu}_L^* (\nu_L^*)^c - m_* \, \bar{\nu}_L^* \nu_R^* + \text{h.c.} \tag{5.1.11}$$

The Lagrangian mass term is easily diagonalised following standard procedures, obtaining two Majorana mass eigenstates, $\nu_{1,2}$, with (positive) mass eigenvalues given by:

$$m_{1,2} = \sqrt{m_*^2 + \left(\frac{m_L}{2}\right)^2} \mp \frac{m_L}{2} \tag{5.1.12}$$

Interacting states can be written as a mixing of the mass eigenstate according to the relation:

$$(\nu_L^*)^c = \; -i \cos\theta \, \nu_{1R} + \sin\theta \, \nu_{2R} \tag{5.1.13a}$$

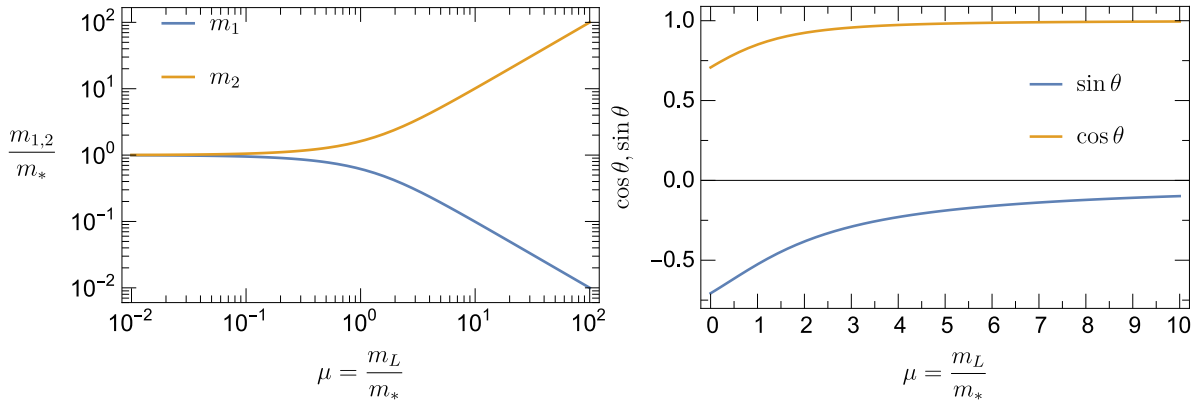

Fig. 5.1.7: Left: mass eigenstates $m_{1,2}$ (in units of m_*) from Eq. (5.1.12) as a function of the parameter $\mu = m_L/m_*$. Right: mixing coefficients $\cos\theta$ and $\sin\theta$ from Eq.s (5.1.13) as a function of the parameter $\mu = m_L/m_*$

$$\nu_R^* = \quad i\sin\theta\,\nu_{1R} + \cos\theta\,\nu_{2R} \tag{5.1.13b}$$

where the mixing angle θ is given in terms of the Dirac and Majorana masses: $\theta = -\frac{1}{2}\arctan\frac{2m_*}{m_L}$.

Now we take into account all the relevant effective couplings of these particles. In the mirror type model, we consider the first lepton family and assume that the excited neutrino and the excited electron are grouped into left handed singlets and a right-handed $SU(2)$ doublet [283]. The corresponding gauge mediated Lagrangian between the left-handed SM doublet L and the right-handed excited doublet R via the $SU(2)_L \times U(1)_Y$ gauge fields [405, 406], which should be of the magnetic type to warrant current conservation, can be written down:

$$\mathcal{L} = \frac{1}{2\Lambda}\,\bar{R}^*\sigma^{\mu\nu}\left(gf\frac{\boldsymbol{\tau}}{2}\cdot\boldsymbol{W}_{\mu\nu} + g'f'YB_{\mu\nu}\right)L + h.c.\,, \tag{5.1.14}$$

where $L^T = (\nu_L, \ell_L)$ is the ordinary $SU(2)_L$ lepton doublet, and $R^T = (\nu_R^*, \ell_R^*)$ is the excited right-handed doublet; g and g' are the $SU(2)_L$ and $U(1)_Y$ gauge couplings and $\boldsymbol{W}_{\mu\nu}$, $B_{\mu\nu}$ are the field strength for the $SU(2)_L$ and $U(1)_Y$ gauge fields; f and f' are dimensionless couplings. The relevant charged current (gauge) interaction of the excited (active) Majorana neutrino ν_R^* is easily derived from Eq. (5.1.14) and can be written out explicitly in terms of the Majorana mass eigenstates through Eq. (5.1.13b):

$$\mathcal{L}_{\rm G} = \frac{gf}{\sqrt{2}\Lambda}\,\left(-i\sin\theta\,\overline{\nu}_1 + \cos\theta\,\overline{\nu}_2\right)\,\sigma^{\mu\lambda}\,\ell_L\,\partial_\mu W_\lambda + h.c. \tag{5.1.15}$$

Contact interactions between ordinary fermions may arise by constituent exchange, if the fermions have common constituents, and/or by exchange of the binding quanta of the new unknown interaction whenever such binding quanta couple to the constituents of both particles [392, 406]. The dominant effect is expected to be given by the dimension 6 four-fermion interactions which scale with the inverse square of the compositeness scale Λ:

$$\mathcal{L}_{\rm CI} = \frac{g_*^2}{\Lambda^2}\frac{1}{2}j^\mu j_\mu \tag{5.1.16a}$$

$$j_\mu = \eta_L\bar{f}_L\gamma_\mu f_L + \eta'_L\bar{f}_L^*\gamma_\mu f_L^* + \eta''_L\bar{f}_L^*\gamma_\mu f_L + h.c. + (L\to R) \tag{5.1.16b}$$

where $g_*^2 = 4\pi$ and the η factors are usually set equal to unity. In this work the right-handed currents will be neglected for simplicity.

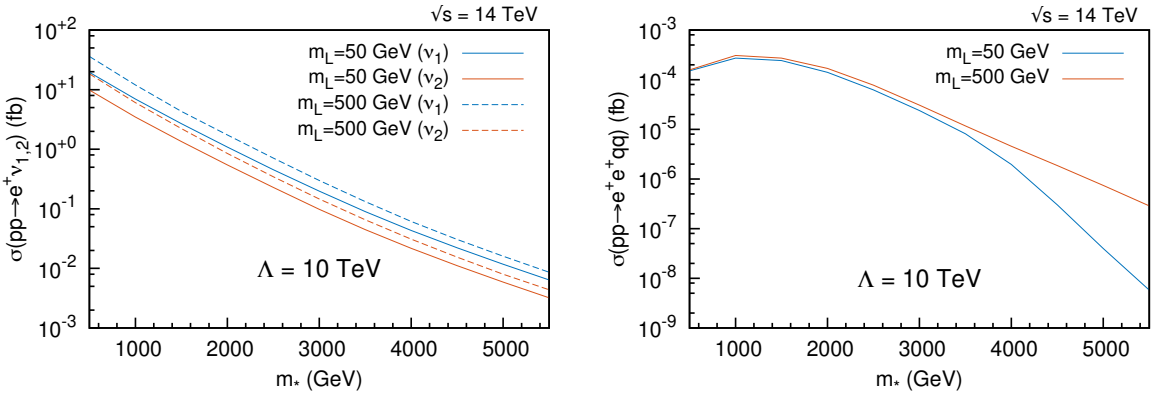

Fig. 5.1.8: Left: production cross section, at $\sqrt{s} = 14$ TeV, for the two mass eigen-states $pp \to e^+\nu_{1,2}$ for two different Majorana mass values, $m_L = 50, 500$ GeV. Right: cross section for the like-sign dileptons signature, $pp \to e^+e^+qq$ at the HL-LHC ($\sqrt{s} = 14$ TeV).

The single production $q\bar{q}' \to \nu^*\ell$ proceeds through flavour conserving but non-diagonal terms, in particular with currents like the third term in Eq. (5.1.16b) which couple excited states with ordinary fermions and the contact interactions in can be written out explicitly in terms of the Majorana mass eigenstates ν_i using Eq. (5.1.13b):

$$\mathcal{L}_{\rm CI} = \frac{g_*^2}{\Lambda^2}\,\bar{q}_L\gamma^\mu q'_L\,\left(-i\cos\theta\,\overline{\nu}_1 + \sin\theta\,\overline{\nu}_2\right)\,\gamma_\mu\ell_L\,. \tag{5.1.17}$$

The gauge interactions in Eq. (5.1.15) and the contact interactions in Eq. (5.1.17) have to be implemented in a MC generator. Here we have mostly used MADGRAPH [67], complementing the results with a validation obtained with the tree-level simulator CALCHEP [407].

In Fig. 5.1.8 is shown the behaviour of production cross section for the two mass eigenstates and for the whole process for different model scenarios. It is worth to notice that in the limit $m_L \to 0$ the cross-section of the like-sign dilepton process goes to zero.

We briefly discuss the potential for discovery at HL-LHC in the three-dimensional parameter space (Λ, m_L, m_*) using the fast simulation framework DELPHES [33] for studying the hypothetical response of the CMS Phase-2 detector. Standard model processes that could mimic the detection of a signal with lepton number violation in this rather clean signature are mainly the triple W boson production, $pp \to W^+W^+W^-$, and the top quark pair production $pp \to t\bar{t}$, the former being the dominant background source. Since the kinematic features of the final state reconstructed objects are similar to those of Ref. [401], we lower the background contribution by imposing two cuts on the leading lepton ($p_T(e_1) > 110$ GeV) and on the second-leading lepton ($p_T(e_2) > 35$ GeV). This particular signal region allows an efficiency in selecting signal around the 80%, while beating the background sources with efficiency of 0.00044% for the $t\bar{t}$ and of 0.0034% for the $W^+W^+W^-$.
We compute, at a c.o.m.energy of $\sqrt{s} = 14$ TeV and with an integrated luminosity of $\mathcal{L} = 3\ \mathrm{ab}^{-1}$, the statistical significance, as defined by the relation $S = \mathcal{L}\sigma_{\rm sig}\epsilon_{\rm sig}/\sqrt{\mathcal{L}\sigma_{\rm bkg}\epsilon_{\rm bkg}}$, where $\epsilon_{\rm sig}, \epsilon_{\rm bkg}$ are respectively the cumulative efficiencies of signal and background due to the event reconstruction. In Fig. 5.1.9 (left) we show the potential for discovery, in the plane (m_*, Λ), of the CMS Phase-2 detector for two different values of the Majorana mass $m_L = 50, 500$ GeV.

Another interesting feature of the present model is that the presence of two heavy neutrino mass eigenstates, which have also opposite CP eigenvalues, can lead to a charge asymmetry, *i.e.* to an asymmetry in the production rate of same-sign dilepton signal versus the opposite-sign dilepton signal [408]. In particular, the charge asymmetry $\mathcal{A} = (\sigma_{e^+e^-jj} - \sigma_{e^+e^+jj})/(\sigma_{e^+e^-jj} + \sigma_{e^+e^+jj})$ could be used to test the relative strength between the Dirac and Majorana nature of the heavy neutrinos at the HL-LHC.

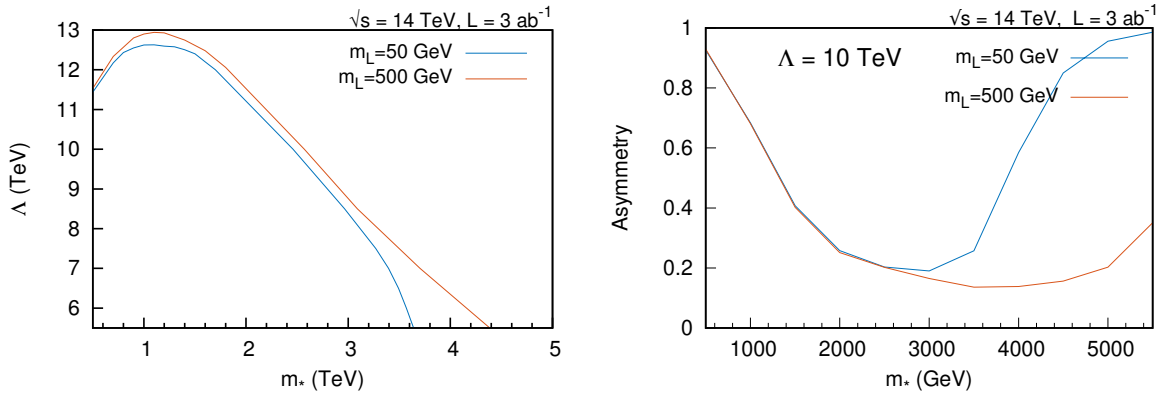

Fig. 5.1.9: Left: the 5σ contour levels curves, at $\sqrt{s} = 14$ TeV and $\mathcal{L} = 3\,\text{ab}^{-1}$, of the statistical significance ($S = 5$) in the parameter plane $[m^*, \Lambda]$, for two different values of the Majorana mass $m_L = 50, 500$ GeV. Right: the expected charge asymmetry at $\sqrt{s} = 14$ TeV and $\mathcal{L} = 3\,\text{ab}^{-1}$ of the same-sign and opposite sign channels for two different values of $m_L = 50, 500$ GeV as function of m_*.

We note that while the same-sign dilepton signature e^+e^+jj is effectively background free (see above), the opposite sign dilepton signature e^+e^-jj is expected to have a substantially larger SM background which however could be subtracted in order to extract the asymmetry $\mathcal{A}$ peculiar of the model features. Figure 5.1.9 (right) shows the charge asymmetry $\mathcal{A}$. In line with expectations that $\mathcal{A} \to 1$ when $\sigma_{e^+e^+jj}$ is suppressed we observe that as a function of m_* after the initial drop in the asymmetry, at fixed m_L, then at larger values of m_* the mass difference of the two eigenstates diminishes and so does the same-sign dilepton yield giving larger asymmetries close to 1 again.

In summary, we have presented a mechanism of lepton number violation within a mirror type compositeness scenario. The mirror model is realised when the left components of the excited states are singlets while the right components are active doublets which do participate to gauge transition interactions with SM fermions. We therefore introduce a *left*-handed Majorana neutrino singlet of mass m_L while the right-handed component belongs to a doublet and has a Dirac mass m_*. This situation is exactly specular to the one encountered in typical see-saw models where the sterile neutrino is the right handed component and the active one is the left handed component. diagonalisation of the mass matrix gives two Majorana mass eigenstates whose phenomenology at the HL-LHC is presented, providing the 5σ contour level curves of the statistical significance for a possible discover by a CMS Phase-2 like detector. We have also shown that the charge asymmetry $\mathcal{A}$ of the like sign dilepton signature is a useful observable for studying the model parameter space.

5.1.3 Search for heavy composite Majorana neutrinos at the HL- and the HE-LHC

Contributors: P. Azzi, C. Cecchi, L. Fanó, A. Gurrola, W. Johns, R. Leonardi, E. Manoni, M. Narain, O. Panella, M. Presilla, F. Romeo, S. Sagir, P. Sheldon, F. Simonetto, E. Usai, W. Zhang, CMS

Compositeness of ordinary fermions is one possible BSM scenario that may lead to a solution of the hierarchy problem or to the explanation of the proliferation of ordinary fermions. Elementary particles are thought to be bound states of some as–yet–unobserved fundamental constituents generically referred to as *preons*. Composite models also predict the existence of excited states of quarks and leptons, with masses lower than or equal to the compositeness scale Λ which interact with SM fermions via both magnetic type gauge couplings and contact interactions.

The heavy composite Majorana neutrino N_ℓ would be a particular case of such excited states. This can be produced in association with a lepton, in pp collisions, via quark–antiquark annihilation ($q\bar{q}' \to \ell N_\ell$). The production and decay processes can occur via both gauge and contact interactions.

The Lagrangian density for gauge mediated interactions is

$$\mathcal{L}_G = \frac{1}{2\Lambda}\overline{L_{\mathrm{R}}^*}\sigma^{\mu\nu}\left(gf\frac{\overrightarrow{\tau}}{2}\cdot\overrightarrow{W}_{\mu\nu} + g'f'YB_{\mu\nu}\right)L_{\mathrm{L}} + h.c., \tag{5.1.18}$$

where L_R^* and L_L are, respectively, the right-handed doublet of the excited fermions and the left-handed doublet of the SM, g and $g^{'}$ are the $SU(2)_L$ and $U(1)_Y$ gauge couplings, and f and f' are dimensionless couplings, which are expected to be of order unity [394] and henceforth simply assumed to be 1. The corresponding Lagrangian describing the four-fermion contact interactions by a dimension-6 effective operator can written as

$$\mathcal{L}_C = \frac{g_*^2}{\Lambda^2}\frac{1}{2}j^\mu j_\mu, \tag{5.1.19}$$

with

$$j_\mu = \eta_L\bar{\psi}_L\gamma_\mu\psi_L + \eta'_L\bar{\psi}_L^*\gamma_\mu\psi_L^* + \eta''_L\bar{\psi}_L^*\gamma_\mu\psi_L + h.c. + (L\to R), \tag{5.1.20}$$

where $g_*^2 = 4\pi$, the η factors that define the chiral structure are usually set equal to 1, and ψ and ψ^* are the SM and excited fermion fields [394].

The production process is dominated by the contact interaction mechanism for all values of the compositeness scale Λ and of the mass of the neutrino $M(N_\ell)$ relevant in this analysis, while for the decay the dominant interaction changes depending on Λ and $M(N_\ell)$ [401].

This study from CMS focuses on the final state signature $\ell\ell q\bar{q}^{'}$, where ℓ is either an electron or a muon [409]. For the HL-LHC sensitivity study, we use MC samples for the signal and the SM backgrounds. The MC samples for the signal are generated with CALCHEP V3.6 [407] using the NNPDF3.0 LO parton distribution functions [121]. The background samples considered are top quark pair production ($\mathrm{t\bar{t}}$), single top quark production (tW), Drell-Yan (DY) process, W+jets and diboson production (WW, WZ, ZZ), and are generated with MADGRAPH5_AMC@NLO [67] using the CTEQ6L1 PDF set [52]. For all of the MC samples the hadronisation of partons is simulated with PYTHIA 8 [68] and the expected response of the upgraded CMS detector is performed with the fast-simulation package DELPHES [33]. The contribution from additional pileup events has been included in the simulation as well.

In order to reduce the contamination from misreconstructed events, a kinematics-based selection is applied. The p_T of the leading lepton is required to be greater than 110 GeV, while the p_T of the subleading lepton must greater than 40 GeV. All lepton candidates are required to be in the pseudorapidity range $|\eta| < 2.4$. Restricting to the high-mass region given by $M(\ell,\ell) > 300$ GeV, where $M(\ell,\ell)$ is the dilepton invariant mass, allows reducing the DY background without affecting the signal acceptance. The large-radius jets are analysed using the PUPPI algorithm [410]. They are reconstructed with a distance parameter of $R = 0.8$ and they are required to have a minimum p_T of 200 GeV, to be within the region $|\eta| < 2.4$ and to be separated from leptons by a distance $\Delta R = \sqrt{(\Delta\eta)^2 + (\Delta\phi)^2} > 0.8$. Requiring one or more large-radius jets is suitable regardless of whether N_ℓ decays through gauge or contact interactions. In fact, for gauge mediated decays of the heavy composite neutrino, the two quarks are expected to overlap and thus form a large-radius jet, while in the case of contact-mediated decays, the two quarks are well separated, but form two large-radius jets because of the overlap with final state radiation. The signal region is therefore defined by requiring two same-flavour isolated leptons (electrons or muons) and at least one large-radius jet.

A shape-based analysis is performed looking at the invariant mass distribution of the two leptons and the leading large-radius jet, $M(\ell\ell J)$. The expected discovery sensitivity of a heavy composite Majorana neutrino, produced in association with a lepton, and decaying into a same-flavour lepton and two jets, is shown in Fig. 5.1.10. The CMS Phase-2 detector will be able to find evidence for a composite neutrino with mass below $M(N_\ell) = 7.6$ TeV. The $M(\ell\ell J)$ distributions of signal and SM backgrounds are also used as input in the computation of an upper limit at the 95% C.L. on the cross section of the

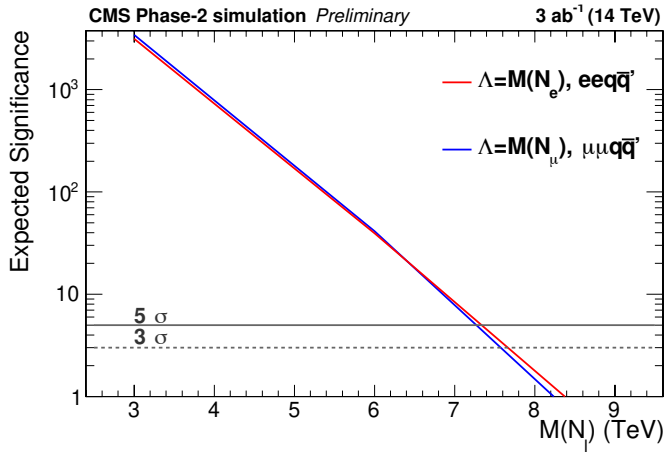

Fig. 5.1.10: Expected statistical significance for the HL-LHC projection of the $eeq\bar{q}'$ (red line) and $\mu\mu q\bar{q}'$ (blue line) channel for the case $\Lambda = M(N_\ell)$. The grey solid (dotted) line represents $5(3)\sigma$, respectively.

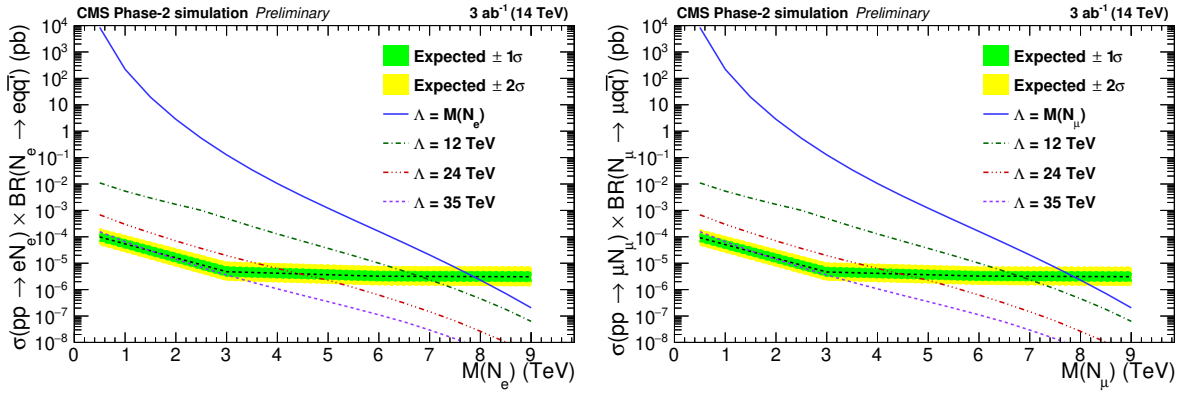

Fig. 5.1.11: Expected 95% C.L. upper limits for the HL-LHC projection (black dotted lines) on $\sigma(pp \to \ell N_\ell) \times \mathcal{B}(N_\ell \to \ell q\bar{q}')$, obtained in the analysis of the $eeq\bar{q}'$ (left) and the $\mu\mu q\bar{q}'$ (right) final states, as a function of the mass of the heavy composite Majorana neutrino. The corresponding green and yellow bands represent the expected variation of the limit to one and two standard deviation(s). The solid blue curve indicates the theoretical prediction of $\Lambda = M(N_l)$. The textured curves give the theoretical predictions for Λ values ranging from 12 to 35 TeV.

heavy composite Majorana neutrino produced in association with a lepton times its branching fraction to a same-flavour lepton and two quarks, $\sigma(pp \to \ell N_\ell) \times \mathcal{B}(N_\ell \to \ell q\bar{q}')$. A CL_s criterion [95] is used to set upper limits. Systematic uncertainties are included on the integrated luminosity (1%), pileup (2%), electron ID (0.5%), electron scale (0.5%), muon ID (0.5%), muon scale (0.5%), jet energy scale (1%), jet energy resolution (1%), the background prediction (0.3%), and Drell-Yan theory (4%), and are evaluated in accordance with the most recent recommendations described in Ref. [411].

The results are shown in Fig. 5.1.11 for the $eeq\bar{q}'$ and $\mu\mu q\bar{q}'$ channels. Figure 5.1.12 displays the corresponding upper limits on the $(\Lambda, M(N_\ell))$ plane. The HL-LHC running conditions and Phase-2 detector will significantly extend the region of parameter space that can be probed. While in Run-2 the mass of the heavy composite Majorana neutrino could be excluded up to 4.60 (4.70) TeV in the $eeq\bar{q}'$ ($\mu\mu q\bar{q}'$) channel [403], for the case of $\Lambda = M(N_\ell)$, for the HL-LHC we could potentially exclude a composite neutrino up to a mass of 8 TeV with the same assumption on the compositeness scale.

The sensitivity of the search is also considered for the High-Energy LHC at $\sqrt{s} = 27$ TeV.

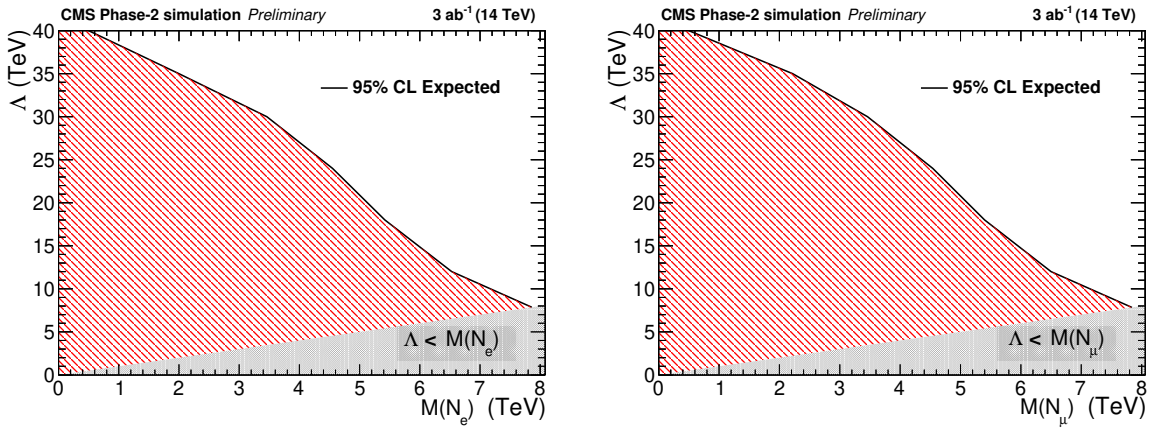

Fig. 5.1.12: Expected 95% C.L. lower limits (black lines) on the compositeness scale Λ, obtained in the analysis of the $eeq\bar{q}'$ (left) and the $\mu\mu q\bar{q}'$ (right) final states, as a function of the mass of the heavy composite Majorana neutrino. The gray zone corresponds to the phase space $\Lambda < M(N_\ell)$ not allowed by the model.

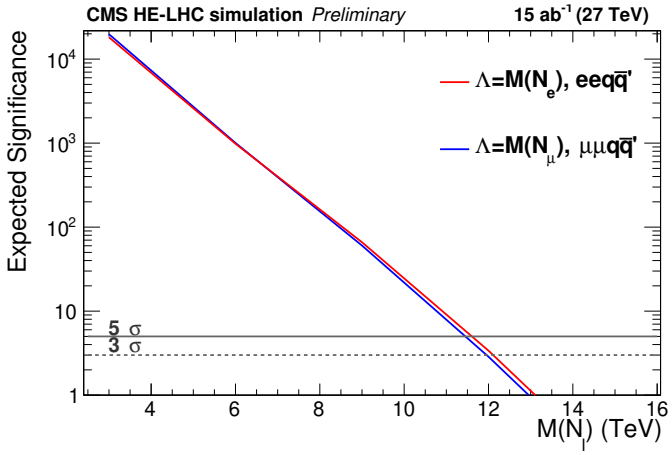

Fig. 5.1.13: Expected statistical significance for the HE-LHC projection of the $eeq\bar{q}'$ (red line) and the $\mu\mu q\bar{q}'$ (blue line) channel for the case $\Lambda = M(N_\ell)$. The gray solid (dotted) line represents $5(3)\sigma$, respectively.

Figure 5.1.13 shows that with the HE-LHC we could find evidence for a composite Majorana neutrino with mass below $M(N_\ell) = 12$ TeV, for $\Lambda = M(N_\ell)$. Figure 5.1.14 shows the results for several values of Λ. The projection of the exclusion limits is also presented in Fig. 5.1.15 for the $(\Lambda, M(N_\ell))$ plane. We conclude that, given the model condition $\Lambda = M(N_\ell)$, the HE-LHC could exclude a heavy composite Majorana neutrino with mass up to 12.5 TeV in both $eeq\bar{q}'$ and $\mu\mu q\bar{q}'$ channels.

5.2 Leptoquarks and Z'

Leptoquarks are hypothetical particles that carry both baryon and lepton quantum numbers. They are colour-triplets and carry fractional electric charge. The spin of a LQ state is either 0 (scalar LQ) or 1 (vector LQ). At the LHC, the pair-production of LQs is possible via gluon-gluon fusion and quark-antiquark annihilation and the production cross section only depends on the mass of the LQ. For scalar LQs, it is known at NLO in perturbative QCD [412]. The LQ may also be singly produced, in association with a lepton, but the cross section is model dependent. New massive vector bosons, Z', are a common feature of NP models. Typically they are assumed to couple in a flavour independent fashion. However, it is possible to build models where these couplings are generation dependent and, after moving to the mass basis, become inter-generational. Constraints on such couplings are weaker for the third generation.

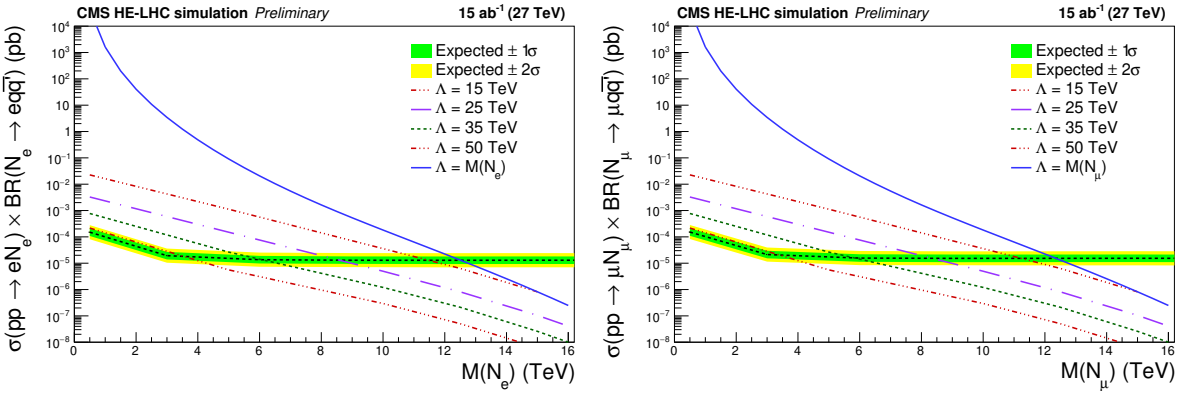

Fig. 5.1.14: Expected 95% C.L. upper limits for the HE-LHC projection of the $eeq\bar{q}'$ channel (left) and the $\mu\mu q\bar{q}'$ channel (right).

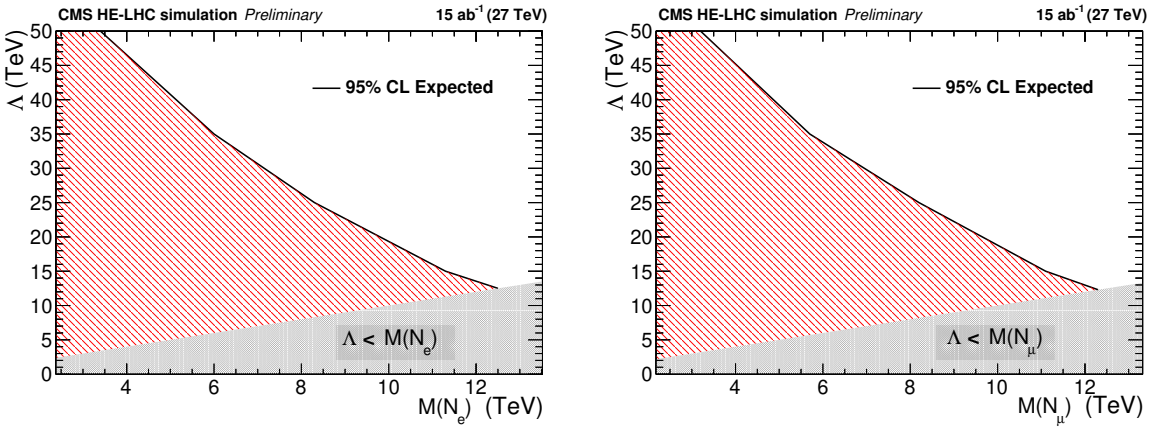

Fig. 5.1.15: Expected 95% C.L. lower limits (black lines) on the compositeness scale Λ, obtained in the analysis of the $eeq\bar{q}'$ (left) and the $\mu\mu q\bar{q}'$ (right) final states, as a function of the mass of the heavy composite Majorana neutrino for the HE-LHC projection. The grey zones are not allowed by the model.

Such models have been invoked to explain several B-physics anomalies.

In this section the reach of the HL-LHC for LQs in the $t + \tau$ and $t + \mu$ channel is discussed in Section 5.2.1. The reach of HL- and HE-LHC for models capable of explaining the B-physics anomalies is addressed in Section 5.2.2. HL-LHC searches for LQs in $b+\tau$ final states is discussed in Section 5.2.3, while the HE-LHC capability is considered in Section 5.2.4.

5.2.1 Leptoquark searches in t+τ and t+μ decays at HL-LHC

Contributors: J. Haller, R. Kogler, A. Reimers, CMS

The reach of searches for pair production of LQs with decays to $t + \mu$ and $t + \tau$ at CMS is studied for the HL-LHC with target integrated luminosities of $\mathcal{L}_{\text{int}}^{\text{target}} = 300\ \text{fb}^{-1}$ and $3\ \text{ab}^{-1}$ [413]. The studies are based on projecting signal and background event yields to HL-LHC conditions from published CMS results of the t+μ [414] and t+τ [415] LQ decay channels which use data from proton-proton collisions at $\sqrt{s} = 13$ TeV corresponding to $\mathcal{L}_{\text{int}} = 35.9\ \text{fb}^{-1}$ recorded in 2016. While the analysis strategies are kept unchanged with respect to the ones in Ref.s [414, 415], different total integrated luminosities, the higher c.o.m. energy of 14 TeV, and different scenarios of systematic uncertainties are considered. In the first scenario (denoted "w/ YR18 syst. uncert."), the relative experimental systematic uncertainties are scaled by a factor of $1/\sqrt{f}$, with $f = \mathcal{L}_{\text{int}}^{\text{target}}/35.9\ \text{fb}^{-1}$, until they reach a defined lower limit based

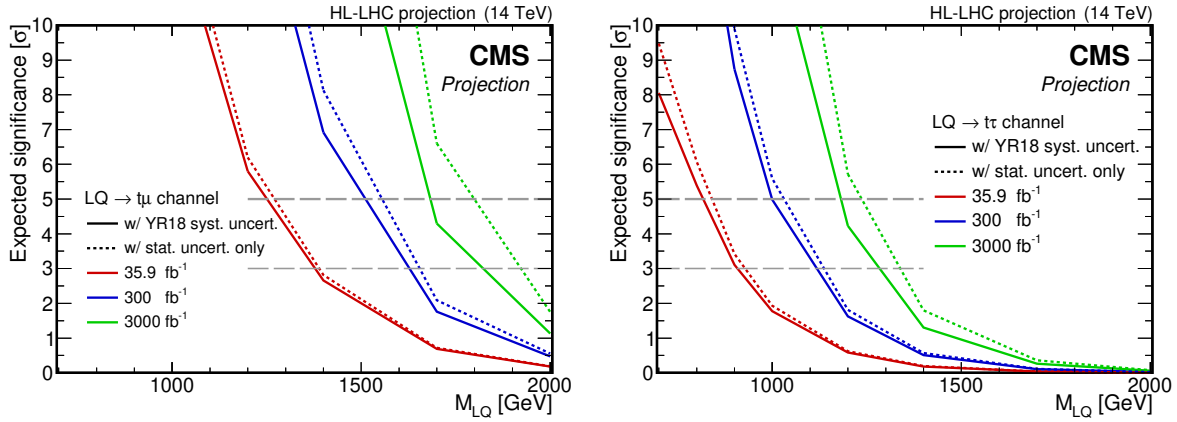

Fig. 5.2.1: Expected significances for an LQ decaying exclusively to top quarks and muons (left) or τ leptons (right).

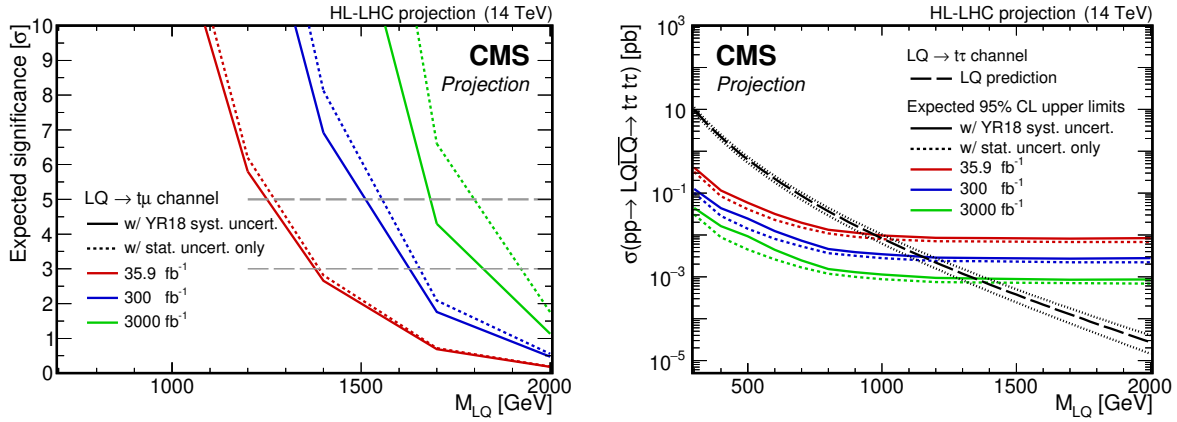

Fig. 5.2.2: Expected upper limits on the LQ pair production cross section at the 95% C.L. for an LQ decaying exclusively to top quarks and muons (left) or τ leptons (right).

on estimates of the achievable accuracy with the upgraded detector [8] as described in Section 1.2. The relative theoretical systematic uncertainties are halved. In the second scenario (denoted "w/ stat. uncert. only"), no systematic uncertainties are considered. The relative statistical uncertainties in both scenarios are scaled by $1/\sqrt{f}$.

Figure 5.2.1 presents the expected signal significances of the analyses as a function of the LQ mass for different assumed integrated luminosities in the "w/ YR18 syst. uncert." and "w/ stat. uncert. only" scenarios. Increasing the target integrated luminosity to $\mathcal{L}_{\text{int}}^{\text{target}} = 3\,\text{ab}^{-1}$ greatly increases the discovery potential of both analyses. The LQ mass corresponding to a discovery at 5σ significance with a dataset corresponding to $3\,\text{ab}^{-1}$increases by more than 500 GeV compared to the situation at $\mathcal{L}_{\text{int}}^{\text{target}} = 35.9\,\text{fb}^{-1}$, from about 1200 GeV to roughly 1700 GeV, in the LQ $\to t\mu$ decay channel. For LQs decaying exclusively to top quarks and τ leptons, a gain of 400 GeV is expected, pushing the LQ mass in reach for a 5σ discovery from 800 GeV to 1200 GeV.

In Fig. 5.2.2, the expected projected exclusion limits on the LQ pair production cross section are shown. Leptoquarks decaying only to top quarks and muons are expected to be excluded below masses of 1900 GeV for $3\,\text{ab}^{-1}$, which is a gain of 500 GeV compared to the limit of 1420 GeV obtained in the published analysis of the 2016 dataset [414]. The mass exclusion limit for LQs decaying exclusively to top quarks and τ leptons are expected to be increased by 500 GeV, from 900 GeV to approximately 1400 GeV.

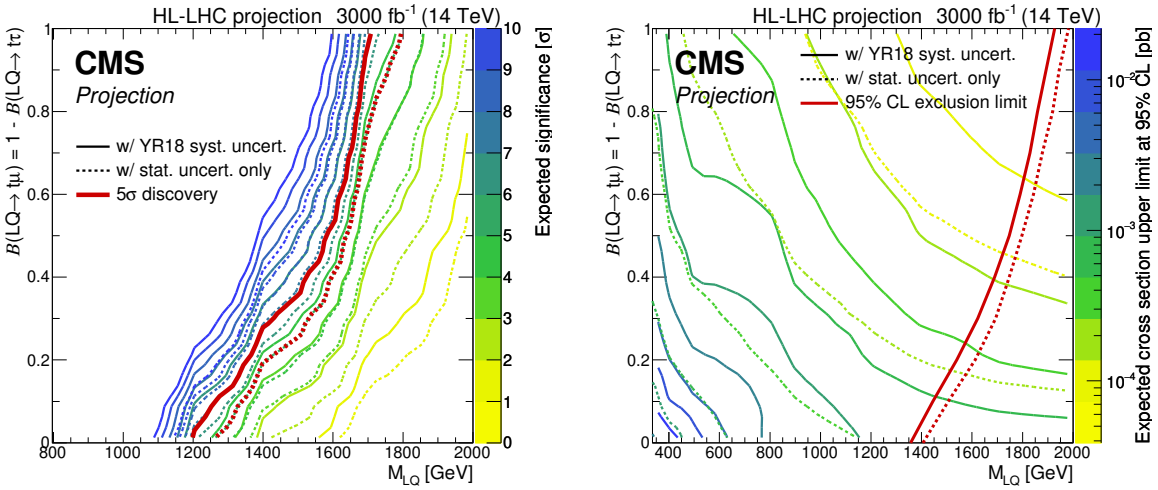

Fig. 5.2.3: Expected significances (left) and expected upper limits on the LQ pair-production cross section at the 95% C.L. (right) as a function of the LQ mass and the branching fraction. Colour-coded lines represent lines of a constant expected significance or cross section limit, respectively. The red lines indicate the 5σ discovery level (left) and the mass exclusion limit (right).

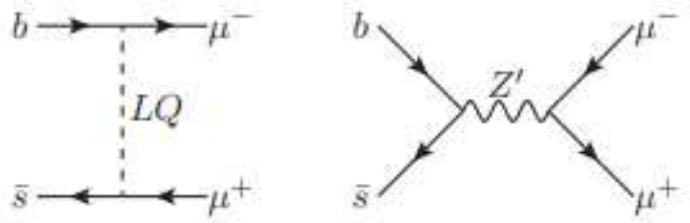

Fig. 5.2.4: Feynman diagrams of two simplified models for mediating an effective operator that explains discrepancies in $B \to K^{(*)}\mu^+\mu^-$ decays as compared to SM predictions. The diagram on the left hand side shows mediation by a scalar LQ, whereas the right-hand side shows mediation by a flavour dependent Z'.

Figure 5.2.3 shows the expected signal significances and upper exclusion limits on the pair production cross section of scalar LQs allowed to decay to top quarks and muons or τ leptons at the 95% C.L. as a function of the LQ mass and a variable branching fraction $\mathcal{B}(\text{LQ} \to t\mu) = 1 - \mathcal{B}(\text{LQ} \to t\tau)$ for an integrated luminosity of 3 ab^{-1}in the two different scenarios. For all values of $\mathcal{B}$, LQ masses up to approximately 1200 GeV and 1400 GeV are expected to be in reach for a discovery at the 5σ level and a 95% C.L. exclusion, respectively.

5.2.2 Z' and leptoquarks for B decay anomalies at HL- and HE-LHC

Contributors: B. Allanach, T. Tevong You

Recent measurements of R_K^* and other b observables indicate that the $\bar{b}P_L s\bar{\mu}P_L\mu$ vertex may be receiving BSM corrections. Here, we examine simplified models that may predict such corrections at the tree-level: Z' models and leptoquark models depicted in Fig. 5.2.4.

The 'naïve' Z' model contains the Lagrangian pieces

$$\mathcal{L}_{Z'}^{\text{min.}} \supset \left(g_L^{sb} Z'_\rho \bar{s}\gamma^\rho P_L b + \text{h.c.}\right) + g_L^{\mu\mu} Z'_\rho \bar{\mu}\gamma^\rho P_L \mu\,, \tag{5.2.1}$$

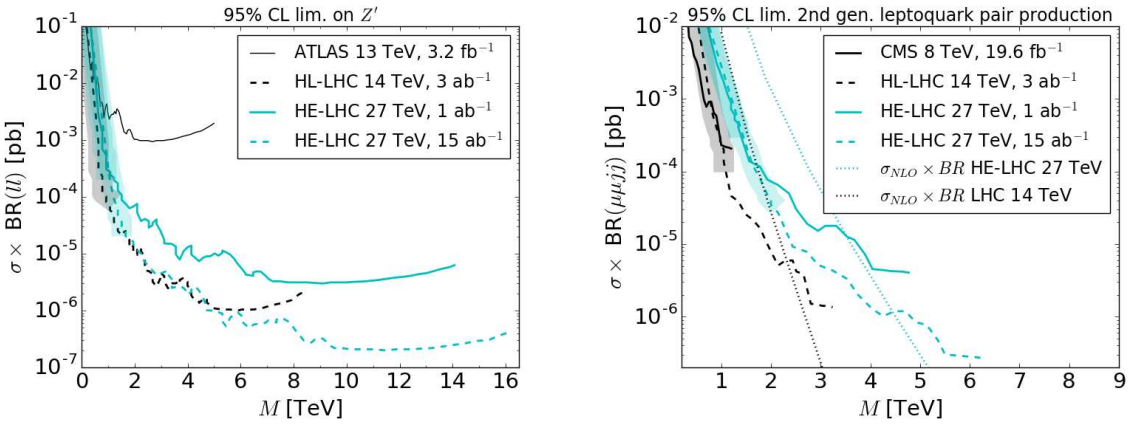

Fig. 5.2.5: Current bounds and projected sensitivities to the naïve Z' model. Left: bounds from a 3.2 fb^{-1} ATLAS Z' search in the $\mu^+\mu^-$ channel [419]. Right: bounds from a 19.6 fb^{-1} search for the process $gg \to \bar{S}_3 S_3 \to (\mu^- j)(\mu^+ j)$, these bounds were then used [420] to extrapolate to the HE-LHC and HL-LHC, and the predicted NLO production cross-sections for the production of the $S_3\bar{S}_3$ pairs.

whereas the more realistic '$33\mu\mu$' Z' model contains more couplings ($SU(2)_L$ and flavour copies):

$$\begin{aligned}\mathcal{L}^{33\mu\mu}_{Z'} \supset\, & g^q_L Z'_\rho \Big[\bar{t}\gamma^\rho P_L t + |V_{tb}|^2 \bar{b}\gamma^\rho P_L b + |V_{td}|^2 \bar{d}\gamma^\rho P_L d + |V_{ts}|^2 \bar{s}\gamma^\rho P_L s \\ & + \left(V_{tb}V^*_{ts}\bar{b}\gamma^\rho P_L s + V^*_{ts}V_{td}\bar{d}\gamma^\rho P_L s + V_{tb}V^*_{td}\bar{b}\gamma^\rho P_L d + \text{h.c.}\right) \\ & + g^{\mu\mu}_L \left(\bar{\mu}\gamma^\rho P_L \mu + \sum_{i,j} \bar{\nu}_i U_{i\mu}\gamma^\rho P_L U^*_{\mu j}\nu_j\right)\Big], \end{aligned} \tag{5.2.2}$$

where U denotes the PMNS matrix involved in lepton mixing. In a fit to 'clean' $b-$observables including $R_{K^{(*)}}$ Ref. [416], we have that, in the naïve Z' model,

$$|g^{sb}_L g^{\mu\mu}_L| = (1.0 \pm 0.25)\left(\frac{M_{Z'}}{31\text{ TeV}}\right)^2, \tag{5.2.3}$$

which we use to constrain the couplings and masses of the Z', (the $33\mu\mu$ model's Z' couplings to $\bar{s}b$ and $\mu^+\mu^-$ can also be matched to Eq. (5.2.1)).

There are particular combinations of quantum numbers allowed for the LQs [416–418], depending upon their spin. For the scalar case this is the triplet LQ S_3, with quantum numbers $(\bar{3}, 3, \frac{1}{3})$ under $SU(3)_c \times SU(2)_L \times U(1)_Y$ and mass M, whose Yukawa couplings to the third family left-handed quark and second family left-handed lepton doublets Q_3 and L_2 are of the form

$$y_{b\mu} Q_3 L_2 S_3 + y_{s\mu} Q_2 L_2 S_3 \text{h.c.}\,. \tag{5.2.4}$$

Its effect on the clean $b-$observables result in a constraint

$$|y_{sb} y_{b\mu}| = (1.00 \pm 0.25)\left(\frac{M}{31\text{ TeV}}\right)^2, \tag{5.2.5}$$

from the fit [416].

In Fig. 5.2.5, we display the projected sensitivities on the naïve Z' and scalar leptoquark models of the HE-LHC and HL-LHC, extrapolated from a 3.2 fb^{-1} ATLAS Z' resonance search in the $\mu^+\mu^-$ model as a function of Z' mass. The extrapolation is performed under the following approximations: changes in efficiency with respect to changing $\sqrt{s}$ or other changes to the operating environment are neglected, and

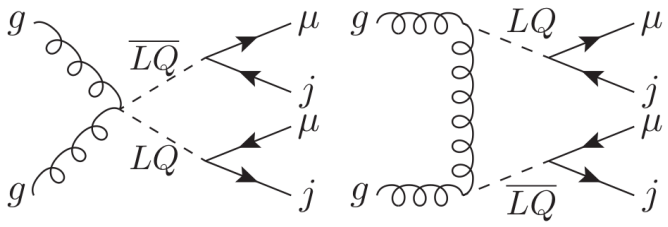

Fig. 5.2.6: Example processes contributing to $S_3\bar{S}_3$ production and subsequent decay at the LHC.

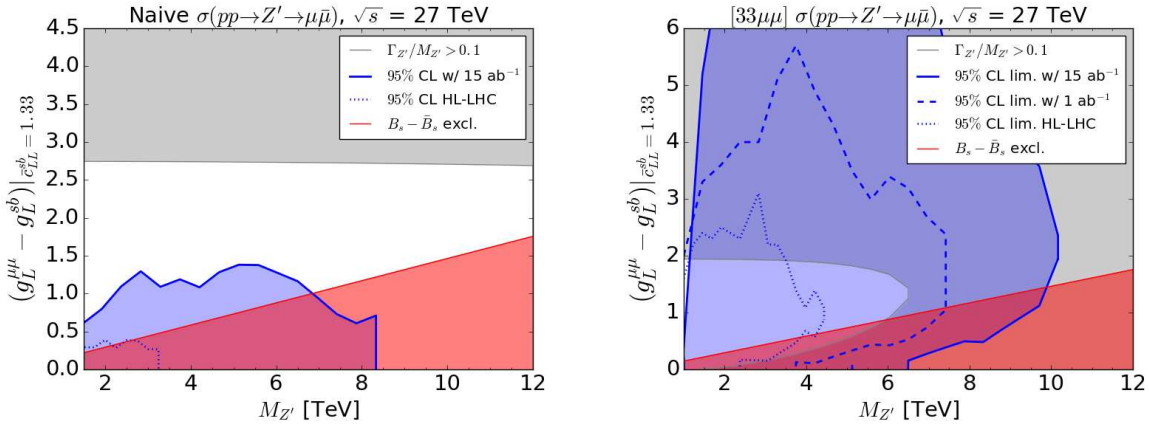

Fig. 5.2.7: Current bounds and projected sensitivities to Z' models explaining $R_{K^{(*)}}$. Each point in the plane has had the couplings adjusted to be consistent with the central value of Eq. (5.2.3). The red region is excluded from $B_s - \bar{B}_s$ mixing measurements, the blue region shows the expected 95% C.L. sensitive region and the greyed region is at width $\Gamma > 0.1 M_{Z'}$, meaning that the extrapolation used to calculate sensitivities (which uses the narrow width approximation) is inaccurate. The blue region shows the region of sensitivity. The vertical axis shows the difference between the muonic and the quark Z' coupling, initially intended to show when one is large compared to the other. However, the $B_s - \bar{B}_s$ mixing constraint implies that $g_L^{sb} \ll g_L^{\mu\mu}$ and so the vertical axis is equal to $g_L^{\mu\mu}$, to a good approximation.

the *narrow width* approximation is used. At strong coupling, the narrow width approximation becomes bad. In the right-hand plot, the sensitivity coming from the process $gg \to \bar{S}_3 S_3 \to \mu^+ j \mu^- j$ depicted in Fig. 5.2.6 is shown. The sensitivities are phrased in terms of production cross-section times BRs of final states on the vertical axis. In the LQ model, the production cross-section depends only upon the mass M of the LQ: its coupling is given by the QCD gauge coupling. We see that HL-LHC(HE-LHC) is sensitive to LQs of mass up to 2.5 (4.2) TeV for this topology. The $B_s - \bar{B}_s$ mixing constraint implies $\left|y_{b\mu} y^*_{s\mu}\right| < M/(26\ \text{TeV})$ for the S_3 LQ case. Combining this with Eq. (5.2.5) yields a bound $M < 40$ TeV[7] [416]. Thus, the HL-LHC and HE-LHC could probe a non-negligible fraction of the viable LQ parameter space.

For the Z' models, the production cross-section depends sensitively upon the coupling g_L^{bs}. If the coupling is large, Z's with masses up to 18 TeV can explain $R_K^{(*)}$ and still be compatible with bounds originating from $B_s - \bar{B}_s$ mixing measurements ($|g_L^{sb}| \leq M_{Z'}/148$ TeV) [416]. We display the relevant sensitivities and bounds upon flavourful Z' models in Fig. 5.2.7 as a function of coupling and mass. From the left hand panel, we see that the HL-LHC only probes a small fraction of the viable naïve Z' parameter space. However, when we examine more realistic model (the $33\mu\mu$ model) in the right-hand

[7] One can also consider singlet or triplet vector LQs whose joint constraints imply $M < 20, 40$ TeV, respectively, but whose sensitivities are equal to those of the S_3.

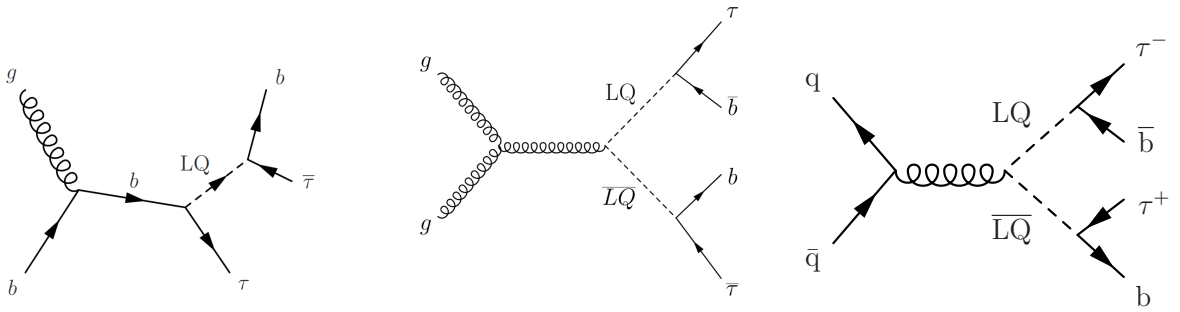

Fig. 5.2.8: Leading order Feynman diagrams for the production of a third-generation LQ in the single production s-channel (left) and the pair production channel via gluon fusion (centre) and quark fusion (right).

panel, we see that a large fraction of parameter space where the narrow width approximation applies is covered. These conclusions become stronger when one examines the sensitivity of the HE-LHC, as the solid lines display: the viable region of the $33\mu\mu$ model with narrow width approximation is completely covered, for example.

We note that the results presented herein represent only a rough estimation and further more detailed studies are desirable. In particular, the narrow width approximation in the case of the LQs is likely to be a rough approximation because one is really producing a pair of LQs. Our approximations effectively assume that they are produced at threshold. At higher luminosities or energies, the efficiency for identifying isolated muons will change, as well as the efficiencies for identifying jets. This could be better estimated by performing Monte-Carlo event generation studies together with a detector simulation rather than extrapolating current limits from the LHC.

5.2.3 Search for leptoquarks decaying to τ and b at HL-LHC

Contributors: Y. Takahashi, P. Matorras, CMS

Third-generation scalar LQs have recently received considerable interest from the theory community, as the existence of leptoquarks with large couplings can explain the anomaly in the $\overline{\mathrm{B}} \to \mathrm{D}\tau\overline{\nu}$ and $\overline{\mathrm{B}} \to \mathrm{D}^{*}\tau\overline{\nu}$ decay rates reported by the BaBar [421, 422], Belle [423–428], and LHCb [429] Collaborations.

This analysis from CMS [430] presents future discovery and exclusion prospects for singly and pair produced third-generation scalar LQs, each decaying to τ_h and a bottom quark. Here, τ_h denotes a hadronically decaying τ lepton. The relevant Feynman diagrams of the signal processes at leading order (LO) are shown in Fig. 5.2.8.

The analysis uses DELPHES [33] event samples of simulated pp collisions at a c.o.m. energy of 14 TeV, corresponding to integrated luminosities of 300 $\mathrm{fb}^{-1}$and 3 ab^{-1}. The matrix elements of LQ signals for both single and pair LQ production are generated at LO using version 2.6.0 of MADGRAPH5_aMC@NLO [67] for $m_{LQ} = 500$, 1000, 1500, and 2000 GeV. The branching fraction β of the LQ to a charged lepton and a quark, in this case LQ$\to \tau b$, is assumed to be $\beta = 1$. The unknown Yukawa coupling λ of the LQ to a τ lepton and a bottom quark is set to $\lambda = 1$. The width Γ is calculated using $\Gamma = m_{LQ}\lambda^2/(16\pi)$ [431], and is less than 10% of the LQ mass for most of the considered search range. The signal samples are normalised to the cross section calculated at LO, multiplied by a K factor to account for higher order contributions [432].

Similar event selections are used in both the singly and pair produced LQ searches, except for the requirement on the number of jets. In both channels, two reconstructed τ_h with opposite-sign charge are required, each with transverse momentum $p_{T,\tau} > 50$ GeV and a maximum pseudorapidity $|\eta_\tau| < 2.3$. In the search for single production, the presence of at least one reconstructed jet with $p_T > 50$ GeV is required, while at least two are required in the search for pair production. Jets are reconstructed with FASTJET [35], using the anti-k_{T} algorithm [34], with a distance parameter of 0.4.

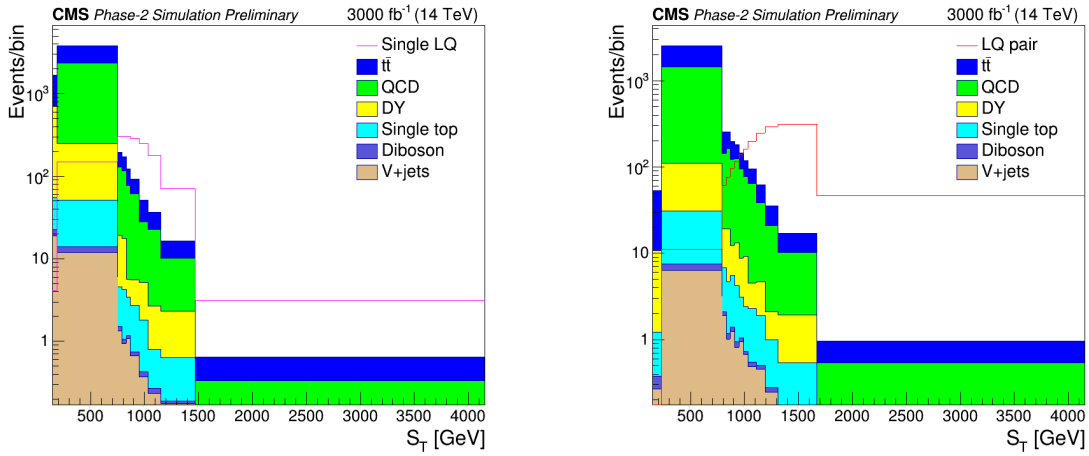

Fig. 5.2.9: Left: scalar sum of the p_T of the two selected τ leptons and the highest-p_T jet in the single LQ selection region. Right: scalar sum of the p_T of the two selected τ leptons and the two highest-p_T jets in the LQ pair search region. The considered backgrounds are shown as stacked histograms, while empty histograms for signals for the single LQ and LQ pair channels (for $m_{LQ} = 1000$ GeV) are overlaid to illustrate the sensitivity. Both signal and background are normalised to a luminosity of 3 ab^{-1}.

To reduce background due to Drell-Yan (particularly Z$\rightarrow \tau\tau$) events, the invariant mass of the two selected τ_h, $m_{\tau\tau}$, is required to be > 95 GeV. In addition, at least one of the previously selected jets is required to be b-tagged to reduce QCD multijet backgrounds. Finally, an event is rejected if it contains an identified and isolated electron (muon), with $p_T > 10$ GeV, $|\eta| < 2.4$ (2.5). The acceptance of the signal events is 4.9% (11%) for single (pair) production, where the branching ratio of two τ leptons decaying hadronically is included in the numerator of the acceptance.

Signal extraction is based on a binned maximum likelihood fit to the distribution of the scalar p_T sum S_T, which is defined as the sum of the transverse momenta of the two τ_h and either the highest-p_T jet in the case of single LQ production, or the two highest-p_T jets in the case of LQ pair production. These distributions are shown in Fig. 5.2.9 for the HL-LHC 3 ab^{-1} scenario.

Systematic uncertainties are calculated by scaling the current experimental uncertainties. For uncertainties limited by statistics, including the uncertainty on the DY (3.3%) and QCD (3.3%) cross sections, a scale factor of $1/\sqrt{\mathcal{L}}$ is applied, for an integrated luminosity ratio $\mathcal{L}$. For uncertainties coming from theoretical calculations, a scale factor of $1/2$ is applied with respect to current uncertainties, as is the case for the uncertainties on the cross section for top (2.8%) or diboson (3%) events. Other experimental systematic uncertainties are scaled by the square root of the integrated luminosity ratio until the uncertainty reaches a minimum value, including uncertainties on the integrated luminosity (1%), τ identification (5%) and b-tagging/misidentification (1%/5%).

Figure 5.2.10 shows an upper limit at 95% C.L. on the cross section times branching fraction β as a function of m_{LQ} by using the asymptotic CLs modified frequentist criterion [94, 95, 257, 433]. Upper limits are calculated considering two different scenarios. The first one, hereafter abbreviated as "stat. only" considers only statistical uncertainties, to observe how the results are affected by the increase of the integrated luminosity. The second scenario, hereafter abbreviated as "stat.+syst.," also includes the estimate of the systematic uncertainties at the HL-LHC. For the single LQ production search, the theoretical prediction for the cross section assumes $\lambda = 1$ and $\beta = 1$.

Comparing the limits with theoretical predictions assuming unit Yukawa coupling $\lambda = 1$, third-generation scalar leptoquarks are expected to be excluded at 95% C.L. for LQ masses below 730 (1250) GeV for a luminosity of 300 fb^{-1}, and below 1130 (1520) GeV for 3 ab^{-1} in the single (pair) production channel, considering both statistical and systematic uncertainties.

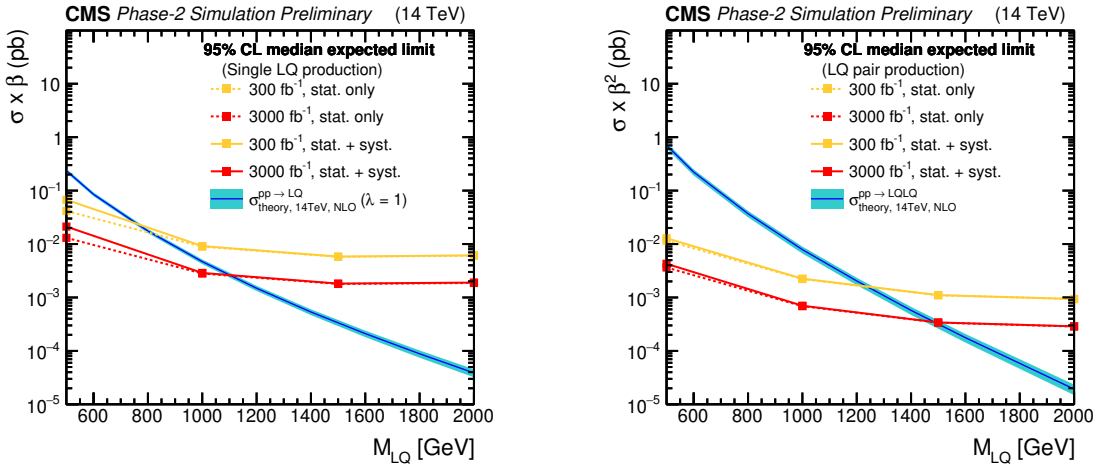

Fig. 5.2.10: Expected limits at 95% C.L. on the product of the cross section σ and the branching fraction β, as a function of the LQ mass, for the two high luminosity projections, 300 fb^{-1} (red) and 3 ab^{-1} (orange), for both the stat. only (dashed lines) and the stat.+syst. scenarios (solid lines). This is shown in conjunction with the theoretical predictions at NLO [432] in cyan. Projections are calculated for both the single LQ (left) and LQ pair production (right).

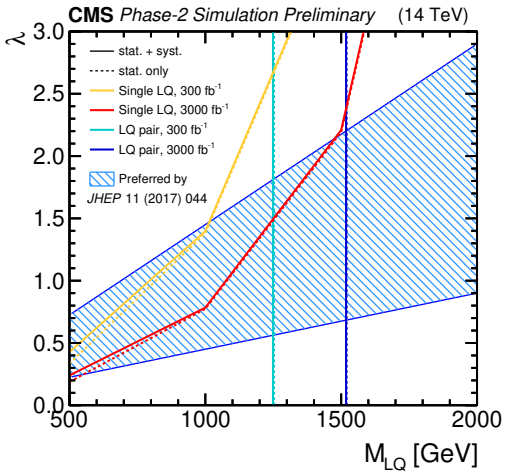

Fig. 5.2.11: Expected exclusion limits at 95% C.L. on the Yukawa coupling λ at the LQ-lepton-quark vertex, as a function of the LQ mass. A unit branching fraction β of the LQ to a τ lepton and a bottom quark is assumed. Future projections for 300 fb^{-1} and 3 ab^{-1} are shown for both the stat. only and stat.+syst. scenarios, shown as dashed and filled lines respectively, and for both the single LQ and LQ pair production, where the latter corresponds to the vertical line (since it does not depend on λ). The left hand side of the lines represents the exclusion region for each of the projections, whereas the region with diagonal blue hatching shows the parameter space preferred by one of the models proposed to explain anomalies observed in B physics [434].

Since the single-LQ signal cross section scales with λ^2, it is straightforward to recast the results presented in Fig. 5.2.10 in terms of expected upper limits on m_{LQ} as a function of λ, as shown in Fig. 5.2.11. The blue band shows the parameter space (95% C.L.) for the scalar LQ preferred by the B physics anomalies: $\lambda = (0.95 \pm 0.50) m_{LQ}(\mathrm{TeV})$ [434]. For the 300 (3000) fb^{-1} luminosity scenario, the leptoquark pair production channel is more sensitive if $\lambda < 2.7$ (2.3), while the single leptoquark production is dominant otherwise.

Using the predicted cross section [432] of the signal, it is also possible to estimate the maximal

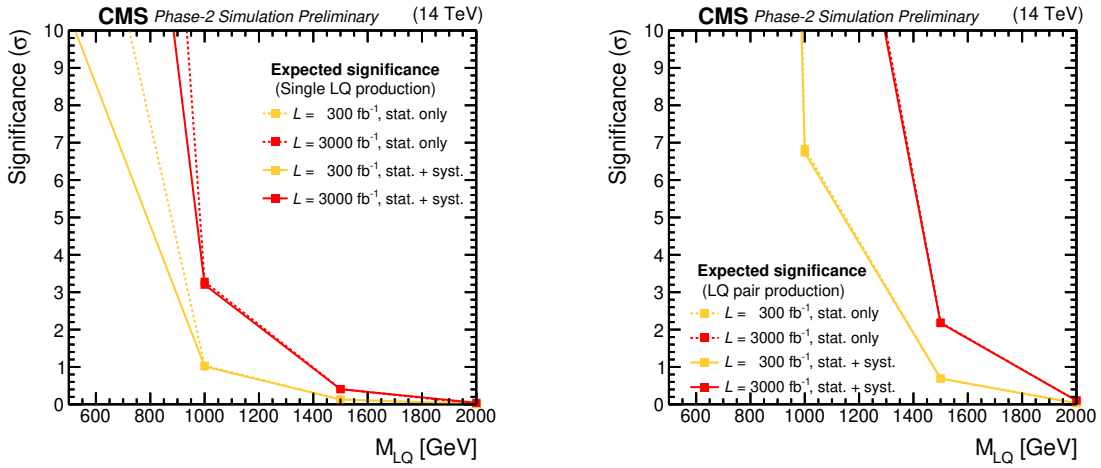

Fig. 5.2.12: Expected local significance of a signal-like excess as a function of the LQ mass, for the two high luminosity projections, 300 fb^{-1} (red) and 3 ab^{-1} (orange), assuming the theoretical prediction for the LQ cross section at NLO [432], calculated with $\lambda = 1$ and $\beta = 1$. Projections are calculated for both single LQ (left) and LQ pair production (right).

LQ mass expected to be in reach for a 5σ discovery. Figure 5.2.12 shows the expected local significance of a signal-like excess as a function of the LQ mass hypothesis.

In summary, this study shows that future LQ searches under higher luminosity conditions are promising, as they are expected to greatly increase the reach of the search. They also show that the pair production channel is expected to be the most sensitive. A significance of 5σ is within reach for LQ masses below 800 (1200) GeV for the single (pair) production channels in the 300 fb^{-1} scenario and 1000 (1500) GeV for the 3 ab^{-1} scenario.

5.2.4 HE-LHC sensitivity study for leptoquarks decaying to $\tau + b$

Contributors: A. Greljo and L. Mittnacht

We analysed the sensitivity of the 27 TeV pp collider with 15 ab^{-1} of integrated luminosity to probe pair production of the scalar and vector leptoquarks decaying to $(b\tau)$ final state. We investigated events containing either one electron or muon, one hadronically decaying tau lepton, and at least two jets. The signal events and the dominant background events $(t\bar{t})$ were generated with MADGRAPH5_aMC@NLO at leading-order. PYTHIA 6 was used to shower and hadronise events and DELPHES 3 was used to simulate the detector response. The scalar leptoquark (r_{23}) and the vector leptoquark (U_1) UFO model files were taken from Ref. [432].

To verify the procedure, we simulated the $t\bar{t}$ background and the scalar leptoquark signal at 13 TeV and compared to the predicted shapes in the S_T distribution from the existing CMS analysis [435]. After we verified the 13 TeV analysis, we simulated the signal and the dominant background events at 27 TeV. From these samples, we selected all events satisfying the particle content requirements and applied the lower cut in the S_T variable. The cut threshold was chosen to maximise $s/\sqrt{b}$ while requiring at least 2 expected signal events at an integrated luminosity of 15 ab^{-1}. In the case of the vector leptoquark we considered the Yang-Mills ($\kappa = 1$) and the minimal coupling ($\kappa = 0$) scenarios [432]. From the simulations of the scalar and vector leptoquark events, we found the ratio of the cross-sections, and assuming similar kinematics, we estimated the sensitivity also for the vector leptoquark U_1.

As shown in Fig. 5.2.13, the HE-LHC collider will be able to probe pair produced third generation scalar leptoquark (decaying exclusively to $b\tau$ final state) up to mass of $\sim$ 4 TeV and vector leptoquark up to $\sim$ 4.5 TeV and $\sim$ 5.2 TeV for the minimal coupling and Yang-Mills scenarios, respectively.

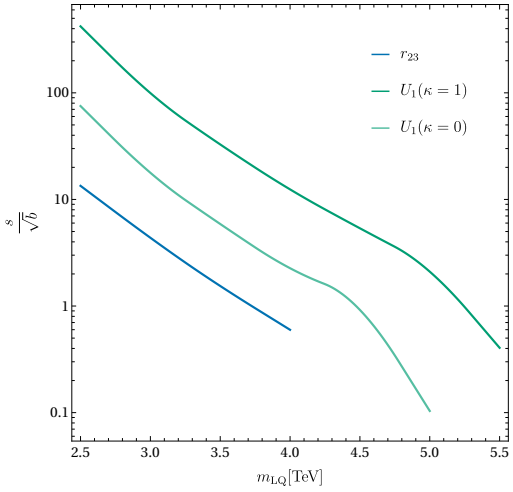

Fig. 5.2.13: Expected sensitivity for pair production of scalar (r_{23}) and vector (U_1) leptoquark at 27 TeV pp collider with an integrated luminosity of 15 ab^{-1}.

While this result is obtained by a rather crude analysis, it shows the impressive reach of the future high-energy pp-collider. In particular, the HE-LHC will cut deep into the relevant perturbative parameter space for $b \to c\tau\nu$ anomaly. As a final comment, this is a rather conservative estimate of the sensitivity to leptoquark models solving $R(D^*)$ anomaly, since a dedicated single leptoquark production search is expected to yield even stronger bounds [432, 434].

5.3 High p_T implications of flavour anomalies

Contributors: A. Celis, A. Greljo, L. Mittnacht, M. Nardecchia, T. You

Precision measurements of flavour transitions at low energies, such as flavour changing B, D and K decays, are sensitive probes of hypothetical dynamics at high energy scales. These can provide the first evidence of new BSM phenomena, even before direct discovery of new particles at high energy colliders. Indeed, the current anomalies observed in B-meson decays, the charge current one in $b \to c\tau\nu$ transitions, and neutral current one in $b \to s\ell^+\ell^-$, may be the first hint of new dynamics which is still waiting to be discovered at high-p_T. When considering models that can accommodate the anomalies, it is crucial to analyse the constraints derived from high-p_T searches at the LHC, since these can often rule out significant regions of model parameter space. Below we review these constraints, and assess the impact of the HL- and HE-LHC upgrades.

5.3.1 EFT analysis

If the dominant NP effects give rise to dimension-six SMEFT operators, the low-energy flavour measurements are sensitive to C/Λ^2, with C the dimensionless NP Wilson coefficient and Λ the NP scale. The size of the Wilson coefficient is model dependent, and thus so is the NP scale required to explain the $R_{D^{(*)}}$ and $R_{K^{(*)}}$ anomalies. Perturbative unitarity sets an upper bound on the energy scale below which new dynamics need to appear [436]. The conservative bounds on the scale of unitarity violation are $\Lambda_U = 9.2$ TeV and 84 TeV for $R_{D^{(*)}}$ and $R_{K^{(*)}}$, respectively, obtained when the flavour structure of NP operators is exactly aligned with what is needed to explain the anomalies. More realistic frameworks for flavour structure, such as MFV, $U(2)$ flavour models, or partial compositeness, give rise to NP effective operators with largest effects for the third generation. This results in stronger unitarity bounds, $\Lambda_U = 1.9$ TeV and 17 TeV for $R_{D^{(*)}}$ and $R_{K^{(*)}}$, respectively. These results mean that: *(i)* the mediators responsible for the $b \to c\tau\nu$ charged current anomalies are expected to be in the energy range of the LHC, *(ii)* the mediators responsible for the $b \to s\ell\ell$ neutral current anomalies could well be above the energy range of the LHC. However, in realistic flavour models also these mediators typically fall within

the (HE-)LHC reach.

If the neutrinos in $b \to c\tau\nu$ are part of a left-handed doublet, the NP responsible for $R_{D^{(*)}}$ anomaly generically implies a sizeable signal in $pp \to \tau^+\tau^-$ production at high-p_T. For realistic flavour structures, in which $b \to c$ transition is $\mathcal{O}(V_{cb})$ suppressed compared to $b \to b$, one expects rather large $bb \to \tau\tau$ NP amplitude. Schematically, $\Delta R_{D^{(*)}} \sim C_{bb\tau\tau}(1 + \lambda_{bs}/V_{cb})$, where $C_{bb\tau\tau}$ is the size of effective dim-6 interactions controlling $bb \to \tau\tau$, and λ_{bs} is a dimensionless parameter controlling the size of flavour violation. Recasting ATLAS 13 TeV, 3.2 fb^{-1} search for $\tau^+\tau^-$ [437], Ref. [438] showed that $\lambda_{bs} = 0$ scenario is already in slight tension with data. For $\lambda_{bs} \sim 5$, which is moderately large, but still compatible with FCNC constraints, HL (or even HE) upgrade of the LHC would be needed to cover the relevant parameter space implied by the anomaly (see Ref. [434]). For large λ_{bs} the limits from $pp \to \tau^+\tau^-$ become comparable with direct the limits on $pp \to \tau\nu$ from the bottom-charm fusion. The limits on the EFT coefficients from $pp \to \tau\nu$ were derived in Ref. [439], and the future LHC projections are promising. The main virtue of this channel is that the same four-fermion interaction is compared in $b \to c\tau\nu$ at low energies and $bc \to \tau\nu$ at high-p_T. Since the effective NP scale in $R(D^{(*)})$ anomaly is low, the above EFT analyses are only indicative. For more quantitative statements we review below bounds on explicit models.

The hints of NP in $R_{K^{(*)}}$ require a $(bs)(\ell\ell)$ interaction. Correlated effects in high-p_T tails of $pp \to \mu^+\mu^-(e^+e^-)$ distributions are expected, if the numerators (denominators) of LFU ratios $R_{K^{(*)}}$ are affected. Reference [440] recast the 13 TeV 36.1 fb^{-1} ATLAS search [441] (see also Ref. [442]), to set limits on a number of semi-leptonic four-fermion operators, and derive projections for HL-LHC (see Ref. [440]). These show that direct limits on the $(bs)(\ell\ell)$ operator from the tails of distributions will never be competitive with those implied by the rare B-decays [440,443]. On the other hand, flavour conserving operators, $(qq)(\ell\ell)$, are efficiently constrained by the high p_T tails of the distributions. The flavour structure of an underlining NP could thus be probed by constraining ratios $\lambda^q_{bs} = C_{bs}/C_{qq}$ with C_{bs} fixed by the $R_{K^{(*)}}$ anomaly. For example, in models with MFV flavour structure, so that $\lambda^{u,d}_{bs} \sim V_{cb}$, the present high-$p_T$ dilepton data is already in slight tension with the anomaly [440]. Instead, if couplings to valence quarks are suppressed, *e.g.*, if NP dominantly couples to the 3rd family SM fermions, then $\lambda^b_{bs} \sim V_{cb}$. Such NP will hardly be probed even at the HL-LHC, and it is possible that NP responsible for the neutral current anomaly might stay undetected in the high-p_T tails at HL-LHC and even at HE-LHC. Future data will cover a significant part of viable parameter space, though not completely, so that discovery is possible, but not guaranteed.

5.3.2 *Constraints on simplified models for $b \to c\tau\nu$*

Since the $b \to c\tau\nu$ decay is a tree-level process in the SM that receives no drastic suppression, models that can explain these anomalies necessarily require a mediator that contributes at tree-level:

- *SM-like W'*: A SM-like W' boson, coupling to left-handed fermions, would explain the approximately equal enhancements observed in $R(D)$ and $R(D^*)$. A possible realisation is a colour-neutral real $SU(2)_L$ triplet of massive vector bosons [444]. However, typical models encounter problems with current LHC data since they result in large contributions to $pp \to \tau^+\tau^-$ cross-section, mediated by the neutral partner of the W' [438,444,445]. For $M_{W'} \gtrsim 500$ GeV, solving the $R(D^{(*)})$ anomaly within the vector triplet model while being consistent with $\tau^+\tau^-$ resonance searches at the LHC is only possible if the related Z' has a large total decay width [438]. Focusing on the W', Ref. [446] analysed the production of this mediator via gg and gc fusion, decaying to $\tau\nu_\tau$. Reference [446] concluded that a dedicated search using that a b-jet is present in the final state would be effective in reducing the SM background compared to an inclusive analysis that relies on τ-tagging and $E_T^{\rm miss}$. Nonetheless, relevant limits will be set by an inclusive search in the future [439].

- *Right-handed W':* Ref.s [447,448] recently proposed that W' could mediate a right-handed interac-

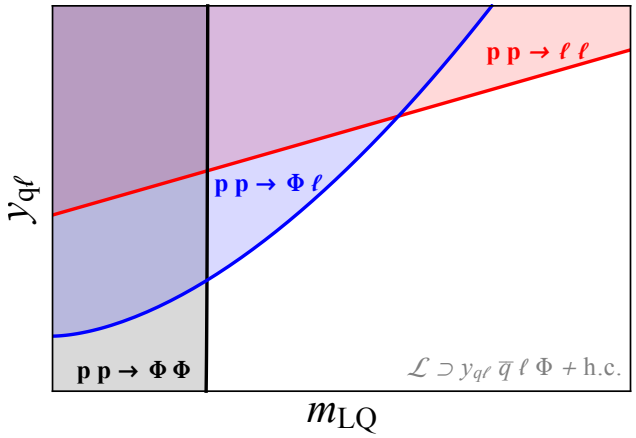

Fig. 5.3.1: Schematic of the LHC bounds on LQ showing complementarity in constraining the (m_{LQ}, y_{q_ℓ}) parameters. The three cases are: pair production $\sigma \propto y^0_{q_\ell}$, single production $\sigma \propto y^2_{q_\ell}$ and Drell-Yan $\sigma \propto y^4_{q_\ell}$ (from Ref. [432]).

tion, with a light sterile right-handed neutrino carrying the missing energy in the B decay. In this case, it is possible to completely uncorrelate FCNC constraints from $R(D^{(*)})$. The most constraining process in this case is instead $pp \to \tau\nu$. Reference [439] performed a recast of the latest ATLAS and CMS searches at 13 TeV and about 36 fb^{-1} to constrain most of the relevant parameter space for the anomaly.

• *Charged Higgs $H^\pm$:* Models that introduce a charged Higgs, for instance a two-Higgs-doublet model, also contain additional neutral scalars. Their masses are constrained by EW precision measurements to be close to that of the charged Higgs. Accommodating the $R(D^{(*)})$ anomalies with a charged Higgs typically implies large new physics contributions to $pp \to \tau^+\tau^-$ via the neutral scalar exchanges, so that current LHC data can challenge this option [438]. Note that a charged Higgs also presents an important tension between the current measurement of $R(D^*)$ and the measured lifetime of the B_c meson [449–452].

• *Leptoquarks:* The observed anomalies in charged and neutral currents appear in semileptonic decays of the B-mesons. This implies that the putative NP has to couple to both quarks and leptons at the fundamental level. A natural BSM option is to consider mediators that couple simultaneously quarks and leptons at the tree level. Such states are commonly referred as leptoquarks. Decay and production mechanisms of the LQ are directly linked to the physics required to explain the anomalous data.

– **Leptoquark decays:** the fit to the $R(D^*)$ observables suggest a rather light leptoquark (at the TeV scale) that couples predominately to the third generation fermions of the SM. A series of constraints from flavour physics, in particular the absence of BSM effects in kaon and charm mixing observables, reinforces this picture.
– **Leptoquark production mechanism:** The size of the couplings required to explain the anomaly is typically very large, roughly $y_{q\ell} \approx m_{LQ}/$ (1 TeV). Depending of the actual sizes of the leptoquark couplings and its mass we can distinguish three regimes that are relevant for the phenomenology at the LHC:

  1. LQ pair production due to strong interactions,
  2. Single LQ production plus lepton via a single insertion of the LQ coupling, and
  3. Non-resonant production of di-lepton through t-channel exchange of the leptoquark.

  Interestingly all three regimes provide complementary bounds in the (m_{LQ}, y_{q_ℓ}) plane, see Fig. 5.3.1.

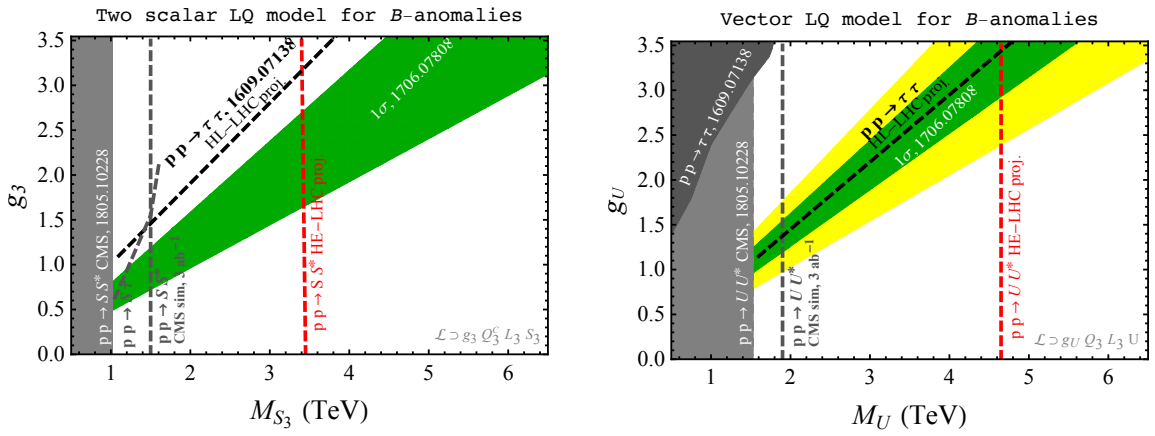

Fig. 5.3.2: Present constraints and HE and HL-LHC reach in the LQ mass versus coupling plane for the scalar leptoquark S_3 (left), and vector leptoquark U_1 (right). The grey and dark grey solid regions are the current exclusions. The grey and black dashed lines are the projected reach for HL-LHC (pair production prospects are based on Section 5.2.3). The red dashed lines are the projected reach at HL-LHC (see Section 5.2.4). The green and yellow bands are the 1σ and 2σ preferred regions from the fit to B physics anomalies. The second coupling required to fit the anomaly does not enter in the leading high-p_T diagrams but is relevant for fixing the preferred region shown in green, for more details see Ref. [434].

Several simplified models with a leptoquark as a mediator were shown to be consistent with the low-energy data. A vector leptoquark with $SU(3)_c \times SU(2)_L \times U(1)_Y$ SM quantum numbers $U_\mu \sim (\mathbf{3}, \mathbf{1}, 2/3)$ was identified as the only single mediator model which can simultaneously fit the two anomalies (see *e.g.* Ref. [434] for a recent fit including leading RGE effects). In order to substantially cover the relevant parameter space, one needs future HL- (HE-) LHC, see Fig. 5.3.2 (right) (see also Ref. [434] for details on the present LHC constraints). A similar statement applies to an alternative model featuring two scalar leptoquarks, S_1, S_3 [453], with the projected reach at CLIC and HL-LHC shown in Fig. 5.3.2 (left) (see Ref. [454] shows details on present LHC constraints).

Leptoquarks states are emerging as the most convincing mediators for the explanations of the flavour anomalies. It is then important to explore all the possible signatures at the the HL- and HE-LHC. The experimental program should focus not only on final states containing quarks and leptons of the third generation, but also on the whole list of decay channels including the off-diagonal ones ($b\mu$, $s\tau$, ...). The completeness of this approach would shed light on the flavour structure of the putative New Physics.

Another aspect to be emphasised concerning leptoquark models for the anomalies is the fact of the possible presence of extra fields required to complete the UV Lagrangian. The accompanying particles would leave more important signatures at high p_T than the leptoquark, this is particularly true for vector leptoquark extensions (see, for example, Ref. [455, 456]).

As a final remark, it is important to remember that the anomalies are not yet experimentally established. Among others, this also means that the statements on whether or not the high p_T LHC constraints rule out certain $R(D^{(*)})$ explanations assumes that the actual values of $R(D^{(*)})$ are given by their current global averages. If future measurements decrease the global average, the high $p_T$constraints can in some cases be greatly relaxed and HL- and/or HE-LHC may be essential for these, at present tightly constrained, cases.

5.3.3 Constraints on simplified models for $b \to sll$

The $b \to sll$ transition is both loop and CKM suppressed in the SM. The explanations of the $b \to sll$ anomalies can thus have both tree level and loop level mediators. Loop-level explanations typically

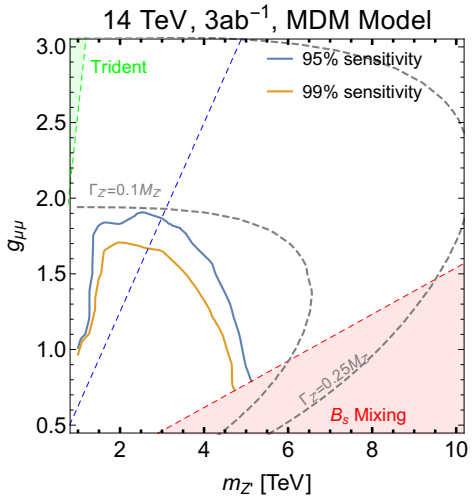

Fig. 5.3.3: HL-LHC 95% (blue) and 99% (orange) C.L. sensitivity contours to Z' in the "mixed-down" model for $g_{\mu\mu}$ vs Z' mass in TeV. The dashed grey contours give the Z' width as a fraction of mass. The green and red regions are excluded by trident neutrino production and B_s mixing, respectively. The dashed blue line is the stronger B_s mixing constraint from Ref. [457]. See also Section 5.2.2.

involve lighter particles. Tree-level mediators can also be light, if sufficiently weakly coupled. However, they can also be much heavier—possibly beyond the reach of the LHC.

• *Tree-level mediators:*
For $b \to sll$ anomaly there are two possible tree-level UV-completions, the Z' vector boson and leptoquarks, either scalar or vector. For leptoquarks, Fig. 5.2.5 (right) shows the current 95% C.L. limits from 8 TeV CMS with 19.6 fb^{-1} in the $\mu\mu jj$ final state (solid black line), as well as the HL-LHC (dashed black line) and 1 (10) ab^{-1} HE-LHC extrapolated limits (solid (dashed) cyan line). Dotted lines give the cross-sections times BR at the corresponding collider energy for pair production of scalar leptoquarks, calculated at NLO using the code of Ref. [412]. We see that the sensitivity to a leptoquark with only the minimal $b-\mu$ and $s-\mu$ couplings reaches around 2.5 and 4.5 TeV at the HL-LHC and HE-LHC, respectively. This pessimistic estimate is a lower bound that will typically be improved in realistic models with additional flavour couplings. Moreover, the reach can be extended by single production searches [420], albeit in a more model-dependent way than pair production. The cross section predictions for vector leptoquark are more model-dependent and are not shown in Fig. 5.2.5 (right). For $\mathcal{O}(1)$ couplings the corresponding limits are typically stronger than for scalar leptoquarks.

For the Z' mediator the minimal couplings in the mass eigenstate basis are obtained by unitary transformations from the gauge eigenstate basis, which necessarily induces other couplings. Reference [458] defined the "mixed-up" model (MUM) and "mixed-down" model (MDM) such that the minimal couplings are obtained via CKM rotations in either the up or down sectors respectively. For MUM there is no sensitivity at the HL-LHC. The predicted sensitivity at the HL-LHC for the MDM is shown in Fig. 5.3.3 as functions of Z' muon coupling $g_{\mu\mu}$ and the Z' mass, setting the Z' coupling to b and s quarks such that it solves the $b \to s\ell\ell$ anomaly. The solid blue (orange) contours give the 95% and 99% C.L. sensitivity. The red and green regions are excluded by B_s mixing [459] and neutrino trident production [460, 461], respectively. The more stringent B_s mixing constraint from Ref. [457] is denoted by the dashed blue line; see, however, Ref. [462] for further discussion regarding the implications of this bound. The dashed grey contours denote the width as a fraction of the mass. We see that the HL-LHC will only be sensitive to Z'' with narrow width, up to masses of 5 TeV.

At the HE-LHC, the reach for 10 ab^{-1} is shown in Fig. 5.3.4 for the MUM and MDM on the left and right, respectively. In this case the sensitivity may reach a Z' with wider widths up to 0.25 and 0.5 of its mass, while the mass extends out to 10 to 12 TeV. We stress that this is a pessimistic estimate of

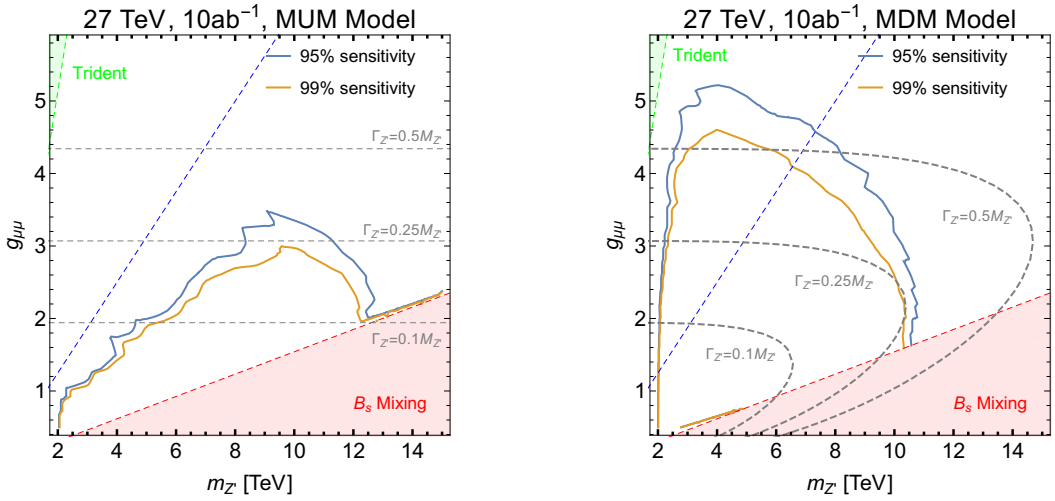

Fig. 5.3.4: HE-LHC 95% (blue) and 99% (orange) C.L. sensitivity contours to Z' in the "mixed-up" (left) and "mixed-down" (right) model in the parameter space of $g_{\mu\mu}$ vs Z' mass in TeV. The dashed grey contours are the width as a fraction of mass. The green and red regions are excluded by trident neutrino production and B_s mixing. The dashed blue line is the stronger B_s mixing constraint from Ref. [457]. See also Section 5.2.2.

the projected sensitivity, particular to the two minimal models; more realistic scenarios will typically be easier to discover.

• *Explanations at the one-loop level:*
It is possible to accommodate the $b \to s\ell^+\ell^-$ anomalies even if mediators only enter at one-loop. One possibility are the mediators coupling to right-handed top quarks and to muons [463–467]. Given the loop and CKM suppression of the NP contribution to the $b \to s\ell^+\ell^-$ amplitude, these models can explain the $b \to s\ell^+\ell^-$ anomalies for a light mediator, with mass around $\mathcal{O}(1)$ TeV or lighter. Constraints from the LHC and future projections for the HL-LHC were derived in Ref. [467] by recasting di-muon resonance, $pp \to t\bar{t}t\bar{t}$ and SUSY searches. Two scenarios were considered: *i)* a scalar LQ $R_2(3, 2, 7/6)$ combined with a vector LQ $\widetilde{U}_{1\alpha}(3, 1, 5/3)$, *ii)* a vector boson Z' in the singlet representation of the SM gauge group. Reference [466] also analysed the HL-LHC projections for the Z'. The constraints from the LHC already rule out part of the relevant parameter space and the HL-LHC will be able to cover much of the remaining regions. Dedicated searches in the $pp \to t\bar{t}t\bar{t}$ channel and a dedicated search for $t\mu$ resonances in $t\bar{t}\mu^+\mu^-$ final state can improve the sensitivity to these models [467].

6 Other BSM signatures

New physics models aimed at extending the SM either to overcome some of its theoretical puzzles, like the EW, flavour and strong CP "hierarchies", or by the need of explaining new phenomena, such as neutrino masses, Dark Matter, and baryogenesis, often predict signatures that are very different from the common SUSY ones, due to the absence of large missing transverse energy. These signatures are instead usually characterised by on-shell resonances, singly or doubly produced, depending on their quantum numbers, that decay into visible SM particles.

The lack so far of hints of new physics at the LHC, has typically required an increased level of complication in models addressing the aforementioned puzzles. Many of these complicated, though well motivated scenarios, are not always the best reference to clearly and simply evaluate the potential of a future collider. Often, as in the case of SUSY, considering simplified models inspired by more motivated, but involved constructions, constitutes the best choice to provide target experimental signatures. These targets are perfectly suited to evaluate the potential of future collider upgrades or new future colliders, and to compare them. Moreover, one can also try to answer questions such as what is the sensitivity to discriminate models given a discovery.

Usual standard scenarios include singly-produced resonances, with integer spin, decaying to two SM fermions or bosons, and pair-produced heavy fermion resonances, decaying to SM bosons and fermions. Most of these cases will be covered in this section, where the main "metric" to evaluate collider performances is the reach in the mass of these resonances, or the reach in covering a mass vs. coupling parameter space. The experimental signatures can be rather clean, like in the case of dilepton resonances, where the reach is usually limited by statistical uncertainties, or they can instead be affected by large SM backgrounds, especially in the hadronic channels, where the reach is typically limited by systematic uncertainties.

This section presents several results considering a broad variety of signatures and new physics scenarios. Of course the list is far from complete in terms of its coverage of possible BSM scenarios. However, it provides a clear and wide enough picture of the potential of the HL- and HE-LHC in terms of reach on heavy states, and coverage of their parameter space.

Finally, notwithstanding that the presented results contain a very detailed study of future prospects, that should serve as a reference for future studies, the global message of this section is that the HL-LHC will be able to extend the present LHC mass reach on heavy objects typically by $\sim 20 - 50\%$. Furthermore, HL-LHC will also be able to constrain, and potentially discover, new physics that is presently unconstrained. Concerning the HE-LHC, the conclusion is often a doubled mass reach, beyond HL-LHC, on heavy objects.

The results are presented considering a categorisation in terms of the spin of the studied resonances, which usually reflects in the final states considered. We therefore present sections containing spin 0 and 2 (Section 6.1), spin 1 (Section 6.2) and spin 1/2 resonances (Section 6.3). Additional prospect analyses that are more signature-based and could enter in more than one of the first three sections, have been collected in the last Section 6.4.

6.1 Spin 0 and 2 resonances

We present here several results concerning the production and decay of spin 0 and 2 particles decaying into several different SM final states. These range from resonant double Higgs production through a spin-2 KK graviton, to heavy scalar singlets that could mix with the Higgs, making the interplay with Higgs coupling measurements a crucial ingredient, from light pseudoscalar and axion-like particles to colour octet scalars.

6.1.1 *Resonant double Higgs production in the 4b final state at the HL-LHC*

Contributors: S. Willocq and A. Miller, ATLAS

The projection study in Ref. [468], summarised here, uses the search for high-mass spin-2 KK gravitons decaying into two Higgs bosons, HH, as a benchmark, with each of the Higgs bosons decaying to $b\bar{b}$, thereby yielding a final state with two highly boosted $b\bar{b}$ systems, which are reconstructed as two large-radius jets. The following strategy is followed to obtain sensitivity estimates at the HL-LHC: (i) signal and background mass distributions for the pair of candidate Higgs bosons in the event are taken from the most recent ATLAS data analysis at $\sqrt{s} = 13$ TeV [274] and scaled to 3 ab^{-1}; (ii) simulated signal and background mass distributions are used to derive mass-dependent scaling functions to extrapolate the distributions from $\sqrt{s} = 13$ TeV to 14 TeV; (iii) simulated signal and background mass distributions are used for further scaling of the distributions to reproduce the impact of additional selection criteria not included in Run-2 searches.

The dominant background for the 13 TeV data analysis stems from multijet production. This background source is estimated directly from data in that analysis and represents about 80%, 90%, and 95% of the total background in the signal region for events with 2, 3, and 4 b-tags (the classification of events based on the number of b-tags is described below). The remaining source of background originates almost completely from $t\bar{t}$ production. The shape of the dijet mass distribution for $t\bar{t}$ events is taken from MC samples. The normalisation of the $t\bar{t}$ background in Ref. [274] is extracted from a fit to the leading large-R jet mass distribution in the 13 TeV data. Samples of simulated multijet background events are generated to derive scaling functions to be applied to the background predictions from the 13 TeV data analysis. These samples are generated at both $\sqrt{s} = 13$ TeV and $\sqrt{s} = 14$ TeV. Two different sets of MC samples are used to study the impact of differences in jet flavour composition on the multijet background scaling functions. The first set of events corresponds to the $2 \to 2$ processes $pp \to jj$ (with $j = g$ or q) generated with PYTHIA 8 with truth jet p_T in the range between 400 and 2500 GeV. The second set of events corresponds to the $2 \to 4$ processes $pp \to bbbb$ generated with MADGRAPH5_aMC@NLO requiring b-quarks to have p_T above 100 GeV and the events are required to have at least one b-quark with p_T above 200 GeV.

Large-radius jets are used in the analysis. They are built from generated particles with the anti-k_t algorithm operating with a radius parameter $R = 1.0$. Previous studies indicate that the trimming effectively removes the impact of pileup up to $\mu = 300$ [469]. Small-radius jets are built from generated charged particles with the anti-k_t algorithm and a radius of $R = 0.2$. Only charged particles with $p_T > 0.5$ GeV are used in the clustering to emulate the track jets used in the 13 TeV data analysis.

The event selection applied to the truth-level analysis proceeds similarly to that used for the 13 TeV data analysis. Three regions in the plane formed by the leading large-R jet mass and the subleading large-R jet mass are used in the analysis. The signal region is defined by the requirement $X_{HH} < 1.6$, with X_{HH} defined as

$$X_{HH} = \sqrt{\left(\frac{m_{\mathrm{J}}^{\mathrm{lead}} - 125\ \mathrm{GeV}}{0.1\, m_{\mathrm{J}}^{\mathrm{lead}}}\right)^2 + \left(\frac{m_{\mathrm{J}}^{\mathrm{subl}} - 120\ \mathrm{GeV}}{0.1\, m_{\mathrm{J}}^{\mathrm{subl}}}\right)^2}, \tag{6.1.1}$$

where m_J is the large-R jet mass. The choices made to define the control and sideband regions are driven by the need to select events that are kinematically similar to those in the signal region while providing sufficiently large samples to derive the background estimate from the sideband region and validate it in the control region.

For the 13 TeV data analysis, the dominant multijet background is estimated with a data-driven approach which utilises events with a smaller number of b-tags in the sideband region. The events used for this estimation are required to have the same track-jet topology as in the event categories in which they are used to model the background. Events with 1 b-tag are used to model the background in the 2-tag category. Likewise, events with 2 b-tags are used to model the background in the 3- and 4-tag

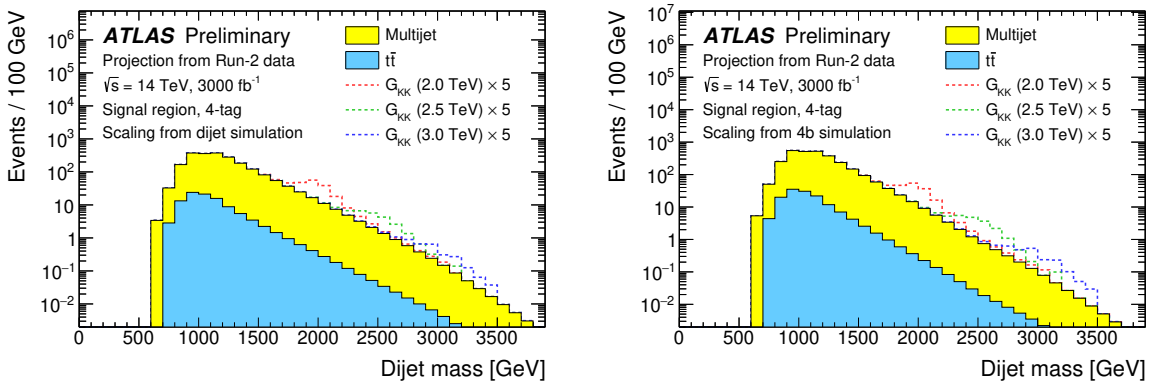

Fig. 6.1.1: Dijet mass distributions from the truth-level analysis for 4-tag events in the signal region for the expected background and signals at the HL-LHC. The multijet background is scaled using either the dijet (left) or the $4b$ multijet (right) MC samples. The event yields for signal events at G_{KK} masses of 2.0, 2.5, and 3.0 TeV are scaled up for visibility.

categories. Various checks performed show that either multijet simulation can be used reliably to predict the shape of the dijet mass distributions. However, differences in the flavour content of the large-R jets in the dijet and $4b$ multijet MC samples do affect the predicted background yields in the following study and the two samples are used to extract a range of projections at the HL-LHC.

As mentioned above, the projection for the HL-LHC proceeds in three steps. At first, the dijet mass distributions for signal and both multijet and $t\bar{t}$ background events from the 13 TeV data analysis in Run-2 are scaled from 36.1 fb^{-1} to 3 ab^{-1}. The background distributions are further scaled with mass-dependent functions to extrapolate from $\sqrt{s} = 13$ TeV to 14 TeV. These functions take into account both increases in cross section and changes in detector performance from the Run-2 ATLAS detector to the future upgraded detector at the HL-LHC. Further mass-dependent scaling is applied to all signal and background distributions to reflect improvements in the reconstruction of highly boosted jets, as obtained by using variable-radius track jets [470] instead of fixed-radius ($R = 0.2$) track jets, or in the background suppression by applying a requirement on the maximum number of charged particles associated with each large-R jet.

The first improvement relative to the 13 TeV data analysis arises from the use of variable-radius track jets. This circumvents the problem that $R = 0.2$ track jets from the $H \to b\bar{b}$ decay start merging for Higgs boson p_T values larger than approximately $2m_H/R = 1250$ GeV. The second improvement relative to the 13 TeV data analysis is the requirement of a maximum number of charged particles associated with large-R jets to exploit differences between quark- and gluon-initiated jets, the latter being an important component of the multijet background. The impact of pileup at $\mu = 200$ has been studied for charged particle tracks with $p_T > 1$ GeV associated with the primary vertex. In the case of $t\bar{t}$ events, the average number of tracks associated with the primary vertex increases by about 15% due to pileup. Further pileup suppression is possible with additional requirements on the longitudinal impact parameter or track-vertex association probability. Both leading and subleading large-R jets are required to have fewer than 20 charged particles with $p_T > 1$ GeV and $\Delta R < 0.6$ with respect to the jet axis.

The dijet mass distributions at $\sqrt{s} = 14$ TeV with 3 ab^{-1}resulting from the scaling procedure described above, including variable-radius track jets and the requirement on the maximum number of charged particles per large-R jet, are shown in Fig. 6.1.1 for 4-tag events in the signal region using either the dijet (left) or the $4b$ multijet (right) MC samples. Systematic uncertainties are scaled down by factors of two or more (where applicable) relative to the values from the 13 TeV data analysis to account for the increased precision available with 3 ab^{-1}at the HL-LHC.

Upper limits on $\sigma \times \mathcal{B}$ at $\sqrt{s} = 14$ TeV range from 1.44 fb (1.82 fb) at a mass of 1.0 TeV to

Model	$\sqrt{s} = 13$ TeV, 36.1 fb^{-1} as in Ref. [274]	$\sqrt{s} = 14$ TeV, 3 ab^{-1} dijet scaling	$\sqrt{s} = 14$ TeV, 3 ab^{-1} $4b$ scaling
$k/\overline{M}_{\mathrm{Pl}} = 0.5$	no limit	2.15 TeV	2.00 TeV
$k/\overline{M}_{\mathrm{Pl}} = 1.0$	1.36 TeV	2.95 TeV	2.75 TeV

Table 6.1.1: Expected 95% C.L. lower limits on G_{KK} mass for the 13 TeV data analysis and the extrapolation to the HL-LHC for $k/\overline{M}_{\mathrm{Pl}} = 0.5$ and 1.0 in the bulk RS model. Different extrapolations are provided based on modelling of the changes in multijet background using either the dijet or the $4b$ multijet MC samples.

0.025 fb (0.040 fb) at a mass of 3.0 TeV when dijet ($4b$) scaling and the variable-radius track jets with a maximum requirement on the number of charged particles are applied. The benefit from the use of variable-radius track jets becomes significant at the highest resonance masses considered here, with an improvement in the upper limits of at least 24% (depending on the choice of scaling) at 3.0 TeV. The additional requirement on the maximum number of charged particles further improves the upper limits by factors of about 20% and 45% at masses of 2.0 and 3.0 TeV, respectively. Systematic uncertainties have a modest impact on the limits with an effect of at most 20% at 1.0 TeV and decreasing to $\sim 5\%$ at high mass. The lower mass limits on KK gravitons are summarised in Table 6.1.1, evaluated at the 95% C.L., using either the dijet MC samples or the $4b$ multijet MC samples to model the changes in the multijet background relative to the background predictions from the 13 TeV data analysis.

6.1.2 VBF production of resonances decaying to HH in the 4b final state at HL-LHC

Contributors: A. Carvalho, J. Komaragiri, D. Majumder, L. Panwar, CMS

Several BSM scenarios predict the existence of resonances decaying to a pair of Higgs bosons, H [3, 4, 471], such as warped extra dimensional (WED) models [472], which have a spin-0 radion [473–475] and a spin-2 first Kaluza–Klein (KK) excitation of the graviton [476–478]. Others, such as the two-Higgs doublet models [479] (particularly, the MSSM [480]) and the Georgi-Machacek model [481] also contain spin-0 resonances. These resonances may have a sizeable branching fraction to a Higgs pair.

Searches for a new particle X in the HH decay channel have been performed by the ATLAS [482–484] and CMS [485–489] Collaborations in proton-proton (pp) collisions at $\sqrt{s} = 7$ and 8 TeV. The ATLAS Collaboration has set limits on the production of a KK bulk graviton decaying to HH in the final state with a pair of b quark and antiquark, $b\bar{b}b\bar{b}$, using pp collision data at $\sqrt{s} = 13$ TeV [274, 490, 491]. The CMS Collaboration has also set limits on the production of a KK bulk graviton and a radion, decaying to HH, in the $b\bar{b}b\bar{b}$ final state, using pp collision data at $\sqrt{s} = 13$ TeV, corresponding to an integrated luminosity of 35.9 fb^{-1} [492, 493]. At present, the searches from ATLAS and CMS set a limit on the production cross sections and the branching fractions $\sigma(pp \to X)\mathcal{B}(X \to HH \to b\bar{b}b\bar{b})$ for masses of X, m_X up to 3 TeV.

The searches were confined to the s-channel production of a narrow resonance X from the SM quark-antiquark or gluon-gluon interactions. The WED models that were used in the interpretations of the results have extra spatial dimension compactified between two branes (called the bulk) via an exponential metric κl, where κ is the warp factor and l the coordinate of the extra spatial dimension [494]. The reduced Planck scale, $\overline{M_{\mathrm{Pl}}} \equiv M_{\mathrm{Pl}}/8\pi$, M_{Pl} being the Planck scale and the ultraviolet cutoff of the theory $\Lambda_{\mathrm{R}} \equiv \sqrt{6}e^{-\kappa l}\overline{M_{\mathrm{Pl}}}$ [473] are fundamental scales in these models. A radion of mass below 1.4 TeV is excluded, assuming $\Lambda_{\mathrm{R}} = 3$ TeV, while the cross section limit for a bulk graviton decaying to $HH \to b\bar{b}b\bar{b}$ is between 1.4 and 4 fb for masses between 1.4 and 3.0 TeV, at 95% C.L. [492, 493].

The search for these resonances in other production modes, such as VBF, as depicted in Fig. 6.1.2, has not yet been explored. While the s-channel production cross section of a bulk graviton, assuming

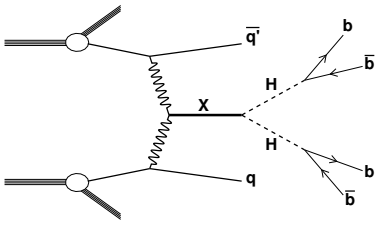

Fig. 6.1.2: Diagrammatic representation of the vector boson fusion production of a resonance X decaying to a pair of Higgs bosons H, with both Higgs bosons decaying to $b\bar{b}$ pairs.

$\kappa/\overline{M_{\rm Pl}} = 0.5$, is in the range $0.05 - 5$ fb for masses between 1.5 and 3 TeV, the VBF production mode is expected to have a cross section an order of magnitude smaller [495]. The absence of a signal from the s-channel process may point to highly suppressed couplings of X with the SM quarks and gluons, making VBF the dominant production process in pp collisions.

Here we explore the prospects for the search for a massive resonance produced through VBF and decaying to HH at the HL-LHC with the upgraded CMS detector. For a very massive resonance, highly Lorentz-boosted Higgs bosons are more efficiently reconstructed as a single large-area jet (Higgs jet). In addition, a signal event will also have two energetic jets at large pseudorapidity η. This study from the CMS Collaboration is reported in detail in Ref. [496]

A simulation of the upgraded Phase 2 CMS detector was used for this study. Signal events for bulk gravitons were simulated at leading order using MADGRAPH5_aMC@NLO 2.4.2 [67] for masses in the range 1.5 to 3 TeV and for a fixed width of 1% of the mass. The NNPDF3.0 leading order PDFs [121], taken from the LHAPDF6 PDF set [497–500], with the four-flavour scheme, were used. The main background is given by multijet events, and has been simulated using PYTHIA 8.212 [68], for events containing two hard partons, with the invariant mass of the two partons required to be greater than 1 TeV.

For both the signal and the background processes, the showering and hadronisation of partons was simulated with PYTHIA 8. The pileup events contribute to the overall event activity in the detector, the effect of which was included in the simulations assuming a pileup distribution averaging to 200. All generated samples were processed through a GEANT4-based [53, 54] simulation of the upgraded CMS detector.

The two leading-p_T large-radius anti-$k_{\rm T}$ jets with a distance parameter of 0.8 (AK8) in the event, J_1 and J_2, are required to have $p_T > 300$ GeV and $|\eta| < 3.0$. To identify the two leading-p_T AK8 jets with the boosted $H \to b\bar{b}$ candidates from the $X \to HH$ decay (H tagging), these jets are groomed [501] to remove soft and wide-angle radiation using the modified mass drop algorithm [502, 503], with the soft radiation fraction parameter z set to 0.1 and the angular exponent parameter β set to 0, also known as the soft-drop algorithm [504, 505]. By undoing the last stage of the jet clustering, one gets two subjets each for J_1 and J_2. The invariant mass of the two subjets is the soft-drop mass of each AK8 jet, which has a distribution with a peak near the Higgs boson mass $m_H = 125$ GeV [506, 507], and a width of about 10%. The soft-drop mass window selection was optimised using a figure of merit of $S/\sqrt{B}$ and required to be in the range $90 - 140$ GeV for both leading jets.

The N-subjettiness ratio $\tau_{21} \equiv \tau_2/\tau_1$ [508] has a value much smaller than unity for a jet with two subjets. For signal selection, J_1 and J_2 are required to have $\tau_{21} < 0.6$ following an optimisation of the above figure of merit.

The H tagging of J_1 and J_2 further requires identifying their subjet pairs to be b tagged with a

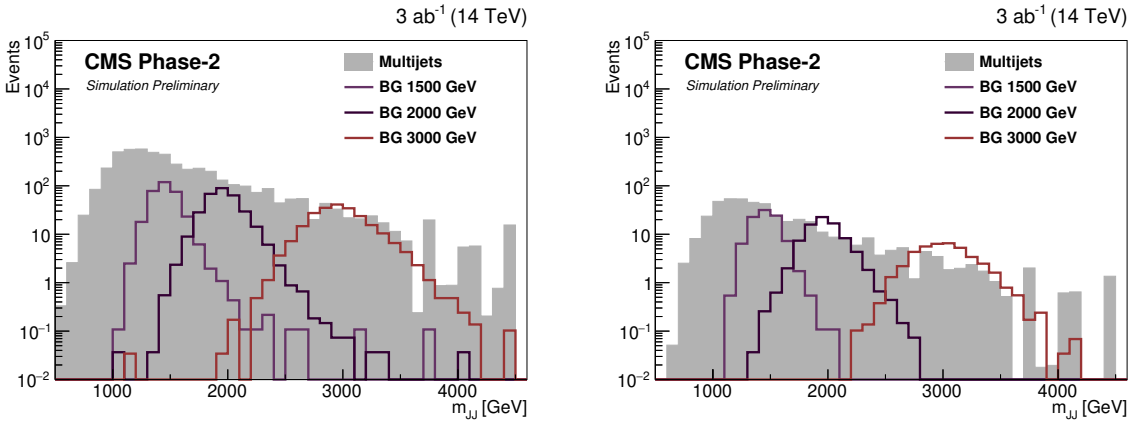

Fig. 6.1.3: Estimated multijet background and the signal m_{JJ} distributions for bulk gravitons (BG) of masses 1.5, 2, and 3 TeV, assuming a signal cross section of 1 fb. The distributions on the left are for the $3b$ and those on the right are for the $4b$ subjet b-tagged categories and for an average pileup of 200.

Process	$3b$ category		$4b$ category	
	Events	Efficiency (%)	Events	Efficiency (%)
Multijets	4755	1.6×10^{-3}	438	1.5×10^{-4}
BG (m_X =1.5 TeV)	326	11	95.2	3.2
BG (m_X =2 TeV)	316	11	81.2	2.7
BG (m_X =3 TeV)	231	7.7	41.4	1.4

Table 6.1.2: Event yields and efficiencies for the signal and multijet background for an average pileup of 200. The product of the cross sections and branching fractions of the signals $\sigma(pp \to X\text{jj} \to HH\text{jj})$ is assumed to be 1 fb. Owing to the large sample sizes of the simulated events, the statistical uncertainties are small.

probability of about 49% to contain at least one b hadron, and a corresponding probability of about 1% of having no b or c hadrons. Events are classified into two categories: those having exactly three out of the four b-tagged subjets ($3b$ category), and those that have all four subjets b-tagged ($4b$ category).

Events are required to have at least two AK4 jets j_1 and j_2, which are separated from the H jets by $\Delta R > 1.2$, with $p_T > 50$ GeV and $|\eta| < 5$. To pass the VBF selections, these jets must lie in opposite η regions of the detector, and a pseudorapidity difference $|\Delta\eta(j_1, j_2)| > 5$. The invariant mass m_{jj} reconstructed using these AK4 jets is required to pass $m_{jj} > 300$ GeV.

The bulk graviton invariant mass m_{JJ} is reconstructed from the 4-momenta of the two Higgs jets in events passing the above mentioned full selection criteria. The main multijet background is smoothly falling, above which the signal is searched for as a localised excess of events for a narrow resonance X.

It is expected that the multijet background component in a true search at the HL-LHC will rely on the data for a precise estimate. Methods such as those described in Ref. [492] are known to provide an accurate prediction of the multijet background m_{JJ} shape as well as the yield.

The simulated multijet background sample consists of ~ 4 million events none of which survive the full selection. To estimate the background, the subjet b-tagging efficiency is determined using a loose set of selection criteria which require events to have J_1 and J_2 passing only the soft-drop mass and τ_{21} requirements. The b-tagging efficiency is obtained for the different subjet flavours and as a function of p_T and η.

Multijet events passing all selection criteria except the subjet b tagging are then reweighted according to the subjet efficiencies to obtain the probability of the event to pass the three of four subjet b-tagging categories. The m_{JJ} distributions for the multijet background after the full selection are then

obtained from the weighted events in these two categories.

From the analysis of current LHC data at $\sqrt{s} = 13$ TeV, it was found that the multijet backgrounds measured in data are a factor of 0.7 smaller than estimated in simulation. Accordingly, the multijet background yield from simulation has been corrected by this factor, assuming this to hold also for the simulations of the multijet processes at $\sqrt{s} = 14$ TeV . The m_{JJ} of the backgrounds thus obtained and the signals are shown in Fig. 6.1.3, while the event yields after full selection are given in Table 6.1.2.

The efficiency of events to pass the VBF jet selection depends strongly on pileup due to the combinatorial backgrounds from pileup jets, which affects both the signal and the background selection. Moreover, the VBF selection efficiency for multijets grows faster than the signal efficiency with pileup, since the latter has true VBF jets which already pass the selection in the absence of pileup. Hence, in the present search, the requirement of additional VBF jets does not result in any appreciable gain in the signal sensitivity. It is anticipated that developments in the rejection of pileup jets in the high η region will eventually help suppress the multijets background and improve the signal sensitivity further.

The expected significance of the signal, assuming a production cross section of 1 fb is estimated. Several systematic uncertainties are considered. The uncertainty in the jet energy scale amounts to 1%. The uncertainty in the subjet b-tagging efficiency difference between the data and simulations is taken to be 1%. An uncertainty of 1% is assigned to the integrated luminosity measurement. These uncertainties are based on the projected values for the full data set at the HL-LHC.

In addition, several measurement uncertainties are considered based on the 2016 search for a resonance decaying to a pair of boosted Higgs bosons [492], which are scaled down by a factor of 0.5 for the HL-LHC study. The H jet selection uncertainties include the uncertainties in the H jet mass scale and resolution (1%), the uncertainty in the data to simulation difference in the selection on τ_{21} (13%), and the uncertainty in the showering and hadronisation model for the H jet (3.5%). The uncertainties in the signal acceptance because of the parton distribution functions (1%) and the simulation of the pileup (1%) are also taken into account

The expected signal significance of a bulk graviton of mass 2000 GeV, produced through vector boson fusion, with an assumed production cross section of 1 fb and decaying into a pair of Higgs bosons, each of which decays to a $b\bar{b}$ pair is found to be 2.6σ for an integrated luminosity of 3 ab^{-1}.

6.1.3 Heavy Higgs bosons in models with vector-like fermions at the HL- and HE-LHC

Contributors: R. Dermisek, E. Lunghi, S. Shin

Among the simplest extensions of the SM are models with extended Higgs sector and models with additional vectorlike matter. Although many search strategies for individual new particles were designed, there are large regions of the parameter space that HL- or HE-LHC will not be sensitive to as a result of either small production rates or large SM backgrounds. However, combined signatures of both extra sectors can lead to many new opportunities to search for heavy Higgs bosons and vectorlike matter simultaneously [509].

For example, in a type-II two Higgs doublet model, the production cross section of the 1 TeV heavy CP-even Higgs boson can be as sizeable as $\sim$ 2 pb (10 pb) at 13 TeV (27 TeV) c.o.m. energy, depending on the values of $\tan\beta$. However, in the decoupling limit, where $H \to ZZ,\ WW$ are suppressed or not present, the dominant decay modes are $t\bar{t}$, hh, $b\bar{b}$ and $\tau^+\tau^-$ which suffer from large SM backgrounds or small branching fractions in some regions of $\tan\beta$. On the other hand, vectorlike leptons typically have very clean signatures but their production rates are very small. Nevertheless, since vectorlike leptons can appear in decay chains of heavy Higgs bosons, the combined signature can feature both the sizeable production rate and clean final states.

We consider a type-II two Higgs doublet model augmented by vectorlike pairs of new quarks ($SU(2)$ doublets $Q_{L,R}$ and SU(2) singlets $U_{L,R}$ and $D_{L,R}$) and vectorlike pairs of new leptons ($SU(2)$ doublets $L_{L,R}$, $SU(2)$ singlets $E_{L,R}$ and SM singlets $N_{L,R}$) [510]. The Q_L, U_R, D_R, L_L and E_R

	ℓ_L^i	e_R^i	q_L^i	u_R^i	d_R^i	$L_{L,R}$	$E_{L,R}$	$N_{L,R}$	$Q_{L,R}$	$T_{L,R}$	$B_{L,R}$	H_d	H_u
$SU(2_L$	**2**	**1**	**2**	**1**	**1**	**2**	**1**	**1**	**2**	**1**	**1**	**2**	**2**
$U(1)_Y$	$-\frac{1}{2}$	-1	$\frac{1}{6}$	$\frac{2}{3}$	-$\frac{1}{3}$	$-\frac{1}{2}$	-1	0	$\frac{1}{6}$	$\frac{2}{3}$	-$\frac{1}{3}$	$\frac{1}{2}$	-$\frac{1}{2}$
Z_2	$+$	$-$	$+$	$+$	$-$	$+$	$-$	$+$	$+$	$+$	$-$	$-$	$+$

Table 6.1.3: Quantum numbers of SM leptons and quarks (ℓ_L^i, e_R^i, q_L^i, u_R^i, d_R^i for $i = 1, 2, 3$), extra vectorlike leptons and quarks and the two Higgs doublets. The electric charge is given by $Q = T_3 + Y$, where T_3 is the weak isospin, which is $+1/2$ for the first component of a doublet and $-1/2$ for the second component.

have the same hypercharges as quarks and leptons in the SM, as summarised in Table 6.1.3. We further assume that the new leptons mix only with one family of SM leptons in order to simply avoid strong constraints from the experiments searching for lepton flavour violation and we consider the mixing with the second family as an example [509–518] (the discovery potential in the case of mixing with the first family would be comparable [516] and in the case of mixing with the third family it would be significantly weaker [516, 519]). This can be achieved by requiring that the individual lepton number is an approximate symmetry (violated only by light neutrino masses). Similarly, we assume that the new quarks mix only with the third family of SM quarks. We consider the most general renormalisable Lagrangian consistent with these assumptions.

Details of the lepton sector of the model were worked out in Ref. [510]. After spontaneous symmetry breaking, $\left\langle H_u^0 \right\rangle = v_u$ and $\left\langle H_d^0 \right\rangle = v_d$ with $\sqrt{v_u^2 + v_d^2} = v = 174$ GeV (we also define $\tan\beta \equiv v_u/v_d$), the model can be summarised by mass matrices in the charged lepton sector, with left-handed fields $(\bar{\mu}_L, \bar{L_L^-}, \bar{E}_L)$ on the left and right-handed fields $(\mu_R, L_R^-, E_R)^T$ on the right [512],

$$M_e = \begin{pmatrix} y_\mu v_d & 0 & \lambda_E v_d \\ \lambda_L v_d & M_L & \lambda v_d \\ 0 & \bar{\lambda} v_d & M_E \end{pmatrix}, \tag{6.1.2}$$

and in the neutral lepton sector, with left-handed fields $(\bar{\nu}_\mu, \bar{L}_L^0, \bar{N}_L)$ on the left and right-handed fields $(\nu_R = 0, L_R^0, N_R)^T$ on the right [510],

$$M_\nu = \begin{pmatrix} 0 & 0 & \kappa_N v_u \\ 0 & M_L & \kappa v_u \\ 0 & \bar{\kappa} v_u & M_N \end{pmatrix}. \tag{6.1.3}$$

The superscripts on vectorlike fields represent the charged and the neutral components (we inserted $\nu_R = 0$ for the right-handed neutrino which is absent in our framework in order to keep the mass matrix 3×3 in complete analogy with the charged sector). The usual SM Yukawa coupling of the muon is denoted by y_μ, the Yukawa couplings to H_d are denoted by various λs, the Yukawa couplings to H_u are denoted by various κs, and finally the explicit mass terms for vectorlike leptons are given by $M_{L,E,N}$. Note that explicit mass terms between SM and vectorlike fields (*i.e.* $\bar{\mu}_L L_R$ and $\bar{E}_L \mu_R$) can be rotated away. These mass matrices can be diagonalised by bi-unitary transformations and we label the two new charged and neutral mass eigenstates by e_4, e_5 and ν_4, ν_5 respectively:

$$U_L^\dagger M_e U_R = \text{diag}\left(m_\mu, m_{e_4}, m_{e_5}\right), \tag{6.1.4}$$

$$V_L^\dagger M_\nu V_R = \text{diag}\left(0, m_{\nu_4}, m_{\nu_5}\right). \tag{6.1.5}$$

Since $SU(2)$ singlets mix with $SU(2)$ doublets, the couplings of all involved particles to the Z, W and Higgs bosons are in general modified. The flavour conserving couplings receive corrections and flavour changing couplings between the muon (or muon neutrino) and heavy leptons are generated. The relevant formulas for these couplings in terms of diagonalisation matrices defined above can be found

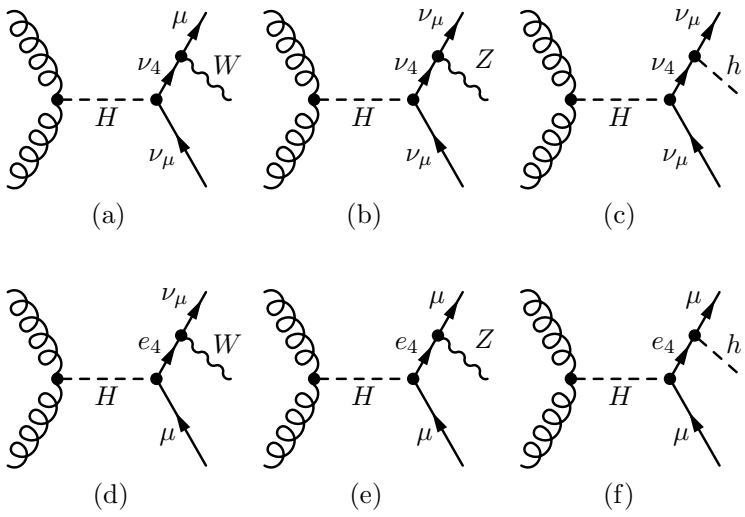

Fig. 6.1.4: Heavy Higgs boson cascade decays through vectorlike leptons.

in Ref.s [510, 512]. In the limit of small mixing, approximate analytic expressions for diagonalisation matrices can be obtained which are often useful for the understanding of numerical results. These are also given in Ref.s [510, 512]. Details of the quark sector of the model can be found in Ref. [520]. The mass matrix in the up and down quark sectors closely follow those for the neutrino and the charged leptons above.

The generated flavour changing couplings between heavy and light leptons lead to new decay modes of heavy CP-even (or CP-odd) Higgs boson: $H \to \nu_4 \nu_\mu$ and $H \to e_4 \mu$, where e_4 and ν_4 are the lightest new charged and neutral leptons. The BRs for these decay modes can be very large when the mass of the heavy Higgs boson is below the $t\bar{t}$ threshold and the light Higgs boson (h) is SM-like so that $H \to ZZ,\ WW$ are suppressed or not present. In this case, flavour changing decays $H \to \nu_4 \nu_\mu$ or $H \to e_4 \mu$ compete only with $H \to b\bar{b}$, and for sufficiently heavy H, also with $H \to hh$. Subsequent decay modes of e_4 and ν_4, $e_4 \to W\nu_\mu$, $e_4 \to Z\mu$, $e_4 \to h\mu$ and $\nu_4 \to W\mu$, $\nu_4 \to Z\nu_\mu$, $\nu_4 \to h\nu_\mu$ lead to the following 6 decay chains of the heavy Higgs boson:

$$H \to \nu_4 \nu_\mu \to W\mu\nu_\mu,\ Z\nu_\mu\nu_\mu,\ h\nu_\mu\nu_\mu\,, \tag{6.1.6}$$

$$H \to e_4 \mu \to W\nu_\mu\mu,\ Z\mu\mu,\ h\mu\mu\,, \tag{6.1.7}$$

which are also depicted in Fig. 6.1.4. In addition, H could also decay into pairs of vectorlike leptons. This is however limited to smaller ranges for masses in which these decays are kinematically open. Moreover, the final states are the same as in pair production of vectorlike leptons. We will not consider these possibilities here. Finally, although we focus on the second family of SM leptons in final states, the modification for a different family of leptons or quarks is straightforward.

In Ref. [509], it was found that in a large range of the parameter space BRs for the decay modes (6.1.6) and (6.1.7) can be sizeable or even dominant while satisfying constraints from searches for heavy Higgs bosons, pair production of vectorlike leptons [516] obtained from searches for anomalous production of multilepton events, and constraints from precision EW observables [283]. Since the Higgs production cross section can be very large, for example the cross section for a 200 GeV Higgs boson at 13 TeV (27 TeV) LHC for $\tan\beta = 1$ is 18 pb (67 pb) [521–523], the final states above can be produced in large numbers. Thus searching for these processes could lead to the simultaneous discovery of a new Higgs boson and a new lepton. Some of the decay modes in Fig. 6.1.4 also allow for full reconstruction of the masses of both new particles in the decay chain.

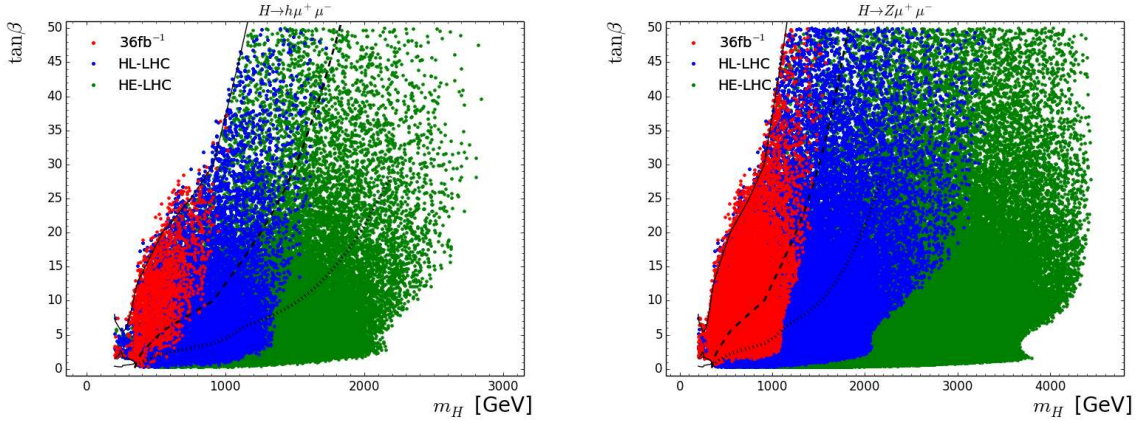

Fig. 6.1.5: Experimental sensitivities for $H \to e_4^\pm \mu^\mp \to h\mu^+\mu^-$ (left) $H \to e_4^\pm \mu^\mp \to Z\mu^+\mu^-$ (right). Red, blue and green points are the regions of the $[m_H, \tan\beta]$ plane which are accessible with LHC with 36 fb^{-1}, at the HL-LHC, and at the HE-LHC, respectively. Black solid, dashed and dotted lines represent the corresponding reaches of $H \to \tau\tau$ searches.

The final states of the processes (6.1.6) and (6.1.7) are the same as final states of $pp \to WW, ZZ, Zh$ production or $H \to WW, ZZ$ decays with one of the gauge bosons decaying into second generation of leptons. Since searching for leptons in final states is typically advantageous, our processes contribute to a variety of existing searches. Even searches for processes with fairly large cross sections can be significantly affected. For example, the contribution of $pp \to H \to \nu_4\nu_\mu \to W\mu\nu_\mu$ to $pp \to WW$ can be close to current limits while satisfying the constraints from $H \to WW$. This has been studied in Ref. [510] in the two Higgs doublet model we consider here, and also in a more model independent way in Ref. [517].

The discussion of the main features of each of the heavy Higgs decay modes, of existing experimental searches to which these new process contribute, and of possible new searches can be found in Ref. [509]. The processes with small SM backgrounds are the best place to look for this scenario. Examples include $H \to h\nu_\mu\nu_\mu$ and $H \to h\mu\mu$ with $h \to \gamma\gamma$.

We now discuss the parameter regions of heavy Higgses and vectorlike leptons which can be accessed by dedicated searches for the modes we propose with current LHC (36 fb^{-1}), HL- and HE-LHC. Among the processes depicted in Fig. 6.1.4, we choose $H \to e_4^\pm \mu^\mp \to h\mu^+\mu^-$ and $H \to e_4^\pm \mu^\mp \to Z\mu^+\mu^-$ as representative examples. These are interesting because they result in additional resonances. The first process was analysed in Ref. [518] for $m_H \leq 340$ GeV. The key selection criterion is an *off-Z* cut ($|m_{\mu^+\mu^-} - M_Z| > 15$ GeV) which exploits the fact that the invariant mass of the two muons in the final state is distributed mostly outside of the Z boson resonance region. This cut removes to a large extent background events from Z + (heavy flavoured) jets with $Z \to \mu^+\mu^-$ and raises enormously the signal significance [518]. In order to maximise the signal cross section, we focus on $h \to b\bar{b}$ (which we studied in detail in Ref. [518]) and $Z \to b\bar{b}$.

To obtain the expected sensitivities, we estimate the number of background events for the HL-LHC by rescaling the results of Ref. [518] (which are based on the search for a heavy resonance decaying to hZ at ATLAS [524]) by the ratio of luminosities. We further estimate that the backgrounds at the HE-LHC increase by a factor 3.6×5 with respect to those at the HL-LHC, where 3.6 is the ratio of the background cross sections calculated with MADGRAPH 5 and 5 comes from the ratio of integrated luminosities (15 ab^{-1}/3 ab^{-1}).

We take a flat signal acceptance of about 30% for $m_H \leq 800$ GeV based on the analysis presented in Ref. [518] for $m_H = 450, 550, 650, 750$ GeV and $m_{e_4} = 250$ GeV. For $m_H \geq 800$ GeV the dimuon invariant mass is much harder and concentrated above the Z resonance; in this region we assume

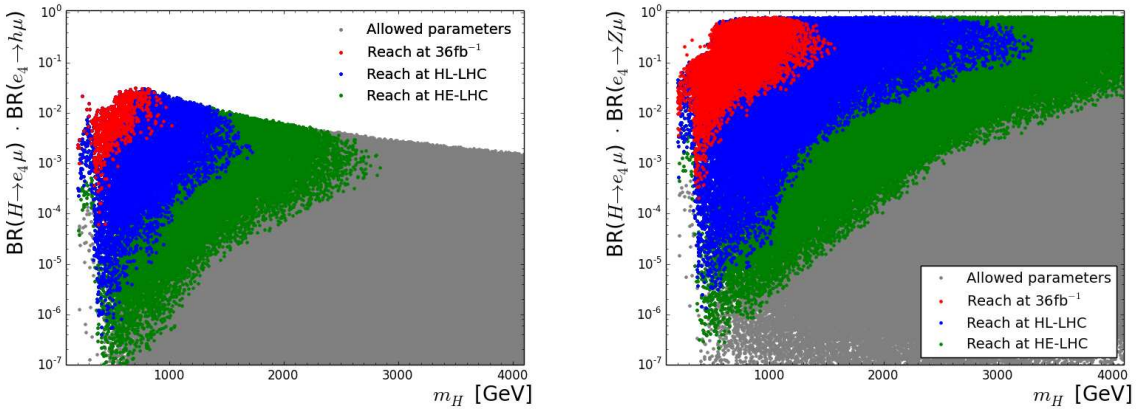

Fig. 6.1.6: Possible values of the BRs $\mathcal{B}(H \to e_4\mu) \times \mathcal{B}(e_4 \to h\mu)$ (left) and $\mathcal{B}(H \to e_4\mu) \times \mathcal{B}(e_4 \to Z\mu)$ (right) as a function of m_H. Note that $\mathcal{B}(H \to e_4\mu)$ includes both $H \to e_4^+\mu$ and $H \to e_4^-\mu^+$ decay modes. See the caption in Fig. 6.1.5 for further details.

an acceptance of about 50%. Furthermore, we consider a flat 50% detector efficiency throughout this analysis.

These estimates of background events, signal acceptances, and detector efficiencies, allow us to calculate the corresponding experimental sensitivities using the condition:

$$N_s^{95} \leq \sigma_H \cdot \mathcal{B}(H \to e_4\mu) \cdot \mathcal{B}(e_4 \to h\mu,\, Z\mu) \cdot A \cdot \epsilon \cdot \mathcal{L}\,, \tag{6.1.8}$$

where σ_H is the $pp \to H$ production cross section, A is the signal acceptance, ϵ is the experimental efficiency, and $\mathcal{L}$ is the integrated luminosity. N_s^{95} is the 95% C.L. upper limit on the expected number of events calculated from the background estimations described above using a modified frequentist construction (CLs) [95] based on a Poisson distribution.

Among the conventional searches of neutral heavy Higgs bosons, $H \to \tau^+\tau^-$ [525] currently provides the strongest constraints on our model, especially for large $\tan\beta$ region; we expect that future analysis improvements may boost the impact of $H \to b\bar{b}$ and $H \to t\bar{t}$. Searches for $H \to WW$ and $H \to ZZ$ are not constraining because these decays are heavily suppressed in the alignment limit in which tree–level couplings of heavy Higgs and weak gauge bosons vanish. Nevertheless, the processes $H \to e_4\ell(\nu_4\nu_\ell) \to \nu_\ell\ell W$ and $H \to e_4\ell \to \ell^+\ell^- Z$ are indirectly constrained by searches for $H \to WW$ and $H \to ZZ$ albeit with different kinematic topologies [509, 510, 517]. The decay $H \to \gamma\gamma$ currently constraints our model at small $\tan\beta \lesssim 1.5$ (at the HL-LHC values of $\tan\beta$ for which we expect constraints raises to about 3.5). Here we focus on $H \to \tau^+\tau^-$ as a competitive search avenue for a heavy neutral Higgs boson.

Let us comment on the extraction of the experimental sensitivities to $H \to \tau\tau$ mentioned above. We assume that there is no change in cut acceptances and detector efficiencies for $H \to \tau\tau$ (for a given m_H) for the HL-LHC and the HE-LHC,[8] implying that $S/\sqrt{B}$ controls to a good approximation the change in sensitivity. With this assumptions, the sensitivity at the HL-LHC increases simply by the square-root of the ratio of the integrated luminosities, *i.e.*, $\sqrt{3000./36.} = 9.13$. For the HE-LHC, we can obtain the sensitivities by further assuming that the background production cross sections ($\sigma_{\text{bkg.}}$) increase by the ratio of Higgs production cross sections for $\tan\beta = 1$, *i.e.*,

$$\sigma_{\text{bkg.}}^{13\text{ TeV}}/\sigma_{\text{bkg.}}^{27\text{ TeV}} = \sigma(pp \to H)_{\tan\beta=1}^{27\text{ TeV}}/\sigma(pp \to H)_{\tan\beta=1}^{13\text{ TeV}}\,, \tag{6.1.9}$$

[8] This is reasonable because the kinematics of H decay products depends almost exclusively on m_H.

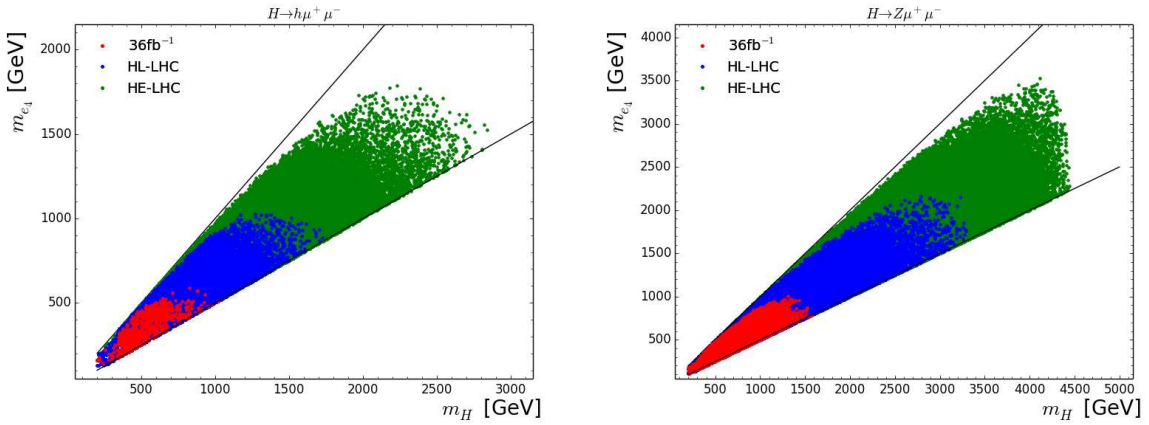

Fig. 6.1.7: Experimental sensitivities for $H \to e_4^\pm \mu^\mp \to h\mu^+\mu^-$ (left) and $H \to e_4^\pm \mu^\mp \to Z\mu^+\mu^-$ (right) in the $[m_H, m_{e_4}]$ plane. Note that we require $m_H > m_{e_4}$ to allow the decay channel, and that we loose sensitivity for $m_H > 2m_{e_4}$, where the $H \to e_4 e_4$ BR dominates. See the caption in Fig. 6.1.5 for further details.

and that the background cut acceptances remain constant. Then, the sensitivity increases as follows:

$$\begin{aligned}\frac{\mathrm{S}^{27\,\mathrm{TeV},\,15\,\mathrm{ab}^{-1}}}{\sqrt{\mathrm{B}^{27\,\mathrm{TeV},\,15\,\mathrm{ab}^{-1}}}} &= \frac{\mathrm{S}^{13\,\mathrm{TeV},\,36\,\mathrm{fb}^{-1}}}{\sqrt{\mathrm{B}^{13\,\mathrm{TeV},\,36\,\mathrm{fb}^{-1}}}} \cdot \frac{\sigma(pp \to H \to \tau^+\tau^-)^{27\,\mathrm{TeV}}}{\sigma(pp \to H \to \tau^+\tau^-)^{13\,\mathrm{TeV}}} \cdot \sqrt{\frac{\sigma_{\mathrm{bkg.}}^{13\,\mathrm{TeV}}}{\sigma_{\mathrm{bkg.}}^{27\,\mathrm{TeV}}} \cdot \frac{\mathcal{L}^{15\,\mathrm{ab}^{-1}}}{\mathcal{L}^{36\,\mathrm{fb}^{-1}}}} \\ &= \frac{\mathrm{S}^{13\,\mathrm{TeV},\,36\,\mathrm{fb}^{-1}}}{\sqrt{\mathrm{B}^{13\,\mathrm{TeV},\,36\,\mathrm{fb}^{-1}}}} \cdot \frac{\sigma(pp \to H \to \tau^+\tau^-)^{27\,\mathrm{TeV}}}{\sigma(pp \to H \to \tau^+\tau^-)^{13\,\mathrm{TeV}}} \cdot 20.4 \cdot \sqrt{\frac{\sigma(pp \to H)^{13\,\mathrm{TeV}}_{\tan\beta=1}}{\sigma(pp \to H)^{27\,\mathrm{TeV}}_{\tan\beta=1}}}\,,\end{aligned} \tag{6.1.10}$$

where $\mathrm{S}^{27\,\mathrm{TeV},\,15\,\mathrm{ab}^{-1}}$ ($\mathrm{S}^{13\,\mathrm{TeV},\,36\,\mathrm{fb}^{-1}}$) and $\mathrm{B}^{27\,\mathrm{TeV},\,15\,\mathrm{ab}^{-1}}$ ($\mathrm{B}^{13\,\mathrm{TeV},\,36\,\mathrm{fb}^{-1}}$) are the number of signal and background events for $H \to \tau^+\tau^-$ at the HE-LHC (at the LHC with 36 fb^{-1}). Note that the estimated sensitivity in Eq. (6.1.10) does not include experimental systematic uncertainties, that would somewhat weaken the reach of $H \to \tau\tau$.

Our main results are presented in Fig.s 6.1.5, 6.1.6 and 6.1.7, where we show the experimental sensitivities for $H \to e_4^\pm \mu^\mp \to h\mu^+\mu^-$ (left) $H \to e_4^\pm \mu^\mp \to Z\mu^+\mu^-$ (right) obtained from re-analysing current data with integrated luminosity 36 fb^{-1} (red), our estimates for the HL-LHC (blue), and HE-LHC (green). For comparison, in Fig. 6.1.5, the reach of $H \to \tau^+\tau^-$ searches in conventional type-II two Higgs doublet model with the current data, at the HL-LHC, and the HE-LHC are shown as black solid, dashed, and dotted lines, respectively. The scatter points satisfy constraints from EWPT, Drell-Yan pair production of vectorlike leptons [516], heavy Higgs searches in the $H \to \tau^+\tau^-$ [525] and $H \to \gamma\gamma$ [526, 527] channels. The range of parameters that we scan over is:

$$M_{L,N} \in [100, 5000]\ \mathrm{GeV}\,, \tag{6.1.11}$$

$$\lambda_L, \lambda_E, \lambda, \bar{\lambda} \in [-1, 1]\,, \tag{6.1.12}$$

$$\kappa_N = \kappa = \bar{\kappa} = 0\,, \tag{6.1.13}$$

$$\tan\beta \in [0.3, 50]\,. \tag{6.1.14}$$

From the inspections of Fig. 6.1.5, we see that searches for heavy Higgs cascade decays into vectorlike leptons considerably extend the reach beyond that of $H \to \tau^+\tau^-$. Searches for $H \to h\mu^+\mu^-$ are sensitive to m_H up to 1.7 TeV (2.9 TeV) and m_{e_4} up to 1 TeV (1.8 TeV) at the HL-LHC (HE-LHC). The decay mode $H \to Z\mu^+\mu^-$ is even more promising and extends the sensitivity to m_H up to 3.3 TeV (4.5 TeV) and m_{e_4} up to 2.2 TeV (3.5 TeV) at the HL-LHC (HE-LHC).

6.1.4 *Heavy singlet scalars at HL- and HE-LHC*

Contributors: D. Buttazzo, F. Sala, A. Tesi

The existence of extended Higgs sectors is predicted in several motivated extensions of the SM. In particular, extra Higgses that are singlets under the SM gauge group arise in some of the most natural BSM constructions, like the next-to-MSSM (NMSSM, see Ref. [528] for a review), as well as in Twin [529] and Composite [530, 531] Higgs models (TH and CH models). Independently of the hierarchy problem of the Fermi scale, extra singlets constitute a minimal possibility to realise a first-order EW phase transition [532–534], which is a necessary condition to achieve EW baryogenesis. These considerations constitute a strong case for the experimental hunt of extra singlet-like scalar particles. It is the purpose of this Section, which summarises and updates the work of Ref.s [535, 536], to review the experimental status of the searches for such scalars, and to determine the reach of the HL- and HE-LHC. To keep this contribution brief, we focus on the case where the extra singlet is heavier than the Higgs boson.

Framework. We add to the SM a real scalar field ϕ, so that the most general renormalisable Lagrangian reads

$$\mathcal{L} = \mathcal{L}_{\rm SM} + \frac{1}{2}(\partial S)^2 - \mu_S^2 S^2 - a_{HS}|H|^2 S - \lambda_{HS}|H|^2 S^2 - a_S S^3 - \lambda_S S^4 \,, \tag{6.1.15}$$

where H is the SM Higgs doublet. Unless a Z_2 symmetry is enforced ($a_{HS} = a_S = 0$), and is not spontaneously broken, the singlet mixes with the SM Higgs as

$$\phi = -s_\gamma\, h_0 + c_\gamma\, s_0, \qquad h = s_\gamma\, s_0 + c_\gamma\, h_0 \,, \tag{6.1.16}$$

where h_0 and s_0 are the neutral CP-even degrees of freedom contained in H and S, h and ϕ are the resulting mass eigenstates, and s_γ, c_γ are the sine and cosine of their mixing angle γ. The signal strengths μ of h and ϕ into SM particles, defined as cross-section times BR, read

$$\mu_h = c_\gamma^2\, \mu_{\rm SM}, \quad \mu_{\phi\to VV,ff} = s_\gamma^2\, \mu_{\rm SM}(m_\phi)\cdot(1-\mathcal{B}(\phi\to hh)), \quad \mu_{\phi\to hh} = s_\gamma^2\, \sigma_{\rm SM}(m_\phi)\cdot\mathcal{B}(\phi\to hh), \tag{6.1.17}$$

where $\sigma_{\rm SM}$ is the production cross-section of a SM Higgs boson, and $\mu_{\rm SM}$ is its signal strength into the pair of SM particles of interest.

Constraints from Higgs couplings. The couplings of the SM-like Higgs boson h to other SM particles are all reduced by the same amount c_γ, independently of m_ϕ. A combined ATLAS and CMS fit to Higgs coupling measurements from 8 TeV data yields the 2σ limit [537] $s_\gamma^2 \lesssim 0.12$, and the sensitivity reached with 36 fb^{-1} of data at 13 TeV is comparable [538, 539]. The HL- and HE-LHC are expected to probe values of s_γ^2 at, and possibly slightly below, the 5% level [32]. The current exclusion and future reach from Higgs coupling measurements is shown in Fig. 6.1.8. Constraints on the mixing angle from EW precision tests are subdominant with respect to those from Higgs coupling measurements, see *e.g.* Ref. [540].

Constraints from Trilinear Higgs coupling. The trilinear Higgs coupling g_{hhh} depends on γ, m_ϕ, and on the singlet VEV v_s, while its dependence on all other parameters is very mild [535] (we fix for definiteness $\lambda_S = \lambda_{HS} = 0.5$). We show its ratio with respect to its SM value in Fig. 6.1.8, for two representative values of v_s. The gray shaded region comes from a rough bound on g_{hhh} that we extract from Ref. [274], using the prediction of Ref. [541].[9] Deviations of order one and larger are allowed by all current and near-future constraints, motivating in particular the HE stage of the LHC, due to the increase of the sensitivity to g_{hhh} with energy [32].

[9] We assume that the only deviation in double Higgs production comes from deviations in g_{hhh}, the contribution from $pp\to\phi\to hh$ is negligibly small due to the large m_ϕ in the excluded region.

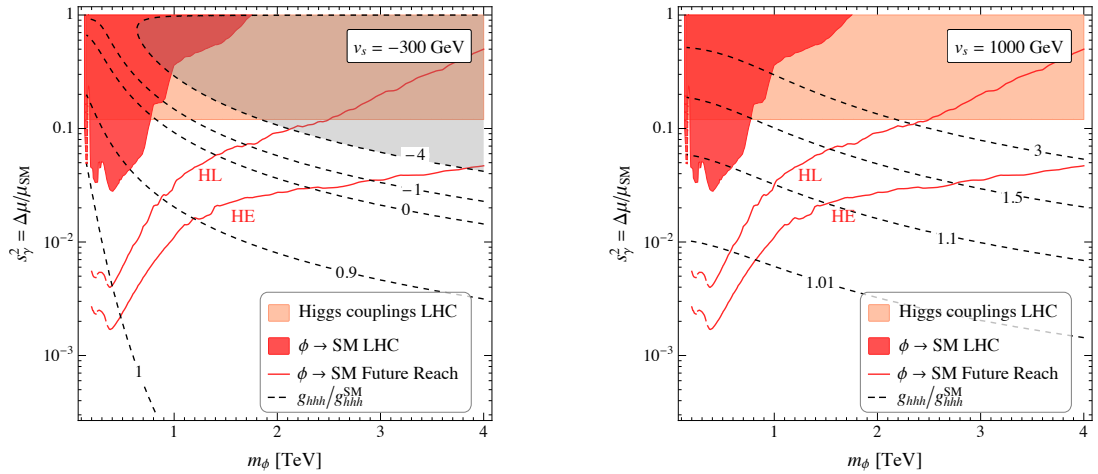

Fig. 6.1.8: Shaded: LHC exclusions from resonance searches (dark red), Higgs coupling measurements (light red) and double Higgs production (gray). Dashed black lines are contours of constant ratio between the trilinear Higgs coupling and its SM value, continuous red lines are expected sensitivities from resonance searches at the HL- and HE-LHC. The singlet VEV v_s is fixed to -300 GeV (left) and to 1000 GeV (right).

Constraints from direct searches of the extra singlet. The collider phenomenology of ϕ is fully controlled by only 3 parameters, m_ϕ, γ and $\mathcal{B}(\phi \to hh)$. Analogously to the case of the triple Higgs coupling g_{hhh}, $\mathcal{B}(\phi \to hh)$ depends dominantly on the model parameters v_s, γ, and m_ϕ [535]. Moreover, because of the Goldstone boson equivalence theorem, it reaches the asymptotic value $\mathcal{B}(\phi \to hh) = \mathcal{B}(\phi \to ZZ) = 25\%$ for $m_\phi \gg m_h$, further reducing the number of parameters relevant for the phenomenology of ϕ. Current resonance searches at the LHC exclude the red shaded area in Fig. 6.1.8, and are dominated by the CMS combined ZZ search in Ref. [542] at 13 TeV with 36 fb^{-1} of data. We rescale the expected sensitivity at 13 TeV [542] at higher energies and luminosities using quark parton luminosities, with a procedure analogous to the one presented in Ref. [535]. Our results for the expected sensitivities at the HL (14 TeV, 3 ab^{-1}) and HE (27 TeV, 15 ab^{-1}) stages of the LHC are also shown in Fig. 6.1.8. Direct searches for the new scalar constitute the strongest probe of the parameter space of these models for m_ϕ below about a TeV, while larger masses are (and will be) probed more efficiently by deviations in Higgs couplings, thus making these two strategies complementary in the exploration of these models.

Implications for the NMSSM. The NMSSM adds to the MSSM particle content a singlet S, so that the superpotential reads $W = W_{\rm MSSM} + \lambda\, S H_u H_d + f(S)$. The fine-tuning needed to reproduce the EW scale is parametrically alleviated, with respect to the MSSM, and for a given value of the stop and gluino masses, by a factor λ/g, see *e.g.* Ref.s [543–546]. Naturalness arguments thus favour a large λ, that is however bounded from above by perturbativity. Assuming the masses of the extra Higgs bosons in the TeV range, a model with $\lambda \simeq 2$ becomes strongly coupled at scales of order 10 TeV, and to have a perturbative coupling up to the GUT scale one needs $\lambda \lesssim 0.7$ [547].[10]

Here we employ the economical parametrisation of the NMSSM scalar sector put forward in Ref.s [548, 549]. We then assume the extra Higgs doublet to be (slightly) decoupled, and we study the phenomenology of the Higgs-singlet scalar sector, which can be described by 4 free parameters

$$m_\phi, \quad \lambda, \quad t_\beta, \quad \Delta_{hh}, \tag{6.1.18}$$

where t_β is the ratio of the up and down Higgs VEVS , and Δ_{hh} encodes the radiative contribution to the SM-like Higgs mass $m_h^2 \lesssim m_Z^2\, c_{2\beta}^2 + \lambda^2\, v^2\, s_{2\beta}^2/2 + \Delta_{hh}^2$. The phenomenology discussed in the previous

[10] It is conceivable that a strong sector exists at the scale where λ becomes non-perturbative, and without affecting the success of GUT in the NMSSM, see *e.g.* the model in Ref. [548] and references therein.

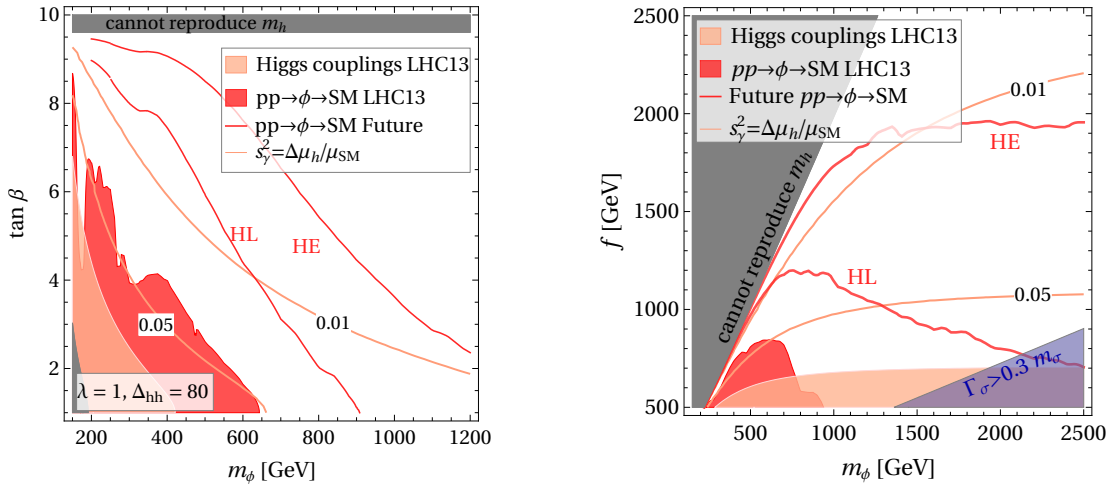

Fig. 6.1.9: Shaded: LHC exclusions from resonance searches (dark red) and Higgs coupling measurements (light red). Left: NMSSM with couplings $\lambda = 1$ and with $\Delta_{hh} = 80$ GeV. Right: Twin and Composite Higgs models. See text for more details.

section is displayed, for the NMSSM, in the left-hand panel of Fig. 6.1.9. We have fixed $\Delta_{hh} = 80$ GeV, a value obtainable for stop masses and mixing in the range of $1 - 2$ TeV. The precise value of Δ_{hh} does not affect the Higgs sector phenomenology as long as it is within order 10% of 80 GeV. We have also fixed $\lambda = 1$, smaller values would make all the exclusions and sensitivities weaker, while larger values would make them stronger.

As seen in Fig. 6.1.9 left, direct searches for the extra singlet are expected to constitute the most promising probe of the $\phi - h$ parameter space. Higgs coupling measurements will give a reach at most comparable to the one of resonance searches, and they will constitute a crucial complementary access to the parameter space of NMSSM scalars. Deviations in the trilinear Higgs coupling depend on more parameters than those in Eq. (6.1.18), and can reach around 50% or more if $\lambda \gtrsim 1$, see Ref. [550] for a precise quantification.

Twin and Composite Higgs. In both TH and CH models, the SM-like Higgs boson is the pseudo-Goldstone boson associated to the spontaneous breaking of a global symmetry at a scale f. The EW fine-tuning of CH models is comparable to the one of typical SUSY constructions, while TH models can achieve a tuning as good as the irreducible factor v^2/f^2 (mainly because the top partners are neutral under colour, and can thus be light). The radial scalar mode σ associated to the pseudo-Goldstone Higgs has a mass $m_\sigma \sim g_* f$, where the size of g_* corresponds to the typical one of the coupling of the UV completion. TH models with weakly coupled UV completions feature an extra scalar singlet that can be light, see *e.g.* Ref.s [551, 552]. The hunt for the extra scalar is a crucial test of TH models, because of the small couplings to the SM of the rest of the "Twin" states.

The scalar potential of TH and CH models has less free parameters, so that all the quantities relevant for the scalar phenomenology (including g_{hhh} and $\mathcal{B}(\phi \to hh)$) are a function of two free parameters only, that we choose to be f and m_σ. One for example obtains $s_\gamma \approx v/f$ and $g_{hhh} \approx 1$ up to terms suppressed by the small ratio v^2/f^2. In TH, an extra freedom is given by the decay channels of ϕ into the Twin sector, whose BR in the limit $m_\sigma \gg gf$ is fixed, through the Goldstone boson equivalence theorem, by the symmetries of the model (3/7 in the cases of $SO(8)/SO(7) \simeq SU(4)/SU(3)$). For simplicity, and because such decay is absent in CH models, we do not include it in our study.

The constraints and sensitivities discussed above are displayed in the right-hand panel of Fig. 6.1.9. Given our considerations above, in the case where these models are not too strongly coupled (we show in Fig. 6.1.9 the region where $\Gamma_\sigma > 0.3 m_\sigma$), they are expected to manifest themselves first via new diboson resonances. On the contrary, their strong-coupling regime is expected to show up first in deviations in

the Higgs couplings.

6.1.5 *Relaxion at the HL-LHC*

Contributors: E. Fuchs, M. Schlaffer

The relaxion mechanism [553] addresses the hierarchy problem differently than conventional symmetry-based solutions. In this framework, the Higgs mass is stabilised dynamically by the relaxion, a pseudo-Nambu-Goldstone boson. The Higgs mass is scanned by the evolution of the relaxion field. Eventually, the relaxion stops at the field value where the Higgs mass is much smaller than the theory's cutoff, hence addressing the fine tuning problem. Relaxion models do not require top, gauge or Higgs partners at the TeV scale. The possible mass range for the relaxion ranges from sub-eV to tens of GeV. Hence this framework can lead to signatures relevant for cosmology, for the low-energy precision frontier, for the intensity frontier, and for the high energy collider frontier. For detailed studies see Ref.s [554–556].

The aspects of the relaxion mechanism that are relevant for the phenomenology at colliders are summarised in the following. The effective scalar potential of the theory depends both on the Higgs doublet H and the relaxion ϕ,

$$V(H,\phi) = \mu^2(\phi) H^\dagger H + \lambda (H^\dagger H)^2 + V_{\rm sr}(\phi) + V_{\rm br}(h,\phi)\,, \tag{6.1.19}$$

$$\mu^2(\phi) = -\Lambda^2 + g\Lambda\phi + \dots\,, \tag{6.1.20}$$

where Λ is the cutoff scale of a Higgs loop. The relaxion scans μ^2 via the slow-roll potential

$$V_{\rm sr}(\phi) = rg\Lambda^3\phi\,, \tag{6.1.21}$$

where g is a small dimension-less coupling and $r > 1/(16\pi^2)$ due to naturalness requirements. Once $\mu^2(\phi)$ becomes negative, the Higgs gets a VEV $v^2(\phi) = -\frac{\mu^2(\phi)}{\lambda}$. The non-zero VEV activates a periodic (model-dependent) backreaction potential $V_{\rm br}$ associated with the backreaction scale $\Lambda_{\rm br}$ that eventually stops the rolling of the relaxion at a value ϕ_0, where $v(\phi_0) = 246$ GeV. Generically, the relaxion mechanism leads to CP violation and as a result, the relaxion ϕ mixes with the Higgs h and inherits its couplings to SM fields [554, 555]. The relaxion mass m_ϕ and the mixing angle $\sin\theta$ can be expressed as

$$m_\phi \simeq \frac{\Lambda_{\rm br}^2}{f}\sqrt{c_0}\,, \tag{6.1.22}$$

$$\sin\theta \simeq 8\frac{\Lambda_{\rm br}^4}{v^3 f} s_0\,, \tag{6.1.23}$$

where $s_0 \equiv \sin\phi_0$, $c_0 \equiv \cos\phi_0$, and f is the scale where the shift symmetry of the backreaction potential is broken. Combining Eq.s (6.1.22) and (6.1.23) with $4\Lambda_{\rm br}^2 s_0 < v^2\sqrt{c_0}$, which is fulfilled due to the suppressed value of s_0 at the endpoint of the rolling [555], the mixing angle as a function of the relaxion mass is approximately bounded by

$$\sin\theta \leq 2\frac{m_\phi}{v}\,. \tag{6.1.24}$$

This upper bound on the relaxion-Higgs mixing is indicated by the black line in Fig. 6.1.10.

Moreover, in the broken phase a trilinear relaxion-relaxion-Higgs coupling $c_{\phi\phi h}$ is generated [554, 556],

$$c_{\phi\phi h} = \frac{\Lambda_{\rm br}^4}{vf^2}c_0 c_\theta^3 - \frac{2\Lambda_{\rm br}^4}{v^2 f}s_0 c_\theta^2 s_\theta - \frac{\Lambda_{\rm br}^4}{2f^3}s_0 c_\theta^2 s_\theta - \frac{2\Lambda_{\rm br}^4}{vf^2}c_0 c_\theta s_\theta^2 + 3v\lambda c_\theta s_\theta^2 + \frac{\Lambda_{\rm br}^4}{v^2 f}s_0 s_\theta^3\,, \tag{6.1.25}$$

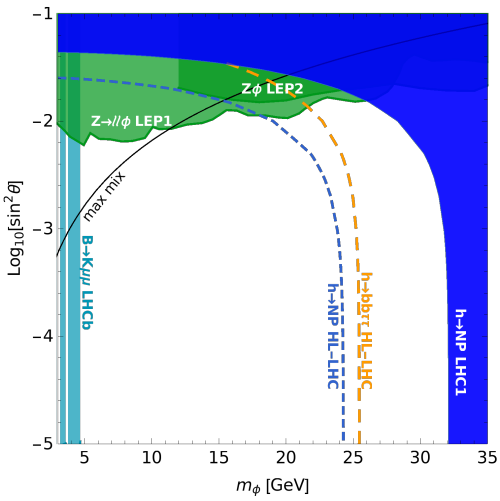

Fig. 6.1.10: Bounds and projections at the 95% C.L. for processes at hadron and lepton colliders. $Z \to Z^*\phi \to \ell\bar{\ell}\phi$ at LEP1 with $\sqrt{s} = M_Z$ [557] and $e^+e^- \to Z\phi$ at LEP2 with $\sqrt{s} = 192 - 202$ GeV [558]. Bound from $B^+ \to K^+\mu^+\mu^-$ at LHCb [559, 560]. Direct searches for exotic Higgs decays at the HL-LHC in the $bb\tau\tau$ channel inferred from Ref. [561] (orange, dashed). Upper bound on $\mathcal{B}(h \to \text{NP})$ from Higgs coupling fits at the LHC Run-1 (blue area) and projection for the HL-LHC with 3 ab^{-1} (blue, dashed). The maximal mixing according to Eq. (6.1.24) is indicated by the black line.

where $s_\theta \equiv \sin\theta$, $c_\theta \equiv \cos\theta$. Thus a bound on $c_{\phi\phi h}$ constrains the $(m_\phi, \sin\theta)$ parameter space. In the limit of small mixing, Eq. (6.1.25) reduces to $c_{\phi\phi h} \simeq m_\phi^2/v$, therefore directly constraining the mass.

There are two complementary ways to constrain $c_{\phi\phi h}$ via the exotic Higgs decay $h \to \phi\phi$: searching directly for the decay products of the ϕ pair, or bounding this BR by a global fit of Higgs couplings.

Concerning the Higgs phenomenology, the relaxion can be viewed as a singlet extension of the SM with a mixing of ϕ and h. The Higgs couplings to SM particles are reduced by the universal coupling modifier $\kappa \equiv \cos\theta$, and the total Higgs width $\Gamma_h^{\text{tot}} = \cos^2\theta\,\Gamma_h^{\text{tot,SM}} + \Gamma_h^{\text{NP}}$ contains the NP contribution $\Gamma_h^{\text{NP}} = \Gamma(h \to \phi\phi)$. For the LHC, $\mathcal{B}(h \to \text{NP})$ has been constrained via a Higgs coupling fit to Run-1 data to be at most 20% at the 95% C.L. while the HL-LHC has the potential to bound this BR to approximately 8.6% at the 95% C.L. Ref. [32, 562]. The resulting bounds in the $(m_\phi, \sin\theta)$ plane are shown in Fig. 6.1.10.

The parameter space probed by the HL-LHC enters the region below the upper bound of the mixing and is therefore relevant for the model. The HL-LHC may exclude a relaxion mass above 24 GeV for vanishing $\sin\theta$. In comparison, direct relaxion production via $B \to K\phi$, $\phi \to \mu\mu$ at LHCb excludes $2m_\mu \leq m_\phi \lesssim 5$ GeV also for $\sin\theta$ smaller than shown in Fig. 6.1.10. In contrast, the bounds set by LEP1 via the 3-body Z-decay into $f\bar{f}\phi$ and by LEP2 via relaxion strahlung in $Z\phi$ production are sensitive only to mixing angles of order $\sin^2\theta \gtrsim 10^{-2}$ and therefore constrain mostly parameter space above the theoretically motivated maximal mixing. Furthermore, the stronger bound reachable at the HL-LHC, compared to the Run-1 one, is highly beneficial for constraining the relaxion mass space down to small mixing angles.

Regarding direct searches for the relaxion decay products, each relaxion from the Higgs decay further decays into a pair of SM particles, resulting in a four-particle final state F. The ATLAS and CMS searches for such signatures yield m_ϕ-dependent bounds on $(\sigma_h/\sigma_h^{\text{SM}}) \times \text{BR}\,(h \to \phi\phi \to F)$. However, none of the current searches [275, 561, 567–572] is sensitive enough to probe parts of the relaxion parameter space displayed in Fig. 6.1.10, *i.e.* 5 GeV $\leq \text{m}_\phi \leq$ 35 GeV and $10^{-5} \leq \sin^2\theta \leq 10^{-1}$. In contrast, the HL-LHC can probe parts of the relevant parameter space via these channels. We estimate the potential reach of the HL-LHC with 3 ab^{-1} by rescaling the current limits by the ratio of luminosities and by the ratio of the Higgs production cross sections in the dominant channels at 8 or 13 TeV with respect to

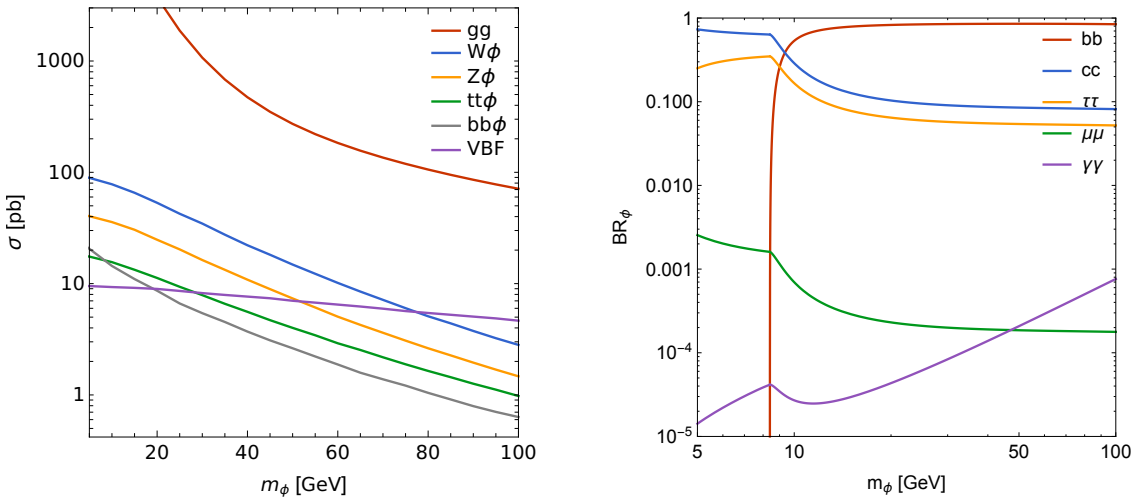

Fig. 6.1.11: Production and decay of ϕ for $\sin^2\theta = 1$. Left: hadronic cross sections, $\sigma(pp \to X)$ at $\sqrt{s} = 14$ TeV for $X = \phi$ (via gluon fusion), $W\phi$, $Z\phi$, $t\bar{t}\phi$, $b\bar{b}\phi$, and ϕjj (via VBF). The $\sigma(pp \to \phi)$ via gluon fusion is calculated using `ggHiggs v3.5` [563–566] at N^{3}LO including N^{3}LL resummation without a p_T-cut. The remaining hadronic cross sections are obtained from MADGRAPH5_aMC@NLO [67] at NLO with $p_T(\phi) > 20$ GeV. Right: BRs $\mathrm{BR}(\phi \to b\bar{b},\, c\bar{c},\, \tau^+\tau^-, \mu^+\mu^-, \gamma\gamma)$.

14 TeV for the search results from Run-1 or Run-2, respectively [573]. According to this scaling, we find that the strongest bound at the HL-LHC is expected in the $bb\tau\tau$ channel (inferred from the CMS search at Run-2 [561]), excluding $m_\phi > 26$ GeV at 95% C.L. as shown in Fig. 6.1.10.

Concerning the relaxion direct production at colliders, similarly to the Higgs, the dominant production modes for the relaxion are gluon fusion ($pp \to \phi$), relaxion strahlung ($pp \to Z\phi,\ W\phi$), $\{t\bar{t},\ b\bar{b}\}$-associated production, and vector boson fusion (VBF, $pp \to \phi jj$). The cross sections of these processes are shown for $\sin\theta = 1$ in the left panel of Fig. 6.1.11. For the HL-LHC, a promising channel is relaxion strahlung due to the relatively large cross sections in combination with the presence of a massive gauge boson that can be tagged. Various decay modes can be considered, see the right panel of Fig. 6.1.11. So far the $Z\phi$ and $W\phi$ searches do not cover the challenging low-mass range. With high luminosity, extending these searches to lower masses could yield complementary bounds.

6.1.6 The HL-LHC and HE-LHC scope for testing compositeness of 2HDMs

Contributors: S. De Curtis, L. Delle Rose, S. Moretti, A. Tesi, K. Yagyu

Much has been written about the ability of TeV scale compositeness to naturally remedy the hierarchy problem of the SM, in particular through the pseudo-Nambu Goldstone boson (pNGB) nature of the Higgs state. This idea is borrowed from QCD: the discovered Higgs boson is the analogue of the pion. Just like there are π, η, *etc.* mesons predicted by QCD, though, there could be several Higgs states predicted by compositeness beyond the one discovered. In this respect, a natural setting [574] is the Composite 2-Higgs Doublet Model (C2HDM) [575–577]. It is built upon the experimentally established existence of a doublet structure triggering Electro-Weak Symmetry Breaking (EWSB), generating the $W^\pm$, Z and SM-like Higgs state h, yet it surpasses it by providing one more composite doublet of Higgs states that can be searched for at the LHC, alongside additional composite gauge bosons (the equivalent of the ρ, ω, *etc.* of QCD) and composite fermions. We concentrate here on the Higgs sector of the C2HDM (see Ref. [578] for a comparative study between the 2HDM based composite solution to the hierarchy problem and the one driven instead by Supersymmetry) based on $SO(6) \to SO(4) \times SO(2)$, in presence of so-called *partial compositeness* [579] realised through the third generation of the SM fermions. The scalar potential and, thus, the masses of the Higgs bosons are generated at one-loop level by the linear mixing between the (elementary) SM and the (composite) strong sector fields. This implies

that masses and couplings are not free parameters, unlike in the elementary realisations, but they depend upon the strong sector dynamics and are strongly correlated. The compositeness scale f is within the energy domain of the LHC and the composite nature of the SM-like Higgs boson in the C2HDM can be revealed through corrections of $\mathcal{O}(\xi)$, where $\xi = v^2/f^2$, with v being the VEV of the SM Higgs field. As current lower limits on f are of order 750 GeV, this implies that such effects enter experimental observables at the $5-10\%$ level. In order to test these effects, the best strategy is to probe gauge interactions of the SM-like Higgs boson, universally affected by $\mathcal{O}(\xi)$ corrections. In particular, these effects are expected to be larger than the corresponding ones in Elementary realisations of a 2HDM (E2HDM) [479], and therefore accessible at the HL-LHC. However, if these were to be found consistent with those of the E2HDM, the last resort in the quest to disentangle the C2HDM from the E2HDM hypothesis would be to exploit the correlation among observable processes involving extra Higgs bosons. Hence, under the above circumstances, it becomes mandatory to assess the scope of the HL- and HE-LHC, the latter being necessary for processes involving Higgs boson self-interactions, which have rather small cross-sections at the current LHC, in exploring the structure of extended Higgs sectors. We shall do so by studying under which LHC machine conditions one could access the processes $gg \to H \to hh \to b\bar{b}\gamma\gamma$ and $gg \to H \to t\bar{t}$ (followed by semi-leptonic top decays), as these will enable one to extract crucial C2HDM parameters, wherein H is the heaviest of the two CP-even (neutral) Higgs states of the C2HDM, the lightest (h) being the SM-like one.

The construction of the model and the fundamental parameters of the C2HDM are described in Ref. [578, 580]. These correspond to the scale of compositeness f, the coupling of the spin-1 resonances, the masses of the heavy top partners, and the mixing between the latter and the elementary top quark (which represents the leading contribution to the effective scalar potential). In order to have phenomenologically acceptable configurations with EW parameters consistent with data, we require: (i) the vanishing of the two tadpoles of the CP-even Higgs bosons, (ii) the value of the top quark mass to match the measured one, and (iii) the value of the Higgs boson mass to match the measured one. Under these constraints, we explore the parameter space by scanning the scale of compositeness in the range $(750, 3000)$ GeV and all the other parameters in the range $(-10, 10)f$. As outputs, we obtain the masses of the charged Higgs boson ($m_{H^\pm}$), the CP-odd Higgs boson (m_A), and the heavier CP-even Higgs boson (m_H), the mixing angle θ between the two CP-even Higgs boson states (h, H), as well as their couplings to fermions and bosons. These quantities are then combined in physics observables and tested against experimental measurements through HiggsBounds [581] and HiggsSignals [582], which include current results from void Higgs boson searches and parameter determinations from the discovered Higgs state, respectively. Further, we extrapolated the latter (at present counting on about 30 fb^{-1} of accumulated luminosity after Run-1 and in Run-2) to $\sqrt{s} = 14$ TeV with 300 fb^{-1}(end of Run-3) and 3 ab^{-1}(HL-LHC), by adopting the expected experimental accuracies given in Ref. [583] (scenario 2 therein). These are listed against the so-called κ's (or 'coupling modifiers') of Ref. [584], among which those interesting us primarily are κ^h_{VV} ($V = W^\pm, Z$), $\kappa^h_{\gamma\gamma}$ and κ^h_{gg}, generally the most constraining ones.

Before proceeding with presenting our results, it is worth mentioning that a generic 2HDM Lagrangian introduces, in general, Flavour Changing Neutral Currents (FCNCs) at tree level via Higgs boson exchanges. To avoid them, we assume here an alignment (in flavour space) between the Yukawa matrices like in the elementary Aligned 2HDM (A2HDM) [585]. In this scenario, the coupling of the heavy Higgs H to the SM top quark is controlled (modulo small corrections induced by the mixing angle $\theta \sim \xi$) by

$$\zeta_t = \frac{\bar{\zeta}_t - \tan\beta}{1 + \bar{\zeta}_t \tan\beta}, \tag{6.1.26}$$

where $\bar{\zeta}_t$ and $\tan\beta$ are predicted, and correlated to each other, in terms of the aforementioned fundamental parameters of the C2HDM. Thus, being interested in the phenomenology of the H state, henceforth we will map the results of our scan in terms of m_H and ζ_t and restrict the parameter space to the region $m_{H,A,H^\pm} > 2m_h$. The ζ_t parameter and the Higgs trilinear coupling λ_{Hhh} set the hierarchy among the

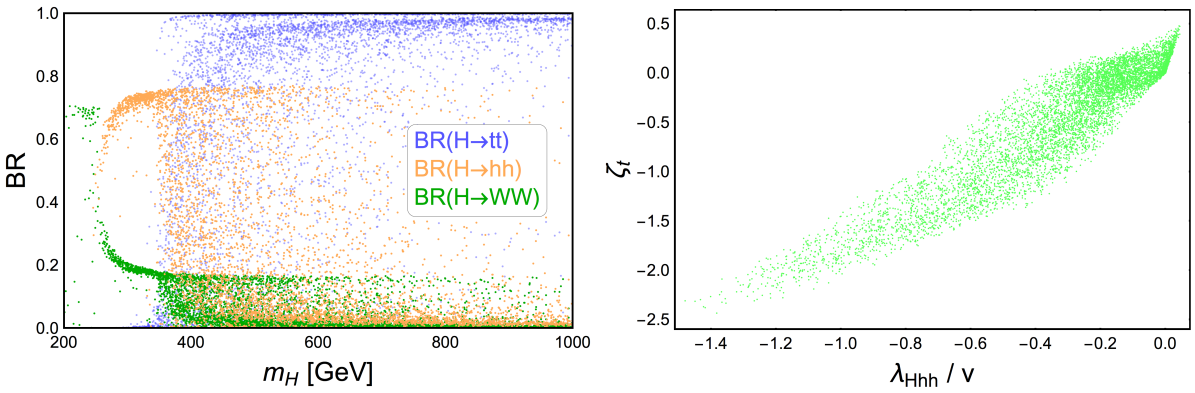

Fig. 6.1.12: Branching ratio of the H state of the C2HDM in the hh (orange) and $t\bar{t}$ (blue) channels (left) and correlation between the ζ_t and λ_{Hhh} couplings obtained upon imposing present HiggsBounds and HiggsSignals constraints at 13 TeV (right).

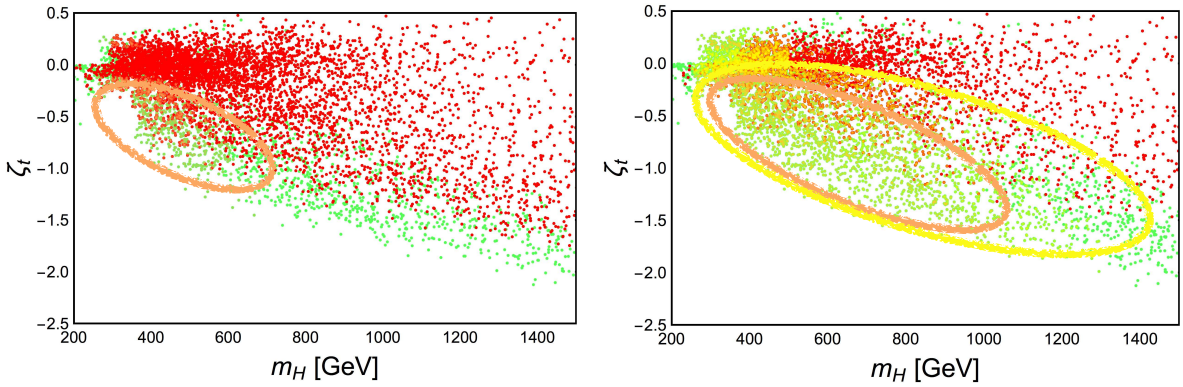

Fig. 6.1.13: Results of the C2HDM scan described in the text. Colour coding is as follows. Green: all points that pass present constraints at 13 TeV. Red: points that, in addition to the above, have κ^h_{VV}, $\kappa^h_{\gamma\gamma}$ and κ^h_{gg} within the 95% C.L. projected uncertainty at 14 TeV with $\mathcal{L} = 300$ fb^{-1} (left) and $\mathcal{L} = 3$ ab^{-1} (right). Orange: points that, in addition to the above, are 95% C.L. excluded by the direct search $gg \to H \to hh \to b\bar{b}\gamma\gamma$, at 14 TeV with $\mathcal{L} = 300$ fb^{-1} (left) and $\mathcal{L} = 3$ ab^{-1} (right). In the right plot the yellow points are 95% C.L. excluded by the same search at the HE-LHC with $\mathcal{L} = 15$ ab^{-1}. The orange and yellow elliptical shapes highlight the regions in which the points of the corresponding colour accumulate.

decay modes of the heavy state H. In particular, $H \to t\bar{t}$, when kinematically allowed, represents the main decay channel. Below the $t\bar{t}$ threshold, the diHiggs $H \to hh$ decay mode can reach, approximately, 80%, with the remaining decay space saturated by $H \to VV$. The corresponding BR observables are shown in Fig. 6.1.12 (left). Both of these can be notably different in the C2HDM with respect to the E2HDM, since the Hhh and $Ht\bar{t}$ couplings can carry the imprint of compositeness (see Fig. 6.1.12 (right) for their correlation). The hierarchy discussed above highlights the key role of the $H \to hh$ and $H \to t\bar{t}$ channels in the discovery and characterisation of the composite heavy Higgs boson.

Figures 6.1.13 and 6.1.14 illustrate the interplay between direct and indirect searches and the ability of the HL- and HE-LHC to discover both the $gg \to H \to hh \to b\bar{b}\gamma\gamma$ and the $gg \to H \to t\bar{t}$ (followed by semi-leptonic top decays) signals, respectively, over regions of the C2HDM parameter space mapped onto the (m_H, ζ_t) plane, even when no deviations are visible in the aforementioned κ's of the SM-like Higgs state h (red points) at the LHC at $\sqrt{s} = 14$ TeV with $\mathcal{L} = 300$ fb^{-1} and $\mathcal{L} = 3$ ab^{-1}. Notice that 95% C.L. exclusion limits are extracted by adopting the sensitivity projections of Ref.s [586, 587] while compliance with the coupling modifiers is here achieved by asking that $|1 - k^h_i|$

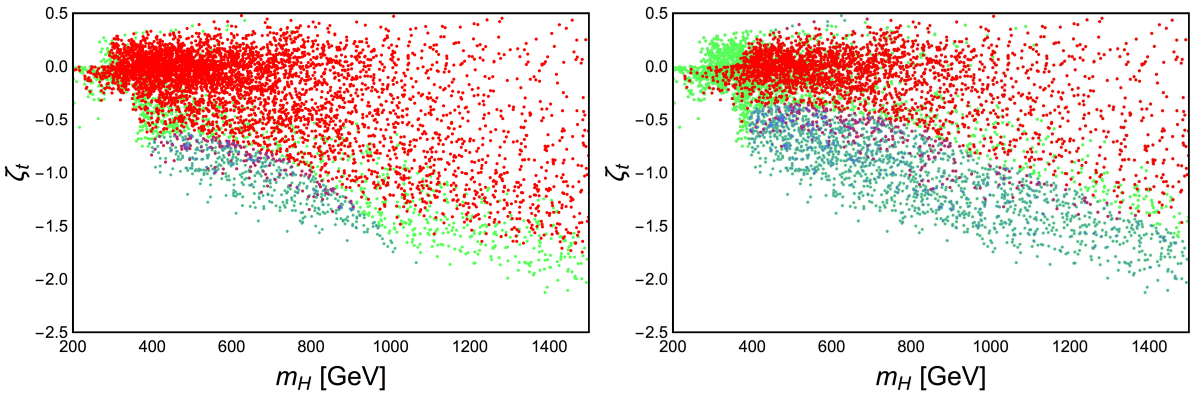

Fig. 6.1.14: Green an red points are as in the previous plot. Blue: points that, in addition to the above, are 95% C.L. excluded by the direct search $gg \to H \to t\bar{t}$, at 14 TeV with $\mathcal{L} = 300$ fb^{-1} (left) and $\mathcal{L} = 3$ ab^{-1} (right).

is less than the percentage uncertainty declared in Ref. [583], where $i = VV, \gamma\gamma$ and gg. Of some relevance, while tensioning the scope of the two search channels to one another, is to note that the orange points have a large overlap with the red ones for small $|\zeta_t|$ values while the corresponding overlap of the blue region is smaller but it reaches larger H masses. Hence, the first channel enables one to cover a larger C2HDM parameter space while the second one higher H masses. Clearly, the combination of the two allows one to combine the benefits of either. The HE-LHC, assuming $\sqrt{s} = 27$ TeV and $\mathcal{L} = 15$ ab^{-1}, will improve the reach in the H high mass region up to 1.2 TeV by studying the process $gg \to H \to hh \to b\bar{b}\gamma\gamma$. For the $gg \to H \to t\bar{t}$ channel, the naive extrapolation of the sensitivity with the parton luminosities is unreliable because it is affected by the SM $t\bar{t}$ threshold effects.

For a proper phenomenological analysis of the $t\bar{t}$ process, one should eventually account for interference effects with gg-induced (irreducible) background. For example, it is well-known that interference effects between the t, u-channel gg-induced Leading Order (LO) QCD diagrams and the one due to a Higgs boson in s-channel via gg-fusion generate a characteristic peak-dip structure of the $M_{t\bar{t}}$ spectrum. However, this contribution is only one of the many entering at the same order in perturbation theory. In fact, Ref. [588] investigated the effect of all one-loop corrections of $\mathcal{O}(\alpha_S^2\alpha_W)$ onto the $t\bar{t}$ invariant mass spectrum at the LHC in presence of both resonant and non-resonant Higgs boson effects. It was shown therein that corrections of $\mathcal{O}(\alpha_S^2\alpha_W)$ involving a non-resonant Higgs boson are comparable to or even larger than those involving interference with the s-channel resonant Higgs boson amplitude and that both of these are subleading with respect to all other (non-Higgs) diagrams through that order. Hence, a complete $\mathcal{O}(\alpha_S^2\alpha_W)$ calculation would be required to phenomenologically assess the relevance of such signal versus background effects in the C2HDM.

In summary, both the HL- and HE-LHC display clear potential in accessing production and decay channels of the heavy CP-even Higgs state of the C2HDM which can give direct access to key interactions that carry the hallmark of compositeness.

6.1.7 Axion-like particles at the HL- and HE-LHC

Contributors: M. Low, A. Mariotti, D. Redigolo, F. Sala, K. Tobioka

The main focus of this contribution is future search strategies for axion-like particles (ALPs) in the mass range between 1 and 90 GeV [589–591]. For simplicity we consider an ALP, a, that couples only to gauge bosons, including a non-zero coupling to gluons. We call this type of ALP a "KSVZ-ALP" because it is inspired by the simplest QCD axion model [592–594]. Such an ALP is perhaps the most theoretically compelling case and also the natural target for hadron colliders, such as the HL-LHC and

the HE-LHC. The effective Lagrangian for the KSVZ-ALP, below the Z mass, is

$$\mathcal{L}_{\rm int} = \frac{a}{4\pi f_a}\left[\alpha_s c_3 G^a\tilde{G}^a + \alpha_2 c_2 W^i\tilde{W}^i + \alpha_1 c_1 B\tilde{B}\right], \tag{6.1.27}$$

$$= \frac{a}{4\pi f_a}\left[\alpha_s c_3 G^a\tilde{G}^a + \alpha_{\rm em} c_\gamma F\tilde{F} + 2\alpha_2 c_W W^-\tilde{W}^+ + \frac{2\alpha_{\rm em}}{t_w} c_{Z\gamma} Z\tilde{F} + \alpha_2 c_w^2 c_Z Z\tilde{Z}\right], \tag{6.1.28}$$

where $\tilde{F}^{\mu\nu} = (1/2)\,\epsilon^{\mu\nu\rho\sigma}F_{\rho\sigma}$ for any field strength, $\alpha_1 = \alpha'$ is the GUT-normalised $U(1)_Y$ coupling constant, and $t_w = s_w/c_w$ where $c_w^2 = 1 - s_w^2 = m_W^2/m_Z^2$. The coefficients c_i encode the Adler-Bell-Jackiw (ABJ) anomalies of the global $U(1)$ symmetry (of which the ALP is the pseudo-Goldstone boson) with $SU(3)$ and $SU(2)\times U(1)_Y$. After EWSB, one can write

$$c_\gamma = c_2 + \frac{5}{3}c_1, \quad c_W = c_2, \quad c_Z = c_2 + t_w^4\frac{5}{3}c_1, \quad c_{Z\gamma} = c_2 - t_w^2\frac{5}{3}c_1. \tag{6.1.29}$$

For $m_a \lesssim m_Z$, the relevant two-body decays of a are to two photons and to two jets, with widths

$$\Gamma_{gg} = \frac{K_g\alpha_s^2 c_3^2}{8\pi^3}\frac{m_a^3}{f_a^2}, \qquad \Gamma_{\gamma\gamma} = \frac{\alpha_{\rm em}^2 c_\gamma^2}{64\pi^3}\frac{m_a^3}{f_a^2}, \tag{6.1.30}$$

where K_g depends on the ALP mass and includes higher-order QCD corrections (see Appendix A in Ref. [590]). The couplings in Eq. (6.1.27) can be generated by heavy vector-like fermions with a mass at $g_* f_a$, where g_* can be as large as 4π. Explicit realisations include: i) KSVZ "heavy axion" models where the axion potential is UV-dominated, the axion mass is heavier than expected from QCD contributions alone, and the decay constant, f_a, can be as low as a TeV solving the axion quality problem (see Ref.s [595–599] for heavy axion models and Ref. [600] for a discussion of the axion quality problem); ii) ALPs arising in standard paradigms addressing the EW hierarchy problem, such as supersymmetry, where spontaneous SUSY-breaking below $M_{\rm Pl}$ predicts, on general grounds, the existence of an R-axion [601, 602]. iii) Axion portal Dark Matter scenarios where the DM is freezing out through its annihilation into gluons pairs [603, 604]. In Fig. 6.1.15 we show the expected decay constant for an accidental Peccei-Quinn symmetry broken by dimension 6 operators at $M_{\rm GUT} = 10^{15}$ GeV, and the one for an axion portal which account for all of the DM relic abundance, see Ref. [590] for more details.

Barring a huge hierarchy among the anomaly coefficients, $c_{1,2} \gtrsim 10^2 c_3$, the width into gluons dominates over the one into photons, $\Gamma_\gamma/\Gamma_{gg} = \alpha_{\rm em}^2/(8K_g\alpha_3^2) \sim 10^{-4}$. ALPs that couple to gluons decay promptly in any kinematical configuration and mass range of interest for the LHC. When accounting for the gluon coupling, searches based on rare decays of SM particles (Higgs, Z, Υ, and B-mesons) into ALPs have a weaker bound on f_a because the dominant BR of the ALP is now into hadronic final states, while the searches look for final states with muons or photons. The only two relevant decay processes for our parameter space are $Z \to \gamma a$ and $\Upsilon_X \to \gamma a$, and the corresponding decay widths are given by

$$\Gamma(Z\to\gamma a) = \frac{\alpha_{\rm em}^2 c_{Z\gamma}^2}{96\pi^2 t_w^2}\frac{m_Z^3}{f_a^2}\left(1 - \frac{m_a^2}{m_Z^2}\right)^3, \tag{6.1.31}$$

$$\Gamma(\Upsilon_X\to\gamma a) = \frac{\alpha_{\rm em} c_{\gamma\gamma}^2}{\pi}\left(\frac{m_{\Upsilon_X}}{4\pi f_a}\right)^2\left(1 - \frac{m_a^2}{m_{\Upsilon_X}^2}\right)^3\Gamma(\Upsilon_X\to ll), \tag{6.1.32}$$

where $\Gamma(\Upsilon_X\to ll) = \Gamma_{\Upsilon_X}\cdot\mathcal{B}(\Upsilon_X\to ll)$, $\mathcal{B}(\Upsilon_{2S,3S}\to ll) \simeq 3.84\,, 4.36\%$ and $\Gamma_{\Upsilon_{2S,3S}} \simeq 20, 32$ KeV. These constraints, together with those from the LHC, are shown in Fig. 6.1.15.

The bound from Z decays, in Eq. (6.1.31), is based on the LEP search in Ref. [608] which has sensitivity down to 12 GeV. In this range, this search is more powerful than the inclusive bound from the total Z-width [283]. The bound from Υ decays, in Eq. (6.1.32), is based on BABAR data [605]

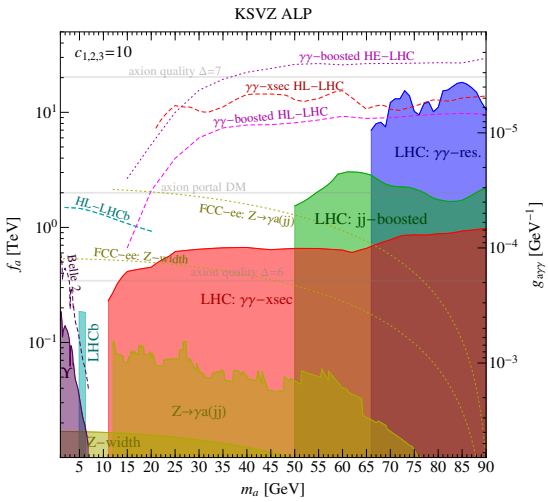

Fig. 6.1.15: Status of the current best experimental constraints on the KSVZ-ALP with ABJ anomalies $c_{1,2,3} = 10$. We include the BABAR bound on $\Upsilon \to \gamma a(jj)$ [605] **(purple)** and its rescaling at Belle II [606] **(purple dotted)**. LHCb bound derived in Ref. [590] from diphoton measurement around the B_s mass [607] **(cyan)**. The projection for HL is also shown **(dashed cyan)**. We also include LEP searches on $Z \to \gamma a(jj)$ [608] and constraints from the Z-width [283] **(yellow)** along with both of their rescalings at FCC-ee [609] **(yellow dotted)**. Constraints from inclusive cross section measurements at the Tevatron [610] and the LHC [611–613] derived in Ref. [589] **(red)** and the rescaled sensitivities of the 8 TeV cross section measurement [613] at the HL-LHC **(dashed red)** are shown. Finally, LHC bounds on boosted dijet resonances [614] reinterpreted for an ALP in Ref. [589] **(green)**, LHC searches for diphoton resonances [615–617] **(blue)**, and the sensitivity of the boosted diphoton resonance search based on the monojet trigger at the HL-LHC (3 ab^{-1}) and the HE-LHC (15 ab^{-1}) [591] **(dashed/dotted magenta)** are plotted. We also display **(gray)** two theory benchmarks motivated by freeze-out of ALP-mediated Dark Matter and by the QCD axion quality problem, see Ref. [590]. On the r.h.s. y-axis we show $g_{a\gamma\gamma} \equiv \frac{\alpha_{\rm em}}{\pi f_a} c_\gamma$ to make contact with the QCD axion notation.

corresponding to $1.21 \cdot 10^8$ Υ_{3S} and $0.98 \cdot 10^8$ Υ_{2S}. "Standard" inclusive diphoton resonance searches at the LHC do not probe masses below 65 GeV [615–617].

A first example of what can be done to improve the low mass reach is the CMS search for a dijet resonance recoiling against a hard jet [614] that we rescale here for an ALP produced in gluon fusion (see Ref. [589] for more details). As we see in Fig. 6.1.15, this probes ALPs down to 50 GeV. A second example is the bound from inclusive cross section measurements, derived in Ref. [589], that reach masses of 10 GeV. References [610–613] provide tables of the measured differential diphoton cross section per invariant mass bin, $\mathrm{d}\sigma_{\gamma\gamma}/\mathrm{d}m_{\gamma\gamma}$, with the relative statistical ($\Delta_{\rm stat}$) and systematical ($\Delta_{\rm sys}$) uncertainties. A conservative bound was derived in Ref. [589] assuming zero knowledge of the background and requiring

$$\sigma^{\rm th}_{\gamma\gamma}(m_a) < \left[m^{\rm Bin}_{\gamma\gamma} \cdot \frac{\mathrm{d}\sigma_{\gamma\gamma}}{\mathrm{d}m_{\gamma\gamma}} \cdot (1 + 2\Delta_{\rm tot}) \right] \cdot \frac{1}{\epsilon_S(m_a)}. \tag{6.1.33}$$

where $\Delta_{\rm tot} = \sqrt{\Delta^2_{\rm stat} + \Delta^2_{\rm sys}}$. The signal efficiency $\epsilon_S(m_a)$ (see Ref. [589] for its computation) does not go to zero below $p^{\rm min}_{T_{\gamma_1}} + p^{\rm min}_{T_{\gamma_2}}$ because the ALP can still pass the cuts recoiling against unvetoed jet activity in the diphoton cross section measurements. A lower limit on the invariant mass that can be measured, and thus on the testable m_a, is set by

$$m_{\gamma\gamma} > \Delta R^{\rm iso}_{\gamma\gamma} \sqrt{p^{\rm min}_{T_{\gamma_1}} p^{\rm min}_{T_{\gamma_2}}} \tag{6.1.34}$$

where $p^{\rm min}_{T_{\gamma_{1,2}}}$ are the minimal cuts on the photon transverse momenta, and $\Delta R^{\rm iso}_{\gamma\gamma} = 0.4$ is the standard

isolation requirement between the photons. A small mass range around the B_s mass is constrained by diphoton measurements at LHCb [607] as first derived in Ref. [590]. Projections for future stages of LHCb have also been derived in Ref. [590].

Here we discuss new LHC search strategies for the HL-LHC and the HE-LHC to improve the coverage in the f_a-m_a plane of KSVZ-like ALPs. The reaches of future experiments are summarised as dashed magenta lines named in Fig. 6.1.15, where we also display, for comparison, LHCb, the Belle II and FCC-ee projections.[11]

We show the reach of the HL-LHC from inclusive cross section measurements with the strategy outlined in the previous section, assuming the same diphoton trigger as in the 8 TeV run. Our signal cross section includes matching up to 2 jets and a K-factor accounting for NLO corrections computed with ggHiggs v3.5 [563–566] which includes full NNLO and approximate N^{3}LO corrections plus threshold resummation at N^{3}LL$'$. The error on the sensitivity is assumed to be dominated by the error on the measurements. In other words, we assume the MC uncertainties will be reduced below $\Delta_{\rm tot}$ (note that, at the present moment, MC uncertainties on the low-mass bins are at the level of 40% using SHERPA [195, 613, 618]). An unexplored direction in diphoton resonance searches is to reduce the photon isolation requirements and pass the trigger making the resonance recoiling against a hard jet. In Fig. 6.1.15 we show the sensitivity at the HL-LHC and the HE-LHC of a search based on this idea. The signal events are required to pass the existing monojet trigger (the leading jet with $p_{T_{j_1}} > 500$ GeV and $|\eta_{j_1}| < 2.5$). As a consequence the two photons produced from the boosted ALP are collimated: $\Delta R_{\gamma\gamma} \simeq 2m_a/p_{T_{j_1}} \lesssim 0.2\left(\frac{m_a}{50\ \text{GeV}}\right)$ where $p_{T_\gamma} \sim p_{T_{j_1}}/2$. To improve $S/\sqrt{B}$ we then require $p_{T_{\gamma_{1,2}}} > 120$ GeV and $\Delta R_{\gamma\gamma} < 0.8$ and bin the events in invariant mass bins with a constant width of 10 GeV. Since two photons fall into one isolation cone, $\Delta R^{\rm iso}_{\gamma\gamma} = 0.4$, standard photon isolation vetos the ALP signal. In order to access lower invariant masses, we modify the standard isolation requirement by simply subtracting the hardest photon (γ_1) in the isolation cone of every test photon, ($\gamma_{\rm test} \neq \gamma_1$). We require[12]

$$E_T^{\rm iso} - E_{T_{\gamma_1}} < 10\ \text{GeV} \quad \text{where} \quad E_T^{\rm iso} \equiv \sum_{i\neq\gamma_{\rm test}}^{\Delta R_{i,\gamma_{\rm test}}<0.4} E_{T_i}\,. \tag{6.1.35}$$

To validate our analysis we first checked that the standard isolation with $E_T^{\rm iso} < 10$ GeV in DELPHES can reproduce the photon fake rate from multijets and the real photon acceptance from the SM Higgs decay, given by Ref. [619]. We find that the isolation in Eq. (6.1.35) gives a similar fake rate and real photon acceptance to the standard ones while the photons from boosted ALP decay now pass the isolation. The modified isolation requirement allows us to go down to two-photon angular separation of $\Delta R \sim 0.1$.[13] Below this value the two photon showers will start to overlap and the photon identification will have to be modified [621, 622]. A similar strategy was employed by ATLAS in $Z \to \gamma a(\gamma\gamma)$ search (see Ref. [623]).

To estimate the sensitivities in Fig. 6.1.15 we simulated the SM background from $2\gamma+nj$, matched for $n = 1, 2$, and from $j\gamma+j$ with a jet faking a photon both at 14 and 27 TeV. We expect the background from $jj+j$ with two jets faking two photons to be subdominant. Finally, notice that the drop of sensitivity in the low mass range of our analysis is expected to ameliorate including the region of phase space with maximally asymmetric photon momenta $p_{T_{\gamma_2}} \ll p_{T_{\gamma_1}}$. Indeed $m^{\rm min}_{\gamma\gamma} = \sqrt{(p_{T_{j_1}} - p_{T_{\gamma_2}})p_{T_{\gamma_2}}}\,\Delta R^{\rm iso}$ after momentum conservation is imposed, so that minimising the momentum of the second photon becomes

[11] The Belle II and FCC-ee lines are obtained by rescaling of the present bounds from BABAR and LEP with the future luminosities of these experiments: 100 times more Υ_{2S}s and Υ_{3S}s are assumed for Belle II and 10^{12} Zs for FCC-ee.

[12] $E_T^{\rm iso}$ is usually calculated using calorimeter cells, while here we also include information of charged tracks. Objects with $E_{T_i} < 0.5$ GeVare not included in the sum [33].

[13] As minimal angular resolution we take for reference the square towers in the Layer 2 region of ATLAS ECAL [620].

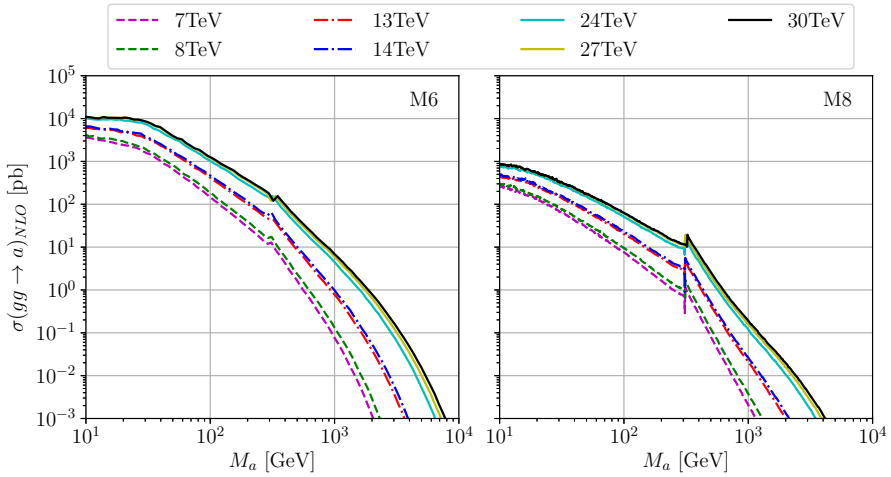

Fig. 6.1.16: Production cross section (dominated by gluon fusion) for the lightest pseudoscalar for the two benchmark models M6 (left) and M8 (right).

beneficial at low invariant masses (see Ref. [591]).

In conclusion, we showed how the sensitivity to KSVZ ALPs can be greatly improved at the HL-LHC and the HE-LHC. Both experiments have sensitivity that exceeds the one of FCC-ee. The type of searches discussed here will probe the parameter space of "heavy axion" models solving the strong CP-problem of the SM and probe SUSY scales, $g_* f_a$, as high as 100 TeV *independently* of any particular assumption on the structure of the SUSY spectrum, it will also probe well motivated scenarios of heavy Dark Matter freeze-in.

Our results have a broader application than the ones discussed here. For example, they can still be the strongest probe in ALP scenarios where the ALP also couples to fermions and the SM Higgs, such as in composite Higgs models [624, 625] where the couplings to photons and gluons are, in fact, generated by top loops. Last but not least, the invariant mass sensitivity can likely be further extended to lower masses by studying to what extent the two collimated photons themselves can trip the monophoton trigger [591], developing techniques to perform bump hunts with L1 triggers [626] and exploring the advantages of converted photons events in the inner tracker.

6.1.8 Search for light pseudoscalar with taus at HL-LHC

Contributors: G. Cacciapaglia, G. Ferretti, T. Flacke, H. Serodio

The discovered Higgs boson may be accompanied by additional light (pseudo-)scalars in models with an extended Higgs sector. We consider a pseudoscalar singlets ϕ, generically coupling as:

$$\mathcal{L} \supset -\sum_{\psi} \frac{iC_{\psi}^{\phi} m_{\psi} \phi}{f_{\phi}} \bar{\psi}\gamma^5\psi + \frac{\phi}{16\pi^2 f_{\phi}} \left(K_G^{\phi} G\tilde{G} + K_W^{\phi} W\tilde{W} + K_B^{\phi} B\tilde{B} \right), \tag{6.1.36}$$

where f_ϕ is a "decay constant" and ψ labels the SM fermions. We focus on models of composite Higgs with partial compositeness described in terms of confining hyper-quarks [624]. A universal feature of all these models is the presence of two such pseudoscalars ($\phi = a, \eta'$), whose couplings in Eq. (6.1.36) can be computed from the underlying model. Additional couplings, including the higher dimensional couplings to the Higgs boson, not included in Eq. (6.1.36), are also determined by the underlying theory (see Ref. [627] for details). In Ref. [627] we narrowed down this class of models to a total of twelve, providing possible benchmarks in the search of new physics.

We present results for two of the twelve models [628, 629], denoted respectively M6 and M8 in Ref. [627], which are those being studied on the lattice [630, 631]. The masses of the pseudoscalars can

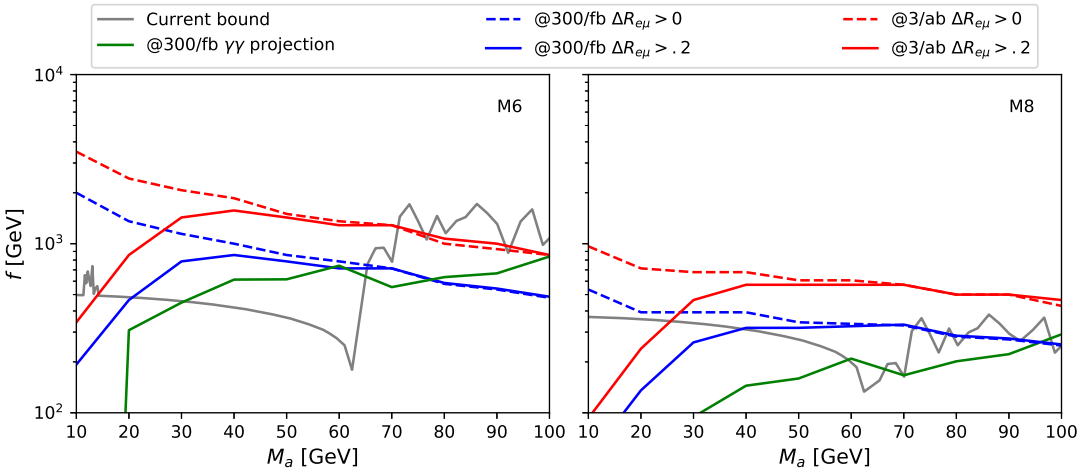

Fig. 6.1.17: Reach of the ditau search for the two models M6 (left) and M8 (right), compared to the existing bounds (gray lines). The existing bounds indicate the strongest exclusion amongst those arising from dimuon searches [632], diphoton searches [615, 617], and BSM decay width of the Higgs [537]. (The bounds from Ref. [300], that can be obtained adapting the analysis of Ref. [633] to these models, may also turn out to be competitive.) We have also indicated the current bounds obtained by adapting the results in Ref. [589] for diphotons (green). The projected reach is computed at 14 TeV using the HL-LHC detector simulation, for a luminosity of 300 fb^{-1}(blue) and 3 ab^{-1} (red), and two distinct cuts on $\Delta R_{\mu e}$.

be considered as free parameters, while their decay constants f_ϕ in Eq. (6.1.36) are related to the composite Higgs decay constant f, defined by $m_W = (g/2) f \sin\theta$, with $\theta \to \pi/2$ being the Technicolour limit [625, 627]. For small underlying hyper-quark masses, the lighter pseudoscalar a is nearly aligned with a spontaneously broken $U(1)$ symmetry and thus can be very light. Its total production cross-section is shown in Fig. 6.1.16 for fixed $f = 1$ TeV. The second pseudoscalar η' is related to an anomalous $U(1)$ (hence the name) and thus receives a larger mass from the strong dynamics.

We observe that the production cross-section of the pseudoscalars is rather large, in contrast to that of other light scalars arising in this class of models that only couple via EW interactions. Nevertheless, as their main decay channels suffer from large backgrounds, they are still fairly unconstrained in the low mass region, particularly between 14 and 65 GeV. In Ref. [625] we proposed a boosted search for the lighter pseudoscalar a in the (fully leptonic, opposite flavour) ditau channel between 10 and 100 GeV. Figure 6.1.17 shows the reach in the M_a/f plane for the two models above. A complementary proposed search in the diphoton channel has been discussed in the previous section, based on Ref. [589].

A crucial discriminating variable in such search, particularly for the low mass region, is the angular separation $\Delta R_{e\mu}$ between the electron and the muon. We present the reach estimated from a cut-and-count simulation with the conservative choice $\Delta R_{e\mu} > 0.2$ included or removed. In the plot we have not taken into account the systematic error in the background, but it is important to remark that, in order to take full advantage of the HL-LHC run, it should be kept below 2%. The additional cuts, discussed in Ref. [625], are: $p_{T\mu} > 50$ GeV, $p_{Te} > 10$ GeV, $\Delta R_{\mu j} > 0.5$, $\Delta R_{ej} > 0.5$, $p_{Tj} > 200$ GeV, $\Delta R_{\mu e} < 1$, $m_{\mu e} < 100$ GeV. Note that we also impose an upper bound on $\Delta R_{\mu e}$ to reduce the (mostly flat) $t\bar{t}$ background.

The heavier pseudoscalar η', not being a true Goldstone boson, could have a mass in the multi TeV range. Nevertheless, it may give observable signals at the LHC because it decays into final states such as $\gamma\gamma$, $Z\gamma$, ZZ, WW, $t\bar{t}$ and Zh (the last one via top loops). In Fig. 6.1.18 we present the lower bounds on f for the two models, in the $(M_a,\, M_{\eta'})$ mass plane. The white region corresponds to masses incompatible with the models [627]. The vertical band with a strong bound for $M_a \sim 215$ GeVcorresponds to Zh searches, which were not included in Ref. [627].

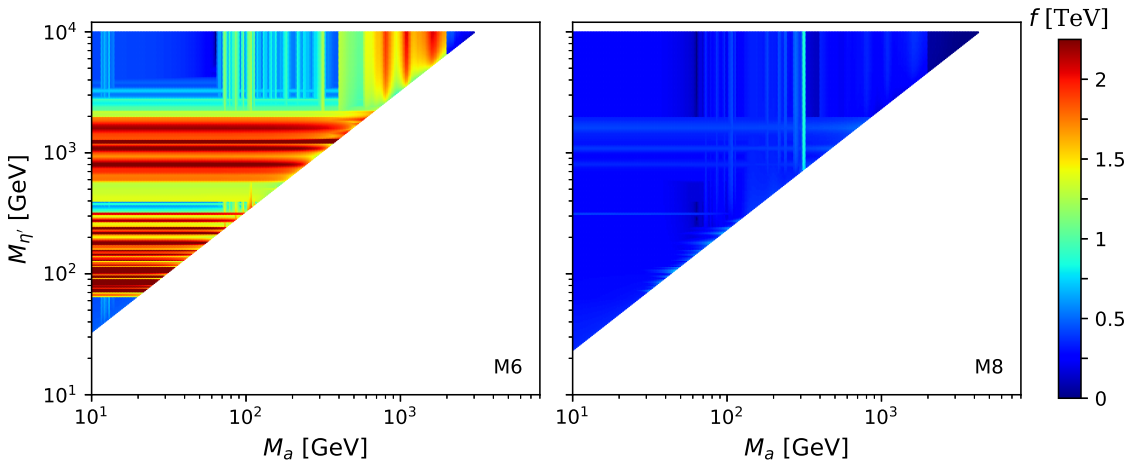

Fig. 6.1.18: Lower bound the Higgs decay constant f for the two benchmark models M6 (left) and M8 (right) in the presence of both pseudoscalars a and η'.

Figure 6.1.18 takes into account the relevant searches performed with the 2016 data of about 36 fb^{-1} of integrated luminosity at 13 TeV. Similar analyses can of course be performed for the remaining models, but the two presented in this work are amongst the least constrained by current data.

In conclusion, the HL and HE phases of the LHC present us with newer possibilities to search for BSM physics. The models discussed here provide concrete examples where new physics could arise both in the high and low mass regime, benefiting from both improvements.

6.1.9 Colour octet scalar into gluons and photons at HL-LHC

Contributors: G. Cacciapaglia, A. Deandrea, A.M. Iyer

We consider a colour octet scalar Φ which is present in various extensions of the SM, and in particular in composite models for the EW sector, where such a state can be a composite object made of fundamental fermions. The colour octet Φ can be produced by single and pair production at the LHC by QCD processes. Due to its nature and quantum numbers, in composite models, it can couple strongly to top quarks and give rise, at one loop in the fundamental theory, to a coupling to gluons and photons via a top loop and the topological anomaly. In particular it also gives rise to an effective vertex with a photon and a gluon which is highly suppressed in SM processes, giving rise to a distinctive mode for its search at the LHC. We therefore consider the decay mode $\Phi \to \gamma g$, thereby making it an exclusive signature for such a state. The effective Lagrangian for this interaction can be written as:

$$\mathcal{L} = a_1 \, f_{abc} G^a_{\mu\nu} G^{b\mu\nu} \Phi^c + a_2 \, f_{abc} f_{ade} \, \Phi^b \, \Phi^d \, G^c_{\mu\nu} \, G^e_{\mu\nu} + c \, G^a_{\mu\nu} \Phi^a B^{\mu\nu} \,, \tag{6.1.37}$$

where a_i are proportional to the strong coupling constant α_s while the ratio c/a depends on the model under consideration. The colour octet can decay into $t\bar{t}$, gg, $g\gamma$, or gZ. The gZ final state is subdominant in comparison to $g\gamma$ as it is suppressed by the Weinberg angle ($\Phi g\gamma$ vertex is derived from the $\Phi G^a_{\mu\nu} B^{\mu\nu}$ term in Lagrangian.). The corresponding comparison of rates of gg with respect to the $t\bar{t}$ final state is parameter dependent and is not considered here. It can however be taken into account by the corresponding reduction of the production rate $\sigma_{eff} = \sigma \times (1 - \mathcal{B}(t\bar{t}))^2$. In this note we are interested in exploring the possibility of the $g\gamma$ decay mode as a possible discovery prospect for the colour octet scalar. For scenarios considered in Ref. [627], where the colour octet arises as a bound state of colour-triplet fermions χ with hyper-charge $1/3$ or $2/3$, the branching fractions amongst the bosonic final states are fixed and given in Table 6.1.4.

We consider the following benchmarks for the mass of the coloured scalar Φ: $m_\Phi = 1, 1.5, 2, 2.5$ TeV. There are existing searches for the pair production of the scalar in the

	$Y_\chi = 1/3$	$Y_\chi = 2/3$
$\frac{\mathcal{B}(\Phi\to g\gamma)}{\mathcal{B}(\Phi\to gg)}$	0.048	0.19

Table 6.1.4: Values of ratios of BRs in di-bosons for the pseudoscalar octet for a mass of 1 TeV. The mass fixes the dependence due to the running of the strong gauge coupling, $\alpha_s(1\text{ TeV}) = 0.0881$ is used for this evaluation.

multi jet channel. For the branching fractions outlined in Table 6.1.4 we compare the efficiency for the multi jet final state corresponding to the existing searches with the following two final states corresponding to the signal: one single photon and three gluons; and two photons and two gluons. The parton level events are simulated at 14 TeV c.o.m. energy using MADGRAPH [67] and showering is done by PYTHIA 8 [50]. We use DELPHES 3 [33] for the detector simulation. The jets are reconstructed using FASTJET [67] with the standard AK4 jet reconstruction algorithm with $R = 0.4$ and $p_T = 60$ GeV. The strategy for the multi-jet final state in this contribution is similar to the analysis in CMS searching in the multi-jet channel for pair produced scalars [634]:

- The jets are reconstructed using the anti-kt algorithm with $R = 0.4$ and $p_T = 60$ GeV. Minimum of 4 jets are required for each event.
- Each jet is required to have a p_T of 80 GeV.
- In order to select the two best di-jet systems compatible with the signal, the four leading jets ordered in p_T are combined to create three unique combinations of di-jet pairs per event. Out of the three combinations, the di-jet configuration with the smallest $\Delta R_{dijet} = \sum_{i=1,2} |\Delta R_i - 0.8|$ is chosen where ΔR^i is the distance in the $\eta - \phi$ plane between the two jets in the i^{th} di-jet pair.
- Asymmetry parameter: Once a configurations is selected, two asymmetry parameters are constructed:

$$M_{asymm} = \frac{|m_{jj1} - m_{jj2}|}{m_{jj1} + m_{jj2}} \quad , \quad \Delta\eta_{asymm} = |\eta_{jj1} - \eta_{jj2}|. \tag{6.1.38}$$

  where m_{jjk} and η_{jjk} is the dijet mass and pseudorapidity combination of the k^{th} di-jet pair. Both these quantities are set < 0.1.

For the 3 jets and 1 photon final state there is no existing search undertaken thus far. Thus we adapt a similar criteria described above. Table 6.1.5 gives the signal and the corresponding background efficiencies (ϵ) for the two topologies and are simply $\epsilon = N_{cut}/N_{gen}$, where N_{cut} is the number of events which pass the cut and N_{gen} are the number of events generated. To facilitate the collider comparison between the gg and the $g\gamma$ decay for the colour octet scalar we define the following ratio:

$$\delta = \frac{S_{ggg\gamma}/\sqrt{B_{jjj\gamma}}}{S_{gggg}/\sqrt{B_{jjjj}}}, \tag{6.1.39}$$

which is computed for the two hypercharge assignments in Table 6.1.4. Here the number of signal or background events (S or B) at a given luminosity $\mathcal{L}$, is simply $\epsilon \times \sigma \times \mathcal{L}$. The ratio however, eliminates the dependence on the luminosity [14]. Using the numbers from Table 6.1.5, the results for the $jjj\gamma$ are given in the first two columns of Table 6.1.6.

The ratio in Eq. (6.1.39) eliminates the dependence on the production cross section and facilitates a transparent comparison of different decay modes. Given the large backgrounds in Table 6.1.5, the signal with the cuts used is not significant, thereby requiring a more detailed analysis. We now discuss the more optimistic 2 gluons and 2 photons final state.

[14] Note that for the $jjj\gamma$ signal $\sigma = \sigma_{prod} 2\,\mathcal{B}(\Phi \to g\gamma)$

	$4j$	$3j$+1γ	$2j$+ 2γ
Signal efficiency ϵ_S ($m_\Phi = 1$ TeV)	0.0067	0.0016	0.0593
Background Efficiency ϵ_B	0.00125	0.00035	0.000114
Background cross section (fb)	6800×10^3	18×10^3	18×10^3

Table 6.1.5: Pair production efficiencies for signal and background. The background cross-section is estimated by requiring the scalar sum of the parton $p_T > 1100$ GeV. The computed efficiencies are simply the ratio of events which pass the cuts to the total number of events generated. The background for $g\gamma g\gamma$ signal is still dominated by QCD $jjja$ background in comparison to the $\gamma\gamma$ + jets. The different efficiencies are a consequence of different selection criteria.

	$S_{ggg\gamma}$		$S_{gg\gamma\gamma}$	
	$Y_\chi = 1/3$	$Y_\chi = 2/3$	$Y_\chi = 1/3$	$Y_\chi = 2/3$
δ	0.84	3.33	1.36	20.56

Table 6.1.6: Comparison of the signal significances ratio δ (defined in Eq. (6.1.39)) between the $ggg\gamma$ and $gggg$ channels for $m_\Phi = 1$ TeV. Similar ratio is computed for the $gg\gamma\gamma$ final state.

In the case of 2 jets + 2 photons, there are only two combinatorial possibilities for the invariant mass reconstruction. Let the isolated photons be denoted as $\gamma_{1,2}$ and the jets as $j_{1,2}$. It is to be noted that the gluon jet and the photon from a given coloured scalar are fairly collimated. Thus in order to identify the correct pair of final states we take the hardest photon γ_1 and compute, $\Delta R_{\gamma_1 j_1}$ and $\Delta R_{\gamma_1 j_2}$ and extract the following:

$$\Delta R_{min} = min(\Delta R_{\gamma_1 j_1}, \Delta R_{\gamma_1 j_2}). \tag{6.1.40}$$

The presence of two photons greatly limits the QCD fake rate. We further impose a hard cut of 180 GeV on the transverse momentum of each photon. The large signal sensitivity in this case is an artefact that a simple p_T cut on the second photon reduces background drastically without affecting the signal significantly. The last two columns of Table 6.1.6 show the comparison of signal sensitivity between the $gg\gamma\gamma$ and $gggg$ channels, implying that they are both similar even for the pessimistic case of smaller branching fraction corresponding to $Y_\chi = 1/3$. The left plot of Fig. 6.1.19 shows the reconstructed invariant mass distribution and the right plot gives the signal significance as a function of luminosity for the optimistic case of $Y_\chi = 2/3$. Using the computation for production cross-sections for 14 TeV in [635], we estimate the sensitivity for different signal benchmarks from 0.3 to 3 ab^{-1}. With a high luminosity run one can reach a sensitivity close to $\sim 2.0\ \sigma$ for $m_\Phi = 1$ TeV. This, as well the sensitivity for the other benchmarks can be further improved by using information of signal kinematics and invariant mass cuts. We have performed a simplified preliminary study of the potential for the study of pair of a colour octet scalar decaying to gluon and photon at the LHC. This opens two additional possibilities for their searches corresponding to the $ggg\gamma$ and $gg\gamma\gamma$ final states. These final states not only serves as an unambiguous signature for colour octets but are also relatively cleaner than the conventional multi jet searches. We demonstrate that for the $gg\gamma\gamma$ channel, we can get a preliminary hint of the existence of the colour octet state at HL-LHC thereby strongly motivating the HE option of the LHC.

6.2 Spin 1 resonances

This section is devoted to the study of the prospects for vector resonances. These are neutral Z' and charged W', which are among the most standard benchmarks usually considered in studying the potential of future colliders, as well as RS gluons and other resonances arising from 2HDMs models.

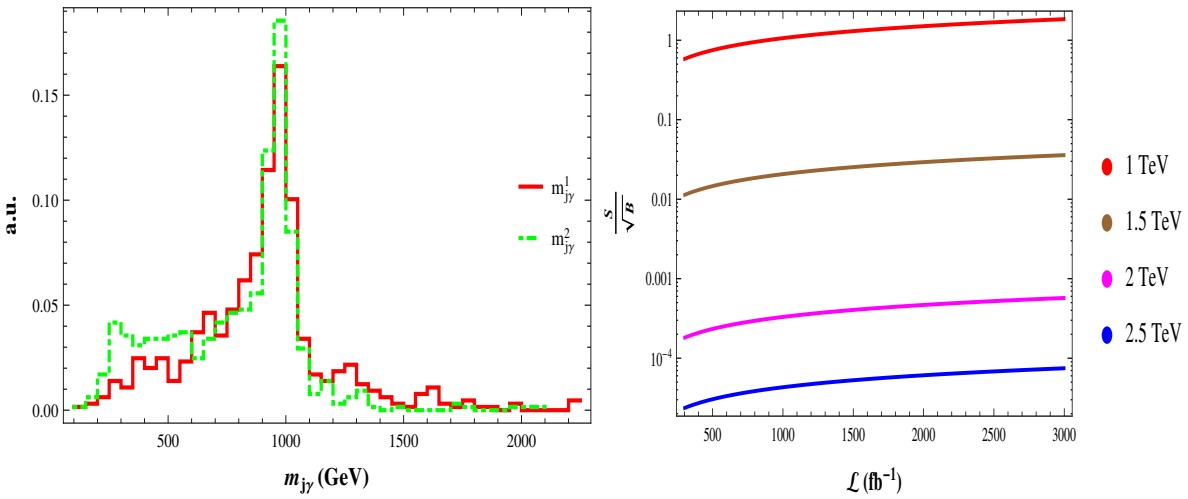

Fig. 6.1.19: Left: distribution of the two reconstructed invariant masses $m_{j\gamma}$ for the 1 TeV benchmark using the criterion in Eq. (6.1.40). $a.u.$ on the Y-axis denotes arbitrary units. Right: Sensitivity for the different signal benchmarks at 14 TeV COM energy for luminosities up to 3 ab^{-1}.

6.2.1 *Precision predictions for new dilepton and $t\bar{t}$ resonances at HL- and HE-LHC*

Contributors: M. Altakach, J. Fiaschi, T. Ježo, M. Klasen, I. Schienbein

We present higher order predictions for spin-1 resonance searches in two classes of observables, top-quark-pair production and dilepton production. In the former case, we use the PBZp code [636] which includes the NLO QCD corrections to the EW production of top-antitop pairs in the presence of a new neutral gauge boson implemented in the parton shower Monte Carlo program POWHEG [637–639]. The dilepton cross sections are calculated using the NLO+NLL code RESUMMINO [640] which matches a soft-gluon resummation at NLL accuracy to a fixed order NLO calculation.

We consider four models: the Un-Unified (UU) [641,642] and the Non-Universal (NU) [643,644] models, a leptophobic topcolour model (TC) (model IV in Ref. [645]), and the SSM [646]. The UU and NU models belong to the general class of G(221)= $SU(2)_1 \times SU(2)_2 \times U(1)_X$ gauge theories with an extra $SU(2)$ gauge symmetry. In the UU model the quarks and leptons belong to different representations of the two $SU(2)$ gauge factors whereas in the NU model the first two generations transform differently than the third generation. Both models take two input parameters, the mixing angle of the first stage symmetry breaking $t = \tan\phi = g_2/g_1$ and the mass of the heavy resonance $M_{Z'}$ (or $M_{W'}$). Exclusion limits on the parameters space for the G(221) models have been derived in Ref. [647] by performing a global analysis of low-energy precision data. Improved limits for the W' and Z' masses were found in Ref. [640] using LHC data at $\sqrt{s} = 7$ and 8 TeV. The TC model has three free parameters in addition to the resonance mass $M_{Z'}$: the width $\Gamma_{Z'}$, the relative strength (f_1) of the Z' coupling to right-handed up-type quarks w.r.t. left-hand up-type quarks, and similarly the relative strength (f_2) of the Z' coupling to right- and left-hand down-type quarks. Finally, in the SSM the only free parameters are the masses $M_{W'}$ and $M_{Z'}$.

We have chosen benchmark points such that the width $\Gamma_{Z'}$ in all models is the same as in the SSM. We have calculated the width in the SSM ($\Gamma^{\rm SSM}_{Z'}$) at leading order using PYTHIA 6 [68] with a running electro-magnetic coupling, $\alpha(M_{Z'})$, such that $\Gamma^{\rm SSM}_{Z'}/M_{Z'}$ slightly increases from 3.48% at $M_{Z'} = 1$ TeV to 3.61% at $M_{Z'} = 10$ TeV. This is achieved by setting the parameter $t = 1$ in the UU and NU models. As a consequence, the W' couplings to the SM fermions are the same in the SSM and NU cases, whereas the Z' couplings are different. For the TC model we set $f_1 = 1$ and $f_2 = 0$ which maximises the fraction of Z' bosons decaying into $t\bar{t}$ pairs. For the parton distribution functions (PDFs), in the $t\bar{t}$ case, we use a NLO PDF4LHC set for Monte Carlo studies (ISET = 90000 in LHAPDF6)

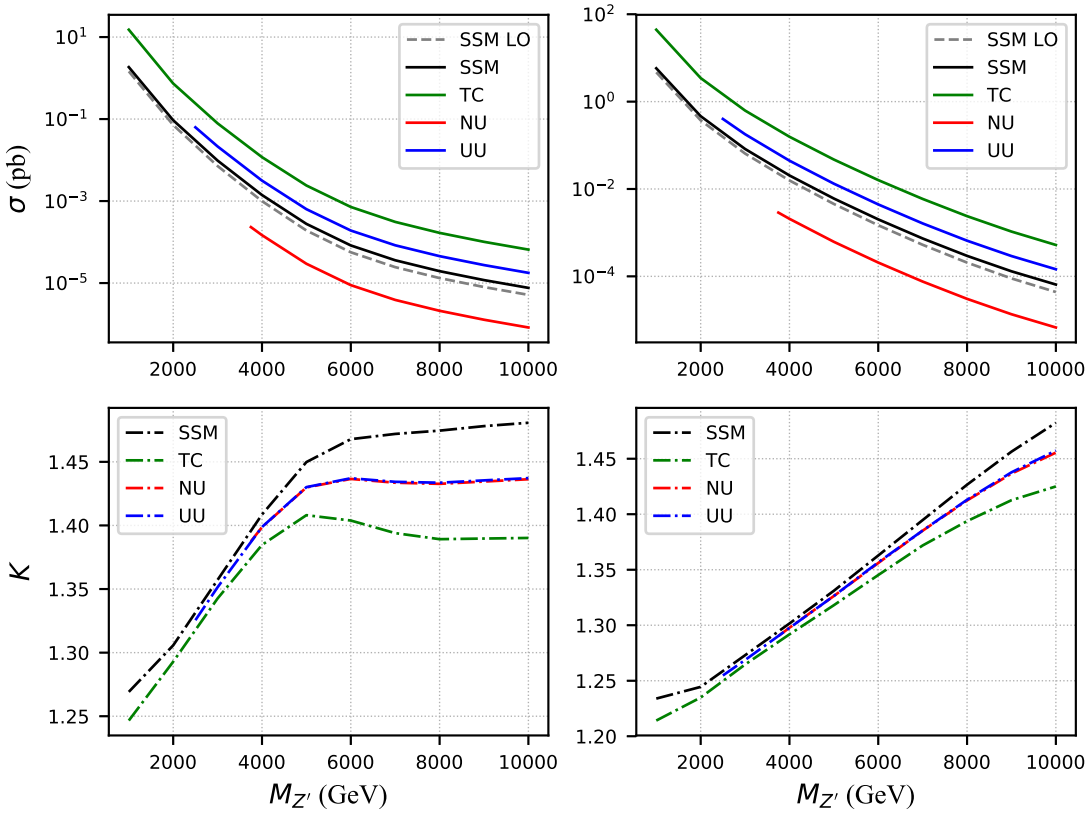

Fig. 6.2.1: Left: LO and NLO total cross section predictions in picobarns for $q\bar{q} \to Z' \to t\bar{t}[+g]$ (top) and the NLO/LO K-factors (bottom) at a c.o.m. energy $\sqrt{s} = 14$ TeV. Right: same as the left for a c.o.m. energy $\sqrt{s} = 27$ TeV.

and the renormalisation and factorisation scales μ_R and μ_F are identified with the invariant mass of the system. On the other hand, in the dilepton case, we use a NLO CT14 (ISET = 13100 in LHAPDF6) and the renormalisation and factorisation scales μ_R and μ_F are identified with the invariant mass of the system.

In Fig. 6.2.1, we show the total cross section for the EW production of $t\bar{t}$ pairs ($q\bar{q} \to Z' \to t\bar{t}[+g]$) in picobarn at a c.o.m. energy $\sqrt{s} = 14$ TeV (left) and 27 TeV (right). The results are given for LO (only for SSM) and NLO cross sections together with the NLO/LO K-factors (bottom) for the SSM, UU, NU, and TC in dependence of the Z' mass. No cut on the invariant mass of the $t\bar{t}$ pair has been applied.

In Fig. 6.2.2 we show the W' production cross sections at a c.o.m. energy $\sqrt{s} = 14$ TeV at NLO and NLO+NLL in the SSM as a function of the heavy gauge boson mass (top left). The ratios of the total cross sections at LHC14 at NLO and NLO+NLL over the LO cross section as a function of the W' mass is also presented (bottom left). Similarly, in the right side of Fig. 6.2.2 we show the same for a c.o.m. energy $\sqrt{s} = 27$ TeV. Interference terms between W and W' gauge bosons are included. The invariant mass of the lepton pair is restricted to $m_{ll} > 3M_{W'}/4$. Increasing the mass the threshold effects become more and more important leading to almost 16% (6%) increase of the cross section at $M_{W'} = 8$ TeV for $\sqrt{s} = 14$ (27) TeV.

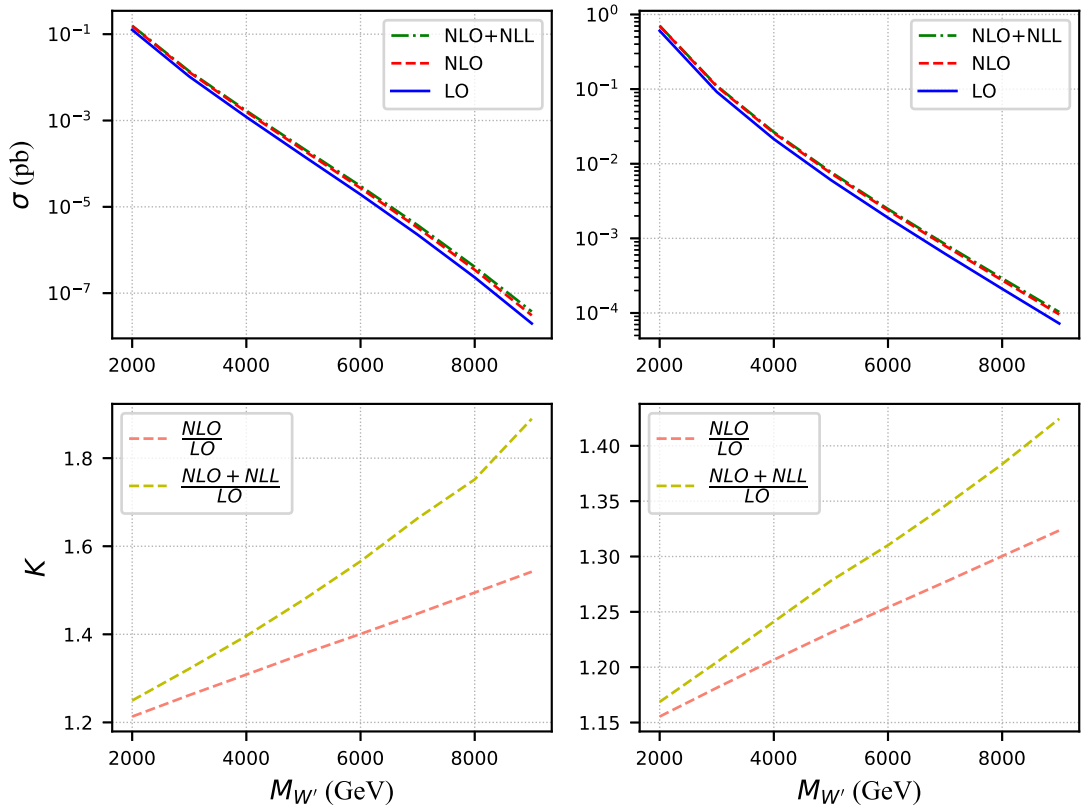

Fig. 6.2.2: Left: LO, NLO, and NLO+NLL total cross section predictions in picobarn for $q\bar{q} \to W|W' \to e\nu$ (top). The NLO/LO and the NLO+NLL/LO K-factors at a c.o.m. energy $\sqrt{s} = 14$ TeV (bottom). Right: same as the left for a c.o.m. energy $\sqrt{s} = 27$ TeV.

6.2.2 Searching for a RS gluon resonance in $t\bar{t}$ at the HL- and HE-LHC

Contributors: M. Narain, K. Pedro, S. Sagir, E. Usai, W. Zhang, CMS

Many models of new physics predict heavy resonances with enhanced couplings to the third generation of the SM [472, 648–654]. Thus, the study of the top quark can give important insight into the validity of such models. This analysis from CMS [655] presents projections for a heavy resonance, in particular a Randall–Sundrum Kaluza–Klein gluon (RSG) [472], decaying into a $t\bar{t}$ pair using the upgraded CMS Phase-2 detector design at HL-LHC, with a c.o.m. energy of 14 TeV. We also present projections for $t\bar{t}$ resonances at a c.o.m. energy of 27 TeV, accessible by the HE-LHC. Two distinct final states with either a single lepton or no leptons are considered. The topology where the hadronic decay products of the top quark are fully merged into a single jet is studied. For top quarks with a large boost (transverse momentum, p_T, greater than 400 GeV), an identification algorithm based on the soft-drop [504] jet grooming algorithm is used in combination with N-subjettiness [508] and subjet b-tagging algorithms to identify the decay of the top quark with no leptons. No lepton isolation is imposed because leptons are not expected to be well separated from other objects in final states.

The RSG signal processes are generated using PYTHIA 8.212 [68] at leading order (LO), assuming a decay width of 17%, and a RS parameter k value of $0.01 \times m_{\text{Planck}}$. The POWHEG 2.0 [638, 639, 656, 657] event generator is used to generate $t\bar{t}$ and single top quark events in the t-channel and tW channel to NLO accuracy. The single top quark events in the s-channel, Z+jets, and W+jets are simulated using MADGRAPH5_aMC@NLO 2.2.2 [67]. The PYTHIA event generator is

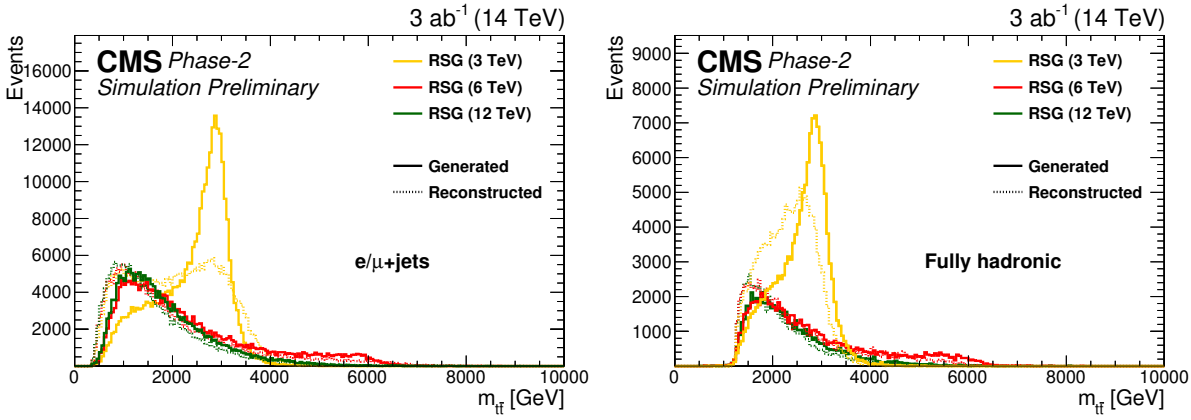

Fig. 6.2.3: Generated and reconstructed RSG mass distributions for the single-lepton (left) and fully hadronic (right) final states. The distributions are shown after full event selection in each final state. The signals are scaled to 1 pb.

used to simulate the QCD multijet and WW events at NLO. Parton showering, hadronisation, and the underlying event are simulated with PYTHIA, using the NNPDF 3.0 parton distribution functions (PDFs) and the CUETP8M1 [658, 659] tune for all Monte Carlo processes, except for the $t\bar{t}$ sample, which is produced with the CUETP8M2T4 [660] tune. The CMS Phase-2 detector simulation and the reconstruction of physics-level objects are simulated with the DELPHES software package [33]. The same signal and background processes are also considered for the HE-LHC projections in both final states at $\sqrt{s} = 27$ TeV, assuming the same number of pileup interactions as the HL-LHC. The reconstruction of physics-level objects for the HE-LHC is simulated with the DELPHES software package with the CMS Phase-2 detector design.

The particle flow (PF) algorithm [661] is used together with the pileup per particle identification (PUPPI) [410] method to reconstruct the final state objects such as electrons, muons, jets, and missing transverse momentum ($\mathbf{p}_{\mathrm{T}}^{\mathrm{miss}}$). In both final states, large-radius anti-k_{T} jets with a distance parameter of 0.8 (AK8) are used. The AK8 jets are required to have $p_T > 400$ GeV, $|\eta| < 4$, soft-drop mass between 105 and 220 GeV, and N-subjettiness ratio $\tau_3/\tau_2 < 0.65$. AK8 jets passing these requirements are referred to as t-tagged jets. In the single-lepton final state, the AK8 jets are selected if they are isolated from lepton by ΔR(lepton, AK8 jet) > 0.8 and events with more than one such AK8 jets are vetoed to be orthogonal to the fully hadronic final state. In the fully hadronic final state, the sum of the p_T of the two AK8 jets, H_{T}, is additionally required to be > 1.2 TeV and the angle between the two AK8 jets, $\Delta\phi$, is required to be > 2.1. We require single-lepton events to have exactly one electron with $p_T > 80$ GeV and $|\eta| < 3$ or one muon with $p_T > 55$ GeV and $|\eta| < 3$. In order to limit the background contribution from QCD multijet events, we require $\mathbf{p}_{\mathrm{T}}^{\mathrm{miss}} > 120$ (50) GeV in the electron (muon) channel, where $\mathbf{p}_{\mathrm{T}}^{\mathrm{miss}}$ is the magnitude of the missing transverse momentum defined as the the negative of the vector p_T sum of all reconstructed PF candidates.

Additionally, the single-muon events are required to have $H_T^{\mathrm{lep}} > 150$ GeV, where $H_T^{\mathrm{lep}} = \mathbf{p}_{\mathrm{T}}^{\mathrm{miss}} + p_T^{\mathrm{lep}}$. The single-lepton events are further required to have at least two AK4 jets with $p_T > 30$ GeV and $|\eta| < 4$. The leading and subleading jets are required to have a p_T greater than 185 (150) and 50 (50) GeV, respectively, in the electron (muon) channel. Because no isolation requirement is imposed on leptons, we require that the AK4 jet that is closest to the lepton is either separated by $\Delta R > 0.4$, or the magnitude of the lepton momentum that is transverse to the jet axis is greater than 25 GeV.

We use the Theta package [662] to derive the expected cross section limits at 95% C.L. on the production of a RSG decaying to $t\bar{t}$. The limits are computed using the asymptotic CLs approach. A binned likelihood fit on the distributions of reconstructed $t\bar{t}$ mass ($m_{t\bar{t}}$), shown in Fig. 6.2.3, is performed

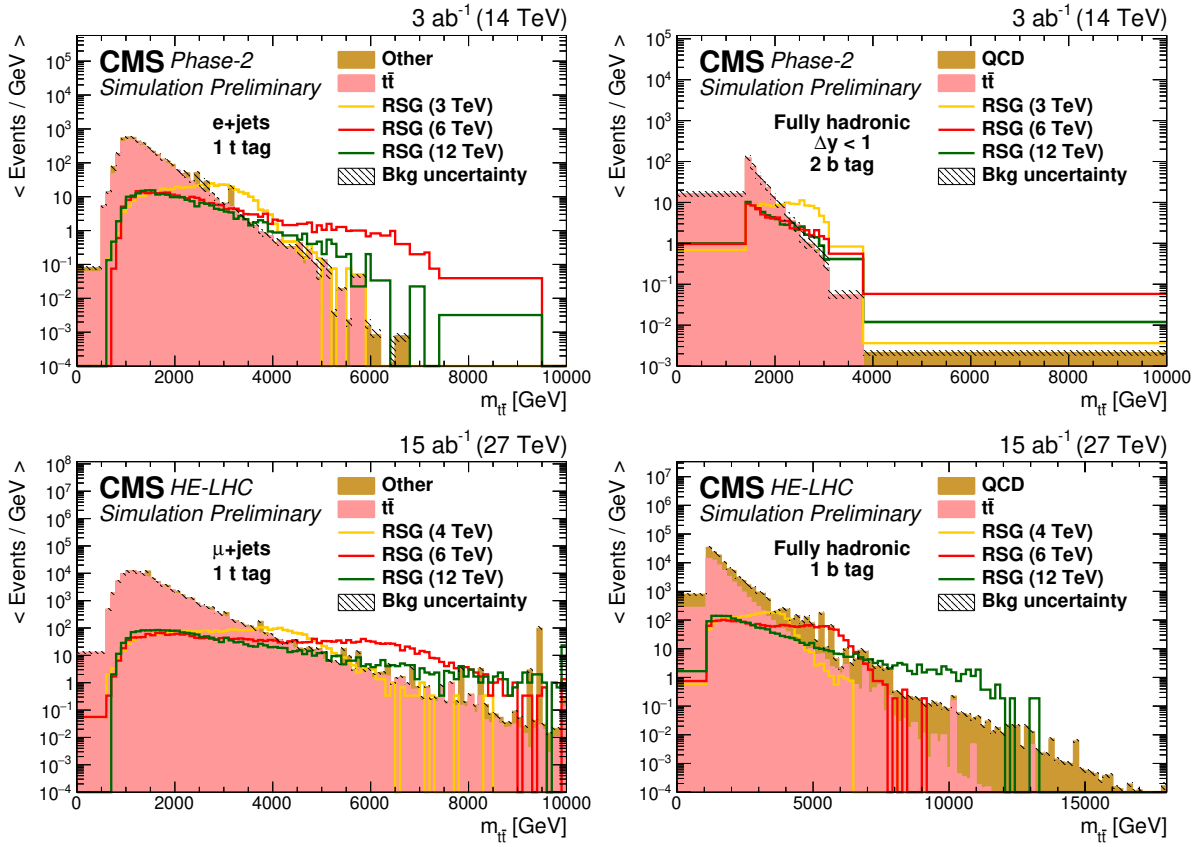

Fig. 6.2.4: Distributions of $m_{t\bar{t}}$ in events with single-electron and one t-tagged jet (top left) or zero lepton, $\Delta y < 1$ and two b tags (top right) for 3 ab^{-1} at 14 TeV. Distributions of $m_{t\bar{t}}$ in events with a single-muon and one t-tagged jet (bottom left) or zero lepton and one b-tag (bottom right) for 15 ab^{-1}at 27 TeV.

in both single-lepton and fully hadronic final states. To improve the sensitivity, the events are categorised based the number of subjet b tags (0, 1, or 2) and the rapidity difference ($|\Delta y(jet_1, jet_2)|$ <1 or >1) in the fully hadronic final state. Similarly, in the single-lepton final state, the categorisation is performed using the number of t-tagged jets (0 or 1) and the flavour of the lepton (e, μ). Example $m_{t\bar{t}}$ distributions of background and signal samples are shown in Fig. 6.2.4. Systematic uncertainties, following the recommendations in Ref. [411], are included in the fit as nuisance parameters with log-normal prior for both HL-LHC and HE-LHC. The results are limited by the statistical uncertainties in the background estimates. These uncertainties are scaled down by the projected integrated luminosity and are treated using the Barlow–Beeston light method [663, 664].

The expected limits at 95% C.L. and discovery reaches at 3 and 5σ for the combined single-lepton and fully hadronic final states are shown in Fig. 6.2.5. The RSG with masses up to 6.6 (10.7) TeV are excluded at 95% C.L. for a projected integrated luminosity of 3 (15) ab^{-1} at the HL-LHC (HE-LHC). This extends the current Run-2 limits of 4.5 TeV based on 36 fb^{-1} [665]. The discovery reach for an RSG is computed to be 5.7 (9.4) TeV at 5σ at the HL-LHC (HE-LHC).

6.2.3 $Z' \to t\bar{t}$ searches at HL-LHC

Contributors: A. Duncan, ATLAS

HL-LHC prospects at for Z' bosons in the $t\bar{t}$ final state were presented in Ref. [666] based on the event selection and systematic uncertainties from the Run-1 analysis with 20.3 fb^{-1} collected at $\sqrt{s} = 8$ TeV in Ref. [667]. These results have been updated [668] using a more recent parameterisation of the b-tagging efficiencies and misidentification rates as shown in Ref. [357] and are summarised below.

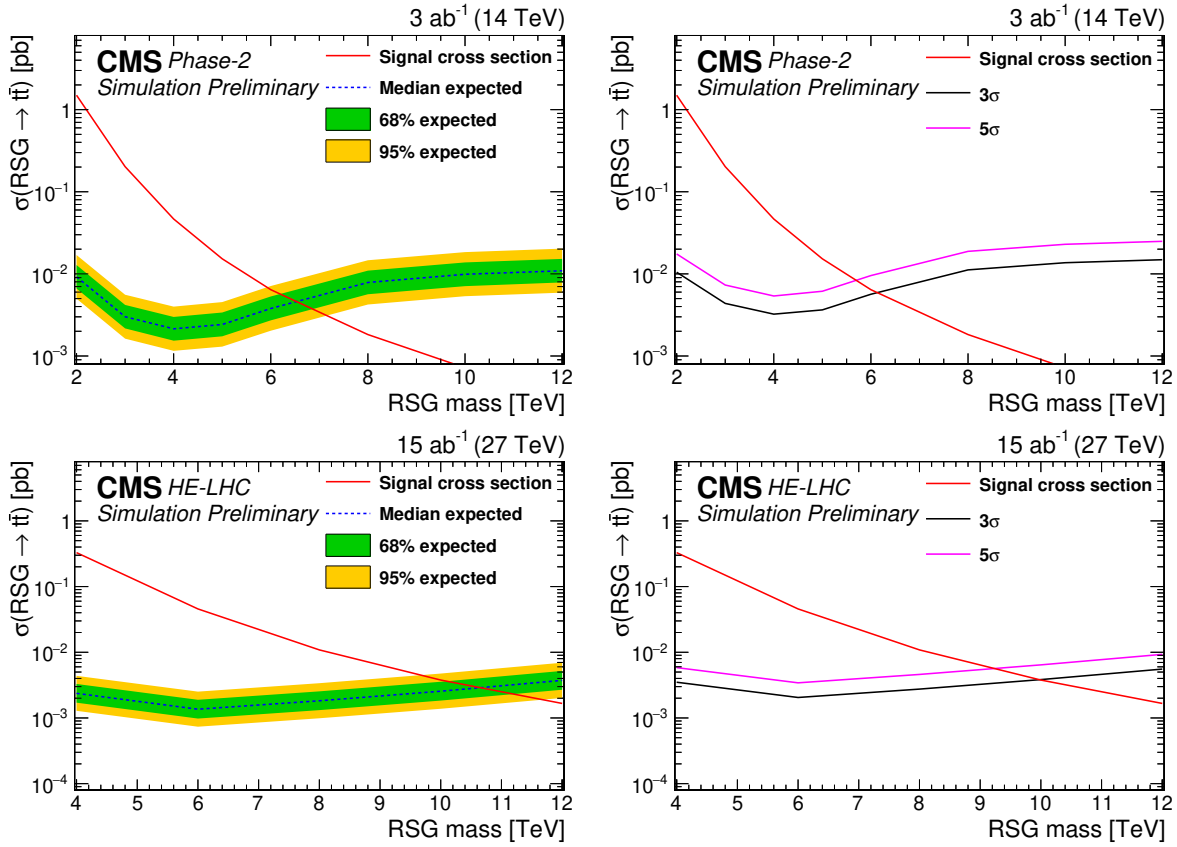

Fig. 6.2.5: 95% C.L. expected upper limits (left) and 3σ and 5σ discovery reaches (right) for a RSG decaying to $t\bar{t}$ at 3 ab^{-1} at 14 TeV (top) and 15 ab^{-1}at 27 TeV (bottom) for the combined single-lepton and fully hadronic final states.

The analysis looks for a narrow width Z' boson in a final state in which one of the W bosons from the top quark decays to two jets and the other decays to a lepton (electron or muon) and a neutrino ($t\bar{t} \to WbWb \to \ell\nu bqq'b$). Events are required to contain exactly one lepton, several jets and at least a moderate amount of missing transverse momentum must be present. Events are separated into boosted and resolved channels with most of the signal events falling in the former category. In the resolved channel the decay products of the hadronic top-quark decay are reconstructed as three separate jets and in total events must contain at least four jets. In the boosted channel, the hadronic top-quark decay products are highly boosted and end up in one broad large-radius jet. Events are selected if at least one large-radius jet and one jet (from the other top-quark decay) is present. Subsequently $m_{t\bar{t}}$ is reconstructed based on the reconstruction of the W bosons and b-jets in the event. Using $m_{t\bar{t}}$ as discriminant, upper limits are set on the signal cross section times BR as a function of the Z' boson mass. Using as benchmark a Topcolour-assisted Technicolour Z'_{TC2} boson with a narrow width of 1.2%, Z'_{TC2} bosons can be excluded up to masses of $\simeq 4$ TeV with 3 $\mathrm{ab}^{-1}$of pp collisions as shown in Fig. 6.2.6. This mass limit is conservative due to the use of systematic uncertainties from the Run-1 analysis [667]. These uncertainties are already smaller in the Run-2 analysis [669] and will be further reduced at the time of the HL-LHC. In particular the systematic uncertainty in the boosted channel is now reduced due to the significant improvements of the performance of boosted jets in Run-2 (in particular using more tracking information to look for sub-jets within the large-radius jets). This gain in performance also improves the signal over background ratio. In addition, the usage of the top-tagger algorithm will help to further reject background.

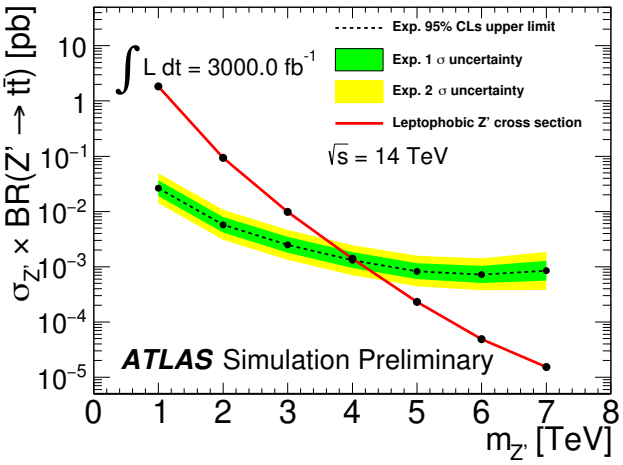

Fig. 6.2.6: Expected upper limits set on the cross section $\times$ BR of the Topcolour Z$'$ boson for masses $1-7$ TeV, with 3 ab^{-1} of simulated 14 TeV pp collisions compared to the theoretical signal cross section.

6.2.4 High mass dilepton (ee, $\mu\mu$, $\tau\tau$) searches at the HE-LHC

Contributors: C. Helsens, D. Jamin, M. Selvaggi

Models with extended gauge groups often feature additional $U(1)$ symmetries with corresponding heavy spin-1 bosons. These bosons, generally referred to as Z', would manifest themselves as a narrow resonance in the dilepton invariant mass spectrum. Among these models are those inspired by Grand Unified Theories, motivated by gauge unification, or a restoration of the left-right symmetry violated by the weak interaction. Examples include the Z' bosons of the E_6 motivated theories [670–672] and Minimal models [673]. The SSM [672] posits a $Z'_{\rm SSM}$ boson with couplings to fermions that are identical to those of the SM Z boson.

The decay products of heavy resonances are in the multi-TeV regime and the capability to reconstruct their momentum imposes stringent requirement on the detector design. In particular, reconstructing the track curvature of multi-TeV muons requires excellent position resolution and a large lever arm. In this section, the expected sensitivity is presented for a $Z' \to \ell\ell$ (where $\ell = {\rm e}, \mu$) and $Z' \to \tau\tau$ separately.

Monte Carlo simulated event samples were used to simulate the response of the future detector to signal and backgrounds. Signals are generated with PYTHIA 8.230 [68] using the leading order cross-section from the generator. All lepton flavour decays of the $Z'_{\rm SSM}$ are generated assuming universality of the couplings. The Drell-Yan background has been generated using MADGRAPH5_aMC@NLO 2.5.2 [67] at leading order only. A conservative overall k-factor of 2 has been applied to all the background processes to account for possibly large higher order QCD corrections.

For the $\ell\ell$ final-states events are required to contain two isolated leptons with $p_T > 500$ GeVand $|\eta| < 4$. For the $\tau\tau$ final state we focus solely on the fully hadronic decay mode which is expected to drive the sensitivity. The $\tau\tau$ event selection requires the presence of two reconstructed jets with $p_T > 500$ GeVand $|\eta| < 2.5$ identified as hadronic τ's. To ensure orthogonality between the ℓ and τ final states, jets overlapping with isolated leptons are vetoed. Additional mass dependent selection criteria on the azimuthal angle between the two reconstructed τ's are applied to further improve the QCD background rejection (see Table 6.2.1).

The left and central panels of Fig. 6.2.7 show the invariant mass distribution for a 6 TeV $Z'_{\rm SSM}$ in the ee and $\mu\mu$ channels. The mass resolution is better for the ee channel, as expected. The right panel of Fig. 6.2.7 shows the transverse mass [15] of a 6 TeV signal for the $\tau\tau$ channel. Because of the presence of neutrinos in τ decays, the true resonance mass cannot be reconstructed. Several arbitrary choices are

[15] The transverse mass is defined as $m_T = \sqrt{2p_{\rm T}^{Z'} * E_{\rm T}^{\rm miss} * (1 - \cos\Delta\phi(Z', E_{\rm T}^{\rm miss}))}$.

Z' mass [TeV]	$\Delta\phi(\tau_1,\tau_2)$	$\Delta R(\tau_1,\tau_2)$	$E_{\mathrm{T}}^{\mathrm{miss}}$
2	> 2.4	> 2.4 and < 3.9	> 80 GeV
4	> 2.4	> 2.7 and < 4.4	> 80 GeV
6	> 2.4	> 2.9 and < 4.4	> 80 GeV
8	> 2.6	> 2.9 and < 4.6	> 80 GeV
10	> 2.8	> 2.9 and < 4.1	> 60 GeV
12	> 2.8	> 3.0 and < 3.6	> 60 GeV
14	> 3.0	> 3.0 and < 3.3	> 60 GeV

Table 6.2.1: List of mass dependent cuts optimised to maximise the sensitivity for the $Z' \to \tau\tau$ search.

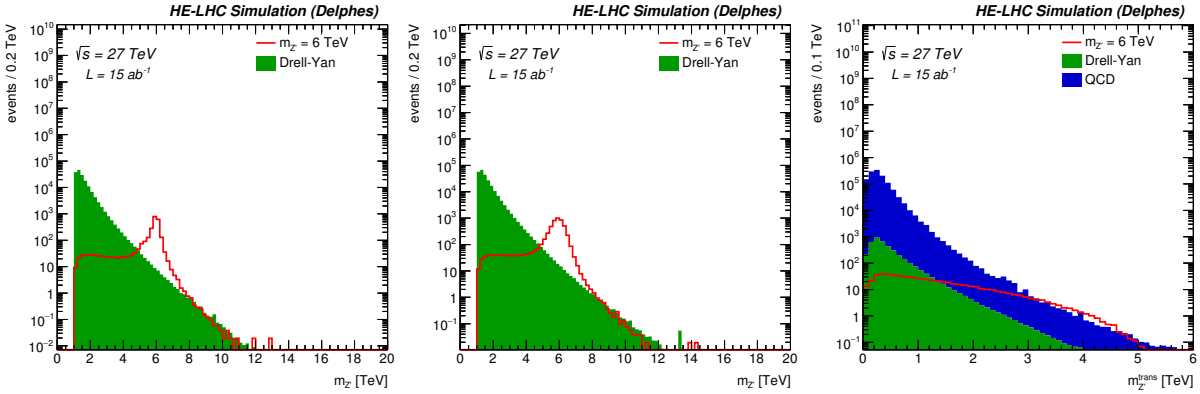

Fig. 6.2.7: Left, centre: Invariant mass for a 6 TeV signal after full event selection for ee channel (left) and $\mu\mu$ channel (centre). Right: Transverse mass for a 6 TeV signal after full event selection for the $\tau\tau$ channel.

possible to approximate the Z' mass. The transverse mass provided the best sensitivity and was therefore used to set limits and determine the discovery reach in $\tau\tau$ decay mode.

Hypothesis testing is performed using a modified frequentist method based on a profile likelihood that takes into account the systematic uncertainties as nuisance parameters that are fitted to the expected background predicted from Monte Carlo. For the ee and $\mu\mu$ analyses, the dilepton invariant mass is used as the discriminant, while for the $\tau\tau$ channel the transverse mass is used. A 50% uncertainty on the background normalisation is assumed.

The 95% C.L. exclusion limit obtained using 15 $\mathrm{ab}^{-1}$of data for the combination of the ee and $\mu\mu$ channels is shown in Fig. 6.2.8 (left) for a list of 6 different Z' models. A detailed discussion on model discrimination at HE-LHC following the observation of an excess at the HL-LHC can be found in Section 6.2.9. We simply note here that it is possible to exclude a Z' with $m_{Z'} \lesssim 10-13$ TeV (depending on the model) at $\sqrt{s} = 27$ TeV with 15 ab^{-1}. Figure 6.2.8 (right) shows the integrated luminosity required to reach a 5σ discovery for a Z'_{SSM} decaying leptonically as a function of the mass of the heavy resonance. Despite a worse di-lepton invariant mass resolution for the $\mu\mu$ final state, the $Z' \to ee$ and $Z' \to \mu\mu$ channel display very similar performances, due to the low background rates and a higher muon reconstruction efficiency. Acceptance for electron could have been recovered by optimising the isolation criteria, but was not done in this study. With the full dataset 15 ab^{-1}, a Z'_{SSM} up to $m_{Z'} \approx 13$ TeV can be discovered. Figure 6.2.9 shows the exclusion limits for 15 ab^{-1} of data (left) and the required integrated luminosity versus mass to reach a 5σ discovery (right) for the $\tau\tau$ resonances. We find that a Z'_{SSM} with $m_{Z'} \approx 6.5$ TeV can be discovered or excluded. As expected, the $Z' \to \tau\tau$ final-state yields to a worse discovery potential compared to the $\ell\ell$ final states because of the presence of a much larger background contribution as well as the absence of narrow mass peak.

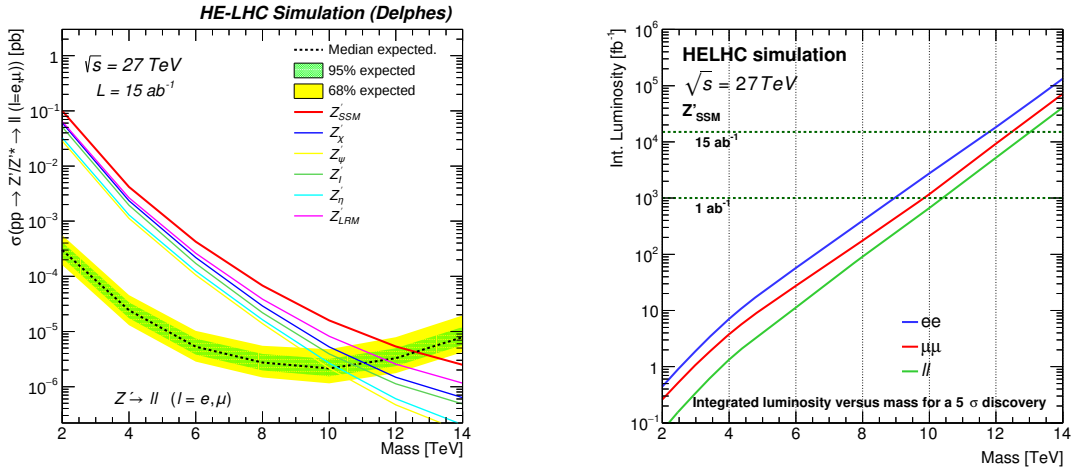

Fig. 6.2.8: Exclusion limit versus mass for the dilepton (ee,$\mu\mu$) channel (left) and luminosity for a 5σ discovery (right) comparing ee, $\mu\mu$ and combined channels.

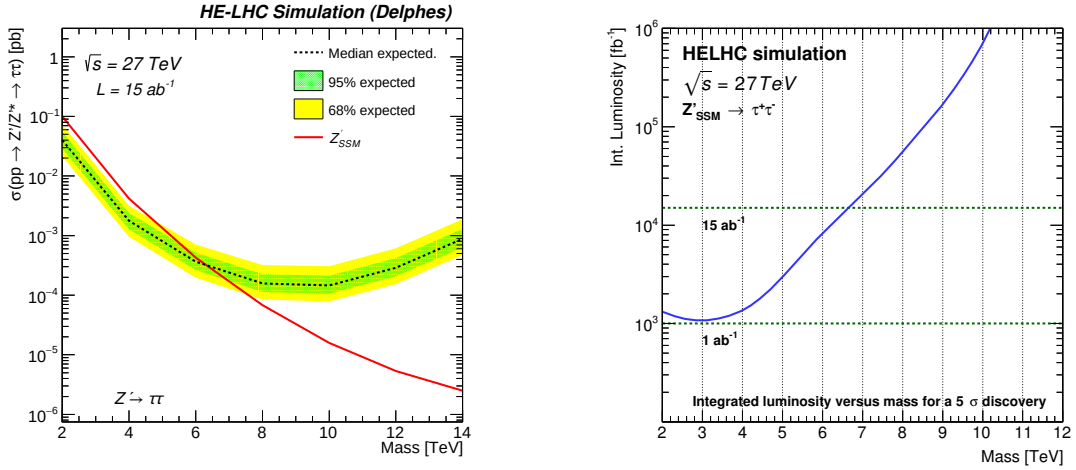

Fig. 6.2.9: Exclusion limit versus mass for the ditau channel (left) and luminosity for a 5σ discovery (right).

6.2.5 *Prospects for $Z' \to e^+e^-, \mu^+\mu^-$ searches at the HL- and HE-LHC*

Contributors: M. Bugge, D. Hayden, S. Kubota, G. Lee, J-P Ochoa, J-C Rivera Vergara, M. Wielers, ATLAS

The sensitivity to narrow Z' bosons decaying into the e^+e^- or $\mu^+\mu^-$ final state is studied for pp collisions at several c.o.m. energies: $\sqrt{s} = 13$, 14, and 15 TeV with 3 ab^{-1}, as well as $\sqrt{s} = 27$ TeV with 15 ab^{-1}. Results are based on studies documented in Ref. [668]. The latter is only studied in the e^+e^- channel since the work presented here is based on the latest layout of the upgraded ATLAS detector for the HL-LHC which is not optimised for extremely high muon momentum measurements. The study supersedes that from Ref. [674] since it uses the latest detector layout and higher pileup conditions. In addition, it was found that the signal cross-sections used in the previous analysis were too high.

The projection study relies on MC simulation for the signal based on PYTHIA 8 [50], the NNPDF23LO PDF set [675], and the A14 set of tuned parameters [676] for the parton shower, hadronisation, and the underlying event. The dominant Drell-Yan background source is generated with POWHEG-BOX [639, 657] and the CTEQ6L1 PDF set [52] interfaced with PYTHIA 8 for the parton shower, hadronisation and the underlying event using the AZNLO set of tuned parameters [677]. Generated samples also include off-shell production.

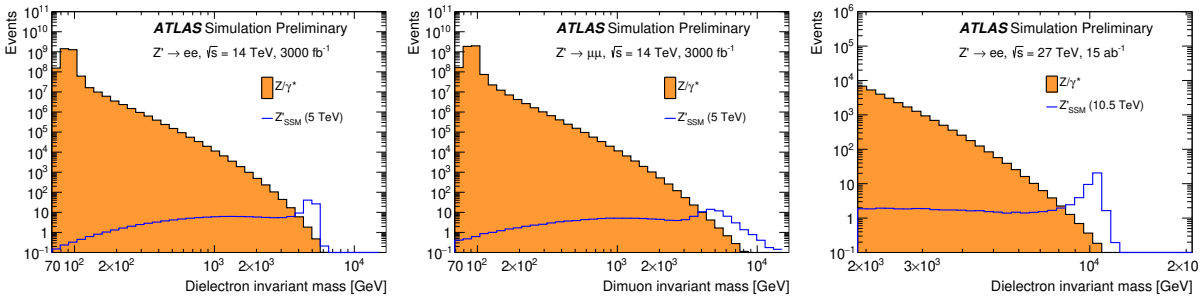

Fig. 6.2.10: Invariant mass distributions for events satisfying all selection criteria in the dielectron and dimuon channels at $\sqrt{s} = 14$ TeV and in the dielectron channel at $\sqrt{s} = 27$ TeV. Distributions of the Drell-Yan background and SSM Z' signal with a mass of 5.0 (10.5) TeV are shown for $\sqrt{s} = 14$ (27) TeV.

The event selection proceeds in a way similar to the analysis of the 13 TeV data with 36.1 fb^{-1} [442]. Events must pass either the single-electron trigger requirements with $p_{\mathrm{T}} > 22$ GeVand $|\eta| < 2.5$ or the single-muon trigger requirements with $p_{\mathrm{T}} > 20$ GeVand $|\eta| < 2.65$. Triggered events are further required to contain exactly two electrons with $p_{\mathrm{T}} > 25$ GeV and $|\eta| < 2.47$ (excluding the barrel-endcap calorimeter transition region $1.37 < |\eta| < 1.52$) or two muons with $p_{\mathrm{T}} > 25$ GeVand $|\eta| < 2.65$. The electrons and muons have to satisfy the *tight* and *high-*p_{T} identification requirements, respectively. Invariant mass distributions of the reconstructed dielectron and dimuon candidates are shown in Fig. 6.2.10 for the Z'_{SSM} signal and the dominant Drell-Yan background. Background from diboson (WW, WZ, ZZ) and top-quark production is not considered as their contribution to the overall SM background is negligible for dilepton invariant masses ($m_{\ell\ell}$) exceeding 2 TeV. This background is more pronounced at lower masses and was found to amount to around 10% (20%) of the total background for an invariant mass of 1 TeV (300 GeV), see Ref. [442]. In the dielectron channel, additional background arises from W+jets and multijet events in which at most one real electron is produced and one or more jets satisfy the electron selection criteria. While this background is negligible in the dimuon channel, it amounts to approximately 15% of the total background for $m_{\ell\ell} > 1$ TeV [442] in the dielectron channel. This source of background is neglected in the analysis below but accounted for in the systematic uncertainties. The differences in the shape of the reconstructed Z' mass distributions in the dielectron and dimuon channels arise from differences in momentum resolution for electron and muon reconstruction. The differences in the shape of the dielectron mass distributions at $\sqrt{s} = 14$ TeV and 27 TeV arise from differences in the rapidity distributions.

The experimental and theoretical uncertainties assumed in this analysis are estimated from the Run-2 results [442] but scaled down to account for the increased statistical precision available at the HL-LHC following the recommendations in Ref. [7]. Only the largest sources of uncertainties are considered. As the uncertainties vary with $m_{\ell\ell}$, the uncertainties are expressed relative to the value of $m_{\ell\ell}$ given in TeV.

The experimental systematic uncertainties due to the reconstruction, identification, and isolation of electrons are negligible while those for muons add up to approximately $2.5\% \times m_{\ell\ell}$ [TeV]. Systematic uncertainties due to the energy resolution and scale are set to $1.5\% \times m_{\ell\ell}$ [TeV]. The uncertainties due to the resolution and reconstruction of the leptons are added in quadrature to the dominant sources of theoretical uncertainty due to the PDFs. The uncertainties due to the choice of PDF set are taken to be $2.5\% \times m_{\ell\ell}$ [TeV] and the uncertainties in the parameters of the nominal PDF set are assumed to be $5\% \times m_{\ell\ell}$ [TeV]. Overall these uncertainties add up to $6.5\% \times m_{\ell\ell}$ [TeV]. As the search looks for an excess in the high $m_{\ell\ell}$ tail, the sensitivity is primarily limited by the statistical uncertainties.

The statistical analysis relies on the Bayesian approach [678] used in Ref. [442]. The same statistical model implementation is used in the following for both the calculation of the exclusion limits and the discovery reach, the latter being based on a profile likelihood ratio test assuming an asymptotic

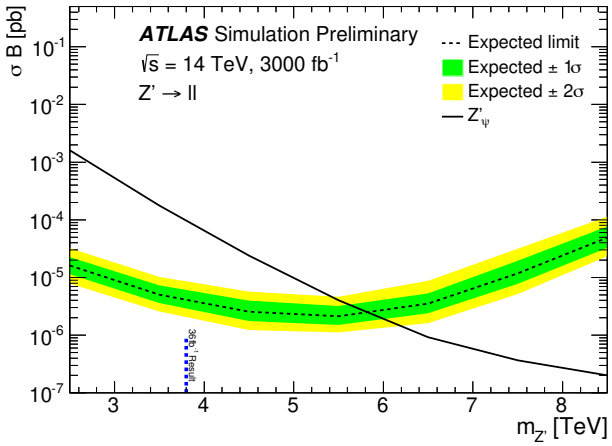

Fig. 6.2.11: Expected (dashed black line) upper limit on cross-section times branching fraction $\sigma \times \mathcal{B}$ as a function of the Z' boson mass in the combined dielectron and dimuon channels for $\sqrt{s} = 14$ TeV collisions and an integrated luminosity value of 3 ab^{-1}. The 1σ (green) and 2σ (yellow) expected limit bands are also shown. The predicted $\sigma \times \mathcal{B}$ for Z'_ψ production is shown as a black line. These limits are based on a NNLO cross-section calculation including off-shell production ($pp \to Z'/Z'^* \to \ell\ell$). The blue marker shows the current limit obtained with the Run-2 analysis based on 36 fb^{-1} of data.

test statistic distribution. In the absence of a signal, 95% C.L. upper limits are placed on the production cross section of a Z' boson times its branching fraction $\sigma \times \mathcal{B}$ to a single lepton generation, assuming lepton universality. These limits are extracted using Z' templates binned in $m_{\ell\ell}$ for a series of Z' masses in the range between 2.5 TeV and 11.5 TeV. The interpretation of results is performed in the context of the SSM and the E_6 ψ model. Exclusion limits are shown in Fig. 6.2.11 assuming the E_6 ψ model as a benchmark. These limits, as well as the ones presented below, are based on a NNLO cross-section calculation including off-shell production.

Lower mass limits and the discovery reach for the different models and $\sqrt{s}$ values at the HL-LHC are summarised in Table 6.2.2. The projected exclusion limits extend the current Z'_{SSM} (Z'_ψ) lower mass limit of 4.5 (3.8) TeV obtained using 36.1 fb^{-1} of data taken at $\sqrt{s} = 13$ TeV to 6.5 (5.8) TeV for $\sqrt{s} = 14$ TeV. Higher limits are obtained in the dielectron channel due to the superior energy resolution of the calorimeter as compared with the momentum resolution for muons in the muon spectrometer. Assuming similar detector performance at the LHC and HL-LHC, a corresponding lower mass limit of 5.4 (4.8) TeV are expected with 300 fb^{-1}at the end of Run-3. The 95% C.L. limits and discovery reach are close due to the absence of background at very high $m_{\ell\ell}$. Compared to the results presented in Ref. [357] the discovery reach reported here is higher due to a change in how the reach is calculated. The analysis described here is based on the shape of the signal and background $m_{\ell\ell}$ distributions while the 5σ significance was calculated in a mass range between $m(Z')/2$ to infinity in Ref. [357].

The discovery reach and lower exclusion limits at 95% C.L. in mass are also calculated for a detector at the HE-LHC in the dielectron channel. This is done assuming the same physics performance as for the ATLAS detector at the HL-LHC. The exclusion limits and the discovery reach are summarised in Table 6.2.3.

At the HE-LHC, Z'_{SSM} and Z'_ψ bosons can be discovered up to 12.8 TeV and 11.2 TeV, respectively, thus increasing their discovery reach by 6.5 TeV compared to the HL-LHC, *i.e.* an increase in the discovery potential by a factor of two. In case Z' bosons are not discovered yet, the HE-LHC will be able to further rule out Z'_{SSM} and Z'_ψ bosons up to 12.8 TeV and 11.4 TeV, respectively.

Decay	$\sqrt{s} = 13$ TeV		$\sqrt{s} = 14$ TeV		$\sqrt{s} = 15$ TeV	
	Exclusion	Discovery	Exclusion	Discovery	Exclusion	Discovery
$Z'_{\mathrm{SSM}} \to ee$	6.0 TeV	5.9 TeV	6.4 TeV	6.3 TeV	6.7 TeV	6.6 TeV
$Z'_{\mathrm{SSM}} \to \mu\mu$	5.5 TeV	5.4 TeV	5.8 TeV	5.7 TeV	6.0 TeV	5.9 TeV
$Z'_{\mathrm{SSM}} \to \ell\ell$	6.1 TeV	6.1 TeV	6.5 TeV	6.4 TeV	6.7 TeV	6.7 TeV
$Z'_{\psi} \to ee$	5.3 TeV	5.3 TeV	5.7 TeV	5.6 TeV	6.1 TeV	6.0 TeV
$Z'_{\psi} \to \mu\mu$	4.9 TeV	4.6 TeV	5.2 TeV	5.0 TeV	5.5 TeV	5.2 TeV
$Z'_{\psi} \to \ell\ell$	5.4 TeV	5.4 TeV	5.8 TeV	5.7 TeV	6.1 TeV	6.1 TeV

Table 6.2.2: Expected 95% C.L. lower limit on the Z' mass in TeV in the dielectron and dimuon channels and their combination for two benchmark Z' models for different centre of mass energies assuming 3 $\mathrm{ab}^{-1}$of data to be taken at the HL-LHC. In addition, the discovery reach for finding such new heavy particles is shown.

Decay	Exclusion [TeV]	Discovery [TeV]
$Z'_{\mathrm{SSM}} \to ee$	12.8	12.8
$Z'_{\psi} \to ee$	11.4	11.2

Table 6.2.3: Lower limits at 95% C.L. and discovery reach on the Z'_{SSM} and Z'_{ψ} boson mass in the dielectron channel assuming 15 $\mathrm{ab}^{-1}$of pp data to be taken at the HE-LHC with $\sqrt{s} = 27$ TeV.

6.2.6 $W' \to e\nu, \mu\nu$ or $tb, t \to b\ell\nu$ searches at HL-LHC

Contributors: M. Bugge, J. Donini, D. Hayden, G. Lee, K. Lin, M. Marjanovic, L. Vaslin, M. Wielers, ATLAS

Resonances decaying into a lepton and missing transverse momentum

The sensitivity to W' resonances decaying into an electron or a muon and a neutrino is studied for $\sqrt{s} = 14$ TeV pp collisions at the HL-LHC [668]. Such resonances would manifest themselves as an excess of events above the SM background at high transverse mass m_{T}. The SM background mainly arises from processes with at least one prompt final-state electron or muon, with the largest source being off-shell charged-current Drell-Yan (DY), leading to a final state with an electron or a muon and a neutrino. Other non-negligible contributions are from top-quark pair and single-top-quark production, neutral-current DY process, diboson production, and from events in which one final-state jet or photon satisfies the lepton selection criteria. This last component of the background, referred to in the following as the multijet background, receives contributions from multijet, heavy-flavour quarks and γ + jet production; it is one of the smallest backgrounds in this analysis. It is evaluated in a data-driven way in the Run-2 analysis and cannot be yet reliably estimated from MC samples and is therefore not considered here. It was found to be negligible in the muon channel at $m_{\mathrm{T}} > 3$ TeV in the Run-2 analysis based on 79.8 fb^{-1} of pp collisions [679]. In the electron channel, the contribution constitutes around 10% of the total background at $m_{\mathrm{T}} \approx 3$ TeV and mainly arises from jets misidentified as electrons.

The projection study relies on MC simulation with the SSM W' signal generated using PYTHIA 8 in the same setup as for the SSM Z' signal described in Section 6.2.5. This also includes off-shell production. The charged and neutral Drell-Yan background is also generated in the same way. Background from $t\bar{t}$ events is produced with POWHEG-BOX and the NNPDFL30NNLO PDF set interfaced with PYTHIA 6 using the A14 tune. Diboson events are generated with SHERPA [195] and the CT10 PDF set [680].

The event selection proceeds similarly to the Run-2 analysis described in Ref. [679]. Events are required to satisfy the single-election or single-muon triggers. The single electron trigger selects events containing at least one electron with $p_{\mathrm{T}} > 22$ GeV and $|\eta| < 2.5$, while the single muon trigger requires a muon with $p_{\mathrm{T}} > 20$ GeV and $|\eta| < 2.65$. Events are required to contain exactly one lepton which can be either an electron or a muon. Muons must have $p_{\mathrm{T}} > 55$ GeV and $|\eta| < 2.65$ as well as satisfy the *high-*p_{T} identification criteria [7]. Electrons must have $p_{\mathrm{T}} > 55$ GeV and $|\eta| < 1.37$ or

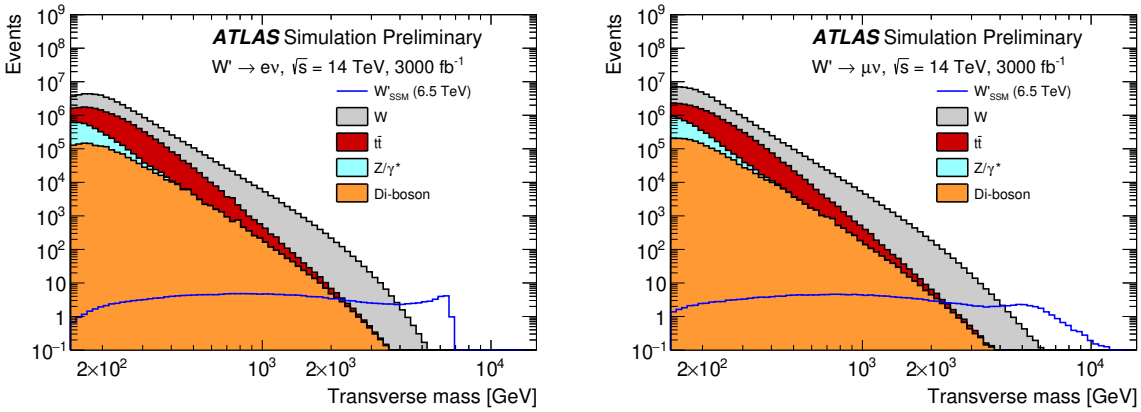

Fig. 6.2.12: Transverse mass distributions for events satisfying all selection criteria in the electron and muon channels of the $W' \to \ell\nu$ search. The different background contributions are shown as a stacked sum and the expected signal distributions for a W' boson with a mass of 6.5 TeV is shown. The bin width is constant in $\log m_{\mathrm{T}}$.

$1.52 < |\eta| < 2.47$, as well as satisfy the *tight* identification criteria. These p_{T} thresholds are the same as in the Run-2 analysis and are motivated by the triggers which select events containing leptons with loose identification criteria and without isolation requirements. Though not applied in this analysis, such events will be needed for the data-driven background subtraction methods, as employed in Run-2, to work. The p_{T} thresholds for these "looser" triggers are not yet available and therefore in the following it is assumed that the thresholds will be similar to those used in Run-2. The magnitude of the missing transverse momentum ($E_{\mathrm{T}}^{\mathrm{miss}}$) must exceed 55 GeV (65 GeV) in the electron (muon) channel. Events in both channels are vetoed if they contain additional leptons satisfying loosened selection criteria, namely electrons with $p_{\mathrm{T}} > 20$ GeVsatisfying the *medium* identification criteria or muons with $p_{\mathrm{T}} > 20$ GeV passing the *loose* muon selection.

The total acceptance times efficiency in the electron (muon) channel decreases from a value of $\sim 85\%$ (70%) at a W' mass of 1 TeV to $\sim 65\%$ (60%) for masses between 5 and 9 TeV. The resulting m_{T} distributions are shown in Fig. 6.2.12 for both the expected background and the W' signal with a mass of 6.5 TeV.

Systematic uncertainties arise from both experimental and theoretical sources. Since the uncertainties from the Run-2 analysis are found to increase as a function of m_{T} these are parametrised as a percentage of the m_{T} value expressed in units of TeV. The uncertainties are then scaled down to account for the increased statistical power at the HL-LHC according to recommendations in Ref. [7]. The experimental systematic uncertainties due to the reconstruction, identification, and isolation of muons result in a value of $2.5\% \times m_{\mathrm{T}}$ [TeV], while these uncertainties are negligible for electrons. Systematic uncertainties due to the energy resolution and scale are set to $2.5\% \times m_{\mathrm{T}}$ [TeV]. The main systematic uncertainties in the $E_{\mathrm{T}}^{\mathrm{miss}}$ calculation and on the jet energy scale are found to be negligible in Run-2 and are therefore not considered in this analysis. Theoretical uncertainties are related to the production cross sections estimated from MC simulation. The effects when propagated to the total background estimate are significant for charged and neutral current DY, and to some extent for top-quark production, but are negligible for diboson production. No theoretical uncertainties are considered for the W' boson signal in the statistical analysis. The largest uncertainties arise from the PDF uncertainty in the DY background. The uncertainties due to the choice of PDF set are taken to be $5\% \times m_{\ell\ell}$ [TeV] and the uncertainties in the parameters of the nominal PDF set are assumed to be $2.5\% \times m_{\ell\ell}$ [TeV]. The uncertainty in the multijet background in the electron channel is assumed to be $2.5\% \times m_{\mathrm{T}}$ [TeV]. Overall these uncertainties in the background event yield add up to $\sim 7\% \times m_{\mathrm{T}}$ [TeV]. As the search looks for an excess in the high m_{T} tail, the sensitivity is primarily limited by the statistical uncertainties.

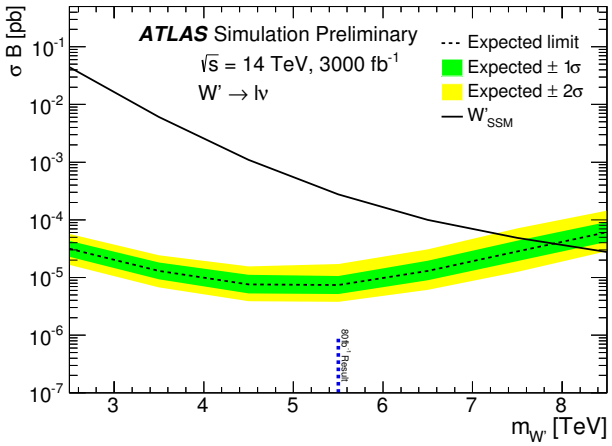

Fig. 6.2.13: Expected (dashed black line) upper limit on cross section times branching fraction ($\sigma \times \mathcal{B}$) as a function of the W' boson mass in the electron, muon, and combined electron and muon channels of the $W' \to \ell\nu$ search assuming $3\,\mathrm{ab}^{-1}$of data. The 1σ (green) and 2σ (yellow) expected limit bands are also shown. The predicted $\sigma \times \mathcal{B}$ for W' production in the SSM is shown as a black line. These limits are based on a NNLO cross-section calculation including off-shell production ($pp \to W^{'}/W^{'*} \to \ell\nu$). The blue marker shows the current limits obtained with the latest Run-2 analysis based on $79.8\,\mathrm{fb}^{-1}$ of data.

The statistical analysis relies on a Bayesian approach to set cross section times branching fraction upper limits and a profile likelihood approach to derive the discovery reach as for the $Z' \to \ell\ell$ search described above. The branching fraction corresponds to that for decays into a single lepton generation, assumed to be universal in the combination of the two channels. The 95% C.L. upper limit on $\sigma \times \mathcal{B}$ as a function of W' mass is shown in Fig. 6.2.13 for an integrated luminosity of $3\,\mathrm{ab}^{-1}$after combination of the electron and muon channels. The upper limits on $\sigma \times \mathcal{B}$ for W' bosons start to weaken above a pole mass of $\sim$ 5 TeV, which is mainly caused by the combined effect of a rapidly falling signal cross section towards the kinematic limit and the increasing proportion of the signal being produced off-shell in the low-m_{T} tail of the signal distribution. The W' bosons in the SSM can be excluded up to masses of 7.6 (7.3) TeV in the electron (muon) channel. These limits are based on a NNLO cross-section calculation including off-shell production for the signal. The limits in the electron channel are stronger due to the superior energy resolution of the calorimeter for high-momentum electrons as compared to that of the muon spectrometer for high-momentum muons. The combination of the two channels increases the limits to just over 7.9 TeV. This is an improvement of more than 2 TeV with respect to the current exclusion limits using $79.8\,\mathrm{fb}^{-1}$ of $\sqrt{s} = 13$ TeV data. For comparison, assuming the performance of the upgraded ATLAS detector and a luminosity of $300\,\mathrm{fb}^{-1}$, W' masses up to 6.7 TeV can be excluded for the combined electron and muon channels. Though the detector resolutions for the upgraded detector at the HL-LHC are applied, this is a good approximation of the reach with the current detector at the end of LHC Run-3.

The discovery reach is based on a 5σ significance. In the context of the SSM, W' bosons can be discovered up to masses of 7.7 TeV. The discovery reach is shown in Table 6.2.4 together with the exclusion limits discussed above. As can be seen, the discovery reach typically is only few hundred GeV lower than the mass limits obtained with a background-only hypothesis. The similarity of the values for the discovery reach and the exclusion limit is expected, as in the high-m_{T} tail the background contribution approaches zero, while the number of signal events is about three. The expected reach with $300\,\mathrm{fb}^{-1}$of data will be 1.2 TeV lower assuming the same detector performance.

Decay	Exclusion [TeV]	Discovery [TeV]
$W'_{\mathrm{SSM}} \to e\nu$	7.6	7.5
$W'_{\mathrm{SSM}} \to \mu\nu$	7.3	7.1
$W'_{\mathrm{SSM}} \to \ell\nu$	7.9	7.7

Table 6.2.4: Expected 95% C.L. lower limit on the W' mass in the electron and muon channels as well as their combination in the context of the SSM assuming 3 $\mathrm{ab}^{-1}$of data. In addition, the discovery reach for finding such new heavy particles is shown. These limits are based on a NNLO cross-section calculation including off-shell production ($pp \to W^{'}/W^{'*} \to \ell\nu$).

Resonances decaying into a top quark and a bottom quark

The search for W' bosons in the lepton plus neutrino channel is sensitive to large mass scales but it is not sensitive to right-handed W' bosons. This can be alleviated by searching for $W'_{\mathrm{R}} \to t\bar{b}$ decays with subsequent decays $t \to Wb$ and $W \to \ell\nu$. The final-state signature consists of two b-quarks, one charged lepton (electron or muon) and $E_{\mathrm{T}}^{\mathrm{miss}}$ from the escaping neutrino.

Events are required to pass one of the single-lepton triggers: at least one electron with $p_{\mathrm{T}} > 22$ GeV and $|\eta| < 2.5$ or at least one muon with $p_{\mathrm{T}} > 20$ GeV and $|\eta| < 2.65$. Electrons must satisfy the *tight* identification requirements [681] requirements and have $p_{\mathrm{T}} > 25$ GeV and $|\eta| < 2.47$ but outside the barrel–endcap transition region, $1.37 < |\eta| < 1.52$. Similarly, muon candidates must meet the *tight* identification criteria [682] and have $p_{\mathrm{T}} > 25$ GeV and $|\eta| < 2.65$.

The projection study relies on MC simulation for the W' signal based on MADGRAPH5_aMC@NLO with the NNPDF23LO PDF set interfaced to PYTHIA 8 and the A14 tune for the parton shower, hadronisation, and the underlying event. Background for the various top-quark production mechanisms is generated by POWHEG-BOX. In the case of the dominant $t\bar{t}$ background, events are produced with the CTEQ6L1 PDF set and interfaced to PYTHIA 6 using the PERUGIA2012 tune [683]. W+jets events are produced with MADGRAPH5_aMC@NLO with the NNPDF23NLO PDF set interfaced to PYTHIA 8 and the A14 tune, whereas Z+jets events are produced with POWHEG-BOXand the CT10 PDF set interfaced to PYTHIA8 and the AU2 tune [684]. Diboson events are generated as for the $W' \to \ell\nu$ search above.

The dominant background processes are the production of $t\bar{t}$ pairs and W+jets. Smaller contributions are also expected from single top quarks (t-channel, Wt and s-channel), Z+jets and diboson (WW, WZ, and ZZ) production. All background processes are modelled with MC simulation. Instrumental background coming from misidentified electrons, referred to as the multijet background, is also present but it is very small and further suppressed by applying dedicated selection criteria, and it is neglected in the following. Events are required to satisfy $E_{\mathrm{T}}^{\mathrm{miss}} > 80$ (30) GeV in the electron (muon) channel as well as $m_{\mathrm{T}}^{W} + E_{\mathrm{T}}^{\mathrm{miss}} > 100$ GeV.

The W' candidates are built from W boson and top-quark candidates. The W bosons are reconstructed from the lepton–$E_{\mathrm{T}}^{\mathrm{miss}}$ system with the longitudinal momentum component of the neutrino from the W decay extracted by imposing a W-boson mass constraint. This W boson candidate is then combined with all selected jets in the event to reconstruct a top-quark candidate as the W+jet combination that has a mass closest to the top-quark mass. The jet used to form the top-quark candidate is referred to as "b_{top}". Finally, the candidate W' boson is reconstructed by combining the top-quark candidate with the highest-p_{T} remaining jet (referred to as "b_1"). The invariant mass of the reconstructed $W' \to t\bar{b}$ system ($m_{t\bar{b}}$) is the discriminating variable of this search. An event selection common to all signal regions is defined as: lepton $p_{\mathrm{T}} > 50$ GeV, $p_{\mathrm{T}}(b_1) > 200$ GeV, and $p_{\mathrm{T}}(\mathrm{top}) > 200$ GeV. As the signal events are expected to be boosted, the angular separation between the lepton and b_{top} is required to satisfy $\Delta R(\ell, b_{\mathrm{top}}) < 1.0$.

The phase space is divided into eight signal regions (SR) defined by the number of jets and b-tagged jets, and are labelled as "X-jet Y-tag" where $X = 2, 3$ and $Y = 1, 2$, that are further sep-

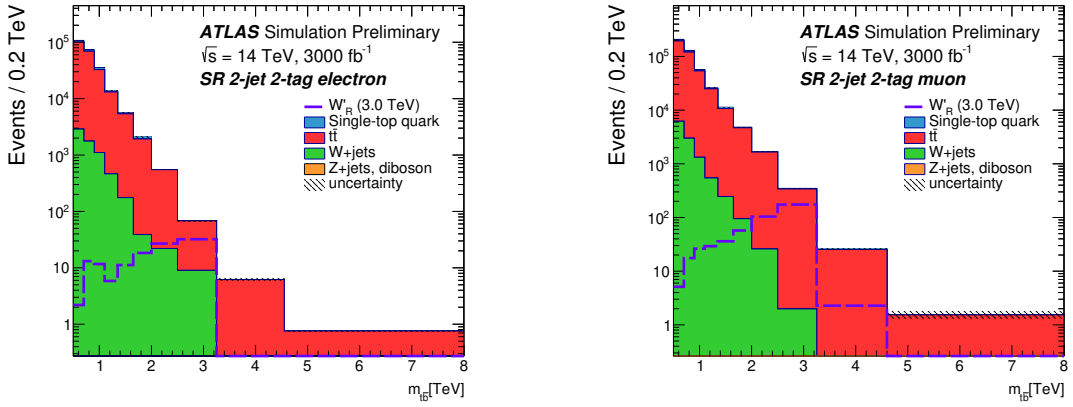

Fig. 6.2.14: Post-fit distributions of the reconstructed mass of the W'_{R} boson candidate in the 2-jet 2-tag signal region for the electron (left) and muon (right) channels. An expected signal contribution corresponding to a W'_{R} boson mass of 3 TeV is shown. Uncertainty bands include all systematic uncertainties.

arated into electron and muon channels. The signal selection acceptance times efficiency rises from $\sim$ 4.4% (7.7%) at a W'_{R} mass of 1 TeV to 4.6% (11.0%) at 2 TeV, then decreasing to 2.6% (8.2%) at 5 TeV in the electron (muon) channel. This decrease is due to the b-tagging performance and the higher boost at higher mass. The muon channel outperforms the electron channel due to overlap removal requirements, as they are relaxed by using a variable ΔR cone size. The variable ΔR cone size is not used for electrons because of the possible double counting of the energies of electron and jet.

Systematic uncertainties are evaluated following the analysis of 36.1 fb^{-1} of $\sqrt{s} = 13$ TeV pp data in Ref. [685] and then scaled according to the recommendations in Ref. [7]. The uncertainty in the luminosity (1%) and in the theory cross sections (5% for diboson, 10% for Z+jets, and 3% for single top) are included in the expected limits and significance calculation. The b-tagging and the modelling uncertainties (which are the dominant uncertainties in the shape of the discriminating variable from the previous analysis) are also included.

The presence of a massive resonance is tested by simultaneously fitting the m_{tb} templates of the signal and background simulated event samples using a binned maximum–likelihood approach (ML). Each signal region is treated as an independent search channel with correlated systematic uncertainties.

The normalisations of the $t\bar{t}$ and W+jets backgrounds were found to be different than those in the analysis of 36.1 fb^{-1}, therefore they are free parameters in the fit. They are constrained by Asimov dataset to one by construction. The other background normalisations are assigned Gaussian priors based on their respective normalisation uncertainties. The signal normalisation is a free parameter in the fit.

As an example, the m_{tb} distributions for two of the eight signal regions after the ML fit are shown in Fig. 6.2.14 for the expected background and signal contribution corresponding to a W'_{R} boson with a mass of 3 TeV. The binning of the m_{tb} distribution is chosen to optimise the search sensitivity while minimising statistical fluctuations.

The limits are evaluated assuming the modified frequentist $\mathrm{CL_s}$ method [95] with a profile-likelihood-ratio test statistic [257] and using the asymptotic approximation. The 95% C.L. upper limits on the production cross section multiplied by the branching fraction for $W'_{\mathrm{R}} \to t\bar{b}$ are shown in Fig. 6.2.15 as a function of the resonance mass for 3 ab^{-1}. The expected exclusion limits range between 0.02 pb and 6×10^{-3} pb for W'_{R} boson masses from 1 TeV to 7 TeV. The existence of W'_{R} bosons with masses below 4.9 TeV is expected to be excluded, assuming that the W'_{R} coupling g' is equal to the SM weak coupling constant g. This would increase the limit obtained with 36.1 fb^{-1} [685] by 1.8 TeV.

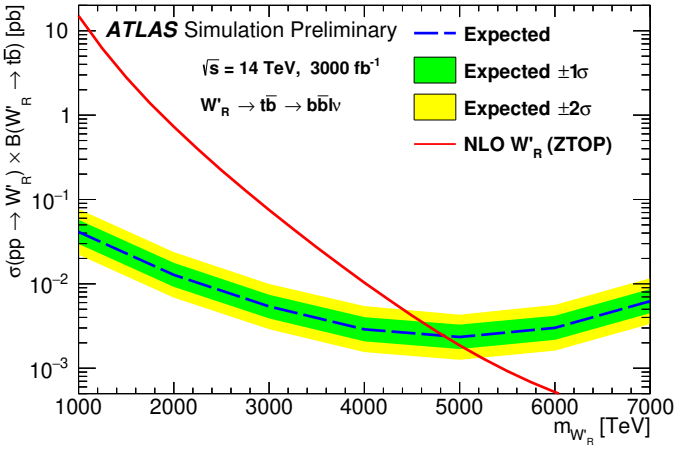

Fig. 6.2.15: Upper limits at the 95% C.L. on the W'_{R} production cross section times branching fraction as a function of resonance mass. The dashed curve and shaded bands correspond to the limit expected in the absence of signal and the regions enclosing one/two standard deviation (s.d.) fluctuations of the expected limit. The theory prediction is also shown.

The expected discovery significance is calculated using the profile likelihood test statistic for different mass hypotheses for a luminosity of $3\ \mathrm{ab}^{-1}$with the asymptotic approximation. Based on 5σ significance, it is found that W'_{R} with masses up to 4.3 TeV can be discovered at the HL-LHC.

6.2.7 Searches for $W' \to \tau + E_{\mathrm{T}}^{\mathrm{miss}}$

Contributors: K. Hoepfner, C. Schuler, CMS

New W′ heavy gauge bosons might decay as $\mathrm{W}' \to \tau\nu$. This yields to final states characterised by a single hadronically decaying tau (τ_h) as the only detectable object, and missing energy due to the neutrinos. Hadronically decaying tau leptons are selected since the corresponding branching fraction, about 60%, is the largest among all τ decays. Tau-jets are experimentally distinctive because of their low charged hadron multiplicity, unlike QCD multi-jets, which have high charged hadron multiplicity, or other leptonic W′ boson decays, which yield no jet. This Phase-2 study [686] follows closely the recently published Run-2 result [687], using hadronically decaying tau leptons.

The signature of a W′ boson (see Fig. 6.2.16), is considered similar to a high-mass W boson. It could be observed in the distribution of the transverse mass (M_T) of the transverse momentum of the τ (p_T^{τ}) and the missing transverse momentum: $M_T = \sqrt{2p_T^{\tau}E_{\mathrm{T}}^{\mathrm{miss}}(1 - cos\Delta\phi(\tau, E_{\mathrm{T}}^{\mathrm{miss}}))}$. Unlike the leptonic search channels, the signal shape of W' bosons with hadronically decaying tau leptons does not show a Jacobian peak structure because of the presence of two neutrinos in the final state. Despite the multi-particle final state, the decay appears as a typical two-body decay; the axis of the hadronic tau jet is back to back with $E_{\mathrm{T}}^{\mathrm{miss}}$ and the magnitude of both is comparable such that their ratio is about unity.

The results are interpreted in the context of the sequential standard model in terms of W′ mass and coupling strength. A model-independent cross section limit allows interpretations in other models. The signal is simulated at LO and the detector performance simulated with DELPHES. The W′ boson coupling strength, $g_{\mathrm{W}'}$, is given in terms of the SM weak coupling strength $g_{\mathrm{W}} = e/\sin^2\theta_W \approx 0.65$. Here, θ_{W} is the weak mixing angle. If the W′ boson is a heavier copy of the SM W boson, their coupling ratio is $g_{\mathrm{W}'}/g_{\mathrm{W}} = 1$ and the SSM W′ boson theoretical cross sections, signal shapes, and widths apply. However, different couplings are possible. Because of the dependence of the width of a particle on its couplings the consequent effect on the transverse mass distribution, a limit can also be set on the coupling strength.

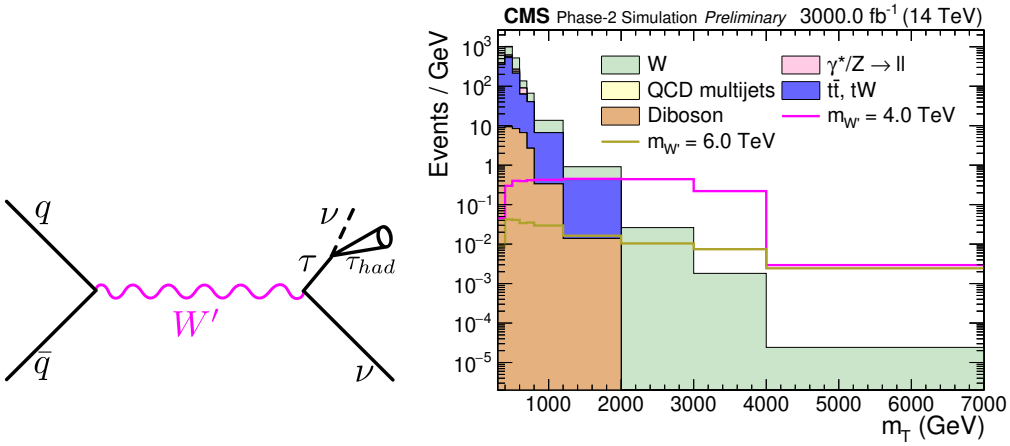

Fig. 6.2.16: Left: Illustration of the studied channel $W' \to \tau\nu$ with the subsequent hadronic decay of the tau (τ_h). Right: The discriminating variable, M_T, after all selection criteria for the HL-LHC conditions of 3 $\mathrm{ab}^{-1}$and 200 PU. The relevant SM backgrounds are shown according to the labels in the legend. Signal examples for W′ boson masses of 4 TeV and 6 TeV are scaled to their SSM LO cross section and 3 ab^{-1}.

The dominant background appears in the high mass tail of the M_T distribution of SM W boson events. Subleading background contributions arise from $t\bar{t}$ and QCD multijet events. These backgrounds primarily arise as a consequence of jets misidentified as τ_h candidates and populate the lower transverse masses while the signal exhibits an excess of events at high M_T. Events with one hadronically decaying τ and $E_{\mathrm{T}}^{\mathrm{miss}}$ are selected if the ratio of p_T^{τ} to $E_{\mathrm{T}}^{\mathrm{miss}}$ satisfies $0.7 < p_T^{\tau}/E_{\mathrm{T}}^{\mathrm{miss}} < 1.3$ and the angle $\Delta\phi(\vec{p_T}^{\,\tau}, E_{\mathrm{T}}^{\mathrm{miss}})$ is greater than 2.4 radians.

The physics sensitivity is studied based on the M_T distribution in Fig. 6.2.16 (right). Signal events are expected to be particularly prominent at the upper end of the M_T distribution, where the expected SM background is low. So far, there are no indications for the existence of a SSM W′ boson [687]. With the high luminosity during Phase-2, the W′ mass reach for potential observation increases to 6.9 TeV and 6.4 TeV for 3σ evidence and 5σ discovery, respectively, as shown in Fig. 6.2.17 (left). Alternatively, in case of no observation, one can exclude SSM W′ boson masses up to 7.0 TeV with 3 ab^{-1}. These are multi-bin limits taking into account the full M_T shape.

While the SSM model assumes SM-like couplings of the fermions, the couplings could well be weaker if further decays occur. The HL-LHC has good sensitivity to study these couplings. The sensitivity to weaker couplings extends significantly. A model-independent cross section limit for new physics with τ+$E_{\mathrm{T}}^{\mathrm{miss}}$ in the final state is depicted in Fig. 6.2.17 (right), calculated as a single-bin limit by counting the number of events above a sliding threshold M_T^{min}.

6.2.8 HL- and HE-LHC sensitivity to 2HDMs with $U(1)_X$ Gauge Symmetries

Contributors: D. A. Camargo, L. Delle Rose, S. Moretti, F. S. Queiroz

Extended Higgs sectors belonging to various BSM scenarios offer the possibility to solve some of the open problems of the SM. Such frameworks with extended Higgs sectors have recently come together with new $U(1)_X$ gauge symmetries, offering a natural solutions to the DM and the neutrino mass problems. These scenarios [688–693] predict a rich new phenomenology due to the presence of a massive Z' gauge boson arising after the $U(1)_X$ spontaneous symmetry breaking.

Our goal is to explore the potential of the HL- and HE-LHC to study such a scenario. To do so, we fist use the latest available dilepton data from the LHC [442,694] to constrain the mass and couplings of such Z' gauge bosons and, consequently, the viable parameter space of the underlying model. Then we use this result to asses the capabilities of the HL- and HE-LHC to test the existence of such heavy

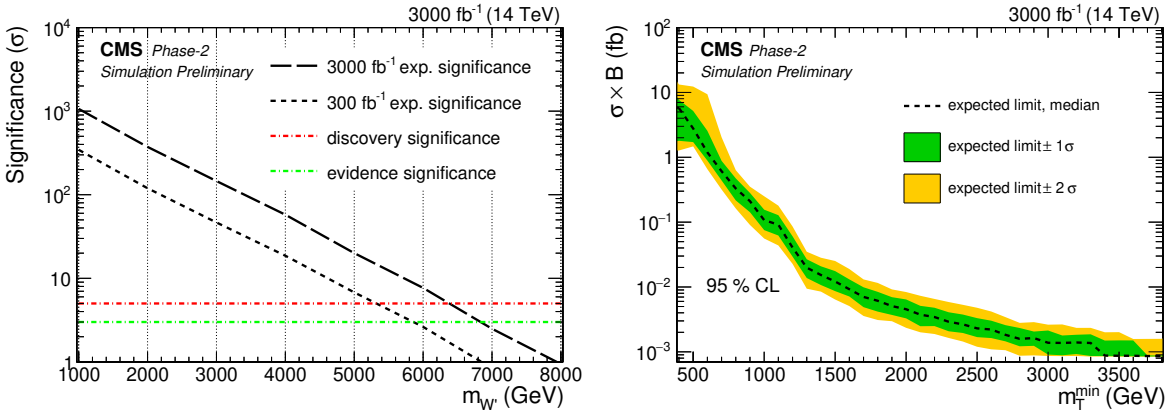

Fig. 6.2.17: Left: Discovery significance for SSM W′ to tau leptons. Right: Model-independent cross section limit. For this, a single-bin limit is calculated for increasing $M_T^{\min}$ while keeping the signal yield constant in order to avoid including any signal shape information on this limit calculation.

neutral vector bosons. An extended version of this contribution can be found in Ref. [695].

The relevant part of the Lagrangian of the model we consider is

$$\mathcal{L}_{\rm NC} \supset -\left(\tfrac{g_Z}{2} J^\mu_{NC} \cos\xi\right) Z_\mu - \left(\tfrac{g_Z}{2} J^\mu_{NC} \sin\xi\right) Z'_\mu \tag{6.2.1}$$

$$+\tfrac{1}{4} g_X \sin\xi \left[\left(Q^R_{Xf} + Q^L_{Xf}\right) \bar\psi_f \gamma^\mu \psi_f + \left(Q^R_{Xf} - Q^L_{Xf}\right) \bar\psi_f \gamma^\mu \gamma_5 \psi_f\right] Z_\mu \tag{6.2.2}$$

$$-\tfrac{1}{4} g_X \cos\xi \left[\left(Q^R_{Xf} + Q^L_{Xf}\right) \bar\psi_f \gamma^\mu \psi_f - \left(Q^L_{Xf} - Q^R_{Xf}\right) \bar\psi_f \gamma^\mu \gamma_5 \psi_f\right] Z'_\mu, \tag{6.2.3}$$

where ξ represents the $Z - Z'$ mixing parameter, g_X the gauge coupling of the new abelian symmetry while $Q^L_X(Q^R_X)$ are the left(right)-handed fermion charges under $U(1)_X$ defined according to Ref. [695]. This interaction Lagrangian represents the key information for the collider phenomenology we are going to tackle, because it dictates Z' production rates at the LHC as well as its most prominent decays to be searched for.

Present LHC bounds are obtained here by simulating at 13 TeV of c.o.m. energy the process

$$pp \to l^+ l^- + X, \tag{6.2.4}$$

where $l = e, \mu$, leading to dilepton signals, and X represents the surrounding hadronic activity. (The dijet signal case was studied in Ref. [695] and found to be less sensitive.) Since this channel is mediated by a heavy Z', alongside γ and Z, a peak around the Z' mass would appear at large values of the invariant mass of the dilepton final state. We describe our results adopting both the Narrow Width Approximation (NWA) and also introducing Finite Width (FW) effects. In this respect, we have implemented in FEYNRULES [696] the models shown in Ref. [695], where the corresponding $U(1)_X$ charge assignment is explicitly shown, and we have simulated the partonic events with MADGRAPH5_aMC@NLO [697]. For hadronisation and detector effects we used PYTHIA 8 [50] and DELPHES [33], respectively.

Assuming, for the sake of definiteness, the NWA with $g_X = 0.1, 0.2$ and 0.3, we project the current experimental limits to the HL- and HE-LHC. In order to extrapolate the current bound to a new collider configuration, one would need to scale the relevant backgrounds and find the new point giving the same number of background events, which, assuming same efficiencies and acceptances, would lead to the same excluded signal cross section, as outlined in Ref. [698]. However, in the case of the dilepton final state, the signal and the background scale equally with energy/luminosity, so that one can employ a simpler strategy, based on a direct rescaling of the bound on the number of signal events. Therefore, in order to find the future sensitivities we just solve an equation for $M_{\rm new}$ (*i.e.*, the new limit on $m_{Z'}$),

Model	13 TeV, 300 fb^{-1}	14 TeV, 3 ab^{-1}	27 TeV, 300 fb^{-1}	27 TeV, 3 ab^{-1}	27 TeV, 15 ab^{-1}
$U(1)_A$	3.07 TeV	4.3 TeV	5.02 TeV	7.03 TeV	8.51 TeV
$U(1)_B$	3.07 TeV	4.3 TeV	5.02 TeV	7.03 TeV	8.51 TeV
$U(1)_C$	2.37 TeV	3.52 TeV	3.73 TeV	5.54 TeV	6.96 TeV
$U(1)_D$	4.45 TeV	5.81 TeV	7.76 TeV	9.89 TeV	11.34 TeV
$U(1)_E$	3.18 TeV	4.45 TeV	5.24 TeV	7.27 TeV	8.75 TeV
$U(1)_F$	4.55 TeV	5.91 TeV	7.97 TeV	10.09 TeV	11.54 TeV
$U(1)_G$	1.73 TeV	2.73 TeV	2.62 TeV	4.16 TeV	5.45 TeV
$U(1)_{B-L}$	2.84 TeV	4.07 TeV	4.60 TeV	6.55 TeV	8.02 TeV

Table 6.2.5: HL-LHC and HE-LHC projected sensitivities for all $U(1)_X$ models studied in this work using dilepton data at 13 TeV, 14 TeV and 27 TeV of CM energy and for $\mathcal{L} = 300$ fb^{-1} and $\mathcal{L} = 3$ and 15 ab^{-1}. Here, $g_X = 0.1$.

Model	13 TeV, 300 fb^{-1}	14 TeV, 3 ab^{-1}	27 TeV, 300 fb^{-1}	27 TeV, 3 ab^{-1}	27 TeV, 15 ab^{-1}
$U(1)_A$	4.14 TeV	5.49 TeV	7.14 TeV	9.26 TeV	10.73 TeV
$U(1)_B$	4.14 TeV	5.49 TeV	7.17 TeV	9.26 TeV	10.73 TeV
$U(1)_C$	3.62 TeV	4.93 TeV	6.09 TeV	8.18 TeV	9.66 TeV
$U(1)_D$	5 TeV	6.43 TeV	9 TeV	11.1 TeV	12.52 TeV
$U(1)_E$	5 TeV	6.43 TeV	9 TeV	11.1 TeV	12.52 TeV
$U(1)_F$	5.53 TeV	6.94 TeV	10.02 TeV	12.09 TeV	13.511 TeV
$U(1)_G$	2.37 TeV	3.52 TeV	3.73 TeV	5.54 TeV	6.96 TeV
$U(1)_{B-L}$	3.83 TeV	5.16 TeV	6.5 TeV	8.62 TeV	10.10 TeV

Table 6.2.6: HL-LHC and HE-LHC projected sensitivities for all $U(1)_X$ models studied in this work using dilepton data at 13 TeV, 14 TeV and 27 TeV of CM energy and for $\mathcal{L} = 300$ fb^{-1} and $\mathcal{L} = 3$ and 15 ab^{-1}. Here, $g_X = 0.2$.

Model	13 TeV, 300 fb^{-1}	14 TeV, 3 ab^{-1}	27 TeV, 300 fb^{-1}	27 TeV, 3 ab^{-1}	27 TeV, 15 ab^{-1}
$U(1)_A$	4.75 TeV	6.12 TeV	8.38 TeV	10.5 TeV	11.94 TeV
$U(1)_B$	4.75 TeV	6.12 TeV	8.38 TeV	10.5 TeV	11.94 TeV
$U(1)_C$	4 TeV	5.38 TeV	6.93 TeV	9.05 TeV	10.52 TeV
$U(1)_D$	5.72 TeV	7.14 TeV	10.4 TeV	12.48 TeV	13.90 TeV
$U(1)_E$	5.14 TeV	6.53 TeV	9.2 TeV	11.3 TeV	12.72 TeV
$U(1)_F$	5.91 TeV	7.34 TeV	10.84 TeV	12.87 TeV	14.28 TeV
$U(1)_G$	4 TeV	5.38 TeV	6.93 TeV	9.05 TeV	10.52 TeV
$U(1)_{B-L}$	4.35 TeV	5.70 TeV	7.55 TeV	9.68 TeV	11.14 TeV

Table 6.2.7: HL-LHC and HE-LHC projected sensitivities for all $U(1)_X$ models studied in this work using dilepton data at 13 TeV, 14 TeV and 27 TeV of CM energy and for $\mathcal{L} = 300$ fb^{-1} and $\mathcal{L} = 3$ and 15 ab^{-1}. Here, $g_X = 0.3$.

knowing the current bound M, as follows:

$$\frac{N_{\text{signal events}}(M^2_{\text{new}}, E_{\text{new}}, \mathcal{L}_{\text{new}})}{N_{\text{signal events}}(M^2, 13\,\text{TeV}, 36\,\text{fb}^{-1})} = 1, \tag{6.2.5}$$

with obvious meaning of the subscripts.

The results from this iteration are summarised in Tables 6.2.5, 6.2.6 and 6.2.7. The lower mass bounds found presently compared to the expected ones at the HL-LHC and/or HE-LHC clearly show how important is any LHC upgrade to test new physics models including a Z'. For some models and benchmark points, such as, *e.g.*, $U(1)_A$ with $g_X = 0.1$, the HE-LHC will potentially probe Z' masses up to 7 TeV, while for others, such as, *e.g.*, $U(1)_F$ with $g_X = 0.3$, it will potentially exclude masses up to 12 TeV. In short, both LHC upgrades can generally extend the current reach in $m_{Z'}$ by a factor 2 to 3. The results are summarised in the tables.

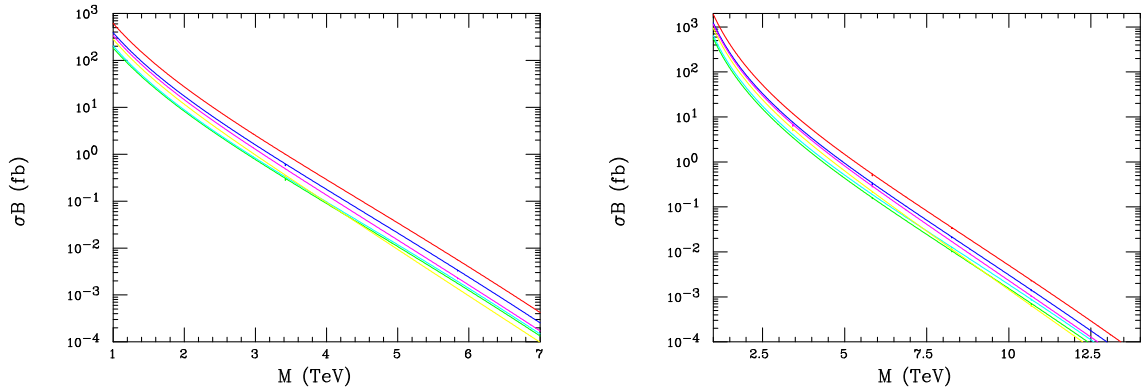

Fig. 6.2.18: Left: σB_l in the NWA for the Z' production at the $\sqrt{s} = 14$ TeV LHC as functions of the Z' mass: SSM(red), LRM (blue), ψ(green), χ(magenta), η(cyan), I(yellow). Right: σB_l of Z' in models described in (left) at $\sqrt{s} = 27$ TeV.

6.2.9 *Z' discrimination at HE-LHC in case of an evidence/discovery after the HL-LHC*

Contributors: C. Helsens, D. Jamin, M. L. Mangano, T. Rizzo, M. Selvaggi

Context of the study and HL-LHC bounds

It is still legitimate to assume that a heavy resonance could be seen at the end of HL-LHC. If that is the case a new collider with higher energy in the c.o.m. is needed to study its properties as too few events will be available at $\sqrt{s} = 14$ TeV. In this section we present the discrimination potential between six Z' models of a HE-LHC with an assumed c.o.m. energy of 27 TeV and an integrated luminosity of $\mathcal{L} = 15\ \text{ab}^{-1}$. Under the assumption that these Z''s decay only to SM particles, we show that there are sufficient observables to perform this model differentiation in most cases.

As a starting point it is needed to estimate what are, for $\sqrt{s} = 14$ TeV, the typical exclusion/discovery reaches for standard reference Z' models assuming $\mathcal{L} = 3\ \text{ab}^{-1}$ employing only the e^+e^- and $\mu^+\mu^-$ channels. The production cross section times leptonic branching fraction is shown in Fig. 6.2.18 (left) for these models at $\sqrt{s} = 14$ TeV in the narrow width approximation (NWA). It has been and will be assumed here that these Z' states only decay to SM particles.

Studies presented in this report on prospects for searches of Z' by ATLAS (see Section 6.2.5) shows that discovery and exclusion reaches are between 5 and 6.5 TeV in $M_{Z'}$ depending on the model assumption. Based on these results, we will assume in our study below that we are dealing with a Z' of mass 6 TeV. Figure 6.2.18 (right) shows the NWA cross sections for the same set of models but now at $\sqrt{s} = 27$ TeV with $\mathcal{L} = 15\ \text{ab}^{-1}$. We note that very large statistical samples will be available for the case of $M_{Z'} = 6$ TeV for each dilepton channel.

Definition of the discriminating variables

The various Z' models can be disentangled with the help of 3 inclusive observables: the production cross section times leptonic branching fraction σB_l, the forward-backward asymmetry A_{FB} and the rapidity ratio r_y. The variable A_{FB} can be seen as an estimate of the charge asymmetry

$$A_{FB} = A_C = \frac{\sigma(\Delta|y| > 0) - \sigma(\Delta|y| < 0)}{\sigma(\Delta|y| > 0) + \sigma(\Delta|y| < 0)}, \tag{6.2.6}$$

where $\Delta|y| = |y_l| - |y_{\bar{l}}|$. It has been checked that this definition is equivalent to defining

$$A_{FB} = \frac{\sigma_F - \sigma_B}{\sigma_F + \sigma_B}, \tag{6.2.7}$$

with $\sigma_F = \sigma(cos\theta^*_{cs}) > 0$ and $\sigma_B = \sigma(cos\theta^*_{cs}) < 0$ where θ^*_{cs} is the Collins-Soper frame angle. The variable r_y is defined as the ratio of central over forward events:

$$r_y = \frac{\sigma(|y_{Z'}| < y_1)}{\sigma(y_1 < |y_{Z'}| < y_2)}, \tag{6.2.8}$$

where $y_1 = 0.5$ and $y_2 = 2.5$.

Model discrimination

The model discrimination presented in this section has been performed assuming the HE-LHC detector parametrisation [699] in DELPHES [33]. In such a detector, muons at $\eta \approx 0$ are assumed to be reconstructed with a resolution $\sigma(p)/p \approx 7\%$ for $p_T = 3$ TeV.

Leptonic final states The potential for discriminating various Z' models is first investigated using the leptonic ee and $\mu\mu$ final states only. The signal samples for the 6 models and the Drell-Yan backgrounds have been generated with PYTHIA 8.230 [68] including the interference between the signal and background. The Z' decays assume lepton flavour universality. For a description of the event selection and a discussion of the discovery potential in leptonic final states for the list of Z' models being discussed here, the reader should refer to Section 6.2.4. We simply point out here that with $\mathcal{L} = 15$ ab^{-1}, all Z' models with $m_{Z'} \lesssim 10$ TeV can be excluded at $\sqrt{s} = 27$ TeV.

Figure 6.2.19 (left) shows the correlated predictions for the A_{FB} and the rapidity ratio r_y observables defined previously for these six models given the above assumptions. Although the interference with the SM background was included in the simulation, its effect is unimportant due to the narrowness of the mass window around the resonance that was employed. Furthermore, the influence of the background uncertainty on the results has been found to have little to no impact on the model discrimination potential. Therefore the displayed errors on A_{FB} and r_y are of statistical origin only. The results show that apart from a possible near degeneracy in models ψ and η, a reasonable Z' model separation can indeed be achieved.

Using a profile likelihood technique, the signal strength μ, or equivalently, σB_l, can be fitted together with its corresponding error using the the di-lepton invariant mass shape. The quantity σB_l and its total estimated uncertainty is shown in Fig. 6.2.19 (centre) as a function of the integrated luminosity. The σB_l measurement seems to be able to resolve the degeneracy between the ψ and η models with $\mathcal{L} = 15$ ab^{-1}. It should be noted however that since the cross-section can easily be modified by an overall rescaling of the couplings, further handles will be needed for a convincing discrimination.

Hadronic final states Model discrimination can be improved by including an analysis involving three Z' addition hadronic final states: $t\bar{t}$, $b\bar{b}$ and $q\bar{q}$, where $q = u, d, c, s$. The sample production and event selection for the $t\bar{t}$, $q\bar{q}$ final states will be described to some extent in Section 6.4.6. We simply remind the reader that the analysis involves requiring the presence of two central high p_T jets. In order to ensure complete orthogonality between the various final states, jets are required to be tagged as follows. In the $Z' \to t\bar{t}$ analysis both jets should be *top-tagged*. For the $Z' \to b\bar{b}$ final state both jets are required to be *b-tagged* and we veto events containing at least one top-tagged jet. Finally, in the $Z' \to q\bar{q}$ analysis, we veto events that contain at least one b-tagged or top-tagged jet.

Figure 6.2.19 (right) summarises the discrimination potential in terms of fitted cross-section of the different models considering the three aforementioned hadronic decays, $t\bar{t}$, $b\bar{b}$ and $q\bar{q}$. An good overall discrimination among the various models can be achieved using all possible final states. For example, the SSM and ψ models, which have very close predictions for r_y and A_{FB}, have measurably different fractions of $t\bar{t}$ or $b\bar{b}$ final states. We note however that the degeneracy between η and ψ can only be partially resolved resolved at $\approx 1\sigma$ by exploiting the difference in $t\bar{t}$ yield.

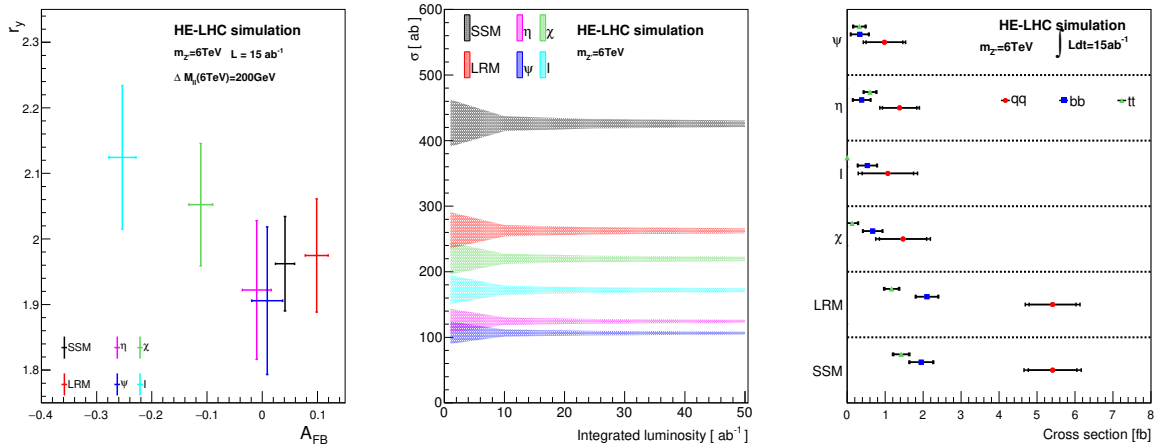

Fig. 6.2.19: Left: scatter plot of r_y versus A_{FB} with 200 GeV and mass window. The full interference is included. Centre: Fitted signal cross-section together with its corresponding error versus integrated luminosity. Right: fitted cross-section of the three hadronic analyses. Statistical and full uncertainties are shown on each point.

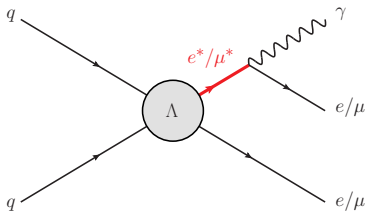

Fig. 6.3.1: Feynman diagram of the production of excited leptons in $\ell\ell\gamma$ final states.

In summary, in this section we studied the discrimination potential of six Z' models at HE-LHC with an assumed c.o.m. energy of 27 TeV and an integrated luminosity of $\mathcal{L} = 15$ ab^{-1}. The exercise has been performed assuming the evidence of an excess observed at $\sqrt{s} = 14$ TeV at a mass $m_{Z'} \approx 6$ TeV. Overall it was found that it is possible to distinguish among most models. Finally, it should be noted that further studies, perhaps employing 3-body decay modes or associated Z' production will be clearly needed to be pursued in case of discovery to further characterise the resonance properties.

6.3 Spin 1/2 resonances

In this section, prospect studies for spin-1/2 resonances are presented, targeting excited leptons and heavy vector-like quarks. Resonances coupled to leptons and quarks or gauge bosons and quarks are considered.

6.3.1 Search for excited leptons at HL-LHC

Contributors: S. Ha, B. Kim, M. S. Kim, K. Nam, S. W. Lee, H. D. Yoo, CMS

A search for excited leptons (electrons and muons) is studied at the HL-LHC with the upgraded CMS detector using simulation [700]. Excited leptons are predicted by many BSM theories where quarks and leptons are not elementary but instead are themselves composite objects. The HL-LHC environment (a c.o.m.energy of 14 TeV and an integrated luminosity of 3 ab^{-1}) allows to extend the discovery potential of excited leptons. This analysis presents a search for excited leptons ($\ell^* = \mathrm{e}^*, \mu^*$) in $\ell\ell\gamma$ ($\ell = \mathrm{e}, \mu$) final states where the excited lepton decays to a SM lepton and a photon ($\ell^* \to \ell\gamma$). An illustration of the production decay mode is shown in Fig. 6.3.1.

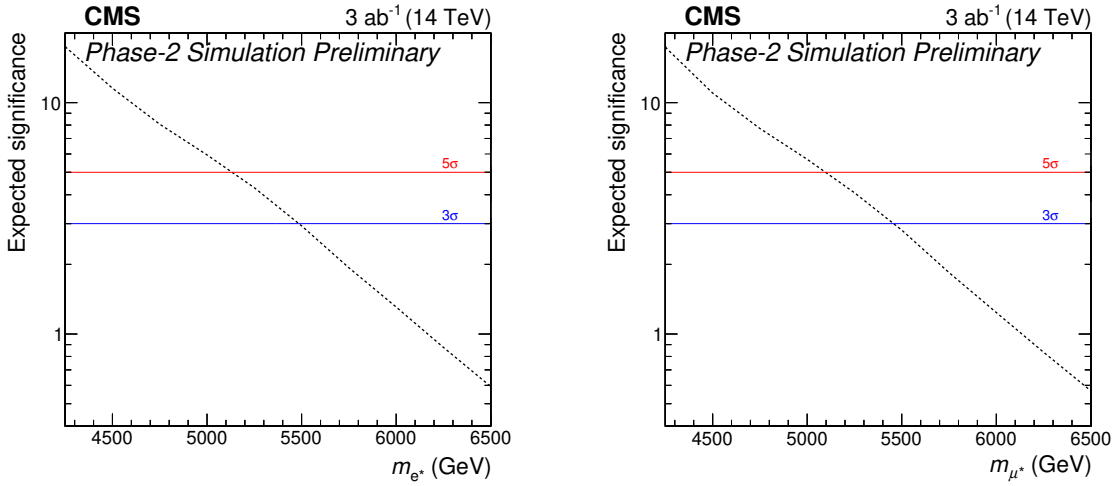

Fig. 6.3.2: Discovery significance for excited electrons (left) and muons (right) with 3 ab^{-1} at the HL-LHC.

In this search, a clear signature of an opposite-sign same-flavour lepton pair and a photon allows highly efficient signal selection to assess the CMS upgrade physics reach. However, an ambiguity between the lepton from the excited lepton decay and the lepton from the contact interaction makes it challenging to identify the reconstructed mass of the excited lepton due to two possible pairings of a lepton and the photon. For this search, information from both invariant mass combinations is used to discriminate the excited lepton signal from SM background processes. We consider a benchmark model based on the formalism described in Ref. [394].

The signal samples are generated with PYTHIA 8.205 [92] at $\Lambda = 10$ TeV for ℓ^* masses ranging from 3.5 TeV to 6.5 TeV in steps of 250 GeV, where Λ is the compositeness scale. The simulated signal samples are generated at leading order (LO) in perturbative quantum chromodynamics. The main background is the SM $\mathrm{Z}\gamma$ process, which is generated at NLO using MADGRAPH5_aMC@NLO 2.3.3 [67, 697]. The generated signal and background samples are interfaced to delphes [33], which features a parametric simulation of the CMS Phase 2 detector at the particle level.

We select events having two isolated electrons or muons and a photon with requirements as follows. Electron and photon candidates are required to have pseudorapidity $|\eta| < 2.5$ and transverse momentum $p_T > 35$ GeV, and they are excluded in the electromagnetic calorimeter barrel-endcap transition region ($1.44 < |\eta| < 1.57$). Muon candidates should be isolated with $|\eta| < 2.4$ and $p_T > 35$ GeV. The leptons are required to have opposite charge and the selected electrons and muons must be separated from the photon by $\Delta R = \sqrt{\Delta\eta^2 + \Delta\phi^2} > 0.7$. In addition, the invariant mass of the two same flavour leptons $m_{\ell\ell}$ is required to be larger than 116 GeV in order to suppress the dominant background contribution from real Z boson production (Z resonance veto criteria).

The main SM background after the event selection is Drell-Yan production associated with a photon ($\mathrm{Z}\gamma$), which has the same signature as the final state of the signal, when the Z boson decays into two leptons. This background is significantly suppressed by the Z boson veto requirement. Contributions of other SM processes like diboson and top quark pair production in association with a photon ($t\bar{t} + \gamma$) are relatively small, in particular in the signal search region of excited lepton masses above 2 TeV. Simulated $t\bar{t} + \gamma$ events are studied in this analysis, however the background events are imperfectly estimated due to the insufficient sample size. Hence, we only consider the dominant $\mathrm{Z}\gamma$ background in this search, and additional background contributions are considered as systematic uncertainties on the total background estimate. The photon misidentification rate under the HL-LHC conditions is studied in Ref. [701] using PHASE-2 DELPHES samples. The photon misidentification rate is expected to be about 1% when the photon p_T is on the order of 100 GeV, which is compatible with the 2016 result. In the previous CMS Run-2 ℓ^* search [702], we observed 20% and 5% contribution from $t\bar{t} + \gamma$ and misidentified photon

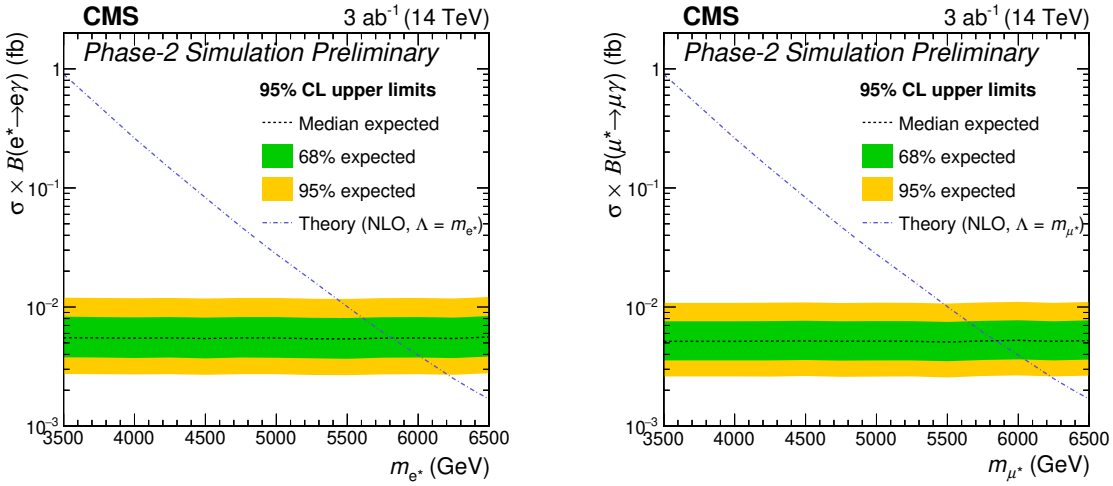

Fig. 6.3.3: Exclusion limits for excited electrons (left) and muons (right) on the product of cross section and branching fraction.

backgrounds, respectively, at $M_{\ell^*} > 1$ TeV; therefore a 25% systematic uncertainty is assigned for the missing background contributions.

To distinguish between signal and background events, a two-dimensional distribution of the two invariant masses $M_{\ell\gamma}^{\text{min}}$ and $M_{\ell\gamma}^{\text{max}}$ is used. A search window is set in the two-dimensional distribution of $M_{\ell\gamma}^{\text{max}}$ versus $M_{\ell\gamma}^{\text{min}}$. For ℓ^* events, either $M_{\ell\gamma}^{\text{min}}$ or $M_{\ell\gamma}^{\text{max}}$ corresponds to the reconstructed invariant mass of ℓ^*. Therefore, the mass resonance of the signal is concentrated in an "L" shape [703,704]. On the other hand, background events have no such correlation in $M_{\ell\gamma}^{\text{min}}$ and $M_{\ell\gamma}^{\text{max}}$ and are scattered around at low masses below about 2 TeV. This distinction between signal and background events in the distribution of $M_{\ell\gamma}^{\text{max}}$ versus $M_{\ell\gamma}^{\text{min}}$ is used to set the search window. We set the lower $M_{\ell\gamma}^{\text{max}}$ bound at 2 TeV in the two-dimensional distribution as the search window in order to maximise the signal yields. The reason why the L-shaped search window is not applied in this analysis is due to the insufficient MC statistics. Therefore the results of the limits presented here are likely to be improved upon with an actual search. The product of signal acceptance and efficiency ($A \times \varepsilon_{\text{sig}}$) is obtained using the simulated DELPHES signal samples and the results are 58% (μ^*) and 45% (e^*) with negligible M_{ℓ^*} dependence.

Systematic uncertainties for the performance of the lepton (0.5%) and photon (2.0%) reconstruction and identification, and the integrated luminosity (1.0%) follow the recommendation for upgrade analyses [705]. The theoretical systematic uncertainty is reduced by a factor of 1/2 with respect to the 2016 result. The statistical uncertainty in the entire signal region is dominant in this analysis. The missing background contribution is considered to be the main systematic uncertainty in the background estimation.

The upper limit of the excited electrons and muons is determined under the the HL-LHC scenario, based on an integrated luminosity of 3 ab^{-1}. We set 95% C.L. upper limits on the production cross sections, which are computed with the modified frequentist CL_s method [94, 95], with a likelihood ratio used as a test statistic. The systematic uncertainties are treated as nuisance parameters with log-normal priors.

The discovery potential as a function of excited lepton mass shown in Fig. 6.3.2 indicates that 3σ evidence (5σ discovery) is possible for both excited electrons and excited muons with masses up to 5.5 (5.1) TeV. Figure 6.3.3 shows the expected upper limits for e^* (left) and μ^* (right). The expected exclusion of the excited leptons is $M_{\ell^*} < 5.8$ TeV for both e^* and μ^* in the case where $M_{\ell^*} = \Lambda$. While the electron channel has a lower signal yield than the muon channel, it also has lower background, and the net result is that the excluded cross sections differ only by about 10%, producing a similar exclusion limit on the excited lepton mass.

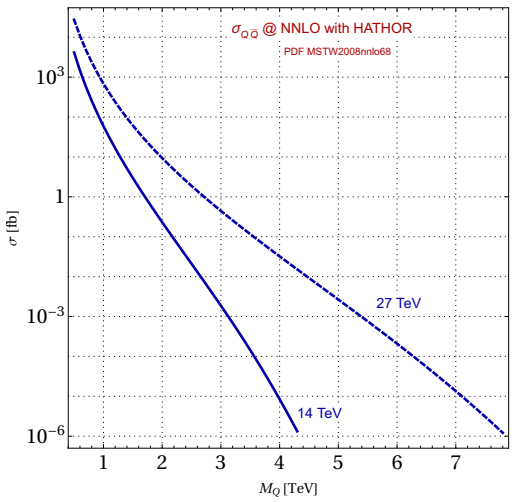

Fig. 6.3.4: VLQ pair production cross section for the 14 and 27 TeV LHC.

6.3.2 VLQs at HL- and HE-LHC: discovery and characterisation

Contributors: D. Barducci, L. Panizzi

Vector Like Quarks (VLQs) are hypothetical heavy quarks whose left- and right-handed chiral components transform under the same representation of the SM gauge group. In minimal extensions of the SM, VLQs couple to SM quarks via Yukawa-type interactions and gauge invariant renormalisable operators can be written only for the singlet, doublet and triplet representations of $SU(2)$ [706]. It can be shown that the couplings of the VLQs with the SM bosons and quarks always have a dominant chiral component [706, 707] and this depends only on whether their weak isospin is integer or half-integer, the other component being suppressed by a factor proportional to $m_q^{\rm SM}/m_{\rm VLQ}$, with $m_q^{\rm SM}$ the mass of the SM quark with which the VLQ mixes.

This property affects the polarisation of the gauge bosons and quarks arising from the VLQs decay. While the gauge bosons tend to have a dominant longitudinal polarisation, the polarisation of the final state quarks allows one to extract useful information. In particular if the VLQ decays into a top quark, its polarisation properties will affect the kinematic distributions of the final decay products. This can slightly affect the reach of new physics searches but, more importantly, in the fortunate event of a signal excess being observed, this difference can be used to probe the structure of the interactions between the VLQs and the SM sector.

In this contribution, based on the results of Ref. [708], we analyse the possibility of discriminating the chiral structure of VLQ couplings at the HL- and HE-LHC, under the hypothesis that the VLQ decays to the SM top quark. This eventually allows one to discriminate its representations under the SM $SU(2)$ gauge group.

The polar angle distribution of the top quark decay product f in the top rest frame is described by

$$\frac{1}{\Gamma_l}\frac{{\rm d}\Gamma_l}{{\rm d}\cos\theta_{f,\rm rest}} = \frac{1}{2}(1 + P_t\cos\theta_{f,\rm rest}) \tag{6.3.1}$$

where Γ_l is the partial width, $\theta_{f,\rm rest}$ is the angle between the momentum of the decay product f and the top spin vector and P_t is the polarisation of the top. From Eq. (6.3.1) one sees that for positive (negative) polarised top quarks most of the decay products come in the forward direction, that is the directions of the would-be momentum of the top quark in the laboratory frame. In the same frame the θ_f distribution is now described by Eq. (6.3.1) combined with a boost from the top rest frame to the laboratory frame. This implies that positive polarised top quarks will produce harder decay products.

To show how the polarisation information can be used to disentangle a VLQ chiral structure we focus on a VLQ with charge $2/3$ interacting exclusively with the top quark and the Z boson. We recast

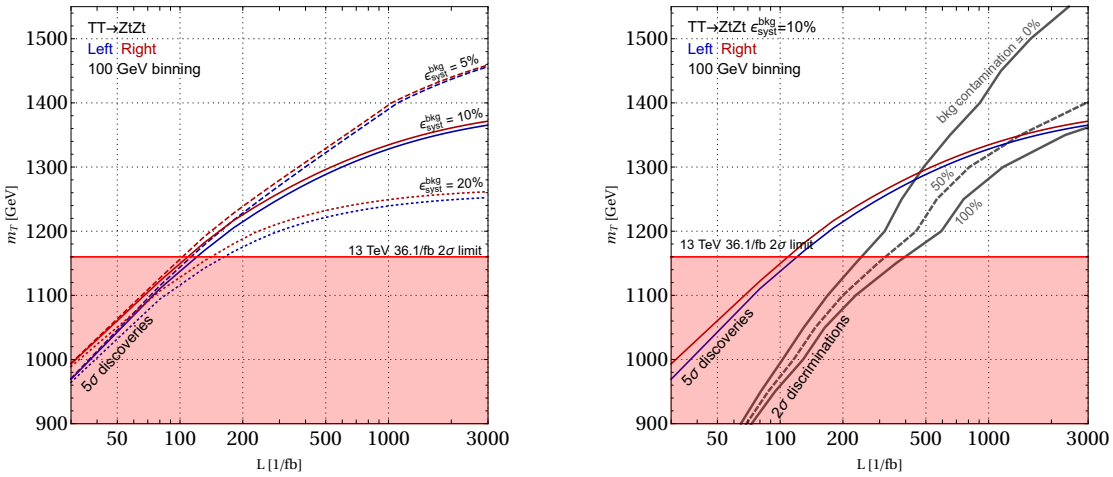

Fig. 6.3.5: Left: projected 5σ discovery (blue and red) for different assumptions for the systematic uncertainties on the background determination of the ATLAS single lepton search [709] for a T VLQ decaying with 100% BR into the Zt final state extrapolated for the 14 TeV LHC (see main text for details). The blue and red lines correspond to the discovery reach for the left-handed and right-handed coupling structure. The red shaded area correspond to the experimental limit from [709] for the 13 TeV LHC from for a VLQ decaying with 100% BR into the Zt final state, namely 1160 GeV. Right: projected 2σ discrimination (gray) reaches assuming $\epsilon^{\rm bkg}_{\rm syst} = 10$ %.

a search for pair produced VLQs performed by the ATLAS collaborations in the single lepton channel with an integrated luminosity of 36.1 fb^{-1} at $\sqrt{s} = 13$ TeV [709]. Throughout this work the VLQ pair production cross sections have been computed with HATHOR [204] and are reported in Fig. 6.3.4.

We then project the discovery and exclusion reach of the ATLAS search for the case of the 14 TeV LHC assuming the same signal acceptances than for the 13 TeV case and rescaling the backgrounds by the relevant parton luminosities ratios. We do these projections for higher values of integrated luminosities and different values of the systematic uncertainties on the background determination, $\epsilon^{\rm bkg}_{\rm syst}$, and then perform a χ^2 fit on the leading lepton p_T between the left- and right-handed coupling scenario considering the number of bins of the distribution as degrees of freedom, and under the simplifying assumption that the background (conservatively assumed to be distributed as the signal) can be subtracted with a certain efficiency, ranging from the extreme scenarios of 0% and 100%: the relation we use is therefore $\chi^2 = \sum_{i=1}^{\rm bins}(L_i - R_i)^2 / \max[\{L_i, R_i\} + \epsilon^{\rm bkg}_{\rm cont}(B + (\epsilon_{\rm syst}B)^2)]$, where L_i and R_i are the number of events in the left- and right-handed coupling scenario, $\epsilon^{\rm bkg}_{\rm cont}$ represents the contamination percentage of background events considered for the discrimination, and we consider Poissonian uncertainties for the signal.

The results are shown in Fig. 6.3.5, where we illustrate the 5σ discovery reaches for different $\epsilon^{\rm bkg}_{\rm syst}$ values (left panel) and the 2σ discrimination contours from the χ^2 fit assuming $\epsilon^{\rm bkg}_{\rm syst} = 10\%$ (right panel). We see that, if it is possible to perform a discrimination χ^2 test after removing all background events, should a VLQ with a mass lighter than around 1300 GeV be discovered, a mild increase in integrated luminosity will be needed to disentangle the two hypotheses, while the collected dataset will already be enough for the discrimination if a VLQ heavier than 1300 GeV is found with a 5σ significance. If background events cannot be removed the discrimination becomes more difficult, as the differences in the shapes become less relevant. The intersection between the discovery reach and the discrimination reach moves therefore towards higher luminosities, and in the limit of 100% background contamination we find that the discovery reach corresponds to the discrimination power at the nominal luminosity of 3 ab^{-1}.

The results obtained for the 14 TeV LHC show that with the signal region currently used in the

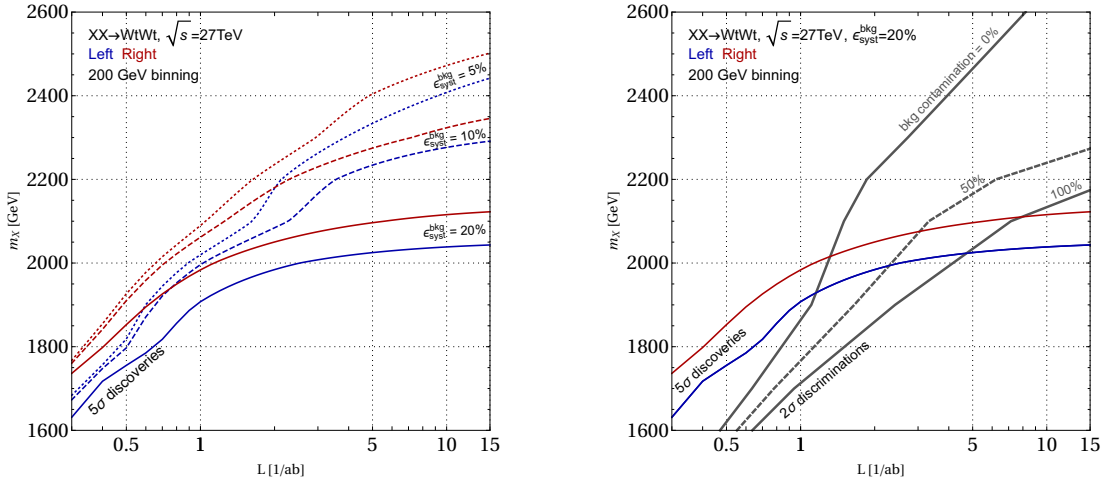

Fig. 6.3.6: Same as Fig. 6.3.5 for the 2SSL search for a X VLQ decaying with 100% BR into the Wt final state at $\sqrt{s} = 27$ TeV. We use the p_T distribution of the sub-leading lepton with a binning of 200 GeV and assume an uncertainty on the background determination of 20% (right).

ATLAS search we have considered, the LHC discovery reach will mildly increase when further data will be collected (unless one assumes a strong reduction of the current systematic uncertainties on the background determination), due to the fact that at hadron colliders the contribution of the PDFs drops when the transferred momentum of the process approaches the kinematic limit $\sqrt{s}/2$.[16] We then estimate here what is the mass reach of the high energy upgrade of the LHC for discovering pair-produced VLQs and discriminate their coupling structure.

We focus on the case of a VLQ with charge $5/3$ decaying into a W boson and a top quark and closely follow the search strategy defined in Ref. [710]. In this case we consider for discrimination the p_T distribution of the sub-leading lepton, which is almost always coming from the SM top decay. With the same statistical procedure adopted above, and rescaling the backgrounds yields given in Ref. [710] for $\sqrt{s} = 27$ TeV we show the results in Fig. 6.3.6. Our results show that a discrimination among the left- and right-handed coupling hypotheses is possible in all the discovery range accessible at the HE-LHC for $\epsilon_{\rm syst}^{\rm bkg} = 20\%$, regardless of the background contamination. In particular, if the background can be entirely subtracted, should a VLQ with mass greater than ~ 2 TeV be discovered, the collected data set will already be sufficient to exclude one of the two coupling structure, while if the background is entirely considered, discrimination is possible at the same time as discovery for a VLQ with mass greater then ~ 2100 GeV.

6.4 Signature based analyses

Several contributions that are constructed around experimental signatures rather than specific theoretical models are presented in this section. This includes analyses of dijets, diphotons, dibosons and ditops final state events at HL- and HE-LHC.

6.4.1 Coloured Resonance Signals at the HL- and HE-LHC

Contributors: T. Han, I. Lewis, Z. Liu

While much of the attention for new physics discovery has centred on precision measurements of the Higgs and EW sectors, the LHC is a QCD machine and most initial states are composed of coloured particles. Hence, new coloured dijet resonances that couple to partons will be produced with favourable rates at the HL-LHC and HE-LHC.

[16] Clearly an optimisation of the signal regions can be performed to increase the sensitivity already at the current LHC energy.

In Ref. [711] we classified the possible coloured resonances at the LHC according to their spin, electric charge, and colour representation. We now update those results for the HE-LHC. This involves comparing the cross sections of the various resonances at the LHC and HE-LHC.

Most initial states at the LHC are composed of coloured particles, *i.e.* quarks and gluons. We now review the possible interactions of coloured resonances with SM partons. A more detailed discussion, including examples of specific realisations of the various resonances in the existing literature, is given in Ref. [711]. All interactions are after EWSB.

Quark-quark annihilation can produce colour antitriplet or sextet scalars and vectors, so-called "diquarks". Please note that the diquarks under discussion here are fundamental particles and not composite. The possible scalar diquark are denoted as E_{N_D}, U_{N_D}, and D_{N_D} with electric charges $4/3, 2/3, -1/3$ respectively. The subscript $N_D = 3,\ 6$ for the $\mathbf{\bar{3}}$ and $\mathbf{6}$ colour representations, respectively. Vector diquarks are represented with an additional Lorentz index μ. The interaction Lagrangian between quarks and diquarks is then

$$\begin{aligned}\mathcal{L}_{qqD} &= K^j_{ab}\Big[\lambda^E_{\alpha\beta}E^j_{N_D}\,\overline{u^C_{\alpha a}}P_\tau u_{\beta b}+\lambda^U_{\alpha\beta}U^j_{N_D}\,\overline{d^C_{\alpha a}}P_\tau d_{\beta b}+\lambda^D_{\alpha\beta}D^j_{N_D}\,\overline{d^C_{\alpha b}}P_\tau u_{\alpha a}\\ &+ \lambda^{E'}_{\alpha\beta}E^{j\mu}_{N_D}\,\overline{u^C_{\alpha a}}\gamma_\mu P_R u_{\beta b}+\lambda^{U'}_{\alpha\beta}U^{j\mu}_{N_D}\,\overline{d^C_{\alpha a}}\gamma_\mu P_R d_{\beta b}+\lambda^{D'}_{\alpha\beta}\,D^{j\mu}_{N_D}\overline{u^C_{\alpha a}}\gamma_\mu P_\tau d_{\beta b}\Big]+\text{h.c.},\end{aligned} \tag{6.4.1}$$

where $P_\tau = \frac{1}{2}(1\pm\gamma_5)$ with $\tau = R, L$ for the right- and left-chirality projection operators, a, b are colour indices for the $SU(3)_C$ fundamental representation, j are colour indices of the N_D representation of $SU(3)_C$, α, β are flavour indices, and K^j_{ab} are $SU(3)_C$ Clebsch-Gordan (CG) coefficients.

Quarks and gluons annihilate into colour triplet or antisextet fermions with $1/2$ or $3/2$ spin. It is possible to produce a $\mathbf{15}$ colour representation, but the existence of such a fermion would spoil asymptotic freedom [712]. The spin $1/2$ $(3/2)$ fermion states are denoted by $d^*_{N_D}, u^*_{N_D}$ $(d^{*\mu}_{N_D}, u^{*\mu}_{N_D})$ with electric charged $-1/3$ and $2/3$, respectively. The lowest order gauge invariant interactions between a gluon, quark, and heavy fermion is dimension five:

$$\begin{aligned}\mathcal{L}_{qgF} &= \frac{g_s}{\Lambda}F^{A,\rho\sigma}\Big[\bar{u}\bar{K}_{N_D,A}(\lambda^U_L P_L+\lambda^U_R P_R)\sigma_{\rho\sigma}u^*_{N_D}+\bar{d}\bar{K}_{N_D,A}(\lambda^D_L P_L+\lambda^D_R P_R)\sigma_{\rho\sigma}d^*_{N_D}\\ &+\bar{u}\bar{K}_{N_D,A}(\lambda^U_L P_L+\lambda^U_R P_R)\sigma_{\rho\sigma}\gamma_\mu u^{*\mu}_{N_D}+\bar{d}\bar{K}_{N_D,A}(\lambda^D_L P_L+\lambda^D_R P_R)\sigma_{\rho\sigma}\gamma_\mu d^{*\mu}_{N_D}\Big]+\text{h.c.}\,,\end{aligned} \tag{6.4.2}$$

where A is the adjoint colour index, $F^{A,\rho\sigma}$ is the gluon field strength tensor, $\sigma_{\rho\sigma} = \frac{i}{2}[\gamma_\rho, \gamma_\sigma]$, Λ is the scale of new physics, and $K_{N_D,A}$ are $3\times N_D$ CG coefficient matrices.

Gluon-gluon annihilation can result in many different representations, that unlike the $\mathbf{15}$ fermion do not spoil asymptotic freedom. A complete list of the possible resonances from gluon-gluon annihilation can be found in Table 1 of Ref. [711]. We will focus on the theoretically motivated colour octet resonances. Two possible resonances that can result from gluon-gluon annihilation are colour octet scalars, S_8, and tensors, $T_8^{\mu\nu}$. These interactions can be described in a gauge invariant way by dimension five operators:

$$\mathcal{L}_{gg8} = g_s d^{ABC}\left(\frac{\kappa_S}{\Lambda_S}S_8^A F^B_{\mu\nu}F^{C,\mu\nu}+\frac{\kappa_T}{\Lambda_T}(T_8^{A,\mu\sigma}F^B_{\mu\nu}F_\sigma^{C\ \nu}+fT_{8\ \rho}^{A,\rho}\,F^{B,\mu\nu}F^C_{\mu\nu})\right), \tag{6.4.3}$$

where $\Lambda_{S,T}$ are the new physics scales, and the relative coupling factor f is expected to be order one.

Finally, quark-antiquark annihilation can produce colour octet or singlet scalars and vectors with zero or unit charge. The neutral vector-octet is denoted by V_8^0 and the charged vector octet states $V_8^\pm$.

Particle Names (leading coupling)	J	$SU(3)_C$	$\lvert Q_e\rvert$	B	Related models
$E^{\mu}_{3,6}\,(uu)$	$0,1$	$\mathbf{3},\ \bar{\mathbf{6}}$	$\frac{4}{3}$	$-\frac{2}{3}$	scalar/vector diquarks
$D^{\mu}_{3,6}\,(ud)$	$0,1$	$\mathbf{3},\ \bar{\mathbf{6}}$	$\frac{1}{3}$	$-\frac{2}{3}$	scalar/vector diquarks; $\tilde{d}$
$U^{\mu}_{3,6}\,(dd)$	$0,1$	$\mathbf{3},\ \bar{\mathbf{6}}$	$\frac{2}{3}$	$-\frac{2}{3}$	scalar/vector diquarks; $\tilde{u}$
$u^{*}_{3,6}\,(ug)$	$\frac{1}{2},\frac{3}{2}$	$\mathbf{3},\ \bar{\mathbf{6}}$	$\frac{2}{3}$	$\frac{1}{3}$	excited u; quixes; stringy
$d^{*}_{3,6}\,(dg)$	$\frac{1}{2},\frac{3}{2}$	$\mathbf{3},\ \bar{\mathbf{6}}$	$\frac{1}{3}$	$\frac{1}{3}$	excited d; quixes; stringy
$S_8\,(gg)$	0	$\mathbf{8}_S$	0	0	$\pi_{TC},\ \eta_{TC}$
$T_8\,(gg)$	2	$\mathbf{8}_S$	0	0	stringy
$V^{0}_8\,(u\bar{u},\ d\bar{d})$	1	$\mathbf{8}$	0	0	axigluon; $g_{KK},\ \rho_{TC}$; coloron
$V^{\pm}_8\,(u\bar{d})$	1	$\mathbf{8}$	1	0	$\rho^{\pm}_{TC}$; coloron

Table 6.4.1: Summary for resonant particle names, their quantum numbers, and possible underlying models.

The interaction Lagrangian is then

$$\begin{aligned}\mathcal{L}_{q\bar{q}V} \;=\; & g_s\Big[V_8{}^{0,A,\mu}\;\bar{u}T^A\gamma_\mu(g^U_L P_L + g^U_R P_R)u + V_8{}^{0,A,\mu}\;\bar{d}T^A\gamma_\mu(g^D_L P_L + g^D_R P_R)d \\ & + \Big(V_8{}^{+,A,\mu}\;\bar{u}T^A\gamma_\mu(C_L V_L^{\text{CKM}} P_L + C_R V_R^{\text{CKM}} P_R)d + \text{h.c.}\Big)\Big]\,,\end{aligned} \tag{6.4.4}$$

where $V^{\text{CKM}}_{L,R}$ are the left- and right-handed Cabibbo-Kobayashi-Maskawa matrices, respectively. To avoid constraints from flavour physics it is assumed that the CKM matrices align with the SM CKM matrices and that there are no tree level flavour changing neutral currents, *i.e.*, $g^{U,D}_{L,R}$ and $C_{L,R}$ are flavour-diagonal. To obtain the interactions with the colour singlet bosons it is sufficient to replace the representation matrices $T^{A,a}{}_b$ with the Kronecker delta $\delta^a{}_b$. The couplings between octet and singlet scalar and light quarks is constrained to be small by minimal flavour violation [713]. It is possible for a new scalar to have substantial couplings to the third generation quarks consistent with minimal flavour violation if it has a non-trivial representation under the SM flavour groups [714]. We will only consider particles that couple to the light quarks and can be resonantly produced at the LHC. Hence, we ignore scalar singlet and octet contributions to s-channel resonances with quark/anti-quark initial states.

In Table 6.4.1 we summarise the different coloured resonances discussed in this section. We list our notation for the different states along with the leading couplings to SM partons and spin, colour representation, and electric charge of each state. The subscript S on $\mathbf{8}_S$ indicates that this colour octet representation is the symmetric combination of two other octets, as shown in Eq. (6.4.3).

Since all of the resonances listed in Table 6.4.1 couple to SM partons, they can decay back into SM partons. Hence, they can be observed as dijet resonances. We assume that the resonances decay exclusively back into (slim) dijets, *i.e.* not new particles or fat jets from top quarks. If there are additional decay channels, our results can be simply rescaled by a BR.

The cross section for resonance R production via quark and/or gluon initial states at the LHC is

$$\sigma = \mathcal{L}_{12}(\tau_0)\frac{4\pi^2}{S_H}\frac{N_D(2J_R+1)}{N_1\,N_2}\frac{\Gamma(R\to X_1X_2)}{M_R}(1+\delta_{X_1X_2}), \tag{6.4.5}$$

where X_1, X_2 are the initial state particles, M_R is the resonance mass, $S_H = 14, 27$ TeV is the c.o.m. energy, and J_R is the spin of the resonance. The dimension of the colour representation of the resonance and initial state particles are denoted by N_D and N_1, N_2, respectively. The parton luminosity is

$$\mathcal{L}_{12}(\tau_0) = \frac{1}{1+\delta_{X_1X_2}}\int_{\tau_0}^1\frac{dx}{x}\left(f_1(x)f_2(\tau_0/x) + f_2(x)f_1(\tau_0/x)\right), \tag{6.4.6}$$

where $\tau_0 = M_R^2/S_H$, f_1 is the PDF of X_1, and f_2 is the PDF of X_2.

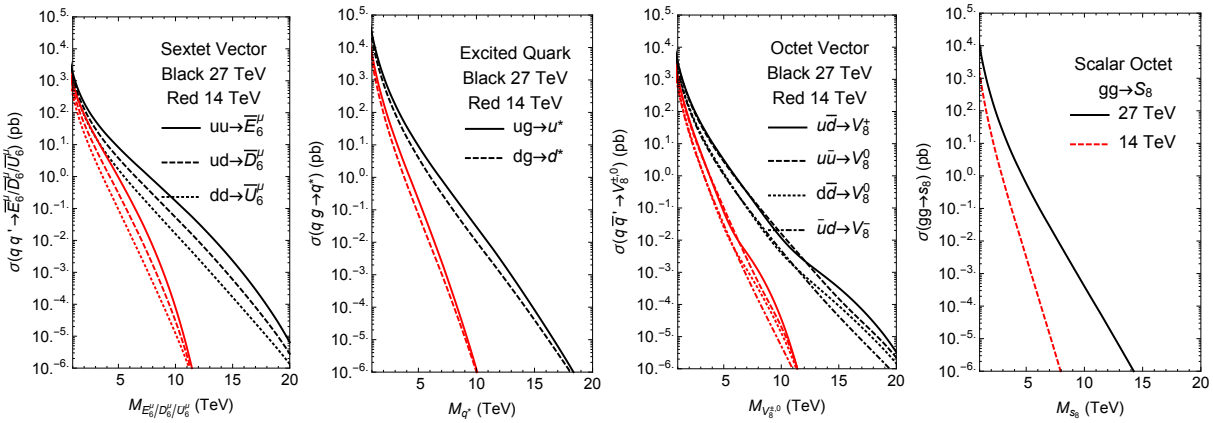

Fig. 6.4.1: Cross sections at HL- and HE-LHC shown in red and black curves, respectively, for (a) sextet diquarks, (b) excited quark, (c) octet vectors, and (d) S_8.

In Fig. 6.4.1 we show the cross sections of (a) sextet diquarks, (b) excited quarks, (c) octet vectors, and (d) S_8 for both the (red) HL- and (black) HE-LHC. These cross sections are calculated using the NNPDF [121] PDF set, the coupling constants $\lambda^{E,U,D}$ and κ_S are set to one, and the new physics scales $\Lambda = \Lambda_S = M_R$. The sextet scalar cross sections are the largest for large resonance mass due to an enhancement from having two valence quarks in the initial state. Somewhat surprisingly, despite the LHC having a reputation as having a large gluon pdf, at very high masses the vector octets produced from quark/anti-quark initial states have larger cross sections than resonances from gluon initial states. This is because the gluon PDF drops precipitously at high momentum fraction. In fact, at the highest resonance masses, S_8 produced from gluon fusion has the lowest cross sections. Although the precise value of these rates depends on the choices of couplings and new physics scale, the gluon pdf suppression is clearly seen by how quickly the excited quark and S_8 cross sections decrease at high resonance masses as compared to the vector octets.

As can be clearly seen, the cross sections greatly increase at the HE-LHC. For a resonance mass around $10 - 11$ TeV, we might expect $\mathcal{O}(1)$ events at the HL-LHC with $3\ \mathrm{ab}^{-1}$ of data for diquarks, excited quarks, and vector octets. For these resonances and resonance mass, at the HE-LHC with $3\ \mathrm{ab}^{-1}$ of data we may expect $\mathcal{O}(10^3 - 10^5)$ events. For S_8, for a resonance mass of 8 TeV for $3\ \mathrm{ab}^{-1}$ we expect $\mathcal{O}(1)$ events at the HL-LHC and $\mathcal{O}(10^4)$ events at the HE-LHC. This is a factor of $\mathcal{O}(10^3 - 10^5)$ increase in the cross sections at the HE-LHC.

Additionally, at the HE-LHC, the mass reach is considerably extended. The baseline for the HE-LHC is $15\ \mathrm{ab}^{-1}$by its end run. For $15\ \mathrm{ab}^{-1}$we expect $\mathcal{O}(10)$ events for 21 TeV diquarks (E_6^u), 19 TeV excited quark (u^*), 21 TeV octet vectors (V_8^+), and 15 TeV octet scalar S_8. Comparing this to the masses for which we expect $\mathcal{O}(10)$ events by the end of the HL-LHC, we see that we may expect the mass reach of the HE-LHC to be twice that of the HL-LHC.

6.4.2 Precision searches in dijets at the HL- and HE-LHC

Contributors: S. V. Chekanov, J. T. Childers, J. Proudfoot, R.Wang, D. Frizzell

Model-independent searches for deviations in dijet invariant mass distributions (M_{jj}) predicted by the SM is one of the central studies at the LHC. The main goal of such searches is to find small deviations from background distributions, under the assumption that a new resonant state decaying to partons that form two jets may introduce an excess in dijet masses localised around the resonance mass. In recent years, such searches for new physics at the LHC have been performed by both ATLAS and CMS collaborations (see the recent studies in Ref. [114, 114, 715–720]), but no statistically significant deviations from background expectations were found. Such searches are usually performed for resonances with a

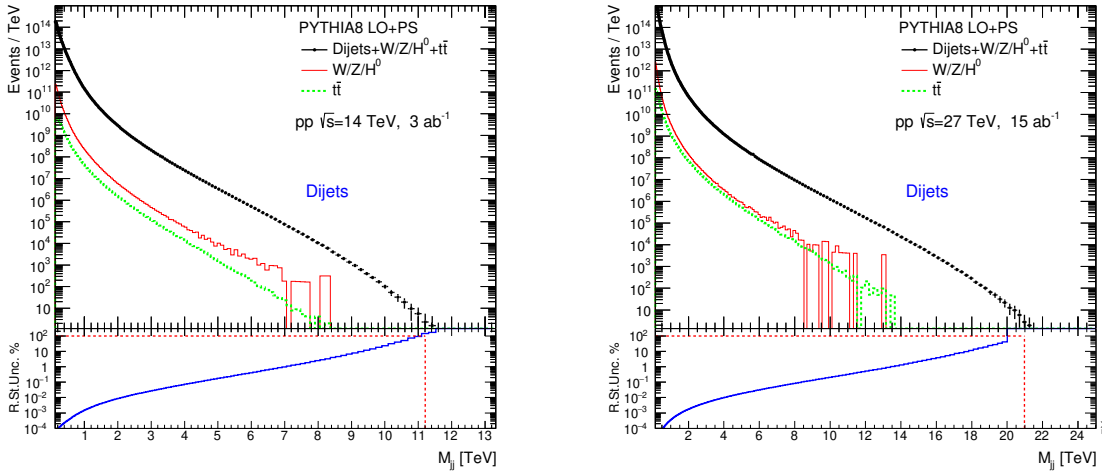

Fig. 6.4.2: Expectations for the dijet invariant mass distribution for 3 ab^{-1}at HL-LHC and 15 ab^{-1} at the HE-LHC using the Pythia generator. Contributions from $W/Z/H^0$ -boson processes and top-quark processes are shown separately (without stacking the histograms). The bottom plots show the relative statistical uncertainties in each bin, together with the line indicating the mass point at which the uncertainty is 100%. The figures are taken from [721].

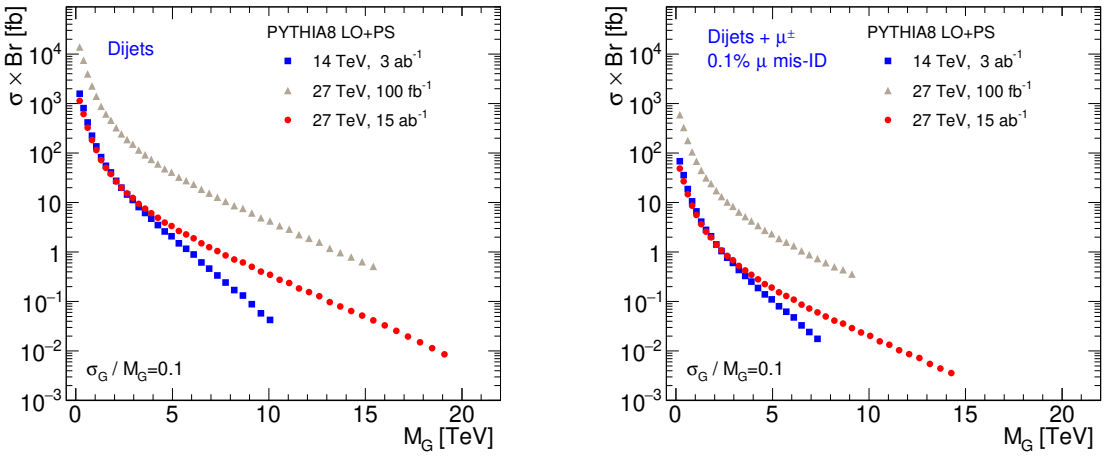

Fig. 6.4.3: Expected 95% C.L. upper limits obtained from the M_{jj} distribution on fiducial cross-section times the BR to two jets for a hypothetical BSM signal approximated by a Gaussian contribution to the dijet mass spectrum. The limits are obtained for the HL-LHC and HE-LHC energies. The figure shows the limits for inclusive dijet production (left) and for events with at least one isolated muon with $p_T > 60$ GeV.

width of up to 15% of the resonance mass. Searches for broader resonances are usually more difficult since the available tools to determine the background hypothesis have a number of limitations that do not allow for reliable estimates of background shapes in the presence of broad resonances. Despite the generality of dijet searches, such studies can exclude a number of BSM models, such as models with quantum black holes, excited quarks, and Z' bosons and so on. Currently, the LHC run II data provide the 95% C.L. exclusion limits on BSM resonances up to 6.5 TeV in masses.

Shapes of the background M_{jj} distributions can be affected by several instrumental factors, making such studies difficult for low-mass regions where statistics are large. In the case of inclusive jet production, the rate of dijets is reduced due to triggers with low acceptance rate, which leads to complicated shapes of in the region of M_{jj} below 1 TeV. This leads to difficulties in interpretation of the shapes

of the M_{jj} distributions using QCD-motivated fit functions. Recently, such searches have been extended to less inclusive events, such as events with $b-$jets and associated leptons [722, 723]. These studies rely on less inclusive triggers with low thresholds, thus accessing regions with small dijet masses.

With the increase of the LHC luminosity, searches for new physics beyond the SM in the invariant mass of two jets become increasingly important since the large event rate allows one to explore a large M_{jj} phase space with improved statistics. The proposed HL-LHC and HE-LHC experiments will open a new chapter in model independent searches, both in terms of the physics reach and the complexity of derivations of data-driven backgrounds. Here we will give an overview of the physics potential for model-independent searches [721] in dijets for the HE-LHC and HL-LHC experiments, as well as describe some technical problems in understanding of "signal-like" feature on a smoothly falling dijet mass distributions. We will cover searches in inclusive jets, as well as more exclusive searches in events with $b-$jets and leptons.

The presented studies use MC event generation with representative for the HL-LHC experiment event statistics. This was achieved using high-performance computers at NERSC. The PYTHIA 8 [50] generator with the default parameter settings and the ATLAS A14 tune [676] was used. The c.o.m. collision energy of pp collisions was set to 14 TeV and 27 TeV for the HL-LHC and HE-LHC respectively. About 100 billion MC events with the multi-jet QCD, $t\bar{t}$ and $W + jet$ categories of processes were simulated using the HepSim software [724] deployed on supercomputers at NERSC. Such a large number of events is required in order to obtain M_{jj} distributions which are sufficiently smooth for calculations of limits. In addition, a phase-space re-weighting was used for $2 \to 2$ processes to increase the statistics in the tail of the M_{jj} distribution as discussed in Ref. [50]. The jets were reconstructed with the anti-k_T algorithm [34], as implemented in the FastJet package [35], using a distance parameter of $R = 0.4$. The minimum transverse momenta of jets was 40 GeV, and the pseudorapidity range was $|\eta| < 2.4$. Dijet invariant masses were reconstructed by combining the two leading jets having the highest transverse momentum. The b-jets are selected by requiring a distance, defined in pseudorapidity and azimuthal angle, between the b-quark and jet to be less than 0.4 and the b-quark p_T to be at least 50% of the jet p_T. A constant 10% mis-tag rate was assumed, which is sufficiently realistic [725] for large $p_T(jet)$.

In addition to jets, muons were also used for such studies. They are required to be isolated using a cone of the size 0.2 in the azimuthal angle and pseudorapidity is defined around the true direction of the lepton. A lepton is considered to be isolated of it carries more than 90% of the cone energy. We also simulated a misidentification rate of muons (or “fake” rate) assuming that a muon can be mis-identified with a rate of 0.1% [726].

Figure 6.4.2 shows two representative M_{jj} distributions using the simulations discussed above. The results are shown for the HL-LHC and HE-LHC colliders using different integrated luminosities, $3\ \mathrm{ab}^{-1}$(for HL-LHC) and $15\ \mathrm{ab}^{-1}$ (for HE-LHC). The figure also shows contributions to the total event rate from $W/Z/H^0$-boson processes combined and top-quark processes from the hard interactions (shown separately). The lower panel shows the relative statistical uncertainty on the data points, *i.e.* $\Delta d_i/d_i$, where d_i is the number of the events in the bins, and Δd_i its statistical uncertainty (which is $\sqrt{d_i}$ in the case of counting statistics). For a quantitative characterisation of the dijet mass reach, the dash lines on the lower panel show the M_{jj} point at which statistical uncertainty in a bin is 100% (or $\Delta d_i/d_i = 1$). We have chosen this point to define the statistical reach for the measurements using the M_{jj} distributions. The M_{jj} mass reach at the HL-LHC is 11.2 TeV, while the mass reach at the c.o.m. of 27 TeV is close to 21 TeV for the the nominal luminosity of $15\ \mathrm{ab}^{-1}$.

The dijet distributions discussed above were used to set the 95% C.L. upper limit on fiducial cross-section times the BR for a generic Gaussian signal with the width (σ_G) being 10% of the Gaussian peak position. Figure 6.4.3 shows the obtained limits. In addition to inclusive dijet events, this figure shows the upper limits for events with at least one isolated muon with transverse momentum above 60 GeV. The results show that even the HE-LHC experiment with an integrated luminosity of $100\ \mathrm{fb}^{-1}$ has advantages over the HL-LHC (with the nominal luminosity of $3\ \mathrm{ab}^{-1}$) in terms of statistical sensitivity to high-mass

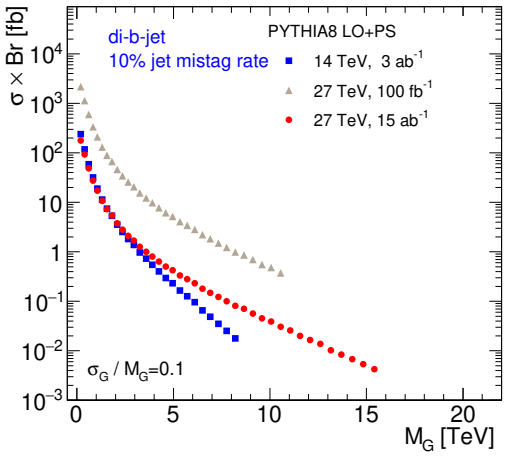

Fig. 6.4.4: Expected 95% C.L. upper limits obtained from the M_{jj} distribution for jets identified as b-jets. The limits are set on fiducial cross-section times the BR to two jets for a hypothetical BSM signal approximated by a Gaussian contribution to the dijet mass spectrum. The limits are obtained for the HL-LHC and HE-LHC energies.

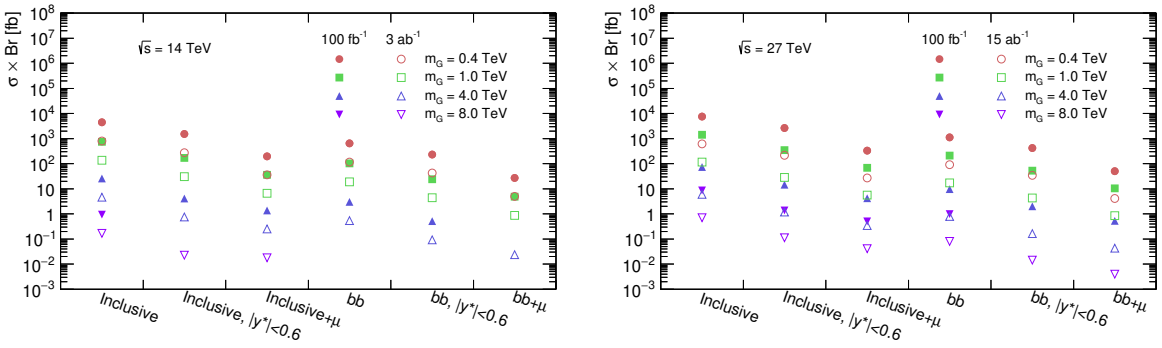

Fig. 6.4.5: Comparisons of the 95% C.L. upper limits obtained from the M_{jj} distribution for the HL-LHC at 14 TeV (left) and the HE-LHC at 27 TeV (right). The limits for the masses 0.4 TeV, 1 TeV, 4 TeV and 8 TeV are shown for 100 fb^{-1}, 3 ab^{-1} and 15 ab^{-1} for different channels with different selections.

states. When using the nominal integrated luminosity of 15 ab^{-1} for HE-LHC, the HE-LHC provides a factor of two larger reach for dijet masses compared to the HL-LHC with the nominal luminosity.

Figure 6.4.4 shows the 95% C.L. upper limits obtained from the M_{jj} distribution for events where both leading jets were identified as $b-$jets. As for the previous simulation based on inclusive jets, the physics reach of the HE-LHC with the nominal luminosity is a factor two larger than that of the HL-LHC.

Figure 6.4.5 shows the comparisons of the limits for dijet and muon associated dijet channels with inclusive or b-tagging selections for the 14 TeV and 27 TeV collision energies. In addition to the inclusive jet case, we also calculated the upper limits after applying the rapidity difference requirement $|y^*| < 0.6$ between two jets [727] in order to enhance the sensitivity to heavy BSM particles decaying to jets.

The studies discussed [721] have also shown that searches for signals in dijets invariant masses require well-understood estimates for the M_{jj} background shape. An example of such challenging background shape is shown in Fig. 6.4.2. A data-driven determination of the shape background at the HL-LHC and HE-LHC should be performed with the relative statistical precision of 0.01% per data point for $M_{jj} < 1$ TeV. Currently, it is difficult to achieve such precision using the available tools used for the

LHC run 2 data.

In conclusion, it was illustrated that the HE-LHC provides substantial improvements for searches of new physics in dijet invariant masses, compared to searches at the HL-LHC. Even for a rather modest $100\ \mathrm{fb}^{-1}$ luminosity of the HE-LHC project, the simulations show that the mass reach for dijet searches is about 50% larger than that from the HL-LHC with the nominal luminosity of $3\ \mathrm{ab}^{-1}$. It was also shown that the HE-LHC project with the nominal luminosity of $15\ \mathrm{ab}^{-1}$ will extend the HL-LHC mass reach by a factor two. The reported limits can be used for exclusions of BSM resonances decaying that decay to form two jets in inclusive dijet events, events with di-b-jets, and events with associated muons. Note that the actual exclusion ranges significantly depend on expected cross-sections and BRs of BSM models for the HL-LHC and HE-LHC collision energies.

6.4.3 Dissecting heavy diphoton resonances at HL- and HE-LHC

Contributors: B. Allanach, D. Bhatia, A. Iyer

We examine the phenomenology of the production of a heavy resonance X, which decays via other new on-shell particles n into multi- (*i.e.* three or more) photon final states. In the limit that n has a much smaller mass than X, the multi-photon final state may dominantly appear as a two photon final state because the γs from the n decay are highly collinear and remain unresolved. We discuss how to discriminate this scenario from $X \to \gamma\gamma$: rather than discarding non-isolated photons, it is better instead to relax the isolation criterion and instead form photon jet substructure variables. The spins of X and n leave their imprint upon the distribution of pseudorapidity gap $\Delta\eta$ between the apparent two photon states. In some models, the heavy resonance X may decay into nn or $n\gamma$, where n is an additional light particle, may further decay into photons leading to a multi-photon[17] final state. Examples of such models include hidden valley models [346, 728], the NMSSM [528] or Higgs portal scenarios [729]. Describing angles in terms of the pseudorapidity η and the azimuthal angle around the beam ϕ, the angular separation between two photons may be quantified by $\Delta R = \sqrt{(\Delta\eta)^2 + (\Delta\phi)^2}$. Neglecting its mass, the opening angle between the two photons coming from a highly boosted on-shell n is

$$\Delta R = \frac{m_n}{\sqrt{z(1-z)}p_T(n)}, \tag{6.4.7}$$

purely from kinematics (this was calculated already in the context of boosted Higgs to $b\bar{b}$ decays [502]), where z and $(1-z)$ are the momentum fractions of the photons[18]. Thus,

$$\Delta R = \frac{m_n}{M_X}\frac{2\cosh\eta(n)}{\sqrt{z(1-z)}}. \tag{6.4.8}$$

In the limit $m_n/M_X \to 0$, $\Delta R \to 0$ and the two photons from n are collinear, appearing as one photon; thus several possible interpretations can be ascribed to an apparent diphoton signal.

We assume that any couplings of new particles such as the X (and the n, to be introduced later) to Higgs fields or $W^{\pm}, Z^0$ bosons are negligible. Eq. (6.4.9) gives an effective field theoretic interaction Lagrangian for the coupling of X to a pair of photons, when X is a scalar (first line) or a graviton (second line).

$$\begin{aligned}
\mathcal{L}^{int}_{X=\text{spin }0} &= -\eta_{GX}\frac{1}{4}G^a_{\mu\nu}G^{\mu\nu a}X - \eta_{\gamma X}\frac{1}{4}F_{\mu\nu}F^{\mu\nu}X, \\
\mathcal{L}^{int}_{X=\text{spin }2} &= -\eta_{T\psi X}T^{\alpha\beta}_{fermion}X_{\alpha\beta} - \eta_{TGX}T^{\alpha\beta}_{gluon}X_{\alpha\beta} - \eta_{T\gamma X}T^{\alpha\beta}_{photon}X_{\alpha\beta}.
\end{aligned} \tag{6.4.9}$$

where $T^{\alpha\beta}_i$ is the stress-energy tensor for the field i and the η_j are effective couplings of mass dimension -1. $F_{\mu\nu}$ is the field strength tensor of the photon (this may be obtained in a SM invariant way from a

[17] In the present paper, whenever we refer to multi-photon final states, we refer to three or more photons.

[18] The decay is strongly peaked towards the minimum opening angle $\Delta R = 2m_n/p_T$ [730].

Model	Process
$S2$	$pp \to S \to \gamma\gamma$
$S4$	$pp \to S \to nn \to \gamma\gamma + \gamma\gamma$
$V3$	$pp \to Z' \to n\gamma \to \gamma + \gamma\gamma$
$G2_{ff}$	$q\bar{q} \to G \to \gamma\gamma$
$G4_{gg}$	$gg \to G \to nn \to \gamma\gamma + \gamma\gamma$
$G4_{ff}$	$\bar{q}q \to G \to nn \to \gamma\gamma + \gamma\gamma$

Table 6.4.2: Cases to discriminate with a scalar n and a heavy resonance which is: scalar (S), spin 1 (Z') or spin 2 (G). We have listed the main signal processes to discriminate between in the second column, ignoring any proton remnants. The notation used for a given model is Xk: $X = S, V, G$ labels the spin of the resonance and k denotes the number of signal photons at the parton level in the final state.

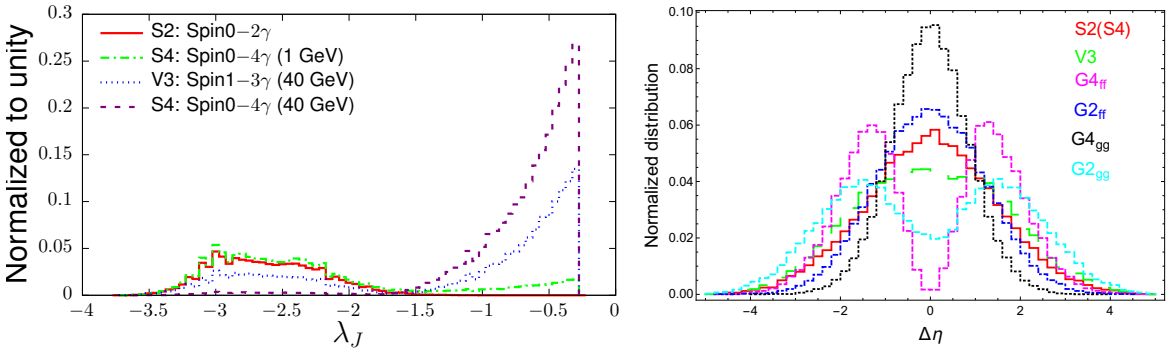

Fig. 6.4.6: Left: distribution of λ_J variable for various signal hypotheses. m_n is noted in parentheses in the legend for the relevant cases. Right: signal $\Delta\eta$ distribution for various different spin combinations at $\sqrt{s} = 27$ TeV, $m_X = 2.5$ TeV. The cases S2 and S4 are practically indistinguishable by eye and so we only plot one histogram for them.

coupling involving the field strength tensor of the hypercharge gauge boson), whereas $G^a_{\mu\nu}$ is the field strength tensor of a gluon of adjoint colour index $a \in \{1, \ldots, 8\}$. As noted earlier, the direct decay of a vector boson into two photons is forbidden by the Landau-Yang theorem [731, 732].

Although we assume that n is electrically neutral, it may decay to two photons through a loop-level process (as is the case for the SM Higgs boson, for instance). Alternatively, if X is a spin 1 particle, it could be produced by quarks in the proton and then decay into $n\gamma$. The Lagrangian terms would be

$$\mathcal{L}^{int}_{X=\text{spin }1,n} = -(\lambda_{\bar{q}Xq}\bar{q}_R\gamma_\mu X^\mu q_R + \lambda_{\bar{Q}XQ}\bar{Q}_L\gamma_\mu X^\mu Q_L + H.c.) - \frac{1}{4}\eta_{nX\gamma} n\tilde{X}_{\mu\nu}F^{\mu\nu}, \qquad (6.4.10)$$

where λ_i are dimensionless couplings, q_R is a right-handed quark, Q_L is a left-handed quark doublet and $\tilde{X}_{\mu\nu} = \partial_\mu X_\nu - \partial_\mu X_\nu$. The decay $X_{spin=1} \to n\gamma$ would have to be a loop-level process, as explicitly exemplified in Ref. [730], since electromagnetic gauge invariance forbids it at tree level. The possible different spins involved in multi-photon production processes, along with our nomenclature for them, are listed in Table 6.4.2. The first tool for model discrimination is the photon sub-jet variable $\lambda_J = \log(1 - p_{T_L}/p_{T_J})$, where P_{T_L} denotes the transverse momentum of the leading photon sub-jet whilst p_{T_J} is the transverse momentum of the whole photon jet. Double pronged photon jets have a peak at $\lambda_J = -0.3$. This may be observed when the signal is multi-photon and m_n is not too small, as Fig. 6.4.6 (left) shows.

Here, we neglect backgrounds and only focus on the signal. This is a good approximation for heavy resonances where backgrounds die off exponentially with invariant mass of the apparent diphoton pair, provided that the signal cross-section is large enough. The signal cross-section is of course set by the size of the couplings in Eq.s (6.4.9) and (6.4.10), which may be adjusted as required. Here, we

N_R	$\sqrt{s}$	$S4$	$G4_{gg}$	$G4_{ff}$
$S4$	14 TeV	∞	23	12
	27 TeV	∞	17	8
$G4_{gg}$	14 TeV	34	∞	5
	27 TeV	24	∞	3
$G4_{ff}$	14 TeV	18	5	∞
	27 TeV	11	4	∞

Table 6.4.3: Spin discrimination in case A: $N_R = \mathcal{L}\sigma_{tot}^{(X)}$, the expected number of total signal events required to be produced to discriminate against the 'true' row model versus a column model by a factor of 20 for $m_n = 100$ GeV.

N_R	$\sqrt{s}$	$S2$	$S4$	$V3$	$G2_{gg}$	$G4_{gg}$	$G2_{ff}$	$G4_{ff}$
$S2$	14 TeV	∞	19270	198	25	13	85	12
	27 TeV	∞	8676	269	26	16	92	14
$S4$	14 TeV	19256	∞	202	25	13	81	13
	27 TeV	8713	∞	311	28	15	83	14
$V3$	14 TeV	186	190	∞	55	7	30	19
	27 TeV	261	299	∞	51	10	40	20
$G2_{gg}$	14 TeV	28	28	66	∞	4	11	35
	27 TeV	31	33	63	∞	5	13	41
$G4_{gg}$	14 TeV	21	21	12	6	∞	47	4
	27 TeV	26	25	16	7	∞	55	5
$G2_{ff}$	14 TeV	101	97	37	11	33	∞	8
	27 TeV	103	93	46	12	39	∞	9
$G4_{ff}$	14 TeV	18	18	26	36	4	12	∞
	27 TeV	19	20	29	41	5	13	∞

Table 6.4.4: Spin discrimination for case B: $N_R = \mathcal{L}\sigma_{tot}^{(X)}$, the expected number of total signal events required to be produced to discriminate against the 'true' row model versus a column model by a factor of 20 at the 14 TeV LHC for $m_n = 10$ GeV.

consider one of the cases in Table 6.4.2 at a time, with cross-sections of all other cases set to zero.

If there is a sizeable peak at $\lambda_J = -0.3$, the model possibilities are $S4, V3, G4_{gg}$ and $G4_{ff}$. Further to this, $V3$ may be further discriminated owing to its double peak structure: at ~ -3 and at -0.3. We call this case A. If there is no sizeable peak, we can either have $S2$ or m_n very small. This latter case we call case B.

After categorisation into case A or B, we can use the fact that each case in Table 6.4.2 corresponds to a different distribution in $\Delta\eta$, the difference in pseudorapidity between the two initially identified photons. We plot the $\Delta\eta$ distributions for the different spin cases in Fig. 6.4.6 (right). We calculate N_R, the expected number of signal events required to disfavour a hypothesis H_S over another hypothesis H_T to an odds factor of $R = 20$ from the $\Delta\eta$ distributions in the discretised Kullback-Leibler method proposed in Ref. [733]. From Tables 6.4.3 and 6.4.4, we see that our estimate of the required number of signal events to discriminate two signal hypotheses does not change much between the HL-LHC and the HE-LHC. For identical input parameters, we would expect the number of signal events to be higher at the higher energies, meaning that spins can be more effectively discriminated to smaller production cross-sections at the HE-LHC.

6.4.4 Prospects for diboson resonances at the HL- and HE-LHC

Contributors: R. Les, V. Cavaliere, T. Nitta, K. Terashi, ATLAS

Prospects are presented [734] for the search for resonances decaying to diboson (WW or WZ, collectively called VV where $V = W$ or Z) in the semileptonic channel where one W-boson decays leptonically and the other W or Z-boson decays to quarks ($\ell\nu qq$ channel). The results include sensitivity for such new resonances based on an integrated luminosity of $300\,\mathrm{fb}^{-1}$or $3\,\mathrm{ab}^{-1}$of pp collisions at $\sqrt{s} = 14\,\mathrm{TeV}$ using the ATLAS upgraded detector. Searches in other semileptonic and fully hadronic decay channels are expected to have similar sensitivities at high masses, as observed in the ATLAS searches with Run-2 data. The analysis is based on event selection and classification similar to those used in the Run-1 and Run-2 ATLAS searches.

The prospect for resonance searches presented in this article are interpreted in the context of three different models: a heavy vector triplet (HVT) [735], a RS model and a narrow heavy scalar resonance. The parameters of these models are chosen such that along the whole generated mass range, the resonance widths are less than 6% of the mass value, which is smaller than the detector resolution. The main background sources are W bosons produced in association with jets (W+jets), with significant contributions from top-quark production (both $t\bar{t}$ pair and single-top), non-resonant vector-boson pair production (ZZ, WZ and WW) and Z bosons produced in association with jets (Z+jets). Background originating from multi-jet processes are expected to be negligible due to the event selection requirements.

Small- and Large-R jets (denoted by j and J) are used in the analysis, reconstructed with the anti-k_t algorithm and radius 0.4 and 1.0 respectively. It is assumed that the performance of a future W/Z-boson tagger at the HL-LHC conditions will have similar, if not better, performance as existing boson taggers.

Events are required to have exactly one lepton satisfying the selection criteria. It is assumed that the effect of trigger thresholds is negligible for the selected leptons with p_T studied in this note. Events are further required to contain a hadronically-decaying W/Z candidate, reconstructed either from two small-R jets, defined as the resolved channel, or from one large-R jet, designated the boosted channel. The missing transverse energy $E_{\mathrm{T}}^{\mathrm{miss}}$ has to be greater than $60\,\mathrm{GeV}$, which suppresses multijet background to a negligible level. By constraining the $E_{\mathrm{T}}^{\mathrm{miss}}$ + lepton system to be consistent with the W mass, the z component of the neutrino momentum can be reconstructed by solving a quadratic equation. The smallest solution is chosen and in the case where the solution is imaginary, only the real part is taken.

The presence of narrow resonances is searched for in the distribution of reconstructed diboson mass using the signal shapes extracted from simulation of benchmark models. The invariant mass of the diboson system ($m(WV)$) is reconstructed from the leptonic W candidate and hadronic W/Z candidate, the latter of which is obtained from two small-R jets in the resolved channel ($m(\ell\nu jj)$) or large-R jet in the boosted channel ($m(\ell\nu J)$). The background shape and normalisation are obtained from MC simulation with dedicated control regions to constrain systematic uncertainties of the background modelling and normalisation. The search is divided into two orthogonal categories to identify the $\mathrm{ggF}/\mathrm{q\bar{q}}$ and VBF production modes by identifying additional forward jets. If an event passes the VBF category selection for the additional forward jets (defined below) it is categorised as a VBF candidate event, otherwise as a $\mathrm{ggF}/\mathrm{q\bar{q}}$ candidate event. Events are then processed by a merged-jet selection then a two resolved-jet selection if they fail the merged selection. This prioritisation strategy provides the optimum signal sensitivity as it favours the merged selection which contains less background contributions. Examples of the final distributions can be seen in Fig. 6.4.7 for the merged $\mathrm{ggF}/\mathrm{q\bar{q}}$ and VBF signal region.

The results are extracted by performing a simultaneous binned maximum-likelihood fit to the $m(WV)$ distributions in the signal regions and the W+jets and $t\bar{t}$ control regions.

The fit includes five background contributions, corresponding to W+jets, $t\bar{t}$, single-top, Z+jets, and diboson. Systematic uncertainties are taken into account as constrained nuisance parameters with

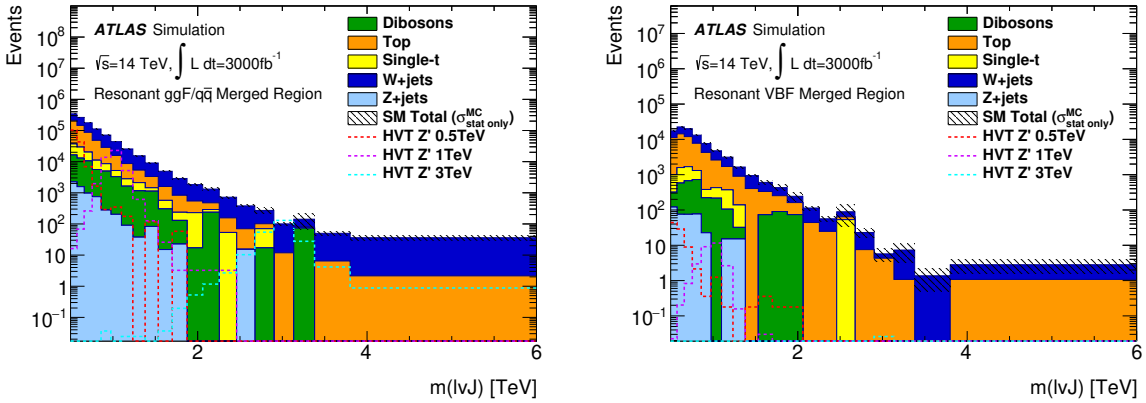

Fig. 6.4.7: Left: final $m(\ell\nu J)$ distribution in the merged signal region for the $\mathrm{ggF/q\bar{q}}$ search. Right: final $m(\ell\nu J)$ distributions in the merged signal region for the VBF search. Background distributions are separated into production type. HVT signals are superimposed as dashed curves where appropriate.

Gaussian or log-normal distributions. For each source of systematic uncertainty, the correlations across bins of $m(WV)$ distributions and between different kinematic regions, as well as those between signal and background, are taken into account. The main background modelling systematics, namely the W+jets and $t\bar{t}$ shape uncertainties, are constrained by the corresponding control regions and are treated as uncorrelated among the resolved and merged signal regions.

The expected upper limits are set on the signal cross section times BR as a function of the signal mass. For the HVT W' and Z' the limits are estimated to be 4.3 TeV with $\mathcal{L} = 300$ fb^{-1} and 4.9 TeV with $\mathcal{L} = 3$ ab^{-1} of pp collisions, using the same detector configuration and pileup conditions. For the Bulk graviton the expected limits are estimated as 2.8 and 3.3 TeV at $\mathcal{L} = 300$ fb^{-1} and $\mathcal{L} = 3$ ab^{-1}. The values at $\mathcal{L} = 3$ ab^{-1} show an expected increase to the sensitivity of the search to the benchmark signals by ~ 1 TeV with respect to existing limits in this channel in Run-2.

Figure 6.4.8 (left) shows one of the upper limit plots for the $\mathrm{ggF/q\bar{q}}$ category at $\mathcal{L} = 3$ ab^{-1}. A line showing the theoretical cross section for the HVT Z' decaying into WW via $\mathrm{ggF/q\bar{q}}$ production at each mass is superimposed and indicates the mass reach of the search. In the circumstance that HL-LHC sees an excess, the expected sensitivity can also be characterised. The discovery significance is defined as the luminosity required to see a 5σ effect of the signal. Figure 6.4.8 (right) shows the expected discovery significance for the resonant search. The signal significance is the quadratic sum of $s/\sqrt{s+b}$, for each bin of the final discriminant distribution at that luminosity, $s(b)$ representing the number of signal(background) events in the bin. In addition to the expected values, dashed curves shows the expected values for a future W/Z-tagger which has a 50% increase in signal efficiency and a further factor of two in background rejection. These values are representative of improvements seen in a recent diboson resonance search in the fully-hadronic $VV \to qqqq$ analysis by using track-calo clusters as opposed to locally-calibrated topologically-clustered calorimeter jets. Other possible improvements in W/Z-tagging in the HL-LHC era can originate from usage of more advanced machine-learning techniques to discriminate against the background contribution and better understanding of jet substructure variables with measurements at higher integrated luminosities.

Resonance search at HE-LHC

The prospect analysis [736] at HE-LHC mimics the analysis at HL-LHC but the DELPHES simulation is used. Results are interpreted in the context of the heavy vector triplet (HVT) model [735]. The major backgrounds W+jets and $t\bar{t}$ production are simulated with MADGRAPH and AMC@NLO respectively, interfaced with Pythia. Z+jets, single top and diboson contribution are not simulated and are expected to contribute at most 10% to the total background.

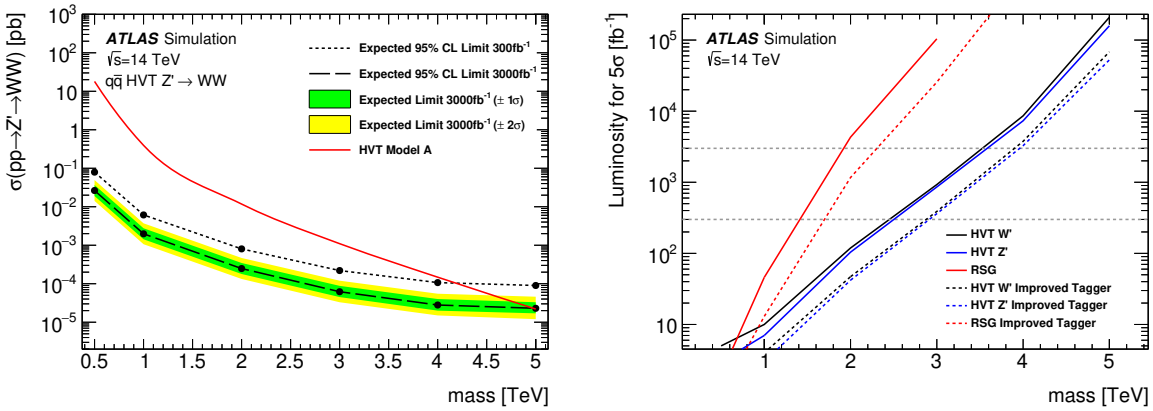

Fig. 6.4.8: Left: 95% C.L. upper limit for the HVT Z' via $\mathrm{ggF/q\bar{q}}$ production. Right: expected luminosity required to observe a 5σ signal significance for the HVT W' (black), HVT Z' (blue) and G_{RS} (red). The solid curves shows the sensitivity using the current W/Z-tagger and the dashed curves for a future tagger that has a 50% increased signal efficiency and a factor two increased rejection of background.

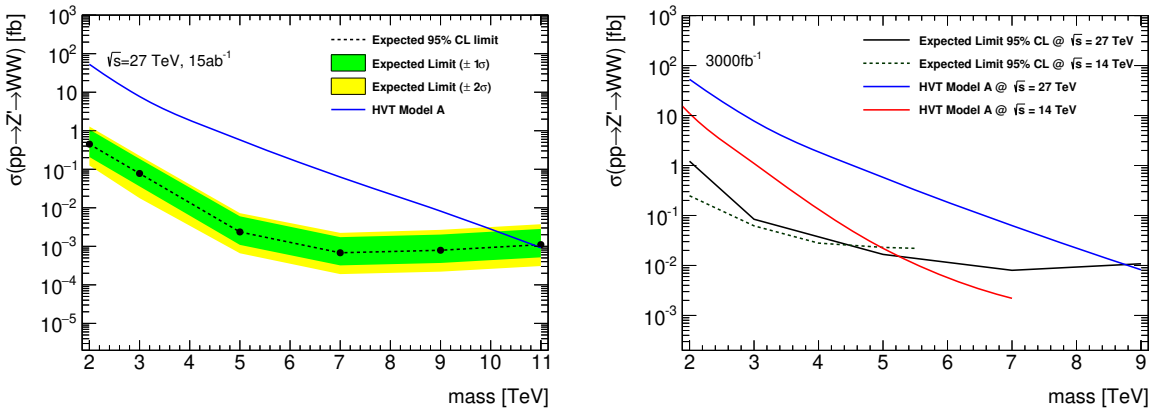

Fig. 6.4.9: 95% C.L. upper limit for the HVT Z' via $\mathrm{ggF/q\bar{q}}$ production for the HE-LHC (left) and HL-LHC (right).

The analysis sensitivities to the resonance signals are extracted by performing a simultaneous binned maximum-likelihood fit to the m_{WW} distributions as in the HL-LHC in the signal regions and the W+jets and $t\bar{t}$ control regions. The signal region and control regions are defined in the same way.

The expected upper limits set on the signal cross section times BR as a function of the signal mass are shown in Fig. 6.4.9 at 27 TeV and compared to the limits obtained for HL-LHC . Based on the Z' production cross section from the HVT signal model the exclusion mass reach is extracted to be 9 and 11 TeV for integrated luminosities of 3 and 15 ab^{-1}at 27 TeV, using DELPHES simulation of a potential detector configuration under no pileup condition.

6.4.5 Prospects for Boosted Object Tagging with Timing Layers at HL-LHC

Contributors: M. D. Klimek

Both CMS and ATLAS are studying new timing detectors to be installed for the high luminosity phase of the LHC. The primary motivation for these new detectors is to aid in mitigating the increased level of pileup that comes along with the increased luminosity. The $\mathcal{O}(30\ \mathrm{ps})$ timing resolution will permit individual proton-proton interactions within a single bunch crossing to be temporally resolved. Beyond pileup mitigation, these detectors may be useful for novel kinds of searches. For example, it has

been proposed in Ref. [737] that they could be used to set limits on long-lived particles. In this section, we point out that this level of timing precision provides the capability of temporally resolving jets for the first time. Currently, jet substructure techniques play a major role in the search for BSM physics. These exploit correlations in momentum and angular distribution of jet constituents to distinguish standard QCD jets from other objects. The capabilities of the new timing layers open up the possibility of extending jet substructure techniques to the time domain. In this section, we will introduce the relevant concepts and suggest that time domain jet substructure can play a complementary role to existing techniques in the search of boosted resonances at the HL-LHC.

Of the various physics objects that are reconstructed by the LHC experiments, jets are unique in that they are collections of particles. The individual jet constituents have some spread in velocity and therefore arrive at the detector over some finite span of time. On dimensional grounds, we can estimate that the typical scale of Lorentz boosts of the jet constituents is $\gamma = E/m \sim E_j/n\Lambda_{\mathrm{QCD}}$, where E_j is the jet energy, n is the hadron multiplicity of the jet, and Λ_{QCD} sets the typical hadron mass. The corresponding scale of the spread in arrival times at a detector a distance R from the interaction point is then of order $\delta t \sim R\delta v \sim R\gamma^{-2}$. For $R \sim 1$ m, $E_j \sim 100$ GeV, $n \sim 10$, and $\Lambda_{\mathrm{QCD}} \sim 1$ GeV, we have $\delta t \sim 100$ ps. Thus we see that at typical LHC energies, the proposed timing detectors with $\mathcal{O}(30\ \mathrm{ps})$ resolution should be sensitive to the temporal structure of jets.

We note that this effect is entirely due to the hadronisation process. Any time differences inherent to the perturbative parton shower should be of order $\Lambda_{\mathrm{QCD}}^{-1}$ and will be far below the resolution of the timing detectors. (In practice, the distance from the interaction point to the timing detector will have some dependence on pseudorapidity η. Because the showering process produces radiation in a cone around the original parton direction, the various jet constituents will then have slightly different distances to travel to the detector. However, for reasonably central jets, this will be a small effect.) If, in the hadronisation process, jet constituents are produced with rapidities y distributed according to $dN/dy = f(y)$, then it is easy to verify that at a detector a distance R in any direction from the interaction point, they will arrive distributed in time according to

$$\frac{dN}{dt} = \frac{cRf(y(t))}{(ct)^2 - R^2}, \tag{6.4.11}$$

with $ct > R$, where c is the speed of light and $y(t) = \operatorname{arctanh}(R/ct)$. Although it is not possible to calculate $f(y)$ from first principles, we note that for any reasonably well-behaved $f(y)$ the arrival time distribution will indicate a burst of jet constituents arriving promptly with a tail extending out to later times.

The hadronisation process is treated phenomenologically by a number of models, and we can verify that this behaviour is borne out. For example, the simplest form of the Lund string hadronisation model [738] predicts $f(y) =$ constant. PYTHIA implements a more complete version of the Lund model, and we use it to verify the predictions of the preceding paragraphs. We generated a sample of 50 GeV quark jets from e^+e^- annihilation in PYTHIA 8, and computed the arrival times of all charged hadrons in each jet at a distance of 1 m from the interaction point. A histogram with 100 ps bin size of the averaged arrival time profile is shown in Fig. 6.4.10. We can see that the PYTHIA output displays the expected behaviour, and we verify that the typical width of the profile is indeed $\mathcal{O}(100\ \mathrm{ps})$.

A study of the rapidity distribution of jet constituents from arrival time profile of QCD jets could provide additional data with which to tune our models of hadronisation. However, we will now argue that this information also provides a novel method for distinguishing normal QCD jets from jets produced by boosted objects. As described in the preceding paragraphs, in a typical jet we expect most hadrons to arrive together and a few to arrive at later times. Note that under a boost, the ordering of the jet constituents in velocity or rapidity is unchanged. Consider a massive particle that decays in its rest frame producing a jet pointing along the negative x axis. The particles in the tail of its velocity distribution have velocities along the x direction that are less negative than the rest of the jet. Now consider the same massive particle but with a large boost in the positive x direction so that this jet is boosted forward into

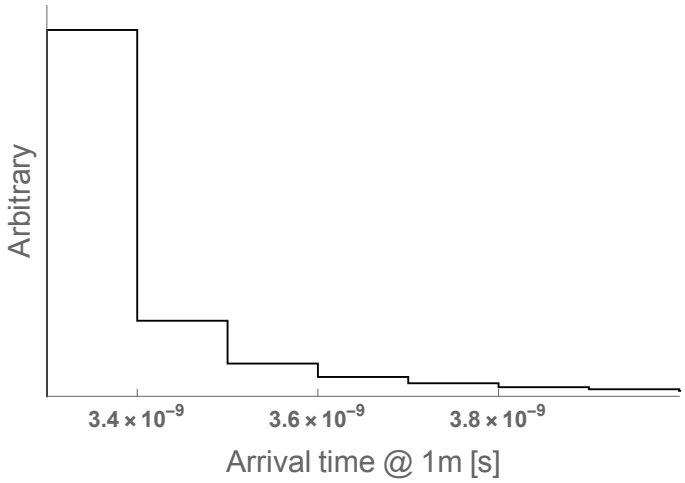

Fig. 6.4.10: Average arrival time profile at $1\ \mathrm{m}$ for charged hadrons in $50\ \mathrm{GeV}$ quark jets from e^+e^- annihilation as simulated by PYTHIA 8.

the positive direction as well. Despite the change in direction, the ordering of the velocities in the jet is the same. The velocities of all jet constituents are now positive, and the tail of the distribution is more positive. We see that if a jet is sufficiently boosted, the tail of its hadron distribution can arrive at the detector first.

In order to quantify this effect, we make use of a simple diagnostic that can distinguish the boosted from the unboosted jets based on their arrival time profiles. Recall that for an unboosted jet, we expect the majority of the charged hadrons to arrive in close temporal proximity with a few arriving later, whereas for a sufficiently boosted jet, one or more charged hadrons may arrive before most of the others. Let t_i and p_i be the arrival times and momenta of the charged hadrons in a jet and $\bar{t}$ be the median charged hadron arrival time. We define the diagnostic function

$$D_\tau = \frac{\sum p_i \Theta(t_i - \bar{t} - \tau)}{\sum p_i}. \tag{6.4.12}$$

The parameter τ should be a value of order the time resolution of the detector. For an unboosted jet, the median arrival time will be in the prompt burst of hadrons. For an appropriate value of τ, none of these hadrons nor any that arrive later will satisfy the theta function, and we will obtain $D_\tau = 0$. However, for boosted jets, some hadrons from the boosted tail may arrive before the main burst. Because the median will still be in the main burst, the early hadrons can satisfy the theta function, in which case we will find $D_\tau > 0$.

To verify this behaviour, we generate two samples of jets in PYTHIA 8. The first is a sample of $500\ \mathrm{GeV}$ quark jets from e^+e^- annihilation. For comparison, we also generate a similar sample of $50\ \mathrm{GeV}$ jets, but then boost them by $v = 0.98$. This is comparable to jets that would be observed from Z decay, where the Z has been produced in the decay of a $1\ \mathrm{TeV}$ diboson resonance. We choose a conservative value of $\tau = 200\ \mathrm{ps}$, which is several times the expected timing detector resolution. In the first sample, we find that our diagnostic is zero in all but 1% of events. However, for the boosted jet sample, we obtain non-zero values in 25% of events.

The actual operating environment of the HL-LHC will present additional challenges coming from the noisy hadronic environment. Jet contamination from pileup and underlying event radiation could mimic the early arrival of the tail of a boosted jet. The information from the timing layers will be used to mitigate pileup and jet grooming techniques can be used to remove stray radiation from the jets before their temporal characteristic are analysed. The timing substructure information can then be combined with existing jet substructure techniques to increase the efficiency for tagging boosted objects, in turn

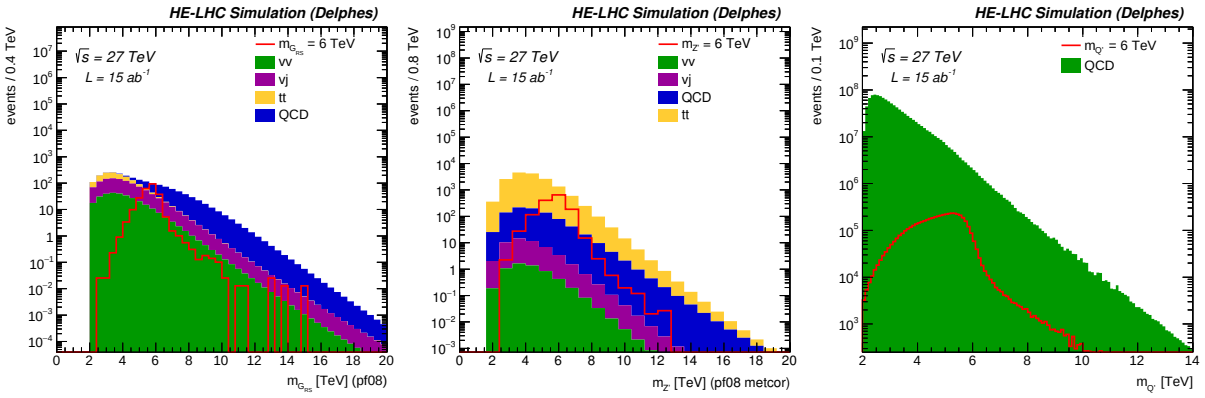

Fig. 6.4.11: Invariant mass distribution of the two selected jets for the full selection for a 6 TeV signal for the three benchmark analyses $G_{RS} \to WW$ (left), $Z' \to t\bar{t}$ (centre) and $Q' \to jj$ (right)

improving the reach of BSM searches. During an HE-LHC phase, even higher boosts can be expected, demanding effective techniques for boosted object tagging. Further details are presented in Ref. [739].

6.4.6 High mass resonance searches at HE-LHC using hadronic final states

Contributors: C. Helsens, D. Jamin, M. Selvaggi

The presence of new resonant states [472,479,740–746] decaying to two highly boosted particles decaying hadronically could be observed as an excess in the invariant mass spectrum of two jets over the large SM background. In this section we present the reach at the HE-LHC for three distinct hadronic signatures: $Z' \to t\bar{t}$, $G_{RS} \to WW$ and $Q' \to jj$. For the $Z' \to t\bar{t}$ decay mode the SSM $Z'_{\rm SSM}$ [672] and a leptophobic $Z'_{\rm TC2}$ [645,747] have been considered as benchmarks Z'models. For the $G_{RS} \to WW$ and $Q' \to jj$ decay modes, a Randall-Sundrum graviton [472] and excited heavy quarks [394,748] have been taken as a benchmarks respectively.

The decay products of the heavy resonances are typically in the multi-TeV regime and their reconstruction imposes stringent requirements on the detector design. Precise jet energy resolution requires full longitudinal shower containment. Highly boosted W bosons and top quarks decay into highly collimated jets that need to be disentangled from standard QCD jets by characterising their substructure. Thus, in order to achieve high sensitivity excellent granularity is needed both in the tracking detectors and in the calorimeters.

Signal events were generated at LO with PYTHIA 8.230 [68]. The considered SM backgrounds are dijet (QCD), top pairs ($t\bar{t}$), VV and $V+$ jets where $V = W/Z$, and were generated at LO using MADGRAPH5_aMC@NLO [67]. A conservative constant k-factor of 2 is applied to all the background processes to account for possibly large higher order corrections. The detector simulation was performed with DELPHES [33] assuming an HE-LHC generic detector [699].

An important ingredient of the $Z' \to t\bar{t}$ and $G_{RS} \to WW$ searches is the identification of hadronically decaying boosted tops and W bosons. To this end, a tagger using jet substructure observables was developed to discriminate W and top jets against QCD jets. It was found that jets using tracking only information (*track-jets*) feature better angular resolution compared to pure calorimeter based jets. Therefore, track-jets are the optimal choice to build jet substructure observables. The boosted top tagger is built from the following jet substructure observables: the soft-dropped jet mass [504] and N-subjettiness [75] variables $\tau_{1,2,3}$ and their ratios τ_2/τ_1 and τ_3/τ_2. In addition, the W-jet versus QCD-jet tagger also uses an "isolation-like" variable that exploits the absence of high $p_{\rm T}$ final state-radiation (FSR) in the vicinity of the W decay products. Following the strategy defined in Ref. [26], we call these variables $E_{\rm F}(\mathrm{n}, \alpha)$ and define them as:

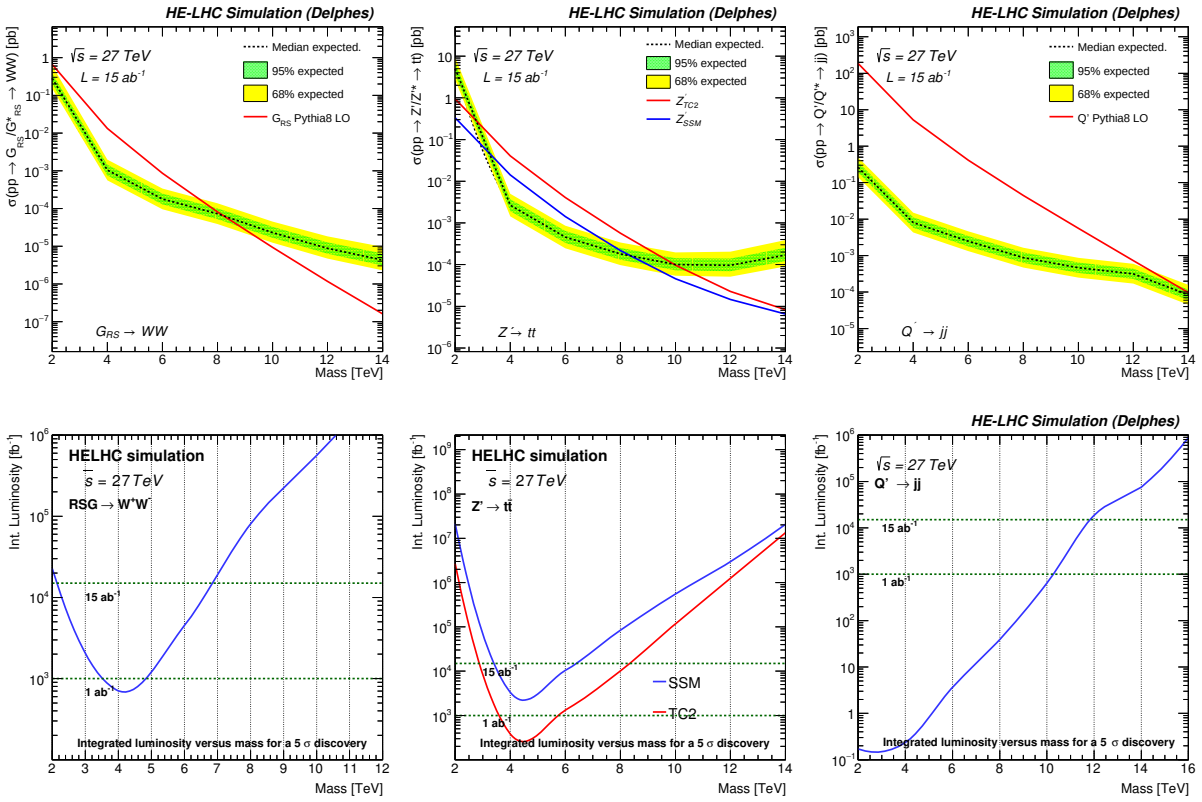

Fig. 6.4.12: Top: exclusion limit at 95% C.L. versus heavy resonance mass for the three benchmark models: $G_{RS} \to WW$ (left), $Z' \to t\bar{t}$ (middle), and $Q' \to jj$ (right). Bottom: integrated luminosity needed for a 5σ discovery as a function of the heavy resonance mass for the three benchmark models.

$$E_{\mathrm{F}}(\mathrm{n},\alpha) = \frac{\sum\limits_{\frac{n-1}{5}\alpha<\Delta R(k,jet)<\frac{n}{5}\alpha} p_{\mathrm{T}}^{(k)}}{\sum\limits_{\Delta R(k,jet)<\alpha} p_{\mathrm{T}}^{(k)}} \tag{6.4.13}$$

We choose $\alpha = 0.05$, construct 5 variables $E_{\mathrm{F}}(\mathrm{n},\alpha)$with $n = 1..5$ and use them as input to the multivariate tagger. The W tagging performance has significantly better performance than the top-tagging due to the use of the energy-flow variables. We choose our working points with a top and W tagging efficiencies of $\epsilon_S^{\mathrm{top}} = 60\%$ and $\epsilon_S^{\mathrm{W}} = 90\%$ corresponding respectively to a background efficiency of $\epsilon_B^{\mathrm{top}} = \epsilon_B^{\mathrm{W}} = 10\%$.

The event selection proceeds as follows: we require two jets with $p_{\mathrm{T}} > 1$ TeV, $|\eta| < 3$ and a small rapidity gap $\Delta\eta < 1.5$ between the two high p_{T} jets. For the $Z' \to t\bar{t}$ and $G_{RS} \to WW$ searches, the rapidity gap selection is relaxed to $\Delta\eta < 2.4$, both jets are required to be respectively top or W-tagged, and, to further reject background QCD jets, we require for both jets a large soft-dropped mass $m_{\mathrm{SD}} > 40$ GeV. Finally, for the $Z' \to t\bar{t}$ search alone, we require that both selected jets must also be b-tagged. Since no lepton veto is applied, there is also some acceptance for leptonic decays. The sensitivity to semi-leptonic $t\bar{t}$ decays is enhanced by adding the $\vec{p_{\mathrm{T}}}^{\mathrm{miss}}$ vector to the closest jet 4-momentum (among the two leading jets). The invariant mass of the two selected jets is used as a discriminant and is shown for the three benchmark analyses in Fig. 6.4.11.

Hypothesis testing is performed using a modified frequentist method based on a profile likelihood fit that takes into account the systematic uncertainties (mostly the background normalisations) as nuisance parameters. The expected exclusion limit at 95% C.L. and discovery reach at 5σ are shown in

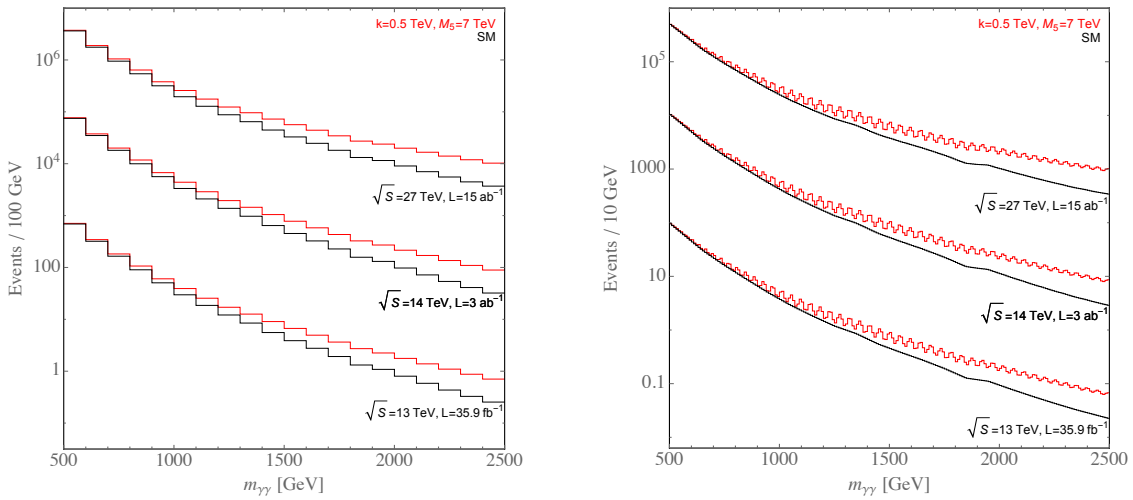

Fig. 6.4.13: Event rates for current integrated luminosity, HL-LHC, and HE-LHC, for the choice $k = 0.5$ TeV and $M_5 = 7$ TeV, which is a parameter point currently on the 95% exclusion contour of a recent CMS analysis [749]. Left: events are shown for a bin width of 100 GeV, as in Ref. [749]. Right: events are shown for a bin width of 10 GeV, which is close to the current experimental resolution, and reveals the oscillating nature of the signal arising due to the closely spaced resonances.

Fig. 6.4.12 (top and bottom) for the various scenarios that have been considered. At $\sqrt{s} = 27$ TeV, and with an integrated luminosity $\mathcal{L} = 15$ ab^{-1}, it is possible to discover a G_{RS} up to $m_G \approx 7$ TeV, and to exclude $m_G \lesssim 8$ TeV. For the $Z' \to t\bar{t}$ search the exclusion reach is $m_{Z'} \lesssim 10(8.5)$ TeV and it is possible to discover it up to $m_{Z'} \approx 8(6.5)$ TeV for the TC2 and SSM models respectively. Finally, for the excited quark model, the exclusion reach is $m_{Q'} \lesssim 14$ TeV and the discovery reach is $m_{Q'} \approx 12$ TeV.

6.4.7 On the power (spectrum) of HL/HE-LHC

Contributors: G. Giudice, Y. Kats, M. McCullough, R. Torre, A. Urbano

Typical searches for heavy new physics beyond the SM focus on particular forms of kinematic features in differential event distributions, such as isolated resonant structures, edges, and fat tails, to name a few. However the space of theoretically consistent BSM signatures extends well beyond these classic signatures.

Recently, in Ref. [750], it was suggested that new physics signatures could give rise to peculiar oscillating patterns in collider data. These signatures may be revealed as a resonance, however rather than being a resonance in the invariant mass distribution within some SM final state, this resonance would show up in Fourier space, after performing a Fourier transform on the relevant collider data.

The particular model studied in Ref. [750], which provides a theoretically robust example of such a signature, is the 'Linear Dilaton Model' which is known to be connected to continuum limit of 'Clockwork' models. We will refer to all classes of models of this form as CW/LD. The CW/LD models can all give rise to various forms of oscillating patterns within SM final states. In particular, the LD model predicts closely packed resonances, starting at some threshold determined by a parameter 'k' which is related to an extra-dimensional geometry. These resonances are predicted to have mass splittings at the $\mathcal{O}(\text{few}\%)$ level. Such mass splittings are still greater than the detector energy resolution in some high-resolution final states, such as $\gamma\gamma$ and l^+l^-.

Motivated by this, in Ref. [750] a detailed proposal for a class of collider searches in Fourier space was discussed. In this contribution we provide a simple extension of this proposal to estimate the expected reach of the HL-LHC and HE-LHC. The analysis is basic and has not been systematically optimised, thus the search reach based on the Fourier space analysis presented here should be considered

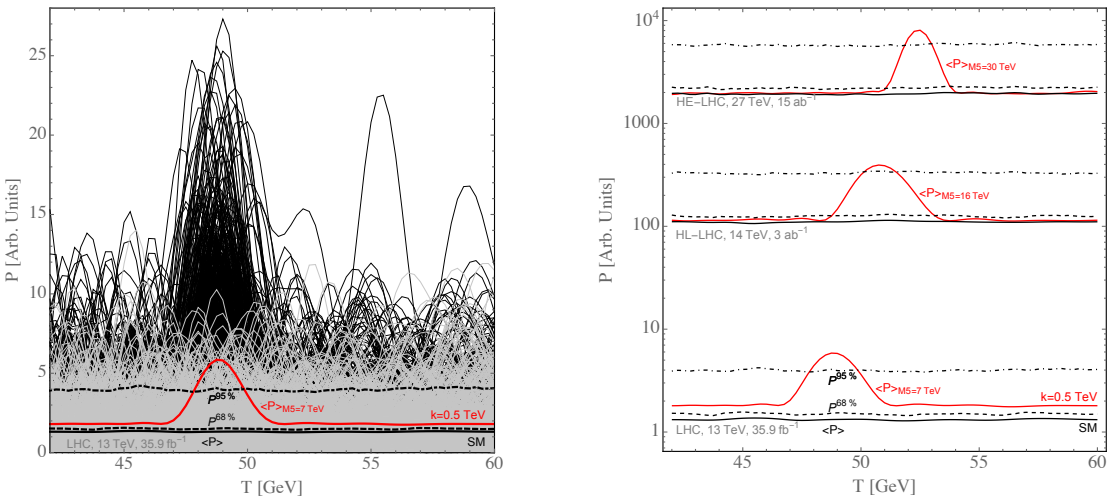

Fig. 6.4.14: Left: example power spectra for 1000 fake experiments at the LHC. The individual SM lines are shown in grey, alongside the mean and confidence intervals. The power with signal ($k = 500$ GeV, $M_5 = 7$ TeV) included is shown in black, alongside the mean in red. Right: the power spectrum, defined in [750], for current integrated luminosity of 35.9 fb^{-1}, HL-LHC, and HE-LHC, for $k = 0.5$ TeV and a variety of values of M_5. The red lines show the average power in the presence of signal and background. The significance of the peak in the power spectrum at $T \approx 50$ GeV, which corresponds to $T = 1/R$, is clearly seen for higher energy and integrated luminosity colliders.

as a preliminary estimate, however it is likely that a dedicated study could perform better.

In Fig. 6.4.13 we show the spectrum of events in the diphoton final state expected for two choices of binning, to reveal the oscillating nature of the signal. The spectrum is calculated for the EBEB selections of the recent analysis [749]. The SM events are taken from the NNLO prediction calculated in Ref. [749]. In Ref. [749] the normalisation of the NNLO prediction is determined by fitting to the data, which is dominated by the low energy events. To obtain the corresponding prediction at 14 TeV and 27 TeV the SM events are rescaled by the ratio of $q\bar{q}$ PDFs at the same $m_{\gamma\gamma}$, relative to 13 TeV. We adopt the diphoton energy resolution detailed in Ref. [750].

Signal events are generated and passed through the acceptance curves for the EBEB category shown in Ref. [749] and we find good agreement with Ref. [749] for the same signal parameters shown in Figure 5 of Ref. [749]. Similarly to the SM events, 14 TeV and 27 TeV predictions are obtained by reweighting according to the PDF ratio.

In Fig. 6.4.13 the oscillatory pattern due to the multiple closely-spaced resonances is clear. We now move to Fourier space, which is suited to searching for such oscillating patterns. We adopt an analogous diphoton 'Power' to the function detailed in Ref. [750], with the modification that, rather than integrating over bins, a discrete Fourier transform, which sums over bin heights at the midpoint energy, is employed. A second modification is that rather than subtracting a fitted curve to find the residuals, we subtract the NNLO prediction detailed in Ref. [749], where the systematics related to the overall normalisation are removed by floating the distribution and fitting to the data.

The resulting power spectrum is illustrated in Fig. 6.4.14. Figure 6.4.14 (right) was obtained by generating 5000 sets of fake experiments, where the number of events in each bin is generated from a Poisson distribution, for both the SM only and SM + signal hypotheses, before subtracting the SM prediction. The curves for $\langle P \rangle$, $P^{68\%}$, and $P^{95\%}$ represent the mean value of $P(T)$ at a given value of T, over all fake experiments, and also the corresponding upper limits at a given C.L. derived from the distributions. The average value, when signal is included, is also shown for a variety of M_5 values.

In each case, the peak in Fourier space is clearly visible and approaches the $P^{95\%}$ line. We will not attempt a robust statistical analysis here, which would require a thorough treatment of systematics in

a likelihood ratio test. Rather, we will focus on the comparison between different colliders. Clearly, if the current LHC data can exclude a parameter point in the ballpark of $k = 0.5$ TeV and $M_5 \approx 7$ TeV, then at the HL-LHC one should be sensitive to $M_5 \approx 16$ TeV, and at the HE-LHC $M_5 \approx 30$ TeV. Furthermore, since the statistics are much higher at these colliders one would presumably benefit from widening the range of $m_{\gamma\gamma}$ considered, thus we expect the reach to exceed these values in a dedicated analysis.

To summarise, in this contribution we have estimated the reach of the HL-LHC and HE-LHC for detecting oscillating patterns in BSM contributions to the differential diphoton spectrum. Such searches have not yet been performed at the LHC and they provide a new target in the search for BSM physics. This estimate is performed in the context of the linear dilaton model, as described in Ref. [750].

We have found that for a warping parameter of $k = 500$ GeV, which sets the mass scale of the first KK graviton resonance, if current limits on the extra-dimensional Planck scale are at the level of $M_5 \approx 7$ TeV, then with HL-LHC they should extend considerably, to around $M_5 \approx 16$ TeV, and at HE-LHC further still, to $M_5 \approx 30$ TeV.

7 Conclusions and Outlook

The LHC is performing superbly and has already moved on from discovering the Higgs boson to accurately measuring its properties. As yet there are no clear deviations from the SM, in Higgs measurements or elsewhere. Nonetheless, with only a fraction of the $150\ \mathrm{fb}^{-1}$ recorded data so far analysed, it is possible that surprises await, or that some of the existing small deviations grow. It is also possible that the new physics has small production cross sections either because it is weakly coupled to the initial state at the LHC, or that it is heavy, or both. Weakly coupled states within kinematic reach of the LHC may require increased data sets to uncover, such as the $3\ \mathrm{ab}^{-1}$ of the HL-LHC each for ATLAS and CMS, and up to $300\ \mathrm{fb}^{-1}$ for the Upgrade II of LHCb. Heavy states instead might require both increased centre-of-mass energy and increased luminosity, such as the 27 TeV and $15\ \mathrm{ab}^{-1}$ of the HE-LHC.

The HL- and HE-LHC will both offer new possibilities to test many BSM scenarios, motivated by long-standing problems such as EW Naturalness, dark matter, the flavour problem, neutrino masses, the strong CP problem, and baryogenesis. All these new physics manifestations predict the existence of new particles, which can be searched for at HL-LHC, profiting from the much larger statistics and slightly higher energy, and at the HE-LHC, profiting from the much larger statistics and much higher energy. In both cases the searches will also benefit from detector upgrades. Careful attention has been paid to the impact of these upgrades and the assessment of the future systematic uncertainties, especially for HL-LHC where concrete proposals for the ATLAS, CMS and LHCb experiments exist.

This document contains numerous studies of the increased reach for many BSM scenarios that can be explored at the HL- and HE-LHC options. As well as determining the reach in sensitivity, several studies analyse the ability for HL- and HE-LHC to characterise potential discoveries and distinguish between possible BSM explanations. Rather than give a complete summary of all prospect analyses in this report, we instead provide representative examples of the scope of the BSM searches for the HL-LHC and HE-LHC. Broadly speaking, in most BSM scenarios, we expect the HL-LHC will increase the present reach in mass and coupling by $20-50\%$ and potentially discover new physics that is currently unconstrained. The reach of the HE-LHC is generically more than double that of the HL-LHC. In Fig. 7.1 we present a summary of the results of SUSY searches (both prompt and long-lived) for sparticles produced via strong- or electroweak interactions, as described in detail in Section 2. Figure 7.2 shows a summary of most of the resonance searches (both single and pair production) presented in Sections 5 and 6.

HL-LHC

Supersymmetry

The extension of the kinematic reach for supersymmetry searches at the HL-LHC is reflected foremost in the sensitivity to EW states, including sleptons, but also for gluinos and squarks. Studies under various hypothesis were made, including prompt and long-lived SUSY particle decays. Wino-like chargino pair production processes are studied considering dilepton final states. Masses up to 840 (660) GeV can be excluded (discovered) for charginos decaying as $\tilde{\chi}_1^{\pm} \to W^{(*)}\tilde{\chi}_1^0$, in R-parity conserving scenarios with $\tilde{\chi}_1^0$ as the lightest supersymmetric particle. The results extend by about 500 GeV the mass reach obtained with $80\ \mathrm{fb}^{-1}$ of 13 TeV pp collisions, and extend beyond the LEP limit by almost an order of magnitude in case of massless neutralinos. Compressed SUSY spectra are theoretically well motivated but are among the most challenging scenarios experimentally, and are barely covered by the Run-2 analyses. HL-LHC searches for low momentum leptons will be sensitive to $\tilde{\chi}^{\pm}$ masses up to 350 GeV for $\Delta m(\tilde{\chi}_1^{\pm}, \tilde{\chi}_1^0) \approx 5$ GeV, and to mass splittings between 0.8 and 50 GeV, thus bringing significant new reach to Higgsino models. Similar search techniques can also be used to target pair produced $\tilde{e}$ and $\tilde{\mu}$ in compressed scenarios. If $\Delta m(\tilde{\chi}_1^{\pm}, \tilde{\chi}_1^0) < 1$ GeV, charginos can decay after the inner layers of the pixel detectors.

Dedicated searches for sleptons, characterised by the presence of at least one hadronically-

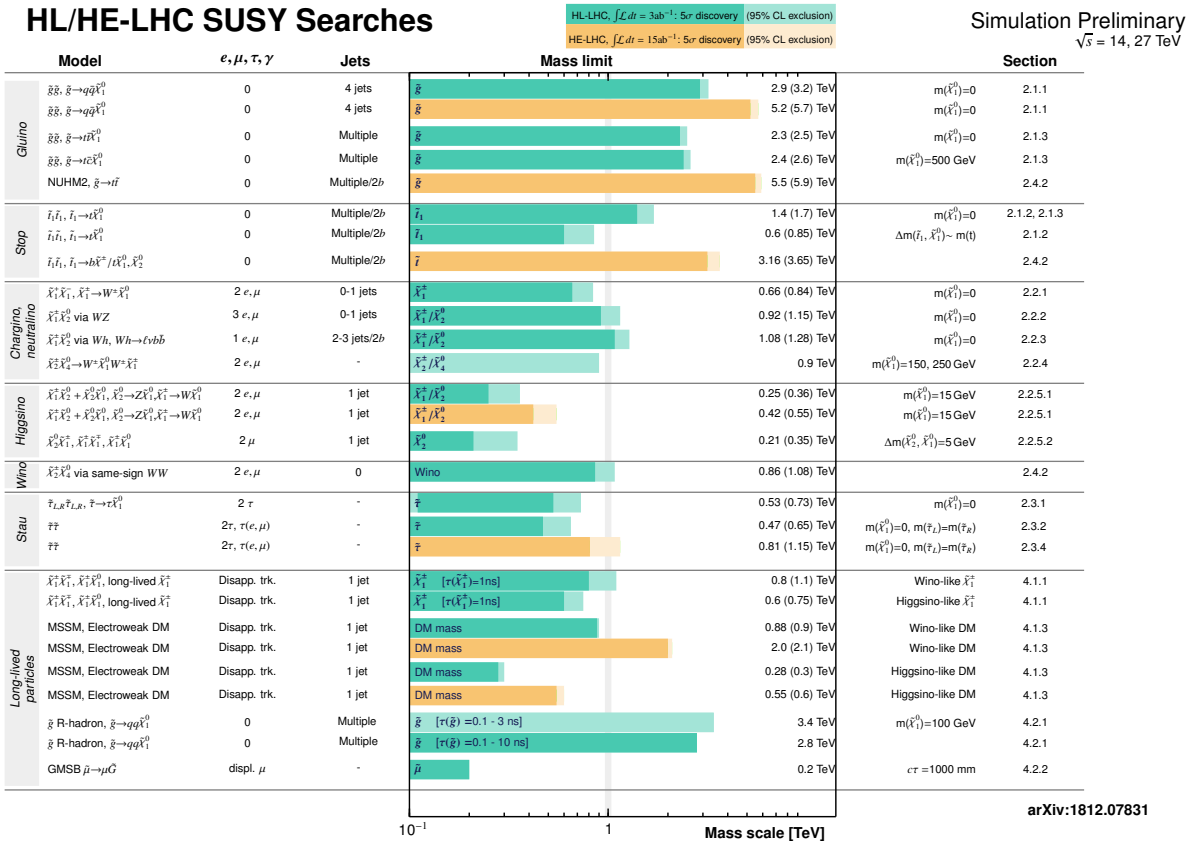

Fig. 7.1: A summary of the expected mass reach for 5σ discovery and 95% C.L. exclusion at the HL/HE-LHC, as presented in Section 2.

decaying τ and missing E_T, will be sensitive to *currently unconstrained* pair-produced $\tilde{\tau}$: exclusion (discovery) for $m_{\tilde{\tau}}$ up to around 700 (500) GeV can be achieved under realistic assumptions of performance and systematic uncertainties.

In the strong SUSY sector, HL-LHC will probe gluino masses up to 3.2 TeV, with discovery reach around 3 TeV, in R-parity conserving scenarios and under a variety of assumptions on the $\tilde{g}$ prompt decay mode. This is about $0.8 - 1$ TeV above the Run-2 $\tilde{g}$ mass reach for 80 fb^{-1}. Pair-production of top squarks has been studied assuming $\tilde{t}_1 \to t\tilde{\chi}_1^0$ and fully hadronic final states with large missing E_T. Top squarks can be discovered (excluded) up to masses of 1.25 (1.7) TeV for massless neutralinos, *i.e.* $\Delta m(\tilde{t}_1, \tilde{\chi}_1^0) \gg m_t$, under realistic uncertainty assumptions. This extends by about 700 GeV the reach of Run-2 for 80 fb^{-1}. The reach in $m_{\tilde{t}}$ degrades for larger $\tilde{\chi}_1^0$ masses. If $\Delta m(\tilde{t}_1, \tilde{\chi}_1^0) \sim m_t$, the discovery (exclusion) reach is 650 (850) GeV.

Dark Matter and Dark Sectors

Compressed SUSY scenarios, as well as other DM models, can be targeted using signatures such as mono-jet, mono-photon and vector-boson-fusion production. Mono-photon and VBF events allow targeting an EW fermionic triplet (minimal DM), equivalent to a wino-like signature in SUSY, for which there is no sensitivity in Run-2 searches with 36 fb^{-1}. Masses of the $\tilde{\chi}_1^0$ up to 310 (130) GeV can be excluded by the mono-photon (VBF) channel, with improvements possible, reducing the theoretical uncertainties. Projections for searches for a mono-Z signature, with $Z \to \ell^+\ell^-$ recoiling against missing E_T, have been interpreted in terms of models with a spin-1 mediator, and models with two Higgs doublets and an additional pseudoscalar mediator a coupling to DM (2HDMa). The exclusion is expected for mediator masses up to 1.5 TeV, and for DM and pseudoscalar masses up to 600 GeV, a

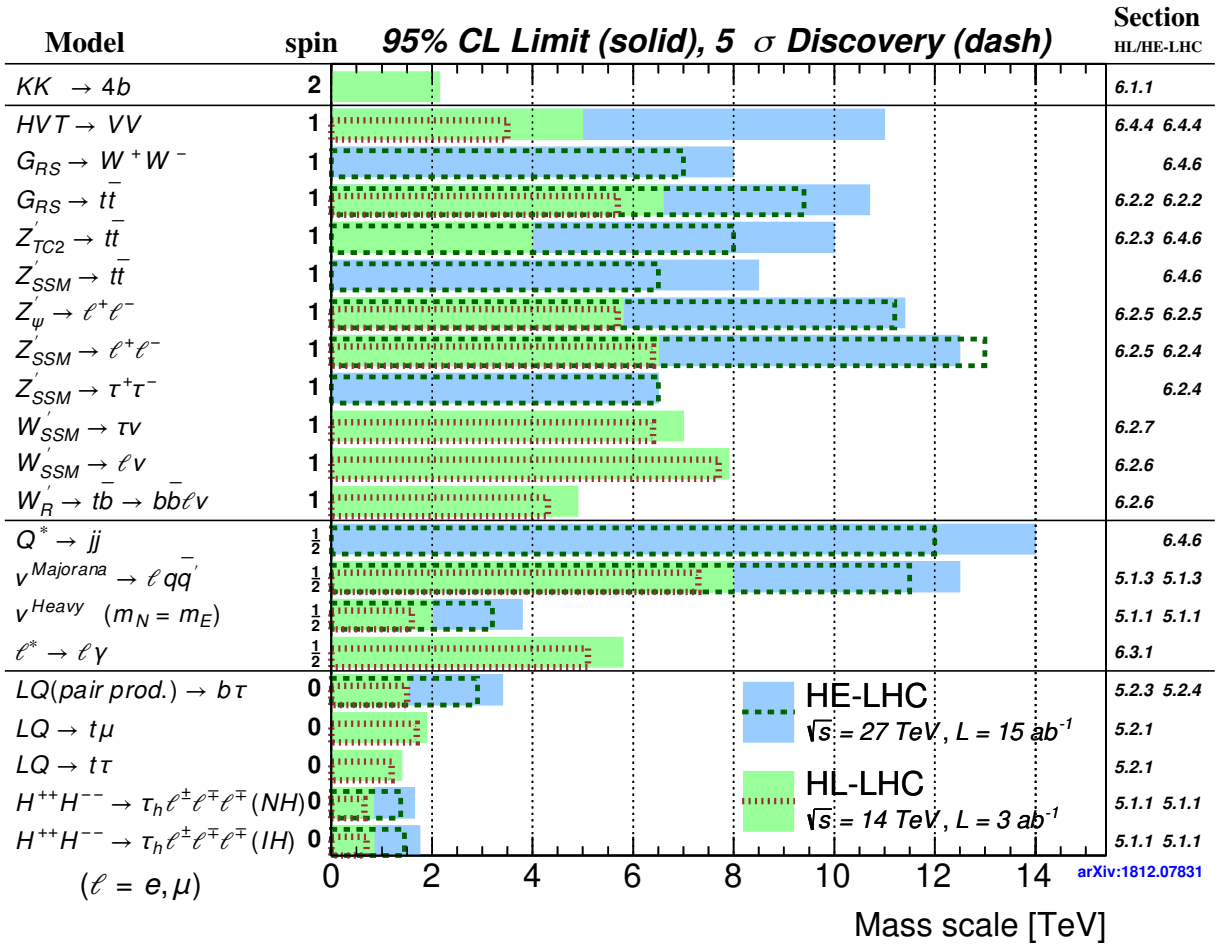

Fig. 7.2: A summary of the expected mass reach for 5σ discovery and 95% C.L. exclusion at the HL/HE-LHC, as presented in Sections 5 and 6.

factor of ~ 3 better than the 36 fb^{-1} Run-2 constraints. The case of 2HDMa models is complemented by 4-top final states, searched in events with two same-charge leptons, or with at least three leptons. While searches using 36 fb^{-1} Run-2 data have limited sensitivity considering the most favourable signal scenarios (*e.g.* $\tan\beta = 0.5$), HL-LHC will probe possible evidence of a signal with $\tan\beta = 1$, $m_H = 600$ GeVand mixing angle of $\sin\theta = 0.35$, assuming m_a masses between 400 GeV and 1 TeV, and will allow exclusion for all 200 GeV $< \mathrm{m_a} <$ 1 TeV. For DM produced in association with bottom or top quarks, where a (pseudo)scalar mediator decays to a DM pair, the HL-LHC will improve the sensitivity to mediator masses by a factor of $3-8$ relative to the Run-2 searches with 36 fb^{-1}.

A compelling scenario in the search for portals between the visible and dark sectors is that of the dark photon A'. Prospects for an inclusive search for dark photons decaying into muon or electron pairs indicate that the HL-LHC could cover a large fraction of the theoretically favoured $\epsilon - m_{A'}$ space, where ϵ is the kinetic mixing between the photon and the dark photon and $m_{A'}$ the dark photon mass.

Resonances

Several studies of resonance searches, in a variety of final states, have been performed and were presented here. A right-handed gauge boson with SM couplings, decaying as $W_R \to bt(\to b\ell\nu)$, can be excluded (discovered) for masses up to 4.9 (4.3) TeV, 1.8 TeV larger than the 36 fb^{-1} Run-2 result. For a sequential SM W' boson in $\ell\nu$ final states ($\ell = e, \mu$), the mass reach improves by more than 2 TeV

w.r.t. Run-2 ($80\,\mathrm{fb}^{-1}$) reach, and by more than 1 TeV w.r.t. $300\,\mathrm{fb}^{-1}$. The HL-LHC bound will be $M_{W'} = 7.9$ TeV, with discovery potential up to $M_{W'} = 7.7$ TeV. Projections for searches of SSM Z' bosons in the dilepton final state predict exclusion (discovery) up to masses of 6.5 (6.4) TeV. The $36\,\mathrm{fb}^{-1}$ Run-2 exclusion is 4.5 TeV, expected to grow to 5.4 TeV after $300\,\mathrm{fb}^{-1}$. Using top-tagging techniques, a Randall–Sundrum Kaluza–Klein gluon decaying to $t\bar{t}$ is expected to be excluded up to 6.6 TeV and discovered up to 5.7 TeV, extending by over 2 TeV the $36\,\mathrm{fb}^{-1}$ bounds.

Models related to the apparent flavour anomalies in B decays suggest the presence of heavy resonances, either Z' or leptoquarks (LQ), coupling to second and/or third generation SM fermions. The HL-LHC will be able to cover a significant portion of the parameter space allowed by flavour constraints, with an exclusion reach up to 4 TeV for the Z', depending on the structure and size of the Z' couplings. Pair produced scalar LQs coupling to μ (τ) and b-quarks, on the other hand, can be excluded up to masses of 2.5 (1.5) TeV, depending on assumptions on couplings. Finally, prospect studies for third generation LQ in the $t\mu$ and $t\tau$ channels deliver mass limits (discovery potential) increased by 500 (400) GeV with respect to $36\,\mathrm{fb}^{-1}$, with prospect discovery in the $t\mu$ channel up to 1.7 TeV.

Long-lived particles

In addition to the significant expansion of expected luminosity, new detector upgrades will enable searches in the long-lived particle regime. Muons displaced from the beamline, such as found in SUSY models with $\tilde{\mu}$ lifetimes of $c\tau > 25\,\mathrm{cm}$, can be excluded at 95% C.L.. New fast timing detectors will also be sensitive to displaced photon signatures arising from LLP in the $0.1 < c\tau < 300\,\mathrm{cm}$ range.

Prospect studies for disappearing tracks searches using simplified models of $\tilde{\chi}^{\pm}$ production lead to exclusions of chargino masses up to $m(\tilde{\chi}_1^{\pm}) = 750$ GeV (1100 GeV) for lifetimes of 1 ns for the higgsino (wino) hypothesis. When considering the lifetime predicted by theory, masses up to 300 GeV and 830 GeV can be excluded in higgsino and wino models, respectively. This improves the $36\,\mathrm{fb}^{-1}$ Run-2 mass reach by a factor of 2-3. The discovery reach is reduced to 160 GeV and 500 GeV respectively, due to the loss in acceptance at low lifetime (0.2 ns), but sensitivity is expected to be recovered with dedicated optimisations.

Several studies are available also for long-lived $\tilde{g}$. As an example, we expect a 1 TeV extension of the $36\,\mathrm{fb}^{-1}$ Run-2 mass reach, for models with $\tilde{g}$ lifetimes $\tau > 0.1$ ns, and an exclusion of $m_{\tilde{g}}$ up to $3.4 - 3.5$ TeV. Finally, the signature of long-lived dark photons decaying to displaced muons can be reconstructed with dedicated algorithms and is sensitive to very small coupling $\epsilon^2 \sim 10^{-14}$ for masses of the dark photons between 10 and 35 GeV. Complementarities in long-lived particle searches and enhancements in sensitivity might be achieved if new proposals of detectors and experiments such as Mathusla, FASER, Codex-B, MilliQan and LHeC are realised in parallel to the HL-LHC.

HE-LHC

Supersymmetry

The increase in energy from 14 TeV to 27 TeV leads to a large increase in the production cross section of heavy coloured states, a 3.5 TeV gluino has nearly a 400-fold increase in production cross section. For supersymmetric spectra without compression the HE-LHC has sensitivity to gluinos up to masses of 6 TeV and discovery potential of 5.5 TeV. The corresponding numbers for stop squarks are 3.5 TeV and 3 TeV, respectively. These results allow to put in perspective the question to what extent classes of "natural" supersymmetric models are within the reach of HE-LHC and can be discovered or excluded conclusively. Examples of specific model scenarios were studied during the Workshop: while HL-LHC can only cover part of the parameter space of the models considered, HE-LHC covers it entirely. The HE-LHC would allow for a 5σ discovery of most natural SUSY models via the observation of both gluinos and stops.

If the coloured states are close in mass to the lightest supersymmetric particle (LSP), the amount

of missing transverse momentum ($E_{\mathrm{T}}^{\mathrm{miss}}$) in the event is decreased. The typical multijet + $E_{\mathrm{T}}^{\mathrm{miss}}$ SUSY searches are less sensitive and must be replaced with monojet-like analyses. Prospect studies show that if for example the gluino-LSP mass splitting is held at $10\ \mathrm{GeV}$, gluino masses can be excluded up to $2.6\ \mathrm{TeV}$. If the lightest coloured state is the stop, and the $\tilde{t}$-LSP splitting is such that final states include very off-shell W and b-jets, $\tilde{t}$ masses up to about $1\ \mathrm{TeV}$ could be excluded, extending the HL-LHC reach by about a factor of two.

The electroweakino sector of supersymmetry presents a particular challenge for hadronic machines. If the LSP is pure higgsino or wino, there is a very small neutralino-chargino mass splitting ($\sim\ 340\ \mathrm{MeV}$, $\sim\ 160\ \mathrm{MeV}$ respectively) and the chargino has a correspondingly long lifetime ($c\tau\ \sim 5,1\ \mathrm{cm}$ respectively). The $E_{\mathrm{T}}^{\mathrm{miss}}$ is again small unless the pair produced electroweakinos recoil against an ISR jet. Taking into account contributions from both chargino and neutralino production the monojet search will deliver a sensitivity for exclusion (discovery) of winos up to $\sim 600\ \mathrm{GeV}$ ($300\ \mathrm{GeV}$) and higgsinos up to $\sim\ 400\ \mathrm{GeV}$ ($150\ \mathrm{GeV}$). Taking advantage of the long lifetime of the charginos allows searches to be done for disappearing charged tracks. Considering a detector similar to the ones available for HL-LHC, winos below $\sim 1800\ \mathrm{GeV}$ ($1500\ \mathrm{GeV}$) can be excluded (discovered), while the equivalent masses for Higgsinos are $\sim 500\ \mathrm{GeV}$ ($450\ \mathrm{GeV}$).

While these results come short of covering the full range of masses for electroweakinos to be a thermal relic and account for all of DM, the mass range accessible to HE-LHC greatly extends the HL-LHC potential and can be complementary to the indirect detection probes using gamma rays from dwarf-spheroidal galaxies.

Dark Matter

Monojet searches, as well as monophoton and vector-boson-fusion production searches, might be sensitive to generic weakly interactive dark matter candidates beyond compressed SUSY scenarios. Analyses of the reach of the HE-LHC under various assumptions of the structure of the DM-SM coupling have been carried out. Models characterised by the presence of an extended Higgs sector, with Higgs doublets mixing with an additional scalar or pseudoscalar mediator that couples to DM have been studied assuming associate production of DM with a pair of top quarks.

Using leptonic decays of the tops, a fit to the distribution of the opening angle between the two leptons can help distinguish signal from SM processes, after other background-suppressing selections. Assuming the DM is lighter than half the mediator mass, a scalar or pseudoscalar mediator can be ruled out at 95% C.L. up to $900\ \mathrm{GeV}$ using this technique, a factor of 2 higher in mass compared to the HL-LHC bounds.

If a dark sector exists and contains heavy coloured particles, $\mathcal{Q}$, nearly degenerate with the DM and decaying to DM and SM coloured particles, a monojet topology could be again the most sensitive. The rate and shape of the monojet distribution depend upon the mass, spin and colour representation of $\mathcal{Q}$. Fermionic colour triplet $\mathcal{Q}$ could be discovered up to $1.1\ \mathrm{TeV}$ at the HE-LHC, a fermionic octet will be ruled out if lighter than $1.8\ \mathrm{TeV}$, and a scalar colour triplet almost degenerate in mass to the DM could be probed up to masses of $600\ \mathrm{GeV}$. Should an excess be observed identifying the spin and colour representation, NNLO precision will be needed for the predictions of the SM backgrounds. Analyses of double-ratios of cross sections at varying p_T could be utilised to partially cancel uncertainties.

Resonances

Searches for heavy resonances will greatly benefit from the increased partonic energy of a $27\ \mathrm{TeV}$ machine. If the resonance is narrow the search can be data driven but if the resonance is wide it will require a precise understanding of the backgrounds, which presents a formidable challenge. The HE-LHC can expect to approximately double the mass reach on dijet resonances of the HL-LHC. For instance, the reach for an excited quark decaying to dijets will be $14\ \mathrm{TeV}$.

Dilepton resonances, *e.g.* Z', are present in many gauge extensions of the SM. The exact reach in any model depends upon the coupling to light quarks and BR to charged leptons. A Z' whose couplings to SM quarks and leptons are as in the SM, a so called sequential Z'_{SSM}, will be discoverable in the dilepton channel up to ~ 13 TeV. In the di-tau channel the reconstruction is harder, reducing the reach to ~ 6 TeV. In the di-top channel a Z'_{SSM} will be discovered up to 6 TeV and excluded up to 8 TeV. It is an interesting question to ask: if a resonance is discovered can we determine the nature of the model? Considering a 6 TeV Z' decaying into e, μ, t, b, q final states, it is sufficient to consider three observables ($\sigma \cdot B$, the forward-backward asymmetry, and the rapidity asymmetry) to distinguish between six Z' models in most cases.

Gauge extensions of the SM also often contain new heavy charged vector bosons, W'. One promising search channel for these new particles is the WZ final state. More generally BSM models can contain resonances decaying to di-bosons WZ/WW. Searching for a RS graviton G_{RS} resonance in WW final states exploiting the all-hadronic signature presents a considerable challenge and requires dedicated identification of boosted W-jets. The estimated reach is ~ 8 TeV, almost a factor of two increase with respect to the HL-LHC. Diboson searches in $WW \to \ell\nu qq$ final states are sensitive also to heavy vector triplet (HVT) model produced via $\mathrm{ggF/q\bar{q}}$. HVT $Z^{'}$ masses up to 11 TeV can be excluded by HE-LHC, extending the HL-LHC reach by about 6 TeV.

Searches for top partners decaying to a top and a W boson in the same-sign dilepton signature can lead to discovery up to more than 2 TeV, with the possibility to discriminate left- and right-handed couplings at the 2σ level in all the accessible discovery range.

Models related to the generation of the observed pattern of neutrino masses and mixings offer a variety of signatures that could profit from the high energy available at HE-LHC. For instance, searches for lepton flavour violating (LFV) final states with two opposite-sign different-flavour leptons and two jets arising from the production of a heavy pseudo-Dirac neutrino and a SM lepton could test heavy neutrino masses in seesaw models up to more than 1 TeV. In left-right symmetric models, a right-handed heavy W_R boson decaying to a Majorana neutrinos can be discovered with 5 ab^{-1} up to ~ 10.5 TeV and excluded up to masses of around ~ 16 TeV with an integrated luminosity of 15 ab^{-1}. This increases the reach of HL-LHC by about 10 TeV. Doubly charged scalars in type-II seesaw models, can also be searched for in multi-lepton signatures, with a reach in the 1.5 TeV region. Heavy leptons in type-III seesaw models, giving rise to final states with two leptons, jets and b-jets can be excluded (discovered) up to 3.8 (3.2) TeV. For comparison, the exclusion reach for the HL-LHC is about 1.6 TeV.

Finally, models related to observed flavour anomalies in neutral-current B decays, suggest the presence of heavy resonances, either Z' or leptoquarks, coupling to muons and b-quarks. The HE-LHC will be able to cover an ample region of the parameter space allowed by flavour constraints, with an exclusion (discovery) reach up to 10 (7) TeV for the Z', depending on the assumptions on the Z' couplings structure and size. Pair produced leptoquarks, on the other hand, can be excluded up to masses of 4.2 TeV, again depending on assumptions on couplings. These masses are typically a factor of 2 to 2.5 higher than the HL-LHC sensitivity.

8 Acknowledgements

We would like to thank the LHC experimental Collaborations and the WLCG for their essential support. We are especially grateful for the efforts by the computing, generator and validation groups who were instrumental for the creation of large simulation samples. We thank the detector upgrade groups as well as the physics and performance groups for their input. Not least, we thank the many colleagues who have provided useful comments on the analyses. The research of A. Aboubrahim and P. Nath was supported in part by NSF Grant PHY-1620575. The research of J. Kalinowski and W. Kotlarski was supported in part by the National Science Centre, Poland, HARMONIA project under contract UMO-2015/18/M/ST2/00518 (2016-2019). The work of T. Han, S. Mukhopadhyay, and X. Wangwas supported in part by the U.S. Department of Energy under grant No. DE-FG02- 95ER40896 and by the PITT PACC. T. Han also acknowledges the hospitality of the Aspen Center for Physics, which is supported by National Science Foundation grant PHY-1607611. The work of S. Chekanov, J. Childers, J. Proudfoot, R. Wang, and D. Frizzell has been created by UChicago Argonne, LLC, Operator of Argonne National Laboratory ("Argonne"). Argonne, a U.S. Department of Energy Office of Science laboratory, is operated under Contract No. DE-AC02-06CH11357. It was also made possible by an allocation of computing time through the ASCR Leadership Computing Challenge (ALCC) program and used resources of the National Energy Research Scientific Computing Center, a DOE Office of Science User Facility supported by the Office of Science of the U.S. Department of Energy under Contract No. DE-AC02-05CH11231. The work of B. Allanach, D. Bhatia, B. Gripaios, A. Iyer, and T. Tevong You has been partially supported by STFC consolidated grants ST/L000385/1, ST/P000681/1. The work of M. Klasen has been supported by the BMBF under contract 05H15PMCCA and the DFG through the Research Training Network 2149 "Strong and weak interactions - from hadrons to dark matter". T. Jezo was supported by the Swiss National Science Foundation (SNF) under contracts BSCGI0-157722 and CRSII2-160814. The work of F. Sala is partly supported by a PIER Seed Project funding (Project ID PIF-2017-72). The work of M. Heikinheimo has been supported by the Academy of Finland, Grant NO. 31013 G. Cacciapaglia is supported by Institut Franco-Suedois (project Tör) and the Labex-LIO (Lyon Institute of Origins) under grant ANR-10-LABX-66, FRAMA (FR3127, Fédération de Recherche "André Marie Ampère"). G. Ferretti is supported by The Knut and Alice Wallenberg Foundation and the Lars Hierta Memorial Foundation. T. Flacke is supported by the IBS under the project code, IBS-R018-D1. H. Serodio is supported by the ERC under the European Union's Horizon 2020 research and innovation programme (grant agreement No 668679). D. Camargo and F. S. Queiroz acknowledge financial support from MEC and UFRN. F. S. Queiroz also acknowledges the ICTP-SAIFR FAPESP grant 2016/01343-7 for additional financial support. S. Moretti is supported in part by the NExT Institute and acknowledges partial financial support from the STFC Consolidated Grant ST/L000296/1 and STFC CG ST/P000711/1, and the H2020-MSCA-RISE-2014 grant no. 645722 (NonMinimal-Higgs).

References

[1] *Final Report of the Workshop on "Physics at HL-LHC, and perspectives on HE-LHC"*, 2018. [CDS].

[2] A. Dainese, M. Mangano, A. Meyer, A. Nisati, G. Salam, M. Vesterinen, et al., *Physics at HL-LHC, and perspectives on HE-LHC*, 2018. [TWIKI].

[3] ATLAS Collaboration, G. Aad et al., *Observation of a new particle in the search for the Standard Model Higgs boson with the ATLAS detector at the LHC*, Phys. Lett. B **716** (2012) 1–29, arXiv:1207.7214 [hep-ex]. [INSPIRE].

[4] CMS Collaboration, S. Chatrchyan, V. Khachatryan, A. M. Sirunyan, A. Tumasyan, W. Adam, E. Aguilo, T. Bergauer, M. Dragicevic, J. Ero", and C. Fabjan, *Observation of a new boson at a mass of* 125 *GeV with the CMS experiment at the LHC*, Phys. Lett. B **716** (2012) 30–61, arXiv:1207.7235 [hep-ex]. [INSPIRE].

[5] *The High-Luminosity LHC*, [WEBPAGE].

[6] G. Apollinari, I. Béjar Alonso, O. Brüning, P. Fessia, M. Lamont, L. Rossi, and L. Tavian, *High-Luminosity Large Hadron Collider (HL-LHC)*, CERN Yellow Report **004** (2017). [INSPIRE].

[7] ATLAS Collaboration, *Expected performance of the ATLAS detector at the HL-LHC*, in progress, 2018.

[8] CMS Collaboration, *Expected performance of the physics objects with the upgraded CMS detector at the HL-LHC*, CMS-NOTE-2018-006, 2018. [CDS].

[9] *HL-LHC CERN Council approval*, [WEBPAGE].

[10] T. Behnke, J. E. Brau, B. Foster, J. Fuster, M. Harrison, J. M. Paterson, M. Peskin, M. Stanitzki, N. Walker, and H. Yamamoto, *The International Linear Collider Technical Design Report - Volume 1: Executive Summary*, arXiv:1306.6327 [physics.acc-ph]. [INSPIRE].

[11] H. Baer, T. Barklow, K. Fujii, Y. Gao, A. Hoang, S. Kanemura, J. List, H. E. Logan, A. Nomerotski, and M. Perelstein, *The International Linear Collider Technical Design Report - Volume 2: Physics*, arXiv:1306.6352 [hep-ph]. [INSPIRE].

[12] C. Adolphsen, M. Barone, B. Barish, K. Buesser, P. Burrows, J. Carwardine, J. Clark, H. Mainaud Durand, G. Dugan, and E. Elsen, *The International Linear Collider Technical Design Report - Volume 3.I: Accelerator & in the Technical Design Phase*, arXiv:1306.6353 [physics.acc-ph]. [INSPIRE].

[13] C. Adolphsen, M. Barone, B. Barish, K. Buesser, P. Burrows, J. Carwardine, J. Clark, H. Mainaud Durand, G. Dugan, and E. Elsen, *The International Linear Collider Technical Design Report - Volume 3.II: Accelerator Baseline Design*, arXiv:1306.6328 [physics.acc-ph]. [INSPIRE].

[14] T. Behnke, J. E. Brau, P. N. Burrows, J. Fuster, M. Peskin, M. Stanitzki, Y. Sugimoto, S. Yamada, H. Yamamoto, and H. Abramowicz, *The International Linear Collider Technical Design Report - Volume 4: Detectors*, arXiv:1306.6329 [physics.ins-det]. [INSPIRE].

[15] L. Linssen, A. Miyamoto, M. Stanitzki, and H. Weerts, *Physics and Detectors at CLIC: CLIC Conceptual Design Report*, arXiv:1202.5940 [physics.ins-det]. [INSPIRE].

[16] M. Aicheler, P. Burrows, M. Draper, T. Garvey, P. Lebrun, K. Peach, N. Phinney, H. Schmickler, D. Schulte, and N. Toge, *A Multi-TeV Linear Collider Based on CLIC Technology*, CERN Yellow Report **007** (2012). [INSPIRE].

[17] *The FCC-ee design study*, [WEBPAGE].

[18] *CEPC-SPPC Preliminary Conceptual Design Report. 1. Physics and Detector*, IHEP-CEPC-DR-2015-01, IHEP-TH-2015-01, IHEP-EP-2015-01, 2015. [INSPIRE].

[19] *CEPC-SPPC Preliminary Conceptual Design Report. 2. Accelerator*, IHEP-CEPC-DR-2015-01,

IHEP-AC-2015-01, 2015. [INSPIRE].

[20] *Muon Accelerator Program*, [WEBPAGE].

[21] M. Antonelli, M. Boscolo, R. D. Nardo, and P. Raimondi, *Novel proposal for a low emittance muon beam using positron beam on target*, Nucl. Instrum. Meth. A **807** (2016) 101–107, arXiv:1509.04454 [physics.acc-ph]. [INSPIRE].

[22] M. Boscolo, M. Antonelli, O. Blanco-García, S. Guiducci, S. Liuzzo, P. Raimondi, and F. Collamati, *Low emittance muon accelerator studies with production from positrons on target*, Phys. Rev. Accel. Beams **21** (2018) no. 6, arXiv:1803.06696 [physics.acc-ph]. [INSPIRE].

[23] *FCC Conceptual Design Report: Volume 4: The High-Energy LHC (HE-LHC)*, 2018. [INDICO].

[24] *FCC Conceptual Design Report*, 2018. [INDICO].

[25] M. Mangano et al., *Physics at the FCC-hh, a* 100 *TeV pp collider*, CERN Yellow Report **003** (2017), arXiv:1710.06353 [hep-ph]. [INSPIRE].

[26] M. Mangano, G. Zanderighi, J. A. Aguilar-Saavedra, S. Alekhin, S. Badger, C. Bauer, T. Becher, V. Bertone, M. Bonvini, and S. Boselli, *Physics at a* 100 *TeV pp Collider: Standard Model Processes*, CERN Yellow Report (2017) 1–254, arXiv:1607.01831 [hep-ph]. [INSPIRE].

[27] R. Contino, D. Curtin, A. Katz, M. Mangano, G. Panico, M. Ramsey-Musolf, G. Zanderighi, C. Anastasiou, W. Astill, and G. Bambhaniya, *Physics at a* 100 *TeV pp collider: Higgs and EW symmetry breaking studies*, CERN Yellow Report **003** (2017) 255–440, arXiv:1606.09408 [hep-ph]. [INSPIRE].

[28] T. Golling, M. Hance, P. Harris, M. Mangano, M. McCullough, F. Moortgat, P. Schwaller, R. Torre, P. Agrawal, and D. Alves, *Physics at a* 100 *TeV pp collider: beyond the Standard Model phenomena*, CERN Yellow Report **003** (2017) 441–634, arXiv:1606.00947 [hep-ph]. [INSPIRE].

[29] LHeC Study Group Collaboration, J. L. Abelleira Fernandez et al., *A Large Hadron Electron Collider at CERN Report on the Physics and Design Concepts for Machine and Detector*, J. Phys. G **39** (2012) 075001. [INSPIRE].

[30] P. Azzi, S. Farry, P. Nason, A. Tricoli, and D. c. Zeppenfeld, *QCD and Standard Model Physics at the HL-LHC and HE-LHC*, CERN-LPCC-2018-03, 2018. [CDS].

[31] A. Cerri, V. Gligorov, S. Malvezzi, J. Martin Camalich, and J. c. Zupan, *Flavour Physics at the HL-LHC and HE-LHC*, CERN-LPCC-2018-06, 2018. [CDS].

[32] S. Gori, F. Riva, M. Kado, M. Cepeda, and P. J. c. Ilten, *Higgs Physics at the HL-LHC and HE-LHC*, CERN-LPCC-2018-04, 2018. [CDS].

[33] DELPHES 3 Collaboration, J. de Favereau, , C. Delaere, P. Demin, A. Giammanco, V. Lemaître, A. Mertens, and M. Selvaggi, *DELPHES 3: a modular framework for fast simulation of a generic collider experiment*, JHEP **02** (2014) 57, arXiv:1307.6346 [hep-ex]. [INSPIRE].

[34] M. Cacciari, G. P. Salam, and G. Soyez, *The anti-k_t jet clustering algorithm*, JHEP **04** (2008) 63, arXiv:0802.1189 [hep-ph]. [INSPIRE].

[35] M. Cacciari, G. P. Salam, and G. Soyez, *FastJet User Manual*, EPJC **72** (2012) no. 3, 1896, arXiv:1111.6097 [hep-ph]. [INSPIRE].

[36] ATLAS Collaboration, *Technical Design Report for the Phase-II Upgrade of the ATLAS TDAQ System*, CERN-LHCC-2017-020, ATLAS-TDR-029, 2017. [CDS].

[37] CMS Collaboration, *The Phase-2 Upgrade of the CMS L1 Trigger Interim Technical Design Report*, CERN-LHCC-2017-013, CMS-TDR-017, 2017. [CDS].

[38] ATLAS Collaboration, *Technical Design Report for the ATLAS Inner Tracker Pixel Detector*, CERN-LHCC-2017-021, ATLAS-TDR-030, 2017. [CDS].

[39] ATLAS Collaboration, *Technical Design Report for the ATLAS Inner Tracker Strip Detector*, CERN-LHCC-2017-005, ATLAS-TDR-025, 2017. [CDS].

[40] CMS Collaboration, *The Phase-2 Upgrade of the CMS Tracker*, CERN-LHCC-2017-009, CMS-TDR-014, 2017. [CDS].

[41] ATLAS Collaboration, *Technical Design Report for the Phase-II Upgrade of the ATLAS LAr Calorimeter*, CERN-LHCC-2017-018, ATLAS-TDR-027, 2017. [CDS].

[42] CMS Collaboration, *The Phase-2 Upgrade of the CMS Barrel Calorimeters Technical Design Report*, CERN-LHCC-2017-011, CMS-TDR-015, 2017. [CDS].

[43] CMS Collaboration, *The Phase-2 Upgrade of the CMS Endcap Calorimeter*, CERN-LHCC-2017-023, CMS-TDR-019, 2017. [CDS].

[44] CMS Collaboration, *Technical Proposal for a MIP Timing Detector in the CMS Experiment Phase-2 Upgrade*, CERN-LHCC-2017-027, LHCC-P-009, 2017. [CDS].

[45] ATLAS Collaboration, *Technical Design Report for the Phase-II Upgrade of the ATLAS Muon Spectrometer*, CERN-LHCC-2017-017, ATLAS-TDR-026, 2017. [CDS].

[46] CMS Collaboration, *The Phase-2 Upgrade of the CMS Muon Detectors*, CERN-LHCC-2017-012, CMS-TDR-016, 2017. [CDS].

[47] ATLAS Collaboration, *Technical Design Report for the Phase-II Upgrade of the ATLAS Tile Calorimeter*, CERN-LHCC-2017-019, ATLAS-TDR-028, 2017. [CDS].

[48] CMS Collaboration, D. Contardo, M. Klute, J. Mans, L. Silvestris, and J. Butler, *Technical Proposal for the Phase-II Upgrade of the CMS Detector*, CERN-LHCC-2015-010, LHCC-P-008, CMS-TDR-15-02, 2015. [INSPIRE].

[49] ATLAS Collaboration, *Technical Proposal: A High-Granularity Timing Detector for the ATLAS Phase-II Upgrade*, CERN-LHCC-2018-023, LHCC-P-012, 2018. [CDS].

[50] T. Sjöstrand, S. Mrenna, and P. Skands, *A Brief Introduction to PYTHIA 8.1*, Comput. Phys. Commun. **178** (2008) no. 11, 852–867, arXiv:0710.3820 [hep-ph]. [INSPIRE].

[51] LHCb Collaboration, I. Belyaev et al., *Handling of the generation of primary events in Gauss, the LHCb simulation framework*, J. Phys. Conf. Ser. **331** (2011) 032047. [INSPIRE].

[52] J. Pumplin, D. R. Stump, J. Huston, H.-L. Lai, P. Nadolsky, and W.-K. Tung, *New generation of parton distributions with uncertainties from global QCD analysis*, JHEP **07** (2002) 12, arXiv:hep-ph/0201195 [hep-ph]. [INSPIRE].

[53] J. Allison, K. Amako, J. Apostolakis, H. Araujo, P. Dubois, M. Asai, G. Barrand, R. Capra, S. Chauvie, and R. Chytracek, *GEANT4 developments and applications*, IEEE Trans. Nucl. Sci. **53** (2006) no. 1, 270. [INSPIRE].

[54] GEANT4 Collaboration, S. Agostinelli, J. Allison, K. Amako, J. Apostolakis, H. Araujo, P. Arce, M. Asai, D. Axen, S. Banerjee, and G. Barrand, *GEANT4: A Simulation toolkit*, Nucl. Instrum. Meth. A **506** (2003) 250–303. [INSPIRE].

[55] LHCb Collaboration, M. Clemencic et al., *The LHCb simulation application, Gauss: Design, evolution and experience*, J. Phys. Conf. Ser. **331** (2011) 032023. [INSPIRE].

[56] R. A. Khalek, S. Bailey, J. Gao, L. Harland-Lang, and J. Rojo, *Towards Ultimate Parton Distributions at the High-Luminosity LHC*, EPJC **78** (2018) no. 11, 962, arXiv:1810.03639 [hep-ph]. [INSPIRE].

[57] T. Han, A. Ismail, and B. Shams Es Haghi, *To appear*, .

[58] C. Borschensky, M. Krämer, A. Kulesza, M. Mangano, S. Padhi, T. Plehn, and X. Portell, *Squark and gluino production cross sections in pp collisions at* $\sqrt{s} = 13$ *, 14, 33 and* 100 *TeV*, EPJC **74** (2014) no. 12, 3174, arXiv:1407.5066 [hep-ph]. [INSPIRE].

[59] B. Fuks, M. Klasen, D. R. Lamprea, and M. Rothering, *Gaugino production in proton-proton collisions at a center-of-mass energy of* 8 *TeV*, JHEP **10** (2012) 81, arXiv:1207.2159 [hep-ph]. [INSPIRE].

[60] B. Fuks, M. Klasen, D. R. Lamprea, and M. Rothering, *Precision predictions for electroweak*

superpartner production at hadron colliders with Resummino, EPJC **73** (2013) no. 7, 2480, arXiv:1304.0790 [hep-ph]. [INSPIRE].

[61] B. Fuks, M. Klasen, D. R. Lamprea, and M. Rothering, *Revisiting slepton pair production at the Large Hadron Collider*, JHEP **01** (2014) 168, arXiv:1310.2621 [hep-ph]. [INSPIRE].

[62] ATLAS Collaboration, *Search for Supersymmetry at the high luminosity LHC with the ATLAS experiment*, ATL-PHYS-PUB-2014-010, 2014. [CDS].

[63] ATLAS Collaboration, *Prospects for a search for direct pair production of top squarks in scenarios with compressed mass spectra at the high luminosity LHC with the ATLAS Detector*, ATL-PHYS-PUB-2016-022, 2016. [CDS].

[64] ATLAS Collaboration, M. Aaboud, G. Aad, B. Abbott, O. Abdinov, B. Abeloos, S. H. Abidi, O. AbouZeid, N. Abraham, H. Abramowicz, and H. Abreu, *Search for squarks and gluinos in final states with jets and missing transverse momentum using* 36 fb^{-1} *of* $\sqrt{s} = 13$ *TeV pp collision data with the ATLAS detector*, Phys. Rev. D **97** (2018) 112001, arXiv:1712.02332 [hep-ex]. [INSPIRE].

[65] CMS Collaboration, A. M. Sirunyan, A. Tumasyan, W. Adam, F. Ambrogi, E. Asilar, T. Bergauer, J. Brandstetter, E. Brondolin, M. Dragicevic, and J. Ero", *Search for natural and split supersymmetry in proton-proton collisions at* $\sqrt{s} = 13$ *TeV in final states with jets and missing transverse momentum*, JHEP **05** (2018) 25, arXiv:1802.02110 [hep-ex]. [INSPIRE].

[66] T. Cohen, T. Golling, M. Hance, A. Henrichs, K. Howe, J. Loyal, S. Padhi, and J. G. Wacker, *SUSY Simplified Models at* 14, 33, *and* 100 *TeV Proton Colliders*, JHEP **04** (2014) 117, arXiv:1311.6480 [hep-ph]. [INSPIRE].

[67] J. Alwall, R. Frederix, S. Frixione, V. Hirschi, F. Maltoni, O. Mattelaer, H. S. Shao, T. Stelzer, P. Torrielli, and M. Zaro, *The automated computation of tree-level and next-to-leading order differential cross sections, and their matching to parton shower simulations*, JHEP **07** (2014) 79, arXiv:1405.0301 [hep-ph]. [INSPIRE].

[68] T. Sjöstrand, S. Ask, J. R. Christiansen, R. Corke, N. Desai, P. Ilten, S. Mrenna, S. Prestel, C. O. Rasmussen, and P. Z. Skands, *An Introduction to PYTHIA 8.2*, Comput. Phys. Commun. **191** (2015) 159–177, arXiv:1410.3012 [hep-ph]. [INSPIRE].

[69] ATLAS Collaboration, M. Aaboud, G. Aad, B. Abbott, J. Abdallah, O. Abdinov, B. Abeloos, R. Aben, O. AbouZeid, N. Abraham, and H. Abramowicz, *Search for squarks and gluinos in final states with jets and missing transverse momentum at* $\sqrt{s} = 13$ *TeV with the ATLAS detector*, EPJC **76** (2016) no. 7, 392, arXiv:1605.03814 [hep-ex]. [INSPIRE].

[70] ATLAS Collaboration, *ATLAS sensitivity to top squark pair production at the HL-LHC*, ATL-PHYS-PUB-2018-021, 2018. [CDS].

[71] ATLAS Collaboration, M. Aaboud et al., *Search for a scalar partner of the top quark in the jets plus missing transverse momentum final state at* $\sqrt{s} = 13$ *TeV with the ATLAS detector*, JHEP **12** (2017) 085, arXiv:1709.04183 [hep-ex]. [INSPIRE].

[72] CMS Collaboration, A. M. Sirunyan et al., *Inclusive search for supersymmetry in pp collisions at* $\sqrt{s} = 13$ *TeV using razor variables and boosted object identification in zero and one lepton final states*, Submitted to: JHEP (2018), arXiv:1812.06302 [hep-ex].

[73] C. Rogan, *Kinematical variables towards new dynamics at the LHC*, 2010.

[74] CMS Collaboration, *HL-LHC and HE-LHC searches for new physics in hadronic final states with boosted W bosons or top quarks using razor variables*, CMS-PAS-FTR-18-037, 2019.

[75] J. Thaler and K. V. Tilburg, *Identifying Boosted Objects with* N*-subjettiness*, JHEP **03** (2011) 15, arXiv:1011.2268 [hep-ph]. [INSPIRE].

[76] A. Pierce and B. Shakya, *Implications of a Stop Sector Signal at the LHC*, JHEP **06** (2018) 91, arXiv:1611.00771 [hep-ph]. [INSPIRE].

[77] S. P. Martin, *A Supersymmetry primer*, Adv. Ser. Direct. High Energy Phys. **2118** (1997) 1–98, arXiv:hep-ph/9709356 [hep-ph]. [INSPIRE].

[78] CMS Collaboration, V. Khachatryan, A. M. Sirunyan, A. Tumasyan, W. Adam, E. Asilar, T. Bergauer, J. Brandstetter, E. Brondolin, M. Dragicevic, and J. Ero", *Search for new physics in same-sign dilepton events in proton-proton collisions at* $\sqrt{s} = 13$ *TeV*, EPJC **76** (2016) no. 8, 439, arXiv:1605.03171 [hep-ex]. [INSPIRE].

[79] CMS Collaboration, *Search for SUSY in same-sign dilepton events at* 13 *TeV*, CMS-PAS-SUS-16-020, 2016. [INSPIRE].

[80] CMS Collaboration, *Search for SUSY with multileptons in* 13 *TeV data*, CMS-PAS-SUS-16-003, 2016. [INSPIRE].

[81] CMS Collaboration, *Search for SUSY with multileptons in* 13 *TeV data*, CMS-PAS-SUS-16-022, 2016. [INSPIRE].

[82] H. Baer and X. Tata, *Weak scale supersymmetry: From superfields to scattering events*. 2006. [INSPIRE].

[83] D. Ghosh, *Boosted dibosons from mixed heavy top squarks*, Phys. Rev. D **88** (2013) 115013, arXiv:1308.0320 [hep-ph]. [INSPIRE].

[84] ATLAS Collaboration, *Prospects for searches for staus, charginos and neutralinos at the high luminosity LHC with the ATLAS Detector*, ATL-PHYS-PUB-2018-048, Geneva, Dec, 2018. [CDS].

[85] ATLAS Collaboration, G. Aad et al., *Search for direct production of charginos, neutralinos and sleptons in final states with two leptons and missing transverse momentum in* pp *collisions at* $\sqrt{s} = 8$ *TeV with the ATLAS detector*, JHEP **05** (2014) 71, arXiv:1403.5294 [hep-ex]. [INSPIRE].

[86] ATLAS Collaboration, *Search for direct chargino pair production with W-boson mediated decays in events with two leptons and missing transverse momentum at* $\sqrt{s} = 13$ *TeV with the ATLAS detector*, ATLAS-CONF-2018-042, 2018. [INSPIRE].

[87] ATLAS Collaboration, M. Aaboud et al., *Search for electroweak production of supersymmetric particles in final states with two or three leptons at* $\sqrt{s} = 13$ *TeV with the ATLAS detector*, EPJC **78** (2018) no. 12, 995, arXiv:1803.02762 [hep-ex]. [INSPIRE].

[88] ATLAS Collaboration, *Prospect for a search for direct pair production of a chargino and a neutralino decaying via a W boson and the lightest Higgs boson in final states with one lepton, two b-jets and missing transverse momentum at the high luminosity LHC with the ATLAS Detector*, ATL-PHYS-PUB-2015-032, 2015. [CDS].

[89] H. Baer, V. Barger, P. Huang, D. Mickelson, A. Mustafayev, W. Sreethawong, and X. Tata, *Radiatively-driven natural supersymmetry at the LHC*, JHEP **1206** (2013) 13, arXiv:1310.4858 [hep-ph]. [INSPIRE].

[90] H. Baer, V. Barger, M. Savoy, and X. Tata, *Multichannel assault on natural supersymmetry at the high luminosity LHC*, Phys. Rev. D **94** (2016) 035025, arXiv:1604.07438 [hep-ph]. [INSPIRE].

[91] CMS Collaboration, *The Phase-2 Upgrade of the CMS Endcap Calorimeter*, CERN-LHCC-2017-023, CMS-TDR-019, 2017. Technical Design Report of the endcap calorimeter for the Phase-2 upgrade of the CMS experiment, in view of the HL-LHC run.

[92] T. Sjöstrand, S. Mrenna, and P. Skands, *PYTHIA 6.4 Physics and Manual*, JHEP **05** (2006) 26, arXiv:hep-ph/0603175 [hep-ph]. [INSPIRE].

[93] CMS Collaboration, A. Sirunyan, A. Tumasyan, W. Adam, F. Ambrogi, E. Asilar, T. Bergauer, J. Brandstetter, E. Brondolin, M. Dragicevic, and J. Ero", *Search for electroweak production of charginos and neutralinos in multilepton final states in proton-proton collisions at* $\sqrt{s} = 13$ *TeV*, JHEP **03** (2018) 166, arXiv:1709.05406 [hep-ex]. [INSPIRE].

[94] T. Junk, *Confidence level computation for combining searches with small statistics*, Nucl. Instrum. Meth. A **434** (1999) 435–443, arXiv:hep-ex/9902006 [hep-ex]. [INSPIRE].

[95] A. L. Read, *Presentation of search results: The CL_s technique*, J. Phys. G **28** (2002) 2693–2704. [INSPIRE].

[96] CMS Collaboration, A. M. Sirunyan, A. Tumasyan, W. Adam, F. Ambrogi, E. Asilar, T. Bergauer, J. Brandstetter, E. Brondolin, M. Dragicevic, and J. Ero", *Search for new physics in events with two soft oppositely charged leptons and missing transverse momentum in proton-proton collisions at $\sqrt{s} = 13$ TeV*, Phys. Lett. B **782** (2018) 440–467, arXiv:1801.01846 [hep-ex]. [INSPIRE].

[97] H. Baer, V. Barger, J. S. Gainer, M. Savoy, D. Sengupta, and X. Tata, *Aspects of the same-sign diboson signature from wino pair production with light higgsinos at the high luminosity LHC*, Phys. Rev. D **97** (2018) 035012, arXiv:1710.09103 [hep-ph]. [INSPIRE].

[98] ATLAS Collaboration, M. Aaboud et al., *Search for electroweak production of supersymmetric states in scenarios with compressed mass spectra at $\sqrt{s} = 13$ TeV with the ATLAS detector*, Phys. Rev. D **97** (2018) 052010, 1712.08119. [INSPIRE].

[99] ALEPH Collaboration, A. Heister et al., *Search for charginos nearly mass degenerate with the lightest neutralino in e^+e^- collisions at center-of-mass energies up to 209 GeV*, Phys. Lett. B **533** (2002) 223–236, arXiv:hep-ex/0203020 [hep-ex]. [INSPIRE].

[100] A. G. Akeroyd, S. Moretti, and M. Song, *Light charged Higgs boson with dominant decay to quarks and its search at LHC and future colliders*, arXiv:1810.05403 [hep-ph]. [INSPIRE].

[101] CMS Collaboration, *Searches for light higgsino-like charginos and neutralinos at the HL-LHC with the Phase-2 CMS detector*, CMS-PAS-FTR-18-001, 2018. [INSPIRE].

[102] ATLAS Collaboration, *ATLAS sensitivity to winos and higgsinos with a highly compressed mass spectrum at the HL-LHC*, ATL-PHYS-PUB-2018-031, 2018. [CDS].

[103] J. C. Pati and A. Salam, *Lepton Number as the Fourth Color*, Phys. Rev. D **1011** (1974) 275–289. [INSPIRE].

[104] R. N. Mohapatra and J. C. Pati, *Left-Right Gauge Symmetry and an Isoconjugate Model of CP Violation*, Phys. Rev. D **11** (1975) 566–571. [INSPIRE].

[105] R. Kuchimanchi and R. N. Mohapatra, *No parity violation without R-parity violation*, Phys. Rev. D **48** (1993) 4352–4360, arXiv:hep-ph/9306290 [hep-ph]. [INSPIRE].

[106] K. Babu and R. N. Mohapatra, *Minimal Supersymmetric Left-Right Model*, Phys. Lett. B **668** (2008) 404–409, arXiv:0807.0481 [hep-ph]. [INSPIRE].

[107] R. N. Mohapatra and A. Rašin, *Simple supersymmetric solution to the strong CP problem*, Phys. Rev. Lett. **76** (1996) no. 19, 3490–3493, arXiv:hep-ph/9511391 [hep-ph]. [INSPIRE].

[108] C. S. Aulakh, K. Benakli, and G. Senjanović, *Reconciling supersymmetry and left-right symmetry*, Phys. Rev. Lett. **79** (1997) no. 12, 2188–2191, arXiv:hep-ph/9703434 [hep-ph]. [INSPIRE].

[109] M. Frank, B. Fuks, K. Huitu, S. K. Rai, and H. Waltari, *Resonant slepton production and right sneutrino dark matter in left-right supersymmetry*, JHEP **05** (2017) 15, arXiv:1702.02112 [hep-ph]. [INSPIRE].

[110] S. Bhattacharya, E. Ma, and D. Wegman, *Supersymmetric left-right model with radiative neutrino mass and multipartite dark matter*, EPJC **74** (2014) no. 6, 2902, arXiv:1308.4177 [hep-ph]. [INSPIRE].

[111] XENON Collaboration, E. Aprile, J. Aalbers, F. Agostini, M. Alfonsi, L. Althueser, F. Amaro, M. Anthony, F. Arneodo, L. Baudis, and B. Bauermeister, *Dark Matter Search Results from a One Ton-Year Exposure of XENON1T*, Phys. Rev. Lett. **121** (2018), arXiv:1805.12562 [astro-ph.CO]. [INSPIRE].

[112] PandaX-II Collaboration, X. Cui, A. Abdukerim, W. Chen, X. Chen, Y. Chen, B. Dong, D. Fang, C. Fu, K. Giboni, and F. Giuliani, *Dark Matter Results From 54-Ton-Day Exposure of PandaX-II Experiment*, Phys. Rev. Lett. **119** (2017), arXiv:1708.06917 [astro-ph.CO]. [INSPIRE].

[113] CMS Collaboration, A. M. Sirunyan, A. Tumasyan, W. Adam, F. Ambrogi, E. Asilar, T. Bergauer, J. Brandstetter, E. Brondolin, M. Dragicevic, and J. Ero", *Search for a heavy right-handed W boson and a heavy neutrino in events with two same-flavor leptons and two jets at* $\sqrt{s} = 13$ *TeV*, JHEP **05** (2018) 148, arXiv:1803.11116 [hep-ex]. [INSPIRE].

[114] ATLAS Collaboration, M. Aaboud, G. Aad, B. Abbott, J. Abdallah, O. Abdinov, B. Abeloos, S. H. Abidi, O. AbouZeid, N. Abraham, and H. Abramowicz, *Search for new phenomena in dijet events using* 37 fb^{-1} *of pp collision data collected at* $\sqrt{s} = 13$ *TeV with the ATLAS detector*, Phys. Rev. D **96** (2017) 052004, arXiv:1703.09127 [hep-ex]. [INSPIRE].

[115] CMS Collaboration, A. M. Sirunyan, A. Tumasyan, W. Adam, F. Ambrogi, E. Asilar, T. Bergauer, J. Brandstetter, E. Brondolin, M. Dragicevic, and J. Ero", *Search for narrow and broad dijet resonances in proton-proton collisions at* $\sqrt{s} = 13$ *TeV and constraints on dark matter mediators and other new particles*, JHEP **08** (2018) 130, arXiv:1806.00843 [hep-ex]. [INSPIRE].

[116] F. Staub, *SARAH 4 : A tool for (not only SUSY) model builders*, Comput. Phys. Commun. **185** (2014) no. 6, 1773–1790, arXiv:1309.7223 [hep-ph]. [INSPIRE].

[117] L. Basso, B. Fuks, M. E. Krauss, and W. Porod, *Doubly-charged Higgs and vacuum stability in left-right supersymmetry*, JHEP **07** (2015) 147, arXiv:1503.08211 [hep-ph]. [INSPIRE].

[118] W. Porod, *SPheno, a program for calculating supersymmetric spectra, SUSY particle decays and SUSY particle production at* e^+e^- *colliders*, Comput. Phys. Commun. **153** (2003) no. 2, 275–315, arXiv:hep-ph/0301101 [hep-ph]. [INSPIRE].

[119] F. Ambrogi, C. Arina, M. Backovic, J. Heisig, F. Maltoni, L. Mantani, O. Mattelaer, and G. Mohlabeng, *MadDM v.3.0: a Comprehensive Tool for Dark Matter Studies*, arXiv:1804.00044 [hep-ph]. [INSPIRE].

[120] C. Degrande, C. Duhr, B. Fuks, D. Grellscheid, O. Mattelaer, and T. Reiter, *UFO - The Universal FeynRules Output*, Comput. Phys. Commun. **183** (2012) no. 6, 1201–1214, arXiv:1108.2040 [hep-ph]. [INSPIRE].

[121] NNPDF Collaboration, R. D. Ball, V. Bertone, S. Carrazza, C. S. Deans, L. Del Debbio, S. Forte, A. Guffanti, N. P. Hartland, J. I. Latorre, and J. Rojo, *Parton distributions for the LHC Run II*, JHEP **04** (2015) 40, arXiv:1410.8849 [hep-ph]. [INSPIRE].

[122] E. Conte, B. Fuks, and G. Serret, *MadAnalysis 5, A User-Friendly Framework for Collider Phenomenology*, Comput. Phys. Commun. **184** (2013) no. 1, 222–256, arXiv:1206.1599 [hep-ph]. [INSPIRE].

[123] E. Conte, B. Dumont, B. Fuks, and C. Wymant, *Designing and recasting LHC analyses with MadAnalysis 5*, EPJC **74** (2014) no. 10, 3103, arXiv:1405.3982 [hep-ph]. [INSPIRE].

[124] B. Dumont, B. Fuks, S. Kraml, S. Bein, G. Chalons, E. Conte, S. Kulkarni, D. Sengupta, and C. Wymant, *Toward a public analysis database for LHC new physics searches using MADANALYSIS 5*, EPJC **75** (2015) no. 2, 56, arXiv:1407.3278 [hep-ph]. [INSPIRE].

[125] B. Fuks and S. Mondal, *MadAnalysis 5 implementation of the CMS search for supersymmetry in the multilepton channel with* 35.9 fb^{-1} *of* 13 *TeV LHC data (CMS-SUS-16-039)*, . [INSPIRE].

[126] ATLAS Collaboration, G. Aad et al., *Search for the electroweak production of supersymmetric particles in* $\sqrt{s} = 8$ *TeV pp collisions with the ATLAS detector*, Phys. Rev. D **93** (2016) 052002, arXiv:1509.07152 [hep-ex]. [INSPIRE].

[127] ATLAS Collaboration, M. Aaboud et al., *Search for the direct production of charginos and neutralinos in final states with tau leptons in* $\sqrt{s} = 13$ *TeV pp collisions with the ATLAS detector*, EPJC **78** (2018) no. 2, 154, arXiv:1708.07875 [hep-ex]. [INSPIRE].

[128] CMS Collaboration, *Search for supersymmetry with direct stau production at the HL-LHC with the CMS Phase-2 detector*, CMS-PAS-FTR-18-010, 2018. [INSPIRE].

[129] W. Beenakker, R. Hoepker, and M. Spira, *PROSPINO: A Program for the production of supersymmetric particles in next-to-leading order QCD*, arXiv:hep-ph/9611232 [hep-ph]. [INSPIRE].

[130] C. Lester and D. Summers, *Measuring masses of semiinvisibly decaying particles pair produced at hadron colliders*, Phys. Lett. B **463** (1999) 99–103, arXiv:hep-ph/9906349 [hep-ph]. [INSPIRE].

[131] A. Barr, C. Lester, and P. Stephens, m_{T2}*: the truth behind the glamour*, J. Phys. G **29** (2003) 2343–2363, arXiv:hep-ph/0304226 [hep-ph]. [INSPIRE].

[132] A. Aboubrahim and P. Nath, *Supersymmetry at a* 28 *TeV hadron collider: HE-LHC*, Phys. Rev. D **98** (2018) 015009, arXiv:1804.08642 [hep-ph]. [INSPIRE].

[133] A. H. Chamseddine, R. L. Arnowitt, and P. Nath, *Locally Supersymmetric Grand Unification*, Phys. Rev. Lett. **49** (1982) 970. [INSPIRE].

[134] P. Nath, R. L. Arnowitt, and A. H. Chamseddine, *Gauge Hierarchy in Supergravity Guts*, Nucl. Phys. B **227** (1983) 121–133. [INSPIRE].

[135] L. Hall, J. Lykken, and S. Weinberg, *Supergravity as the Messenger of Supersymmetry Breaking*, Phys. Rev. D **27** (1983) 2359–2378. [INSPIRE].

[136] R. L. Arnowitt and P. Nath, *SUSY mass spectrum in* $SU(5)$ *supergravity grand unification*, Phys. Rev. Lett. **69** (1992) 725–728. [INSPIRE].

[137] K. L. Chan, U. Chattopadhyay, and P. Nath, *Naturalness, weak scale supersymmetry and the prospect for the observation of supersymmetry at the Tevatron and at the CERN LHC*, Phys. Rev. D **58** (1998) 096004, arXiv:hep-ph/9710473 [hep-ph]. [INSPIRE].

[138] A. Aboubrahim and P. Nath, *Supergravity models with* $50 - 100$ *TeV scalars, supersymmetry discovery at the LHC, and gravitino decay constraints*, Phys. Rev. D **96** (2017) 075015, arXiv:1708.02830 [hep-ph]. [INSPIRE].

[139] A. Aboubrahim, P. Nath, and A. B. Spisak, *Stau coannihilation, compressed spectrum, and SUSY discovery potential at the LHC*, Phys. Rev. D **95** (2017) 115030, arXiv:1704.04669 [hep-ph]. [INSPIRE].

[140] P. Nath and A. B. Spisak, *Gluino Coannihilation and Observability of Gluinos at LHC RUN II*, Phys. Rev. D **93** (2016) 095023, arXiv:1603.04854 [hep-ph]. [INSPIRE].

[141] H. Baer, V. Barger, J. S. Gainer, P. Huang, M. Savoy, D. Sengupta, and X. Tata, *Gluino reach and mass extraction at the LHC in radiatively-driven natural SUSY*, EPJC **77** (2017) no. 7, 499, arXiv:1612.00795 [hep-ph]. [INSPIRE].

[142] H. Baer, V. Barger, J. S. Gainer, H. Serce, and X. Tata, *Reach of the high-energy LHC for gluinos and top squarks in SUSY models with light Higgsinos*, Phys. Rev. D **96** (2017) 115008, arXiv:1708.09054 [hep-ph]. [INSPIRE].

[143] H. Baer, V. Barger, J. S. Gainer, D. Sengupta, H. Serce, and X. Tata, *LHC luminosity and energy upgrades confront natural supersymmetry models*, Phys. Rev. D **98** (2018) 075010, arXiv:1808.04844 [hep-ph]. [INSPIRE].

[144] H. Baer, V. Barger, N. Nagata, and S. Michael, *Phenomenological profile of top squarks from natural supersymmetry at the LHC*, Phys. Rev. D **95** (2017) 055012, arXiv:1611.08511 [hep-ph]. [INSPIRE].

[145] ATLAS Collaboration, *Prospects for benchmark Supersymmetry searches at the high luminosity LHC with the ATLAS Detector*, ATL-PHYS-PUB-2013-011, 2013. [CDS].

[146] H. Baer, V. Barger, P. Huang, A. Mustafayev, and X. Tata, *Radiative natural SUSY with a* 125 *GeV Higgs boson*, Phys. Rev. Lett. **109** (2012) no. 16, arXiv:1207.3343 [hep-ph].

[INSPIRE].

[147] H. Baer, V. Barger, P. Huang, D. Mickelson, A. Mustafayev, and X. Tata, *Radiative natural supersymmetry: Reconciling electroweak fine-tuning and the Higgs boson mass*, Phys. Rev. D **87** (2013) 115028, arXiv:1212.2655 [hep-ph]. [INSPIRE].

[148] H. Baer, V. Barger, and M. Savoy, *Upper bounds on sparticle masses from naturalness or how to disprove weak scale supersymmetry*, Phys. Rev. D **93** (2016) 035016, arXiv:1509.02929 [hep-ph]. [INSPIRE].

[149] H. Baer, A. Mustafayev, S. Profumo, A. Belyaev, and X. Tata, *Direct, indirect and collider detection of neutralino dark matter in SUSY models with non-universal Higgs masses*, JHEP **07** (2005) 65, arXiv:hep-ph/0504001 [hep-ph]. [INSPIRE].

[150] H. Baer, V. Barger, H. Serce, and X. Tata, *Natural generalized mirage mediation*, Phys. Rev. D **94** (2016) 115017, arXiv:1610.06205 [hep-ph]. [INSPIRE].

[151] H. Baer, V. Barger, and D. Sengupta, *Anomaly mediated SUSY breaking model retrofitted for naturalness*, Phys. Rev. D **98** (2018) 015039, arXiv:1801.09730 [hep-ph]. [INSPIRE].

[152] H. Baer, V. Barger, P. Huang, D. Mickelson, A. Mustafayev, W. Sreethawong, and X. Tata, *Same sign diboson signature from supersymmetry models with light higgsinos at the LHC*, Phys. Rev. Lett. **110** (2013) no. 15, arXiv:1302.5816 [hep-ph]. [INSPIRE].

[153] H. Baer, V. Barger, D. Sengupta, and X. Tata, *Is natural higgsino-only dark matter excluded?*, EPJC **78** (2018) no. 10, 838, arXiv:1803.11210 [hep-ph]. [INSPIRE].

[154] H. Baer, A. Mustafayev, and X. Tata, *Monojets and mono-photons from light higgsino pair production at LHC14*, Phys. Rev. D **89** (2014) 055007, arXiv:1401.1162 [hep-ph]. [INSPIRE].

[155] T. Han, S. Mukhopadhyay, and X. Wang, *Electroweak Dark Matter at Future Hadron Colliders*, Phys. Rev. D **98** (2018) 035026, arXiv:1805.00015 [hep-ph]. [INSPIRE].

[156] H. Baer, A. Mustafayev, and X. Tata, *Monojet plus soft dilepton signal from light higgsino pair production at LHC14*, Phys. Rev. D **90** (2014) 115007, arXiv:1409.7058 [hep-ph]. [INSPIRE].

[157] H. Baer, V. Barger, H. Serce, and K. Sinha, *Higgs and superparticle mass predictions from the landscape*, JHEP **03** (2018) 2, arXiv:1712.01399 [hep-ph]. [INSPIRE].

[158] MSSM Working Group Collaboration, A. Djouadi, S. Rosier-Lees, M. Bezouh, M. Bizouard, C. Boehm, F. Borzumati, C. Briot, J. Carr, M. Causse, and F. Charles, *The Minimal supersymmetric standard model: Group summary report*, arXiv:hep-ph/9901246 [hep-ph]. [INSPIRE].

[159] A. Arbey, M. Battaglia, and F. Mahmoudi, *Implications of LHC Searches on SUSY Particle Spectra: The pMSSM Parameter Space with Neutralino Dark Matter*, EPJC **72** (2012) no. 1, 1847, arXiv:1110.3726 [hep-ph]. [INSPIRE].

[160] A. Arbey, M. Battaglia, and F. Mahmoudi, *Constraints on the MSSM from the Higgs Sector: A pMSSM Study of Higgs Searches, $B_s^0 \to \mu^+\mu^-$ and Dark Matter Direct Detection*, EPJC **72** (2012) no. 3, 1906, arXiv:1112.3032 [hep-ph]. [INSPIRE].

[161] A. Arbey, M. Battaglia, and F. Mahmoudi, *The Higgs boson, Supersymmetry and Dark Matter: Relations and Perspectives*, Annalen Phys. **528** (2016) no. 1-2, 179–186, arXiv:1504.05091 [hep-ph]. [INSPIRE].

[162] ATLAS Collaboration, G. Aad et al., *Search for squarks and gluinos with the ATLAS detector in final states with jets and missing transverse momentum using $\sqrt{s} = 8$ TeV proton–proton collision data*, JHEP **09** (2014) 176, arXiv:1405.7875 [hep-ex]. [INSPIRE].

[163] ATLAS Collaboration, G. Aad et al., *ATLAS Run 1 searches for direct pair production of third-generation squarks at the Large Hadron Collider*, EPJC **75** (2015) no. 10, 510,

arXiv:1506.08616 [hep-ex]. [Erratum: Eur. Phys. J.C76,no.3,153(2016)] [INSPIRE].

[164] ATLAS Collaboration, G. Aad et al., *Search for direct top-squark pair production in final states with two leptons in pp collisions at $\sqrt{s} = 8$ TeV with the ATLAS detector*, JHEP **06** (2014) 124, arXiv:1403.4853 [hep-ex]. [INSPIRE].

[165] ATLAS Collaboration, G. Aad et al., *Search for squarks and gluinos in events with isolated leptons, jets and missing transverse momentum at $\sqrt{s} = 8$ TeV with the ATLAS detector*, JHEP **04** (2015) 116, arXiv:1501.03555 [hep-ex]. [INSPIRE].

[166] ATLAS Collaboration, G. Aad et al., *Search for direct pair production of a chargino and a neutralino decaying to the 125 GeV Higgs boson in $\sqrt{s} = 8$ TeV pp collisions with the ATLAS detector*, EPJC **75** (2015) no. 5, 208, arXiv:1501.07110 [hep-ex]. [INSPIRE].

[167] ATLAS Collaboration, G. Aad et al., *Search for direct production of charginos and neutralinos in events with three leptons and missing transverse momentum in $\sqrt{s} = 8$ TeV pp collisions with the ATLAS detector*, JHEP **04** (2014) 169, arXiv:1402.7029 [hep-ex]. [INSPIRE].

[168] ATLAS Collaboration, G. Aad et al., *Search for pair-produced third-generation squarks decaying via charm quarks or in compressed supersymmetric scenarios in pp collisions at $\sqrt{s} = 8$ TeV with the ATLAS detector*, Phys. Rev. D **90** (2014) 052008, arXiv:1407.0608 [hep-ex]. [INSPIRE].

[169] CMS Collaboration, V. Khachatryan et al., *Search for dark matter, extra dimensions, and unparticles in monojet events in protonproton collisions at $\sqrt{s} = 8$ TeV*, EPJC **75** (2015) no. 5, 235, arXiv:1408.3583 [hep-ex]. [INSPIRE].

[170] A. Arbey, M. Battaglia, L. Covi, J. Hasenkamp, and F. Mahmoudi, *LHC constraints on Gravitino Dark Matter*, Phys. Rev. D **92** (2015) 115008, arXiv:1505.04595 [hep-ph]. [INSPIRE].

[171] S. Dawson et al., *Working Group Report: Higgs Boson*, FERMILAB-CONF-13-671-T, 2013. arXiv:1310.8361 [hep-ex]. [INSPIRE].

[172] A. Arbey, M. Battaglia, and F. Mahmoudi, *Monojet Searches for MSSM Simplified Models*, Phys. Rev. D **94** (2016) 055015, arXiv:1506.02148 [hep-ph]. [INSPIRE].

[173] G. Corcella and S. Gentile, *Heavy Neutral Gauge Bosons at the LHC in an Extended MSSM*, Nucl. Phys. B **866868** (2013) 293–336, arXiv:1205.5780 [hep-ph]. [INSPIRE].

[174] G. Corcella, *Phenomenology of supersymmetric Z' decays at the Large Hadron Collider*, EPJC **75** (2015) no. 6, 264, arXiv:1412.6831 [hep-ph]. [INSPIRE].

[175] J. Y. Araz, G. Corcella, M. Frank, and B. Fuks, *Loopholes in Z' searches at the LHC: exploring supersymmetric and leptophobic scenarios*, JHEP **02** (2018) 92, arXiv:1711.06302 [hep-ph]. [INSPIRE].

[176] J. Erler, P. Langacker, and T. Li, *The $Z - Z'$ mass hierarchy in a supersymmetric model with a secluded $U(1)'$ breaking sector*, Phys. Rev. D **66** (2002) 015002, arXiv:hep-ph/0205001 [hep-ph]. [INSPIRE].

[177] K. S. Babu, C. Kolda, and J. March-Russell, *Leptophobic $U(1)'$s and the $R_b - R_c$ crisis*, Phys. Rev. D **54** (1996) 4635–4647, arXiv:hep-ph/9603212 [hep-ph]. [INSPIRE].

[178] W. Porod and F. Staub, *SPheno 3.1: Extensions including flavour, CP-phases and models beyond the MSSM*, Comput. Phys. Commun. **183** (2012) no. 11, 2458–2469, arXiv:1104.1573 [hep-ph]. [INSPIRE].

[179] J. Anderson, A. Avetisyan, R. Brock, S. Chekanov, T. Cohen, N. Dhingra, J. Dolen, J. Hirschauer, K. Howe, and A. Kotwal, *Snowmass Energy Frontier Simulations*, arXiv:1309.1057 [hep-ex]. [INSPIRE].

[180] A. Avetisyan, J. M. Campbell, T. Cohen, N. Dhingra, J. Hirschauer, K. Howe, S. Malik, M. Narain, S. Padhi, and M. E. Peskin, *Methods and Results for Standard Model Event Generation at $\sqrt{s} = 14$ TeV, 33 TeV and 100 TeV Proton Colliders (A Snowmass Whitepaper)*,

arXiv:1308.1636 [hep-ex]. [INSPIRE].

[181] M. W. Goodman and E. Witten, *Detectability of Certain Dark Matter Candidates*, Phys. Rev. D **31** (1985) 3059. [INSPIRE].

[182] J. E. Gunn, B. W. Lee, I. Lerche, D. N. Schramm, and G. Steigman, *Some Astrophysical Consequences of the Existence of a Heavy Stable Neutral Lepton*, Astrophys. J. **223** (1978) 1015–1031. [INSPIRE].

[183] F. W. Stecker, *The Cosmic Gamma-Ray Background from the Annihilation of Primordial Stable Neutral Heavy Leptons*, Astrophys. J. **223** (1978) 1032–1036. [INSPIRE].

[184] J. Silk and M. Srednicki, *Cosmic Ray anti-Protons as a Probe of a Photino Dominated Universe*, Phys. Rev. Lett. **53** (1984) 624. [INSPIRE].

[185] L. M. Krauss, K. Freese, W. Press, and D. Spergel, *Cold dark matter candidates and the solar neutrino problem*, Astrophys. J. **299** (1985) 1001. [INSPIRE].

[186] J. Silk, K. A. Olive, and M. Srednicki, *The Photino, the Sun and High-Energy Neutrinos*, Phys. Rev. Lett. **55** (1985) 257–259. [INSPIRE].

[187] D. N. Spergel and P. J. Steinhardt, *Observational evidence for selfinteracting cold dark matter*, Phys. Rev. Lett. **84** (2000) 3760–3763, arXiv:astro-ph/9909386 [astro-ph]. [INSPIRE].

[188] O. Buchmueller, C. Doglioni, and L. T. Wang, *Search for dark matter at colliders*, Nature Phys. **13** (2017) no. 3, 217–223. [INSPIRE].

[189] B. Penning, *The pursuit of dark matter at colliders—an overview*, J. Phys. G **45** (2018) 063001, arxiv:1712.01391 [hep-ex]. [INSPIRE].

[190] ATLAS Collaboration, *Extrapolation of E_{T}^{miss}+ jet search results to an integrated luminosity of* 300 *fb*$^{-1}$ *and* 3000 *fb*$^{-1}$, ATL-PHYS-PUB-2018-043, 2018. [CDS].

[191] ATLAS Collaboration, M. Aaboud, G. Aad, B. Abbott, O. Abdinov, B. Abeloos, S. H. Abidi, O. AbouZeid, N. Abraham, H. Abramowicz, and H. Abreu, *Search for dark matter and other new phenomena in events with an energetic jet and large missing transverse momentum using the ATLAS detector*, JHEP **01** (2018) 126, arXiv:1711.03301 [hep-ex]. [INSPIRE].

[192] J. Lindert, S. Pozzorini, R. Boughezal, J. Campbell, A. Denner, S. Dittmaier, A. Gehrmann-De Ridder, T. Gehrmann, N. Glover, and A. Huss, *Precise predictions for V+jets dark matter backgrounds*, EPJC **77** (2017) no. 12, 829, arXiv:1705.04664 [hep-ph]. [INSPIRE].

[193] U. Haisch, F. Kahlhoefer, and E. Re, *QCD effects in mono-jet searches for dark matter*, JHEP **12** (2013) 7, arXiv:1310.4491 [hep-ph]. [INSPIRE].

[194] J. Bellm, S. Gieseke, D. Grellscheid, S. Pla"tzer, M. Rauch, C. Reuschle, P. Richardson, P. Schichtel, M. H. Seymour, and A. Sio'dmok, *Herwig 7.0/Herwig++ 3.0 release note*, EPJC **76** (2016) no. 4, 196, arXiv:1512.01178 [hep-ph]. [INSPIRE].

[195] T. Gleisberg, S. Höche, F. Krauss, M. Schönherr, S. Schumann, F. Siegert, and J. Winter, *Event generation with SHERPA 1.1*, JHEP **02** (2009) 7, arXiv:0811.4622 [hep-ph]. [INSPIRE].

[196] C. Degrande, *Automatic evaluation of UV and R_2 terms for beyond the Standard Model Lagrangians: a proof-of-principle*, Comput. Phys. Commun. **197** (2015) 239–262, arXiv:1406.3030 [hep-ph]. [INSPIRE].

[197] A. Chakraborty, S. Kuttimalai, S. H. Lim, M. M. Nojiri, and R. Ruiz, *Monojet Signatures from Heavy Colored Particles: Future Collider Sensitivities and Theoretical Uncertainties*, EPJC **78** (2018) no. 8, 679, arXiv:1805.05346 [hep-ph]. [INSPIRE].

[198] ATLAS Collaboration, *Search for dark matter and other new phenomena in events with an energetic jet and large missing transverse momentum using the ATLAS detector*, ATLAS-CONF-2017-060, 2017. [INSPIRE].

[199] CMS Collaboration, A. M. Sirunyan, A. Tumasyan, W. Adam, F. Ambrogi, E. Asilar,

T. Bergauer, J. Brandstetter, E. Brondolin, M. Dragicevic, and J. Ero", *Search for new physics in final states with an energetic jet or a hadronically decaying W or Z boson and transverse momentum imbalance at $\sqrt{s} = 13$ TeV*, Phys. Rev. D **97** (2018) 092005, arXiv:1712.02345 [hep-ex]. [INSPIRE].

[200] B. Fuks and H.-S. Shao, *QCD next-to-leading-order predictions matched to parton showers for vector-like quark models*, EPJC **77** (2017) no. 2, 135, arXiv:1610.04622 [hep-ph]. [INSPIRE].

[201] *FeynRules models to be used for NLO calculations with aMC@NLO*, . [WEBPAGE].

[202] C. Degrande, B. Fuks, V. Hirschi, J. Proudom, and H.-S. Shao, *Matching next-to-leading order predictions to parton showers in supersymmetric QCD*, Phys. Lett. B **755** (2016) 82–87, arXiv:1510.00391 [hep-ph]. [INSPIRE].

[203] *Workshop on the physics of HL-LHC, and perspectives at HE-LHC*, . [INDICO].

[204] M. Aliev, H. Lacker, U. Langenfeld, S. Moch, P. Uwer, and M. Wiedermann, *HATHOR: HAdronic Top and Heavy quarks crOss section calculatoR*, Comput. Phys. Commun. **182** (2011) no. 4, 1034–1046, arXiv:1007.1327 [hep-ph]. [INSPIRE].

[205] M. Czakon and A. Mitov, *Top++: A Program for the Calculation of the Top-Pair Cross-Section at Hadron Colliders*, Comput. Phys. Commun. **185** (2014) no. 11, 2930, arXiv:1112.5675 [hep-ph]. [INSPIRE].

[206] J. Hisano, S. Matsumoto, and M. M. Nojiri, *Explosive dark matter annihilation*, Phys. Rev. Lett. **92** (2004) no. 3, arXiv:hep-ph/0307216 [hep-ph]. [INSPIRE].

[207] J. Hisano, S. Matsumoto, M. M. Nojiri, and O. Saito, *Non-perturbative effect on dark matter annihilation and gamma ray signature from galactic center*, Phys. Rev. D **71** (2005) 063528, arXiv:hep-ph/0412403 [hep-ph]. [INSPIRE].

[208] J. Hisano, S. Matsumot, M. Nagai, O. Saito, and M. Senami, *Non-perturbative effect on thermal relic abundance of dark matter*, Phys. Lett. B **646** (2007) 34–38, arXiv:hep-ph/0610249 [hep-ph]. [INSPIRE].

[209] S. Mizuta and M. Yamaguchi, *Coannihilation effects and relic abundance of Higgsino-dominant LSPs*, Phys. Lett. B **298** (1993) 120–126, arXiv:hep-ph/9208251 [hep-ph]. [INSPIRE].

[210] M. Ibe, S. Matsumoto, and R. Sato, *Mass Splitting between Charged and Neutral Winos at Two-Loop Level*, Phys. Lett. B **721** (2013) 252–260, arXiv:1212.5989 [hep-ph]. [INSPIRE].

[211] S. Thomas and J. D. Wells, *Phenomenology of Massive Vectorlike Doublet Leptons*, Phys. Rev. Lett. **81** (1998) no. 1, 34–37, arXiv:hep-ph/9804359 [hep-ph]. [INSPIRE].

[212] ATLAS Collaboration, *ATLAS sensitivity to dark matter produced in association with heavy quarks at the HL-LHC*, ATL-PHYS-PUB-2018-036, 2018. [CDS].

[213] ATLAS Collaboration, M. Aaboud, G. Aad, B. Abbott, O. Abdinov, B. Abeloos, S. H. Abidi, O. AbouZeid, N. Abraham, H. Abramowicz, and H. Abreu, *Search for dark matter produced in association with bottom or top quarks in $\sqrt{s} = 13$ TeV pp collisions with the ATLAS detector*, EPJC **78** (2018) no. 1, 18, arXiv:1710.11412 [hep-ex]. [INSPIRE].

[214] CMS Collaboration, A. M. Sirunyan, A. Tumasyan, W. Adam, F. Ambrogi, E. Asilar, T. Bergauer, J. Brandstetter, M. Dragicevic, J. Ero", and A. Escalante Del Valle, *Search for dark matter particles produced in association with a top quark pair at $\sqrt{s} = 13$ TeV*, arXiv:1807.06522 [hep-ex]. [INSPIRE].

[215] A. Boveia, O. Buchmueller, G. Busoni, F. D'Eramo, A. De Roeck, A. De Simone, C. Doglioni, M. J. Dolan, M.-H. Genest, and K. Hahn, *Recommendations on presenting LHC searches for missing transverse energy signals using simplified s-channel models of dark matter*, arXiv:1603.04156 [hep-ex]. [INSPIRE].

[216] U. Haisch, P. Pani, and G. Polesello, *Determining the CP nature of spin-0 mediators in*

associated production of dark matter and $t\bar{t}$ pairs, JHEP **02** (2017) 131, arXiv:1611.09841 [hep-ph]. [INSPIRE].

[217] P. Pani and G. Polesello, *Dark matter production in association with a single top-quark at the LHC in a two-Higgs-doublet model with a pseudoscalar mediator*, Phys. Dark Univ. **21** (2018) 8–15, arXiv:1712.03874 [hep-ph]. [INSPIRE].

[218] G. Brooijmans, M. Dolan, S. Gori, F. Maltoni, M. McCullough, P. Musella, L. Perrozzi, P. Richardson, F. Riva, and A. Angelescu, *Les Houches 2017: Physics at TeV Colliders New Physics Working Group Report*, arXiv:1803.10379 [hep-ph]. [INSPIRE].

[219] D. Abercrombie, N. Akchurin, E. Akilli, J. Alcaraz Maestre, B. Allen, B. Alvarez Gonzalez, J. Andrea, A. Arbey, G. Azuelos, and P. Azzi, *Dark Matter Benchmark Models for Early LHC Run-2 Searches: Report of the ATLAS/CMS Dark Matter Forum*, arXiv:1507.00966 [hep-ex]. [INSPIRE].

[220] LHC Dark Matter Working Group Collaboration, T. Abe, Y. Afik, A. Albert, C. R. Anelli, L. Barak, M. Bauer, J. Katharina Behr, N. F. Bell, A. Boveia, and O. Brandt, *LHC Dark Matter Working Group: Next-generation spin-0 dark matter models*, arXiv:1810.09420 [hep-ex]. [INSPIRE].

[221] S. Ipek, D. McKeen, and A. E. Nelson, *A Renormalizable Model for the Galactic Center Gamma Ray Excess from Dark Matter Annihilation*, Phys. Rev. D **90** (2014) 055021, arXiv:1404.3716 [hep-ph]. [INSPIRE].

[222] J. M. No, *Looking through the pseudoscalar portal into dark matter: Novel mono-Higgs and mono-Z signatures at the LHC*, Phys. Rev. D **93** (2016) 031701, arXiv:1509.01110 [hep-ph]. [INSPIRE].

[223] D. Gonçalves, P. A. Machado, and J. M. No, *Simplified Models for Dark Matter Face their Consistent Completions*, Phys. Rev. D **95** (2017) 055027, arXiv:1611.04593 [hep-ph]. [INSPIRE].

[224] M. Bauer, U. Haisch, and F. Kahlhoefer, *Simplified dark matter models with two Higgs doublets: I. Pseudoscalar mediators*, JHEP **05** (2017) 138, arXiv:1701.07427 [hep-ph]. [INSPIRE].

[225] P. Tunney, J. M. No, and M. Fairbairn, *Probing the pseudoscalar portal to dark matter via $\bar{b}bZ(\to \ell\ell) + E_T^{miss}$: From the LHC to the Galactic Center excess*, Phys. Rev. D **96** (2017) 095020, arXiv:1705.09670 [hep-ph]. [INSPIRE].

[226] ATLAS Collaboration, *Search for charged Higgs bosons in the $H^{\pm} \to tb$ decay channel in pp collisions at $\sqrt{s} = 13$ TeV using the ATLAS detector*, ATLAS-CONF-2016-089, 2016. [INSPIRE].

[227] ATLAS Collaboration, *Prospects for a search of invisible particles produced in association with single-top quarks with the ATLAS detector at the HL-LHC*, ATL-PHYS-PUB-2018-024, 2018. [CDS].

[228] J. Andrea, B. Fuks, and F. Maltoni, *Monotops at the LHC*, Phys. Rev. D **84** (2011) 074025, arXiv:1106.6199 [hep-ph]. [INSPIRE].

[229] P. Speckmayer, A. Hocker, J. Stelzer, and H. Voss, *The toolkit for multivariate data analysis, TMVA 4*, J. Phys. Conf. Ser. **219** (2010) 032057. [INSPIRE].

[230] ATLAS Collaboration, *ATLAS sensitivity to Two-Higgs-Doublet models with an additional pseudoscalar exploiting four top quark signatures with 3 ab^{-1} of $\sqrt{s} = 14$ TeV proton-proton collisions*, ATL-PHYS-PUB-2018-027, 2018. [CDS].

[231] CMS Collaboration, *Projections of sensitivities for tttt production at HL-LHC and HE-LHC*, CMS-PAS-FTR-18-031, 2018. [INSPIRE].

[232] ATLAS Collaboration, *HL-LHC prospects for the measurement of the Standard Model four-top-quark production cross-section*, ATL-PHYS-PUB-2018-047, 2018. [CDS].

[233] CMS Collaboration, A. Sirunyan, A. Tumasyan, W. Adam, F. Ambrogi, E. Asilar, T. Bergauer, J. Brandstetter, E. Brondolin, M. Dragicevic, and J. Ero", *Search for new physics in events with a leptonically decaying Z boson and a large transverse momentum imbalance in proton-proton collisions at $\sqrt{s} = 13$ TeV*, EPJC **78** (2018) no. 4, 291, arXiv:1711.00431 [hep-ex]. [INSPIRE].

[234] CMS Collaboration, *Projection of the Mono-Z search for dark matter to the HL-LHC*, CMS-PAS-FTR-18-007, 2018. [INSPIRE].

[235] CMS Collaboration, A. M. Sirunyan et al., *Search for dark matter produced in association with a Higgs boson decaying to a pair of bottom quarks in proton-proton collisions at $\sqrt{s} = 13$ TeV*, arXiv:1811.06562 [hep-ex]. [INSPIRE].

[236] Planck Collaboration, P. Ade, N. Aghanim, M. Arnaud, M. Ashdown, J. Aumont, C. Baccigalupi, A. Banday, R. Barreiro, J. Bartlett, and N. Bartolo, *Planck 2015 results. XIII. Cosmological parameters*, Astron. Astrophys. **594** (2016) A13, arXiv:1502.01589 [astro-ph.CO]. [INSPIRE].

[237] A. Albert, M. Backovic', A. Boveia, O. Buchmueller, G. Busoni, A. De Roeck, C. Doglioni, T. DuPree, M. Fairbairn, and M.-H. Genest, *Recommendations of the LHC Dark Matter Working Group: Comparing LHC searches for heavy mediators of dark matter production in visible and invisible decay channels*, arXiv:1703.05703 [hep-ex]. [INSPIRE].

[238] ATLAS Collaboration, *Prospects for Dark Matter searches in mono-photon and VBF+E_T^{miss} final states in ATLAS*, ATL-PHYS-PUB-2018-038, 2018. [CDS].

[239] L. Randall and R. Sundrum, *Out of this world supersymmetry breaking*, Nucl. Phys. B **557** (1999) 79–118, arXiv:hep-th/9810155 [hep-th]. [INSPIRE].

[240] G. F. Giudice, R. Rattazzi, M. A. Luty, and H. Murayama, *Gaugino mass without singlets*, JHEP **12** (1998) 27, arXiv:hep-ph/9810442 [hep-ph]. [INSPIRE].

[241] T. Moroi and L. Randall, *Wino cold dark matter from anomaly mediated SUSY breaking*, Nucl. Phys. B **570** (2000) 455–472, arXiv:hep-ph/9906527 [hep-ph]. [INSPIRE].

[242] M. Cirelli, N. Fornengo, and A. Strumia, *Minimal dark matter*, Nucl. Phys. B **753** (2006) 178–194, arXiv:hep-ph/0512090 [hep-ph]. [INSPIRE].

[243] M. Cirelli, A. Strumia, and M. Tamburini, *Cosmology and astrophysics of minimal dark matter*, Nucl. Phys. B **787** (2007) 152–175, arXiv:hep-ph/07064071 [hep-ph]. [INSPIRE].

[244] M. Cirelli and A. Strumia, *Minimal Dark Matter: Model and results*, New J. Phys. **11** (2009) 105005, arXiv:0903.3381 [hep-ph]. [INSPIRE].

[245] ATLAS Collaboration, M. Aaboud et al., *Search for dark matter at $\sqrt{s} = 13$ TeV in final states containing an energetic photon and large missing transverse momentum with the ATLAS detector*, EPJC **77** (2017) no. 6, 393, arXiv:1704.03848 [hep-ex]. [INSPIRE].

[246] ATLAS Collaboration, M. Aaboud et al., *Search for invisible Higgs boson decays in vector boson fusion at $\sqrt{s} = 13$ TeV with the ATLAS detector*, arXiv:1809.06682 [hep-ex]. [INSPIRE].

[247] M. Cirelli, F. Sala, and M. Taoso, *Wino-like Minimal Dark Matter and future colliders*, JHEP **10** (2014) 033, arXiv:1407.7058 [hep-ph]. [Erratum: JHEP01, 041 (2015)] [INSPIRE].

[248] M. Low and L.-T. Wang, *Neutralino dark matter at 14 TeV and 100 TeV*, JHEP **08** (2014) 161, arXiv:1404.0682 [hep-ph]. [INSPIRE].

[249] A. Berlin, T. Lin, M. Low, and L.-T. Wang, *Neutralinos in Vector Boson Fusion at High Energy Colliders*, Phys. Rev. D **91** (2015) 115002, arXiv:1502.05044 [hep-ph]. [INSPIRE].

[250] J. L. Feng, T. Moroi, L. Randall, M. Strassler, and S.-f. Su, *Discovering supersymmetry at the Tevatron in wino LSP scenarios*, Phys. Rev. Lett. **83** (1999) 1731–1734, arXiv:hep-ph/9904250 [hep-ph]. [INSPIRE].

[251] OPAL Collaboration, G. Abbiendi et al., *Search for nearly mass degenerate charginos and*

neutralinos at LEP, EPJC **C29** (2003) 479–489, arXiv:hep-ex/0210043 [hep-ex]. [INSPIRE].

[252] J. L. Feng, J.-F. Grivaz, and J. Nachtman, *Searches for Supersymmetry at High-Energy Colliders*, Rev. Mod. Phys. **82** (2010) 699–727, arXiv:0903.0046 [hep-ex]. [Reprint: Adv. Ser. Direct. High Energy Phys. 21, 351 (2010)].

[253] ATLAS Collaboration, *The simulation principle and performance of the ATLAS fast calorimeter simulation FastCaloSim*, ATL-PHYS-PUB-2010-013, 2010. [CDS].

[254] ATLAS Collaboration, G. Aad et al., *The ATLAS simulation Infrastructure*, EPJC **70** (2010) 823, arXiv:1005.4568 [hep-ex]. [INSPIRE].

[255] ATLAS Collaboration, *Technical Design Report for the ATLAS Inner Tracker Strip Detector*, CERN-LHCC-2017-005, ATLAS-TDR-025, 2017. [CDS].

[256] ATLAS Collaboration, *Technical Design Report for the ATLAS Inner Tracker Pixel Detector*, CERN-LHCC-2017-021, ATLAS-TDR-030, 2017. [CDS].

[257] G. Cowan, K. Cranmer, E. Gross, and O. Vitells, *Asymptotic formulae for likelihood-based tests of new physics*, EPJC **7173** (2011) no. 2, 1554, arXiv:1007.1727 [physics.data-an]. [Erratum: Eur. Phys. J.C73,2501(2013)] [INSPIRE].

[258] ATLAS Collaboration, M. Aaboud et al., *Jet energy scale measurements and their systematic uncertainties in proton–proton collisions at* $\sqrt{s} = 13$ *TeV with the ATLAS detector*, Phys. Rev. D **96** (2017) 072002, arXiv:1703.09665 [hep-ex]. [INSPIRE].

[259] ATLAS Collaboration, M. Aaboud, G. Aad, B. Abbott, J. Abdallah, O. Abdinov, B. Abeloos, S. H. Abidi, O. AbouZeid, N. Abraham, and H. Abramowicz, *Jet reconstruction and performance using particle flow with the ATLAS Detector*, EPJC **77** (2017) no. 7, 466, arXiv:1703.10485 [hep-ex]. [INSPIRE].

[260] ATLAS Collaboration, G. Aad, B. Abbott, J. Abdallah, O. Abdinov, R. Aben, M. Abolins, O. AbouZeid, H. Abramowicz, H. Abreu, and R. Abreu, *Performance of pile-up mitigation techniques for jets in pp collisions at* $\sqrt{s} = 8$ *TeV using the ATLAS detector*, EPJC **76** (2016) no. 11, 581, arXiv:1510.03823 [hep-ex]. [INSPIRE].

[261] V. Silveira and A. Zee, *Scalar Phantoms*, Phys. Lett. B **161** (1985) 136–140. [INSPIRE].

[262] C. Burgess, M. Pospelov, and T. ter Veldhuis, *The Minimal model of nonbaryonic dark matter: A Singlet scalar*, Nucl. Phys. B **619** (2001) 709–728, arXiv:hep-ph/0011335 [hep-ph]. [INSPIRE].

[263] Y. G. Kim and K. Y. Lee, *The Minimal model of fermionic dark matter*, Phys. Rev. D **75** (2007) 115012, arXiv:hep-ph/0611069 [hep-ph]. [INSPIRE].

[264] K. Y. Lee, Y. G. Kim, and S. Shin, *Singlet fermionic dark matter*, JHEP **05** (2008) 100, arXiv:0803.2932 [hep-ph]. [INSPIRE].

[265] L. Lopez-Honorez, T. Schwetz, and J. Zupan, *Higgs portal, fermionic dark matter, and a Standard Model like Higgs at* 125 *GeV*, Phys. Lett. B **716** (2012) 179–185, arXiv:1203.2064 [hep-ph]. [INSPIRE].

[266] M. A. Fedderke, J.-Y. Chen, E. W. Kolb, and L.-T. Wang, *The Fermionic Dark Matter Higgs Portal: an effective field theory approach*, JHEP **08** (2014) 122, arXiv:1404.2283 [hep-ph]. [INSPIRE].

[267] K. Ghorbani, *Fermionic dark matter with pseudo-scalar Yukawa interaction*, JCAP **01** (2015) 015, arXiv:1408.4929 [hep-ph]. [INSPIRE].

[268] Y. G. Kim, K. Y. Lee, C. B. Park, and S. Shin, *Secluded singlet fermionic dark matter driven by the Fermi gamma-ray excess*, Phys. Rev. D **93** (2016) 075023, arXiv:1601.05089 [hep-ph]. [INSPIRE].

[269] Y. G. Kim, C. B. Park, and S. Shin, *Collider probes of singlet fermionic dark matter scenarios for*

the Fermi gamma-ray excess, arXiv:1809.01143 [hep-ph]. [INSPIRE].

[270] Y. G. Kim and S. Shin, *Singlet Fermionic Dark Matter explains DAMA signal*, JHEP **05** (2009) 036, arXiv:0901.2609 [hep-ph]. [INSPIRE].

[271] W. Chao and M. J. Ramsey-Musolf, *Catalysis of Electroweak Baryogenesis via Fermionic Higgs Portal Dark Matter*, arXiv:1503.00028 [hep-ph]. [INSPIRE].

[272] O. Lebedev, H. M. Lee, and Y. Mambrini, *Vector Higgs-portal dark matter and the invisible Higgs*, Phys. Lett. B **707** (2012) 570–576, arXiv:1111.4482 [hep-ph]. [INSPIRE].

[273] S. Shin, *Light neutralino dark matter in light Higgs scenario related with the CoGeNT and DAMA/LIBRA results*, PoS **IDM2010** (2011) 94, arXiv:1011.6377 [hep-ph]. [INSPIRE].

[274] ATLAS Collaboration, M. Aaboud et al., *Search for pair production of Higgs bosons in the $b\bar{b}b\bar{b}$ final state using proton-proton collisions at $\sqrt{s} = 13$ TeV with the ATLAS detector*, arXiv:1804.06174 [hep-ex]. [INSPIRE].

[275] ATLAS Collaboration, M. Aaboud, G. Aad, B. Abbott, O. Abdinov, B. Abeloos, D. K. Abhayasinghe, S. H. Abidi, O. Abouzeid, N. Abraham, and H. Abramowicz, *Search for the Higgs boson produced in association with a vector boson and decaying into two spin-zero particles in the $H \to aa \to 4b$ channel in pp collisions at $\sqrt{s} = 13$ TeV with the ATLAS detector*, JHEP **10** (2018) 31, arXiv:1806.07355 [hep-ex]. [INSPIRE].

[276] M. J. Baker and A. Thamm, *Leptonic WIMP Coannihilation and the Current Dark Matter Search Strategy*, JHEP **10** (2018) 187, arXiv:1806.07896 [hep-ph]. [INSPIRE].

[277] G. Bélanger, F. Boudjema, A. Pukhov, and A. Semenov, *micrOMEGAs4.1: two dark matter candidates*, Comput. Phys. Commun. **192** (2015) 322–329, arXiv:1407.6129 [hep-ph]. [INSPIRE].

[278] *Workshop Physics of the HL-LHC, and Perspectives at the HE-LHC*, 2018. [TWIKI].

[279] I. Hinchliffe, A. Kotwal, M. L. Mangano, C. Quigg, and L.-T. Wang, *Luminosity goals for a 100-TeV pp collider*, Int. J. Mod. Phys. A **30** (2015) no. 23, 1544002, arXiv:1504.06108 [hep-ph]. [INSPIRE].

[280] F. Staub, *SARAH*, arXiv:0806.0538 [hep-ph]. [INSPIRE].

[281] FCC Working Group Collaboration, Z. Drasal, *FCCSW Main page for documentation and resources.*, .

[282] A. J. Barr, B. Gripaios, and C. G. Lester, *Transverse masses and kinematic constraints: from the boundary to the crease*, JHEP **11** (2009) 96, arXiv:0908.3779 [hep-ph]. [INSPIRE].

[283] Particle Data Group Collaboration, C. Patrignani, K. Agashe, G. Aielli, C. Amsler, M. Antonelli, D. Asner, H. Baer, S. Banerjee, R. Barnett, and T. Basaglia, *Review of Particle Physics*, Chin. Phys. **C 40** (2016) no. 10, 100001. [INSPIRE].

[284] S. Gori, S. Jung, and L.-T. Wang, *Cornering electroweakinos at the LHC*, JHEP **10** (2013) 191, arXiv:1307.5952 [hep-ph]. [INSPIRE].

[285] P. Schwaller and J. Zurita, *Compressed electroweakino spectra at the LHC*, JHEP **03** (2014) 60, arXiv:1312.7350 [hep-ph]. [INSPIRE].

[286] J. A. Evans and J. Shelton, *Long-Lived Staus and Displaced Leptons at the LHC*, JHEP **04** (2016) 56, arXiv:1601.01326 [hep-ph]. [INSPIRE].

[287] V. V. Khoze, A. D. Plascencia, and K. Sakurai, *Simplified models of dark matter with a long-lived co-annihilation partner*, JHEP **06** (2017) 41, arXiv:1702.00750 [hep-ph]. [INSPIRE].

[288] R. Mahbubani, P. Schwaller, and J. Zurita, *Closing the window for compressed Dark Sectors with disappearing charged tracks*, JHEP **0610** (2017) 119, arXiv:1703.05327 [hep-ph]. [INSPIRE].

[289] LUX Collaboration, D. S. Akerib et al., *Improved Limits on Scattering of Weakly Interacting Massive Particles from Reanalysis of 2013 LUX Data*, Phys. Rev. Lett. **116** (2016) no. 16,

161301, arXiv:1512.03506 [astro-ph.CO]. [INSPIRE].

[290] DARWIN Collaboration, J. Aalbers et al., *DARWIN: towards the ultimate dark matter detector*, JCAP **1611** (2016) 017, arXiv:1606.07001 [astro-ph.IM]. [INSPIRE].

[291] B.-A. Gradwohl and J. A. Frieman, *Dark matter, long range forces, and large scale structure*, Astrophys. J. **398** (1992) 407–424. [INSPIRE].

[292] E. D. Carlson, M. E. Machacek, and L. J. Hall, *Self-interacting dark matter*, Astrophys. J. **398** (1992) 43–52. [INSPIRE].

[293] R. FOOT, *Mirror matter-type dark matter*, Int. J. Mod. Phys. D **13** (2004) no. 10, 2161–2192, arXiv:astro-ph/0407623 [astro-ph]. [INSPIRE].

[294] L. Ackerman, M. R. Buckley, S. M. Carroll, and M. Kamionkowski, *Dark Matter and Dark Radiation*, Phys. Rev. D **79** (2009) 277–286, arXiv:0810.5126 [hep-ph]. [INSPIRE].

[295] J. Fan, A. Katz, L. Randall, and M. Reece, *Dark-Disk Universe*, Phys. Rev. Lett. **110** (2013) no. 21, arXiv:1303.3271 [hep-ph]. [INSPIRE].

[296] P. Agrawal, F.-Y. Cyr-Racine, L. Randall, and J. Scholtz, *Make Dark Matter Charged Again*, JCAP **05** (2017) no. 05, 22, arXiv:1610.04611 [hep-ph]. [INSPIRE].

[297] R. Foot and S. Vagnozzi, *Dissipative hidden sector dark matter*, Phys. Rev. D **91** (2015) 023512, arXiv:1409.7174 [hep-ph]. [INSPIRE].

[298] M. Heikinheimo, M. Raidal, C. Spethmann, and H. Veermäe, *Dark matter self-interactions via collisionless shocks in cluster mergers*, Phys. Lett. B **749** (2015) 236–241, arXiv:1504.04371 [hep-ph]. [INSPIRE].

[299] J. Alexander, M. Battaglieri, B. Echenard, R. Essig, M. Graham, E. Izaguirre, J. Jaros, G. Krnjaic, J. Mardon, and D. Morrissey, *Dark Sectors 2016 Workshop: Community Report*, arXiv:1608.08632 [hep-ph]. [INSPIRE].

[300] LHCb Collaboration, R. Aaij, B. Adeva, M. Adinolfi, Z. Ajaltouni, S. Akar, J. Albrecht, F. Alessio, M. Alexander, A. Alfonso Albero, and S. Ali, *Search for Dark Photons Produced in* 13 *TeV pp Collisions*, Phys. Rev. Lett. **120** (2018), arXiv:1710.02867 [hep-ex]. [INSPIRE].

[301] P. Ilten, J. Thaler, M. Williams, and W. Xue, *Dark photons from charm mesons at LHCb*, Phys. Rev. D **92** (2015) 115017, arXiv:1509.06765 [hep-ph]. [INSPIRE].

[302] P. Ilten, Y. Soreq, J. Thaler, M. Williams, and W. Xue, *Proposed Inclusive Dark Photon Search at LHCb*, Phys. Rev. Lett. **116** (2016) no. 25, arXiv:1603.08926 [hep-ph]. [INSPIRE].

[303] P. Ilten, Y. Soreq, M. Williams, and W. Xue, *Serendipity in dark photon searches*, JHEP **06** (2018) 4, arXiv:1801.04847 [hep-ph]. [INSPIRE].

[304] M. Baumgart, C. Cheung, J. T. Ruderman, L.-T. Wang, and I. Yavin, *Non-Abelian Dark Sectors and Their Collider Signatures*, JHEP **04** (2009) 14, arXiv:0901.0283 [hep-ph]. [INSPIRE].

[305] A. Falkowski, J. T. Ruderman, T. Volansky, and J. Zupan, *Hidden Higgs Decaying to Lepton Jets*, JHEP **05** (2010) 77, arXiv:1002.2952 [hep-ph]. [INSPIRE].

[306] CMS Collaboration, *Search sensitivity for dark photons decaying to displaced muons with CMS at the high-luminosity LHC*, CMS-PAS-FTR-18-002, 2018. [INSPIRE].

[307] CMS Collaboration, *Muon Reconstruction and Identification Improvements for Run-2 and First Results with 2015 Run Data*, CMS Detector Performance Note CMS-DP-2015-015, 2015. [CDS].

[308] CMS Collaboration, *A search for pair production of new light bosons decaying into muons at* $\sqrt{s} = 13$ *TeV*, CMS-PAS-HIG-18-003, 2018. [INSPIRE].

[309] CMS Collaboration, V. Khachatryan, A. M. Sirunyan, A. Tumasyan, W. Adam, E. Asilar, T. Bergauer, J. Brandstetter, E. Brondolin, M. Dragicevic, and J. Ero", *Searches for invisible decays of the Higgs boson in pp collisions at* $\sqrt{s} = 7$, 8, *and* 13 *TeV*, JHEP **02** (2017) 135, arXiv:1610.09218 [hep-ex]. [INSPIRE].

[310] LHC Higgs Cross Section Working Group Collaboration, S. Dittmaier, C. Mariotti, G. Passarino, R. Tanaka, J. Baglio, P. Bolzoni, R. Boughezal, O. Brein, C. Collins-Tooth, and S. Dawson, *Handbook of LHC Higgs Cross Sections: 1. Inclusive Observables*, arXiv:1101.0593 [hep-ph]. [INSPIRE].

[311] ATLAS Collaboration, *Search prospects for dark-photons decaying to displaced collimated jets of muons at HL-LHC*, ATL-PHYS-PUB-2019-002, Geneva, Jan, 2019. [CDS].

[312] E. Gabrielli and M. Raidal, *Exponentially spread dynamical Yukawa couplings from nonperturbative chiral symmetry breaking in the dark sector*, Phys. Rev. D **89** (2014) 015008, arXiv:1310.1090 [hep-ph]. [INSPIRE].

[313] E. Gabrielli, L. Marzola, and M. Raidal, *Radiative Yukawa Couplings in the Simplest Left-Right Symmetric Model*, Phys. Rev. D **95** (2017) 035005, arXiv:1611.00009 [hep-ph]. [INSPIRE].

[314] B. Holdom, *Two $U(1)$'s and Epsilon Charge Shifts*, Phys. Lett. B **166** (1986) 196–198. [INSPIRE].

[315] E. Gabrielli, M. Heikinheimo, B. Mele, and M. Raidal, *Dark photons and resonant monophoton signatures in Higgs boson decays at the LHC*, Phys. Rev. D **90** (2014) 055032, arXiv:1405.5196 [hep-ph]. [INSPIRE].

[316] S. Biswas, E. Gabrielli, M. Heikinheimo, and B. Mele, *Dark-photon searches via ZH production at e^+e^- colliders*, Phys. Rev. D **96** (2017) 055012, arXiv:1703.00402 [hep-ph]. [INSPIRE].

[317] S. Biswas, E. Gabrielli, M. Heikinheimo, and B. Mele, *Dark-Photon searches via Higgs-boson production at the LHC*, Phys. Rev. D **93** (2016) 093011, arXiv:1603.01377 [hep-ph]. [INSPIRE].

[318] CMS Collaboration, V. Khachatryan, A. M. Sirunyan, A. Tumasyan, W. Adam, E. Asilar, T. Bergauer, J. Brandstetter, E. Brondolin, M. Dragicevic, and J. Ero", *Search for exotic decays of a Higgs boson into undetectable particles and one or more photons*, Phys. Lett. B **753** (2016) 363–388, arXiv:1507.00359 [hep-ex]. [INSPIRE].

[319] V. V. Gligorov, S. Knapen, B. Nachman, M. Papucci, and D. J. Robinson, *Leveraging the ALICE/L3 cavern for long-lived exotics*, arXiv:1810.03636 [hep-ph]. [INSPIRE].

[320] V. V. Gligorov, S. Knapen, M. Papucci, and D. J. Robinson, *Searching for Long-lived Particles: A Compact Detector for Exotics at LHCb*, Phys. Rev. D **97** (2018) 015023, arXiv:1708.09395 [hep-ph]. [INSPIRE].

[321] J. L. Feng, I. Galon, F. Kling, and S. Trojanowski, *ForwArd Search ExpeRiment at the LHC*, Phys. Rev. D **97** (2018) 035001, arXiv:1708.09389 [hep-ph]. [INSPIRE].

[322] J. L. Feng, I. Galon, F. Kling, and S. Trojanowski, *Dark Higgs bosons at the ForwArd Search ExpeRiment*, Phys. Rev. D **97** (2018) 055034, arXiv:1710.09387 [hep-ph]. [INSPIRE].

[323] F. Kling and S. Trojanowski, *Heavy Neutral Leptons at FASER*, Phys. Rev. D **97** (2018) 095016, arXiv:1801.08947 [hep-ph]. [INSPIRE].

[324] A. Haas, C. S. Hill, E. Izaguirre, and I. Yavin, *Looking for milli-charged particles with a new experiment at the LHC*, Phys. Lett. B **746** (2015) 117–120, arXiv:1410.6816 [hep-ph]. [INSPIRE].

[325] A. Ball, J. Brooke, C. Campagnari, A. De Roeck, B. Francis, M. Gastal, F. Golf, J. Goldstein, A. Haas, and C. S. Hill, *A Letter of Intent to Install a milli-charged Particle Detector at LHC P5*, arXiv:1607.04669 [physics.ins-det]. [INSPIRE].

[326] J. P. Chou, D. Curtin, and H. Lubatti, *New Detectors to Explore the Lifetime Frontier*, Phys. Lett. B **767** (2017) 29–36, arXiv:1606.06298 [hep-ph]. [INSPIRE].

[327] D. Curtin, M. Drewes, M. McCullough, P. Meade, R. Mohapatra, J. Shelton, B. Shuve, E. Accomando, C. Alpigiani, and S. Antusch, *Long-Lived Particles at the Energy Frontier: The MATHUSLA Physics Case*, arXiv:1806.07396 [hep-ph]. [INSPIRE].

[328] S. Alekhin, W. Altmannshofer, T. Asaka, B. Batell, F. Bezrukov, K. Bondarenko, A. Boyarsky, K.-Y. Choi, C. Corral, and N. Craig, *A facility to Search for Hidden Particles at the CERN SPS: the SHiP physics case*, Rept. Prog. Phys. **79** (2016), arXiv:1504.04855 [hep-ph]. [INSPIRE].

[329] SHiP Collaboration, M. Anelli, S. Aoki, G. Arduini, J. Back, A. Bagulya, W. Baldini, A. Baranov, G. Barker, S. Barsuk, and M. Battistin, *A facility to Search for Hidden Particles (SHiP) at the CERN SPS*, arXiv:1504.04956 [physics.ins-det]. [INSPIRE].

[330] D. Curtin, K. Deshpande, O. Fischer, and J. Zurita, *New Physics Opportunities for Long-Lived Particles at Electron-Proton Colliders*, JHEP **07** (2018) 24, arXiv:1712.07135 [hep-ph]. [INSPIRE].

[331] ATLAS Collaboration, *Search for long-lived charginos based on a disappearing-track signature in pp collisions at* $\sqrt{s} = 13$ *TeV with the ATLAS detector*, ATLAS-CONF-2017-017, 2017. [INSPIRE].

[332] ATLAS Collaboration, M. Aaboud, G. Aad, B. Abbott, O. Abdinov, B. Abeloos, S. H. Abidi, O. AbouZeid, N. Abraham, H. Abramowicz, and H. Abreu, *Search for long-lived charginos based on a disappearing-track signature in pp collisions at* $\sqrt{s} = 13$ *TeV with the ATLAS detector*, JHEP **06** (2018) 22, arXiv:1712.02118 [hep-ex]. [INSPIRE].

[333] ATLAS Collaboration, M. Aaboud et al., *Search for long-lived, massive particles in events with displaced vertices and missing transverse momentum in* $\sqrt{s} = 13$ *TeV pp collisions with the ATLAS detector*, Phys. Rev. D **97** (2018) 052012, arXiv:1710.04901 [hep-ex]. [INSPIRE].

[334] CMS Collaboration, A. M. Sirunyan, A. Tumasyan, W. Adam, F. Ambrogi, E. Asilar, T. Bergauer, J. Brandstetter, E. Brondolin, M. Dragicevic, and J. Ero", *Search for new long-lived particles at* $\sqrt{s} = 13$ *TeV*, Phys. Lett. B **780** (2018) 432–454, arXiv:1711.09120 [hep-ex]. [INSPIRE].

[335] CMS Collaboration, A. M. Sirunyan, A. Tumasyan, W. Adam, F. Ambrogi, E. Asilar, T. Bergauer, J. Brandstetter, M. Dragicevic, J. Ero", and A. Escalante Del Valle, *Search for long-lived particles decaying into displaced jets in proton-proton collisions at* $\sqrt{s} = 13$ *TeV*, arXiv:1811.07991 [hep-ex]. [INSPIRE].

[336] ATLAS Collaboration, *Sensitivity of the ATLAS experiment to long-lived particles with a displaced vertex and* E_T^{miss} *signature at the HL-LHC*, ATL-PHYS-PUB-2018-033, 2018. [CDS].

[337] G. Giudice and A. Romanino, *Split supersymmetry*, Nucl. Phys. B **699706** (2004) 65–89, arXiv:hep-ph/0406088 [hep-ph]. [INSPIRE].

[338] ATLAS Collaboration, *Further ATLAS tunes of PYTHIA6 and Pythia 8*, ATL-PHYS-PUB-2011-014, ATL-COM-PHYS-2011-1507, 2011. [INSPIRE].

[339] HL-LHC Physics WG 3, *Gluino pair cross-sections*, 2018. [TWIKI].

[340] ATLAS Collaboration, *HepData record for Search for long-lived, massive particles in events with displaced vertices and missing transverse momentum in* $\sqrt{s} = 13$ *TeV pp collisions with the ATLAS detector*, 2017. [HEPDATA].

[341] CMS Collaboration, *The Phase-2 Upgrade of the CMS Muon Detectors*, CERN-LHCC-2017-012, CMS-TDR-016, 2017. [CDS].

[342] L. Lee, C. Ohm, A. Soffer, and T.-T. Yu, *Collider Searches for Long-Lived Particles Beyond the Standard Model*, arXiv:1810.12602 [hep-ph]. [INSPIRE].

[343] LHCb Collaboration, *Prospects for searches for long-lived particles after the LHCb detector upgrades*, LHCb-CONF-2018-006, CERN-LHCb-CONF-2018-006, 2018. [INSPIRE].

[344] LHCb Collaboration, R. Aaij, B. Adeva, M. Adinolfi, Z. Ajaltouni, S. Akar, J. Albrecht, F. Alessio, M. Alexander, S. Ali, and G. Alkhazov, *Search for massive long-lived particles decaying semileptonically in the LHCb detector*, EPJC **77** (2017) no. 4, 224, arXiv:1612.00945 [hep-ex]. [INSPIRE].

[345] LHC Higgs Cross Section Working Group Collaboration, D. de Florian, C. Grojean, F. Maltoni, C. Mariotti, A. Nikitenko, M. Pieri, P. Savard, M. Schumacher, R. Tanaka, and R. Aggleton, *Handbook of LHC Higgs Cross Sections: 4. Deciphering the Nature of the Higgs Sector*, CERN Yellow Report **002** (2017), arXiv:1610.07922 [hep-ph]. [INSPIRE].

[346] M. J. Strassler and K. M. Zurek, *Echoes of a hidden valley at hadron colliders*, Phys. Lett. B **651** (2007) 374–379, arXiv:hep-ph/0604261 [hep-ph]. [INSPIRE].

[347] A. Pierce, B. Shakya, Y. Tsai, and Y. Zhao, *Searching for confining hidden valleys at LHCb, ATLAS, and CMS*, Phys. Rev. D **97** (2018) 095033, arXiv:1708.05389 [hep-ph]. [INSPIRE].

[348] LHCb Collaboration, R. Aaij, B. Adeva, M. Adinolfi, Z. Ajaltouni, S. Akar, J. Albrecht, F. Alessio, M. Alexander, S. Ali, and G. Alkhazov, *Updated search for long-lived particles decaying to jet pairs*, EPJC **77** (2017) no. 12, 812, arXiv:1705.07332 [hep-ex]. [INSPIRE].

[349] P. Bokan, *Reconstructing low mass boosted $A \to bb$ at LHCb. A: scalar particle in low mass region.*, . [CDS].

[350] CMS Collaboration, V. Khachatryan, A. M. Sirunyan, A. Tumasyan, W. Adam, T. Bergauer, M. Dragicevic, J. Ero", M. Friedl, R. Fruehwirth, and V. M. Ghete, *Constraints on the pMSSM, AMSB model and on other models from the search for long-lived charged particles in proton-proton collisions at $\sqrt{s} = 8$ TeV*, EPJC **75** (2015) no. 7, 325, arXiv:1502.02522 [hep-ex]. [INSPIRE].

[351] CMS Collaboration, *Search for heavy stable charged particles with $12.9\ fb^{-1}$ of 2016 data*, CMS-PAS-EXO-16-036, 2016. [INSPIRE].

[352] CMS Collaboration, *The Phase-2 Upgrade of the CMS Tracker*, CERN-LHCC-2017-009, CMS-TDR-014, 2017. [CDS].

[353] CMS Collaboration, *Technical proposal for a MIP timing detector in the CMS experiment Phase-2 upgrade*, CERN-LHCC-2017-027, LHCC-P-009, 2017. [CDS].

[354] P. Meade, M. Reece, and D. Shih, *Long-Lived Neutralino NLSPs*, JHEP **10** (2010) 67, arXiv:1006.4575 [hep-ph]. [INSPIRE].

[355] CMS Collaboration, S. Chatrchyan, V. Khachatryan, A. M. Sirunyan, A. Tumasyan, W. Adam, T. Bergauer, M. Dragicevic, J. Ero", C. Fabjan, and M. Friedl, *Description and performance of track and primary-vertex reconstruction with the CMS tracker*, JINST **9** (2014), arXiv:1405.6569 [physics.ins-det]. [INSPIRE].

[356] CMS Collaboration, S. Chatrchyan, V. Khachatryan, A. M. Sirunyan, A. Tumasyan, W. Adam, E. Aguilo, T. Bergauer, M. Dragicevic, J. Ero", and C. Fabjan, *Search for long-lived particles decaying to photons and missing energy in proton-proton collisions at $\sqrt{s} = 7$ TeV*, Phys. Lett. B **722** (2013) 273–294, arXiv:1212.1838 [hep-ex]. [INSPIRE].

[357] ATLAS Collaboration, *Technical Design Report for the ATLAS LAr Calorimeter Phase-II Upgrade*, CERN-LHCC-2017-018, ATLAS-TDR-027, 2017. [CDS].

[358] R. Alonso, M. Dhen, M. B. Gavela, and T. Hambye, *Muon conversion to electron in nuclei in type-I seesaw models*, JHEP **01** (2013) 118, arXiv:1209.2679 [hep-ph]. [INSPIRE].

[359] CMS Collaboration, V. Khachatryan et al., *Search for heavy Majorana neutrinos in $e^{\pm}e^{\pm}$+ jets and $e^{\pm}\mu^{\pm}$+ jets events in proton-proton collisions at $\sqrt{s} = 8$ TeV*, JHEP **04** (2016) 169, arXiv:1603.02248 [hep-ex]. [INSPIRE].

[360] A. Atre, T. Han, S. Pascoli, and B. Zhang, *The Search for Heavy Majorana Neutrinos*, JHEP **05** (2009) 30, arXiv:0901.3589 [hep-ph]. [INSPIRE].

[361] Y. Cai, T. Han, T. Li, and R. Ruiz, *Lepton Number Violation: Seesaw Models and Their Collider Tests*, Front. in Phys. **6** (2018) 40, arXiv:1711.02180 [hep-ph]. [INSPIRE].

[362] S. Antusch, E. Cazzato, and O. Fischer, *Sterile neutrino searches at future e^-e^+, pp, and e^-p colliders*, Int. J. Mod. Phys. A **32** (2017) no. 14, 1750078, arXiv:1612.02728 [hep-ph].

[INSPIRE].

[363] C. Weiland, *Effects of fermionic singlet neutrinos on high- and low-energy observables*, Master's thesis, 2013. [INSPIRE].

[364] R. E. Ruiz, *Hadron Collider Tests of Neutrino Mass-Generating Mechanisms*, Master's thesis, 2015. [INSPIRE].

[365] X. Marcano, *Lepton flavor violation from low scale seesaw neutrinos with masses reachable at the LHC*, Master's thesis, 2017. [INSPIRE].

[366] J. Kersten and A. Y. Smirnov, *Right-Handed Neutrinos at CERN LHC and the Mechanism of Neutrino Mass Generation*, Phys. Rev. D **76** (2007) 073005, arXiv:0705.3221 [hep-ph]. [INSPIRE].

[367] *Equivalence between massless neutrinos and lepton number conservation in fermionic singlet extensions of the Standard Model*, arXiv:1712.07611 [hep-ph]. [INSPIRE].

[368] R. Ruiz, M. Spannowsky, and P. Waite, *Heavy neutrinos from gluon fusion*, Phys. Rev. D **96** (2017) 055042, arXiv:1706.02298 [hep-ph]. [INSPIRE].

[369] C. Degrande, O. Mattelaer, R. Ruiz, and J. Turner, *Fully-Automated Precision Predictions for Heavy Neutrino Production Mechanisms at Hadron Colliders*, Phys. Rev. D **94** (2016) 053002, arXiv:1602.06957 [hep-ph]. [INSPIRE].

[370] D. Alva, T. Han, and R. Ruiz, *Heavy Majorana neutrinos from $W\gamma$ fusion at hadron colliders*, JHEP **02** (2015) 72, arXiv:1411.7305 [hep-ph]. [INSPIRE].

[371] A. Hessler, A. Ibarra, E. Molinaro, and S. Vogl, *Impact of the Higgs boson on the production of exotic particles at the LHC*, Phys. Rev. D **91** (2015) 115004, arXiv:1408.0983 [hep-ph]. [INSPIRE].

[372] S. Pascoli, R. Ruiz, and C. Weiland, *Safe Jet Vetoes*, Phys. Lett. B **786** (2018) 106–113, arXiv:1805.09335 [hep-ph]. [INSPIRE].

[373] S. Pascoli, R. Ruiz, and C. Weiland, *Heavy Neutrinos with Dynamic Jet Vetoes: Multilepton Searches at $\sqrt{s} = 14,\ 27,$ and 100 TeV*, arXiv:1812.08750 [hep-ph].

[374] E. Fernandez-Martinez, J. Hernandez-Garcia, and J. Lopez-Pavon, *Global constraints on heavy neutrino mixing*, JHEP **08** (2016) 33, arXiv:1605.08774 [hep-ph]. [INSPIRE].

[375] E. Arganda, M. Herrero, X. Marcano, and C. Weiland, *Exotic $\mu\tau jj$ events from heavy ISS neutrinos at the LHC*, Phys. Lett. B **752** (2016) 46–50, arXiv:1508.05074 [hep-ph]. [INSPIRE].

[376] MEG Collaboration, J. Adam, X. Bai, A. Baldini, E. Baracchini, C. Bemporad, G. Boca, P. Cattaneo, G. Cavoto, F. Cei, and C. Cerri, *New constraint on the existence of the $\mu^+ \to e^+\gamma$ decay*, Phys. Rev. Lett. **110** (2013), arXiv:1303.0754 [hep-ex]. [INSPIRE].

[377] E. Arganda, M. Herrero, X. Marcano, and C. Weiland, *Imprints of massive inverse seesaw model neutrinos in lepton flavor violating Higgs boson decays*, Phys. Rev. D **91** (2015) 015001, arXiv:1405.4300 [hep-ph]. [INSPIRE].

[378] *Lepton Number Violation at Colliders from Kinematically Inaccessible Gauge Bosons*, EPJC **77** (2017) no. 6, 375, arXiv:1703.04669 [hep-ph]. [INSPIRE].

[379] W.-Y. Keung and G. Senjanović, *Majorana Neutrinos and the Production of the Right-handed Charged Gauge Boson*, Phys. Rev. Lett. **50** (1983) no. 19, 1427. [INSPIRE].

[380] M. Mitra, R. Ruiz, D. J. Scott, and M. Spannowsky, *Neutrino Jets from High-Mass W_R Gauge Bosons in TeV-Scale Left-Right Symmetric Models*, Phys. Rev. D **94** (2016) 095016, arXiv:1607.03504 [hep-ph]. [INSPIRE].

[381] *Automated Neutrino Jet and Top Jet Predictions at Next-to-Leading-Order with Parton Shower Matching in Effective Left-Right Symmetric Models*, arXiv:1610.08985 [hep-ph]. [INSPIRE].

[382] B. Fuks and R. Ruiz, *A comprehensive framework for studying W' and Z' bosons at hadron*

colliders with automated jet veto resummation, JHEP **05** (2017) 32, arXiv:1701.05263 [hep-ph]. [INSPIRE].

[383] T. Han, I. Lewis, R. Ruiz, and Z. guo Si, *Lepton Number Violation and W' Chiral Couplings at the LHC*, Phys. Rev. D **8787** (2013) 035011, arXiv:1211.6447 [hep-ph]. [INSPIRE].

[384] A. Ferrari, J. Collot, M.-L. Andrieux, B. Belhorma, P. de Saintignon, J.-Y. Hostachy, P. Martin, and M. Wielers, *Sensitivity study for new gauge bosons and right-handed Majorana neutrinos in pp collisions at $\sqrt{s} = 14$ TeV*, Phys. Rev. D **62** (2000) 013001. [INSPIRE].

[385] P. F. Pérez, T. Han, G. Huang, T. Li, and K. Wang, *Neutrino Masses and the CERN LHC: Testing Type II Seesaw*, Phys. Rev. D **78** (2008) 015018, arXiv:0805.3536 [hep-ph]. [INSPIRE].

[386] T. Li, *Type II Seesaw and tau lepton at the HL-LHC, HE-LHC and FCC-hh*, JHEP **09** (2018) 79, arXiv:1802.00945 [hep-ph]. [INSPIRE].

[387] H. Sugiyama, K. Tsumura, and H. Yokoya, *Discrimination of models including doubly charged scalar bosons by using tau lepton decay distributions*, Phys. Lett. B **717** (2012) 229–234, arXiv:1207.0179 [hep-ph]. [INSPIRE].

[388] R. Ruiz, *QCD Corrections to Pair Production of Type III Seesaw Leptons at Hadron Colliders*, JHEP **12** (2015) 165, arXiv:1509.05416 [hep-ph]. [INSPIRE].

[389] A. Arhrib, B. Bajc, D. K. Ghosh, T. Han, G.-Y. Huang, I. Puljak, and G. Senjanović, *Collider Signatures for Heavy Lepton Triplet in Type I+III Seesaw*, Phys. Rev. D **82** (2010) 053004, arXiv:0904.2390 [hep-ph]. [INSPIRE].

[390] T. Li and X.-G. He, *Neutrino Masses and Heavy Triplet Leptons at the LHC: Testability of Type III Seesaw*, Phys. Rev. D **80** (2009) 093003, arXiv:0907.4193 [hep-ph]. [INSPIRE].

[391] E. Eichten, K. D. Lane, and M. E. Peskin, *New Tests for Quark and Lepton Substructure*, Phys. Rev. Lett. **50** (1983) 811–814. [INSPIRE].

[392] M. E. Peskin, *Substructure and strong interactions at the TeV scale*, SLAC-PUB-3852, 1985. [INSPIRE].

[393] N. Cabibbo, L. Maiani, and Y. Srivastava, *Anomalous Z Decays: Excited Leptons?*, Phys. Lett. B **139** (1984) 459–463. [INSPIRE].

[394] U. Baur, M. Spira, and P. M. Zerwas, *Excited quark and lepton production at hadron colliders*, Phys. Rev. D **42** (1990) 815–824. [INSPIRE].

[395] O. Panella, R. Leonardi, G. Pancheri, Y. Srivastava, M. Narain, and U. Heintz, *Production of exotic composite quarks at the LHC*, Phys. Rev. D **96** (2017) 075034, arXiv:1703.06913 [hep-ph]. [INSPIRE].

[396] S. Biondini, O. Panella, G. Pancheri, Y. N. Srivastava, and L. Fanò, *Phenomenology of excited doubly charged heavy leptons at LHC*, Phys. Rev. D **85** (2012) 095018, arXiv:1201.3764 [hep-ph]. [INSPIRE].

[397] R. Leonardi, O. Panella, and L. Fanò, *Doubly charged heavy leptons at LHC via contact interactions*, Phys. Rev. D **90** (2014) 035001, arXiv:1405.3911 [hep-ph]. [INSPIRE].

[398] S. Biondini and O. Panella, *Leptogenesis and composite heavy neutrinos with gauge mediated interactions*, EPJC **77** (2017) no. 9, 644, 1707.00844. [INSPIRE].

[399] ATLAS Collaboration, G. Aad et al., *Search for excited electrons and muons in $\sqrt{s} = 8$ TeV proton-proton collisions with the ATLAS detector*, New J. Phys. **15** (2013) 093011, arXiv:1308.1364 [hep-ex]. [INSPIRE].

[400] CMS Collaboration, V. Khachatryan et al., *Search for excited leptons in proton-proton collisions at $\sqrt{s} = 8$ TeV*, JHEP **03** (2016) 125, arXiv:1511.01407 [hep-ex]. [INSPIRE].

[401] R. Leonardi, L. Alunni, F. Romeo, L. Fanò, and O. Panella, *Hunting for heavy composite Majorana neutrinos at the LHC*, EPJC **76** (2016) no. 11, 593, arXiv:1510.07988 [hep-ph]. [INSPIRE].

[402] CMS Collaboration, *Search for heavy composite Majorana neutrinos produced in association with a lepton and decaying into a same-flavour lepton plus two quarks at $\sqrt{s} = 13$ TeV with the CMS detector*, CMS-PAS-EXO-16-026, 2016. [INSPIRE].

[403] CMS Collaboration, A. Sirunyan, A. Tumasyan, W. Adam, F. Ambrogi, E. Asilar, T. Bergauer, J. Brandstetter, E. Brondolin, M. Dragicevic, and J. Ero", *Search for a heavy composite Majorana neutrino in the final state with two leptons and two quarks at $\sqrt{s} = 13$ TeV*, Phys. Lett. B **775** (2017) 315–337, arXiv:1706.08578 [hep-ex]. [INSPIRE].

[404] *Like-sign dileptons with mirror type composite neutrinos at the HL-LHC*, arXiv:1811.00374 [hep-ph]. [INSPIRE].

[405] E. Takasugi, *Composite neutrinos and double beta decay*, Prog. Theor. Phys. **94** (1995) no. 6, 1097–1104, arXiv:hep-ph/9506379 [hep-ph]. [INSPIRE].

[406] Particle Data Group Collaboration, K. A. Olive et al., *Review of Particle Physics*, Chin. Phys. **C 38** (2014) no. 9, 090001. [INSPIRE].

[407] A. Belyaev, N. D. Christensen, and A. Pukhov, *CalcHEP 3.4 for collider physics within and beyond the Standard Model*, Comput. Phys. Commun. **184** (2013) no. 7, 1729–1769, arXiv:1207.6082 [hep-ph]. [INSPIRE].

[408] P. S. B. Dev and R. Mohapatra, *Unified explanation of the $eejj$, diboson and dijet resonances at the LHC*, Phys. Rev. Lett. **115** (2015) no. 18, arXiv:1508.02277 [hep-ph]. [INSPIRE].

[409] CMS Collaboration, *Search for heavy composite Majorana neutrinos at the High-Luminosity and the High-Energy LHC*, CMS-PAS-FTR-18-006, 2018. [INSPIRE].

[410] D. Bertolini, P. Harris, M. Low, and N. Tran, *Pileup Per Particle Identification*, JHEP **10** (2014) 59, arXiv:1407.6013 [hep-ph]. [INSPIRE].

[411] *Recommendations for Systematic Uncertainties HL-LHC*, 2018. [TWIKI].

[412] M. Krämer, T. Plehn, M. Spira, and P. M. Zerwas, *Pair production of scalar leptoquarks at the CERN LHC*, Phys. Rev. D **71** (2005) 057503, arXiv:hep-ph/0411038 [hep-ph]. [INSPIRE].

[413] CMS Collaboration, *Projection of searches for pair production of scalar leptoquarks decaying to a top quark and a charged lepton at the HL-LHC*, CMS-PAS-FTR-18-008, 2018. [INSPIRE].

[414] CMS Collaboration, A. M. Sirunyan, A. Tumasyan, W. Adam, F. Ambrogi, E. Asilar, T. Bergauer, J. Brandstetter, M. Dragicevic, J. Ero", and A. Escalante Del Valle, *Search for leptoquarks coupled to third-generation quarks in proton-proton collisions at $\sqrt{s} = 13$ TeV*, Phys. Rev. Lett. **121** (2018) no. 24, 241802, arXiv:1809.05558 [hep-ex]. [INSPIRE].

[415] CMS Collaboration, A. M. Sirunyan, A. Tumasyan, W. Adam, F. Ambrogi, E. Asilar, T. Bergauer, J. Brandstetter, E. Brondolin, M. Dragicevic, and J. Ero", *Search for third-generation scalar leptoquarks decaying to a top quark and a τ lepton at $\sqrt{s} = 13$ TeV*, EPJC **78** (2018) 707, arXiv:1803.02864 [hep-ex]. [INSPIRE].

[416] G. D'Amico, M. Nardecchia, P. Panci, F. Sannino, A. Strumia, R. Torre, and A. Urbano, *Flavour anomalies after the R_{K^*} measurement*, JHEP **09** (2017) 10, arXiv:1704.05438 [hep-ph]. [INSPIRE].

[417] G. Hiller and I. Nišandžić, *R_K and R_{K^*} beyond the standard model*, Phys. Rev. D **96** (2017) 035003, arXiv:1704.05444 [hep-ph]. [INSPIRE].

[418] B. Capdevila, A. Crivellin, S. Descotes-Genon, J. Matias, and J. Virto, *Patterns of New Physics in $b \to s\ell^+\ell^-$ transitions in the light of recent data*, JHEP **01** (2018) 93, arXiv:1704.05340 [hep-ph]. [INSPIRE].

[419] ATLAS Collaboration, M. Aaboud, G. Aad, B. Abbott, J. Abdallah, O. Abdinov, B. Abeloos, R. Aben, O. AbouZeid, N. Abraham, and H. Abramowicz, *Search for high-mass new phenomena in the dilepton final state using proton-proton collisions at $\sqrt{s} = 13$ TeV with the ATLAS detector*, Phys. Lett. B **761** (2016) 372–392, arXiv:1607.03669 [hep-ex]. [INSPIRE].

[420] B. C. Allanach, B. Gripaios, and T. You, *The case for future hadron colliders from $B \to K^{(*)}\mu^+\mu^-$ decays*, JHEP **03** (2018) 21, arXiv:1710.06363 [hep-ph]. [INSPIRE].

[421] BaBar Collaboration, J. Lees, V. Poireau, V. Tisserand, J. Garra Tico, E. Grauges, A. Palano, G. Eigen, B. Stugu, D. N. Brown, and L. Kerth, *Evidence for an excess of $\bar{B} \to D^{(*)}\tau^-\bar{\nu}_\tau$ decays*, Phys. Rev. Lett. **109** (2012), arXiv:1205.5442 [hep-ex]. [INSPIRE].

[422] BaBar Collaboration, J. Lees, V. Poireau, V. Tisserand, E. Grauges, A. Palano, G. Eigen, B. Stugu, D. N. Brown, L. Kerth, and Y. Kolomensky, *Measurement of an Excess of $\bar{B} \to D^{(*)}\tau^-\bar{\nu}_\tau$ Decays and Implications for Charged Higgs Bosons*, Phys. Rev. D **88** (2013) 072012, arXiv:1303.0571 [hep-ex]. [INSPIRE].

[423] Belle Collaboration, A. Matyja, M. Rozanska, I. Adachi, H. Aihara, V. Aulchenko, T. Aushev, S. Bahinipati, A. Bakich, V. Balagura, and E. Barberio, *Observation of $B^0 \to D^*\tau^+\nu_\tau$ decay at Belle*, Phys. Rev. Lett. **99** (2007), arXiv:0706.4429 [hep-ex]. [INSPIRE].

[424] Belle Collaboration, A. Bozek, M. Rozanska, I. Adachi, H. Aihara, K. Arinstein, V. Aulchenko, T. Aushev, T. Aziz, A. Bakich, and V. Bhardwaj, *Observation of $B^+ \to \bar{D}^{*0}\tau^+\nu_\tau$ and Evidence for $B^+ \to \bar{D}^0\tau^+\nu_\tau$ at Belle*, Phys. Rev. D **82** (2010) 072005, arXiv:1005.2302 [hep-ex]. [INSPIRE].

[425] Belle Collaboration, M. Huschle, T. Kuhr, M. Heck, P. Goldenzweig, A. Abdesselam, I. Adachi, K. Adamczyk, H. Aihara, S. Said, and K. Arinstein, *Measurement of the branching ratio of $\bar{B} \to D^{(*)}\tau^-\bar{\nu}_\tau$ relative to $\bar{B} \to D^{(*)}\ell^-\bar{\nu}_\ell$ decays with hadronic tagging at Belle*, Phys. Rev. D **92** (2015) 072014, arXiv:1507.03233 [hep-ex]. [INSPIRE].

[426] Belle Collaboration, Y. Sato, T. Iijima, K. Adamczyk, H. Aihara, D. Asner, H. Atmacan, T. Aushev, R. Ayad, T. Aziz, and V. Babu, *Measurement of the branching ratio of $\bar{B}^0 \to D^{*+}\tau^-\bar{\nu}_\tau$ relative to $\bar{B}^0 \to D^{*+}\ell^-\bar{\nu}_\ell$ decays with a semileptonic tagging method*, Phys. Rev. D **94** (2016) 072007, arXiv:1607.07923 [hep-ex]. [INSPIRE].

[427] Belle Collaboration, S. Hirose, T. Iijima, I. Adachi, K. Adamczyk, H. Aihara, S. Al Said, D. Asner, H. Atmacan, V. Aulchenko, and T. Aushev, *Measurement of the τ lepton polarization and $R(D^*)$ in the decay $\bar{B} \to D^*\tau^-\bar{\nu}_\tau$*, Phys. Rev. Lett. **118** (2017), arXiv:1612.00529 [hep-ex]. [INSPIRE].

[428] Belle Collaboration, S. Hirose, T. Iijima, I. Adachi, K. Adamczyk, H. Aihara, S. Al Said, D. Asner, H. Atmacan, T. Aushev, and R. Ayad, *Measurement of the τ lepton polarization and R_{D^*} in the decay $\bar{B} \to D^*\tau^-\bar{\nu}_\tau$ with one-prong hadronic τ decays at Belle*, Phys. Rev. D **97** (2018) 012004, arXiv:1709.00129 [hep-ex]. [INSPIRE].

[429] LHCb Collaboration, R. Aaij, B. Adeva, M. Adinolfi, A. Affolder, Z. Ajaltouni, S. Akar, J. Albrecht, F. Alessio, M. Alexander, and S. Ali, *Measurement of the ratio of branching fractions $\mathcal{B}(\bar{B}^0 \to D^{*+}\tau^-\bar{\nu}_\tau)/\mathcal{B}(\bar{B}^0 \to D^{*+}\mu^-\bar{\nu}_\mu)$*, Phys. Rev. Lett. **115115** (2015), arXiv:1506.08614 [hep-ex]. [INSPIRE].

[430] CMS Collaboration, *Prospects for exclusion or discovery of a third generation leptoquark decaying into a τ lepton and a b quark at CMS*, CMS-PAS-FTR-18-028, 2018. [INSPIRE].

[431] T. Plehn, H. Spiesberger, M. Spira, and P. Zerwas, *Formation and decay of scalar leptoquarks / squarks in ep collisions*, Z. Phys. C **74** (1997) no. 4, 611–614, arXiv:hep-ph/9703433 [hep-ph]. [INSPIRE].

[432] I. Doršner and A. Greljo, *Leptoquark toolbox for precision collider studies*, JHEP **05** (2018) 126, arXiv:1801.07641 [hep-ph]. [INSPIRE].

[433] ATLAS and CMS and LHC Higgs Combination Group Collaborations, *Procedure for the LHC Higgs boson search combination in summer 2011*, ATL-PHYS-PUB-2011-011, CMS-NOTE-2011-005, 2011. [INSPIRE].

[434] D. Buttazzo, A. Greljo, G. Isidori, and D. Marzocca, *B-physics anomalies: a guide to combined explanations*, JHEP **11** (2017) 44, arXiv:1706.07808 [hep-ph]. [INSPIRE].

[435] CMS Collaboration, A. M. Sirunyan, A. Tumasyan, W. Adam, E. Asilar, T. Bergauer, J. Brandstetter, E. Brondolin, M. Dragicevic, J. Ero", and M. Flechl, *Search for third-generation scalar leptoquarks and heavy right-handed neutrinos in final states with two tau leptons and two jets in proton-proton collisions at* $\sqrt{s} = 13$ *TeV*, JHEP **07** (2017) 121, arXiv:1703.03995 [hep-ex]. [INSPIRE].

[436] L. D. Luzio and M. Nardecchia, *What is the scale of new physics behind the* B*-flavour anomalies?*, EPJC **77** (2017) no. 8, 536, arXiv:1706.01868 [hep-ph]. [INSPIRE].

[437] ATLAS Collaboration, M. Aaboud, G. Aad, B. Abbott, J. Abdallah, O. Abdinov, B. Abeloos, R. Aben, O. AbouZeid, N. Abraham, and H. Abramowicz, *Search for Minimal Supersymmetric Standard Model Higgs bosons* H/A *and for* a' *boson in the* $\tau\tau$ *final state produced in* pp *collisions at* $\sqrt{s} = 13$ *TeV with the ATLAS Detector*, EPJC **76** (2016) no. 11, 585, arXiv:1608.00890 [hep-ex]. [INSPIRE].

[438] D. A. Faroughy, A. Greljo, and J. F. Kamenik, *Confronting lepton flavor universality violation in* B *decays with high-*p_T *tau lepton searches at LHC*, Phys. Lett. B **764** (2017) 126–134, arXiv:1609.07138 [hep-ph]. [INSPIRE].

[439] A. Greljo, J. M. Camalich, and J. D. Ruiz-Álvarez, *The Mono-Tau Menace: From* B *Decays to High-*p_T *Tails*, arXiv:1811.07920 [hep-ph]. [INSPIRE].

[440] A. Greljo and D. Marzocca, *High-*p_T *dilepton tails and flavor physics*, EPJC **77** (2017) no. 8, 548, arXiv:1704.09015 [hep-ph]. [INSPIRE].

[441] ATLAS Collaboration, *Search for new high-mass phenomena in the dilepton final state using* $36.1\ fb^{-1}$ *of proton-proton collision data at* $\sqrt{s} = 13$ *TeV with the ATLAS detector*, ATLAS-CONF-2017-027, 2017. [INSPIRE].

[442] ATLAS Collaboration, M. Aaboud, G. Aad, B. Abbott, O. Abdinov, B. Abeloos, S. H. Abidi, O. AbouZeid, N. Abraham, H. Abramowicz, and H. Abreu, *Search for new high-mass phenomena in the dilepton final state using* $36\ fb^{-1}$ *of proton-proton collision data at* $\sqrt{s} = 13$ *TeV with the ATLAS detector*, JHEP **10** (2017) 182, arXiv:1707.02424 [hep-ex]. [INSPIRE].

[443] Y. Afik, J. Cohen, E. Gozani, E. Kajomovitz, and Y. Rozen, *Establishing a Search for* $b \to s\ell^+\ell^-$ *Anomalies at the LHC*, JHEP **08** (2018) 56, arXiv:1805.11402 [hep-ph]. [INSPIRE].

[444] A. Greljo, G. Isidori, and D. Marzocca, *On the breaking of Lepton Flavor Universality in* B *decays*, JHEP **07** (2015) 142, arXiv:1506.01705 [hep-ph]. [INSPIRE].

[445] S. M. Boucenna, A. Celis, J. Fuentes-Martín, A. Vicente, and J. Virto, *Phenomenology of an* $SU(2) \times SU(2) \times U(1)$ *model with lepton-flavour non-universality*, JHEP **12** (2016) 59, arXiv:1608.01349 [hep-ph]. [INSPIRE].

[446] M. Abdullah, J. Calle, B. Dutta, A. Flórez, and D. Restrepo, *Probing a simplified,* W' *model of* $R_{D^{(*)}}$ *anomalies using b-tags,* τ *leptons and missing energy*, Phys. Rev. D **98** (2018) 055016, arXiv:1805.01869 [hep-ph]. [INSPIRE].

[447] A. Greljo, D. J. Robinson, B. Shakya, and J. Zupan, $R_{D^{(*)}}$ *from* W' *and right-handed neutrinos*, JHEP **09** (2018) 169, arXiv:1804.04642 [hep-ph]. [INSPIRE].

[448] P. Asadi, M. R. Buckley, and D. Shih, *It's all right(-handed neutrinos): a new* W' *model for the* $R_{D^{(*)}}$ *anomaly*, JHEP **09** (2018) 10, arXiv:1804.04135 [hep-ph]. [INSPIRE].

[449] X.-Q. Li, Y.-D. Yang, and X. Zhang, *Revisiting the one leptoquark solution to the* $R_{D^{(*)}}$ *anomalies and its phenomenological implications*, JHEP **08** (2016) 54, arXiv:1605.09308 [hep-ph]. [INSPIRE].

[450] R. Alonso, B. Grinstein, and J. M. Camalich, *Lifetime of* B_c^- *Constrains Explanations for Anomalies in* $B \to D^{(*)}\tau\nu$, Phys. Rev. Lett. **118** (2017) no. 8, arXiv:1611.06676 [hep-ph]. [INSPIRE].

[451] A. Celis, M. Jung, X.-Q. Li, and A. Pich, *Scalar contributions to* $b \to c(u)\tau\nu$ *transitions*, Phys.

Lett. B **771** (2017) 168–179, arXiv:1612.07757 [hep-ph]. [INSPIRE].

[452] A. Akeroyd and C.-H. Chen, *Constraint on the branching ratio of $B_c \to \tau\bar{\nu}$ from LEP1 and consequences for $R_{D^{(*)}}$ anomaly*, Phys. Rev. D **96** (2017) 075011, arXiv:1708.04072 [hep-ph]. [INSPIRE].

[453] A. Crivellin, D. Müller, and T. Ota, *Simultaneous explanation of $R(D^*)$ and $btos\mu^+\mu^-$: the last scalar leptoquarks standing*, JHEP **09** (2017) 40, arXiv:1703.09226 [hep-ph]. [INSPIRE].

[454] D. Marzocca, *Addressing the B-physics anomalies in a fundamental Composite Higgs Model*, JHEP **07** (2018) 121, arXiv:1803.10972 [hep-ph]. [INSPIRE].

[455] L. D. Luzio, A. Greljo, and M. Nardecchia, *Gauge leptoquark as the origin of B-physics anomalies*, Phys. Rev. D **96** (2017) 115011, arXiv:1708.08450 [hep-ph]. [INSPIRE].

[456] L. D. Luzio, J. Fuentes-Martin, A. Greljo, M. Nardecchia, and S. Renner, *Maximal Flavour Violation: a Cabibbo mechanism for leptoquarks*, JHEP **11** (2018) 81, arXiv:1808.00942 [hep-ph]. [INSPIRE].

[457] Fermilab Lattice and MILC Collaborations, A. Bazavov, C. Bernard, C. Bouchard, C. Chang, C. DeTar, D. Du, A. El-Khadra, E. Freeland, E. Ga'miz, and S. Gottlieb, *$B^0_{(s)}$-mixing matrix elements from lattice QCD for the Standard Model and beyond*, Phys. Rev. D **93** (2016) 113016, arXiv:1602.03560 [hep-lat]. [INSPIRE].

[458] *Hadron Collider Sensitivity to Fat Flavourful Z's for $R_{K^{(*)}}$*, arXiv:1810.02166 [hep-ph]. [INSPIRE].

[459] P. Arnan, A. Crivellin, L. Hofer, and F. Mescia, *Loop effects of heavy new scalars and fermions in $b \to s\mu^+\mu^-$*, JHEP **04** (2017) 43, arXiv:1608.07832 [hep-ph]. [INSPIRE].

[460] A. Falkowski, M. González-Alonso, and K. Mimouni, *Compilation of low-energy constraints on 4-fermion operators in the SMEFT*, JHEP **08** (2017) 123, arXiv:1706.03783 [hep-ph]. [INSPIRE].

[461] A. Falkowski, S. F. King, E. Perdomo, and M. Pierre, *Flavourful Z' portal for vector-like neutrino Dark Matter and $R_{K^{(*)}}$*, JHEP **08** (2018) 61, arXiv:1803.04430 [hep-ph]. [INSPIRE].

[462] *Combined Explanations of the $b \to s\mu^+\mu^-$ and $b \to c\tau^-\bar{\nu}$ Anomalies: a General Model Analysis*, arXiv:1806.07403 [hep-ph]. [INSPIRE].

[463] A. Celis, J. Fuentes-Martín, A. Vicente, and J. Virto, *Gauge-invariant implications of the LHCb measurements on lepton-flavor nonuniversality*, Phys. Rev. D **96** (2017) 035026, arXiv:1704.05672 [hep-ph]. [INSPIRE].

[464] D. Bečirević and O. Sumensari, *A leptoquark model to accommodate $R_K^{\rm exp} < R_K^{\rm SM}$ and $R_{K^*}^{\rm exp} < R_{K^*}^{\rm SM}$*, JHEP **08** (2017) 104, arXiv:1704.05835 [hep-ph]. [INSPIRE].

[465] J. F. Kamenik, Y. Soreq, and J. Zupan, *Lepton flavor universality violation without new sources of quark flavor violation*, Phys. Rev. D **97** (2018) 035002, arXiv:1704.06005 [hep-ph]. [INSPIRE].

[466] P. J. Fox, I. Low, and Y. Zhang, *Top-philic Z' forces at the LHC*, JHEP **03** (2018) 74, arXiv:1801.03505 [hep-ph]. [INSPIRE].

[467] J. E. Camargo-Molina, A. Celis, and D. A. Faroughy, *Anomalies in Bottom from new physics in Top*, Phys. Lett. B **784** (2018) 284–293, arXiv:1805.04917 [hep-ph]. [INSPIRE].

[468] ATLAS Collaboration, *Search prospects for resonant Higgs boson pair production in the $b\bar{b}b\bar{b}$ final state with large-radius jets from pp collisions at the HL-LHC*, ATL-PHYS-PUB-2018-028, 2018. [CDS].

[469] ATLAS Collaboration, *Jet substructure at very high luminosity*, 2014. [TWIKI].

[470] ATLAS Collaboration, *Boosted Object Tagging with Variable-R Jets in the ATLAS Detector*, ATL-PHYS-PUB-2016-013, 2016. [CDS].

[471] CMS Collaboration, S. Chatrchyan et al., *Observation of a new boson with mass near* 125 *GeV in pp collisions at* $\sqrt{s} = 7$ *and* 8 *TeV*, JHEP **06** (2013) 081, arXiv:1303.4571 [hep-ex]. [INSPIRE].

[472] L. Randall and R. Sundrum, *A large mass hierarchy from a small extra dimension*, Phys. Rev. Lett. **83** (1999) 3370, arXiv:hep-ph/9905221. [INSPIRE].

[473] W. D. Goldberger and M. B. Wise, *Modulus stabilization with bulk fields*, Phys. Rev. Lett. **83** (1999) no. 24, 4922–4925, arXiv:hep-ph/9907447 [hep-ph]. [INSPIRE].

[474] C. Csáki, M. Graesser, L. Randall, and J. Terning, *Cosmology of brane models with radion stabilization*, Phys. Rev. D **62** (2000) 045015, arXiv:hep-ph/9911406 [hep-ph]. [INSPIRE].

[475] C. Csáki, M. L. Graesser, and G. D. Kribs, *Radion dynamics and electroweak physics*, Phys. Rev. D **63** (2001) 065002, arXiv:hep-th/0008151 [hep-th]. [INSPIRE].

[476] H. Davoudiasl, J. L. Hewett, and T. G. Rizzo, *Phenomenology of the Randall-Sundrum Gauge Hierarchy Model*, Phys. Rev. Lett. **84** (2000) no. 10, 2080, arXiv:hep-ph/9909255 [hep-ph]. [INSPIRE].

[477] O. DeWolfe, D. Z. Freedman, S. S. Gubser, and A. Karch, *Modeling the fifth-dimension with scalars and gravity*, Phys. Rev. D **62** (2000) 046008, arXiv:hep-th/9909134 [hep-th]. [INSPIRE].

[478] K. Agashe, H. Davoudiasl, G. Perez, and A. Soni, *Warped Gravitons at the LHC and Beyond*, Phys. Rev. D **76** (2007) 036006, arXiv:hep-ph/0701186 [hep-ph]. [INSPIRE].

[479] G. Branco, P. Ferreira, L. Lavoura, M. Rebelo, M. Sher, and J. P. Silva, *Theory and phenomenology of two-Higgs-doublet models*, Phys. Rept. **516** (2012) 1–102, arXiv:1106.0034 [hep-ph]. [INSPIRE].

[480] A. Djouadi, *The Anatomy of electro-weak symmetry breaking. II. The Higgs bosons in the minimal supersymmetric model*, Phys. Rept. **459** (2008) 1–241, arXiv:hep-ph/0503173 [hep-ph]. [INSPIRE].

[481] H. Georgi and M. Machacek, *Doubly charged Higgs bosons*, Nucl. Phys. B **262** (1985) 463–477. [INSPIRE].

[482] ATLAS Collaboration, G. Aad, B. Abbott, J. Abdallah, S. Abdel Khalek, O. Abdinov, R. Aben, B. Abi, M. Abolins, O. AbouZeid, and H. Abramowicz, *Search For Higgs Boson Pair Production in the* $\gamma\gamma b\bar{b}$ *Final State using pp Collision Data at* $\sqrt{s} = 8$ *TeV from the ATLAS Detector*, Phys. Rev. Lett. **114** (2015), arXiv:1406.5053 [hep-ex]. [INSPIRE].

[483] ATLAS Collaboration, G. Aad, B. Abbott, J. Abdallah, O. Abdinov, R. Aben, M. Abolins, O. AbouZeid, H. Abramowicz, H. Abreu, and R. Abreu, *Search for Higgs boson pair production in the* $b\bar{b}b\bar{b}$ *final state from pp collisions at* $\sqrt{s} = 8$ *TeVwith the ATLAS detector*, EPJC **75** (2015) no. 9, 412, arXiv:1506.00285 [hep-ex]. [INSPIRE].

[484] ATLAS Collaboration, G. Aad, B. Abbott, J. Abdallah, O. Abdinov, R. Aben, M. Abolins, O. AbouZeid, H. Abramowicz, H. Abreu, and R. Abreu, *Searches for Higgs boson pair production in the* $hh \to bb\tau\tau, \gamma\gamma WW^*, \gamma\gamma bb, bbbb$ *channels with the ATLAS detector*, Phys. Rev. D **92** (2015) 092004, arXiv:1509.04670 [hep-ex]. [INSPIRE].

[485] CMS Collaboration, V. Khachatryan, A. M. Sirunyan, A. Tumasyan, W. Adam, T. Bergauer, M. Dragicevic, J. Ero", C. Fabjan, M. Friedl, and R. Fruehwirth, *Searches for heavy Higgs bosons in two-Higgs-doublet models and for* $t \to ch$ *decay using multilepton and diphoton final states in pp collisions at* 8 *TeV*, Phys. Rev. D **90** (2014) 112013, arXiv:1410.2751 [hep-ex]. [INSPIRE].

[486] CMS Collaboration, V. Khachatryan et al., *Search for resonant pair production of Higgs bosons decaying to two bottom quark-antiquark pairs in proton-proton collisions at* 8 *TeV*, Phys. Lett. B **749** (2015) 560, arXiv:1503.04114 [hep-ex]. [INSPIRE].

[487] CMS Collaboration, V. Khachatryan, A. M. Sirunyan, A. Tumasyan, W. Adam, E. Asilar,

T. Bergauer, J. Brandstetter, E. Brondolin, M. Dragicevic, and J. Ero", *Searches for a heavy scalar boson H decaying to a pair of* 125 *GeV Higgs bosons hh or for a heavy pseudoscalar boson A decaying to Zh, in the final states with* $h \to \tau\tau$, Phys. Lett. B **755** (2016) 217–244, arXiv:1510.01181 [hep-ex]. [INSPIRE].

[488] CMS Collaboration, V. Khachatryan, A. M. Sirunyan, A. Tumasyan, W. Adam, E. Asilar, T. Bergauer, J. Brandstetter, E. Brondolin, M. Dragicevic, and J. Ero", *Search for two Higgs bosons in final states containing two photons and two bottom quarks in proton-proton collisions at* 8 *TeV*, Phys. Rev. D **94** (2016) 052012, arXiv:1603.06896 [hep-ex]. [INSPIRE].

[489] CMS Collaboration, V. Khachatryan, A. M. Sirunyan, A. Tumasyan, W. Adam, E. Asilar, T. Bergauer, J. Brandstetter, E. Brondolin, M. Dragicevic, and J. Ero", *Search for heavy resonances decaying to two Higgs bosons in final states containing four b quarks*, EPJC **76** (2016) no. 7, 371, arXiv:1602.08762 [hep-ex]. [INSPIRE].

[490] ATLAS Collaboration, M. Aaboud, G. Aad, B. Abbott, J. Abdallah, O. Abdinov, B. Abeloos, R. Aben, O. AbouZeid, N. Abraham, and H. Abramowicz, *Search for pair production of Higgs bosons in the* $b\bar{b}b\bar{b}$ *final state using proton–proton collisions at* $\sqrt{s} = 13$ *TeV with the ATLAS detector*, Phys. Rev. D **94** (2016) 052002, arXiv:1606.04782 [hep-ex]. [INSPIRE].

[491] ATLAS Collaboration, *Search for pair production of Higgs bosons in the* $b\bar{b}b\bar{b}$ *final state using proton−proton collisions at* $\sqrt{s} = 13$ *TeV with the ATLAS detector*, ATLAS-CONF-2016-049, 2016. [INSPIRE].

[492] CMS Collaboration, A. Sirunyan, A. Tumasyan, W. Adam, F. Ambrogi, E. Asilar, T. Bergauer, J. Brandstetter, E. Brondolin, M. Dragicevic, and J. Ero", *Search for a massive resonance decaying to a pair of Higgs bosons in the four b quark final state in proton-proton collisions at* $\sqrt{s} = 13$ *TeV*, Phys. Lett. B **781** (2018) 244–269, arXiv:1710.04960 [hep-ex]. [INSPIRE].

[493] CMS Collaboration, A. M. Sirunyan, A. Tumasyan, W. Adam, F. Ambrogi, E. Asilar, T. Bergauer, J. Brandstetter, M. Dragicevic, J. Ero", and A. Escalante Del Valle, *Search for production of Higgs boson pairs in the four b quark final state using large-area jets in proton-proton collisions at* $\sqrt{s} = 13$ *TeV*, arXiv:1808.01473 [hep-ex]. [INSPIRE].

[494] G. F. Giudice, R. Rattazzi, and J. D. Wells, *Graviscalars from higher dimensional metrics and curvature Higgs mixing*, Nucl. Phys. B **595** (2001) 250–276, arXiv:hep-ph/0002178 [hep-ph]. [INSPIRE].

[495] A. Carvalho, *Gravity particles from Warped Extra Dimensions, predictions for LHC*, arXiv:1404.0102 [hep-ph]. [INSPIRE].

[496] CMS Collaboration, *Search for vector boson fusion production of a massive resonance decaying to a pair of Higgs bosons in the four b quark final state at the HL-LHC using the CMS Phase 2 detector*, CMS-PAS-FTR-18-003, 2018. [INSPIRE].

[497] L. A. Harland-Lang, A. D. Martin, P. Motylinski, and R. S. Thorne, *Parton distributions in the LHC era: MMHT 2014 PDFs*, EPJC **75** (2015) no. 5, 204, arXiv:1412.3989 [hep-ph]. [INSPIRE].

[498] A. Buckley, J. Ferrando, S. Lloyd, K. Nordström, B. Page, M. Rüfenacht, M. Schönherr, and G. Watt, *LHAPDF6: parton density access in the LHC precision era*, EPJC **75** (2015) no. 3, 132, arXiv:1412.7420 [hep-ph]. [INSPIRE].

[499] S. Carrazza, J. I. Latorre, J. Rojo, and G. Watt, *A compression algorithm for the combination of PDF sets*, EPJC **75** (2015) no. 10, 474, arXiv:1504.06469 [hep-ph]. [INSPIRE].

[500] J. Butterworth, S. Carrazza, A. Cooper-Sarkar, A. De Roeck, J. Feltesse, S. Forte, J. Gao, S. Glazov, J. Huston, and Z. Kassabov, *PDF4LHC recommendations for LHC Run II*, J. Phys. G **43** (2016) 023001, arXiv:1510.03865 [hep-ph]. [INSPIRE].

[501] G. P. Salam, *Towards Jetography*, EPJC **67** (2010) no. 3-4, 637–686, arXiv:0906.1833 [hep-ph]. [INSPIRE].

[502] J. M. Butterworth, A. R. Davison, M. Rubin, and G. P. Salam, *Jet substructure as a new Higgs search channel at the LHC*, Phys. Rev. Lett. **100** (2008) no. 24, arXiv:0802.2470 [hep-ph]. [INSPIRE].

[503] M. Dasgupta, A. Fregoso, S. Marzani, and G. P. Salam, *Towards an understanding of jet substructure*, JHEP **09** (2013) 29, arXiv:1307.0007 [hep-ph]. [INSPIRE].

[504] A. J. Larkoski, S. Marzani, G. Soyez, and J. Thaler, *Soft Drop*, JHEP **05** (2014) 146, arXiv:1402.2657 [hep-ph]. [INSPIRE].

[505] CMS Collaboration, *Jet algorithms performance in* 13 *TeV data*, CMS-PAS-JME-16-003, 2017. [INSPIRE].

[506] ATLAS and CMS Collaborations, G. Aad, B. Abbott, J. Abdallah, O. Abdinov, R. Aben, M. Abolins, O. AbouZeid, H. Abramowicz, H. Abreu, and R. Abreu, *Combined Measurement of the Higgs Boson Mass in pp Collisions at* $\sqrt{s} = 7$ *and* 8 *TeV with the ATLAS and CMS Experiments*, Phys. Rev. Lett. **114** (2015), arXiv:1503.07589 [hep-ex]. [INSPIRE].

[507] CMS Collaboration, A. M. Sirunyan, A. Tumasyan, W. Adam, F. Ambrogi, E. Asilar, T. Bergauer, J. Brandstetter, E. Brondolin, M. Dragicevic, and J. Ero", *Measurements of properties of the Higgs boson decaying into the four-lepton final state in pp collisions at* $\sqrt{s} = 13$ *TeV*, JHEP **11** (2017) 47, arXiv:1706.09936 [hep-ex]. [INSPIRE].

[508] J. Thaler and K. Van Tilburg, *Maximizing boosted top identification by minimizing* N*-subjettiness*, JHEP **02** (2012) 093, arXiv:1108.2701 [hep-ph]. [INSPIRE].

[509] R. Dermíšek, E. Lunghi, and S. Shin, *New decay modes of heavy Higgs bosons in a two Higgs doublet model with vectorlike leptons*, JHEP **05** (2016) 148, arXiv:1512.07837 [hep-ph]. [INSPIRE].

[510] R. Dermíšek, E. Lunghi, and S. Shin, *Two Higgs doublet model with vectorlike leptons and contributions to* $pp \to WW$ *and* $H \to WW$, JHEP **02** (2016) 119, arXiv:1509.04292 [hep-ph]. [INSPIRE].

[511] K. Kannike, M. Raidal, D. M. Straub, and A. Strumia, *Anthropic solution to the magnetic muon anomaly: the charged see-saw*, JHEP **0210** (2012) 106, arXiv:1111.2551 [hep-ph]. [INSPIRE].

[512] R. Dermíšek and A. Raval, *Explanation of the Muon* $g-2$ *Anomaly with Vectorlike Leptons and its Implications for Higgs Decays*, Phys. Rev. D **88** (2013) 013017, arXiv:1305.3522 [hep-ph]. [INSPIRE].

[513] A. Falkowski, D. M. Straub, and A. Vicente, *Vector-like leptons: Higgs decays and collider phenomenology*, JHEP **05** (2014) 92, arXiv:1312.5329 [hep-ph]. [INSPIRE].

[514] A. Falkowski and R. Vega-Morales, *Exotic Higgs decays in the golden channel*, JHEP **12** (2014) 37, arXiv:1405.1095 [hep-ph]. [INSPIRE].

[515] R. Dermíšek, A. Raval, and S. Shin, *Effects of vectorlike leptons on* $h \to 4\ell$ *and the connection to the muon* $g-2$ *anomaly*, Phys. Rev. D **90** (2014) 034023, arXiv:1406.7018 [hep-ph]. [INSPIRE].

[516] R. Dermíšek, J. P. Hall, E. Lunghi, and S. Shin, *Limits on Vectorlike Leptons from Searches for Anomalous Production of Multi-Lepton Events*, JHEP **12** (2014) 13, arXiv:1408.3123 [hep-ph]. [INSPIRE].

[517] R. Dermíšek, E. Lunghi, and S. Shin, *Contributions of flavor violating couplings of a Higgs boson to* $pp \to WW$, JHEP **08** (2015) 126, arXiv:1503.08829 [hep-ph]. [INSPIRE].

[518] R. Dermíšek, E. Lunghi, and S. Shin, *New constraints and discovery potential for Higgs to Higgs cascade decays through vectorlike leptons*, JHEP **10** (2016) 81, arXiv:1608.00662 [hep-ph]. [INSPIRE].

[519] N. Kumar and S. P. Martin, *Vectorlike Leptons at the Large Hadron Collider*, Phys. Rev. D **92**

(2015) 115018, arXiv:1510.03456 [hep-ph]. [INSPIRE].

[520] R. Dermisek, E. Lunghi, and S. Shin, *Heavy Higgs cascade decay into a vectorlike quark* , .

[521] LHC Higgs Cross Section Working Group Collaboration, S. Heinemeyer, C. Mariotti, G. Passarino, R. Tanaka, J. R. Andersen, P. Artoisenet, E. A. Bagnaschi, A. Banfi, T. Becher, and F. U. Bernlochner, *Handbook of LHC Higgs Cross Sections: 3. Higgs Properties*, arXiv:1307.1347 [hep-ph]. [INSPIRE].

[522] R. V. Harlander, S. Liebler, and H. Mantler, *SusHi: A program for the calculation of Higgs production in gluon fusion and bottom-quark annihilation in the Standard Model and the MSSM*, Comput. Phys. Commun. **184** (2013) no. 6, 1605–1617, arXiv:1212.3249 [hep-ph]. [INSPIRE].

[523] R. V. Harlander, S. Liebler, and H. Mantler, *SusHi Bento: Beyond NNLO and the heavy-top limit*, Comput. Phys. Commun. **212** (2017) 239–257, arXiv:1605.03190 [hep-ph]. [INSPIRE].

[524] ATLAS Collaboration, *Search for a CP-odd Higgs boson decaying to Zh in pp collisions at $\sqrt{s} = 13$ TeV with the ATLAS detector*, ATLAS-CONF-2016-015, 2016. [INSPIRE].

[525] ATLAS Collaboration, M. Aaboud, G. Aad, B. Abbott, O. Abdinov, B. Abeloos, S. H. Abidi, O. AbouZeid, N. Abraham, H. Abramowicz, and H. Abreu, *Search for additional heavy neutral Higgs and gauge bosons in the ditau final state produced in 36 fb^{-1} of pp collisions at $\sqrt{s} = 13$ TeV with the ATLAS detector*, JHEP **01** (2018) 55, arXiv:1709.07242 [hep-ex]. [INSPIRE].

[526] CMS Collaboration, V. Khachatryan, A. M. Sirunyan, A. Tumasyan, W. Adam, E. Asilar, T. Bergauer, J. Brandstetter, E. Brondolin, M. Dragicevic, and J. Ero", *Search for high-mass diphoton resonances in proton-proton collisions at 13 TeV and combination with 8 TeV search*, Phys. Lett. B **767** (2017) 147–170, arXiv:1609.02507 [hep-ex]. [INSPIRE].

[527] ATLAS Collaboration, M. Aaboud, G. Aad, B. Abbott, O. Abdinov, B. Abeloos, S. H. Abidi, O. AbouZeid, N. Abraham, H. Abramowicz, and H. Abreu, *Search for new phenomena in high-mass diphoton final states using 37 fb^{-1} of proton–proton collisions collected at $\sqrt{s} = 13$ TeV with the ATLAS detector*, Phys. Lett. B **775** (2017) 105–125, arXiv:1707.04147 [hep-ex]. [INSPIRE].

[528] U. Ellwanger, C. Hugonie, and A. M. Teixeira, *The Next-to-Minimal Supersymmetric Standard Model*, Phys. Rept. **496** (2010) 1–77, arXiv:0910.1785 [hep-ph]. [INSPIRE].

[529] Z. Chacko, H.-S. Goh, and R. Harnik, *The Twin Higgs: Natural electroweak breaking from mirror symmetry*, Phys. Rev. Lett. **96** (2006) no. 23, arXiv:hep-ph/0506256 [hep-ph]. [INSPIRE].

[530] R. Contino, *The Higgs as a Composite Nambu-Goldstone Boson*, arXiv:1005.4269 [hep-ph]. [INSPIRE].

[531] G. Panico and A. Wulzer, *The Composite Nambu-Goldstone Higgs*, vol. 913. Springer International Publishing, 2016. arXiv:1506.01961 [hep-ph]. [INSPIRE].

[532] M. Pietroni, *The Electroweak phase transition in a nonminimal supersymmetric model*, Nucl. Phys. B **402** (1993) 27–45, arXiv:hep-ph/9207227 [hep-ph]. [INSPIRE].

[533] D. Curtin, P. Meade, and C.-T. Yu, *Testing Electroweak Baryogenesis with Future Colliders*, JHEP **11** (2014) 127, arXiv:1409.0005 [hep-ph]. [INSPIRE].

[534] N. Craig, H. K. Lou, M. McCullough, and A. Thalapillil, *The Higgs Portal Above Threshold*, JHEP **02** (2016) 127, arXiv:1412.0258 [hep-ph]. [INSPIRE].

[535] D. Buttazzo, F. Sala, and A. Tesi, *Singlet-like Higgs bosons at present and future colliders*, JHEP **11** (2015) 158, arXiv:1505.05488 [hep-ph]. [INSPIRE].

[536] D. Buttazzo, D. Redigolo, F. Sala, and A. Tesi, *Fusing Vectors into Scalars at High Energy Lepton Colliders*, JHEP **11** (2018) 144, arXiv:1807.04743 [hep-ph]. [INSPIRE].

[537] ATLAS and CMS Collaborations, G. Aad, B. Abbott, J. Abdallah, O. Abdinov, B. Abeloos,

R. Aben, O. AbouZeid, N. Abraham, H. Abramowicz, and H. Abreu, *Measurements of the Higgs boson production and decay rates and constraints on its couplings from a combined ATLAS and CMS analysis of the LHC pp collision data at $\sqrt{s} = 7$ and 8 TeV*, JHEP **08** (2016) 45, arXiv:1606.02266 [hep-ex]. [INSPIRE].

[538] CMS Collaboration, *Combined measurements of the Higgs boson's couplings at $\sqrt{s} = 13$ TeV*, CMS-PAS-HIG-17-031, 2018. [INSPIRE].

[539] ATLAS Collaboration, *Measurement of gluon fusion and vector boson fusion Higgs boson production cross-sections in the $H \to WW^* \to e\nu\mu\nu$ decay channel in pp collisions at $\sqrt{s} = 13$ TeV with the ATLAS detector*, ATLAS-CONF-2018-004, 2018. [INSPIRE].

[540] M. Carena, Z. Liu, and M. Riembau, *Probing the electroweak phase transition via enhanced di-Higgs boson production*, Phys. Rev. D **97** (2018) 095032, arXiv:1801.00794 [hep-ph]. [INSPIRE].

[541] J. Baglio, A. Djouadi, R. Gröber, M. Mühlleitner, J. Quevillon, and M. Spira, *The measurement of the Higgs self-coupling at the LHC: theoretical status*, JHEP **04** (2013) 151, arXiv:1212.5581 [hep-ph]. [INSPIRE].

[542] CMS Collaboration, A. M. Sirunyan, A. Tumasyan, W. Adam, F. Ambrogi, E. Asilar, T. Bergauer, J. Brandstetter, E. Brondolin, M. Dragicevic, and J. Ero", *Search for a new scalar resonance decaying to a pair of Z bosons in proton-proton collisions at $\sqrt{s} = 13$ TeV*, JHEP **06** (2018) 127, arXiv:1804.01939 [hep-ex]. [INSPIRE].

[543] R. Barbieri, L. J. Hall, Y. Nomura, and V. S. Rychkov, *Supersymmetry without a Light Higgs Boson*, Phys. Rev. D **75** (2007) 035007, arXiv:hep-ph/0607332 [hep-ph]. [INSPIRE].

[544] L. J. Hall, D. Pinner, and J. T. Ruderman, *A Natural SUSY Higgs Near 126 GeV*, JHEP **04** (2012) 131, arXiv:1112.2703 [hep-ph]. [INSPIRE].

[545] K. Agashe, Y. Cui, and R. Franceschini, *Natural Islands for a 125 GeV Higgs in the scale-invariant NMSSM*, JHEP **02** (2013) 31, arXiv:1209.2115 [hep-ph]. [INSPIRE].

[546] T. Gherghetta, B. von Harling, A. D. Medina, and M. A. Schmidt, *The Scale-Invariant NMSSM and the 126 GeV Higgs Boson*, JHEP **02** (2013) 32, arXiv:1212.5243 [hep-ph]. [INSPIRE].

[547] J. Espinosa and M. Quirós, *On Higgs boson masses in nonminimal supersymmetric standard models*, Phys. Lett. B **279** (1992) 92–97. [INSPIRE].

[548] R. Barbieri, D. Buttazzo, K. Kannike, F. Sala, and A. Tesi, *Exploring the Higgs sector of a most natural NMSSM*, Phys. Rev. D **87** (2013) 115018, arXiv:1304.3670 [hep-ph]. [INSPIRE].

[549] R. Barbieri, D. Buttazzo, K. Kannike, F. Sala, and A. Tesi, *One or more Higgs bosons?*, Phys. Rev. D **88** (2013) 055011, arXiv:1307.4937 [hep-ph]. [INSPIRE].

[550] F. Sala, *Higgs and flavour as doors to new physics*, Eur. Phys. J. Plus **131** (2016) no. 4, 79, arXiv:1509.08655 [hep-ph]. [INSPIRE].

[551] A. Katz, A. Mariotti, S. Pokorski, D. Redigolo, and R. Ziegler, *SUSY Meets Her Twin*, JHEP **01** (2017) 142, arXiv:1611.08615 [hep-ph]. [INSPIRE].

[552] M. Badziak and K. Harigaya, *Supersymmetric D-term Twin Higgs*, JHEP **06** (2017) 65, arXiv:1703.02122 [hep-ph]. [INSPIRE].

[553] P. W. Graham, D. E. Kaplan, and S. Rajendran, *Cosmological Relaxation of the Electroweak Scale*, Phys. Rev. Lett. **115** (2015) no. 22, arXiv:1504.07551 [hep-ph]. [INSPIRE].

[554] T. Flacke, C. Frugiuele, E. Fuchs, R. S. Gupta, and G. Perez, *Phenomenology of relaxion-Higgs mixing*, JHEP **06** (2017) 50, arXiv:1610.02025 [hep-ph]. [INSPIRE].

[555] K. Choi and S. H. Im, *Constraints on Relaxion Windows*, JHEP **12** (2016) 93, arXiv:1610.00680 [hep-ph]. [INSPIRE].

[556] C. Frugiuele, E. Fuchs, G. Perez, and M. Schlaffer, *Relaxion and light (pseudo)scalars at the HL-LHC and lepton colliders*, JHEP **10** (2018) 151, arXiv:1807.10842 [hep-ph]. [INSPIRE].

[557] L3 Collaboration, M. Acciarri, O. Adriani, M. Aguilar-Benitez, S. Ahlen, B. Alpat, J. Alcaraz, G. Alemanni, J. Allaby, A. Aloisio, and G. Alverson, *Search for neutral Higgs boson production through the process* $e^+e^- \to Z^*H^0$, Phys. Lett. B **385** (1996) 454–470. [INSPIRE].

[558] ALEPH and DELPHI and L3 and OPAL and LEP Working Group for Higgs Boson Searches Collaborations, S. Schael, R. Barate, R. Bruneliere, I. De Bonis, D. Decamp, C. Goy, S. Jezequel, J. Lees, F. Martin, and E. Merle, *Search for neutral MSSM Higgs bosons at LEP*, EPJC **47** (2006) 547–587, arXiv:hep-ex/0602042 [hep-ex]. [INSPIRE].

[559] LHCb Collaboration, R. Aaij, C. Abellan Beteta, A. Adametz, B. Adeva, M. Adinolfi, C. Adrover, A. Affolder, Z. Ajaltouni, J. Albrecht, and F. Alessio, *Differential branching fraction and angular analysis of the* $B^+ \to K^+\mu^+\mu^-$ *decay*, JHEP **02** (2013) 105, arXiv:1209.4284 [hep-ex]. [INSPIRE].

[560] LHCb Collaboration, R. Aaij, B. Adeva, M. Adinolfi, A. Affolder, Z. Ajaltouni, S. Akar, J. Albrecht, F. Alessio, M. Alexander, and S. Ali, *Search for hidden-sector bosons in* $B^0 \to K^{*0}\mu^+\mu^-$ *decays*, Phys. Rev. Lett. **115** (2015), arXiv:1508.04094 [hep-ex]. [INSPIRE].

[561] CMS Collaboration, *Search for the exotic decay of the Higgs boson to a pair of light pseudoscalars in the final state with two b quarks and two* τ *leptons*, CMS-PAS-HIG-17-024, 2018. [INSPIRE].

[562] P. Bechtle, S. Heinemeyer, O. Stål, T. Stefaniak, and G. Weiglein, *Probing the Standard Model with Higgs signal rates from the Tevatron, the LHC and a future ILC*, JHEP **11** (2014) 39, arXiv:1403.1582 [hep-ph]. [INSPIRE].

[563] R. D. Ball, M. Bonvini, S. Forte, S. Marzani, and G. Ridolfi, *Higgs production in gluon fusion beyond NNLO*, Nucl. Phys. B **874** (2013) 746–772, arXiv:1303.3590 [hep-ph]. [INSPIRE].

[564] M. Bonvini, R. D. Ball, S. Forte, S. Marzani, and G. Ridolfi, *Updated Higgs cross section at approximate* N^3LO, J. Phys. G **41** (2014) 095002, arXiv:1404.3204 [hep-ph]. [INSPIRE].

[565] M. Bonvini, S. Marzani, C. Muselli, and L. Rottoli, *On the Higgs cross section at* N^3LO+N^3LL *and its uncertainty*, JHEP **08** (2016) 105, arXiv:1603.08000 [hep-ph]. [INSPIRE].

[566] T. Ahmed, M. Bonvini, M. C. Kumar, P. Mathews, N. Rana, V. Ravindran, and L. Rottoli, *Pseudo-scalar Higgs boson production at* N^3 LO_A +N^3 LL', EPJC **76** (2016) no. 12, 663, arXiv:1606.00837 [hep-ph]. [INSPIRE].

[567] CMS Collaboration, V. Khachatryan, A. M. Sirunyan, A. Tumasyan, W. Adam, E. Asilar, T. Bergauer, J. Brandstetter, E. Brondolin, M. Dragicevic, and J. Ero", *Search for light bosons in decays of the* 125 *GeV Higgs boson in proton-proton collisions at* $\sqrt{s} = 8$ *TeV*, JHEP **10** (2017) 76, arXiv:1701.02032 [hep-ex]. [INSPIRE].

[568] ATLAS Collaboration, M. Aaboud, G. Aad, B. Abbott, O. Abdinov, B. Abeloos, D. K. Abhayasinghe, S. H. Abidi, O. Abouzeid, N. Abraham, and H. Abramowicz, *Search for Higgs boson decays into a pair of light bosons in the* $bb\mu\mu$ *final state in pp collision at* $\sqrt{s} = 13$ *TeV with the ATLAS detector*, arXiv:1807.00539 [hep-ex]. [INSPIRE].

[569] CMS Collaboration, *Search for the exotic decay of the Higgs boson to a pair of light pseudoscalars in the final state of two muons and two* τ *leptons at* $\sqrt{s} = 13$ *TeV.*, CMS-PAS-HIG-17-029, 2018. [INSPIRE].

[570] CMS Collaboration, *A Search for Beyond Standard Model Light Bosons Decaying into Muon Pairs*, CMS-PAS-HIG-16-035, 2016. [INSPIRE].

[571] ATLAS Collaboration, M. Aaboud, G. Aad, B. Abbott, O. Abdinov, B. Abeloos, S. H. Abidi, O. AbouZeid, N. Abraham, H. Abramowicz, and H. Abreu, *Search for Higgs boson decays to beyond-the-Standard-Model light bosons in four-lepton events with the ATLAS detector at* $\sqrt{s} = 13$ *TeV*, JHEP **06** (2018) 166, arXiv:1802.03388 [hep-ex]. [INSPIRE].

[572] ATLAS Collaboration, M. Aaboud, G. Aad, B. Abbott, O. Abdinov, B. Abeloos, S. H. Abidi,

O. Abouzeid, N. Abraham, H. Abramowicz, and H. Abreu, *Search for Higgs boson decays into pairs of light (pseudo)scalar particles in the $\gamma\gamma jj$ final state in pp collisions at $\sqrt{s} = 13$ TeV with the ATLAS detector*, Phys. Lett. B **782** (2018) 750–767, arXiv:1803.11145 [hep-ex]. [INSPIRE].

[573] LHC Higgs cross section working group. [WEBPAGE].

[574] J. Mrazek, A. Pomarol, R. Rattazzi, M. Redi, J. Serra, and A. Wulzer, *The Other Natural Two Higgs Doublet Model*, Nucl. Phys. B **853** (2011) 1–48, arXiv:1105.5403 [hep-ph]. [INSPIRE].

[575] S. D. Curtis, S. Moretti, K. Yagyu, and E. Yildirim, *Perturbative unitarity bounds in composite two-Higgs doublet models*, Phys. Rev. D **94** (2016) 055017, arXiv:1602.06437 [hep-ph]. [INSPIRE].

[576] S. D. Curtis, S. Moretti, K. Yagyu, and E. Yildirim, *LHC Phenomenology of Composite 2-Higgs Doublet Models*, EPJC **77** (2017) no. 8, 513, arXiv:1610.02687 [hep-ph]. [INSPIRE].

[577] S. D. Curtis, S. Moretti, K. Yagyu, and E. Yildirim, *Single and double SM-like Higgs boson production at future electron-positron colliders in composite 2HDMs*, Phys. Rev. D **95** (2017) 095026, arXiv:1702.07260 [hep-ph]. [INSPIRE].

[578] S. D. Curtis, L. D. Rose, S. Moretti, and K. Yagyu, *Supersymmetry versus Compositeness: 2HDMs tell the story*, Phys. Lett. B **786** (2018) 189–194, arXiv:1803.01865 [hep-ph]. [INSPIRE].

[579] D. B. Kaplan, *Flavor at SSC energies: A New mechanism for dynamically generated fermion masses*, Nucl. Phys. B **365** (1991) 259–278. [INSPIRE].

[580] S. D. Curtis, L. D. Rose, S. Moretti, and K. Yagyu, *A Concrete Composite 2-Higgs Doublet Model*, arXiv:1810.06465 [hep-ph]. [INSPIRE].

[581] P. Bechtle, O. Brein, S. Heinemeyer, O. Stål, T. Stefaniak, G. Weiglein, and K. E. Williams, HiggsBounds $-$ 4*: Improved Tests of Extended Higgs Sectors against Exclusion Bounds from LEP, the Tevatron and the LHC*, EPJC **74** (2014) no. 3, 2693, arXiv:1311.0055 [hep-ph]. [INSPIRE].

[582] P. Bechtle, S. Heinemeyer, O. Stål, T. Stefaniak, and G. Weiglein, *HiggsSignals: Confronting arbitrary Higgs sectors with measurements at the Tevatron and the LHC*, EPJC **74** (2014) no. 2, 2711, arXiv:1305.1933 [hep-ph]. [INSPIRE].

[583] CMS Collaboration, *Projected Performance of an Upgraded CMS Detector at the LHC and HL-LHC: Contribution to the Snowmass Process*, arXiv:1307.7135 [hep-ex]. [INSPIRE].

[584] LHC Higgs Cross Section Working Group Collaboration, A. David, A. Denner, M. Duehrssen, M. Grazzini, C. Grojean, G. Passarino, M. Schumacher, M. Spira, G. Weiglein, and M. Zanetti, *LHC HXSWG interim recommendations to explore the coupling structure of a Higgs-like particle*, arXiv:1209.0040 [hep-ph]. [INSPIRE].

[585] A. Pich and P. Tuzón, *Yukawa Alignment in the Two-Higgs-Doublet Model*, Phys. Rev. D **80** (2009) 091702, arXiv:0908.1554 [hep-ph]. [INSPIRE].

[586] ATLAS Collaboration, M. Aaboud, G. Aad, B. Abbott, O. Abdinov, B. Abeloos, S. H. Abidi, O. Abouzeid, N. Abraham, H. Abramowicz, and H. Abreu, *Search for heavy particles decaying into top-quark pairs using lepton-plus-jets events in proton-proton collisions at $\sqrt{s} = 13$ TeV with the ATLAS detector*, EPJC **78** (2018) no. 7, 565, arXiv:1804.10823 [hep-ex]. [INSPIRE].

[587] CMS Collaboration, *Search for Higgs boson pair production in the final state containing two photons and two bottom quarks in proton-proton collisions at $\sqrt{s} = 13$ TeV*, CMS-PAS-HIG-17-008, 2017. [INSPIRE].

[588] S. Moretti and D. Ross, *On the top-antitop invariant mass spectrum at the LHC from a Higgs boson signal perspective*, Phys. Lett. B **712** (2012) 245–249, arXiv:1203.3746 [hep-ph].

[INSPIRE].

[589] A. Mariotti, D. Redigolo, F. Sala, and K. Tobioka, *New LHC bound on low-mass diphoton resonances*, Phys. Lett. B **783** (2018) 13–18, arXiv:1710.01743 [hep-ph]. [INSPIRE].

[590] *New Axion Searches at Flavor Factories*, arXiv:1810.09452 [hep-ph]. [INSPIRE].

[591] M. Low, A. Mariotti, D. Redigolo, F. Sala, and K. Tobioka, *Boosted Axion-like particles*, .

[592] R. D. Peccei and H. R. Quinn, *CP Conservation in the Presence of Instantons*, Phys. Rev. Lett. **38** (1977) 1440–1443. [INSPIRE].

[593] J. E. Kim, *Weak Interaction Singlet and Strong CP Invariance*, Phys. Rev. Lett. **43** (1979) 103. [INSPIRE].

[594] M. A. Shifman, A. I. Vainshtein, and V. I. Zakharov, *Can Confinement Ensure Natural CP Invariance of Strong Interactions?*, Nucl. Phys. B **166** (1980) 493–506. [INSPIRE].

[595] Z. Berezhiani, L. Gianfagna, and M. Giannotti, *Strong CP problem and mirror world: The Weinberg-Wilczek axion revisited*, Phys. Lett. B **500** (2001) 286–296, arXiv:hep-ph/0009290 [hep-ph]. [INSPIRE].

[596] A. Hook, *Anomalous solutions to the strong CP problem*, Phys. Rev. Lett. **114** (2015) no. 14, arXiv:1411.3325 [hep-ph]. [INSPIRE].

[597] H. Fukuda, K. Harigaya, M. Ibe, and T. T. Yanagida, *Model of visible QCD axion*, Phys. Rev. D **92** (2015) 015021, arXiv:1504.06084 [hep-ph]. [INSPIRE].

[598] S. Dimopoulos, A. Hook, J. Huang, and G. Marques-Tavares, *A collider observable QCD axion*, JHEP **11** (2016) 52, arXiv:1606.03097 [hep-ph]. [INSPIRE].

[599] P. Agrawal and K. Howe, *Factoring the Strong CP Problem*, arXiv:1710.04213 [hep-ph]. [INSPIRE].

[600] M. Kamionkowski and J. March-Russell, *Planck scale physics and the Peccei-Quinn mechanism*, Phys. Lett. B **282** (1992) 137–141, arXiv:hep-th/9202003 [hep-th]. [INSPIRE].

[601] A. E. Nelson and N. Seiberg, *R symmetry breaking versus supersymmetry breaking*, Nucl. Phys. B **416** (1994) 46–62, arXiv:hep-ph/9309299 [hep-ph]. [INSPIRE].

[602] B. Bellazzini, A. Mariotti, D. Redigolo, F. Sala, and J. Serra, *R-axion at colliders*, Phys. Rev. Lett. **119** (2017) no. 14, arXiv:1702.02152 [hep-ph]. [INSPIRE].

[603] J. Mardon, Y. Nomura, and J. Thaler, *Cosmic Signals from the Hidden Sector*, Phys. Rev. D **80** (2009) 035013, arXiv:0905.3749 [hep-ph]. [INSPIRE].

[604] J. Fan, J. Thaler, and L.-T. Wang, *Dark matter from dynamical SUSY breaking*, JHEP **06** (2010) 45, arXiv:1004.0008 [hep-ph]. [INSPIRE].

[605] BaBar Collaboration, J. Lees, V. Poireau, V. Tisserand, J. Garra Tico, E. Grauges, M. Martinelli, D. Milanes, A. Palano, M. Pappagallo, and G. Eigen, *Search for hadronic decays of a light Higgs boson in the radiative decay* $\Upsilon \to \gamma A^0$, Phys. Rev. Lett. **107** (2011), arXiv:1108.3549 [hep-ex]. [INSPIRE].

[606] BELLE-II Collaboration, R. de Sangro, *SuperKEKB and Belle II Status Report*, PoS **FPCP2017** (2017) 037. [INSPIRE].

[607] S. Benson and A. Puig Navarro, *Triggering* $B_s^0 \to \gamma\gamma$ *at LHCb*, LHCb-PUB-2018-006, CERN-LHCb-PUB-2018-006, 2018. [CDS].

[608] L3 Collaboration, O. Adriani, M. Aguilar-Benitez, S. Ahlen, H. Akbari, J. Alcaraz, A. Aloisio, G. Alverson, M. Alviggi, G. Ambrosi, and Q. An, *Isolated hard photon emission in hadronic* Z^0 *decays*, Phys. Lett. B **292** (1992) 472–484. [INSPIRE].

[609] M. Koratzinos, *The FCC-ee design study: luminosity and beam polarization*, PoS **EPS-HEP2015** (2015) 518, arXiv:1511.01021 [physics.acc-ph]. [INSPIRE].

[610] CDF Collaboration, T. Aaltonen, S. Amerio, D. Amidei, A. Anastassov, A. Annovi, J. Antos, G. Apollinari, J. Appel, T. Arisawa, and A. Artikov, *Measurement of the Cross Section for*

Prompt Isolated Diphoton Production Using the Full CDF Run II Data Sample, Phys. Rev. Lett. **110** (2013), arXiv:1212.4204 [hep-ex]. [INSPIRE].

[611] ATLAS Collaboration, G. Aad, T. Abajyan, B. Abbott, J. Abdallah, S. Abdel Khalek, A. A. Abdelalim, O. Abdinov, R. Aben, B. Abi, and M. Abolins, *Measurement of isolated-photon pair production in pp collisions at $\sqrt{s} = 7$ TeV with the ATLAS detector*, JHEP **01** (2013) 86, arXiv:1211.1913 [hep-ex]. [INSPIRE].

[612] CMS Collaboration, S. Chatrchyan, V. Khachatryan, A. M. Sirunyan, A. Tumasyan, W. Adam, T. Bergauer, M. Dragicevic, J. Ero", C. Fabjan, and M. Friedl, *Measurement of differential cross sections for the production of a pair of isolated photons in pp collisions at $\sqrt{s} = 7$ TeV*, EPJC **74** (2014) no. 11, 3129, arXiv:1405.7225 [hep-ex]. [INSPIRE].

[613] ATLAS Collaboration, M. Aaboud, G. Aad, B. Abbott, J. Abdallah, O. Abdinov, B. Abeloos, S. H. Abidi, O. AbouZeid, N. Abraham, and H. Abramowicz, *Measurements of integrated and differential cross sections for isolated photon pair production in pp collisions at $\sqrt{s} = 8$ TeV with the ATLAS detector*, Phys. Rev. D **95** (2017) 112005, arXiv:1704.03839 [hep-ex]. [INSPIRE].

[614] CMS Collaboration, A. M. Sirunyan, A. Tumasyan, W. Adam, F. Ambrogi, E. Asilar, T. Bergauer, J. Brandstetter, E. Brondolin, M. Dragicevic, and J. Ero", *Search for low mass vector resonances decaying into quark-antiquark pairs in proton-proton collisions at $\sqrt{s} = 13$ TeV*, JHEP **01** (2018) 97, arXiv:1710.00159 [hep-ex]. [INSPIRE].

[615] ATLAS Collaboration, G. Aad, B. Abbott, J. Abdallah, S. Abdel Khalek, O. Abdinov, R. Aben, B. Abi, O. AbouZeid, H. Abramowicz, and H. Abreu, *Search for Scalar Diphoton Resonances in the Mass Range $65 - 600$ GeV with the ATLAS Detector in pp Collision Data at $\sqrt{s} = 8$ TeV*, Phys. Rev. Lett. **113** (2014), arXiv:1407.6583 [hep-ex]. [INSPIRE].

[616] CMS Collaboration, *Search for new resonances in the diphoton final state in the mass range between 80 and 115 GeV in pp collisions at $\sqrt{s} = 8$ TeV*, CMS-PAS-HIG-14-037, 2015. [INSPIRE].

[617] CMS Collaboration, *Search for new resonances in the diphoton final state in the mass range between 70 and 110 GeV in pp collisions at $\sqrt{s} = 8$ and 13 TeV*, CMS-PAS-HIG-17-013, 2017. [INSPIRE].

[618] S. Catani, L. Cieri, D. de Florian, G. Ferrera, and M. Grazzini, *Diphoton production at the LHC: a QCD study up to NNLO*, JHEP **04** (2018) 142, arXiv:1802.02095 [hep-ph]. [INSPIRE].

[619] ATLAS Collaboration, *Expected performance for an upgraded ATLAS detector at High-Luminosity LHC*, ATL-PHYS-PUB-2016-026, 2016. [CDS].

[620] ATLAS Collaboration, M. Aaboud, G. Aad, B. Abbott, J. Abdallah, O. Abdinov, B. Abeloos, R. Aben, O. AbouZeid, N. Abraham, and H. Abramowicz, *Measurement of the photon identification efficiencies with the ATLAS detector using LHC Run-1 data*, EPJC **76** (2016) no. 12, 666, arXiv:1606.01813 [hep-ex]. [INSPIRE].

[621] S. D. Ellis, T. S. Roy, and J. Scholtz, *Jets and Photons*, Phys. Rev. Lett. **110** (2013) no. 12, arXiv:1210.1855 [hep-ph]. [INSPIRE].

[622] S. D. Ellis, T. S. Roy, and J. Scholtz, *Phenomenology of Photon-Jets*, Phys. Rev. D **87** (2013) 014015, arXiv:1210.3657 [hep-ph]. [INSPIRE].

[623] ATLAS Collaboration, G. Aad, B. Abbott, J. Abdallah, O. Abdinov, R. Aben, M. Abolins, O. AbouZeid, H. Abramowicz, H. Abreu, and R. Abreu, *Search for new phenomena in events with at least three photons collected in pp collisions at $\sqrt{s} = 8$ TeV with the ATLAS detector*, EPJC **76** (2016) no. 4, 210, arXiv:1509.05051 [hep-ex]. [INSPIRE].

[624] G. Ferretti and D. Karateev, *Fermionic UV completions of Composite Higgs models*, JHEP **03** (2014) 77, arXiv:1312.5330 [hep-ph]. [INSPIRE].

[625] G. Cacciapaglia, G. Ferretti, T. Flacke, and H. Serôdio, *Revealing timid pseudo-scalars with taus*

at the LHC, EPJC **78** (2018) no. 9, 724, arXiv:1710.11142 [hep-ph]. [INSPIRE].

[626] CMS Collaboration, *The Phase-2 Upgrade of the CMS L1 Trigger Interim Technical Design Report*, CERN-LHCC-2017-013, CMS-TDR-017, 2017. [CDS].

[627] A. Belyaev, G. Cacciapaglia, H. Cai, G. Ferretti, T. Flacke, A. Parolini, and H. Serodio, *Di-boson signatures as Standard Candles for Partial Compositeness*, JHEP **0112** (2017) 94, arXiv:1610.06591 [hep-ph]. [INSPIRE].

[628] G. Ferretti, *UV Completions of Partial Compositeness: The Case for a $SU(4)$ Gauge Group*, JHEP **06** (2014) 142, arXiv:1404.7137 [hep-ph]. [INSPIRE].

[629] J. Barnard, T. Gherghetta, and T. S. Ray, *UV descriptions of composite Higgs models without elementary scalars*, JHEP **02** (2014) 2, arXiv:1311.6562 [hep-ph]. [INSPIRE].

[630] E. Bennett, D. K. Hong, J.-W. Lee, C.-J. D. Lin, B. Lucini, M. Piai, and D. Vadacchino, *$Sp(4)$ gauge theory on the lattice: towards $SU(4)/Sp(4)$ composite Higgs (and beyond)*, JHEP **03** (2018) 185, arXiv:1712.04220 [hep-lat]. [INSPIRE].

[631] V. Ayyar, T. DeGrand, D. C. Hackett, W. I. Jay, E. T. Neil, Y. Shamir, and B. Svetitsky, *Baryon spectrum of $SU(4)$ composite Higgs theory with two distinct fermion representations*, Phys. Rev. D **97** (2018) 114505, arXiv:1801.05809 [hep-ph]. [INSPIRE].

[632] CMS Collaboration, S. Chatrchyan, V. Khachatryan, A. M. Sirunyan, A. Tumasyan, W. Adam, T. Bergauer, M. Dragicevic, J. Ero", C. Fabjan, and M. Friedl, *Search for a light pseudoscalar Higgs boson in the dimuon decay channel in pp collisions at $\sqrt{s} = 7$ TeV*, Phys. Rev. Lett. **109** (2012), arXiv:1206.6326 [hep-ex]. [INSPIRE].

[633] U. Haisch, J. F. Kamenik, A. Malinauskas, and M. Spira, *Collider constraints on light pseudoscalars*, JHEP **03** (2018) 178, arXiv:1802.02156 [hep-ph]. [INSPIRE].

[634] CMS Collaboration, A. M. Sirunyan, A. Tumasyan, W. Adam, F. Ambrogi, E. Asilar, T. Bergauer, J. Brandstetter, M. Dragicevic, J. Ero", and A. Escalante Del Valle, *Search for pair-produced resonances decaying to quark pairs in proton-proton collisions at $\sqrt{s} = 13$ TeV*, arXiv:1808.03124 [hep-ex]. [INSPIRE].

[635] M. I. Gresham and M. B. Wise, *Color octet scalar production at the LHC*, Phys. Rev. **D76** (2007) 075003, arXiv:0706.0909 [hep-ph].

[636] R. Bonciani, T. Ježo, M. Klasen, F. Lyonnet, and I. Schienbein, *Electroweak top-quark pair production at the LHC with Z' bosons to NLO QCD in POWHEG*, JHEP **02** (2016) 141, arXiv:1511.08185 [hep-ph]. [INSPIRE].

[637] S. Frixione and B. R. Webber, *Matching NLO QCD computations and parton shower simulations*, JHEP **06** (2002) 29, arXiv:hep-ph/0204244 [hep-ph]. [INSPIRE].

[638] S. Frixione, P. Nason, and C. Oleari, *Matching NLO QCD computations with Parton Shower simulations: the POWHEG method*, JHEP **11** (2007) 70, arXiv:0709.2092 [hep-ph]. [INSPIRE].

[639] S. Alioli, P. Nason, C. Oleari, and E. Re, *A general framework for implementing NLO calculations in shower Monte Carlo programs: the POWHEG BOX*, JHEP **06** (2010) 43, arXiv:1002.2581 [hep-ph]. [INSPIRE].

[640] T. Ježo, M. Klasen, D. R. Lamprea, F. Lyonnet, and I. Schienbein, *NLO+NLL limits on W' and Z' gauge boson masses in general extensions of the Standard Model*, JHEP **12** (2014) 92, arXiv:1410.4692 [hep-ph]. [INSPIRE].

[641] H. Georgi, E. E. Jenkins, and E. H. Simmons, *Ununifying the Standard Model*, Phys. Rev. Lett. **6263** (1989) no. 24, 2789. [INSPIRE].

[642] H. Georgi, E. E. Jenkins, and E. H. Simmons, *The Ununified Standard Model*, Nucl. Phys. B **331** (1990) 541–555. [INSPIRE].

[643] E. Malkawi, T. Tait, and C.-P. Yuan, *A Model of strong flavor dynamics for the top quark*, Phys.

Lett. B **385** (1996) 304–310, arXiv:hep-ph/9603349 [hep-ph]. [INSPIRE].

[644] X. Li and E. Ma, *Gauge Model of Generation Nonuniversality*, Phys. Rev. Lett. **47** (1981) 1788. [INSPIRE].

[645] R. M. Harris, C. T. Hill, and S. J. Parke, *Cross-Section for Topcolor Z'_t Decaying to $t\bar{t}$*, arXiv:hep-ph/9911288 [hep-ph]. [INSPIRE].

[646] G. Altarelli, B. Mele, and M. Ruiz-Altaba, *Searching for New Heavy Vector Bosons in $p\bar{p}$ Colliders*, Z. Phys. C **4547** (1989) no. 1, 109. [INSPIRE].

[647] K. Hsieh, K. Schmitz, J.-H. Yu, and C.-P. Yuan, *Global Analysis of General $SU(2) \times SU(2) \times U(1)$ Models with Precision Data*, Phys. Rev. D **82** (2010) 035011, arXiv:1003.3482 [hep-ph]. [INSPIRE].

[648] S. Dimopoulos and H. Georgi, *Softly Broken Supersymmetry and $SU(5)$*, Nucl. Phys. B **193** (1981) 150–162. [INSPIRE].

[649] L. Susskind, *Dynamics of Spontaneous Symmetry Breaking in the Weinberg-Salam Theory*, Phys. Rev. D **20** (1979) 2619–2625. [INSPIRE].

[650] C. T. Hill and S. J. Parke, *Top production: Sensitivity to new physics*, Phys. Rev. D **49** (1994) 4454–4462, arXiv:hep-ph/9312324. [INSPIRE].

[651] R. S. Chivukula, B. A. Dobrescu, H. Georgi, and C. T. Hill, *Top quark seesaw theory of electroweak symmetry breaking*, Phys. Rev. D **59** (1999) 075003, arXiv:hep-ph/9809470. [INSPIRE].

[652] N. Arkani-Hamed, A. G. Cohen, and H. Georgi, *Electroweak symmetry breaking from dimensional deconstruction*, Phys. Lett. B **513** (2001) 232, arXiv:hep-ph/0105239. [INSPIRE].

[653] N. Arkani-Hamed, S. Dimopoulos, and G. R. Dvali, *The hierarchy problem and new dimensions at a millimeter*, Phys. Lett. B **429** (1998) 263, arXiv:hep-ph/9803315. [INSPIRE].

[654] L. Randall and R. Sundrum, *An alternative to compactification*, Phys. Rev. Lett. **83** (1999) 4690, arXiv:hep-th/9906064. [INSPIRE].

[655] CMS Collaboration, *Search for ttbar resonances at the HL-LHC and HE-LHC with the Phase-2 CMS detector*, CMS-PAS-FTR-18-009, 2018. [INSPIRE].

[656] P. Nason, *A New method for combining NLO QCD with shower Monte Carlo algorithms*, JHEP **11** (2004) 40, arXiv:hep-ph/0409146 [hep-ph]. [INSPIRE].

[657] S. Frixione, G. Ridolfi, and P. Nason, *A Positive-weight next-to-leading-order Monte Carlo for heavy flavour hadroproduction*, JHEP **09** (2007) 126, arXiv:0707.3088 [hep-ph]. [INSPIRE].

[658] CMS Collaboration, V. Khachatryan et al., *Event generator tunes obtained from underlying event and multiparton scattering measurements*, EPJC **76** (2016) no. 3, 155, arXiv:1512.00815 [hep-ex]. [INSPIRE].

[659] P. Skands, S. Carrazza, and J. Rojo, *Tuning PYTHIA 8.1: the Monash 2013 Tune*, EPJC **74** (2014) no. 8, 3024, arXiv:1404.5630 [hep-ph]. [INSPIRE].

[660] CMS Collaboration, *Investigations of the impact of the parton shower tuning in Pythia 8 in the modelling of $t\bar{t}$ at $\sqrt{s} = 8$ and 13 TeV*, CMS-PAS-TOP-16-021, 2016. [INSPIRE].

[661] CMS Collaboration, A. Sirunyan, A. Tumasyan, W. Adam, E. Asilar, T. Bergauer, J. Brandstetter, E. Brondolin, M. Dragicevic, J. Ero", and M. Flechl, *Particle-flow reconstruction and global event description with the CMS detector*, JINST **12** (2017), arXiv:1706.04965 [physics.ins-det]. [INSPIRE].

[662] J. Ott, THETA—*A framework for template-based modeling and inference*, 2010. [WEBPAGE].

[663] R. J. Barlow and C. Beeston, *Fitting using finite Monte Carlo samples*, Comput. Phys. Commun. **77** (1993) no. 2, 219. [INSPIRE].

[664] J. S. Conway, *Incorporating nuisance parameters in likelihoods for multisource spectra*, in *Proceedings, PHYSTAT 2011 Workshop on Statistical Issues Related to Discovery Claims in*

Search Experiments and Unfolding, p. 115. 2011. arXiv:1103.0354 [physics.data-an]. [INSPIRE].

[665] CMS Collaboration, A. M. Sirunyan, A. Tumasyan, W. Adam, F. Ambrogi, E. Asilar, T. Bergauer, J. Brandstetter, M. Dragicevic, J. Ero", and A. Escalante Del Valle, *Search for resonant $\mathrm{t\bar{t}}$ production in proton-proton collisions at $\sqrt{s} = 13$ TeV*, arXiv:1810.05905 [hep-ex]. [INSPIRE].

[666] ATLAS Collaboration, *Study on the prospects of a $t\bar{t}$ resonance search in events with one lepton at a High Luminosity LHC*, ATL-PHYS-PUB-2017-002, 2017. [CDS].

[667] ATLAS Collaboration, G. Aad, B. Abbott, J. Abdallah, O. Abdinov, R. Aben, M. Abolins, O. AbouZeid, H. Abramowicz, H. Abreu, and R. Abreu, *A search for $t\bar{t}$ resonances using lepton-plus-jets events in proton-proton collisions at $\sqrt{s} = 8$ TeV with the ATLAS detector*, JHEP **08** (2015) 148, arXiv:1505.07018 [hep-ex]. [INSPIRE].

[668] ATLAS Collaboration, *Prospects for searches for heavy Z' and W' bosons in fermionic final states with the ATLAS experiment at the HL-LHC*, ATL-PHYS-PUB-2018-044, 2018. [CDS].

[669] ATLAS Collaboration, M. Aaboud, G. Aad, B. Abbott, O. Abdinov, B. Abeloos, S. H. Abidi, O. AbouZeid, N. Abraham, H. Abramowicz, and H. Abreu, *Search for $W' \to tb$ decays in the hadronic final state using pp collisions at $\sqrt{s} = 13$ TeV with the ATLAS detector*, Phys. Lett. B **781** (2018) 327–348, arXiv:1801.07893 [hep-ex]. [INSPIRE].

[670] D. London and J. L. Rosner, *Extra Gauge Bosons in E_6*, in *Proceedings, 23RD International Conference on High Energy Physics, JULY 16-23, 1986, Berkeley, CA*. 1986. [INSPIRE].

[671] A. Joglekar and J. L. Rosner, *Searching for signatures of E_6*, Phys. Rev. D **96** (2017) 015026, arXiv:1607.06900 [hep-ph]. [INSPIRE].

[672] P. Langacker, *The Physics of Heavy Z' Gauge Bosons*, Rev. Mod. Phys. **81** (2009) no. 3, 1199–1228, arXiv:0801.1345 [hep-ph]. [INSPIRE].

[673] E. Salvioni, G. Villadoro, and F. Zwirner, *Minimal Z' models: Present bounds and early LHC reach*, JHEP **11** (2009) 68, arXiv:0909.1320 [hep-ph]. [INSPIRE].

[674] ATLAS Collaboration, *Studies of Sensitivity to New Dilepton and Ditop Resonances with an Upgraded ATLAS Detector at a High-Luminosity LHC*, ATL-PHYS-PUB-2013-003, 2013. [CDS].

[675] R. D. Ball, V. Bertone, S. Carrazza, C. S. Deans, L. Del Debbio, S. Forte, A. Guffanti, N. P. Hartland, J. I. Latorre, and J. Rojo, *Parton distributions with LHC data*, Nucl. Phys. B **867** (2013) 244–289, arXiv:1207.1303 [hep-ph]. [INSPIRE].

[676] ATLAS Collaboration, *ATLAS Run 1 Pythia8 tunes*, ATL-PHYS-PUB-2014-021, 2014. [CDS].

[677] ATLAS Collaboration, G. Aad et al., *Measurement of the Z/γ^* boson transverse momentum distribution in pp collisions at $\sqrt{s} = 7$ TeV with the ATLAS detector*, JHEP **09** (2014) 55, arXiv:1406.3660 [hep-ex]. [INSPIRE].

[678] A. Caldwell, D. Kollár, and K. Kröninger, *BAT: The Bayesian Analysis Toolkit*, Comput. Phys. Commun. **180** (2009) no. 11, 2197–2209, arXiv:0808.2552 [physics.data-an]. [INSPIRE].

[679] ATLAS Collaboration, *Search for a new heavy gauge boson resonance decaying into a lepton and missing transverse momentum in 79.8 fb^{-1} of pp collisions at $\sqrt{s} = 13$ TeV with the ATLAS experiment*, ATLAS-CONF-2018-017, 2018. [INSPIRE].

[680] H.-L. Lai, M. Guzzi, J. Huston, Z. Li, P. M. Nadolsky, J. Pumplin, and C.-P. Yuan, *New parton distributions for collider physics*, Phys. Rev. D **82** (2010) 074024, arXiv:1007.2241 [hep-ph]. [INSPIRE].

[681] ATLAS Collaboration, G. Aad et al., *Electron reconstruction and identification efficiency measurements with the ATLAS detector using the 2011 LHC proton-proton collision data*, EPJC **74** (2014) no. 7, 2941, arXiv:1404.2240 [hep-ex]. [INSPIRE].

[682] ATLAS Collaboration, G. Aad et al., *Muon reconstruction performance of the ATLAS detector in proton–proton collision data at $\sqrt{s} = 13$ TeV*, EPJC **76** (2016) no. 5, 292, arXiv:1603.05598 [hep-ex]. [INSPIRE].

[683] P. Z. Skands, *Tuning Monte Carlo Generators: The Perugia Tunes*, Phys. Rev. D **82** (2010) 074018, arXiv:1005.3457 [hep-ph]. [INSPIRE].

[684] ATLAS Collaboration, *Summary of ATLAS Pythia 8 tunes*, ATL-PHYS-PUB-2012-003, ATL-COM-PHYS-2012-738, 2012. [INSPIRE].

[685] ATLAS Collaboration, M. Aaboud, G. Aad, B. Abbott, O. Abdinov, B. Abeloos, D. K. Abhayasinghe, S. H. Abidi, O. Abouzeid, N. Abraham, and H. Abramowicz, *Search for vector-boson resonances decaying to a top quark and bottom quark in the lepton plus jets final state in pp collisions at $\sqrt{s} = 13$ TeV with the ATLAS detector*, Phys. Lett. B **788** (2019) 347–370, arXiv:1807.10473 [hep-ex]. [INSPIRE].

[686] CMS Collaboration, *Sensitivity study for a heavy guage boson W' in the decay channel with a tau lepton and a neutrino at the High-Luminosity LHC*, CMS-PAS-FTR-18-030, 2019. [CDS].

[687] CMS Collaboration, A. M. Sirunyan et al., *Search for a W' boson decaying to a τ lepton and a neutrino in proton-proton collisions at $\sqrt{s} = 13$ TeV*, arXiv:1807.11421 [hep-ex]. [INSPIRE].

[688] P. Ko, Y. Omura, and C. Yu, *Higgs phenomenology in Type-I 2HDM with $U(1)_H$ Higgs gauge symmetry*, JHEP **01** (2014) 16, arXiv:1309.7156 [hep-ph]. [INSPIRE].

[689] P. Ko, Y. Omura, and C. Yu, *Dark matter and dark force in the type-I inert 2HDM with local $U(1)_H$ gauge symmetry*, JHEP **11** (2014) 54, arXiv:1405.2138 [hep-ph]. [INSPIRE].

[690] A. Berlin, T. Lin, and L.-T. Wang, *Mono-Higgs Detection of Dark Matter at the LHC*, JHEP **06** (2014) 78, arXiv:1402.7074 [hep-ph]. [INSPIRE].

[691] W.-C. Huang, Y.-L. S. Tsai, and T.-C. Yuan, *G2HDM : Gauged Two Higgs Doublet Model*, JHEP **04** (2016) 19, arXiv:1512.00229 [hep-ph]. [INSPIRE].

[692] L. D. Rose, S. Khalil, and S. Moretti, *Explanation of the 17 MeV Atomki anomaly in a $U(1)$-extended two Higgs doublet model*, Phys. Rev. D **96** (2017) 115024, arXiv:1704.03436 [hep-ph]. [INSPIRE].

[693] M. D. Campos, D. Cogollo, M. Lindner, T. Melo, F. S. Queiroz, and W. Rodejohann, *Neutrino Masses and Absence of Flavor Changing Interactions in the 2HDM from Gauge Principles*, JHEP **08** (2017) 92, arXiv:1705.05388 [hep-ph]. [INSPIRE].

[694] CMS Collaboration, A. M. Sirunyan, A. Tumasyan, W. Adam, F. Ambrogi, E. Asilar, T. Bergauer, J. Brandstetter, E. Brondolin, M. Dragicevic, and J. Ero", *Search for high-mass resonances in dilepton final states in proton-proton collisions at $\sqrt{s} = 13$ TeV*, JHEP **06** (2018) 120, arXiv:1803.06292 [hep-ex]. [INSPIRE].

[695] D. A. Camargo, L. D. Rose, S. Moretti, and F. S. Queiroz, *Collider Bounds on 2-Higgs Doublet Models with $U(1)_X$ Gauge Symmetries*, arXiv:1805.08231 [hep-ph]. [INSPIRE].

[696] A. Alloul, N. D. Christensen, C. Degrande, C. Duhr, and B. Fuks, *FeynRules 2.0 - A complete toolbox for tree-level phenomenology*, Comput. Phys. Commun. **185** (2014) no. 8, 2250–2300, arXiv:1310.1921 [hep-ph]. [INSPIRE].

[697] J. Alwall, M. Herquet, F. Maltoni, O. Mattelaer, and T. Stelzer, *MadGraph 5 : Going Beyond*, JHEP **06** (2011) 128, arXiv:1106.0522 [hep-ph]. [INSPIRE].

[698] A. Thamm, R. Torre, and A. Wulzer, *Future tests of Higgs compositeness: direct vs indirect*, JHEP **07** (2015) 100, arXiv:1502.01701 [hep-ph]. [INSPIRE].

[699] *High Energy LHC main page*, 2018. [TWIKI].

[700] CMS Collaboration, *Search for excited leptons in $\ell\ell\gamma$ final states in proton-proton collisions at the HL-LHC*, CMS-PAS-FTR-18-029, 2018. [INSPIRE].

[701] CMS Collaboration, *Constraints on the Higgs boson self-coupling from $ttH + tH$, $H \to \gamma\gamma$ differential measurements at the HL-LHC*, CMS-PAS-FTR-18-020, 2018. [INSPIRE].

[702] CMS Collaboration, *Search for excited leptons in $\ell\ell\gamma$ final states in proton-proton collisions at $\sqrt{s} = 13$ TeV*, CMS-PAS-EXO-18-004, 2018. [CDS].

[703] CMS Collaboration, S. Chatrchyan et al., *Search for excited leptons in pp collisions at $\sqrt{s} = 7$ TeV*, Phys. Lett. B **720** (2013) 309–329, arXiv:1210.2422 [hep-ex]. [INSPIRE].

[704] CMS Collaboration, V. Khachatryan et al., *Search for excited leptons in proton-proton collisions at $\sqrt{s} = 8$ TeV*, JHEP **03** (2016) 125, arXiv:1511.01407 [hep-ex]. [INSPIRE].

[705] CMS Collaboration, *Projected performance of Higgs analyses at the HL-LHC for ECFA 2016*, CMS-PAS-FTR-16-002, 2017. [INSPIRE].

[706] F. del Aguila, J. Santiago, and M. Pérez-Victoria, *Observable contributions of new exotic quarks to quark mixing*, JHEP **09** (2000) 11, arXiv:hep-ph/0007316 [hep-ph]. [INSPIRE].

[707] M. Buchkremer, G. Cacciapaglia, A. Deandrea, and L. Panizzi, *Model Independent Framework for Searches of Top Partners*, Nucl. Phys. B **876** (2013) 376–417, arXiv:1305.4172 [hep-ph]. [INSPIRE].

[708] D. Barducci and L. Panizzi, *Vector-like quarks coupling discrimination at the LHC and future hadron colliders*, JHEP **12** (2017) 57, arXiv:1710.02325 [hep-ph]. [INSPIRE].

[709] ATLAS Collaboration, M. Aaboud, G. Aad, B. Abbott, O. Abdinov, B. Abeloos, S. H. Abidi, O. AbouZeid, N. Abraham, H. Abramowicz, and H. Abreu, *Search for pair production of vector-like top quarks in events with one lepton, jets, and missing transverse momentum in $\sqrt{s} = 13$ TeV pp collisions with the ATLAS detector*, JHEP **08** (2017) 52, arXiv:1705.10751 [hep-ex]. [INSPIRE].

[710] A. Avetisyan and T. Bose, *Search for top partners with charge $5e/3$*, arXiv:1309.2234 [hep-ex]. [INSPIRE].

[711] T. Han, I. Lewis, and Z. Liu, *Colored Resonant Signals at the LHC: Largest Rate and Simplest Topology*, JHEP **12** (2010) 85, arXiv:1010.4309 [hep-ph]. [INSPIRE].

[712] R. Chivukula, M. Golden, and E. H. Simmons, *Six jet signals of highly colored fermions*, Phys. Lett. B **257** (1991) 403–408. [INSPIRE].

[713] A. V. Manohar and M. B. Wise, *Flavor changing neutral currents, an extended scalar sector, and the Higgs production rate at the CERN LHC*, Phys. Rev. D **74** (2006) 035009, arXiv:hep-ph/0606172 [hep-ph]. [INSPIRE].

[714] J. M. Arnold, M. Pospelov, M. Trott, and M. B. Wise, *Scalar Representations and Minimal Flavor Violation*, JHEP **01** (2010) 73, arXiv:0911.2225 [hep-ph]. [INSPIRE].

[715] ATLAS Collaboration, G. Aad, B. Abbott, J. Abdallah, O. Abdinov, R. Aben, M. Abolins, O. AbouZeid, H. Abramowicz, H. Abreu, and R. Abreu, *Dijet production in $\sqrt{s} = 7$ TeV pp collisions with large rapidity gaps at the ATLAS experiment*, Phys. Lett. B **754** (2016) 214–234, arXiv:1511.00502 [hep-ex]. [INSPIRE].

[716] ATLAS Collaboration, G. Aad et al., *Search for resonances in the mass distribution of jet pairs with one or two jets identified as b-jets in proton–proton collisions at $\sqrt{s} = 13$ TeV with the ATLAS detector*, Phys. Lett. B **759** (2016) 229 – 246. [INSPIRE].

[717] CMS Collaboration, V. Khachatryan, A. M. Sirunyan, A. Tumasyan, W. Adam, T. Bergauer, M. Dragicevic, J. Ero", C. Fabjan, M. Friedl, and R. Fruehwirth, *Search for Dijet Resonances in 7 TeV pp Collisions at CMS*, Phys. Rev. Lett. **105** (2010), arXiv:1010.0203 [hep-ex]. [INSPIRE].

[718] CMS Collaboration, S. Chatrchyan, V. Khachatryan, A. M. Sirunyan, A. Tumasyan, W. Adam, E. Aguilo, T. Bergauer, M. Dragicevic, J. Ero", and C. Fabjan, *Search for narrow resonances using the dijet mass spectrum in pp collisions at $\sqrt{s} = 8$ TeV*, Phys. Rev. D **87** (2013) 114015,

arXiv:1302.4794 [hep-ex]. [INSPIRE].

[719] CMS Collaboration, A. M. Sirunyan, A. Tumasyan, W. Adam, E. Asilar, T. Bergauer, J. Brandstetter, E. Brondolin, M. Dragicevic, J. Ero", and M. Flechl, *Search for dijet resonances in proton-proton collisions at $\sqrt{s} = 13$ TeV and constraints on dark matter and other models*, Phys. Lett. B **769772** (2017) 520–542, arXiv:1611.03568 [hep-ex]. [INSPIRE].

[720] ATLAS Collaboration, M. Aaboud, G. Aad, B. Abbott, O. Abdinov, B. Abeloos, S. H. Abidi, O. Abouzeid, N. Abraham, H. Abramowicz, and H. Abreu, *Search for low-mass dijet resonances using trigger-level jets with the ATLAS detector in pp collisions at $\sqrt{s} = 13$ TeV*, Phys. Rev. Lett. **121** (2018), arXiv:1804.03496 [hep-ex]. [INSPIRE].

[721] S. V. Chekanov, J. T. Childers, J. Proudfoot, R. Wang, and D. Frizzell, *Precision searches in dijets at the HL-LHC and HE-LHC*, JINST **13** (2018) no. 05, 05022, arXiv:1710.09484 [hep-ex]. [INSPIRE].

[722] ATLAS Collaboration, M. Aaboud, G. Aad, B. Abbott, O. Abdinov, B. Abeloos, D. K. Abhayasinghe, S. H. Abidi, O. Abouzeid, N. Abraham, and H. Abramowicz, *Search for resonances in the mass distribution of jet pairs with one or two jets identified as b-jets in proton-proton collisions at $\sqrt{s} = 13$ TeV with the ATLAS detector*, Phys. Rev. D **98** (2018) 032016, arXiv:1805.09299 [hep-ex]. [INSPIRE].

[723] ATLAS Collaboration, *Search for dijet resonances in events with an isolated lepton using $\sqrt{s} = 13$ TeV proton–proton collision data collected by the ATLAS detector*, ATLAS-COM-CONF-2018-020, 2018. [CDS].

[724] S. V. Chekanov, *HepSim: a repository with predictions for high-energy physics experiments*, Adv. High Energy Phys. **2015** (2015) 1–7, arXiv:1403.1886 [hep-ph]. [INSPIRE].

[725] ATLAS Collaboration, G. Aad, B. Abbott, J. Abdallah, O. Abdinov, R. Aben, M. Abolins, O. AbouZeid, H. Abramowicz, H. Abreu, and R. Abreu, *Performance of b-Jet Identification in the ATLAS Experiment*, JINST **11** (2016), arXiv:1512.01094 [hep-ex]. [INSPIRE].

[726] ATLAS Collaboration, G. Aad, E. Abat, B. Abbott, J. Abdallah, A. Abdelalim, A. Abdesselam, O. Abdinov, B. Abi, M. Abolins, and H. Abramowicz, *Expected Performance of the ATLAS Experiment - Detector, Trigger and Physics*, arXiv:0901.0512 [hep-ex]. [INSPIRE].

[727] ATLAS Collaboration, G. Aad, B. Abbott, J. Abdallah, O. Abdinov, B. Abeloos, R. Aben, M. Abolins, O. AbouZeid, H. Abramowicz, and H. Abreu, *Search for new phenomena in dijet mass and angular distributions from pp collisions at $\sqrt{s} = 13$ TeV with the ATLAS detector*, Phys. Lett. B **754** (2016) 302–322, arXiv:1512.01530 [hep-ex]. [INSPIRE].

[728] M. J. Strassler and K. M. Zurek, *Discovering the Higgs through highly-displaced vertices*, Phys. Lett. B **661** (2008) 263–267, arXiv:hep-ph/0605193 [hep-ph]. [INSPIRE].

[729] R. Schabinger and J. D. Wells, *A Minimal spontaneously broken hidden sector and its impact on Higgs boson physics at the large hadron collider*, Phys. Rev. D **72** (2005) 093007, arXiv:hep-ph/0509209 [hep-ph]. [INSPIRE].

[730] M. Chala, M. Duerr, F. Kahlhoefer, and K. Schmidt-Hoberg, *Tricking Landau-Yang: How to obtain the diphoton excess from a vector resonance*, Phys. Lett. B **755** (2016) 145–149, arXiv:1512.06833 [hep-ph]. [INSPIRE].

[731] *On the angular momentum of a system of two photons*, Dokl. Akad. Nauk Ser. Fiz. **60** (1948) 207–209. [INSPIRE].

[732] C.-N. Yang, *Selection Rules for the Dematerialization of a Particle Into Two Photons*, Phys. Rev. **77** (1950) no. 2, 242–245. [INSPIRE].

[733] B. C. Allanach, D. Bhatia, and A. M. Iyer, *Dissecting Multi-Photon Resonances at the Large Hadron Collider*, EPJC **77** (2017) no. 9, 595, arXiv:1706.09039 [hep-ph]. [INSPIRE].

[734] ATLAS Collaboration, *HL-LHC prospects for diboson resonance searches and electroweak vector boson scattering in the $WW/WZ \to \ell\nu qq$ final state*, ATL-PHYS-PUB-2018-022, 2018.

[CDS].

[735] D. Pappadopulo, A. Thamm, R. Torre, and A. Wulzer, *Heavy Vector Triplets: Bridging Theory and Data*, JHEP **09** (2014) 60, arXiv:1402.4431 [hep-ph]. [INSPIRE].

[736] V. Cavaliere, R. Les, T. Nitta, and K. Terashi, *HE-LHC prospects for diboson resonance searches and electroweak WW/WZ production via vector boson scattering in the semi-leptonic final states*, arXiv:1812.00841 [hep-ex]. [INSPIRE].

[737] J. Liu, Z. Liu, and L.-T. Wang, *Long-lived particles at the LHC: catching them in time*, arXiv:1805.05957 [hep-ph]. [INSPIRE].

[738] B. Andersson, G. Gustafson, G. Ingelman, and T. Sjöstrand, *Parton Fragmentation and String Dynamics*, Phys. Rept. **97** (1983) 31–145. [INSPIRE].

[739] M. Klimek, *In preparation*, .

[740] R. M. HARRIS and K. KOUSOURIS, *Searches for Dijet Resonances at Hadron Colliders*, Int. J. Mod. Phys. A **26** (2011) no. 30n31, 5005–5055, arXiv:1110.5302 [hep-ex]. [INSPIRE].

[741] N. Boelaert and T. Åkesson, *Dijet angular distributions at* $\sqrt{s} = 14$ *TeV*, EPJC **66** (2010) 343–357, arXiv:0905.3961 [hep-ph]. [INSPIRE].

[742] T. D. Lee, *A Theory of Spontaneous T Violation*, Phys. Rev. D **8** (1973) 1226–1239. [INSPIRE].

[743] C. T. Hill, *Topcolor assisted technicolor*, Phys. Lett. B **345** (1995) 483–489, arXiv:hep-ph/9411426 [hep-ph]. [INSPIRE].

[744] D. B. Kaplan, H. Georgi, and S. Dimopoulos, *Composite Higgs Scalars*, Phys. Lett. B **136** (1984) 187–190. [INSPIRE].

[745] B. Bellazzini, C. Csáki, and J. Serra, *Composite Higgses*, EPJC **74** (2014) no. 5, 2766, arXiv:1401.2457 [hep-ph]. [INSPIRE].

[746] A. Pomarol, *Gauge bosons in a five-dimensional theory with localized gravity*, Phys. Lett. B **486** (2000) 153–157, arXiv:hep-ph/9911294 [hep-ph]. [INSPIRE].

[747] R. M. Harris and S. Jain, *Cross Sections for Leptophobic Topcolor* Z' *Decaying to Top-Antitop*, EPJC **72** (2012) no. 7, 2072, arXiv:1112.4928 [hep-ph]. [INSPIRE].

[748] U. Baur, I. Hinchliffe, and D. Zeppenfeld, *Excited Quark Production at Hadron Colliders*, Int. J. Mod. Phys. A **2** (1987) no. 04, 1285. [INSPIRE].

[749] CMS Collaboration, A. M. Sirunyan et al., *Search for physics beyond the standard model in high-mass diphoton events from proton-proton collisions at* $\sqrt{s} = 13$ *TeV*, Phys. Rev. D **98** (2018) 092001, arXiv:1809.00327 [hep-ex]. [INSPIRE].

[750] G. F. Giudice, Y. Kats, M. McCullough, R. Torre, and A. Urbano, *Clockwork/linear dilaton: structure and phenomenology*, JHEP **06** (2018) 009, arXiv:1711.08437 [hep-ph]. [INSPIRE].

Report from Working Group 4: Opportunities in flavour physics at the HL-LHC and HE-LHC

Physics of the HL-LHC, and Perspectives at the HE-LHC

Conveners:
A. Cerri[1] , V.V. Gligorov[2] , S. Malvezzi[3] , J. Martin Camalich[4,5] , J. Zupan[6]

Contributors:
S. Akar[6] , J. Alimena[7] , B.C. Allanach[8] , W. Altmannshofer[9] , L. Anderlini[10] , F. Archilli[11] , P. Azzi[12] , S. Banerjee[13] , W. Barter[14] , A.E. Barton[15] , M. Bauer[13] , I. Belyaev[16] , S. Benson[11] , M. Bettler[17] , R. Bhattacharya[18] , S. Bifani[19] , A. Birnkraut[20] , F. Bishara[21] , T. Blake[22] , S. Blusk[23] , E. Boos[24] , M. Borsato[25] , C. Bozzi[26,27] , A. Bragagnolo[28,12] , J. Brod[6] , J. Brodzicka[29] , A. J. Buras[30] , L. Cadamuro[31] , A. Carbone[32,33] , M. Carena[34,35] , I. Carli[151] , A. Carmona[36] , F.R. Cavallo[32] , A. Celis[37] , M. Cepeda[38,39] , G. S. Chahal[40,41] , M. Chala[13] , J. Charles[42] , M. Charles[2] , K.F. Chen[43] , V. Chobanova[44] , M. Chrzaszcz[27] , G. Ciezarek[27] , V. Cirigliano[45] , M. Ciuchini[46] , H. Cliff[17] , J. Cogan[47] , G. Colangelo[48] , A. Contu[49] , R. Covarelli[50,51] , G. Cowan[52] , A. Crivellin[53] , G. D'Ambrosio[54] , M. D'Onofrio[55] , N.P. Dang[56] , A. Davis[57] , O. A. De Aguiar Francisco[27] , K. De Bruyn[27] , U. De Sanctis[58,59] , H. De la Torre[60] , W. Dekens[45,61] , F. Deliot[62] , M. Della Morte[63] , S. Demers[64] , D. Derkach[65] , O. Deschamps[66] , S. Descotes-Genon[67] , F. Dettori[68] , A. Di Canto[27] , M. Dinardo[3,69] , P. Dini[3] , F. Dordei[49] , M. Dorigo[27,70] , A. dos Reis[181] , L. Dudko[24] , L. Dufour[11] , G. Durieux[71,21] , S. Dutta[18] , A. Dziurda[29] , U. Eitschberger[20] , A. Esposito[72] , M. Estevez[73] , S. Fajfer[74,75] , A. Falkowski[67] , D.A. Faroughy[74] , G. Fedi[76] , S. Fiorendi[3,69] , F. Fiori[77,76] , C. Fitzpatrick[27] , R. Fleischer[11] , M. Fontana[27] , P.J. Fox[34] , M. Freytsis[78,106] , E. Gámiz[79] , E. Gabriel[52] , P. Gambino[80] , J. García Pardiñas[81] , L.S. Geng[82] , E. Gersabeck[57] , M. Gersabeck[57] , T. Gershon[22] , A. Gilbert[38] , M. Gonzalez-Alonso[83] , P. Govoni[3,69] , G. Graziani[10] , A. Greljo[83] , L. Grillo[57] , B. Grinstein[61] , A. Grohsjean[84] , Y. Grossman[85] , D. Guadagnoli[86] , F.-K. Guo[87,88] , L. Guzzi[3,69] , J. Haller[89] , B. Hamilton[90] , T. Han[91] , R. Harnik[34] , D. Hill[92] , G. Hiller[93] , K. Hoepfner[94] , J.M. Hogan[95,96] , T. Hurth[36] , O. Igonkina[97,98] , P. Ilten[19] , G. Isidori[99] , Sa. Jain[100] , M. John[92] , D. Johnson[27] , M. Jung[101] , N. Jurik[92] , S. Jäger[102] , M. Kado[103,104,105] , A. L. Kagan[6] , J.F. Kamenik[74,75] , M. Karliner[106] , M. Kenzie[17] , B. Khanji[27] , J. Kieseler[38] , T. Kitahara[107] , T. Klijnsma[108] , M. Knecht[42] , N. Košnik[74,75] , R. Kogler[89] , P. Koppenburg[11] , A. Korytov[31] , M. Kreps[22] , C. Langenbruch[109] , U. Langenegger[110] , T. Latham[22] , R.F. Lebed[111] , A. J. Lenz[13] , N. Leonardo[135] , O. Leroy[47] , Q. Li[112] , T. Li[113] , F. Ligabue[76,77] , Z. Ligeti[114] , K. Long[115] , E. Lunghi[116] , F. Mahmoudi[117] , G. Mancinelli[47] , P. Mandrik[118] , T. Mannel[119] , X. Marcano[67] , J. F. Marchand[120] , D. Martínez Santos[121] , A. Martin[122] , M. Martinelli[27] , F. Martinez Vidal[123] , D. Marzocca[124] , J. Matias[125] , P. Matorras Cuevas[126] , O. Matsedonskyi[127] , A. Mauri[81] , K. Mazumdar[100] , M. Merk[11] , A.B. Meyer[84] , E. Michielin[12] , G. Mitselmakher[31] , L. Mittnacht[36] , S. Monteil[66] , M. J. Morello[76,128] , M. Morgenstern[97] , M. Narain[96] , M. Nardecchia[83] , M. Needham[52] , N. Neri[129,130] , M. Neubert[131] , S. Neubert[25] , U. Nierste[132] , J. Nieves[133] , Y. Nir[127] , A. Nisati[104,105] , D. P. O'Hanlon[32] , E. Oset[133] , P. Owen[81] , O. Ozcelik[134,135] , S. Pagan Griso[136,137] , E. Palencia Cortezon[138] , F. Palla[76] , M. Palutan[139] , M. Pappagallo[52] , C. Parkes[57,27] , S. Pascoli[13] , G. Passaleva[10,27] , E. Passemar[116,140,141] , M. Patel[14] , A. Pearce[27] , K. Pedro[142] , S. Perazzini[27] , M. Perfilov[24] , L. Perrozzi[108] , L. Pescatore[143] , B.A. Petersen[144] , A. A. Petrov[145] , A. Pich[133] , A. Pilloni[146,141] , F. Polci[2] , A.D. Polosa[147] , S. Prelovsek[75,74,148] , A. Puig Navarro[81] , G. Punzi[76,149] , J. Rademacker[150] , M. Rama[76] , M. Reboud[120] , A. Reimers[89] , P. Reznicek[151] , D. J. Robinson[9,114] , J. L. Rosner[152] , R. Ruiz[153,13] , S. Saito[100] , S. Sarkar[18] , A. Savin[115] , S. Sawant[100] , S. Schacht[85] , M. Schlaffer[127] , A. Schmidt[94] , B. Schneider[142] , A. Schopper[27] , M. H. Schune[154] , J. Segovia[155] , M. Selvaggi[38] , N. Serra[81] , G. Servant[21,156] , L. Sestini[12] , D. Shih[157] , R. Silva Coutinho[81] , L. Silvestrini[147,83] , K. Skovpen[158] , T. Skwarnicki[23] , M. Smizanska[15] , A. Soni[159] , Y. Soreq[83,71] ,

https://doi.org/10.23731/CYRM-2019-007.867

M. Spannowsky[160] , P. Spradlin[161] , E. Stamou[35] , S. Stone[23] , S. Stracka[76] , D. M. Straub[101] , A.P Szczepaniak[116,140,141] , S. T'Jampens[120] , Y. Takahashi[126] , F. Teubert[27] , E. Thomas[27] , V. Tisserand[66] , R. Torre[162,83] , F. Tresoldi[1] , D. Tsiakkouri[163] , S. Turchikhin[164] , K.A. Ulmer[165] , V. Vagnoni[32] , D. van Dyk[168] , J. van Tilburg[11] , S. Vecchi[26] , R. Venditti[166] , M. Vesterinen[22] , J. Virto[167,168] , P. Volkov[24] , G. Vorotnikov[24] , E. Vryonidou[83] , J. Walder[15] , W. Walkowiak[169] , J. Wang[31] , W. Wang[170] , C. Weiland[171,13] , M. Whitehead[109] , G. Wilkinson[92] , J. M. Williams[172] , M. R. J. Williams[57] , F. Wilson[173] , Y. Xie[174] , Z. Yang[175] , E. Yazgan[176] , T. You[177,178] , F. Yu[36,179] , C. Zhang[180] , L. Zhang[175] , W. Zhang[96]

[1]Department of Physics and Astronomy, University of Sussex, Brighton, United Kingdom, [2]LPNHE, Sorbonne Université, Paris Diderot Sorbonne Paris Cité, CNRS/IN2P3, Paris, France, [3]INFN Sezione di Milano-Bicocca, Milano, Italy, [4]Universidad de La Laguna, Facultad de Física, Avda. Astrofísico Fco. Sanchez s/n, 38206, La Laguna, Tenerife, Spain, [5]Instituto de Astrofísica de Canarias (IAC) C/ Vía Lactea, s/n E-38205, La Laguna, Tenerife, Spain, [6]University of Cincinnati, Cincinnati, OH, United States, [7]The Ohio State University, Columbus, USA, [8]Department of Applied Mathematics and Theoretical Physics, University of Cambridge, Wilberforce Road, United Kingdom, CB1 3BZ, [9]Santa Cruz Institute for Particle Physics (SCIPP), 1156 High Street, Santa Cruz, CA 95064, USA, [10]INFN Sezione di Firenze, Firenze, Italy, [11]Nikhef National Institute for Subatomic Physics, Amsterdam, Netherlands, [12]INFN Sezione di Padova, Padova, Italy, [13]Durham University, Institute for Particle Physics Phenomenology, Ogden Centre for Fundamental Physics, South Road, Durham DH1 3LE, United Kingdom, [14]Imperial College, London, United Kingdom, [15]Physics Department, Lancaster University, Lancaster, United Kingdom, [16]Institute of Theoretical and Experimental Physics (ITEP), Moscow, Russia, [17]Cavendish Laboratory, University of Cambridge, Cambridge, United Kingdom, [18]Saha Institute of Nuclear Physics, HBNI, Kolkata, India, [19]University of Birmingham, Birmingham, United Kingdom, [20]Fakultät Physik, Technische Universität Dortmund, Dortmund, Germany, [21]Deutsches Elektronen-Synchrotron (DESY), Notkestrasse 85, 22607 Hamburg, Germany, [22]Department of Physics, University of Warwick, Coventry, United Kingdom, [23]Syracuse University, Syracuse, NY, United States, [24]Skobeltsyn Institute of Nuclear Physics, Lomonosov Moscow State University, Moscow, Russia, [25]Physikalisches Institut, Ruprecht-Karls-Universität Heidelberg, Heidelberg, Germany, [26]INFN Sezione di Ferrara, Ferrara, Italy, [27]European Organization for Nuclear Research (CERN), Geneva, Switzerland, [28]Università di Padova, Padova, Italy, [29]Henryk Niewodniczanski Institute of Nuclear Physics Polish Academy of Sciences, Kraków, Poland, [30]TUM-IAS, Lichtenbergstr. 2a, D-85748 Garching, Germany, [31]University of Florida, Gainesville, USA, [32]INFN Sezione di Bologna, Bologna, Italy, [33]Università di Bologna, Dipartimento di Fisica, Bologna, Italy, [34]Theoretical Physics Department, Fermilab, Batavia, IL 60510, USA, [35]Enrico Fermi Institute and Kavli Institute for Cosmological Physics, University of Chicago, Chicago, IL 60637, USA, [36]PRISMA Cluster of Excellence and Institute for Physics (THEP), Johannes Gutenberg University Mainz, D-55099 Mainz, Germany, [37]Ludwig-Maximilians-Universität (LMU) Müchen, [38]CERN, European Organization for Nuclear Research, Geneva, Switzerland, [39]Centro de Investigaciones Energéticas Medioambientales y Tecnológicas (CIEMAT), Madrid, Spain, [40]Imperial College, London, UK, [41]Institute for Particle Physics Phenomenology, University of Durham, Durham, UK, [42]Aix-Marseille Univ, Universitè de Toulon, CNRS, CPT, Marseille, France, [43]National Taiwan University (NTU), Taipei, Taiwan, [44]Instituto Galego de Física de Altas Enerxías (IGFAE), Spain, [45]Theoretical Division, Los Alamos National Laboratory, MS B283, Los Alamos, NM 87545, USA, [46]INFN Sezione di Roma Tre, Via della Vasca Navale 84, I-00146 Roma, Italy, [47]Aix Marseille Univ, CNRS/IN2P3, CPPM, Marseille, France, [48]Institute for Theoretical Physics, Albert Einstein Center for Fundamental Physics, University of Bern, Sidlerstrasse 5, 3012 Bern, Switzerland, [49]INFN Sezione di Cagliari, Monserrato, Italy, [50]Università di Torino, Torino, Italy, [51]INFN Sezione di Torino, Torino, Italy, [52]School of Physics and Astronomy, University of Edinburgh, Edinburgh, United Kingdom,

[53]Paul Scherrer Institut, CH-5232 Villigen PSI, Switzerland, [54]Istituto Nazionale di Fisica Nucleare (INFN), Sezione di Napoli,via Cintia, I-80126 Napoli, [55]Oliver Lodge Laboratory, University of Liverpool, Liverpool, United Kingdom, [56]University of Louisville; United States of America, [57]School of Physics and Astronomy, University of Manchester, Manchester, United Kingdom, [58]INFN Roma Tor Vergata, Roma, Italy, [59]Università di Roma Tor Vergata, Dipartimento di Fisica, Roma, Italy, [60]Michigan State University, Department of Physics and Astronomy; United States of America, [61]University of California (UC), Department of physics, 9500 Gilman Dr. La Jolla, CA 92093-0319, USA, [62]IRFU, CEA, Université Paris-Saclay, Gif-sur-Yvette, France, [63]CP3-Origins, Syddansk Unversitet, Campusvej 55, DK-5230 Odense M, Denmark, [64]Department of Physics, Yale University, New Haven CT, United States of America, [65]National Research University Higher School of Economics, Moscow, Russia, [66]Universit'e Clermont Auvergne, CNRS/IN2P3, LPC, F-63000 Clermont-Ferrand, France , [67]Laboratoire de Physique Théorique (UMR8627), CNRS, Univ. Paris-Sud, Université Paris-Saclay, 91405 Orsay, France, [68]Oliver Lodge Laboratory, University of Liverpool, Liverpool, United Kingdom, [69]Università di Milano-Bicocca, Milano, Italy, [70]INFN Sezione di Trieste, Trieste, Italy, [71]Department of Physics, Technion, Haifa 32000, Israel, [72]Theoretical Particle Physics Laboratory (LPTP), Institute of Physics, EPFL, Lausanne, Switzerland, [73]International Center for Advanced Studies (ICAS), 25 de Mayo y Francia, San Martin, Pcia. de Buenos Aires, Argentina, [74]Jožef Stefan Institute, Jamova 39, P.O.B. 3000, SI-1001 Ljubljana, Slovenia, [75]University of Ljubljana, Faculty of Mathematics and Physics, Jadranska ulica 19, SI-1000 Ljubljana, Slovenia, [76]INFN Sezione di Pisa, Pisa, Italy, [77]Scuola Normale Superiore di Pisa, Pisa, Italy, [78]Princeton, Institute for Advanced Study (IAS), Einstein Drive Princeton, NJ, 08540, USA , [79]CAFPE and Departamento de Física Teórica y del Cosmos, Universidad de Granada, Granada, Spain , [80]Dipartimento di Fisica, Universita di Torino and INFN, Sezione di Torino, I-10125 Torino, Italy, [81]Physik-Institut, Universität Zürich, Zürich, Switzerland, [82]School of Physics, Beihang University, Beijing 100191, China, [83]CERN, TH Department, Geneva, Switzerland, [84]Deutsches Elektronen-Synchrotron, Hamburg, Germany, [85]Department of Physics, LEPP, Cornell University, Ithaca, NY 14853, USA, [86]LAPTh, 9 Chemin de Bellevue, F-74941 Annecy Cedex, France, [87]CAS Key Laboratory of Theoretical Physics, Institute of Theoretical Physics, Chinese Academy of Sciences, Zhong Guan Cun East Street 55, Beijing 100190, China, [88]School of Physical Sciences, University of Chinese Academy of Sciences, Beijing 100049, China , [89]University of Hamburg, Hamburg, Germany, [90]University of Maryland, College Park, MD, United States, [91]University of Pittsburgh, [92]Department of Physics, University of Oxford, Oxford, United Kingdom, [93]Fakultät Physik, TU Dortmund, Otto-Hahn-Str.4, D-44221 Dortmund, Germany, [94]RWTH Aachen University, III. Physikalisches Institut A, Aachen, Germany, [95]Bethel University, St. Paul, USA, [96]Brown University, Providence, USA, [97]Nikhef National Institute for Subatomic Physics and University of Amsterdam, Amsterdam, Netherlands, [98]Institute for Mathematics, Astrophysics and Particle Physics, Radboud University Nijmegen/Nikhef, Nijmegen, Netherlands, [99]Universit'at Zurich, Physik-Institut. Winterthurerstrasse 190, CH-8057 Zurich, Switzerland, [100]Tata Institute of Fundamental Research-B, Mumbai, India, [101]Excellence Cluster Universe, TUM, Boltzmannstr. 2, 85748 Garching, Germany, [102]Department of Physics and Astronomy, University of Sussex, Brighton BN1 6NL, United Kingdom, [103]LAL, Univ. Paris-Sud, IN2P3/CNRS, Université Paris-Saclay, Paris, France, [104]Sezione di Roma, Istituto Nazionale di Fisica Nucleare, Roma, Italy, [105]Sapienza Università di Roma, Dipartimento di Fisica, Roma, Italy, [106]School of Physics and Astronomy, Tel Aviv University, Israel, [107]Nagoya University, Furo-cho, Chikusa-ku, Nagoya-shi 464-6802, Japan, [108]ETH Zurich - Institute for Particle Physics and Astrophysics (IPA), Zurich, Switzerland, [109]I. Physikalisches Institut, RWTH Aachen University, Aachen, Germany, [110]Paul Scherrer Institut, Villigen, Switzerland, [111]Department of Physics, Arizona State University, Tempe, AZ 85287, USA, [112]State Key Laboratory of Nuclear Physics and Technology, Peking University, Beijing, China, [113]Department of Physics, Nankai University, [114]Lawrence Berkeley National Laboratory ; University of California, Berkeley, USA, [115]University of Wisconsin - Madison, Madison, USA, [116]Indiana University, 727 E 3rd St, Bloomington, IN 47405, USA, [117]Univ. Lyon,

Univ. Lyon 1, CNRS/IN2P3, Institut de Physique Nucléaire de Lyon, UMR5822, F-69622 Villeurbanne, France, [118]Institute for High Energy Physics of National Research Centre 'Kurchatov Institute', Protvino, Russia, [119]Physics Department, University of Siegen, 57072 Siegen, Germany , [120]Univ. Grenoble Alpes, Univ. Savoie Mont Blanc, CNRS, IN2P3-LAPP, Annecy, France, [121]Instituto Galego de Fisica de Altas Enerxias (IGFAE), Universidade de Santiago de Compostela, [122]University of Notre Dame, Notre Dame, Indiana 46556, USA, [123]Instituto de Fisica Corpuscular, Centro Mixto Universidad de Valencia - CSIC, Valencia, Spain, [124]INFN, Sezione di Trieste, Trieste, Italy, [125]Universitat Autonoma de Barcelona and IFAE, 08193 Bellaterra (Barcelona), [126]Universität Zürich, Zurich, Switzerland, [127]Department of Particle Physics and Astrophysics, Weizmann Institute of Science, Rehovot, Israel 7610001, [128]Pisa, Scuola Normale Superiore, Pisa, Italy, [129]INFN Sezione di Milano, Milano, Italy, [130]Università degli Studi di Milano, Milano, Italy, [131]Johannes Gutenberg University, Mainz, Germany, [132]Institute for Theoretical Particle Physics, Karlsruhe Institute of Technology (KIT), Wolfgang-Gaede-Str. 1, 76131 Karlsruhe, Germany , [133]Instituto de Fisica Corpuscular (IFIC), Centro Mixto Universidad de Valencia - CSIC , [134]Bogazici University, Istanbul, Turkey, [135]Laboratório de Instrumentacao Física Experimental de Partículas, Lisboa, Portugal, [136]Physics Division, Lawrence Berkeley National Laboratory and University of California, Berkeley CA, United States of America, [137]Department of Physics, University of California (UC), Berkeley, United States of America, [138]Universidad de Oviedo, Oviedo, Spain, [139]INFN Laboratori Nazionali di Frascati, Frascati, Italy, [140]Center for Exploration of Energy and Matter, Indiana University, Bloomington, IN 47408, USA, [141]Theory Center, Thomas Jefferson National Accelerator Facility, 12000 Jefferson Ave, Newport News VA 23606, USA, [142]Fermi National Accelerator Laboratory, Batavia, USA, [143]Institute of Physics, Ecole Polytechnique Fédérale de Lausanne (EPFL), Lausanne, Switzerland, [144]European Laboratory for Particle Physics, CERN, Geneva, Switzerland, [145]Department of Physics and Astronomy, Wayne State University, Detroit, MI 48201, USA, [146]European Centre for Theoretical Studies in Nuclear Physics and Related Areas (ECT*)) and Fondazione Bruno Kessler, Strada delle Tabarelle 286, I-38123 Villazzano (TN), Italy, [147]Sapienza Università di Roma and INFN, Piazzale Aldo Moro 2, I-00185, Rome, Italy, [148]Universitàt Regensburg, Fakultàt für Physik, Universitatsstr. 31, 93053 Regensburg, Germany, [149]Università di Pisa, Pisa, Italy, [150]H.H. Wills Physics Laboratory, University of Bristol, Bristol, United Kingdom, [151]Charles University, Faculty of Mathematics and Physics, Prague, Czech Republic, [152]University of Chicago, Enrico Fermi Institute, 5640 S Ellis Ave, Chicago IL 60637, USA, [153]Université Catholique de Louvain, Centre for Cosmology, Particle Physics, and Phenomenology, Louvain-la-Neuve, Belgium, [154]LAL, Univ. Paris-Sud, CNRS/IN2P3, Université Paris-Saclay, Orsay, France, [155]Departamento de Sistemas Físicos, Químicos y Naturales, Universidad Pablo de Olavide, E-41013 Sevilla, Spain, [156] Universitàt Hamburg, II Institut für Theoretische Physik, Luruper Chaussee 149, 22761 Hamburg, Germany, [157]NHETC, Dept of Physics and Astronomy, Rutgers University, 136 Frelinghuysen Rd, Piscataway, NJ 08854 USA, [158]Vrije Universiteit Brussel, Brussel, Belgium, [159]High Energy Theory, Brookhaven National Lab, Upton, NY 11973, USA, [160]Department of Physics, Durham University, [161]School of Physics and Astronomy, University of Glasgow, Glasgow, United Kingdom, [162]INFN, Genoa Istituto Nazionale di Fisica Nucleare (INFN) Sezione di Genova Via Dodecaneso, 33 I-16146 Genova Italy, [163]University of Cyprus, Nicosia, Cyprus, [164]JINR, Joint Institute for Nuclear Research, Dubna, Russia, [165]University of Colorado Boulder, Boulder, USA, [166]INFN Sezione di Bari, Bari, Italy, [167]Center for Theoretical Physics, Massachusetts Institute of Technology 77 Massachusetts Ave, Cambridge, MA 02139, USA, [168]Physik Department, Technische Universität München, James-Franck-Strasse 1, D-85748 Garching, Germany, [169]Department Physik, Universität Siegen, Siegen, Germany, [170]SKLPPC, School of Physics and Astronomy, Shanghai Jiao Tong University, Shanghai 200240, China, [171]University of Pittsburgh, Department of Physics and Astronomy, 3941 O'Hara Street, Pittsburgh, PA 15260, USA, [172]Massachusetts Institute of Technology, Cambridge, MA, United States, [173]STFC Rutherford Appleton Laboratory, Didcot, United Kingdom, [174]Institute of Particle Physics, Central China Normal University, Wuhan, Hubei, China, [175]Center for High Energy Physics, Tsinghua University, Beijing, China, [176]Institute of High Energy Physics, Beijing, China,

[177]University of Cambridge, Cavendish Laboratory, Madingley Road, Cambridge, CB3 0HE, United Kingdom, [178]Department of Applied Mathematics and Theoretical Physics, University of Cambridge, Wilberforce Road, United Kingdom, [179]Johannes Gutenberg Universitàt Mainz, Intitut für Physik, Staudinger Weg 7, 55128 Mainz, Germany, [180]Institute of High Energy Physics (IHEP), Chinese Academy of Sciences (CAS), [181]Centro Brasileiro de Pesquisas Físicas (CBPF), Rio de Janeiro, Brazil

Abstract

Motivated by the success of the flavour physics programme carried out over the last decade at the Large Hadron Collider (LHC), we characterize in detail the physics potential of its High-Luminosity and High-Energy upgrades in this domain of physics. We document the extraordinary breadth of the HL/HE-LHC programme enabled by a putative Upgrade II of the dedicated flavour physics experiment LHCb and the evolution of the established flavour physics role of the ATLAS and CMS general purpose experiments. We connect the dedicated flavour physics programme to studies of the top quark, Higgs boson, and direct high-p_T searches for new particles and force carriers. We discuss the complementarity of their discovery potential for physics beyond the Standard Model, affirming the necessity to fully exploit the LHC's flavour physics potential throughout its upgrade eras.

Contents

1 Introduction . . . 875
1.1 Theoretical considerations . . . 875
1.2 Experimental considerations and the breadth of flavour physics . . . 880
2 Testing the CKM unitarity and related observables . . . 886
2.1 Structure of the CKM matrix . . . 886
2.2 Current status of the constraints . . . 887
2.3 Combined constraints on the CKM parameters . . . 891
2.4 Theoretical prospects . . . 893
2.5 Experimental prospects . . . 894
2.6 Future of global CKM fits . . . 916
2.7 Future extrapolation of constraints on NP in $\Delta F = 2$ amplitudes . . . 920
3 Charm-quark probes of new physics . . . 923
3.1 Charm mixing . . . 923
3.2 CP violation in $D^0 - \overline{D}^0$ mixing . . . 925
3.3 Direct CP violating probes . . . 927
3.4 Null tests from isospin sum rules . . . 928
3.5 Radiative and leptonic charm decays . . . 928
3.6 Inputs for B physics . . . 931
3.7 Experimental prospects . . . 931
4 Strange-quark probes of new physics . . . 943
4.1 The (HL) LHC as a strangeness factory . . . 943
4.2 $K_S^0 \to \mu^+\mu^-$ and $K_L^0 \to \mu^+\mu^-$ decays . . . 944
4.3 $K_S \to \mu^+\mu^-\gamma$, $K_S \to \mu^+\mu^- e^+e^-$ and $K_S \to \mu^+\mu^-\mu^+\mu^-$ . . . 947
4.4 $K_S \to \pi^0\ell^+\ell^-$ and $K^\pm \to \pi^\pm\ell^+\ell^-$ . . . 947
4.5 $K_S \to \pi^+\pi^- e^+e^-$ . . . 949
4.6 LFV modes . . . 949
4.7 Hyperons at HL-LHC . . . 950
5 Tau leptons . . . 952
5.1 Lepton-flavour-conserving processes . . . 952
5.2 Lepton Flavour Violation . . . 954
6 Hadron spectroscopy and QCD exotica . . . 960
6.1 Open questions in spectroscopy . . . 960
6.2 Hadrons with a single heavy quark . . . 963
6.3 Hadrons containing $\bar{c}c$, $\bar{b}b$ or $\bar{c}b$ . . . 966
6.4 Experimental prospects . . . 968
7 Bottom-quark probes of new physics and prospects for B-anomalies . . . 975
7.1 Phenomenology of $b \to s\ell\ell$ decays . . . 975
7.2 Phenomenology of $b \to c\ell\nu$ decays . . . 983
7.3 Experimental perspectives . . . 989
8 The top quark and flavour physics . . . 1011

8.1 Global effective-field-theory interpretation of top-quark FCNCs . . . 1011
8.2 Anomalous Wtb vertices and CP-violation effects from T-odd kinematic distributions . 1020
8.3 Determinations of V_{tx} . . . 1022
9 The Higgs boson and flavour physics . . . 1026
9.1 New Physics benchmarks for modified Higgs couplings . . . 1026
9.2 Probing charm and light quark Yukawa couplings . . . 1028
9.3 LFV decays of the Higgs . . . 1036
9.4 CP violating Yukawa couplings . . . 1036
10 The high p_{T} flavour physics programme . . . 1039
10.1 Models of flavour and TeV Physics . . . 1039
10.2 Flavour implications for high p_{T} new physics searches . . . 1043
10.3 Implications of TeV scale flavour models for electroweak baryogenesis . . . 1050
10.4 Phenomenology of high p_{T} searches in the context of flavour anomalies . . . 1052
11 Lattice QCD in the HL/HE-LHC era . . . 1067
12 Conclusions . . . 1073
13 Acknowledgements . . . 1074
A Details on experimental extrapolations . . . 1076
A.1 Analysis methods and objects definitions . . . 1076
A.2 Treatment of systematic uncertainties . . . 1077

1 Introduction

The past decade has witnessed a highly successful programme of flavour physics at the LHC, building on and greatly expanding the pioneering work at the Tevatron's CDF and DØ. The unprecedented breadth and precision of the physics results produced by the LHC's dedicated flavour physics experiment, LHCb, has been complemented by crucial measurements at ATLAS and CMS. Together, they have probed the Standard Model at energy scales complementary to the direct LHC searches, and proven that it is possible to carry out a broad programme of precision flavour physics in such a challenging hadronic environment. This document offers a glimpse of the future – the potential for flavour physics in the High-Luminosity phase of the Large Hadron Collider (HL-LHC) and its possible upgrade to a 27 TeV proton collider, the High-Energy LHC (HE-LHC). The landscape of flavour physics is considered and theoretical arguments are presented for measurements with higher precision and of qualitatively new observables. The prospective experimental sensitivities for the HL-LHC assume 3000 fb^{-1} recorded by ATLAS and CMS, and 300 fb^{-1} recorded by a proposed Upgrade II of LHCb.

The main points, detailed in the subsequent sections, are:

- The flavour physics programme at the LHC comprises many different probes: the weak decays of beauty, charm, strange and top quarks, as well as of the τ lepton and the Higgs;
- CP violation and Flavour Changing Neutral Currents (FCNCs) are sensitive probes of short-distance physics, within the Standard Model (SM) and beyond (BSM);
- Flavour physics probes scales much greater than 1 TeV, with the sensitivity often limited by statistics and not by theory;
- For most FCNC processes, a New Physics (NP) contribution at 20% of the SM is still allowed, so there is plenty of discovery potential;
- Spectroscopy and flavour changing transitions serve as laboratories for a better understanding of nonperturbative Quantum Chromodynamics (QCD);
- Some of the several tensions between flavour physics data and the SM may soon become decisive;
- Precision tests of the SM flavour sector will improve by orders of magnitude including Charged Lepton Flavour Violating transitions (CLFV);
- Flavour physics will teach us about physics at shorter distances, complementary to the high-$p_{\rm T}$ physics programme, whether NP is seen or not, and could point to the next energy scale to explore.

1.1 Theoretical considerations

Authors (TH): G. Isidori, Z. Ligeti.

As a community, we are now in a strikingly different position than we were a decade ago, before the LHC turned on. Already before the start of the LHC it was clear from unitarity considerations that the LHC experiments were basically guaranteed to uncover the origin of the electroweak symmetry breaking, i.e., the breaking of the $SU(2)_L \times U(1)_Y$ gauge symmetry to the $U(1)$ of electromagnetism. The discovery of the Higgs boson by ATLAS and CMS in 2012 was a triumph, confirming these expectations. Since then we have learned that the properties of the Higgs boson are in increasing agreement with the SM. Coupled with the lack of direct signals of BSM particles so far, this increasingly points to a mass gap between the SM particle spectrum and the BSM one.

After completion of the first phase of the LHC programme, the field entered into a more uncertain, yet possibly more exciting exploratory era. We are still faced by a number of key open questions, e.g., the need for dark matter and how to generate the baryon asymmetry. We thus do know that BSM physics must exist. However, we do not know which experiments, at what energy scale, and probing which aspects of our understanding of nature, may provide the first unambiguous evidence for BSM phenomena. The phenomenological successes of the SM, in conjunction with being a renormalizable quantum field theory,

means that there is no clear guidance where to search for clues on how to extend the SM. [1] This calls for a diversified programme of BSM searches, with no stone left unturned. A deeper study of the properties of the Higgs boson is one of the pillars of this programme, and will be the central focus of the HL-LHC. The same programme also offers unique opportunities for tremendous improvements in indirect NP searches via precision studies of low-energy flavour-changing observables. Here the expected increase in statistics may be even larger than in the Higgs sector. As explained below, this programme is complementary to both the high-$p_{\rm T}$ NP searches as well as to the indirect NP searches performed via the Higgs precision measurements. To show this, we first give a brief introduction to flavour physics, starting with the "flavour puzzle" and the general discussion of probing BSM through flavour transitions.

1.1.1 The flavour puzzle

Flavour is the label generically used to differentiate the 12 fermions which, according to the SM, are the basic constituents of matter. These particles can be grouped into 3 families, each containing two quarks and two leptons. The particles within a given family have different combinations of strong, weak, and electromagnetic charges. This in turn implies differing behaviors under the SM interactions. Across the three families the particle content is identical except for the masses. That is, the second and third family are copies of the first family, with the same SM quantum numbers for the copies of particles across generations, but with different masses. Ordinary matter consists of particles of the first family: the up and down quarks that form atomic nuclei, as well as the electrons and the corresponding neutrinos. The question why there are three almost identical replicas of quarks and leptons as well as the origin of their different mass matrices are among the big open questions in fundamental physics, often referred to as the "SM flavour puzzle".

Within the SM, the hierarchy of fermion masses originates from the hierarchy in the strengths of interactions between the fermions and the Higgs field, namely from the structure of the Yukawa couplings. However, this prescription does not provide any explanation for the origin of the large hierarchies observed among fermion masses. Putting aside the special case of neutrinos, there are five orders of magnitudes between the mass of an electron and a top quark. Similarly, we do not know what determines the peculiar and rather different mixing structure in the quark and lepton mass matrices observed through the misalignment of mass and weak-interaction eigenstates in flavour space. We do know experimentally, that the Higgs field is responsible for the bulk of the heaviest quark and lepton masses: the top and bottom quarks and the tau leptons. The generation of at least some of the quark masses and mixing angles is thus connected to the Higgs sector. This suggests a possible connection between the flavour puzzle and the electroweak hierarchy puzzle, another big open question pointing toward some form of new physics.

1.1.2 Model-independent considerations

The above puzzling aspects make flavour physics, i.e., the precision study of flavour-changing processes in the quark and lepton sector, a very interesting window on possible physics beyond the SM. We do not know if there is an energy scale at which the flavour structure observed assumes a simpler form, i.e., we do not know if the masses and mixing angles, as observed at low energies, can be predicted in terms of a reduced number of more fundamental parameters in a theory valid at some high scale. On the other hand, precision measurements of flavour-changing transitions may probe such scales, even if they are well above the LHC center-of-mass energy.

This statement can be made quantitative by considering the SM as a low-energy effective theory that is valid up to a cut-off scale Λ, taken to be bigger than the electroweak scale $v = (\sqrt{2}\,G_F)^{-1/2} \approx$

[1] The only clearly established exception are neutrino masses which require non-renormalizable operators (or new degrees of freedom) and seem to point toward a very high scale of new physics that is not accessible in practice. However, the existence of a high new scale connected to neutrino mass generation does not prevent other BSM physics to appear at lower scales.

246 GeV. According to such an assumption of heavy NP, the amplitudes describing a flavour changing transition of a fermion ψ_i to a fermion ψ_j can be cast into the following general form

$$\mathcal{A}(\psi_i \to \psi_j + X) = \mathcal{A}_0 \left(\frac{c_{\rm SM}}{v^2} + \frac{c_{\rm NP}}{\Lambda^2} \right). \tag{1}$$

Since in many cases $c_{\rm SM} \ll 1$, NP effects can have a large impact even if $\Lambda \gg v$. For instance, in the quark sector the reason that often $c_{\rm SM} \ll 1$ stems from the facts that:

(i) $c_{\rm SM}$ can be proportional to small entries of the Cabibbo-Kobayashi-Maskawa (CKM) matrix and/or to small SM Yukawa couplings;

(ii) $c_{\rm SM}$ may include a loop factor $1/(16\pi^2)$, if the corresponding transition is forbidden at tree level, as is the case for flavour-changing neutral-current (FCNC) transitions or meson-antimeson mixing transitions.

As a result, these low-energy processes can probe indirectly, via quantum effects, scales of order $v/\sqrt{c_{\rm SM}}$. These can easily exceed those directly reachable via production of on-shell states in current and planned accelerators. As an explicit example, in the case of $B-\bar{B}$ mixing, $\sqrt{c_{\rm SM}} \sim |V_{td}|/(4\pi) \sim 10^{-3}$, hence this observable can probe NP scales up to 10^3 TeV in models with $c_{\rm NP} \sim 1$.

The precise values of the NP scale probed at present vary over a wide range, depending on the specific observable and the specific NP model ($c_{\rm NP}$ can span a large range, too). However, the form of Eq. (1) does allow us to predict how the bounds will improve with increasing datasets. For the observables that are SM dominated, are already observed, and whose uncertainties are dominated by statistics, the corresponding bound on Λ scales as $N^{1/4}$, where N is the relative increase in the number of events. The same scaling occurs for forbidden or highly suppressed SM processes, i.e., in the limit $c_{\rm SM} \ll c_{\rm NP}$, if the search is not background dominated. Thus, with two orders of magnitude increase in statistics one can probe scales roughly 3 times higher than at present. This is well above the increase in NP scale probed in on-shell heavy particle searches at high-$p_{\rm T}$ that can be achieved at fixed collider energy by a similar increase in statistics.

While theoretical uncertainties are often important, there are enough measurements which are known not to be limited by theoretical uncertainties. Improved experimental results will therefore directly translate to better NP sensitivity. There are also several cases of observables sensitive to NP where the theoretical uncertainties are mainly of parametric nature (e.g., our ability to precisely compute $c_{\rm SM}$ is dominated by the knowledge of CKM elements, quark masses, etc.). For such cases, we can expect significant increase in precision with higher statistics thanks to the improvement in the reduction of parametric uncertainties. This also highlights the importance of a broad flavour physics programme where the focus is not only on rare or CP violating processes "most likely" affected by NP but also on core SM measurements which help to reduce the theoretical uncertainties.

1.1.3 Current anomalies and historical comments

Due to the generic sensitivity to high scales, flavour physics has historically played a major role in developing and understanding the Standard Model. Flavour physics measurements signalled the presence of "new" particles well before these were directly observed (this was the case for charm and top quarks from $K_L \to \mu^+\mu^-$ decays and K-meson mixing, and from B-meson mixing, respectively). With the completion of the SM, and the increasingly precise tests that the SM predictions have successfully passed, one may draw the naive conclusion that the discovery potential of precision experiments has declined in the last decades. However, the opposite is true. First of all, a qualitative change in our understanding has been achieved during that time. Before the asymmetric B factory experiments, BaBar and Belle, it was not known whether the SM accounted for the dominant or just a small part of CP violation observed in kaon mixing. We now know that the bulk of it is due to the SM Kobayashi-Maskawa mechanism. However, even after decades of progress, for most FCNC amplitudes the NP is still allowed to contribute at $\sim 20\%$ of the SM contribution.

The great improvements in precision for several flavour-changing processes achieved in the last 20 years, both at experimental and theoretical levels, represent a very important advancement of the field. We learned that either NP is much heavier than the electroweak scale, or, if it is not far above the electroweak scale as required by most solutions of the hierarchy puzzle, it must have a highly nontrivial flavour structure that is able to mimic the strong suppression of FCNC transitions in the SM. The latter statement has often been oversimplified, assuming that there is little hope to observe significant deviations from the SM in flavour physics. The anomalies recently observed in semileptonic B decays clearly demonstrated a genuine discovery potential, regardless of whether or not their significance increase with improved measurements.

Recent measurements, both in charged-current and in neutral-current semileptonic B decays, hint at a violation of one of the key predictions of the SM – the universality of interactions for leptons of different generations (in the limit where their masses can be neglected). These anomalies represent the strongest tensions with the SM predictions currently observed in laboratory experiments. The statistical significance of the anomalies is not high enough to claim a discovery but the situation is very interesting. More precise measurements of some of these observables, in particular the lepton flavour universality violating ratios $R_{K^{(*)}} = \Gamma(B \to K^{(*)}\mu^+\mu^-)/\Gamma(B \to K^{(*)}e^+e^-)$ and $R(D^{(*)}) = \Gamma(B \to D^{(*)}\tau\bar{\nu})/\Gamma(B \to D^{(*)}l\bar{\nu})$, where $l = e,\ \mu$, could establish the presence of NP even with modest improvements in statistics. At the current central values for these anomalies, analyzing all of the Run 1 and Run 2 data could already establish a discrepancy with the SM expectation in a single observable with $5\,\sigma$ significance.

Whether or not these anomalies will gain significance to become unambiguous signals of physics beyond the SM, they have clearly exemplified the discovery potential of flavour-physics observables and enlarged our horizon regarding possible BSM scenarios. Before the appearance of these anomalies, lepton flavour universality (LFU) was an implicit assumption adopted by the vast majority of BSM scenarios proposed . It is now better appreciated that LFU is an accidental property of the SM. It is well tested in transitions involving only the first two generations of quarks and leptons, while it is rather poorly tested in processes involving the third generation (and may indeed be violated at a detectable level in B decays). A deeper scrutiny of this SM property has highlighted the interest in a large variety of observables, with small theoretical uncertainties, which would strongly benefit from more statistics. Similarly, it has often (though not always) been taken for granted that NP effects in tree-level dominated processes, such as those affecting $R(D^{(*)})$, are negligible, while it is now clear that there are many NP scenarios where this assumption does not hold. This observation has important phenomenological consequences and signals the limitation of a significant fraction of current NP analyses. Last but not least, theoretical models addressing the anomalies have highlighted the interest of BSM constructions containing heavy leptoquark fields – a class of NP models that was not popular until a few years ago.

The current central values of $R_{K^{(*)}}$ and, especially, $R(D^{(*)})$ imply that NP needs to be at a fairly low scale: below few tens of TeV in the former, and a few TeV in the latter case. This can be easily understood given that the NP effects need to give $\mathcal{O}(10\% - 20\%)$ corrections to the amplitudes which are one-loop and tree level in the SM, respectively. Models addressing the anomalies are therefore a perfect laboratory to explore the interplay between indirect NP searches from flavour observables and direct searches at high-$p_{\rm T}$. Interestingly enough, even in the low-scale models addressing $R(D^{(*)})$, with or without $R_{K^{(*)}}$, there exist ample regions of parameter space that are able to explain the anomalies and that are at the same time consistent with the null results of NP searches performed so far at high $p_{\rm T}$.

1.1.4 Connections to lepton flavour violation

The CLFV processes, such as $\tau \to 3\mu$, are essential parts of the flavour-physics programme. CLFV amplitudes can also be decomposed as in Eq. (1), with the advantage that in this case $c_{\rm SM}$ vanish. If the SM is extended to describe neutrino masses, non-zero predictions arise but are suppressed by m_ν^2/m_W^2.

The predicted CLFV rates are thus many orders of magnitudes below the detection reach of any present or planned facility. As a consequence the searches for CLFV are very clean and powerful ways to search for physics beyond the SM.

Any attempt to solve the flavour puzzle with new dynamics not far from the TeV scale, such that the observed hierarchies in the Yukawa couplings are accounted for by the new dynamics, naturally leads to CLFV rates not far from the present bounds. The recent LFU anomalies have strengthened the case further. Many models explaining these anomalies predict CLFV at a detectable level, in many cases just below the current bounds. Of noteworthy interest, triggered by the recent anomalies, are processes that violate both quark and lepton flavour, such as $B \to K\tau\mu$. There is a large variety of observables of this type that, together with purely leptonic observables, form a large and very promising sub-field of NP probes. Such searches can be organized in a large matrix, with the row and column indices determined by lepton and quark flavours, which is largely unexplored at present. For any NP model that may populate entries in this matrix, there is a large complementarity between the HL-LHC experiments, Belle-II, and dedicated experiments at muon beams searching for $\mu \to e$ conversion, $\mu \to e\gamma$, and $\mu \to 3e$, as well as with the flavour diagonal probes such as the measurements of the $(g-2)$ of the muon and the electron, or the searches for electric dipole moment of the electron.

1.1.5 Connections with the hierarchy problem and complementarity with high-p_{T} searches

BSM models proposed to address the electroweak hierarchy problem, such as supersymmetric models or composite Higgs models, predict new particles around the TeV scale. For all these models, flavour physics imposes very stringent bounds, requiring a flavour structure not far from that in the SM. This was the main rationale underlying the hypothesis of Minimal flavour Violation (MFV). The MFV hypothesis is an ansatz for the flavour structure of NP that assumes that the SM Yukawa couplings are the only sources of flavour non-degeneracy even beyond the SM. This requirement is nowadays partially relaxed by the absence of direct signals of NP in high-p_{T} experiments, allowing non-trivial modifications from the strict MFV. This example illustrates nicely the importance of flavour physics in reconstructing the structure of any NP model addressing the electroweak hierarchy problem. But it also reveals its complementarity with the high-p_{T} experiments, where improved direct bounds relax the flavour structure requirements.

If there are new particles which couple to the SM quarks or leptons, then, in general, there are corresponding new flavour parameters. Measuring them would be very important in order to understand the structure of NP. This has been studied in great detail in the context of Supersymmetry (SUSY) (alignment mechanism of the soft-breaking terms) and in composite models (partial-compositeness mechanism). In the specific case of low energy supersymmetry, the squark and slepton couplings may yield measurable effects in FCNC processes and CP violating observables and may give rise to detectable CLFV transitions. Observable CP violation is also possible in neutral currents and in electric dipole moments, for which the SM predictions are below the near future experimental sensitivities. The supersymmetric flavour problems, namely the observation that TeV-scale SUSY models with generic parameters are excluded by FCNC and CP violation measurements, can be alleviated in several scenarios: (i) universal squark masses (e.g., gauge mediation); (ii) quark–squark alignment, (e.g., horizontal symmetry); (iii) very heavy squarks (e.g., split SUSY). All viable models incorporate some of these ingredients. Conversely, if SUSY is discovered, mapping out its flavour structure, with the help of future more precise flavour tests, may help answer questions about even higher scales, the mechanism of SUSY breaking and the way it is communicated to the Minimal Supersymmetric Standard Model (MSSM), etc.

1.1.6 Nonperturbative QCD and its role in flavour physics

Of special interest are the theoretical uncertainties due to our incomplete understanding of QCD dynamics at low energies. In order to extract information on short-distance physics from weak decays of

hadrons, knowledge of nonperturbative matrix elements, encoded in decay constants and form factors, is usually needed. Refinements in the effective-field-theory (EFTs) approaches exploiting heavy-quark and/or low-energy perturbative expansions and, especially, major progress in lattice QCD calculations seen in the last decade, make possible a full exploitation of the BSM flavour physics programme. Some of the hadronic uncertainties have already reached the per-mille level, e.g., the theoretical precision in the calculation of nonperturbative quantities crucial for the extraction of the CKM matrix element $|V_{us}|$, and many more are at the percent level, for instance, the theory prediction for the rare FCNC decay $B_q \to \mu^+\mu^-$.

On the other hand, there are many other transitions that would benefit from further theoretical breakthroughs. In the past, large increases in available data always triggered new theory developments, and better understanding of the domain of applicability and accuracy of existing theoretical tools. It can be anticipated that these fruitful cross-fertilizations will continue to occur in the HL-LHC era between flavour physics experiments and theory. While there is a substantial suite of measurements whose interpretations will not be limited by hadronic uncertainties, the experimental programme can still benefit a lot from theoretical improvements. For many observables, lattice QCD improvements are important. The anticipated improvements in experimental precision also pose interesting challenges for lattice QCD, to robustly address isospin violating and electromagnetic effects in flavour observables. For many nonleptonic decays, relevant for CP violation, lattice QCD is unlikely to make a big impact. Nevertheless, developing new methods based on effective theories and testing existing approaches can be expected to improve the theoretical understanding of many observables, further enhancing the sensitivity of the experimental programme to possible BSM phenomena.

Understanding the nonperturbative structure of QCD of course has significant scientific merit per se, independent of the searches for NP. A very active area of research that will benefit from the flavour programme at HL/HE-LHC is hadron spectroscopy. A plethora of new states, many of which were unexpected or show intriguing features, have been discovered at the B-factories, Tevatron and the LHC. The increase of data samples at the HL-LHC will make it possible to discover many more of these states and chart their quantum numbers and properties. Accommodating them into our theoretical understanding of the nonperturbative regime of QCD will be a major challenge for the next decades.

1.1.7 Unexpected discoveries

It goes without saying that it is impossible to predict truly unexpected future discoveries. However, it cannot be emphasized enough that the large increase in datasets has the potential to revolutionize the field by unexpected discoveries and trigger entirely new areas of experimentation. It should be obvious that exact and approximate conservation laws should be tested as precisely as possible, especially when the experimental sensitivity can substantially increase. Recall that the discovery of CP violation itself was unexpected, in an experiment whose primary goal was checking an anomalous kaon regeneration result. New particles with surprising properties were in fact discovered at each of BaBar, Belle, and LHCb, respectively: the discoveries of the $D_{sJ}(2317)$ meson with a mass much below expectations, the discovery of the unexpectedly narrow charmonium-like state $X(3872)$ and the $Z(4430)$, and the discovery of pentaquarks. Thus, beside the "classical" searches for flavour-violating processes mentioned so far, both in quark and lepton sectors, other searches like those related to dark sectors in many channels or BSM searches not yet conceived will all form important parts of the flavour physics programme in the HL-LHC era.

1.2 Experimental considerations and the breadth of flavour physics

At the end of the HL-LHC the useful datasets will have increased by a factor of order 30–100 compared to the present ones. However, due to improvements in detector capabilities and changing running conditions, robust estimates of sensitivity improvements are complicated tasks discussed in details in the next

sections. At LHCb, in most analyses, one may expect faster improvements in the results than simply scaling with collected total luminosity, due to improvements in detector capabilities in the upcoming upgrades. At ATLAS and CMS the large number of interactions per bunch crossing during the HL-LHC will be a challenge. However, the upgraded detectors will have higher granularity and timing information to mitigate pileup effects [1,2]. It is important to pursue as broad a programme as possible, since several key channels are expected to remain competitive with LHC.

In many cases Belle-II and tau-charm factories such as BES III will provide competition and cross-checks of LHCb results. However, especially in the very low rate modes, such as $B_d \to \mu^+\mu^-$, it is ATLAS and CMS and not Belle-II which are expected to best compete with LHCb. If there are anomalies in B_s, and especially in Λ_b decays, they can only be cross-checked at the LHC experiments.

As mentioned above, our ignorance about BSM physics requires a diversified programme that, even within the flavour-physics domain, calls for a large set of complementary measurements. To properly identify the BSM model, if deviations are observed, measuring its imprint on different observables is very important, as stressed, e.g., in Ref. [3]. These measurements cannot all be performed at a single facility. There is full complementarity and many potential synergies in case some BSM signal emerges, among different b-hadron decays ($B_{u,d}$, B_s, Λ_b, etc.), CP violating and rare processes involving charm and kaons, as well as possible FCNC transitions with top-quark. For instance, the measurements of theoretically precisely known $s \to d\nu\nu$ FCNC transitions are expected from NA62 and KOTO, and will be directly complementary to the results from the flavour programme at the LHC. Such measurements of different flavour transitions are important to determine the BSM flavour structure, while measurements of the same quark level transition, but with different hadronic initial and final states determine the chiral structure of the BSM model.

1.2.1 Key experimental capabilities at ATLAS and CMS

The upgraded high-luminosity LHC (HL-LHC) will deliver to the CMS and ATLAS experiments proton-proton collisions at a center-of-mass energy of 14 TeV for a total integrated luminosity of about 3000 fb^{-1}. This goal will be achieved through a high instantaneous luminosity which implies up to 200 proton-proton interactions per bunch-crossing. In this regime, the experimental sensitivity to new physics is enhanced and complemented by flavour physics measurements, with sensitivities in specific modes (e.g., $B_{s,d} \to \mu\mu$, $B_s^0 \to J/\psi\phi$, $B^0 \to K^{*0}\mu\mu$) comparable to those of dedicated experiments. The ability of general purpose detectors to make precision heavy flavour measurements has been clearly demonstrated by the results from Run-1 and Run-2 data. HL-LHC can be a unique test bench for B physics studies in ATLAS and CMS: $\sim 10^{15}$ $b\bar{b}$ pairs will be produced for the integrated luminosity goal.

ATLAS and CMS will exploit this potential thanks to some projected Phase-2 upgrades which promise good detection capability at low momenta, good pileup effect mitigation and even, in some cases, an improved performance. Examples are the new inner trackers, improvements of the muon systems, topological trigger capabilities, and the possibility to use tracking in the early stages of the trigger chain [1,2].

The high integrated luminosity expected will allow ATLAS and CMS to study some rare processes at a precision never attained before. The excellent tracking and muon identification performances are highlighted by a number of benchmark channels, $B_{s,d} \to \mu\mu$, $B^0 \to K^{*0}\mu\mu$, $B_s \to J/\psi\phi$, and $\tau \to 3\mu$, that are used for projections. Precision measurements at the level of 5% to 10% for the $B_s^0 \to \mu^+\mu^-$ branching fraction, are expected, along with the observation of the $B^0 \to \mu^+\mu^-$ decay with more than 5σ, and a measurement of the $B_s^0 \to \mu^+\mu^-$ effective lifetime with a 3% statistical precision. The sensitivity to the CP-violating phase ϕ_s in the $B_s^0 \to J/\psi\phi$ mode is estimated to be at the level of $\sim$ 5 mrad, i.e., a factor of ~ 20 better than the corresponding Run-1 analyses values (a factor of ~ 5 with respect to the current combination of $b \to \bar{c}cs$ measurements). The uncertainty on the angular variable P_5' in $B^0 \to K^{*0}\mu^+\mu^-$ as a function of the dimuon squared invariant mass (q^2) is expected to improve

by a factor of 15 with respect to the published Run-1 measurements. With the HL-LHC high statistics the $B^0 \to K^{*0}\mu^+\mu^-$ analysis can be performed in narrow bins of q^2 to reach a more precise determination of the angular observables. Finally, the $\tau \to 3\mu$ decay is expected to be probed down to $\mathcal{O}(10^{-9})$.

The lack of particle-ID detectors is bound to limit the investigation of fully hadronic final states at ATLAS and CMS. Nevertheless, some capability is retained through the early use of tracking in the trigger selection. The $B_s \to \phi\phi \to 4K$ decay is an example of a hadronic final state that would benefit from the tracking performance at trigger level and the ϕ resonance signature. Furthermore, the precision time information from the timing detector [4] will bring new and unique capabilities to the detectors in the heavy flavour sector.

The heavy flavour programme at ATLAS and CMS requires dedicated low-$p_{\rm T}$ triggers, in contention for bandwidth with high-$p_{\rm T}$ measurements and searches. The physics scenario at the time of HL-LHC will motivate the optimal trigger bandwidth allocation for low-$p_{\rm T}$ studies. Indeed, considering the tenfold increase in the High Level Trigger rates and pileup mitigation, it could be conceivable to think of analysis dedicated streams to be performed with the whole 3000 fb^{-1} statistics or in dedicated runs, with minimal impact on the high-$p_{\rm T}$ physics. Still unexplored options, such as 40MHz data scouting, will be also studied. Furthermore, the high-$p_{\rm T}$ searches in ATLAS and CMS will allow for a programme of measurements which are complementary to the low-$p_{\rm T}$ flavour investigations and will help to build a coherent theoretical picture.

1.2.2 Key experimental capabilities at LHCb

The Upgrade II of LHCb will enable a very wide range of flavour observables to be determined with unprecedented precision, which will give the experiment sensitivity to NP scales several orders of magnitude above those accessible to direct searches. The expected uncertainties for a few key measurements with 300 fb^{-1} are presented in Table 1. The future LHCb estimates are all based on extrapolations from current measurements, and take no account of detector improvements apart from an approximate factor two increase in efficiency for hadronic modes, arising from the full software trigger that will be deployed from Run 3 onwards. Three principal arguments motivate the Upgrade II of LHCb, and the full exploitation of the HL-LHC for flavour physics.

1. There is a host of measurements of *theoretically clean* observables, such as the CP-violating phase γ, the lepton-universality ratios R_K, R_{K^*} etc., or the ratio of branching fractions $R \equiv \mathcal{B}(B^0 \to \mu^+\mu^-)/\mathcal{B}(B^0_s \to \mu^+\mu^-)$, where knowledge will still be statistically limited after Run 4. The same conclusion applies for other observables such as ϕ_s and $\sin 2\beta$, where strategies exist to monitor and control possible Penguin pollution. The HL-LHC and the capabilities of LHCb Upgrade II offer a unique opportunity to take another stride forward in precision for these quantities. Advances in lattice-QCD calculations will also motivate better measurements of other critical observables, e.g. $|V_{ub}|/|V_{cb}|$.
   The anticipated impact of the improved knowledge of Unitarity Triangle parameters can be seen in Fig. 1, which shows the evolving constraints in the $\bar{\rho} - \bar{\eta}$ plane from LHCb inputs and lattice-QCD calculations, alone. The increased sensitivity will allow for extremely precise tests of the CKM paradigm. In particular, it will permit the tree-level observables, which provide SM benchmarks, to be assessed against those with loop contributions, which are more susceptible to NP. In practice, this already very powerful ensemble of constraints will be augmented by complementary measurements from Belle-II, particularly in the case of $|V_{ub}|/|V_{cb}|$.
   The increasing precision of observables from measurements of statistically-limited FCNC processes will provide significant improvements in sensitivity to the scale of NP. As an example, Table 2 shows the expected improvement with integrated luminosity in the knowledge of the Wilson coefficients C_9 (vector current) and C'_{10} (right-handed axial-vector current), and the corresponding 90% exclusion limits to the NP scale Λ under various scenarios. The reach for generic NP at

Table 1: Summary of prospects for future measurements of selected flavour observables for LHCb. The projected LHCb sensitivities take no account of potential detector improvements, apart from in the trigger. See subsequent chapters for definitions.

Observable	Current LHCb	LHCb 2025	Upgrade II
EW Penguins			
R_K $(1 < q^2 < 6\,\mathrm{GeV}^2c^4)$	0.1 [5]	0.025	0.007
R_{K^*} $(1 < q^2 < 6\,\mathrm{GeV}^2c^4)$	0.1 [6]	0.031	0.008
R_ϕ, R_{pK}, R_π	–	0.08, 0.06, 0.18	0.02, 0.02, 0.05
CKM tests			
γ, with $B_s^0 \to D_s^+ K^-$	$(^{+17}_{-22})^\circ$ [7]	4°	1°
γ, all modes	$(^{+5.0}_{-5.8})^\circ$ [8]	1.5°	0.35°
$\sin 2\beta$, with $B^0 \to J/\psi K^0_S$	0.04 [9]	0.011	0.003
ϕ_s, with $B_s^0 \to J/\psi\phi$	49 mrad [10]	14 mrad	4 mrad
ϕ_s, with $B_s^0 \to D_s^+ D_s^-$	170 mrad [11]	35 mrad	9 mrad
$\phi_s^{s\bar{s}s}$, with $B_s^0 \to \phi\phi$	154 mrad [12]	39 mrad	11 mrad
a^s_{sl}	33×10^{-4} [13]	10×10^{-4}	3×10^{-4}
$\lvert V_{ub}\rvert/\lvert V_{cb}\rvert$	6% [14]	3%	1%
$B_s^0, B^0 \to \mu^+\mu^-$			
$\mathcal{B}(B^0 \to \mu^+\mu^-)/\mathcal{B}(B_s^0 \to \mu^+\mu^-)$	90% [15]	34%	10%
$\tau_{B_s^0 \to \mu^+\mu^-}$	22% [15]	8%	2%
$S_{\mu\mu}$	–	–	0.2
$b \to c\ell^-\bar{\nu}_l$ LUV studies			
$R(D^*)$	0.026 [16, 17]	0.0072	0.002
$R(J/\psi)$	0.24 [18]	0.071	0.02
Charm			
$\Delta A_{CP}(KK - \pi\pi)$	8.5×10^{-4} [19]	1.7×10^{-4}	3.0×10^{-5}
A_Γ $(\approx x \sin\phi)$	2.8×10^{-4} [20]	4.3×10^{-5}	1.0×10^{-5}
$x \sin\phi$ from $D^0 \to K^+\pi^-$	13×10^{-4} [21]	3.2×10^{-4}	8.0×10^{-5}
$x \sin\phi$ from multibody decays	–	$(K3\pi)$ 4.0×10^{-5}	$(K3\pi)$ 8.0×10^{-6}

tree-level in Upgrade II is found to exceed 100 TeV.

2. It will be essential to *widen the set of observables under study* beyond those accessible at the current LHCb experiment or its first upgrade, *e.g.* by including additional important measurements involving $b \to s\ell^+\ell^-$, $b \to d\ell^+\ell^-$ and $b \to c\ell^-\bar{\nu}_l$ decays. Improving our knowledge of the flavour sector both through better measurements and through new observables will be essential in searching for and then characterising NP in the HL-LHC era.
3. Due to its ability to reconstruct and analyze all collisions in real-time and the statistical power of the HL-LHC dataset, LHCb Upgrade II will be able to collect a unique dataset for hadronic spectroscopy. This will enable not only the precise understanding of higher-excited states of mesons and baryons, but also a detailed and broad understanding of multiquark systems, containing (or not) multiple heavy quarks, and other yet-to-be-discovered exotic states of matter. While not directly sensitive to BSM effects, these measurements will play an important role in sharpening our understanding of QCD at the energy scales relevant for flavour physics, and hence make an important contribution to the accurate interpretation of any BSM anomalies observed.

The intention to operate a flavour-physics experiment at luminosities of $10^{34}\,\mathrm{cm}^{-2}\mathrm{s}^{-1}$ is already an

Table 2: Uncertainty on Wilson coefficients and 90% exclusion limits on NP scales Λ for different data samples. The C_9 analysis is based on the ratio of branching fractions R_K and R_{K^*} in the range $1 < q^2 < 6\,\mathrm{GeV}^2/c^4$. The C'_{10} analysis exploits the angular observables S_i from the decay $B^0 \to K^{*0}\mu^+\mu^-$ in the ranges $1 < q^2 < 6\,\mathrm{GeV}^2/c^4$ and $15 < q^2 < 19\,\mathrm{GeV}^2/c^4$. The limits on the scale of NP, Λ_{NP}, are given for the following scenarios: tree-level generic, tree-level minimum flavour violation, loop-level generic and loop-level minimal flavour violation. More information on the fits may be found in [22].

Integrated Luminosity	$3\,\mathrm{fb}^{-1}$	$23\,\mathrm{fb}^{-1}$	$300\,\mathrm{fb}^{-1}$
R_K and R_{K^*} measurements			
$\sigma(C_9)$	0.44	0.12	0.03
$\Lambda^{\text{tree generic}}$ [TeV]	40	80	155
$\Lambda^{\text{tree MFV}}$ [TeV]	8	16	31
$\Lambda^{\text{loop generic}}$ [TeV]	3	6	12
$\Lambda^{\text{loop MFV}}$ [TeV]	0.7	1.3	2.5
$B^0 \to K^{*0}\mu^+\mu^-$ angular analysis			
$\sigma^{\text{stat}}(S_i)$	0.034–0.058	0.009–0.016	0.003–0.004
$\sigma(C'_{10})$	0.31	0.15	0.06
$\Lambda^{\text{tree generic}}$ [TeV]	50	75	115
$\Lambda^{\text{tree MFV}}$ [TeV]	10	15	23
$\Lambda^{\text{loop generic}}$ [TeV]	4	6	9
$\Lambda^{\text{loop MFV}}$ [TeV]	0.8	1.2	1.9

ambitious one, but the planned improvements to the detector's capabilities will extend the physics gains still further. These gains are not included in Table 1 as full simulations have not yet been performed, but a summary of the expected benefits can be found in [22]. It is intended to take first steps towards some of these detector enhancements already in LS3, before the start of the HL-LHC, thereby improving the performance of the first LHCb upgrade, and laying the foundations for Upgrade II. Finally, it must be emphasised that the raw gain in sample sizes during the HL-LHC era will have great consequences for the physics reach, irrespective of any detector improvements. The energy scale probed by virtual loops in flavour observables will rise by a factor of up to 1.9 with respect to the pre-HL-LHC era, with a corresponding gain in discovery potential similar to what will apply for direct searches if the beam energy is doubled, as proposed for the HE-LHC.

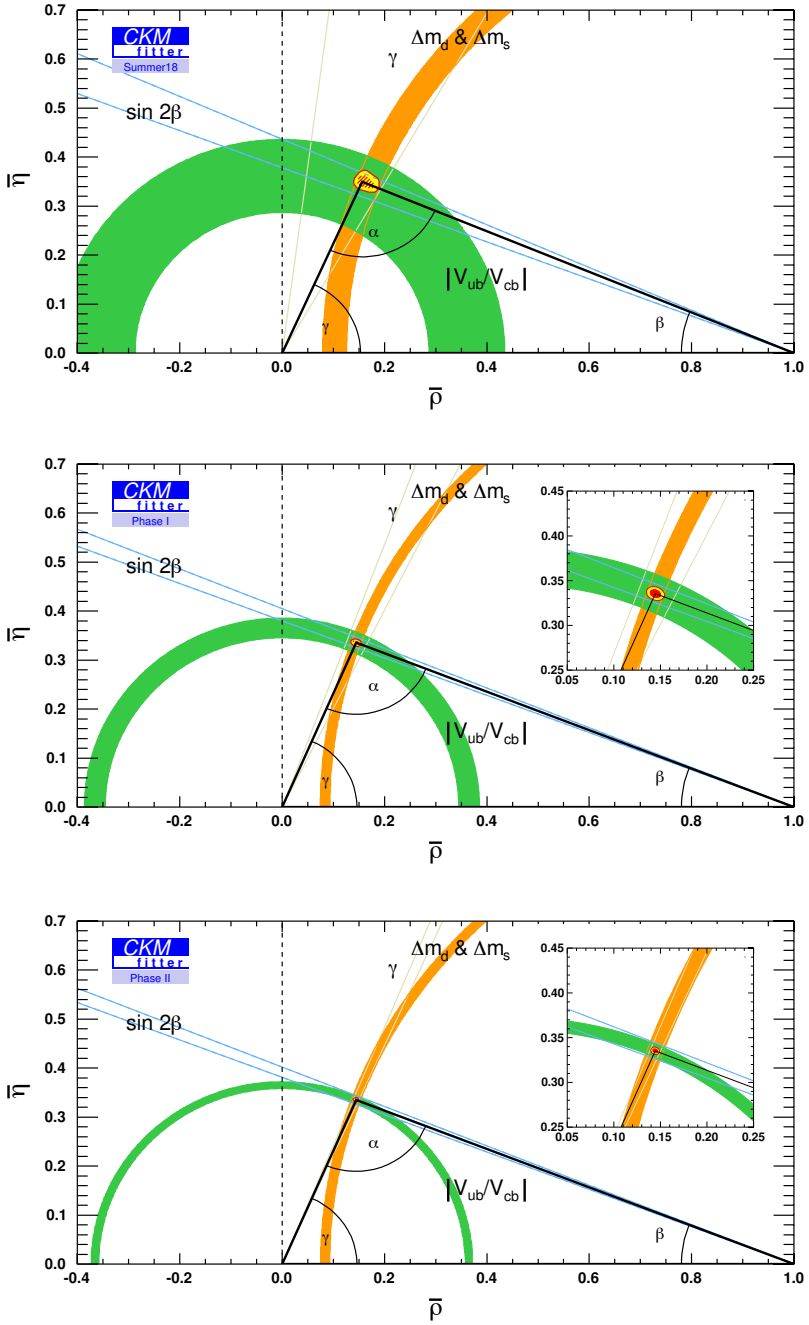

Fig. 1: Evolving constraints in the $\bar{\rho} - \bar{\eta}$ plane from LHCb measurements and lattice QCD calculations, alone, with current inputs (2018), and the anticipated improvements from the data accumulated by 2025 ($23\,\text{fb}^{-1}$) and 2035 ($300\,\text{fb}^{-1}$). More information on the fits may be found in Sec. 2 and [22].

2 Testing the CKM unitarity and related observables

Authors (TH): Jérôme Charles, Marco Ciuchini, Olivier Deschamps, Sébastien Descotes-Genon, Luca Silvestrini, Vincenzo Vagnoni.

In the SM, the weak charged-current transitions mix quarks of different generations, which is encoded in the unitary Cabibbo-Kobayashi-Maskawa (CKM) matrix [23, 24]. The SM does not predict the values of the weak flavour-couplings, and so all matrix elements must be measured experimentally. However, the unitary nature of the CKM matrix, and the assumptions of the SM, impose relations between the elements that are often expressed graphically in the complex plane as the so-called unitarity triangle. Overconstraining the apex of this unitarity triangle from tree- and loop-level quark mixing processes is therefore a powerful way to probe for virtual BSM effects at mass scales complementary or superior to those which can be directly searched for at the HL-LHC. As we shall see below, in many cases such indirect probes of BSM physics will not be limited by either experimental or theoretical systematics in the HL-LHC era.

2.1 Structure of the CKM matrix

The part of the SM Lagrangian which is relevant for describing quark mixing is

$$\mathcal{L}_{W^\pm} = -\frac{g}{\sqrt{2}} \left(V_{\rm CKM}\right)_{ij} \left(\overline{u}_i \gamma^\mu \tfrac{(1-\gamma_5)}{2} d_j\right) W^+_\mu + \text{h.c.}, \tag{2}$$

where g is the electroweak coupling constant, and $V_{\rm CKM}$ the unitary CKM matrix,

$$V_{\rm CKM} = \begin{pmatrix} V_{ud} & V_{us} & V_{ub} \\ V_{cd} & V_{cs} & V_{cb} \\ V_{td} & V_{ts} & V_{tb} \end{pmatrix}. \tag{3}$$

The CKM matrix induces flavour-changing transitions inside and between generations in the charged currents at tree level ($W^\pm$ interaction). By contrast, there are no flavour-changing transitions in the neutral currents at tree level.

Experimentally, a strong hierarchy is observed among the CKM matrix elements: transitions within the same generation are characterised by $V_{\rm CKM}$ elements of $\mathcal{O}(1)$, whereas there is a suppression of $\mathcal{O}(10^{-1})$ between 1st and 2nd generations, $\mathcal{O}(10^{-2})$ between 2nd and 3rd and $\mathcal{O}(10^{-3})$ between 1st and 3rd. This hierarchy is expressed by defining the four phase convention–independent quantities,

$$\lambda^2 = \frac{|V_{us}|^2}{|V_{ud}|^2 + |V_{us}|^2}, \qquad A^2\lambda^4 = \frac{|V_{cb}|^2}{|V_{ud}|^2 + |V_{us}|^2}, \qquad \bar\rho + i\bar\eta = -\frac{V_{ud}V^*_{ub}}{V_{cd}V^*_{cb}}. \tag{4}$$

The four independent quantities, λ, A, $\bar\rho$, $\bar\eta$, fully determine the CKM matrix in the SM.

The CKM matrix can be expanded in powers of the small parameter λ (which corresponds to the Cabibbo parameter $\sin\theta_C \simeq 0.22$) [25] by exploiting the unitarity of $V_{\rm CKM}$. This expansion yields the following parametrisation, valid up to $\mathcal{O}\left(\lambda^6\right)$,

$$V_{\rm CKM} = \begin{pmatrix} 1 - \frac{1}{2}\lambda^2 - \frac{1}{8}\lambda^4 & \lambda & A\lambda^3\left(\bar\rho - i\bar\eta\right) \\ -\lambda + \frac{1}{2}A^2\lambda^5\left[1 - 2(\bar\rho + i\bar\eta)\right] & 1 - \frac{1}{2}\lambda^2 - \frac{1}{8}\lambda^4(1 + 4A^2) & A\lambda^2 \\ A\lambda^3\left[1 - (\bar\rho + i\bar\eta)\right] & -A\lambda^2 + \frac{1}{2}A\lambda^4\left[1 - 2(\bar\rho + i\bar\eta)\right] & 1 - \frac{1}{2}A^2\lambda^4 \end{pmatrix}. \tag{5}$$

The CKM matrix is complex, i.e., it contains a phase that cannot be rotated away, if $\bar\eta \neq 0$. Furthermore, CP is violated, if and only if $\bar\eta$ differs from zero.

Orthogonality relations can be written involving two columns or two rows of the unitary CKM matrix, and they can be represented as triangles in the complex plane. It is standard to focus on the following orthogonality relation,

$$V_{ud}V^*_{ub} + V_{cd}V^*_{cb} + V_{td}V^*_{tb} = 0, \tag{6}$$

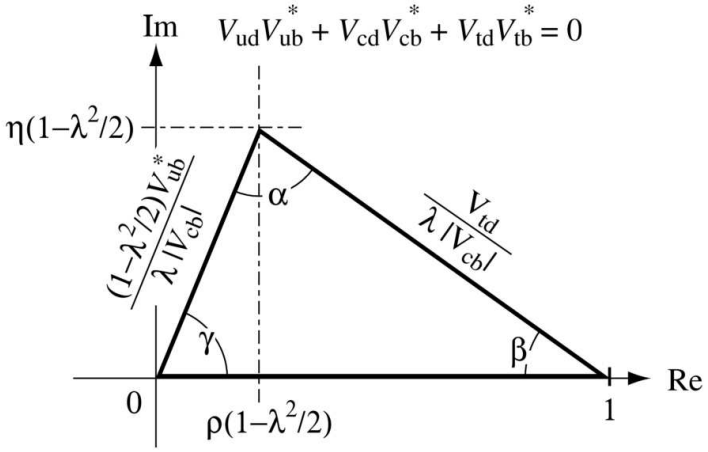

Fig. 2: The standard CKM unitarity triangle. The parameters ρ and η are defined as $\rho + i\eta = \left(\bar{\rho} + i\bar{\eta}\right)\left(1 - \lambda^2/2 + O(\lambda^4)\right)$, with $\bar{\rho}, \bar{\eta}$ defined in (4).

as the three products of CKM elements are of similar size, $\mathcal{O}(\lambda^3)$. Fig. 2 shows the standard unitarity triangle (UT), obtained from Eq. (6) by rescaling the three terms in the orthogonality relation by $V_{cd}V_{cb}^*$.

The apex of the UT is at $(\bar{\rho}, \bar{\eta})$, while the angles are related to the CKM matrix elements as

$$\alpha = \arg\left(-\frac{V_{td}V_{tb}^*}{V_{ud}V_{ub}^*}\right), \qquad \beta = \arg\left(-\frac{V_{cd}V_{cb}^*}{V_{td}V_{tb}^*}\right), \qquad \gamma \equiv \arg\left(-\frac{V_{ud}V_{ub}^*}{V_{cd}V_{cb}^*}\right). \tag{7}$$

2.2 Current status of the constraints

2.2.1 $|V_{ud}|, |V_{us}|, |V_{cd}|, |V_{cs}|$

Accurate constraints on the first and second rows and columns of the CKM matrix come from leptonic decays, $\pi \to e\nu$, $K \to e\nu$, $K \to \mu\nu$, $\tau \to \pi\nu_\tau$, $\tau \to K\nu_\tau$, $D \to \mu\nu$, $D_s \to \mu\nu$, and from semileptonic decays, $K \to \pi e\nu$, $D \to \pi e\nu$, $D_s \to K e\nu$. The extraction of CKM matrix elements requires knowledge of hadronic inputs (decay constants for the leptonic decays, normalisations of the form factors at $q^2 = 0$ for the semileptonic decays) and electromagnetic/isospin corrections when available (i.e., for kaon and pion decays) [26]. Another prominent input for the $|V_{ud}|$ determination comes from the consideration of the superallowed β decays of 20 different nuclei [27–29], which provides a very accurate constraint on $|V_{ud}|$. There are also other constraints, but less powerful due to experimental uncertainties and/or theoretical systematics that are difficult to assess.

2.2.2 $|V_{cb}|$ and $|V_{ub}|$

Tree-level semileptonic decays of beauty mesons and baryons allow for the extraction of $|V_{cb}|$ and $|V_{ub}|$. The current determination is dominated by the B-factories data on B decays and by the measurement of $|V_{ub}|/|V_{cb}|$ from baryonic decays at LHCb. For B decays, both inclusive and exclusive semileptonic decays have been used to extract $|V_{cb}|$ and $|V_{ub}|$. The two approaches have different sources of theoretical uncertainties: inclusive analyses rely on quark-hadron duality, involve hadronic matrix elements in subleading powers of the heavy quark expansion and, for $|V_{ub}|$, on additional hadronic quantities called shape functions; exclusive analyses require the knowledge of the relevant form factors over the entire kinematic range, a very difficult task for lattice QCD. Currently, the HFLAV averages for inclusive and exclusive determinations of $|V_{cb}|$ and $|V_{ub}|$ disagree at the 3σ level. While recently the choice of the parameterization of the form factor dependence on the recoil for $B \to D^*$ decays has been shown to have a large impact on the extracted value of $|V_{cb}|$ [30–32], the situation is still rather unclear.

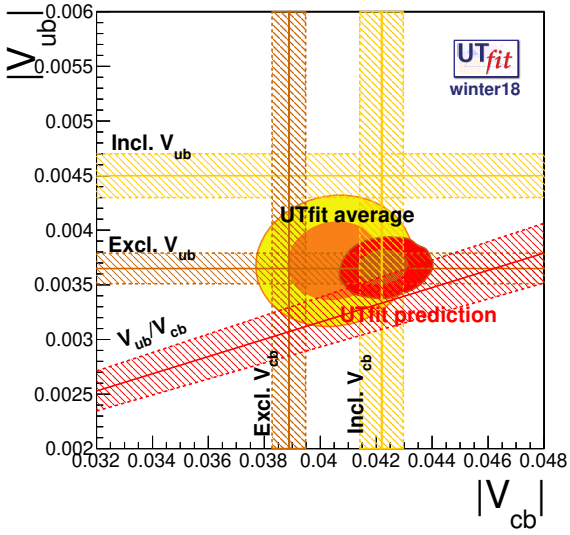

Fig. 3: Measurements of $|V_{cb}|$ and $|V_{ub}|$ from exclusive and inclusive B decays (vertical and horizontal bands) and from $\Lambda_b^0 \to p\mu^-\overline{\nu}_\mu$ and $\Lambda_b^0 \to \Lambda_c^+\mu^-\overline{\nu}_\mu$ (diagonal band), skeptical average and indirect determination of $|V_{cb}|$ and $|V_{ub}|$.

One way to deal with this, followed by the UTFit collaboration, is to assume that the uncertainty of each determination of $|V_{cb}|$ and $|V_{ub}|$ might have been underestimated, and perform a "skeptic combination" of all available data following the method of Ref. [33], which is equivalent to the PDG prescription in one dimension, and is a straightforward generalization to the two-dimensional case of $|V_{cb}|$ and $|V_{ub}|$. The result is reported in Fig. 3, where in addition to the average we also plot the "indirect determination" obtained from all the other flavour observables. The numerical results of the skeptic average are $|V_{cb}| = 0.0405 \pm 0.0011$, $|V_{ub}| = 0.00374 \pm 0.00023$, with correlation $\rho = 0.09$. CKMfitter collaboration uses instead the exclusive value for V_{cb} from $B \to D^*\ell\nu$ that was obtained using more model independent BGL parametrisation, and which is in agreement with both $B \to D\ell\nu$ and the inclusive extraction. This leads to the combined value $|V_{cb}| = (41.8 \pm 0.4(\text{exp}) \pm 0.6(\text{theory})) \cdot 10^{-3}$. For V_{ub} the CKMfitter collaboration performs an R-fit of inclusive and exclusive determinations to obtain $|V_{ub}| = (3.98 \pm 0.08(\text{exp}) \pm 0.22(\text{LQCD})) \cdot 10^{-3}$.

Lattice QCD determinations of the form factors in a large kinematic range are under way. It is expected that they will allow Belle-II to perform a much more parameterization-independent extraction of V_{cb} from exclusive decays, hopefully reconciling it with the inclusive one. Also for $|V_{ub}|$, the much larger statistics should allow to get an insight on the origin of the discrepancy between inclusive and exclusive determinations, and provide a consistent determination of $|V_{ub}|$.

2.2.3 Angle α

The constraints on the CKM angle α are derived from the isospin analysis of the charmless decay modes $B \to \pi\pi$, $B \to \rho\rho$ and $B \to \rho\pi$ [34–36]. This approach has the interesting feature of being almost free from hadronic uncertainties. Assuming isospin symmetry and neglecting the electroweak penguin contributions, the amplitudes of the isospin $SU(2)$-conjugated modes are related. The measured branching fractions and asymmetries in the $B^{\pm,0} \to (\pi\pi)^{\pm,0}$ and $B^{\pm,0} \to (\rho\rho)^{\pm,0}$ modes and the bilinear form factors in the Dalitz analysis of the neutral $B^0 \to (\rho\pi)^0 \to \pi^+\pi^-\pi^0$ decays thus provide enough observables to simultaneously extract the weak phase $\beta + \gamma = \pi - \alpha$ together with the hadronic tree and penguin contribution to each mode. The combination of the experimental data for the three decay modes above, mostly provided by the B-factories, gives the world-average value at 68% Confidence

Level (CL) [37]: $\alpha_{\rm dir} = (86.2^{+4.4}_{-4.0} \cup 178.4^{+3.9}_{-5.1})^\circ$. The experimental uncertainty is so far significantly larger than the theoretical uncertainty due to isospin $SU(2)$ breaking, which may affect the $\alpha_{\rm dir}$ determination at around 2°. The solution near 90° is in good agreement with the indirect determination obtained by the global fit of the flavour data [38].

A detailed analysis of the prospects for the CKM angle α has been performed in [37]. The global determination of α is dominated by the $B \to \rho\rho$ data, constraining α with about 5% uncertainty. Improving the measurements of the neutral modes, especially the colour-suppressed $B^0 \to \rho^0\rho^0$ decay, can have a sizeable impact. In the $B \to \pi\pi$ system any sizable improvement is driven by the increased accuracy in the measurement of the direct CP asymmetry in the colour-suppressed decay $B^0 \to \pi^0\pi^0$, potentially reachable through Dalitz decays $\pi^0 \to \gamma e^+ e^-$. However, all α measurements at subdegree precision must address isospin-breaking effects such as electroweak penguin contributions [37, 39].

2.2.4 Angle β

The CKM angle β is measured from the time-dependent CP asymmetry of $b \to c\bar{c}s$ decays, such as $B \to J/\psi K_S$. The decay amplitude, $A_{J/\psi K_S} = V_{cs}V_{cb}^* T + V_{us}V_{ub}^* P$, is dominated by the isoscalar tree-level amplitude T, while the subleading term P is both loop and doubly Cabibbo suppressed. Neglecting P, the time-dependent CP asymmetry, $a_t^{CP}(B \to J/\psi K_S) = \sin 2\beta \, \sin(\Delta m_B \, t)$, has a single oscillatory term, the amplitude of which gives experimental access to $\sin 2\beta$ (the fourfold ambiguity in β can be reduced through time-dependent transversity analysis of $B \to J/\psi K^*$, sensitive to $\cos 2\beta$). The $P = 0$ approximation is justified as long as the relative error on $\sin 2\beta$ is larger than the correction induced by the subleading term $\sim \lambda^2 P/T$. The present relative uncertainty on $\sin 2\beta$ from various charmonium states, including J/ψ / $\psi(2S)$ / χ_{c1} / η_c K_S, $J/\psi K_L$, $\psi(nS)K^0$, is about 2.4%. Double Cabibbo suppression amounts to 5% and $|P/T| < 1$ is expected. Yet the precise suppression due to P/T is unknown, likely ranging between some tens and a few percent, the latter estimate given by the perturbative estimate of the penguin amplitude. Thus, depending on the actual value of P/T, the subleading amplitude could be a limiting factor for the extraction of $\sin 2\beta$ already now or, in the opposite case, be safely neglected down to an experimental precision of few permille. In order to place a bound on the subleading amplitude, one can use $SU(3)$ flavour (or U-spin) related decays where the penguin contribution is not suppressed, such as $B_s \to J/\psi K_s$ or $B \to J/\psi\pi$ [40–45]. Measuring branching ratios and (time-dependent) CP asymmetries, it is possible to extract the correction to $\sin 2\beta$ induced by the subleading term and the corresponding uncertainty, due to the experimental errors and $SU(3)$-breaking effects. The latter, being proportional to a CKM suppressed amplitude, are expected to be at the permille level.

With present data, the typical shift in β is 0.5–1° with about 100% uncertainty, dominated by the experimental uncertainties. Improvements in the measurement of the time-dependent asymmetry in $B \to J/\psi K_S$ should therefore be accompanied by a corresponding improvement in the measurement of the control channels in order to keep the subleading amplitude under control and extract $\sin 2\beta$ with a subpercent precision. It is worth mentioning that a complemetary approach proposing a theoretical computation of the subleading amplitude using an OPE based on soft-collinear factorization in QCD can be found in Ref. [46]. Assuming that the subleading amplitude is kept under control, the uncertainty on the indirect determination of $\sin 2\beta$ from the UT analysis is expected to go from the present 4.5% down to 0.6%, providing an improved sensitivity to NP in the B–$\bar{B}$ mixing amplitude, as discussed further below.

2.2.5 Angle γ

The current best sensitivity is obtained from charged B decays into $\tilde{D}K^-$, $\tilde{D}^*K^-$, $\tilde{D}K^{*-}$, and $\tilde{D}K^-\pi^+\pi$ where $\tilde{D}$ is a D^0 or $\overline{D}^0$ meson decaying to the same final state. The D^0 is produced through the leading $b \to c$ transition, with the amplitude $\mathcal{A}_{b\to c} \propto \lambda^3$, and $\overline{D}^0$ in the CKM and colour-suppressed $b \to u$

transition, $\mathcal{A}_{b\to u} \propto \lambda^3\left(\bar{\eta}^2+\bar{\rho}^2\right)^{1/2} e^{i(\delta_B-\gamma)}$. Since D^0 and $\overline{D}^0$ decay to a common final state, the interference between the two tree amplitudes leads to observables that depend on the relative weak phase γ and results in different B^+ and B^- decay rates. The size of this interference also depends on the magnitude of the ratio of the two amplitudes, $r_B \equiv |\mathcal{A}_{b\to u}/\ \mathcal{A}_{b\to c}|$, and the relative strong phase δ_B. The value of r_B, which determines the size of the direct CP asymmetry, is predicted [47] to lie in the range 0.05–0.2. Experimental sensitivity to γ decreases with smaller r_B.

There are several different methods that exploit the above interference pattern: the Gronau-London-Wyler (GLW) method [48, 49] where the neutral D meson is reconstructed in a CP eigenstate; the Atwood-Dunietz-Soni (ADS) method [50–52] where the D^0 meson, associated with the $\mathcal{A}_{b\to c}$ amplitude, is required to decay to a doubly Cabibbo-suppressed decay (DCSD), while the $\overline{D}^0$ meson, associated with the $\mathcal{A}_{b\to u}$ amplitude, decays to a Cabibbo-favoured final state, such as $K^+\pi^-$; the Giri-Grossman-Soffer-Zupan (GGSZ) method [53] where the neutral D meson is reconstructed in self-conjugate three-body final state such as $K^0_S h^+ h^-$ (where $h = \pi$ or K). These γ extraction techniques rely on clean theoretical assumptions since the decay amplitudes are completely tree-level dominated, to an excellent approximation [54]. All variants are sensitive to the same B decay parameters and can therefore be combined in a single fit to extract the common weak phase γ, as well as the hadronic parameters associated with each method.

In addition to the above approaches, it is also possible to measure γ from time-dependent analyses of B^0 and B^0_s decays, as well as from decays of b-baryons. These methods offer significant additional sensitivity and are discussed further in Sec. 2.5.

2.2.6 Angle β_s

The angle $\beta_s = \arg\left(-V_{ts}V^*_{tb}/V_{cs}V^*_{cb}\right)$ belongs to the squeezed UT $\sum_{q_u} V^*_{q_u b}V_{q_u s} = 0$ instead of the usual $\sum_{q_u} V^*_{q_u b}V_{q_u d} = 0$. Given its reduced sensitivity to $\bar{\rho}$ and $\bar{\eta}$, it is not a strong constraint in the UT plane. On the other hand, the UT analysis provides a very precise indirect determination of its value that can be compared with the direct determination extracted from time-dependent transversality analysis of $B_s \to J/\psi\phi$. At present, we have $\beta_s^{\rm direct} = (0.60 \pm 0.88)^\circ$ and $\beta_s^{\rm UTA} = (1.06 \pm 0.03)^\circ$. The future uncertainties of the direct and indirect determinations are expected to be ± 0.01 and ± 0.007 respectively, allowing for a deeper investigation of BSM contributions to B_s–$\bar{B}_s$ mixing amplitude. It is worth noting that, similarly to the measurement of phase β, the shifts of a few degrees in the value of β_s extracted from the time-dependent analysis caused by the subleading amplitude P cannot be excluded. These shifts, however, now produce a much larger relative uncertainty, since β_s itself is doubly Cabibbo suppressed. Some control of doubly Cabibbo suppressed contributions is thus required to meaningfully extract β_s at the SM level. This can be achieved by using the $SU(3)_f$ related channels, with the additional caveat that ϕ is an (almost equal) admixture of $SU(3)_f$ octet and singlet, introducing an additional source of uncertainty.

2.2.7 $K - \bar{K}$ mixing

The CP-violating parameter ε_K, historically the first constraint in the UT plane, is becoming limited by long-distance contributions. In the last years, the improvements in the constraining power of ε_K have come from new determination of the bag parameter, B_K, on the lattice. Nowadays, the theoretical error on B_K is approaching percent level. The dominating uncertainty in the SM prediction of ε_K comes from the long-distance contributions, the best estimate of which has an error of 2% [55]. A breakthrough could come from developing ideas for computing these terms on the lattice, using recent techniques to cope with the non-local operators that were used to obtain predictions for a closely related quantity, Δm_K [56, 57].

2.2.8 $B_d - \bar{B}_d$ and $B_s - \bar{B}_s$ mixing

The dispersive and absorptive contributions to B_d and B_s mixing are described by 2×2 matrices, $M^q = M^{q\dagger}$ and $\Gamma^q = \Gamma^{q\dagger}$, respectively ($q = d, s$). They describe the quantum-mechanical evolution of the $B_q - \overline{B}_q$ system. Their diagonalisation defines the physical eigenstates $|B_H^q\rangle$ and $|B_L^q\rangle$ with masses M_H^q, M_L^q and decay rates Γ_H^q, Γ_L^q. One can reexpress these quantities in terms of three parameters: $|M_{12}^q|$, $|\Gamma_{12}^q|$ and the relative phase $\phi_q = \arg(-M_{12}^q/\Gamma_{12}^q)$. The SM prediction for the mass splitting, $\Delta m_q = M_H^q - M_L^q$, is dominated by boxes involving top quarks, and is given by

$$\Delta m_q = \frac{G_F^2}{6\pi^2} \eta_B m_{B_q} f_{B_q}^2 \hat{B}_q m_W^2 S(x_t) \left| V_{tq} V_{tb}^* \right|^2 , \tag{8}$$

with the Inami-Lim function $S(x_t)$ [58] evaluated at $x_t = \overline{m}_t^2/m_W^2$, while η_B encodes the perturbative QCD corrections, originally estimated at NLO in Ref. [59]. Using up-to-date α_s and the top-quark mass gives $\eta_B = 0.5510 \pm 0.0022$ [60]. The decay constant f_{B_q} and the so-called bag parameter, $\hat{B}_q$, parametrize the nonperturbative hadronic matrix elements.

The translation of the measured value for Δm_d into constraints on the CKM parameter combination $|V_{td}V_{tb}^*|^2$ is limited at present by uncertainties in the lattice QCD calculation of the hadronic parameters $f_{B_d}, \hat{B}_d$. The ratios f_{B_s}/f_{B_d} and $\hat{B}_s/\hat{B}_d$ are much better determined, so that $\Delta m_d/\Delta m_s$ gives a much better constraint in the $(\bar{\rho}, \bar{\eta})$ plane, see Fig. 4. The hadronic parameters, f_{B_s}, $\hat{B}_s$, as well as f_{B_s}/f_{B_d} and $\hat{B}_s/\hat{B}_d$, are set to have their errors significantly reduced by future lattice QCD computations, see Sec. 11.

2.3 Combined constraints on the CKM parameters

Due to its economical structure in terms of only four parameters the CKM matrix can be determined through many different quark transitions, both the $\Delta F = 1$ decays and the $\Delta F = 2$ neutral-meson mixing transitions. A consistent determination of the four CKM parameters from all these processes is a fundamental test of the Kobayashi-Maskawa mechanism. Extracting the information on the four CKM parameters from data poses both experimental and theoretical challenges. First of all, the SM depends on a number of other parameters, masses and couplings, which are not predicted within the SM, but rather need to also be determined experimentally. An additional difficulty relates to the presence of strong interactions, binding quarks into hadrons. This is responsible for most of the theoretical uncertainties in the determinations of CKM matrix elements.

2.3.1 Statistical approaches

The CKMfitter group determines the CKM parameters from a large set of flavour physics constraints using a standard χ^2-like frequentist approach, in addition to a specific (Rfit) scheme to treat theoretical uncertainties [61–63]. The set of experimental observables, denoted $\vec{\mathcal{O}}_{exp}$, is measured in terms of likelihoods that can be used to build a χ^2-like test statistic, $\chi^2(\vec{p}) = -2 \log \mathcal{L}(\vec{\mathcal{O}}_{exp} - \vec{\mathcal{O}}_{th}(\vec{p}))$, with $\vec{\mathcal{O}}_{th}(\vec{p})$ the theoretical values of the observables depending on N fixed parameters $\vec{p}$. The absolute minimum value of the test statistic, $\chi^2_{\rm min}$, quantifies the agreement of the data with the theoretical model, once converted into a p-value (interpreting $\chi^2(\vec{p})$ as a random variable distributed according to a χ^2 law). It is also possible to perform the metrology of specific parameters of the model, by considering the hadronic parameters $\vec{\mu}$ as "nuisance parameters" and defining the test statistic, $\Delta\chi^2(\alpha) = \min_{\vec{\mu}}[\chi^2(\alpha)] - \chi^2_{\rm min}$ [61, 64, 65]. Here, $\min_{\vec{\mu}}[\chi^2(\alpha)]$ is the value of χ^2, minimised with respect to the nuisance parameters for a fixed α value. This test statistic assesses how a given hypothesis on the true value of α agrees with the data, irrespective of the value of the nuisance parameters. Confidence intervals on α can be derived from the resulting p-value, which is computed assuming that $\Delta\chi^2(\alpha)$ is χ^2-distributed with one degree of

freedom,

$$p(\alpha) = \mathrm{Prob}(\Delta\chi^2(\alpha), N_{dof} = 1)\,, \qquad \mathrm{Prob}\Big(\Delta\chi^2, N_{dof}\Big) = \frac{\Gamma(N_{dof}/2, \Delta\chi^2/2)}{\Gamma(N_{dof}/2)}\,, \tag{9}$$

where $\Gamma(x)$ is the usual Euler factorial function, and $\Gamma(s,x)$ is the upper incomplete gamma function. Confidence intervals at a given confidence level (CL) are obtained by selecting the values of α with p-value larger than $1-$CL.

In addition to the frequentist statistical treatment outline above, the CKMfitter collaboration relies on a specific treatment of theoretical uncertainties (e.g., systematics due to uncertainties on hadronic matrix elements not scaling with the size of the sample). The current approach is the so-called Rfit [61, 64,65] model, where the theoretical parameter/observable is restricted to a range, without any possibility to exceed this range. Most of the systematic uncertainties come from lattice QCD. The CKMfitter collaboration follows the recommendations of the Flavour Lattice Averaging Group [66] and uses a specific procedure to perform the average of the lattice inputs based on the Rfit model combined with a linear addition of systematic uncertainties for the individual inputs [65].

The UTfit collaboration follows a Bayesian approach to combine the constraints in the UT plane. Bayesian statistics allows for a unified treatment of systematic and theoretical uncertainties in a scheme of "updating of knowledge" from prior to posterior distributions. Following Bayes' theorem, the unnormalized posterior probability density function (p.d.f.) for $\bar\rho$ and $\bar\eta$ (given the constraints) is,

$$f(\bar\rho, \bar\eta | \hat{\mathbf{c}}, \hat{\mathbf{f}}) \propto \mathcal{L}(\hat{\mathbf{c}} \,|\, \bar\rho, \bar\eta, \mathbf{f})\, f_0(\bar\rho, \bar\eta). \tag{10}$$

Here $\hat{\mathbf{c}} = \{c_1, c_2, \ldots, c_M\}$ is a set of measured constraints, whose theoretical expressions are given by functions $c_j(\bar\rho, \bar\eta; \mathbf{x})$ that depend on $\bar\rho$, $\bar\eta$, and a set of additional experimental and theoretical parameters $\mathbf{x} = \{x_1, x_2, \ldots, x_N\}$. The $f_0(\bar\rho, \bar\eta)$ is the prior p.d.f. for $\bar\rho$ and $\bar\eta$, assumed to be flat on the UT plane, and is multiplied by the effective overall likelihood,

$$\mathcal{L}(\hat{\mathbf{c}} \,|\, \bar\rho, \bar\eta, \mathbf{f}) = \int \prod_{j=1,\mathrm{M}} f_j(\hat{c}_j \,|\, \bar\rho, \bar\eta, \mathbf{x}) \prod_{i=1,\mathrm{N}} f_i(x_i)\, \mathrm{d}x_i\,. \tag{11}$$

The p.d.f. $f_i = \{f_1, f_2, \ldots, f_N\}$ are the prior distributions of the parameters, while $f_j(\hat{c}_j \,|\, \bar\rho, \bar\eta, \mathbf{x})$ are the conditional probabilities of $\hat{c}_j$ given $\bar\rho$, $\bar\eta$, and $\mathbf{x}$, that in the Gaussian approximation become

$$f_j(\hat{c}_j \,|\, \bar\rho, \bar\eta, \mathbf{x}) = \frac{1}{\sqrt{2\pi}\,\sigma(c_j)} \exp\left[-\frac{(c_j(\bar\rho, \bar\eta; \mathbf{x}) - \hat{c}_j)^2}{2\,\sigma^2(c_j)} \right]. \tag{12}$$

The integration in Eq. (11) is usually carried out using Monte Carlo methods. More details on the Bayesian approach of the UTfit collaboration can be found in Ref. [67].

2.3.2 Current combined constraints on the CKM parameters

From the SM global fit the CKMfitter collaboration finds for the four CKM parameters,

$$A = 0.8403^{\,+0.0056}_{\,-0.0201}, \quad \lambda = 0.224747^{\,+0.000254}_{\,-0.000059}, \quad \bar\rho = 0.1577^{\,+0.0096}_{\,-0.0074}, \quad \bar\eta = 0.3493^{\,+0.0095}_{\,-0.0071}. \tag{13}$$

The asymmetric errors come from the combination of several constraints containing both statistical and systematic uncertainties, so that the resulting χ^2 has a rather complicated asymmetric shape. The corresponding results are shown in Fig. 4. The fit shows a good overall consistency among the various constraints. The main pulls come from the kaon and charm sector, but nothing exceeds the 2-σ level, confirming the very good overall agreement of the various constraints involved here.

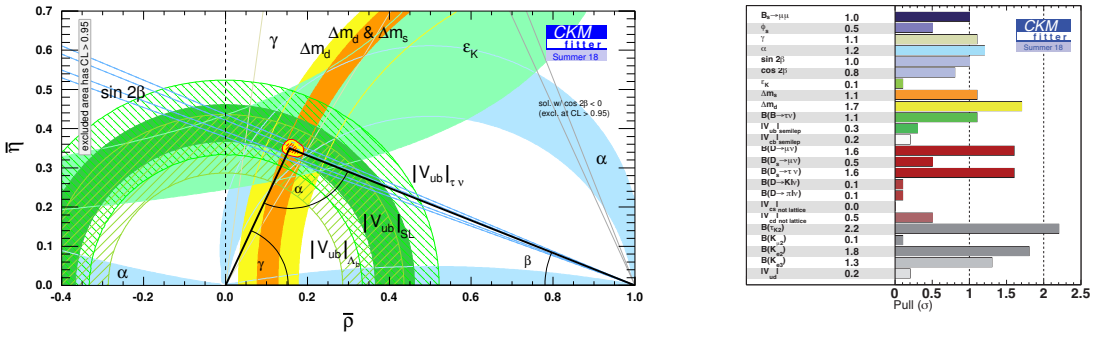

Fig. 4: Results for the CKMfitter global fit of the CKM parameters as of Summer 2018. See Ref. [38] for more detail.

Detailed input values as well as predictions for various CKM-related parameters and observables in the SM from the UTfit collaboration can be found in the Summer 2018 update page on the UTfit website [68]. The CKM matrix is determined as

$$V_{\rm CKM} = \begin{pmatrix} 0.97431(12) & 0.22514(55) & 0.00365(10)e^{-i66.8(2.0)^\circ} \\ -0.22500(54)e^{i0.0351(10)^\circ} & 0.97344(12)e^{-i0.00188(5)^\circ} & 0.04241(65) \\ 0.00869(14)e^{-i22.2(0.6)^\circ} & -0.04124(56)e^{i1.056(32)^\circ} & 0.999112(24) \end{pmatrix} . \quad (14)$$

while the Wolfenstein parameters are,

$$A = 0.826\pm, 0.012, \quad \lambda = 0.2255 \pm 0.0005, \quad \bar{\rho} = 0.148 \pm 0.013, \quad \bar{\eta} = 0.348 \pm 0.010, \quad (15)$$

in good agreement with the CKMfitter determination in (13).

2.4 Theoretical prospects

2.4.1 Lattice extrapolations

Advancement in the lattice QCD determination of hadronic matrix elements, used in the extraction of CKM elements, need to go hand in hand with the improved experimental precision. The projections on the expected errors for the most important hadronic matrix elements are discussed in detail in Sec. 11 with the main results collected in Table 41.

The accuracy of the projections below will also require an improvement in the understanding of electromagnetic corrections, which for the moment are only partially addressed in theoretical predictions. Further details on the inclusion of QED corrections in lattice predictions are discussed in Sec. 11.

2.4.2 Other theoretical issues

The determination of γ has negligible theoretical errors. In contrast, extractions of β and β_s from $b \to c\bar{c}s$ transitions receive small theoretical uncertainty from penguin diagrams. For present data the penguin contributions in $b \to c\bar{c}s$ are assumed to be negligible. However, they may compete with the statistical errors in the future. Techniques to estimate the penguin contributions from data on SU(3)-related channels are described in Sec. 2.5.10. An independent, more theory-driven, cross-check of the SU(3) approach was suggested in Ref. [46] – to use Operator Product Expansion to calculate the penguin-to-tree ratio. It is important to note that the penguin contributions in various $b \to c\bar{c}s$ channels are different, so that with increased precision of the measurements one cannot anymore average $\sin 2\beta$ from

$B \to J/\psi K_S, B \to \eta_c K_S, \ldots$, without first correcting for the penguin contributions on a channel by channel basis.

In the determination of α, the small penguin contributions are avoided using isospin symmetry. The associated theory error on α due to isospin breaking has been estimated to be at sub degree level [37]. It is neglected at present, but will need to be taken into account in significantly larger statistics samples.

An open issue is the (in)compatibility of the inclusive and exclusive determinations of $|V_{cb}|$ and $|V_{ub}|$, where a $\sim 3\sigma$ discrepancy has been observed ever since the first precise measurements. Recently, the $|V_{cb}|$ discrepancy was shown to depend significantly on the choice of the form factor parametrisation, and on the hypotheses made about the underlying heavy quark symmetry [31, 32]. Relaxing these choices leads to an exclusive determination of $|V_{cb}|$ that is in good agreement with the inclusive one, but with unexpectedly large corrections to the heavy quark symmetry predictions [69], unless one employs additional theoretical information, as shown in Ref. [70]. Lattice calculations should soon settle the matter. As for $|V_{ub}|$ no satisfying explanation of the discrepancy has been found so far. In the future more precise exclusive measurements by LHCb and Belle-II, and more precise inclusive analysis by Belle-II, should shed light on this topic by investigating whether or not it could be an experimental effect.

2.5 Experimental prospects

2.5.1 $|V_{ub}|$ and $|V_{cb}|$ from semileptonic decays

LHCb is well suited to measuring ratios of $b \to u\ell\nu$ to $b \to c\ell\nu$ decay rates, in which the unknown b production cross sections, and to some extent also efficiency corrections, cancel. LHCb reported the first study of the $\Lambda_b^0 \to p\mu^-\overline{\nu}_\mu$ and $\Lambda_b^0 \to \Lambda_c^+\mu^-\overline{\nu}_\mu$ decays with Run 1 data, which resulted in a determination of $|V_{ub}|/|V_{cb}|$ [14], exploiting precise lattice QCD calculations of the decay form factors [71, 72].

LHCb Upgrade II presents an exciting opportunity for new measurements of this type. An excellent example is an analogous analysis of $B_s^0 \to K^-\mu^+\nu_\mu$ and $B_s^0 \to D_s^-\mu^+\nu_\mu$ decays. The relatively large spectator s quark mass allows the form factors of these decays to be computed with lattice QCD to higher precision than decays of other b hadrons. There are also good prospects to extend the approach of [14], with a single q^2 bin, to perform a differential measurement in many fine bins of q^2 [73], which clearly demands substantially larger sample sizes. Furthermore, there are several reasons to expect that, compared to the study of Λ_b^0 decays [14], far larger luminosities are required for the ultimate precision with B_s^0 decays. Firstly, the $B_s^0 \to K^-\mu^+\nu_\mu$ signal rate is roughly one order of magnitude smaller compared to $\Lambda_b^0 \to p\mu^-\overline{\nu}_\mu$. Secondly, the $B_s^0 \to K^-\mu^+\nu_\mu$ decay is subject to backgrounds from all b meson species, whereas $\Lambda_b^0 \to p\mu^-\overline{\nu}_\mu$ is primarily contaminated by other Λ_b^0 decays. Thirdly, the $B_s^0 \to K^-\mu^+\nu_\mu$ decay rate is further suppressed with respect to $\Lambda_b^0 \to p\mu^-\overline{\nu}_\mu$ at the higher q^2 values at which the lattice QCD uncertainties are smallest.

LHCb Upgrade II should also include several potential gains in the detector performance which are highly relevant to the reconstruction of decays like $B_s^0 \to K^-\mu^+\nu_\mu$. The key variable which distinguishes the signal from background processes is the *corrected mass*, which depends on the reconstructed line-of-flight between the primary vertex (PV) and the B_s^0 decay vertex. It is the resolution on this direction which dominates the corrected mass resolution. The removal, or further thinning, of the RF foil is therefore a very appealing prospect, since this would reduce the multiple scattering contribution to the corrected mass resolution. Fig. 5 shows the potential gain in effective luminosity that can be achieved by reducing the RF foil thickness. This analysis only considers the effect of the improved corrected mass resolution, while further improvements are expected in the selection efficiency, purity and q^2 resolution.

The dominant systematic uncertainty in the Λ_b^0 analysis [14] (material budget and its effect on the charged hadron reconstruction efficiency) can be tightly constrained with new methods, the performance of which will be greatly enhanced by any reduction in the RF foil. The lattice QCD form factors are most precise at large q^2 values, which correspond to low momentum kaons that are not efficiently identified with the RICH approach of the current detector. The low momentum particle identification (PID) per-

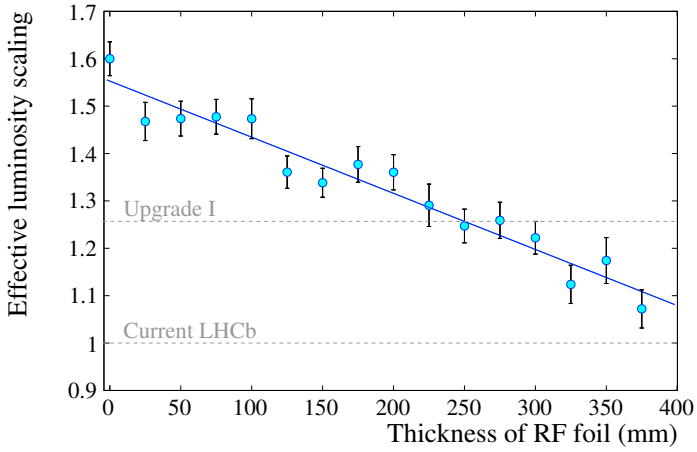

Fig. 5: The factor by which the effective luminosity in LHCb would be increased in an analysis of $B_s^0 \to K^-\mu^+\nu_\mu$ decays, as a function of the thickness of the RF foil. This factor is defined to be with respect to the vertex resolution of the current detector. It is determined using pseudo experiments in which the $B_s^0 \to K^-\mu^+\nu_\mu$ signal yield is extracted through a likelihood fit to the corrected mass distribution. The other parameters affecting the vertex resolution are assumed to be the same as in the upgraded LHCb detector, which will have a baseline foil thickness of 250 μm.

formance of the proposed TORCH detector would greatly enhance our capabilities with $B_s^0 \to K^-\mu^+\nu_\mu$ decays at high q^2.

The combination of these detector improvements with the LHCb Upgrade II data set is expected to reduce the experimental systematic uncertainties on $|V_{ub}|/|V_{cb}|$ to the 0.5% level. External branching ratio uncertainties will also be greatly reduced at the BESIII experiment. For example, $\mathcal{B}(D_s^+ \to K^+K^-\pi^+)$ will be determined at the 1% level, translating to a $\sim 0.5\%$ uncertainty on $|V_{ub}|/|V_{cb}|$. Combined with the differential shape information of the signals and continued improvements to the lattice calculations this will lead to a $|V_{ub}|/|V_{cb}|$ measurement uncertainty of less than 1% with the LHCb Upgrade II data set.

LHCb Upgrade II will allow several currently inaccessible decays, not least those of the rarely produced B_c^+ mesons, to be studied in detail. A prime example is the decay $B_c^+ \to D^0\mu^+\nu_\mu$, which is potentially very clean from a theory point of view, once lattice QCD calculations of the form factor become available. Approximately 30,000 reconstructed candidates can be expected with the 300 fb^{-1} LHCb Upgrade II data set, which could lead to a competitive measurement of $|V_{ub}|$ in this, currently unexplored, system. Purely leptonic decays, such as $B^+ \to \mu^+\mu^-\mu^+\nu_\mu$, will also become competitive, with similar signal yields, and can provide information on the B-meson light cone distribution amplitude, which is a crucial input to the widely used theoretical tool of QCD factorisation [74, 75].

The standalone determination of $|V_{cb}|$ will also be increasingly important when other measurements get more precise, as it will become the limiting factor in many SM predictions such as the branching fraction of $B_s^0 \to \mu^+\mu^-$ [76], as well as $K \to \pi\nu\bar{\nu}$, and for ϵ_K. The current uncertainty is inflated due to the disagreement between measurements from inclusive and exclusive final states and currently appears to critically depend on the parametrisation used to fit the form factors [31, 32]. LHCb has already performed a measurement of the differential rate of the decay $\Lambda_b^0 \to \Lambda_c^+\mu\nu$, allowing a determination of the form factors of that decay [77]. A first determination of the absolute value of $|V_{cb}|$, exploiting theoretical predictions for the ratios of semileptonic decay widths between different b hadron species [78], is in progress. The LHCb Upgrade II data set would provide large samples of exclusive $b \to c\ell\nu$ decays, with the full range of b hadron species, with which very precise shape measurements could be performed,

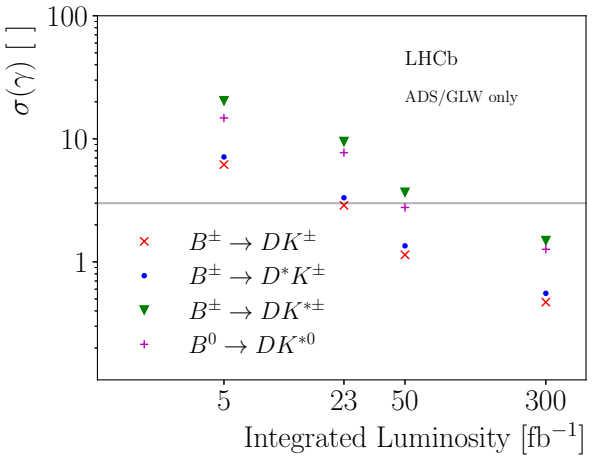

Fig. 6: Extrapolation of γ sensitivity from the ADS/GLW analyses at LHCb, ignoring disfavoured ambiguities. The expected Belle-II precision on γ at an integrated luminosity of 50 ab^{-1} is shown by the horizontal grey line.

as a crucial ingredient to reach the ultimate precision on $|V_{cb}|$.

2.5.2 Time-integrated tree-level measurements of γ

LHCb has observed and studied two-body ADS/GLW modes during Run 1 and Run 2 [79, 80]; all ADS/GLW asymmetries are statistically limited. The systematic uncertainties are small and arise predominantly from sources that will naturally decrease with increasing data, notably knowledge of instrumentation asymmetries. Methods for measuring and correcting for the B-meson production asymmetry and the $K^\pm/\pi^\pm$ reconstruction asymmetries are established using calibration samples; such samples will continue to be collected. The dominant systematic uncertainties for GLW decays are due to background contributions from $\Lambda_b^0 \to \Lambda_c^+ K^-$ decays and charmless decays, while the dominant uncertainty for ADS decays arises from the $B_s^0 \to \overline{D}^0 K^- \pi^+$ background. All will be better determined with dedicated studies as the sample size increases.

LHCb is expanding the ADS/GLW technique to the other $B \to DK$ decays, which share the same quark-level transition. An analysis of GLW observables in $B^\pm \to D^{*0}K^\pm$ decays has been developed for the case where the D^{*0} vector meson is not fully reconstructed [80]. This partial reconstruction has larger background uncertainties but these will improve with more data as dedicated studies of the background are performed. Furthermore, ADS/GLW analyses have been developed and published in quasi-two-body modes, $B^\pm \to DK^{*\pm}$ [81] and $B^0 \to DK^{*0}$ [82]. As in the case of $B^\pm \to D^{(*)0}K^\pm$ decays, these modes have no limiting systematic and they will make competitive contributions with the Upgrade II data sets.

Under the assumption that systematic uncertainties decrease in parallel with the statistical uncertainties as $\propto 1/\sqrt{\mathcal{L}}$, the future precision on γ is predicted in Fig. 6. Fig. 6 uses central values and uncertainties in the published analyses of $B^\pm \to DK^\pm$, $B^\pm \to DK^{*\pm}$ and $B^0 \to DK^{*0}$ decays. For $B^\pm \to D^{*0}K^\pm$ both the partial and full reconstruction techniques are used in this study albeit with unpublished central values and uncertainties.

For the GGSZ family of measurements, the model-independent method is expected to be the baseline for LHCb Upgrade II , and its uncertainty is currently statistically dominated. Although systematic uncertainties will already become significant compared to the statistical uncertainty in Run 3, studies performed so far give confidence that the systematic uncertainties will generally scale with the statistical reach well into the Upgrade II period. An example of the bin definitions and expected per-bin asymme-

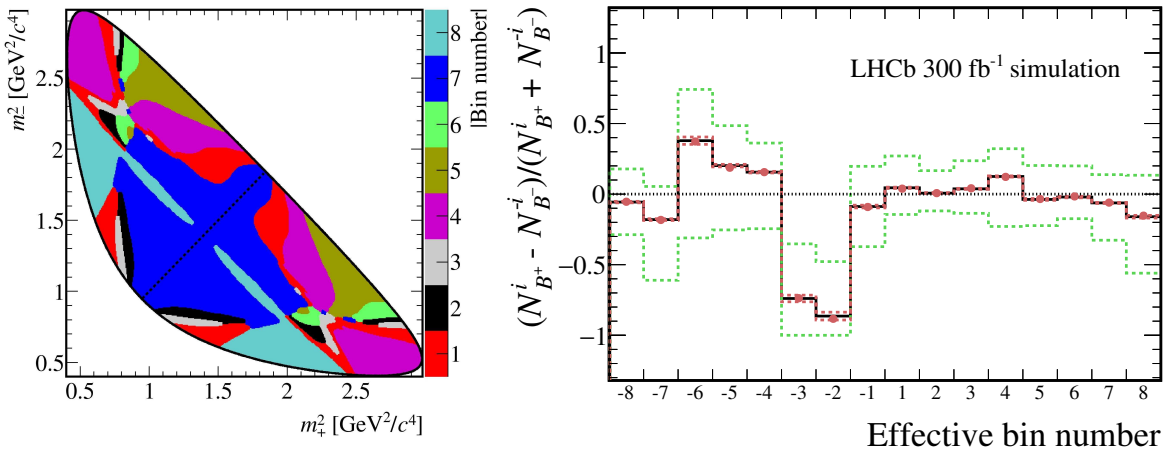

Fig. 7: (Left) Bin definitions for $D \to K^0_S\pi^+\pi^-$ as a function of m^2_- and m^2_+, the invariant masses squared of the $K^0_S h^-$ and $K^0_S h^+$. (Right) Asymmetry between yields for $B^\pm \to DK^\pm$ decays, with $D \to K^0_S\pi^+\pi^-$ in bin i (for B^+) and $-i$ (for B^-). The data points are obtained from simulation with the expected sample size at 300 fb^{-1}, assuming the current performance of the LHCb experiment. The black histogram shows the predicted asymmetry based on the current world average values of γ and relevant hadronic parameters, the red dots show the result of a single pseudoexperiment, while the red bands show the expected uncertainties from an ensemble. The green bands show the corresponding uncertainties with the current LHCb data set.

tries in LHCb Upgrade II can be seen in Fig. 7.

The largest systematic uncertainty is due to the precision of the external strong-phase inputs coming from the CLEO-c data which currently contribute approximately 2° to the overall uncertainty on γ [83]. The impact of this uncertainty on GGSZ measurements is estimated in Fig. 8 which compares a $\sqrt{N}$ improvement with the expected yield increase and the projected uncertainty if the current external information on c_i and s_i is not improved. It can be seen that this starts to approach a limit originating from the fixed size of the quantum-correlated charm input from CLEO-c. This contribution will naturally decrease with larger $B^\pm \to D^0K^\pm$ samples, however, as the B decays themselves also have sensitivity to c_i and s_i. Studies performed using pseudoexperiments with different size quantum correlated D samples and LHCb B data suggest that the optimal sensitivity is only reached when the size of the input D sample is at least as big as the overall B sample. More precise measurements with data already recorded by the BESIII experiment will be able to reduce the external contribution to the uncertainty by around 50% but analysis of future larger data sets with BESIII and at LHCb will be vital in order to avoid the external input compromising the ultimate sensitivity to γ.

The current second largest source of systematic uncertainty comes from the knowledge of the distribution of D decays over the Dalitz plane in the flavour-specific B final state, with reconstruction and efficiency effects incorporated. These are determined with a flavour-specific control decay mode $B^0 \to D^{*\pm}\mu^\mp\nu_\mu X$, where the D^{*-} decays to $\overline{D}^0\pi^-$ and X represents any unreconstructed particles. The ultimate systematic uncertainty is particularly sensitive to data-simulation agreement and size of simulated samples because of a need to model unavoidable differences in the signal and control modes. Fast simulation techniques which are being deployed and further developed at LHCb will therefore be crucial for keeping up with the large data samples, while a fully software-based trigger will allow for a better alignment of the signal and control channel selections compared to today. Uncertainties from sources such as low mass backgrounds can be expected to remain subdominant with higher statistics, as further studies will give better understanding to their rates and shapes. Some additional complications

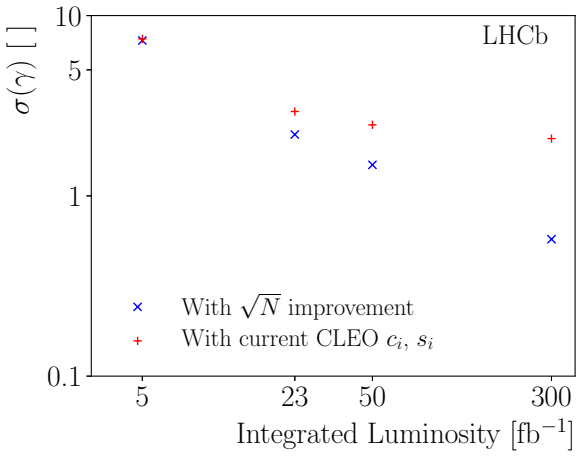

Fig. 8: Expected evolution of γ sensitivity with (red crosses) current CLEO inputs and with (blue x-marks) $\sqrt{N}$ improvements on their uncertainty.

will present themselves as the yields will eventually be high enough that it will become necessary to take into account effects induced from asymmetries in the K^0_S system, and eventually through mixing in the D^0 system. However these are tractable problems, and studies have already been done to understand when these effects will become important.

There are many prospects for adding orthogonal information on γ by applying the ADS/GLW and GGSZ techniques to modes that have an additional π^0. The first use of π^0 mesons in an LHCb γ analysis occurred with the Run 1 ADS/GLW analysis of $B^\pm \to DK^\pm$ decays with $D \to K\pi\pi^0$, $KK\pi^0, \pi\pi\pi^0$ final states [84]. The $K\pi\pi^0$ and $\pi\pi\pi^0$ modes have branching fractions 3 and 10 times larger than their two-body equivalents. However, the π^0 reconstruction+selection efficiency in these decays is low, around 3% with the current calorimeter. Also the analysis is complicated by a combinatorial background arising from random π^0 association. Improvements to the Upgrade II calorimeter granularity and energy resolution will therefore be crucial in achieving the ultimate sensitivity with these modes, especially by improving the resolution of merged π^0, their separation for photons, and improving the π^0 mass resolution.

An important mode under development for the upgrade era is $B^\pm \to D^{*0}K^\pm$ decays, with $D^{*0} \to D^0\pi^0$ and $D^{*0} \to D^0\gamma$ decays. These twin modes provide an excellent sensitivity to γ as an exact phase difference between the two D^{*0} modes can be exploited [85]. For this case, the efficient distinction of π^0 and γ calorimeter objects is critical as the two D^{*0} modes exhibit opposite CP asymmetries. The initial studies show small, but clean signals. As long as the fully and partially reconstructed data sets are kept statistically independent, the final sensitivity from $B^\pm \to D^{*0}K^\pm$ decays will be around 0.5° as seen in Fig. 6.

A GGSZ-like analysis of $B^\pm \to D[\to K^0_s\pi\pi\pi^0]K^\pm$ decays has recently been proposed for Belle II, where a sensitivity approaching that of the $D \to K^0_s\pi\pi$ GGSZ analysis is expected [86]. With improved π^0 efficiency, LHCb Upgrade II can exploit this mode competitively. Lastly, higher π^0 efficiency will merit the analysis of $B^\pm \to DK^{*\pm}[\to K^\pm\pi^0]$ decays. The π^0 reconstruction efficiency is typically a factor 3-4 lower than that of the K^0_S so the $K^0_S\pi^\pm$ mode is preferred. However the $B^\pm \to DK^\pm\pi^0$ Dalitz analysis for γ should share many advantages of the isospin-conjugate decays $B^0 \to DK^+\pi^-$ analysis (discussed next) but with reduced B^0_s feed down and large asymmetries in the ADS-like region of the Dalitz space.

Analogously to the neutral modes, a variety of high-multiplicity B and D modes are already being established and will play an important role in a future determination of γ. The most developed multi-body B decay channel is $B^0 \to DK^+\pi^-$ decays, where the D meson is found in an ADS/GLW-like

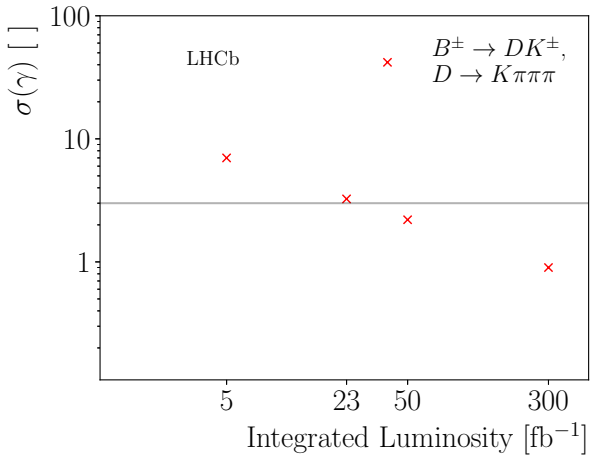

Fig. 9: Projected sensitivity to γ from a binned analysis of $B^\pm \to D[\to \pi K\pi\pi]K^\pm$ decays. The expected Belle-II precision on γ at an integrated luminosity of 50 ab^{-1} is shown by the horizontal grey line.

($K\pi$, KK, $\pi\pi$, $K3\pi$, ...) or GGSZ-like ($K^0_S\pi\pi$, $K^0_S KK$, ...) final states. These modes are less abundant than the equivalent $B^\pm$ modes but the fact that both the $b \to c\bar{u}s$ and $b \to u\bar{c}s$ transitions proceed by colour-suppressed amplitudes means the GLW asymmetries can be very large. Furthermore, understanding the pattern of asymmetry across the B^0 Dalitz plane quashes the trigonometric ambiguities. This analysis has been established with the KK and $\pi\pi$ modes using Run 1 data in Ref. [87] after the development of the $B^0 \to \overline{D}^0 K^+\pi^-$ amplitude model [88]. Although the statistical sensitivity to CP violation using Run 1 data alone was not significant, the method remains promising for future analysis given the high value of r_B in this mode (~ 0.25). The extension to $B^0 \to D[\to K^0_S\pi^+\pi^-]K^+\pi^-$ decays is of particular importance as it allows for a so-called "double Dalitz" model-independent analysis to be performed [89, 90]. Extrapolating yields from a Run 1 $B^0 \to D^0 K^{*0}$ analysis to a dataset corresponding to an integrated luminosity of 23 fb^{-1}, sensitivity studies indicate that a precision on γ of 3° can be expected [91], thus by extension, a sub-degree precision is expected for Upgrade II. Another high-multiplicity mode that holds promise is $B^\pm \to DK^\pm\pi^+\pi^-$, which has been studied with Run 1 data with two-body D decays [92], though due to the unknown Dalitz structure of the B decay a much larger dataset is needed to fully exploit this mode.

Another exciting extension to the standard ADS technique uses $B^\pm \to D[\to \pi K\pi\pi]K^\pm$ decays where the five-dimensional (5D) Dalitz volume of the D decay is split into bins. Excellent sensitivity to γ is achieved as long as the D-system parameters (r_D, δ_D, κ) in each bin are known. An optimal binning scheme is soon to be defined from the amplitude analysis of the suppressed and favoured $D^0 \to \pi K\pi\pi$ and $D^0 \to K\pi\pi\pi$ decays [93]. The expected sensitivity is shown in Fig. 9. An additional irreducible uncertainty from the D system measurements of $< 1^\circ$ is expected.

Other multibody D decays are under development with reciprocal charm-system measurements underway: a $B^\pm \to D[\to 4\pi]K^\pm$ analysis can build on the D-system knowledge gathered in Ref. [94]; an ADS analysis of $B^\pm \to D[\to K^0_S K\pi]K^\pm$ decays has been demonstrated with Run 1 [95]; and work on $B^\pm \to D[\to KK\pi\pi]K^\pm$ decays is envisaged.

2.5.3 Time-integrated loop-level measurements of γ

There are numerous methods that allow the extraction of CKM information by combining amplitude measurements made in different decay channels, in particular the $B^0_{(s)} \to K^0_S h^+h^-$, $B^0_{(s)} \to h^+h^-\pi^0$, and $B^+ \to h^+h^+h^-$ families. Some such methods exploit the interference between various $K^*\pi$ or ρK con-

tributions, which can be related using isospin symmetry [96–101]. Constructing such relations enables the determination of the angle γ, up to corrections for contributions from electroweak penguins. These methods are particularly promising when using decays such as $B_s^0 \to K_S^0\pi^+\pi^-$ and $B_s^0 \to K^-\pi^+\pi^0$, since here the electroweak penguin contributions are expected to be negligible. Other methods use the whole Dalitz plot amplitude and relate numerous decays via flavour symmetries [102–104] or exploit interference between the charmless decays and those that proceed via intermediate charmonium states such as $B^+ \to \chi_{c0}\pi^+$ [105, 106].

Extrapolating the observed yields in Ref. [107] to the data sample expected to be collected at the end of LHCb Upgrade II gives signal yields of between 1.2 and 36 million depending on the $B^+ \to h^+h^+h^-$ final state. These can be compared to an extrapolation of the yields obtained by the B factories [108, 109] to the expected 50 ab^{-1} sample to be collected by Belle II, which gives approximately 47,000 to 660,000 events for the same range of modes. The far larger yields, combined with the much better signal to background ratios, mean that LHCb will continue to dominate the precision in these modes.

Amplitude analyses cannot benefit from cancellations of systematic effects to the same degree as the binned measurements of asymmetries performed in Ref. [107], and are more likely to become systematically limited. On the other hand, the extremely large $B^+ \to h^+h^+h^-$ signal samples will allow new information to be extracted. In particular, by performing coupled-channel analyses of these decay modes, contributions from $\pi^+\pi^- \leftrightarrow K^+K^-$ rescattering processes can be better understood and constrained. The development of such new, improved models will also be of enormous benefit to analyses of many other decay modes, such as the closely related $B \to K_S^0h^+h^-$ and $B \to h^+h^-\pi^0$ families. This will help to reduce the corresponding uncertainty on the CKM phases that can be determined from those channels.

2.5.4 Time-dependent measurements of γ

Using Run 1 data, LHCb has determined the $B_s^0 \to D_s^\mp K^\pm$ oscillation parameters, which determine $\gamma - 2\beta_s$, from a sample of about 6000 signal decays [7]. From the measured parameters, a value of γ of $(128^{+17}_{-22})^\circ$ (modulo 180°) is determined. The result is dominated by statistical uncertainties thanks to the wide use of data-driven methods to determine the decay-time acceptance and resolution, and to calibrate the flavour tagging. The systematic uncertainties are, in decreasing order of importance, related to background from b-hadron decays, to uncertainty on the value of Δm_s, to the calibration of the decay-time resolution and to the flavour tagging. The first contribution can be significantly reduced by a tighter signal selection or by using a different fitting approach; the remaining contributions are expected to scale with the statistics accumulated due to their data-driven nature.

In the case of $B^0 \to D^\mp\pi^\pm$ decays, the smallness of the ratio of amplitudes, $r_{D\pi}$, which limits the sensitivity to S_f and $S_{\bar{f}}$, is compensated for by a large signal yield. About 480 000 flavour-tagged signal decays are available in the Run 1 LHCb data sample [110]. Analysis of this sample gives measurements of S_f and $S_{\bar{f}}$ that are more precise than those from BaBar and Belle [111, 112]. Also in this case the precision is limited by the statistical uncertainty. The dominant sources of systematic uncertainty, such as due to knowledge of Δm_d and of background subtraction, are expected to be reducible with larger samples.

In $B^0 \to D^\mp\pi^\pm$ decays there are only two observables, S_f and $S_{\bar{f}}$, that depend on three unknown quantities, $r_{D\pi}$, $\delta_{D\pi}$ and $2\beta + \gamma$. External input must thus be used to obtain a constraint on $2\beta + \gamma$. A common approach is to determine $r_{D\pi}$ from the branching fraction of $B^0 \to D_s^+\pi^-$ decays, assuming SU(3) symmetry,

$$r_{D\pi} = \tan\theta_c \frac{f_{D^+}}{f_{D_s}} \sqrt{\frac{\mathcal{B}(B^0 \to D_s^+\pi^-)}{\mathcal{B}(B^0 \to D^-\pi^+)}}\,, \tag{16}$$

where $\tan\theta_c$ is the tangent of the Cabibbo angle and f_{D^+}/f_{D_s} is the ratio of decay constants. Using the resulting value of $r_{D\pi} = 0.0182 \pm 0.0012 \pm 0.0036$, where the second uncertainty accounts for

Table 3: Expected statistical uncertainties from LHCb on parameters of $B_s^0 \to D_s^{\mp} K^{\pm}$ and $B^0 \to D^{\mp}\pi^{\pm}$ decays.

	$B_s^0 \to D_s^{\mp} K^{\pm}$				$B^0 \to D^{\mp}\pi^{\pm}$			
Parameters	Run 1	23 fb^{-1}	50 fb^{-1}	300 fb^{-1}	23 fb^{-1}	50 fb^{-1}	300 fb^{-1}	
S_f, $S_{\bar{f}}$	0.20	0.043	0.027	0.011	0.02	0.0041	0.0026	0.0010
$A_f^{\Delta\Gamma}$, $A_{\bar{f}}^{\Delta\Gamma}$	0.28	0.065	0.039	0.016	–	–	–	
C_f	0.14	0.030	0.017	0.007	–	–	–	

Table 4: Current LHCb measurements of $C_{\pi^+\pi^-}$, $S_{\pi^+\pi^-}$, $C_{K^+K^-}$, $S_{K^+K^-}$ and $A_{K^+K^-}^{\Delta\Gamma}$ using the full sample of pp collisions collected during Run 1, where the first uncertainty is statistical and the second systematic. The projection of statistical precisions for each variables are also reported.

Data sample	$C_{\pi^+\pi^-}$	$S_{\pi^+\pi^-}$	$C_{K^+K^-}$	$S_{K^+K^-}$	$A_{K^+K^-}^{\Delta\Gamma}$
Run 1 (3 fb^{-1} [114])	$-0.34 \pm 0.06 \pm 0.01$	$-0.63 \pm 0.05 \pm 0.01$	$0.20 \pm 0.06 \pm 0.02$	$0.18 \pm 0.06 \pm 0.02$	$-0.79 \pm 0.07 \pm 0.10$
			σ (stat.)		
Run 1-3 (23 fb^{-1})	0.015	0.013	0.015	0.015	0.018
Run 1-6 (300 fb^{-1})	0.004	0.004	0.004	0.004	0.005

possible nonfactorisable SU(3)-breaking effects [113], the intervals $|\sin(2\beta+\gamma)| \in [0.77, 1.00]$ and $\gamma \in [5, 86]^\circ \cup [185, 266]^\circ$ are obtained, at the 68% CL. The uncertainties on $r_{D\pi}$ and β have negligible impact on these intervals, as the dominant uncertainties are from the S_f and $S_{\bar{f}}$ measurements.

The expected statistical sensitivities for the CP violation parameters in $B_s^0 \to D_s^{\mp} K^{\pm}$ and $B^0 \to D^{\mp}\pi^{\pm}$ decays are shown in Table 3. These are based on scaling of yields, and as such assume that the same detector performance as achieved in Run I can be maintained. In particular, the sensitivity depends strongly on the performance of the particle identification, decay time resolution and flavour tagging. The results can be complemented by studies of the related $B_s^0 \to D_s^{*\mp} K^{\pm}$ and $B^0 \to D^{*\mp}\pi^{\pm}$ channels. In particular, the $D^{*\mp}\pi^{\pm}$ mode has an all charged final state, and with a possible gain in the acceptance of slow pions from D^* decays from the addition of magnet side stations, comparable precision to that for $B^0 \to D^{\mp}\pi^{\pm}$ may be possible.

The corresponding expected sensitivities of γ from $B_s^0 \to D_s^{\mp} K^{\pm}$ decays are about 4°, 2.5° and 1° after collecting 23, 50 and 300 fb^{-1}, respectively. It is more challenging to estimate the constraints on $\sin(2\beta+\gamma)$ and γ from $B^0 \to D^{\mp}\pi^{\pm}$ decays, since the precision of the external value of $r_{D\pi}$ will become the dominant source of systematic uncertainty. Theoretical advancements on understanding the nonfactorisable SU(3)-breaking effects are thus required.

LHCb has measured the CP violation parameters in $B^0 \to \pi^+\pi^-$ and $B_s^0 \to K^+K^-$ decays ($C_{\pi^+\pi^-}$, $S_{\pi^+\pi^-}$, $C_{K^+K^-}$, $S_{K^+K^-}$ and $A_{K^+K^-}^{\Delta\Gamma}$) using the full sample of pp collisions collected during Run 1 corresponding to 3.0 fb^{-1} of integrated luminosity [114]. The results are reported in Table 4, together with the projections of the statistical uncertainties to larger samples. The scaling of statistical uncertainties assumes the same detector performances as in Run 1, in particular regarding the flavour tagging, the decay-time resolution and the particle identification performance, which are particularly important for the determination of these observables. The main sources of systematic uncertainties are due to limited knowledge of: the variation of the selection efficiency as a function of the B_q meson decay time, the parameters Γ_s and $\Delta\Gamma_s$, and the calibration of the decay-time resolution. The evaluation of these uncertainties is based on the study of control modes, and hence they are expected to decrease in a statistical manner as the available sample size grows.

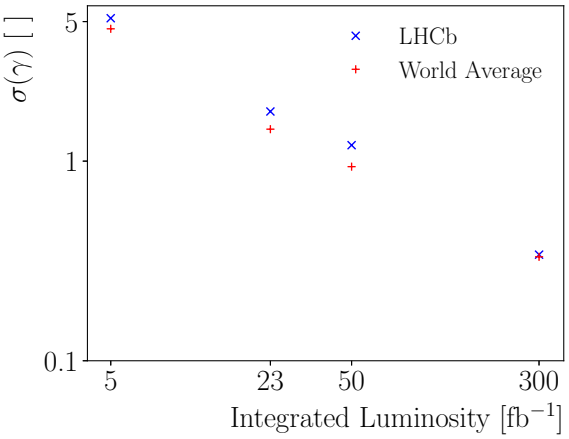

Fig. 10: Projected sensitivity for the LHCb γ combination with the currently used strategies and the world average using projections from Belle II in addition.

2.5.5 Gamma combination and impact of external inputs

Projections for the expected precision of the LHCb γ combination are shown in Fig. 10, estimating the uncertainty on γ to be 1.5° and 0.35° with 23 fb^{-1} and 300 fb^{-1} data samples, respectively. The LHCb projections assume that the statistical uncertainty scales with the data sample size and include the effect of the increased centre-of-mass energy, increased trigger performance and increased integrated luminosity. Most of the systematic uncertainties are driven by the size of the data samples and corresponding simulation samples. The overall sensitivity is predominantly driven by the GLW modes which provide the narrowest solutions for γ. The dominant systematic uncertainty for these modes will depend on knowledge of both the shape and rate of the background from $\Lambda_b^0 \to \Lambda_c^+ K^-$, as well as uncertainties arising from particle identification calibration and instrumental charge asymmetries. In order to obtain the best possible precision on γ it will be necessary to ascertain the correlation of these uncertainties between different GLW modes. The ultimate sensitivity to these modes from Belle II will be considerably less than that at LHCb, however detailed analysis from both experiments will provide an important cross check. For decays with neutrals in the final state, particularly the *CP*-odd GLW mode with $D^0 \to K_S^0 \pi^0$, the LHCb detector has considerable disadvantages over Belle II. These would be mitigated by an improved electromagnetic calorimeter for the LHCb Upgrade II. The GGSZ modes are a powerful way to unambiguously resolve the multiple solutions of the GLW method and furthermore offer considerable standalone sensitivity to γ. Accurate knowledge of the selection efficiency across the Dalitz plane is vital for these modes and contributes a considerable systematic uncertainty. This will naturally reduce with larger datasets as it is obtained via semi-leptonic $B^0 \to D^{*+}\mu^-\overline{\nu}_\mu X$ control modes but requires large simulation samples. More precise measurement of important external parameters, particularly c_i and s_i from BESIII, will be required to reduce the uncertainty associated with the model independent GGSZ method. The uncertainties of inputs from charm threshold data collected by CLEO-c will begin to limit the sensitivity by the end of Run 2, so it is essential to work together with BESIII to provide updated measurements for the suite of charm decays and $D \to K_S^0 h^+ h^-$ in particular. Provided that the charm inputs are improved sub-degree level precision on γ is attainable. Understanding the correlations between different B decay modes that all use these external parameters will be vitally important as they are likely to contribute one of the largest overall systematic uncertainties in the combination. A comparison between the current LHCb GGSZ and GLW/ADS measurements [80, 115] with their future projections at 300 fb^{-1} is shown in Fig. 11. The order of magnitude increase in precision is very apparent and the importance of the combination clear, given the multiple ambiguous solutions for GLW/ADS measurements is not resolved with increased luminosity.

The GGSZ modes are considered the *golden modes* at Belle II and drive the overall uncertainty on

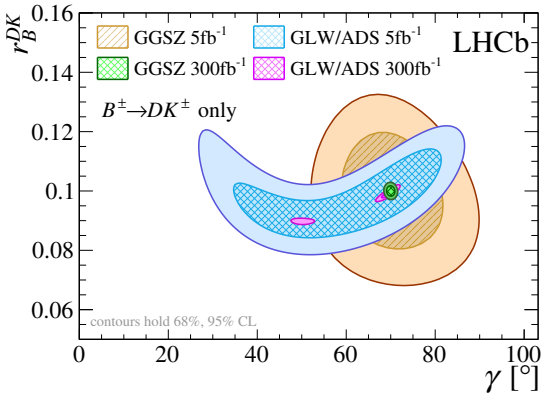

Fig. 11: Comparison between the current LHCb 3-body GGSZ and 2-body GLW/ADS measurements alongside their future projections with 300 fb^{-1} in the plane of γ vs. r_B^{DK} (note the curtailed y-axis for r_B^{DK}). The scan is produced using a pseudo-experiment, centred at $\gamma = 70^\circ$, $r_B^{DK} = 0.1$, with $B^\pm \to DK^\pm$ decays only.

γ which is expected to reach 1.5° with a data sample of $50\ \mathrm{ab}^{-1}$. This is comparable to the sensitivity that the LHCb γ combination will achieve with a data sample corresponding to approximately $23\,\mathrm{fb}^{-1}$. Subsequently input from Belle II will still contribute towards the world average by the end of Run 4 but LHCb will dominate γ measurements with Upgrade II ($300\,\mathrm{fb}^{-1}$) contributing entirely towards a world average precision of $\sim 0.35^\circ$. It should be emphasised that this projection includes only the currently used strategies, and does not include improvements from other approaches. A comparison between the projected uncertainties for LHCb and the world average as a function of integrated luminosity is shown in Fig. 10.

2.5.6 *Determinations of Δm_s, Δm_d, and interplay with b-hadron lifetimes*

The world-leading measurements of both Δm_d and Δm_s are from LHCb [116, 117], and can be improved further assuming that good flavour tagging performance can be maintained. This will not only reduce systematic uncertainties in CP-violation measurements but also provide a strong constraint on the length of one side of the unitarity triangle, although progress here is mainly dependent on improvements in lattice QCD calculations. The decay-time-dependent angular analysis of $B_s^0 \to J/\psi\,\phi$ allows measurement of $\Delta\Gamma_s$ simultaneously with CP-violation parameters. Therefore, improved knowledge of $\Delta\Gamma_s$ will be obtained together with measurements of $\phi_s^{c\bar{c}s}$. Precision at the LHC is expected not to be systematically limited. The LHCb Upgrade II will allow to exploit measurements in various channels. ATLAS and CMS projections in the $B_s \to J/\psi\,\phi$ decay mode can be found in 2.5.8.1. For theory predictions of $\Delta\Gamma_s$ see Ref. [118].

Width differences between different types of b hadrons, such as $\Gamma_s - \Gamma_d$, are also of interest. They test the heavy-quark expansion, used to make theoretical predictions. In addition, their precise knowledge is important to control systematic uncertainties in measurements where a decay mode of one type of b hadron is used as a control channel in studies of a decay of another. Detailed understanding of acceptances is necessary for such measurements, which can be achieved using topologically similar final states (see, e.g., Ref. [119]). These measurements are therefore expected to be significantly improved with LHCb Upgrade II.

2.5.7 *Semileptonic asymmetries and prospects for $\Delta\Gamma_d$*

Semileptonic decays, being flavour specific, provide a unique probe of B_q^0, where $q = s, d$, meson mixing phenomena. In particular, CP violation in B_q^0 meson mixing can be expressed through the semileptonic

asymmetries

$$a^q_{\rm sl} = \frac{\Gamma(\overline{B}^0_q \to f) - \Gamma(B^0_q \to \bar{f})}{\Gamma(\overline{B}^0_q \to f) + \Gamma(B^0_q \to \bar{f})} \approx \frac{\Delta\Gamma_q}{\Delta M_q} \tan\phi^q_{12}, \tag{17}$$

where f is a flavour-specific final state that is only accessible through the decay of the B^0_q state. Mixing is required to mediate the transition $\overline{B}^0_q \to B^0_q \to f$, and its conjugate. Semileptonic decays of the type $B^0_q \to D^-_q \mu^+ \nu_\mu X$ are well suited because (i) they are immune to any unknown CP violation in decay and (ii) they have large branching ratios.

Including the effect of an unknown production asymmetry, a_p, the time-dependent *untagged* asymmetry is defined as:

$$A^q_{\rm sl}(t) \equiv \frac{N - \bar{N}}{N + \bar{N}} = \frac{a^q_{\rm sl}}{2} - \left[a_p + \frac{a^q_{\rm sl}}{2}\right] \cdot \left[\frac{\cos\Delta M_q t}{\cosh\Delta\Gamma_q t/2}\right], \tag{18}$$

where N and $\bar{N}$ denote the number of observed decays to f and $\bar{f}$ final states, respectively. A decay-time-dependent fit can disentangle the $B^0_d - \bar{B}^0_d$ production asymmetry from $a^d_{\rm sl}$ [120]. In the B^0_s case the *time integrated* asymmetry is employed [13]. Owing to the large value of Δm_s the term containing a_p is suppressed to a calculable correction of a few $\times 10^{-4}$, after integrating over decay time. These approaches have been applied in the measurements with the Run 2 dataset that are listed in Table 5, giving the world's best single measurements. These measurements are far from any uncertainty floor in the SM predictions, and are sensitive to anomalous NP contributions to Γ^q_{12} and M^q_{12}. The difference $\Gamma_d - \Gamma_s$ further probes NP in penguin coefficients [121].

The following briefly reviews the dominant sources of uncertainty on the current LHCb measurements, and considers strategies to fully exploit the potential of the LHCb Upgrade II. All uncertainties are as evaluated on a^q_{sl} (i.e., all sources of raw asymmetry, and their uncertainties, are scaled by a factor of two as expected from Eq. 18).

Statistical precision: The statistical uncertainty on $a^s_{\rm sl}$ straightforwardly extrapolates to 2.1×10^{-4}. In the case of $a^d_{\rm sl}$ it should be noted that stringent fiducial cuts and weights were imposed on the signal sample to control certain tracking asymmetries that were not well known at the time. By the time of the subsequent $a^s_{\rm sl}$ measurement, a new method with $J/\psi \to \mu^+\mu^-$ decays had been developed, and others are in the pipeline. A further factor of two increase in yields is therefore assumed, which extrapolates to an uncertainty of 1.1×10^{-4}.

Detection asymmetries: The single largest contributor is the $K^-\pi^+$ asymmetry in $a^d_{\rm sl}$. This asymmetry was determined with a single method using D^+ decays to the $K^-\pi^+\pi^+$ and $K^0_{\rm S}\pi^+$ final states, with a precision of around 2.0×10^{-3} [120]. Thanks to trigger improvements, a factor of two increase in the effective yield of the most limiting $K^0_{\rm S}\pi^+$ final state [122, 123] can be anticipated. This will extrapolate to an uncertainty of 1.1×10^{-4}. Improvements in the reconstruction of downstream tracks in the earliest stage of the software trigger may also allow us to exploit $K^0_{\rm S}\pi^+$ final states with $K^0_{\rm S}$ decays downstream of the LHCb vertex detector (VELO). Further methods have since been proposed using partially reconstructed D^{*+} decays and $D^0 \to K^-K^+$ decays. The partial reconstruction method will be greatly improved by the reduction of material before the first VELO measurement point. The systematic uncertainties in these approaches will be controlled by using ultra high statistics fast simulations to track the kinematic dependencies in the asymmetries. The target uncertainty is 1.0×10^{-4}, including systematic uncertainties. The equivalent K^+K^- asymmetry in the $a^s_{\rm sl}$ measurement will be smaller and more precisely controlled. The $\mu^+\pi^-$ asymmetry will be controlled by a combination of $J/\psi \to \mu^+\mu^-$ decays, partially reconstructed D^{*+} decays, $D^0 \to h^-h^+$ decays, and high statistics fast simulations.

Background asymmetries: These measurements are challenging because the $B^0_q \to D^-_q \mu^+ \nu_\mu X$ final states can be fed by the decays of other b hadron species. This dilutes the relation between the

Table 5: Current theoretical and experimental determinations of the semileptonic asymmetries $a^d_{\rm sl}$ and $a^s_{\rm sl}$.

Sample ($\mathcal{L}$)	$\delta a^s_{\rm sl}/10^{-4}$	$\delta a^d_{\rm sl}/10^{-4}$
Run 1 (3 fb^{-1}) [13, 120]	33	36
Run 1-3 (23 fb^{-1})	10	8
Run 1-5 (300 fb^{-1})	3	2
Current theory [118, 126]	0.03	0.6

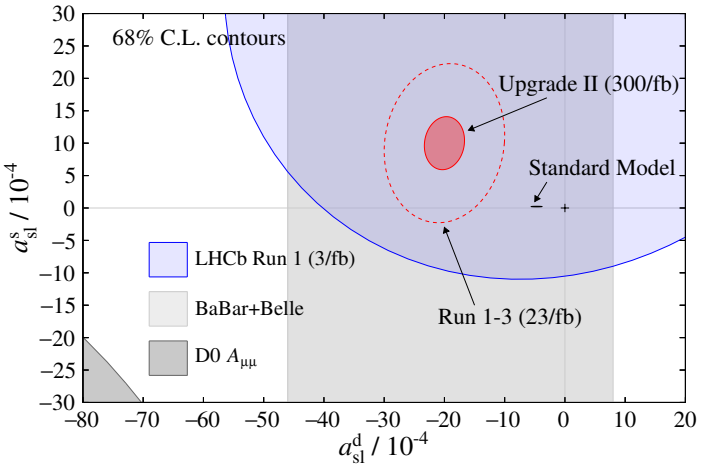

Fig. 12: Current and future landscape for the semileptonic asymmetries. The grey vertical band indicates the current B-Factory average for $a^d_{\rm sl}$. The blue ellipse represents the current LHCb Run 1 measurements [13, 120]. The red ellipse, which is arbitrarily centred, delineates the LHCb Upgrade II projected precision. The black ellipse shows the SM prediction, the uncertainty of which is barely visible.

raw asymmetry and $a^q_{\rm sl}$ and leads to a cocktail of production asymmetry corrections. We assume that these backgrounds can be statistically subtracted by extending the signal fits to include the $D^-_q\mu^+$ corrected mass dimension. It is assumed that the background asymmetry uncertainties can be controlled to the 1.0×10^{-4} level.

Other considerations: We must carefully consider the impact of having unequal sample sizes in the two polarities. This can be partially compensated for by assigning weights to one polarity [124]. We note that the choice of crossing angles should be carefully considered [125]. While we do not account for them in the current estimation, we could consider using other D^+_q decay modes to better align the detection asymmetries between $a^s_{\rm sl}$ and $a^d_{\rm sl}$. For example, $D^+\to K^-K^+\pi^+$ and $D^+\to K^0_{\rm S}\pi^+$ decays can be used, taking advantage of possible improvements in the trigger efficiency for $K^0_{\rm S}$ decays in LHCb Upgrade II. While the former decay is singly Cabibbo suppressed, its CP asymmetry could be measured using promptly produced D^+ mesons.

In summary the LHCb Upgrade II dataset should allow both $a^s_{\rm sl}$ and $a^d_{\rm sl}$ asymmetries to be measured to the level of a few parts in 10^{-4}, see Table 5. This will give unprecedented new physics sensitivity, and is still far from saturating the *current* theory uncertainties in the SM predictions. Fig. 12 shows the prospective LHCb Upgrade II measurement, arbitrarily centred at a value that differs from the SM prediction at the 10^{-3} level.

The ratio $\Delta\Gamma_d/\Gamma_d$, is typically measured from the difference in effective lifetimes between B^0 decays to final states that are flavour-specific, namely $J/\psi\,K^{*0}$, and CP-eigenstates, namely $J/\psi\,K^0_{\rm S}$ [127].

With this approach LHCb determined $\Delta\Gamma_d/\Gamma_d = -0.044 \pm 0.025 \pm 0.011$ using $1\,\text{fb}^{-1}$ of data [128]. ATLAS and CMS published competitive measurements [129, 130] reaching at their best statistical and systematic uncertainties of 0.011 and 0.009 respectively. The expected statistical uncertainty for LHCb Upgrade II, taking into account the larger centre-of-mass energy and the increase in luminosity, is $\sigma(\Delta\Gamma_d/\Gamma_d) \sim 0.001$. This can be compared with the SM prediction $\Delta\Gamma_d^{\rm SM}/\Gamma_d^{\rm SM} = (0.00397 \pm 0.00090)$ [126]. Thus, if systematic uncertainties can be controlled sufficiently, it will be possible to measure a significantly non-zero value of $\Delta\Gamma_d$ even if it is not enhanced above its SM prediction.

The challenge in controlling the systematic uncertainty is to understand precisely the decay-time acceptance difference between the $J/\psi K^{*0}$ and $J/\psi K^0_{\rm S}$ decay topologies. However, if the B^0 vertex position is reconstructed identically, namely using only the J/ψ decay products, and only $K^0_{\rm S}$ mesons decaying inside the VELO are considered, the largest sources of systematic uncertainty should cancel almost exactly and therefore not dominate the measurement. Similarly, the asymmetry in production rate between B^0 and $\overline{B}^0$ is expected to be precisely measured in independent control samples, and thus will not limit the achievable precision. In addition to the intrinsic interest in determining $\Delta\Gamma_d$, precise knowledge of its value will benefit many other studies of B^0 decay modes, since any systematic uncertainties associated with the assumption that $\Delta\Gamma_d = 0$ can be removed.

2.5.8 Measurements of ϕ_s from $b \to c\bar{c}s$ transitions

The single statistically most sensitive measurement of $\phi_s^{c\bar{c}s}$ is given by the flavour-tagged decay-time-dependent angular analysis of $B^0_s \to J/\psi(\mu^+\mu^-)\phi(K^+K^-)$ decay. The current world average is consistent with the SM prediction [63, 126], with new physics effects of a few tens of miliradians still allowed **??**. As the experimental precision improves it will be essential to have good control over possible hadronic effects [131, 132] that could mimic the BSM signal. It will also be crucial to achieve precise control of penguin pollution, both in $B^0_s \to J/\psi(\mu^+\mu^-)\phi(K^+K^-)$ and in other $b \to c\bar{c}s$ transitions. The wide range of $b \to c\bar{c}s$ modes accessible at LHCb Upgrade II will be vital to achieving both of these, and therefore contribute significantly more than their naive statistical sensitivity to the overall reach of this physics programme.

2.5.8.1 Projections for $B^0_s \to J/\psi(\mu^+\mu^-)\phi(K^+K^-)$

Fully exploiting the statistical power of HL-LHC for measurements of $\Delta\Gamma_s$ and the weak phase difference ϕ_s will require excellent flavour tagging performance, invariant mass resolution and proper-time resolution. The planned detector improvements in all three experiments are critical to deliver these requirements despite the much higher HL-LHC pileup.

Improvements in the decay time resolution are expected in ATLAS and CMS thanks to their upgraded inner detectors. Fig. 13 shows the ATLAS proper time resolution for Run-1, Run-2, and HL-LHC as a function of the B meson transverse momentum. Similarly Fig. 14 shows the CMS [133] expected HL-LHC performances in the proper decay length uncertainty, obtained from a simulation of of an ideal Phase-2 detector response. Besides the improvements in the tracker, which include the L1 trigger capability to reconstruct charged tracks above 2 GeV in transverse momentum with almost offline-like resolutions, the extended pseudorapidity coverage (up to $|\eta| = 4$) will increase the CMS acceptance for track reconstruction [1]. The CMS Phase-2 L1 (hardware) and HLT (software) trigger performances are expected to be comparable to those in Run 2 and sustainable in terms of rates; the offline selections for this projection are thus the same as in the 2012 data analysis [134]. The same signal purity is assumed as in the previous analysis; this assumption also relies on the future presence of the timing layer [4] which will mitigate the background pollution due to tracks coming from pileup vertices.

The ATLAS sensitivity study [135] follows the same approach as the previous study found in [136] and is based on the extrapolation of the ATLAS 2012 analysis [137], correcting for the full-simulation based observation of the signal invariant mass and proper-time resolutions. A full simulation of the HL-

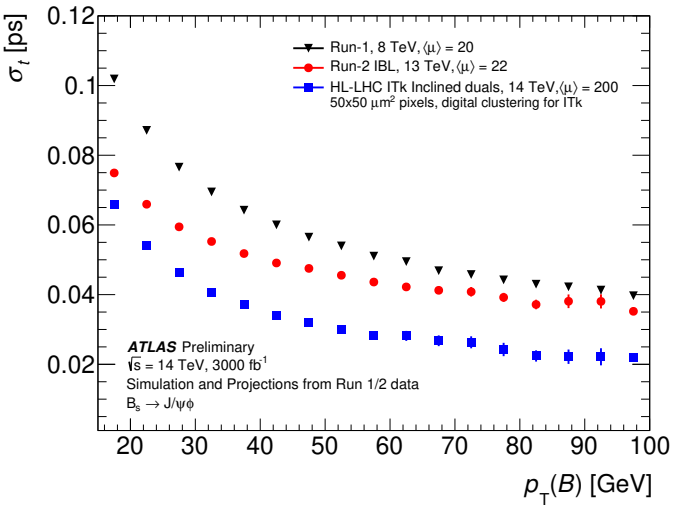

Fig. 13: The proper decay time resolution of the B_s^0 meson in ATLAS for the signal $B_s \to J/\psi\phi$ decay as function of the B meson p_{T}. Per-candidate resolutions corrected for scale-factors are shown, comparing the performance in Run 1, Run 2 and upgrade HL-LHC MC simulations. All samples use 6 GeV muon p_{T} cuts.

Table 6: Summary of the ATLAS $B_s \to J/\psi\phi$ performance at the HL-LHC compared with the Run 1 measurements and projections (numbers in parenthesis are predictions). The ϵ is the flavour-tagging efficiency, $D = 1-2\omega$ is the dilution factor, ω the wrong tag fraction, and $\sigma(t)$ the proper time resolution.

Period	L_{int} [fb^{-1}]	N_{sig}	ϵD^2	$\sigma\,(t)$ [ps]	$\delta_{\phi_s}^{stat}$ [rad]	$\delta_{\Delta\Gamma_s}^{stat}$ [ps^{-1}]
2011	4.9	22700	1.45	0.1	0.25 (0.22)	0.021
2012	14.3	73700	1.5	0.09	0.082	0.013
HL-LHC $\mu6\mu6$	3000	$9.7 \cdot 10^6$	1.5	0.05	(0.004)	(0.0011)
HL-LHC $\mu10\mu6$	3000	$5.9 \cdot 10^6$	1.5	0.04	(0.005)	(0.0014)
HL-LHC $\mu10\mu10$	3000	$1.7 \cdot 10^6$	1.5	0.04	(0.009)	(0.003)

LHC ATLAS tracking system is employed, including the effect of an average of 200 pile-up event per bunch crossing. An offline emulation of HL-LHC trigger responses is employed to evaluate the signal yield expectations corresponding to different dimuon transverse momentum thresholds: (p_T^1, p_T^2)= (6 GeV, 6 GeV), (6 GeV, 10 GeV) and (10 GeV, 10 GeV). Table 6 summarises the expected sensitivities, compared to the ATLAS Run-1 measurements and Fig. 15 left shows the $\delta\phi_s$ distributions. The CMS study is based on fully simulated signal events using the same model as in the previous CMS analysis [134] and toy Monte Carlo experiments for three different tagging scenarios: a where the flavour tagging performance is based on opposite-side muons and jet-charge, b where a muon and electron flavour tagging is used (as in the CMS 2012 data analysis), and c where a well performing flavour tagging based on leptons, jet-charge, and same side jet-charge/kaon tagging is tested. Fig. 15 right shows the CMS ϕ_s statistical uncertainty predictions for the different tagging scenarios. Assuming the new tagging power to be in the range 1.2-2.4% , and a total of 9 million fully reconstructed $B_s^0 \to J/\psi\phi(1020)$ candidates, CMS expects the ϕ_s statistical uncertainty to be 5-6 mrad at the end of the HL-LHC data taking. Both ATLAS and CMS systematic uncertainties are expected to be reduced to 1 mrad in the HL-LHC period, and thus the total ϕ_s uncertainty will still be statistically limited.

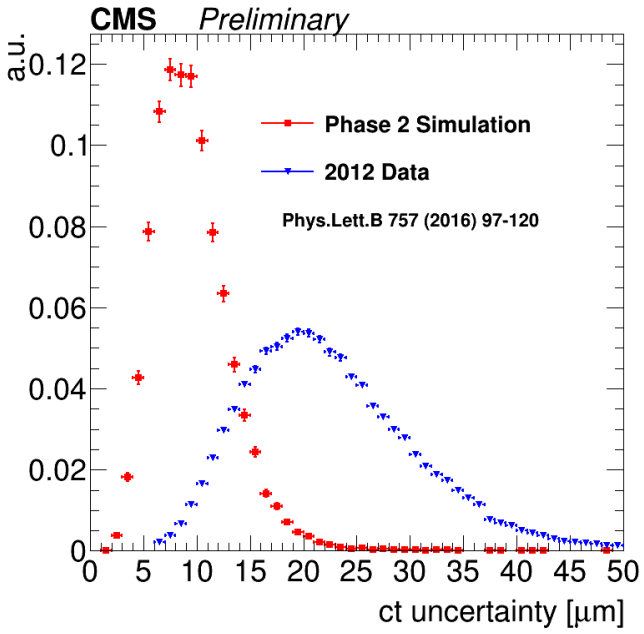

Fig. 14: CMS ct uncertainty distribution in 2012 data (blue) and HL-LHC Monte Carlo (red) samples (taken from [133]).

The ϕ_s measurement is usually illustrated as a constraint in the ϕ_s-$\Delta\Gamma_s$ plane. Fig. 16 summarises the projected contours in the $\Delta\Gamma_s$ vs φ_s plane for the ATLAS, CMS and LHCb experiments, with the CMS systematic uncertainty on $\Delta\Gamma_s$ assumed to be equal to the statistical uncertainty and an ATLAS estimated systematic uncertainty on the same parameter of approximately 0.0005 ps^{-1}. The red contour in the figure illustrates the combined HL-LHC sensitivity, equivalent to ~ 2 mrad in φ_s and ~ 5 ps^{-1} in $\Delta\Gamma_s$.

The expected LHCb precision on $\phi_s^{c\bar{c}s}$ after Upgrade II has been estimated based on the current published results, assuming that the detector performance remains the same in the HL-LHC period. Because of the data-driven nature of the LHCb analysis systematic uncertainties are expected to scale with luminosity and the overall sensitivity is expected to be $\sim 4\,\mathrm{mrad}$. This will be at the same level as the current precision on the indirect determination based on the CKM fit using tree-level measurements, which in turn is expected to improve with better measurements of the other CKM matrix parameters. Fig. 17 left shows the signal-yield asymmetry as a function of the B_s^0 decay time, folded at the frequency of B_s^0 oscillations, for $B_s^0 \to J/\psi\,\phi$ decays from a simulated data set corresponding to $300\,\mathrm{fb}^{-1}$. It clearly shows that a visible CP-violation effect will be observable.

2.5.8.2 *Projections for other $b \to c\bar{c}s$ transitions*

LHCb foresees extending the study of $b \to c\bar{c}s$ transitions to cover multiple independent precision measurements. It permits not only improved precision of the average, but a powerful consistency check of the SM. One important way in which this can be done is by allowing independent CP-violation effects for each polarisation state in the $B_s^0 \to J/\psi\,\phi$. This has been done as a cross-check in the LHCb Run I analysis [10], but this strategy will become the default in LHCb Upgrade II. Additional information can be obtained from $B_s^0 \to J/\psi\,K^+K^-$ decays with K^+K^- invariant mass above the $\phi(1020)$ meson, where higher spin K^+K^- resonances such as $f_2'(1525)$ meson contribute [140]. Among other channels, competitive precision can be obtained with $B_s^0 \to J/\psi\,\pi^+\pi^-$ decays [141], which have been found to be dominated by the CP-odd component. The $B_s^0 \to D_s^+D_s^-$ [11] and $B_s^0 \to \psi(2S)\phi$ [142] modes

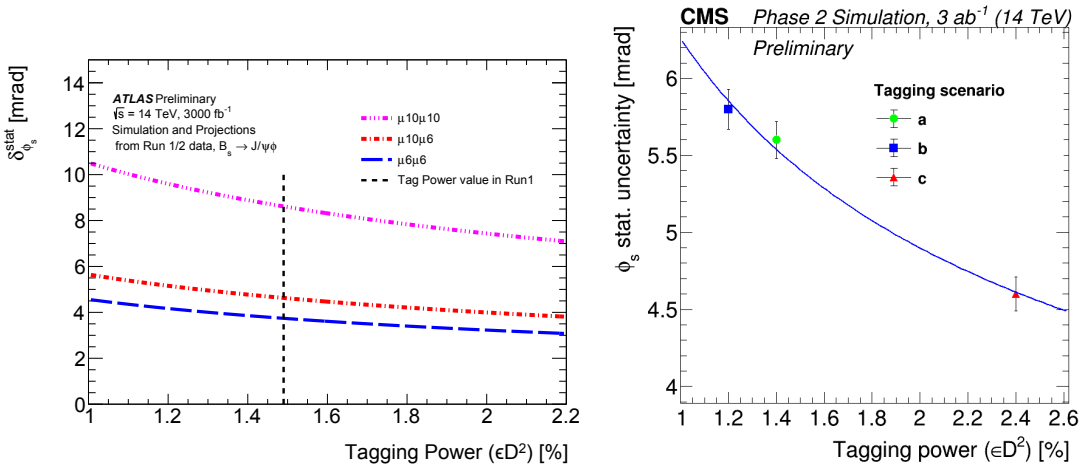

Fig. 15: Variation of the ϕ_s statistical uncertainty in ATLAS (left) and CMS (right) as function of the tagging power (ϵD^2). The behaviour is shown for different ATLAS triggers and CMS flavour tagging scenarios as explained in the text. The vertical dashed line in the ATLAS plot corresponds to the value assumed in the analysis extrapolation. A function proportional to $1/\sqrt{\epsilon D^2}$ is shown in the CMS plot to describe the ϕ_s uncertainty behaviour in a continuous range of the tagging power from 1.0 to 2.6 % (The CMS plot is taken from [133]).

have also been studied with LHCb, and give less precise but still important complementary results. Other channels, which have not been exploited yet, but could be important in LHCb Upgrade II, if good calorimeter performance can be achieved, include $B^0_s \to J/\psi\,\phi$ with $J/\psi \to e^+e^-$ and $B^0_s \to J/\psi\,\eta^{(\prime)}$ with $\eta' \to \rho^0\gamma$ or $\eta\pi^+\pi^-$, and $\eta \to \pi^+\pi^-\pi^0$ or $\gamma\gamma$ [143, 144].

The scaling of the $\phi_s^{c\bar{c}s}$ precision with integrated luminosity for individual decay modes and for their combination is shown in Fig. 18. These uncertainties are statistical only and are scaled from existing results, taking into account the gain in efficiency expected for $B^0_s \to D^+_s D^-_s$ from the removal of the hardware trigger. Maintaining the current performance will put stringent constraints on the design of the detector with regards to the momentum and vertex position resolution, as well as particle identification performance. A key ingredient is the flavour tagging that is very sensitive to event and track multiplicity. Systematic uncertainties are mainly based on the sizes of control samples, and are therefore expected to remain subdominant even with very large samples. Therefore, it is expected that the small value of $-2\beta_s$ predicted in the SM can be measured to be significantly non-zero in several channels. The expected precision on $\phi_s^{c\bar{c}s}$ after LHCb Upgrade II will be $\sim 3\,\mathrm{mrad}$ from all modes combined.

2.5.9 *Measurements of ϕ_d from $b \to c\bar{c}s$ transitions*

The world average of $\sin 2\beta$ is dominated by results from BaBar, Belle and LHCb using $B^0 \to J/\psi\,K^0_S$ decays. The single most precise measurement is from Belle ($\sin\phi_d^{c\bar{c}s} = 0.670 \pm 0.029 \pm 0.013$ [145]), while the LHCb result has competitive uncertainty ($0.731 \pm 0.035 \pm 0.020$ [139]). With $50\,\mathrm{fb}^{-1}$ of data, LHCb will reach a precision on $\sin\phi_d^{c\bar{c}s}$ of about 0.006 with $B^0 \to J/\psi\,K^0_S$ decays. The Belle II experiment is expected to achieve a precision of about 0.005 after accumulating $50\,\mathrm{ab}^{-1}$ [146]. After Upgrade II, LHCb will be able to reach a statistical precision below 0.003. Fig. 17(right) shows the signal-yield asymmetry as a function of the B^0 decay time for $B^0 \to J/\psi\,K^0_S$ decays from a simulated data set corresponding to $300\,\mathrm{fb}^{-1}$.

The majority of systematic uncertainties on $\sin\phi_d^{c\bar{c}s}$ depend on the size of control samples, and are therefore not expected to be limiting. However, at this level of precision it will be necessary to understand possible biases on the result due to CP violation in K^0–$\overline{K}^0$ mixing, and from the difference in

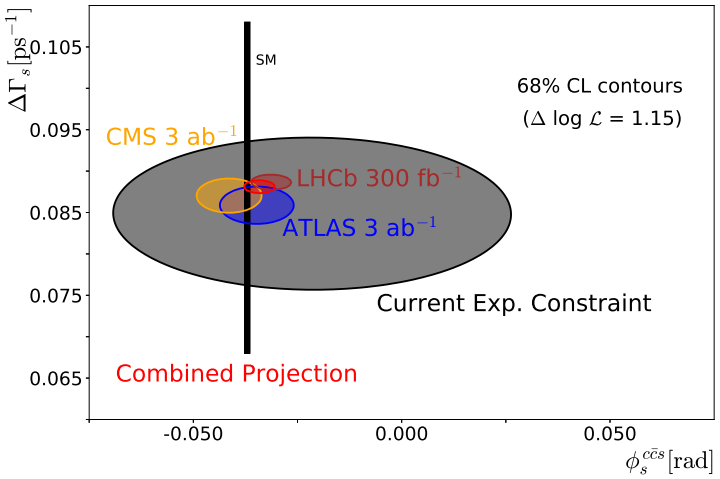

Fig. 16: Projected 68% confidence-level contour in the $\Delta\Gamma_s$ vs φ_s plane for the ATLAS, CMS (still preliminary) and LHCb sensitivity at the HL-LHC compared with the current experimental limit. For clarity of the representation each projection is centered on a random value generated with its uncertainty assuming the SM value as truth. The combined contour is obtained following the HFLAV approach for averages for the PDG 2018 review [138].

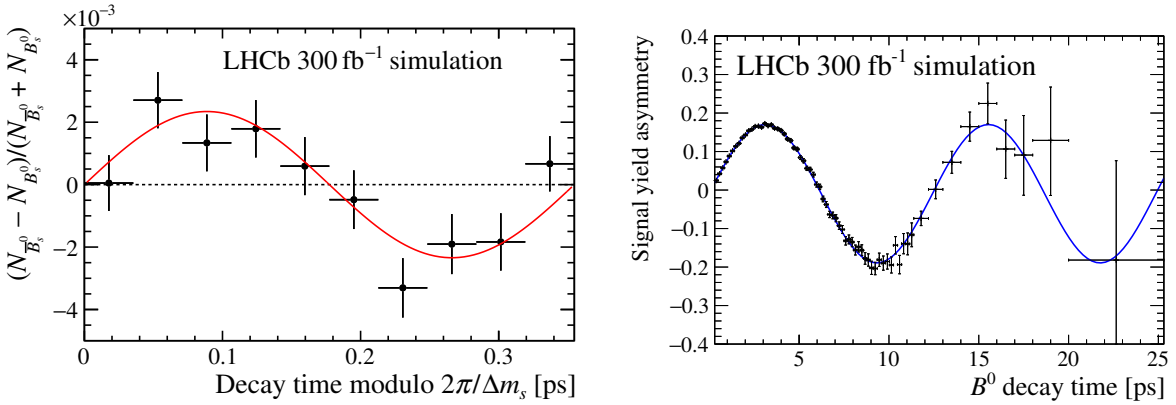

Fig. 17: Signal-yield asymmetry as a function of the $B^0_{(s)}$ decay time, $(N_{\overline{B}^0_{(s)}} - N_{B^0_{(s)}})/(N_{\overline{B}^0_{(s)}} + N_{B^0_{(s)}})$. Here, $N_{\overline{B}^0_{(s)}}$ ($N_{B^0_{(s)}}$) is the number of (left) $B^0_s \to J/\psi\,\phi$ or (right) $B^0 \to J/\psi\,K^0_S$ decays with a $\overline{B}^0_{(s)}$ ($B^0_{(s)}$) flavour tag. The data points are obtained from simulation with the expected sample size at 300 fb^{-1}, and assuming the current performance of the LHCb experiment. The solid curves represent the expected asymmetries for $\phi_s^{c\bar{c}s} = -36.4\,\text{mrad}$ [63] and $\sin\phi_d^{c\bar{c}s} = 0.731$ [139]), the values used in the simulation. The height of the oscillation is diluted from $\sin\phi_{d(s)}^{c\bar{c}s}$ due to mistagging, decay time resolution, and, for $B^0_s \to J/\psi\,\phi$, the mixture of CP-even and CP-odd components in the final state.

the nuclear cross-sections in material between K^0 and $\overline{K}^0$ states. Therefore, some irreducible systematic uncertainties are unavoidable. It is notable that the leading sources of systematic uncertainty are different for Belle II and LHCb, so that having measurements from both experiments will be important. As for the $\phi_s^{c\bar{c}s}$ case, continued good flavour tagging performance and improved understanding of subleading contributions to the decay amplitudes will be required.

The decay $\overline{B}^0 \to D^0\pi^+\pi^-$, and related decays involving excited charm mesons, offer a purely tree-level measurement of $\phi_d = 2\beta$. BaBar and Belle have performed measurements using $B^0 \to D^{(*)}h^0$ with both D decays to CP eigenstates [147] and to the three-body $K^0_S\pi^+\pi^-$ final state [148, 149], where

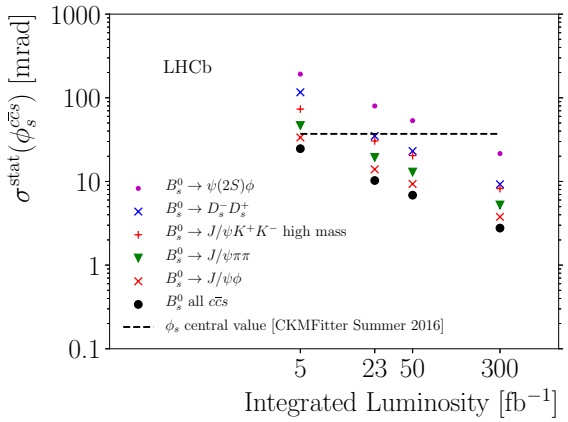

Fig. 18: Scaling of the LHCb statistical precision on ϕ_s from several tree-dominated B_s^0 meson decay modes.

h^0 is a light neutral meson such as π^0. The combined results are $\sin\phi_d = 0.71 \pm 0.09$ and $\cos\phi_d = 0.91 \pm 0.25$ including all uncertainties. While $B^0 \to Dh^0$ can also be studied at LHCb, it is more attractive to measure the same quantities using the $B^0 \to D\pi^+\pi^-$ mode (here D indicates an admixture of D^0 and $\overline{D}^0$ states). The Dalitz-plot structure of the decay $B^0 \to \overline{D}^0\pi^+\pi^-$ has been previously studied [150–152], and the models obtained from these studies could be used in a decay-time-dependent amplitude analysis using the $D \to K^+K^-$ and $D \to \pi^+\pi^-$ channels to determine ϕ_d [153, 154]. In practice it will be more convenient to perform a simultaneous fit including also the $\overline{D}^0 \to K^+\pi^-$ mode, which acts as a control mode to determine the amplitude model, flavour-tagging response and decay-time acceptance.

An estimate of the achievable sensitivity has been made using pseudoexperiments. The expected statistical precisions on $\sin\phi_d$ and $\cos\phi_d$ are ±0.06 and ±0.10, respectively, for the LHCb Run 1 and 2 data samples combined. Extrapolating this to $300\,\text{fb}^{-1}$ gives ±0.007 for $\sin\phi_d$ and ±0.017 for $\cos\phi_d$. Further experimental studies are needed to understand the impact of systematic uncertainties, although the use of the $\overline{D}^0 \to K^+\pi^-$ control sample is expected to minimise effects from many potential sources of systematic bias. In case model uncertainties become a limiting factor, a model-independent version of the method can be used instead [155]. Thus, it is expected that a penguin-free measurement of ϕ_d can be achieved with sensitivity better than Belle II, and comparable to that with $B^0 \to J/\psi K^0_{\rm S}$.

2.5.10 Measurements of penguin pollution in $b \to c\bar{c}s$

Strategies to measure penguin pollution have already been tested using $B^0 \to J/\psi\rho^0$ [156] and $B_s^0 \to J/\psi\overline{K}^{*0}$ [157] decays. These modes constrain the penguin contribution in $B^0 \to J/\psi K^{*0}$. The best constraint on penguin pollution in $\phi_s^{c\bar{c}s}$ is currently obtained from the $B^0 \to J/\psi\rho^0$ channel, benefiting from the fact that $S_{J/\psi\rho^0}$ and $C_{J/\psi\rho^0}$ have been measured, giving a constraint on ${\phi_d}^{J/\psi\rho^0}$. Following Ref. [156], the bias on ϕ_s is

$$\Delta\phi_s^{c\bar{c}s} \approx -\epsilon\left({\phi_d}^{J/\psi\rho^0} - 2\beta\right), \tag{19}$$

where $\epsilon = |V_{us}|^2/(1-|V_{us}|^2) = 0.0534$, and 2β is mainly determined by $B^0 \to J/\psi K^0_{\rm S}$. Since 2β is, and will continue to be, determined precisely, the sensitivity on $\Delta\phi_s^{c\bar{c}s}$ will be driven by the precision on ${\phi_d}^{J/\psi\rho^0}$. Scaling the uncertainties obtained from Ref. [156], the expected statistical precision on ${\phi_d}^{J/\psi\rho^0}$ will be $\lesssim 1^\circ$ with $300\,\text{fb}^{-1}$. It is expected that systematic uncertainties, such as those from modelling the S-wave component in $B^0 \to J/\psi\pi^+\pi^-$ decays, can be kept under control, so that the uncertainty due to penguin pollution is expected to be $\lesssim 1.5\,\text{mrad}$. Thus, this is not expected to limit the sensitivity of the ϕ_s measurement with $B_s^0 \to J/\psi\phi$. However, if significant effects of penguin pollution become

apparent it may complicate the combination of results from different modes, since a separate correction will be required for each. For some modes such as $B_s^0 \to J/\psi\, f_0(980)$ this may be challenging, since the identification of the states in the SU(3) multiplet is not trivial. However, this is not a problem for $B_s^0 \to D_s^+ D_s^-$, related by U-spin subgroup to $B^0 \to D^+ D^-$, which can be used to control penguin pollution [158–161].

Similar strategies can be applied using $B_s^0 \to J/\psi\, K_S^0$ and $B^0 \to J/\psi\, \pi^0$ decays to control the penguin contributions in $\phi_d^{c\bar{c}s}$ [41, 42, 45]. A first analysis of $B_s^0 \to J/\psi\, K_S^0$ decays has been performed [162] as a proof of concept for constraining $\Delta\phi_d^{c\bar{c}s}$ with larger datasets. The CP violation parameters in $B^0 \to J/\psi\, \pi^0$ have been previously measured by BaBar and Belle [163, 164], and the Belle II experiment is expected to reach a sensitivity to $S_{J/\psi\,\pi^0}$ of ~ 0.03, which should be sufficient to keep penguin pollution under control. LHCb can also study $B^0 \to J/\psi\, \pi^0$ decays, although the presence of a neutral pion in the final state makes the analysis more challenging and there is currently no public result from which to extrapolate the sensitivity. Improving the capabilities of LHCb's electromagnetic calorimeter (ECAL) will enhance prospects for studying this mode.

It should be stressed that the methods to constrain penguin pollution rely on SU(3) symmetry, and the approximations associated with the method and inherent in Eq. (19) must also be investigated. This can be done by studying the full set of modes related by SU(3), namely $B_{(s)}^0 \to J/\psi \{\pi^0, \eta, \eta', K^0, \overline{K}^0\}$ and $B^\pm \to J/\psi \{\pi^\pm, K^\pm\}$ for the vector-pseudoscalar final states and $B_{(s)}^0 \to J/\psi \{\rho^0, \omega, \phi, K^{*0}, \overline{K}^{*0}\}$ and $B^\pm \to J/\psi \{\rho^\pm, K^{*\pm}\}$ for the vector-vector final states. Several of these modes have not yet been measured, but with the data sample of LHCb Upgrade II it should be possible to measure all branching fractions and CP asymmetry parameters, allowing a full theoretical treatment and more detailed understanding of subleading contributions. An alternative approach to controlling penguin contributions, which does not involve $SU(3)$ symmetry, can be found in Ref. [46].

2.5.11 Measurements of ϕ_d and ϕ_s in charmless decays

The $B_s^0 \to \phi\phi$ decay is forbidden at tree level in the SM and proceeds predominantly via a gluonic penguin $\bar{b} \to \bar{s}s\bar{s}$ loop process. Hence, this channel provides an excellent probe of physics beyond the SM that may contribute to the penguin diagram [165–167]. This mode is well suited for study at the LHC, as both ϕ mesons can be reconstructed through their decay to K^+K^-, leading to clean signatures even in the absence of hadronic particle identification.

2.5.11.1 CMS $B_s \to \phi\phi$ studies

The lack of particle-ID detectors will limit the CMS investigation of fully hadronic final states. However, some capability is retained through the early use of tracking in the trigger selection. The $B_s \to \phi\phi \to 4K$ is an example of a hadronic final state that would benefit from the tracking performance at trigger level and the ϕ resonance signature. While the full study of the sensitivity to the ϕ measurement in this channel is still ongoing, an analysis was performed by CMS to see if $B_s^0 \to \phi\phi \to 4K$ events can be triggered with high efficiency at L1 using only the tracks reconstructed at that level (L1 tracks) [168].

The L1 track finder will allow identification of $B_s^0 \to \phi\phi \to 4K$ candidates at L1 by forming ϕ candidates from pairs of oppositely charged L1 tracks constrained to come from the same vertex and then combining pairs of such candidates into a B_s^0 candidate. The p_T of the lowest-p_T kaon lies very close to the lowest possible trigger threshold of the L1 tracking of 2 GeV, possibly causing loss of signal efficiency.

Fig. 19 shows the invariant mass of the $B_s^0 \to \phi\phi$ candidates for all ϕ-pairs having separation along the beam axis (z) of $\Delta z(\phi\text{-pair}) < 1$ cm, distance in the plane perpendicular to the beam axis $\Delta xy(\phi\text{-pair}) < 1$ cm, $0.2 < \Delta R(\phi\text{-pair}) < 1$, and $\Delta R(K^+, K^-) < 0.12$, in events with 200 pile-up (PU) interactions. Simulations show that an efficiency of 30-35 % can be achieved at L1 trigger

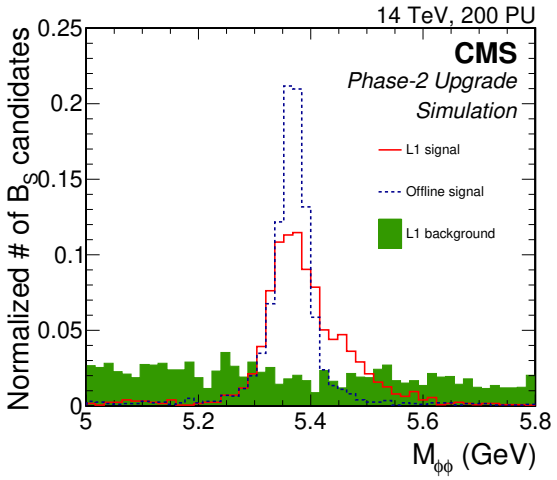

Fig. 19: Normalized invariant mass distribution in CMS of all the ϕ-pairs with $\Delta z(\phi\text{-pair}) < 1$ cm, $\Delta xy(\phi\text{-pair}) < 1$ cm, $0.2 < \Delta R(\phi\text{-pair}) < 1$, $\Delta R(K^+, K^-) < 0.12$. The blue dashed line corresponds to the signal events reconstructed with offline tracks. The signal and background distributions obtained using L1 tracks are shown as red solid line and green histograms, respectively. A pile up scenario of 200 interactions is assumed (taken from [168]).

level, depending on the track candidate selection, and that the events selected at L1 would be accepted by the subsequent offline analysis with high efficiency. For the scenario with 200 PU and a moderate signal efficiency of around 30%, the expected L1 trigger rate is about 15 kHz, within the acceptable limit according to the present understanding of the expected detector performance.

2.5.11.2 LHCb $B_s \to \phi\phi$ projections

The measured and extrapolated LHCb statistical sensitivities for $\phi_s^{s\bar{s}s}$ and similar CP-violating phases measured in other decay modes are shown in Fig. 20. A statistical uncertainty on $\phi_s^{s\bar{s}s}$ of $0.011\,\text{rad}$ can be achieved with $300\,\text{fb}^{-1}$ of data collected at LHCb Upgrade II. Similarly to other measurements of CP violation parameters from decay-time-dependent analyses, many systematic uncertainties are evaluated from control samples, and are therefore expected to scale accordingly with integrated luminosity. Among others, there is an important uncertainty associated with knowledge of the angular acceptance, which is determined from simulation. This therefore relies on good agreement between data and simulation, which can be validated using control channels such as $B^0 \to \phi K^{*0}$. Thus the determination of $\phi_s^{s\bar{s}s}$ is expected to remain statistically limited even with the full LHCb Upgrade II data sample.

2.5.11.3 LHCb projections for ϕ_s from other charmless decays

Another way of measuring ϕ_s is the $B_s^0 \to K^*(892)^0 \overline{K}^*(892)^0$ family of decays, which in the SM is dominated by a gluonic penguin $b \to d\bar{d}s$ diagram. LHCb has recently published the first measurement of $\phi_s^{d\bar{d}s}$ [169] using Run 1 data. In this groundbreaking analysis, it was realised that a significant gain in sensitivity can be obtained by including the full $B_s^0 \to (K^+\pi^-)(K^-\pi^+)$ phase space in the $K\pi$-mass window from 750 to $1600\,\text{MeV}/c^2$, since the fraction of $B_s^0 \to K^*(892)^0 \overline{K}^*(892)^0$ in this region is only $f_{VV} = 0.067 \pm 0.004 \pm 0.024$ (the other contributions are from $K\pi$ S-wave and the $K_2^*(1430)^0$ resonance). The result, $\phi_s^{d\bar{d}s} = -0.10 \pm 0.13 \pm 0.14\,\text{rad}$, is compatible with the SM expectation.

The current result has statistical and systematic uncertainties of comparable size, but both are expected to be reducible with larger data samples. The largest systematic uncertainty, corresponding to

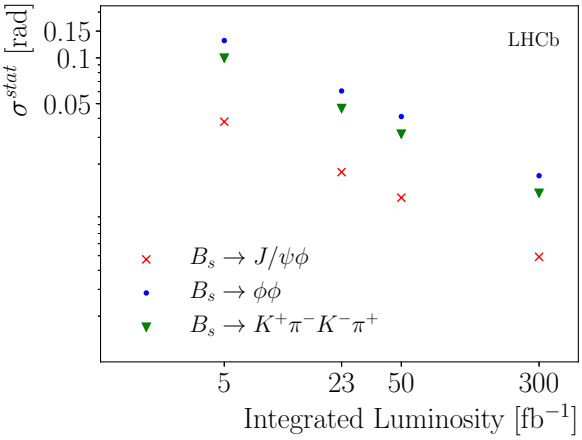

Fig. 20: Comparison of ϕ_s statistical sensitivity at LHCb from different decay modes.

Table 7: Statistical sensitivity on $\phi_s^{s\bar{s}s}$ and $\phi_s^{d\bar{d}s}$ at LHCb.

Decay mode	σ(stat.) [rad]			
	3 fb^{-1}	23 fb^{-1}	50 fb^{-1}	300 fb^{-1}
$B_s^0 \to \phi\phi$	0.154	0.039	0.026	0.011
$B_s^0 \to (K^+\pi^-)(K^-\pi^+)$ (inclusive)	0.129	0.033	0.022	0.009
$B_s^0 \to K^*(892)^0\overline{K}^*(892)^0$	–	0.127	0.086	0.035

the treatment of the acceptance, is mostly driven by the limited size of the simulation samples — due to the large phase space investigated in this analysis, very large simulation samples are required. In order to produce significantly larger samples it will be necessary to exploit rapid simulation production mechanisms, since increases in available CPU power are not expected to keep pace with the size of the data samples. Another important systematic uncertainty due to the modelling of the $K\pi$ resonant and non-resonant components can be reduced by incorporating results of state-of-the-art studies of the $K\pi$ system, but some component of this may be irreducible. Other systematic uncertainties are mainly based on control samples. Therefore it is expected that the limiting systematic uncertainty will be not larger than $\sigma(\text{syst.}) \sim 0.03\,\text{rad}$.

The measured and extrapolated statistical sensitivities for $\phi_s^{d\bar{d}s}$ are given in Table 7, both for the average over the $B_s^0 \to (K^+\pi^-)(K^-\pi^+)$ system and for the exclusive $B_s^0 \to K^*(892)^0\overline{K}^*(892)^0$ decay. The sensitivities for $B_s^0 \to (K^+\pi^-)(K^-\pi^+)$ are also included in Fig. 20. In the current analysis, the same weak phase is assumed for all contributions, but as the precision increases it will be possible to determine $\phi_s^{d\bar{d}s}$ separately for each, including possible polarisation dependence in the $B_s^0 \to K^*(892)^0\overline{K}^*(892)^0$ decay. The systematic uncertainty related to modelling of components is expected to be smaller when focusing on the $K^*(892)$ resonance, since its lineshape is well known. Moreover, by making similar studies with the $B^0 \to (K^+\pi^-)(K^-\pi^+)$ mode, it will be possible to obtain all necessary inputs for the U-spin analysis of each component separately, leading to good control of the theoretical uncertainty on the prediction for $\phi_s^{d\bar{d}s}$.

Finally, LHCb can also make measurements of $\phi_s^{d\bar{u}u}$ using a decay-time-dependent flavour-tagged Dalitz-plot analysis of $B_s^0 \to K_S^0\pi^+\pi^-$ decays [170]. Preliminary sensitivity studies indicate that the precision achievable on $\phi_s^{d\bar{u}u}$ with the full Run 1 + Run 2 dataset is approximately $0.4\,\text{rad}$. Extrapolation to

$300\,\text{fb}^{-1}$ indicates potential for a precision of around $0.07\,\text{rad}$. Similar studies for the $B_s^0 \to K_S^0 K^\pm \pi^\mp$ decay mode can be performed, which requires a more complicated analysis since both $K_S^0 K^- \pi^+$ and $K_S^0 K^+ \pi^-$ final states are accessible to both B_s^0 and $\overline{B}_s^0$ decays with comparable magnitude. Although currently the precision of such measurements are dominated by the statistical uncertainty [171], the expected yields of more than 10^6 signal decays for $300\,\text{fb}^{-1}$ will allow a complete understanding of the $B_s^0 \to K_S^0 K^\pm \pi^\mp$ phase space.

2.5.11.4 LHCb projections for ϕ_d from other charmless decays

The large yields of $B^0 \to K_S^0 h^+ h^-$ decays available [172] at LHCb enable a relevant reach for ϕ_d from these modes. For the $B^0 \to K_S^0 \pi^+ \pi^-$ mode, a decay-time-integrated analysis has been performed resulting in the first observation of CP violation in the $B^0 \to K^{*+}\pi^-$ channel [173]; with more data this analysis can be updated to include decay-time-dependence and determine also CP-violating parameters for the $B^0 \to \rho^0 K_S^0$ and $f_0(980) K_S^0$ channels.

Studies of $B_{(s)}^0 \to h^+ h^- \pi^0$ decays will provide further sensitivity. For example, resonant contributions of the type $K^{*\pm} h^\mp$ will decay to the final state $K^\pm h^\mp \pi^0$ in addition to $K_S^0 \pi^\pm h^\mp$, and therefore a combined analysis of both can provide additional information that helps to test the SM prediction [96–99]. Large yields will be available and the improved capabilities of the Upgrade II ECAL will allow backgrounds to be controlled. Two particularly important features of these decays are that background from $B \to V\gamma$ decays, where $V \to h^+ h^-$, must be suppressed and that it must be possible to resolve B^0 and B_s^0 decays to the same final state. Thus, it will be important to have both good γ–π^0 separation and good mass resolution.

2.5.12 Measurements of α

The main input from LHCb to the isospin analysis determination of α from $B \to \pi\pi$ decays will be world-leading measurements of the CP-violating parameters in $B^0 \to \pi^+\pi^-$ decay. Important input can also be expected on the $B^+ \to \pi^+\pi^0$ decay, using the method pioneered in Ref. [174] for $B^+ \to K^+\pi^0$ decays. Clearly, good performance of the electromagnetic calorimeter will be critical for such a measurement. Progress on the $B^0 \to \pi^0\pi^0$ mode, which is currently limiting the precision of α determination from $B \to \pi\pi$ decays, will mainly come from the Belle II experiment.

The situation is quite different for the $B \to \rho\rho$ system, which currently provides the strongest constraints on α. Although the presence of two vector particles in the final state makes the analysis more complicated in principle [34, 175–177], the observed dominance of longitudinal polarisation and the smaller penguin contribution compared to $B \to \pi\pi$ lead to good sensitivity on α. The rarest of the three isospin-partner modes is the $B^0 \to \rho^0\rho^0$ decay, which has a final state of four charged tracks following $\rho^0 \to \pi^+\pi^-$ decays, making it well suited for study at LHCb. Indeed, this decay was first observed by LHCb, and a time-integrated angular analysis on Run 1 data was performed [178]. With larger data samples it will be possible not only to improve the measurements of the branching fraction and longitudinal polarisation fraction, but to make precise determinations of the CP-violating parameters. Consequently, the determination of α from $B \to \rho\rho$ decays will benefit from the additional information inherent in $S_{\rho^0\rho^0}$, compared to the $B \to \pi\pi$ system for which $S_{\pi^0\pi^0}$ is barely measurable (Belle II plans to measure $S_{\pi^0\pi^0}$ using Dalitz decay of π^0, but only rather limited sensitivity is possible).

First measurements of $B^0 \to \rho\pi$ have been published by BaBar and Belle [179–181], but do not yet provide strong constraints on α. LHCb has not yet published any result on this channel, but it is expected that large yields will be available in LHCb Upgrade II, and that it should be possible to control backgrounds with good understanding of π^0 reconstruction. It is worth noting that a significant proportion of the photons from neutral pions produced at the B decay vertex convert into e^+e^- pairs in the LHCb detector material, with approximately half of these conversions occurring before the magnet. Tracks from these converted photons provide additional information with which to constrain the B decay

vertex and the neutral pion momentum, resulting in improved resolution and background rejection.

2.5.13 *Measurements of CP violation in baryon decays*[2]

In contrast with the study of CP violation in beauty-meson decays, the sector of beauty baryons remains almost unexplored. Previous to the LHC era, only a measurement of direct CP asymmetries in $\Lambda_b^0 \to pK^-$ and $\Lambda_b^0 \to p\pi^-$ decays was available with $\mathcal{O}(0.1)$ precision [182]. Thanks to the large production cross-section of beauty baryons in pp collisions at the LHC, the LHCb experiment is the only experiment capable of expanding our knowledge in this sector, as these decays are not accessible at the e^+e^- KEK collider. Hence, even though a handful of CP asymmetries of Λ_b^0 decays have been measured so far by LHCb [183–186], the landscape of CP violation in the decays of beauty baryons is expected to change rapidly in the next few years.

The unprecedented number of beauty baryons available with the data sample expected to be collected in the LHCb Upgrade II phase, will allow a precision measurement programme of CP violation observables in b-baryon decays to be pursued, analogously to b-meson decays. A very interesting example is the study of decays governed by $b \to u$ and $b \to c$ tree-level transitions, like the decays $\Lambda_b^0 \to D^0\Lambda$ and $\Lambda_b^0 \to D^0 pK^-$. These decays can be used to measure the angle γ of the unitarity triangle [187–189] in a similar way to what can be done with $B^0 \to DK^+\pi^-$ decays. The LHCb experiment reported the first observation of the $\Lambda_b^0 \to D^0(K^-\pi^+)pK^-$, based on a signal yield of 163 ± 18 using a sample of pp collisions corresponding to $1\,\text{fb}^{-1}$ of integrated luminosity at a centre-of-mass energy of 7 TeV [190]. Extrapolating to Upgrade II approximately 95000 signal decays are expected. However, extrapolating the sensitivity to γ is not easy, since it strongly depends on the values of the hadronic parameters involved in the process. In addition, even though the determination of γ from the analysis of these decays is expected to be theoretically very clean, the possible polarisation of Λ_b^0 baryons produced in pp collisions has to be taken into account and might represent a limiting factor for high-precision measurements.

Another very interesting sector is that of beauty baryons decaying to final states without a charm quark. These decays receive relevant contributions from $b \to d$, s loop-level transitions, where new physics beyond the SM may appear. Also in this case, similar quantities to those measured with B-meson decays are available. For example, statistical precisions of $\mathcal{O}(10^{-3})$ and $\mathcal{O}(10^{-2})$ are expected for the CP asymmetries of $\Lambda_b^0 \to ph^-$ and $\Lambda_b^0 \to \Lambda h^+h^-$ decays (with $h = K, \pi$), respectively. Very large signal yields are also expected in several multibody final states of Λ_b^0 and Ξ_b decays: about 10^6 $\Lambda_b^0 \to p\pi^-\pi^+\pi^-$ and $\Lambda_b^0 \to pK^-K^+K^-$ decays, and about 10^5 $\Xi_b^0 \to pK^-\pi^+K^-$ decays [191, 192]. Such a signal yield will allow very precise measurements of CP-violating quantities to be made over the phase space of these decays, characterised by a rich set of resonances. Unfortunately, as for the charmless decays of B mesons, the interpretation of these quantities in terms of CKM parameters is still unclear from the theoretical point of view. Hence, more theoretical work is crucial to exploit the full potential of beauty baryons.

Experimentally, the main issues are the determination of particle-antiparticle production asymmetries and detection asymmetries that could mimic CP-violation effects. This task is generally more difficult for heavy baryons, with respect to B mesons, since methods used for measuring meson production asymmetries [193] cannot be applied. In addition, different interactions of baryons and antibaryons with the detector material are difficult to calibrate. Nonetheless, several quantities can be measured in b-baryon decays that are sensitive to different manifestations of CP violation and are largely unaffected by experimental effects. A few examples are the difference of CP-violating asymmetries of particles decaying to a similar final state, ΔA_{CP} [194], triple-product asymmetries (TPA) [191] and energy-test (ET) [195]. It is important to note that TPA and ET are important tools for discovery of CP violation in multibody decays, while an amplitude analysis is required to study the source of CP violation.

[2]We thank I. Bigi for stressing the importance of baryon decays.

Table 8: Uncertainties on inputs for the CKMfitter and UTFit projections.

	Current	Phase 1	Phase 2	Ref.
$\|V_{ud}\|$	± 0.00021	± 0.00021	± 0.00021	[38]
$\|V_{us}\| f_+^{K\to\pi}(0)$	± 0.0004	± 0.0004	± 0.0004	[38]
$\|\epsilon_K\| \times 10^3$	± 0.011	± 0.011	± 0.011	[38]
Δm_d [ps^{-1}]	± 0.0019	± 0.0019	± 0.0019	[197]
Δm_s [ps^{-1}]	± 0.021	± 0.021	± 0.021	[197]
$\|V_{ub}\| \times 10^3$ ($b \to u\ell\bar{\nu}$)	± 0.23	± 0.04	± 0.04	[196]
$\|V_{cb}\| \times 10^3$ ($b \to c\ell\bar{\nu}$)	± 0.7	± 0.5	± 0.5	[196]
$\|V_{ub}/V_{cb}\|$ (Λ_b)	± 0.0050	± 0.0025	± 0.0008	See above
$\sin 2\beta$	± 0.017	± 0.005	± 0.003	Above & [196]
α [°]	± 4.4	± 0.6	± 0.6	[196]
γ [°]	± 5.6	± 1	± 0.35	Above & [196]
β_s [rad]	± 0.031	± 0.014	± 0.004	See above
$\mathcal{B}(B \to \tau\nu) \times 10^4$	± 0.21	± 0.04	± 0.04	[196]
$\bar{m}_c$ [GeV]	± 0.012 (0.9%)	± 0.005 (0.4%)	± 0.005 (0.4%)	See Sec. 11
$\bar{m}_t$ [GeV]	± 0.73 (0.4%)	± 0.35 (0.2%)	± 0.35 (0.2%)	[38]
$\alpha_s(m_Z)$	± 0.0011 (0.9%)	± 0.0011 (0.9%)	± 0.0011 (0.9%)	[38]
$f_+^{K\to\pi}(0)$	± 0.0026 (0.3%)	± 0.0012 (0.12%)	± 0.0012 (0.12%)	See Sec. 11
f_K	± 0.0006 (0.5%)	± 0.0005 (0.4%)	± 0.0005 (0.4%)	See Sec. 11
B_K	± 0.012 (1.6%)	± 0.005 (0.7%)	± 0.004 (0.5%)	See Sec. 11
f_{B_s} [GeV]	± 0.0025 (1.1%)	± 0.0011 (0.5%)	± 0.0011 (0.5%)	See Sec. 11
B_{B_s}	± 0.034 (2.8%)	± 0.010 (0.8%)	± 0.007 (0.5%)	See Sec. 11
f_{B_s}/f_{B_d}	± 0.007 (0.6%)	± 0.005 (0.4%)	± 0.005 (0.4%)	See Sec. 11
B_{B_s}/B_{B_d}	± 0.020 (1.9%)	± 0.005 (0.5%)	± 0.003 (0.3%)	See Sec. 11

2.6 Future of global CKM fits

2.6.1 Summary of the projections

As discussed above, HL-LHC will improve the determination of several flavour observables crucial for the extraction of CKM parameters. We consider two phases for the HL-LHC projections: in Phase 1, we assume an integrated luminosity of 23 fb^{-1} for LHCb and 300 fb^{-1} for CMS/ATLAS; in Phase 2 we have 300 fb^{-1} for LHCb and 3000 fb^{-1} for CMS/ATLAS. Several observables will be measured more precisely at Belle-II. For uncertainties on these observables we use the 50 ab^{-1} projections in Ref. [196]. Since we are interested in the future sensitivity for Phase 1 and Phase 2, we choose the central values of future measurements to coincide with their SM predictions using the current best-fit values of $\overline{\rho}$ and $\overline{\eta}$.

2.6.2 CKMfitter results

The inputs used by CKMfitter collaboration for the fits are shown in Table 8. For easier comparison the "Current" column shows present uncertainties, taking central values corresponding to a perfect agreement of the various constraints in the SM. Note that this choice does change slightly the present determination of CKM parameters – the global fit described in Sec. 2.3 exhibits slight discrepancies, in particular for $|V_{us}|$, which currently increases the accuracy of the determination of the CKM parameters. In order to determine the increase in accuracy on the CKM parameters in a fair way, we therefore compare the three scenarios presented in Table 8 with the same central values taken to have perfect agreement (rather

Table 9: The 68% CL uncertainties on the determination from the CKMfitter global fit.

	Summer 18	Current	Phase I	Phase II
A	0.0129	0.0120	0.0058	0.0057
λ	0.0002	0.0007	0.0004	0.0004
$\bar{\rho}$	0.0085	0.0085	0.0027	0.0018
$\bar{\eta}$	0.0083	0.0087	0.0024	0.0015
$\lvert V_{ub}\rvert$	0.000076	0.000096	0.000027	0.000023
$\lvert V_{cb}\rvert$	0.00073	0.00070	0.00026	0.00025
$\lvert V_{td}\rvert$	0.00017	0.00014	0.00006	0.00006
$\lvert V_{ts}\rvert$	0.00068	0.00054	0.00026	0.00025
$\sin 2\beta$	0.012	0.015	0.004	0.003
$\alpha\ (^\circ)$	1.4	1.4	0.4	0.3
$\gamma\ (^\circ)$	1.3	1.3	0.4	0.3
β_s (rad)	0.00042	0.00042	0.00012	0.00010

than comparing the future projections with the CKMfitter results for the Summer 2018 update).

From the global fit we determine the 68% CL intervals for the 4 CKM parameters and other parameters of interest. In Fig. 21 we show the Phase 1 (left panels) and Phase 2 (right panels) determinations in the standard UT plane for a global fit (upper), as well as when using only subsets of constraints, tree only (middle) or loop only (lower panels). The uncertainties obtained are listed in Table 9. We show the corresponding constraints for the B_s meson system also in Fig. 22, defining the apex of the B_s unitarity triangle as [63]

$$\bar{\rho}_{sb} + i\bar{\eta}_{sb} = -\frac{V_{us}V_{ub}^*}{V_{cs}V_{cb}^*}. \tag{20}$$

2.6.3 UTfit results

The projection of the UT analysis in the HL-LHC era is obtained by performing a global fit using the same future expected values of experimental and theoretical input parameters as CKMfitter, Table 8. In particular, the lattice uncertainties for Phase 1 and Phase 2 are the same as Table 41 in Sec. 11. For both theoretical and experimental parameters the SM expectations were taken as central values, in order to ensure the compatibility of the extrapolated constraints.

The improvement of the UT global analysis can be appreciated in Fig. 23, where the present and future Phase 1 and Phase 2 constraints on the standard UT plane are shown next to each other, after zooming into the SM preferred region. For a more quantitative comparison we collect in Table 10 the uncertainties on the indirect determination of CKM parameters and angles, obtained from the predictive posterior p.d.f.'s (i.e., obtained without including the corresponding direct measurements in the fit). These uncertainties are reduced by a factor 3–5 for Phase 1, and are further reduced by up to a factor of 2 for Phase 2, allowing for an increasingly improved tests of the SM, as discussed next. A similar progression of improvements is seen in the projections from CKMfitter collaboration, cf. Fig. 21.

2.7 Future extrapolation of constraints on NP in $\Delta F = 2$ amplitudes

The Unitarity Triangle Analysis can be generalized beyond the SM to obtain a simultaneous determination of CKM parameters and NP contributions to $\Delta F = 2$ amplitudes [60, 198]. Assuming that NP is absent (or negligible) in charged current amplitudes, but allowing for NP to be present in FCNC

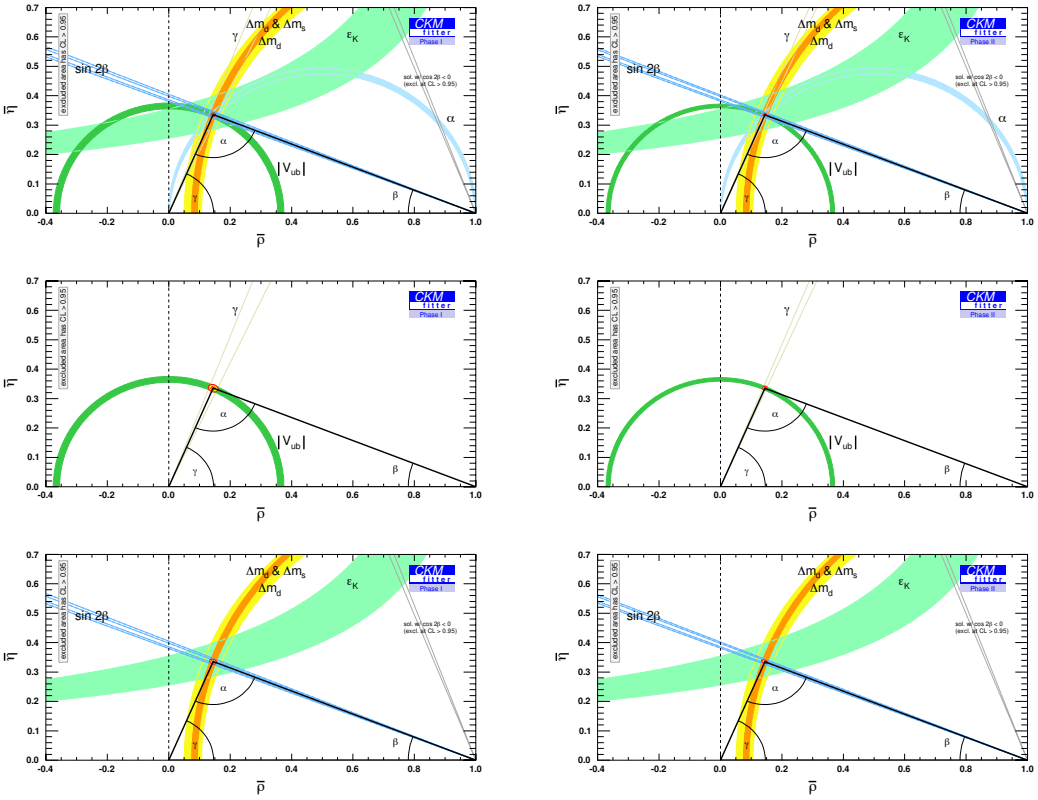

Fig. 21: Constraints on the unitarity triangle from the CKMfitter global analysis: global fit (top), tree only (center), loop only (bottom), for Phase 1 (left) and Phase 2 (right).

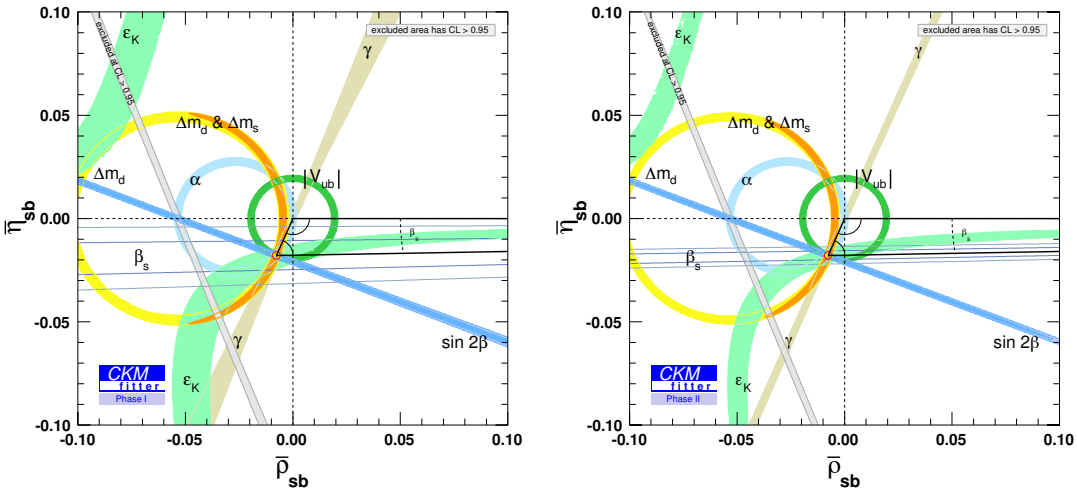

Fig. 22: Constraints on the unitarity triangle for the B_s meson from the CKMfitter global analysis for Phase 1 (left) and Phase 2 (right).

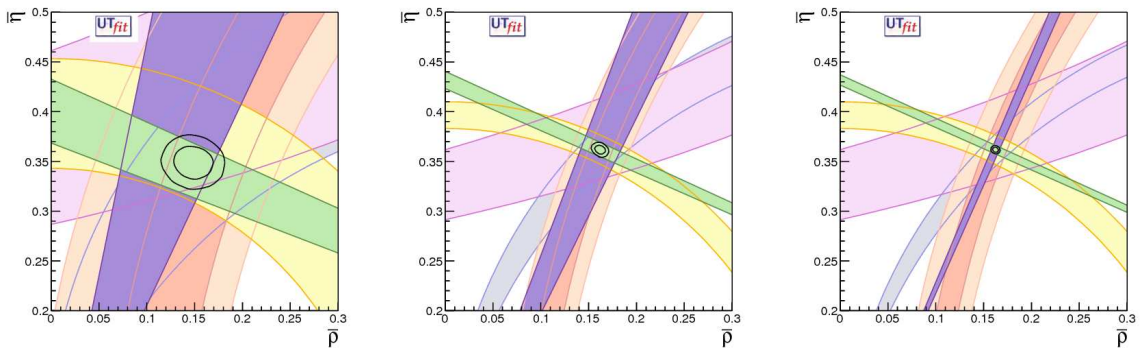

Fig. 23: Present (left) and future (center: phase 1, right: phase 2) constraints in the $(\bar{\rho}, \bar{\eta})$ plane (UTfit collaboration).

Table 10: Relative uncertainties on the predictions of UT parameters and angles, using current and extrapolated input values for measurements and theoretical parameters (UTfit collaboration).

	λ	$\bar{\rho}$	$\bar{\eta}$	A	$\sin 2\beta$	γ	α	β_s
Current	0.12%	9%	3%	1.5%	4.5%	3%	2.5%	3%
Phase 1	0.12%	2%	0.8%	0.6%	0.9%	0.9%	0.7%	0.8%
Phase 2	0.12%	1%	0.6%	0.5%	0.6%	0.8%	0.4%	0.5%

amplitudes, where its virtual effects compete with loop-level SM amplitudes, we can still use the measurements of $|V_{ud}|$, $|V_{us}|$, $|V_{cb}|$, $|V_{ub}|$, γ and α (allowing for NP contributions in penguins, but barring order-of-magnitude enhancements of electroweak penguins) to obtain the "tree-level" determination of the UT. This allows us to obtain the SM prediction for K, B_d and B_s mixing amplitudes. Comparing them with the experimental results we can extract $C_{\varepsilon_K} = \varepsilon_K/\varepsilon_K^{\rm SM}$ and

$$C_{B_q} e^{i\phi_{B_q}} = \frac{\langle B_q | H^{\rm SM+NP} | \bar{B}_q \rangle}{\langle B_q | H^{\rm SM} | \bar{B}_q \rangle} \,. \tag{21}$$

The SM point is $C_i = 1, \phi_i = 0$. Using semileptonic asymmetries it is possible to break the degeneracy for $\gamma \leftrightarrow \gamma + 180^\circ$ present in the tree-level determination of the CKM matrix [199], getting rid of the solution in the third quadrant. We then obtain the results in Table 11 for the projected errors on CKM parameters and on the NP parameters. Note that at present the NP contribution that are about an order of magnitude smaller than the SM are still perfectly allowed. At the end of Phase 2 we will be able to probe amplitudes that are another factor of 4 smaller than possible at present (corresponding to about a factor of 2 higher reach in the NP scale for dimension 6 NP operators). The corresponding two-dimensional distributions for B_d and B_s mixing are shown in Fig. 24.

Combining the results of the generalized UT analysis with the constraints on CP violation in D mixing from Sec. 3.7.5, we can consider the most general $\Delta F = 2$ effective Hamiltonian and place bounds on its coefficients (barring accidental cancellations). The most general effective Hamiltonians for $\Delta F = 2$ processes beyond the SM have the following form [200] (with $q_1 q_2 = sd, uc, bq$ for $M = K, D, B_q$)

$$\mathcal{H}_{\rm eff}^{M-\bar{M}} = \sum_{i=1}^{5} C_i \, Q_i^{q_1 q_2} + \sum_{i=1}^{3} \tilde{C}_i \, \tilde{Q}_i^{q_1 q_2} , \tag{22}$$

Table 11: Present and future uncertainties on CKM and NP parameters from the generalized UT analysis (UTfit collaboration).

	$\bar{\rho}$	$\bar{\eta}$	C_{ε_K}	C_{B_d}	$\phi_{B_d}[^\circ]$	C_{B_s}	$\phi_{B_s}[^\circ]$
Current	0.030	0.028	0.12	0.11	1.8	0.09	0.89
Phase 2	0.0047	0.0040	0.036	0.030	0.28	0.026	0.29

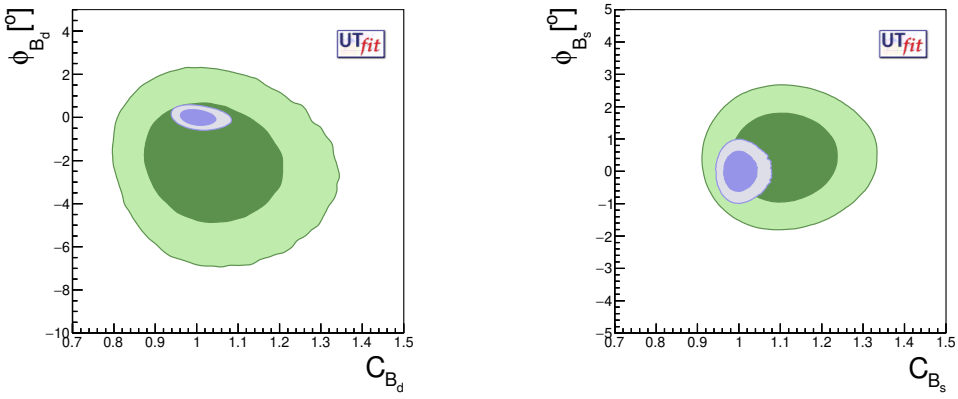

Fig. 24: The present (green) and future Phase 2 (blue) constraints on NP contributions to B_d-$\bar{B}_d$ (left) and B_s-$\bar{B}_s$ (right) mixing, with 1σ (2σ) regions shown with darker (lighter) shading.

where the operator basis consists of dimension 6 operators $Q_1^{q_iq_j} = (\bar{q}_{jL}^{\alpha}\gamma_\mu q_{iL}^{\alpha})(\bar{q}_{jL}^{\beta}\gamma^\mu q_{iL}^{\beta})$, $Q_2^{q_iq_j} = (\bar{q}_{jR}^{\alpha}q_{iL}^{\alpha})(\bar{q}_{jR}^{\beta}q_{iL}^{\beta})$, $Q_3^{q_iq_j} = (\bar{q}_{jR}^{\alpha}q_{iL}^{\beta})(\bar{q}_{jR}^{\beta}q_{iL}^{\alpha})$, $Q_4^{q_iq_j} = (\bar{q}_{jR}^{\alpha}q_{iL}^{\alpha})(\bar{q}_{jL}^{\beta}q_{iR}^{\beta})$, $Q_5^{q_iq_j} = (\bar{q}_{jR}^{\alpha}q_{iL}^{\beta})(\bar{q}_{jL}^{\beta}q_{iR}^{\alpha})$, and the operators $\tilde{Q}_{1,2,3}^{q_iq_j}$ that are obtained from the $Q_{1,2,3}^{q_iq_j}$ by exchanging $L \leftrightarrow R$. Here $q_{R,L} = P_{R,L}\, q$, with $P_{R,L} = (1 \pm \gamma_5)/2$, and α and β are colour indices. Following the procedure detailed in Ref. [198], the UTFit collaboration obtained p.d.f.'s for the Wilson coefficients based on the extrapolated UT and D mixing analyses. For self-consistency, the coefficients are computed at a scale μ_H roughly corresponding to the bound on the NP scale Λ that one obtains from the analysis (see below). The present and expected Phase 2 allowed regions at 95% probability on the Wilson coefficients

$$C_i(\Lambda) = \frac{F_i L_i}{\Lambda^2}\,, \tag{23}$$

are reported in Fig. 25. In the left panel in Fig. 25 the flavour and loop factors were set to $F_i = L_i = 1$, i.e., this shows the limits on the mass of NP states that contribute to meson mixing at tree level and couple with $\mathcal{O}(1)$ strength to the corresponding SM fermions. In Fig. 25 right, the flavour factor was set to $F_i = V_{tq_1}V_{tq_2}^*$, and the loop factor to $L_i = \alpha_2^2$, with α_2 the weak structure constant. That is, the right panel of Fig. 25 shows the reach for masses of NP states that have MFV-like couplings to SM fermions and contribute only at one loop level.

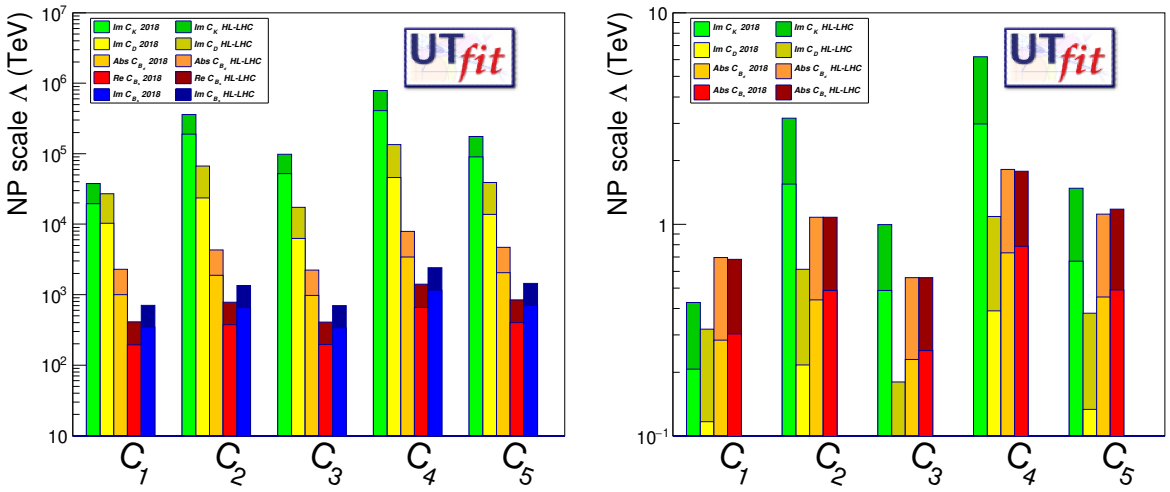

Fig. 25: Present (lighter) and future Phase 2 (darker) constraints on the NP scale from the UTfit NP analysis. The right panel shows constraints assuming NP is weakly coupled, has MFV structure of couplings, and enters observables only at one loop, see text for details.

3 Charm-quark probes of new physics

Authors (TH): J. Brod, S. Fajfer, A. Kagan, A. Lenz, L. Silvestrini.

In the SM, the FCNC processes involving charmed hadrons are suppressed compared to those involving strange or beauty hadrons since they are proportional to the small breaking of the GIM mechanism by the bottom quark mass. This also means that the contributions from long-distance physics, due to intermediate d, s quarks, are relatively more important, complicating the predictions. Moreover, due to small off-diagonal CKM matrix elements the third generation approximately factorizes from the first two generations, leading to additional suppression of the CP violating effects in charmed hadrons. The charmed hadrons can then be used as sensitive probes of new physics in the up-quark sector, to the extent that theoretical uncertainties can be brought under control, e.g., by constructing null tests, or circumvented by using experimental data.

3.1 Charm mixing

Weak interactions mix D^0 and $\bar{D}^0$ mesons, so that the mass eigenstates are $|D_{1,2}\rangle = p|D^0\rangle \pm q|\bar{D}^0\rangle$. By convention $|D_2\rangle$ is CP-even in the absence of CP violation. The mass and width differences, $\Delta M = m_2 - m_1$, and $\Delta\Gamma = \Gamma_2 - \Gamma_1$, are parametrized as

$$x \equiv \Delta M^D/\Gamma^D = 0.46\% \pm 0.13\%\,, \qquad y \equiv \Delta\Gamma^D/(2\Gamma^D) = 0.62\% \pm 0.07\%. \tag{24}$$

Here Γ is the total decay rate of the neutral D mesons, while the numerical values are from the fits to the experimental measurements [197]. As follows from Eq. (24), it appears that in D system $x \sim y$ or $\Gamma_{12} \sim M_{12}$. This is to be contrasted with the B system, where $|\Gamma_{12}/M_{12}| \ll 1$ holds. We also define the "theoretical" mixing parameters,

$$x_{12} \equiv \frac{2|M_{12}^D|}{\Gamma^D}\,, \quad y_{12} \equiv \frac{|\Gamma_{12}^D|}{\Gamma^D}\,, \quad \phi_{12} \equiv \arg\left(\frac{M_{12}^D}{\Gamma_{12}^D}\right)\,, \tag{25}$$

where M_{12}^D and Γ_{12}^D are the dispersive and absorptive contributions to the $D^0 - \overline{D}^0$ mixing amplitude, $\langle D^0|H|\bar{D}^0\rangle = M_{12}^D - \frac{i}{2}\Gamma_{12}^D$. The phase ϕ_{12} gives rise to CP violation in mixing, cf. Sec. 3.2. Its magnitude is currently bounded to lie below ~ 100 mrad at 95% CL [197, 201]. These parameters are related to x and y as,

$$(x - iy)^2 = x_{12}^2 - y_{12}^2 - 2\,i\,x_{12}y_{12}\cos\phi_{12}\,, \tag{26}$$

so that, up to negligible corrections quadratic in $\sin\phi_{12}$ (in general, $|y| \leq y_{12}$ [202, 203]),

$$|x| = x_{12}, \quad |y| = y_{12}\,. \tag{27}$$

It is convenient to begin the discussion of the SM mixing amplitudes with their U-spin flavor symmetry decomposition [204, 205]. Employing CKM unitarity, $\lambda_d + \lambda_s + \lambda_b = 0$, with $\lambda_x = V_{cx}V_{ux}^*$, Γ_{12}^D can be written as

$$\Gamma_{12}^D = \frac{(\lambda_s - \lambda_d)^2}{4}\,\Gamma_2 + \frac{(\lambda_s - \lambda_d)\lambda_b}{2}\,\Gamma_1 + \frac{\lambda_b^2}{4}\,\Gamma_0\,, \tag{28}$$

where

$$\begin{aligned}
\Gamma_2 &= \Gamma_{ss} + \Gamma_{dd} - 2\Gamma_{sd} \;\sim\; (\bar{s}s - \bar{d}d)^2 = \mathcal{O}(\epsilon^2)\,,\\
\Gamma_1 &= \Gamma_{ss} - \Gamma_{dd} \;\sim\; (\bar{s}s - \bar{d}d)(\bar{s}s + \bar{d}d) = \mathcal{O}(\epsilon)\,,\\
\Gamma_0 &= \Gamma_{ss} + \Gamma_{dd} + 2\Gamma_{sd} \;\sim\; (\bar{s}s + \bar{d}d)^2 = \mathcal{O}(1)\,,
\end{aligned} \tag{29}$$

with $\epsilon \sim 0.2$ denoting the U-spin breaking parameter. The $\Gamma_{2,1,0}$ are the $\Delta U_3 = 0$ elements of the U-spin 5-plet, triplet, and singlet, respectively. The individual Γ_{ij} are identified, at the quark level, with box

diagrams containing on-shell internal i and j quarks. They possess flavor structure $\Gamma_{ij} \sim (\bar{i}i)(\bar{j}j)(\bar{u}c)^2$, where the external u and c quarks are irrelevant for the U-spin decomposition. The U-spin decomposition of M_{12}^D is analogous to Eq. (28), with $\Gamma \to M$ replacement everywhere. At the level of quark box diagrams, $M_{1,0}$ also receive contributions containing internal b quarks. The small value of $\lambda_b \sim \mathcal{O}(10^{-4})$ implies that we can neglect the $\Delta U = 1, 0$ contributions to the mass and width differences, even though the $\Delta U = 2$ piece is higher order in ϵ.

Evaluation of the SM mixing amplitudes is very challenging, because the charm quark mass lies at an intermediate scale between the masses of the light quarks and the bottom quark. Broadly speaking, there are two approaches: (i) an inclusive one employing the operator product expansion (OPE), which expands in powers of $\Lambda_{\rm QCD}/m_c$, as in the heavy quark expansion (HQE), and assumes that local quark-hadron duality holds [206–209]; and (ii) an exclusive one in which y is estimated by summing over contributions of exclusive states, and x is estimated via a dispersion relation which relates it to y. In the first approach, the HQE applied to Γ_{12}^D, combined with the relevant non-perturbative dimension six operator matrix elements evaluated in [210–213], yields contributions of the individual Γ_{ij} to y that are five times larger than the experimental value [214]. This corresponds to $\Gamma_{ij} \sim \Gamma^D$, which is not surprising, given that the HQE can accommodate the charm meson lifetimes [213, 215]. However, the result for Γ_2, cf. Eqs. (28), (29), yields a value of y lying about four orders of magnitude below experiment, due to large GIM-cancellations between the Γ_{ij} contributions. Evidently, the inclusive approach is not well suited for analyzing the U-spin breaking responsible for $D^0 - \overline{D}^0$ mixing, i.e., the charm quark is not sufficiently massive, and $(m_s - m_d)/\Lambda_{\rm QCD}$ is not sufficiently small. First estimates of the dimension nine contribution in the HQE [216] indicate an enhancement compared to the leading dimension six terms, but do not alter this conclusion. The HQE result $\theta_c^2\, \Gamma_{ij} \sim 5\, y$ would require large U-spin violation, e.g. $\mathcal{O}(\epsilon^2) = 20\%$ in Γ_2, cf. (29), which could be attributed to long-distance duality violation [203]. One possibility for directly addressing the origin of U-spin violation in $D^0 - \overline{D}^0$ mixing is the second (exclusive) approach mentioned above.

The starting point for the exclusive approach [204, 205, 217–219] is a sum over the decay modes contributing to the absorptive and dispersive mixing amplitudes, see e.g. [220],

$$\Gamma_{12}^D = \sum_f \rho_f A_f^* \, \bar{A}_f \,; \qquad M_{12}^D = \langle D^0 | H^{\Delta D=2} | \bar{D}^0 \rangle + P \sum_f \frac{A_f^* \, \bar{A}_f}{m_{D^0}^2 - E_f^2} \,, \tag{30}$$

where $A_f = \langle f | H_{\Delta c=1} | D^0 \rangle$ and $\bar{A}_f = \langle f | H_{\Delta c=1} | \bar{D}^0 \rangle$ are the $D^0 \to f$ and $\bar{D}^0 \to f$ decay amplitudes, respectively, ρ_f is the density of the state f, and P is the principal value. Unfortunately, the charm quark mass is not sufficiently light for D meson decays to be dominated by a few final states. Moreover, the strong phase differences entering Γ_{12}^D, and the off-shell decay amplitudes entering M_{12}^D are not calculable from first principles. Thus, simplified treatments of $SU(3)_F$ flavor symmetry breaking have been utilized. A rough U-spin based estimate for y is simply obtained from the first term in (28),

$$y \;=\; \sin^2\theta_c \times \Gamma_2/\Gamma^D \;\sim\; \sin^2\theta_C \;\times\; \epsilon^2 \sim (0.2 - 5)\%, \tag{31}$$

where we have taken $\Gamma_2 \sim \Gamma^D \epsilon^2$ (which can be motivated by the HQE result $\Gamma_{ij} \sim \Gamma^D$); and $\epsilon \sim 0.2 - 1$, corresponding to variation from nominal to maximal U-spin breaking. The authors of [204, 217] only took $SU(3)_F$-breaking phase space effects into account in the exclusive sum. They found that $y \lesssim 1\%$ could naturally be realized, where a value at the high end would require contributions from higher multiplicity final states, due to the larger $SU(3)_F$ breaking effects near threshold (consistent with the large U-spin breaking required from duality violations in the OPE/HQE approach). This conclusion was subsequently supported in [218, 219], which added experimental branching ratio inputs together with factorization based models for dynamical $SU(3)_F$ breaking effects, e.g., in the form factors and strong phases. Rough dispersion relation estimates in [217, 218] suggested that $|x/y| \sim 0.1 - 1$.

We conclude that the estimates of x and y in the SM are consistent with their measured values, cf. (24). Unfortunately, the large theoretical uncertainties eliminate the window for NP in these quantities.

The situation is markedly different for the CPV mixing observables, due to their large suppression in the SM, as discussed below. On a very long time-scale, direct lattice calculations might be able to predict the SM values of x and y by building on the methods described in [221].

3.2 CP violation in $D^0 - \overline{D}^0$ mixing

In the SM, *CP* violation (CPV) in $D^0 - \overline{D}^0$ mixing is highly suppressed, entering at $\mathcal{O}(|V_{cb}V_{ub}/V_{cs}V_{us}|) \sim 10^{-3}$. This raises several questions, which we briefly address, based on work to appear in [222]: What is the resulting theoretical uncertainty on the indirect CPV observables? How large is the current window for New Physics (NP)? What is an appropriate parametrization for indirect CPV effects, given the expected sensitivity in the LHCb/Belle-II era?

There are two types of CPV due to mixing; both are referred to as "indirect" CPV. The first is CPV due to interference between the dispersive and absorptive mixing amplitudes ("CPVMIX"), which arises when $\phi_{12} \neq 0$. CPVMIX can be directly measured via the semileptonic *CP* asymmetry

$$A_{\rm SL} \equiv \frac{\Gamma(D^0 \to K^+\ell^-\nu) - \Gamma(\bar{D}^0 \to K^-\ell^+\nu)}{\Gamma(D^0 \to K^+\ell^-\nu) + \Gamma(\bar{D}^0 \to K^-\ell^+\nu)} = \frac{|q/p|^4 - 1}{|q/p|^4 + 1} = \frac{2x_{12}y_{12}}{x_{12}^2 + y_{12}^2}\sin\phi_{12}\,. \tag{32}$$

The second type of indirect CPV is due to interference between a direct decay amplitude and a "mixed" amplitude followed by decay ("CPVINT"), i.e., interference between $D^0 \to f$ and $D^0 \to \bar{D}^0 \to f$. For decays to a *CP* eigenstate final state, there are two CPVINT observables [223, 224],

$$\lambda_f^M \equiv \frac{M_{12}}{|M_{12}|}\frac{A_f}{\overline{A}_f} = \eta_f^{CP}\left|\frac{A_f}{\overline{A}_f}\right| e^{i\phi_f^M}\,, \quad \lambda_f^\Gamma \equiv \frac{\Gamma_{12}}{|\Gamma_{12}|}\frac{A_f}{\overline{A}_f} = \eta_f^{CP}\left|\frac{A_f}{\overline{A}_f}\right| e^{i\phi_f^\Gamma}\,, \tag{33}$$

parametrizing the interference for a dispersive and absorptive mixing amplitudes, respectively. The ϕ_f^M and ϕ_f^Γ are CPV weak phases, with $\phi_{12} = \phi_f^M - \phi_f^\Gamma$, while $\eta_f^{CP} = +(-)$ for *CP* even (odd) final states. In general, ϕ_f^M and ϕ_f^Γ are final-state specific due to non-universal weak and strong phases entering the CKM suppressed SM (and potential NP) contributions to the subleading decay amplitudes.

Non-vanishing ϕ_f^M and ϕ_f^Γ yield *time-dependent CP* asymmetries. For example, in singly Cabibbo suppressed (SCS) decays to CP-eigenstates, $f = K^+K^-$, $\pi^+\pi^-$, ..., the effective decay widths, $\hat{\Gamma}$, for D^0 and $\bar{D}^0$ decays (the time-dependence of these decays can, to good approximation, be parametrized in exponential form $\propto e^{-\hat{\Gamma}\tau}$, where $\tau \equiv \Gamma_D t$) will differ,

$$\Delta Y_f \equiv \frac{\hat{\Gamma}_{\bar{D}^0\to f} - \hat{\Gamma}_{D^0\to f}}{2\Gamma_D} = -x_{12}\sin\phi_f^M + a_f^d\, y_{12}\,. \tag{34}$$

The first and second terms on the RHS are the dispersive CPVINT and direct CPV contributions, respectively, where the direct *CP* asymmetry is defined as $a_f^d = 1 - \left|\bar{A}_f/A_f\right|$. They can, in principle, be disentangled via measurements of the corresponding time-integrated *CP* asymmetries (43), which satisfy $A_{CP}(D^0 \to h^+h^-) = \Delta Y_{h^+h^-}\,\langle t\rangle/\tau_D + a^d_{h^+h^-}$. Examples of time-dependent *CP* asymmetries in decays to non-CP eigenstates include the SCS final states $f = K^*K$ or $f = \rho\pi$, and the Cabibbo favored/doubly Cabibbo suppressed (CF/DCS) final states $f = K^\pm\pi^\mp$. These asymmetries generally depend on both ϕ_f^M and ϕ_f^Γ, unlike decays to *CP* eigenstates, due to the additional strong phases [222].

The dispersive and absorptive observables are simply related [222] to the more familiar parametrization of indirect CPV, see, e.g., [220]. The latter consists of $|q/p| - 1$, and

$$\lambda_f \equiv \frac{q}{p}\frac{\bar{A}_f}{A_f} = -\eta_f^{CP}\left|\lambda_f\right| e^{i\,\phi_{\lambda_f}}\,, \tag{35}$$

for *CP* eigenstate final states, and pairs of observables λ_f, $\lambda_{\bar{f}}$ for non-CP eigenstate final states. The same number of independent parameters is employed in each case (recall that $\phi_{12} = \phi_f^M - \phi_f^\Gamma$).

Single mrad precision for ϕ_{12} could become a realistic target at LHCb, see below and Sec. 3.7, to be compared with the current $\sim 50 - 100$ mrad bounds [95% CL] quoted by HFLAV and UTfit Collaboration [197, 201]. Thus, we must estimate the final state dependence in ϕ_f^M, ϕ_f^Γ due to the subleading decay amplitudes, and consider how to best parameterize this. This is accomplished via the U-spin flavor symmetry decomposition of the $D^0 - \overline{D}^0$ mixing amplitudes given in Eq. (28). We define three theoretical CPV phases

$$\phi_2^\Gamma \equiv \arg\left(\frac{\Gamma_{12}}{\Gamma_{12}^{\Delta U=2}}\right), \quad \phi_2^M \equiv \arg\left(\frac{M_{12}}{\Gamma_{12}^{\Delta U=2}}\right), \quad \phi_2 \equiv \arg\left(\frac{q}{p}\Gamma_{12}^{\Delta U=2}\right), \tag{36}$$

which are the theoretical analogs of the final state dependent phases ϕ_f^M, ϕ_f^Γ, and ϕ_{λ_f}, respectively. The U-spin breaking hierarchy $\Gamma_1/\Gamma_2 = \mathcal{O}(1/\epsilon)$ yields the estimate

$$\phi_2^\Gamma \approx \mathrm{Im}\left(\frac{2\lambda_b}{\lambda_s - \lambda_d}\frac{\Gamma_1}{\Gamma_2}\right) \sim \left|\frac{\lambda_b}{\theta_c}\right| \sin\gamma \times \frac{1}{\epsilon}, \tag{37}$$

and similarly for ϕ_2^M (the $O(\lambda_b^2)$ contributions are negligible). Taking the nominal value $\epsilon \sim 0.2$ for U-spin breaking, we obtain the rough SM estimates

$$\phi_{12} \sim \phi_2^\Gamma \sim \phi_2^M \sim 3 \times 10^{-3}\,. \tag{38}$$

Comparison with the current 95% CL bounds on ϕ_{12} implies that there is an $\mathcal{O}(10)$ window for NP in indirect CPV. An alternative expression for ϕ_2^Γ follows from (37) via the relation $\Gamma_2 \cong y\,\Gamma^D$,

$$|\phi_2^\Gamma| = \left|\frac{\sin\gamma\ \lambda_b\,\lambda_s}{y}\right| \frac{|\Gamma_1|}{\Gamma^D} \approx 0.005\,\frac{|\Gamma_1|}{\Gamma^D} \sim 0.005\,\epsilon\,, \tag{39}$$

where in the last relation we have taken $\Gamma_1 \sim \Gamma^D\epsilon$ (recall that the HQE yields $\Gamma_{ij} \sim \Gamma^D$). In principle, Γ_1 can be estimated via the exclusive approach as more data on SCS D^0 decay branching ratios and direct CP asymmetries becomes available.

The misalignments between ϕ_f^M, ϕ_f^Γ, ϕ_{λ_f} in (33), (35), and their theoretical counterparts satisfy

$$\delta\phi_f \equiv \phi_f^\Gamma - \phi_2^\Gamma = \phi_f^M - \phi_2^M = \phi_2 - \phi_{\lambda_f}\,. \tag{40}$$

We can characterize the magnitude of the misalignment $\delta\phi_f$ in the SM as follows: (i) For CF/DCS decays it is precisely known and negligible, i.e., $\delta\phi_f = \mathcal{O}(\lambda_b^2/\theta_c^2)$; (ii) In SCS decays, $\delta\phi_f$ is related to direct CPV as $\delta\phi_f = a_f^d \cot\delta$ via the U-spin decomposition of the decay amplitudes [225], where a strong phase $\delta = \mathcal{O}(1)$ is expected due to large rescattering at the charm mass scale. Thus, for $f = \pi^+\pi^-, K^+K^-$, the experimental bounds $a_f^d \lesssim \mathcal{O}(10^{-3})$ imply that $\delta\phi_f \lesssim \mathcal{O}(10^{-3})$; (iii) In SCS decays, $\delta\phi_f = \mathcal{O}(\lambda_b \sin\gamma/\theta_c) \times \cot\delta$, i.e., it is $\mathcal{O}(1)$ in $SU(3)_F$ breaking. Thus, (37) yields $\delta\phi_f/\phi_2^\Gamma = \mathcal{O}(\epsilon)$, implying an order of magnitude suppression of the misalignment. An exception to property (iii) arises in $D^0 \to K_sK_s$, where the leading "tree-level" decay amplitude enters at $O(\epsilon)$ [226], thus yielding $\delta\phi_{K_sK_s}/\phi_2^\Gamma = \mathcal{O}(1)$. Note that $\delta\phi_{K^{*0}K_S}$ could also be enhanced due to a suppression of the leading amplitudes [227].

In the HL-LHC era, a single pair of dispersive and absorptive phases, identified with ϕ_2^M and ϕ_2^Γ, respectively, should suffice to parametrize all indirect CPV effects. We refer to this fortunate circumstance as *approximate universality*. Moreover, approximate universality generalizes beyond the SM under the following conservative assumptions about NP contributions: (i) they can be neglected in CF/DCS decays (a highly exotic NP flavor structure would otherwise be required in order to evade the ϵ_K constraint [228]); (ii) in SCS decays they are of similar size or smaller than the SM QCD penguin amplitudes,

as already hinted at by the experimental bounds on the direct CP asymmetries $a^d_{K^+K^-}$, $a^d_{\pi^+\pi^-}$. These assumptions can be tested by future direct CPV measurements.

Under approximate universality, $\phi_f^M \to \phi_2^M$ and $\phi_f^\Gamma \to \phi_2^\Gamma$ in expressions for time-dependent CP asymmetries. A global fit to the CPV data for any two of the three phases, ϕ_2^M, ϕ_2^Γ, ϕ_{12}, is equivalent to the traditional two-parameter fit for $|q/p|$ and ϕ , where ϕ is identified with ϕ_2 [222]. The relations

$$\left|\frac{q}{p}\right| - 1 \approx \frac{|x||y|}{x^2+y^2}\sin\phi_{12}, \qquad \tan 2(\phi_2+\phi^\Gamma) \approx -\frac{x_{12}^2}{x_{12}^2+y_{12}^2}\sin 2\phi_{12}\,, \tag{41}$$

together with $\phi_{12} = \phi_2^M - \phi_2^\Gamma$, allow one to translate between $(\phi_2, |q/p|)$ and $(\phi_2^M, \phi_2^\Gamma)$. To illustrate the potential reach of LHCb in ϕ_2^M and ϕ_2^Γ from prompt charm production at 300 fb^{-1}, the projected statistical errors on ϕ, $|q/p|$, x, y from $D^0 \to K_s\pi^+\pi^-$ (combined with the Belle error correlation matrix [229]), and on $\Delta Y_f = -A_\Gamma$, given in the last rows of Tables 14 and 16, and assuming the central values $|q/p| = 1$, $\phi = 0$, $x = 0.57\%$, and $y = 0.7\%$, yield

$$\sigma(\phi_2^M) = 2 \text{ mrad}, \quad \sigma(\phi_2^\Gamma) = 5 \text{ mrad}\,. \tag{42}$$

The projected statistical errors are smaller for $D^0 \to K^+\pi^-\pi^-\pi^+$ than for $D^0 \to K_s\pi^+\pi^-$, cf. Tab. 15. Thus, if the systematic errors are not prohibitively large, cf. Sec. 3.7, LHCb could probe indirect CPV in the SM.

Finally, we remark, that if NP predominantly couples to left-handed quark currents, there are strong correlations between NP contributions to $D-\bar{D}$ and $K-\bar{K}$ mixing [230, 231]. In such a case, the combination of measurements in these two systems is particularly powerful.

3.3 Direct *CP* violating probes

Direct CP asymmetries,

$$A_{CP}(D^0 \to h^-h^+) \equiv \frac{\Gamma(D^0 \to h^-h^+) - \Gamma(\overline{D}^0 \to h^-h^+)}{\Gamma(D^0 \to h^-h^+) + \Gamma(\overline{D}^0 \to h^-h^+)}, \tag{43}$$

with h a light meson, are suppressed in the SM but could be enhanced by NP. A prominent test of direct CPV in charm is the observable

$$\Delta A_{CP} = A_{CP}(K^-K^+) - A_{CP}(\pi^-\pi^+), \tag{44}$$

which measures the difference between direct CPV in SCS modes $D^0 \to K^+K^-$ and $D^0 \to \pi^+\pi^-$. This is despite that the SM prediction is hard to obtain. However, assuming nominal breaking of the $SU(3)$ flavor symmetry, $\epsilon \approx f_K/f_\pi - 1 \approx \mathcal{O}(20\,\%)$, one can infer from the observed branching ratios of the CF decay$D^0 \to \pi^+K^-$ and DCS decay $D^0 \to \pi^-K^+$ a consistent picture involving large matrix elements for U-spin breaking penguin [225, 232–236] (see also [237]). These can account, in the presence of large strong phases, for values of $\Delta A_{CP} \lesssim 0.2\%$ [238], in accordance with the current measurements. Light cone QCD sum rule calculations, on the other hand, predict a much smaller quantity, $\Delta A_{CP} = (0.020 \pm 0.003)\%$ [239]. LHCb is expected to probe far into this region after Upgrade II (see Sec. 3.7.6).

SCS D decay modes are sensitives probes of CP violation in and beyond the SM [240]. Other decay modes can also be sensitive to CP asymmetries of the same order, both in the SM and in NP extensions that modify the QCD penguin operators. Besides the modes $D^+ \to K^+\bar{K}^0$ and $D_s^+ \to \pi^+K^0$, obtained from the above via exchange of the spectator quark, the mode $D^0 \to K_SK_S$ is particularly interesting, because a large CP asymmetry $\lesssim 1\,\%$ can be expected [226, 238]. The related $D \to KK^*$ modes have smaller asymmetries, but this can be compensated by the higher experimental efficiency [227]. Such quasi two-body decays can interfere, if they contribute to the same three- or four-body final state, which

needs to be taken into account in the analysis (for theory discussion, see, e.g., [241], for experimental prospects at LHCb Upgrade II see Sec. 3.7.6).

Another interesting class of observables are the semileptonic D decays, $D \to P\ell^+\ell^-$ and $D \to P_1P_2\ell^+\ell^-$, where P, P_1, P_2 are light pseudoscalars. In analogy to the well-studied corresponding semileptonic B decay modes, interesting null tests of CP violation can be constructed [242–244]. In certain regions of phase space, the CP asymmetries can be largely enhanced via interferences with resonances, which makes these decays an interesting class of observables for LHCb [245].

A set of observables related to direct CP asymmetry are $\widehat{T}$-violating triple products [246] (see also Sec. 3.7.6). To be nonzero they require a source of CPV, and at least three independent momenta or polarization vectors in the final state, such as in $D \to VV$ decays or decays to four pseudoscalars. Unlike direct CP asymmetry, the $\widehat{T}$-violating triple products can be nonzero even in the case of vanishing strong phase differences.

3.4 Null tests from isospin sum rules

SM predictions for hadronic D decays are notoriously difficult. In some cases it is possible to obtain strong indications for the presence of NP by relating various modes using the approximate flavor symmetry $SU(3)$ (invariance under interchange of up, down, and strange quarks) or the more precise isospin (invariance under interchange of up and down quarks).

Probably the simplest example is the $D^+ \to \pi^+\pi^0$ decay [238]. The final state has isospin $I = 2$ which cannot be reached from the $I = 1/2$ initial state via the $\Delta I = 1/2$ QCD penguin operators, predicting very suppressed direct CPV in the SM. An important question in this context is the size of isospin-breaking effects. Isospin-breaking due to QED and the difference of up- and down-quark mass is CP conserving and can be safely neglected. The electroweak penguin contribution is relatively suppressed by α/α_s in the SM. Thus, enhanced direct CPV in $D^+ \to \pi^+\pi^0$ would signal the presence of isospin-violating NP.

Another example is the sum of rate differences [247]

$$\begin{aligned} &|A_{\pi^+\pi^-}|^2 - |\bar{A}_{\pi^+\pi^-}|^2 + |A_{\pi^0\pi^0}|^2 - |\bar{A}_{\pi^0\pi^0}|^2 \\ &\qquad - \frac{3}{2}\left(|A_{\pi^+\pi^0}|^2 - |\bar{A}_{\pi^-\pi^0}|^2\right) = 3\left(|A_{1/2}|^2 - |\bar{A}_{1/2}|^2\right), \end{aligned} \tag{45}$$

which depends only on $\Delta I = 1/2$ amplitudes. There are two possibilities. If the sum is non-zero, there are $\Delta I = 1/2$ contributions to CP violation; they can be due to SM or NP. If the sum is zero, but the individual asymmetries are non-zero, the CP asymmetries are likely dominated by $\Delta I = 3/2$ NP contributions. More sum rules, involving also vector meson final states, can be devised for the decay modes $D \to \rho\pi$, $D \to K^{(*)}\bar{K}^{(*)}\pi(\rho)$, $D_s^+ \to K^*\pi(\rho)$ [247]. For an exhaustive list of sum rules based on the flavor $SU(3)$ or its subgroups, see Refs. [248–250]. For decays with only charged particles in the final state a significant improvement in precision is projected at LHCb Upgrade II. The final states with neutral pions are more challenging (for experimental prospects at LHCb Upgrade II see Sec. 3.7.6). However, precise information on these CP asymmetries is expected from Belle-II.

3.5 Radiative and leptonic charm decays

In the down-type quark sector the GIM suppression is less effective because of the large top quark mass, so that the diagrams with the top-quark running in the loop dominate. In the *charm* sector the GIM suppression is more efficient at least at the perturbative level, since none of the down-type quarks are heavy. The exact suppression for a particular FCNC decay depends on how well the GIM suppression is carried over to the non-perturbative contributions ("long distance" physics). The result is that the SM branching ratios for radiative and leptonic charm decays, while suppressed, are in general not too small to be out of reach. The branching ratios for semi-leptonic FCNC decays, such as $D \to P\ell\ell$, $D \to V\ell\ell$,

and $D \to PP\ell\ell$ are at the level of $10^{-7} - 10^{-6}$, while for the radiative decays, $D \to V\gamma$, they are at the level of $10^{-4} - 10^{-5}$. The branching ratios for these decays are resonance dominated, and this holds true even in the presence of new physics. However, one can still search for new physics effects by using appropriate observables such as CP asymmetries, polarization asymmetries, and angular observables, as well as enhancements of differential rates away from resonance regions.

3.5.1 *Radiative Decays*

The effective weak Lagrangian for the exclusive $c \to u\gamma$ FCNC transitions $D \to V\gamma$ is, see, e.g., [243],

$$\mathcal{L}_{\text{eff}}^{\text{weak}} = \frac{4G_F}{\sqrt{2}} \left(\sum_{q\in\{d,s\}} V_{cq}^* V_{uq} \sum_{i=1}^{2} C_i O_i^{(q)} + \sum_{i=3}^{6} C_i O_i + \sum_{i=7}^{8} \left(C_i O_i + C_i' O_i' \right) \right), \tag{46}$$

with the operators $\mathcal{O}_{2(1)} = (\bar{u}_L \gamma_\mu (T^a) q_L)(\bar{q}_L \gamma^\mu (T^a) c_L)$, $\mathcal{O}_7^{(\prime)} = e\, m_c/16\pi^2 (\bar{u}_{L(R)} \sigma^{\mu\nu} c_{R(L)}) F_{\mu\nu}$ and $\mathcal{O}_8^{(\prime)} = g_s\, m_c/16\pi^2 (\bar{u}_{L(R)} \sigma^{\mu\nu} T^a c_{R(L)}) G^a_{\mu\nu}$. The SM effective Wilson coefficients $C_i^{(\text{eff})}$, which absorb the universal long-distance effects from quark loops in perturbation theory, are known at two-loop level in QCD [243, 251–253]. The authors of Ref. [243] improved the SM prediction for the branching ratios of $D \to V\gamma$, by including power corrections and updating the hybrid model predictions. The hybrid model combines the heavy quark effective theory and chiral perturbation theory using experimentally measured parameters [254, 255]. They also included corrections to the perturbative Wilson coefficients by employing a QCD based approach, worked out for B physics as reviewed in [243]. Updated values for the SM Wilson coefficients at leading order in α_s are given in [242, 243, 251]. The GIM mechanism suppresses strongly C_8^{eff} in the SM. The experimental branching ratio for the Cabibbo allowed decay is $\mathcal{B}(D^0 \to K^*(892)\gamma) = (4.1 \pm 0.7) \times 10^{-4}$ and for the Cabibbo suppressed decays $\mathcal{B}(D^0 \to \phi\gamma) = (2.74 \pm 0.19) \times 10^{-5}$, $\mathcal{B}(D^0 \to \rho^0\gamma) = (1.76 \pm 0.31) \times 10^{-5}$ [256]. The hybrid model predicts in the SM $\mathcal{B}(D^0 \to \rho^0\gamma)_{\text{SM}} = (0.041 - 1.17) \times 10^{-5}$, $\mathcal{B}(D^0 \to \phi\gamma)_{\text{SM}} = (0.24 - 2.8)) \times 10^{-5}$, $\mathcal{B}(D^0 \to \bar{K}^{*0}\gamma)_{\text{SM}} = (0.26 - 4.6) \times 10^{-4}$ [243, 257]. The NP scenarios discussed in Ref. [257] can contribute at the loop level to $C_{7,8}^{\text{eff}}$, and cannot significantly modify the branching ratios. However, the NP induced CPV asymmetry was found to still be modest, e.g., $\sim \mathcal{O}(10\%)$ for $D^0 \to \rho^0\gamma$. In the case of baryonic mode $\Lambda_c \to p\gamma$ the rate is estimated to be $\sim \mathcal{O}(10^{-5})$. The forward-backward asymmetry of photon momentum relative to Λ_c boost probes the handedness of $c \to u\gamma$ transitions. It can be 0.2 in the SM, and somewhat smaller within scenarios of NP discussed in [243, 257]. The probes of photon polarization include time-dependent analysis in $D^0, \bar{D}^0 \to V\gamma$, where $V = \rho^-, K^0, \phi$, or an up-down asymmetry in $D_{(s)} \to K_1(\to K\pi\pi)\gamma$ [258].

3.5.2 *Rare leptonic decays of charm*

To describe NP effects the effective Lagrangian for the $c \to u\bar{\ell}\ell$ has to be extended by the following operators

$$\begin{aligned} \mathcal{O}_{9(10)} &= \frac{e^2}{(4\pi)^2} (\bar{u}\gamma^\mu P_L c)(\bar{\ell}\gamma_\mu(\gamma_5)\ell)\,, & \mathcal{O}_{S(P)} &= \frac{e^2}{(4\pi)^2} (\bar{u} P_R c)(\bar{\ell}(\gamma_5)\ell)\,, \\ \mathcal{O}_T &= \frac{e^2}{(4\pi)^2} (\bar{u}\sigma_{\mu\nu} c)(\bar{\ell}\sigma^{\mu\nu}\ell)\,, & \mathcal{O}_{T5} &= \frac{e^2}{(4\pi)^2} (\bar{u}\sigma_{\mu\nu} c)(\bar{\ell}\sigma^{\mu\nu}\gamma_5\ell). \end{aligned} \tag{47}$$

Among these only C_9 is nonzero in the SM. For each $\mathcal{O}_i$ one can introduce $\mathcal{O}_i'$ with the corresponding Wilson coefficient C_i' by replacing the chirality operator $P_L = 1/2(1-\gamma^5)$ by $P_R = 1/2(1+\gamma^5)$ [259]. In Ref. [242] the authors obtained (N)NLO QCD SM Wilson coefficients at $\mu_c = m_c$, $C_7 \simeq (-0.0011 - 0.0041i)$ and $C_9 \simeq -0.021 X_{ds}$, where $X_{ds} = V_{cd}^* V_{ud} L(m_d^2, q^2) + V_{cs}^* V_{us} L(m_s^2, q^2)$, with $L(m^2, q^2)$ defined in eq. (B1) of [242]. In the range of $m_c/\sqrt{2} \le \mu_c \le \sqrt{2} m_c$ the effective Wilson

Table 12: Maximal experimentally allowed magnitudes of the Wilson coefficients, $|\tilde{C}_i| = |V_{ub}V_{cb}^* C_i|$, obtained from non-resonant part of $D^+ \to \pi^+\mu^+\mu^-$ decay, low q^2 region I: $q^2 \in [0.0625, 0.276]\,\text{GeV}^2$; high q^2 region: $q^2 \in [1.56, 4.00]\text{GeV}^2$); and from $\mathcal{B}(D^0 \to \mu^+\mu^-) < 7.6 \times 10^{-9}$ at 95% C.L. [260]. The last row applies to the case $\tilde{C}_9 = \pm\tilde{C}_{10}$. All the bounds assume real C_i, and also apply to coefficients with flipped chirality, $\tilde{C}'_j$.

	$\dfrac{|\tilde{C}_i|_{\max}}{\mathcal{B}(\pi\mu\mu)_I}$	$\mathcal{B}(\pi\mu\mu)_{II}$	$\mathcal{B}(D^0 \to \mu\mu)$
$\tilde{C}_7$	2.4	1.6	-
$\tilde{C}_9$	2.1	1.3	-
$\tilde{C}_{10}$	1.4	0.92	0.63
$\tilde{C}_S$	4.5	0.38	0.049
$\tilde{C}_P$	3.6	0.37	0.049
$\tilde{C}_T$	4.1	0.76	-
$\tilde{C}_{T5}$	4.4	0.74	-
$\tilde{C}_9 = \pm\tilde{C}_{10}$	1.3	0.81	0.63

coefficients were found to be $(-0.0014 - 0.0054i) \leq C_7 \leq (-0.00087 - 0.0033i)$ and $-0.060 X_{ds}(\mu_c = \sqrt{2}m_c) \leq C_9 \leq 0.030 X_{ds}(\mu_c = m_c/\sqrt{2})$. In the small $q^2 \gtrsim 1\,\text{GeV}^2$ region $|C_9| \lesssim 5 \cdot 10^{-4}$.

One can consider contributions of this effective Lagrangian in the exclusive decay channels. For the D meson di-leptonic decays the best upper bound to date is obtained by the LHCb collaboration at the 90% CL [260] $\mathcal{B}(D^0 \to \mu^+\mu^-) < 6.2 \times 10^{-9}$. In the decay $D^+ \to \pi^+\mu^+\mu^-$ the LHCb experiment determined bounds on the branching ratio in the two kinematic regions of the di-lepton mass, chosen to be either below or above the dominant resonant contributions. The measured total branching ratio, obtained by extrapolating spectra over the non-resonant region, is [261] $\mathcal{B}(D^+ \to \pi^+\mu^+\mu^-) < 8.3 \times 10^{-8}$, while the separate branching fractions in the low- and high-q^2 bins are bounded to be below $\mathcal{B}(\pi^+\mu^+\mu^-)_I < 2.5 \times 10^{-8}$ for region I, $q^2 \in [0.0625, 0.276]\,\text{GeV}^2$, and $\mathcal{B}(\pi^+\mu^+\mu^-)_{II} < 2.9 \times 10^{-8}$ for region II, $q^2 \in [1.56, 4.00]\text{GeV}^2$ [261]. These can be used to put bounds on Wilson coefficients. Allowing for NP contributions to only one Wilson coefficient at a time gives the upper bounds listed in Table 12, where $\tilde{C}_i = V_{ub}V_{cb}^* C_i$ [259]. The bound on $\mathcal{B}(D^0 \to \mu^+\mu^-)$ gives the most stringent bounds on $C_{S,P,10}$ Wilson coefficients.

For baryonic $c \to u\ell^+\ell^-$ transitions the relevant form factors are known from lattice QCD calculations for the $\Lambda_c \to p\ell^+\ell^-$ decay [262]. The dominant contributions to the branching ratio come from resonant regions of $\Lambda_c \to p\rho, (\omega, \phi)$ with ρ, ω and ϕ decaying to $\mu^+\mu^-$. This permits to investigate the impact of NP on the differential branching ratio, the fraction of longitudinally polarized di-muons and the forward-backward asymmetry. The upper 90% CL bound $\mathcal{B}(\Lambda_c \to p\mu^+\mu^-)_{exp} < 7.7 \times 10^{-8}$ [263], obtained by excluding the ± 40 MeV intervals around resonances still allows NP contribution in C_9 and C_{10}. The $\Lambda_c \to p\mu^+\mu^-$ forward-backward asymmetry appears as a result of a nonzero C_{10} Wilson coefficient, generated by the NP. Therefore this observable provides a clean null test of the SM as suggested in Ref. [262].

The above bounds allow for appreciable NP contributions. An example are leptoquark mediators [264], which are well motivated as the NP explanations of the B-meson anomalies, see, e.g., [265]. Refs. [242] and [259] showed that leptoquark exchanges do not affect much the branching ratios, but can lead to CP asymmetries in $D \to \pi l^+ l^-$ and $D_s \to K l^+ l^-$ of a few percent [242, 266]. Namely, such CP asymmetries are defined close to the ϕ resonance that couples to the lepton pair and they can be generated by imaginary parts of the C_7 Wilson coefficients in the effective Lagrangian for $c \to u l^+ l^-$

processes. In the case of any NP scenario one cannot consider any charm rare decays without considering bounds from the $D^0 - \bar{D}^0$ oscillation as pointed out in [267]. In some particular NP scenarios, bounds on NP are stronger if from the $D^0 - \bar{D}^0$ oscillation.

In addition, if the NP is realized by the left-handed doublets of the weak isospin, then NP present in B physics also inevitably appears in charm physics, accompanied with the appropriate CKM matrix elements. Tests of lepton flavour universality are of particular interest, such as the observable $R_{hh} = \mathcal{B}(D \to hh\mu^+\mu^-)/\mathcal{B}(D \to hhe^+e^-)$. The ratio R_{hh} is theoretically clean, but only when both numerator and denominator have the same kinematic cuts, and when these are well above the muon threshold [244, 259]. LHCb has already measured $D \to \pi^+\pi^-\mu^+\mu^-$ and $D \to K^+K^-\mu^+\mu^-$ [268], and BESIII set upper limits on the electron modes [269], but with different cuts on q^2.

3.6 Inputs for B physics

If discovered, the presence of direct CP violation in D decays can affect the extraction of the CKM angle γ from the "tree-level" decays $B \to DK$ [48,49,51,53]. If one includes the $B \to D\pi$ modes, the effect can be of order one [270]. One of the advantages of obtaining γ from tree decays is that all hadronic parameters can be fit from data. This remains essentially true even if direct CPV is present in the decays of the final-state D mesons [270–272], as long as one includes all direct CP asymmetries in the fit – there are still more observables than parameters in the fit. However, one can show that there remains an ambiguity: A shift in the angle γ can be compensated by a corresponding, unobservable shift in the contributing strong phases. This shift symmetry can be broken by assuming the absence of CPV in one of the D decay modes (for instance, in the SM this is the case for CF and DCS decay modes). Alternatively, one could consider ratios of $B \to f_D K$ and $B \to f_D \pi$ modes where the strong phase cancels, or use information on the relative strong phases, e.g., by measuring entangled decays at D factories [270].

3.7 Experimental prospects

We now summarize the status of experimental measurements and their prospects for the future. We generally follow the notation of Sec. 3.2. In the case of time-dependent CPV, we also define the parameters x' and y' which depend linearly on the mixing parameters, $x' \equiv x\cos\delta + y\sin\delta$ and $y' \equiv y\cos\delta - x\sin\delta$. Here δ is the strong phase difference between the favoured and doubly Cabibbo suppressed final states.

3.7.1 Mixing and time-dependent CPV in two-body decays

The mixing and CPV parameters in D^0–$\overline{D}^0$ oscillations can be accessed by comparing the decay-time-dependent ratio of $D^0 \to K^+\pi^-$ to $D^0 \to K^-\pi^+$ rates with the corresponding ratio for the charge-conjugate processes.

The latest measurement from LHCb [21] uses Run 1 and early Run 2 (2015–2016) data, corresponding to a total sample of about $\mathcal{L} = 5\,\text{fb}^{-1}$ of integrated luminosity. Assuming CP conservation, the mixing parameters are measured to be $x'^2_{K\pi} = (3.9 \pm 2.7) \times 10^{-5}$, $y'_{K\pi} = (5.28 \pm 0.52) \times 10^{-3}$, and $R_D^{K\pi} = (3.454 \pm 0.031) \times 10^{-3}$. Studying D^0 and $\overline{D}^0$ decays separately shows no evidence for CP violation and provides the current most stringent bounds on the parameters $A_D^{K\pi}$ and $|q/p|$ from a single measurement, $A_D^{K\pi} = (-0.1 \pm 9.1) \times 10^{-3}$ and $1.00 < |q/p| < 1.35$ at the 68.3% confidence level.

In Table 13 the signal yields and the statistical precision from Ref. [21] are extrapolated to the end of Run 2 and to the end of Upgrade II, assuming that the central values of the measurements stay the same. This assumption is particularly important for the CP-violation parameters, as their precision may depend on the measured values.

Systematic uncertainties are estimated using control samples of data and none of them are foreseen to have irreducible contributions that exceed the ultimate statistical precision, if the detector performance (particularly in terms of vertexing/tracking and particle identification capabilities) is kept at least in line with what is currently achieved at LHCb.

Table 13: Extrapolated signal yields, and statistical precision on the mixing and CP-violation parameters, from the analysis of promptly produced DCS $D^{*+} \to D^0(\to K^+\pi^-)\pi^+$ decays. Signal yields of promptly produced CF $D^{*+} \to D^0(\to K^-\pi^+)\pi^+$ decays are typically 250 times larger.

Sample ($\mathcal{L}$)	Yield ($\times 10^6$)	$\sigma(x'^2_{K\pi})$	$\sigma(y'_{K\pi})$	$\sigma(A_D)$	$\sigma(\lvert q/p\rvert)$	$\sigma(\phi)$
Run 1–2 (9 fb^{-1})	1.8	1.5×10^{-5}	2.9×10^{-4}	0.51%	0.12	10°
Run 1–3 (23 fb^{-1})	10	6.4×10^{-6}	1.2×10^{-4}	0.22%	0.05	4°
Run 1–4 (50 fb^{-1})	25	3.9×10^{-6}	7.6×10^{-5}	0.14%	0.03	3°
Run 1–5 (300 fb^{-1})	170	1.5×10^{-6}	2.9×10^{-5}	0.05%	0.01	1°

3.7.2 Mixing and time-dependent CPV in $D^0 \to K^0_S\pi^+\pi^-$

The self-conjugate decay $D^0 \to K^0_S\pi^+\pi^-$ includes both CF and DCS, as well as CP-eigenstate processes reconstructed in the same final state. This allows for the relative strong phase between different contributions to be determined from data, and, in turn, enables both the mixing parameters x and y, as well as the CP-violation parameters $|q/p|$ and ϕ to be directly measured without need for external input. As a result, this channel provides the dominant constraint on the parameter x in the global fits.

The mixing and CPV parameters modulate the time-dependence of the complex amplitudes, and these amplitudes themselves vary over the two-dimensional final state phase-space. As such, the measurement relies both on the precise understanding of the detector acceptance as a function of phase-space and decay time, and on the accurate description of the evolution of the underlying decay amplitudes over the Dalitz plane. Both model-dependent and model-independent approaches using quantum-correlated $D\bar{D}$ pairs from $\psi(3770)$ decays can be applied.

Previous measurements from the CLEO [273], BaBar [274], and Belle [229] collaborations have used the model-dependent approach, with the Belle measurement having the best precision to date, $x = (0.56^{+0.20}_{-0.23})\%$, $y = (0.30^{+0.16}_{-0.17})\%$ (assuming CP symmetry), and $|q/p| = 0.90^{+0.18}_{-0.16}$, $\phi = (-6 \pm 12)^\circ$. The one published LHCb result was based on 1 fb^{-1} of Run 1 data [275], and used a model-independent approach with strong phases taken from the CLEO measurement [276] to determine $x = (-0.86 \pm 0.56)\%$, $y = (0.03 \pm 0.48)\%$. This analysis used around 2×10^5 $D^{*+} \to D^0\pi^+$, $D^0 \to K^0_S\pi^+\pi^-$ decays from 2011, which suffered from low K^0_S trigger efficiencies that were significantly increased for 2012 and beyond, and will benefit further from software trigger innovations at the LHCb in the upgrade era.

At LHCb these decays can be reconstructed either through semileptonic decays, for instance $B^- \to D^0\mu^-\bar{\nu}_\mu$, where the muon charge is used to tag the initial D^0 flavour, or through prompt charm production, where the charge of the slow pion in the decay $D^{*+} \to D^0\pi^+$ tags the initial flavour. The two channels have complementary properties and both will be important components of future mixing and CP violation analyses at LHCb.

The prompt charm yields are significantly larger than for the semileptonic channel, due to the increased production cross-section. However, for the semileptonic channel the triggering on signal candidates is much more efficient, and introduces fewer non-uniformities in the acceptance. The estimated future yields are presented in Table 14. Also shown are projected statistical precisions on the four mixing and CPV parameters, which have been extrapolated from complete analyses of the Run 1 data for both the semileptonic and prompt cases.

For this channel the dominant systematic uncertainties on mixing parameters come from two main sources. First is the precision with which the non-uniformities in detector acceptance can be determined versus as a function of phase space and decay time. Second is the knowledge of the strong-phase variation across the Dalitz plane. For the LHCb Run 2 analysis, both contributions are significantly smaller than the statistical precision. In the longer term new approaches will be necessary to further reduce these systematic uncertainties. Trigger and event selection techniques should be adapted to emphasise

Table 14: Extrapolated signal yields at LHCb, together with statistical precision on the mixing and CP violation parameters, for the analysis of the decay $D^0 \to K^0_S \pi^+ \pi^-$. Candidates tagged by semileptonic B decay (SL) and those from prompt charm meson production are shown separately.

Sample (lumi $\mathcal{L}$)	Tag	Yield	$\sigma(x)$	$\sigma(y)$	$\sigma(\lvert q/p \rvert)$	$\sigma(\phi)$
Run 1–2 (9 fb^{-1})	SL	10M	0.07%	0.05%	0.07	4.6°
	Prompt	36M	0.05%	0.05%	0.04	1.8°
Run 1–3 (23 fb^{-1})	SL	33M	0.036%	0.030%	0.036	2.5°
	Prompt	200M	0.020%	0.020%	0.017	0.77°
Run 1–4 (50 fb^{-1})	SL	78M	0.024%	0.019%	0.024	1.7°
	Prompt	520M	0.012%	0.013%	0.011	0.48°
Run 1–5 (300 fb^{-1})	SL	490M	0.009%	0.008%	0.009	0.69°
	Prompt	3500M	0.005%	0.005%	0.004	0.18°

uniform acceptance, a task made easier by the removal of the calorimeter-based hardware trigger. New techniques, such as the bin-flip method [277], can further reduce dependence on the non-uniform acceptance, although at the cost of degraded statistical precision on the mixing and CP-violation parameters. In the model-dependent approach many of the model systematic uncertainties may reduce or vanish with increased integrated luminosity, as currently fixed parameters are incorporated into the data fit, and the data become increasingly capable of rejecting unsuitable models provided that there is suitable evolution in the model descriptions. For the model-independent approach, the uncertainty from external inputs (currently from CLEO-c, later with 50% reduction from BESIII) will also reduce with luminosity as the LHCb data starts to provide constraining power. There are no systematic uncertainties which are known to have irreducible contributions that exceed the ultimate statistical precision.

For the CP violation parameters additional sources of systematic uncertainty come from the knowledge of detector-induced asymmetries. In particular, there is a known asymmetry between K^0 and $\bar{K}^0$ in their interactions with material. The limitation here will be the precision with which the material traversed by each K^0_S meson can be determined. The LHCb Upgrade II detector will be constructed to minimise material, and to allow precise evaluation of the remaining contributions. In summary, this channel has comparable power on CP violating parameters, but with a simpler two-dimensional phase space and complementary detector systematic uncertainties, as the four-body decays that we discuss next.

3.7.3 Mixing and time-dependent CPV in four-body decays

Like $D^0 \to K^-\pi^+$ and $D^0 \to K^+\pi^-$, the decays $D^0 \to K^-\pi^+\pi^-\pi^+$ and $D^0 \to K^+\pi^-\pi^-\pi^+$ are a pair of CF and DCS decays with high sensitivity to charm mixing. However, the rich amplitude structure across the five dimensional phase space of the latter decays offers unique opportunities (and challenges) in these four-body modes.

In the phase-space integrated analysis using 3fb^{-1} of data, LHCb made the first observation of mixing in this decay mode, and measured quantities $R_D^{K3\pi} = (3.21 \pm 0.014) \cdot 10^{-3}$, as well as $R_{\rm coher}^{K3\pi} y'_{K3\pi} = (0.3 \pm 1.8) \cdot 10^{-3}$, and $\frac{1}{4}(x^2 + y^2) = (4.8 \pm 1.8) \cdot 10^{-5}$ [278]. The coherence factor, $R_{\rm coher}^{K3\pi}$, measures the effect of integrating over the entire four-body phase space [279, 280].

The unique power of multibody decays lies to a large extent in the fact that the strong phase difference between the interfering D^0 and $\bar{D}^0$ amplitudes varies across the phase space. This can be fully exploited only by moving away from the phase-space-integrated approach to the analyses of phase

Table 15: Extrapolated signal yields for LHCb, and sensitivity to the mixing and CP-violation parameters, from the analysis of $D^0 \to K^+\pi^-\pi^-\pi^+$ decays (statistical uncertainties only).

Sample ($\mathcal{L}$)	Yield ($\times 10^6$)	$\sigma(x'_{K\pi\pi\pi})$	$\sigma(y'_{K\pi\pi\pi})$	$\sigma(\lvert q/p\rvert)$	$\sigma(\phi)$
Run 1-2 (9 fb^{-1})	0.22	2.3×10^{-4}	2.3×10^{-4}	0.020	1.2°
Run 1-3 (23 fb^{-1})	1.29	0.9×10^{-4}	0.9×10^{-4}	0.008	0.5°
Run 1-4 (50 fb^{-1})	3.36	0.6×10^{-4}	0.6×10^{-4}	0.005	0.3°
Run 1-5 (300 fb^{-1})	22.5	0.2×10^{-4}	0.2×10^{-4}	0.002	0.1°

space distributions, either in bins or unbinned. Such a "phase space resolved" approach allows a direct measurement of $x'_{K\pi\pi\pi}$ and $y'_{K\pi\pi\pi}$ (rather than only the x'^2 and y' as in the 2-body case), and, crucially, provides high sensitivity to the CP violating variables ϕ and $|q/p|$.

On the other hand, the same phase variations that make multibody decays so powerful, are also a major challenge, as they need to be known precisely in order to cleanly extract the mixing and CP violation parameters of interest. In principle, the relevant phases can be inferred from an amplitude model such as that obtained from 3fb^{-1} of LHCb data [93]. Such models may introduce theoretical uncertainties that are unacceptably large for the precision era of LHCb Upgrade II, unless there are significant innovations in the theoretical description of four-body amplitudes. The alternative is to use model-independent approaches. These use quantum-correlated events at the charm threshold to infer the required phase information in a model-unbiased way. BESIII is working closely with LHCb [281] to provide the necessary model-independent inputs for $D^0 \to K^+\pi^-\pi^-\pi^+$ across different regions of phase space for measurements of the γ angle as well as charm mixing and CP violation measurements.

Sensitivity studies with model-dependent approaches give a useful indication of the precision that can be achieved. A recent such study, Ref. [282], uses LHCb's latest $D^0 \to K^+\pi^-\pi^-\pi^+$ amplitude model [93]. Table 15 gives the yields and sensitivities scaled from the study in [282], illustrating the impressive sensitivity of this decay mode. The study is based on promptly produced D^{*+} mesons, decaying in the flavour-conserving $D^{*+} \to D^0\pi^+$ channel. Several systematic uncertainties require improvements in the analysis method in order to scale with increasing sample sizes. However, given the huge potential of this channel, sufficient effort is expected to be dedicated to this challenge, such that adequate methods can be developed, and that the necessary input from threshold measurements is both generated at BESIII and exploited optimally at LHCb. Indeed, once these are in place, this channel has the potential for probing CP violation at the $\mathcal{O}(10^{-5})$ level, given the current world average value of x.

3.7.4 *Measurement of A_Γ*

The parameter A_Γ is related to indirect CP violation ($\simeq -A_{CP}^{\text{indir}}$) and is defined as

$$A_\Gamma \equiv \frac{\hat{\Gamma}(D^0 \to h^+h^-) - \hat{\Gamma}(\overline{D}^0 \to h^+h^-)}{\hat{\Gamma}(D^0 \to h^+h^-) + \hat{\Gamma}(\overline{D}^0 \to h^+h^-)} \tag{48}$$

Neglecting contributions from subleading amplitudes, A_Γ is independent of the final state f.

The large yields available in the SCS modes, $f = \pi^+\pi^-$ or $f = K^+K^-$, together with tagging from the $D^{*\pm}$ decay, allow for a precise measurement of A_Γ, provided the systematic uncertainties can be controlled with high degree of precision. Tagging based on semileptonic decays of a parent bottom hadron is also possible and has been used in a published LHCb measurement [283], but contributes significantly lower yields.

Most potential systematic effects are essentially constant in t and therefore cause little uncertainties in the observed decay time evolution of the asymmetry. However, second-order effects and detector–induced correlation between momentum and proper decay time are sufficient to produce spu-

Table 16: Extrapolated signal yields at LHCb, and statistical precision on indirect CP violation from A_Γ.

Sample ($\mathcal{L}$)	Tag	Yield K^+K^-	$\sigma(A_\Gamma)_{K^+K^-}$	Yield $\pi^+\pi^-$	$\sigma(A_\Gamma)_{\pi^+\pi^-}$
Run 1–2 (9 fb^{-1})	Prompt	60M	0.013%	18M	0.024%
Run 1–3 (23 fb^{-1})	Prompt	310M	0.0056%	92M	0.0104 %
Run 1–4 (50 fb^{-1})	Prompt	793M	0.0035%	236M	0.0065 %
Run 1–5 (300 fb^{-1})	Prompt	5.3G	0.0014%	1.6G	0.0025 %

rious asymmetries, that must be appropriately corrected. In addition, contamination from secondary decays is a first-order effect in time that must be suppressed, and its residual bias accounted for. Both corrections are dependent on the availability of a large number of CF $D^0 \to K^-\pi^+$ decays as calibration, and can be expected to scale with statistics; collection of this sample with the same trigger as for the signal modes is therefore a crucial tool for performing this measurement with high precision in the future.

The Run 1 LHCb measurement of this quantity gave consistent results in the two h^+h^- modes, averaging $A_\Gamma = (-0.13 \pm 0.28 \pm 0.10) \times 10^{-3}$ [20], which is still statistically dominated. For the reasons mentioned above, this precision is at the threshold of becoming physically interesting, making it a worthy target to pursue with more data. It seems highly unlikely that any experiment built in the foreseeable future will be able to do this, except for an upgrade of LHCb to higher luminosity.

Table 16 shows expected yields and precisions attainable in LHCb Upgrade II, under the same assumptions on efficiencies adopted in the previous sections; this must include provisions for acquiring and storing 5×10^{10} CF decays. The ultimate combined precision is 1×10^{-5}.

3.7.5 Combined mixing and time dependent CPV sensitivity

The projected precisions of the analyses presented in the previous sections are shown in Fig. 26, and are compared with the expected precisions at Belle II. The expected LHCb constraints on ϕ are translated into asymmetry constraints ($A_{CP}^{ind.} \approx x\sin(\phi)$) by multiplying by the current HFLAV average of x and neglecting the uncertainty on this under the assumption that x will be comparatively well determined in the future. This comparison neglects additional constraining power from $|q/p|$. The relative values of these asymmetry constraints with those from A_Γ is indicative only.

The analyses presented in the previous sections are also combined to establish the sensitivity to the CP-violating parameters $|q/p|$ and ϕ. The combination is performed using the method described in Ref. [284]. At an integrated luminosity of 300 fb^{-1} the sensitivity to $|q/p|$ is expected to be 0.001 and that to ϕ to be 0.1°. This remarkable sensitivity is contrasted in Fig. 27 with the HFLAV world average as of 2017. We can conclude that the LHCb Upgrade II will have impressive power to characterise NP contributions to CP violation and is the only foreseen facility with strong potential of probing the SM contribution.

3.7.6 Direct CP violation

The SCS decays $D^0 \to K^-K^+$ and $D^0 \to \pi^-\pi^+$ play a critical role in the measurement of time-integrated direct CP violation through time-integrated CP asymmetry in the h^-h^+ decay rates, Eq. (43). The sensitivity to direct CP violation is enhanced through a measurement of the difference in CP asymmetries between $D^0 \to K^-K^+$ and $D^0 \to \pi^-\pi^+$ decays, ΔA_{CP}, Eq. (44). The individual asymmetries $A_{CP}(K^-K^+)$ and $A_{CP}(\pi^-\pi^+)$ can also be measured.

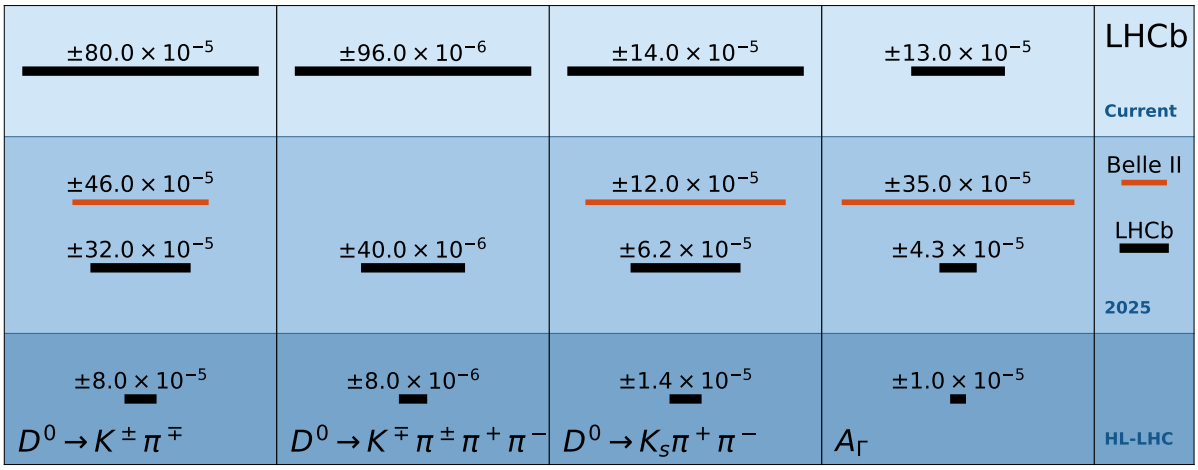

Fig. 26: The predicted constraints on the indirect *CP* violation asymmetry in charm from the decay channels indicated in the labels at the bottom of the columns. Predictions are shown in LS2 (2020) from LHCb, LS3 (2025) from LHCb, at the end of Belle II (2025), and at the end of the HL-LHC LHCb Upgrade II programme.

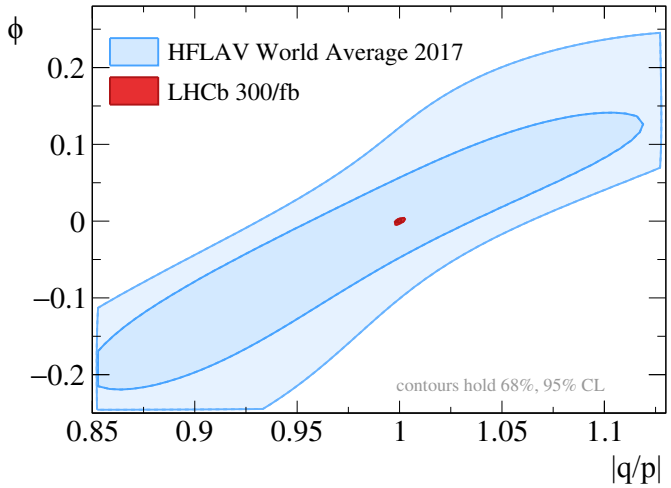

Fig. 27: The estimated constraints for LHCb Upgrade II on ϕ, $|q/p|$ from the combination of the analyses (red), see main text for details, compared to the current world-average precision (light blue). The notation on the axes or lowercase a corresponds to the uppercase A used in the section text.

A measurement of the time-integrated *CP* asymmetry in $D^0 \to K^-K^+$ has been performed in LHCb with 3 fb^{-1} collected at centre-of-mass energies of 7 and 8 TeV. The flavour of the charm meson at production is determined from the charge of the pion in $D^{*+} \to D^0\pi^+$ decays, or via the charge of the muon in semileptonic b-hadron decays, $\overline{B} \to D^0\mu^-\overline{\nu}_\mu X$. The analysis strategy so far relies on the $D^+ \to K^+\pi^+\pi^-$, $D^+ \to K^0_s\pi^+$ and $D^{*+} \to D^0(\to K^-\pi^+)\pi^+$ decays as control samples [285]. In this case, due to the weighting procedures aiming to fully cancel the production and reconstruction asymmetries, the effective prompt signal yield for $A_{CP}(K^-K^+)$ is reduced. The expected signal yields and the corresponding statistical precision in LHCb Upgrade II are summarised in Table 17.

The observable ΔA_{CP} is robust against systematic uncertainties. The main sources of systematic uncertainties are inaccuracies in the fit model, the weighting procedure, the contamination of the prompt sample with secondary D^0 mesons and the presence of peaking backgrounds. There are no systematic

Table 17: Extrapolated signal yields at LHCb and statistical precision on direct *CP* violation observables for the promptly produced samples.

Sample ($\mathcal{L}$)	Tag	Yield $D^0 \to K^-K^+$	Yield $D^0 \to \pi^-\pi^+$	$\sigma(\Delta A_{CP})$ [%]	$\sigma(A_{CP}(hh))$ [%]
Run 1-2 (9 fb^{-1})	Prompt	52M	17M	0.03	0.07
Run 1-3 (23 fb^{-1})	Prompt	280M	94M	0.013	0.03
Run 1-4 (50 fb^{-1})	Prompt	1G	305M	0.01	0.03
Run 1-5 (300 fb^{-1})	Prompt	4.9G	1.6G	0.003	0.007

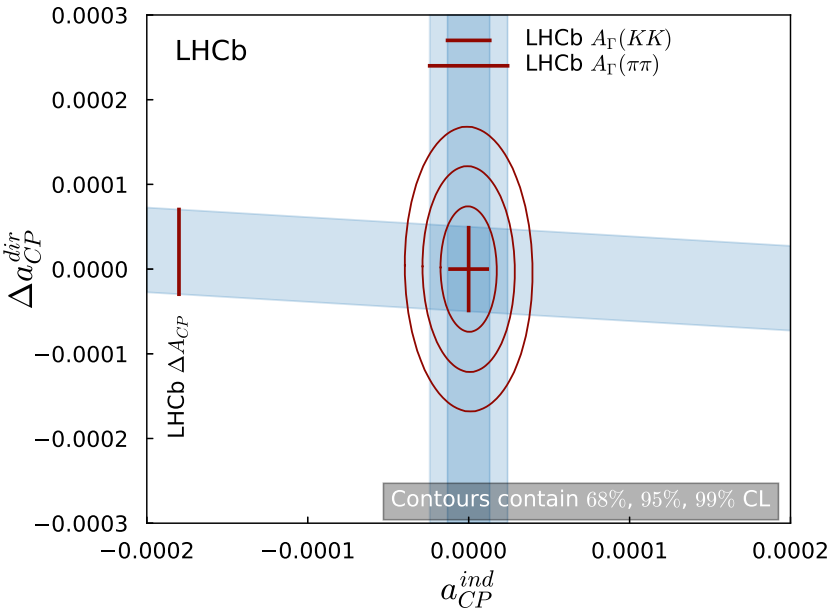

Fig. 28: The estimated constraints for LHCb Upgrade II on indirect and direct charm *CP* violation from the analysis of two-body *CP* eigenstates. The current world-average precision [286] is $\pm 2.6 \times 10^{-4}$ for indirect and $\pm 18 \times 10^{-4}$ for direct *CP* violation and thus larger than the full scale of this plot.

uncertainties with expected irreducible contributions above the ultimate statistical precision. This channel is already entering the upper range of the physically interesting sensitivities, and will likely continue to provide the world's best sensitivity to direct *CP* violation in charm at LHCb Upgrade II. The power of these two-body *CP* eigenstates at LHCb Upgrade II is illustrated in Fig. 28, which shows the indirect (see Sect. 3.7.4) and direct *CP* constraints that will come from these modes.

There are a number of other two-body modes of strong physics interest for which Upgrade II will also make important contributions. These include the decay modes $D^0 \to K^0_S K^0_S$ (0.28%), $D^0 \to K^0_S \bar{K}^{*0}$ (0.21%), $D^0 \to K^0_S K^{*0}$ (0.15%), $D_s^+ \to K^0_S \pi^+$ (3.2×10^{-4}), $D^+ \to K^0_S K^+$ (1.2×10^{-4}), $D^+ \to \phi\pi^+$ (6×10^{-5}), $D^+ \to \eta'\pi^+$ (3.2×10^{-5}), $D_s^+ \to \eta'\pi^+$ (3.2×10^{-4}), where the projected statistical only *CP* asymmetry sensitivities are given in brackets after the decay mode. The first three modes mentioned are notable as they receive sizeable contributions from exchange amplitudes at tree-level and could have a relatively enhanced contribution from penguin annihilation diagrams which are sensitive to NP. Consequently, they could be potential *CP* violation discovery channels [226], [227].

Searches for direct *CP* violation in the phase space of SCS $D^+ \to h_1h_2h_3$ decays, hereafter referred to as $D \to 3h$, are complementary to that of $D^{(0,+)} \to h_1h_2$ ($h_i = \pi, K$). In charged D systems, only *CP* violation in the decay is possible. The main observable is the *CP* asymmetry, which, in

Table 18: Extrapolated signal yields at LHCb, in units of 10^6, for the SCS decays $D^+ \to K^-K^+\pi^+$, $D^+ \to \pi^-\pi^+\pi^+$, and for the DCS decays $D^+ \to K^-K^+K^+$, $D^+ \to \pi^-K^+\pi^+$.

Sample ($\mathcal{L}$)	$K^-K^+\pi^+$	$\pi^-\pi^+\pi^+$	$K^-K^+K^+$	$\pi^-K^+\pi^+$
Run 1–2 ($9\,\text{fb}^{-1}$)	200	100	14	8
Run 1–4 ($23\,\text{fb}^{-1}$)	1,000	500	70	40
Run 1–4 ($50\,\text{fb}^{-1}$)	2,600	1,300	182	104
Run 1–6 ($300\,\text{fb}^{-1}$)	17,420	8,710	1,219	697

Table 19: Sensitivities to several illustrative CP-violation scenarios in $D^+ \to \pi^-\pi^+\pi^+$ decay. Simulated D^+ and D^- Dalitz plots are generated with relative changes in the phase of the $R\pi^\pm$ amplitude, $R = \rho^0(770)$, $f_0(500)$ or $f_2(1270)$. The values of the phase difference are given in degrees and correspond to a 5σ CP-violation effect. Simulations are performed with $3\,\text{fb}^{-1}$ and extrapolated to the expected luminosities.

resonant channel	$9\,\text{fb}^{-1}$	$23\,\text{fb}^{-1}$	$50\,\text{fb}^{-1}$	$300\,\text{fb}^{-1}$
$f_0(500)\pi$	0.30	0.13	0.083	0.032
$\rho^0(770\pi$	0.50	0.22	0.14	0.054
$f_2(1270)\pi$	1.0	0.45	0.28	0.11

the case of two-body decays, is a single number. In contrast, $D \to 3h$ decays allow to study the variation of the CP asymmetry across the two-dimensional phase space (usually represented by the Dalitz plot).

The estimated signal yields in future LHCb upgrades are summarised in Table 18, based on an extrapolation of the Run 2 yields per unit luminosity. The estimated sensitivities to observation of CP violation, using $D^+ \to \pi^-\pi^+\pi^+$ as an example, are presented in Table 19.

The SM generated CP violation could be observed in the SCS decays, such as $D^0 \to \pi^+\pi^-\pi^+\pi^-$ and $D^0 \to K^+K^-\pi^+\pi^-$, while NP is needed to justify any observation of CP violation in the DCS decays, such as $D^0 \to K^+\pi^-\pi^+\pi^-$. Many techniques can be adopted to search for CP violation, all of them exploiting the rich resonant structure of the decays. The methods used so far at LHCb are based on $\widehat{T}$-odd asymmetries and the energy test, while studies are ongoing to measure model-dependent CP asymmetries in the decay amplitudes.

The study of $\widehat{T}$-odd asymmetries exploits potential P-odd CP violation from the interference between different amplitude structures in the decay, as described in Ref. [287]. This uses a triple product $C_T = \vec{p}_A \cdot (\vec{p}_B \times \vec{p}_C)$ constructed from the momenta of three of the final state particles $\vec{p}_A, \vec{p}_B, \vec{p}_C$. LHCb has studied T-odd asymmetries using $3\,\text{fb}^{-1}$ data from the Run 1 dataset, and obtained a sensitivity of 2.9×10^{-3} with very small systematic uncertainties [288]. The peculiarity of this measurement is the absence of instrumental asymmetries, since it is given by the difference of two asymmetries measured separately on D^0 and $\overline{D}^0$ decays, $a_{CP} = (A_T - \bar{A}_T)/2$, where

$$A_T = \frac{(\Gamma(D^0, C_T > 0) - \Gamma(D^0, C_T < 0))}{(\Gamma(D^0, C_T > 0) + \Gamma(D^0, C_T < 0))}, \quad \bar{A}_T = \frac{(\Gamma(\overline{D}^0, \bar{C}_T > 0) - \Gamma(\overline{D}^0, \bar{C}_T < 0))}{(\Gamma(\overline{D}^0, \bar{C}_T > 0) + \Gamma(\overline{D}^0, \bar{C}_T < 0))}. \tag{49}$$

One can therefore expect the errors to scale with luminosity to reach a sensitivity down to 2.9×10^{-5} (9.4×10^{-5}) for $D^0 \to \pi^+\pi^-\pi^+\pi^-$ ($D^0 \to K^+K^-\pi^+\pi^-$) decays, as detailed in Table 20.

The energy test method is insensitive to global asymmetries. However, it is expected that it will become sensitive to variations in phase space of production and detection asymmetries. These can be controlled in data by application of the method to CF decays, such as $D^0 \to K^-\pi^+\pi^+\pi^-$. Assuming scaling with the square-root of the ratio of sample sizes, the same p-values can be expected for the CP

Table 20: Extrapolated signal yields, and statistical precision on $\widehat{T}$-odd CP-violation observables at LHCb.

	$D^0 \to \pi^+\pi^-\pi^+\pi^-$		$D^0 \to K^+K^-\pi^+\pi^-$	
Sample ($\mathcal{L}$)	Yield ($\times 10^6$)	$\sigma(a_{CP}^{\widehat{T}\text{-odd}})$	Yield ($\times 10^6$)	$\sigma(a_{CP}^{\widehat{T}\text{-odd}})$
Run 1–2 (9 fb^{-1})	13.5	2.4×10^{-4}	4.7	5.4×10^{-4}
Run 1–3 (23 fb^{-1})	69	1.1×10^{-4}	12	3.4×10^{-4}
Run 1–5 (300 fb^{-1})	900	2.9×10^{-5}	156	9.4×10^{-5}

Table 21: Overview of sensitivities to various CP-violation scenarios for $D^0 \to \pi^+\pi^-\pi^+\pi^-$ decays as extrapolated from Ref. [289]. The relative changes in magnitude and phase of the amplitude of the resonance R to which sensitivity is expected are given in % and $^\circ$, respectively. The P-wave $\rho^0(770)$ is a P-odd component. The phase change in this resonance is tested with the P-odd CP-violation test. Results for all the other scenarios are given with the standard P-even test.

R (partial wave)	9 fb^{-1}	23 fb^{-1}	300 fb^{-1}
$a_1 \to \rho^0\pi$ (S)	1.4%	0.6%	0.17%
$a_1 \to \rho^0\pi$ (S)	0.8°	0.35°	0.10°
$\rho^0\rho^0$ (D)	1.4%	0.6%	0.17%
$\rho^0\rho^0$ (P)	0.8°	0.35°	0.10°

asymmetries given in Table 21.

Charm decays with neutrals in the final state can help to shed light on the SM or beyond-SM origin of possible CP-violation signals by testing correlations between CP asymmetries measured in various flavour-SU(3) or isospin related decays, see Sec. 3.4 and Refs. [233, 234, 290]. These modes are, however, particularly challenging in hadronic collisions, where the calorimeter background for low energy clusters is high, while the trigger retention rate needs to be kept low to allow for affordable rates.

Nevertheless, good performances are achieved when considering decays with at least two charged particles in the final states, such as $D^0 \to \pi^+\pi^-\pi^0$, since the charged particles help to identify the displaced decay vertex of the charm meson. In only 2 fb^{-1} of data, collected during 2012, LHCb has reconstructed about 660,000 $D^0 \to \pi^+\pi^-\pi^0$ decays [195], i.e., about five times more than Babar from its full data set [291], with comparable purity. Preliminary estimates for Run 2 data, give about 500 000 signal decays per fb^{-1}, making future CP-violation searches in this channel very promising. Similarly, large samples of $D^+_{(s)} \to \eta^{(\prime)}\pi^+$ decays, with $\eta^{(\prime)} \to \pi^+\pi^-\gamma$, or $D^+ \to \pi^+\pi^0$ decays, with $\pi^0 \to e^+e^-\gamma$, are already possible with the current detector. The $D^+_{(s)} \to \eta'\pi^+$ mode, as an example, has been used by LHCb during Run 1 to perform the most precise measurement of CP asymmetries in these channels to date, with uncertainties below the 1% level [292].

More challenging final states consisting only of neutral particles, such as $\pi^0\pi^0$ or $\eta\eta$, can still be reconstructed with $\pi^0 \to \gamma\gamma$ or $\eta \to \gamma\gamma$ candidates made of photons which, after interacting with the detector material, have converted into an e^+e^- pair. Such conversions must occur before the tracking system to have electron tracks reconstructed. Although the reconstruction efficiency of these "early" converted photons in the current detector reaches only a few percent of the calorimetric photon efficiency, their purity is much higher. This approach may become interesting only with the large data sets that are expected to be collected by the end of Upgrade II. The η decays can also be reconstructed through the $\pi^+\pi^-\gamma$ final state.

Unlike the D^0 decays which are usually tagged with a soft pion from D^{*+} decays, there is no easy tagging of the D^+ modes, which thus often suffer from a high combinatorial background. Employing a

π^0 tag using $D^{*+} \to D^+\pi^0$ decays could facilitate future studies of D^+ decays, in particular those with challenging and/or high multiplicity final states.

The study of these modes may be challenging in Run 3 due to the cluster pile-up at higher luminosities and radiation damage of the current calorimeter. The new calorimeter proposed for LHCb Upgrade II would have an improved granularity. It would therefore improve the efficiency for $\pi^0 \to \gamma\gamma$ decays and, in particular, could make the π^0 tag feasible.

3.7.7 Rare leptonic and radiative charm decays

The most experimentally accessible very rare charm decay is $D^0 \to \mu^+\mu^-$. The world's best limit on $\mathcal{B}(D^0 \to \mu^+\mu^-)$ was obtained by LHCb with $0.9\,\text{fb}^{-1}$ of 2011 data [260], resulting in

$$\mathcal{B}(D^0 \to \mu^+\mu^-) < 6.2 \times 10^{-9} \text{ at } 90\% \text{ CL}. \tag{50}$$

Extrapolating the current detector performance, the expected limit is about 5.9×10^{-10} with 23 fb^{-1} and 1.8×10^{-10} with 300 fb^{-1} of integrated luminosity, covering a large part of the unambiguous space to search for NP without being affected by long distance uncertainties in the SM predictions.

The next class of rare charm decays which are particularly suited for experiments at hadron colliders are three-body decays with a pair of leptons in the final state, such as $D^+_{(s)}/\Lambda_c^+ \to h^+\ell^+\ell^-$ and $D^0 \to h^+h^-\ell^+\ell^-$. In some NP scenarios the short distance contributions can be enhanced by several orders of magnitude allowing NP to manifest as an enhancement of the branching fraction. An example of such a model is shown in Fig. 29, where the Wilson coefficients were assumed to obtain NP contributions, $C_9^{\text{NP}} = -0.6$ and $C_{10}^{\text{NP}} = 0.6$ (cf. Eqs. (46), (47)). Outside of the resonance regions the short distance contributions are comparable to the long distance effects. The chosen NP benchmark point leads to branching ratios just below the current LHCb limit [263]

$$\mathcal{B}(\Lambda_c^+ \to p\mu^+\mu^-) < 5.9 \times 10^{-8} \text{ at } 90\% \text{ CL}. \tag{51}$$

In the Upgrade II LHCb is expected to improve the limit to

$$\mathcal{B}(\Lambda_c^+ \to p\mu^+\mu^-) < 4.4 \times 10^{-9} \text{ at } 90\% \text{ CL}. \tag{52}$$

An order of magnitude improvement is expected for the limit on $\mathcal{B}(D^+_{(s)} \to \pi^+\mu^+\mu^-)$ decays, which is currently at 7.3×10^{-8} at 90% CL [261]. The expected upper limits are about 1.3×10^{-8} with $23\,\text{fb}^{-1}$ and 0.37×10^{-8} with $300\,\text{fb}^{-1}$. In addition, LHCb will have the ability to measure angular observables such as the forward-background asymmetry, A_{FB}, or time integrated A_{CP}, which will provide additional handles to separate the long distance from the short distance contributions, and for which some theoretical predictions in NP scenarios already exist [242], as shown in Fig. 30.

Last but not least with a sample corresponding to an integrated luminosity of 300 fb^{-1} LHCb will be able to perform searches for the LFV decays $D^+_{(s)}/\Lambda_c^+ \to h^+\ell^+\ell'^-$ and perform tests of lepton universality via the ratios $\mathcal{B}(D^+_{(s)}/\Lambda_c^+ \to h^+\mu^+\mu^-)/\mathcal{B}(D^+_{(s)}/\Lambda_c^+ \to h^+e^+e^-)$.

The decays $D^0 \to h^+h^-\ell^+\ell^-$ have richer dynamics than the two- and three-body decays, allowing for a variety of differential distributions to be investigated. Due to the huge charm production cross-section at the LHC, and LHCb's ability to trigger on low p_{T} dimuons, LHCb has unique physics reach in studying these decays. In fact, significant progress has already been made with the observation of the CF decay $D^0 \to K^-\pi^+\mu^-\mu^+$ (with the dimuon mass in the ρ/ω region) with a branching fraction $(4.17 \pm 0.42) \times 10^{-6}$ [293] and the SCS decays $D^0 \to \pi^+\pi^-\mu^+\mu^-$ and $D^0 \to K^+K^-\mu^+\mu^-$ with branching fractions of $(9.64 \pm 1.20) \times 10^{-7}$ and $(1.54 \pm 0.33) \times 10^{-7}$, respectively [268]. For the latter, also the differential branching fraction as a function of the dimuon mass squared, q^2, was measured. Furthermore, LHCb has performed the first measurement of CP- and angular asymmetries

the D mesons, which decreases the power of selections based on the displacement of the charm vertex, increasing the prompt combinatorial background, which mainly comprises low-momentum pions and kaons. Selections of charm baryons then heavily rely on good discrimination between proton, kaon, and pion hypotheses in the reconstruction of charged tracks, and on a precise secondary vertex reconstruction. The latter is also necessary when reconstructing charm baryons originating from semileptonic b-hadron decays, which has the advantage of both a simple trigger path (a high-p_{T}, displaced muon) and a cleaner experimental signature due to the large b-hadron lifetime. The presence of the proton in the final state, whilst a useful handle for selections, poses experimental challenges for CP-violation measurements in addition to those present for measurements with D mesons, as the proton-antiproton detection asymmetry must be accounted for. This has not yet been measured at LHCb due to the lack of a suitable control mode.

The most precise measurement of CP violation in charm baryons was made recently by the LHCb collaboration using Run 1 data, corresponding to $3\,\mathrm{fb}^{-1}$ of integrated luminosity [194]. The difference between the phase-space-averaged CP asymmetries in $\Lambda_c^+ \to pK^-K^+$ and $\Lambda_c^+ \to p\pi^-\pi^+$ decays was found to be consistent with CP symmetry to a statistical precision of $0.9\,\%$. This difference is largely insensitive to the proton detection asymmetry, but masks like-sign CP asymmetries between the two modes. Further studies must then gain a precise understanding of the proton detection asymmetry, in addition to measuring the variation of CP violation across the decay phase space.

Although there is little literature on the subject, the magnitude of direct CP violation in charm baryon decays is expected to be similar to that for charmed mesons [294], and so the first step in furthering our understanding is to reach a precision of 0.5×10^{-4}. This can be met by LHCb given the $300\,\mathrm{fb}^{-1}$ of integrated luminosity collected by the end of Run 5. The acquisition of more data is vital in enabling studies of states heavier than the Λ_c^+ baryon, as their alternate compositions may permit considerably different dynamics. In this respect it is interesting to note that the Ξ_{cc}^{++} baryon was discovered [295] by LHCb using the $\Lambda_c^+ K^-\pi^+\pi^+$ final state with data taken in 2016, corresponding to an integrated luminosity of $1.7\,\mathrm{fb}^{-1}$. A signal yield of 313 ± 33 was determined, which can be extrapolated to around $100,000$ such decays obtainable with data corresponding to $300\,\mathrm{fb}^{-1}$, allowing asymmetry measurements with a precision of $0.4\,\%$. The flexible trigger and real-time analysis concept of LHCb's Upgrade II will however enable not only this measurement but a detailed mapping of the entire landscape of multiply-heavy charmed hadrons.

4 Strange-quark probes of new physics

Authors (TH): Giancarlo D'Ambrosio, Diego Guadagnoli, Teppei Kitahara, Diego Martinez Santos.

Although not specifically built for the study of strange hadrons, LHCb's forward geometry allows for a rich physics programme with strange hadrons. LHCb Upgrade II phase will substantially enlarge in scope this programme. Its relevance is evident from the fact that kaon physics provides among the most stringent constraints on new-physics interactions. As with the charm and beauty counterparts, the HL-LHC will be a uniquely powerful factory for strange baryons which the LHCb Upgrade II is well placed to exploit.

4.1 The (HL) LHC as a strangeness factory

The capabilities of LHCb for strangeness decays are due to the large strange-hadron production rates at the LHC, combined with the specific features of LHCb in comparison with the other LHC detectors. These are the higher efficiency for low transverse-momentum particles and the better invariant-mass and vertex resolutions. A simple estimate with `Pythia 8.226` yields a K^0 cross section in 14 TeV pp collisions of about 0.6 barn, as well as another 0.6 barn for $K^\pm$. These are roughly 1000 times larger than the production cross sections for B mesons. Hyperon cross sections are also large, attaining in `Pythia` 0.14, 0.04, 0.01 barn for Λ^0, Σ^+, and Ξ^-, respectively (including their antiparticles), while the cross section for Ω^- is similar to that of B's.

The LHCb capabilities for strange decays were first demonstrated in Ref. [296], which achieved the world's best result in $\mathcal{B}(K^0_S \to \mu^+\mu^-)$ even though the trigger efficiency on well reconstructed decays was only $\sim 1\%$ (to be compared to $\sim 90\%$ for $B^0_s \to \mu^+\mu^-$). In Run 2, dedicated trigger lines have been implemented, selecting muons down to 80 MeV in transverse momentum and increasing the trigger efficiency by one order of magnitude for strangeness decays to dimuons [297]. The main limitation is the hardware trigger (L0). In Run 3 the LHCb trigger will be fully software-based, which can in principle allow for efficiencies as high as those achieved for B's. The main challenge for LHCb Upgrade II will be to fully exploit the software trigger, and enable high trigger efficiency at low transverse momentum using the displacement of the decay products. In addition, using downstream reconstruction in the trigger may boost the LHCb capabilities for charged kaon decays by up to a factor 5 [298].

Among the different strange hadron species, the LHCb detector layout is particularly suitable for K^0_S and hyperons, which have relatively shorter lifetimes compared to $K^\pm$ or K^0_L, which mostly decay outside the detector. An approximate acceptance ratio for $K^0_S : K^\pm : K^0_L$ is estimated as $1 : 0.01 : 3 \times 10^{-3}$ [298] for full tracking and $1 : 0.02 : 0.01$ for downstream tracking (i.e, no usage of VELO information). Hence, measurements with $K^\pm$ decays will also be possible, with potential overlap with NA62. LHCb Upgrade II will reach sensitivities for $\mathcal{B}(K^0_S \to \mu^+\mu^-)$ below the 10^{-11} level if it keeps the performance of the current detector [299], taking into account that the full software trigger will allow for very high trigger efficiencies. Similarly, sensitivities at the 10^{-10} level are expected for $\mathcal{B}(K^0_S \to \pi^0\mu^+\mu^-)$ [300].

The same analysis strategy as $\mathcal{B}(K^0_S \to \pi^0\mu^+\mu^-)$ can be applied to other decays, such as $K^0_S \to \gamma\mu^+\mu^-$, although the sensitivity will be worse due to poorer mass resolution [298]. Other kaon decays that can be studied at LHCb include $K^+ \to \pi\mu\mu$ (both with opposite-sign and same-sign muon pairs), $K^0_S \to 4\mu$, or decays involving electrons, especially interesting in order to search for lepton flavor violation (LFV) and lepton-flavor universality violation (LFUV). The LHCb Upgrade II will also have an abundant enough sample of $\Sigma^+ \to p\mu^+\mu^-$ to do precise study of the differential decay rate. The $\Sigma^+ \to pe^+e^-$ can be studied using dedicated triggers. Semileptonic hyperon decays are reconstructed in LHCb [298] and kinematic constraints can be used to reconstruct the mass peak of the hyperon. Since the expected yields for these decays can be very large, the main challenge is the fight against peaking backgrounds, such as $\Lambda \to p\pi^-$ or $\Xi^- \to \Lambda\pi^-$. LHCb Upgrade II will also be able to update existing limits on LFV kaon decays [301]. A longer list of decays that LHCb will be able to probe can be found

in Ref. [298].

4.2 $K_S^0 \to \mu^+\mu^-$ and $K_L^0 \to \mu^+\mu^-$ decays

LHCb Upgrade I and Upgrade II are expected to be able to probe short-distance physics using the $K^0 \to \mu^+\mu^-$ decay. In the SM, $K_S \to \mu^+\mu^-$ is significantly dominated by P-wave CP-conserving long-distance (LD) contribution, while S-wave CP-violating short-distance (SD) contributions from Z-penguin and W-box are small [302–304]:

$$\mathcal{B}(K_S \to \mu^+\mu^-)_{\rm SM} = [(4.99 \pm 1.50)_{\rm LD} + (0.19 \pm 0.02)_{\rm SD}] \times 10^{-12}. \tag{53}$$

The large uncertainty comes from the LD contribution which has been computed in ChPT [302]. This uncertainty is expected to be reduced by a dispersive treatment of $K_S \to \gamma^*\gamma^*$ [305], where $K_S \to \gamma\gamma$, $K_S \to \mu^+\mu^-\gamma$, $K_S \to \mu^+\mu^-e^+e^-$ and $K_S \to \mu^+\mu^-\mu^+\mu^-$ are measurable in LHCb experiment and KLOE-2 experiment at DAΦNE [306]. It is important to note that, in contrast to the $K_L \to \mu^+\mu^-$ decay:

- The decay $K_S \to \mu^+\mu^-$ provides another sensitive probe of *imaginary* parts of SD couplings and consequently is very sensitive to new sources of CP violation. This is not the case of $K_L \to \mu^+\mu^-$ which is governed by *real* couplings.
- As seen in Eq. (53) the LD and SD contributions to the total rate are added incoherently [302,303], which represents a big theoretical advantage over $K_L \to \mu^+\mu^-$, where LD and SD amplitudes interfere.

This means that in BSMs in which the SD contribution is significantly enhanced, the LD-uncertainty in $K_S \to \mu^+\mu^-$ ceases to be important, and theoretically clean tests of new-physics scenarios are possible. In particular, being the SD contribution dominant, correlations of $K_S \to \mu^+\mu^-$ with ε'/ε and also $K_L \to \pi^0\nu\bar{\nu}$ are present within many new-physics models.

Indeed, within concrete BSMs, $\mathcal{B}(K_S \to \mu^+\mu^-)$ can be modified substantially, for example $\mathcal{B} \sim \mathcal{O}(10^{-10})$ in the leptoquark models [307] and $\mathcal{B} \sim \mathcal{O}(10^{-11})$, or even saturate the current experimental bound in certain MSSM parameter space [308], albeit somewhat fine-tuned. Already the present upper bound from LHCb can have some impact on the allowed parameter range of certain models. This shows that future improvement of this bound can have important impact on various BSM scenarios.

The LHCb full Run1 analysis has set the upper limit for $K_S \to \mu^+\mu^-$ [309],

$$\mathcal{B}(K_S \to \mu^+\mu^-)_{\text{LHCb Run1}} < 0.8\,(1.0) \times 10^{-9} \text{ at } 90\%\,(95\%)\text{ CL}, \tag{54}$$

which is 2 orders of magnitude larger than the SM sensitivity. With LHCb upgrades the sensitivity is significantly improved. Using the upgraded software trigger, the LHCb experiment is aiming to reach the SM sensitivity, as shown in Fig. 31.

A crucial aspect of the $K^0 \to \mu^+\mu^-$ decay is a flavor-tagged measurement which can probe CP-violating SD contributions directly. Its numerical effect is $\mathcal{O}(1)$ compared to the prediction in Eq. (53) even in the SM [304]. While K_L decays typically outside the LHCb fiducial volume, for K_S the interference between K_L and K_S affects the number of signal events as $\Gamma_{\text{int.}} \propto \mathcal{A}(K_L \to \mu^+\mu^-)\mathcal{A}(K_S \to \mu^+\mu^-)^*$ when the flavor tagging, K^0 or $\overline{K}^0$ at $t = 0$, is performed. An effective branching ratio into $\mu^+\mu^-$, which includes the interference correction and would correspond to experimental event numbers after the removal of $K_L \to \mu^+\mu^-$ background, is given by [304],

$$\begin{aligned}\mathcal{B}(K_S \to \mu^+\mu^-)_{\text{eff}} =& \tau_S \left[\int_{t_{\min}}^{t_{\max}} dt e^{-\frac{t}{\tau_S}}\varepsilon(t)\right]^{-1} \int_{t_{\min}}^{t_{\max}} dt \Bigg\{ \Gamma(K_S \to \mu^+\mu^-)e^{-\frac{t}{\tau_S}} \\ &+ \frac{D f_K^2 m_K^3 \beta_\mu}{8\pi} \text{Re}\left[i\left(A_S A_L - \beta_\mu^2 B_S^* B_L\right) e^{-i\Delta m_K t}\right] e^{-\frac{t}{2\tau_S}\left(1+\frac{\tau_S}{\tau_L}\right)} \Bigg\} \varepsilon(t),\end{aligned} \tag{55}$$

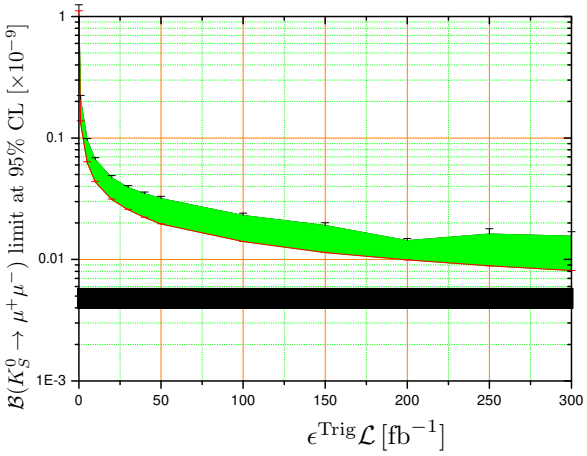

Fig. 31: Projected LHCb reach for $\mathcal{B}(K_S^0 \to \mu^+\mu^-)$ as a function of the integrated luminosity times trigger efficiency (which is expected to be $\mathcal{O}(1)$ in LHCb Upgrade II. The black band is the SM prediction. Figure adapted from Ref. [299], which is based on the data used in [309].

with $\Gamma(K_S \to \mu^+\mu^-) = f_K^2 m_K^3 \beta_\mu \left(A_S^2 + \beta_\mu^2 |B_S|^2\right)/(16\pi)$, where final-state muon polarizations are summed over, $t_{\rm min}$ to $t_{\rm max}$ corresponds to a range of detector for K_S tagging, $\varepsilon(t)$ is the decay-time acceptance of the detector, $\beta_\mu = \left(1 - 4m_\mu^2/m_K^2\right)^{1/2}$, and $f_K = (155.9 \pm 0.4)$ MeV [310]. The $K_L \to \mu^+\mu^-$ background can be subtracted by a combination of the simultaneous measurement of $K_S \to \pi^+\pi^-$ and the knowledge of the observed value of $\mathcal{B}(K_L \to \mu^+\mu^-)$ [304]. The dilution factor D is a measure of the initial K^0–$\overline{K}^0$ asymmetry,

$$D = \left(K^0 - \overline{K}^0\right)/\left(K^0 + \overline{K}^0\right). \tag{56}$$

The $A_{S,L}$ and $B_{S,L}$ are the S-wave and P-wave contributions in $K_{S,L} \to \mu^+\mu^-$ transitions, respectively. The expressions for them are given in Ref. [308] using the general $\Delta S = 1$ effective Hamiltonian. Note that A_S and B_L are real, while B_S and A_L are complex.

The interference contribution is proportional to the dilution factor, D, which requires flavor tagging. This can be done by detecting the accompanying K^- in the process $pp \to K^0 K^- X$, Λ^0 in the process $pp \to K^0 \Lambda^0 X$, or π^+ in the process $pp \to K^{*+} X \to K^0 \pi^+ X$ [304].

In the SM, the effective branching ratio in Eq. (55) can be reduced to [304, 308]

$$A_S A_L - \beta_\mu^2 B_S^* B_L = \frac{4G_F^2 M_W^2 m_\mu^2}{m_K^2 \pi^2} \underbrace{{\rm Im}C_{A,{\rm SM}}}_{\rm SD\ (CPV)} \left(\underbrace{A^\mu_{L\gamma\gamma}}_{\rm LD\ (CPC)} - \frac{\pi^2}{G_F^2 M_W^2} \underbrace{{\rm Re}C_{A,{\rm SM}}}_{\rm SD\ (CPC)} \right). \tag{57}$$

The Wilson coefficient C_A is defined by, $\mathcal{H}_{\rm eff} = -C_A(\bar{s}\gamma^\mu P_L d)(\bar{\ell}\gamma_\mu\gamma_5\ell) + {\rm h.c.}$, and

$$C_{A,{\rm SM}} = -\frac{[\alpha_2(M_Z)]^2}{2M_W^2}\left(V_{ts}^* V_{td} Y_t + V_{cs}^* V_{cd} Y_c\right), \tag{58}$$

where $\alpha_2 = g^2/(4\pi)$, $Y_t = 0.950 \pm 0.049$ and $Y_c = (2.95 \pm 0.46) \times 10^{-4}$ [311]. The large CP-conserving LD two-photon contribution to K_L is [303, 312]

$$A^\mu_{L\gamma\gamma} = \pm 2.01(1) \times 10^{-4} \times (0.71(101) - i\,5.21), \tag{59}$$

where the sign is theoretically and experimentally unknown. The large imaginary (absorptive) component in $A^\mu_{L\gamma\gamma}$ can amplify the small CP-violating SD contribution in $K_S \to \mu^+\mu^-$. Fig. 32 shows the

effective branching ratio and time distributions in the SM, where the interference of the CP-violating contribution can affect $K_S \to \mu^+\mu^-$ decay up to $\mathcal{O}(60)\%$. This quantity is also sensitive to NP contributions to the electroweak penguin, that contributes to ε'/ε (direct CP violation in $K_L^0 \to \pi\pi$). To illustrate this correlation we plot with a green band in Fig. 32 (left) the effect in the effective lifetime (as a function of D) of a Z penguin BSM contribution that would explain the experimental value of ε'/ε assuming the SM predictions obtained in Refs. [313, 314]. These are based on the current lattice result [315] or in Ref. [316], although it is important to note that there are SM calculations of ε'/ε consistent with the experimental data [317, 318]. Some studies in new physics models are also given in Refs. [308, 319].

Using the effective branching ratio in Eq. (55), one can define the flavor-tagging asymmetry in $K_S \to \mu^+\mu^-$ by [308]

$$A_{CP}(K_S \to \mu^+\mu^-)_{D,D'} = \frac{\mathcal{B}(K_S \to \mu^+\mu^-)_{\rm eff}(D) - \mathcal{B}(K_S \to \mu^+\mu^-)_{\rm eff}(D')}{\mathcal{B}(K_S \to \mu^+\mu^-)_{\rm eff}(D) + \mathcal{B}(K_S \to \mu^+\mu^-)_{\rm eff}(D')}, \tag{60}$$

where D' is obtained by requiring an opposite flavor tagging. For instance, when a positive dilution factor is achieved by collecting the di-muon signals accompanying K^-, the negative dilution factor, that is expressed as D', can be obtained by collecting the signals accompanying K^+. This asymmetry is a theoretically clean quantity that emerges from a genuine direct CP violation in general new-physics models. In the SM, $A_{CP}(K_S \to \mu^+\mu^-)^{\rm SM}_{D,-D} = \mathcal{O}(0.7) \times D$ is predicted in the case of $D' = -D$ and it is sensitive to a new CP-violating phase beyond the SM [308].

In a similar way, the CP asymmetry of $B_{d,s} \to \mu^+\mu^-$ has been studied [320, 321]. However, for the B_s system the situation differs substantially from K_S, since the LD contributions are negligible and the life-time difference between the two mass eigenstates is small compared to $K_{S,L}$. The CP asymmetry in $B_{d,s} \to \mu^+\mu^-$ vanishes in the SM, but is also sensitive to a new CP-violating phase.

Before closing this section, we briefly comment on $K_L \to e^+e^-$. Both $K_L \to e^+e^-$ and $K_L \to \mu^+\mu^-$ are dominated by LD two-photon contributions [322,323]. The branching ratio for $K_L \to e^+e^-$ is dominated by the double logarithm contribution, $\propto \log^2(m_e/m_K)$. The subdominant local term is fixed, up to a two-fold ambiguity, from the measured $\mathcal{B}(K_L \to \mu^+\mu^-)$; so that $\mathcal{B}(K_L \to e^+e^-)/\mathcal{B}(K_L \to \gamma\gamma) = (1.552 \pm 0.014) \times 10^{-8}$ or $\mathcal{B}(K_L \to e^+e^-)/\mathcal{B}(K_L \to \gamma\gamma) = (1.406 \pm 0.013) \times 10^{-8}$ is predicted [323]. The measured value $(1.65 \pm 0.91) \times 10^{-8}$ [310] is not yet precise enough to resolve the ambiguity.

4.3 $K_S \to \mu^+\mu^-\gamma$, $K_S \to \mu^+\mu^-e^+e^-$ and $K_S \to \mu^+\mu^-\mu^+\mu^-$

To improve the LD determination of $\mathcal{B}(K_S \to \mu^+\mu^-)$, it is important to measure $K_S \to \mu^+\mu^-\gamma$, $K_S \to \mu^+\mu^-e^+e^-$ and $K_S \to \mu^+\mu^-\mu^+\mu^-$. These channels are at reach for LHCb Upgrade II and thus may give necessary LD information needed for a better control of $K_L \to \mu^+\mu^-$. These four body decays have a peculiar feature: similarly to $K_{S,L} \to \pi^+\pi^-e^+e^-$ [323], the two different helicity amplitudes interfere. One can then measure the sign of $K_L \to \gamma^*\gamma^* \to \ell^+\ell^-\ell^+\ell^-$ by studying the time interference between K_S and K_L, which has a decay length $2\Gamma_S$ [324].

The ChPT prediction for $\mathcal{B}(K_S \to \gamma\gamma)$ [325], which has been experimentally confirmed, allows one to make a prediction for $\mathcal{B}(K_S \to \mu^+\mu^-\gamma) = 7.25 \times 10^{-10}$; this value is increased by vector meson dominance (VMD) and unitarity corrections to $\mathcal{B}(K_S \to \mu^+\mu^-\gamma) = (1.45 \pm 0.27) \times 10^{-9}$ [305].

4.4 $K_S \to \pi^0\ell^+\ell^-$ and $K^\pm \to \pi^\pm\ell^+\ell^-$

At low dilepton mass squared, q^2, the dominant contribution to $K^\pm(K_S) \to \pi^\pm(\pi^0)\ell^+\ell^-$ is due to a single virtual-photon exchange. The resulting amplitude involves a vector form factor $V_i(z)$ $(i = \pm, S)$,

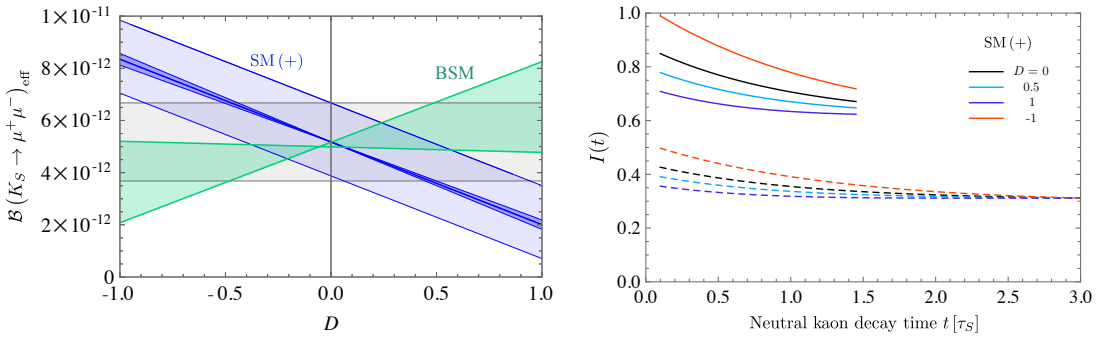

Fig. 32: Left panel: The effective branching ratios with the blue (gray) band denoting the SM prediction with (without) taking into account the dilution D. The green band corresponds to a BSM scenario entering through electroweak penguins studied in Ref. [304]. Right panel: The $K \to \mu^+\mu^-$ time distributions in the SM for several choices of D. The $D = 0$ decay intensity is normalized, either over the interval $0.1\tau_S$ to $1.45\tau_S$ (solid lines) or $0.1\tau_S$ to $3\tau_S$ (dashed lines). Positive sign of $A^{\mu}_{L\gamma\gamma}$ is assumed in Eq. (59). A detailed explanation and results for the negative sign of $A^{\mu}_{L\gamma\gamma}$ are given in Ref. [304].

Table 22: Fitted values of coefficients entering the vector form factor in Eq. (61).

Channel	a_+	b_+	Reference
ee	-0.587 ± 0.010	-0.655 ± 0.044	E865 [328]
ee	-0.578 ± 0.016	-0.779 ± 0.066	NA48/2 [329]
$\mu\mu$	-0.575 ± 0.039	-0.813 ± 0.145	NA48/2 [330]

which can be decomposed in the general form up to $\mathcal{O}(p^6)$ in the chiral expansion as [326, 327],

$$V_i(z) = a_i + b_i z + V_i^{\pi\pi}(z)\,, \quad z = q^2/m_K^2\,, \quad \text{for} \quad i = \pm, S. \tag{61}$$

Here the low energy constants (LECs), a_i and b_i, parametrize the polynomial part of the amplitude, while the rescattering contribution $V_i^{\pi\pi}$ can be determined from fits to $K \to \pi\pi$ and $K \to \pi\pi\pi$ data (no $\Delta I = 1/2$ contribution to $V_S^{\pi\pi}$). The chiral loops, encoded in $V_i^{\pi\pi}$, have been computed, model-independently and at leading order, in the framework of chiral perturbation theory [326, 327]. Chiral symmetry alone does not constrain the values of the LECs, so instead, we consider the differential decay rate $d\Gamma/dz \propto |V_+(z)|^2$ as a means to extract a_+ and b_+ from experiment. The resulting fit to the decay spectra from all available high-statistics experiments is given in Table 22. The experimental size of the b_+/a_+ ratio exceeds the naive dimensional analysis estimate, calling for a large VMD contribution.

The branching ratios of $K_S \to \pi^0\ell^+\ell^-$, on the other hand, are approximately

$$\mathcal{B}(K_S \to \pi^0 e^+ e^-) \approx 5 \times 10^{-9} \cdot a_S^2, \qquad \mathcal{B}(K_S \to \pi^0 \mu^+ \mu^-) \approx 1.2 \times 10^{-9} \cdot a_S^2, \tag{62}$$

and NA48, assuming just a VMD form factor, finds respectively [331, 332]

$$|a_S|_{ee} = 1.06^{+0.26}_{-0.21} \pm 0.07, \qquad |a_S|_{\mu\mu} = 1.54^{+0.40}_{-0.32} \pm 0.06. \tag{63}$$

The uncertainty of $|a_S|_{\mu\mu}$ gives the dominant theoretical uncertainty in $K_L \to \pi^0\mu^+\mu^-$. Therefore, this measurement is a crucial piece of information required to establish the relative roles of indirect CP violation vs. direct CP violation in $K_L \to \pi^0\mu^+\mu^-$, in order to probe SD effects [312]. The LHCb Upgrade II can reach a precision in $\mathcal{B}(K_S^0 \to \pi^0\mu^+\mu^-)$ at the 10^{-10} level (see Fig. 33), and, through an analysis of the differential decay rate, a 10% statistical precision on the form factor term $|a_S|$ with free b_S [298].

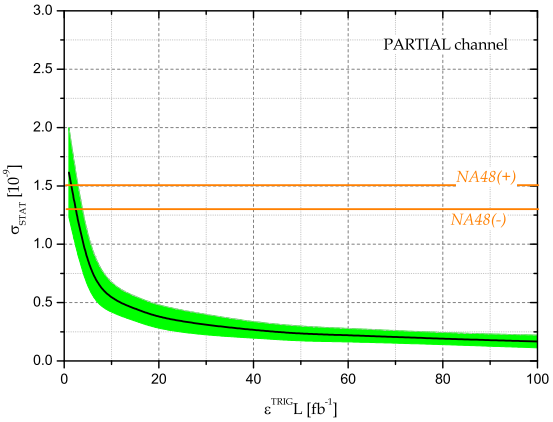

Fig. 33: Projected LHCb reach for $\mathcal{B}(K_S^0 \to \pi^0\mu^+\mu^-)$ as a function of the integrated luminosity times trigger efficiency (which is expected to be $\mathcal{O}(1)$ in LHCb Upgrade II. Figure adapted from Ref. [300].

4.4.1 Lepton flavor universality violation in $K^\pm \to \pi^\pm\ell^+\ell^-$

The coefficients a_+ and b_+ can be used to test for LFUV. If lepton flavour universality applies, each of the two coefficients, averaged over different experiments, have to be equal for the ee and $\mu\mu$ channels. Within errors this is indeed the case, see Table 22. Since the SM interactions are lepton flavour universal, deviations from zero in differences, such as $a_+^{\mu\mu} - a_+^{ee}$, would be a sign of NP. Such a test is especially interesting in view of the B-physics anomalies (see Sec. 7), with rare kaon decays providing a complementary role in testing the NP explanations. Our analysis [333] is based on the observation that at low energy scales, $\mu \ll m_{t,b,c}$, the strangeness-changing transitions are described in terms of the effective Lagrangian [323]

$$\mathcal{L}_{\rm eff}^{|\Delta S|=1} = -\frac{G_F}{\sqrt{2}} V_{ud}V_{us}^* \sum_i C_i(\mu)Q_i(\mu) + \text{h.c.}\,, \tag{64}$$

which contains semileptonic operators

$$Q_{7V} = [\bar{s}\gamma^\mu(1-\gamma_5)d] \sum_{\ell=e,\mu} \left[\bar{\ell}\gamma_\mu\ell\right], \quad \text{and} \quad Q_{7A} = [\bar{s}\gamma^\mu(1-\gamma_5)d] \sum_{\ell=e,\mu} \left[\bar{\ell}\gamma_\mu\gamma_5\ell\right], \tag{65}$$

that are the $s \to d$ analogues of the $b \to s$ operators, $Q_{9,10}^B$. In the framework of minimal flavour violation (MFV), the Wilson coefficients of the two sectors are correlated. We use this feature to convert knowledge of $C_{7V,7A}$ into bounds on $C_{9,10}^B$.

To convert the allowed range on $a_+^{\rm NP}$ into a corresponding range in the Wilson coefficients $C_{7V}^{\ell\ell}$, we make use of the $\mathcal{O}(p^2)$ chiral realization of the $SU(3)_L$ current

$$\bar{s}\gamma^\mu(1-\gamma_5)d \leftrightarrow i f_\pi^2 (U\partial^\mu U^\dagger)_{23}\,, \qquad U = U(\pi, K, \eta)\,, \tag{66}$$

to obtain

$$a_+^{\rm NP} = \frac{2\pi\sqrt{2}}{\alpha} V_{ud}V_{us}^* C_{7V}^{\rm NP}\,. \tag{67}$$

Contributions due to NP in $K^+ \to \pi^+\ell^+\ell^-$ can then be probed by considering the difference between the two channels

$$C_{7V}^{\mu\mu} - C_{7V}^{ee} = \alpha \frac{a_+^{\mu\mu} - a_+^{ee}}{2\pi\sqrt{2}V_{ud}V_{us}^*}\,. \tag{68}$$

Assuming MFV, this can be converted into a constraint on the NP contribution to C_9^B,

$$C_9^{B,\mu\mu} - C_9^{B,ee} = -\frac{a_+^{\mu\mu} - a_+^{ee}}{\sqrt{2}V_{td}V_{ts}^*} \approx -19 \pm 79\,, \tag{69}$$

where we have averaged over the two electron experiments listed in Table 22.

The determination of $a_+^{\mu\mu} - a_+^{ee}$ needs to be improved by an $\mathcal{O}(10)$ factor in order to probe the parameter space relevant for the B-anomalies, which require Wilson coefficients $C_{9,10}^B = \mathcal{O}(1)$ [334]. Improvements of this size may be possible at NA62, especially for the experimentally cleaner dimuon mode which currently has the larger uncertainty.

4.5 $K_S \to \pi^+\pi^- e^+ e^-$

The $K_S \to \pi^+\pi^- e^+ e^-$ decays can be interesting, if one can test beyond the dominant bremsstrahlung contribution, performing ChPT tests. In principle, CP violation is also of interest for NP searches. So far, NA48 has, using 676 events, obtained a measurement $\mathcal{B}(K_S \to \pi^+\pi^- e^+ e^-) = (4.79 \pm 0.15) \times 10^{-5}$, [310] to be compared with the theoretical prediction [335]

$$\mathcal{B}(K_S \to \pi^+\pi^- e^+ e^-) = \underbrace{4.74 \cdot 10^{-5}}_{\text{Brems.}} + \underbrace{4.39 \cdot 10^{-8}}_{\text{Int.}} + \underbrace{1.33 \cdot 10^{-10}}_{\text{DE}}\,. \tag{70}$$

Similarly, one can predict for the dimuon channel,

$$\mathcal{B}(K_S \to \pi^+\pi^- \mu^+ \mu^-) = \underbrace{4.17 \cdot 10^{-14}}_{\text{Brems.}} + \underbrace{4.98 \cdot 10^{-15}}_{\text{Int.}} + \underbrace{2.17 \cdot 10^{-16}}_{\text{DE}}\,. \tag{71}$$

The LHCb upgrade expects a yield of up to 5×10^{-4} events per fb-1 [336].

4.6 LFV modes

Modes with LFV, such as $K \to (n\pi)\mu^\pm e^\mp$, provide null tests of the SM. The interest on such processes has been renewed because they can receive sizable contributions from BSM addressing the hints for LFUV in $B \to K^{(*)}\ell^+\ell^-$. Both types of processes can arise from NP contributions to the product of the two neutral currents, composed of the down-type quarks and charged leptons. The only difference between the two is the strength of the flavour couplings involved. Using general EFT arguments, the amount of LFUV hinted at in $B \to K^{(*)}\ell^+\ell^-$ decays, generically imply $B \to K^{(*)}$ LFV rates of the order of 10^{-8} [337]. (More quantitative estimates require introduction of flavour models [265, 333, 338–348].)

As discussed in Ref. [301], such arguments can be extended to $K \to (\pi)\mu^\pm e^\mp$, with fairly general assumptions on different flavour couplings involved. Expected rates can be as large as $10^{-10} - 10^{-13}$ for the $K_L \to \mu^\pm e^\mp$ mode and a factor of ~ 100 smaller for the $K^+ \to \pi^+\mu^\pm e^\mp$ one. Taking into account the suppression mechanisms at play, such "large" rates are a non-trivial finding. The relatively wide predicted ranges are due to the inherent model dependence, especially in the choice of the leptonic coupling and of the overall scale of the new interaction, typically between 5 and 15 TeV [301]. On the experimental side, the limits on $K \to (\pi)\mu^\pm e^\mp$ modes are, somewhat surprisingly, decades-old

$$\begin{aligned} &\mathcal{B}(K_L \to e^\pm\mu^\mp) < 4.7 \times 10^{-12} \quad [349]\,, && \mathcal{B}(K_L \to \pi^0 e^\pm\mu^\mp) < 7.6 \times 10^{-11} \quad [350]\,, \\ &\mathcal{B}(K^+ \to \pi^+ e^-\mu^+) < 1.3 \times 10^{-11} \quad [351]\,, && \mathcal{B}(K^+ \to \pi^+ e^+\mu^-) < 5.2 \times 10^{-10} \quad [352]\,. \end{aligned} \tag{72}$$

These modes can be profitably pursued at the upgraded LHCb, which will benefit from huge yields. Ref. [301] presented a feasibility study for the modes in Eq. (72), taking $K^+ \to \pi^+\mu^\pm e^\mp$ as a benchmark. The expected reach is displayed in Fig. 34 as a function of the integrated luminosity and for different

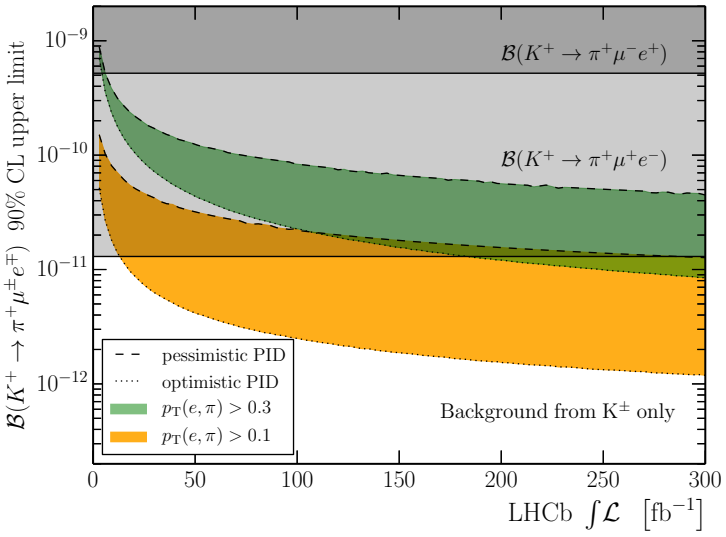

Fig. 34: Expected reach for $K^+ \to \pi^+\mu^\pm e^\mp$ as a function of the integrated luminosity with 13 TeV pp collisions based on a fast simulation of LHCb. Different scenarios in terms of PID performance and p_T thresholds of the π^+ and $e^\pm$ candidates are shown. Combinatorial background is neglected in the study. Figure adapted from Ref. [301].

scenarios of detector performance. This shows that LHCb Upgrade II could update some of the existing limits, a result that per se already makes these searches promising. Even more interestingly, LHCb Upgrade II could probe part of the parameter space for LFV kaon decays suggested by the B-physics anomalies. This conclusion in turn calls attention to other running and upcoming facilities, including Belle-II, NA62 [353], as well as the newly proposed TauFV [354]. Dedicated sensitivity studies for these facilities are required in order to make more quantitative statements. Yet, the experimental outlook for all these modes is certainly promising.

4.7 Hyperons at HL-LHC

The LHCb can contribute significantly to the strangeness-physics programme with measurements of hyperon decays. There is vast room for improvement in this sector as most of the data for the standard modes, both in nonleptonic and semileptonic decays, is about 40 years old, and many of the rare decays sensitive to SD physics have not even been searched for. An exploratory study of the LHCb's potential in hyperon physics was presented in [355]; here we summarize the main conclusions.

Current experimental data on the semileptonic hyperon decays $\Lambda \to p\mu^-\bar{\nu}$, $\Xi^- \to \Lambda\mu^-\bar{\nu}$ and $\Xi^- \to \Sigma^0\mu^-\bar{\nu}$ is quite poor, with relative uncertainties in the range of 20%-100%. These decay modes can be partially reconstructed at the LHCb, where the kinematic distributions allow one to discriminate from the peaking backgrounds of $\Lambda \to p\pi^-$ and $\Xi^- \to \Lambda\pi^-$. Besides testing lepton-universality by comparing with the semi-electronic modes, these decays are sensitive to BSM scalar and tensor currents [356]. If percent precision is achieved in the measurement of semi-muonic branching fractions, they could contribute to a better determination of the CKM matrix element $|V_{us}|$ from hyperon decays [357–360].

A golden mode among the rare hyperon decays is $\Sigma^+ \to p\mu^+\mu^-$, to which LHCb recently contributed with an evidence for the decay at 4.1σ and a di-muon invariant distribution consistent with the SM [361], thus challenging the HyperCP anomaly [362]. With dedicated triggers and the upgraded LHCb detector in the HL phase about a thousand events per year of data-taking could be measured, which will allow one to measure angular distributions or direct CP asymmetries that have been shown to be sensitive to SD physics [262, 363]. The equivalent channel with lepton number violation, $\Sigma \to \bar{p}\mu^+\mu^+$ can also be searched for, with potential sensitivities at the 10^{-9} level. Other $\Delta S = 1$ semileptonic rare hyperon

decays, except those of the Ω^- (which will be produced at a rate similar to that of a B-meson), must have electrons in the final state due to phase space. Sensitivity to $\mathcal{B}(\Sigma^+ \to pe^+e^-) \sim 10^{-6}$ should be accessible at LHCb, whereas other modes like $\Lambda \to p\pi^-e^+e^-$ suffer from low electron reconstruction efficiency. More exotic modes, probing baryon-number violation, lepton-flavor violation, or $\Delta S = 2$, can also be measured with projected sensitivities improving by orders of magnitude the current limits [355]. Radiative decays such as $\Lambda \to p\pi\gamma$ are also accessible to LHCb.

5 Tau leptons

Authors (TH): Vincenzo Cirigliano, Martin Gonzalez-Alonso, Adam Falkowski, Emilie Passemar.

The physics of the tau lepton is an exceptionally broad topic, both experimentally and theoretically. A large variety of processes involving taus have been used in the last decades to learn about fundamental physics [364]. In some cases the results obtained in e^+e^- machines [365] are very hard to improve in the LHC environment, due to large backgrounds, even if the number of taus produced is much larger. This is the case, *e.g.*, for the study of basic tau properties (mass, lifetime, etc.) or the standard tau decay channels. However, there are also many processes involving taus that are relevant for HL/HE-LHC. Here we focus on those that are more directly connected to flavour and that are not covered by other sections (for instance $h \to \tau\tau$, $h \to \tau\ell$, Sec. 9 or heavy meson decays to taus, Sec. 7).

To simplify the discussion we will assume that the scale of New Physics (NP) relevant for the processes under consideration is much heavier than the energy scales probed by the LHC. We can then use the SMEFT framework [366]. We first discuss lepton flavour conserving observables, where the SM contribution has to be calculated with some accuracy in order to probe NP. In contrast, the SM contribution is negligible for lepton flavour violating processes, where the challenges are purely experimental. As a result, the NP scales that are probed are much higher in the latter case.

5.1 Lepton-flavour-conserving processes

Collider phenomenology is usually very different for the so-called vertex corrections and contact interactions. For vertex corrections the NP contributions mimic the structure of the SM gauge couplings, $Z\tau\tau$ and $W\tau\nu$. Their study requires, in most cases, very precise measurements, which are challenging in a hadron collider. On the other hand, four-fermion contact interactions (generated for example by the tree-level exchange of a heavy mediator) give a contribution to high-energy observables qualitatively different from the SM one. For instance, a contribution from an off-shell mediator grows with the partonic center of mass energy, and thus one does not require very high precision in order for the measurements to probe interesting NP scales [367, 368]. For these contact interactions, we focus on flavour-diagonal couplings involving first-generation quarks and third-generation leptons.

5.1.1 High-energy tails

LHC measurements of differential distributions in the Drell-Yan lepton production can be sensitive to new effective interactions between leptons and quarks [367, 368]. As an example, consider that the following dimension-6 interaction is added to the SM Lagrangian,

$$\mathcal{L} \supset \frac{C_{lq}^{(3)}}{\Lambda^2}(\bar{L}_3\gamma_\mu\sigma^i L_3)(Q_1\gamma^\mu\sigma^i Q_1), \tag{73}$$

where σ^i are the Pauli matrices, $L_3 = (\nu_L^\tau, \tau_L)$ is the 3rd generation lepton doublet, and $Q_1 = (u_L, d_L)$ is the 1st generation quark doublet. This interaction term can be interpreted as an effective field theory (EFT) description of a more fundamental theory, for example an exchange of an $SU(2)$ triplet of vector bosons with masses $m_V = \Lambda \gg v$ that couples to L_3 and Q_1 with coupling strength $g_V \approx 2|C_{lq}^{(3)}|^{1/2}$. Even when m_V is too heavy to be directly produced at the LHC, the effective interaction in Eq. (73) may produce observable effects, and therefore provide information about the theory that completes the SM.

At the LHC, contact interactions between quarks and 3rd generation leptons can be probed via the processes $pp \to \tau^+\tau^- X$ and $pp \to \tau\nu X$ [369, 370]. Here we focus on the latter, taking as a template the existing Run-2 ATLAS analysis in Ref. [371]. This measured the $\tau\nu$ transverse mass distribution, where the transverse mass is given by $m_T = \sqrt{2p_{\rm T}E_T(1-\cos\phi)}$, with $\vec{p_{\rm T}}$ the transverse momentum of the (hadronic) tau candidate, $\vec{E}_T$ the missing transverse momentum, and ϕ the azimuthal angle between the two. The effects of the interaction in Eq. (73) are most pronounced at higher m_T.

To estimate the current and future sensitivity, we pick $m_T > 1.8$ TeV as our signal region (a more elaborate analysis with a wider, binned, m_T range would lead to stronger bounds [370]). Using the `Madgraph` [372]/`Pythia 8` [373]/`Delphes` [374] simulation chain and imposing the selection cuts we can estimate the expected number of events in the presence of the interaction in Eq. (73):

$$N_{pp\to\tau\tau}^{m_T>1.8\ \text{TeV}} \approx \left(\frac{\mathcal{L}}{36.1\ \text{fb}^{-1}}\right)\left[0.36 + 4.0\times 10^3 \frac{C_{lq}^{(3)} v^2}{\Lambda^2} + 3.6\times 10^5 \left(\frac{C_{lq}^{(3)} v^2}{\Lambda^2}\right)^2\right], \qquad (74)$$

where $\mathcal{L}$ is the integrated luminosity, $v \approx 246$ GeV, and we will ignore the theoretical error of this estimation. The ATLAS collaboration observed 0 events in $\mathcal{L} = 36.1\ \text{fb}^{-1}$ [371], from which one can derive the 68% CL limit on the Wilson coefficient in Eq. (73): $-(5.3\ \text{TeV})^{-2} \le C_{lq}^{(3)}/\Lambda^2 \le (7.7\ \text{TeV})^{-2}$. For the HL-LHC with $\mathcal{L} = 3000\ \text{fb}^{-1}$, assuming the observed number of events will be exactly equal to the SM prediction, the expected limit becomes

$$-\frac{1}{(17.5\ \text{TeV})^2} \le \frac{C_{lq}^{(3)}}{\Lambda^2} \le \frac{1}{(20.5\ \text{TeV})^2} \qquad @\ 68\%\ \text{CL}. \qquad (75)$$

Compared to the present LHC bound, this represents an $\mathcal{O}(10)$ stronger bound on $C_{lq}^{(3)}/\Lambda^2$, or $\mathcal{O}(3)$ times improvement in the reach for the mass scale of NP. Assuming maximally strongly coupled NP, $g_V \sim 4\pi$, the HL-LHC can probe particles even as heavy as $m_V \sim 100$ TeV.

There are 3 more independent dimension-6 operators that can be probed by the $pp \to \tau\nu$ process: $O_{ledq} = (\bar{L}_3\tau_R)(\bar{d}_R Q_1)$, $O_{lequ} = (\bar{L}_3\tau_R)(Q_1 u_R)$, and $O_{lequ}^{(3)} = (\bar{L}_3\sigma_{\mu\nu}\tau_R)(\bar{Q}_1\sigma^{\mu\nu}u_R)$ [367, 375]. We estimate that the HL-LHC will be sensitive to $C/\Lambda^2 \sim (10\ \text{TeV})^{-2}$ through a one-bin analysis like the one presented above. The slightly smaller sensitivity than for the operator in Eq. (73) follows from the fact that these do not interfere with the SM amplitudes, and thus their effect enters only at quadratic order in C/Λ^2. [3]

We expect that our simple analysis provides a good qualitative estimate of the HL-LHC reach. However, a more sophisticated analysis using the full information about the m_T distribution (such as in Ref. [370]), and possibly also about the τ polarization, should lead to a further $\mathcal{O}(1)$ increase of sensitivity. Ideally, the optimal analysis should be able to distinguish between different dimension-6 operators (except between O_{ledq} and O_{lequ}, which give exactly the same contribution to the $pp \to \tau\nu$ cross section), and provide constraints on the Wilson coefficients in the situation when all the independent operators are simultaneously present. Furthermore, the process $pp \to \tau^+\tau^-$ probes a large set of dimension-6 operators: $O_{lq} = (\bar{L}_3\gamma_\mu L_3)(Q_1\gamma^\mu Q_1)$, $O_{lu} = (\bar{L}_3\gamma_\mu L_3)(\bar{u}_R\gamma^\mu u_R)$, $O_{ld} = (\bar{L}_3\gamma_\mu L_3)(\bar{d}_R\gamma^\mu d_R)$, $O_{eq} = (\bar{\tau}_R\gamma_\mu\tau_R)(\bar{Q}_1\gamma^\mu Q_1)$, $O_{eu} = (\bar{\tau}_R\gamma_\mu\tau_R)(\bar{u}_R\gamma^\mu u_R)$, and $O_{ed} = (\bar{\tau}_R\gamma_\mu\tau_R)\ (\bar{d}_R\gamma^\mu d_R)$, in addition to the operators discussed above. We expect comparable sensitivity of $pp \to \tau^+\tau^-$ to C/Λ^2 as in the case of $pp \to \tau\nu$ [367]. It is unlikely that the LHC alone can discriminate between all these operators; to this end combining with low energy precision measurements of τ decays will be necessary. Finally, we mention that $\tau\tau$ and $\tau\nu$ production also probes analogous operators with heavier (s, c, b) quarks instead of the 1st generation ones [369, 377, 378]. The presence of such operators in the Lagrangian can be motivated by the anomalies observed by BaBar and LHCb in the $B \to D^{(*)}\tau\nu$ decays [379–381] (see Sec 7).

5.1.2 Beyond tails: lepton flavour universality

It has been pointed out recently that there is an interesting complementarity between the high-energy searches and low-energy precision studies, presented above, and hadronic tau decays [370]. The latter

[3] Contributions from SMEFT dim-8 operators are assumed to be subleading with respect to dim-6 squared terms. Although not true in general, this is indeed the case for strongly coupled UV completions [376].

are equally sensitive to vertex and contact interactions, and thus effectively become model-independent probes of LFU violations in the $W\tau\nu$ vertex once the strong LHC bounds described above are taken into account. This is interesting because the only low-energy model-independent measurement of this effect, which was carried out at LEP2, found a $\sim 2\sigma$ tension with LFU [382, 383]. Including also hadronic tau decays and LHC bounds on contact interactions, the result is improved by a factor of two, but the (dis)agreement with LFU remains at the $\sim 2\sigma$ level: $\delta g_L^{W\tau} - \delta g_L^{We} = 0.0134(74)$ [370].

Finally, it is interesting to mention the possibility of accessing LFU violations in the vertex corrections at the (HL/HE) LHC. In the ratio of $W \to \tau\nu$ and $W \to \ell\nu$ many experimental and QCD uncertainties cancel, which make a per-cent level extraction a bit less complicated. In fact, past studies carried out by the D0 collaboration [384] showed that such precision is indeed possible in a collider environment.

5.2 Lepton Flavour Violation

Lepton Flavour Violating (LFV) processes involving charged leptons are very interesting because their observation would be a clear indication of physics beyond the SM. While lepton family number is an accidental symmetry of the SM, we know it must be broken in order to account for neutrino masses and mixings. If the only low-energy manifestations of LFV are neutrino masses and mixings (which corresponds to a very high scale for LFV), then charged LFV amplitudes are suppressed by the GIM mechanism and the predicted rates are un-observably small, e.g., $\mathcal{B}(\mu \to e\gamma) \sim 10^{-52}$, $\mathcal{B}(\tau \to \mu\gamma) \sim 10^{-45}$ and $\mathcal{B}(\tau \to 3\mu) \sim 10^{-54}$ [385–388]). However, if the breaking of the lepton family symmetry happens not too much above the electroweak symmetry breaking scale, as borne out in many NP scenarios, then one can expect charged LFV BRs quite close to existing limits, and therefore within reach of ongoing searches. In fact in some cases experimental limits are already excluding regions of parameter space in specific weak scale NP models. While less severe than in the quark sector, one has a "flavour problem" in the lepton sector as well.

A rich literature exists on this topic, including studies in supersymmetric extensions of the SM, little Higgs models, low-scale seesaw models, leptoquark models, Z' models, left-right symmetric models, and extended Higgs models. For recent reviews on both theoretical and experimental aspects we refer the reader to Refs. [389, 390]. Current limits on BRs in μ-e transitions are at the level of 10^{-13} (e.g. $\mathcal{B}(\mu^+ \to e^+\gamma) < 4.2 \times 10^{-13}$ (90% CL) [391]), while τ-μ and τ-e BRs are bound at the 10^{-8} level [197]. As discussed below, improvements in LFV τ decays will offer the opportunity to explore *(i)* correlations with μ-e transitions, probing underlying sources of flavour breaking; *(ii)* correlations among different LFV τ decays, probing the nature of the underlying mechanism. In parallel to the ambitious programme constraining LFV for tau lepton, a similar programme exists in the muonic sector improving the limit on $\mu \to e\gamma$ with MEGII [392, 393], $\mu \to 3e$ with Mu3e [394, 395], and $\mu \to e$ conversion on Aluminium target with Mu2e [396] at Fermilab and COMET [397] at JPARC and on silicon-carbide and graphite target with DeeMe at JPARC [398, 399]. LFV studies can also be performed in B and D decays, as well as the decays of $c\bar{c}$ and $b\bar{b}$ quarkonia, though the effective NP scale reach is lower, see, e.g., [400, 401]. Probing the relative strength of $\mu \to e$ and $\tau \to \mu$ LFV transitions will shed light on the underlying sources of family symmetry breaking in the lepton sector and their link to the quark sector in grand unified scenarios.

Finally, LFV decay modes of the Z^0 are also of considerable interest. Their BRs in the SM are again negligible, $\mathcal{B}(Z \to e^\pm\mu^\mp) \sim \mathcal{B}(Z \to e^\pm\tau^\mp) \sim 10^{-54}$, $\mathcal{B}(Z \to \mu^\pm\tau^\mp) \sim 10^{-60}$ and the LHC can obtain competitive bounds in some of these channels [402]. The current upper limits are due to LEP measurements (at 95% CL) [403–406],

$$\mathcal{B}(Z \to e^\pm\mu^\mp) < 1.7 \times 10^{-6}, \quad \mathcal{B}(Z \to e^\pm\tau^\mp) < 9.8 \times 10^{-6}, \quad \mathcal{B}(Z \to \mu^\pm\tau^\mp) < 1.2 \times 10^{-5}, \tag{76}$$

while the ATLAS Collaboration has recently obtained the following 95% CL upper limits: $\mathcal{B}(Z \to e^\pm\tau^\mp) < 5.8 \times 10^{-5}$ [407], and $\mathcal{B}(Z \to \mu^\pm\tau^\mp) < 1.3 \times 10^{-5}$ [407]. The HL/HE LHC will therefore

provide the best limit on LFV Z decays. The detection of a signal in the $Z^0 \to \ell\ell'$ channel, in combination with the information from charged lepton LFV decays, would also allow one to learn about features of the underlying LFV dynamics. An explicit example is provided by the Inverse Seesaw (ISS) and "3+1" effective models which add one or more sterile neutrinos to the particle content of the SM [408] (see also, e.g., Ref. [409–411]).

5.2.1 Lepton Flavour Violation in τ decays

Tau decays offer a rich landscape to search for CLFV. The τ lepton is heavy enough to decay into hadrons. Until now already 48 LFV modes have been bounded at the level of 10^{-8} [197], as can be seen in Fig. 35.

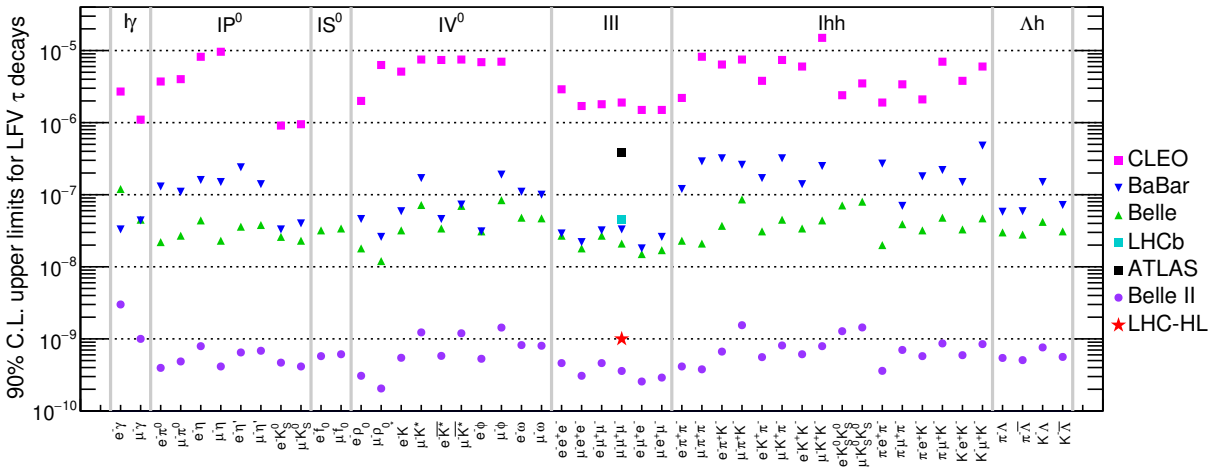

Fig. 35: Bounds on Tau Lepton Flavour Data from the existing experiments are compiled by HFLAV [197]; projections of the Belle-II bounds were performed by the Belle-II collaboration assuming 50 ab^{-1} of integrated luminosity [196].

The B factories, BaBar and Belle, have improved by more than an order of magnitude [412–424] the previous CLEO bounds [425–427] for a significant number of modes. Some of the modes, for instance, $\tau \to \ell\omega$, have been bounded for the first time [413].

Table 23 shows a list of limits obtained for the $\tau \to 3\mu$ channel by different experiments. The strongest limits come from the B-factories, with a competitive limit obtained by LHCb [428]. Table 23 also contains the recent measurement by ATLAS [429], as well as the expected limit from the Belle-II experiment at the SuperKEKB collider, which will improve current limits by almost two orders of magnitude [196]. Finally, Table 23 also summarizes the expected limits from the HL-LHC that we discuss in more detail below.

The physics reach and model-discriminating power of LFV tau decays is most efficiently analyzed above the electroweak scale using SMEFT, and in a corresponding low-energy EFT when below the weak scale [430]. Several classes of dimension-six operators contribute to LFV tau decays at the low-scale, with effective couplings denoted by C_i/Λ^2. Loop-induced dipole operators mediate radiative decays $\tau \to \ell\gamma$ as well as purely leptonic $\tau \to 3\ell$ and semi-leptonic decays. Four-fermion – both four-lepton and semi-leptonic – operators with different Dirac structures can be induced at tree-level or loop-level, and contribute to $\tau \to 3\ell$ and $\tau \to \ell + \text{hadrons}$. As a typical example, we note that current limits on $\tau \to \mu\gamma$ probe scales on the order of $\Lambda/\sqrt{C_{\text{Dipole}}} \sim 500$ TeV. Besides probing high scales, LFV τ decays offer two main handles to discriminate among underlying models of NP, i.e., to identify which operators are present at low energy and what is their relative strength: (i) correlations among different LFV τ decay rates [430]; (ii) differential distributions in higher multiplicity decays, such as the $\pi\pi$ invariant mass in $\tau \to \mu\pi\pi$ [430] and the Dalitz plot in $\tau \to 3\mu$ [431, 432].

Table 23: Actual and expected limits on BR($\tau \to 3\mu$) for different experiments and facilities. The ATLAS projections are given for the medium background scenario, see main text for further details.

BR($\tau \to 3\mu$) (90% CL limit)	Ref.	Comments
3.8×10^{-7}	ATLAS [429]	Actual limit (Run 1)
4.6×10^{-8}	LHCb [428]	Actual limit (Run 1)
3.3×10^{-8}	BaBar [417]	Actual limit
2.1×10^{-8}	Belle [423]	Actual limit
3.7×10^{-9}	CMS HF-channel at HL-LHC	Expected limit (3000 fb^{-1})
6×10^{-9}	ATLAS W-channel at HL-LHC	Expected limit (3000 fb^{-1})
2.3×10^{-9}	ATLAS HF-channel at HL-LHC	Expected limit (3000 fb^{-1})
$\mathcal{O}(10^{-9})$	LHCb at HL-LHC	Expected limit (300 fb^{-1})
3.3×10^{-10}	Belle-II [196]	Expected limit (50 ab^{-1})

In addition to Belle-II, HL/HE LHC will be able to search for the "background-free" $\tau \to 3\mu$. A detailed summary of projected sensitivities is given below. This is a particularly crucial discovery mode when LFV is introduced at tree-level, for example by the exchange of Z' or doubly charged Higgs bosons. Efforts should also go into understanding the backgrounds and improving the sensitivity in semi-leptonic three-body decays $\tau \to \mu\pi^+\pi^-$ and $\tau \to \mu K\bar{K}$, which have a particularly high discovery potential in Higgs-mediated [433–435] or leptoquark-mediated LFV. If LFV is discovered, these modes also have significant model-diagnosing power because of their Dalitz structure, and therefore also probe a wider class of models than the dominant one-loop-induced LFV process $\tau \to \mu\gamma$. Of particular interest is the sensitivity of $\tau \to \mu\pi\pi$ to extended Higgs sectors and to non-standard Yukawa couplings of the SM Higgs to light quarks and leptons [430, 434]. This channel also allows a particularly robust theoretical interpretation thanks to advances in the calculation of all the relevant hadronic form factors [434].

5.2.2 HL-LHC experimental prospects

The LHC proton collisions at 13 TeV produce τ leptons with a cross-section five orders of magnitude larger than at Belle II. As a result, during the HL-LHC running period, about 10^{15} τ leptons will be produced in 4π. Most will be produced in the decay of heavy flavour hadrons, specifically D_s meson decays. This high production cross-section compensates for the higher background levels and lower integrated luminosity, in particular for the $\tau \to 3\mu$ golden mode. Background events arise dominantly from badly reconstructed heavy flavour decays like $D_s^+ \to \eta(\mu^+\mu^-\gamma)\mu^+\nu_\mu$, lepton fakes from hadrons ($c\bar{c}/b\bar{b} \to X\mu\mu$), and pile-up. A particular challenge for this production channel is the soft momentum spectrum of the τ decay products, which places stringent requirements on both the trigger and offline reconstructions of all the HL-LHC experiments.

W and Z bosons offer a complementary source of τ leptons. Their production cross sections are considerably smaller than those for B and D mesons, but τ leptons from W and Z afford much cleaner experimental signatures with far better signal-to-background ratios for CMS and ATLAS; the LHCb forward geometry is less well suited to exploting these decays. For instance, in a $\tau \to 3\mu$ search relying on $W \to \tau\nu$ decays as a source of τ leptons, one can benefit from τ leptons having relatively large transverse momenta and being isolated, from large missing transverse momentum $p_{\mathrm{T}}^{\mathrm{miss}}$ in an event, and from the transverse mass of the τ-$p_{\mathrm{T}}^{\mathrm{miss}}$ system being close to the W mass.

Detector improvements planned for the HL-LHC period will significantly enhance the capabilities of all three experiments in this area. In the case of ATLAS, the installation of a new tracking system will improve the vertex and momentum resolution. The trigger system upgrade will include additional capabilities, ultimately improving the online selection, and allowing to maintain a low muon triggering

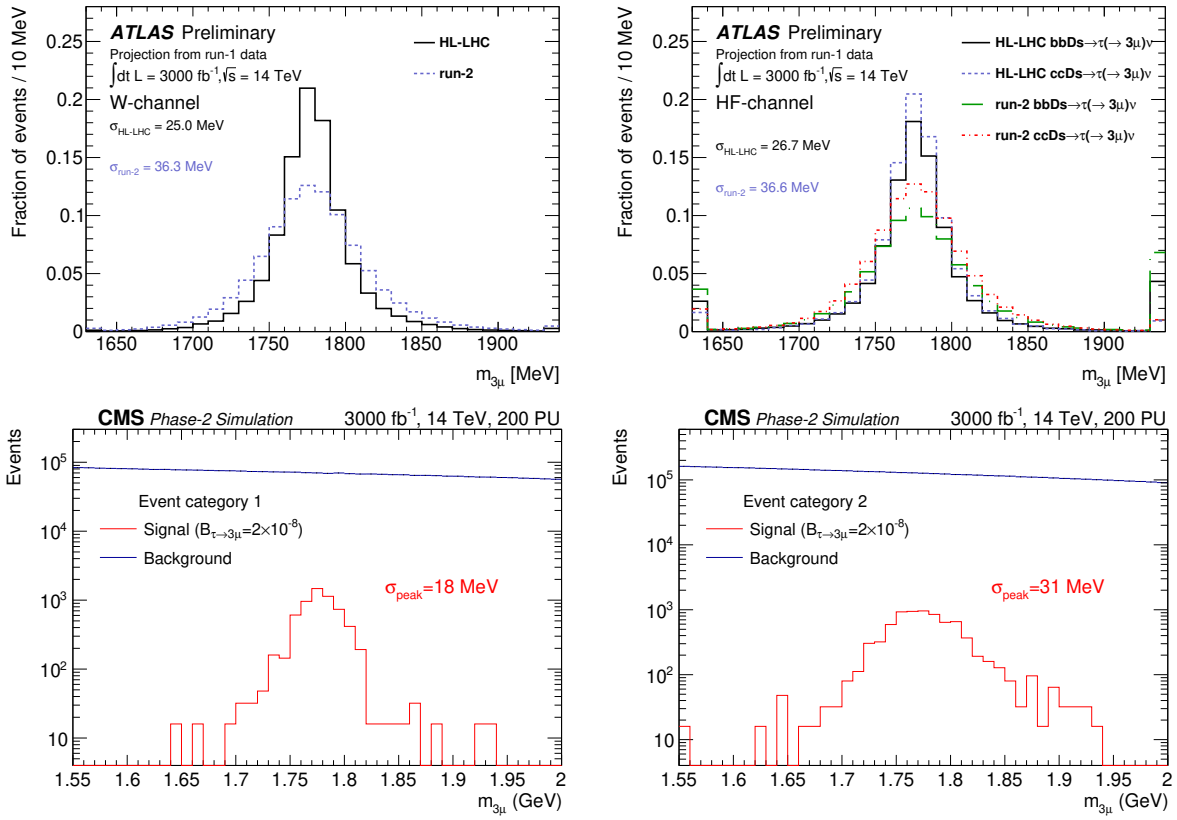

Fig. 36: (Top) Comparison of ATLAS tau mass resolutions in the W- (left) and HF-channels (right) in Run-2 and under HL-LHC detector conditions. Widths are estimated from a double-Gaussian fit. (Bottom) CMS trimuon invariant mass $m_{3\mu}$ for the $\tau \to 3\mu$ signal (red) and background (blue) after all event selection cuts, for Category 1 (left) and Category 2 (right) events, as defined in the text. The signal is shown for $\mathcal{B}(\tau \to 3\mu) = 2 \times 10^{-8}$. CMS results refer to the HF channel; plots are taken from [436] .

threshold. The CMS upgraded muon system, whose coverage is extended from $|\eta|$ = 2.4 to 2.8, increases the signal fiducial acceptance by a factor of two and, also, enhances the capability to trigger on and reconstruct low momentum muons [436]. The additional events with muons at high $|\eta|$ have worse trimuon mass resolution. Hence, two event categories are introduced: Category 1 for events with all three muons reconstructed only with the Phase-1 detectors, and Category 2 for events with at least one muon reconstructed by the new triple Gas Electron Multiplier (GEM) detectors, which will be installed in the first station of the upgraded muon system. The impact of the proposed ATLAS detector upgrades and CMS event categories is shown in Fig. 36. In the case of LHCb, the deployment of a fully software trigger will remove one of the key sources of inefficiency in the current analysis. In addition, the proposed calorimeter improvements during the LHCb Upgrade II will play an important role in suppressing backgrounds such as $D_s^+ \to \eta(\mu^+\mu^-\gamma)\mu^+\nu_\mu$.

The extrapolated sensitivities for ATLAS and CMS are shown in Fig. 37 and Tables 24 and 25. The ATLAS sensitivities [437] are extrapolated based on the Run 1 measurement [429] taking into account the expected detector improvements. Three scenarios for the acceptance, efficiency and background yields are considered. Systematic uncertainties are extrapolated from the Run-1 measurement scaling down by the increased statistics with preserved constant terms for the reconstruction efficiency. A 15% systematic uncertainty dominated by the background estimation is derived. Varying the systematic uncertainty by 5% translates into a 10% change of the expected upper limit. Limits of up to $\mathcal{B}(\tau \to 3\mu) = 1.03(5.36) \times$

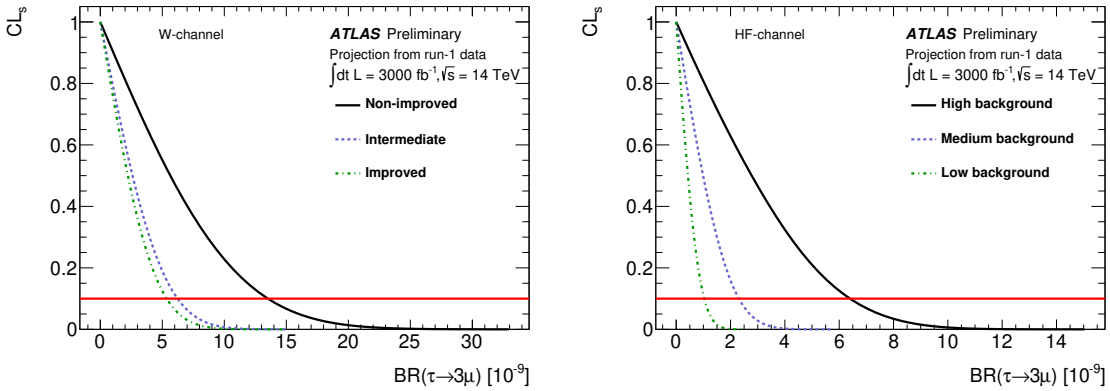

Fig. 37: ATLAS extrapolated CL_s versus the $\tau \to 3\mu$ branching fraction, BR($\tau \to 3\mu$) for each of the discussed scenarios in the W-channel (left) and HF-channel (right). The horizontal red line denotes the 90% CL. The limit is obtained from the intersection of the CLs and this line.

Table 24: Summary of the ATLAS expected 90% CL upper limit on $\mathcal{B}(\tau \to 3\mu)$ for an assumed luminosity of 3 ab^{-1} of pp collisions at $\sqrt{s} = 14$ TeV in the W and Heavy Flavour (HF) channels, for different signal and background yield scenarios.

Scenario	W-channel 90% CL UL [10^{-9}]	HF-channel 90% CL UL [10^{-9}]
ATLAS High	5.4	1
ATLAS Medium	6.2	2.3
ATLAS Low	13.5	6.4

10^{-9} are derived in the HF-(W-)channel. In the case of CMS, the absence of tails in the signal trimuon mass distribution, shown in Fig. 36, demonstrates the robustness of the reconstruction even at the high pileup (PU=200) of HL-LHC. The projected exclusion sensitivity in the absence of a signal is $\mathcal{B}(\tau \to 3\mu) < 3.7 \times 10^{-9}$ at 90% CL, while the expected 5 σ-observation sensitivity is $\mathcal{B}(\tau \to 3\mu) = 1.1 \times 10^{-8}$. CMS studies focusing on τ leptons originating from W boson decays are ongoing.

Extrapolations based on the current LHCb $\tau \to 3\mu$ result [428] and assuming no detector or trigger improvements show that, similarly to Belle II, CMS, and ATLAS, Upgrade II LHCb would also be able to probe branching ratios down to $\mathcal{O}(10^{-9})$. This will allow Upgrade II LHCb to independently confirm any earlier Belle II discovery, or to significantly improve the combined limit.

Table 25: (Top) The expected numbers of signal and background events in the mass window 1.55 -2.0 GeV for CMS. An integrated luminosity of 3000 fb^{-1} and a signal $\mathcal{B}(\tau \to 3\mu)$ = 2 $\times 10^{-8}$ is assumed. (Bottom) The search sensitivities for the combined categories.

	Category 1	Category 2
Number of background events	2.4 $\times 10^{6}$	2.6 $\times 10^{6}$
Number of signal events	4580	3640
Trimuon mass resolution	18 MeV	31 MeV
$\mathcal{B}(\tau \to 3\mu)$ limit per event category	4.3 $\times 10^{-9}$	7.0 $\times 10^{-9}$
$\mathcal{B}(\tau \to 3\mu)$ 90% C.L. limit	3.7×10^{-9}	
$\mathcal{B}(\tau \to 3\mu)$ for 3-σ evidence	6.7×10^{-9}	
$\mathcal{B}(\tau \to 3\mu)$ for 5-σ observation	1.1×10^{-8}	

6 Hadron spectroscopy and QCD exotica

Authors (TH): Angelo Esposito, Feng-Kun Guo, Juan Nieves, Alessandro Pilloni, Antonio Polosa, Sasa Prelovsek.

Determination of hadron spectrum is key to understanding the strong interactions, in particular the mechanisms underlying color confinement. While BESIII is the leading experiment in the charm region, and Belle II will make a major impact in the study of excited mesons and lighter exotic hadrons, only the HL-LHC experiments have the potential to comprehensively study the full range of possible excited hadronic states. Such a comprehensive understanding and characterisation of quark structures would not only, in some sense, greatly enhance the taxonomy of the SM particles, but would also sharpen our understanding of QCD in a particularly difficult energy regime. Moreover, while not directly probing BSM physics, spectroscopy measurements will continue to make essential contributions to the interpretation of any observed BSM effects in the flavour sector. In addition, spectroscopy can provide tools to probe BSM effects by using a new observed state as a tagger [438], [439].

While the Upgrade II of LHCb will by design offer unparalleled capabilities in this area, the legacy of HL-LHC for spectroscopy will be much stronger, if ATLAS and CMS are also able to continue to pursue this work in the HL-LHC period. The planned hardware tracking triggers and much higher data rates sent to their software triggers are promising in this respect, and we encourage further study of what capabilities they might bring to this area of physics. In particular, heavy-ion experiments might have an advantage for doubly-heavy exotics, if they can improve their particle identification.

Gauge theories play a major role in BSM and some of them might be strongly coupled. In this sense, QCD serves as a prototype of a strongly-coupled gauge theory. By studying hadron spectroscopy and the QCD exotica we learn about the range of possibilities of analogous states in BSM theories.

6.1 Open questions in spectroscopy

A large number of "exotic" experimental discoveries, which did not fit the expectations of the (until then) very successful valence quark model, as well as the unprecedented statistical precision obtained by LHCb, BESIII, and other experiments, have led to a recent renaissance of hadron spectroscopy. For recent reviews, see [196, 310, 440–448]. Understanding strong interactions at low energies requires an explanation of how the emergent hadron spectrum is organized, which can shed light on the confinement property of QCD.

To answer this question, a joint effort by experimental and theoretical communities is needed, making a combined use of all available tools, including lattice QCD results and effective field theory (EFT) methods, as well as phenomenological tools. The spectra of weakly decaying hadrons, as postdicted or predicted by lattice QCD, generally agree with the observed ones. Valuable conclusions can be drawn from the lattice also for several strongly decaying resonances, where the challenge increases with the number of open strong decay channels. From the phenomenological side, quark potential models, inspired by QCD, describe mesons as bound states of a valence quark-antiquark pair, and baryons as bound states of three valence quarks. One would expect these models [449–451] to work particularly well in describing the heavy quarkonium sector. They indeed do a very good job for the spectrum of charmonia and bottomonia below their respective open-flavor thresholds. This success can be connected with QCD by using nonrelativistic EFTs such as the ones described in Refs. [452–455].

However, other color configurations are allowed, such as mesons with two quarks and two antiquarks, and baryons with four quarks and one anti-quark, dubbed tetraquarks and pentaquarks, respectively.[4] These are examples of the so-called exotic hadrons which also include glueballs and hybrid hadrons with gluonic excitations. As already mentioned, their search has been an important theme in high-energy experiments, although plagued by several ambiguous claims. The key questions are: Can

[4] In fact, such configurations were already suggested in Gell-Mann's seminal paper on the quark model [456]. Multiquark configurations are also suggested, but not listed, in Zweig's original paper [457]. The name of "pentaquark" and a pioneering dynamical model first appeared in Ref. [458].

new states be unambiguously extracted from the experimental data? Are exotic hadrons really allowed by QCD? If yes, what kinds are allowed? Why are they so scarce? Can lattice QCD predict their spectrum? Is it possible to construct QCD-based phenomenological models for (at least) some of them?

The situation dramatically changed in 2003, when the charm-strange mesons $D^*_{s0}(2317)$, $D_{s1}(2460$ and the charmonium-like $X(3872)$ were discovered by the BaBar, CLEO and Belle Collaborations, respectively. None of them is in line with the predictions from potential quark models. For instance, their masses are lower than the predictions by Godfrey and Isgur by about 160 MeV, 70 MeV and 80 MeV, respectively [451]. As time passed, more and more unknown resonant structures were reported from various high-energy experiments, mostly BaBar, Belle, BESIII and LHCb. Many new structures, not compatible with predictions, have been found in the charmonium mass region. These are traditionally called XYZ states.[5] In particular, the isovector Z states are explicitly exotic, because they have nonzero isospin and at the same time contain a heavy $Q\bar{Q}$ pair. Similarly, LHCb [459] reported two structures in the $J/\psi\, p$ spectrum. If these were produced by real QCD baryon resonances (P_c), these states would contain at least five valence quarks/antiquarks. So far, there has been no consensus about the nature of these resonances, and some of the related experimental peaks might even receive large contributions from kinematical effects, making their interpretation as real states ambiguous. To resolve these issues, high statistics data and the search for signatures of these states in several different processes are highly desirable.

Next, we introduce briefly a few main types of models beyond the naive quark model for these intriguing exotic hadron candidates.

6.1.1 Tetraquarks

Two quarks and two antiquarks can lead to color singlets in different ways, which are difficult to choose from first principles. One possibility is for the constituents to be bound in a compact tetraquark (see, e.g., [460, 461]). For experimental reasons, the most studied systems are of the form $Q\bar{Q}q\bar{q}'$, where $Q = c, b$ and $q^{(\prime)}$ are light quarks. Their spectrum is well described in terms of diquarks, with a spin-spin interaction between the constituents given by $H_I = 2\kappa_{Qq}\big(\boldsymbol{S}_Q \cdot \boldsymbol{S}_q + \boldsymbol{S}_{\bar{Q}} \cdot \boldsymbol{S}_{\bar{q}'}\big)$, with no coupling between the constituents of different diquarks [461]. The chromomagnetic couplings κ are extracted from observed masses. It is found that two quasi-degenerate 1^{++} and 1^{+-} states are expected (identified with the $X(3872)$ and $Z_c(3900)$), together with a higher 1^{+-} state (the $Z'_c(4020)$). The same pattern should be replicated in the beauty system, where the two $Z_b(1^{+-})$'s have been discovered but the $X_b(1^{++})$ is still missing. The Z_c's and Z_b's are expected to fill in triplets of states, as confirmed experimentally. The X is an exception: only the neutral state is observed. This could be due to its accidental vicinity to threshold [462]. Moreover, the remarkable isospin violation observed in its decays can be explained by the fact that, being $\alpha_s(2m_c)$ small, the mixing between the mass eigenstates is suppressed [460, 463]. The $X^{\pm}$ components are forced to decay only into charmonia, and the computed rates lie below the current exclusion limits set experimentally. Decay modes such as, for example, $X^{\pm} \to J/\psi\rho^{\pm}$ should be eagerly sought in data.

Radial excitations are also possible, the charged $Z(4430)$ being the most remarkable example [460, 464, 465]. Its mass and decay modes fit perfectly a picture where it is the first radial excitation of the Z_c. Lastly, one also has orbital excitations, allowing for a 1^- spectroscopy. Prominent candidates are the observed $Y(1^-)$ states. An example is the $Y(4630) - Y(4660)$ system (identified as a single particle in [466]). Its mass fits the diquarkonium spectroscopy and its strong preference to decay into two baryons is easily explained by the breaking of the QCD string between the diquarks. For reviews see [440, 442, 443, 445, 467]. Remarkably, the X, $Z_c^{(\prime)}$ and $Z_b^{(\prime)}$ resonances are found experimentally

[5] Note that the naming scheme was changed in the 2018 edition of the Reviews of Particle Physics (RPP) by the Particle Data Group [310]. For charmonium(-like) states, the isoscalar states with quantum numbers J^{--}, J^{++} are called ψ_J, χ_{cJ}, respectively, and the isovector states with J^{--}, J^{+-} are called R_{cJ}, Z_{cJ}, respectively.

$\delta \lesssim 10$ MeV *above* their related meson-meson thresholds ($D^0\bar{D}^{*0}$ for the X, etc.). Their measured widths follow a $\Gamma = A\sqrt{\delta}$ law, with the same coefficient A for both charm and beauty states, as first observed in [468].

The above feature, the suppression of the interactions across different diquarks and the preference for decaying into open-flavour mesons, can be qualitatively explained with a separation in space of the two diquarks due to a (tiny) potential barrier between the two [462, 469–471]. With this conjecture, one can also understand why the discrepancy between the decay into quarkonia and open flavor is more prominent in the bottom sector than in the charm one. This would also make these exotic hadrons slightly larger than the standard ones (≈ 1.3 fm) [471]. The idea of the diquark–antidiquark pair being slightly separated in space has also been presented in [472], where it was shown that considering diquarks as dynamical and moving with respect to each other leads to an interesting way of computing tetraquark decays. The same picture has also been employed to study the spectrum of tetraquarks and possible selection rules for their decays [473], as well as to study pentaquarks [474]. Among other proposals to calculate the tetraquark spectrum, we recall the Born-Oppenheimer approximation, where the tetraquark is described as a heavy $Q\bar{Q}$ pair in color octet, immersed into an effective potential generated by the light pair, again in color octet. Under the assumption that the effective potential is the same as the one calculated on the lattice for heavy hybrids, the spectrum is derived [475]. Lastly, it was also proposed that the scaling of the tetraquark exclusive production cross section with the center-of-mass energy might reveal important information on the composite nature of these states [476, 477]. It follows that the study of production of exotic states is crucial.

6.1.2 Hadronic molecules

These are complex systems for which the dominant components are two or more interacting hadrons. For a review of theoretical and phenomenological aspects of hadronic molecules, with a focus on the new heavy-flavour hadrons, we refer to [444]. For a review focusing on the $X(3872)$, see [478].

The simplest hadronic molecule would be a loosely bound state of two hadrons (H_1, H_2) with a sizable extension. Such an object would be the analog to a neutron-proton pair bound to form a deuteron. If the physical state is located slightly below an S-wave threshold of two hadrons H_1 and H_2, the scattering length (a) and effective range (r) of the continuum $H_1 + H_2 \to H_1 + H_2$ scattering amplitude would be approximately given by

$$a = -2\frac{1-\lambda^2}{2-\lambda^2}\frac{1}{\gamma} + \mathcal{O}(\gamma/\beta), \qquad r = -\frac{\lambda^2}{1-\lambda^2}\frac{1}{\gamma} + \mathcal{O}(\gamma/\beta), \tag{77}$$

where $\gamma = \sqrt{2\mu E_B}$, with μ the H_1, H_2 reduced mass and $E_B > 0$ the binding energy of the physical state (i.e., the difference between the H_1, H_2 threshold and its mass), β the inverse range of forces and λ^2 the wave function renormalization constant, which for a pure molecule vanishes. There is also a relation for the effective coupling of the physical state to H_1 and H_2, given by (using the non-relativistic normalization)

$$g^2_{\text{NR,eff}} = \frac{2\pi\gamma}{\mu}(1-\lambda^2) + \mathcal{O}(\gamma/\beta). \tag{78}$$

The $(1-\lambda^2)$ factor gives the molecular probability, i.e., the probability of finding the H_1H_2 component in the physical state (the Weinberg compositeness criterion [479]). Thus, for a pure molecule ($\lambda^2 = 0$), one finds that the scattering length takes its maximum value, $a = -1/\gamma$, and in addition $r = \mathcal{O}(1/\beta)$, while for a compact state ($\lambda^2 = 1$) one gets $a = \mathcal{O}(1/\beta)$ and $r \to -\infty$. In addition, the effective coupling takes the maximal value for a pure molecule and it vanishes when there is no H_1H_2 component in the physical state. These differences produce distinctive signatures in the line shapes of near-threshold states (see, e.g., the discussion in [444, 480]) and not-so-near-threshold states [481]. In the case of coupled-channel dynamics, one might also find states that can decay into some of the open channels. These may

still qualify as hadronic molecules, were they to couple strongly to one of the channels considered in the dynamical space. A detailed review on weak decays of heavy hadrons leading to molecular states in the final state is given in [482].

The hadron-hadron interactions are usually taken from EFTs based on exact or approximate QCD symmetries, which are employed to construct amplitudes satisfying unitarity in coupled channels. The undetermined low-energy constants (LECs) are fitted to data or lattice QCD results, both in the perturbative expansion (implicit in the EFT) and in the unitarization procedure.

6.1.2.1 Effect of meson-meson channels on naive quark-antiquark bound states

Many of the hadronic structures discovered since 2003 appear close to hadron-hadron thresholds, and thus their dynamics can be strongly dictated by the nearby multiquark hadron-hadron channels. In fact, the discovery of the XYZ particles is opening the door to systematically explore higher Fock components of the hadron wave function [483–485]. When the hadron-hadron channels dominate, one gets states that can be approximately by hadronic molecules introduced above. Within quark models, the hadron-hadron effects can be calculated as pioneered in Refs. [449, 450, 486].

Within the quark model picture, the coupling between the quark-antiquark and meson-meson sectors requires that the hadronic state is written as [487, 488]

$$|\Psi\rangle = \sum_\alpha c_\alpha |\psi_\alpha\rangle + \sum_\beta \chi_\beta(P)|\phi_A\phi_B\beta\rangle, \tag{79}$$

where $|\psi_\alpha\rangle$ are eigenstates of the quark-antiquark Hamiltonian [489, 490], $|\phi_A\phi_B\beta\rangle$ is the two-meson state with β quantum numbers and $\chi_\beta(P)$ is the relative wave function between the two mesons. In principle one should couple with an infinite number of hadron-hadron channels. However, it has been argued in Refs. [491, 492] that the only relevant thresholds are those close to the naive states, while the rest have only little effect, which can be absorbed in the quark model parameters. The reason is that the energy nonanalyticity at thresholds does not cause any nontrivial behavior, if the thresholds are far away.

The meson-meson interaction can be derived from the quark-antiquark one using the resonating group method (RGM) [493, 494]. The coupling between the quark-antiquark and meson-meson sectors requires the creation of a light quark-antiquark pair, and thus the operator associated with this should describe also the open-flavor meson strong decays of heavy quarkonia. The most simple decay model is the well-known $^3P_0$ model [495–497], in which the transition potential between quark-antiquark and meson-meson sectors can be defined as

$$\langle\phi_A\phi_B\beta|T|\psi_\alpha\rangle = P\, h_{\beta\alpha}(P)\, \delta^{(3)}(\vec{P}_{\rm cm})\,, \tag{80}$$

where P denotes the relative momentum of the two-meson state.

Using Eq. (79) and the transition potential in Eq. (80), one gets the coupled equations

$$c_\alpha M_\alpha + \sum_\beta \int h_{\alpha\beta}(P)\chi_\beta(P)P^2 dP = E\, c_\alpha\,, \tag{81}$$

$$\sum_\beta \int H_{\beta'\beta}(P', P)\chi_\beta(P)P^2 dP + \sum_\alpha h_{\beta'\alpha}(P')\, c_\alpha = E\, \chi_{\beta'}(P')\,, \tag{82}$$

where M_α are the masses of the bare quark-antiquark mesons and $H_{\beta'\beta}$ is the RGM Hamiltonian for the two-meson states. Solving the coupled-channel equations, Eqs. (81) and (82), as indicated, e.g., in Ref. [498], allows to study hadronic states as poles of the S-matrix in any possible Riemann sheet.

6.2 Hadrons with a single heavy quark

6.2.1 Mesons

The lowest positive-parity states include the very narrow charm-strange mesons $D_{s0}^*(2317)$, $D_{s1}(2460)$, and the very broad charm-nonstrange mesons $D_0^*(2400)$ and $D_1(2430)$ [310]. Their bottom partners are still waiting for discovery, likely by LHC experiments. Bottom partners of the first two might be also accessible at Belle-II, though being at the upper edge of its energy reach.

6.2.1.1 Phenomenology

There were attempts trying to interpret the $D_{s0}^*(2317)$ and $D_{s1}(2460)$ as $c\bar{s}$ mesons, see, e.g., [499–502], or as the positive-parity chiral partners of the ground-state D_s and D_s^* [503, 504]. In these cases, the isospin-breaking hadronic decay widths are predicted to be of the order of only 10 keV. Predictions for the radiative decays can be found in [499, 503]. An updated calculation of the excited $c\bar{q}$ ($q = u, d, s$) meson spectrum and the decay properties in the relativized quark model can be found in [505].

The $D_{s0}^*(2317)$ and $D_{s1}(2460)$ states could be compact tetraquarks, namely $[cq][\bar{s}\bar{q}']$ states, where the two quarks and the two antiquarks are coupled to form a color singlet, see, e.g., [460, 506]. Having a single heavy quark, the mechanism driving isospin violation described in [460, 463] is expected not to be as effective as for the $X(3872)$, making the D_{sJ} states isosinglet. The only kinematically allowed hadronic decay channel is the isovector $D_s^{(*)}\pi$ state. Hence, the lack of isospin violation, together with the predilection for tetraquarks to decay into baryons, explains the narrowness of the states. Using the mass of the $X(3872)$ to fix the chromomagnetic coupling in the tetraquark model, one can indeed accommodate both of them. Of course, this predicts other similar states with quantum numbers $(0, 1, 2)^+$, all expected to decay into $D_s^{(*)+}\pi^0$. The $D^{(*)}K$ mode should be open for the heavier members in the multiplet.

Another possibility is to describe the $D_{s0}^*(2317)$ and $D_{s1}(2460)$ as DK and D^*K molecules [507, 508]. Dynamically they can be generated from charmed-meson–light-meson scattering in unitarized heavy-meson chiral effective theory (UHMChPT) [509–512], using as input the scattering lengths calculated on the lattice [513]. Such scheme predicts a (strangeness, isospin) $(S, I) = (1, 0)$ state with a mass 2315^{+18}_{-28} MeV, in agreement with that of the $D_{s0}^*(2317)$ resonance. Applying the Weinberg's compositeness condition allows one to estimate the size of the molecular component to be about 70% [513]. Such a picture is supported by the lattice energy levels reported in [514, 515], as discussed in [516, 517].

A decisive measurement is that of the width of the $D_{s0}^*(2317)$, which is expected to be around 100 keV in the molecular picture and smaller in other models [499, 500]. So far, only an upper limit has been provided. It would be difficult to measure such a tiny width at LHC experiments for two reasons: because it requires a very high mass resolution, and because there is a neutral pion in the dominant decay mode $D_s^+\pi^0$. However, it could be possible to measure the width of its spin partner $D_{s1}(2460)$, which carries similar information, through the decay mode $D_s\pi^+\pi^-$ and the Dalitz decay $D_{s1}(2460) \to D_s\gamma(\to \mu^+\mu^-)$. Dalitz decays have already been probed successfully for the χ_c states [518]. Both decay modes benefit from a very good mass resolution (~ 1 MeV), given the small Q values of the reactions. Though a measurement of the width with a precision of 100 keV might be optimistic, LHCb should at least be able to improve on the current upper limit (< 3.5 MeV). The proposed decay modes suffer from tiny branching fractions, but the large integrated luminosity in the HL-HE era would help cope with that.

In the $(S, I) = (0, 1/2)$ sector, UHMChPT suggests the presence of two broad D_0^* states at about $2.10 - i\,0.10$ GeV and $2.45 - i\,0.13$ GeV [519], which would have masses different from the $D_0^*(2400)$ given in the RPP [310], determined from fitting to the $D\pi$ mass distributions using a single Breit–Wigner function. Ref. [520] showed that these amplitudes can reproduce well the $B^- \to D^+\pi^-\pi^-$ process measured by the LHCb Collaboration [521]. The combination of angular moments, $\langle P_1\rangle - \frac{14}{9}\langle P_3\rangle$, is particularly sensitive to the $D\pi$ S-wave, and a higher-statistics measurement in the energy range between 2.4 and 2.5 GeV will provide invaluable information on the $D\pi$–$D\eta$–$D_s\bar{K}$ coupled-channel dynamics. Ref. [520] also finds two broad D_1 states at $2.25 - i\,0.11$ GeV and $2.56 - i\,0.20$ GeV, in addition to

the relatively well-understood narrow $D_1(2420)$. A precise study of $\langle P_1\rangle - \frac{14}{9}\langle P_3\rangle$ for the $D^*\pi$ S-wave is needed in the $\bar{B} \to D^*\pi\pi$ channel, as well as in $\bar{B} \to D^{(*)}\eta\pi$, $\bar{B} \to D_s^{(*)}\bar{K}\pi$, $\bar{B} \to D_s^{(*)}\bar{K}\bar{K}$, $\bar{B}_s \to D^{(*)}\bar{K}\pi$, $\bar{B}_s \to D_s^{(*)}\eta\pi$, etc. In particular, signals of the predicted higher D_0^* and D_1 states, coupled dominantly to $D_s^{(*)}\bar{K}$, could be near-threshold enhancements in the $D_s^{(*)}\bar{K}$ spectrum. Such enhancements exist in low-statistics data by BaBar [522] and Belle [523,524], and need to be investigated at LHCb using data sets with much higher statistics.

Heavy-quark flavour symmetry allows one to predict the bottom partners of charmed mesons. The lowest B_{s0}^* and B_{s1} are predicted to be at about 5.72 GeV and 5.77 GeV [519, 520], consistent with lattice results [525]. A good channel to search for both of them is $B_s^*\gamma$ [503, 526]. They can also decay into the isospin-breaking hadronic channels $B_s^{(*)}\pi^0$, whose widths are expected to be smaller than those of their charm partners because the isospin splitting between B^0 and $B^\pm$ is an order of magnitude smaller than that between D^0 and $D^\pm$. The axial state B_{s1} can decay into $B_s\gamma$ as well. Both the $B_s\gamma$ and $B_s^*\gamma$ decay modes should appear in the $B_s\gamma$ spectrum with similar efficiencies (similarly to the $B_{s2}^*(5840) \to B^*K$ decay, which peaks in the BK spectrum as well [527]). Large integrated luminosity will cope with the low efficiency for detecting soft photons, and the LHCb experiment will have sensitivity to observe such states for the first time. The predicted poles for the B_0^* mesons are at about $5.54 - i\,0.11$ GeV and $5.85 - i\,0.04$ GeV, while those for the B_1 mesons they are at about $5.58 - i\,0.12$ GeV and $5.91 - i\,0.04$ GeV [519, 520]. The bottom meson spectrum in quark models is different. For an updated calculation of the excited $b\bar{q}$ ($q = u, d, s$) meson spectrum and the decay properties in the relativized quark model can be found in [528]. And the predictions of bottom mesons in the parity-doubling model can be found in [503]. These resonances can be searched for in $B\pi$ and, for higher excited states, in $B_s\bar{K}$ final states.

The $D_{sJ}(2860)$ discovered by BaBar [529] was split into a 1^- state, the $D_{s1}^*(2860)$, and a 3^- state, the $D_{s3}^*(2860)$ by the LHCb measurement with higher statistics [530]. Yet, the ratio of two branching fractions $\mathcal{B}(D^*K)/\mathcal{B}(DK) = 1.10 \pm 0.24$ [531] is assigned to the spin-1 $D_{s1}^*(2860)$ in the RPP2018 [310]. This value is much larger than the expectations in Ref. [532], based on heavy quark spin symmetry (HQSS) and the leading order chiral Lagrangian, for the D-wave $c\bar{s}$ mesons, which are the only available quark-model option in that mass region. The predictions in [532] are 0.06 and 0.39 for the 1^- and 3^- D-wave states, respectively. However, the quark-model calculation in Ref. [533] gives larger values, 0.72 and 0.68 for the 1^- and 3^- D-wave states, respectively. On the other hand, in the picture for the $D_{s1}^*(2860)$ as mainly a $D_1(2420)K$ bound state, the ratio is predicted to be 1.23 as a natural consequence of HQSS [534]. Heavy quark symmetries allow to predict several related mesons in this picture: a 2^- spin partner at about 2.91 GeV, decaying into D^*K and $D_s^*\eta$; the bottom partners at about 6.15 GeV and 6.17 GeV, decaying into $B^{(*)}\bar{K}$ and $B_s^{(*)}\eta$ [534].

6.2.1.2 Lattice QCD

The most extensive spectrum of higher-lying D and D_s mesons on the lattice [535] was obtained in the single-hadron approximation, in which the decays of resonances and the effects of thresholds are not taken into account. This lattice study predicts a large number of states with $J \leq 4$ [535], most of which have not been discovered yet. Some of them might contain substantial gluonic components (hybrid mesons).

A proper treatment of a strongly decaying resonance $R \to H_1H_2$, with one open channel, requires simulations of single-channel H_1H_2 scattering. This has been accomplished recently by several lattice collaborations for a series of resonances. Mostly, resonances composed of u, d, s were considered. The infinite-volume scattering matrix $T(E)$ is extracted from the energies of H_1H_2 eigenstates on the finite lattice via the rigorous Lüscher's formalism [536]. The resulting scattering matrix $T(E)$ renders resonance masses, M, and decay widths, Γ, via Breit–Wigner-type fits. A related strategy is to analytically continue $T(E_c)$ to the complex-energy plane, where the pole positions, $E_c \simeq M - \frac{i}{2}\Gamma$, are related to the

resonance parameters. The resonances that strongly decay to several final states require simulation of coupled-channel scattering, which is much more challenging. The Hadron Spectrum Collaboration managed to extract the coupled-channel scattering matrix for a few selected channels, while most channels are awaiting future simulations.

Strong decays of resonances containing a single heavy quark were considered only for the low-lying charmed resonances with $J^P = 0^+, 1^\pm, 2^+$ [537, 538]. The $N_f = 2$ simulation of $D\pi$ scattering [537] finds a broad D_0^*, in rough agreement with experiment. As commented above, a reanalysis of $D\pi$–$D\eta$–$D_s\bar{K}$ coupled channels [538] for $N_f = 2 + 1$ suggests two D_0^* states, with masses located around 2.10 and 2.45 GeV [519].

The strongly stable states that lie closely below the H_1H_2 threshold might be sensitive to threshold effects. A proper way to treat these is to simulate H_1H_2 scattering. The mass of a shallow bound state corresponds to an energy $E < m_1 + m_2$, of which the scattering matrix, $T(E)$, has a pole. In this way, the effects of D^*K thresholds were found to push the masses of the D_{s0}^* and D_{s1}^* down, bringing them close to the experimental values [514, 515]. Analogously, the yet-undiscovered strongly stable B_{s0}^* and B_{s1}^0 were predicted at 5.71 and 5.75 GeV, respectively [525]. For the decay modes that can be used in searching, we refer to the discussion in 6.2.1.1.

6.2.2 Baryons

The most extensive spectrum of yet-undiscovered singly charmed baryons was predicted in 2013 [539]. It predicted five Ω_c baryons in the region 3.0-3.2 GeV, in impressive agreement with the 2017 LHCb discovery [540]. This work predicted also up to ten Λ_c, Σ_c, Ω_c, Ξ_c states in each channel with $J \leq 7/2$, where resonances are treated in a simplified single-hadron approach. A follow-up precision lattice study of the five discovered Ω_c resonances confirms their most likely quantum numbers [541].

The experimental discovery of the five Ω_c states has triggered extensive theoretical activity, with some of the quark models revisited in view of the new result [542–547]. The role of diquarks in the Ω_c spectrum was discussed in [542, 548, 549], while the odd-parity molecular interpretation for two or three of the states seen by LHCb was proposed in Refs. [550–552]. The meson-baryon interactions used in the molecular schemes, derived in [550, 552], are consistent with both chiral and heavy-quark spin symmetries, and lead to successful descriptions of the observed lowest-lying odd parity $\Lambda_c(2595)$, $\Lambda_c(2625)$ [553–556] and $\Lambda_b(5912)$, $\Lambda_b(5920)$ [557] resonances. Some of the Ω_c states observed by LHCb could thus be spin-flavour symmetry partners of these $\Lambda_{Q=c,b}^*$ baryons. However, the masses and decay widths of $\Lambda_{Q=c,b}^*$, at least the charmed ones, can also be accommodated within usual constituent quark models (see for instance [558, 559]), and thus the importance of the molecular components in their structure has not been settled yet. Information obtained from the $\Lambda_b \to \bar{\nu}_\ell \ell \Lambda_c(2595)$, $\Lambda_b \to \bar{\nu}_\ell \ell \Lambda_c(2625)$, and related reactions will put some constraints on these models, as shown in [560].

Molecular schemes also predict partners of the Ω_c baryons in the bottom sector (see for instance, Ref. [561]). LHCb recently reported [562] a peak in both the $\Lambda_b^0 K^-$ and $\Xi_b^0\pi^-$ invariant mass spectra that might correspond to either a radially or orbitally excited quark-model $\Xi_b^-(6627)$ resonance with quark content bds, or to a hadron molecule. In the latter, it would be dynamically generated from the coupled-channel interaction between Goldstone bosons and the lowest even-parity bottom baryons [557, 563–565]. For a review of recent observations and phenomenological models of open-flavour heavy hadrons, we refer to [566].

6.3 Hadrons containing $\bar{c}c$, $\bar{b}b$ or $\bar{c}b$

The current experimental status for the hadrons containing a heavy quark-antiquark pair can be found in several recent reviews [196, 310, 440–448], and will not be repeated here. In the following, we discuss isospin-scalar quarkonium(-like) states and, separately, exotic charged states, and focus on a few selected important issues.

6.3.1 Quarkonia

6.3.1.1 Phenomenology

The $J^{PC} = 1^{++}$ $X(3872)$ state has several salient features: the central value of its mass coincides with the $D^0\bar{D}^*$ threshold within a small uncertainty of 180 keV [310]; despite the tiny phase space, its decay branching fraction into $D^0\bar{D}^0\pi^0$ is larger than 40% [310]; it decays into $\omega J/\psi$ ($I = 0$) and $\rho J/\psi$ ($I = 1$) with similar partial decay widths.

This state could be interpreted in terms of a $[cq][\bar{c}\bar{q}]$ compact tetraquark. In this case, the isospin violation is explained by the smallness of $\alpha_s(m_c)$ [460, 463], which suppresses the mixing between the almost degenerate mass eigenstates $X_u = [cu][\bar{c}\bar{u}]$ and $X_d = [cd][\bar{c}\bar{d}]$. Isospin symmetry predicts a degenerate charged partner X^+– experimental search for which has so far been unsuccessful. Similarly, degenerate isoscalar and isovector states with signature 0^{++}, $0^{++\prime}$ and 2^{++} are expected, with masses around $M(0^{++}) \simeq 3.8$ GeV and $M(0^{++\prime}) \simeq M(2^{++}) \simeq 4$ GeV [461]. Were the $Z_c(4050)$ a scalar or a tensor, it would have been a suitable candidate for one of the above isovector states (see e.g. [567]). If confirmed, another possible candidate for the heavier scalar state could be the resonance observed by LHCb in $\eta_c\pi$ [568]; see also Ref. [475].

Given the expected mass, the charged partner predicted in the tetraquark picture, X^+, might only decay into a charmonium and a light meson. As discussed in Sec. 6.1.1, a potential barrier between the diquarks has been conjectured [462, 469–471]. This would solve the issue about the elusive X^+: the decay into J/ψ plus hadrons would be largely suppressed by the tunneling factor for a heavy quark, and could make the hadronic decay comparable to the electromagnetic one, as is indeed observed in data. Although physically and phenomenologically motivated, such a picture awaits experimental confirmation. Specifically, the charged partners of the X could be searched in the $J/\psi\rho^\pm$ channel.

The properties of the $X(3872)$, on the other hand, indicate that it couples strongly to $D\bar{D}^*$. This leads to the proposal that it could have a large $D\bar{D}^*$ molecular component [569–571]. The isospin violation in this case stems from the difference of masses between the neutral $D^0\bar{D}^{*0}$ and charge D^+D^{*-} in the loops [572–574]. The line shapes of the $X(3872)$ in both $J/\psi\pi^+\pi^-$ and $D^0\bar{D}^{*0}$ modes are crucial to reveal its nature and binding mechanism [575–579] (for a review, see [478]). Improved measurements at the LHC experiments are foreseen. In the hadronic molecular picture, the 2^{++} heavy-quark spin partner of the X, dubbed X_2, would decay into $D\bar{D}^*$ and $D\bar{D}$ in a D wave, and it is expected to be narrow [580, 581]. However, it has been suggested [582] that the mixing of the $D^*\bar{D}^*$ molecule with bare charmonium $\chi_{c2}(2P)$ might destabilize the X_2 [583], making it hardly visible. Better experimental information on the 2^{++} spectrum around 4 GeV is hence of great importance, and the X_2 can be searched for in $D\bar{D}$ and $J/\psi\omega$. So far, there is only one observed state, $\chi_{c2}(3930)$, compatible with a standard charmonium assignment, and its mass is lower than what is normally expected for the X_2. No evidence for an additional 2^{++} state that could be identified as the X_2 has been observed so far. Hence, the existence of the $\chi_{c1}(2P)$ and/or the X_2, in addition to the $X(3872)$ and $\chi_{c2}(2P)$ states, respectively, are still open questions which need to be addressed and that will definitely shed light into the dynamics of the mysterious $X(3872)$ [582].

The 0^{++} spectrum is also still unclear: the spin of the narrow $X(3915)$ is not fixed, and the broad $X(3860)$ [584,585] needs confirmation. Since the $(0, 1, 2)^{++}$ and 1^{+-} heavy quarkonia differ from each other only by the quark polarization, it is necessary to consider systematically physical states with these quantum numbers [582, 586]. Thus, searching for an isoscalar 1^{+-} state around 3.9 GeV is also of high interest [587]. Its important decay modes include $D\bar{D}^*$, $J/\psi\eta$ and $J/\psi\pi\pi$. Hints for such a state have been seen by COMPASS [588], albeit with low statistics.

The $X(3872)$ could emerge as a dynamically generated mixed state of a DD^* molecule and the $\chi_{c1}(2P)$ as shown in [589], see also Refs. [484, 576, 586, 590–594]. The $c\bar{c}$ mixture is less than 10% but it is important to bind the molecular state. The proposed structure would allow to understand the origin of its prompt production rate and to describe correctly its isospin violating decays and radiative

transitions. The original $c\bar{c}(2^3P_1)$ state is dressed by meson-meson coupled-channel effects and goes up in the spectrum allowing its identification with the $X(3940)$. Within the same coupled-channels scheme, Ref. [583] analyzes the $J^{PC} = 0^{++}$ and 2^{++} charmonium sectors. The two hadron states found in the 0^{++} channel were assigned to the $Y(3940)$ and to the recently identified resonance $X(3860)$ [584, 585]. The bound state with quantum numbers 2^{++} found in [583] is interesting because, within the uncertainties of the model, its mass and decay properties suggest that the $X(3915)$ and $X(3930)$ meson-like structures could correspond to the same state, as also claimed in Ref. [595].

It is also crucial to look for the analogue of the $X(3872)$ in the bottom sector. Such a state could decay, for example, into $B\bar{B}\gamma$, $\chi_{bJ}\pi\pi$, $\Upsilon\pi\pi\pi$ and $\Upsilon\gamma$ [596–598]. The $X_b \to \Upsilon\rho$ channel has already been investigated, with no observation [599,600]. It should be noticed, however, that this channel should be highly suppressed due to G-parity violation. There is an important difference between the $X(3872)$ and the X_b: The mass difference between the charged and neutral charmed mesons is one order of magnitude larger than that for the bottom mesons, because of the different interference between the QCD and QED contributions [601], and thus the X_b should be a well-defined isoscalar state [596]. The null results of Refs. [599, 600] are perfectly consistent with the existence of an isoscalar X_b [597, 598]. Note that in the tetraquark model one would expect isospin violation, while the opposite is true in a molecular scheme. The isospin-conserving channel $X_b \to \Upsilon\omega$ has found no evidence for the state either [602]. The spin-2 bottomonium-like X_{b2} and B_c-like state X_{bc2} [596] can instead be searched for in D-wave $B\bar{B}$ and DB final states, respectively.

Vector 1^{--} states have also been observed at e^+e^- colliders (see, e.g., [603–607]). The number of observed vector charmonium-like states far exceeds the predictions in the $c\bar{c}$ potential quark models, and thus some of them must have an exotic origin. In the tetraquark model these are diquarkonia with orbital angular momentum $L = 1$, and their spectrum easily matches the experimental observations [461] (see also [608]), which also leads to a distinctive spectrum with a low-mass 3^{--} state [609]. Complexity in understanding these structures also comes from the many S-wave thresholds of hadron pairs, such as the $\bar{D}D_1(2420)$ for the $Y(4260)$ [610] and $\psi' f_0(980)$ for the $Y(4660)$ [611]. Effects of open charm channels for the $Y(4260)$ are considered in a quark model framework in Ref. [612]. The $Y(4260)$ is also widely regarded as a candidate for a hybrid charmonium [613–617]. The hadro-charmonium model for the $Y(4260)$ and $Y(4360)$ [618] can hardly explain why the $Y(4260)$ was seen in several different channels including $J/\psi\pi^+\pi^-$, $h_c\pi^+\pi^-$, $\chi_{c0}\omega$ and $D^0D^{*-}\pi^+ + c.c.$ (the data are nicely summarized in Ref. [448] and a combined fit in these channels leads to a lower mass around 4.22 GeV for the $Y(4260)$ [619]. The search for these states in, for example, prompt production and/or B decays can help to understand their nature.

6.3.1.2 Lattice QCD

The lattice spectrum of bottomonia presented in [620] contains almost all the observed $\bar{b}b$ states up to the $\bar{B}B$ threshold. It also predicts a plethora of undiscovered states where the $\bar{b}b$ pair carries an orbital angular momentum $L = 2, 3, 4$, and total angular momentum $J \leq 4$. Fourteen B_c mesons with $J \leq 3$ are predicted up to the BD threshold [620]. Only two of them have been discovered so far.

All the charmonia below the $D\bar{D}$ threshold have been experimentally discovered, while the treatment of strongly decaying resonances is much more challenging. The most extensive spectrum obtained in the simplified single-hadron approach predicts several excited $\bar{c}c$ states, as well as $\bar{c}cg$ hybrids up to 4.7 GeV, carrying $J \leq 4$ [535], also including exotic 1^{-+}, 0^{+-}, 2^{+-} quantum numbers. Most of them have not been observed yet. Only one exploratory study considered the resonant nature of charmonia above the open-charm threshold [621], and underlines the need to experimentally explore further $\bar{D}D$ in S and D waves. A neutral is found as a state slightly below $D\bar{D}^*$ [622].

Table 26: Expected data samples at LHCb Upgrade II and Belle II for key decay modes for the spectroscopy of heavy flavoured hadrons. The expected yields at Belle II are estimated by assuming similar efficiencies as at Belle.

		LHCb		Belle II
Decay mode	$23\,\text{fb}^{-1}$	$50\,\text{fb}^{-1}$	$300\,\text{fb}^{-1}$	$50\,\text{ab}^{-1}$
$B^+ \to X(3872)(\to J/\psi\pi^+\pi^-)K^+$	14k	30k	180k	11k
$B^+ \to X(3872)(\to \psi(2S)\gamma)K^+$	500	1k	7k	4k
$B^0 \to \psi(2S)K^-\pi^+$	340k	700k	4M	140k
$B_c^+ \to D_s^+ D^0 \overline{D}^0$	10	20	100	—
$\Lambda_b^0 \to J/\psi p K^-$	340k	700k	4M	—
$\Xi_b^- \to J/\psi \Lambda K^-$	4k	10k	55k	—
$\Xi_{cc}^{++} \to \Lambda_c^+ K^-\pi^+\pi^+$	7k	15k	90k	< 6k
$\Xi_{bc}^+ \to J/\psi \Xi_c^+$	50	100	600	—

6.4 Experimental prospects

The LHCb Upgrade II detector will have a large impact on sensitivity in searches for heavy states. Aside from the much larger integrated luminosity, many of the detector improvements planned for LHCb Upgrade II may have significant benefits for spectroscopy studies. For example, the potential removal of the VELO RF foils, together with the improved particle identification provide by the TORCH, will enhance the reconstruction efficiency for multibody B decays, such as $B_c^+ \to D_s^+ D^0 \overline{D}^0$; the selection of short-lived particles (*e.g.*, B_c^+, Ξ_{cc}, Ω_{cc}^+, Ξ_{bc}, etc) will also benefit from an improved vertex resolution; the Magnet Side Stations will help in studying di-pion transitions such as $X(3872) \to \chi_{c1}\pi^+\pi^-$ or $B_c^{**+} \to B_c^+\pi^+\pi^-$; improved π^0 and η mass resolutions will increase the sensitivity in searching for the C-odd and charged partners of the $X(3872)$ meson by $X(3872)^{C-\text{odd}} \to J/\psi\,\eta$ and $X(3872)^{\pm} \to J/\psi\,\pi^0$. A summary of the expected yields in certain important modes, and a comparison with Belle II, is given in Table 26. Below we give further details on the prospects for specific studies and analyses.

6.4.1 Taxonomy of tetraquarks and pentaquarks

To advance our understanding of the $X(3872)$ state, it will be very important to learn even more about its decay pattern. In particular, if it really has a strong $\chi_{c1}(2P)$ component, it should have $\pi^+\pi^-$ transitions to the $\chi_{c1}(1P)$ state. Unfortunately at LHCb, the reconstruction efficiency for the dominant $\chi_{c1}(1P)$ decay to $\gamma J/\psi$ decay is low, making this prediction hard to test. The very large data set of LHCb Upgrade II will allow one to overcome this problem, and will be essential in detecting or refuting such transitions. Studies of the $X(3872)$ lineshape by a simultaneous fit to all detected channels are important for pinning down the location of its resonant pole and determining its natural width; both are very important inputs in helping with the understanding of the state. Therefore a very large data set will be essential for the statistical precision of such studies and reconstruction of decays to $D^0\overline{D}^{*0}$, which are relevant given the proximity of the $X(3872)$ mass to the $D^0\overline{D}^{*0}$ threshold.

Searching for prompt production of any known exotic hadron candidates at the LHC remains an important task, since its detection would signify a compact component, either conventional quarkonium, or a tightly bound tetraquark or pentaquark. To date, the $X(3872)$ is the only exotic hadron candidate with $Q\overline{Q}$ content that has been confirmed to be produced promptly. However, it will be important to quantify the upper limits in negative searches to allow more rigorous phenomenological analysis.

Many puzzling charged exotic meson candidates (e.g., $Z(4430)^+$) decaying to J/ψ, $\psi(2S)$ or χ_{c1} plus a charged pion have been observed in B decays. Some of them are broad, and none can be satisfactorily explained by any of the available phenomenological models. The hidden-charm mesons, observed

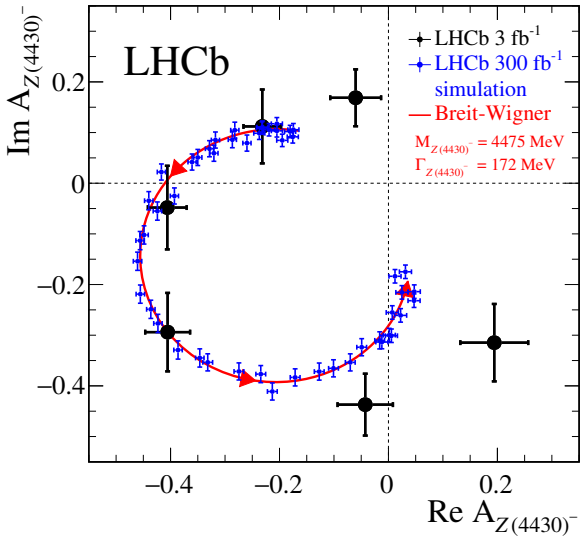

Fig. 38: Argand diagram of the $Z(4430)^-$ amplitude ($\mathrm{A}_{Z(4430)^-}$) in bins of $m^2_{\psi(2S)\pi^-}$ from a fit to the $B^0 \to \psi(2S)K^+\pi^-$ decays. The black points are the results based on Run 1 data [737] while the blue points correspond to an extrapolation to an integrated luminosity of 300 fb^{-1} expected at the LHCb Upgrade II. The red curve is the prediction from the Breit-Wigner formula with a resonance mass (width) of 4475 (172) MeV. Units are arbitrary.

in the $J/\psi\,\phi$ decay [738–740], also belong to this category. The determination of their properties, or even the claim of their existence, relies on an advanced amplitude analysis, which allows the exotic contributions to be separated from the typically dominant non-exotic components. Further investigation of these $Q\overline{Q}q\overline{q}$ structures will require much larger data samples and refinement of theoretical approaches to parametrisations of hadronic amplitudes. Similar comments apply to improvements in the determination of the properties of the pentaquark candidates $P_c(4380)^+$ and $P_c(4450)^+$ and to the spectroscopy of excited Λ baryons in $\Lambda_b^0 \to J/\psi\,pK$ decays. The large data set collected during the LHCb Upgrade II would allow one to test further the resonant character of the $P_c(4380)^+$, $P_c(4450)^+$ and $Z(4430)^+$ states (Fig. 38), while improvements in calorimetry would help in searching for new decay modes (e.g., $P_c^+ \to \chi_{c1,2}(\to J/\psi\,\gamma)p$) by amplitude analyses of $\Lambda_b^0 \to \chi_{c1,2}pK^-$ decays [657, 741].

6.4.2 *Searches for further tetra- and pentaquarks*

Though the true nature of the $X(3872)$ meson is still unclear, both the molecular [742] and tetraquark [460] models predict that a C-odd partner ($X(3872)^{C-\mathrm{odd}}$) and charged partners ($X(3872)^{\pm}$) may exist and decay to $J/\psi\,\eta/\gamma\chi_{cJ}$ and $J/\psi\,\pi^0\pi^{\pm}$ respectively.

Similarly, the existence of the $P_c(4380)^+$ and $P_c(4450)^+$ pentaquark states raises the question of whether there is a large pentaquark multiplet. The observed states have an isospin 3-component of $I_3 = +\frac{1}{2}$. If they are part of an isospin doublet with $I = \frac{1}{2}$, there should be a neutral $I_3 = -\frac{1}{2}$ state decaying to $J/\psi\,n$ [474]. However this final state does not lend itself well to observation. Instead, the search for the neutral pentaquark candidate can be carried out using decays into pairs of open charm, in particular in the process $\Lambda_b^0 \to \Lambda_c^+ D^- \overline{K}^{*0}$, where the neutral pentaquark states would appear as resonances in the $\Lambda_c^+ D^-$ subsystem (Fig. 39 left). Such decays can be very well reconstructed, but the total reconstruction efficiency suffers from the large number of tracks and the small branching fractions of Λ_c^+ and D^- reconstructable final states; the total reconstruction efficiency is about a factor 50 smaller than the efficiency for the $\Lambda_b^0 \to J/\psi\,pK^-$ channel. If there could exist pentaquarks of an isospin quadruplet,

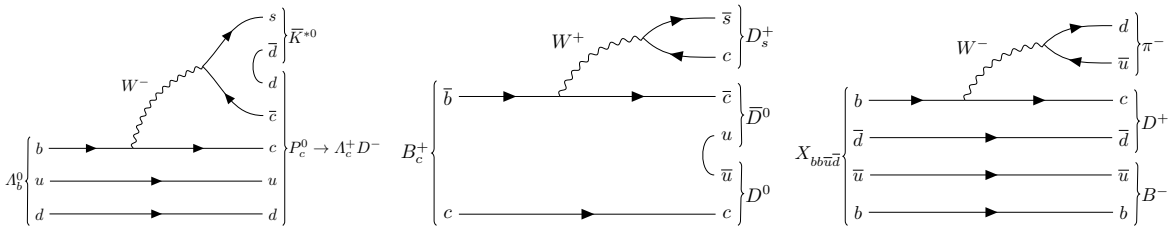

Fig. 39: Schematic Feynman diagrams for decays of $\Lambda_b^0 \to \bar{K}^{*0}\Lambda_c^+ D^-$, $B_c^+ \to D^0 \bar{D}^0 D_s^+$, and $X_{bb\bar{u}\bar{d}} \to B^- D^+ \pi^-$ (from left to right).

then there is the interesting possibility to find doubly charged pentaquarks decaying into $\Sigma_c^{++}\overline{D}^0$. Channels such as these require very large data sets to offset the low efficiency. The magnet side stations will also improve the reconstruction efficiency of such decay modes with several tracks in the final states.

The relative coupling of the pentaquark states to their decays into the double open-charm channels will depend on their internal structure and the spin structure of the respective decay. For that reason it is important to study decays involving D^{*+} resonances as well (e.g., $P_c^+ \to D^{*-}\Sigma_c^{++}$) to investigate the internal structure of pentaquarks [665]. Since these decays require the reconstruction of slow pions from the D^{*+} decays, the proposed tracking stations inside the magnet, enhancing the acceptance for low-momentum particles, will be highly beneficial for this study.

Invoking $\mathrm{SU}(3)$ flavour symmetry, one would expect the existence of pentaquarks with strangeness, which would decay into channels like $J/\psi\,\Lambda$ or $\Lambda_c^+ D_s^-$. Such states and their decays into these channels were investigated in [649, 743]. To explore the potential of the former case, the decay $\Xi_b^- \to J/\psi\,\Lambda K^-$ has been studied using Run 1 data at LHCb, with about 300 signal decays observed [744]. Complementary information can be achieved by a study of the $\Lambda_b^0 \to J/\psi\,\Lambda\phi$ decays. An increase of the available integrated luminosity by a factor of 100 would allow detailed amplitude analyses to be performed for these final states, with a similar sensitivity as was the case for the pentaquark discovery channel.

The history of $X(3872)$ studies illustrates well the difficulty of distinguishing between exotic and conventional explanations for a hidden-charm state. Therefore, it is appealing to search for states with uncontroversial exotic signatures. A good candidate in this category would be a $\mathcal{T}_{cc}$ doubly charmed tetraquark [443, 643, 696, 702–704, 745–755], being a meson with constituent-quark content $cc\overline{q}\overline{q}'$, where the light quarks q and q' could be u, d or s. If the masses of the doubly charmed tetraquarks are below their corresponding open-charm thresholds, they would manifest as weakly decaying hadrons with properties including masses, lifetimes and decay modes not too different from the recently observed Ξ_{cc}^{++} baryons [756], and, as for the Ξ_{cc} baryons, the most promising searches are in prompt production. Instead, if the masses of $\mathcal{T}_{cc}$ states are above the open-charm threshold and their widths are broad, it will be very challenging to observe these states via prompt production. Instead, B_c^+ decays to open-charm mesons can offer unique opportunity to test for their existence. In Run 5 the B_c^+ mesons will be copiously produced at the LHC, because of the large production cross-sections of $b\bar{b}$ and $c\bar{c}$ pairs and of the enormous data sample. Similarly to the amplitude analysis of the $\Lambda_b^0 \to J/\psi\,pK^-$ decay, which led to the observation of the P_c^+ pentaquark candidates [757], studying the angular distributions of the multi-body final states of the B_c^+ meson has the potential of indicating new states, e.g., $\mathcal{T}_{cc}$, inaccessible through decays of lighter hadrons. It also allows for the determination of the spin-parity quantum numbers of any state that is observed. A good example is to study the $\mathcal{T}_{cc}^+$ state in the decay mode $B_c^+ \to D_s^+ D^0 \overline{D}^0$ (Fig. 39 middle) through the decay chain $B_c^+ \to \mathcal{T}_{cc}^+ \overline{D}^0$ and $\mathcal{T}_{cc}^+ \to D_s^+ D^0$, as discussed in Ref. [702].

The decay $B_c^+ \to D_s^+ D^0 \overline{D}^0$ has not been observed with the Run 1 data, and predictions on the branching fractions of B_c^+ decays are subject to very large uncertainties. Estimates of the integrated luminosity needed to perform a full amplitude analysis are therefore imprecise, and can only be formulated through considerations of other decay modes such as $B_c^+ \to J/\psi\,D_s^+$. The signal yield of $B_c^+ \to J/\psi\,D_s^+(\to \phi\pi^+)$ decays observed in Run 1 data is 30 ± 6 [758]. Considering the branching

fraction of the decay of the additional charm hadron and the lower efficiency due to the higher track multiplicity, the estimated number of signal of $B_c^+ \to D_s^+ D^0 \overline{D}^0$ decays is $\mathcal{O}(10^2)$ in a future dataset corresponding to an integrated luminosity of 300 fb^{-1}, collected with $\mathcal{O}(100\%)$ trigger efficiency [758]. Since the D^0 and D_s^+ mesons are pseudoscalars, the amplitude analysis simplifies, and can provide conclusive results already with a few hundred decays.

Finally, strongly decaying doubly charmed tetraquarks with a narrow decay width, as predicted by pure tetraquark models with spin-parity quantum numbers of 0^+, 1^+ and 2^+, can also be searched for in prompt production. The expected yields can be estimated by the associated production of open-charm mesons measured with a fraction of the Run 1 data [759]. With a data sample of 300 fb^{-1}, the yield for D^+D^+ ($D^+D_s^+$) associated production is around 750k (150k), which is a very promising sample in which to search for narrow $\mathcal{T}_{cc}$ states.

If the coincidence of the $\chi_{c1}(2P)$ charmonium state with the $D^0\overline{D}^{*0}$ threshold is responsible for the $X(3872)$ state, there is likely no bottomonium analogue of it, since the $\chi_{b1}(3P)$ state was detected well below the $B\overline{B}^*$ threshold, and the $\chi_{b1}(4P)$ state is predicted to be too far above it. However, if molecular forces dominate its dynamics, there could be an isosinglet state below this threshold decaying to $\omega\Upsilon(1S)$, where ω could be reconstructed via the decay to $\pi^+\pi^-\pi^0$. Unfortunately, its prompt production would likely be very small unless driven by tightly bound tetraquark dynamics or by the $b\bar{b}$ Fock-state component of the same quantum numbers [597]. The improved π^0 reconstruction in the LHCb Upgrade II will help for these searches.

The prompt production at the LHC remains the best hope for unambiguously establishing the existence of a stable, weakly decaying $bb\bar{u}\bar{d}$ tetraquark predicted by both lattice QCD and phenomenological models. However, the inclusive reconstruction efficiencies for such states are tiny due to the small branching fractions of B and D meson decays to low-multiplicity final states (Fig. 39c). Recently, there have been also several predictions for an exotic state with quark composition $b\bar{b}b\bar{b}$ [711–721] with a mass below the $2m_{\eta_b}$ threshold, which implies that it can decay to $\Upsilon\mu^+\mu^-$. However, lattice QCD calculations do not find evidence for such a state in the hadron spectrum [710]. Given the presence of four muons in the final state, LHCb will have good sensitivity for observing the first exotic state composed of more than two heavy quarks [760].

Motivated by the discovery of the hidden-charm pentaquarks, theorists have extended the respective models for multiplet systems to include beauty quarks. In Ref. [668] $Q\overline{Q}qqq$ ground states were investigated in an effective-Hamiltonian framework assuming a colour-magnetic interaction between colour-octet qqq and $Q\overline{Q}$ subsystems. Several resonant states are predicted. Such beautiful pentaquarks could be searched for in the Υp, $\Upsilon\Lambda$, $B_c^\pm p$ and $B_c^\pm\Lambda$ mass spectra. In analogy with the popular $\Sigma_c\overline{\Lambda}_c^-$ molecular model, Refs. [669] and [670] investigate similar dynamics in the hidden-bottom sector and predict a large number of exotic resonances. Indeed, in the hidden-beauty sector the theory calculations are found to be even more stable than for hidden charm, motivating searches for resonances close to the $B^*\Sigma_b$, $B\Sigma_b^*$, $B^*\Sigma_b^*$ and $B\Lambda_b^{*0}$, $B^*\Lambda_b^0$ thresholds.

Another possibility is the existence of pentaquarks with open beauty and quark contents such as $\bar{b}duud$, $b\bar{u}udd$, $b\bar{d}uud$ and $\bar{b}suud$ [761, 762]. If those states lie below the respective baryon-meson thresholds containing beauty, then they could be stable against strong decay and would predominantly decay through the weak transition $b \to c\bar{c}s$. A search using a 3 fb^{-1} data set in four decay channels $J/\psi p h^+ h^-$ (h = K, π) has been performed in Ref. [763]. No signals were found and 90% CL limits were set on the production cross section times branching fraction relative to the Λ_b^0 in the $J/\psi pK^-$ mode. The obtained limits are of the order of 10^{-3}, which does not yet rule out the estimates for the production of such an object provided in Ref. [761]. Similar searches in channels with open-charm hadrons in the final state again lead to large multiplicities and the respective small reconstruction efficiencies, but could profit from favoured branching fractions. Investigations of a large number of channels will maximise sensitivity for weakly decaying exotic hadrons. It has also been proposed to search for excited Ω_b^- states [561] in analogy to the recently discovered excited Ω_c^0 states [764]. Such open-beauty excited

states could be searched for in decays to the $\Xi_b K$ final state.

6.4.3 Study of doubly-heavy baryons

The discovery of the Ξ_{cc}^{++} baryon has opened an exciting new line of research that LHCb is avidly pursuing. Measurements of the lifetime and relative production cross-section of Ξ_{cc}^{++}, searches for additional decay modes, and searches for its isospin partner Ξ_{cc}^{+} and their strange counterpart Ω_{cc}^{+} are underway.

A signal yield of 313 ± 33 $\Xi_{cc}^{++} \to \Lambda_c^+ K^- \pi^+ \pi^+$ decays was observed by LHCb in $1.7\,\text{fb}^{-1}$ of Run 2 data [756]. Improvements in the trigger for the LHCb Upgrade II detector are projected to increase selection efficiencies by a factor two for most charm decays, with decays to high-multiplicity final states, such as those from the cascade decays of doubly charmed baryons, potentially benefiting much more [765, 766]. Thus the Run 5 sample will contain more than 90 000 decays of this mode. The branching fraction for $\Xi_{cc}^{++} \to \Lambda_c^+ K^- \pi^+ \pi^+$ is theoretically estimated to be up to 10%, making it one of the most frequent nonleptonic decay modes. Several other lower multiplicity modes with $\mathcal{O}(1\%)$ predicted branching fractions will yield samples of comparable size [295, 681, 767, 768].

The efficiency with which LHCb can disentangle weak decays of doubly charmed baryons from prompt backgrounds depends on the lifetime of the baryon [769]. Although the predicted lifetimes for the Ξ_{cc}^{+}, Ξ_{cc}^{++}, and Ω_{cc}^{+} baryons span almost an order of magnitude, the relative lifetimes of Ξ_{cc}^{+} and Ω_{cc}^{+} are expected to be approximately $1/3$ that of the Ξ_{cc}^{++} baryon [674, 679, 770–775]. Assuming a relative efficiency of 0.25 with respect to Ξ_{cc}^{++} due to the shorter lifetimes and an additional production suppression of $\sigma(\Omega_{cc}^{+})/\sigma(\Xi_{cc}^{++}) \sim 0.2$ for Ω_{cc}^{+} [674], LHCb will have Run 5 yields of around 25 000 for Ξ_{cc}^{+} and 4500 for Ω_{cc}^{+} in each of several decay modes.

LHCb will be the primary experiment for studies of the physics of doubly charmed baryons for the foreseeable future, and its potential will not be exhausted by the end of Run 5. With the data collected in Run 2, LHCb should observe all three weakly decaying doubly charmed baryons and characterise their physical properties. Run 5 will supply precision measurements of doubly differential cross sections that will provide insight into production mechanisms of doubly heavy baryons. In addition Run 5 will allow the spectroscopy of excited states and bring studies of the rich decay structure of doubly charmed hadrons into the domain of precision physics.

The production cross section of the Ξ_{bc} baryons within the LHCb acceptance is expected to be about 77 nb [776]. This value is about 1/6 of the expected production cross-section of a B_c^+ meson [777, 778]. It should be noted that the relative Λ_b^0 production rate is $p_{\rm T}$-dependent. In the typical $p_{\rm T}$ range in the LHCb acceptance, a ratio of production rates, $\sigma(pp \to \Lambda_b^0 X)/\sigma(pp \to \overline{B}^0 X) \sim 0.5$ [779, 780] is measured. It is therefore conceivable that the Ξ_{bc} production rates are also larger than predicted by the above calculations.

It is quite challenging to observe and study Ξ_{bc} and Ω_{bc}^0 baryons because of the low production rates, the small product of branching fractions and the selection efficiencies for reconstructing all of the final-state particles. To collect a large sample of Ξ_{bc} baryons will require the higher integrated luminosity and detector enhancements planned for in the LHCb Upgrade II. Using the notation that X_c is a charmed baryon containing a single charm quark, some of the most promising decay modes to detect Ξ_{bc} and Ω_{bc}^0 baryons are: *(i)* $J/\psi\, X_c$ modes $J/\psi\, \Xi_c^+$, $J/\psi\, \Xi_c^0$, $J/\psi\, \Lambda_c^+$, $J/\psi\, \Lambda_c^+ K^-$; *(ii)* Ξ_{cc} modes $\Xi_{cc}\pi^-$; *(iii)* doubly charmed modes $D^0 \Lambda_c^+$, $D^0 \Lambda_c^+ \pi^-$, $D^0 D^0 p$; *(iv)* penguin-topology modes $\Lambda_c^+ K^-$, $\Xi_c^+ \pi^-$; *(v)* the Ξ_b , B^0 or Λ_b^0 modes $\Xi_b \pi^+$, $\Lambda_b^0 \pi^+$, $B^0 p$, using fully reconstructed or semileptonic B^0, Λ_b^0 or Ξ_b decays [781]; *(vi)* the decays due to W-exchange between b-c quarks, that is not helicity suppressed, and which can give rise to a final state with just one charmed particle, *e.g.*, $\Lambda_c^+ K^-$.

To put this in context, the LHCb collaboration observed 30 ± 6 $B_c^+ \to J/\psi\, D_s^+ (\to \phi\pi^+)$ decays with $3\,\text{fb}^{-1}$ data at 7 and 8 TeV [758]. With looser selections about 100 signal decays can be obtained with reasonably good signal-to-background ratio. The $\Xi_{bc}^+ \to J/\psi\, \Xi_c^+$ decay is kinematically

very similar. Assuming $f_{\Xi_{bc}^+}/f_{B_c^+} \sim 0.2$, with $\mathcal{B}(\Xi_{bc}^+ \to J/\psi\,\Xi_c^+)/\mathcal{B}(B_c^+ \to J/\psi\,D_s^+) \sim 1$, while $\mathcal{B}(\Xi_c^+ \to pK^-\pi^+)/\mathcal{B}(D_s^+ \to K^+K^-\pi^+) \sim 0.1$, and $\epsilon_{\Xi_{bc}^+}/\epsilon_{B_c^+} \sim 0.5$, a signal yield of about 600 $\Xi_{bc}^+ \to J/\psi\,\Xi_c^+$ decays is expected in Run 5, albeit with sizeable uncertainties. Other modes could also provide sizeable signal samples. It is likely LHCb will observe the Ξ_{bc} baryons in Run 3/4, and further probe the spectrum of other doubly heavy baryons with the large samples accessible in the proposed Upgrade II.

6.4.4 Precision measurements of quarkonia

The correct interpretation of the experimental polarisation results for S-wave quarkonia requires a rigorous analysis of the feed-down contributions from higher excited states [782, 783]. The direct measurement of the polarisation for χ_c and χ_b states is necessary to decrease this model dependence. Since P-wave states are practically free from the feed-down from higher excited states, any χ_c and χ_b polarisation measurements could be interpreted in a robust manner without additional model assumptions.

The recent discovery of the $\chi_{c1,2} \to J/\psi\,\mu^+\mu^-$ decays [784] opens the possibility to perform a detailed study of χ_c production, allowing almost background-free measurements even for a very low transverse momentum of χ_c candidates. Due to the excellent mass resolution, the vector state χ_{c1} and the tensor state χ_{c2} are well separated, eliminating the possible systematic uncertainty caused by the large overlap of these states in the $\chi_c(\chi_b) \to J/\psi\,(\Upsilon)\gamma$ decay [782, 783, 785–788]. An integrated luminosity of 300 fb^{-1} will allow one to probe the high-multipole contributions to the $\chi_c \to J/\psi\,\mu^+\mu^-$ amplitude, namely the magnetic-dipole contribution for χ_{c1} decays and the magnetic-dipole and electric-octupole contributions for χ_{c2} decays. Use of the Run 5 data set is also necessary to measure the $(p_{\rm T}, y)$ dependence of χ_c polarisation parameters. In addition, the effect of the form factor in the decays $\chi_c \to J/\psi\,\mu^+\mu^-$ [789, 790] could be probed with the precision of several percent from the shape of the $m(\mu^+\mu^-)$ spectra.

Studies of double quarkonia production allows independent tests for the quarkonia production mechanism, and in particular for the role of the colour octet. So far the LHCb collaboration has analysed double-J/ψ production in 7 TeV and 13 TeV data with relatively small datasets [791, 792]. Using 280 pb^{-1} of data collected at $\sqrt{s} = 13$ TeV, $(1.05 \pm 0.05) \times 10^3$ signal $J/\psi\,J/\psi$ events are observed. However, even with the larger sample of $J/\psi\,J/\psi$ events now available, it is not possible to distinguish between different theory descriptions of the single-parton scattering (SPS) mechanism [793–801], nor to separate the contributions from the SPS and double-parton scattering (DPS) mechanisms [802, 803]. Though the larger samples collected during Runs 3 and 4 will allow some progress on these questions, the measurement of the correlation of J/ψ polarisation parameters will only be possible with the Upgrade II data set.

In addition, while it is likely that $\Upsilon\Upsilon$ and $J/\psi\,\Upsilon$ production will be observed in the near future (assuming the dominance of the DPS mechanism), the determination of the relative SPS and DPS contributions, as well as the discrimination between different SPS theory models, will require precision measurements only possible with Run 5 data.

7 Bottom-quark probes of new physics and prospects for B-anomalies

A key contribution of the HL-LHC data sets will be a comprehensive global picture of rare and (semi)-leptonic quark transitions. This has value whether or not the current "flavour anomalies" are confirmed with Run 2 or Run 3 LHC data. If the improvements on statistically limited observables, $R_{K^{(*)}}$ and $R(D^{(*)})$, confirm the anomalies, a global analysis of all related channels may discriminate between different BSM explanations. Such a global analysis will also help to constrain the mass scale of the BSM particles and mediators, which, together with the direct HL-LHC searches, will further restrict the range of possible explanations for the anomalies. On the other hand, if the signifcance of the anomalies decreases, or they even disappear with Run 2 and Run 3 data, we should still search for small BSM effects on top of the dominant SM amplitudes. In this case, global analyses of the data would lead to improved bounds on the BSM affecting these flavor observables. The statistical power of the HL-LHC datasets will also enable a unique reach for other BSM signatures such as Lepton-Flavour Violation (LFV) and Baryon-Number Violation (BNV), particularly in the baryon and heavy-meson sectors.

We would like to stress that, in the HL-LHC era, many rare beauty decays will become abundant and enter the precision-measurement regime. Therefore, it will become increasingly important that the LHC collaborations and Belle II publish results in such a way that systematic uncertainties can be treated in a coherent manner and their correlations taken into account. A good example of this is the treatment of the ratio of hadronization fractions f_s/f_d in any LHC $B_q \to \ell\ell$ combination, discussed in Sec. 7.3. It will also be important to correctly treat systematic uncertainties due to the use of common software packages, e.g., the use of `PHOTOS` by the LHC experiments and Belle II, in future lepton universality measurements.

While much of the power of the HL-LHC and Belle II datasets will lie in the breadth of precisely measured rare and (semi-)leptonic decays, practical considerations mean that experiments will continue to publish analyses of individual decay modes as each is completed. Systematically publishing experimental likelihoods, efficiency maps, and resolution unfoldings, as already done for some of the most important analyses, should be strongly encouraged even now. This facilitates both the combination of results between experimental collaborations, and the inclusion of the results in global fits and in tests of phenomenological models [804–806].

7.1 Phenomenology of $b \to s\ell\ell$ decays

Authors (TH): Wolfgang Altmannshofer, David Straub, Javier Virto.

In this section we discuss the status of the interpretation of $b \to s$ transitions in and beyond the SM, the prospects for future sensitivities at the LHC, and the complementarity with Belle-II. All current and planned measurements of processes involving $b \to s$ transitions are related to weak decays of b-hadrons. At present, most of the data is on B decays, with a smaller fraction on B_s decays. LHCb has already provided a few measurements on Λ_b decays, with data sets that will increase dramatically in future runs, including a significant output on decays of other b-hadrons such as Ω_b or Ξ_b [807] (see Sec. 7.3).

Theoretically, the decays of b-hadrons are best described within the Weak Effective Theory (WET), where flavor-changing transitions are mediated by "effective" dimension-six operators with Wilson coefficients (WCs) that encapsulate all SM and heavy NP effects. Thus all observables can be calculated in full generality, model-independently in terms of the WCs and hadronic matrix elements. The relevant effective Lagrangian for $b \to s$ transitions at low-energies in the SM is [808]

$$\mathcal{H}_{\text{eff}}^{\text{SM}} = \frac{4G_F}{\sqrt{2}} \sum_{p=u,c} \lambda_{ps} \left(C_1 O_1^p + C_2 O_2^p + \sum_{i=3}^{10} C_i O_i \right), \tag{83}$$

with $\lambda_{ps} = V_{pb} V_{ps}^*$. As defined in Ref. [808], the $O_{1,2}^p$, $O_{3,\ldots,6}$, and O_8 are the so-called "current-current", "QCD-penguin" and "chromo-dipole" operators, respectively, and they contribute to the $b \to s\gamma$ and $b \to$

$s\ell\ell$ transitions via an electromagnetic interaction. The $O_{7\gamma}$ and $O_{9,10}$ are the "electromagnetic dipole" and the "semileptonic" operators, respectively. The BSM can enter through the WCs $C_1, \ldots, C_{10}$, or the chirally-flipped versions, $P_{L(R)} \to P_{R(L)}$, giving $O'_{7\gamma,\ldots,10}$, or through scalar and tensor semileptonic operators [809]. Furthermore, beyond the SM, semileptonic operators can induce lepton-flavor universality violation (LFUV) or charged-lepton flavor violation (CLFV). For the purpose of this Section, the relevant operators for the interpretation of $b \to s\gamma$ and $b \to s\ell\ell'$ data are

$$\begin{aligned} O_{7\gamma}^{(\prime)} &= \frac{e\, m_b}{16\pi^2}(\bar{s}\sigma_{\mu\nu}P_{R(L)}b)F^{\mu\nu}, \\ O_9^{\ell\ell'(\prime)} &= \frac{\alpha_{\rm em}}{4\pi}(\bar{s}\gamma_\mu P_{L(R)}b)(\bar{\ell}\gamma^\mu \ell'), \qquad O_{10}^{\ell\ell'(\prime)} = \frac{\alpha_{\rm em}}{4\pi}(\bar{s}\gamma_\mu P_{L(R)}b)(\bar{\ell}\gamma^\mu\gamma_5 \ell'), \end{aligned} \tag{84}$$

where we have added leptonic flavor labels ($C_i^\ell \equiv C_i^{\ell\ell}$).

By calculating and measuring a large set of independent observables, one can perform global fits to all the relevant WCs, and by comparing with their SM values, extract information on NP model-independently. This programme has been carried out since the start of the LHC, and culminated in the current $b \to s\ell\ell$ anomalies [810–820]. The future runs of the LHC will allow either to establish the anomalies or to refine our understanding of these transitions.

7.1.1 Observables and Hadronic Matrix Elements

7.1.1.1 $B_q \to \ell^+\ell^-$

From a theoretical perspective the purely leptonic decay, $B_s \to \ell^+\ell^-$, is the cleanest exclusive $b \to s\ell\ell$ process. Up to QED corrections [821], all QCD effects are contained in a decay constant, which is precisely and reliably computed using lattice QCD, giving $f_{B_s} = 230.7(1.3)$ MeV [822]. [6] Going beyond this accuracy in f_{B_s} is difficult (see Sec. 11), and the current theoretical error is less than 5% [821, 822],

$$\mathcal{B}(B_s \to \mu^+\mu^-)_{\rm SM} = (3.64 \pm 0.11) \cdot 10^{-9}, \tag{85}$$

which is dominated by the uncertainties of the relevant CKM parameters. The latest measurements by LHCb and ATLAS [15, 825], have an error of $\sim 25\%$ (see Sec. 7.3 for HL-LHC prospects). Beyond the SM, the decay $B_s \to \mu^+\mu^-$ gives very strong constraints on the scalar and pseudoscalar operators [826, 827], and also on $C_{10}^{\mu(\prime)}$, which has an impact on the fits and the $b \to s\mu\mu$ anomalies. Searches for the CLFV channels $B_s \to \tau\mu$ and $B_s \to \mu e$ are important, because an observation would be an unambiguous signal of NP, which can be connected to the LFUV signals in $R_{K^{(*)}}$ [337, 339, 341, 828, 829]. Besides the branching fractions, an effective lifetime observable and the CP-violating observable $S_{\mu\mu}$ are accessible by exploiting the nonvanishing width difference, $\Delta\Gamma_s$, in the B_s system [320, 830]. This provides complementary constraints on the WCs [831], and a precise measurement will be possible at the LHCb.

These measurements are simultaneously sensitive to the decay $B_d \to \mu^+\mu^-$, although its branching fraction is further suppressed by a CKM factor [822, 832],

$$\mathcal{B}(B_d \to \mu^+\mu^-)_{\rm SM} = (1.00 \pm 0.03) \cdot 10^{-10}. \tag{86}$$

The ratio $\mathcal{B}(B_s \to \mu^+\mu^-)/\mathcal{B}(B_d \to \mu^+\mu^-)$ can be predicted more accurately in the SM and models with Minimal-Flavor Violation (MFV) than the single branching ratios, testing the flavor structure of the short-distance dynamics. In particular, it is related to the ratio $\Delta m_s/\Delta m_d$ [833] with small uncertainties from hadronic inputs and none from CKM ones. A similar comment applies to the ratios $\mathcal{B}(B_q \to$

[6] The average of lattice $N_f = 2 + 1$ results from FLAG 2016 [66] and other recent $N_f = 2 + 1 + 1$ lattice calculations of the decay constant [823, 824] give similar central values but with larger errors.

$\mu^+\mu^-)/\Delta m_q$ [833]. It is important to emphasize that the measurements of $\mathcal{B}(B_d \to \mu^+\mu^-)$ that can be done at the LHC are of utmost importance as they cannot be done in any other facility in the coming decade.

Finally, the $m_{\mu^+\mu^-}$ spectrum is sensitive to the decay $B_s \to \mu^+\mu^-\gamma$ (where the photon is not detected) [834]. Theoretically, this mode is interesting because the extra photon lifts the chiral suppression of the leptonic mode and gives access to the WC C_9^μ. However, it is also challenging to predict because of long-distance hadronic contributions [835].

7.1.1.2 $B_q \to M\ell^+\ell^-$

The most prominent semileptonic decay modes are $B \to K^{(*)}\mu^+\mu^-$ and $B_s \to \phi\mu^+\mu^-$. These are sensitive to all the WCs and they currently dominate the global fits to $b \to s\ell\ell$ data because of the experimental precision achieved and the large number of observables they give access to. This allows one to constrain some independent combinations of WCs and hadronic parameters. Since there is no experimental information related to the polarization of the final-state leptons, the measurable observables arise from the kinematic differential distributions of the final-state momenta. These are customarily written as angular distributions with coefficients that depend on the dilepton invariant mass squared q^2, measured in specific bins of q^2.

In the case of the three-body mode $B \to K\mu^+\mu^-$, there are three observables: the differential branching fraction, $d\mathcal{B}/dq^2$, the forward-backward asymmetry, $A_{\rm FB}(q^2)$, and the "flat term", $F_H(q^2)$ [809]. The kinematic distribution of the four-body decay, $B \to V(\to M_1M_2)\ell^+\ell^-$, contains many more independent angular coefficients, up to 11 in the most general case (plus the total rate), called $I_i(q^2)$ or $J_i(q^2)$ [836–838]. Normalizing these by the total differential rate $d\Gamma/dq^2$ and symmetrizing or antisymmetrizing with respect to the two charge-conjugate modes leads to the observables S_i, A_i [837]. A subset of these observables can also be constructed for $B_s \to \phi\mu^+\mu^-$ [839]. It is convenient to define certain combinations of angular observables where form-factor uncertainties largely cancel in the heavy-quark limit, called "optimized observables". An independent set of these, optimized at low-q^2, is given by the $P_i^{(\prime)}$ basis [838, 840, 841]. Optimized observables at large-q^2 also exist [841, 842].

The observables in exclusive semileptonic decays, $B \to M\ell^+\ell^-$, are specified by transversity (or helicity) amplitudes. They depend on two types of hadronic matrix elements: "local" (form factors) and "non-local" (see, e.g., [843–845]). Local form factors for $B \to K$, $B \to K^*$ and $B_s \to \phi$ transitions can be calculated at low-q^2 in two different versions of light-cone sum rules (LCSRs) [846–849], and at large-q^2 using Lattice QCD [850, 851] (LQCD). A comparison between both determinations can be done by parametrizing the q^2 dependence via the z-expansion [852–854], which is based on the analytic structure of the matrix elements. Future prospects for the theoretical precision of the form factors rely on improvements in LQCD calculations. Note that both LQCD and LCSRs work in the narrow-width limit for vector mesons. A calculation beyond this approximation is possible within the LCSRs [855, 856], and points to a correction of up to 10%. There are prospects for treating hadronic resonances on the lattice [857], and calculating directly the $B \to K\pi$ form factors should play an important role in the next decade.

Non-local effects are significantly more difficult to estimate [858–860]. Data-driven methods might be able to reduce the uncertainties on these hadronic contributions and will benefit significantly from the high statistics collected by LHCb in the HL phase. All of these methods are based on precise measurements of the q^2 spectra in conjunction with a theoretically motivated parametrization of the q^2 dependence of the amplitudes and a theory benchmark that allows one to separate short-distance contributions from long-distance contributions.

At low q^2, the theory input is based on the light-cone Operator Product Expansion (OPE) at very low (or negative) q^2 [858, 859], an expansion that breaks down at the perturbative $c\bar{c}$ threshold $q^2 \simeq 4m_c^2$. Parametrizations of the q^2 dependence are based on a Taylor expansion in powers of q^2 [819, 844] or on

dispersion relations [859] such as in the z-expansion [845]. The latter two parametrizations implement analyticity constraints and use extra information, such as data on (or in between) the $B \to \psi K^*$ decays, with $\psi = \{J/\psi, \psi(2S)\}$. Short- and long-distance effects are disentangled by the experimental input from $B \to \psi K^*$, the fixed q^2 dependence of the NP contribution, and by the theory constraints at negative q^2. The experimental prospects for this data-driven approach were studied in [861], showing that future LHC data could provide a higher level of control over the long-distance contribution at low q^2.

At high q^2, the theory input is based on the low-recoil OPE [842, 860, 862]. This method relies on the theoretical assumption that resonant effects from "above-threshold" charmonia average out within sufficiently broad q^2 bins ("quark-hadron duality"). Thus, only a single bin in the whole high-q^2 region is typically considered in the global fits. The q^2 spectrum can be used to give estimates and test models of the intrinsically nonperturbative "duality-violating" effects. Currently, these analyses are carried out within the "Krüger-Sehgal" (naive factorization) approach [863], which allows one to use data on the $R(s)$ ratio in e^+e^- annihilation [860, 864, 865]. Ref. [865] uses all currently available data on $B \to K^*\mu^+\mu^-$ at low recoil and finds agreement with the OPE within $\sim 20\%$ in all the bins. Notably, future precision data from the LHC with the expected fine binning will be essential in refining these data-driven methods and to disentangle NP contributions. As in the low-q^2 case, combined fits to hadronic parameters and NP are also beneficial [865].

Hadronic uncertainties largely cancel in the SM in lepton-universality ratios such as $R_{K^{(*)}}$ [866],

$$R_{K^{(*)}} = \frac{\mathcal{B}(B \to K^{(*)}\mu^+\mu^-)}{\mathcal{B}(B \to K^{(*)}e^+e^-)}. \tag{87}$$

The SM predictions are thus limited only by the size of the electromagnetic corrections [867]. Current LHCb measurements show tensions with the SM in R_K [868] and in two bins of R_{K^*} [869] at approximately $\sim 2.5\,\sigma$ each. Much higher precision will be achieved with future data at LHCb [807]. and, independently, with Belle-II, which can confirm R_K at $5\,\sigma$ with $20\,\text{ab}^{-1}$ [196] at the current experimental central value. In the presence of LFUV contributions the predictions are less precise and "optimized" observables based on angular analyses of muonic and electronic modes can improve the sensitivity to different BSM scenarios [870, 871]. In fact, LFUV and CLFV can be connected, and decays such as $B \to K^{(*)}\tau\mu$ and $B \to K^{(*)}\mu e$ become clear targets for the HL-LHC. Semitauonic decays $B \to K^{(*)}\tau^+\tau^-$ are very challenging at the LHC but theoretically interesting because their branching fractions can receive enhancements of several orders of magnitude in BSM [341, 872] (see also [873] and [874]). Assuming that the LFUV anomalies persist and the BSM contributions are in the muonic WCs, as the global fits to $b \to s\mu\mu$ currently suggest, one can use future precise and fine-binned measurements in $b \to se^+e^-$ exclusive modes to fit the hadronic parameters directly [875].

Other measurements with potential impact on the $b \to s\ell\ell$ fits will be possible at the HL-LHC. The LHC experiments have a unique opportunity to measure the $\Lambda_b \to \Lambda\mu^+\mu^-$ decays [186], probing the $b \to s\mu^+\mu^-$ transition in a baryonic system [876–878]. For $B_s \to \phi\mu^+\mu^-$, a flavor-tagged time-dependent analysis allows one to access independent observables [879] sensitive to BSM. The expected sensitivity to the B_s and Λ_b decay measurements will make it possible to extend the global fit programme, outlined above, to these modes. Finally, the study of exclusive $b \to d\mu^+\mu^-$ transitions will reach the level of precision we have now in $b \to s\mu^+\mu^-$ (see Sec. 7.3). This will allow one to extend the programme of the global fits to $b \to d\mu^+\mu^-$ transitions, setting constraints in a different flavor sector or, if the $b \to s\ell\ell$ anomalies remain, to give further insights on the BSM flavour structure. The $b \to d\mu^+\mu^-$ modes are theoretically more challenging than their $b \to s\ell\ell$ counterparts, since new large long-distance contributions appear at low q^2, e.g., in the form of light resonances [880].

7.1.1.3 Radiative decays: $B_s \to \phi\gamma$ and related modes

Radiative decays are obvious probes of the electromagnetic dipole operators. Strategies to determine with these decays the helicity of the photon (and therefore the presence of BSM WC $C'_{7\gamma}$ have intensively been investigated [881–886]. Approaches based on the CP-averaged exclusive decay rates are prone to hadronic uncertainties and depend quadratically on $C'_{7\gamma}$ [885–887]. In contrast, interference between helicity amplitudes of the $B^0_{(s)}$ and $\bar{B}^0_{(s)}$ decays is directly sensitive to the photon polarization. This can be measured by constructing time-dependent CP-asymmetries in $B \to V\gamma$ (the $S_{V\gamma}$ observable), or those induced by the width-differences $\Delta\Gamma_q$, shown to be clean null tests of the SM [881, 888]. Experimentally, $S_{K^*\gamma}$ has been measured in the B-factories [889, 890], while a measurement of the width-difference effects has been achieved at LHCb [891]. Prospects in the HL-LHC include reaching a few-percent precision in this observable, which will provide a strong constraint on the chirality of the electromagnetic dipole operators.

The $B \to K^{(*)}\ell^+\ell^-$ decays are also sensitive to the interference of the two helicities through the angular observables P_1 (also called $A_{\rm T}^{(2)}$) and P_3^{CP} close to the photon pole $q^2 \simeq 0$, region where these observables are particularly clean from hadronic uncertainties [844]. Thus, the electronic mode is especially suited for these measurements, providing a theoretically clean window to right-handed currents beyond the SM. This has been measured by LHCb with a $\sim 20\%$ precision with data of Run 1 [892] and will be improved to a few-percent precision in the HL-LHC.

7.1.1.4 Interplay with Belle-II: Inclusive B decays and $B_q \to M\nu\bar{\nu}$

Apart from contributing to the above-mentioned measurements [196], Belle-II will also measure decays which are very challenging in the LHC environment. This comprises inclusive decays and the $b \to s\nu\bar{\nu}$ transitions. The inclusive observables used in the current fits are $\mathcal{B}(B \to X_s\gamma)$ and $\mathcal{B}(B \to X_s\ell^+\ell^-)$. Belle-II will improve these, including precise measurements of the forward-backward asymmetry in $B \to X_s\ell^+\ell^-$, which will impact the fits [196]. In particular, Belle-II measurements of $B \to X_s\mu^+\mu^-$ will be able to test the LHCb anomalies independently by 2024 [196]. Theoretically, these inclusive rates can be calculated perturbatively in terms of the partonic decay of the b quark up to small non-perturbative effects [893, 894]. These include local power corrections, non-local shape function-like effects, and additional contributions to the absence of an OPE for some operator insertion. The latter effects represent irreducible uncertainties which cannot be removed by relaxing the experimentally necessary cuts in the hadronic mass spectrum [894]. Calculations of both rates have been done with high accuracy [895, 896]. The exclusive decays $B \to K^{(*)}\nu\bar{\nu}$ and related modes [897], on the other hand, depend only on local form factors. Belle-II is expected to provide measurements of these modes with an uncertainty of about 10%, assuming the rates are SM-like [196]. These decays do not probe directly the WCs entering the $b \to s\nu\bar{\nu}$ transitions. However, they can be correlated through $SU(2)_L$ gauge invariance in the SMEFT if the BSM is realized above the EW scale, and direct correlations are obtained in specific models of NP (see e.g. [341, 898]).

7.1.2 Model-Independent Fits

Existing measurements show hints of deviations from the SM expectations in three different classes of measurements: in $B \to K^*\mu^+\mu^-$ angular observables [899], in branching fractions of exclusive $b \to s\mu^+\mu^-$ decays (in particular $B_s \to \phi\mu^+\mu^-$ [900]), and in μ-e universality (LFU) tests [5, 6]. None of the individual measurements is in tension with the SM by more than 4σ. However, a global significance of the tensions can be defined in a specific framework of NP, such as the model-independent framework provided by the weak effective Hamiltonian.

Several groups have performed global fits of the WCs to existing $b \to s\ell\ell$ data (see [815–820, 827] for recent fits). Three classes of fits can be distinguished: fits to $b \to s\mu\mu$ data only, fits to μ-e LFU ratios only, and combined fits assuming no NP in $b \to see$ transitions. All these fits agree – up to differences

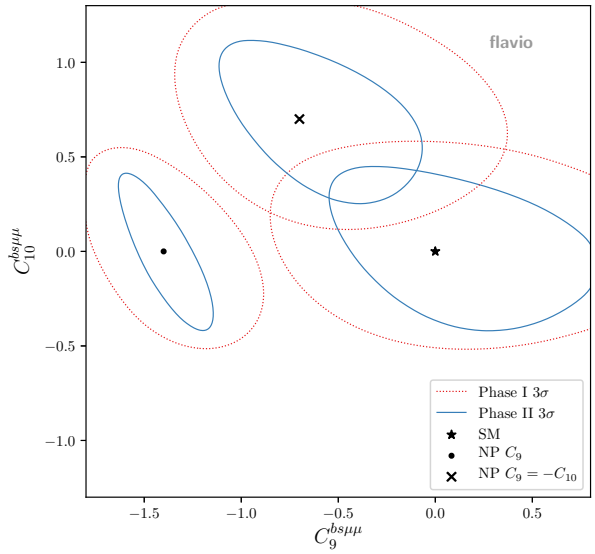

Fig. 40: Potential sensitivity to the SM and to NP scenarios motivated by the anomalies of LHCb, ATLAS and CMS combined after the HL-LHC phase. These scenarios are $C_9 = -1.4$ (vector current) and $C_9 = -C_{10} = -0.7$ (pure left-handed current). The observables included are the branching fraction of $B_s \to \mu^+\mu^-$ and the angular observables of the decay $B^0 \to K^{*0}\mu^+\mu^-$ in the low-q^2 region (e.g., P_5'). To produce the P_5' expectation for ATLAS and CMS in Phase I, the result from a CMS projection was scaled by $1/\sqrt{2}$, assuming that the two experiments have the same sensitivity and the uncertainties are uncorrelated. This plot has been done using the `flavio` software package [903].

that can be attributed to different theoretical inputs or different selection of observables – and arrive at two basic conclusions. First, there is a tension in $b \to s\mu\mu$ data alone, and could be explained by a NP shift in the WC C_9^μ [811] (maybe combined with C_{10}^μ), or by a not well understood hadronic effect. Second, the LHCb measurements of $R_{K^{(*)}}$, if combined,are already in tension with the SM and lepton-flavor universality at 4σ, assuming there is no experimental correlation between R_K and R_{K^*}. This cannot be explained by hadronic effects. Assuming that it is due to NP coupling only to muons, one finds that it is consistent with the NP contribution needed to accommodate the $b \to s\mu\mu$ anomaly [826]. Singling out the WC C_9^μ in the muonic transition and performing a global fit to all the data, the log-likelihood ratio between the best-fit point and the SM hypothesis corresponds to a deviation ranging from 4σ to more than 6σ, depending on the theoretical assumptions [815–820].

Clearly, future experimental efforts that can clarify the origin of the above tensions are of utmost importance. If LFU is indeed violated in $b \to s\ell\ell$ transitions, then R_K and R_{K^*} are theoretically clean smoking guns that allow one to establish a possible deviation from the SM. At the same time, global fits to all the relevant observables will remain relevant for several reasons: *(i)* if the hints for LFUV disappear with more statistics, LFU new physics effects [820, 901, 902] might still hide in observables that are theoretically less clean ; *(ii)* to identify the nature of NP (and not just its presence), the values of the BSM Wilson coefficients have to be determined; *(iii)* in particular, if LFUV persists, to understand whether the NP effects are due to the muons, the electrons, or to which part of admixture one needs to perform lepton specific measurements and corresponding global fits; and *(iv)* they allow one to simultaneously determine poorly known hadronic effects from the data.

Extrapolations of global fits to the LHC data after the HL phase, in the (C_9^μ, C_{10}^μ) plane, are shown in Fig. 40. Further improvements beyond those taken into account in projections in Fig. 40 are: *(i)* $B \to K^* e^+ e^-$ angular analysis can be included, where for LFUV NP a simultaneous amplitude analysis of $B \to K^*\mu^+\mu^-$ and $B \to K^* e^+ e^-$ decays is more powerful than separate analyses [875];

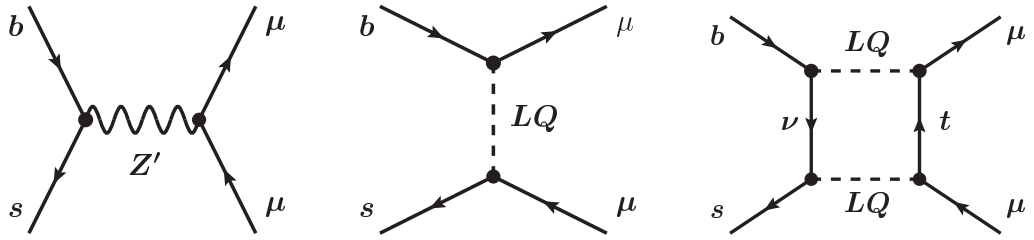

Fig. 41: Examples of NP contributions to $b \to s\mu\mu$ transitions. Left: tree-level Z' contribution. Center: tree-level leptoquark contribution. Right: One-loop leptoquark contribution.

(ii) combined fits to semi-leptonic and non-leptonic decays as well as the precise dilepton invariant mass spectra will allow one to better disentangle long- and short-distance effects in $B \to K^* \mu^+ \mu^-$ [861]; *(iii)* unbinned determination of Wilson coefficients [804] will fully exploit the experimental potential.

7.1.3 Models of NP for $b \to s\ell\ell$

Finally, we briefly review the NP models that can explain the $b \to s\ell\ell$ anomalies, assuming these become statistically significant. The model-independent analysis gives for the NP scale of a tree-level mediator with couplings of $\mathcal{O}(1)$,

$$\Lambda_{\rm NP} = \frac{4\pi}{e} \frac{1}{\sqrt{|V_{tb}V_{ts}^*|}} \frac{1}{\sqrt{|\Delta C_9^\mu|}} \frac{v}{\sqrt{2}} \simeq \frac{35\ \text{TeV}}{\sqrt{|\Delta C_9^\mu|}}\,, \tag{88}$$

where ΔC_i^ℓ denotes the NP contribution to C_i^ℓ. The actual mass of the NP degrees of freedom responsible for the anomalies can be much smaller if the NP couplings are small and/or if the NP contributions arise at loop level, instead of at tree level.

At tree level there are two types of NP particles that can contribute to $b \to s\ell\ell$ transitions: Z' and leptoquarks (see left and center diagrams in Fig. 41). Loop-level contributions of leptoquarks have been studied extensively in the literature (see right diagram in Fig. 41). Other loop-level models have been put forward, see, e.g., Refs. [342, 904–908], but we will not discuss them in detail.

7.1.3.1 Z' models

Models with a Z' that has flavour-violating couplings to quarks and that couples non-universally to leptons can explain the observed anomalies in $b \to s\ell\ell$. In a "simplified model" approach, treating the Z' mass and its couplings to the SM fermions as free parameters, irreducible constraints arise from B_s mixing, neutrino-trident production and LEP bounds on four-lepton contact interactions.

Combining these constraints gives the following maximal values for the Z' contributions to the relevant Wilson coefficients $\Delta C_{9,10}^{e,\mu}$ in the case of *(i)* left-handed lepton couplings (89), or *(ii)* in the case of vectorial lepton couplings (90) [909],

$$|\Delta C_9^\mu| = |\Delta C_{10}^\mu| \lesssim 5.4\,, \quad |\Delta C_9^e| = |\Delta C_{10}^e| \lesssim 0.64\,, \tag{89}$$

$$|\Delta C_9^\mu| \lesssim 9.3\,, \quad |\Delta C_9^e| \lesssim 0.72\,, \quad \Delta C_{10}^\mu = \Delta C_{10}^e = 0\,. \tag{90}$$

The Z' coupling to muons can comfortably explain the anomalies in R_K and R_{K^*} and the other anomalies in $b \to s\mu\mu$ transitions. Addressing R_K and R_{K^*} through a Z' coupling to electrons is possible only in the parameter region close to the current upper bounds from B_s meson mixing and four-lepton contact interactions. The sensitivity to NP of B_s-mixing [910, 911] will become stronger at the time scale of the HL/HE-LHC due to improved lattice predictions of hadronic matrix elements (see Secs. 2 and 11). The Z' mass can be at most several TeV; otherwise an explanation of the anomalies requires couplings to

leptons that are non-perturbatively large. If the Z' has very weak couplings to light quarks and electrons, its production cross section at colliders is tiny. Therefore the Z' could in principle be light, for example at the electroweak scale, or in certain models even much lighter [912–914].

A popular class of UV-complete Z' models is based on gauging the difference of muon-number and tau-number, $L_\mu - L_\tau$. Once physics is introduced that generates flavor-violating couplings of the Z' to quarks, the observed tensions in $b \to s\ell\ell$ decays can be explained [915–922]. $L_\mu - L_\tau$ models predict

$$\Delta C_9^e = 0\,, \quad \Delta C_9^\mu = -\Delta C_9^\tau\,, \quad \Delta C_{10}^e = \Delta C_{10}^\mu = \Delta C_{10}^\tau = 0\,. \tag{91}$$

Besides $L_\mu - L_\tau$, various other combinations of gauged flavor symmetries have been used to construct Z' models that can address the $b \to s\ell\ell$ anomalies [340, 923–936]. Also, scenarios where the Z' couples to both quarks and leptons indirectly through the mixing with heavy vectorlike fermions have been considered [347, 937, 938].

In models with partial compositeness the Z' can be identified with a heavy neutral spin-1 resonance of the composite sector, typically denoted as ρ. Such a resonance generically features flavor-violating couplings to quarks. A large degree of compositeness of the left-handed muons is required to explain the B-decay anomalies [939–944]. The generic expectation in models with partial compositeness is that the ρ couplings are strongest to SM fermions of the third generation, reflecting the mass hierarchy of the SM fermions that is related to their degree of compositeness. Assuming the dominance of couplings to left-handed leptons, these models suggest the pattern

$$\Delta C_9^e \simeq -\Delta C_{10}^e \ll \Delta C_9^\mu \simeq -\Delta C_{10}^\mu \ll \Delta C_9^\tau \simeq -\Delta C_{10}^\tau\,. \tag{92}$$

Models in which the Z' is part of a $SU(2)_L$ triplet have been suggested as a simultaneous explanation of the $b \to s\ell\ell$ anomalies and hints for LFUV in semileptonic charged-current decays, $R(D)$ and $R(D^*)$ [265, 925, 926, 945–948].

Different Z' models predict different patterns of NP effects in $b \to s\ell\ell$ and the related $b \to s\nu\nu$ transitions. Future measurements of these transitions at LHCb and Belle II will therefore allow one to narrow down viable Z' models. For example, the Z' models based on the gauged $L_\mu - L_\tau$ symmetry predict effects in the semileptonic $b \to s\mu^+\mu^-$ and $b \to s\tau^+\tau^-$ transitions of opposite sign, while $b \to se^+e^-$ transitions remain SM-like. In these models, the purely leptonic $B_s \to \mu^+\mu^-$ and $B_s \to \tau^+\tau^-$ decays, as well as the neutrino modes $B \to K^{(*)}\nu\bar{\nu}$, are predicted to be SM-like [915].

A markedly different pattern arises in the Z' scenarios based on dominant couplings to left-handed fermions of the third generation. In those models the $b \to s\tau^+\tau^-$ and $B \to K^{(*)}\nu\bar{\nu}$ rates are typically enhanced compared to the SM predictions by a factor of a few. The $B_s \to \mu^+\mu^-$ rate is predicted to be suppressed by approximately 25% compared to the SM prediction. Finally, in contrast to the $L_\mu - L_\tau$ models, rare lepton flavor-violating decays like $B \to K^{(*)}\tau\mu$ are predicted at levels of $O(10^{-8})$ [337] which might be in reach at the HL-/HE-LHC.

7.1.3.2 Leptoquark models

There are seven quantum number assignments for leptoquarks that allow tree-level couplings to down-type quarks and charged leptons of the SM. These are [264] $S_3 = (\bar{3}, 3, 1/3)$, $R_2 = (3, 2, 7/6)$, $\tilde{R}_2 = (3, 2, 1/6)$, $\tilde{S}_1 = (\bar{3}, 1, 4/3)$, $U_3 = (3, 3, 2/3)$, $V_2 = (\bar{3}, 2, 5/3)$ and $U_1 = (3, 1, -1/3)$. Among these, the couplings of R_2, $\tilde{R}_2$, $\tilde{S}_1$, and V_2 necessarily involve right-handed currents and therefore cannot explain the anomalies. Thus one is left with the triplet scalar S_3, the singlet vector U_1, and the triplet vector U_3. They all contribute at tree level to the operator $(\bar{s}\gamma_\alpha P_L b)(\bar{\mu}\gamma^\alpha P_L \mu)$ and can explain the $b \to s\ell\ell$ anomalies.

In a simplified model approach the constraints on the leptoquark models are very weak. While the leptoquarks S_3, U_1, and U_3 contribute to B_s-mixing, they only do so at the 1-loop level. Correspondingly,

the bounds on the leptoquark couplings from B_s mixing allow leptoquark masses as high as several 10's of TeV. Lower bounds on the leptoquark masses come from direct searches at hadron colliders. All leptoquarks are charged under color and can be pair-produced through strong interactions in pp collisions. Bounds from direct searches at the LHC are currently above 1 TeV in all different channels [949].

There is an additional leptoquark that has been identified as a possible explanation of the rare B-decay anomalies. With the appropriate couplings, the scalar-doublet leptoquark $R_2 = (3, 2, 7/6)$ can contribute to $b \to s\ell\ell$ transitions through 1-loop box diagrams [346] (for an earlier attempt with the scalar singlet leptoquark S_1 see [950]). The R_2 model largely avoids constraints from the neutrino modes $B \to K^{(*)}\nu\bar{\nu}$, and B_s mixing as well as from lepton universality in $b \to c\mu\nu$ and $b \to ce\nu$ transitions. If R_2 is responsible for the anomalies, it is expected to be very close to the current sensitivity of direct searches.

Most studies treat leptoquarks in the simplified-model approach [341, 344, 947, 948, 950–955]. Going beyond simplified models, one finds that the leptoquark couplings required to explain the anomalies are likely not of Minimal-Flavor Violation type [956], and constitute new sources of flavor violation beyond the SM Yukawa couplings. Both scalar and vector leptoquarks could arise, for example, in composite models [957, 958]. The vector leptoquarks could also be the gauge bosons of an enlarged gauge group that is broken not far above the TeV scale [348, 959–965]. The scalar-singlet leptoquark that contributes to $b \to s\ell\ell$ transitions at the loop level can be identified with the right-handed sbottom in the Minimal Supersymmetric Standard Model with R-parity violation [966, 967].

Some leptoquark scenarios are also able to address simultaneously the $b \to s\ell\ell$ anomalies as well as the hints for LFUV in $R(D^{(*)})$ [265, 348, 947, 948, 950, 954, 955, 958, 959, 962–964, 968]. However, many of the models that attempt a simultaneous explanation are strongly constrained by measurements of the $\tau^+\tau^-$ invariant mass spectrum at the LHC [369]; by existing bounds on $B \to K\nu\nu$ and $B \to K^*\nu\nu$ from BaBar and Belle; by existing bounds on LFV tau decays like $\tau \to 3\mu$; from precision measurements of the leptonic couplings of the Z at LEP [969–971], and by lepton-universality tests in leptonic tau decays $\tau \to \ell\nu_\tau\bar{\nu}_\ell$ [969–971].

7.2 Phenomenology of $b \to c\ell\nu$ decays

Authors (TH): Marat Freytsis, Martin Jung, Dean Robinson, Stefan Schacht.

7.2.1 $B \to D^{(*)}l\nu$ form factors and anatomy of $R(D^{(*)})$

Signs of LFUV have not only been seen in loop-suppressed flavor-changing neutral currents discussed above, but also in tree-level decays, namely, in tensions with the SM predictions for the ratios

$$R(D^{(*)}) = \frac{\mathcal{B}(B \to D^{(*)}\tau\nu)}{\mathcal{B}(B \to D^{(*)}l\nu)}, \qquad (l = \mu,\ e). \tag{93}$$

Assuming for the moment the SM particle content only, the $b \to c\ell\nu_{\ell'}$ transitions at scales near m_b can be described by an $SU(3) \times U(1)$-invariant effective Hamiltonian,

$$\mathcal{H}_{\text{eff}}^{b\to c\tau\nu} = \frac{4G_F}{\sqrt{2}} V_{cb} \sum_{\ell\ell'} \Big((\delta_{\ell\ell'} + C_L^{\ell\ell'}) O_{V_L}^{\ell\ell'} + \sum_i C_i^{\ell\ell'} O_i^{\ell\ell'} + \text{h.c.} \Big), \tag{94}$$

where $\ell, \ell' = e, \mu, \tau$ denotes the charged-lepton and neutrino flavor, respectively, and the sum over i runs over the following operators,

$$\begin{aligned} O_{V_{L,R}}^{\ell\ell'} &= (\bar{c}_{L,R}\gamma^\mu b_{L,R})(\bar{\ell}_L\gamma_\mu\nu_{\ell' L}), \qquad & O_{S_{L,R}}^{\ell\ell'} &= (\bar{c}_{R,L} b_{L,R})(\bar{\ell}_R\nu_{\ell' L}), \\ O_T^{\ell\ell'} &= (\bar{c}_R\sigma^{\mu\nu} b_L)(\bar{\ell}_R\sigma_{\mu\nu}\nu_{\ell' L}). \end{aligned} \tag{95}$$

The NP coefficients $C_i^{\ell\ell'}$ depend, in general, on both charged-lepton and neutrino flavor. These operators arise from more fundamental interactions at a higher scale Λ which, in accordance with available LHC data, can be taken to be larger than the electroweak scale v˜. The operators of Eq. (95) should then be embedded into $SU(2)_L \times U(1)$ invariant operators composed of the full SM field content. For C_{V_R} there is no contribution violating lepton-universality at dimension-6, leading to a parametric suppression of at least v^2/Λ^2 for tree-level ultraviolet (UV) completions. Linearly realized electroweak symmetry breaking, captured by the Standard Model effective field theory (SMEFT) [366,375], also yields the prediction $C_{V_R}^{\ell\ell'} \equiv C_{V_R}\delta_{\ell\ell'}$ [972,973]. In this case, sizable contributions to C_{V_R} are excluded by $b \to c(e,\mu)\nu$ [974]. While deviations from this prediction are possible in a non-linear realization of electroweak symmetry breaking [973], at least one of the above-named sources of suppression always remains and right-handed currents do not play a role.

The relevant hadronic matrix elements of the SM operator $O_{V_L}^{\ell\ell}$, i.e., $\langle D|\,\bar{c}\gamma^\mu b\,|\bar{B}\rangle$, $\langle D^*|\,\bar{c}\gamma^\mu b\,|\bar{B}\rangle$, and $\langle D^*|\,\bar{c}\gamma^\mu\gamma_5 b\,|\bar{B}\rangle$, are parametrized using one, two, and three form factors, respectively [975]. The helicity form factors obey unitarity bounds which can be written in an elegant way using the parametrization of Boyd-Grinstein-Lebed (BGL) [976]. The contributions of the helicity form factors S_1 and P_1 (as defined in [975]) to the branching ratios of $B \to Dl\nu$ and $B \to D^*l\nu$ are suppressed by the mass of the final-state lepton. In view of the lack of experimental information on these form factors we need input from theory. In the case of $B \to D$, we are in the fortunate position that lattice results for both V_1 and S_1 at $w \geq 1$ exist [66,977,978], where $w = (m_B^2 + m_{D^{(*)}}^2 - q^2)/(2m_B m_{D^{(*)}})$. This is the reason for the very good agreement of all SM predictions in this case, see Table 27. Recently, also soft photon corrections to $R(D)$ have been discussed [979]. For $B \to D^*$, we have only one data point from lattice, namely $A_1(w=1)$ [980,981] so that it is necessary to use Heavy Quark Effective Theory (HQET) [975,982–988] to relate the $B \to D$ and $B \to D^*$ form factors order-by-order in the heavy quark expansion in terms of Isgur–Wise functions in order to obtain a prediction for P_1 and hence $R(D^*)$.

At NLO in the heavy-quark expansion, i.e., expanding to linear order in α_s/π and $1/m_{c,b}$, there is sufficient differential information in the $B \to D^{(*)}l\nu$ decays to fit to the four Isgur-Wise functions that arise at this order [982,989]. In the literature the theoretical error from using NLO HQET results is under discussion, leading to different results for the error of the SM prediction. HQET can also be used to obtain a stronger version of the unitarity bounds (see Refs. [70,976] for details). Additional model-dependent theoretical input at maximal w can be provided by Light Cone Sum Rules (LCSR) [849,990], or at zero recoil by QCD sum rules [985–988]. We give a summary of theoretical predictions for $R(D^{(*)})$ in Table 27.

Since lattice data is presently available only at zero recoil for $B \to D^*$ and the kinematic suppression requires $d\Gamma[B \to D^*l\nu]/dw$ to vanish at $w = 1$, $|V_{cb}|$ can be obtained from $B \to D^*l\nu$ only by extrapolating $d\Gamma[B \to D^*l\nu]/dw$ back to zero recoil. This procedure can be highly sensitive to the chosen form-factor parameterization and other theoretical inputs; for recent analyses, see Refs. [31,32,69,70,981,982,989,991,992]. Lattice data beyond zero recoil is expected soon (see [993] for preliminary results) from both domain wall and AsqTad ensemble approaches. Combined with abundant future data for $B \to D^*l\nu$ from HL-LHC, extractions of $|V_{cb}|$ that are less sensitive to theoretical inputs will become possible, thereby either resolving or more concretely establishing tensions between exclusive and inclusive measurements of $|V_{cb}|$.

With future experimental data and lattice QCD results (see Sec. 11 and Table 41 therein) the SM prediction of $R(D^*)$ will improve considerably. For an estimate, one may note that the dependence of $d\Gamma/dw$ on the P_1 form factor arises only incoherently, via a contribution of the form $m_l^2|P_1(w)|^2$. This P_1 term contributes approximately 10% of the total integrated $B \to D^*\tau\nu$ rate, which suggests that the dependence of $R(D^*)$ on this form factor should be limited. Assuming a 1% future precision for P_1, using the 50 ab^{-1} which Belle II will presumably gather by 2025, and taking into account the expected improvement of the form factors $A_{1,5}$ and V_4 from the lattice, it is hence reasonable to assume that an

Table 27: Current SM $R(D^{(*)})$ theory predictions and their deviation from experiment $R(D)^{\rm exp} = 0.407(39)(24)$ [197,379,380,994] and $R(D^*) = 0.306(13)(7)$ [16,17,197,379–381,994–997] (HFLAV 2018 summer update). For older SM predictions see Refs. [998–1000]. Table adapted and extended from Ref. [992].

Ref.	$R(D)$	Exp. deviation
[1001]	0.299(3)	2.4σ
[982]	0.299(3)	2.4σ
[989]	0.302(3)	2.3σ

Ref.	$R(D^*)$	Exp. deviation
[982]	0.257(3)	3.3σ
[70]	0.260(8)	2.7σ
[989]	0.257(5)	3.1σ

error of 0.001 for the SM value of $R(D^*)$ might be achieved.

7.2.2 Excited states and other b hadrons: $R(D^{**})$, $R(J/\psi)$, $R(\Lambda_c^{(*)})$ and $R(X_c)$

Measurements of $|V_{cb}|$ and lepton universality can also be probed via B decays to the D^{**} excited states, as well as decays of strange or charmed b hadrons, including $B_s \to D_s^{(*)}$, $B_c \to J/\psi$, and the baryonic $\Lambda_b \to \Lambda_c^{(*)}$ transitions. In comparison to the $B \to D^{(*)}\ell\nu$ decay modes, these modes may variously exhibit higher sensitivities to specific NP operators or, in some cases, may be theoretically cleaner than the decays to the $D^{(*)}$ ground states. These modes can also be important downfeed or crossfeed backgrounds to the $B \to D^{(*)}\ell\nu$ decays and, to the extent they are affected by the same NP operators, must also be understood and measured carefully. The HL-LHC is the only experiment planned that will yield significant samples of these heavier b-hadrons, with precision analyses anticipated from the LHCb experiment. In this subsection we present the motivations and theoretical prospects for the measurement of each of these exclusive decay modes, as well as for measurement of inclusive semileptonic B decays.

The D^{**} excited states comprise four different charmed hadrons: The D_0^*, D_1^*, D_1, D_2^*. In the language of HQET, these furnish two doublets, $\{D_0^*, D_1^*\}$ and $\{D_1, D_2^*\}$, with spin-parity $s_\ell^{\pi_\ell} = \frac{1}{2}^+$ and $\frac{3}{2}^+$, respectively. (In the heavy-quark limit, spin-parity is a conserved quantum number.) The $\frac{3}{2}^+$ states are narrow, with $\Gamma \sim 30$–$50\,\text{MeV}$, because their hadronic decays to $D^{(*)}\pi$ either proceed via a D-wave or violate heavy quark-symmetry, while the $\frac{1}{2}^+$ states are quite broad. Although isolating these excited-state decays will likely be simpler at e^+e^- B factories, which can more easily reconstruct π^0's and photons, analyses of $B \to D^{**}\ell\nu$ decays are also feasible at LHCb Upgrade II, especially for the narrow $\frac{3}{2}^+$ states subsequently decaying to charged hadrons.

The crucial attractive feature of the $B \to D^{**}$ transitions is that various leading-order contributions to the form factors vanish in the heavy-quark limit at zero recoil ($w = 1$), so that $\mathcal{O}(\alpha_s)$ and $\mathcal{O}(1/m_{c,b})$ corrections become important [1002–1005]. The richer structure of the subleading form-factor contributions has the consequence that sensitivity to various NP currents can be much larger than in the ground state decays [1005, 1006]. For example, including only a NP tensor operator, $O_T^{\ell\ell'}$, one finds the ratios $R(X)/R(X)_{\rm SM} \simeq \{1.5, 1.3\}$ for $X = \{D, D^*\}$ at the best fit to the $R(D^{(*)})$ data. However, the same Wilson coefficients result in $R(X)/R(X)_{\rm SM}$ greater than 4.0 or less than 0.5 for $X = \{D_0^*, D_1^*, D_1, D_2^*\}$. Interference between different $B \to D^{**}$ transitions also offers the possibility to probe for new CP-violating phases in the NP operators [1007]. The current SM predictions for all four modes, from fits to Belle data including NLO HQET contributions, are [1006]

$$R(D_0^*) = 0.08\pm0.03, \quad R(D_1^*) = 0.05\pm0.02, \quad R(D_1) = 0.10\pm0.02, \quad R(D_2^*) = 0.07\pm0.01\,. \tag{96}$$

Decays of B mesons to these excited states have total SM branching ratios comparable to the $B \to D^{(*)}\ell\nu$ decays themselves. Combined with the possible large enhancement of the semitauonic

modes by NP contributions, this means that the subsequent $D^{**} \to D^{(*)}X$ decays can then induce important downfeed backgrounds to the $D^{(*)}$ measurements. Analyses of $B \to D^{(*)}\ell\nu$ will therefore typically have to fold in contributions from these excited states. Moreover, anticipated analyses for the inclusive $B \to D\pi\ell\nu$ decays provide an opportunity to probe these excited-state decays and their associated larger NP sensitivities collectively with the ground-state decays. In this context, rather than being thought of as a background, these contributions should be more properly thought of as additional sources of (NP) signal. The large data sets from HL-LHC will then provide a very sensitive set of channels for probing NP contributions to $b \to c\ell\nu$.

The B_s and B_c mesons have production ratios $\sigma(B_s)/\sigma(b\bar{b}) \sim 10\%$ [1008] and $\sigma(B_c)/\sigma(b\bar{b}) \sim 0.2\%$ [1009] in Run 1 LHC. A much smaller sample of B_s mesons may also be produced at B factories running on the $\Upsilon(5S)$ resonance. However, for the B_c the only significant sample of mesons will be produced at HL-LHC. At first glance, the theoretical structure of $B_s \to D_s^{(*,**)}\ell\nu$ can be mapped directly from $B \to D^{(*,**)}\ell\nu$ via the approximate $SU(3)$ flavor symmetry. Some crucial differences are that $\mathcal{B}(D_s^* \to D_s\gamma) \simeq 94\%$, which will be difficult to see at LHCb Upgrade II, while the four D_s^{**} excited states are all narrow, and therefore may be easier to resolve.

The leptonic $B_c \to (J/\psi \to \mu\mu)\ell\nu$ decay mode is reasonably clean experimentally, with measurements for $R(J/\psi)$ already available from LHCb Run 1 data, $R(J/\psi) = 0.71 \pm 0.17\,(\text{stat}) \pm 0.18\,(\text{sys})$ [18], albeit with large uncertainties at present. A central difficulty in probing this mode lies in the large theoretical uncertainties for the $B_c \to J/\psi$ form-factor parameterizations. Predictions for the form factors are typically hadronic-model-dependent, making use of either perturbative QCD, the constituent-quark model, the (non)relativitistic quark model, or QCD sum rules [1010–1018]. The LHCb results have motivated several studies of the form factors [1019–1022]. A recent, more model-independent result combines preliminary lattice QCD results with dispersive bounds and zero-recoil heavy-quark relations, leading to the prediction $0.20 \leq R(J/\psi) \leq 0.39$ [1023], at 95% CL, implying a mild tension at the 1.3σ level with the data.

Abundant samples of Λ_b's will be produced only at (HL-)LHC, with a production cross-section $\sigma(\Lambda_b)/\sigma(b\bar{b}) \sim 10\%$ [779]. From an HQET point of view, the $\Lambda_b \to \Lambda_c$ transitions are theoretically cleaner than the $B \to D^{(*)}$ decays, because the "brown muck" dressing the heavy quark lies in the $s_\ell^{\pi\ell} = 0^+$ ground state. A consequence of this is a relatively simpler form-factor structure, where not only the $\mathcal{O}(\alpha_s)$ but also the $\mathcal{O}(1/m_{c,b})$ and $\mathcal{O}(\alpha_s/m_{c,b})$ subleading contributions are fully fixed by the leading-order HQET structure, reducing the number of free parameters in the form-factor fits. These modes are therefore promising, clean candidates for testing the behavior of the HQET expansion itself, by e.g., assessing the impact of $\mathcal{O}(1/m_c^2)$ contributions. Fitting the subsubleading $\mathcal{O}(\alpha_s, \alpha_s/m_{c,b}, 1/m_c^2)$ HQET structure to existing LHCb data [77] and lattice form factor results [71] implies such terms are of the expected size [1024]. More $\Lambda_b \to \Lambda_c\ell\nu$ data from LHCb will improve the precision of these results, allowing access to other subleading terms. Moreover, with precision lattice calculations of the form factors (see, e.g., Ref. [71]), additional data for these modes may permit precision measurement of $|V_{cb}|$ in an environment with reduced theoretical uncertainties.

The heavy quark expansion is also applicable to Λ_b transitions into excited $\Lambda_c^* = \Lambda_c(2595)$, $\Lambda_c(2625)$ states [1025]. The complexity of the HQET description lies between that of $\Lambda_b \to \Lambda_c$ and $B \to D^{(*)}$ transitions, with two unknown functions up to $\mathcal{O}(1/m_{c,b})$. It was recently demonstrated that simultaneous binned likelihood fits to the rich angular distributions of $\Lambda_b \to \Lambda_c^*\mu\bar{\nu}$ decays can determine these two functions and produce data-driven predictions of $R(\Lambda_c^*)$ [1026]. The projected precision due to parametric effects reaches $\sim 2\%$ for the LHCb Upgrade 1 data set. Due to the spin structure of the Λ_c^* states, these decays provide a complementary LFU probe with a different set of systematic uncertainties when compared to $R(D^{(*)})$ and $R(\Lambda_c)$. More data from LHCb will similarly improve the precision of these results.

Also of interest is the measurement of the inclusive process $B \to X_c\ell\nu$, where X_c can be a

multibody charmed state of arbitrary invariant mass, and the associated ratio $R(X_c)$. In the heavy quark limit $m_b \to \infty$, the amplitude for this process corresponds simply to that of the free quark decay $b \to c\ell\nu$. Corrections to the heavy quark limit are obtained via an OPE in terms of local heavy-quark operators: SM predictions exist at $\mathcal{O}(1/m_b^2)$ including two-loop QCD corrections [1027, 1028], yielding

$$R(X_c) = 0.223 \pm 0.004\,, \tag{97}$$

although recent analyses [1029, 1030] have shown that $1/m_b^3$ corrections can decrease $R(X_c)$ by as much as 5%. Combining this with the inclusive measurement $\mathcal{B}(B \to X_c e\nu) = (10.65 \pm 0.16)\%$ [197] implies $\text{Br}(B \to X_c\tau\nu) = (2.38 \pm 0.05)\%$. This is in good agreement with the LEP measurement $\mathcal{B}(b \to X\tau\nu) = (2.41 \pm 0.23)\%$ [310], where X can be any multibody state. However, the present measurements for $\mathcal{B}(B \to D\tau\nu) + \mathcal{B}(B \to D^*\tau\nu) = (2.71 \pm 0.18)\%$ [1028], when further combined with the SM predictions for $\mathcal{B}(B \to D^{**}\tau\nu)$ [1005, 1006], implies $\mathcal{B}(B \to X_c\tau\nu) > (2.8 \pm 0.2)\%$, already well in excess of the SM prediction for the semitauonic inclusive process. An indirect $R(X_c)$ anomaly then arises independent from the details of the form factor parameterizations involved in $R(D^{(*)})$. Given these tensions, and since measurement of the inclusive process would involve both different theory uncertainties and different systematics compared to the exclusive modes, direct measurement of $B \to X_c\tau\nu$ is of high interest in further understanding the $b \to c\tau\nu$ anomalies.

7.2.3 *Models of NP for $b \to c\tau\nu$*

A possible NP origin of the deviations in $R(D^{(*)})$ requires a large contribution with respect to the SM. Defining $\hat{R}(X) = R(X)/R(X)|_{\text{SM}}$, we have with present data $\hat{R}(D) = 1.36 \pm 0.15$ and $\hat{R}(D^*) = 1.19 \pm 0.06$. This points to $\gtrsim 10\%$ NP contribution to the amplitude when the SM and NP contributions interfere, and $\gtrsim 40\%$ if they do not. The scale of NP for the $R(D^{(*)})$ anomaly is then

$$\Lambda_{\text{NP}} = \frac{1}{\sqrt{|V_{cb}|}} \frac{1}{\sqrt{|\Delta C_i|}} \frac{v}{\sqrt{2}} \sim \frac{1\text{ TeV}}{\sqrt{|\Delta C_i|}}\,, \tag{98}$$

and the contributions are expected to enter at tree level. Possible mediators, assuming they couple only to SM fields, were classified in [1028]. If the present central values $R(D^{(*)})$ are sustained, this anomaly will be established by the time of the measurements at HL/HE-LHC, cf. Fig. 42 left. The focus will hence shift to model differentiation in $b \to c\tau\nu$ and the analysis of the lepton- and quark-flavor structure of the NP contributions. A completely general NP analysis will require theoretical care. For instance, form-factor determinations from $b \to c\ell\nu$ decays could also be sensitive to NP contributions, subject to the constraint that extractions of $|V_{cb}|$ from these decays can be made consistent with all other global data on CKM unitarity. Consequently, experimentally determined form-factor parameters may require a simultaneous fit to the deviations or additional determinations of form-factor ratios, which, however, are expected to be available at the required precision by the start of HL/HE-LHC. See Sec. 11 for corresponding prospects from lattice QCD.

The tree-level mediators that can explain the $R(D)$-$R(D^*)$ anomaly are a W' [925, 926, 943, 946] generating C_{V_L}, a charged color-neutral scalar [999, 1031–1037] generating $C_{S_{L,R}}$ in Eq. (94), and leptoquarks [341,377,828,950,952,954,958,959,962,963,968,1038–1048] generating various couplings, mostly C_{V_L} or $C_{S_L} \sim C_T$. For comparisons between these models, see for instance [1000, 1028, 1049–1053]. Allowing for additional light particles opens up the possibility to address the anomalies with contributions involving right-handed neutrinos [1047, 1054–1060], since the neutrino is not detected.

In order to differentiate between the different combinations of NP operators that these models produce at low energies, information beyond $R(D^{(*)})$ is needed [1030, 1061]. Presently, the available additional observables in $b \to c\tau\nu$ transitions are: *(i)* differential distributions in q^2 [379, 380] already excluding some fine-tuned scenarios despite their large uncertainties; *(ii)* the first measurements of the τ polarization asymmetry and the longitudinal fraction in $B \to D^*\tau\nu$ [995, 996]; *(iii)* the measurement

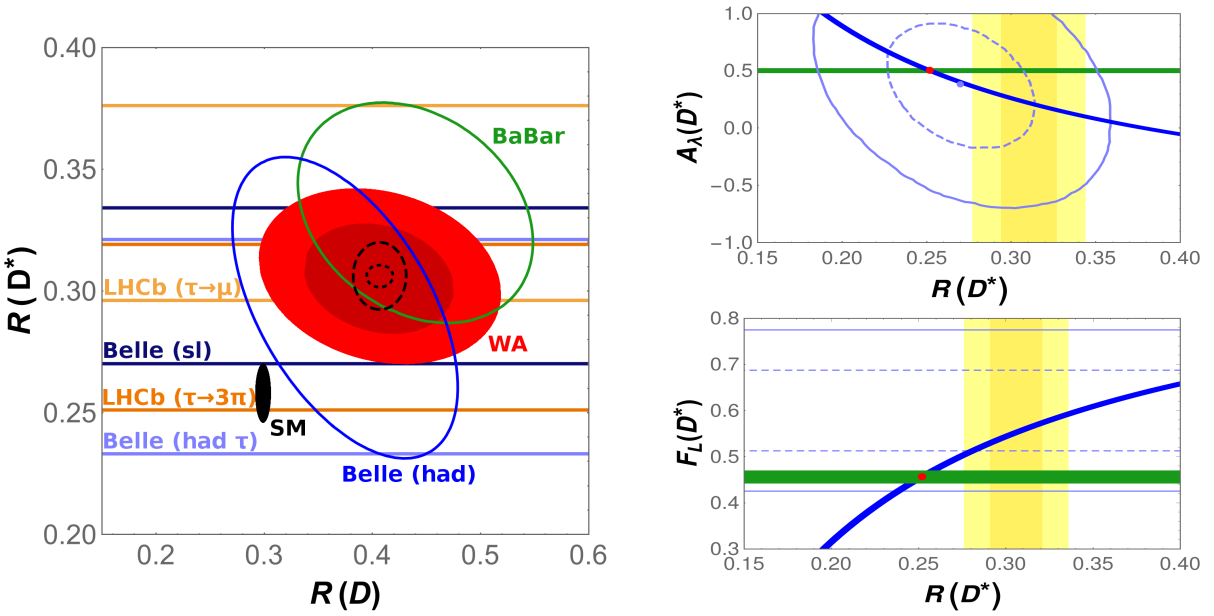

Fig. 42: Left: Present status of the $R(D)$-$R(D^*)$ anomaly, showing the individual measurements (68% CL contours), the world average (68% and 95% CL filled ellipses), the SM prediction (95% CL filled ellipse) as well as the projections for LHCb measurements by 2025 (dashed contour), and Upgrade II (dotted contour, both at 68% CL, assuming the present central value). Right: Correlations between $R(D^*)$ and the τ-polarization asymmetry $A_\lambda(D^*)[= -P_\tau(D^*)]$ (upper panel) and the longitudinal fraction $F_L(D^*)$ (lower panel) for NP scenarios with only a left-handed vector coupling (green) or only scalar couplings (blue), together with the first measurements [995, 996] (light blue) and the experimental average for $R(D^*)$ (yellow bands), excluding [995] in the upper panel. Updated and adapted from Ref. [1031].

of $R(J/\psi)$ [18], which is up to 2σ above the SM prediction, as well as that of any NP model (see the previous subsection); *(iv)* the measurement of the inclusive rate $b \to X\tau\nu$ at LEP [310, 1062], yielding $\hat{R}(X_c) = 1.01 \pm 0.10$, in slight tension with the measurements for $R(D^{(*)})$ [1027–1029, 1031]; *(v)* the (indirect) bound on $B_c \to \tau\nu$ from the B_c lifetime [1046, 1063, 1064], providing a strong constraint on models with only scalar couplings and disfavoring them as a solution for $R(D^*)$ for values close to the present central value.

Additional indirect constraints apply within UV-complete NP models: high-p_T searches for signatures related to potential mediators of these transitions often provide strong constraints via, e.g., $b\bar{b} \to \tau\tau$ [369], $b\bar{c} \to \tau\nu$ [378] or $h \to \tau\tau$ [1065], while radiative corrections can result in constraints from lepton universality in τ decays [970], lepton-flavor violating decays [970], charged-lepton magnetic moments [1065] and electric dipole moments [1066]. Current data on $\Upsilon(1S) \to \tau\tau$ decays also constrain most mediator models, and a future programme of measuring both Υ and ψ decays can have sensitivity to all NP UV completions [1067]. The current bounds on $b \to s\nu\bar{\nu}$, now only $\mathcal{O}(1)$ above the SM [1068, 1069], can also put severe constraints on particular NP models [1070, 1071]. Finally, it is interesting to note that contributions to $b \to s\ell\ell$ and $b \to s\gamma$ are also generically produced at loop level [908].

At the HL/HE-LHC qualitative progress in identifying potential NP in $b \to c\tau\nu$ can be understood chiefly in terms of two classes of observables:

- Precision results for $R(X)$: $R(D^{(*)})$ can establish NP and give basic model differentiation. $R(\Lambda_c^{(*)})$ is a measurement with independent systematics that improves model discrimination since it is sensitive to a different combination of NP parameters. The same applies to inclusive $R(X_c)$, to be

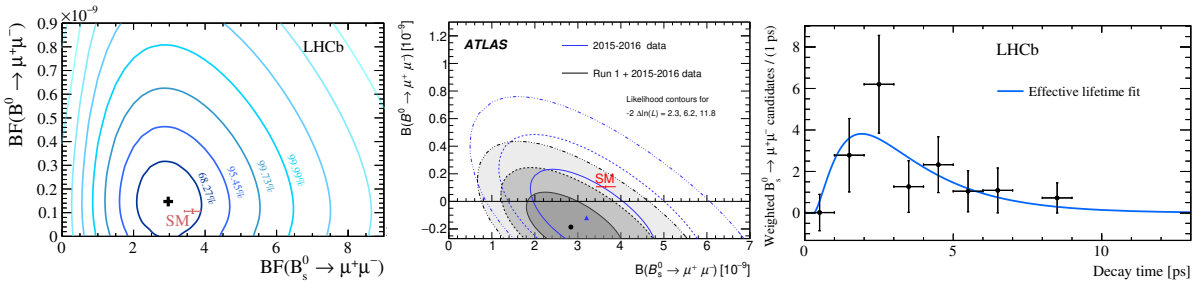

Fig. 43: A two-dimensional representation of the LHCb (left) and ATLAS (middle) branching fraction measurements for $B^0 \to \mu^+\mu^-$ and $B^0_s \to \mu^+\mu^-$. The central values are indicated with the marker. The profile likelihood contours for 1,2,3...Gaussian σ are shown as blue contours (left) and grey shaded areas (middle). The red cross labelled SM reports the Standard Model predictions. Right: background-subtracted $B^0_s \to \mu^+\mu^-$ decay-time distribution with the LHCb fit result superimposed.

measured by Belle II. Other modes, like $R(D_s^{(*)})$ or $R(J/\psi)$, will add to these and provide cross-checks with independent systematic uncertainties.

- Differential-rate measurements in $B \to X\tau\nu$: Differential measurements in q^2 as well as in the helicity angles and the τ-polarization are powerful discriminators between the SM and NP, as well as between different NP models [974, 998, 999, 1031, 1050, 1072–1084]. For instance, the low-recoil region in $B \to D\tau\nu$ is very sensitive to scalar contributions, tensor contributions change the polarization in the high-recoil region in $B \to D^*$ in a unique manner, and left-handed vector contributions leave normalized quantities unchanged while affecting the total rates sizably. Examples for the discriminating power of such measurements are given in Fig. 42 (right), where correlations in NP models are shown together with the first measurements of two proposed quantities by Belle [995, 996]. First studies regarding the reach of LHCb for such observables are presented in Sec. 7.3.7. Already semi-integrated quantities like the forward-backward asymmetry or the observables shown in Fig. 42 can be very powerful in distinguishing different NP scenarios.

At high $p_{\rm T}$, $bc\tau\nu$ operators can also be directly probed by the $pp \to \tau X$+MET (missing transverse energy) signature at the LHC, inclusively [378], or with a b-tag in the final state, with model discrimination possible at the beyond the 3σ level in at the HL-LHC [817]. This channel would allow one to probe all the NP scenarios addressing the $R(D^{(*)})$ anomalies in the HL-LHC phase (see Sec. 10). Analysis of NP effects in $b \to c\tau\nu$ will be made more powerful and self-consistent by the development of dedicated NP reweighting tools such as `Hammer` [1085]. These tools will permit experimental collaborations to efficiently reweight their very large simulated datasets to arbitrary NP models and thus fit for WCs as part of experimental analyses. Observation of NP in $b \to c\tau\nu$ would warrant precise measurements at HL-/HE-LHC of related modes, $b \to c(e,\mu)\nu$, $b \to u\tau\nu$ and $t \to b\tau\nu$ transitions.

7.3 Experimental perspectives

7.3.1 Measurements of $B_q \to ll$ from LHCb/ATLAS/CMS

Following the observation of $B^0_s \to \mu^+\mu^-$ by the CMS and LHCb collaborations [1086], the most stringent constraints on $B^0_s \to \mu^+\mu^-$ and $B^0 \to \mu^+\mu^-$ have been set by the LHCb [15] and ATLAS [825, 1087] collaborations, cf., Fig. 43. Both sets of measurements are compatible with the SM predictions.

HL-LHC will offer a compelling opportunity to extend the ATLAS and CMS $B^0_s \to \mu^+\mu^-$ and $B^0 \to \mu^+\mu^-$ studies to the expected integrated high luminosity. Flexible trigger systems and inner tracker improvements will allow both experiments to maintain efficient low-$p_{\rm T}$ dimuon triggers and achieve good mass resolution, which are the key ingredients for the $B_{s,d} \to \mu^+\mu^-$ analysis. Fig. 44 demonstrates the ATLAS and CMS $B \to \mu^+\mu^-$ invariant mass reconstruction capabilities in the HL-

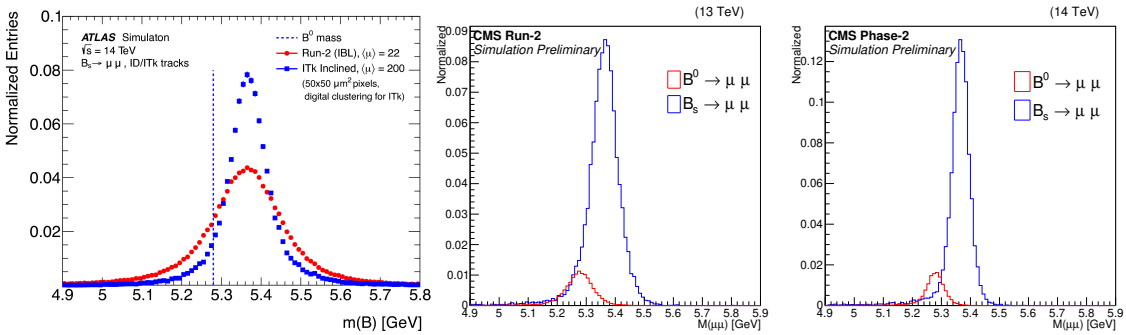

Fig. 44: Left: comparison of the ATLAS invariant mass spectra for simulated $B_s^0 \to \mu^+\mu^-$ events with the current (Run-2) and upgraded (ITk) detectors. A vertical line at the B_d mass value is drawn to visualize the B_s-B_d signals separation. Middle and right plots: CMS B_s^0 and B^0 invariant mass distributions in the Run-2 and Phase-2 scenario respectively. The B_s^0 distribution is normalized to unity and the B^0 distribution is normalized according to the SM expectation. CMS plots are taken from [1088].

LHC era. The pseudorapidity $|\eta_f|$ of the most forward muon (of the candidate) is used to visualize the CMS results and compare the performance of Phase-2 against Run-2. In Fig. 44 the signal mass distributions for $|\eta_f| < 1.4$ are overlaid. The CMS improved separation between $B^0 \to \mu^+\mu^-$ and $B_s^0 \to \mu^+\mu^-$ in Phase-2 is evident; this will help to separate the B^0 signal from the tails of the B_s^0 signal,which now becomes a background for the B^0 measurement.

The LHCb detector is already well optimised for this decay, and planned improvements to the tracking and muon detector shielding in LHCb's upgrades will ensure that the muon reconstruction and identification performance does not degrade with increasing pileup. Both ATLAS and CMS make HL-LHC extrapolations with a PU scenario of 200 interactions per bunch-crossing, which was found not to have strong impact on the analysis performance. While the uncertainty on $\mathcal{B}(B^0 \to \mu^+\mu^-)$ remains statistically limited for HL-LHC projections (300 fb^{-1}/3 ab^{-1}), the projected uncertainty on $\mathcal{B}(B_s^0 \to \mu^+\mu^-)$ depends on the assumptions made for the systematic uncertainties. The current systematic uncertainty is dominated by sources external to the analysis, such as the relative uncertainty associated with the b-quark fragmentation probability ratio, f_s/f_d [1089], followed by the branching fractions of the normalisation modes and less significant systematics arising from internal analysis effects (e.g., 2% each from particle identification and track reconstruction in the case of LHCb, individual efficiencies in the case of ATLAS and CMS).

Systematic uncertainties are treated slightly differently in the projections of the three experiments. ATLAS conservatively assumes in the HL-LHC projections that the f_s/f_d and the normalization modes branching fraction uncertainties will be at the same level as previously used, i.e., 5.8% and 3%, while CMS and LHCb project them to be 3.5% and 1.4%, respectively, based on reasonable assumptions about additional Belle II inputs and improvements in the knowledge of form-factor ratios and branching fraction measurements. A more complete discussion of sensitivity projections and systematics therein from ATLAS and CMS are presented in Refs [1090] and [1088]. For LHCb, the remaining experimental systematic uncertainties are already at the $\sim$ 3 percent level, and because they rely on data-driven corrections from calibration samples they can be expected to be reduced to the $\sim$ 1.4 percent level in Upgrade II. The resulting HL-LHC projected statistical and systematic uncertainties for the three experiments are summarized in table 28; for the comparisons of the ATLAS, CMS and LHCb reaches (such as the one carried out in Fig. 47) , the reference scenarios considered are respectively the "3 ab^{-1} Intermediate", "3 ab^{-1}" and "300 fb^{-1}".

At the end of the Upgrade II data taking period, LHCb assumes to achieve an overall uncertainty

Table 28: Projected ATLAS, CMS and LHCb uncertainty on $\mathcal{B}(B_s^0 \to \mu^+\mu^-)$ and $\mathcal{B}(B^0 \to \mu^+\mu^-)$.The HL-LHC scenario corresponds to an integrated luminosity of 300 fb^{-1} for LHCb and 3 ab^{-1} for ATLAS and CMS. For each extrapolation the total (statistical+systematic) uncertainties are reported.

		$\mathcal{B}(B_s^0 \to \mu^+\mu^-)$	$\mathcal{B}(B^0 \to \mu^+\mu^-)$
Experiment	Scenario	stat + syst %	stat + syst %
LHCb	23 fb^{-1}	8.2	33
LHCb	300 fb^{-1}	4.4	9.4
CMS	300 fb^{-1}	12	46
CMS	3 ab^{-1}	7	16
ATLAS	Run 2	22.7	135
ATLAS	3 ab^{-1} Conservative	15.1	51
ATLAS	3 ab^{-1} Intermediate	12.9	29
ATLAS	3 ab^{-1} High-yield	12.6	26

on $\mathcal{B}(B_s^0 \to \mu^+\mu^-)$ of about 4.4%, which would imply an uncertainty on $\mathcal{B}(B_s^0 \to \mu^+\mu^-)$ to be approximately 0.30×10^{-9} with 23 fb^{-1} and 0.16×10^{-9} with 300 fb^{-1}. The LHCb reach on the ratio of branching fractions $\mathcal{B}(B^0 \to \mu^+\mu^-)/\mathcal{B}(B_s^0 \to \mu^+\mu^-)$ is expected to remain limited by statistics and decrease from 90% for the current measurement to $\sim 34\%$ with 23 fb^{-1} and $\sim 10\%$ with 300 fb^{-1}.

The CMS projections are obtained by extrapolating the Run-2 analysis performances to the HL-LHC scenario. Trigger efficiencies comparable to those of Run-2, with manageable rates, are expected to be attained [1091] and are here assumed. The effect of the increased pileup on the signal selection efficiency was also found to be manageable. The inner tracker of the CMS HL-LHC detector is estimated to provide a 40-50% improvement relative to Run-2 on the dimuon mass resolution. This results in an improved separation of the B_s^0 and B^0 signals, lowering the signal cross-feed contamination that is specially crucial for the B^0 observation, and a reduction of the level of the semileptonic background in the signal region (see Fig. 44). With the full Phase-2 integrated luminosity of 3000 fb^1, CMS expects to measure the $B_s^0 \to \mu^+\mu^-$ branching fraction at the level of 7%. precision, and observe the $B^0 \to \mu^+\mu^-$ decay with a significance in excess of 5σ. Fig. 45 shows the invariant mass fit projections for the $B_{s,d} \to \mu^+\mu^-$ analyses for an integrated luminosity of 3000 fb^{-1}.

The ATLAS projections [1090] are extrapolated from the ATLAS Run 1 analysis [1092]. Assumptions include the training of a multivariate classifier capable of similar background rejection and signal purities and an analysis selection with comparable pile-up immunity as Run 1. The study takes into account the scaling of B production cross-section and integrated luminosity relative to Run 1, and explores different triggering scenarios corresponding to different dimuon transverse momentum thresholds, $(p_T^{\mu_1}, p_T^{\mu_2})$: $(6\,\text{GeV}, 6\,\text{GeV})$, $(6\,\text{GeV}, 10\,\text{GeV})$ and $(10\,\text{GeV}, 10\,\text{GeV})$. For each of these scenarios the sensitivity is categorized on the basis of the signal statistics expected relative to the Run 1 analysis (x15, x60 and x75 respectively, in 3 ab^{-1} of HL-LHC ATLAS data), yielding the projected 68.3%, 95.5% and 99.7% likelihood contours in Fig. 46.

Fig. 47 compares the projected experimental sensitivities of ATLAS, CMS, and LHCb with the BR predictions from a particular class of BSM models [1094]. All estimates use the quoted SM predictions

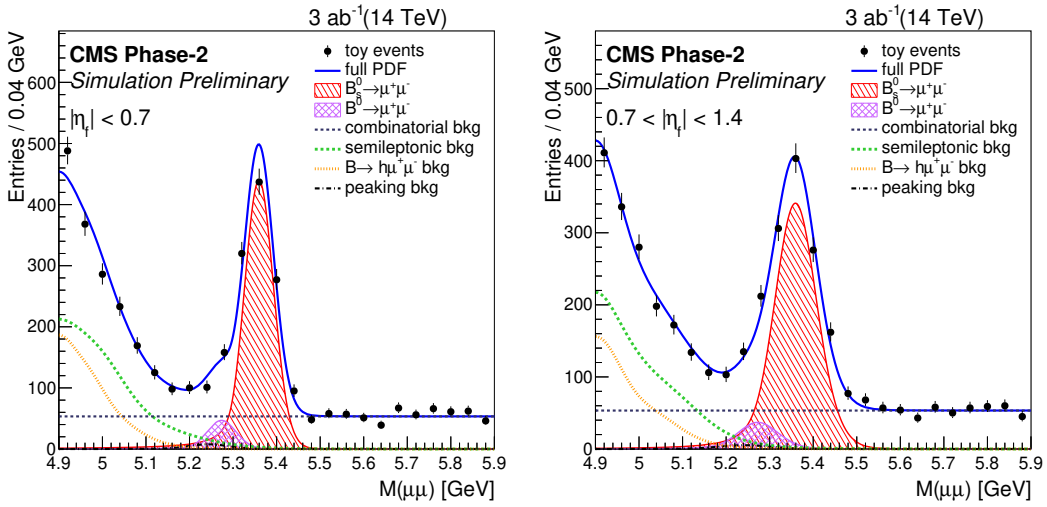

Fig. 45: Projected dimuon invariant mass distributions with overlaid fit results for the $B_{d,s} \to \mu^+\mu^-$ analyses by CMS, with an integrated luminosity of 3000 fb^{-1}. Events where the most forward muon lies in the barrel (left) and forward (right) regions of the detector display different mass resolutions and are categorized accordingly in the analysis. The SM relative B_s^0 and B^0 contributions are here assumed. (Plots are taken from [1088]).

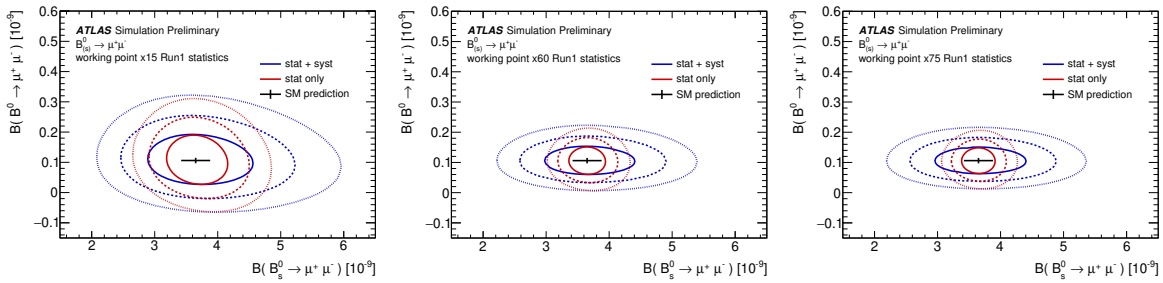

Fig. 46: ATLAS projected 68.3% (solid), 95.5% (dashed) and 99.7% (dotted) confidence level profiled likelihood ratio contours for the "conservative" (top), "intermediate" (middle) and "high-yield" HL-LHC extrapolations. Red contours do not include the systematic uncertainties, which are then included in the blue ellipsoids. The black point shows the SM theoretical prediction and its uncertainty [1093].

as central values for the branching fractions. The estimated experimental sensitivity at HL-LHC is close to the uncertainty of the current SM prediction from theory, which is dominated by the uncertainty on the B_s^0 decay constant, f_{B_s}, determined from lattice QCD calculations, and the CKM matrix elements. Both are expected to improve in precision in the future. The power of the HL-LHC data set to discriminate not only between the SM and BSM models, but also within the parameter space of those BSM models, is clear.

With the HL-LHC data set, precise measurements of additional observables are possible, namely the effective lifetime, $\tau^{\text{eff}}_{\mu\mu}$, and the time-dependent CP asymmetry of $B_s^0 \to \mu^+\mu^-$ decays. Both quantities are sensitive to possible new contributions from the scalar and pseudo-scalar sector in a way complementary to the branching ratio measurement [320]. The effective lifetime is related to the mean B_s^0 lifetime τ_{B_s} through the relation

$$\tau^{\text{eff}}_{\mu\mu} = \frac{\tau_{B_s}}{1-y_s^2}\frac{1+2A^{\mu\mu}_{\Delta\Gamma}y_s+y_s^2}{1+A^{\mu\mu}_{\Delta\Gamma}y_s}\,, \tag{99}$$

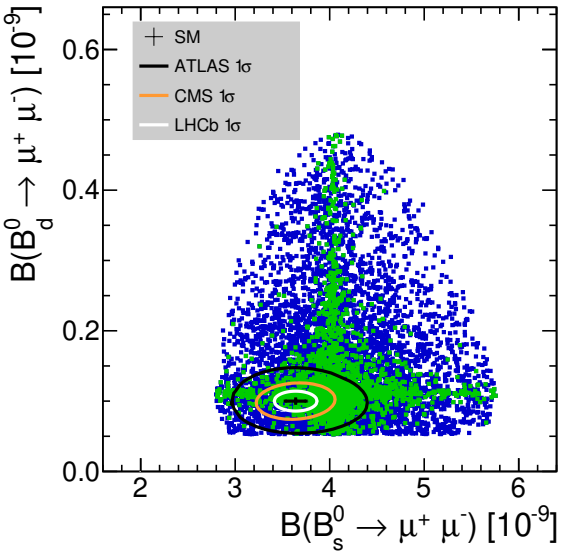

Fig. 47: $B_s^0 \to \mu^+\mu^-$ and $B^0 \to \mu^+\mu^-$ branching ratios as computed using new sources of flavour-changing neutral currents, as discussed in Ref. [1094]. The green points are the subset consistent with other measurements. The black cross point is the SM prediction, while the coloured contours show the expected 1-sigma HL-LHC sensitivites of ATLAS, CMS, and LHCb.

where $y_s = \tau_{B_s}\Delta\Gamma_s/2$, and $\Delta\Gamma_s = \Gamma_{B^0_{sL}} - \Gamma_{B^0_{sH}}$. In the SM, $A^{\mu\mu}_{\Delta\Gamma} = 1$, with only the heavy mass eigenstate decaying to $\mu^+\mu^-$. In BSM scenarios it can take any value between -1 and 1. LHCb has performed the first measurement of the $B_s^0 \to \mu^+\mu^-$ effective lifetime using a dataset of 4.4 fb^{-1}, resulting in $\tau^{\rm eff}_{\mu\mu} = 2.04 \pm 0.44 \pm 0.05$ ps [15] (Fig. 43, right). The relative uncertainty on $\tau^{\rm eff}_{\mu\mu}$ is expected to decrease to approximately 8% with 23 fb^{-1} and 2% with 300 fb^{-1}, being statistically limited.

The CMS sensitivity for a measurement of the $B_s^0 \to \mu^+\mu^-$ effective lifetime is estimated using an ensemble of pseudo-experiments generated with parameters reflecting the projected Phase-2 conditions. The signal lifetime distribution for each pseudo-experiment is obtained using the sPlot technique [1095] to separate out the background, and then fitted with a model consisting of an exponential function, convolved with a Gaussian function that describes the expected decay time resolution, and multiplied by an efficiency function that accounts for reconstruction effects. The outcome of such a pseudo-experiment is shown in Fig. 48. The effective lifetime is expected to be measured with a statistical precision of 3% at 3000 fb^{-1}.

While the current experimental uncertainty is larger than for $\tau_{B^0_{sH}} - \tau_{B^0_{sL}}$, a $2-3\%$ uncertainty on $\tau^{\rm eff}_{\mu\mu}$ would allow to set stringent constraints on $A^{\mu\mu}_{\Delta\Gamma}$ and in particular would allow to break the degeneracy between any possible contribution from new scalar and pseudoscalar mediators.

Assuming a tagging power of about 3.7% [10], a dataset of 300 fb^{-1} allows LHCb to reconstruct a pure sample of more than 100 flavour-tagged $B_s^0 \to \mu^+\mu^-$ decays (effective yield) and measure their time-dependent CP asymmetry. From the relation

$$\frac{\Gamma(B_s^0(t) \to \mu^+\mu^-) - \Gamma(\bar{B}_s^0 \to \mu^+\mu^-)}{\Gamma(B_s^0(t) \to \mu^+\mu^-) + \Gamma(\bar{B}_s^0 \to \mu^+\mu^-)} = \frac{S_{\mu\mu}\sin(\Delta m_s t)}{\cosh(y_s t/\tau_{B_s}) + A^{\mu\mu}_{\Delta\Gamma}\sinh(y_s t/\tau_{B_s})}\,, \tag{100}$$

where t is the signal proper time and Δm_s is the mass difference of the heavy and light B_s^0 mass eigenstates, $S_{\mu\mu}$ can be measured with an uncertainty of about 0.2. The signal yield expected in a 23 fb^{-1} dataset, on the other hand, is too low to allow a meaningful constraint to be set on $S_{\mu\mu}$. A nonzero value for $S_{\mu\mu}$ would automatically indicate evidence of CP-violating phases beyond the SM.

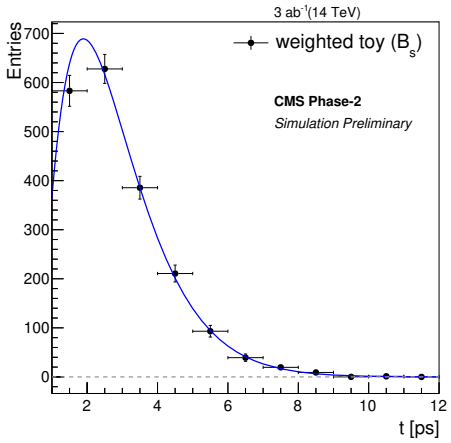

Fig. 48: Projection of a background-subtracted proper decay time distribution, with fit result overlaid, with the CMS experiment and 3000 fb^{-1}. The estimated uncertainty in the $B_s^0 \to \mu^+\mu^-$ effective lifetime is obtained by fitting an ensemble of corresponding pseudo-experiments. (The plot is taken from [1088]).

Being sensitive to a wider set of effective operators (O_7, O_9 and O_{10}) [1096], the $B_s^0 \to \mu^+\mu^-\gamma$ decay offers an interesting counterpart to $B_s^0 \to \mu^+\mu^-$. The theoretical branching fraction is expected to be one order of magnitude larger than the $B_s^0 \to \mu^+\mu^-$ one [1097], owing to the removal of the helicity suppression, when integrated over the full q^2 spectrum. However, the presence of the photon makes the direct reconstruction challenging at LHCb. No limit exist today on the $B_s^0 \to \mu^+\mu^-\gamma$ channel, while the $B^0 \to \mu^+\mu^-\gamma$ is limited at 1×10^{-7} at 90% CL by the BaBar experiment [1098].

Given the experimental difficulty, two complementary techniques are employed for the study of the $B_s^0 \to \mu^+\mu^-\gamma$ decay at LHCb. The first is a full reconstruction which is more sensitive at low and mid q^2, where the photon energy is higher, and the second, recently proposed in Ref. [834], without photon reconstruction but only sensitive at high q^2.

The only non-negligible partially reconstructed background is the not yet measured $B_d \to \mu^+\mu^-\pi^0$, whose branching fraction is theoretically estimated to be of the same order of magnitude as the signal. The main difficulty of the measurement is therefore the combinatorial background, because the uncertainty on the photon momentum enlarges the signal width and blurs its kinematics. Based on current reconstruction efficiencies, the expected sensitivity at the end of Run 3 (Upgrade II) is $\sim 9\sigma$ ($\sim 22\sigma$). The use of $B_s \to J/\psi\eta$ and $B_d \to K\pi\gamma$ as normalisation channels reduces the systematic uncertainties due to the selection.

The partially reconstructed method consists of studying the $B_s^0 \to \mu^+\mu^-\gamma$ decay as a shoulder on the left of the $B_s^0 \to \mu^+\mu^-$ peak in the dimuon mass distribution. The SM contribution as background has been considered negligible so far. Conversely, large branching fractions could be easily excluded [834] when considering this as an additional component. The SM branching fraction for this region would be around 2×10^{-10}, implying a first observation would be possible with Run 3 and certainly with Run 4 data, while extremely tight limits could already be determined with Run 2.

7.3.2 Measurements of $b \to s\ell\ell$ from LHCb/ATLAS/CMS

7.3.2.1 Yield and systematics evolution

With the large data set that will be collected at the end of Run 5, it will be possible to make a precise determination of the angular observables in narrow bins of q^2 or using a q^2-unbinned approach [804,806];

LHCb foresees to achieve around 440 000 fully reconstructed $B^0 \to K^{*0}\mu^+\mu^-$ decays, CMS around 700 000 excluding the q^2 range overlapping with the resonant decays [1099].

The current ATLAS, CMS and LHCb measurements are statistically limited. For LHCb the major systematics are those which affect the calculation of the angular acceptance. Most of the systematic uncertainties are expected to reduce significantly with more integrated luminosity due to larger control samples. Both the LHCb statistical and systematic uncertainties are therefore scaled with integrated luminosity when obtaining the projections. In this context it is interesting to note that Upgrade II will provide signal yields that are of the order of the current tree-level control modes $B^0 \to J/\psi K^{*0}$ and $B_s^0 \to J/\psi\,\phi$. In the most recent measurement of ϕ_s from $B_s^0 \to J/\psi\,\phi$, the systematic uncertainties on the decay amplitudes due to modeling of the angular acceptance were already at the 0.001-0.002 level. Therefore, even without considering further improvements from the larger control samples available in Upgrade II, these uncertainties will not systematically limit the Upgrade II analysis.

The CMS sensitivity for the measurement of the P_5' parameter at HL-LHC is extrapolated [1099] from the CMS Run-1 results [1100] under some assumptions: effects of improvements in the analysis strategy (e.g., different selection criteria or fits) are not considered and the trigger thresholds and efficiency are assumed to remain the same. The latter is likely to be a conservative assumption since the availability of tracking information at the first level trigger may result in a higher efficiency than in Run-1. The extrapolation method also assumes that the signal-to-background is the same; indeed, the main source of background is from other b-hadron decays, whose cross-section scales the same as the signal. Samples of simulated events are used to evaluate three relevant aspects of the analysis, namely mass resolution, CP mistagged rate, and the effect of pileup, to justify the extrapolation method; no degradation in the projected analysis performance was found. For each q^2 bin, the expected $B^0 \to K^{*0}\mu^+\mu^-$ signal yields are obtained from a sample of simulated signal events generated with the Phase-2 conditions, including an average of 200 pileup, and scaled to the integrated luminosity of 3000 fb $^{-1}$.

The estimated statistical uncertainty on the P_5' parameter at 3000 fb^{-1} is obtained by scaling the statistical uncertainty measured in Run-1 by the square root of the ratio between the yields observed in Run-1 and the Phase-2 simulation. The evolution of the systematic uncertainties is also extrapolated from the Run-1 analysis. Improved understanding of theory and the experimental apparatus is expected to reflect in a factor of 2 reduction in many uncertainties in the Phase-2 scenario. The uncertainties which depend on the available amount of data are scaled the same as the statistical uncertainties. The uncertainty related to the limited number of simulation events is neglected, under the assumption that sufficiently large simulation samples will be available by the time the HL-LHC becomes operational.

The ATLAS study extrapolates the signal and background yields based on the Run 1 analysis data observations [1101], accounting for 3000 fb^{-1} of integrated luminosity and a $\times 1.7$ increase in the b production cross-section. Monte-Carlo simulations are employed to estimate the experimental precision achievable, including the improved 4-prong invariant mass resolution projected with the ATLAS upgraded tracking system [1102]. Particular care is taken in applying likely trigger selections, emulating trigger thresholds and accounting for the q^2-dependency of the trigger efficiency. Three different sets of di-muon trigger threshold scenarios are considered: two 6 GeV muons, the combinaton of 6 GeV and a 10 GeV muon, or two muons of 10 GeV. Although not dominant in the result, systematic uncertainties are carefully extrapolated as well: signal and background fit model accuracies are expected to improve in proportion to the available data statistics, detector acceptance and mistagging accuracy are driven by MC statistics and thus assumed to produce negligible effects, the inclusion of S-wave contributions to the data fit is extrapolated to improve the effect of this systematic by a factor 5, and detector alignment and B-field systematic uncertainties are expected to improve approximately by a factor 4 with larger calibration samples and the use of new techniques [1103].

The precision of the future $b \to s\ell\ell$ branching fraction measurements from the LHC experiments will be limited also by the knowledge of the $B \to J/\psi X$ decay modes that are used to normalise the

Table 29: Wilson coefficients in benchmark NP scenarios. The first scenario is inspired by the present discrepancies in the rare decays, including the angular distributions of the decay $B^0 \to K^{*0}\mu^+\mu^-$ and the measurements of the branching fraction ratios R_K and R_{K^*}. The second scenario is inspired by the possibility of explaining the rare decays discrepancies and those measured in the observables $R(D^{(*)})$. The third and fourth scenarios assume small nonzero right-handed couplings.

scenario	$C_9^{\rm NP}$	$C_{10}^{\rm NP}$	C_9'	C_{10}'
I	-1.4	0	0	0
II	-0.7	0.7	0	0
III	0	0	0.3	0.3
IV	0	0	0.3	-0.3

observed signals. The knowledge of these branching fractions will be improved by the Belle II collaboration but will inevitably limit the precision of the absolute branching fractions of rare $b \to s\ell^+\ell^-$ processes. The comparison between the predicted and measured branching fractions will in any case be limited by the theoretical knowledge of the form factors.

7.3.2.2 Sensitivity projections

In order to estimate the sensitivity to BSM effects in $b \to s\ell\ell$ decays, a number of benchmark NP scenarios are considered, see Table 29. Scenarios I and II are inspired by the current discrepancies. The first scenario is the one that best explains the present $b \to s\mu\mu$ decay data. The second is the best explaining the rare semileptonic measurements within a purely left-handed scenario. This requirement is theoretically well motivated and arises in models designed to simultaneously explain the discrepancies seen in both tree-level semitauonic and loop-level semileptonic decays. The third and fourth scenarios assume that the current discrepancies are not confirmed but there is instead a small contribution from right-handed currents that would not be visible with the current level of experimental precision. These scenarios will serve to illustrate the power of the large LHCb Upgrade II data set to distinguish between different NP models. This power relies critically on the ability to exploit multiple related decay channels.

Unlike the systematics limited branching fractions, a more precise comparison between theory and experiment can be achieved by studying isospin and CP asymmetries, which will be experimentally probed at percent-level precision with the LHCb Upgrade II data set. This will also enable new decay modes to be studied, for example higher spin K^* states and modes with larger numbers of decay products. It is also possible to reduce theoretical and experimental uncertainties by comparing regions in angular phase-space of $b \to s\ell\ell$ decays. The angular distribution of $B \to V\ell^+\ell^-$ decays, where V is a vector meson, can be expressed in terms of eight q^2-dependent angular coefficients that depend on the Wilson coefficients and the form factors. Measurements of angular observables in $B^0 \to K^{*0}\mu^+\mu^-$ decays show a discrepancy with respect to the SM predictions [813, 814, 899, 1100, 1101, 1104–1118]. This discrepancy is largest in the so-called optimized observable P_5' [899]. The decay $B_s^0 \to \phi\mu^+\mu^-$ can also be described by the same angular formalism as the $B^0 \to K^{*0}\mu^+\mu^-$ decay. However, in this case the B_s^0 and $\overline{B}_s^0$ mesons decay to a common final state and it is not possible to determine the full set of observables without tagging the initial flavour of the B_s^0.

The expected precision of an unbinned LHCb-only determination of P_5' in the SM and in Scenarios I and II is illustrated in Fig. 49, where we have followed the theoretical approaches in Refs. [804, 806] for the predictions. Upgrade II will enable these scenarios to be clearly separated from the SM and from each other. By combining information from all of the angular observables in the decay, it will also be possible for LHCb to distinguish models with much smaller NP contributions. Fig. 50 shows the expected $3\,\sigma$ sensitivity to NP in the Wilson coefficients $C_{9,10}'$ assuming the central values for the SM,

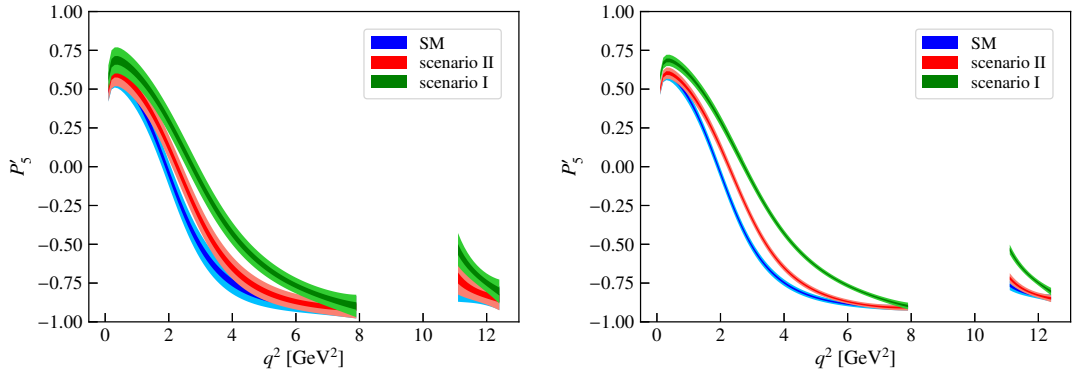

Fig. 49: Total experimental sensitivity, including systematics, at LHCb to the P_5' angular observable in the SM, Scenarios I and II for the Run 3 (left) and the Upgrade II (right) data sets. The sensitivity is computed assuming that the charm-loop contribution is determined from the data.

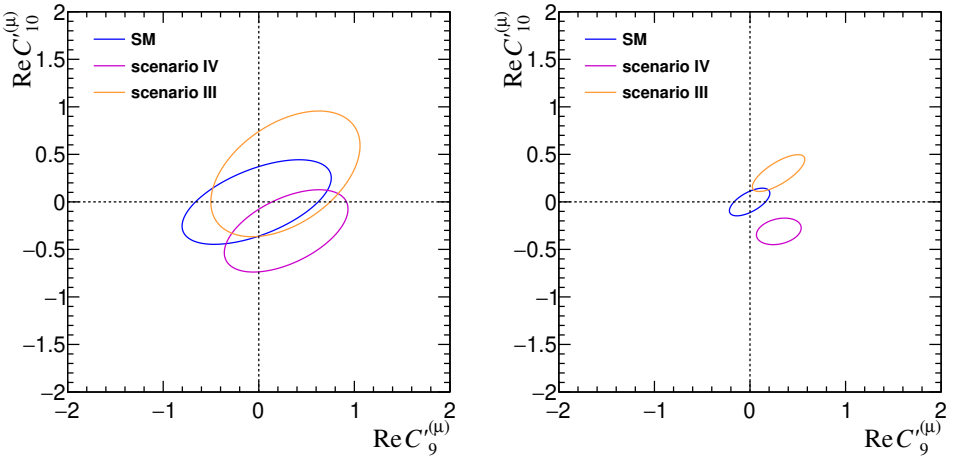

Fig. 50: Expected sensitivity to the Wilson coefficients C_9' and C_{10}' from the future LHCb analysis of the $B^0 \to K^{*0}\mu^+\mu^-$ decay. The ellipses correspond to 3 σ contours for the SM, Scenario III and Scenario IV for the Run 3 (left) and the Upgrade II (right) data sets.

Scenario III and Scenario IV. These scenarios are also clearly distinguishable with the precision that will be available with the Upgrade II data set.

The CMS projected statistical uncertainties and total uncertainties for the measurement of P_5' versus q^2 for an integrated luminosity of 3000 fb^{-1} are shown in Fig. 51, along with the Run 1 results.

The P_5' total uncertainties in the q^2 bins are estimated to improve up to a factor of 15 in the 3000 fb^{-1} scenario [1099], compared to those quoted in the Run-1 analysis. The extrapolation to 300 fb^{-1} integrated luminosity is also estimated by CMS [1099] and provides an improvement of up to a factor of 7 with respect to the Run-1 analysis. These results are among the inputs of the global fit to the HL-LHC experimental projections shown in Fig. 40, which indicates the potential sensitivity to the SM and NP scenarios in the C_9- C_{10} Wilson-coefficient plane.

The foreseen Phase-2 total integrated luminosity offers the opportunity to perform the angular analysis in narrower q^2 bins, in order to measure the P_5' shape as a function of q^2 with finer granularity. The q^2 region below the J/ψ mass(-squared), which is more sensitive to possible new physics effects, is considered. Each Run-1 q^2 bin is split into smaller and equal-size bins to achieve a statistical uncertainty of the order of the total systematic uncertainty in the same bin. With respect to the Phase-2 systematic

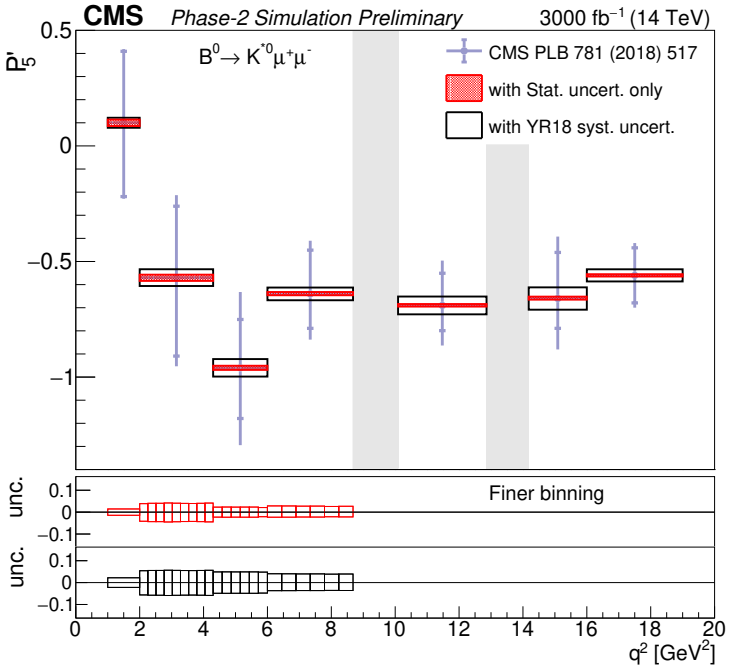

Fig. 51: Projected statistical (hatched regions) and total (open box) uncertainties on the CMS P_5' parameter versus q^2 in the Phase-2 scenario at 3000 fb^{-1}. The CMS Run-1 measurement of P_5' is also shown by circles with inner vertical bars representing the statistical uncertainties and outer vertical bars representing the total uncertainties. The vertical shaded regions correspond to the J/Ψ and ψ' resonances. The two lower pads represent the statistical (upper pad) and total (lower pad) uncertainties with the finer q^2 binning. (The plot is taken from [1099]).

uncertainties with wider bins, the systematic uncertainties that were scaled the same as the statistical uncertainties are adjusted to account for less data in each finer bin while the other uncertainties are unchanged. The corresponding statistical and total uncertainties on P_5' are shown in the lower two pads of Fig. 51.

The analysis in narrow q^2 bins provides a better determination of the P_5' parameter shape which will allow for testing theoretical predictions. The CMS available projection is for the single P_5' angular parameter; with the foreseen HL-LHC statistics, CMS will have the capability to perform a full angular analysis of the $B^0 \to K^{*0}\mu^+\mu^-$ decay mode.

The ATLAS [1119] projected statistical and systematic uncertainties are provided in the same q^2 bins employed in the Run 1 analysis, and for the same set of angular parameters already published. Table 30 reports the combined statistical and systematic uncertainty expectations for the different trigger scenarios considered, with the projected uncertainties for all the angular parameters compared to current theoretical predictions in figure 52. Reference [1119] includes full detail on the breakdown of statistical and systematic contributions. The precision in measuring e.g. the P_5' parameter is expected to improve by a factor between 5 and 9 relative to the Run 1 result, depending on the trigger scenario considered.

Furthermore, with large data sets expected at the HL-LHC it will be possible for the LHC experiments to probe $B \to V\ell^+\ell^-$ SM contributions, under the premise that a genuine NP contribution is expected to have no q^2 dependence, while, e.g., a charm loop contribution is expected to grow when approaching the pole of the charmonia resonances. A measurement using Breit-Wigner functions to parametrise the resonances, and their interference with the short-distance contributions to the decay, was

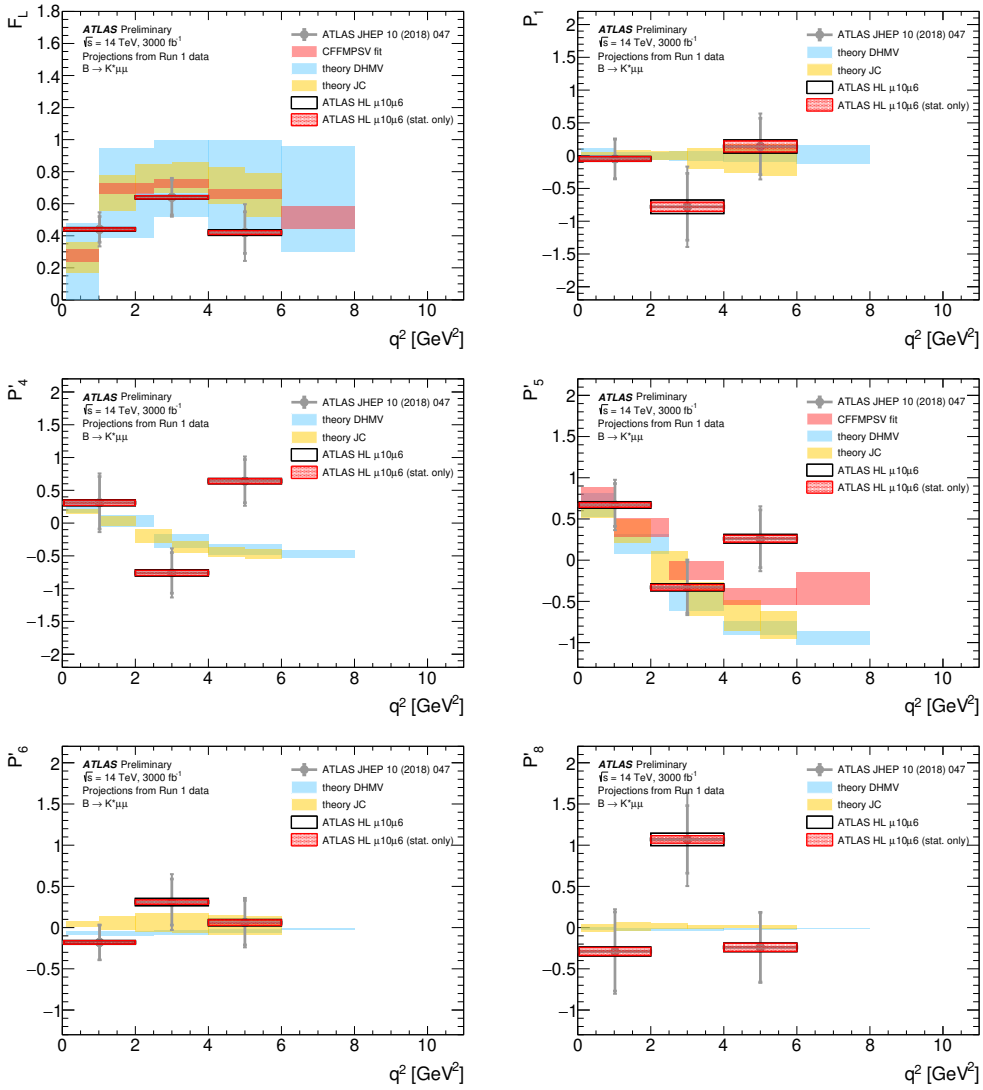

Fig. 52: Projected ATLAS HL-LHC measurement precision in the $F_{\rm L}$, P_1, P_4', P_5', P_6' and P_8' parameters for the intermediate μ10μ6 trigger scenario compared to the ATLAS Run 1 measurement. Alongside theory predictions (CFFMPSV [1120], DHMV [1121], JC [843]) are also shown. Both the projected statistical and the total (statistical and systematic) uncertainties are shown. While the HL-LHC toy-MC were generated with the DHMV central values of the $F_{\rm L}$ and $P_i^{(\prime)}$ parameters, in these plots the central values are moved to the ATLAS Run 1 measurement for better visualization of the improvement in the precision.

proposed in Ref. [805]. A similar technique has already been applied by LHCb to the Run-1 data for the $B^+ \to K^+\mu^+\mu^-$ decay [1122]. An alternative approach using additional phenomenological inputs has also been proposed [1123]. Such a combination of phenomenological and experimental methods may improve our knowledge of the charm-loop contribution and form factors, which would allow C_9^μ and C_{10}^μ to be determined with great precision in $b \to s\mu\mu$ transitions.

7.3.3 Measurements of b → dll

Thanks to LHCb's particle identification capabilities, the Upgrade II data set will provide a unique opportunity to make precise measurements of $b \to d\ell\ell$ processes. Using the Run 1 and 2 data sets, LHCb data

Table 30: Combined systematic and statistical uncertainties on the $F_{\rm L}$ and $P_i^{(\prime)}$ parameters from the 2012 ATLAS data measurement and projected to the HL-LHC phase for the three trigger scenarios discussed in the text.

LHC phase	$q^2[\,\mathrm{GeV}^2]$	$\delta^{\rm tot}_{F_L}$	$\delta^{\rm tot}_{P_1}$	$\delta^{\rm tot}_{P'_4}$	$\delta^{\rm tot}_{P'_5}$	$\delta^{\rm tot}_{P'_6}$	$\delta^{\rm tot}_{P'_8}$
Run 1	$[0.04, 2.0]$	0.11	0.31	0.45	0.31	0.21	0.51
	$[2.0, 4.0]$	0.12	0.61	0.37	0.34	0.34	0.57
	$[4.0, 6.0]$	0.18	0.50	0.38	0.39	0.30	0.43
HL-LHC μ6μ6	$[0.04, 2.0]$	0.010	0.027	0.037	0.037	0.019	0.046
	$[2.0, 4.0]$	0.008	0.093	0.040	0.038	0.040	0.070
	$[4.0, 6.0]$	0.016	0.083	0.032	0.047	0.033	0.041
HL-LHC μ10μ6	$[0.04, 2.0]$	0.011	0.037	0.046	0.040	0.023	0.055
	$[2.0, 4.0]$	0.011	0.103	0.047	0.042	0.044	0.075
	$[4.0, 6.0]$	0.018	0.100	0.040	0.053	0.038	0.052
HL-LHC μ10μ10	$[0.04, 2.0]$	0.018	0.065	0.076	0.059	0.041	0.093
	$[2.0, 4.0]$	0.017	0.15	0.074	0.068	0.059	0.100
	$[4.0, 6.0]$	0.026	0.17	0.074	0.082	0.063	0.090

have been used to observe the decays $B^+ \to \pi^+\mu^+\mu^-$ [1124, 1125] and $\Lambda_b^0 \to p\pi^-\mu^+\mu^-$ [1126], and to find evidence for the decays $B^0 \to \pi^+\pi^-\mu^+\mu^-$ (in a $\pi^+\pi^-$ mass region that is expected to be dominated by $B^0 \to \rho^0\mu^+\mu^-$) and $B_s^0 \to \overline{K}^{*0}\mu^+\mu^-$ [1127] with branching fractions at the $\mathcal{O}(10^{-8})$ level. The existing data samples comprise $\mathcal{O}(10)$ decays in these decay modes. The upgrade will provide samples of thousands, or tens of thousands of such decays. The ability to measure the properties of these processes depends heavily on the PID performance of the LHCb subdetectors. In the case of the $B_s^0 \to \overline{K}^{*0}\mu^+\mu^-$ decay, excellent mass resolution is also critical to separate B_s^0 and B^0 decays.

The ratio of branching fractions between the CKM-suppressed $b \to d\ell\ell$ transitions and their CKM-favoured $b \to s\ell^+\ell^-$ counterparts, together with theoretical input on the ratio of the relevant form factors, enables the ratio of CKM elements $|V_{td}|/|V_{ts}|$ to be determined. The precision on $|V_{td}|/|V_{ts}|$ from such decays is dominated at present by the statistical uncertainty on the experimental measurements of $B^+ \to \pi^+\mu^+\mu^-$, and is much less precise than the determination from mixing measurements. The theoretical uncertainty at high-q^2 is at the level of 4% and is expected to improve with further progress on the form factors from lattice QCD [1128]. Around 17 000 $B^+ \to \pi^+\mu^+\mu^-$ decays are expected in the full 300 fb^{-1} dataset, allowing an experimental precision better than 2%.

The current set of measurements of $b \to s\ell\ell$ processes have demonstrated the importance of angular measurements in the precision determination of Wilson coefficients. With the LHCb Upgrade II dataset, where a sample of 4300 $B_s^0 \to \overline{K}^{*0}\mu^+\mu^-$ decays is expected, it will be possible to make a full angular analysis of a $b \to d\ell^+\ell^-$ transition. The $B_s^0 \to \overline{K}^{*0}\mu^+\mu^-$ decay is both self-tagging and has a final state involving only charged particles. The LHCb Upgrade II data set will allow the angular observables in this decay to be measured with better precision than the existing measurements of the $B^0 \to K^{*0}\mu^+\mu^-$ angular distribution.

The LHCb Upgrade II dataset will also give substantial numbers of $B^{0,+} \to \rho^{0,+}\mu^+\mu^-$ and $\Lambda_b^0 \to N\mu^+\mu^-$ decays. Although the $B^0 \to \rho^0\mu^+\mu^-$ decay does not give the flavour of the initial B meson, untagged measurements will give sensitivity to a subset of the interesting angular observables. Analysis of the

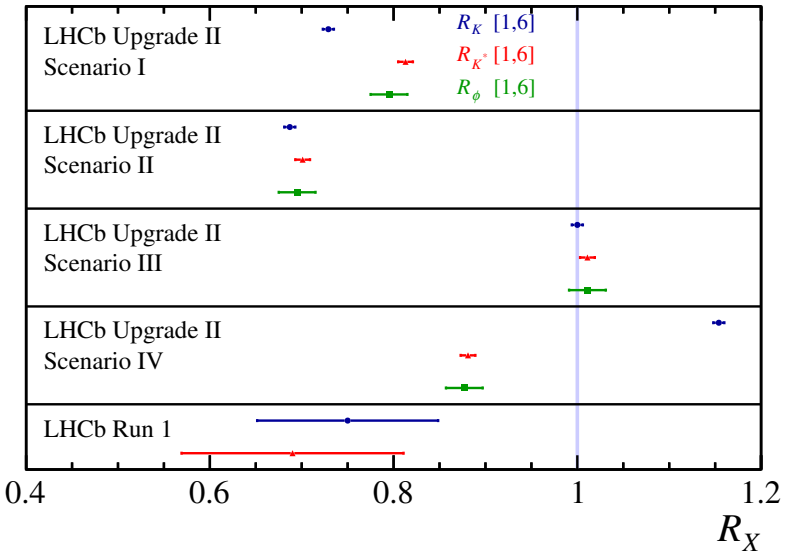

Fig. 53: Projected sensitivity for the R_K, R_{K^*} and R_ϕ measurements in different NP scenarios with the Upgrade II data set. The existing Run 1 measurements of R_K and R_{K^*} are shown for comparison.

$\Lambda_b^0 \to N^* \mu^+ \mu^-$ decay will require statistical separation of overlapping $p\pi^-$ resonances with different J^P by performing an amplitude analysis of the final-state particles.

The combination of information from $\mathcal{B}(B^0 \to \mu^+\mu^-)$, the differential branching fraction of the $B^+ \to \pi^+\mu^+\mu^-$ decay, and angular measurements, notably of $B_s^0 \to \overline{K}^{*0}\mu^+\mu^-$, will indicate whether NP effects are present in $b \to d$ transitions at the level of 20% of the SM amplitude with more than 5σ significance.

7.3.4 LFU tests in $b \to (s,d)\ell\ell$

The Run 1 LHCb data have been used to perform the most precise measurements of R_K and R_{K^*} to-date [5,6] (see Fig. 53). These measurements are compatible with the SM at the level of 2.1–2.6 standard deviations. Assuming the current detector performance, approximately 46 000 $B^+ \to K^+e^+e^-$ and 20 000 $B^0 \to K^{*0}e^+e^-$ candidates are expected in the range $1.1 < q^2 < 6.0\,\text{GeV}^2/c^4$ in the Upgrade II data set. The ultimate precision on R_K and R_{K^*} will be better than 1%. The importance of the Upgrade II data set in distinguishing between different NP scenarios is highlighted in Fig. 53. With this data set all four NP scenarios could be distinguished at more than $5\,\sigma$ significance.

The Upgrade II data set will also enable the measurement of other R_X ratios e.g., R_ϕ, R_{pK} and the ratios in CKM suppressed decays. For example, with $300\,\text{fb}^{-1}$, it will be possible to determine $R_\pi = \mathcal{B}(B^+ \to \pi^+\mu^+\mu^-)/\mathcal{B}(B^+ \to \pi^+e^+e^-)$ with a few percent statistical precision. A summary of the expected performance for a number of different R_X ratios is indicated in Table 31.

In addition to improvements in the R_X measurements, the enlarged Upgrade II data set will give access to new observables. For example, the data will allow precise comparisons of the angular distribution of dielectron and dimuon final-states. Differences between angular observables in $B \to X\mu^+\mu^-$ and $B \to Xe^+e^-$ decays are theoretically pristine [1129, 1130] and are sensitive to different combinations of Wilson coefficients compared to the R_X measurements. Fig. 54 shows that an upgraded LHCb detector will enable such decays to be used to discriminate between different NP models, for example separating between Scenarios I and II [1131]. Excellent NP sensitivity can be achieved irrespective of the assumptions made about the hadronic contributions to the decays.

In the existing LHCb detector, electron modes have an approximately factor five lower efficiency

Table 31: Estimated yields of $b \to se^+e^-$ and $b \to de^+e^-$ processes and the statistical uncertainty on R_X in the range $1.1 < q^2 < 6.0\,\text{GeV}^2/c^4$ extrapolated from the Run 1 data. A linear dependence of the $b\bar{b}$ production cross section on the pp centre-of-mass energy and unchanged Run 1 detector performance are assumed. Where modes have yet to be observed, a scaled estimate from the corresponding muon mode is used.

Yield	Run 1 result	$9\,\text{fb}^{-1}$	$23\,\text{fb}^{-1}$	$50\,\text{fb}^{-1}$	$300\,\text{fb}^{-1}$
$B^+ \to K^+e^+e^-$	254 ± 29 [5]	1 120	3 300	7 500	46 000
$B^0 \to K^{*0}e^+e^-$	111 ± 14 [6]	490	1 400	3 300	20 000
$B_s^0 \to \phi e^+e^-$	–	80	230	530	3 300
$\Lambda_b^0 \to pKe^+e^-$	–	120	360	820	5 000
$B^+ \to \pi^+e^+e^-$	–	20	70	150	900
R_X precision	Run 1 result	$9\,\text{fb}^{-1}$	$23\,\text{fb}^{-1}$	$50\,\text{fb}^{-1}$	$300\,\text{fb}^{-1}$
R_K	$0.745 \pm 0.090 \pm 0.036$ [5]	0.043	0.025	0.017	0.007
$R_{K^{*0}}$	$0.69 \pm 0.11 \pm 0.05$ [6]	0.052	0.031	0.020	0.008
R_ϕ	–	0.130	0.076	0.050	0.020
R_{pK}	–	0.105	0.061	0.041	0.016
R_π	–	0.302	0.176	0.117	0.047

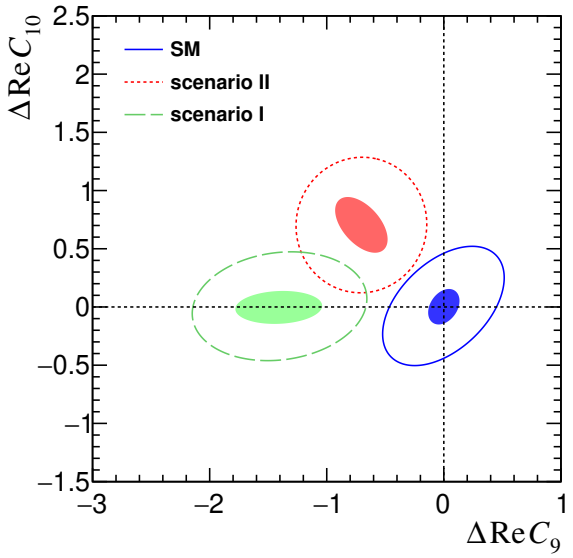

Fig. 54: Constraints on the difference in the C_9 and C_{10} Wilson coefficients from angular analyses of the electron and muon modes with the Run 3 and Upgrade II data sets. The 3σ regions for the Run 3 data sample are shown for the SM (solid blue), a vector-axial-vector new physics contribution (red dotted) and for a purely vector new physics contribution (green dashed). The shaded regions denote the corresponding constraints for the Upgrade II data set.

than the corresponding muon modes, owing to the tendency for the electrons to lose a significant fraction of their energy through bremsstrahlung in the detector. This loss impacts on the ability to reconstruct, trigger and select the electron modes. The precision with which observables can be extracted therefore depends primarily on the electron modes and not the muon modes. In order for R_X measurements to

benefit from the large Upgrade II data samples, it will be necessary to reduce systematic uncertainties to the percent level. These uncertainties are controlled by taking a double ratio between R_X and the decays $B \to J/\psi X$, where the J/ψ decays to $\mu^+\mu^-$ and e^+e^-. This approach is expected to work well, even with very large data sets.

Other sources of systematic uncertainty can be mitigated through design choices for the upgraded detector. The recovery of bremsstrahlung photons is inhibited by the ability to find the relevant photons in the ECAL (over significant backgrounds) and by the energy resolution. A reduced amount of material before the magnet would reduce the amount of bremsstrahlung and hence would increase the electron reconstruction efficiency and improve the electron momentum resolution. Higher transverse granularity would aid signal selection and help reduce the backgrounds. With a large number of primary pp collisions, the combinatorial background will increase and will need to be controlled with the use of timing information. However, the Run 1 data set indicates that it may be possible to tolerate a significant (i.e., larger than a factor two) increase in combinatorial backgrounds without destroying the signal selection ability.

7.3.5 *Time dependent angular analyses in $b \to (s,d)ll$*

Time dependent analyses of rare decays into CP-eigenstates can deliver orthogonal experimental information to time-integrated observables. So far, no time-dependent measurement of the $B^0_s \to \phi\mu^+\mu^-$ decay has been performed due to the limited signal yield of 432 ± 24 in the Run 1 data sample [900]. However, the larger data samples available in Upgrade II will enable time-dependent studies. The framework describing $\overline{B}$ and $B \to V\ell^+\ell^-$ transitions to a common final-state is discussed in Ref. [1132], where several observables are discussed that can be accessed with and without flavour tagging. Two observables called s_8 and s_9, which are only accessible through a time-dependent flavour-tagged analysis, are of particular interest. These observables are proportional to the mixing term $\sin(\Delta m_s t)$ and provide information that is not available through flavour specific decays. Assuming a time resolution of around $45\,\text{fs}$ and an effective tagging power of 5% results in an effective signal yield of 2000 decays for the Upgrade II data set.

As a first step towards a full time-dependent analysis, the effective lifetime of the decay $B^0_s \to \phi\mu^+\mu$ can be studied. The untagged time-dependent decay rate is given by

$$\frac{\mathrm{d}\Gamma}{\mathrm{d}t} \propto e^{-\Gamma_s}\left[\cosh\left(\frac{\Delta\Gamma_s t}{2}\right) + A^{\Delta\Gamma}\sinh\left(\frac{\Delta\Gamma_s t}{2}\right)\right]. \tag{101}$$

The observable $A^{\Delta\Gamma}$ can be related to the angular observables F_L and S_3 via $A^{\Delta\Gamma} = 2S_3 - F_\mathrm{L}$. Due to the significant lifetime difference $\Delta\Gamma_s$ in the B^0_s system, even an untagged analysis can probe right-handed currents. For the combined low- and high-q^2 regions, preliminary studies suggest a statistical sensitivity to $A^{\Delta\Gamma}$ of 0.05 can be achieved with a $300\,\text{fb}^{-1}$ data set.

With the Upgrade II data set it will also be possible to perform a time-dependent angular analysis of the $b \to d$ process $B^0 \to \rho^0\mu^+\mu^-$. This process differs from $B^0_s \to \phi\mu^+\mu^-$ in two important regards: it is CKM suppressed and therefore has a smaller SM branching fraction; and $\Delta\Gamma_d \approx 0$, removing sensitivity to $A^{\Delta\Gamma}$. The uncertainties on the angular observables are expected to be of the order of 0.1 for this case.

The time-dependent angular analyses will still be statistically limited even with $300\,\text{fb}^{-1}$. It will be important to maintain good decay-time resolution and the performance of the particle identification will be crucial to control backgrounds, as well as to improve flavour tagging performance.

7.3.6 *Measurements of $b \to s\gamma$*

The time dependent CP asymmetry of $B \to f_{CP}\gamma$ arises from the interference between decay amplitudes with and without $B^0_{(s)} - \overline{B}^0_{(s)}$ mixing and is predicted to be small in the SM [881, 1133, 1134]. As a

consequence, a large asymmetry due to interference between the B mixing and decay diagrams can only be present if the two photon helicities contribute to both B and $\overline{B}$ decays. From the time dependent decay rate

$$\Gamma(B^0_{(s)}(\overline{B}^0_{(s)}) \to f_{CP}\gamma)(t) \sim e^{-\Gamma_s t}\Big[\cosh\left(\frac{\Delta\Gamma_{(s)}}{2}\right) - \mathcal{A}^{\Delta}\sinh\left(\frac{\Delta\Gamma_{(s)}}{2}\right) \pm \\ \pm \mathcal{C}_{CP}\cos\left(\Delta m_{(s)}t\right) \mp \mathcal{S}_{CP}\sin\left(\Delta m_{(s)}t\right)\Big], \tag{102}$$

where A^{Δ}, $\mathcal{C}_{CP}$ and $\mathcal{S}_{CP}$ depend on the photon polarisation [888]. Two strategies can be devised: one studying the decay rate independently of the flavour of the B meson, which allows A^{Δ} to be accessed, and one tagging the flavour of the B meson, which accesses $\mathcal{S}_{CP}$ and $\mathcal{C}_{CP}$. The first strategy has been exploited at LHCb to study the 4000 $B^0_s \to \phi\gamma$ candidates collected in Run 1 to obtain $A^{\Delta} = -0.98^{+0.46}_{-0.52}\,(\text{stat})^{+0.23}_{-0.20}\,(\text{syst})$ [891], compatible at two standard deviations from the prediction of $A^{\Delta}_{\text{SM}} = 0.047^{+0.029}_{-0.025}$.

With $\sim$ 60k signal candidates expected with 50 fb^{-1}, the full analysis, including flavour tagging information, will improve the statistical uncertainty on A^{Δ} to ~ 0.07, and will need a careful control of the systematic uncertainties. The analysis performed with $\sim$ 800k signal decays expected with 300 fb^{-1}, with a statistical uncertainty to ~ 0.02, requires some of the possible improvements in π^0 reconstruction of the Upgrade II detector to be able to use the full statistical power of the data.

In addition to studying the B^0_s system, LHCb can study the time-dependent decay rate of $B^0 \to K^0_S\pi^+\pi^-\gamma$ decays, which permits access of the photon polarisation through the $\mathcal{S}_{CP}$ term. With $\mathcal{O}(1000)$ signal events in Run 1, around 35k and 200k are expected at the end of Run 4 and Upgrade II, respectively (1.75k and 10k when considering the flavour tagging efficiency), opening the doors to a very competitive measurement of $\mathcal{S}_{CP}$ in the B^0 system.

Another way to study the photon polarisation is through the angular correlations among the three-body decay products of a kaonic resonance in $B \to K_{\text{res}}(\to K\pi\pi)\gamma$, which allows the direct measurement of the photon polarisation parameter in the effective radiative weak Hamiltonian [883]. As a first step towards the photon polarisation measurement, LHCb observed nonzero photon polarisation for the first time by studying the photon angular distribution in bins of $K^+\pi^-\pi^+$ invariant mass [1135], but the determination of the value of this polarisation could not be performed due to the lack of knowledge of the hadronic system. To overcome this problem, a method to measure the photon polarisation using a full amplitude analysis of $B \to K\pi\pi\gamma$ decays is currently under development [1136], with an expected statistical sensitivity on the photon polarisation parameter of $\sim 5\%$ in the charged mode with the Run 1 dataset. The extrapolation of the precision to 300 fb^{-1} results in a statistical precision better than 1%, and hence control of the systematic uncertainties will be crucial.

The polarisation of the photon emitted in $b \to s\gamma$ transitions can also be accessed via semileptonic $b \to s\ell\ell$ transitions, for example in the decay $B^0 \to K^{*0}\ell^+\ell^-$. Indeed, as mentioned in previous sections, at very low q^2 these decays are dominated by the electromagnetic dipole operator $\mathcal{O}^{(\prime)}_7$. Namely, the longitudinal polarisation fraction (F_{L}) is expected to be below 20% for $q^2 < 0.2\,\text{GeV}^2/c^4$. In this q^2 region, the angle ϕ between the planes defined by the dilepton system and the $K^{*0} \to K^+\pi^-$ decay is sensitive to the $b \to s\gamma$ photon helicity.

While the $K^{*0}\mu^+\mu^-$ final state is experimentally easier to select and measure at LHCb, the $K^{*0}e^+e^-$ final state allows q^2 values below $4m^2_\mu$ to be probed, where the sensitivity to the photon helicity is maximal. Compared to the radiative channels used for polarisation measurements, the $B^0 \to K^{*0}e^+e^-$ final state is fully charged and gives better mass resolution and therefore better separation from partially reconstructed backgrounds.

The sensitivity of this decay channel at LHCb was demonstrated by an angular analysis performed with Run 1 data [1137]. The angular observables most sensitive to the photon polarisation at low q^2 are $A^{(2)}_{\text{T}}$ and A^{Im}_{T}, as defined in Ref. [1137, 1138]. Indeed, in the limit $q^2 \to 0$, these observables can

be expressed by the following functions of $C_{7\gamma}^{(\prime)}$ (assuming NP contributions to be much smaller than $|C_{7\gamma}^{\rm SM}|$):

$$A_{\rm T}^{(2)}(q^2 \to 0) \simeq 2\frac{\mathcal{R}e(C_7^{\prime *})}{|C_7|} \quad \text{and} \quad A_{\rm T}^{\rm Im}(q^2 \to 0) \simeq 2\frac{\mathcal{I}m(C_7^{\prime *})}{|C_7|}. \tag{103}$$

In order to maximise the sensitivity to the photon polarisation, the angular analysis should be performed as close as possible to the low q^2 endpoint. However, the events at extremely low q^2 have worse ϕ resolution (because the two electrons are almost collinear) and are polluted by $B^0 \to K^{*0}\gamma$ decays with the γ converting in the VELO material. In the Run 1 analysis [1137] the minimum required $m(e^+e^-)$ was set at $20\,\text{MeV}/c^2$, but this should be reduced as the Upgrade II VELO detector will have a significantly lower material budget (multiple scattering is the main effect worsening the ϕ resolution). Similarly, the background from γ conversions will be reduced with a lighter RF-foil or with the complete removal of it in Upgrade II [807].

Using the signal yield as given in Table 31 leads to the following statistical sensitivities to $A_{\rm T}^{(2)}$ and $A_{\rm T}^{\rm Im}$: 12% with $8\,\text{fb}^{-1}$, 7% with $23\,\text{fb}^{-1}$ and 2% with $300\,\text{fb}^{-1}$. The theoretical uncertainty induced when this observable is translated into a photon polarisation measurement is currently at the level of 2% but should improve by the time of the Upgrade II analyses. The current measurements performed with Run 1 data have a systematic uncertainty of order 5% coming mainly from the modelling of the angular acceptance and from the uncertainty on the angular shape of the combinatorial background. The acceptance is independent of ϕ at low q^2 and its modelling can be improved with larger simulation samples and using the proxy channel $B^0 \to K^{*0}J/\psi(\to e^+e^-)$.

Weak radiative decays of b baryons are largely unexplored, with the best limits coming from CDF: $\mathcal{B}(\Lambda_b^0 \to \Lambda\gamma) < 1.3 \times 10^{-3}$ at 90% CL [1139]. They offer a unique sensitivity to the photon polarisation through the study of their angular distributions, and will constitute one of the main topics in the radiative decays programme in the LHCb Upgrade II.

With predicted branching fractions of $O(10^{-5} - 10^{-6})$, the first challenge for LHCb will be their observation, as the production of long-lived particles in their decay, in addition to the photon, means in most cases that the b-baryon secondary vertex cannot be reconstructed. This makes their separation from background considerably more difficult than in the case of regular radiative b decays.

The most abundant of these decays is $\Lambda_b^0 \to \Lambda(\to p\pi^-)\gamma$, which is sensitive to the photon polarisation mainly[7] through the distribution of the angle between the proton and the Λ momentum in the rest frame of the Λ (θ_p),

$$\frac{\mathrm{d}\,\Gamma}{\mathrm{d}\cos\theta_p} \propto 1 - \alpha_\gamma \alpha_{p,1/2} \cos\theta_p, \tag{104}$$

where α_γ is the asymmetry between left- and right-handed amplitudes and $\alpha_{p,1/2} = 0.642 \pm 0.013$ [310] is the $\Lambda \to p\pi^-$ decay parameter. Using specialised trigger lines for this mode $15 - 150$ signal events are expected using the Run 2 dataset. Preliminary studies show that a statistical sensitivity to α_γ of $(20 - 25)\%$ is expected with these data, which would be reduced to $\sim 15\%$ with $23\,\text{fb}^{-1}$ and below 4% with $300\,\text{fb}^{-1}$. In the LHCb Upgrade II, the addition of timing information in the calorimeter will be important to be able to study this combinatorial-background dominated decay; additionally, improved downstream reconstruction would allow the use of downstream Λ decays, which make up more than 2/3 of the total signal.

The $\Xi_b \to \Xi^-(\to \Lambda(\to p\pi^-)\pi^-)\gamma$ decay presents a richer angular distribution, with dependence to the photon polarisation in both the Λ angle (θ_Λ) and proton angle (θ_p),

$$\frac{\mathrm{d}\,\Gamma}{\mathrm{d}\cos\theta_\Lambda \cos\theta_p} \propto 1 - \alpha_\gamma \alpha_\Xi \cos\theta_\Lambda + \alpha_{p,1/2} \cos\theta_p \left(\alpha_\Xi - \alpha_\gamma \cos\theta_\Lambda\right), \tag{105}$$

[7] In the following, we assume that the Λ_b^0 (and any other beauty baryon) polarisation is zero [1140], removing part of the photon polarisation dependence.

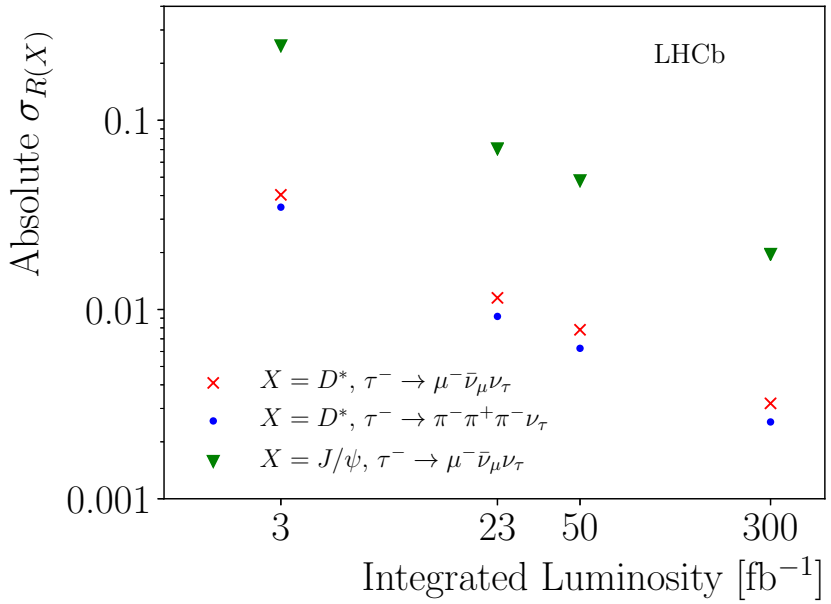

Fig. 55: The projected absolute uncertainties on $\mathcal{R}(D^*)$ and $\mathcal{R}(J/\psi)$ from the current sensitivities (at 3 fb^{-1}) to 23 fb^{-1}, 50 fb^{-1}, and 300 fb^{-1}.

but the lower $\sigma(pp \to \Xi_b)$, combined with a lower reconstruction efficiency due to the presence of one extra track, results in an order of magnitude fewer events than in the Λ_b^0 case, making the increase of statistics from the Upgrade II even more relevant. With a similar sensitivity to the photon polarisation to that of $\Lambda_b^0 \to \Lambda(\to p\pi^-)\gamma$, $\Xi_b \to \Xi^-\gamma$ decays will allow this parameter to be probed with a precision of 40% and 10% with 23 and 300 fb^{-1}, respectively.

7.3.7 *Measurements of $b \to c\ell\nu$ including B_c and b-baryon prospects*

LHCb has made measurements of $R(D^{(*)})$ using both muonic ($\tau^+ \to \mu^+\nu\nu$) and hadronic ($\tau^+ \to \pi^+\pi^-\pi^+\nu$) decays of the tau lepton [16, 17, 997]. Due to the presence of multiple neutrinos these decays are extremely challenging to measure. The measurements rely on isolation techniques to suppress partially reconstructed backgrounds, B meson flight information to constrain the kinematics of the unreconstructed neutrinos, and a multidimensional template fit to determine the signal yield. Fig. 55 shows how the absolute uncertainties on the LHCb muonic and hadronic $\mathcal{R}(D^*)$ measurements are projected to evolve with respect to the current status. The major uncertainties are the statistical uncertainty from the fit, the uncertainties on the background modelling and the limited size of simulated samples. A major effort is already underway to commission fast simulation tools. The background modelling is driven by a strategy of dedicated control samples in the data, and so this uncertainty will continue to improve with larger data samples. From Run 3 onward it is assumed that, taking advantage of the full software HLT, the hadronic analysis can normalise directly to the $B^0 \to D^{*-}\mu^+\nu_\mu$ decay, thus eliminating the uncertainty from external measurements of $\mathcal{B}(B^0 \to D^{*-}\pi^+\pi^-\pi^+)$. It is assumed that all other sources of systematic uncertainty will scale as $\sqrt{\mathcal{L}}$. With these assumptions, an absolute uncertainty on $\mathcal{R}(D^*)$ of 0.003 will be achievable for the muonic and hadronic modes with the 300 fb^{-1} Upgrade II dataset.

On the timescale of Upgrade II, interest will shift toward new observables beyond the branching fraction ratio [1141]. The kinematics of the $B \to D^*\tau\nu$ decays is fully described by the dilepton mass, and three angles which are denoted χ, θ_L and θ_D. LHCb is capable of resolving these three angles, as can be seen in Fig. 56. However, the broad resolutions demand very large samples to extract the underlying physics. The decay distributions within this kinematic space are governed by the underlying spin

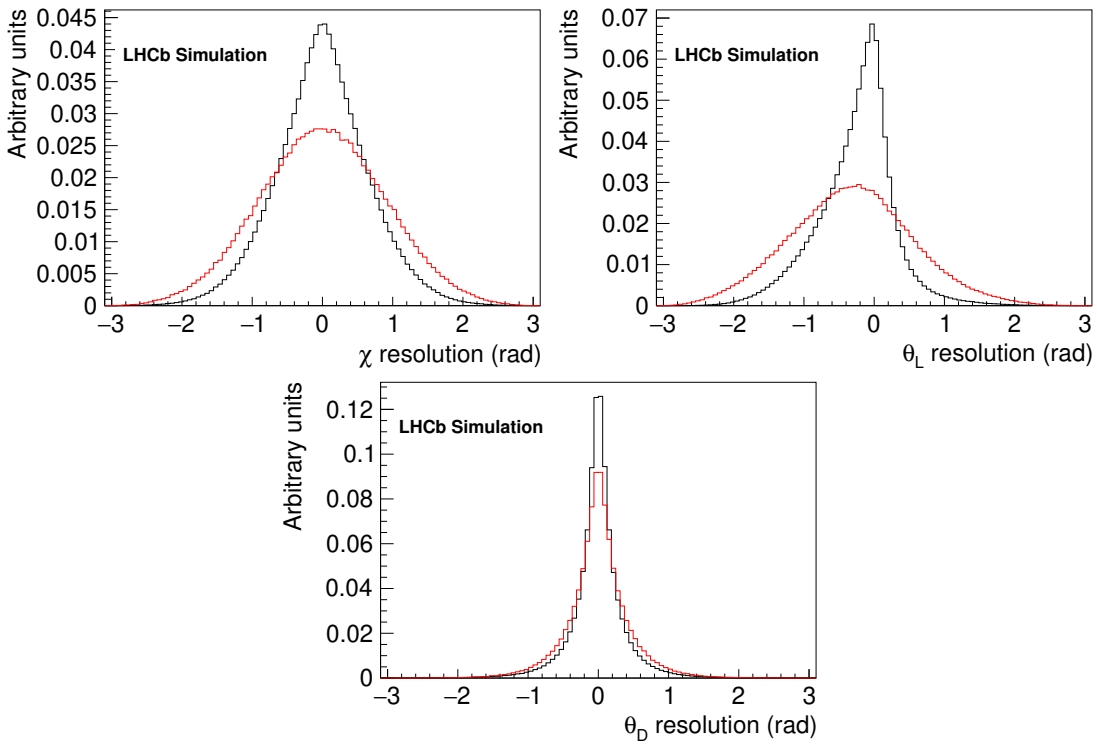

Fig. 56: Angular resolution for simulated $B \to D^* \mu\nu$ (black) and $B \to D^* \tau\nu$ (red) decays, with $\tau^+ \to \mu^+ \nu\nu$. This demonstrates our ability to resolve the full angular distribution, with some level of statistical dilution.

structure, and precise measurements of these distributions will allow the different helicity amplitudes to be disentangled. This can be used both to constrain the Lorentz structure of any potential NP contribution, and to measure the hadronic parameters governing the $B \to D^* \tau\nu$ decay, serving as an essential baseline for SM and non-SM studies. The helicity-suppressed amplitude which presently dominates the theoretical uncertainty on $R(D^{(*)})$ is too strongly suppressed in the $B \to D^{(*)} \mu\nu$ decays to be measurable, however this can be accessed in the $B \to D^{(*)} \tau\nu$ decay directly. If any potential NP contributions are assumed not to contribute via the helicity-suppressed amplitude then the combined measurements of $B \to D^{(*)} \mu\nu$ and $B \to D^{(*)} \tau\nu$ decays will allow for a fully data-driven prediction for $R(D^{(*)})$ under the assumption of lepton universality, eliminating the need for any theory input relating to hadronic form factors. However, these measurements have yet to be demonstrated with existing data. This exciting programme of differential measurements needs to be developed on Run 1 and 2 data before any statement is made about the precise sensitivity, but it offers unparalleled potential to fully characterise both the SM and non-SM contributions to the $b \to c\tau\nu$ transition.

As measurements in $\mathcal{R}(D^*)$ become more statistically precise, it will become increasingly more urgent to provide supplementary measurements in other b-hadron species with different background structure and different sources of systematic uncertainties. For example, the $\overline{B}{}^0_s \to D^+_s \tau^- \overline{\nu}$ and $\overline{B}{}^0_s \to D^{*+}_s \tau^- \overline{\nu}$ decays will allow supplementary measurements at high yields, and do not suffer as badly from cross-feed backgrounds from other mesons, unlike, for example, $\overline{B}{}^0 \to D^{*+} \tau^- \overline{\nu}$, where the B^+ and B^0_s both contribute to the $D^{*+} \mu X$ or $D^{*+} \pi^- \pi^+ \pi^- X$ final states. Furthermore, the comparison of decays with different spins of the b and c hadrons can enhance our sensitivity to different NP scenarios [77,1142]. No published measurements exist for the B^0_s case yet, but based on known relative efficiencies and assuming the statistical power of this mode tracks $\mathcal{R}(D^{(*)})$, we expect less than 6% relative uncertainty after Run 3, and 2.5% with the Upgrade II data, where limiting systematic uncertainties are currently

expected to arise from corrections to simulated pointing and vertex resolutions, from knowledge of particle identification efficiencies, and from knowledge of the backgrounds from random combinations of charm and muons. It is conceivable that new techniques and control samples could further increase the precision of these measurements.

Methods are currently under development for separating the $\overline{B}{}^0_s \to D_s^{*+}\ell^-\overline{\nu}$ and $\overline{B}{}^0_s \to D_s^+\ell^-\overline{\nu}$ modes, and given the relative slow pion ($D^{*+} \to D^0\pi^+$) and soft photon ($D_s^{*+} \to D_s^+\gamma$) efficiencies, the precision in $\overline{B}{}^0_s \to D_s^+\tau\nu$ decays can be expected to exceed that in $\overline{B}{}^0_s \to D_s^{*+}\tau\nu$, the reverse of the situation for $\mathcal{R}(D^{(*)})$. An upgraded ECAL would extend the breadth and sensitivity of $\mathcal{R}(D_s^{*(*)+})$ measurements possible in the Upgrade II scenario above and beyond the possible benefits of improved neutral isolation in $\mathcal{R}(D)$ or $\mathcal{R}(D_s^+)$ measurements.

Of particular interest are the semitauonic decays of b baryons and of B_c^+ mesons. The former provides probes of entirely new Lorentz structures of NP operators which pseudoscalar to pseudoscalar or vector transitions simply do not access. The value of probing this supplementary space of couplings has already been demonstrated by LHCb with its Run 1 measurement of $|V_{ub}|$ via the decay $\Lambda_b^0 \to p\mu^-\overline{\nu}$, which places strong constraints on right-handed currents sometimes invoked to explain the inclusive-exclusive tensions in that quantity. By the end of Run 3, it is expected that the relative uncertainty for $\mathcal{R}(\Lambda_c^+)$ will reach below 4%, and 2.5% by the end of Upgrade II. A further exciting prospect is the study of $b \to u\mu\nu$ decays, which have been beyond experimental reach thus far. For example the decay $B^+ \to p\bar{p}\mu\nu$ offers a clean experimental signature. Our capabilities with this decay could benefit from the enhanced low momentum proton identification with the TORCH subdetector.

Meanwhile, the $B_c^+ \to J/\psi\,\tau^-\overline{\nu}$ decay is an entirely unique state among the flavoured mesons as the bound state of two distinct flavors of heavy quark, and, through its abundant decays to charmonium final states, provides a highly efficient signature for triggering and reconstruction at high instantaneous luminosities. Measurements of $B_c^+ \to J/\psi\,\ell\overline{\nu}$ decays involve a trade-off between the approximately 100 times smaller production cross-section for B_c^+ verses the extremely efficient $J/\psi \to \mu^+\mu^-$ signature in the LHCb trigger. For illustration, in Run 1, LHCb reconstructed and selected 19 000 $B_c^+ \to J/\psi\,\mu^-\overline{\nu}$ decays, compared with 360 000 $\overline{B}{}^0 \to D^{*+}\mu^-\overline{\nu}$. This resulted in a measurement of $\mathcal{R}(J/\psi) = 0.71 \pm 0.17 \pm 0.18$ [18]. As a result of the smaller production cross-section, the muonic measurements have large backgrounds from $h \to \mu$ misidentification from the relatively abundant $B \to J/\psi\,X_h$ decays, where X_h is any collection of hadrons, and so they are very sensitive to the performance of the muon system and PID algorithms in the future. Here it is assumed that it will be possible to achieve similar performance to Run 1 in the upgraded system.

To project the sensitivity for $B_c^+ \to J/\psi\,\tau^-\overline{\nu}$ based on Ref. [18], it is assumed that all the systematic uncertainties can be reduced with the size of the input data except for those that were assumed not to scale with data for the previous predictions. For these, we assume that they can be reduced down until they reach the same absolute size as the corresponding systematic uncertainties in the Run 1 muonic $\mathcal{R}(D^*)$ analysis. In addition, it is assumed that sometime in the 2020s lattice QCD calculations of the form factors for this process will allow the systematic uncertainty due to signal form factors to be reduced by an additional factor of two. This results in a projected absolute uncertainty for the muonic mode of 0.07 at the end of Run 3 and 0.02 by the end of Upgrade II, as can be seen in Fig. 55. Measurements in the hadronic mode can be expected to reach similar sensitivities.

7.3.8 Searches for LFV, LNV, BNV and interplay with tests of LU

The LHCb collaboration has recently published [1143] the world's best limits on the branching fractions of the $B_s^0 \to e^\pm\mu^\mp$ and $B^0 \to e^\pm\mu^\mp$ decays using the first $3\,\text{fb}^{-1}$ collected in 2011 and 2012 at 7 and 8 TeV respectively. The acceptance of the $B_s^0 \to e^\pm\mu^\mp$ decays can be affected by the relative contribution of the two B_s^0 mass eigenstates to the total decay amplitude, due to their large lifetime difference. Therefore, the upper limit on the branching fraction of $B_s^0 \to e^\pm\mu^\mp$ decays is evaluated in two extreme

hypotheses: where the amplitude is completely dominated by the heavy eigenstate or by the light eigenstate. The results are $\mathcal{B}(B_s^0 \to e^\pm\mu^\mp) < 6.3\,(5.4) \times 10^{-9}$ and $\mathcal{B}(B_s^0 \to e^\pm\mu^\mp) < 7.2\,(6.0) \times 10^{-9}$ at 95% (90%) CL, respectively. The limit for the branching fraction of the B^0 mode is $\mathcal{B}(B^0 \to e^\pm\mu^\mp) < 1.3\,(1.0) \times 10^{-9}$ at 95% (90%) CL.

Assuming similar performances in background rejection and signal retention as in the current analysis, at the end of Run 4 the LHCb experiment will be able to probe branching fractions of $B_s^0 \to e^\pm\mu^\mp$ and $B^0 \to e^\pm\mu^\mp$ decays down to 8×10^{-10} and 2×10^{-10}, respectively. The additional statistics accumulated during the Upgrade II data taking period will push down these limits to 3×10^{-10} and 9×10^{-11} respectively, close to the interesting region where NP effects may appear. The Upgrade II improvement in electron reconstruction will be very important in attaining, or exceeding, this goal.

An upper limit on the $B^0 \to \tau^\pm\mu^\mp$ channel has been already set by BaBar: $\mathcal{B}\left(B^0 \to \tau^\pm\mu^\mp\right) < 2.2 \times 10^{-5}$ at 90% CL [1144]. The first search for the $B_s^0 \to \tau^\pm\mu^\mp$ channel is in progress in LHCb and the results are expected soon on data recorded in 2011 and 2012 using the $\tau^\pm \to \pi^\pm\pi^\mp\pi^\pm\nu$ and $\tau^\pm \to \pi^\pm\pi^\mp\pi^\pm\pi^0\nu$ decay modes. Given the presence of a neutrino that escapes detection this kind of analysis is much more complicated than those investigating electron or muon final states. A specific reconstruction technique is used in order to infer the energy of the ν, taking advantage of the known τ vertex position given by the 3π reconstructed vertex. This way, the complete kinematics of the process can be solved up to a two-fold ambiguity. LHCb expects to reach sensitivities of a few times 10^{-5} with the Run 1 and 2 data sets. Extrapolating the current measurements to the Upgrade II LHCb could reach $\mathcal{B}\left(B^0 \to \tau^\pm\mu^\mp\right) < 3 \times 10^{-6}$ at 90% CL. The mass reconstruction technique depends heavily on the uncertainty on the primary and the τ decay vertices, hence improvement in the tracking system in Upgrade II, including a removal or reduction in material of the VELO RF foil, will be very valuable.

In many generic NP models with LFUV, CLFV decays of b-hadrons can be linked with the anomalies recently measured in $b \to s\ell\ell$ decays [5, 6, 899]. If NP indeed allows for CLFV then the branching fractions of $B \to K\ell\ell'$ or $\Lambda_b^0 \to \Lambda\ell\ell'$ will be enhanced with respect to their purely leptonic counterparts, since the helicity suppression is lower. Furthermore, if observed, they would allow the measurement of more observables with respect to the lepton flavour violating decays discussed in the previous sections, thanks to their multi-body final states and, in the case of Λ_b^0, to the non-zero initial spin.

The current limits set by the B-Factories on the branching fractions of $B \to Ke\mu$ and $B \to K\tau\mu$ decays are $< 13 \times 10^{-8}$ [1107] and $< 4.8 \cdot 10^{-5}$ [1145] at 90% confidence level, respectively.

At LHCb, searches for $B^+ \to K^+e^\pm\mu^\mp$, $B^0 \to K^{*0}\tau^\pm\mu^\mp$, $B^+ \to K^+\tau^\pm\mu^\mp$ and $\Lambda_b^0 \to \Lambda e^\pm\mu^\mp$ are ongoing. These searches are complementary, as charged lepton flavour violation couplings among different families are expected to be different. The analyses involving τ leptons reconstruct candidates via the $\tau^- \to \pi^-\pi^-\pi^+\nu_\tau$ channel, which allows the reconstruction of the τ decay vertex.[8] All these decays contain at least one muon, which is used to efficiently trigger on the event. Usually, since these decays involve combinations of leptons that are not allowed in the SM, the backgrounds can be kept well under control, leaving very clean samples only polluted by candidates formed by the random combinations of tracks. This combinatorial effect is higher for the channel with a τ in the final state decaying into three charged pions. The other relevant background comes from chains of semileptonic decays, where two or more neutrinos are emitted and therefore combinations of leptons of different flavours are possible. These decays have typically a low reconstructed invariant mass, due to the energy carried away by the neutrinos, and so they do not significantly pollute the signal region.

The expected upper limits at LHCb using the first $9\,\text{fb}^{-1}$ of data taken are $\mathcal{O}(10^{-9})$ and $\mathcal{O}(10^{-6})$ for the $B^+ \to K^+e^\pm\mu^\mp$ and $B^0 \to K^{*0}\tau^\pm\mu^\mp$ decays respectively, at 90% confidence level. The limit for $B^+ \to K^+\tau^\pm\mu^\mp$ is expected to be similar to $B^0 \to K^{*0}\tau^\pm\mu^\mp$. The sensitivity of these analyses

[8] It should be noted that searches for $B^+ \to K^+\tau^\pm\mu^\mp$ from B_{s2}^* without τ reconstruction can give complementary information.

scales almost linearly with luminosity for $B^+ \to K^+ e^\pm \mu^\mp$, and with the square root of the luminosity for $B^0 \to K^{*0} \tau^\pm \mu^\mp$. In both cases, the expected limits using the Upgrade II data are in the region of interest of the models currently developed for explaining the B anomalies, so they will provide strong constraints on the NP scenarios with CLFV

Experimentally, Lepton-Number Violating (LNV) and Baryon-Number Violating (BNV) measurements are null searches, so sensitivity is assumed to scale linearly with luminosity $\mathcal{L}$ when the background is negligible and as $\sqrt{\mathcal{L}}$ if the background is significant. LHCb has already published searches in certain channels, and others are in progress:

- Searches for LNV in various B-meson decays of the form $B \to X\mu^+\mu^+$, where X is a system of one or more hadrons. The principal motivation is the sensitivity to contributions from Majorana neutrinos [1146], which may be on-shell or off-shell, depending on the decay mode. The published results consist of searches for $B^+ \to K^-\mu^+\mu^+$, $B^+ \to \pi^-\mu^+\mu^+$ and $B^+ \to D^+_{(s)}\mu^-\mu^-$ [1147–1149]. A limit of $\mathcal{B}(B^+ \to \pi^-\mu^+\mu^+) < 4 \times 10^{-9}$ is set at the 95% confidence level, along with more detailed limits as a function of the Majorana neutrino mass. Since the combinatorial background was found to be low but not negligible with the Run 1 data, we estimate that the limit can be improved by a factor of ten with the full Upgrade II dataset.
- Search for BNV in Ξ_b^0 oscillations [438]. Six-fermion, flavour-diagonal operators, involving two fermions from each generation, could give rise to BNV without violating the nucleon stability limit [1150,1151]. Since the Ξ_b^0 (bsd) has one valence quark from each generation, it could couple directly to such an operator and oscillate to $\overline{\Xi}_b^0$. The published search used the Run 1 data and set a lower limit on the oscillation period of 80 ps. Since events are tagged by decays of the $\Xi_b^{\prime-}$ and Ξ_b^{*-} resonances, with the former being particularly clean, and since the analysis also uses the decay-time distribution of events, the sensitivity is expected to scale linearly. Although the decay mode used in the published analysis is hadronic ($\Xi_b^0 \to \Xi_c^+\pi^-$), future work could also benefit from the lower-purity but higher-yield semileptonic mode $\Xi_b^0 \to \Xi_c^+\mu^-\overline{\nu}_\mu$.
- $\Lambda_c^+ \to \overline{p}\mu^+\mu^+$. This channel has previously been investigated at the e^+e^- B-Factories. The current upper limit, obtained by BaBar [1152], is $\mathcal{B}(\Lambda_c^+ \to \overline{p}\mu^+\mu^+) < 9.4 \times 10^{-6}$ at the 90% confidence level. With Run 1 and 2 data alone, it should be possible to reduce this to 1×10^{-6}. Further progress depends on the background level, but an additional factor of 5–10 with the full Upgrade II statistics is likely.
- $\Lambda_c^+ \to \mu^+\mu^-\mu^+$. Experimentally, this is a particularly promising decay mode: the final state with three muons is very clean, and there are no known sources of peaking background. This search could be added for little extra effort to the $\tau^- \to \mu^+\mu^-\mu^-$ search described in the preceding section.

8 The top quark and flavour physics

Among the SM fermions the top quark stands out. It has a large mass and an $\mathcal{O}(1)$ coupling to the Higgs, quite distinct from any other SM fermion. Studying top quark properties may shed light on the resolution of the SM flavour puzzle, or at least as to why one and only one Yukawa coupling is large. The large Higgs-top coupling is also the reason for the weak scale hierarchy problem to be so acute – the quadratic divergent corrections to the Higgs mass are driven almost completely by this coupling. BSM models addressing the hierarchy problem may thus well leave an imprint in the top quark properties and decays. For instance, the FCNC top decays, $t \to c\gamma, cZ, cg$, are null tests of the SM and are used as BSM probes.

Top quark also directly enters the flavour phenomenology. Loops with the top quark are responsible for the largest short-distance contributions to the down-quark FCNCs. The SM predictions are thus controlled by the flavour couplings of the top – with B and K transitions determining the CKM matrix elements V_{tb}, V_{ts}, V_{td} through these virtual effects. Determining V_{tx} directly from high $p_{\rm T}$ transitions, as well as the structure of the Wtb vertices, can then serve as independent consistency checks of the SM.

Top quarks can also be used as a clean source of tagged B mesons. Ref. [1153], for instance, suggested to use top-pair events, where at least one of the tops decays semi-leptonically, to measure CP violation in heavy flavor mixing and decays. This measurement was then performed for the first time at by ATLAS in Ref. [1154].

The LHC is already a top factory and the currently available statistics has allowed ATLAS and CMS to perform a vast campaign of top related measurements. However, the larger number of top quarks at HL-LHC and HE-LHC will open new possibilities for precise measurements of top-quark properties and for significant improvements probing NP, such as the rare FCNC decays.

8.1 Global effective-field-theory interpretation of top-quark FCNCs

Authors (TH): Gauthier Durieux, Teppei Kitahara, Cen Zhang.

8.1.1 Effective operators

Starting from an Effective Field Theory (EFT) with full $SU(3)_C \times SU(2)_L \times U(1)_Y$ gauge symmetry and matter content of the SM, one can show that odd-dimensional operators all violate baryon or lepton numbers [1155]. Imposing the conservation of these quantum numbers, the leading higher dimensional operators of the SM arise at dimension six. We follow the top-quark EFT conventions set by the LHC TOP WG in Ref. [1156]. The LHC TOP WG employs linear combinations of Warsaw-basis operators [375] which appear in interactions with physical fields after electroweak symmetry breaking.

The operators contributing to top-quark FCNC processes fall into several categories. We consider operators involving exactly two quarks, as well as those involving two quarks and two leptons. Operators containing four quarks only start contributing at next-to-leading order in QCD in most of the measurements we consider ($pp \to tj$ is the exception). The corresponding Warsaw-basis operators are [1156]

$$
\begin{aligned}
O_{u\varphi}^{(ij)} &= \bar{q}_i u_j \tilde{\varphi}\,(\varphi^\dagger\varphi), & O_{lq}^{1(ijkl)} &= (\bar{l}_i\gamma^\mu l_j)(\bar{q}_k\gamma^\mu q_l),\\
O_{\varphi q}^{1(ij)} &= (\varphi^\dagger i\overleftrightarrow{D}_\mu\varphi)(\bar{q}_i\gamma^\mu q_j), & O_{lq}^{3(ijkl)} &= (\bar{l}_i\gamma^\mu\tau^I l_j)(\bar{q}_k\gamma^\mu\tau^I q_l),\\
O_{\varphi q}^{3(ij)} &= (\varphi^\dagger i\overleftrightarrow{D}^I_\mu\varphi)(\bar{q}_i\gamma^\mu\tau^I q_j), & O_{lu}^{(ijkl)} &= (\bar{l}_i\gamma^\mu l_j)(\bar{u}_k\gamma^\mu u_l),\\
O_{\varphi u}^{(ij)} &= (\varphi^\dagger i\overleftrightarrow{D}_\mu\varphi)(\bar{u}_i\gamma^\mu u_j), & O_{eq}^{(ijkl)} &= (\bar{e}_i\gamma^\mu e_j)(\bar{q}_k\gamma^\mu q_l),\\
O_{\varphi ud}^{(ij)} &= (\tilde{\varphi}^\dagger iD_\mu\varphi)(\bar{u}_i\gamma^\mu d_j), & O_{eu}^{(ijkl)} &= (\bar{e}_i\gamma^\mu e_j)(\bar{u}_k\gamma^\mu u_l),\\
O_{uW}^{(ij)} &= (\bar{q}_i\sigma^{\mu\nu}\tau^I u_j)\,\tilde{\varphi}W^I_{\mu\nu}, & O_{lequ}^{1(ijkl)} &= (\bar{l}_i e_j)\,\varepsilon\,(\bar{q}_k u_l),\\
O_{dW}^{(ij)} &= (\bar{q}_i\sigma^{\mu\nu}\tau^I d_j)\,\varphi W^I_{\mu\nu}, & O_{lequ}^{3(ijkl)} &= (\bar{l}_i\sigma^{\mu\nu} e_j)\,\varepsilon\,(\bar{q}_k\sigma_{\mu\nu} u_l),\\
O_{uB}^{(ij)} &= (\bar{q}_i\sigma^{\mu\nu} u_j)\quad\tilde{\varphi}B_{\mu\nu}, & O_{ledq}^{(ijkl)} &= (\bar{l}_i e_j)(\bar{d}_k q_l)\\
O_{uG}^{(ij)} &= (\bar{q}_i\sigma^{\mu\nu}T^A u_j)\,\tilde{\varphi}G^A_{\mu\nu}
\end{aligned}
\tag{106}
$$

The operators $O_{\varphi ud}$, O_{dW}, and O_{ledq}, only contribute to charged top-quark currents (not considering SM electroweak corrections) and are therefore not relevant for our purposes. The EFT degrees of freedom appearing in top-quark FCNC processes were defined in Appendices E.1-2 of Ref. [1156]. They are:

$$
\begin{aligned}
c_{t\varphi}^{[I](3a)} &\equiv \underset{\text{Re}}{[\text{Im}]}\{C_{u\varphi}^{(3a)}\}, & c_{uA}^{[I](3a)} &\equiv \underset{\text{Re}}{[\text{Im}]}\{c_W C_{uB}^{(3a)} + s_W C_{uW}^{(3a)}\}, &(107)\\
c_{t\varphi}^{[I](a3)} &\equiv \underset{\text{Re}}{[\text{Im}]}\{C_{u\varphi}^{(a3)}\}, & c_{uA}^{[I](a3)} &\equiv \underset{\text{Re}}{[\text{Im}]}\{c_W C_{uB}^{(a3)} + s_W C_{uW}^{(a3)}\}, &(108)\\
c_{\varphi q}^{-[I](3+a)} &\equiv \underset{\text{Re}}{[\text{Im}]}\{C_{\varphi q}^{1(3a)} - C_{\varphi q}^{3(3a)}\}, & c_{uZ}^{[I](3a)} &\equiv \underset{\text{Re}}{[\text{Im}]}\{-s_W C_{uB}^{(3a)} + c_W C_{uW}^{(3a)}\}, &(109)\\
c_{\varphi u}^{[I](3+a)} &\equiv \underset{\text{Re}}{[\text{Im}]}\{C_{\varphi u}^{(3a)}\}, & c_{uZ}^{[I](a3)} &\equiv \underset{\text{Re}}{[\text{Im}]}\{-s_W C_{uB}^{(a3)} + c_W C_{uW}^{(a3)}\}, &(110)
\end{aligned}
$$

as well as $c_{uG}^{[I](3a)} \equiv \underset{\text{Re}}{[\text{Im}]}\{C_{uG}^{(3a)}\}$, $c_{uG}^{[I](a3)} \equiv \underset{\text{Re}}{[\text{Im}]}\{C_{uG}^{(a3)}\}$, and

$$
\begin{aligned}
c_{lq}^{-[I](\ell,3+a)} &\equiv \underset{\text{Re}}{[\text{Im}]}\{C_{lq}^{-(\ell\ell 3a)}\}, & c_{lequ}^{S[I](\ell,3a)} &\equiv \underset{\text{Re}}{[\text{Im}]}\{C_{lequ}^{1(\ell\ell 3a)}\}, &(111)\\
c_{eq}^{[I](\ell,3+a)} &\equiv \underset{\text{Re}}{[\text{Im}]}\{C_{eq}^{(\ell\ell 3a)}\}, & c_{lequ}^{S[I](\ell,a3)} &\equiv \underset{\text{Re}}{[\text{Im}]}\{C_{lequ}^{1(\ell\ell a3)}\}, &(112)\\
c_{lu}^{[I](\ell,3+a)} &\equiv \underset{\text{Re}}{[\text{Im}]}\{C_{lu}^{(\ell\ell 3a)}\}, & c_{lequ}^{T[I](\ell,3a)} &\equiv \underset{\text{Re}}{[\text{Im}]}\{C_{lequ}^{3(\ell\ell 3a)}\}, &(113)\\
c_{eu}^{[I](\ell,3+a)} &\equiv \underset{\text{Re}}{[\text{Im}]}\{C_{eu}^{(\ell\ell 3a)}\}, & c_{lequ}^{T[I](\ell,a3)} &\equiv \underset{\text{Re}}{[\text{Im}]}\{C_{lequ}^{3(\ell\ell a3)}\}. &(114)
\end{aligned}
$$

Compared to the anomalous coupling parametrization, the EFT approach has two features that are worth emphasizing. First, it includes four-fermion operators, which have been unduly neglected in most experimental analyses (apart from Ref. [1158]). Second, the EFT approach captures the correlations between interaction terms that derive from electroweak gauge invariance. For instance, the $\bar{t}\sigma^{\mu\nu}T^A q\; h\; G^A_{\mu\nu}$ and $\bar{t}\sigma^{\mu\nu}T^A q\; G^A_{\mu\nu}$ interactions arise from the same O_{uG} operator and their coefficients are thus related. In Fig. 57, we show examples of four-point interactions contributing to single top-quark FCNC production. Correlations also arise from the fact that left-handed down- and up-type quarks belong to a single gauge-eigenstate doublet. Operator coefficients measurable in B-meson physics are thus related to those relevant to top-quark physics (see Secs. 8.1.5 and 8.2.2).

8.1.2 Theory predictions

Because the LHC is a hadron collider, theory predictions at LO are often not sufficient when an accurate interpretation of observables in terms of theory parameters is needed. Typical NLO QCD corrections in top-decay processes [1159–1164] amount to approximately 10%, while in production processes they can reach between about 30% and 80% [1165–1169]. Theory predictions for top-quark FCNC processes are in general available at NLO accuracy in QCD. Complete results at NLO in QCD for top-quark FCNC

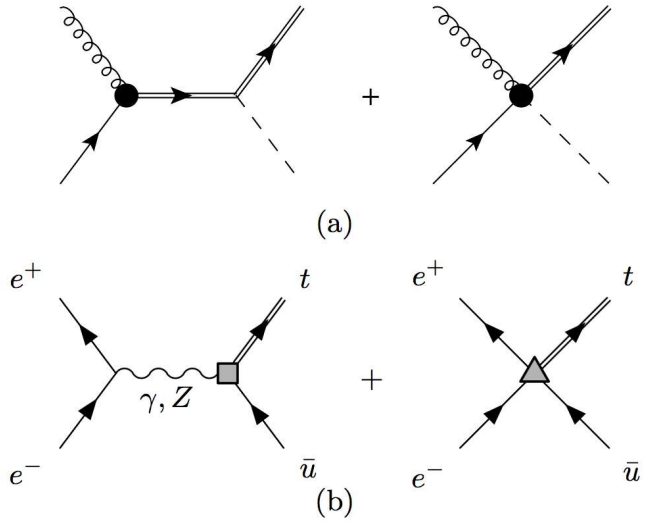

Fig. 57: Effective operators give rise to four-point contact interactions that are overlooked in the approach with anomalous couplings, although they contribute to FCNC processes at the same order in $1/\Lambda^2$ as the three-point ones. Representative diagrams are shown for $ug \to th$ production (or radiative $t \to hug$ decay), and $e^+e^- \to t\,\bar{u}$ (or $t \to u\,e^+e^-$ decay). Figure taken from Ref. [1157].

decays through two-quark and two-quark–two-lepton operators can be found in Ref. [1164]. Single top-quark production associated with a neutral gauge boson, γ, Z, or the scalar boson h have also been studied. Two-quark operators have been implemented in the `FeynRules/MadGraph5_aMC@NLO` simulation chain [372, 1170, 1171], allowing for automated NLO QCD predictions matched to parton shower. Details on this implementation have been presented in Ref. [1172]. Two-quark-two-lepton operators are now also available in `MadGraph5_aMC@NLO` (see Ref. [1173]). Finally, the direct top-quark production with decay process, $pp \to bW^+$, involves additional technical difficulties due to the intermediate top-quark resonance. It is now being studied, and the corresponding NLO generator matched to parton shower will be available in the future [1174].

8.1.3 Existing limits

Table 32 lists the existing limits on FCNC processes. We follow Ref. [1157] and interpret them in a global EFT analysis. Several additional remarks are in order:

- For $t \to q\ell\ell$ we use the predictions at NLO in QCD provided in Ref. [1157] for the $m_{\ell\ell} \in [78, 102]$ GeV range although the most stringent constraints by ATLAS are set using $|m_{\ell\ell} - m_Z| < 15$ GeV. The CMS bounds obtained by combining production and decay process cannot be reinterpreted to include four-fermion operators.
- For single top-quark production through the tqg interaction, we use the best constraints: in the up-quark channel by CMS and in the charm-quark channel by ATLAS. We naively combine them using the numerical value at NLO in QCD for the $t \to jj$ branching fraction provided in Sec. V.B of Ref. [1157].
- For single top-quark production in association with a photon, we note the very interesting fiducial limit provided by Ref. [1175] which allows for an accurate reinterpretation. However, we use the simplified approach of Ref. [1157] based on the limit quoted on the total cross section and use the numerical values computed at NLO in QCD for $pp \to t\gamma + \bar{t}\gamma$ with a 30 GeV cut on the photon $p_{\rm T}$ although a 50 GeV cut was applied in Ref. [1175].
- For $t \to hj$ decay we use the most stringent limits set by ATLAS in the multilepton channel. The

Table 32: Summary of the existing 95% C.L. limits on top-quark FCNC branching fractions obtained at the LHC. A summary plot is available at https://twiki.cern.ch/twiki/bin/view/LHCPhysics/LHCTopWGSummaryPlots#table21. Ref. [1175] has set limits in a fiducial volume at the particle level for $pp \to t\gamma$ (not displayed in this table). Numbers in bold are used as inputs to the global EFT analysis.

Mode	$\mathrm{Br}^{95\%\mathrm{CL}}$	Ref.	exp.	$\sqrt{s}$	$\mathcal{L}$	remarks
$t \to qZ$						
u	$\mathbf{1.7 \times 10^{-4}}$	[1176]	ATLAS	13 TeV	$36.1\,\mathrm{fb}^{-1}$	decay, $\lvert m_{\ell\ell} - m_Z \rvert < 15$ GeV
c	$\mathbf{2.4 \times 10^{-4}}$					
u	2.4×10^{-4}	[1177]	CMS	13 TeV	$35.9\,\mathrm{fb}^{-1}$	production plus decay
c	4.5×10^{-4}					
u	2.2×10^{-4}	[1178]	CMS	8 TeV	$19.7\,\mathrm{fb}^{-1}$	production, $76 < m_{\ell\ell} < 106$ GeV
c	4.9×10^{-4}					
$t \to qg$						
u	0.40×10^{-4}	[1179]	ATLAS	8 TeV	$20.3\,\mathrm{fb}^{-1}$	$\sigma(pp \to t) \times \mathrm{Br}(t \to bW) < 3.4$ pb
c	$\mathbf{2.0 \times 10^{-4}}$					
u	$\mathbf{0.20 \times 10^{-4}}$	[1180]	CMS	7, 8 TeV	$5.0, 17.9\,\mathrm{fb}^{-1}$	in $pp \to tj$
c	4.1×10^{-4}					
$t \to q\gamma$						
u	$\mathbf{1.3 \times 10^{-4}}$	[1175]	CMS	8 TeV	$19.8\,\mathrm{fb}^{-1}$	$\sigma(pp \to t\gamma) \times \mathrm{Br}(t \to bl\nu) < 26$ fb
c	$\mathbf{17 \times 10^{-4}}$					$\sigma(pp \to t\gamma) \times \mathrm{Br}(t \to bl\nu) < 37$ fb
$t \to qh$						
u	$\mathbf{19 \times 10^{-4}}$	[1181]	ATLAS	13 TeV	$36.1\,\mathrm{fb}^{-1}$	multilepton channel
c	$\mathbf{16 \times 10^{-4}}$					
u	55×10^{-4}	[1182]	CMS	8 TeV	$19.7\,\mathrm{fb}^{-1}$	multilepton, $\gamma\gamma$, $b\bar{b}$
c	40×10^{-4}					
u	47×10^{-4}	[1183]	CMS	13 TeV	$35.9\,\mathrm{fb}^{-1}$	$b\bar{b}$
c	47×10^{-4}					

dependence on all operator coefficients, except $C_{t\phi}$ and C_{tG}, is assumed to be negligible.

- Limits on $e^+e^- \to tj + \bar{t}j$ obtained at LEP II [1184] still dominate constraints on four-fermion operators involving electrons, while $t \to q\ell\ell$ at hadron colliders are the only measurements constraining four-fermion operators featuring a pair of muons. However, the latter limits are not explicitly shown below. We use the limit from the highest LEP II centre-of-mass energy, $\sqrt{s} = 207$ GeV, which is the most sensitive to four-fermion operators, $\sigma(e^+e^- \to tj + \bar{t}j) < 170$ fb.

The global analysis based on existing data gives 95% C.L. limits on the EFT Wilsons coefficients in the notation of Ref. [1156], shown in Fig. 58 (left panel). As explained in Ref. [1157], no statistical combination is attempted, i.e., limits from different measurements are only overlaid. Fig. 59 (left panel) show two-dimensional constraints in the $c^-_{\varphi q,\varphi u}$,$c_{eq,eu}$ plane. This illustrates the complementarity between the LHC and the LEP II measurements; the former gives better constraints on two-fermion operators, the latter on four-fermion operators.

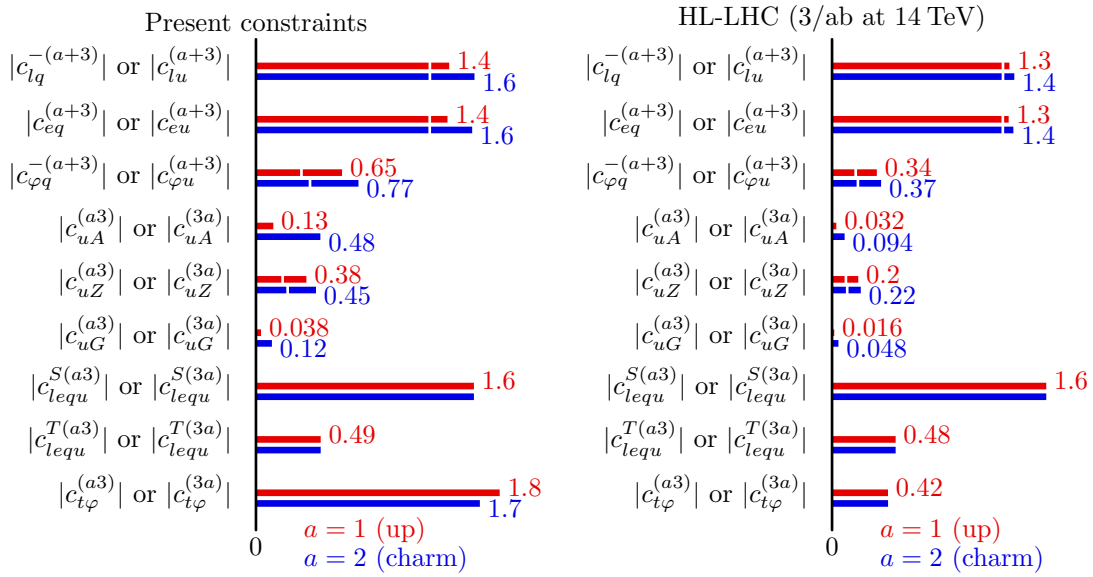

Fig. 58: Current (left) and projected HL-LHC (right) 95% C.L. limits on top-quark FCNC operator coefficients in the conventions of Ref. [1156]. Red and blue bars denote top-up and top-charm FCNCs, respectively. White marks indicate individual limits, obtained under the unrealistic assumption that all the other operator coefficients vanish.

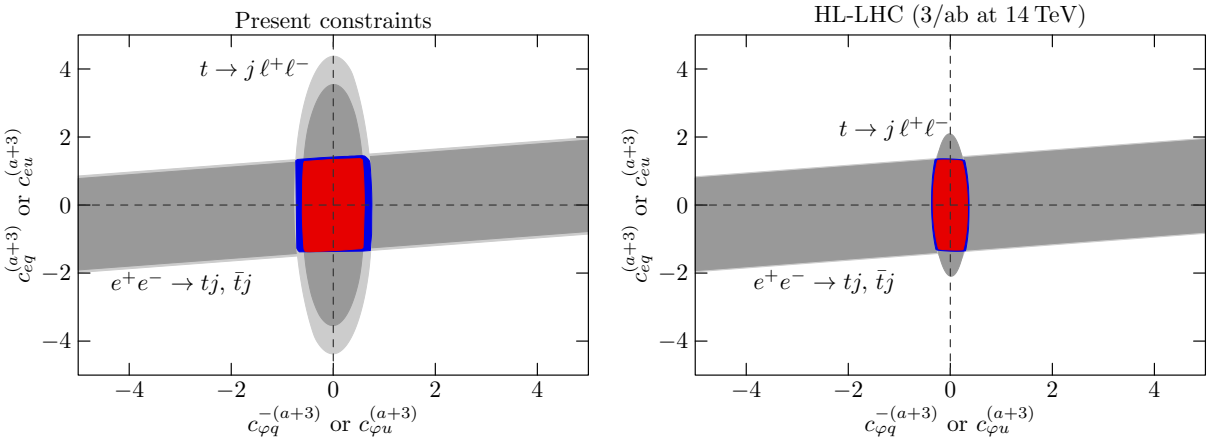

Fig. 59: Current (left) and prospective HL-LHC (right) 95% C.L. limits on top-quark FCNC operator coefficients in a two-dimensional plane formed by two- (x axis) and four-fermion (y axis) operator coefficients. Other parameters are marginalized over, within the constraints obtained when all measurements are included. Red and blue regions are the combined constraints for top-up and top-charm FCNCs. The impact of $t \to j\ell^+\ell^-$ and $e^+e^- \to tj, \bar{t}j$ measurements is displayed separately in dark and light gray colors for top-up and top-charm FCNCs, respectively.

8.1.4 Future limits

We use the prospects presented in Sec. 8.1.6 to estimate the future reach of global constraints for the HL-LHC scenario. As previously, we assume that the limits quoted on the $\mathrm{Br}(t \to qZ)$ branching fraction are derived using the dilepton decays of the Z boson, in a $m_{\ell\ell} \in [78, 102]$ GeV window for the dilepton invariant mass. This determines the sensitivity to four-fermion operators. The limits on the $tq\gamma$ interaction were derived by a combination of production and decay processes [1185]. Since the only prospect provided is on the $\mathcal{B}(t \to q\gamma)$ branching fraction, we approximate it as though it is from the measurement of the decay process only. This assumption affects primarily the dependence of bounds on

tqg interactions.

The results of a global fit based on the HL-LHC prospects are displayed in Fig. 58 (right panel). Comparing with the left panel, constraints on two-fermion operators are typically improved by a factor of a few, while those on four-fermion operators are only marginally improved, mostly indirectly through the improvement of the limits on other operator coefficients. The two dimensional plane of Fig. 59 (right panel) shows that LEP II constraints on $e^+e^- \to tj, \bar{t}j$ production will start having little impact, even on the four-fermion operators, after the HL-LHC phase.

8.1.5 *Complementarity with B-meson and kaon rare processes*

The NP effective operators which include the top quark also contribute to the low-scale effective Hamiltonian for meson decays, and hence, precision measurements of the B-meson and kaon rare processes provide complementary constraints to the NP top-quark operators [1186–1188].

In the framework of SMEFT, the $SU(2)_L$ gauge symmetry between t_L and b_L provides a direct constraint to the NP top-quark operators arising from the tree-level matching onto the B physics Hamiltonian [904, 1187]. For instance, in the flavour basis, the following operators

$$O_{\ell q}^{1(ij32)} = (\bar{\ell}_i \gamma_\mu P_L \ell_j)(\bar{q}_3 \gamma^\mu P_L q_2) = (\bar{\ell}_i \gamma_\mu P_L \ell_j)(\bar{t} \gamma^\mu P_L c) + (\bar{\ell}_i \gamma_\mu P_L \ell_j)(\bar{b} \gamma^\mu P_L s)\,, \tag{115}$$

$$O_{\ell equ}^{1(ij32)} = (\bar{\ell}_i P_R e_j)\varepsilon(\bar{q}_3 P_R c) = -(\bar{\ell}_i{}^+ P_R e_j)(\bar{t} P_R c) + (\bar{\nu}_i P_R e_j)(\bar{b} P_R c)\,, \tag{116}$$

are constrained from $B_s \to \ell^+\ell^-$, $B \to K^{(*)}\bar{\nu}\nu$, $b \to s\ell^+\ell^-$, and $b \to c\ell^-\bar{\nu}$ observables. Each of the constraints significantly depends on the lepton-flavour dependence (*e.g.*, see Ref. [952]).

Also, the NP operators which include single top quark, *e.g.*,

$$O_{\varphi q}^{1(32)} = (\varphi^\dagger i\overleftrightarrow{D}_\mu \varphi)(\bar{t} \gamma^\mu P_L c) + (\varphi^\dagger i\overleftrightarrow{D}_\mu \varphi)(\bar{b} \gamma^\mu P_L s)\,, \tag{117}$$

and two top quarks, *e.g.*,

$$O_{qd}^{1(33kl)} = (\bar{t} \gamma_\mu P_L t)(\bar{d}^k \gamma^\mu P_R d^l) + (\bar{b} \gamma_\mu P_L b)(\bar{d}^k \gamma^\mu P_R d^l) \quad \text{with } k \neq l\,, \tag{118}$$

can contribute to the low-scale effective Hamiltonian through the one-loop matching conditions at the electroweak symmetry breaking scale by integrating out the top quark, W, Z and the SM Higgs boson. These one-loop contributions are enhanced by the top-quark mass. Although such a two top-quark operator does not contribute to the single top-quark production mentioned in this section, once a UV completion is considered, single and two top-quarks operators could be related. The one-loop matching conditions onto $\Delta F = 1$ processes are given in Ref. [904], while the conditions onto $\Delta F = 2$ ones are given in Ref. [1189]. Besides, one-loop matching conditions to $\Delta F = 0$, *e.g.*, $h \to \tau^+\tau^-$ and the leptonic dipole moments, are investigated in Ref. [1065].

8.1.6 *Experimental perspectives*

8.1.6.1 *Signal modeling*

The generation of signal events at ATLAS is done at NLO with `MadGraph5_aMC@NLO` [372, 1190] and the effective field theory framework developed in the TopFCNC model is used [1157, 1172]. In the case of gqt coupling, the MEtop generator is used instead [1191]. At CMS signal events are simulated at LO with `MadGraph5_aMC@NLO` with the effective lagrangian implemented by means of the `FEYNRULES` package, except in the simulation of signal events for gqt and γqt couplings where `CompHEP` [1192] and `PROTOS 2.0` [1193] are used, respectively. In both experiments `Pythia 8` is used to simulate the parton showering and hadronization. The generation of signal events is done under the assumption of only one non-vanishing FCNC coupling at a time.

Table 33: Summary of the projected reach for the 95% C.L. limits on the branching ratio for anomalous flavor changing top couplings.

$\mathcal{B}$ limit at 95%C.L.	3 ab^{-1}, 14 TeV	15ab^{-1}, 27 TeV	Ref.
$t \to gu$	3.8×10^{-6}	5.6×10^{-7}	[1194]
$t \to gc$	32.1×10^{-6}	19.1×10^{-7}	[1194]
$t \to Zq$	$2.4 - 5.8 \times 10^{-5}$		[1195]
$t \to \gamma u$	8.6×10^{-6}		[1196]
$t \to \gamma c$	7.4×10^{-5}		[1196]
$t \to Hq$	10^{-4}		[1195]

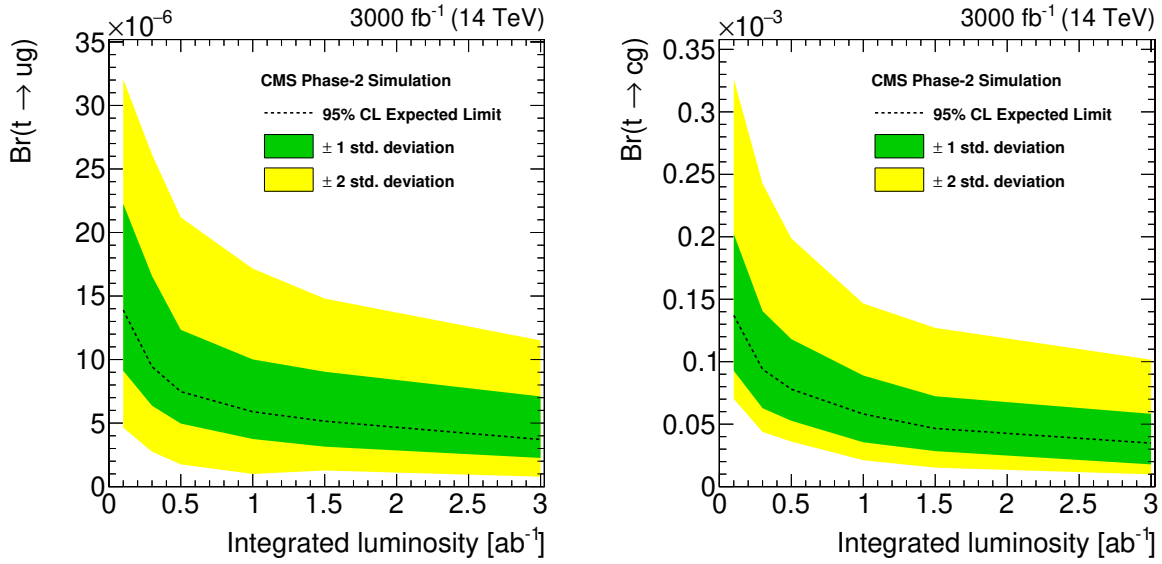

Fig. 60: The expected exclusion limits at 95% C.L. on the branching fractions for the $t \to ug$ (left panel) and $t \to cg$ (right panel) FCNC processes as a function of integrated luminosity.

8.1.6.2 Top-gluon

The gqt FCNC process was studied by ATLAS [1179] and CMS [1180] in single top quark events. The event signature includes the requirement of one isolated lepton and the presence of a significant amount of transverse missing energy (E_T^{miss}). The analysis at CMS requires exactly one b and one non-b jet to be present in the final state with the dominant background arising from the $t\bar{t}$+jets production, while the analysis at ATLAS vetoes any additional jets resulting in the dominant source of background associated with the W+jets production. A neural network-based technique is used to separate signal from background events. The observed (expected) 95% C.L. upper limits in the CMS analysis are $\mathcal{B}(t \to gu) < 2.0\ (2.8) \times 10^{-5}$ and $\mathcal{B}(t \to gc) < 4.1\ (2.8) \times 10^{-4}$, while the resultant limits in case of ATLAS are $\mathcal{B}(t \to gu) < 4.0\ (3.5) \times 10^{-5}$ and $\mathcal{B}(t \to gc) < 2.0\ (1.8) \times 10^{-4}$. The projected limits for 3 ab^{-1} are $\mathcal{B}(t \to gu) < 3.8 \times 10^{-6}$ and $\mathcal{B}(t \to gc) < 32.1 \times 10^{-6}$ [1194].

The dependence of the $\mathcal{B}(t \to ug)$ and $\mathcal{B}(t \to cg)$ exclusion upper limits on integrated luminosity is shown in Fig. 60 with 1 and 2 σ bands corresponding to 68 % and 95 % C.L intervals of distributions of the limits . In addition the two-dimensional contour that reflects the possible simultaneous presence of both FCNC processes. is shown in Fig. 61.

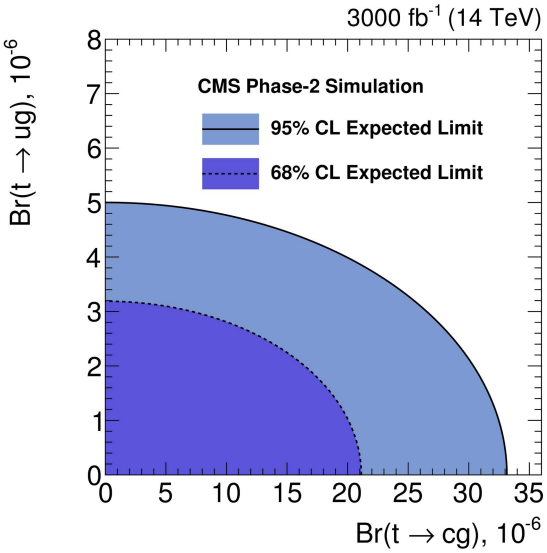

Fig. 61: Two-dimensional expected limits on the $t \to ug$ vs and $t \to cg$ branching fractions at 68% and 95% C.L. for an integrated luminosity of 3000 fb^{-1}

8.1.6.3 Top-Z

ATLAS studied the sensitivity to the tqZ interaction, by performing an analysis [1197] based on simulated samples and following both the strategy of its 13 TeV data analysis on the same subject [1176] and of the general recommendations for this HL-LHC study. The study is performed in the three charged lepton final state of $t\bar{t}$ events, in which one of the top quarks decays to qZ, $(q = u, c)$ and the other one decays to bW ($t\bar{t} \to bWqZ \to b\ell\nu q\ell\ell$). The kinematics of the events are reconstructed through a χ^2 minimisation and dedicated control regions are used to normalize the main backgrounds and constrain systematic uncertainties. The main uncertainties, in both the background and signal estimations, are expected to come from theoretical normalization uncertainties and uncertainties in the modeling of background processes in the simulation. Different scenarios for the systematic uncertainties are considered, ranging from the full estimations obtained with the 13 TeV data analysis, to the ones expected with improvements in theoretical predictions, which should be half of the former ones. A binned likelihood function $L(\mu, \theta)$ is used to do the statistical analysis and extract the signal normalisation. An improvement by a factor of five is expected in relation to the current 13 TeV data analysis results. Obtained branching ratio limits are at the level of 4 to 5 $\times 10^{-5}$ depending on the considered scenarios for the systematic uncertainties.

8.1.6.4 Top-gamma

The $t\gamma q$ anomalous interactions have been probed by CMS at 8 TeV in events with single top quarks produced in association with a photon [1175] and the resulting exclusion limits are $\mathcal{B}(t \to \gamma u) < 1.3\ (1.9) \times 10^{-4}$ and $\mathcal{B}(t \to \gamma c) < 2.0\ (1.7) \times 10^{-3}$.

In this section, the sensitivity of the upgraded CMS detector to $tq\gamma$ FCNC transitions is estimated for integrated luminosities of 300 and 3000 fb^{-1} using single top quark production via $q \to q\gamma$, with q being a u or a charm quark [1196]. This analysis focuses on subsequent SM decays of the top quark in a W boson and bottom quark, with the W boson decays leptonically to a muon or electron and a neutrino. The final state signature is the presence of a single muon or electron, large missing transverse momentum, a b jet, and an isolated high energy photon, with a broad η spectrum. The photon properties themselves provide good separation with respect to the dominant background processes from W+jets, and single top

or top quark pair production in association with photons. For the discrimination of signal and background events, and to set the limits on the FCNC couplings, the events are split into two categories depending on the pseudo-rapidity of the photon (central region with $|\eta_\gamma| < 1.4$ and forward region with $1.6 < |\eta_\gamma| < 2.8$). In the central (forward) region the photon p_{T} (energy) is used as a discriminating distribution: the low p_{T} (energy) is background dominated, while the high p_{T} (energy) region is populated by signal events. The distributions are shown in Fig. 62.

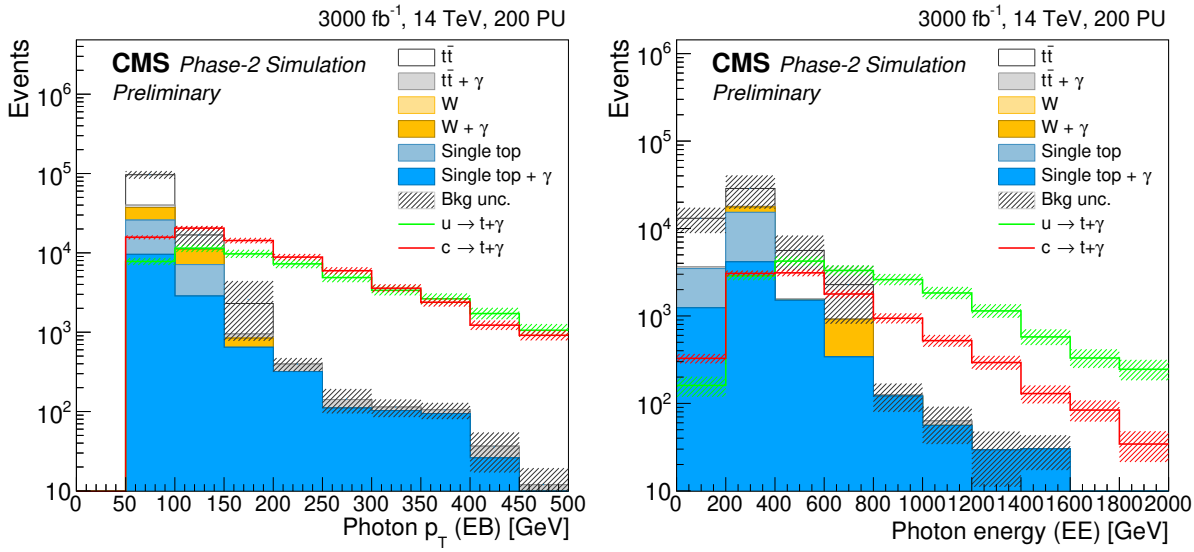

Fig. 62: Transverse momentum of photon candidates for the central η region (left) and energy of photon candidates in the forward region (right).

The limits on the cross section for the single top quark production via $tq\gamma$ are obtained considering systematic uncertainties from variations of the renormalization and factorization scale, b-tagging and jet energy scale corrections and their effects as propagated to missing transverse energy, lepton efficiency and luminosity.

These studies yield the following upper limite on the branching ratios at 95%C.L.: $\mathcal{B}(t \to \gamma u) < 8.6 \times 10^{-6}$, $\mathcal{B}(t \to \gamma c) < 7.4 \times 10^{-5}$.

8.1.6.5 Top-Higgs

The tHq interactions are studied by ATLAS in top quark pair events with $t \to qH, H \to \gamma\gamma$ [1198] and $H \to WW$ [1181] at 13 TeV. The former analysis explores the final state with two isolated photons. For leptonic top quark decays the selection criteria includes the requirement of one isolated lepton, exactly one b jet, and at least one non-b jet. In case of hadronic top quark decays the analysis selects events with no isolated leptons, at least one b jet, and at least three additional non-b jets. The dominant background processes are associated with the production of non-resonant $\gamma\gamma$+jets, $t\bar{t}$+jets and W+$\gamma\gamma$ events. The resultant limits are $\mathcal{B}(t \to Hu) < 2.4\ (1.7) \times 10^{-3}$ and $\mathcal{B}(t \to Hc) < 2.2\ (1.6) \times 10^{-3}$. The search for FCNC in $H \to WW$ includes the analysis of multilepton final states with either two same-sign or three leptons. The dominant backgrounds arising from the ttW, ttZ and non-prompt lepton production are suppressed with a BDT. The obtained limits are $\mathcal{B}(t \to Hu) < 1.9\ (1.5) \times 10^{-3}$ and $\mathcal{B}(t \to Hc) < 1.6\ (1.5) \times 10^{-3}$. The tHq anomalous couplings are probed by CMS in $H \to b\bar{b}$ channel in top quark pair events, as well as in single top associated production with a Higgs boson, at 13 TeV [1183]. The event selection includes the requirement of one isolated lepton, at least two b jets, and at least one additional non-b jet. The dominant $t\bar{t}$ background is suppressed with a BDT discriminant to set the exclusion limits of $\mathcal{B}(t \to Hu) < 4.7\ (3.4) \times 10^{-3}$ and $\mathcal{B}(t \to Hc) < 4.7\ (4.4) \times 10^{-3}$.

Table 34: The current and projected 95% C.L. constraints from direct observables on the real and imaginary parts of the Wilson coefficients that contribute to the Wtb vertex, assuming $\Lambda = 1$ TeV and $c_{\varphi q}^{-} = 0$.

	Coeff.	c_{tW}	c_{bW}	$c_{\varphi tb}$
Current	Re(...)	$[-0.70, 0.82]$	$[-2.2, 2.2]$	$[-8.9, 10.9]$
	Im(...)	$[-1.5, 2.2]$	$[-2.1, 2.2]$	$[-9.9, 9.9]$
3000 fb^{-1}	Re(...)	$[-0.23, 0.58]$	$[-2.2, 2.0]$	$[-9.3, 10.6]$
	Im(...)	$[-1.2, 1.3]$	$[-2.2, 2.1]$	$[-9.9, 9.9]$

Preliminary projections suggest $\mathcal{B}(t \to Hq) < \mathcal{O}(10^{-4})$ [1195, 1199].

8.2 Anomalous Wtb vertices and CP-violation effects from T-odd kinematic distributions

Authors (TH): Frederic Deliot, Wouter Dekens.

Beyond the SM, contributions to the Wtb vertex have been widely studied in the literature [1187, 1188, 1200–1214]. Assuming that new physics is much heavier than the electroweak scale, the BSM corrections to the Wtb vertex can be described using an EFT. The first contributions appear at dimension six and, in the conventions of [1156], take the following form

$$\mathcal{L}_{tb} = -\bar{t}\left[\frac{g}{\sqrt{2}}\gamma^{\mu}\left(V_{tb}\left(1+\tfrac{v^2}{2}c_{\varphi q}^{-}\right)P_L + \tfrac{v^2}{2}C_{\varphi tb}P_R\right)W_{\mu}^{+} - v\sigma^{\mu\nu}W_{\mu\nu}^{+}\left(C_{bW}P_R + C_{tW}^{*}P_L\right)\right]b + \text{h.c.}\,, \tag{119}$$

where $C_i = (c_i + ic_i^{[I]})/\Lambda^2$. In writing (119) we follow Ref. [1200] and enforce $C_{\varphi q}^{1(33)} + C_{\varphi q}^{3(33)} = 0$ to avoid tree-level FCNC decays of the Z (one also obtains a strong constraint from $Z \to bb$ decays [1208]), such that only the real combination $c_{\varphi q}^{-} = C_{\varphi q}^{1(33)} - C_{\varphi q}^{3(33)}$ appears.

The Wilson coefficients in Eq. (119) are in terms of the often-used anomalous couplings [1202, 1215] given by

$$V_L = V_{tb}^{*}\left(1+\tfrac{v^2}{2}c_{\varphi q}^{-}\right), \qquad V_R = \tfrac{v^2}{2}C_{\varphi tb}^{*}, \qquad g_L = -\sqrt{2}v^2C_{bW}^{*}, \qquad g_R = -\sqrt{2}v^2C_{tW}. \tag{120}$$

Note that within SMEFT gauge invariance links the above vertices to additional interactions. The full form of the relevant SMEFT operators is given in Sec. 8.1.

The above interactions give tree-level contributions to single-top production and to the observables in $t \to W^{+}b$ decay, in particular, to the W-boson helicity fractions. Apart from these processes that are "directly" sensitive to the Wtb vertices, there are "indirect" observables that receive contributions from the same operators through loop diagrams. Examples are $h \to \bar{b}b$, $B \to X_s\gamma$, and searches for electric dipole moments (EDMs). Below we discuss briefly both the direct and indirect limits on the operators in Eq. (119), as well as the projections for the HL-LHC (see also Working-Group 1 Section on this topic).

8.2.1 Direct probes

The Wtb interactions can be probed directly in single-top production and through the W boson helicity fractions in top decays. In the case of polarized top quarks it is possible to construct additional T-odd observables that are sensitive to CP-violating phases in the Wtb couplings. Here we discuss briefly these observables and the resulting (projected) constraints.

Single top production The single-top production cross section has been measured in the t and s channels at the LHC at $\sqrt{s} = 7$, 8, and 13 TeV [1216–1221]. In principle, these cross sections receive contributions from all Wtb couplings. The measurements can be compared with the SM prediction [1222] at NNLO in QCD, while BSM contributions have been evaluated at NLO [1223–1226]. In

Table 35: Indicative constraints on the SMEFT operators contributing to the Wtb vertex from indirect observables. A single Wilson coefficient is taken to be nonzero at a time, and we set $\Lambda = 1$ TeV.

Coeff.	$h \to \bar{b}b$	EWPT	$B \to X_s\gamma$	EDMs
$c_{\varphi q}^-$	–	–	$[-2.0, 2.2]$	–
$c_{\varphi tb}$	$[-0.3, 4.3]$	–	$[-4.6, 4.9] \cdot 10^{-2}$	–
c_{tW}	–	$[-1.1, 0.7]$	$[-0.22, 0.89]$	–
c_{bW}	–	–	$[-13, 3.5] \cdot 10^{-3}$	–
$c_{\varphi tb}^{[I]}$	$[-7.3, 7.3]$	–	$[-0.20, 0.20]$	$[-0.019, 0.019]$
$c_{tW}^{[I]}$	–	–	$[-2.4, 4.5]$	$[-1.0, 1.0] \cdot 10^{-3}$
$c_{bW}^{[I]}$	–	–	$[-4.3, 2.3] \cdot 10^{-2}$	$[-5.5, 5.5] \cdot 10^{-4}$

SMEFT the single-top cross sections can receive contributions from other operators, in particular, from several four-quark operators, see, e.g., Refs. [1210,1211]. Thus, in order to perform an exhaustive global analysis one would have to include these effects as well.

Top quark decays The helicity fractions of the W boson in top decays are mostly sensitive to c_{tW}, c_{bW}, and $c_{\varphi tb}$, and have been measured both at the Tevatron and the LHC [1227–1232]. In addition, the phase δ^- between the amplitudes of longitudinally and transversely polarized W bosons, recoiling against a left-handed b quark, carries information on the imaginary part of C_{tW} [1230, 1233]. The SM predictions for the helicity fractions are known to NNLO in QCD [1234], while the BSM contributions have been computed to NLO [1164, 1201].

As mentioned above, in the case of polarized top-quark decays, it becomes possible to construct additional observables that are sensitive to both the real and imaginary parts of the Wtb couplings. In particular, both the asymmetries constructed in Ref. [1235,1236] and the triple-differential measurements of Ref. [1237] are sensitive to $c_{tW}^{[I]}$ (see also Ref. [1206]). As a result, the limits on $c_{tW}^{[I]}$ already improve noticeably when including current experimental measurements of these angular asymmetries [1214].

After taking into account the current experimental results on single-top production, the helicity fractions, and angular asymmetries one obtains the current (projected) limits in the left (right) panel of Table 34 [1214, 1238]. For an analysis focused on single-top production see Ref. [1239]. These limits were obtained by assuming that $c_{\varphi q}^- = 0$. [9] Comparing the two panels one sees that the current and projected limits on the c_{bW} and $c_{\varphi tb}$ couplings are very similar, while the projected limits on the real and imaginary parts of c_{tW} are roughly a factor of 2 stronger than the current constraints.

Top decays can also be used to probe physics beyond that of the top sector. For example, Ref. [1240] recently suggested that the process $t \to bW \to b\bar{b}c$ can be used to measure V_{cb} at the m_W scale, instead of $V_{cb}(m_b)$ which is probed in B decays.

8.2.2 Indirect probes

The anomalous Wtb interactions contribute to other processes through loop diagrams. Although this can give rise to stringent constraints, their interpretation requires some care. As indirect observables receive contributions from additional operators apart from the Wtb couplings, cancellations between different Wilson coefficients are possible. We will assume this is not the case and derive limits for the case that a single dimension-six operator is generated at the BSM scale.

[9] This coupling is harder to constrain as it is degenerate with a shift in V_{tb}, see Eq. (119). This degeneracy can be broken by using CKM unitarity tests, or by considering additional interactions, such as the Wts, Wtd, and Ztt vertices, that are linked to $c_{\varphi q}^-$ by gauge invariance. A more naive constraint, obtained by setting $V_{tb} = 1$, leads to $|c_{\varphi q}^-| \lesssim 1$ [1225].

Electric dipole moments. Electric dipole moments are probes of CP violation and, therefore, receive contributions from the imaginary parts of the Wtb couplings. The most stringent experimental limits have been obtained on the EDMs of the neutron, mercury, and the ThO molecule, the latter of which can be interpreted as a limit on the electron EDM for our purposes. To obtain the contributions to EDMs one first has to evolve the Wtb operators to low energies, $\mu \sim 2$ GeV. QCD becomes non-perturbative below this scale, and one has to match to Chiral perturbation theory, which describes the CP-odd interactions in terms of hadrons, photons, and electrons. These interactions can then be used to calculate the EDMs of nucleons, atoms, and molecules.

Among the operators in Eq. (119), the $c_{\varphi tb}^{[I]}$ and $c_{bW}^{[I]}$ couplings are mainly constrained by the neutron EDM, while $c_{tW}^{[I]}$ contributes to the electron EDM. The $c_{\varphi tb}^{[I]}$ and $c_{bW}^{[I]}$ first generate the bottom-quark chromo EDM, $O_{dG}^{(33)}$ (in the notation of [1200]), through one-loop diagrams [1225, 1241, 1242], which subsequently induces the Weinberg operator, $O_{\tilde{G}}$, after integrating out the bottom quark [1243–1246]. The hadronic matrix element of the Weinberg operator contributing to the neutron EDM is poorly known. Combining naive-dimensional-analysis and sum-rule estimates [1244, 1247, 1248], one has $|d_n| = 6|e\,(50\,\mathrm{MeV})\,C_{\tilde{G}}(1\,\mathrm{GeV})|$, with an $\mathcal{O}(100\%)$ uncertainty.

The contributions to the electron EDM also arise from a two-step process: $c_{tW}^{[I]}$ first induces CP-odd operators of the form $X_{\mu\nu}\tilde{X}^{\mu\nu}\varphi^\dagger\varphi$, with $X_{\mu\nu}$ a $SU(2)_L$ or $U(1)_Y$ field strength, as well as semileptonic interactions of the form, $(\bar{e}_L\sigma_{\mu\nu}\,e_R)\,(\bar{t}_L\sigma^{\mu\nu}t_R)$, through the renormalization group equations [1224, 1249, 1250]. These additional operators then induce the electron EDM at one loop. Using the above contributions and the current experimental limits [1251–1253], we obtain the constraints in Table 35. The limits from the neutron EDM are expected to improve by 1 to 2 orders of magnitude in the next generation of experiments [1254], while proposals exist to improve the electron EDM limits by several orders of magnitude [1255–1257].

Rare B decays. Unlike EDMs, measurements of $B \to X_s\gamma$ are sensitive to both the real and imaginary parts of the couplings. Although all four of the Wtb vertices give rise to flavour-changing $b \to s$ transitions through one-loop diagrams [904, 1188, 1200], the largest effects are due to $C_{\varphi tb}$ and C_{bW}. Both of these couplings induce contributions proportional to m_t instead of m_b that appears in SM (as well as for $c_{\varphi q}^-$ and C_{tW}), leading to a relative enhancement of m_t/m_b. Here we consider the constraints from measurements of the $B \to X_s\gamma$ branching ratio and the CP asymmetry [197], for which we use the theoretical expressions of [1258] and [1259], respectively. This leads to the constraints in Table 35, which are expected to improve by a factor of a few in the future. In particular, the uncertainty on the branching ratio is expected to decrease by a factor of 2 to 3 at Belle II, while the improvement is projected to be a factor of 5 for the CP asymmetry [196].

Electroweak precision tests. The Wtb operators also modify the self energies of the SM gauge bosons through one-loop diagrams, which are often parametrized by the S, T, and U parameters [1260–1262]. Taking into account the RGE contributions, only c_{tW} induces the S parameter by mixing with the $O_{\varphi WB}$ operator (c_{bW} contributions are proportional to m_b), which leads to the limits in Table 35. Here we assumed only a single dimension-six operator is present at $\mu = \Lambda$, but one can include the couplings of the operators that induce S and T at tree level, $O_{\varphi WB}$ and O_{HD}, and marginalize over them. This can be done because electroweak precision observables carry more information than is captured by the S, T, and U parameters alone. This approach is discussed Ref. [1208, 1263] and leads to weaker limits, $c_{tW} \in [-1.6, 0.8]$, $c_{bW} \in [-2, 24]$, $c_{\varphi q}^- \in [-0.7, 4.7]$ for $\Lambda = 1$ TeV.

Higgs decays. Finally, the Wtb interactions contribute to the process $h \to \bar{b}b$ by inducing corrections to the SM bottom-quark Yukawa coupling [1225]. In particular, the $C_{\varphi tb}$ coupling generates a contribution to the Yukawa coupling that scales as $y_b \sim y_t v^2 C_{\varphi tb}/(4\pi)^2$. Thus, although this contribution only appears at one loop, the suppression is offset by the appearance of the top-quark Yukawa instead of that of the bottom quark. Using the combined ATLAS and CMS analysis [1264] of the Higgs

decays to $\gamma\gamma$, WW, ZZ, $\tau\tau$, $\mu\mu$, and $\bar{b}b$ signal strengths we obtain the limits in Table 35.

8.3 Determinations of V_{tx}

Authors (TH): Mariel Estevez, Darius Faroughy, Jernej Kamenik.

The LHC as a top-quark factory has the ability to directly probe the V_{tx} matrix elements. In particular, measuring the fractions of b-tagged jets in leptonic top decays $t \to Wj$ allows one to set a limit on the ratio

$$\mathcal{R} = \frac{\mathrm{Br}(t \to bW)}{\sum_{x=d,s,b} \mathrm{Br}(t \to Wx)} > 0.995 \tag{121}$$

at 95% CL [1265]. This result, when combined with measurements of t-channel single-top production [1217], provides a direct determination of $|V_{tb}| = 1.07 \pm 0.09$ in the limit $|V_{tb}| \gg |V_{ts}|, |V_{td}|$. Given that these measurements are already dominated by systematic effects, in particular the knowledge of the b-tagging efficiencies and theoretical uncertainties in single-top production, significant improvement in precision of V_{tb} measurement at the HL-LHC or HE-LHC would arguably require novel strategies.

8.3.1 Measuring $|V_{td}|$ at HL-LHC and HE-LHC

A possible experimental strategy to probe the $|V_{td}|$ matrix element directly at the HL(HE)-LHC is using single top production associated with a W boson, $pp \to tW$. The idea is to exploit the production cross-section enhancement, as well as boosts of the top quarks coming from initial state valence d-partons. The d-quark is a valence constituent of the proton and there is an imbalance with the $\bar{d}$-quark that motivates to explore charge asymmetries as possible V_{td}-sensitive observables. The main backgrounds, contrary to t-channel single top production, are charge symmetric or have very small charge asymmetries. The $dg \to tW$ associated production process is interesting because of its sizeable charge asymmetry in proton collisions and also because its kinematics predicts a characteristic angular distribution. We expect a relatively large incoming momentum on average from the valence d-quark. Consequently, a forward W^- is preferred in the lab frame, which is supposed to produce a forward ℓ^- in signal events. The main two backgrounds to the $\ell^+\ell^- bE_T^{\mathrm{miss}}$ final state are the dileptonic $t\bar{t}$ production (missing one of the b-jets from top decays) and $gb \to tW$ associated production, proportional to $|V_{tb}|^2$. Both backgrounds have very small charge asymmetries. In order to increase the sensitivity and enhance the signal cuts can be imposed that reduce the cross-sections of the backgrounds, see Ref. [1266] for details. The most important difference between signal and background comes from the $\eta(\ell^-)$ distribution, where the signal clearly prefers forward negatively charged leptons. The asymmetry

$$A(\eta, p_T) = \frac{N^+ - N^-}{N^+ + N^-}, \tag{122}$$

where $N^\pm = N\left(\Delta|\eta(\ell)| \gtrless 0 \,\&\, \Delta p_T(\ell) \gtrless 0\right)$, is a $|V_{td}|$ sensitive observable. Each process contributes with $N_i^+ - N_i^- = \sigma_i \cdot \mathcal{A}_i \cdot \epsilon_i \cdot A_i(\eta, p_T)$, where the factors on the right hand side are the cross-section, acceptance, selection efficiency and asymmetry, respectively. To quantify the versatility of the proposed charge asymmetry we study the prospective experimental reach in $r \equiv |V_{td}/V_{td}^{\mathrm{SM}}|$ by computing the difference of $A(\eta, p_T)$ to its SM expectation in units of the uncertainty. Based on existing experimental studies of charge asymmetries in top production [1267] we include an estimate for the systematic uncertainty of $\Delta_{sys} = 0.2\%$, and define the significance as

$$\text{significance} = \left|A(\eta, p_T) - A(\eta, p_T)^{\mathrm{SM}}\right| \Big/ \sqrt{(N^+ + N^-)^{-1} + \Delta^2_{\mathrm{syst}}}. \tag{123}$$

Fig. 63 shows the contours of expected experimental significance for $A(\eta, p_T)$ (and r) as functions of luminosity, for 13 TeV and 27 TeV LHC. As a rough guidance we also show with dashed lines the significance for the case that the dominant $t\bar{t}$ background were further reduced by a factor of 2, e.g., by

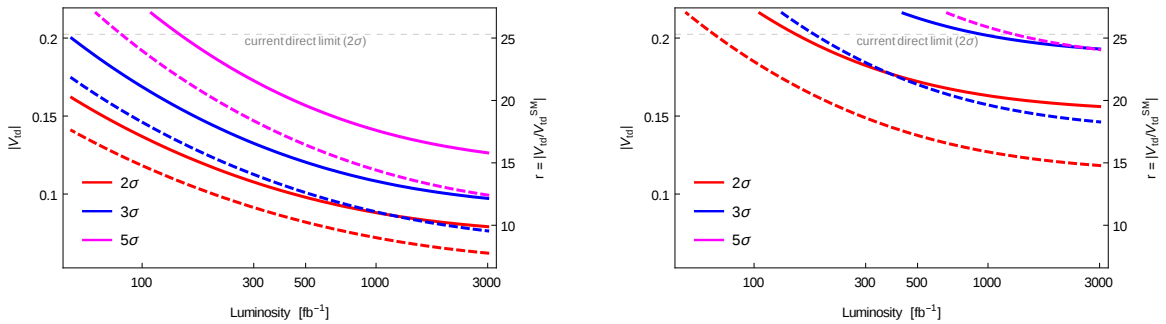

Fig. 63: Contour lines for the projected 2σ, 3σ and 5σ upper bounds on $|V_{td}|$ (and $r \equiv |V_{td}/V_{td}^{\rm SM}|$) as functions of the LHC luminosity at 13 TeV (left) and 27 TeV (right). Dashed lines follow if the dominant $t\bar{t}$ background is reduced by half, see text for details.

using multivariate discrimination techniques as already done in existing single top analyses [1268–1270]. Values of $r < 10$ could be directly accessible at the LHC@13TeV, improving the existing best direct constraint [1265] by roughly a factor of three. The current direct bound on $|V_{td}|$ can be surpassed with the Run 2 dataset, while with $3000\,\text{fb}^{-1}$ it could be possible to probe $|V_{td}| \sim |V_{ts}^{\rm SM}| \simeq 0.04$.

The dominant $t\bar{t}$ background is mostly generated via gluon fusion, which is charge symmetric. There are subleading contributions from processes like $u\bar{u} \to t\bar{t}$ which are charge asymmetric, but only enter at higher orders in QCD. This is the main reason the dominant $t\bar{t}$ background has a strongly suppressed charge asymmetry. At higher collision energies, the probability of finding energetic enough gluons in the proton increases faster than that of valence quarks. Consequently, the fraction of $t\bar{t}$ events from the quark-antiquark initial state is reduced [1267]. This leads to a shrinking charge asymmetry with growing collision energy. Unfortunately, the same happens to the signal, this time because at higher energies the asymmetry between d and $\bar{d}$ partons inside the proton is reduced. The net effect is a severely diminished significance at 27 TeV compared to 13 TeV for comparable luminosities.

8.3.2 Measuring Cabibbo-suppressed decays of the top quark at HL-LHC and HE-LHC

With the large $t\bar{t}$ statistics at the LHC, one might attempt a direct measurement of Cabibbo-suppressed decays of the top quark, $t \to (s,d)\,W^{\pm}$, in leptonic $t\bar{t}$ events. Since there is no practical way to distinguish between strange and down quark jets at the detector level (without dedictated PID systems), one measures

$$\rho \equiv \sqrt{\big(\mathcal{B}(t \to sW) + \mathcal{B}(t \to dW)\big)/\mathcal{B}(t \to bW)}\,. \tag{124}$$

This gives a direct information on $(|V_{ts}|^2 + |V_{td}|^2)^{1/2}$, but not on V_{ts} and V_{td} separately. In the SM, $\rho \approx |V_{ts}| \approx 0.04$.

To perform the measurement it is necessary to discriminate between heavy-flavoured jets, e.g., b-jets from the $t \to bW$ background, gluons from ISR/FSR contamination, and the signal – the light-quark jets (q-jets) from the Cabibbo-suppressed top decays. This can be achieved through a q-tagger based on existing techniques used for b-tagging and quark/gluon jet discrimination [1271]. There are several known useful observables which can be used in a q-tagger. In the following we use: (i) the multiplicity $N_{\rm SV}$ of secondary vertices (SV) in the jet within a fiducial volume of the tracker, (ii) the fraction of longitudinal momentum of the jet carried by the hardest prompt charged track $z_{\rm max} \equiv \max\big[\vec{p}_x \cdot \vec{p}_{\rm jet}/|\vec{p}_{\rm jet}|^2\big]_{x\in{\rm jet}}$, and (iii) the 2-point energy correlation function $U_1^{\beta} = \sum_{i,j\in{\rm jet}} z_T^i z_T^j\,(R_{ij})^{\beta}$, $z_T^i \equiv p_T^i/p_T^{\rm jet}$, where $R_{ij}^2 = (\eta_i-\eta_j)^2 + (\phi_i-\phi_j)^2$ and β is a free real parameter for which quark/gluon discrimination is optimized at $\beta = 0.2$ [1272, 1273], see Ref. [1274] for more details.

For the projections we use the reference working point shown in Table 36. We bin preselected events into one of the six tagged dijet categories $\{jj, jb, jq, qb, qq, bb\}$ where q, b and j represent q -jets,

Table 36: Tagging and mis-tagging efficiencies for the q-tagging working point used in the V_{tq} analysis.

(t) type	Cuts	ϵ_q^t	ϵ_b^t	ϵ_c^t	ϵ_g^t
q-tagger	$N_{SV} = 0$ & $z_{max} > 0.3$	0.18	0.0031	0.038	0.049
b-tagger	$N_{SV} > 3$	0.0091	0.64	0.09	0.016

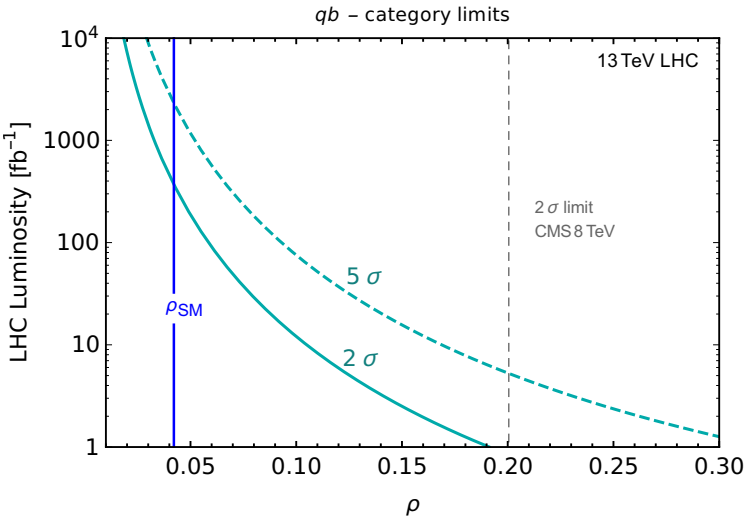

Fig. 64: Illustration of statistical limits on the ratio $\rho \simeq \left(|V_{ts}|^2 + |V_{td}|^2\right)^{1/2}/|V_{tb}|$ from an analysis of Cabbibo-suppressed top decays in leptonic $t\bar{t}$ events at 13TeV LHC. See text for details.

b-jets and non-tagged jets (a jet failing both taggers), respectively. Fig. 64 shows the resulting upper limits on ρ taking into account only statistical uncertainties in the qb category for the signal significance $S/\sqrt{B}$ at 2σ (solid boundary) and 5σ (dashed boundary) as a function of the LHC luminosity, compared to the current best limit by CMS shown by the gray dashed curve. The results suggest that the HL-LHC could find evidence of Cabbibo-suppressed top decays and determine V_{ts} CKM element directly, though the precise precision depends crucially on how well systematic uncertainties can be controlled. The uncertainties in q- and b-tagging efficiencies could be controlled using Zj production. Then a fit of the categorized dijet data $\{jj, jb, jq, qb, qq, bb\}$ in inclusive dilepton events to a probabilistic model taking into account the tagging efficiencies could be performed, similar to that performed in [1265,1275] for the extraction of V_{tb}. Especially relevant for the HE-LHC would be to measure $t \to (s,d)W$ from boosted semi-leptonic $t\bar{t}$ events. Events with one top-tagged fat jet, one narrow jet and one lepton (both daughter candidates of the leptonic top) can be categorized by the flavour content of the narrow jet. A preliminary analysis [1274] suggests comparable sensitivity to the leptonic $t\bar{t}$ dataset already at the 13TeV LHC.

9 The Higgs boson and flavour physics

Authors (TH): F. Bishara, R. Harnik, A. Martin, M. Schlafer, Y. Soreq, E. Stamou, F. Yu.

In the SM the Higgs couplings to the fermions are the origin of the flavour structure. In the SM the Yukawa couplings, y_f, are CP conserving and proportional to the fermion masses, m_f, with a common proportionality factor,

$$y_f^{\rm SM} = \sqrt{2} m_f / v \,, \tag{125}$$

while the tree-level flavour changing couplings are zero. Currently, only the third generation Yukawa couplings have been measured and found to be in agreement with the SM predictions, see Refs. [1276–1282]. For the Higgs couplings to the first two generations, only upper bounds exist at present [1283–1287].

To parametrize the deviations from the SM, it is useful to introduce a generalized κ framework (the summation is over fermion type $f = u, d, \ell$ and generations $i, j = 1, 2, 3$)

$$\mathcal{L}_{\rm eff} = -\kappa_{f_i} \frac{m_{f_i}}{v} h \bar{f}_i f_i + i \tilde{\kappa}_{f_i} \frac{m_{f_i}}{v} h \bar{f}_i \gamma_5 f_i - \left[\left(\kappa_{f_i f_j} + i \tilde{\kappa}_{f_i f_j} \right) h \bar{f}^i_L f^j_R + \text{h.c.} \right]_{i \neq j} . \tag{126}$$

Experimentally, we want to test a number of SM predictions: *(i)* proportionality, $y_f \propto m_f$; *(ii)* the factor of proportionality, $\kappa_{f_i} = 1$; *(iii)* diagonality (no off-diagonal flavour violation), $\kappa_{f_i f_j} = 0$; *(iv)* reality (no CP violation), $\tilde{\kappa}_{f_i} = \tilde{\kappa}_{f_i f_j} = 0$ [1288]. Different Higgs Yukawa couplings are probed both directly and indirectly. Direct methods are: for top Yukawa the $t\bar{t}h$ production [1276–1278]); for bottom and charm, $pp \to Vh, h \to b\bar{b}, c\bar{c}$ [1281–1283]; for leptons $pp \to h \to \ell^+\ell^-$ [1279, 1280, 1284]; for light quarks the exclusive $h \to V\gamma$ decays [1289–1292]. The kinematical distributions [1293, 1294] and global fits to all the Higgs data also provide bounds on different Yukawa couplings.

The Higgs production and decay signal strengths from the CMS collaboration [1295], and from ATLAS for $h \to c\bar{c}$ [1283] from a global fit, which includes the direct observation of $t\bar{t}h$ production, gives for the signal strengths $\mu_{tth} = 1.18^{+0.30}_{-0.27}, \mu_{bb} = 1.12^{+0.29}_{-0.29}, \mu_{cc} < 105, \mu_{\tau\tau} = 1.20^{+0.26}_{-0.24}, \mu_{\mu\mu} = 0.68^{+1.25}_{-1.24}$. In terms of modifications of the flavour-diagonal CP-conserving Yukawas, the best fit values are, see also [1264, 1295],

$$\kappa_t = 1.11^{+0.12}_{-0.10}, \qquad \kappa_b = -1.10^{+0.33}_{-0.23}, \qquad \kappa_\tau = 1.01^{+0.16}_{-0.20}, \qquad \kappa_\mu = 0.79^{+0.58}_{-0.79}. \tag{127}$$

The u, d, s, and charm Yukawa couplings can be constrained from a global fit to the Higgs data and the precision electroweak measurements at LEP. Floating all the couplings in the fit gives [1285, 1287],

$$\kappa_u < 3.4 \cdot 10^3, \qquad \kappa_d < 1.7 \cdot 10^3, \qquad \kappa_s < 42, \qquad \kappa_c \lesssim 6.2. \tag{128}$$

The upper bound on $\mathcal{B}(h \to e^+e^-)$ gives for the electron Yukawa $|\kappa_e| < 611$ [1286, 1296]. The upper bounds on $\kappa_{c,s,d,u}$ roughly correspond to the size of the SM bottom Yukawa coupling and are thus much bigger than the corresponding SM Yukawa couplings. The upper bounds can be saturated only if one allows for large cancellations between the contribution to fermion masses from the Higgs vev and an equally large contribution from NP, but with an opposite sign. In models of NP motivated by the hierarchy problem, the effects of NP are generically well below these bounds.

In the rest of this section we first briefly discuss the expected deviations in a set of NP models, and give the prospects for HL-/HE-LHC (see also [1289, 1297–1301]). An expanded version of the discussion is available in write-up of WG2, Sec. 7.

9.1 New Physics benchmarks for modified Higgs couplings

The expected sizes of effective Yukawa couplings, κ_f, $\tilde{\kappa}_f$ and $\kappa_{ff'}, \tilde{\kappa} f f'$, in popular models of weak scale NP models, some of them motivated by the hierarchy problem are shown in Tables 37 and 38,

Model	κ_t	$\kappa_{c(u)}/\kappa_t$	$\tilde{\kappa}_t/\kappa_t$	$\tilde{\kappa}_{c(u)}/\kappa_t$
SM	1	1	0	0
MFV	$1+\frac{\mathrm{Re}(a_u v^2+2b_u m_t^2)}{\Lambda^2}$	$1-\frac{2\,\mathrm{Re}(b_u)m_t^2}{\Lambda^2}$	$\frac{\mathrm{Im}(a_u v^2+2b_u m_t^2)}{\Lambda^2}$	$\frac{\mathrm{Im}(a_u v^2)}{\Lambda^2}$
NFC	$V_{hu}\,v/v_u$	1	0	0
F2HDM	$\cos\alpha/\sin\beta$	$-\tan\alpha/\tan\beta$	$\mathcal{O}\left(\frac{m_c}{m_t}\frac{\cos(\beta-\alpha)}{\cos\alpha\cos\beta}\right)$	$\mathcal{O}\left(\frac{m^2_{c(u)}}{m_t^2}\frac{\cos(\beta-\alpha)}{\cos\alpha\cos\beta}\right)$
MSSM	$\cos\alpha/\sin\beta$	1	0	0
FN	$1+\mathcal{O}\left(\frac{v^2}{\Lambda^2}\right)$	$1+\mathcal{O}\left(\frac{v^2}{\Lambda^2}\right)$	$\mathcal{O}\left(\frac{v^2}{\Lambda^2}\right)$	$\mathcal{O}\left(\frac{v^2}{\Lambda^2}\right)$
GL2	$\cos\alpha/\sin\beta$	$\simeq 3(7)$	0	0
RS	$1-\mathcal{O}\left(\frac{v^2}{m_{KK}^2}\bar{Y}^2\right)$	$1+\mathcal{O}\left(\frac{v^2}{m_{KK}^2}\bar{Y}^2\right)$	$\mathcal{O}\left(\frac{v^2}{m_{KK}^2}\bar{Y}^2\right)$	$\mathcal{O}\left(\frac{v^2}{m_{KK}^2}\bar{Y}^2\right)$
pNGB	$1+\mathcal{O}\left(\frac{v^2}{f^2}\right)+\mathcal{O}\left(y_*^2\lambda^2\frac{v^2}{M_*^2}\right)$	$1+\mathcal{O}\left(y_*^2\lambda^2\frac{v^2}{M_*^2}\right)$	$\mathcal{O}\left(y_*^2\lambda^2\frac{v^2}{M_*^2}\right)$	$\mathcal{O}\left(y_*^2\lambda^2\frac{v^2}{M_*^2}\right)$

Table 37: Predictions for the flavour-diagonal up-type Yukawa couplings in a sample of NP models (see text for details).

Model	$\kappa_{ct(tc)}/\kappa_t$	$\kappa_{ut(tu)}/\kappa_t$	$\kappa_{uc(cu)}/\kappa_t$
MFV	$\frac{\mathrm{Re}\left(c_u m_b^2 V_{cb}^{(*)}\right)}{\Lambda^2}\frac{\sqrt{2}m_{t(c)}}{v}$	$\frac{\mathrm{Re}\left(c_u m_b^2 V_{ub}^{(*)}\right)}{\Lambda^2}\frac{\sqrt{2}m_{t(u)}}{v}$	$\frac{\mathrm{Re}\left(c_u m_b^2 V_{ub(cb)}V^*_{cb(ub)}\right)}{\Lambda^2}\frac{\sqrt{2}m_{c(u)}}{v}$
F2HDM	$\mathcal{O}\left(\frac{m_c}{m_t}\frac{\cos(\beta-\alpha)}{\cos\alpha\cos\beta}\right)$	$\mathcal{O}\left(\frac{m_u}{m_t}\frac{\cos(\beta-\alpha)}{\cos\alpha\cos\beta}\right)$	$\mathcal{O}\left(\frac{m_c m_u}{m_t^2}\frac{\cos(\beta-\alpha)}{\cos\alpha\cos\beta}\right)$
FN	$\mathcal{O}\left(\frac{v m_{t(c)}}{\Lambda^2}\lvert V_{cb}\rvert^{\pm 1}\right)$	$\mathcal{O}\left(\frac{v m_{t(u)}}{\Lambda^2}\lvert V_{ub}\rvert^{\pm 1}\right)$	$\mathcal{O}\left(\frac{v m_{c(u)}}{\Lambda^2}\lvert V_{us}\rvert^{\pm 1}\right)$
GL2	$\epsilon(\epsilon^2)$	$\epsilon(\epsilon^2)$	ϵ^3
RS	$\sim\lambda^{(-)2}\frac{m_{t(c)}}{v}\bar{Y}^2\frac{v^2}{m_{KK}^2}$	$\sim\lambda^{(-)3}\frac{m_{t(u)}}{v}\bar{Y}^2\frac{v^2}{m_{KK}^2}$	$\sim\lambda^{(-)1}\frac{m_{c(u)}}{v}\bar{Y}^2\frac{v^2}{m_{KK}^2}$
pNGB	$\mathcal{O}(y_*^2\frac{m_t}{v}\frac{\lambda_{L(R),2}\lambda_{L(R),3}m_W^2}{M_*^2})$	$\mathcal{O}(y_*^2\frac{m_t}{v}\frac{\lambda_{L(R),1}\lambda_{L(R),3}m_W^2}{M_*^2})$	$\mathcal{O}(y_*^2\frac{m_c}{v}\frac{\lambda_{L(R),1}\lambda_{L(R),2}m_W^2}{M_*^2})$

Table 38: Same as Table 37 but for flavour-violating up-type Yukawa couplings. In the SM, NFC and the tree-level MSSM the Higgs Yukawa couplings are flavour diagonal. The CP-violating $\tilde{\kappa}_{ff'}$ are obtained by replacing the real part, Re, with the imaginary part, Im. All the other models predict a zero contribution to these flavour changing couplings.

adapted from [1302–1306]. The predictions are shown for the Standard Model, multi-Higgs-doublet models (MHDM) with natural flavour conservation (NFC) [1307,1308], a "flavourful" two-Higgs-doublet model beyond NFC (F2HDM) [1309–1312] the MSSM at tree level, a single Higgs doublet with a Froggat-Nielsen mechanism (FN) [1313], the Giudice-Lebedev model of quark masses modified to 2HDM (GL2) [1314], NP models with minimal flavour violation (MFV) [1315], Randall-Sundrum models (RS) [1316], and models with a composite Higgs where Higgs is a pseudo-Nambu-Goldstone boson (pNGB) [1317–1320]. Tables 37 and 38 only show predictions for up-quark sector, while the results for down-quark and lepton sectors can be found in (see also Sec. 7 of WG2 write-up).

In Tables 37 and 38, $v = 246$ GeV is the electroweak vev, while Λ is the typical NP scale. For instance, if SM is corrected by dimension six operators with Minimal Flavour Violation (MFV), then the up-quark couplings receive a contribution $Y'_u \bar{Q}_L H^c u_R/\Lambda^2$, so that the Yukawa coupling is $y_u = Y_u + 3Y'_u v^2/(2\Lambda^2)$, with $Y'_u = a_u Y_u + b_u Y_u Y_u^\dagger Y_u + c_u Y_d Y_d^\dagger Y_u + \cdots$, where $Y_{u,d}$ are the SM

Yukawas. The v^2/Λ^2 contributions correct both the diagonal Yukawa couplings, and lead to off-diagonal, flavour violating, couplings.

Not all NP models lead to flavour-violating Yukawa couplings. For instance, in multi-Higgs-doublet models with natural flavour conservation by assumption only one doublet, H_u, couples to the up-type quarks, only one Higgs doublet, H_d, couples to the down-type quarks, and only one doublet, H_ℓ couples to leptons (it is possible that any of these coincide, as in the SM where $H = H_u = H_d = H_\ell$) [1307, 1308]. This only modifies diagonal Yukawa couplings, while off-diagonal remain to be zero, as in the SM. Similar result applies to the MSSM tree-level Higgs potential where $h_{u,d}$ mix into the Higgs mass-eigenstates h and H as $h_u = \cos\alpha h + \sin\alpha H$, $h_d = -\sin\alpha h + \cos\alpha H$, where h is the observed SM-like Higgs, and the vevs are $v_u = \sin\beta\, v$, $v_d = \cos\beta$. Flavourful two-Higgs-doublet model [1309], on the other hand, introduces mass suppressed off-diagonal and CP violating contributions, a direct consequence of the fact that one Higgs doublet couples only to top, bottom and tau, and a second Higgs doublet couples to the remaining fermions (see also [1321–1324]). Off-diagonal and CP violating Yukawa couplings are typical of any model of flavour with new degrees of freedom that are light enough, such as if the Higgs mixes with the flavon from the Froggatt-Nielsen (FN) mechanism [1313], or if FN mechanism gives the structure of both dimension 4 and dimension 6 operators in SMEFT. Another example is the model of quark masses introduced by Giudice and Lebedev [1314], where the quark masses, apart from the top mass, are small, because they arise from higher dimensional operators.

In Randall-Sundrum warped extra-dimensional models, that address simultaneously the hierarchy problem and the hierarchy of the SM fermion masses [1316, 1325–1328], the corrections to the Yukawa couplings are suppressed by the masses of Kaluza-Klein (KK) modes, m_{KK}. If Higgs is a pseudo-Goldstone boson arising from the spontaneous breaking of a global symmetry in a strongly coupled sector, coupling to the composite sector with a typical coupling y_* [1317–1320] (for a review, see [1329]), the corrections to the Yukawa couplings are suppressed by the mass of composite resonance with a typical mass $M_* \sim \Lambda$.

In conclusion, we see that the NP effects in Higgs couplings to the SM fermions are either suppressed by $1/\Lambda^2$, where Λ is the NP scale, or are proportional to the mixing angles with the extra scalars. This means that in the decoupling limit, $\Lambda \to \infty$ and/or small mixing angles, all the NP effects vanish. In the decoupling limit the Higgs couplings coincide with the SM predictions, $\kappa_f = 1$, while $\tilde{\kappa}_f = 0, \kappa_{ff'} = 0, \tilde{\kappa}_{ff'} = 0$.

9.2 Probing charm and light quark Yukawa couplings

The inclusive method of probing the charm-quark Yukawa is in many ways complementary to searches for exclusive decays (see discussion of Sec. 9.2.3) or searches for deviations in Higgs distributions (see Sec. 9.2.4). For example, in the inclusive approach an underlying assumption is that the Higgs coupling to WW and ZZ —entering Higgs production— is SM-like, while the interpretation of Higgs distributions assumes no additional new physics contribution that affects them in a significant way. An important difference between the inclusive and the exclusive approach is that the latter relies on interference with the SM $H \to \gamma\gamma$ amplitude while the former does not. Therefore, in principle the exclusive approach may be sensitive to the sign and CP properties of the coupling to which the inclusive approach is insensitive to. At the same time, measurements of exclusive decays of the Higgs are challenging due to the small probability of fragmenting into the specific final state and large QCD backgrounds, which is why the inclusive approach appears to be the most promising one to probe deviations in the magnitude of the Higgs to charm coupling.

The summary of the projections that are discussed in the following sections, is given in Fig. 66. Shown are the expected HL-LHC constraints from exclusive decays (blue), from Higgs kinematic distributions (purple) and from inclusive c-tagging measurements (yellow), as well as the constraints from the combined $h \to \gamma\gamma$ and $h \to ZZ$ line shapes (dashed lines), from the total width using off-shell methods (green), and from the global fits to Higgs data (red). For the global fit one assumes $\mathcal{B}(h \to \text{BSM}) < 5\%$,

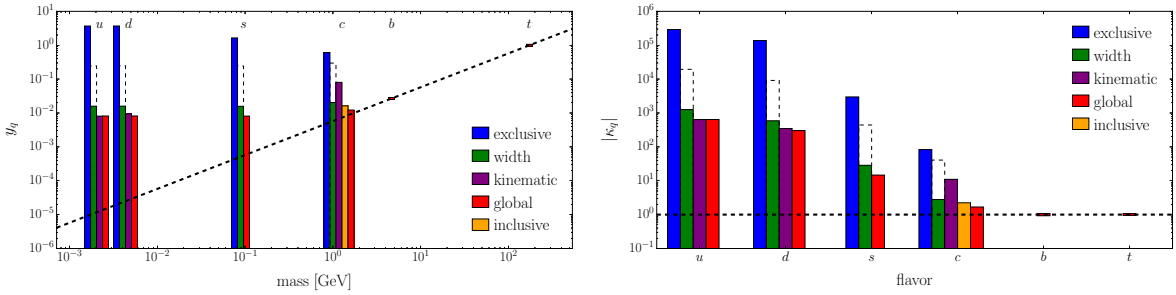

Fig. 65: Summary of the HL-LHC projections for measurements of Higgs Yukawa couplings to quarks discussed in the main text: from exclusive decays (blue), from Higgs kinematic distributions (purple) and from inclusive constraints (yellow), from off-shell bounds on total decay width (green), from the $h \to \gamma\gamma$ and ZZ line shapes (dashed), and from global fits (red).

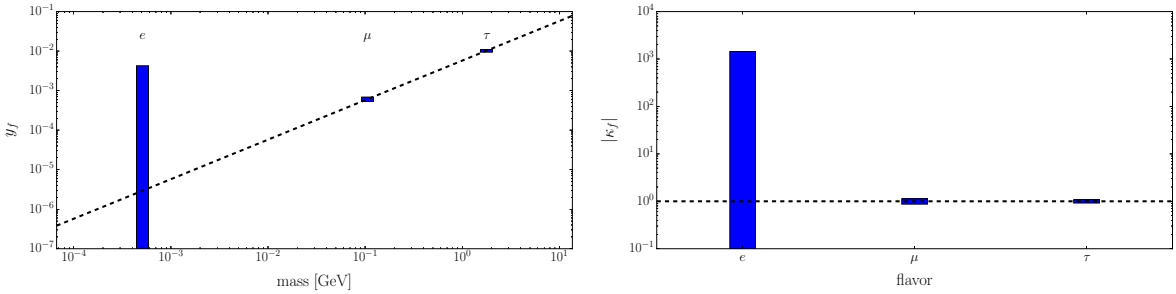

Fig. 66: Summary of the HL-LHC projections for measurements of Higgs Yukawa couplings to leptons from searches for $h \to \ell^+\ell^-$ decays.

while the constraints from the total width assume that one will be able to constrain $\Gamma < 1.2\Gamma_{\rm SM}$ (green bars), and that the resolution for the $\gamma\gamma/ZZ$ line shape will be 200MeV at the HL-LHC. Note that the off-shell constraints are model dependent.

9.2.1 Inclusive charm quark tagging

The most straight-forward way of inclusively probing charm quark Yukawa is to expand the $h \to b\bar{b}$ search with a search for $pp \to (Z/W \to \ell\ell/\nu)(h \to c\bar{c})$ [1285]. Another possibility is to search for $pp \to hc$ production [1298]. The search for $h \to c\bar{c}$ from $pp \to Zh$ at $\sqrt{s} = 13$ TeV was recently performed on a 36.1 fb^{-1} sample by ATLAS [1283]. The c-tagging algorithms are similar to b-tagging ones, with the most relevant quantities the displaced vertices due to a finite lifetime of c-hadrons. Prior to its use in Higgs physics, c-tagging was used early on in Run I of the LHC by ATLAS and CMS in searches for supersymmetry [1330, 1331]. Its usefulness in relations to Higgs physics was first discussed in Ref. [1332] and subsequently used in Ref. [1285] to recast ATLAS and CMS Run I analyses for $h \to b\bar{b}$ to provide the first direct LHC constraint on charm Yukawa.

The efficiency of jet flavour tagging algorithms in associating a jet to a specific quark is correlated with the confidence to reject other hypotheses, e.g., production from light-quarks. Given the rather similar lifetimes of b and c hadrons, there is always a non-negligible contamination of the c-jet sample with b jets [1285]. The ATLAS analysis [1283] used a working point with an efficiency of approximately 41% to tag c-jets and rejection factors of roughly 4 and 20 for b- and light-quark-jets, respectively. An inclusive $h \to c\bar{c}$ analysis must thus either assume a SM value for the bottom Yukawa (as in Ref. [1283]), or break the degeneracy between y_b and y_c, e.g., by using more than one tagging working point with different ratios of c-tagging to b-tagging efficiencies [1285, 1297].

The prospects for measuring $pp \to Zh(\to c\bar{c})$ at the HL-LHC were obtained in Ref. [1333], by

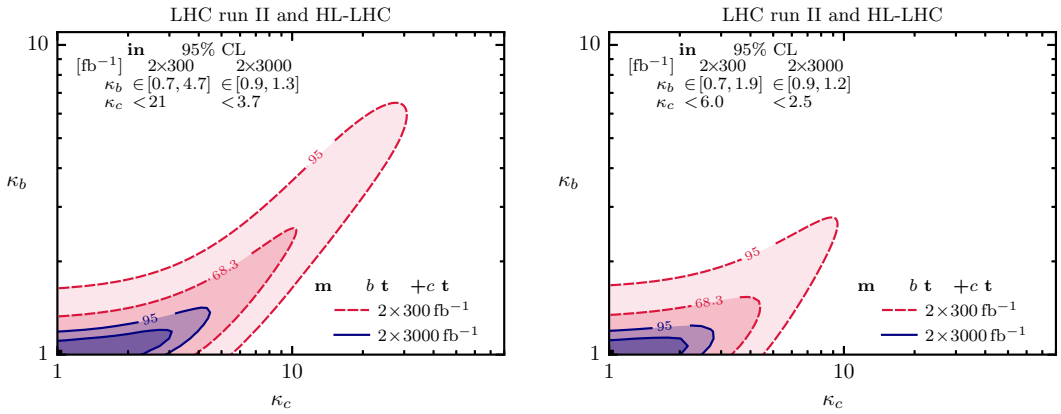

Fig. 67: Projections for measuring charm Yukawa modifications from an inclusive $H \to c\bar{c}$ search at $\sqrt{s} = 14\,\text{TeV}$ using two different c-taggers (left and right panel) [1297]. In red the 95% CL region employing an integrated luminosity of 2×300 fb^{-1} and in blue the region employing 2×3000 fb^{-1}.

rescaling the Run 2 analysis [1283] to an integrated luminosity of 3000 fb^{-1}. Possibilities to reduce the systematic uncertainties were discussed as well. Assuming $\kappa_b = 1$, an upper bound on the signal strength of $\mu_{Zh(c\bar{c})} < 6.3$ at 95% CL can be set. In Ref. [1297] instead, the prospects for measuring $h \to b\bar{b}$ at $\sqrt{s} = 14\,\text{TeV}$ [1334] were recast to obtain the projection for an inclusive $h \to c\bar{c}$ measurement. Both κ_c and κ_b are treated as free variables. Fig. 67 shows results for two flavour tagging working points: a c-tagging efficiency of 30% (c-tag II, left panel) or 50% (c-tag III, right panel), while in both cases the b(light)-jet rejection is 5(200). The κ_b direction is profiled away, giving the HL-LHC sensitivity of $\kappa_c \simeq 21(6)$ at 95% CL with c-tag II (c-tag III) and $2 \times 3000\,\text{fb}^{-1}$ at $\sqrt{s} = 14\,\text{TeV}$, indicated by the blue regions in Fig. 67.

Even though the LHCb experiment operates at lower luminosity compared to ATLAS and CMS, it has unique capabilities for discrimination between b- and c-jets thanks to its excellent vertex reconstruction system [1335]. With the secondary vertex tagging (SV-tagging) LHCb achieved an identification efficiency of 60% on b-jets, of 25% on c-jets and a light jets (light quarks or gluons) mis-identification probability of less than 0.2%. Further discrimination between light and heavy jets and between b- and c-jets is achieved by exploiting the secondary vertex kinematic properties, using Boosted Decision Tree techniques (BDTs). For instance, an additional cut on the BDT that separates b- from c-jets removes 90% of $h \to b\bar{b}$ while retaining 62% of $h \to c\bar{c}$ events [1336].

The LHCb acceptance covers $\sim 5\%$ of the associated production of $W/Z + h$ at 13 TeV. Fig. 68 (left) shows the coverage of LHCb for the $b\bar{b}$ pair produced in the decay of the Higgs boson in association with a vector boson. When the two b-jets are within the acceptance, the lepton from W/Z tends to be in acceptance as well ($\sim$ 60% of the time). Due to the forward geometry, Lorentz-boosted Higgs bosons are likely to be properly reconstructed.

LHCb set upper limits on the $V + h(\to b\bar{b})$ and $V + h(\to c\bar{c})$ production [1336] with data from LHC Run 1. Without any improvements in the analysis or detector, the extrapolation of this to 300fb^{-1} at 14 TeV leads to a sensitivity of $\mu_{Zh(cc)} \lesssim 50$. Detector improvements are expected in future upgrades, in particular in impact parameter resolution which directly affects the c-tagging performance. If the detector improvement is taken into account, the c-jet tagging efficiency with the SV-tagging is expected to improve as shown in Fig. 68 (right). Further improvement is expected from the electron reconstruction due to upgraded versions of the electromagnetic calorimeter. Electrons are used in the identification of the vector bosons associated with the Higgs. With these improvements, the expected limit can be pushed down to $\mu_{Zh(cc)} \lesssim 5 - 10$ which corresponds to a limit of 2-3 times the Standard Model prediction on

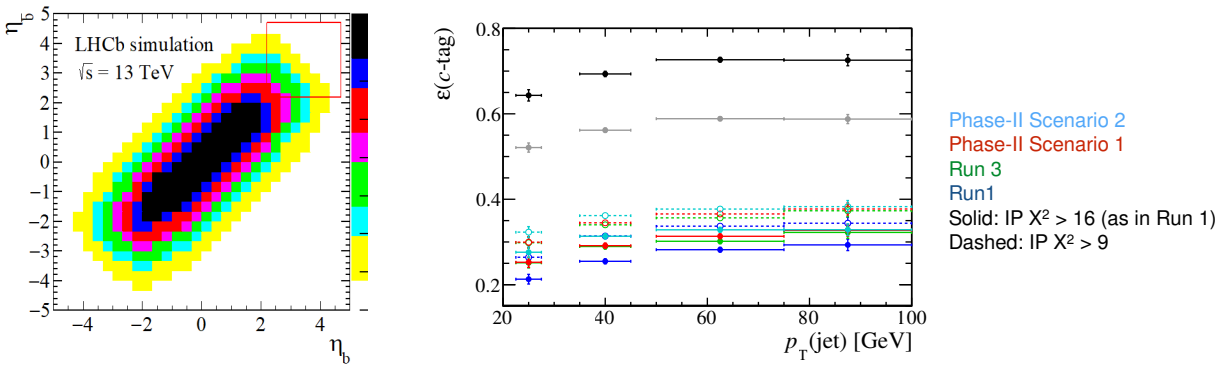

Fig. 68: Left: 2D histogram showing the coverage of the LHCb acceptance for the $b\bar{b}$ pair produced by the Higgs decay in associated production with a W or a Z boson. Right: LHCb c-jet SV-tagging efficiency for different scenarios in the HL-LHC conditions.

the charm Yukawa coupling. This extrapolation does not include improvements in analysis techniques: for instance Deep Learning methods can be applied to exploit correlations in jets substructure properties to reduce the backgrounds.

9.2.2 Strange quark tagging

The main idea behind the strange tagger described in Ref. [1337] is that strange quarks—more than other partons—hadronize to prompt kaons which carry a large fraction of the jet momentum. Although the current focus at LHC is mainly on charm and bottom tagging, recognizing strange jets has been attempted before at DELPHI [1338] and SLD [1339], albeit in Z decays.

Fig. 69 shows results for a strange tagger based on an analysis of event samples of Higgs and W events generated with PYTHIA 8.219 [373, 1340]. In each of the two hemispheres of the resonance decay, the charged pions and kaons stemming from the resonance are selected with an assumed efficiency of 95%. Similarly, K_S are identified with an efficiency of 85% if they decay via $K_S \to \pi^+\pi^-$ within 80 cm of the interaction point, which allows one to reconstruct the decaying neutral kaon. Among the two lists of kaon candidates—one per hemisphere—one kaon in each list is chosen for further analysis such that the scalar sum of their momenta is maximized while rejecting charged same-sign pairs. The events are separated into the categories charged-charged (CC), charged-neutral (CN) and neutral-neutral (NN) with relative abundances of about CC:CN:NN$\approx 9:6:1$.

All selected candidates are required to carry a large momentum $p_{||}$ along the hemisphere axis. This cut reduces the background from gluon jets as gluons radiate more than quarks and therefore tend to spread their energy among more final state particles. In addition, charged kaons need to be produced promptly, in order to reject heavy flavour jets. The latter requirement is implemented by a cut on the impact parameter d_0 after the truth value has been smeared by the detector resolution.

The efficiencies obtained in the CC and CN channel for a cut of $d_0 < 14$ μm are shown in Fig. 69. While there is clearly still ample room for improvement, this simple tagger already shows a good suppression of the bottom, charm and gluon background by orders of magnitude. Due to missing particle identification at ATLAS and CMS, the efficiencies for first-generation jets and strange jets are degenerate in the CC channel. However, in the CN channel, due to the required K_S, a suppression of pions is achieved that breaks this degeneracy. This is particularly interesting in light of the HL-LHC, where a large background from first generation jets is expected.

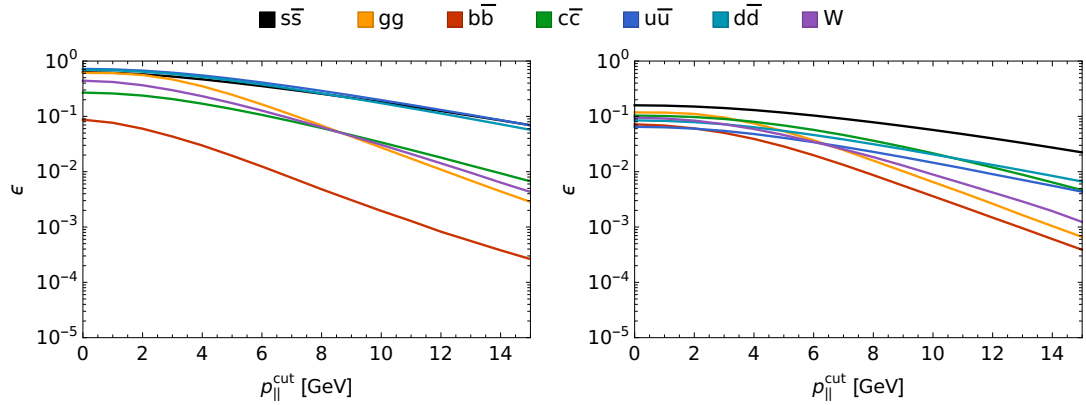

Fig. 69: Efficiencies as function of the cut on $p_{||}$ and for d_0 <14 μm to reconstruct the different Higgs decay channels and W decays as $s\bar{s}$ event by the described tagger. The left plot shows the CC channel, the right the CN channel.

mode	$\mathcal{B}_{h\to V\gamma}<$	$\mathcal{R}_{V\gamma,ZZ^*}<$	Yukawa range
$J/\psi\,\gamma$	$1.5\cdot10^{-3}$ [1289, 1290]	9.3	$-295\kappa_Z+16\kappa_{\gamma\gamma}^{\rm eff}<\kappa_c<295\kappa_Z+16\kappa_{\gamma\gamma}^{\rm eff}$
$\phi\,\gamma$	$4.8\cdot10^{-4}$ [1292, 1341]	3.2	$-140\kappa_Z+10\kappa_{\gamma\gamma}^{\rm eff}<\bar{\kappa}_s<140\kappa_Z+10\kappa_{\gamma\gamma}^{\rm eff}$
$\rho\,\gamma$	$8.8\cdot10^{-4}$ [1292]	5.8	$-285\kappa_Z+42\kappa_{\gamma\gamma}^{\rm eff}<2\bar{\kappa}_u+\bar{\kappa}_d<285\kappa_Z+42\kappa_{\gamma\gamma}^{\rm eff}$

Table 39: The current 95% C.L. upper bounds, assuming SM Higgs production, on different exclusive $h\to V\gamma$ decays, and the interpretation in terms of the Higgs Yukawa couplings. Note that $\bar{\kappa}_q=y_q/y_b^{\rm SM}$.

9.2.3 Exclusive Higgs decays

Exclusive Higgs decays to a vector meson, V, and a photon, $h\to V\gamma$, can directly probe bottom, charm [1300,1301], strange, down and up [1287] quark Yukawas. On the experimental side, both ATLAS and CMS reported first upper bounds on $h\to\Upsilon\gamma$, $J/\psi\gamma$ [1289,1290], $h\to\phi\gamma$ and $h\to\rho\gamma$ [1292,1341], sensitive to diagonal Yukawa couplings. The $h\to V\gamma$ decays receive two contributions, from $h\to\gamma\gamma^*$ decay followed by a $\gamma^*\to V$ fragmentation, and from a numerically smaller amplitude that involves the direct coupling of quarks to the Higgs [1287, 1300, 1301, 1342]. The sensitivity to the quark Yukawa couplings thus comes mostly from the interference of the two amplitudes.

Normalizing to the $h\to ZZ^*\to4\ell$ channel the total Higgs width cancels [1285, 1299],

$$\mathcal{R}_{V\gamma,ZZ^*}\equiv\frac{\mu_{V\gamma}}{\mu_{ZZ^*}}\frac{\mathcal{B}_{h\to V\gamma}^{\rm SM}}{\mathcal{B}_{h\to ZZ^*}^{\rm SM}}\simeq\frac{\Gamma_{h\to V\gamma}}{\Gamma_{h\to ZZ^*}}, \tag{129}$$

where $\mathcal{B}_{h\to ZZ^*}^{\rm SM}$ is the SM branching ratio for $h\to ZZ^*\to4\ell$. In the last equality we also assumed perfect cancellation of the production mechanisms (this is entirely correct, if $h\to\gamma\gamma$ is used as normalization channel, but at present this leads to slightly worse bounds on light quark Yukawas). Using predictions from Ref. [1299] gives the currently allowed ranges for light quark Yukawa couplings, collected in Table 39 (here κ_Z and $\kappa_{\gamma\gamma}^{\rm eff}$ parametrize deviations of $h\to ZZ,\gamma\gamma$ amplitudes relative to their SM values).

For prospects to probe light quark Yukawa at HL-/HE-LHC we follow Ref. [1297]. Rescaling with luminosity and the increased production cross sections both the signal and backgrounds, while ignoring any changes to the analysis that may change the ratios of the two, gives the projected sensitivities listed in Table 40. The estimates in Table 40 are in agreement with the ATLAS projection for $h\to J/\psi\gamma$ [1343], which quotes $\mathcal{R}_{J/\psi\gamma,ZZ^*}<0.34^{+0.14}_{-0.1}$. We see that only large enhancements, with Yukawa coupling of

mode	collider energy	$\mathcal{R}_{V\gamma,ZZ^*} <$	Yukawa range ($\kappa_V = \kappa_{\gamma\gamma}^{\rm eff} = 1$)
$J/\psi\,\gamma$	14 TeV	$0.47\sqrt{L_3}$	$16 - 67L_3^{1/4} < \kappa_c < 16 + 67L_3^{1/4}$
	27 TeV	$0.28\sqrt{L_3}$	$16 - 52L_3^{1/4} < \kappa_c < 16 + 52L_3^{1/4}$
$\phi\,\gamma$	14 TeV	$0.33\sqrt{L_3}$	$11 - 46L_3^{1/4} < \bar{\kappa}_s < 11 + 46L_3^{1/4}$
	27 TeV	$0.20\sqrt{L_3}$	$11 - 35L_3^{1/4} < \bar{\kappa}_s < 11 + 35L_3^{1/4}$
$\rho\,\gamma$	14 TeV	$0.60\sqrt{L_3}$	$44 - 93L_3^{1/4} < 2\bar{\kappa}_u + \bar{\kappa}_d < 44 + 93L_3^{1/4}$
	27 TeV	$0.36\sqrt{L_3}$	$44 - 72L_3^{1/4} < 2\bar{\kappa}_u + \bar{\kappa}_d < 44 + 72L_3^{1/4}$

Table 40: The projections of bounds on Yukawa couplings for HL-/HE-LHC as functions of integrated luminosity, $L_3 \equiv (3/\text{ab})/\mathcal{L}$. Note that $\bar{\kappa}_q = y_q/y_b^{\rm SM}$.

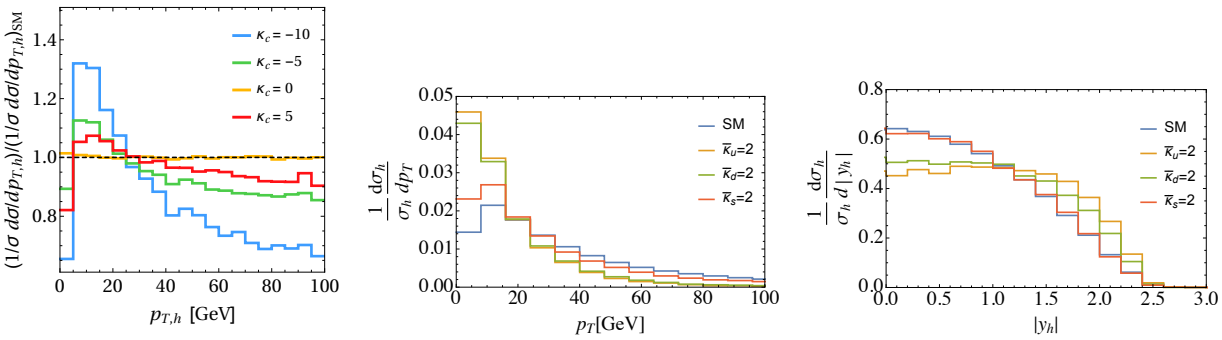

Fig. 70: Normalized Higgs $p_{\rm T}$ and rapidity distributions for modified charm (left) and u, d and s Yukawas (middle and right). Taken from [1294] and [1293].

light quarks well above the values of bottom Yukawa will be probed. To be phenomenologically viable, these would require large cancellations in the contributions to the light quark masses (and a mechanism to avoid indirect bounds from global fits to the Higgs data).

Higgs exclusive decays can in principle also probe off-diagonal couplings by measuring modes such as $h \to B_s^*\gamma$ [1287]. However, the Higgs flavour violating couplings are strongly constrained by meson mixing [1344, 1345], so that the expected rates are too small to be observed. For a detailed discussion of $h \to MZ, MW$ channels see [1346].

9.2.4 Yukawa constraints from Higgs distributions

9.2.4.1 Higgs $p_{\rm T}$ and rapidity distributions

In general, the Higgs $p_{\rm T}$ distribution probes whether NP particles are running in the $gg \to h + (g)$ loops [1347–1358]. However, the soft part of the $p_{\rm T}$ spectrum is also an indirect probe of light quark Yukawas [1293, 1294]. If Higgs, unlike in the SM, is produced from the $u\bar{u}$ or $d\bar{d}$ fusion, then *(i)* the Sudakov peak is shifted to $p_T \sim 5\,$GeV from $\sim 10\,$GeV in the SM [1293, 1359], and *(ii)* the rapidity distributions are more forward, i.e., shifted toward larger η [1293], see Fig. 70. Enhanced s or c Yukawa couplings also lead to softer Higgs $p_{\rm T}$ spectrum. The dominant effect for charm quark is due to one loop contributions to $gg \to hj$ process that are enhanced by double logarithms [1360], while for strange quark it is due to $s\bar{s}$ fusion production of the Higgs [1293]. Fig. 70 shows the corresponding normalized distributions, for which many theoretical and experimental uncertainties cancel.

The 8 TeV ATLAS results on Higgs $p_{\rm T}$ distributions [1361] were converted to the following 95 %

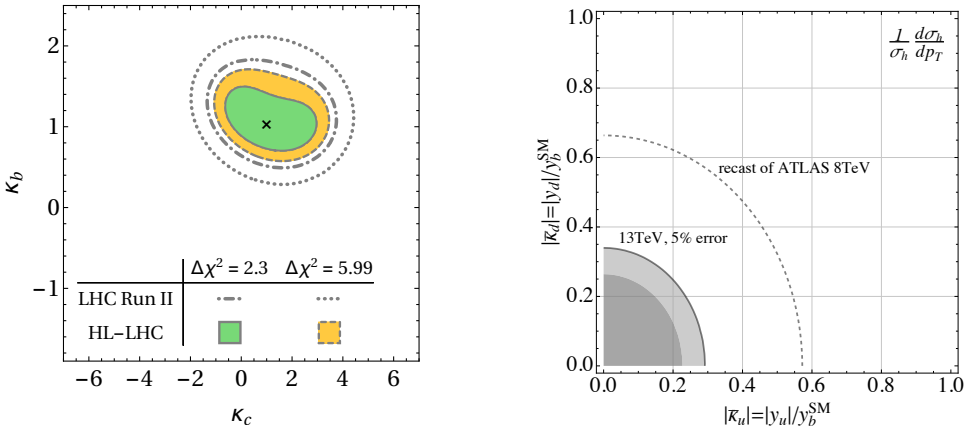

Fig. 71: The sensitivity of Higgs $p_{\rm T}$ distributions to the light quark Yukawa couplings at 13 TeV LHC Run2 and HL-LHC: to charm and bottom [1294] (left) and to up and down [1293] (right, assuming total 5% systematic+statistical uncertainty).

CL bounds in Ref. [1293]

$$\bar{\kappa}_u = y_u/y_b^{\rm SM} < 0.46\,, \qquad \bar{\kappa}_d = y_d/y_b^{\rm SM} < 0.54\,, \tag{130}$$

stronger than the corresponding bounds from fits to the inclusive Higgs production cross sections. The sensitivities expected at HL-LHC are shown in Fig. 71 (right), assuming a 5% total uncertainty in each $p_{\rm T}$ bin. CMS interpreted the 35.9 fb^{-1} measurement of 13 TeV Higgs $p_{\rm T}$ spectrum in terms of 95 % CL bounds on c and b Yukawa couplings [1362]

$$-4.9(-33) < \kappa_c < 4.8(38), \qquad -1.1(-8.5) < \kappa_b < 1.1(18), \tag{131}$$

assuming the branching fractions depend only on κ_c or κ_b (in addition the total decay width is allowed to float freely). These bounds on the c and b Yukawa are weaker than the bounds from the global fit of the 8 TeV Higgs data along with the electroweak precision data allowing all Higgs coupling to float [1285] and from the direct measurement of $h \to b\bar{b}$ by using b-tagging. The projected HL-LHC sensitivity for $\kappa_{c,b}$ from higgs p_T distributions, while assuming SM branching ratios, is shown in Fig. 71 (left). For the case that tha bounds depends only on the κ_c and κ_b, the bound on the c Yukawa is stronger than the bound from the global fit of the 8 TeVHiggs data along with the electroweak precision data, allowing all Higgs couplings to float [1285]. However, it relies on strong assumptions that the Higgs couplings (besides c or b) are SM like, and it is mostly sensitive to the cross section and not to the angular shape as the latter bound.

Fig. 72 shows expected one sigma κ_c, κ_b contours from 3000fb^{-1} global fits, obtained by extrapolating the measured constraints in Ref. [1363]. The fit uses expected differential distributions, obtained by extrapolating the $\sqrt{s} = 13$ TeV $p_{\rm T}$ distributions in the $h \to \gamma\gamma$ [1364] and $h \to ZZ^{(*)} \to 4\ell$ [1365] ($\ell = e$ or μ) decay channels, as well as a search for $h \to b\bar{b}$ at large $p_{\rm T}$ [1366], which enhances the sensitivity to κ_t. The simultaneous extended maximum likelihood fit to the diphoton mass, four-lepton mass, and soft-drop mass, $m_{\rm SD}$, [1367, 1368] spectra in all the analysis categories of the $h \to \gamma\gamma$, $h \to ZZ$, and $h \to b\bar{b}$ channels, gives the results in Fig. 72 (left) when only κ_c and κ_b are varied, while all the other couplings are set to the SM value, and in Fig. 72 (right), if in addition the Higgs total decay width is allowed to float. In the fit for Fig. 72 (left) the largest sensitivity to κ_c, κ_b comes from the total cross sections times branching ratios, while for Fig. 72 (right) it is due to normalized differential distributions $(1/\sigma)(d\sigma/dp_T)$. In Fig. 72 the systematic uncertainties are conservatively kept at current level (dubbed Scenario 1). There is only a minor change in the projected constraints on κ_c, κ_b in case of reduced systematic uncertainties (Scenario 2) compared to Scenario 1.

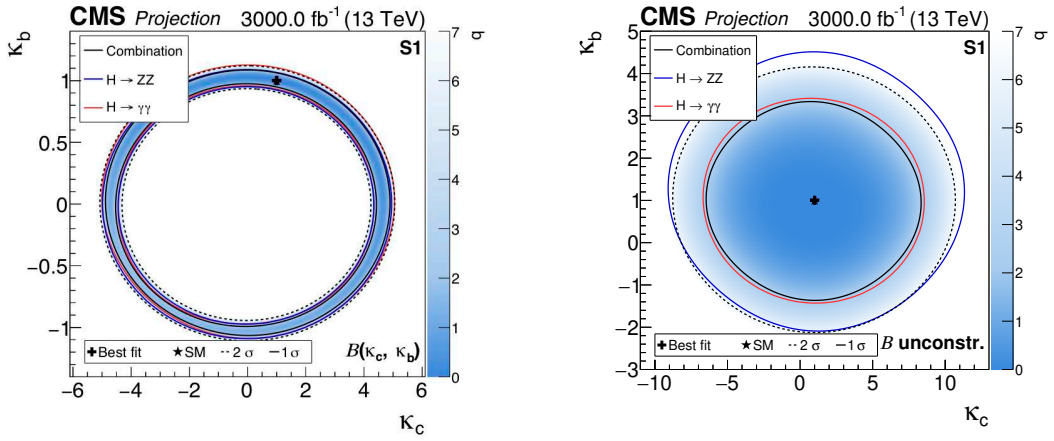

Fig. 72: Left: projected simultaneous fit of κ_b and κ_c from 3ab^{-1} 13 TeV data, assuming current systematics (Scenario 1). The one standard deviation contours are drawn for the $h \to \gamma\gamma$ channel (the $h \to ZZ$, the combination of $h \to \gamma\gamma$ and $h \to ZZ$) with solid red (blue, black). For the combination the two standard deviation contour is drawn as a black dashed line. The negative log-likelihood value are given on the coloured axis. Right: same as left, but with the branching fractions implemented as nuisance parameters with no prior constraint, i.e., the total Higgs width is floated freely. (Taken from [1369].).

9.2.4.2 $W^{\pm}h$ charge asymmetry

The $W^{\pm}h$ charge asymmetry,

$$A = \frac{\sigma(W^+h) - \sigma(W^-h)}{\sigma(W^+h) + \sigma(W^-h)}, \tag{132}$$

is a production-based probe of light quark Yukawa couplings [1370]. In the SM, the inclusive HE-LHC charge asymmetry is expected to be 17.3%, while the HL-LHC charge asymmetry is expected to be 21.6%. The dominant $W^{\pm}h$ production mode is due to Higgs boson radiating from $W^{\pm}$ intermediate lines, if the Yukawa-mediated diagrams are negligible. If the quark Yukawas are not SM-like, however, the charge asymmetry can either increase or decrease, depending on the overall weight of the relevant PDFs. In particular, the charge asymmetry will increase if the down or up quark Yukawa couplings are large, reflecting the increased asymmetry of $u\bar{d}$ vs. $\bar{u}d$ PDFs; the charge asymmetry will decrease if the strange or charm Yukawa couplings are large, reflecting the symmetric nature of $c\bar{s}$ vs. $\bar{c}s$ PDFs. The subleading correction from the Cabibbo angle-suppressed PDF contributions determines the asymptotic behavior for extremely large Yukawa enhancements.

The effect of individual d, u, s, or c quark Yukawa enhancements on the inclusive charge asymmetry is shown in Fig. 73, in units of $\bar{\kappa}_f = y_f/y_{b,\text{SM}}$, evaluated at the Higgs mass scale. Since $W^{\pm}h$ production probes lower Bjorken-x at the HE-LHC compared to the HL-LHC, the expected SM charge asymmetry is lower at the higher energy collider. The bands denote the change in the charge asymmetry from varying the renormalization and factorization scales within a factor of 2. The error bars denote the expected 0.45% (0.25%) statistical sensitivity to the charge asymmetry at HL-LHC (HE-LHC) in the $W^{\pm}h \to \ell^{\pm}\ell^{\pm}jj\nu\nu$ final state [1370]. The HE-LHC sensitivity was estimated by simply rescaling with the appropriate luminosity ratio, since we expect the increases in both signal and background electroweak rates to largely cancel. The constraint from the CMS Run I direct Higgs width upper bound is also shown [1370]. If the signal strengths are fixed to the SM expectation and the central prediction is used, the HE-LHC charge asymmetry measurement could constrain $\bar{\kappa}_f \lesssim 2-3$ for up and charm quarks, and $\bar{\kappa}_f \lesssim 7$ for down or strange quarks.

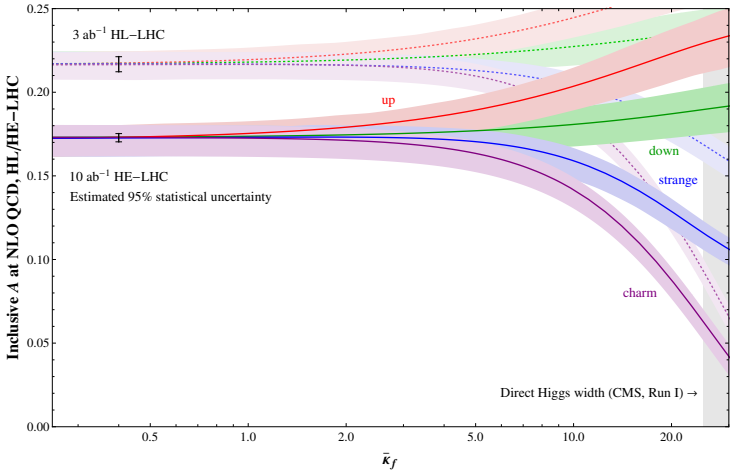

Fig. 73: Inclusive charge asymmetry for $W^{\pm}h$ production at the 27 TeV HE-LHC (solid colored bands), and 14 TeV HL-LHC (dotted colored bands), calculated at NLO QCD from MadGraph_aMC@NLO using NNPDF 2.3 as a function of individual Yukawa rescaling factors $\bar{\kappa}_f$ for $f = u$ (red), d (green), s (blue), and c (purple). Shaded bands correspond to scale uncertainties at 1σ from individual $\sigma(W^+h)$ and $\sigma(W^-h)$ production, which are conservatively taken to be fully uncorrelated. The expected statistical errors from this measurement using 10 ab^{-1} of HE-LHC data and 3 ab^{-1} of HL-LHC data are also shown.

9.3 LFV decays of the Higgs

The flavour violating Yukawa couplings are well constrained by the low-energy flavour-changing neutral current measurements [1344,1345,1371]. For instance, CMS bounds $\kappa^2_{\mu e}+\kappa^2_{e\mu} < (5.4\times10^{-4})^2$ from the $h \to e\mu$ search [1372], compared to indirect bound from $\mu \to e\gamma$, which is $\kappa^2_{\mu e} + \kappa^2_{e\mu} < (3.6 \times 10^{-6})^2$ [1345]. A notable exception are the flavour-violating couplings involving a tau lepton, where the strongest constraints on $\kappa_{\tau\mu}, \kappa_{\mu\tau}, \kappa_{\tau e}, \kappa_{e\tau}$ are from direct searches for flavour-violating Higgs decays at the LHC [1373, 1374]. Currently, the CMS 13 TeV search with 35.9 fb^{-1} [1373] gives the strongest constraint

$$\sqrt{\kappa^2_{\mu\tau} + \kappa^2_{\tau\mu}} < 1.43 \times 10^{-3}\,, \qquad \sqrt{\kappa^2_{e\tau} + \kappa^2_{\tau e}} < 2.26 \times 10^{-3}\,, \tag{133}$$

obtained from 95 % CL upper limits $\mathcal{B}(h \to \mu\tau) < 0.25\%$ and $\mathcal{B}(h \to e\tau) < 0.61\%$, respectively. One can also directly measure the difference between the branching ratios of $h \to \tau e$ and $h \to \tau\mu$, as proposed in [1375]. Assuming naively that both systematics and statistical error scale with square root of the luminosity, one can expect that the sensitivity of 3000 fb^{-1} HL-LHC will be around the half per-mil level for both the $h \to e\tau$ and $h \to \mu\tau$ branching ratios.

The LHC can also set bounds on rare FCNC top decays involving a Higgs [1182,1198,1376,1377]. The strongest current bounds are $|\kappa_{ct}|^2 + |\kappa_{tc}|^2 < (0.06)^2$ and $|\kappa_{ut}|^2 + |\kappa_{tu}|^2 < (0.07)^2$ at 95 % CL.

9.4 CP violating Yukawa couplings

The CP-violating flavour-diagonal Yukawa couplings, $\tilde{\kappa}_{f_i}$, are well constrained from bounds on the electric dipole moments (EDMs) [1286, 1378–1381] under the assumption of no cancellation with other contributions to EDMs. For the electron Yukawa, the latest ACME measurement [1253, 1382] results in an upper bound of $\tilde{\kappa}_e < 1.9 \times 10^{-3}$ [1286]. For the bottom and charm Yukawas the strongest limits come from the neutron EDM [1381]. Using the NLO QCD theoretical prediction, this translates into the upper bounds $\tilde{\kappa}_b < 5$ and $\tilde{\kappa}_c < 21$ when theory errors are taken into account. For the light quark

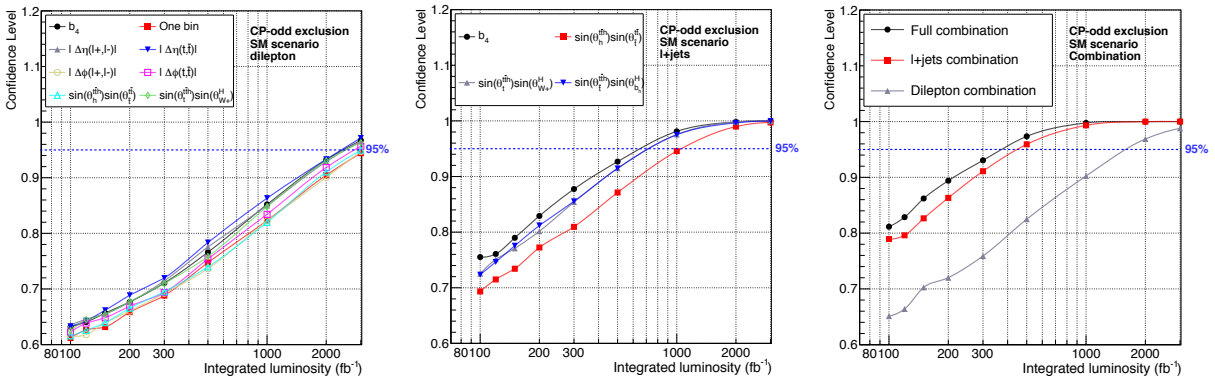

Fig. 74: Expected CL, assuming the SM, for exclusion of the pure CP-odd scenario, $\kappa_t = 0, \tilde{\kappa}_t = 1$, as a function of the integrated luminosity. Left: using the $t\bar{t}h$ ($h \to b\bar{b}$) dileptonic analysis only, middle: using the $t\bar{t}h$ ($h \to b\bar{b}$) semileptonic analysis only, right: combining observables in each individual channel and combining both channels, treating the observables as uncorrelated. A likelihood ratio computed from the binned distribution of the corresponding discriminant observable was used as test statistic.

CPV Yukawas, measurements of the Mercury EDM place strong bounds on the up and down Yukawas of $\tilde{\kappa}_u < 0.06$ and $\tilde{\kappa}_d < 0.03$ [1383] (no theory errors, 90% CL), while the neutron EDM measurement gives a weaker constraint on the strange quark Yukawa of $\tilde{\kappa}_s < 2.2$ [1383] (no theory errors, 90% CL).

The top and τ Yukawa phases can be directly probed at HL-LHC, as we discuss below. For constraints from EDMs and other phases see [1253, 1286, 1286, 1378, 1379, 1381, 1382].

9.4.1 $t\bar{t}h$

CP violation in the top quark-Higgs coupling is strongly constrained by EDM measurements [1378], if the light quark Yukawa couplings and hWW couplings have their SM values. If this is not the case, the indirect constraints on the phase of the top Yukawa coupling can be substantially relaxed. Assuming the EDM constraints can be avoided, the CP structure of the top quark Yukawa can be probed directly in $pp \to t\bar{t}h$. Many simple observables, such as $m_{t\bar{t}h}$ and $p_{T,h}$ are sensitive to the CP structure, but require reconstructing the top quarks and Higgs.

Recently, several $t\bar{t}h$ observables have been proposed that access the CP structure without requiring full event reconstruction. These include the azimuthal angle between the two leptons in a fully leptonic $t/\bar{t}$ decay with the additional requirement that the $p_{T,h} > 200\,\text{GeV}$ [1384], and the angle between the leptons, in a fully leptonic $t/\bar{t}$ system, projected onto the plane perpendicular to the h momentum [1385]. These observables only require that the Higgs is reconstructed and are inspired by the sensitivity of $\Delta\phi_{\ell^+\ell^-}$ to top/anti-top spin correlations in $pp \to t\bar{t}$ [1386]. The sensitivity of both of these observables improves at higher Higgs boost, and therefore higher energy, making them promising targets for the HE-LHC, though no dedicated studies have been carried out to date.

Fig. 74 shows the expected CL, assuming the SM, for exclusion of the pure CP-odd scenario, $\kappa_t = 0, \tilde{\kappa}_t = 1$, as a function of the integrated luminosity. Samples of $t\bar{t}h(h \to b\bar{b})$ events were generated at the LHC for $\sqrt{s} = 13$ TeV, with `MadGraph5_aMC@NLO` [372] using the `HC_NLO_X0` model [1387], as were all relevant SM background processes. The analyses of the $t\bar{t}h$ ($h \to b\bar{b}$) events were carried out in the dileptonic and semileptonic decay channels of the $t\bar{t}$ system. `Delphes` [374] was used for a parametrised detector simulation and both analyses used kinematic fits to fully reconstruct the $t\bar{t}h$ system. The results were extrapolated, as a function of luminosity, up to the 3000 fb^{-1}.

Fig. 74 left (middle) shows results using the dileptonic (semileptonic) analysis only. The CL were obtained from a signal-enriched region (with at least 3 b-tagged jets) in which a likelihood ratio was computed from binned distributions of various discriminant observables [1388, 1389]. Only statistical

uncertainties were considered. Fig. 74 right shows CL obtained from the combination of different observables in each channel i.e., $\Delta\eta(\ell^+,\ell^-)$, $\Delta\phi(t,\bar{t})$ and $\sin(\theta_t^{t\bar{t}H})\sin(\theta_{W^+}^{H})$ in the dileptonic channel and, b_4 and $\sin(\theta_{\bar{t}}^{t\bar{t}H})\sin(\theta_{b_H}^{H})$ in the semileptonic channel. The combination of the two channels is also shown for comparison. The observables were treated as uncorrelated.

The main conclusions of these studies can be summarized in what follows: *i)* many angular observables are available with the potential of discriminating between values of $\kappa_t, \tilde{\kappa}_t$ in the top quark Yukawa coupling; *ii)* the sensitivity of the semileptonic final state of $t\bar{t}h(h \to b\bar{b})$ is roughly a factor 3 better than that of the dileptonic channel alone (Fig. 74 left); *iii)* the combination of the two channels (semi- and dileptonic) is roughly a factor 5 more sensitive than the dileptonic channel, providing a powerful test of the top quark-Higgs interactions in the fermionic sector.

9.4.2 $\tau\bar{\tau}h$

The most promising direct probe of CP violation in fermionic Higgs decays is the $\tau^+\tau^-$ decay channel, which benefits from a relatively large τ Yukawa, resulting in a SM branching fraction of 6.3%. Measuring the CP violating phase in the tau Yukawa requires a measurement of the linear polarizations of both τ leptons and the azimuthal angle between them. This can be done by analyzing tau substructure, namely the angular distribution of the various components of the tau decay products.

The main τ decay modes studied include $\tau^\pm \to \rho^\pm(770)\nu$, $\rho^\pm \to \pi^\pm\pi^0$ [1390–1395] and $\tau^\pm \to \pi^\pm\nu$ [1396–1398]. Assuming CPT symmetry, collider observables for CP violation must be built from differential distributions based on triple products of three-vectors. In the first case, $h \to \pi^\pm\pi^0\pi^\mp\pi^0\nu\nu$, angular distributions built only from the outgoing charged and neutral pions are used to determine the CP properties of the initial τ Yukawa coupling. In the second case, $h \to \pi^\pm\pi^\mp\nu\nu$, there are not enough reconstructible independent momenta to construct an observable sensitive to CP violation, requiring additional kinematic information such as the τ decay impact parameter.

In the kinematic limit when each outgoing neutrino is taken to be collinear with its corresponding reconstructed $\rho^\pm$ meson, the acoplanarity angle, denoted Φ, between the two decay planes spanned by the $\rho^\pm \to \pi^\pm\pi^0$ decay products is exactly analogous to the familiar acoplanarity angle from $h \to 4\ell$ CP-property studies. Hence, by measuring the τ decay products in the single-prong final state, suppressing the irreducible $Z \to \tau^+\tau^-$ and reducible QCD backgrounds, and reconstructing the acoplanarity angle of ρ^+ vs. ρ^-, the differential distribution in Φ gives a sinusoidal shape whose maxima and minima correspond to the CP-phase in the τ Yukawa coupling, $\varphi_\tau = \arctan(\tilde{\kappa}_\tau/\kappa_\tau)$.

An optimal observable using the colinear approximation was derived in [1393]. Assuming 70% efficiency for tagging hadronic τ final states, and neglecting detector effects, the estimated sensitivity for the CP-violating phase φ_τ using 3 ab^{-1} at the HL-LHC is 8.0°. A more sophisticated analysis [1394] found that detector resolution effects on the missing transverse energy distribution degrade the expected sensitivity considerably, and as such, about 1 ab^{-1} is required to distinguish a pure scalar coupling ($\kappa_\tau = 1, \tilde{\kappa}_\tau = 0$) from a pure pseudoscalar coupling ($\kappa_\tau = 0, \tilde{\kappa}_\tau = 1$).

At the HE-LHC, the increased signal cross section for Higgs production is counterbalanced by the increased background rates, and so the main expectation is that improvements in sensitivity will be driven by the increased luminosity and more optimized experimental methodology. Rescaling with the appropriate luminosity factors, the optimistic sensitivity to the τ Yukawa phase φ_τ from acoplanarity studies is 4-5°, while the more conservative estimate is roughly an order of magnitude worse.

10 The high $p_{\rm T}$ flavour physics programme

Flavour and high $p_{\rm T}$ searches are intertwined in several ways. On the one hand the stringent bounds from low-energy constraints put severe bounds on the NP models that contain states with TeV masses with couplings to quarks. On the other hand, TeV scale New Physics is suggested by several solutions of long standing problems of the SM, e.g., the hierarchy problem. Quite often the low energy constraints are avoided by assuming Minimal Flavour Violation (MFV), where the only flavour breaking, even in the NP sector, is due to the SM Yukawa matrices. However, more general flavour structures for the NP states are still allowed. In fact such non-MFV couplings can have interesting consequences. In general we can group the NP models into two broad classes: *(i)* models that address outstanding problems of the SM, such at the SM flavour puzzle, the origin of dark matter, or the hierarchy problem, which may have non trivial flavour structure, and *(ii)* models designed to explain the $b \to s\ell\ell$ and $b \to c\tau\nu$ flavour anomalies, that almost inevitably have quite a distinct flavour structure. The NP mediators potentially responsible for the anomalies, Z', W' or leptoquarks, could be found at high $p_{\rm T}$ searches in the HL- or HE-LHC.

In the rest of this section we first briefly review the models that address the SM flavour puzzle and have states that could be probed at the HL-/HE-LHC, and their implications for high $p_{\rm T}$ searches. The second part of this section is devoted to high $p_{\rm T}$ implications of B physics anomalies.

10.1 Models of flavour and TeV Physics

10.1.1 Randall-Sundrum models of flavour

Models of flavour based on warped extra dimension [1316] attempt to simultaneously solve the hierarchy problem as well as the SM flavour problem [1325, 1326]. In the Randall-Sundrum (RS) models the 5-dimensional space-time has anti-de Sitter geometry (AdS_5), truncated by flat 4D boundaries, the Planck (UV) and the TeV (IR) branes. This setup gives a warped metric in the bulk [1316] $ds^2 = \exp(-2kr_c|\phi|)\eta_{\mu\nu}dx^\mu dx^\nu - r_c^2 d\phi^2$, where k is the 5D curvature scale, r_c the radius of compactification and $\phi \in [-\pi, \pi]$ the coordinate along the 5-th dimension. The warp factor, $\exp(-2kr_c|\phi|)$, leads to different length scales in different 4D slices along the ϕ direction, which provides a solution to the hierarchy problem. In particular, the Higgs field is assumed to be localized near the TeV-brane so that the metric "warps" $\langle H\rangle_5 \sim M_5 \sim M_P \sim 10^{19}$ GeV down to the weak scale, $\langle H\rangle_4 = \exp(-kr_c\pi)\langle H\rangle_5$. For $kr_c \approx 12$ then $\langle H\rangle_{\rm SM} \equiv \langle H\rangle_4 \sim 1$ TeV.

The hierarchies among the quark masses can be realized by localizing the Higgs on the IR brane, while the fermions have different profiles in the 5-th dimension. The first and second generation zero mode fermions are localized close to the UV-brane and have small overlaps with the Higgs, giving small effective 4D SM Yukawa interactions, and thus small quark masses after electroweak symmetry breaking. The top quark, on the other hand, is localized near the TeV brane resulting in a large top Yukawa coupling.

This configuration has a built in automatic suppression of FCNCs, which are suppressed by the same zero mode overlaps that gives the hierarchy of masses [1325, 1326]. This feature of the RS framework plays a similar role as the SM Glashow-Iliopoulos-Maiani (GIM) mechanism, and was dubbed RS-GIM in [1399, 1400]. Similarly to the SM GIM, the RS GIM is violated by the large top quark mass. In particular, $(t, b)_L$ needs to be localized near the TeV brane, otherwise the 5D Yukawa coupling becomes too large and makes the theory strongly coupled at the scale of the first Kaluza-Klein (KK) excitation. In general this leads to sizeable corrections to electroweak precision observables, such as the Zb_Lb_L couplings. Such problems can be largely ameliorated by enlarging the bulk symmetry such that it contains a custodial $SU(2)_L \times SU(2)_R$ symmetry [1401], which for instance lowers the KK scale bounds from EW precision tests from 5 TeV to about 2TeV [1402]. The consequences for flavour phenomenology have been worked out in a series of papers, see, e.g., [1403–1406], with $K - \bar{K}$ mixing for instance requiring the KK scale to be above 8 TeV [1402]. With flavour alignment the scale of KK modes could be substantially lowered [1407] and could be reachable by HL/HE-LHC.

The KK gluon resonances cannot be produced from gluons [1408], so that the LHC production is restricted to the quark-antiquark fusion, even though this is suppressed by the flavor dependent zero mode overlaps. This means that the LHC cross section for the first KK gluon resonances are small, suppressed also by the quark-anti-quark parton density functions (PDFs). The dominant decay mode is into $t\bar{t}$ final state, due to the large zero mode overlaps [1409]. Using the benchmark RS model from [1410], the most recent CMS analysis for $t\bar{t}$ resonance searches, using both hadronic and leptonic tops, sets a lower bound of 4.55 TeV on the mass of the KK gluon [1411]. The projected reach for 33TeV and 100TeV pp colliders can be found in [1402].

10.1.2 Partial compositeness

Partial compositeness as the origin of the flavour hierarchies in composite Higgs models [1412] is the holographic dual to the RS models of flavour. While the Higgs is the lightest state of the composite sector, usually a pseudo-Nambu Goldstone boson from global symmetry breaking, the SM fermions and gauge bosons are elementary (for a review, see, e.g, [1329]). The elementary fermions, Q, U, D, are coupled to the composite sector through linear mixing with the composite operators, $\mathcal{O}_Q$, $\mathcal{O}_U$, $\mathcal{O}_D$,

$$\mathcal{L} \supset \epsilon_Q \bar{Q}_L \mathcal{O}_Q + \epsilon_U \bar{U}_R \mathcal{O}_U + \epsilon_D \bar{D}_R \mathcal{O}_D. \tag{134}$$

The mixing parameters ϵ_a exhibit exponentially large hierarchies because of large, yet still $\mathcal{O}(1)$, differences in anomalous dimensions of the corresponding composite operators. This is the analog of the zero mode overlaps in the RS models. The SM Yukawa are given by $(Y_{U(D)})_{ij} \sim \epsilon^i_Q \epsilon^j_{U(D)}$. For $\epsilon^1_Q \ll \epsilon^2_Q \ll \epsilon^3_Q \sim 1$, $\epsilon^1_U \ll \epsilon^2_U \ll \epsilon^3_U \sim 1$, $\epsilon^1_D \ll \epsilon^2_D \ll \epsilon^3_D \ll 1$ one can obtain the SM structure of quark masses and CKM mixings.

The composite Higgs models are described by the compositeness scale f and the mass of the first composite resonances, $M_* \sim g_* f$, with g_* the typical strength of the resonances in the composite sector. The searches at the HL-/HE-LHC consist of Higgs coupling measurements, including deviations in Higgs Yukawa couplings, and searches for composite resonances preferably coupled to third generation fermions, electroweak gauge bosons, or the Higgs. Flavour observables put strong bounds on M_*, if the flavour structure is assumed to be generic. Such bounds can be relaxed in the case of approximate flavour symmetries, see, e.g., Ref. [1329] for a review.

10.1.3 Low scale gauge flavour symmetries

The SM has in the limit of vanishing Yukawa couplings a large global symmetry. In the quark sector this is $G_F = SU(3)_Q \times SU(3)_U \times SU(3)_D$. Ref. [1413] showed that the SM flavor symmetry group G_F is anomaly free, if one adds a set of fermions that are vector-like under the SM gauged group, but chiral under the G_F. This means that G_F can be gauged. It is broken by a set of scalar fields that have hiearchical vevs and lead to hierarchy of SM quark masses. This also implies a hierarchy for the masses of the flavoured gauge bosons, with gauge bosons that more strongly couple to third generation being lighter, while the flavoured gauge bosons that couple more strongly to the first two generations are significantly heavier. This pattern in the spectrum of flavoured gauge bosons then avoids too large contributions to FCNCs [1414].

At the LHC one searches for the lightest flavoured gauge bosons, with $\mathcal{O}(\mathrm{TeV})$ masses, which couple mostly to b quarks and t quarks, but could also have non-negligible couplings to the first two generations. The di-jet and $t\bar{t}$ resonance searches are thus sensitive probes. A signal could also come from production of the lightest vectorlike fermions, t', or b' [1413]. For several further benchmarks see, e.g., Ref. [1415], where also a connection with dark matter was explored.

10.1.4 2HDM and low scale flavour models

Authors (TH): Martin Bauer, Marcela Carena and Adrián Carmona.

In 2 Higgs Doublet Models (2HDMs), the two Higgs doublets, H_1 and H_2 are usually assumed not to carry flavour quantum numbers. The collider phenomenology, on the other hand, changes substantially, if they do. This is an interesting possibility that could solve the SM flavour puzzle via the Froggatt-Nielsen (FN) mechanism where the flavon is replaced by the $H_1 H_2 \equiv H_1^T (i\sigma_2) H_2$ operator. In this way, the NP scale Λ where the higher dimensional FN operators are generated is tied to the electroweak scale, leading to much stronger phenomenological consequences. Let us assume for concreteness a type-I like 2DHM with the following Yukawa Lagrangian in the quark sector [1306, 1416]

$$\mathcal{L}_Y \supset y^u_{ij} \left(\frac{H_1 H_2}{\Lambda^2}\right)^{n_{u_{ij}}} \bar{q}^i_L H_1 u^j_R + y^d_{ij} \left(\frac{H_1^\dagger H_2^\dagger}{\Lambda^2}\right)^{n_{d_{ij}}} \bar{q}^i_L \tilde{H}_1 d^j_R + \text{h.c.}\,, \tag{135}$$

where $\tilde{H}_1 \equiv i\sigma_2 H_1^*$ as usual, and the charges $n_{u,d,e}$ are a combination of the $U(1)$ charges of H_1, $(H_1 H_2)$ and the different SM fermion fields (for an alternative discussion, where H_1, H_2 carry flavour charges, but the Yukawa interactions are taken to be renormalizable, see [1417]). For simplicity, we set the flavour charges of H_1 and H_2 to 0 and 1, respectively, such that $n_{u_{ij}} = a_{q_i} - a_{u_j}, n_{d_{ij}} = -a_{q_i} + a_{d_j}$, if we denote by $a_{q_i}, a_{u_i}, \ldots,$ the $U(1)$ charges of the SM fermions. In general, the fermion masses are given by

$$m_\psi = y_\psi \varepsilon^{n_\psi} \frac{v}{\sqrt{2}}, \qquad \varepsilon = \frac{v_1 v_2}{2\Lambda^2} = \frac{t_\beta}{1+t_\beta^2} \frac{v^2}{2\Lambda^2}, \tag{136}$$

with the vacuum expectation values $\langle H_{1,2} \rangle = v_{1,2}$ and $t_\beta \equiv v_1/v_2$. For the right assignment of flavour charges one is able to accommodate the observed hierarchy of SM fermion masses and mixing angles. This framework also leads to enhanced diagonal Yukawa couplings between the Higgs and the SM fermions, while FCNCs are suppressed. If we denote by h and H the two neutral scalar mass eigenstates, with h the observed 125 GeV Higgs, the couplings between the scalars $\varphi = h, H$ and SM fermions $\psi_{L_i,R_i} = P_{L,R}\psi_i$ in the mass eigenbasis read

$$\mathcal{L} = g_{\varphi \psi_{L_i} \psi_{R_j}}\, \varphi\, \bar{\psi}_{L_i} \psi_{R_j} + \text{h.c.} \tag{137}$$

with i, such that $u_i = u, c, t,\ d_i = d, s, b$ and $e_i = e, \mu, \tau$. This induces flavour-diagonal couplings

$$g_{\varphi \psi_{L_i} \psi_{R_i}} = \kappa^\varphi_{\psi_i} \frac{m_{\psi_i}}{v} = \left(g^\varphi_{\psi_i}(\alpha,\beta) + n_{\psi_i}\, f^\varphi(\alpha,\beta)\right) \frac{m_{\psi_i}}{v}, \tag{138}$$

as well as flavour off-diagonal couplings

$$g_{\varphi \psi_{L_i} \psi_{R_j}} = f^\varphi(\alpha,\beta) \left(\mathcal{A}_{ij} \frac{m_{\psi_j}}{v} - \frac{m_{\psi_i}}{v} \mathcal{B}_{ij}\right). \tag{139}$$

The flavour universal functions in (138) and (139) are $g^h_{\psi_i} = c_{\beta-\alpha}/t_\beta + s_{\beta-\alpha}$, $g^H_{\psi_i} = c_{\beta-\alpha} - s_{\beta-\alpha}/t_\beta$, and $f^h(\alpha,\beta) = c_{\beta-\alpha}\big(1/t_\beta - t_\beta\big) + 2 s_{\beta-\alpha}$, $f^H(\alpha,\beta) = -s_{\beta-\alpha}\big(1/t_\beta - t_\beta\big) + 2 c_{\beta-\alpha}$, where $c_x \equiv \cos x$, $s_x \equiv \sin x$. The entries in matrices $\mathcal{A}$ and $\mathcal{B}$ are proportional to the flavour charges of the corresponding fermions that define the coefficients in (135). Unless all flavour charges for a given type of fermions are equal, the off-diagonal elements in matrices $\mathcal{A}$ and $\mathcal{B}$ lead to FCNCs which are chirally suppressed by powers of the ratio ε, see [1418] for more details and explicit examples for scalings of matrix elements in $\mathcal{A}$ and $\mathcal{B}$.

10.1.5 A Clockwork solution to the flavour puzzle

Author (TH): Adrián Carmona.

The clockwork mechanism, introduced in [1419, 1420] and later generalized to a broader context in Ref. [1421], allows one to obtain large hierarchies in couplings or mass scales. Ref. [1422] showed that

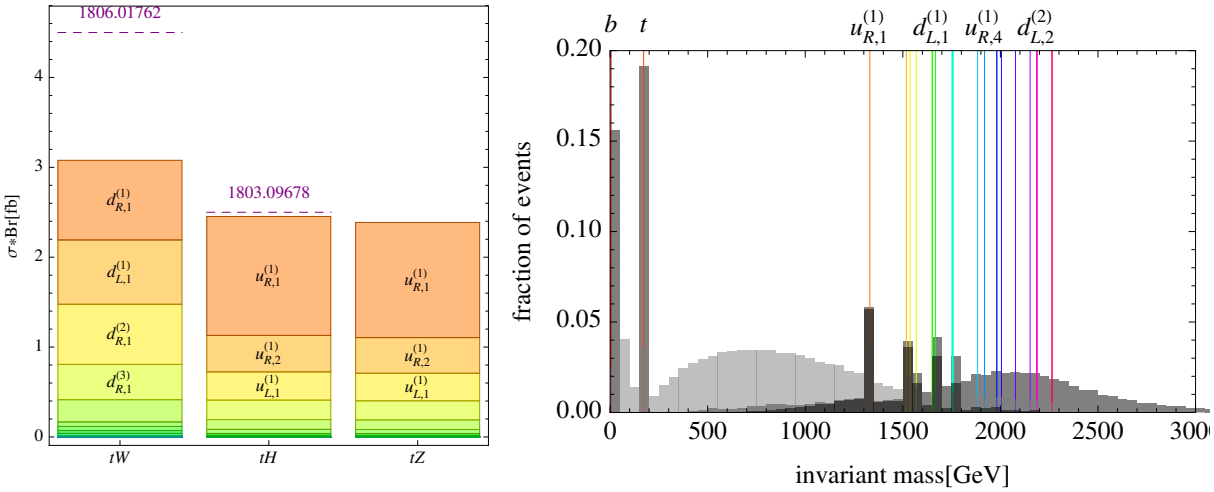

Fig. 75: *Left:* The total gear pair production cross-sections in the final states $tW + X$, $tH + X$ and $tZ + X$ for the benchmark model from Ref. [1422], with contributions from individual gears shown stacked. The currently most stringent upper bounds [1423, 1424] are denoted with dashed lines (for the $tZ + X$ [1424] final state the bound is too weak to be shown). *Right:* Invariant mass spectrum of individual pseudojets clustered using the hemisphere algorithm applied to partonic gear pair production and decay at the 13 TeV LHC. The original hemisphere clustering results are shown in light gray, and the modified hemisphere clustering results in mid-gray (dark gray if in addition the masses of the two pseudojets are required to differ by less than 30%)

it can also be used to generate the observed hierarchy of quark masses and mixing angles with anarchic Yukawa couplings, providing a solution to the flavour puzzle.

In the clockwork solution to the flavour puzzle, each SM chiral fermion ψ is accompanied with a N_ψ-node chain of vector-like fermions, $\psi_{L,j}, \psi_{R,j}$, with masses m, and a series of nearest neighbour mass terms, $qm\bar{\psi}_{L,j}\psi_{R,j-1}$, between the nodes, where $j = 1, \ldots, N_\psi$. The mass spectrum of each chain has one chiral zero mode, the would-be SM fermion, and N_ψ heavy Dirac fermion mass-eigenstates – the gears. For $q \gg 1$, the spectrum of the gears is compressed in a $2m$ band around qm, with $(M_{N_\psi} - M_1) \ll M_1$. The massless zero-mode interacts with the SM Higgs, which is on the 0-th node, through a set of Yukawa interactions described by $\mathcal{O}(1)$ Yukawa matrices, $Y_{U,D}$. The component of the massless mode on the 0-th node is, in the large q limit, given by $1/q^{N_\psi}$. This suppression is the origin of the SM Yukawa hierarchies,

$$\left(Y_u^{\rm SM}\right)_{ij} \sim q_{Q(i)}^{-N_{Q(i)}} \, (Y_U)_{ij} \, q_{u(j)}^{-N_{u(j)}}, \quad \left(Y_d^{\rm SM}\right)_{ij} \sim q_{Q(i)}^{-N_{Q(i)}} \, (Y_D)_{ij} \, q_{d(j)}^{-N_{d(j)}}. \tag{140}$$

The hierarchy of quark masses can be then naturally obtained for anarchical Y_U and Y_D Yukawa matrices if $q^{-N_{Q(i)}} \ll q^{-N_{Q(j)}}$, $q_{u(i)}^{-N_{u(i)}} \ll q_{u(j)}^{-N_{u(j)}}$, $q_{d(i)}^{-N_{d(i)}} \ll q_{d(j)}^{-N_{d(j)}}$, for $i < j$ (in the benchmark below we take q_i to be universal and equal to q).

The clockwork models of flavour are endowed with a powerful flavour protection against FCNCs, very similar to the RS models. The FCNCs with light quarks on the external legs are suppressed by the same small overlaps of the zero-modes, giving rise to hierarchies between the SM quark masses. This clockwork-GIM mechanism, along with the constraints on $Y_{U,D}$ arising from the stability of the Higgs potential, suffices to alleviate the flavour constraints to the level that TeV scale gear masses are compatible with experimental bounds [1422].

TeV scale gears can be searched for at the LHC, where they are produced through QCD pair production. The collider signatures depend on the gear decay patterns. The gears decay predominantly

through their coupling to the Higgs doublet into gears from a different-chirality chain. The lightest gears decay directly to SM fermions, mostly t and b, via the emission of W, Z or h, as do heavier gears for which these are the only kinematically allowed channels. The main existing collider constraints are from searches for pair production of vector-like quarks, in final states involving third generation SM quarks. Ref. [1422] found the two 35 fb^{-1} 13 TeV ATLAS searches for vector-like quarks decaying into tW final states [1423], as well as the analogous search employing the tZ and tH final states [1424], to be currently most sensitive, see Fig. 75.

The dense spectrum of gears and the potentially complex pattern of gear decays poses an experimental challenge. In the conventional vector-like quark searches the clockwork signal will appear as an excess of events with high transverse energies or H_T, but without a dominant single peak in the invariant mass of any particular final state, such as tH or tW. Ref. [1422] proposed a novel reconstruction strategy targeting pair production of heavy quarks with a-priori unknown but potentially long decay chains that result in a single heavy flavoured quark, t or b, plus any number of massive weak or Higgs bosons per decay chain. The proposed search strategy uses a modified hemisphere clustering algorithm, with $t-$ and $b-$tagged jets as seeds for clustering into exactly two pseudo-jets (the invariant mass of these is shown as mid-gray distribution in Fig. 75 right). The original hemisphere clustering uses instead the jets with highest invariant mass as seeds and shows no sharp features (light gray). Requiring that the masses of the two pseudo-jets differ by less then 30% gives the dark grey distribution, with clearly visible gears (in the exploratory study of [1422] tops, b-quarks, W, Z and the Higgs were not decayed).

10.2 Flavour implications for high p_{T} new physics searches

In this subsection we collect several signatures of flavour models or models where nontrivial flavour structure is relevant for high p_{T} searches: the FCNC top decays to exotica, the (model dependent) implications for di-Higgs production, and the set of signatures that are related to neutrino mass models.

10.2.1 Top decays to exotica

Authors (TH): S. Banerjee, M. Chala, M. Spannowsky.

The FCNC mediated processes are rare within the SM. However, LHC is a top factory and significant number of events are expected even for top decays with very small branching ratios. In light of this, studies of top FCNC decays to SM particles have garnered a strong interest in the community [1175, 1176, 1180, 1181, 1198, 1239, 1425–1434]. The FCNC top decays to SM particles, $t \to qZ, q\gamma, qg, qH$, $q = u, c$, and the related constraints from FCNC production processes, were discussed in Sections 8.1 and 8.1.6.

In the presence of light NP, other exotic top FCNC decays are possible. We highlight one such possibility, where the NP spectrum contains a light scalar singlet, S, with mass m_S below the top quark mass. Such a scalar particle is predicted in a number of well-motivated NP models, e.g., in the NMSSM [1435] and in non-minimal composite Higgs models [1319, 1320, 1329, 1436]. Moreover, quite often the induced $t \to cS, uS$ FCNC decays are easier to probe than, for instance the ones involving the SM Higgs, $t \to ch, uh$ [1437]. The reason is three-fold; *(i)* The top FCNCs mediated by S are usually suppressed by one less power of the heavy physics scale; *(ii)* S may have a larger decay width into cleaner final states, such as $\ell^+\ell^-$, $b\bar{b}$ or $\gamma\gamma$; *(iii)* S can be much lighter than the Higgs, reducing the phase space suppression. Note that very light S, i.e., with $m_S < m_h/2 \sim 62.5$ GeV, need not be excluded by the LHC constraints on the Higgs width, $\Gamma(h \to SS) \lesssim 10$ MeV [1438]. Indeed, for a quartic coupling $\lambda_{HS} S^2 |H|^2$, this bound is avoided for $\lambda_{HS} < 0.05$.

There are no direct experimental limits on $t \to qS$ from colliders. The indirect constraints from 1-loop box diagrams in $D^0 - \bar{D}^0$ oscillations constrain the products of two S Yukawas, $\tilde{Y}_{ut}\tilde{Y}_{ct(tc)}$, and $\tilde{Y}_{tu}\tilde{Y}_{ct(tc)}$, to be small [198, 1345, 1439]. The $S\bar{t}c$ or $S\bar{t}u$ couplings can still be sizeable, but not both at the same time. Inspired by the CMS $t \to hc$ search [1183], Ref. [1440] developed a dedicated analysis

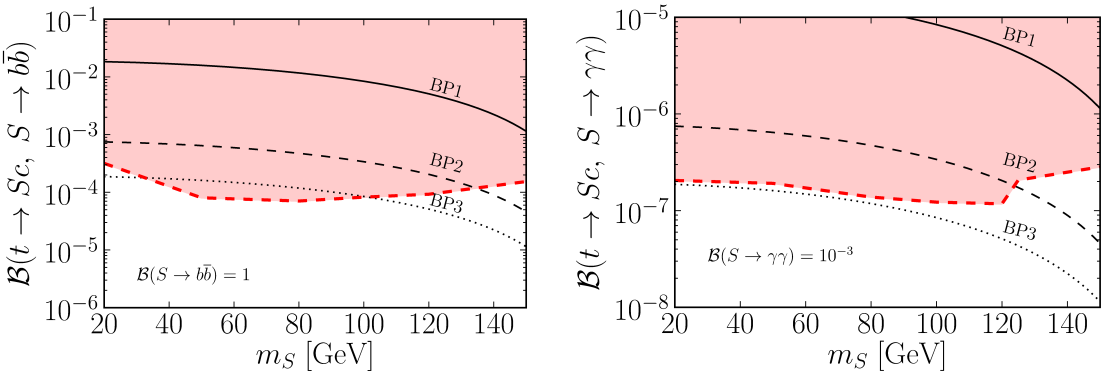

Fig. 76: Branching ratios that can be tested in the $b\bar{b}$ (left) and $\gamma\gamma$ (right) channels at 14 TeV HL-LHC with 3000 fb^{-1} (95% CL upper limit is denoted by red dashed line). The three benchmark points, Eq. (142), are denoted with black lines.

for $t \to qS$, by varying m_S, the mass of S. The projections at the 14 TeV LHC for $S \to b\bar{b}$ and $S \to \gamma\gamma$ decays are shown in Fig. 76 . Assuming that S is the only light NP state, its couplings to the SM quarks are induced by dimension 5 effective operator (not displaying generational indices)

$$\mathcal{L} = -\bar{q}_L \tilde{Y} \frac{S}{f} \tilde{H} u_R + \text{h.c.} \supset \tilde{g} \frac{m_t}{f} \bar{t}_L S c_R + \text{h.c.}, \tag{141}$$

where f is the NP scale, and on the r.h.s. we introduced a new flavour violating coupling $\tilde{g}$. The three Benchmark Points (BP) shown in Figs. 76 are

$$\text{BP1(2,3)}: \quad \tilde{g} = 1.0(1.0, 0.1),\ f = 2(10, 2)\ \text{TeV} \implies \mathcal{B}(t \to Sc) \sim 10^{-3(4,5)} - 10^{-2(3,4)}. \tag{142}$$

If the flavour conserving couplings of S to the SM fermions, ψ, are $c_\psi m_\psi S(\bar{\psi}\psi)/f$, and to the photons $c_\gamma \alpha S F_{\mu\nu}\tilde{F}^{\mu\nu}/(4\pi f)$, then $\mathcal{B}(S \to \gamma\gamma)/\mathcal{B}(S \to \overline{\psi}\psi) \sim (\alpha/\pi)^2 (m_S/m_\psi)^2$, taking $c_\psi \sim c_\gamma \sim \mathcal{O}(1)$. The suppression of $S \to \gamma\gamma$ can be partially compensated by scaling with m_S, so that $\mathcal{B}(S \to \gamma\gamma)$ can possibly be significantly larger than $\mathcal{B}(h \to \gamma\gamma)$. Searches should thus use both $S \to b\bar{b}$ and $S \to \gamma\gamma$. The details on how to reduce the backgrounds can be found in [1440]. Current searches for $S \to b\bar{b}$ in the gluon fusion channel [1441] constrain only values of c_ψ above ~ 10 for $f \sim 1$ TeV. Our analysis works instead for very small values of c_ψ provided the branching ratio is sizable.

For projections at future colliders we find that the increase in cross-section for the background at $\sqrt{s} = 27$ TeV (100 TeV) when compared to $\sqrt{s} = 14$ TeV is similar to that for the signal, and is $\sim 4(40)$. Assuming an integrated luminosity of 10 ab^{-1}, we expect an increase in significance by a factor of ~ 3.7 (~ 11.5). Similar results hold for the $b\bar{b}$ channel.

10.2.2 Implications for di-Higgs production

Authors (TH): Martin Bauer, Marcela Carena and Adrián Carmona.

Interestingly, in some models the flavour structure can feed back into nontrivial constraints on the scalar potential. This was demonstrated in the 2HDM model with FN charges, introduced in Sec. 10.1.4. The scalar couplings to gauge bosons are the same as in the normal type-I 2HDM while the scalar coupling between the heavy Higgs H and two SM Higgs scalars h, as well as the triple Higgs coupling can be expressed as [1442, 1443]

$$g_{Hhh} = \frac{c_{\beta-\alpha}}{v}\left[\left(1 - f^h(\alpha,\beta) s_{\beta-\alpha}\right)\left(3M_A^2 - 2m_h^2 - M_H^2\right) - M_A^2\right], \tag{143}$$

$$g_{hhh} = -\frac{3}{v}\left[f^h(\alpha,\beta) c_{\beta-\alpha}^2 (m_h^2 - M_A^2) + m_h^2 s_{\beta-\alpha}\right], \tag{144}$$

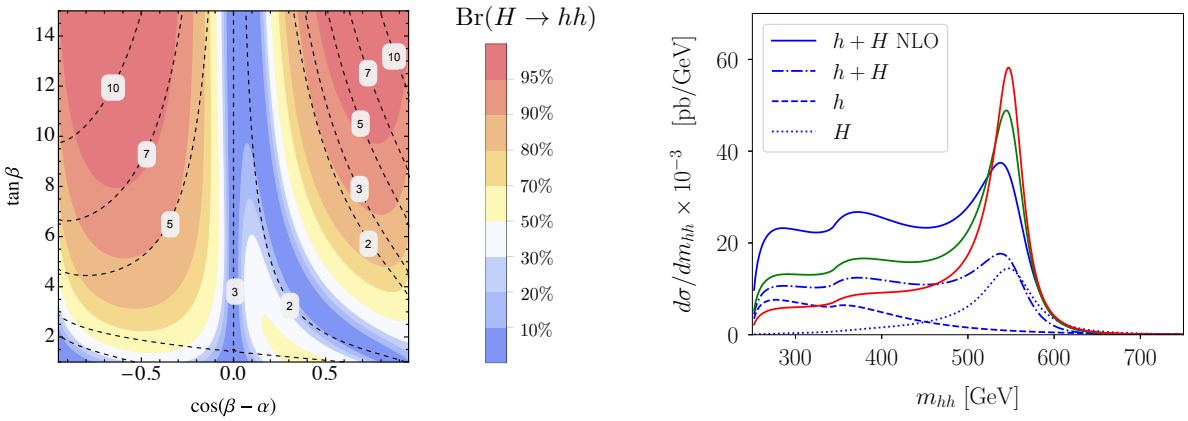

Fig. 77: Left: Br($H \to hh$) as a function of $\cos(\beta - \alpha)$ and $\tan\beta$ for $M_H = M_{H^\pm} = 550$ GeV and $M_A = 450$ GeV. The dashed contours correspond to constant $|\kappa^h_\psi|$ (we set $n_\psi = 1$). Right: Invariant mass distribution for the different contributions to the $pp \to hh$ signal with $c_{\beta-\alpha} = -0.45$ and $\kappa^h_\psi = 5$ (blue), $\kappa^h_\psi = 4$ (green) and $\kappa^h_\psi = 3$ (red) at $\sqrt{s} = 27$ TeV, respectively.

where M_A is the pseudoscalar mass. The $U(1)$ flavour symmetry restricts the number of allowed terms in the scalar potential forbidding, e.g., terms proportional to $H_1 H_2$. Interestingly, one can rewrite such self scalar interactions with the help of function $f^h(\alpha, \beta)$, since it is related to the combination $H_1 H_2^\dagger$ appearing in both the scalar potential and the higher dimensional operators generating different Yukawa couplings. Therefore, the parameter space for which $f^h(\alpha, \beta) \gg 1$ and $c_{\beta-\alpha} \neq 0$ leads to maximally enhanced diagonal couplings of the SM Higgs to fermions (138) as well as to enhanced trilinear couplings (143) and (144). For maximally enhanced Yukawa couplings, the mass of the heavy Higgs H cannot be taken arbitrarily large and resonant Higgs pair production has to be present. This correlation between the enhancement of the Higgs Yukawa couplings κ^h_ψ and Br($H \to hh$) is illustrated for $M_H = M_A = M_{H^\pm} = 500$ GeV in Fig. 77 (left) where we plot the dependence of Br($H \to hh$) on $c_{\beta-\alpha}$ and t_β [1418]. The dashed contours correspond to constant values of $|\kappa^h_\psi|$ for $n_\psi = 1$. The correlation does not depend on the factor n_ψ, although $n_\psi > 1$ leads to a larger enhancement. The two exceptions for which this correlation breaks down are the limits $c_{\beta-\alpha} \approx 0$ (disfavored in the flavour model) and $c_{\beta-\alpha} \approx \pm 1$ (disfavoured by SM Higgs couplings strength measurements). Depending on the structure of the Yukawa couplings, the value of κ^h_ψ in Fig. 77 (left) can be larger or smaller than the value $n = 1$ chosen to illustrate the relation between g_{Hhh} and κ^h_ψ. Current experimental limits constrain this structure. For example, since $\kappa^h_\mu < 2.1$ [1444], either $n = 0$ for the muon, or one is constrained to the $\kappa^h_\mu < 2.1$ parameter space in Fig. 77 (left).

There is a non-trivial interplay between resonant and non-resonant contributions to $pp \to hh$, as shown in Fig. 77 (right), for $\sqrt{s} = 27$ TeV, setting $M_A = 450$ GeV and $M_H = M_{H^\pm} = 550$ GeV, $c_{\beta-\alpha} = -0.45$ and three different values of $\kappa^h_\psi = 3, 4$ and 5. When the enhancement in the Higgs Yukawa couplings is large enough, the interference between non-resonant and resonant contributions turns the broad peak into a shoulder in the $d\sigma/dm_{hh}$ distribution for the total cross section, as shown for the case $\kappa^h_\psi = 5$ by the blue line.

10.2.3 Neutrino Mass Models at the HL/HE LHC

Authors (TH): T. Han, T. Li, X. Marcano, S. Pascoli, R. Ruiz, C. Weiland.

The questions pertaining to neutrino masses: whether or not neutrinos are Majorana particles, the origin of smallness of the neutrino masses, as well as the reason for large mixing angles, remain some of the most pressing open issues in particle physics today. A set of potential solutions is provided by the

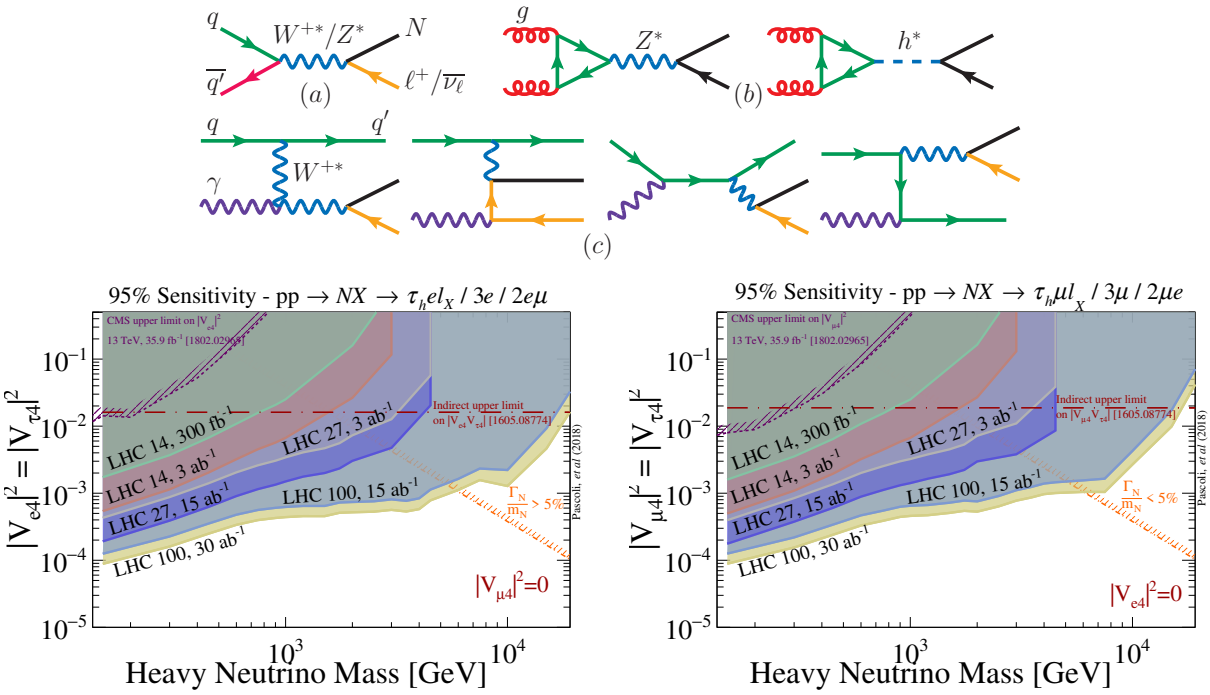

Fig. 78: Upper: Born-level diagrams for heavy neutrino, N, production via (a) Drell-Yan (DY), (b) gluon fusion (GF), and (c) vector boson fusion (VBF). Lower: for the benchmark mixing hypotheses $|V_{e4}| = |V_{\tau 4}|$ with $|V_{\mu 4}| = 0$ (left panel) and $|V_{\mu 4}| = |V_{\tau 4}|$ with $|V_{e4}| = 0$ (right panel), the projected sensitivity at $\sqrt{s} = 14,\ 27$ and 100 TeV using the tri-lepton + dynamic jet veto analysis of Ref. [1451].

seesaw models. These postulate new particles that couple to SM fields via mixing/Yukawa couplings, SM gauge currents, and/or new gauge symmetries. If accessible, a plethora of rich physics can be studied in considerable detail at hadron colliders. This would complement low energy and oscillation probes of neutrinos [1146, 1445]. In the following, we summarize the discovery potential of seesaw models at hadron colliders with collision energies of $\sqrt{s} = 14$ and 27 TeV. For a more comprehensive reviews on the sensitivity of colliders to neutrino mass models, see [1146, 1445–1448] and references therein.

The Type I Seesaw and Variants

In Type I seesaw the light neutrino masses and mixing are generated from couplings of SM leptons to new fermionic gauge singlets with Majorana masses. For low-scale seesaw models with only fermionic singlets, lepton number has to be nearly conserved and light neutrino masses are proportional to small lepton number violating (LNV) parameters [1449, 1450]. For high-scale seesaws with only fermionic singlets, light neutrino masses are inversely proportional to large LNV mass scales, and again lepton number is approximately conserved at low energies. Thus LNV processes are suppressed in type I seesaw models (unless additional particles are introduced to decouple the light neutrino mass generation from heavy neutrino production).

If kinematically accessible, heavy neutrinos N can be produced in hadron collisions through neutral current and charged current processes, as shown in Fig. 78 (upper). The expected suppression of LNV processes in type I seesaw models motivates the study of lepton number conserving (LNC) processes, such as the heavy neutrino N production via DY and VBF, with subsequent decays to only leptons,

$$pp \to \ell_N N + X \to \ell_N \ell_W W + X \to \ell_N \ell_W \ell_\nu \nu + X, \tag{145}$$

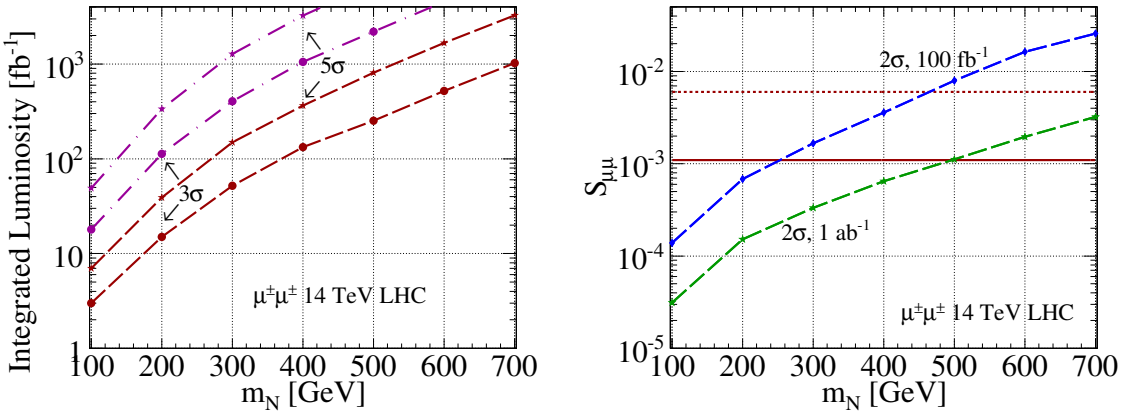

Fig. 79: Left: required luminosity for 3 $(5)\sigma$ evidence (discovery) using the LNV final state $\mu^{\pm}\mu^{\pm}jj$, as a function of the heavy neutrino mass, m_N, assuming optimistic (brown) and pessimistic (purple) mixing scenarios [1454]. Right: sensitivity to $N-\mu$ mixing [1454] with the optimistic (pessimistic) mixing scenario is given by the horizontal dashed (full) line.

giving the trilepton final state, $\ell_i^{\pm}\ell_j^{\mp}\ell_k^{\pm}+$MET. Projections from a new tri-lepton search strategy recently proposed in Ref. [1451], based on a dynamical jet veto selection cut, are shown in Fig. 78, assuming the benchmark mixing hypotheses $|V_{e4}| = |V_{\tau 4}|$ with $|V_{\mu 4}| = 0$ (left panel) and $|V_{\mu 4}| = |V_{\tau 4}|$ with $|V_{e4}| = 0$ (right panel), for $\sqrt{s} = 14,\ 27$ and 100 TeV. For benchmark luminosities, the colliders can probe active-sterile mixing as small as (approximately) $|V_{\ell 4}|^2 \sim 5\times 10^{-4} - 9\times 10^{-5}$ and masses as heavy as (approximately) $1.5-15$ TeV for $|V_{\ell 4}|^2 \sim 10^{-2}$.

Another possibility is to search for lepton flavor violating (LFV) final states such as

$$q\,\overline{q}' \to\ N\,\ell_1^{\pm} \to\ \ell_1^{\pm}\,\ell_2^{\mp}\,W^{\mp} \to\ \ell_1^{\pm}\,\ell_2^{\mp}\,j\,j. \tag{146}$$

This was, e.g., studied in Ref [1452] in the context of the inverse seesaw (ISS), a low-scale variant of the type I seesaw. Due to strong experimental limits on $\mu \to e\gamma$ by MEG [1453], the event rates involving taus are more promising than those for $e^{\pm}\mu^{\mp}jj$. After $\mathcal{L} = 3\ \mathrm{ab}^{-1}$ of data taking, more than 100 LFV events of $\tau^{\pm}\mu^{\mp}jj$ type could be produced for neutrino masses below 700 (1000) GeV for pp collisions at 14 (27) TeV.

In the presence of additional particles that can decouple the heavy neutrino production from the light neutrino mass generation, e.g., new but far off-shell gauge bosons [1455], the Majorana nature of the heavy neutrinos can lead to striking LNV collider signatures, such as the well-studied same-sign dilepton and jets process [1456]

$$pp \to\ N\,\ell_1^{\pm} \to\ \ell_1^{\pm}\,\ell_2^{\pm}\,W^{\mp} \to\ \ell_1^{\pm}\,\ell_2^{\pm} + nj. \tag{147}$$

Assuming that a low-scale type I seesaw is responsible for the heavy neutrino production, Fig. 79 displays the discovery potential and active-heavy mixing sensitivity of the $\mu^{\pm}\mu^{\pm}$ channel [1454]. Assuming the pessimistic/conservative mixing scenario of $S_{\mu\mu} = 1.1\times 10^{-3}$ [1454], the HL-LHC with 3 ab^{-1} would be able to discover a heavy neutrino with a mass of $m_N \simeq 400\,\mathrm{GeV}$ and is sensitive to masses up to $550\,\mathrm{GeV}$ at 3σ. Using only 1 ab^{-1}, the HL-LHC can improve on the preexisting mixing constraints summarized in the pessimistic scenario for neutrino masses up to $500\,\mathrm{GeV}$.

Heavy Neutrinos and the Left-Right Symmetric Model

The Left-Right Symmetric Model (LRSM) addresses the origin of both tiny neutrino masses via a Type I+II seesaw hybrid mechanism as well as the SM $V-A$ chiral structure through spontaneous breaking

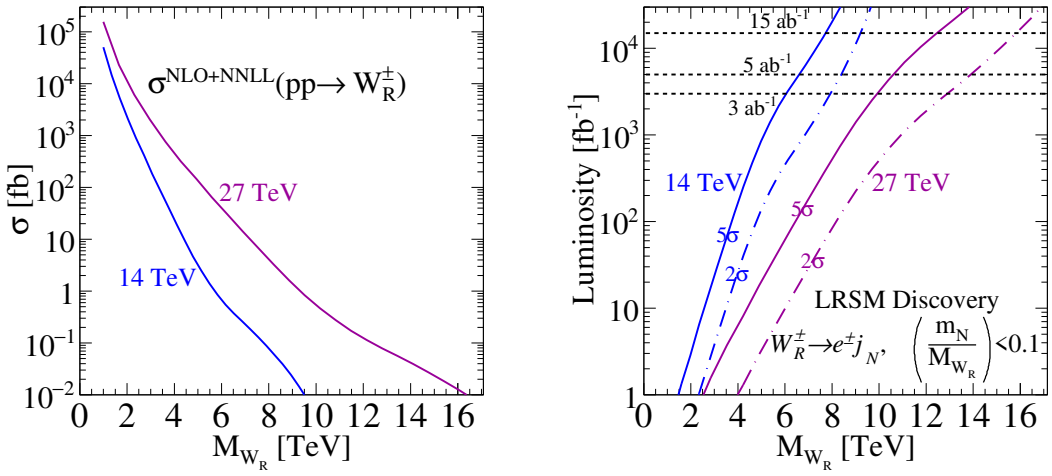

Fig. 80: Left: The total $pp \to W_R$ cross section at NLO+NNLL(Threshold). Right: $5(2)\sigma$ discovery potential (sensitivity) via W_R decaying to an electron and neutrino jet (j_N), as a function of W_R mass, at $\sqrt{s} = 14$ and 27 TeV [1457].

of the $SU(2)_L \times SU(2)_R$ symmetry. The model predicts new heavy gauge bosons $(W_R^{\pm},\ Z_R')$, heavy Majorana neutrinos (N), and a plethora of neutral and electrically charged scalars $(H_i^0,\ H_j^{\pm},\ H_k^{\pm\pm})$. The LRSM gauge couplings are fixed to the SM Weak coupling constant, up to (small) RG-running corrections. As a result, the Drell-Yan production mechanisms for W_R and Z_R result in large rates at hadron colliders.

One of the most promising discovery channels is the production of heavy Majorana neutrinos from resonant W_R, with N decaying via a lepton number-violating final state. At the partonic level, the process is [1456] (for details see [1445] and references therein)

$$q_1\overline{q}_2 \to W_R \to N\,\ell_i^{\pm} \to \ell_i^{\pm}\ell_j^{\pm}W_R^{\mp *} \to \ell_i^{\pm}\ell_j^{\pm}q_1'\overline{q_2'}. \tag{148}$$

Due to the ability to fully reconstruct the final state of Eq. (148), many properties of W_R and N can be extracted, including a complete determination of W_R chiral couplings to quarks independent of leptons [1458]. Beyond the canonical $pp \to W_R \to N\ell \to 2\ell + 2j$ channel, it may be the case that the heavy neutrino is hierarchically lighter than the right-handed (RH) gauge bosons. Notably, for $(m_N/M_{W_R}) \lesssim 0.1$, N is sufficiently Lorentz boosted that its decay products, particularly the charged lepton, are too collimated to be resolved experimentally [1457, 1459]. Instead, one can consider the $(\ell_j^{\pm}q_1'\overline{q_2'})$-system as a single object, a *neutrino jet* [1457, 1460]. The hadronic process is then $pp \to W_R \to N\ell_i^{\pm} \to j_N\,\ell_i^{\pm}$, and inherits much of the desired properties of (148), such as the simultaneous presence of high-$p_{\rm T}$ charged leptons and lack of MET [1457, 1460], resulting in a very strong discovery potential. Fig. 80 (right) shows the requisite integrated luminosity for $5(2)\sigma$ discovery at $\sqrt{s} = 14$ and 27 TeV.

Type II Scalars

Type II seesaw introduces a new scalar $\mathrm{SU}(2)_L$ triplet that couples to SM leptons. The light neutrinos obtain Majorana masses through $\mathrm{SU}(2)_L$ triplet vev, so that type II scenario notably does not have sterile neutrinos. The most appealing production mechanisms at hadron colliders of triplet Higgs bosons are

$$pp \to Z^*/\gamma^* \to H^{++}H^{--}, \quad pp \to W^* \to H^{\pm\pm}H^{\mp}, \tag{149}$$

followed, by lepton flavor- and lepton number-violating decays to the SM charged leptons. In Type II scenarios, $H^{\pm\pm}$ decays to $\tau^{\pm}\tau^{\pm}$ and $\mu^{\pm}\mu^{\pm}$ pairs are comparable or greater than the $e^{\pm}e^{\pm}$ channel by two

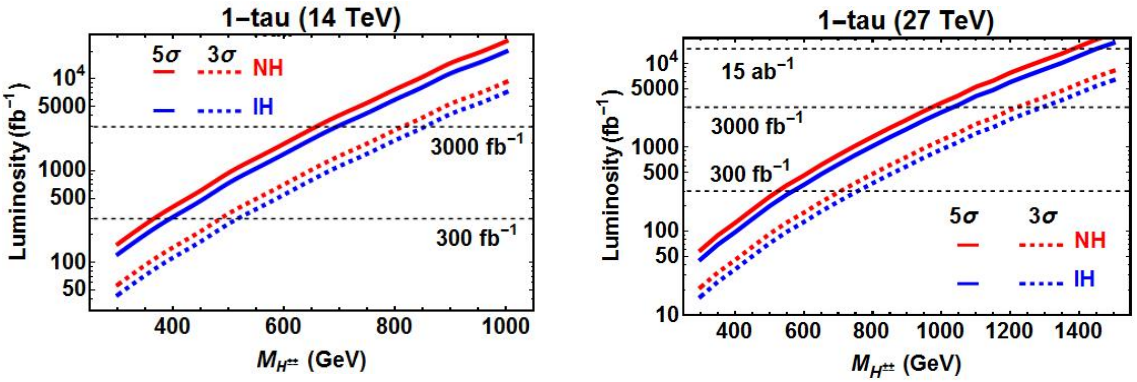

Fig. 81: Requisite luminosity for $5(3)\sigma$ discovery (evidence) as a function of $M_{H^{\pm\pm}}$ for the process $pp \to H^{++}H^{--} \to \tau_h \ell^{\pm}\ell^{\mp}\ell^{\mp}$, where $\tau^{\pm} \to \pi^{\pm}\nu$, for the NH and IH at $\sqrt{s} = 14, 27$ TeV.

orders of magnitude. Moreover, the $\tau\mu$ channel is typically dominant in decays involving different lepton flavors [1461, 1462]. If such a seesaw is realized in nature, tau polarizations can help to determine the chiral property of triplet scalars. One can discriminate between different heavy scalar mediated neutrino mass mechanisms, e.g., between Type II seesaw and Zee-Babu model, by studying the distributions of tau lepton decay products [1462,1463]. Due to the low τ_h identification efficiencies, future colliders with high energy and/or luminosity enables one to investigate and search for doubly charged Higgs decaying to τ_h pairs. Accounting for constraints from neutrino oscillation data on the doubly charged Higgs branching ratios, as well as tau polarization effects [1462], Figs. 81 displays the 3σ and 5σ significance in the plane of integrated luminosity versus doubly charged Higgs mass for $pp \to H^{++}H^{--} \to \tau^{\pm}\ell^{\pm}\ell^{\mp}\ell^{\mp}$ at $\sqrt{s} = 14, 27$ TeV, for single τ channel with $\tau \to \pi\nu$, both for normal (NH) and inverted hierarchy (IH).

Type III Leptons

Low-scale Type III seesaws introduce heavy electrically charged $(E^{\pm})$ and neutral (N) leptons, part of $\mathrm{SU}(2)_L$ triplet, that couple to both SM charged and neutral leptons through mixing/Yukawa couplings. Triplet leptons couple appreciably to EW gauge bosons, and thus do not have suppressed production cross section, contrary to seesaw scenarios with gauge singlet fermions. Up to small (and potentially negligible) mixing effects the triplet lepton pair production cross sections are fully determined, see Fig. 82 (upper) for relevant tree level diagrams for the production of heavy charged leptons. Drell-Yan processes are the dominant production channel of triplet leptons when kinematically accessible [1445]. Fig. 82 (lower left) shows the summed cross sections for the Drell-Yan processes, $pp \to \gamma^*/Z^* \to E^+E^-$, and $pp \to W^{\pm *} \to E^{\pm}N$, at NLO in QCD, following [1464], as a function of triplet masses (assuming $m_N = m_E$), at $\sqrt{s} = 14$ and 27 TeV.

Another consequence of the triplet leptons coupling to all EW bosons is the adherence to the Goldstone Equivalence Theorem. This implies that triplet leptons with masses well above the EW scale will preferentially decay to longitudinal polarized W and Z bosons as well as to the Higgs bosons. For decays of EW boson to jets or charged lepton pairs, triplet lepton can be fully reconstructed from their final-state enabling their properties to be studied in detail. For fully reconstructible final-states,

$$NE^{\pm} \to \ell\ell' + WZ/Wh \to \ell\ell' + nj + mb, \tag{150}$$

$$E^+E^- \to \ell\ell' + ZZ/Zh/hh \to \ell\ell' + nj + mb, \tag{151}$$

which correspond approximately to the branching fractions $\mathcal{B}(NE) \approx 0.115$ and $\mathcal{B}(EE) \approx 0.116$, search strategies such as those considered in [1465, 1466] can be enacted. Assuming a fixed detector

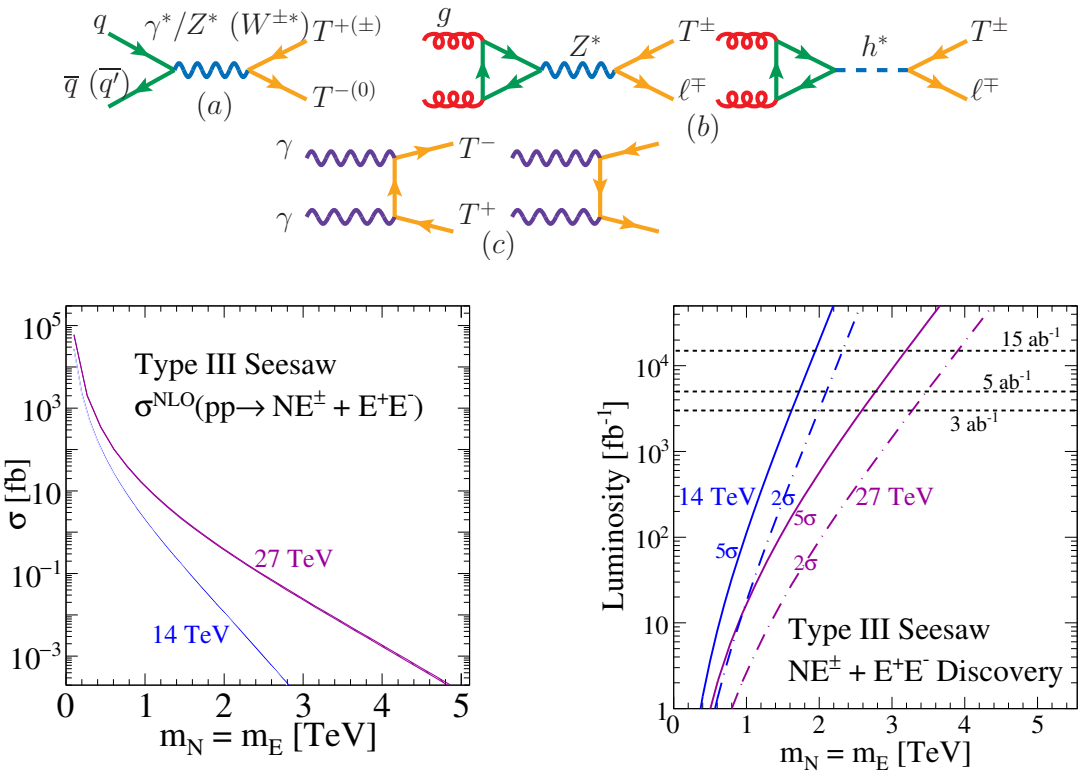

Fig. 82: Upper: Born level production of Type III leptons via (a) Drell-Yan, (b) gluon fusion, and (c) photon fusion; from [1445]. Lower left: the inclusive production cross section for $pp \to NE^{\pm} + E^+E^-$, at NLO in QCD [1464] for $\sqrt{s} = 14$ and 27 TeV, as a function of heavy triplet lepton mass. Lower right: the required integrated luminosity for 5(2)σ discovery (sensitivity) to $NE^{\pm} + E^+E^-$, based on the analyses of [1465, 1466].

acceptance and efficiency of $\mathcal{A} = 0.75$, which is in line to those obtained by [1465, 1466], Fig. 82(lower right) shows as a function of triplet mass the requisite luminosity for a 5σ discovery (solid) and 2σ evidence (dash-dot) of triplet leptons at $\sqrt{s} = 14$ and 27 TeV. With $\mathcal{L} = 3 - 5$ ab^{-1}, the 14 TeV HL-LHC can discover states as heavy as $m_N, m_E = 1.6 - 1.8$ TeV. For the same amount of data, the 27 TeV HE-LHC can discover heavy leptons $m_N, m_E = 2.6 - 2.8$ TeV; with $\mathcal{L} = 15$ ab^{-1}, one can discover (probe) roughly $m_N, m_E = 3.2$ (3.8) TeV.

10.3 Implications of TeV scale flavour models for electroweak baryogenesis

Authors (TH): Oleksii Matsedonskyi, Geraldine Servant.

In most solutions to the SM flavour puzzle, Yukawa couplings have a dynamical origin, which means that they potentially impact the cosmological evolution. In Refs. [1467–1474], such connections between flavour and cosmology, in particular with the electroweak baryogenesis, have been investigated in detail.

Electroweak baryogenesis (EWBG) is a framework where the matter-antimatter asymmetry of the universe was created during the electroweak phase transition. It relies on a charge transport mechanism in the vicinity of bubble walls during a first-order electroweak (EW) phase transition. EWBG uses EW scale physics only and is therefore testable experimentally. It requires an extension of the Higgs sector, giving a first-order EW phase transition as well as new sources of *CP* violation. Typically, there are stringent constraints on EWBG models from bounds on Electric Dipole Moments. In the following, we

consider situations where the source of CP violation has changed with time, which is a natural way to evade constraints. The main motivation is to link EWBG to low-scale flavour models. If the physics responsible for the structure of the Yukawa couplings is linked to EW symmetry breaking, we can expect the Yukawa couplings to vary at the same time as the Higgs is acquiring a VEV, in particular if the flavour structure is controlled by a new scalar field which couples to the Higgs. This is precisely what can happen in Composite Higgs (CH) models [1320, 1329], on which we focus in the following.

The Composite Higgs (CH) models assume that the Higgs boson arises as a bound state of a new strong interaction, confining around the TeV scale f. Other composite resonances are naturally heavier than the Higgs, due to an approximate Goldstone symmetry suppressing the Higgs mass. The rest of the SM fields do not belong to the strong sector and are elementary. The nature of the EW phase transition in CH models can be substantially different with respect to the SM. One of the reasons is that the CH models naturally feature new scalar resonances that participate in the EW phase transition and change its properties (see Refs. [1475, 1476]). On the other hand, the EW transition may become strongly first order even without the help of such additional states, if the EW transition happens simultaneously with the deconfinement-confinement phase transition of the new strong sector (see Refs. [1471, 1472] and also Refs. [1469, 1477] for the dual description in the warped 5D space).

The flavour structure of the CH models is intimately tied with the viability of EWBG. The requirement of having a sizeable top quark Yukawa coupling, while suppressing the unwanted flavour-violating effects, suggests that the new sector is nearly scale-invariant for a large range of energies above the confinement scale. As a result, one may expect that the transition dynamics is mostly determined by a single light field – the dilaton χ (see e.g Ref. [1478]). Depending on its mass, whose size can be related to the separation of the UV flavour scale and the EW scale, the EW phase transition may happen separately from the confinement, or simultaneously with it [1471, 1472].

Moreover, the mechanism for generating the SM flavour hierarchy in CH models may also be a source of CP asymmetry during the EW phase transition. The hierarchy of SM Yukawas λ_q is generated by the renormalization group running of the couplings y_q between the elementary fermions and the strong sector operators,

$$\lambda_q \propto y_q^2, \quad \text{with} \quad y_q = y_q^{\rm UV} \left(\frac{\mu}{\Lambda_{\rm UV}}\right)^{\gamma_{y_q}}, \tag{152}$$

where $\mu \sim \chi$ is the confinement scale, $\Lambda_{\rm UV}$ is some large scale at which all the mixings are generated with a similar size, $y_q^{\rm UV}$, and γ_{y_q} is the anomalous dimension of the operator responsible for the mixing. This means that the size of the Yukawa couplings changes with the evolution of the confinement scale during the confinement phase transition. Such a change of the Yukawa interactions may efficiently source the CP-violation required for the baryogenesis [1470].

For both types of transitions mentioned, one can expect to observe deviations of the Higgs couplings from the SM predictions. These deviations are a result of contributions generic to CH models, as well as those linked to the features of the phase transition and new sources of CP-violation. For concreteness we focus on the more minimal example, the combined electroweak and strong sector phase transition. The potential of the Higgs boson can be parametrized in terms of trigonometric functions of h/f, with the overall size of the potential controlled by the mixings between the elementary and composite fermions [1480, 1481],

$$V = c_1 \sin^2 \frac{h}{f} + c_2 \sin^4 \frac{h}{f}, \tag{153}$$

where $c_1 \sim c_2 \sim \sum_q (3y_q^2/(4\pi)^2) g_\star^2 f^4$. The dependence of the y_q mixings on the dilaton field is responsible for the mass mixing between the dilaton and the Higgs field, which we parametrise by an angle δ. To generate sufficient amount of CP violation, such mass mixing needs to be sizeable. Let us

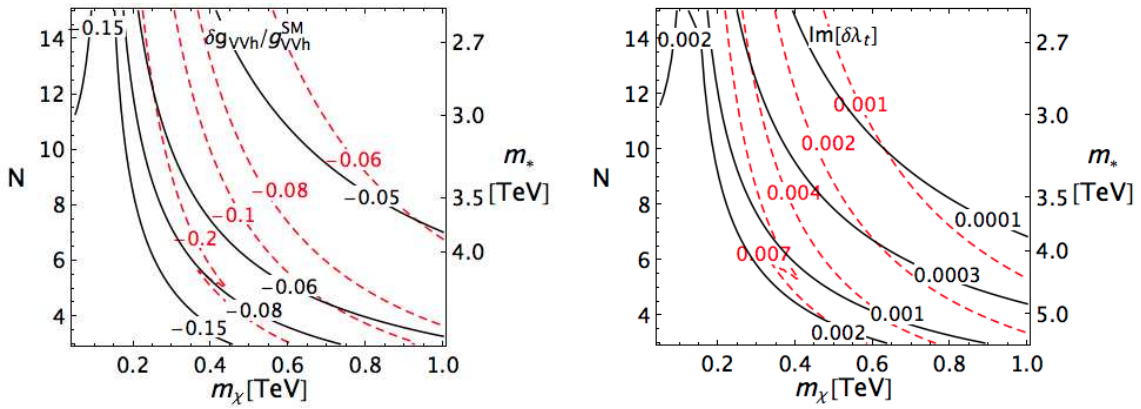

Fig. 83: Relative deviation of the Higgs couplings to W and Z bosons (left panel) and the imaginary part of the correction to the top quark Yukawa coupling (right panel), as functions of the dilaton mass, m_χ, the number of colours, N, in the new confining sector, and generic mass of composite states, m_*. Solid black (red dashed) contours correspond to the glueball-like (meson-like) dilaton. The current and near future experimental sensitivities of electron EDM experiments to the imaginary part of the top yukawa correspond respectively to approximately 2×10^{-3} [1253, 1378] and 2×10^{-4} [1479].

consider its effect on the quark Yukawa coupling:

$$\mathcal{L}_{\text{Yukawa}} = \lambda(\chi)\left(\chi \sin\frac{h}{f}\right)\bar{q}_L q_R = \bar{q}_L q_R h\left(\lambda(f)\frac{\chi}{f} + \beta_\lambda \frac{\chi - f}{f}\right) + \ldots, \tag{154}$$

where we performed an expansion in χ around its present day value, f. Similar, but CP-preserving, modifications are also generated in the couplings of the Higgs boson to the SM gauge fields and the Higgs self-interactions. The complex phase of the Yukawa beta-function, β_λ, in (154) has to be different from that of the quark mass $\lambda(f)h$, as the Yukawa phase changes with energy. Choosing the mass parameter to be real, the CP-violating interaction resides in the term $\propto \beta_\lambda$. Rotating the h and χ fields to the mass basis, the CP-even and CP-odd corrections to the Higgs Yukawa interaction are

$$\text{Re}[\delta\lambda] \sim \text{Re}[\beta_\lambda]\delta(v/f) + \lambda(\delta^2/2 + \delta(v/f)), \quad \text{Im}[\delta\lambda] \sim \text{Im}[\beta_\lambda]\delta(v/f). \tag{155}$$

In Fig. (83) we show the values of the CP-violating top quark Yukawa modification and the deviations of the Higgs couplings to the W and Z bosons. Such couplings can be tested directly at the LHC, and also in the measurements of electric dipole moments. The strength of the phase transition can be tested in gravitational waves signals at the future space-based observatory LISA [1482].

10.4 Phenomenology of high p_{T} searches in the context of flavour anomalies

Authors (TH): Alejandro Celis, Admir Greljo, Lukas Mittnacht, Marco Nardecchia, Tevong You.

Precision measurements of flavour transitions at low energies, such as flavour changing B, D and K decays, are sensitive probes of hypothetical dynamics at high energy scales. These can provide the first evidence of new phenomena beyond the SM, even before direct discovery of new particles at high energy colliders. Indeed, the current anomalies observed in B-meson decays, in particular, the charged current one in $b \to c\tau\nu$ transitions, and neutral current one in $b \to s\ell^+\ell^-$, may be the first hint of new dynamics which is still waiting to be discovered at high-p_{T}. When considering models that can accommodate the anomalies, it is crucial to analyse the constraints derived from high-p_{T} searches at the LHC, since these can often rule out significant regions of model parameter space. Below we review these constrains, and assess the impact of the High Luminosity and High Energy LHC upgrades (see also the discussion in Sections 7.1.3,7.1.2, and 7.2.3).

10.4.1 EFT analysis

If the dominant NP effects give rise to dimension-six SMEFT operators, the low-energy flavour measurements are sensitive to C/Λ^2, with C the dimensionless NP Wilson coefficient and Λ the NP scale. The size of the Wilson coefficient is model dependent, and thus so is the NP scale required to explain the $R_{D^{(*)}}$and $R_{K^{(*)}}$ anomalies. Perturbative unitarity sets an upper bound on the energy scale below which new dynamics need to appear [1483]. The conservative bounds on the scale of unitarity violation are $\Lambda_U = 9.2$ TeV and 84 TeV for $R_{D^{(*)}}$and $R_{K^{(*)}}$, respectively, obtained when the flavour structure of NP operators is exactly aligned with what is needed to explain the anomalies. More realistic frameworks for flavour structure, such as MFV, $U(2)$ flavour models, or partial compositeness, give rise to NP effective operators with largest effects for the third generation. This results in stronger unitarity bounds, $\Lambda_U = 1.9$ TeV and 17 TeV for $R_{D^{(*)}}$ and $R_{K^{(*)}}$, respectively. These results mean that: *(i)* the mediators responsible for the $b \to c\tau\nu$ charged current anomalies are expected to be in the energy range of the LHC, *(ii)* the mediators responsible for the $b \to s\ell\ell$ neutral current anomalies could well be above the energy range of the LHC. However, in realistic flavour models also these mediators typically fall within the (HE-)LHC reach.

If the neutrinos in $b \to c\tau\nu$ are part of a left-handed doublet, the NP responsible for $R_{D^{(*)}}$ anomaly generically implies a sizeable signal in $pp \to \tau^+\tau^-$ production at high-$p_{\rm T}$. For realistic flavour structures, in which $b \to c$ transition is $\mathcal{O}(V_{cb})$ suppressed compared to $b \to b$, one expects rather large $bb \to \tau\tau$ NP amplitude. Schematically, $\Delta R_{D^{(*)}} \sim C_{bb\tau\tau}(1 + \lambda_{bs}/V_{cb})$, where $C_{bb\tau\tau}$ is the size of effective dim-6 interactions controlling $bb \to \tau\tau$, and λ_{bs} is a dimensionless parameter controlling the size of flavour violation. Recasting ATLAS 13 TeV, 3.2 fb^{-1} search for $\tau^+\tau^-$ [1484], Ref. [369] showed that $\lambda_{bs} = 0$ scenario is already in slight tension with data. For $\lambda_{bs} \sim 5$, which is moderately large, but still compatible with FCNC constraints, HL (or even HE) upgrade of the LHC would be needed to cover the relevant parameter space implied by the anomaly (see Fig. [5] in [265]). For large λ_{bs} the limits from $pp \to \tau^+\tau^-$ become comparable with direct the limits on $pp \to \tau\nu$ from the bottom-charm fusion. The limits on the EFT coefficients from $pp \to \tau\nu$ were derived in Ref. [378], and the future LHC projections are promising. The main virtue of this channel is that the same four-fermion interaction is compared in $b \to c\tau\nu$ at low energies and $bc \to \tau\nu$ at high-$p_{\rm T}$. Since the effective NP scale in $R(D^{(*)})$ anomaly is low, the above EFT analyses are only indicative. For more quantitative statements we review below bounds on explicit models.

The hints of NP in $R_{K^{(*)}}$ require a $(bs)(\ell\ell)$ interaction. Correlated effects in high-$p_{\rm T}$ tails of $pp \to \mu^+\mu^-(e^+e^-)$ distributions are expected, if the numerators (denominators) of LFU ratios $R_{K^{(*)}}$ are affected. Ref. [1485] recast the 13 TeV 36.1 fb^{-1} ATLAS search [1486] (see also [1487]), to set limits on a number of semi-leptonic four-fermion operators, and derive projections for HL-LHC (see Table 1 in [1485]). These show that direct limits on the $(bs)(\ell\ell)$ operator from the tails of distributions will never be competitive with those implied by the rare B-decays [1485, 1488]. On the other hand, flavour conserving operators, $(qq)(\ell\ell)$, are efficiently constrained by the high $p_{\rm T}$ tails of the distributions. The flavour structure of an underlining NP could thus be probed by constraining ratios $\lambda^q_{bs} = C_{bs}/C_{qq}$ with C_{bs} fixed by the $R_{K^{(*)}}$ anomaly. For example, in models with MFV flavour structure, so that $\lambda^{u,d}_{bs} \sim V_{cb}$, the present high-$p_{\rm T}$ dilepton data is already in slight tension with the anomaly [1485]. Instead, if couplings to valence quarks are suppressed, e.g., if NP dominantly couples to the 3rd family SM fermions, then $\lambda^b_{bs} \sim V_{cb}$. Such NP will hardly be probed even at the HL-LHC, and it is possible that NP responsible for the neutral current anomaly might stay undetected in the high-$p_{\rm T}$ tails at HL-LHC and even at HE-LHC. Future data will cover a significant part of viable parameter space, though not completely, so that discovery is possible, but not guaranteed.

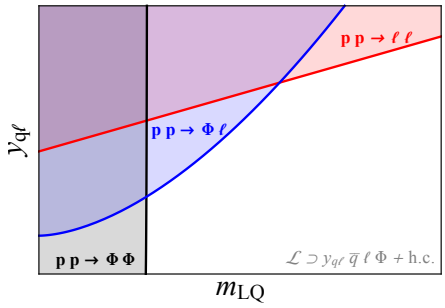

Fig. 84: Schematic of the LHC bounds on LQ showing complementarity in constraining the (m_{LQ}, y_{q_ℓ}) parameters. The three cases are: pair production $\sigma \propto y^0_{q_\ell}$, single production $\sigma \propto y^2_{q_\ell}$ and Drell-Yan $\sigma \propto y^4_{q_\ell}$ (from [1490]).

10.4.2 Constraints on simplified models for $b \to c\tau\nu$

Since the $b \to c\tau\nu$ decay is a tree-level process in the SM that receives no drastic suppression, models that can explain these anomalies necessarily require a mediator that contributes at tree-level:

- *SM-like W'*: A SM-like W' boson, coupling to left-handed fermions, would explain the approximately equal enhancements observed in $R(D)$ and $R(D^*)$. A possible realization is a color-neutral real $SU(2)_L$ triplet of massive vector bosons [946]. However, typical models encounter problems with current LHC data since they result in large contributions to $pp \to \tau^+\tau^-$ cross-section, mediated by the neutral partner of the W' [369, 926, 946]. For $M_{W'} \gtrsim 500$ GeV, solving the $R(D^{(*)})$ anomaly within the vector triplet model while being consistent with $\tau^+\tau^-$ resonance searches at the LHC is only possible if the related Z' has a large total decay width [369]. Focusing on the W', Ref. [1489] analyzed the production of this mediator via gg and gc fusion, decaying to $\tau\nu_\tau$. Ref. [1489] concluded that a dedicated search using that b-jet is present in the final state would be effective in reducing the SM background compared to an inclusive analysis that relies on τ-tagging and E_T^{miss}. Nonetheless, relevant limits will be set by an inclusive search in the future [378].

- *Right-handed W':* Refs. [1056, 1057] recently proposed that W' could mediate a right-handed interaction, with a light sterile right-handed neutrino carrying the missing energy in the B decay. In this case, it is possible to completely decorelate FCNC constraints from $R(D^{(*)})$. The most constraining process in this case is instead $pp \to \tau\nu$. Ref. [378] performed a recast of the latest ATLAS and CMS searches at 13 TeV and about 36 fb^{-1} to constrain most of the relevant parameter space for the anomaly.

- *Charged Higgs $H^\pm$:* Models that introduce a charged Higgs, for instance a two-Higgs-doublet model, also contain additional neutral scalars. Their masses are constrained by electroweak precision measurements to be close to that of the charged Higgs. Accommodating the $R(D^{(*)})$ anomalies with a charged Higgs typically implies large new physics contributions to $pp \to \tau^+\tau^-$ via the neutral scalar exchanges, so that current LHC data can challenge this option [369]. Note that a charged Higgs also presents an important tension between the current measurement of $R(D^*)$ and the measured lifetime of the B_c meson [1031, 1046, 1063, 1064].

- *Leptoquarks:*

The observed anomalies in charged and neutral currents appear in semileptonic decays of the B-mesons. This implies that the putative NP has to couple to both quarks and leptons at the fundamental level. A natural BSM option is to consider mediators that couple simultaneously quarks and leptons at the tree level. Such states are commonly referred as leptoquarks. Decay and production mechanisms of the LQ are directly linked to the physics required to explain the anomalous data.

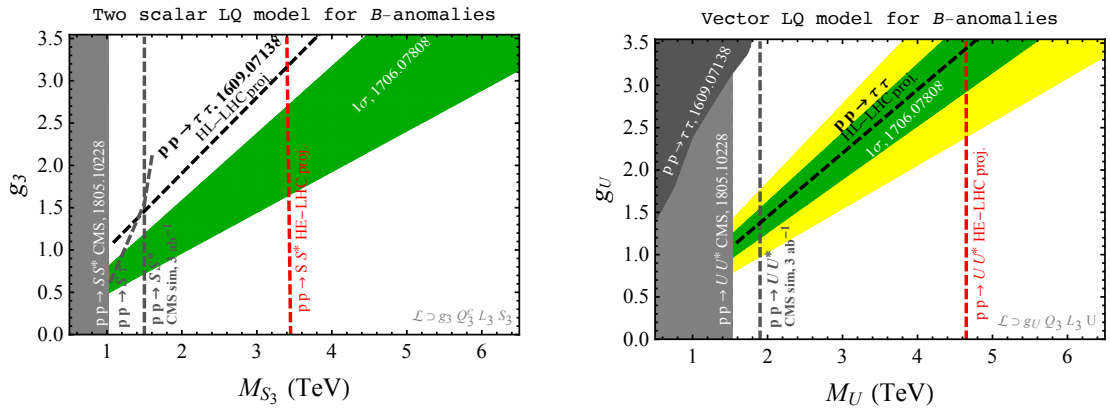

Fig. 85: Present constraints and HL(HE)-LHC projections in the leptoquark mass versus coupling plane for the scalar leptoquark S_3 (left), and vector leptoquark U_1 (right). The grey and dark grey solid regions are the current exclusions. The grey and black dashed lines are the projected reach for HL-LHC (pair and single leptoquark production prospects are based on the CMS simulation from Section 10.4.5). The red dashed lines are the projected reach at HE-LHC (see Section 10.4.6). The green and yellow bands are the 1σ and 2σ preferred regions from the fit to B physics anomalies. The second coupling required to fit the anomaly does not enter in the leading high-$p_{\rm T}$ diagrams but it is relevant for fixing the preferred region shown in green, for more details see Ref. [265].

– **Leptoquark decays:** the fit to the $R(D^*)$ observables suggest a rather light leptoquark (at the TeV scale) that couples predominately to the third generation fermions of the SM. A series of constraints from flavour physics, in particular the absence of BSM effects in kaon and charm mixing observables, reinforces this picture.
– **Leptoquark production mechanism:** The size of the couplings required to explain the anomaly is typically very large, roughly $y_{q\ell} \approx m_{LQ}/$ (1 TeV). Depending of the actual sizes of the leptoquark couplings and its mass we can distinguish three regimes that are relevant for the phenomenology at the LHC:

  1. LQ pair production due to strong interactions,
  2. Single LQ production plus lepton via a single insertion of the LQ coupling, and
  3. Non-resonant production of di-lepton through t-channel exchange of the leptoquark.

  Interestingly all three regimes provide complementary bounds in the (m_{LQ}, y_{q_ℓ}) plane, see Fig. 84.

Several simplified models with leptoquark as a mediator were shown to be consistent with the low-energy data. A vector leptoquark with $SU(3)_c \times SU(2)_L \times U(1)_Y$ SM quantum numbers $U_\mu \sim (\mathbf{3}, \mathbf{1}, 2/3)$ was identified as the only single mediator model which can simultaneously fit the two anomalies (see e.g. [265] for a recent fit including leading RGE effects). In order to substantially cover the relevant parameter space, one needs future HL- (HE-) LHC, see Fig. 85 (right) (see also Fig. 5 of [265] for details on the present LHC constraints). A similar statement applies to an alternative model featuring two scalar leptoquarks, S_1, S_3 [955]. The pair of plots in Fig. 85 summaries the current exclusion and the discovery reach for the HE and HL-LHC in the LQ coupling versus mass plane.

Leptoquarks states are emerging as the most convincing mediators for the explanations of the flavour anomalies. It is then important to explore all the possible signatures at the HL- and HE-LHC. The experimental programme should focus not only on the final states containing quarks and leptons of the third generation, but also on the whole list of decay channels including the off-diagonal ones ($b\mu$, $s\tau, \ldots$). The completeness of this approach would allow to shed light on the flavour structure of the putative New Physics.

Another aspect to be emphasized regarding leptoquark models is that the UV complete models often require extra fields. The accompanying particles would leave more important signatures at high

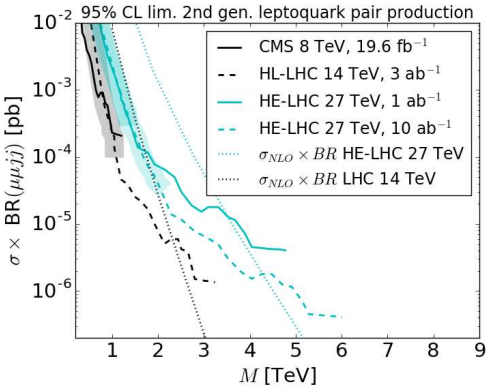

Fig. 86: Current and projected 95% CL limits on $\mu\mu jj$ final state at CMS (solid black) and HL-LHC (cyan) with 1 (10) ab^{-1} in solid (dashed) lines. The pair production cross-section for scalar leptoquarks is shown in dotted lines for 14 (27) TeV in black (cyan) (Fig. taken from [1493]).

p_T than the leptoquarks, which is particularly true for vector leptoquark extensions (see for example [963, 1491])

10.4.3 Constraints on simplified models for $b \to sll$

The $b \to sll$ transition is both loop and CKM suppressed in the SM. The explanations of the $b \to sll$ anomalies can thus have both tree level and loop level mediators. Loop-level explanations typically involve lighter particles. Tree-level mediators can also be light, if sufficiently weakly coupled. However, they can also be much heavier—possibly beyond the reach of the LHC.

• *Tree-level mediators:*
For $b \to sll$ anomaly there are two possible tree-level UV-completions, the Z' vector boson and leptoquarks, either scalar or vector (see Fig. 41 in Sec. 7.1.3). For leptoquarks, Fig. 86 shows the current 95% CL limits from 8 TeV CMS with 19.6 fb^{-1} in the $\mu\mu jj$ final state (solid black line), as well as the HL-LHC (dashed black line) and 1 (10) ab^{-1} HE-LHC extrapolated limits (solid (dashed) cyan line). Dotted lines give the cross-sections times branching ratio at the corresponding collider energy for pair production of scalar leptoquarks, calculated at NLO using the code of Ref. [1492]. We see that the sensitivity to a leptoquark with only the minimal $b-\mu$ and $s-\mu$ couplings reaches around 2.5 and 4.5 TeV at the HL-LHC and HE-LHC, respectively. This pessimistic estimate is a lower bound that will typically be improved in realistic models with additional flavour couplings. Moreover, the reach can be extended by single production searches [1493], albeit in a more model-dependent way than pair production. The cross section predictions for vector leptoquark are more model-dependent and are not shown in Fig. 86. For $\mathcal{O}(1)$ couplings the corresponding limits are typically stronger than for scalar leptoquarks. Searches in other decay channels should also be considered, such at $t\bar{t}$+MET for which HL-LHC projections can be found in Ref. [1494].

For the Z' mediator the minimal couplings in the mass eigenstate basis are obtained by unitary transformations from the gauge eigenstate basis, which necessarily induces other couplings. Ref. [1496] defined the "mixed-up" model (MUM) and "mixed-down" model (MDM) such that the minimal couplings are obtained via CKM rotations in either the up or down sectors respectively. For MUM there is no sensitivity at the HL-LHC. The predicted sensitivity at the HL-LHC for the MDM is shown in Fig. 87 as functions of Z' muon coupling $g_{\mu\mu}$ and the Z' mass, setting the Z' coupling to b and s quarks such that it solves the $b \to s\ell\ell$ anomaly. The solid blue (orange) contours give the 95% and 99% CL sensitivity. The red and green regions are excluded by B_s mixing [906] and neutrino trident production [1497, 1498], respectively. The more stringent B_s mixing constraint from Ref. [1495] is denoted by the dashed blue

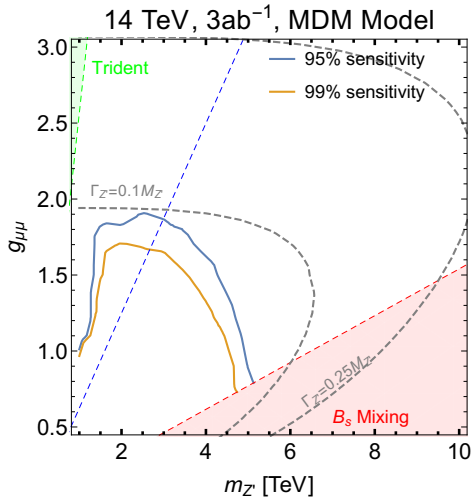

Fig. 87: HL-LHC 95% (blue) and 99% (orange) CL sensitivity contours to Z' in the "mixed-down" model for $g_{\mu\mu}$ vs Z' mass in TeV. The dashed grey contours give the Z' width as a fraction of mass. The green and red regions are excluded by trident neutrino production and B_s mixing, respectively. The dashed blue line is the stronger B_s mixing constraint from Ref. [1495] (Fig. taken from [1496]).

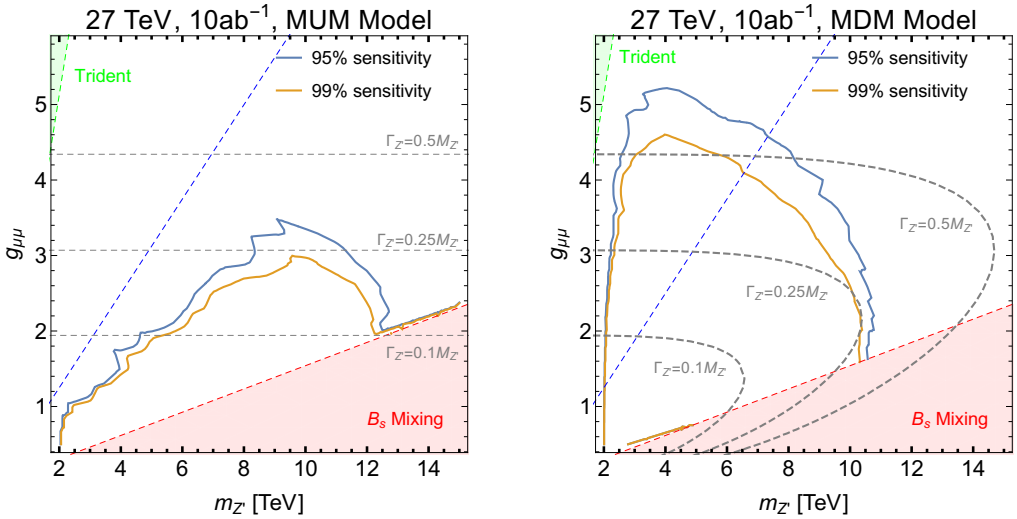

Fig. 88: HE-LHC 95% (blue) and 99% (orange) CL sensitivity contours to Z' in the "mixed-up" (left) and "mixed-down" (right) model in the parameter space of $g_{\mu\mu}$ vs Z' mass in TeV. The dashed grey contours are the width as a fraction of mass. The green and red regions are excluded by trident neutrino production and B_s mixing. The dashed blue line is the stronger B_s mixing constraint from Ref. [1495] (Figs. taken from [1496]).

line; see, however, Ref. [948] for further discussion regarding the implications of this bound. The dashed grey contours denote the width as a fraction of the mass. We see that the HL-LHC will only be sensitive to Z' with narrow width, up to masses of 5 TeV.

At the HE-LHC, the reach for 10 ab^{-1} is shown in Fig. 88 for the MUM and MDM on the left and right, respectively. In this case the sensitivity may reach a Z' with wider widths up to 0.25 and 0.5 of its mass, while the mass extends out to 10 to 12 TeV. We stress that this is a pessimistic estimate of the projected sensitivity, particular to the two minimal models; more realistic scenarios will typically be easier to discover.

• *Explanations at the one-loop level:*
It is possible to accomodate the $b \to s\ell^+\ell^-$ anomalies even if mediators only enter at one-loop. One possibility is the mediators coupling to right-handed top quarks and to muons [346, 907, 1499–1501]. Given the loop and CKM suppression of the NP contribution to the $b \to s\ell^+\ell^-$ amplitude, these models can explain the $b \to s\ell^+\ell^-$ anomalies for a light mediator, with mass around $\mathcal{O}(1)$ TeV or lighter. Constraints from the LHC and future projections for the HL-LHC were derived in [1501] by recasting di-muon resonance, $pp \to t\bar{t}t\bar{t}$ and SUSY searches. Two scenarios were considered: *i)* a scalar LQ $R_2(3, 2, 7/6)$ combined with a vector LQ $\widetilde{U}_{1\alpha}(3, 1, 5/3)$, *ii)* a vector boson Z' in the singlet representation of the SM gauge group. Ref. [1500] also analyzed the HL-LHC projections for the Z'. The constraints from the LHC already rule out part of the relevant parameter space and the HL-LHC will be able to cover much of the remaining regions. Dedicated searches in the $pp \to t\bar{t}t\bar{t}$ channel and a dedicated search for $t\mu$ resonances in $t\bar{t}\mu^+\mu^-$ final state can improve the sensitivity to these models [1501].

10.4.4 Conclusions regarding high p_{T} probes of flavour anomalies

The anomalous results in B-meson decays cannot be considered yet as a convincing evidence of New Physics. On the other hand, the number (and quality) of observables that are not in complete agreement with the SM prediction is growing with time in a coherent way. If true, the implications for HEP will be profound. The conclusions we draw are the following:

- A conservative argument based on perturbative unitarity [1483] sets an upper bound on the New Physics scale to be 9 TeV for charged current anomalies and 80 TeV for neutral current ones. The analysis of explicit models show that the high-luminosity programme has a clear potential to probe a large portion of the possible BSM options.
- The explanation of the anomalies in $b \to c\tau\nu$ transitions requires non trivial model building. In particular, it is not possible to simply isolate the physics that mediate the flavour anomalous transitions. In complete models other signature have to be considered. Typically it would be very difficult to escape direct detection at HL/HE-LHC.
- Even though the naive scale associated with the $b \to s\ell\ell$ anomalies is much higher than the energy accessible at HL/HE-LHC, in motivated models the flavour suppressions and weak couplings guarantee a large coverage of the parameter space for leptoquark and Z' mediators [1496].

More generally, the probes of lepton flavour universality such as the ratios of inclusive $\tau^+\tau^-$ vs. $\mu^+\mu^-$ (or $\mu^+\mu^-$ vs. e^+e^-) mass distributions, are important, theoretically clean, tests of the SM and are well motivated observables both at HL- and HE-LHC, whether or not the current B-meson anomalies become statistically significant.

As a final remark, it is important to remember that the anomalies are not yet experimentally established. Among others, this also means that the statements on whether or not the high p_T LHC constraints rule out certain $R(D^{(*)})$ explanations assumes that the actual values of $R(D^{(*)})$ are given by their current global averages. If future measurements decrease the global average, the high p_T constraints can in some cases be greatly relaxed so that HL- and/or HE-LHC may be essential even for these, at present tightly constrained, cases.

10.4.5 Experimental prospects for high p_T searches at HL-LHC relevant for B anomalies

We give next the experimental prospects for leptoquark searches, with leptoquarks decaying to the final states relevant for B physics anomalies.

10.4.5.1 Prospects for leptoquark searches assuming t+τ and/or t+μ decays

The reach of searches for pair production of leptoquarks (LQs) with decays to $t + \mu$ and $t + \tau$ is studied for the HL-LHC with target integrated luminosities of $\mathcal{L}_{\text{int}}^{\text{target}} = 300$ and $3000\,\text{fb}^{-1}$ [1502]. The studies

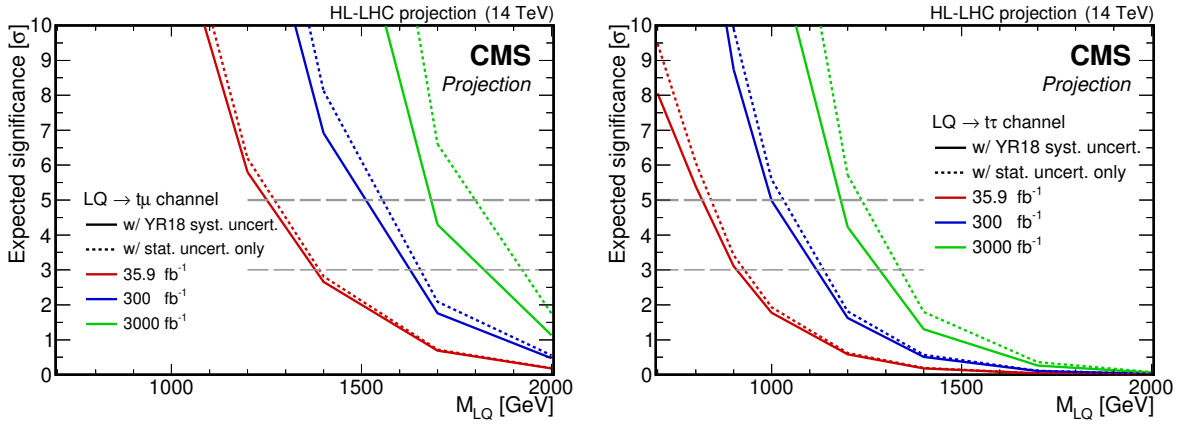

Fig. 89: Expected significances for an LQ decaying exclusively to top quarks and muons (left) or top quarks and τ leptons (right).

are based on published CMS results of the t+μ [1503] and t+τ [1504] LQ decay channels which use data of proton-proton collisions at $\sqrt{s} = 13\,\text{TeV}$ corresponding to $\mathcal{L}_{\text{int}} = 35.9\,\text{fb}^{-1}$ recorded in 2016. While the analysis strategies are kept unchanged with respect to the ones in Refs. [1503, 1504], different total integrated luminosities, the higher center-of-mass energy of 14 TeV, and different scenarios of systematic uncertainties are considered. In the first scenario (denoted "w/ YR18 syst. uncert."), the relative experimental systematic uncertainties are scaled by a factor of $1/\sqrt{f}$, with $f = \mathcal{L}_{\text{int}}^{\text{target}}/35.9\,\text{fb}^{-1}$, until they reach a defined lower limit based on estimates of the achievable accuracy with the upgraded detector [1]. The relative theoretical systematic uncertainties are halved. In the second scenario (denoted "w/ stat. uncert. only"), no systematic uncertainties are considered. The relative statistical uncertainties in both scenarios are scaled by $1/\sqrt{f}$.

Figure 89 presents the expected signal significances of the analyses as a function of the LQ mass for different assumed integrated luminosities in the "w/ YR18 syst. uncert." and "w/ stat. uncert. only" scenarios. Increasing the target integrated luminosity to $\mathcal{L}_{\text{int}}^{\text{target}} = 3000\,\text{fb}^{-1}$ greatly increases the discovery potential of both analyses. The LQ mass corresponding to a discovery at 5σ significance with a dataset corresponding to $3000\,\text{fb}^{-1}$ increases by more than 500 GeV compared to the situation at $\mathcal{L}_{\text{int}}^{\text{target}} = 35.9\,\text{fb}^{-1}$, from about 1200 GeV to roughly 1700 GeV, in the LQ $\to t\mu$ decay channel. For LQs decaying exclusively to top quarks and τ leptons, a gain of 400 GeV is expected, pushing the LQ mass in reach for a 5σ discovery from 800 GeV to 1200 GeV.

In Fig. 90, the expected projected exclusion limits on the LQ pair production cross section are shown. Leptoquarks decaying only to top quarks and muons are expected to be excluded below masses of 1900 GeV for $3000\,\text{fb}^{-1}$, which is a gain of 500 GeV compared to the limit of 1420 GeV obtained in the published analysis of the 2016 dataset [1503]. The mass exclusion limit for LQs decaying exclusively to top quarks and τ leptons are expected to be increased by 500 GeV, from 900 GeV to approximately 1400 GeV.

Figure 91 shows the expected signal significances and upper exclusion limits on the pair production cross section of scalar LQs allowed to decay to top quarks and muons or τ leptons at the 95% CL as a function of the LQ mass and a variable branching fraction $\mathcal{B}(\text{LQ} \to t\mu) = 1 - \mathcal{B}(\text{LQ} \to t\tau)$ for an integrated luminosity of $3000\,\text{fb}^{-1}$ in the two different scenarios. For all values of $\mathcal{B}$, LQ masses up to approximately 1200 GeV and 1400 GeV are expected to be in reach for a discovery at the 5σ level and a 95% CL exclusion, respectively.

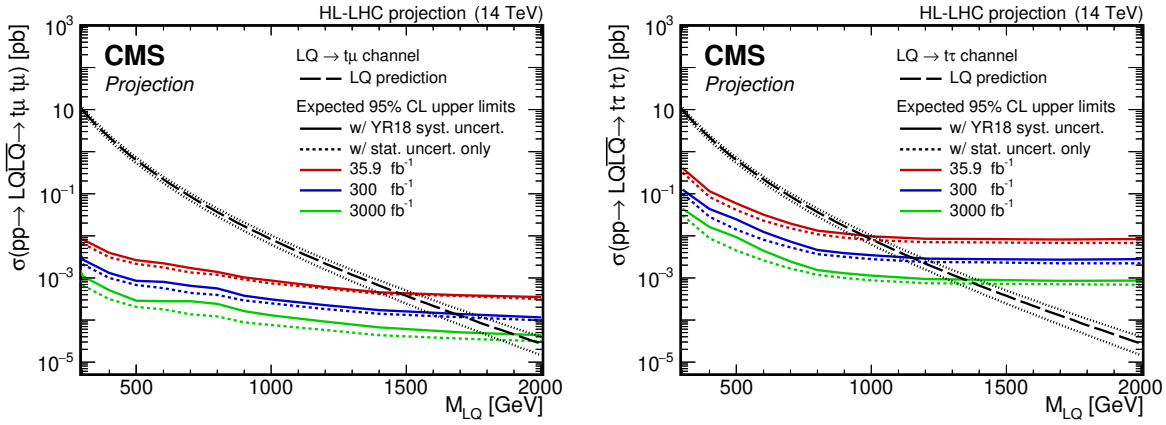

Fig. 90: Expected upper limits on the LQ pair production cross section at the 95% CL for an LQ decaying exclusively to top quarks and muons (left) or τ leptons (right).

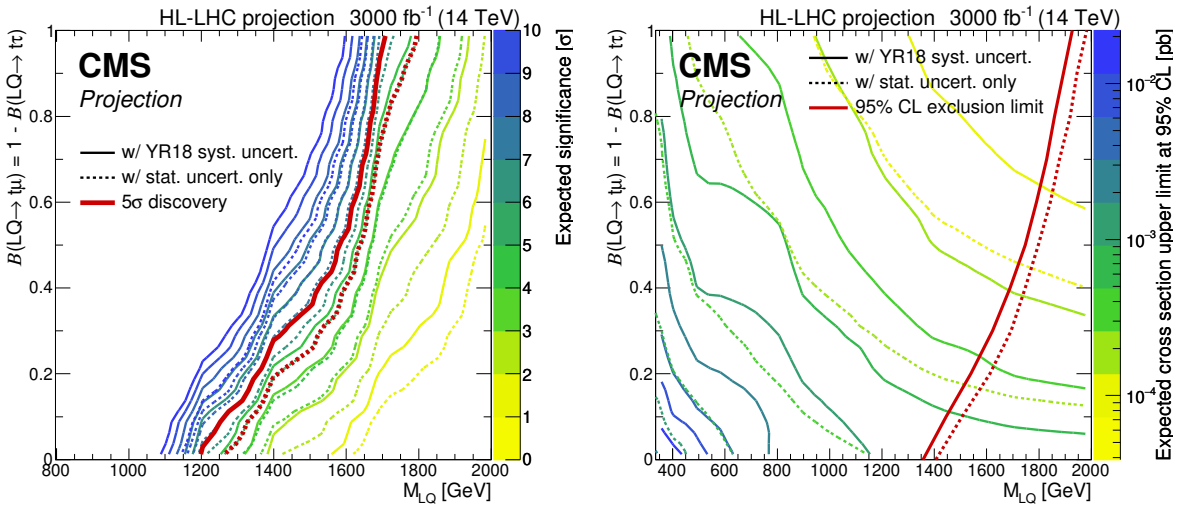

Fig. 91: Expected significances (left) and expected upper limits on the LQ pair-production cross section at the 95% CL (right) as a function of the LQ mass and the branching fraction. Color-coded lines represent lines of a constant expected significance or cross section limit, respectively. The red lines indicate the 5σ discovery level (left) and the mass exclusion limit (right).

10.4.5.2 CMS Search for leptoquarks decaying to τ and b

This analysis from CMS [1505] presents future discovery and exclusion prospects for singly and pair produced third-generation scalar LQs, each decaying to τ_h and a bottom quark. Here, τ_h denotes a hadronically decaying τ lepton. The relevant Feynman diagrams of the signal processes at leading order (LO) are shown in Fig. 92.

The analysis uses DELPHES [374] event samples of simulated pp collisions at a center-of-mass energy of 14 TeV, corresponding to integrated luminosities of 300 and 3000 fb^{-1}. The matrix elements of LQ signals for both single and pair LQ production are generated at LO using version 2.6.0 of `MadGraph5_aMC@NLO` [372] for m_{LQ} =500, 1000, 1500, and 2000 GeV. The branching fraction β of the LQ to a charged lepton and a quark, in this case LQ$\rightarrow \tau b$, is assumed to be $\beta = 1$. The unknown Yukawa coupling λ of the LQ to a τ lepton and a bottom quark is set to $\lambda = 1$. The width Γ is calculated using $\Gamma = m_{LQ}\lambda^2/(16\pi)$ [1506], and is less than 10% of the LQ mass for most of the considered search range. The signal samples are normalized to the cross section calculated at LO, multiplied by a K factor to account for higher order contributions [1490].

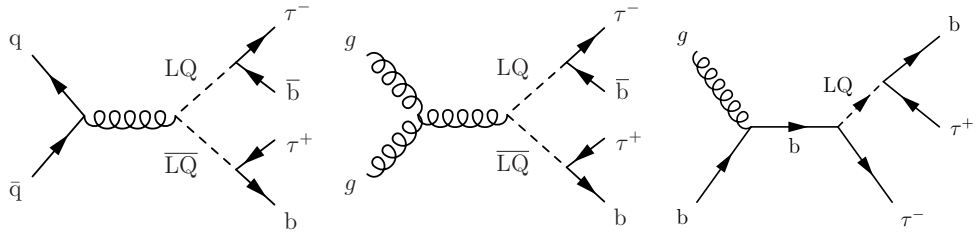

Fig. 92: Leading order Feynman diagrams for the production of a third-generation LQ in the single production s-channel (left) and the pair production channel via gluon fusion (center) and quark fusion (right).

Similar event selections are used in both the singly and pair produced LQ searches, except for the requirement on the number of jets. In both channels, two reconstructed τ_h with opposite-sign charge are required, each with transverse momentum $p_{T,\tau} > 50$ GeV and a maximum pseudorapidity $|\eta_\tau| < 2.3$. In the search for single production, the presence of at least one reconstructed jet with $p_T > 50$ GeV is required, while at least two are required in the search for pair production. Jets are reconstructed with FASTJET [1507], using the anti-k_{T} algorithm [1508], with a distance parameter of 0.4.

To reduce background due to Drell-Yan (particularly Z$\rightarrow \tau\tau$) events, the invariant mass of the two selected τ_h, $m_{\tau\tau}$, is required to be > 95 GeV. In addition, at least one of the previously selected jets is required to be b-tagged to reduce QCD multijet backgrounds. Finally, an event is rejected if it contains identified and isolated electrons (muons), with $p_T > 10$ GeV, $|\eta|$ <2.4 (2.5). The acceptance of the signal events is 4.9% (11%) for single (pair) production, where the branching ratio of two τ leptons decaying hadronically is included in the numerator of the acceptance.

Signal extraction is based on a binned maximum likelihood fit to the distribution of the scalar p_T sum $\mathrm{S_T}$, which is defined as the sum of the transverse momenta of the two τ_h and either the highest-p_T jet in the case of single LQ production, or the two highest-p_T jets in the case of LQ pair production. These distributions are shown in Fig. 93 for the HL-LHC 3000 fb^{-1} scenario.

Systematic uncertainties are calculated by scaling the current experimental uncertainties. For uncertainties limited by statistics, including the uncertainty on the DY (3.3%) and QCD (3.3%) cross sections, a scale factor of $1/\sqrt{L}$ is applied, for an integrated luminosity ratio L. For uncertainties coming from theoretical calculations, a scale factor of 1/2 is applied with respect to current uncertainties, as is the case for the uncertainties on the cross section for top (2.8%) or diboson (3%) events. Other experimental systematic uncertainties are scaled by the square root of the integrated luminosity ratio until the uncertainty reaches a minimum value, including uncertainties on the integrated luminosity (1%), τ identification (5%) and b-tagging/misidentification (1%-5%).

Figure 94 shows an upper limit at 95% CL on the cross section times branching fraction β as a function of m_{LQ} by using the asymptotic CLs modified frequentist criterion [1509–1512]. Upper limits are calculated considering two different scenarios. The first one, hereafter abbreviated as "stat. only" considers only statistical uncertainties, to observe how the results are affected by the increase of the integrated luminosity. The second scenario, hereafter abbreviated as "stat.+syst.," also includes the estimate of the systematic uncertainties at the HL-LHC. For the single LQ production search, the theoretical prediction for the cross section assumes $\lambda = 1$ and $\beta = 1$.

Comparing the limits with theoretical predictions assuming unit Yukawa coupling $\lambda = 1$, third-generation scalar leptoquarks are expected to be excluded at 95% confidence level for LQ masses below 732 (1249) GeV for a luminosity of 300 fb^{-1}, and below 1130 (1518) GeV for 3000 fb^{-1} in the single (pair) production channel, considering both statistical and systematic uncertainties.

Since the single-LQ signal cross section scales with λ^2, it is straightforward to recast the results presented in Fig. 94 in terms of expected upper limits on m_{LQ} as a function of λ, as shown in Fig. 95. The

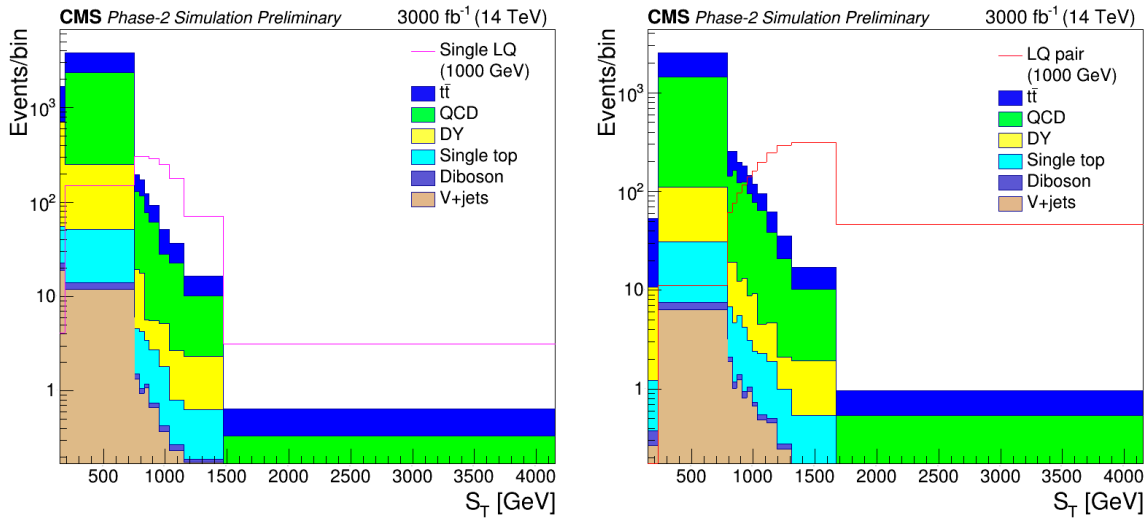

Fig. 93: Left: scalar sum of the p_{T} of the two selected τ leptons and the highest-p_T jet in the single LQ selection region. Right: scalar sum of the p_T of the two selected τ leptons and the two highest-p_T jets in the LQ pair search region. The considered backgrounds are shown as stacked histograms, while empty histograms for signals for the single LQ and LQ pair channels (for $m_{LQ} = 1000$ GeV) are overlaid to illustrate the sensitivity. Both signal and backround are normalised to a luminosity of 3000 fb^{-1}.

blue band shows the parameter space (95% CL) for the scalar LQ preferred by the B physics anomalies: $\lambda = (0.95 \pm 0.50) m_{LQ}(\text{ TeV})$ [265]. For the 300 (3000) fb^{-1} luminosity scenario, the leptoquark pair production channel is more sensitive if $\lambda < 2.7\ (2.3)$, while the single leptoquark production is dominant otherwise.

Using the predicted cross section [1490] of the signal, it is also possible to estimate the maximal LQ mass expected to be in reach for a 5σ discovery. Figure 96 shows the expected local significance of a signal-like excess as a function of the LQ mass hypothesis.

In summary, this study shows that future LQ searches under higher luminosity conditions are promising, as they are expected to greatly increase the reach of the search. They also show that the pair production channel is expected to be the most sensitive. A significance of 5σ is within reach for LQ masses below 800 (1200) FeV for the single (pair) production channels in the 300 fb^{-1} scenario and 1000 (1500) GeV for the 3000 fb^{-1} scenario.

10.4.5.3 CMS Searches for $W' \to \tau + E_{\mathrm{T}}^{\mathrm{miss}}$

New heavy gauge bosons are predicted by various SM extensions. The charged version of such heavy gauge bosons is generally referred to as W$'$. The decay W$' \to \tau\nu$ yields a single hadronically decaying tau (τ_h) as the only detectable object and missing energy due to the neutrinos. Hadronically decaying tau leptons are selected since the corresponding branching fraction, about 60%, is the largest among all τ decays. Tau-jets are experimentally distinctive because of their low charged hadron multiplicity, unlike QCD multi-jets, which have high charged hadron multiplicity, or other leptonic W$'$ boson decays, which yield no jet. This Phase-2 study [1513] follows closely the recently published Run 2 result [1514], using hadronically decaying tau leptons.

The signature of a W$'$ boson (see Fig. 97), is considered similar to a high-mass W boson. It could be observed in the distribution of the transverse mass (M_T) of the transverse momentum of the τ (p_T^τ) and the missing transverse momentum ($\mathbf{p}_{\mathrm{T}}^{\mathrm{miss}}$): $M_T = \sqrt{2 p_T^\tau p_T^{miss} (1 - cos\Delta\phi(\tau, p_T^{miss}))}$. Unlike the

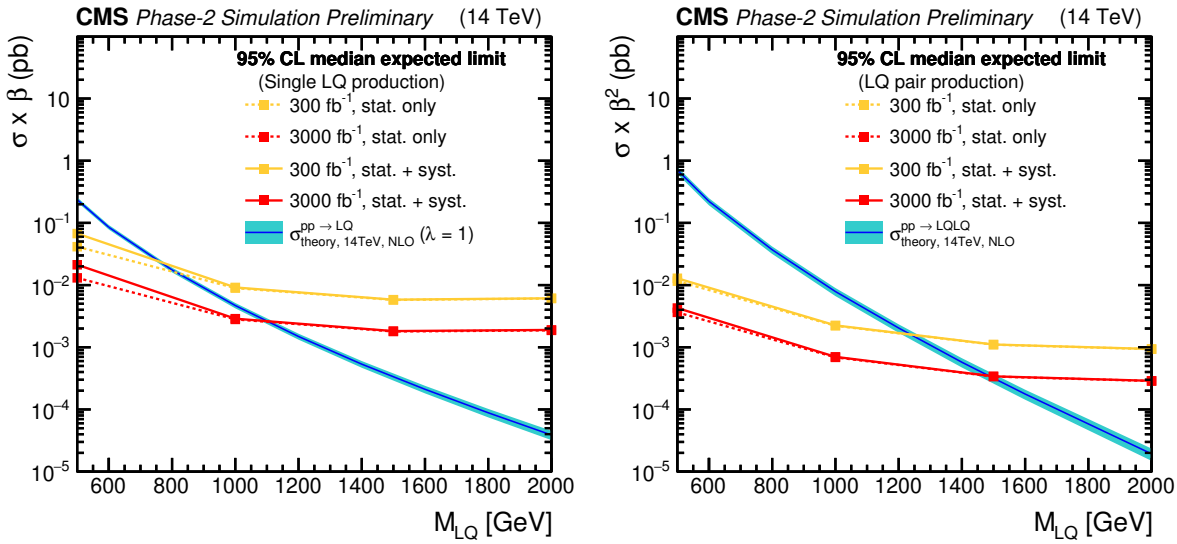

Fig. 94: Expected limits at 95% CL on the product of the cross section σ and the branching fraction β, as a function of the LQ mass, for the two high luminosity projections, 300 fb^{-1} (red) and 3000 fb^{-1} (orange), for both the stat. only (dashed lines) and the stat.+syst. scenarios (solid lines). This is shown in conjunction with the theoretical predictions at NLO [1490] in cyan. Projections are calculated for both the single LQ (left) and LQ pair production (right).

leptonic search channels, the signal shape of W' bosons with hadronically decaying tau leptons does not show a Jacobian peak structure because of the presence of two neutrinos in the final state. Despite the multi-particle final state, the decay appears as a typical two-body decay; the axis of the hadronic tau jet is back to back with $\mathbf{p}_{\mathrm{T}}^{\mathrm{miss}}$ and the magnitude of both is comparable such that their ratio is about unity.

The results are interpreted in the context of the sequential standard model (SSM) [1515] in terms of W$'$ mass and coupling strength. A model-independent cross section limit allows interpretations in other models. The signal was simulated in LO and the detector performance simulated with DELPHES. The W$'$ boson coupling strength, $g_{\mathrm{W}'}$, is given in terms of the SM weak coupling strength $g_W = e/\sin^2\theta_W \approx 0.65$. Here, θ_W is the weak mixing angle. If the W$'$ boson is a heavier copy of the SM W boson, their coupling ratio is $g_{\mathrm{W}'}/g_W = 1$ and the SSM W$'$ boson theoretical cross sections, signal shapes, and widths apply. However, different couplings are possible. Because of the dependence of the width of a particle on its couplings the consequent effect on the transverse mass distribution, a limit can also be set on the coupling strength.

The dominant background appears in the off-shell tail of the M_T distribution of the SM W boson. Subleading background contributions arise from $t\bar{t}$ and QCD multijet events. The number of background events is reduced by the event selection. These backgrounds primarily arise as a consequence of jets misidentified as τ_h candidates and populate the lower transverse masses while the signal exhibits an excess of events at high M_T. Events with one hadronically decaying τ and $\mathbf{p}_{\mathrm{T}}^{\mathrm{miss}}$ are selected if the ratio of p_{T}^{τ} to $\mathbf{p}_{\mathrm{T}}^{\mathrm{miss}}$ satisfies $0.7 < p_{\mathrm{T}}^{\tau}/\mathbf{p}_{\mathrm{T}}^{\mathrm{miss}} < 1.3$ and the angle $\Delta\phi(\vec{p_T}^{\,\tau}, \vec{p_T}_{miss})$ is greater than 2.4 radians.

The physics sensitivity is studied based on the M_T distribution in Fig. 97-right. Signal events are expected to be particularly prominent at the upper end of the M_T distribution, where the expected SM background is low. So far, there are no indications for the existence of a SSM W$'$ boson [1514]. With the high luminosity during Phase-2, the W$'$ mass reach for potential observation increases to 6.9 TeV and 6.4 TeV for 3 σ evidence and 5 σ discovery, respectively, as shown in Fig. 98-left. Alternatively, in case of no observation, one can exclude SSM W$'$ boson masses up to 7.0 TeV with 3 ab^{-1}. These are multi-bin limits taking into account the full M_T shape.

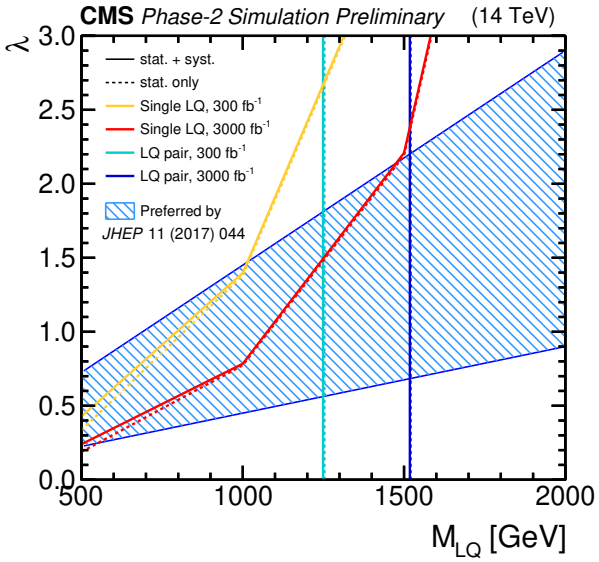

Fig. 95: Expected exclusion limits at 95% CL on the Yukawa coupling λ at the LQ-lepton-quark vertex, as a function of the LQ mass. A unit branching fraction β of the LQ to a τ lepton and a bottom quark is assumed. Future projections for 300 and 3000 fb^{-1} are shown for both the stat. only and stat.+syst. scenarios, shown as dashed and filled lines respectively, and for both the single LQ and LQ pair production, where the latter corresponds to the vertical line (since it does not depend on λ). The left hand side of the lines represents the exclusion region for each of the projections, whereas the region with diagonal blue hatching shows the parameter space preferred by one of the models proposed to explain anomalies observed in B physics [265].

While the SSM model assumes SM-like couplings of the fermions, the couplings could well be weaker if further decays occur. The HL-LHC has good sensitivity to study these couplings. The sensitivity to weaker couplings extends significantly. A model-independent cross section limit for new physics with τ+MET in the final state is depicted in Fig. 98-right, calculated as a single-bin limit by counting the number of events above a sliding threshold $M_T^{\min}$.

10.4.6 High p_T searches at HE-LHC relevant for B physics anomalies

We show next the sensitivity of the 27 TeV pp collider with 15 ab^{-1} integrated luminosity to probe pair production of the scalar and vector leptoquarks decaying to $(b\tau)$ final state. The investigated events contain either one electron or muon, one hadronically decaying tau lepton, and at least two jets. The signal events and the dominant background events ($t\bar{t}$) were generated with `MadGraph5_aMC@NLO` at leading-order. `Pythia6` was used to shower and hadronise events and `DELPHES3` was used to simulate the detector response. The scalar leptoquark (S_3) and the vector leptoquark (U_1) UFO model files were taken from [1490].

To verify the procedure, the $t\bar{t}$ background and the scalar leptoquark signal were simulated at 13 TeV and compared to the predicted shapes in the S_T distribution from the existing CMS analysis [1516]. After verifying the 13 TeV analysis, the signal and the dominant background events at 27 TeV were simulated. From these samples, all events satisfying the particle content requirements and applied the lower cut in the S_T variable were selected. The cut threshold was chosen to maximize $S/\sqrt{B}$ while requiring at least 2 expected signal events at an integrated luminosity of 15 ab^{-1}. In the case of the vector leptoquark two options were considered, the Yang-Mills ($\kappa = 1$), and the minimal coupling ($\kappa = 0$) scenario for the couplings to the gluon field strength, $\mathcal{L} \supset -ig\kappa U_{1\mu}^{\dagger} T^a U_{1\nu} G^a_{\mu\nu}$ [1490]. From the simulations of the scalar and vector leptoquark events, the ratio of the cross-sections was obtained,

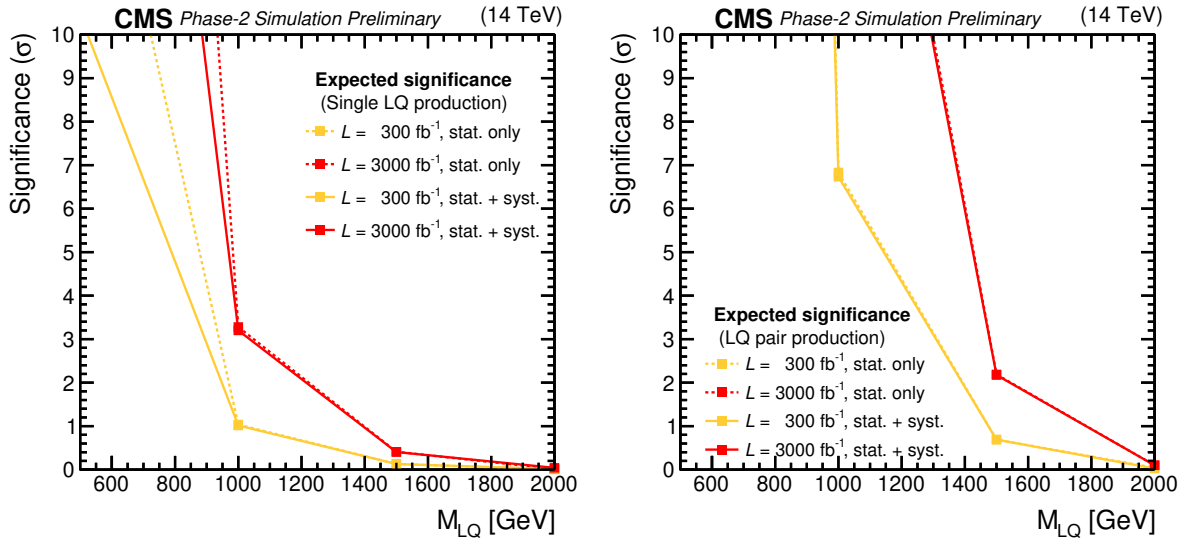

Fig. 96: Expected local significance of a signal-like excess as a function of the LQ mass, for the two high luminosity projections, 300 fb^{-1} (red) and 3000 fb^{-1} (orange), assuming the theoretical prediction for the LQ cross section at NLO [1490], calculated with $\lambda = 1$ and $\beta = 1$. Projections are calculated for both single LQ (left) and LQ pair production (right).

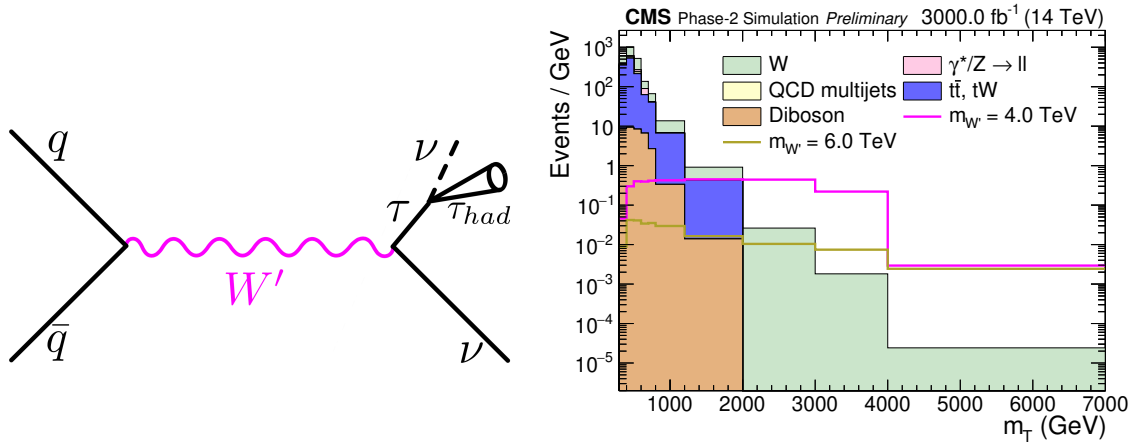

Fig. 97: Left: Illustration of the studied channel $W' \to \tau\nu$ with the subsequent hadronic decay of the tau (τ_h). Right: The discriminating variable, M_T, after all selection criteria for the HL-LHC conditions of 3 ab^{-1} and 200 PU. The relevant SM backgrounds are shown according to the labels in the legend. Signal examples for W′ boson masses of 1 TeV, 5 TeV and 6 TeV are scaled to their SSM LO cross section and 3 ab^{-1}.

and assuming similar kinematics, also the sensitivity for the vector leptoquark U_1.

As shown in Fig. 99, the HE-LHC collider will be able to probe pair produced third generation scalar leptoquark (decaying exclusively to $b\tau$ final state) up to mass of ~ 4 TeV and vector leptoquark up to ~ 4.5 TeV and ~ 5.2 TeV for the minimal coupling and Yang-Mills scenarios, respectively. While this result is obtained by a rather crude analysis, it shows the impressive reach of the future high-energy pp-collider. In particular, the HE-LHC will cut deep into the relevant perturbative parameter space for $b \to c\tau\nu$ anomaly. As a final comment, this is a rather conservative estimate of the sensitivity to leptoquark models solving $R(D^*)$ anomaly, since a dedicated single leptoquark production search is

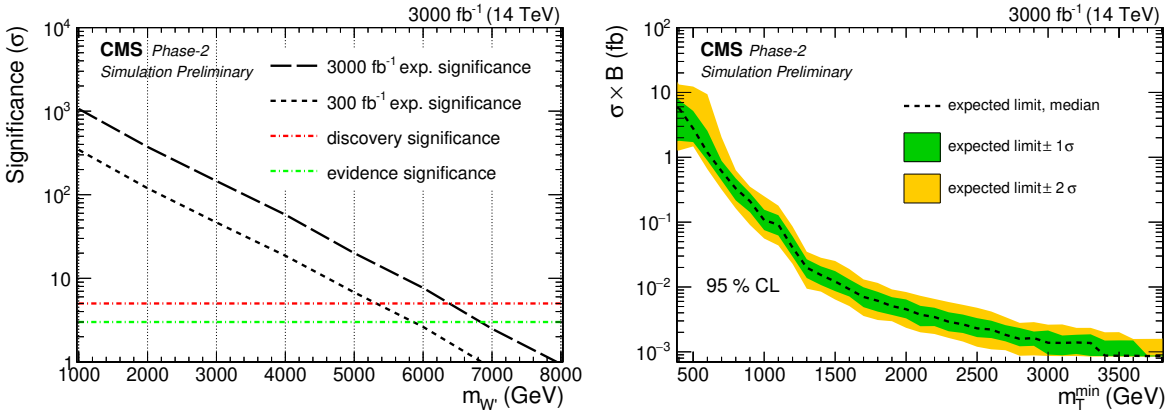

Fig. 98: Left: Discovery significance for SSM W′ to tau leptons. Right: Model-independent cross section limit. For this, a single-bin limit is calculated for increasing $M_T^{\min}$ while keeping the signal yield constant in order to avoid including any signal shape information on this limit calculation.

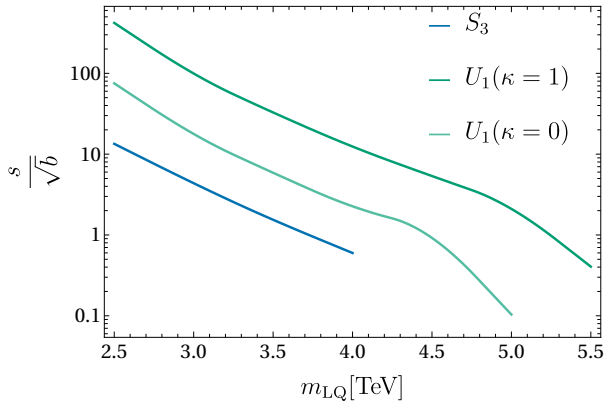

Fig. 99: Expected sensitivity for pair production of scalar (S_3) and vector (U_1) leptoquark at 27 TeV pp collider with an integrated luminosity of 15 ab^{-1}.

expected to yield even stronger bounds [265, 1490].

11 Lattice QCD in the HL/HE-LHC era

Authors (TH): Michele Della Morte, Elvira Gámiz, Enrico Lunghi.

We discuss the ten-year projections described in Sect. 2 for the lattice inputs on hadronic parameters, by presenting the current status and reviewing the main sources of uncertainty for different quantities. A naive application of Moore's law (computing power doubling each two years) would give a reduction in the errors by a factor around 3 by 2025. However, such an extrapolation is not always appropriate since the dominant uncertainties are often systematic. For this reason attempting to extrapolate even farther in the future is subject to very large uncertainties. The lattice approach is systematically improvable by construction, however in order to almost completely remove the main systematic affecting current computations one would have to extrapolate the performance of present algorithms to unexplored regions of parameters. Any such extrapolation would be quite unreliable. It is anyway reasonable to expect that by 2030 the uncertainties related to the inclusion of electromagnetic effects, where relevant, will be removed.

The last FLAG review [66], or its online version [10], still provides an almost up-to-date picture of the precision reached so far. For example, the target accuracy on f_{B_s} and the ratio f_{B_s}/f_{B_d} of about 0.4% has already been achieved. The latest $N_f = 2+1+1$ results by the FNAL/MILC Collaboration in [822] quote very similar errors for those two quantities. Electromagnetic corrections (together with the known long- and short-distance electroweak contributions) in that case are directly subtracted from the experimental decay rate quoted by PDG, such that the decay constant, which is purely a QCD quantity, is the only hadronic parameter needed for the extraction of $|V_{ub}|$ from leptonic B-decays. Alternatively, one could consider the full transition rate on the lattice, as proposed in [1517], and further discussed in [1518] concerning several subtleties arising in a straightforward application of the method to heavy-meson decays.

In addition to the inclusion of isospin breaking corrections, the most important limiting factor in the achievable precision of future lattice computations of decay constants is probably going to be the scale setting, i.e., the conversion from lattice units to MeV. This is quite obviously important for dimensionful quantities, but it is also critical for some dimensionless ones, e.g., the hadronic contribution to the anomalous magnetic moment of the muon, where one needs to convert the muon mass to lattice units (see [1519] for a detailed discussion of this point). The current precision in the knowledge of the lattice spacing is at the half-percent level. Going beyond that is challenging, as one needs a quantity which is both very well known experimentally and precisely computable on the lattice, with both small statistical as well as systematic uncertainties. Future strategies may involve combining/averaging several quantities for the scale setting. [11] On the other hand, ratios of decay constants can be obtained very precisely from lattice simulations, especially for light mesons, in which case discretization effects are not as severe as for heavy-light mesons. For example, the last calculations of the ratio of decay constants $f_{K^\pm}/f_{\pi^\pm}$ has reached a 0.15% error [822].

We turn next to the bag parameter B_K, relevant for the theoretical prediction of ε_K, which encodes indirect CP-violation in the neutral kaon system. The global estimate from FLAG for the $N_f = 2+1$ theory has a 1.3% error. Again, the error is systematic-dominated. In particular, one of the largest uncertainties comes from the conversion between the lattice renormalization scheme (e.g., Schrödinger Functional (SF) or MOM) and $\overline{\text{MS}}$. This is typically done at one-loop and to improve on that one needs either a higher order computation [12], or to follow the non-perturbative running up to as large a scale as possible. In the SF scheme, but only in the two-flavor case, the matching scale has been pushed to the elctroweak scale, where truncation errors can be safely neglected [1521]. The FLAG averages of the B_K parameter have been very stable throughout different reviews. The main reason is, at least for the

[10] `http://flag.unibe.ch/`

[11] We acknowledge S. Gottlieb and R. Van de Water for a discussion on this issue.

[12] See Ref. [1520] for recent work in this direction.

2+1 flavor setup, that the final value is dominated by a single computation from 2011 [1522]. It should therefore be possible to significantly reduce the error in the next few years. In fact, with current methods and existing configurations several collaborations can probably reach that precision.

The main hadronic uncertainty in the theoretical prediction of ε_K is currently due to long-distance contributions not captured by the short-distance parameter B_K. An approach for computing those non-perturbatively has been put forward in [1523] and preliminary results have been reported at the last Lattice conferences, with the most recent update in [1524]. Although the parameters in the lattice simulations are not physical, producing rather heavy pions (329 MeV), and only one lattice resolution with $a > 0.1$ fm has been considered, the long distance correction to ε_K is found to be rather large, amounting to about 8(5)% of the experimental value. For a more accurate estimate, the calculation is being repeated with physical kinematics and finer lattice spacings [13]. It is worth pointing out that other approaches (e.g., in [55]) produce values corresponding to a 4% contribution at most. Finally, it has been emphasized in [1525] that the theoretical estimate of ε_K based on lattice inputs strongly depends on the value of V_{cb}. Its current uncertainty, due to the tension between inclusive and exclusive determinations, represents then the largest source of systematic error.

In the B-sector, theoretical predictions of $B_q - \bar{B}_q$ mixing observables in the SM and beyond depend on hadronic matrix elements of local four-fermion operators. Historically, these matrix elements have been parametrized in terms of the so-called bag parameters. In the SM, the mass difference for a B_q^0 meson depends on a single matrix element, proportional to $f_{B_q}^2 \hat{B}_{B_q}$, or, equivalently, on a single bag parameter, $\hat{B}_{B_q}$.

There has been steady progress in the last decade in lattice determinations of these matrix elements, with errors $\sim 4 - 5\%$ for $\hat{B}_{B_q}$ [66]. However, there is still a lot of room for improvement. First of all, current calculations are not done on the last generation ensembles with $N_f = 2 + 1 + 1$, physical light-quark masses, the smallest lattice spacings, and/or the most improved lattice actions. Performing simulations on those ensembles will reduce, and in some cases eliminate, the dominant errors in B-mixing: statistics, continuum and chiral extrapolations, no inclusion of charm quarks on the sea, and heavy-quark discretization. In addition, current calculations with $N_f = 2 + 1$ flavors of sea quarks rely on effective field theories for the description of the b quark. Using a fully relativistic description instead, will further reduce the heavy-quark discretization uncertainty and will also allow more precise renormalization techniques, the other large source of uncertainty. For a particular lattice calculation, either the decay constants f_B and f_{B_s} are obtained within the same analysis in a correlated way, or external inputs are used to get the bag parameters from the extracted matrix elements. The recent and projected progress on the determination of these decay constants will thus partly contribute to the reduction in the bag parameters uncertainty.

All the improvements described above could considerably reduce the error in $\hat{B}_{B_s}$ to a 0.8% level. For the ratio of bag parameters, B_{B_s}/B_{B_d}, the error could be reduced from the current 2% to 0.5% or even less. A similar reduction can be achieved for the bag parameters describing the BSM contributions to the mixing. On-going calculations of hadronic matrix elements of NLO operators [1526] will also contribute to a substantial reduction in the uncertainty of $\Delta\Gamma_q$ in the next years.

Matrix elements describing the short-distance contribution to D-meson mixing in the SM and beyond could benefit from a similar error reduction. However, in contrast to B-mixing, D-mixing is dominated by long-distance contributions and thus reducing the error of the short-distance contribution is not so pressing.

Next we review the status and the prospects for lattice computations of form factors for a number of semileptonic decays. The vector form factor at zero momentum transfer, $f_+^{K^0\pi^-}(q^2 = 0)$, needed to extract $|V_{us}|$ from experimental measurements of $K \to \pi\ell\nu$ decay widths, is among the most accurate quantities obtained on the lattice. The most recent calculation of this form factor, not included in the last

[13] See `https://indico.fnal.gov/event/15949/session/3/contribution/151/material/slides/0.pdf`.

FLAG review, has reduced the error to 0.20% [1527], the same level as the experimental error [1528]. The main source of uncertainty on the lattice side is now statistics, which could be reduced by several lattice collaborations, both with $N_f = 2+1$ and $N_f = 2+1+1$, extending their simulations to existing and planned ensembles. Those ensembles include set of configurations with smaller lattice spacings than those that are currently being used for calculations of $f_+^{K^0\pi^-}(q^2=0)$, which will further reduce the total uncertainty. Other important sources of error on current calculations arise from the scale setting and the uncertainty in the input parameters: quark masses and ChPT low energy constants. Better determinations of those parameters, which are needed in the analyses of many observables, are underway or expected. With those improvements the error in $f_+^{K^0\pi^-}(q^2=0)$, including strong isospin-breaking corrections, will be soon enterely dominated by statistics and could achieve the 0.12% level in ten years.

The uncertainty of the experimental average $|V_{us}|f_+^{K^0\pi^-}$, 0.19%, includes errors of the estimated long-distance electromagnetic effects and the difference between strong isospin-breaking effects in charged and neutral modes. Those estimates, which use phenomenology and ChPT techniques, will become dominant sources of error in the future. There are proposals to extend the study of full leptonic transition rates to semileptonic decays [14]. Future calculations on the lattice thus should be able to not only reduce the error on the QCD form factor, but also the electromagnetic and strong isospin-breaking corrections contributing to the experimental uncertainty.

Lattice calculations are not limited to $q^2 = 0$ determination of $f_+^{K^0\pi^-}$. There exist results for the momentum depedence of both the vector and scalar form factors [1529]. The q^2 dependence of $f_+^{K\pi}(q^2)$ obtained in Ref. [1529] agrees very well with experimental data, although the determination of the constants entering in the dispersive parametrization of the energy dependence, usually adopted in experiment, is still less precise when using lattice data. However, in the future, with the improvements discussed above, lattice could provide the most precise evaluation of the phase-space integral for kaon semileptonic decays.

We discuss next three groups of b-hadron form factors of crucial phenomenological importance: heavy meson to stable pseudoscalar meson transitions, $B \to (\pi, K, D)$ and $B_s \to (K, D_s)$; heavy meson to unstable vector meson transitions, $B \to (D^*, K^*))$; and heavy baryon to baryon transitions, $\Lambda_b \to (p, \Lambda_c)$. Form factors in the first group have been calculated by several collaborations, since the presence of a stable final state particle simplifies the analysis. Form factors in the second group are complicated by the presence of an unstable final state meson. While there is a solid theoretical foundation to treat such situation on the lattice [1530], it should be noted that the huge hierarchy $\Gamma_{D^*}/M_{D^*} \sim 4\times10^{-5} \ll \Gamma_{K^*}/M_{K^*} \sim 6\times10^{-2}$ reduces the impact of the final state meson decay for the D^* case. In all cases, lattice calculations have higher accuracy for kinematical configurations in which the final state hadron has low recoil(large q^2) while experimental measurements tend to have better efficiency at large recoil (small q^2).

Moreover, it is important to stress the role of form factors parametrizations which must be used to extrapolate the lattice results at low-q^2, for example the $B \to D^{(*)}$ form factors, or when combining lattice and experimental results in order to extract CKM parameters, e.g., $|V_{cb}|$ and $|V_{ub}|$. As mentioned above, lattice and experiments present differential (binned) distributions which tend to have higher accuracy at low and high recoil, respectively. Their combination covers the whole kinematic spectrum, thus reducing drastically the sensitivity to any given form factor parametrization. In situations in which experiments and/or lattice collaborations perform one sided extrapolations, the impact of the chosen parametrization can be very large (see, for instance, the extraction of $|V_{cb}|$ from $B \to D^*\ell\nu$ discussed in Refs. [31, 32]).

The state of the art for the form factor determinations is represented by the averages in the latest FLAG review [66]. In the following we estimate the theoretical accuracy on the form factors that can

[14] See talk by Chris Sachrajda at Lattice 2018, https://indico.fnal.gov/event/15949/session/3/contribution/163

be achieved over the next eight years and their impact on the extraction of $|V_{ub}|$ and $|V_{cb}|$. As a general rule, we estimate the overall drop in uncertainty to be a factor of 3 both in its statistical and systematic components. Thus, for many calculations the total extrapolated lattice uncertainty drops below the 1% level, at which point QED effects need to be included. This can be done on the lattice either in the quenched QED limit or by explicitly generating mixed QCD-QED configurations. The inclusion of QED corrections to form factors is complicated by IR safety issues which can, nonetheless, be addressed in lattice calculations [1517]. It is likely, but not guaranteed, that QED corrections to the form factors we discuss below will be calculated in the time frame we consider. We consider two scenarios according to whether QED corrections have or have not been calculated; in the latter case we add in quadrature an extra 1% uncertainty.

- $B \to \pi$ and $|V_{ub}|$. The overall point-by-point uncertainty should reduce to the sub-percent level due the adoption of Highly Improved Staggered Quark (HISQ) for heavy quarks on the finer lattices and physical light quark masses. Currently the uncertainty on the extraction of $|V_{ub}|$ from a simultaneous fit of lattice form factors [72, 1531] and binned measurements of the semileptonic branching ratio is 3.7%. The theoretical and experimental contributions to this error can be estimated at the 2.9% and 2.3% level, respectively. A reduction of the lattice uncertainties along the lines mentioned above would naively reduce the former uncertainty to about 1%. As a cautionary note we point out that these estimates are sensitive to the information pertaining to the shape of the form factor, which is controlled by the correlation in the synthetic data and by the accuracy of future experimental results. In conclusion, the theory uncertainty on $|V_{ub}|$ is expected to decrease from 2.9% to 1% (1.4% if QED corrections are not calculated).
- $B \to K$. These form factors have been calculated in Refs. [1532, 1533]. The FLAG average of the various form factors has uncertainties on the first coefficient in the BCL z-expansion of about 2%. Future improvements can push this uncertainty to the 0.7% (1.2%) level according to the assumption on the inclusion of QED corrections.
- $B \to D$ and $|V_{cb}|$. A simultaneous fit of the lattice $B \to D$ form factor [977,978], and experimental data on the semileptonic $B \to D\ell\nu$ branching ratio yields an uncertainty on $|V_{cb}|$ at the 2.5% level. The theoretical and experimental contributions to this error can be estimated as 1.4% and 2.0%, respectively. The lattice contribution to the uncertainty is essentially controlled by the 1.5% error on the coefficients a_0^+ of the BCL z-expansion. Note that in the FLAG fit the zero-recoil value has an uncertainty of only 0.7%: $\mathcal{G}^{B\to D}(1) = 1.059(7)$. Leaving aside the issue that this uncertainty is lower than the conservative ballpark of the missing QED corrections, in order to use this very precise result one needs the corresponding zero-recoil experimental branching ratio which has an uncertainty of about 3%. Clearly the zero-recoil extraction of $|V_{cb}|$ is inferior to the simultaneous fit method. The uncertainty on the form factors is expected to drop by about a factor of 3 and to reach the 0.5% (1.1%) level. Correspondingly, the theory uncertainty on $|V_{cb}|$ is expected to decrease from 1.4% to 0.3% (1%).
- $B_s \to K$, $B_s \to D_s$ and $|V_{ub}|/|V_{cb}|$. These form factors have been calculated in Refs. [72, 1534]. The FLAG average of the various form factors has uncertainties on the first coefficient in the BCL z-expansion of about 4%. Future improvements can push this uncertainty to the 1.3% (1.7%) level according to the assumption on the inclusion of QED corrections. Very recently the authors of Ref. [1535] presented a calculation of the ratio $f_+^{(B\to K)}(0)/f_+^{(B_s\to D_s)}(0)$ with a total uncertainty of 13%, which is expected to reduce to about 4% in the time frame we consider. This would also be the expected theory uncertainty on the extraction of the CKM ratio $|V_{ub}|/|V_{cb}|$ from future measurements. Note that Ref. [1535] presents full information on the q^2 distribution of the two form factors and that once differential experimental results become available the above mentioned theory uncertainty will further decrease.
- $B \to D^*$ and $|V_{cb}|$. There are two calculations of the form factor at zero-recoil [980, 981]. The most precise one in Ref. [980] quotes an uncertainty of 1.4% on $\mathcal{F}^{B\to D^*}(1)$. This uncertainty

includes an estimate of the size of missing QED effects at the 0.5% level. Assuming a factor 3 reduction on lattice uncertainties one projects uncertainties on this form factor at the 0.4% level (the estimate increases to 0.7%, (1.1%) in case QED corrections are not calculated, and are estimated to be 0.5% (1%) in size). We should point out that the Fermilab/MILC collaboration is about to publish a calculation of the form factor at non-zero recoil. This will allow simultaneous theory/experiment fits which are expected to further reduce the uncertainty on $|V_{cb}|$.

- $B \to K^*$. The $B \to K^*$ form factors have been calculated in Refs. [1536, 1537]. These calculations are performed for a stable K^* and, as we mentioned, receive potentially large corrections from the relatively large K^* width. Currently an effort towards implementing the proper decay chain $B \to K^* \to K\pi$ along the lines described in Refs. [221, 536, 1530, 1538–1544] is undergoing. This type of calculation will remove the uncontrolled uncertainty due to the assumption of a stable final state vector meson. Unfortunately, it is too soon to present an estimate on what the expected form factor uncertainty is going to be. Once the first complete result will become available, it will be possible to estimate the expected progression in error reduction as for all the other quantities we have considered.
- $\Lambda_b \to p$, $\Lambda_b \to \Lambda_c$ and $|V_{ub}|/|V_{cb}|$. Currently there is only one calculation of these form factors [71] which allows an extraction of the ratio $|V_{ub}|/|V_{cb}|$ with a theory uncertainty of 4.9%. Over the next few years the total lattice uncertainty on these form factors is expected to reduce by a factor of 2 [1545]. We estimate the improvement over the following decade to be another factor of 2 [15]. This implies that in the time frame we are considering we expect a reduction in the theory uncertainty on $|V_{ub}|/|V_{cb}|$ to the 1.2% (1.6%) level.

An important development from the phenomenological point of view is related to the computation of long-distance effects for rare decays as $K \to \pi\ell^+\ell^-$. A lattice approach has been put forward in [1546] and exploratory results have appeared in [1547]. The extension to $b \to s$ transitions however is by no means straightforward.

In order to make it easily accessible, we collect all the information presented in this Section, including our projections for 2025, in Table 41:

- In the second and third columns we quote the current published best averages of lattice results with references.
- In the fourth column we quote the error corresponding to the published value in the second column and, in parenthesis, the error coming from a couple of recent calculations, significantly reducing current errors, but that either are not published yet ($f_+(0)^{K\to\pi}$) or are not included in the FLAG-2016 averages (decay constants). The latest will be included in the next release of the FLAG averages in 2019.
- Significant reduction of current errors in the decay constants are very unlikely, so we did not quote any numbers for these quantities.
- For semileptonic decays:
  - $X \to Y$ for $|V_{ab}|$ means the theory error in the extraction of $|V_{ab}|$ from that exclusive mode.
  - Fifth column: The two errors correspond to assuming that isospin breaking corrections are calculated by that time (first number) or that they are still estimated phenomenologically (second number in parenthesis).

[15] We thank S. Meinel for a discussion on this point.

Quantity	Published averages	Reference	error (to be published/not in FLAG-2016)	Phase I	Phase II
$f_{K^\pm}$	155.7(7) MeV	$N_f = 2+1$ [66]	0.4%	0.4%	0.4%
$f_{K^\pm}/f_{\pi^\pm}$	1.193(3)	$N_f = 2+1+1$ [66]	0.25%(0.15%, symmet. [822])	0.15%	0.15%
$f_+^{K\to\pi}(0)$	0.9706(27)	$N_f = 2+1+1$ [66]	0.28% (0.20% [1527])	0.12%	0.12%
B_K	0.7625(97)	$N_f = 2+1$ [66]	1.3%	0.7%	0.5%
f_{D_s}	248.83(1.27)	$N_f = 2+1+1$ [66]	0.5%(0.16% [822])	0.16%	0.16%
f_{D_s}/f_{D^+}	1.1716(32)	$N_f = 2+1+1$ [66]	0.27%(0.14% [822])	0.14%	0.14%
f_{B_s}	228.4(3.7)	$N_f = 2+1$ [66]	1.6%(0.56% [822])	0.5%	0.5%
f_{B_s}/f_{B^+}	1.205(7)	$N_f = 2+1+1$ [66]	0.6%(0.4% [822])	0.4%	0.4%
B_{B_s}	1.32(5)/1.35(6)	$N_f = 2/N_f = 2+1$ [66]	$\sim 4\%$	0.8%	0.5%
B_{B_s}/B_{B_d}	1.007(21)/1.032(28)	$N_f = 2/N_f = 2+1$ [66]	2.1%/2.7%	0.5%	0.3%
ξ	1.206(17)	$N_f = 2+1$ [66]	1.4%	0.3%	0.3%
$\overline{m}_c(\overline{m}_c)$	1.275(8) GeV	$N_f = 2+1$ [66]	0.6%	0.4%	0.4%
$B\to\pi$ for $\lvert V_{ub}\rvert_{\rm theor}$		$N_f = 2+1$ [66]	2.9%	1%(1.4%)	1%
$B\to D$ for $\lvert V_{cb}\rvert_{\rm theor}$		$N_f = 2+1$ [66]	1.4%	0.3%(1%)	0.3%
(first param. BCL z-exp.)		$N_f = 2+1$ [66]	1.5%	0.5%(1.1%)	0.5%
$B\to D^*$ for $\lvert V_{cb}\rvert_{\rm theor}$ $h_{A_1}^{B\to D^*}(\omega=1)$		$N_f = 2+1$ [66]	1.4%	0.4%(0.7%)	0.4%
$P_1^{B\to D^*}(\omega=1)$		No LQCD available		1-1.5%	1%
$\Lambda_b\to p(\Lambda_c)$ for $\lvert V_{ub}/V_{cb}\rvert_{\rm theor}$		[71]	4.9%	1.2%(1.6%)	1.2%
$B\to K$ (first param. BCL z-exp.)		$N_f = 2+1$ [66]	2%	0.7%(1.2%)	0.7%
$B_s\to K$ (first param. BCL z-exp.)		$N_f = 2+1$ [66]	4%	1.3%(1.7%)	1.3%

Table 41: Current estimates and projections for lattice QCD determinations of hadronic inputs. In the fourth column we quote the error corresponding to the published value in the second column and, in parenthesis, the error for forthcoming calculations that either are not published yet or are not included in the FLAG-2016 averages. See text for further explanations.

12 Conclusions

Flavour physics has many faces. This becomes already obvious in the Standard Model (SM), where the origin of the flavour structure are the Higgs Yukawa couplings, but which exhibits itself in the flavour non-diagonal couplings of W boson, once we rotate to the quark mass eigenbases. As a result, we can search for signs of New Physics (NP) using flavour probes in many sectors: the Higgs couplings to the SM fermions, be it deviations in the flavour diagonal Yukawa couplings or in searches for flavour violating couplings, or in the flavour changing transitions of top, bottom, charm and strange quarks or of leptons.

HL-LHC and HE-LHC experiments are set to make great strides in almost all of these probes, as exhibited in great detail in this document. The high luminosity programs at ATLAS and CMS are unmatched in their ability to push the precision frontier in measuring Higgs couplings and searching for rare top decays, at the same time expanding their flavour-physics contribution. LHCb with its planned Upgrade II can quite impressively cover a very wide range of low-energy probes in bottom, charm and strange flavor transitions.

These low-energy measurements will bloom in competition with the upgraded Belle-II super B factory, which is coming on line at this very moment. There is also large complementarity between the two programs: The LHC hadronic environment gives access to a larger set of hadronic states such as heavy baryons and a larger sample of B_s mesons. The HL/HE-LHC upgrades will push well past the benchmarks set by Belle-II for many measurements in the near future.

In turn, this complementarity is very timely, given the tantalizing hints for NP surfacing in measurements of semi-tauonic and rare semi-muonic B-decays which suggest that Lepton Universality may be broken by new dynamics in the TeV range. The flavor anomalies thus lead to a different type of complementarity, between the low-energy flavor probes and the direct searches of NP at high $p_{\rm T}$ in ATLAS and CMS. This interplay is especially prolific in the context of model building, where the anomalies can be fitted into the more ambitious BSM program. Therefore, the HL/HE-LHC programme has the potential to shape the NP to come, in case the anomalies are confirmed in the coming years.

Finally, it is important to note that the projected advancements in experiments are set to be accompanied by improvements in theory most notably in the calculations of the hadronic matrix elements by lattice QCD simulations. These matrix elements are required for the precision flavour-physics program, to convert the measurements in constraints or to lead to unambiguous discoveries of NP through the effects of their virtual corrections. In addition, the capabilities of LHCb to chart the spectrum and properties of resonances and exotic states in QCD, will lead to a better understanding of the nonperturbative phenomena. The combined improvements in the theoretical predictions, along with HL/HE-LHC experimental achievements are set to enhance the current reach on the NP physics mass scale by a factor as large as four. This represents a significant advance, with real discovery potential.

13 Acknowledgements

We would like to thank the LHC experimental Collaborations and the WLCG for their essential support. We are especially grateful for the efforts by the computing, generator and validation groups who were instrumental for the creation of large simulation samples. We thank the detector upgrade groups as well as the physics and performance groups for their input. We acknowledge support from CERN and from the national agencies: CAPES, CNPq, FAPERJ and FINEP (Brazil); MOST and NSFC (China); CNRS/IN2P3 (France); BMBF, DFG and MPG (Germany); INFN (Italy); NWO (Netherlands); MNiSW and NCN (Poland); MEN/IFA (Romania); MSHE (Russia); MinECo (Spain); SNSF and SER (Switzerland); NASU (Ukraine); STFC (United Kingdom); NSF (USA). We acknowledge the computing resources that are provided by CERN, IN2P3 (France), KIT and DESY (Germany), INFN (Italy), SURF (Netherlands), PIC (Spain), GridPP (United Kingdom), RRCKI and Yandex LLC (Russia), CSCS (Switzerland), IFIN-HH (Romania), CBPF (Brazil), PL-GRID (Poland) and OSC (USA). We are indebted to the communities behind the multiple open-source software packages on which we depend. Individual authors have received support from AvH Foundation (Germany); EPLANET, Marie Skłodowska-Curie Actions and ERC (European Union); ANR, Labex P2IO and OCEVU, and Région Auvergne-Rhône-Alpes (France); Key Research Program of Frontier Sciences of CAS, CAS PIFI, and the Thousand Talents Program (China); RFBR, RSF and Yandex LLC (Russia); GVA, XuntaGal and GENCAT (Spain); the Royal Society and the Leverhulme Trust (United Kingdom); Laboratory Directed Research and Development program of LANL (USA). Not least, we thank the many colleagues who have provided useful comments on the analyses. We thank I. Bigi, S. Hudan, A. Khodjamirian, E. Kou, L. Maiani, J. Portolés and K. Trabelsi for useful comments. J. Martín Camalich acknowledges support from the Spanish MINECO through the "Ramón y Cajal" program RYC-2016-20672. J. Zupan acknowledges support in part by the DOE grant de-sc0011784. W. Altmannshofer acknowledges the National Science Foundation under Grant No. NSF-1912719. F. Bishara acknowledges the Marie Skłodowska-Curie Individual Fellowship of the European Commission's Horizon 2020 Programme under contract number 745954 Tau-SYNERGIES. A. Carmona acknowledges the Cluster of Excellence Precision Physics, Fundamental Interactions and Structure of Matter (PRISMA-EXC1098) and grant 05H18UMCA1 of the German Federal Ministry for Education and Research (BMBF). M. Chala acknowledges the Royal Society under the Newton International Fellowship programme. A. Crivellin acknowledges the Ambizione grant of the Swiss National Science Foundation (PZ00P2 154834). W. Dekens acknowledges the US Department of Energy Grant No. DE-SC0009919. S. Descotes-Genon acknowledges the EU Horizon 2020 program from the grants No. 690575, No. 674896 and No. 692194. A. Esposito acknowledges the Swiss National Science Foundation under contract 200020-169696 and through the National Center of Competence in Research SwissMAP R. Fleischer acknowledges the Dutch National Organisation for Scientific Research (NWO). E. Gámiz acknowledges the Spanish State Research Agency (FPA2016-78220-C3-3-P) and Junta de Andalucía (FQM 101). L.-S. Geng acknowledges the National Science Foundation of China, Grant Nos. 11522539 and 11735003. B. Grinstein acknowledges the US Depatment of Energy, Grant DE-SC0009919. F.-K. Guo acknowledges the National Natural Science Foundation of China (NSFC) (Grant Nos. 11621131001, 11747601, and 11835015), the CAS Key Research Program of Frontier Sciences (Grant No. QYZDB-SSWSYS013), the CAS Key Research Program (Grant No. XDPB09), the CAS Center for Excellence in Particle Physics. S. Jäger acknowledges the UK STFC Consolidated Grant ST/P000819/1. R. Lebed acknowledges the U.S. National Science Foundation, Grant No. PHY-1803912. A. Lenz acknowledges the STFC through the IPPP grant. J. Matias has been supported by the Catalan ICREA Academia Program and acknowledges the FPA2014-55613-P and FPA2017-86989-P and 2017 SGR 1069. O. Matsedonskyi acknowledges the IASH postdoctoral fellowship for foreign researchers. J. Nieves acknowledges the Spanish State Research Agency (FIS2017-84038-C2-1-P and SEV-2014-0398). Y. Nir acknowledges the ISF, BSF, I-CORE, Minerva. A. A. Petrov acknowledges the U.S. Department of Energy, DE-SC0007983. T. Pich acknowledges the Spanish State Research Agency (FPA2017-84445-P) and Generalitat Valenciana [Prometeo/2017/053]. S. Prelovsek acknowledges the Slovenian Research Agency (No. J1-8137 and No. P1-0035) and DFG Grant SFB/TRR 55. S. Schacht ac-

knowledges the DFG Forschungsstipendium under contract no. SCHA 2125/1-1. D. Shih acknowledges the US Department of Energy Grant SC0010008. L. Silvestrini acknowledges the European Research Council (ERC) under the European Union's Horizon 2020 research and innovation program (grant agreement n^o 772369). D. van Dyk acknowledges the Deutsche Forschungsgemeinschaft (DFG) within the Emmy Noether programme under grant DY 130/1-1 and through the DFG Collaborative Research Center 110 "Symmetries and the Emergence of Structure in QCD". J. Virto acknowledges the European Union's Horizon 2020 research and innovation programme under the Marie Sklodowska-Curie grant agreement No 700525, 'NIOBE'. W. Wang acknowledges the National Science Foundation of China, Grant Nos. 11575110, 11655002, 11735010.

Appendices

A Details on experimental extrapolations

A.1 Analysis methods and objects definitions

Different approaches have been used by the experiments and in theoretical prospect studies, hereafter named projections, to assess the sensitivity in searching for new physics at the HL-LHC and HE-LHC. For some of the projections, a mix of the approaches described below is used, in order to deliver the most realistic result. The total integrated luminosity for the HL-LHC dataset is assumed to be 3000 fb^{-1} at a center-of-mass energy of 14 TeV. For HE-LHC studies the dataset is assumed to be 15 ab^{-1} at a center-of-mass of 27 TeV. The effect of systematic uncertainties is taken into account based on the studies performed for the existing analyses and using common guidelines for projecting the expected improvements that are foreseen thanks to the large dataset and upgraded detectors, as described in Section A.2.

Detailed-simulations are used to assess the performance of reconstructed objects in the upgraded detectors and HL-LHC conditions, as described in Sections A.1.1,A.1.2. For some of the projections, such simulations are directly interfaced to different event generators, parton showering (PS) and hadronisation generators. Monte Carlo (MC) generated events are used for standard model (SM) and beyond-the-standard-model (BSM) processes, and are employed in the various projections to estimate the expected contributions of each process.

Extrapolations of existing results rely on the existent statistical frameworks to estimate the expected sensitivity for the HL-LHC dataset. The increased center-of-mass energy and the performance of the upgraded detectors are taken into account for most of the extrapolations using scale factors on the individual processes contributing to the signal regions. Such scale factors are derived from the expected cross sections and from detailed simulation studies.

Fast-simulations are employed for some of the projections in order to produce a large number of Monte Carlo events and estimate their reconstruction efficiency for the upgraded detectors. The upgraded CMS detector performance is taken into account encoding the expected performance of the upgraded detector in `Delphes` [374], including the effects of pile-up interactions. Theoretical contributions use `Delphes` [374] with the commonly accepted HL-LHC card corresponding to the upgraded ATLAS and CMS detectors.

Parametric-simulations are used for some of the projections to allow a full re-optimization of the analysis selections that profit from the larger available datasets. Particle-level definitions are used for electrons, photons, muons, taus, jets and missing transverse momentum. These are constructed from stable particles of the MC event record with a lifetime larger than 0.3×10^{-10} s within the observable pseudorapidity range. Jets are reconstructed using the anti-k_t algorithm [1508] implemented in the `Fastjet` [1548] library, with a radius parameter of 0.4. All stable final-state particles are used to reconstruct the jets, except the neutrinos, leptons and photons associated to W or Z boson or τ lepton decays. The effects of an upgraded ATLAS detector are taken into account by applying energy smearing, efficiencies and fake rates to generator level quantities, following parameterisations based on detector performance studies with the detailed simulations. The effect of the high pileup at the HL-LHC is incorporated by overlaying pileup jets onto the hard-scatter events. Jets from pileup are randomly selected as jets to be considered for analysis with $\sim 2\%$ efficiency, based on studies of pile-up jet rejection and current experience.

A.1.1 ATLAS and CMS performance

The expected performance of the upgraded ATLAS and CMS detectors has been studied in detail in the context of the Technical Design Reports and subsequent studies; the assumptions used for this report and a more detailed description are available in Ref. [1,1549]. For CMS, the object performance in the central region assumes a barrel calorimeter aging corresponding to an integrated luminosity of 1000 fb^{-1}.

The triggering system for both experiments will be replaced and its impact on the triggering abilities of each experiment assessed; new capabilities will be added, and, despite the more challenging conditions, most of the trigger thresholds for common objects are expected to either remain similar to the current ones or to even decrease [1550, 1551]. The inner detector is expected to be completely replaced by both experiments, notably extending its coverage to $|\eta| < 4.0$. The performance for reconstructing charged particles has been studied in detail in Ref. [168, 1552, 1553]. Electrons and photons are reconstructed from energy deposits in the electromagnetic calorimeter and information from the inner tracker [4, 1554–1556]. Several identification working points have been studied and are employed by the projection studies as most appropriate. Muons are reconstructed combining muon spectrometer and inner tracker information [436, 1557].

Jets are reconstructed by clustering energy deposits in the electromagnetic and hadronic calorimeters [1554, 1555, 1558] using the anti-k_T algorithm [1508]. B-jets are identified via b-tagging algorithms. B-tagging is performed if the jet is within the tracker acceptance ($|\eta| < 4.0$). Multivariate techniques are employed in order to identify $b-$jets and $c-$jets, and were fully re-optimized for the upgraded detectors [168, 1552]. An 70% $b-$jet efficiency working point is used, unless otherwise noted. High p_T boosted jets are reconstructed using large-radius anti-k_T jets with a distance parameter of 0.8. Various jet substructure variables are employed to identify boosted W/Z/Higgs boson and top quark jets with good discrimination against generic QCD jets.

Missing transverse energy is reconstructed following similar algorithms as employed in the current data taking. Its performance has been evaluated for standard processes, such as top pair production [1552, 1559]. The addition of new precise-timing detectors and its effect on object reconstruction has also been studied in Ref. [4, 1560], although its results are only taken into account in a small subset of the projections in this report.

A.1.2 LHCb

The LHCb upgrades are shifted with respect to those of ATLAS and CMS. A first upgrade will happen at the end of Run 2 of the LHC, to run at a luminosity five times larger ($2 \times 10^{33}\text{cm}^{-2}\text{s}^{-1}$) in LHC Run 3 compared to those in Runs 1 and 2, while maintaining or improving the current detector performance. This first upgrade phase (named Upgrade I) will be followed by by the so-called Upgrade II phase (planned at the end of Run 4) to run at an even more challenging luminosity of $\sim 2\times10^{34}\text{cm}^{-2}\text{s}^{-1}$.

The LHCb MC simulation used in this document mainly relies on the `Pythia8` generator [1561] with a specific LHCb configuration [1562], using the CTEQ6 leading-order set of parton density functions [1563]. The interaction of the generated particles with the detector, and its response, are implemented using the `Geant4` toolkit [1564, 1565], as described in Ref. [1566].

The reconstruction of jets is done using a particle flow algorithm, with the output of this clustered using the anti-kT algorithm as implemented in `Fastjet`, with a distance parameter of 0.5. Requirements are placed on the candidate jet in order to reduce the background formed by particles which are either incorrectly reconstructed or produced in additional pp interactions in the same event. Concerning the increased pile-up, different assumptions are made, but in general the effect is assumed to be similar to the one in Run 2.

A.2 Treatment of systematic uncertainties

It is a significant challenge to predict the expected systematic uncertainties of physics results at the end of HL-LHC running. It is reasonable to anticipate improvements to techniques of determining systematic uncertainties over an additional decade of data-taking. To estimate the expected performance, experts in the various physics objects and detector systems from ATLAS and CMS have looked at current limitations to systematic uncertainties in detail to determine which contributions are limited by statistics and where there are more fundamental limitations. Predictions were made taking into account the increased

integrated luminosity and expected potential gains in technique. These recommendations were then harmonized between the experiments to take advantage of a wider array of expert opinions and to allow the experiments to make sensitivity predictions on equal footing [1, 1549]. For theorists' contributions, a simplified approach is often adopted, loosely inspired by the improvements predicted by experiments.

General guide-lining principles were defined in assessing the expected systematic uncertainties. Theoretical uncertainties are assumed to be reduced by a factor of two with respect to the current knowledge, thanks to both higher-order calculation as well as reduced PDF uncertainties [1567]. All the uncertainties related to the limited number of simulated events are neglected, under the assumption that sufficiently large simulation samples will be available by the time the HL-LHC becomes operational. For all scenarios, the intrinsic statistical uncertainty in the measurement is reduced by a factor $1/\sqrt{\mathrm{L}}$, where L is the projection integrated luminosity divided by that of the reference Run 2 analysis. Systematics driven by intrinsic detector limitations are left unchanged, or revised according to detailed simulation studies of the upgraded detector. Uncertainties on methods are kept at the same value as in the latest public results available, assuming that the harsher HL-LHC conditions will be compensated by method improvements.

The uncertainty in the integrated luminosity of the data sample is expected to be reduced down to 1% by a better understanding of the calibration methods and their stability employed in its determination, and making use of the new capabilities of the upgraded detectors.

In addition to the above scenario (often referred to as "YR18 systematics uncertainties" scenario), results are often compared to the case where the current level of understanding of systematic uncertainties is assumed ("Run 2 systematic uncertainties") or to the case of statistical-only uncertainties.

References

[1] The CMS Collaboration, *Expected performance of the physics objects with the upgraded CMS detector at the HL-LHC*, CERN-CMS-NOTE-2018-006, CERN, Geneva, Dec, 2018. https://cds.cern.ch/record/2650976.

[2] ATLAS Collaboration, *Expected performance of the ATLAS detector at the High-Luminosity LHC*, ATL-PHYS-PUB-2019-005, CERN, Geneva, Jan, 2019. http://cds.cern.ch/record/2655304.

[3] A. J. Buras and J. Girrbach, *Towards the Identification of New Physics through Quark Flavour Violating Processes*, Rept. Prog. Phys. **77** (2014) 086201, arXiv:1306.3775 [hep-ph].

[4] The CMS Collaboration, *TECHNICAL PROPOSAL FOR A MIP TIMING DETECTOR IN THE CMS EXPERIMENT PHASE 2 UPGRADE* , CERN-LHCC-2017-027 ; LHCC-P-009, CERN, Geneva, 2017. https://cds.cern.ch/record/2296612.

[5] LHCb collaboration, R. Aaij et al., *Test of lepton universality using $B^+ \to K^+\ell^+\ell^-$ decays*, Phys. Rev. Lett. **113** (2014) 151601, arXiv:1406.6482 [hep-ex].

[6] LHCb collaboration, R. Aaij et al., *Test of lepton universality with $B^0 \to K^{*0}\ell^+\ell^-$ decays*, JHEP **08** (2017) 055, arXiv:1705.05802 [hep-ex].

[7] LHCb collaboration, R. Aaij et al., *Measurement of CP asymmetry in $B_s^0 \to D_s^{\mp}K^{\pm}$ decays*, JHEP **03** (2018) 059, arXiv:1712.07428 [hep-ex].

[8] LHCb collaboration, *Update of the LHCb combination of the CKM angle γ using $B \to DK$ decays*, May, 2018.

[9] LHCb collaboration, R. Aaij et al., *Measurement of CP violation in $B^0 \to J/\psi K_S^0$ and $B^0 \to \psi(2S)K_S^0$ decays*, JHEP **11** (2017) 170, arXiv:1709.03944 [hep-ex].

[10] LHCb collaboration, R. Aaij et al., *Precision measurement of CP violation in $B_s^0 \to J/\psi K^+K^-$ decays*, Phys. Rev. Lett. **114** (2015) 041801, arXiv:1411.3104 [hep-ex].

[11] LHCb collaboration, R. Aaij et al., *Measurement of the CP-violating phase ϕ_s in $\overline{B}_s^0 \to D_s^+D_s^-$ decays*, Phys. Rev. Lett. **113** (2014) 211801, arXiv:1409.4619 [hep-ex].

[12] LHCb collaboration, R. Aaij et al., *Measurement of CP violation in $B_s^0 \to \phi\phi$ decays*, Phys. Rev. **D90** (2014) 052011, arXiv:1407.2222 [hep-ex].

[13] LHCb collaboration, R. Aaij et al., *Measurement of the CP asymmetry in B_s^0–$\overline{B}_s^0$ mixing*, Phys. Rev. Lett. **117** (2016) 061803, arXiv:1605.09768 [hep-ex].

[14] LHCb collaboration, R. Aaij et al., *Determination of the quark coupling strength $|V_{ub}|$ using baryonic decays*, Nature Physics **11** (2015) 743, arXiv:1504.01568 [hep-ex].

[15] LHCb collaboration, R. Aaij et al., *Measurement of the $B_s^0 \to \mu^+\mu^-$ branching fraction and effective lifetime and search for $B^0 \to \mu^+\mu^-$ decays*, Phys. Rev. Lett. **118** (2017) 191801, arXiv:1703.05747 [hep-ex].

[16] LHCb collaboration, R. Aaij et al., *Measurement of the ratio of branching fractions $\mathcal{B}(\overline{B}^0 \to D^{*+}\tau^-\overline{\nu}_\tau)/\mathcal{B}(\overline{B}^0 \to D^{*+}\mu^-\overline{\nu}_\mu)$*, Phys. Rev. Lett. **115** (2015) 111803, arXiv:1506.08614 [hep-ex].

[17] LHCb collaboration, R. Aaij et al., *Test of lepton flavor universality by the measurement of the $B^0 \to D^{*-}\tau^+\nu_\tau$ branching fraction using three-prong τ decays*, Phys. Rev. **D97** (2018) 072013, arXiv:1711.02505 [hep-ex].

[18] LHCb collaboration, R. Aaij et al., *Measurement of the ratio of branching fractions $\mathcal{B}(B_c^+ \to J/\psi\tau^+\nu_\tau)/\mathcal{B}(B_c^+ \to J/\psi\mu^+\nu_\mu)$*, Phys. Rev. Lett. **120** (2018) 121801, arXiv:1711.05623 [hep-ex].

[19] LHCb collaboration, R. Aaij et al., *Measurement of the difference of time-integrated CP asymmetries in $D^0 \to K^-K^+$ and $D^0 \to \pi^-\pi^+$ decays*, Phys. Rev. Lett. **116** (2016) 191601, arXiv:1602.03160 [hep-ex].

[20] LHCb collaboration, R. Aaij et al., *Measurement of the CP violation parameter A_Γ in $D^0 \to K^+K^-$ and $D^0 \to \pi^+\pi^-$ decays*, Phys. Rev. Lett. **118** (2017) 261803, arXiv:1702.06490 [hep-ex].

[21] LHCb collaboration, R. Aaij et al., *Updated determination of D^0-$\overline{D}^0$ mixing and CP violation parameters with $D^0 \to K^+\pi^-$ decays*, Phys. Rev. **D97** (2018) 031101, arXiv:1712.03220 [hep-ex].

[22] LHCb Collaboration, R. Aaij et al., *Physics case for an LHCb Upgrade II - Opportunities in flavour physics, and beyond, in the HL-LHC era*, arXiv:1808.08865.

[23] N. Cabibbo, *Unitary Symmetry and Leptonic Decays*, Phys. Rev. Lett. **10** (1963) 531–533.

[24] M. Kobayashi and T. Maskawa, *CP Violation in the Renormalizable Theory of Weak Interaction*, Prog. Theor. Phys. **49** (1973) 652–657.

[25] L. Wolfenstein, *Parametrization of the Kobayashi-Maskawa Matrix*, Phys. Rev. Lett. **51** (1983) 1945.

[26] FlaviaNet Working Group on Kaon Decays Collaboration, M. Antonelli et al., *An Evaluation of $|V_{us}|$ and precise tests of the Standard Model from world data on leptonic and semileptonic kaon decays*, Eur. Phys. J. **C69** (2010) 399–424, arXiv:1005.2323 [hep-ph].

[27] J. C. Hardy and I. S. Towner, *Superallowed $0^+ \to 0^+$ nuclear decays: 2014 critical survey, with precise results for V_{ud} and CKM unitarity*, Phys. Rev. **C91** (2015) no. 2, 025501, arXiv:1411.5987 [nucl-ex].

[28] I. S. Towner and J. C. Hardy, *Theoretical corrections and world data for the superallowed ft values in the β decays of ^{42}Ti, ^{46}Cr, ^{50}Fe and ^{54}Ni*, Phys. Rev. **C92** (2015) no. 5, 055505, arXiv:1510.03793 [nucl-th].

[29] J. C. Hardy and I. S. Towner, *Nuclear beta decays and CKM unitarity*, in *13th Conference on the Intersections of Particle and Nuclear Physics (CIPANP 2018) Palm Springs, California, USA, May 29-June 3, 2018*. 2018. arXiv:1807.01146 [nucl-ex].

[30] Belle Collaboration, A. Abdesselam et al., *Measurement of CKM Matrix Element $|V_{cb}|$ from $\bar{B} \to D^{*+}\ell^-\bar{\nu}_\ell$*, arXiv:1809.03290 [hep-ex].

[31] D. Bigi, P. Gambino, and S. Schacht, *A fresh look at the determination of $|V_{cb}|$ from $B \to D^*\ell\nu$*, Phys. Lett. **B769** (2017) 441–445, arXiv:1703.06124 [hep-ph].

[32] B. Grinstein and A. Kobach, *Model-independent extraction of $|V_{cb}|$ from $\bar{B} \to D^*\ell\overline{\nu}$*, Phys. Lett. **B771** (2017) 359–364, arXiv:1703.08170 [hep-ph].

[33] G. D'Agostini, *Sceptical combination of experimental results: General considerations and application to epsilon-prime / epsilon*, Submitted to: Phys. Rev. D (1999) , arXiv:hep-ex/9910036 [hep-ex].

[34] M. Gronau and D. London, *Isospin analysis of CP asymmetries in B decays*, Phys. Rev. Lett. **65** (1990) 3381–3384.

[35] H. J. Lipkin, Y. Nir, H. R. Quinn, and A. Snyder, *Penguin trapping with isospin analysis and CP asymmetries in B decays*, Phys. Rev. **D44** (1991) 1454–1460.

[36] A. E. Snyder and H. R. Quinn, *Measuring CP asymmetry in B —> rho pi decays without ambiguities*, Phys. Rev. **D48** (1993) 2139–2144.

[37] J. Charles, O. Deschamps, S. Descotes-Genon, and V. Niess, *Isospin analysis of charmless B-meson decays*, Eur. Phys. J. **C77** (Aug, 2017) 574, arXiv:1705.02981 [hep-ph]. https://doi.org/10.1140/epjc/s10052-017-5126-9.

[38] CKMfitter collaboration, *Summer 2018 update available on http://ckmfitter.in2p3.fr/*, .

[39] M. Gronau and J. Zupan, *Isospin-breaking effects on alpha extracted in $B \to \pi\pi, \rho\rho, \rho\pi$*, Phys. Rev. **D71** (2005) 074017, arXiv:hep-ph/0502139 [hep-ph].

[40] R. Fleischer, *Extracting γ from $B(s/d) \to J/\psi K_S$ and $B(d/s) \to D^+(d/s)D^-(d/s)$*, Eur.

Phys. J. **C10** (1999) 299–306, arXiv:hep-ph/9903455 [hep-ph].

[41] M. Ciuchini, M. Pierini, and L. Silvestrini, *The effect of penguins in the $B^0 \to J/\psi K^0$ CP asymmetry*, Phys. Rev. Lett. **95** (2005) 221804, arXiv:hep-ph/0507290 [hep-ph].

[42] S. Faller, M. Jung, R. Fleischer, and T. Mannel, *The golden modes $B^0 \to J/\psi K_{\rm S,L}$ in the era of precision flavour physics*, Phys. Rev. **D79** (2009) 014030, arXiv:0809.0842 [hep-ph].

[43] M. Ciuchini, M. Pierini, and L. Silvestrini, *Theoretical uncertainty in sin 2β: An Update*, in *CKM unitarity triangle. Proceedings, 6th International Workshop, CKM 2010, Warwick, UK, September 6-10, 2010*. 2011. arXiv:1102.0392 [hep-ph].

[44] M. Jung, *Determining weak phases from $B \to J/\psi P$ decays*, Phys. Rev. **D86** (2012) 053008, arXiv:1206.2050 [hep-ph].

[45] K. De Bruyn and R. Fleischer, *A roadmap to control penguin effects in $B^0_d \to J/\psi K^0_{\rm S}$ and $B^0_s \to J/\psi\phi$*, JHEP **1503** (2015) 145, arXiv:1412.6834 [hep-ph].

[46] P. Frings, U. Nierste, and M. Wiebusch, *Penguin contributions to CP phases in $B_{d,s}$ decays to charmonium*, arXiv:1503.00859 [hep-ph].

[47] M. Gronau, *Improving bounds on γ in $B^\pm \to DK^\pm$ and $B^{\pm,0}$ßDX$^{\pm,0}_s$*, Phys. Lett. **B557** (2003) 198–206, arXiv:hep-ph/0211282 [hep-ph].

[48] M. Gronau and D. London, *How to determine all the angles of the unitarity triangle from $B^0_{(d)} \to DK_{(s)}$ and $B^0_{(s)} \to D^0\Phi$*, Phys. Lett. **B253** (1991) 483–488.

[49] M. Gronau and D. Wyler, *On determining a weak phase from CP asymmetries in charged B decays*, Phys. Lett. **B265** (1991) 172–176.

[50] D. Atwood, G. Eilam, M. Gronau, and A. Soni, *Enhancement of CP violation in $B^\pm - \to K^\pm_i D^0$ by resonant effects*, Phys. Lett. **B341** (1995) 372–378, arXiv:hep-ph/9409229 [hep-ph].

[51] D. Atwood, I. Dunietz, and A. Soni, *Enhanced CP violation with $B \to KD^0(\bar{D}^0)$ modes and extraction of the CKM angle γ*, Phys.Rev.Lett. **78** (1997) 3257, arXiv:hep-ph/9612433 [hep-ph].

[52] D. Atwood, I. Dunietz, and A. Soni, *Improved methods for observing CP violation in $B^\pm \to KD$ and measuring the CKM phase gamma*, Phys. Rev. **D63** (2001) 036005, arXiv:hep-ph/0008090 [hep-ph].

[53] A. Giri, Y. Grossman, A. Soffer, and J. Zupan, *Determining gamma using $B^\pm \to DK^\pm$ with multibody D decays*, Phys. Rev. **D68** (2003) 054018, arXiv:hep-ph/0303187 [hep-ph].

[54] J. Brod and J. Zupan, *The ultimate theoretical error on γ from $B \to DK$ decays*, JHEP **01** (2014) 051, arXiv:1308.5663 [hep-ph].

[55] A. J. Buras, D. Guadagnoli, and G. Isidori, *On ϵ_K Beyond Lowest Order in the Operator Product Expansion*, Phys. Lett. **B688** (2010) 309–313, arXiv:1002.3612 [hep-ph].

[56] Z. Bai, N. H. Christ, T. Izubuchi, C. T. Sachrajda, A. Soni, and J. Yu, *$K_L - K_S$ Mass Difference from Lattice QCD*, Phys. Rev. Lett. **113** (2014) 112003, arXiv:1406.0916 [hep-lat].

[57] B. Wang, *Results for the mass difference between the long- and short- lived K mesons for physical quark masses*, 2018. arXiv:1812.05302 [hep-lat].

[58] T. Inami and C. S. Lim, *Effects of Superheavy Quarks and Leptons in Low-Energy Weak Processes $K_L \to \mu\bar{\mu}$, $K^+ \to \pi^+\nu\bar{\nu}$ and $K^0 - \bar{K}^0$*, Prog. Theor. Phys. **65** (1981) 297. [Erratum: Prog. Theor. Phys.65,1772(1981)].

[59] A. J. Buras, M. Jamin, and P. H. Weisz, *Leading and Next-to-leading QCD Corrections to ϵ Parameter and $B^0 - \bar{B}^0$ Mixing in the Presence of a Heavy Top Quark*, Nucl. Phys. **B347** (1990) 491–536.

[60] A. Lenz, U. Nierste, J. Charles, S. Descotes-Genon, A. Jantsch, C. Kaufhold, H. Lacker, S. Monteil, V. Niess, and S. T'Jampens, *Anatomy of New Physics in $B - \bar{B}$ mixing*, Phys. Rev.

D83 (2011) 036004, arXiv:1008.1593 [hep-ph].

[61] CKMfitter Group Collaboration, J. Charles, A. Hocker, H. Lacker, S. Laplace, F. R. Le Diberder, J. Malcles, J. Ocariz, M. Pivk, and L. Roos, *CP violation and the CKM matrix: Assessing the impact of the asymmetric B factories*, Eur. Phys. J. **C41** (2005) no. 1, 1–131, arXiv:hep-ph/0406184 [hep-ph].

[62] J. Charles et al., *Predictions of selected flavor observables within the Standard Model*, Phys. Rev. **D84** (2011) 033005, arXiv:1106.4041 [hep-ph].

[63] J. Charles et al., *Current status of the Standard Model CKM fit and constraints on $\Delta F = 2$ New Physics*, Phys. Rev. **D91** (2015) 073007, arXiv:1501.05013 [hep-ph].

[64] A. Hocker, H. Lacker, S. Laplace, and F. Le Diberder, *A New approach to a global fit of the CKM matrix*, Eur. Phys. J. **C21** (2001) 225–259, arXiv:hep-ph/0104062 [hep-ph].

[65] J. Charles, S. Descotes-Genon, V. Niess, and L. Vale Silva, *Modeling theoretical uncertainties in phenomenological analyses for particle physics*, Eur. Phys. J. **C77** (2017) no. 4, 214, arXiv:1611.04768 [hep-ph].

[66] S. Aoki et al., *Review of lattice results concerning low-energy particle physics*, Eur. Phys. J. **C77** (2017) no. 2, 112, arXiv:1607.00299 [hep-lat].

[67] M. Ciuchini, G. D'Agostini, E. Franco, V. Lubicz, G. Martinelli, F. Parodi, P. Roudeau, and A. Stocchi, *2000 CKM triangle analysis: A Critical review with updated experimental inputs and theoretical parameters*, JHEP **07** (2001) 013, arXiv:hep-ph/0012308 [hep-ph].

[68] UTfit collaboration, *Summer 2018 update available at http://www.utfit.org/UTfit/ResultsSummer2018*, .

[69] F. U. Bernlochner, Z. Ligeti, M. Papucci, and D. J. Robinson, *Tensions and correlations in $|V_{cb}|$ determinations*, Phys. Rev. **D96** (2017) no. 9, 091503, arXiv:1708.07134 [hep-ph].

[70] D. Bigi, P. Gambino, and S. Schacht, *$R(D^*)$, $|V_{cb}|$, and the Heavy Quark Symmetry relations between form factors*, JHEP **11** (2017) 061, arXiv:1707.09509 [hep-ph].

[71] W. Detmold, C. Lehner, and S. Meinel, *$\Lambda_b \to p\ell^-\bar{\nu}_\ell$ and $\Lambda_b \to \Lambda_c\ell^-\bar{\nu}_\ell$ form factors from lattice QCD with relativistic heavy quarks*, Phys. Rev. **D92** (2015) 034503, arXiv:1503.01421 [hep-lat].

[72] J. M. Flynn, T. Izubuchi, T. Kawanai, C. Lehner, A. Soni, R. S. Van de Water, and O. Witzel, *$B \to \pi\ell\nu$ and $B_s \to K\ell\nu$ form factors and $|V_{ub}|$ from 2+1-flavor lattice QCD with domain-wall light quarks and relativistic heavy quarks*, Phys. Rev. **D91** (2015) 074510, arXiv:1501.05373 [hep-lat].

[73] G. Ciezarek, A. Lupato, M. Rotondo, and M. Vesterinen, *Reconstruction of semileptonically decaying beauty hadrons produced in high energy pp collisions*, JHEP **02** (2017) 021, arXiv:1611.08522 [hep-ex].

[74] M. Beneke, G. Buchalla, M. Neubert, and C. T. Sachrajda, *QCD factorization for B —> pi pi decays: Strong phases and CP violation in the heavy quark limit*, Phys. Rev. Lett. **83** (1999) 1914–1917, arXiv:hep-ph/9905312 [hep-ph].

[75] M. Beneke, G. Buchalla, M. Neubert, and C. T. Sachrajda, *QCD factorization for exclusive, nonleptonic B meson decays: General arguments and the case of heavy light final states*, Nucl. Phys. **B591** (2000) 313–418, arXiv:hep-ph/0006124 [hep-ph].

[76] A. J. Buras, J. Girrbach, D. Guadagnoli, and G. Isidori, *On the Standard Model prediction for $\mathcal{B}(B_{s,d} \to \mu^+\mu^-)$*, Eur. Phys. J. **C72** (2012) 2172, arXiv:1208.0934 [hep-ph].

[77] LHCb collaboration, R. Aaij et al., *Measurement of the shape of the $\Lambda_b^0 \to \Lambda_c^+\mu^-\bar{\nu}_\mu$ differential decay rate*, Phys. Rev. **D96** (2017) 112005, arXiv:1709.01920 [hep-ex].

[78] I. I. Bigi, T. Mannel, and N. Uraltsev, *Semileptonic width ratios among beauty hadrons*, Journal of High Energy Physics **2011** (Sep, 2011) 12.

https://doi.org/10.1007/JHEP09(2011)012.

[79] LHCb collaboration, R. Aaij et al., *Measurement of CP observables in $B^\pm \to DK^\pm$ and $B^\pm \to D\pi^\pm$ with two- and four-body D decays*, Phys. Lett. **B760** (2016) 117, arXiv:1603.08993 [hep-ex].

[80] LHCb collaboration, R. Aaij et al., *Measurement of CP observables in $B^\pm \to D^{(*)}K^\pm$ and $B^\pm \to D^{(*)}\pi^\pm$ decays*, Phys. Lett. **B777** (2017) 16, arXiv:1708.06370 [hep-ex].

[81] LHCb collaboration, R. Aaij et al., *Measurement of CP observables in $B^\pm \to DK^{*\pm}$ decays using two- and four-body D-meson final states*, JHEP **11** (2017) 156, arXiv:1709.05855 [hep-ex].

[82] LHCb collaboration, R. Aaij et al., *Measurement of CP violation parameters in $B^0 \to DK^{*0}$ decays*, Phys. Rev. **D90** (2014) 112002, arXiv:1407.8136 [hep-ex].

[83] S. S. Malde, *Synergy of BESIII and LHCb physics programmes*, Oct, 2016. https://cds.cern.ch/record/2223391.

[84] LHCb collaboration, R. Aaij et al., *A study of CP violation in $B^\mp \to Dh^\mp$ ($h = K, \pi$) with the modes $D \to K^\mp\pi^\pm\pi^0$, $D \to \pi^+\pi^-\pi^0$ and $D \to K^+K^-\pi^0$*, Phys. Rev. **D91** (2015) 112014, arXiv:1504.05442 [hep-ex].

[85] A. Bondar and T. Gershon, *On ϕ_3 measurements using $B^- \to D^*K^-$ decays*, Phys. Rev. **D70** (2004) 091503, arXiv:hep-ph/0409281 [hep-ph].

[86] P. K. Resmi, J. Libby, S. Malde, and G. Wilkinson, *Quantum-correlated measurements of $D \to K^0_S\pi^+\pi^-\pi^0$ decays and consequences for the determination of the CKM angle γ*, JHEP **01** (2018) 082, arXiv:1710.10086 [hep-ex].

[87] LHCb collaboration, R. Aaij et al., *Constraints on the unitarity triangle angle γ from Dalitz plot analysis of $B^0 \to DK^+\pi^-$ decays*, Phys. Rev. **D93** (2016) 112018, arXiv:1602.03455 [hep-ex].

[88] LHCb collaboration, R. Aaij et al., *Amplitude analysis of $B^0 \to \overline{D}^0K^+\pi^-$ decays*, Phys. Rev. **D92** (2015) 012012, arXiv:1505.01505 [hep-ex].

[89] T. Gershon and V. V. Gligorov, *CP violation in the B system*, Rept. Prog. Phys. **80** (2017) 046201, arXiv:1607.06746 [hep-ex].

[90] T. Gershon, *On the measurement of the Unitarity Triangle angle γ from $B^0 \to DK^{*0}$ decays*, Phys. Rev. **D79** (2009) 051301, arXiv:0810.2706 [hep-ph].

[91] D. Craik, T. Gershon, and A. Poluektov, *Optimising sensitivity to γ with $B^0 \to DK^+\pi^-$, $D \to K^0_S\pi^+\pi^-$ double Dalitz plot analysis*, Phys. Rev. **D97** (2018) 056002, arXiv:1712.07853 [hep-ph].

[92] LHCb collaboration, R. Aaij et al., *Study of $B^- \to DK^-\pi^+\pi^-$ and $B^- \to D\pi^-\pi^+\pi^-$ decays and determination of the CKM angle γ*, Phys. Rev. **D92** (2015) 112005, arXiv:1505.07044 [hep-ex].

[93] LHCb collaboration, R. Aaij et al., *Studies of the resonance structure in $D^0 \to K^\mp\pi^\pm\pi^+\pi^-$ decays*, Eur. Phys. J. **C78** (2018) 443, arXiv:1712.08609 [hep-ex].

[94] S. Harnew, P. Naik, C. Prouve, J. Rademacker, and D. Asner, *Model-independent determination of the strong phase difference between D^0 and $\bar{D}^0 \to \pi^+\pi^-\pi^+\pi^-$ amplitudes*, JHEP **01** (2018) 144, arXiv:1709.03467 [hep-ex].

[95] LHCb collaboration, R. Aaij et al., *A study of CP violation in $B^\pm \to DK^\pm$ and $B^\pm \to D\pi^\pm$ decays with $D \to K^0_S K^\pm\pi^\mp$ final states*, Phys. Lett. **B733** (2014) 36, arXiv:1402.2982 [hep-ex].

[96] M. Ciuchini, M. Pierini, and L. Silvestrini, *New bounds on the CKM matrix from $B \to K\pi\pi$ Dalitz plot analyses*, Phys. Rev. **D74** (2006) 051301, arXiv:hep-ph/0601233 [hep-ph].

[97] M. Ciuchini, M. Pierini, and L. Silvestrini, *Hunting the CKM weak phase with time-integrated*

Dalitz analyses of $B_s \to K\pi\pi$ decays, Phys. Lett. **B645** (2007) 201–203, arXiv:hep-ph/0602207 [hep-ph].

[98] M. Gronau, D. Pirjol, A. Soni, and J. Zupan, *Improved method for CKM constraints in charmless three-body B and B_s^0 decays*, Phys.Rev. **D75** (2007) 014002, arXiv:hep-ph/0608243 [hep-ph].

[99] M. Gronau, D. Pirjol, A. Soni, and J. Zupan, *Constraint on $\bar{\rho}, \bar{\eta}$ from $B \to K^*\pi$*, Phys.Rev. **D77** (2008) 057504, arXiv:0712.3751 [hep-ph].

[100] I. Bediaga, G. Guerrer, and J. M. de Miranda, *Extracting the quark mixing phase γ from $B^\pm \to K^\pm\pi^+\pi^-$, $B^0 \to K_S\pi^+\pi^-$, and $\bar{B}^0 \to K_S\pi^+\pi^-$*, Phys.Rev. **D76** (2007) 073011, arXiv:hep-ph/0608268 [hep-ph].

[101] J. Charles, S. Descotes-Genon, J. Ocariz, and A. Perez Perez, *Disentangling weak and strong interactions in $B \to K^*(\to K\pi)\pi$ Dalitz-plot analyses*, Eur. Phys. J. **C77** (2017) 561, arXiv:1704.01596 [hep-ph].

[102] N. Rey-Le Lorier and D. London, *Measuring γ with $B \to K\pi\pi$ and $B \to KK\overline{K}$ Decays*, Phys. Rev. **D85** (2012) 016010, arXiv:1109.0881 [hep-ph].

[103] B. Bhattacharya, M. Imbeault, and D. London, *Extraction of the CP-violating phase γ using $B \to K\pi\pi$ and $B \to KK\overline{K}$ decays*, Phys. Lett. **B728** (2014) 206–209, arXiv:1303.0846 [hep-ph].

[104] B. Bhattacharya and D. London, *Using U spin to extract γ from charmless $B \to PPP$ decays*, JHEP **04** (2015) 154, arXiv:1503.00737 [hep-ph].

[105] I. Bediaga, R. E. Blanco, C. Gobel, and R. Mendez-Galain, *A Direct measurement of the CKM angle gamma*, Phys. Rev. Lett. **81** (1998) 4067–4070, arXiv:hep-ph/9804222 [hep-ph].

[106] R. E. Blanco, C. Gobel, and R. Mendez-Galain, *Measuring the CP violating phase gamma using $B^+ \to \pi^+\pi^+\pi^-$ and $B^+ \to K^+\pi^+\pi^-$ decays*, Phys. Rev. Lett. **86** (2001) 2720–2723, arXiv:hep-ph/0007105 [hep-ph].

[107] LHCb collaboration, R. Aaij et al., *Measurement of CP violation in the three-body phase space of charmless $B^\pm$ decays*, Phys. Rev. **D90** (2014) 112004, arXiv:1408.5373 [hep-ex].

[108] BaBar collaboration, B. Aubert et al., *Evidence for direct CP violation from Dalitz-plot analysis of $B^\pm \to K^\pm\pi^\mp\pi^\pm$*, Phys. Rev. **D78** (2008) 012004, arXiv:0803.4451 [hep-ex].

[109] Belle collaboration, C. L. Hsu et al., *Measurement of branching fraction and direct CP asymmetry in charmless $B^+ \to K^+K^-\pi^+$ decays at Belle*, Phys. Rev. **D96** (2017) 031101, arXiv:1705.02640 [hep-ex].

[110] LHCb collaboration, R. Aaij et al., *Measurement of CP violation in $B^0 \to D^\pm\pi^\mp$ decays*, JHEP **06** (2018) 084, arXiv:1805.03448 [hep-ex].

[111] BaBar collaboration, B. Aubert et al., *Measurement of time-dependent CP asymmetries in $B^0 \to D^{(*)\pm}\pi^\mp$ and $B^0 \to D^\pm\rho^\mp$ decays*, Phys. Rev. **D73** (2006) 111101, arXiv:hep-ex/0602049 [hep-ex].

[112] Belle collaboration, F. Ronga et al., *Measurements of CP violation in $B^0 \to D^{*-}\pi^+$ and $B^0 \to D^-\pi^+$ decays*, Phys. Rev. **D73** (2006) 092003, arXiv:hep-ex/0604013 [hep-ex].

[113] K. De Bruyn, R. Fleischer, R. Knegjens, M. Merk, M. Schiller, and N. Tuning, *Exploring $B_s \to D_s^{(*)\pm}K^\mp$ decays in the presence of a sizable width difference $\Delta\Gamma_s$*, Nucl. Phys. **B868** (2013) 351–367, arXiv:1208.6463 [hep-ph].

[114] LHCb collaboration, R. Aaij et al., *Measurement of CP asymmetries in two-body $B^0_{(s)}$-meson decays to charged pions and kaons*, Phys. Rev. **D98** (2018) 032004, arXiv:1805.06759 [hep-ex].

[115] LHCb collaboration, R. Aaij et al., *Measurement of the CKM angle γ using $B^\pm \to DK^\pm$ with $D \to K^0_S\pi^+\pi^-$, $K^0_S K^+K^-$ decays*, JHEP **08** (2018) 176, arXiv:1806.01202 [hep-ex].

[116] LHCb collaboration, R. Aaij et al., *A precise measurement of the B^0 meson oscillation frequency*, Eur. Phys. J. **C76** (2016) 412, arXiv:1604.03475 [hep-ex].

[117] LHCb collaboration, R. Aaij et al., *Precision measurement of the B_s^0–$\overline{B}_s^0$ oscillation frequency in the decay $B_s^0 \to D_s^- \pi^+$*, New J. Phys. **15** (2013) 053021, arXiv:1304.4741 [hep-ex].

[118] A. Lenz and U. Nierste, *Theoretical update of $B_s^0 - \overline{B}_s^0$ mixing*, JHEP **06** (2007) 072, arXiv:hep-ph/0612167 [hep-ph].

[119] LHCb collaboration, R. Aaij et al., *Precision measurement of the ratio of the Λ_b^0 to $\overline{B}^0$ lifetimes*, Phys. Lett. **B734** (2014) 122, arXiv:1402.6242 [hep-ex].

[120] LHCb collaboration, R. Aaij et al., *Measurement of the semileptonic CP asymmetry in B^0–$\overline{B}^0$ mixing*, Phys. Rev. Lett. **114** (2015) 041601, arXiv:1409.8586 [hep-ex].

[121] Y.-Y. Keum and U. Nierste, *Probing penguin coefficients with the lifetime ratio tau (B-s) / tau (B-d)*, Phys. Rev. **D57** (1998) 4282–4289, arXiv:hep-ph/9710512 [hep-ph].

[122] A. Davis, L. Dufour, F. Ferrari, S. Stahl, M. A. Vesterinen, and J. Van Tilburg, *Measurement of the instrumental asymmetry for $K^-\pi^+$-pairs at LHCb in Run 2*, Mar, 2018. https://cds.cern.ch/record/2310213.

[123] A. Davis, L. Dufour, F. Ferrari, S. Stahl, M. A. Vesterinen, and J. Van Tilburg, *Measurement of the $K^-\pi^+$ two-track detection asymmetry in Run 2 using the Turbo stream*, Sep, 2017. https://cds.cern.ch/record/2284097.

[124] M. Vesterinen, on behalf of the LHCb collaboration, *Considerations on the LHCb dipole magnet polarity reversal*, Apr, 2014. https://cds.cern.ch/record/1642153.

[125] L. Dufour and J. Van Tilburg, *Decomposition of simulated detection asymmetries in LHCb*, Feb, 2018. https://cds.cern.ch/record/2304546.

[126] M. Artuso, G. Borissov, and A. Lenz, *CP violation in the B_s^0 system*, Rev. Mod. Phys. **88** (2016) 045002, arXiv:1511.09466 [hep-ph].

[127] T. Gershon, *$\Delta\Gamma_d$: A forgotten null test of the Standard Model*, J. Phys. **G38** (2011) 015007, arXiv:1007.5135 [hep-ph].

[128] LHCb collaboration, R. Aaij et al., *Measurements of the B^+, B^0, B_s^0 meson and Λ_b^0 baryon lifetimes*, JHEP **04** (2014) 114, arXiv:1402.2554 [hep-ex].

[129] ATLAS collaboration, M. Aaboud et al., *Measurement of the relative width difference of the B^0–$\overline{B}^0$ system with the ATLAS detector*, JHEP **06** (2016) 081, arXiv:1605.07485 [hep-ex].

[130] CMS collaboration, A. M. Sirunyan et al., *Measurement of b hadron lifetimes in pp collisions at $\sqrt{s} = 8$ TeV*, Eur. Phys. J. **C78** (2018) no. 6, 457, arXiv:1710.08949 [hep-ex].

[131] S. Faller, R. Fleischer, and T. Mannel, *Precision physics with $B_s^0 \to J/\psi\phi$ at the LHC: The quest for new physics*, Phys.Rev. **D79** (2009) 014005, arXiv:0810.4248 [hep-ph].

[132] B. Bhattacharya, A. Datta, and D. London, *Reducing penguin pollution*, Int. J. Mod. Phys. **A28** (2013) 1350063, arXiv:1209.1413 [hep-ph].

[133] CMS Collaboration, *CP-Violation studies at the HL-LHC with CMS using B_s^0 decays to $J/\psi\phi(1020)$*, CMS Physics Analysis Summary CMS-PAS-FTR-18-041, 2018. http://cdsweb.cern.ch/record/2650772.

[134] CMS Collaboration, V. Khachatryanand et al., *Measurement of the CP-violating weak phase ϕ_s and the decay width difference $\Delta\Gamma_s$ using the $B_s^0 \to J/\psi\phi(1020)$ decay channel in pp collisions at $\sqrt{s} = 8$ TeV*, Phys. Lett. **B757** (2016) 97, arXiv:1507.07527 [hep-ex].

[135] ATLAS Collaboration, *CP-violation measurement prospects in the $B_s^0 \to J/\psi\phi$ channel with the upgraded ATLAS detector at the HL-LHC*, ATL-PHYS-PUB-2018-041, CERN, Geneva, Dec, 2018. http://cds.cern.ch/record/2649881.

[136] *ATLAS B-physics studies at increased LHC luminosity, potential for CP-violation measurement in the B0s → J/ψφ decay*, ATL-PHYS-PUB-2013-010, CERN, Geneva, Sep, 2013.

http://cds.cern.ch/record/1604429.

[137] ATLAS Collaboration, G. Aad et al., *Measurement of the CP-violating phase ϕ_s and the B_s^0 meson decay width difference with $B_s^0 \to J/\psi\phi$ decays in ATLAS*, JHEP **08** (2016) 147, arXiv:1601.03297 [hep-ex].

[138] Heavy Flavour Averaging Group Collaboration, Y. Amhisand et al., *Averages of b-hadron, c-hadron, and τ-lepton properties as of summer 2016*, Eur. Phys. **J77** (2017) 895, arXiv:arXiv:1612.07233 [hep-ex]. and online update http://www.slac.stanford.edu/xorg/hfag.

[139] LHCb collaboration, R. Aaij et al., *Measurement of CP violation in $B^0 \to J/\psi K_S^0$ decays*, Phys. Rev. Lett. **115** (2015) 031601, arXiv:1503.07089 [hep-ex].

[140] LHCb collaboration, R. Aaij et al., *Resonances and CP-violation in $\overline{B}_s^0$ and $B_s^0 \to J/\psi K^+K^-$ decays in the mass region above the $\phi(1020)$*, JHEP **08** (2017) 037, arXiv:1704.08217 [hep-ex].

[141] LHCb collaboration, R. Aaij et al., *Measurement of the CP-violating phase ϕ_s in $\overline{B}_s^0 \to J/\psi\pi^-\pi^-$ decays*, Phys. Lett. **B736** (2014) 186, arXiv:1405.4140 [hep-ex].

[142] LHCb collaboration, R. Aaij et al., *Measurement of the CP violating phase and decay-width difference in $B_s^0 \to \psi(2S)\phi$ decays*, Phys. Lett. **B762** (2016) 253, arXiv:1608.04855 [hep-ex].

[143] LHCb collaboration, R. Aaij et al., *Study of η–η' mixing from measurement of $B_{(s)}^0 \to J/\psi\eta^{(\prime)}$ decay rates*, JHEP **01** (2015) 024, arXiv:1411.0943 [hep-ex].

[144] LHCb collaboration, R. Aaij et al., *Measurement of the $B_s^0 \to J/\psi\eta$ lifetime*, Phys. Lett. **B762** (2016) 484, arXiv:1607.06314 [hep-ex].

[145] I. Adachi et al., *Precise measurement of the CP violation parameter $\sin 2\phi_1$ in $B^0 \to (c\bar{c})K^0$ decays*, Phys. Rev. Lett. **108** (2012) 171802, arXiv:1201.4643 [hep-ex].

[146] A. Gaz, *Physics prospects at SuperKEKB/Belle II*, PoS **KMI2017** (2017) 005.

[147] Belle and BaBar collaborations, A. Abdesselam et al., *First observation of CP violation in $\overline{B}^0 \to D_{CP}^{(*)}h^0$ decays by a combined time-dependent analysis of BaBar and Belle data*, Phys. Rev. Lett. **115** (2015) no. 12, 121604, arXiv:1505.04147 [hep-ex].

[148] Belle and BaBar collaborations, I. Adachi et al., *First evidence for $\cos 2\beta > 0$ and resolution of the CKM Unitarity Triangle ambiguity by a time-dependent Dalitz plot analysis of $B^0 \to D^{(*)}h^0$ with $D \to K_S^0\pi^+\pi^-$ decays*, arXiv:1804.06152 [hep-ex].

[149] Belle and BaBar collaboration, I. Adachi et al., *Measurement of $\cos 2\beta$ in $B^0 \to D^{(*)}h^0$ with $D \to K_S^0\pi^+\pi^-$ decays by a combined time-dependent Dalitz plot analysis of BaBar and Belle data*, arXiv:1804.06153 [hep-ex].

[150] Belle collaboration, A. Kuzmin et al., *Study of $\overline{B}^0 \to D^0\pi^+\pi^-$ decays*, Phys. Rev. **D76** (2007) 012006, arXiv:hep-ex/0611054 [hep-ex].

[151] BaBar collaboration, P. del Amo Sanchez et al., *Dalitz plot analysis of $B^0 \to \overline{D}^0\pi^+\pi^-$*, PoS **ICHEP2010** (2010) 250, arXiv:1007.4464 [hep-ex].

[152] LHCb collaboration, R. Aaij et al., *Dalitz plot analysis of $B^0 \to \overline{D}^0\pi^+\pi^-$ decays*, Phys. Rev. **D92** (2015) 032002, arXiv:1505.01710 [hep-ex].

[153] J. Charles, A. Le Yaouanc, L. Oliver, O. Pene, and J. Raynal, *$B_d^0(t) \to DPP$ time dependent Dalitz plots, CP-violating angles 2β, $2\beta+\gamma$, and discrete ambiguities*, Phys.Lett. **B425** (1998) 375, arXiv:hep-ph/9801363 [hep-ph].

[154] T. Latham and T. Gershon, *A method to measure $\cos(2\beta)$ using time-dependent Dalitz plot analysis of $B^0 \to D_{CP}\pi^+\pi^-$*, J. Phys. **G36** (2009) 025006, arXiv:0809.0872 [hep-ph].

[155] A. Bondar, A. Kuzmin, and V. Vorobyev, *A method for model-independent measurement of the CKM angle β via time-dependent analysis of the $B^0 \to D\pi^+\pi^-$, $D \to K_S^0\pi^+\pi^-$ decays*, JHEP

03 (2018) 195, arXiv:1802.00200 [hep-ph].

[156] LHCb collaboration, R. Aaij et al., *Measurement of the CP-violating phase β in $\overline{B}^0 \to J/\psi\pi^+\pi^-$ decays and limits on penguin effects*, Phys. Lett. **B742** (2015) 38, arXiv:1411.1634 [hep-ex].

[157] LHCb collaboration, R. Aaij et al., *Measurement of CP violation parameters and polarisation fractions in $B_s^0 \to J/\psi \overline{K}^{*0}$ decays*, JHEP **11** (2015) 082, arXiv:1509.00400 [hep-ex].

[158] R. Fleischer, *Exploring CP violation and penguin effects through $B_d^0 \to D^+D^-$ and $B_s^0 \to D_s^+D_s^-$*, Eur. Phys. J. **C51** (2007) 849–858, arXiv:0705.4421 [hep-ph].

[159] M. Jung and S. Schacht, *Standard model predictions and new physics sensitivity in $B \to DD$ decays*, Phys. Rev. **D91** (2015) no. 3, 034027, arXiv:1410.8396 [hep-ph].

[160] L. Bel, K. De Bruyn, R. Fleischer, M. Mulder, and N. Tuning, *Anatomy of $B \to D\overline{D}$ decays*, JHEP **07** (2015) 108, arXiv:1505.01361 [hep-ph].

[161] LHCb collaboration, R. Aaij et al., *Measurement of CP violation in $B \to D^+D^-$ decays*, Phys. Rev. Lett. **117** (2016) 261801, arXiv:1608.06620 [hep-ex].

[162] LHCb collaboration, R. Aaij et al., *Measurement of the time-dependent CP asymmetries in $B_s^0 \to J/\psi K_{\rm S}^0$*, JHEP **06** (2015) 131, arXiv:1503.07055 [hep-ex].

[163] BaBar collaboration, B. Aubert et al., *Evidence for CP violation in $B^0 \to J/\psi\pi^0$ decays*, Phys. Rev. Lett. **101** (2008) 021801, arXiv:0804.0896 [hep-ex].

[164] Belle collaboration, S. E. Lee et al., *Improved measurement of time-dependent CP violation in $B^0 \to J/\psi\pi^0$ decays*, Phys. Rev. **D77** (2008) 071101, arXiv:0708.0304 [hep-ex].

[165] M. Bartsch, G. Buchalla, and C. Kraus, *$B \to V_L V_L$ decays at next-to-leading order in QCD*, arXiv:0810.0249 [hep-ph].

[166] M. Beneke, J. Rohrer, and D. Yang, *Branching fractions, polarisation and asymmetries of $B \to VV$ decays*, Nucl. Phys. **B774** (2007) 64–101, arXiv:hep-ph/0612290 [hep-ph].

[167] H.-Y. Cheng and C.-K. Chua, *QCD factorization for charmless hadronic B_s decays revisited*, Phys. Rev. **D80** (2009) 114026, arXiv:0910.5237 [hep-ph].

[168] CMS Collaboration, *The Phase-2 Upgrade of the CMS Tracker*, CERN-LHCC-2017-009 ; CMS-TDR-014, CERN, Geneva, 2017. https://cds.cern.ch/record/2272264.

[169] LHCb collaboration, R. Aaij et al., *First measurement of the CP-violating phase $\phi_s^{d\bar{d}}$ in $B_s^0 \to (K^+\pi^-)(K^-\pi^+)$ decays*, JHEP **03** (2018) 140, arXiv:1712.08683 [hep-ex].

[170] T. Gershon, T. Latham, and R. Silva Coutinho, *Probing CP violation in $B_s^0 \to K_{\rm S}^0\pi^+\pi^-$ decays*, Nucl. Part. Phys. Proc. **273-275** (2016) 1417–1422, arXiv:1411.2018 [hep-ph].

[171] R. Silva Coutinho, *Studies of charmless three-body b-hadron decays at LHCb*, Apr, 2015. http://cds.cern.ch/record/2045786.

[172] LHCb collaboration, R. Aaij et al., *Updated branching fraction measurements of $B_{(s)}^0 \to K_{\rm S}^0 h^+h'^-$ decays*, JHEP **11** (2017) 027, arXiv:1707.01665 [hep-ex].

[173] LHCb collaboration, R. Aaij et al., *Amplitude analysis of the decay $\overline{B}^0 \to K_{\rm S}^0\pi^+\pi^-$ and first observation of CP asymmetry in $\overline{B}^0 \to K^*(892)^-\pi^+$*, Phys. Rev. Lett. **120** (2018) 261801, arXiv:1712.09320 [hep-ex].

[174] LHCb collaboration, *Study of the decay $B^+ \to K^+\pi^0$ at LHCb*, Mar, 2015.

[175] I. Dunietz, H. R. Quinn, A. Snyder, W. Toki, and H. J. Lipkin, *How to extract CP violating asymmetries from angular correlations*, Phys. Rev. **D43** (1991) 2193–2208.

[176] A. F. Falk, Z. Ligeti, Y. Nir, and H. Quinn, *Comment on extracting α from $B \to \rho\rho$*, Phys. Rev. **D69** (2004) 011502, arXiv:hep-ph/0310242 [hep-ph].

[177] M. Beneke, M. Gronau, J. Rohrer, and M. Spranger, *A Precise determination of α using $B^0 \to \rho^+\rho^-$ and $B^0 \to K^{*+}\rho^-$*, Phys. Lett. **B638** (2006) 68–73, arXiv:hep-ph/0604005

[hep-ph].

[178] LHCb collaboration, R. Aaij et al., *Observation of the $B^0 \to \rho^0\rho^0$ decay from an amplitude analysis of $B^0 \to (\pi^+\pi^-)(\pi^+\pi^-)$ decays*, Phys. Lett. **B747** (2015) 468, arXiv:1503.07770 [hep-ex].

[179] BaBar collaboration, J. P. Lees et al., *Measurement of CP-violating asymmetries in $B^0 \to (\rho\pi)^0$ decays using a time-dependent Dalitz plot analysis*, Phys. Rev. **D88** (2013) no. 1, 012003, arXiv:1304.3503 [hep-ex].

[180] Belle collaboration, A. Kusaka et al., *Measurement of CP asymmetry in a time-dependent Dalitz analysis of $B^0 \to (\rho\pi)^0$ and a constraint on the CKM angle ϕ_2*, Phys. Rev. Lett. **98** (2007) 221602, arXiv:hep-ex/0701015 [hep-ex].

[181] Belle collaboration, A. Kusaka et al., *Measurement of CP asymmetries and branching fractions in a time-dependent Dalitz analysis of $B^0 \to (\rho\pi)^0$ and a constraint on the quark mixing angle ϕ_2*, Phys. Rev. **D77** (2008) 072001, arXiv:0710.4974 [hep-ex].

[182] CDF collaboration, T. A. Aaltonen et al., *Measurements of direct CP-violating asymmetries in charmless decays of bottom baryons*, Phys. Rev. Lett. **113** (2014) 242001, arXiv:1403.5586 [hep-ex].

[183] LHCb collaboration, R. Aaij et al., *Searches for Λ_b^0 and Ξ_b^0 decays to $K^0_S p\pi^-$ and $K^0_S pK^-$ final states with first observation of the $\Lambda_b^0 \to K^0_S p\pi^-$ decay*, JHEP **04** (2014) 087 LHCb-PAPER-2013-061, CERN-PH-EP-2014-012, arXiv:1402.0770 [hep-ex].

[184] LHCb collaboration, R. Aaij et al., *Observations of $\Lambda_b^0 \to \Lambda K^+\pi^-$ and $\Lambda_b^0 \to \Lambda K^+K^-$ decays and searches for other Λ_b^0 and Ξ_b^0 decays to Λh^+h^- final states*, JHEP **05** (2016) 081, arXiv:1603.00413 [hep-ex].

[185] LHCb collaboration, R. Aaij et al., *Measurement of branching fractions of charmless four-body Λ_b^0 and Ξ_b^0 decays*, JHEP **02** (2018) 098, arXiv:1711.05490 [hep-ex].

[186] LHCb collaboration, R. Aaij et al., *Observation of the decay $\Lambda_b^0 \to pK^-\mu^+\mu^-$ and search for CP violation*, JHEP **06** (2017) 108, arXiv:1703.00256 [hep-ex].

[187] I. Dunietz, *CP violation with beautiful baryons*, Z. Phys. **C56** (1992) 129–144.

[188] Fayyazuddin, *$\Lambda_b^0 \to \Lambda + D^0(\bar{D}^0)$ decays and CP violation*, Mod. Phys. Lett. **A14** (1999) 63–70, arXiv:hep-ph/9806393 [hep-ph].

[189] A. K. Giri, R. Mohanta, and M. P. Khanna, *Possibility of extracting the weak phase γ from $\Lambda_b^0 \to \Lambda D^0$ decays*, Phys. Rev. **D65** (2002) 073029, arXiv:hep-ph/0112220 [hep-ph].

[190] LHCb collaboration, R. Aaij et al., *Study of beauty baryon decays to D^0ph^- and $\Lambda_c^+h^-$ final states*, Phys. Rev. **D89** (2014) 032001 CERN-PH-EP-2013-207, LHCb-PAPER-2013-056, arXiv:1311.4823 [hep-ex].

[191] LHCb collaboration, R. Aaij et al., *Measurement of matter-antimatter differences in beauty baryon decays*, Nature Physics **13** (2017) 391, arXiv:1609.05216 [hep-ex].

[192] LHCb collaboration, R. Aaij et al., *Search for CP violation using triple product asymmetries in $\Lambda_b^0 \to pK^-\pi^+\pi^-$, $\Lambda_b^0 \to pK^-K^+K^-$, and $\Xi_b^0 \to pK^-K^-\pi^+$ decays*, JHEP **08** (2018) 039, arXiv:1805.03941 [hep-ex].

[193] LHCb collaboration, R. Aaij et al., *Measurement of B^0, B_s^0, B^+ and Λ_b^0 production asymmetries in 7 and 8 TeV pp collisions*, Phys. Lett. **B774** (2017) 139, arXiv:1703.08464 [hep-ex].

[194] LHCb collaboration, R. Aaij et al., *Search for CP violation in $\Lambda_c^+ \to pK^-K^+$ and $\Lambda_c^+ p\pi^-\pi^+$ decays*, JHEP **03** (2018) 182, arXiv:1712.07051 [hep-ex].

[195] LHCb collaboration, R. Aaij et al., *Search for CP violation in $D^0 \to \pi^-\pi^+\pi^0$ decays with the energy test*, Phys. Lett. **B740** (2015) 158, arXiv:1410.4170 [hep-ex].

[196] Belle II Collaboration, E. Kou et al., *The Belle II Physics Book*, arXiv:1808.10567

[hep-ex].

[197] HFLAV Collaboration, Y. Amhis et al., *Averages of b-hadron, c-hadron, and τ-lepton properties as of summer 2016*, Eur. Phys. J. **C77** (2017) no. 12, 895, arXiv:1612.07233 [hep-ex].

[198] UTfit Collaboration, M. Bona et al., *Model-independent constraints on $\Delta F = 2$ operators and the scale of new physics*, JHEP **03** (2008) 049, arXiv:0707.0636 [hep-ph].

[199] S. Laplace, Z. Ligeti, Y. Nir, and G. Perez, *Implications of the CP asymmetry in semileptonic B decay*, Phys. Rev. **D65** (2002) 094040, arXiv:hep-ph/0202010 [hep-ph].

[200] F. Gabbiani, E. Gabrielli, A. Masiero, and L. Silvestrini, *A Complete analysis of FCNC and CP constraints in general SUSY extensions of the standard model*, Nucl. Phys. **B477** (1996) 321–352, arXiv:hep-ph/9604387 [hep-ph].

[201] L. Silvestrini. talk at Implications of LHCb measurements and future prospects, CERN, Nov 3-5, 2015.

[202] U. Nierste, *Three Lectures on Meson Mixing and CKM phenomenology*, in *Heavy quark physics. Proceedings, Helmholtz International School, HQP08, Dubna, Russia, August 11-21, 2008*, pp. 1–38. 2009. arXiv:0904.1869 [hep-ph]. http://inspirehep.net/record/817820/files/arXiv:0904.1869.pdf.

[203] T. Jubb, M. Kirk, A. Lenz, and G. Tetlalmatzi-Xolocotzi, *On the ultimate precision of meson mixing observables*, Nucl. Phys. **B915** (2017) 431–453, arXiv:1603.07770 [hep-ph].

[204] A. F. Falk, Y. Grossman, Z. Ligeti, and A. A. Petrov, *SU(3) breaking and D0 - anti-D0 mixing*, Phys. Rev. **D65** (2002) 054034, arXiv:hep-ph/0110317 [hep-ph].

[205] M. Gronau and J. L. Rosner, *Revisiting D0-D0bar mixing using U-spin*, Phys. Rev. **D86** (2012) 114029, arXiv:1209.1348 [hep-ph].

[206] H. Georgi, *D - anti-D mixing in heavy quark effective field theory*, Phys. Lett. **B297** (1992) 353–357, arXiv:hep-ph/9209291 [hep-ph].

[207] T. Ohl, G. Ricciardi, and E. H. Simmons, *D - anti-D mixing in heavy quark effective field theory: The Sequel*, Nucl. Phys. **B403** (1993) 605–632, arXiv:hep-ph/9301212 [hep-ph].

[208] I. I. Y. Bigi and N. G. Uraltsev, *D0 - anti-D0 oscillations as a probe of quark hadron duality*, Nucl. Phys. **B592** (2001) 92–106, arXiv:hep-ph/0005089 [hep-ph].

[209] M. Bobrowski, A. Lenz, J. Riedl, and J. Rohrwild, *How Large Can the SM Contribution to CP Violation in $D^0 - \bar{D}^0$ Mixing Be?*, JHEP **03** (2010) 009, arXiv:1002.4794 [hep-ph].

[210] N. Carrasco et al., *$D^0 - \bar{D}^0$ mixing in the standard model and beyond from N_f =2 twisted mass QCD*, Phys. Rev. **D90** (2014) no. 1, 014502, arXiv:1403.7302 [hep-lat].

[211] ETM Collaboration, N. Carrasco, P. Dimopoulos, R. Frezzotti, V. Lubicz, G. C. Rossi, S. Simula, and C. Tarantino, *$\Delta S = 2$ and $\Delta C = 2$ bag parameters in the standard model and beyond from N_f=2+1+1 twisted-mass lattice QCD*, Phys. Rev. **D92** (2015) no. 3, 034516, arXiv:1505.06639 [hep-lat].

[212] A. Bazavov et al., *Short-distance matrix elements for D^0-meson mixing for $N_f = 2 + 1$ lattice QCD*, Phys. Rev. **D97** (2018) no. 3, 034513, arXiv:1706.04622 [hep-lat].

[213] M. Kirk, A. Lenz, and T. Rauh, *Dimension-six matrix elements for meson mixing and lifetimes from sum rules*, JHEP **12** (2017) 068, arXiv:1711.02100 [hep-ph].

[214] A. Lenz, *Theory Overview*, PoS **CHARM2016** (2017) 003, arXiv:1610.07943 [hep-ph].

[215] A. Lenz and T. Rauh, *D-meson lifetimes within the heavy quark expansion*, Phys. Rev. **D88** (2013) 034004, arXiv:1305.3588 [hep-ph].

[216] M. Bobrowski, A. Lenz, and T. Rauh, *Short distance D-Dbar mixing*, in *Proceedings, 5th International Workshop on Charm Physics (Charm 2012): Honolulu, Hawaii, USA, May 14-17, 2012*. 2012. arXiv:1208.6438 [hep-ph]. http://inspirehep.net/record/1184026/files/arXiv:1208.6438.pdf.

[217] A. F. Falk, Y. Grossman, Z. Ligeti, Y. Nir, and A. A. Petrov, *The D0 - anti-D0 mass difference from a dispersion relation*, Phys. Rev. **D69** (2004) 114021, arXiv:hep-ph/0402204 [hep-ph].

[218] H.-Y. Cheng and C.-W. Chiang, *Long-Distance Contributions to $D^0 - \bar{D}^0$ Mixing Parameters*, Phys. Rev. **D81** (2010) 114020, arXiv:1005.1106 [hep-ph].

[219] H.-Y. Jiang, F.-S. Yu, Q. Qin, H.-n. Li, and C.-D. Lu, *D^0-$\overline{D}^0$ mixing parameter y in the factorization-assisted topological-amplitude approach*, arXiv:1705.07335 [hep-ph]. [Chin. Phys.C42,063101(2018)].

[220] Y. Nir, *CP violation*, Conf. Proc. **C9207131** (1992) 81–136. [,81(1992)].

[221] M. T. Hansen and S. R. Sharpe, *Multiple-channel generalization of Lellouch-Luscher formula*, Phys. Rev. **D86** (2012) 016007, arXiv:1204.0826 [hep-lat].

[222] Y. Grossman, A. Kagan, Z. Ligeti, G. Perez, A. Petrov, and L. Silvestrini. in preparation.

[223] G. C. Branco, L. Lavoura, and J. P. Silva, *CP Violation*, Int. Ser. Monogr. Phys. **103** (1999) 1–536.

[224] I. I. Bigi and A. I. Sanda, *CP violation*, . [Camb. Monogr. Part. Phys. Nucl. Phys. Cosmol.9,1(2009)].

[225] J. Brod, Y. Grossman, A. L. Kagan, and J. Zupan, *A consistent picture for large penguins in $Dto\pi^+\pi^-, K^+K^-$*, JHEP **10** (2012) 161, arXiv:1203.6659 [hep-ph].

[226] U. Nierste and S. Schacht, *CP Violation in $D^0 \to K_S K_S$*, Phys. Rev. **D92** (2015) no. 5, 054036, arXiv:1508.00074 [hep-ph].

[227] U. Nierste and S. Schacht, *Neutral $D \to K K^*$ decays as discovery channels for charm CP violation*, Phys. Rev. Lett. **119** (2017) no. 25, 251801, arXiv:1708.03572 [hep-ph].

[228] S. Bergmann and Y. Nir, *New physics effects in doubly Cabibbo suppressed D decays*, JHEP **09** (1999) 031, arXiv:hep-ph/9909391 [hep-ph].

[229] Belle collaboration, T. Peng et al., *Measurement of $D^0 - \overline{D}^0$ mixing and search for indirect CP violation using $D^0 \to K^0_S \pi^+ \pi^-$ decays*, Phys. Rev. **D89** (2014) 091103, arXiv:1404.2412 [hep-ex].

[230] K. Blum, Y. Grossman, Y. Nir, and G. Perez, *Combining $K^0 - \bar{K}^0$ mixing and $D^0 - \bar{D}^0$ mixing to constrain the flavor structure of new physics*, Phys. Rev. Lett. **102** (2009) 211802, arXiv:0903.2118 [hep-ph].

[231] A. L. Kagan and M. D. Sokoloff, *On Indirect CP Violation and Implications for $D^0 - \bar{D}^0$ and $B_{(s)} - \bar{B}_{(s)}$ mixing*, Phys. Rev. **D80** (2009) 076008, arXiv:0907.3917 [hep-ph].

[232] M. J. Savage, *SU(3) violations in the nonleptonic decay of charmed hadrons*, Phys. Lett. **B257** (1991) 414–418.

[233] D. Pirtskhalava and P. Uttayarat, *CP violation and flavor $SU(3)$ breaking in D-meson decays*, Phys. Lett. **B712** (2012) 81–86, arXiv:1112.5451 [hep-ph].

[234] T. Feldmann, S. Nandi, and A. Soni, *Repercussions of flavour symmetry breaking on CP violation in D-meson decays*, JHEP **06** (2012) 007, arXiv:1202.3795 [hep-ph].

[235] E. Franco, S. Mishima, and L. Silvestrini, *The Standard Model confronts CP violation in $D^0 \to \pi^+\pi^-$ and $D^0 \to K^+K^-$*, JHEP **05** (2012) 140, arXiv:1203.3131 [hep-ph].

[236] G. Hiller, M. Jung, and S. Schacht, *SU(3)-flavor anatomy of nonleptonic charm decays*, Phys. Rev. **D87** (2013) no. 1, 014024, arXiv:1211.3734 [hep-ph].

[237] D. Atwood and A. Soni, *Searching for the Origin of CP violation in Cabibbo Suppressed D-meson Decays*, PTEP **2013** (2013) no. 9, 093B05, arXiv:1211.1026 [hep-ph].

[238] J. Brod, A. L. Kagan, and J. Zupan, *Size of direct CP violation in singly Cabibbo-suppressed D decays*, Phys. Rev. **D86** (2012) 014023, arXiv:1111.5000 [hep-ph].

[239] A. Khodjamirian and A. A. Petrov, *Direct CP asymmetry in $D \to \pi^-\pi^+$ and $D \to K^-K^+$ in*

QCD-based approach, Phys. Lett. **B774** (2017) 235–242, arXiv:1706.07780 [hep-ph].

[240] Y. Grossman, A. L. Kagan, and Y. Nir, *New physics and CP violation in singly Cabibbo suppressed D decays*, Phys. Rev. **D75** (2007) 036008, arXiv:hep-ph/0609178 [hep-ph].

[241] A. Ryd and A. A. Petrov, *Hadronic D and D(s) Meson Decays*, Rev. Mod. Phys. **84** (2012) 65–117, arXiv:0910.1265 [hep-ph].

[242] S. de Boer and G. Hiller, *Flavor and new physics opportunities with rare charm decays into leptons*, Phys. Rev. **D93** (2016) no. 7, 074001, arXiv:1510.00311 [hep-ph].

[243] S. de Boer and G. Hiller, *Rare radiative charm decays within the standard model and beyond*, JHEP **08** (2017) 091, arXiv:1701.06392 [hep-ph].

[244] S. de Boer and G. Hiller, *Null tests from angular distributions in $D \to P_1 P_2 l^+ l^-$, $l = e, \mu$ decays on and off peak*, arXiv:1805.08516 [hep-ph].

[245] LHCb collaboration, R. Aaij et al., *Measurement of angular and CP asymmetries in $D^0 \to \pi^+\pi^-\mu^+\mu^-$ and $D^0 \to K^+K^-\mu^+\mu^-$ decays*, Phys. Rev. Lett. **121** (2018) 091801, arXiv:1806.10793 [hep-ex].

[246] A. Datta and D. London, *Triple-product correlations in $B \to V_1 V_2$ decays and new physics*, Int. J. Mod. Phys. **A19** (2004) 2505–2544, arXiv:hep-ph/0303159 [hep-ph].

[247] Y. Grossman, A. L. Kagan, and J. Zupan, *Testing for new physics in singly Cabibbo suppressed D decays*, Phys. Rev. **D85** (2012) 114036, arXiv:1204.3557 [hep-ph].

[248] Y. Grossman and D. J. Robinson, *SU(3) Sum Rules for Charm Decay*, JHEP **04** (2013) 067, arXiv:1211.3361 [hep-ph].

[249] Y. Grossman, Z. Ligeti, and D. J. Robinson, *More Flavor SU(3) Tests for New Physics in CP Violating B Decays*, JHEP **01** (2014) 066, arXiv:1308.4143 [hep-ph].

[250] S. Muller, U. Nierste, and S. Schacht, *Sum Rules of Charm CP Asymmetries beyond the $SU(3)_F$ Limit*, Phys. Rev. Lett. **115** (2015) no. 25, 251802, arXiv:1506.04121 [hep-ph].

[251] S. de Boer, B. Muller, and D. Seidel, *Higher-order Wilson coefficients for $c \to u$ transitions in the standard model*, JHEP **08** (2016) 091, arXiv:1606.05521 [hep-ph].

[252] C. Greub, T. Hurth, M. Misiak, and D. Wyler, *The $c \to u$ gamma contribution to weak radiative charm decay*, Phys. Lett. **B382** (1996) 415–420, arXiv:hep-ph/9603417 [hep-ph].

[253] S. Fajfer, P. Singer, and J. Zupan, *The Radiative leptonic decays $D^0 \to e^+e^-\gamma, \mu^+\mu^-\gamma$ in the standard model and beyond*, Eur. Phys. J. **C27** (2003) 201–218, arXiv:hep-ph/0209250 [hep-ph].

[254] S. Fajfer and P. Singer, *Long distance $c \to u$ gamma effects in weak radiative decays of D mesons*, Phys. Rev. **D56** (1997) 4302–4310, arXiv:hep-ph/9705327 [hep-ph].

[255] S. Fajfer, S. Prelovsek, and P. Singer, *Long distance contributions in $D \to V\gamma$ decays*, Eur. Phys. J. **C6** (1999) 471–476, arXiv:hep-ph/9801279 [hep-ph].

[256] Particle Data Group Collaboration, M. Tanabashi et al., *Review of Particle Physics*, Phys. Rev. **D98** (2018) no. 3, 030001.

[257] S. de Boer, *Rare radiative charm decays in the standard model and beyond*, PoS **EPS-HEP2017** (2017) 209, arXiv:1710.06670 [hep-ph].

[258] S. de Boer and G. Hiller, *The photon polarization in radiative D decays, phenomenologically*, Eur. Phys. J. **C78** (2018) no. 3, 188, arXiv:1802.02769 [hep-ph].

[259] S. Fajfer and N. Košnik, *Prospects of discovering new physics in rare charm decays*, Eur. Phys. J. **C75** (2015) no. 12, 567, arXiv:1510.00965 [hep-ph].

[260] LHCb collaboration, R. Aaij et al., *Search for the rare decay $D^0 \to \mu^+\mu^-$*, Phys. Lett. **B725** (2013) 15, arXiv:1305.5059 [hep-ex].

[261] LHCb collaboration, R. Aaij et al., *Search for $D^+_{(s)} \to \pi^+\mu^+\mu^-$ and $D^+_{(s)} \to \pi^-\mu^+\mu^+$ decays*, Phys. Lett. **B724** (2013) 203, arXiv:1304.6365 [hep-ex].

[262] S. Meinel, $\Lambda_c \to N$ *form factors from lattice QCD and phenomenology of* $\Lambda_c \to n\ell^+\nu_\ell$ *and* $\Lambda_c \to p\mu^+\mu^-$ *decays*, Phys. Rev. **D97** (2018) no. 3, 034511, arXiv:1712.05783 [hep-lat].

[263] LHCb collaboration, R. Aaij et al., *Search for the rare decay* $\Lambda_c^+ \to p\mu^+\mu^-$, Phys. Rev. **D97** (2018) 091101, arXiv:1712.07938 [hep-ex].

[264] I. Doršner, S. Fajfer, A. Greljo, J. F. Kamenik, and N. Košnik, *Physics of leptoquarks in precision experiments and at particle colliders*, Phys. Rept. **641** (2016) 1–68, arXiv:1603.04993 [hep-ph].

[265] D. Buttazzo, A. Greljo, G. Isidori, and D. Marzocca, *B-physics anomalies: a guide to combined explanations*, JHEP **11** (2017) 044, arXiv:1706.07808 [hep-ph].

[266] S. Fajfer and N. Košnik, *Resonance catalyzed CP asymmetries in* $D \to P\ell^+\ell^-$, Phys. Rev. **D87** (2013) no. 5, 054026, arXiv:1208.0759 [hep-ph].

[267] E. Golowich, J. Hewett, S. Pakvasa, and A. A. Petrov, *Relating D0-anti-D0 Mixing and D0 —> l+ l- with New Physics*, Phys. Rev. **D79** (2009) 114030, arXiv:0903.2830 [hep-ph].

[268] LHCb collaboration, R. Aaij et al., *Observation of* D^0 *meson decays to* $\pi^+\pi^-\mu^+\mu^-$ *and* $K^+K^-\mu^+\mu^-$ *final states*, Phys. Rev. Lett. **119** (2017) 181805, arXiv:1707.08377 [hep-ex].

[269] BESIII Collaboration, M. Ablikim et al., *Search for the rare decays* $D \to h(h')e^+e^-$, Phys. Rev. **D97** (2018) no. 7, 072015, arXiv:1802.09752 [hep-ex].

[270] M. Martone and J. Zupan, $B^\pm \to DK^\pm$ *with direct CP violation in charm*, Phys. Rev. **D87** (2013) no. 3, 034005, arXiv:1212.0165 [hep-ph].

[271] W. Wang, *CP Violation Effects on the Measurement of the Cabibbo-Kobayashi-Maskawa Angle* γ *from* $B \to D\,K$, Phys. Rev. Lett. **110** (2013) no. 6, 061802, arXiv:1211.4539 [hep-ph].

[272] B. Bhattacharya, D. London, M. Gronau, and J. L. Rosner, *Shift in weak phase* γ *due to CP asymmetries in D decays to two pseudoscalar mesons*, Phys. Rev. **D87** (2013) no. 7, 074002, arXiv:1301.5631 [hep-ph].

[273] CLEO collaboration, D. M. Asner et al., *Search for* $D^0 - \overline{D}^0$ *mixing in the Dalitz plot analysis of* $D^0 \to K^0_S\pi^+\pi^-$, Phys. Rev. **D72** (2005) 012001, arXiv:hep-ex/0503045 [hep-ex].

[274] BaBar collaboration, P. del Amo Sanchez et al., *Measurement of* $D^0 - \overline{D}^0$ *mixing parameters using* $D^0 \to K^0_S\pi^+\pi^-$ *and* $D^0 \to K^0_S K^+K^-$ *decays*, Phys. Rev. Lett. **105** (2010) 081803, arXiv:1004.5053 [hep-ex].

[275] LHCb collaboration, R. Aaij et al., *Model-independent measurement of mixing parameters in* $D^0 \to K^0_S\pi^+\pi^-$ *decays*, JHEP **04** (2016) 033, arXiv:1510.01664 [hep-ex].

[276] CLEO collaboration, J. Libby et al., *Model-independent determination of the strong-phase difference between* D^0 *and* $\bar{D}^0 \to K^0_{S,L}h^+h^-$ $(h = \pi, K)$ *and its impact on the measurement of the CKM angle* γ/ϕ_3, Phys. Rev. **D82** (2010) 112006, arXiv:1010.2817 [hep-ex].

[277] A. Di Canto, J. G. Ticó, T. Gershon, N. Jurik, M. Martinelli, T. Pilař, S. Stahl, and D. Tonelli, *A novel method for measuring charm-mixing parameters using multibody decays*, arXiv:1811.01032 [hep-ex].

[278] LHCb collaboration, R. Aaij et al., *First observation of* $D^0 - \overline{D}^0$ *oscillations in* $D^0 \to K^+\pi^+\pi^-\pi^-$ *decays and a measurement of the associated coherence parameters*, Phys. Rev. Lett. **116** (2016) 241801, arXiv:1602.07224 [hep-ex].

[279] D. Atwood and A. Soni, *Role of charm factory in extracting CKM phase information via* $B \to DK$, Phys. Rev. **D68** (2003) 033003, arXiv:hep-ph/0304085 [hep-ph].

[280] T. Evans, S. Harnew, J. Libby, S. Malde, J. Rademacker, and G. Wilkinson, *Improved determination of the* $D \to K^-\pi^+\pi^+\pi^-$ *coherence factor and associated hadronic parameters from a combination of* $e^+e^- \to \psi(3770) \to c\bar{c}$ *and* $pp \to c\bar{c}X$ *data*, Phys. Lett. **B757** (2016) 520–527, arXiv:1602.07430 [hep-ex]. [Erratum: Phys. Lett.B765,402(2017)].

[281] S. S. Malde, *Synergy of BESIII and LHCb physics programmes*, Oct, 2016. http://cds.cern.ch/record/2223391.

[282] D. Müller, M. Gersabeck, and C. Parkes, *Measurements of production cross-sections and mixing of charm mesons at LHCb*, Nov, 2017. http://cds.cern.ch/record/2297069.

[283] LHCb collaboration, R. Aaij et al., *Measurement of indirect CP asymmetries in $D^0 \to K^-K^+$ and $D^0 \to \pi^-\pi^+$ decays*, JHEP **04** (2015) 043, arXiv:1501.06777 [hep-ex].

[284] LHCb collaboration, R. Aaij et al., *Measurement of the CKM angle γ from a combination of LHCb results*, JHEP **12** (2016) 087, arXiv:1611.03076 [hep-ex].

[285] LHCb collaboration, R. Aaij et al., *Measurement of CP asymmetry in $D^0 \to K^+K^-$ decays*, Phys. Lett. **B767** (2017) 177, arXiv:1610.09476 [hep-ex].

[286] Heavy Flavor Averaging Group Collaboration, Y. Amhis et al., *Averages of b-hadron, c-hadron, and τ-lepton properties as of summer 2016*, Eur. Phys. J. **C77** (2017) 895, arXiv:1612.07233 [hep-ex]. updated results and plots available at https://hflav.web.cern.ch.

[287] G. Durieux and Y. Grossman, *Probing CP violation systematically in differential distributions*, Phys. Rev. **D92** (2015) 076013, arXiv:1508.03054 [hep-ph].

[288] LHCb collaboration, R. Aaij et al., *Search for CP violation using T-odd correlations in $D^0 \to K^+K^-\pi^+\pi^-$ decays*, JHEP **10** (2014) 005, arXiv:1408.1299 [hep-ex].

[289] LHCb collaboration, R. Aaij et al., *Search for CP violation in the phase space of $D^0 \to \pi^+\pi^-\pi^+\pi^-$ decays*, Phys. Lett. **B769** (2017) 345, arXiv:1612.03207 [hep-ex].

[290] B. Bhattacharya, M. Gronau, and J. L. Rosner, *CP asymmetries in singly-Cabibbo-suppressed D decays to two pseudoscalar mesons*, Phys. Rev. **D85** (2012) 079901, arXiv:1201.2351 [hep-ph].

[291] BaBar collaboration, J. P. Lees et al., *Measurement of the neutral D meson mixing parameters in a time-dependent amplitude analysis of the $D^0 \to \pi^+\pi^-\pi^0$ decay*, Phys. Rev. **D93** (2016) 112014, arXiv:1604.00857 [hep-ex].

[292] LHCb collaboration, R. Aaij et al., *Measurement of CP asymmetries in $D^\pm \to \eta'\pi^\pm$ and $D_s^\pm \to \eta'\pi^\pm$ decays*, Phys. Lett. **B771** (2017) 21, arXiv:1701.01871 [hep-ex].

[293] LHCb collaboration, R. Aaij et al., *First observation of the decay $D^0 \to K^-\pi^+\mu^+\mu^-$ in the $\rho^0 - \omega$ region of the dimuon mass spectrum*, Phys. Lett. **B757** (2016) 558, arXiv:1510.08367 [hep-ex].

[294] I. I. Bigi, *Probing CP asymmetries in charm baryons decays*, arXiv:1206.4554 [hep-ph].

[295] LHCb collaboration, R. Aaij et al., *First observation of the doubly charmed baryon decay $\Xi_{cc}^{++} \to \Xi_c^+\pi^+$ decay*, Phys. Rev. Lett. **121** (2018) 162002, arXiv:1807.01919 [hep-ex].

[296] LHCb collaboration, R. Aaij et al., *Search for the rare decay $K_S^0 \to \mu^+\mu^-$*, JHEP **01** (2013) 090, arXiv:1209.4029 [hep-ex].

[297] F. Dettori, D. Martinez Santos, and J. Prisciandaro, *Low-p_T dimuon triggers at LHCb in Run 2*, LHCb-PUB-2017-023. CERN-LHCb-PUB-2017-023, CERN, Geneva, Dec, 2017. http://cds.cern.ch/record/2297352.

[298] A. A. Alves Junior et al., *Prospects for Measurements with Strange Hadrons at LHCb*, arXiv:1808.03477 [hep-ex].

[299] D. Martinez Santos. https://cds.cern.ch/record/2270191/files/fpcp2017-MartinezSantos.pdf. LHCb-TALK-2017-164, at FPCP 2017.

[300] V. G. Chobanova, X. Cid Vidal, J. P. Dalseno, M. Lucio Martinez, D. Martinez Santos, and V. Renaudin, *Sensitivity of LHCb and its upgrade in the measurement of $\mathcal{B}(K_S^0 \to \pi^0\mu^+\mu^-)$*, LHCb-PUB-2016-017, CERN, Geneva, Oct, 2016. http://cds.cern.ch/record/2195218.

[301] M. Borsato, V. V. Gligorov, D. Guadagnoli, D. Martinez Santos, and O. Sumensari, *The strange*

side of LHCb, arXiv:1808.02006 [hep-ph].

[302] G. Ecker and A. Pich, *The Longitudinal muon polarization in $K_L \to \mu^+\mu^-$*, Nucl. Phys. **B366** (1991) 189–205.

[303] G. Isidori and R. Unterdorfer, *On the short distance constraints from $K_{L,S} \to \mu^+\mu^-$*, JHEP **01** (2004) 009, arXiv:hep-ph/0311084 [hep-ph].

[304] G. D'Ambrosio and T. Kitahara, *Direct CP Violation in $K \to \mu^+\mu^-$*, Phys. Rev. Lett. **119** (2017) no. 20, 201802, arXiv:1707.06999 [hep-ph].

[305] G. Colangelo, R. Stucki, and L. C. Tunstall, *Dispersive treatment of $K_S \to \gamma\gamma$ and $K_S \to \gamma\ell^+\ell^-$*, Eur. Phys. J. **C76** (2016) no. 11, 604, arXiv:1609.03574 [hep-ph].

[306] G. Amelino-Camelia et al., *Physics with the KLOE-2 experiment at the upgraded DAϕNE*, Eur. Phys. J. **C68** (2010) 619–681, arXiv:1003.3868 [hep-ex].

[307] C. Bobeth and A. J. Buras, *Leptoquarks meet ε'/ε and rare Kaon processes*, JHEP **02** (2018) 101, arXiv:1712.01295 [hep-ph].

[308] V. Chobanova, G. D'Ambrosio, T. Kitahara, M. Lucio Martinez, D. Martinez Santos, I. S. Fernandez, and K. Yamamoto, *Probing SUSY effects in $K_S^0 \to \mu^+\mu^-$*, JHEP **05** (2018) 024, arXiv:1711.11030 [hep-ph].

[309] LHCb collaboration, R. Aaij et al., *Improved limit on the branching fraction of the rare decay $K_S^0 \to \mu\mu$*, Eur. Phys. J. **C77** (2017) 678, arXiv:1706.00758 [hep-ex].

[310] Particle Data Group Collaboration, M. Tanabashi et al., *Review of Particle Physics*, Phys. Rev. **D98** (2018) 030001.

[311] M. Gorbahn and U. Haisch, *Charm Quark Contribution to $K_L \to \mu^+\mu^-$ at Next-to-Next-to-Leading*, Phys. Rev. Lett. **97** (2006) 122002, arXiv:hep-ph/0605203 [hep-ph].

[312] F. Mescia, C. Smith, and S. Trine, *$K_L \to \pi^0 e^+ e^-$ and $K_L \to \pi^0 \mu^+ \mu^-$: A Binary star on the stage of flavor physics*, JHEP **08** (2006) 088, arXiv:hep-ph/0606081 [hep-ph].

[313] A. J. Buras, M. Gorbahn, S. Jäger, and M. Jamin, *Improved anatomy of ε'/ε in the Standard Model*, JHEP **11** (2015) 202, arXiv:1507.06345 [hep-ph].

[314] T. Kitahara, U. Nierste, and P. Tremper, *Singularity-free next-to-leading order $\Delta S = 1$ renormalization group evolution and ϵ'_K/ϵ_K in the Standard Model and beyond*, JHEP **12** (2016) 078, arXiv:1607.06727 [hep-ph].

[315] RBC, UKQCD Collaboration, Z. Bai et al., *Standard Model Prediction for Direct CP Violation in $K \to \pi\pi$ Decay*, Phys. Rev. Lett. **115** (2015) no. 21, 212001, arXiv:1505.07863 [hep-lat].

[316] A. J. Buras and J.-M. Gérard, *Upper bounds on ε'/ε parameters $B_6^{(1/2)}$ and $B_8^{(3/2)}$ from large N QCD and other news*, JHEP **12** (2015) 008, arXiv:1507.06326 [hep-ph].

[317] E. Pallante and A. Pich, *Strong enhancement of epsilon-prime / epsilon through final state interactions*, Phys. Rev. Lett. **84** (2000) 2568–2571, arXiv:hep-ph/9911233 [hep-ph].

[318] H. Gisbert and A. Pich, *Direct CP violation in $K^0 \to \pi\pi$: Standard Model Status*, Rept. Prog. Phys. **81** (2018) no. 7, 076201, arXiv:1712.06147 [hep-ph].

[319] M. Endo, T. Goto, T. Kitahara, S. Mishima, D. Ueda, and K. Yamamoto, *Gluino-mediated electroweak penguin with flavor-violating trilinear couplings*, JHEP **04** (2018) 019, arXiv:1712.04959 [hep-ph].

[320] K. De Bruyn, R. Fleischer, R. Knegjens, P. Koppenburg, M. Merk, A. Pellegrino, and N. Tuning, *Probing New Physics via the $B_s^0 \to \mu^+\mu^-$ Effective Lifetime*, Phys. Rev. Lett. **109** (2012) 041801, arXiv:1204.1737 [hep-ph].

[321] A. J. Buras, R. Fleischer, J. Girrbach, and R. Knegjens, *Probing New Physics with the $B_s \to \mu^+\mu^-$ Time-Dependent Rate*, JHEP **07** (2013) 77, arXiv:1303.3820 [hep-ph].

[322] D. Gomez Dumm and A. Pich, *Long distance contributions to the $K_L \to \mu^+\mu^-$ decay width*, Phys. Rev. Lett. **80** (1998) 4633–4636, arXiv:hep-ph/9801298 [hep-ph].

[323] V. Cirigliano, G. Ecker, H. Neufeld, A. Pich, and J. Portoles, *Kaon Decays in the Standard Model*, Rev. Mod. Phys. **84** (2012) 399, arXiv:1107.6001 [hep-ph].

[324] G. D'Ambrosio, D. Greynat, and G. Vulvert, *Standard Model and New Physics contributions to K_L and K_S into four leptons*, Eur. Phys. J. **C73** (2013) no. 12, 2678, arXiv:1309.5736 [hep-ph].

[325] G. D'Ambrosio and D. Espriu, *Rare Decay Modes of the K Mesons in the Chiral Lagrangian*, Phys. Lett. **B175** (1986) 237–242.

[326] G. D'Ambrosio, G. Ecker, G. Isidori, and J. Portoles, *The Decays $K \to \pi\ell^+\ell^-$ beyond leading order in the chiral expansion*, JHEP **08** (1998) 004, arXiv:hep-ph/9808289 [hep-ph].

[327] G. D'Ambrosio, D. Greynat, and M. Knecht, *On the amplitudes for the CP-conserving $K^\pm(K_S) \to \pi^\pm(\pi^0)\ell^+\ell^-$ rare decay modes*, arXiv:1812.00735 [hep-ph].

[328] E865 Collaboration, R. Appel et al., *A New measurement of the properties of the rare decay $K^+ \to \pi^+e^+e^-$*, Phys. Rev. Lett. **83** (1999) 4482–4485, arXiv:hep-ex/9907045 [hep-ex].

[329] NA48/2 Collaboration, J. R. Batley et al., *Precise measurement of the $K^\pm \to \pi^\pm e^+e^-$ decay*, Phys. Lett. **B677** (2009) 246–254, arXiv:0903.3130 [hep-ex].

[330] NA48/2 Collaboration, J. R. Batley et al., *New measurement of the $K^\pm \to \pi^\pm\mu^+\mu^-$ decay*, Phys. Lett. **B697** (2011) 107–115, arXiv:1011.4817 [hep-ex].

[331] NA48/1 Collaboration, J. R. Batley et al., *Observation of the rare decay $K_S \to \pi^0e^+e^-$*, Phys. Lett. **B576** (2003) 43–54, arXiv:hep-ex/0309075 [hep-ex].

[332] NA48/1 Collaboration, J. R. Batley et al., *Observation of the rare decay $K_S \to \pi^0\mu^+\mu^-$*, Phys. Lett. **B599** (2004) 197–211, arXiv:hep-ex/0409011 [hep-ex].

[333] A. Crivellin, G. D'Ambrosio, M. Hoferichter, and L. C. Tunstall, *Violation of lepton flavor and lepton flavor universality in rare kaon decays*, Phys. Rev. **D93** (2016) no. 7, 074038, arXiv:1601.00970 [hep-ph].

[334] S. Descotes-Genon, L. Hofer, J. Matias, and J. Virto, *Global analysis of $b \to s\ell\ell$ anomalies*, JHEP **06** (2016) 092, arXiv:1510.04239 [hep-ph].

[335] L. Cappiello, O. Catà, and G. D'Ambrosio, *Closing in on the radiative weak chiral couplings*, Eur. Phys. J. **C78** (2018) no. 3, 265, arXiv:1712.10270 [hep-ph].

[336] C. Marin Benito, L. Garrido Beltran, and X. Cid Vidal, *Feasibility study of $K^0_S \to \pi^+\pi^-e^+e^-$ at LHCb* , LHCb-PUB-2016-016. CERN-LHCb-PUB-2016-016, CERN, Geneva, Oct, 2016. https://cds.cern.ch/record/2193358.

[337] S. L. Glashow, D. Guadagnoli, and K. Lane, *Lepton Flavor Violation in B Decays?*, Phys. Rev. Lett. **114** (2015) 091801, arXiv:1411.0565 [hep-ph].

[338] D. Guadagnoli and K. Lane, *Charged-Lepton Mixing and Lepton Flavor Violation*, Phys. Lett. **B751** (2015) 54–58, arXiv:1507.01412 [hep-ph].

[339] S. M. Boucenna, J. W. F. Valle, and A. Vicente, *Are the B decay anomalies related to neutrino oscillations?*, Phys. Lett. **B750** (2015) 367–371, arXiv:1503.07099 [hep-ph].

[340] A. Celis, J. Fuentes-Martin, M. Jung, and H. Serodio, *Family nonuniversal Z' models with protected flavor-changing interactions*, Phys. Rev. **D92** (2015) no. 1, 015007, arXiv:1505.03079 [hep-ph].

[341] R. Alonso, B. Grinstein, and J. Martin Camalich, *Lepton universality violation and lepton flavor conservation in B-meson decays*, JHEP **10** (2015) 184, arXiv:1505.05164 [hep-ph].

[342] B. Gripaios, M. Nardecchia, and S. A. Renner, *Linear flavour violation and anomalies in B physics*, JHEP **06** (2016) 083, arXiv:1509.05020 [hep-ph].

[343] D. Bečirević, O. Sumensari, and R. Zukanovich Funchal, *Lepton flavor violation in exclusive*

$b \to s$ *decays*, Eur. Phys. J. **C76** (2016) no. 3, 134, arXiv:1602.00881 [hep-ph].

[344] D. Bečirević, N. Košnik, O. Sumensari, and R. Zukanovich Funchal, *Palatable Leptoquark Scenarios for Lepton Flavor Violation in Exclusive $b \to s\ell_1\ell_2$ modes*, JHEP **11** (2016) 035, arXiv:1608.07583 [hep-ph].

[345] G. Hiller, D. Loose, and K. Schönwald, *Leptoquark Flavor Patterns & B Decay Anomalies*, JHEP **12** (2016) 027, arXiv:1609.08895 [hep-ph].

[346] D. Bečirević and O. Sumensari, *A leptoquark model to accommodate $R_K^{\rm exp} < R_K^{\rm SM}$ and $R_{K^*}^{\rm exp} < R_{K^*}^{\rm SM}$*, JHEP **08** (2017) 104, arXiv:1704.05835 [hep-ph].

[347] S. F. King, *Flavourful Z models for $R_{K^{(*)}}$*, JHEP **08** (2017) 019, arXiv:1706.06100 [hep-ph].

[348] M. Bordone, C. Cornella, J. Fuentes-Martín, and G. Isidori, *Low-energy signatures of the $\rm PS^3$ model: from B-physics anomalies to LFV*, JHEP **10** (2018) 148, arXiv:1805.09328 [hep-ph].

[349] BNL Collaboration, D. Ambrose et al., *New limit on muon and electron lepton number violation from $K_L^0 \to \mu^\pm e^\mp$ decay*, Phys. Rev. Lett. **81** (1998) 5734–5737, arXiv:hep-ex/9811038 [hep-ex].

[350] KTeV Collaboration, E. Abouzaid et al., *Search for lepton flavor violating decays of the neutral kaon*, Phys. Rev. Lett. **100** (2008) 131803, arXiv:0711.3472 [hep-ex].

[351] A. Sher et al., *An Improved upper limit on the decay $K^+ \to \pi^+\mu^+e^-$*, Phys. Rev. **D72** (2005) 012005, arXiv:hep-ex/0502020 [hep-ex].

[352] R. Appel et al., *Search for lepton flavor violation in K+ decays*, Phys. Rev. Lett. **85** (2000) 2877–2880, arXiv:hep-ex/0006003 [hep-ex].

[353] NA62 Collaboration, C. NA62, *2018 NA62 Status Report to the CERN SPSC*, CERN-SPSC-2018-010. SPSC-SR-229, CERN, Geneva, Apr, 2018. http://cds.cern.ch/record/2312430.

[354] G. Wilkinson. https://indico.cern.ch/event/706741/contributions/3017537/attachments/1667814/2703428/TauFV_PBC.pdf. Talk at Physics Beyond Colliders, June 2018.

[355] A. A. Alves Junior et al., *Prospects for Measurements with Strange Hadrons at LHCb*, arXiv:1808.03477 [hep-ex].

[356] H.-M. Chang, M. González-Alonso, and J. Martin Camalich, *Nonstandard Semileptonic Hyperon Decays*, Phys. Rev. Lett. **114** (2015) no. 16, 161802, arXiv:1412.8484 [hep-ph].

[357] N. Cabibbo, E. C. Swallow, and R. Winston, *Semileptonic hyperon decays*, Ann. Rev. Nucl. Part. Sci. **53** (2003) 39–75, arXiv:hep-ph/0307298 [hep-ph].

[358] N. Cabibbo, E. C. Swallow, and R. Winston, *Semileptonic hyperon decays and CKM unitarity*, Phys. Rev. Lett. **92** (2004) 251803, arXiv:hep-ph/0307214 [hep-ph].

[359] V. Mateu and A. Pich, *V_{us} determination from hyperon semileptonic decays*, JHEP **10** (2005) 041, arXiv:hep-ph/0509045 [hep-ph].

[360] S. Sasaki, *Continuum limit of hyperon vector coupling $f_1(0)$ from 2+1 flavor domain wall QCD*, Phys. Rev. **D96** (2017) no. 7, 074509, arXiv:1708.04008 [hep-lat].

[361] LHCb collaboration, R. Aaij et al., *Evidence for the rare decay $\Sigma^+ \to p\mu^+\mu^-$*, Phys. Rev. Lett. **120** (2018) 221803, arXiv:1712.08606 [hep-ex].

[362] HyperCP Collaboration, H. Park et al., *Evidence for the decay $\Sigma^+ \to p\mu^+\mu^-$*, Phys. Rev. Lett. **94** (2005) 021801, arXiv:hep-ex/0501014 [hep-ex].

[363] X.-G. He, J. Tandean, and G. Valencia, *Decay rate and asymmetries of $\Sigma^+ \to p\mu^+\mu^-$*, JHEP **10** (2018) 040, arXiv:1806.08350 [hep-ph].

[364] A. Pich, *Precision Tau Physics*, Prog. Part. Nucl. Phys. **75** (2014) 41–85, arXiv:1310.7922

[hep-ph].

[365] ALEPH Collaboration, S. Schael et al., *Branching ratios and spectral functions of tau decays: Final ALEPH measurements and physics implications*, Phys. Rept. **421** (2005) 191–284, arXiv:hep-ex/0506072.

[366] W. Buchmuller and D. Wyler, *Effective Lagrangian Analysis of New Interactions and Flavor Conservation*, Nucl.Phys. **B268** (1986) 621.

[367] V. Cirigliano, M. Gonzalez-Alonso, and M. L. Graesser, *Non-standard Charged Current Interactions: beta decays versus the LHC*, JHEP **02** (2013) 046, arXiv:1210.4553 [hep-ph].

[368] J. de Blas, M. Chala, and J. Santiago, *Global Constraints on Lepton-Quark Contact Interactions*, Phys. Rev. **D88** (2013) 095011, arXiv:1307.5068 [hep-ph].

[369] D. A. Faroughy, A. Greljo, and J. F. Kamenik, *Confronting lepton flavor universality violation in B decays with high-p_T tau lepton searches at LHC*, Phys. Lett. **B764** (2017) 126–134, arXiv:1609.07138 [hep-ph].

[370] V. Cirigliano, A. Falkowski, M. González-Alonso, and A. Rodríguez-Sánchez, *Hadronic tau decays as New Physics probes in the LHC era*, arXiv:1809.01161 [hep-ph].

[371] ATLAS Collaboration, M. Aaboud et al., *A search for high-mass resonances decaying to $\tau\nu$ in pp collisions at $\sqrt{s}$ = 13 TeV with the ATLAS detector*, arXiv:1801.06992 [hep-ex].

[372] J. Alwall, R. Frederix, S. Frixione, V. Hirschi, F. Maltoni, O. Mattelaer, H. S. Shao, T. Stelzer, P. Torrielli, and M. Zaro, *The automated computation of tree-level and next-to-leading order differential cross sections, and their matching to parton shower simulations*, JHEP **07** (2014) 079, arXiv:1405.0301 [hep-ph].

[373] T. Sjöstrand, S. Ask, J. R. Christiansen, R. Corke, N. Desai, P. Ilten, S. Mrenna, S. Prestel, C. O. Rasmussen, and P. Z. Skands, *An Introduction to PYTHIA 8.2*, Comput. Phys. Commun. **191** (2015) 159–177, arXiv:1410.3012 [hep-ph].

[374] J. de Favereau, C. Delaere, P. Demin, A. Giammanco, V. Lemaître, et al., *DELPHES 3, A modular framework for fast simulation of a generic collider experiment*, arXiv:1307.6346 [hep-ex].

[375] B. Grzadkowski, M. Iskrzynski, M. Misiak, and J. Rosiek, *Dimension-Six Terms in the Standard Model Lagrangian*, JHEP **10** (2010) 085, arXiv:1008.4884 [hep-ph].

[376] R. Contino, A. Falkowski, F. Goertz, C. Grojean, and F. Riva, *On the Validity of the Effective Field Theory Approach to SM Precision Tests*, JHEP **07** (2016) 144, arXiv:1604.06444 [hep-ph].

[377] W. Altmannshofer, P. Bhupal Dev, and A. Soni, *$R_{D^{(*)}}$ anomaly: A possible hint for natural supersymmetry with R-parity violation*, Phys. Rev. **D96** (2017) no. 9, 095010, arXiv:1704.06659 [hep-ph].

[378] A. Greljo, J. Martin Camalich, and J. D. Ruiz-Álvarez, *The Mono-Tau Menace: From B Decays to High-p_T Tails*, arXiv:1811.07920 [hep-ph].

[379] BaBar Collaboration, J. P. Lees et al., *Measurement of an Excess of $\bar{B} \to D^{(*)}\tau^-\bar{\nu}_\tau$ Decays and Implications for Charged Higgs Bosons*, Phys. Rev. **D88** (2013) no. 7, 072012, arXiv:1303.0571 [hep-ex].

[380] Belle Collaboration, M. Huschle et al., *Measurement of the branching ratio of $\bar{B} \to D^{(*)}\tau^-\bar{\nu}_\tau$ relative to $\bar{B} \to D^{(*)}\ell^-\bar{\nu}_\ell$ decays with hadronic tagging at Belle*, Phys. Rev. **D92** (2015) no. 7, 072014, arXiv:1507.03233 [hep-ex].

[381] Belle Collaboration, Y. Sato et al., *Measurement of the branching ratio of $\bar{B}^0 \to D^{*+}\tau^-\bar{\nu}_\tau$ relative to $\bar{B}^0 \to D^{*+}\ell^-\bar{\nu}_\ell$ decays with a semileptonic tagging method*, Phys. Rev. **D94** (2016) no. 7, 072007, arXiv:1607.07923 [hep-ex].

[382] Particle Data Group Collaboration, C. Patrignani et al., *Review of Particle Physics*, Chin. Phys.

C40 (2016) no. 10, 100001.

[383] A. Filipuzzi, J. Portoles, and M. Gonzalez-Alonso, *U(2)^5 flavor symmetry and lepton universality violation in $W \to \tau\nu_\tau$*, Phys. Rev. **D85** (2012) 116010, arXiv:1203.2092 [hep-ph].

[384] D0 Collaboration, B. Abbott et al., *A measurement of the $W \to \tau\nu$ production cross section in $p\bar{p}$ collisions at $\sqrt{s} = 1.8$ TeV*, Phys. Rev. Lett. **84** (2000) 5710–5715, arXiv:hep-ex/9912065 [hep-ex].

[385] T.-P. Cheng and L.-F. Li, *Muon Number Nonconservation Effects in a Gauge Theory with V A Currents and Heavy Neutral Leptons*, Phys. Rev. **D16** (1977) 1425.

[386] B. W. Lee and R. E. Shrock, *Natural Suppression of Symmetry Violation in Gauge Theories: Muon - Lepton and Electron Lepton Number Nonconservation*, Phys. Rev. **D16** (1977) 1444.

[387] S. T. Petcov, *The Processes $mu \to e\gamma$, $\mu \to ee\bar{e}$, $\nu' \to \nu\gamma$ in the Weinberg-Salam Model with Neutrino Mixing*, Sov. J. Nucl. Phys. **25** (1977) 340. [Erratum: Yad. Fiz.25,1336(1977)].

[388] G. Hernández-Tomé, G. López Castro, and P. Roig, *Flavor violating leptonic decays of τ and μ leptons in the Standard Model with massive neutrinos*, arXiv:1807.06050 [hep-ph].

[389] L. Calibbi and G. Signorelli, *Charged Lepton Flavour Violation: An Experimental and Theoretical Introduction*, Riv. Nuovo Cim. **41** (2018) no. 2, 1, arXiv:1709.00294 [hep-ph].

[390] R. H. Bernstein and P. S. Cooper, *Charged Lepton Flavor Violation: An Experimenter's Guide*, Phys. Rept. **532** (2013) 27–64, arXiv:1307.5787 [hep-ex].

[391] MEG Collaboration, A. M. Baldini et al., *Search for the lepton flavour violating decay $\mu^+ \to e^+\gamma$ with the full dataset of the MEG experiment*, Eur. Phys. J. **C76** (2016) no. 8, 434, arXiv:1605.05081 [hep-ex].

[392] A. M. Baldini et al., *MEG Upgrade Proposal*, arXiv:1301.7225 [physics.ins-det].

[393] MEG II Collaboration, A. M. Baldini et al., *The design of the MEG II experiment*, Eur. Phys. J. **C78** (2018) no. 5, 380, arXiv:1801.04688 [physics.ins-det].

[394] A. Blondel et al., *Research Proposal for an Experiment to Search for the Decay $\mu \to eee$*, arXiv:1301.6113 [physics.ins-det].

[395] Mu3e Collaboration, N. Berger, *The Mu3e Experiment*, Nucl. Phys. Proc. Suppl. **248-250** (2014) 35–40.

[396] Mu2e Collaboration, L. Bartoszek et al., *Mu2e Technical Design Report*, arXiv:1501.05241 [physics.ins-det].

[397] COMET Collaboration, *COMET Phase-I technical design report*, (2014) .

[398] DeeMe Collaboration, *DeeMe KEK J-PARC Proposal*, (2010) .

[399] DeeMe Collaboration, T. M. Nguyen, *Search for $\mu \to e$ conversion with DeeMe experiment at J-PARC MLF*, PoS **FPCP2015** (2015) 060.

[400] D. E. Hazard and A. A. Petrov, *Radiative lepton flavor violating B, D, and K decays*, Phys. Rev. **D98** (2018) no. 1, 015027, arXiv:1711.05314 [hep-ph].

[401] D. E. Hazard and A. A. Petrov, *Lepton flavor violating quarkonium decays*, Phys. Rev. **D94** (2016) no. 7, 074023, arXiv:1607.00815 [hep-ph].

[402] S. Davidson, S. Lacroix, and P. Verdier, *LHC sensitivity to lepton flavour violating Z boson decays*, JHEP **09** (2012) 092, arXiv:1207.4894 [hep-ph].

[403] ALEPH Collaboration, D. Decamp et al., *Searches for new particles in Z decays using the ALEPH detector*, Phys. Rept. **216** (1992) 253–340.

[404] L3 Collaboration, O. Adriani et al., *Search for lepton flavor violation in Z decays*, Phys. Lett. **B316** (1993) 427–434.

[405] OPAL Collaboration, R. Akers et al., *A Search for lepton flavor violating Z^0 decays*, Z. Phys. **C67** (1995) 555–564.

[406] DELPHI Collaboration, P. Abreu et al., *Search for lepton flavor number violating Z^0 decays*, Z. Phys. **C73** (1997) 243–251.

[407] ATLAS Collaboration, M. Aaboud et al., *A search for lepton-flavor-violating decays of the Z boson into a τ-lepton and a light lepton with the ATLAS detector*, Submitted to: Phys. Rev. (2018) , arXiv:1804.09568 [hep-ex].

[408] A. Abada, V. De Romeri, and A. M. Teixeira, *Effect of steriles states on lepton magnetic moments and neutrinoless double beta decay*, JHEP **09** (2014) 074, arXiv:1406.6978 [hep-ph].

[409] V. De Romeri, M. J. Herrero, X. Marcano, and F. Scarcella, *Lepton flavor violating Z decays: A promising window to low scale seesaw neutrinos*, Phys. Rev. **D95** (2017) no. 7, 075028, arXiv:1607.05257 [hep-ph].

[410] B. Bhattacharya, R. Morgan, J. Osborne, and A. A. Petrov, *Studies of Lepton Flavor Violation at the LHC*, Phys. Lett. **B785** (2018) 165–170, arXiv:1802.06082 [hep-ph].

[411] Y. Cai, M. A. Schmidt, and G. Valencia, *Lepton-flavour-violating gluonic operators: constraints from the LHC and low energy experiments*, JHEP **05** (2018) 143, arXiv:1802.09822 [hep-ph].

[412] BaBar Collaboration, B. Aubert et al., *Search for Lepton Flavor Violating Decays $\tau^\pm \to \ell^\pm\pi^0$, $\ell^\pm\eta$, $\ell^\pm\eta'$*, Phys. Rev. Lett. **98** (2007) 061803, arXiv:hep-ex/0610067 [hep-ex].

[413] BaBar Collaboration, B. Aubert et al., *Search for lepton flavor violating decays $\tau^\pm \to \ell^\pm\omega$ ($\ell = e,\ \mu$)*, Phys. Rev. Lett. **100** (2008) 071802, arXiv:0711.0980 [hep-ex].

[414] BaBar Collaboration, B. Aubert et al., *Searches for Lepton Flavor Violation in the Decays $\tau^\pm \to e^\pm\gamma$ and $\tau^\pm \to \mu^\pm\gamma$*, Phys. Rev. Lett. **104** (2010) 021802, arXiv:0908.2381 [hep-ex].

[415] BaBar Collaboration, B. Aubert et al., *Search for Lepton Flavor Violating Decays $\tau \to \ell^- K^0_S$ with the BABAR Experiment*, Phys. Rev. **D79** (2009) 012004, arXiv:0812.3804 [hep-ex].

[416] BaBar Collaboration, B. Aubert et al., *Improved limits on lepton flavor violating tau decays to $\ell\phi$, $\ell\rho$, ℓK^* and $\ell\bar{K}^*$*, Phys. Rev. Lett. **103** (2009) 021801, arXiv:0904.0339 [hep-ex].

[417] BaBar Collaboration, J. P. Lees et al., *Limits on tau Lepton-Flavor Violating Decays in three charged leptons*, Phys. Rev. **D81** (2010) 111101, arXiv:1002.4550 [hep-ex].

[418] Belle Collaboration, Y. Miyazaki et al., *Search for lepton and baryon number violating tau-decays into anti-Lambda pi- and Lambda pi-*, Phys. Lett. **B632** (2006) 51–57, arXiv:hep-ex/0508044 [hep-ex].

[419] Belle Collaboration, K. Hayasaka et al., *New Search for $\tau \to \mu\gamma$ and $\tau \to e\gamma$ Decays at Belle*, Phys. Lett. **B666** (2008) 16–22, arXiv:0705.0650 [hep-ex].

[420] Belle Collaboration, Y. Miyazaki et al., *Search for lepton flavor violating τ^- decays into $\ell^-\eta$, $\ell^-\eta'$ and $\ell^-\pi^0$*, Phys. Lett. **B648** (2007) 341–350, arXiv:hep-ex/0703009 [HEP-EX].

[421] Belle Collaboration, Y. Miyazaki et al., *Search for Lepton-Flavor-Violating tau Decays into Lepton and $f_0(980)$ Meson*, Phys. Lett. **B672** (2009) 317–322, arXiv:0810.3519 [hep-ex].

[422] Belle Collaboration, Y. Miyazaki et al., *Search for Lepton Flavor Violating tau^- Decays into $\ell^- K^0_S$ and $\ell^- K^0_S K^0_S$*, Phys. Lett. **B692** (2010) 4–9, arXiv:1003.1183 [hep-ex].

[423] K. Hayasaka et al., *Search for Lepton Flavor Violating Tau Decays into Three Leptons with 719 Million Produced $\tau^+\tau^-$ Pairs*, Phys. Lett. **B687** (2010) 139–143, arXiv:1001.3221 [hep-ex].

[424] Belle Collaboration, Y. Miyazaki et al., *Search for Lepton-Flavor-Violating tau Decays into a Lepton and a Vector Meson*, Phys. Lett. **B699** (2011) 251–257, arXiv:1101.0755 [hep-ex].

[425] CLEO Collaboration, T. J. V. Bowcock et al., *Search for Neutrinoless Decays of the τ Lepton*, Phys. Rev. **D41** (1990) 805.

[426] CLEO Collaboration, G. Bonvicini et al., *Search for neutrinoless tau decays involving pi0 or eta mesons*, Phys. Rev. Lett. **79** (1997) 1221–1224, arXiv:hep-ex/9704010 [hep-ex].

[427] CLEO Collaboration, S. Chen et al., *Search for neutrinoless tau decays involving the K^0_S meson*, Phys. Rev. **D66** (2002) 071101, arXiv:hep-ex/0208019 [hep-ex].

[428] LHCb collaboration, R. Aaij et al., *Search for the lepton flavour violating decay $\tau^- \to \mu^-\mu^+\mu^-$*, JHEP **02** (2015) 121, arXiv:1409.8548 [hep-ex].

[429] ATLAS Collaboration, G. Aad et al., *Probing lepton flavour violation via neutrinoless $\tau \to 3\mu$ decays with the ATLAS detector*, Eur. Phys. J. **C76** (2016) no. 5, 232, arXiv:1601.03567 [hep-ex].

[430] A. Celis, V. Cirigliano, and E. Passemar, *Model-discriminating power of lepton flavor violating τ decays*, Phys. Rev. **D89** (2014) no. 9, 095014, arXiv:1403.5781 [hep-ph].

[431] B. M. Dassinger, T. Feldmann, T. Mannel, and S. Turczyk, *Model-independent analysis of lepton flavour violating tau decays*, JHEP **10** (2007) 039, arXiv:0707.0988 [hep-ph].

[432] A. Matsuzaki and A. I. Sanda, *Analysis of lepton flavor violating $\tau^\pm \to \mu^\pm\mu^\pm\mu^\mp$ decays*, Phys. Rev. **D77** (2008) 073003, arXiv:0711.0792 [hep-ph].

[433] P. Paradisi, *Higgs-mediated $\tau \to \mu$ and $\tau \to e$ transitions in II Higgs doublet model and supersymmetry*, JHEP **02** (2006) 050, arXiv:hep-ph/0508054 [hep-ph].

[434] A. Celis, V. Cirigliano, and E. Passemar, *Lepton flavor violation in the Higgs sector and the role of hadronic τ-lepton decays*, Phys. Rev. **D89** (2014) 013008, arXiv:1309.3564 [hep-ph].

[435] A. A. Petrov and D. V. Zhuridov, *Lepton flavor-violating transitions in effective field theory and gluonic operators*, Phys. Rev. **D89** (2014) no. 3, 033005, arXiv:1308.6561 [hep-ph].

[436] CMS Collaboration, *The Phase-2 Upgrade of the CMS Muon Detectors* , CERN-LHCC-2017-012 ; CMS-TDR-016, CERN, Geneva, 2017. https://cds.cern.ch/record/2283189/.

[437] ATLAS Collaboration, *Prospects for lepton flavour violation measurements in $\tau \to 3\mu$ decays with the ATLAS detector at the HL-LHC*, ATL-PHYS-PUB-2018-032, CERN, Geneva, Nov, 2018. http://cds.cern.ch/record/2647956.

[438] LHCb collaboration, R. Aaij et al., *Search for baryon-number-violating Ξ^0_b oscillations*, Phys. Rev. Lett. **119** (2017) 181807, arXiv:1708.05808 [hep-ex].

[439] LHCb collaboration, R. Aaij et al., *New algorithms for identifying the flavour of B^0 mesons using pions and protons*, Eur. Phys. J. **C77** (2017) 238, arXiv:1610.06019 [hep-ex].

[440] H.-X. Chen, W. Chen, X. Liu, and S.-L. Zhu, *The hidden-charm pentaquark and tetraquark states*, Phys. Rept. **639** (2016) 1–121, arXiv:1601.02092 [hep-ph].

[441] A. Hosaka, T. Iijima, K. Miyabayashi, Y. Sakai, and S. Yasui, *Exotic hadrons with heavy flavors: X, Y, Z, and related states*, PTEP **2016** (2016) no. 6, 062C01, arXiv:1603.09229 [hep-ph].

[442] R. F. Lebed, R. E. Mitchell, and E. S. Swanson, *Heavy-quark QCD exotica*, Prog. Part. Nucl. Phys. **93** (2017) 143–194, arXiv:1610.04528 [hep-ph].

[443] A. Esposito, A. Pilloni, and A. D. Polosa, *Multiquark Resonances*, Phys. Rept. **668** (2016) 1–97, arXiv:1611.07920 [hep-ph].

[444] F.-K. Guo, C. Hanhart, U.-G. Meißner, Q. Wang, Q. Zhao, and B.-S. Zou, *Hadronic molecules*, Rev. Mod. Phys. **90** (2018) no. 1, 015004, arXiv:1705.00141 [hep-ph].

[445] A. Ali, J. S. Lange, and S. Stone, *Exotics: Heavy pentaquarks and tetraquarks*, Prog. Part. Nucl. Phys. **97** (2017) 123–198, arXiv:1706.00610 [hep-ph].

[446] S. L. Olsen, T. Skwarnicki, and D. Zieminska, *Nonstandard heavy mesons and baryons: Experimental evidence*, Rev. Mod. Phys. **90** (2018) no. 1, 015003, arXiv:1708.04012 [hep-ph].

[447] M. Karliner, J. L. Rosner, and T. Skwarnicki, *Multiquark states*, arXiv:1711.10626 [hep-ph].

[448] C.-Z. Yuan, *The XYZ states revisited*, Int. J. Mod. Phys. **A33** (2018) no. 21, 1830018, arXiv:1808.01570 [hep-ex].

[449] E. Eichten, K. Gottfried, T. Kinoshita, K. D. Lane, and T.-M. Yan, *Charmonium: The model*, Phys. Rev. **D17** (1978) 3090.

[450] E. Eichten, K. Gottfried, T. Kinoshita, K. D. Lane, and T.-M. Yan, *Charmonium: Comparison with Experiment*, Phys. Rev. **D21** (1980) 203.

[451] S. Godfrey and N. Isgur, *Mesons in a Relativized Quark Model with Chromodynamics*, Phys. Rev. **D32** (1985) 189–231.

[452] W. E. Caswell and G. P. Lepage, *Effective lagrangians for bound state problems in QED, QCD, and other field theories*, Phys. Lett. **167B** (1986) 437–442.

[453] G. T. Bodwin, E. Braaten, and G. P. Lepage, *Rigorous QCD analysis of inclusive annihilation and production of heavy quarkonium*, Phys. Rev. **D51** (1995) 1125–1171, arXiv:hep-ph/9407339 [hep-ph].

[454] N. Brambilla, A. Pineda, J. Soto, and A. Vairo, *Effective field theories for heavy quarkonium*, Rev. Mod. Phys. **77** (2005) 1423, arXiv:hep-ph/0410047 [hep-ph].

[455] A. Pineda, *Review of Heavy Quarkonium at weak coupling*, Prog. Part. Nucl. Phys. **67** (2012) 735–785, arXiv:1111.0165 [hep-ph].

[456] M. Gell-Mann, *A Schematic Model of Baryons and Mesons*, Phys. Lett. **8** (1964) 214–215.

[457] G. Zweig, *An SU(3) model for strong interaction symmetry and its breaking. Version 2*, in *DEVELOPMENTS IN THE QUARK THEORY OF HADRONS. VOL. 1. 1964 - 1978*, D. Lichtenberg and S. P. Rosen, eds., pp. 22–101. 1964.

[458] H. J. Lipkin, *NEW POSSIBILITIES FOR EXOTIC HADRONS*, in *HADRONS, QUARKS AND GLUONS. PROCEEDINGS, HADRONIC SESSION OF THE 22ND RENCONTRES DE MORIOND, LES ARCS, FRANCE, MARCH 15-21, 1987*, pp. 691–696. 1987.

[459] LHCb Collaboration, R. Aaij et al., *Observation of $J/\psi p$ Resonances Consistent with Pentaquark States in $\Lambda_b^0 \to J/\psi K^- p$ Decays*, Phys. Rev. Lett. **115** (2015) 072001, arXiv:1507.03414 [hep-ex].

[460] L. Maiani, F. Piccinini, A. D. Polosa, and V. Riquer, *Diquark-antidiquarks with hidden or open charm and the nature of X(3872)*, Phys. Rev. **D71** (2005) 014028, arXiv:hep-ph/0412098 [hep-ph].

[461] L. Maiani, F. Piccinini, A. D. Polosa, and V. Riquer, *The Z(4430) and a New Paradigm for Spin Interactions in Tetraquarks*, Phys. Rev. **D89** (2014) 114010, arXiv:1405.1551 [hep-ph].

[462] L. Maiani, A. D. Polosa, and V. Riquer, *A Theory of X and Z Multiquark Resonances*, Phys. Lett. **B778** (2018) 247–251, arXiv:1712.05296 [hep-ph].

[463] G. C. Rossi and G. Veneziano, *Isospin mixing of narrow pentaquark states*, Phys. Lett. **B597** (2004) 338–345, arXiv:hep-ph/0404262 [hep-ph].

[464] L. Maiani, A. D. Polosa, and V. Riquer, *The charged Z(4430) in the diquark-antidiquark picture*, New J. Phys. **10** (2008) 073004.

[465] L. Maiani, A. D. Polosa, and V. Riquer, *The Charged Z(4433): Towards a new spectroscopy*, arXiv:0708.3997 [hep-ph].

[466] G. Cotugno, R. Faccini, A. D. Polosa, and C. Sabelli, *Charmed Baryonium*, Phys. Rev. Lett. **104** (2010) 132005, arXiv:0911.2178 [hep-ph].

[467] A. Esposito, A. L. Guerrieri, F. Piccinini, A. Pilloni, and A. D. Polosa, *Four-Quark Hadrons: an Updated Review*, Int. J. Mod. Phys. **A30** (2015) 1530002, arXiv:1411.5997 [hep-ph].

[468] A. Esposito, A. Pilloni, and A. D. Polosa, *Hybridized Tetraquarks*, Phys. Lett. **B758** (2016)

292–295, arXiv:1603.07667 [hep-ph].

[469] R. L. Jaffe and F. Wilczek, *Diquarks and exotic spectroscopy*, Phys. Rev. Lett. **91** (2003) 232003, arXiv:hep-ph/0307341 [hep-ph].

[470] A. Selem and F. Wilczek, *Hadron systematics and emergent diquarks*, in *Proceedings, Ringberg Workshop on New Trends in HERA Physics 2005: Ringberg Castle, Tegernsee, Germany, October 2-7, 2005*, pp. 337–356. 2006. arXiv:hep-ph/0602128 [hep-ph].

[471] A. Esposito and A. D. Polosa, *A $bb\bar{b}\bar{b}$di-bottomonium at the LHC?*, arXiv:1807.06040 [hep-ph].

[472] S. J. Brodsky, D. S. Hwang, and R. F. Lebed, *Dynamical Picture for the Formation and Decay of the Exotic XYZ Mesons*, Phys. Rev. Lett. **113** (2014) no. 11, 112001, arXiv:1406.7281 [hep-ph].

[473] R. F. Lebed, *Spectroscopy of Exotic Hadrons Formed from Dynamical Diquarks*, Phys. Rev. **D96** (2017) no. 11, 116003, arXiv:1709.06097 [hep-ph].

[474] R. F. Lebed, *The Pentaquark Candidates in the Dynamical Diquark Picture*, Phys. Lett. **B749** (2015) 454–457, arXiv:1507.05867 [hep-ph].

[475] E. Braaten, *How the $Z_c(3900)$ Reveals the Spectra of Quarkonium Hybrid and Tetraquark Mesons*, Phys. Rev. Lett. **111** (2013) 162003, arXiv:1305.6905 [hep-ph].

[476] S. J. Brodsky and R. F. Lebed, *QCD dynamics of tetraquark production*, Phys. Rev. **D91** (2015) 114025, arXiv:1505.00803 [hep-ph].

[477] R. F. Lebed, *Constituent Counting Rules and Exotic Hadrons*, Few Body Syst. **59** (2018) no. 5, 106, arXiv:1807.01650 [hep-ph].

[478] Y. S. Kalashnikova and A. V. Nefediev, *$X(3872)$ in the molecular model*, arXiv:1811.01324 [hep-ph].

[479] S. Weinberg, *Evidence That the Deuteron Is Not an Elementary Particle*, Phys. Rev. **137** (1965) B672–B678.

[480] T. Sekihara, T. Hyodo, and D. Jido, *Comprehensive analysis of the wave function of a hadronic resonance and its compositeness*, PTEP **2015** (2015) 063D04, arXiv:1411.2308 [hep-ph].

[481] R. Molina, M. Döring, and E. Oset, *Determination of the compositeness of resonances from decays: the case of the $B_s^0 \to J/\psi f_1(1285)$*, Phys. Rev. **D93** (2016) no. 11, 114004, arXiv:1604.02574 [hep-ph].

[482] E. Oset et al., *Weak decays of heavy hadrons into dynamically generated resonances*, Int. J. Mod. Phys. **E25** (2016) 1630001, arXiv:1601.03972 [hep-ph].

[483] E. J. Eichten, K. Lane, and C. Quigg, *New states above charm threshold*, Phys. Rev. **D73** (2006) 014014, arXiv:hep-ph/0511179 [hep-ph]. [Erratum: Phys. Rev.D73,079903(2006)].

[484] Yu. S. Kalashnikova, *Coupled-channel model for charmonium levels and an option for X(3872)*, Phys. Rev. **D72** (2005) 034010, arXiv:hep-ph/0506270 [hep-ph].

[485] V. Baru, C. Hanhart, Yu. S. Kalashnikova, A. E. Kudryavtsev, and A. V. Nefediev, *Interplay of quark and meson degrees of freedom in a near-threshold resonance*, Eur. Phys. J. **A44** (2010) 93–103, arXiv:1001.0369 [hep-ph].

[486] N. A. Törnqvist, *The Meson Mass Spectrum and Unitarity*, Annals Phys. **123** (1979) 1.

[487] P. G. Ortega, D. R. Entem, and F. Fernandez, *Molecular Structures in Charmonium Spectrum: The XYZ Puzzle*, J. Phys. **G40** (2013) 065107, arXiv:1205.1699 [hep-ph].

[488] J. Segovia, P. G. Ortega, D. R. Entem, and F. Fernández, *Bottomonium spectrum revisited*, Phys. Rev. **D93** (2016) no. 7, 074027, arXiv:1601.05093 [hep-ph].

[489] J. Vijande, F. Fernandez, and A. Valcarce, *Constituent quark model study of the meson spectra*, J. Phys. **G31** (2005) 481, arXiv:hep-ph/0411299 [hep-ph].

[490] J. Segovia, D. R. Entem, F. Fernandez, and E. Hernandez, *Constituent quark model description*

of charmonium phenomenology, Int. J. Mod. Phys. **E22** (2013) 1330026, arXiv:1309.6926 [hep-ph].

[491] E. S. Swanson, *Unquenching the quark model and screened potentials*, J. Phys. **G31** (2005) 845–854, arXiv:hep-ph/0504097 [hep-ph].

[492] T. Barnes and E. S. Swanson, *Hadron loops: General theorems and application to charmonium*, Phys. Rev. **C77** (2008) 055206, arXiv:0711.2080 [hep-ph].

[493] Y. C. Tang, M. Lemere, and D. R. Thompson, *Resonating-group method for nuclear many-body problems*, Phys. Rept. **47** (1978) 167–223.

[494] D. R. Entem, F. Fernandez, and A. Valcarce, *Chiral quark model of the N N system within a Lippmann-Schwinger resonating group method*, Phys. Rev. **C62** (2000) 034002.

[495] L. Micu, *Decay rates of meson resonances in a quark model*, Nucl. Phys. **B10** (1969) 521–526.

[496] A. Le Yaouanc, L. Oliver, O. Pene, and J. C. Raynal, *Naive quark pair creation model of strong interaction vertices*, Phys. Rev. **D8** (1973) 2223–2234.

[497] A. Le Yaouanc, L. Oliver, O. Pene, and J. C. Raynal, *Naive quark pair creation model and baryon decays*, Phys. Rev. **D9** (1974) 1415–1419.

[498] P. G. Ortega, J. Segovia, D. R. Entem, and F. Fernandez, *Canonical description of the new LHCb resonances*, Phys. Rev. **D94** (2016) no. 11, 114018, arXiv:1608.01325 [hep-ph].

[499] S. Godfrey, *Testing the nature of the D(sJ)*(2317)+ and D(sJ)(2463)+ states using radiative transitions*, Phys. Lett. **B568** (2003) 254–260, arXiv:hep-ph/0305122 [hep-ph].

[500] P. Colangelo and F. De Fazio, *Understanding D(sJ)(2317)*, Phys. Lett. **B570** (2003) 180–184, arXiv:hep-ph/0305140 [hep-ph].

[501] T. Mehen and R. P. Springer, *Even- and odd-parity charmed meson masses in heavy hadron chiral perturbation theory*, Phys. Rev. **D72** (2005) 034006, arXiv:hep-ph/0503134 [hep-ph].

[502] O. Lakhina and E. S. Swanson, *A Canonical Ds(2317)?*, Phys. Lett. **B650** (2007) 159–165, arXiv:hep-ph/0608011 [hep-ph].

[503] W. A. Bardeen, E. J. Eichten, and C. T. Hill, *Chiral multiplets of heavy - light mesons*, Phys. Rev. **D68** (2003) 054024, arXiv:hep-ph/0305049 [hep-ph].

[504] M. A. Nowak, M. Rho, and I. Zahed, *Chiral doubling of heavy light hadrons: BABAR 2317 MeV/c^2 and CLEO 2463 MeV/c^2 discoveries*, Acta Phys. Polon. **B35** (2004) 2377–2392, arXiv:hep-ph/0307102 [hep-ph].

[505] S. Godfrey and K. Moats, *Properties of Excited Charm and Charm-Strange Mesons*, Phys. Rev. **D93** (2016) no. 3, 034035, arXiv:1510.08305 [hep-ph].

[506] T. E. Browder, S. Pakvasa, and A. A. Petrov, *Comment on the new $D_s^{*+}\pi^0$ resonances*, Phys. Lett. **B578** (2004) 365–368, arXiv:hep-ph/0307054 [hep-ph].

[507] T. Barnes, F. E. Close, and H. J. Lipkin, *Implications of a DK molecule at 2.32-GeV*, Phys. Rev. **D68** (2003) 054006, arXiv:hep-ph/0305025 [hep-ph].

[508] E. van Beveren and G. Rupp, *Observed D(s)(2317) and tentative D(2030) as the charmed cousins of the light scalar nonet*, Phys. Rev. Lett. **91** (2003) 012003, arXiv:hep-ph/0305035 [hep-ph].

[509] E. E. Kolomeitsev and M. F. M. Lutz, *On Heavy light meson resonances and chiral symmetry*, Phys. Lett. **B582** (2004) 39–48, arXiv:hep-ph/0307133 [hep-ph].

[510] F.-K. Guo, P.-N. Shen, H.-C. Chiang, R.-G. Ping, and B.-S. Zou, *Dynamically generated 0^+ heavy mesons in a heavy chiral unitary approach*, Phys. Lett. **B641** (2006) 278–285, arXiv:hep-ph/0603072 [hep-ph].

[511] F.-K. Guo, P.-N. Shen, and H.-C. Chiang, *Dynamically generated 1^+ heavy mesons*, Phys. Lett. **B647** (2007) 133–139, arXiv:hep-ph/0610008 [hep-ph].

[512] D. Gamermann, E. Oset, D. Strottman, and M. J. Vicente Vacas, *Dynamically generated open and hidden charm meson systems*, Phys. Rev. **D76** (2007) 074016, arXiv:hep-ph/0612179 [hep-ph].

[513] L. Liu, K. Orginos, F.-K. Guo, C. Hanhart, and U.-G. Meißner, *Interactions of charmed mesons with light pseudoscalar mesons from lattice QCD and implications on the nature of the* $D^*_{s0}(2317)$, Phys. Rev. **D87** (2013) no. 1, 014508, arXiv:1208.4535 [hep-lat].

[514] G. S. Bali, S. Collins, A. Cox, and A. Schäfer, *Masses and decay constants of the* $D^*_{s0}(2317)$ *and* $D_{s1}(2460)$ *from* $N_f = 2$ *lattice QCD close to the physical point*, Phys. Rev. **D96** (2017) no. 7, 074501, arXiv:1706.01247 [hep-lat].

[515] C. B. Lang, L. Leskovec, D. Mohler, S. Prelovsek, and R. M. Woloshyn, *Ds mesons with DK and D*K scattering near threshold*, Phys. Rev. **D90** (2014) no. 3, 034510, arXiv:1403.8103 [hep-lat].

[516] A. Martínez Torres, E. Oset, S. Prelovsek, and A. Ramos, *Reanalysis of lattice QCD spectra leading to the* $D^*_{s0}(2317)$ *and* $D^*_{s1}(2460)$, JHEP **05** (2015) 153, arXiv:1412.1706 [hep-lat].

[517] M. Albaladejo, P. Fernandez-Soler, J. Nieves, and P. G. Ortega, *Contribution of constituent quark model* $c\bar{s}$ *states to the dynamics of the* $D^*_{s0}(2317)$ *and* $D_{s1}(2460)$ *resonances*, Eur. Phys. J. **C78** (2018) no. 9, 722, arXiv:1805.07104 [hep-ph].

[518] LHCb Collaboration, R. Aaij et al., χ_{c1} *and* χ_{c2} *Resonance Parameters with the Decays* $\chi_{c1,c2} \to J/\psi\mu^+\mu^-$, Phys. Rev. Lett. **119** (2017) no. 22, 221801, arXiv:1709.04247 [hep-ex].

[519] M. Albaladejo, P. Fernandez-Soler, F.-K. Guo, and J. Nieves, *Two-pole structure of the* $D^*_0(2400)$, Phys. Lett. **B767** (2017) 465–469, arXiv:1610.06727 [hep-ph].

[520] M.-L. Du, M. Albaladejo, P. Fernandez-Soler, F.-K. Guo, C. Hanhart, U.-G. Meißner, J. Nieves, and D.-L. Yao, *A new paradigm for heavy-light meson spectroscopy*, arXiv:1712.07957 [hep-ph].

[521] LHCb Collaboration, R. Aaij et al., *Amplitude analysis of* $B^- \to D^+\pi^-\pi^-$ *decays*, Phys. Rev. **D94** (2016) no. 7, 072001, arXiv:1608.01289 [hep-ex].

[522] BaBar Collaboration, B. Aubert et al., *Observation of tree-level* B *decays with s anti-s production from gluon radiation.*, Phys. Rev. Lett. **100** (2008) 171803, arXiv:0707.1043 [hep-ex].

[523] Belle Collaboration, J. Wiechczynski et al., *Measurement of* $B \to D_s^{(*)} K\pi$ *branching fractions*, Phys. Rev. **D80** (2009) 052005, arXiv:0903.4956 [hep-ex].

[524] Belle Collaboration, J. Wiechczynski et al., *Measurement of* $B^0 \to D_s^- K^0_S \pi^+$ *and* $B^+ \to D_s^- K^+ K^+$ *branching fractions*, Phys. Rev. **D91** (2015) no. 3, 032008, arXiv:1411.2035 [hep-ex].

[525] C. B. Lang, D. Mohler, S. Prelovsek, and R. M. Woloshyn, *Predicting positive parity* B_s *mesons from lattice QCD*, Phys. Lett. **B750** (2015) 17–21, arXiv:1501.01646 [hep-lat].

[526] M. Cleven, H. W. Grießhammer, F.-K. Guo, C. Hanhart, and U.-G. Meißner, *Strong and radiative decays of the* $D^*_{s0}(2317)$ *and* $D_{s1}(2460)$, Eur. Phys. J. **A50** (2014) 149, arXiv:1405.2242 [hep-ph].

[527] LHCb Collaboration, R. Aaij et al., *First observation of the decay* $B^*_{s2}(5840)^0 \to B^{*+}K^-$ *and studies of excited* B^0_s *mesons*, Phys. Rev. Lett. **110** (2013) no. 15, 151803, arXiv:1211.5994 [hep-ex].

[528] S. Godfrey, K. Moats, and E. S. Swanson, B *and* B_s *Meson Spectroscopy*, Phys. Rev. **D94** (2016) no. 5, 054025, arXiv:1607.02169 [hep-ph].

[529] BaBar Collaboration, B. Aubert et al., *Observation of a New* D_s *Meson Decaying to* DK *at a*

Mass of 2.86 GeV/c^2, Phys. Rev. Lett. **97** (2006) 222001, arXiv:hep-ex/0607082 [hep-ex].

[530] LHCb Collaboration, R. Aaij et al., *Observation of overlapping spin-1 and spin-3 $\bar{D}^0 K^-$ resonances at mass* $2.86\text{GeV}/c^2$, Phys. Rev. Lett. **113** (2014) 162001, arXiv:1407.7574 [hep-ex].

[531] BaBar Collaboration, B. Aubert et al., *Study of D_{sJ} decays to $D^* K$ in inclusive e^+e^- interactions*, Phys. Rev. **D80** (2009) 092003, arXiv:0908.0806 [hep-ex].

[532] P. Colangelo, F. De Fazio, and S. Nicotri, *$D_{sJ}(2860)$ resonance and the $s_l^P = 5/2^-$ $c\bar{s}(c\bar{q})$ doublet*, Phys. Lett. **B642** (2006) 48–52, arXiv:hep-ph/0607245 [hep-ph].

[533] J. Segovia, D. R. Entem, and F. Fernandez, *Charmed-strange Meson Spectrum: Old and New Problems*, Phys. Rev. **D91** (2015) no. 9, 094020, arXiv:1502.03827 [hep-ph].

[534] F.-K. Guo and U.-G. Meißner, *More kaonic bound states and a comprehensive interpretation of the D_{sJ} states*, Phys. Rev. **D84** (2011) 014013, arXiv:1102.3536 [hep-ph].

[535] Hadron Spectrum Collaboration, G. K. C. Cheung, C. O'Hara, G. Moir, M. Peardon, S. M. Ryan, C. E. Thomas, and D. Tims, *Excited and exotic charmonium, D_s and D meson spectra for two light quark masses from lattice QCD*, JHEP **12** (2016) 089, arXiv:1610.01073 [hep-lat].

[536] M. Luscher, *Two particle states on a torus and their relation to the scattering matrix*, Nucl. Phys. **B354** (1991) 531–578.

[537] D. Mohler, S. Prelovsek, and R. M. Woloshyn, *$D\pi$ scattering and D meson resonances from lattice QCD*, Phys. Rev. **D87** (2013) no. 3, 034501, arXiv:1208.4059 [hep-lat].

[538] G. Moir, M. Peardon, S. M. Ryan, C. E. Thomas, and D. J. Wilson, *Coupled-Channel $D\pi$, $D\eta$ and $D_s\bar{K}$ Scattering from Lattice QCD*, JHEP **10** (2016) 011, arXiv:1607.07093 [hep-lat].

[539] M. Padmanath, R. G. Edwards, N. Mathur, and M. Peardon, *Excited-state spectroscopy of singly, doubly and triply-charmed baryons from lattice QCD*, in *Proceedings, 6th International Workshop on Charm Physics (Charm 2013): Manchester, UK, August 31-September 4, 2013*. 2013. arXiv:1311.4806 [hep-lat]. http://inspirehep.net/record/1265083/files/arXiv:1311.4806.pdf.

[540] LHCb Collaboration, R. Aaij et al., *Observation of five new narrow Ω_c^0 states decaying to $\Xi_c^+ K^-$*, Phys. Rev. Lett. **118** (2017) no. 18, 182001, arXiv:1703.04639 [hep-ex].

[541] M. Padmanath and N. Mathur, *Quantum Numbers of Recently Discovered Ω_c^0 Baryons from Lattice QCD*, Phys. Rev. Lett. **119** (2017) no. 4, 042001, arXiv:1704.00259 [hep-ph].

[542] M. Karliner and J. L. Rosner, *Very narrow excited Ω_c baryons*, Phys. Rev. **D95** (2017) no. 11, 114012, arXiv:1703.07774 [hep-ph].

[543] K.-L. Wang, L.-Y. Xiao, X.-H. Zhong, and Q. Zhao, *Understanding the newly observed Ω_c states through their decays*, Phys. Rev. **D95** (2017) no. 11, 116010, arXiv:1703.09130 [hep-ph].

[544] B. Chen and X. Liu, *New Ω_c^0 baryons discovered by LHCb as the members of $1P$ and $2S$ states*, Phys. Rev. **D96** (2017) no. 9, 094015, arXiv:1704.02583 [hep-ph].

[545] H.-Y. Cheng and C.-W. Chiang, *Quantum numbers of Ω_c states and other charmed baryons*, Phys. Rev. **D95** (2017) no. 9, 094018, arXiv:1704.00396 [hep-ph].

[546] W. Wang and R.-L. Zhu, *Interpretation of the newly observed Ω_c^0 resonances*, Phys. Rev. **D96** (2017) no. 1, 014024, arXiv:1704.00179 [hep-ph].

[547] G. Yang and J. Ping, *Dynamical study of Ω_c^0 in the chiral quark model*, Phys. Rev. **D97** (2018) no. 3, 034023, arXiv:1703.08845 [hep-ph].

[548] A. Ali, L. Maiani, A. V. Borisov, I. Ahmed, M. Jamil Aslam, A. Ya. Parkhomenko, A. D. Polosa, and A. Rehman, *A new look at the Y tetraquarks and Ω_c baryons in the diquark model*,

Eur. Phys. J. **C78** (2018) no. 1, 29, arXiv:1708.04650 [hep-ph].

[549] H.-C. Kim, M. V. Polyakov, and M. Praszałowicz, *Possibility of the existence of charmed exotica*, Phys. Rev. **D96** (2017) no. 1, 014009, arXiv:1704.04082 [hep-ph]. [Addendum: Phys. Rev.D96,no.3,039902(2017)].

[550] J. Nieves, R. Pavao, and L. Tolos, Ω_c *excited states within a* $\mathrm{SU}(6)_{\mathrm{lsf}}\times$ *HQSS model*, Eur. Phys. J. **C78** (2018) no. 2, 114, arXiv:1712.00327 [hep-ph].

[551] G. Montaña, A. Feijoo, and A. Ramos, *A meson-baryon molecular interpretation for some* Ω_c *excited states*, Eur. Phys. J. **A54** (2018) no. 4, 64, arXiv:1709.08737 [hep-ph].

[552] V. R. Debastiani, J. M. Dias, W. H. Liang, and E. Oset, *Molecular* Ω_c *states generated from coupled meson-baryon channels*, Phys. Rev. **D97** (2018) no. 9, 094035, arXiv:1710.04231 [hep-ph].

[553] C. Garcia-Recio, V. K. Magas, T. Mizutani, J. Nieves, A. Ramos, L. L. Salcedo, and L. Tolos, *The s-wave charmed baryon resonances from a coupled-channel approach with heavy quark symmetry*, Phys. Rev. **D79** (2009) 054004, arXiv:0807.2969 [hep-ph].

[554] O. Romanets, L. Tolos, C. Garcia-Recio, J. Nieves, L. L. Salcedo, and R. G. E. Timmermans, *Charmed and strange baryon resonances with heavy-quark spin symmetry*, Phys. Rev. **D85** (2012) 114032, arXiv:1202.2239 [hep-ph].

[555] W. H. Liang, T. Uchino, C. W. Xiao, and E. Oset, *Baryon states with open charm in the extended local hidden gauge approach*, Eur. Phys. J. **A51** (2015) no. 2, 16, arXiv:1402.5293 [hep-ph].

[556] W. H. Liang, C. W. Xiao, and E. Oset, *Baryon states with open beauty in the extended local hidden gauge approach*, Phys. Rev. **D89** (2014) no. 5, 054023, arXiv:1401.1441 [hep-ph].

[557] C. Garcia-Recio, J. Nieves, O. Romanets, L. L. Salcedo, and L. Tolos, *Odd parity bottom-flavored baryon resonances*, Phys. Rev. **D87** (2013) no. 3, 034032, arXiv:1210.4755 [hep-ph].

[558] T. Yoshida, E. Hiyama, A. Hosaka, M. Oka, and K. Sadato, *Spectrum of heavy baryons in the quark model*, Phys. Rev. **D92** (2015) no. 11, 114029, arXiv:1510.01067 [hep-ph].

[559] H. Nagahiro, S. Yasui, A. Hosaka, M. Oka, and H. Noumi, *Structure of charmed baryons studied by pionic decays*, Phys. Rev. **D95** (2017) no. 1, 014023, arXiv:1609.01085 [hep-ph].

[560] W.-H. Liang, E. Oset, and Z.-S. Xie, *Semileptonic* $\Lambda_b \to \bar{\nu}_l l \Lambda_c(2595)$ *and* $\Lambda_b \to \bar{\nu}_l l \Lambda_c(2625)$ *decays in the molecular picture of* $\Lambda_c(2595)$ *and* $\Lambda_c(2625)$, Phys. Rev. **D95** (2017) no. 1, 014015, arXiv:1611.07334 [hep-ph].

[561] W.-H. Liang, J. M. Dias, V. R. Debastiani, and E. Oset, *Molecular* Ω_b *states*, Nucl. Phys. **B930** (2018) 524–532, arXiv:1711.10623 [hep-ph].

[562] LHCb Collaboration, R. Aaij et al., *Observation of a new* Ξ_b^- *resonance*, Phys. Rev. Lett. **121** (2018) no. 7, 072002, arXiv:1805.09418 [hep-ex].

[563] J.-X. Lu, Y. Zhou, H.-X. Chen, J.-J. Xie, and L.-S. Geng, *Dynamically generated* $J^P = 1/2^-(3/2^-)$ *singly charmed and bottom heavy baryons*, Phys. Rev. **D92** (2015) no. 1, 014036, arXiv:1409.3133 [hep-ph].

[564] Y. Huang, C.-j. Xiao, L.-S. Geng, and J. He, *Strong decays of the* $\Xi_b(6227)$ *as a* $\Sigma_b\bar{K}$ *molecule*, arXiv:1811.10769 [hep-ph].

[565] Q. X. Yu, R. Pavao, V. R. Debastiani, and E. Oset, *Description of the* Ξ_c *and* Ξ_b *states as molecular states*, arXiv:1811.11738 [hep-ph].

[566] H.-X. Chen, W. Chen, X. Liu, Y.-R. Liu, and S.-L. Zhu, *A review of the open charm and open bottom systems*, Rept. Prog. Phys. **80** (2017) no. 7, 076201, arXiv:1609.08928 [hep-ph].

[567] S. L. Olsen, *XYZ Meson Spectroscopy*, in *Proceedings, 53rd International Winter Meeting on*

Nuclear Physics (Bormio 2015): Bormio, Italy, January 26-30, 2015. 2015. arXiv:1511.01589 [hep-ex]. https://inspirehep.net/record/1402960/files/arXiv:1511.01589.pdf.

[568] LHCb Collaboration, R. Aaij et al., *Evidence for an $\eta_c(1S)\pi^-$ resonance in $B^0 \to \eta_c(1S)K^+\pi^-$ decays*, Submitted to: Eur. Phys. J. (2018) , arXiv:1809.07416 [hep-ex].

[569] N. A. Törnqvist, *Isospin breaking of the narrow charmonium state of Belle at 3872-MeV as a deuson*, Phys. Lett. **B590** (2004) 209–215, arXiv:hep-ph/0402237 [hep-ph].

[570] E. S. Swanson, *Short range structure in the X(3872)*, Phys. Lett. **B588** (2004) 189–195, arXiv:hep-ph/0311229 [hep-ph].

[571] M. T. AlFiky, F. Gabbiani, and A. A. Petrov, *X(3872): Hadronic molecules in effective field theory*, Phys. Lett. **B640** (2006) 238–245, arXiv:hep-ph/0506141 [hep-ph].

[572] D. Gamermann and E. Oset, *Isospin breaking effects in the X(3872) resonance*, Phys. Rev. **D80** (2009) 014003, arXiv:0905.0402 [hep-ph].

[573] C. Hanhart, Yu. S. Kalashnikova, A. E. Kudryavtsev, and A. V. Nefediev, *Remarks on the quantum numbers of X(3872) from the invariant mass distributions of the rho J/psi and omega J/psi final states*, Phys. Rev. **D85** (2012) 011501, arXiv:1111.6241 [hep-ph].

[574] N. Li and S.-L. Zhu, *Isospin breaking, Coupled-channel effects and Diagnosis of X(3872)*, Phys. Rev. **D86** (2012) 074022, arXiv:1207.3954 [hep-ph].

[575] C. Hanhart, Yu. S. Kalashnikova, A. E. Kudryavtsev, and A. V. Nefediev, *Reconciling the X(3872) with the near-threshold enhancement in the D0 anti-D*0 final state*, Phys. Rev. **D76** (2007) 034007, arXiv:0704.0605 [hep-ph].

[576] Yu. S. Kalashnikova and A. V. Nefediev, *Nature of X(3872) from data*, Phys. Rev. **D80** (2009) 074004, arXiv:0907.4901 [hep-ph].

[577] P. Artoisenet, E. Braaten, and D. Kang, *Using Line Shapes to Discriminate between Binding Mechanisms for the X(3872)*, Phys. Rev. **D82** (2010) 014013, arXiv:1005.2167 [hep-ph].

[578] V. Baru, A. A. Filin, C. Hanhart, Y. S. Kalashnikova, A. E. Kudryavtsev, and A. V. Nefediev, *Three-body $D\bar{D}\pi$ dynamics for the X(3872)*, Phys. Rev. **D84** (2011) 074029, arXiv:1108.5644 [hep-ph].

[579] X.-W. Kang and J. A. Oller, *Different pole structures in line shapes of the $X(3872)$*, Eur. Phys. J. **C77** (2017) no. 6, 399, arXiv:1612.08420 [hep-ph].

[580] M. Albaladejo, F. K. Guo, C. Hidalgo-Duque, J. Nieves, and M. P. Valderrama, *Decay widths of the spin-2 partners of the X(3872)*, Eur. Phys. J. **C75** (2015) no. 11, 547, arXiv:1504.00861 [hep-ph].

[581] V. Baru, E. Epelbaum, A. A. Filin, C. Hanhart, U.-G. Meißner, and A. V. Nefediev, *Heavy-quark spin symmetry partners of the X (3872) revisited*, Phys. Lett. **B763** (2016) 20–28, arXiv:1605.09649 [hep-ph].

[582] E. Cincioglu, J. Nieves, A. Ozpineci, and A. U. Yilmazer, *Quarkonium Contribution to Meson Molecules*, Eur. Phys. J. **C76** (2016) no. 10, 576, arXiv:1606.03239 [hep-ph].

[583] P. G. Ortega, J. Segovia, D. R. Entem, and F. Fernández, *Charmonium resonances in the 3.9 GeV/c^2 energy region and the $X(3915)/X(3930)$ puzzle*, Phys. Lett. **B778** (2018) 1–5, arXiv:1706.02639 [hep-ph].

[584] F.-K. Guo and U.-G. Meißner, *Where is the $\chi_{c0}(2P)$?*, Phys. Rev. **D86** (2012) 091501, arXiv:1208.1134 [hep-ph].

[585] Belle Collaboration, K. Chilikin et al., *Observation of an alternative $\chi_{c0}(2P)$ candidate in $e^+e^- \to J/\psi D\bar{D}$*, Phys. Rev. **D95** (2017) 112003, arXiv:1704.01872 [hep-ex].

[586] Z.-Y. Zhou and Z. Xiao, *Understanding $X(3862)$, $X(3872)$, and $X(3930)$ in a*

Friedrichs-model-like scheme, Phys. Rev. **D96** (2017) no. 5, 054031, arXiv:1704.04438 [hep-ph]. [Erratum: Phys. Rev.D96,no.9,099905(2017)].

[587] R. F. Lebed and E. S. Swanson, *Quarkonium h States As Arbiters of Exoticity*, Phys. Rev. **D96** (2017) no. 5, 056015, arXiv:1705.03140 [hep-ph].

[588] COMPASS Collaboration, M. Aghasyan et al., *Search for muoproduction of $X(3872)$ at COMPASS and indication of a new state $\widetilde{X}(3872)$*, Phys. Lett. **B783** (2018) 334–340, arXiv:1707.01796 [hep-ex].

[589] P. G. Ortega, J. Segovia, D. R. Entem, and F. Fernandez, *Coupled channel approach to the structure of the X(3872)*, Phys. Rev. **D81** (2010) 054023, arXiv:0907.3997 [hep-ph].

[590] I. V. Danilkin and Yu. A. Simonov, *Channel coupling in heavy quarkonia: Energy levels, mixing, widths and new states*, Phys. Rev. **D81** (2010) 074027, arXiv:0907.1088 [hep-ph].

[591] M. Takizawa and S. Takeuchi, *X(3872) as a hybrid state of charmonium and the hadronic molecule*, PTEP **2013** (2013) 093D01, arXiv:1206.4877 [hep-ph].

[592] C. Meng, H. Han, and K.-T. Chao, *$X(3872)$ and its production at hadron colliders*, Phys. Rev. **D96** (2013) no. 7, 074014, arXiv:1304.6710 [hep-ph].

[593] S. Takeuchi, K. Shimizu, and M. Takizawa, *On the origin of the narrow peak and the isospin symmetry breaking of the $X(3872)$*, PTEP **2014** (2014) no. 12, 123D01, arXiv:1408.0973 [hep-ph]. [Erratum: PTEP2015,no.7,079203(2015)].

[594] Z.-Y. Zhou and Z. Xiao, *Comprehending Isospin breaking effects of $X(3872)$ in a Friedrichs-model-like scheme*, Phys. Rev. **D97** (2018) no. 3, 034011, arXiv:1711.01930 [hep-ph].

[595] Z.-Y. Zhou, Z. Xiao, and H.-Q. Zhou, *Could the $X(3915)$ and the $X(3930)$ Be the Same Tensor State?*, Phys. Rev. Lett. **115** (2015) no. 2, 022001, arXiv:1501.00879 [hep-ph].

[596] F.-K. Guo, C. Hidalgo-Duque, J. Nieves, and M. P. Valderrama, *Consequences of Heavy Quark Symmetries for Hadronic Molecules*, Phys. Rev. **D88** (2013) 054007, arXiv:1303.6608 [hep-ph].

[597] F.-K. Guo, U.-G. Meißner, W. Wang, and Z. Yang, *Production of the bottom analogs and the spin partner of the X(3872) at hadron colliders*, Eur. Phys. J. **C74** (2014) no. 9, 3063, arXiv:1402.6236 [hep-ph].

[598] M. Karliner and J. L. Rosner, *$X(3872)$, X_b, and the $\chi_{b1}(3P)$ state*, Phys. Rev. **D91** (2015) no. 1, 014014, arXiv:1410.7729 [hep-ph].

[599] CMS Collaboration, S. Chatrchyan et al., *Search for a new bottomonium state decaying to $\Upsilon(1S)\pi^+\pi^-$ in pp collisions at $\sqrt{s}$ = 8 TeV*, Phys. Lett. **B727** (2013) 57–76, arXiv:1309.0250 [hep-ex].

[600] ATLAS Collaboration, G. Aad et al., *Search for the X_b and other hidden-beauty states in the $\pi^+\pi^-\Upsilon(1S)$ channel at ATLAS*, Phys. Lett. **B740** (2015) 199–217, arXiv:1410.4409 [hep-ex].

[601] F.-K. Guo, C. Hanhart, and U.-G. Meißner, *Mass splittings within heavy baryon isospin multiplets in chiral perturbation theory*, JHEP **09** (2008) 136, arXiv:0809.2359 [hep-ph].

[602] Belle Collaboration, X. H. He et al., *Observation of $e^+e^- \to \pi^+\pi^-\pi^0\chi_{bJ}$ and Search for $X_b \to \omega\Upsilon(1S)$ at $\sqrt{s} = 10.867$ GeV*, Phys. Rev. Lett. **113** (2014) no. 14, 142001, arXiv:1408.0504 [hep-ex].

[603] BaBar Collaboration, B. Aubert et al., *Observation of a broad structure in the $\pi^+\pi^- J/\psi$ mass spectrum around 4.26-GeV/c^2*, Phys. Rev. Lett. **95** (2005) 142001, arXiv:hep-ex/0506081 [hep-ex].

[604] Belle Collaboration, Z. Q. Liu et al., *Study of $e^+e^- \to \pi^+\pi^- J/\psi$ and Observation of a Charged Charmoniumlike State at Belle*, Phys. Rev. Lett. **110** (2013) 252002,

arXiv:1304.0121 [hep-ex].

[605] BESIII Collaboration, M. Ablikim et al., *Observation of $e^+e^- \to \gamma X(3872)$ at BESIII*, Phys. Rev. Lett. **112** (2014) no. 9, 092001, arXiv:1310.4101 [hep-ex].

[606] Belle Collaboration, X. L. Wang et al., *Measurement of $e^+e^- \to \pi^+\pi^-\psi(2S)$ via Initial State Radiation at Belle*, Phys. Rev. **D91** (2015) 112007, arXiv:1410.7641 [hep-ex].

[607] BaBar Collaboration, J. P. Lees et al., *Study of the reaction $e^+e^- \to \psi(2S)\pi^-\pi^-$ via initial-state radiation at BaBar*, Phys. Rev. **D89** (2014) no. 11, 111103, arXiv:1211.6271 [hep-ex].

[608] Z.-G. Wang, *Lowest vector tetraquark states: $Y(4260/4220)$ or $Z_c(4100)$*, Eur. Phys. J. **C78** (2018) no. 11, 933, arXiv:1809.10299 [hep-ph].

[609] M. Cleven, F.-K. Guo, C. Hanhart, Q. Wang, and Q. Zhao, *Employing spin symmetry to disentangle different models for the XYZ states*, Phys. Rev. **D92** (2015) no. 1, 014005, arXiv:1505.01771 [hep-ph].

[610] Q. Wang, C. Hanhart, and Q. Zhao, *Decoding the riddle of $Y(4260)$ and $Z_c(3900)$*, Phys. Rev. Lett. **111** (2013) no. 13, 132003, arXiv:1303.6355 [hep-ph].

[611] F.-K. Guo, C. Hanhart, and U.-G. Meißner, *Evidence that the $Y(4660)$ is a $f_0(980)\psi'$ bound state*, Phys. Lett. **B665** (2008) 26–29, arXiv:0803.1392 [hep-ph].

[612] Y. Lu, M. N. Anwar, and B.-S. Zou, *$X(4260)$ Revisited: A Coupled Channel Perspective*, Phys. Rev. **D96** (2017) no. 11, 114022, arXiv:1705.00449 [hep-ph].

[613] S.-L. Zhu, *The Possible interpretations of Y(4260)*, Phys. Lett. **B625** (2005) 212, arXiv:hep-ph/0507025 [hep-ph].

[614] Y. S. Kalashnikova and A. V. Nefediev, *Spectra and decays of hybrid charmonia*, Phys. Rev. **D77** (2008) 054025, arXiv:0801.2036 [hep-ph].

[615] M. Berwein, N. Brambilla, J. Tarrus Castella, and A. Vairo, *Quarkonium Hybrids with Nonrelativistic Effective Field Theories*, Phys. Rev. **D92** (2015) no. 11, 114019, arXiv:1510.04299 [hep-ph].

[616] Y. Chen, W.-F. Chiu, M. Gong, L.-C. Gui, and Z. Liu, *Exotic vector charmonium and its leptonic decay width*, Chin. Phys. **C40** (2016) no. 8, 081002, arXiv:1604.03401 [hep-lat].

[617] R. Oncala and J. Soto, *Heavy Quarkonium Hybrids: Spectrum, Decay and Mixing*, Phys. Rev. **D96** (2017) no. 1, 014004, arXiv:1702.03900 [hep-ph].

[618] X. Li and M. B. Voloshin, *$Y(4260)$ and $Y(4360)$ as mixed hadrocharmonium*, Mod. Phys. Lett. **A29** (2014) no. 12, 1450060, arXiv:1309.1681 [hep-ph].

[619] X. Y. Gao, C. P. Shen, and C. Z. Yuan, *Resonant parameters of the $Y(4220)$*, Phys. Rev. **D95** (2017) no. 9, 092007, arXiv:1703.10351 [hep-ex].

[620] M. Wurtz, R. Lewis, and R. M. Woloshyn, *Free-form smearing for bottomonium and B meson spectroscopy*, Phys. Rev. **D92** (2015) no. 5, 054504, arXiv:1505.04410 [hep-lat].

[621] C. B. Lang, L. Leskovec, D. Mohler, and S. Prelovsek, *Vector and scalar charmonium resonances with lattice QCD*, JHEP **09** (2015) 089, arXiv:1503.05363 [hep-lat].

[622] S. Prelovsek and L. Leskovec, *Evidence for X(3872) from DD^* scattering on the lattice*, Phys.Rev.Lett. **111** (2013) 192001, arXiv:1307.5172 [hep-lat].

[623] M. Padmanath, C. B. Lang, and S. Prelovsek, *X(3872) and Y(4140) using diquark-antidiquark operators with lattice QCD*, Phys. Rev. **D92** (2015) no. 3, 034501, arXiv:1503.03257 [hep-lat].

[624] A. Ali, C. Hambrock, and W. Wang, *Tetraquark Interpretation of the Charged Bottomonium-like states $Z_b^{+-}(10610)$ and $Z_b^{+-}(10650)$ and Implications*, Phys. Rev. **D85** (2012) 054011, arXiv:1110.1333 [hep-ph].

[625] A. Esposito, A. L. Guerrieri, and A. Pilloni, *Probing the nature of $Z_c^{()}$ states via the $h_c r$ decay*,

Phys. Lett. **B746** (2015) 194–201, arXiv:1409.3551 [hep-ph].

[626] S. S. Agaev, K. Azizi, and H. Sundu, *Strong $Z_c^+(3900) \to J/\psi\pi^+; \eta_c\rho^+$ decays in QCD*, Phys. Rev. **D93** (2016) no. 7, 074002, arXiv:1601.03847 [hep-ph].

[627] S. S. Agaev, K. Azizi, and H. Sundu, *Treating $Z_c(3900)$ and $Z(4430)$ as the ground-state and first radially excited tetraquarks*, Phys. Rev. **D96** (2017) no. 3, 034026, arXiv:1706.01216 [hep-ph].

[628] C.-J. Xiao, D.-Y. Chen, Y.-B. Dong, W. Zuo, and T. Matsuki, *Understanding the $\eta_c\rho$ decay mode of $Z_c^{(\prime)}$ via final state interactions*, arXiv:1811.04688 [hep-ph].

[629] JPAC Collaboration, A. Pilloni, C. Fernandez-Ramirez, A. Jackura, V. Mathieu, M. Mikhasenko, J. Nys, and A. P. Szczepaniak, *Amplitude analysis and the nature of the $Z_c(3900)$*, Phys. Lett. **B772** (2017) 200–209, arXiv:1612.06490 [hep-ph].

[630] M. Albaladejo, F.-K. Guo, C. Hidalgo-Duque, and J. Nieves, *$Z_c(3900)$: What has been really seen?*, Phys. Lett. **B755** (2016) 337–342, arXiv:1512.03638 [hep-ph].

[631] M. Albaladejo, P. Fernandez-Soler, and J. Nieves, *$Z_c(3900)$: Confronting theory and lattice simulations*, Eur. Phys. J. **C76** (2016) no. 10, 573, arXiv:1606.03008 [hep-ph].

[632] S. Prelovsek, C. B. Lang, L. Leskovec, and D. Mohler, *Study of the Z_c^+ channel using lattice QCD*, Phys. Rev. **D91** (2015) no. 1, 014504, arXiv:1405.7623 [hep-lat].

[633] F. K. Guo, C. Hanhart, Yu. S. Kalashnikova, P. Matuschek, R. V. Mizuk, A. V. Nefediev, Q. Wang, and J. L. Wynen, *Interplay of quark and meson degrees of freedom in near-threshold states: A practical parametrization for line shapes*, Phys. Rev. **D93** (2016) no. 7, 074031, arXiv:1602.00940 [hep-ph].

[634] Q. Wang, V. Baru, A. A. Filin, C. Hanhart, A. V. Nefediev, and J. L. Wynen, *The line shapes of the $Z_b(10610)$ and $Z_b(10650)$ in the elastic and inelastic channels revisited*, arXiv:1805.07453 [hep-ph].

[635] F.-K. Guo, C. Hanhart, Q. Wang, and Q. Zhao, *Could the near-threshold XYZ states be simply kinematic effects?*, Phys. Rev. **D91** (2015) no. 5, 051504, arXiv:1411.5584 [hep-ph].

[636] Q. Wang, C. Hanhart, and Q. Zhao, *Systematic study of the singularity mechanism in heavy quarkonium decays*, Phys. Lett. **B725** (2013) no. 1-3, 106–110, arXiv:1305.1997 [hep-ph].

[637] A. P. Szczepaniak, *Triangle Singularities and XYZ Quarkonium Peaks*, Phys. Lett. **B747** (2015) 410–416, arXiv:1501.01691 [hep-ph].

[638] Q.-R. Gong, J.-L. Pang, Y.-F. Wang, and H.-Q. Zheng, *The $Z_c(3900)$ peak does not come from the triangle singularity*, Eur. Phys. J. **C78** (2018) no. 4, 276, arXiv:1612.08159 [hep-ph].

[639] A. E. Bondar and M. B. Voloshin, *$\Upsilon(6S)$ and triangle singularity in $e^+e^- \to B_1(5721)\bar{B} \to Z_b(10610)\,\pi$*, Phys. Rev. **D93** (2016) no. 9, 094008, arXiv:1603.08436 [hep-ph].

[640] D0 Collaboration, V. M. Abazov et al., *Evidence for $Z_c^{\pm}(3900)$ in semi-inclusive decays of b-flavored hadrons*, arXiv:1807.00183 [hep-ex].

[641] M. B. Voloshin, *Radiative transitions from Upsilon(5S) to molecular bottomonium*, Phys. Rev. **D84** (2011) 031502, arXiv:1105.5829 [hep-ph].

[642] HAL QCD Collaboration, Y. Ikeda, S. Aoki, T. Doi, S. Gongyo, T. Hatsuda, T. Inoue, T. Iritani, N. Ishii, K. Murano, and K. Sasaki, *Fate of the Tetraquark Candidate $Z_c(3900)$ from Lattice QCD*, Phys. Rev. Lett. **117** (2016) no. 24, 242001, arXiv:1602.03465 [hep-lat].

[643] Hadron Spectrum Collaboration, G. K. C. Cheung, C. E. Thomas, J. J. Dudek, and R. G. Edwards, *Tetraquark operators in lattice QCD and exotic flavour states in the charm sector*, JHEP **11** (2017) 033, arXiv:1709.01417 [hep-lat].

[644] A. Peters, P. Bicudo, and M. Wagner, *$b\bar{b}u\bar{d}$ four-quark systems in the Born-Oppenheimer approximation: prospects and challenges*, EPJ Web Conf. **175** (2018) 14018,

arXiv:1709.03306 [hep-lat].

[645] L. Maiani, A. D. Polosa, and V. Riquer, *The New Pentaquarks in the Diquark Model*, Phys. Lett. **B749** (2015) 289–291, arXiv:1507.04980 [hep-ph].

[646] L. Maiani, A. D. Polosa, and V. Riquer, *From pentaquarks to dibaryons in $\Lambda_b(5620)$ decays*, Phys. Lett. **B750** (2015) 37–38, arXiv:1508.04459 [hep-ph].

[647] A. Ali, I. Ahmed, M. J. Aslam, and A. Rehman, *Heavy quark symmetry and weak decays of the b-baryons in pentaquarks with a $c\bar{c}$ component*, Phys. Rev. **D94** (2016) no. 5, 054001, arXiv:1607.00987 [hep-ph].

[648] A. Ali, I. Ahmed, M. J. Aslam, and A. Rehman, *Mass spectrum of spin-1/2 pentaquarks with a $c\bar{c}$ component and their anticipated discovery modes in b-baryon decays*, arXiv:1704.05419 [hep-ph].

[649] J.-J. Wu, R. Molina, E. Oset, and B. S. Zou, *Prediction of narrow N^* and Λ^* resonances with hidden charm above 4 GeV*, Phys. Rev. Lett. **105** (2010) 232001, arXiv:1007.0573 [nucl-th].

[650] W. L. Wang, F. Huang, Z. Y. Zhang, and B. S. Zou, *$\Sigma_c\bar{D}$ and $\Lambda_c\bar{D}$ states in a chiral quark model*, Phys. Rev. **C84** (2011) 015203, arXiv:1101.0453 [nucl-th].

[651] Z.-C. Yang, Z.-F. Sun, J. He, X. Liu, and S.-L. Zhu, *The possible hidden-charm molecular baryons composed of anti-charmed meson and charmed baryon*, Chin. Phys. **C36** (2012) 6–13, arXiv:1105.2901 [hep-ph].

[652] J.-J. Wu, T. S. H. Lee, and B. S. Zou, *Nucleon Resonances with Hidden Charm in Coupled-Channel Models*, Phys. Rev. **C85** (2012) 044002, arXiv:1202.1036 [nucl-th].

[653] M. Karliner and J. L. Rosner, *New Exotic Meson and Baryon Resonances from Doubly-Heavy Hadronic Molecules*, Phys. Rev. Lett. **115** (2015) no. 12, 122001, arXiv:1506.06386 [hep-ph].

[654] L. Roca, J. Nieves, and E. Oset, *LHCb pentaquark as a $\bar{D}^*\Sigma_c - \bar{D}^*\Sigma_c^*$ molecular state*, Phys. Rev. **D92** (2015) no. 9, 094003, arXiv:1507.04249 [hep-ph].

[655] L. Roca and E. Oset, *On the hidden charm pentaquarks in $\Lambda_b \to J/\psi K^- p$ decay*, Eur. Phys. J. **C76** (2016) no. 11, 591, arXiv:1602.06791 [hep-ph].

[656] C. W. Xiao, J. Nieves, and E. Oset, *Combining heavy quark spin and local hidden gauge symmetries in the dynamical generation of hidden charm baryons*, Phys. Rev. **D88** (2013) 056012, arXiv:1304.5368 [hep-ph].

[657] F.-K. Guo, U.-G. Meißner, W. Wang, and Z. Yang, *How to reveal the exotic nature of the $P_c(4450)$*, Phys. Rev. **D92** (2015) no. 7, 071502, arXiv:1507.04950 [hep-ph].

[658] X.-H. Liu, Q. Wang, and Q. Zhao, *Understanding the newly observed heavy pentaquark candidates*, Phys. Lett. **B757** (2016) 231–236, arXiv:1507.05359 [hep-ph].

[659] M. Bayar, F. Aceti, F.-K. Guo, and E. Oset, *A Discussion on Triangle Singularities in the $\Lambda_b \to J/\psi K^- p$ Reaction*, Phys. Rev. **D94** (2016) no. 7, 074039, arXiv:1609.04133 [hep-ph].

[660] N. P. Jurik, *Observation of J/ψ p resonances consistent with pentaquark states in$\Lambda_b^0 \to J/\psi K^- p$ decays*. PhD thesis, Syracuse U., 2016-08-08.

[661] V. Kubarovsky and M. B. Voloshin, *Formation of hidden-charm pentaquarks in photon-nucleon collisions*, Phys. Rev. **D92** (2015) no. 3, 031502, arXiv:1508.00888 [hep-ph].

[662] A. N. Hiller Blin, C. Fernández-Ramírez, A. Jackura, V. Mathieu, V. I. Mokeev, A. Pilloni, and A. P. Szczepaniak, *Studying the $P_c(4450)$ resonance in J/ψ photoproduction off protons*, Phys. Rev. **D94** (2016) no. 3, 034002, arXiv:1606.08912 [hep-ph].

[663] M. Karliner and J. L. Rosner, *Photoproduction of Exotic Baryon Resonances*, Phys. Lett. **B752** (2016) 329–332, arXiv:1508.01496 [hep-ph].

[664] C.-W. Shen, F.-K. Guo, J.-J. Xie, and B.-S. Zou, *Disentangling the hadronic molecule nature of the $P_c(4380)$ pentaquark-like structure*, Nucl. Phys. **A954** (2016) 393–405, arXiv:1603.04672 [hep-ph].

[665] Y.-H. Lin, C.-W. Shen, F.-K. Guo, and B.-S. Zou, *Decay behaviors of the P_c hadronic molecules*, Phys. Rev. **D95** (2017) no. 11, 114017, arXiv:1703.01045 [hep-ph].

[666] M. I. Eides and V. Yu. Petrov, *Decays of Pentaquarks in Hadrocharmonium and Molecular Pictures*, arXiv:1811.01691 [hep-ph].

[667] J.-J. Wu and B. S. Zou, *Prediction of super-heavy N^* and Λ^* resonances with hidden beauty*, Phys. Lett. **B709** (2012) 70–76, arXiv:1011.5743 [hep-ph].

[668] J. Wu, Y.-R. Liu, K. Chen, X. Liu, and S.-L. Zhu, *Hidden-charm pentaquarks and their hidden-bottom and B_c-like partner states*, Phys. Rev. **D95** (2017) no. 3, 034002, arXiv:1701.03873 [hep-ph].

[669] Y. Yamaguchi, A. Giachino, A. Hosaka, E. Santopinto, S. Takeuchi, and M. Takizawa, *Hidden-charm and bottom meson-baryon molecules coupled with five-quark states*, Phys. Rev. **D96** (2017) no. 11, 114031, arXiv:1709.00819 [hep-ph].

[670] C.-W. Shen, D. Rönchen, U.-G. Meißner, and B.-S. Zou, *Exploratory study of possible resonances in heavy meson - heavy baryon coupled-channel interactions*, Chin. Phys. **C42** (2018) no. 2, 023106, arXiv:1710.03885 [hep-ph].

[671] Y.-H. Lin, C.-W. Shen, and B.-S. Zou, *Decay behavior of the strange and beauty partners of P_c hadronic molecules*, Nucl. Phys. **A980** (2018) 21–31, arXiv:1805.06843 [hep-ph].

[672] G. Yang, J. Ping, and J. Segovia, *Hidden-Bottom Pentaquarks*, arXiv:1809.06193 [hep-ph].

[673] S. S. Gershtein, V. V. Kiselev, A. K. Likhoded, and A. I. Onishchenko, *Spectroscopy of doubly heavy baryons*, Phys. Rev. **D62** (2000) 054021.

[674] V. V. Kiselev and A. K. Likhoded, *Baryons with two heavy quarks*, Phys. Usp. **45** (2002) 455–506, arXiv:hep-ph/0103169 [hep-ph]. [Usp. Fiz. Nauk172,497(2002)].

[675] D. Ebert, R. N. Faustov, V. O. Galkin, and A. P. Martynenko, *Mass spectra of doubly heavy baryons in the relativistic quark model*, Phys. Rev. **D66** (2002) 014008, arXiv:hep-ph/0201217 [hep-ph].

[676] V. V. Kiselev, A. K. Likhoded, O. N. Pakhomova, and V. A. Saleev, *Mass spectra of doubly heavy Omega QQ' baryons*, Phys. Rev. **D66** (2002) 034030, arXiv:hep-ph/0206140 [hep-ph].

[677] C. Albertus, E. Hernandez, J. Nieves, and J. M. Verde-Velasco, *Static properties and semileptonic decays of doubly heavy baryons in a nonrelativistic quark model*, Eur. Phys. J. **A32** (2007) 183–199, arXiv:hep-ph/0610030 [hep-ph]. [Erratum: Eur. Phys. J.A36,119(2008)].

[678] M. Padmanath, R. G. Edwards, N. Mathur, and M. Peardon, *Spectroscopy of doubly-charmed baryons from lattice QCD*, Phys. Rev. **D91** (2015) no. 9, 094502, arXiv:1502.01845 [hep-lat].

[679] M. Karliner and J. L. Rosner, *Baryons with two heavy quarks: Masses, production, decays, and detection*, Phys. Rev. **D90** (2014) no. 9, 094007, arXiv:1408.5877 [hep-ph].

[680] F.-S. Yu, H.-Y. Jiang, R.-H. Li, C.-D. Lü, W. Wang, and Z.-X. Zhao, *Discovery Potentials of Doubly Charmed Baryons*, Chin. Phys. **C42** (2018) no. 5, 051001, arXiv:1703.09086 [hep-ph].

[681] W. Wang, F.-S. Yu, and Z.-X. Zhao, *Weak decays of doubly heavy baryons: the $1/2 \to 1/2$ case*, Eur. Phys. J. **C77** (2017) no. 11, 781, arXiv:1707.02834 [hep-ph].

[682] L.-Y. Xiao, K.-L. Wang, Q.-f. Lu, X.-H. Zhong, and S.-L. Zhu, *Strong and radiative decays of the doubly charmed baryons*, Phys. Rev. **D96** (2017) no. 9, 094005, arXiv:1708.04384 [hep-ph].

[683] E.-L. Cui, H.-X. Chen, W. Chen, X. Liu, and S.-L. Zhu, *Suggested search for doubly charmed baryons of $J^P = 3/2^+$ via their electromagnetic transitions*, Phys. Rev. **D97** (2018) no. 3, 034018, arXiv:1712.03615 [hep-ph].

[684] L.-Y. Xiao, Q.-F. Lü, and S.-L. Zhu, *Strong decays of the 1P and 2D doubly charmed states*, Phys. Rev. **D97** (2018) no. 7, 074005, arXiv:1712.07295 [hep-ph].

[685] H.-S. Li, L. Meng, Z.-W. Liu, and S.-L. Zhu, *Radiative decays of the doubly charmed baryons in chiral perturbation theory*, Phys. Lett. **B777** (2018) 169–176, arXiv:1708.03620 [hep-ph].

[686] LHCb Collaboration, R. Aaij et al., *Observation of the doubly charmed baryon Ξ_{cc}^{++}*, Phys. Rev. Lett. **119** (2017) no. 11, 112001, arXiv:1707.01621 [hep-ex].

[687] SELEX Collaboration, M. Mattson et al., *First Observation of the Doubly Charmed Baryon Ξ_{cc}^{+}*, Phys. Rev. Lett. **89** (2002) 112001, arXiv:hep-ex/0208014 [hep-ex].

[688] S. J. Brodsky, F.-K. Guo, C. Hanhart, and U.-G. Meißner, *Isospin splittings of doubly heavy baryons*, Phys. Lett. **B698** (2011) 251–255, arXiv:1101.1983 [hep-ph].

[689] M. Karliner and J. L. Rosner, *Isospin splittings in baryons with two heavy quarks*, Phys. Rev. **D96** (2017) no. 3, 033004, arXiv:1706.06961 [hep-ph].

[690] M.-J. Yan, X.-H. Liu, S. Gonzàlez-Solís, F.-K. Guo, C. Hanhart, U.-G. Meißner, and B.-S. Zou, *New spectrum of negative parity doubly charmed baryons: Possibility of two quasi-stable states*, arXiv:1805.10972 [hep-ph].

[691] Z.-H. Guo, *Prediction of exotic doubly charmed baryons within chiral effective field theory*, Phys. Rev. **D96** (2017) no. 7, 074004, arXiv:1708.04145 [hep-ph].

[692] J. M. Dias, V. R. Debastiani, J. J. Xie, and E. Oset, *Doubly charmed Ξ_{cc} molecular states from meson-baryon interaction*, Phys. Rev. **D98** (2018) no. 9, 094017, arXiv:1805.03286 [hep-ph].

[693] M. Karliner and J. L. Rosner, *Strange baryons with two heavy quarks*, Phys. Rev. **D97** (2018) no. 9, 094006, arXiv:1803.01657 [hep-ph].

[694] N. Mathur and M. Padmanath, *On the discovery of next doubly charmed baryon*, arXiv:1807.00174 [hep-lat].

[695] N. Mathur, M. Padmanath, and S. Mondal, *Precise predictions of charmed-bottom hadrons from lattice QCD*, arXiv:1806.04151 [hep-lat].

[696] E. J. Eichten and C. Quigg, *Heavy-quark symmetry implies stable heavy tetraquark mesons $Q_iQ_j\bar{q}_k\bar{q}_l$*, Phys. Rev. Lett. **119** (2017) no. 20, 202002, arXiv:1707.09575 [hep-ph].

[697] A. Czarnecki, B. Leng, and M. B. Voloshin, *Stability of tetrons*, Phys. Lett. **B778** (2018) 233–238, arXiv:1708.04594 [hep-ph].

[698] M. Karliner and J. L. Rosner, *Discovery of doubly-charmed Ξ_{cc} baryon implies a stable ($bb\bar{u}\bar{d}$) tetraquark*, Phys. Rev. Lett. **119** (2017) no. 20, 202001, arXiv:1707.07666 [hep-ph].

[699] J. P. Ader, J. M. Richard, and P. Taxil, *Do narrow heavy multi-quark states exist?*, Phys. Rev. **D25** (1982) 2370.

[700] A. V. Manohar and M. B. Wise, *Exotic $QQ\bar{q}\bar{q}$ states in QCD*, Nucl. Phys. **B399** (1993) 17–33, arXiv:hep-ph/9212236 [hep-ph].

[701] T. Mehen, *Implications of Heavy Quark-Diquark Symmetry for Excited Doubly Heavy Baryons and Tetraquarks*, Phys. Rev. **D96** (2017) no. 9, 094028, arXiv:1708.05020 [hep-ph].

[702] A. Esposito, M. Papinutto, A. Pilloni, A. D. Polosa, and N. Tantalo, *Doubly charmed tetraquarks in B_c and Ξ_{bc} decays*, Phys. Rev. **D88** (2013) no. 5, 054029, arXiv:1307.2873 [hep-ph].

[703] S.-Q. Luo, K. Chen, X. Liu, Y.-R. Liu, and S.-L. Zhu, *Exotic tetraquark states with the $qq\bar{Q}\bar{Q}$ configuration*, Eur. Phys. J. **C77** (2017) no. 10, 709, arXiv:1707.01180 [hep-ph].

[704] Y.-q. Chen and S.-z. Wu, *Production of four-quark states with double heavy quarks at LHC*,

Phys. Lett. **B705** (2011) 93–97, arXiv:1101.4568 [hep-ph].

[705] A. Ali, Q. Qin, and W. Wang, *Discovery potential of stable and near-threshold doubly heavy tetraquarks at the LHC*, arXiv:1806.09288 [hep-ph].

[706] T. Gershon and A. Poluektov, *Displaced B_c^- mesons as an inclusive signature of weakly decaying double beauty hadrons*, arXiv:1810.06657 [hep-ph].

[707] European Twisted Mass Collaboration, P. Bicudo and M. Wagner, *Lattice QCD signal for a bottom-bottom tetraquark*, Phys. Rev. **D87** (2013) no. 11, 114511, arXiv:1209.6274 [hep-ph].

[708] A. Francis, R. J. Hudspith, R. Lewis, and K. Maltman, *Lattice Prediction for Deeply Bound Doubly Heavy Tetraquarks*, Phys. Rev. Lett. **118** (2017) no. 14, 142001, arXiv:1607.05214 [hep-lat].

[709] P. Bicudo, K. Cichy, A. Peters, B. Wagenbach, and M. Wagner, *Evidence for the existence of $ud\bar{b}\bar{b}$ and the non-existence of $ss\bar{b}\bar{b}$ and $cc\bar{b}\bar{b}$ tetraquarks from lattice QCD*, Phys. Rev. **D92** (2015) no. 1, 014507, arXiv:1505.00613 [hep-lat].

[710] C. Hughes, E. Eichten, and C. T. H. Davies, *Searching for beauty-fully bound tetraquarks using lattice nonrelativistic QCD*, Phys. Rev. **D97** (2018) no. 5, 054505, arXiv:1710.03236 [hep-lat].

[711] L. Heller and J. A. Tjon, *On Bound States of Heavy $Q^2\bar{Q}^2$ Systems*, Phys. Rev. **D32** (1985) 755.

[712] A. V. Berezhnoy, A. V. Luchinsky, and A. A. Novoselov, *Heavy tetraquarks production at the LHC*, Phys. Rev. **D86** (2012) 034004, arXiv:1111.1867 [hep-ph].

[713] J. Wu, Y.-R. Liu, K. Chen, X. Liu, and S.-L. Zhu, *Heavy-flavored tetraquark states with the $QQ\bar{Q}\bar{Q}$ configuration*, Phys. Rev. **D97** (2018) 094015, arXiv:1605.01134 [hep-ph].

[714] W. Chen, H.-X. Chen, X. Liu, T. G. Steele, and S.-L. Zhu, *Hunting for exotic doubly hidden-charm/bottom tetraquark states*, Phys. Lett. **B773** (2017) 247–251, arXiv:1605.01647 [hep-ph].

[715] M. Karliner, S. Nussinov, and J. L. Rosner, *$QQ\bar{Q}\bar{Q}$ states: masses, production, and decays*, Phys. Rev. **D95** (2017) no. 3, 034011, arXiv:1611.00348 [hep-ph].

[716] Y. Bai, S. Lu, and J. Osborne, *Beauty-full Tetraquarks*, arXiv:1612.00012 [hep-ph].

[717] Z.-G. Wang, *Analysis of the $QQ\bar{Q}\bar{Q}$ tetraquark states with QCD sum rules*, Eur. Phys. J. **C77** (2017) 432, arXiv:1701.04285 [hep-ph].

[718] J.-M. Richard, A. Valcarce, and J. Vijande, *String dynamics and metastability of all-heavy tetraquarks*, Phys. Rev. **D95** (2017) 054019, arXiv:1703.00783 [hep-ph].

[719] M. N. Anwar, J. Ferretti, F.-K. Guo, E. Santopinto, and B.-S. Zou, *Spectroscopy and decays of the fully-heavy tetraquarks*, arXiv:1710.02540 [hep-ph].

[720] Y. Chen and R. Vega-Morales, *Golden probe of the di-Υ threshold*, arXiv:1710.02738 [hep-ph].

[721] E. Eichten and Z. Liu, *Would a Deeply Bound $b\bar{b}b\bar{b}$ Tetraquark Meson be Observed at the LHC?*, arXiv:1709.09605 [hep-ph].

[722] K.-T. Chao, *The $cc\bar{c}\bar{c}$ (diquark-antidiquark) states in e^+e^- annihilation*, Z. Phys. **C7** (1981) 317.

[723] M. Padmanath, R. G. Edwards, N. Mathur, and M. Peardon, *Spectroscopy of triply-charmed baryons from lattice QCD*, Phys. Rev. **D90** (2014) no. 7, 074504, arXiv:1307.7022 [hep-lat].

[724] C. Bignamini, B. Grinstein, F. Piccinini, A. D. Polosa, and C. Sabelli, *Is the X(3872) Production Cross Section at Tevatron Compatible with a Hadron Molecule Interpretation?*, Phys. Rev. Lett. **103** (2009) 162001, arXiv:0906.0882 [hep-ph].

[725] P. Artoisenet and E. Braaten, *Production of the X(3872) at the Tevatron and the LHC*, Phys.

Rev. **D81** (2010) 114018, arXiv:0911.2016 [hep-ph].

[726] C. Bignamini, B. Grinstein, F. Piccinini, A. D. Polosa, V. Riquer, and C. Sabelli, *More loosely bound hadron molecules at CDF?*, Phys. Lett. **B684** (2010) 228–230, arXiv:0912.5064 [hep-ph].

[727] P. Artoisenet and E. Braaten, *Estimating the Production Rate of Loosely-bound Hadronic Molecules using Event Generators*, Phys. Rev. **D83** (2011) 014019, arXiv:1007.2868 [hep-ph].

[728] A. Esposito, F. Piccinini, A. Pilloni, and A. D. Polosa, *A Mechanism for Hadron Molecule Production in p pbar(p) Collisions*, J. Mod. Phys. **4** (2013) 1569–1573, arXiv:1305.0527 [hep-ph].

[729] A. Guerrieri, F. Piccinini, A. Pilloni, and A. Polosa, *Production of Tetraquarks at the LHC*, Phys. Rev. **D90** (2014) 034003, arXiv:1405.7929 [hep-ph].

[730] M. Albaladejo, F.-K. Guo, C. Hanhart, U.-G. Meißner, J. Nieves, A. Nogga, and Z. Yang, *Note on $X(3872)$ production at hadron colliders and its molecular structure*, Chin. Phys. **C41** (2017) 121001, arXiv:1709.09101 [hep-ph].

[731] A. Esposito, B. Grinstein, L. Maiani, F. Piccinini, A. Pilloni, A. D. Polosa, and V. Riquer, *Comment on 'Note on $X(3872)$ production at hadron colliders and its molecular structure'*, arXiv:1709.09631 [hep-ph].

[732] E. Braaten, L.-P. He, and K. Ingles, *Predictive Solution to the $X(3872)$ Collider Production Puzzle*, arXiv:1811.08876 [hep-ph].

[733] A. Esposito, A. L. Guerrieri, L. Maiani, F. Piccinini, A. Pilloni, A. D. Polosa, and V. Riquer, *Observation of light nuclei at ALICE and the $X(3872)$ conundrum*, Phys. Rev. **D92** (2015) no. 3, 034028, arXiv:1508.00295 [hep-ph].

[734] W. Wang, *On the production of hidden-flavored hadronic states at high energy*, Chin. Phys. **42** (2018) 043103, arXiv:1709.10382 [hep-ph].

[735] F.-K. Guo, U.-G. Meißner, and W. Wang, *Production of charged heavy quarkonium-like states at the LHC and the Tevatron*, Commun. Theor. Phys. **61** (2014) 354–358, arXiv:1308.0193 [hep-ph].

[736] F.-K. Guo, U.-G. Meißner, W. Wang, and Z. Yang, *Production of charm-strange hadronic molecules at the LHC*, JHEP **05** (2014) 138, arXiv:1403.4032 [hep-ph].

[737] LHCb collaboration, R. Aaij et al., *Observation of the resonant character of the $Z(4430)^-$ state*, Phys. Rev. Lett. **112** (2014) 222002, arXiv:1404.1903 [hep-ex].

[738] LHCb collaboration, R. Aaij et al., *Observation of exotic $J/\psi\,\phi$ structures from amplitude analysis of $B^+ \to J/\psi\,\phi K^+$ decays*, Phys. Rev. Lett. **118** (2016) 022003, arXiv:1606.07895 [hep-ex].

[739] CMS collaboration, S. Chatrchyan et al., *Observation of a peaking structure in the $J/\psi\phi$ mass spectrum from $B^\pm \to J/\psi\phi K^\pm$ decays*, Phys. Lett. **B734** (2014) 261–281, arXiv:1309.6920 [hep-ex].

[740] CDF collaboration, T. Aaltonen et al., *Evidence for a narrow near-threshold structure in the $J/\psi\phi$ mass spectrum in $B^+ \to J/\psi\phi K^+$ Decays*, Phys. Rev. Lett. **102** (2009) 242002, arXiv:0903.2229 [hep-ex].

[741] LHCb collaboration, R. Aaij et al., *Observation of the decays $\Lambda_b^0 \to \chi_{c1} p K^-$ and $\Lambda_b^0 \to \chi_{c2} p K^-$*, Phys. Rev. Lett. **119** (2017) 062001, arXiv:1704.07900 [hep-ex].

[742] J. Nieves and M. P. Valderrama, *The heavy quark spin symmetry partners of the X(3872)*, Phys. Rev. **D86** (2012) 056004, arXiv:1204.2790 [hep-ph].

[743] J.-J. Wu, R. Molina, E. Oset, and B. S. Zou, *Dynamically generated N^* and Λ^* resonances in the hidden charm sector around 4.3 GeV*, Phys. Rev. **C84** (2011) 015202, arXiv:1011.2399

[nucl-th].

[744] LHCb collaboration, R. Aaij et al., *Observation of the $\Xi_b^- \to J/\psi \Lambda K^-$ decay*, Phys. Lett. **B772** (2017) 265, arXiv:1701.05274 [hep-ex].

[745] M. A. Moinester, *How to search for doubly charmed baryons and tetraquarks*, Z. Phys. **A355** (1996) 349–362, arXiv:hep-ph/9506405 [hep-ph].

[746] A. Del Fabbro, D. Janc, M. Rosina, and D. Treleani, *Production and detection of doubly charmed tetraquarks*, Phys. Rev. **D71** (2005) 014008, arXiv:hep-ph/0408258 [hep-ph].

[747] T. F. Caramés, A. Valcarce, and J. Vijande, *Doubly charmed exotic mesons: A gift of nature?*, Phys. Lett. **B699** (2011) 291–295.

[748] T. Hyodo, Y.-R. Liu, M. Oka, K. Sudoh, and S. Yasui, *Production of doubly charmed tetraquarks with exotic color configurations in electron-positron collisions*, Phys. Lett. **B721** (2013) 56–60, arXiv:1209.6207 [hep-ph].

[749] Y. Ikeda, B. Charron, S. Aoki, T. Doi, T. Hatsuda, T. Inoue, N. Ishii, K. Murano, H. Nemura, and K. Sasaki, *Charmed tetraquarks T_{cc} and T_{cs} from dynamical lattice QCD simulations*, Phys. Lett. **B729** (2014) 85–90, arXiv:1311.6214 [hep-lat].

[750] A. L. Guerrieri, M. Papinutto, A. Pilloni, A. D. Polosa, and N. Tantalo, *Flavored tetraquark spectroscopy*, PoS **LATTICE2014** (2015) 106, arXiv:1411.2247 [hep-lat].

[751] R. Maciuła, V. A. Saleev, A. V. Shipilova, and A. Szczurek, *New mechanisms for double charmed meson production at the LHCb*, Phys. Lett. **B758** (2016) 458–464, arXiv:1601.06981 [hep-ph].

[752] J.-M. Richard, *Exotic hadrons: review and perspectives*, Few Body Syst. **57** (2016) no. 12, 1185–1212, arXiv:1606.08593 [hep-ph].

[753] T. Hyodo, Y.-R. Liu, M. Oka, and S. Yasui, *Spectroscopy and production of doubly charmed tetraquarks*, arXiv:1708.05169 [hep-ph].

[754] Z.-G. Wang and Z.-H. Yan, *Analysis of the scalar, axialvector, vector, tensor doubly charmed tetraquark states with QCD sum rules*, Eur. Phys. J. **C78** (2018) no. 1, 19, arXiv:1710.02810 [hep-ph].

[755] X. Yan, B. Zhong, and R. Zhu, *Doubly charmed tetraquarks in a diquark-antidiquark model*, arXiv:1804.06761 [hep-ph].

[756] LHCb collaboration, R. Aaij et al., *Observation of the doubly charmed baryon Ξ_{cc}^{++}*, Phys. Rev. Lett. **119** (2017) 112001, arXiv:1707.01621 [hep-ex].

[757] LHCb collaboration, R. Aaij et al., *Observation of $J/\psi p$ resonances consistent with pentaquark states in $\Lambda_b^0 \to J/\psi p K^-$ decays*, Phys. Rev. Lett. **115** (2015) 072001, arXiv:1507.03414 [hep-ex].

[758] LHCb collaboration, R. Aaij et al., *Observation of $B_c^+ \to J/\psi D_s^+$ and $B_c^+ \to J/\psi D_s^{*+}$ decays*, Phys. Rev. **D87** (2013) 112012, arXiv:1304.4530 [hep-ex].

[759] LHCb collaboration, R. Aaij et al., *Observation of double charm production involving open charm in pp collisions at $\sqrt{s} = 7$ TeV*, JHEP **06** (2012) 141, arXiv:1205.0975 [hep-ex].

[760] LHCb collaboration, R. Aaij et al., *Search for beautiful tetraquarks in the $\Upsilon\mu^+\mu^-$ invariant-mass spectrum*, JHEP **10** (2018) 086, arXiv:1806.09707 [hep-ex].

[761] I. W. Stewart, M. E. Wessling, and M. B. Wise, *Stable heavy pentaquark states*, Phys. Lett. **B590** (2004) 185–189, arXiv:hep-ph/0402076 [hep-ph].

[762] Y.-s. Oh, B.-Y. Park, and D.-P. Min, *Pentaquark exotic baryons in the Skyrme model*, Phys. Lett. **B331** (1994) 362–370, arXiv:hep-ph/9405297 [hep-ph].

[763] LHCb collaboration, R. Aaij et al., *Search for weakly decaying b-flavored pentaquarks*, Phys. Rev. **D97** (2018) 032010, arXiv:1712.08086 [hep-ex].

[764] LHCb collaboration, R. Aaij et al., *Observation of five new narrow Ω_c^0 states decaying to*

$\Xi_c^+ K^-$, Phys. Rev. Lett. **118** (2017) 182001, arXiv:1703.04639 [hep-ex].

[765] LHCb collaboration, *Framework TDR for the LHCb Upgrade: Technical Design Report*, 2012. LHCb-TDR-012.

[766] LHCb collaboration, R. Aaij *et al.*, and A. Bharucha et al., *Implications of LHCb measurements and future prospects*, Eur. Phys. J. **C73** (2013) 2373, arXiv:1208.3355 [hep-ex].

[767] T. Gutsche, M. A. Ivanov, J. G. Körner, and V. E. Lyubovitskij, *Decay chain information on the newly discovered double charm baryon state Ξ_{cc}^{++}*, Phys. Rev. **D96** (2017) 054013, arXiv:1708.00703 [hep-ph].

[768] N. Sharma and R. Dhir, *Estimates of W-exchange contributions to Ξ_{cc} decays*, Phys. Rev. **D96** (2017) 113006, arXiv:1709.08217 [hep-ph].

[769] LHCb collaboration, R. Aaij et al., *Search for the doubly charmed baryon Ξ_{cc}^+*, JHEP **12** (2013) 090, arXiv:1310.2538 [hep-ex].

[770] S. Fleck and J.-M. Richard, *Baryons with double charm*, Prog. Theor. Phys. **82** (1989) 760–774.

[771] B. Guberina, B. Melić, and H. Štefančić, *Inclusive decays and lifetimes of doubly charmed baryons*, Eur.Phys.J. **C9** (1999) 213–219, arXiv:hep-ph/9901323 [hep-ph].

[772] V. Kiselev, A. Likhoded, and A. Onishchenko, *Lifetimes of doubly charmed baryons: Ξ_{cc}^+ and Ξ_{cc}^{++}*, Phys.Rev. **D60** (1999) 014007, arXiv:hep-ph/9807354 [hep-ph].

[773] C.-H. Chang, T. Li, X.-Q. Li, and Y.-M. Wang, *Lifetime of doubly charmed baryons*, Commun.Theor.Phys. **49** (2008) 993–1000, arXiv:0704.0016 [hep-ph].

[774] A. V. Berezhnoy and A. K. Likhoded, *Doubly heavy baryons*, Phys. Atom. Nucl. **79** (2016) 260–265.

[775] LHCb collaboration, R. Aaij et al., *Measurement of the lifetime of the doubly charmed baryon Ξ_{cc}^{++}*, Phys. Rev. Lett. **121** (2018) 052002, arXiv:1806.02744 [hep-ex].

[776] J.-W. Zhang, X.-G. Wu, T. Zhong, Y. Yu, and Z.-Y. Fang, *Production of the doubly heavy baryon Ξ_{bc} at LHC*, Phys. Rev. **D83** (2011) 034026, arXiv:1101.1130 [hep-ph].

[777] C.-H. Chang and X.-G. Wu, *Uncertainties in estimating hadronic production of the meson B_c and comparisons between TEVATRON and LHC*, Eur. Phys. J. **C38** (2004) 267–276, arXiv:hep-ph/0309121 [hep-ph].

[778] Y.-N. Gao, J. He, P. Robbe, M.-H. Schune, and Z.-W. Yang, *Experimental prospects of the B_c studies of the LHCb experiment*, Chin. Phys. Lett. **27** (2010) 061302.

[779] LHCb collaboration, R. Aaij et al., *Measurement of b hadron production fractions in 7 TeV pp collisions*, Phys. Rev. **D85** (2012) 032008, arXiv:1111.2357 [hep-ex].

[780] LHCb collaboration, R. Aaij et al., *Study of the kinematic dependences of Λ_b^0 production in pp collisions and a measurement of the $\Lambda_b^0 \to \Lambda_c^+ \pi^-$ branching fraction*, JHEP **08** (2014) 143, arXiv:1405.6842 [hep-ex].

[781] LHCb collaboration, R. Aaij et al., *Observation of two resonances in the $\Lambda_b^0 \pi^\pm$ systems and precise measurement of $\Sigma_b^\pm$ and $\Sigma_b^{*\pm}$ properties*, arXiv:1809.07752 [hep-ex].

[782] LHCb collaboration, R. Aaij et al., *Measurement of the ratio of prompt χ_c to J/ψ production in pp collisions at $\sqrt{s} = 7$ TeV*, Phys. Lett. **B718** (2012) 431, arXiv:1204.1462 [hep-ex].

[783] LHCb collaboration, R. Aaij et al., *Study of χ_b meson production in pp collisions at $\sqrt{s} = 7$ and 8 TeV and observation of the decay $\chi_b \to \Upsilon(3S)\gamma$*, Eur. Phys. J. **C74** (2014) 3092, arXiv:1407.7734 [hep-ex].

[784] LHCb collaboration, R. Aaij et al., *χ_{c1} and χ_{c2} resonance parameters with the decays $\chi_{c1,c2} \to J/\psi \mu^+ \mu^-$*, Phys. Rev. Lett. **119** (2017) 221801, arXiv:1709.04247 [hep-ex].

[785] LHCb collaboration, R. Aaij et al., *Measurement of the cross-section ratio $\sigma(\chi_{c2})/\sigma(\chi_{c1})$ for prompt χ_c production at $\sqrt{s} = 7$ TeV*, Phys. Lett. **B714** (2012) 215–223, arXiv:1202.1080 [hep-ex].

[786] LHCb collaboration, R. Aaij et al., *Measurement of the fraction of $\Upsilon(1S)$ originating from $\chi_b(1P)$ decays in pp collisions at $\sqrt{s} = 7$ TeV*, JHEP **11** (2012) 031, arXiv:1209.0282 [hep-ex].

[787] LHCb collaboration, R. Aaij et al., *Measurement of the relative rate of prompt χ_{c0}, χ_{c1} and χ_{c2} production at $\sqrt{s} = 7$ TeV*, JHEP **10** (2013) 115, arXiv:1307.4285 [hep-ex].

[788] LHCb collaboration, R. Aaij et al., *Measurement of the $\chi_b(3P)$ mass and of the relative rate of $\chi_{b1}(1P)$ and $\chi_{b2}(1P)$ production*, JHEP **10** (2014) 088, arXiv:1409.1408 [hep-ex].

[789] A. Faessler, C. Fuchs, and M. I. Krivoruchenko, *Dilepton spectra from decays of light unflavored mesons*, Phys. Rev. **C61** (2000) 035206, arXiv:nucl-th/9904024 [nucl-th].

[790] A. V. Luchinsky, *Muon pair production in radiative decays of heavy quarkonia*, Mod. Phys. Lett. **A33** (2017) 1850001, arXiv:1709.02444 [hep-ph].

[791] LHCb collaboration, R. Aaij et al., *Observation of J/ψ-pair production in pp collisions at $\sqrt{s} = 7$ TeV*, Phys. Lett. **B707** (2012) 52, arXiv:1109.0963 [hep-ex].

[792] LHCb collaboration, R. Aaij et al., *Measurement of the J/ψ pair production cross-section in pp collisions at $\sqrt{s} = 13$ TeV*, JHEP **06** (2017) 047, arXiv:1612.07451 [hep-ex].

[793] L.-P. Sun, H. Han, and K.-T. Chao, *Impact of J/ψ pair production at the LHC and predictions in nonrelativistic QCD*, Phys. Rev. **D94** (2016) 074033, arXiv:1404.4042 [hep-ph].

[794] A. K. Likhoded, A. V. Luchinsky, and S. V. Poslavsky, *Production of $J/\psi + \chi_c$ and $J/\psi + J/\psi$ with real gluon emission at LHC*, Phys. Rev. **D94** (2016) 054017, arXiv:1606.06767 [hep-ph].

[795] J.-P. Lansberg and H.-S. Shao, *Production of $J/\psi + \eta_c$ versus $J/\psi + J/\psi$ at the LHC: Importance of real α_s^5 corrections*, Phys. Rev. Lett. **111** (2013) 122001, arXiv:1308.0474 [hep-ph].

[796] J.-P. Lansberg and H.-S. Shao, *J/ψ-pair production at large momenta: indications for double parton scatterings and large α_s^5 contributions*, Phys. Lett. **B751** (2015) 479, arXiv:1410.8822 [hep-ph].

[797] J.-P. Lansberg and H.-S. Shao, *Double-quarkonium production at a fixed-target experiment at the LHC (AFTER@LHC)*, Nucl. Phys. **B900** (2015) 273–294, arXiv:1504.06531 [hep-ph].

[798] H.-S. Shao, HELAC-ONIA*: An automatic matrix element generator for heavy quarkonium physics*, Comput. Phys. Commun. **184** (2013) 2562, arXiv:1212.5293 [hep-ph].

[799] H.-S. Shao, HELAC-ONIA 2.0*: An upgraded matrix-element and event generator for heavy quarkonium physics*, Comput. Phys. Commun. **198** (2016) 238, arXiv:1507.03435 [hep-ph].

[800] S. P. Baranov, *Pair production of J/ψ mesons in the k_T-factorization approach*, Phys. Rev. **D84** (2011) 054012.

[801] S. P. Baranov and H. Jung, *Double J/ψ production: A probe of gluon polarization?*, Z. Phys. **C66** (1995) 647.

[802] S. Bansal et al., *Progress in double parton scattering studies*, in *Workshop on Multi-Parton Interactions at the LHC (MPI @ LHC 2013) Antwerp, Belgium, December 2-6, 2013*. arXiv:1410.6664 [hep-ph]. https://inspirehep.net/record/1323623/files/arXiv:1410.6664.pdf.

[803] I. Belyaev and D. Savrina, *Study of double parton scattering processes with heavy quarks*, . arXiv:1711.10877 [hep-ex]. http://inspirehep.net/record/1639442/files/arXiv:1711.10877.pdf.

[804] T. Hurth, C. Langenbruch, and F. Mahmoudi, *Direct determination of Wilson coefficients using $B^0 \to K^{*0}\mu^+\mu^-$ decays*, JHEP **11** (2017) 176, arXiv:1708.04474 [hep-ph].

[805] T. Blake, U. Egede, P. Owen, K. A. Petridis, and G. Pomery, *An empirical model to determine*

the hadronic resonance contributions to $\overline{B}^0 \to \overline{K}^{*0}\mu^+\mu^-$ transitions, Eur. Phys. J. **C78** (2018) no. 6, 453, arXiv:1709.03921 [hep-ph].

[806] M. Chrzaszcz, A. Mauri, N. Serra, R. Silva Coutinho, and D. van Dyk, *Prospects for disentangling long- and short-distance effects in the decays $B \to K^*\mu^+\mu^-$*, arXiv:1805.06378 [hep-ph].

[807] LHCb Collaboration, R. Aaij et al., *Expression of Interest for a Phase-II LHCb Upgrade: Opportunities in flavour physics, and beyond, in the HL-LHC era*, CERN-LHCC-2017-003, CERN, Geneva, Feb, 2017. http://cds.cern.ch/record/2244311.

[808] G. Buchalla, A. J. Buras, and M. E. Lautenbacher, *Weak decays beyond leading logarithms*, Rev. Mod. Phys. **68** (1996) 1125–1144, arXiv:hep-ph/9512380 [hep-ph].

[809] C. Bobeth, G. Hiller, and G. Piranishvili, *Angular distributions of $\bar{B} \to \bar{K}\ell^+\ell^-$ decays*, JHEP **12** (2007) 040, arXiv:0709.4174 [hep-ph].

[810] LHCb Collaboration, R. Aaij et al., *Differential branching fraction and angular analysis of the decay $B^0 \to K^{*0}\mu^+\mu^-$*, JHEP **08** (2013) 131, arXiv:1304.6325 [hep-ex].

[811] S. Descotes-Genon, J. Matias, and J. Virto, *Understanding the $B \to K^*\mu^+\mu^-$ Anomaly*, Phys. Rev. **D88** (2013) 074002, arXiv:1307.5683 [hep-ph].

[812] W. Altmannshofer and D. M. Straub, *New Physics in $B \to K^*\mu\mu$?*, Eur. Phys. J. **C73** (2013) 2646, arXiv:1308.1501 [hep-ph].

[813] F. Beaujean, C. Bobeth, and D. van Dyk, *Comprehensive Bayesian analysis of rare (semi)leptonic and radiative B decays*, Eur. Phys. J. **C74** (2014) 2897, arXiv:1310.2478 [hep-ph].

[814] T. Hurth and F. Mahmoudi, *On the LHCb anomaly in $B \to K^*\ell^+\ell^-$*, JHEP **04** (2014) 097, arXiv:1312.5267 [hep-ph].

[815] W. Altmannshofer, C. Niehoff, P. Stangl, and D. M. Straub, *Status of the $B \to K^*\mu^+\mu^-$ anomaly after Moriond 2017*, Eur. Phys. J. **C77** (2017) no. 6, 377, arXiv:1703.09189 [hep-ph].

[816] B. Capdevila, A. Crivellin, S. Descotes-Genon, J. Matias, and J. Virto, *Patterns of New Physics in $b \to s\ell^+\ell^-$ transitions in the light of recent data*, JHEP **01** (2018) 093, arXiv:1704.05340 [hep-ph].

[817] W. Altmannshofer, P. Stangl, and D. M. Straub, *Interpreting Hints for Lepton Flavor Universality Violation*, Phys. Rev. **D96** (2017) no. 5, 055008, arXiv:1704.05435 [hep-ph].

[818] T. Hurth, F. Mahmoudi, D. Martinez Santos, and S. Neshatpour, *Lepton nonuniversality in exclusive $b \to s\ell\ell$ decays*, Phys. Rev. **D96** (2017) no. 9, 095034, arXiv:1705.06274 [hep-ph].

[819] M. Ciuchini, A. M. Coutinho, M. Fedele, E. Franco, A. Paul, L. Silvestrini, and M. Valli, *On Flavourful Easter eggs for New Physics hunger and Lepton Flavour Universality violation*, Eur. Phys. J. **C77** (2017) no. 10, 688, arXiv:1704.05447 [hep-ph].

[820] L.-S. Geng, B. Grinstein, S. Jäger, J. Martin Camalich, X.-L. Ren, and R.-X. Shi, *Towards the discovery of new physics with lepton-universality ratios of $b \to s\ell\ell$ decays*, arXiv:1704.05446 [hep-ph].

[821] M. Beneke, C. Bobeth, and R. Szafron, *Enhanced electromagnetic correction to the rare B-meson decay $B_{s,d} \to \mu^+\mu^-$*, Phys. Rev. Lett. **120** (2018) no. 1, 011801, arXiv:1708.09152 [hep-ph].

[822] A. Bazavov et al., *B- and D-meson leptonic decay constants from four-flavor lattice QCD*, arXiv:1712.09262 [hep-lat].

[823] ETM Collaboration, A. Bussone et al., *Mass of the b quark and B -meson decay constants from N_f=2+1+1 twisted-mass lattice QCD*, Phys. Rev. **D93** (2016) no. 11, 114505,

arXiv:1603.04306 [hep-lat].

[824] C. Hughes, C. T. H. Davies, and C. J. Monahan, *New methods for B meson decay constants and form factors from lattice NRQCD*, Phys. Rev. **D97** (2018) no. 5, 054509, arXiv:1711.09981 [hep-lat].

[825] ATLAS Collaboration, M. Aaboud et al., *Study of the rare decays of B_s^0 and B^0 mesons into muon pairs using data collected during 2015 and 2016 with the ATLAS detector*, arXiv:1812.03017 [hep-ex].

[826] R. Alonso, B. Grinstein, and J. Martin Camalich, *$SU(2) \times U(1)$ gauge invariance and the shape of new physics in rare B decays*, Phys. Rev. Lett. **113** (2014) 241802, arXiv:1407.7044 [hep-ph].

[827] A. Arbey, T. Hurth, F. Mahmoudi, and S. Neshatpour, *Hadronic and New Physics Contributions to $b \to s$ Transitions*, Phys. Rev. **D98** (2018) no. 9, 095027, arXiv:1806.02791 [hep-ph].

[828] L. Calibbi, A. Crivellin, and T. Ota, *Effective Field Theory Approach to $b \to \ell\ell^{(\prime)}$, $B \to K^{(*)}\nu\overline{\nu}$ and $B \to D^{(*)}\tau\nu$ with Third Generation Couplings*, Phys. Rev. Lett. **115** (2015) 181801, arXiv:1506.02661 [hep-ph].

[829] A. Crivellin, L. Hofer, J. Matias, U. Nierste, S. Pokorski, and J. Rosiek, *Lepton-flavour violating B decays in generic Z' models*, Phys. Rev. **D92** (2015) 054013, arXiv:1504.07928 [hep-ph].

[830] K. De Bruyn, R. Fleischer, R. Knegjens, P. Koppenburg, M. Merk, and N. Tuning, *Branching Ratio Measurements of B_s Decays*, Phys. Rev. **D86** (2012) 014027, arXiv:1204.1735 [hep-ph].

[831] W. Altmannshofer, C. Niehoff, and D. M. Straub, *$B_s \to \mu^+\mu^-$ as current and future probe of new physics*, JHEP **05** (2017) 076, arXiv:1702.05498 [hep-ph].

[832] C. Bobeth, M. Gorbahn, T. Hermann, M. Misiak, E. Stamou, et al., *$B_{s,d} \to \ell^+\ell^-$ in the Standard Model with reduced theoretical uncertainty*, Phys. Rev. Lett. **112** (2014) 101801, arXiv:1311.0903 [hep-ph].

[833] A. J. Buras, *Relations between $\Delta M_{s,d}$ and $B_{s,d} \to \mu\bar{\mu}$ in models with minimal flavor violation*, Phys. Lett. **B566** (2003) 115–119, arXiv:hep-ph/0303060 [hep-ph].

[834] F. Dettori, D. Guadagnoli, and M. Reboud, *$B_s^0 \to \mu^+\mu^-\gamma$ from $B_s^0 \to \mu^+\mu^-$*, Phys. Lett. **B768** (2017) 163–167, arXiv:1610.00629 [hep-ph].

[835] D. Guadagnoli, M. Reboud, and R. Zwicky, *$B_s^0 \to \ell^+\ell\gamma$ as a test of lepton flavor universality*, JHEP **11** (2017) 184, arXiv:1708.02649 [hep-ph].

[836] D. Melikhov, N. Nikitin, and S. Simula, *Probing right-handed currents in $B \to K^*\ell^+\ell^-$ transitions*, Phys. Lett. **B442** (1998) 381–389, arXiv:hep-ph/9807464 [hep-ph].

[837] W. Altmannshofer, P. Ball, A. Bharucha, A. J. Buras, D. M. Straub, and M. Wick, *Symmetries and Asymmetries of $B \to K^*\mu^+\mu^-$ Decays in the Standard Model and Beyond*, JHEP **01** (2009) 019, arXiv:0811.1214 [hep-ph].

[838] J. Matias, F. Mescia, M. Ramon, and J. Virto, *Complete Anatomy of $\bar{B}_d \to \bar{K}^{*0}(\to K\pi)l^+l^-$ and its angular distribution*, JHEP **04** (2012) 104, arXiv:1202.4266 [hep-ph].

[839] C. Bobeth, G. Hiller, and G. Piranishvili, *CP Asymmetries in bar $B \to \bar{K}^*(\to \bar{K}\pi)\bar{\ell}\ell$ and Untagged $\bar{B}_s$, $B_s \to \phi(\to K^+K^-)\bar{\ell}\ell$ Decays at NLO*, JHEP **07** (2008) 106, arXiv:0805.2525 [hep-ph].

[840] S. Descotes-Genon, J. Matias, M. Ramon, and J. Virto, *Implications from clean observables for the binned analysis of $B \to K^*\mu^+\mu^-$ at large recoil*, JHEP **01** (2013) 048, arXiv:1207.2753 [hep-ph].

[841] S. Descotes-Genon, T. Hurth, J. Matias, and J. Virto, *Optimizing the basis of $B \to K^*ll$ observables in the full kinematic range*, JHEP **05** (2013) 137, arXiv:1303.5794 [hep-ph].

[842] C. Bobeth, G. Hiller, and D. van Dyk, *The Benefits of $\bar{B} \to \bar{K}^* l^+ l^-$ Decays at Low Recoil*, JHEP **07** (2010) 098, arXiv:1006.5013 [hep-ph].

[843] S. Jäger and J. Martin Camalich, *On $B \to V\ell\ell$ at small dilepton invariant mass, power corrections, and new physics*, JHEP **05** (2013) 043, arXiv:1212.2263 [hep-ph].

[844] Jäger, Sebastian and Martin Camalich, Jorge, *Reassessing the discovery potential of the $B \to K^* \ell^+ \ell^-$ decays in the large-recoil region: SM challenges and BSM opportunities*, Phys. Rev. **D93** (2016) no. 1, 014028, arXiv:1412.3183 [hep-ph].

[845] C. Bobeth, M. Chrzaszcz, D. van Dyk, and J. Virto, *Long-distance effects in $B \to K^* \ell\ell$ from analyticity*, Eur. Phys. J. **C78** (2018) no. 6, 451, arXiv:1707.07305 [hep-ph].

[846] A. Khodjamirian, T. Mannel, and N. Offen, *Form-factors from light-cone sum rules with B-meson distribution amplitudes*, Phys. Rev. **D75** (2007) 054013, arXiv:hep-ph/0611193 [hep-ph].

[847] A. Bharucha, D. M. Straub, and R. Zwicky, *$B \to V\ell^+\ell^-$ in the Standard Model from light-cone sum rules*, JHEP **08** (2016) 098, arXiv:1503.05534 [hep-ph].

[848] A. Khodjamirian and A. V. Rusov, *$B_s \to K\ell\nu_\ell$ and $B_{(s)} \to \pi(K)\ell^+\ell^-$ decays at large recoil and CKM matrix elements*, JHEP **08** (2017) 112, arXiv:1703.04765 [hep-ph].

[849] N. Gubernari, A. Kokulu, and D. van Dyk, *$B \to P$ and $B \to V$ Form Factors from B-Meson Light-Cone Sum Rules beyond Leading Twist*, arXiv:1811.00983 [hep-ph].

[850] J. A. Bailey et al., *$B \to K l^+ l^-$ decay form factors from three-flavor lattice QCD*, Phys. Rev. **D93** (2016) no. 2, 025026, arXiv:1509.06235 [hep-lat].

[851] R. R. Horgan, Z. Liu, S. Meinel, and M. Wingate, *Lattice QCD calculation of form factors describing the rare decays $B \to K^* \ell^+ \ell^-$ and $B_s \to \phi \ell^+ \ell^-$*, Phys. Rev. **D89** (2014) no. 9, 094501, arXiv:1310.3722 [hep-lat].

[852] N. Meiman, Analytic Expressions for Upper Limits of Coupling Constants in Quantum Field Theory, Zh. Eksp. Teor. Fiz. **44** (1963) 1228. [Sov. Phys. JETP **17**, 830 (1963)].

[853] C. G. Boyd, B. Grinstein, and R. F. Lebed, *Constraints on form-factors for exclusive semileptonic heavy to light meson decays*, Phys. Rev. Lett. **74** (1995) 4603–4606, arXiv:hep-ph/9412324 [hep-ph].

[854] C. Bourrely, I. Caprini, and L. Lellouch, *Model-independent description of $B \to \pi l \nu$ decays and a determination of $|V_{ub}|$*, Phys. Rev. **D79** (2009) 013008, arXiv:0807.2722 [hep-ph]. [Erratum: Phys. Rev.D82,099902(2010)].

[855] S. Cheng, A. Khodjamirian, and J. Virto, *$B \to \pi\pi$ Form Factors from Light-Cone Sum Rules with B-meson Distribution Amplitudes*, JHEP **05** (2017) 157, arXiv:1701.01633 [hep-ph].

[856] S. Cheng, A. Khodjamirian, and J. Virto, *Timelike-helicity $B \to \pi\pi$ form factor from light-cone sum rules with dipion distribution amplitudes*, Phys. Rev. **D96** (2017) no. 5, 051901, arXiv:1709.00173 [hep-ph].

[857] C. Alexandrou, L. Leskovec, S. Meinel, J. Negele, S. Paul, M. Petschlies, A. Pochinsky, G. Rendon, and S. Syritsyn, *P-wave $\pi\pi$ scattering and the ρ resonance from lattice QCD*, Phys. Rev. **D96** (2017) no. 3, 034525, arXiv:1704.05439 [hep-lat].

[858] M. Beneke, T. Feldmann, and D. Seidel, *Systematic approach to exclusive $B \to V l^+ l^-$, $V\gamma$ decays*, Nucl. Phys. **B612** (2001) 25–58, arXiv:hep-ph/0106067 [hep-ph].

[859] A. Khodjamirian, T. Mannel, A. A. Pivovarov, and Y. M. Wang, *Charm-loop effect in $B \to K^{(*)} \ell^+ \ell^-$ and $B \to K^* \gamma$*, JHEP **09** (2010) 089, arXiv:1006.4945 [hep-ph].

[860] M. Beylich, G. Buchalla, and T. Feldmann, *Theory of $B \to K^{(*)} \ell^+ \ell^-$ decays at high q^2: OPE and quark-hadron duality*, Eur. Phys. J. **C71** (2011) 1635, arXiv:1101.5118 [hep-ph].

[861] M. Chrzaszcz, A. Mauri, N. Serra, R. Silva Coutinho, and D. van Dyk, *Prospects for disentangling long- and short-distance effects in the decays $B \to K^* \mu^+ \mu^-$*,

arXiv:1805.06378 [hep-ph].

[862] B. Grinstein and D. Pirjol, *Exclusive rare $B \to K^* \ell^+ \ell^-$ decays at low recoil: Controlling the long-distance effects*, Phys. Rev. **D70** (2004) 114005, arXiv:hep-ph/0404250 [hep-ph].

[863] F. Kruger and L. M. Sehgal, *Lepton polarization in the decays $b \to X_s \mu^+ \mu^-$ and $B \to X_s \tau^+ \tau^-$*, Phys. Lett. **B380** (1996) 199–204, arXiv:hep-ph/9603237 [hep-ph].

[864] J. Lyon and R. Zwicky, *Resonances gone topsy turvy - the charm of QCD or new physics in $b \to s \ell^+ \ell^-$?*, arXiv:1406.0566 [hep-ph].

[865] S. Braß, G. Hiller, and I. Nisandzic, *Zooming in on $B \to K^* \ell\ell$ decays at low recoil*, Eur. Phys. J. **C77** (2017) no. 1, 16, arXiv:1606.00775 [hep-ph].

[866] G. Hiller and F. Kruger, *More model-independent analysis of $b \to s$ processes*, Phys. Rev. **D69** (2004) 074020, arXiv:hep-ph/0310219 [hep-ph].

[867] M. Bordone, G. Isidori, and A. Pattori, *On the Standard Model predictions for R_K and R_{K^*}*, Eur. Phys. J. **C76** (2016) 440, arXiv:1605.07633 [hep-ph].

[868] LHCb Collaboration, R. Aaij et al., *Test of lepton universality using $B^+ \to K^+ \ell^+ \ell^-$ decays*, Phys. Rev. Lett. **113** (2014) 151601, arXiv:1406.6482 [hep-ex].

[869] LHCb Collaboration, R. Aaij et al., *Test of lepton universality with $B^0 \to K^{*0} \ell^+ \ell^-$ decays*, JHEP **08** (2017) 055, arXiv:1705.05802 [hep-ex].

[870] B. Capdevila, S. Descotes-Genon, J. Matias, and J. Virto, *Assessing lepton-flavour non-universality from $B \to K^* \ell\ell$ angular analyses*, JHEP **10** (2016) 075, arXiv:1605.03156 [hep-ph].

[871] Belle Collaboration, S. Wehle et al., *Lepton-Flavor-Dependent Angular Analysis of $B \to K^* \ell^+ \ell^-$*, Phys. Rev. Lett. **118** (2017) no. 11, 111801, arXiv:1612.05014 [hep-ex].

[872] B. Capdevila, A. Crivellin, S. Descotes-Genon, L. Hofer, and J. Matias, *Searching for New Physics with $b \to s \tau^+ \tau^-$ processes*, Phys. Rev. Lett. **120** (2018) no. 18, 181802, arXiv:1712.01919 [hep-ph].

[873] J. F. Kamenik, S. Monteil, A. Semkiv, and L. V. Silva, *Lepton polarization asymmetries in rare semi-tauonic $b \to s$ exclusive decays at FCC-ee*, Eur. Phys. J. **C77** (2017) no. 10, 701, arXiv:1705.11106 [hep-ph].

[874] D. Das, *On the angular distribution of $\Lambda_b \to \Lambda(\to N\pi)\tau^+\tau^-$ decay*, JHEP **07** (2018) 063, arXiv:1804.08527 [hep-ph].

[875] A. Mauri, N. Serra, and R. Silva Coutinho, *Towards establishing Lepton Flavour Universality violation in $\bar{B} \to \bar{K}^* \ell^+ \ell^-$ decays*, arXiv:1805.06401 [hep-ph].

[876] P. Böer, T. Feldmann, and D. van Dyk, *Angular Analysis of the Decay $\Lambda_b \to \Lambda(\to N\pi)\ell^+\ell^-$*, JHEP **01** (2015) 155, arXiv:1410.2115 [hep-ph].

[877] D. Das, *Model independent New Physics analysis in $\Lambda_b \to \Lambda \mu^+ \mu^-$ decay*, Eur. Phys. J. **C78** (2018) no. 3, 230, arXiv:1802.09404 [hep-ph].

[878] T. Blake and M. Kreps, *Angular distribution of polarised Λ_b baryons decaying to $\Lambda \ell^+ \ell^-$*, JHEP **11** (2017) 138, arXiv:1710.00746 [hep-ph].

[879] S. Descotes-Genon and J. Virto, *Time dependence in $B \to V \ell\ell$ decays*, JHEP **04** (2015) 045, arXiv:1502.05509 [hep-ph]. [Erratum: JHEP07,049(2015)].

[880] C. Hambrock, A. Khodjamirian, and A. Rusov, *Hadronic effects and observables in $B \to \pi \ell^+ \ell^-$ decay at large recoil*, Phys. Rev. **D92** (2015) 074020, arXiv:1506.07760 [hep-ph].

[881] D. Atwood, M. Gronau, and A. Soni, *Mixing induced CP asymmetries in radiative B decays in and beyond the standard model*, Phys. Rev. Lett. **79** (1997) 185–188, arXiv:hep-ph/9704272 [hep-ph].

[882] M. Gronau, Y. Grossman, D. Pirjol, and A. Ryd, *Measuring the photon polarization in*

$B \to K\pi\pi\gamma$, Phys. Rev. Lett. **88** (2002) 051802, arXiv:hep-ph/0107254 [hep-ph].

[883] M. Gronau and D. Pirjol, *Photon polarization in radiative B decays*, Phys. Rev. **D66** (2002) 054008, arXiv:hep-ph/0205065 [hep-ph].

[884] P. Ball, G. W. Jones, and R. Zwicky, $B \to V\gamma$ *beyond QCD factorisation*, Phys. Rev. **D75** (2007) 054004, arXiv:hep-ph/0612081 [hep-ph].

[885] E. Kou, A. Le Yaouanc, and A. Tayduganov, *Determining the photon polarization of the* $b \to s\gamma$ *using the* $B \to K_1(1270)\gamma \to (K\pi\pi)\gamma$ *decay*, Phys. Rev. **D83** (2011) 094007, arXiv:1011.6593 [hep-ph].

[886] D. Becirevic, E. Kou, A. Le Yaouanc, and A. Tayduganov, *Future prospects for the determination of the Wilson coefficient* $C'_{7\gamma}$, JHEP **08** (2012) 090, arXiv:1206.1502 [hep-ph].

[887] S. Descotes-Genon, D. Ghosh, J. Matias, and M. Ramon, *Exploring New Physics in the C7-C7' plane*, JHEP **06** (2011) 099, arXiv:1104.3342 [hep-ph].

[888] F. Muheim, Y. Xie, and R. Zwicky, *Exploiting the width difference in* $B_s \to \phi\gamma$, Phys. Lett. **B664** (2008) 174–179, arXiv:0802.0876 [hep-ph].

[889] BaBar Collaboration, B. Aubert et al., *Measurement of the time-dependent CP-violating asymmetry in* $B^0 \to K^0_S\pi^0\gamma$ *decays*, Phys. Rev. **D72** (2005) 051103, arXiv:hep-ex/0507038 [hep-ex].

[890] Belle Collaboration, Y. Ushiroda et al., *Time-Dependent CP Asymmetries in* $B^0 \to K^0_S\pi^0\gamma$ *transitions*, Phys. Rev. **D74** (2006) 111104, arXiv:hep-ex/0608017 [hep-ex].

[891] LHCb collaboration, R. Aaij et al., *First experimental study of photon polarization in radiative* B^0_s *decays*, Phys. Rev. Lett. **118** (2017) 021801, arXiv:1609.02032 [hep-ex].

[892] LHCb Collaboration, R. Aaij et al., *Angular analysis of the* $B^0 \to K^{*0}e^+e^-$ *decay in the low-*q^2 *region*, JHEP **04** (2015) 064, arXiv:1501.03038 [hep-ex].

[893] M. Benzke, S. J. Lee, M. Neubert, and G. Paz, *Factorization at Subleading Power and Irreducible Uncertainties in* $\bar{B} \to X_s\gamma$ *Decay*, JHEP **08** (2010) 099, arXiv:1003.5012 [hep-ph].

[894] M. Benzke, T. Hurth, and S. Turczyk, *Subleading power factorization in* $\bar{B} \to X_s\ell^+\ell^-$, JHEP **10** (2017) 031, arXiv:1705.10366 [hep-ph].

[895] M. Misiak et al., *Updated NNLO QCD predictions for the weak radiative B-meson decays*, Phys. Rev. Lett. **114** (2015) no. 22, 221801, arXiv:1503.01789 [hep-ph].

[896] T. Huber, T. Hurth, and E. Lunghi, *Inclusive* $\overline{B} \to X_s\ell^+\ell^-$ *: complete angular analysis and a thorough study of collinear photons*, JHEP **06** (2015) 176, arXiv:1503.04849 [hep-ph].

[897] A. J. Buras, J. Girrbach-Noe, C. Niehoff, and D. M. Straub, $B \to K^{(*)}\nu\bar{\nu}$ *decays in the Standard Model and beyond*, JHEP **02** (2015) 184, arXiv:1409.4557 [hep-ph].

[898] A. J. Buras, J. Girrbach-Noe, C. Niehoff, and D. M. Straub, $B \to K^{(*)}\nu\bar{\nu}$ *decays in the Standard Model and beyond*, arXiv:1409.4557 [hep-ph].

[899] LHCb collaboration, R. Aaij et al., *Angular analysis of the* $B^0 \to K^{*0}\mu^+\mu^-$ *decay using* $3\,fb^{-1}$ *of integrated luminosity*, JHEP **02** (2016) 104, arXiv:1512.04442 [hep-ex].

[900] LHCb collaboration, R. Aaij et al., *Angular analysis and differential branching fraction of the decay* $B^0_s \to \phi\mu^+\mu^-$, JHEP **09** (2015) 179, arXiv:1506.08777 [hep-ex].

[901] S. Jager, K. Leslie, M. Kirk, and A. Lenz, *Charming new physics in rare B-decays and mixing?*, Phys. Rev. **D97** (2018) no. 1, 015021, arXiv:1701.09183 [hep-ph].

[902] M. Algueró, B. Capdevila, S. Descotes-Genon, P. Masjuan, and J. Matias, *Are we overlooking Lepton Flavour Universal New Physics in* $b \to s\ell\ell$ *?*, arXiv:1809.08447 [hep-ph].

[903] D. M. Straub, *flavio: a Python package for flavour and precision phenomenology in the Standard Model and beyond*, arXiv:1810.08132 [hep-ph].

[904] J. Aebischer, A. Crivellin, M. Fael, and C. Greub, *Matching of gauge invariant dimension-six operators for $b \to s$ and $b \to c$ transitions*, JHEP **05** (2016) 037, arXiv:1512.02830 [hep-ph].

[905] G. Belanger, C. Delaunay, and S. Westhoff, *A Dark Matter Relic From Muon Anomalies*, Phys. Rev. **D92** (2015) 055021, arXiv:1507.06660 [hep-ph].

[906] P. Arnan, L. Hofer, F. Mescia, and A. Crivellin, *Loop effects of heavy new scalars and fermions in $b \to s\mu^+\mu^-$*, JHEP **04** (2017) 043, arXiv:1608.07832 [hep-ph].

[907] J. F. Kamenik, Y. Soreq, and J. Zupan, *Lepton flavor universality violation without new sources of quark flavor violation*, Phys. Rev. **D97** (2018) no. 3, 035002, arXiv:1704.06005 [hep-ph].

[908] A. Crivellin, C. Greub, F. Saturnino, and D. Müller, *Importance of Loop Effects in Explaining the Accumulated Evidence for New Physics in B Decays with a Vector Leptoquark*, arXiv:1807.02068 [hep-ph].

[909] W. Altmannshofer and D. M. Straub, *New physics in $b \to s$ transitions after LHC run 1*, Eur. Phys. J. **C75** (2015) no. 8, 382, arXiv:1411.3161 [hep-ph].

[910] L. Di Luzio, M. Kirk, and A. Lenz, *One constraint to kill them all?*, arXiv:1712.06572 [hep-ph].

[911] L. Di Luzio, M. Kirk, and A. Lenz, *B_s-$\bar{B}_s$ mixing interplay with B anomalies*, in *10th International Workshop on the CKM Unitarity Triangle (CKM 2018) Heidelberg, Germany, September 17-21, 2018*. 2018. arXiv:1811.12884 [hep-ph].

[912] A. Datta, J. Liao, and D. Marfatia, *A light Z' for the R_K puzzle and nonstandard neutrino interactions*, Phys. Lett. **B768** (2017) 265–269, arXiv:1702.01099 [hep-ph].

[913] F. Sala and D. M. Straub, *A New Light Particle in B Decays?*, Phys. Lett. **B774** (2017) 205–209, arXiv:1704.06188 [hep-ph].

[914] W. Altmannshofer, M. J. Baker, S. Gori, R. Harnik, M. Pospelov, E. Stamou, and A. Thamm, *Light resonances and the low-q^2 bin of R_{K^*}*, JHEP **03** (2018) 188, arXiv:1711.07494 [hep-ph].

[915] W. Altmannshofer, S. Gori, M. Pospelov, and I. Yavin, *Quark flavor transitions in $L_\mu - L_\tau$ models*, Phys. Rev. **D89** (2014) 095033, arXiv:1403.1269 [hep-ph].

[916] A. Crivellin, G. D'Ambrosio, and J. Heeck, *Explaining $h \to \mu^\pm\tau^\mp$, $B \to K^*\mu^+\mu^-$ and $B \to K\mu^+\mu^-/B \to Ke^+e^-$ in a two-Higgs-doublet model with gauged $L_\mu - L_\tau$*, Phys. Rev. Lett. **114** (2015) 151801, arXiv:1501.00993 [hep-ph].

[917] W. Altmannshofer and I. Yavin, *Predictions for lepton flavor universality violation in rare B decays in models with gauged $L_\mu - L_\tau$*, Phys. Rev. **D92** (2015) no. 7, 075022, arXiv:1508.07009 [hep-ph].

[918] K. Fuyuto, W.-S. Hou, and M. Kohda, *Z' -induced FCNC decays of top, beauty, and strange quarks*, Phys. Rev. **D93** (2016) no. 5, 054021, arXiv:1512.09026 [hep-ph].

[919] W. Altmannshofer, S. Gori, S. Profumo, and F. S. Queiroz, *Explaining dark matter and B decay anomalies with an $L_\mu - L_\tau$ model*, JHEP **12** (2016) 106, arXiv:1609.04026 [hep-ph].

[920] S. Baek, *Dark matter contribution to $b \to s\mu^+\mu^-$ anomaly in local $U(1)_{L_\mu - L_\tau}$ model*, arXiv:1707.04573 [hep-ph].

[921] C.-H. Chen and T. Nomura, *Penguin $b \to s\ell'^+\ell'^-$ and B-meson anomalies in a gauged $L_\mu - L_\tau$*, Phys. Lett. **B777** (2018) 420–427, arXiv:1707.03249 [hep-ph].

[922] W. Altmannshofer, M. Carena, and A. Crivellin, *$L_\mu - L_\tau$ theory of Higgs flavor violation and $(g-2)_\mu$*, Phys. Rev. **D94** (2016) no. 9, 095026, arXiv:1604.08221 [hep-ph].

[923] A. Crivellin, G. D'Ambrosio, and J. Heeck, *Addressing the LHC flavor anomalies with horizontal gauge symmetries*, Phys. Rev. **D91** (2015) no. 7, 075006, arXiv:1503.03477

[hep-ph].

[924] A. Falkowski, M. Nardecchia, and R. Ziegler, *Lepton Flavor Non-Universality in B-meson Decays from a U(2) Flavor Model*, JHEP **11** (2015) 173, arXiv:1509.01249 [hep-ph].

[925] S. M. Boucenna, A. Celis, J. Fuentes-Martin, A. Vicente, and J. Virto, *Non-abelian gauge extensions for B-decay anomalies*, Phys. Lett. **B760** (2016) 214–219, arXiv:1604.03088 [hep-ph].

[926] S. M. Boucenna, A. Celis, J. Fuentes-Martin, A. Vicente, and J. Virto, *Phenomenology of an $SU(2) \times SU(2) \times U(1)$ model with lepton-flavour non-universality*, JHEP **12** (2016) 059, arXiv:1608.01349 [hep-ph].

[927] A. Celis, W.-Z. Feng, and M. Vollmann, *Dirac dark matter and $b \to s\ell^+\ell^-$ with $\mathrm{U}(1)$ gauge symmetry*, Phys. Rev. **D95** (2017) no. 3, 035018, arXiv:1608.03894 [hep-ph].

[928] A. Crivellin, J. Fuentes-Martin, A. Greljo, and G. Isidori, *Lepton Flavor Non-Universality in B decays from Dynamical Yukawas*, Phys. Lett. **B766** (2017) 77–85, arXiv:1611.02703 [hep-ph].

[929] R. Alonso, P. Cox, C. Han, and T. T. Yanagida, *Anomaly-free local horizontal symmetry and anomaly-full rare B-decays*, Phys. Rev. **D96** (2017) no. 7, 071701, arXiv:1704.08158 [hep-ph].

[930] J. Ellis, M. Fairbairn, and P. Tunney, *Anomaly-Free Models for Flavour Anomalies*, arXiv:1705.03447 [hep-ph].

[931] R. Alonso, P. Cox, C. Han, and T. T. Yanagida, *Flavoured $B - L$ local symmetry and anomalous rare B decays*, Phys. Lett. **B774** (2017) 643–648, arXiv:1705.03858 [hep-ph].

[932] C. Bonilla, T. Modak, R. Srivastava, and J. W. F. Valle, *$U(1)_{B_3-3L_\mu}$ gauge symmetry as the simplest description of $b \to s$ anomalies*, arXiv:1705.00915 [hep-ph].

[933] K. S. Babu, A. Friedland, P. A. N. Machado, and I. Mocioiu, *Flavor Gauge Models Below the Fermi Scale*, JHEP **12** (2017) 096, arXiv:1705.01822 [hep-ph].

[934] L. Bian, S.-M. Choi, Y.-J. Kang, and H. M. Lee, *A minimal flavored $U(1)'$ for B-meson anomalies*, Phys. Rev. **D96** (2017) no. 7, 075038, arXiv:1707.04811 [hep-ph].

[935] Y. Tang and Y.-L. Wu, *Flavor non-universal gauge interactions and anomalies in B-meson decays*, Chin. Phys. **C42** (2018) no. 3, 033104, arXiv:1705.05643 [hep-ph].

[936] J. M. Cline and J. Martin Camalich, *B decay anomalies from nonabelian local horizontal symmetry*, Phys. Rev. **D96** (2017) no. 5, 055036, arXiv:1706.08510 [hep-ph].

[937] D. Aristizabal Sierra, F. Staub, and A. Vicente, *Shedding light on the $b \to s$ anomalies with a dark sector*, Phys. Rev. **D92** (2015) no. 1, 015001, arXiv:1503.06077 [hep-ph].

[938] K. Fuyuto, H.-L. Li, and J.-H. Yu, *Implications of hidden gauged $U(1)$ model for B anomalies*, arXiv:1712.06736 [hep-ph].

[939] C. Niehoff, P. Stangl, and D. M. Straub, *Violation of lepton flavour universality in composite Higgs models*, Phys. Lett. **B747** (2015) 182–186, arXiv:1503.03865 [hep-ph].

[940] A. Carmona and F. Goertz, *Lepton Flavor and Nonuniversality from Minimal Composite Higgs Setups*, Phys. Rev. Lett. **116** (2016) no. 25, 251801, arXiv:1510.07658 [hep-ph].

[941] E. Megias, G. Panico, O. Pujolas, and M. Quiros, *A Natural origin for the LHCb anomalies*, JHEP **09** (2016) 118, arXiv:1608.02362 [hep-ph].

[942] A. Carmona and F. Goertz, *Recent B Physics Anomalies - a First Hint for Compositeness?*, arXiv:1712.02536 [hep-ph].

[943] E. Megias, M. Quiros, and L. Salas, *Lepton-flavor universality violation in R_K and $R_{D^{(*)}}$ from warped space*, JHEP **07** (2017) 102, arXiv:1703.06019 [hep-ph].

[944] F. Sannino, P. Stangl, D. M. Straub, and A. E. Thomsen, *Flavor Physics and Flavor Anomalies in Minimal Fundamental Partial Compositeness*, arXiv:1712.07646 [hep-ph].

[945] B. Bhattacharya, A. Datta, D. London, and S. Shivashankara, *Simultaneous Explanation of the R_K and $R(D^{(*)})$ Puzzles*, Phys. Lett. **B742** (2015) 370–374, arXiv:1412.7164 [hep-ph].

[946] A. Greljo, G. Isidori, and D. Marzocca, *On the breaking of Lepton Flavor Universality in B decays*, JHEP **07** (2015) 142, arXiv:1506.01705 [hep-ph].

[947] B. Bhattacharya, A. Datta, J.-P. Guevin, D. London, and R. Watanabe, *Simultaneous Explanation of the R_K and $R_{D^{(*)}}$ Puzzles: a Model Analysis*, JHEP **01** (2017) 015, arXiv:1609.09078 [hep-ph].

[948] J. Kumar, D. London, and R. Watanabe, *Combined Explanations of the $b \to s\mu^+\mu^-$ and $b \to c\tau^-\bar{\nu}$ Anomalies: a General Model Analysis*, arXiv:1806.07403 [hep-ph].

[949] B. Diaz, M. Schmaltz, and Y.-M. Zhong, *The leptoquark Hunter's guide: Pair production*, JHEP **10** (2017) 097, arXiv:1706.05033 [hep-ph].

[950] M. Bauer and M. Neubert, *Minimal Leptoquark Explanation for the $R_{D^{(*)}}$, R_K , and $(g-2)_g$ Anomalies*, Phys. Rev. Lett. **116** (2016) no. 14, 141802, arXiv:1511.01900 [hep-ph].

[951] G. Hiller and M. Schmaltz, *R_K and future $b \to s\ell\ell$ physics beyond the standard model opportunities*, Phys. Rev. **D90** (2014) 054014, arXiv:1408.1627 [hep-ph].

[952] S. Fajfer and N. Kosnik, *Vector leptoquark resolution of R_K and $R_{D^{(*)}}$ puzzles*, Phys. Lett. **B755** (2016) 270–274, arXiv:1511.06024 [hep-ph].

[953] G. Hiller and I. Nisandzic, *R_K and R_{K^*} beyond the standard model*, Phys. Rev. **D96** (2017) no. 3, 035003, arXiv:1704.05444 [hep-ph].

[954] C.-H. Chen, T. Nomura, and H. Okada, *Excesses of muon $g-2$, $R_{D^{(*)}}$, and R_K in a leptoquark model*, Phys. Lett. **B774** (2017) 456–464, arXiv:1703.03251 [hep-ph].

[955] A. Crivellin, D. Mueller, and T. Ota, *Simultaneous explanation of $R_{D^{()}}$ and $b \to s\mu^+\mu^-$: the last scalar leptoquarks standing*, JHEP **09** (2017) 040, arXiv:1703.09226 [hep-ph].

[956] D. Aloni, A. Dery, C. Frugiuele, and Y. Nir, *Testing minimal flavor violation in leptoquark models of the $R_{K^{(*)}}$ anomaly*, JHEP **11** (2017) 109, arXiv:1708.06161 [hep-ph].

[957] B. Gripaios, M. Nardecchia, and S. A. Renner, *Composite leptoquarks and anomalies in B-meson decays*, JHEP **05** (2015) 006, arXiv:1412.1791 [hep-ph].

[958] R. Barbieri, C. W. Murphy, and F. Senia, *B-decay Anomalies in a Composite Leptoquark Model*, Eur. Phys. J. **C77** (2017) no. 1, 8, arXiv:1611.04930 [hep-ph].

[959] D. Das, C. Hati, G. Kumar, and N. Mahajan, *Towards a unified explanation of $R_{D^{(*)}}$, R_K and $(g-2)_\mu$ anomalies in a left-right model with leptoquarks*, Phys. Rev. **D94** (2016) 055034, arXiv:1605.06313 [hep-ph].

[960] B. Fornal, S. A. Gadam, and B. Grinstein, *Left-Right SU(4) Vector Leptoquark Model for Flavor Anomalies*, arXiv:1812.01603 [hep-ph].

[961] N. Assad, B. Fornal, and B. Grinstein, *Baryon Number and Lepton Universality Violation in Leptoquark and Diquark Models*, Phys. Lett. **B777** (2018) 324–331, arXiv:1708.06350 [hep-ph].

[962] M. Bordone, C. Cornella, J. Fuentes-Martin, and G. Isidori, *A three-site gauge model for flavor hierarchies and flavor anomalies*, Phys. Lett. **B779** (2018) 317–323, arXiv:1712.01368 [hep-ph].

[963] L. Di Luzio, A. Greljo, and M. Nardecchia, *Gauge leptoquark as the origin of B-physics anomalies*, Phys. Rev. **D96** (2017) no. 11, 115011, arXiv:1708.08450 [hep-ph].

[964] M. Blanke and A. Crivellin, *B Meson Anomalies in a Pati-Salam Model within the Randall-Sundrum Background*, Phys. Rev. Lett. **121** (2018) no. 1, 011801, arXiv:1801.07256 [hep-ph].

[965] L. Calibbi, A. Crivellin, and T. Li, *A model of vector leptoquarks in view of the B-physics anomalies*, arXiv:1709.00692 [hep-ph].

[966] D. Das, C. Hati, G. Kumar, and N. Mahajan, *Scrutinizing R-parity violating interactions in light of $R_{K^{(*)}}$ data*, Phys. Rev. **D96** (2017) no. 9, 095033, arXiv:1705.09188 [hep-ph].

[967] K. Earl and T. Gregoire, *Contributions to $b \to s\ell\ell$ Anomalies from R-Parity Violating Interactions*, arXiv:1806.01343 [hep-ph].

[968] D. Bečirevic, I. Doršner, S. Fajfer, N. Košnik, D. A. Faroughy, and O. Sumensari, *Scalar leptoquarks from grand unified theories to accommodate the B-physics anomalies*, Phys. Rev. **D98** (2018) no. 5, 055003, arXiv:1806.05689 [hep-ph].

[969] F. Feruglio, P. Paradisi, and A. Pattori, *Revisiting Lepton Flavor Universality in B Decays*, Phys. Rev. Lett. **118** (2017) no. 1, 011801, arXiv:1606.00524 [hep-ph].

[970] F. Feruglio, P. Paradisi, and A. Pattori, *On the Importance of Electroweak Corrections for B Anomalies*, JHEP **09** (2017) 061, arXiv:1705.00929 [hep-ph].

[971] C. Cornella, F. Feruglio, and P. Paradisi, *Low-energy Effects of Lepton Flavour Universality Violation*, arXiv:1803.00945 [hep-ph].

[972] V. Cirigliano, J. Jenkins, and M. Gonzalez-Alonso, *Semileptonic decays of light quarks beyond the Standard Model*, Nucl. Phys. **B830** (2010) 95–115, arXiv:0908.1754 [hep-ph].

[973] O. Catá and M. Jung, *Signatures of a nonstandard Higgs boson from flavor physics*, Phys. Rev. **D92** (2015) no. 5, 055018, arXiv:1505.05804 [hep-ph].

[974] M. Jung and D. M. Straub, *Constraining new physics in $b \to c\ell\nu$ transitions*, arXiv:1801.01112 [hep-ph].

[975] I. Caprini, L. Lellouch, and M. Neubert, *Dispersive bounds on the shape of anti-B $\to$ D(*) lepton anti-neutrino form-factors*, Nucl. Phys. **B530** (1998) 153–181, arXiv:hep-ph/9712417 [hep-ph].

[976] C. G. Boyd, B. Grinstein, and R. F. Lebed, *Precision corrections to dispersive bounds on form-factors*, Phys. Rev. **D56** (1997) 6895–6911, arXiv:hep-ph/9705252 [hep-ph].

[977] MILC Collaboration, J. A. Bailey et al., *$B \to Dl\nu$ form factors at nonzero recoil and $|V_{cb}|$ from 2+1-flavor lattice QCD*, Phys. Rev. **D92** (2015) no. 3, 034506, arXiv:1503.07237 [hep-lat].

[978] HPQCD Collaboration, H. Na, C. M. Bouchard, G. P. Lepage, C. Monahan, and J. Shigemitsu, *$B \to Dl\nu$ form factors at nonzero recoil and extraction of $|V_{cb}|$*, Phys. Rev. **D92** (2015) no. 5, 054510, arXiv:1505.03925 [hep-lat]. [Erratum: Phys. Rev.D93,no.11,119906(2016)].

[979] S. de Boer, T. Kitahara, and I. Nisandzic, *Soft-Photon Corrections to $\bar{B} \to D\tau^-\bar{\nu}_\tau$ Relative to $\bar{B} \to D\mu^-\bar{\nu}_\mu$*, Phys. Rev. Lett. **120** (2018) no. 26, 261804, arXiv:1803.05881 [hep-ph].

[980] Fermilab Lattice, MILC Collaboration, J. A. Bailey et al., *Update of $|V_{cb}|$ from the $\bar{B} \to D^*\ell\bar{\nu}$ form factor at zero recoil with three-flavor lattice QCD*, Phys. Rev. **D89** (2014) no. 11, 114504, arXiv:1403.0635 [hep-lat].

[981] HPQCD Collaboration, J. Harrison, C. Davies, and M. Wingate, *Lattice QCD calculation of the $B_{(s)} \to D^*_{(s)}\ell\nu$ form factors at zero recoil and implications for $|V_{cb}|$*, Phys. Rev. **D97** (2018) no. 5, 054502, arXiv:1711.11013 [hep-lat].

[982] F. U. Bernlochner, Z. Ligeti, M. Papucci, and D. J. Robinson, *Combined analysis of semileptonic B decays to D and D^*: $R(D^{(*)})$, $|V_{cb}|$, and new physics*, Phys. Rev. **D95** (2017) no. 11, 115008, arXiv:1703.05330 [hep-ph]. [Erratum: Phys. Rev.D97,no.5,059902(2018)].

[983] M. E. Luke, *Effects of subleading operators in the heavy quark effective theory*, Phys. Lett. **B252** (1990) 447–455.

[984] M. Neubert and V. Rieckert, *New approach to the universal form-factors in decays of heavy mesons*, Nucl. Phys. **B382** (1992) 97–119.

[985] M. Neubert, *Heavy quark symmetry*, Phys. Rept. **245** (1994) 259–396,

arXiv:hep-ph/9306320 [hep-ph].

[986] M. Neubert, Z. Ligeti, and Y. Nir, *QCD sum rule analysis of the subleading Isgur-Wise form-factor* $\chi_2(v - v')$, Phys. Lett. **B301** (1993) 101–107, arXiv:hep-ph/9209271 [hep-ph].

[987] M. Neubert, Z. Ligeti, and Y. Nir, *The Subleading Isgur-Wise form-factor* $\chi_3(v, v')$ *to order* α_s *in QCD sum rules*, Phys. Rev. **D47** (1993) 5060–5066, arXiv:hep-ph/9212266 [hep-ph].

[988] Z. Ligeti, Y. Nir, and M. Neubert, *The Subleading Isgur-Wise form-factor* $xi_3(v - v')$ *and its implications for the decays* $\bar{B} \to D * l\bar{\nu}$, Phys. Rev. **D49** (1994) 1302–1309, arXiv:hep-ph/9305304 [hep-ph].

[989] S. Jaiswal, S. Nandi, and S. K. Patra, *Extraction of* $|V_{cb}|$ *from* $B \to D^{(*)}\ell\nu_\ell$ *and the Standard Model predictions of* $R(D^{(*)})$, JHEP **12** (2017) 060, arXiv:1707.09977 [hep-ph].

[990] S. Faller, A. Khodjamirian, C. Klein, and T. Mannel, $B \to D^{(*)}$ *Form Factors from QCD Light-Cone Sum Rules*, Eur. Phys. J. **C60** (2009) 603–615, arXiv:0809.0222 [hep-ph].

[991] Belle Collaboration, A. Abdesselam et al., *Precise determination of the CKM matrix element* $|V_{cb}|$ *with* $\bar{B}^0 \to D^{*+}\ell^-\bar{\nu}_\ell$ *decays with hadronic tagging at Belle*, arXiv:1702.01521 [hep-ex].

[992] S. Schacht, *The role of theory input for exclusive* V_{cb} *determinations*, PoS **EPS-HEP2017** (2017) 241, arXiv:1710.07948 [hep-ph].

[993] A. Vaquero Avilés-Casco, C. DeTar, D. Du, A. El-Khadra, A. S. Kronfeld, J. Laiho, and R. S. Van de Water, $\overline{B} \to D^*\ell\overline{\nu}$ *at Non-Zero Recoil*, EPJ Web Conf. **175** (2018) 13003, arXiv:1710.09817 [hep-lat].

[994] BaBar Collaboration, J. P. Lees et al., *Evidence for an excess of* $\bar{B} \to D^{(*)}\tau^-\bar{\nu}_\tau$ *decays*, Phys. Rev. Lett. **109** (2012) 101802, arXiv:1205.5442 [hep-ex].

[995] Belle Collaboration, S. Hirose et al., *Measurement of the* τ *lepton polarization and* $R(D^*)$ *in the decay* $\bar{B} \to D^*\tau^-\bar{\nu}_\tau$, Phys. Rev. Lett. **118** (2017) no. 21, 211801, arXiv:1612.00529 [hep-ex].

[996] Belle Collaboration, S. Hirose et al., *Measurement of the* τ *lepton polarization and* $R(D^*)$ *in the decay* $\bar{B} \to D^*\tau^-\bar{\nu}_\tau$ *with one-prong hadronic* τ *decays at Belle*, Phys. Rev. **D97** (2018) no. 1, 012004, arXiv:1709.00129 [hep-ex].

[997] LHCb collaboration, R. Aaij et al., *Measurement of the ratio of the* $\mathcal{B}(B^0 \to D^{*-}\tau^+\nu_\tau)$ *and* $\mathcal{B}(B^0 \to D^{*-}\mu^+\nu_\mu)$ *branching fractions using three-prong* τ*-lepton decays*, Phys. Rev. Lett. **120** (2018) 171802, arXiv:1708.08856 [hep-ex].

[998] S. Fajfer, J. F. Kamenik, and I. Nisandzic, *On the* $B \to D^*\tau\bar{\nu}_\tau$ *Sensitivity to New Physics*, Phys. Rev. **D85** (2012) 094025, arXiv:1203.2654 [hep-ph].

[999] A. Celis, M. Jung, X.-Q. Li, and A. Pich, *Sensitivity to charged scalars in* $\boldsymbol{B \to D^{(*)}\tau\nu_\tau}$ *and* $\boldsymbol{B \to \tau\nu_\tau}$ *decays*, JHEP **01** (2013) 054, arXiv:1210.8443 [hep-ph].

[1000] M. Tanaka and R. Watanabe, *New physics in the weak interaction of* $\bar{B} \to D^{(*)}\tau\bar{\nu}$, Phys. Rev. **D87** (2013) no. 3, 034028, arXiv:1212.1878 [hep-ph].

[1001] D. Bigi and P. Gambino, *Revisiting* $B \to D\ell\nu$, Phys. Rev. **D94** (2016) no. 9, 094008, arXiv:1606.08030 [hep-ph].

[1002] A. K. Leibovich, Z. Ligeti, I. W. Stewart, and M. B. Wise, *Model independent results for* $B \to D_1(2420)\ell\bar{\nu}$ *and* $B \to D_2^*(2460)\ell\bar{\nu}$ *at order* $\Lambda_{\rm QCD}/mc, b$, Phys. Rev. Lett. **78** (1997) 3995–3998, arXiv:hep-ph/9703213 [hep-ph].

[1003] A. K. Leibovich, Z. Ligeti, I. W. Stewart, and M. B. Wise, *Semileptonic B decays to excited charmed mesons*, Phys. Rev. **D57** (1998) 308–330, arXiv:hep-ph/9705467 [hep-ph].

[1004] F. U. Bernlochner, Z. Ligeti, and S. Turczyk, *A Proposal to solve some puzzles in semileptonic B decays*, Phys. Rev. **D85** (2012) 094033, arXiv:1202.1834 [hep-ph].

[1005] F. U. Bernlochner and Z. Ligeti, *Semileptonic $B_{(s)}$ decays to excited charmed mesons with e, μ, τ and searching for new physics with $R(D^{**})$*, Phys. Rev. **D95** (2017) no. 1, 014022, arXiv:1606.09300 [hep-ph].

[1006] F. U. Bernlochner, Z. Ligeti, and D. J. Robinson, *Model independent analysis of semileptonic B decays to D^{**} for arbitrary new physics*, Phys. Rev. **D97** (2018) no. 7, 075011, arXiv:1711.03110 [hep-ph].

[1007] D. Aloni, Y. Grossman, and A. Soffer, *Measuring CP violation in $b \to c\tau^-\bar{\nu}_\tau$ using excited charm mesons*, Phys. Rev. **D98** (2018) no. 3, 035022, arXiv:1806.04146 [hep-ph].

[1008] LHCb collaboration, R. Aaij et al., *Measurement of B meson production cross-sections in proton-proton collisions at $\sqrt{s} = 7$ TeV*, JHEP **08** (2013) 117 CERN-PH-EP-2013-095, LHCb-PAPER-2013-004, arXiv:1306.3663 [hep-ex].

[1009] LHCb collaboration, R. Aaij et al., *Observation of the decay $B_c^+ \to B_s^0\pi^+$*, Phys. Rev. Lett. **111** (2013) 181801 CERN-PH-EP-2013-136, LHCb-PAPER-2013-044, arXiv:1308.4544 [hep-ex].

[1010] A. Yu. Anisimov, I. M. Narodetsky, C. Semay, and B. Silvestre-Brac, *The B_c meson lifetime in the light front constituent quark model*, Phys. Lett. **B452** (1999) 129–136, arXiv:hep-ph/9812514 [hep-ph].

[1011] V. V. Kiselev, A. K. Likhoded, and A. I. Onishchenko, *Semileptonic B_c meson decays in sum rules of QCD and NRQCD*, Nucl. Phys. **B569** (2000) 473–504, arXiv:hep-ph/9905359 [hep-ph].

[1012] M. A. Ivanov, J. G. Korner, and P. Santorelli, *The Semileptonic decays of the B_c meson*, Phys. Rev. **D63** (2001) 074010, arXiv:hep-ph/0007169 [hep-ph].

[1013] V. V. Kiselev, *Exclusive decays and lifetime of B_c meson in QCD sum rules*, arXiv:hep-ph/0211021 [hep-ph].

[1014] E. Hernandez, J. Nieves, and J. M. Verde-Velasco, *Study of exclusive semileptonic and non-leptonic decays of B_c - in a nonrelativistic quark model*, Phys. Rev. **D74** (2006) 074008, arXiv:hep-ph/0607150 [hep-ph].

[1015] M. A. Ivanov, J. G. Korner, and P. Santorelli, *Exclusive semileptonic and nonleptonic decays of the B_c meson*, Phys. Rev. **D73** (2006) 054024, arXiv:hep-ph/0602050 [hep-ph].

[1016] W.-F. Wang, Y.-Y. Fan, and Z.-J. Xiao, *Semileptonic decays $B_c \to (\eta_c, J/\Psi) l\nu$ in the perturbative QCD approach*, Chin. Phys. **C37** (2013) 093102, arXiv:1212.5903 [hep-ph].

[1017] C.-F. Qiao and R.-L. Zhu, *Estimation of semileptonic decays of B_c meson to S-wave charmonia with nonrelativistic QCD*, Phys. Rev. **D87** (2013) no. 1, 014009, arXiv:1208.5916 [hep-ph].

[1018] Z. Rui, H. Li, G.-x. Wang, and Y. Xiao, *Semileptonic decays of B_c meson to S-wave charmonium states in the perturbative QCD approach*, Eur. Phys. J. **C76** (2016) no. 10, 564, arXiv:1602.08918 [hep-ph].

[1019] R. Dutta and A. Bhol, *$B_c \to (J/\psi,\ \eta_c)\tau\nu$ semileptonic decays within the standard model and beyond*, Phys. Rev. **D96** (2017) no. 7, 076001, arXiv:1701.08598 [hep-ph].

[1020] C.-T. Tran, M. A. Ivanov, J. G. Körner, and P. Santorelli, *Implications of new physics in the decays $B_c \to (J/\psi, \eta_c)\tau\nu$*, Phys. Rev. **D97** (2018) no. 5, 054014, arXiv:1801.06927 [hep-ph].

[1021] A. Issadykov and M. A. Ivanov, *The decays $B_c \to J/\psi + \bar{\ell}\nu_\ell$ and $B_c \to J/\psi + \pi(K)$ in covariant confined quark model*, Phys. Lett. **B783** (2018) 178–182, arXiv:1804.00472 [hep-ph].

[1022] R. Watanabe, *New Physics effect on $B_c \to J/\psi\tau\bar{\nu}$ in relation to the $R_{D^{(*)}}$ anomaly*, Phys. Lett. **B776** (2018) 5–9, arXiv:1709.08644 [hep-ph].

[1023] T. D. Cohen, H. Lamm, and R. F. Lebed, *Model-Independent Bounds on $R(J/\psi)$*,

arXiv:1807.02730 [hep-ph].

[1024] F. U. Bernlochner, Z. Ligeti, D. J. Robinson, and W. L. Sutcliffe, *New predictions for $\Lambda_b \to \Lambda_c$ semileptonic decays and tests of heavy quark symmetry*, arXiv:1808.09464 [hep-ph].

[1025] A. K. Leibovich and I. W. Stewart, *Semileptonic Lambda(b) decay to excited Lambda(c) baryons at order Lambda(QCD) / m(Q)*, Phys. Rev. **D57** (1998) 5620–5631, arXiv:hep-ph/9711257 [hep-ph].

[1026] P. Böer, M. Bordone, E. Graverini, P. Owen, M. Rotondo, and D. Van Dyk, *Testing lepton flavour universality in semileptonic $\Lambda_b \to \Lambda_c^*$ decays*, JHEP **06** (2018) 155, arXiv:1801.08367 [hep-ph].

[1027] Z. Ligeti and F. J. Tackmann, *Precise predictions for $B \to X_c \tau \bar{\nu}$ decay distributions*, Phys. Rev. **D90** (2014) no. 3, 034021, arXiv:1406.7013 [hep-ph].

[1028] M. Freytsis, Z. Ligeti, and J. T. Ruderman, *Flavor models for $\bar{B} \to D^{(*)} \tau \bar{\nu}$*, Phys. Rev. **D92** (2015) no. 5, 054018, arXiv:1506.08896 [hep-ph].

[1029] T. Mannel, A. V. Rusov, and F. Shahriaran, *Inclusive semitauonic B decays to order $\mathcal{O}(\Lambda_{QCD}^3/m_b^3)$*, Nucl. Phys. **B921** (2017) 211–224, arXiv:1702.01089 [hep-ph].

[1030] S. Bhattacharya, S. Nandi, and S. Kumar Patra, *$b \to c \tau \nu_\tau$ Decays: A Catalogue to Compare, Constrain, and Correlate New Physics Effects*, arXiv:1805.08222 [hep-ph].

[1031] A. Celis, M. Jung, X.-Q. Li, and A. Pich, *Scalar contributions to $b \to c(u)\tau\nu$ transitions*, Phys. Lett. **B771** (2017) 168–179, arXiv:1612.07757 [hep-ph].

[1032] A. Crivellin, C. Greub, and A. Kokulu, *Explaining $B \to D\tau\nu$, $B \to D^*\tau\nu$ and $B \to \tau\nu$ in a 2HDM of type III*, Phys. Rev. **D86** (2012) 054014, arXiv:1206.2634 [hep-ph].

[1033] A. Crivellin, J. Heeck, and P. Stoffer, *A perturbed lepton-specific two-Higgs-doublet model facing experimental hints for physics beyond the Standard Model*, Phys. Rev. Lett. **116** (2016) no. 8, 081801, arXiv:1507.07567 [hep-ph].

[1034] C.-H. Chen and T. Nomura, *Charged-Higgs on $R_{D^{(*)}}$, τ polarization, and FBA*, Eur. Phys. J. **C77** (2017) no. 9, 631, arXiv:1703.03646 [hep-ph].

[1035] S. Iguro and K. Tobe, *$R(D^{(*)})$ in a general two Higgs doublet model*, Nucl. Phys. **B925** (2017) 560–606, arXiv:1708.06176 [hep-ph].

[1036] C.-H. Chen and T. Nomura, *Charged-Higgs on $B_q^- \to \ell\bar{\nu}$ and $\bar{B} \to (P,V)\ell\bar{\nu}$ in a generic two-Higgs doublet model*, arXiv:1803.00171 [hep-ph].

[1037] S.-P. Li, X.-Q. Li, Y.-D. Yang, and X. Zhang, *$R_{D^{(*)}}$, $R_{K^{(*)}}$ and neutrino mass in the 2HDM-III with right-handed neutrinos*, JHEP **09** (2018) 149, arXiv:1807.08530 [hep-ph].

[1038] S. Fajfer, J. F. Kamenik, I. Nisandzic, and J. Zupan, *Implications of Lepton Flavor Universality Violations in B Decays*, Phys. Rev. Lett. **109** (2012) 161801, arXiv:1206.1872 [hep-ph].

[1039] N. G. Deshpande and A. Menon, *Hints of R-parity violation in B decays into $\tau\nu$*, JHEP **01** (2013) 025, arXiv:1208.4134 [hep-ph].

[1040] Y. Sakaki, M. Tanaka, A. Tayduganov, and R. Watanabe, *Testing leptoquark models in $\bar{B} \to D^{(*)}\tau\bar{\nu}$*, Phys. Rev. **D88** (2013) no. 9, 094012, arXiv:1309.0301 [hep-ph].

[1041] M. Duraisamy, P. Sharma, and A. Datta, *Azimuthal $B \to D^*\tau^-\bar{\nu}_\tau$ angular distribution with tensor operators*, Phys. Rev. **D90** (2014) no. 7, 074013, arXiv:1405.3719 [hep-ph].

[1042] R. Barbieri, G. Isidori, A. Pattori, and F. Senia, *Anomalies in B-decays and $U(2)$ flavour symmetry*, Eur. Phys. J. **C76** (2016) no. 2, 67, arXiv:1512.01560 [hep-ph].

[1043] N. G. Deshpande and X.-G. He, *Consequences of R-parity violating interactions for anomalies in $\bar{B} \to D^{(*)}\tau\bar{\nu}$ and $b \to s\mu^+\mu^-$*, Eur. Phys. J. **C77** (2017) no. 2, 134, arXiv:1608.04817 [hep-ph].

[1044] S. Sahoo, R. Mohanta, and A. K. Giri, *Explaining the R_K and $R_{D^{(*)}}$ anomalies with vector*

leptoquarks, Phys. Rev. **D95** (2017) no. 3, 035027, arXiv:1609.04367 [hep-ph].

[1045] B. Dumont, K. Nishiwaki, and R. Watanabe, *LHC constraints and prospects for S_1 scalar leptoquark explaining the $\bar{B} \to D^{(*)}\tau\bar{\nu}$ anomaly*, Phys. Rev. **D94** (2016) no. 3, 034001, arXiv:1603.05248 [hep-ph].

[1046] X.-Q. Li, Y.-D. Yang, and X. Zhang, *Revisiting the one leptoquark solution to the R(D$^{(*)}$) anomalies and its phenomenological implications*, JHEP **08** (2016) 054, arXiv:1605.09308 [hep-ph].

[1047] D. Bečirević, S. Fajfer, N. Košnik, and O. Sumensari, *Leptoquark model to explain the B-physics anomalies, R_K and R_D*, Phys. Rev. **D94** (2016) 115021, arXiv:1608.08501 [hep-ph].

[1048] S. Iguro, T. Kitahara, Y. Omura, R. Watanabe, and K. Yamamoto, *D^* polarization vs. $R_{D^{(*)}}$ anomalies in the leptoquark models*, arXiv:1811.08899 [hep-ph].

[1049] S. Bhattacharya, S. Nandi, and S. K. Patra, *Looking for possible new physics in $B \to D^{(*)}\tau\nu_\tau$ in light of recent data*, Phys. Rev. **D95** (2017) no. 7, 075012, arXiv:1611.04605 [hep-ph].

[1050] M. A. Ivanov, J. G. Körner, and C.-T. Tran, *Probing new physics in $\bar{B}^0 \to D^{(*)}\tau^-\bar{\nu}_\tau$ using the longitudinal, transverse, and normal polarization components of the tau lepton*, Phys. Rev. **D95** (2017) no. 3, 036021, arXiv:1701.02937 [hep-ph].

[1051] A. K. Alok, D. Kumar, J. Kumar, S. Kumbhakar, and S. U. Sankar, *New physics solutions for R_D and R_{D^*}*, JHEP **09** (2018) 152, arXiv:1710.04127 [hep-ph].

[1052] S. Bifani, S. Descotes-Genon, A. Romero Vidal, and M.-H. Schune, *Review of Lepton Universality tests in B decays*, arXiv:1809.06229 [hep-ex].

[1053] M. Blanke, A. Crivellin, S. de Boer, T. Kitahara, M. Moscati, U. Nierste, and I. Nišandžić, *Impact of polarization observables and $B_c \to \tau\nu$ on new physics explanations of the $b \to c\tau\nu$ anomaly*, arXiv:1811.09603 [hep-ph].

[1054] X.-G. He and G. Valencia, *B decays with τ leptons in nonuniversal left-right models*, Phys. Rev. **D87** (2013) no. 1, 014014, arXiv:1211.0348 [hep-ph].

[1055] X.-G. He and G. Valencia, *Lepton universality violation and right-handed currents in $b \to c\tau\nu$*, Phys. Lett. **B779** (2018) 52–57, arXiv:1711.09525 [hep-ph].

[1056] A. Greljo, D. J. Robinson, B. Shakya, and J. Zupan, *$R(D^{(*)})$ from W' and right-handed neutrinos*, JHEP **09** (2018) 169, arXiv:1804.04642 [hep-ph].

[1057] P. Asadi, M. R. Buckley, and D. Shih, *It's all right(-handed neutrinos): a new W' model for the $R_{D^{(*)}}$ anomaly*, JHEP **09** (2018) 010, arXiv:1804.04135 [hep-ph].

[1058] D. J. Robinson, B. Shakya, and J. Zupan, *Right-handed Neutrinos and $R(D^{(*)})$*, arXiv:1807.04753 [hep-ph].

[1059] A. Azatov, D. Barducci, D. Ghosh, D. Marzocca, and L. Ubaldi, *Combined explanations of B-physics anomalies: the sterile neutrino solution*, arXiv:1807.10745 [hep-ph].

[1060] J. Heeck and D. Teresi, *Pati-Salam explanations of the B-meson anomalies*, arXiv:1808.07492 [hep-ph].

[1061] S. Bhattacharya, S. Nandi, and S. K. Patra, *Optimal-observable analysis of possible new physics in $B \to D^{(*)}\tau\nu_\tau$*, Phys. Rev. **D93** (2016) no. 3, 034011, arXiv:1509.07259 [hep-ph].

[1062] CDF, DELPHI, ALEPH, SLD, OPAL, L3 Collaboration, D. Abbaneo et al., *Combined results on b hadron production rates and decay properties*, arXiv:hep-ex/0112028 [hep-ex].

[1063] R. Alonso, B.-n. Grinstein, and J. Martin Camalich, *Lifetime of B_c^- Constrains Explanations for Anomalies in $B \to D^{(*)}\tau\nu$*, Phys. Rev. Lett. **118** (2017) no. 8, 081802, arXiv:1611.06676 [hep-ph].

[1064] A. G. Akeroyd and C.-H. Chen, *Constraint on the branching ratio of $B_c \to \tau\bar{\nu}$ from LEP1 and*

consequences for $R(D^{(*)})$ anomaly, Phys. Rev. **D96** (2017) no. 7, 075011, arXiv:1708.04072 [hep-ph].

[1065] F. Feruglio, P. Paradisi, and O. Sumensari, *Implications of scalar and tensor explanations of $R_{D^{(*)}}$*, arXiv:1806.10155 [hep-ph].

[1066] W. Dekens, J. de Vries, M. Jung, and K. K. Vos, *The phenomenology of electric dipole moments in models of scalar leptoquarks*, arXiv:1809.09114 [hep-ph].

[1067] D. Aloni, A. Efrati, Y. Grossman, and Y. Nir, *Υ and ψ leptonic decays as probes of solutions to the $R_D^{(*)}$ puzzle*, JHEP **06** (2017) 019, arXiv:1702.07356 [hep-ph].

[1068] BaBar Collaboration, J. P. Lees et al., *Search for $B \to K^{(*)}\nu\bar{\nu}$ and invisible quarkonium decays*, Phys. Rev. **D87** (2013) no. 11, 112005, arXiv:1303.7465 [hep-ex].

[1069] Belle Collaboration, J. Grygier et al., *Search for $\boldsymbol{B \to h\nu\bar{\nu}}$ decays with semileptonic tagging at Belle*, Phys. Rev. **D96** (2017) no. 9, 091101, arXiv:1702.03224 [hep-ex]. [Addendum: Phys. Rev.D97,no.9,099902(2018)].

[1070] T. Blake, G. Lanfranchi, and D. M. Straub, *Rare B Decays as Tests of the Standard Model*, Prog. Part. Nucl. Phys. **92** (2017) 50–91, arXiv:1606.00916 [hep-ph].

[1071] Y. Cai, J. Gargalionis, M. A. Schmidt, and R. R. Volkas, *Reconsidering the One Leptoquark solution: flavor anomalies and neutrino mass*, JHEP **10** (2017) 047, arXiv:1704.05849 [hep-ph].

[1072] J. G. Körner and G. A. Schuler, *Exclusive Semileptonic Decays of Bottom Mesons in the Spectator Quark Model*, Z. Phys. **C38** (1988) 511. [Erratum: Z. Phys.C41,690(1989)].

[1073] K. Hagiwara, A. D. Martin, and M. F. Wade, *Helicity Amplitude Analysis of $B \to D^* \ell$ Neutrino Decays*, Phys. Lett. **B228** (1989) 144–148.

[1074] M. Tanaka, *Charged Higgs effects on exclusive semitauonic B decays*, Z. Phys. **C67** (1995) 321–326, arXiv:hep-ph/9411405 [hep-ph].

[1075] C.-H. Chen and C.-Q. Geng, *Lepton angular asymmetries in semileptonic charmful B decays*, Phys. Rev. **D71** (2005) 077501, arXiv:hep-ph/0503123 [hep-ph].

[1076] C.-H. Chen and C.-Q. Geng, *Charged Higgs on $B^- \to \tau\bar{\nu}_\tau$ and $\bar{B} \to P(V)\ell\bar{\nu}_\ell$*, JHEP **10** (2006) 053, arXiv:hep-ph/0608166 [hep-ph].

[1077] U. Nierste, S. Trine, and S. Westhoff, *Charged-Higgs effects in a new $B \to D\tau\nu$ differential decay distribution*, Phys. Rev. **D78** (2008) 015006, arXiv:0801.4938 [hep-ph].

[1078] M. Tanaka and R. Watanabe, *Tau longitudinal polarization in B -> D tau nu and its role in the search for charged Higgs boson*, Phys. Rev. **D82** (2010) 034027, arXiv:1005.4306 [hep-ph].

[1079] A. Datta, M. Duraisamy, and D. Ghosh, *Diagnosing New Physics in $b \to c\,\tau\,\nu_\tau$ decays in the light of the recent BaBar result*, Phys. Rev. **D86** (2012) 034027, arXiv:1206.3760 [hep-ph].

[1080] Y. Sakaki and H. Tanaka, *Constraints on the charged scalar effects using the forward-backward asymmetry on $B^- \to D^{(*)}\tau^-\nu_\tau$*, Phys. Rev. **D87** (2013) no. 5, 054002, arXiv:1205.4908 [hep-ph].

[1081] M. Duraisamy and A. Datta, *The Full $B \to D^*\tau^-\bar{\nu_\tau}$ Angular Distribution and CP violating Triple Products*, JHEP **09** (2013) 059, arXiv:1302.7031 [hep-ph].

[1082] R. Alonso, A. Kobach, and J. Martin Camalich, *New physics in the kinematic distributions of $\bar{B} \to D^{(*)}\tau^-(\to \ell^-\bar{\nu}_\ell\nu_\tau)\bar{\nu}_\tau$*, Phys. Rev. **D94** (2016) no. 9, 094021, arXiv:1602.07671 [hep-ph].

[1083] Z. Ligeti, M. Papucci, and D. J. Robinson, *New Physics in the Visible Final States of $B \to D^{(*)}\tau\nu$*, JHEP **01** (2017) 083, arXiv:1610.02045 [hep-ph].

[1084] R. Alonso, J. Martin Camalich, and S. Westhoff, *Tau properties in $B \to D\tau\nu$ from visible final-state kinematics*, Phys. Rev. **D95** (2017) no. 9, 093006, arXiv:1702.02773 [hep-ph].

[1085] S. Duell, F. Bernlochner, Z. Ligeti, M. Papucci, and D. Robinson, *HAMMER: Reweighting tool for simulated data samples*, PoS **ICHEP2016** (2017) 1074.

[1086] LHCb, CMS Collaboration, V. Khachatryan et al., *Observation of the rare $B^0_s \to \mu^+\mu^-$ decay from the combined analysis of CMS and LHCb data*, Nature **522** (2015) 68–72, arXiv:1411.4413 [hep-ex].

[1087] ATLAS Collaboration, *Study of the rare decays of B0s and B0 into muon pairs from data collected during 2015 and 2016 with the ATLAS detector*, ATLAS-CONF-2018-046, CERN, Geneva, Sep, 2018. https://cds.cern.ch/record/2639673.

[1088] CMS Collaboration, *Measurement of rare $B \to \mu^+\mu^-$ decays with the Phase-2 upgraded CMS detector at the HL-LHC*, CMS Physics Analysis Summary CMS-PAS-FTR-18-013, 2018. http://cdsweb.cern.ch/record/2650545.

[1089] LHCb collaboration, R. Aaij et al., *Measurement of the fragmentation fraction ratio f_s/f_d and its dependence on B meson kinematics*, JHEP **04** (2013) 001, arXiv:1301.5286 [hep-ex]. f_s/f_d value updated in LHCb-CONF-2013-011.

[1090] ATLAS Collaboration, *Prospects for the $\mathcal{B}(B^0_{(s)} \to \mu^+\mu^-)$ measurements with the ATLAS detector in the Run 2 and HL-LHC data campaigns*, ATL-PHYS-PUB-2018-005, CERN, Geneva, May, 2018. https://cds.cern.ch/record/2317211.

[1091] CMS Collaboration, *B Physics analyses for the Phase-II Upgrade Technical Proposal*, CMS Physics Analysis Summary CMS-PAS-FTR-14-015, 2014. https://cds.cern.ch/record/2036007.

[1092] ATLAS Collaboration, M. Aaboud et al., *Study of the rare decays of B^0_s and B^0 into muon pairs from data collected during the LHC Run 1 with the ATLAS detector*, Eur. Phys. J **C76** (2016) 513, arXiv:1604.04263 [hep-ex].

[1093] C. Bobeth, M. Gorbahn, T. Hermann, M. Misiak, E. Stamou, and M. Steinhauser, *$B_{s,d} \to l^+l^-$ in the Standard Model with Reduced Theoretical Uncertainty*, Phys. Rev. Lett. **112** (2014) 101801, arXiv:1311.0903 [hep-ph].

[1094] B. Dutta and Y. Mimura, *Enhancement of $Br(B_d \to \mu^+\mu^-)/Br(B_s \to \mu^+\mu^-)$ in supersymmetric unified models*, Phys. Rev. **D91** (2015) no. 9, 095011, arXiv:1501.02044 [hep-ph].

[1095] M. Pivk and F. R. Le Diberder, *sPlot: a statistical tool to unfold data distributions*, Nucl. Instrum. Method. **A555** (2005) 356, arXiv:0402083 [physics].

[1096] F. Kruger and D. Melikhov, *Gauge invariance and form-factors for the decay $B \to \gamma\ell^+\ell^-$*, Phys. Rev. **D67** (2003) 034002, arXiv:hep-ph/0208256 [hep-ph].

[1097] D. Melikhov and N. Nikitin, *Rare radiative leptonic decays $B_{d,s} \to \ell^+\ell^-\gamma$*, Phys. Rev. **D70** (2004) 114028, arXiv:hep-ph/0410146 [hep-ph].

[1098] BaBar collaboration, B. Aubert et al., *Search for the decays $B^0 \to e^+e^-\gamma$ and $B^0 \to \mu^+\mu^-\gamma$*, Phys. Rev. **D77** (2008) 011104, arXiv:0706.2870 [hep-ex].

[1099] CMS Collaboration, *Study of the expected sensitivity to the P'_5 parameter in the $B^0 \to K^{*0}\mu^+\mu^-$ decay at the HL-LHC*, CMS Physics Analysis Summary CMS-PAS-FTR-18-033, 2018. http://cds.cern.ch/record/2651298.

[1100] CMS collaboration, A. M. Sirunyan et al., *Measurement of angular parameters from the decay $\mathrm{B}^0 \to \mathrm{K}^{*0}\mu^+\mu^-$ in proton-proton collisions at $\sqrt{s} = 8$ TeV*, Phys. Lett. **B781** (2018) 517–541, arXiv:1710.02846 [hep-ex].

[1101] ATLAS collaboration, M. Aaboud et al., *Angular analysis of $B^0_d \to K^*\mu^+\mu^-$ decays in pp collisions at $\sqrt{s} = 8$ TeV with the ATLAS detector*, arXiv:1805.04000 [hep-ex].

[1102] A. Collaboration, *Technical Design Report for the ATLAS Inner Tracker Pixel Detector*, CERN-LHCC-2017-021. ATLAS-TDR-030, CERN, Geneva, Sep, 2017.

https://cds.cern.ch/record/2285585.

[1103] ATLAS Collaboration, *Studies of radial distortions of the ATLAS Inner Detector*, ATL-PHYS-PUB-2018-003, CERN, Geneva, Mar, 2018. https://cds.cern.ch/record/2309785.

[1104] LHCb collaboration, R. Aaij et al., *Measurement of form-factor-independent observables in the decay* $B^0 \to K^{*0}\mu^+\mu^-$, Phys. Rev. Lett. **111** (2013) 191801, arXiv:1308.1707 [hep-ex].

[1105] LHCb collaboration, R. Aaij et al., *Differential branching fractions and isospin asymmetries of* $B \to K^*\mu^+\mu^-$ *decays*, JHEP **06** (2014) 133, arXiv:1403.8044 [hep-ex].

[1106] LHCb collaboration, R. Aaij et al., *Differential branching fraction and angular analysis of the decay* $B^0 \to K^{*0}\mu^+\mu^-$, JHEP **08** (2013) 131, arXiv:1304.6325 [hep-ex].

[1107] BaBar collaboration, B. Aubert et al., *Measurements of branching fractions, rate asymmetries, and angular distributions in the rare decays* $B \to K\ell^+\ell^-$ *and* $B \to K^*\ell^+\ell^-$, Phys. Rev. **D73** (2006) 092001, arXiv:hep-ex/0604007 [hep-ex].

[1108] BaBar collaboration, J. P. Lees et al., *Measurement of angular asymmetries in the decays* $B \to K^*\ell^+\ell^-$, Phys. Rev. **D93** (2016) 052015, arXiv:1508.07960 [hep-ex].

[1109] Belle Collaboration, J. T. Wei et al., *Measurement of the Differential Branching Fraction and Forward-Backword Asymmetry for* $B \to K^{(*)}\ell^+\ell^-$, Phys. Rev. Lett. **103** (2009) 171801, arXiv:0904.0770 [hep-ex].

[1110] CDF Collaboration, T. Aaltonen et al., *Measurements of the Angular Distributions in the Decays* $B \to K^{(*)}\mu^+\mu^-$ *at CDF*, Phys. Rev. Lett. **108** (2012) 081807, arXiv:1108.0695 [hep-ex].

[1111] CMS Collaboration, S. Chatrchyan et al., *Angular analysis and branching fraction measurement of the decay* $B^0 \to K^{*0}\mu^+\mu^-$, Phys. Lett. **B727** (2013) 77–100, arXiv:1308.3409 [hep-ex].

[1112] CMS collaboration, V. Khachatryan et al., *Angular analysis of the decay* $B^0 \to K^{*0}\mu^+\mu^-$ *from pp collisions at* $\sqrt{s} = 8$ *TeV*, Phys. Lett. **B753** (2016) 424–448, arXiv:1507.08126 [hep-ex].

[1113] M. Beneke, T. Feldmann, and D. Seidel, *Exclusive radiative and electroweak* $b \to d$ *and* $b \to s$ *penguin decays at NLO*, Eur. Phys. J. **C41** (2005) 173–188, arXiv:hep-ph/0412400 [hep-ph].

[1114] U. Egede, M. Patel, and K. A. Petridis, *Method for an unbinned measurement of the* q^2 *dependent decay amplitudes of* $\overline{B}^0 \to K^{*0}\mu^+\mu^-$ *decays*, JHEP **06** (2015) 084, arXiv:1504.00574 [hep-ph].

[1115] F. Kruger and J. Matias, *Probing new physics via the transverse amplitudes of* $B^0 \to K^{*0}(\to K^-\pi^+)l^+l^-$ *at large recoil*, Phys. Rev. **D71** (2005) 094009, arXiv:hep-ph/0502060 [hep-ph].

[1116] J. Lyon and R. Zwicky, *Resonances gone topsy turvy - the charm of QCD or new physics in* $b \to s\ell^+\ell^-$*?*, arXiv:1406.0566 [hep-ph].

[1117] W. Altmannshofer and D. M. Straub, *New Physics in* $B \to K^*\mu\mu$*?*, Eur. Phys. J. **C73** (2013) 2646, arXiv:1308.1501 [hep-ph].

[1118] S. Descotes-Genon, J. Matias, and J. Virto, *Understanding the* $B \to K^*\mu^+\mu^-$ *anomaly*, Phys. Rev. **D88** (2013) 074002, arXiv:1307.5683 [hep-ph].

[1119] ATLAS Collaboration, $B_d^0 \to K^{*0}\mu\mu$ *angular analysis prospects with the upgraded ATLAS detector at the HL-LHC*, ATL-PHYS-PUB-2019-003, CERN, Geneva, Jan, 2019. https://cds.cern.ch/record/2654519.

[1120] M. Ciuchini, M. Fedele, E. Franco, S. Mishima, A. Paul, L. Silvestrini, and M. Valli, $B \to K^*\ell^+\ell^-$ *decays at large recoil in the Standard Model: a theoretical reappraisal*, JHEP **06** (2016) 116, arXiv:1512.07157 [hep-ph].

[1121] S. Descotes-Genon, L. Hofer, J. Matias, and J. Virto, *On the impact of power corrections in the prediction of $B \to K^* \mu^+ \mu^-$ observables*, JHEP **12** (2014) 125, arXiv:1407.8526 [hep-ph].

[1122] LHCb collaboration, R. Aaij et al., *Measurement of the phase difference between the short- and long-distance amplitudes in the $B^+ \to K^+ \mu^+ \mu^-$ decay*, Eur. Phys. J. **C77** (2017) 161, arXiv:1612.06764 [hep-ex].

[1123] C. Bobeth, M. Chrzaszcz, D. van Dyk, and J. Virto, *Long-distance effects in $B \to K^* \ell\ell$ from Analyticity*, arXiv:1707.07305 [hep-ph].

[1124] LHCb collaboration, R. Aaij et al., *First observation of the decay $B^+ \to \pi^+ \mu^+ \mu^-$*, JHEP **12** (2012) 125, arXiv:1210.2645 [hep-ex].

[1125] LHCb collaboration, R. Aaij et al., *First measurement of the differential branching fraction and CP asymmetry of the $B^+ \to \pi^+ \mu^+ \mu^-$ decay*, JHEP **10** (2015) 034, arXiv:1509.00414 [hep-ex].

[1126] LHCb collaboration, R. Aaij et al., *Observation of the suppressed decay $\Lambda_b^0 \to p\pi^- \mu^+ \mu^-$*, JHEP **04** (2017) 029, arXiv:1701.08705 [hep-ex].

[1127] LHCb collaboration, R. Aaij et al., *Evidence for the decay $B_s^0 \to \overline{K}^{*0} \mu^+ \mu^-$*, JHEP **07** (2018) 020, arXiv:1804.07167 [hep-ex].

[1128] D. Du, A. X. El-Khadra, S. Gottlieb, A. S. Kronfeld, J. Laiho, E. Lunghi, R. S. Van de Water, and R. Zhou, *Phenomenology of semileptonic B-meson decays with form factors from lattice QCD*, Phys. Rev. **D93** (2016) 034005, arXiv:1510.02349 [hep-ph].

[1129] B. Capdevila, S. Descotes-Genon, J. Matias, and J. Virto, *Assessing lepton-flavour non-universality from $B \to K^* \ell\ell$ angular analyses*, JHEP **10** (2016) 075, arXiv:1605.03156 [hep-ph].

[1130] N. Serra, R. Silva Coutinho, and D. van Dyk, *Measuring the breaking of lepton flavor universality in $B \to K^* \ell^+ \ell^-$*, Phys. Rev. **D95** (2017) no. 3, 035029, arXiv:1610.08761 [hep-ph].

[1131] A. Mauri, N. Serra, and R. Silva Coutinho, *Towards establishing Lepton Flavour Universality violation in $\bar{B} \to \bar{K}^* \ell^+ \ell^-$ decays*, arXiv:1805.06401 [hep-ph].

[1132] S. Descotes-Genon and J. Virto, *Time dependence in $B \to V \ell^+ \ell^-$ decays*, JHEP **04** (2015) 045, arXiv:1502.05509 [hep-ph].

[1133] P. Ball and R. Zwicky, *Time-dependent CP asymmetry in $B \to K^* \gamma$ as a (quasi) null test of the Standard Model*, Phys. Lett. **B642** (2006) 478–486, arXiv:hep-ph/0609037 [hep-ph].

[1134] M. Matsumori and A. I. Sanda, *The mixing-induced CP asymmetry in $B \to K^* \gamma$ decays with perturbative QCD approach*, Phys. Rev. **D73** (2006) 114022, arXiv:hep-ph/0512175 [hep-ph].

[1135] LHCb collaboration, R. Aaij et al., *Observation of photon polarization in the $b \to s\gamma$ transition*, Phys. Rev. Lett. **112** (2014) 161801, arXiv:1402.6852 [hep-ex].

[1136] V. Bellée, F. Blanc, P. Pais, A. Puig, O. Schneider, and K. Trabelsi, *Measuring photon polarisation in $B \to K\pi\pi\gamma$ decays*, 2018. in preparation.

[1137] LHCb collaboration, R. Aaij et al., *Angular analysis of the $B^0 \to K^* e^+ e^-$ decay in the low-q^2 region*, JHEP **04** (2015) 064, arXiv:1501.03038 [hep-ex].

[1138] D. Becirevic and E. Schneider, *On transverse asymmetries in $B \to K^* \ell^+ \ell^-$*, Nucl. Phys. **B854** (2012) 321–339, arXiv:1106.3283 [hep-ph].

[1139] CDF collaboration, D. Acosta et al., *Search for radiative b-hadron decays in $p\bar{p}$ collisions at $\sqrt{s} = 1.8$ TeV*, Phys. Rev. **D66** (2002) 112002, arXiv:hep-ex/0208035 [hep-ex].

[1140] LHCb collaboration, R. Aaij et al., *Measurements of the $\Lambda_b^0 \to J/\psi \Lambda$ decay amplitudes and the Λ_b^0 polarisation in pp collisions at $\sqrt{s} = 7$ TeV*, Phys. Lett. **B724** (2013) 27, arXiv:1302.5578 [hep-ex].

[1141] D. Becirevic, S. Fajfer, I. Nisandzic, and A. Tayduganov, *Angular distributions of $\bar{B} \to D^{(*)}\ell\bar{\nu}_\ell$ decays and search of New Physics*, arXiv:1602.03030 [hep-ph].

[1142] A. Azatov, D. Bardhan, D. Ghosh, F. Sgarlata, and E. Venturini, *Anatomy of $b \to c\tau\nu$ anomalies*, arXiv:1805.03209 [hep-ph].

[1143] LHCb collaboration, R. Aaij et al., *Search for the lepton-flavour violating decays $B^0_{(s)} \to e^\pm\mu^\mp$*, JHEP **03** (2018) 078, arXiv:1710.04111.

[1144] BaBar collaboration, B. Aubert et al., *Searches for the decays $B^0 \to \ell^\pm\tau^\mp$ and $B^+ \to \ell^+\nu$ (l=e, μ) using hadronic tag reconstruction*, Phys. Rev. **D77** (2008) 091104, arXiv:0801.0697 [hep-ex].

[1145] BaBar collaboration, J. P. Lees et al., *A search for the decay modes $B^{+-} \to h^{+-}\tau^{+-}l$*, Phys. Rev. **D86** (2012) 012004, arXiv:1204.2852 [hep-ex].

[1146] A. Atre, T. Han, S. Pascoli, and B. Zhang, *The search for heavy Majorana neutrinos*, JHEP **05** (2009) 030, arXiv:0901.3589 [hep-ph].

[1147] LHCb collaboration, R. Aaij et al., *Search for lepton number violating decays $B^+ \to \pi^-\mu^+\mu^+$ and $B^+ \to K^-\mu^+\mu^+$*, Phys. Rev. Lett. **108** (2012) 101601, arXiv:1110.0730 [hep-ex].

[1148] LHCb collaboration, R. Aaij et al., *Searches for Majorana neutrinos in B^- decays*, Phys. Rev. **D85** (2012) 112004, arXiv:1201.5600 [hep-ex].

[1149] LHCb collaboration, R. Aaij et al., *Search for Majorana neutrinos in $B^- \to \pi^+\mu^-\mu^-$ decays*, Phys. Rev. Lett. **112** (2014) 131802, arXiv:1401.5361 [hep-ex].

[1150] C. Smith, *Proton stability from a fourth family*, Phys.Rev. **D85** (2012) 036005, arXiv:1105.1723 [hep-ph].

[1151] G. Durieux, J.-M. Gérard, F. Maltoni, and C. Smith, *Three-generation baryon and lepton number violation at the LHC*, Phys. Lett. **B721** (2013) 82–85, arXiv:1210.6598 [hep-ph].

[1152] BaBar collaboration, J. P. Lees et al., *Searches for rare or forbidden semileptonic charm decays*, Phys. Rev. **D84** (2011) 072006, arXiv:1107.4465 [hep-ex].

[1153] O. Gedalia, G. Isidori, F. Maltoni, G. Perez, M. Selvaggi, and Y. Soreq, *Top B Physics at the LHC*, Phys. Rev. Lett. **110** (2013) no. 23, 232002, arXiv:1212.4611 [hep-ph].

[1154] ATLAS Collaboration, M. Aaboud et al., *Measurements of charge and CP asymmetries in b-hadron decays using top-quark events collected by the ATLAS detector in pp collisions at $\sqrt{s} = 8$ TeV*, JHEP **02** (2017) 071, arXiv:1610.07869 [hep-ex].

[1155] C. Degrande, N. Greiner, W. Kilian, O. Mattelaer, H. Mebane, T. Stelzer, S. Willenbrock, and C. Zhang, *Effective Field Theory: A Modern Approach to Anomalous Couplings*, Annals Phys. **335** (2013) 21–32, arXiv:1205.4231 [hep-ph].

[1156] D. Barducci et al., *Interpreting top-quark LHC measurements in the standard-model effective field theory*, arXiv:1802.07237 [hep-ph].

[1157] G. Durieux, F. Maltoni, and C. Zhang, *Global approach to top-quark flavor-changing interactions*, Phys. Rev. **D91** (2015) no. 7, 074017, arXiv:1412.7166 [hep-ph].

[1158] L3 Collaboration, P. Achard et al., *Search for single top production at LEP*, Phys.Lett. **B549** (2002) 290–300, arXiv:hep-ex/0210041 [hep-ex].

[1159] N. Kidonakis and A. Belyaev, *FCNC top quark production via anomalous tqV couplings beyond leading order*, JHEP **0312** (2003) 004, arXiv:hep-ph/0310299 [hep-ph].

[1160] J. J. Zhang, C. S. Li, J. Gao, H. Zhang, Z. Li, et al., *Next-to-leading order QCD corrections to the top quark decay via model-independent FCNC couplings*, Phys.Rev.Lett. **102** (2009) 072001, arXiv:0810.3889 [hep-ph].

[1161] J. Drobnak, S. Fajfer, and J. F. Kamenik, *Flavor Changing Neutral Coupling Mediated Radiative Top Quark Decays at Next-to-Leading Order in QCD*, Phys.Rev.Lett. **104** (2010) 252001, arXiv:1004.0620 [hep-ph].

[1162] J. Drobnak, S. Fajfer, and J. F. Kamenik, *QCD Corrections to Flavor Changing Neutral Coupling Mediated Rare Top Quark Decays*, Phys.Rev. **D82** (2010) 073016, arXiv:1007.2551 [hep-ph].

[1163] J. J. Zhang, C. S. Li, J. Gao, H. X. Zhu, C.-P. Yuan, et al., *Next-to-leading order QCD corrections to the top quark decay via the Flavor-Changing Neutral-Current operators with mixing effects*, Phys.Rev. **D82** (2010) 073005, arXiv:1004.0898 [hep-ph].

[1164] C. Zhang, *Effective field theory approach to top-quark decay at next-to-leading order in QCD*, Phys. Rev. **D90** (2014) no. 1, 014008, arXiv:1404.1264 [hep-ph].

[1165] J. J. Liu, C. S. Li, L. L. Yang, and L. G. Jin, *Next-to-leading order QCD corrections to the direct top quark production via model-independent FCNC couplings at hadron colliders*, Phys.Rev. **D72** (2005) 074018, arXiv:hep-ph/0508016 [hep-ph].

[1166] J. Gao, C. S. Li, J. J. Zhang, and H. X. Zhu, *Next-to-leading order QCD corrections to the single top quark production via model-independent t-q-g flavor-changing neutral-current couplings at hadron colliders*, Phys.Rev. **D80** (2009) 114017, arXiv:0910.4349 [hep-ph].

[1167] Y. Zhang, B. H. Li, C. S. Li, J. Gao, and H. X. Zhu, *Next-to-leading order QCD corrections to the top quark associated with γ production via model-independent flavor-changing neutral-current couplings at hadron colliders*, Phys.Rev. **D83** (2011) 094003, arXiv:1101.5346 [hep-ph].

[1168] B. H. Li, Y. Zhang, C. S. Li, J. Gao, and H. X. Zhu, *Next-to-leading order QCD corrections to tZ associated production via the flavor-changing neutral-current couplings at hadron colliders*, Phys.Rev. **D83** (2011) 114049, arXiv:1103.5122 [hep-ph].

[1169] Y. Wang, F. P. Huang, C. S. Li, B. H. Li, D. Y. Shao, et al., *Constraints on flavor-changing neutral-current Htq couplings from the signal of tH associated production with QCD next-to-leading order accuracy at the LHC*, Phys.Rev. **D86** (2012) 094014, arXiv:1208.2902 [hep-ph].

[1170] A. Alloul, N. D. Christensen, C. Degrande, C. Duhr, and B. Fuks, *FeynRules 2.0 - A complete toolbox for tree-level phenomenology*, Comput.Phys.Commun. **185** (2014) 2250–2300, arXiv:1310.1921 [hep-ph].

[1171] C. Degrande, C. Duhr, B. Fuks, D. Grellscheid, O. Mattelaer, et al., *UFO - The Universal FeynRules Output*, Comput.Phys.Commun. **183** (2012) 1201–1214, arXiv:1108.2040 [hep-ph].

[1172] C. Degrande, F. Maltoni, J. Wang, and C. Zhang, *Automatic computations at next-to-leading order in QCD for top-quark flavor-changing neutral processes*, Phys. Rev. **D91** (2015) 034024, arXiv:1412.5594 [hep-ph].

[1173] G. Durieux, M. Perelló, M. Vos, and C. Zhang, *Global and optimal probes for the top-quark effective field theory at future lepton colliders*, JHEP **10** (2018) 168, arXiv:1807.02121 [hep-ph].

[1174] C. Degrande, A. S. Papanastasiou, and C. Zhang , work in progress.

[1175] CMS Collaboration, V. Khachatryan et al., *Search for anomalous single top quark production in association with a photon in pp collisions at $\sqrt{s} = 8$ TeV*, JHEP **04** (2016) 035, arXiv:1511.03951 [hep-ex].

[1176] ATLAS Collaboration, M. Aaboud et al., *Search for flavour-changing neutral current top-quark decays $t \to qZ$ in proton-proton collisions at $\sqrt{s} = 13$ TeV with the ATLAS detector*, JHEP **07** (2018) 176, arXiv:1803.09923 [hep-ex].

[1177] CMS Collaboration, *Search for flavour changing neutral currents in top quark production and decays with three-lepton final state using the data collected at $\sqrt{s} = 13$ TeV*, CMS-PAS-TOP-17-017 . http://cds.cern.ch/record/2292045.

[1178] CMS Collaboration, A. M. Sirunyan et al., *Search for associated production of a Z boson with*

a single top quark and for tZ flavour-changing interactions in pp collisions at $\sqrt{s} = 8$ TeV, JHEP **07** (2017) 003, arXiv:1702.01404 [hep-ex].

[1179] ATLAS Collaboration, G. Aad et al., *Search for single top-quark production via flavour-changing neutral currents at 8 TeV with the ATLAS detector*, Eur. Phys. J. **C76** (2016) no. 2, 55, arXiv:1509.00294 [hep-ex].

[1180] CMS Collaboration, V. Khachatryan et al., *Search for anomalous Wtb couplings and flavour-changing neutral currents in t-channel single top quark production in pp collisions at $\sqrt{s} = 7$ and 8 TeV*, JHEP **02** (2017) 028, arXiv:1610.03545 [hep-ex].

[1181] ATLAS Collaboration, M. Aaboud et al., *Search for flavor-changing neutral currents in top quark decays $t \to Hc$ and $t \to Hu$ in multilepton final states in proton-proton collisions at $\sqrt{s} = 13$ TeV with the ATLAS detector*, Phys. Rev. **D98** (2018) no. 3, 032002, arXiv:1805.03483 [hep-ex].

[1182] CMS Collaboration, V. Khachatryan et al., *Search for top quark decays via Higgs-boson-mediated flavor-changing neutral currents in pp collisions at $\sqrt{s} = 8$ TeV*, JHEP **02** (2017) 079, arXiv:1610.04857 [hep-ex].

[1183] CMS Collaboration, A. M. Sirunyan et al., *Search for the flavor-changing neutral current interactions of the top quark and the Higgs boson which decays into a pair of b quarks at $\sqrt{s} =$ 13 TeV*, JHEP **06** (2018) 102, arXiv:1712.02399 [hep-ex].

[1184] Aleph, Delphi, L3, Opal Collaborations, and the LEP Exotica Working Group, *Search for single top production via flavour changing neutral currents: preliminary combined results of the LEP experiments*, DELPHI-2001-119 CONF 542 (2001) . https://cds.cern.ch/record/1006392.

[1185] CMS Collaboration, *ECFA 2016: Prospects for selected standard model measurements with the CMS experiment at the High-Luminosity LHC*, CMS-PAS-FTR-16-006 (2017) . http://cds.cern.ch/record/2262606.

[1186] P. J. Fox, Z. Ligeti, M. Papucci, G. Perez, and M. D. Schwartz, *Deciphering top flavor violation at the LHC with B factories*, Phys. Rev. **D78** (2008) 054008, arXiv:0704.1482 [hep-ph].

[1187] J. Drobnak, S. Fajfer, and J. F. Kamenik, *Probing anomalous tWb interactions with rare B decays*, Nucl. Phys. **B855** (2012) 82–99, arXiv:1109.2357 [hep-ph].

[1188] J. Brod, A. Greljo, E. Stamou, and P. Uttayarat, *Probing anomalous $t\bar{t}Z$ interactions with rare meson decays*, JHEP **02** (2015) 141, arXiv:1408.0792 [hep-ph].

[1189] M. Endo, T. Kitahara, and D. Ueda, *SMEFT top-quark effects on $\Delta F = 2$ observables*, arXiv:1811.04961 [hep-ph].

[1190] M. L. Mangano, M. Moretti, F. Piccinini, and M. Treccani, *Matching matrix elements and shower evolution for top-quark production in hadronic collisions*, JHEP **01** (2007) 013, arXiv:hep-ph/0611129 [hep-ph].

[1191] R. Coimbra, A. Onofre, R. Santos, and M. Won, *MEtop - a generator for single top production via FCNC interactions*, Eur. Phys. J. **C72** (2012) 2222, arXiv:1207.7026 [hep-ph].

[1192] CompHEP Collaboration, E. Boos, V. Bunichev, M. Dubinin, L. Dudko, V. Ilyin, A. Kryukov, V. Edneral, V. Savrin, A. Semenov, and A. Sherstnev, *CompHEP 4.4: Automatic computations from Lagrangians to events*, Nucl. Instrum. Meth. **A534** (2004) 250–259, arXiv:hep-ph/0403113 [hep-ph].

[1193] J. Aguilar-Saavedra, *Zt, gamma t and t production at hadron colliders via strong flavour-changing neutral couplings*, Nucl.Phys. **B837** (2010) 122–136, arXiv:1003.3173 [hep-ph].

[1194] CMS Collaboration, *Prospects for the search for gluon-mediated FCNC in top quark production with the CMS Phase-2 detector at the HL-LHC*, CMS Physics Analysis Summary CMS-PAS-FTR-18-004, 2018. https://cds.cern.ch/record/2638815.

[1195] ATLAS Collaboration, *Expected sensitivity of ATLAS to FCNC top quark decays $t \to Zu$ and $t \to Hq$ at the High Luminosity LHC*, ATL-PHYS-PUB-2016-019, CERN, Geneva, Aug, 2016. http://cds.cern.ch/record/2209126.

[1196] CMS Collaboration, *The Phase-2 Upgrade of the CMS Endcap Calorimeter*, CERN-LHCC-2017-023. CMS-TDR-019, CERN, Geneva, Nov, 2017. https://cds.cern.ch/record/2293646. Technical Design Report of the endcap calorimeter for the Phase-2 upgrade of the CMS experiment, in view of the HL-LHC run.

[1197] ATLAS Collaboration, *Sensitivity of searches for the flavour-changing neutral current decay $t \to qZ$ using the upgraded ATLAS experiment at the High Luminosity LHC*, ATL-PHYS-PUB-2019-001, 2019. https://cds.cern.ch/record/2653389.

[1198] ATLAS Collaboration, M. Aaboud et al., *Search for top quark decays $t \to qH$, with $H \to \gamma\gamma$, in $\sqrt{s} = 13$ TeV pp collisions using the ATLAS detector*, JHEP **10** (2017) 129, arXiv:1707.01404 [hep-ex].

[1199] *Sensitivity of ATLAS at HL-LHC to flavour changing neutral currents in top quark decays $t \to cH$, with $H \to \gamma\gamma$* , ATL-PHYS-PUB-2013-012, CERN, Geneva, Sep, 2013. https://cds.cern.ch/record/1604506.

[1200] B. Grzadkowski and M. Misiak, *Anomalous Wtb coupling effects in the weak radiative B-meson decay*, Phys. Rev. D **78** (2008) 077501, arXiv:0802.1413 [hep-ph].

[1201] J. Drobnak, S. Fajfer, and J. F. Kamenik, *New physics in $t \to bW$ decay at next-to-leading order in QCD*, Phys. Rev. **D82** (2010) 114008, arXiv:1010.2402 [hep-ph].

[1202] J. A. Aguilar-Saavedra, *A Minimal set of top anomalous couplings*, Nucl. Phys. **B812** (2009) 181–204, arXiv:0811.3842 [hep-ph].

[1203] G. A. Gonzalez-Sprinberg, R. Martinez, and J. Vidal, *Top quark tensor couplings*, JHEP **07** (2011) 094, arXiv:1105.5601 [hep-ph]. [Erratum: JHEP05,117(2013)].

[1204] Q.-H. Cao, B. Yan, J.-H. Yu, and C. Zhang, *A General Analysis of Wtb anomalous Couplings*, arXiv:1504.03785 [hep-ph].

[1205] Z. Hioki and K. Ohkuma, *Full analysis of general non-standard tbW couplings*, Phys. Lett. **B752** (2016) 128–130, arXiv:1511.03437 [hep-ph].

[1206] M. Schulze and Y. Soreq, *Pinning down electroweak dipole operators of the top quark*, arXiv:1603.08911 [hep-ph].

[1207] J. F. Kamenik, M. Papucci, and A. Weiler, *Constraining the dipole moments of the top quark*, Phys. Rev. D **85** (2012) 071501, arXiv:1107.3143 [hep-ph]. [Erratum: Phys. Rev.D88,no.3,039903(2013)].

[1208] C. Zhang, N. Greiner, and S. Willenbrock, *Constraints on Non-standard Top Quark Couplings*, Phys. Rev. **D86** (2012) 014024, arXiv:1201.6670 [hep-ph].

[1209] J. de Blas, M. Chala, and J. Santiago, *Renormalization Group Constraints on New Top Interactions from Electroweak Precision Data*, JHEP **09** (2015) 189, arXiv:1507.00757 [hep-ph].

[1210] A. Buckley, C. Englert, J. Ferrando, D. J. Miller, L. Moore, M. Russell, and C. D. White, *Global fit of top quark effective theory to data*, Phys. Rev. **D92** (2015) no. 9, 091501, arXiv:1506.08845 [hep-ph].

[1211] A. Buckley, C. Englert, J. Ferrando, D. J. Miller, L. Moore, M. Russell, and C. D. White, *Constraining top quark effective theory in the LHC Run II era*, JHEP **04** (2016) 015, arXiv:1512.03360 [hep-ph].

[1212] O. B. Bylund, F. Maltoni, I. Tsinikos, E. Vryonidou, and C. Zhang, *Probing top quark neutral couplings in the Standard Model Effective Field Theory at NLO QCD*, arXiv:1601.08193 [hep-ph].

[1213] N. Castro, J. Erdmann, C. Grunwald, K. Kröninger, and N.-A. Rosien, *EFTfitter—A tool for interpreting measurements in the context of effective field theories*, Eur. Phys. J. **C76** (2016) no. 8, 432, arXiv:1605.05585 [hep-ex].

[1214] F. Déliot, R. Faria, M. C. N. Fiolhais, P. Lagarelhos, A. Onofre, C. M. Pease, and A. Vasconcelos, *Global Constraints on Top Quark Anomalous Couplings*, Phys. Rev. **D97** (2018) no. 1, 013007, arXiv:1711.04847 [hep-ph].

[1215] J. A. Aguilar-Saavedra, J. Carvalho, N. F. Castro, F. Veloso, and A. Onofre, *Probing anomalous Wtb couplings in top pair decays*, Eur. Phys. J. **C50** (2007) 519–533, arXiv:hep-ph/0605190 [hep-ph].

[1216] ATLAS Collaboration, G. Aad et al., *Comprehensive measurements of t-channel single top-quark production cross sections at $\sqrt{s} = 7$ TeV with the ATLAS detector*, Phys. Rev. **D90** (2014) no. 11, 112006, arXiv:1406.7844 [hep-ex].

[1217] ATLAS Collaboration, M. Aaboud et al., *Measurement of the inclusive cross-sections of single top-quark and top-antiquark t-channel production in pp collisions at $\sqrt{s}$ = 13 TeV with the ATLAS detector*, arXiv:1609.03920 [hep-ex].

[1218] ATLAS Collaboration, M. Aaboud et al., *Fiducial, total and differential cross-section measurements of t-channel single top-quark production in pp collisions at 8 TeV using data collected by the ATLAS detector*, arXiv:1702.02859 [hep-ex].

[1219] CMS Collaboration, S. Chatrchyan et al., *Measurement of the single-top-quark t-channel cross section in pp collisions at $\sqrt{s} = 7$ TeV*, JHEP **12** (2012) 035, arXiv:1209.4533 [hep-ex].

[1220] CMS Collaboration, V. Khachatryan et al., *Measurement of the t-channel single-top-quark production cross section and of the $| V_{tb} |$ CKM matrix element in pp collisions at $\sqrt{s}$= 8 TeV*, JHEP **06** (2014) 090, arXiv:1403.7366 [hep-ex].

[1221] CMS Collaboration, A. M. Sirunyan et al., *Cross section measurement of t-channel single top quark production in pp collisions at $\sqrt{s} = 13$ TeV*, arXiv:1610.00678 [hep-ex].

[1222] M. Brucherseifer, F. Caola, and K. Melnikov, *On the NNLO QCD corrections to single-top production at the LHC*, Phys. Lett. **B736** (2014) 58–63, arXiv:1404.7116 [hep-ph].

[1223] C. Zhang, *Single Top Production at Next-to-Leading Order in the Standard Model Effective Field Theory*, Phys. Rev. Lett. **116** (2016) no. 16, 162002, arXiv:1601.06163 [hep-ph].

[1224] V. Cirigliano, W. Dekens, J. de Vries, and E. Mereghetti, *Constraining the top-Higgs sector of the Standard Model Effective Field Theory*, Phys. Rev. **D94** (2016) no. 3, 034031, arXiv:1605.04311 [hep-ph].

[1225] S. Alioli, V. Cirigliano, W. Dekens, J. de Vries, and E. Mereghetti, *Right-handed charged currents in the era of the Large Hadron Collider*, JHEP **05** (2017) 086, arXiv:1703.04751 [hep-ph].

[1226] M. de Beurs, E. Laenen, M. Vreeswijk, and E. Vryonidou, *Effective operators in t-channel single top production and decay*, Eur. Phys. J. **C78** (2018) no. 11, 919, arXiv:1807.03576 [hep-ph].

[1227] CDF, D0 Collaboration, T. Aaltonen et al., *Combination of CDF and D0 measurements of the W boson helicity in top quark decays*, Phys. Rev. **D85** (2012) 071106, arXiv:1202.5272 [hep-ex].

[1228] ATLAS Collaboration, G. Aad et al., *Measurement of the W boson polarization in top quark decays with the ATLAS detector*, JHEP **06** (2012) 088, arXiv:1205.2484 [hep-ex].

[1229] CMS Collaboration, S. Chatrchyan et al., *Measurement of the W-boson helicity in top-quark decays from $t\bar{t}$ production in lepton+jets events in pp collisions at $\sqrt{s} = 7$ TeV*, JHEP **10** (2013) 167, arXiv:1308.3879 [hep-ex].

[1230] ATLAS Collaboration, G. Aad et al., *Search for anomalous couplings in the Wtb vertex from*

the measurement of double differential angular decay rates of single top quarks produced in the t-channel with the ATLAS detector, JHEP **04** (2016) 023, arXiv:1510.03764 [hep-ex].

[1231] CMS Collaboration, V. Khachatryan et al., *Measurement of the W boson helicity in events with a single reconstructed top quark in pp collisions at $\sqrt{s} = 8$ TeV*, JHEP **01** (2015) 053, arXiv:1410.1154 [hep-ex].

[1232] ATLAS Collaboration, M. Aaboud et al., *Measurement of the W boson polarisation in $t\bar{t}$ events from pp collisions at $\sqrt{s}$ = 8 TeV in the lepton+jets channel with ATLAS*, arXiv:1612.02577 [hep-ex].

[1233] J. Boudreau, C. Escobar, J. Mueller, K. Sapp, and J. Su, *Single top quark differential decay rate formulae including detector effects*, arXiv:1304.5639 [hep-ex].

[1234] A. Czarnecki, J. G. Korner, and J. H. Piclum, *Helicity fractions of W bosons from top quark decays at NNLO in QCD*, Phys. Rev. **D81** (2010) 111503, arXiv:1005.2625 [hep-ph].

[1235] J. A. Aguilar-Saavedra and J. Bernabeu, *Breaking down the entire W boson spin observables from its decay*, Phys. Rev. **D93** (2016) no. 1, 011301, arXiv:1508.04592 [hep-ph].

[1236] J. A. Aguilar-Saavedra and J. Bernabeu, *W polarisation beyond helicity fractions in top quark decays*, Nucl. Phys. **B840** (2010) 349–378, arXiv:1005.5382 [hep-ph].

[1237] ATLAS Collaboration, M. Aaboud et al., *Analysis of the Wtb vertex from the measurement of triple-differential angular decay rates of single top quarks produced in the t-channel at $\sqrt{s}$ = 8 TeV with the ATLAS detector*, arXiv:1707.05393 [hep-ex].

[1238] F. Déliot, M. C. N. Fiolhais, and A. Onofre, *Top Quark Anomalous Couplings at the High-Luminosity Phase of the LHC*, arXiv:1811.02492 [hep-ph].

[1239] CMS Collaboration, *Search for flavour changing neutral currents in top quark production and decays with three-lepton final state using the data collected at sqrt(s) = 13 TeV*, CMS-PAS-TOP-17-017, CERN, Geneva, 2017. https://cds.cern.ch/record/2292045.

[1240] P. F. Harrison and V. E. Vladimirov, *A Method to Determine $|V_{cb}|$ at the Weak Scale in Top Decays at the LHC*, arXiv:1810.09424 [hep-ph].

[1241] W. Dekens and J. de Vries, *Renormalization Group Running of Dimension-Six Sources of Parity and Time-Reversal Violation*, JHEP **1305** (2013) 149, arXiv:1303.3156 [hep-ph].

[1242] R. Alonso, E. E. Jenkins, A. V. Manohar, and M. Trott, *Renormalization Group Evolution of the Standard Model Dimension Six Operators III: Gauge Coupling Dependence and Phenomenology*, JHEP **04** (2014) 159, arXiv:1312.2014 [hep-ph].

[1243] D. A. Dicus, *Neutron Electric Dipole Moment From Charged Higgs Exchange*, Phys.Rev. **D41** (1990) 999.

[1244] S. Weinberg, *Larger Higgs Exchange Terms in the Neutron Electric Dipole Moment*, Phys. Rev. Lett. **63** (1989) 2333.

[1245] E. Braaten, C.-S. Li, and T.-C. Yuan, *The Evolution of Weinberg's Gluonic CP Violation Operator*, Phys. Rev. Lett. **64** (1990) 1709.

[1246] G. Boyd, A. K. Gupta, S. P. Trivedi, and M. B. Wise, *Effective Hamiltonian for the Electric Dipole Moment of the Neutron*, Phys.Lett. **B241** (1990) 584.

[1247] D. A. Demir, M. Pospelov, and A. Ritz, *Hadronic EDMs, the Weinberg operator, and light gluinos*, Phys. Rev. D **67** (2003) 015007, arXiv:hep-ph/0208257 [hep-ph].

[1248] J. de Vries, R. G. E. Timmermans, E. Mereghetti, and U. van Kolck, *The Nucleon Electric Dipole Form Factor From Dimension-Six Time-Reversal Violation*, Phys. Lett. **B695** (2011) 268–274, arXiv:1006.2304 [hep-ph].

[1249] V. Cirigliano, W. Dekens, J. de Vries, and E. Mereghetti, *Is there room for CP violation in the top-Higgs sector?*, Phys. Rev. **D94** (2016) no. 1, 016002, arXiv:1603.03049 [hep-ph].

[1250] K. Fuyuto and M. Ramsey-Musolf, *Top Down Electroweak Dipole Operators*,

arXiv:1706.08548 [hep-ph].

[1251] J. Pendlebury et al., *Revised experimental upper limit on the electric dipole moment of the neutron*, Phys. Rev. **D92** (2015) no. 9, 092003, arXiv:1509.04411 [hep-ex].

[1252] C. A. Baker, D. D. Doyle, P. Geltenbort, K. Green, M. G. D. van der Grinten, et al., *An Improved experimental limit on the electric dipole moment of the neutron*, Phys. Rev. Lett. **97** (2006) 131801, arXiv:hep-ex/0602020 [hep-ex].

[1253] ACME Collaboration, V. Andreev et al., *Improved limit on the electric dipole moment of the electron*, Nature **562** (2018) no. 7727, 355–360.

[1254] T. Chupp, P. Fierlinger, M. Ramsey-Musolf, and J. Singh, *Electric Dipole Moments of the Atoms, Molecules, Nuclei and Particles*, arXiv:1710.02504 [physics.atom-ph].

[1255] I. Kozyryev and N. R. Hutzler, *Precision Measurement of Time-Reversal Symmetry Violation with Laser-Cooled Polyatomic Molecules*, Phys. Rev. Lett. **119** (2017) no. 13, 133002, arXiv:1705.11020 [physics.atom-ph].

[1256] A. C. Vutha, M. Horbatsch, and E. A. Hessels, *Oriented polar molecules in a solid inert-gas matrix: a proposed method for measuring the electric dipole moment of the electron*, arXiv:1710.08785 [physics.atom-ph].

[1257] J. Lim, J. R. Almond, M. A. Trigatzis, J. A. Devlin, N. J. Fitch, B. E. Sauer, M. R. Tarbutt, and E. A. Hinds, *Laser Cooled YbF Molecules for Measuring the Electron's Electric Dipole Moment*, Phys. Rev. Lett. **120** (Mar, 2018) 123201. https://link.aps.org/doi/10.1103/PhysRevLett.120.123201.

[1258] T. Hurth, E. Lunghi, and W. Porod, *Untagged $\bar{B} \to X_{s+d}\gamma$ CP asymmetry as a probe for new physics*, Nucl. Phys. B **704** (2005) 56–74, arXiv:hep-ph/0312260 [hep-ph].

[1259] M. Benzke, S. J. Lee, M. Neubert, and G. Paz, *Long-Distance Dominance of the CP Asymmetry in $B \to X_{s,d} + \gamma$ Decays*, Phys. Rev. Lett. **106** (2011) 141801, arXiv:1012.3167 [hep-ph].

[1260] M. E. Peskin and T. Takeuchi, *A New constraint on a strongly interacting Higgs sector*, Phys. Rev. Lett. **65** (1990) 964–967.

[1261] M. E. Peskin and T. Takeuchi, *Estimation of oblique electroweak corrections*, Phys. Rev. **D46** (1992) 381–409.

[1262] R. Barbieri, A. Pomarol, R. Rattazzi, and A. Strumia, *Electroweak symmetry breaking after LEP-1 and LEP-2*, Nucl. Phys. **B703** (2004) 127–146, arXiv:hep-ph/0405040 [hep-ph].

[1263] N. Greiner, S. Willenbrock, and C. Zhang, *Effective Field Theory for Nonstandard Top Quark Couplings*, Phys. Lett. **B704** (2011) 218–222, arXiv:1104.3122 [hep-ph].

[1264] ATLAS, CMS Collaboration, G. Aad et al., *Measurements of the Higgs boson production and decay rates and constraints on its couplings from a combined ATLAS and CMS analysis of the LHC pp collision data at $\sqrt{s} = 7$ and 8 TeV*, JHEP **08** (2016) 045, arXiv:1606.02266 [hep-ex].

[1265] CMS Collaboration, V. Khachatryan et al., *Measurement of the ratio $\mathcal{B}(t \to Wb)/\mathcal{B}(t \to Wq)$ in pp collisions at $\sqrt{s}$ = 8 TeV*, Phys. Lett. **B736** (2014) 33–57, arXiv:1404.2292 [hep-ex].

[1266] E. Alvarez, L. Da Rold, M. Estevez, and J. F. Kamenik, *Measuring $|V_{td}|$ at the LHC*, Phys. Rev. **D97** (2018) no. 3, 033002, arXiv:1709.07887 [hep-ph].

[1267] CMS Collaboration, V. Khachatryan et al., *Measurements of $t\bar{t}$ charge asymmetry using dilepton final states in pp collisions at $\sqrt{s} = 8$ TeV*, Phys. Lett. **B760** (2016) 365–386, arXiv:1603.06221 [hep-ex].

[1268] CMS Collaboration, S. Chatrchyan et al., *Observation of the associated production of a single top quark and a W boson in pp collisions at $\sqrt{s}$ =8 TeV*, Phys. Rev. Lett. **112** (2014) no. 23, 231802, arXiv:1401.2942 [hep-ex].

[1269] ATLAS Collaboration, G. Aad et al., *Measurement of the production cross-section of a single*

top quark in association with a W boson at 8 TeV with the ATLAS experiment, JHEP **01** (2016) 064, arXiv:1510.03752 [hep-ex].

[1270] ATLAS Collaboration, M. Aaboud et al., *Measurement of the cross-section for producing a W boson in association with a single top quark in pp collisions at $\sqrt{s} = 13$ TeV with ATLAS*, JHEP **01** (2018) 063, arXiv:1612.07231 [hep-ex].

[1271] J. Gallicchio and M. D. Schwartz, *Quark and Gluon Tagging at the LHC*, Phys. Rev. Lett. **107** (2011) 172001, arXiv:1106.3076 [hep-ph].

[1272] A. J. Larkoski, G. P. Salam, and J. Thaler, *Energy Correlation Functions for Jet Substructure*, JHEP **06** (2013) 108, arXiv:1305.0007 [hep-ph].

[1273] I. Moult, L. Necib, and J. Thaler, *New Angles on Energy Correlation Functions*, JHEP **12** (2016) 153, arXiv:1609.07483 [hep-ph].

[1274] D. Faroughy, J. F. Kamenik, M. Patra, and J. Zupan, , to appear (2018) .

[1275] P. Silva and M. Gallinaro, *Probing the flavor of the top quark decay*, Nuovo Cim. **B125** (2010) 983–998, arXiv:1010.2994 [hep-ph].

[1276] ATLAS Collaboration, M. Aaboud et al., *Evidence for the associated production of the Higgs boson and a top quark pair with the ATLAS detector*, Phys. Rev. **D97** (2018) no. 7, 072003, arXiv:1712.08891 [hep-ex].

[1277] ATLAS Collaboration, M. Aaboud et al., *Observation of Higgs boson production in association with a top quark pair at the LHC with the ATLAS detector*, Phys. Lett. **B784** (2018) 173–191, arXiv:1806.00425 [hep-ex].

[1278] CMS Collaboration, A. M. Sirunyan et al., *Evidence for associated production of a Higgs boson with a top quark pair in final states with electrons, muons, and hadronically decaying τ leptons at $\sqrt{s} = 13$ TeV*, JHEP **08** (2018) 066, arXiv:1803.05485 [hep-ex].

[1279] ATLAS Collaboration, G. Aad et al., *Evidence for the Higgs-boson Yukawa coupling to tau leptons with the ATLAS detector*, JHEP **04** (2015) 117, arXiv:1501.04943 [hep-ex].

[1280] ATLAS Collaboration, M. Aaboud et al., *Cross-section measurements of the Higgs boson decaying into a pair of tau-leptons in proton-proton collisions at $\sqrt{s} = 13$ TeV with the ATLAS detector*, arXiv:1811.08856 [hep-ex].

[1281] CMS Collaboration, A. M. Sirunyan et al., *Observation of Higgs boson decay to bottom quarks*, Phys. Rev. Lett. **121** (2018) no. 12, 121801, arXiv:1808.08242 [hep-ex].

[1282] ATLAS Collaboration, M. Aaboud et al., *Observation of $H \to b\bar{b}$ decays and VH production with the ATLAS detector*, Phys. Lett. **B786** (2018) 59–86, arXiv:1808.08238 [hep-ex].

[1283] ATLAS Collaboration, M. Aaboud et al., *Search for the Decay of the Higgs Boson to Charm Quarks with the ATLAS Experiment*, Phys. Rev. Lett. **120** (2018) no. 21, 211802, arXiv:1802.04329 [hep-ex].

[1284] ATLAS Collaboration, M. Aaboud et al., *Search for the dimuon decay of the Higgs boson in pp collisions at $\sqrt{s}$ = 13 TeV with the ATLAS detector*, Phys. Rev. Lett. **119** (2017) no. 5, 051802, arXiv:1705.04582 [hep-ex].

[1285] G. Perez, Y. Soreq, E. Stamou, and K. Tobioka, *Constraining the charm Yukawa and Higgs-quark coupling universality*, Phys. Rev. **D92** (2015) no. 3, 033016, arXiv:1503.00290 [hep-ph].

[1286] W. Altmannshofer, J. Brod, and M. Schmaltz, *Experimental constraints on the coupling of the Higgs boson to electrons*, JHEP **05** (2015) 125, arXiv:1503.04830 [hep-ph].

[1287] A. L. Kagan, G. Perez, F. Petriello, Y. Soreq, S. Stoynev, and J. Zupan, *Exclusive Window onto Higgs Yukawa Couplings*, Phys. Rev. Lett. **114** (2015) no. 10, 101802, arXiv:1406.1722 [hep-ph].

[1288] Y. Nir, *Flavour Physics and CP Violation*, in *Proceedings, 7th CERN Latin-American School of*

High-Energy Physics (CLASHEP2013): Arequipa, Peru, March 6-19, 2013, pp. 123–156. 2015. arXiv:1605.00433 [hep-ph]. http://inspirehep.net/record/1454240/files/arXiv:1605.00433.pdf.

[1289] ATLAS Collaboration, G. Aad et al., *Search for Higgs and Z Boson Decays to $J/\psi\gamma$ and $\Upsilon(nS)\gamma$ with the ATLAS Detector*, Phys. Rev. Lett. **114** (2015) no. 12, 121801, arXiv:1501.03276 [hep-ex].

[1290] CMS Collaboration, V. Khachatryan et al., *Search for a Higgs boson decaying into $\gamma^*\gamma \to \ell\ell\gamma$ with low dilepton mass in pp collisions at $\sqrt{s} = 8$ TeV*, Phys. Lett. **B753** (2016) 341–362, arXiv:1507.03031 [hep-ex].

[1291] ATLAS Collaboration, M. Aaboud et al., *Searches for exclusive Higgs and Z boson decays into $J/\psi\gamma$, $\psi(2S)\gamma$, and $\Upsilon(nS)\gamma$ at $\sqrt{s} = 13$ TeV with the ATLAS detector*, Phys. Lett. **B786** (2018) 134–155, arXiv:1807.00802 [hep-ex].

[1292] ATLAS Collaboration, M. Aaboud et al., *Search for exclusive Higgs and Z boson decays to $\phi\gamma$ and $\rho\gamma$ with the ATLAS detector*, arXiv:1712.02758 [hep-ex].

[1293] Y. Soreq, H. X. Zhu, and J. Zupan, *Light quark Yukawa couplings from Higgs kinematics*, JHEP **12** (2016) 045, arXiv:1606.09621 [hep-ph].

[1294] F. Bishara, U. Haisch, P. F. Monni, and E. Re, *Constraining Light-Quark Yukawa Couplings from Higgs Distributions*, Phys. Rev. Lett. **118** (2017) no. 12, 121801, arXiv:1606.09253 [hep-ph].

[1295] CMS Collaboration, A. M. Sirunyan et al., *Combined measurements of Higgs boson couplings in proton-proton collisions at $\sqrt{s} = 13$ TeV*, Submitted to: Eur. Phys. J. (2018) , arXiv:1809.10733 [hep-ex].

[1296] CMS Collaboration, V. Khachatryan et al., *Search for a standard model-like Higgs boson in the $\mu^+\mu^-$ and e^+e^- decay channels at the LHC*, Phys. Lett. **B744** (2015) 184–207, arXiv:1410.6679 [hep-ex].

[1297] G. Perez, Y. Soreq, E. Stamou, and K. Tobioka, *Prospects for measuring the Higgs boson coupling to light quarks*, Phys. Rev. **D93** (2016) no. 1, 013001, arXiv:1505.06689 [hep-ph].

[1298] I. Brivio, F. Goertz, and G. Isidori, *Probing the Charm Quark Yukawa Coupling in Higgs+Charm Production*, Phys. Rev. Lett. **115** (2015) no. 21, 211801, arXiv:1507.02916 [hep-ph].

[1299] M. Koenig and M. Neubert, *Exclusive Radiative Higgs Decays as Probes of Light-Quark Yukawa Couplings*, JHEP **08** (2015) 012, arXiv:1505.03870 [hep-ph].

[1300] G. T. Bodwin, H. S. Chung, J.-H. Ee, J. Lee, and F. Petriello, *Relativistic corrections to Higgs boson decays to quarkonia*, Phys. Rev. **D90** (2014) no. 11, 113010, arXiv:1407.6695 [hep-ph].

[1301] G. T. Bodwin, F. Petriello, S. Stoynev, and M. Velasco, *Higgs boson decays to quarkonia and the $H\bar{c}c$ coupling*, Phys. Rev. **D88** (2013) no. 5, 053003, arXiv:1306.5770 [hep-ph].

[1302] F. Bishara, J. Brod, P. Uttayarat, and J. Zupan, *Nonstandard Yukawa Couplings and Higgs Portal Dark Matter*, JHEP **01** (2016) 010, arXiv:1504.04022 [hep-ph].

[1303] A. Dery, A. Efrati, Y. Nir, Y. Soreq, and V. Susic, *Model building for flavor changing Higgs couplings*, Phys. Rev. **D90** (2014) 115022, arXiv:1408.1371 [hep-ph].

[1304] A. Dery, A. Efrati, G. Hiller, Y. Hochberg, and Y. Nir, *Higgs couplings to fermions: 2HDM with MFV*, JHEP **08** (2013) 006, arXiv:1304.6727 [hep-ph].

[1305] A. Dery, A. Efrati, Y. Hochberg, and Y. Nir, *What if $BR(h \to \mu\mu)/BR(h \to \tau\tau)$ does not equal m_μ^2/m_τ^2?*, JHEP **05** (2013) 039, arXiv:1302.3229 [hep-ph].

[1306] M. Bauer, M. Carena, and K. Gemmler, *Creating the fermion mass hierarchies with multiple Higgs bosons*, Phys. Rev. **D94** (2016) no. 11, 115030, arXiv:1512.03458 [hep-ph].

[1307] S. L. Glashow and S. Weinberg, *Natural Conservation Laws for Neutral Currents*, Phys. Rev. **D15** (1977) 1958.

[1308] E. A. Paschos, *Diagonal Neutral Currents*, Phys. Rev. **D15** (1977) 1966.

[1309] W. Altmannshofer, S. Gori, A. L. Kagan, L. Silvestrini, and J. Zupan, *Uncovering Mass Generation Through Higgs Flavor Violation*, Phys. Rev. **D93** (2016) no. 3, 031301, arXiv:1507.07927 [hep-ph].

[1310] W. Altmannshofer, J. Eby, S. Gori, M. Lotito, M. Martone, and D. Tuckler, *Collider Signatures of Flavorful Higgs Bosons*, Phys. Rev. **D94** (2016) no. 11, 115032, arXiv:1610.02398 [hep-ph].

[1311] W. Altmannshofer, S. Gori, D. J. Robinson, and D. Tuckler, *The Flavor-locked Flavorful Two Higgs Doublet Model*, JHEP **03** (2018) 129, arXiv:1712.01847 [hep-ph].

[1312] W. Altmannshofer and B. Maddock, *Flavorful Two Higgs Doublet Models with a Twist*, Phys. Rev. **D98** (2018) no. 7, 075005, arXiv:1805.08659 [hep-ph].

[1313] C. D. Froggatt and H. B. Nielsen, *Hierarchy of Quark Masses, Cabibbo Angles and CP Violation*, Nucl. Phys. **B147** (1979) 277–298.

[1314] G. F. Giudice and O. Lebedev, *Higgs-dependent Yukawa couplings*, Phys. Lett. **B665** (2008) 79–85, arXiv:0804.1753 [hep-ph].

[1315] G. D'Ambrosio, G. F. Giudice, G. Isidori, and A. Strumia, *Minimal flavor violation: An Effective field theory approach*, Nucl. Phys. **B645** (2002) 155–187, arXiv:hep-ph/0207036 [hep-ph].

[1316] L. Randall and R. Sundrum, *A Large mass hierarchy from a small extra dimension*, Phys. Rev. Lett. **83** (1999) 3370–3373, arXiv:hep-ph/9905221 [hep-ph].

[1317] M. J. Dugan, H. Georgi, and D. B. Kaplan, *Anatomy of a Composite Higgs Model*, Nucl. Phys. **B254** (1985) 299–326.

[1318] H. Georgi, D. B. Kaplan, and P. Galison, *Calculation of the Composite Higgs Mass*, Phys. Lett. **143B** (1984) 152–154.

[1319] D. B. Kaplan, H. Georgi, and S. Dimopoulos, *Composite Higgs Scalars*, Phys. Lett. **136B** (1984) 187–190.

[1320] D. B. Kaplan and H. Georgi, *SU(2) x U(1) Breaking by Vacuum Misalignment*, Phys. Lett. **136B** (1984) 183–186.

[1321] F. J. Botella, G. C. Branco, M. N. Rebelo, and J. I. Silva-Marcos, *What if the masses of the first two quark families are not generated by the standard model Higgs boson?*, Phys. Rev. **D94** (2016) no. 11, 115031, arXiv:1602.08011 [hep-ph].

[1322] D. Ghosh, R. S. Gupta, and G. Perez, *Is the Higgs Mechanism of Fermion Mass Generation a Fact? A Yukawa-less First-Two-Generation Model*, Phys. Lett. **B755** (2016) 504–508, arXiv:1508.01501 [hep-ph].

[1323] A. K. Das and C. Kao, *A Two Higgs doublet model for the top quark*, Phys. Lett. **B372** (1996) 106–112, arXiv:hep-ph/9511329 [hep-ph].

[1324] A. E. Blechman, A. A. Petrov, and G. Yeghiyan, *The Flavor puzzle in multi-Higgs models*, JHEP **11** (2010) 075, arXiv:1009.1612 [hep-ph].

[1325] T. Gherghetta and A. Pomarol, *Bulk fields and supersymmetry in a slice of AdS*, Nucl. Phys. **B586** (2000) 141–162, arXiv:hep-ph/0003129 [hep-ph].

[1326] Y. Grossman and M. Neubert, *Neutrino masses and mixings in nonfactorizable geometry*, Phys. Lett. **B474** (2000) 361–371, arXiv:hep-ph/9912408 [hep-ph].

[1327] S. J. Huber and Q. Shafi, *Fermion masses, mixings and proton decay in a Randall-Sundrum model*, Phys. Lett. **B498** (2001) 256–262, arXiv:hep-ph/0010195 [hep-ph].

[1328] S. J. Huber, *Flavor violation and warped geometry*, Nucl. Phys. **B666** (2003) 269–288,

arXiv:hep-ph/0303183 [hep-ph].

[1329] G. Panico and A. Wulzer, *The Composite Nambu-Goldstone Higgs*, Lect. Notes Phys. **913** (2016) pp.1–316, arXiv:1506.01961 [hep-ph].

[1330] ATLAS Collaboration, G. Aad et al., *Search for pair-produced third-generation squarks decaying via charm quarks or in compressed supersymmetric scenarios in pp collisions at $\sqrt{s} = 8$ TeV with the ATLAS detector*, Phys. Rev. **D90** (2014) no. 5, 052008, arXiv:1407.0608 [hep-ex].

[1331] ATLAS Collaboration, G. Aad et al., *Search for Scalar Charm Quark Pair Production in pp Collisions at $\sqrt{s} = 8$ TeV with the ATLAS Detector*, Phys. Rev. Lett. **114** (2015) no. 16, 161801, arXiv:1501.01325 [hep-ex].

[1332] C. Delaunay, T. Golling, G. Perez, and Y. Soreq, *Enhanced Higgs boson coupling to charm pairs*, Phys. Rev. **D89** (2014) no. 3, 033014, arXiv:1310.7029 [hep-ph].

[1333] ATLAS Collaboration, *Prospects for $H \to c\bar{c}$ using Charm Tagging with the ATLAS Experiment at the HL-LHC*, ATL-PHYS-PUB-2018-016, CERN, Geneva, Aug, 2018. https://cds.cern.ch/record/2633635.

[1334] ATLAS Collaboration, *Physics at a High-Luminosity LHC with ATLAS*, 2012. ATL-PHYS-PUB-2012-004, ATL-COM-PHYS-2012-1455.

[1335] LHCb collaboration, R. Aaij et al., *Identification of beauty and charm quark jets at LHCb*, JINST **10** (2015) P06013, arXiv:1504.07670 [hep-ex].

[1336] LHCb Collaboration, T. L. Collaboration, *Search for $H^0 \to b\bar{b}$ or $c\bar{c}$ in association with a W or Z boson in the forward region of pp collisions*, .

[1337] J. Duarte-Campderros, G. Perez, M. Schlaffer, and A. Soffer, *Probing the strange Higgs coupling at lepton colliders using light-jet flavor tagging*, arXiv:1811.09636 [hep-ph].

[1338] E. Boudinov, P. Kluit, F. Cossutti, K. Huet, M. Gunther, and O. Botner, *Measurement of the strange quark forward- backward asymmetry around the Z peak*, .

[1339] SLD Collaboration, M. Kalelkar et al., *Light quark fragmentation in polarized Z0 decays at SLD*, Nucl. Phys. Proc. Suppl. **96** (2001) 31–35, arXiv:hep-ex/0008032 [hep-ex]. [,31(2000)].

[1340] T. Sjöstrand, S. Mrenna, and P. Z. Skands, *PYTHIA 6.4 Physics and Manual*, JHEP **05** (2006) 026, arXiv:hep-ph/0603175 [hep-ph].

[1341] ATLAS Collaboration, M. Aaboud et al., *Search for Higgs and Z Boson Decays to $\phi\gamma$ with the ATLAS Detector*, Phys. Rev. Lett. **117** (2016) no. 11, 111802, arXiv:1607.03400 [hep-ex].

[1342] W.-Y. Keung, *THE DECAY OF THE HIGGS BOSON INTO HEAVY QUARKONIUM STATES*, Phys. Rev. **D27** (1983) 2762.

[1343] *Search for the Standard Model Higgs and Z Boson decays to $J/\psi\,\gamma$: HL-LHC projections*, ATL-PHYS-PUB-2015-043, CERN, Geneva, Sep, 2015. http://cds.cern.ch/record/2054550.

[1344] G. Blankenburg, J. Ellis, and G. Isidori, *Flavour-Changing Decays of a 125 GeV Higgs-like Particle*, Phys. Lett. **B712** (2012) 386–390, arXiv:1202.5704 [hep-ph].

[1345] R. Harnik, J. Kopp, and J. Zupan, *Flavor-violating Higgs decays*, JHEP **03** (2013) 026, arXiv:1209.1397 [hep-ph].

[1346] S. Alte, M. König, and M. Neubert, *Exclusive Weak Radiative Higgs Decays in the Standard Model and Beyond*, JHEP **12** (2016) 037, arXiv:1609.06310 [hep-ph].

[1347] C. Arnesen, I. Z. Rothstein, and J. Zupan, *Smoking Guns for On-Shell New Physics at the LHC*, Phys. Rev. Lett. **103** (2009) 151801, arXiv:0809.1429 [hep-ph].

[1348] A. Biekötter, J. Brehmer, and T. Plehn, *Extending the limits of Higgs effective theory*, Phys. Rev. **D94** (2016) no. 5, 055032, arXiv:1602.05202 [hep-ph].

[1349] J. Brehmer, A. Freitas, D. Lopez-Val, and T. Plehn, *Pushing Higgs Effective Theory to its Limits*, Phys. Rev. **D93** (2016) no. 7, 075014, arXiv:1510.03443 [hep-ph].

[1350] S. Dawson, I. M. Lewis, and M. Zeng, *Usefulness of effective field theory for boosted Higgs production*, Phys. Rev. **D91** (2015) 074012, arXiv:1501.04103 [hep-ph].

[1351] M. Schlaffer, M. Spannowsky, M. Takeuchi, A. Weiler, and C. Wymant, *Boosted Higgs Shapes*, Eur. Phys. J. **C74** (2014) no. 10, 3120, arXiv:1405.4295 [hep-ph].

[1352] C. Grojean, E. Salvioni, M. Schlaffer, and A. Weiler, *Very boosted Higgs in gluon fusion*, JHEP **05** (2014) 022, arXiv:1312.3317 [hep-ph].

[1353] U. Langenegger, M. Spira, and I. Strebel, *Testing the Higgs Boson Coupling to Gluons*, arXiv:1507.01373 [hep-ph].

[1354] J. Bramante, A. Delgado, L. Lehman, and A. Martin, *Boosted Higgses from chromomagnetic b's: $b\bar{b}h$ at high luminosity*, Phys. Rev. **D93** (2016) no. 5, 053001, arXiv:1410.3484 [hep-ph].

[1355] M. Buschmann, C. Englert, D. Goncalves, T. Plehn, and M. Spannowsky, *Resolving the Higgs-Gluon Coupling with Jets*, Phys. Rev. **D90** (2014) no. 1, 013010, arXiv:1405.7651 [hep-ph].

[1356] A. Azatov and A. Paul, *Probing Higgs couplings with high p_T Higgs production*, JHEP **01** (2014) 014, arXiv:1309.5273 [hep-ph].

[1357] A. Banfi, A. Martin, and V. Sanz, *Probing top-partners in Higgs+jets*, JHEP **08** (2014) 053, arXiv:1308.4771 [hep-ph].

[1358] M. Buschmann, D. Goncalves, S. Kuttimalai, M. Schonherr, F. Krauss, and T. Plehn, *Mass Effects in the Higgs-Gluon Coupling: Boosted vs Off-Shell Production*, JHEP **02** (2015) 038, arXiv:1410.5806 [hep-ph].

[1359] J. C. Collins, D. E. Soper, and G. F. Sterman, *Transverse Momentum Distribution in Drell-Yan Pair and W and Z Boson Production*, Nucl. Phys. **B250** (1985) 199–224.

[1360] U. Baur and E. W. N. Glover, *Higgs Boson Production at Large Transverse Momentum in Hadronic Collisions*, Nucl. Phys. **B339** (1990) 38–66.

[1361] ATLAS Collaboration, G. Aad et al., *Measurements of the Total and Differential Higgs Boson Production Cross Sections Combining the $H \to \gamma\gamma$ and $H \to ZZ^* \to 4\ell$ Decay Channels at $\sqrt{s} = 8$TeV with the ATLAS Detector*, Phys. Rev. Lett. **115** (2015) no. 9, 091801, arXiv:1504.05833 [hep-ex].

[1362] CMS Collaboration, A. M. Sirunyan et al., *Measurement and interpretation of differential cross sections for Higgs boson production at $\sqrt{s} = 13$ TeV*, Submitted to: Phys. Lett. (2018) , arXiv:1812.06504 [hep-ex].

[1363] CMS Collaboration, *Combined measurement and interpretation of differential Higgs boson production cross sections at $\sqrt{s}$=13 TeV*, . http://cdsweb.cern.ch/record/2628757.

[1364] CMS Collaboration, A. M. Sirunyan et al., *Measurement of inclusive and differential Higgs boson production cross sections in the diphoton decay channel in proton-proton collisions at $\sqrt{s} = 13$ TeV*, arXiv:1807.03825 [hep-ex].

[1365] CMS Collaboration, A. M. Sirunyan et al., *Measurements of properties of the Higgs boson decaying into the four-lepton final state in pp collisions at $\sqrt{s}$ = 13 TeV*, JHEP **11** (2017) 047, arXiv:1706.09936 [hep-ex].

[1366] CMS Collaboration, A. M. Sirunyan et al., *Inclusive search for a highly boosted Higgs boson decaying to a bottom quark-antiquark pair*, Phys. Rev. Lett. **120** (2018) 071802, arXiv:1709.05543 [hep-ex].

[1367] M. Dasgupta, A. Fregoso, S. Marzani, and G. P. Salam, *Towards an understanding of jet substructure*, JHEP **09** (2013) 029, arXiv:1307.0007 [hep-ph].

[1368] A. J. Larkoski, S. Marzani, G. Soyez, and J. Thaler, *Soft Drop*, JHEP **05** (2014) 146, arXiv:1402.2657 [hep-ph].

[1369] CMS Collaboration, *Sensitivity projections for Higgs boson properties measurements at the HL-LHC*, CMS-PAS-FTR-18-011, CERN, Geneva, 2018. http://cds.cern.ch/record/2647699?ln=en.

[1370] F. Yu, *Phenomenology of Enhanced Light Quark Yukawa Couplings and the $W^{\pm}h$ Charge Asymmetry*, JHEP **02** (2017) 083, arXiv:1609.06592 [hep-ph].

[1371] M. Gorbahn and U. Haisch, *Searching for $t \to c(u)h$ with dipole moments*, JHEP **06** (2014) 033, arXiv:1404.4873 [hep-ph].

[1372] CMS Collaboration, V. Khachatryan et al., *Search for lepton flavour violating decays of the Higgs boson to $e\tau$ and $e\mu$ in proton-proton collisions at $\sqrt{s} = 8$ TeV*, Phys. Lett. **B763** (2016) 472–500, arXiv:1607.03561 [hep-ex].

[1373] CMS Collaboration, A. M. Sirunyan et al., *Search for lepton flavour violating decays of the Higgs boson to $\mu\tau$ and $e\tau$ in proton-proton collisions at $\sqrt{s} = 13$ TeV*, JHEP **06** (2018) 001, arXiv:1712.07173 [hep-ex].

[1374] ATLAS Collaboration, G. Aad et al., *Search for lepton-flavour-violating decays of the Higgs and Z bosons with the ATLAS detector*, Eur. Phys. J. **C77** (2017) no. 2, 70, arXiv:1604.07730 [hep-ex].

[1375] S. Bressler, A. Dery, and A. Efrati, *Asymmetric lepton-flavor violating Higgs boson decays*, Phys. Rev. **D90** (2014) no. 1, 015025, arXiv:1405.4545 [hep-ph].

[1376] ATLAS Collaboration, G. Aad et al., *Search for flavour-changing neutral current top quark decays $t \to Hq$ in pp collisions at $\sqrt{s} = 8$ TeV with the ATLAS detector*, JHEP **12** (2015) 061, arXiv:1509.06047 [hep-ex].

[1377] ATLAS Collaboration, G. Aad et al., *Search for top quark decays $t \to qH$ with $H \to \gamma\gamma$ using the ATLAS detector*, JHEP **1406** (2014) 008, arXiv:1403.6293 [hep-ex].

[1378] J. Brod, U. Haisch, and J. Zupan, *Constraints on CP-violating Higgs couplings to the third generation*, JHEP **11** (2013) 180, arXiv:1310.1385 [hep-ph].

[1379] Y. T. Chien, V. Cirigliano, W. Dekens, J. de Vries, and E. Mereghetti, *Direct and indirect constraints on CP-violating Higgs-quark and Higgs-gluon interactions*, JHEP **02** (2016) 011, arXiv:1510.00725 [hep-ph]. [JHEP02,011(2016)].

[1380] D. Egana-Ugrinovic and S. Thomas, *Higgs Boson Contributions to the Electron Electric Dipole Moment*, arXiv:1810.08631 [hep-ph].

[1381] J. Brod and E. Stamou, *Electric dipole moment constraints on CP-violating heavy-quark Yukawas at next-to-leading order*, arXiv:1810.12303 [hep-ph].

[1382] ACME Collaboration, J. Baron et al., *Order of Magnitude Smaller Limit on the Electric Dipole Moment of the Electron*, Science **343** (2014) no. 6168, 269–272, arXiv:1310.7534 [physics.atom-ph].

[1383] J. Brod and D. Skodras, *Electric dipole moment constraints on CP-violating light-quark Yukawas*, arXiv:1811.05480 [hep-ph].

[1384] M. R. Buckley and D. Goncalves, *Boosting the Direct CP Measurement of the Higgs-Top Coupling*, Phys. Rev. Lett. **116** (2016) no. 9, 091801, arXiv:1507.07926 [hep-ph].

[1385] F. Boudjema, R. M. Godbole, D. Guadagnoli, and K. A. Mohan, *Lab-frame observables for probing the top-Higgs interaction*, Phys. Rev. **D92** (2015) no. 1, 015019, arXiv:1501.03157 [hep-ph].

[1386] G. Mahlon and S. J. Parke, *Angular correlations in top quark pair production and decay at hadron colliders*, Phys. Rev. **D53** (1996) 4886–4896, arXiv:hep-ph/9512264 [hep-ph].

[1387] P. Artoisenet et al., *A framework for Higgs characterisation*, JHEP **11** (2013) 043,

arXiv:1306.6464 [hep-ph].

[1388] S. Amor Dos Santos et al., *Probing the CP nature of the Higgs coupling in $t\bar{t}h$ events at the LHC*, Phys. Rev. **D96** (2017) no. 1, 013004, arXiv:1704.03565 [hep-ph].

[1389] F. Demartin, F. Maltoni, K. Mawatari, B. Page, and M. Zaro, *Higgs characterisation at NLO in QCD: CP properties of the top-quark Yukawa interaction*, Eur. Phys. J. **C74** (2014) no. 9, 3065, arXiv:1407.5089 [hep-ph].

[1390] G. R. Bower, T. Pierzchala, Z. Was, and M. Worek, *Measuring the Higgs boson's parity using $\tau \to \rho\nu$*, Phys. Lett. **B543** (2002) 227–234, arXiv:hep-ph/0204292 [hep-ph].

[1391] K. Desch, Z. Was, and M. Worek, *Measuring the Higgs boson parity at a linear collider using the tau impact parameter and $\tau \to \rho\nu$ decay*, Eur. Phys. J. **C29** (2003) 491–496, arXiv:hep-ph/0302046 [hep-ph].

[1392] K. Desch, A. Imhof, Z. Was, and M. Worek, *Probing the CP nature of the Higgs boson at linear colliders with tau spin correlations: The Case of mixed scalar - pseudoscalar couplings*, Phys. Lett. **B579** (2004) 157–164, arXiv:hep-ph/0307331 [hep-ph].

[1393] R. Harnik, A. Martin, T. Okui, R. Primulando, and F. Yu, *Measuring CP violation in $h \to \tau^+\tau^-$ at colliders*, Phys. Rev. **D88** (2013) no. 7, 076009, arXiv:1308.1094 [hep-ph].

[1394] A. Askew, P. Jaiswal, T. Okui, H. B. Prosper, and N. Sato, *Prospect for measuring the CP phase in the $h\tau\tau$ coupling at the LHC*, Phys. Rev. **D91** (2015) no. 7, 075014, arXiv:1501.03156 [hep-ph].

[1395] R. Józefowicz, E. Richter-Was, and Z. Was, *Potential for optimizing the Higgs boson CP measurement in $H \to \tau\tau$ decays at the LHC including machine learning techniques*, Phys. Rev. **D94** (2016) no. 9, 093001, arXiv:1608.02609 [hep-ph].

[1396] S. Berge, W. Bernreuther, and J. Ziethe, *Determining the CP parity of Higgs bosons at the LHC in their tau decay channels*, Phys. Rev. Lett. **100** (2008) 171605, arXiv:0801.2297 [hep-ph].

[1397] S. Berge and W. Bernreuther, *Determining the CP parity of Higgs bosons at the LHC in the tau to 1-prong decay channels*, Phys. Lett. **B671** (2009) 470–476, arXiv:0812.1910 [hep-ph].

[1398] S. Berge, W. Bernreuther, B. Niepelt, and H. Spiesberger, *How to pin down the CP quantum numbers of a Higgs boson in its tau decays at the LHC*, Phys. Rev. **D84** (2011) 116003, arXiv:1108.0670 [hep-ph].

[1399] K. Agashe, G. Perez, and A. Soni, *Flavor structure of warped extra dimension models*, Phys. Rev. **D71** (2005) 016002, arXiv:hep-ph/0408134 [hep-ph].

[1400] K. Agashe, G. Perez, and A. Soni, *B-factory signals for a warped extra dimension*, Phys. Rev. Lett. **93** (2004) 201804, arXiv:hep-ph/0406101 [hep-ph].

[1401] K. Agashe, A. Delgado, M. J. May, and R. Sundrum, *RS1, custodial isospin and precision tests*, JHEP **08** (2003) 050, arXiv:hep-ph/0308036 [hep-ph].

[1402] K. Agashe, M. Bauer, F. Goertz, S. J. Lee, L. Vecchi, L.-T. Wang, and F. Yu, *Constraining RS Models by Future Flavor and Collider Measurements: A Snowmass Whitepaper*, arXiv:1310.1070 [hep-ph].

[1403] M. Blanke, A. J. Buras, B. Duling, K. Gemmler, and S. Gori, *Rare K and B Decays in a Warped Extra Dimension with Custodial Protection*, JHEP **03** (2009) 108, arXiv:0812.3803 [hep-ph].

[1404] M. E. Albrecht, M. Blanke, A. J. Buras, B. Duling, and K. Gemmler, *Electroweak and Flavour Structure of a Warped Extra Dimension with Custodial Protection*, JHEP **09** (2009) 064, arXiv:0903.2415 [hep-ph].

[1405] S. Casagrande, F. Goertz, U. Haisch, M. Neubert, and T. Pfoh, *The Custodial Randall-Sundrum Model: From Precision Tests to Higgs Physics*, JHEP **09** (2010) 014, arXiv:1005.4315

[hep-ph].

[1406] S. Casagrande, F. Goertz, U. Haisch, M. Neubert, and T. Pfoh, *Flavor Physics in the Randall-Sundrum Model: I. Theoretical Setup and Electroweak Precision Tests*, JHEP **10** (2008) 094, arXiv:0807.4937 [hep-ph].

[1407] C. Csaki, G. Perez, Z. Surujon, and A. Weiler, *Flavor Alignment via Shining in RS*, Phys. Rev. **D81** (2010) 075025, arXiv:0907.0474 [hep-ph].

[1408] B. C. Allanach, F. Mahmoudi, J. P. Skittrall, and K. Sridhar, *Gluon-initiated production of a Kaluza-Klein gluon in a Bulk Randall-Sundrum model*, JHEP **03** (2010) 014, arXiv:0910.1350 [hep-ph].

[1409] K. Agashe, A. Belyaev, T. Krupovnickas, G. Perez, and J. Virzi, *LHC Signals from Warped Extra Dimensions*, Phys. Rev. **D77** (2008) 015003, arXiv:hep-ph/0612015 [hep-ph].

[1410] B. Lillie, L. Randall, and L.-T. Wang, *The Bulk RS KK-gluon at the LHC*, JHEP **09** (2007) 074, arXiv:hep-ph/0701166 [hep-ph].

[1411] CMS Collaboration, A. M. Sirunyan et al., *Search for resonant $\mathrm{t\bar{t}}$ production in proton-proton collisions at $\sqrt{s} = 13$ TeV*, Submitted to: JHEP (2018) , arXiv:1810.05905 [hep-ex].

[1412] D. B. Kaplan, *Flavor at SSC energies: A New mechanism for dynamically generated fermion masses*, Nucl. Phys. **B365** (1991) 259–278.

[1413] B. Grinstein, M. Redi, and G. Villadoro, *Low Scale Flavor Gauge Symmetries*, JHEP **11** (2010) 067, arXiv:1009.2049 [hep-ph].

[1414] A. J. Buras, M. V. Carlucci, L. Merlo, and E. Stamou, *Phenomenology of a Gauged $SU(3)^3$ Flavour Model*, JHEP **03** (2012) 088, arXiv:1112.4477 [hep-ph].

[1415] F. Bishara, A. Greljo, J. F. Kamenik, E. Stamou, and J. Zupan, *Dark Matter and Gauged Flavor Symmetries*, JHEP **12** (2015) 130, arXiv:1505.03862 [hep-ph].

[1416] M. Bauer, M. Carena, and K. Gemmler, *Flavor from the Electroweak Scale*, JHEP **11** (2015) 016, arXiv:1506.01719 [hep-ph].

[1417] A. Dery and Y. Nir, *FN-2HDM: Two Higgs Doublet Models with Froggatt-Nielsen Symmetry*, JHEP **04** (2017) 003, arXiv:1612.05219 [hep-ph].

[1418] M. Bauer, M. Carena, and A. Carmona, *Higgs Pair Production as a Signal of Enhanced Yukawa Couplings*, Phys. Rev. Lett. **121** (2018) no. 2, 021801, arXiv:1801.00363 [hep-ph].

[1419] K. Choi and S. H. Im, *Realizing the relaxion from multiple axions and its UV completion with high scale supersymmetry*, JHEP **01** (2016) 149, arXiv:1511.00132 [hep-ph].

[1420] D. E. Kaplan and R. Rattazzi, *Large field excursions and approximate discrete symmetries from a clockwork axion*, Phys. Rev. **D93** (2016) no. 8, 085007, arXiv:1511.01827 [hep-ph].

[1421] G. F. Giudice and M. McCullough, *A Clockwork Theory*, JHEP **02** (2017) 036, arXiv:1610.07962 [hep-ph].

[1422] R. Alonso, A. Carmona, B. M. Dillon, J. F. Kamenik, J. Martin Camalich, and J. Zupan, *A clockwork solution to the flavor puzzle*, arXiv:1807.09792 [hep-ph].

[1423] ATLAS Collaboration, M. Aaboud et al., *Search for pair production of heavy vector-like quarks decaying into high-p_T W bosons and top quarks in the lepton-plus-jets final state in pp collisions at $\sqrt{s} = 13$ TeV with the ATLAS detector*, arXiv:1806.01762 [hep-ex].

[1424] ATLAS Collaboration, M. Aaboud et al., *Search for pair production of up-type vector-like quarks and for four-top-quark events in final states with multiple b-jets with the ATLAS detector*, arXiv:1803.09678 [hep-ex].

[1425] K. Agashe and R. Contino, *Composite Higgs-Mediated FCNC*, Phys. Rev. **D80** (2009) 075016, arXiv:0906.1542 [hep-ph].

[1426] B. Mele, S. Petrarca, and A. Soddu, *A New evaluation of the $t \to cH$ decay width in the standard model*, Phys.Lett. **B435** (1998) 401–406, arXiv:hep-ph/9805498 [hep-ph].

[1427] A. Greljo, J. F. Kamenik, and J. Kopp, *Disentangling Flavor Violation in the Top-Higgs Sector at the LHC*, JHEP **1407** (2014) 046, arXiv:1404.1278 [hep-ph].

[1428] A. Azatov, G. Panico, G. Perez, and Y. Soreq, *On the Flavor Structure of Natural Composite Higgs Models & Top Flavor Violation*, JHEP **12** (2014) 082, arXiv:1408.4525 [hep-ph].

[1429] F. J. Botella, G. C. Branco, M. Nebot, and M. N. Rebelo, *Flavour Changing Higgs Couplings in a Class of Two Higgs Doublet Models*, Eur. Phys. J. **C76** (2016) no. 3, 161, arXiv:1508.05101 [hep-ph].

[1430] D. Bardhan, G. Bhattacharyya, D. Ghosh, M. Patra, and S. Raychaudhuri, *Detailed analysis of flavor-changing decays of top quarks as a probe of new physics at the LHC*, Phys. Rev. **D94** (2016) no. 1, 015026, arXiv:1601.04165 [hep-ph].

[1431] M. Badziak and K. Harigaya, *Asymptotically Free Natural SUSY Twin Higgs*, Phys. Rev. Lett. **120** (2018) 211803, arXiv:1711.11040 [hep-ph].

[1432] E. Gabrielli, B. Mele, M. Raidal, and E. Venturini, *FCNC decays of standard model fermions into a dark photon*, Phys. Rev. **D94** (2016) no. 11, 115013, arXiv:1607.05928 [hep-ph].

[1433] A. Papaefstathiou and G. Tetlalmatzi-Xolocotzi, *Rare top quark decays at a 100 TeV proton–proton collider: $t \to bWZ$ and $t \to hc$*, Eur. Phys. J. **C78** (2018) no. 3, 214, arXiv:1712.06332 [hep-ph].

[1434] G. Abbas, A. Celis, X.-Q. Li, J. Lu, and A. Pich, *Flavour-changing top decays in the aligned two-Higgs-doublet model*, JHEP **06** (2015) 005, arXiv:1503.06423 [hep-ph].

[1435] U. Ellwanger, C. Hugonie, and A. M. Teixeira, *The Next-to-Minimal Supersymmetric Standard Model*, Phys. Rept. **496** (2010) 1–77, arXiv:0910.1785 [hep-ph].

[1436] S. Dimopoulos and J. Preskill, *Massless Composites With Massive Constituents*, Nucl. Phys. **B199** (1982) 206–222.

[1437] C. Zhang and F. Maltoni, *Top-quark decay into Higgs boson and a light quark at next-to-leading order in QCD*, Phys.Rev. **D88** (2013) 054005, arXiv:1305.7386 [hep-ph].

[1438] CMS Collaboration, V. Khachatryan et al., *Search for Higgs boson off-shell production in proton-proton collisions at 7 and 8 TeV and derivation of constraints on its total decay width*, JHEP **09** (2016) 051, arXiv:1605.02329 [hep-ex].

[1439] Top Quark Working Group Collaboration, K. Agashe et al., *Working Group Report: Top Quark*, in *Proceedings, 2013 Community Summer Study on the Future of U.S. Particle Physics: Snowmass on the Mississippi (CSS2013): Minneapolis, MN, USA, July 29-August 6, 2013*. 2013. arXiv:1311.2028 [hep-ph]. https://inspirehep.net/record/1263763/files/arXiv:1311.2028.pdf.

[1440] S. Banerjee, M. Chala, and M. Spannowsky, *Top quark FCNCs in extended Higgs sectors*, arXiv:1806.02836 [hep-ph].

[1441] CMS Collaboration, A. M. Sirunyan et al., *Search for low-mass resonances decaying into bottom quark-antiquark pairs in proton-proton collisions at $\sqrt{s} = 13$ TeV*, Submitted to: Phys. Rev. (2018) , arXiv:1810.11822 [hep-ex].

[1442] F. Boudjema and A. Semenov, *Measurements of the SUSY Higgs selfcouplings and the reconstruction of the Higgs potential*, Phys. Rev. **D66** (2002) 095007, arXiv:hep-ph/0201219 [hep-ph].

[1443] J. F. Gunion and H. E. Haber, *The CP conserving two Higgs doublet model: The Approach to the decoupling limit*, Phys. Rev. **D67** (2003) 075019, arXiv:hep-ph/0207010 [hep-ph].

[1444] ATLAS Collaboration, T. A. collaboration, *A search for the rare decay of the Standard Model Higgs boson to dimuons in pp collisions at $\sqrt{s} = 13$ TeV with the ATLAS Detector*, .

[1445] Y. Cai, T. Han, T. Li, and R. Ruiz, *Lepton Number Violation: Seesaw Models and Their Collider Tests*, Front.in Phys. **6** (2018) 40, arXiv:1711.02180 [hep-ph].

[1446] C. Weiland, *Effects of fermionic singlet neutrinos on high- and low-energy observables*. PhD thesis, Orsay, LPT, 2013. arXiv:1311.5860 [hep-ph].

[1447] R. E. Ruiz, *Hadron Collider Tests of Neutrino Mass-Generating Mechanisms*. PhD thesis, Pittsburgh U., 2015. arXiv:1509.06375 [hep-ph].

[1448] X. Marcano Imaz, *Lepton flavor violation from low scale seesaw neutrinos with masses reachable at the LHC*. PhD thesis, U. Autonoma, Madrid (main), Cham, 2017-06. arXiv:1710.08032 [hep-ph]. https://repositorio.uam.es/handle/10486/681399.

[1449] J. Kersten and A. Yu. Smirnov, *Right-Handed Neutrinos at CERN LHC and the Mechanism of Neutrino Mass Generation*, Phys. Rev. **D76** (2007) 073005, arXiv:0705.3221 [hep-ph].

[1450] K. Moffat, S. Pascoli, and C. Weiland, *Equivalence between massless neutrinos and lepton number conservation in fermionic singlet extensions of the Standard Model*, arXiv:1712.07611 [hep-ph].

[1451] S. Pascoli, R. Ruiz, and C. Weiland, *Safe Jet Vetoes*, Phys. Lett. **B786** (2018) 106, arXiv:1805.09335 [hep-ph].

[1452] E. Arganda, M. J. Herrero, X. Marcano, and C. Weiland, *Exotic $\mu\tau jj$ events from heavy ISS neutrinos at the LHC*, Phys. Lett. **B752** (2016) 46–50, arXiv:1508.05074 [hep-ph].

[1453] MEG Collaboration, J. Adam et al., *New constraint on the existence of the $\mu^+ \to e^+\gamma$ decay*, Phys. Rev. Lett. **110** (2013) 201801, arXiv:1303.0754 [hep-ex].

[1454] D. Alva, T. Han, and R. Ruiz, *Heavy Majorana neutrinos from $W\gamma$ fusion at hadron colliders*, JHEP **02** (2015) 072, arXiv:1411.7305 [hep-ph].

[1455] R. Ruiz, *Lepton Number Violation at Colliders from Kinematically Inaccessible Gauge Bosons*, Eur. Phys. J. **C77** (2017) no. 6, 375, arXiv:1703.04669 [hep-ph].

[1456] W.-Y. Keung and G. Senjanovic, *Majorana Neutrinos and the Production of the Right-handed Charged Gauge Boson*, Phys. Rev. Lett. **50** (1983) 1427.

[1457] M. Mitra, R. Ruiz, D. J. Scott, and M. Spannowsky, *Neutrino Jets from High-Mass W_R Gauge Bosons in TeV-Scale Left-Right Symmetric Models*, Phys. Rev. **D94** (2016) no. 9, 095016, arXiv:1607.03504 [hep-ph].

[1458] T. Han, I. Lewis, R. Ruiz, and Z.-g. Si, *Lepton Number Violation and W' Chiral Couplings at the LHC*, Phys. Rev. **D87** (2013) no. 3, 035011, arXiv:1211.6447 [hep-ph]. [Erratum: Phys. Rev.D87,no.3,039906(2013)].

[1459] A. Ferrari, J. Collot, M.-L. Andrieux, B. Belhorma, P. de Saintignon, J.-Y. Hostachy, P. Martin, and M. Wielers, *Sensitivity study for new gauge bosons and right-handed Majorana neutrinos in pp collisions at s = 14-TeV*, Phys. Rev. **D62** (2000) 013001.

[1460] O. Mattelaer, M. Mitra, and R. Ruiz, *Automated Neutrino Jet and Top Jet Predictions at Next-to-Leading-Order with Parton Shower Matching in Effective Left-Right Symmetric Models*, arXiv:1610.08985 [hep-ph].

[1461] P. Fileviez Perez, T. Han, G.-y. Huang, T. Li, and K. Wang, *Neutrino Masses and the CERN LHC: Testing Type II Seesaw*, Phys. Rev. **D78** (2008) 015018, arXiv:0805.3536 [hep-ph].

[1462] T. Li, *Type II Seesaw and tau lepton at the HL-LHC, HE-LHC and FCC-hh*, JHEP **09** (2018) 079, arXiv:1802.00945 [hep-ph].

[1463] H. Sugiyama, K. Tsumura, and H. Yokoya, *Discrimination of models including doubly charged scalar bosons by using tau lepton decay distributions*, Phys. Lett. **B717** (2012) 229–234, arXiv:1207.0179 [hep-ph].

[1464] R. Ruiz, *QCD Corrections to Pair Production of Type III Seesaw Leptons at Hadron Colliders*, JHEP **12** (2015) 165, arXiv:1509.05416 [hep-ph].

[1465] A. Arhrib, B. Bajc, D. K. Ghosh, T. Han, G.-Y. Huang, I. Puljak, and G. Senjanovic, *Collider Signatures for Heavy Lepton Triplet in Type I+III Seesaw*, Phys. Rev. **D82** (2010) 053004,

arXiv:0904.2390 [hep-ph].

[1466] T. Li and X.-G. He, *Neutrino Masses and Heavy Triplet Leptons at the LHC: Testability of Type III Seesaw*, Phys. Rev. **D80** (2009) 093003, arXiv:0907.4193 [hep-ph].

[1467] I. Baldes, T. Konstandin, and G. Servant, *A First-Order Electroweak Phase Transition in the Standard Model from Varying Yukawas*, arXiv:1604.04526 [hep-ph].

[1468] I. Baldes, T. Konstandin, and G. Servant, *Flavor Cosmology: Dynamical Yukawas in the Froggatt-Nielsen Mechanism*, JHEP **12** (2016) 073, arXiv:1608.03254 [hep-ph].

[1469] B. von Harling and G. Servant, *Cosmological evolution of Yukawa couplings: the 5D perspective*, JHEP **05** (2017) 077, arXiv:1612.02447 [hep-ph].

[1470] S. Bruggisser, T. Konstandin, and G. Servant, *CP-violation for Electroweak Baryogenesis from Dynamical CKM Matrix*, JCAP **1711** (2017) no. 11, 034, arXiv:1706.08534 [hep-ph].

[1471] S. Bruggisser, B. Von Harling, O. Matsedonskyi, and G. Servant, *The Baryon Asymmetry from a Composite Higgs*, Phys. Rev. Lett. **121** (2018) no. 13, 131801, arXiv:1803.08546 [hep-ph].

[1472] S. Bruggisser, B. Von Harling, O. Matsedonskyi, and G. Servant, *Electroweak Phase Transition and Baryogenesis in Composite Higgs Models*, arXiv:1804.07314 [hep-ph].

[1473] I. Baldes and G. Servant, *High Scale Electroweak Phase Transition: Baryogenesis & Symmetry Non-Restoration*, arXiv:1807.08770 [hep-ph].

[1474] G. Servant, *The serendipity of electroweak baryogenesis*, Phil. Trans. Roy. Soc. Lond. **A376** (2018) no. 2114, 20170124, arXiv:1807.11507 [hep-ph].

[1475] J. R. Espinosa, B. Gripaios, T. Konstandin, and F. Riva, *Electroweak Baryogenesis in Non-minimal Composite Higgs Models*, JCAP **1201** (2012) 012, arXiv:1110.2876 [hep-ph].

[1476] M. Chala, G. Nardini, and I. Sobolev, *Unified explanation for dark matter and electroweak baryogenesis with direct detection and gravitational wave signatures*, Phys. Rev. **D94** (2016) no. 5, 055006, arXiv:1605.08663 [hep-ph].

[1477] E. Megias, G. Nardini, and M. Quiros, *Cosmological Phase Transitions in Warped Space: Gravitational Waves and Collider Signatures*, arXiv:1806.04877 [hep-ph].

[1478] F. Coradeschi, P. Lodone, D. Pappadopulo, R. Rattazzi, and L. Vitale, *A naturally light dilaton*, JHEP **11** (2013) 057, arXiv:1306.4601 [hep-th].

[1479] K. Kumar, Z.-T. Lu, and M. J. Ramsey-Musolf, *Working Group Report: Nucleons, Nuclei, and Atoms*, in *Fundamental Physics at the Intensity Frontier*, pp. 159–214. 2013. arXiv:1312.5416 [hep-ph]. https://inspirehep.net/record/1272872/files/arXiv:1312.5416.pdf.

[1480] O. Matsedonskyi, G. Panico, and A. Wulzer, *Light Top Partners for a Light Composite Higgs*, JHEP **01** (2013) 164, arXiv:1204.6333 [hep-ph].

[1481] G. Panico, M. Redi, A. Tesi, and A. Wulzer, *On the Tuning and the Mass of the Composite Higgs*, JHEP **03** (2013) 051, arXiv:1210.7114 [hep-ph].

[1482] C. Caprini et al., *Science with the space-based interferometer eLISA. II: Gravitational waves from cosmological phase transitions*, JCAP **1604** (2016) no. 04, 001, arXiv:1512.06239 [astro-ph.CO].

[1483] L. Di Luzio and M. Nardecchia, *What is the scale of new physics behind the B-flavour anomalies?*, Eur. Phys. J. **C77** (2017) no. 8, 536, arXiv:1706.01868 [hep-ph].

[1484] ATLAS Collaboration, M. Aaboud et al., *Search for Minimal Supersymmetric Standard Model Higgs bosons H/A and for a Z' boson in the $\tau\tau$ final state produced in pp collisions at $\sqrt{s} = 13$ TeV with the ATLAS Detector*, Eur. Phys. J. **C76** (2016) no. 11, 585, arXiv:1608.00890 [hep-ex].

[1485] A. Greljo and D. Marzocca, *High-p_T dilepton tails and flavor physics*, Eur. Phys. J. **C77** (2017) no. 8, 548, arXiv:1704.09015 [hep-ph].

[1486] ATLAS Collaboration, T. A. collaboration, *Search for new high-mass phenomena in the dilepton final state using 36.1 fb^{-1} of proton-proton collision data at $\sqrt{s} = 13$ TeV with the ATLAS detector*, .

[1487] ATLAS Collaboration, M. Aaboud et al., *Search for new high-mass phenomena in the dilepton final state using 36 fb^{-1} of proton-proton collision data at $\sqrt{s} = 13$ TeV with the ATLAS detector*, JHEP **10** (2017) 182, arXiv:1707.02424 [hep-ex].

[1488] Y. Afik, J. Cohen, E. Gozani, E. Kajomovitz, and Y. Rozen, *Establishing a Search for $b \to s\ell^+\ell^-$ Anomalies at the LHC*, arXiv:1805.11402 [hep-ph].

[1489] M. Abdullah, J. Calle, B. Dutta, A. Florez, and D. Restrepo, *Probing a simplified, W' model of $R(D^{(*)})$ anomalies using b-tags, τ leptons and missing energy*, arXiv:1805.01869 [hep-ph].

[1490] I. Dorsner and A. Greljo, *Leptoquark toolbox for precision collider studies*, JHEP **05** (2018) 126, arXiv:1801.07641 [hep-ph].

[1491] L. Di Luzio, J. Fuentes-Martin, A. Greljo, M. Nardecchia, and S. Renner, *Maximal Flavour Violation: a Cabibbo mechanism for leptoquarks*, JHEP **11** (2018) 081, arXiv:1808.00942 [hep-ph].

[1492] M. Kramer, T. Plehn, M. Spira, and P. M. Zerwas, *Pair production of scalar leptoquarks at the CERN LHC*, Phys. Rev. **D71** (2005) 057503, arXiv:hep-ph/0411038 [hep-ph].

[1493] B. C. Allanach, B. Gripaios, and T. You, *The case for future hadron colliders from $B \to K^{(*)}\mu^+\mu^-$ decays*, JHEP **03** (2018) 021, arXiv:1710.06363 [hep-ph].

[1494] N. Vignaroli, *Seeking LQs in the $\mathrm{t\bar{t}}$ plus missing energy channel at the high-luminosity LHC*, arXiv:1808.10309 [hep-ph].

[1495] Fermilab Lattice, MILC Collaboration, A. Bazavov et al., *$B^0_{(s)}$-mixing matrix elements from lattice QCD for the Standard Model and beyond*, Phys. Rev. **D93** (2016) 113016, arXiv:1602.03560 [hep-lat].

[1496] B. C. Allanach, T. Corbett, M. J. Dolan, and T. You, *Hadron Collider Sensitivity to Fat Flavourful Z's for $R_{K^{(*)}}$*, arXiv:1810.02166 [hep-ph].

[1497] A. Falkowski, M. Gonzalez-Alonso, and K. Mimouni, *Compilation of low-energy constraints on 4-fermion operators in the SMEFT*, JHEP **08** (2017) 123, arXiv:1706.03783 [hep-ph].

[1498] A. Falkowski, S. F. King, E. Perdomo, and M. Pierre, *Flavourful Z' portal for vector-like neutrino Dark Matter and $R_{K^{(*)}}$*, JHEP **08** (2018) 061, arXiv:1803.04430 [hep-ph].

[1499] A. Celis, J. Fuentes-Martin, A. Vicente, and J. Virto, *Gauge-invariant implications of the LHCb measurements on lepton-flavor nonuniversality*, Phys. Rev. **D96** (2017) no. 3, 035026, arXiv:1704.05672 [hep-ph].

[1500] P. J. Fox, I. Low, and Y. Zhang, *Top-philic Z' Forces at the LHC*, JHEP **03** (2018) 074, arXiv:1801.03505 [hep-ph].

[1501] J. E. Camargo-Molina, A. Celis, and D. A. Faroughy, *Anomalies in Bottom from new physics in Top*, arXiv:1805.04917 [hep-ph].

[1502] CMS Collaboration, *Projection of searches for pair production of scalar leptoquarks decaying to a top quark and a charged lepton at the HL-LHC*, CMS-PAS-FTR-18-008, CERN, Geneva, 2018. https://cds.cern.ch/record/2645611.

[1503] CMS Collaboration, A. M. Sirunyan et al., *Search for leptoquarks coupled to third-generation quarks in proton-proton collisions at $\sqrt{s} = 13$ TeV*, Phys. Rev. Lett. **121** (2018) 241802, arXiv:1809.05558 [hep-ex].

[1504] CMS Collaboration, A. M. Sirunyan et al., *Search for third-generation scalar leptoquarks decaying to a top quark and a τ lepton at $\sqrt{s} = 13$ TeV*, Eur. Phys. J. C **78** (2018) 707, arXiv:1803.02864 [hep-ex].

[1505] CMS Collaboration, *Prospects for exclusion or discovery of a third generation leptoquark decaying into a τ lepton and a b quark at CMS*, CMS-PAS-FTR-18-028, CERN, Geneva, 2018. http://cds.cern.ch/record/2652363.

[1506] T. Plehn, H. Spiesberger, M. Spira, and P. M. Zerwas, *Formation and decay of scalar leptoquarks / squarks in ep collisions*, Z. Phys. C **74** (1997) 611, arXiv:hep-ph/9703433 [hep-ph].

[1507] M. Cacciari, G. P. Salam, and G. Soyez, *FastJet User Manual*, Eur. Phys. J. **C72** (2012) 1896, arXiv:1111.6097 [hep-ph].

[1508] M. Cacciari, G. P. Salam, and G. Soyez, *The Anti-k(t) jet clustering algorithm*, JHEP **04** (2008) 063, arXiv:0802.1189 [hep-ph].

[1509] G. Cowan, K. Cranmer, E. Gross, and O. Vitells, *Asymptotic formulae for likelihood-based tests of new physics*, Eur. Phys. J. **C71** (2011) 1554, arXiv:1007.1727 [physics.data-an]. [Erratum: Eur. Phys. J.C73,2501(2013)].

[1510] T. Junk, *Confidence level computation for combining searches with small statistics*, Nucl. Instrum. Meth. **A434** (1999) 435–443, arXiv:hep-ex/9902006 [hep-ex].

[1511] A. L. Read, *Presentation of search results: The CL(s) technique*, J. Phys. **G28** (2002) 2693–2704. [,11(2002)].

[1512] ATLAS, CMS, LHC Higgs Combination Group Collaboration, *Procedure for the LHC Higgs boson search combination in summer 2011*, .

[1513] CMS Collaboration, *Sensitivity study for $W' \to \tau\nu$ at the HL-LHC*, CMS Physics Analysis Summary CMS-PAS-FTR-18-030, 2018. http://cdsweb.cern.ch/record/2655312.

[1514] CMS Collaboration, A. M. Sirunyan et al., *Search for a W' boson decaying to a τ lepton and a neutrino in proton-proton collisions at $\sqrt{s} = 13$ TeV*, Submitted to: Phys. Lett. (2018) , arXiv:1807.11421 [hep-ex].

[1515] G. Altarelli, B. Mele, and M. Ruiz-Altaba, *Searching for New Heavy Vector Bosons in $p\bar{p}$ Colliders*, Z. Phys. **C45** (1989) 109. [Erratum: Z. Phys.C47,676(1990)].

[1516] CMS Collaboration, A. M. Sirunyan et al., *Search for third-generation scalar leptoquarks and heavy right-handed neutrinos in final states with two tau leptons and two jets in proton-proton collisions at $\sqrt{s} = 13$ TeV*, JHEP **07** (2017) 121, arXiv:1703.03995 [hep-ex].

[1517] N. Carrasco, V. Lubicz, G. Martinelli, C. T. Sachrajda, N. Tantalo, C. Tarantino, and M. Testa, *QED Corrections to Hadronic Processes in Lattice QCD*, Phys. Rev. **D91** (2015) no. 7, 074506, arXiv:1502.00257 [hep-lat].

[1518] A. Patella, *QED Corrections to Hadronic Observables*, PoS **LATTICE2016** (2017) 020, arXiv:1702.03857 [hep-lat].

[1519] M. Della Morte, A. Francis, V. Guelpers, G. Herdoiza, G. von Hippel, H. Horch, B. Jaeger, H. B. Meyer, A. Nyffeler, and H. Wittig, *The hadronic vacuum polarization contribution to the muon $g-2$ from lattice QCD*, JHEP **10** (2017) 020, arXiv:1705.01775 [hep-lat].

[1520] D. Giusti, V. Lubicz, G. Martinelli, C. Sachrajda, F. Sanfilippo, S. Simula, and N. Tantalo, *Radiative corrections to decay amplitudes in lattice QCD*, in *36th International Symposium on Lattice Field Theory (Lattice 2018) East Lansing, MI, United States, July 22-28, 2018*. 2018. arXiv:1811.06364 [hep-lat].

[1521] ALPHA Collaboration, P. Dimopoulos, G. Herdoiza, F. Palombi, M. Papinutto, C. Pena, A. Vladikas, and H. Wittig, *Non-perturbative renormalisation of Delta F=2 four-fermion operators in two-flavour QCD*, JHEP **05** (2008) 065, arXiv:0712.2429 [hep-lat].

[1522] S. Durr et al., *Precision computation of the kaon bag parameter*, Phys. Lett. **B705** (2011) 477–481, arXiv:1106.3230 [hep-lat].

[1523] RBC, UKQCD Collaboration, N. H. Christ, T. Izubuchi, C. T. Sachrajda, A. Soni, and J. Yu,

Long distance contribution to the KL-KS mass difference, Phys. Rev. **D88** (2013) 014508, arXiv:1212.5931 [hep-lat].

[1524] Z. Bai, *Long distance part of ϵ_K from lattice QCD*, PoS **LATTICE2016** (2017) 309, arXiv:1611.06601 [hep-lat].

[1525] J. A. Bailey, S. Lee, W. Lee, J. Leem, and S. Park, *Updated evaluation of ϵ_K in the standard model with lattice QCD inputs*, Phys. Rev. **D98** (2018) no. 9, 094505, arXiv:1808.09657 [hep-lat].

[1526] C. Davies, J. Harrison, G. P. Lepage, C. Monahan, J. Shigemitsu, and M. Wingate, *Improving the theoretical prediction for the $B_s - \bar{B}_s$ width difference: matrix elements of next-to-leading order $\Delta B = 2$ operators*, EPJ Web Conf. **175** (2018) 13023, arXiv:1712.09934 [hep-lat].

[1527] A. Bazavov et al., *$|V_{us}|$ from $K_{\ell 3}$ decay and four-flavor lattice QCD*, arXiv:1809.02827 [hep-lat].

[1528] M. Moulson, *Experimental determination of V_{us} from kaon decays*, PoS **CKM2016** (2017) 033, arXiv:1704.04104 [hep-ex].

[1529] N. Carrasco, P. Lami, V. Lubicz, L. Riggio, S. Simula, and C. Tarantino, *$K \to \pi$ semileptonic form factors with $N_f = 2 + 1 + 1$ twisted mass fermions*, Phys. Rev. **D93** (2016) no. 11, 114512, arXiv:1602.04113 [hep-lat].

[1530] R. A. Briceño, M. T. Hansen, and A. Walker-Loud, *Multichannel $1 \to 2$ transition amplitudes in a finite volume*, Phys. Rev. **D91** (2015) no. 3, 034501, arXiv:1406.5965 [hep-lat].

[1531] Fermilab Lattice, MILC Collaboration, J. A. Bailey et al., *$|V_{ub}|$ from $B \to \pi \ell \nu$ decays and (2+1)-flavor lattice QCD*, Phys. Rev. **D92** (2015) no. 1, 014024, arXiv:1503.07839 [hep-lat].

[1532] HPQCD Collaboration, C. Bouchard, G. P. Lepage, C. Monahan, H. Na, and J. Shigemitsu, *Rare decay $B \to K \ell^+ \ell^-$ form factors from lattice QCD*, Phys. Rev. **D88** (2013) no. 5, 054509, arXiv:1306.2384 [hep-lat]. [Erratum: Phys. Rev.D88,no.7,079901(2013)].

[1533] J. A. Bailey et al., *$B \to K l^+ l^-$ decay form factors from three-flavor lattice QCD*, Phys. Rev. **D93** (2016) no. 2, 025026, arXiv:1509.06235 [hep-lat].

[1534] C. M. Bouchard, G. P. Lepage, C. Monahan, H. Na, and J. Shigemitsu, *$B_s \to K \ell \nu$ form factors from lattice QCD*, Phys. Rev. **D90** (2014) 054506, arXiv:1406.2279 [hep-lat].

[1535] C. J. Monahan, C. M. Bouchard, G. P. Lepage, H. Na, and J. Shigemitsu, *Form factor ratios for $B_s \to K \, \ell \, \nu$ and $B_s \to D_s \, \ell \, \nu$ semileptonic decays and $|V_{ub}/V_{cb}|$*, arXiv:1808.09285 [hep-lat].

[1536] R. R. Horgan, Z. Liu, S. Meinel, and M. Wingate, *Lattice QCD calculation of form factors describing the rare decays $B \to K^* \ell^+ \ell^-$ and $B_s \to \phi \ell^+ \ell^-$*, Phys. Rev. **D89** (2014) no. 9, 094501, arXiv:1310.3722 [hep-lat].

[1537] R. R. Horgan, Z. Liu, S. Meinel, and M. Wingate, *Calculation of $B^0 \to K^{*0} \mu^+ \mu^-$ and $B_s^0 \to \phi \mu^+ \mu^-$ observables using form factors from lattice QCD*, Phys. Rev. Lett. **112** (2014) 212003, arXiv:1310.3887 [hep-ph].

[1538] M. Luscher, *Volume Dependence of the Energy Spectrum in Massive Quantum Field Theories. 2. Scattering States*, Commun. Math. Phys. **105** (1986) 153–188.

[1539] M. Luscher, *Signatures of unstable particles in finite volume*, Nucl. Phys. **B364** (1991) 237–251.

[1540] M. Lage, U.-G. Meissner, and A. Rusetsky, *A Method to measure the antikaon-nucleon scattering length in lattice QCD*, Phys. Lett. **B681** (2009) 439–443, arXiv:0905.0069 [hep-lat].

[1541] V. Bernard, M. Lage, U. G. Meissner, and A. Rusetsky, *Scalar mesons in a finite volume*, JHEP **01** (2011) 019, arXiv:1010.6018 [hep-lat].

[1542] M. Doring, U.-G. Meissner, E. Oset, and A. Rusetsky, *Unitarized Chiral Perturbation Theory in*

a finite volume: Scalar meson sector, Eur. Phys. J. **A47** (2011) 139, arXiv:1107.3988 [hep-lat].

[1543] R. A. Briceno and Z. Davoudi, *Moving multichannel systems in a finite volume with application to proton-proton fusion*, Phys. Rev. **D88** (2013) no. 9, 094507, arXiv:1204.1110 [hep-lat].

[1544] Hadron Spectrum Collaboration, J. J. Dudek, R. G. Edwards, C. E. Thomas, and D. J. Wilson, *Resonances in coupled $\pi K - \eta K$ scattering from quantum chromodynamics*, Phys. Rev. Lett. **113** (2014) no. 18, 182001, arXiv:1406.4158 [hep-ph].

[1545] S. Meinel, $\Lambda_b \to \Lambda_c^{(*)}$ *form factors from lattice QCD*, https://indico.mitp.uni-mainz.de/event/129/session/0/contribution/2/material/slides/0.pdf. Talk at the workshop "Challenges in Semileptonic B Decays" held 9-13 April 2018 at the Mainz Institute for Theoretical Physics, Johannes Gutenberg University.

[1546] RBC, UKQCD Collaboration, N. H. Christ, X. Feng, A. Portelli, and C. T. Sachrajda, *Prospects for a lattice computation of rare kaon decay amplitudes: $K \to \pi\ell^+\ell^-$ decays*, Phys. Rev. **D92** (2015) no. 9, 094512, arXiv:1507.03094 [hep-lat].

[1547] N. H. Christ, X. Feng, A. Juttner, A. Lawson, A. Portelli, and C. T. Sachrajda, *First exploratory calculation of the long-distance contributions to the rare kaon decays $K \to \pi\ell^+\ell^-$*, Phys. Rev. **D94** (2016) no. 11, 114516, arXiv:1608.07585 [hep-lat].

[1548] M. Cacciari, G. P. Salam, and G. Soyez, *FastJet User Manual*, Eur. Phys. J. **C72** (2012) 1896, arXiv:1111.6097 [hep-ph].

[1549] ATLAS Collaboration, ATLAS Collaboration, *Expected performance of the ATLAS detector at HL-LHC*, in progress, CERN, Geneva, Dec, 2018.

[1550] A. Collaboration, *Technical Design Report for the Phase-II Upgrade of the ATLAS TDAQ System*, CERN-LHCC-2017-020. ATLAS-TDR-029, CERN, Geneva, Sep, 2017. http://cds.cern.ch/record/2285584.

[1551] CMS Collaboration, *The Phase-2 Upgrade of the CMS L1 Trigger Interim Technical Design Report*, CERN-LHCC-2017-013. CMS-TDR-017, CERN, Geneva, Sep, 2017. https://cds.cern.ch/record/2283192. This is the CMS Interim TDR devoted to the upgrade of the CMS L1 trigger in view of the HL-LHC running, as approved by the LHCC.

[1552] A. Collaboration, *Technical Design Report for the ATLAS Inner Tracker Pixel Detector*, CERN-LHCC-2017-021. ATLAS-TDR-030, CERN, Geneva, Sep, 2017. http://cds.cern.ch/record/2285585.

[1553] A. Collaboration, *Technical Design Report for the ATLAS Inner Tracker Strip Detector*, CERN-LHCC-2017-005. ATLAS-TDR-025, CERN, Geneva, Apr, 2017. http://cds.cern.ch/record/2257755.

[1554] A. Collaboration, *Technical Design Report for the Phase-II Upgrade of the ATLAS LAr Calorimeter*, CERN-LHCC-2017-018. ATLAS-TDR-027, CERN, Geneva, Sep, 2017. http://cds.cern.ch/record/2285582.

[1555] CMS Collaboration, *The Phase-2 Upgrade of the CMS Barrel Calorimeters Technical Design Report*, CERN-LHCC-2017-011. CMS-TDR-015, CERN, 2017. https://cds.cern.ch/record/2283187.

[1556] CMS Collaboration, *The Phase-2 Upgrade of the CMS Endcap Calorimeter*, CERN-LHCC-2017-023. CMS-TDR-019, 2017. https://cds.cern.ch/record/2293646.

[1557] A. Collaboration, *Technical Design Report for the Phase-II Upgrade of the ATLAS Muon Spectrometer*, CERN-LHCC-2017-017. ATLAS-TDR-026, CERN, Geneva, Sep, 2017. http://cds.cern.ch/record/2285580.

[1558] A. Collaboration, *Technical Design Report for the Phase-II Upgrade of the ATLAS Tile Calorimeter*, CERN-LHCC-2017-019. ATLAS-TDR-028, CERN, Geneva, Sep, 2017.

http://cds.cern.ch/record/2285583.

[1559] CMS Collaboration, D. Contardo, M. Klute, J. Mans, L. Silvestris, and J. Butler, *Technical Proposal for the Phase-II Upgrade of the CMS Detector*, CERN-LHCC-2015-010. LHCC-P-008. CMS-TDR-15-02, 2015. https://cds.cern.ch/record/2020886.

[1560] A. Collaboration, *Technical Proposal: A High-Granularity Timing Detector for the ATLAS Phase-II Upgrade*, CERN-LHCC-2018-023. LHCC-P-012, CERN, Geneva, Jun, 2018. http://cds.cern.ch/record/2623663.

[1561] T. Sjostrand, S. Mrenna, and P. Z. Skands, *A Brief Introduction to PYTHIA 8.1*, Comput. Phys. Commun. **178** (2008) 852–867, arXiv:0710.3820 [hep-ph].

[1562] I. Belyaev et al., *Handling of the generation of primary events in Gauss, the LHCb simulation framework*, J. Phys. Conf. Ser. **331** (2011) 032047.

[1563] J. Pumplin, D. Stump, J. Huston, H. Lai, P. M. Nadolsky, et al., *New generation of parton distributions with uncertainties from global QCD analysis*, JHEP **07** (2002) 012, arXiv:hep-ph/0201195 [hep-ph].

[1564] J. Allison et al., *Geant4 developments and applications*, IEEE Trans. Nucl. Sci. **53** (2006) 270.

[1565] GEANT4 Collaboration, S. Agostinelli et al., *GEANT4: A Simulation toolkit*, Nucl. Instrum. Meth. **A506** (2003) 250–303.

[1566] M. Clemencic et al., *The LHCb simulation application, Gauss: Design, evolution and experience*, J. Phys. Conf. Ser. **331** (2011) 032023.

[1567] R. A. Khalek, S. Bailey, J. Gao, L. Harland-Lang, and J. Rojo, *Towards Ultimate Parton Distributions at the High-Luminosity LHC*, Eur. Phys. J. **C78** (2018) no. 11, 962, arXiv:1810.03639 [hep-ph].

Report from Working Group 5: Future physics opportunities for high-density QCD at the LHC with heavy-ion and proton beams

Physics of the HL-LHC, and Perspectives at the HE-LHC

Conveners:
Z. Citron[3], *A. Dainese*[24], *J.F. Grosse-Oetringhaus*[6], *J.M. Jowett*[6], *Y.-J. Lee*[53], *U.A. Wiedemann*[6], *M. Winn*[33,43]

Chapter coordinators:
A. Andronic[52], *F. Bellini*[6], *E. Bruna*[26], *E. Chapon*[6], *H. Dembinski*[51], *D. d'Enterria*[6], *I. Grabowska-Bold*[1], *G.M. Innocenti*[6,53], *C. Loizides*[61], *S. Mohapatra*[13], *C.A. Salgado*[38], *M. Verweij*[68,101], *M. Weber*[74]

Contributors:
J. Aichelin[71], *A. Angerami*[48], *L. Apolinario*[35,44], *F. Arleo*[45], *N. Armesto*[38], *R. Arnaldi*[26], *M. Arslandok*[19], *P. Azzi*[24], *R. Bailhache*[39], *S.A. Bass*[16], *C. Bedda*[99], *N.K. Behera*[36], *R. Bellwied*[88], *A. Beraudo*[26], *R. Bi*[53], *C. Bierlich*[50,59], *K. Blum*[6,103], *A. Borissov*[52], *P. Braun-Munzinger*[17], *R. Bruce*[6], *G.E. Bruno*[65], *S. Bufalino*[66], *J. Castillo Castellanos*[33], *R. Chatterjee*[100], *Y. Chen*[6], *Z. Chen*[69], *C. Cheshkov*[31], *T. Chujo*[97], *Z. Conesa del Valle*[8], *J.G. Contreras Nuno*[14], *L. Cunqueiro Mendez*[61], *T. Dahms*[18], *N.P. Dang*[92], *H. De la Torre*[54], *A.F. Dobrin*[6], *B. Doenigus*[39], *L. Van Doremalen*[99], *X. Du*[77], *A. Dubla*[17], *M. Dumancic*[103], *M. Dyndal*[15], *L. Fabbietti*[76], *E.G. Ferreiro*[38], *F. Fionda*[83], *F. Fleuret*[45], *S. Floerchinger*[19], *G. Giacalone*[32], *A. Giammanco*[81], *P.B. Gossiaux*[71], *G. Graziani*[23], *V. Greco*[82], *A. Grelli*[99], *F. Grosa*[66], *M. Guilbaud*[6], *T. Gunji*[10], *V. Guzey*[20,64,90], *C. Hadjidakis*[30], *S. Hassani*[34], *M. He*[56], *I. Helenius*[80,90], *P. Huo*[75], *P.M. Jacobs*[47], *P. Janus*[1], *M.A. Jebramcik*[6,39], *J. Jia*[4,75], *A.P. Kalweit*[6], *H. Kim*[12], *M. Klasen*[52], *S.R. Klein*[47], *M. Klusek-Gawenda*[21], *M. Konyushikhin*[102], *J. Kremer*[1], *G.K. Krintiras*[81], *F. Krizek*[2], *E. Kryshen*[64], *A. Kurkela*[6,73], *A. Kusina*[21], *J.-P. Lansberg*[30], *R. Lea*[96], *M. van Leeuwen*[60,99], *W. Li*[69], *J. Margutti*[99], *A. Marin*[17], *C. Marquet*[9], *J. Martin Blanco*[45], *L. Massacrier*[30], *A. Mastroserio*[86], *E. Maurice*[45], *C. Mayer*[21], *C. Mcginn*[53], *G. Milhano*[6,35,44], *A. Milov*[103], *V. Minissale*[29], *C. Mironov*[53], *A. Mischke*[*99], *N. Mohammadi*[6], *M. Mulders*[6], *M. Murray*[91], *M. Narain*[5], *P. Di Nezza*[28], *A. Nisati*[25], *J. Noronha-Hostler*[70], *A. Ohlson*[19], *V. Okorokov*[58], *F. Olness*[72], *P. Paakkinen*[90], *L. Pappalardo*[85], *J. Park*[42], *H. Paukkunen*[20,90], *C.C. Peng*[67], *H. Pereira Da Costa*[33], *D.V. Perepelitsa*[84], *D. Peresunko*[57], *M. Peters*[53], *N.E. Pettersson*[93], *S. Piano*[27], *T. Pierog*[40], *J. Pires*[7,35], *M. Płoskoń*[47], *S. Plumari*[82], *F. Prino*[26], *M. Puccio*[95], *R. Rapp*[77], *K. Redlich*[17,98], *K. Reygers*[19], *C.L. Ristea*[37], *P. Robbe*[43], *A. Rossi*[94], *A. Rustamov*[17,19,55], *M. Rybar*[13], *M. Schaumann*[6], *B. Schenke*[4], *I. Schienbein*[46], *L. Schoeffel*[34], *I. Selyuzhenkov*[17,58], *A.M. Sickles*[89], *M. Sievert*[70], *P. Silva*[6], *T. Song*[87], *M. Spousta*[11], *J. Stachel*[19], *P. Steinberg*[4], *D. Stocco*[71], *M. Strickland*[41], *M. Strikman*[63], *J. Sun*[78], *D. Tapia Takaki*[91], *K. Tatar*[53], *C. Terrevoli*[88], *A. Timmins*[88], *S. Trogolo*[95], *B. Trzeciak*[99], *A. Trzupek*[21], *R. Ulrich*[40], *A. Uras*[31], *R. Venugopalan*[4], *I. Vitev*[49], *G. Vujanovic*[62,102], *J. Wang*[53], *T.W. Wang*[53], *R. Xiao*[67], *Y. Xu*[16], *C. Zampolli*[6,22], *H. Zanoli*[79], *M. Zhou*[75], *Y. Zhou*[59]
[*] *deceased*

https://doi.org/10.23731/CYRM-2019-007.1159

[1] AGH University of Science and Technology, Kraków, Poland, [2] Academy of Sciences, Prague, Czech Republic,
[3] Ben-Gurion University of the Negev, Beersheba, Israel, [4] Brookhaven National Laboratory, Upton, USA,
[5] Brown University, Rhode Island, USA, [6] CERN, Geneva, Switzerland, [7] CFTP, Lisbon, Portugal,
[8] CNRS/IN2P3, Université Paris-Sud, Université Paris-Saclay, Orsay, France,
[9] CPHT, CNRS, École polytechnique, Université Paris-Saclay, Palaiseau, France,
[10] Center for Nuclear Study, Graduate School of Science, The University of Tokyo, Japan,
[11] Charles University, Prague, Czech Republic, [12] Chonnam National University, Gwangju, China,
[13] Columbia University, New York City, USA, [14] Czech Technical University in Prague, Czech Republic,
[15] DESY, Hamburg, Germany, [16] Duke University, Durham, USA,
[17] EMMI/GSI Helmholtzzentrum für Schwerionenforschung GmbH, Darmstadt, Germany,
[18] Excellence Cluster Universe, Technical University Munich, Germany, [19] Heidelberg University, Germany,
[20] Helsinki Institute of Physics, Finland, [21] IFJ PAN, PL-31342 Kraków, Poland, [22] INFN - Sezione di Bologna, Italy,
[23] INFN - Sezione di Firenze, Italy, [24] INFN - Sezione di Padova, Italy, [25] INFN - Sezione di Roma, Roma, Italy,
[26] INFN - Sezione di Torino, Italy, [27] INFN - Sezione di Trieste, Italy, [28] INFN-LNF, Frascati, Italy,
[29] INFN-LNS, Catania, Italy, [30] IPN Orsay, CNRS/IN2P3, Université Paris-Sud, Université Paris-Saclay, Orsay, France,
[31] IPN-Lyon, CNRS/IN2P3, Université de Lyon, Lyon, France,
[32] IPhT, CEA Saclay, CNRS, Université Paris-Saclay, Saclay, France,
[33] IRFU/DPhN, CEA Saclay, Université Paris-Saclay, Saclay, France,
[34] IRFU/DPhP, CEA Saclay, Université Paris-Saclay, Saclay, France, [35] IST Lisbon, Portugal,
[36] Inha University, Incheon, Korea, [37] Institute of Space Science, Bucharest, Romania,
[38] Instituto Galego de Fisica de Altas Enerxias (IGFAE), Universidade de Santiago de Compostela, Spain,
[39] Johann-Wolfgang-Goethe Universität, Frankfurt, Germany, [40] Karlsruhe Institute of Technology, Germany,
[41] Kent State University, USA, [42] Korea University, Seoul, Korea,
[43] LAL, CNRS/IN2P3, Université Paris-Sud, Université Paris-Saclay, Orsay, France, [44] LIP, Lisbon, Portugal,
[45] LLR, CNRS/IN2P3, École polytechnique, Université Paris-Saclay, Palaiseau, France,
[46] LPSC Grenoble, CNRS/IN2P3, Grenoble INP, Université Grenoble Alpes, Grenoble, France,
[47] Lawrence Berkeley National Laboratory, Berkeley, USA, [48] Lawrence Livermore National Laboratory, Livermore, USA,
[49] Los Alamos National Laboratory, Los Alamos, USA, [50] Lund University, Sweden,
[51] MPI for Nuclear Physics, Heidelberg, Germany, [52] Münster University, Germany,
[53] Massachusetts Institute of Technology, Cambridge, USA, [54] Michigan State University, East Lansing, USA,
[55] NNRC, Baku, Azerbaijan, [56] Nanjing University of Science and Technology, China,
[57] National Research Centre Kurchatov Institute, Moscow, Russia,
[58] National Research Nuclear University MEPhI, Moscow, Russia, [59] Niels Bohr Institute, Copenhagen, Denmark,
[60] Nikhef, Amsterdam, The Netherlands, [61] Oak Ridge National Laboratory, Oak Ridge, USA,
[62] Ohio State University, Columbus, USA, [63] Pennsylvania State University, University Park, USA,
[64] Petersburg Nuclear Physics Institute, Gatchina, Russia, [65] Politecnico di Bari and INFN - Sezione di Bari, Italy,
[66] Politecnico di Torino and INFN - Sezione di Torino, Italy, [67] Purdue University, West Lafayette, USA,
[68] RIKEN BNL Research Center, Upton, USA, [69] Rice University, Houston, USA,
[70] Rutgers University, New Brunswick, USA, [71] SUBATECH, CNRS/IN2P3, IMT Atlantique, Université de Nantes, France,
[72] Southern Methodist University, Dallas, USA, [73] Stavanger University, Norway,
[74] Stefan Meyer Institute Vienna, Austria, Austrian Academy of Sciences, [75] Stony Brook University, USA,
[76] Technical University Munich, Germany, [77] Texas A&M University, College Station, USA,
[78] Tsinghua University, Beijing, China, [79] Universidade de Sao Paulo, Brazil, [80] Universität Tübingen, Germany,
[81] Université catholique de Louvain, Louvain-la-Neuve, Belgium, [82] Università di Catania and INFN-LNS, Catania, Italy,
[83] University of Bergen, Norway, [84] University of Colorado Boulder, USA,
[85] University of Ferrara and INFN - Sezione di Ferrara, Italy, [86] University of Foggia and INFN - Sezione di Bari, Italy,
[87] University of Gießen, Germany, [88] University of Houston, USA, [89] University of Illinois, Urbana-Champaign, USA,
[90] University of Jyvaskyla, Finland, [91] University of Kansas, Lawrence, USA, [92] University of Louisville, USA,
[93] University of Massachusetts, Amherst, USA, [94] University of Padova and INFN - Sezione di Padova, Italy,

[95] University of Torino and INFN - Sezione di Torino, Italy, [96] University of Trieste and INFN - Sezione di Trieste, Italy,
[97] University of Tsukuba, Japan, [98] University of Wroclaw, Poland, [99] Utrecht University, The Netherlands,
[100] VECC Calcutta, India, [101] Vanderbilt University, Nashville, USA, [102] Wayne State University, Detroit, USA,
[103] Weizmann Institute of Science, Rehovot, Israel

Abstract

The future opportunities for high-density QCD studies with ion and proton beams at the LHC are presented. Four major scientific goals are identified: the characterisation of the macroscopic long wavelength Quark-Gluon Plasma (QGP) properties with unprecedented precision, the investigation of the microscopic parton dynamics underlying QGP properties, the development of a unified picture of particle production and QCD dynamics from small (pp) to large (nucleus–nucleus) systems, the exploration of parton densities in nuclei in a broad (x, Q^2) kinematic range and the search for the possible onset of parton saturation. In order to address these scientific goals, high-luminosity Pb–Pb and p–Pb programmes are considered as priorities for Runs 3 and 4, complemented by high-multiplicity studies in pp collisions and a short run with oxygen ions. High-luminosity runs with intermediate-mass nuclei, for example Ar or Kr, are considered as an appealing case for extending the heavy-ion programme at the LHC beyond Run 4. The potential of the High-Energy LHC to probe QCD matter with newly-available observables, at twice larger center-of-mass energies than the LHC, is investigated.

Contents

1 Introduction . . . 1165
1.1 Macroscopic QGP properties . . . 1167
1.2 Accessing the inner workings of hot QCD matter . . . 1168
1.3 Developing a unified picture of QCD collectivity across system size . . . 1170
1.4 Nuclear parton densities and search for non-linear QCD evolution . . . 1171
1.5 Physics performance studies by ALICE, ATLAS, CMS and LHCb . . . 1172
2 Heavy-ion performance of LHC, HL-LHC and HE-LHC . . . 1173
2.1 Heavy-ion performance of LHC in Runs 1 and 2 . . . 1173
2.2 Pb–Pb luminosity in Run 3 and Run 4 (HL-LHC) . . . 1173
2.3 Proton-lead operation in Run 3 and HL-LHC . . . 1176
2.4 Colliding lighter nuclei at HL-LHC . . . 1177
2.5 Short run for O–O and p–O . . . 1179
2.6 Heavy-ion performance of HE-LHC . . . 1180
3 Light flavour sector: (anti-)(hyper-)nuclei and fluctuations of conserved charges . . . 1182
3.1 Introduction . . . 1182
3.2 (Anti-)(hyper-)nuclei production . . . 1183
3.3 Fluctuations of conserved charges . . . 1191
4 Flow and Correlations . . . 1197
4.1 Introduction . . . 1197
4.2 Review of current status of theory on bulk and flow observables . . . 1197
4.3 Experimental constraints from Run 3 and 4 . . . 1200
4.4 Vorticity and polarization . . . 1204
4.5 Chiral Magnetic Effect . . . 1205
4.6 Summary . . . 1208
5 Open heavy flavour . . . 1209
5.1 Perspectives for heavy-flavour observables in LHC Run 3 and 4 . . . 1209
5.2 Impact of detector upgrades on heavy-flavour measurements . . . 1210
5.3 Nuclear modification factor and collective flow . . . 1211
5.4 Studies of heavy-quark hadronisation . . . 1215
5.5 Heavy-flavour correlations and jets . . . 1219
5.6 Sensitivity to early magnetic fields and vorticity phenomena . . . 1221
5.7 Heavy flavour measurements in small colliding systems . . . 1222
6 Jets and parton energy loss . . . 1226
6.1 Introduction . . . 1226
6.2 Out-of-cone radiation . . . 1227
6.3 Jet deflection . . . 1228
6.4 Jet internal structure . . . 1232
6.5 Opportunities for jet quenching studies with light-ion collisions . . . 1239

7 Quarkonia . . . 1242
7.1 Introduction . . . 1242
7.2 Charmonia in Pb–Pb collisions . . . 1244
7.3 Bottomonia in Pb–Pb collisions . . . 1246
7.4 Quarkonia in p–Pb and pp collisions . . . 1249
8 Electromagnetic radiation . . . 1253
8.1 Thermal radiation and in-medium spectral function . . . 1253
8.2 Two-photon and photonuclear interactions . . . 1261
8.3 Dark photons . . . 1265
8.4 Limitations and outlook . . . 1266
9 Emergence of hot and dense QCD matter in small systems . . . 1269
9.1 Introduction . . . 1269
9.2 Overview of experimental results and critical assessment . . . 1271
9.3 Open questions and new opportunities at HL-LHC . . . 1275
9.4 Proton–proton collisions at extreme multiplicities . . . 1276
9.5 Global-event properties . . . 1278
9.6 Particle correlations . . . 1279
9.7 Strangeness enhancement . . . 1282
9.8 Energy loss . . . 1283
9.9 Thermal Radiation . . . 1285
9.10 Potential of O–O Collisions . . . 1285
9.11 Summary . . . 1287
10 High energy QCD with proton-nucleus collisions and ultra-peripheral collisions . . . 1290
10.1 Introduction . . . 1290
10.2 The physics of ultra-peripheral collisions . . . 1292
10.3 The physics of inelastic p-Pb collisions . . . 1303
10.4 Constraints on nuclear PDFs . . . 1310
10.5 Perspectives with lighter ions . . . 1315
11 Other opportunities with ion and proton beams at the LHC . . . 1318
11.1 Physics motivation for collisions of light ions . . . 1318
11.2 Physics of $\gamma\gamma$ interactions in heavy-ion collisions . . . 1322
11.3 Proton-oxygen collisions for cosmic ray research . . . 1329
11.4 Fixed-target prospects with LHC beams . . . 1332
12 Summary of luminosity requirements and proposed run schedule . . . 1338
13 First considerations on a heavy-ion programme at a High Energy LHC (HE-LHC) . . . 1340
13.1 Introduction . . . 1340
13.2 Global characteristics of nucleus–nucleus collisions at the HE-LHC . . . 1341
13.3 QGP studies with hard probes . . . 1341
13.4 Nuclear PDF measurements and search for parton saturation . . . 1345

13.5 Photon–photon collisions 1346

1 Introduction

Experiments with heavy-ion collisions at the LHC create and diagnose strongly-interacting matter under the most extreme conditions of high density and temperature accessible in the laboratory. Under these conditions, QCD calculations on the lattice predict that matter undergoes a phase transition to a Quark–Gluon Plasma (QGP) in which colour charges are deconfined and chiral symmetry is restored. Aside of its intrinsic interest, this line of research is central to our understanding of the Early Universe and the evolution of ultra-dense stars. In practice, the main focus of experimentation with nuclear beams at the LHC is on learning how collective phenomena and macroscopic properties, involving many degrees of freedom, emerge under extreme conditions from the microscopic laws of strong-interaction physics. In doing so, proton–nucleus (p–A) and nucleus–nucleus (A–A) collision experiments at the LHC aim at applying and extending the Standard Model of particle physics to matter properties that govern dynamically evolving systems of finite size.

Recent experiments with nuclear beams at collider energies have identified opportunities to further strengthen the connection between the rich phenomenology of ultra-dense matter, and its understanding in terms of the fundamental laws of strong-interaction physics. Two broad classes of phenomena may be highlighted in this context.

First, the observation of flow-like phenomena in essentially all measured soft particle spectra and particle correlations lends strong support to understanding bulk properties of heavy-ion collisions in terms of viscous fluid dynamics. The fluid-dynamic evolution is solely based on combining conservation laws with thermodynamic transport theories that are calculable from first principles in quantum field theory. Hence, this provides an experimentally accessible inroad to constraining QCD matter properties via soft flow, correlation and fluctuation measurements. As further explained in this document, this motivates future improved measurements of flow and transport phenomena, including in particular measurements of soft heavy flavour and electromagnetic radiation. It also motivates improved experimental control over the system-size dependence of flow phenomena to better constrain under which conditions and in which kinematic regime ultra-relativistic p–A and A–A collisions show fluid dynamic behaviour and where this picture fails.

Second, the observation of quantitatively-large quenching phenomena in essentially all measured hard hadronic observables in A–A collisions has established the feasibility of testing the produced QCD matter with a broad set of probes whose production rates are controlled with good precision with pp reference measurements and perturbative QCD calculations. Hard quarks and gluons are known to interact with the medium and they thus *probe* medium properties. As detailed in this document, important physics opportunities are related to analysing hard probes in p–A and A–A collisions with the greater precision and kinematic reach accessible in future LHC runs. For instance, the identification of (Rutherford-type) large-angle jet-medium scattering could constrain the quasi-particle nature of the fluid-like medium. This is of central importance since it critically tests the working hypothesis that the matter produced in A–A collisions is a fluid with a ratio of shear viscosity over entropy density η/s close to the theoretical minimum value. Such a fluid would be void of quasi-particles, while QCD is definitive in predicting that a microscope with sufficiently high resolution will reveal partonic (quasi-)particle structure. Identifying the scale at which inner structure (such as quasi-particles and related non-vanishing mean free paths) arises would provide a microscopic understanding of how fluid-like behaviour arises in nucleus–nucleus collisions. Therefore, probing the inner workings of the QGP by resolving its properties at shorter and shorter length scales is one of the main motivations for future experimentation with hard probes. Also at intermediate transverse momentum, this document identifies important questions that will be accessible experimentally. For instance, more differential studies of quarkonium bound-state dissociation as a function of transverse momentum, rapidity and system size are expected to yield further insights into the mechanisms of colour deconfinement and recombination. Moreover, there is the general question of how fluid-like phenomena at low momentum scales transition

to quenching phenomena at intermediate and high momentum scales.

Capitalizing on previous discoveries at RHIC, the LHC experimental programme with Pb–Pb and p–Pb collisions has significantly advanced the state of the art in both the soft- and the hard-physics sector. In the soft-physics sector, differential measurements at the LHC have in particular allowed for precise p_{T}, particle species and rapidity-dependent measurements of all higher flow harmonics v_{n}, their mode–mode couplings and the resulting reaction-plane correlations. This flow systematics extends to charmed flavoured hadrons and possibly even to beauty ones. It is at the basis of constraining QCD transport properties today. In the hard-physics sector, the wider kinematic reach of LHC has given qualitatively novel access to quarkonium suppression and jet-quenching phenomenology, including precision measurements of bottomonium, novel observations of charmonium enhancement, and a rich phenomenology of calorimetrically defined jets and jet substructure in nuclear collisions.

LHC experiments have also led to surprises that pose significant novel challenges for the understanding of p–A and A–A collisions. Most notable in this context is the discovery that flow-like phenomena are not limited to nucleus–nucleus collisions but they persist with significant magnitude in p–A collisions and in high-multiplicity pp collisions at the LHC and some of their signatures have been observed even in minimum-bias pp collisions. However, pp collisions are typically expected to show vanishingly small re-interaction rates between produced final-state particles. In contrast, the perfect-fluid paradigm, that underlies the successful phenomenology of flow-like phenomena in nucleus–nucleus collisions implicitly, assumes that re-interaction rates are so large that even the notions of quasi-particle and mean-free path become meaningless. Does the persistence of flow-like phenomena in p–A and pp collisions indicate, in contrast to previous belief, that the perfect-fluid paradigm applies to these smaller collision systems? Or, if the prefect-fluid paradigm is not applicable to pp and p–A collisions, is it conceivable that significant corrections to a fluid-dynamic picture of vanishing mean free path persist also in the larger A–A collision systems? The LHC discoveries in pp and p–A collisions that give rise to these questions provide arguably the strongest motivation for a future programme of detailed experimentation that aims at constraining microscopic structures and length-scales in the produced QGP matter and that is expected to clarify in this way the microscopic mechanisms underlying the apparent fluid-dynamic behaviour of pp, p–A and A–A collisions.

Historically, experimental heavy-ion programmes have always addressed a very diverse set of phenomenological opportunities. Some of the proposed experimental measurements have always reached out to other areas of science and could be clearly related to fundamental open question such as the origin of mass in the Universe, QCD deconfinement, or the determination of thermodynamic transport properties (that led in the past to unforeseen connections between string theory and the thermodynamics of quantum field theories). Other parts of the experimental programme were originally not related to a working hypothesis based on an open fundamental question, but they sometimes revealed themselves a posteriori as elements of crucial insight. This can be said for instance about the LHC p–A programme, that was not part of the original LHC design, that was first conceived mainly as a set of benchmark measurements for establishing the cold nuclear matter baseline for interpretation of heavy-ion data, and that has resulted in one of the most surprising discoveries made in the LHC nuclear-beams programme. We therefore emphasize that heavy-ion physics at the LHC, in the future as well as in the past, is likely to have multiple ways of reaching out and contributing to physics at large. At the time of writing this report, questions about the origin of collectivity in small pp and p–A collision systems, and their implications for the interpretation of collective phenomena observed in A–A collisions, are arguably identified as the most pressing conceptual issue in the scientific debate. As outlined so far, they are clearly related to further experimentation with soft processes, and to research on the internal structure of QGP matter utilizing hard processes. However, future experimentation at the LHC is not limited to this set of questions. From improved constraints on nuclear parton distribution functions that may inform us about the physics reach of future electron–ion facilities, to improved measurements of anti-nuclei, to ultra-peripheral colli-

sions of electromagnetic Weizsäcker-Williams photons at unprecedented field strength, to the search for qualitatively novel signatures of ultra-strong QED magnetic fields, the LHC nuclear beams programme can provide new insight in a much broader range of subject areas.

As detailed in this report, the HL/HE-LHC physics working group 5 has identified future physics opportunities for high-density QCD with ions and proton beams that can be grouped broadly into the following four goals that are coming now within experimental reach:

1. Characterizing the macroscopic long-wavelength QGP properties with unprecedented precision.
2. Accessing the microscopic parton dynamics underlying QGP properties.
3. Developing a unified picture of particle production from small (pp) to larger (p–A and A–A) systems.
4. Probing parton densities in nuclei in a broad $(x,\, Q^2)$ kinematic range and searching for the possible onset of parton saturation.

In the following, we summarize how the four general goals are addressed by the measurements discussed in this report. As the density and temperature attained in hadronic collisions changes mildly but distinctly with the centre-of-mass energy, the physics opportunities listed below can be further enhanced by a combined interpretation of future measurements at the LHC and at RHIC. In particular, new or upgraded experiments at RHIC aim at providing measurements of highly-improved quality and precision in the sectors of hard probes (jets and jet correlations, heavy flavour, quarkonia) and electromagnetic observables.

1.1 Macroscopic QGP properties

At sufficiently long wavelength, essentially all forms of matter can be described by fluid dynamics. The observation of flow-like behaviour in nucleus–nucleus collisions and in smaller collision systems demonstrates that this universal long-wavelength limit of hot and dense QCD matter can be accessed experimentally at the LHC. This provides an experimental inroad to fundamental questions about QCD thermodynamics and hydrodynamics since i) the QGP properties entering a fluid dynamic description are calculable from first principles in quantum field theory, and ii) hydrodynamic long wavelength properties depend on the effective physical degrees of freedom in the plasma and they are thus sensitive to the microscopic dynamics that governs their interactions. The following properties of the QCD matter produced in TeV-scale collisions are accessible via future measurements at the LHC

1. *Temperature*
   Within the programme of determining the QCD equation of state, QCD lattice simulations at finite temperature have established since long a precise relation between the QCD energy density and pressure that determine the fluid dynamic expansion, and the temperature of QCD matter. While energy density and pressure can be constrained experimentally by many measurements, an independent determination of temperature is of great value for testing the idea of local equilibration in heavy-ion collisions or for establishing deviations thereof. Future LHC experiments will constrain the temperature and its time evolution with unprecedented precision, in particular via thermal radiation of real and virtual (dileptons) photons (Chapter 8).
2. *QCD phase transition at* $\mu_B \simeq 0$
   Collisions at the LHC realize systems of close-to-zero baryo-chemical potential. QCD calculations on the lattice predict in this regime a smooth cross-over transition from a hot partonic plasma

to a cold hadron gas. Fluctuation measures of conserved charges are sensitive to the characteristics of the phase transition. In future LHC experiments, they are accessible with unprecedented precision and completeness (Chapter 3). Future measurements of low-mass dileptons will also be, for the first time at the TeV-scale, sensitive to in-medium modifications of the ρ-spectral function (Chapter 8). This provides unique access to the transition between phases with restored and broken chiral symmetry that is predicted by lattice QCD.

3. *Viscosity and further QCD transport coefficients*
   Existing flow measurements provide tight upper bounds on the value of η/s and they have been a cornerstone in supporting the perfect-fluid paradigm. In the future, measuring higher-order cross-correlations of flow coefficients will significantly extend this line of research. In addition, we note that the value of η/s can be related to the existence and size of the mean free path (isotropization length scale), which in turn results from the existence of (quasi-)particle-like excitations in the produced matter. This motivates increasing the precision on η/s with the aim of establishing the tightest lower bound on this quantity (Chapter 4), and it motivates detailed studies of flow in smaller systems with the idea of identifying the scale at which the system size becomes comparable to the mean free path (Chapter 9). Also, measurements of soft dileptons will give access to the electric conductivity of the strongly interacting medium (Chapter 8), and flow and correlation measurements may help to constrain the bulk viscous corrections (Chapter 4).

4. *Heavy-quark transport coefficients*
   Heavy quarks provide unique tools for testing collective phenomena in nuclear collisions. As they are produced in initial hard-scattering processes and flavour is conserved throughout the collective dynamical evolution, they are the best experimental proxy to the idea of putting coloured test charges of well-defined mass into the medium and testing how they participate in the evolution. Of particular interest are precision measurements of transverse-momentum anisotropies v_{n} and nuclear-modification factors of open heavy-flavoured mesons that are known to constrain e.g. the heavy-quark diffusion coefficient $2\pi T D_s$ and its dependence on the temperature T, that can be compared to first-principle calculations of QCD on the lattice (Chapter 5).

5. *Searching for transport phenomena related to the presence of strong electrodynamic fields.*
   Heavy-ion collisions produce the largest electromagnetic field of any system accessible to laboratory experiments. The field is largest in the early phase of the collision, thus the early-produced heavy quarks are expected to be the most sensitive to its strength (Chapter 5). As the maximal field strengths are estimated to be of the order of the pion mass ($e\,B^2 \sim m_\pi^2$), effects are also likely to be present for light-flavour charged hadrons (Chapter 4). Other measurements of interest include transport coefficients such as the electric conductivity with which the plasma responds to an electromagnetic field, and that are calculable within QCD. In addition, as a consequence of the chiral anomaly, QCD coupled to QED gives rise to *anomalous hydrodynamics* that displays various qualitatively novel phenomena, including for instance a component of the electromagnetic currents that flows parallel to the magnetic field. The existence of these anomalous phenomena follows from first principles in field theory and thermodynamics, but the size of potential experimental signatures is model-dependent. Beyond determining conventional QED transport phenomena, LHC allows to search with increased precision for these intriguing signatures of anomalous fluid dynamics (Chapter 4).

1.2 Accessing the inner workings of hot QCD matter

Previous experiments at the LHC and at lower centre-of-mass energy have established that the QCD matter produced in nucleus–nucleus collisions is subject to strong collective evolution. However, the

nature of the effective constituents of that matter, and its characteristic inner length scales (such as screening lengths or mean scattering times, if any) are not yet understood. The scale dependence of QCD implies that one must be able to resolve partonic constituents of hot QCD matter at sufficiently high resolution scale. This motivates the use of high-momentum transfer processes (hard probes) to study the inner workings of hot QCD matter. In addition, the current status of phenomenological modelling does not exclude the existence of a sizeable mean free path of hot QCD matter (which is assumed in transport model simulations of heavy-ion collisions, but which is not assumed in almost perfect fluid dynamic models). This motivates to learn about the inner workings at hot QCD matter also from particle production at intermediate transverse momentum (such as heavy quark transport at intermediate and low p_{T}). Here, we highlight the following opportunities for further experimentation.

1. *Constraining with jet quenching the colour field strength of the medium*
   In general, the fragments of jets produced in nucleus–nucleus collisions are medium-modified due to interactions with the hot QCD matter. These jet quenching effects depend on the inner structure of that matter. In particular, the average medium-induced colour field strength experienced by the escaping jet can be quantified e.g. with the quenching parameter $\hat{q}$, which measures the average exchanged transverse momentum squared per unit path length. Experiments at the LHC will provide improved constraints on this field strength measurement (Chapter 6). Qualitatively novel opportunities for testing the time evolution of the medium opacity to hard partons could arise if boosted tops could be studied in nuclear matter. A run at the LHC with lighter (than Pb) nuclei, like e.g. $^{40}\mathrm{Ar}$, would provide sufficient luminosity to this end, as well as largely enhanced kinematic and statistics reach for γ–jet and Z–jet recoil measurements (Chapter 11.1). The opportunities for boosted top measurements in Pb–Pb and lighter nuclei collisions at the HE-LHC are also discussed (Chapter 13).

2. *Investigating the quasi-particle structure of QCD matter with jet and heavy-quark measurements*
   Hard quarks and gluons with different energies can be used to investigate the constituents of the QCD matter at various resolution scales. On one side of the scale, high-energy quarks and gluons (leading to high-energy jets) address the smallest spatial scale. While $\hat{q}$ characterizes the effects of jet–medium interactions in the coherent regime in which individual constituents in the medium are not resolved, Z/γ–jet correlations and modern jet substructure measurements on the high-statistics samples of future LHC Runs are expected to access a regime of Rutherford-type large angle jet–medium scattering, in which the detection of recoil or of large angle deflections gives insight into the microscopic structure of the produced matter (Chapter 6). On the other side of the scale, the scattering of low-momentum heavy quarks, characterized using for example the diffusion coefficient, addresses the nature of the QCD constituents at long-wavelength scale (Chapter 5).

3. *Testing colour screening with bottomonium production*
   The family of bottomonium bound states gives access to a set of well-defined length scales that are embedded in the hot and dense QCD matter. As a consequence, the dissociation of the various bound states sensitively depends on the interplay of color screening and the coupling to the strongly interacting medium through dissociation reactions. This opens a unique window on the in-medium modifications of the fundamental QCD force that binds bottomonium. Increasingly-tight bound states are expected to melt with increasing temperature, providing a laboratory for in-medium spectroscopy. The increased precision of future measurements will allow to test for additional physics mechanisms in the production of bottomonium, such as regeneration processes that may affect the yield of $\Upsilon(2\mathrm{S})$ and $\Upsilon(3\mathrm{S})$. Also, the higher rates of future experiments will allow one to cross-correlate measurements of bottomonium suppression with other manifestations of collectivity, such as elliptic flow (Chapter 7).

4. *Testing colour screening and regeneration dynamics with charmonium production*
   In close similarity to bottomonium, the medium-modification of charmonium bound states is sensitive to colour screening and it is subject to the same QCD dissociation dynamics. However, since charm quarks and anti-quarks are produced abundantly in nucleus–nucleus collisions at the TeV scale, c and $\bar{\mathrm{c}}$ produced in different hard processes can form bound states. Indications of this qualitatively novel bound-state formation process are accessible at low and intermediate transverse momentum, and they motivate high-precision measurements of nuclear modification factor R_{AA} and elliptic flow v_2. In addition, future open heavy-flavour measurements reaching down to zero p_{T} with high precision will help to determine the total charm cross section which is a central input for the precise quantification of regeneration (Chapters 5 and 7).

5. *Formation of hadrons and light nuclei from a dense partonic system*
   The question of how a collective partonic system of many degrees of freedom evolves into the hadronic phase and produces colour singlet hadrons and light nuclei is essential for a complete dynamical understanding of nucleus–nucleus collisions. Recent LHC measurements in proton–proton and proton–nucleus collisions suggest that also in small-system hadronic collisions the hadronization process may be modified with respect to elementary $\mathrm{e}^+\mathrm{e}^-$ collisions. Future measurements at the LHC will enable comparative and multi-differential studies of these modifications with unprecedented precision, for both the heavy-flavour sector (D_s^+, B_s^0, charm and beauty baryons, see Chapter 5) and for light nuclei and hyper-nuclei (Chapter 3). For open heavy flavour, these measurements are also crucial to disentangle the role of mass-dependent radial flow and of recombination, as well as to constrain the parameters of hadronization in the models that are used to estimate QGP properties like the heavy-quark diffusion coefficients. For light nuclei, precise measurements of nuclei and hyper-nuclei with mass numbers 3 and 4 as well as possible observation of exotic baryonic states will address the question whether their production is dominated by coalescence of protons, neutrons and Λ baryons or by statistical hadronization of a partonic system. These measurements, in addition to that of high-momentum deuteron production, also have important astrophysical implications (dense compact stars as well as dark matter searches in the Cosmos).

1.3 Developing a unified picture of QCD collectivity across system size

As discussed at the beginning of this chapter, recent LHC discoveries of signatures of collectivity in proton–nucleus and in proton–proton collisions question common beliefs. For the smallest collision systems, these measurements indicate that more physics effects are at work in multi-particle production than traditionally assumed in the modelling of proton–proton collisions. For the larger collision systems (proton–nucleus and nucleus–nucleus collisions), they question whether the origin of signatures of collectivity is solely (perfect) fluid dynamical, given that these signatures persist in proton–proton collisions. This raises important qualitative questions like: What is the smallest length scale on which QCD displays fluid-dynamic behaviour? Is there a non-vanishing characteristic mean free path for the production of soft and intermediate p_{T} hadrons, and if so, is it smaller or larger than the proton diameter? What are the novel physics concepts with which underlying event simulations in proton–proton collisions need to be supplemented (e.g. in multi-purpose event generators) to account for the totality of observed phenomena? While some of these questions sound technical, it needs to be emphasized that the size of dissipative properties of QCD matter, such as its shear viscosity, are quantitatively related to the presence or absence of intrinsic length scales such as a mean free path. Any systematic experimental variation of the system size therefore relates directly to a search for intrinsic length scales that determine the dissipative properties of hot QCD matter. Within the present report, we identify in particular the following future opportunities for an improved understanding of the system-size dependence of collective phenomena (Chapter 9):

1. *Flow measurements in* pp *and* p–A *systems: Onset and higher-order correlations*
While flow signals have been established in smaller collision systems in recent years, their detailed characterization lacks behind the state of the art achieved in nucleus–nucleus collisions. Future measurements will allow for characterizing higher-order cumulants in largely non-flow suppressed multi-particle correlations, and test whether there is a system-size dependence in the characteristic correlations between different flow harmonics v_{n}, or the characteristic reaction plane correlations.

2. *Flow of heavy flavour and quarkonium in smaller systems*
Is there a minimal system size needed to transport heavy quarks within a common flow field? Given that the local hard production of heavy flavour is expected to be independent of any collective direction, precision measurements of heavy-flavour flow in pp and p–A collisions will provide decisive tests of heavy quark transport, thus experimentally addressing the question of how QCD flow field build up efficiently and on short length and time scales.

3. *Strangeness production as a function of system size*
One of the recent surprising LHC discoveries that is not accounted for in traditional models of minimum-bias pp collisions but that may be accounted for in a thermal picture is the smooth increase of strangeness with event multiplicity across system size. We discuss in detail how future measurement at the LHC, such as the study of strange D-mesons or baryons, can extend the systematics underlying this observation (Chapters 5 and Section 9.7).

4. *Searching for the onset/existence of energy-loss effects in small systems*
All dynamical models of collectivity involve final-state interactions. This implies the existence of jet–medium final-state interactions and, a fortiori, the existence of parton energy-loss effects. The latter have not been identified experimentally, yet. In this report, we discuss novel opportunities to test for their existence, including tests in future p–Pb collisions, as well as opportunities specific to O–O collisions.

5. *Searching for the onset/existence of thermal radiation in small systems*
If the collectivity observed in smaller collision systems is due to final-state isotropization and equilibration phenomena, it must be accompanied by thermal radiation. The search for the corresponding conceptually clean electromagnetic signatures, such as thermal dilepton and photon production in p–Pb collisions, is an important part in developing a unified picture of QCD collectivity. This report discusses the experimental opportunities in light of experimental upgrades.

1.4 Nuclear parton densities and search for non-linear QCD evolution

Future experiments at the LHC offer a variety of opportunities for precision measurements with nuclear beams. Here, we highlight three opportunities that are clearly related to the main physics challenges of the heavy-ion programme (Chapter 10):

1. *Precise determination of nuclear PDFs at high* Q^2
As high-momentum transfer processes have a short space-time scale, they are not affected by the long-wavelength particle excitations of the QCD matter in nuclear collisions. This implies that the primary production rates of hard processes in nucleus–nucleus collisions are determined perturbatively, whereas their medium modifications arise from traversing a dense QCD matter of considerable spatial extent and considerable colour-field strength. For a dynamical understanding of jet quenching, control over primary-production rates is indispensable and this necessitates the knowledge of nuclear parton distribution functions. Global nPDF-fits that reflect the current state of the art of nuclear parton distributions could be improved at the LHC in the near future at high

Q^2 and $x \sim 10^{-3}$–10^{-2} in particular with high-precision W, Z and dijets measurements in p–Pb and Pb–Pb collisions (Sections 10.3 and 10.4). High-luminosity Ar–Ar collisions would enable for the first time using top quarks to constrain nuclear PDFs at very high Q^2 and large $x \sim 10^{-2}$–10^{-1} and would contribute to constraining experimentally the nuclear mass number A dependence of nuclear PDFs.

2. *Constraining nuclear PDFs at low Q^2*
   Drell-Yan and photon measurements (Section 10.3) in p–Pb collisions could provide significantly improved constraints on the nuclear parton distribution functions at low Q^2 and low $x \sim 10^{-5}$–10^{-3}, where nuclear effects are larger. In addition, although so far global PDFs do not use measurements from ultra-peripheral collisions (UPC), it is thought that quarkonia and dijet production in UPC can constrain nuclear PDFs in the future. This report identifies opportunities for the corresponding measurements (Section 10.2).

3. *Access to non-linear QCD evolution at small-x*
   The scale-dependence of parton distribution functions is known to obey linear QCD evolution equations within a logarithmically wide range in Q^2 and $\ln x$. However, where partonic density in the incoming hadronic wave function are not perturbatively small, qualitatively novel non-linear density effects are expected to affect the QCD evolution. For Q^2 smaller than a characteristic saturation scale $Q_s^2(x)$, these effects are dominant, and as the saturation scale $Q_s^2(x)$ increases with decreasing x, one expects on general grounds at sufficiently small $\ln x$ a qualitatively novel saturation regime in which non-linear QCD evolution occurs at perturbatively large Q^2. Future measurements at LHC will provide novel test for these saturation effects with previously unexplored measurements (Section 10.3). The larger centre-of-mass energy of the HE-LHC would extend the small-x coverage by an additional factor two. Measurements of relevance include in p–Pb collisions dilepton and photon production at small-x and forward measurements of dihadron and dijet correlations. The perspectives for such measurements are discussed in Chapter 13.

1.5 Physics performance studies by ALICE, ATLAS, CMS and LHCb

The performance results presented in this report were obtained by experimental groups within the four Collaborations and they are described in more detail in these documents: ALICE [1–4], ATLAS [5–7], CMS [8–12], LHCb [13]. Two types of results are included: *simulation* studies used full or fast simulations of the detector setups for Run 3 and/or Run 4; *projection* studies are based on existing measurements where their uncertainties have been reduced as expected with the future detectors and data samples. The impact of the detector upgrades on the various observables is discussed in the corresponding chapters and in more detail in the referenced documents by the Collaborations. The integrated luminosities used for the physics studies are summarised in Chapter 12.

2 Heavy-ion performance of LHC, HL-LHC and HE-LHC

Coordinator: John M. Jowett (CERN)

Contributors: R. Bruce (CERN), M. Schaumann (CERN), M.A. Jebramcik (Johann-Wolfgang-Goethe Universität, Frankfurt & CERN)

2.1 Heavy-ion performance of LHC in Runs 1 and 2

The 2018 Pb–Pb run of the LHC brought Run 2 to an end and launched the hardware upgrades to the collider, and to the ALICE experiment, that should allow the full "HL-LHC" heavy-ion performance to be delivered from 2021 onward. Beyond pp collisions, the 2004 LHC Design Report [14], specified only Pb–Pb collisions with a peak Pb–Pb luminosity of $L = 1 \times 10^{27}\,\mathrm{cm}^{-2}\mathrm{s}^{-1}$. Now, much of the upgraded performance is already in hand. Not only has that peak Pb–Pb luminosity goal been exceeded by a factor of more than 6, but the p–Pb collision mode—an upgrade beyond the initial design whose feasibility was widely doubted—has yielded similarly high luminosity in multiple operating conditions (see Ref. [15] and references therein). Table 1 summarises the main parameters of the runs to date. Additionally, in 2017, the LHC has collided beams of Xe nuclei [16], providing many new results and demonstrating the potential for colliding lighter species. The goal for 2018 was to complete the accumulation of an integrated Pb–Pb luminosity of $1\,\mathrm{nb}^{-1}$ to each of the ALICE, ATLAS and CMS experiments and this was substantially exceeded. The LHCb experiment also received over $0.26\,\mathrm{nb}^{-1}$.

2.2 Pb–Pb luminosity in Run 3 and Run 4 (HL-LHC)

The High Luminosity LHC (HL-LHC) is an upgrade of the LHC to achieve instantaneous pp luminosities a factor of five larger than the LHC nominal value. Its operational phase is scheduled to start in LHC Run 4, in the second half of the 2020s, for the pp physics programmes described in the other chapters of this report. The HL-LHC project also includes hardware upgrades of the present LHC that will allow the LHC to operate with potential peak Pb–Pb luminosities an order of magnitude larger than the nominal [14]. These upgrades will be completed during Long Shutdown 2 and can already be exploited in Run 3, starting in 2021. Upgrades to the heavy-ion injector chain, in the framework of the LHC Injectors Upgrade project will increase the total stored intensity of heavy-ion beams and will also be completed for Run 3. Finally, the ALICE experiment will be upgraded to accept higher peak luminosity.

The heavy-ion performance of the LHC will be similar in Run 3 and in Run 4. Therefore, the two Runs are discussed together in this report in terms of their contribution to the HL-LHC heavy-ion physics programme. Presently achieved performance of the injectors [18] and collider [19] indicate that the performance parameters given in the last column of Table 1 will be achieved the upgrades planned for the LHC's Long Shutdown 2. In a typical one-month Pb–Pb run, this will yield an integrated luminosity of $3.1\,\mathrm{nb}^{-1}$. The necessary single-bunch intensities have already been attained but an implementation of slip-stacking in the SPS will be required to obtain a basic bunch spacing of 50 ns and store over 1200 Pb bunches in each LHC ring. The necessary upgrades of the SPS RF system will be implemented during LS2 and it is planned to commission this new mode of operation in 2021.

2.2.1 Secondary beams from the IPs

Ultra-peripheral electromagnetic interactions of Pb nuclei lead to copious lepton-pair production. Most of this is innocuous except for the (single) bound-free pair production (BFPP1):

$$^{208}\mathrm{Pb}^{82+} + ^{208}\mathrm{Pb}^{82+} \longrightarrow ^{208}\mathrm{Pb}^{82+} + ^{208}\mathrm{Pb}^{81+} + e^{+}, \tag{1}$$

in which the electron is bound to one nucleus. As extensively discussed in e.g. Refs. [20–22] and elsewhere, the modified nuclei emerge from the collision point, as a narrow secondary beam with modified

Table 1: Representative simplified beam parameters at the start of the highest luminosity physics fills, in conditions that lasted for $> 5\,\mathrm{days}$, in each annual Pb–Pb run (Ref. [15] and references therein). The original design values for Pb–Pb [14] collisions and future upgrade Pb–Pb goals are also shown (in this column the integrated luminosity goal is to be attained over the 4 Pb–Pb runs in the 10-year periods before and after 2020). Peak luminosities are averages for ATLAS and CMS (ALICE being levelled). The smaller luminosities delivered to LHCb from 2013–2018 are not shown. Emittance and bunch length are RMS values. The series of runs with $\sqrt{s_{\mathrm{NN}}} = 5.02\,\mathrm{TeV}$ also included pp reference runs, not shown here. Design and record achieved nucleon-pair luminosities are boxed, and some key parameters related to p–Pb parameters in Table 2 are set in red type, for easy comparison. The upgrade peak luminosity is reduced by a factor $\simeq 3$ from its potential value by levelling.

Quantity	design	achieved				upgrade
Year	(2004)	2010	2011	2015	2018	≥2021
Weeks in physics	-	4	3.5	2.5	3.5	-
Fill no. (best)		1541	2351	4720	7473	-
Beam energy $E[Z\,\mathrm{TeV}]$	7	3.5		6.37	6.37	7
Pb beam energy $E[A\,\mathrm{TeV}]$	2.76	1.38		2.51	2.51	2.76
Collision energy $\sqrt{s_{\mathrm{NN}}}\,[\mathrm{TeV}]$	5.52	2.51		**5.02**	**5.02**	5.52
Bunch intensity $N_b\,[10^8]$	0.7	1.22	1.07	2.0	2.2	1.8
No. of bunches k_b	592	137	338	518	733	1232
Pb norm. emittance $\epsilon_N\,[\mu\mathrm{m}]$	1.5	2.	2.0	2.1	2.0	1.65
Pb bunch length σ_z m	0.08			0.07–0.1		0.08
β^* [m]	0.5	3.5	1.0	0.8	0.5	0.5
Pb stored energy MJ/beam	3.8	0.65	1.9	8.6	13.3	21
Luminosity $L_{\mathrm{AA}}\,[10^{27}\mathrm{cm}^{-2}\mathrm{s}^{-1}]$	1	0.03	0.5	3.6	6.1	7
NN luminosity $L_{\mathrm{NN}}\,[10^{30}\mathrm{cm}^{-2}\mathrm{s}^{-1}]$	43	1.3	22.	156	264	303
Integrated luminosity/experiment $[\mu\mathrm{b}^{-1}]$	1000	9	160	433,585	900,1800	10^4
Int. NN lumi./expt. $[\mathrm{pb}^{-1}]$	43	0.38	6.7	19,25.3	39,80	4.3×10^5

magnetic rigidity, following a dispersive trajectory that impacts on the beam screen in a superconducting magnet in the dispersion suppressor (DS) downstream. These secondary beams emerge in both directions from every interaction point (IP) where ions collide. Each carries a power of

$$\mathrm{P}_{\mathrm{BFPP}} = L\sigma_{\mathrm{BFPP}}E_b, \tag{2}$$

where L is the luminosity and $\sigma_{\mathrm{BFPP}} \simeq 276\,\mathrm{b}$ is the cross-section at the 2015/18 run energy of $E_b = 6.37Z\,\mathrm{TeV}$. These losses carry much greater power than the luminosity debris (generated by the nuclear collision cross-section of 8 b) and can quench magnets and directly limit luminosity. With a peak luminosity of $L = 6.1 \times 10^{27}\,\mathrm{cm}^{-2}\mathrm{s}^{-1}$ each secondary beam carries $\mathrm{P}_{\mathrm{BFPP}} \lesssim 120\,\mathrm{W}$, which is more than enough to quench an LHC dipole as demonstrated in 2015 [23].

To reduce the risk of quenching these magnets, orbit bumps were implemented around the impact locations in IP1 and IP5 in order to move the losses out of the dipole and into the adjacent connection

Table 2: Representative simplified beam parameters at the start of the highest luminosity physics fills, in conditions that lasted for $> 5\,\mathrm{days}$, in the one-month p–Pb runs (Ref. [15] and references therein). The very short pilot run in 2012 is not shown. The original "design" values for p–Pb [17] collisions are also shown (in this column the integrated luminosity goal was supposed to be obtained over a few runs. Peak luminosities are averages for ATLAS and CMS (ALICE being levelled). The smaller luminosities delivered to LHCb from 2013–2016 and in the minimum-bias part of the run in 2016 are not shown. Emittance and bunch length are RMS values. Single bunch parameters for these p–Pb or Pb–p runs are generally those of the Pb beam. Design and record achieved nucleon-pair luminosities are boxed, and some key parameters related to p–Pb parameters in Table 1 are set in red type, for easy comparison.

Quantity	"design"	achieved	
Year	(2011)	2012–13	2016
Weeks in physics	-	3	1, 2
Fill no. (best)		3544	5562
Beam energy $E[Z\,\mathrm{TeV}]$	7	4	4,6.5
Pb beam energy $E[A\,\mathrm{TeV}]$	2.76	2.51	1.58,2.56
Collision energy $\sqrt{s_{\mathrm{NN}}}\,[\mathrm{TeV}]$	5.52	**5.02**	**5.02**,8.16
Bunch intensity $N_b\,[10^8]$	0.7	1.2	2.1
No. of bunches k_b	592	358	540
Pb norm. emittance $\epsilon_N\,[\mu\mathrm{m}]$	1.5	2.	1.6
Pb bunch length σ_z m	0.08	0.07–0.1	
β^* [m]	0.5	0.8	10, 0.6
Pb stored energy MJ/beam	3.8	2.77	9.7
Luminosity $L_{\mathrm{AA}}\,[10^{27}\mathrm{cm}^{-2}\mathrm{s}^{-1}]$	150	116	850
NN luminosity $L_{\mathrm{NN}}\,[10^{30}\mathrm{cm}^{-2}\mathrm{s}^{-1}]$	43	24	177
Integrated luminosity/experiment $[\,\mu\mathrm{b}^{-1}]$	10^5	32000	1.9×10^5
Int. NN lumi./expt. $[\,\mathrm{pb}^{-1}]$	21	6.7	40

cryostat ("missing dipole" in the DS) that does not contain a superconducting magnet coil and therefore is less likely to quench. This technique was first used in 2015. It was almost fully proved in 2018 when the ATLAS and CMS Pb–Pb luminosities were sustained at values very close to the nominal levelling values for Runs 3 and 4. Beam-loss monitor thresholds were set, based on the measured quench level in 2015 and it was clear that there was sufficient margin for still higher luminosity. In IP2, the method of orbit bumps alone is not applicable with present optics and layout. It is therefore foreseen to install an additional collimator in the connection cryostat on the outgoing beam on each side of IP2. In combination with this, orbit bumps will then be deployed to steer the BFPP beams onto the collimators. The installation will take place in LS2 in order to allow the HL-LHC design luminosity for ALICE (corresponding to a hadronic event rate of 50 kHz) in subsequent runs.

2.2.2 Collimation and intensity limit

While the LHC stores unprecedented beam energies, superconducting magnets are needed to bend and focus these beams, most of which are operated at 1.9 K. A loss of a tiny fraction of the beam is enough to induce a magnet quench, and it is therefore vital to avoid any uncontrolled beam losses. To safely intercept losses and provide protection of the magnets, the LHC uses a multi-stage collimation system [24–27]. During the first two runs of the LHC, this system has shown a very good performance with proton beams [28–31] and ion beams [32, 33].

LHC collimation is much less efficient with heavy-ion beams than with protons, since ions have a high cross section for undergoing nuclear fragmentation inside the primary collimators [34]. The angular offsets of the out-scattered fragments are frequently not large enough to reach the secondary collimators in the straight collimation insertion (IR7). At the same time these fragments have a magnetic rigidity different from the main beam, so that they risk being lost where the dispersion starts to rise in the first few dipoles of the DS. This was the most critical beam loss location during the Pb ion runs in Run 1 and Run 2, with a local cleaning inefficiency of about a factor 100 worse than for protons [32, 33]. Therefore, even though the total stored beam energy is about a factor 10 lower with Pb ions than with protons, collimation of heavy ions is critical. Still, ion collimation has worked well in the LHC and did not introduce operational bottlenecks so far. However, extrapolations of the losses in the DS from a 2015 experimental tests to Run 3 and HL-LHC show that, if nothing is done, the total stored Pb beam energy is limited to around 10 MJ, if drops of the instantaneous beam lifetime down to 12 minutes are assumed [35]. At the same time, it is foreseen to increase the stored Pb beam energy to about 24 MJ. To alleviate this limitation and safely intercept the losses, it is planned to install additional collimators, called TCLDs, in the dispersion suppressors [36–38]. On the other hand, the LHC was successfully operated with Pb beams containing over 13.5 MJ each in 2018 thanks to good control of beam lifetimes. In order to make space for the TCLDs, standard 8.3 T LHC dipoles will be replaced by an assembly consisting of two shorter higher-field 11 T dipoles with the TCLD in between [38]. The solution that gives the best simulated Pb cleaning efficiency uses two TCLDs per side of IR7. However, this is not possible within tight constraints of long shutdown 2 and the HL-LHC project, and the baseline is therefore to install one TCLD per side. If this turns out to be a real limitation, it could be considered at a later stage to install a second TCLD. As an alternative and complementary alleviation method, it is under study whether crystal collimation could help in reducing the losses in the DS. In this collimation scheme, bent crystals are used instead of the standard LHC primary collimators [39]. Incoming beam particles follow the curvature of the crystal planes, the so-called channelling, and exit with a significant angular kick. They can then be efficiently steered onto an absorber. Nuclear interactions inside the the channels of well-aligned crystals are significantly suppressed. Initial experiments using an LHC test installation [40] have shown very promising results with Xe and proton beams [41]. Channelling has very recently also been observed with Pb beams in 2018 and potential improvements of the collimation system are presently being assessed experimentally. Studies with Pb beams are not yet conclusive but it is hoped that this will be further clarified by analysis of data taken during the 2018 Pb ion run.

Collimation of lighter ion species has not yet been studied in detail, although some first simulations are presented in Ref. [32]. Results for Ar and Xe beams show that the amount of expected losses in the DS is similar to Pb but the longitudinal loss distribution changes. The fractional change in magnetic rigidity for every lost nucleon in the collimators is larger for light ions, and it is hence expected that out-scattered fragments have larger effective energy deviations and are lost more upstream. It is thus likely that the TCLD should help significantly also for lighter ions, although comparative studies on intensity limits for different ion species still remain to be done.

2.3 Proton-lead operation in Run 3 and HL-LHC

Within colliding nuclei, with charges Z_1, Z_2 and nucleon numbers A_1, A_2, in rings with magnetic field set for protons of momentum p_p[1], the colliding nucleon pairs will have an average centre-of-mass energy

$$\sqrt{s_{\mathrm{NN}}} \approx 2c\,p_p\sqrt{\frac{Z_1 Z_2}{A_1 A_2}} \approx 2c\,p_p \begin{cases} 1 & \mathrm{pp} \\ 0.628 & \mathrm{p\text{–}Pb} \\ 0.394 & \mathrm{Pb\text{–}Pb} \end{cases} \tag{3}$$

[1] Conditions imposed by the two-in-one magnet design of the LHC.

and a central rapidity shift in the direction of the (Z_1, A_1) beam

$$y_{\text{NN}} \approx \frac{1}{2}\log\left(\frac{Z_1 A_2}{A_1 Z_2}\right) \approx \begin{cases} 0 & \text{pp, Pb–Pb} \\ 0.465 & \text{p–Pb} \\ -0.465 & \text{Pb–p} \end{cases} . \tag{4}$$

We present parameters for operation at the nominal LHC momentum $p_p c = 7\,\text{TeV}$ extrapolating from the experience of the last p–Pb run in 2016.

The injection and ramp of protons and lead ions with equal magnetic rigidity leads to moving long-range beam-beam encounters in the four interaction regions of the LHC. These beam-beam encounters were one of the reasons why the feasibility of p–Pb operation in the LHC was initially questioned. This effect has been proven small in the LHC and calculations have this will remain true for the HL-LHC era despite larger bunch numbers and higher proton bunch intensities. The dynamic range of the interlock strip-line BPMs, common for the lead and proton beam, limited the proton intensity to $N_b < 5 \times 10^{10}$ protons per bunch during Run 1. Gating the stripline BPM read-out appropriately removed this constraint a few days before the end of the 2016 run. The higher proton intensity of $N_b = 2.8 \times 10^{10}$ protons per bunch resulted in increased luminosities at the IPs but also led to the substantial deposition of collision debris from the Pb beam in the dispersion suppressors at ATLAS and CMS risking a beam dump [42]. The collision debris collimators (TCLs), which could have intercepted emerging fragments from the IPs, were not commissioned at tighter settings for the 2016 p–Pb run. Appropriate TCL settings are expected to neutralise these fragments and should allow for higher peak luminosities in the future.

A potential p–Pb run during Run 3 and beyond will greatly benefit from the longitudinal slip stacking in the SPS and the small $\beta^* = 0.5\,\text{m}$ in three experiments. The proton intensity cannot be pushed to values much larger than the maximum achieved in 2016 as bunches colliding in multiple IPs and especially in ATLAS and CMS will approach the interlock BPM threshold of 2×10^9 charges per bunch too quickly if the luminosities of ATLAS and CMS are not levelled. This would lead to an undesirable early beam dumps while ALICE is still levelled. In order to predict the potential performance of a future p–Pb run, the expected Pb–Pb filling pattern [19] is used providing 1136 collisions in ATLAS/CMS, 1120 collisions in ALICE and 81 collisions in LHCb. This approximation is made since the proton injection should be flexible enough to reproduce most of the respective Pb pattern. This calculations assumes $N_b = 3 \times 10^{10}$ protons per bunch and ALICE being levelled to the instantaneous luminosity of $L_{\text{AA}} = 5 \times 10^{29}\,\text{cm}^{-2}\text{s}^{-1}$. $L_{\text{AA}} = 5 \times 10^{29}\,\text{cm}^{-2}\text{s}^{-1}$ ATLAS and CMS are not luminosity levelled in this scenario since the loss of integrated luminosity for ATLAS and CMS outweighs the marginal gain for ALICE. A simulation of the beam evolution based on ordinary differential equations including intra-beam scattering and radiation damping leads to a luminosity evolution in the different IPs as displayed in Fig. 1.

At around 6.1 h, the bunch intensity of the bunches colliding in ATLAS, ALICE and CMS drop below the interlock BPM threshold ultimately limiting the fill length, even though the potential levelling time for ALICE has not been reached. Detailed engineering of the filling scheme might avoid this. Key results from the beam evolution study are listed in Tab. 3. The expected peak luminosity in ATLAS and CMS is at around $L_{\text{AA}} = 17.4 \times 10^{29}\,\text{cm}^{-2}\text{s}^{-1}$, i.e., roughly a factor 2 larger than in 2016. The integrated luminosity in ATLAS and CMS are expected to approach $0.7\,\text{pb}^{-1}$ outperforming the 2016 integrated luminosity by a rough factor 3.5. Since the nominal HL-LHC normalised proton emittance of $\epsilon_N = 2.5\,\mu\text{m}$ is assumed, the actual performance may exceed these predictions since normalised proton emittances in the range of $\epsilon_N = 1.3\,\mu\text{m}$ have already been achieved.

2.4 Colliding lighter nuclei at HL-LHC

The bunch intensity limits in the injectors depend largely on the ion charge which changes at the various stripping stages which must be optimised for space-charge limits, intra-beam scattering, efficiency of

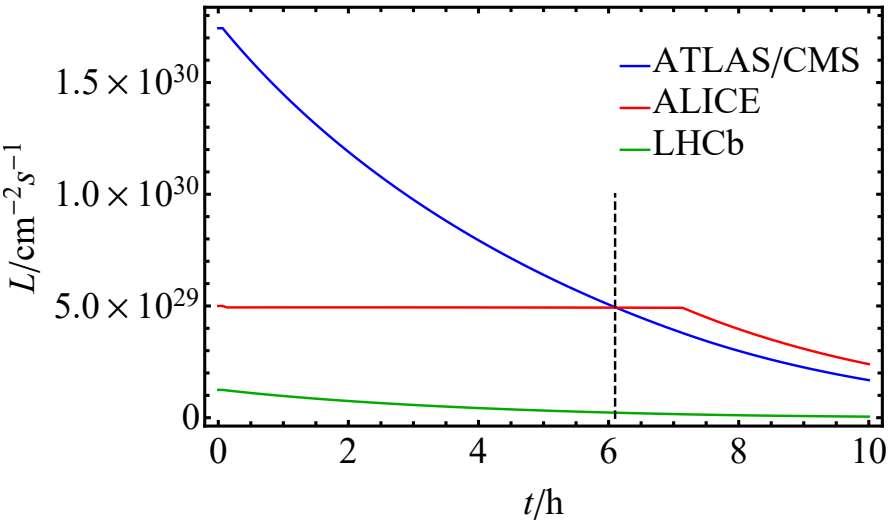

Fig. 1: Evolution of the instantaneous luminosity in the LHC experiments during a p-Pb fill. At around 6.1 h (dashed line), the interlock BPM threshold is reached for some bunches, limiting the fill length.

Table 3: Key parameters and results of the p–Pb beam evolution calculation. A turn-around time, i.e., the time between Beam Dump and Stable Beams, of 3 h and an operational efficiency factor of 0.5 is assumed. The final result was scaled down by additional 5 % to take potential deviations of the proton filling pattern into account. The time the first bunches need to reach the interlock BPM threshold is used as the fill time.

Species	p	Pb	
Beam energy $E[Z\,\mathrm{TeV}]$	7		
Collision energy $\sqrt{s_{\mathrm{NN}}}$ [TeV]	8.78		
Bunch intensity N_b [10^8]	300	1.8	
No, of bunches k_b	1232	1232	
Norm. emittance ϵ_N [μm]	2.5	1.65	
Bunch length σ_z [m]	0.09	0.08	
Fill time t_{fill} [h]	6.1		
IP	ATLAS/CMS	ALICE	LHCb
β^* [m]	0.5	0.5	0.5
Colliding bunches k_c	1136	1120	81
Luminosity L_{AA} [$10^{29}\mathrm{cm}^{-2}\mathrm{s}^{-1}$]	17.4	5.0	1.2
NN luminosity L_{NN} [$10^{31}\mathrm{cm}^{-2}\mathrm{s}^{-1}$]	36.3	10.4	2.6
$\int_{\mathrm{month}} L_{\mathrm{AA}}$ dt [nb^{-1}]	674	328	41.1
$\int_{\mathrm{month}} L_{\mathrm{NN}}$ dt [pb^{-1}]	140	68	8.5

electron-cooling, beam losses on residual gas and other effects in the ion source, Linac4, LEIR, the PS and SPS. Given the uncertainties, the deliverable intensity for other species can only be determined after sufficient time spend commissioning and empirically optimising the many parameters and operating modes of the whole injector chain. To simplify present considerations, we postulate a simple form relating the number of ions per bunch, N_b, to the well-established value (N_b(82,208)=1.9×10^8) for Pb beams

$$N_b(Z,A) = N_b(82,208)\left(\frac{Z}{82}\right)^{-p} \tag{5}$$

Fitting such an expression to the limited information [43] from the few species used for SPS fixed-target in recent years (since the commissioning of the present ECR ion source and LEIR) yields a value of the fit parameter $p = 1.9$. Beam quality requirements for fixed-target beams are, of course, less stringent than for injection into the collider. Fitting to the first commissioning of Xe beams for the LHC [16], on the other hand, gives a much less optimistic $p = 0.75$. Although this was the only occasion where any other species than Pb was delivered to the collider, only the simplest version of the injection scheme was used and it is clear that, given time, significantly higher intensities could be achieved. We consider that $1.5 \leq p \leq 1.9$ corresponds to a representative range of possibilities that could be realised in fully-prepared future operation.

In addition, we make a number of simplifying assumptions to allow a simplified, yet meaningful, comparison between species

- The *geometric* transverse beam emittances at the start of collisions will be equal to those of Pb beams [19]. This is justified, at least at the level of the LHC, since the scaling of intra-beam scattering with N_b, Z and A, given by the parameter f_{IBS}/(m Hz) is generally smaller than for Pb as long as $p \lesssim 1.9$. A similar scaling should hold in the injectors such as the SPS where intra-beam scattering may also blow up the emittances. This ignores possible space-charge limits in the injectors which should also be considered once the appropriate stripping schemes and charge states have been defined.
- Same filling scheme and number of bunches.
- No luminosity-levelling in any experiment.
- Fill length optimised for intensity evolution dominated by luminosity burn-off.
- Equal operational efficiency of 50%. Following conventional practice for HL-LHC, the integrated luminosity for a 1-month run is estimated assuming back-to-back ideal fills of optimal length and a turn-around time of 2.5 h between the end of one fill and the resumption of "Stable Beams" for collisions in the next. The operational efficiency factor is then applied as a way of taking into account the time needed for commissioning, intensity ramp-up, faults and other non-availability of LHC and injector systems.

The parameters are estimated using analytical approximations unlike the more elaborate simulations used in Section 2.2. Together with the assumption that there is no luminosity levelling, these lead to a higher estimate of integrated luminosity in a one-month run. Nevertheless they can be used as a guide to the relative gain factors in integrated nucleon-nucleon luminosity by changing from Pb to a lighter nucleus.

2.5 Short run for O–O and p–O

As discussed in Section 11.3, a short p–O collision run is of interest for cosmic-ray physics. If O beams were available from the injectors, this could be combined with a short, low-luminosity, O–O run, which would be of value for the main high-density QCD programme. Limiting the beams to low-intensities would allow a rapid set-up in LHC on the successful model of the 2012 p–Pb run which was later re-used in the 2017 Xe–Xe run [16]. Each of those runs took about 16 h of LHC operation time, including set-up and physics data-taking but a combination O–O/p–O run could take a few days.

Because oxygen is used as the carrier gas in the CERN heavy-ion source, the idea has been mooted that it may be possible to switch from Pb to $^{16}O^{8+}$ beams for the LHC, and back, somewhat more rapidly than other species. Commissioning of the O beam in the injectors for single-bunch injection into the LHC would need to be scheduled, in parallel with pp operation, and use of the injectors for other programmes, in the period preceding the O–O/p–O run. The possibilities are under study and include either inserting the run at the end of one of the annual Pb–Pb runs or scheduling it earlier in the year in order to provide time for the source to be switched back to Pb operation afterwards.

Table 4: Parameters and performance for a range of light nuclei with a moderately optimistic value of the scaling parameter $p = 1.5$ in (5).

	$^{16}O^{8+}$	$^{40}Ar^{18+}$	$^{40}Ca^{20+}$	$^{78}Kr^{36+}$	$^{129}Xe^{54+}$	$^{208}Pb^{82+}$
γ	3760.	3390.	3760.	3470.	3150.	2960.
$\sqrt{s_{NN}}$/TeV	7.	6.3	7.	6.46	5.86	5.52
σ_{had}/b	1.41	2.6	2.6	4.06	5.67	7.8
σ_{BFPP}/b	2.36×10^{-5}	0.00688	0.0144	0.88	15.	280.
σ_{EMD}/b	0.0738	1.24	1.57	12.2	51.8	220.
σ_{tot}/b	1.48	3.85	4.18	17.1	72.5	508.
N_b	6.24×10^9	1.85×10^9	1.58×10^9	6.53×10^8	3.56×10^8	1.9×10^8
ϵ_{xn}/μm	2.	1.8	2.	1.85	1.67	1.58
f_{IBS}/(m Hz)	0.0662	0.0894	0.105	0.13	0.144	0.167
W_b/MJ	68.9	45.9	43.6	32.5	26.5	21.5
$L_{AA0}/\mathrm{cm}^{-2}s^{-1}$	1.46×10^{31}	1.29×10^{30}	9.38×10^{29}	1.61×10^{29}	4.76×10^{28}	1.36×10^{28}
$L_{NN0}/\mathrm{cm}^{-2}s^{-1}$	3.75×10^{33}	2.06×10^{33}	1.5×10^{33}	9.79×10^{32}	7.93×10^{32}	5.88×10^{32}
P_{BFPP}/W	0.0031	0.179	0.303	5.72	43.4	350.
P_{EMD1}/W	4.98	16.5	16.9	40.5	76.7	141.
τ_{L0}/h	16.4	21.3	23.	13.5	5.87	1.57
T_{opt}/h	9.04	10.3	10.7	8.23	5.42	2.8
$\langle L_{AA} \rangle$ $\mathrm{cm}^{-2}\mathrm{s}^{-1}$	8.99×10^{30}	8.34×10^{29}	6.17×10^{29}	9.46×10^{28}	2.23×10^{28}	3.8×10^{27}
$\langle L_{NN} \rangle$ $\mathrm{cm}^{-2}\mathrm{s}^{-1}$	2.3×10^{33}	1.33×10^{33}	9.87×10^{32}	5.76×10^{32}	3.71×10^{32}	1.64×10^{32}
$\int_{month} L_{AA}$ dt/nb^{-1}	1.17×10^4	1080.	799.	123.	28.9	4.92
$\int_{month} L_{NN}$ dt/pb^{-1}	2980.	1730.	1280.	746.	481.	213.
R_{had}/kHz	2.07×10^4	3340.	2440.	653.	270.	106.
μ	1.64	0.266	0.194	0.0518	0.0215	0.00842

2.6 Heavy-ion performance of HE-LHC

Heavy-ion operation of HE-LHC awaits a fully detailed study. First results were presented in [44]. Since the HE-LHC would occupy the same tunnel as the LHC, one can, for the moment, assume the same injected beams as HL-LHC. Future possible upgrades to the injectors might improve this. The total integrated luminosity obtainable per fill, summed over all experiments, is bounded by the total intensity divided by the burn-off cross-section and will therefore be similar to the HL-LHC. The same can be said for time taken to inject a fill. Only a modest increase in integrated luminosity, given by somewhat shorter times spent in collision and, most likely, a reduction in the number of experiments, can be envisaged. For purposes of this report, we estimate that the integrated luminosity obtained by each of two experiments in a one-month run will be of order $6\,\mathrm{nb}^{-1}$. However, the BFPP power with Pb–Pb collisions will be very high and this could be a strong argument for running with somewhat lighter species. In that case, one can expect the luminosity to scale similarly to HL-LHC in Sect. 2.4.

Table 5: Parameters and performance for a range of light nuclei with an optimistic value of the scaling parameter $p = 1.9$ in (5).

	$^{16}O^{8+}$	$^{40}Ar^{18+}$	$^{40}Ca^{20+}$	$^{78}Kr^{36+}$	$^{129}Xe^{54+}$	$^{208}Pb^{82+}$
γ	3760.	3390.	3760.	3470.	3150.	2960.
$\sqrt{s_{NN}}$/TeV	7.	6.3	7.	6.46	5.86	5.52
σ_{had}/b	1.41	2.6	2.6	4.06	5.67	7.8
σ_{BFPP}/b	2.36×10^{-5}	0.00688	0.0144	0.88	15.	280.
σ_{EMD}/b	0.0738	1.24	1.57	12.2	51.8	220.
σ_{tot}/b	1.48	3.85	4.18	17.1	72.5	508.
N_b	1.58×10^{10}	3.39×10^{9}	2.77×10^{9}	9.08×10^{8}	4.2×10^{8}	1.9×10^{8}
ϵ_{xn}/μm	2.	1.8	2.	1.85	1.67	1.58
f_{IBS}/(m Hz)	0.168	0.164	0.184	0.18	0.17	0.167
W_b/MJ	175.	84.3	76.6	45.2	31.4	21.5
$L_{AA0}/\text{cm}^{-2}s^{-1}$	9.43×10^{31}	4.33×10^{30}	2.9×10^{30}	3.11×10^{29}	6.66×10^{28}	1.36×10^{28}
$L_{NN0}/\text{cm}^{-2}s^{-1}$	2.41×10^{34}	6.93×10^{33}	4.64×10^{33}	1.89×10^{33}	1.11×10^{33}	5.88×10^{32}
P_{BFPP}/W	0.0199	0.601	0.935	11.	60.6	350.
P_{EMD1}/W	32.	55.6	52.2	78.3	107.	141.
τ_{L0}/h	6.45	11.6	13.1	9.74	4.96	1.57
T_{opt}/h	5.68	7.62	8.08	6.98	4.98	2.8
$\langle L_{AA} \rangle$ $\text{cm}^{-2}\text{s}^{-1}$	4.54×10^{31}	2.45×10^{30}	1.69×10^{30}	1.68×10^{29}	2.95×10^{28}	3.8×10^{27}
$\langle L_{NN} \rangle$ $\text{cm}^{-2}\text{s}^{-1}$	1.16×10^{34}	3.93×10^{33}	2.71×10^{33}	1.02×10^{33}	4.91×10^{32}	1.64×10^{32}
$\int_{month} L_{AA}$ dt/nb^{-1}	5.89×10^{4}	3180.	2190.	218.	38.2	4.92
$\int_{month} L_{NN}$ dt/pb^{-1}	1.51×10^{4}	5090.	3510.	1330.	636.	213.
R_{had}/kHz	1.33×10^{5}	1.12×10^{4}	7540.	1260.	378.	106.
μ	10.6	0.893	0.598	0.1	0.03	0.00842

3 Light flavour sector: (anti-)(hyper-)nuclei and fluctuations of conserved charges

Coordinator: Francesca Bellini (CERN)

Contributors: M. Arslandok (Heidelberg University), N. K. Behera (Inha University), R. Bellwied (Houston University), K. Blum (CERN and Weizmann Institute of Science), A. Borissov (Münster University), P. Braun-Munzinger (EMMI/GSI Helmholtzzentrum für Schwerionenforschung GmbH), B. Doenigus (Frankfurt University), L. Fabbietti (TU Munich), S. Floerchinger (Heidelberg University), A.P. Kalweit (CERN), R. Lea (University and INFN, Trieste), A. Mastroserio (Foggia University and INFN, Bari), A. Ohlson (Heidelberg University), V. Okorokov (National Research Nuclear University MEPhI, Moscow), S. Piano (INFN Trieste), M. Puccio (University and INFN, Torino), K. Redlich (University of Wroclaw and EMMI/GSI Helmholtzzentrum für Schwerionenforschung GmbH), A. Rustamov (NNRC Baku, GSI Helmholtzzentrum für Schwerionenforschung GmbH and Heidelberg University), J. Stachel (Heidelberg University), A. Timmins (University of Houston), S. Trogolo (University and INFN, Torino).

3.1 Introduction

The analysis of the data collected at the LHC during Run 1 and Run 2 has consolidated our understanding of a standard model for the production of light-flavour hadrons (containing u, d and s quarks) in heavy-ion collisions: particle chemistry (described by integrated particle yields) is well described by the thermal-statistical model [45, 46] and kinetic equilibrium (reflected in the p_{T}-dependence of particle production) is well described by a common radial expansion governed by hydrodynamics [47, 48]. While the physics of light-flavour particles is often perceived as not statistics hungry, the unprecedented large integrated luminosities expected in Run 3 and Run 4 at the LHC offer a unique physics potential. Despite containing only u, d and s valence quarks, light (anti-)(hyper-)nuclei are very rarely produced because of their composite nature and very large mass. Their study will enormously profit from the significant increase in luminosity for heavy-ion collisions expected in the years 2021 until 2029. The same holds true for the study of event-by-event fluctuations of the produced particles, which is closely linked to the production of light (anti-)(hyper-)nuclei in the scenario of a common chemical freeze-out determining light-flavour hadrons and (hyper-)nuclei abundances. If, as indicated by the recent experimental findings [46], the thermal-statistical approach is the correct model to describe (anti-)(hyper-)nuclei production, the chemical freeze-out temperature is most precisely determined by measurements of light (anti-)(hyper-)nuclei as they are not subject to feed-down corrections from strong decays [45]. This is the same temperature at which event-by-event fluctuations of conserved quantities are compared to lattice QCD (lQCD). The physics of light (anti-)(hyper-)nuclei and exotic multi-quark states together with the related observables that will become experimentally accessible in Pb–Pb collisions at the LHC Runs 3 and 4 are discussed in Sec. 3.2. In Sec. 3.3, measurements of fluctuations of particle production and conserved charges are discussed as they give experimental access to fundamental properties of the QCD phase transition at μ_{B} and allow for direct comparison with lQCD calculations.
In small collision systems (pp, p–Pb), measurements of light-flavour hadrons provide fundamental input to the study of particle production mechanisms and collectivity across systems, as discussed in Ch. 9. At the same time, the physics programme with pp and p–Pb collisions in Runs 3 and 4 will open the possibility for system-size dependent studies of (anti-)nuclei production and for precision measurements of the hyperon-nucleon potentials. The physics case for these measurements in small colliding systems is motivated in this chapter in Sec. 3.2.6, as well as the implications of the findings at the LHC for astrophysics and searches for dark matter in space-based experiments.

3.2 (Anti-)(hyper-)nuclei production

3.2.1 Testing thermal production and nucleon coalescence models

The production of light (hyper-)nuclei and their anti-matter counterparts is modeled within the scenarios of thermal-statistical hadronisation and nucleon coalescence. In the thermal-statistical approach [45, 49], particles are produced from a fireball in thermal equilibrium with temperatures of the order of $T_{\rm chem} \approx 156$ MeV that are near the temperature of the QCD phase transition boundary, as predicted by lQCD calculations [50, 51]. The yields of the produced objects depend on the chemical freeze-out temperature $T_{\rm chem}$ (when inelastic collisions cease) and the mass m of the object, and approximately scale as $\mathrm{d}N/\mathrm{d}y \propto \exp(-m/T_{\rm chem})$. Thermal-statistical models have been successful in describing light-flavour particle production across a wide range of energies in nucleus-nucleus collisions [45, 46]. Due to their large mass, light (anti-)(hyper-)nuclei are particularly sensitive to $T_{\rm chem}$ and since they are not affected by feed-down from higher mass states [45], the measurement of their production constitutes a precision test for the thermal model.

In the coalescence scenario, composite objects are formed at kinetic freeze-out by coalescence of nucleons that are close in configuration and momentum space [52–57]. Calculations of the coalescence probability based on a density matrix approach [57] require the knowledge of the nucleus wave function and identify the volume of the particle source as the homogeneity volume that can be extracted via Hanbury-Brown–Twiss interferometry [58]. The size of the (hyper-)nucleus is identified with the size parameter of its wave-function, which is related to the (measurable) rms of the charge distribution by simple relations [55, 59].

While there are several theory groups working on the calculation of the expected coalescence [57, 60–63] and thermal production rates [49,64,65], predictions reported in Fig. 2 rely on the study presented in [59], which contrasts the two production scenarios. In order to distinguish them, a measurement of the coalescence parameter for (anti-)(hyper-)nuclei that differ by mass, spin and size as a function of source volume (or source radius) is proposed. The coalescence parameter $B_{\rm A}$ is defined as

$$E_A \frac{\mathrm{d}^3 N_A}{\mathrm{d}p_A^3} = B_A \left(E_{\rm p,n} \frac{\mathrm{d}^3 N_{\rm p,n}}{\mathrm{d}p_{\rm p,n}^3} \right)^A \Bigg|_{\vec{p}_{\rm p}=\vec{p}_{\rm n}=\frac{\vec{p}_A}{A}} , \tag{6}$$

where $p_{\rm p,n}$ are the momenta of the proton and neutron and $E_{p,n}$ their energies. In the coalescence model (black curves in top panels of Fig. 2), the coalescence parameter is determined analytically. The thermal model predicts $p_{\rm T}$-independent particle yields at a given $T_{\rm chem}$, therefore a Blast-Wave (BW) model is used in [59] to describe the $p_{\rm T}$-dependence of (hyper-)nuclei and nucleon production. With the $p_{\rm T}$ spectra of (hyper-)nuclei and protons obtained in this way, Eq. 6 is used to extract $B_{\rm A}$ (dashed blue curve in top panels of Fig. 2). Similarly, the coalescence parameter is obtained experimentally from Eq. 6 using the measured (hyper-)nucleus and proton $p_{\rm T}$ distributions as input. It is considered that for BW, little energy dependence of the fit parameters is observed in Pb–Pb collisions from $\sqrt{s_{\rm NN}}$ = 2.76 to 5.02 TeV. The thermal model yields only depend on temperature and no collision energy dependence of the temperature is expected in the LHC energy range. The size of the source can be sampled by means of multiplicity- and centrality-differential measurements.

The particle with the strongest sensitivity to the production mechanism appears to be the hypertriton (a pΛn bound state) with its large charge rms radius of about 10 fm, for which the coalescence and the thermal model predictions differ by up to three orders of magnitude as a function of the source radius. While the hypertriton seems to be largely suppressed with respect to ^{3}He (pnn), the $^4_\Lambda$H (ppΛn) is predicted to have only a slightly lower coalescence probability with respect to ^{4}He (ppnn). Moreover, for small R, i.e. in small systems as those formed in pp and p–Pb collisions, $^3_\Lambda$H is predicted by coalescence to be suppressed by about a factor of 100 with respect to ^{3}He. These considerations motivate systematic multi-differential measurements of A = 3 and A = 4 nuclei and hyper-nuclei as a function of

multiplicity and from small (pp, p–Pb) to large systems (Pb–Pb) to test the validity of the coalescence picture as opposed to thermal production.

With an integrated luminosity $L_{\rm int}$ = 10 $\rm nb^{-1}$ in Pb–Pb collisions in Runs 3 and 4, $B_{\rm A}$ for ^{3}He, $^3_\Lambda$H and ^{4}He can be measured in ALICE in up to ten centrality classes with a statistical precision lower than 5%, 10% and 20%, respectively. The projected relative statistical uncertainties on $B_{\rm A}$ ($\sigma_{\rm stat}/B_{\rm A}$) for (hyper-)nuclei with A > 2 are reported in the central row of panels of Fig. 2. These uncertainties have been estimated by scaling the significance of the nuclei and hyper-nuclei spectra measurements in Pb–Pb collisions at $\sqrt{s_{\rm NN}}$ = 5.02 TeV [66, 67] to the expected integrated luminosity of Runs 3 and 4 and assuming thermal production for the states with A = 4. The uncertainties on the proton spectra are negligible already in the existing measurements.

The experimental discrimination power between the models has been extracted as $(B_{\rm A}^{therm} - B_{\rm A}^{coal})/\sigma$, where $\sigma = \sqrt{\sigma_{\rm stat}^2 + \sigma_{\rm sys}^2}$, and is reported in the lower panels of Fig. 2. Relative systematic uncertainties $\sigma_{\rm sys}/B_{\rm A}$ = 10% and 20% have been considered, to be compared with a typical 15% uncertainty of the Run 1 and 2 measurements. Measurements of $^3_\Lambda$H allow for a 10σ discrimination between models, even in a pessimistic scenario in all centralities. The discrimination power rises above the 10σ level for ^{4}He in semi-central and peripheral collisions.

3.2.2 *Light (anti-)(hyper-)nuclei observables in Runs 3 and 4*

Measurements of (anti-)(hyper-)nuclei and exotic QCD bound states require large event samples collected with a minimum-bias trigger, as well as high tracking precision for the separation of secondary vertices and charged-hadron (light nucleus) identification. The upgraded ALICE detector after LS2 [3, 68–70] fulfills these requirements, developing further the potential already explored in Runs 1 and 2. The yields of (hyper-)nuclei (d, ^{3}He, ^{4}He, $^3_\Lambda$H, $^4_\Lambda$H, $^4_\Lambda$He) and their anti-particles in Pb–Pb collisions at the LHC in Runs 3 and 4 have been estimated for measurements with ALICE. The detectable yield and significance for (anti-)(hyper-)nuclei have been estimated for 0–10% central Pb–Pb collisions considering the acceptance and detection efficiency in the nominal magnetic field of the ALICE detector (B = 0.5 T). These projections are reported for anti-particles in Fig. 3 as a function of the minimum-bias integrated luminosity. The detectable particle and anti-particle yields are equivalent in the considered $p_{\rm T}$ range. All projections have been extracted in the $2 < p_{\rm T} < 10$ GeV/c range, where the lower limit is given by the $p_{\rm T}$ down to which nuclei with A $\geq$ 3 can be reconstructed without ambiguity in ALICE. In a scenario in which ALICE will take data with a central-barrel low-field configuration (B = 0.2 T), it will be possible to extend the low-$p_{\rm T}$ limit for (anti-)nuclei identification down to 1 GeV/c, increasing the expected number of detectable light (anti-)(hyper-)nuclei (by about 20% for ^{3}He). In Fig. 3, the bands indicate the uncertainty on the yield (significance) associated with different model predictions: the central line is obtained assuming statistical-thermal production with $T_{\rm chem}$ = 156 MeV [49], the upper line is the yield (significance) assuming thermal production at $T_{\rm chem}$ = 158 MeV, and the lower one using for the yields the expectation from coalescence (see Sec. 3.2.1). The arrow represents the recorded luminosity at the end of the LHC Run 2. It has to be noted that for this study, the geometry of the ALICE Inner Tracking System (ITS) in Run 2 has been considered. The new geometry and acceptance of the upgraded ITS system [3] are expected to increase the detection efficiency by up to 20%.

The expected yield per unit of rapidity at mid-rapidity are reported for $\overline{\rm d}$, $^3\overline{\rm He}$ and $^4\overline{\rm He}$ in left panel of Fig. 3. With $L_{\rm int}$ = 10 $\rm nb^{-1}$ recorded with the nominal magnetic field, a measurement of the elliptic flow (v_2) of ^{3}He and ^{3}H (and anti-nuclei) in Pb–Pb collisions will become feasible with ALICE with a statistical precision better than 5% in the 2–10 GeV/c transverse momentum range in at least eight centrality intervals. Elliptic flow measurements for anti-nuclei provide a powerful independent test of coalescence scenarios as already demonstrated with deuterons [71] and might provide an indirect assessment of the neutron flow comparing the ^{3}He and ^{3}H results. In addition, the large data sample

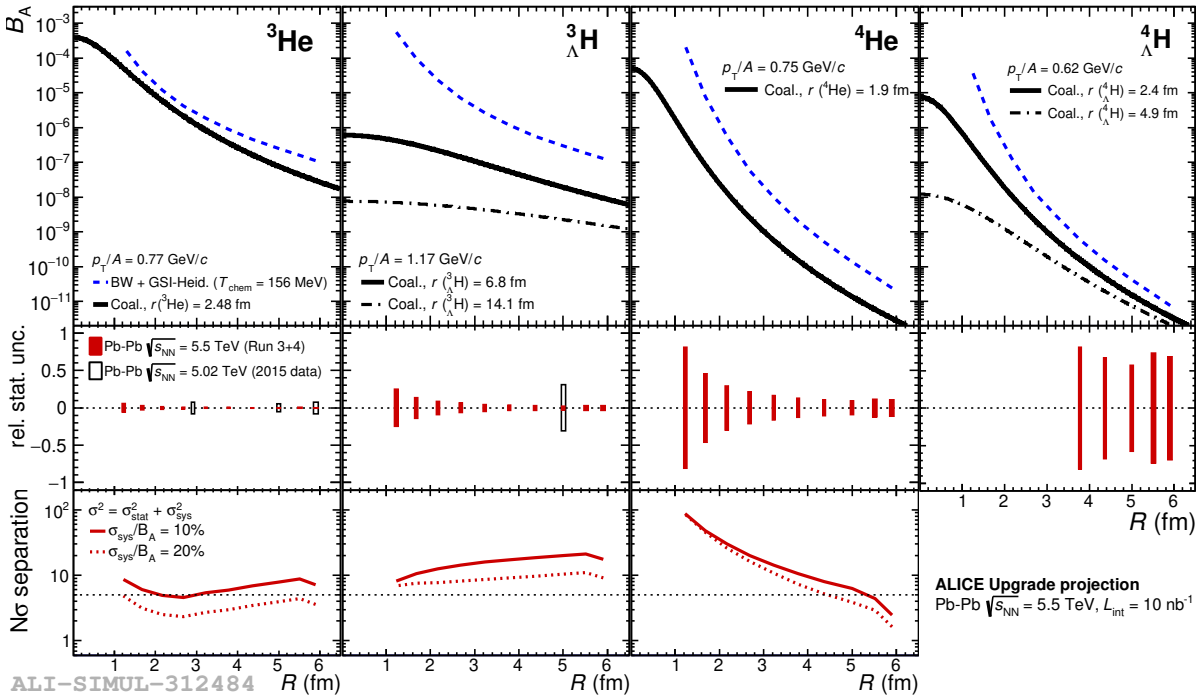

Fig. 2: Top: comparison of predictions for the coalescence parameters for (hyper-)nuclei with A = 3, 4 from the Blast-Wave + GSI-Heidelberg thermal statistical model and nucleon coalescence as a function of the radius (R) of the particle emitting source. For each (hyper-)nucleus, the radius r considered by the coalescence model is reported in the legend. For $^3_\Lambda$H ($^4_\Lambda$H), two values of the radius are considered: the lower value represents the average separation of the three (four) constituents, whereas the larger r corresponds to the average separation between the Λ and the deuteron (triton) core. See [59] for full details on the models. Middle: projection of the relative statistical uncertainty achievable with a minimum bias Pb–Pb integrated luminosity of $L_{\rm int}$= 10 nb^{-1} and the upgraded ALICE detector (in red) compared to the relative statistical uncertainty of the Run 2 measurements (in black). Bottom: significance in the discrimination between the two models, assuming 10% and 20% systematic uncertainty in addition to the statistical uncertainty expected with $L_{\rm int}$= 10 nb^{-1}. For $^3_\Lambda$H, the coalescence prediction considered is for r = 6.8 fm (corresponding to the black continuous lines in the top panel). Figure from Ref. [1].

that will be collected for light anti-nuclei will lead to the first precise measurements of the mass of light anti-nuclei with A = 3, by means of the Time-Of-Flight detector [72]. This measurement will make it possible to test Charge Symmetry Breaking (CSB) in the anti-nuclei sector due to the differences in the up and down quark masses and due to electromagnetic effects [73]. The differences in A = 3 systems are extensions of the neutron-proton difference. Although the mass difference for the lightest "mirror pair" with A = 3 (i.e. ^{3}H,^{3}He), is well known (at the level of O(eV) [74]), no measurement has been performed in the anti-matter sector and will be accessible with $L_{\rm int}$ = 10 nb^{-1}.

In the right panel of Fig. 3, the expected significance of anti-hyper-nuclei measurements in central Pb–Pb collisions is reported as a function of the minimum bias integrated luminosity. For each species, the decay channels with the minimum number of charged particles in the final state and with the highest detection efficiency in ALICE have been considered for this study, as reported in the legend of Fig. 3. The study of other decay channels, e.g. the three body decay of $^3_\Lambda$H that has larger theoretical branching ratio with respect to the 2-body decay [75], but lower detection efficiency in ALICE, will be also carried out profiting from the large integrated luminosity. Considering the thermal model predictions

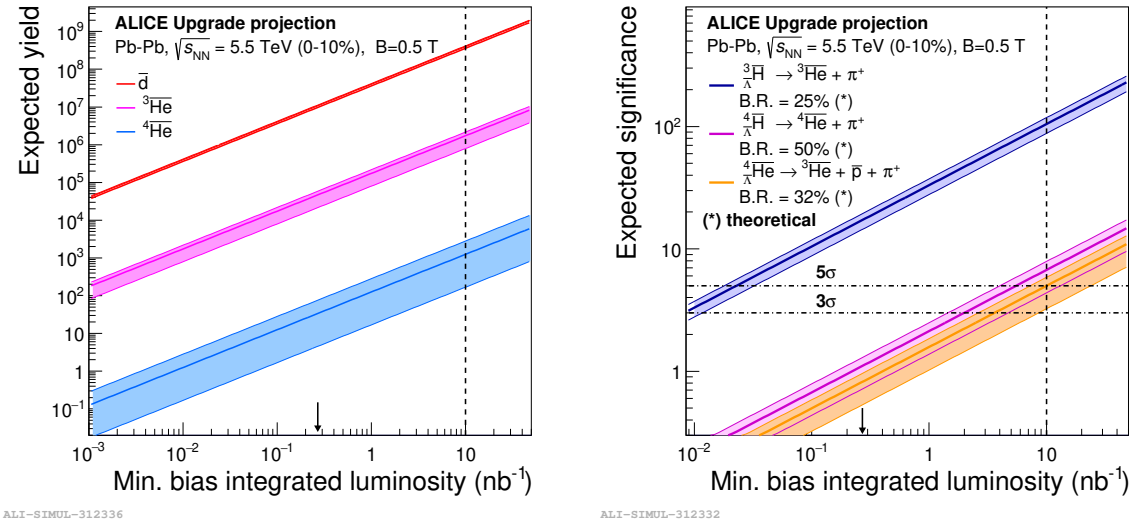

Fig. 3: Left: (raw) yield of anti-nuclei in the $2 < p_{\rm T} < 10$ GeV/c interval, detectable in 0–10% central Pb–Pb collisions with the ALICE detector as a function of the minimum bias luminosity. Right: Projected significance of anti-hyper-nuclei measurements in central Pb–Pb collisions in Runs 3 and 4 with ALICE as a function of the integrated minimum-bias luminosity. In both panels, the arrow represents the minimum bias Pb–Pb luminosity anticipated for the end of Run 2. The dashed vertical line marks the projections with $L_{\rm int} = 10\ {\rm nb}^{-1}$. The bands represents the uncertainty on model prediction for the yield (see text for details). Figures from Ref. [1].

at $T_{\rm chem}$ = 156 MeV, the expected significance of $^3_\Lambda\overline{\rm H}$, $^4_\Lambda\overline{\rm H}$ and $^4_\Lambda\overline{\rm He}$ at $L_{\rm int} = 10\ {\rm nb}^{-1}$ is 100, 7 and 5, respectively. The collected sample will enable very precise measurements of the production of $^3_\Lambda$H and $^3_\Lambda\overline{\rm H}$ and the first ever measurement of their elliptic flow as a function of $p_{\rm T}$. The discovery of $^4_\Lambda\overline{\rm H}$ and $^4_\Lambda\overline{\rm He}$ will be in reach with $L_{\rm int} = 10\ {\rm nb}^{-1}$ at the end of Run 4.

3.2.3 The hypertriton lifetime

The experimental measurement of the Λ separation energy of the $^3_\Lambda$H, $B_\Lambda = 0.13 \pm 0.05$ (stat.) $\pm$ 0.04 (syst.) MeV [76], led to the hypothesis that the lifetime of the hypertriton is equal to or only slightly below the free Λ lifetime $\tau(\Lambda) = 263.2 \pm 0.2$ ps [77]. Three different experimental techniques have been used to tackle this question: photographic emulsion, He bubble chambers, and counter experiments. The average for the emulsion experiments is 203^{+40}_{-31} ps [78], for the He bubble chambers is 193^{+15}_{-13} ps [78], and for the combination of both visualizing techniques is 193^{+14}_{-13} ps [78]. The most recent results, 181 $^{+54}_{-39}\pm$ 33 ps and 142 $^{+24}_{-21}\pm$ 29 ps, have been obtained with the counter technique in heavy-ion collisions by the ALICE [79] and STAR [80] experiments, respectively. This technique is currently the one with the highest precision (14-16%) and the weighted average of heavy-ion experiments results is 185^{+28}_{-23} ps [78]. However, the few existing theoretical calculations point in the direction of the hypothesis mentioned at the beginning of this section. The first theoretical determination of $\tau(^3_\Lambda{\rm H})$ (by Dalitz and Rayet, [81]) ranged from 239.3 to 255.5 ps. More recent calculations from Congleton [82] and Kamada [75] estimated values of 232 ps and 256 ps, respectively. The deviation of the experimental results from the theoretical calculations and the free Λ lifetime, by more than 2σ, is known as the "hypertriton lifetime puzzle".

With the expected integrated Pb–Pb luminosity at the end of the LHC Run 4, the statistical uncer-

tainty on the lifetime will be reduced down to 1%. In parallel, a reduction of the systematic uncertainty ($\sim$ 10% in the most recent ALICE measurements), will be achieved with the upgraded ALICE ITS that will allow for a reduction of the uncertainty due to tracking and material budget. To improve even further down the control on the systematic uncertainty, a better understanding of the corrections for the absorption in the material will be crucial.

3.2.4 Σ-hypernuclei

In addition to measurements of Λ-hypernuclei, also the search for Σ-hypernuclei is to be considered with the luminosities forseen for the LHC Runs 3 and 4. Theory calculations for the ΣNN system suggest the presence of a near-threshold narrow ($\sim$2 MeV wide) quasi-bound state in the I = 1 and J = 1/2 configuration, where the possible isospin and spin states are 0, 1, 2 and 1/2, 3/2, respectively [83]. Among Σ-hypernuclei, only the ${}^{4}_{\Sigma^0}\mathrm{He}$ bound state has been observed so far, using the ${}^{4}\mathrm{He}(K^-,\pi^-)$ reaction [84]. When the Σ^0 hyperon is bound inside a nucleus, the electromagnetic decay is dominated by the conversion reaction $\Sigma^0\mathrm{N} \rightarrow \Lambda\mathrm{N}$, thus the partial width of electromagnetic decay is expected to be reduced substantially. However, for the I = 2 state the conversion reaction is not allowed and the electromagnetic decay becomes prominent. Experimental searches for Σ-hypertriton bound states will also profit from the Pb–Pb data-taking programme of the LHC Runs 3 and 4 to exploit the strong decay ${}^{3}_{\Sigma^0}\mathrm{H}$ $({}^{3}_{\bar{\Sigma}^0}\overline{\mathrm{H}})$ $\rightarrow$ Λ $(\overline{\Lambda})$ + d and the decay ${}^{3}_{\Sigma^0}\mathrm{H}$ $({}^{3}_{\bar{\Sigma}^0}\overline{\mathrm{H}})$ $\rightarrow$ ${}^{3}_{\Lambda}\mathrm{H}$ $({}^{3}_{\bar{\Lambda}}\overline{\mathrm{H}})$ + γ following a similar strategy to the detected electromagnetic decay of Σ^0 $(\overline{\Sigma}^0)$ $\rightarrow$ Λ $(\overline{\Lambda})$ + γ [85]. The signal of hypertriton can be reconstructed in ALICE as discussed in Sec. 3.2.2. The soft photon can be identified by exploiting the conversion into electron pairs in the detector material of the ITS and Time Projection Chamber ($X/X_0 \approx 9\,\%$ considering the upgraded ITS and the TPC together), covering the pseudorapidity range $|\eta| < 0.8$, over the full azimuth ($\Delta\varphi = 2\pi$) [86]. Alternatively, the photon can be detected in the PHOS calorimeter, but with limited acceptance of $\Delta\varphi = 100^{\mathrm{o}}$ and $|\eta| < 0.12$ [86]. The search for Σ-hypernuclei via electromagnetic decay will be carried out in ALICE profiting from the expected detector performance and detection of about 10^5 hypertriton candidates (see Fig. 3) in 0–10% central Pb–Pb collisions at L_{int} = 10 nb^{-1}.

3.2.5 Exotic QCD bound states

At LHC energies, potential QCD bound states that have more complex structures such as pentaquarks, tetraquarks, hadron molecules or dibaryon states could be produced. In particular, the possibility to detect and measure f_0(980), N(1875), NΞ, NΩ and NΛ_c in heavy-ion collisions with the unprecedented statistics of the LHC Runs 3 and 4 programme has been investigated. The advanced capabilities of the ALICE experiment in terms of hadron identification, including topological reconstruction of weak decays, are particularly suited for these studies.

The per-event yields of these states $(\mathrm{d}N/\mathrm{d}y)_{\mathrm{th}}$ predicted by quark- and hadron-coalescence models [60] and the statistical-thermal model [45] are reported in Tab. 6.

The total number of signals ($\mathrm{S}_{\mathrm{raw}}$) detectable in ALICE with a minimum bias Pb–Pb integrated luminosity of 10 nb^{-1} have been estimated assuming the same detector performance as in Run 2 [87,88]. The significance is defined as $\frac{\mathrm{S}}{\sqrt{\mathrm{S+B}}}$, where S and B are the integrals of the signal and background distributions, respectively, in a $\pm$ 3 σ window centered at the nominal mass from [77]. σ is $\Gamma/2.35$, where Γ is the resonance width taken from [77]. The significance for f_0(980) and N(1835) was extracted assuming a combinatorial background in the invariant mass range under study. Such combinatorics was computed based on particle species that can populate the invariant mass distribution, making use of the corresponding momentum distribution as measured in ALICE in Run 2 (e.g. individual primary charged pions paired as candidates for the $\mathrm{f}_0(980) \rightarrow \pi^+ + \pi^-$ channel) and assuming a uniform distribution in φ

and η [2]. The resulting significance is reported in the last row of Tab. 6 for the most pessimistic scenario, in which production occurs via quark coalescence, and the most optimistic scenario, corresponding to thermal production.

Measurements of $f_0(980)$ and N(1875) will be feasible in Runs 3 and 4 and will shed light on the highly-debated nature of the states (hadrons or hadronic molecules). In particular, the N(1875) can be considered a molecular bound state and at the same time the strange partner of the recently discovered pentaquark P_c [90]. Because the structure of exotic states is related to the fundamental properties of Quantum Chromodynamics (QCD), their observation can provide new insights on the properties of QCD at finite temperature and density, for instance that tetraquark condensation may lead to a second chiral phase transition [60]. Several possible states have been studied and predictions are available on the expected yields at LHC energies [60]. Among the possible dibaryon bound states, the NΩ, NΞ and NΛ_c look promising in terms of detection feasibility. Their detection and baryon-baryon correlations will be useful for hyperon correlation studies, providing new insights into the baryon-baryon attractive potential as well as upper limits on the formation of such bound states in central heavy-ion collisions.

Very recently, a study was reported on the production of exotic charmonia, specifically the possible tetraquark state X(3872), in Pb-Pb and Kr-Kr collisions at LHC collision energies [91]. For X(3872) production in Pb-Pb collisions the authors predict, using the statistical hadronization model for charm, a transverse momentum distribution similar in shape to that for J/ψ mesons with a strong enhancement at low transverse momenta and a production yield of about 1% relative to that for J/ψ. It would be interesting and feasible to test this prediction in LHC Run 3 and especially Run 4.

[2] An additional factor is introduced if the decay particle is reconstructed via invariant mass, since the candidate may belong also to the background.

Table 6: Properties and yields of exotic states in 0–10% central Pb–Pb collisions at $\sqrt{s_{\rm NN}} = 5.5$ TeV. Theoretical predictions of yields per event, $(\mathrm{d}N/\mathrm{d}y)_{\rm th}$, are given in three different scenarios: quark- and hadron-coalescence [60], and thermal model [49]. $S_{\rm raw}$ represents the total detectable yield at the Pb–Pb luminosity of 10 nb^{-1}, taking into account the branching ratios (B.R.) of the decay channels considered and assuming the ALICE detector performance as in Run 2 [87, 88]. For $f_0(980)$, a $\mathrm{K\overline{K}}$ state and a decay into $\mathrm{K\overline{K}}$ with B.R. = 10^{-3} is assumed for hadron coalescence †. A tetraquark state is assumed for quark coalescence and a decay into $\pi\pi$. The same decay channel is assumed for the thermal production case. Masses are from [89].

	Model	$f_0(980)$	N(1875)	NΞ	NΩ	NΛ_c
Structure		$\mathrm{qq\bar{q}\bar{q}}$ or $\mathrm{K\overline{K}}$	hadron molecule	dibaryon	dibaryon	dibaryon
$\left(\frac{\mathrm{d}N}{\mathrm{d}y}\right)_{\rm th}$	q-coal.	5.4×10^{-2}	-	-	1.8×10^{-3}	1.5×10^{-3}
	h-coal.	3.2 †	-	-	1.6×10^{-3}	5×10^{-3}
	thermal	10	3×10^{-1}	8.7×10^{-3}	5.7×10^{-3}	4×10^{-3}
Decay channel		$\pi\pi$ / $\mathrm{K\overline{K}}$	$\Sigma^*(\to \Lambda\pi)\mathrm{K}$	$\Xi \to \Lambda\pi$	$\Omega \to \Lambda\mathrm{K}$	$\Lambda_c \to \pi\mathrm{Kp}$ + $\Lambda_c \to \mathrm{K^0_S p}$
B.R. (%)		dominant / seen†	unknown (87)	99.9	67.8	6.2 + 1.58
Mass (MeV/c^2)		990	1850 – 1920	-	-	-
Width (MeV/c^2)		10 – 100	120 – 250	-	-	-
$S_{\rm raw}$	q-coal.	1.8×10^8	-	-	6.2×10^4	1.5×10^4
	h-coal.	6.4×10^6 †	-	-	5.5×10^4	5.1×10^4
	thermal	3.6×10^{10}	5.5×10^7	6.7×10^5	1.9×10^5	4.1×10^4
$\frac{\mathrm{S}}{\sqrt{\mathrm{S+B}}}$	q-coal.	130-3.5	-	-	-	-
	h-coal.	-	-	-	-	-
	thermal	2600-70	520-360	-	-	-

3.2.6 Implications of anti-nuclei measurements for cosmic-ray physics and dark-matter searches

The HL-LHC physics program with pp and p–Pb collisions will allow for precision measurements of anti-nuclei production and related observables that have implications for cosmic-ray physics and dark-matter searches. Cosmic-ray (CR) anti-nuclei $\overline{\mathrm{p}}$, $\overline{\mathrm{d}}$, and $^3\overline{\mathrm{He}}$ have long been considered as probes of new physics, such as dark matter annihilation [92–103]. Detecting these particles is one of the main goals of various CR experiments (e.g. AMS-02 [104, 105], GAPS [106, 107], BESS-Polar [108]).

The galaxy produces CR anti-nuclei as secondaries, due to collisions of CR protons and helium with interstellar matter. Information from accelerator experiments is essential for the theoretical description of the background constituted by these secondary anti-nuclei. The flux of secondary anti-nuclei can be calculated with only minor sensitivity to the details of CR astrophysics. The point is to use secondary-to-secondary flux ratios, where astrophysical uncertainties largely cancel. Secondary $\overline{\mathrm{p}}$, $\overline{\mathrm{d}}$, and $^3\overline{\mathrm{He}}$ are all formed dominantly by the same set of reactions. Using this basic fact, an explicit prediction for the locally observable flux of secondary $\overline{\mathrm{d}}$, relative to the flux of secondary $\overline{\mathrm{p}}$ can be derived [109–111]:

$$\frac{J_{\overline{\mathrm{d}}}(\mathcal{R})}{J_{\overline{\mathrm{p}}}(\mathcal{R})} = \frac{\int \mathrm{d}\epsilon\, J_{\mathrm{p}}(\epsilon)\, \frac{\mathrm{d}\sigma_{\mathrm{pp}\to\overline{\mathrm{d}}}(\epsilon,\epsilon_{\overline{\mathrm{d}}})}{\mathrm{d}\epsilon_{\overline{\mathrm{d}}}}}{\int \mathrm{d}\epsilon\, J_{\mathrm{p}}(\epsilon)\, \frac{\mathrm{d}\sigma_{\mathrm{pp}\to\overline{\mathrm{p}}}(\epsilon,\epsilon_{\overline{\mathrm{p}}})}{\mathrm{d}\epsilon_{\overline{\mathrm{p}}}} + \left(\sigma_{\overline{\mathrm{d}}}(\epsilon_{\overline{\mathrm{d}}}) - \sigma_{\overline{\mathrm{p}}}(\epsilon_{\overline{\mathrm{p}}})\right) J_{\overline{\mathrm{p}}}(\mathcal{R})}. \tag{7}$$

Here $J_{\overline{\mathrm{d}}}(\mathcal{R})$ is the predicted $\overline{\mathrm{d}}$ flux, given at magnetic rigidity $\mathcal{R} = p/Z$, where p is the momentum and Z is the electric charge. $J_{\overline{\mathrm{p}}}(\mathcal{R})$ is the (already well-measured [112]) $\overline{\mathrm{p}}$ flux at the same rigidity, and $J_{\mathrm{p}}(\epsilon)$ is the proton flux [113] at energy ϵ. $\frac{\mathrm{d}\sigma_{\mathrm{pp}\to\bar{x}}(\epsilon,\epsilon_{\bar{x}})}{\mathrm{d}\epsilon_{\bar{x}}}$ and $\sigma_{\bar{x}}(\epsilon_{\bar{x}})$ are the inclusive production and inelastic cross sections, respectively, with $x = \mathrm{d}, \mathrm{p}$. The particle energy $\epsilon_{\bar{x}}$ for a nucleus with mass number A is evaluated at $\mathcal{R}$: $\epsilon_{\overline{\mathrm{p}}} = \sqrt{\mathcal{R}^2 + \mathrm{A}^2 m_{\mathrm{p}}^2}$. To describe $^3\overline{\mathrm{He}}$ we use an analogous expression to Eq. (7), adding the production of $\overline{\mathrm{t}}$ which decays to $^3\overline{\mathrm{He}}$. More details, including the relation of the differential cross section appearing in Eq. (7) to the Lorentz-invariant differential cross section measurable at the LHC, can be found in [111].

The cross section for producing an anti-nucleus can be parameterized in terms of the anti-proton cross section, using the coalescence factor B_{A}: $(\epsilon_{\mathrm{A}}\mathrm{d}\sigma/\mathrm{d}^3p)_{\mathrm{pp}\to\mathrm{A}} = B_{\mathrm{A}}/\sigma_{\mathrm{pp}}^{\mathrm{A}-1}[(\epsilon_{\overline{\mathrm{p}}}\mathrm{d}\sigma/\mathrm{d}^3p)_{\mathrm{pp}\to\overline{\mathrm{p}}}]^{\mathrm{A}}$, where σ_{pp} is the total inelastic pp cross section. Here, for simplicity, threshold effects are omitted [111, 114, 115]. Using Eq. (7), and plugging in the coalescence factors experimentally obtained at the LHC [116], the predicted flux ratios can be obtained. Secondary CR production is dominated by the low p_{T} region. As a result, the impact on the CR flux, due to p_{T}-dependent B_{A}, can be factored out to good approximation, allowing us to derive simple approximate formulae [3] [111]:

$$\frac{J_{\overline{\mathrm{d}}}(\mathcal{R})}{J_{\overline{\mathrm{p}}}(\mathcal{R})}|_{\mathcal{R}=100\mathrm{GV}} \approx 4\times10^{-4}\left(\frac{B_2}{1.5\times10^{-2}\ \mathrm{GeV}^2}\right), \tag{8}$$

$$\frac{J_{^3\overline{\mathrm{He}}}(\mathcal{R})}{J_{\overline{\mathrm{p}}}(\mathcal{R})}|_{\mathcal{R}=100\mathrm{GV}} \approx 2\times10^{-7}\left(\frac{B_3}{1.5\times10^{-4}\ \mathrm{GeV}^4}\right), \tag{9}$$

where, for CR studies, the B_2 and B_3 values should be read from the average yield in the range $p_{\mathrm{T}}/\mathrm{A} = (0-0.5)\ \mathrm{GeV}/c$ in the accelerator analysis. The precision requirements (O(10%)) on the flux ratio determination for the astrophysical applications discussed here will be matched by measuring B_2 and B_3 in the lowest p_{T} bin with a relative systematic uncertainty of the order of 10% [116]. The latter largely dominates the statistical uncertainty that is expected to be of O(0.1%) already with $L_{\mathrm{int}} = 6\ \mathrm{pb}^{-1}$ in pp collisions at $\sqrt{s} = 5.5$ TeV. Moreover, a first measurement of B_4 in pp collisions will be achievable in the same sample. The statistical precision on B_4 can be lowered to the 10% level if a

[3] Note that the rigidity $\mathcal{R} = 100$ GV refers to the CR experiment rest frame, which is boosted w.r.t. the proton-proton collision centre of mass frame. In the proton-proton collision centre of mass frame, the anti-nuclei are formed close to threshold.

luminosity of 200 pb^{-1} in pp collisions at $\sqrt{s} = 14$ TeV can be inspected with a dedicated trigger for (anti-)nuclei.

It is important to note that the B_{A} measurement [116] performed by ALICE during the LHC Run 1 was confined to mid-rapidity, $|y| < 0.5$. Possible y dependence of the coalescence factor B_{A} at $y = \mathcal{O}(1)$, or variation of the $\overline{\mathrm{p}}$ differential cross section with respect to current parameterisations [117], would affect the prediction in Eqs. (8-9). It would be an important task of future LHC measurements to test these effects. Similarly important, albeit – possibly – beyond the reach of the LHC, would be to study the low $\sqrt{s} = \mathcal{O}(10)$ GeV behaviour of B_{A} [111].

3.2.7 Implications of anti-nuclei measurements and hyperon-nucleon correlations for neutron star physics

Although the neutron star crust is composed of neutrons, within the innermost core hyperons could be present [118]. Whether or not this scenario holds true depends on the two- and three-body hyperon nucleon interactions (YN and YNN) that are still only rather scarcely constrained experimentally.
At present the mass range for observed neutron stars is about (0.9 – 3.0)$M_{\odot}$ within errors [119], where $M_{\odot}$ stands for the solar mass. The equation of state (EoS) of neutron stars is constrained by the mass-radius relationship, in particular, the maximum mass (M_{max}). An EoS with "conventional" (N+π) degrees of freedom provides M_{max} invariably above $2M_{\odot}$ [120–122]. However, adding the Λ hyperon in the hadronic basis softens the EoS and, as a consequence, significantly reduces M_{max}. The solution of this so-called "hyperon puzzle" is non-trivial, and is presently the subject of very active research.

Thanks to the large yields of free hyperons and exotic (anti-)hyper-nuclei that can be produced in collider experiments and the excellent particle identification capabilities of the ALICE experiment, the upcoming experimental campaigns in Runs 3 and 4 at the LHC offer a unique opportunity to quantitatively characterise hypermatter under controlled (laboratory) conditions and infer on the equation of state of compact objects as neutron stars.

One of the crucial element to solve the “hyperon puzzle” is the determination of the ΛNN three-body forces. Calculations show that with a parameterization of these forces compatible with the hypernuclear binding energies, the admixture of Λ’s in neutron star matter gets strongly reduced such that the pressure to support a $2M_{\odot}$ neutron star can be maintained [123]. The observation of neutron-rich Λ hyper-nuclei like ${}^{4}_{\Lambda}\mathrm{H}$ etc. at colliders could be very promising for studying the effects of the three-body ΛNN forces in dense strongly interacting matter since a precise knowledge of light neutron-rich hypernuclei energy level structure could imply far-reaching consequences for dense strange stellar matter properties.

Another promising way to contribute to the understanding of the hyperon puzzle is to pin down the hyperon-nucleon two-body interaction for hyperons such as Σ^{-} and Ξ^{-}. These hyperons can also be produced within neutron rich matter (n + n $\rightarrow \Sigma^{-}+$ p, Λ + n $\rightarrow \Xi^{-}+$ p) depending on their interaction with the surrounding neutrons. Some models assume a repulsive pΣ interaction and postulate that Σ^{-} can appear in neutron rich matter only starting from baryon densities $\rho \simeq 4\rho_0$ (where ρ_0 is the density of standard nuclear matter) [124]. For Ξ, no reliable experimental information about the interaction is available. Recent studies [125] showed that the femtoscopy technique applied to pp and p–Pb collisions at LHC energies are particularly suited to study the final state interaction between nucleons and strange baryons (e.g.: Λ–p) and between two strange baryons (e.g.: Λ–Λ). Indeed, small colliding systems such as pp and p–Pb lead to hadron sources of rather small dimensions, of the order of 1 fm, in the range where the strong interaction is mostly evident. Also, the production mechanism of hadrons in minimum bias pp and p–Pb collisions is not affected by the intermediate creation of a QGP and its time-dependent evolution as in Pb–Pb collisions at LHC energies. This allows for a more precise study of the hadron-hadron interactions.

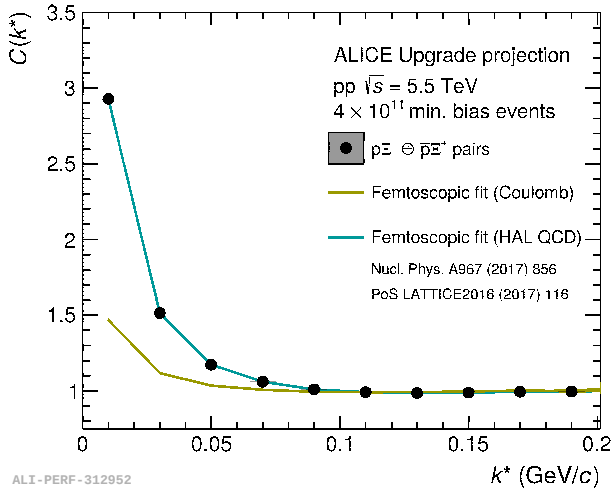

Fig. 4: Expected $\mathrm{p\Xi^-}$ + $\mathrm{\bar{p}\Xi^+}$ correlation for pp collisions at $\sqrt{s} = 5.5$ TeV and 4×10^{11} minimum bias events, corresponding to $L_{\mathrm{int}} = 6\ \mathrm{pb}^{-1}$. Only statistical errors have been estimated. Figure from Ref. [1].

Among the quantitative results obtained by ALICE in Run 2 at the LHC is the first observation of the attractive $\mathrm{p\Xi^-}$ interaction. Figure 4 shows the expected $\mathrm{p\Xi}$ correlation for the Run 3 pp sample as a function of the relative momentum $k*$. The projection is obtained on the basis of the current prediction by the HAL-QCD lQCD group [126,127] that is in agreement with the Run 2 results. The clear deviation from the Coulomb-only correlation function shows the effect of the strong attractive interaction and the expected statistics will allow for a quantitative determination of the scattering parameters and the test of different hadronic models [128, 129]. The investigation will also be extended to the Σ^0 hyperon, since in Run 3 and 4 we expect a total of 500,000 $\mathrm{p\Sigma^0}$ pairs to be used to study the femtoscopy correlation.

In summary, massive neutron stars with $M \sim 2M_{\odot}$ are very intriguing recent observations in relativistic astrophysics. An improved account of the two-body YN interaction, the three-body ΛNN forces, and the contribution of multi-strange hyperons in the EoS is crucially important for more realistic description of compact astrophysical objects, in particular neutron and hybrid stars. The measurement of hyper-nuclei and hyperon correlations with the HL-LHC project are suggested as a promising tool for astrophysical applications.

3.3 Fluctuations of conserved charges

3.3.1 Physics introduction and observables

In the phase diagram of strongly interacting matter at zero net baryon density, the presence of a chiral phase transition between hadronic matter and a QGP has been conjectured [130], and arguments have been presented [131, 132] in lQCD that the transition, for vanishing light quark masses, is of second order and belongs to the O(4) universality class. Due to the small but finite physical quark masses, in lQCD a rapid crossover is found [133–137] which, however, exhibits pseudo-critical features due to the smallness of the u- and d-quark masses and the proximity of the crossover region to the O(4) line [131, 138].

In general, fluctuations can be linked to critical behaviour associated with a phase transition, and it has been pointed out that fluctuations of conserved charges in heavy-ion collisions can provide an experimental observable to test for critical behaviour in the phase diagram of strongly interacting matter [139–142]. These fluctuations can be related to susceptibilities, specifically to the derivatives of the pressure with respect to the chemical potentials corresponding to the conserved charges. Here, the

relevant 'charges' are baryon number B, strangeness S, and electrical charge Q, and the corresponding chemical potentials are μ_B, μ_S, and μ_Q. The susceptibilities are defined (see e.g. [142, 143]) in terms of dimensionless normalized chemical potentials $\hat{\mu}_X \equiv \mu_X/T$ as

$$\chi^{BQS}_{ijk}(T) = \left.\frac{\partial P(T,\hat{\mu})/T^4}{\partial \hat{\mu}_B^i \partial \hat{\mu}_Q^j \partial \hat{\mu}_S^k}\right|_{\hat{\mu}=0} . \tag{10}$$

The generalized susceptibilities can be computed in lQCD at vanishing chemical potential, exactly the conditions probed by experiments at the LHC. Within the Grand Canonical Ensemble (GCE), these generalized susceptibilities can be related to experimental measurements of the fluctuations of particle multiplicities, such as the net number of baryons. For instance, a measurement of higher moments or cumulants of net baryon number in relativistic nuclear collisions can be directly related [144–149] to theoretical predictions from lQCD or from more phenomenological models of the chiral phase transition [150, 151] to shed light on the possible critical behaviour near the QCD phase boundary. For a distribution of the net baryon number, $\Delta N_B = N_B - N_{\overline{B}}$, with moments defined as

$$\mu_i = \langle (\Delta N_B - \langle \Delta N_B \rangle)^i \rangle, \tag{11}$$

the cumulants κ_i can be directly linked to the generalized susceptibilities such as

$$\kappa_2 = \mu_2 = VT^3\chi_2^B \tag{12}$$

$$\kappa_3 = \mu_3 = VT^3\chi_3^B \tag{13}$$

$$\kappa_4 = \mu_4 - 3\mu_2^2 = VT^3\chi_4^B . \tag{14}$$

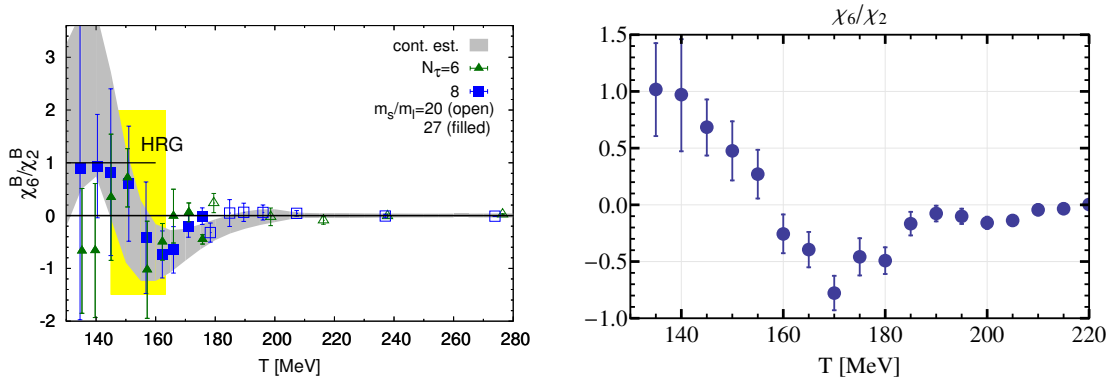

Fig. 5: Ratio of sixth to second-order baryon number susceptibilities from lQCD. The left-hand figure is from [140]. The right-hand figure is calculated from recent lQCD data on sixth and second order susceptibilities from [152].

In the O(4) universality class, a singular contribution to the pressure shows up for higher order moments. More specifically, at vanishing chemical potential, all odd susceptibilities of the net baryon number vanish. In addition, in the O(4) universality class, the second- and fourth-order susceptibilities remain finite at the phase transition temperature at $\mu_B = 0$ in the chiral limit, implying that only sixth- and higher-order susceptibilities diverge [139, 141]. Thus, for physical quark masses and at $\mu_B = 0$,

only higher order cumulants κ_n with $n \geq 6$ can exhibit O(4) criticality, whereas at finite μ_B this is already the case for κ_n with $n \geq 3$.

Sensitivity to chiral criticality due to the vicinity of the O(4) line at $\mu_B = 0$ is borne out in phenomenological models as is shown in [141, 150], and in lQCD predictions [140, 152], by strong deviations of χ_6^B/χ_2^B from unity as shown in Fig. 5.

We note that a convenient baseline for the cumulants of multiplicity distributions and fluctuations of produced particles in relativistic nuclear collisions can be obtained in the framework of the hadron resonance gas (HRG) [144, 152–155]. In this model, uncorrelated Poissonian fluctuations of baryon and anti-baryon multiplicities result in a Skellam distribution for the net baryon number, in which the higher moments and cumulants can all be related to the first moments in the following way [154, 156, 157]:

$$\kappa_n(N_B - N_{\overline{B}}) = \langle (N_B + (-1)^n N_{\overline{B}}) \rangle \tag{15}$$

For zero net baryon number then all odd cumulants vanish and all even cumulants are identical.

Measuring such cumulants with precision poses a formidable experimental challenge due to the requirement of very large data sets ($> 10^9$ events of a particular event or centrality class) with superb control of systematic uncertainties. As a first physics case to consider along this line, the impact of measuring the distribution of net protons as a proxy for net baryons needs to be studied further. We note that, at LHC energy and low transverse momentum, particle production near mid-rapidity takes place mostly in gluonic processes, implying that isospin asymmetries, as in the colliding nuclei, are absent. As a consequence, the production yields of protons and neutrons should be very close. For light nuclei this isospin symmetry has been checked experimentally, albeit with significant uncertainties. In addition, non-critical contributions to the cumulants from volume fluctuations and global baryon number conservation [145, 157, 158] need to be evaluated and the data corrected accordingly. Furthermore, in particular for comparison to lQCD predictions, care needs to be taken to keep experimental cuts such as in p_{T} to a minimum insofar as such cuts cannot be introduced in lQCD [159, 160].

Two-particle correlations with net baryons can also be used to explore transport properties of the hydrodynamic evolution. The baryon diffusion constant D is a fundamental transport property of the quark-gluon plasma, similar to shear viscosity η or bulk viscosity ζ. It characterizes the mobility of baryon number, and is predicted to be finite at the LHC despite the fact that $\mu_B \sim 0$. A two-particle correlation function as been proposed [161], which explores correlations of net-baryon fluctuations as a function of separations in azimuthal angle and rapidity, and can provide experimental constraints on the diffusion coefficient D. As $\mu_B \sim 0$ at the LHC, such an analysis has yet to be carried out in Run 1 and 2 data since it is statistically challenging, and will be greatly aided by the increase by about a factor 100 in the Pb–Pb integrated luminosity foreseen for Runs 3 and 4.

3.3.2 State of the art experimental measurements and present limitations

Net proton fluctuations measured by the ALICE experiment and in the STAR beam energy scan program provide interesting and stimulating results. The measurements at STAR [162] complement the corresponding measurements from ALICE, which will make it possible to pin down the global structure of the phase diagram of strongly interacting matter in a wide range of temperatures and net-baryon densities. However, before drawing firm conclusions by confronting theoretical calculations with data, non-dynamical contributions stemming from unavoidable fluctuations of participant nucleons and overall baryon number conservation have to be subtracted from the experimental measurements. Both of these non-dynamical contributions, which exist neither in lQCD nor in the HRG model, lead to deviations from the baseline as defined in Eq. 15. Indeed, the acceptance dependence of the second-order cumulants of net-protons measured by ALICE [163] exhibits deviations from the non-critical (Skellam) baseline. However, these deviations were explained by global baryon number conservation [157, 158, 163], which,

in accordance with the experimental findings, decreases the amount of fluctuations with the increasing acceptance. This is the first experimental verification of the lQCD predictions for the second-order cumulants of net-baryon distributions. This also serves as a strong support of the HRG model, in that experimental measurements of the second cumulants of net-protons do not show any evidence of criticality and actually coincide with the second cumulants of the Skellam distribution. In order to probe critical phenomena, higher cumulants beyond the second order have to be addressed.

As mentioned in the previous section, even at vanishing net-baryon densities, lQCD and other theoretical calculations such as Polyakov-loop extended Quark- Meson model (PQM) [150] predict critical fluctuations encoded in the deviations of net-baryon κ_4/κ_2 and κ_6/κ_2 from unity. Moreover, at the pseudo critical temperature of about 156 MeV the magnitudes of κ_4/κ_2 and κ_6/κ_2 are predicted in Ref. [150] to be 0.5 and -0.39, respectively. Similar values of κ_6/κ_2 are quoted in different lQCD calculations as presented in Fig 5. These numbers, shown in Fig. 6, do not take into account experimental artefacts such as global net-baryon number conservation and unavoidable fluctuations of participating nucleons from event to event. Also shown are the values of of κ_4/κ_2 and κ_6/κ_2 after accounting for these non-dynamical effects using the procedure in Refs. [157, 158, 164]. Even after accounting for participant fluctuations and global baryon number conservation we observe deviations in κ_4/κ_2 and κ_6/κ_2 from unity, although they are somewhat reduced. This motivates our experimental program of measuring higher moments of net-proton distributions at the LHC energies. Also, fluctuation measurements are underway in the strange baryon sector to approach measurements of net baryon number fluctuations. All this will be greatly helped by the anticipated dramatic increase in statistics in Runs 3 and 4.

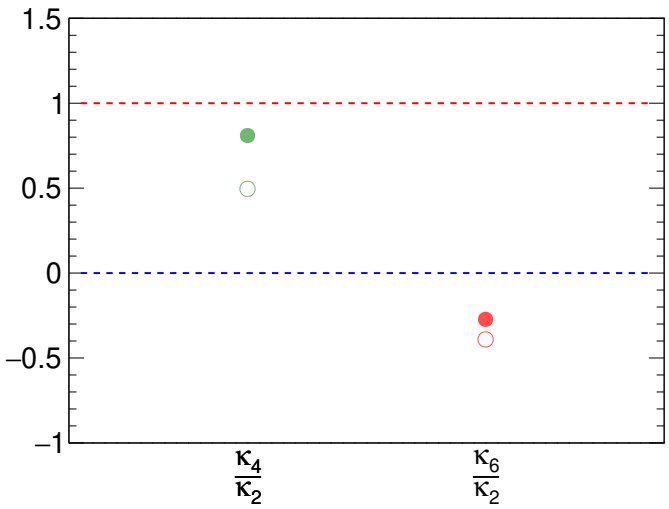

Fig. 6: κ_4/κ_2 and κ_6/κ_2 as calculated within PQM [150] model (open symbols). After taking into account contributions from participant nucleon fluctuations and global baryon number conservation [157, 158], the deviations from unity decrease (closed symbols).

3.3.3 Projections for HL-LHC

As discussed above, precise studies of the higher-order cumulants of particle multiplicity distributions are needed to verify theoretical predictions. In this section we estimate the statistics needed to address these measurements with the ALICE experiment. For this purpose two distinct Monte Carlo simulations

have been developed. In the first approach, following recent developments in [165], the probability distribution function of net-protons is approximated by a superposition of two Gaussian distributions which has four free parameters. Using the experimentally measured second cumulant of net-protons for 0-5 % most central Pb–Pb collisions [163] and the κ_4/κ_2 and κ_6/κ_2 ratios from the PQM model [150], absolute values for κ_4 and κ_6 were obtained first. These values were adjusted to account for fluctuations from participant nucleons in 0-5% most central Pb–Pb collisions and global baryon number conservation [157, 158]. Finally, the free parameters of the double Gaussian distribution were fixed using the expected values of κ_1 , κ_2 , κ_4 and κ_6 , where κ_1 equals zero by definition. The event-by-event net-proton number was sampled from the double Gaussian function thus generating the net-proton distribution for a given number of events. In the second approach the probability distribution functions of protons and anti-protons are calculated separately by exploiting the Pearson curve method [166]. This approach also needs four measurements as inputs, which are taken as the first four cumulants of the proton and anti-proton multiplicities measured by ALICE [167]. The net-proton distribution for a given number of events is constructed by sampling the obtained proton and anti-proton probability distribution functions. In each approach, the resulting statistical uncertainties are obtained using the subsample method.

The obtained results for κ_4/κ_2 and κ_6/κ_2 and their corresponding statistical uncertainties are shown in Fig. 7 as a function of the simulated event statistics. The dashed red lines correspond to the input values predicted by PQM calculations of critical fluctuations (CF) and assuming a double Gaussian net-proton distribution, while the green dashed lines come from the Pearson curve method based on the lower-order cumulants measured by ALICE. As expected, with increasing statistics both κ_4/κ_2 and κ_6/κ_2 approach their nominal values. The statistics necessary to measure these cumulants are presented in the bottom panels of Fig. 7, where the deviations of the expected values from unity are quantified in units of the magnitudes of the statistical uncertainty (σ). As seen from the left panel of Fig. 7, for κ_4/κ_2 already 10 million events are sufficient to distinguish the expected critical fluctuations signal from unity with a statistical significance of 4σ. Similar conclusions are obtained with the Pearson curve method. Several times this amount of data has already been recorded by ALICE, and the expected statistics in Runs 3 and 4 will make it possible to measure κ_4/κ_2 with unprecedented precision.

For κ_6/κ_2, however, significantly larger event sample is needed. As seen from the right panel of Fig. 7, more than 5 billion 0-5 % central events generated with the double Gaussian approach are needed in order to observe statistically significant deviations from unity in favor of the critical values indicated with the red dashed line. These would correspond to a minimum bias Pb–Pb integrated luminosity of 12.5 nb^{-1} in Runs 3 and 4. Results obtained with the Pearson curve method indicate that more than 200 million 0-5 % central events (corresponding to a minimum bias Pb–Pb integrated luminosity of 0.5 nb^{-1}) would be sufficient in order to claim a significant deviation from unity in favour of the corresponding expected value. This difference in the estimation of the required statistics for κ_6/κ_2 comes mainly from the different baseline values of -1.43 and -0.27 used in the Pearson and double-Gaussian methods, respectively. In addition, the value of κ_2 used in the Pearson method is about two times smaller than measured in the experiment and used in the double Gaussian method. Track reconstruction and particle identification efficiency in the fiducial acceptance in η and p_{T} efficiencies, which would increase the required number of events for a given statistical precision, are not included in the study presented here because they depend on the details of the analysis. Considering that these efficiencies are expected to range from 60% to 80%, we conclude that the Pb–Pb integrated luminosity of 13 nb^{-1} foreseen in Runs 3 and 4 (see Ch. 12) will be sufficient to probe the critical phenomena contained in κ_6/κ_2.

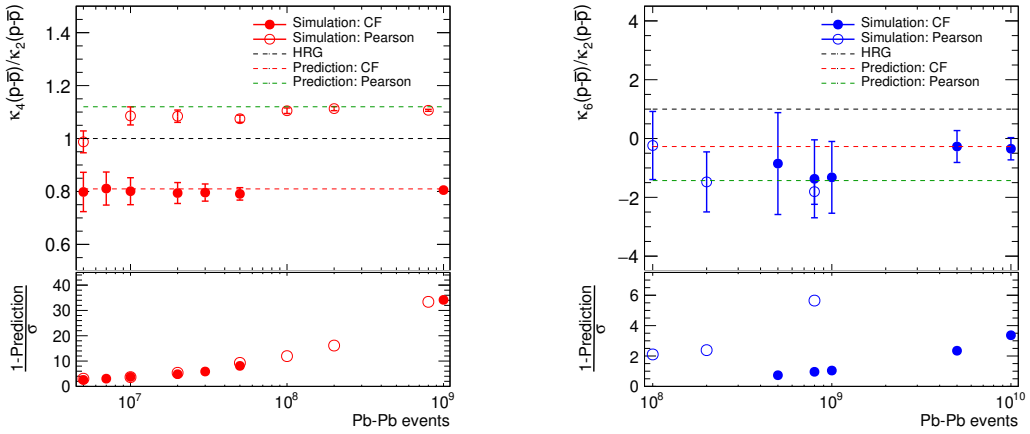

Fig. 7: Simulated values of κ_4/κ_2 (left panel) and κ_6/κ_2 (right panel) as functions of the generated number of events. Full symbols represent results obtained with the double Gaussian approach adjusted to reproduce critical fluctuations (CF) predicted in the PQM model [150]. Open symbols are obtained with the Pearson Curve Method [166].

4 Flow and Correlations

Coordinators: Soumya Mohapatra (Nevis Labs, Columbia University)

Contributors: A.F. Dobrin (CERN), S. Floerchinger (Heidelberg University), P. Huo (Stony Brook University), M. Konyushikhin (Wayne State University), W. Li (Rice University), J. Noronha-Hostler (Rutgers University), V. Okorokov (National Research Nuclear University MEPhI), B. Schenke (Brookhaven National Laboratory), M. Sievert (Rutgers University), A. Trzupek (IFJ PAN, Kraków), U.A. Wiedemann (CERN)

4.1 Introduction

It is particularly interesting to study the macroscopic properties of the QGP fluid because - at least conceptually - they are fully fixed by the microscopic properties of a renormalizable, fundamental quantum field theory, namely QCD. One key question is how macroscopic properties of QGP arise from its microscopic interactions. Many theoretical methods ranging from perturbative to non-perturbative techniques are being developed to understand this in detail and one can expect that the insights gained here will be valuable for many related problems in fields ranging from condensed matter theory to cosmology in the future. Many different fronts of research are being explored at the moment. This ranges from conceptual questions on how to consistently formulate relativistic fluid dynamics or how to solve quantum field theory in non-equilibrium situations to very concrete practical questions about the thermodynamic and transport properties (such as viscosities or conductivities) of the QGP. The description of the initial state – prior to QGP formation – and the mechanism by which the products of the collision rapidly thermalize are also under investigation. Besides the role of strong interactions, also electromagnetic interactions and in particular the role of magnetic fields are being explored. Other fronts of research concern the role of quantum anomalies, chirality and vorticity or the dependence of collective behavior on system size (nucleus-nucleus versus proton-nucleus and proton-proton collisions), on centrality and collision energy, the initial state directly after the collision, or various types of fluctuations. These challenges are discussed in more detail in this section.

4.2 Review of current status of theory on bulk and flow observables

4.2.1 QCD Equation of State

The QCD equation of state, accessible in high-energy collisions (and in the region around mid-rapidity) is one that has vanishing baryon chemical potential. It has been established for some time that it features a crossover transition to a chirally symmetric quark gluon plasma [133]. Most recent lattice calculations [168] have determined the cross-over temperature to be $T_c \simeq 156.5 \pm 1.5\,\mathrm{MeV}$. Recent efforts are also exploring the equation of state at finite μ_B, which at LHC would have relevance mainly at very forward rapidities. Here, because of the fermion sign problem in lattice QCD, methods like Taylor expansion [169–172] or imaginary chemical potentials [173–177] have to be used. To employ lattice QCD based equations of state in hydrodynamic calculations, they need to be matched to a hadron resonance gas model at low temperatures. Various equations of state [50, 178, 179], using different lattice data and different matching conditions have been used in simulations. A comparison of some of them can be found in [180], where the sensitivity of observables to the choice of equation of state was studied. For a recent theoretical proposal on how to gain experimental sensitivity on the equation of state, see ref. [181]. Currently available data are consistent with the lattice QCD equation of state, however with an $\sim 50\,\%$ error. To reduce the uncertainty, measurements of particle spectra over a wide range of colliding energies using a single detector with good particle identification, especially at low transverse momentum, would be needed. Another possibility to constrain the equation of state from experimental

data would be to extend state of the art Bayesian techniques [182] to include free parameters describing the equation of state and fit them along with other free parameters such as shear and bulk viscosities.

4.2.2 *Shear and bulk viscosities of hot nuclear matter*

Ideal fluid dynamics has been very successful in describing a variety of bulk observables in heavy ion collisions [183–185], indicating early on that the shear and bulk viscosities of the produced matter cannot be large. Calculations in the strong coupling limit using gauge gravity duality have found a value of $\eta/s = 1/4\pi$ for an $N = 4$ Supersymmetric Yang-Mills quantum system [186, 187]. This value was significantly smaller than the η/s obtained in perturbative QCD calculations, which were however, beset by significant uncertainties, mainly resulting from uncertainties in the relevant scales [188]. Recently, such perturbative calculations have been extended to include next-to-leading order corrections and a significant reduction compared to the leading order result was found [189]: At temperatures of the order of the QCD transition the η/s obtained using NLO corrections is smaller by a factor of 5 compared to the LO result, and reaches values of approximately $2/4\pi$. Extractions of transport coefficients from lattice QCD calculations [190–192] are extraordinarily hard, because a numerically difficult analytic continuation from imaginary to real times is necessary.

There are also several theoretical indications that bulk viscosity could play an important role in the QGP to hadron gas transition region (see [193] and references therein). Perturbative calculations have shown that the simple estimate $\zeta \approx 15\eta(1/3 - c_s^2)^2$ [194] is parametrically correct for QCD [195], where $(1/3 - c_s^2)$ is the deviation from conformal symmetry. Lattice calculations using the Kubo formula yield large values of ζ/s (~ 1) around T_c [196, 197] with large uncertainties [198]. The calculations also show a fast drop of ζ/s with increasing T. Parametrizations of the bulk viscosity over entropy density's temperature dependence were performed in [199] with input from [196] for the QGP phase and [200] for the hadronic phase. Similar to the case of shear viscosity, bulk viscosity over entropy density ratios have been determined also in holographic models that are supplemented with non-conformal features [201, 202]. In this approach, the ζ/s reaches a much lower peak value ~ 0.05 at temperatures slightly above T_c [202]. It remains to be understood to what extent this provides semi-quantitative guidance for the value in QCD.

Apart from theoretical calculations of the shear and bulk viscous properties, one may also constrain them by means of fluid dynamic simulations and comparison to experimental data [203, 204]. This method suffers mainly from uncertainties in the initial state (see also Section 4.2.3) and has an uncertainty of approximately a factor of 3 (for η/s) at this point. Some of the latest constraints come from simulations using the IP-Glasma initial state [205, 206], the EKRT model [207] and Bayesian analyses employing the Trento initial state model [182]. In terms of the Viscous corrections to the distribution function at freeze-out, the low-p_{T} range of the spectrum is more sensitive to the bulk viscosity than to the shear viscosity [208, 209]. Consequently, the uncertainties resulting from bulk viscous corrections are typically larger than for shear when studying p_{T} integrated observables. Precise measurements of the low-p_{T} spectra and mean-p_{T} in different collision systems will help in lowering the current uncertainties, specifically in the extraction of ζ/s. In order to disentangle features of the initial state and medium properties, it might be useful to study additional collision systems such as Ar–Ar or O–O and to perform a more detailed global analysis including refined data on harmonic flow coefficients for identified particles that become available during Run 3 and 4 (see Section 4.3.1).

4.2.3 *Initial conditions*

Modelling the exact geometry and initial conditions for a fluid dynamic description of heavy ion collisions is not a simple task, because it involves non-perturbative physics. The available descriptions for the initial state thus range from very simplistic models that assign deposited energy densities based on the wounded nucleons or binary collisions determined in a Monte-Carlo Glauber prescription, to classi-

cal effective theories of QCD that are valid in the high energy limit. The major ingredient that needs to be provided by an initial state model is the geometry of the interaction region in the plane transverse to the beam. It is entirely dominated by the positions of incoming nucleons whose fluctuations also play an important role.

Initial conditions for hydrodynamic simulations have to provide, in principle, all components of the energy momentum tensor as a function of spatial position (and initial conditions for other conserved charges, if considered). This includes, apart from the always included energy density distribution, the initial flow as well as initial viscous corrections. Initial flow is included in many recently developed models, that either assume free streaming [182], including Yang-Mills evolution, which is close to free streaming [210] or an initial flow distribution motivated by strong coupling calculations [211]. Initial viscous corrections are often set to zero. Only a few works [182,212,213] include the full viscous stress tensor provided by the initial state description.

Since the initial state models that provide the entire $T^{\mu\nu}$ all switch from essentially a freely streaming system to strongly interacting hydrodynamics at a fixed time τ, that transition is somewhat abrupt and unphysical. To improve over this situation an intermediate step using effective kinetic theory has been introduced [214, 215]. This procedure allows for a somewhat smoother matching but has yet to be used in full fledged hydrodynamic simulations. A first study that matches full kinetic theory to full viscous fluid dynamics indicates that the intermediate kinetic transport formulation becomes more important with decreasing system size [216].

As already discussed in Section 4.2.2, the choice of initial state has a significant effect on the extraction of transport coefficients. A more compact initial state and the presence of initial flow lead to a larger transverse flow, which requires a larger bulk viscosity to compensate for it and produce agreement with experimental data [213]. In addition the initial flow also affects the value of the extracted shear viscosity. Also, the models' eccentricities will affect the final momentum anisotropies, influencing the extracted shear viscosity to entropy density ratio. Two possible attempts to solve this problem have been pursued: the first is to perform a combined Bayesian analysis of all parameters [182], including those of the initial state, to find the best fit for all transport coefficients along with the initial state description. The second is to constrain an initial state description as well as possible using data from experiments other than heavy ion collisions e.g. e–p scattering data, which will hopefully be extended to e–A in a future electron ion collider facility. As mentioned above, at the moment the two approaches lead to some similar features of the initial state (product of thickness functions, presence of subnucleon structure), but also show discrepancies (size of the nucleon and sub-nucleon scales along with the size of the extracted bulk viscosity). In the near future, flow measurements in light ion collisions such as Ar–Ar, O–O etc. can also provide independent experimental constraints on initial conditions (see Section 4.3.2). Similarly, new flow observables can also help constrain the initial conditions. In particular the measurement of flow fluctuations has provided constraints on initial geometry models, in both the approaches discussed above. Analogously, the more recent studies of longitudinal flow fluctuations [217–219] and their extensions in Run 3 and 4 (see Section 4.3.3) can provide additional constraints.

4.2.4 Response functions

In a fluid dynamic description of heavy ion collisions, one can understand the azimuthal harmonic flow coefficients $v_{\rm n}$ as a response to deviations of the initial state from an azimuthally isotropic form. Mathematically, one can formulate this in terms of response functions that describe how the solution of the fluid dynamic evolution equations, as well as resulting experimental observables such as azimuthal particle distributions, get modified when the initial values of the fluid fields are changed [220–222]. In the simplest implementation, linear response functions describe the linear response of flow coefficients to eccentricities $v_n \sim \epsilon_n$, while the quadratic response functions describe terms like $v_n \sim \epsilon_a \epsilon_b$ where symmetry reasons imply $|n| = |a \pm b|$ [223,224]. Response functions can not only be used to study deviations

from azimuthal rotation symmetry but also for deviations from (approximate) Bjorken boost invariance, vanishing baryon number density, for electric fields and so on. Quite generally, response functions carry interesting information about fluid properties such as thermodynamic and transport properties. Where the response functions are known, one can infer properties of the initial state by reverse engineering. Experimentally, one can constrain properties of response functions indirectly via measurements of various particle correlation functions. It is particularly interesting to compare situations with strong deviations from a symmetry (such as peripheral collisions for the case of azimuthal rotation invariance) to situations with small deviations (such as central collisions) in order to differentiate between linear and non-linear response. For existing experimental work in this direction see [225–227] and for an example of a recent further going theoretical proposal see [228].

Detailed comparison of flow observables between experiment and theoretical calculations, especially regarding the dependence on external parameters like system size and collision energy as well as differential information such as on centrality, or particle identification will be helpful to make further progress in constraining response functions. Improvements in particle identification, transverse momentum and longitudinal coverage in Run 3 and 4 will be particularly valuable to this end.

4.3 Experimental constraints from Run 3 and 4

Since measurements of flow and correlations provide arguably the most direct manifestations of collectivity, they play naturally a central role in the scientific programme of exploring finite temperature QCD via collectivity. At the HL-LHC, much more stringent tests of the collective dynamics in nucleus–nucleus collisions will be possible. These will constrain QGP medium properties and initial conditions, as discussed in the previous section, in great detail. In the following, these newly arising opportunities are illustrated with a set of physics performance studies exploiting: 1) high-statistics particle-identified flow measurements, 2) system-size dependence of flow, and 3) longitudinal flow fluctuations.

4.3.1 Identified particle v_n

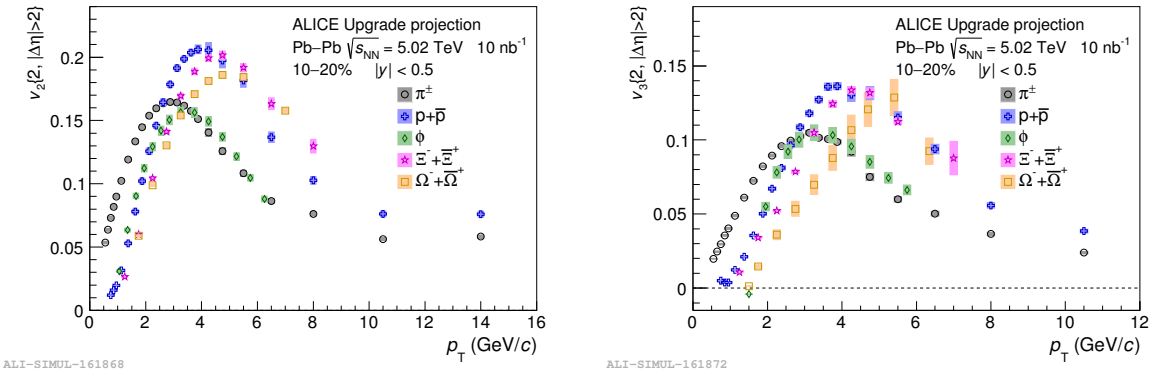

Fig. 8: ALICE projections for v_2 (left) and v_3 (right) of $\pi^{\pm}$, p+$\overline{\text{p}}$, Ξ+$\overline{\Xi}$, Ω+$\overline{\Omega}$, and the ϕ-meson in the 10–20% centrality interval for an integrated luminosity of 10 nb^{-1}. Error bars (shaded boxes) represent the projected statistical (systematic) uncertainties. Figures from Ref. [1].

In a fluid dynamic picture of A–A collisions, hadrons decouple from the fluid at late times, when the density of the system is sufficiently low and the mean-free path is sufficiently large so that a fluid dynamic description ceases to apply. Therefore, it is a direct consequence of this late time-scale, that the PID-dependence of v_n measurements tests a limitation of fluid dynamic behavior. Do all hadron

species emerge from the same common flow field? Or can one see at the higher accuracy of future v_n measurements particle specific differences in the decoupling which are related to the differences in hadronic cross sections? Quantitative questions of this kind will allow one to better constrain how significant the hadronic stage of A–A collisions contribute to v_n, and since the viscous properties of QCD change significantly in the hadronic stage, this is of direct relevance for extracting information about viscous transport coefficients with higher precision. The same class of improved PID-sensitive v_n measurements is also important for testing different dynamical pictures of hadronization. In particular since fragmentation is expected to be the dominant hadronization mechanism at high p_T while recombination becomes relevant at lower p_T, extending these PID measurements with precision over the largest possible transverse momentum range will be of interest. To this end, figure 8 shows projections from the ALICE collaboration for the v_2 and v_3 of several light-flavor species, that are expected for an integrated luminosity of 10 nb^{-1} expected in Run 3 and 4. The projected statistical uncertainties are typically negligible over the entire p_T range and in most cases the systematic uncertainties are quite small as well. These measurements will be much more precise compared to those in Run 1 and 2, and will allow for the recombination/fragmentation descriptions to be examined with unprecedented accuracy. Similar projections for heavy-flavor particles are discussed further in Chapter 5 together with their physics implications.

4.3.2 System size dependence

In Pb–Pb collisions, previous v_n measurements at the LHC have accessed the system size dependence of flow via the centrality dependence. However, this centrality dependence is biased by a strong variation of the spatial eccentricity of the nuclear overlap. While modelling allows one to control this eccentricity dependence to some extent, studying smaller collision systems at highest centrality (i.e. impact parameter close to zero) remains conceptually the cleanest way of establishing the system size dependence of flow. It also provides a way of disentangling the event-averaged spatial eccentricity from the event-by-event eccentricity fluctuations, and can thus contribute significantly to constraining the initial condition from which collective behaviour emerges. These are important motivations for studying soft multi-particle production and its transverse asymmetries in the collision of lighter nuclei.

Figure 9 shows ATLAS comparisons of the v_n in Xe–Xe and Pb–Pb collisions as a function of centrality (left panels) and their ratios (right panels). Also shown for comparison in the right panels are theoretical predictions for the ratios from Ref. [229]. It is seen that in most central collisions the ratio v_n (Xe–Xe)/v_n (Pb–Pb) is larger than unity for $n = 2$ and 3. With decreasing centrality the ratios for all harmonics show a decreasing trend. These trends can be explained as follows: Xe–Xe being a smaller system than Pb–Pb, the effect of fluctuations is more important. The fluctuations increase the initial eccentricities of the collision geometry and therefore enhance the v_n. However, because Xe–Xe is a smaller collision system the viscous effects (which suppress the v_n) are larger, and play a bigger role with decreasing centrality and increasing harmonic order. In most central events, the effect of the increased fluctuations wins for v_2. But with increasing harmonic order and/or decreasing centrality, eventually the viscous effects reduce the v_n compared to Pb–Pb. These observations indicate the ability of such cross-system v_n measurements to be very sensitive to initial conditions of the heavy ion collision as well as the transport coefficients of the QGP. The measured ratios for the v_n (Xe–Xe)/v_n (Pb–Pb) are qualitatively reproduced by the theory predictions from Ref. [229]. In order to illustrate the sensitivity of such models to the collision species, predictions are also presented for Ar–Ar and O–O collisions. The predictions show considerably larger variation of the centrality dependence of the v_n going from Xe–Xe to Ar–Ar to O–O, as compared to the variation going from Pb–Pb to Xe–Xe. Given such strong trends in the theory predictions, performing v_n measurements in light ion species such as Ar–Ar and O–O in Run 3 can provide strong constrains on the theoretical models.

Furthermore, there has been much work in studying long-range correlations observed in p–A,

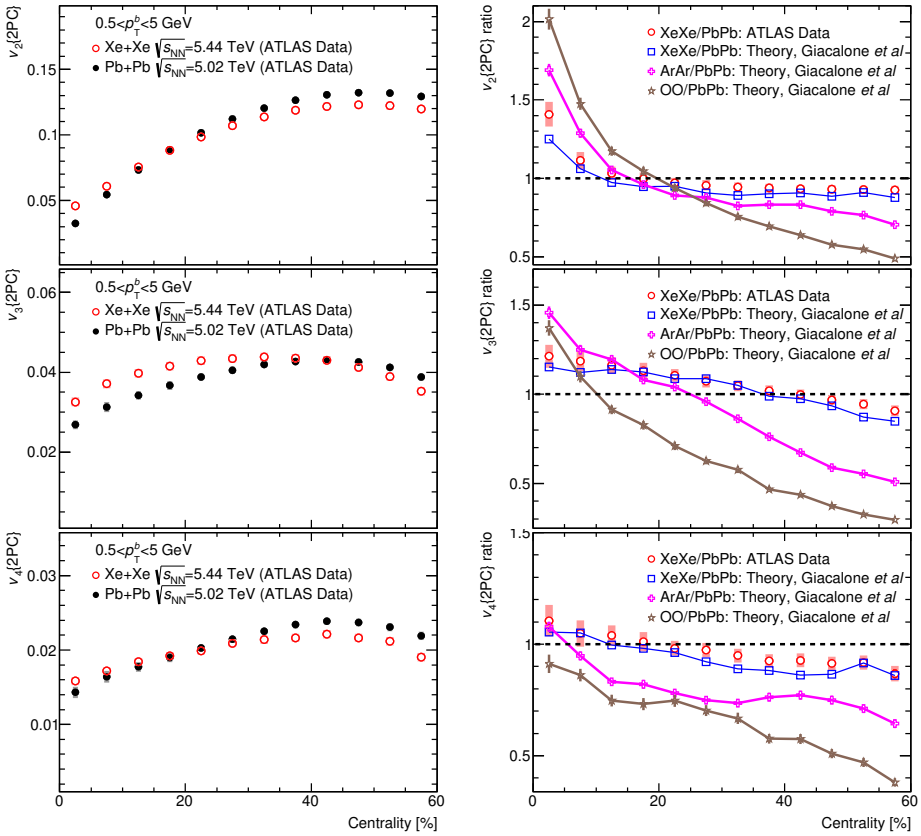

Fig. 9: Left panels: comparisons of the centrality dependence of the v_{n} measured in Pb–Pb collisions at $\sqrt{s_{\mathrm{NN}}}$=5.02 TeV to Xe–Xe measurements. The plots are for the 0.5–5 GeV/c p_{T} interval. From top to bottom each row corresponds to a different harmonic order n. The ratios are compared to theoretical predictions from Ref. [229]. Also shown are theory calculations of the ratios for Ar–Ar and O–O. ATLAS Data taken from Ref. [230].

d–A, ^{3}He–A, and more recently in pp collisions (see Chapter 9). Measuring flow in medium and light ions would allow for a continuous study of how collective phenomena vary from large (Pb–Pb) to small (p–A and pp) systems.

4.3.3 Longitudinal flow fluctuations

The characterization of how the longitudinal scales at which the symmetry planes Ψ_n associated to v_{n} decorrelate, and how this relates to the variation of the signal strength v_{n} with rapidity is still far from the state of the art reached in v_{n} measurements at mid-rapidity. However, any deviation from the simple picture of a rapidity-independent (Bjorken-like) longitudinal dynamics directly impacts our understanding of the time evolution of matter in all rapidity windows, including the well studied mid-rapidity one. Multiple recent measurements at the LHC indicate the presence of considerable longitudinal dynamics. These include measurements from CMS of event-plane decorrelation in p–Pb and Pb–Pb collisions [217, 218] and from ATLAS on flow-decorrelations [219] and forward-backward multiplicity fluctuations [231]. It is therefore important that experiments at the HL-LHC will parallel higher precision measurements at mid-rapidity with improved experimental control over the longitudinal evolution.

In the ATLAS measurements in Ref. [219], the flow decorrelation is quantified by constructing a

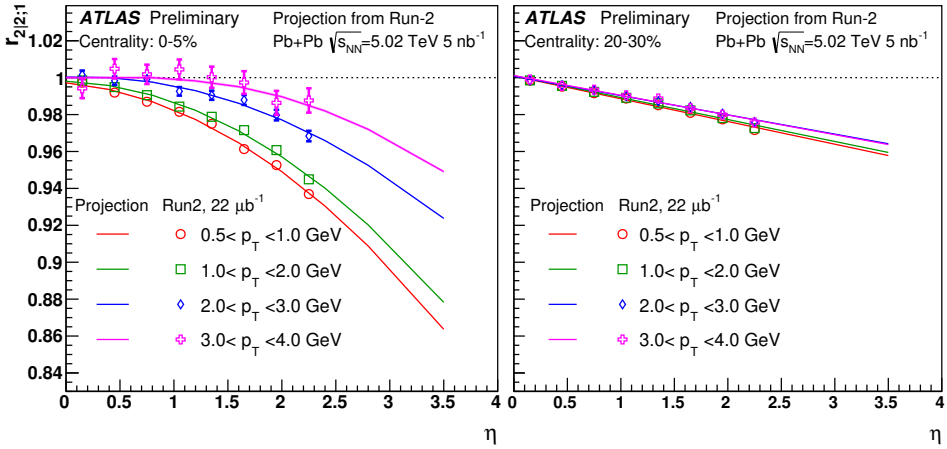

Fig. 10: ATLAS projections of the flow-decorrelation observable $r_{2|2;1}$ as a function of η (lines). The markers indicate the present measurements from Ref. [219]. The left and right panels show projections for the 0–5% and 20–30% centrality intervals, respectively. The width of the projection bands indicates the expected statistical uncertainty.

correlator $r_{n|n;1}$ defined as:

$$r_{n|n;1}(\eta) = \frac{\langle \mathbf{v}_n(-\eta)\mathbf{v}_n^*(\eta_{\rm ref})\rangle}{\langle \mathbf{v}_n(\eta)\mathbf{v}_n^*(\eta_{\rm ref})\rangle}, \tag{16}$$

where $\mathbf{v}_n$ is the normalized flow vector, and $\eta_{\rm ref}$ is the reference pseudo-rapidity [219]. The correlator, $r_{n|n;1}$, measures the relative difference between flow $v_n e^{in\Psi_n}$ at η and $-\eta$. If flow were boost-invariant, then $r_{n|n;1}$ would equal unity. However any difference in the η dependence of the flow magnitude $v_{\rm n}$ and the event plane angle Ψ_n will lead to $r_{n|n;1}$ become smaller than unity. The ATLAS measurements of $r_{2|2;1}$ over the 0–2.5 η range are shown in Figure 10 by the markers. It is observed that the $r_{2|2;1}$ is significantly smaller than unity in central collisions, which indicates stronger flow decorrelation. For a given centrality, $r_{2|2;1}$ decreases faster at low $p_{\rm T}$ that at higher-$p_{\rm T}$. In the 20–30% mid-central $r_{2|2;1}$ decreases linearly with η, however in the 0–5% most central collisions there are indications that the decorrelations are possibly quadratic.

Repeating this measurement in Run 4 will lead to significant improvements due to increased luminosity and especially due to increased tracking acceptance in η to ± 4 units. Figure 10 also shows the ATLAS projections for $r_{2|2;1}$ made for Run 4, indicated as dashed lines. The ATLAS tracking acceptance in Run 4 will extend the η range to ± 4 units, but the projected measurement is made to ± 3.5 units, in order to leave a gap between the ITk and the region of the forward calorimeter in which the reference measurement is made ($4.4 < |\eta| < 4.9$). The projections are made by fitting the existing data with a linear function for the 20–30% centrality range and with a quadratic function for the 0–5% centrality range. It is seen that with the increased η acceptance the non-linearity in the flow decorrelation can be studied in much more detail.

The longitudinal flow-decorrelation observables are sensitive to the event by event fluctuations of the initial energy density profile in the longitudinal direction. Thus precise measurement of these decorrelations should give a better understanding of the initial conditions along the longitudinal direction and in the development of full three-dimensional viscous hydrodynamic models. These would in turn result in a more accurate estimation of η/s.

4.4 Vorticity and polarization

An interesting open question for relativistic fluids is to what extent the spin degrees of freedom thermalize locally and to what extend spin polarization results as a consequence of the fluid motion. Intuitively, one might expect that spin aligns locally with the rotational motion of the fluid as measured by vorticity, corresponding to the curl of the fluid velocity.

The relativistic generalization of the non-relativistic fluid vorticity is not unambiguous, however. The vorticity of a fluid in local equilibrium is characterized by the so-called thermal vorticity tensor, corresponding to $\omega_{\mu\nu} = \frac{1}{2}(\nabla_\nu \beta_\mu - \nabla_\mu \beta_\nu)$ where $\beta_\mu = u_\mu/T$ is the ratio of fluid velocity to temperature [232]. This thermal vorticity includes contributions from global rotational motion, local fluid acceleration, and temperature gradients. It has been argued that this thermal vorticity should lead to local spin polarization. If this holds at chemical freeze-out, one should be able to find traces of the thermal vorticity in the spin polarization of particles and resonances, such as Λ ($\overline{\Lambda}$) particles.

Spin polarization is in this picture closely tied to angular momentum of the expanding fireball. For non-central events, the angular momentum of the produced matter is perpendicular to the event plane. Via the spin-vorticity coupling mechanism, this leads to a global polarization in the transverse plane aligning with the global angular momentum (also known as the "transverse polarization"). This global transverse polarization has recently been observed in the measurement of Λ spin polarization at RHIC [233]. For this global effect following global angular momentum, one expects a decreasing magnitude with increasing collision energy and the effect is expected to be relatively small at LHC energies.

Figure 11 shows the energy dependence of the global transverse polarization of Λ and $\overline{\Lambda}$ for semi-central heavy ion collisions. The RHIC results show the decrease of polarization with increasing $\sqrt{s_{\rm NN}}$. The preliminary ALICE data point at $\sqrt{s_{\rm NN}} = 2.76$ TeV is consistent with zero within 1σ statistical/systematic uncertainties. However it is also consistent with the predicted maximum value (blue line) within $\sim 2\sigma$ statistical/systematic uncertainties. But the ALICE upgrade projection at twice large collision energy, (assuming zero signal) shows that the polarization in Run 3 and 4 can be measured with very high precision. Therefore the study of global polarization of Λ and $\overline{\Lambda}$ within HL–LHC project allows the unambiguous conclusion with regard of the values of this physics quantity in the TeV-energy domain.

In addition to the transverse polarization, an azimuthal-dependent, longitudinal polarization (in the direction of the beam pipe) has also been predicted and recently observed at RHIC [236]. This is mainly a consequence of an azimuthal dependence of local acceleration and temperature gradient (e.g., the elliptic flow), which could lead to an elliptic modulation of longitudinal spin polarization in non-central collisions. Unlike the global transverse polarization, this longitudinal polarization effect has a much weaker dependence on collision energy from RHIC to the LHC [237], mainly because the anisotropic flow has a weak collision energy dependence. With increased data sample and upgraded detectors covering a wider rapidity range in the HL–LHC era, there will be exciting opportunities for precision study of the Λ polarization and to map out the dependence on variables such as azimuthal angle, rapidity, transverse momentum.

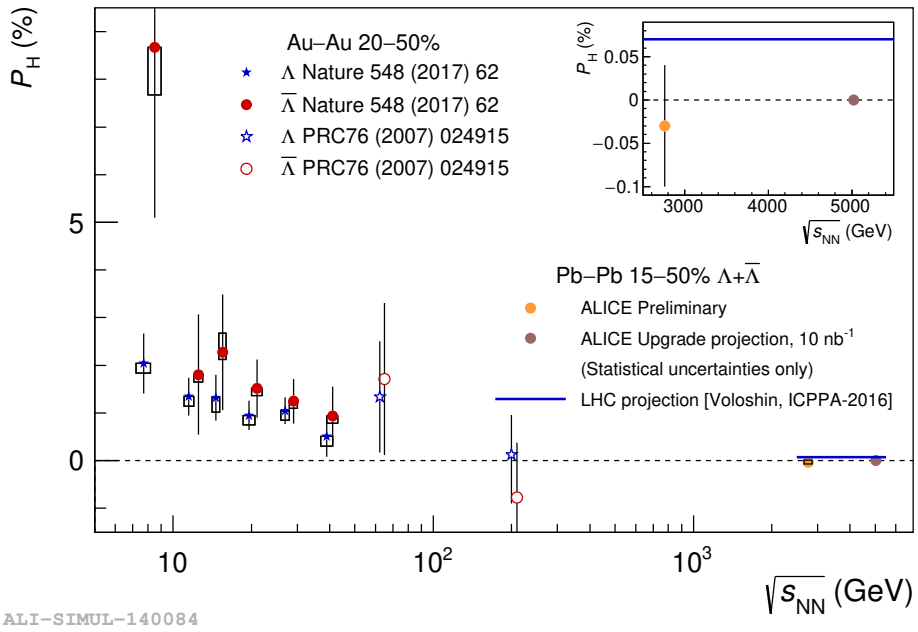

Fig. 11: ALICE projections for the Global hyperon polarization in Pb–Pb collisions at $\sqrt{s_{\rm NN}} = 2.76$ TeV for an integrated luminosity of 10 nb^{-1} (blush symbol), together with the present measurements (orange symbol) compared to analogous measurements at various collision energies from the STAR collaboration [233, 234] (blue and red symbols). The blue line indicates the prediction for the maximum value at the LHC [235]. The inlay plot shows a zoomed in version of the plot around the ALICE measurement and Run 3 and 4 projection, together with the prediction for the maximum value at the LHC. The points for $\overline{\Lambda}$ are slightly shifted along the horizontal axis for visibility. Error bars (open boxes) represent the statistical (systematic) uncertainties. Figure from Ref. [1].

4.5 Chiral Magnetic Effect

An important property of the strong interaction which is potentially observable in heavy-ion collisions is parity violation. Although it is allowed by quantum chromodynamics (QCD), global parity violation is not observed in strong interaction. However, QCD predicts the existence of topologically non-trivial configurations of the gluonic field, instantons and sphalerons, which might be responsible for local parity violation in microscopic QCD domains at finite temperature [238–241]. The P- and CP-odd interactions between quarks and such fields with non-zero topological charge [242] change the quark chirality, breaking parity symmetry by creating an imbalance between the number of left- and right-handed quarks. Furthermore, an extremely strong magnetic field is expected to be produced in heavy-ion collisions [243, 244] (of the order of 10^{19} Gauss at the LHC) because the charges of initial ions add coherently. This strong magnetic field aligns the spins of the positively (negatively) charged quarks in the direction parallel (anti-parallel) to magnetic field orientation. Moreover, right-handed (left-handed) quarks have their direction of momentum parallel (anti-parallel) to the spin orientation. The spin alignment coupled with the local imbalance between the number of left- and right-handed quarks leads to the development of a quark current. The current moves the positively charged quarks along its direction and the negatively charged quarks in the opposite direction. This implies a charge separation along the direction of the magnetic field, which is on average perpendicular to the reaction plane, a phenomenon called Chiral Magnetic Effect (CME) [245–248].

The sign of the topological charge can give rise to a positive or negative current in the magnetic

field direction with equal probability. Therefore, the charge separation averaged over many events is zero. This makes the observation of the CME experimentally difficult and possible only via azimuthal particle correlations, which introduces a large flow related background into the measurements.

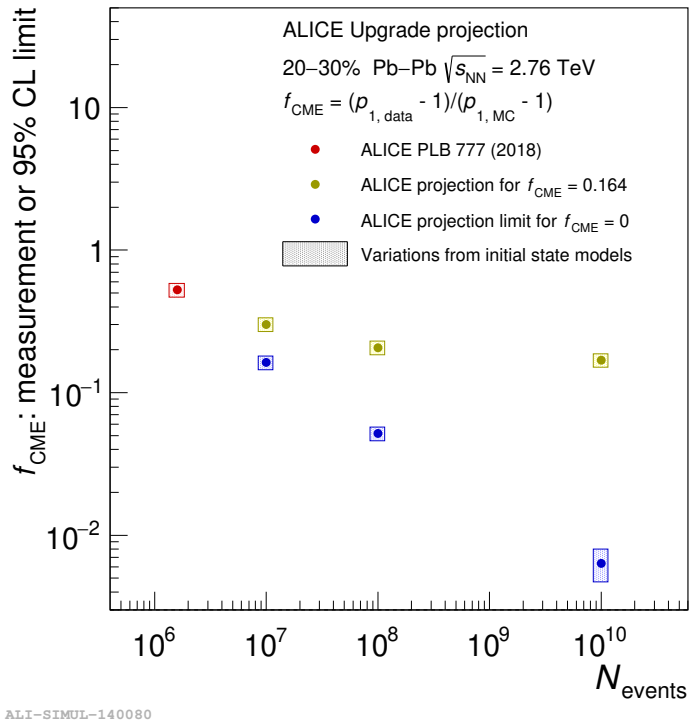

Fig. 12: ALICE projections for the upper limit on the CME fraction at 95% confidence level as a function of the number of events in the 20–30% centrality interval. The right-most projection point corresponds to an integrated luminosity of 10 nb^{-1}. The result reported by the ALICE collaboration [249] is shown together with expectations for $f_{\rm CME} = 0.164$ (current estimate) and $f_{\rm CME} = 0$ (null hypothesis). The shaded boxes denote variations from various initial state models (see text for details). Figure from Ref. [1].

The three-particle correlator $\gamma_{\alpha\beta} = \langle\cos(\varphi_\alpha + \varphi_\beta - 2\Psi_2)\rangle$ [250], where φ_α is the azimuthal angle of the particle of charge α and Ψ_2 is the second harmonic symmetry plane angle, was proposed to measure charge-dependent azimuthal correlations. This correlator eliminates correlations independent of symmetry plane orientation, suppressing background contributions at the level of $\sim v_2$. However, the interpretation of the experimental results is complicated by the remaining background (e.g. local charge conservation (LCC) coupled with elliptic flow [251,252]). Recent observation of similar charge-dependent azimuthal correlations in p–Pb (where the CME is not expected) and Pb–Pb collisions [253] indicates the $\gamma_{\alpha\beta}$ correlator be dominated, if not all, by the background effect. The ALICE [249] and CMS [254] collaborations have used the Event Shape Engineering (ESE) technique [255] to estimate the CME fraction to the charge dependence of $\gamma_{\alpha\beta}$, $f_{\rm CME}$, in Pb–Pb collisions. ALICE extracted $f_{\rm CME}$ by relating measurements of the charge dependence of $\gamma_{\alpha\beta}$ from the ESE analysis to CME signal expectations from various initial state model calculations including a magnetic field. It has been assumed that the CME signal is proportional to $\langle|B|^2\cos(2(\Psi_{\rm B} - \Psi_2))\rangle$, where $|B|$ and $\Psi_{\rm B}$ are the magnitude and direction of the magnetic field, respectively. Within current experimental uncertainties, the CME signal contribution to the $\gamma_{\alpha\beta}$ correlator is consistent with zero.

Figure 12 shows the upper limit on $f_{\rm CME}$ at 95% confidence level for the 20–30% centrality

interval reported by the ALICE collaboration together with expectations for $f_{\mathrm{CME}} = 0.164$ (current estimate) and $f_{\mathrm{CME}} = 0$ as a function of the number of events. The shaded boxes denote variations due to different estimates of the magnetic field from the investigated models. The ALICE upgrade projection indicates that stringent constraints for the CME contribution to the charge dependence of $\gamma_{\alpha\beta}$ can be achieved at a level of less than 1% with the expected HL–LHC statistics.

One key ingredient needed for the observation of the CME is the strong magnetic field in the QGP medium. It is important to establish direct evidence for this field and determine its strength, which will help significantly constrain theoretical predictions on the magnitude of the CME signal. Measurement of the pseudorapidity-odd component of directed flow, v_1^{odd}, separately for positive and negative charged particles has been proposed as a probe to the magnetic field [244]. Any difference will indicate the presence of induced electromagnetic currents and will allow to estimate the magnitude of the effect. It will also provide information on the electric conductivity of the QGP medium.

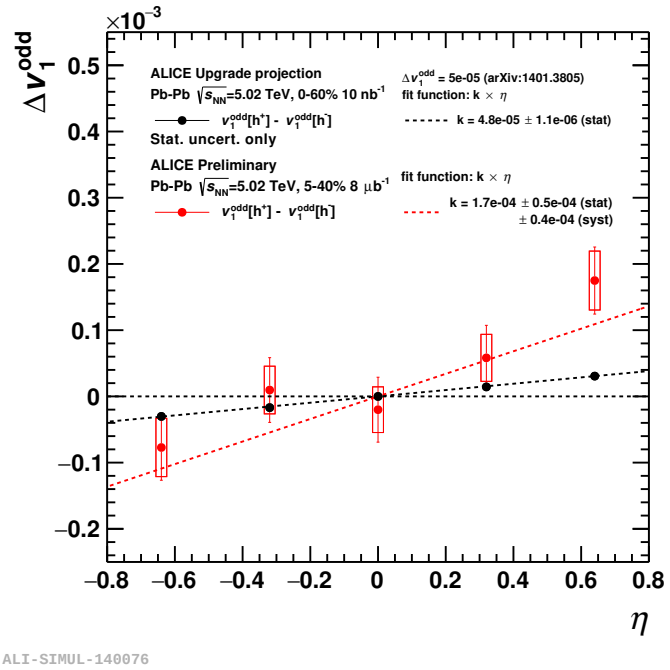

Fig. 13: Charge difference of v_1^{odd} as a function of pseudorapidity measured by the ALICE collaboration in Pb–Pb collisions at $\sqrt{s_{\mathrm{NN}}} = 5.02$ TeV [256] (red symbols) and the projection for a 5×10^{-5} difference [244] from 10 nb^{-1} (black symbols) together with linear fits (dashed lines). Error bars (open boxes) represent the statistical (systematic) uncertainties. Figure from Ref. [1].

Figure 13 shows the charge difference of v_1^{odd}, $\Delta v_1^{\mathrm{odd}} = v_1^{\mathrm{odd}+} - v_1^{\mathrm{odd}-}$, as a function of pseudorapidity measured by the ALICE collaboration in Pb–Pb collisions at $\sqrt{s_{\mathrm{NN}}} = 5.02$ TeV [256] together with a linear fit. A hint of a charge-dependent difference is observed and quantified by the slope k with a total significance of 2.6 σ. This difference, which differs both in magnitude and sign compared to predictions for $\pi^{\pm}$ at $\sqrt{s_{\mathrm{NN}}} = 2.76$ TeV and similar $\langle p_{\mathrm{T}} \rangle$ [244], needs to be measured with better precision. This will be achieved with the large data sample expected at the HL–LHC which will be sensitive to a difference as small as 5×10^{-5} (about three times smaller that the current measurement), as reported by the ALICE upgrade projection in Fig. 13. Furthermore, similar measurement can also be performed in the heavy flavor sector, e.g., for D^0 and $\overline{\mathrm{D}^0}$ meson directed flow [257], this is further discussed in Chapter 5. Heavy flavor quarks have the advantage of being produced at a very early stage, and thus

potentially have a better sensitivity to the magnetic field at its evolution at early time.

4.6 Summary

The measurements of inclusive hadron $v_{\rm n}$ by traditional methods such as two-particle correlations, event-plane/scalar-product methods, multi-particle cumulants etc. have been performed with high precision by the ALICE, ATLAS and CMS experiments at the LHC. These inclusive hadron $v_{\rm n}$ measurements are not statistically limited across most of the centrality-$p_{\rm T}$ phase space and further improvement in the measurements is not a high priority for Run 3 and 4. However, in the case of identified hadrons the increased statistics will lead to further improvement in the $v_{\rm n}$ measurements. This is true for both light hadrons such as pions, protons, ϕ-mesons as shown in Figure 8, as well as for heavy-flavor particles such as $\rm D^0$, $\rm D^{\pm}$, J/ψ, Υ which are discussed in Chapters 5 and 7, respectively. Significant improvements are expected in measurements of longitudinal flow fluctuations, which have only been briefly investigated in Run 1 and 2. These are largely driven by the increases η acceptance of the ATLAS and CMS tracking detectors in Run 4, the acceptance is planned to reach $\pm$5 units. The study of longitudinal flow fluctuations will allow comparisons to predictions of 3+1D hydro models. Flow measurements in light ions such as Ar–Ar and O–O, will lead to stronger constraints on theoretical models describing different stages of a heavy ion collision – initial conditions, equation of state, transport coefficients etc. This is difficult presently, as flow observables are dependent on all of these, so it becomes difficult to constrain any one of these without full knowledge of the others. Flow measurements across a variety of colliding species will provide independent data that will improve our understanding of the different stages of heavy ion collisions. Further physics motivations for colliding light ions are discussed in Chapter 11.1.

Other observables related to collective phenomena where current measurements are statistics limited and are expected to improve considerably are related to effects of vorticity and magnetic fields. The current measurements of Λ polarization from ALICE are statistics limited and consistent with both the null hypothesis as well as with the theoretically predicated value. The ALICE projections for Λ polarization in Run 3 and 4 show that the measurements will have significantly smaller statistical uncertainties and will differentiate between the null and predicted values. ALICE and CMS have measured the fraction of the three-particle correlator $\gamma_{\alpha\beta}$ that arises from CME effects: $f_{\rm CME}$. The measured $f_{\rm CME}$ by ALICE is consistent with zero but due to large uncertainties its upper limit at 95% CL can be as large as $\sim$0.5. ALICE projections for Run 3 and 4 show that the $f_{\rm CME}$ can be determined with a precision of better than 1%.

5 Open heavy flavour

Coordinators: Elena Bruna (INFN Torino) and Gian Michele Innocenti (Massachusetts Institute of Technology, CERN)

Contributors: J. Aichelin (SUBATECH, CNRS/IN2P3, IMT Atlantique, Université de Nantes), S.A. Bass (Duke University), C. Bedda (Utrecht University), A. Beraudo (INFN Torino), G.E. Bruno (Politecnico di Bari and INFN), Z. Citron (Ben-Gurion University of the Negev), Z. Conesa del Valle (CNRS/IN2P3, Université Paris-Sud, Université Paris-Saclay, Orsay), A. Dainese (INFN Padova), A. Dubla (GSI Helmholtzzentrum für Schwerionenforschung GmbH), F. Fionda (University of Bergen), P.B. Gossiaux (SUBATECH, CNRS/IN2P3, IMT Atlantique, Université de Nantes), V. Greco (INFN Catania, Università di Catania, INFN-LNS), F. Grosa (Politecnico di Torino and INFN), Y.-J. Lee (Massachusetts Institute of Technology), J. Margutti (Utrecht University), V. Minissale (INFN-LNS, Catania), A. Mischke (Utrecht University), S. Mohapatra (Columbia University, New York), C.C. Peng (Purdue University), M. Peters (Massachusetts Institute of Technology), S. Plumari (Università di Catania), F. Prino (INFN Torino), A. Rossi (Padova University and INFN), J. Sun (Tsinghua University, Beijing), C. Terrevoli (Padova University and INFN), B. Trzeciak (Utrecht University), A. Uras (Université de Lyon, CNRS/IN2P3, IPN-Lyon), L. Van Doremalen (Utrecht University, Utrecht), I. Vitev (Los Alamos National Laboratory), J. Wang (Massachusetts Institute of Technology), T.-W. Wang (Massachusetts Institute of Technology), M. Winn (LAL, now DPhN, CEA/IRFU), R. Xiao (Purdue University), Y. Xu (Duke University)

This chapter is dedicated to the memory of our colleague Andre Mischke.

5.1 Perspectives for heavy-flavour observables in LHC Run 3 and 4

Charm and beauty quarks are produced in hard scattering processes occurring in the early stage of heavy-ion collisions. They subsequently traverse the QGP medium and interact with its constituents through inelastic (gluon radiation) and elastic (or collisional) processes. These interactions may lead to the thermalisation of low-momentum heavy quarks, which would thus take part in the expansion and hadronisation of the medium. For these reasons, heavy-flavour hadrons provide information on all stages of the system evolution and they uniquely probe the quark-mass dependence of the QGP inner workings (see Refs. [258–260] for recent reviews).

Many experimental observations from RHIC and LHC showed evidence that charm and beauty quarks interact strongly with the QGP and that beauty quarks lose less energy at low transverse momentum compared to charm quarks [261, 262]. While data are becoming more and more precise to start imposing constraints on theoretical calculations, there are still several unresolved questions: What are the microscopic mechanisms that drive heavy-flavour interaction and diffusion in the QGP, and what are their implications for the QCD matter structure? What is the relative relevance of collisional and radiative processes? Can the same QCD process can describe both the heavy-quark interaction with the strongly coupled plasma and the mechanisms of hadronisation?

The Run 3 and 4 of the LHC will open a new precision era for heavy-flavour measurements in heavy-ion collisions that will address the above questions. With the upgrades of the machine and of the tracking detectors, the higher accumulated statistics and higher precision will make it possible to quantify the properties of the QGP with heavy-flavour probes. This high-precision era will also make new and more differential observables accessible for the first time. The key measurements that are expected to have a strong impact on the characterisation of the QGP with heavy-flavour observables are discussed in this chapter and summarized below.

– Nuclear modification factor and flow harmonics: these measurements for particles with charm and beauty in the large kinematic range covered by combining the different LHC experiments will put the strongest constraints on the transport coefficients of the QGP, clarifying the microscopic

mechanisms governing the interactions of heavy quarks with the medium, and quantifying their degree of thermalisation.

– Strange D and B mesons, charm and beauty baryons: currently limited by statistics, these measurements will help to quantify not only the degree of thermalisation of heavy quarks, but also the contribution of recombination with lighter quarks to the hadronisation process. They are also sensitive to the mass scaling of the hyrodynamical flow in the heavy-flavour sector.
– Heavy-flavour correlations and jet observables: they will provide new insights on the parton mass effects in parton showers, on the redistribution of the radiated energy, and on the role of collisional and radiative energy loss.

5.2 Impact of detector upgrades on heavy-flavour measurements

The upgrades of the four large LHC experiments during LS2 and LS3 will strongly enhance their performance for open heavy-flavour measurements. The detector improvements that will have the largest impact are the new silicon trackers, with higher granularity and precision, as well as extended pseudo-rapidity coverage. Brief descriptions of these improvements are reported in the following.

– ALICE. The new Inner Tracking System [263], which will be installed during LS2, is composed of seven layers of pixel detectors with an intrinsic spatial precision of about 5×5 μm^2 and a material thickness of 0.3% of the radiation length in the innermost layers. The track pointing resolution will be improved by a factor 3 in the direction transverse to the beam line and by a factor 5 in the longitudinal direction, down to values of about 20 μm for tracks with $p_{\mathrm{T}} = 1$ GeV/c. A Muon Forward Tracker [4], composed of 5 disks of pixel detectors with the same spatial resolution as the Inner Tracking System, will instrument the region $2.5 < \eta < 3.6$, in front of the muon spectrometer, enabling the separation from the primary vertex of single and dimuons from D, B and J/ψ decays. The upgraded TPC with GEM-based readout chambers, together with readout upgrades of several other detectors and with a new Online-Offline computing system, will enable the full recording of Pb–Pb interactions with a minimum-bias trigger at a rate of 50 kHz, which is 50-fold larger than for the present apparatus.
– ATLAS. The Inner Tracker (ITk) [264] will be an all-silicon tracker composed of pixels and strips installed during LS3 for ATLAS phase II. The ITk will provide charged-particle tracking acceptance for $|\eta| < 4$. The performance of the ITk in Pb–Pb collisions is expected to be comparable to pp collisions. The High Granularity Timing Detector [265] has been proposed to complement the spatial information of the ITk with timing information. These detectors will improve jet reconstruction capabilities, and in particular tagging of heavy-flavour jets, as well as all studies using charged particles.
– CMS. The following upgrades scheduled for LS3 will largely enhance the performance for heavy-flavour measurements, in particular in the low-momentum region [266]. The upgraded inner tracker will cover a large acceptance up to $|\eta| < 4$ [267]. The improved L1 and DAQ rate (up to 60 GB/s) will allow more sophisticated triggers and to record a larger number of minimum-bias triggered events. In addition, the proposed MIP Timing Detector [268] with a radius of 1.16 m and a time resolution of ≈ 30 ps could provide, in conjunction with other detectors, proton, pion and kaon separation in the interval $0.7 < p_{\mathrm{T}} < 2$ GeV/c in $|\eta| < 1.5$.
– LHCb. The experiment is preparing to run at five times larger instantaneous luminosities in pp collisions, processing the full event rate with a software trigger and preserving or exceeding the present performance. All tracking detectors will be upgraded during LS2 [269,270]. Most notably for heavy-flavour observables, the active area of the upgraded Vertex Locator, the pixel detector replacing the present silicon strip detector, will move as close as 5.1 mm to the nominal beam spot. The larger granularity for the majority of phase space will improve the performance in Pb–Pb

collisions whereas proton-induced reactions will result in average in lower detector occupancies than the standard pp running.

5.3 Nuclear modification factor and collective flow

The standard observable used to study the medium effects on heavy-flavour meson production is the nuclear modification factor ($R_{\rm AA}$), defined as the ratio of the Pb–Pb yield to the pp cross-section scaled by the nuclear overlap function. In the view of the pQCD-based models, heavy quarks interact with the medium constituents via radiative and collisional processes. While radiative interactions only lead to energy loss, collisional ones can also result in an increase of the heavy-quark momentum. The dead-cone effect [271] is expected to reduce small-angle gluon radiation of heavy quarks when compared to both gluons and light quarks. At low $p_{\rm T}$, the production rate of heavy-flavour mesons in heavy-ion collisions is sensitive to the elastic energy loss of the heavy quark in medium, the nuclear shadowing effect in the initial state, and the recombination of the heavy quark with light quarks at the hadronization stage. At high $p_{\rm T}$, the nuclear modification factor is sensitive to the medium-induced radiative energy loss of heavy quarks. Precise measurements of the $R_{\rm AA}$ thus provide insights on the momentum dependence of heavy quark energy loss, and provide important tests of QCD predictions, in particular for the expected flavour and mass dependence of the energy loss processes.

Another interesting observable is the azimuthal anisotropy of open heavy flavour production, which can be characterized by the Fourier coefficients v_n in the azimuthal angle (φ) distribution of the heavy-flavour hadron yield with respect to the reaction plane in non-central Pb–Pb collisions. At low $p_{\rm T}$, the v_2 measurements can provide important insights into the mechanisms of interaction of heavy quarks with the medium and on their strength (as discussed in more details in Sec. 5.3.2). Heavy quarks are indeed expected to acquire a positive v_2 mostly as a consequence of their interaction with the light quarks of the medium. Measurements of elliptic flow of heavy hadrons are also sensitive to hadronisation processes. In particular, they can be used to study the relevance of heavy-flavour recombination (see Sect. 5.4.1) in which heavy-quarks can acquire additional v_2 by combining with light quarks at the hadronisation stage. At high $p_{\rm T}$, v_2 of heavy-flavour hadrons is sensitive to the path-length dependence of heavy quark energy loss. The simultaneous description of $R_{\rm AA}$ and v_2 for heavy-flavour hadrons is still challenging for most of the theoretical calculations, because it entails accurate modelling of the initial heavy-quark production and its modification in nuclei, of the medium and its expansion, of the various quark-medium interaction mechanisms and of the possible modification of hadronisation processes.

5.3.1 Experimental performance of the ALICE, ATLAS and CMS experiments

Figure 14 shows the projected performance for the $R_{\rm AA}$ of several heavy-flavour hadrons or decay channels with $L_{\rm int} = 10\ {\rm nb}^{-1}$. The left panel presents the projection of charged particles, $\rm D^0$, $\rm B^+$ and non-prompt J/ψ from b-hadron decay which can be measured by CMS. The right panel shows the ALICE simulation results for $\rm D^0$, non-prompt J/ψ, non-prompt $\rm D^0$, $\rm B^+$ ($\rightarrow$ $\rm D^0\pi^+$) —in addition, the $\rm B^0 \rightarrow D^{*+}\pi^-$ reconstruction was studied by ALICE and it provides an alternative channel for the study of the beauty meson $R_{\rm AA}$ with a significance of larger than $5\,\sigma$ at $p_{\rm T} > 3$ GeV/c. With the high luminosity and the Inner Tracking System Upgrade in ALICE, the $R_{\rm AA}$ of light hadrons, charm hadrons and beauty hadrons can be clearly separated in a wide kinematic range.

Figure 15 shows the projected performance for v_2 of charm hadrons with $L_{\rm int} = 10\ {\rm nb}^{-1}$. The left panel shows the projection for $\rm D^0$ in CMS, with the charged particle v_2 also shown for comparison. The right panel presents the projection for $\rm D^0$, $\rm D_s$ and Λ_c in ALICE [263]. Precise measurements of charm hadron v_2 will allow the study of the thermalization of heavy quarks and the wide kinematic range allows to get insights on different process, as coalescence hadronization and energy loss. Figure 16 (left) shows

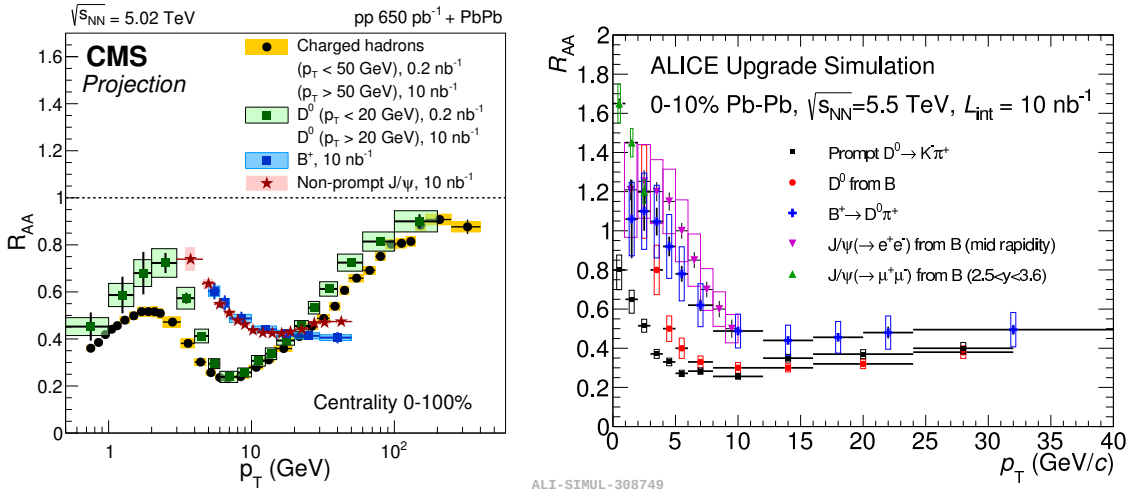

Fig. 14: Nuclear modification factors of charged particles, D^0, B^+ and non-prompt J/ψ in CMS [8] (left). R_{AA} of D^0, non-prompt J/ψ and non-prompt D^0 in ALICE in central Pb–Pb collisions for $L_{\mathrm{int}} = 10\ \mathrm{nb}^{-1}$ [1, 263] (right).

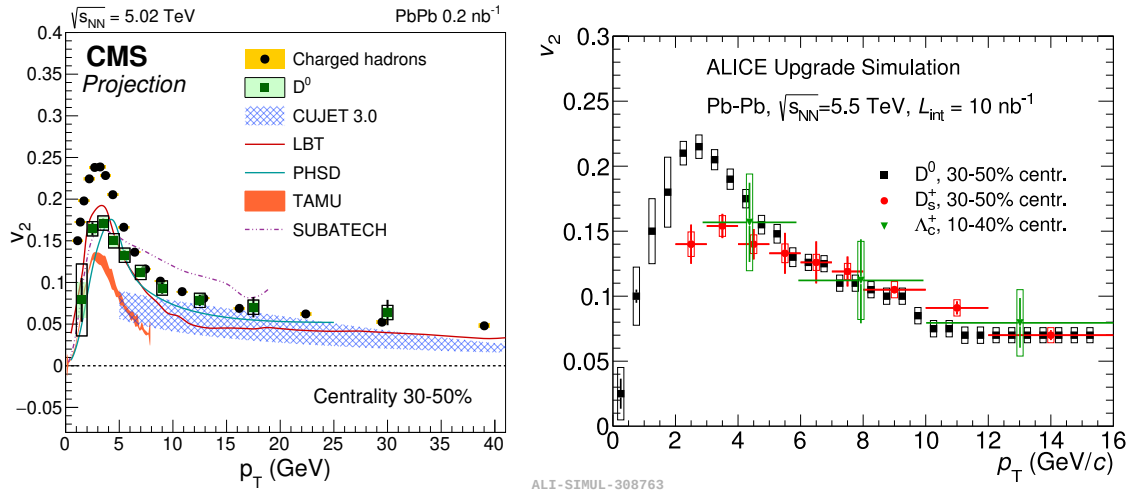

Fig. 15: v_2 of charged particles and D^0 in CMS [8] (left), charm hadrons (D^0, $\mathrm{D_s}$, Λ_c) in ALICE (right) in Pb–Pb collisions with $L_{\mathrm{int}} = 10\ \mathrm{nb}^{-1}$ [1, 263].

the projected performance for v_2 of B^+ mesons, non-prompt D^0 and non-prompt J/ψ. These will be the first precise measurements of B meson elliptic flow at the LHC. Heavy-flavour flow will also be measured with high precision using decay electrons and muons. As an example the projection for the measurement with muons by ATLAS is shown in Fig. 16 (right) [6].

5.3.2 Constraining the heavy-quark diffusion coefficient $2\pi TD_\mathrm{s}$

Many theoretical efforts have been recently undertaken to understand the properties of the QGP medium and the interaction between heavy quarks and the medium constituents, see Refs. [258–260] for recent reviews. Although the interaction mechanism can widely vary among different theoretical models, the

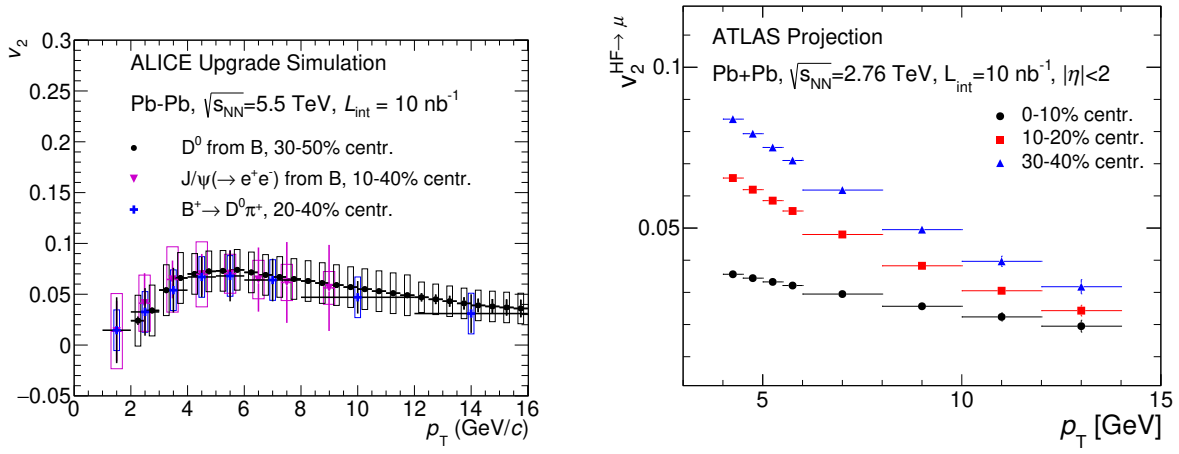

Fig. 16: v_2 of non-prompt D^0, non-prompt J/ψ and B^+ ($\rightarrow \mathrm{D}^0$) in ALICE (left) [1, 263] and of heavy-flavour decay muons in ATLAS (right) [6] in Pb–Pb collisions for $L_{\mathrm{int}} = 10\ \mathrm{nb}^{-1}$.

reduction to a few transport coefficients allows one to compare these models and evaluate different microscopic pictures. Most of the present theoretical models explain the interactions of heavy quarks as dominated by collisional (elastic) processes in the low transverse momentum region (up to about 5–10 GeV/c) and by radiative energy loss (inelastic process with gluon radiation off the heavy quark) at higher p_{T}.

The extraction of the heavy-quark spatial diffusion coefficient, which is one of the main QGP properties regulating the strength of collisional processes, is considered here to illustrate the impact of the high-precision measurements in Run 3 and Run 4. In particular, the p_{T}-dependence of this coefficient provides important constraints on the weakening of the interaction strength with increasing p_{T}. For illustration, the extracted values of D_s is considered at a fixed p_{T} value. The heavy-quark spatial diffusion coefficient D_s in the QGP is related to the relaxation (equilibration) time of heavy quarks $\tau_{\mathrm{Q}} = \frac{m_{\mathrm{Q}}}{T} D_s$, where m_{Q} is the quark mass and T is the medium temperature [272].

Figure 17 shows the constraining power of future experimental measurements of R_{AA} and v_2 on the heavy quark diffusion coefficient ($2\pi T D_{\mathrm{s}}$) using two different transport models: Catania model with Fokker-Plank equation [273,274] on the left and a modified Langevin framework on the right [275]. The left figure presents a normalized χ^2 as a function of spatial diffusion coefficient by comparing the model calculation [273, 274] of D-meson R_{AA} in Pb–Pb collisions at 5.02 TeV in a single centrality class (0–10%). The cases of the present experimental uncertainties (2015 Pb–Pb sample) and of these uncertainties reduced factors of two or five are considered for illustration. In the projections for $L_{\mathrm{int}} = 10\ \mathrm{nb}^{-1}$ shown in the previous section, the D-meson R_{AA} uncertainties are reduced by a factor between two and five, depending on p_{T}, with respect to the present measurements. Considering the $2\pi T D_{\mathrm{s}}$ range with $\chi^2_{R_{\mathrm{AA}}}/\mathrm{n.d.f} < 1.5$ (corresponding to 85% confidence), it is found that by reducing the present experimental uncertainty by a factor two or five, the uncertainty on the estimation $2\pi T D_{\mathrm{s}}$ would be also reduced almost to 50% or 20%, respectively. The right panel presents the diffusion coefficient as a function of temperature, which is estimated using a Bayesian calibration on D-meson R_{AA} and v_2 in Pb–Pb collisions at 5.02 TeV for different centralities. The $2\pi T D_{\mathrm{s}}$ shows a positive temperature dependence with the minimum value around T_{c}. Such behaviour is consistent with the Bayesian estimation for shear viscosity η/s. The potential improvement with Run 3 and Run 4 measurements is estimated using the R_{AA} and v_2 projections by ALICE and CMS shown in the previous section and it is shown by the red band. With these future experimental measurements, the diffusion coefficient around T_{c} could be

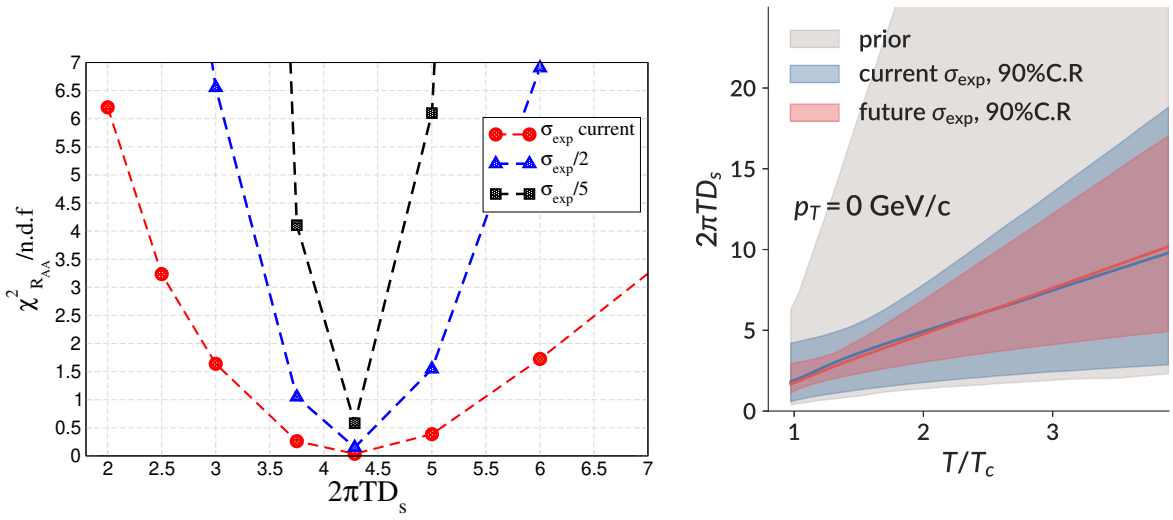

Fig. 17: Left: Normalized χ^2 as a function of spatial diffusion coefficient ($2\pi TD_{\rm s}$) for different experimental precision levels from the Catania Fokker-Plank transport model [273, 274]. Right: Coefficient range (90% credibility region) for $2\pi TD_{\rm s}$ as a function of $T/T_{\rm c}$ for different experimental precision levels, estimated by a model-to-data Bayesian analysis using a modified Langevin framework [275].

constrained with an uncertainty of about 30–50% of the present one.

5.3.3 D-meson analyses with Event Shape Engineering

Further insight into the dynamics of heavy quarks in the medium can be obtained from measurements of the yield and elliptic flow of heavy-flavour particles with the Event Shape Engineering (ESE) technique [255]. This technique consists of selecting events with the same centrality but different magnitude of the average bulk elliptic flow and therefore initial-state geometry eccentricity. The analyses with ESE will allow us to investigate the correlation between the flow coefficients of heavy-flavour hadrons and soft hadrons, to study the interplay between elliptic and radial flow, and to further constrain the path-length dependence of the energy loss suffered by the heavy quarks in the QGP. A first analysis was published by ALICE using 2015 Pb–Pb data [278]. In the left-hand panel of Fig. 18, the prospects for the measurement of the $\rm D^0$-meson v_2 with the ESE technique in the 30–50% centrality class with $L_{\rm int} = 10\ \rm nb^{-1}$ are shown. In particular, the ratio between the v_2 of D mesons in the 10% of the events with larger (smaller) elliptic flow of the bulk (quantified through the magnitude of the so-called reduced flow vector q_2) and the v_2 in all the collisions in the considered centrality class is reported as a function of $p_{\rm T}$. It is compared to the current measurement of the same ratio for charged particles, which is dominated by light-flavour hadrons. The expected statistical uncertainties for the $\rm D^0$-meson v_2 in the 0–10% of events with larger (smaller) q_2 are of the order of about 1–2% in the interval $1 < p_{\rm T} < 8$ GeV/c. This will allow us to resolve a possible difference of a few percent in the response of the v_2 to the ESE selection between the $\rm D^0$ mesons and the light hadrons, providing new insight on the coupling of the charm quark with the medium constituents and on its degree of thermalisation. The performance for the measurements of $\rm D^0$-meson $p_{\rm T}$-differential yield in event-shape classes is displayed in the right-hand panel of Fig. 18. The expected performance will provide a sensitivity of a few percent for the modification of the D-meson $p_{\rm T}$ spectra in events with small (large) initial geometrical anisotropy. This will open the way for precise studies on the interplay between the initial geometrical anisotropy (the collective flow of the bulk) and the heavy-flavour radial flow and energy loss.

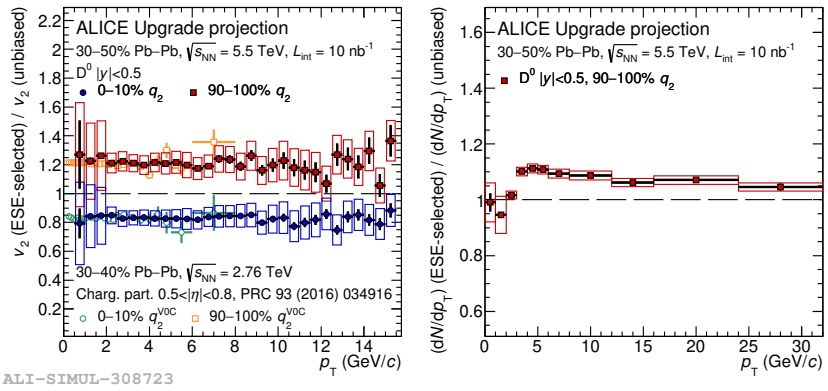

Fig. 18: Left: projection of the expected ratio of D^0-meson v_2 in the 10% events with larger (smaller) q_2 with respect to the unbiased one as a function of p_T for the 30–50% centrality class. The modification of the D^0-meson v_2 was assumed to be equal to that measured for the charged particles in Pb–Pb collisions at $\sqrt{s_{NN}} = 2.76$ TeV in the the 30–40% centrality class (superimposed for comparison) [276]. Right: projection of the expected ratio of D^0-meson p_T-differential yield in the 10% events with larger q_2 with respect to the unbiased one, estimated considering the prediction provided by the POWLANG model [277]. Figure from Ref. [1].

5.4 Studies of heavy-quark hadronisation

5.4.1 Hadronisation mechanisms for c and b quarks

The hadronisation mechanisms belong to the non-perturbative domain of QCD and a first-principle description of these processes is still missing, for both light and heavy flavours. However, from the study of charm dynamics in nucleus–nucleus collisions in the last decade there is a general consensus that the details of hadronisation have a large effect on both the heavy-flavour observables R_{AA} and v_2 [260, 279, 280]. This section introduces the two main microscopic hadronisation mechanisms for the production of heavy-flavour hadrons: fragmentation and coalescence (also denoted as recombination). Fragmentation is one of the most common approaches for the calculation of inclusive hadron production and it is appropriate for high-momentum partons emerging from initial hard processes, where high-momentum quarks fragment directly and independently into high-momentum hadrons. Independent fragmentation has also been widely applied at low momentum in e^+e^-, ep and pp collisions. On the other hand, coalescence is expected to dominate in the low-momentum regime in nucleus–nucleus collisions, where partons are abundant and heavy quarks can hadronise by recombination with light quarks [281–283]. Recent measurements at the LHC indicate that fragmentation may not be sufficient to describe charm quark hadronisation at low momentum in pp and p–Pb collisions, at least for what concerns baryon production [284, 285].

The hadron momentum spectra produced by heavy-quark fragmentation are given by:

$$\frac{\mathrm{d}N_{\mathrm{had}}}{\mathrm{d}^2p_{\mathrm{T}}\,\mathrm{d}y} = \sum \int \mathrm{d}z \frac{\mathrm{d}N_{\mathrm{fragm}}}{\mathrm{d}^2p_{\mathrm{T}}\,\mathrm{d}y} \frac{D_{\mathrm{had/Q}}(z, Q^2)}{z^2} \tag{17}$$

where $z = p_{\mathrm{had}}/p_{\mathrm{Q}}$ is the fraction of quark momentum carried by the hadron, $Q^2 = (p_{\mathrm{had}}/2z)^2$ is the momentum scale for the fragmentation process and $D_{\mathrm{had/Q}}$ is the fragmentation function.

In the basic coalescence model developed in Refs. [286–292] and used here for illustration, the

spectrum of heavy-flavour hadrons formed by coalescence of heavy-light quarks can be written as

$$\frac{\mathrm{d}^2N_{\mathrm{had}}}{\mathrm{d}p_{\mathrm{T}}^2} = g_{\mathrm{had}} \int \prod_{i=1}^{n} \frac{\mathrm{d}^3p_i}{(2\pi)^3E_i} p_i \cdot \mathrm{d}\sigma_i \cdot f_{q_i}(x_i,p_i) f_{\mathrm{had}}(x_1...x_n,p_1...p_n)\, \delta^{(2)}\left(p_{\mathrm{T,had}} - \sum_{i=1}^{n} p_{\mathrm{T},i}\right) \tag{18}$$

where $\mathrm{d}\sigma_i$ denotes an element of a space-like hypersurface and f_{q_i} are the quark (antiquark) phase-space distribution functions for i-th quark (antiquark), while g_{had} is the statistical factor to form a colourless hadron from quarks and antiquarks with spin 1/2. An alternative approach proposes resonance formation in quark-antiquark scatterings as the main production channel of D mesons through coalescence. In this approach, the same QCD process is responsible for both the interaction of charm quarks with the strongly-coupled medium and for the process of D-meson formation through recombination [293, 294].

Hadronisation via coalescence leads to a modification of the relative abundance of the various heavy-flavour hadron species produced. The most striking effect is an enhancement of the baryon-to-meson ratios for heavy-flavour hadrons. First studies of these ratios [290, 292] indicated a significant change in the relative abundances of the heavy-flavour hadron species, and in particular a ratio of $\Lambda_{\mathrm{c}}/\mathrm{D}^0$ close to unity, which is nearly an order of magnitude larger than what predicted by the fragmentation process implemented in the PYTHIA event generator. This value is also much larger than the prediction of the statistical hadronisation model [295], in which the hadronisation occurs by recombination of an equilibrated system of quarks and the hadron abundances are mainly determined by their masses. In addition, hadronisation via coalescence in a strangeness-rich Quark-Gluon Plasma is predicted to lead to a large enhancement in the production of strange heavy-flavour hadrons, like $\mathrm{D_s}$ and $\mathrm{B_s}$ [296–298]. Hints of an enhancement of the $\mathrm{D_s}/\mathrm{D}^0$ and $\Lambda_{\mathrm{c}}/\mathrm{D}^0$ ratios in nucleus–nucleus collisions have recently been reported by ALICE at the LHC [299, 300] and by STAR at RHIC [301].

The hadronisation by coalescence plus fragmentation also affects the p_{T} distribution of heavy-flavour hadrons. For D mesons the effect can be roughly seen as a shift in p_{T} of about 1.0–1.5 GeV/c in the region of p_{T} of 1.5–6 GeV/c, resulting in a significant enhancement of $R_{\mathrm{AA}}(p_{\mathrm{T}})$. The degree of these enhancements for D mesons, however, is significantly different among the different implementations of the hadronisation by coalescence and it is nearly unknown for heavy-flavour baryons, like Λ_{b} and Λ_{c}.

Finally, the coalescence process leads to a significant enhancement of the $v_2(p_{\mathrm{T}})$ in the intermediate p_{T} region that, for D mesons, amounts to about 20–40% depending on the specific modelling. The Λ_{c} is expected to acquire instead a much larger enhancement of at least a factor of two for the v_2. Therefore, a combined measurement of the $\Lambda_{\mathrm{c}}/\mathrm{D}$ and $\Lambda_{\mathrm{b}}/\mathrm{B}$ ratios and of the baryon elliptic flow would impose strong constraints on the hadronisation mechanism and lead to a better determination of the diffusion transport coefficient of heavy quarks (see Section 5.4.3).

5.4.2 Measurement performance studies (ALICE and CMS)

Simulation studies for the measurement of the $\mathrm{D_s}$, Λ_{c} and Λ_{b} production were carried out by the ALICE Collaboration [263] and are updated in the present document. A projection of the performance for the $\mathrm{B_s^0}$ meson by the CMS Collaboration is also reported [8]. The $\mathrm{D_s}$, Λ_{c} and Λ_{b} ($\rightarrow \Lambda_c\pi$) reconstruction strongly benefits from the improved track spatial resolution of the ALICE Inner Tracking System Upgrade, because they have small mean proper decay lengths (e.g. about 60 μm for Λ_{c}) and large combinatorial backgrounds. The Λ_{c}, Λ_{b} and $\mathrm{B_s^0}$, in particular, require very large integrated luminosities, because the decay branching ratios are very small (e.g. about 3×10^{-4} for $\Lambda_{\mathrm{b}} \rightarrow \Lambda_{\mathrm{c}}(\rightarrow \mathrm{pK}\pi)\pi$) and the combinatorial background is very large, in case for the Λ_{c}, which has a small separation from the interaction vertex and lower invariant-mass than the b-hadrons. In [8] it has been shown that the statistical uncertainty in the lowest accessible p_{T} intervals for these hadrons would increase above 20–30% with integrated luminosity significantly lower than 10 nb^{-1}.

Figure 19 shows the performance for the R_{AA} of $\mathrm{D_s}$ (left) and $\mathrm{B_s^0}$ (right), compared with the cor-

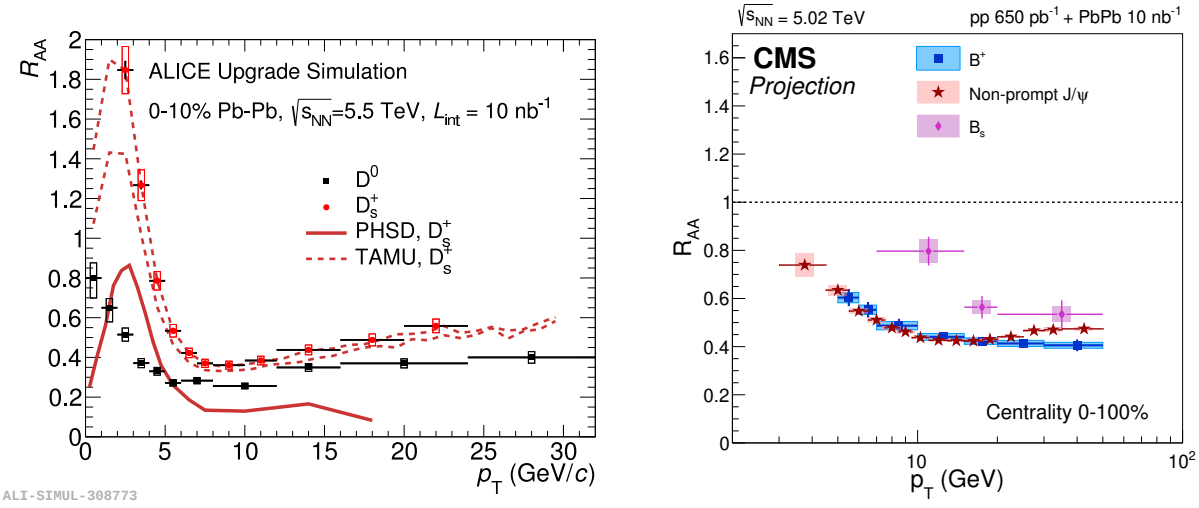

Fig. 19: Measurement performance projections for the nuclear modification factor R_{AA} of $\mathrm{D_s}$ (left) and $\mathrm{B_s^0}$ (right) mesons in Pb–Pb collisions ($L_{\mathrm{int}} = 10\ \mathrm{nb}^{-1}$). The ALICE study for $\mathrm{D_s}$ is based on full simulation [1, 263]. The CMS projection is based on scaling of uncertainties from existing measurements [8, 9].

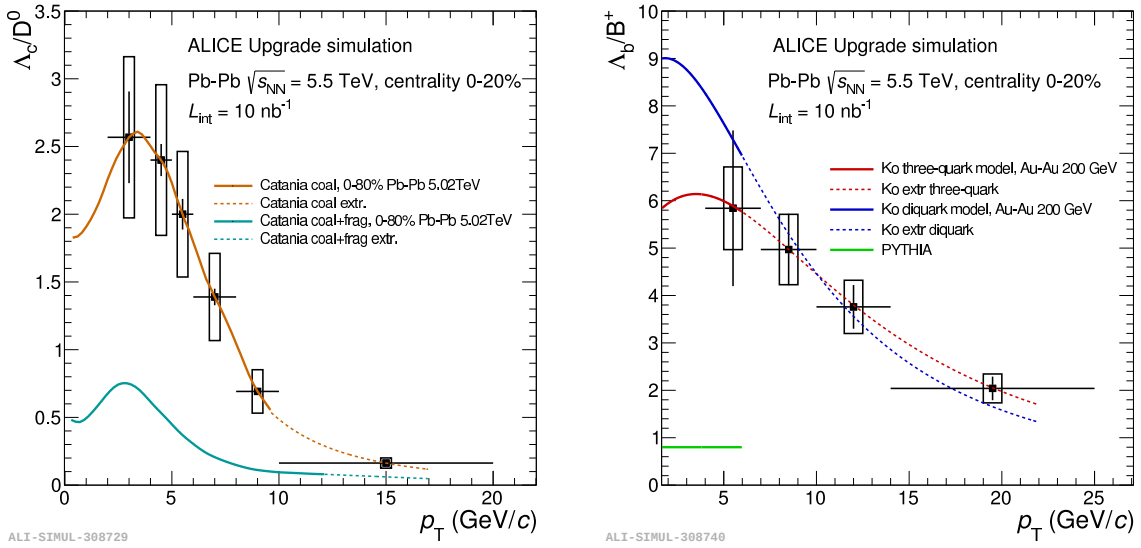

Fig. 20: ALICE measurement performance for the Λ_c/D^0 (left) and Λ_b/B^+ ratios in central Pb–Pb collisions ($L_{\mathrm{int}} = 10\ \mathrm{nb}^{-1}$), based on studies from [263]. Figures from Ref. [1].

responding non-strange mesons. The predicted difference between the D^0 and $\mathrm{D_s}$ R_{AA} will be measured very precisely and the difference in the beauty sector could be observed with a significance of about $3\,\sigma$. The measurements were studied only for $p_{\mathrm{T}} > 2$ and 8 GeV/c, respectively, but an extension to lower p_{T} is considered within reach.

Figure 20 shows the performance for the charm and beauty baryon-to-meson ratios as they can be measured by ALICE with $L_{\mathrm{int}} = 10\ \mathrm{nb}^{-1}$ [263]. The measurements are compared with predictions based on various mechanisms for heavy-quark recombination in the medium [290, 292]. Figure 15 (right) shows the performance for the elliptic flow coefficient v_2 of D^0, $\mathrm{D_s}$ and Λ_{c} in semi-central Pb–Pb

collisions [263]. The precision of the D_s v_2 should be sufficient to enable a significant comparison with D^0 and with model calculations, in which the observable is found to be sensitive to the interactions of D mesons in the hadronic phase that characterises the late stages of the collision [297]. Both measurements cannot be extended to the very-low-momentum region, where the separation of the heavy-flavour secondary vertex from the primary vertex is small. This limitation motivates studies for a further improvement of the ALICE inner tracker during LS3 [302]. A more precise measurement would open the possibility to test in the charm sector some features at present only observed for the v_2 of light-flavour hadrons: the mass scaling at low p_{T} and the baryon–meson grouping at high p_{T}. Finally, the detection of baryons with multiple-heavy-flavour content, like e.g. the Ω_{cc} and Ω_{ccc} states that are predicted to have enhancements of several orders of magnitude if heavy quarks recombine in the QGP [303–305], is one of the main physics goals driving the concept for a possible new heavy-ion experiment at the LHC [306]. This experiment, which could be a follow-up of the ALICE experiment in the 2030s, would be mainly based on ultra-thin and granular silicon pixel detectors.

5.4.3 *Impact of hadronisation models on QGP characterisation*

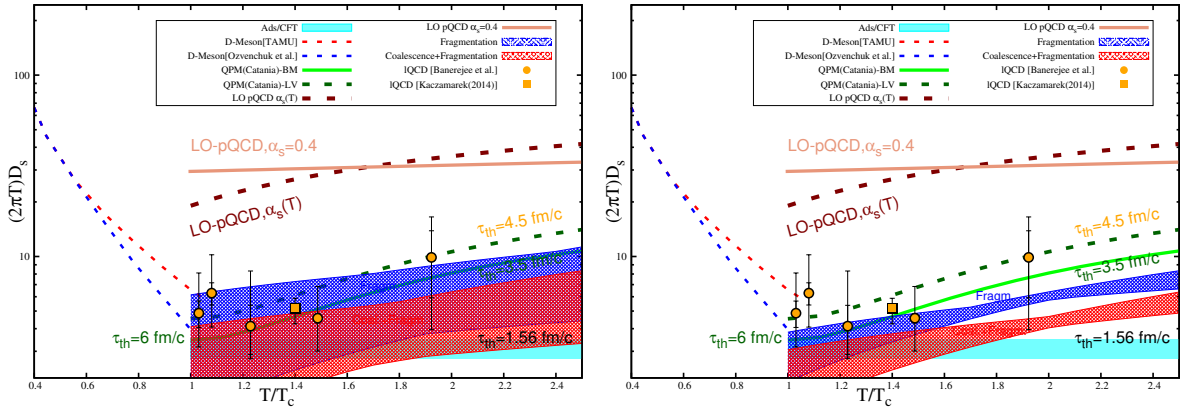

Fig. 21: Illustration of charm diffusion coefficient $2\pi T D_s(T)$ estimate from D meson $R_A A$ data using different hadronisation assumptions in the Catania model [273, 274] as a function of temperature. The blue band refers to fit with fragmentation only, the red band to the fit with coalescence plus fragmentation. In the left panel the D_s estimation obtained with the current experimental uncertainties is shown, while in the right panel the estimation considering the case with more precise measurements as expected with $L_{\mathrm{int}} = 10\ \mathrm{nb}^{-1}$ is shown.

The hadronisation mechanism of heavy quarks is important for the description of the measured heavy-flavour R_{AA} and v_2 at RHIC and LHC energies. In particular, it has been recognized that recombination play a dominant role in describing simultaneously both D meson R_{AA} and v_2 [280, 307–309]. Moreover, as discussed in Section 5.4.1, the charm baryon-to-meson ratio Λ_c/D^0 measured at RHIC and LHC is not consistent with a fragmentation only scenario [290, 292]. Therefore, a combined study including also the heavy baryon-to-meson ratio provides further information to solve the ambiguity on the recombination fraction. In the following, the sensitivity of the QGP characterisation to the recombination fractions described in Section 5.4.1 is illustrated. To estimate how different model implementations of the hadronisation mechanisms can affect the extraction of the charm quark diffusion coefficient $2\pi T D_s$, a global quantitative χ^2 analysis was carried out by comparing experimental data on the D meson R_{AA} with theoretical results obtained using the Fokker-Planck equation under a standard bulk medium evolving hydrodynamically with $\eta/s = 0.1$ [310, 311]. The model developed in [273, 274] with diffusion and drag coefficients related by the fluctuation-dissipation theorem was used, considering two differ-

ent implementations of the hadronisation process: one using only fragmentation of charm quarks to D mesons (with the Peterson function) and another one including a hybrid hadronisation by coalescence plus fragmentation [280, 292]. For the estimate of the temperature dependence of $2\pi TD_s$, a schematic model in which the drag coefficient is parametrized as $\gamma = \gamma_0(T/T_c)^{\beta}$ was used. The two parameters γ_0 and β were determined by minimizing the $\chi^2/\mathrm{n.d.f.}$ of the model with respect to the measured D meson R_{AA}. The exercise could in principle be repeated using both R_{AA} and v_2. The spatial diffusion coefficient is directly related to the drag coefficient by $D_s = T/(M \cdot \gamma(p=0))$, where M is the charm quark mass. The left panel of Fig. 21 shows the spatial diffusion coefficient $2\pi TD_s(T)$ estimated from the fit to the present data with $\chi^2/\mathrm{n.d.f} < 2.5$. The blue band corresponds to the fragmentation only results and the red band to the coalescence plus fragmentation result. The right panel shows the same calculations obtained with experimental data with smaller error bars on the D-meson R_{AA} as expected with $L_{\mathrm{int}} = 10\ \mathrm{nb}^{-1}$. The comparison between the two cases highlights the difference in the estimation of the D_s coefficient obtained with the two different hadronisation mechanism. Clearly, an optimal estimate of the diffusion coefficient requires an accurate description of the hadronisation mechanisms in the model.

5.5 Heavy-flavour correlations and jets

5.5.1 Heavy-flavour correlations

Although heavy quarks at the LHC energies are mostly produced in primary hard scatterings between the incoming partons in hadronic collisions, a non negligible fraction of c and b quarks are originated from processes of gluon splitting. At the leading order, $\mathrm{c\overline{c}}$ pairs are produced with an azimuthal opening angle of 180°. At the next to leading order, gluon splitting and flavour excitation processes can generate $\mathrm{c\overline{c}}$ pairs typically at small opening angles. The role of next-to-leading order production is currently poorly understood even in proton-proton collisions [312, 313] and introduces sizeable uncertainties in the models for Pb–Pb collisions. As a result, heavy-ion calculations which use proton-proton generators as baseline can be biased because of the different energy loss of quarks and gluons. Correlations between D and $\overline{\mathrm{D}}$ represent a promising way to study the relevance of these mechanisms in different kinematic ranges of the charm quarks. In p–Pb collisions, the study of open heavy-flavour correlations at forward and backward rapidity provides information to test modifications of parton distribution functions in nuclei (see Sect. 10.3.3).

Figure 22 shows the LHCb projections for the azimuthal $\mathrm{D\overline{D}}$ correlations at forward rapidity in pp and p–Pb collisions at the same collision energy per nucleon-nucleon-pair of 8.8 TeV. The figure shows only statistical uncertainties (dominant with respect to the systematic uncertainties) as expected with the Run 3 and 4 integrated luminosity. The measurement of the $\mathrm{D\overline{D}}$ correlation can be performed in intervals of D meson p_{T}, providing differential information to test theoretical models with precision. The experimental projections are compared with predictions obtained with EPOS3-HQ event generator for two different kinematic selections in case of pPb collisions. In particular, the two selected p_{T} ranges, 2-3 GeV/c and 3-12 GeV/c, yield to significantly different correlation shapes in the calculation. This dynamic change of shape demonstrates the necessity to provide precise quantitative tests of the importance of different production mechanism at the partonic level, the hadronisation and potential medium effects in pp and in p–Pb collisions across different kinematic configurations.

In nucleus-nucleus collisions, $\mathrm{D\overline{D}}$ correlations are sensitive observables to discriminate among different mechanisms of in-medium energy loss of heavy-quarks, like radiative and collisional processes. Such measurements, presently challenged by statistical limitations, will greatly benefit from future high-luminosity heavy-ions runs.

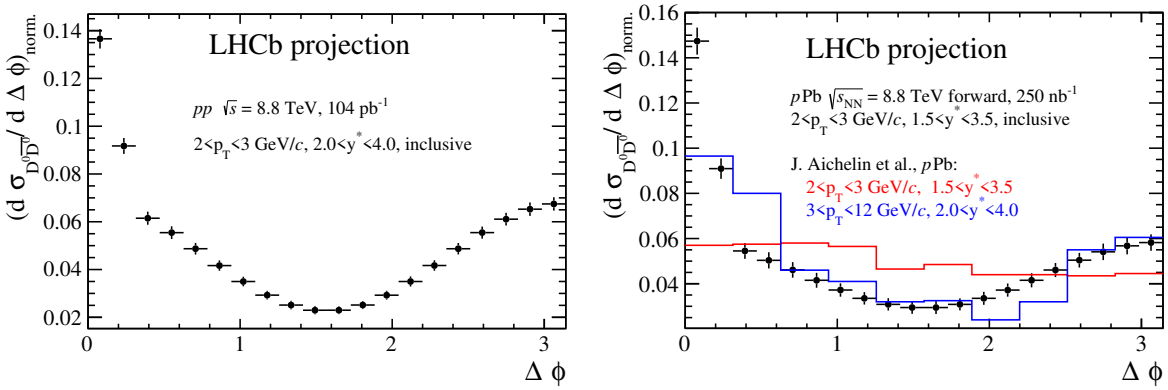

Fig. 22: LHCb projection of the azimuthal $\mathrm{D\overline{D}}$ correlations in p–Pb and in pp collisions at $\sqrt{s} = 8.8$ TeV for the integrated Run 3 and Run 4 luminosity. The p–Pb panel shows a calculation for two different kinematic selection in p–Pb collisions within the EPOS3-HQ generator. A detailed description of the experimental estimates can be found in Ref. [13].

5.5.2 Heavy-flavour jet measurements

Further insights into the mechanism of parton energy loss in the QGP can be provided by the study of reconstructed heavy-flavour jets. These measurements provide complementary information to the studies of D and B mesons since they enable to better determine the energy of the initial heavy quark and give access to the jet energy profile. By comparing the production of heavy-flavour jets with light jets one can test the expected flavour dependence of the in-medium energy loss in a wide transverse momentum range and study the different energy loss mechanism of quarks and gluons. The study of more differential observables related to the production of heavy-flavour particles in jets, like the fragmentation function and the angular correlations, provides additional constraints into the mechanisms of redistribution of the energy lost by the parton inside the medium.

Figure 23 (left) shows the projections for the nuclear modification factor of D^0-meson tagged jets in Pb–Pb collisions at $\sqrt{s_{\mathrm{NN}}} = 5.02$ TeV with ALICE. The measurement will provide a precise estimation of the suppression of D^0-tagged jets down to low p_{T}, opening the way to study possible modifications of charm fragmentation. Future measurements of the fragmentation functions of charmed hadrons in pp collisions will also help to reduce the uncertainties on the charm fragmentation mechanisms, which are currently among the main sources of uncertainties for theoretical calculations that describe heavy-quark production at the LHC.

Figure 23 (right) shows the CMS projection for the distribution of D mesons as a function of the distance from the jet axis for jets of $p_{\mathrm{T}} > 60$ GeV/c in Pb–Pb collisions divided by the distribution in pp collisions. With the precision achievable with the high-luminosity data, one would be able to measure precisely the effect of heavy-quark in-medium energy loss and the redistribution of the energy at large angle with respect to the jet axis. This is expected to provide new constraints on in-medium energy loss calculations. By comparing the ratio measured for D mesons with the one obtained for charged particles, it will be possible to assess the relevance of medium response phenomena, which can induce modification of the jet shape at large angles and are expected to be less relevant for heavy quarks due to their large masses.

Another area of research where the LHC experiments can make key contributions is the study of heavy-flavour jet substructure. New experimental observables related to the inner structure of heavy-flavour jets, like the splitting functions, can provide insights into the mass dependence of the parton shower in new kinematic regimes. A precise measurement of these observables at the LHC down to low p_{T} would also provide a unique opportunity to further investigate the dead cone effect [271], currently

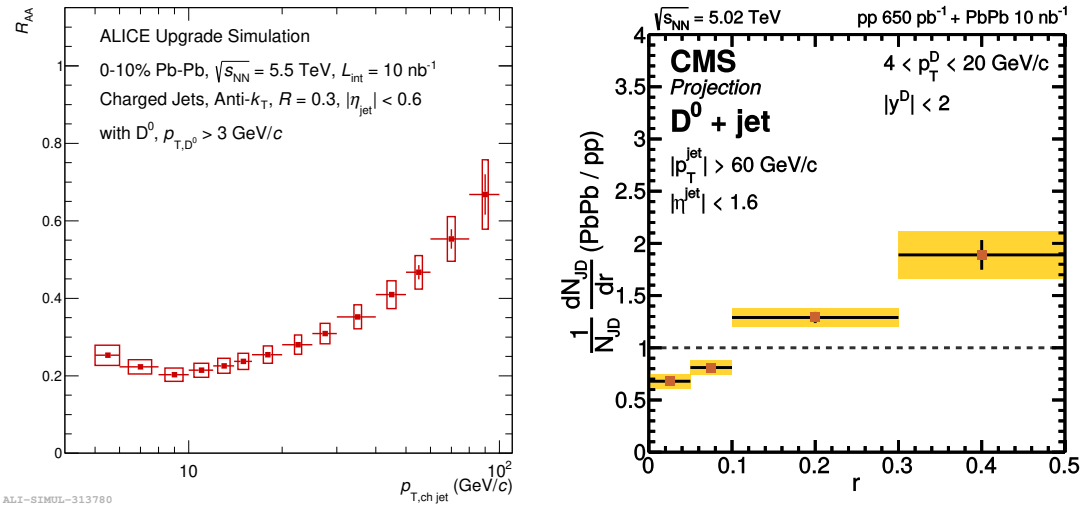

Fig. 23: (Left) ALICE simulation results for the nuclear modification factor of D^0-meson tagged jets in central Pb–Pb collisions [1]. (Right) CMS projection for the distribution of D mesons in jets as a function of the distance from the jet axis for jets of $p_{\mathrm{T}} > 60\,\mathrm{GeV}/c$ in Pb–Pb collisions divided by the distribution in pp collisions.

not well understood and constrained.

5.6 Sensitivity to early magnetic fields and vorticity phenomena

Recently, it has been recognized that very strong electric and magnetic fields are created at early times of ultra-relativistic heavy-ion collisions. In Fig. 24 (left), the time dependence of the magnetic ($\mathrm{B_y}$) and electric ($\mathrm{E_x}$) fields in Pb–Pb collisions at $\sqrt{s_{\mathrm{NN}}} = 2.76$ TeV with impact parameter b=9.5 fm is presented for a system with electric conductivity σ_{el} =0.023 fm^{-1}. The space-time evolution is obtained as solution of the Maxwell's equations as developed in [244]. The magnetic field produced in non-central heavy ion collisions is dominated by the $\mathrm{B_y}$ component which induces a current in the xz plane while the time dependence of $\mathrm{B_y}$ generates an electric field which is directed in the x direction. The combined effect of both fields is a current in the xz plane.

The presence of early magnetic fields produced in heavy-ion collisions is expected to have an effect on the charm directed flow [257, 314], resulting in a v_1 value larger than that of lighter particles (short charm formation time and therefore sensitive to the maximum magnetic field strength), and opposite for particles with charm and anti-charm (due to the Lorentz force). Also the initial vorticity of non-central collision is expected to affect the directed flow observable. The STAR collaboration recently presented the first measurements of the directed flow v_1 coefficient for mesons. This first observation of non-zero v_1 for charm mesons, larger than that of lighter particles, is in qualitative agreement with theoretical models including both electromagnetic and vorticity effects. The uncertainties on the difference between the v_1 of D^0 and $\overline{\mathrm{D}}^0$ from STAR are still too large to draw conclusions on the effects of the early magnetic fields. The LHC Run 3 and 4 will enable more precise measurements on the charm directed flow, which will give additional insights into the initial vorticity of the Quark Gluon Plasma and the strength of the electromagnetic fields. Figure 24 (right) shows the precision level for the difference of directed flow v_1 for D^0 and $\overline{\mathrm{D}}^0$ which ALICE can measure as a function of pseudorapidity in semi-central Pb–Pb collisions at $\sqrt{s_{\mathrm{NN}}} = 5.5$ TeV.

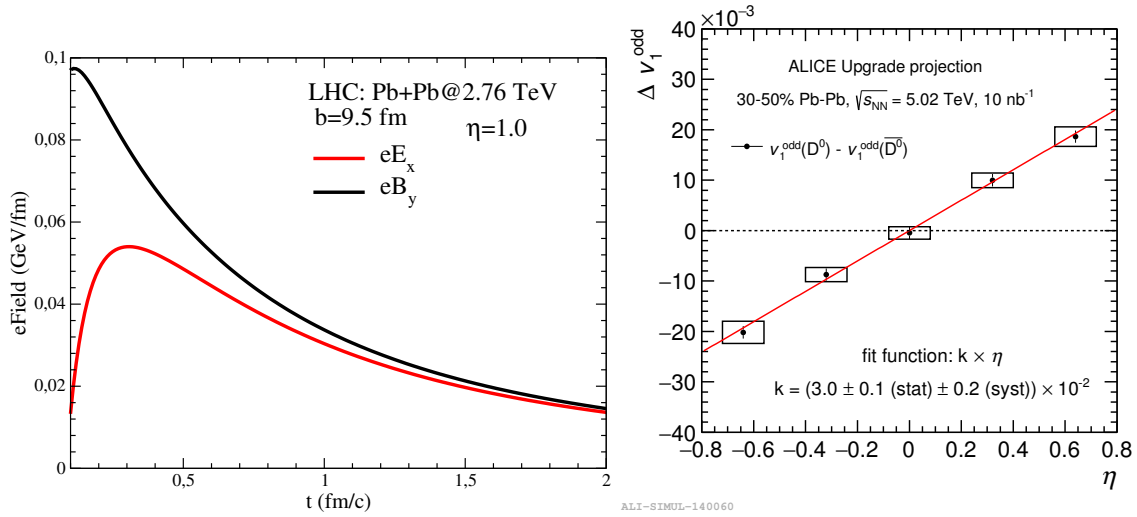

Fig. 24: Left: Time evolution in the forward rapidity region of the magnetic field $\mathrm{B_y}$ and electric field $\mathrm{E_x}$ in Pb–Pb collisions at $\sqrt{s_{\mathrm{NN}}} = 2.76$ TeV with impact parameter $b = 9.5$ fm [257]. Right: ALICE projection of the difference of directed flow v_1 for $\mathrm{D^0}$ and $\overline{\mathrm{D}}^0$ as a function of pseudorapidity in semi-central Pb–Pb collisions at $\sqrt{s_{\mathrm{NN}}} = 5.5$ TeV [1].

5.7 Heavy flavour measurements in small colliding systems

Traditionally, proton-nucleus collisions were considered just as a benchmark to investigate Cold-Nuclear-Matter (CNM) effects in the absence of a deconfined medium. As discussed in the devoted section, recent results suggest to partially reconsider such a paradigm. In particular, the study of soft observables in high-multiplicity p–Pb (and even pp) collisions led to the observation of signals traditionally attributed to the formation of a hot deconfined medium: long-range azimuthal 2-particle correlations [315–318], non-vanishing flow harmonics [319, 320], increasing baryon/meson ratio as a function of p_{T} [321], enhancement of strange-hadron production [322]. Many authors interpreted these observations as indications that the same strongly-interacting medium – with a collective hydrodynamic expansion driven by pressure gradients – supposed to be formed in nucleus-nucleus collisions is also produced in smaller systems. If the hydrodynamic scheme provides a consistent framework describing the above observations, its strong assumptions (e.g. a mean-free-path much smaller than the system size $\lambda_{\mathrm{mfp}} \ll L$) look challenging to satisfy for such small systems. Hence, some authors looked for alternative interpretation of the data in terms, for instance, of initial-state effects (Color-Glass-Condensate [323]), of the formation of a system with small parton-parton cross-sections [324], of the presence of anisotropic parton escape mechanisms [325] or of quantum-mechanical interference in the presence of multiple sources of particle production, entailing to reconsider the no-interaction baseline before looking for final-state collective effects [326] .

On the other hand, no signature of jet-quenching or suppression of high-p_{T} particle production was observed in high-multiplicity proton-nucleus collisions [327]. At first glance this appears in contradiction with the measurements involving soft observables. One should in any case consider that the quenching of jets due to parton energy-loss in the QGP has a strong dependence on the thickness of the crossed matter. On the contrary, if one accepts the hydrodynamic paradigm, the smaller size of the medium with respect to the nucleus-nucleus case would lead to even larger pressure gradients and hence to a larger acceleration of the fluid, compensating its shorter lifetime.

In light of the above findings, as an independent probe, it is clearly of interest to address the study of small systems also through heavy-flavour observables. Due to their large mass c and b quarks are in

fact produced in the very first instants in hard processes described by pQCD, at most affected by nuclear modifications of the Parton Distribution Functions (nPDFs) and by an initial transverse-momentum broadening acquired in CNM. It looks then natural to extend transport calculations, developed to describe heavy-flavour propagation through the plasma formed in nucleus-nucleus collisions, also to the case of small systems, assuming as a working hypothesis that also in this case a hot deconfined medium is formed. The theoretical modelling involves the same processes as in the heavy-ion case: the so-called CNM effects (nPDFs and initial k_{T}-broadening) modifying the hard $Q\overline{Q}$ production, the propagation of the heavy quarks throughout the fireball and finally their hadronization in the presence of a hot medium. The only difference is that, in the case of small systems, it is mandatory to include event-by-event fluctuations in the initial conditions.

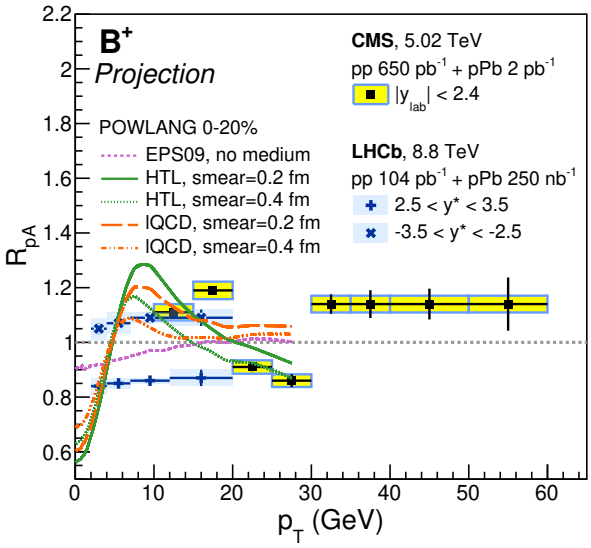

Fig. 25: Projection for the measurement of the nuclear modification factor of B mesons in p–Pb collisions achievable by CMS [9] and LHCb at $\sqrt{s_{\mathrm{NN}}} = 5.02$ TeV and 8.8 TeV respectively. The predictions of the POWLANG model with different choices of the transport coefficients and of the smearing of the initial condition at $\sqrt{s_{\mathrm{NN}}} = 5.02$ TeV are shown. Also reported, in magenta, the curve containing only Cold-Nuclear-Matter effects.

In order to illustrate the level of precision which future experimental measurements must reach to discriminate among different scenarios of initial and final-state effects, various sets of predictions based on the POWLANG model are reported in the following [328]. In Fig. 25 results of transport calculations for the nuclear modification factor of beauty hadrons in p–Pb collisions at $\sqrt{s_{\mathrm{NN}}} = 5.02$ TeV are displayed and compared to experimental projections by CMS for the B-meson R_{pPb} obtained from Run 2 data and projections of LHCb at lower transverse momentum for the B-meson R_{pPb} [13] obtained using as central points the calculations based on Ref. [329]. As can be seen, model predictions are sensitive to the different choices of the transport coefficients (see discussion in [328]) and of the initial conditions (each nucleon-nucleon collision is assumed to deposit some entropy with a Gaussian smearing). In order to answer the question about possible final-state hot-medium effects, experimental measurements should be extended to lower p_{T}, as planned for the different experiments (see ALICE plans to perform beauty measurements down to low p_{T} in nucleus-nucleus collisions in Sec. 5.3.1). In fact, for p_{T} larger than 10–15 GeV/c the curves accounting for the transport and hadronization of the heavy quarks in a hot medium (green curves) are very close to the (magenta) one which includes only the effect of the nPDF's and of the initial k_{T}-broadening acquired in CNM, all of them being very close to unity as the experimental projections by CMS. On the contrary, at lower p_{T} the radial flow of the beauty hadrons, acquired in part

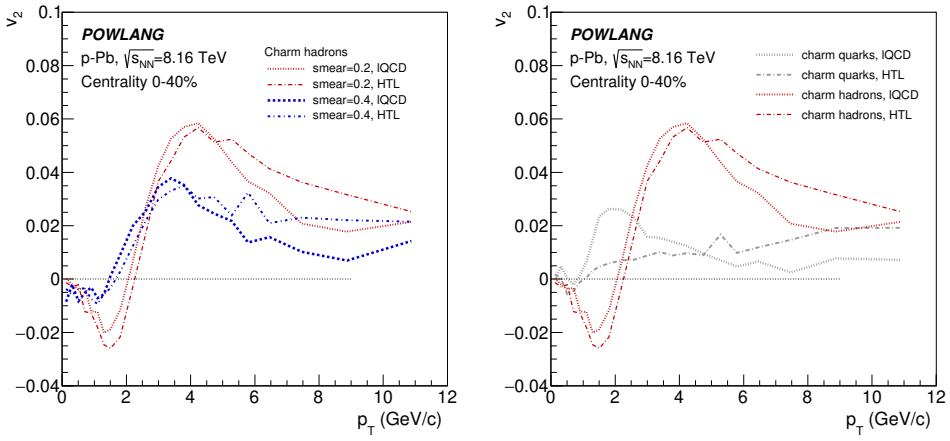

Fig. 26: Left: The elliptic flow of charmed hadrons in the 0-40% most central p–Pb collisions at $\sqrt{s_{\rm NN}} = 8.16$ TeV. Results of the POWLANG model with different choices of the transport coefficients and of the smearing of the initial condition are shown. Right: a comparison of the results at the level of charm quarks and hadrons. An important fraction of the flow is acquired at hadronization via recombination with light partons from the medium.

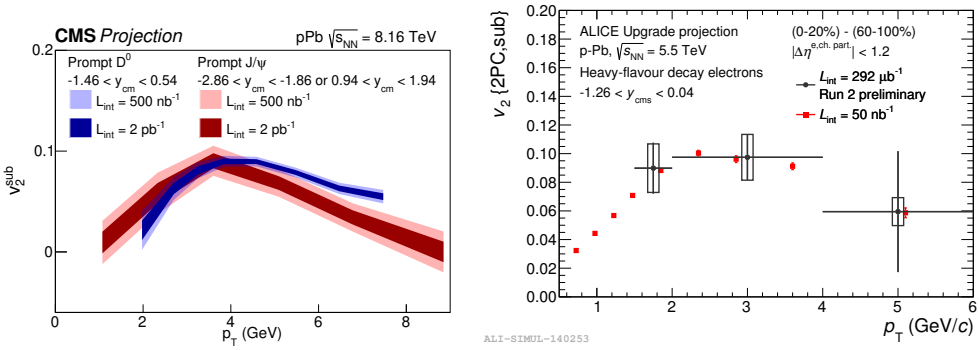

Fig. 27: Left: projection of prompt D-meson and prompt J/ψ elliptic flow as a function of $p_{\rm T}$ in high-multiplicity p–Pb collisions at $\sqrt{s_{\rm NN}} = 8.16$ TeV with CMS [11]. Right: projection of elliptic flow of electrons from heavy-flavour hadron decays as a function of $p_{\rm T}$ in 0–20% central p–Pb collisions at $\sqrt{s_{\rm NN}} = 5.02$ TeV with ALICE [1].

during the propagation through the hot medium and in part at hadronization via recombination, leads to a depletion of the spectrum at low $p_{\rm T}$ and to an enhancement at intermediate $p_{\rm T}$ which would allow one to distinguish this scenario from the case of pure CNM effects.

As displayed in Fig. 26 the possible production of a hot deconfined medium in proton-nucleus collisions would also leave its fingerprints in the azimuthal distribution of the final hadrons, leading in particular to a non-vanishing elliptic-flow coefficient. Notice how one gets a positive v_2 for charmed hadrons only starting from $p_T \approx 2$ GeV/c, in agreement with recent CMS data [330]. Differently from the heavy-ion case, in such small systems it is important how the initial entropy deposition is modelled with varying the smearing parameter (left panel). As displayed in the right panel of Fig. 26, within the framework of the model, an important role is played by hadronization via recombination with light partons from the fireball, whose collective flow enhances the azimuthal asymmetry of the charmed hadrons.

The projected precision with p–Pb integrated luminosities $L_{\rm int} \sim 2$ pb^{-1} (ATLAS and CMS)

and ~ 1 pb^{-1} (ALICE) has the potential to shed light on the different mechanisms behind the observed anisotropy (see Fig. 27 for D mesons and prompt J/ψ with CMS [11] and electrons from heavy-flavour hadron decays with ALICE).

Besides the analysis of kinematic distributions (in momentum and angle) of heavy-flavour particles, further interesting information on the onset of possible medium effects may come from the study of the yields of the various charm and beauty hadrons as a function of charged-particle multiplicity going from pp to p–Pb and Pb–Pb, as done in the past for the case of strangeness production. As an example, with high-multiplicity triggers in pp collisions at $\sqrt{s} = 14$ TeV ($L_{\rm int} = 200$ pb^{-1}), the ALICE experiment will have the potential to detect D mesons with a precision better than 10% in a wide kinematic range up to about 10–12 times the average charged-particle multiplicity.

6 Jets and parton energy loss

Coordinators: Marta Verweij (Vanderbilt University and RIKEN BNL Research Center)

Contributors: L. Apolinario (LIP and IST Lisbon), R. Bi (Massachusetts Institute of Technology), Z. Citron (Ben-Gurion University of the Negev), Y. Chen (CERN), L. Cunqueiro Mendez (Oak Ridge National Laboratory), D. d'Enterria (CERN), P.M. Jacobs (Lawrence Berkeley National Laboratory), F. Krizek (Academy of Sciences, Prague), Y.-J. Lee (Massachusetts Institute of Technology), M. van Leeuwen (NIKHEF), C. Mcginn (Massachusetts Institute of Technology), G. Milhano (LIP and IST Lisbon, CERN), D.V. Perepelitsa (University of Colorado Boulder), M. Płoskoń (Lawrence Berkeley National Laboratory), M. Rybar (Columbia University), A.M. Sickles (U. Illinois, Urbana-Champaign), M. Spousta (Charles University), K. Tatar (Massachusetts Institute of Technology), J. Wang (Massachusetts Institute of Technology)

6.1 Introduction

The most direct way to measure the structure of matter is the controlled scattering of a beam of probe particles. This approach was used to discover the atomic nucleus, and quarks and gluons, and it is employed today to explore the partonic structure of nucleons and nuclei. However, the partonic phase of the QGP lives for $\sim 10^{-23}$ seconds before breaking up into its hadronic remnants, so that probing it by the scattering of an externally-generated beam is impossible in practical terms. As an alternative, energetic jets arising from high-Q^2 processes in the same nuclear collision that generates the QGP provide internally-generated probes that may be applied for this purpose [331–336].

Jets, observed as collimated sprays of energetic particles, were predicted by Quantum Chromo Dynamics (QCD) to form in high energy collisions. They constitute a substantial part of the background in beyond the Standard Model physics searches and were instrumental in the Higgs boson discovery. While jet evolution in vacuum is well understood, the question of how jets interact with a dense deconfined medium remains an active field of study, that is largely driven in the recent years by the unprecedented experimental capabilities of the RHIC and LHC accelerators and detectors. Understanding from first principles how a jet evolves as a multi-partonic system, spanning a large range of scales (from $\sim$1 GeV to $\sim$1 TeV) is crucial to quantitatively probe the Quark Gluon Plasma (QGP). The successful description of bulk observables by viscous hydrodynamic calculations with a small viscosity to entropy ratio have led to the standard picture of a strongly coupled plasma. However, due to the property of asymptotic freedom in QCD, the produced matter is expected to behave differently at smaller and smaller distances which can only be accessed with well calibrated probes, namely, QCD jets.

High-Q^2 processes between the partonic constituents of colliding nucleons occur early in the collision. Further interactions of the outgoing partons with the hot and dense QCD medium produced in heavy ion collisions are expected to modify the angular and momentum distributions of final-state jet fragments relative to those in proton-proton collisions. This process, known as jet quenching, can be used to probe the properties of the QGP [331–336]. Jet quenching was first observed at RHIC, BNL [337–347] and then at the CERN LHC [348–358] by studying the redistribution of energy radiated from the parton because of interactions with the QGP. More recent detailed analyses have focused on modifications to the distribution of final-state particles emitted in the parton's shower [359–365].

One of the main goals of the RHIC and LHC heavy ion physics programs is utilization of jets and their decay products, including high p_{T} hadrons formed by light and heavy quarks, to investigate the QGP properties. A milestone in this program is the extraction of the transport coefficient $\hat{q}$ by the JET Collaboration [366], based on inclusive hadron suppression measurements at RHIC and the LHC. However, this result has significant systematic uncertainties, due both to theoretical issues and to the limited view provided by inclusive hadron suppression measurements into the fundamental processes underlying jet quenching. A more complete picture requires measurements of reconstructed jets and their in-medium modification.

At the LHC, the collision energy is over an order of magnitude larger than at RHIC. Jet production cross-sections are correspondingly larger, enabling the study of hard processes over a wider kinematic range. Detectors at both facilities have extensive capabilities to study fully-reconstructed jets by grouping the detected particles within a given angular region into a jet, thereby capturing a significant fraction of the parton shower. Jets are a key diagnostic of the QGP, as their interactions with this new state of matter reveal its properties. The interaction with the medium can result in a broadening of the jet profile with respect to vacuum fragmentation. In this case, for a given jet size and a fixed initial parton energy, the energy of the jet reconstructed in heavy ion collisions will be smaller than in vacuum. In the case where the gluons are radiated inside the cone, the jet is expected to have a softer fragmentation and a modified density profile compared to jets in vacuum. Jets may also scatter coherently in the medium, and measurements of jet deflection may provide a direct probe of the micro-structure of the QGP. Fully reconstructed jets provide better theoretical control than high p_{T} hadrons because they are less sensitive to non-perturbative physics and therefore have the potential to provide a better characterization of the QGP. Furthermore, major theoretical and experimental advances were made recently in understanding the evolution of parton showers in a QCD medium with the development of novel jet substructure observables.

In the following sections the expected performance using a total integrated luminosity of 10 nb^{-1} of Pb–Pb data, which is expected for HL-LHC, for a selection of key jet observables will be discussed.

6.2 Out-of-cone radiation

One of the classic observables to measure the out-of-cone radiation due to jet quenching is the jet nuclear modification factor R_{AA} defined as:

$$R_{\mathrm{AA}} = \frac{\frac{1}{N_{\mathrm{evt}}} \frac{\mathrm{d}^2 N_{\mathrm{jet}}}{\mathrm{d}p_{\mathrm{T}}\mathrm{d}y}\Big|_{\mathrm{cent}}}{T_{\mathrm{AA}} \frac{\mathrm{d}^2 \sigma_{\mathrm{jet}}}{\mathrm{d}p_{\mathrm{T}}\mathrm{d}y}\Big|_{pp}}, \tag{19}$$

where N_{jet} and σ_{jet} are the jet yield in Pb–Pb collisions and the jet production cross-section in pp collisions, respectively, both measured as a function of transverse momentum, p_{T}, and rapidity, y, and where N_{evt} is the total number of Pb–Pb collisions within a chosen centrality interval. Measurements of the jet R_{AA} at the LHC have shown a suppression of a factor of two in central collisions over a wide range of jet transverse momentum [354, 355, 367]. Figure 28 shows the current precision obtained with 0.5 nb^{-1} and what can be achieved at the HL-LHC with a factor of 20 more data (10 nb^{-1}). Especially at high transverse momentum a strong reduction of the experimental uncertainties is expected, which will allow a detailed study of the momentum dependence of the out-of-cone radiation. The jet R_{AA} is sensitive to various physics mechanisms such as color coherence, flavor dependence of energy loss, and the medium response to the jet. Models incorporating these various physics effects can be confronted with the high precision data from HL-LHC with a goal of determining what the relative contribution of each of these phenomena is. The expected performance is compared with several recent model predictions: the Linear Boltzmann Transport model (LBT) [368], three calculations using Soft Collinear Effective Theory (SCET) [369–372], and the Effective Quenching model (EQ) [373]. The higher precision data will allow tighter constraints on or falsification of theoretical model predictions. In addition to the inclusive jet R_{AA} it is particularly interesting to study the mid- and forward rapidity region separately since it allows to study the interplay between flavor and spectral steepness, and the path-length dependence of jet quenching. The right panel of Fig. 28 shows the improvement in statistical precision in the forward rapidity region. The statistical precision should be sufficient to quantitatively assess the rapidity dependence of the R_{AA} up to a rapidity of $|y| = 2.8$. Both of these predictions

indicate that HL-LHC should bring a definitive understanding of the intriguing features of the jet R_{AA} as seen in the current data.

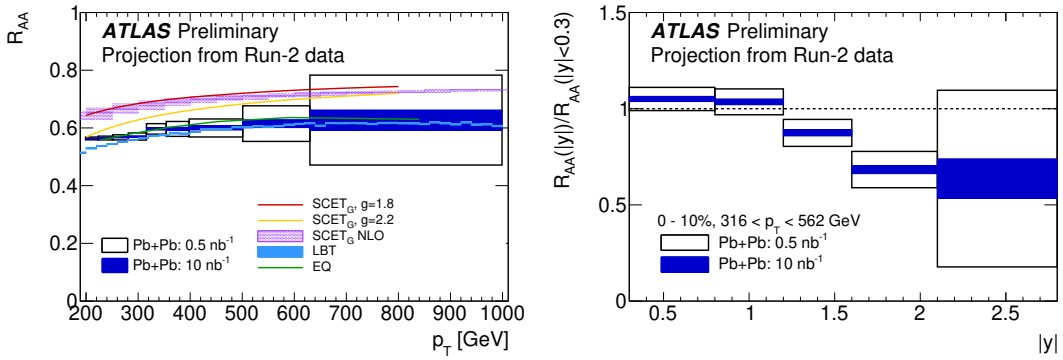

Fig. 28: Projection of the precision that can be reached for jet R_{AA} at the HL-LHC using calorimeter jets at ATLAS as function of p_{T} (left panel) and rapidity (right panel) [5]. See text for model details.

Parton energy loss can be studied more differentially using boson tagged jets. The bosons (photons or Z^0 bosons) escape the region of the hot dense medium unmodified. This has been confirmed through the absence of significant modification of both photon and Z^0 boson production rates in Pb–Pb collisions relative to expectations from measured cross section in pp collisions by both ATLAS and CMS collaborations [374–377]. However, the partons recoiling from the boson is modified in heavy ion collisions due to interactions with the QCD medium. Furthermore, jets produced opposite to the isolated boson are more likely to originate from quarks, while dijet and hadron+jet correlations usually involve significant gluon contributions. Comparing Z+jet and γ+jet observables to dijets [353, 378] (or hadron+jets [358]) allows to explore the difference between energy loss for quark and gluon initiated jets. Figures 29 and 30 show the expected performance at the HL-LHC for the transverse momentum balance between the jet and the boson. The central values are based on the smoothed data from the previous CMS publications [379, 380]. The systematic uncertainties are reduced by a factor of two with respect to the results with the 2015 Pb–Pb data due to improvements on the jet energy scale and jet energy resolution uncertainties available with the larger data sample at the HL-LHC. The collected number of γ+jet events will also be sufficient to study the path length dependence of jet quenching by performing measurements as a function of angle with the reaction plane for the first time. In addition to the smaller uncertainties due to the enhanced statistics at the HL-LHC, it will also be possible to utilize higher momentum photons and Z^0 bosons allowing the measurement of larger jet energy losses. The LHC experiments also envision extending the jet momentum reach to lower transverse momentum in certain analyses, allowing to recover those heavily quenched jets which are currently not selected for such measurements due to limitation arising from the fluctuating background. A distinct effect due to large backgrounds is that of limited jet energy resolution, which can be improved by using more sophisticated techniques for the background correction as was recently shown in Ref. [381].

6.3 Jet deflection

Angular deflection of the jet relative to its initial direction due to momentum transfer with the medium can be used as a direct probe of the QGP. Jet deflection can be measured by coincidence observables, in which an axis is determined by a hard reference object, and the deflection of the jet recoiling from hard object is measured relative to that axis. Such scattering measurements, carried out over a wide range in energy and resolution scale, can be used to explore the microscopic structure of the QGP. Modification of the rate of rare, large-angle jets with respect to the hard reference object in nuclear collisions compared

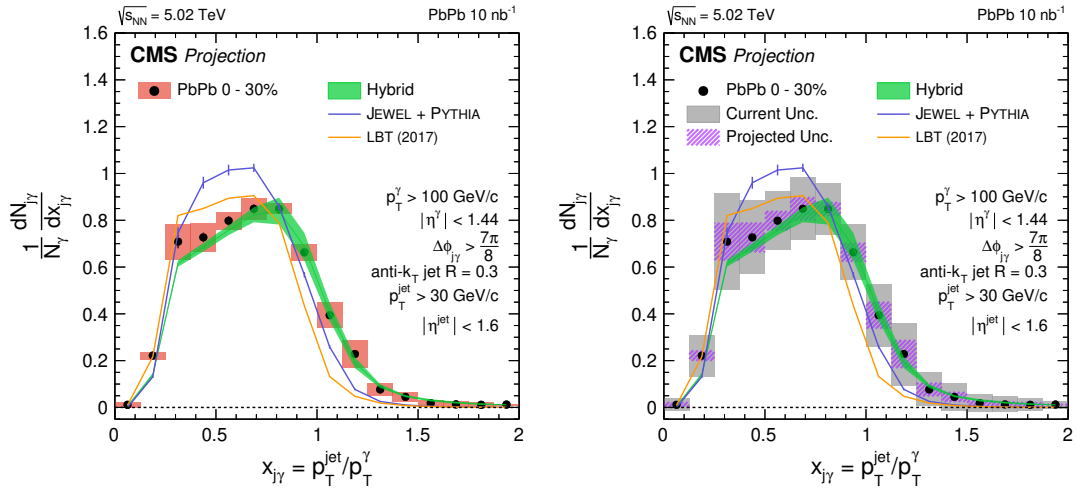

Fig. 29: (Left Panel) Photon-jet momentum balance $x_{j\gamma}$ distribution for isolated-photon+jets of $p_{\gamma} > 100$ GeV/c and $|\eta_{\gamma}| < 1.44$, $p_{\mathrm{jet}} > 30$ GeV/c and $|\eta_{\mathrm{jet}}| < 1.6$ in the HL-LHC data (Right Panel). Comparison between the current performance with 0.4 nb^{-1} of Pb–Pb data collected in 2015 and with HL-LHC data [8].

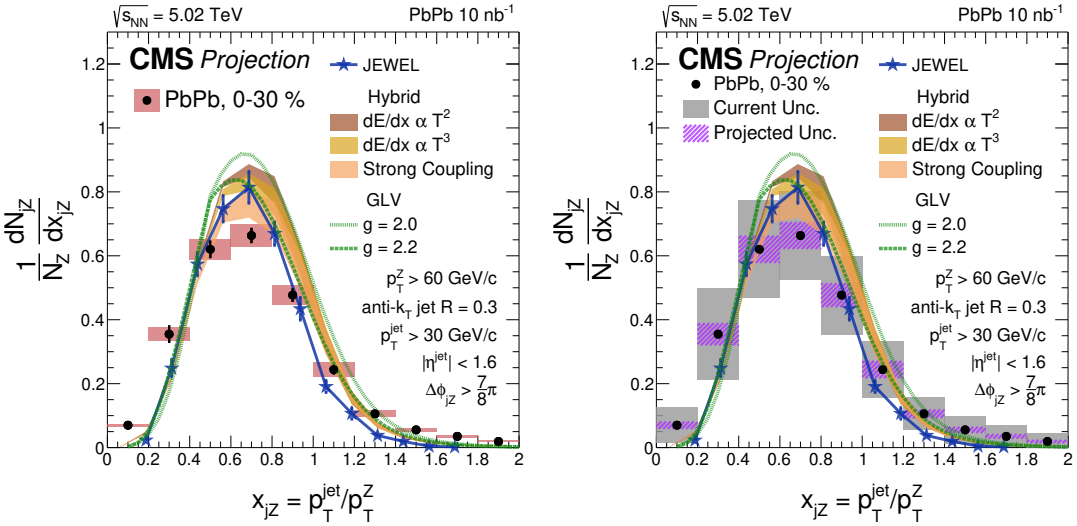

Fig. 30: (Left Panel) X_{jZ} distribution for Z boson-jet pairs with $p_{\mathrm{T}}^{Z} > 60$ GeV/c, $p_{\mathrm{jet}} > 30$ GeV/c and $|\eta_{\mathrm{jet}}| < 1.6$ in the HL-LHC data (Right Panel) Comparison between the current performance with 0.4 nb^{-1} of Pb–Pb data collected in 2015 and with HL-LHC data [8].

to the production rate in vacuum may arise from the scattering off quasi-particles (quarks and gluons or composite objects) of the QGP, thereby probing their nature [382]. In addition, the recoil jet distribution at small recoil angles relative to the reference axis (the axis of the hard object selected at the opposite hemisphere) may be modified by soft multiple scattering in the QGP, which can be used to extract the jet transport parameter $\hat{q}$ by comparison to models [383].

Measurements of the angular distribution of jets relative to a reference axis have been reported for either dijet, photon-jet, Z^0-jet and hadron-jet coincidences, at RHIC [347] and LHC [353,358,379,380,

384]. These current measurements exhibit no significant evidence of in-medium modification of angular distributions, both at small and large angles to the reference axis. While they impose constraints on the magnitude of in-medium scattering effects, their statistical precision is limited. Measurements during HL-LHC will either discover in-medium modification to the recoil jet angular distributions, or improve these constraints substantially.

There is an intensive ongoing effort to develop analysis tools and calculable approaches that discriminate the various contributions to in-medium jet deflection and shower modification, in both experiment and theory [385] (see Sec. 6.2 and 6.4). In this section we focus solely on jet-centroid deflection measurements, without consideration of the effects of shower broadening or other shower modification (see Sec. 6.4). Measurements of both classes of jet quenching observable must ultimately be interpretable in a single consistent picture, but such an approach is beyond current experimental and theoretical capabilities.

The most significant background to the measurement of medium-induced jet deflection is broadening of the angular difference between the two leading jets due to well-established vacuum QCD effects, in particular Sudakov radiation, which is radiation outside the jet cone that generates a broad peak in the recoil jet angular distribution relative to a reference axis (for example a high momentum hadron) [383, 386].

Low-energy jet measurements are expected to experience larger deflection for a given momentum transfer between the jet and medium [387, 388] and are therefore more likely to show large angle deflection. A recent calculation, that includes the effects of vacuum Sudakov radiation and jet-medium interactions based on the few-hard (GLV) or multiple-soft (BDMPS) scattering approaches to jet quenching, finds that the acoplanarity distributions for these different jet quenching pictures differ by a few percent in the range $20 < p_{\mathrm{T,jet}} < 40$ GeV/c [388]. This sets the precision required for the observation of medium-induced jet deflection during HL-LHC. Additional theoretical considerations of in-medium p_{T}-broadening can be found in [334, 389].

In light of such considerations, it is necessary to utilize analysis techniques that can attain few percent precision in the measurement of recoil jet angular distributions for low $p_{\mathrm{T,jet}}$ and large jet radius R, over the large and complex uncorrelated backgrounds in central Pb–Pb collisions at the LHC. This precision is achievable using the statistical approach to jet background correction [347, 358, 379, 380], in which the discrimination of correlated and uncorrelated recoil jet yield is carried out in a fully data-driven way, at the level of ensemble-averaged distributions. The statistical correction approach has been used to measure the azimuthal distribution for charged jets with $R = 0.5$ and $40 < p_{\mathrm{T,jet}}^{\mathrm{ch}} < 60$ GeV/c recoiling from a high-p_{T} hadron in central Pb–Pb collisions at the LHC [358], and for charged jets with $R = 0.5$ and $p_{\mathrm{T,jet}}^{\mathrm{ch}} \sim 10$ GeV/c in central Au–Au collisions at RHIC [347], as well as for photon-jet and Z-jet correlations [379, 380]. We expect that reaching as low as $p_{\mathrm{T,jet}} = 10$ GeV/c is likewise achievable at the LHC, with good systematic precision.

The required experimental approach is therefore in hand, and we explore here the statistical precision achievable using it for such measurements during HL-LHC. We utilize the JEWEL event generator [390] for these projections, which incorporates medium-induced interactions of partons propagating in the QGP. Calculations are carried out for central Pb–Pb collisions at $\sqrt{s_{\mathrm{NN}}} = 5.02$ TeV with integrated luminosity of 10 nb^{-1} , and pp collisions at $\sqrt{s} = 5.02$ TeV with integrated luminosity of 6 pb^{-1}. The JEWEL calculations for central Pb–Pb collisions are carried out with the “Recoil off" configuration in which the partons from the medium response are neglected.

Figure 31 shows the recoil jet azimuthal angle, $\Delta\varphi$, defined with respect to the reference axis [358] as simulated by the JEWEL event generator. The background-corrected azimuthal distribution of recoil jets recoiling from a high-p_{T} hadron, with the statistics expected by ALICE for central Pb–Pb and pp collisions during the HL-LHC phase is shown. The distribution for central Pb–Pb collisions exhibits an overall yield suppression, corresponding to jet quenching, but also a slight narrowing of the main peak at

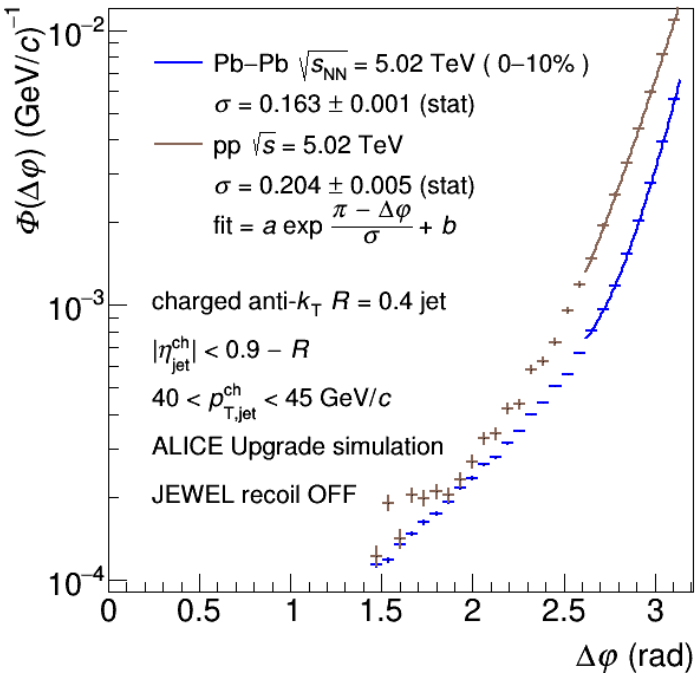

Fig. 31: JEWEL simulation of the angular distribution of charged jet yield in the ALICE acceptance for $40 < p_{\mathrm{T,jet}}^{\mathrm{ch}} < 45$ GeV/c and $R = 0.4$ recoiling from a high-p_{T} reference hadron ($20 < p_{\mathrm{T,trig}} < 50$ GeV/c), for central Pb–Pb collisions at $\sqrt{s_{\mathrm{NN}}} = 5.02$ TeV with 10 nb^{-1} int. luminosity, and pp collisions at $\sqrt{s} = 5.02$ TeV with 6 pb^{-1} int. luminosity. The recoil jet azimuthal angle $\Delta\varphi$ is defined with respect to the reference axis. The observable shown is $\Phi(\Delta\varphi)$ which incorporates statistical suppression of uncorrelated background. Figure from Ref. [1].

$\Delta\varphi \sim \pi$ and an enhancement at large deflection angle. The narrowing is characterized by extracting the width of the $\Delta\varphi$distribution which is 0.204 ± 0.005 in the pp simulation and 0.163 ± 0.001 for the Pb–Pb simulation with JEWEL İn order to quantify the difference at large recoil jet deflection angle between pp and central Pb–Pb collisions, we integrate the $\Phi(\Delta\varphi)$ from $\pi/2$ to a threshold angle $\Delta\varphi_{\mathrm{thresh}}$ [358],

$$\Sigma(\Delta\varphi_{\mathrm{thresh}}) = \int_{\pi/2}^{\pi-\Delta\varphi_{\mathrm{thresh}}} \Phi(\Delta\varphi)\mathrm{d}\Delta\varphi. \tag{20}$$

Figure 32 shows $\Sigma(\Delta\varphi_{\mathrm{thresh}})$ for the $\Phi(\Delta\varphi)$ distributions in Fig. 31, together with their ratio. In this calculation, the value of Σ at $\Delta\varphi_{\mathrm{thresh}} = 0$ is around 0.5, which is the yield suppression averaged over the full recoil hemisphere. The ratio grows to $\Sigma \sim 1$ at $\Delta\varphi_{\mathrm{thresh}} = 1.2$, indicating a factor two enhancement in large-angle yield relative to the hemisphere average. The statistics of the measurement are clearly sufficient to measure the effect predicted by this calculation. However, the calculation in [388] predicts a difference of only a few percent in these distributions for GLV-like and BDMPS-like in-medium scattering, which is more difficult to discriminate. The statistical error in the ratio in Fig. 32 is

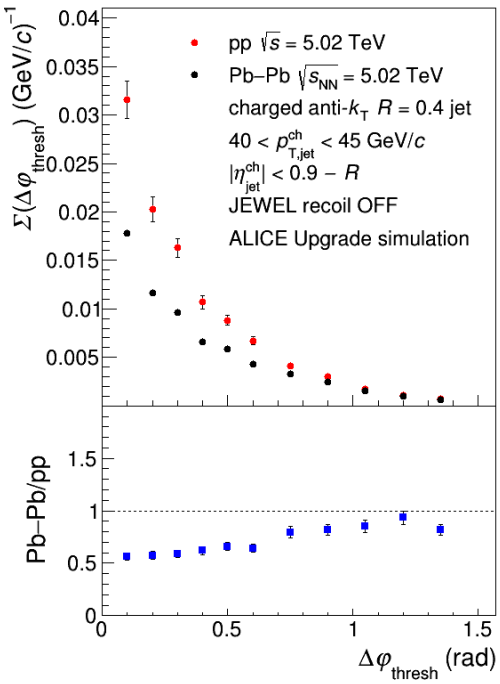

Fig. 32: Cumulative large-angle yield $\Sigma(\Delta\varphi_{\mathrm{thresh}})$ (Eq. 20) vs. $\Delta\varphi_{\mathrm{thresh}}$ for the pp and central Pb–Pb distributions $\Phi(\Delta\varphi)$ in Fig. 31. See text for details. Figure from Ref. [1].

around 5% at $\Delta\varphi_{\mathrm{thresh}} \sim 1$, due predominantly to the statistical precision of the pp distribution.

6.4 Jet internal structure

The first measurements of jet quenching through full jet reconstruction at the LHC revolutionized our understanding of parton energy loss in a hot and dense medium. Nevertheless, there remains a gap in our understanding of the jet quenching mechanism that could be resolved by measuring the exact properties of the parton evolution through the medium. High statistics of collected jets during HL-LHC will provide a prime opportunity to explore the details of the internal structure of high energy jets that undergo interactions with the QGP. Observables probing the internal structure of jets can be defined using all measured hadrons in a jet or by using subjet techniques selecting only a specific region of the radiation phase space. In the following sections both approaches and their potential will be discussed.

6.4.1 Substructure with hadrons

Inclusive measurements of the longitudinal and transverse momentum distribution of hadrons in inclusive jets have been performed with high accuracy at the LHC [391, 392]. The modification due to jet quenching is studied by comparing the results in pp and Pb–Pb collisions. For certain kinematic selections, for example at large z where the leading particle in the jet is carrying a large fraction of the total jet momentum, the current experimental uncertainties are however large (see left panel of Fig. 33) limiting the constraints on the jet quenching mechanism that can be extracted by comparing data to theoretical models. The expected statistical precision at HL-LHC for the ratio of fragmentation functions in Pb–Pb and pp collisions is shown in Fig. 33. This precision will allow detailed characterization of the excess in yield of hard (large z) and soft (small z) fragments and the suppression in the region between these two excesses providing strong constraints to theoretical models. Measurements of the rapidity dependence of jet observables are of great interest since the fraction of quark- and gluon-initiated jets

varies with rapidity. However, current measurements of the fragmentation function are statistics limited and no significant rapidity dependence is observed [391]. The right panel of Fig. 33 shows the ratio of fragmentation functions of high momentum jets for most central collisions with the expected accuracy at the HL-LHC. The projection are compared to the hybrid model [393, 394] which implements energy loss according to the strong coupling description of the radiation of low energy gluons associated with the hot QCD matter which predicts a rapidity-dependent suppression of particle yield at high z.

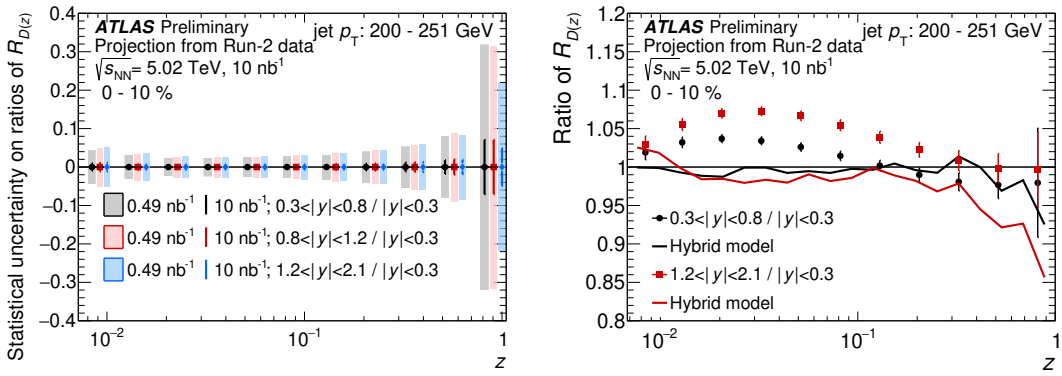

Fig. 33: Projection of the precision that can be reached for the modification of jet fragmentation function, $R_{D(z)}$, measured in jet p_{T} interval $200 - 251$ GeV/c. In the left panel the statistical uncertainty on the measurement with the shaded boxes corresponding to 0.49 nb^{-1} while the vertical bars are for 10 nb^{-1}. The right panel shows a comparison of $R_{D(z)}$ with a theory model (see text for more details) [5].

When interpreting the modification of inclusive jets one has to realize that by requiring a certain jet momentum range a different sample of partons initiating the jet is selected in pp and Pb–Pb collisions. Incorporation of this effect in model calculations introduces an additional uncertainty limiting the constraints that can be put on a model. This can be overcome by using the rare process of jets recoiling from photons. The expected performance of the radial p_{T} profile in jets recoiling from a high momentum photon at HL-LHC is shown in Fig.34. The central values of the extrapolated spectra are obtained by smoothing the results from [395] by a third order polynomial. The systematic uncertainties shown are obtained by reducing by a factor of two those from the 2015 Pb–Pb data results, considering the expected improvements on the jet energy scale and jet energy resolution uncertainties. The results show that the photon-tagged jet shape could be measured with high precision providing insights about the modification of the jet transverse structure of quark initiated jets in the strongly interacting medium. Figure 35 shows the expected statistical precision of the fragmentation function on photon-tagged events. The larger data sample will enable the measurement for finer centrality selections with respect to the current preliminary results [396] allowing an exploration of the temperature and path length dependence of jet quenching.

6.4.2 Substructure with subjets

Early hard splittings in a parton shower may result in two partons with high transverse momentum that are well separated in angle. Information about these leading partonic components can be obtained by removing the softer wide-angle radiation contributions. This is done through the use of a jet grooming algorithm called "soft drop", an extension of the modified mass drop tagger (mMDT), that attempt to split a single jet into two subjets, a process referred to as "declustering" [397–401]. For a parton shower in vacuum, these subjets provide access to the properties of the first splitting in the parton evolution [402, 403]. Figure 36 shows the expected performance for the momentum sharing fraction, z_{g} [403], in the

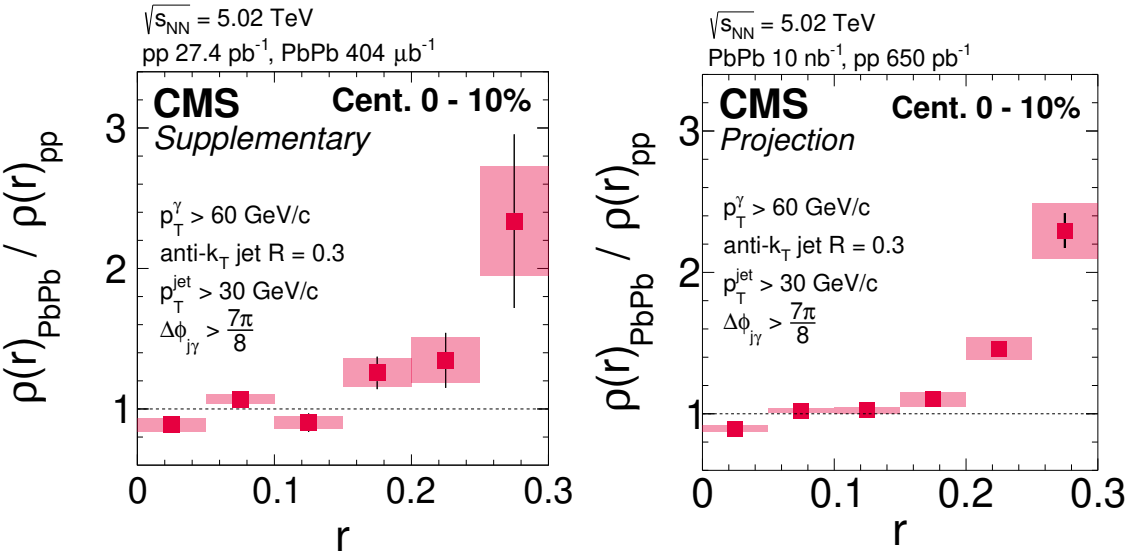

Fig. 34: (Left Panel:) The ratio of measured photon-tagged jet shape in Pb–Pb and pp collisions with the 2015 Pb–Pb data [395]. (Right Panel:) The expected performance of the jet shape ratio in the HL-LHC data, using a third-order polynomial for smoothing the data. [REF to be added when note is public]

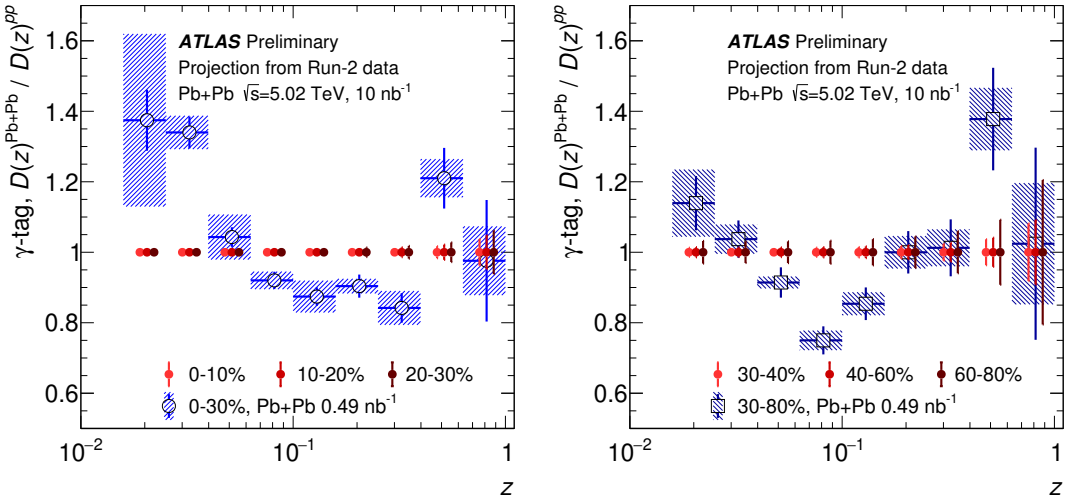

Fig. 35: Projection of the statistical precision that can be reached for the ratio of jet fragmentation functions in Pb–Pb and pp collisions, $R_{D(z)}$, of jets recoiling from a photon. The left panel shows the projection for the most central collisions while the right panel for the more peripheral events [5].

HL-LHC phase. The central values of z_g and jet mass are from previous CMS publications [364, 365]. The systematic uncertainties are reduced by a factor of two with respect to the results with 2015 Pb–Pb data due to the expected improvements on the jet energy scale and jet energy resolution uncertainties. While the current data is not precise enough to constrain the medium properties further, the expected luminosity at the HL-LHC will allow more detailed constraints as can be observed from the different results of the BDMPS [404] and SCETg [405] calculations when the medium density ($\hat{q}$ for BDMPS and g for SCETg) is varied. In addition, the expected precision will also provide the ability to distinguish

different physical mechanisms and scales relevant for jet quenching as is shown for the role of coherence in Fig. 36 in the HT theoretical calculations [406]. A measurement of the groomed jet mass with the 2015 LHC Pb–Pb data already showed that jet quenching might cause an increase of high mass jets [365]. Figure 37 shows the expected performance for the groomed jet mass at HL-LHC which will allow measuring the high mass region with higher precision.

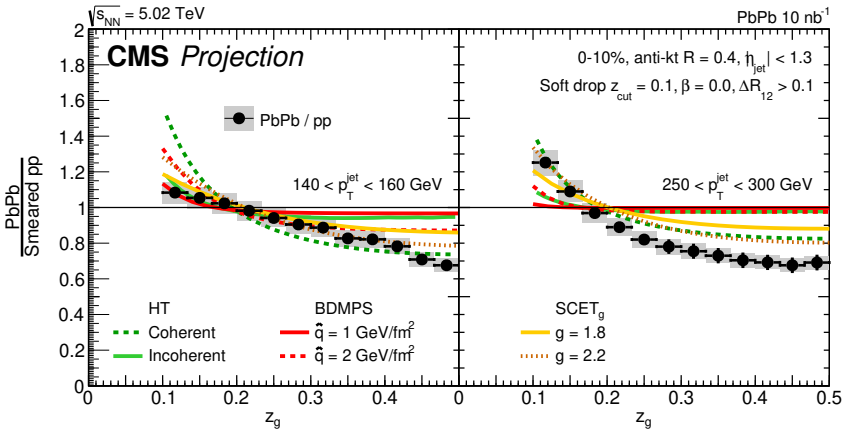

Fig. 36: Performance of jet splitting function measurement with HL-LHC data in Pb–Pb collisions for two different selections in jet transverse momentum. [8]

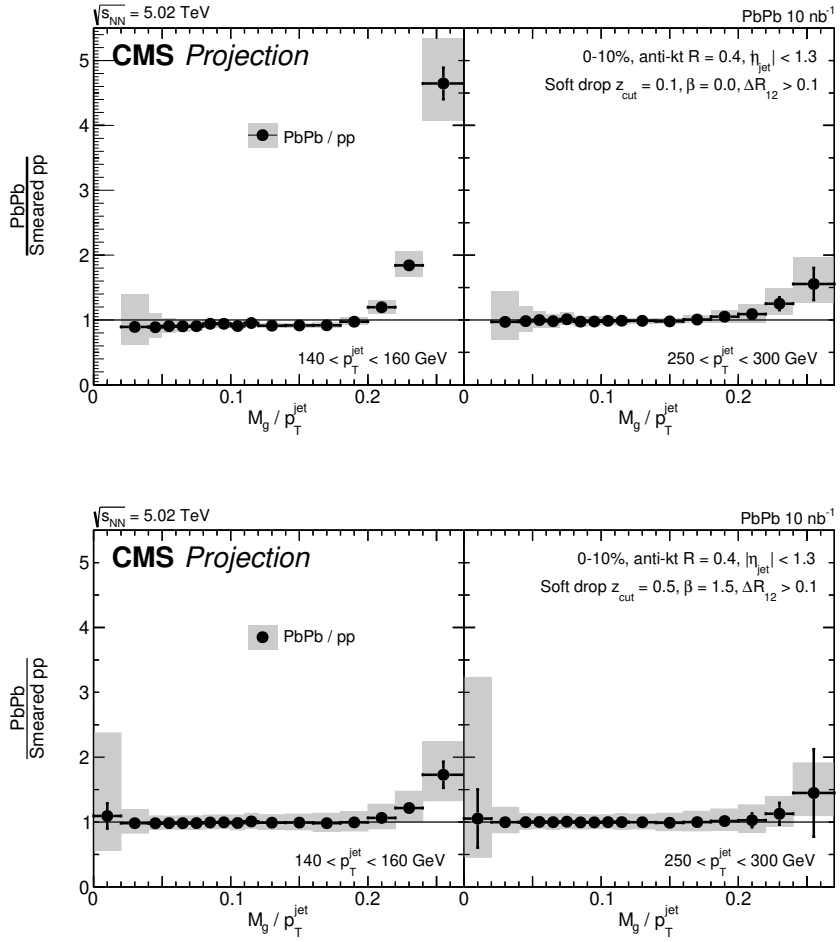

Fig. 37: Jet mass distribution with grooming setting $(z_{cut}, \beta) = (0.1, 0.0)$ (Upper panels) and $(z_{cut}, \beta) = (0.5, 1.5)$ (Lower panels). [8]

6.4.3 Radiation phase space with Lund diagram

Recently, a theoretical representation of the radiation phase space within jets inspired by Lund diagrams [407] has been proposed [385] to study medium modification of the radiation pattern. The so-called Lund jet plane [408] - a portrayal of the internal structure of jets - was designed to build a conceptual connection between manually constructed observables and approaches that use Machine Learning techniques to study QCD jets and/or discriminate between signal and background jets. The diagram is constructed by mapping the available phase-space within a jet to a triangle in a two dimensional (logarithmic) plane that shows the transverse momentum and the angle of any given emission with respect to its emitter. Such a triangular diagram, a representation of the radiation within any given jet, can be created through repeated Cambridge/Aachen declustering.

To demonstrate the potential of future measurements at the LHC we constructed Lund diagrams using the JEWEL Monte Carlo event generator [390]. To study the differences in the Lund diagram due to medium effects the results are compared to a vacuum reference (jets produced in pp collisions). For the simulations the JEWEL generator with the default settings is used without the optional calculation of the so-called medium response retaining the partons / scattering centres that interacted with the jet was not used (i.e. *recoils off* setting of the MC generator was used). The substructure of jets was analysed

by reclustering the constituents of the jet with the Cambridge/Aachen (C/A) algorithm as implemented in the FASTJET package [409, 410] for two selections of jet p_{T} 80–120 GeV/c and 200–250 GeV/c.

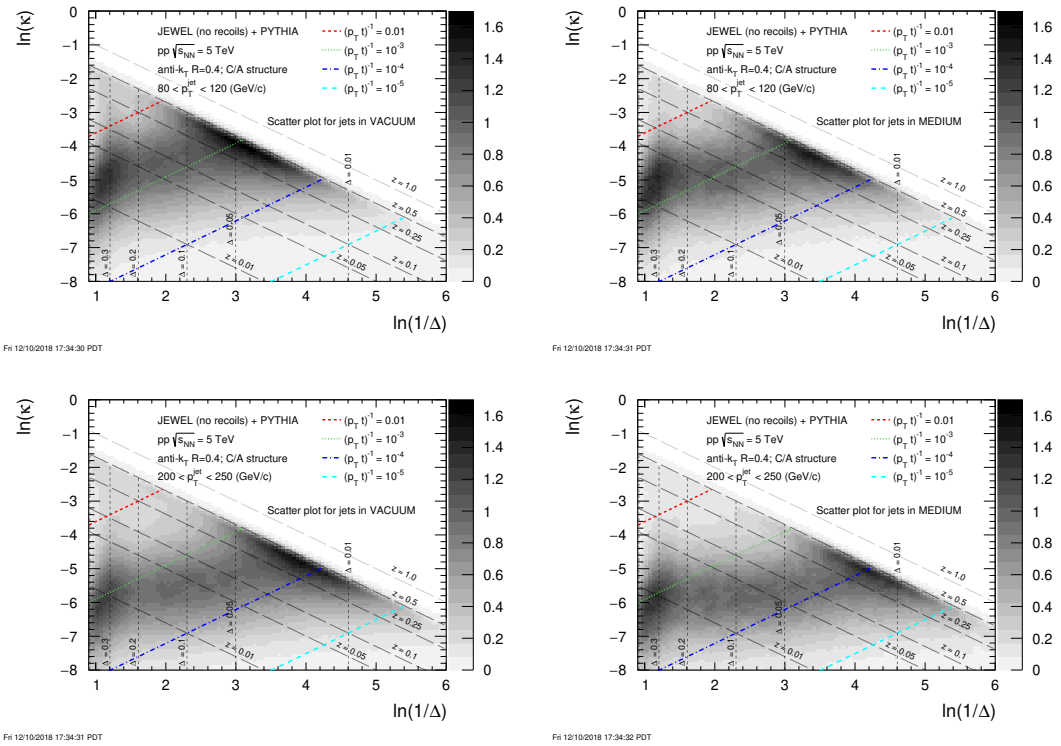

Fig. 38: The density of points of a Lund diagram for anti-k_{T} $R = 0.4$ jets for two p_{T} selections: $80 < p_{\mathrm{T}} < 120$ GeV/c in the upper row and $200 < p_{\mathrm{T}} < 250$ GeV/c in the lower row. Result of the JEWEL Monte Carlo generator with left column: jets in pp collisions; Right column: jets from Pb–Pb collisions - some with in-medium modifications. Each of the density plots shows curves of the average quantities of the densities over the other axis.

The Lund diagram density can be constructed experimentally and compared to analytic predictions and parton-shower Monte-Carlo simulations, such as JEWEL. For this purpose a density map of points (emissions) is defined following formulations in [408]:

$$\bar{\rho}(\Delta,\kappa) = \frac{1}{N_{\mathrm{jet}}} \frac{\mathrm{d}n_{\mathrm{emission}}}{\mathrm{d}\ln\kappa\,\mathrm{d}\ln 1/\Delta}, \tag{21}$$

where for two clusters 1 and 2 labeled such that $p_{\mathrm{T},1} > p_{\mathrm{T},2}$, $\Delta^2 = (y_1 - y_2)^2 + (\varphi_1 - \varphi_2)^2$ with φ being the azimuthal angle and y the rapidity of a cluster, and $\kappa = \frac{p_{T,2}}{p_{\mathrm{T},1}+p_{\mathrm{T},2}}\Delta$. Figure 38 shows the density $\bar{\rho}$ from the JEWEL simulation without (left panels) and with (right panels) medium effects. The z_g variable which was defined in [403] and studied in heavy-ion collisions [364] is related to the variables in the Lund plane in the following way: $z_{\mathrm{g}} = \kappa/\Delta$ from the first of the entries $(1...i...N)$ in the primary declustering sequence that satisfies $z^{(i)} \geq z_{\mathrm{cut}}(\Delta^{(i)})^{\beta}$ [408] resulting in diagonal lines with negative slope in the Lund diagram for a constant value of z_{g}.

The effect of jet quenching on the Lund diagram is quantified by taking the difference between the diagram with and without medium effects as shown in Fig. 39 for the two transverse momentum ranges considered in this study. The average density integrated over $\ln\kappa$ calculated for Pb–Pb (MEDIUM) case shows little deviation from the pp (VACUUM) reference. The most pronounced differences between

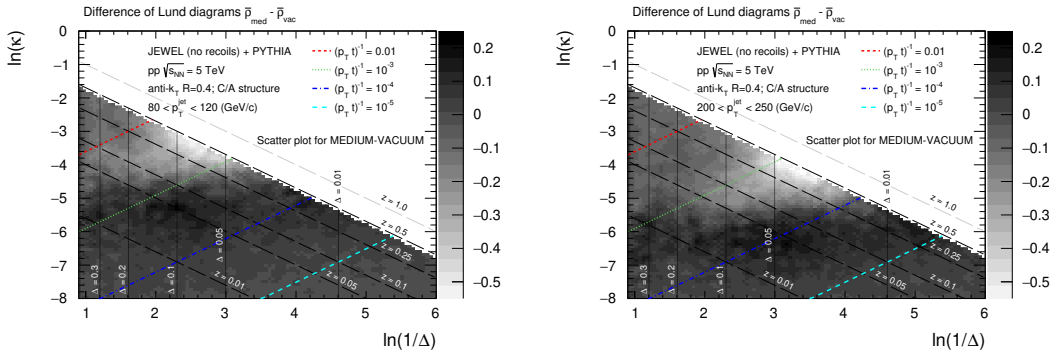

Fig. 39: Result of the JEWEL+PYTHIA MC simulation: MEDIUM-VACUUM difference of the calculations shown in Fig. 38 for two jet p_{T} selections.

VACUUM and MEDIUM calculations are visible for the region of $-3 < \ln\kappa < -3$ and large $\ln 1\Delta$ which correspond to the hard-collinear splittings (Region-A), and a band along $\ln 1/\Delta$ for small $\ln\kappa$ (Region-B): $-5 < \ln\kappa < -6$ for the lower p_{T} selection and $-5.5 < \ln\kappa < -7$ for higher p_{T} jets; that corresponds to an enhancement of soft (moderate $\ln 1/\Delta$) and hard collinear splittings (large $\ln 1/\Delta$). These observations are consistent with soft and hard collinear splittings being modified by the medium.

To illustrate the different modifications of the Lund diagram density for the two regions identified in Fig. 39, projections along $\ln 1/\Delta$ are shown in Fig. 40. For Region-A we observe 30%-40% depletion of splittings for the MEDIUM case whereas in Region-B a moderate increase of splittings induced by the medium is visible. The depletion in Region-A is consistent a sample of more collimated jets consistent with previous measurements in heavy-ion collisions [363, 392]. The increase seen in Region-B is consistent with a small in-medium enhancement of splittings with moderate dependency on the angle of the splitting but favoring the soft collinear medium-induced radiation (moderate $ln1/\Delta$).

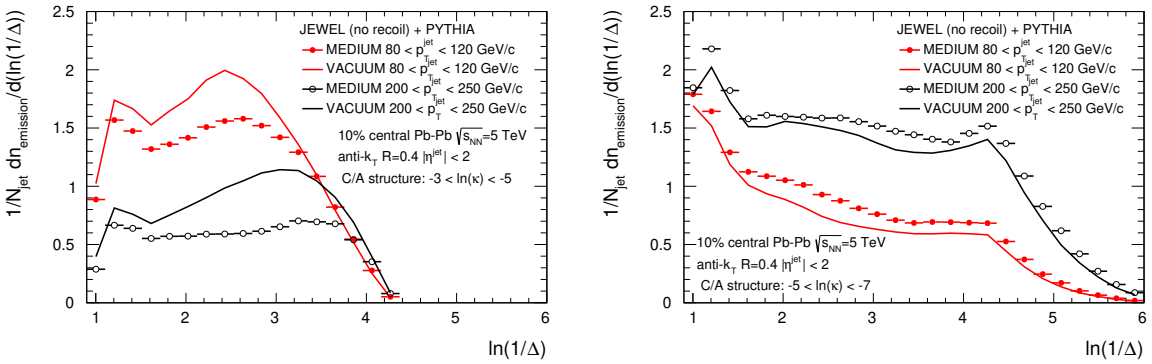

Fig. 40: Projections of the lund diagram along the angular separation $\ln 1/\Delta$ of the splittings for the two selections of jet p_{T}. In-medium suppression of splittings for moderate $\ln\kappa$ according to JEWEL (left). Enhancement for small $\ln\kappa$ (right).

As discussed in Ref. [385] specific regions in the Lund plane are sensitive to different type of parton splittings. These regions can be identified by selecting the desired area using linear functions $\ln\kappa = \ln 1/\Delta + \ln\frac{1}{p_{\mathrm{T}}t}$, where t is related to the decoherence time (thus formation time). Depending on the selection, different formation times are probed and splittings will occur within or outside the medium. Several arbitrary regions selected by the diagonal lines for constant $\frac{1}{p_{\mathrm{T}}t}$ are indicated in Fig. 38.

To illustrate the in-medium effects and their dependence on the jet momentum, the p_{T} and the formation (decoherence) time the density of the splittings can be projected along the momentum imbalance $z = p_{\mathrm{T},2}/(p_{\mathrm{T},1} + p_{\mathrm{T},2})$. In the left panel of Fig. 41 we show the relative difference of the splitting density $\Delta\bar{\rho} = (\bar{\rho}_{med} - \bar{\rho}_{vac})/\bar{\rho}_{vac}$ for a selection of $p_{\mathrm{T}}t$. For small $p_{\mathrm{T}}t$ the splitting density is suppressed for the in-medium calculations whereas for large $p_{\mathrm{T}}t$ the modification is smaller. This is consistent with the expectation that for large formation times the medium effects should be of smaller magnitude as compared to splittings formed early. As the suppression seen in $\Delta\bar{\rho}$ selected on $p_{\mathrm{T}}t$ depends on the jet p_{T} we find similar suppression for high- and low-p_{T} jet selection for substantially different product of the p_{T} and formation time. In particular, for low momentum jets the modifications of $\Delta\bar{\rho}$ for large $p_T t$ is small. To further exploit the formula providing the approximate formation time dependence of the splittings we select two regions of the Lund diagram: "late" $t > 10$ and "early" $t < 10$. The "early" region should be dominated by splittings that form within the medium, whereas the "late" splittings are to be dominated by the shower evolution outside the medium of length $L \sim t$. In the right panel of Fig. 41 we present $\Delta\bar{\rho}$ for two selections of decoherence time. As expected, a small dependence on jet p_{T} for "late" and "early" splittings is seen - a similar suppression for "early" splittings independent of jet p_{T} and almost identical $\Delta\bar{\rho}$, with small deviations from unity, for "late" emmissions. The residual differences could be attributed to different fractions of the splittings resolved by the medium, and likely, different impact of non-perturbative effects (such as hadronization) for the two jet p_{T} selections.

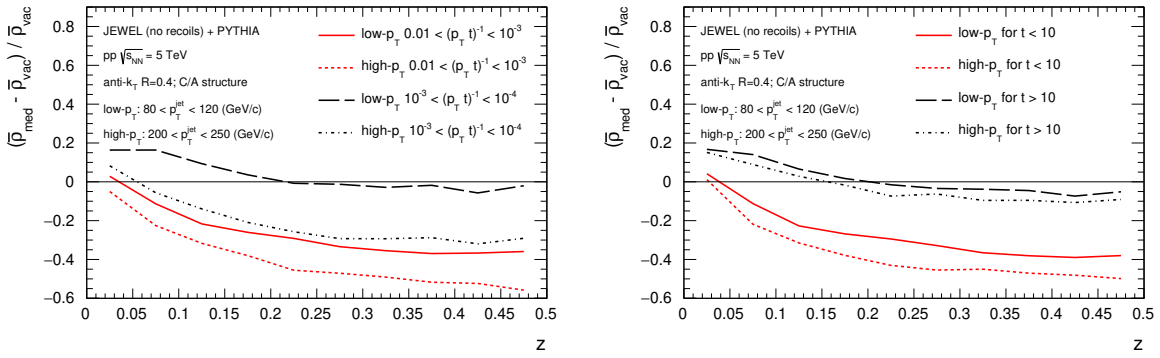

Fig. 41: Projections of the relative difference of the Lund diagram onto momentum imbalance of the splittings for two selections of jet p_{T}. Left: selection of splittings for different $\frac{1}{p_{\mathrm{T}}t}$. Right: selection of splittings for different t.

6.5 Opportunities for jet quenching studies with light-ion collisions

The ability of the LHC to collide ions lighter than Pb as discussed in section 2.4 provides an opportunity to enhance the heavy-ion programme with a very large number of rare probes as summarized in Sect. 11.1. Ar–Ar collisions are used as a test case for light ion running, although the optimal choice of ion is still under study. It is clear that due to the larger integrated luminosity obtainable for a given heavy-ion running period the number of jets produced in Ar–Ar collisions will be significantly larger than in Pb–Pb collisions. The question which will determine the value of the of light-ion running to the study of jets and parton energy loss is to what extent jet suppression effects will be reduced in smaller systems. To address this question, projections for Ar–Ar and Xe–Xe collisions at the LHC are considered using the JEWEL Monte Carlo event generator [390].

The jet nuclear modification factor R_{AA} (discussed in Sect. 6.2) in Ar–Ar collisions is here computed as the ratio of the jet transverse momentum spectrum in medium (Ar–Ar) over that in vacuum

(pp)

$$R_{\mathrm{AA}}^{\mathrm{jet}} = \frac{(\mathrm{d}N_{\mathrm{jets}}/\mathrm{d}p_{\mathrm{T}})^{\mathrm{med}}}{(\mathrm{d}N_{\mathrm{jets}}/\mathrm{d}p_{\mathrm{T}})^{\mathrm{vac}}} \,. \tag{22}$$

Table 7 summarizes the parameters used in JEWEL to calculate this quantity in 0–10% centrality Ar–Ar collisions, compared with the parameterization for Pb–Pb and Xe–Xe. The T_i^{v1} values were obtained assuming the same pre-factors as in [411]:

$$T(t) = \left(\epsilon(t)\frac{30}{47.5\,\pi^2}\right)^{1/4} , \tag{23}$$

where the energy density $\epsilon(t)$ follows a Bjorken evolution:

$$\epsilon(t) = \frac{1}{\pi R_{nucl}^2 t}\frac{\mathrm{d}E}{\mathrm{d}\eta} \,. \tag{24}$$

The energy per unit of pseudo-rapidity is taken from centrality-dependent measurements in Pb–Pb collisions. Finally the temperature T_i^{v1} is evaluated at τ_i.

Table 7: Energy and medium parameter used in JEWEL simulation of dijets and Z+jet events.

	Pb–Pb	Xe–Xe	Ar–Ar
$\sqrt{s_{\mathrm{NN}}}$ (TeV)	5.02	5.80	6.30
$\langle N_{\mathrm{part}} \rangle$	353	210	66
R_{nucl} (fm)	6.6	5.4	3.6
τ_i (fm/c)	0.6	0.57	0.63
T_i^{v1} (MeV)	360	350	318
T_i^{v2} (MeV)	260	250	218

With these medium parameters, JEWEL results lie quite below the ATLAS R_{AA} results for the Pb–Pb 0–10% centrality class [412]. JEWEL was run with medium recoil effects off, although they are known to contribute to increase the jet R_{AA} by $\sim$ 0.1–0.2 in the most central events [413]. This may explain the discrepancy. Alternatively, the discrepancy can be eliminated by reducing the temperature in JEWEL. Starting from the Pb–Pb temperature changed in order to match the ATLAS results for the Pb–Pb 0–10% centrality class, temperatures for Xe–Xe and Ar–Ar are obtained by assuming that the energy density scales with $A^{1/3}$. Thus, for an arbitrary collision system XX one has:

$$\left(\frac{T_{XX}}{T_{\mathrm{Pb-Pb}}}\right)^4 = \left(\frac{A_{XX}}{A_{\mathrm{Pb}}}\right)^{1/3} . \tag{25}$$

This parameterisation is used to obtain the T_i^{v2} values listed in Table 7 which are used to calculate the jet R_{AA} shown in Figure 42. The figure shows the JEWEL calculations for Pb–Pb, Xe–Xe, and Ar–Ar along with ATLAS Pb–Pb measurements in centrality classes chosen to match the $\langle N_{\mathrm{part}} \rangle$ values in Table 7.

To further investigate jet energy loss in Ar–Ar collisions, Z boson + jet events are studied within the same JEWEL framework. The importance of boson + jet events for the precision study of energy loss is discussed in Sect. 6.2. Events with a Z boson decaying into $\mu^+\mu^-$ associated with a jet were simulated with JEWEL + PYTHIA Monte Carlo [414]. Events were selected for a reconstructed Z boson with a mass within 70–110 GeV, a minimum p_{T} of 10 GeV/c for its decay muons, and an associated jet with a $p_{\mathrm{T}} > 30$ GeV/c and a $|\delta\varphi| > 7\pi/8$ with respect to the boson momentum direction. The resulting energy asymmetry distributions, $x_{\mathrm{jZ}} = p_{\mathrm{T}}^{\mathrm{jet}}/p_{\mathrm{T}}^{\mathrm{Z}}$, normalized to the number of reconstructed Z bosons are

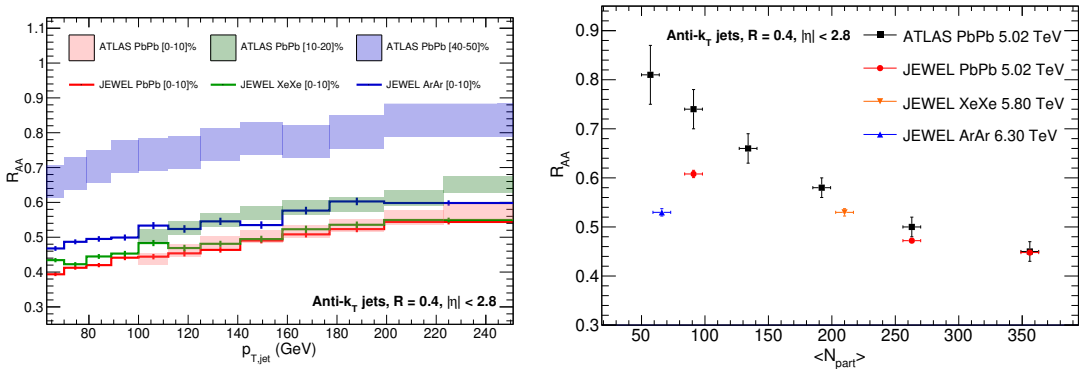

Fig. 42: Jet R_{AA} obtained from a JEWEL simulations using the medium parameters listed in Table 7, with the temperatures listed as T_i^{v2}. On the left, the jet R_{AA} is shown as a function of the jet p_{T}, and on the right as a function of $\langle N_{\mathrm{part}} \rangle$ for a jet $100 < p_{\mathrm{T}} < 126$ GeV/c.

shown in Figure 43.The distribution for central Ar–Ar collisions is similar to those for central and semi-central Pb–Pb collisions. The effect of jet quenching is very significant, as apparent in the comparison with the distribution in pp collisions.

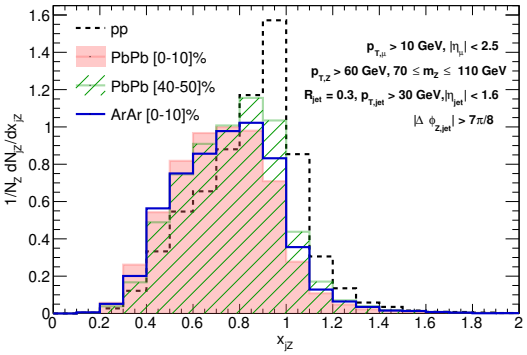

Fig. 43: Boson-Jet energy asymmetry, x_{jZ} obtained from JEWEL simulations using the medium parameters listed in table 7, with the temperatures listed as T_i^{v2}.

Taken together, these studies suggest that JEWEL does somewhat over-predict suppression in smaller systems, e.g. Xe–Xe. However, considering that central collisions are reproduced well by this model and that allowing as an upper limit the suppression measured in the Pb–Pb 40–50% centrality class, a significant suppression is expected in central Ar–Ar collisions. The expected suppression combined with the much larger nucleon–nucleon integrated luminosity (e.g. 8–25 larger with Ar–Ar than with Pb–Pb collisions) makes lighter ion collisions at the LHC an attractive possibility for the study of parton energy loss.

7 Quarkonia

Coordinators: Anton Andronic (Münster University) and Emilien Chapon (CERN)

Contributors: E. G. Ferreiro (Instituto Galego de Fisica de Altas Enerxias (IGFAE) Universidade de Santiago de Compostela), J.-P. Lansberg (Institut de Physique Nucléaire d'Orsay), R. Rapp (Texas A&M University, College Station), J. Castillo Castellanos (IRFU/DPhN, CEA Saclay), C. Cheshkov (IPN Lyon), J. Martin Blanco (Laboratoire Leprince Ringuet), J. Park (Korea University), X. Du (Texas A&M University, College Station), M. Strickland (Kent State University), R. Venugopalan (BNL), I. Vitev (Los Alamos National Laboratory)

7.1 Introduction

A key objective in high-energy heavy-ion physics is to determine the in-medium forces that give rise to the remarkable many-body features of the QGP. In the QCD vacuum, the unravelling of the fundamental force between two static Color charges was made possible by the discovery of the charmonium and bottomonium states in the 1970's. Subsequent quantitative analyses of the bound-state spectra established a phenomenological potential of the Cornell type [415],

$$V(r) = -\frac{4}{3}\frac{\alpha_s}{r} + \sigma r \,, \tag{26}$$

with a colour-Coulomb term due to gluon exchange dominant at short distances, and a linear term with string tension $\sigma \simeq 0.9\,\mathrm{GeV/fm}$ to account for confinement at large distance. This potential has also been quantitatively confirmed by lattice-QCD (lQCD) calculations [416, 417]. The corresponding effective field theory of QCD, potential non-relativistic QCD (pNRQCD), allows for the definition of the static potential [418] in a $1/m_Q$ expansion for large heavy-quark mass, m_Q [419, 420]. The heavy-quark (HQ) potential thus provides a well calibrated starting point to probe the QCD medium, and the in-medium spectroscopy of quarkonia is the natural tool to carry this out in heavy-ion collisions, cf. [421–425] for recent reviews. The string term in the HQ potential, eq. (26), characterises the long-range nonperturbative part of the force and is associated with the confining property of QCD. It is expected to play a critical role in the transition from hadronic to partonic degrees of freedom, and may be responsible for the remarkable transport properties of the QGP, *i.e.*, its strongly coupled nature, up to temperatures of 2-3 times the (pseudo-)critical temperature, T_c [426].

Much like in vacuum, a systematic investigation of the in-medium force must involve the *spectroscopy* of different states, as they subsequently dissolve with increasing temperature. The complexity in describing the in-medium properties of quarkonia and their implementation into transport calculations in heavy-ion collisions prevents their use as a straightforward thermometer of the medium produced in these reactions. On the contrary, using information on the space-time and temperature evolution in heavy-ion collisions from other sources (e.g.,, hydrodynamics and electromagnetic radiation), on can utilize quarkonium observables to deduce their in-medium properties and infer the fundamental interactions in QCD matter. In the vacuum, only the 1S ground-state bottomonia ($\Upsilon(1S)$ and η_b) are small enough in size to be mostly bound by the colour-Coulomb force. All excited bottomonia and all charmonia are predominantly bound by the nonperturbative string term (and/or residual mesonic forces). Thus, charmonia and excited bottomonia are excellent probes of the in-medium confining force, as originally envisioned for the J/ψ [427]. However, in the cooling of the expanding fireball, quarkonia can also be "(re)generated" through recombination of individual heavy quarks and anti-quarks diffusing through the medium. It is important to emphasise that quarkonium formation occurs also from quarks and antiquarks from different initial pairs. This mechanism [428–430] has turned out to be critical in understanding the rise of J/ψ production from RHIC to the LHC where (re)generation seems to constitute the major part of the yield observed in central Pb–Pb collisions [431]. The data is also compatible with production of J/ψ exclusively through statistical hadronisation at the crossover phase boundary [432]. Precise measurements of the $c\bar{c}$ production cross section and the extraction of the charm-quark diffusion coefficient

in Runs 3 & 4 will be important for making a more definite statement; these are key objectives discussed in the chapter 5 on open heavy-flavor production. Information from p_{T} spectra and elliptic flow will help to complete the picture.

Regarding bottomonia, the current understanding suggests that (re)generation is less important for $\Upsilon(1\mathrm{S})$, but possibly figures as a major component in the strongly suppressed yield of excited states [433, 434]. It is therefore of great importance to obtain additional information about the typical time at which quarkonia are produced, in particular through p_{T} spectra and elliptic flow which contain information about the fireball collectivity imprinted on the quarkonia by the time of their decoupling. A schematic illustration of the current knowledge extracted from in-medium quarkonium spectroscopy, *i.e.*, their production systematics in heavy-ion collisions is shown in Fig. 44.

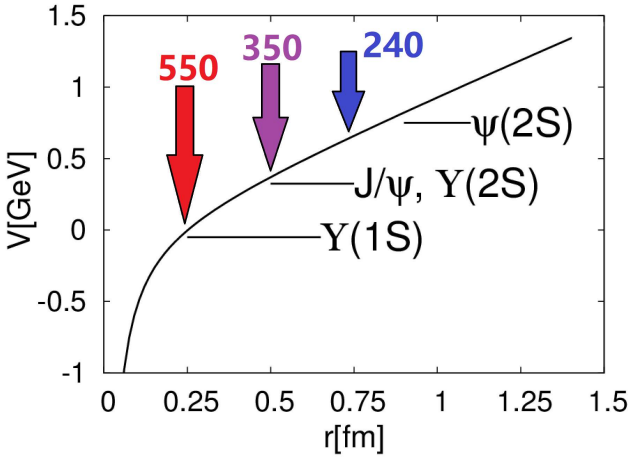

Fig. 44: The vacuum heavy-quark potential as a function of $Q\bar{Q}$ separation. The horizontal lines indicate the approximate locations of the vacuum bound states while the vertical arrows indicate the minimal screening distances of the media produced at the SPS, RHIC and LHC, as deduced from approximate initial temperatures reached in these collisions extracted from data (indicated above the arrows in MeV) and from quarkonium production systematics in Pb–Pb and Au-Au collisions. Figure taken from Ref. [431].

On the theoretical side, the basic objects are the quarkonium spectral functions which encode the information on the quarkonium binding energies, in-medium HQ masses and the (inelastic) reaction rates. Ample constraints on the determination of the quarkonium spectral functions are available from thermal lQCD, *e.g.*, in terms of the heavy-quark free energy, euclidean and spatial quarkonium correlation functions, and HQ susceptibilities, and are being implemented into potential model calculations [435–441]. In particular, the role of dissociation reactions has received increasing attention. Early calculations of gluo-dissociation [442, 443] or inelastic parton scattering [444] have been revisited and reformulated, e.g., as a singlet-to-octet transition mechanism [438] or in terms of an imaginary part of a two-body potential [445], respectively. In particular, the latter accounts for interference effects which reduce the rate relative to "quasi-free" dissociation [444] in the limit of small binding; interference effects can also be calculated diagrammatically [446]; they ensure that, in the limit of vanishing size, a Color-neutral $Q\bar{Q}$ dipole becomes "invisible" to the Color charges in the QGP.

The information from the spectral functions can then be utilised in heavy-ion phenomenology via transport models. The latter provide the connection between first-principles information from lQCD and experiment that greatly benefits the extraction of robust information on the in-medium QCD force and its emergent transport properties, most notably the (chemical) equilibration rates of quarkonia. Thus far

most transport models are based on rate equations and/or semiclassical Boltzmann equations. In recent years quantum transport approaches have been developed using, e.g., a Schrödinger-Langevin [447–450] or density-matrix [451, 452] formulation. These will enable to test the classical approximation underlying the Boltzmann and rate equation treatments and ultimately quantify the corrections. Quantum effects may be particularly relevant at high p_{T} in connection with the in-medium formation times of quarkonia, augmented by the Lorentz time dilation in the moving frame; schematic treatments of this effect in semiclassical approaches suggest that varying formation times can leave observable differences for high-momentum charmonia and bottomonia [433, 434, 453–455]. Finally, the implementation of phase-space distributions of explicitly diffusing heavy quarks into quarkonium transport is being investigated by various groups (see, e.g., Ref. [456]), which, as mentioned above, will provide valuable constraints on the magnitude and p_{T} dependence of (re)generation processes. In particular, the role of non-perturbative effects in the HQ interactions in the QGP (which are believed to be essential to explain the large elliptic flow observed for D-mesons [260]) needs to be accounted for; the associated large scattering widths are likely to require quarkonium transport implementations beyond semi-classical (or perturbative) approximations, which reiterates the need for a quantum treatment of recombination processes.

The larger experimental data samples in Runs 3 & 4, combined with improved detector performance and measurement techniques, will allow one to significantly improve over the current measurements, with extended kinematic coverage (in p_{T}) and allowing one to reach also currently-unobserved quarkonium states, like $\Upsilon(3S)$. The complementarity (and overlap) of all 4 LHC experiments is crucial in this endeavour and will call for a data combination strategy, for instance for Υ azimuthal anisotropy. Quarkonia are measured in the dimuon channel in ATLAS ($|y| < 2.0$), CMS ($|y| < 2.4$), LHCb ($2.0 < y < 4.5$), and ALICE ($2.5 < y < 4.0$), and in the dielectron channel with ALICE ($|y| < 0.9$). We present below data projections and simulations for a selection of observables and compare to model predictions (which sometimes constitute the basis for the projections). The model uncertainties shown in this section represent the current knowledge; significant improvements are expected both in what concerns the conceptual aspects discussed above as well for the input parameters, which will be constrained by data and theory (for instance in what concerns nuclear PDFs, see also Section 10.4).

All four LHC experiments will benefit from a large upgrade program, during the Long Shutdown 2 (2019–2020) for ALICE and LHCb, and during Long Shutdown 3 (2024–2025) for ATLAS and CMS. The addition of the Muon Forward Tracker (MFT) will allow ALICE to separate the prompt charmonium from the contribution from B meson decays. In addition, the background will be reduced, yielding to better signal over background ratios. Regarding ATLAS and CMS, the upgraded inner tracker will extend to $|\eta| \lesssim 4.0$ after LS3, and the muon system coverage to $|\eta| \lesssim 2.7$ (3.0) for ATLAS (CMS). While the detector improvements will have a smaller impact than the increase in data sample size, this increase in pseudorapidity coverage is appreciable in also giving an overlap with the range of ALICE and LHCb. Better track momentum resolution is also expected from these upgraded inner trackers, with an improvement of about 30% of the mass resolution of quarkonia for CMS [457]. The expected improvement in the relative statistical uncertainty, due to a better signal over background ratio, is in the range 10–25% [9].

7.2 Charmonia in Pb–Pb collisions

A remarkable discovery at the LHC was that the suppression of J/ψ is significantly reduced in comparison to lower energies [458] and that this reduction is concentrated at lower p_{T} [459, 460], compatible with predictions of (re)generation at the phase boundary of QCD [428] or throughout the deconfined phase [429, 461, 462], via recombination of diagonal (correlated pairs) or off-diagonal $\mathrm{c\bar{c}}$ pairs [430]. No significant difference is however found between measurements at $\sqrt{s_{\mathrm{NN}}} = 2.76\,\mathrm{TeV}$ and $\sqrt{s_{\mathrm{NN}}} = 5.02\,\mathrm{TeV}$ [460, 463]. Recently, the measurement of a significant elliptic flow coefficient v_2 both for D mesons [464–466] and J/ψ [262, 467–470], which was shown to be correlated to

the flow of the bulk particles [278, 470], can be seen as another indication for the thermalisation of charm quarks in the QGP. Transport model calculations [471, 472] currently underestimate the data for $p_{\mathrm{T}} \gtrsim 6$ GeV/c [262, 468, 469].

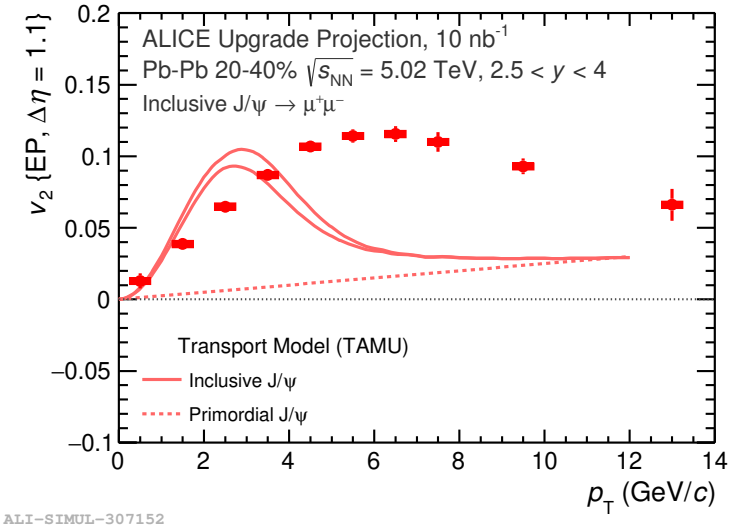

Fig. 45: Projected measurement of elliptic flow coefficient v_2 as a function of p_{T} for J/ψ mesons (measured in ALICE, for $2.5 < y < 4$), for the centrality class 20–40%, in comparison to model calculations [472]. Figure from Ref. [1].

The projected ALICE measurement of inclusive J/ψ v_2 as a function of p_{T} for the centrality class 20–40%, for $2.5 < y < 4$, in comparison to model calculations [472] is shown in Fig. 45. Disentangling the contributions of prompt and non-prompt J/ψ and considering (path-length dependent) energy loss seems mandatory to understand the details of the J/ψ v_2 pattern, which will be facilitated with the detector upgrades and higher luminosity of Runs 3 & 4. The measurement of higher harmonics, e.g., v_3, which are sensitive to initial state energy density fluctuations, will also become available and provide further insight into the charmonium production mechanisms. Precise prompt and non-prompt J/ψ v_2 and v_3 measurements at low p_{T} will be reachable using the ALICE central barrel. Polarisation will be measured too [2], providing further insight in the different production mechanisms involved in Pb–Pb collisions as compared to pp. Under the statistical hadronisation paradigm, the prompt J/ψ yield in Pb–Pb collisions should be unpolarised with the 3 polarisation states equally populated.

At high p_{T}, where a raising trend is currently hinted by Run 2 R_{AA} measurements [463, 473], the production mechanisms cannot currently be resolved, given the statistical limitation in the data (see Fig. 46, left). The high p_{T} reach of Runs 3 & 4 data (illustrated in Fig. 46 (right) for CMS) will allow one to conclude on the important question of whether J/ψ formation at high p_{T} is determined by the Debye screening mechanism [455, 474], or by energy loss of the charm quark or the c$\bar{\mathrm{c}}$ pair [475, 476].

The measurement of $\psi(2S)$ mesons is more difficult than that of J/ψ, because of a much smaller production cross section times branching ratio and even larger suppression in Pb–Pb, yielding a very low signal to background ratio. The projections for the measurement of the $\psi(2S)$ state in ALICE are shown in Fig. 47 as a function of centrality and compared to model predictions in the transport approach [472] and from the statistical hadronisation model [432]. This (p_{T}-integrated) measurement will significantly contribute to make a distinction between the two models. Projections are also available from the CMS experiment [8]. Other states, for instance χ_{c}, may be measured too, albeit the measurement down to $p_{\mathrm{T}} = 0$ will remain challenging. $\mathrm{B_c^+}$ mesons can also be measured, either in the J/$\psi\pi$ or

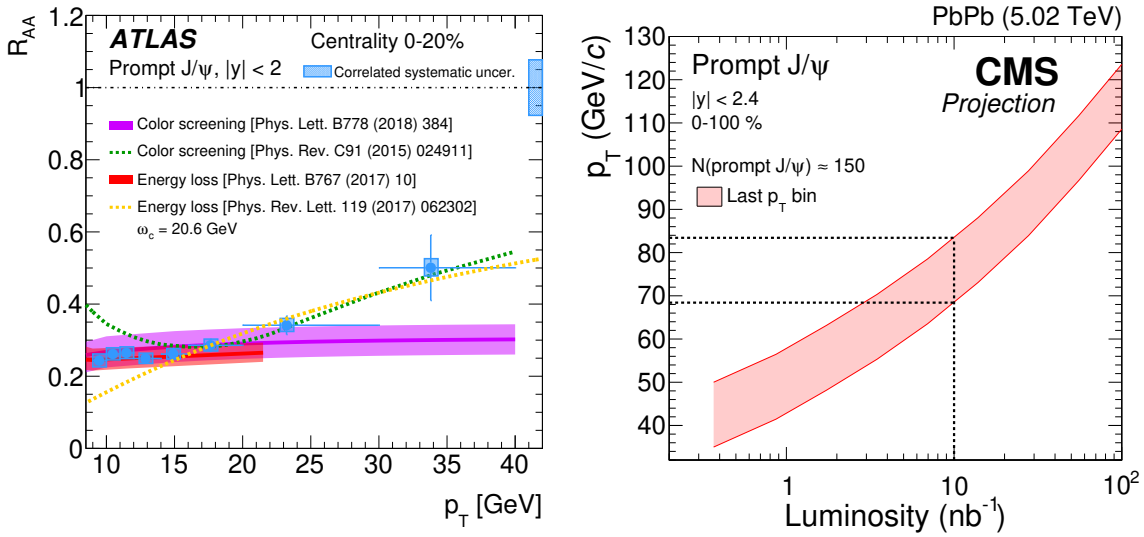

Fig. 46: Left: R_{AA} vs p_{T} for prompt J/ψ in central (0–20%) collisions (ATLAS, $|y| < 2$, [473]). Right: Prompt J/ψ high p_{T} bin boundaries as a function of luminosity with the CMS experiment [9]. The boundaries are chosen in such a way the number of mesons in the bin for the corresponding luminosity equals the number of mesons found in the last p_{T} bin of the current measurement [463].

J/$\psi\mu\nu_{\mu}$ channel, to further study recombination in the beauty sector.

7.3 Bottomonia in Pb–Pb collisions

The study of bottomonia with Pb–Pb data from the Runs 3 & 4 of the LHC will bring further information on the physics aspects described above. Although their production is a priori sensitive to the same effects as charmonia, in practice the two quarkonium families feature some fundamental differences. Binding energies differ, which is reflected in the different dissociation temperatures. Experimentally, compared to charmonia, the absence of contribution from B meson decays and the more similar cross section times branching ratio between the ground and excited states make bottomonia measurements easier. At the same time, in pp collisions, up to 30–50% of the measured $\Upsilon(1S)$ and $\Upsilon(2S)$ yields actually result from the feed-down from other states [258, 478]: a large portion of measured $\Upsilon(1S)$ suppression can be due to the stronger suppression of the feed-down states – $\Upsilon(2S)$ and $\Upsilon(3S)$ mesons also receive a significant contribution from feed-down. The impact of (re)generation from uncorrelated $b\bar{b}$ is also expected to be much smaller than for charmonia, because of the much smaller number of $b\bar{b}$ pairs per Pb–Pb event compared to that of $c\bar{c}$ pairs. The importance of regeneration for bottomonia, from correlated or uncorrelated pairs [450], is however still very model dependent, and no unambiguous experimental signal for it has been found yet. Possible ways of constraining this contribution will be discussed in this section.

Experimentally, the higher mass of bottomonia compared to charmonia implies higher p_{T} decay leptons, allowing the ATLAS and CMS experiments to measure the production down to zero transverse momentum, as is possible for ALICE for both charmonia and bottomonia [479, 480]. The proximity in mass between the different mass states, especially between the $\Upsilon(2S)$ and $\Upsilon(3S)$ states, also means that good muon (or electron) momentum resolution is essential to their measurement, especially for excited states.

It is useful to remind quickly the status in 2018, based on results from Run 1 and early Run 2 LHC data as well as RHIC data. Υ production is found to be suppressed in Pb–Pb compared to expectations

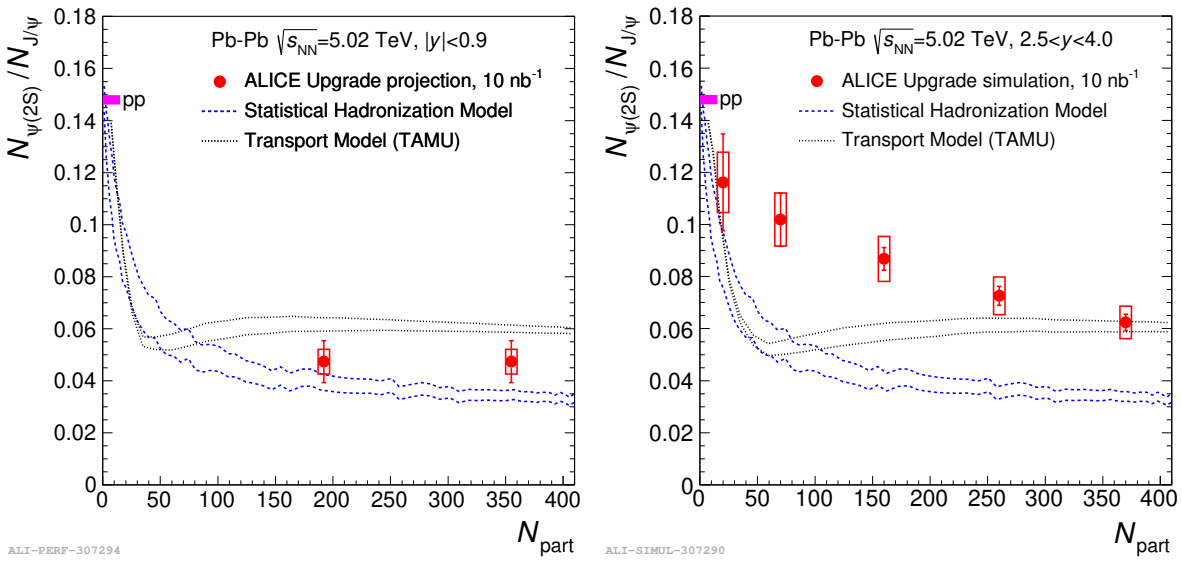

Fig. 47: Production ratio $\psi(2S)/J/\psi$ vs. N_{part} for $|y| < 0.9$ (left) and $2.5 < y < 4$ (right) [2, 477]. Model predictions in the transport approach [472] and from statistical hadronisation [432] are included. The values of the ratio used for the projections are quasi-arbitrary. Figures from Ref. [1].

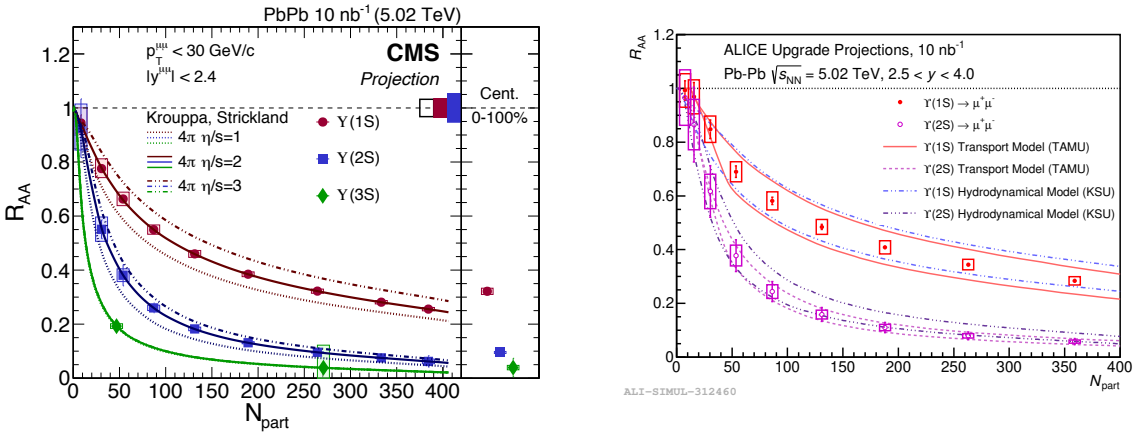

Fig. 48: Centrality dependence of $\Upsilon(1S)$, $\Upsilon(2S)$ and $\Upsilon(3S)$ R_{AA}, as projected by the CMS [8,484] (left) and ALICE [1] (right) experiments, and from a transport model [433]

from a scaling of incoherent pp collisions, in all rapidity, p_T and centrality ranges measured [479–482]. Suppression is stronger in central events, as expected from the hotter and longer-lived medium in such events. The results from the most central collisions suggest that a certain amount of suppression of the directly produced $\Upsilon(1S)$ might be needed to explain the data in addition to cold nuclear matter effects and melting of the excited Υ and χ_b states. The excited states $\Upsilon(2S)$ and $\Upsilon(3S)$ show higher suppression wrt the ground state, with R_{AA} values which respect the hierarchy expected based on their binding energies. The $\Upsilon(3S)$ is still unobserved in Pb–Pb collisions ($R_{AA}(\Upsilon(3S)) < 0.094$ at 95% confidence level, for $\sqrt{s_{NN}} = 5.02$ TeV [481, 483]). No significant dependence of the suppression of Υ states is found at the LHC on collision energy or rapidity.

Differences exist between models in the theoretical treatment of the suppression of the bottomonia in the medium, as summarised earlier in Section. 7.1. Different assumptions are used regarding the

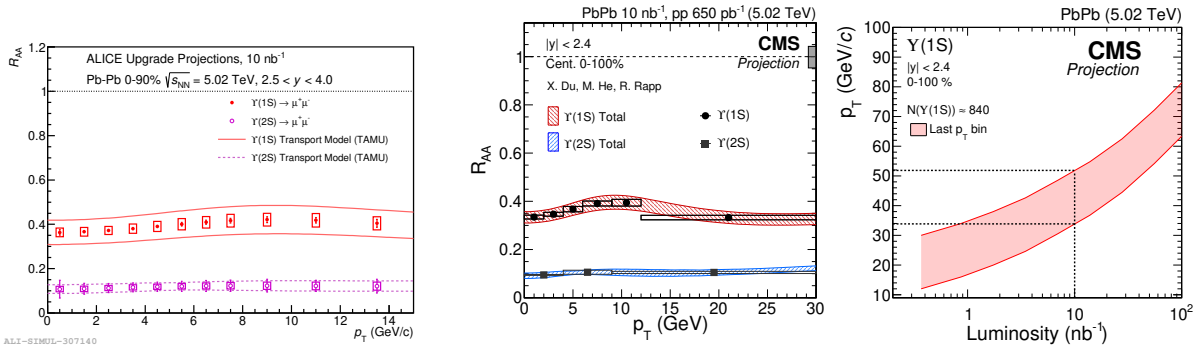

Fig. 49: Projected R_{AA} for $\Upsilon(1\mathrm{S})$ and $\Upsilon(2\mathrm{S})$ expected from the ALICE [1] (left) and CMS [9] (center) experiments, as a function of p_{T}, with $10\,\mathrm{nb}^{-1}$ of Pb–Pb data. The expected p_{T} reach for $\Upsilon(1\mathrm{S})$ from the CMS experiment is also shown [9], as the position of the last p_{T} bin of the measurement, with constant number of observed $\Upsilon(1\mathrm{S})$, as a function of integrated luminosity.

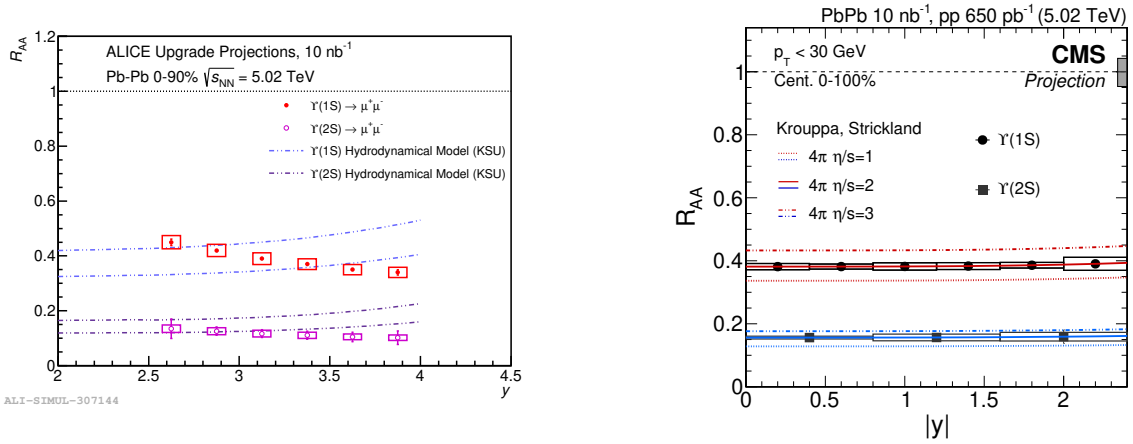

Fig. 50: Projected R_{AA} for $\Upsilon(1\mathrm{S})$ and $\Upsilon(2\mathrm{S})$ expected from the ALICE [1] (left) and CMS [9] (right) experiments, as a function of rapidity, with $10\,\mathrm{nb}^{-1}$ of Pb–Pb data.

production mechanism, the heavy quark potential, or the evolution of the quarkonia with the medium. The understanding of hot medium effects will be also improved thanks to higher precision measurements in pp collisions of the feed-down fractions and to stronger constrains of the cold nuclear matter and initial state effects (including nPDF or coherent energy loss effects [485]) from p–Pb collision measurements. Figure 48 shows that the projected uncertainty on the R_{AA} of Υ with $10\,\mathrm{nb}^{-1}$ will be much smaller than the current model uncertainties. Bottomonia may bring information complementary to other probes, using the sensitivity of the suppression to the medium shear viscosity or to the initial temperature of the fireball.

A precise measurement of the p_{T} dependence of the $\Upsilon(1\mathrm{S})$ R_{AA} will be possible using LHC data from Runs 3 & 4. At low and medium p_{T}, the measurement is sensitive to the possible regeneration component in Υ meson production [433]. Projections for the expected precision of Υ measurements from the ALICE and CMS detectors using an integrated luminosity of $10\,\mathrm{nb}^{-1}$ after the Runs 3 & 4 are shown as a function of p_{T} in Fig. 49 and y in Fig. 50, and compared to the expectations from two models [433, 434]. In the Kent state model calculations [434] (not shown), where Υ mesons are originating only from the primordial production, with no regeneration component, the R_{AA} is rather flat in the low and medium p_{T} range. Only at higher p_{T} (above 10–15 GeV/c) is a small rise predicted, which

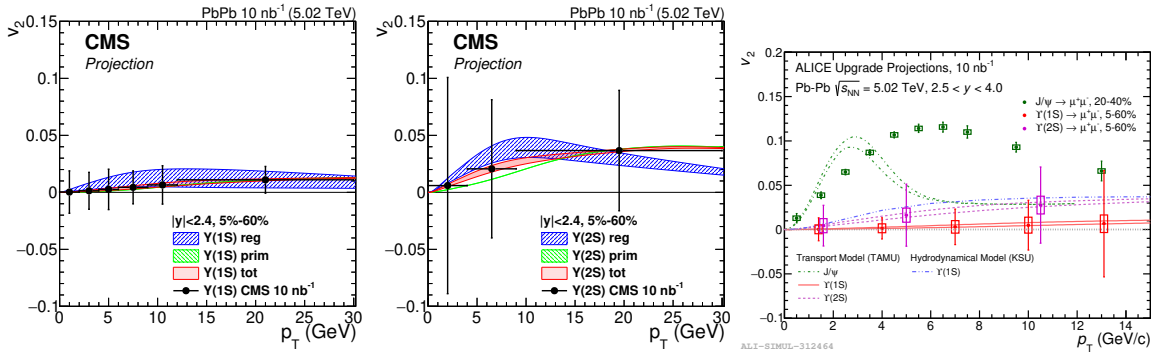

Fig. 51: v_2 projections for the CMS [9] (left and centre) and ALICE [1] (right) experiments for the $\Upsilon(1S)$ and $\Upsilon(2)$ mesons, assuming the predictions from a transport model [433].

can be looked for in Runs 3 & 4 data: as can be seen in Fig. 49, it is expected that a measurement up to a p_T of about 50 GeV/c can be performed with the ATLAS and CMS detectors with 10 nb^{-1} of data. In the TAMU model [433] however, a regeneration component is considered, and several assumptions are explored, especially on the degree of thermalisation of the bottom quarks. It predicts a maximum in the $\Upsilon(1S)$ R_{AA} at a p_T around 10 GeV/c. The current data is not precise enough to confirm or disfavour such a local maximum in the R_{AA}, but Runs 3 & 4 data will allow to conclude.

Almost no rapidity dependence is expected at the LHC for the nuclear modification factor of Υ mesons within the acceptance of ATLAS and CMS ($|\eta| \lesssim 2.5 - 3$), which can be better tested using Runs 3 & 4 data. This will be further made significant considering the ALICE acceptance ($2.5 < y < 4$), allowing to confirm or disprove the prediction of the hydrodynamic model, see Fig. 50.

Coming back to the matter of regeneration, much can be learnt about it by a measurement of the elliptic flow of $\Upsilon(1S)$ mesons [486], unmeasured to date in any collision system. A parallel can be drawn with that of J/ψ, which is still not properly described by models. This observable requires a more detailed implementation of the dynamics of the interactions between the quarkonium and the medium: thermalisation of the heavy quarks, time dependence of regeneration, path length dependence of energy loss, as well as initial geometry fluctuations and elastic rescattering of the quarkonia in the medium. Thus, collective flow brings complementary information to the R_{AA}, and its measurement can help disentangle some effects. In the case of $\Upsilon(1S)$ mesons, a small v_2 (order of 1–2%) is expected [433,487, 488], as can be seen in Fig. 51. The elliptic flow of $\Upsilon(2S)$ could be significantly higher [433,488], both from the regenerated and primordial components. For both states, projections show that experimental precision may not be enough for a significant v_2 measurement, assuming v_2 values as in Ref. [433]. For this reason, combining results between the different LHC experiments would be beneficial to reach a better sensitivity.

While we have focused on the R_{AA} and v_2 in this section, bottomonium production can be studied using other observables. For instance, fully corrected yields or cross sections in Pb–Pb can be studied, without making the ratio to a pp measurement in a R_{AA}. Such a measurement, already reported in some of the available experimental results [481], can directly be compared to production models.

7.4 Quarkonia in p–Pb and pp collisions

7.4.1 p–Pb *collisions*

Quarkonium-production studies in high-energy p–Pb collisions are usually carried out to measure how much specific nuclear effects, those which do *not* result from the creation of a deconfined state of matter, can alter the quarkonium yields. They should indeed be accounted for in the interpretation of Pb–Pb

results. They are also interesting on their own as they provide means to probe the modification of the gluon densities in the nuclei, the interaction between such pure heavy-quark bound states and light hadrons, or phenomena such as the coherent medium-induced energy loss of these quark-antiquark pairs. The measurements as a function of event activity brought several surprises, hotly discussed presently.

Usually, a separation into initial-state and final-state effects is done (coherent energy loss effects [489] can be seen as an interplay between the two types of effects). Yet, it is probably more instructive to separate out the effects which are believed to impact *all* the states of the charmonium or the bottomonium family with the *same* magnitude from those which are expected to impact differently the ground and the excited states. In principle, initial-state effects (in particular gluon shadowing [329]) are of the first kind as the nature of the to-be-produced quarkonium state is not yet fixed when the effects are at work. On the contrary, final-state effects (like regeneration [490]) do depend on the properties of the produced quarkonium state and are thus be of the second kind.

However, in p–Pb collisions at LHC energies, final-state interactions between the heavy-quark pair and the nuclear matter likely occur *before* the pair hadronises. This is due to the large boost between the nucleus and the pair – and thus the quarkonium. At rest, a $c\bar{c}$ or $b\bar{b}$ pair takes 0.3–0.4 fm/c to hadronise; seen from the nucleus, at, for instance $y^{\rm lab}_{\rm pair} - y_{\rm beam} \sim 7$, it takes $\gamma = \cosh(7) \simeq 500$ times longer. As such, final-state interactions with the compounds nucleus likely do not discriminate ground and excited quarkonium states, unless rescattering in the nucleus affects the $\rm Q\bar{Q}$ wave function, overlapping with the quarkonium wave function at large distance [491]. Such an argument based on the existence of a large boost is nevertheless not applicable if one considers effects arising from the interactions between the pair and other particles *produced* by the p–Pb collisions, not those contained in the Pb nucleus. The former are indeed not moving at the Pb projectile rapidity. In fact, some of these particles can have similar rapidities as the quarkonium and can thus be considered as comoving with it [492–494].

The simultaneous study of open-heavy flavoured hadrons along with both ground and excited quarkonium states can shed light on all these phenomena. Along the lines exposed above, one expects forward-quarkonium production in p–Pb collisions (namely when the quarkonia flies in the direction of the proton) to be sensitive to low-x phenomena (like the gluon shadowing or saturation in the lead ion) and to the coherent energy loss. On the contrary, the backward production should be sensitive to the gluon antishadowing and to fully coherent energy loss. Moreover, the scatterings of quarkonia with comoving particles occur more often backward than forward, due to the rapidity-asymmetric particle multiplicities, and more often as well with the larger and less tightly bound excited states.

With a wide rapidity coverage spanning from about -5 to 5, the LHC data from the 4 experiments are unique as they allow one to probe much smaller x values than at RHIC and with a larger reach in $p_{\rm T}$. The higher c.m.s. energy, the competitive luminosities and the resolution of the detectors also allow for more extensive studies of the bottomonium family. In fact, an important observation made with Run 1 data was that of a relative suppression in p–Pb collisions of the excited $\Upsilon(2S)$,$\Upsilon(3S)$ states compared to that of the $\Upsilon(1S)$ observed by CMS [495] as a function of the event activity (recently confirmed by ATLAS [496], but also observed in pp collisions by CMS [497]). Not only was it unexpected, but it constitutes a challenge to the conventional interpretation of suppression observed in Pb–Pb collisions [481, 483, 498], which is of a significantly larger magnitude, but of a similar pattern. Such a relative suppression was also observed in the charmonium sector [499], where it is as well remarkable.

As far as the suppression of the $\Upsilon(1S)$ and J/ψ is concerned, they seem to follow the expectations based on the RHIC results with a strong forward suppression described by shadowing – of a compatible magnitude to that observed with HF data [329], or with the coherent energy loss mechanism [489]. More data, including that on $\Upsilon(nS)$ and Drell-Yan production, are clearly needed to disentangle both effects [500] (see also Section 10.3.4). More precision for $\Upsilon(nS)$ and non-prompt J/ψ is in general critically needed as the typical experimental uncertainties are still on the order of the expected effects.

As a case in point, backward y data are not yet precise enough to quantify the magnitude of the gluon antishadowing, see Section 10 for the possible relevance of quarkonium p–Pb LHC data on nuclear PDF fits. Direct inclusion of this data in nPDF fits is however not yet possible, pending unambiguous clarification of the different effects impacting quarkonium production in p–Pb collisions.

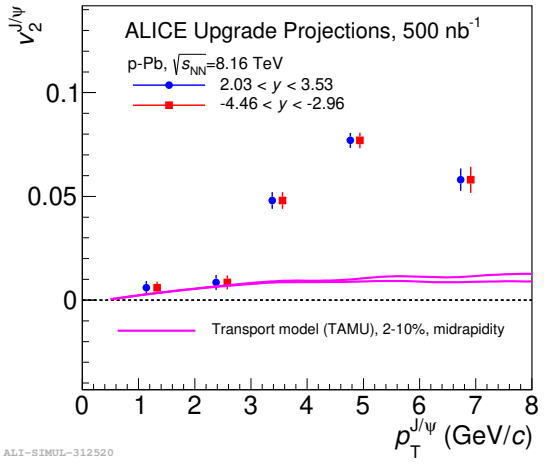

Fig. 52: The p_{T} dependence of the v_2 coefficient of J/ψ mesons in p–Pb collisions, for 500 nb^{-1} (ALICE). The projections are based on current ALICE data for 0–20% centrality [501] and are shown separately for negative and positive y_{CM}), assuming the same magnitude and are compared with transport model (TAMU) calculations [490] for midrapidity. Figure from Ref. [1].

Recently, the measurement of v_2 of J/ψ in p–Pb collisions became available [501,502], indicating a large azimuthal anisotropy, $v_2 \lesssim 0.1$ up to $p_{\mathrm{T}} \lesssim 8$ GeV/c. Recent transport model calculations [490], which are successful in describing the features of the data, including the transverse momentum and centrality dependence of J/ψ and $\psi(2S)$ production in p–Pb, cannot reach the high value of the v_2 coefficient seen in data [501, 502] (see Fig. 52), suggesting that the observed v_2 in p–Pb collisions might also originate from initial state effects. A precision measurement in Runs 3 & 4 for a broad rapidity range will clarify this.

In addition to conventional LHC collider data, one should not overlook the discriminating power of data which can be collected in the fixed-target mode [503, 504]. Not only they correspond to completely different energy and (c.m.s.) rapidity ranges, but extremely competitive luminosities, up to a few fb^{-1}, are easily reachable, beyond what can be reached in the collider mode during Runs 3 & 4. The LHCb collaboration has paved the way for a full fixed-target program at the LHC with their SMOG luminosity monitor [505] used as an internal (He, Ne, Ar) gas target [506] (see also Section 11.4). It is now clear that corresponding studies to those suggested above are possible [507] with the LHCb and ALICE detectors with minor technical adjustments. They would drastically expand the scope of current proton-nucleus quarkonium studies.

7.4.2 High-multiplicity pp *collisions*

Systematic studies of the quarkonium production in high-multiplicity pp events can play an important role in understanding hadronisation. In particular, the correlation of the quarkonium yields with the charged-particle multiplicity can provide new insights into the interplay between hard and soft processes in particle production. Hidden and open heavy-flavour production measurements as a function of the event activity were carried out at the LHC during Run 1 [495, 508]. The striking feature of the data is that the production yields of quarkonia in high multiplicity events are significantly enhanced

relative to minimum bias events, like for D mesons [509]. Specifically, the measurements of the self-normalised yields (the yield divided by the mean yield in minimum bias collisions) as a function of the self-normalised charged-particle multiplicity show an increase which is stronger than linear at the highest multiplicities. The similarity between the D-meson and J/ψ results [508, 509] suggests that this behaviour is most likely related to the production processes, and that hadronisation may only play a secondary role. When comparing J/ψ preliminary results at $\sqrt{s} = 13$ TeV [510] to the ones previously obtained at $\sqrt{s} = 7$ TeV [508], no significant energy dependence is observed, *i.e.* the relative J/ψ yields for events with identical relative multiplicities give similar results. In addition, a dependence of the excited-to-ground-state ratio with charged particle multiplicity is observed in the bottomonium sector in pp collisions [495, 497].

The data are described both by initial-state models as well as by a model assuming hydrodynamic evolution [511], considering that the energy density reached in pp collisions at LHC is high enough to apply such evolution. Initial-state (saturation) effects are considered within i) the Color-Glass-Condensate (CGC) framework [512]; ii) the percolation approach [513, 514]; iii) a model with higher Fock states [515], based on parameters derived from p–Pb collisions. The energy dependence of the cross sections is controlled by the saturation momentum $Q_s(x)$ in the case of the CGC or density of colour ropes $\rho_s(y, p_T)$ in the percolation model, which also governs the charged-hadron multiplicity; events at different energies with the same Q_s or ρ_s are therefore identical. For a given event multiplicity, they predict the relative yields to be almost energy independent. It seems that, in any case, multiple interactions at the partonic level need to be taken into account in order to reproduce the data [516–518].

Runs 3 & 4 data, reaching unprecedented high multiplicities because of larger data samples, and allowing for differential studies in $p_{\rm T}$, will certainly help discriminate models. For instance, in the percolation model, where colour interactions produce a reduction of the charged-particle multiplicities, the deviation from the linear behaviour is expected to be steeper for high-$p_{\rm T}$ quarkonia (and D mesons). Moreover, measurements of J/ψ yields relative to those of D mesons with the same transverse mass could help elucidate the relative contribution of hadronisation and initial-state effects.

Studies of double differential ratios of excited-to-ground quarkonium states versus relative multiplicity could help clarify the presence of final-state effects, either QGP-like or the ones proposed by the comover model [519, 520]. Also, within the CGC+NRQCD framework [512], the relative contributions of the 4 leading J/ψ Fock states have been calculated as a function of the event activity, showing a different dependence for different Fock states.

8 Electromagnetic radiation

Coordinator: Michael Weber (Stefan Meyer Institute Vienna, Austrian Academy of Sciences)

Contributors: R. Bailhache (Goethe-University Frankfurt), R. Chatterjee (VECC Calcutta), T. Dahms (Excellence Cluster Universe, Technical University Munich), T. Gunji (Center for Nuclear Study, Graduate School of Science, the University of Tokyo), M. He (Nanjing University of Science and Technology), S.R. Klein (Lawrence Berkeley National Laboratory), A. Marin (GSI Helmholtzzentrum für Schwerionenforschung GmbH), D. Peresunko (National Research Centre Kurchatov Institute, Moscow), R. Rapp (Texas A&M University, College Station), K. Reygers (Heidelberg University), T. Song (University of Gießen), A. Uras (Université de Lyon, CNRS/IN2P3, IPN-Lyon), G. Vujanovic (Ohio State University and Wayne State University)

The strongly interacting system formed in ultrarelativistic heavy-ion collisions emits electromagnetic radiation that can be detected using different probes: real *direct* photons or virtual photons measurable via dilepton pairs. Direct photons can be split into *prompt* photons, emitted by the partons of colliding nuclei during their inter-penetration, and *thermal* photons, emitted by the almost thermalized hot system. For dileptons these contributions are called Drell-Yan and thermal, respectively. In contrast to real photons, dileptons carry a mass and thus can be used to study the decay of massive particles, such as the in-medium modified spectral shape of vector mesons, the ρ meson being the most prominent one, and the search for particles beyond the Standard Model, e.g., dark photons. In this section, we outline the measurement of photons via calorimetry and the so-called photon conversion method, as well as dielectron (e^+e^-), and dimuon ($\mu^+\mu^-$) pairs in A–A collisions in the ALICE detector at the LHC. Moreover, the photoproduction of dilepton pairs in peripheral collisions and the expected sensitivity for the search of dark photons are discussed in subsections 8.2 and 8.3, respectively. We begin with a short review of previous experimental results together with a summary of the basic theoretical models employed to describe these data.

8.1 Thermal radiation and in-medium spectral function

Electromagnetic radiation from the hot and dense system formed in ultrarelativistic heavy-ion collisions in the form of real photons was measured for the first time at the SPS by WA98 [521]. The direct photon spectrum measured in Pb–Pb collisions at $\sqrt{s_{\rm NN}} = 17.3$ GeV showed an excess above the extrapolated prompt photon signal based on measurements in proton induced reactions. The excess is described by a large variety of hydrodynamic and cascade models (see [522] for review), most of which assume the formation of a QGP phase. Also at the SPS, a modification of low-mass dilepton pairs in S–Au and Pb–Au collisions relative to the expectation of in-vacuum hadron decays was observed by CERES [523–527] and studied with high precision by NA60 in In–In collisions [528–531]. The data are consistent with an in-medium ρ spectral function that, driven by the coupling to baryons, melts and approaches the one from $q\bar{q}$ annihilation in the vicinity of the phase transition [532–534], which is compatible with chiral symmetry restoration [136, 535]. On the other hand, the data cannot be described with a dropping mass scenario, in which the ρ mass drops to zero as chiral symmetry is restored [536]. Beyond the issue of chiral symmetry restoration, NA60 measured an excess of prompt dimuons in the intermediate mass region between the ϕ and the J/ψ masses [529, 530]. Contrary to transverse-mass spectra of the dimuon continuum at lower masses, this excess shows no increase of the exponential inverse slope with mass, i.e., blue shift, that is typical for radial flow. This suggests that the source of this enhancement is from the earliest phase of the collision, before significant radial flow has built up. This supports the idea that the inverse slope of the invariant mass spectrum is insensitive to the expansion of the medium and therefore a true measure of the average temperature. NA60 measured a value of $T = 205 \pm 12$ MeV [531], which significantly exceeds the temperature of 154 ± 9 MeV, above which the formation of a QGP has been predicted [50, 135].

At RHIC energies, PHENIX and STAR have measured an enhancement of e^+e^- pairs in the low mass region in Au–Au collisions [537–540] that can be described with the same model of collisional

broadening as used at the SPS. STAR measured that the enhancement above the hadron decay background does not change with collision energy between $\sqrt{s_{\rm NN}} = 19$ and 200 GeV [540]. Despite a marked decrease of the net-baryon chemical potential in this energy range, the total baryon plus antibaryon density does not change much, providing further evidence that the ρ coupling to baryons and antibaryons is responsible for the enhancement. Real direct photon production in Au–Au collisions was measured by PHENIX [541–543]. An excess was observed compared to binary scaled direct photon production in pp collisions. The signal was measured via quasi-real virtual photons, i.e., e^+e^- pairs with small invariant mass, as well as real photons converting in detector material. The excess yield at low $p_{\rm T}$ appears to have a universal multiplicity dependence, scaling with the charged-particle multiplicity at midrapidity to the power of about 1.25, independent of collision energy between $\sqrt{s_{\rm NN}} = 39$ and 200 GeV [543]. The transverse momentum spectrum of the excess yield has an exponential inverse slope of $T = 221 \pm 19\ (\text{stat.}) \pm 19\ (\text{syst.})$ MeV for central collisions and values close to that for other centralities. The spectrum, however, is strongly blue shifted by radial flow in the later stages of the fireball radiation, which is further supported by a sizeable elliptic flow (v_2) of the direct photon signal [544]. Therefore, the inverse slope cannot directly be interpreted as an average temperature, which highlights the importance of thermal dilepton measurements as a function of invariant mass. However, the modelling of the space-time evolution offers the possibility of extracting temperature information from the photon data [545]. The direct photon v_2 is indeed comparable to the v_2 of pions, which suggests late emission of direct photons dominated by the hadronic phase [546]. A simultaneous description of the elliptic flow effect, as well as the large direct photon excess, which implies early production, poses a significant challenge to theoretical models.

The first measurement of direct photon production in Pb–Pb collisions with the ALICE detector [547] at the LHC also show an excess of thermal production at low $p_{\rm T} < 3$ GeV/c with respect to the prompt direct photon expectation [548]. The extracted effective temperatures $T = 297 \pm 12\ (\text{stat.}) \pm 41\ (\text{syst.})$ MeV in central collisions and $T = 410 \pm 84\ (\text{stat.}) \pm 140\ (\text{syst.})$ MeV in semi-central collisions are higher than those at RHIC energies, as expected. The direct photon elliptic flow was also extracted in central and semi-central collisions [549]. The measured flow is close to the one at RHIC energy and at low $p_{\rm T} < 4$ GeV/c to the one of final hadrons. However, this measurement does not cause the same challenges to models, since the experimental uncertainties are still large at this point. The reduction of systematic uncertainties of the direct photon measurement is the main objective for Run 3 to improve its significance. Moreover, a low magnetic field run will allow one to access the $p_{\rm T} < 1$ GeV/c region where the thermal photon production increases rapidly. Theoretical calculations of thermal and prompt photon productions are available at $\sqrt{s_{\rm NN}} = 5.02$ TeV (Fig. 53) [209, 550–552]. The thermal contribution dominant at low $p_{\rm T}$ is given by the QGP photon emission rates and the hadronic photon production rates, integrated over the space-time evolution of the system. In [209] a (2+1)D hydrodynamic evolution with IP-Glasma initial conditions with initial flow and finite shear and bulk viscosity is followed by a hadronic phase modelled using UrQMD. A longitudinal boost invariant (2+1)D ideal hydrodynamics is used in [551], while in [552] a (2+1)D ideal hydrodynamic model including non-vanishing initial flow is employed. The prompt photon component, dominant at high $p_{\rm T}$, is very similar in all models. It is obtained from NLO pQCD calculations using the BFG-II photon fragmentation function and the CTEQ6.6 [551] or nCTEQ15 parton distribution function [550]. An increase by a factor $\sim$ 1.5 at about $p_{\rm T} \approx 1$ GeV/c and by a factor 1.5 to 2 for the prompt photons is predicted compared to yields at $\sqrt{s_{\rm NN}} = 2.76$ TeV. The predicted thermal photon elliptic flow parameters for central collisions are close to each other at the two LHC energies and are very small. Differences become larger as one goes towards peripheral collisions. Simultaneous measurements of photon yields and photon flow with high accuracy and lower $p_{\rm T}$ reach will provide constraints to theoretical models.

Dilepton measurements by ALICE at the LHC are not yet sensitive to possible low-mass enhancement and thermal signals [555]. A precise measurement of the low-mass dielectron continuum will be one of the main objectives of the ALICE physics programme during the LHC Run 3 and 4. In the mean-

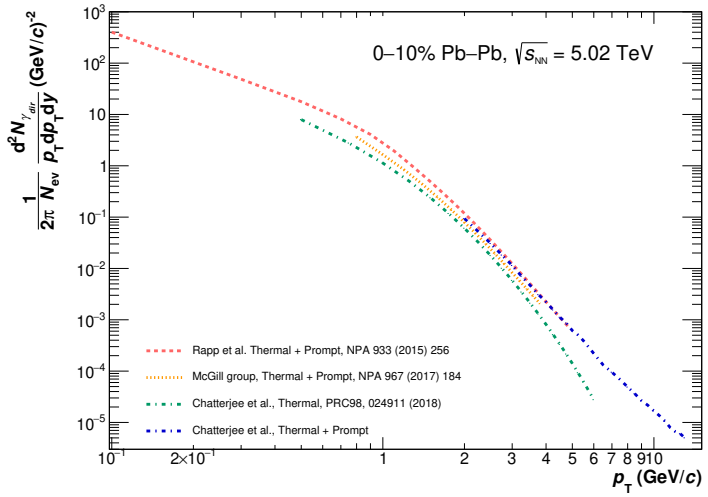

Fig. 53: Direct photon differential invariant yield for central 0–10% Pb–Pb collisions at $\sqrt{s_{\rm NN}} = 5.02$ TeV as predicted by several models [209, 551–554].

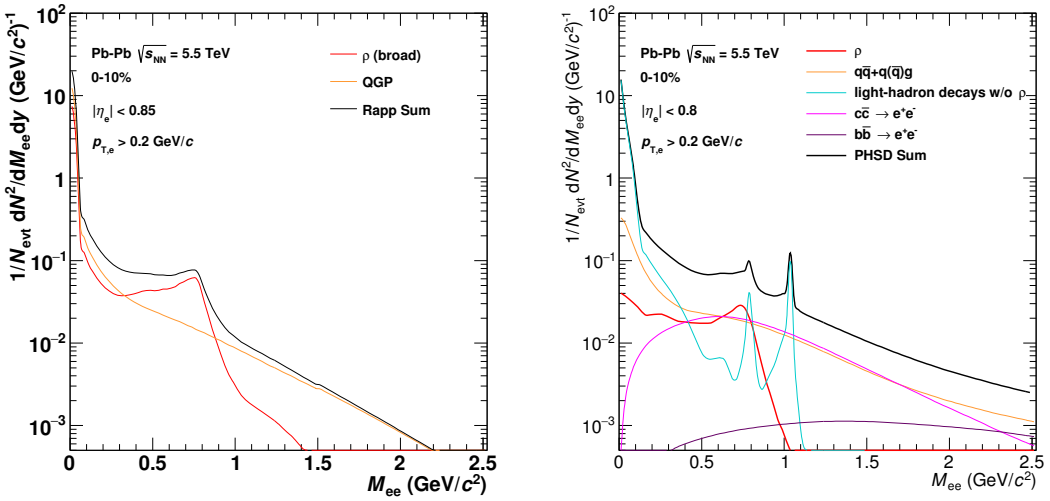

Fig. 54: Model predictions for the invariant mass spectrum of e^+e^- pairs in central (0–10%) Pb–Pb collisions at $\sqrt{s_{\rm NN}} = 5.5$ TeV. Left panel: in-medium radiation plus decays of the ρ meson at the end of the system evolution by R. Rapp *et al.*. Right panel: Expectations from the PHSD model including the in-medium ρ meson, $q\bar{q} \rightarrow e^+e^-$, $q\bar{q} \rightarrow e^+e^-g$, and $q(\bar{q})g \rightarrow e^+e^-q(\bar{q})$, hadronic sources, and semileptonic decays of $c\bar{c}$ and $b\bar{b}$.

while, the dominant background of dielectrons from correlated semileptonic open heavy-flavour decays is utilised to learn more about open heavy-flavour production in pp collisions at LHC energies [556,557].

The model by R. Rapp *et al.*, an approach that has been proven to provide a quantitative description of the existing dilepton results [558], is based on two ingredients that are put into a realistic space-time evolution [559]. The thermal dilepton radiation is modelled by emission rates from the hadronic phase and the Quark–Gluon Plasma [534, 560]. A hadronic many-body approach [533] is used for the medium-modified spectral functions of ρ and ω mesons. In addition, the equation of state is updated to a cross-over transition around $T_{\rm c} = 170$ MeV extracted from with recent lattice QCD computations, and hadro-chemical freezeout at $T_{\rm chem} = 160$ MeV [561]. Figure 54 (left) shows the calculations performed

for central Pb–Pb collisions at $\sqrt{s_{\rm NN}} = 5.5$ TeV for in-medium radiation plus decays of the ρ meson at the end of the system evolution. The pair-yield is estimated for the rapidity range $|y_{\rm e}| < 0.85$ and transverse momentum of single electrons $p_{\rm T}^{\rm e} > 0.2$ GeV/c and is normalized to the number of events $N_{\rm evt}$.

A complementary approach to study dilepton spectra and thermal radiation is provided by the parton-hadron-string dynamics (PHSD) transport approach, which also successfully describes the existing experimental data [562, 563]. The in-medium modification of the ρ meson is incorporated in PHSD by an off-shell transport of vector mesons with a dynamically changing set of spectral functions [564] evolving towards the vacuum spectral function at the end of the collision history. The electromagnetic radiation of the QGP is modelled by $q\bar{q} \rightarrow e^+e^-$, $q\bar{q} \rightarrow e^+e^-g$, and $q(\bar{q})g \rightarrow e^+e^-q(\bar{q})$ using effective propagators for quarks and gluons from a dynamical quasi-particle model [565]. Figure 54 (right) shows both contributions to the dielectron spectrum in central Pb–Pb collisions at $\sqrt{s_{\rm NN}} = 5.5$ TeV calculated from PHSD together with other sources of dielectrons: decays of long-lived light mesons into e^+e^- (the so-called hadronic cocktail) and the semileptonic decay of hadrons containing heavy quarks, such as D and B mesons.

Important input for models aiming to describe the dilepton yield at LHC energies are the in-medium spectral functions for the vector mesons, most importantly the ρ meson, as well as the photon and dilepton rates from the QGP. For the latter, Lattice QCD calculations, which are currently limited to the quenched approximation, will hopefully be extended (e.g., larger lattices, especially in the time direction, or facilitating extrapolations to the continuum limit) and be available at higher accuracy for realistic systems including light dynamical degrees of freedom in the future. Recent updates on calculations of the photon rate [566], the electrical conductivity [567], and dilepton rates [568] are promising. The photons and dilepton rates from Lattice calculations should in the future be combined with dynamical models like those in Fig. 54, thus improving their results. In addition, the in-medium spectral functions could also use direct input from Lattice QCD [569, 570] or from a functional renormalization group approach [571]. These models can further be refined by including the effects of dissipation, and in that case the electrical conductivity will become of interest to both the dynamical evolution of the medium as well as the electromagnetic rates. In order for that to be achieved self-consistently, the evolution of the medium and the electromagnetic rates need to be modified to account for dissipative effects, which is a currently ongoing effort [209, 572, 573].

More differential information can be used to study the equation of state of the system throughout the full collision history. The measurement of the elliptic flow coefficient v_2 of thermal photons and dileptons, especially if combined with results from hadronic channels, should put tighter constraints on fundamental properties of the medium (e.g., transport coefficients), as well as its "initial conditions" or "pre-equilibrium" dynamics [574]. For example, owing to the penetrating nature of dileptons, the invariant mass dependence of the dilepton v_2 is sensitive to the temperature dependence of both shear [573] and bulk viscosity [572] in a way that is difficult to access using hadronic observables alone.

8.1.1 Real photons

ALICE has measured direct photon spectra in three centrality classes in Pb–Pb collisions at $\sqrt{s_{\rm NN}} = 2.76$ TeV [548]. An excess of direct photons was quantified by the $p_{\rm T}$ dependent double ratio

$$R_\gamma \equiv \frac{\gamma_{\rm incl}}{\pi^0_{\rm param}} \Big/ \frac{\gamma_{\rm decay}}{\pi^0_{\rm param}} = \frac{\gamma_{\rm incl}}{\gamma_{\rm decay}}, \tag{27}$$

where $\gamma_{\rm incl}$ is the measured inclusive photon spectrum, $\pi^0_{\rm param}$ a parametrization of the measured π^0 spectrum, and $\gamma_{\rm decay}$ the calculated decay photon spectrum. The double ratio has the advantage that some of the largest systematic uncertainties cancel partially or completely. The measurement combines

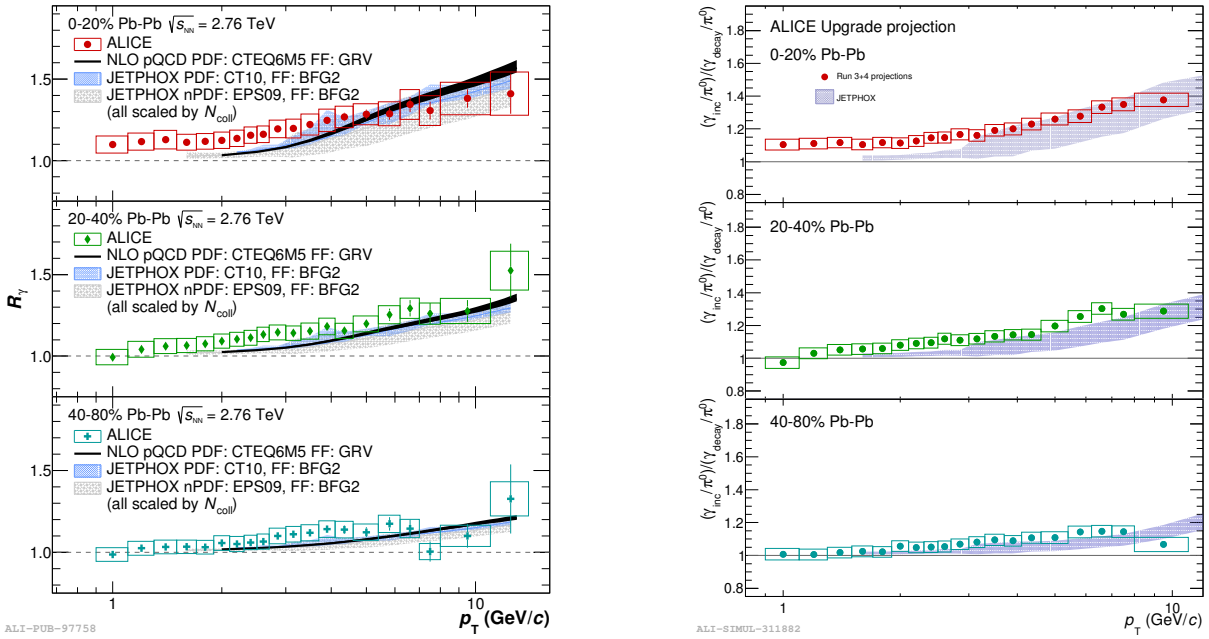

Fig. 55: R_γ measured [548] (left) and R_γ projected [1] keeping the measured values of R_γ and recalculating the uncertainties as explained in the text.

results of the Photon Conversion Method (PCM) and of the Photon Spectrometer (PHOS), see Fig. 55, left. In central collisions at low $p_{\mathrm{T}} < 4$ GeV/c an excess with respect to prompt photon predictions is observed that is attributed to thermal photon emission from the QGP. In the 20% most central collisions the low p_{T} excess is of the order of 10–15%, while the total uncertainty of the order of 6%. A signal of direct photons is found in central collisions, but on the level of $\sim 2\sigma$, while in mid-central and especially in peripheral the significance is even smaller. On the other hand, peripheral collisions are important since there one can estimate and restrict the contribution from prompt direct photons.

For Run 3 the PCM measurement will be influenced by the ALICE Inner Tracking System (ITS) and Time Projection Chamber (TPC) upgrades, while PHOS and the Electromagnetic Calorimeter (EMCal) will be kept unchanged. The new ITS shows an improved low p_{T} tracking efficiency, that will partially compensate the efficiency loss due to the $\sim$ 30% reduction of its material thickness. Two 1 mm tungsten wires with well known thickness will be installed parallel to the beam direction for precise calibration of the material thickness as described later. The TPC continuous readout mode together with large pile-up may prevent the use of photon conversions beyond a radius of 35 cm. This restriction will translate into a $\sim$ 35% lower photon efficiency. On the other hand, the PCM measurement will also profit from the dedicated heavy-ion run with reduced magnetic field of the ALICE solenoid, which will considerably increase the low p_{T} reconstruction efficiency. To estimate how one can improve the accuracy of the measurement, the uncertainties are split into three classes: those which can be improved with increase of statistics (statistical uncertainties, uncertainties related to π^0 spectrum extraction, η/π^0 ratio); uncertainties which can be reduced using new techniques and some special methods (material budget estimate - with calibrated material analysis, energy scale in calorimeters with new hybrid π^0 methods); and uncertainties related to the properties of the detector which can not be improved (hadron contamination in calorimeters, electron identification in conversion method etc.). To estimate the improvement of the uncertainties it is assumed that the integrated luminosity will reach $L_{\mathrm{int}} = 3.1$ nb^{-1} per Pb–Pb run and in total $L_{\mathrm{int}} = 13$ nb^{-1} at the end of Run 4, which is more than a factor of 100 larger the than integrated luminosity $L_{\mathrm{int}} = 10$ µb^{-1} used in the published analysis [548]. The major improvement foreseen for Run 3 is the use of calibrated tungsten wires inserted into the ITS to determine

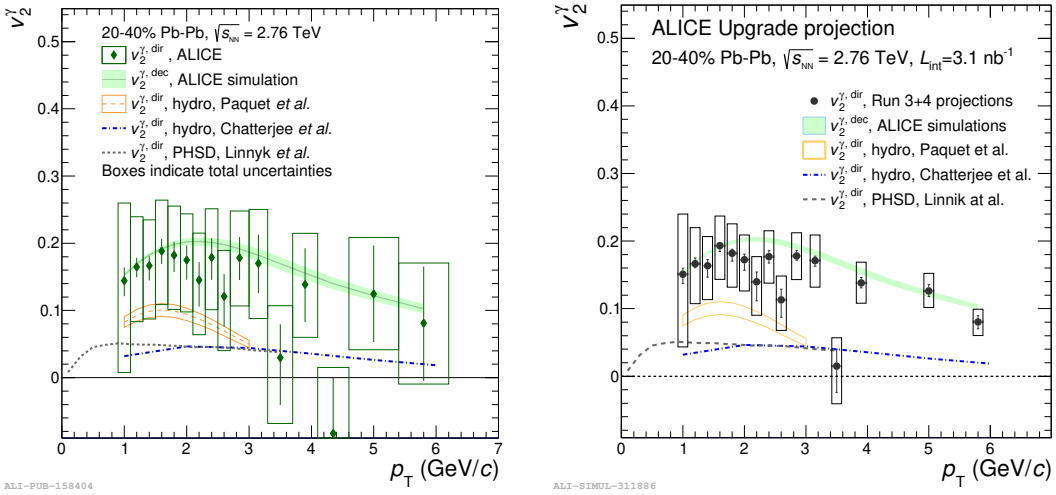

Fig. 56: Direct photon flow in mid-central collisions. Left: direct photon collective flow measured in Pb–Pb collisions compared to decay photon flow and several theoretical predictions. Right: expected accuracy in Run 3 keeping the measured values of R_γ and v_2^γ and recalculating the uncertainties as explained in the text. Figure from Ref. [1].

the product of the photon flux times the γ reconstruction efficiency. This product would then be used to precisely determine the material thickness in the rest of the ITS (assuming φ-independent photon flux and taking the radial dependence of the reconstruction efficiency from simulation). The proposed calibration method is based on weights calculated as the double ratio:

$$\omega_i = \left(\frac{N_\gamma^{\rm rec}(r_i)}{N_\gamma^{\rm rec}(r_{\rm wire})} \right)^{\rm data} \Big/ \left(\frac{N_\gamma^{\rm rec}(r_i)}{N_\gamma^{\rm rec}(r_{\rm wire})} \right)^{\rm MC} \tag{28}$$

where $N_\gamma^{\rm rec}(r_i)$ and $N_\gamma^{\rm rec}(r_{\rm wire})$ are the number of reconstructed γ's in data or in MC simulations in a given radial bin and the calibrated wire, respectively. For the Run 3 projections a systematic uncertainty of 1% on the ITS thickness is taken. The uncorrelated systematic uncertainties on the π^0 and η measurements will be reduced by a factor 10 due to the increased luminosity as they are defined mostly by the raw yield extraction uncertainties which scale proportional to statistical uncertainties. The systematic uncertainties on the photon selection and particle identification are expected to be reduced by 50%. Figure 55 (right) shows the projection of the R_γ measurement for Run 3 calculated with these assumptions: the measured values of R_γ are kept but the uncertainties are recalculated. The total errors are reduced by $\sim$ 50%. In addition to the reduction of the uncertainties, the large data set foreseen for Run 3 will allow exploration of the 0–1% centrality range.

The ALICE Collaboration carried out measurements of the direct photon elliptic flow [549] in Pb–Pb collisions at $\sqrt{s_{\rm NN}} = 2.76$ TeV for the two centrality classes, 0–20% and 20–40%, see Fig. 56, left plot for 20–40% centrality. The measured direct photon elliptic flow $v_2^{\gamma,{\rm dir}}$ is compared to the estimated decay photon elliptic flow $v_2^{\gamma,{\rm dec}}$, marked as cocktail, and to the predictions of several theoretical models. Similar to RHIC measurements, the direct and decay photon elliptic flow are very close and systematically higher than theoretical predictions of hydrodynamic [575, 576] and the transport [577]

models. However, because of the large uncertainties one can not presently exclude either of theoretical calculations. Using the same assumption concerning photon and neutral measurements in Run 3 as for R_γ, the expected accuracy of $v_2^{\gamma,\mathrm{dir}}$ measurements in Run 3 is estimated, see Fig. 56 (right). The mean values are kept the same but the uncertainties are reduced as expected. Similar to R_γ with the current assumptions the total errors will be reduced by factor ~ 2 and one will be able to exclude or confirm available theoretical calculations.

8.1.2 Dileptons

The sensitivity to the expected signal of thermal radiation and an in-medium modification of the ρ spectral function in the dielectron and dimuon channels with the ALICE detector [86, 547] was studied already in preparation for ITS upgrade in 2019/20 [2,3,68,477]. The measurement of low-mass dileptons after this upgrade will profit from

- an improved vertex resolution, which leads to a better separation of electrons from prompt sources, like thermal radiation, and electrons from the decays of heavy-flavour hadrons, for which $c\tau$ is about 150 μm (open-charm hadrons) or 400 μm (open-beauty hadrons),
- a reduced material budget and improved tracking efficiency at low transverse momentum p_T, which leads to a smaller background of electrons and positrons from photon conversion in the detector material,
- the installation of the muon forward tracker, that will lead to an improved mass resolution and reduced background in the dimuon channel,
- and a higher rate capability (50 kHz in Pb–Pb collisions) that will increase the expected number of events in the central barrel detector by a factor of 100. The increased rate capability also enables the possibility to record in a single Pb–Pb run a large data sample with reduced magnetic field value in the ALICE central barrel ($B = 0.2$ T instead of 0.5 T), which increases the phase-space acceptance and the reconstruction efficiency of low momentum electrons and positrons.

The expected measured spectra discussed in this section closely follow the strategy that is discussed in more detail in [2, 3, 68, 477].

For the dielectron channel an integrated luminosity $L_\mathrm{int} \approx 3$ nb^{-1} is assumed, which should be collected in the dedicated Pb–Pb run at low field. The corresponding number of events in central (0–10%) collisions is 2.5×10^9. The input for the signal is composed of:

- contributions from the decays of long-lived light pseudoscalar and vector mesons (hadronic cocktail consisting of π^0,η,η',ω, and ϕ), with particle ratios and spectral shapes extrapolated from existing heavy-ion data at lower energies,
- correlated semileptonic charm decays based on calculations from the PYTHIA event generator [578],
- and the radiation of thermal dileptons and a medium-modified spectral function for the ρ meson in a realistic space-time evolution (see Fig. 54 (left)).

With respect to earlier calculations [2, 3, 68] a fast simulation of central Pb–Pb collisions is used here to estimate the combinatorial background and the statistical significance of the signal. The particles are produced with the event generator HIJING [579] and then propagated through the detector material by GEANT3 [580]. An updated geometry of the ITS is utilised in the detector description and leads to a more realistic treatment of conversion electrons and the subsequent background. Electrons are reconstructed and identified via signals in the ALICE Time Projection Chamber (TPC) and Time-Of-Flight (TOF) detector, a parametrised efficiency from runs at low magnetic field during LHC Run 2

is applied. After pairing electrons and positrons an additional selection on the pair distance of closest approach

$$DCA_{ee}(\sigma) = \sqrt{\left(\mathrm{DCA}_{\mathrm{xy},1}/\sigma_{\mathrm{xy},1}\right)^2 + \left(\mathrm{DCA}_{\mathrm{xy},2}/\sigma_{\mathrm{xy},2}\right)^2} \tag{29}$$

is applied to reduce the contribution from correlated semileptonic charm decays. The selection is chosen such that 95% of these pairs are rejected, while having an efficiency for prompt pairs of $\sim$ 17%. The signal distribution S, which includes the remaining charm and beauty hadron decays, is obtained by subtraction of the combinatorial background from all $\mathrm{e}^+\mathrm{e}^-$ pairs. The combinatorial background B is estimated from like-sign pairs and a correction factor R that takes into account the different acceptance of the apparatus for unlike- and like-sign pairs [555–557]. The significance that is used to project the statistical uncertainty on the measurement is calculated as $S/\sqrt{S+2B}$. The signal S is shown in Fig. 57 (left) together with all input distributions. In order to extract the QGP component and the in-medium modified ρ spectral function, the hadronic cocktail and the contribution from correlated semileptonic charm decays is subtracted and shown in Fig. 58 (left). In addition, the systematic uncertainties from the combinatorial background and signal extraction, as well as physical backgrounds after subtraction are shown. The relative systematic uncertainty of the signal, from tracking, track matching, and particle identification, is assumed to be 10%. For the systematic uncertainty of B a mass independent uncertainty of the R factor of 0.02% is used. Relative systematic uncertainties from the light-hadron cocktail and the total charm cross section of 10% and 15%, respectively, are applied.

In the dimuon channel, the integrated luminosity of Pb–Pb collisions ($L_{\mathrm{int}} \approx 10\mathrm{nb}^{-1}$) is used. In this channel, the main source of background is represented by the combinatorial pairs of muons coming from uncorrelated semimuonic decays of light-flavoured mesons, mainly pions and kaons, copiously produced in high-energy nuclear collisions. The opposite-sign dimuon mass spectrum obtained after the subtraction of the combinatorial background evaluated by means of an event mixing technique, results from the superposition of several opposite-sign correlated dimuon sources, represented in the right panel of Fig. 57. In order to isolate the thermal dimuon radiation and the in-medium modified line shapes of the ρ meson, the known and well-identifiable sources of the hadronic cocktail — 2-body and Dalitz decays of the η, ω, ϕ mesons, for which no in-medium effect is expected — are subtracted from the total opposite-sign correlated dimuon mass spectrum. A 10% systematic uncertainty in the evaluation of the shape and the normalization of these sources has been considered in the performance studies. The same procedure has been also applied for the subtraction of the dimuons from the open charm and open beauty processes; alternatively, these two sources could be separated from the prompt ones by means of an analysis based on the discrimination of the dimuon offset at the primary vertex.

The spectral function of low-mass dielectrons and dimuons in the mass region of the modified ρ-meson spectral function $M_{\mathrm{ee}} \approx 0.5$ GeV/c^2 can be extracted with a systematic uncertainty of $\approx$ 15% and $\approx$ 20%, respectively (see Fig. 58). The sizeable contribution of thermal dilepton pairs above $M_{\mathrm{ee}} > 1.1$ GeV/c^2 can be used to extract the temperature of the system. An exponential fit with $\mathrm{d}N/\mathrm{d}M_{\mathrm{ee}} \sim M_{\mathrm{ee}}^{3/2} \exp(-M_{\mathrm{ee}}/T_{\mathrm{fit}})$ to the subtracted $\mathrm{e}^+\mathrm{e}^-$ spectra in the invariant mass region $1.1 < M_{\mathrm{ee}} < 2.0$ GeV/c^2 was performed. Comparing the fit parameter T_{fit} to the real temperature T_{real} from the fit to the thermal contribution, a statistical uncertainty of 5% and systematic uncertainty of 10% and 20% for the background and the charm subtraction, respectively, were estimated. The same kind of measurement is also expected to be possible in the dimuon channel, considering a dedicated set of cuts optimized for the analysis of the intermediate mass region (the cuts considered in the right panel of Fig. 58 being optimized for the signal extraction in the mass region below ~ 1 GeV/c^2).

An alternative method to separate the thermal component from the modified heavy-flavour production in the intermediate mass range, is to fit the measured DCA_{ee} distribution as a function of the dielectron invariant mass and pair transverse momentum with a three component function, including the contributions from prompt dielectron sources, from open-charm hadron decays and from open-beauty hadron decays. Since the shape of the heavy-flavour DCA_{ee} spectra is quasi model independent, the

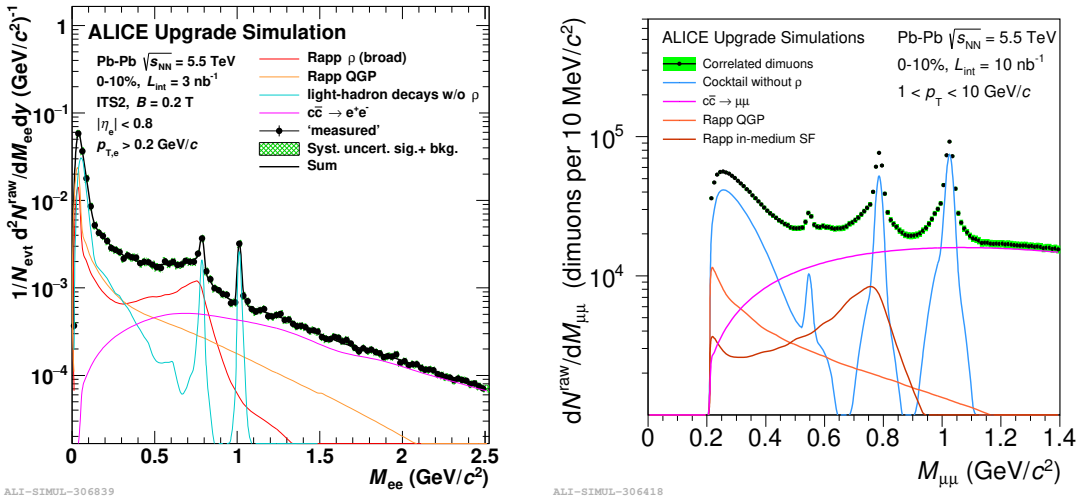

Fig. 57: Inclusive e^+e^- (left) and $\mu^+\mu^-$ (right) invariant mass spectrum for 0–10% most central Pb–Pb collisions at $\sqrt{s_{NN}} = 5.5$ TeV. The green boxes show the systematic uncertainties from the combinatorial background subtraction. Figures from Ref. [1].

dielectron yield of open heavy-flavour decays in the ALICE acceptance can be determined from the data with small uncertainties, without relying on theoretical calculations. Such fits were performed already with the Run 1 data in pp collisions at $\sqrt{s} = 7$ TeV [556]. Nevertheless, the statistics available did not allow for a differential study.

The measurement of the dielectron elliptic flow coefficient v_2 as a function of M_{ee} in peripheral Pb–Pb collisions (40–60%) was studied already in [2]. It was shown that an absolute statistical uncertainty on v_2 of $\sigma_{v_2} \approx 0.01$ can be achieved. Such uncertainties present a very encouraging prospect for dilepton studies since temperature dependent shear viscosity [573], bulk viscosity [572, 581], and early stages of reaction dynamics [574] have effects on the order of a few up to tens of percent on dilepton v_2, and thus future constraints on these properties will greatly benefit from a statistically improved dilepton v_2 measurement.

8.2 Two-photon and photonuclear interactions

Heavy ions carry strong electromagnetic fields. Their electric and magnetic fields are perpendicular, so may be treated as a flux of nearly-real photons [582]. These photon fields can give rise to photonuclear (photon on nucleus) and two-photon interactions. Although these interactions are expected to occur in both ultra-peripheral (UPC) and more central collisions, they were not generally expected to be visible in non-UPC collisions. The few final state particles from the photon-mediated interactions were expected to be swamped by the more copious hadronically produced particles. That expectation changed recently, when ALICE [583] and then STAR [584, 585] and ATLAS [586] observed excesses of dileptons produced at very small pair p_T, $p_T < 100$ MeV/c. These pairs were prominent in Pb–Pb and Au–Au collisions, but not in pp interactions; the excess corresponded to $R_{AA} > 5$. This is inconsistent with all expectations for hadroproduction, but consistent with photoproduction, where the pair p_T scale is set by the nuclear radius R_A, with $p_T \approx \hbar/R_A$. The kinematics of these pairs may be affected by the medium in which they are produced or propagate, so they may probe the evolving Quark–Gluon Plasma or associated magnetic fields.

UPC photon-mediated interactions have been studied at both RHIC and the LHC [582, 587–590]. The agreement between data and calculations is quite good. Photoproduction of ρ, ω, ρ' , J/ψ, J/ψ',

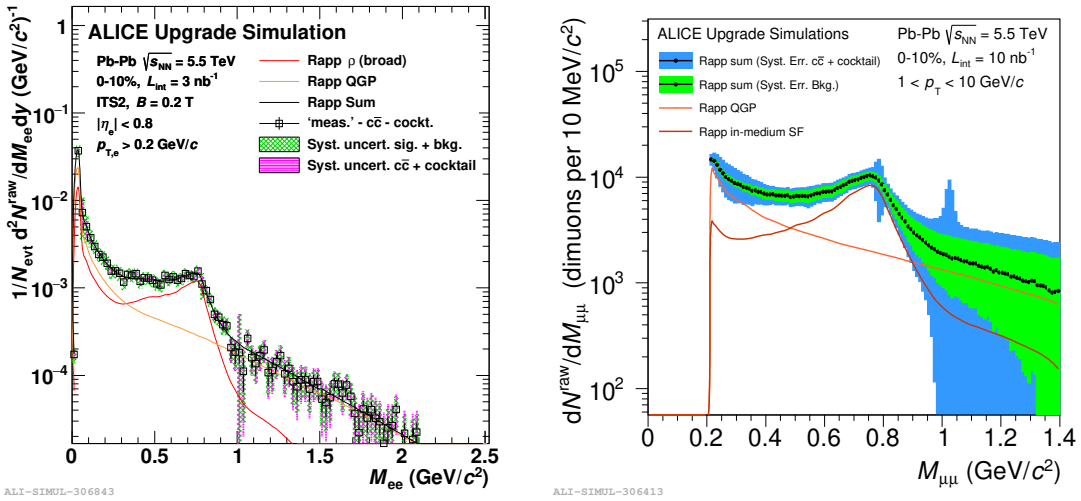

Fig. 58: Excess (after subtraction of light hadron decays and from correlated charm semileptonic decays) e^+e^- (left) and $\mu^+\mu^-$ (right) invariant mass spectrum for 0–10% most central Pb–Pb collisions at $\sqrt{s_{NN}} = 5.5$ TeV. The green boxes show the systematic uncertainties from the combinatorial background subtraction, the magenta (left) and blue (right) boxes indicate systematic errors related to the subtraction of the cocktail and charm contribution. Figures from Ref. [1].

Υ and direct π^+ π^- pairs has been observed, along with two-photon production of dilepton pairs and light-by-light scattering. In peripheral collisions, photon-mediated interactions might be used to probe the nuclear medium that they may occur in, including the QGP [584, 586]. The produced leptons may interact with this medium, leading to alterations in their momentum.

Peripheral collisions introduce several new considerations for photon-mediated reactions, particularly evolving coherence conditions for both photon emission and coherent photon-nucleus scattering. Photon emission in both γγ and photonuclear interactions is expected to be completely coherent, governed by the nuclear form factor $F(q)$ [591]. The photon emission from a nucleus moving with Lorentz boost γ should occur before the hadronic interaction (which is taken to occur at $t = 0$), at a retarded time, $t - x/c$ [592], where $x = |b|/\gamma$; $|b|$ is the transverse distance from the photon emission point to where it interacts. For very small impact parameters, some coherence may be lost, and a more detailed calculation is needed. For photon-nucleus collisions, the situation is more complicated, and will be discussed below.

Here, two-photon interactions and coherent photonuclear interactions are discussed.

8.2.1 Two-photon interactions

In two-photon interactions, each nucleus emits a photon, which then interact and form a lepton pair. In UPCs, this process is well described by the Weizsäcker-Williams approach (where each photon is treated as real), except at very low pair p_{T}, where a lowest-order QED calculation works better [593]. UPC calculations can be easily extended to include peripheral collisions [594–596]. The kinematic distributions are similar to those in UPCs, and the cross-section depends on the range of impact parameters.

Recently, the ATLAS collaboration [586] presented results showing a dramatic modification to $\gamma\gamma \to \mu^+\mu^-$ in peripheral collisions. Figure 59 shows the pair acoplanarity α, the azimuthal angular deviation from being perfectly back-to-back, and A, the energy imbalance between the two leptons. For UPCs, they found good agreement with the STARlight [597, 598] reference, with the data and

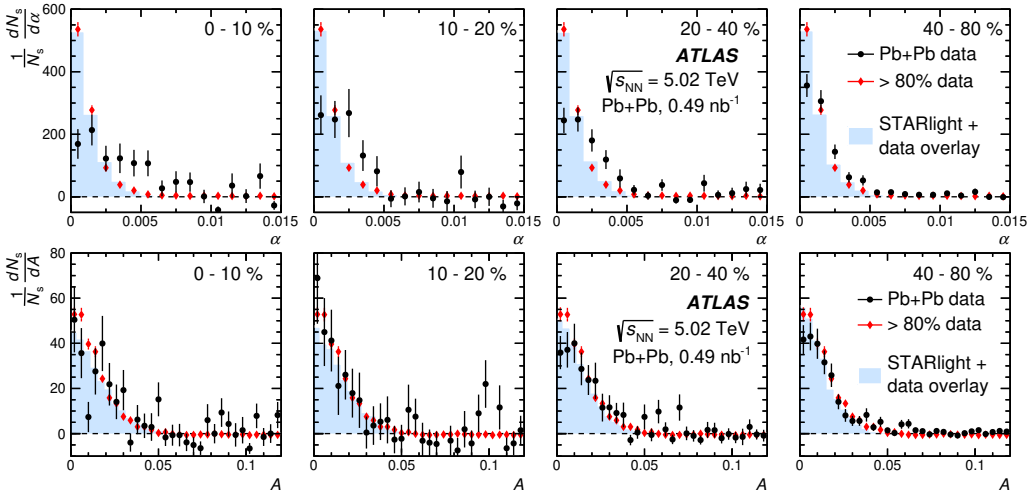

Fig. 59: Acoplanarity (α, top) and lepton energy imbalance (A, bottom) as a function of centrality, for dimuon pairs with pair mass above 10 GeV/c^2, observed in the ATLAS detector. From Ref. [586].

calculations peaked at small α and A. More central collisions show dramatic changes with the low-α peak largely disappearing, and the A distributions only minimally changed. ATLAS described this as "Consistent with order of magnitude estimates from kinetic theory for multiple scattering off electric charges in thermal plasma." Multiple scattering would remove the peak at low α, but leave A largely unaffected. A recent calculation finds that the magnitude of the change in α is at least roughly consistent with that expected for leptons propagating through a Quark–Gluon Plasma [599]. If multiple scattering is large, though, one might also expect some bremsstrahlung, which should increase A. To evaluate this further requires a calculation of how many of the produced leptons are produced in the medium, and/or traverse it. An alternate explanation could involve the leptons bending in the magnetic field from the QGP. If a QGP is electrically conducting, then it may acquire an induced magnetic field from the short-lived magnetic fields carried by the two nuclei [600]. The QGP field, however, will be longer lived, and could bend the produced leptons in opposite directions, reducing their coplanarity. Symmetry also predicts that it should disappear for the most central collisions [599], except possibly for event-by-event fluctuations.

The STAR Collaboration also has studied two-photon e^+e^- production in peripheral Au–Au collisions; they found a small difference between their pair p_T spectrum and calculations, and suggest that it might be due to medium effects [584]. ALICE has not yet seen these pairs [583], likely because their pair acceptance requires lepton $p_T > 1$ GeV/c, eliminating most pairs from $\gamma\gamma$ reactions.

Coupled with better theoretical calculations, the large Pb–Pb integrated luminosity in Run 3 and 4 can confirm and dramatically expand our understanding of this effect. One important goal is to expand the study to cover a much wider range of masses. Figure 60 shows the expected mass spectrum obtainable by ATLAS for a 13 nb^{-1} integrated luminosity run, assuming no changes in the trigger; masses up to 100 GeV/c^2 should be accessible. These high mass pairs correspond to two-photon interactions in or very near the two nuclei, so should show increased effects due to interactions with the medium or magnetic fields associated with the Quark–Gluon Plasma.

In contrast, lower masses correspond to larger distances between the dilepton production point and the nuclei, so in-medium effects may be smaller. These lower masses should be accessible with a softer requirement on the muon momentum. It would also be interesting to compare e^+e^- with $\mu^+\mu^-$ (and possibly $\tau^+\ \tau^-$), since the lighter leptons should interact more. If the leptons interact with the medium, then the electron A distribution should show more change than that for muons.

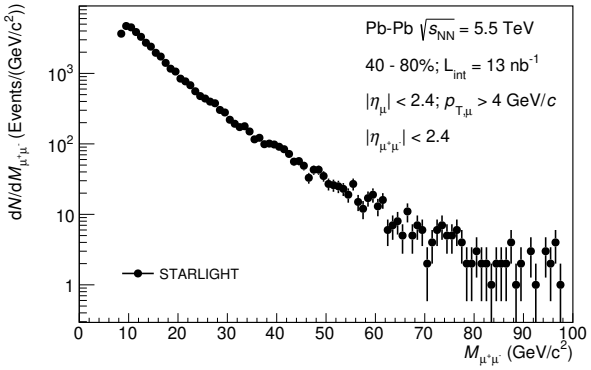

Fig. 60: Expected dimuon yield in ATLAS acceptance (both muons with $p_{\mathrm{T}} > 4$ GeV/c and $|\eta| < 2.4$), for 40–80% centrality Pb–Pb collisions and the expected Run 3/4 integrated luminosity of 13 nb^{-1}. Masses up to 100 GeV/c^2 are accessible. The effective 8 GeV/c^2 minimum mass is because of the nearly back-to-back topology and the 4 GeV/c minimum muon p_{T} cut. This was calculated using STARlight [594, 598].

8.2.2 Photonuclear interactions

In photonuclear interactions, a photon emitted by one nucleus fluctuates to a quark-antiquark dipole, which then scatters elastically from the other (target) nucleus, emerging as a real vector meson. The scattering occurs via Pomeron exchange, which preserves the photon quantum numbers. In perturbative QCD, Pomerons are made up of gluons, so the process is sensitive to the gluon distribution in the target nucleus. UPC measurements are consistent with moderate gluon shadowing. In coherent scattering, the typical pair p_{T} is $\hbar/R_{\mathrm{A}}$. Incoherent scattering is also possible, with a lower cross-section. There the quark-antiquark dipole scatters elastically from a single nucleon (or, at still higher p_{T} inelastically from a single nucleon), producing a vector meson with a typical p_{T} of a few hundred MeV/c.

Both ALICE [583] and STAR [585] have observed coherent J/ψ photoproduction in peripheral heavy-ion collisions. There are a number of parallel theoretical calculations [592, 601]. The photon emission process is similar to the two-photon case, but the dipole-nucleons scattering happens at the same time as the hadronic interaction, introducing several complications to the calculations. This immediately raises several questions: What happens to the coherence if a target nucleon is involved in an interaction? Does the dipole-nucleon interaction occur before or after the nuclear collisions? If the hadronic interaction occurs first, the target nucleon will have lost energy, so the photon-nucleon cross-section will be smaller. A detailed calculation should consider both possibilities. There is also destructive interference between photoproduction from the two possible target nuclei [602]; this interference extends to higher p_{T} for more central collisions, and should reduce the cross-section for the region where nuclear collisions occur. At $b = 0$, we expect complete destructive interference. Ref. [592] makes predictions for a variety of coherence conditions, and as Fig. 61 shows, finds that the ALICE and STAR data likely lie below the region where there is complete coherence for both photon emission and scattering, but probably above that where coherence is limited to only the spectator nucleons. This is not surprising, but there is at least one element missing from this calculation. The lifetime of J/ψ particles is of the order 10^{-20} s, far shorter than that of the expanding Quark–Gluon Plasma. Coherently photoproduced J/ψ have $p_{\mathrm{T}} \sim 100$ MeV/c, so, near mid-rapidity, are moving at a small fraction of the speed of light. Particularly for more central collisions, one would expect many of them to be engulfed by the expanded QGP, before they have a chance to decay.

The ALICE error bars are large, and more data, from the current and future runs are needed to pin down the centrality dependence of the cross section. More data will also allow access to additional observables. A detailed study of the shape of $\mathrm{d}\sigma/\mathrm{d}p_{\mathrm{T}}$ would shed more light on the possible loss of

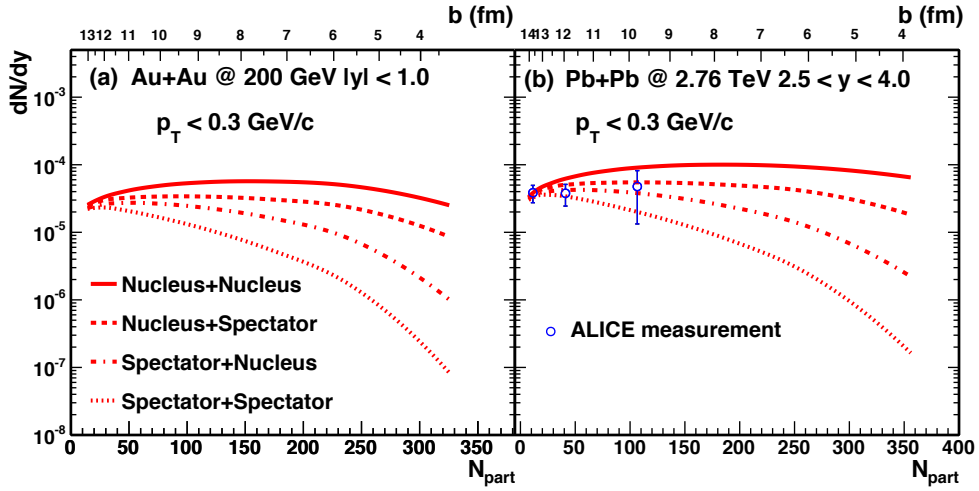

Fig. 61: J/ψ coherent photoproduction cross-sections in peripheral collisions, as a function of the number of participants (bottom), and impact parameter (top) with Au–Au collisions at RHIC (left) and Pb–Pb at the LHC (right). The four curves are for different assumptions regarding centrality for the photon emitter (first particle listed) and the target (second particle listed). From Ref. [583, 592].

coherence in more central collisions. There are also expected correlations between the reaction plane, which can be determined from the hadronic part of the collision, with the photonuclear interaction. Because the destructive interference between photoproduction at mid-rapidity on the two nuclei goes as $\sigma \sim |1 - \exp{(i\vec{b} \cdot \vec{p_{\rm T}})}|^2$ [603], the azimuthal direction of $\vec{p_{\rm T}}$ provides information about the azimuthal direction of $\vec{b}$, i.e., the reaction plane. Thus, it can be used either as an independent measurement of the reaction plane, or as a test of the loss of correlation. Also, the J/ψ polarization follows that of the photon that produced it, so it also follows $\vec{b}$, providing another probe of the reaction plane. With a large data sample, one may also be able to probe incoherent J/ψ photoproduction, at least in very peripheral hadronic collisions, where the signal-to-noise ratio is high.

It will be very interesting to study ψ' and Υ photoproduction in peripheral collisions. Since these mesons have different sizes from the J/ψ, they should interact with the medium with different strengths. These studies should be possible at HL-LHC.

8.3 Dark photons

Dark Matter is a hypothetical form of matter that is responsible for accounting for approximately 80% of the matter in the Universe [604]. Dark matter cannot be incorporated into the Standard Model, so the introduction of dark matter requires new interactions between dark matter particles and the ordinary Standard Model particles via unknown dark-sector forces [605]. The dark sector could have a rich structure with a few possible candidates, where one of them is regarded as Dark Photon (A') with $L_{mix} \propto \frac{g}{2} F^{\mu\nu} X_{\mu\nu}$. The dark photon is introduced as an extra-$U(1)$ gauge boson and acts as a messenger particle of a dark sector with the residual interaction (g) to the Standard Model particles. Understanding of possible interactions of dark photons has been motivated by a number of astrophysical anomalies such as antiproton spectrum in the cosmic rays measured by AMS Collaboration, positron excess in the cosmic rays observed earlier by PAMELA [606] and confirmed by FERMI [607] and AMS [608], and the long standing discrepancy between the measured and the calculated anomalous magnetic moment of the muon $(g-2)_\mu$, where the difference is more than three standard deviations away from zero [609].

If the dark photon is the lightest state of the dark sector and therefore can decay only into the

Standard Model particles, dark photons with mass $m_{A'} \leq 2m_{\mu}$ decay only into electron-positron pairs. For dark photons above 2 muon threshold ($m_{A'} \geq 2m_{\mu}$), dark photons can decay into muon pairs. For ($m_{A'} \geq 2m_{\pi}$), dark photons can decay into hadrons as well. A lot of experimental activities have been seen recently and constraints of mixing parameter (g^2) as a function of dark photon mass ($m_{A'}$) has been done from many experiments. They are, for example, beam-dump experiments (measurement of lepton pairs from dark photons behind a sufficiently long shield. Examples are E141 [610] and E137 [611] at SLAC, E774 [612] at Fermilab), fixed-target experiments (by scattering the electron beam on a nuclear target, the dark photon may be emitted in the initial or final state and coupling to electron-positron pairs is studied by looking for a bump in the electron-positron invariant mass. Examples are A1 [613] at MAMI in Mainz, APEX [614] at JLAB, DarkLight [615] at JLAB) and collider experiments (BABAR [616], NA48/2 [617] at SPS, WASA [618] at COSY, HADES [619] at GSI, PHENIX [620] at RHIC, LHCb [621] and ALICE at LHC). Since any process in which a virtual photon couples to lepton pairs or hadrons can be used to search for dark photons, following processes are used in the collider experiments: measurements of Dalitz decays of the $\pi^0/\eta/\eta' \rightarrow \gamma A'$ mesons and rare meson decays such as $K \rightarrow \pi A'$, $\phi \rightarrow \eta A'$, and $D^* \rightarrow D^0 A'$, Bremsstrahlung process ($e^- Z \rightarrow e^- Z A'$ with A' emitted at very forward direction), radiative decay of vector resonances and initial state radiation (done by BABAR using radiative decays of $\Upsilon(3S)$ and done by KLOE [622] using $\phi \rightarrow e^+e^-$). The 79-string IceCube search for dark matter in the Sun public data is used to test Secluded Dark Matter models [623]. Dark matter particles can be captured by the Sun, annihilate, and produce a neutrino flux that can be observed at Earth and that depends on the dark matter scattering cross section off nuclei and on the dark matter annihilation rate and final states. This analysis constrains a kinetic mixing parameter $g \sim 10^{-9}$ between 0.22 and ~ 1 GeV [623].

ALICE has good capabilities for electron identification in the low transverse momentum region, that enables the measurement of a large sample of the π^0 Dalitz decays [556]. ALICE searches for possible decays of $\pi^0 \rightarrow \gamma A'$, $A' \rightarrow e^+e^-$ by examining the electron-positron invariant mass in a large sample of π^0 Dalitz decay for $20 \leq M_{ee} \leq 90$ MeV/c^2 in pp collisions at 7 TeV ($L_{\rm int} \sim 4$ nb^{-1}) and p–Pb collisions at 5.0 TeV ($L_{\rm int} \sim 40$ μb^{-1}) as shown in Fig. 62.
LHCb has good capabilities to measure muons and hardware and software triggers enable the accumulation of a large sample of dimuon pairs. LHCb searches for prompt-like and long-lived dark photons produced in pp collisions at 13 TeV, using $A' \rightarrow \mu^+\mu^-$ decays from a large data sample corresponding to $L_{\rm int} \sim 1.6$ fb^{-1} collected during 2016, where the prompt-like A' search is shown in Fig. 62 [621].

The ALICE upgrade during LS2 will greatly improve the efficiency of electron-positron measurements and data taking capability. Figure 63 shows expected constraints that will be achieved by ALICE and LHCb together with the future experiments. After the major ALICE upgrade, ALICE will accumulate 6 pb^{-1}, 0.3 pb^{-1}, 10 nb^{-1}, 0.3 pb^{-1}, and 3 nb^{-1} of pp, p–Pb, and Pb–Pb collisions at 0.5 T, and p–Pb and Pb–Pb collisions at 0.2 T, respectively. LHCb will improve sensitivity of dark photon searches to large regions of the unexplored space. These new constraints leverage the improved invariant-mass and vertex resolution, as well as the unique capabilities of the particle-identification and real-time data-analysis with triggerless readout, that enables to accumulate $L_{\rm int} \sim 15$ fb^{-1} [625].

8.4 Limitations and outlook

While the statistical precision for the measurement of low mass dielectrons and dimuons as well as real photons will be sufficient in LHC Run 3 and 4 to study their yield as a function transverse momentum and with respect to the event plane (elliptic flow), more differential measurements might still be limited. The measurement of the photon polarization via the angular distribution of dileptons can not only provide information on the thermalization of the system, but also on the early stages of the collision [626]. Experimentally these distributions have been measured in the NA60 experiment [627], where no polarization was found concluding that the observed excess dimuons are in agreement with the thermal

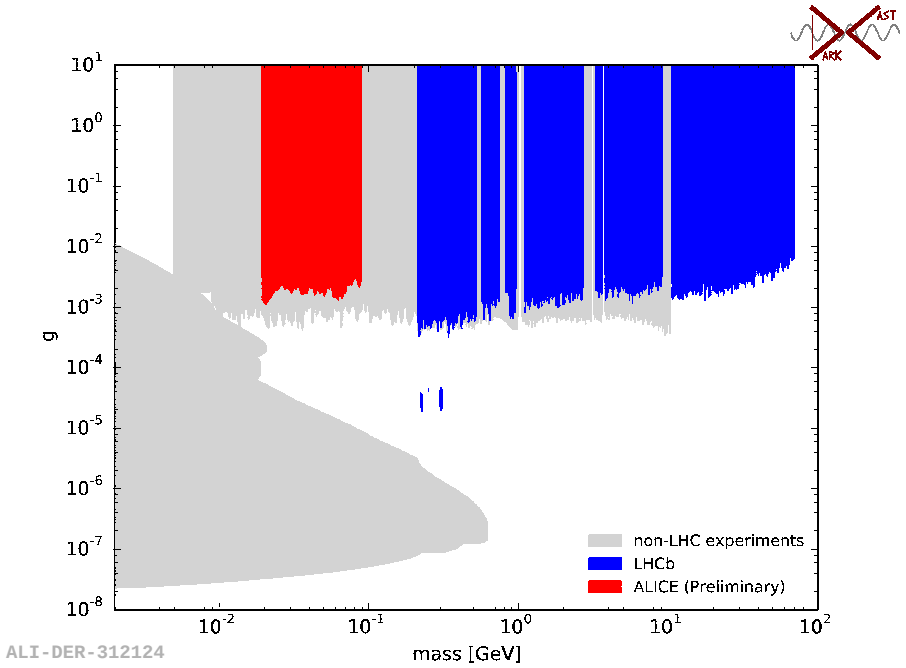

Fig. 62: 90% of confidence level of mixing parameter as a function of dark photon mass. Figure is adapted from Ref. [624]. Red and blue are from ALICE and LHCb [621]. Light grey band contains results from BABAR, KLOE, A1, APEX, NA48/2, E774, E141, E137, KEK, Orsay, BESIII, CHARM, HPS, NA64, NOMAD, NuCAL, and PS191 [624].

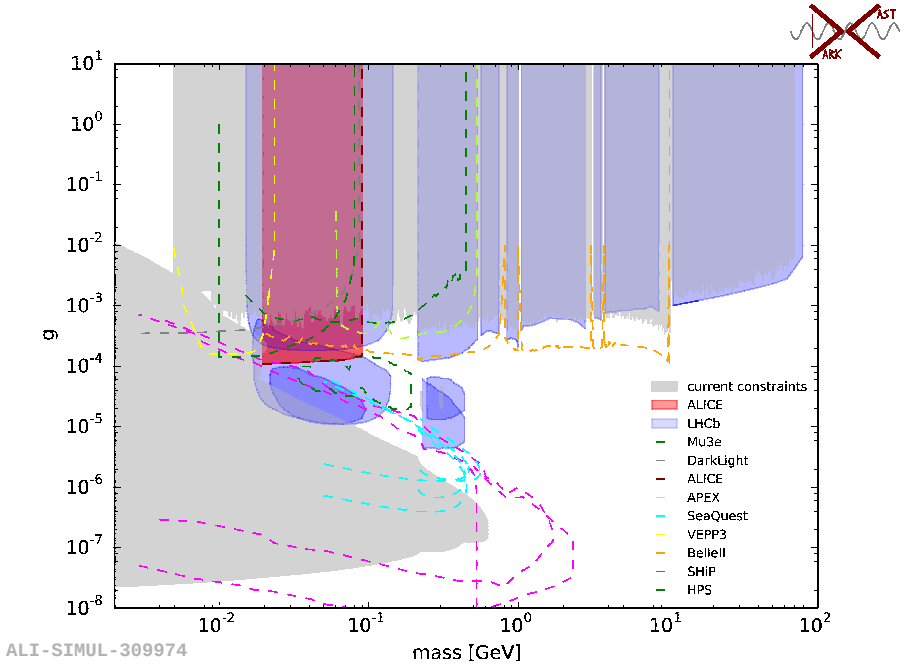

Fig. 63: 90% of CL constrained by ALICE and LHCb in HL-LHC era. Constraints by ALICE are based on 6 pb^{-1}, 0.3 pb^{-1}, 10 nb^{-1}, 0.3 pb^{-1}, and 3 nb^{-1} of pp, p–Pb, and Pb–Pb collisions at 0.5 T, and p–Pb and Pb–Pb collisions at 0.2 T and by LHCb are based on 15 fb^{-1}. ALICE projection from Ref. [1]. The other projections are adopted from Ref. [624].

emission from a a randomized system. In order to study the angular distributions, for example in the Collins-Soper reference frame [628–630] in the polar angle θ and the azimuthal angle φ, a large data set is needed (NA60 used ~ 50000 excess $\mu^+\mu^-$ pairs).

Another promising direction is measurement of Bose-Einstein (BE) correlations of direct photons. With this probe one can trace space-time dimensions of the hottest part of the fireball and moreover, varying k_{T} of the photon pair, one can select pairs coming mostly from earlier or later stages of the collision and thus look at evolution of the fireball. On the other hand, from the correlation strength parameter one can extract the direct photon spectrum down to very low $p_{\mathrm{T}} \sim 100$ MeV/c. So far there was one successful measurement of direct photon BE correlations by the WA98 Collaboration [631], while at RHIC and LHC energies these measurements are still unavailable. The reason is that the expected strength of these correlations $\lambda_{PGg} = 1/2(N_\gamma^{\mathrm{dir}}/N_\gamma^{\mathrm{tot}})^2$ is extremely small. Moreover, in contrast to massive particles, averaging of full 3D correlation function $C_2(q_{\mathrm{out}}, q_{\mathrm{side}}, q_{\mathrm{long}})$ to 1D $C_2(q_{\mathrm{inv}})$ results in further dramatic decrease of correlation strength [631]. This requires very large statistics in addition to understanding the detector response.

A first step to increase the statistical precision and the available data set for low-mass dileptons could be a further upgrade of the inner barrel of silicon detectors of the ALICE apparatus that is currently under discussion [302]. The planned reduction of the material budget would reduce conversion probability. In addition, an improvement of the tracking efficiency especially at low momentum would increase the conversion rejection efficiency even further. First studies [302] showed that the statistical uncertainty can be reduced by a factor 1.3, while the systematic uncertainty from the subtraction of the combinatorial background would be reduced by a factor of two. With a better pointing resolution the rejection of charm background is improved and would lead to a reduced systematic uncertainty from the subtraction of the light-hadron and charm decay backgrounds by a factor of two.

Finally, the detection of thermal radiation using low invariant mass and transverse momentum dielectron pairs is one of the main physics goals driving the concept for a possible new heavy-ion experiment at the LHC [306]. This experiment, which could be a follow-up of the ALICE experiment in the 2030s, would be mainly based on ultra-thin and granular silicon pixel detectors.

9 Emergence of hot and dense QCD matter in small systems

Coordinators: Jan Fiete Grosse-Oetringhaus (CERN) and Constantin Loizides (Oak Ridge National Laboratory)

Contributors: R. Bi (Massachusetts Institute of Technology), C. Bierlich (Lund University and Niels Bohr Institute), E. Bruna (University and INFN Torino), Z. Chen (Rice University), C. Cheshkov (IPN Lyon), Z. Citron (Ben-Gurion University of the Negev), A.F. Dobrin (CERN), M. Dumancic (Weizmann Institute of Science), M. Guilbaud (CERN), P.M. Jacobs (Lawrence Berkeley National Laboratory), J. Jia (Stony Brook University and Brookhaven National Lab), A.P. Kalweit (CERN), F. Krizek (Academy of Sciences, Prague), A. Kurkela (CERN and Stavanger University), Y.-L. Lee (Massachusetts Institute of Technology), N. Mohammadi (CERN), D.V. Perepelitsa (University of Colorado Boulder), R. Rapp (Texas A&M University, College Station), B. Schenke (Brookhaven National Lab), K. Tatar (Massachusetts Institute of Technology), M. Weber (Austrian Academy of Sciences), H. Zanoli (Universidade de Sao Paulo), M. Zhou (Stony Brook University)

9.1 Introduction

In the program of proton–proton collisions at the LHC, the main effort is focused on hard processes which are embedded in an underlying event consisting of soft low-p_{T} particles. The underlying event is described using models, such as Pythia [516] or HERWIG [632], based on essentially free streaming (i.e. no final-state interactions) of the produced particles, supplemented by a non-perturbative cluster or string fragmentation picture [633, 634] to model the non-perturbative soft-particle production. The same models are used to describe minimum-bias events, i.e. events without any signal trigger, primarily consisting of soft QCD interactions. In the past years at LHC, during Run 1 and 2, this picture was challenged by several observations that qualitatively differ from the model expectations and cannot be accommodated by tuning of the existing models used to describe minimum-bias collisions and the underlying event [635].

The first such observation was the unexpected discovery in 2010 of azimuthal correlations of final-state hadrons in very high multiplicity proton–proton collisions [315], referred to by *the ridge*. These persist at large separation in rapidity on the near side surrounding the jet-like peak. A few years later, a similar observation was made in high multiplicity p–Pb collisions [316]. By subtracting the jet-like contribution in p–Pb collisions, a second long-range rapidity correlation on the away side, back-to-back in azimuth to the first observed correlation, was extracted [317, 318]. Even later, the procedure was adapted to pp collisions, allowing one to identify two long-range contributions also in high-multiplicity pp collisions [636,637]. Under certain assumptions even lower-multiplicity pp collisions show the same features [636]. With these observations the similarity of small and large collision systems with respect to azimuthal correlations had been clearly demonstrated.

The second observation was that of enhanced production of multi-strange hadrons in high-multiplicity pp collisions extending the puzzle from final-state particle kinematics to include also hadrochemistry. Already after Run 1, several experiments reported that ratios of strange to non-strange particle yields, in minimum-bias collisions, could not be described using model fits obtained from LEP data [638–641]. After systematic studies of this discrepancy, it was found that not only does strangeness increase smoothly with particle density at mid-rapidity in pp collisions, the dependence on this observable continues smoothly to p–Pb and Pb–Pb collisions [642].

Initially, these collision systems were thought as a reference for the effects observed in Pb–Pb collisions. But the discovery of these qualitatively new features has turned the study of small systems into a field on its own, with significant interest in both the heavy-ion and the high-energy physics community.

In ultra-relativistic nucleus–nucleus collisions, ranging from early SPS experiments at CERN through the Relativistic Heavy-Ion Collider (RHIC) at Brookhaven National Laboratory (BNL) to LHC, similar observations have been interpreted as evidence of formation of a droplet of thermalised Quark–

Gluon Plasma. The long-range azimuthal correlations, and in particular their lowest harmonic component v_2, have been used in combination with relativistic fluid-dynamical modeling to constrain the material properties of the plasma. The striking result from RHIC was that the plasma formed in central nucleus–nucleus collisions flows as a liquid nearly without dissipation such that its specific shear viscosity η/s – quantifying the dissipative properties of the medium – was found to be smaller than that of any other known substance. The inferred value of the specific shear viscosity $\eta/s \sim 0.07 - 0.16$ was found to be significantly smaller than the expectation from perturbative QCD and other quasiparticle models, and closer to the expectation of holographic model calculations of strongly coupled (maximally supersymmetric $N = 4$) gauge theories in the limit of large number of colors $N_c \to \infty$. These models can be seen as models of fluids with minimal dissipation allowed by basic principles of quantum mechanics thus giving rise to the paradigm of Quark–Gluon Plasma as a perfect liquid. Perfect liquid models do, by definition, not have any quasi-particle structure. This means that they do not have any degrees of freedom which can free stream for an appreciable amount of time, compared to their de Broglie wavelength. In that context it is notable that the observation of fluid–like signatures in small systems can be described as a small modification of the free streaming evolution, challenging the perfect-fluid paradigm.

There are several theoretical pictures that have been suggested to explain the smooth onset of signals of collectivity in small systems. The pp event generators have been supplemented on the one hand with elements describing string or cluster fragmentation in a dense medium [643, 644] to address the hadrochemistry, and on the other hand with final-state interactions between the fragmenting strings to account for the final-state kinematical correlations [645]. The models underlying pp event generators can then in turn be extrapolated to cover p–Pb and Pb–Pb collision systems, which is an approach used since the 1980's [579, 646]. Recent theoretical developments [647, 648] have improved the state of such extrapolations to a degree where also the supplemented hadronisation models can be extrapolated in order to provide a microscopic picture of the QGP even in large systems. The question whether such extrapolations will give even a qualitative description of the observed features is still open.

At the same time, the description of large systems has been employed in regimes initially thought to be not accessible by models implementing the perfect-fluid paradigm. Their application down to proton–proton collisions [211, 649, 650], taken at face value, would imply the formation of a nearly perfect liquid even in the smallest collision systems. Furthermore, pQCD based saturation models can describe the emergence of charged-particle azimuthal anisotropy ($v_{\rm n}$) [651]. In these models the final-state azimuthal correlations can arise either from the intrinsic correlations in the nuclear wave function (initial-state correlations) as correlated anisotropic particle production or as a final-state interaction after the initial particle production. In heavy-ion collisions, statistical models [652] have been very successful in describing the hadrochemistry of particle yields. Their extension to pp collisions shows promise, but similarly with points of tension [653]. Regardless of whether the approach is to extrapolate from pp to Pb–Pb collisions or the other way around, it is crucial to establish that any such model can capture the essential features of intermediate systems. Asymmetric collision systems such as p–Pb, provide challenges and opportunities for both approaches. They may be used as a necessary intermediate stepping stone for pp to A–A extrapolations, and they provide possible discrimination between saturation and fluid approaches as a possible point of tension [654, 655].

A question remains to what extent these different models are describing qualitatively different physical phenomena or to what extent they are different representations of the same underlying physics of final-state interactions. For this reason it is important to develop theoretical tools that encompass both the fluid-dynamic limit and the free-streaming limit to theoretically describe how the microscopic physics that leads to fluid-dynamic behavior in A–A collisions should represent itself in small systems. An attempt to do so comes from transport theory, which can describe microscopic interactions but in the limit of large number of final-state interactions allows for a coarse-grained effective description in terms of fluid dynamics. As such, transport theory has the potential to bridge the gap between small

systems, where final-state interactions act as small modification to the free-streaming evolution, and central nucleus–nucleus collisions where the final-state interactions bring the matter to the fluid-dynamical limit [216].

The experimental program in the large intermediate region — spanning from mid-central Pb–Pb and Xe–Xe collisions, through p–Pb collisions down to minimum-bias pp collisions — offers a possibility to bridge the difference between the two limits by providing a setup where the microscopic final-state interactions that lead in central Pb–Pb collision to the formation of a QGP may be studied in isolation in the limit of small number of final-state interactions.

The suggested theoretical pictures may have implications for high-energy physics analyses, which depend on reliable models of the underlying event. As an example, it has been recently shown that the discussed long-range correlations are also present in the underlying event of Z-tagged pp collisions [656]. The direct implication is the necessity for questioning the correct description of the underlying event of MC models. As the usual models used to describe the underlying event do not describe such long-range correlations, even qualitatively, the uncertainty introduced by imposing a model dependence, might be larger than expected, as *e.g.* shown for colour reconnection effects on $t\bar{t}$ final states [657]. As such, better descriptions of collective effects in small systems could also probe vital for reducing uncertainties in high-energy physics analyses.

The main experimental task in future years is a detailed examination and characterization of the observed effects in pp, p–Pb and Pb–Pb collisions, in order to understand whether such effects are different or similar in origin in small and large systems. For such a task to be successful, all three types of collision systems, pp, p–Pb and Pb–Pb must be utilized, as they each offer unique features not obtainable from the other systems. The central Pb–Pb collision system is so far the only one where all features of collectivity (including multi–particle correlations, jet quenching, quarkonia supression, thermal photons and hadrochemistry) have been observed. For the study of small collision systems, central Pb–Pb offers the only viable *true collective* reference. Conversely, pp is so far the smallest collision system where collective effects have been observed, and the only system where a smooth transition to the e^+e^- expectation could be reasonably expected. In the intermediate region p–Pb collisions are the only one of the three collision systems which offer, both, a saturation dominated initial state with a well known geometry, and, in a single event the Pb-going and p-going direction allowing the study between both regimes. The potential study of O–O collisions provides an interesting system with smaller fluctuations in the number of participating nucleons. Furthermore, the detailed study of asymmetric collision systems provides valuable input both to models extrapolating pp dynamics to Pb–Pb collisions, and for providing quantitative distinction between initial-state saturation effects and final-state interactions.

This chapter is structured as follows: Section 9.2 gives an overview presenting the observations that have been made and comparing them between pp, p–Pb and Pb–Pb collisions. Subsequently, Sect. 9.3 summarizes the open questions and discusses how these can be addressed at HL-LHC. Sect. 9.4 details the multiplicity distribution which needs to be extrapolated to be used for performance studies, the expected energy densities and the data-taking conditions assumed. A set of performance studies which address the open questions are introduced in Sect. 9.5–9.9 ranging from correlation measures, over hadrochemistry to signatures of energy loss and thermal radiation. Finally, Sect. 9.10 presents the opportunities of a short run of O–O collisions.

9.2 Overview of experimental results and critical assessment

This section will give an overview where the measurements in Pb–Pb, p–Pb and pp collisions at LHC provide a consistent picture and where differences emerge. In addition, it is pointed out where measurements are missing and where additional data is needed which forms the basis for the projections given in the subsequent sections of this chapter. Table 8 lists the different observables and if they have been

Table 8: Summary of bulk observables or effects in Pb–Pb collisions, as well as in high multiplicity p–Pb and pp collisions at the LHC. References to key measurements for the various observables and systems are given. See text for details. Table adapted from Ref. [669].

Observable or effect	Pb–Pb	p–Pb (high mult.)	pp (high mult.)	Refs.
Low p_{T} spectra ("radial flow")	yes	yes	yes	[47, 71, 321, 322, 658, 660, 666, 667, 670, 671]
Intermediate p_{T} ("recombination")	yes	yes	yes	[321, 660–666]
Particle ratios Statistical model	GC level $\gamma_s^{\mathrm{GC}} = 1$, 10–30%	GC level except Ω $\gamma_s^{\mathrm{GC}} \approx 1$, 20–40%	GC level except Ω MB: $\gamma_s^{\mathrm{C}} < 1$, 20–40%	[322, 642, 667, 668] [322, 642, 672]
HBT radii ($R(k_{\mathrm{T}})$, $R(\sqrt[3]{N_{\mathrm{ch}}})$)	$R_{\mathrm{out}}/R_{\mathrm{side}} \approx 1$	$R_{\mathrm{out}}/R_{\mathrm{side}} \lesssim 1$	$R_{\mathrm{out}}/R_{\mathrm{side}} \lesssim 1$	[673–680]
Azimuthal anisotropy (v_{n}) (from two particle correlations)	v_1–v_7	v_1–v_5	v_2–v_4	[48, 316–318, 636, 637, 656, 681–691]
Characteristic mass dependence	v_2–v_5	v_2, v_3	v_2	[48, 319, 330, 686, 689, 692–694]
Directed flow (from spectators)	yes	no	no	[695]
Charge-dependent correlations	yes	yes	yes	[249, 253, 254, 696–699]
Higher-order cumulants (mainly $v_2\{n\}$, $n \geq 4$)	"$4 \approx 6 \approx 8 \approx$ LYZ" +higher harmonics	"$4 \approx 6 \approx 8 \approx$ LYZ" +higher harmonics	"$4 \approx 6$"	[218, 320, 686, 691, 700–710]
Symmetric cumulants	up to $\mathrm{SC}(5,3)$	only $\mathrm{SC}(4,2), \mathrm{SC}(3,2)$	only $\mathrm{SC}(4,2), \mathrm{SC}(3,2)$	[227, 690, 711–714]
Non-linear flow modes	up to v_6	not measured	not measured	[715]
Weak η dependence	yes	yes	not measured	[218, 231, 688, 716–720]
Factorization breaking	yes ($n = 2, 3$)	yes ($n = 2, 3$)	not measured	[217, 219, 685, 687, 721]
Event-by-event v_{n} distributions	$n = 2$–4	not measured	not measured	[722–724]
Direct photons at low p_{T}	yes	not measured	not observed	[548, 725]
Jet quenching through dijet asymmetry	yes	not observed	not observed	[352, 364, 378, 726–728]
Jet quenching through R_{AA}	yes	not observed	not observed	[327, 348, 350, 351, 356, 729–736]
Jet quenching through correlations	yes (Z–jet, γ–jet, h–jet)	not observed (h–jet)	not measured	[358, 361, 379, 380, 384, 392, 732, 737–739]
Heavy flavor anisotropy	yes	yes	not measured	[262, 330, 464–468, 501, 740–744]
Quarkonia production	suppressed†	suppressed	not measured	[262, 458, 460, 463, 482, 483, 495, 496, 498, 499, 501, 583, 745–754]

† J/ψ $\uparrow$, $\Upsilon(\downarrow)$ w.r.t. RHIC energies.

measured in the Pb–Pb, p–Pb and pp collision systems. In the following a critical assessment of the findings is performed.

Particle spectra In all three systems, the p_{T} spectra of identified particles harden with increasing multiplicity. If this is interpreted by using a combined blast-wave parametrisation in Pb–Pb collisions[4] a larger radial flow is observed in pp and p–Pb collisions at the same multiplicity [653] as expected by Ref. [659]. In the intermediate p_{T} region ($2 < p_{\mathrm{T}} < 5$ GeV/c), enhancement of baryon-to-meson ratios is observed in all three systems. Recombination models suggest that the number of constituent quarks of the hadrons determine this enhancement [321, 660–666]. Particle ratios and yields are described as in the Grand Canonical ensemble by the statistical model with the strangeness undersaturation factor $\gamma_S \approx 1$ with an accuracy of approximately 10–30% for Pb–Pb collisions and at 20–40% level for p–Pb collisions (except for the Ω meson). The statistical model has been so far applied to minimum-bias pp collisions and when treated as a canonical ensemble, was found to describe the yields with $\gamma_S^C < 1$ and deviations of only about 20–40% from the expected yields [322, 642, 667, 668].

Pressure-driven expansion and anisotropies Assuming that the pressure gradients build up early in the evolution of the created system, initial spatial anisotropies (ε_{n}) translate into final momentum anisotropies, namely anisotropic flow (v_{n}) in a system with small viscosity. A large number of detailed studies have been done on different coefficients of anisotropic flow. Higher-order flow harmonics are in particular more sensitive to initial-state fluctuations and therefore can constrain the initial conditions of the system. Anisotropic flow has been measured with two-particle correlation techniques up to v_7 in Pb–Pb, v_5 in p–Pb, and v_4 in pp collisions for charged particles. These v_{n} coefficients exhibit weaker multiplicity dependence in pp and p–Pb collisions than in Pb–Pb collisions where this is closely related to the shape of the overlap region [48, 316–318, 636, 637, 681–691].

Higher-order cumulants have been measured using Lee-Yang Zeros (LYZ) method and multi-particle correlation techniques with up to 8 particles in both Pb–Pb and p–Pb collisions and up to 6 particles in pp collisions [218, 320, 686, 691, 700–710]. Interestingly, for each collision system, the measurements of the cumulants at different orders ($n \geq 4$) are similar within 10%. The presence of non-zero higher-order cumulants with similar magnitude can be interpreted as evidence for a hydrodynamically evolving system. However, some disfavor this interpretation since models that do not incorporate hydrodynamics have also been able to reproduce these results [755–757]. The p_{T}-differential v_{n} measurements for identified particles show the characteristic mass dependence of anisotropic flow up to v_5 in Pb–Pb, v_3 in p–Pb, and v_2 in pp collisions where heavier particles are depleted at low p_{T} [48, 319, 330, 686, 689, 692–694]. In Pb–Pb collisions this is ascribed to the interplay between radial flow and anisotropic flow harmonics at low p_{T} and recombination at higher p_{T}. This characteristic mass dependence has been described by hydrodynamic calculations to a good approximation in all three systems. In the intermediate p_{T} values in all three systems a meson-baryon grouping can be observed which points to a combination of hydrodynamics and quark coalescence (or recombination).

The non-linear hydrodynamic response of the system has been probed using symmetric cumulants which quantify the correlation between different anisotropic flow harmonics. Symmetric cumulants, that are also known as mixed harmonics, have been measured in all three systems up to SC(5,3) in Pb–Pb and SC(4,2) in p–Pb and pp collisions [227, 690, 711–714]. Different order harmonic correlations have different sensitivities to the transport properties of the system and the initial conditions. Based on the hydrodynamic calculations the data favour a small shear viscosity [758]. In addition, the linear and non-linear hydrodynamic response has been investigated in Pb–Pb collisions up to the sixth order flow harmonic [715]. These new observables, i.e. linear and non-linear flow modes, are very sensitive to details of the hydrodynamic modelling, i.e. initial conditions and the transport properties of the

[4] A combined blast-wave parametrisation model is a blast-wave model that fits charged pions, kaons and (anti-)protons simultaneously. In [658], combined blast-wave parametrisation perfectly describes $\pi^{\pm}$ ($0.5 < p_{\mathrm{T}} < 1$ GeV/c), $K^{\pm}$ ($0.2 < p_{\mathrm{T}} < 1.5$ GeV/c) and $\mathrm{p} + \overline{\mathrm{p}}$ ($0.3 < p_{\mathrm{T}} < 3$ GeV/c).

system. Current data–model comparison show this sensitivity which help to constrain the transport properties of the QGP created in Pb–Pb collisions [715]. Linear ($v_{\rm n}^{\rm L}$) and non-linear ($v_{\rm n}^{\rm NL}$) flow modes in pp and p–Pb collisions are not yet measured and can constrain the transport properties as well as initial conditions of these small systems. Furthermore, hydrodynamic calculations capture qualitatively "higher-order" details, such as the breaking of factorization due to event-plane angle decorrelations in $p_{\rm T}$ and η measured in both Pb–Pb and p–Pb collisions [217, 687, 721]. With the existing data such measurements are not yet possible in pp collisions. Similarly, event-by-event $v_{\rm n}$ measurements have only been done in Pb–Pb collisions [722–724] and it would be interesting to study those in both p–Pb and pp collisions.

Directed flow, for the rapidity-odd as well as the rapidity-even components, of charged particles at mid-rapidity was measured relative to the collision symmetry plane defined by the spectator nucleons, and evidence for dipole-like initial-state density fluctuations in the overlap region was found in Pb–Pb collisions [695]. In small systems, the concept of directed flow is less clear, especially in pp collisions. If there is collectivity in pp collisions, one could also expect a non-zero directed flow measurement. This is technically challenging since the measurement of the spectator plane is not feasible in small systems and, hence, v_1 could only be measured using higher-order ($n \geq 4$) cumulants. The width of the balance functions, $\langle\Delta\eta\rangle$ and $\langle\Delta\varphi\rangle$, have been measured for charged particles in pp, p–Pb and Pb–Pb collisions [696, 698]. The balance function probes the charge creation time and the development of collectivity in the produced system. These measurements are consistent with the picture of a system exhibiting larger radial flow with increasing multiplicity but also whose charges are created at the later stages of the collision. The charge-dependent azimuthal correlations are measured in both Pb–Pb and p–Pb collisions [675–678, 680]. These correlations quantify the influence of the chiral magnetic effect (CME) and the chiral magnetic wave (CMW) on the produced particles. These correlators are also sensitive to strong background contributions, for example from local charge conservation and possibly radial and anisotropic flow.

The freeze-out radii in three orthogonal directions ("out", "side", "long") can be deduced from measurements of quantum-statistic correlations between pairs of same-charge pions and kaons (HBT) at low-momentum transfer. The HBT radii in all collision systems are found to scale with $\sqrt[3]{N_{\rm ch}}$ indicating a constant density at freeze-out, and to decrease with increasing pair momentum $k_{\rm T}$ as expected from hydrodynamics. The size along the emission direction is similar to the geometric size of the system ($R_{\rm out}/R_{\rm side} \approx 1$) in Pb–Pb collisions [673–675, 678, 679, 679] and $R_{\rm out}/R_{\rm side} \leq 1$ for both p–Pb and pp collisions [675–678, 680].

Direct photons Direct-photon measurements in the low $p_{\rm T}$ region are so far performed in Pb–Pb and pp collisions. The measurements are reproduced by models assuming the formation of a QGP in Pb–Pb collisions [548]. In this measurement, one cannot discriminate between the available models due to the large systematic uncertainties: models incorporating different initial temperatures, i.e. from 385 to 740 MeV in the most central Pb–Pb collisions, are able to reproduce the measurements. Nevertheless, the comparison among these models suggests that the initial temperature in central Pb–Pb collisions must exceed about 400 MeV [548]. No significant direct-photon signal has been extracted in pp collisions at current available center-of-mass energies [725].

Energy loss The created system in Pb–Pb collisions is opaque for high-$p_{\rm T}$ colored probes. Due to radiational and collisional energy loss high-$p_{\rm T}$ colored probes are strongly suppressed (jet quenching) whereas the system is transparent for photons and other colorless probes [327, 348, 350, 351, 356, 729–731, 734]. Jet quenching leads to a large asymmetry in back-to-back jet $p_{\rm T}$ and slightly modified jet fragmentation functions inside small jet cone sizes ($\mathrm{R} = 0.4$). Most of the radiated energy appears at large angles ($\mathrm{R} > 0.8$) [352, 364, 378, 726, 727].

On the contrary, the picture is different in p–Pb collisions: measurements of inclusive high-$p_{\rm T}$ hadron and inclusive jet yields in minimum-bias p–Pb collisions at the LHC are consistent with

$R_{\rm pPb} = 1$ within the current accuracy of approximately 20%; i.e. no evidence of medium-induced modification is observed [327, 732, 733, 735, 736]. For event classes split by event activity, neither medium-induced modification in inclusive hadron production nor dijet transverse momentum imbalance are observed [327, 728, 736]; in contrast, for inclusive jet yields $R_{\rm pPb}$ is strongly suppressed relative to unity in "central" p–Pb collisions, and strongly enhanced in "peripheral" p–Pb collisions [735], attributed to selection biases [737].

The semi-inclusive yield of jets recoiling from a high-$p_{\rm T}$ trigger hadron has been used to search for jet quenching in p–Pb collisions [737]. This observable is trigger-normalized and semi-inclusive, and it therefore has greater systematic sensitivity to jet quenching effects in small systems than inclusive jet observables. Nevertheless, no significant jet quenching effects within the uncertainties of the measurement have been observed. These uncertainties can be expressed as an upper limit of 400 MeV (at 90% CL) on medium-induced energy transport outside a jet cone with $R = 0.4$. This value is a factor 20 smaller than the magnitude of out-of-cone energy transport measured by a similar approach in Pb–Pb collisions [358].

Heavy flavour Due to interactions and rescattering with the medium, also heavy-flavour particles exhibit finite anisotropies as shown with non-zero v_2 measurements for heavy flavour particles in both Pb–Pb and p–Pb collisions [262, 330, 464–468, 501, 740–744], see also Chapter 5. In addition, J/ψ suppression in Pb–Pb collisions shows an enhancement w.r.t. RHIC energies [749]. Models incorporating a J/ψ regeneration component from deconfined charm quarks in the medium can reproduce these measurements [458, 749]. The limited understanding of cold nuclear matter effects in the open charm cross section determination, however, restricts the ability of these models to fully describe the experimental data on J/ψ production in Pb–Pb collisions [754]. The size of these effects can be quantified by measurements in p–Pb collision. In p–Pb collisions, J/ψ is suppressed relative to pp collisions [754]. The production of the excited charmonium state, $\Psi(2S)$ as well as different bottomonium states (Υ(nS)) have been measured in both Pb–Pb and p–Pb collisions [482, 496, 747, 749, 753] which shows a suppression w.r.t. the ground state.

9.3 Open questions and new opportunities at HL-LHC

The previous section has extensively reviewed the state-of-the-art experimental knowledge of pp and p–Pb collisions. Certain gaps in knowledge became apparent due to either insufficient available data or shortcomings in the present detectors. The HL era of LHC can make a significant step ahead in many areas. The most relevant ones are discussed with dedicated performance projections in the remainder of this chapter.

Run 3 and 4 will allow the study of unprecedentedly high-multiplicity pp collisions. In order to do estimates in this regime, Sect. 9.4 will establish a firm extrapolation of the multiplicity distribution based on current LHC data together with a review of the data sample to expect. The large multiplicities bring a qualitatively new feature: a wide overlap between pp and Pb–Pb collisions up to about 65% central collisions allowing a unique opportunity to compare observables in a small (pp) and large (Pb–Pb) system at the same multiplicity. Studies in p–Pb collisions amend the picture. Given that multiplicity is not the only driving variable of a system, comparisons of estimates of the energy density in pp, p–Pb and Pb–Pb collisions are made below. The uniqueness of these extreme multiplicity pp collisions warrants that the study of their global-event properties are an interesting subject in itself, see Sect. 9.5.

Subsequently, a set of key observables is presented which require either the large data samples or the upgraded detectors. In particular the measurement of thermal dileptons profits from the new ALICE pixel detector with reduced material budget, and the measurement of higher-order correlations from the extended tracker acceptance in Run 4 in ATLAS and CMS. Correlations at higher orders using the subevent method will provide an essentially non-flow free measurement of $v_{\rm n}$ coefficients and their inter-correlations measured through symmetric cumulants, see Sect. 9.6. These measurements focus on

two interesting regimes: at high multiplicity where the overlap with Pb–Pb collisions will be studied, and at low multiplicity to answer the question on the onset of collective phenomena. This section also shows that the measurement of the probability distribution of event-by-event v_2 becomes for the first time feasible in small systems, a quantity presently completely unknown in pp collisions.

The smooth increase of strange-particle production across system size is one of the key surprising findings from Run 2 pp physics. A projection of the reach at HL-LHC is given in Sect. 9.7 showing that the question if the thermal limit, given by statistical models in Pb–Pb collisions, is reached also in pp collisions can be answered. A puzzling finding is the absence of jet quenching in p–Pb collisions with the measurements performed in Run 1 and 2. If final-state interactions are to explain the observed collective phenomena, also energy loss of traversing partons should be measurable. Section 9.8 discusses how jet quenching can be observed in Run 3 and 4 if present, or alternatively how a stringent limit can be set. Performance studies are presented for hadron–jet, γ–jet and Z–jet correlations, both, in p–Pb and pp collisions. Finally, the potential to detect thermal radiation and extract a medium temperature in p–Pb collisions is presented in Sect. 9.9. Such a measurement would constitute a strong indication of the formation of an emitting medium. Finally, the potential of colliding smaller nuclei, in particular oxygen, is assessed in Sect. 9.10.

9.4 Proton–proton collisions at extreme multiplicities

9.4.1 Multiplicity distribution

For the performance estimates at high multiplicity in pp collisions, a multiplicity-distribution extrapolation has been used which is based on existing ALICE ($|\eta| < 1.5$) [759] and ATLAS ($|\eta| < 2.5$) [760,761] data. Data from CMS [762] is compatible with the used distributions and is therefore not explicitly included in the extrapolation. A parameterisation with a single[5] negative binomial distribution is used to characterize the multiplicity distribution [763, 764].

The data is shown in Fig. 64 overlaid with the fit with a single negative binomial distribution of the tail of the distribution (20–40% of the cross-section). The three parameters of this fit are itself fit with a power law to extrapolate to $\sqrt{s} = 14$ TeV.

The resulting extrapolated multiplicity distribution for 14 TeV is shown in Fig. 65 for the ALICE and ATLAS case. In addition, these are compared scaled by their respective average multiplicities. The agreement is rather good, with some discrepancy in the tail of the distribution. The extrapolation based on the smaller phase-space region falls off more quickly with multiplicity, and is therefore used as the conservative estimate for the extrapolations in this chapter.

9.4.2 Energy density

While the multiplicity is a convenient and well-defined observable to compare different collision systems, the underlying dynamics may be driven by other properties. In large collision systems, the energy density ϵ is often used to characterize the system and the expected effects. Figure 66 shows an estimate of the energy density for pp, p–Pb and Pb–Pb collisions based on IP-Glasma [765] as well as on the Bjorken estimate:

$$\epsilon = \frac{1}{A\tau}\langle E\rangle \frac{3}{2}\frac{dN_{ch}}{dy}. \tag{30}$$

For the latter, the input is the multiplicity-dependent $\langle p_{\mathrm{T}}\rangle$ [734,766] as well as the multiplicity-dependent transverse overlap from a Glauber MC [767]. The energy density is calculated at fixed $\tau = 0.2\,\mathrm{fm/c}$. It should be noted that these assumptions can be challenged and other ways to calculate ϵ are available which can lead to largely different value in particular in pp and p–Pb collisions. Here the aim is only to

[5] At LHC energies two NBDs are needed for a good fit to the full distribution, but one is sufficient for the tail of the distribution.

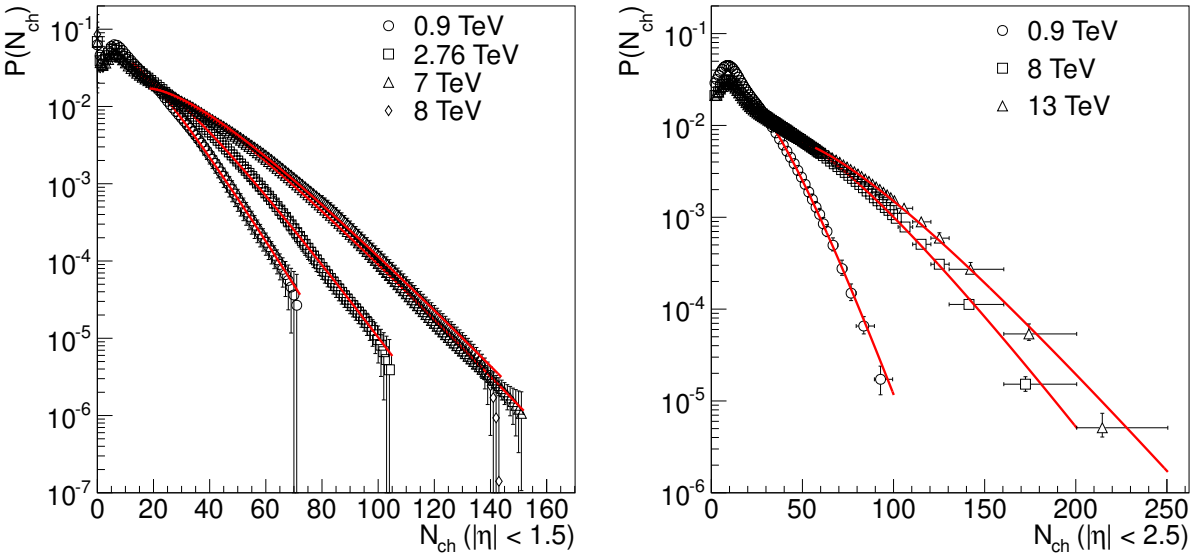

Fig. 64: Multiplicity distributions measured by ALICE [759] (left panel) and ATLAS [760, 761] (right panel) overlaid by the fit with a negative binomial distribution. For details see text.

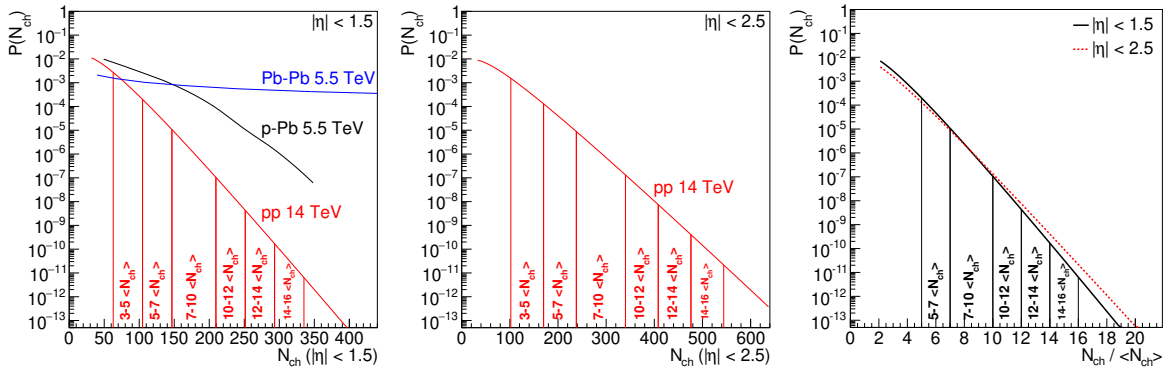

Fig. 65: Extrapolated multiplicity distributions in pp collisions within $|\eta| < 1.5$ (left panel) and $|\eta| < 2.5$ (centre panel). The indicated regions are (from left to right) 5–7, 7–10, 10–12, 12–14, 14–16 times the average multiplicity. In the left panel the multiplicity distribution of Pb–Pb and p–Pb collisions is also plotted. The right panel compares these two distributions scaled by the average multiplicity. The extrapolation for $|\eta| < 2.5$ turns out to be a bit wider at large multiplicities; therefore the one based on $|\eta| < 1.5$ is used as baseline.

show that the energy density depends on the system at a fixed multiplicity, and can reach large values in pp and p–Pb collisions, of the order of central Pb–Pb collisions.

9.4.3 Data-taking conditions and integrated luminosity for pp *collisions*

For the performance studies in this chapter, a high-multiplicity sample of $L_{\text{int}} = 200\,\text{pb}^{-1}$ is assumed per experiment. In order to assure a clean trigger, collisions at low $\mu \approx 1$ are needed which requires special runs or special conditions at the end of fill for ATLAS and CMS. For LHCb, the comparatively low pileup and good vertex resolution should allow for recording high-multiplicity events during normal running conditions at a pile up of about five visible pp interactions. ALICE generally runs at low μ and can collect a similar sample over a longer data-taking period. For Run 4, the upgraded tracking and vertex detectors in ATLAS and CMS may allow to isolate high-multiplicity collisions also in a large μ

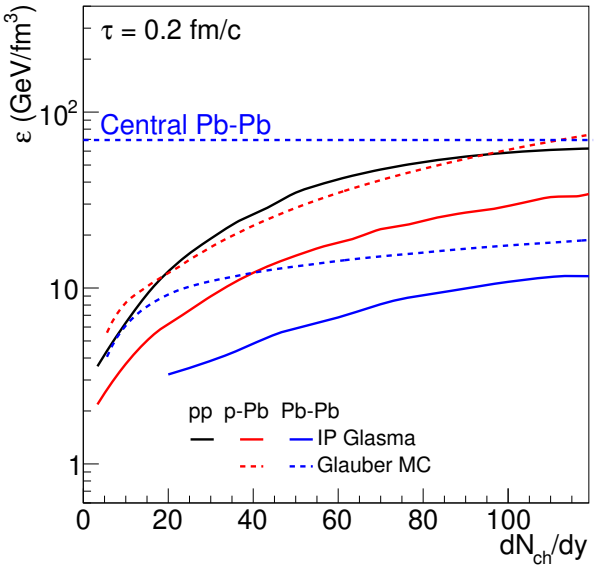

Fig. 66: Energy density as a function of $\mathrm{d}N_{\mathrm{ch}}/\mathrm{d}y$ calculated by IP-Glasma (solid lines) and with MC Glauber and the Bjorken formula (dashed lines); for details see text. Compared are pp ($\sqrt{s} = 7$ TeV), p–Pb ($\sqrt{s_{\mathrm{NN}}} = 5.02$ TeV) and Pb–Pb ($\sqrt{s_{\mathrm{NN}}} = 5.02$ TeV) collisions at $\tau = 0.2\,\mathrm{fm/c}$. The horizontal line indicates the energy density reached in central Pb–Pb collisions ($\mathrm{d}N_{\mathrm{ch}}/\mathrm{d}y \approx 2000$).

Table 9: Number of pp events at $\sqrt{s} = 14$ TeV in selected high-multiplicity bins.

Range	$\mathrm{d}N_{\mathrm{ch}}/\mathrm{d}\eta$	Fraction	Events per pb^{-1}	Events in 200 pb^{-1}
5–7 $\langle N_{\mathrm{ch}} \rangle$	35–49	2.4e-03	1.9e+08	3.7e+10
7–10 $\langle N_{\mathrm{ch}} \rangle$	49–70	1.3e-04	1.0e+07	2.0e+09
10–12 $\langle N_{\mathrm{ch}} \rangle$	70–84	1.1e-06	9.0e+04	1.8e+07
12–14 $\langle N_{\mathrm{ch}} \rangle$	84–98	4.7e-08	3.7e+03	7.3e+05
14–16 $\langle N_{\mathrm{ch}} \rangle$	98–112	1.8e-09	1.4e+02	2.8e+04

environment. This option needs to be carefully studied.

Table 9 gives the fraction of cross-section and the number of events in five multiplicity classes: 5–7, 7–10, 10–12, 12–14 and 14–16 times the average multiplicity. Table 10 gives the number of events of bins with equivalent multiplicity than commonly measured multiplicity bins in p–Pb and Pb–Pb collisions. For the calculation of the number of events $\sigma_{\mathrm{inel}} = 78.4\,\mathrm{mb}$ [767] is used. These tables are the key input for the performance figures presented in this chapter. The conversion of the provided $\mathrm{d}N_{\mathrm{ch}}/\mathrm{d}\eta$ to multiplicity ranges with larger pseudorapidity coverage is done for simplicity assuming a flat pseudorapidity distribution within $|\eta| < 2.5$. For the conversion to a phase space with a p_{T} cut as employed in many current measurements a set of conversation factors is used, listed in Tab. 11.

9.5 Global-event properties

The measurement of global-event observables in rare high-multiplicity pp collisions are of interest in itself. The shape of the multiplicity distribution, which has been largely extrapolated in the previous section, is today a challenge for models. The dynamics of producing very large multiplicity events is not understood in detail and therefore the shape of the distribution is an important input. Furthermore, studies of $\langle p_{\mathrm{T}} \rangle$ as a function of multiplicity [766] have shown a strong increase with multiplicity. However, those measurements exist only up to $\mathrm{d}N_{\mathrm{ch}}/\mathrm{d}\eta \approx 55$, while the measurements at HL-LHC promise

Table 10: Number of events in pp collisions at $\sqrt{s} = 14$ TeV sliced in equivalent multiplicity bins as in p–Pb and Pb–Pb collisions.

Range	$\mathrm{d}N_{\mathrm{ch}}/\mathrm{d}\eta$	Events per pb^{-1}	Events in 200 pb^{-1}
0–5% p–Pb	41–56	4.9e+07	9.8e+09
5–10% p–Pb	34–41	1.9e+08	3.8e+10
10–20% p–Pb	27–34	6.6e+08	1.3e+11
60–65% Pb–Pb	98–137	1.5e+02	3.0e+04
65–70% Pb–Pb	68–98	1.6e+05	3.1e+07
70–75% Pb–Pb	45–68	2.1e+07	4.2e+09
75–80% Pb–Pb	29–45	5.9e+08	1.2e+11

Table 11: Conversion factors between N_{ch} with a p_{T} threshold, and N_{ch} including particles down to $p_{\mathrm{T}} = 0$. The factor shown is $N_{\mathrm{ch}}/N_{\mathrm{ch}}(p_{\mathrm{T}} > X)$, extracted with Pythia 8, tune CUETP8M1 [768]. A potential multiplicity dependence of this factor is neglected for the projections in this chapter.

$\lvert\eta\rvert$ \ p_{T}	> 0.1 GeV/c	> 0.2 GeV/c	> 0.3 GeV/c	> 0.4 GeV/c	> 0.5 GeV/c
$\lvert\eta\rvert < 1.5$	1.03	1.11	1.22	1.31	1.40
$\lvert\eta\rvert < 2.4$	1.04	1.14	1.27	1.42	1.55

a measurement beyond twice that value.

The shape of the multiplicity distribution and the growth of $\langle p_{\mathrm{T}} \rangle$ are closely connected to the physics of multiple parton interactions: high-multiplicity collisions are understood as originating from the collision of multiple partons within the same pp collisions. It has been shown that the number of (low momentum transfer) parton interactions increases linearly with multiplicity with a possible saturation at large multiplicity [769]. The prospect of showing that adding another parton interaction to an already busy event may be strongly suppressed, is an important ingredient to a revised conceptual understanding of particle production in high-energy pp collisions. Together with the studies of symmetric cumulants (see the subsequent Section), HL-LHC will determine not only if there is a saturation limit for multiple parton interactions, but also the parton structure within the proton.

9.6 Particle correlations

The measurements of two-particle correlations and higher-order cumulants have been the initial observations of collective-like effects in small systems. In pp collisions, two distinct regions are of interest at HL-LHC: the high-multiplicity tail to compare to p–Pb and Pb–Pb collisions and the low-multiplicity region to investigate the onset of these effects. In the following, several performance estimates are given as examples for the rich physics which can be addressed.

State-of-the-art measured 4-particle cumulants of v_3 ($c_3\{4\}$) in pp and p–Pb collisions are presented in Fig. 67 overlaid with the projection for HL-LHC. In order to remove non-flow contributions, the 3-subevent method is applied. In pp collisions, with the data collected in Run 2, the statistical uncertainties are large and the $c_3\{4\}$ values are consistent with zero in most of the N_{ch} range. On the contrary, in large systems, significant non-zero $c_3\{4\}$ up to $-0.4 \cdot 10^{-6}$ depending on centrality has been measured [707], which reflects the nucleonic fluctuations in the initial state. Whether similar behaviour is observed in small systems still needs to be studied. The increase in luminosity in Run 3 and 4 provides a great opportunity to measure $c_3\{4\}$ in pp collisions with high precision: the statistics are sufficient to measure a signal as small as $v_3\{4\} = 1.5\%$ for $N_{\mathrm{ch}} \gtrapprox 170$, while 2% are accessible with large significance over a wide multiplicity range ($N_{\mathrm{ch}} \gtrapprox 100$). Similarly, in p–Pb collision, the current result shows

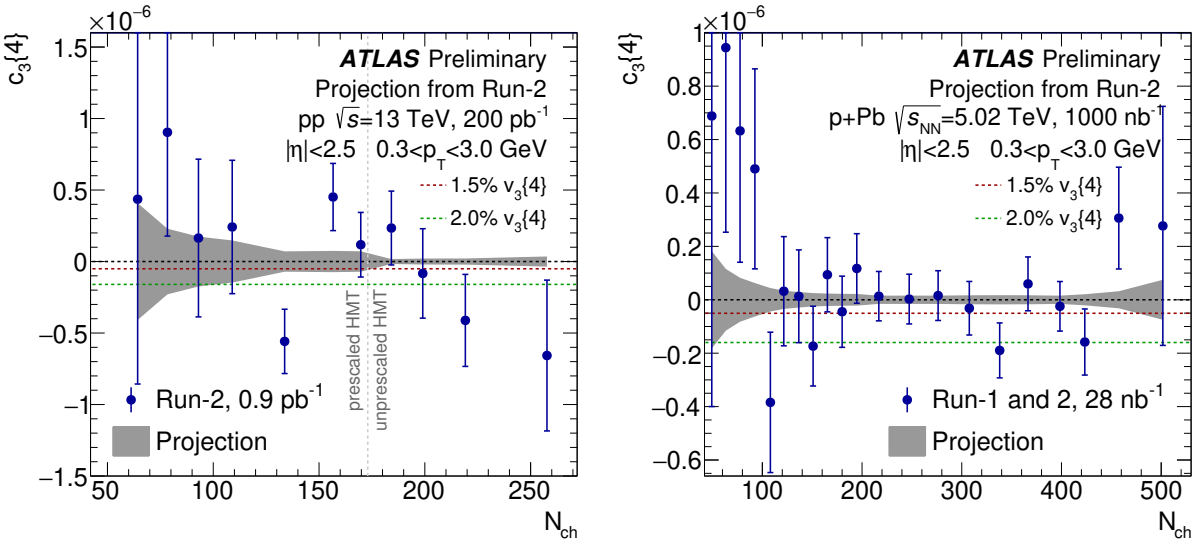

Fig. 67: 4-particle cumulants $c_3\{4\}$ measured with 3-subevent method for pp (left panel) and p–Pb collisions (right panel) as a function of $N_{\rm ch}$ ($|\eta| < 2.5$ and $0.3 < p_{\rm T} < 3$ GeV/c). Only statistical uncertainties are shown in the figure and the gray band represents the projected statistical uncertainty, with $c_3\{4\}$ assumed to be zero. The red and green dash lines represent 1.5% and 2.0% $v_3\{4\}$ signal, respectively. The vertical line in the left panel indicates the transition between minimum-bias and high-multiplicity triggered data. Figures from Ref. [6].

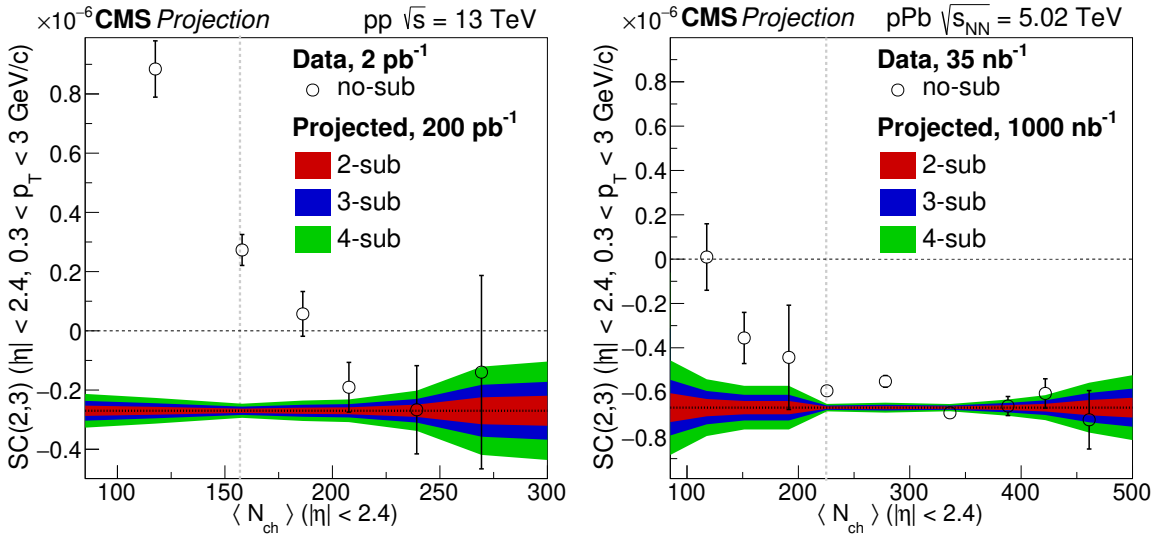

Fig. 68: Symmetric cumulants extracted with and without applying subevents for pp (left panel) and p–Pb collisions (right panel) as a function of $N_{\rm ch}$ ($|\eta| < 2.4$ and $0.3 < p_{\rm T} < 3$ GeV/c). The projected reach is shown for the case of 2, 3 and 4 subevents assuming a constant signal as a function of multiplicity indicated by the lower horizontal line. The vertical line indicates the transition between minimum-bias and high-multiplicity triggered data. Figures from Ref. [11].

that $c_3\{4\}$ is consistent with zero, but increased statistics will help to detect a potential non-zero $c_3\{4\}$ smaller than 1.5% for $100 \lessapprox N_{\rm ch} \lessapprox 500$. Similarly, the precision of the already measured non-zero $c_2\{4\}$ will be greatly improved [6].

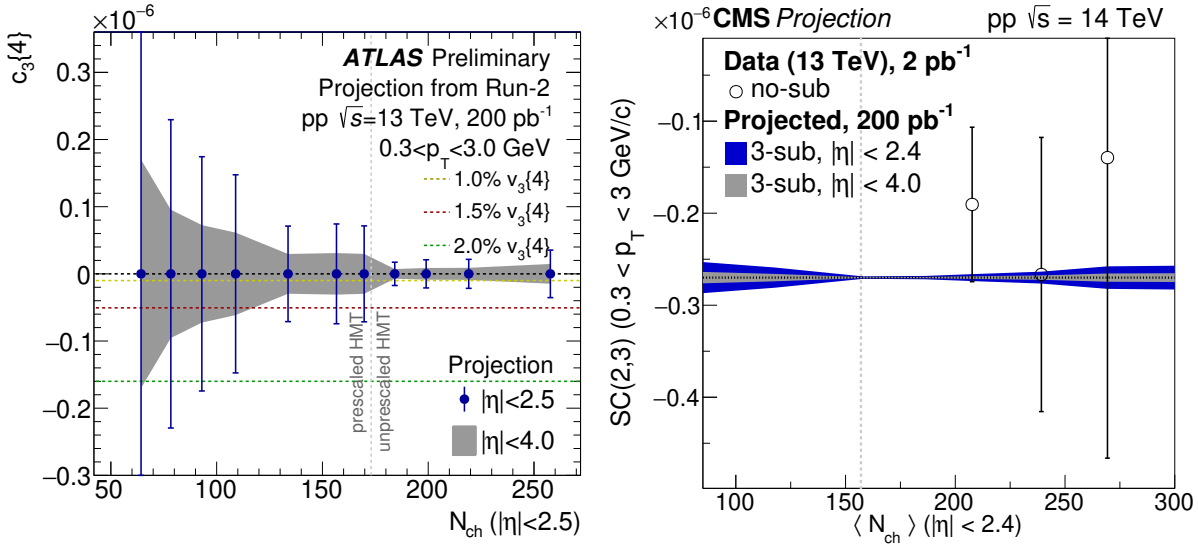

Fig. 69: Demonstration of the influence of the larger tracking acceptances for ATLAS and CMS available in Run 4. Left panel: 4-particle cumulant $c_3\{4\}$ (as in the left panel of Fig. 67) for pp collisions with $L_{\text{int}} = 200\,\text{pb}^{-1}$. The data points indicate the reach with the detector in Run 3 ($|\eta| < 2.5$) while the gray band the enlarged acceptance of $|\eta| < 4$ in Run 4. The yellow, red and green dash lines represent 1.0%, 1.5% and 2.0% $v_3\{4\}$ signal, respectively. Figure from Ref. [6]. Right panel: Symmetric cumulants with 3 subevents (as in left panel of Fig. 68) for pp collisions with $L_{\text{int}} = 200\,\text{pb}^{-1}$. The blue (gray) area indicates the projected uncertainty for Run 3 (4). Figure from Ref. [11].

The correlations of flow harmonics between different orders, called symmetric cumulants, are very sensitive to the initial state and the hydrodynamic evolution in heavy-ion collisions. In Pb–Pb collisions these are, for instance, used to constrain the shear viscosity over entropy ratio η/s. In addition, they challenge the description of the observed phenomena within initial-state saturation models. Their measurement in small systems can provide important insight in the validity of the hydrodynamic description of the observed phenomena. Here, symmetric cumulants probe in particular the proton substructure [770] which is needed to provide a solid description of the initial state, a necessary ingredient for the hydrodynamic description. The present uncertainties of such measurement in small systems are too large for a definitive conclusion, in particular in pp collisions, due to the dominance of non-flow like jets and resonance decays. Figure 68 shows the performance projection of $\text{SC}(2,3) = \langle v_2^2 v_3^2 \rangle - \langle v_2^2 \rangle \langle v_3^2 \rangle$ for HL-LHC for pp and p–Pb collisions. The uncertainties of the measurement without subevents would become practically invisible, however, those stay dominated by non-flow effects. A measurement requiring two, three and even four subevents becomes possible with uncertainties of the order of a few times 10^{-7} depending on multiplicity. Such results can give a definitive answer if a similar hydrodynamic footprint is observed in small and large systems.

Figure 69 illustrates the reduction of the statistical uncertainty due to the larger tracker acceptance in Run 4 for ATLAS and CMS. For this 4-particle correlator a reduction of the uncertainties of about 2.5 is expected, and therefore even the measurement of a 1% $v_3\{4\}$ signal comes into reach. The influence of the acceptance increase on the uncertainties of 6- and 8-particle cumulants will be larger, factor 4 and 6.5, respectively. Similarly, the uncertainties on the SC measurement reduce significantly at larger p_{T}.

Figure 70 (left panel) illustrates the reach which can be obtained for the v_2 measurement of heavy-flavoured objects in p–Pb collisions. Shown are projections for heavy-flavour electrons and inclusive J/ψ by ALICE as well as for prompt D and J/ψ by CMS. Minor uncertainties are expected for this observable with the potential to demonstrate for the first time with significance the final-state interaction

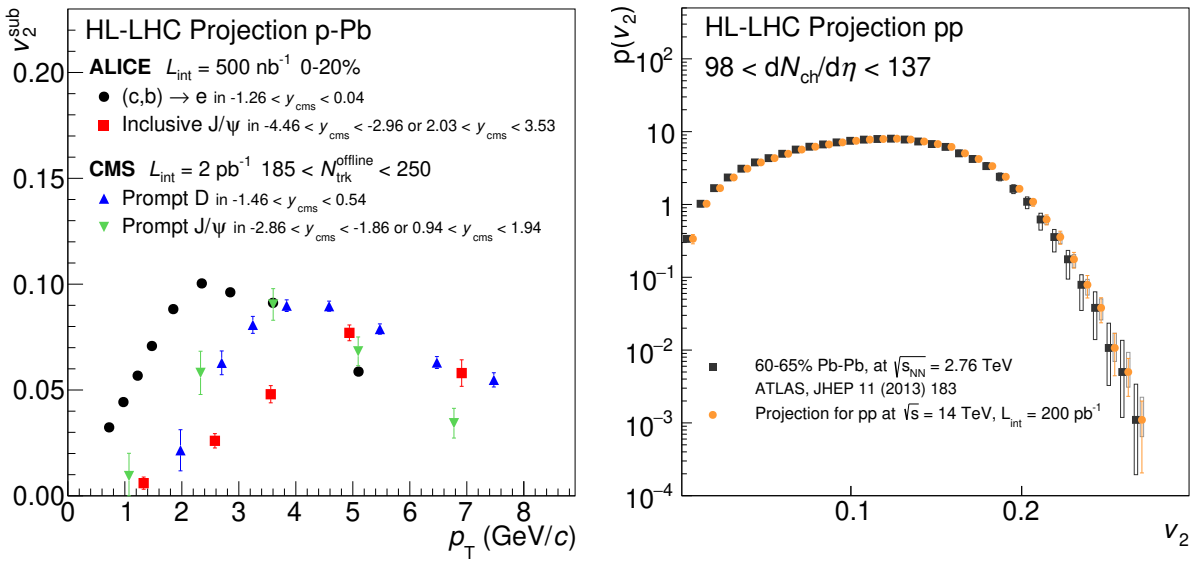

Fig. 70: Left panel: Particle identified v_2 coefficients for p–Pb collisions as a function of p_{T}. Two different cases are shown: the ALICE projections are for the 20% highest-multiplicity collision ($L_{\mathrm{int}} = 500\,\mathrm{nb}^{-1}$) demonstrating the negligible statistical uncertainties for heavy-flavour decay electrons and J/ψ, while the CMS projection is for a bin with $4 - 5\langle N_{\mathrm{ch}}\rangle$ ($L_{\mathrm{int}} = 2\,\mathrm{pb}^{-1}$) demonstrating the wide reach in multiplicity achievable for D mesons and J/ψ. Right panel: Projection of the measurement in pp collisions of the probability distribution of v_2. To illustrate the reach the same signal as in Pb–Pb [722] is assumed although the mean and the width of the distribution is most likely smaller in pp collisions. The projection is for the equivalent pp multiplicity (circles) as in 60–65% centrality in Pb–Pb collisions (squares).

of charm and beauty in a small collision system.

The v_{n} fluctuates on an event-by-event basis as no two nuclei have identical parton distribution. The probability density distribution of v_{n}, $\mathrm{p}(v_{\mathrm{n}})$ is closely related to event-by-event fluctuations of the eccentricities, $\mathrm{p}(\varepsilon_{\mathrm{n}})$ as $v_2 \propto k_2\epsilon_2$. Therefore its measurement provides crucial information about the initial conditions and the final-state dynamics of the medium. To characterise the initial-state spatial anisotropy these measurements are fitted with Bessel-Gaussian and elliptic power functions. The measurements of probability density distributions for v_2 at Pb–Pb collisions are described well by the Bessel-Gaussian function at central collisions and less in peripheral collisions [722–724]. This deviation from the Bessel-Gaussian function is expected in peripheral collisions as k_2 increases slightly at large ϵ_2 values [771]. Measurements are well described by the elliptic power functions in all centrality intervals of Pb–Pb collisions [723]. These measurement have not yet been attempted in small systems due to the insufficient available statistics. Figure 70 (right panel) presents a projection for the measurement of $\mathrm{p}(v_{\mathrm{n}})$ in pp collisions. This extrapolation is based on the $\mathrm{p}(v_2)$ measurement in 60–65% centrality Pb–Pb collisions at $\sqrt{s_{\mathrm{NN}}} = 2.76$ TeV [722]. In this simple study, the same signal is assumed although the mean and width of the distribution is most likely smaller in pp collisions. Such a measurement would constitute the first measurement of $\mathrm{p}(v_{\mathrm{n}})$ in pp collisions, and can shed important light on the nature of the observed v_2 coefficients.

9.7 Strangeness enhancement

The unexpected increase of the strange-particle yield normalized by the pion yield as a function of N_{ch} is one of the key observations in small systems. In pp collisions these ratios are measured up

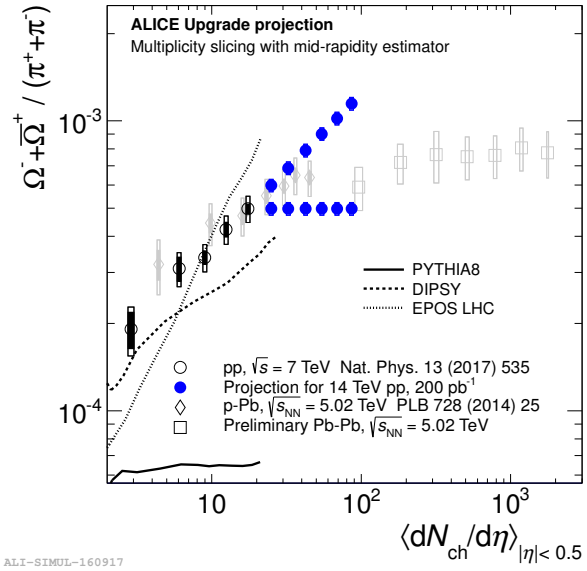

Fig. 71: Ω/π ratio as a function of $\mathrm{d}N_{\mathrm{ch}}/\mathrm{d}\eta$ for pp, p–Pb, and Pb–Pb collisions. The existing data (from Ref. [642]) is shown in open black symbols (pp), grey diamonds (p–Pb) and grey squares (Pb–Pb), while the extrapolation for pp collision is shown in blue filled circles. Two scenarios are shown: a) assuming that the ratio continues increasing following the measured trend, and b) assuming that the value stays the same as at the largest measured $\mathrm{d}N_{\mathrm{ch}}/\mathrm{d}\eta$. Figure from Ref. [1].

to $\mathrm{d}N_{\mathrm{ch}}/\mathrm{d}\eta \approx 17$ with some overlap with p–Pb collisions. The most peripheral Pb–Pb collisions measured have a $\mathrm{d}N_{\mathrm{ch}}/\mathrm{d}\eta \approx 96$, nearly 6 times larger. Figure 71 presents the expected reach of the Ω/π ratio in pp collisions which will bridge the present gap between pp and Pb–Pb collisions. In particular, if the measured increasing trend would continue, the Ω/π ratio would grow larger than in peripheral Pb–Pb collisions. Assuming that strangeness enhancement scales with the energy density of the system, Fig. 66 suggests that it should indeed be possible to see that the high-multiplicity pp results exceed the low multiplicity Pb–Pb results (crossover). Whether the signature will be as striking as the projection in Fig. 71, depends on the details of the assumed scaling law. At this point simulations are not precise enough to provide quantitative predictions of such a crossover, and HL-LHC experimental results on strangeness enhancement will as such be driving the theoretical development. The scenario with a clear crossover will be immediately distinguishable from a scenario where the Ω/π ratio flattens, and connects smoothly with the Pb–Pb result. Such a result will in itself also be groundbreaking, as it will indicate that the thermal limit reached in Pb–Pb collisions will already be realized in high-multiplicity pp collision.

9.8 Energy loss

As discussed in Sect. 9.2, inclusive high-p_{T} hadron and jet yields show at present no evidence of medium-induced energy loss in p–Pb collisions, and suffer from selection biases if measured in event classes. Inclusive measurements with the large event set expected at HL-LHC therefore do not help to resolve the question of energy loss in small systems. However, coincidence measurements of jets recoiling against a trigger object are not subject to such biases, and have the potential to identify small energy-loss effects or put stringent upper limits. In this section, projections are given for correlations between high-p_{T} hadrons and jets, as well as jets and γ and Z.

Figure 72 shows a projection of the measurement of semi-inclusive hadron–jet correlations in LHC Run 3 and 4, for pp collisions at $\sqrt{s} = 14$ TeV and p–Pb collisions at $\sqrt{s_{\mathrm{NN}}} = 5.02$ TeV. The

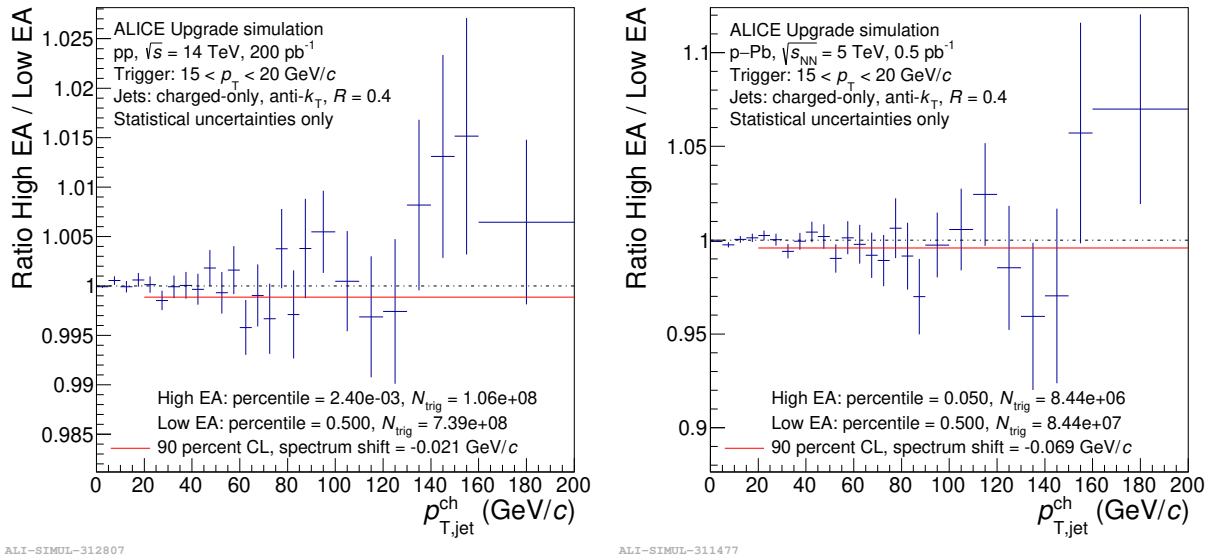

Fig. 72: Modification of jet-recoil yields extracted from semi-inclusive hadron–jet correlations for pp collisions (left) and p–Pb collisions (right) within the ALICE acceptance. Shown is the ratio of high event-activity (EA) and low-EA recoil spectra as a function of $p_{\mathrm{T,jet}}^{\mathrm{ch}}$, with high-EA corresponding to 5–7 $\langle N_{\mathrm{ch}} \rangle$ in pp collisions (left panel), and the 0–5% bin for p–Pb collisions (right panel). Since no EA-dependent shift is imposed, the parent distribution of the ratio has the value of unity at all p_{T}. The red lines show the 90% CL limit for a possible EA-dependent spectrum shift. Figures from Ref. [1].

figure shows the ratio of trigger-normalized recoil spectra for events selected on high and low event-activity (EA) classes. This projection is based on Pythia simulations for pp collisions, which gives the expected number of charged-hadron triggers in the interval $15 < p_{\mathrm{T,trig}} < 20$ GeV (scaled by A to model p–Pb collisions), and the per-trigger recoil jet spectrum. The measured enhancement in the per-event high-p_{T} hadron yield for pp collisions in high-multiplicity collisions [653] has been taken into account.

The projection represents the case where no energy loss occurs for high-EA relative to low-EA collisions, and demonstrates the statistically achievable limit. The 90% confidence level for a possible EA-dependent spectrum shift due to large-angle energy transport from jet quenching [737] is 70 MeV/c for p–Pb (5% highest EA) and 21 MeV/c for pp collisions (5–7 $\langle N_{\mathrm{ch}} \rangle$). These values are over 100 times smaller than the spectrum shift measured in Pb–Pb collisions [358]. The high statistics of the HL-LHC dataset enables this approach to be applied to yet more stringent EA selections; for 7–10 $\langle N_{\mathrm{ch}} \rangle$ (10–12 $\langle N_{\mathrm{ch}} \rangle$) the corresponding 90% CL limit on energy loss is expected to be 69 MeV/c (590 MeV/c).

Projections for the correlation of jets and γ as well as jets and Z are presented in Fig. 73 for pp and p–Pb collisions. Shown are distribution of the momentum fraction $x_{jX} = p_{\mathrm{T}}^{\mathrm{jet}}/p_{\mathrm{T}}^{X}$ where X is the γ or Z. Given that the γ and Z can be considered unmodified by final-state interactions, a potential energy loss acting on the jet would directly alter the x_{jX} distribution. For pp collisions, the left panel of Fig. 73 presents the distribution for different classes in multiplicity based on Pythia, demonstrating the reach. It can be also seen that the distribution shifts significantly as a function of multiplicity without final-state interactions, but purely due to the presence of an underlying event. This shift is caused by selection biases, e.g. the likelihood of multi-jet events is increased by requiring higher event multiplicity. In order to extract a firm conclusion on energy loss, this observable needs to be compared to theoretical calculations or tuned generators which reproduce multiplicity and underlying-event fluctuations in $\mathrm{e^+e^-}$ and pp collisions. The right panel of Fig. 73 presents the projection for p–Pb collisions for MB collisions but in different pseudorapidity intervals sensitive to potential differences in

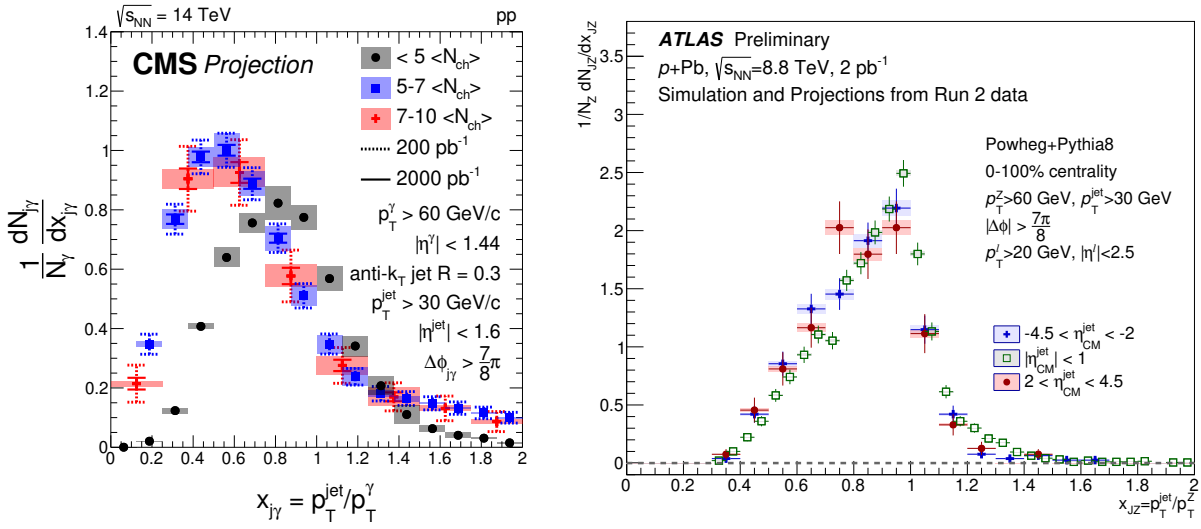

Fig. 73: Left panel: CMS projection of the measurement of the jet–γ momentum fraction $x_{j\gamma}$ in pp collisions for selected high-multiplicity bins. A jet with $p_{\mathrm{T}} > 30$ GeV/c is required to be back-to-back ($\Delta\varphi > 7/8\pi$) with a γ with $p_{\mathrm{T}} > 60$ GeV/c. The shape is based on Pythia and shifts due to selection biases as a function of multiplicity (see text). Figure from Ref. [10]. Right panel: ATLAS projection of the measurement of the Z–jet momentum fraction x_{jZ} in p–Pb collisions in different pseudorapidity intervals. The momentum requirements are also 30 GeV/c for the jet and at least 60 GeV/c for the Z, with the same back-to-back requirement ($\Delta\varphi > 7/8\pi$). The projection is based on Powheg + Pythia 8 Monte Carlo samples with the CT10 PDF set. Figure from Ref. [7].

the p and Pb hemisphere.

9.9 Thermal Radiation

The measurement of thermal radiation in p–Pb collisions can be considered as a smoking gun for the formation of a system with an energy scale above the phase-transition temperature, see Chapter 8. In order to estimate the sensitivity to the thermal radiation in p–Pb collisions, a similar strategy as in Sec. 8.1.2 was used. The combinatorial background was scaled from Pb–Pb collisions to the expected number of pairs in p–Pb collisions. The pair efficiency (including the efficiency for rejecting $\mathrm{e}^+\mathrm{e}^-$ pairs from semileptonic charm decays) is assumed to be the same as in Pb–Pb collisions. Subsequently, the temperature of the QGP is extracted in the same way as in Sec. 8.1.2. The minimum thermal photon to π^0 (both decaying into $\mathrm{e}^+\mathrm{e}^-$) ratio that is needed for a fit to the invariant mass spectrum with a statistical uncertainty $\sigma_{\mathrm{T,stat}} = 10\%$ as a function of L_{int} up to 2000 nb^{-1} is shown in Fig. 74. If the considered prediction is accurate, an integrated luminosity of about 50 nb^{-1} is sufficient for the measurement. In case the signal is 50% smaller about 4–5 times the statistics is needed.

9.10 Potential of O–O Collisions

A promising opportunity to study the emergence of collective phenomena further as well as the presence of possible parton energy loss in small collision systems, are collisions of smaller nuclei. In particular, collisions of oxygen are an efficient way of investigating the properties of low-multiplicity heavy-ion collisions, which in large A–A systems only occurs for peripheral geometries. The achieved multiplicities in O–O collisions are similar to p–Pb collisions with the significant advantage that the collision geometry is much better defined. This is demonstrated in Fig. 75, which shows the correlations between number of participants, multiplicities and impact parameter in O–O and p–Pb collisions. The correla-

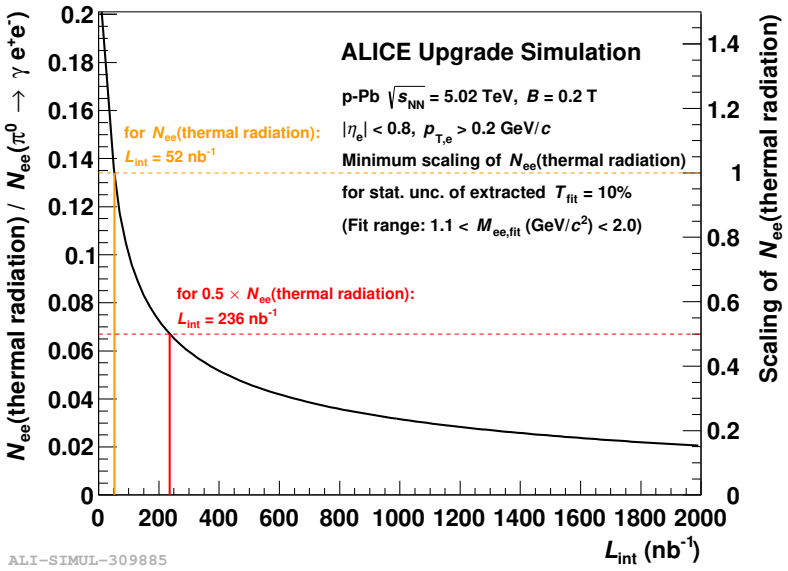

Fig. 74: Projection of the measurement of the medium temperature extracted from thermal dileptons in p–Pb collisions. As the expected signal is uncertain, the figure presents the required integrated luminosity relative to the prediction based on Ref. [558] denoted by $N_{\rm ee}$(thermal radiation). It is expressed as the minimum thermal photon $N_{\rm ee}$(thermal radiation) to π^0 ratio (left axis) and scaling of $N_{\rm ee}$(thermal radiation) (right axis) for achieving a 10% statistical uncertainty on the extracted temperature. Figure from Ref. [1].

tions between $N_{\rm part}$ and impact parameter as well as multiplicity and $N_{\rm part}$ is much narrower in O–O collisions as compared to p–Pb collisions. Consequently, highest multiplicities in p–Pb collisions are only accessible in the tail of the distribution while similar multiplicities are already reached in O–O collisions in the plateau region. This is shown in Fig. 76 illustrated for the 20–40% event class.

Scaling the measured nuclear-modification factor in Pb–Pb collisions at 5.02 TeV [327] at similar multiplicities as for central O–O collisions while roughly accounting for the artificial suppression caused by the multiplicity bias present in such peripheral Pb–Pb collisions [734], allows to estimate the expected effect on the $R_{\rm AA}$ in O–O collisions to about 20%. Out of this deviation from unity, about half can be attributed to biases due to the multiplicity selection in such small collision systems already in absence of nuclear effects [772]. An observable deviations from unity of about 10% caused by energy loss in the produced medium remains. While this expected suppression may seem small, it should be possible to measure it already with an $L_{\rm int}$ of a few 100 μb^{-1}. In case such a suppression was absent, the conclusion can be drawn that small collision systems do not exhibit measurable energy loss, while other collective features are present, challenging the role of significant final-state interactions as underlying mechanism. It should be noted that the absence of suppression can most likely not be taken as a proof against the formation of the QGP, as it may be that the fast partons are emerging without seeing the medium, either because they are emitted from the surface or because their formation time is longer than the time within the medium. On the contrary, as discussed in Sect. 9.8 the first observation of energy loss in small systems would clearly confirm models in which final-state interactions play an important role

The study of bulk particle production in O–O collisions has twofold interest: Firstly, the dependence of the pseudorapidity density of charged particles scaled by participant pairs on $\sqrt{s}$ is stronger in A–A collisions than in pp and p–A collisions [775]. The rise for p–Pb and d–Au collisions is simi-

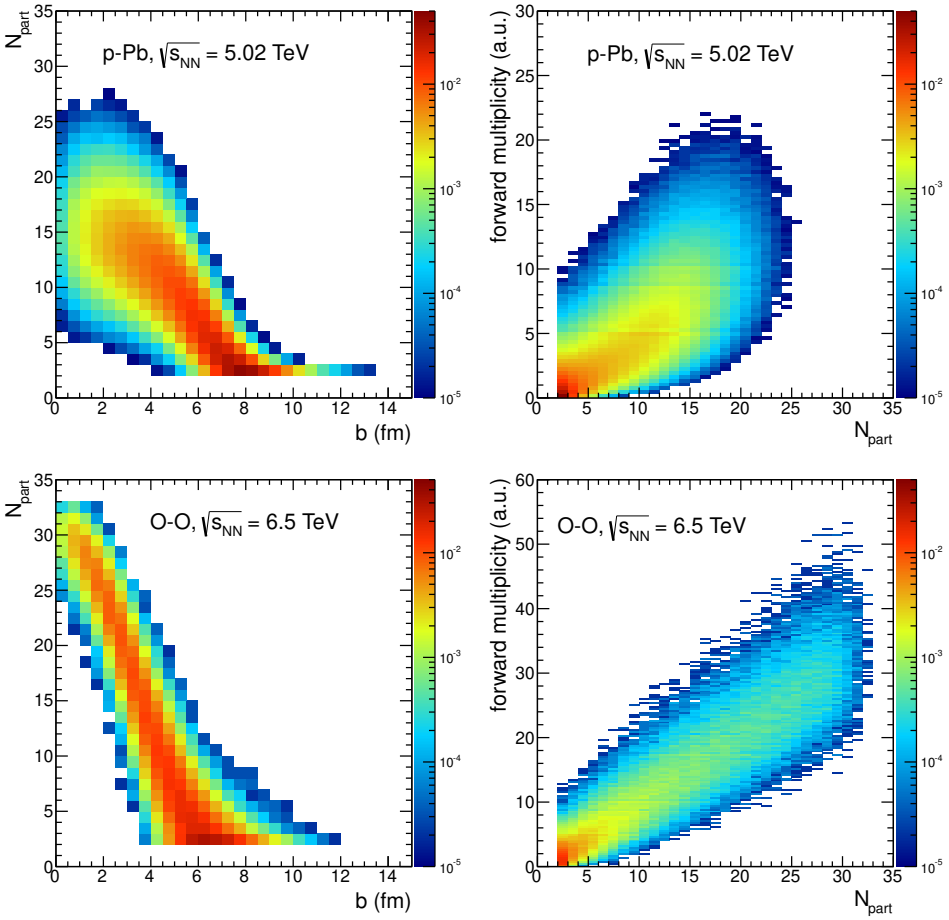

Fig. 75: Glauber MC calculations are presented for for p–Pb (top panels) and O–O collisions (bottom panels). Shown are N_{part} as a function of impact parameter (left panels) and forward multiplicity as a function of N_{part} (right panels).

lar to the one of inelastic pp collisions indicating that the stronger rise in A–A collisions might not be solely related to the multiple collisions undergone by the participants since the proton in p–A collisions also encounters multiple nucleons. High-energy O–O collisions promise to study this $\sqrt{s}$ dependence further in a regime of small number of participants. Secondly, a strong correlation between initial state geometry (collision eccentricity) and observed flow has been established since RHIC [776], and pertains at LHC, in Pb–Pb and Xe–Xe collisions [777]. As shown in Fig. 77, the eccentricity profiles of Xe–Xe and Pb–Pb collisions are, however, quite similar, and collision systems exhibiting a different geometry as O–O could therefore provide further insight into the connection between initial-state geometry and multi-particle correlations [778].

9.11 Summary

The discoveries made in recent years in small collision systems have challenged two paradigms, the modelling of heavy-ion collisions, as well as the modelling of the underlying event of elementary pp collisions. The experimental observations of strangeness enhancement and multi-particle correlations suggests that energy loss should also be present, as both are a consequence of significant final-state interactions. But up to this point no hint of energy loss in pp or p–Pb collisions has been seen. The increased luminosity will allow both for precision studies of the established signatures of small system

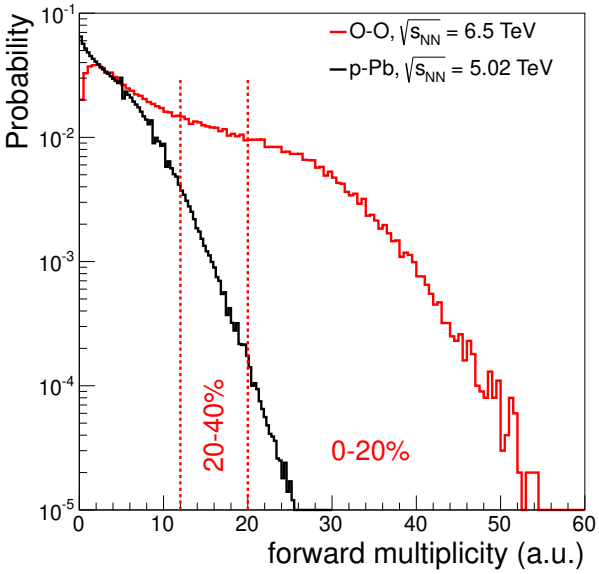

Fig. 76: Estimated multiplicity distributions in the forward region in O–O and p–Pb collisions. The event classes of highest multiplicity in O–O collisions are indicated with 0–20% and 20–40%. The O–O studies have been been performed for the 2018 beam configurations at $\sqrt{s_{\rm NN}} = 6.5$ TeV, while the Run 3 configuration would yield $\sqrt{s_{\rm NN}} = 7$ TeV, with the advantage that a large pp reference data set already exists from earlier LHC running (2010–11).

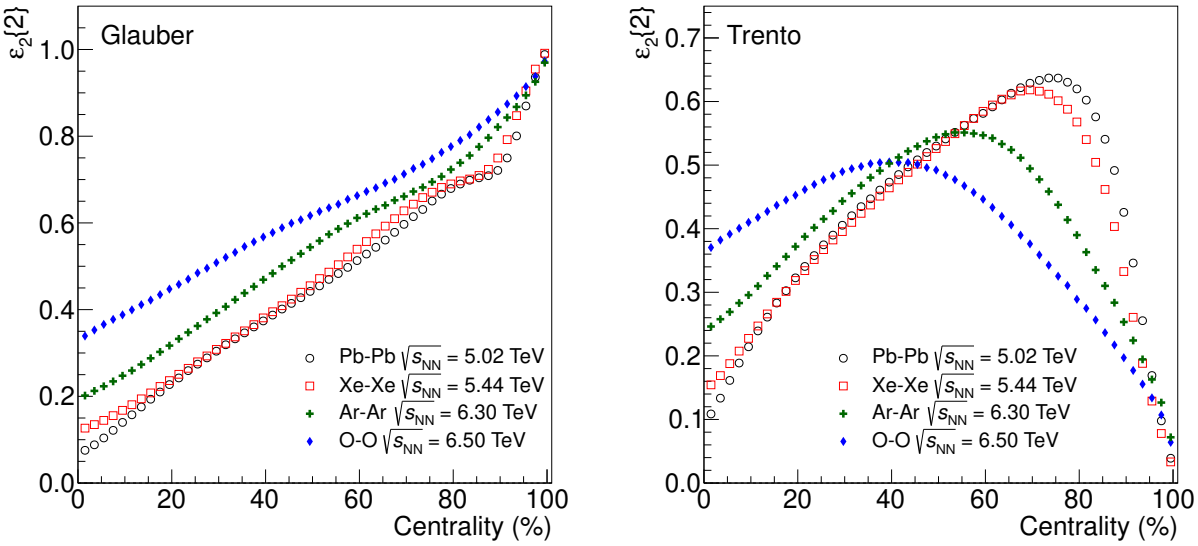

Fig. 77: Second-order eccentricity coefficient ϵ_2 as a function of centrality for O–O, Ar–Ar, Xe–Xe and Pb–Pb collisions from MC-Glauber (left panel) [767, 773] and Trento (right panel) [774] initial conditions.

collectivity, and to either establish evidence or place exclusion limits on the latter.

This chapter has presented a HL-LHC small system experimental program promising significant progress shown by the set of performance studies, ranging from largely non-flow suppressed high-order correlations, over measurement of strange-particle yields and thermal radiation, to energy-loss signals. In addition, new theoretical insights and phenomenological developments are also needed for developing

a unified picture of parton dynamics and particle production valid for both small and large systems. This working group encourages both investment in the necessary theoretical development, and facilitation of collaboration between theorists and experimentalists.

The physics community can look forward to a deepened understanding of hot and dense QCD and a universal description of small to large collision systems.

10 High energy QCD with proton-nucleus collisions and ultra-peripheral collisions

Coordinator: Michael Winn (LAL and IRFU/DPhN, CEA Saclay)

Contributors: A. Angerami (LLNL Livermore), F. Arleo (LLR/École Polytechnique), N. Armesto (Instituto Galego de Fisica de Altas Enerxias (IGFAE) Universidade de Santiago de Compostela), R. Bi (Massachusetts Institute of Technology), É. Chapon (CERN), Z. Citron (Ben-Gurion University of the Negev), J. G. Contreras Nuno (Czech Technical University in Prague), M. Dumancic (Weizmann Institute of Science), D. d'Enterria (CERN), G. Giacalone (IPhT, CNRS/CEA), A. Giammanco (Université Louvain), V. Guzey (Helsinki University, University of Jyvaskyla, Kurchatov institute, Gatchina),I. Helenius (University of Jyvaskyla and Universität Tübingen), P. Janus (AGH University of Science and Technology), H. Kim (Chonnam National University), M. Klasen (Münster University), S.R. Klein (Lawrence Berkeley National Laboratory), J. Kremer (AGH University of Science and Technology), G. Krintiras (Université Louvain), E. Kryshen (Kurchatov institute, Gatchina), A. Kusina (IFJ PAN, PL-31342 Kraków, Poland), Y.-J. Lee (Massachusetts Institute of Technology), M. van Leeuwen (Utrecht University/Nikhef), C. Marquet (CPHT/École Polytechnique), C. Mayer (IFJ PAN, Kraków, Poland), M. Mulders (CERN), M. Murray (University of Kansas), F. Olness (SMU Dallas), P. Paakkinen (University of Jyvaskyla), H. Paukkunen (University of Jyvaskyla, Helsinki Institute of Physics), I. Schienbein (LPSC/Université Grenoble Alpes), P. Silva (CERN), D. Stocco (Subatech Nantes), M. Strikman (Pennsylvania State University), D. Tapia Takaki (University of Kansas).

10.1 Introduction

Proton-nucleus [17] and ultraperipheral (UPC) [587] collisions offer the opportunity to study the behaviour of QCD at high energies and large partonic densities [779]. As the theory of the strong interaction, QCD is analytically well understood only in a perturbative regime of small coupling constant and where radiation of gluons and quarks is a linear process that can be described with linear evolution equations of the non-perturbative parton densities, i.e., hadrons and nuclei are considered as dilute partonic objects. However, non-linear effects are unavoidable in QCD, and they should in principle dominate at large densities reached at high collision energies and for large nuclei. It was proposed long ago [780,781] that at such large densities a resummation of powers of density scaled by the strong coupling constant is possible, resulting in a non-perturbative but weak coupling regime where parton densities saturate, and whose effective field theory incarnation is the Color Glass Condensate (CGC) [782]. Particle production in p–A collisions in the forward rapidity region is dominated by small$-x$ partons in the nucleus. Therefore, saturation effects are expected to be largest there. Furthermore, UPCs as a source of large fluxes of quasi-real photons, provide the opportunity to study the partonic structure of protons (in pp and p–A) and nuclei (in p–A and A–A).

The structure of nucleons and nuclei, and the mechanism of particle production at small x, are also key ingredients for a detailed description of heavy-ion collisions and for the characterisation of the produced hot and dense medium. For hard probes, the nuclear modification of standard collinear parton densities is one of the uncertainties in the extraction of medium characteristics [260, 385]. For soft and semihard observables, both the parton densities and the detailed transverse spatial structure of nucleons and nuclei are crucial ingredients for their description, e.g. for the initial conditions for hydrodynamical evolution [211, 212, 783].

In the collinear framework, parton densities inside nuclei (nPDFs) [784, 785] are poorly constrained due to two primary factors. On the one hand, data come from a large variety of nuclei and the number of data points for any of them is very small compared to the proton analysis. In particular, for the Pb nucleus, there are less than 50 points coming from fixed target Deep Inelastic Scattering (DIS) and Drell-Yan experiments and from p–Pb collisions at the LHC. The fit for a single nucleus is therefore impossible and the modeling of the A-dependence of the parameters in the initial conditions becomes mandatory [786, 787]. On the other hand, the kinematic coverage in Q^2 and x with existing data is very small compared to the requirements of present hadronic colliders, see Fig. 78. In spite of the

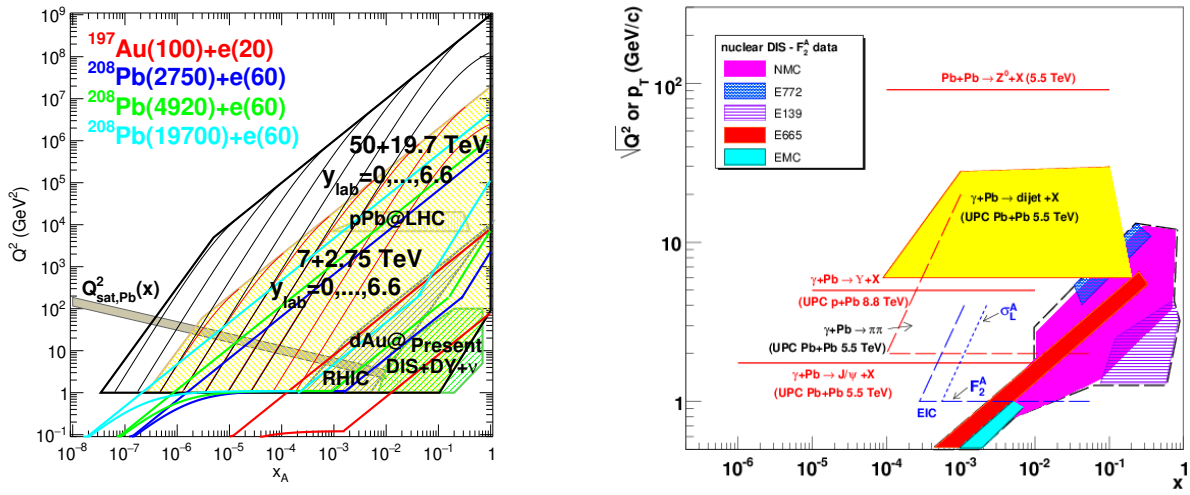

Fig. 78: Left: x-Q^2 plane to be explored in proton-nucleus at the LHC and the FCC, and in proposed electron-nucleus colliders, compared with the regions where the experimental data presently used in the EPPS16 analysis [786] lie. Right: x-Q^2 plane to be explored in UPCs, taken from [587].

uncertainties in the applicability of collinear factorisation, scale choices and other theoretical caveats for nPDFs extraction in hadronic collisions and UPCs, these are the only experimental collision systems where the nPDFs can be constrained before electron-ion colliders become available. The most up to date analyses include between 1000 and 2000 data points for 14 nuclei and are performed at next-to-leading accuracy [786–788], there even exists a first attempt at next-to-next-to-leading [789]. Differences between them mainly arise from the different sets of data included in the analysis and from the different functional forms employed for the initial conditions. All in all, all parton species are very weakly constrained at small $x < 10^{-2}$, gluons at large $x > 0.2$, and the flavour decomposition is largely unknown - a natural fact for u and d due to the approximate isospin symmetry in nuclei. The impact of presently available LHC data, studied in [786], is quite modest with some constrains on the gluon in the region $0.01 < x < 0.3$. On the other hand, theoretical predictions for nuclear shadowing of quark and gluon PDFs based on s-channel unitarity and diffractive nucleon PDFs are available down to $x \sim 10^{-4}$ –10^{-5} [790, 791].

In the context of phenomena beyond collinear factorisation and PDF evolution in $\ln(Q^2)$, there have been recent claims [792, 793] that resummation of logarithms of x may be required for a better description of DIS data from HERA at small x, and searches for long range azimuthal correlations are undergoing [794]. But no conclusive evidence of saturation, i.e., of non-linear dynamics, has been found in hadronic collisions. While the CGC provides a calculational framework for several observables in pp, p–A and A–A, see e.g. the reviews [795, 796], like the ridge, back-to-back hadron correlations in the forward region, multiplicities and transverse momentum distributions,. . . , there is no consensus in the field in the interpretation of these results, or they involve non-perturbative modeling, or they are affected by large theoretical uncertainties and, for some of them, higher-order calculations are missing, or the data lie at the border of phase space where extracting clear conclusions is very delicate. Therefore, high-energy p–A collisions and UPCs are two promising systems where data can offer clear evidences of non-linear effects.

In Fig. 78, the kinematic regions covered by proton-nucleus collisions at the LHC and the FCC (the left panel, [411]) and UPCs at the LHC (right) are shown and compared with the regions where data currently used to constrain nPDFs lie. A huge enlargement is evident with respect to the presently existing data at the LHC. The HL-LHC offers new improved detectors and larger statistics for some observables

like dijets or photon-jet correlations. The HE-LHC would enlarge the kinematic plane in a region intermediate between the LHC and the FCC. On the other hand, electron-nucleus collisions [797, 798], if they eventually happen in the 2030's, would be complementary. They offer measurements in a cleaner experimental environment (no pileup, full kinematic reconstruction) and under better theoretical control as first-principle calculations are easier in DIS albeit in a more restricted kinematical region. The comparison between the kinematic regions covered by the LHC and Future Circular Collider (FCC) in p–A mode, and the Electron-Ion Collider (EIC) [798] (10-20 GeVelectrons combined with the RHIC nuclear beams or with a new hadron machine at Jefferson Lab) and the LHeC [797] (60 GeVelectrons colliding with the HL-LHC, HE-LHC or FCC nuclear beams) is shown in Fig. 78 (left).

10.2 The physics of ultra-peripheral collisions

Ultra-peripheral collisions are interactions with impact parameter larger than the radial size of the colliding nuclei or protons. In these collisions, one nucleus acts as a source of quasi-real photons that interact with the crossing nucleus or proton. The electromagnetic field intensity and hence the photon flux scales with the charge number squared. At the LHC, these collisions occur abundantly and serve as a laboratory for strong and electromagnetic interactions [587]. After an experimental overview discussing the opportunities, the discussion focuses on vector meson production studies to probe nuclear gluons and dijet production in photonuclear or photon-proton interactions in LHC Run 3 and 4 as a direct access of nPDFs. A dedicated section 11.2 addresses the physics of $\gamma\gamma$ interactions as a probe of QED and beyond the standard model physics. The investigation of γ-proton interactions in pp collision allowed interesting measurements on vector meson production by LHCb [799–802] and will allow for interesting measurements with already recorded and future data. This possibility will not be discussed in detail because the standard running conditions in terms of pile-up and beam optics relevant for forward proton tagging in ATLAS/CMS and the pile-up in LHCb in Run 3 and Run 4 will make comparatively low Q^2 measurements primarily discussed here challenging and likely restricted to short special runs whereas in ALICE, the equivalent luminosity γ-proton luminosity will be smaller or similar than in p–Pb collisions but with the ambiguity which beam emitted the photon.

10.2.1 Experimental overview

An overview of the detector capabilities in Run 3 and Run 4 is given by the four collaborations ALICE,ATLAS,CMS and LHCb in the following. Subsequently, the expected statistics for vector meson observables is given in Tab. 13,14,15 followed by an estimate of the available precision for coherent heavy vector meson production and the theoretical assessment of vector mesons and dijet production in UPCs.

- **ALICE** [2] will take data in both in triggered and in continuous readout mode during Run 3 and Run 4 [70]. Using continuous readout [69] essentially the full delivered luminosity can be integrated without significant trigger and dead-time inefficiencies. Therefore the total acceptance-efficiency factor for UPC events is significantly larger than in LHC Runs 1 and 2; it is determined by the tracking efficiencies and the geometrical acceptances of the Inner Tracking System (ITS) [3], of the Time Projection Chamber (TPC) [68], and of the Muon Spectrometer [803]. The geometrical acceptances of these detectors correspond to the narrow central and forward acceptances defined in Tab. 12. Vector meson yields in the corresponding acceptance are given in Tab. 13,14,15. Final-state neutron emission in UPC events can be detected by the zero-degree calorimeters (ZDC) which will also take data in continuous readout mode, and vetoes can be imposed using the fast interaction trigger detector (FIT).
- **ATLAS** UPC measurements in Run 3 and Run 4 will continue to be an important part of the experiments heavy-ion programme and will benefit from several detector upgrades in that period.

Prior to Run 3, the Zero Degree Calorimeter (ZDC), which is key for UPC event identification by measuring forward neutrons, will be upgraded. At mid-rapidity, the Inner Tracker (ITk) upgrade [264] will increase the acceptance for charged particles to $|\eta| < 4$ for Run 4. The High Granularity Timing Detector (HGTD) [265] will complement the spatial information of the ITk with timing information in the region $2.4 < \eta < 4.0$, with a resolution of 30 ps. In addition, upgrades to the ATLAS trigger and data-acquisition system will take place prior to both Run 3 and Run 4 [804], and will enable advanced triggering capabilities. Together these will aid the study of low-mass resonances and the continuum as well as jets in UPC events.

- **CMS** UPC studies will benefit from the upgraded inner tracker for Run 4 which will provide a large acceptance for charged particles up to $|\eta| < 4$ [457]. The improved CMS level-1 trigger and data acquisition rate (up to 60 GB/s) will provide opportunities for more innovative and sophisticated triggers to capture a wide variety of processes. In addition, the proposed MIP Timing Detector [805], which is around 1.16 m away from the beam pipe could provide a time resolution around 30 ps. By combining it with other detectors, MIP will provide proton, pion, and kaon separation for p_{T} values between 0.7 to 2 GeV/$c$in the midrapidity region ($|\eta| < 1.5$). These detector upgrades and the increased trigger performance summarised in [806] will facilitate the study low-mass UPC resonant states and UPC heavy flavour studies. In addition, the reconstruction algorithms will be improved with the addition of the four-layer pixel system. The CMS-acceptance in Run 3 corresponds to the wide central range defined in Tab. 12. Yields in acceptance for vector mesons are provided in Tab. 13,14,15.
- **LHCb** is well suited for exclusive production studies in ultra-peripheral collisions. In particular, its optimisation for flavour physics within its acceptance $2 < \eta < 5$ provides an excellent resolution for typical momenta in quarkonium and heavy-flavour exclusive production as demonstrated in Ref. [807]. Its particle identification capabilities allow to measure final states with charged muons, pions, kaons and protons. The upgraded detector will be able to efficiently sample the full delivered luminosity for UPC final states based on a purely software based trigger scheme [808]. Exclusive diphoton analyses as pioneered in ATLAS [809] and CMS [810] are also conceivable with lower E_{T}-thresholds discussed in Section 11.2. The feasibility of inclusive γ-induced measurements in LHCb will require further studies. In Tab. 13,14,15 conceivable vector meson final states are given for LHCb represented by the wide forward acceptance defined in Tab. 12.

10.2.2 Vector meson production

10.2.2.1 Experimental reach

The number of vector mesons expected in the upcoming runs provides an estimate of the expected physics reach. Four toy-model experimental acceptances are shown in Tab. 12. The effects of cuts on the p_{T} of the final state daughter particles are not estimated, because this depends on the analysis and trigger conditions. In general, for two-prong decays, as long as the minimum detectable p_{T} is less than about 1/4 of the final state mass, the effect on the efficiency is limited. The acceptance cuts are applied to both the vector meson rapidity and the daughter particle pseudorapidities. These two selection types have similar effects on the production phase space, and the results would not be very different without the cut on the vector meson rapidity.

Table 13 shows the expected cross sections and rates for five representative vector meson decays, including the decay branching ratios. The rates are calculated using STARlight [598], which has been shown to predict the cross sections for all mesons on proton targets and for ρ photoproduction on heavy targets [811, 812]. Since the ρ vector resonance is broad, the mass range from $2m_{\pi}$ up to $M_{\rho} + 5\Gamma_{\rho}$ is considered. Non-resonant $\pi^{+}\pi^{-}$ production is not included which would lead to a 8% increase of the production rate. The ρ' state represents $\pi^{+}\pi^{-}\pi^{+}\pi^{-}$ states with masses in the range from $4m_{\pi}$ up to

2.5 GeV/c^2. In absence of other guidance and the possibility of more complex resonance structure, the calculation is anchored to the STAR measurement of the $\pi^+\pi^-\pi^+\pi^-$ final state in Au–Au collisions at $\sqrt{s_{\rm NN}} = 200$ Gev [813] and uses STARlight to extrapolate in collision energy and collision system.

Since STARlight does not include nuclear shadowing, a rapidity-dependent nuclear shadowing correction following Ref. [814] for the heavy quarkonium (J/ψ, ψ(2S) and Υ(1S) was applied. The cross sections and rates are hence reduced by factors of 0.42, 0.475 and 0.77 for the J/ψ, ψ(2S) and Υ(1S) respectively.

Table 12: Table of toy-model acceptance cuts for the different experiments.

Condition	Tot.	Central 1 Narrow	Central 2 Wide	Forward 1 Narrow	Forward 2 Wide
Rapidity	-	$\|y\| < 0.9$	$\|y\| < 2.4$	$2.5 < y < 4.0$	$2 < y < 5$
e/π/μ pseudorapidity	-	$\|\eta\| < 0.9$	$\|\eta\| < 2.4$	$2.5 < \eta < 4.0$	$2 < \eta < 5$

Table 13: Table of cross sections and numbers of events in 13 nb^{-1} integrated luminosity for the different mesons in Pb–Pb collisions. B, M and K denote 10^9, 10^6 and 10^3 respectively. Both the rates and cross sections include the relevant branching ratios. The cross sections and toy-model acceptances are determined using STARlight [598]. For the J/ψ, ψ(2S) and Υ(1S), rapidity-dependent nuclear shadowing cross sections have been applied following the approach in Ref. [814].

PbPb						
Meson	σ	All Total	Central 1 Total	Central 2 Total	Forward 1 Total l	Forward 2 Total
$\rho \to \pi^+\pi^-$	5.2b	68 B	5.5 B	21B	4.9 B	13 B
$\rho' \to \pi^+\pi^-\pi^+\pi^-$	730 mb	9.5 B	210 M	2.5 B	190 M	1.2 B
$\phi \to \mathrm{K}^+\mathrm{K}^-$	0.22b	2.9 B	82 M	490 M	15 M	330 M
J/$\psi \to \mu^+\mu^-$	1.0 mb	14 M	1.1 M	5.7 M	600 K	1.6 M
ψ(2S) $\to \mu^+\mu^-$	30μb	400 K	35 K	180 K	19 K	47 K
Υ(1S) $\to \mu^+\mu^-$	2.0 μb	26 K	2.8 K	14 K	880	2.0 K

The rates for light mesons are very large, enough to support billion-event samples of the ρ and ρ', and hundreds of millions of ϕ, allowing the studies discussed below. Beyond precise cross section measurements detailed below, the rates for J/ψ, ψ(2S) and Υ(1S) should allow tomographic measurements which can be used to infer information on the nuclear wave function and which is outlined in Section 10.2.2.3. In the $\pi^+\pi^-$ channel, the study of pairs with masses above 2 Gev/c^2 comes in reach.

In the hadronic decay $\phi \to K^+K^-$, the kaons have a momentum of only 135 MeV/c in the ϕ rest frame. Since the kaon momentum is dominated by the longitudinal momentum acquired from the ϕ-meson, the kaons are produced with large pseudorapidity. Therefore, the acceptance for this channel is low at around midrapidity even without a considering a minimal kaon-$p_{\rm T}$. Consequently, an observation is very difficult with the potential exception of the far forward region where the kaons are significantly Lorentz boosted. Alternately, measurements exploiting the leptonic decay channels $\phi \to \mu^+\mu^-$ore$^+$e$^-$ despite the small branching ratios. The feasibility can be conservatively estimated by scaling the $\phi \to \mathrm{K}^+\mathrm{K}^-$ rates down by Br ($\phi \to \mu^+\mu^-$)/Br($\phi \to \mathrm{K}^+\mathrm{K}^-$)$\approx 5.9 \times 10^{-4}$ neglecting the acceptance increase for leptons w.r.t. kaons.

The exploration of double vector mesons photoproduction by a single ion-ion pair by exchange of two independent photons becomes available. The expected ratio of $\rho\rho$ photoproduction to single ρ photoproduction is about $1:600$ while the predicted ratio of ρJ/ψ to ρ is about $1:160$ [815]. These

events should display significant quantum correlations.

In p–Pb collisions, the per-nucleon centre-of-mass system is boosted by 0.465 units of rapidity from the lab frame, and there are two possible directions for the beams, protons from the $+z$ direction, or from the $-z$ direction influencing strongly the available kinematics for the forward detectors. Furthermore, there are two possibilities for the photon emitter, 'lead-shine' (γp), the photon from the lead nucleus, or 'proton-shine' (γPb), the photon from the proton. These two vector meson production channels can be in principle separated by their different p_{T} scale corresponding to $\hbar/R_{\mathrm{proton}}$ for 'lead-shine' (γp) and $\hbar/R_{\mathrm{Pb}}$ for 'proton-shine' (γPb). The rates are calculated for these two possibilities in separate tables.

The total p–Pb luminosity of 2000 nb^{-1} assumed to be equally divided between the two possible proton beam directions. For the asymmetric (around $y = 0$) detectors, these two Runs are considered separately, listing them as 'forward' (in the proton-going hemisphere) and 'backward' (in the lead-going hemisphere).

Tables 14 and 15 show the cross sections and rates for the lead-shine and proton-shine cases respectively. Lead-shine is dominant, with proton-shine contributing less than 10% to the total rate. The extraction of the proton-shine component by fitting to the different p_{T} spectra for proton-shine and lead-shine will be challenging and the measurement precision depends strongly of the momentum resolution of the detector. Nuclear shadowing corrections are not applied, the reduction factors are similar for the proton-shine cross sections as for the lead-lead collisions. No attempt to calculate the rates for the ρ' on proton targets is undertaken due to the large rate uncertainties.

Table 14: Table of cross sections and numbers of events for the different mesons in p–Pb collisions for 'lead-shine' (a photon from the lead scattering from the proton). The rates are for the 2000 nb^{-1} integrated luminosity noted above, split evenly between the two possible proton directions. For the central regions, the net luminosity is 2000 nb^{-1} since both directions contribute, but for the forward (FW) and backward (BW) directions, the net luminosity is only 1000 nb^{-1} each. B, M and K denote 10^9, 10^6 and 10^3 respectively. Both the rates and cross sections include the relevant branching ratios.

pPb - lead shine, γp								
Meson	σ	All Total	Ctl. 1 Total	Ctl. 2 Total	FW 1 Total	FW 2 Toal	BW 1 Total	BW 2 Total
$\rho \to \pi^+\pi^-$	35 mb	70 B	3.9 B	15 B	2.0 B	5.5 B	850 M	2.0 B
$\phi \to \mathrm{K}^+\mathrm{K}^-$	870 μb	1.7 B	65 M	290 M	22 M	120 M	9.7 M	52 M
$\mathrm{J}/\psi \to \mu^+\mu^-$	6.2 μb	12 M	1.0 M	5.2 M	260 K	800 K	180 K	430 K
$\psi(2\mathrm{S}) \to \mu^+\mu^-$	134 nb	270 K	22 K	110 K	6.0 K	18 K	3.2 K	7.7 K
$\Upsilon(1\mathrm{S}) \to \mu^+\mu^-$	5.74 nb	11 K	1.1 K	5.4 K	310	880	41	100

In case of coherent heavy vector meson production in UPC of lead nuclei, the expected experimental uncertainties are evaluated by the ALICE and CMS collaborations. The vector meson cross section in Pb–Pb UPC can be expressed as a sum of two terms reflecting the fact that either of the colliding ions can serve as a photon source:

$$\sigma(y) = n(+y)\sigma_{\gamma\mathrm{Pb}}(+y) + n(-y)\sigma_{\gamma\mathrm{Pb}}(-y) \tag{31}$$

The photoproduction cross sections $\sigma_{\gamma\mathrm{Pb}}(y)$ and $\sigma_{\gamma\mathrm{Pb}}(-y)$ are coupled and cannot be extracted unambiguously from the measured rapidity differential cross section. However, one can decouple them by measuring vector meson production in UPC with and without additional neutron activity in Zero Degree Calorimeters [816]. Measurement of $\sigma_{0\mathrm{N}0\mathrm{N}}(y)$ (no neutrons on both sides) and $\sigma_{0\mathrm{N}\mathrm{X}\mathrm{N}}(y)$ (at least one neutron on one of the sides) cross sections provides a system of two equations of two unknown

Table 15: Table of cross sections and rates for the different mesons in p–Pb collisions for 'proton-shine' (a photon from the proton scattering from the lead nucleus). The rates are for the 2000 nb^{-1} integrated luminosity noted above, split evenly between the two possible proton directions. For the central regions, the net luminosity is 2000 nb^{-1} since both directions contribute, but for the forward (FW) and backward (BW) directions, the net luminosity is only 1000 nb^{-1} each. B, M and K denote 10^9, 10^6 and 10^3 respectively. Both the rates and cross sections include the relevant branching ratios.

pPb - proton shine, γA								
Meson	σ	All Total	Ctl. 1 Total	Ctl. 2 Total	FW 1 Total	FW 2 Total	BW 1 Total	BW 2 Total
$\rho \to \pi^+\pi^-$	531μb	1.1 B	83 M	360 M	20 M	44 M	56 M	150 M
$\phi \to \mathrm{K}^+\mathrm{K}^-$	23 μb	46 M	1.3 M	8.0 M	120 K	1.7 M	210 K	3.9 M
$\mathrm{J}/\psi \to \mu^+\mu^-$	333 nb	670 K	55 K	290 K	14K	36 K	15 K	41 K
$\psi(2\mathrm{S}) \to \mu^+\mu^-$	8.9 nb	18 K	1.5 K	7.9 K	380	990	380	1.0 K
$\Upsilon(1\mathrm{S}) \to \mu^+\mu^-$	0.43 nb	860	93	460	14	34	14	30

photoproduction cross sections $\sigma_{\gamma\mathrm{Pb}}(\pm y)$:

$$\sigma_{0\mathrm{N}0\mathrm{N}}(y) = n_{0\mathrm{N}0\mathrm{N}}(+y)\sigma_{\gamma\mathrm{Pb}}(+y) + n_{0\mathrm{N}0\mathrm{N}}(-y)\sigma_{\gamma\mathrm{Pb}}(-y), \quad (32)$$

$$\sigma_{0\mathrm{N}\mathrm{X}\mathrm{N}}(y) = n_{0\mathrm{N}\mathrm{X}\mathrm{N}}(+y)\sigma_{\gamma\mathrm{Pb}}(+y) + n_{0\mathrm{N}\mathrm{X}\mathrm{N}}(-y)\sigma_{\gamma\mathrm{Pb}}(-y), \quad (33)$$

where $n_{0\mathrm{N}0\mathrm{N}}(\pm y)$ and $n_{0\mathrm{N}\mathrm{X}\mathrm{N}}(\pm y)$ are corresponding photon fluxes, calculable with high accuracy. Solutions of this system of equations can be used to extract photoproduction cross section $\sigma_{\gamma\mathrm{Pb}}$.

The expected experimental uncertainties are evaluated in terms of the nuclear suppression factor R_{Pb} which is defined as root square of the ratio of photoproduction cross section $\sigma_{\gamma\mathrm{Pb}}$ measured in Pb–Pb UPC and photoproduction cross section in the Impulse Approximation calculated as a reference photoproduction cross section off proton scaled by the integral over squared Pb form factor [817]:

$$R_{\mathrm{Pb}}(x) = \left(\frac{\sigma_{\gamma\mathrm{Pb}}(x)}{\sigma_{\mathrm{IA}}(x)}\right)^{1/2}, \qquad \text{where} \qquad x = \frac{m_V}{\sqrt{s_{\mathrm{NN}}}}\exp(-y). \quad (34)$$

Under the assumption that the coherent photoproduction cross section is proportional to the squared gluon density at the scale $Q = m_V/2$, where m_V is the mass of the produced vector meson, this nuclear suppression factor can be used to constrain nuclear shadowing at different scales Q. The theoretical discussion is given in the following Section 10.2.2.2.

The ALICE and CMS collaborations estimate that the uncertainties on luminosity (4%), reference cross section (5%) and photon flux (5%) result in $\sim$ 8% systematic uncertainty on the ratio $\sigma_{\gamma\mathrm{Pb}}(x)/\sigma_{\mathrm{IA}}(x)$ and $\sim$ 4% uncertainty on the nuclear suppression factor $R_{\mathrm{Pb}}(x)$. Detailed information about the uncertainty calculation can be found in existing publications [818–820]. The pseudodata projections for the nuclear suppression factor are shown in Fig. 79 at different scales corresponding to J/ψ, $\psi(2\mathrm{S})$ and $\Upsilon(1\mathrm{S})$ photoproduction measurements demonstrating that precision measurements with a range of different scales become available.

10.2.2.2 Coherent vector meson production off nuclei

Extensive data were produced in the previous LHC heavy ion Runs on coherent photoproduction of ρ mesons [811], J/ψ [818, 819, 821] and to a lesser extent $\psi(2\mathrm{S})$ [820]: $\gamma + A \to V + A$. Due to the presence of two photon sources, the x-range of these studies is largely limited to $x \geq m_V/\sqrt{s}$. For light mesons these measurements provide information on the pattern of interactions of extended

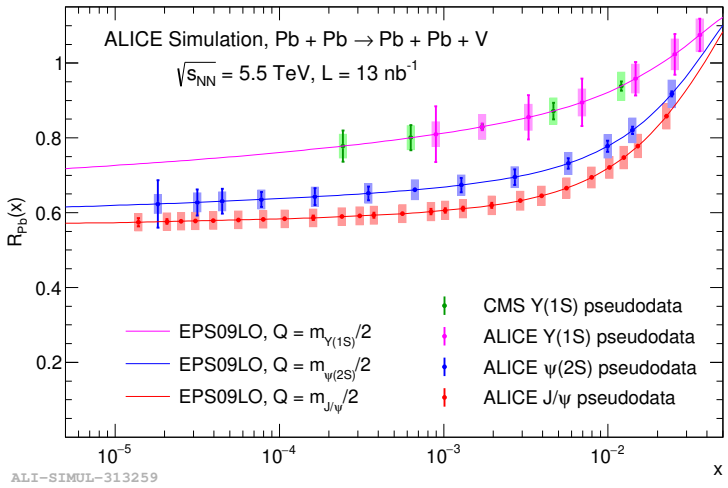

Fig. 79: Pseudodata projections for the nuclear suppression factor by ALICE [1] and CMS measured with the photoproduction of three heavy vector mesons in Pb–Pb ultra-peripheral collisions are shown. The pseudodata points are derived from EPS09-based photoproduction cross section projections following the method described in Ref. [817].

pion-size mesons and such phenomena as shadowing and color fluctuations. For small dipoles like J/ψ and $\Upsilon(1S)$, it provided information on the leading twist nuclear shadowing at moderate Q^2, which is difficult to obtain using other hard probes. The measured factor of $\sim$ 3 reduction of the J/ψ cross section compared to the γp case has significantly constrained the gluon distribution in leading twist approaches [817, 822–824]. In the dipole model framework, e.g., [825, 826], have had a tendency to predict less supression than seen in the data (in this case, the shape and normalisation of the rapidity distribution rather strongly depends on the form of the dipole cross section and charmonium wave function). The gluon nuclear shadowing in coherent J/ψ photoproduction in UPCs was also studied in the k_t-factorization approach [827] in terms of the unintegrated nuclear gluon distribution, which determines the initial condition for the non-linear evolution equation. In the case of ρ meson production, shadowing is a factor of $\sim$ 2 stronger [828] than in the approach based on the Glauber model and the vector meson dominance model.

The higher LHC luminosity and experimental upgrades will allow us to collect vastly improved samples of UPC events. In particular, the planned ALICE continuous readout [829], will eliminate many of the trigger-based constraints that have limited UPC data collection, allowing for high-efficiency collection of large samples of photoproduced light mesons. The increases in sample sizes should be considerably larger than one would expect from merely scaling the luminosity.

In order to conclude this section on the opportunities with vector meson production, we want to give a list of not yet exploited measurements that provide further insight into photonuclear interactions with heavy, light and multiple vector meson production:

– Extend substantially the x range for coherent J/ψ photoproduction on nuclei using information on the impact parameter distribution in peripheral and ultra-peripheral collisions provided by forward neutron production [816]. The impact parameter distribution can be accessed in the context of UPCs by exploiting the properties of additional photon or hadronic interactions in addition to the photon that produces the vector meson. The rates for the combined processed can be found in [830] and the relationship between impact parameter and additional photon interactions is discussed in [831]. The x-range can be also extended by using p–A collisions to probe the nucleus. In the latter case, one would have to separate coherent J/ψ production in γA and γp using a

much more narrow p_{T} distribution of J/ψ produced in coherent γA scattering and very good p_{T} resolution for the transverse momentum of the pair (LHCb).

- Measure with high enough statistics coherent $\Upsilon(1\mathrm{S})$ production in γp and γA scattering to check the expectation of the 20% reduction of the coherent cross section, which would allow one to probe gluon shadowing at a factor of ~ 10 higher Q^2 than in J/ψ production.
- Study coherent production of two pions with masses above 1 GeV/$c^2$to study an interplay of soft and hard dynamics as a function of $M_{\pi\pi}$ and $p_{\mathrm{T}}(\pi)$.
- Measure the production of heavier 2π [832], 4π and other resonances on ion targets, and search for the photoproduction of the observed exotic mesons. By using data from both proton targets (at HERA or the LHC) and ion targets, it is possible to separate the photon-meson coupling constant and the meson-nucleon interaction cross sections.
- Study the photoproduction of multiple vector mesons by a single ion pair [815]. Double photoproduction introduces many quantum correlations, including the possibility of observing stimulated decays of vector mesons. Since the two photons share the same linear polarisation, it will be possible to study photoproduction with polarised photons. In the discussed process, the charged particles from the vector meson decays are aligned (as $cos^2(\theta)$) with the plane of the linear polarization. If the two vector mesons are aligned along the same plane, then the planes formed by the decay particles will be correlated [831].

10.2.2.3 Nuclear imaging with coherent photoproduction

In coherent photoproduction, production amplitudes from each individual scattering site add with a phase factor $\exp i(\vec{x}\cdot\vec{k})$, where $\vec{x}$ is the location within the nucleus and $\vec{k}$ is the momentum transfer from the nucleus to the vector meson. So, one can Fourier transform the coherent photoproduction cross section, $\mathrm{d}\sigma_{\mathrm{coherent}}/\mathrm{d}t$ to find the location of the scattering sites within the nucleus. This can provide information on the spatial dependence of nuclear shadowing, allowing us to compare shadowing in the centre of nuclei vs. shadowing in the periphery through the transverse profile $F(b)$. Assuming azimuthal symmetry [833, 834]

$$F(b) \propto \frac{1}{2\pi}\int_0^\infty p_{\mathrm{T}} dp_{\mathrm{T}} J_0(bp_T)\sqrt{\frac{\mathrm{d}\sigma_{\mathrm{coherent}}}{\mathrm{d}t}}. \tag{35}$$

One complication is that it is necessary to flip the sign of $\sqrt{\mathrm{d}\sigma_{\mathrm{coherent}}/\mathrm{d}t}$ when crossing each diffractive minimum in the sample.

This calculation is data-hungry, and is subject to a number of theoretical uncertainties. It is also necessary to separate the cross section into its coherent and incoherent components. Nevertheless, the STAR Collaboration applied it to ρ^0 photoproduction in UPCs [835], finding a relatively boxy shape, inconsistent with a Woods-Saxon distribution, but seemingly consistent with expectations from nuclear shadowing. A follow-on study explored the Q^2 evolution of this transverse distribution by dividing the sample into three bins with different dipion mass [836]. That study also considered some of the uncertainties inherent in the analysis, including the finite experimental reach in p_{T} and the effects of the photon p_{T}, and the impact of the vector meson wave function.

Studies at the LHC could avoid many of these issues, by triggering on exclusive vector mesons (STAR required that the vector mesons be accompanied by neutrons from mutual Coulomb excitation). This would expand the p_{T} range where a meaningful $\mathrm{d}\sigma_{\mathrm{coherent}}/\mathrm{d}t$ can be extracted, increasing the accuracy of the transform. Also, because of the higher beam energies, the photon p_{T} is less important than it is at RHIC. More importantly, LHC Run 3 and 4 could also extend this study to a wider variety of mesons, including the ρ' (generically, 4π final states with a mass in the 1-2 GeV/c^2range) and the J/ψ. The latter is of particular interest because it is heavy enough to probe gluon shadowing, rather than just nuclear shadowing.

10.2.2.4 Incoherent vector meson production off nuclei

Incoherent diffractive processes provide information on nuclear dynamics, which is complementary to the information one can obtain from coherent scattering. In particular, incoherent J/ψ photoproduction probes quantum fluctuations of the target gluon density [837–842]. The corresponding cross section can be measured in a much larger range of $W_{\gamma N}$ than in the coherent case. This is possible since the activity in the nucleus fragmentation region, for example, neutrons in a ZDC can be used to determine which of two nuclei was a source of photons almost in each event.

One can distinguish two contributions to incoherent diffraction: quasielastic, when the nucleus involved in the strong interaction breaks down into nucleons and nuclear fragments, and inelastic, when hadrons are produced in the nucleus fragmentation region. At small t the second mechanism gives a $\sim 20\%$ contribution to the incoherent cross section [837, 843]. However, since the t-dependence of the inelastic mechanism is weaker, it dominates the nuclear incoherent cross section for $|t| \geq 0.5$ GeV/c^2.

While it is generally understood and accepted that J/ψ photoproduction with target dissociation is sensitive to fluctuations of the gluon density of the target, practical realisations of this notion require modeling. Notably, proton size fluctuations at $t = 0$ [837] should be contrasted with proton shape fluctuations [838–840], which in turn can be refined by including fluctuations of number of subnucleonic degrees of freedoms representing regions of high-gluon density, so-called hot spots [841,842]. The latter two approaches are assumed to be valid in an entire range of $|t|$. Hence, studies of incoherent diffraction in γp scattering via p–A UPCs and γA scattering via A–A UPCs would allow one to map variations of the gluon fluctuations with energy (x) including a possible approach to the black disk regime, where the fluctuations are strongly suppressed [841].

For very large $|t| \geq 1 - 2$ GeV/c^2one enters the regime of pQCD, which corresponds to elastic scattering of small-size dipoles off individual small-x partons of the nuclear target [844, 845].

Note also that for the proton target, one can use the process $\gamma + p \to VM(\mathrm{J}/\psi) + gap + Y$ at $-t \geq$ few GeV/c^2 to study the perturbative Pomeron. In the kinematics, where Δy is fixed, $\mathrm{d}\sigma/\mathrm{d}y_{VM} \propto (y_{VM} - \Delta y)^{2\alpha_{Pomeron}-2}$. In BFKL one expects $2\alpha_{Pomeron} - 2 \sim 0.4$ and, hence, a strong rapidity dependence of the corresponding cross section. A larger acceptance of the ATLAS and CMS detectors should allow for a more effective study of these processes than at HERA.

By studying the t-dependence and activity in the nucleus fragmentation region it would be possible to separate the two mechanisms of incoherent nuclear scattering as a function of t. For small $|t| \leq 0.3 - 0.5$ GeV^2, one can calculate nuclear shadowing for both mechanisms within the leading twist shadowing framework [816]. The shadowing turns out to be large and sensitive to the details of the leading twist shadowing dynamics. At large $|t|$, one can study the A dependence of the discussed reaction for different rapidity gap intervals to track propagation of a small dipole through the nuclear medium. By changing Δy it would be possible to vary strongly the relative role of the initial and final state interaction.

10.2.3 Inclusive and diffractive dijet production in UPC

Ultra-peripheral heavy-ion collisions provide an opportunity to study nuclear modifications of the PDFs in clean photon-nucleus interactions. One possible observable is dijet production as suggested in Ref. [846]. Compared to the dijet production in p–Pb collisions the photo-nuclear events have less underlying event activity since multiparton interactions are significantly suppressed. This enables jet reconstruction at lower transverse momenta allowing to study nPDFs at smaller scales Q^2 and x where the current PDF uncertainties are more pronounced. As the virtuality of the photons emitted by the nucleus is negligible, there are two components that need to be taken into account: the photons may interact as unresolved particles or the quasi-real photons may fluctuate into a hadronic state described with photon PDFs. The relative contribution of the direct and resolved components depends on the kinematics of the final state

jets. Hence, the uncertainty related to weakly-constrained photon PDFs can be reduced by focusing on the region where direct processes dominate the dijet production.

Here, the photoproduction framework is applied which has been recently implemented into the PYTHIA 8 Monte-Carlo event generator [516] and validated against HERA data [847], to study the potential of the Run 3 and Run 4 program to constrain nPDFs using photo-nuclear dijets. The relevant part of the photon flux is obtained by integrating the impact-parameter dependent flux from $b_{\mathrm{min}} = 2R_{\mathrm{Pb}} \approx 13.27$ fm. Two different jet kinematics are considered, one corresponding to the preliminary ATLAS measurement [848] with $p_{\mathrm{T}}^{\mathrm{lead}} > 20$ GeV/c and $m_{\mathrm{jets}} > 35$ GeV/$c^2$and one similar to HERA dijet photoproduction data [849, 850] with $p_{\mathrm{T}}^{\mathrm{lead}} > 8$ GeV/c and $m_{\mathrm{jets}} > 14$ GeV/c^2. In both cases the jets were reconstructed from the generated events using the anti-k_{T} algorithm with $R = 0.4$ implemented in the FASTJET package [409]. The differential cross sections are shown as a function of x_A in Fig. 80 using NNPDF2.3LO proton PDFs [851] with and without EPPS16 nuclear modifications [786]. The kinematic variables used in the ATLAS study [848] are defined as

$$\begin{aligned} x_A &= \frac{m_{\mathrm{jets}}}{\sqrt{s_{\mathrm{NN}}}} e^{-y_{\mathrm{jets}}}, \qquad z_\gamma = \frac{m_{\mathrm{jets}}}{\sqrt{s_{\mathrm{NN}}}} e^{y_{\mathrm{jets}}}, \\ m_{\mathrm{jets}} &= \left[\left(\sum_i E_i \right)^2 - \left| \sum_i \vec{p}_i \right|^2 \right]^{1/2}, \qquad y_{\mathrm{jets}} = \frac{1}{2} \ln \left(\frac{\sum_i E_i + p_{i,z}}{\sum_i E_i - p_{i,z}} \right). \end{aligned} \tag{36}$$

where the index i runs over all accepted jets; E_i and $\vec{p}_i$ denote the jet energy and momentum, respectively. Note that in a leading-order (LO) parton-level calculation, the definitions of x_A and z_γ would exactly match the momentum fractions probed in the PDFs of the nucleus and the photon. The parton-shower emissions and MPIs, and NLO corrections considered below, smear this connection but x_A and z_γ do serve as rather precise hadron-level estimators for the momentum fractions [852].

The uncertainty bands are derived from the EPPS16 error sets and reflect the uncertainties in the current nPDF analyses which are compared to the expected statistical uncertainties of the data in the ratio. Also the contributions from direct and resolved processes are separately plotted. Furthermore, results with the default CJKL photon PDFs [853] are compared to GRV [854] and SASGAM [855] analyses to study the underlying photon PDF uncertainty.

As shown in Figure 80(left), the contribution from resolved processes becomes dominant around $x_A > 0.02$ for $p_{\mathrm{T}}^{\mathrm{lead}} > 20$ GeV/c. This leads to a more pronounced dependence on the photon PDFs in this region, partly hindering the use of the data from this region in a global nPDF analysis. However, at small-x region, where the nPDF uncertainties are currently large and the dijets in p–Pb do not provide additional constraints, the direct processes dominate the dijet production and the dependence on the photon PDFs is negligible. The dijet cross sections fall off rapidly at small-x_A region which increases the expected statistical uncertainty limiting the small-x_A reach of the observable. With an integrated luminosity of $L_{\mathrm{int}} = 2$ nb^{-1} in Pb–Pb collisions and jet kinematics of the ATLAS preliminary study the expected statistical uncertainties become significant at $x_A \lesssim 2 \cdot 10^{-3}$. The increased luminosity of the LHC Run 3 and 4 increases the potential small-x_A reach only slightly but in the region where nPDF constraints are currently sparse. An effective way to extend the small-x_A reach is to consider jets with lower p_{T} as demonstrated in Figure 80(right). With a cut of $p_{\mathrm{T}}^{\mathrm{lead}} > 8$ GeV/c and an integrated luminosity $L_{\mathrm{int}} = \mathrm{nb}^{-1}13$ in Runs 3 and 4 it is possible to obtain nPDF constraints down to $x_A \approx 10^{-4}$. Also, the small-x nPDF uncertainties are more pronounced with a lower $p_{\mathrm{T}}^{\mathrm{lead}}$-cut since the nuclei are probed at smaller scales. The theoretical uncertainty related to the limited precision of the photon PDFs could be reduced by performing a similar measurement in p–Pb collisions where the photon flux would be dominantly provided by the Pb ion and the jets produced by γ-p system without any nuclear modifications. This measurement would constrain also the uncertainty related to the impact-parameter rejection that removes the events with hadronic interactions. However, as the minimum allowed impact

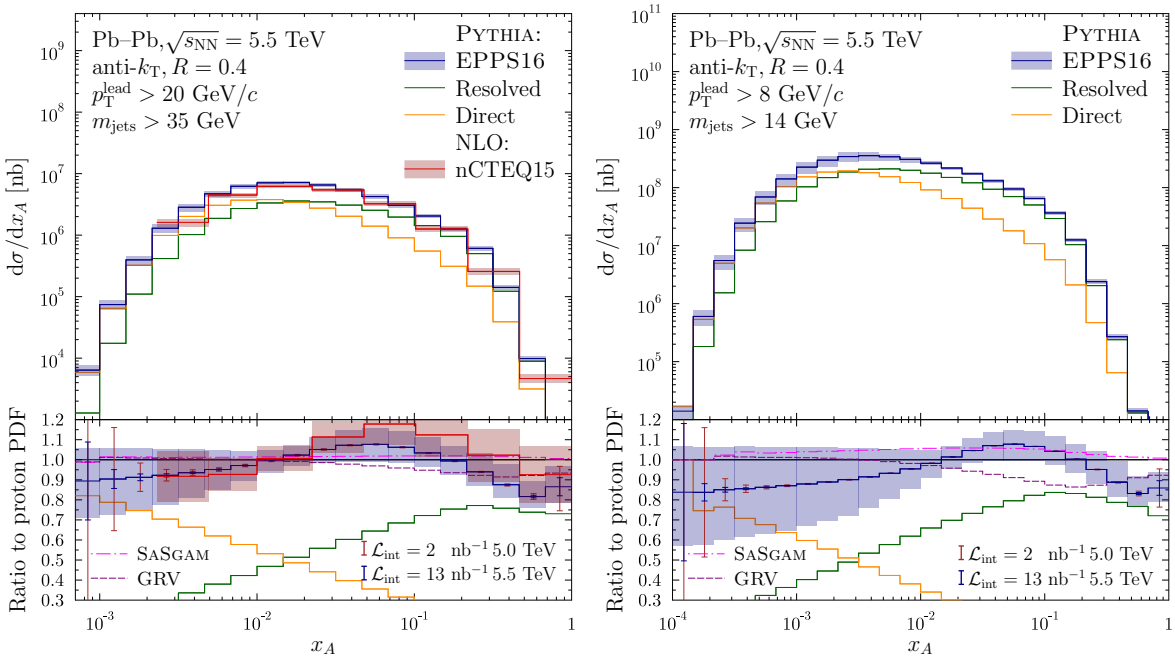

Fig. 80: Photo-nuclear dijet cross sections in ultra-peripheral Pb–Pb collisions at $\sqrt{s_{\rm NN}} = 5.5$ TeV with leading jet $p_{\rm T}$ cut of 20 GeV/c (left) and 8 GeV/c (right). Results based on PYTHIA simulations are calculated with EPPS16 nuclear modification (blue) and the contributions from resolved (green) and direct (orange) photons are separately shown. Ratio plots show also results with different photon PDF sets and the expected statistical uncertainties corresponding to the LHC (brown) and the Run 3 and and Run 4 (dark blue) luminosities. Corresponding results based on NLO calculations for Pb–Pb collisions at $\sqrt{s_{\rm NN}} = 5.02$ TeV with nCTEQ15 nPDFs [856] (red) are shown in case leading jet $p_{\rm T}$ cut of 20 GeV/c.

parameter is smaller in case of p–Pb compared to Pb–Pb and the spectrum of photons is correlated with the impact parameter cut, the kinematics would not be fully comparable preventing a full calibration of the photon flux. As the nPDFs mainly vary the shape of the x_A distributions, part of the theoretical and experimental uncertainties could also be reduced by considering x_A distributions normalized with the integrated cross section.

Inclusive dijet photoproduction in UPCs can also be evaluated to the next-to-leading order (NLO) accuracy of perturbative QCD. The corresponding cross section can be written in the following form [857]:

$$\mathrm{d}\sigma(AA \to A + 2\mathrm{jets} + X) = \tag{37}$$

$$\sum_{a,b} \int \mathrm{d}y \int \mathrm{d}x_\gamma \int \mathrm{d}x_b f_{\gamma/A}(y) f_{a/\gamma}(x_\gamma, \mu^2) f_{b/A}(x_A, \mu^2) \mathrm{d}\hat{\sigma}(ab \to \mathrm{jets}) \,, \tag{38}$$

where a, b are parton flavours; $f_{\gamma/A}(y)$ is the flux of equivalent photons emitted by one ion, which depends on the photon light-cone momentum fraction y; $f_{a/\gamma}(x_\gamma, \mu^2)$ is the PDF of the photon, which depends on the momentum fraction x_γ and the factorisation scale μ; $f_{b/A}(x_A, \mu^2)$ is the nPDF with x_A being the corresponding parton momentum fraction; $\mathrm{d}\hat{\sigma}(ab \to \mathrm{jets})$ is the elementary cross section for production of two- and three-parton final states emerging as jets in the interaction of partons a and b. The sum over a involves quarks and gluons for the resolved photon contribution and the photon for the direct photon contribution dominating at $x_\gamma \approx 1$.

Figure 80 (left) presents predictions of Eq. (38) for the cross section of dijet photoproduction in Pb–Pb UPCs at $\sqrt{s_{\rm NN}} = 5.02$ TeV in the ATLAS kinematics as a function of x_A. The red solid lines and the associated shaded band correspond to the central fit of nCTEQ15 nPDFs and their uncertainty,

respectively. The top panel of this figure demonstrates that NLO pQCD correctly reproduces the shape and, at least semi-quantitatively, the normalisation of the preliminary ATLAS data. The lower panel of Fig. 80 shows the ratio of the curves from the upper panel to the result of the calculation, where nCTEQ15 nPDFs are substituted by free proton and neutron PDFs. One can see from this panel that the central value of the ratio of the two cross sections reveals the expected trend of nuclear modifications of nPDFs: $\sim 10\%$ shadowing for small $x_A < 0.01$, which is followed by $\sim 20\%$ antishadowing (enhancement) around $x = 0.1$ and then $\sim 10\%$ suppression for $x_A > 0.3$. Note that since the uncertainties of nCTEQ15 nPDFs are of the same magnitude as the effect of nuclear modifications, inclusion of this dijet data if global QCD fits of nPDFs should in principle reduce the existing uncertainty.

It is also important to study diffractive dijet photoproduction in UPCs in the reaction $A + A \to A{+}jet1{+}jet2{+}X{+}A$. NLO pQCD predictions for the cross section of this process in pp, p–A, and A–A UPCs in the LHC kinematics were made in [858]. It was shown that studies of this process on nuclei may shed some light on the mechanism of QCD factorisation breaking in diffractive photoproduction and, for the first time, give access to nuclear diffractive PDFs and test their models.

10.2.4 Photoproduction of heavy quarks

Photoproduction of open charm and bottom is a direct probe of the gluon content of the target nucleus [859, 860]. The lowest order process, $\gamma + gluon \to c\bar{c}$ (or $b\bar{b}$) dominates over higher order, resolved processes, in which the photon radiates before it interacts with the target gluon [859]. This process type is a subset of flavour untagged dijets, discussed above. However, open charm and bottom offer some advantages, including very high rates. Based on the leading order calculations in Ref. [859] with the EKS nPDF [861], a total number of 22 billion (10 million) $c\bar{c}$ ($b\bar{b}$) pairs are produced in γPb interactions in a 13 nb^{-1} PbPb data set at $\sqrt{s_{NN}}$=5.5 TeV. In pPb collisions at $\sqrt{s_{NN}}$ =8.8 TeV with a luminosity of 2 pb^{-1}, 18 billion (100 million) $c\bar{c}$ ($b\bar{b}$) pairs are produced. The measurement of both of these processes should be well feasible despite the small experimental acceptances and branching ratios.

Vertex detectors can detect separated vertices from charm production if the charm is moderately relativistic [862], so it should be possible to study pairs with an invariant mass of $M_{c\bar{c}} \approx 4m_c \approx 6$ GeV/c^2. This will enable to study gluon distributions down to Bjorken$-x$ values of around: $x \approx M_{Q\overline{Q}}/(4\gamma m_p)\exp(y)$, where the relativistic boost of the nucleus γ, the rapidity y of the $Q\overline{Q}$ and the proton mass m_p appear. The corresponding scale is $Q^2 \approx M_{Q\overline{Q}}$. Assuming scales down to $M_{c\bar{c}} \approx 6$ GeV/c^2, a Bjorken$-x$ lower by a factor 6 can be reached compared to the kinematic selection in the preliminary inclusive dijet ATLAS analysis [848] for which the Bjorken-x reach is depicted in Fig. 80(left). By comparing results from proton targets (in p–A collisions) and heavy-ion targets (in A–A collisions), it is possible to make a direct measurement of nuclear shadowing.

The clear experimental signature for this process consists of a pair of separated vertices each corresponding to a D-meson decay in an event with one large rapidity gap. The ion moving in the same direction as the rapidity gap should remain intact. The full reconstruction of both D-mesons, the cleanest channel, the in specific decay channels requires large large event statistics and might be complemented by an analysis with one D-meson decaying semileptonically. However, the charm production rates are high enough that the low efficiency should be affordable for a precise measurement.

In addition to charm and bottom, it may also be possible to study the photoproduction of top [863, 864]. The rates are small for lead-lead collisions at the LHC (7 pairs in 13 nb^{-1}), but for pPb collisions at $\sqrt{s_{NN}}$ =8.8 TeV, the calculation of Ref. [863] finds that an integrated luminosity of 2 pb^{-1} corresponds to a production of 110 pairs. These pairs are mostly at fairly central rapidities and the large top semileptonic branching ratio should provide a clear experimental tag. This process could provide a separate probe of gluon distributions at larger x, and very high Q^2. It would also allow a direct measurement of the electric charge of the top quark.

10.3 The physics of inelastic p-Pb collisions

10.3.1 Experimental overview

Proton-lead collisions are an integral part of the LHC program since the 2012 pilot run. Within collinear factorisation, constraints on our knowledge of the nuclear wave functions could be extended at high Q^2 by dijets and heavy gauge boson available for the first time in nuclear collisions [786]. Insights have been gained at lower Q^2 with heavy-flavour production based on the assumption that their nuclear production modification is dominated by nPDFs [329]. In Run 3 and 4, the increased luminosities and detector upgrades will allow to improve the statistical precision, to extent the kinematic reach and the available processes. The detector capabilities and observables are outlined in view of high-energy QCD studies in p–Pb collisions and experimental measurement projections on selected observables are shown. One upgrade dedicated to low-x physics is separately discussed. In all cases, the statistical and point-by-point uncorrelated systematic uncertainties are not taking into account to place the central point. After this introduction, two theory contributions zoom in on specific aspects of Run 3-4 data.

- **ALICE** will measure heavy flavour and charged particle production at mid-rapidity in p–Pb collisions during Run 3 and Run 4. These measurements will constrain the parton densities in the nucleus at moderate x. At forward and backward rapidity, measurements of W and Z-boson production, as well as a range of quarkonia (J/ψ, $\psi(2S)$, and the Υ(nS) family) will be performed. In particular the W and Z boson measurements will constrain the nuclear PDFs, while the quarkonia are also sensitive to final state effects. An example is given for the Z boson in Fig. 83 on the right.
- **ATLAS** will measure heavy electro-weak bosons, W and Z, with the larger p–Pb dataset which will be available in Run 3-4. The much larger luminosity will allow precision in these measurements significantly surpassing the one currently available. Projected W and Z boson cross sections published in Ref. [7] are shown in Figure 81. Previous results have suggested that the modification of EW boson cross sections that is described with nPDFs, appears to be stronger in more central collisions [865, 866]. Figure 82 (left) shows the projected boson yield ratio of central to peripheral collisions, $R_{\rm CP}$, for different centrality bins from Ref. [7]. Figure 82(right) shows the yield of Z bosons scaled by the nuclear overlap function, $\rm T_{AB}$, as a function of centrality. It indicates that the Z boson yield uncertainties will be considerably smaller than the $\rm T_{AB}$ uncertainty.
- **CMS** will exploit the larger p–Pb dataset available during Run 3–4 and it will hence further improve the precision on differential measurements of W and Z bosons (constraining quark and antiquark nPDFs) [867, 868], as well as dijet and top quark pair ($t\bar{t}$) production (gluon nPDFs) [869, 870]. While first Run 2 results on W boson production already feature experimental uncertainties smaller than the nPDF ones [871], the larger luminosity by a factor 5 to 10 expected in Runs 3–4 will allow for another large jump in the constraints on nPDFs from data. The CMS dijet capabilities with Run 3–4 data [12] are shown in Fig. 84. In addition, novel studies will become possible, such as the measurement of differential cross sections for $t\bar{t}$ production, for an improved constraining power on nPDFs, as well as the mass dependence of Drell-Yan production down to the Υ meson mass region. The projection for $t\bar{t}$ production [12] is shown together with the precise W boson asymmetry measurement in Run 3–4 [8] in Fig. 85. Heavy flavour meson cross sections will also be measured, which are sensitive to low-x gluon nPDFs: D mesons ($p_{\rm T} > 0.5$ GeV/c), B mesons ($p_{\rm T} > 5$ GeV/c), prompt and non-prompt J/ψ ($p_{\rm T} > 3$ GeV/c), and Υ(nS) down to $p_{\rm T} = 0$. These measurements will benefit from the improved detector and trigger performance in Run 4 [806].
- **LHCb** will operate during Run 3 and Run 4 with the average charged particle multiplicity in p–Pb and Pb–p collisions that are smaller than the nominal conditions in pp running with an average pile-up of 5 interactions. All p–Pb collisions will be processed in the software trigger. Hence, LHCb can fully profit from the luminosity increase including $p_{\rm T} = 0$ heavy-flavour production.

A natural focus is the study of open and hidden beauty and charm production with improved precision. A novel measurement in the p–Pb collision system is discussed in detail in view of saturation physics in section 10.3.3 and is shown in Fig. 87. A new focus of LHCb, profitting from the increased ion in one of the considered rapidity range is shown in Fig. 83 down to 5 GeV/c^2. Direct photon studies in the conversion channel will strongly profit from the increased luminosity. The projections of the LHCb collaboration for p–Pb collisions are discussed in detail in Ref. [13].

10.3.2 Forward calorimeter upgrade of ALICE

The ALICE collaboration is considering to add a high-granularity forward calorimeter (FOCAL) to the experiment to measure direct photon production in the rapidity range 3.0–5.0 and at low p_{T}, to probe the gluon density in protons and nuclei at $x \sim 10^{-5}$ where gluon saturation and non-linear effects in the gluon density may become apparent. The FOCAL design is based on the Si-W calorimeter technology, with two or three high-granularity layers with silicon pixel sensors that allow to separate electromagnetic showers with only a few mm distance between them. This unique high granularity makes it possible to reconstruct neutral pions in the forward direction and to reject the decay photon background for the direct photon measurement.

Figure 86 shows the expected performance of the FOCAL detector for the direct photon measurement in p–Pb collisions. The left panel shows the projected uncertainties, which are 7-8% at high p_T and increase at lower momentum due to the combinatorial background. The right panel shows the impact of the measurement on our knowledge of the nuclear modification of the gluon distribution; the red lines show the current uncertainty, based on the EPS09 nPDFs, but using a broader set of parametrisations for the nuclear PDFs at the initial scale Q_0, similar to [873]. The grey band shows the uncertainty after including the FOCAL pseudo-data. The improvement in the uncertainty is about a factor 2, but it should be noted that the direct photon measurements probes the gluon distribution at low x directly, while the most of the existing data only probe $x \gtrsim 10^{-3}$ (see Fig. 78). At present, the only measurements that probe the very low x region for nuclear PDFs are forward heavy flavour measurements from LHCb [754, 874] and ALICE [875]; theoretical developments are under way to use these data to constrain the PDFs [329, 876]. The FOCAL program will probe small x in different production channels (quark-gluon Compton scattering vs gluon fusion) and therefore also further test universality and factorisation in this regime [877]. Future measurements of Drell-Yan production in LHCb, as shown in Fig. 91, will also probe this region, but will have a weaker impact for gluons at small Q^2 according to current experimental uncertainty estimates.

In addition to the inclusive direct photon measurement, the FOCAL program will measure forward π^0 production in pp, p–Pb and Pb–Pb collisions, which also provides important constraints for the nuclear PDFs and parton energy loss in Pb–Pb collisions at large rapidity. Correlation measurements of neutral pions and photons will be used to further probe the gluon density and to search for evidence of multiple-gluon interactions which are expected to be important in the high gluon density of the Color Glass Condensate [878, 879].

10.3.3 Transverse momentum dependent and low-x phenomena sensitive observables in $c\bar{c}$ and $b\bar{b}$ production

In recent years, many efforts have been devoted to elucidate the properties of transverse-momentum-dependent gluon distributions in the high-energy or small-x limit, and in particular to determine how non-linear saturation effects impact the various distributions. A process which is particularly interesting in this regard is the forward production of a heavy quark-antiquark pair, in high-energy proton-proton or proton-nucleus collisions. For kinematical reasons, in the proton-nucleus case, the proton side of the collision involves large-x partons, while on the nucleus side, small-x gluons participate. Hence,

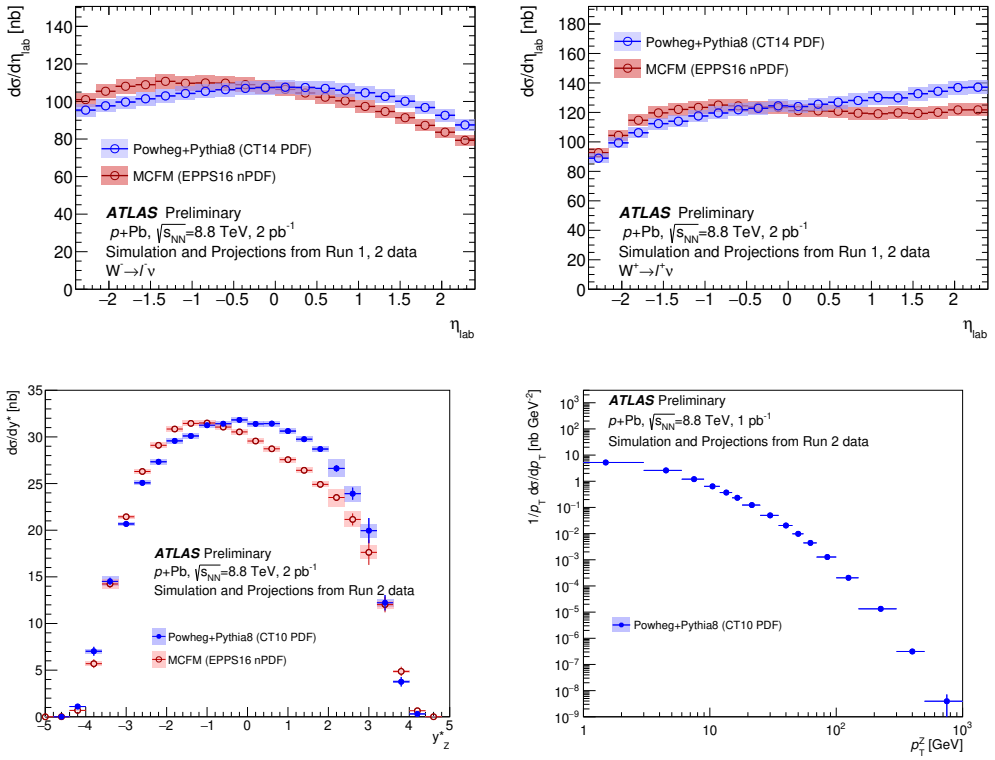

Fig. 81: Top row: Fiducial cross sections for W^+ (left) and W^- (right) boson production in p–Pb collisions at $\sqrt{s_{\mathrm{NN}}} = 8.8$ TeV differential in the charged lepton pseudorapidity measured in the laboratory frame η_{lab} [7]. The cross sections are projected with nuclear effects described by the EPPS16 nPDF set and without any nuclear effects. The boxes represent the projected total uncertainties (quadratic sum of statistical and systematic uncertainties), while vertical bars represent statistical uncertainties (smaller than the marker size). Botton row: Z boson rapidity (left) and transverse momentum (right) differential cross sections [7].

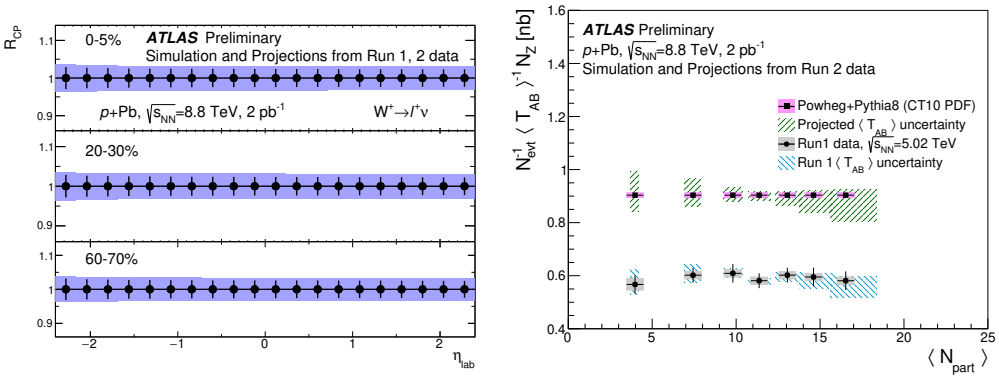

Fig. 82: Left: Uncertainties on measurments of the W^+ (left) and W^- (right) boson yield ratio of central to peripheral collisions R_{CP}. The boxes represent the projected total uncertainties (quadratic sum of statistical and systematic uncertainties), while vertical bars represent statistical uncertainties [7]. Right: Projected Z boson yields scaled by $\mathrm{T_{AB}}$ as a function of the number of nucleon participants [7]. Statistical uncertainties are everywhere smaller than the marker size, and projected systematic uncertainties (green) are described in the text. The projections are compared with a previous run 1 analysis [865].

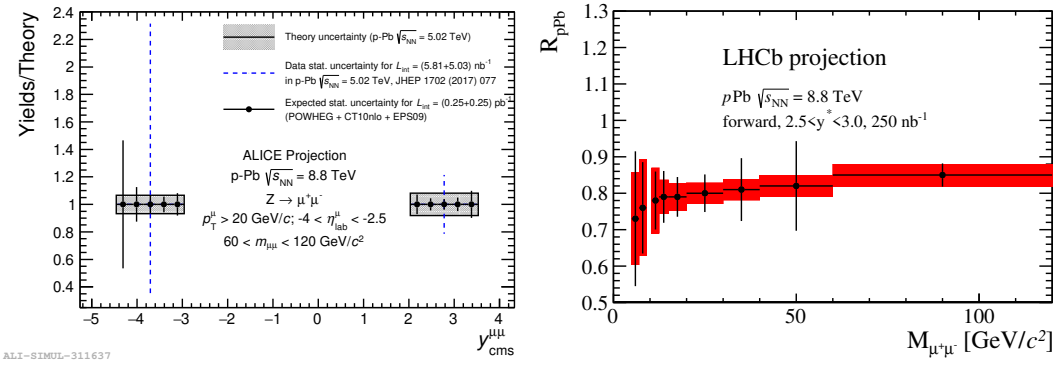

Fig. 83: Left: Expected statistical significance of the Z boson rapidity distribution for p–Pb collisions at $\sqrt{s_{\rm NN}} = 8.8$ TeV in Run 3-4 assuming an integrated luminosity of 0.25/pb (0.25/pb) obtained with the proton (Pb ion) going toward the ALICE muon spectrometer [1]. The results are compared with the statistical significance of the published data collected in p–Pb collisions in 2013. Right: $R_{\rm pPb}$ of inclusive Drell-Yan production in $2.5 < y_{cms} < 3.0$, one of five rapidity bins accessible with LHCb. The projection is detailed in Ref. [13].

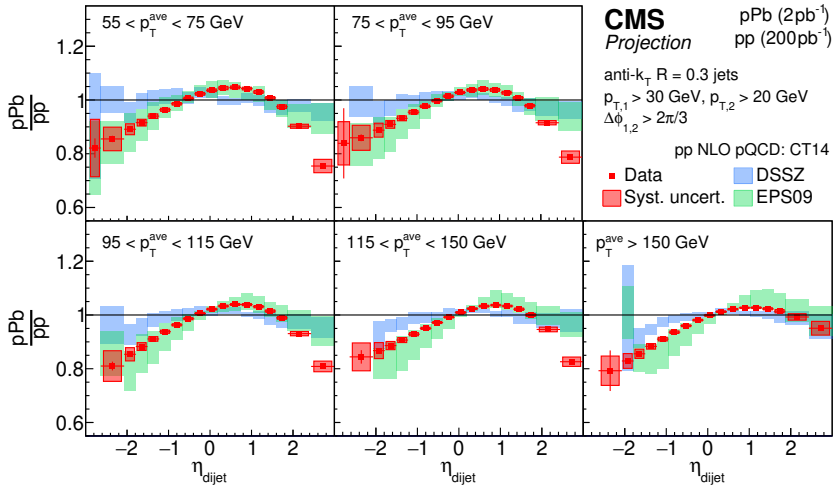

Fig. 84: Projected dijet η measurements in p–Pb collisions with combined Run 3 and Run 4 data [12].

this process can be described in a hybrid approach in which the proton content is described by regular, integrated PDFs, while the small-x dynamics in the nuclear wave function is dealt with using the Color Glass Condensate (CGC) effective theory, from which the gluon transverse momentum dependent distributions (TMDs) naturally emerge [880, 881].

In terms of sensitivity to the QCD saturation regime, the same manifestations are expected than with light quarks [882], although smaller values of x can be reached in the latter case. From the point of view of the TMD content however, heavy quarks are interesting because their production involves linearly-polarized gluons TMDs [883], in addition to the usual unpolarized gluon TMDs, and because, due to non-linear effects, the linearly-polarized TMDs generally differ from their unpolarized partners [884]. The LHCb detector is well-suited to measure heavy hadrons in the forward rapidity region, and given large-enough statistics, one could potentially try and extract information about the linearly-polarized gluons in protons and lead nuclei, from data obtained with LHC unpolarized beams. Before giving cross section estimates, let us briefly give a bit more details about the process and the physics involved.

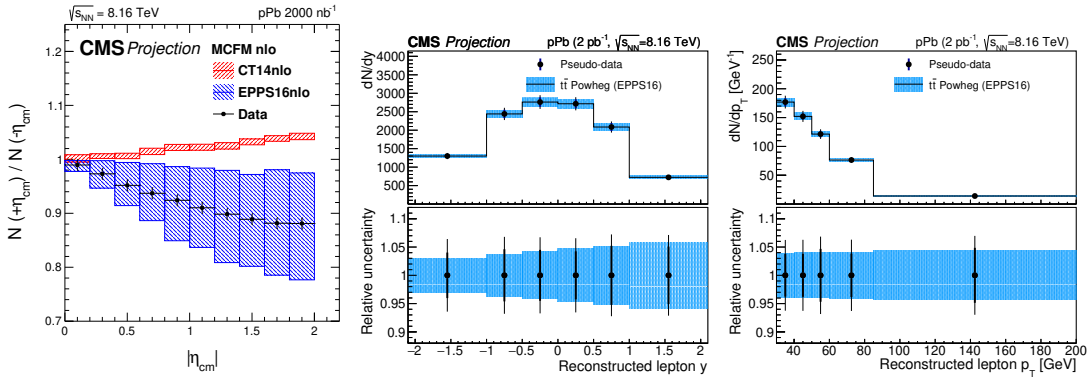

Fig. 85: Left: W boson asymmetry measurement with Run 3 and Run 4 with CMS [8]. Middle and right: CMS projected differential $t\bar{t}$ production cross section as a function of the reconstructed lepton p_{T} (middle) and rapidity (right) [12]. The total and statistical uncertainties are represented by the outer and inner error bars, respectively. The bottom panels represent the relative uncertainties (68 confidence-level error bands) in the projected data and theory predictions employing the CT14NLO [872] free proton and EPPS16NLO [786] bound nucleon PDF sets.

.

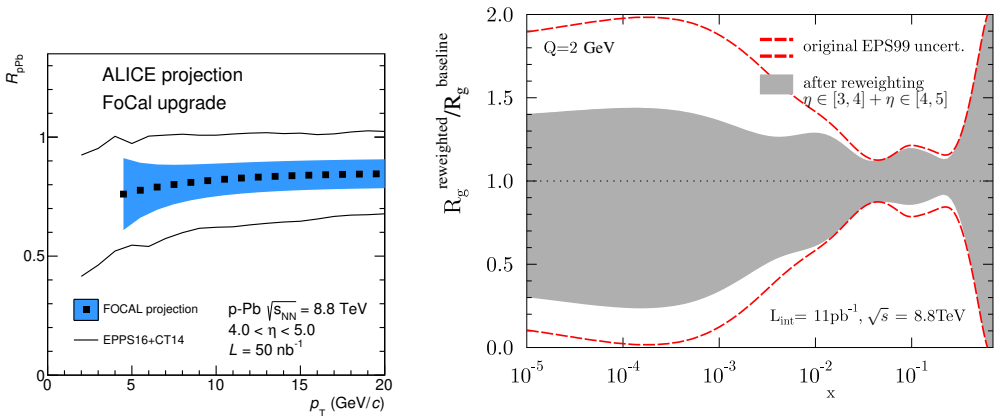

Fig. 86: Left: Projected uncertainties on the nuclear modification factor for the forward direct photon measurement in p–Pb collisions with the ALICE FOCAL upgrade. Right: Uncertainty on the modification ratio of the gluon density in the Pb nucleus from a fit to FOCAL pseudo-data. The red lines show the current uncertainty and the grey band shows the uncertainty after including the FOCAL pseudo-data. Figures from Ref. [1].

Forward quark-antiquark pair production in dilute-dense collisions is characterized by three momentum scales: P_t, the typical transverse momentum of a single quark, and always one of the largest scales; k_t, the total transverse momentum of the pair, which is a measure of the transverse momentum of the small-x gluons coming from the target; and Q_s, the saturation scale of the target, which is always one of the softest scales. The value of k_t with respect to Q_s and P_t governs which factorisation scheme is relevant. Indeed, when $k_t \sim Q_s \ll P_t$ (the quark and the antiquark are almost back-to-back), there are effectively two strongly ordered scales k_t and P_t in the problem and TMD factorisation applies [880], implying the involvement of several gluon TMDs that differ significantly from each other, especially in the saturation regime, when $k_t \leq Q_s$ [881]. In the other regime which shall not be discussed here (away from back-to-back production), k_t and P_t are of the same order and far above the saturation scale, only the linear small-x dynamics is important and the various TMDs differ no more.

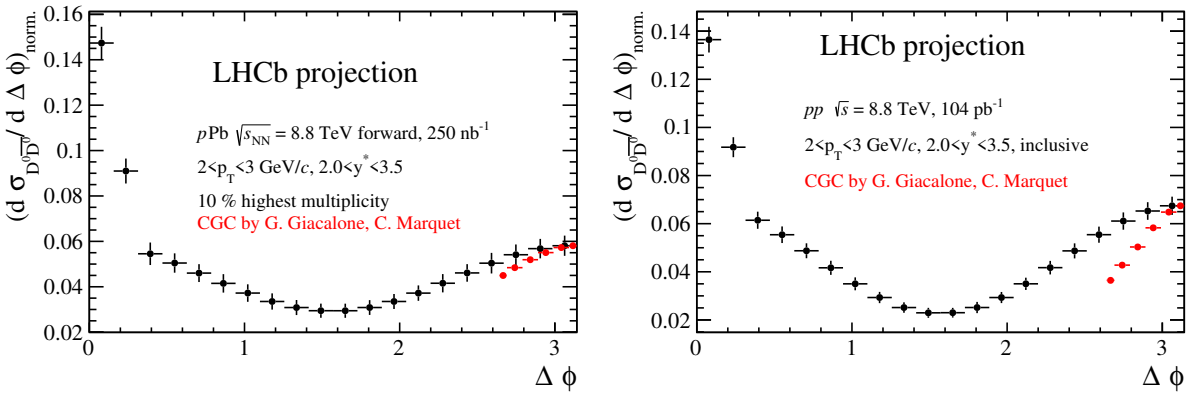

Fig. 87: LHCb projections [13] for $D^0\overline{D^0}$ in LHC Run 3 and Run 4 compared with theoretical calculations decribed in section 10.3.3 in 10 % largest multiplicity p–Pb collisions (left panel) and minimum bias, i.e., inclusive, pp collisions (right panel). The D-mesons are both reconstructed in the πK-decay channel.

In [880, 885], the cross section for forward di-jet production in proton-nucleus collisions was calculated within the CGC. It was then shown that, in the back-to-back limit, a TMD factorisation formula could be extracted, the result being the same as in a direct TMD approach (i.e., without resorting to the CGC). However, in contrast to the direct TMD approach, the calculation in the CGC yields explicit expressions for the TMDs in terms of Wilson lines, which can be evolved in rapidity through the non-linear Jalilian-Marian-Iancu-McLerran-Weigert-Leonidov-Kovner (JIMWLK) equation. In [884], those results were extended to the case of a forward heavy quark-antiquark pair. As already observed earlier (see for instance [883, 886–890]), by keeping a non-zero quark mass, the cross section becomes sensitive to additional TMDs, which describe the linearly-polarized gluon content of the unpolarized target.

The three unpolarized gluon TMDs which describe the quark-antiquark pair production are the adjoint-dipole TMD, the Weizsäcker-Williams TMD, and a third one which is roughly a convolution of two fundamental-dipole TMDs. They are accompanied by three 'polarized' partners, which couple through the quark mass and via azimuthal-angle modulation. This is analogous to what happens in the $\gamma^* A \to q\bar{q}$ process (in that case not only a non-zero quark mass but also a non-zero photon virtuality brings sensitivity to linearly-polarized gluons) described in Section 10.2.4,10.2.3, although there, only one unpolarized gluon TMD is involved (the Weizsäcker-Williams distribution), along with its polarized partner [889, 890].

Predictions for D mesons are presented in Figure 87 as a function of their relative azimuthal angle near π, along with projections from the LHCb experiment. In the p–Pb kinematical range that is investigated here, roughly 2.800 raw counts are expected over the full azimuthal range for the specified decay channel that can be complemented with other channels as in pp collisions in Ref. [891].

10.3.4 Fully coherent energy loss effects on different final states

The multiple scattering of quarks and gluons traveling in a QCD medium induces the radiation of gluons which carry away some energy of the propagating parton, leading for instance to the jet quenching phenomenon. Therefore, a key ingredient of any parton energy loss calculation is the medium-induced gluon spectrum radiated by the fast propagating color charge. It is of course of crucial importance to know the correct parametric dependence of the induced spectrum, which in general depends on the parton properties (in particular its energy and mass) and those of the medium, since it has a direct impact on the phenomenology of particle production in p–A and A–A collisions. The emission of a gluon

radiated by an energetic parton experiencing multiple scattering in a medium takes a typical formation time, t_f, which needs to be compared to the length of the medium, L.

Over the last few years, it has been realized that in a hard process involving incoming and outgoing energetic color charges (which do not have to be identical) being quasi-collinear in the rest frame of the medium, the associated medium-induced gluon spectrum is dominated by *large* gluon formation times, $t_f \gg L$ [489, 892, 893]. In this so-called fully coherent (FC) region, the medium-induced radiated energy is similar to the energy loss of an asymptotic charge. In particular it scales as the energy, and thus exceeds at high energy the average parton energy loss in the Landau–Pomeranchuk–Migdal (LPM) regime, $t_f \lesssim L$, for which the energy dependence is at most logarithmic. This different parametric behavior has important consequences on the phenomenology of hadron production in p–A collisions. In particular, a model based on the fully coherent induced gluon spectrum was shown to describe accurately the quarkonium suppression observed in p–A collisions at all centre-of-mass energies, from the SPS fixed-target experiments ($\sqrt{s} \simeq 20$ GeV) to the LHC ($\sqrt{s} = 5.02$ TeVand $\sqrt{s} = 8.16$ TeV) [894–896]. It is therefore necessary to investigate further the role of fully coherent energy loss on other processes. Because the fully coherent induced gluon spectrum arises from the interference between the emission amplitudes off the initial charge and that off the final state, the effects of FC energy loss are process dependent. Let us review, at a qualitative level, the expected nuclear dependence of different processes which could be measured at the LHC with a high luminosity.

In the absence of color charge in the partonic final state, the energy loss in Drell-Yan (DY) production at leading order is expected to be that of a suddenly decelerated parton, that is, independent of its energy (LPM regime). The effects of parton energy loss in nuclei should therefore play almost no role on DY production in high-energy p–A collisions, since $\Delta E/E \to 0$ in the high-energy limit. The inclusive production of DY lepton pairs in p–A collisions at the LHC should therefore be free of any parton energy loss effect. As a result, this process might be used advantageously in order to probe possible nuclear PDF effects at small values of x, see e.g., Fig. 83 and Ref. [500] for more details. Assuming a luminosity of $L_{\text{int}} = 250$ nb^{-1} and taking the conservative value for the cross section in p–Pb collisions at $\sqrt{s} = 5$ TeV, $\mathrm{d}\sigma/\mathrm{d}y = 40$ nb [500], the number of forward DY lepton pairs, which could be measured by the LHCb experiment is typically 10^4 per rapidity unit. Also interesting, and accessible with a high luminosity, would be the production of diphotons in p–A collisions. This process would be free of energy loss effects, for the same reasons as the DY process, while being sensitive to nPDF in the quark sector, $q\bar{q} \to \gamma\gamma$, and in the gluon sector through the 'box diagram', $gg \to \gamma\gamma$.

Note that the energy loss scaling as E (FC regime) would come into play only if *another* energetic charged particle is produced in the final-state in association with the virtual photon (or the diphoton), such that the final state carries a global color charge. Such a situation typically occurs in DY+jet production in p–A collisions. Consider for instance the Compton scattering process, $qg \to q\gamma^\star$. At forward rapidity, an incoming quark from the proton projectile scatters in the medium to produce the final state in a color triplet representation. In this peculiar case of quark to a color triplet final state, one would expect a negative *medium-induced* gluon spectrum (i.e., with stronger gluon radiation in pp than in p–A collisions), leading to an energy *gain* (with respect to pp collisions), $\Delta E \propto (-1/2N_c) \times E$ [893]. Such an unusual dependence would manifest by a slight *enhancement* of DY+jet production in p–A collisions with respect to pp collisions [500], although a quantitative study would be needed to answer whether this effect could be visible in the experiment. Similarly, should this enhancement be small or negligible, the associate production of a prompt photon with a heavy-quark jet might be sensitive to the nPDF of heavy quarks and gluons, as emphasized in Ref. [897]. Using $\sigma_{\gamma c} = 1.2 \times 10^5$ pb in the acceptance of the ALICE calorimeter [897] leads to 2.4×10^5 $\gamma + c$-jet events in p–Pb collisions at $\sqrt{s} = 8.8$ TeV assuming $\mathcal{L} = 2$ pb^{-1}. This observable should be also accessible in ATLAS, CMS and LHCb acceptances as well.

More pronounced effects of fully coherent energy loss are expected when the final state is in a

color octet state, or possibly in higher color representations. An example is the production of a jet pair with not too large transverse momenta (ideally only a few times the saturation scale of the target nucleus). In the case of di-gluon production, the final state can be produced in the 27-plet color representation (with Casimir $C_{27} = 8$) that would lead to an average coherent energy loss proportional to $(N_c + C_{27})/2 = 11/2$, that is almost twice larger that expected if the final state is in a color octet state. Such higher color representations could also be probed in the production of B_c mesons (or in the associate production of a D and a B meson), with a complex final state $\mathrm{c\,\bar{c}\,b\,\bar{b}}$. From the number of fitted signal candidates $\mathcal{N} = 10^4$ B_c mesons extracted at LHCb in the semileptonic decay channel in pp collisions at $\sqrt{s} = 8$ TeV with $\mathcal{L} = 2$ fb^{-1} [898], the expected $\mathrm{B_c}$ rate in the LHCb acceptance using $\mathcal{L} = 0.5$ pb^{-1} in p–Pb collisions at the same energy is $\mathcal{N} = 5 \times 10^2$ $\mathrm{B_c}$ mesons.

10.4 Constraints on nuclear PDFs

10.4.1 Overview

As previously discussed in Sec. 10.1, the nuclear Parton Distribution Functions (nPDFs) are poorly constrained as compared to the proton PDFs. This is mainly due to the lack of high statistics data across the very large nuclear mass number (A) range. In fact, even the precision of the proton PDFs rely crucially on nuclear target data [872, 899, 900]; for example, the neutrino-nucleon deep-inelastic-scattering (DIS) structure functions are essential for decomposing the flavour components of the proton [901–905]. Consequently, improved determinations of the nuclear PDFs and nuclear correction factors could improve the proton PDF precision. Thus, the future LHC Runs 3 and 4 could provide the opportunity to precisely constrain the nPDFs for the Pb-nucleus and, in Run 5 and later, one or more lighter nuclei, and thereby disentangle the nuclear effects from the individual flavour components.

In Fig. 88 selected nPDFs from the literature are displayed.

10.4.2 W and Z boson production

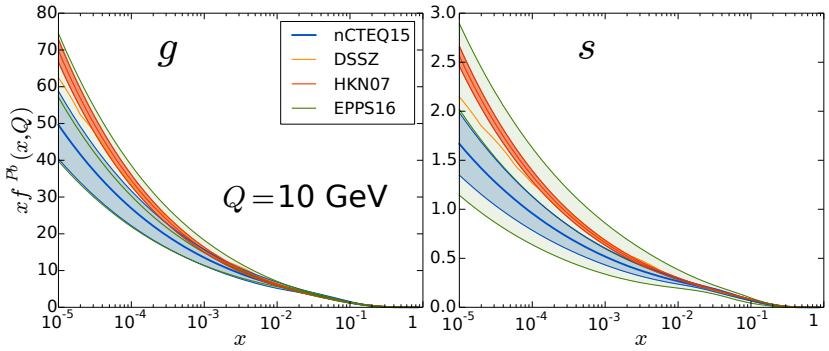

Fig. 88: Comparison of the gluon (left) and strange (right) quark nPDF for a lead nucleus as a function of x for a selection of nuclear PDF sets: HKN07 [906], DSSZ [788], EPPS16 [786], and nCTEQ15 [787].

Inclusive W and Z boson production: Inclusive production of W and Z bosons in pp collisions at the LHC can provide new information on the strange, charm and beauty quark PDFs. Additionally, heavy-ion W and Z production data from p–Pb and Pb–Pb can provide insight on the nuclear corrections, and this complements other data on nuclear targets as it is at large A (lead) and high energy (and thus, smaller x) [865–868, 871, 910, 911]. For example, ATLAS used inclusive W/Z production data to extract the strange quark component of the proton as displayed in Fig. 89 (left). This yielded a larger strange quark PDF than commonly expected [907, 912]. A recent analysis of the ATLAS and CMS inclusive W and Z differential cross section data at 7 and 8 TeV [913] and the combined HERA inclusive data indicates that while there is no tension between the data sets, the LHC data does support unsuppressed

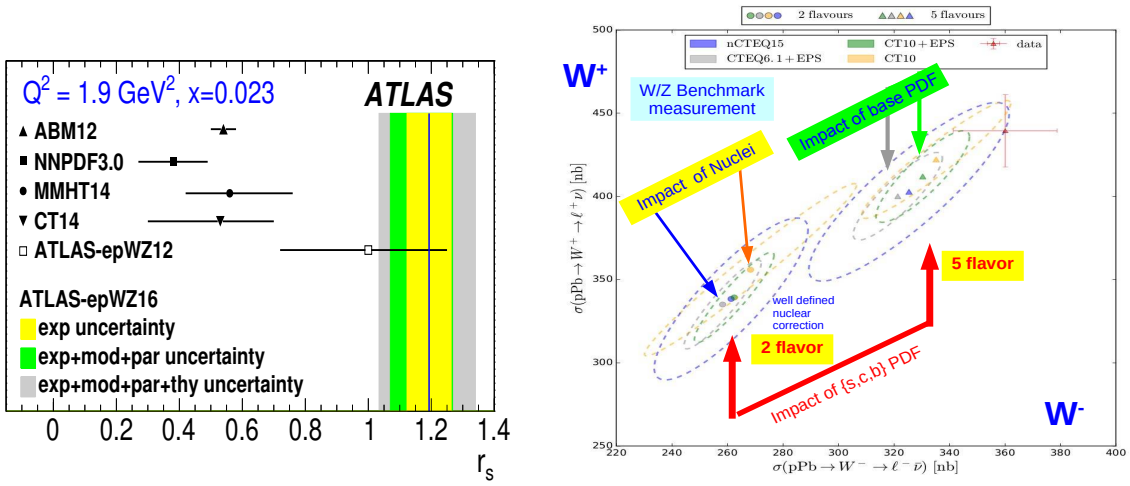

Fig. 89: Left: The relative strange-to-down sea quark fractions $r_s = 0.5(s + \bar{s})/\bar{d}$ as compared with predictions from different NNLO PDF sets; figure from Ref. [907]. Right: correlations between W^+ and W^- p–Pb cross sections calculated with different input PDFs and assumptions to illustrate the separate impact of the i) nuclear corrections, ii) heavy flavour components, and iii) base PDFs [908,909].

strangeness in the proton at low x at both low and high scales. Certainly this is an area that warrants further study.

To highlight the sensitivity of the heavy ion W/Z production to both the heavy flavour components and the nuclear corrections, in Fig. 89 (right), the correlations between W^+ and W^- cross sections for proton-lead interactions calculated with different input PDFs and assumptions [908] are shown. By comparing the results with and without the strange, charm, beauty quark flavours, it can be observed that these quarks do have a large impact on this observable; hence, this process can provide incisive information about the corresponding PDFs. To see the effect of the nuclear corrections, the CT10 proton result is compared with the other calculations. For the case that only two flavours are considered, the separation of the proton result (CT10) and the nuclear results are quite distinct. In this case, the effect of the specific nuclear correction (nCTEQ15 or EPS09) or the effect of the underling base PDF (CTEQ6.1 or CT10) is minimal. In contrast, when this picture is compared to the five flavour results, the division between the proton and nuclear result is not as simple as the different nuclear corrections and proton baseline PDFs yield a broader range of results. In particular, the strange quark PDFs in the CTEQ6.1 and CT10 proton baseline PDFs are quite different, and this will contribute to the spread of results. Thus, proton-lead production of W/Z is an ideal "laboratory" as this process is sensitive to i) the heavy flavour components, ii) the nuclear corrections, and iii) the underlying "baseline" proton PDF. Thus, high-statistics heavy-ion run data during Run 3 and Run 4 has the potential to reduce the current uncertainties and improve the nuclear PDF determination as illustrated by the projections from ATLAS in Fig. 81 and CMS 85.

$W^{\pm}$ asymmetries: A way to disentangle the nuclear effects from proton PDF and other theory uncertainties like higher-order corrections even in the absence of a pp reference, is the forward-to-backward ratio [914]. To showcase the potential in the case of $W^{\pm}$ projections (shown in Fig. 85), Fig. 90 presents the effect that PDF reweighting [915] analysis with these data has on EPPS16 nuclear PDFs and the corresponding theory predictions for the asymmetry. The most notable effect is the dramatic reduction in the uncertainties of the gluon PDF. Indeed, $W^{\pm}$ production takes place at a high scale $Q^2 \sim M_W^2$ and even though it is mostly $q_i\bar{q}_j$ processes that make the W bosons, the $\bar{q}_j$ PDFs probed at $\eta_{CM} \gtrsim 0$ are, in practice, dominated by the evolution effects at small x. Thus, it is not that surprising that it is predominantly the gluon component that gets tightly constrained by the W data. The improvement for the light

Fig. 90: Left: The CMS projections [8] for the forward-backward asymmetry in $W^{\pm}$ production (Fig. 85) compared to the original EPPS16 90% confidence-level error bands and those after reweighting with these $W^{\pm}$ data. Right: The change in EPPS16 nuclear PDF modifications for sea quarks and gluons at $Q^2 = 100$ GeV^2 upon reweighting with the data shown in the left-hand panel.

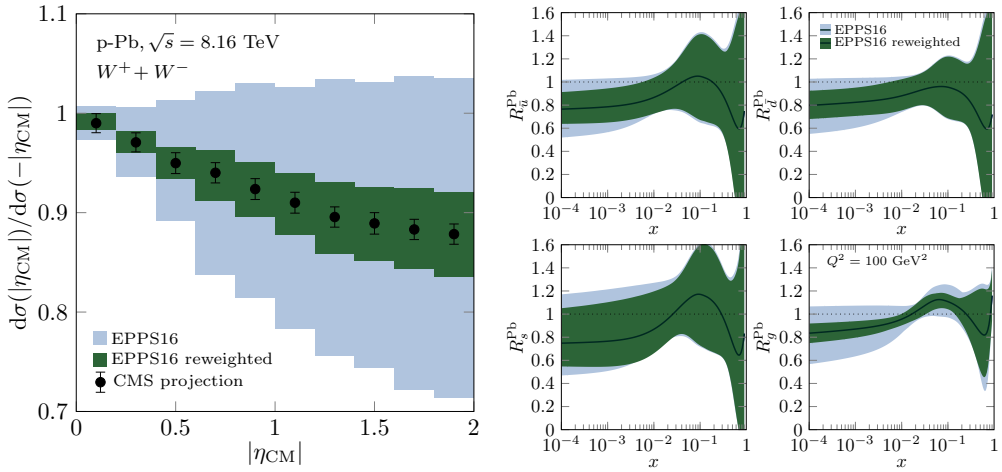

sea quarks (d,u,s) is merely a consequence of better constrained gluons, through QCD dynamics. The large-x ($x \gtrsim 0.1$) part is not really affected by the $W^{\pm}$ data.

Another $W^{\pm}$ observable that would benefit from a high luminosity is an asymmetry

$$[\sigma^{W^+}(y_{\mathrm{CM}}) - \sigma^{W^+}(-y_{\mathrm{CM}})]/[\sigma^{W^-}(y_{\mathrm{CM}}) - \sigma^{W^-}(-y_{\mathrm{CM}})]$$

proposed in Ref. [914]. In order to measure such a quantity involving four cross sections and subtractions among them (particularly in the denominator which may fluctuate between positive and negative), an excellent statistical precision — like that achievable during Run 3 and 4 at the LHC would be advantageous. With the present Run 2 luminosity it appears that the data [871] are still not accurate enough to measure this across the full rapidity acceptance.

Low-mass Drell-Yan: The Drell-Yan process at low invariant masses is a luminosity-hungry process where LHC Run 3 and Run 4 can make a difference. It would be very much advantageous to reach this low-mass region experimentally as it offers a possibility to constrain the nuclear PDFs at lower factorisation scale where the nuclear effects are larger. The estimated impact is shown in Fig. 91 where the LHCb estimates for R_{pPb} are compared to the reduction of EPPS16 uncertainties upon performing a PDF reweighting [915] with these data described in detail in Ref. [13]. In the calculation, a full decay-lepton phase space has been assumed, but this has a feeble effect on R_{pPb}. Although the Drell-Yan process occurs predominantly via $q\bar{q}$ annihilation, the scale-evolution effects are large and these data mostly constrain the gluon PDFs. Here, it should be noted that the probed x values are already so small, that the parametrisation bias which is prominent at small x [873, 916] is probably significant and understates the "true" effect of these measurements. This kind of scan over a wide range of invariant masses with the LHC Run 3 and 4 precision would offer a possibility to test the Q^2 evolution of nuclear PDFs – whether there are corrections to standard DGLAP – much more systematically than only on-shell $W^{\pm}$- and Z-production measurements do (involving only one scale).

10.4.3 Heavy quark production

Inclusive Heavy Quark Production: A recent study of inclusive heavy quark production in proton–lead collisions at the LHC demonstrates this can also help constrain the gluon distribution in nuclei.

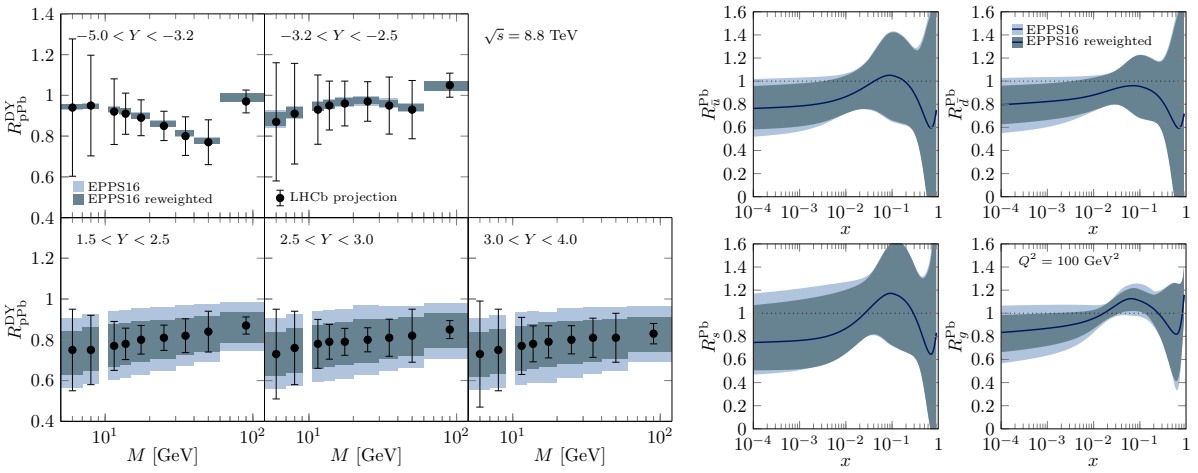

Fig. 91: Left: The LHCb projections [13] on R_{pPb} in Drell-Yan process compared to the original EPPS16 error bands and those after reweighting with these data. Right: The improvement in EPPS16 nuclear PDFs for sea quarks and gluons at $Q^2 = 100$ GeV^2 upon reweighting with the data shown in the left-hand panel.

Specifically, Ref. [917] makes use of LHC p–Pb data on $\mathrm{D}^0, \mathrm{J}/\psi, \mathrm{B} \to \mathrm{J}/\psi, \Upsilon(1\mathrm{S})$ meson production [496, 506, 754, 874, 918–929]. They obtain a consistent description of these data assuming nPDF modifications are the dominant source of nuclear modifications in p–Pb collisions. Under this assumption, a clear confirmation of gluon shadowing at small x is found. Additionally, they demonstrate that the inclusion of such heavy-flavour data in a global fit can significantly reduce the uncertainty on the gluon density down to $x \simeq 7 \times 10^{-6}$ while keeping an agreement with the other data of the global fits. A reweighting of the current nPDFs sets with the LHC heavy-flavour data was performed for the nCTEQ15 and EPPS16 sets. In a recent analysis of beauty hadrons by the LHCb collaboration [754, 922, 923] excellent agreement between the reweighted predictions and the measured data for the nuclear modification factor R_{pPb} was found. Furthermore, the precision of these data will allow to further reduce the uncertainty of the low-x nuclear gluon distribution. Due to the lower production rates for beauty hadrons, this kind of observables would clearly profit from a higher luminosity as shown in Fig. 25 in the heavy-flavour chapter. Note that heavy flavour measurements from LHCb extending to larger transverse momenta have also the potential to constrain the intrinsic heavy quark component [930–932].

Prompt Diphoton Production: As discussed in Sec. 10.3.4, other nuclear effects such as coherent small angle gluon radiation may explain the heavy-flavour data without a strong shadowing of the small-x gluon. A way to contrast parton shadowing against effects from coherent energy loss discussed in section 10.3.4, will be to study hard processes with color neutral final states in the context of a global analysis in order to see whether a coherent description of all the data remains possible. The case of vector boson production has already been discussed above which is rather sensitive to the quark distributions. Interesting processes (with more or less color neutral final states) which are sensitive to the gluon distribution are inclusive prompt photon production and diphoton production. The prompt photon observable has been discussed in Section 10.3.2 in the context of the ALICE upgrade. The diphoton production is rather clean with an essentially color neutral final state assuming that the contribution from the fragmentation of quarks and gluons into photons can be strongly suppressed by photon isolation criteria [725, 933]. Due to the small diphoton cross section, this measurement requires high luminosities. Based on the available calculations at next-to-leading order [934, 935], about 6000 events within the fiducial experimental acceptance used in pp collisions by ATLAS can be expected with 2 pb^{-1} p–Pb collisions.

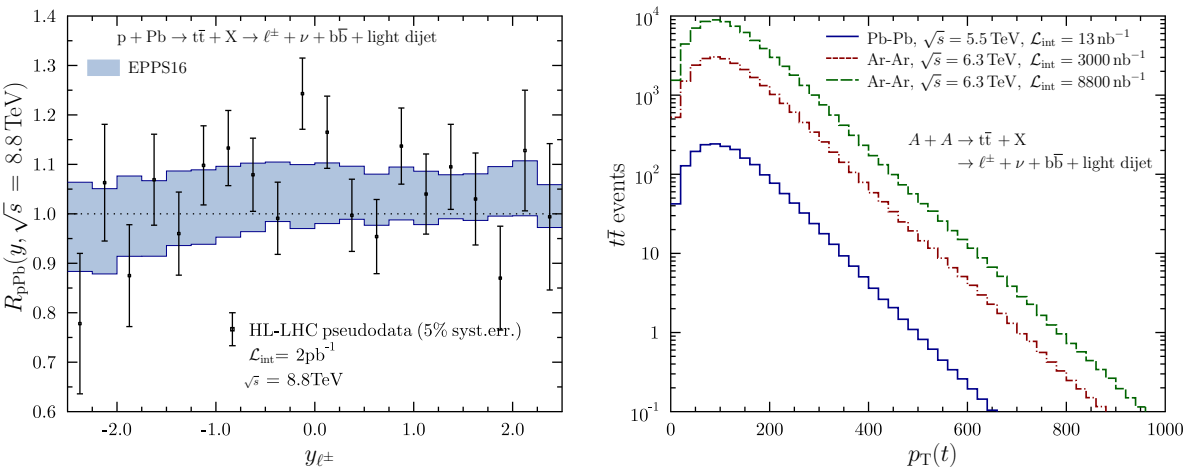

Fig. 92: Left: Projected data for $t\bar{t}$ production during Run 3 and 4 compared with uncertanties of the EPPS16 pdf-set. Right: Number of expected $t\bar{t}$ events in Ar–Ar collisions and in Pb–Pb as a function of the top-quark transverse momentum. the used luminosities are discussed in the text.

Heavy Quark Associated Production: The associated production of a heavy quark Q and a vector boson $\gamma/Z/W^{\pm}$ also provides incisive information about the PDFs. For all these processes, the LO contribution comes from the gluon–heavy-quark (gQ) initiated subprocess, making this process very sensitive to the gluon and the heavy quark nuclear parton densities. For the neutral current processes, a prompt photon γ or Z together with a c or b quark can be considered to obtain information of the c and b PDFs, respectively; for the charged current process, the Wc and Wb final states are sensitive to the strange and charm quark, respectively. These channels have been analysed for the LHC pp data [936–941] and the Wc channel is a key input for the ATLAS/CMS comparison of the strange sea quark content of the proton [913]. The event statistics in 2 pb^{-1} p–Pb collisions can be expected to be a factor 10 smaller than in the Run 1 CMS [940] and ATLAS [941] allowing for a first measurement in p–Pb collisions.

Additionally, the γ/Z transverse momentum can be used to gauge the initial energy of the massive parton propagating through the dense QCD medium produced in those collisions, making γ/Z+ Q production a powerful process in order to probe energy loss dynamics in the heavy-quark sector. Furthermore, the comparison of the photon-jet pair momentum, from pp to Pb–Pb collisions, is sensitive to the amount of energy lost by the heavy-quarks and could therefore be used in order to better understand parton energy loss processes in the heavy quark sector.

10.4.4 Top production

The $t\bar{t}$ production provides a complementary observable to the dijets for probing high-x gluons [870, 942]. For the very short t-quark life time, they decay, in practice exclusively, to W boson and b quarks. Although, the cleanest channel is the one where both W bosons decay leptonically, it has been recently demonstrated [870] that it is possible to get a clear signal when one of the two W bosons decays leptonically and the other one goes to light-quark jets. This is the preferred observable as the yields are 3 times higher than when both W bosons decay leptonically. The cross sections using the MCFM code [943], process 146 (where the leptonically decaying W comes from top quark) have been estimated at NLO level. The following fiducial cuts have been applied:

$$p_{\rm T}^{\ell^\pm} > 30\ \text{GeV/c},\ |y^{\ell^\pm}| < 2.5,\ p_{\rm T}^{\rm missing} > 30\ \text{GeV/c},$$

$$p_{\mathrm{T}}^{\mathrm{jets}} > 30 \text{ GeV/c}, \ |y^{\mathrm{jets}}| < 2.5, R_{\mathrm{isolation}}^{\mathrm{jets}} = 0.5.$$

In this setup, the NLO calculation with the factorisation and renormalisation scales set to the top-quark mass yields, per-nucleon, $\sigma_{\mathrm{n-n}} \approx 4200\,\mathrm{fb}$ in p–Pb collisions at $\sqrt{s} = 8.8\,\mathrm{TeV}$, with CT14NLO [872] proton PDFs and EPPS16 [786] nuclear corrections. This is to be multiplied by a factor two to account for the electron and muon final states and by a factor of two to account for the process where the antitop is the one from which the leptonically decaying W originates from. Since this is the nucleon-nucleon cross section, a factor of 208 has to be still multiplied to get the p–Pb cross section. This yields $\sigma_{\mathrm{pPb}} \approx 3.5\,\mathrm{nb}$. Considering the $2000\,\mathrm{nb}^{-1}$ scenario, and efficiency of 0.75 [942] in b-jet tagging, around 5200 events are expected. Based on this number, the expected nuclear modification factor R_{pPb} following the steps of Ref. [942] has been estimated, assigning each data point a 5% uncorrelated systematic uncertainty (in the current p–Pb measurement of CMS [870] the systematic uncertainty is ∼20%). Dividing the $|y^{\ell^{\pm}}| < 2.5$ interval to 20 bins, the statistical uncertainty varies from 5% ($|y^{\ell^{\pm}}| < 1$) to 10% (most forward/backward). The resulting R_{pPb} is compared in Fig. 92 with the EPPS16 uncertainty band. In the considered kinematic configuration the expected R_{pPb} is typically a bit above unity for the gluon antishadowing in EPPS16. As can be seen from the left-hand panel of Fig. 92, the expected precision of the measurement is not enough to give significant constraints on nuclear PDFs. In particular, the dijets considered in Section 11.4.3 will probe the same kinematic configuration with a clearly higher precision. However, here much depends on the expected systematic error (taken here to be 5% for each data point separately) and how large are the bin-to-bin correlations. In the p-Ar mode, the higher c.m. energy of $\sqrt{s} \approx 9.4\,\mathrm{TeV}$ increases the yields around 50% and would also benefit from the higher luminosities, see the next subsection and Sec. 2.4.

This, plus a higher achievable nucleon-nucleon luminosity would render the above case almost completely systematics dominated.

Using the same framework and assumptions as above, the fiducial $t\bar{t}$ yields in A-A collisions have been estimated. Here, the Pb–Pb and Ar–Ar cases have been considered. In Pb–Pb collisions at $\sqrt{s_{\mathrm{NN}}} = 5.5\,\mathrm{TeV}$, the per-nucleon cross section is $\sigma_{\mathrm{n-n}} \approx 1200\,\mathrm{fb}$ which translates to around 2000 reconstructed events for $13\,\mathrm{nb}^{-1}$ ion-ion luminosity. In the Ar–Ar option, the c.m. energy is slightly higher, $\sqrt{s} = 6.3\,\mathrm{TeV}$, which increases the cross section by some 50%. In addition, the achievable ion-ion luminosity is much higher, $3000\,\mathrm{nb}^{-1}$-$8800\,\mathrm{nb}^{-1}$ within 2.75 months of running, see Tables in Chapter 2.4. Thus, the estimated amount of $t\bar{t}$ events is clearly larger, around 30000. The right-hand panel of Fig. 92 shows the event distributions as a function of top-quark transverse momentum $p_{\mathrm{T}}(t)$. This shows that, the HL-LHC may allow to probe the space-time picture of heavy-ion collisions using top quarks [944] up to $p_{\mathrm{T}}(t) \approx 400$ GeV/c in the Pb–Pb case, and up to $p_{\mathrm{T}}(t) \approx 700$ GeV/c in the Ar–Ar alternative.

10.5 Perspectives with lighter ions

Lighter ions, with the possibility to achieve large integrated luminosities in modest running times, see Sect. 2.4 in the accelerator chapter, offer several interesting opportunities for the study of the initial stage of ion collisions, for small-x physics and for the determination of nuclear parton densities, see Section 10.1.

First, concerning nPDFs, it should be noted that due to the scarcity of nuclear data, a PDF fit or a single nucleus is impossible as discussed in Section 10.1. The different groups [786–788] have adopted different strategies but, generically, they give the parameters in the initial condition to be fitted a dependence on the nuclear mass number. Such dependence acquires different functional forms and, therefore, it constitutes part of the parametrisation bias in the nPDF set. Data on lighter nuclei may help to constrain such parametrisations, see the discussions for UPCs and p–A collisions in Section 10.4. To highlight the current unknowns, Fig. 93 compares the nuclear modifications for Argon and Lead, as

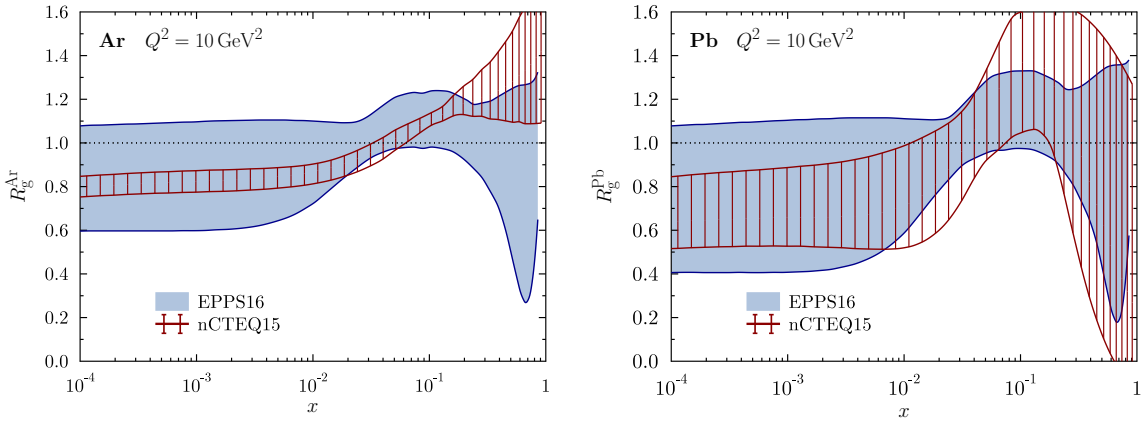

Fig. 93: The EPPS16 and nCTEQ15 nuclear PDF modifications for gluons at $Q^2 = 10\,\mathrm{GeV}^2$. Left-hand panel corresponds to the Argon nucleus and the right-hand panel to the Lead nucleus. From Ref. [945]

given by the EPPS16 and nCTEQ15 global analyses. In particular, the nCTEQ15 prediction varies, even qualitatively, quite significantly between Argon and Lead. This underscores the usefulness of e.g. a p-Ar run at the LHC.

On the other hand, the impact parameter dependence of nPDFs is linked to their dependence on nuclear size. Several models exist (see e.g. [946, 947]), and even less model-dependent approaches like the EPS09s analysis [948] where the dependence on nuclear size was used to constrain the impact parameter dependence. First-principle calculations combining the Gribov theory of inelastic shadowing and factorisation theorems for hard diffraction and DIS relate diffraction in electron-proton collisions with nuclear shadowing. This has been used to predict nuclear shadowing [790, 791], including its nuclear size and impact parameter dependence. While such relation is exact for the deuteron, its extension to larger nuclei has some degree of model dependence. Lighter ions are the ideal place to test the nuclear size dependence without resorting to centrality selection, whose relation with impact parameter is doomed to be as problematic - at least - as found in p–Pb collisions at the LHC.

Lighter ions also offer large luminosities that are important for several aspects:

- Data on beauty mesons and bottomonium in p–A collisions can be used to constrain nPDFs [329] better than their charm counterparts, because of the larger scale given by the mass and by the opportunity that they are less affected by collective effects. But they demand large statistics that can be achieved with lighter ions.
- Larger luminosities will benefit measurements in p–A collisions for observables with large scales, like high-mass DY or dijets, for precise determination of nPDFs.
- UPCs and photon-photon studies [587] in A–A collisions will greatly benefit in spite of the $Z^{2(4)}$ factor for the photon luminosities that can be overcompensated by the larger nucleon-nucleon luminosity.
- Larger luminosities can also benefit small-x forward observables that, like dijets [411], aim to reach quite large transverse momenta in p–A collisions.

Lighter ions offer a bridge between small systems and Pb–Pb without requiring centrality selection that is problematic both in pp, p–A and peripheral A–A. In the framework of saturation models [782] that aim to describe collective effects in small systems without requiring final state interactions (see e.g. [949] and references therein), the extension from the proton to the nuclear case in some of the phenomenological realisations is done by a simple rescaling of the squared saturation momentum

$Q_s^2 \propto A^{1/3}$. And the centrality dependence is assumed to be proportional to the nuclear profile, which leads to strong problems in the nuclear periphery where a dilute situation is restored. Lighter ions offer a check of our ideas on the nuclear size versus energy leading the density that determines saturation, and the use of minimum bias observables instead of centrality-sliced ones that would greatly simplify the phenomenology.

To conclude, lighter ions offer several advantages and disadvantages for initial stage studies. The main disadvantage is the fact that theory calculations usually assume the limit of scattering of a dilute projectile (proton) on a dense target (nucleus). Lighter ion-ion collisions are further from this limit. On the other hand, they offer: (i) a bridge between small and large systems without resorting to centrality selection that would be useful for constraining the nuclear wave function, the collision dynamics and the interpretation of collectivity; (ii) the possibility of larger luminosities for UPCs and forward observables for nPDFs determination and small-x studies; and (iii) a more affordable setup for microscopic calculations of nuclear corrections.

11 Other opportunities with ion and proton beams at the LHC

11.1 Physics motivation for collisions of light ions

Coordinator: Zvi Citron (Ben-Gurion University of the Negev)

Contributors: L. Apolinario (LIP and IST Lisbon), A. Dainese (INFN Padova), J.F. Grosse-Oetringhaus (CERN), J.M. Jowett (CERN), Y.-J. Lee (Massachusetts Institute of Technology), C. Loizides (Oak Ridge National Laboratory), G. Milhano (LIP and IST Lisbon, CERN), A. Milov (Weizmann Institute of Science), J. Pires (CFTP and IST Lisbon), A.M. Sickles (U. Illinois, Urbana-Champaign), U. Wiedemann (CERN), M. Winn (LAL, Orsay and IRFU/DPhN, Saclay)

The collision of ion species with $A \ll A_{\mathrm{Pb}}$ is an appealing opportunity to expand the physics programme presented in this document. The recent Xe–Xe run of only eight hours has provided valuable input for the physics performance of ion collisions lighter than Pb at the LHC. Broadly, the advantages of using $A \ll A_{\mathrm{Pb}}$ collisions are twofold: smaller collision systems sample key physical parameters beyond what can be probed with Pb–Pb and p–Pb collisions, and they allow higher luminosity running to maximize the accumulation of rare events in heavy-ion collisions. This higher luminosity would enable high-precision measurements for currently rare observables in Pb–Pb collisions as well as the study of observables totally inaccessible in Pb–Pb collisions.

A scenario is envisioned in which the programme is extended in two directions: a) a short run of O–O ($A = 16$) to study system-size dependence and b) longer running of a species of intermediate A to achieve a large luminosity increase. The choice of the intermediate species will be dictated by the competition of increased luminosity with lower A against the goal of studying the properties of an extended QGP system. Optimizing the choice of species will require further study from the accelerator, experimental, and theoretical communities; in this document Ar–Ar ($A = 40$) collisions are considered as a test-case for the choice of intermediate ion. It is understood that any choice of collision species will likely require a pilot run prior to beginning dedicated collisions.

Section 2.4 describes the technical capabilities of the LHC to provide lighter-ion collisions, as well as the expected performance for several ion species. For example, for Ar–Ar the expectation for one month of collisions is $1080\,\mathrm{nb}^{-1}$ ($p = 1.5$). In order to compare across different collisions species we consider the nucleon–nucleon integrated luminosity per month of running, which could be larger by a factor 8–25 (for $p = 1.5$–1.9) with respect to Pb–Pb collisions, i.e. one month of Ar–Ar collisions would be equivalent to ~ 25–$80\,\mathrm{nb}^{-1}$ of Pb–Pb collisions. This gain would be the same in all centrality classes (defined in terms of percentiles of the hadronic cross section). Jet quenching estimates for light ion (Ar–Ar) collisions are presented in Sect. 6.5. Section 4.3.2 discusses flow measurements with light ions. A discussion of the role that light ion collisions can play for small-x and nPDF studies is reported in Sect. 10.5. Finally, the implications of Ar–Ar collisions for the study of light-by-light scattering are discussed in Sect. 11.2.

Even a short O–O run can help clarify the uncertainty concerning the onset of QGP or QGP-like phenomena in high-multiplicity pA and pp collisions, as discussed in section 9.10. The search for signals associated with the QGP in O–O collisions should complement the searches in pp and p–Pb collisions.In particular, the O–O system has well-understood collision geometry as described in detail in Sect. 9.10, enabling the study of collisions with low values of $\langle N_{\mathrm{part}} \rangle$ that are difficult to select and study in Pb–Pb collisions and that are similar to those associated to high-multiplicity p–Pb events. Colliding O–O at the LHC naturally dovetails with p–O collisions whose significance for cosmic-ray physics is detailed in Sect. 11.3.

Complementing Pb–Pb collisions, the possibility of high-luminosity extended LHC runs with intermediate-A nuclei (e.g. Ar–Ar or Kr–Kr) is an appealing long-term option. The chief promise of these collisions is the possibility of reaching much higher luminosity than Pb–Pb collisions while still producing a QGP over an extended volume of ~ 1000 fm^3 in central events. Based on a Glauber Monte

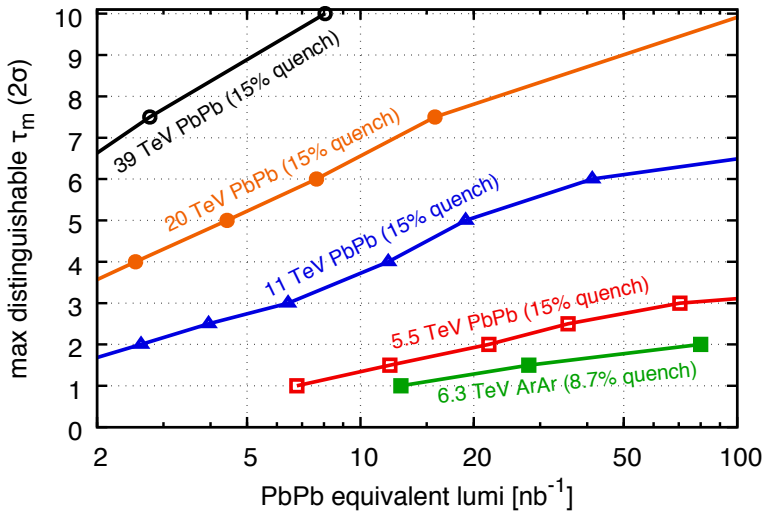

Fig. 94: Maximum medium lifetime that can be distinguished from a full quenching baseline with a statistical significance of two standard deviations ($2\,\sigma$), as a function of luminosity (shown in terms of equivalent Pb–Pb luminosity) for different species and collider energies. A single Ar–Ar run is expected to provide $\sim$ 25–80 nb^{-1} of Pb–Pb equivalent luminosity. Adapted from [944].

Carlo simulation [767], the mean number of participants for Ar–Ar ranges from $\langle N_{\mathrm{part}} \rangle \sim 7$ for 60–80% centrality to $\sim$ 70 for 0–5% centrality collisions. QGP effects are observed in Pb–Pb collisions with similar number of participants (see e.g. [950, 951]). In addition, the much lower underlying event multiplicity in Ar–Ar relative to central Pb–Pb collisions is expected to lead to reduced systematic uncertainties for several observables, from reconstructed jets to all signal affected by large combinatorial backgrounds. These features, combined with the possibility to increase the nucleon–nucleon luminosity by more than one order of magnitude, make Ar–Ar collisions an extremely attractive option for hard-probe measurements that in Pb–Pb collisions are limited or impossible, such as boosted top-quark decay chains for QGP studies [944]. Figure 94 extends the analysis to lighter nuclei and shows that one month of Ar–Ar collisions, with nucleon–nucleon luminosity equivalent to 25–80 nb^{-1} for Pb–Pb, allows a similar physics reach as the entire Pb–Pb future programme (13 nb^{-1}), namely to probe the QGP density evolution up to a time of about 1.5–2 fm/c. Top quark studies in Ar–Ar collisions in the context of constraints on nPDFs are discussed in Sect. 10.4.4.

Studies with Z bosons are representative examples of the types of measurements that may be undertaken in a lighter ion rare-probes programme. In Fig. 95 the expected number of Z boson candidates (assuming a selection similar to that used by ATLAS and CMS in previous studies) for one month of heavy-ion running as a function of $\langle N_{\mathrm{part}} \rangle$ is shown for several colliding ion species, and compared with the expectation for the full Pb–Pb and p–Pb programmes of Runs 3 and 4. The figure demonstrates that the overall yield of Z bosons would be considerably higher for one Ar–Ar run than for several years of Pb–Pb running including both a sufficient number of candidates to study low $\langle N_{\mathrm{part}} \rangle$ collisions unreachable with Pb–Pb collisions as well as moderate $\langle N_{\mathrm{part}} \rangle$ values in which QGP formation is expected. Z bosons are a powerful tool to probe the properties of the QGP in particular in Z+jet events. In these studies the energy of the Z is a direct measurement of the energy of parton that initiated the recoil jet. Therefore, the coverage of a broad range in Z momentum gives access to a jet-energy differential study of jet quenching. the The expected number of Z+jet events from the 0–10% centrality class above a given p_{T} of the Z boson is calculated at NLO (and without including jet suppression) and shown in Fig. 96 as a function of Pb–Pb equivalent luminosity. The Pb–Pb programme in Runs 3 and 4 (13 nb^{-1}) gives 1000 events with Z $p_{\mathrm{T}} > 120$ GeV/c, while a single Ar–Ar one-month run extends the coverage

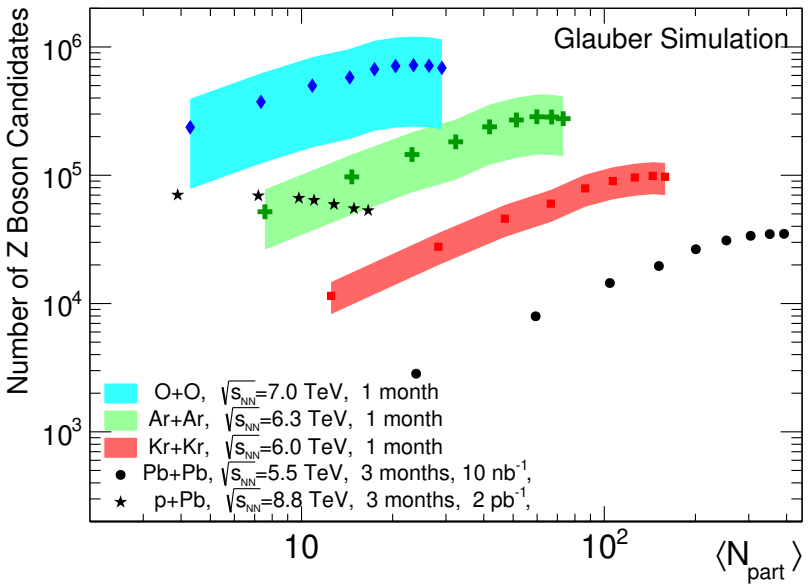

Fig. 95: The number of Z bosons as a function of $\langle N_{\mathrm{part}} \rangle$ expected for one month of O–O,Ar–Ar, and Kr–Kr collisions at the LHC and for the full expected Pb–Pb and p–Pb programmes. The Z bosons are reconstructed via the di-lepton decay channel with leptonic $p_{\mathrm{T}} > 20$ GeV/c and $|\eta| < 2.5$, and a mass selection of $66 < M_{\ell\ell} < 116$ GeV. The bands shown indicate the range of the expected luminosity ranging from $p = 1.5$ to $p = 1.9$, as discussed in section 2.4.

with the same number of events to 140–180 GeV/c. A three-months Ar–Ar programme extends well above 200 GeV/c.

For further study, Z+jet events were simulated in the 10% most central events in Ar–Ar collisions using Jewel [952] to estimate the expected jet-quenching effects. Details of the use of and limitations of JEWEL for this purpose are discussed in Sect. 6.5. Figure 97 shows the distribution of x_{jZ}, the ratio of the jet transverse momentum to that of the Z boson for 0–10% centrality Ar–Ar events, as well as pp collisions and 0–10% centrality Pb–Pb events ($N_{\mathrm{part}} = 356$, $T = 260$ MeV at thermalization time $\tau = 0.6$ fm/c for $\sqrt{s} = 5.02$ TeV). The Z boson must have $p_{\mathrm{T}} > 60$ GeV/c and be back-to-back ($|\Delta\varphi| > 7/8\pi$) to a jet with $p_{\mathrm{T}} > 30$ GeV/c. The Figure clearly shows that for this observable the jet-quenching phenomena observed in Pb–Pb collisions as modelled by JEWEL are present also in Ar–Ar collisions. More studies are needed to refine modelling of more dilute systems and optimize the choice of colliding species, but taken together the available information suggests the potential of light ion collision systems like Ar–Ar for a heavy-ion rare-probes programme.

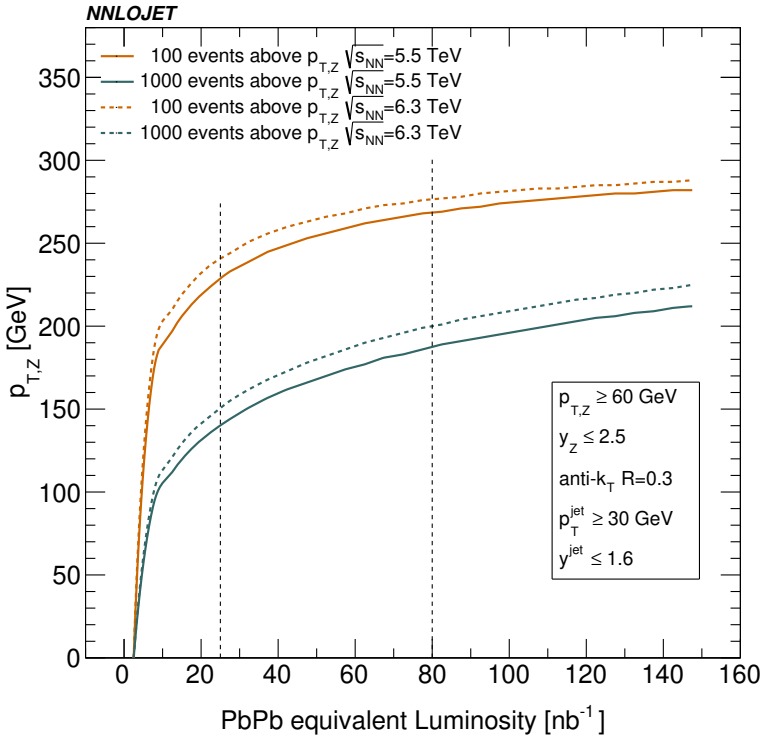

Fig. 96: The kinematic reach of Z+jet events as a function of Pb–Pb equivalent luminosity. The curves indicate the maximum p_{T} of the Z boson for which 100 (or 1000) events are expected from 0–10% centrality collisions for a given Pb–Pb equivalent luminosity. 25 and $80\,\mathrm{nb}^{-1}$, corresponding to the upper and lower expectations for one month of Ar–Ar collisions, are indicated by the vertical lines.

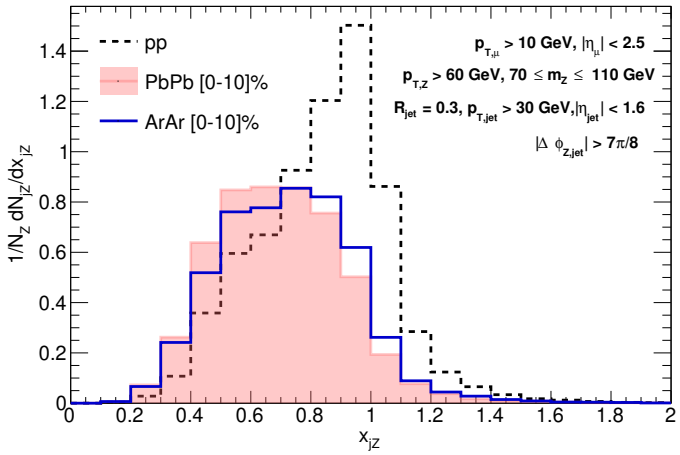

Fig. 97: The x_{jZ} distribution for pp, Pb–Pb, and Ar–Ar collisions calculated with JEWEL. The 10% most central events are shown for Pb–Pb and Ar–Ar. Ar–Ar collisions are calculated as $N_{\mathrm{part}} = 60$, $T = 318\,\mathrm{MeV}$ at thermalization time $\tau = 0.63$ fm/c for $\sqrt{s} = 6.3$ TeV. The Z boson must have $p_{\mathrm{T}} > 60$ GeV/c and be back-to-back ($|\Delta\varphi| > 7/8\pi$) to a jet with $p_{\mathrm{T}} > 30$ GeV/c.

11.2 Physics of $\gamma\gamma$ interactions in heavy-ion collisions

Coordinators: Iwona Grabowska-Bold (AGH University of Science and Technology)

Contributors: M. Dyndal (DESY), S. Hassani (Université Paris-Saclay), M. Klusek-Gawenda (IFJ PAN, PL-31342 Kraków, Poland), L. Schoeffel (Université Paris-Saclay), Peter Steinberg (BNL)

Heavy-ion beams are composed of nuclei which carry electric charge Ze (e is the electron charge and Z is the atomic number). They are accelerated to nearly the speed of light, thus they generate large electromagnetic (EM) fields. The EM fields generated by the relativistic ion can interact with the other nucleus or its EM fields. Therefore, besides nuclear hadronic interactions, EM interactions also occur in ultra-relativistic heavy-ion collisions. These EM interactions can be studied in so-called ultra-peripheral collisions (UPC) which occur when the distance between two nuclei in the transverse plane is larger than two times the nuclear radius, and hadronic interactions are thus suppressed [582].

A broad range of processes can be studied with $\gamma\gamma$ interactions in UPC. In the following, a few examples of photon-induced processes are considered at the HL-LHC: exclusive production of $\mu^+\mu^-$ or $p\bar{p}$ pairs, a rare process of light-by-light (LbyL) scattering and a potential of searches for axion-like particles (ALP).

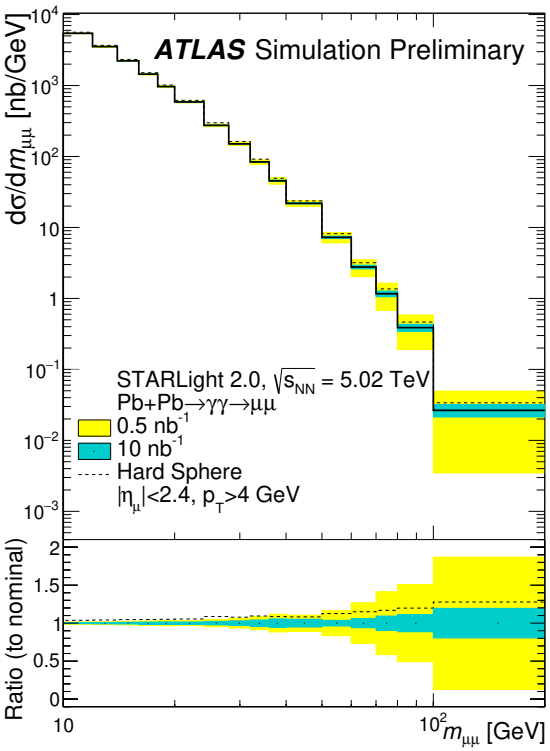

Fig. 98: (Upper) Differential cross section for exclusive production of the di-muon pairs as a function of the di-muon mass for $10 < m_{\mu\mu} < 200$ GeV extracted from STARLight. Two scenarios are considered for the nuclear geometry: a realistic skin depth of the nucleus (solid line) or a hard sphere (dashed line). (Bottom) Ratio to nominal as a function of the di-muon mass, where "nominal" stands for the realistic skin depth of the nucleus. Shaded bands represent expected statistical uncertainties associated with a number of signal events in each bin for integrated luminosity of $0.5\ \mathrm{nb}^{-1}$ (yellow), and $10\ \mathrm{nb}^{-1}$ (cyan).

Exclusive production of di-muon pairs ($\gamma\gamma \to \mu^+\mu^-$) in UPC can offer a precision measurement of photon fluxes associated with ion beams, and as such can be used to constrain predictions for the

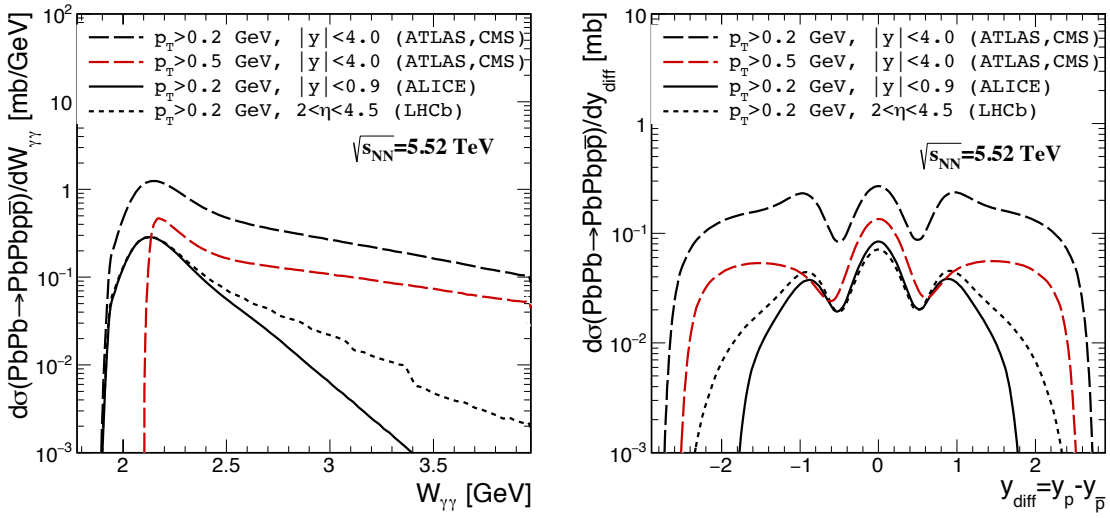

Fig. 99: Differential cross sections as a function of $\mathrm{p\bar{p}}$ invariant mass (left) and rapidity distance between proton and anti-proton (right) in Pb–Pb collisions at $\sqrt{s_{\mathrm{NN}}} = 5.52$ TeV for four experimental acceptance requirements. For ATLAS and CMS experiments two requirements for proton $p_{\mathrm{T}} > 0.2$ GeV/c or $p_{\mathrm{T}} > 0.5$ GeV/c are considered.

other processes covered in this section. The cross section at high pair mass is also sensitive to the nuclear geometry assumed in the calculations. Figure 98 presents a differential cross section as a function of the invariant mass of the di-muon system in the range of 10–200 GeV with expected statistical uncertainties represented by two bands corresponding to integrated luminosities of $0.5\ \mathrm{nb}^{-1}$ and $10\ \mathrm{nb}^{-1}$. Two scenarios are considered for the nuclear geometry: a realistic skin depth of the nucleus or a hard sphere [953]. For the $10\ \mathrm{nb}^{-1}$ scenario, a significant reduction of the statistical uncertainty is expected. This will help in reducing uncertainties from the modelling of the nuclear geometry. The expected upgrades of the ATLAS Zero Degree Calorimeters (ZDC) in the LHC Run 3 will also be important for isolating the contributions to the cross section stemming from dissociative processes.

Exclusive production of $\mathrm{p\bar{p}}$ pairs ($\gamma\gamma \to \mathrm{p\bar{p}}$) in heavy-ion collisions is considered as a process which can help verify the existing theoretical approaches. It has been demonstrated that the $\gamma\gamma \to \mathrm{p\bar{p}}$ experimental data [954] from the Belle Collaboration can be successfully described by implementation of several components [955]: the non-resonant proton exchange, s-channel tensor meson exchange and the hand-bag model [956]. Figure 99 shows the calculated distributions of invariant mass of the $\mathrm{p\bar{p}}$ system, $W_{\gamma\gamma} = M_{\mathrm{p\bar{p}}}$ (left panel) and of the difference of rapidities for protons and anti-protons, $y_{\mathrm{diff}} = y_{\mathrm{p}} - y_{\bar{\mathrm{p}}}$ (right panel). The ALICE Collaboration can measure $\mathrm{p\bar{p}}$ pairs in Pb–Pb collisions at mid-rapidity ($|y| < 0.9$). The LHCb Collaboration could also provide a complementary measurement of $\mathrm{p\bar{p}}$ production in the forward region ($2 < \eta < 4.5$). The upgraded charged particle tracking capabilities of ATLAS and CMS experiments for Run 4 will measure in $|y| < 4.0$. Corresponding kinematic requirements on transverse momenta and rapidity or pseudorapidity specific for each experiment are presented in the figure legend. The calculations are made for Pb–Pb collisions with $\sqrt{s_{\mathrm{NN}}} = 5.52$ TeV. The total cross section predicted for the ATLAS and CMS acceptances for $p_{\mathrm{T}} > 0.2$ GeV/c ($p_{\mathrm{T}} > 0.5$ GeV/c) is $\sigma = 793$ μb (248 μb), while LHCb and ALICE requirements lead to $\sigma = 125$ and 105 μb, respectively.

From the left panel of Fig. 99 one can deduce that the dependence on invariant mass of the $\mathrm{p\bar{p}}$ pair is sensitive to the rapidity/pseudorapidity of the outgoing particle. The cut-off at the minimal value of $W_{\gamma\gamma}$ is determined by the minimum p_{T} requirement. The y_{diff} distribution shown in the right panel of Fig. 99 is of particular interest. The broad maximum at $y_{\mathrm{diff}} = 0$ corresponds to the region with $|\cos\theta| <$

0.6, where θ denotes the angle of the outgoing nucleon relative to the beam direction in the centre-of-mass frame. An observation of peaks at $y_{\rm diff} = \pm 1$ could be a good test to constraint the theoretical models which predict the elementary cross section. The proposed model has a few parameters (i.e. vertex form factors for the proton exchange, tensor meson s-channel exchanges and a form factor in the hand-bag contribution) which could be constrained with the help of the $y_{\rm diff}$ distributions. The fiducial acceptance requirements imposed on $p_{\rm T}$ do not distort the maxima. If the structures in the $y_{\rm diff}$ distributions indeed exist, the study of $\rm p\bar{p}$ production in UPC can provide an important complimentary information to the existing $\gamma\gamma \to \ell^+\ell^-$ and $\rm J/\psi \to \ell^+\ell^-$ data with $\ell = e, \mu$ [819, 957].

Evidence of the rare process of LbyL scattering has been established by the ATLAS and CMS Collaborations using Pb–Pb data obtained in 2015 [809, 958] with an integrated luminosity of about $0.4\ \rm nb^{-1}$. That process can be studied with higher precision using heavy-ion data collected at the HL-LHC. The left panel of Fig. 100 presents a differential cross section as a function of the di-photon rapidity for LbyL scattering for photons with $|\eta^\gamma| < 4$ with two photon $p_{\rm T}^\gamma$ thresholds: 2.0 and 2.5 GeV/c. The LbyL scattering occurs in the central region: 91% of the integrated cross section resides within $|\eta^\gamma| < 2.37$. A strong dependence on the $p_{\rm T}^\gamma$ requirement is observed. The cross section increases by a factor of two when the single photon $p_{\rm T}^\gamma$ threshold is lowered by half a GeV/c from 2.5 to 2.0 GeV/c. The corresponding integrated cross sections in the fiducial region are 112 nb for $p_{\rm T}^\gamma > 2.5$ GeV/c and 221 nb for $p_{\rm T}^\gamma > 2.0$ GeV/c.

The right panel of Fig. 100 shows a detector-level acoplanarity (=$1 - |\varphi_1^\gamma - \varphi_2^\gamma|/\pi$) distribution for the di-photon system from LbyL signal and two background processes originating from exclusive production of di-electron pairs ($\gamma\gamma \to \rm e^+e^-$) and di-photons produced in central exclusive production ($\rm gg \to \gamma\gamma$). The distributions depict simulated events which passed a full simulation of the ATLAS detector with the extended acceptance in pseudorapidity. About 640 LbyL events pass the selection requirements for acoplanarity below 0.01 and $p_{\rm T}^\gamma > 2.5$ GeV/c in 5.02 TeV Pb–Pb collisions with an integrated luminosity of $10\,\rm nb^{-1}$, in comparison to about 13 events observed in the 2015 data set with the $p_{\rm T}^\gamma > 3.0$ GeV/c requirement. The signal events are peaked at acoplanarities close to zero, while the background processes are distributed either uniformly (di-photons from central exclusive production) or even grow with acoplanarity ($\rm e^+e^-$ pairs from exclusive di-electron production). The latter originates from $\rm e^+e^-$ pairs which trajectories have been bent in the magnetic field before emitting hard-bremsstrahlung photons. A limitation of the current analysis is lack of simulation of the trigger response. Based on experience from the analyses of 2015 Pb–Pb data, triggering on photons with $p_{\rm T}^\gamma < 3.0$ GeV/c is challenging, and therefore a dedicated trigger strategy needs to be developed for LbyL event candidates exploiting new features of the upgraded trigger system [959, 960].

The LbyL process can also be studied at lower di-photon masses. The differential cross sections as a function of the di-photon mass can be evaluated taking into account acceptance of the ALICE experiment, i.e. pseudorapidity limited to $|\eta^\gamma| < 0.9$ or in the forward region defined by $2 < \eta^\gamma < 4.5$ in the LHCb experiment, and relatively low energies of outgoing photons [962]. At lower energies ($W_{\gamma\gamma} < 4$ GeV) meson resonances [963] may play an important role in addition to the Standard Model box diagrams [964, 965] or double photon fluctuations into light vector mesons [965] or two-gluon exchanges [966]. Figure 101 shows predictions for LbyL and background processes in the ALICE and LHCb experiments with photon acceptance in $|\eta^\gamma| < 0.9$ and E_γ > 200 MeV (top panel) or $2 < \eta^\gamma < 4.5$ and $E_{{\rm T},\gamma}$ > 200 MeV (bottom panel), respectively, for two systems: Pb–Pb collisions at 5.52 TeV (left panel) and Ar–Ar collisions at 6.3 TeV (right panel). Presented results include the effect of the experimental energy resolution [967, 968]. The black-solid lines depict the LO QED fermionic box mechanism with leptons and quarks. Presented results for the $\gamma\gamma \to \gamma\gamma$ process are in agreement with calculations from Refs. [969–971]. The green-solid lines show results for the s-channel $\gamma\gamma \to$pseudoscalar/scalar/tensor resonances that contribute to the LbyL process. In the present analysis, η, $\eta'(958)$, $\eta_c(1S)$, $\eta_c(2S)$, $\chi_{c0}(1P)$ mesons are considered. Their masses, total widths and branching

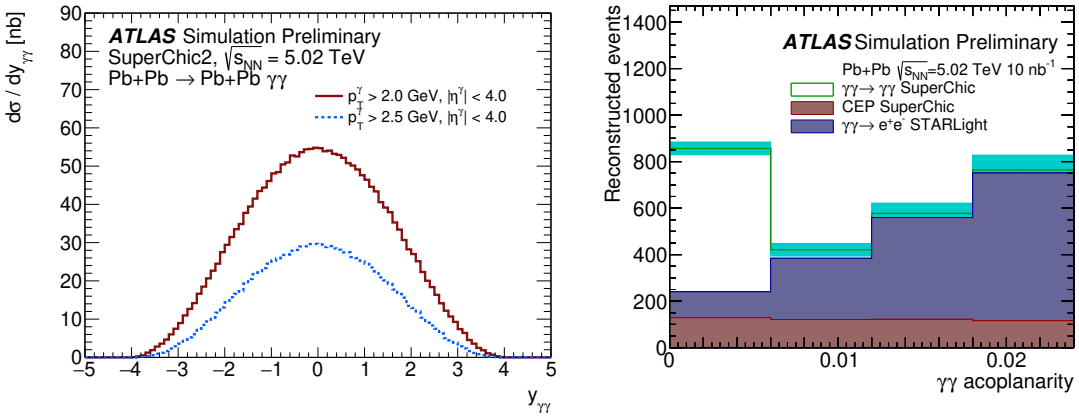

Fig. 100: (Left) Predicted differential cross section as a function of the di-photon rapidity for LbyL scattering for photons with $p_{\mathrm{T}}^{\gamma} > 2.5$ GeV/c (dashed) or $p_{\mathrm{T}}^{\gamma} > 2.0$ GeV/c (solid), and $|\eta^{\gamma}| < 4$ extracted from SuperChic [961]. (Right) Detector-level acoplanarity distribution of the di-photon system for photons from the LbyL signal and background processes in 5.02 TeV Pb–Pb collisions with an integrated luminosity of 10 nb^{-1}. The shaded band in cyan represents expected statistical uncertainties.

ratios are taken from the PDG [972]. The contributions of pseudoscalar mesons from radiative decays of a coherently-produced vector meson could be sizeable [973] and should be quantified in future studies. The dominant background from the $\gamma\gamma \to \pi^0\pi^0$ process is shown by the blue lines. It becomes non-negligible only when one photon from each $\pi^0 \to \gamma\gamma$ decay is reconstructed in the detector. Two scenarios with and without the acoplanarity requirement of 0.01 are considered. The acoplanarity requirement reduces this background contribution by a factor of 5 in the full $W_{\gamma\gamma}$ region. The experimental data for the $\gamma\gamma \to \pi\pi$ elementary cross section were very well described in Ref. [974]. There simultaneously the total cross section and angular distributions for both charged and neutral pions are shown. Following Ref. [974], here nine resonances, $\gamma\gamma \to \rho^{\pm} \to \pi^0\pi^0$ continuum, Brodsky-Lepage and hand-bag mechanism are included. Figure 101 shows that pionic background dominates at low invariant di-photon mass (below 2 GeV). In the same energy region, one can observe a very clear dominance of η, $\eta'(958)$ mesons over other processes. The inclusion of energy resolution introduces mainly smearing of the contribution from $\gamma\gamma \to \eta, \eta' \to \gamma\gamma$ resonance scattering. This contribution is supposed to be measured with good precision. These results suggest that both ALICE and LHCb Collaborations could measure LbyL scattering for $W_{\gamma\gamma} > 2$ GeV in Pb–Pb collisions.

In the case of Ar–Ar collisions, the cross sections are about two orders of magnitude lower, because of the smaller electric charge of Ar nulcei with respect to Pb nuclei. Assuming integrated luminosities of $3.0 - 8.8$ pb^{-1} in a dedicated Ar–Ar run, the LbyL production cross section leads to 1460–4280 signal events for ALICE and 11–34 events for LHCb in a range of $W_{\gamma\gamma} > 2$ GeV. A background contribution from $\gamma\gamma \to \pi^0\pi^0$ is at the level of 20% for ALICE and 134% for LHCb in this region.

Axions and axion-like particles (ALP) are fundamental components of extensions of the Standard Model, occurring in most solutions of the strong CP problem [975,976]. Recently an increasing interest has been paid to ALP masses above 1 GeV [977–981]. In particular the Higgs discovery has set spin zero particles in the spotlight of searches for new physics, with scalar and pseudo-scalar particles (elementary or not) as heralds of new phenomena. An interesting feature is that ALP (generically labelled as a in the following) in this mass range would induce an anomalous contribution to the LbyL, via the reaction: $\gamma\gamma \to \mathrm{a} \to \gamma\gamma$, under the condition that the magnitudes of the EM fields associated with the incident photon are large enough, typically $|\vec{E}| > 10^{18}$ V/m. This has triggered the study presented

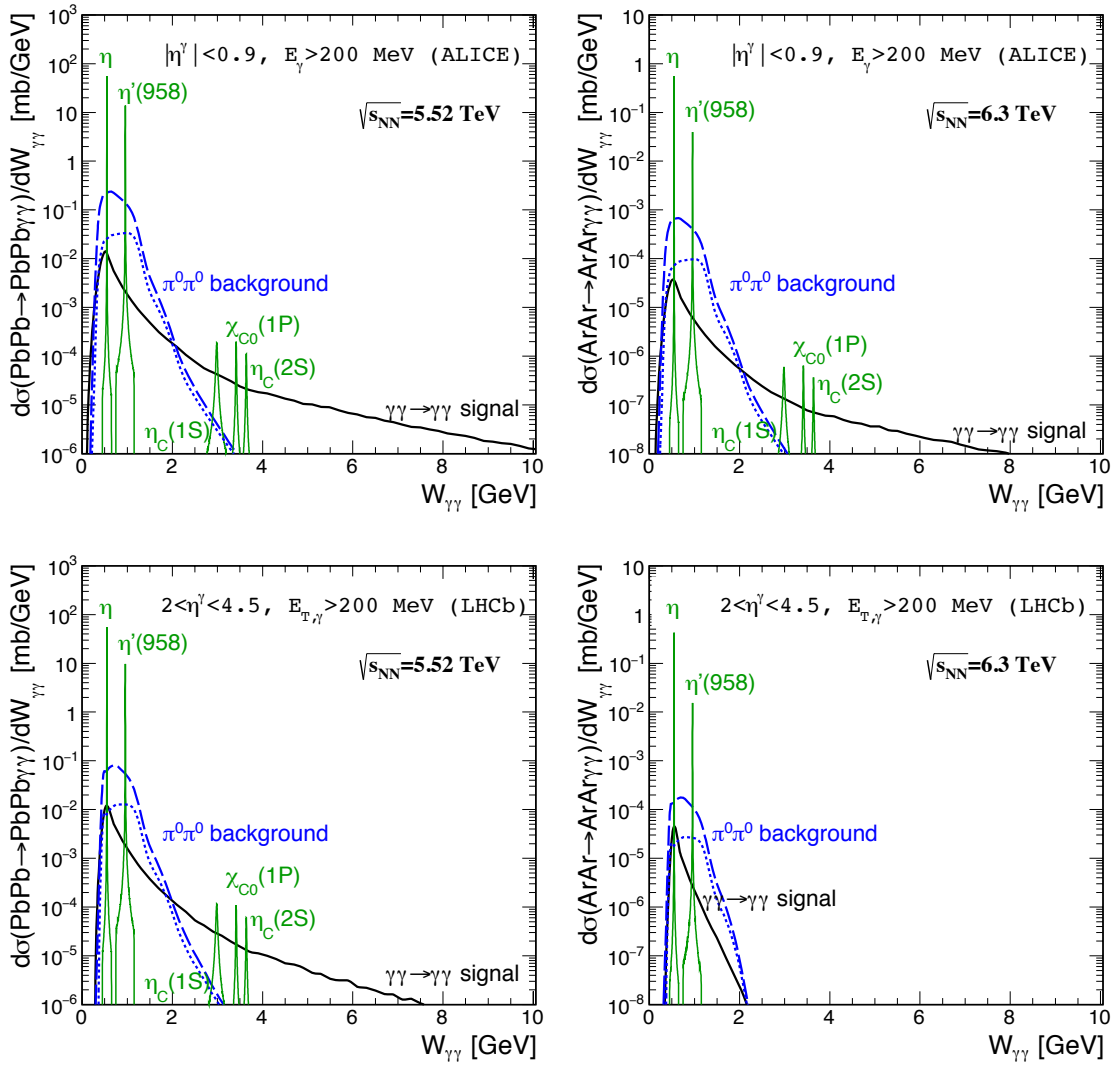

Fig. 101: Di-photon invariant mass distributions for Pb–Pb collisions at $\sqrt{s_{\rm NN}} = 5.52\,\text{TeV}$ (left) and Ar–Ar collisions at $\sqrt{s_{\rm NN}} = 6.3\,\text{TeV}$ (right) for ALICE at mid-rapidity (top) and LHCb at forward pseudorapidity (bottom). The $\pi^0\pi^0$ background is shown with the acoplanarity requirement of 0.01 (dotted line) and also without it (dashed line).

in Ref. [980], and then in Ref. [982] using the recent observation of LbyL scattering published by the ATLAS experiment in Pb–Pb collisions [809], where the electric field produced by the ultra-relativistic Pb is of the order of 10^{25} V/m (thus satisfying the above condition).

The potential of ALP searches in UPC Pb–Pb collisions is studied using detector-level quantities after the LbyL selection requirements are imposed. The overall selection efficiency (times acceptance) relative to generated events increases from about 40% to 65% for ALP masses ranging from 7 GeV to 80 GeV. Also, the mass resolution varies from 0.5 GeV at low masses (below 15 GeV) up to 1 GeV for larger masses. In the left panel of Fig. 102 the expected mass distributions for three ALP signal mass values, and the main background from LbyL normalised to integrated luminosity of 10 nb^{-1} are shown. In this study, other sources of backgrounds are neglected, since they have been found to be small in the LbyL measurement [809]. The invariant mass distribution is used as the discriminating variable, with bin widths comparable to the expected resolution of a narrow resonant signal. Upper limits are set on

the product of the production cross section of new resonances and their decay branching ratio into $\gamma\gamma$. Exclusion intervals are derived using the CLs method [983] in the asymptotic approximation. The limit set on the signal strength μ is then translated into a limit on the signal cross section times branching ratio as presented in the right panel of Fig. 102.

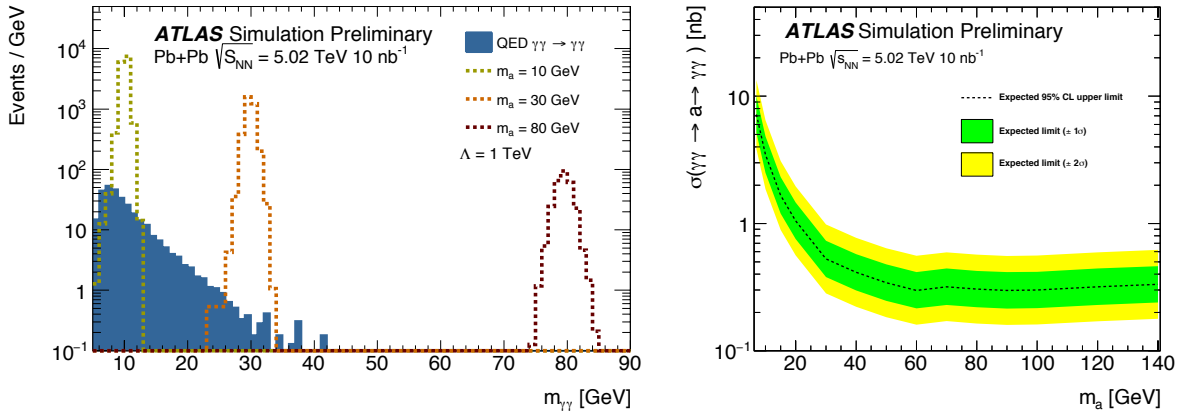

Fig. 102: (Left) Mass distribution for the ALP signal shown for three values of the ALP mass: $m_{\mathrm{a}} = 10, 30$ and 80 GeV (in red). Also shown (in blue) the LbyL background (see text). All ALP mass points are generated with $\Lambda = 1$ TeV ($1/\Lambda$ is the coupling of the interaction) which follows a convention defined in Ref. [980]. (Right) Expected 95% CLs upper limits on $\sigma_{\mathrm{a}\to\gamma\gamma}$.

In Fig. 103 exclusion limits on the coupling, $1/\Lambda$, as a function of m_{a} are presented along with the existing results from the compilation discussed in Ref. [984]. The ATLAS 20 nb^{-1} limit is derived using Pb–Pb collisions at 5.52 TeV. These results demonstrate that heavy-ion collisions have unique sensitivity to ALP searches in the range of $m_{\mathrm{a}} = 7 - 140$ GeV, where the previous results based on available Pb–Pb data by ATLAS and CMS [958, 980] are also shown (labelled as ATLAS $\gamma\gamma \to \gamma\gamma$ and CMS $\gamma\gamma \to \gamma\gamma$ in the figure).

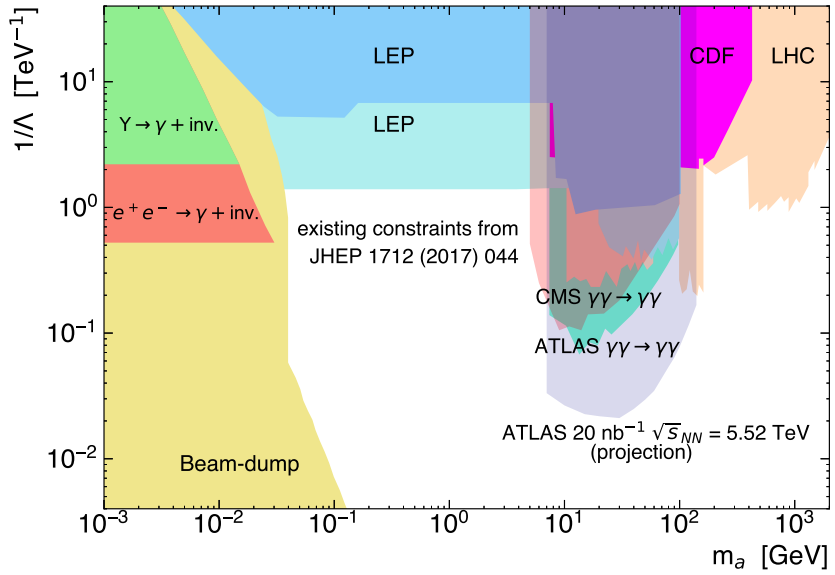

Fig. 103: Compilation of exclusion limits obtained by different experiments (see text). In light grey, the ATLAS 20 nb^{-1} limit at $\sqrt{s_{\mathrm{NN}}} = 5.52$ TeV is presented. The ATLAS $\gamma\gamma \to \gamma\gamma$ represents the exclusion limit derived from the LbyL cross section measured in Pb—Pb collisions by ATLAS [809], while the CMS $\gamma\gamma \to \gamma\gamma$ limit comes from the recent analysis described in Ref. [958]. A more complete version of the existing constraints on ALPs masses versus coupling, including the constraints in the sub meV range from astrophysical observations and from dedicated experiments such as CAST can be found in Ref. [977].

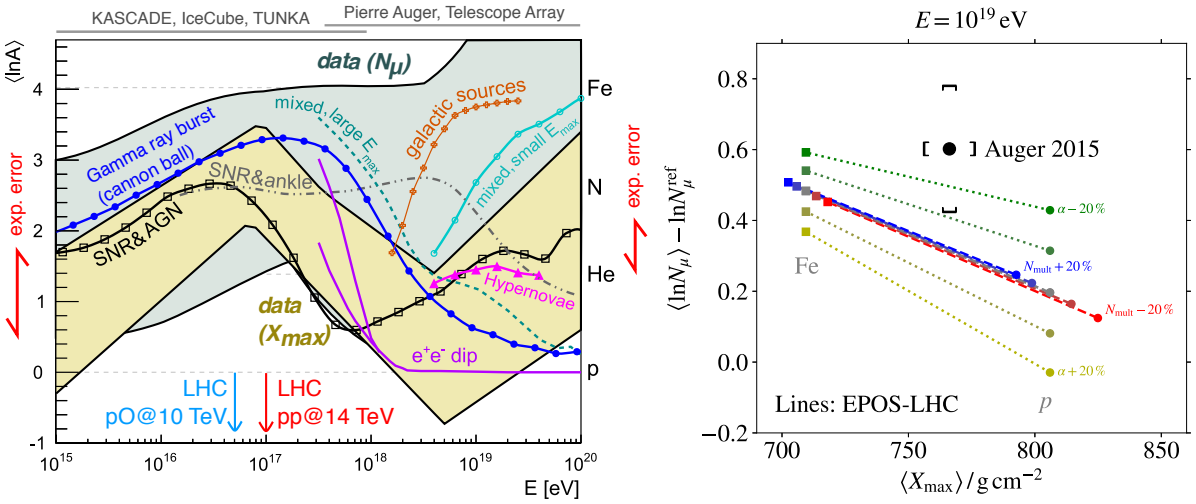

Fig. 104: Left: Mass composition of cosmic rays quantified by $\langle \ln A \rangle$ as a function of cosmic ray energy E. See Ref. [985] for references to data (bands) and model predictions (markers and lines), and the text for a discussion. Right: Impact of changes of the hadron multiplicity $N_{\rm mult}$ (dashed lines) and the energy fraction α (dotted lines) which goes into neutral pions in collisions at the LHC energy scale on EPOS-LHC predictions for $X_{\rm max}$ and $\ln N_\mu$ in 10^{19} eV air showers, compared to Auger data [986]. The model lines represent all values that can be obtained for any mixture of cosmic nuclei from proton (bottom right) to iron (top left). The dashed and dotted lines represent modifications of $N_{\rm mult}$ and α in steps of $\pm 10\%$ from their nominal values.

11.3 Proton-oxygen collisions for cosmic ray research

Coordinators: Hans Dembinski (MPI for Nuclear Physics, Heidelberg)

Contributors: T. Pierog (Karlsruhe Institute of Technology), R. Ulrich (Karlsruhe Institute of Technology)

The recent coincident observations of gamma rays and neutrinos from the flaring blazar TXS 0506+056 confirmed that active galactic nuclei produce high-energy cosmic rays [987]. This long awaited finding demonstrates that sources of cosmic rays are linked to the most violent places in our universe. Measurements of cosmic rays contribute to the understanding of the high-energy universe. Since cosmic rays are charged and bent by magnetic fields in space onto chaotic paths, their arrival directions at Earth are highly isotropic, but their mass composition carries an imprint of the source physics. Precision measurements of minimum-bias events in proton-oxygen collisions have the unique power to resolve current ambiguities in the mass composition measured with atmospheric air-shower techniques.

Cosmic rays are nuclei from protons to iron (heavier elements are negligible). The energy-dependent mass composition of cosmic rays is characteristic for different source scenarios, as shown in Fig. 104, left-hand-side, which displays predictions (lines and markers) of the mean-logarithmic-mass $\langle \ln A \rangle$ of cosmic rays. Above particle energies of 10^{15} eV, $\langle \ln A \rangle$ can only be indirectly inferred from extensive air showers, huge secondary particle cascades produced by collisions between cosmic rays and nuclei in the atmosphere. The two leading observables to infer $\langle \ln A \rangle$ are the depth $X_{\rm max}$ of the shower maximum in the atmosphere (yellow band in Fig. 104), and the number N_μ of muons produced in the shower (green band in Fig. 104). The width of those bands has two main contributions: the experimental uncertainties, and the hadronic model uncertainties inherent in converting the air shower observables into $\langle \ln A \rangle$.

Leading experiments achieve an instrumental accuracy of 10 % of the proton-iron difference, which would strongly discriminate between source scenarios, but air shower simulations are required

to convert N_μ and X_{max} to $\langle \ln A \rangle$ and this adds a large model uncertainty. The simulations use the multi-purpose heavy-ion event generator EPOS-LHC [988], or specialized hadronic interaction models such as QGSJet-II.04 [989] and SIBYLL-2.3c [990]. All are designed to describe nucleus-nucleus and soft-QCD interactions by extrapolating combinations of Regge field theory tuned to available data and perturbative QCD. Uncertainties in these models arise from a lack of data on multiparticle production in the very forward phase-space in hadron-nucleus interactions at the TeV scale.

LHC measurements have already reduced the spread of model predictions for X_{max} in the latest generation of models. This big improvement was due to high-precision measurements of the inelastic cross-section (see e.g. [991] and references therein). Further measurements now have the potential to make the spread negligible. The model spread for N_μ is still large and predictions are not consistent with X_{max} for cosmic rays with the same mass. There is overwhelming evidence from air shower experiments [986, 992–995] that the muon number N_μ is underestimated in simulations starting at about 10^{16} eV. This corresponds to a cms energy of 4.3 TeV, well accessible by the LHC. Shown in Fig. 104, right-hand-side, is a representative data point from the Pierre Auger Observatory, which is well above EPOS-LHC predictions – and EPOS-LHC and SIBYLL-2.3c are already models which produce the highest muon number of all hadronic interaction models models. This is called the *Muon Puzzle*.

Two aspects of multi-particle production with a strong effect on N_μ have been identified [996], the hadron multiplicity N_{mult} and the energy fraction α that goes into neutral pions. The impact of changing these variables in EPOS-LHC at 13 TeV cms energy and extrapolating upward in energy is also shown in Fig.104, right-hand-side. A combined measurement to 5 % accuracy of both variables at the LHC would reduce the model uncertainty for the conversion of X_{max} to $\langle \ln A \rangle$ well below the experimental uncertainty of 10 %, and has the clear potential to resolve the discrepancy in the muon number N_μ. To reach the accuracy goal, the following minimum-bias measurements are desired:

- Double-differential production cross-section for charged pions, kaons, and protons:
  ALICE $|\eta| < 0.9$, LHCb $2 < \eta < 5$
- Production cross-section for neutral pions and neutrons: LHCf $\eta > 8.4$.
- Energy flow over pseudo-rapidity, separated for hadrons and gammas:
  CMS+CASTOR $-6.6 < \eta < 5.2$, ATLAS $-4.5 < \eta < 4.5$.

Energy flow measurements separated by hadronic and electromagnetic energy deposit constrain both N_{mult} and α, and can be done further forward than direct measurements of charged tracks. The particle identification provided by the ALICE and LHCb experiments provides important additional information, needed to tune and test internal parameters of hadronic interaction models. In particular, the number of produced baryons was found to strongly affect the number of muons in air showers at ground, despite their small number compared to pions [997].

To meet the accuracy goal, N_{mult} and α need to be measured in proton-oxygen collisions at the LHC, which directly mimic interactions of cosmic rays with the atmosphere. Constraining α and N_{mult} to 5 % with existing and future pp and p–Pb data is very challenging [999], since forward-produced hadrons experience strong nuclear modification [327, 754, 1000]. A sufficiently accurate theory to predict nuclear modification in the p–O system based on pp and p–Pb data is not yet available, and a simple interpolation is not reliable since both systems are far away in $\ln A$. The difficulty of predicting hadron production in ion collisions is demonstrated in Fig. 105. EPOS-LHC predictions for Xe–Xe collisions significantly underestimate the observed yields in the central region, despite a satisfactory description of pp, p–Pb, and Pb–Pb collisions. The deviations in Xe–Xe are much larger than what is expected from a simple interpolation [998]. The dominant nuclear effects are expected to be different for light and heavy collision partners. Light nuclei are described by the shell model and nucleon correlations are important. Lead nuclei can be described by a simpler model, essentially a Wood-Saxon potential with reduced nucleon correlations that cannot be probed well in experiments.

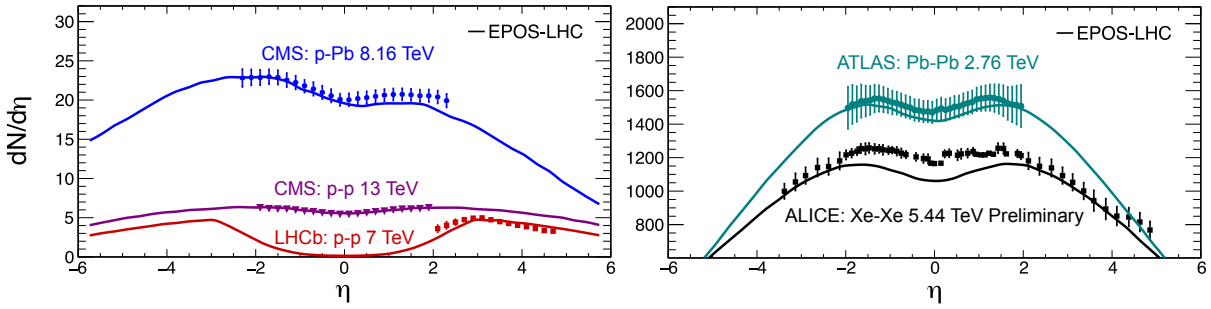

Fig. 105: Comparison of charged particle multiplicity measurements at different center-of-mass energies and in different colliding systems with the EPOS-LHC model [998]. Shown in both plots is $\mathrm{d}N/\mathrm{d}\eta$.

Selecting peripheral p–Pb collisions to mimic p-air collisions with the same number of binary collisions was considered as an alternative to direct p–O measurements, but this option also increases the uncertainty too much. Centrality in p–Pb collisions is extracted from the data using various centrality estimators with different selection biases. These biases would increase the uncertainty of the proposed measurements well beyond the target of 5 % [772]. However, p–O measurements could provide a sensitive test of centrality estimators since the thickness of the oxygen nucleus and hence the average number of wounded nucleons is about a factor of two smaller. The advantages of estimating centrality in a small ion system are discussed in Sect. 9.10.

In conclusion, collisions of p–O at the LHC are highly desirable to solve the outlined questions. The corresponding measurements would be a crucial input to cosmic ray physics and have the potential to result in significant advances in the century-long ridde of the origin of cosmic rays. The luminosity requirements to reach the physics goals are moderate. A statistical accuracy better than 5 % can be achieved with 100 M minimum-bias events. Luminosity calculations for light ion systems are given in Sect. 2.4. The setup of p–O collisions would follow the successful rapid set-up procedure previously used in the 2012 p–Pb run and the 2017 Xe–Xe run, as described in Sect. 2.5.

It is worthwhile noting that a period of oxygen acceleration in the SPS would also provide the opportunity to complement cosmic-ray related measurements of nuclear fragmentation at NA61/SHINE [1001, 1002] at beam momenta of $150\,A\,\mathrm{GeV}/c$. These measurements aim at improving our understanding of the cosmic-ray propagation in the Galaxy and to evaluate the cosmic-ray background for signatures of astrophysical dark matter [1003]. Another opportunity is the study of very forward production of hadrons in the p–O system at $\sqrt{s_{\mathrm{NN}}} \sim 100\,\mathrm{GeV}$ at the LHCb experiment, by colliding the oxygen beam with proton gas provided by an upgraded SMOG system, as described in Sect. 11.4.

11.4 Fixed-target prospects with LHC beams

Contributors: F. Fleuret (LLLR, Palaiseau), G. Graziani (INFN, Firenze), C. Hadjidakis (IPNO, Orsay), E. Maurice (LLR, Palaiseau), L. Massacrier (IPNO, Orsay), P. Di Nezza (INFN, Frascati), L. Pappalardo (University and INFN Ferrara), P. Robbe (LAL, Orsay), B. Trzeciak (Institute for Subatomic Physics, Utrecht)

Fixed target experiments present many advantages having the versatility of polarised and nuclear targets and allowing one to reach high luminosities with dense and long targets. The 7 TeV proton and 2.76 A.TeV lead beams allow one to reach a centre-of-mass energy per nucleon pair of $\sqrt{s_{\rm NN}} = 115$ GeV and $\sqrt{s_{\rm NN}} = 72$ GeV with a centre-of-mass rapidity boost of 4.8 and 4.2 units, respectively. These energies correspond to an energy domain between the SPS and nominal RHIC energies. The large rapidity boost implies that the backward rapidity region ($y_{\rm cms} \leq 0$) is easily accessible by using standard experimental techniques or existing LHC experiments such as ALICE or LHCb.

The physics opportunities offered by a fixed-target programme at the LHC have been developed in several publications of the AFTER@LHC study group [503, 507, 1004] and can be summarised as follows:

- advance our understanding of the large-x gluon, sea quark and heavy-quark content in the nucleon and nucleus,
- advance our understanding of the dynamics and spin of gluons inside polarised nucleons (if a polarised target were used),
- advance our understanding of the properties of the Quark-Gluon Plasma formed in heavy-ion collisions between SPS and RHIC energies.

11.4.1 Status and future plans in LHCb

The LHCb experiment has pioneered fixed target physics at the LHC since Run 2, using noble-gas targets (helium, neon and argon) obtained by injecting the gas directly in the LHC vacuum pipe in the proximity of the LHCb collision point through the SMOG device [1005]. The nominal target gas pressure of 2×10^{-7} mbar corresponds, for a typical LHC beam of 10^{14} protons, to a luminosity of $6 \times 10^{29} \mathrm{cm}^{-2}\mathrm{s}^{-1}$ for collisions occurring in one meter of gas along the beam direction, which is roughly the acceptance of the LHCb vertex detector.

The forward geometry of the detector is particularly well suited for this configuration. It provides three units of pseudorapidity corresponding to mid and backward rapidities ($-2.8 < y_{cms} < 0.2$ for a beam energy of 6.5 TeV), fully equipped with tracking and particle identification. Proton-nucleus and Pb-nucleus collisions using fixed targets of different nuclear size can be studied at the energy scale of $\sqrt{s_{\rm NN}} \sim 100$ GeV with unique coverage of the high-x regime in the target nucleon.

The samples collected during Run 2, corresponding to integrated luminosities up to about $100\ \mathrm{nb}^{-1}$, allowed to perform studies of particle production which are of particular relevance to cosmic ray physics [100 and to collect unprecedented samples of charmed hadrons in fixed-target collisions at this energy scale [506]. These data can provide unique inputs to discriminate cold nuclear matter effects in heavy-flavour production from the effect of deconfinement, and to study nuclear PDFs at large x. The physics reach of heavy-flavour studies is presently limited by the size of these samples. Measurements of absolute cross-sections are also limited in accuracy by the determination of the luminosity, since the gas pressure can be controlled only within $\pm 50\%$ with the SMOG device. For the first fixed-target physics results, the integrated luminosity has been determined from the rate of elastically scattered atomic electrons with a precision of 6% [1006].

An upgraded gas target device, named SMOG2, is currently being developed, and expected to be operational already during Run 3. In the new setup, the gas is contained in a storage cell, consisting of a 20-cm-long open-ended tube with a diameter of 1 cm, fed by a capillary. It allows to increase the gas

Table 16: Expected yields of reconstructed events for some benchmark channels using the largest fixed-target data sample acquired with SMOG during the LHC Run 2, and possible with SMOG2, using as example a p–Ar sample of 0.1 fb^{-1}.

	SMOG largest sample p–Ne@68 GeV	SMOG2 example p–Ar@115 GeV
Integrated luminosity	~ 100 nb^{-1}	100 pb^{-1}
syst. error on J/ψ x-sec.	6–7%	2–3 %
J/ψ yield	15k	35M
D^0 yield	100k	350M
Λ_c yield	1k	3.5M
ψ(2S) yield	150	400k
$\Upsilon(1S)$ yield	4	15k
Low-mass ($5 < M_{\mu\mu} < 9$ GeV/c^2) Drell-Yan yield	5	20k

density in the target by at least one order of magnitude with respect to SMOG, reaching luminosities of order 10^{31} cm^{-2}s^{-1} with proton beams. The target is placed upstream, from -50 to -30 cm, the nominal LHCb collision point and is thus not overlapping the luminous pp region. This opens the possibility to acquire fixed target events simultaneously with collision events with negligible impact to the pp physics program. The new setup would also allow other gases to be injected, notably hydrogen and deuterium, providing pp collisions in fixed-target mode as a reference for all pA collision samples, and extending the physics case to the study of the three-dimensional structure functions of the nucleon through spin-independent observables [1007]. Heavy noble gases as Kr and Xe would also be usable. The device will be equipped with a gas feed system, allowing to know the target gas density at 1% level.

Assuming that about 10% of the beam intensity can be exploited for fixed-target physics, either in synergy with pp data taking or through dedicated runs, samples corresponding to integrated luminosities of order 0.1 fb^{-1} (using proton beams) and 0.1 pb^{-1} (using Pb beams) can be collected per year, also profiting from the increased beam intensity provided by the HL-LHC.

Samples of this size would allow copious production of Drell-Yan and heavy flavour states, including $b\bar{b}$ mesons. As an example, rough estimates are provided in Table 16 for the yields of reconstructed events in an assumed sample of p–Ar collisions corresponding to 0.1 fb^{-1}. Substantial advancements in the understanding of parton distributions for gluons, antiquark and heavy-quarks at large x, where PDFs are now poorly constrained, are foreseeable [507, 1004]. The precise determination of heavy hadron production at large x is expected to clarify the extent of the intrinsic heavy quark content in the nucleon [931, 1008], and to constrain modifications of the nuclear PDFs due to initial state effects (anti-shadowing and EMC effect [1009], saturation effects [1010]). Sequential quarkonia suppression is a main signature for deconfinement [427], but is also affected by final state effects as break-up of the heavy quark pair [1011] and statistical recombination [428]. The rich samples of different quarkonia states reconstructed in fixed target data will allow to investigate sequential suppression at an energy scale between the SPS and RHIC/LHC, for collision systems ranging from pp to Pb–Xe. The study of collisions of Pb beams on heavy nuclei has been limited in Run 2 by the detector tracking capabilities and would greatly profit from the higher detector granularity offered by the LHCb upgrade 1 and upgrade 2 detectors.

The fixed-target program also presents a very good testbed for the hydrodynamic description of the QCD medium produced in heavy-ion collisions down to the energy of $\sqrt{s_{\rm NN}} \sim 100$ GeV, thanks to the considerable pseudorapidity coverage, with particle identification capability for pions, kaons and protons as well as neutral particles ϕ, K^0_S and Λ^0. Measurements of flow observables and correlations

can contribute in particular to shed light on the extension of the hydrodynamic description [1012, 1013] successful at top RHIC energy and at the LHC towards lower beam energies requiring an appropriate treatment of baryon density [1014], and a fully 3 dimensional initial state [1015]. This can provide important inputs to the search for the critical point in the QCD phase diagram [155, 1016]. In addition, the extension of the fluid dynamical paradigm towards smaller collision systems as an explanation of the experimental findings in proton(deuteron)-nucleus and pp collisions at the LHC [315–318, 720] and at RHIC [1017] can be probed in a novel kinematic regime.

The study of ultra-peripheral collisions in the fixed target configuration also offers a complementary kinematic regime to the similar studies in beam-beam collisions discussed in Section 10. An intriguing possibility would be the observation of η_c photoproduction in the PbAr sample, where the cross section is estimated to be of order 1 nb [1018] provided that the signal can be cleanly separated from the background due to radiative J/ψ decays. This would constitute a confirmation for the existence of the odderon, since the η_c state cannot be produced in the γ-pomeron process and would be under threshold for the γ-γ process in fixed-target PbA collisions. Large samples of exclusively produced ρ^0 and ω are also expected [1019].

Studies of proton collisions on light nuclei provide crucial inputs to the understanding of cosmic ray propagation in the interstellar medium (using H and He targets) and in the atmosphere (using N and O targets). The interpretation of the precise measurements of the antiproton component in cosmic rays, performed in the last decade by the PAMELA [1020] and AMS-02 [1021] space-based missions, is presently limited by the knowledge of the antiproton production in the interstellar medium. The first measurement of antiproton production in pHe collisions has been performed by LHCb with Run 2 data [1006] and has been used to improve the sensitivity to a possible dark matter contribution to the cosmic antiproton flux [1022, 1023]. During Run 3, it is planned to extend these studies with a hydrogen target. The production of antineutrons can also be inferred indirectly by evaluating isospin violation in antiproton production from proton-hydrogen and proton-deuterium collisions.

A better understanding of the bulk of particle production in high-energy hadronic collisions is also crucial to the modeling of atmospheric showers induced by ultra-high-energy cosmic rays. Despite the moderate energy scale, fixed target data offer the unique possibility to use a wide range of nuclear targets, including nitrogen and oxygen, and to study production at large x. The main background for the observation of the astrophysical high-energy neutrino flux, recently established by the IceCube collaboration [1024], originates from neutrinos of PeV energy produced from decays of charmed hadrons in atmospheric showers. A relevant uncertainty on this background is related to the possible intrisic charm contribution to the charm PDF at large x [1025]. Knowledge of light hadron production, notably baryons, at large x will allow to improve the modeling of the number of muons produced in the lateral development of the showers, which is a key observable to infer the mass composition of ultra-high-energy cosmic rays, as discussed in Sect. 11.3.

More ambitious projects for future target upgrades have also been proposed for a possible installation in LHCb on the time scale of HL-LHC. These are beyond the baseline LHCb Upgrade 2. A polarised gas target similar to that used in HERMES [1026], installed upstream of the LHCb vertex detector, would make LHCb a key contributor to spin physics. With this option, LHCb would have access to single spin asymmetries in an unique kinematic range for a variety of final states, including unique measurements with quarkonium and Drell-Yan lepton pairs [1027]. Measurements of the three-dimensional structure of nucleons from hadron collisions would be highly complementary to the program at the electron-ion collider, which is proposed on a comparable time scale.

11.4.2 Opportunities with ALICE

The ALICE detector provides many physics opportunities if running in the fixed-target mode with the LHC proton and lead beams. One of the main strengths of ALICE in the fixed-target mode would be

its large rapidity coverage. Assuming a target location at $z = 0$, the ALICE muon spectrometer would access the mid- to backward rapidity in the centre-of-mass frame ($-2.3 < y_{\rm cms}$[6] < -0.8) considering an incident proton beam on the target. For an incident lead beam, the muon spectrometer rapidity coverage is $-1.8 < y_{\rm cms} < -0.3$. In addition, the absorber in front of the muon tracking stations is an asset for background rejection and Drell-Yan studies. The ALICE central barrel offers a complementary coverage to the muon arm by accessing the very backward rapidity region ($-5.7 < y_{\rm cms} < -3.9$ with the proton beam and $-5.2 < y_{\rm cms} < -3.4$ with the lead beam), reaching the end of the phase space for several probes. Thanks to its excellent particle identification capabilities, particle detection and identification down to low $p_{\rm T}$, unique measurements of soft probes and open heavy flavours can be pursued. Another asset of the ALICE apparatus is the capability to operate with good performance in a high particle density environment. Access to the most central AA collisions at $\sqrt{s_{\rm NN}} = 72$ GeV should be possible if the detector occupancy does not exceed the one expected in Pb–Pb collisions at 50 kHz. In addition, the ALICE Collaboration could potentially devote a significant data taking time to a fixed-target programme (especially with the proton beam), allowing the collection of large integrated luminosities and the investigation of several target species.

Two main solutions are being investigated to deliver fixed-target collisions to ALICE: an internal gaseous target or an internal solid target (coupled to a bent crystal to deflect the beam halo). On the one hand, a gas-jet or a storage cell with levelled gas pressure would allow to deliver about 45 pb^{-1} of proton-polarised hydrogen collisions to ALICE (260 pb^{-1} in case of unpolarised H_2 collisions), and 8 nb^{-1} of Pb–Xe collisions per year. For the luminosity calculation, a time duration of 10^7 s and 10^6 s, corresponding to one LHC year, is considered for the proton and lead beams, respectively. With a gas system the target can be polarised, but requires large space to be installed, most likely outside the ALICE barrel magnet, 7 metres from the nominal Interaction Point (IP). In that case, additional detectors for vertexing are needed as well as studies of the tracking performances of the TPC in such conditions. A simple unpolarised storage cell might potentially be used closer to the current ALICE IP. On the other hand, the usage of an internal solid target coupled to a bent crystal has the advantage of more portability, allowing one to install the target closer to the IP, from 2.75 to 4.7 m to the IP, and thus benefiting of better performances from the current ALICE apparatus. With such a device 37 pb^{-1} (6 pb^{-1}) of p–C (p–W) collisions, and 5 nb^{-1} (3 nb^{-1}) of Pb–C (Pb–W) collisions could be registered in ALICE per year. One of these solutions could be installed during LS3.

The performance for several key probes has been investigated using fast simulations [507] and it is summarised in the following.

- Quarkonia: Very large yields are expected for charmonia (up to $\sim 10^6$ J/ψ) in the ALICE muon spectrometer both in pp and Pb-A collisions[7] considering one LHC year of data taking. The $\Upsilon(1S)$ will also be within reach. Looking at quarkonium suppression as a function of rapidity and the system size would allow one to search for the onset of the QGP formation, and to determine the in-medium modification of the QCD forces for centre-of-mass energies between the ones probed at RHIC and the SPS. In pA collisions, $\Upsilon(1S)$ could be used to probe large-x gluons in the target ($0.1 < x < 1$), in order to constrain the anti-shadowing and EMC effects.
- Drell-Yan: A precise measurement of the Drell-Yan process with the muon spectrometer can probe initial state effects on quarks of momentum fraction $0.05 < x < 0.8$ at a mass scale of $M_{\mu\mu} > 4$ GeV/c^2 from pA to A- collisions. The correlated background from $\rm b\bar{b}$ and $\rm c\bar{c}$ pairs in the dimuon decay channel is largely reduced at the lower centre-of-mass energy of the fixed-target mode, with respect to the TeV energy range.
- Open heavy flavour: At $y_{\rm lab} \sim 1$ about 3000 (up to 100) D^0 are expected to be produced per 0.1

[6] The rapidity is calculated assuming massless particles.

[7] The largest atomic mass number considered here is W for the solid target and Xe for the gas target.

rapidity unit per year in pp (Pb-A) collisions, respectively. The ALICE central barrel probes the end of the D meson phase-space, in particular if the vertex is located at $z < 4$ m from the IP. This would allow one to reach very large-x gluon close to 1 at low mass scale, where the contribution of the intrinsic charm component in the proton could largely increase the D meson yield. Hence the ALICE central barrel is well suited to study the large-x intrinsic charm component in the proton.

– Identified charged hadrons: In few hours of Pb–A data taking, it would be already possible to collect up to 10^6 minimum bias events with the ALICE central barrel which would allow one to reach an absolute statistical uncertainty of 0.01 on the elliptic flow coefficient v_2 for pions and protons, 0.02 for kaons, and 0.05 for antiprotons in semi-central events. Measurements of identified particles up to very large rapidities would complement the limiting fragmentation studies carried out by the BRAHMS and PHOBOS experiments at RHIC. In addition, particle yields and flow coefficients measured at large rapidities are powerful tools to constrain the temperature dependence of the medium shear viscosity [1028]. Thermal model calculations also indicate that the temperature and baryonic chemical potential depend on the rapidity [1029–1031] suggesting that one can perform a rapidity scan of the QGP phase diagram in a complementary approach to the Beam Energy Scan programme of RHIC.
– Antiproton production: Measurements of antiproton production cross sections in p–H, p–He, p–C, p–N and p–O collisions are important inputs for theoretical calculations of the secondary cosmic antiproton spectrum [1032–1034], where secondary antiprotons originate from the high energy scattering between the interstellar matter and the primary cosmic rays. The measurement of a cosmic antiproton excess with respect to expectations from secondary antiproton production would open new perspectives on the indirect detection of dark matter or unknown astrophysical mechanisms of cosmic ray acceleration. Complementarily to LHCb [1006], the ALICE central barrel can measure very slow antiprotons down to few hundred MeV momentum. Measuring slow antiprotons produced with the LHC proton beam on a nuclear target is equivalent to the case where the nuclear target travels at TeV energies, hit an interstellar proton at rest and produces an antiproton with high energy. Thanks to the large antiproton yields expected in p–H_2 collisions (larger than 10^8 per 0.1 rapidity unit per year), the ALICE central barrel is well placed to help constraining the uncertainty on the cosmic antiproton spectrum.
– Strangeness: Thanks to the large yields ($\sim 10^8$ per 0.1 rapidity unit per year at $y_{\rm lab} \sim 1$) of Λ hyperons expected to be produced in the ALICE central barrel by using a longitudinally polarised target with the proton beam, a precise measurement of the longitudinal spin transfer D_{LL} of the Λ hyperon could be carried out. So far only limited experimental results exist with poor precision [1035, 1036]. Measurements with ALICE would give a unique opportunity to study the spin-dependent strange quark (antiquark) densities at $0.35 < x < 0.7$.
– Charmonium and pentaquark photoproduction: Exclusive J/ψ photoproduction is known to be sensitive to gluon Generalised Parton Distributions (GPD) at leading order [1037]. ALICE in fixed target mode would have a unique opportunity to study the yet unknown GPD $E_{\rm g}$ thanks to the measurement of single transverse spin asymmetries of photoproduced J/ψ by using a transversally polarised H target with the proton beam [1038, 1039]. About 200 photoproduced J/ψ per year are expected to be produced in the muon spectrometer acceptance. Moreover, the photoproduction of hidden charm pentaquark states [1040] might be possible in the central barrel acceptance which allows for the access to low photon-proton centre-of-mass energies ($W_{\gamma p} \sim 5$ GeV). About 2 to 20 pentaquarks are expected to be produced in the ALICE central barrel per year in p–H_2 collisions.

Note that these studies were performed assuming a vertex position at the ALICE IP for the quarkonia, identified hadron production, as well as for charmonium and pentaquark photoproduction, and a vertex position at 4.7 m from the IP for the antiproton and strangeness production.

Studies are ongoing to address the technical feasibility of the target system integration in the

experiment, as well as simulation studies to evaluate the ALICE apparatus tracking performance for target positions displaced by a few metres from the IP. Moreover, investigations are ongoing to extend the ALICE rapidity coverage for several observables thanks to combined measurements of muons detected both in the ALICE central and the muon spectrometer (see as an example the work in [1041] in collider mode).

12 Summary of luminosity requirements and proposed run schedule

The physics programme presented in this report requires data-taking campaigns with various colliding systems with centre-of-mass energies and integrated luminosities $L_{\rm int}$ as outlined in the following. In some cases the requirements are updated or new with respect to the present baseline LHC programme (see Sec. 2.2 and Ref. [2]). The main variations are: a much larger $L_{\rm int}$ target for p–Pb collisions, motivated by high-precision studies of both initial and final-state effects, following the surprising discoveries of collective-like effects in small collision systems; a large sample of pp collisions at top LHC energy to reach the highest possible multiplicities with the smallest hadronic colliding system; moderate-statistics samples of O–O (as mentioned in 2.5, this would be a limited "pilot-run" scenarion that could not achieve the values listed in Tables 4 and 5) and p–O collisions, to study the onset of hot-medium effects and to tune cosmic-ray particle production models, respectively. Finally, as discussed in Sec. 11.1, extended LHC running with colliding intermediate-mass nuclei (as, for example, Ar–Ar or Kr–Kr), offers the unique opportunity of a large increase in nucleon–nucleon luminosity to access novel probes of the QGP and to open a precision era for probes which are still rare with the Pb–Pb system. The working group considers the high-luminosity Pb–Pb and p–Pb programmes to be the priorities that should be pursued in Run 3 and Run 4. High-luminosity runs with intermediate-mass nuclei are regarded as an appealing case for extending the heavy-ion programme at the LHC after LS4. This case, including the choice of the optimal nuclear species, should be studied further from the theoretical and operational points of view, both of which could be informed with one or two pilot runs with different species.

- **Pb–Pb at $\sqrt{s_{\rm NN}} = 5.5$ TeV**, $L_{\rm int} = 13\ {\rm nb}^{-1}$ (ALICE, ATLAS, CMS), $2\ {\rm nb}^{-1}$ (LHCb)
- **pp at $\sqrt{s} = 5.5$ TeV**, $L_{\rm int} = 600\ {\rm pb}^{-1}$ (ATLAS, CMS), $6\ {\rm pb}^{-1}$ (ALICE), $50\ {\rm pb}^{-1}$ (LHCb)
- **pp at $\sqrt{s} = 14$ TeV**, $L_{\rm int} = 200\ {\rm pb}^{-1}$ with low pileup (ALICE, ATLAS, CMS)
- **p–Pb at $\sqrt{s_{\rm NN}} = 8.8$ TeV**, $L_{\rm int} = 1.2\ {\rm pb}^{-1}$ (ATLAS, CMS), $0.6\ {\rm pb}^{-1}$ (ALICE, LHCb)
- **pp at $\sqrt{s} = 8.8$ TeV**, $L_{\rm int} = 200\ {\rm pb}^{-1}$ (ATLAS, CMS, LHCb), $3\ {\rm pb}^{-1}$ (ALICE)
- **O–O at $\sqrt{s_{\rm NN}} = 7$ TeV**, $L_{\rm int} = 500\ \mu{\rm b}^{-1}$ (ALICE, ATLAS, CMS, LHCb)
- **p–O at $\sqrt{s_{\rm NN}} = 9.9$ TeV**, $L_{\rm int} = 200\ \mu{\rm b}^{-1}$ (ALICE, ATLAS, CMS, LHCb)
- **Intermediate AA**, e.g. $L_{\rm int}^{\rm Ar-Ar} = 3$–$9\ {\rm pb}^{-1}$ (about 3 months) gives NN luminosity equivalent to Pb–Pb with $L_{\rm int} = 75$–$250\ {\rm nb}^{-1}$

Based on these requirements, the proposed updated running schedule is reported in the following table. It can be seen that the physics programme for Run 3 and Run 4 discussed in this report is achievable by a modest increase of the "heavy-ion running" time from 12 to 14 weeks per run.

Year	Systems, $\sqrt{s_{\rm NN}}$	Time	$L_{\rm int}$
2021	Pb–Pb 5.5 TeV	3 weeks	$2.3\ \mathrm{nb}^{-1}$
	pp 5.5 TeV	1 week	$3\ \mathrm{pb}^{-1}$ (ALICE), $300\ \mathrm{pb}^{-1}$ (ATLAS, CMS), $25\ \mathrm{pb}^{-1}$ (LHCb)
2022	Pb–Pb 5.5 TeV	5 weeks	$3.9\ \mathrm{nb}^{-1}$
	O–O, p–O	1 week	$500\ \mu\mathrm{b}^{-1}$ and $200\ \mu\mathrm{b}^{-1}$
2023	p–Pb 8.8 TeV	3 weeks	$0.6\ \mathrm{pb}^{-1}$ (ATLAS, CMS), $0.3\ \mathrm{pb}^{-1}$ (ALICE, LHCb)
	pp 8.8 TeV	few days	$1.5\ \mathrm{pb}^{-1}$ (ALICE), $100\ \mathrm{pb}^{-1}$ (ATLAS, CMS, LHCb)
2027	Pb–Pb 5.5 TeV	5 weeks	$3.8\ \mathrm{nb}^{-1}$
	pp 5.5 TeV	1 week	$3\ \mathrm{pb}^{-1}$ (ALICE), $300\ \mathrm{pb}^{-1}$ (ATLAS, CMS), $25\ \mathrm{pb}^{-1}$ (LHCb)
2028	p–Pb 8.8 TeV	3 weeks	$0.6\ \mathrm{pb}^{-1}$ (ATLAS, CMS), $0.3\ \mathrm{pb}^{-1}$ (ALICE, LHCb)
	pp 8.8 TeV	few days	$1.5\ \mathrm{pb}^{-1}$ (ALICE), $100\ \mathrm{pb}^{-1}$ (ATLAS, CMS, LHCb)
2029	Pb–Pb 5.5 TeV	4 weeks	$3\ \mathrm{nb}^{-1}$
Run-5	Intermediate AA	11 weeks	e.g. Ar–Ar 3–9 pb^{-1} (optimal species to be defined)
	pp reference	1 week	

13 First considerations on a heavy-ion programme at a High Energy LHC (HE-LHC)

Coordinators: Andrea Dainese (INFN Padova), David d'Enterria (CERN) and Carlos A. Salgado (Instituto Galego de Fisica de Altas Enerxias (IGFAE) Universidade de Santiago de Compostela)

Contributors: L. Apolinario (LIP and IST Lisbon), N. Armesto (Instituto Galego de Fisica de Altas Enerxias (IGFAE) Universidade de Santiago de Compostela), J. Jowett (CERN), G. Milhano (LIP and IST Lisbon, CERN), U.A. Wiedemann (CERN)

13.1 Introduction

In this section the physics opportunities associated with the operation of the HE-LHC with heavy-ion beams are discussed. These first considerations are based on studies carried out in the scope of the Future Circular Collider (FCC) Study group [411, 1042]. For a centre-of-mass energy $\sqrt{s} = 27$ TeV for pp collisions, the relation $\sqrt{s_{\rm NN}} = \sqrt{s}\sqrt{Z_1 Z_2 / A_1 A_2}$ gives the energy per nucleon–nucleon collision of $\sqrt{s_{\rm NN}} = 10.6$ TeV for Pb–Pb ($Z = 82$, $A = 208$) and 17 TeV for p–Pb collisions. The present estimate of the integrated luminosity per month of running is larger by a factor two with respect to the current projection for the future LHC runs, i.e. $L_{\rm int} \approx 6\ {\rm nb}^{-1}$ per experiment, see Section 2.2. The possibility of using nuclei smaller than Pb, like e.g. ^{40}Ar or ^{129}Xe, to achieve larger instantaneous luminosity is also under consideration. For example, the integrated nucleon–nucleon (NN) luminosity per run for Xe–Xe collisions at $\sqrt{s_{\rm NN}} = 11.5$ TeV could be 2–3 times larger than for Pb–Pb collisions (see integrated $L_{\rm NN}$ values in Tables 4 and 5).

The increase in the centre-of-mass energy and integrated luminosity at the FCC with respect to the LHC opens up novel opportunities for physics studies of the Quark-Gluon Plasma (QGP) described in a recent CERN Yellow Report [411]. Most of these opportunities also apply to the HE-LHC scenario, although with more moderate reach in terms of available probes and kinematics coverage. The main scientific motivations for a heavy-ion programme at the HE-LHC can be summarized as follows.

Novel access to QCD thermodynamics and QCD equilibration processes. Substantially increasing the centre-of-mass energy leads to the creation of initially denser and hotter strongly-interacting systems that expand for a longer duration and over a larger volume, thereby developing stronger collective phenomena. Extrapolations of LHC measurements indicate that the initial energy density increases by a factor about 1.4 from $\sqrt{s_{\rm NN}} = 5.5$ TeV to 10.6 TeV, up to values of about 22–24 GeV/fm^3 (at $\tau = 1$ fm/c). These estimates are presented in Section 13.2. The QGP formed at the HE-LHC collision energies reaches closer to a range of temperatures ($T \sim 1$ GeV) where charm quarks start to contribute as active thermal degrees of freedom in the QGP equation of state, thus playing a novel role in QCD equilibration processes.

Characterisation of dense QCD matter through hard-scattering processes. As detailed in Section 13.3, the HE-LHC would provide a much larger abundance of hard-scattering processes than the LHC, as well as novel probes like the top quark and, potentially, the Higgs boson [942, 944, 1043]. A notable example is provided by high-momentum (thus, highly boosted) $\mathrm{t} \to \mathrm{W} \to \mathrm{q\bar{q}}$ decay chains, which are promising probes of the QGP time evolution and of the role of colour coherence [944]. The secondary production of charm quarks in scatterings between quark and gluon constituents of the hot QCD medium could reach a substantial fraction of the initial production in partonic hard scatterings and be observed for the first time.

Exploration of saturated parton densities in a previously-uncharted, ultra-dense kinematic domain. As discussed in Section 13.4, the higher centre-of-mass energy of the HE-LHC allows one to explore a wide previously-uncharted kinematic range at low x and Q^2, where parton saturation is expected to set in. Proton–nucleus collisions would have a coverage down to $x \sim 5 \times 10^{-6}$ in the Pb nucleus at a rapidity of $y \approx 5$.

Table 17: Global properties measured in central Pb–Pb collisions (0–5% centrality class) at $\sqrt{s_{\rm NN}} = 2.76$ TeV and extrapolated to 5.5, 10.6 and 39 TeV. The values for Pb–Pb collisions at the LHC and FCC are from Ref. [411]. The values for Pb–Pb collisions at the HE-LHC are estimated using the same parametrisations as used for the FCC. The values for Xe–Xe collisions at the HE-LHC are all estimated on the basis of the multiplicity extrapolation from the measurement by the ALICE Collaboration [1045] (it is assumed that the transverse energy density scales only with the multiplicity, neglecting possible differences of the average energy per particle between Pb–Pb and Xe–Xe and between the LHC and the HE-LHC).

System, $\sqrt{s_{\rm NN}}$ (Tev)	Pb–Pb, 2.76	Pb–Pb, 5.5	Pb–Pb, 10.6	Xe–Xe, 11.5	Pb–Pb, 39.4
$\mathrm{d}N_{\rm ch}/\mathrm{d}\eta$ at $\eta = 0$	1600	2000	2400	1500	3600
$\mathrm{d}E_{\rm T}/\mathrm{d}\eta$ at $\eta = 0$ (TeV)	1.7–2.0	2.3–2.6	3.1–3.4	≈ 1.5	5.2–5.8
Homogeneity volume fm^3	5000	6200	7400	4500	11000
Decoupling time (fm/c)	10	11	11.5	10	13
ε at $\tau = 1$ fm/c (GeV/fm^3)	12–13	16–17	22–24	≈ 15	35–40

13.2 Global characteristics of nucleus–nucleus collisions at the HE-LHC

Extrapolating measurements of charged particle multiplicity, transverse energy and femtoscopic correlations at lower energies, one can obtain estimates for the growth of global event characteristics from the LHC to the HE-HC and the FCC. In particular, up to the top LHC energy, the growth of charged-particle multiplicity per participant pair per unit rapidity in nucleus–nucleus collisions is consistent with a slowly-rising power-law: $\mathrm{d}N_{\rm ch}/\mathrm{d}\eta\,(\eta = 0) \propto (\sqrt{s_{\rm NN}})^{0.3}$ (see e.g. [1044]). As shown in Table 17, for Pb–Pb this amounts to an increase of a factor ~ 1.2 from the LHC to the HE-LHC. The multiplicity in central Xe–Xe collisions is expected to be lower by 35% with respect to Pb–Pb collisions at the HE-LHC, and similar to that of Pb–Pb collisions at 2.76 TeV.

In general, the global event characteristics listed in Table 17 determine the spatio-temporal extent QGP system, and they constrain the thermodynamic conditions that apply after thermalization. The measured transverse energy per unit rapidity $\mathrm{d}E_{\rm T}/\mathrm{d}\eta$ (see Table 17) is of particular importance since it constrains the initial energy density. The energy density is expected to increase by a factor 1.4 from the LHC to the HE-LHC, reaching a value of 22–24 GeV/fm^3 at the time of 1 fm/c [411]. Using the arguments presented in Ref. [411], an initial temperature as large as $T_0 \approx 600$–800 MeV is expected at the time $\mathcal{O}(0.05\,\mathrm{fm}/c)$ after which both nuclei traverse each other at HE-LHC energies. In the case of Xe–Xe collisions the energy density is estimated to be significantly lower than that for Pb–Pb and similar to that of Pb–Pb at LHC energies.

13.3 QGP studies with hard probes

13.3.1 Hard processes in nucleus–nucleus collisions at the HE-LHC

The increase in energy and luminosity (in the case of Xe–Xe) from the LHC to the HE-LHC provides new tools to study the matter created in the collisions of heavy ions. In Fig. 106 (left), cross sections for different processes and different energies are computed with MCFM [1046] at the highest available order. The increases amount to a factor ~ 2 for charm, beauty, W and Z production, ~ 4 for jets with $p_{\rm T} > 100$ GeV/c and for Higgs, and ~ 6 for top-pair production.

The motivations for measurements of top quarks in heavy-ion collisions are multifold. In p–Pb collisions the cross sections efficiently probe the nuclear gluon PDFs in a wide range in momentum fraction x at high scale $Q \sim m_{\rm t}$ [942] (see Section 10.4.4). In Pb–Pb collisions, the top-quark observables are sensitive to the energy-loss of heavy quarks [1047] and by selecting boosted (very high $p_{\rm T}$)

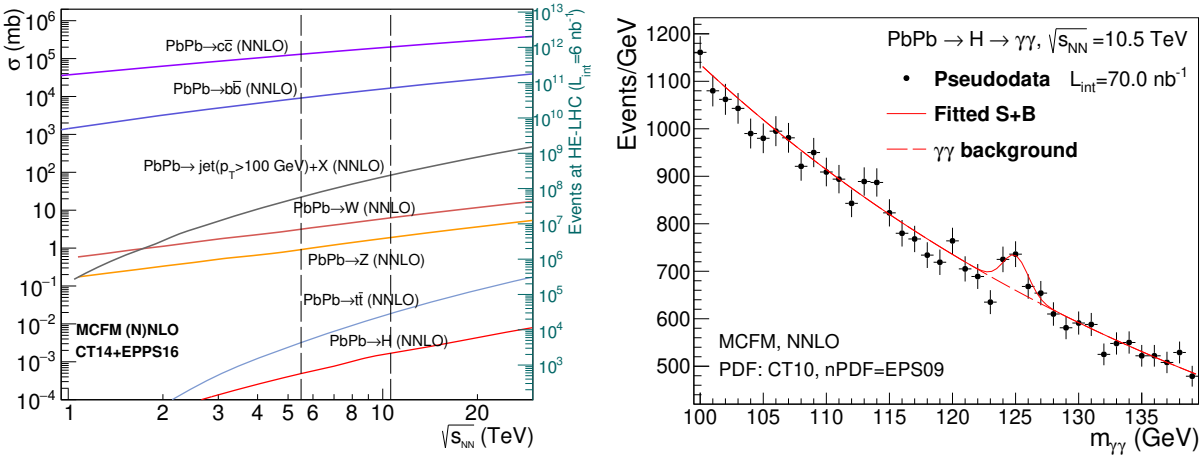

Fig. 106: Left: $\sqrt{s}$-dependence of the cross sections for hard processes of interest for a heavy-ion programme, calculated with MCFM [1046] at the highest available order. The yields for a one month Pb–Pb run ($L_{\rm int} = 6\ {\rm nb}^{-1}$) are also shown. Right: invariant mass distribution for Higgs boson search in the $\gamma\gamma$ decay channel in Pb–Pb collisions at the HE-LHC with $L_{\rm int} = 70\ {\rm nb}^{-1}$ using the selections described in Ref. [1043].

top quarks one could also probe the QGP medium at later times as the decays of boosted top quarks get Lorentz time dilated (see next section). For example, the estimated measurable yields for $\rm t\bar{t} \to b\bar{b}\,\ell\ell\,\nu\nu$ (using the per-month luminosities discussed in Section 13.1) with realistic analysis cuts and conservative 50% efficiency for b-jet tagging are about 10^4 in Pb–Pb collisions and 3×10^4 in Xe–Xe collisions (for the case of three-fold increase of NN integrated luminosity with respect to Pb–Pb).

Another potential novel probe of the QGP medium at HE-LHC and FCC energies is the Higgs boson. The Higgs boson has a lifetime of $\tau \approx 50$ fm/c, which is much larger than the time extent of the QGP phase [1048, 1049]. In Ref. [1048] it has been argued that the Higgs boson interacts strongly with the quarks and gluons of the QGP and the interactions induce its decay in the gluon–gluon or quark–antiquark channels, thus depleting the branching ratio to the most common "observation" channels $\gamma\gamma$ or $\rm ZZ^\star$. More recent detailed theoretical calculations, including virtual corrections, predict however no visible suppression of the scalar boson [1050]. The cross section for Higgs boson production in Pb–Pb collisions is expected to increase by a factor about 4 when going from $\sqrt{s_{\rm NN}} = 5.5$ TeV to $\sqrt{s_{\rm NN}} = 10.6$ TeV [1043]. A statistically-significant Higgs boson observation in the $\gamma\gamma$ decay channel in Pb–Pb collisions at the HE-LHC requires an integrated luminosity of 70 ${\rm nb}^{-1}$ (estimated as in Ref. [1043]), which corresponds to about 12 months with the present machine performance projections. The analysis used similar photon selections as used by ATLAS and CMS in pp collisions: $p_{\rm T} > 30, 40$ GeV/c, $|\eta| < 4$, $R_{\rm isol} = 0.3$. The backgrounds included the irreducible QCD diphoton continuum plus 30% of events coming from misidentified γ-jet and jet-jet processes. The corresponding invariant mass distribution is shown in the right-hand panel of Fig. 106. With Xe–Xe collisions the same statistical significance could be reached in 4 months.

13.3.2 Boosted tops and the time evolution of QGP opacity

The HE-LHC would provide large rates of highly-boosted heavy particles, such as tops, Z and W bosons. It is expected that when these particles decay the density profile of the QGP has already evolved. It has been argued that the hadronically-decaying W bosons in events with a $\rm t\bar{t}$ pair can provide unique insights into the time structure of the QGP [944]. This is because the time decays of the top and the W bosons are

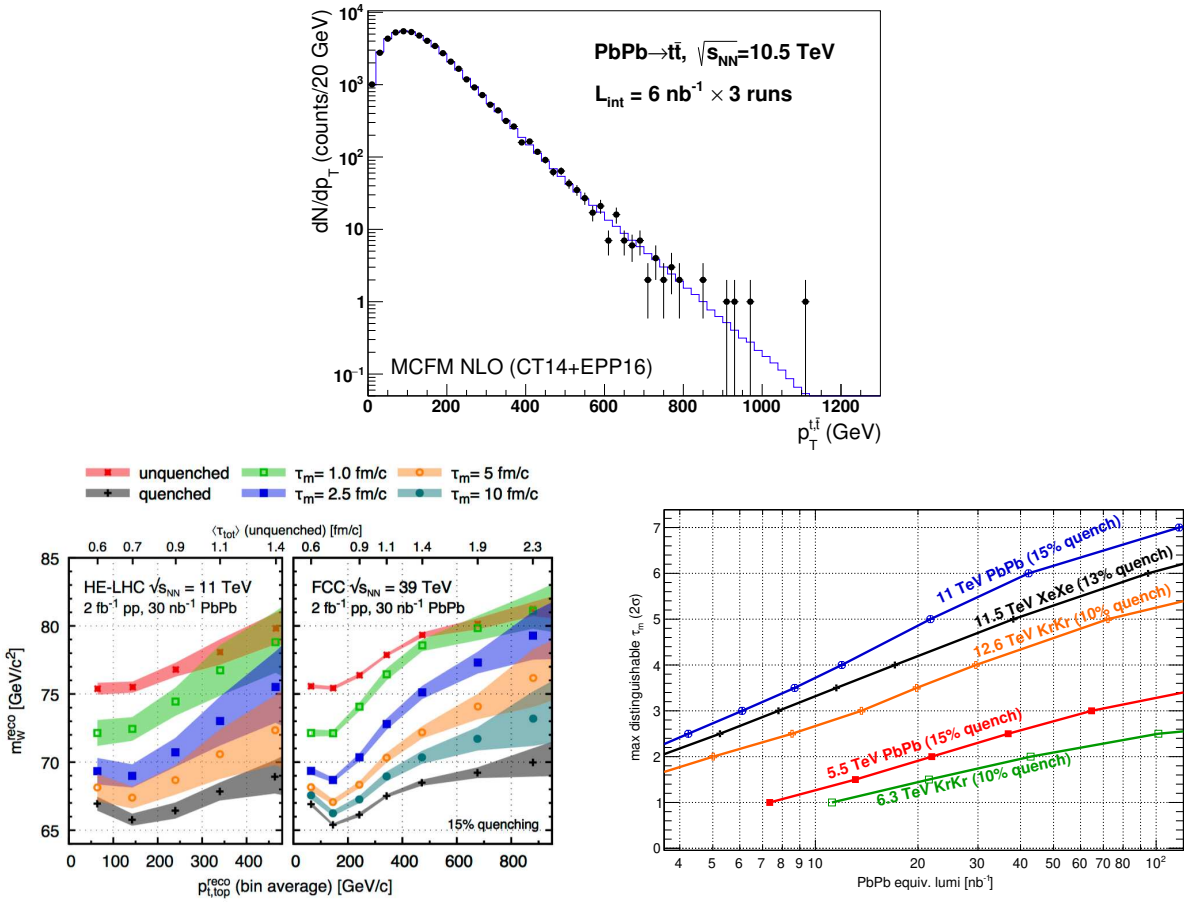

Fig. 107: Upper panel: expected top-quark p_{T} distribution in Pb–Pb in the decay channels of interest for the boosted top analysis at $\sqrt{s_{\mathrm{NN}}} = 10.6$ TeV after acceptance and efficiency cuts with the statistical uncertainties for $L_{\mathrm{int}} = 18$ nb^{-1}, corresponding to three months of data taking (adapted from [942]). Lower-left panel: reconstructed W boson mass at HE-LHC and FCC energies, as a function of the top p_{T}. The upper axis refers to the average total time delay of the corresponding top p_{T} bin. Lower-right panel: maximum medium quenching end-time, τ_m, that can be distinguished from full quenching at two standard deviations, as a function of luminosity for various species at LHC and HE-LHC energies. The luminosity for nuclei lighter than Pb is scaled to the Pb–Pb equivalent nucleon–nucleon luminosity. Figures adapted from Ref. [944].

followed by a time-delay in the interaction of the decay products of the W boson with the surrounding medium due to a colour coherence effect. The sum of these three times, several fm/c for boosted tops, would be the time at which the interaction with the QGP begins, providing a unique way to directly measure the time structure of the QGP evolution. In addition, due to colour coherence effects, energy loss would be initially absent for the colour-singlet $\mathrm{q\bar{q}}$ decay products of a highly-boosted W boson: the two quarks would start to be quenched only when their distance becomes larger than the colour correlation length of the medium, which depends on the transport coefficient $\hat{q}$ (the average transverse momentum squared that particles exchange with the medium per unit mean-free path) [1051]. The effect on the reconstructed masses of the top and W was studied with different energy loss scenarios as a proof of concept of the potential of these observables to access completely novel quantities in heavy-ion collisions [944].

For this study, the p_{T} reach of top quarks in Pb–Pb collisions is of special importance, because it determines the maximum time delay for probing the QGP. The upper panel of Fig. 107 shows the estimated p_{T} distribution of the reconstructed top yields in Pb–Pb collisions at the HE-LHC with an integrated luminosity of 18 nb^{-1}, corresponding to three months of data taking. The figure indicates that events with top p_{T} up to about 500 GeV/c can be studied. The reconstructed W-boson mass as a function of top transverse momentum is shown in Fig. 107 (lower-left panel), together with the FCC case. For details on the simulation and reconstruction procedure see [944]. The scale on the upper horizontal axis shows that a p_{T} reach of 500 GeV/c corresponds to an average total time delay $\langle\tau_{\mathrm{tot}}\rangle \sim 1.5$ fm/c. The shaded region corresponds to the statistical uncertainty estimated in central Pb–Pb collisions for $L_{\mathrm{int}} = 30$ nb^{-1} (corresponding to 5 Pb–Pb months or 1.5 Xe–Xe months with the present luminosity estimates) and $L_{\mathrm{int}} = 2$ fb^{-1} for the pp reference. Energy loss was simulated by assuming that all particles, except the W-boson decay products, lose 15% of their initial momentum. Average time delays $\tau_m = 1; 2.5; 5$ and 10 fm/c were considered as effective QGP time evolution profiles. Fig. 107 (right) shows the maximum medium quenching end-time, τ_m, that can be distinguished from full quenching with two standard deviations, as a function of luminosity for various collider energies and species. For Pb–Pb with $L_{\mathrm{int}} = 30$ nb^{-1} (5 months) at the HE-LHC a maximum time of 5–6 fm/c can be accessed, which is much larger than the time up to 1.5 fm/c that can be probed at the LHC with the nominal programme of 10 nb^{-1}. For Xe–Xe collisions, with equivalent NN luminosity larger by a factor 2–3 with respect to Pb-Pb, a time range longer by $\sim$ 1–2 fm/c can be covered in the same running period.

13.3.3 Heavy flavour and quarkonia

Heavy quarks (charm and bottom) are among the hard probes that have provided important insights on the formation and the characterics of the QGP, see Sections 5 and 7, and Ref. [258]. In this section, a few selected aspects that could represent novel or particularly remarkable observations at HE-LHC energy are discussed, namely: i) large production of thermal charm from interactions of light quarks and gluons within the QGP; ii) observation of an enhancement of charmonium production with respect to the binary scaling of the yields in pp collisions, as consequence of (re)generation; iii) observation of a colour screening and (re)generation for the most tightly-bound quarkonium state, the Υ(1S).

Interactions between gluons or light quarks of the QGP can lead to the production of $\mathrm{c\bar{c}}$ pairs if the energy in the centre of mass of the interaction is of the order of twice the charm quark mass $\sqrt{\hat{s}} \sim 2\,m_c \sim 3$ GeV. In Section 13.2 we have estimated that an initial temperature T_0 of 600–800 MeV could be reached at the HE-LHC. With these QGP temperatures a sizeable fraction of the gluons and light quarks have energies larger than the charm quark mass and $\mathrm{c\bar{c}}$ pairs can be produced in their interactions. Figure 108 shows the prediction [1052] for the time-dependence of the $\mathrm{c\bar{c}}$ rapidity density at mid-rapidity in central Pb–Pb collisons at the HE-LHC. The value at the initial time τ_0 corresponds to the initial hard-scattering cross section. Both calculations show a rapid increase after τ_0 with a final value that is larger by up to 20% than the initial production. This enhancement could be observed for the first time at the HE-LHC and provide a handle on the initial temperature of the QGP. The abundance of charm quarks also has an effect on the QGP equation of the state: the inclusion of the charm quark in lattice-QCD calculations results in a sizeable increase of $P/T^4 \propto n_{\mathrm{d.o.f.}}$ for $T > 400$ MeV, as discussed in the context of the FCC [411].

The measurements of the nuclear modification factor of J/ψ at the LHC [745, 749, 1053] are described by models that include dissociation caused by colour-charge screening and a contribution of recombination (usually denoted (re)generation) from deconfined c and $\mathrm{\bar{c}}$ quarks in the QGP [461, 1054, 1055]. The (re)generation contribution the charmonium yield is expected to be proportional to the square of the rapidity density of $\mathrm{c\bar{c}}$ pairs in the QGP. Therefore, it is predicted to be much larger at HE-LHC than LHC energies, as a consequence of the larger hard-scattering production cross section of $\mathrm{c\bar{c}}$ pairs and the possible sizeable thermal production. This could lead to the observation of an enhancement of

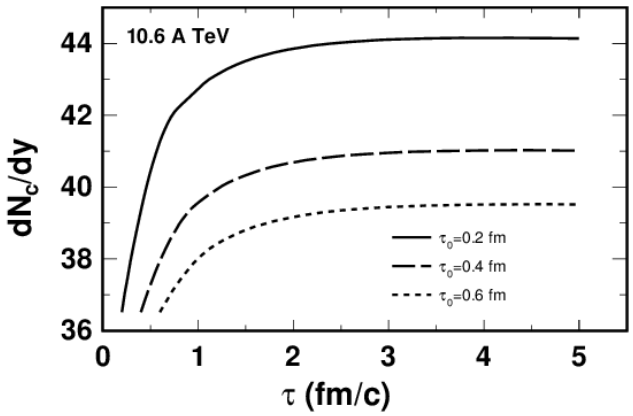

Fig. 108: Time-evolution of the $\mathrm{c\overline{c}}$ yield (per unit of rapidity at midrapidity) for central Pb–Pb collisions at $\sqrt{s_{\mathrm{NN}}} = 10.6$ TeV, obtained as described in Ref. [1052].

J/ψ production with respect to binary scaling of the yield in pp collisions, i.e. $R_{\mathrm{AA}} > 1$, which would be striking evidence of $c\overline{c}$ recombination from a deconfined QGP.

The measurement of Υ production would be particularly interesting at the high energies and temperatures reached at the HE-LHC. The LHC data are consistent with a scenario in which the excited states 2S and 3S are partially or totally suppressed by colour screening, while the 1S, which is the most tightly bound state, has no or little direct melting. Its suppression by about 60% could be explained by the lack of feed-down from the (melted) higher states and the effect of nuclear PDF suppression (see e.g. Ref. [258] for a recent review). At HE-LHC energies, on the one hand, the temperature could be large enough to determine a full melting even of the tightly-bound 1S state, on the other hand the large abundance of $\mathrm{b\overline{b}}$ pairs in the QGP could induce substantial Υ (re)generation. The role of the two effects —degree of survival of initial bottomonia and contribution of (re)generation— could be separated by means of precise measurements of the $\mathrm{b\overline{b}}$ cross section and of the B meson and Υ R_{AA} and elliptic flow v_2 (the regenerated Υ states could exhibit a v_2 such that $0 < v_2^{\Upsilon} < v_2^{\mathrm{B}}$).

13.4 Nuclear PDF measurements and search for parton saturation

Parton saturation [780, 781] is based on the idea that standard linear parton branching leads, at small values of momentum fraction x, to parton densities so high that non-linear dynamics (like gluon recombination) becomes important and parton densities are tamed to grow from power-like to logarithmically. Non-linear effects are expected to become important when the density of gluons per unit transverse area exceeds a certain limit, the *saturation density*.

In the framework of QCD collinear factorization, Parton Distribution Functions of nucleons inside nuclei (nuclear PDFs) can be obtained in standard global fit analysis with usual linear evolution equations. The differences with respect to free nuclon PDFs are parametrized in a nuclear modification factor $R_i^{\mathrm{A}}(x, Q^2)$ with $i = \mathrm{g}$, $\mathrm{q_{valence}}$, $\mathrm{q_{sea}}$ (see e.g. Ref. [1056]). Collinear factorization is expected to break down when the gluon phase-space becomes saturated. The onset of saturation is usually discussed in terms of the saturation momentum Q_{S}^2, defined as the scale at which the transverse area of the nucleus is completely saturated and gluons start to overlap. It can be shown that $Q_{\mathrm{S}}^2 \sim A^{1/3}\left(\sqrt{s_{\mathrm{NN}}}\right)^{\lambda} e^{\lambda y}$, with $\lambda \approx 0.3$ [411]. Therefore, the regime of high gluon density is best accessed at a high-$\sqrt{s_{\mathrm{NN}}}$ hadron collider with measurements at low p_{T} and forward rapidity, which probe small x and small Q^2. In order to firmly establish the existence of this new high-energy regime of QCD and clarify the validity of the different approaches to factorisation and evolution, new kinematic regions must be explored using

higher collision energies in order to have a large lever arm in Q^2 in a region that, while perturbative, lies inside the saturation domain. The HE-LHC extends the small-x coverage by a factor of two with respect to the LHC, as shown in Fig. 109.

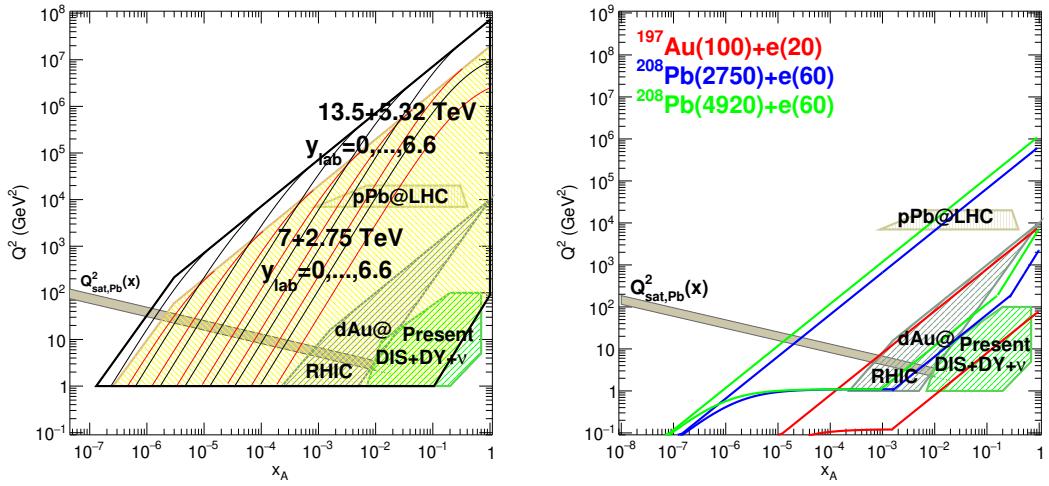

Fig. 109: Regions of the x–Q^2 plane covered by the data used for present nuclear PDF fits (nuclear DIS and Drell-Yan, p–Pb and d–Au at the LHC and RHIC), shown in both panels, by p–Pb collisions at the LHC and the HE-LHC (left) and by e–A collisions at the EIC, LHeC and HE-LHC (right). In the left panel, the thin lines correspond to different rapidities in the laboratory frame $y_{\rm lab}$ = 0,1, 2, 3, 4, 5, 6 from right to left, with the left edge defined by $y_{\rm lab} = 6.6$. Values of $Q^2_{\rm S}(x)$ for Pb are shown for illustration in both panels.

There is a strong complementarity between the physics programmes at hadron colliders and at the proposed electron–hadron colliders (Electron-Ion Collider in the USA [798], Large Hadron Electron Collider LHeC [797]). With kinematic reach at the TeV scale in the c.m.s. (Fig. 109, left), the electron–nucleus option at the HE-LHC would be well-positioned to reach conclusive evidence for the existence of a new non-linear regime of QCD. It would be clearly complementary with the p–Pb case, providing a precise knowledge on the partonic structure of nucleons and nuclei and on the small-x dynamics. A specific discussion can be found in the electron–nucleus part of the FCC Conceptual Design Report.

13.5 Photon–photon collisions

Photon–photon collisions in UPCs of proton [1057] and lead (Pb) beams [587] have been experimentally observed at the LHC [819, 1058–1060]. The future prospects at the LHC are extensively discussed in Sect. 11.2. Although the γ spectrum is harder for smaller charges –which favours proton over nuclear beams in the production of heavy diphoton systems– each photon flux scales with the squared charge of the hadron, Z^2, and thus $\gamma\gamma$ luminosities are extremely enhanced for ion beams ($Z^4 = 5 \cdot 10^7$ in the case of Pb–Pb). The Pb beam Lorentz factor at HE-LHC ($\gamma = 5\,650$) determines the "maximum" quasireal photon energy $\omega_{\rm max} = \gamma/{\rm R_{Pb}} \approx 160$ GeV, leading to photon–photon collisions up to centre-of-mass energies of $\sqrt{s_{\gamma\gamma}} \approx 320$ GeV, twice larger than those reachable at the LHC.

The very rare elastic scattering of two photons in vacuum $\gamma\gamma \to \gamma\gamma$ was recently observed for the first time in UPCs at the LHC [809, 810]. At the HE-LHC, due to the higher diphoton masses reached, this process may be sensitive to physics beyond the SM through new heavy charged particles contributing to the virtual loop such as, e.g., from SUSY particles [1061]. Light-by-light (LbyL) scattering has also been proposed as a tool to search for monopoles [1062], axions [1063], unparticles [1064], low-scale

gravity effects [1065], and non-commutative interactions [1066].

Acknowledgements

We would like to thank the LHC experimental Collaborations and the WLCG for their essential support. We are especially grateful for the efforts by the computing, generator and validation groups who were instrumental for the creation of large simulation samples. We thank the detector upgrade groups as well as the physics and performance groups for their input. Not least, we thank the many colleagues who have provided useful comments on the analyses.

Specific authors acknowledge the following forms of support:

- Nestor Armesto, Elena G. Ferreiro and Carlos Salgado acknowledge the support of the Ministerio de Ciencia e Innovación of Spain under projects FPA2014-58293-C2-1-P, FPA2017-83814-P and Unidad de Excelencia María de Maetzu under project MDM-2016-0692, by Xunta de Galicia (Consellería de Educación) within the Strategic Unit AGRUP2015/11, and by FEDER.
- Raphaelle Bailhache acknowledges the support of the German Federal Ministry of Education and Research (BMBF).
- Zvi Citron acknowledges the support of the ISRAEL SCIENCE FOUNDATION (grant No. 91/6491).
- Torsten Dahms acknowledges the support of the DFG cluster of excellence "Origin and Structure of the Universe".
- Stefan Floerchinger acknowledges the support of the DFG Collaborative Research Centre SFB 1225 (ISOQUANT).
- Iwona Grabowska-Bold acknowledges the support of the Polish National Science Centre grant DEC-2016/23/B/ST2/01409, of the AGH UST statutory tasks No. 11.11.220.01/4 within subsidy of the Ministry of Science and Higher Education, and of the PL-Grid Infrastructure.
- Ilkka Helenius acknowledges the support of the Carl Zeiss Foundation and the Academy of Finland, Project 308301.
- Peter Jacobs and Mateusz Płoskoń acknowledge the support of the U.S. Department of Energy, Office of Science, Office of Nuclear Physics, under contract DE-AC02-05CH11231.
- Jiangyong Jia, Peng Huo and Mingliang Zhou acknowledges the support of the U.S. National Science Foundation under grant number PHY-1613294.
- Spencer Klein acknowledges the support of the U.S. DOE under contract number DE-AC02-05-CH11231.
- Filip Krizek acknowledges the support of the Ministry of Education of the Czech Republic (grant InterExcellence LT17018)
- Mariola Klusek-Gawenda acknowledges the support of the Polish National Science Center Grant No. DEC-2014/15/B/ST2/02528.
- Nirbhay Kumar Behera acknowledges the support of National Research Foundation of Korea (NRF), Basic Science Research Program, funded by the Ministry of Education, Science and Technology (Grant No. NRF-2014R1A1A1008246).
- Constantin Loizides acknowledges the support of of the U.S. Department of Energy, Office of Science, Office of Nuclear Physics, under contract number DE-AC05-00OR22725.
- Laure Massacrier acknowledges the support of CNRS under the grant RFBR/CNRS 18-52-15007.
- Christoph Mayer acknowledges the support of the Polish Ministry of Science and Higher Education and from the Polish National Science Center.
- Alexander Milov acknowledges the support of the Israel Science Foundation (grant 1065/15), and the MINERVA Stiftung with the funds from the BMBF of the Federal Republic of Germany.
- Soumya Mohapatra acknowledges the support of the Division of Nuclear Physics of the US Department of Energy under grant DE-FG02-86ER40281.

– Petja Paakkinen acknowledges the support of the Magnus Ehrnrooth Foundation.
– Hannu Paukkunen acknowledges the support by his Academy-of-Finland project 308301.
– Dmitri Peresunko acknowledges the support of the Russian Science Foundation grant 17-72-20234.
– Ralf Rapp acknowledges the support of the U.S. National Science Foundation under grant number PHY-1614484, and in part by the ExtreMe Matter Institute EMMI at the GSI Helmholtzzentrum für Schwerionenforschung (Darmstadt,Germany).
– Kristof Redlich acknowledges the support of the Polish National Science Center NCN under Maestro grant DEC-2013/10/A/ST2/00106.
– Mark Strikman acknowledges the support of the U.S. Department of Energy, Office of Science, Office of Nuclear Physics, under Award No. DE-FG02-93ER40771.
– Adam Trzupek acknowledges the support of the National Science Centre, Poland under the grant no 2016/23/B/ST2/00702.
– Michael Weber acknowledges the support of the Austrian Academy of Sciences and the Nationalstiftung für Forschung, Technologie und Entwicklung, Austria.
– Michael Winn acknowledges the support of the European Research Council (ERC) through the project EXPLORINGMATTER, funded by the ERC through a ERC-Consolidator-Grant.

References

[1] ALICE Collaboration, *ALICE upgrade physics performance studies for 2018 Report on HL/HE-LHC physics*, ALICE-PUBLIC-2019-001, Feb, 2019. https://cds.cern.ch/record/2661798.

[2] ALICE Collaboration, B. Abelev et al., *Upgrade of the ALICE Experiment: Letter Of Intent*, J. Phys. **G41** (2014) 087001.

[3] ALICE Collaboration, B. Abelev et al., *Technical Design Report for the Upgrade of the ALICE Inner Tracking System*, J. Phys. **G41** (2014) 087002.

[4] ALICE Collaboration, B. Abelev et al., *Technical Design Report for the Muon Forward Tracker*, CERN-LHCC-2015-001. ALICE-TDR-018, Jan, 2015. https://cds.cern.ch/record/1981898.

[5] ATLAS Collaboration, *Projections for ATLAS Measurements of Jet Modifications in Pb+Pb Collisions in LHC Runs 3 and 4*, ATL-PHYS-PUB-2018-019, CERN, Geneva, Oct, 2018. http://cds.cern.ch/record/2644406.

[6] ATLAS Collaboration, *Projections for ATLAS Measurements of Bulk Properties of Pb+Pb, p+Pb, and pp Collisions in LHC Runs 3 and 4*, ATL-PHYS-PUB-2018-020, CERN, Geneva, Oct, 2018. http://cds.cern.ch/record/2644407.

[7] ATLAS Collaboration, *Expected ATLAS Measurement Capabilities of Observables Sensitive to Nuclear Parton Distributions*, ATL-PHYS-PUB-2018-039 (Nov, 2018) . https://cds.cern.ch/record/2649445.

[8] CMS Collaboration, *Projected Heavy Ion Physics Performance at the High Luminosity LHC Era with the CMS Detector*, CMS-PAS-FTR-17-002, CERN, Geneva, 2017. https://cds.cern.ch/record/2291105.

[9] CMS Collaboration, *Performance of heavy flavor and quarkonia in heavy ion collisions at HL-LHC*, CMS-PAS-FTR-18-024, CERN, Geneva, 2018. http://cds.cern.ch/record/2650897.

[10] CMS Collaboration, *Performance of jet quenching measurements in pp and PbPb collisions with CMS at the HL-LHC*, CMS-PAS-FTR-18-025, CERN, Geneva, 2018. https://cds.cern.ch/record/2651892.

[11] CMS Collaboration, *Predictions on the precision achievable for small system flow observables in the context of HL-LHC*, CMS-PAS-FTR-18-026, CERN, Geneva, 2018. http://cds.cern.ch/record/2650773.

[12] CMS Collaboration, *Constraining nuclear parton distributions with heavy ion collisions at HL-LHC with the CMS experiment*, CMS-PAS-FTR-18-027 (2018) . https://cds.cern.ch/record/2652030.

[13] LHCb Collaboration, *LHCb projections for proton-lead collisions during LHC Runs 3 and 4*, LHCb-CONF-2018-005. CERN-LHCb-CONF-2018-005, CERN, Geneva, Nov, 2018. http://cds.cern.ch/record/2648625.

[14] O. S. Brüning, P. Collier, P. Lebrun, et al., *LHC Design Report*. CERN Yellow Reports: Monographs. CERN, Geneva, 2004. https://cds.cern.ch/record/782076.

[15] J.M. Jowett, *Colliding Heavy Ions in the LHC*, in *Proc. 9th International Particle Accelerator Conference (IPAC'18)*, pp. 584–589. JACoW Publishing, Geneva, Switzerland, June, 2018.

[16] M. Schaumann et al., *First Xenon-Xenon Collisions in the LHC*, in *Proc. 9th International Particle Accelerator Conference (IPAC'18), Vancouver, BC, Canada, April 29-May 4, 2018*, pp. 180–183. JACoW Publishing, Geneva, Switzerland, June, 2018.

[17] C. A. Salgado et al., *Proton-Nucleus Collisions at the LHC: Scientific Opportunities and Requirements*, J. Phys. **G39** (2012) 015010, arXiv:1105.3919 [hep-ph].

[18] H. Bartosik et al., *LIU baseline for ions*, LHC Performance Workshop (Chamonix 2017) . https://indico.cern.ch/event/580313/contributions/2359517/attachments/1401284/2138778/LIU_baseline_for_ions.pdf.

[19] J. M. Jowett et al., *HL-LHC beam parameters for ions*, LHC Performance Workshop (Chamonix 2017) . https://indico.cern.ch/event/580313/contributions/2359507/attachments/1401326/2138794/Chamonix2017_Jowett.pdf.

[20] S. R. Klein, *Localized beam pipe heating due to e- capture and nuclear excitation in heavy ion colliders*, Nucl.Instrum.Meth. **A459** (2001) 51–57, arXiv:physics/0005032 [physics].

[21] J. M. Jowett, *Ions in the LHC ring*, in *LHC performance. Proceedings, 12th Workshop, Chamonix, France, March 3-8, 2003*, pp. 84–90. 2003. http://ab-div.web.cern.ch/ab-div/Conferences/Chamonix/chamx2003/PAPERS/2_6_JJ.pdf.

[22] R. Bruce, S. Gilardoni, J. M. Jowett, and D. Bocian, *Beam losses from ultra-peripheral nuclear collisions between (Pb-208)**82+ ions in the Large Hadron Collider and their alleviation*, Phys. Rev. ST Accel. Beams **12** (2009) 071002, arXiv:0908.2527 [physics.acc-ph].

[23] C. Bahamonde Castro et al., *Power Deposition in LHC Magnets Due to Bound-Free Pair Production in the Experimental Insertions*, in *Proceedings, 7th International Particle Accelerator Conference (IPAC 2016): Busan, Korea, May 8-13, 2016*, p. TUPMW006. 2016.

[24] R. W. Assmann, *Collimators and beam absorbers for cleaning and machine protection*, in *LHC Project Workshop 14th Chamonix Workshop Chamonix, Switzerland, January 17-21, 2005*, p. 54. 2005. http://ab-div.web.cern.ch/ab-div/Conferences/Chamonix/chamx2005/PAPERS/8_02.pdf.

[25] G. Robert-Demolaize, *Design and performance optimization of the LHC collimation system*. PhD thesis, LPSC, Grenoble, 2006. http://cds.cern.ch/record/1004869.

[26] R. Assmann et al., *The final collimation system for the LHC*, Conf. Proc. **C060626** (2006) 986–988. https://inspirehep.net/record/727805.

[27] C. Bracco, *Commissioning scenarios and tests for the LHC collimation system*. PhD thesis, Milan U., 2009. http://weblib.cern.ch/abstract?CERN-THESIS-2009-031.

[28] R. Bruce, R. W. Assmann, V. Boccone, et al., *Simulations and measurements of beam loss patterns at the CERN Large Hadron Collider*, Phys. Rev. ST Accel. Beams **17** (Aug, 2014) 081004.

[29] G. Valentino, R. Bruce, M. Fiascaris, et al., *Performance of the LHC collimation system during 2015*, CERN-ACC-2015-376, Proceedings of the 6th Evian Workshop, Evian, France (2015) . http://cds.cern.ch/record/2156966?ln=en.

[30] D. Mirarchi, R.Bruce, M. Fiascaris, et al., *Collimation: experience and performance*, CERN-ACC-2017-094, Proceedings of the 7th Evian Workshop, Evian, France (2016) . http://cds.cern.ch/record/2289585?ln=en.

[31] R. Bruce, C. Bracco, R. De Maria, et al., *Reaching record-low b^* at the CERN Large Hadron Collider using a novel scheme of collimator settings and optics*, Nucl. Instrum. Meth. **A848** (2017) 19–30.

[32] P. D. Hermes, *Heavy-Ion Collimation at the Large Hadron Collider: Simulations and Measurements*. PhD thesis, Univ. of Muenster, Sep, 2016. https://cds.cern.ch/record/2241364.

[33] P. D. Hermes, R. Bruce, J. M. Jowett, et al., *Measured and simulated heavy-ion beam loss patterns at the CERN Large Hadron Collider*, Nucl. Instrum. Meth. **A819** (2016) 73–83.

[34] H.-H. Braun, R. W. Assmann, A. Ferrari, et al., *Collimation of Heavy Ion Beams in LHC*, in *9th European Particle Accelerator Conference (EPAC 2004) Lucerne, Switzerland, July 5-9, 2004*. 2004. http://accelconf.web.cern.ch/AccelConf/e04/PAPERS/MOPLT010.PDF.

[35] P. D. Hermes, B. Auchmann, R. Bruce, et al., *LHC Heavy-Ion Collimation Quench Test at 6.37Z TeV*, CERN-ACC-NOTE-2016-0031, Mar, 2016. http://cds.cern.ch/record/2136828.

[36] R. Bruce, A. Marsili, and S. Redaelli, *Cleaning Performance with 11T Dipoles and Local Dispersion Suppressor Collimation at the LHC*, in *Proceedings of the International Particle Accelerator Conference 2014, Dresden, Germany*, p. 170. 2014.

[37] A. Lechner, B. Auchmann, R. Bruce, et al., *Power Deposition in LHC Magnets With and Without Dispersion Suppressor Collimators Downstream of the Betatron Cleaning Insertion*, in *Proceedings of the International Particle Accelerator Conference 2014, Dresden, Germany*, p. 112. 2014.

[38] Apollinari G. and Béjar Alonso I. and Brüning O. and Fessia P. and Lamont M. and Rossi L. and Tavian L., *High-Luminosity Large Hadron Collider (HL-LHC): Technical Design Report V. 0.1*. CERN Yellow Reports: Monographs. CERN, Geneva, 2017.

[39] D. Mirarchi, *Crystal Collimation for LHC*. PhD thesis, Imperial College, London, Aug, 2015. http://cds.cern.ch/record/2036210.

[40] D. Mirarchi, G. Hall, S. Redaelli, and W. Scandale, *Design and implementation of a crystal collimation test stand at the Large Hadron Collider*, Eur. Phys. J. **C77** (2017) no. 6, 424.

[41] W. Scandale et al., *Observation of channeling for 6500 GeV/ c protons in the crystal assisted collimation setup for LHC*, Phys. Lett. **B758** (2016) 129–133.

[42] J. Jowett, R. Alemany-Fernández, G. Baud, et al., *The 2016 Proton-Nucleus Run of the LHC*, TUPVA014 (2017) no. CERN-ACC-2017-143, . https://cds.cern.ch/record/2289686.

[43] D. Manglunki et al., *CERN's Fixed Target Primary Ion Programme*, in *Proceedings, 7th International Particle Accelerator Conference (IPAC 2016): Busan, Korea, May 8-13, 2016*, p. TUPMR027. 2016.

[44] J.M. Jowett, *Nuclear beams at HE-LHC*, in *FCC Week, Amsterdam*. 2018. https://indico.cern.ch/event/656491/contributions/2923429/.

[45] A. Andronic, P. Braun-Munzinger, K. Redlich, and J. Stachel, *Decoding the phase structure of QCD via particle production at high energy*, Nature **561** (2018) no. 7723, 321–330, arXiv:1710.09425 [nucl-th].

[46] ALICE Collaboration, S. Acharya et al., *Production of ^{4}He and $^4\overline{He}$ in Pb-Pb collisions at $\sqrt{s_{\rm NN}}$ = 2.76 TeV at the LHC*, Nucl. Phys. **A971** (2018) 1–20, arXiv:1710.07531 [nucl-ex].

[47] ALICE Collaboration, B. Abelev et al., *Centrality dependence of π, K, p production in PbPb collisions at $\sqrt{s_{\rm NN}} = 2.76$ TeV*, Phys. Rev. **C88** (2013) 044910, arXiv:1303.0737 [hep-ex].

[48] ALICE Collaboration, S. Acharya et al., *Anisotropic flow of identified particles in Pb-Pb collisions at $\sqrt{s_{\rm NN}} = 5.02$ TeV*, JHEP **09** (2018) 006, arXiv:1805.04390 [nucl-ex].

[49] A. Andronic, P. Braun-Munzinger, J. Stachel, and H. Stöcker, *Production of light nuclei, hypernuclei and their antiparticles in relativistic nuclear collisions*, Phys. Lett. **B697** (2011) 203–207, arXiv:1010.2995 [nucl-th].

[50] HotQCD Collaboration, A. Bazavov et al., *Equation of state in (2+1)-flavor QCD*, Phys. Rev. D **90** (2014) 094503, arXiv:1407.6387 [hep-lat].

[51] R. Bellwied, S. Borsanyi, Z. Fodor, S. D. Katz, and C. Ratti, *Is there a flavor hierarchy in the deconfinement transition of QCD?*, Phys. Rev. Lett. **111** (2013) 202302, arXiv:1305.6297 [hep-lat].

[52] S. T. Butler and C. A. Pearson, *Deuterons from High-Energy Proton Bombardment of Matter*, Phys. Rev. **129** (1963) 836–842.

[53] J. I. Kapusta, *Mechanisms for deuteron production in relativistic nuclear collisions*, Phys. Rev. **C21** (1980) 1301–1310.

[54] J. C. Bergstrom, *^{6}Li electromagnetic form factors and phenomenological cluster models*, Nucl. Phys. **A327** (1979) 458–476.

[55] H. Sato and K. Yazaki, *On the coalescence model for high-energy nuclear reactions*, Phys. Lett. **B98** (1981) 153–157.

[56] J. L. Nagle, B. S. Kumar, D. Kusnezov, H. Sorge, and R. Mattiello, *Coalescence of deuterons in relativistic heavy ion collisions*, Phys. Rev. **C53** (1996) 367–376.

[57] R. Scheibl and U. W. Heinz, *Coalescence and flow in ultrarelativistic heavy ion collisions*, Phys. Rev. **C59** (1999) 1585–1602, arXiv:nucl-th/9809092 [nucl-th].

[58] U. A. Wiedemann and U. W. Heinz, *Particle interferometry for relativistic heavy ion collisions*, Phys. Rept. **319** (1999) 145–230, arXiv:nucl-th/9901094 [nucl-th].

[59] F. Bellini and A. P. Kalweit, *Testing coalescence and statistical-thermal production scenarios for (anti-)(hyper-)nuclei and exotic QCD objects at LHC energies*, Phys. Rev. **C99** (2019) 054905, arXiv:1807.05894 [hep-ph].

[60] ExHIC Collaboration, S. Cho et al., *Exotic Hadrons from Heavy Ion Collisions*, Prog. Part. Nucl. Phys. **95** (2017) 279–322, arXiv:1702.00486 [nucl-th].

[61] Z. Zhang and C. M. Ko, *Hypertriton production in relativistic heavy ion collisions*, Phys. Lett. **B780** (2018) 191–195.

[62] S. Bazak and S. Mrowczynski, *^{4}He vs. ^{4}Li and production of light nuclei in relativistic heavy-ion collisions*, Mod. Phys. Lett. **A33** (2018) no. 25, 1850142, arXiv:1802.08212 [nucl-th].

[63] W. Zhao, L. Zhu, H. Zheng, C. M. Ko, and H. Song, *Spectra and flow of light nuclei in relativistic heavy ion collisions at energies available at the BNL Relativistic Heavy Ion Collider and at the CERN Large Hadron Collider*, Phys. Rev. **C98** (2018) no. 5, 054905, arXiv:1807.02813 [nucl-th].

[64] S. Wheaton and J. Cleymans, *THERMUS: A Thermal model package for ROOT*, Comput. Phys. Commun. **180** (2009) 84–106, arXiv:hep-ph/0407174 [hep-ph].

[65] M. Petran, J. Letessier, J. Rafelski, and G. Torrieri, *SHARE with CHARM*, Comput. Phys. Commun. **185** (2014) 2056–2079, arXiv:1310.5108 [hep-ph].

[66] ALICE Collaboration, *Preliminary Physics Summary: Deuteron and anti-deuteron production in pp collisions at $\sqrt{s} = 13$ TeV and in Pb–Pb collisions at $\sqrt{s_{\rm NN}} = 5.02$ TeV*, ALICE-PUBLIC-2017-006, Jul, 2017. https://cds.cern.ch/record/2272148.

[67] ALICE Collaboration, S. Trogolo, *Recent results on (anti-)(hyper-)nuclei production in pp, p-Pb and Pb-Pb collisions with ALICE*, PoS **EPS-HEP2017** (2017) 200.

[68] ALICE Collaboration, *Upgrade of the ALICE Time Projection Chamber*, CERN-LHCC-2013-020. ALICE-TDR-016, Oct, 2013. http://cds.cern.ch/record/1622286.

[69] ALICE Collaboration, P. Antonioli, A. Kluge, and W. Riegler, *Upgrade of the ALICE Readout and Trigger System*, CERN-LHCC-2013-019. ALICE-TDR-015, Sep, 2013. https://cds.cern.ch/record/1603472.

[70] P. Buncic, M. Krzewicki, and P. Vande Vyvre, *Technical Design Report for the Upgrade of the Online-Offline Computing System*, CERN-LHCC-2015-006. ALICE-TDR-019, Apr, 2015. https://cds.cern.ch/record/2011297.

[71] ALICE Collaboration, S. Acharya et al., *Measurement of deuteron spectra and elliptic flow in Pb?Pb collisions at* $\sqrt{s_{\rm NN}}$ *= 2.76 TeV at the LHC*, Eur. Phys. J. **C77** (2017) no. 10, 658, arXiv:1707.07304 [nucl-ex].

[72] ALICE Collaboration, J. Adam et al., *Precision measurement of the mass difference between light nuclei and anti-nuclei*, Nature Phys. **11** (2015) no. 10, 811–814, arXiv:1508.03986 [nucl-ex].

[73] G. A. Miller, *Charge symmetry breaking*, Nucl. Phys. **A518** (1990) 345–357.

[74] G. Audi, A. H. Wapstra, and C. Thibault, *The Ame2003 atomic mass evaluation (II). Tables, graphs and references*, Nucl. Phys. **A729** (2002) 337–676.

[75] H. Kamada, J. Golak, K. Miyagawa, H. Witala, and W. Gloeckle, *Pi mesonic decay of the hypertriton*, Phys. Rev. **C57** (1998) 1595–1603, arXiv:nucl-th/9709035 [nucl-th].

[76] D. H. Davis, *50 years of hypernuclear physics. I. The early experiments*, Nucl. Phys. **A754** (2005) 3–13.

[77] Particle Data Group Collaboration, M. Tanabashi et al., *Review of Particle Physics*, Phys. Rev. **D98** (2018) no. 3, 030001.

[78] M. Agnello, E. Botta, T. Bressani, S. Bufalino, and A. Feliciello, *On the use of the* (π^-, K_0) *reaction on nuclear targets for the precise determination of the lifetime of the hydrogen hyperisotopes and other neutron-rich* Λ*-hypernuclei*, Nucl. Phys. **A954** (2016) 176–198.

[79] ALICE Collaboration, J. Adam et al., ${}^{3}_{\Lambda}\mathrm{H}$ *and* ${}^{3}_{\Lambda}\overline{\mathrm{H}}$ *production in Pb-Pb collisions at* $\sqrt{s_{\rm NN}} =$ *2.76 TeV*, Phys. Lett. **B754** (2016) 360–372, arXiv:1506.08453 [nucl-ex].

[80] STAR Collaboration, L. Adamczyk et al., *Measurement of the* ${}^{3}_{\Lambda}H$ *lifetime in Au+Au collisions at the BNL Relativistic Heavy Ion Collider*, Phys. Rev. **C97** (2018) no. 5, 054909, arXiv:1710.00436 [nucl-ex].

[81] M. Rayet and R. H. Dalitz, *Lifetime of H-3*, Nuovo Cim. **A46** (1966) 786.

[82] J. G. Congleton, *A Simple model of the hypertriton*, J. Phys. **G18** (1992) 339–357.

[83] F.-C. T. Garcilazo H., Valcarce A., ΛNN *and* ΣNN *systems at threshold. II. The effect of D waves*, Phys. Rev. C **76** (2007) 034001.

[84] T. Nagae et al., *Observation of a* ${}^{4}_{\Sigma^0}\mathrm{He}$ *Bound State in the* ${}^{4}\mathrm{He}(\mathrm{K}^-, \pi^-)$ *Reaction at 600 MeV/c*, Phys. Rev. Lett. **80** (1998) 1605–1609.

[85] ALICE Collaboration, A. Borissov, *Hyperon Production in pp Collisions at* $\sqrt{s}$ *= 7 TeV at the LHC with ALICE*, EPJ Web Conf. **97** (2015) 00005.

[86] ALICE Collaboration, B. B. Abelev et al., *Performance of the ALICE Experiment at the CERN LHC*, Int. J. Mod. Phys. **A29** (2014) 1430044, arXiv:1402.4476 [nucl-ex].

[87] ALICE Collaboration, N. Jacazio, *Production of identified charged hadrons in Pb–Pb collisions at* $\sqrt{s_{NN}} = 5.02$ *TeV*, Nucl. Phys. **A967** (2017) 421–424, arXiv:1704.06030 [nucl-ex].

[88] ALICE Collaboration, S. Acharya et al., $\Lambda_{\rm c}^{+}$ *production in Pb-Pb collisions at* $\sqrt{s_{\rm NN}} = 5.02$ *TeV*, Phys. Lett. **B793** (2019) 212–223, arXiv:1809.10922 [nucl-ex].

[89] Particle Data Group Collaboration, C. Patrignani et al., *Review of Particle Physics*, Chin. Phys. **C40** (2016) no. 10, 100001.

[90] J. He, *Nucleon resonances* $N(1875)$ *and* $N(2100)$ *as strange partners of LHCb pentaquarks*, Phys. Rev. **D95** (2017) no. 7, 074031, arXiv:1701.03738 [hep-ph].

[91] A. Andronic, P. Braun-Munzinger, M. K. Köhler, K. Redlich, and J. Stachel, *Transverse momentum distributions of charmonium states with the statistical hadronization model*, arXiv:1901.09200 [nucl-th].

[92] F. Donato, N. Fornengo, and P. Salati, *Anti-deuterons as a signature of supersymmetric dark matter*, Phys. Rev. **D62** (2000) 043003, arXiv:hep-ph/9904481 [hep-ph].

[93] H. Baer and S. Profumo, *Low energy antideuterons: shedding light on dark matter*, JCAP **0512** (2005) 008, arXiv:astro-ph/0510722 [astro-ph].

[94] F. Donato, N. Fornengo, and D. Maurin, *Antideuteron fluxes from dark matter annihilation in diffusion models*, Phys. Rev. **D78** (2008) 043506, arXiv:0803.2640 [hep-ph].

[95] C. B. Brauninger and M. Cirelli, *Anti-deuterons from heavy Dark Matter*, Phys. Lett. **B678** (2009) 20–31, arXiv:0904.1165 [hep-ph].

[96] M. Kadastik, M. Raidal, and A. Strumia, *Enhanced anti-deuteron Dark Matter signal and the implications of PAMELA*, Phys. Lett. **B683** (2010) 248–254, arXiv:0908.1578 [hep-ph].

[97] Y. Cui, J. D. Mason, and L. Randall, *General Analysis of Antideuteron Searches for Dark Matter*, JHEP **11** (2010) 017, arXiv:1006.0983 [hep-ph].

[98] L. A. Dal and M. Kachelriess, *Antideuterons from dark matter annihilations and hadronization model dependence*, Phys. Rev. **D86** (2012) 103536, arXiv:1207.4560 [hep-ph].

[99] A. Ibarra and S. Wild, *Prospects of antideuteron detection from dark matter annihilations or decays at AMS-02 and GAPS*, JCAP **1302** (2013) 021, arXiv:1209.5539 [hep-ph].

[100] N. Fornengo, L. Maccione, and A. Vittino, *Dark matter searches with cosmic antideuterons: status and perspectives*, JCAP **1309** (2013) 031, arXiv:1306.4171 [hep-ph].

[101] E. Carlson, A. Coogan, T. Linden, et al., *Antihelium from Dark Matter*, Phys. Rev. **D89** (2014) no. 7, 076005, arXiv:1401.2461 [hep-ph].

[102] T. Aramaki et al., *Review of the theoretical and experimental status of dark matter identification with cosmic-ray antideuterons*, Phys. Rept. **618** (2016) 1–37, arXiv:1505.07785 [hep-ph].

[103] M. Korsmeier, F. Donato, and N. Fornengo, *Prospects to verify a possible dark matter hint in cosmic antiprotons with antideuterons and antihelium*, Phys. Rev. **D97** (2018) no. 10, 103011, arXiv:1711.08465 [astro-ph.HE].

[104] AMS Collaboration, F. Giovacchini and V. Choutko, *Cosmic Rays Antideuteron Sensitivity for AMS-02 Experiment*, in *Proceedings, 30th International Cosmic Ray Conference (ICRC 2007): Merida, Yucatan, Mexico, July 3-11, 2007*, vol. 4, pp. 765–768. 2007. http://indico.nucleares.unam.mx/contributionDisplay.py?contribId=1112&confId=4.

[105] AMS Collaboration, A. Kounine, *AMS Experiment on the International Space Station*, in *Proceedings, 32nd International Cosmic Ray Conference (ICRC 2011): Beijing, China, August 11-18, 2011*, vol. c, p. 5. 2011. https://inspirehep.net/record/1352202/files/vc_I02.pdf.

[106] GAPS Collaboration, P. von Doetinchem, T. Aramaki, S. Boggs, et al., *GAPS - Dark matter search with low-energy cosmic-ray antideuterons and antiprotons*, PoS **ICRC2015** (2016) 1219, arXiv:1507.02717 [astro-ph.IM]. [34,1218(2015)].

[107] T. Aramaki, C. J. Hailey, S. E. Boggs, et al., *Antideuteron Sensitivity for the GAPS Experiment*, Astropart. Phys. **74** (2016) 6–13, arXiv:1506.02513 [astro-ph.HE].

[108] K. Abe et al., *Measurement of the cosmic-ray antiproton spectrum at solar minimum with a long-duration balloon flight over Antarctica*, Phys. Rev. Lett. **108** (2012) 051102, arXiv:1107.6000 [astro-ph.HE].

[109] V. S. Berezinsky, S. V. Bulanov, V. A. Dogiel, and V. L. Ginzburg, *Astrophysics of cosmic rays*. North-Holland, Amsterdam, 1990. ISBN 0444886419. https://cds.cern.ch/record/216576. Trans. from the Russian.

[110] B. Katz, K. Blum, and E. Waxman, *What can we really learn from positron flux 'anomalies'?*, Mon. Not. Roy. Astron. Soc. **405** (2010) 1458, arXiv:0907.1686 [astro-ph.HE].

[111] K. Blum, K. C. Y. Ng, R. Sato, and M. Takimoto, *Cosmic rays, antihelium, and an old navy spotlight*, Phys. Rev. **D96** (2017) no. 10, 103021, arXiv:1704.05431 [astro-ph.HE].

[112] AMS Collaboration, M. Aguilar et al., *Antiproton Flux, Antiproton-to-Proton Flux Ratio, and Properties of Elementary Particle Fluxes in Primary Cosmic Rays Measured with the Alpha Magnetic Spectrometer on the International Space Station*, Phys. Rev. Lett. **117** (2016) no. 9, .

[113] AMS Collaboration, M. Aguilar et al., *Precision Measurement of the Proton Flux in Primary Cosmic Rays from Rigidity 1 GV to 1.8 TV with the Alpha Magnetic Spectrometer on the International Space Station*, Phys. Rev. Lett. **114** (2015) 171103.

[114] R. P. Duperray, K. V. Protasov, and A. Yu. Voronin, *Anti-deuteron production in proton proton and proton nucleus collisions*, Eur. Phys. J. **A16** (2003) 27–34, arXiv:nucl-th/0209078 [nucl-th].

[115] R. P. Duperray, K. V. Protasov, L. Derome, and M. Buenerd, *A Model for A = 3 anti-nuclei production in proton nucleus collisions*, Eur. Phys. J. **A18** (2003) 597–604, arXiv:nucl-th/0301103 [nucl-th].

[116] ALICE Collaboration, S. Acharya et al., *Production of deuterons, tritons, ^{3}He nuclei and their antinuclei in pp collisions at $\sqrt{s}$ = 0.9, 2.76 and 7 TeV*, Phys. Rev. **C97** (2018) no. 2, 024615, arXiv:1709.08522 [nucl-ex].

[117] F. Donato, M. Korsmeier, and M. Di Mauro, *Prescriptions on antiproton cross section data for precise theoretical antiproton flux predictions*, Phys. Rev. **D96** (2017) no. 4, 043007, arXiv:1704.03663 [astro-ph.HE].

[118] A. Gal, E. V. Hungerford, and D. J. Millener, *Strangeness in nuclear physics*, Rev. Mod. Phys. **88** (2016) 035004, arXiv:1605.00557 [nucl-th].

[119] J. M. Lattimer, *The nuclear equation of state and neutron star masses*, Annu. Rev. Nucl. Part. Sci. **62** (2012) 485, arXiv:1305.3510 [nucl-th].

[120] W. Weise, *Topics in low-energy QCD with strange quarks*, Hyperfine Interact. **233** (2015) no. 1–3, 131, arXiv:1412.7838 [nucl-th].

[121] P. B. Demorest, T. Pennucci, S. M. Ransom, M. S. E. Roberts, and J. W. T. Hessels, *A two-solar-mass neutron star measured using Shapiro delay*, Nature **467** (2010) 1081.

[122] E. Fonseca, T. T. Pennucci, J. A. Ellis, et al., *The NANOGrav nine-year data set: mass and geometric measurements of binary millisecond pulsars*, Astrophys. J. **832** (2016) no. 2, 167, arXiv:1603.00545 [astro-ph.HE].

[123] D. Lonardoni, A. Lovato, S. Gandolfi, and F. Pederiva, *Hyperon Puzzle: Hints from Quantum Monte Carlo Calculations*, Phys. Rev. Lett. **114** (2015) no. 9, 092301, arXiv:1407.4448 [nucl-th].

[124] H. Togashi, E. Hiyama, Y. Yamamoto, and M. Takano, *Equation of state for neutron stars with hyperons using a variational method*, Phys. Rev. C **93** (2016) no. 3, 035808, arXiv:1602.08106 [nucl-th].

[125] ALICE Collaboration, S. Acharya et al., *p-p, p-Λ and Λ-Λ correlations studied via femtoscopy in pp reactions at $\sqrt{s}$ = 7 TeV*, Phys. Rev. **C99** (2019) no. 2, 024001, arXiv:1805.12455 [nucl-ex].

[126] K. Sasaki et al., *Baryon interactions from lattice QCD with physical masses – $S = -2$ sector –*, PoS **LATTICE2016** (2017) 116, arXiv:1702.06241 [hep-lat].

[127] T. Hatsuda, K. Morita, A. Ohnishi, and K. Sasaki, *$p\Xi^-$ Correlation in Relativistic Heavy Ion Collisions with Nucleon-Hyperon Interaction from Lattice QCD*, Nucl. Phys. **A967** (2017) 856–859, arXiv:1704.05225 [nucl-th].

[128] J. Haidenbauer, *Coupled-channel effects in hadron-hadron correlation functions*, Nucl. Phys. **A981** (2019) 1–16, arXiv:1808.05049 [hep-ph].

[129] T. A. Rijken and Y. Yamamoto, *Extended-soft-core baryon-baryon model III: S=-2 hyperon-hyperon/nucleon interaction*, arXiv:nucl-th/0608074 [nucl-th].

[130] R. D. Pisarski and F. Wilczek, *Remarks on the Chiral Phase Transition in Chromodynamics*, Phys. Rev. **D29** (1984) 338–341.

[131] S. Ejiri, F. Karsch, E. Laermann, et al., *On the magnetic equation of state in (2+1)-flavor QCD*, Phys. Rev. **D80** (2009) 094505, arXiv:0909.5122 [hep-lat].

[132] H. T. Ding, P. Hegde, F. Karsch, et al., *Chiral phase transition of (2+1)-flavor QCD*, Nucl. Phys. **A982** (2019) 211–214, arXiv:1807.05727 [hep-lat].

[133] Y. Aoki, G. Endrodi, Z. Fodor, S. D. Katz, and K. K. Szabo, *The Order of the quantum chromodynamics transition predicted by the standard model of particle physics*, Nature **443** (2006) 675–678, arXiv:hep-lat/0611014 [hep-lat].

[134] Y. Aoki, S. Borsanyi, S. Durr, et al., *The QCD transition temperature: results with physical masses in the continuum limit II.*, JHEP **06** (2009) 088, arXiv:0903.4155 [hep-lat].

[135] Wuppertal-Budapest Collaboration, S. Borsanyi, Z. Fodor, C. Hoelbling, et al., *Is there still any T_c mystery in lattice QCD? Results with physical masses in the continuum limit III*, JHEP **09** (2010) 073, arXiv:1005.3508 [hep-lat].

[136] A. Bazavov et al., *The chiral and deconfinement aspects of the QCD transition*, Phys. Rev. D **85** (2012) 054503, arXiv:1111.1710 [hep-lat].

[137] T. Bhattacharya et al., *QCD Phase Transition with Chiral Quarks and Physical Quark Masses*, Phys. Rev. Lett. **113** (2014) no. 8, 082001, arXiv:1402.5175 [hep-lat].

[138] H. T. Ding, A. Bazavov, F. Karsch, et al., *Chiral phase transition of N_f=2+1 QCD with the HISQ action*, PoS **LATTICE2013** (2014) 157, arXiv:1312.0119 [hep-lat].

[139] S. Ejiri, F. Karsch, and K. Redlich, *Hadronic fluctuations at the QCD phase transition*, Phys. Lett. **B633** (2006) 275–282, arXiv:hep-ph/0509051 [hep-ph].

[140] A. Bazavov et al., *The QCD Equation of State to $\mathcal{O}(\mu_B^6)$ from Lattice QCD*, Phys. Rev. **D95** (2017) no. 5, 054504, arXiv:1701.04325 [hep-lat].

[141] B. Friman, F. Karsch, K. Redlich, and V. Skokov, *Fluctuations as probe of the QCD phase transition and freeze-out in heavy ion collisions at LHC and RHIC*, Eur. Phys. J. **C71** (2011) 1694, arXiv:1103.3511 [hep-ph].

[142] HotQCD Collaboration, A. Bazavov et al., *Fluctuations and Correlations of net baryon number, electric charge, and strangeness: A comparison of lattice QCD results with the hadron resonance gas model*, Phys. Rev. **D86** (2012) 034509, arXiv:1203.0784 [hep-lat].

[143] R. Bellwied, S. Borsanyi, Z. Fodor, et al., *Fluctuations and correlations in high temperature QCD*, Phys. Rev. **D92** (2015) no. 11, 114505, arXiv:1507.04627 [hep-lat].

[144] F. Karsch and K. Redlich, *Probing freeze-out conditions in heavy ion collisions with moments of charge fluctuations*, Phys. Lett. **B695** (2011) 136–142, arXiv:1007.2581 [hep-ph].

[145] V. Skokov, B. Friman, and K. Redlich, *Volume Fluctuations and Higher Order Cumulants of the Net Baryon Number*, Phys. Rev. **C88** (2013) 034911, arXiv:1205.4756 [hep-ph].

[146] F. Karsch, *Determination of Freeze-out Conditions from Lattice QCD Calculations*, Central Eur. J. Phys. **10** (2012) 1234–1237, arXiv:1202.4173 [hep-lat].

[147] F. Karsch, *QCD thermodynamics in the crossover/freeze-out region*, Acta Phys. Polon. Supp. **10** (2017) 615, arXiv:1703.06702 [hep-lat].

[148] S. Borsanyi, Z. Fodor, S. D. Katz, et al., *Freeze-out parameters: lattice meets experiment*, Phys. Rev. Lett. **111** (2013) 062005, arXiv:1305.5161 [hep-lat].

[149] S. Borsanyi, Z. Fodor, S. D. Katz, et al., *Freeze-out parameters from electric charge and baryon number fluctuations: is there consistency?*, Phys. Rev. Lett. **113** (2014) 052301, arXiv:1403.4576 [hep-lat].

[150] G. A. Almasi, B. Friman, and K. Redlich, *Baryon number fluctuations in chiral effective models and their phenomenological implications*, Phys. Rev. **D96** (2017) no. 1, 014027, arXiv:1703.05947 [hep-ph].

[151] P. Parotto, M. Bluhm, D. Mroczek, et al., *Lattice-QCD-based equation of state with a critical point*, arXiv:1805.05249 [hep-ph].

[152] S. Borsanyi, Z. Fodor, J. N. Guenther, et al., *Higher order fluctuations and correlations of conserved charges from lattice QCD*, JHEP **10** (2018) 205, arXiv:1805.04445 [hep-lat].

[153] C. R. Allton, M. Doring, S. Ejiri, et al., *Thermodynamics of two flavor QCD to sixth order in quark chemical potential*, Phys. Rev. **D71** (2005) 054508, arXiv:hep-lat/0501030 [hep-lat].

[154] P. Braun-Munzinger, B. Friman, F. Karsch, K. Redlich, and V. Skokov, *Net-charge probability distributions in heavy ion collisions at chemical freeze-out*, Nucl. Phys. **A880** (2012) 48–64, arXiv:1111.5063 [hep-ph].

[155] X. Luo and N. Xu, *Search for the QCD Critical Point with Fluctuations of Conserved Quantities in Relativistic Heavy-Ion Collisions at RHIC : An Overview*, Nucl. Sci. Tech. **28** (2017) no. 8, 112, arXiv:1701.02105 [nucl-ex].

[156] P. Braun-Munzinger, B. Friman, F. Karsch, K. Redlich, and V. Skokov, *Net-proton probability distribution in heavy ion collisions*, Phys. Rev. **C84** (2011) 064911, arXiv:1107.4267 [hep-ph].

[157] P. Braun-Munzinger, A. Rustamov, and J. Stachel, *Experimental results on fluctuations of conserved charges confronted with predictions from canonical thermodynamics*, Nucl. Phys. **A982** (2019) 307–310, arXiv:1807.08927 [nucl-th].

[158] P. Braun-Munzinger, A. Rustamov, and J. Stachel, *Bridging the gap between event-by-event fluctuation measurements and theory predictions in relativistic nuclear collisions*, Nucl. Phys. **A960** (2017) 114–130, arXiv:1612.00702 [nucl-th].

[159] F. Karsch, K. Morita, and K. Redlich, *Effects of kinematic cuts on net-electric charge fluctuations*, Phys. Rev. **C93** (2016) no. 3, 034907, arXiv:1508.02614 [hep-ph].

[160] P. Alba, R. Bellwied, M. Bluhm, et al., *Sensitivity of multiplicity fluctuations to freeze-out conditions in heavy ion collisions*, Phys. Rev. **C92** (2015) no. 6, 064910, arXiv:1504.03262 [hep-ph].

[161] S. Floerchinger and M. Martinez, *Fluid dynamic propagation of initial baryon number perturbations on a Bjorken flow background*, Phys. Rev. **C92** (2015) no. 6, 064906, arXiv:1507.05569 [nucl-th].

[162] STAR Collaboration, L. Adamczyk et al., *Energy Dependence of Moments of Net-proton Multiplicity Distributions at RHIC*, Phys. Rev. Lett. **112** (2014) 032302, arXiv:1309.5681 [nucl-ex].

[163] ALICE Collaboration, A. Rustamov, *Net-baryon fluctuations measured with ALICE at the CERN LHC*, Nucl. Phys. **A967** (2017) 453–456, arXiv:1704.05329 [nucl-ex].

[164] A. Bzdak, V. Koch, and V. Skokov, *Baryon number conservation and the cumulants of the net proton distribution*, Phys. Rev. **C87** (2013) no. 1, 014901, arXiv:1203.4529 [hep-ph].

[165] A. Bzdak and V. Koch, *Mapping the QCD phase diagram with statistics friendly distributions*, arXiv:1811.04456 [nucl-th].

[166] N. K. Behera, *Constructing probability density function of net-proton multiplicity distributions using Pearson curve method*, arXiv:1706.06558 [nucl-ex].

[167] ALICE Collaboration, N. K. Behera, *Higher moment fluctuations of identified particle distributions from ALICE*, Nucl. Phys. **A982** (2019) 851–854, arXiv:1807.06780 [hep-ex].

[168] P. Steinbrecher, *The QCD crossover at zero and non-zero baryon densities from Lattice QCD*, arXiv:1807.05607 [hep-lat].

[169] O. Kaczmarek, F. Karsch, E. Laermann, et al., *Phase boundary for the chiral transition in (2+1) -flavor QCD at small values of the chemical potential*, Phys. Rev. **D83** (2011) 014504, arXiv:1011.3130 [hep-lat].

[170] G. Endrodi, Z. Fodor, S. D. Katz, and K. K. Szabo, *The QCD phase diagram at nonzero quark density*, JHEP **04** (2011) 001, arXiv:1102.1356 [hep-lat].

[171] A. Bazavov et al., *Curvature of the freeze-out line in heavy ion collisions*, Phys. Rev. **D93** (2016) no. 1, 014512, arXiv:1509.05786 [hep-lat].

[172] C. Bonati, M. D'Elia, F. Negro, F. Sanfilippo, and K. Zambello, *Curvature of the pseudocritical line in QCD: Taylor expansion matches analytic continuation*, Phys. Rev. **D98** (2018) no. 5, 054510, arXiv:1805.02960 [hep-lat].

[173] P. Cea, L. Cosmai, and A. Papa, *Critical line of 2+1 flavor QCD*, Phys. Rev. **D89** (2014) no. 7, 074512, arXiv:1403.0821 [hep-lat].

[174] C. Bonati, P. de Forcrand, M. D'Elia, O. Philipsen, and F. Sanfilippo, *Chiral phase transition in two-flavor QCD from an imaginary chemical potential*, Phys. Rev. **D90** (2014) no. 7, 074030, arXiv:1408.5086 [hep-lat].

[175] C. Bonati, M. D'Elia, M. Mariti, et al., *Curvature of the chiral pseudocritical line in QCD: Continuum extrapolated results*, Phys. Rev. **D92** (2015) no. 5, 054503, arXiv:1507.03571 [hep-lat].

[176] R. Bellwied, S. Borsanyi, Z. Fodor, et al., *The QCD phase diagram from analytic continuation*, Phys. Lett. **B751** (2015) 559–564, arXiv:1507.07510 [hep-lat].

[177] P. Cea, L. Cosmai, and A. Papa, *Critical line of 2+1 flavor QCD: Toward the continuum limit*, Phys. Rev. **D93** (2016) no. 1, 014507, arXiv:1508.07599 [hep-lat].

[178] P. Huovinen and P. Petreczky, *QCD Equation of State and Hadron Resonance Gas*, Nucl. Phys. **A837** (2010) 26–53, arXiv:0912.2541 [hep-ph].

[179] S. Borsanyi, Z. Fodor, C. Hoelbling, et al., *Full result for the QCD equation of state with 2+1 flavors*, Phys. Lett. **B730** (2014) 99–104, arXiv:1309.5258 [hep-lat].

[180] J. S. Moreland and R. A. Soltz, *Hydrodynamic simulations of relativistic heavy-ion collisions with different lattice quantum chromodynamics calculations of the equation of state*, Phys. Rev. **C93** (2016) no. 4, 044913, arXiv:1512.02189 [nucl-th].

[181] A. Monnai and J.-Y. Ollitrault, *Constraining the equation of state with identified particle spectra*, Phys. Rev. **C96** (2017) no. 4, 044902, arXiv:1707.08466 [nucl-th].

[182] J. S. Moreland, J. E. Bernhard, and S. A. Bass, *Estimating initial state and quark-gluon plasma medium properties using a hybrid model with nucleon substructure calibrated to p-Pb and Pb-Pb collisions at* $\sqrt{s_{\rm NN}} = 5.02$ *TeV*, arXiv:1808.02106 [nucl-th].

[183] P. F. Kolb and U. W. Heinz, *Hydrodynamic description of ultrarelativistic heavy ion collisions*, in *Hwa, R.C. (ed.) et al.: Quark gluon plasma*, pp. 634–714. 2003. arXiv:nucl-th/0305084 [nucl-th].

[184] P. Huovinen, *Hydrodynamical description of collective flow. Chapter 1.*, in *Hwa, R.C. (ed.) et al.: Quark gluon plasma*, pp. 600–633. 2003. arXiv:nucl-th/0305064 [nucl-th].

[185] T. Hirano and K. Tsuda, *Collective flow and two pion correlations from a relativistic hydrodynamic model with early chemical freezeout*, Phys. Rev. **C66** (2002) 054905, arXiv:nucl-th/0205043 [nucl-th].

[186] G. Policastro, D. T. Son, and A. O. Starinets, *Shear Viscosity of Strongly Coupled $N = 4$ Supersymmetric Yang-Mills Plasma*, Phys. Rev. Lett. **87** (Aug, 2001) 081601. https://link.aps.org/doi/10.1103/PhysRevLett.87.081601.

[187] P. K. Kovtun, D. T. Son, and A. O. Starinets, *Viscosity in Strongly Interacting Quantum Field Theories from Black Hole Physics*, Phys. Rev. Lett. **94** (Mar, 2005) 111601. https://link.aps.org/doi/10.1103/PhysRevLett.94.111601.

[188] P. B. Arnold, G. D. Moore, and L. G. Yaffe, *Transport coefficients in high temperature gauge theories. 2. Beyond leading log*, JHEP **05** (2003) 051, arXiv:hep-ph/0302165 [hep-ph].

[189] J. Ghiglieri, G. D. Moore, and D. Teaney, *Second-order Hydrodynamics in Next-to-Leading-Order QCD*, Phys. Rev. Lett. **121** (2018) no. 5, 052302, arXiv:1805.02663 [hep-ph].

[190] A. Nakamura and S. Sakai, *Transport coefficients of gluon plasma*, Phys. Rev. Lett. **94** (2005) 072305, arXiv:hep-lat/0406009 [hep-lat].

[191] H. B. Meyer, *A Calculation of the shear viscosity in SU(3) gluodynamics*, Phys. Rev. **D76** (2007) 101701, arXiv:0704.1801 [hep-lat].

[192] S. Borsányi, Z. Fodor, M. Giordano, et al., *High statistics lattice study of stress tensor correlators in pure $SU(3)$ gauge theory*, Phys. Rev. **D98** (2018) no. 1, 014512, arXiv:1802.07718 [hep-lat].

[193] S. Ryu, J.-F. Paquet, C. Shen, et al., *Effects of bulk viscosity and hadronic rescattering in heavy ion collisions at energies available at the BNL Relativistic Heavy Ion Collider and at the CERN Large Hadron Collider*, Phys. Rev. **C97** (2018) no. 3, 034910, arXiv:1704.04216 [nucl-th].

[194] R. Horsley and W. Schoenmaker, *Quantum Field Theories Out of Thermal Equilibrium. 1. General Considerations*, Nucl. Phys. **B280** (1987) 716–734.

[195] P. B. Arnold, C. Dogan, and G. D. Moore, *The Bulk Viscosity of High-Temperature QCD*, Phys. Rev. **D74** (2006) 085021, arXiv:hep-ph/0608012 [hep-ph].

[196] F. Karsch, D. Kharzeev, and K. Tuchin, *Universal properties of bulk viscosity near the QCD phase transition*, Phys. Lett. **B663** (2008) 217–221, arXiv:0711.0914 [hep-ph].

[197] H. B. Meyer, *A Calculation of the bulk viscosity in SU(3) gluodynamics*, Phys. Rev. Lett. **100** (2008) 162001, arXiv:0710.3717 [hep-lat].

[198] D. Kharzeev and K. Tuchin, *Bulk viscosity of QCD matter near the critical temperature*, JHEP **09** (2008) 093, arXiv:0705.4280 [hep-ph].

[199] G. S. Denicol, T. Kodama, T. Koide, and P. Mota, *Effect of bulk viscosity on Elliptic Flow near QCD phase transition*, Phys. Rev. **C80** (2009) 064901, arXiv:0903.3595 [hep-ph].

[200] J. Noronha-Hostler, J. Noronha, and C. Greiner, *Transport Coefficients of Hadronic Matter near T(c)*, Phys. Rev. Lett. **103** (2009) 172302, arXiv:0811.1571 [nucl-th].

[201] A. Buchel, *Bulk viscosity of gauge theory plasma at strong coupling*, Phys. Lett. **B663** (2008) 286–289, arXiv:0708.3459 [hep-th].

[202] S. I. Finazzo, R. Rougemont, H. Marrochio, and J. Noronha, *Hydrodynamic transport coefficients for the non-conformal quark-gluon plasma from holography*, JHEP **02** (2015) 051, arXiv:1412.2968 [hep-ph].

[203] C. Gale, S. Jeon, and B. Schenke, *Hydrodynamic Modeling of Heavy-Ion Collisions*, Int. J. Mod. Phys. **A28** (2013) 1340011, arXiv:1301.5893 [nucl-th].

[204] U. Heinz and R. Snellings, *Collective flow and viscosity in relativistic heavy-ion collisions*, Ann. Rev. Nucl. Part. Sci. **63** (2013) 123–151, arXiv:1301.2826 [nucl-th].

[205] B. Schenke, P. Tribedy, and R. Venugopalan, *Fluctuating Glasma initial conditions and flow in heavy ion collisions*, Phys. Rev. Lett. **108** (2012) 252301, arXiv:1202.6646 [nucl-th].

[206] B. Schenke, P. Tribedy, and R. Venugopalan, *Event-by-event gluon multiplicity, energy density, and eccentricities in ultrarelativistic heavy-ion collisions*, Phys. Rev. **C86** (2012) 034908, arXiv:1206.6805 [hep-ph].

[207] H. Niemi, K. J. Eskola, and R. Paatelainen, *Event-by-event fluctuations in a perturbative QCD + saturation + hydrodynamics model: Determining QCD matter shear viscosity in ultrarelativistic heavy-ion collisions*, Phys. Rev. **C93** (2016) no. 2, 024907, arXiv:1505.02677 [hep-ph].

[208] P. Bozek, *Bulk and shear viscosities of matter created in relativistic heavy-ion collisions*, Phys. Rev. **C81** (2010) 034909, arXiv:0911.2397 [nucl-th].

[209] J.-F. Paquet, C. Shen, G. S. Denicol, et al., *Production of photons in relativistic heavy-ion collisions*, Phys. Rev. **C93** (2016) no. 4, 044906, arXiv:1509.06738 [hep-ph].

[210] C. Gale, S. Jeon, B. Schenke, P. Tribedy, and R. Venugopalan, *Event-by-event anisotropic flow in heavy-ion collisions from combined Yang-Mills and viscous fluid dynamics*, Phys. Rev. Lett. **110** (2013) no. 1, 012302, arXiv:1209.6330 [nucl-th].

[211] R. D. Weller and P. Romatschke, *One fluid to rule them all: viscous hydrodynamic description of event-by-event central p+p, p+Pb and Pb+Pb collisions at* $\sqrt{s} = 5.02$ *TeV*, Phys. Lett. **B774** (2017) 351–356, arXiv:1701.07145 [nucl-th].

[212] H. Mäntysaari, B. Schenke, C. Shen, and P. Tribedy, *Imprints of fluctuating proton shapes on flow in proton-lead collisions at the LHC*, Phys. Lett. **B772** (2017) 681–686, arXiv:1705.03177 [nucl-th].

[213] B. Schenke, C. Shen, and P. Tribedy, *Features of the IP-Glasma*, Nucl. Phys. **A982** (2019) 435–438, arXiv:1807.05205 [nucl-th].

[214] A. Kurkela, A. Mazeliauskas, J.-F. Paquet, S. Schlichting, and D. Teaney, *Matching the Nonequilibrium Initial Stage of Heavy Ion Collisions to Hydrodynamics with QCD Kinetic Theory*, Phys. Rev. Lett. **122** (2019) no. 12, 122302, arXiv:1805.01604 [hep-ph].

[215] A. Kurkela, A. Mazeliauskas, J.-F. Paquet, S. Schlichting, and D. Teaney, *Effective kinetic description of event-by-event pre-equilibrium dynamics in high-energy heavy-ion collisions*, Phys. Rev. **C99** (2019) no. 3, 034910, arXiv:1805.00961 [hep-ph].

[216] A. Kurkela, U. A. Wiedemann, and B. Wu, *Kinetic transport is needed to reliably extract shear viscosity from pA and AA data*, arXiv:1805.04081 [hep-ph].

[217] CMS Collaboration, V. Khachatryan et al., *Evidence for transverse momentum and pseudorapidity dependent event plane fluctuations in* Pb–Pb *and* p–Pb *collisions*, Phys. Rev. **C92** (2015) no. 3, 034911, arXiv:1503.01692 [nucl-ex].

[218] CMS Collaboration, A. M. Sirunyan et al., *Pseudorapidity and transverse momentum dependence of flow harmonics in pPb and PbPb collisions*, Phys. Rev. **C98** (2018) no. 4, 044902, arXiv:1710.07864 [nucl-ex].

[219] ATLAS Collaboration, M. Aaboud et al., *Measurement of longitudinal flow decorrelations in Pb+Pb collisions at $\sqrt{s_{NN}} = 2.76$ and 5.02 TeV with the ATLAS detector*, Eur. Phys. J. **C78** (2018) no. 2, 142, arXiv:1709.02301 [nucl-ex].

[220] D. Teaney and L. Yan, *Triangularity and Dipole Asymmetry in Heavy Ion Collisions*, Phys. Rev. **C83** (2011) 064904, arXiv:1010.1876 [nucl-th].

[221] S. Floerchinger and U. A. Wiedemann, *Mode-by-mode fluid dynamics for relativistic heavy ion collisions*, Phys. Lett. **B728** (2014) 407–411, arXiv:1307.3453 [hep-ph].

[222] S. Floerchinger and U. A. Wiedemann, *Statistics of initial density perturbations in heavy ion collisions and their fluid dynamic response*, JHEP **08** (2014) 005, arXiv:1405.4393 [hep-ph].

[223] D. Teaney and L. Yan, *Non linearities in the harmonic spectrum of heavy ion collisions with ideal and viscous hydrodynamics*, Phys. Rev. **C86** (2012) 044908, arXiv:1206.1905 [nucl-th].

[224] S. Floerchinger, U. A. Wiedemann, A. Beraudo, et al., *How (non-)linear is the hydrodynamics of heavy ion collisions?*, Phys. Lett. **B735** (2014) 305–310, arXiv:1312.5482 [hep-ph].

[225] ATLAS Collaboration, *Measurement of event-plane correlations in $\sqrt{s_{\rm NN}} = 2.76$ TeV lead–lead collisions with the ATLAS detector*, Phys. Rev. C **90** (2014) 024905, arXiv:1403.0489 [hep-ex].

[226] ATLAS Collaboration, *Measurement of the correlation between flow harmonics of different order in lead–lead collisions at $\sqrt{s_{\rm NN}} = 2.76$ TeV with the ATLAS detector*, Phys. Rev. C **92** (2015) 034903, arXiv:1504.01289 [hep-ex].

[227] ALICE Collaboration, J. Adam et al., *Correlated event-by-event fluctuations of flow harmonics in Pb-Pb collisions at $\sqrt{s_{\rm NN}} = 2.76$ TeV*, Phys. Rev. Lett. **117** (2016) 182301, arXiv:1604.07663 [nucl-ex].

[228] G. Giacalone, J. Noronha-Hostler, and J.-Y. Ollitrault, *Relative flow fluctuations as a probe of initial state fluctuations*, Phys. Rev. **C95** (2017) no. 5, 054910, arXiv:1702.01730 [nucl-th].

[229] G. Giacalone, J. Noronha-Hostler, M. Luzum, and J.-Y. Ollitrault, *Hydrodynamic predictions for 5.44 TeV Xe+Xe collisions*, Phys. Rev. **C97** (2018) no. 3, 034904, arXiv:1711.08499 [nucl-th]. Predictions for O+O and Ar+Ar obtained by private communications.

[230] ATLAS Collaboration, *Measurement of the azimuthal anisotropy of charged particle production in Xe+Xe collisions at $\sqrt{s_{\rm NN}}$=5.44 TeV with the ATLAS detector*, ATLAS-CONF-2018-011, CERN, Geneva, May, 2018. https://cds.cern.ch/record/2318870.

[231] ATLAS Collaboration, M. Aaboud et al., *Measurement of forward-backward multiplicity correlations in lead-lead, proton-lead, and proton-proton collisions with the ATLAS detector*, Phys. Rev. **C95** (2017) no. 6, 064914, arXiv:1606.08170 [hep-ex].

[232] F. Becattini, V. Chandra, L. Del Zanna, and E. Grossi, *Relativistic distribution function for particles with spin at local thermodynamical equilibrium*, Annals Phys. **338** (2013) 32–49, arXiv:1303.3431 [nucl-th].

[233] STAR Collaboration, L. Adamczyk et al., *Global Λ hyperon polarization in nuclear collisions: evidence for the most vortical fluid*, Nature **548** (2017) 62, arXiv:1701.06657 [nucl-ex].

[234] STAR Collaboration, B. I. Abelev et al., *Global polarization measurement in Au+Au collisions*, Phys. Rev. **C76** (2007) 024915, arXiv:0705.1691 [nucl-ex]. [Erratum: Phys. Rev.C95,no.3,039906(2017)].

[235] S. A. Voloshin, *Vorticity in heavy ion collisions: directed flow, global polarization, CVE, and more*, Oct., 2016. https://doi.org/10.5281/zenodo.3241492. Presented at the 2nd International Conference on Particle Physics and Astrophysics, 10-14 October 2016 Milan Hotel, Moscow, Russia.

[236] STAR Collaboration, T. Niida, *Global and local polarization of Λ hyperons in Au+Au collisions at 200 GeV from STAR*, 2018. arXiv:1808.10482 [nucl-ex].

[237] I. Karpenko and F. Becattini, *Study of Lambda polarization at RHIC BES and LHC energies*, arXiv:1710.09726 [nucl-th]. [EPJ Web Conf.171, 17001(2018)].

[238] T. D. Lee, *A Theory of Spontaneous T Violation*, Phys. Rev. **D8** (1973) 1226–1239.

[239] T. D. Lee and G. C. Wick, *Vacuum Stability and Vacuum Excitation in a Spin 0 Field Theory*, Phys. Rev. **D9** (1974) 2291–2316.

[240] P. D. Morley and I. A. Schmidt, *Strong P, CP, T Violations in Heavy Ion Collisions*, Z. Phys. **C26** (1985) 627.

[241] D. Kharzeev, R. D. Pisarski, and M. H. G. Tytgat, *Possibility of spontaneous parity violation in hot QCD*, Phys. Rev. Lett. **81** (1998) 512–515, arXiv:hep-ph/9804221 [hep-ph].

[242] S.-S. Chern and J. Simons, *Characteristic forms and geometric invariants*, Annals Math. **99** (1974) 48–69.

[243] W.-T. Deng and X.-G. Huang, *Event-by-event generation of electromagnetic fields in heavy-ion collisions*, Phys. Rev. **C85** (2012) 044907, arXiv:1201.5108 [nucl-th].

[244] U. Gursoy, D. Kharzeev, and K. Rajagopal, *Magnetohydrodynamics, charged currents and directed flow in heavy ion collisions*, Phys. Rev. **C89** (2014) no. 5, 054905, arXiv:1401.3805 [hep-ph].

[245] D. Kharzeev, *Parity violation in hot QCD: Why it can happen, and how to look for it*, Phys. Lett. **B633** (2006) 260–264, arXiv:hep-ph/0406125 [hep-ph].

[246] D. Kharzeev and A. Zhitnitsky, *Charge separation induced by P-odd bubbles in QCD matter*, Nucl. Phys. **A797** (2007) 67–79, arXiv:0706.1026 [hep-ph].

[247] D. E. Kharzeev, L. D. McLerran, and H. J. Warringa, *The Effects of topological charge change in heavy ion collisions: 'Event by event P and CP violation'*, Nucl. Phys. **A803** (2008) 227–253, arXiv:0711.0950 [hep-ph].

[248] K. Fukushima, D. E. Kharzeev, and H. J. Warringa, *The Chiral Magnetic Effect*, Phys. Rev. **D78** (2008) 074033, arXiv:0808.3382 [hep-ph].

[249] ALICE Collaboration, S. Acharya et al., *Constraining the magnitude of the Chiral Magnetic Effect with Event Shape Engineering in Pb-Pb collisions at $\sqrt{s_{\rm NN}}$ = 2.76 TeV*, Phys. Lett. **B777** (2018) 151–162, arXiv:1709.04723 [nucl-ex].

[250] S. A. Voloshin, *Parity violation in hot QCD: How to detect it*, Phys. Rev. **C70** (2004) 057901, arXiv:hep-ph/0406311 [hep-ph].

[251] S. Schlichting and S. Pratt, *Charge conservation at energies available at the BNL Relativistic Heavy Ion Collider and contributions to local parity violation observables*, Phys. Rev. **C83** (2011) 014913, arXiv:1009.4283 [nucl-th].

[252] S. Pratt, S. Schlichting, and S. Gavin, *Effects of Momentum Conservation and Flow on Angular Correlations at RHIC*, Phys. Rev. **C84** (2011) 024909, arXiv:1011.6053 [nucl-th].

[253] CMS Collaboration, V. Khachatryan et al., *Observation of charge-dependent azimuthal correlations in p-Pb collisions and its implication for the search for the chiral magnetic effect*, Phys. Rev. Lett. **118** (2017) 122301, arXiv:1610.00263 [nucl-ex].

[254] CMS Collaboration, A. M. Sirunyan et al., *Constraints on the chiral magnetic effect using charge-dependent azimuthal correlations in pPb and PbPb collisions at the CERN Large Hadron Collider*, Phys. Rev. **C97** (2018) no. 4, 044912, arXiv:1708.01602 [nucl-ex].

[255] J. Schukraft, A. Timmins, and S. A. Voloshin, *Ultra-relativistic nuclear collisions: event shape engineering*, Phys. Lett. **B719** (2013) 394–398, arXiv:1208.4563 [nucl-ex].

[256] ALICE Collaboration, J. Margutti, *The search for magnetic-induced charged currents in Pb–Pb collisions with ALICE*, in *12th Workshop on Particle Correlations and Femtoscopy (WPCF 2017) Amsterdam, Netherdands, June 12-16, 2017*. 2017. arXiv:1709.05618 [nucl-ex].

[257] S. K. Das, S. Plumari, S. Chatterjee, et al., *Directed Flow of Charm Quarks as a Witness of the Initial Strong Magnetic Field in Ultra-Relativistic Heavy Ion Collisions*, Phys. Lett. **B768** (2017) 260–264, arXiv:1608.02231 [nucl-th].

[258] A. Andronic et al., *Heavy-flavour and quarkonium production in the LHC era: from proton–proton to heavy-ion collisions*, Eur. Phys. J. **C76** (2016) no. 3, 107, arXiv:1506.03981 [nucl-ex].

[259] F. Prino and R. Rapp, *Open Heavy Flavor in QCD Matter and in Nuclear Collisions*, J. Phys. **G43** (2016) no. 9, 093002, arXiv:1603.00529 [nucl-ex].

[260] A. Beraudo et al., *Extraction of Heavy-Flavor Transport Coefficients in QCD Matter*, Nucl. Phys. **A979** (2018) 21–86, arXiv:1803.03824 [nucl-th].

[261] ALICE Collaboration, J. Adam et al., *Centrality dependence of high-p_T D meson suppression in Pb-Pb collisions at $\sqrt{s_{\rm NN}} = 2.76$ TeV*, JHEP **11** (2015) 205, arXiv:1506.06604 [nucl-ex]. [Addendum: JHEP06,032(2017)].

[262] CMS Collaboration, V. Khachatryan et al., *Suppression and azimuthal anisotropy of prompt and nonprompt J/ψ production in PbPb collisions at $\sqrt{s_{\rm NN}} = 2.76$ TeV*, Eur. Phys. J. **C77** (2017) no. 4, 252, arXiv:1610.00613 [nucl-ex].

[263] ALICE Collaboration, B. Abelev et al., *Technical Design Report for the Upgrade of the ALICE Inner Tracking System*, CERN-LHCC-2013-024. ALICE-TDR-017, Nov, 2013. https://cds.cern.ch/record/1625842.

[264] ATLAS Collaboration, *Expected Performance of the ATLAS Inner Tracker at the High-Luminosity LHC*, ATL-PHYS-PUB-2016-025, CERN, Geneva, Oct, 2016. https://cds.cern.ch/record/2222304.

[265] ATLAS Collaboration, *Technical Proposal: A High-Granularity Timing Detector for the ATLAS Phase-II Upgrade*, CERN-LHCC-2018-023. LHCC-P-012, CERN, Geneva, Jun, 2018. https://cds.cern.ch/record/2623663.

[266] CMS Collaboration, *Expected performance of the physics objects with the upgraded CMS detector at the HL-LHC*, CMS Physics Analysis Summary CMS-PAS-FTR-18-012, CERN, Geneva, 2018.

[267] CMS Collaboration, D. Contardo, M. Klute, J. Mans, L. Silvestris, and J. Butler, *Technical Proposal for the Phase-II Upgrade of the CMS Detector*, CERN-LHCC-2015-010. LHCC-P-008. CMS-TDR-15-02, Geneva, Jun, 2015. https://cds.cern.ch/record/2020886.

[268] CMS Collaboration, *The Phase-2 Upgrade of the CMS Tracker*, CERN-LHCC-2017-009. CMS-TDR-014, CERN, Geneva, Jun, 2017. https://cds.cern.ch/record/2272264.

[269] LHCb Collaboration, *LHCb VELO Upgrade Technical Design Report*, CERN-LHCC-2013-021. LHCB-TDR-013, Nov, 2013. http://cds.cern.ch/record/1624070.

[270] LHCb Collaboration, *LHCb Tracker Upgrade Technical Design Report*, CERN-LHCC-2014-001. LHCB-TDR-015, Feb, 2014. https://cds.cern.ch/record/1647400.

[271] Y. Dokshitzer and D. Kharzeev, *Heavy-quark colorimetry of QCD matter*, Physics Letters B **519** (2001) no. 3, 199 – 206.

[272] G. D. Moore and D. Teaney, *How much do heavy quarks thermalize in a heavy ion collision?*, Phys. Rev. **C71** (2005) 064904, arXiv:hep-ph/0412346 [hep-ph].

[273] S. K. Das, F. Scardina, S. Plumari, and V. Greco, *Toward a solution to the R_{AA} and v_2 puzzle for heavy quarks*, Phys. Lett. **B747** (2015) 260–264, arXiv:1502.03757 [nucl-th].

[274] S. K. Das, F. Scardina, S. Plumari, and V. Greco, *Heavy-flavor in-medium momentum evolution: Langevin versus Boltzmann approach*, Phys. Rev. **C90** (2014) 044901, arXiv:1312.6857 [nucl-th].

[275] Y. Xu, J. E. Bernhard, S. A. Bass, M. Nahrgang, and S. Cao, *Data-driven analysis for the temperature and momentum dependence of the heavy-quark diffusion coefficient in relativistic heavy-ion collisions*, Phys. Rev. **C97** (2018) no. 1, 014907, arXiv:1710.00807 [nucl-th].

[276] ALICE Collaboration, J. Adam et al., *Event shape engineering for inclusive spectra and elliptic flow in Pb-Pb collisions at $\sqrt{s_{\rm NN}} = 2.76$ TeV*, Phys. Rev. **C93** (2016) no. 3, 034916, arXiv:1507.06194 [nucl-ex].

[277] A. Beraudo, A. De Pace, M. Monteno, M. Nardi, and F. Prino, *Heavy-flavor flow-harmonics in high-energy nuclear collisions: time-development and eccentricity fluctuations*, Nuclear Physics A **982** (2019) 675–678, arXiv:1807.03180 [hep-ph].

[278] ALICE Collaboration, S. Acharya et al., *Event-shape engineering for the D-meson elliptic flow in mid-central Pb-Pb collisions at $\sqrt{s_{\rm NN}} = 5.02$ TeV*, JHEP **02** (2019) 150, arXiv:1809.09371 [nucl-ex].

[279] X. Dong and V. Greco, *Heavy quark production and properties of Quark-Gluon Plasma*, Prog. Part. Nucl. Phys **104** (2018) no. 5, 1–47.

[280] F. Scardina, S. K. Das, V. Minissale, S. Plumari, and V. Greco, *Estimating the charm quark diffusion coefficient and thermalization time from D meson spectra at energies available at the BNL Relativistic Heavy Ion Collider and the CERN Large Hadron Collider*, Phys. Rev. **C96** (2017) no. 4, 044905, arXiv:1707.05452 [nucl-th].

[281] Z.-w. Lin and D. Molnar, *Quark coalescence and elliptic flow of charm hadrons*, Phys. Rev. **C68** (2003) 044901, arXiv:nucl-th/0304045 [nucl-th].

[282] V. Greco, C. Ko, and R. Rapp, *Quark coalescence for charmed mesons in ultrarelativistic heavy-ion collisions*, Physics Letters B **595** (2004) no. 1, 202 – 208.

[283] R. J. Fries, V. Greco, and P. Sorensen, *Coalescence Models For Hadron Formation From Quark Gluon Plasma*, Ann.Rev.Nucl.Part.Sci. **58** (2008) 177–205, arXiv:0807.4939 [nucl-th].

[284] ALICE Collaboration, S. Acharya et al., *$\Lambda_{\rm c}^+$ production in pp collisions at $\sqrt{s} = 7$ TeV and in p-Pb collisions at $\sqrt{s_{\rm NN}} = 5.02$ TeV*, JHEP **04** (2018) 108, arXiv:1712.09581 [nucl-ex].

[285] ALICE Collaboration, S. Acharya et al., *First measurement of $\Xi_{\rm c}^0$ production in pp collisions at $\sqrt{\rm s} = 7$ TeV*, Phys. Lett. **B781** (2018) 8–19, arXiv:1712.04242 [hep-ex].

[286] V. Greco, C. M. Ko, and P. Levai, *Parton coalescence at RHIC*, Phys. Rev. **C68** (2003) 034904, arXiv:nucl-th/0305024 [nucl-th].

[287] V. Greco, C. M. Ko, and R. Rapp, *Quark coalescence for charmed mesons in ultrarelativistic heavy ion collisions*, Phys. Lett. **B595** (2004) 202–208, arXiv:nucl-th/0312100 [nucl-th].

[288] R. J. Fries, B. Muller, C. Nonaka, and S. A. Bass, *Hadron production in heavy ion collisions: Fragmentation and recombination from a dense parton phase*, Phys. Rev. **C68** (2003) 044902, arXiv:nucl-th/0306027 [nucl-th].

[289] R. J. Fries, B. Muller, C. Nonaka, and S. A. Bass, *Hadronization in heavy ion collisions: Recombination and fragmentation of partons*, Phys. Rev. Lett. **90** (2003) 202303, arXiv:nucl-th/0301087 [nucl-th].

[290] Y. Oh, C. M. Ko, S. H. Lee, and S. Yasui, *Heavy baryon/meson ratios in relativistic heavy ion collisions*, Phys. Rev. **C79** (2009) 044905, arXiv:0901.1382 [nucl-th].

[291] V. Minissale, F. Scardina, and V. Greco, *Hadrons from coalescence plus fragmentation in AA collisions at energies available at the BNL Relativistic Heavy Ion Collider to the CERN Large Hadron Collider*, Phys. Rev. **C92** (2015) no. 5, 054904, arXiv:1502.06213 [nucl-th].

[292] S. Plumari, V. Minissale, S. K. Das, G. Coci, and V. Greco, *Charmed Hadrons from Coalescence plus Fragmentation in relativistic nucleus-nucleus collisions at RHIC and LHC*, Eur. Phys. J. **C78** (2018) no. 4, 348, arXiv:1712.00730 [hep-ph].

[293] L. Ravagli and R. Rapp, *Quark coalescence based on a transport equation*, Physics Letters B **655** (2007) no. 3, 126 – 131.

[294] M. He, R. J. Fries, and R. Rapp, *Heavy-Quark Diffusion and Hadronization in Quark-Gluon Plasma*, Phys. Rev. **C86** (2012) 014903, arXiv:1106.6006 [nucl-th].

[295] A. Andronic, P. Braun-Munzinger, K. Redlich, and J. Stachel, *Charmonium and open charm production in nuclear collisions at SPS/FAIR energies and the possible influence of a hot hadronic medium*, Phys. Lett. **B659** (2008) 149–155, arXiv:0708.1488 [nucl-th].

[296] I. Kuznetsova and J. Rafelski, *Charmed hadrons from strangeness-rich QGP*, J. Phys. **G32** (2006) S499–S504, arXiv:hep-ph/0605307 [hep-ph].

[297] M. He, R. J. Fries, and R. Rapp, *Heavy Flavor at the Large Hadron Collider in a Strong Coupling Approach*, Phys. Lett. **B735** (2014) 445–450, arXiv:1401.3817 [nucl-th].

[298] T. Song, H. Berrehrah, D. Cabrera, W. Cassing, and E. Bratkovskaya, *Charm production in Pb + Pb collisions at energies available at the CERN Large Hadron Collider*, Phys. Rev. **C93** (2016) no. 3, 034906, arXiv:1512.00891 [nucl-th].

[299] ALICE Collaboration, S. Acharya et al., *Measurement of D^0, D^+, D^{*+} and D_s^+ production in Pb-Pb collisions at $\sqrt{s_{NN}} = 5.02$ TeV*, JHEP (2018) 174, arXiv:1804.09083 [nucl-ex].

[300] ALICE Collaboration, X. Peng, *Non-strange and strange D-meson and charm-baryon production in heavy-ion collisions measured with ALICE at the LHC*, Nuclear Physics A **982** (2019) 667–670, arXiv:1807.07286 [nucl-ex].

[301] STAR Collaboration, S. K. Radhakrishnan, *Measurements of Open Charm and Bottom Production in Au+Au Collisions at $\sqrt{s_{NN}}$ = 200 GeV with the STAR Experiment at RHIC*, Nuclear Physics A **982** (2019) 659–662.

[302] ALICE Collaboration, S. Acharya et al., *Expression of Interest for an ALICE ITS Upgrade in LS3*, ALICE-PUBLIC-2018-013, CERN, 2018. https://cds.cern.ch/record/2644611.

[303] F. Becattini, *Production of multiply heavy flavored baryons from quark gluon plasma in relativistic heavy ion collisions*, Phys. Rev. Lett. **95** (2005) 022301, arXiv:hep-ph/0503239 [hep-ph].

[304] H. He, Y. Liu, and P. Zhuang, *Ω_{ccc} production in high energy nuclear collisions*, Phys. Lett. **B746** (2015) 59–63, arXiv:1409.1009 [hep-ph].

[305] J. Zhao, H. He, and P. Zhuang, *Searching for Ξ_{cc}^+ in Relativistic Heavy Ion Collisions*, Phys. Lett. **B771** (2017) 349–353, arXiv:1603.04524 [nucl-th].

[306] D. Adamová et al., *A next-generation LHC heavy-ion experiment*, arXiv:1902.01211 [physics.ins-det].

[307] H. van Hees, V. Greco, and R. Rapp, *Heavy-quark probes of the quark-gluon plasma at RHIC*, Phys. Rev. **C73** (2006) 034913, arXiv:nucl-th/0508055 [nucl-th].

[308] P. B. Gossiaux and J. Aichelin, *Towards an understanding of the RHIC single electron data*, Phys. Rev. **C78** (2008) 014904, arXiv:0802.2525 [hep-ph].

[309] M. He, R. J. Fries, and R. Rapp, *Heavy-Quark Diffusion and Hadronization in Quark-Gluon Plasma*, Phys. Rev. **C86** (2012) 014903, arXiv:1106.6006 [nucl-th].

[310] S. Plumari, G. L. Guardo, F. Scardina, and V. Greco, *Initial state fluctuations from mid-peripheral to ultra-central collisions in a event-by-event transport approach*, Phys. Rev. **C92** (2015) no. 5, 054902, arXiv:1507.05540 [hep-ph].

[311] M. Ruggieri, F. Scardina, S. Plumari, and V. Greco, *Thermalization, Isotropization and Elliptic Flow from Nonequilibrium Initial Conditions with a Saturation Scale*, Phys. Rev. **C89** (2014) no. 5, 054914, arXiv:1312.6060 [nucl-th].

[312] LHCb collaboration, R. Aaij et al., *Observation of double charm production involving open charm in proton-proton collisions at* $\sqrt{s} = 7$ *TeV*, JHEP **06** (2012) 141 CERN-PH-2012-109, LHCb-PAPER-2012-003, arXiv:1205.0975 [hep-ex].

[313] G. Aarts et al., *Heavy-flavor production and medium properties in high-energy nuclear collisions –What next?*, Eur. Phys. J. A **53** (2017) no. 5, 93.

[314] S. Chatterjee and P. Bozek, *Interplay of drag by hot matter and electromagnetic force on the directed flow of heavy quarks*, , arXiv:1804.04893 [nucl-th].

[315] CMS Collaboration, V. Khachatryan et al., *Observation of Long-Range Near-Side Angular Correlations in Proton-Proton Collisions at the LHC*, JHEP **09** (2010) 091, arXiv:1009.4122 [hep-ex].

[316] CMS Collaboration, S. Chatrchyan et al., *Observation of long-range near-side angular correlations in proton-lead collisions at the LHC*, Phys. Lett. **B718** (2013) 795–814, arXiv:1210.5482 [nucl-ex].

[317] ALICE Collaboration, B. Abelev et al., *Long-range angular correlations on the near and away side in p-Pb collisions at* $\sqrt{s_{NN}} = 5.02$ *TeV*, Phys. Lett. **B719** (2013) 29–41, arXiv:1212.2001 [nucl-ex].

[318] ATLAS Collaboration, G. Aad et al., *Observation of Associated Near-Side and Away-Side Long-Range Correlations in* $\sqrt{s_{NN}}$*=5.02 TeV Proton-Lead Collisions with the ATLAS Detector*, Phys. Rev. Lett. **110** (2013) no. 18, 182302, arXiv:1212.5198 [hep-ex].

[319] ALICE Collaboration, B. B. Abelev et al., *Long-range angular correlations of* π*, K and p in p-Pb collisions at* $\sqrt{s_{\rm NN}}$ *= 5.02 TeV*, Phys. Lett. **B726** (2013) 164–177, arXiv:1307.3237 [nucl-ex].

[320] CMS Collaboration, V. Khachatryan et al., *Evidence for Collective Multiparticle Correlations in p-Pb Collisions*, Phys. Rev. Lett. **115** (2015) no. 1, 012301, arXiv:1502.05382 [nucl-ex].

[321] ALICE Collaboration, B. B. Abelev et al., *Multiplicity Dependence of Pion, Kaon, Proton and Lambda Production in p-Pb Collisions at* $\sqrt{s_{NN}}$ *= 5.02 TeV*, Phys. Lett. **B728** (2014) 25–38, arXiv:1307.6796 [nucl-ex].

[322] ALICE Collaboration, J. Adam et al., *Multi-strange baryon production in p-Pb collisions at* $\sqrt{s_{\rm NN}} = 5.02$ *TeV*, Phys. Lett. **B758** (2016) 389–401, arXiv:1512.07227 [nucl-ex].

[323] K. Dusling and R. Venugopalan, *Comparison of the color glass condensate to dihadron correlations in proton-proton and proton-nucleus collisions*, Phys. Rev. **D87** (2013) no. 9, 094034, arXiv:1302.7018 [hep-ph].

[324] A. Bzdak and G.-L. Ma, *Elliptic and triangular flow in p+Pb and peripheral Pb+Pb collisions from parton scatterings*, Phys. Rev. Lett. **113** (2014) no. 25, 252301, arXiv:1406.2804 [hep-ph].

[325] L. He, T. Edmonds, Z.-W. Lin, et al., *Anisotropic parton escape is the dominant source of azimuthal anisotropy in transport models*, Physics Letters B **753** (2016) 506 – 510.

[326] B. Blok, C. D. Jäkel, M. Strikman, and U. A. Wiedemann, *Collectivity from interference*, JHEP **12** (2017) 074, arXiv:1708.08241 [hep-ph].

[327] ALICE Collaboration, S. Acharya et al., *Transverse momentum spectra and nuclear modification factors of charged particles in pp, p-Pb and Pb-Pb collisions at the LHC*, JHEP **11** (2018) 013, arXiv:1802.09145 [nucl-ex].

[328] A. Beraudo, A. De Pace, M. Monteno, M. Nardi, and F. Prino, *Heavy-flavour production in high-energy d-Au and p-Pb collisions*, JHEP **03** (2016) 123, arXiv:1512.05186 [hep-ph].

[329] A. Kusina, J.-P. Lansberg, I. Schienbein, and H.-S. Shao, *Gluon shadowing in heavy-flavor production at the LHC*, Phys. Rev. Lett. **121** (2018) 052004, arXiv:1712.07024 [hep-ph].

[330] CMS Collaboration, A. M. Sirunyan et al., *Elliptic flow of charm and strange hadrons in high-multiplicity pPb collisions at* $\sqrt{s_{\rm NN}} = 8.16$ *TeV*, Phys. Rev. Lett. (2018) , arXiv:1804.09767 [hep-ex].

[331] J. D. Bjorken, *Energy Loss of Energetic Partons in Quark - Gluon Plasma: Possible Extinction of High p(t) Jets in Hadron - Hadron Collisions*, FERMILAB-PUB-82-059-THY, FERMILAB-PUB-82-059-T (1982) .

[332] M. Gyulassy and M. Plumer, *Jet quenching in dense matter*, Phys. Lett. B **243** (1990) 432.

[333] R. Baier, Y. L. Dokshitzer, S. Peigne, and D. Schiff, *Induced gluon radiation in a QCD medium*, Phys. Lett. B **345** (1995) 277, arXiv:hep-ph/9411409 [hep-ph].

[334] B. G. Zakharov, *Radiative Quark* $p_\perp$*-Broadening in a Quark–Gluon Plasma beyond the Soft Gluon Approximation*, JETP Lett. **108** (2018) no. 8, 508, arXiv:1807.09742 [hep-ph].

[335] M. Gyulassy, P. Levai, and I. Vitev, *Jet quenching in thin quark gluon plasmas. 1. Formalism*, Nucl. Phys. **B571** (2000) 197–233, arXiv:hep-ph/9907461 [hep-ph].

[336] U. A. Wiedemann, *Jet Quenching in Heavy Ion Collisions*, in *Landolt-Bornstein 23, 521 (2010)*, pp. 521–562. 2010. arXiv:0908.2306 [hep-ph].

[337] PHENIX Collaboration, K. Adcox et al., *Suppression of hadrons with large transverse momentum in central Au+Au collisions at* $\sqrt{s_{\rm NN}}$ *= 130 GeV*, Phys. Rev. Lett. **88** (2002) 022301, arXiv:nucl-ex/0109003 [nucl-ex].

[338] PHENIX Collaboration, S. S. Adler et al., *Suppressed* π^0 *production at large transverse momentum in central Au+Au collisions at* $\sqrt{s_{\rm NN}}$ *= 200 GeV*, Phys. Rev. Lett. **91** (2003) 072301, arXiv:nucl-ex/0304022 [nucl-ex].

[339] STAR Collaboration, C. Adler et al., *Centrality dependence of high* p_T *hadron suppression in Au+Au collisions at* $\sqrt{s}_{NN}$ *= 130-GeV*, Phys. Rev. Lett. **89** (2002) 202301, arXiv:nucl-ex/0206011 [nucl-ex].

[340] STAR Collaboration, C. Adler et al., *Disappearance of back-to-back high* p_T *hadron correlations in central Au+Au collisions at* $\sqrt{s_{NN}}$ *= 200-GeV*, Phys. Rev. Lett. **90** (2003) 082302, arXiv:nucl-ex/0210033 [nucl-ex].

[341] STAR Collaboration, J. Adams et al., *Transverse momentum and collision energy dependence of high $p_{\rm T}$ hadron suppression in Au+Au collisions at ultrarelativistic energies*, Phys. Rev. Lett. **91** (2003) 172302, arXiv:nucl-ex/0305015 [nucl-ex].

[342] STAR Collaboration, J. Adams et al., *Evidence from d + Au measurements for final state suppression of high p(T) hadrons in Au+Au collisions at RHIC*, Phys. Rev. Lett. **91** (2003) 072304, arXiv:nucl-ex/0306024 [nucl-ex].

[343] STAR Collaboration, J. Adams et al., *Direct observation of dijets in central Au+Au collisions at s(NN)**(1/2) = 200-GeV*, Phys. Rev. Lett. **97** (2006) 162301, arXiv:nucl-ex/0604018 [nucl-ex].

[344] BRAHMS Collaboration, I. Arsene et al., *Transverse momentum spectra in Au+Au and d+Au collisions at $\sqrt{s_{\rm NN}}$ = 200 GeV and the pseudorapidity dependence of high $p_{\rm T}$ suppression*, Phys. Rev. Lett. **91** (2003) 072305, arXiv:nucl-ex/0307003 [nucl-ex].

[345] PHOBOS Collaboration, B. B. Back et al., *Charged hadron transverse momentum distributions in Au+Au collisions at $\sqrt{s_{\rm NN}}$ = 200 GeV*, Phys. Lett. B **578** (2004) 297, arXiv:nucl-ex/0302015 [nucl-ex].

[346] STAR Collaboration, L. Adamczyk et al., *Dijet imbalance measurements in Au+Au and pp collisions at $\sqrt{s_{\rm NN}} = 200$ GeV at STAR*, Phys. Rev. Lett. **119** (2017) 062301, arXiv:1609.03878 [nucl-ex].

[347] STAR Collaboration, L. Adamczyk et al., *Measurements of jet quenching with semi-inclusive hadron+jet distributions in Au+Au collisions at $\sqrt{s_{\rm NN}}$ = 200 GeV*, Phys. Rev. C **96** (2017) 024905, arXiv:1702.01108 [nucl-ex].

[348] ALICE Collaboration, K. Aamodt et al., *Suppression of charged particle production at large transverse momentum in central* Pb–Pb *collisions at $s_{_{NN}} = 2.76$ TeV*, Phys. Lett. **B696** (2011) 30–39, arXiv:1012.1004 [nucl-ex].

[349] ALICE Collaboration, K. Aamodt et al., *Particle-Yield Modification in Jetlike Azimuthal Dihadron Correlations in Pb-Pb Collisions at $\sqrt{s_{\rm NN}} = 2.76$ TeV*, Phys. Rev. Lett. **108** (2012) 092301, arXiv:1110.0121 [nucl-ex].

[350] ATLAS Collaboration, G. Aad et al., *Measurement of charged-particle spectra in* Pb–Pb *collisions at $s_{_{NN}} = 2.76$ TeV with the ATLAS detector at the LHC*, JHEP **09** (2015) 050, arXiv:1504.04337 [hep-ex].

[351] CMS Collaboration, S. Chatrchyan et al., *Study of high-$p_{\rm T}$ charged particle suppression in* Pb–Pb *compared to* pp *collisions at $s_{_{NN}} = 2.76$ TeV*, Eur. Phys. J. **C72** (2012) 1945, arXiv:1202.2554 [nucl-ex].

[352] ATLAS Collaboration, G. Aad et al., *Observation of a centrality-dependent dijet asymmetry in lead-lead collisions at $s_{_{NN}} = 2.76$ TeV with the ATLAS Detector at the LHC*, Phys. Rev. Lett. **105** (2010) 252303, arXiv:1011.6182 [hep-ex].

[353] CMS Collaboration, S. Chatrchyan et al., *Jet momentum dependence of jet quenching in PbPb collisions at $\sqrt{s_{\rm NN}} = 2.76$ TeV*, Phys. Lett. B **712** (2012) 176, arXiv:1202.5022 [nucl-ex].

[354] ATLAS Collaboration, G. Aad et al., *Measurement of the jet radius and transverse momentum dependence of inclusive jet suppression in lead-lead collisions at $\sqrt{s_{\rm NN}} = 2.76$ TeV with the ATLAS detector*, Phys. Lett. B **719** (2013) 220, arXiv:1208.1967 [hep-ex].

[355] ALICE Collaboration, B. Abelev et al., *Measurement of charged jet suppression in Pb-Pb collisions at $\sqrt{s_{\rm NN}}$ = 2.76 TeV*, JHEP **03** (2014) 013, arXiv:1311.0633 [nucl-ex].

[356] ALICE Collaboration, J. Adam et al., *Measurement of jet suppression in central* Pb–Pb *collisions at $s_{_{NN}} = 2.76$ TeV*, Phys. Lett. **B746** (2015) 1–14, arXiv:1502.01689 [nucl-ex].

[357] CMS Collaboration, V. Khachatryan et al., *Charged-particle nuclear modification factors in PbPb and pPb collisions at* $\sqrt{s_{\rm NN}} = 5.02$ *TeV*, JHEP **04** (2017) 039, arXiv:1611.01664 [nucl-ex].

[358] ALICE Collaboration, J. Adam et al., *Measurement of jet quenching with semi-inclusive hadron-jet distributions in central Pb-Pb collisions at* $\sqrt{s_{\rm NN}} = 2.76$ *TeV*, JHEP **09** (2015) 170, arXiv:1506.03984 [nucl-ex].

[359] CMS Collaboration, S. Chatrchyan et al., *Modification of jet shapes in PbPb collisions at* $\sqrt{s_{\rm NN}} = 2.76$ *TeV*, Phys. Lett. B **730** (2014) 243, arXiv:1310.0878 [nucl-ex].

[360] CMS Collaboration, S. Chatrchyan et al., *Measurement of jet fragmentation in PbPb and pp collisions at* $\sqrt{s_{\rm NN}} = 2.76$ *TeV*, Phys. Rev. C **90** (2014) 024908, arXiv:1406.0932 [nucl-ex].

[361] ATLAS Collaboration, M. Aaboud et al., *Measurement of jet fragmentation in Pb+Pb and pp collisions at* $\sqrt{s_{\rm NN}} = 2.76$ *TeV with the ATLAS detector at the LHC*, Eur. Phys. J. **C77** (2017) no. 6, 379, arXiv:1702.00674 [hep-ex].

[362] ALICE Collaboration, S. Acharya et al., *First measurement of jet mass in Pb–Pb and p–Pb collisions at the LHC*, Phys. Lett. **B776** (2018) 249–264, arXiv:1702.00804 [nucl-ex].

[363] ALICE Collaboration, S. Acharya et al., *Medium modification of the shape of small-radius jets in central Pb-Pb collisions at* $\sqrt{s_{\rm NN}} = 2.76$ TeV, JHEP **10** (2018) 139, arXiv:1807.06854 [nucl-ex].

[364] CMS Collaboration, A. M. Sirunyan et al., *Measurement of the Splitting Function in pp and Pb-Pb Collisions at* $\sqrt{s_{\rm NN}} = 5.02$ *TeV*, Phys. Rev. Lett. **120** (2018) no. 14, 142302, arXiv:1708.09429 [nucl-ex].

[365] CMS Collaboration, A. M. Sirunyan et al., *Measurement of the groomed jet mass in PbPb and pp collisions at* $\sqrt{s_{\rm NN}} = 5.02$ *TeV*, JHEP **10** (2018) 161, arXiv:1805.05145 [hep-ex].

[366] JET Collaboration, K. M. Burke et al., *Extracting the jet transport coefficient from jet quenching in high-energy heavy-ion collisions*, Phys. Rev. **C90** (2014) no. 1, 014909, arXiv:1312.5003 [nucl-th].

[367] CMS Collaboration, V. Khachatryan et al., *Measurement of inclusive jet cross sections in pp and PbPb collisions at* $\sqrt{s_{NN}} = 2.76$ *TeV*, Phys. Rev. C **96** (2017) no. 1, 015202, arXiv:1609.05383 [nucl-ex].

[368] Y. He, T. Luo, X.-N. Wang, and Y. Zhu, *Linear Boltzmann Transport for Jet Propagation in the Quark-Gluon Plasma: Elastic Processes and Medium Recoil*, Phys. Rev. **C91** (2015) 054908, arXiv:1503.03313 [nucl-th]. [Erratum: Phys. Rev.C97,no.1,019902(2018)].

[369] Y.-T. Chien, A. Emerman, Z.-B. Kang, G. Ovanesyan, and I. Vitev, *Jet Quenching from QCD Evolution*, Phys. Rev. **D93** (2016) no. 7, 074030, arXiv:1509.02936 [hep-ph].

[370] Y.-T. Chien and I. Vitev, *Towards the understanding of jet shapes and cross sections in heavy ion collisions using soft-collinear effective theory*, JHEP **05** (2016) 023, arXiv:1509.07257 [hep-ph].

[371] I. Vitev, S. Wicks, and B.-W. Zhang, *A Theory of jet shapes and cross sections: From hadrons to nuclei*, JHEP **11** (2008) 093, arXiv:0810.2807 [hep-ph].

[372] Z.-B. Kang, F. Ringer, and I. Vitev, *Inclusive production of small radius jets in heavy-ion collisions*, Phys. Lett. **B769** (2017) 242–248, arXiv:1701.05839 [hep-ph].

[373] M. Spousta and B. Cole, *Interpreting single jet measurements in Pb + Pb collisions at the LHC*, Eur. Phys. J. **C76** (2016) no. 2, 50, arXiv:1504.05169 [hep-ph].

[374] ATLAS Collaboration, G. Aad et al., *Measurement of Z boson Production in Pb+Pb Collisions at* $\sqrt{s_{NN}} = 2.76$ *TeV with the ATLAS Detector*, Phys. Rev. Lett. **110** (2013) no. 2, 022301, arXiv:1210.6486 [hep-ex].

[375] ATLAS Collaboration, G. Aad et al., *Centrality, rapidity and transverse momentum dependence of isolated prompt photon production in lead-lead collisions at* $\sqrt{s_{\rm NN}} = 2.76$ *TeV measured with the ATLAS detector*, Phys. Rev. **C93** (2016) no. 3, 034914, arXiv:1506.08552 [hep-ex].

[376] CMS Collaboration, S. Chatrchyan et al., *Measurement of isolated photon production in pp and PbPb collisions at* $\sqrt{s_{NN}} = 2.76$ *TeV*, Phys. Lett. **B710** (2012) 256–277, arXiv:1201.3093 [nucl-ex].

[377] CMS Collaboration, S. Chatrchyan et al., *Study of Z production in PbPb and pp collisions at* $\sqrt{s_{\rm NN}} = 2.76$ *TeV in the dimuon and dielectron decay channels*, JHEP **03** (2015) 022, arXiv:1410.4825 [nucl-ex].

[378] CMS Collaboration, S. Chatrchyan et al., *Observation and studies of jet quenching in* Pb–Pb *collisions at nucleon-nucleon center-of-mass energy = 2.76 TeV*, Phys. Rev. **C84** (2011) 024906, arXiv:1102.1957 [nucl-ex].

[379] CMS Collaboration, A. M. Sirunyan et al., *Study of Jet Quenching with* Z *+ jet Correlations in Pb-Pb and pp Collisions at* $\sqrt{s_{NN}} = 5.02$ TeV, Phys. Rev. Lett. **119** (2017) no. 8, 082301, arXiv:1702.01060 [nucl-ex].

[380] CMS Collaboration, A. M. Sirunyan et al., *Study of jet quenching with isolated-photon+jet correlations in PbPb and pp collisions at* $\sqrt{s_{\rm NN}} = 5.02$ *TeV*, arXiv:1711.09738 [nucl-ex].

[381] R. Haake and C. Loizides, *Machine Learning based jet momentum reconstruction in heavy-ion collisions*, arXiv:1810.06324 [nucl-ex].

[382] F. D'Eramo, M. Lekaveckas, H. Liu, and K. Rajagopal, *Momentum Broadening in Weakly Coupled Quark-Gluon Plasma (with a view to finding the quasiparticles within liquid quark-gluon plasma)*, JHEP **05** (2013) 031, arXiv:1211.1922 [hep-ph].

[383] L. Chen, G.-Y. Qin, S.-Y. Wei, B.-W. Xiao, and H.-Z. Zhang, *Probing Transverse Momentum Broadening via Dihadron and Hadron-jet Angular Correlations in Relativistic Heavy-ion Collisions*, Phys. Lett. **B773** (2017) 672–676, arXiv:1607.01932 [hep-ph].

[384] ATLAS Collaboration, M. Aaboud et al., *Measurement of jet* $p_{\rm T}$ *correlations in Pb+Pb and pp collisions at* $\sqrt{s_{\rm NN}} = 2.76$ *TeV with the ATLAS detector*, Phys. Lett. **B774** (2017) 379–402, arXiv:1706.09363 [hep-ex].

[385] H. A. Andrews et al., *Novel tools and observables for jet physics in heavy-ion collisions*, arXiv:1808.03689 [hep-ph].

[386] A. H. Mueller, B. Wu, B.-W. Xiao, and F. Yuan, *Medium Induced Transverse Momentum Broadening in Hard Processes*, Phys. Rev. **D95** (2017) no. 3, 034007, arXiv:1608.07339 [hep-ph].

[387] F. D'Eramo, K. Rajagopal, and Y. Yin, *Molière scattering in quark-gluon plasma: finding point-like scatterers in a liquid*, JHEP **01** (2019) 172, arXiv:1808.03250 [hep-ph].

[388] M. Gyulassy, P. Levai, J. Liao, et al., *Precision Dijet Acoplanarity Tomography of the Chromo Structure of Perfect QCD Fluids*, Nucl. Phys. **A982** (2019) 627–630, arXiv:1808.03238 [hep-ph].

[389] J. Ghiglieri and H. Kim, *Transverse momentum broadening and collinear radiation at NLO in the* $\mathcal{N} = 4$ *SYM plasma*, JHEP **12** (2018) 049, arXiv:1809.01349 [hep-ph].

[390] K. C. Zapp, *JEWEL 2.0.0: directions for use*, Eur. Phys. J. **C74** (2014) no. 2, 2762, arXiv:1311.0048 [hep-ph].

[391] ATLAS Collaboration, M. Aaboud et al., *Measurement of jet fragmentation in Pb+Pb and pp collisions at $\sqrt{s_{NN}} = 5.02$ TeV with the ATLAS detector*, Phys. Rev. **C98** (2018) no. 2, 024908, arXiv:1805.05424 [nucl-ex].

[392] CMS Collaboration, A. M. Sirunyan et al., *Jet properties in PbPb and pp collisions at $\sqrt{s_{\mathrm{N\,N}}} = 5.02$ TeV*, JHEP **05** (2018) 006, arXiv:1803.00042 [nucl-ex].

[393] J. Casalderrey-Solana, D. C. Gulhan, J. G. Milhano, D. Pablos, and K. Rajagopal, *A Hybrid Strong/Weak Coupling Approach to Jet Quenching*, JHEP **10** (2014) 019, arXiv:1405.3864 [hep-ph]. [Erratum: JHEP09,175(2015)].

[394] Z. Hulcher, D. Pablos, and K. Rajagopal, *Resolution Effects in the Hybrid Strong/Weak Coupling Model*, JHEP **03** (2018) 010, arXiv:1707.05245 [hep-ph].

[395] CMS Collaboration, A. M. Sirunyan et al., *Jet shapes of isolated photon-tagged jets in PbPb and pp collisions at $\sqrt{s_{\mathrm{NN}}} = 5.02$ TeV*, Phys. Rev. Lett. **122** (2019) no. 15, 152001, arXiv:1809.08602 [hep-ex].

[396] ATLAS Collaboration, *Measurement of the fragmentation function for photon-tagged jets in $\sqrt{s_{\mathrm{NN}}} = 5.02$ TeV Pb+Pb and pp collisions with the ATLAS detector*, ATLAS-CONF-2017-074, CERN, Geneva, Sep, 2017. https://cds.cern.ch/record/2285812.

[397] S. D. Ellis, C. K. Vermilion, and J. R. Walsh, *Recombination algorithms and jet substructure: Pruning as a tool for heavy particle searches*, Phys. Rev. D **81** (2010) 094023, arXiv:0912.0033 [hep-ph].

[398] J. M. Butterworth, A. R. Davison, M. Rubin, and G. P. Salam, *Jet substructure as a new Higgs search channel at the LHC*, Phys. Rev. Lett. **100** (2008) 242001, arXiv:0802.2470 [hep-ph].

[399] D. Krohn, J. Thaler, and L.-T. Wang, *Jet trimming*, JHEP **02** (2010) 084, arXiv:0912.1342 [hep-ph].

[400] M. Dasgupta, A. Fregoso, S. Marzani, and G. P. Salam, *Towards an understanding of jet substructure*, JHEP **09** (2013) 029, arXiv:1307.0007 [hep-ph].

[401] A. J. Larkoski, S. Marzani, G. Soyez, and J. Thaler, *Soft drop*, JHEP **05** (2014) 146, arXiv:1402.2657 [hep-ph].

[402] G. Altarelli and G. Parisi, *Asymptotic freedom in parton language*, Nucl. Phys. B **126** (1977) 298.

[403] A. J. Larkoski, S. Marzani, and J. Thaler, *Sudakov Safety in Perturbative QCD*, Phys. Rev. D **91** (2015) 111501, arXiv:1502.01719 [hep-ph].

[404] Y. Mehtar-Tani and K. Tywoniuk, *Groomed jets in heavy-ion collisions: sensitivity to medium-induced bremsstrahlung*, JHEP **04** (2017) 125, arXiv:1610.08930 [hep-ph].

[405] Y.-T. Chien and I. Vitev, *Probing the Hardest Branching within Jets in Heavy-Ion Collisions*, Phys. Rev. Lett. **119** (2017) 112301, arXiv:1608.07283 [hep-ph].

[406] N.-B. Chang, S. Cao, and G.-Y. Qin, *Probing medium-induced jet splitting and energy loss in heavy-ion collisions*, Phys. Lett. **B781** (2018) 423–432, arXiv:1707.03767 [hep-ph].

[407] B. Andersson, G. Gustafson, L. Lonnblad, and U. Pettersson, *Coherence Effects in Deep Inelastic Scattering*, Z. Phys. **C43** (1989) 625.

[408] F. A. Dreyer, G. P. Salam, and G. Soyez, *The Lund Jet Plane*, JHEP **12** (2018) 064, arXiv:1807.04758 [hep-ph].

[409] M. Cacciari, G. P. Salam, and G. Soyez, *FastJet User Manual*, Eur. Phys. J. **C72** (2012) 1896, arXiv:1111.6097 [hep-ph].

[410] M. Cacciari and G. P. Salam, *Dispelling the N^3 myth for the k_t jet-finder*, Phys. Lett. **B641** (2006) 57–61, arXiv:hep-ph/0512210 [hep-ph].

[411] A. Dainese et al., *Heavy ions at the Future Circular Collider*, CERN Yellow Report (2017) no. 3, 635–692, arXiv:1605.01389 [hep-ph].

[412] ATLAS Collaboration, M. Aaboud et al., *Measurement of the nuclear modification factor for inclusive jets in Pb+Pb collisions at $\sqrt{s_{\rm NN}} = 5.02$ TeV with the ATLAS detector*, Phys. Lett. **B790** (2019) 108–128, arXiv:1805.05635 [nucl-ex].

[413] R. Kunnawalkam Elayavalli and K. C. Zapp, *Medium response in JEWEL and its impact on jet shape observables in heavy ion collisions*, JHEP **07** (2017) 141, arXiv:1707.01539 [hep-ph].

[414] R. Kunnawalkam Elayavalli and K. C. Zapp, *Simulating V+jet processes in heavy ion collisions with JEWEL*, Eur. Phys. J. **C76** (2016) no. 12, 695, arXiv:1608.03099 [hep-ph].

[415] E. Eichten, K. Gottfried, T. Kinoshita, K. D. Lane, and T.-M. Yan, *Charmonium: Comparison with Experiment*, Phys. Rev. **D21** (1980) 203.

[416] G. S. Bali, *QCD forces and heavy quark bound states*, Phys. Rept. **343** (2001) 1–136, arXiv:hep-ph/0001312 [hep-ph].

[417] N. Brambilla, A. Pineda, J. Soto, and A. Vairo, *Effective field theories for heavy quarkonium*, Rev. Mod. Phys. **77** (2005) 1423, arXiv:hep-ph/0410047 [hep-ph].

[418] Y. Schroder, *The Static potential in QCD to two loops*, Phys. Lett. **B447** (1999) 321–326, arXiv:hep-ph/9812205 [hep-ph].

[419] N. Brambilla, A. Pineda, J. Soto, and A. Vairo, *Potential NRQCD: An Effective theory for heavy quarkonium*, Nucl. Phys. **B566** (2000) 275, arXiv:hep-ph/9907240 [hep-ph].

[420] Quarkonium Working Group Collaboration, N. Brambilla et al., *Heavy quarkonium physics*, FERMILAB-FN-0779, CERN-2005-005 (2004) , arXiv:hep-ph/0412158 [hep-ph].

[421] R. Rapp, D. Blaschke, and P. Crochet, *Charmonium and bottomonium production in heavy-ion collisions*, Prog. Part. Nucl. Phys. **65** (2010) 209–266, arXiv:0807.2470 [hep-ph].

[422] P. Braun-Munzinger and J. Stachel, *Charmonium from Statistical Hadronization of Heavy Quarks: A Probe for Deconfinement in the Quark-Gluon Plasma*, Landolt-Bornstein **23** (2010) 424, arXiv:0901.2500 [nucl-th].

[423] L. Kluberg and H. Satz, *Color Deconfinement and Charmonium Production in Nuclear Collisions*, arXiv:0901.3831 [hep-ph].

[424] A. Mocsy, P. Petreczky, and M. Strickland, *Quarkonia in the Quark Gluon Plasma*, Int. J. Mod. Phys. **A28** (2013) 1340012, arXiv:1302.2180 [hep-ph].

[425] Y. Liu, K. Zhou, and P. Zhuang, *Quarkonia in high energy nuclear collisions*, Int. J. Mod. Phys. **E24** (2015) no. 11, 1530015.

[426] S. Y. F. Liu and R. Rapp, *Spectral and Transport Properties of a Non-Perturbative Quark-Gluon Plasma*, arXiv:1612.09138 [nucl-th].

[427] T. Matsui and H. Satz, *J/ψ Suppression by Quark-Gluon Plasma Formation*, Phys. Lett. **B178** (1986) 416–422.

[428] P. Braun-Munzinger and J. Stachel, *(Non)thermal aspects of charmonium production and a new look at J / psi suppression*, Phys. Lett. **B490** (2000) 196–202, arXiv:nucl-th/0007059 [nucl-th].

[429] R. L. Thews, M. Schroedter, and J. Rafelski, *Enhanced J/ψ production in deconfined quark matter*, Phys. Rev. **C63** (2001) 054905, arXiv:hep-ph/0007323 [hep-ph].

[430] C. Young and E. Shuryak, *Charmonium in strongly coupled quark-gluon plasma*, Phys. Rev. **C79** (2009) 034907, arXiv:0803.2866 [nucl-th].

[431] R. Rapp and X. Du, *Theoretical Perspective on Quarkonia from SPS via RHIC to LHC*, Nucl. Phys. **A967** (2017) 216–224, arXiv:1704.07923 [hep-ph].

[432] A. Andronic, P. Braun-Munzinger, K. Redlich, and J. Stachel, *Decoding the phase structure of QCD via particle production at high energy*, Nature **561** (2018) 321–330, arXiv:1710.09425 [nucl-th].

[433] X. Du, R. Rapp, and M. He, *Color Screening and Regeneration of Bottomonia in High-Energy Heavy-Ion Collisions*, Phys. Rev. **C96** (2017) no. 5, 054901, arXiv:1706.08670 [hep-ph].

[434] B. Krouppa, A. Rothkopf, and M. Strickland, *Bottomonium suppression using a lattice QCD vetted potential*, Phys. Rev. **D97** (2018) no. 1, 016017, arXiv:1710.02319 [hep-ph].

[435] C.-Y. Wong, *Heavy quarkonia in quark-gluon plasma*, Phys. Rev. **C72** (2005) 034906, arXiv:hep-ph/0408020 [hep-ph].

[436] A. Mocsy and P. Petreczky, *Quarkonia correlators above deconfinement*, Phys. Rev. **D73** (2006) 074007, arXiv:hep-ph/0512156 [hep-ph].

[437] W. M. Alberico, A. Beraudo, A. De Pace, and A. Molinari, *Quarkonia in the deconfined phase: Effective potentials and lattice correlators*, Phys. Rev. **D75** (2007) 074009, arXiv:hep-ph/0612062 [hep-ph].

[438] N. Brambilla, J. Ghiglieri, A. Vairo, and P. Petreczky, *Static quark-antiquark pairs at finite temperature*, Phys. Rev. **D78** (2008) 014017, arXiv:0804.0993 [hep-ph].

[439] F. Riek and R. Rapp, *Selfconsistent Evaluation of Charm and Charmonium in the Quark-Gluon Plasma*, New J. Phys. **13** (2011) 045007, arXiv:1012.0019 [nucl-th].

[440] Y. Burnier, O. Kaczmarek, and A. Rothkopf, *Quarkonium at finite temperature: Towards realistic phenomenology from first principles*, JHEP **12** (2015) 101, arXiv:1509.07366 [hep-ph].

[441] S. Y. F. Liu and R. Rapp, *T-matrix Approach to Quark-Gluon Plasma*, Phys. Rev. **C97** (2018) no. 3, 034918, arXiv:1711.03282 [nucl-th].

[442] G. Bhanot and M. E. Peskin, *Short Distance Analysis for Heavy Quark Systems. 2. Applications*, Nucl. Phys. **B156** (1979) 391–416.

[443] D. Kharzeev and H. Satz, *Quarkonium interactions in hadronic matter*, Phys. Lett. **B334** (1994) 155–162, arXiv:hep-ph/9405414 [hep-ph].

[444] L. Grandchamp and R. Rapp, *Thermal versus direct J/ψ production in ultrarelativistic heavy ion collisions*, Phys. Lett. **B523** (2001) 60–66, arXiv:hep-ph/0103124 [hep-ph].

[445] M. Laine, O. Philipsen, P. Romatschke, and M. Tassler, *Real-time static potential in hot QCD*, JHEP **03** (2007) 054, arXiv:hep-ph/0611300 [hep-ph].

[446] Y. Park, K.-I. Kim, T. Song, S. H. Lee, and C.-Y. Wong, *Widths of quarkonia in quark gluon plasma*, Phys. Rev. **C76** (2007) 044907, arXiv:0704.3770 [hep-ph].

[447] J.-P. Blaizot, D. De Boni, P. Faccioli, and G. Garberoglio, *Heavy quark bound states in a quark-gluon plasma: Dissociation and recombination*, Nucl. Phys. **A946** (2016) 49–88, arXiv:1503.03857 [nucl-th].

[448] R. Katz and P. B. Gossiaux, *The Schrödinger-Langevin equation with and without thermal fluctuations*, Annals Phys. **368** (2016) 267–295, arXiv:1504.08087 [quant-ph].

[449] S. Kajimoto, Y. Akamatsu, M. Asakawa, and A. Rothkopf, *Dynamical dissociation of quarkonia by wave function decoherence*, Phys. Rev. **D97** (2018) no. 1, 014003, arXiv:1705.03365 [nucl-th].

[450] P. Petreczky and C. Young, *Sequential bottomonium production at high temperatures*, Few Body Syst. **58** (2017) no. 2, 61, arXiv:1606.08421 [nucl-th].

[451] Y. Akamatsu, *Heavy quark master equations in the Lindblad form at high temperatures*, Phys. Rev. **D91** (2015) no. 5, 056002, arXiv:1403.5783 [hep-ph].

[452] N. Brambilla, M. A. Escobedo, J. Soto, and A. Vairo, *Quarkonium suppression in heavy-ion collisions: an open quantum system approach*, Phys. Rev. **D96** (2017) no. 3, 034021, arXiv:1612.07248 [hep-ph].

[453] T. Song, C. M. Ko, and S. H. Lee, *Quarkonium formation time in relativistic heavy-ion collisions*, Phys. Rev. **C91** (2015) no. 4, 044909, arXiv:1502.05734 [nucl-th].

[454] J. Hoelck, F. Nendzig, and G. Wolschin, *In-medium Υ suppression and feed-down in UU and PbPb collisions*, Phys. Rev. **C95** (2017) no. 2, 024905, arXiv:1602.00019 [hep-ph].

[455] S. Aronson, E. Borras, B. Odegard, R. Sharma, and I. Vitev, *Collisional and thermal dissociation of J/ψ and Υ states at the LHC*, Phys. Lett. **B778** (2018) 384–391, arXiv:1709.02372 [hep-ph].

[456] X. Yao and B. Müller, *Approach to equilibrium of quarkonium in quark-gluon plasma*, Phys. Rev. **C97** (2018) no. 1, 014908, arXiv:1709.03529 [hep-ph]. [Erratum: Phys. Rev.C97,no.4,049903(2018)].

[457] D. Contardo, M. Klute, J. Mans, L. Silvestris, and J. Butler, *Technical proposal for the Phase-II upgrade of the CMS detector*, CERN-LHCC-2015-010, 2015. https://cds.cern.ch/record/2020886.

[458] ALICE Collaboration, B. Abelev et al., *J/ψ suppression at forward rapidity in Pb-Pb collisions at $\sqrt{s_{NN}} = 2.76$ TeV*, Phys. Rev. Lett. **109** (2012) 072301, arXiv:1202.1383 [hep-ex].

[459] ALICE Collaboration, B. B. Abelev et al., *Centrality, rapidity and transverse momentum dependence of J/ψ suppression in Pb-Pb collisions at $\sqrt{s_{\rm NN}}$=2.76 TeV*, Phys. Lett. **B734** (2014) 314–327, arXiv:1311.0214 [nucl-ex].

[460] ALICE Collaboration, J. Adam et al., *J/ψ suppression at forward rapidity in Pb-Pb collisions at $\sqrt{\mathbf{s}_{\rm NN}} = \mathbf{5.02}$ TeV*, Phys. Lett. **B766** (2017) 212–224, arXiv:1606.08197 [nucl-ex].

[461] X. Zhao and R. Rapp, *Medium Modifications and Production of Charmonia at LHC*, Nucl. Phys. **A859** (2011) 114–125, arXiv:1102.2194 [hep-ph].

[462] L. Yan, P. Zhuang, and N. Xu, *Competition between J / psi suppression and regeneration in quark-gluon plasma*, Phys. Rev. Lett. **97** (2006) 232301, arXiv:nucl-th/0608010 [nucl-th].

[463] CMS Collaboration, A. M. Sirunyan et al., *Measurement of prompt and nonprompt charmonium suppression in PbPb collisions at 5.02 TeV*, Eur. Phys. J. **C78** (2018) no. 6, 509, arXiv:1712.08959 [nucl-ex].

[464] ALICE Collaboration, B. B. Abelev et al., *Azimuthal anisotropy of D meson production in Pb-Pb collisions at $\sqrt{s_{\rm NN}} = 2.76$ TeV*, Phys. Rev. **C90** (2014) no. 3, 034904, arXiv:1405.2001 [nucl-ex].

[465] ALICE Collaboration, S. Acharya et al., *D-meson azimuthal anisotropy in midcentral Pb-Pb collisions at $\sqrt{\mathbf{s}_{\rm NN}} = \mathbf{5.02}$ TeV*, Phys. Rev. Lett. **120** (2018) no. 10, 102301, arXiv:1707.01005 [nucl-ex].

[466] CMS Collaboration, A. M. Sirunyan et al., *Measurement of prompt D^0 meson azimuthal anisotropy in Pb-Pb collisions at $\sqrt{s_{NN}}$ = 5.02 TeV*, Phys. Rev. Lett. **120** (2018) no. 20, 202301, arXiv:1708.03497 [nucl-ex].

[467] ALICE Collaboration, E. Abbas et al., *J/Psi Elliptic Flow in Pb-Pb Collisions at $\sqrt{s_{\rm NN}}$ = 2.76 TeV*, Phys. Rev. Lett. **111** (2013) 162301, arXiv:1303.5880 [nucl-ex].

[468] ALICE Collaboration, S. Acharya et al., *J/ψ elliptic flow in Pb-Pb collisions at $\sqrt{s_{\rm NN}} = 5.02$ TeV*, Phys. Rev. Lett. **119** (2017) no. 24, 242301, arXiv:1709.05260 [nucl-ex].

[469] ATLAS Collaboration, M. Aaboud et al., *Prompt and non-prompt J/ψ elliptic flow in Pb+Pb collisions at $\sqrt{s_{NN}} = 5.02$ Tev with the ATLAS detector*, Eur. Phys. J. **C78** (2018) no. 9, 784, arXiv:1807.05198 [nucl-ex].

[470] ALICE Collaboration, S. Acharya et al., *Study of J/ψ azimuthal anisotropy at forward rapidity in Pb-Pb collisions at $\sqrt{s_{\rm NN}} = 5.02$ TeV*, JHEP **02** (2019) 012, arXiv:1811.12727 [nucl-ex].

[471] K. Zhou, N. Xu, Z. Xu, and P. Zhuang, *Medium effects on charmonium production at ultrarelativistic energies available at the CERN Large Hadron Collider*, Phys. Rev. **C89** (2014) no. 5, 054911, arXiv:1401.5845 [nucl-th].

[472] X. Du and R. Rapp, *Sequential Regeneration of Charmonia in Heavy-Ion Collisions*, Nucl. Phys. **A943** (2015) 147–158, arXiv:1504.00670 [hep-ph].

[473] ATLAS Collaboration, M. Aaboud et al., *Prompt and non-prompt J/ψ and $\psi(2S)$ suppression at high transverse momentum in 5.02 TeV Pb+Pb collisions with the ATLAS experiment*, Eur. Phys. J. **C78** (2018) no. 9, 762, arXiv:1805.04077 [nucl-ex].

[474] B. Z. Kopeliovich, I. K. Potashnikova, I. Schmidt, and M. Siddikov, *Survival of charmonia in a hot environment*, Phys. Rev. **C91** (2015) no. 2, 024911, arXiv:1409.5147 [hep-ph].

[475] M. Spousta, *On similarity of jet quenching and charmonia suppression*, Phys. Lett. **B767** (2017) 10–15, arXiv:1606.00903 [hep-ph].

[476] F. Arleo, *Quenching of Hadron Spectra in Heavy Ion Collisions at the LHC*, Phys. Rev. Lett. **119** (2017) no. 6, 062302, arXiv:1703.10852 [hep-ph].

[477] ALICE Collaboration, *Addendum of the Letter of Intent for the upgrade of the ALICE experiment : The Muon Forward Tracker*, CERN-LHCC-2013-014. LHCC-I-022-ADD-1, CERN, Geneva. https://cds.cern.ch/record/1592659.

[478] LHCb Collaboration, R. Aaij et al., *Study of $\chi_{\rm b}$ meson production in* p p *collisions at $\sqrt{s} = 7$ and* 8 TeV *and observation of the decay $\chi_{\rm b}(3{\rm P}) \to \Upsilon(3{\rm S})\gamma$*, Eur. Phys. J. **C74** (2014) no. 10, 3092, arXiv:1407.7734 [hep-ex].

[479] ALICE Collaboration, B. B. Abelev et al., *Suppression of $\Upsilon(1S)$ at forward rapidity in Pb-Pb collisions at $\sqrt{s_{\rm NN}} = 2.76$ TeV*, Phys. Lett. **B738** (2014) 361–372, arXiv:1405.4493 [nucl-ex].

[480] ALICE Collaboration, S. Acharya et al., *Υ suppression at forward rapidity in Pb-Pb collisions at $\sqrt{s_{\rm NN}}$ = 5.02 TeV*, Phys. Lett. **B790** (2019) 89–101, arXiv:1805.04387 [nucl-ex].

[481] CMS Collaboration, A. M. Sirunyan et al., *Measurement of nuclear modification factors of Υ(1S), Υ(2S), and Υ(3S) mesons in PbPb collisions at $\sqrt{s_{\rm NN}} = 5.02$ TeV*, arXiv:1805.09215 [hep-ex].

[482] CMS Collaboration, V. Khachatryan et al., *Suppression of $\Upsilon(1S)$, $\Upsilon(2S)$ and $\Upsilon(3S)$ production in PbPb collisions at $\sqrt{s_{\rm NN}}$ = 2.76 TeV*, Phys. Lett. **B770** (2017) 357–379, arXiv:1611.01510 [nucl-ex].

[483] CMS Collaboration, A. M. Sirunyan et al., *Suppression of Excited Υ States Relative to the Ground State in Pb-Pb Collisions at $\sqrt{s_{\rm NN}}$=5.02 TeV*, Phys. Rev. Lett. **120** (2018) no. 14, 142301, arXiv:1706.05984 [hep-ex].

[484] B. Krouppa and M. Strickland, *Predictions for bottomonia suppression in 5.023 TeV Pb-Pb collisions*, Universe **2** (2016) no. 3, 16, arXiv:1605.03561 [hep-ph].

[485] F. Arleo and S. Peigné, *Quarkonium suppression in heavy-ion collisions from coherent energy loss in cold nuclear matter*, JHEP **10** (2014) 73, arXiv:1407.5054 [hep-ph].

[486] D. Das and N. Dutta, *Anisotropic flow: A case for Bottomonia*, Int. J. Mod. Phys. **A33** (2018) no. 16, 1850092, arXiv:1802.00414 [nucl-ex].

[487] X. Yao, W. Ke, Y. Xu, S. Bass, and B. Müller, *Quarkonium production in heavy ion collisions: coupled Boltzmann transport equations*, Nucl. Phys. **A982** (2019) 755–758, arXiv:1807.06199 [nucl-th].

[488] P. P. Bhaduri, N. Borghini, A. Jaiswal, and M. Strickland, *Anisotropic escape mechanism and elliptic flow of bottomonia*, arXiv:1809.06235 [hep-ph].

[489] F. Arleo, S. Peigné, and T. Sami, *Revisiting scaling properties of medium-induced gluon radiation*, Phys. Rev. **D83** (2011) 114036, arXiv:1006.0818 [hep-ph].

[490] X. Du and R. Rapp, *In-Medium Charmonium Production in Proton-Nucleus Collisions*, JHEP (2019) 015, arXiv:1808.10014 [nucl-th].

[491] C. J. Benesh, J. Qiu, and J. P. Vary, *J/ψ suppression in hadron-nucleus collisions*, Phys. Rev. C **50** (1994) 1015–1023, arXiv:hep-ph/9403265 [hep-ph].

[492] S. Gavin and R. Vogt, *Charmonium suppression by Comover scattering in Pb + Pb collisions*, Phys. Rev. Lett. **78** (1997) 1006–1009, arXiv:hep-ph/9606460 [hep-ph].

[493] S. J. Brodsky and A. H. Mueller, *Using Nuclei to Probe Hadronization in QCD*, Phys. Lett. **B206** (1988) 685–690.

[494] A. Capella, E. G. Ferreiro, and A. B. Kaidalov, *Nonsaturation of the J / psi suppression at large transverse energy in the comovers approach*, Phys. Rev. Lett. **85** (2000) 2080–2083, arXiv:hep-ph/0002300 [hep-ph].

[495] CMS Collaboration, S. Chatrchyan et al., *Event activity dependence of Y(nS) production in $\sqrt{s_{NN}}$=5.02 TeV pPb and $\sqrt{s}$=2.76 TeV pp collisions*, JHEP **04** (2014) 103, arXiv:1312.6300 [nucl-ex].

[496] ATLAS Collaboration, M. Aaboud et al., *Measurement of quarkonium production in proton-lead and proton-proton collisions at* 5.02 TeV *with the ATLAS detector*, Eur. Phys. J. **C78** (2018) no. 3, 171, arXiv:1709.03089 [nucl-ex].

[497] CMS Collaboration, *Dependence of the Υ(nS) production ratios on charged particle multiplicity in pp collisions at $\sqrt{s} = 7$* TeV, CMS-PAS-BPH-14-009, CERN, 2016. https://cds.cern.ch/record/2223879.

[498] CMS Collaboration, S. Chatrchyan et al., *Observation of sequential Upsilon suppression in PbPb collisions*, Phys. Rev. Lett. **109** (2012) 222301, arXiv:1208.2826 [nucl-ex].

[499] ALICE Collaboration, B. B. Abelev et al., *Suppression of ψ(2S) production in pPb collisions at $\sqrt{s_{\rm NN}} = 5.02$ TeV*, JHEP **12** (2014) 073, arXiv:1405.3796 [nucl-ex].

[500] F. Arleo and S. Peigné, *Disentangling Shadowing from Coherent Energy Loss using the Drell-Yan Process*, Phys. Rev. D **95** (2017) no. 1, 011502, arXiv:1512.01794 [hep-ph].

[501] ALICE Collaboration, S. Acharya et al., *Search for collectivity with azimuthal J/ψ-hadron correlations in high multiplicity p-Pb collisions at $\sqrt{s_{\rm NN}}$ = 5.02 and 8.16 TeV*, Phys. Lett. **B780** (2018) 7–20, arXiv:1709.06807 [nucl-ex].

[502] CMS Collaboration, A. M. Sirunyan et al., *Observation of prompt J/ψ meson elliptic flow in high-multiplicity pPb collisions at $\sqrt{s_{\rm NN}} = 8.16$ TeV*, Phys. Lett. **B791** (2019) 172–194, arXiv:1810.01473 [hep-ex].

[503] S. J. Brodsky, F. Fleuret, C. Hadjidakis, and J. P. Lansberg, *Physics Opportunities of a Fixed-Target Experiment using the LHC Beams*, Phys. Rept. **522** (2013) 239–255, arXiv:1202.6585 [hep-ph].

[504] J. P. Lansberg, S. J. Brodsky, F. Fleuret, and C. Hadjidakis, *Quarkonium Physics at a Fixed-Target Experiment using the LHC Beams*, Few Body Syst. **53** (2012) 11–25, arXiv:1204.5793 [hep-ph].

[505] M. Ferro-Luzzi, *Proposal for an absolute luminosity determination in colliding beam experiments using vertex detection of beam-gas interactions*, Nucl. Instrum. Meth. **A553** (2005) 388–399.

[506] LHCb Collaboration, R. Aaij et al., *First Measurement of Charm Production in its Fixed-Target Configuration at the LHC*, Phys. Rev. Lett. **122** (2019) no. 13, 132002, arXiv:1810.07907 [hep-ex].

[507] C. Hadjidakis et al., *A Fixed-Target Programme at the LHC: Physics Case and Projected Performances for Heavy-Ion, Hadron, Spin and Astroparticle Studies*, arXiv:1807.00603 [hep-ex].

[508] ALICE Collaboration, B. Abelev et al., *J/ψ Production as a Function of Charged Particle Multiplicity in pp Collisions at $\sqrt{s} = 7$ TeV*, Phys. Lett. **B712** (2012) 165–175, arXiv:1202.2816 [hep-ex].

[509] ALICE Collaboration, J. Adam et al., *Measurement of charm and beauty production at central rapidity versus charged-particle multiplicity in proton-proton collisions at $\sqrt{s} = 7$ TeV*, JHEP **09** (2015) 148, arXiv:1505.00664 [nucl-ex].

[510] ALICE Collaboration, S. G. Weber, *Measurement of J/ψ production as a function of event multiplicity in pp collisions at $\sqrt{s} = 13$ TeV with ALICE*, Nucl. Phys. **A967** (2017) 333–336, arXiv:1704.04735 [hep-ex].

[511] K. Werner, B. Guiot, I. Karpenko, and T. Pierog, *Analysing radial flow features in p-Pb and p-p collisions at several TeV by studying identified particle production in EPOS3*, Phys. Rev. **C89** (2014) no. 6, 064903, arXiv:1312.1233 [nucl-th].

[512] Y.-Q. Ma, P. Tribedy, R. Venugopalan, and K. Watanabe, *Event engineering studies for heavy flavor production and hadronization in high multiplicity hadron-hadron and hadron-nucleus collisions*, Phys. Rev. **D98** (2018) no. 7, 074025, arXiv:1803.11093 [hep-ph].

[513] E. G. Ferreiro and C. Pajares, *High multiplicity pp events and J/ψ production at LHC*, Phys. Rev. **C86** (2012) 034903, arXiv:1203.5936 [hep-ph].

[514] E. G. Ferreiro and C. Pajares, *Open charm production in high multiplicity proton-proton events at the LHC*, arXiv:1501.03381 [hep-ph].

[515] B. Z. Kopeliovich, H. J. Pirner, I. K. Potashnikova, K. Reygers, and I. Schmidt, *J/ψ in high-multiplicity pp collisions: Lessons from pA collisions*, Phys. Rev. **D88** (2013) no. 11, 116002, arXiv:1308.3638 [hep-ph].

[516] T. Sjöstrand, S. Ask, J. R. Christiansen, et al., *An Introduction to PYTHIA 8.2*, Comput. Phys. Commun. **191** (2015) 159–177, arXiv:1410.3012 [hep-ph].

[517] P. Skands, S. Carrazza, and J. Rojo, *Tuning PYTHIA 8.1: the Monash 2013 Tune*, Eur. Phys. J. **C74** (2014) no. 8, 3024, arXiv:1404.5630 [hep-ph].

[518] T. Sjöstrand, *The Development of MPI Modeling in Pythia*, Adv. Ser. Direct. High Energy Phys. **29** (2018) 191–225, arXiv:1706.02166 [hep-ph].

[519] E. G. Ferreiro, *Excited charmonium suppression in proton–nucleus collisions as a consequence of comovers*, Phys. Lett. **B749** (2015) 98–103, arXiv:1411.0549 [hep-ph].

[520] E. G. Ferreiro and J.-P. Lansberg, *Is bottomonium suppression in proton-nucleus and nucleus-nucleus collisions at LHC energies due to the same effects?*, JHEP **10** (2018) 094, arXiv:1804.04474 [hep-ph].

[521] WA98 Collaboration, M. M. Aggarwal et al., *Observation of direct photons in central 158 AGeV ^{208}Pb + ^{208}Pb collisions*, Phys. Rev. Lett. **85** (2000) 3595, arXiv:nucl-ex/0006008 [nucl-ex].

[522] T. Peitzmann and M. H. Thoma, *Direct photons from relativistic heavy ion collisions*, Phys. Rept. **364** (2002) 175–246, arXiv:hep-ph/0111114 [hep-ph].

[523] CERES Collaboration, G. Agakichiev et al., *Enhanced production of low mass electron pairs in 200 GeV/nucleon S–Au collisions at the CERN Super Proton Synchrotron*, Phys. Rev. Lett. **75** (1995) 1272–1275.

[524] CERES Collaboration, G. Agakishiev et al., *Low mass e^+e^- pair production in 158 AGeV Pb–Au collisions at the CERN SPS, its dependence on multiplicity and transverse momentum*, Phys. Lett. B **422** (1998) 405–412, arXiv:nucl-ex/9712008 [nucl-ex].

[525] CERES/NA45 Collaboration, D. Adamova et al., *Enhanced production of low mass electron pairs in 40-AGeV Pb - Au collisions at the CERN SPS*, Phys. Rev. Lett. **91** (2003) 042301, arXiv:nucl-ex/0209024 [nucl-ex].

[526] CERES Collaboration, G. Agakichiev et al., *e^+e^--pair production in Pb–Au collisions at 158 GeV per nucleon*, Eur. Phys. J. C **41** (2005) 475–513, arXiv:nucl-ex/0506002 [nucl-ex].

[527] CERES Collaboration, D. Adamova et al., *Modification of the ρ meson detected by low-mass electron–positron pairs in central Pb–Au collisions at 158 AGeV/c*, Phys. Lett. B **666** (2008) 425, arXiv:nucl-ex/0611022 [nucl-ex].

[528] NA60 Collaboration, R. Arnaldi et al., *First measurement of the ρ spectral function in high-energy nuclear collisions*, Phys. Rev. Lett. **96** (2006) 162302, arXiv:nucl-ex/0605007 [nucl-ex].

[529] NA60 Collaboration, R. Arnaldi et al., *Evidence for radial flow of thermal dileptons in high-energy nuclear collisions*, Phys. Rev. Lett. **100** (2008) 022302, arXiv:0711.1816 [nucl-ex].

[530] NA60 Collaboration, R. Arnaldi et al., *NA60 results on thermal dimuons*, Eur. Phys. J. C **61** (2009) 711, arXiv:0812.3053 [nucl-ex].

[531] NA60 Collaboration, H. J. Specht, *Thermal Dileptons from Hot and Dense Strongly Interacting Matter*, AIP Conf. Proc. **1322** (2010) 1, arXiv:1011.0615 [nucl-ex].

[532] R. Rapp, G. Chanfray, and J. Wambach, *Medium modifications of the rho meson at CERN SPS energies*, Phys. Rev. Lett. **76** (1996) 368, arXiv:hep-ph/9508353 [hep-ph].

[533] R. Rapp and J. Wambach, *Low mass dileptons at the CERN SPS: Evidence for chiral restoration?*, Eur. Phys. J. **A6** (1999) 415–420, arXiv:hep-ph/9907502 [hep-ph].

[534] R. Rapp, J. Wambach, and H. van Hees, *The Chiral Restoration Transition of QCD and Low Mass Dileptons*, Landolt-Bornstein **23** (2010) 134, arXiv:0901.3289 [hep-ph].

[535] P. M. Hohler and R. Rapp, *Is ρ-Meson Melting Compatible with Chiral Restoration?*, Phys. Lett. **B731** (2014) 103–109, arXiv:1311.2921 [hep-ph].

[536] G. Brown and M. Rho, *Scaling effective Lagrangians in a dense medium*, Phys. Rev. Lett. **66** (1991) 2720.

[537] PHENIX Collaboration, A. Adare et al., *Detailed measurement of the e^+e^- pair continuum in pp and Au–Au collisions at $\sqrt{s_{\rm NN}}$ = 200 GeV and implications for direct photon production*, Phys. Rev. C **81** (2010) 034911, arXiv:0912.0244 [nucl-ex].

[538] PHENIX Collaboration, A. Adare et al., *Dielectron production in Au–Au collisions at $\sqrt{s_{\rm NN}}$ = 200 GeV*, Phys. Rev. C **93** (2016) 014904, arXiv:1509.04667 [nucl-ex].

[539] STAR Collaboration, L. Adamczyk et al., *Dielectron mass spectra from Au–Au collisions at* $\sqrt{s_{\rm NN}}$ *= 200 GeV*, Phys. Rev. Lett. **113** (2014) 022301, arXiv:1312.7397 [hep-ex].

[540] STAR Collaboration, L. Adamczyk et al., *Energy dependence of acceptance-corrected dielectron excess mass spectrum at mid-rapidity in Au–Au collisions at* $\sqrt{s_{\rm NN}}$ *= 19.6 and 200 GeV*, Phys. Lett. B **750** (2015) 64, arXiv:1501.05341 [hep-ex].

[541] PHENIX Collaboration, A. Adare et al., *Enhanced production of direct photons in Au–Au collisions at* $\sqrt{s_{\rm NN}}$ *= 200 GeV and implications for the initial temperature*, Phys. Rev. Lett. **104** (2010) 132301, arXiv:0804.4168 [nucl-ex].

[542] PHENIX Collaboration, A. Adare et al., *Centrality dependence of low-momentum direct-photon production in Au–Au collisions at* $\sqrt{s_{\rm NN}}$ *= 200 GeV*, Phys. Rev. C **91** (2015) 064904, arXiv:1405.3940 [nucl-ex].

[543] PHENIX Collaboration, A. Adare et al., *Beam-energy and centrality dependence of direct-photon emission from ultra-relativistic heavy-ion collisions*, Submitted to: Phys. Rev. Lett. (2018) , arXiv:1805.04084 [hep-ex].

[544] PHENIX Collaboration, A. Adare et al., *Observation of direct-photon collective flow in Au–Au collisions at* $\sqrt{s_{\rm NN}}$ *= 200 GeV*, Phys. Rev. Lett. **109** (2012) 122302, arXiv:1105.4126 [nucl-ex].

[545] C. Shen, U. W. Heinz, J.-F. Paquet, and C. Gale, *Thermal photons as a quark-gluon plasma thermometer reexamined*, Phys. Rev. **C89** (2014) no. 4, 044910, arXiv:1308.2440 [nucl-th].

[546] H. van Hees, C. Gale, and R. Rapp, *Thermal Photons and Collective Flow at the Relativistic Heavy-Ion Collider*, Phys. Rev. **C84** (2011) 054906, arXiv:1108.2131 [hep-ph].

[547] ALICE Collaboration, K. Aamodt et al., *The ALICE experiment at the CERN LHC*, JINST **3** (2008) S08002.

[548] ALICE Collaboration, J. Adam et al., *Direct photon production in Pb–Pb collisions at* $\sqrt{s_{\rm NN}}$ *= 2.76 TeV*, Phys. Lett. B **754** (2016) 235, arXiv:1509.07324 [nucl-ex].

[549] ALICE Collaboration, S. Acharya et al., *Direct photon elliptic flow in Pb-Pb collisions at* $\sqrt{s_{\rm NN}}$ *= 2.76 TeV*, Phys. Lett. **B789** (2019) 308–322, arXiv:1805.04403 [nucl-ex].

[550] C. Shen, J.-F. Paquet, G. S. Denicol, S. Jeon, and C. Gale, *Collectivity and electromagnetic radiation in small systems*, Phys. Rev. **C95** (2017) no. 1, 014906, arXiv:1609.02590 [nucl-th].

[551] P. Dasgupta, S. De, R. Chatterjee, and D. K. Srivastava, *Photon production from Pb+Pb collisions at* $\sqrt{s_{\rm NN}}$ *= 5.02 TeV at LHC and at* $\sqrt{s_{\rm NN}}$ *= 39 TeV at FCC*, Phys. Rev. **C98** (2018) no. 2, 024911, arXiv:1804.02828 [nucl-th].

[552] H. van Hees, M. He, and R. Rapp, *Pseudo-critical enhancement of thermal photons in relativistic heavy-ion collisions?*, Nucl. Phys. **A933** (2015) 256–271, arXiv:1404.2846 [nucl-th].

[553] J.-F. Paquet, *Electromagnetic probes of heavy ion collisions: recent developments*, Nucl. Part. Phys. Proc. **289-290** (2017) 89–94, arXiv:1612.07359 [nucl-th].

[554] J.-F. Paquet, *Probing the space-time evolution of heavy ion collisions with photons and dileptons*, Nucl. Phys. **A967** (2017) 184–191, arXiv:1704.07842 [nucl-th].

[555] ALICE Collaboration, S. Acharya et al., *Measurement of dielectron production in central Pb-Pb collisions at* $\sqrt{s_{\rm NN}}$ *= 2.76 TeV*, Phys. Rev. **C99** (2019) no. 2, 024002, arXiv:1807.00923 [nucl-ex].

[556] ALICE Collaboration, S. Acharya et al., *Dielectron production in proton-proton collisions at* $\sqrt{s} = 7$ *TeV*, JHEP **09** (2018) 064, arXiv:1805.04391 [hep-ex].

[557] ALICE Collaboration, S. Acharya et al., *Dielectron and heavy-quark production in inelastic and high-multiplicity proton–proton collisions at $\sqrt{s_{NN}} = 13TeV$*, Phys. Lett. **B788** (2019) 505–518, arXiv:1805.04407 [hep-ex].

[558] R. Rapp, *Theory of Soft Electromagnetic Emission in Heavy-Ion Collisions*, Acta Phys. Polon. **B42** (2011) 2823–2852, arXiv:1110.4345 [nucl-th].

[559] R. Rapp, *Signatures of thermal dilepton radiation at RHIC*, Phys. Rev. **C63** (2001) 054907, arXiv:hep-ph/0010101 [hep-ph].

[560] H. van Hees and R. Rapp, *Dilepton Radiation at the CERN Super Proton Synchrotron*, Nucl. Phys. **A806** (2008) 339–387, arXiv:0711.3444 [hep-ph].

[561] M. He, R. J. Fries, and R. Rapp, *Ideal Hydrodynamics for Bulk and Multistrange Hadrons in $\sqrt{s_{NN}}$=200 AGeV Au-Au Collisions*, Phys. Rev. **C85** (2012) 044911, arXiv:1112.5894 [nucl-th].

[562] O. Linnyk, E. L. Bratkovskaya, and W. Cassing, *Effective QCD and transport description of dilepton and photon production in heavy-ion collisions and elementary processes*, Prog. Part. Nucl. Phys. **87** (2016) 50–115, arXiv:1512.08126 [nucl-th].

[563] W. Cassing and E. L. Bratkovskaya, *Parton-Hadron-String Dynamics: an off-shell transport approach for relativistic energies*, Nucl. Phys. **A831** (2009) 215–242, arXiv:0907.5331 [nucl-th].

[564] E. L. Bratkovskaya and W. Cassing, *Dilepton production and off-shell transport dynamics at SIS energies*, Nucl. Phys. **A807** (2008) 214–250, arXiv:0712.0635 [nucl-th].

[565] O. Linnyk, *Dilepton production by dynamical quasiparticles in the strongly interacting quark gluon plasma*, J. Phys. **G38** (2011) 025105, arXiv:1004.2591 [hep-ph].

[566] J. Ghiglieri, O. Kaczmarek, M. Laine, and F. Meyer, *Lattice constraints on the thermal photon rate*, Phys. Rev. **D94** (2016) no. 1, 016005, arXiv:1604.07544 [hep-lat].

[567] G. Aarts, C. Allton, A. Amato, et al., *Electrical conductivity and charge diffusion in thermal QCD from the lattice*, JHEP **02** (2015) 186, arXiv:1412.6411 [hep-lat].

[568] H.-T. Ding, O. Kaczmarek, and F. Meyer, *Thermal dilepton rates and electrical conductivity of the QGP from the lattice*, Phys. Rev. **D94** (2016) no. 3, 034504, arXiv:1604.06712 [hep-lat].

[569] G. Aarts and J. M. Martinez Resco, *Continuum and lattice meson spectral functions at nonzero momentum and high temperature*, Nucl. Phys. **B726** (2005) 93–108, arXiv:hep-lat/0507004 [hep-lat].

[570] B. B. Brandt, A. Francis, B. Jäger, and H. B. Meyer, *Charge transport and vector meson dissociation across the thermal phase transition in lattice QCD with two light quark flavors*, Phys. Rev. **D93** (2016) no. 5, 054510, arXiv:1512.07249 [hep-lat].

[571] C. Jung, F. Rennecke, R.-A. Tripolt, L. von Smekal, and J. Wambach, *In-Medium Spectral Functions of Vector- and Axial-Vector Mesons from the Functional Renormalization Group*, Phys. Rev. **D95** (2017) no. 3, 036020, arXiv:1610.08754 [hep-ph].

[572] G. Vujanovic, J.-F. Paquet, S. Ryu, et al., *Bulk viscous effects on flow and dilepton radiation in a hybrid approach*, Nucl. Phys. **A967** (2017) 692–695, arXiv:1704.04687 [nucl-th].

[573] G. Vujanovic, G. S. Denicol, M. Luzum, S. Jeon, and C. Gale, *Investigating the temperature dependence of the specific shear viscosity of QCD matter with dilepton radiation*, Phys. Rev. **C98** (2018) no. 1, 014902, arXiv:1702.02941 [nucl-th].

[574] G. Vujanovic, J.-F. Paquet, G. S. Denicol, et al., *Electromagnetic radiation as a probe of the initial state and of viscous dynamics in relativistic nuclear collisions*, Phys. Rev. **C94** (2016) no. 1, 014904, arXiv:1602.01455 [nucl-th].

[575] C. Gale, Y. Hidaka, S. Jeon, et al., *Production and Elliptic Flow of Dileptons and Photons in a Matrix Model of the Quark-Gluon Plasma*, Phys. Rev. Lett. **114** (2015) 072301, arXiv:1409.4778 [hep-ph].

[576] R. Chatterjee, P. Dasgupta, and D. K. Srivastava, *Anisotropic flow of thermal photons at energies available at the BNL Relativistic Heavy Ion Collider and at the CERN Large Hadron Collider*, Phys. Rev. **C96** (2017) no. 1, 014911, arXiv:1702.02378 [nucl-th].

[577] O. Linnyk, V. Konchakovski, T. Steinert, W. Cassing, and E. L. Bratkovskaya, *Hadronic and partonic sources of direct photons in relativistic heavy-ion collisions*, Phys. Rev. **C92** (2015) no. 5, 054914, arXiv:1504.05699 [nucl-th].

[578] T. Sjostrand, S. Mrenna, and P. Z. Skands, *PYTHIA 6.4 Physics and Manual*, JHEP **05** (2006) 026, arXiv:hep-ph/0603175 [hep-ph].

[579] X.-N. Wang and M. Gyulassy, *HIJING: A Monte Carlo model for multiple jet production in p p, p A and A A collisions*, Phys. Rev. **D44** (1991) 3501–3516.

[580] R. Brun, F. Bruyant, F. Carminati, et al., *GEANT: Detector Description and Simulation Tool; Oct 1994*, , Geneva, 1993. Long Writeup W5013.

[581] G. Vujanovic, J.-F. Paquet, C. Shen, et al., *Dilepton radiation and bulk viscosity in heavy-ion collisions*, Nucl. Part. Phys. Proc. **289-290** (2017) 165–168, arXiv:1703.06164 [nucl-th].

[582] C. A. Bertulani, S. R. Klein, and J. Nystrand, *Physics of ultra-peripheral nuclear collisions*, Ann. Rev. Nucl. Part. Sci. **55** (2005) 271–310, arXiv:nucl-ex/0502005 [nucl-ex].

[583] ALICE Collaboration, J. Adam et al., *Measurement of an excess in the yield of J/ψ at very low $p_{\rm T}$ in Pb-Pb collisions at $\sqrt{s_{\rm NN}}$ = 2.76 TeV*, Phys. Rev. Lett. **116** (2016) no. 22, 222301, arXiv:1509.08802 [nucl-ex].

[584] STAR Collaboration, J. Adam et al., *Low-p_T e^+e^- pair production in Au+Au collisions at $\sqrt{s_{NN}}$ = 200 GeV and U+U collisions at $\sqrt{s_{NN}}$ = 193 GeV at STAR*, Phys. Rev. Lett. **121** (2018) no. 13, 132301, arXiv:1806.02295 [hep-ex].

[585] W. Zha, *Excess of J/ψ Production at Very Low Transverse Momenta in A+A Collisions from STAR*, Int. J. Mod. Phys. Conf. Ser. **46** (2018) 1860012.

[586] ATLAS Collaboration, M. Aaboud et al., *Observation of centrality-dependent acoplanarity for muon pairs produced via two-photon scattering in Pb+Pb collisions at $\sqrt{s_{\rm NN}} = 5.02$ TeV with the ATLAS detector*, Phys. Rev. Lett. **121** (2018) no. 21, 212301, arXiv:1806.08708 [nucl-ex].

[587] A. J. Baltz, *The Physics of Ultraperipheral Collisions at the LHC*, Phys. Rept. **458** (2008) 1–171, arXiv:0706.3356 [nucl-ex].

[588] S. Klein and J. Nystrand, *Ultraperipheral nuclear collisions*, Phys. Today **70** (2017) no. 10, 40–47.

[589] C. A. Bertulani and G. Baur, *Electromagnetic Processes in Relativistic Heavy Ion Collisions*, Phys. Rept. **163** (1988) 299.

[590] G. Baur, K. Hencken, D. Trautmann, S. Sadovsky, and Y. Kharlov, *Coherent gamma gamma and gamma-A interactions in very peripheral collisions at relativistic ion colliders*, Phys. Rept. **364** (2002) 359–450, arXiv:hep-ph/0112211 [hep-ph].

[591] M. Vidovic, M. Greiner, C. Best, and G. Soff, *Impact parameter dependence of the electromagnetic particle production in ultrarelativistic heavy ion collisions*, Phys. Rev. **C47** (1993) 2308–2319.

[592] W. Zha, S. R. Klein, R. Ma, et al., *Coherent J/ψ photoproduction in hadronic heavy-ion collisions*, Phys. Rev. **C97** (2018) no. 4, 044910, arXiv:1705.01460 [nucl-th].

[593] STAR Collaboration, J. Adams et al., *Production of e+ e- pairs accompanied by nuclear dissociation in ultra-peripheral heavy ion collision*, Phys. Rev. **C70** (2004) 031902, arXiv:nucl-ex/0404012 [nucl-ex].

[594] S. R. Klein, *Two-photon production of dilepton pairs in peripheral heavy ion collisions*, Phys. Rev. **C97** (2018) no. 5, 054903, arXiv:1801.04320 [nucl-th].

[595] W. Zha, L. Ruan, Z. Tang, Z. Xu, and S. Yang, *Coherent lepton pair production in hadronic heavy ion collisions*, Phys. Lett. **B781** (2018) 182–186, arXiv:1804.01813 [hep-ph].

[596] M. Kłusek-Gawenda, R. Rapp, W. Schäfer, and A. Szczurek, *Dilepton Radiation in Heavy-Ion Collisions at Small Transverse Momentum*, Phys. Lett. **B790** (2019) 339–344, arXiv:1809.07049 [nucl-th].

[597] A. J. Baltz, Y. Gorbunov, S. R. Klein, and J. Nystrand, *Two-Photon Interactions with Nuclear Breakup in Relativistic Heavy Ion Collisions*, Phys. Rev. **C80** (2009) 044902, arXiv:0907.1214 [nucl-ex].

[598] S. R. Klein, J. Nystrand, J. Seger, Y. Gorbunov, and J. Butterworth, *STARlight: A Monte Carlo simulation program for ultra-peripheral collisions of relativistic ions*, Comput. Phys. Commun. **212** (2017) 258–268, arXiv:1607.03838 [hep-ph].

[599] S. Klein, A. H. Mueller, B.-W. Xiao, and F. Yuan, *Acoplanarity of a Lepton Pair to Probe the Electromagnetic Property of Quark Matter*, Phys. Rev. Lett. **122** (2019) no. 13, 132301, arXiv:1811.05519 [hep-ph].

[600] D. E. Kharzeev, K. Landsteiner, A. Schmitt, and H.-U. Yee, *'Strongly interacting matter in magnetic fields': an overview*, Lect. Notes Phys. **871** (2013) 1–11, arXiv:1211.6245 [hep-ph].

[601] M. Klusek-Gawenda and A. Szczurek, *Photoproduction of J/ψ mesons in peripheral and semicentral heavy ion collisions*, Phys. Rev. **C93** (2016) no. 4, 044912, arXiv:1509.03173 [nucl-th].

[602] STAR Collaboration, B. I. Abelev et al., *Observation of Two-source Interference in the Photoproduction Reaction Au Au —> Au Au rho0*, Phys. Rev. Lett. **102** (2009) 112301, arXiv:0812.1063 [nucl-ex].

[603] S. R. Klein and J. Nystrand, *Interference in exclusive vector meson production in heavy ion collisions*, Phys. Rev. Lett. **84** (2000) 2330–2333, arXiv:hep-ph/9909237 [hep-ph].

[604] Planck Collaboration, P. A. R. Ade et al., *Planck 2013 results. XXII. Constraints on inflation*, Astron. Astrophys. **571** (2014) A22, arXiv:1303.5082 [astro-ph.CO].

[605] J. Alexander et al., *Dark Sectors 2016 Workshop: Community Report*, 2016. arXiv:1608.08632 [hep-ph]. http://lss.fnal.gov/archive/2016/conf/fermilab-conf-16-421.pdf.

[606] PAMELA Collaboration, O. Adriani et al., *An anomalous positron abundance in cosmic rays with energies 1.5-100 GeV*, Nature **458** (2009) 607–609, arXiv:0810.4995 [astro-ph].

[607] Fermi-LAT Collaboration, M. Ackermann et al., *Measurement of separate cosmic-ray electron and positron spectra with the Fermi Large Area Telescope*, Phys. Rev. Lett. **108** (2012) 011103, arXiv:1109.0521 [astro-ph.HE].

[608] AMS Collaboration, M. Aguilar et al., *First Result from the Alpha Magnetic Spectrometer on the International Space Station: Precision Measurement of the Positron Fraction in Primary Cosmic Rays of 0.5-350 GeV*, Phys. Rev. Lett. **110** (2013) 141102.

[609] Muon g-2 Collaboration, G. W. Bennett et al., *Final Report of the Muon E821 Anomalous Magnetic Moment Measurement at BNL*, Phys. Rev. **D73** (2006) 072003, arXiv:hep-ex/0602035 [hep-ex].

[610] E. M. Riordan et al., *A Search for Short Lived Axions in an Electron Beam Dump Experiment*, Phys. Rev. Lett. **59** (1987) 755.

[611] J. D. Bjorken, S. Ecklund, W. R. Nelson, et al., *Search for Neutral Metastable Penetrating Particles Produced in the SLAC Beam Dump*, Phys. Rev. **D38** (1988) 3375.

[612] A. Bross, M. Crisler, S. H. Pordes, et al., *A Search for Shortlived Particles Produced in an Electron Beam Dump*, Phys. Rev. Lett. **67** (1991) 2942–2945.

[613] H. Merkel et al., *Search at the Mainz Microtron for Light Massive Gauge Bosons Relevant for the Muon g-2 Anomaly*, Phys. Rev. Lett. **112** (2014) no. 22, 221802, arXiv:1404.5502 [hep-ex].

[614] APEX Collaboration, S. Abrahamyan et al., *Search for a New Gauge Boson in Electron-Nucleus Fixed-Target Scattering by the APEX Experiment*, Phys. Rev. Lett. **107** (2011) 191804, arXiv:1108.2750 [hep-ex].

[615] J. Balewski et al., *DarkLight: A Search for Dark Forces at the Jefferson Laboratory Free-Electron Laser Facility*, in *Proceedings, 2013 Community Summer Study on the Future of U.S. Particle Physics: Snowmass on the Mississippi (CSS2013): Minneapolis, MN, USA, July 29-August 6, 2013*. 2013. arXiv:1307.4432 [physics.ins-det]. https://misportal.jlab.org/ul/publications/view_pub.cfm?pub_id=12467.

[616] BaBar Collaboration, J. P. Lees et al., *Search for a Dark Photon in e^+e^- Collisions at BaBar*, Phys. Rev. Lett. **113** (2014) no. 20, 201801, arXiv:1406.2980 [hep-ex].

[617] NA48/2 Collaboration, J. R. Batley et al., *Search for the dark photon in π^0 decays*, Phys. Lett. **B746** (2015) 178–185, arXiv:1504.00607 [hep-ex].

[618] WASA-at-COSY Collaboration, P. Moskal, *Search for a dark photon with the WASA detector at COSY*, in *Proceedings, 49th Rencontres de Moriond on QCD and High Energy Interactions: La Thuile, Italy, March 22-29, 2014*, pp. 237–242. 2014. arXiv:1406.5738 [nucl-ex].

[619] HADES Collaboration, G. Agakishiev et al., *Searching a Dark Photon with HADES*, Phys. Lett. **B731** (2014) 265–271, arXiv:1311.0216 [hep-ex].

[620] PHENIX Collaboration, A. Adare et al., *Search for dark photons from neutral meson decays in $p+p$ and d + Au collisions at $\sqrt{s_{NN}} = 200$ GeV*, Phys. Rev. **C91** (2015) no. 3, 031901, arXiv:1409.0851 [nucl-ex].

[621] LHCb Collaboration, R. Aaij et al., *Search for Dark Photons Produced in 13 TeV pp Collisions*, Phys. Rev. Lett. **120** (2018) no. 6, 061801, arXiv:1710.02867 [hep-ex].

[622] KLOE-2 Collaboration, F. Archilli et al., *Search for a vector gauge boson in ϕ meson decays with the KLOE detector*, Phys. Lett. **B706** (2012) 251–255, arXiv:1110.0411 [hep-ex].

[623] M. Ardid, I. Felis, A. Herrero, and J. A. Martínez-Mora, *Constraining Secluded Dark Matter models with the public data from the 79-string IceCube search for dark matter in the Sun*, JCAP **1704** (2017) no. 04, 010, arXiv:1701.08863 [astro-ph.HE].

[624] P. Ilten, Y. Soreq, M. Williams, and W. Xue, *Serendipity in dark photon searches*, JHEP **06** (2018) 004, arXiv:1801.04847 [hep-ph].

[625] P. Ilten, Y. Soreq, J. Thaler, M. Williams, and W. Xue, *Proposed Inclusive Dark Photon Search at LHCb*, Phys. Rev. Lett. **116** (2016) no. 25, 251803, arXiv:1603.08926 [hep-ph].

[626] G. Baym, T. Hatsuda, and M. Strickland, *Virtual photon polarization in ultrarelativistic heavy-ion collisions*, Phys. Rev. **C95** (2017) no. 4, 044907, arXiv:1702.05906 [nucl-th].

[627] NA60 Collaboration, R. Arnaldi et al., *First results on angular distributions of thermal dileptons in nuclear collisions*, Phys. Rev. Lett. **102** (2009) 222301, arXiv:0812.3100 [nucl-ex].

[628] J. C. Collins and D. E. Soper, *Angular Distribution of Dileptons in High-Energy Hadron Collisions*, Phys. Rev. **D16** (1977) 2219.

[629] C. S. Lam and W.-K. Tung, *A Systematic Approach to Inclusive Lepton Pair Production in Hadronic Collisions*, Phys. Rev. **D18** (1978) 2447.

[630] C. S. Lam and W.-K. Tung, *A Parton Model Relation Sans QCD Modifications in Lepton Pair Productions*, Phys. Rev. **D21** (1980) 2712.

[631] WA98 Collaboration, M. M. Aggarwal et al., *Interferometry of direct photons in central Pb-208+Pb-208 collisions at 158-A-GeV*, Phys. Rev. Lett. **93** (2004) 022301, arXiv:nucl-ex/0310022 [nucl-ex].

[632] J. Bellm et al., *Herwig 7.0/Herwig++ 3.0 release note*, Eur. Phys. J. **C76** (2016) no. 4, 196, arXiv:1512.01178 [hep-ph].

[633] B. Andersson, G. Gustafson, G. Ingelman, and T. Sjostrand, *Parton Fragmentation and String Dynamics*, Phys. Rept. **97** (1983) 31–145.

[634] B. R. Webber, *A QCD Model for Jet Fragmentation Including Soft Gluon Interference*, Nucl. Phys. **B238** (1984) 492–528.

[635] N. Fischer and T. Sjöstrand, *Thermodynamical String Fragmentation*, JHEP **01** (2017) 140, arXiv:1610.09818 [hep-ph].

[636] ATLAS Collaboration, G. Aad et al., *Observation of Long-Range Elliptic Azimuthal Anisotropies in $\sqrt{s}$ =13 and 2.76 TeV pp Collisions with the ATLAS Detector*, Phys. Rev. Lett. **116** (2016) no. 17, 172301, arXiv:1509.04776 [hep-ex].

[637] CMS Collaboration, V. Khachatryan et al., *Measurement of long-range near-side two-particle angular correlations in pp collisions at $\sqrt{s}$ =13 TeV*, Phys. Rev. Lett. **116** (2016) no. 17, 172302, arXiv:1510.03068 [nucl-ex].

[638] CMS Collaboration, V. Khachatryan et al., *Strange Particle Production in pp Collisions at $\sqrt{s} = 0.9$ and 7 TeV*, JHEP **05** (2011) 064, arXiv:1102.4282 [hep-ex].

[639] LHCb Collaboration, R. Aaij et al., *Measurement of prompt hadron production ratios in pp collisions at $\sqrt{s} = 0.9$ and 7 TeV*, Eur. Phys. J. **C72** (2012) 2168, arXiv:1206.5160 [hep-ex].

[640] ALICE Collaboration, K. Aamodt et al., *Strange particle production in proton-proton collisions at sqrt(s) = 0.9 TeV with ALICE at the LHC*, Eur. Phys. J. **C71** (2011) 1594, arXiv:1012.3257 [hep-ex].

[641] ALICE Collaboration, B. Abelev et al., *Multi-strange baryon production in pp collisions at $\sqrt{s} = 7$ TeV with ALICE*, Phys. Lett. **B712** (2012) 309–318, arXiv:1204.0282 [nucl-ex].

[642] ALICE Collaboration, J. Adam et al., *Enhanced production of multi-strange hadrons in high-multiplicity proton-proton collisions*, Nature Phys. **13** (2017) 535–539, arXiv:1606.07424 [nucl-ex].

[643] C. Bierlich, G. Gustafson, L. Lönnblad, and A. Tarasov, *Effects of Overlapping Strings in pp Collisions*, JHEP **03** (2015) 148, arXiv:1412.6259 [hep-ph].

[644] S. Gieseke, P. Kirchgaeßer, and S. Plätzer, *Baryon production from cluster hadronisation*, Eur. Phys. J. **C78** (2018) no. 2, 99, arXiv:1710.10906 [hep-ph].

[645] C. Bierlich, G. Gustafson, and L. Lönnblad, *Collectivity without plasma in hadronic collisions*, Phys. Lett. **B779** (2018) 58–63, arXiv:1710.09725 [hep-ph].

[646] B. Andersson, G. Gustafson, and B. Nilsson-Almqvist, *A Model for Low p(t) Hadronic Reactions, with Generalizations to Hadron - Nucleus and Nucleus-Nucleus Collisions*, Nucl. Phys. **B281** (1987) 289–309.

[647] C. Bierlich, G. Gustafson, L. Lönnblad, and H. Shah, *The Angantyr model for Heavy-Ion Collisions in PYTHIA8*, JHEP **10** (2018) 134, arXiv:1806.10820 [hep-ph]. [JHEP18,134(2020)].

[648] J. Bellm and C. Bierlich, *PISTA: Posterior Ion STAcking*, arXiv:1807.01291 [hep-ph].

[649] K. Werner, *Core-corona separation in ultra-relativistic heavy ion collisions*, Phys. Rev. Lett. **98** (2007) 152301, arXiv:0704.1270 [nucl-th].

[650] PHENIX Collaboration, C. Aidala et al., *Creation of quark–gluon plasma droplets with three distinct geometries*, Nature Phys. **15** (2019) no. 3, 214–220, arXiv:1805.02973 [nucl-ex].

[651] B. Schenke, S. Schlichting, P. Tribedy, and R. Venugopalan, *Mass ordering of spectra from fragmentation of saturated gluon states in high multiplicity proton-proton collisions*, Phys. Rev. Lett. **117** (2016) no. 16, 162301, arXiv:1607.02496 [hep-ph].

[652] P. Braun-Munzinger, K. Redlich, and J. Stachel, *Particle production in heavy ion collisions*, arXiv:nucl-th/0304013 [nucl-th].

[653] ALICE Collaboration, S. Acharya et al., *Multiplicity dependence of light-flavor hadron production in pp collisions at* $\sqrt{s}$ *= 7 TeV*, Phys. Rev. **C99** (2019) no. 2, 024906, arXiv:1807.11321 [nucl-ex].

[654] M. Mace, V. V. Skokov, P. Tribedy, and R. Venugopalan, *Hierarchy of azimuthal anisotropy harmonics in collisions of small systems from the Color Glass Condensate*, Phys. Rev. Lett. **121** (2018) no. 5, 052301, arXiv:1805.09342 [hep-ph].

[655] J. L. Nagle and W. A. Zajc, *Assessing saturation physics explanations of collectivity in small collision systems with the IP-Jazma model*, arXiv:1808.01276 [nucl-th].

[656] ATLAS Collaboration, *Measurement of long-range azimuthal correlations in* Z*-boson tagged* pp *collisions at* $\sqrt{s} = 8$ *TeV*, ATLAS-CONF-2017-068, CERN, Geneva, Sep, 2017. http://cds.cern.ch/record/2285806.

[657] S. Argyropoulos and T. Sjöstrand, *Effects of color reconnection on* $t\bar{t}$ *final states at the LHC*, JHEP **11** (2014) 043, arXiv:1407.6653 [hep-ph].

[658] ALICE Collaboration, B. Abelev et al., *Pion, kaon, and proton production in central PbPb collisions at* $\sqrt{s_{\rm NN}} = 2.76$ *TeV*, Phys. Rev. Lett. **109** (2012) 252301, arXiv:1208.1974 [hep-ex].

[659] E. Shuryak and I. Zahed, *High-multiplicity pp and pA collisions: Hydrodynamics at its edge*, Phys. Rev. **C88** (2013) no. 4, 044915, arXiv:1301.4470 [hep-ph].

[660] ALICE Collaboration, C. Andrei, *Light flavor hadron spectra at low* p_T *and search for collective phenomena in high multiplicity pp, p–Pb and Pb–Pb collisions measured with the ALICE experiment*, Nucl. Phys. **A931** (2014) 888–892, arXiv:1408.0093 [hep-ex].

[661] ALICE Collaboration, B. Abelev et al., K^0_S *and* Λ *production in PbPb collisions at* $\sqrt{s_{\rm NN}} = 2.76$ *TeV*, Phys. Rev. Lett. **111** (2013) 222301, arXiv:1307.5530 [nucl-ex].

[662] ALICE Collaboration, B. B. Abelev et al., $K^*(892)^0$ *and* $\phi(1020)$ *production in PbPb collisions at* $\sqrt{s_{\rm NN}} = 2.76$ *TeV*, Phys. Rev. **C91** (2015) 024609, arXiv:1404.0495 [nucl-ex].

[663] CMS Collaboration, V. Khachatryan et al., *Multiplicity and rapidity dependence of strange hadron production in pp, pPb, and PbPb collisions at the LHC*, Phys. Lett. **B768** (2017) 103–129, arXiv:1605.06699 [nucl-ex].

[664] ALICE Collaboration, J. Adam et al., ϕ*-meson production at forward rapidity in p-Pb collisions at* $\sqrt{s_{\rm NN}}$ *= 5.02 TeV and in pp collisions at* $\sqrt{s}$ *= 2.76 TeV*, Phys. Lett. **B768** (2017) 203–217, arXiv:1506.09206 [nucl-ex].

[665] ALICE Collaboration, J. Adam et al., *Multiplicity dependence of charged pion, kaon, and (anti)proton production at large transverse momentum in p-Pb collisions at* $\sqrt{s_{\rm NN}}$ *= 5.02 TeV*, Phys. Lett. **B760** (2016) 720–735, arXiv:1601.03658 [nucl-ex].

[666] ALICE Collaboration, J. Adam et al., $K^*(892)^0$ *and* $\phi(1020)$ *meson production at high transverse momentum in pp and Pb-Pb collisions at* $\sqrt{s_{\rm NN}}$ *= 2.76 TeV*, Phys. Rev. **C95** (2017) no. 6, 064606, arXiv:1702.00555 [nucl-ex].

[667] ALICE Collaboration, J. Adam et al., *Production of* $K^*(892)^0$ *and* $\phi(1020)$ *in p?Pb collisions at* $\sqrt{s_{NN}}$ *= 5.02 TeV*, Eur. Phys. J. **C76** (2016) no. 5, 245, arXiv:1601.07868 [nucl-ex].

[668] ALICE Collaboration, B. B. Abelev et al., *Multi-strange baryon production at mid-rapidity in PbPb collisions at* $\sqrt{s_{\rm NN}} = 2.76$ *TeV*, Phys. Lett. **B728** (2014) 216–227, arXiv:1307.5543 [nucl-ex].

[669] C. Loizides, *Experimental overview on small collision systems at the LHC*, Nucl. Phys. **A956** (2016) 200–207, arXiv:1602.09138 [nucl-ex].

[670] CMS Collaboration, S. Chatrchyan et al., *Study of the production of charged pions, kaons, and protons in pPb collisions at* $\sqrt{s_{\rm NN}} = 5.02$ *TeV*, Eur. Phys. J. **C74** (2014) no. 6, 2847, arXiv:1307.3442 [hep-ex].

[671] CMS Collaboration, S. Chatrchyan et al., *Study of the inclusive production of charged pions, kaons, and protons in pp collisions at* $\sqrt{s} = 0.9$*, 2.76, and 7 TeV*, Eur. Phys. J. **C72** (2012) 2164, arXiv:1207.4724 [hep-ex].

[672] M. Floris, *Hadron yields and the phase diagram of strongly interacting matter*, Nucl. Phys. **A931** (2014) 103–112, arXiv:1408.6403 [nucl-ex].

[673] ALICE Collaboration, J. Adam et al., *Centrality dependence of pion freeze-out radii in Pb-Pb collisions at* $\sqrt{s}_{NN} = 2.76$ *TeV*, Phys. Rev. **C93** (2016) no. 2, 024905, arXiv:1507.06842 [nucl-ex].

[674] ALICE Collaboration, J. Adam et al., *One-dimensional pion, kaon, and proton femtoscopy in PbPb collisions at* $\sqrt{s_{\rm NN}} = 2.76$ *TeV*, Phys. Rev. **C92** (2015) no. 5, 054908, arXiv:1506.07884 [nucl-ex].

[675] ALICE Collaboration, B. Abelev et al., *Freeze-out radii extracted from three-pion cumulants in pp, pPb and PbPb collisions at the LHC*, Phys. Lett. **B739** (2014) 139–151, arXiv:1404.1194 [nucl-ex].

[676] ALICE Collaboration, J. Adam et al., *Two-pion femtoscopy in pPb collisions at* $\sqrt{s_{\rm NN}} = 5.02$ *TeV*, Phys. Rev. **C91** (2015) 034906, arXiv:1502.00559 [nucl-ex].

[677] ALICE Collaboration, K. Aamodt et al., *Femtoscopy of pp collisions at* $\sqrt{s} = 0.9$ *and 7 TeV at the LHC with two-pion Bose-Einstein correlations*, Phys. Rev. **D84** (2011) 112004, arXiv:1101.3665 [hep-ex].

[678] CMS Collaboration, *Femtoscopy with identified charged hadrons in pp, pPb, and peripheral PbPb collisions at LHC energies*, CMS-PAS-HIN-14-013, CERN, Geneva, 2014. https://cds.cern.ch/record/1703272.

[679] ALICE Collaboration, S. Acharya et al., *Kaon femtoscopy in Pb-Pb collisions at* $\sqrt{s_{\rm NN}}$ *= 2.76 TeV*, Phys. Rev. **C96** (2017) no. 6, 064613, arXiv:1709.01731 [nucl-ex].

[680] ATLAS Collaboration, M. Aaboud et al., *Femtoscopy with identified charged pions in proton-lead collisions at* $\sqrt{s_{\rm NN}} = 5.02$ *TeV with ATLAS*, Phys. Rev. **C96** (2017) no. 6, 064908, arXiv:1704.01621 [hep-ex].

[681] ALICE Collaboration, K. Aamodt et al., *Harmonic decomposition of two-particle angular correlations in* Pb–Pb *collisions at* $s_{NN} = 2.76$ *TeV*, Phys. Lett. **B708** (2012) 249–264, arXiv:1109.2501 [nucl-ex].

[682] CMS Collaboration, S. Chatrchyan et al., *Long-range and short-range dihadron angular correlations in central* Pb–Pb *collisions at a nucleon-nucleon center of mass energy of 2.76 TeV*, JHEP **07** (2011) 076, arXiv:1105.2438 [nucl-ex].

[683] CMS Collaboration, S. Chatrchyan et al., *Centrality dependence of dihadron correlations and azimuthal anisotropy harmonics in* Pb–Pb *collisions at* $s_{_{NN}} = 2.76$ *TeV*, Eur. Phys. J. **C72** (2012) 2012, arXiv:1201.3158 [nucl-ex].

[684] ATLAS Collaboration, G. Aad et al., *Measurement of the azimuthal anisotropy for charged particle production in* $s_{_{NN}} = 2.76$ *TeV lead-lead collisions with the ATLAS detector*, Phys. Rev. **C86** (2012) 014907, arXiv:1203.3087 [hep-ex].

[685] ATLAS Collaboration, G. Aad et al., *Measurement of long-range pseudorapidity correlations and azimuthal harmonics in* $\sqrt{s_{_{NN}}} = 5.02$ *TeV proton-lead collisions with the ATLAS detector*, Phys. Rev. **C90** (2014) no. 4, 044906, arXiv:1409.1792 [hep-ex].

[686] CMS Collaboration, V. Khachatryan et al., *Evidence for collectivity in pp collisions at the LHC*, Phys. Lett. **B765** (2017) 193–220, arXiv:1606.06198 [nucl-ex].

[687] ALICE Collaboration, S. Acharya et al., *Searches for transverse momentum dependent flow vector fluctuations in Pb-Pb and p-Pb collisions at the LHC*, JHEP **09** (2017) 032, arXiv:1707.05690 [nucl-ex].

[688] ALICE Collaboration, J. Adam et al., *Pseudorapidity dependence of the anisotropic flow of charged particles in Pb-Pb collisions at* $\sqrt{s_{\rm NN}} = 2.76$ *TeV*, Phys. Lett. **B762** (2016) 376–388, arXiv:1605.02035 [nucl-ex].

[689] ALICE Collaboration, J. Adam et al., *Higher harmonic flow coefficients of identified hadrons in Pb-Pb collisions at* $\sqrt{s_{\rm NN}}$ *= 2.76 TeV*, JHEP **09** (2016) 164, arXiv:1606.06057 [nucl-ex].

[690] CMS Collaboration, A. M. Sirunyan et al., *Observation of Correlated Azimuthal Anisotropy Fourier Harmonics in pp and* $p+Pb$ *Collisions at the LHC*, Phys. Rev. Lett. **120** (2018) no. 9, 092301, arXiv:1709.09189 [nucl-ex].

[691] ATLAS Collaboration, M. Aaboud et al., *Measurement of multi-particle azimuthal correlations in pp, p+Pb and low-multiplicity Pb+Pb collisions with the ATLAS detector*, Eur. Phys. J. **C77** (2017) no. 6, 428, arXiv:1705.04176 [hep-ex].

[692] ALICE Collaboration, B. Abelev et al., *Elliptic flow of identified hadrons in* Pb–Pb *collisions at* $s_{_{NN}} = 2.76$ *TeV*, JHEP **06** (2015) 190, arXiv:1405.4632 [nucl-ex].

[693] ALICE Collaboration, B. Abelev et al., *Anisotropic flow of charged hadrons, pions and (anti-)protons measured at high transverse momentum in* Pb–Pb *collisions at* $s_{_{NN}} = 2.76$ *TeV*, Phys. Lett. **B719** (2013) 18–28, arXiv:1205.5761 [nucl-ex].

[694] CMS Collaboration, V. Khachatryan et al., *Long-range two-particle correlations of strange hadrons with charged particles in* p–Pb *and* Pb–Pb *collisions at LHC energies*, Phys. Lett. **B742** (2015) 200–224, arXiv:1409.3392 [nucl-ex].

[695] ALICE Collaboration, B. Abelev et al., *Directed flow of charged particles at midrapidity relative to the spectator plane in* Pb–Pb *collisions at* $s_{_{NN}} = 2.76$ *TeV*, Phys. Rev. Lett. **111** (2013) no. 23, 232302, arXiv:1306.4145 [nucl-ex].

[696] ALICE Collaboration, B. Abelev et al., *Charge correlations using the balance function in Pb-Pb collisions at* $\sqrt{s_{_{NN}}}$ *= 2.76 TeV*, Phys. Lett. **B723** (2013) 267–279, arXiv:1301.3756 [nucl-ex].

[697] ALICE Collaboration, J. Adam et al., *Charge-dependent flow and the search for the chiral magnetic wave in Pb-Pb collisions at* $\sqrt{s_{\rm NN}} = 2.76$ *TeV*, Phys. Rev. **C93** (2016) no. 4, 044903, arXiv:1512.05739 [nucl-ex].

[698] ALICE Collaboration, J. Adam et al., *Multiplicity and transverse momentum evolution of charge-dependent correlations in pp, p-Pb, and Pb-Pb collisions at the LHC*, Eur. Phys. J. **C76** (2016) no. 2, 86, arXiv:1509.07255 [nucl-ex].

[699] CMS Collaboration, A. M. Sirunyan et al., *Challenges to the chiral magnetic wave using charge-dependent azimuthal anisotropies in pPb and PbPb collisions at* $\sqrt{s_{\rm NN}} = 5.02$ *TeV*, arXiv:1708.08901 [nucl-ex].

[700] ATLAS Collaboration, G. Aad et al., *Measurement with the ATLAS detector of multi-particle azimuthal correlations in* p–Pb *collisions at* $s_{NN} = 5.02$ *TeV*, Phys. Lett. **B725** (2013) 60–78, arXiv:1303.2084 [hep-ex].

[701] CMS Collaboration, S. Chatrchyan et al., *Multiplicity and transverse momentum dependence of two- and four-particle correlations in* p–Pb *and* Pb–Pb *collisions*, Phys. Lett. **B724** (2013) 213–240, arXiv:1305.0609 [nucl-ex].

[702] ALICE Collaboration, K. Aamodt et al., *Elliptic flow of charged particles in* Pb–Pb *collisions at 2.76 TeV*, Phys. Rev. Lett. **105** (2010) 252302, arXiv:1011.3914 [nucl-ex].

[703] ALICE Collaboration, K. Aamodt et al., *Higher harmonic anisotropic flow measurements of charged particles in* Pb–Pb *collisions at* $s_{NN} = 2.76$ *TeV*, Phys. Rev. Lett. **107** (2011) 032301, arXiv:1105.3865 [nucl-ex].

[704] CMS Collaboration, S. Chatrchyan et al., *Measurement of the elliptic anisotropy of charged particles produced in* Pb–Pb *collisions at* $s_{NN} = 2.76$ *TeV*, Phys. Rev. **C87** (2013) no. 1, 014902, arXiv:1204.1409 [nucl-ex].

[705] ALICE Collaboration, B. Abelev et al., *Multiparticle azimuthal correlations in* p–Pb *and* Pb–Pb *collisions at the CERN Large Hadron Collider*, Phys. Rev. **C90** (2014) no. 5, 054901, arXiv:1406.2474 [nucl-ex].

[706] CMS Collaboration, S. Chatrchyan et al., *Measurement of higher-order harmonic azimuthal anisotropy in* Pb–Pb *collisions at* $s_{NN} = 2.76$ *TeV*, Phys. Rev. **C89** (2014) no. 4, 044906, arXiv:1310.8651 [nucl-ex].

[707] ATLAS Collaboration, G. Aad et al., *Measurement of flow harmonics with multi-particle cumulants in* Pb–Pb *collisions at* $s_{NN} = 2.76$ *TeV with the ATLAS detector*, Eur. Phys. J. **C74** (2014) no. 11, 3157, arXiv:1408.4342 [hep-ex].

[708] ALICE Collaboration, J. Adam et al., *Anisotropic flow of charged particles in Pb-Pb collisions at* $\sqrt{s_{\rm NN}} = 5.02$ *TeV*, Phys. Rev. Lett. **116** (2016) no. 13, 132302, arXiv:1602.01119 [nucl-ex].

[709] CMS Collaboration, A. M. Sirunyan et al., *Azimuthal anisotropy of charged particles with transverse momentum up to 100 GeV/ c in PbPb collisions at* $\sqrt{s_{NN}}$*=5.02 TeV*, Phys. Lett. **B776** (2018) 195–216, arXiv:1702.00630 [hep-ex].

[710] ATLAS Collaboration, M. Aaboud et al., *Measurement of long-range multiparticle azimuthal correlations with the subevent cumulant method in* pp *and* $p + Pb$ *collisions with the ATLAS detector at the CERN Large Hadron Collider*, Phys. Rev. **C97** (2018) no. 2, 024904, arXiv:1708.03559 [hep-ex].

[711] ATLAS Collaboration, G. Aad et al., *Measurement of event-plane correlations in* $s_{NN} = 2.76$ *TeV lead-lead collisions with the ATLAS detector*, Phys. Rev. **C90** (2014) no. 2, 024905, arXiv:1403.0489 [hep-ex].

[712] ATLAS Collaboration, G. Aad et al., *Measurement of the correlation between flow harmonics of different order in lead–lead collisions at* $\sqrt{s_{\rm NN}}$*=2.76 TeV with the ATLAS detector*, Phys. Rev. **C92** (2015) no. 3, 034903, arXiv:1504.01289 [hep-ex].

[713] ALICE Collaboration, S. Acharya et al., *Systematic studies of correlations between different order flow harmonics in Pb-Pb collisions at* $\sqrt{s_{\rm NN}}$ *= 2.76 TeV*, Phys. Rev. **C97** (2018) no. 2, 024906, arXiv:1709.01127 [nucl-ex].

[714] ATLAS Collaboration, M. Aaboud et al., *Correlated long-range mixed-harmonic fluctuations measured in pp, p+Pb and low-multiplicity Pb+Pb collisions with the ATLAS detector*, Phys. Lett. **B789** (2019) 444–471, arXiv:1807.02012 [nucl-ex].

[715] ALICE Collaboration, S. Acharya et al., *Linear and non-linear flow modes in Pb-Pb collisions at* $\sqrt{s_{\rm NN}} = 2.76$ *TeV*, Phys. Lett. **B773** (2017) 68–80, arXiv:1705.04377 [nucl-ex].

[716] ATLAS Collaboration, G. Aad et al., *Measurement of the centrality and pseudorapidity dependence of the integrated elliptic flow in lead-lead collisions at* $\sqrt{s_{\rm NN}} = 2.76$ *TeV with the ATLAS detector*, Eur. Phys. J. **C74** (2014) no. 8, 2982, arXiv:1405.3936 [hep-ex].

[717] ATLAS Collaboration, G. Aad et al., *Measurement of the pseudorapidity and transverse momentum dependence of the elliptic flow of charged particles in lead-lead collisions at* $\sqrt{s_{\rm NN}} = 2.76$ *TeV with the ATLAS detector*, Phys. Lett. **B707** (2012) 330–348, arXiv:1108.6018 [hep-ex].

[718] CMS Collaboration, V. Khachatryan et al., *Pseudorapidity dependence of long-range two-particle correlations in pPb collisions at* $\sqrt{s_{NN}} = 5.02$ *TeV*, Phys. Rev. **C96** (2017) no. 1, 014915, arXiv:1604.05347 [nucl-ex].

[719] ALICE Collaboration, J. Adam et al., *Forward-central two-particle correlations in pPb collisions at* $\sqrt{s_{\rm NN}} = 5.02$ *TeV*, Phys. Lett. **B753** (2016) 126–139, arXiv:1506.08032 [nucl-ex].

[720] LHCb Collaboration, R. Aaij et al., *Measurements of long-range near-side angular correlations in* $\sqrt{s_{NN}} = 5$*TeV proton-lead collisions in the forward region*, Phys. Lett. **B762** (2016) 473–483, arXiv:1512.00439 [nucl-ex].

[721] CMS Collaboration, A. M. Sirunyan et al., *Principal-component analysis of two-particle azimuthal correlations in PbPb and pPb collisions at CMS*, Phys. Rev. **C96** (2017) no. 6, 064902, arXiv:1708.07113 [nucl-ex].

[722] ATLAS Collaboration, G. Aad et al., *Measurement of the distributions of event-by-event flow harmonics in lead-lead collisions at* $s_{_{NN}} = 2.76$ *TeV with the ATLAS detector at the LHC*, JHEP **11** (2013) 183, arXiv:1305.2942 [hep-ex].

[723] CMS Collaboration, A. M. Sirunyan et al., *Non-Gaussian elliptic-flow fluctuations in PbPb collisions at* $\sqrt{s_{_{NN}}} = 5.02$ *TeV*, Phys. Lett. **B789** (2019) 643–665, arXiv:1711.05594 [nucl-ex].

[724] ALICE Collaboration, S. Acharya et al., *Energy dependence and fluctuations of anisotropic flow in Pb-Pb collisions at* $\sqrt{s_{\rm NN}} = 5.02$ *and 2.76 TeV*, JHEP **07** (2018) 103, arXiv:1804.02944 [nucl-ex].

[725] ALICE Collaboration, S. Acharya et al., *Direct photon production at low transverse momentum in proton-proton collisions at* $\sqrt{\rm s} = \mathbf{2.76}$ *and 8 TeV*, Phys. Rev. **C99** (2019) no. 2, 024912, arXiv:1803.09857 [nucl-ex].

[726] CMS Collaboration, A. M. Sirunyan et al., *Comparing transverse momentum balance of b jet pairs in pp and PbPb collisions at* $\sqrt{s_{\rm NN}} = 5.02$ *TeV*, JHEP **03** (2018) 181, arXiv:1802.00707 [hep-ex].

[727] CMS Collaboration, V. Khachatryan et al., *Decomposing transverse momentum balance contributions for quenched jets in PbPb collisions at* $\sqrt{s_{\rm N\,N}} = 2.76$ *TeV*, JHEP **11** (2016) 055, arXiv:1609.02466 [nucl-ex].

[728] CMS Collaboration, S. Chatrchyan et al., *Studies of dijet transverse momentum balance and pseudorapidity distributions in pPb collisions at* $\sqrt{s_{\rm NN}} = 5.02$ *TeV*, Eur. Phys. J. **C74** (2014) no. 7, 2951, arXiv:1401.4433 [nucl-ex].

[729] ALICE Collaboration, B. Abelev et al., *Centrality dependence of charged particle production at large transverse momentum in* Pb–Pb *collisions at* $s_{_{NN}} = 2.76$ *TeV*, Phys. Lett. **B720** (2013) 52–62, arXiv:1208.2711 [hep-ex].

[730] ALICE Collaboration, B. Abelev et al., *Suppression of high transverse momentum D mesons in central* Pb–Pb *collisions at* $s_{_{NN}} = 2.76$ *TeV*, JHEP **09** (2012) 112, arXiv:1203.2160 [nucl-ex].

[731] ATLAS Collaboration, G. Aad et al., *Measurements of the nuclear modification factor for jets in* Pb–Pb *collisions at* $s_{_{NN}} = 2.76$ *TeV with the ATLAS Detector*, Phys. Rev. Lett. **114** (2015) no. 7, 072302, arXiv:1411.2357 [hep-ex].

[732] ALICE Collaboration, J. Adam et al., *Centrality dependence of charged jet production in p-Pb collisions at* $\sqrt{s_{\rm NN}}$ *= 5.02 TeV*, Eur. Phys. J. **C76** (2016) no. 5, 271, arXiv:1603.03402 [nucl-ex].

[733] CMS Collaboration, A. M. Sirunyan et al., *Measurements of the charm jet cross section and nuclear modification factor in pPb collisions at* $\sqrt{s_{_{NN}}}$ *= 5.02 TeV*, Phys. Lett. **B772** (2017) 306–329, arXiv:1612.08972 [nucl-ex].

[734] ALICE Collaboration, S. Acharya et al., *Analysis of the apparent nuclear modification in peripheral Pb-Pb collisions at 5.02 TeV*, arXiv:1805.05212 [nucl-ex].

[735] ATLAS Collaboration, G. Aad et al., *Centrality and rapidity dependence of inclusive jet production in* $\sqrt{s_{\rm NN}} = 5.02$ *TeV proton-lead collisions with the ATLAS detector*, Phys. Lett. **B748** (2015) 392–413, arXiv:1412.4092 [hep-ex].

[736] CMS Collaboration, V. Khachatryan et al., *Nuclear Effects on the Transverse Momentum Spectra of Charged Particles in pPb Collisions at* $\sqrt{s_{\rm NN}} = 5.02$ *TeV*, Eur. Phys. J. **C75** (2015) no. 5, 237, arXiv:1502.05387 [nucl-ex].

[737] ALICE Collaboration, S. Acharya et al., *Constraints on jet quenching in p-Pb collisions at* $\sqrt{\rm s_{NN}}$ *= 5.02 TeV measured by the event-activity dependence of semi-inclusive hadron-jet distributions*, Phys. Lett. **B783** (2018) 95–113, arXiv:1712.05603 [nucl-ex].

[738] ALICE Collaboration, J. Adam et al., *Jet-like correlations with neutral pion triggers in pp and central Pb?Pb collisions at 2.76 TeV*, Phys. Lett. **B763** (2016) 238–250, arXiv:1608.07201 [nucl-ex].

[739] CMS Collaboration, A. M. Sirunyan et al., *Observation of medium induced modifications of jet fragmentation in PbPb collisions using isolated-photon-tagged jets*, Phys. Rev. Lett. **121** (2018) 242301, arXiv:1801.04895 [hep-ex].

[740] ALICE Collaboration, B. Abelev et al., *D meson elliptic flow in non-central* Pb–Pb *collisions at* $s_{_{NN}} = 2.76$ *TeV*, Phys. Rev. Lett. **111** (2013) 102301, arXiv:1305.2707 [nucl-ex].

[741] ALICE Collaboration, J. Adam et al., *Elliptic flow of muons from heavy-flavour hadron decays at forward rapidity in* Pb–Pb *collisions at* $s_{_{NN}} = 2.76$ *TeV*, Phys. Lett. **B753** (2016) 41–56, arXiv:1507.03134 [nucl-ex].

[742] ALICE Collaboration, J. Adam et al., *Elliptic flow of electrons from heavy-flavour hadron decays at mid-rapidity in Pb-Pb collisions at* $\sqrt{\rm s_{NN}} = 2.76$ *TeV*, JHEP **09** (2016) 028, arXiv:1606.00321 [nucl-ex].

[743] ALICE Collaboration, J. Adam et al., *Measurement of azimuthal correlations of D mesons and charged particles in pp collisions at* $\sqrt{s} = 7$ *TeV and p-Pb collisions at* $\sqrt{s_{\rm NN}} = 5.02$ *TeV*, Eur. Phys. J. **C77** (2017) no. 4, 245, arXiv:1605.06963 [nucl-ex].

[744] ALICE Collaboration, S. Acharya et al., *Azimuthal Anisotropy of Heavy-Flavor Decay Electrons in p-Pb Collisions at $\sqrt{s_{\rm NN}}$ = 5.02 TeV*, Phys. Rev. Lett. **122** (2019) no. 7, 072301, arXiv:1805.04367 [nucl-ex].

[745] ALICE Collaboration, J. Adam et al., *Inclusive, prompt and non-prompt J/ψ production at mid-rapidity in PbPb collisions at $\sqrt{s_{\rm NN}} = 2.76$ TeV*, JHEP **07** (2015) 051, arXiv:1504.07151 [nucl-ex].

[746] ALICE Collaboration, J. Adam et al., *Centrality dependence of inclusive J/ψ production in pPb collisions at $\sqrt{s_{\rm NN}} = 5.02$ TeV*, JHEP **11** (2015) 127, arXiv:1506.08808 [nucl-ex].

[747] ALICE Collaboration, J. Adam et al., *Centrality dependence of ψ(2S) suppression in p-Pb collisions at $\sqrt{s_{\rm NN}}$ = 5.02 TeV*, JHEP **06** (2016) 050, arXiv:1603.02816 [nucl-ex].

[748] ALICE Collaboration, J. Adam et al., *Inclusive quarkonium production at forward rapidity in pp collisions at $\sqrt{s} = 8$ TeV*, Eur. Phys. J. **C76** (2016) no. 4, 184, arXiv:1509.08258 [hep-ex].

[749] ALICE Collaboration, J. Adam et al., *Differential studies of inclusive J/Ψ and Ψ(2S) production at forward rapidity in Pb-Pb collisions at $\sqrt{s_{\rm NN}} = 2.76$ TeV*, JHEP **05** (2016) 179, arXiv:1506.08804 [nucl-ex].

[750] ALICE Collaboration, D. Adamová et al., *J/ψ production as a function of charged-particle pseudorapidity density in p-Pb collisions at $\sqrt{s_{\rm NN}} = 5.02$ TeV*, Phys. Lett. **B776** (2018) 91–104, arXiv:1704.00274 [nucl-ex].

[751] ALICE Collaboration, S. Acharya et al., *Energy dependence of forward-rapidity* J/ψ *and* ψ(2S) *production in pp collisions at the LHC*, Eur. Phys. J. **C77** (2017) no. 6, 392, arXiv:1702.00557 [hep-ex].

[752] CMS Collaboration, A. M. Sirunyan et al., *Measurement of prompt and nonprompt* J/ψ *production in* pp *and* pPb *collisions at $\sqrt{s_{\rm NN}} = 5.02$ TeV*, Eur. Phys. J. **C77** (2017) no. 4, 269, arXiv:1702.01462 [nucl-ex].

[753] CMS Collaboration, A. M. Sirunyan et al., *Relative Modification of Prompt ψ(2S) and J/ψ Yields from pp to PbPb Collisions at $\sqrt{s_{NN}} = 5.02$?TeV*, Phys. Rev. Lett. **118** (2017) no. 16, 162301, arXiv:1611.01438 [nucl-ex].

[754] LHCb Collaboration, R. Aaij et al., *Prompt and nonprompt J/ψ production and nuclear modification in pPb collisions at $\sqrt{s_{NN}} = 8.16$ TeV*, Phys. Lett. **B774** (2017) 159–178, arXiv:1706.07122 [hep-ex].

[755] J. Jia and S. Radhakrishnan, *Limitation of multiparticle correlations for studying the event-by-event distribution of harmonic flow in heavy-ion collisions*, Phys. Rev. **C92** (2015) no. 2, 024911, arXiv:1412.4759 [nucl-ex].

[756] M. Gyulassy, P. Levai, I. Vitev, and T. S. Biro, *Non-Abelian bremsstrahlung and azimuthal asymmetries in high energy p-A reactions*, Phys. Rev. **D90** (2014) no. 5, 054025, arXiv:1405.7825 [hep-ph].

[757] L. McLerran and V. V. Skokov, *The eccentric collective BFKL pomeron*, Acta Phys. Polon. **B46** (2015) no. 8, 1513, arXiv:1407.2651 [hep-ph].

[758] X. Zhu, Y. Zhou, H. Xu, and H. Song, *Correlations of flow harmonics in 2.76A TeV Pb–Pb collisions*, Phys. Rev. **C95** (2017) no. 4, 044902, arXiv:1608.05305 [nucl-th].

[759] ALICE Collaboration, J. Adam et al., *Charged-particle multiplicities in proton?proton collisions at $\sqrt{s} = 0.9$ to 8 TeV*, Eur. Phys. J. **C77** (2017) no. 1, 33, arXiv:1509.07541 [nucl-ex].

[760] ATLAS Collaboration, G. Aad et al., *Charged-particle multiplicities in pp interactions measured with the ATLAS detector at the LHC*, New J. Phys. **13** (2011) 053033, arXiv:1012.5104 [hep-ex].

[761] ATLAS Collaboration, G. Aad et al., *Charged-particle distributions in pp interactions at $\sqrt{s} =$ 8 TeV measured with the ATLAS detector*, Eur. Phys. J. **C76** (2016) no. 7, 403, arXiv:1603.02439 [hep-ex].

[762] CMS Collaboration, V. Khachatryan et al., *Charged particle multiplicities in pp interactions at $\sqrt{s} = 0.9$, 2.36, and 7 TeV*, JHEP **01** (2011) 079, arXiv:1011.5531 [hep-ex].

[763] J. F. Grosse-Oetringhaus and K. Reygers, *Charged-Particle Multiplicity in Proton-Proton Collisions*, J. Phys. **G37** (2010) 083001, arXiv:0912.0023 [hep-ex].

[764] ALICE Collaboration, S. Acharya et al., *Charged-particle multiplicity distributions over a wide pseudorapidity range in proton-proton collisions at $\sqrt{s} = 0.9$, 7, and 8 TeV*, Eur. Phys. J. **C77** (2017) no. 12, 852, arXiv:1708.01435 [hep-ex].

[765] A. Bzdak, B. Schenke, P. Tribedy, and R. Venugopalan, *Initial state geometry and the role of hydrodynamics in proton-proton, proton-nucleus and deuteron-nucleus collisions*, Phys. Rev. **C87** (2013) no. 6, 064906, arXiv:1304.3403 [nucl-th].

[766] ALICE Collaboration, B. B. Abelev et al., *Multiplicity dependence of the average transverse momentum in pp, p-Pb, and Pb-Pb collisions at the LHC*, Phys. Lett. **B727** (2013) 371–380, arXiv:1307.1094 [nucl-ex].

[767] C. Loizides, J. Kamin, and D. d'Enterria, *Improved Monte Carlo Glauber predictions at present and future nuclear colliders*, Phys. Rev. **C97** (2018) no. 5, 054910, arXiv:1710.07098 [nucl-ex].

[768] CMS Collaboration, V. Khachatryan et al., *Event generator tunes obtained from underlying event and multiparton scattering measurements*, Eur. Phys. J. **C76** (2016) no. 3, 155, arXiv:1512.00815 [hep-ex].

[769] ALICE Collaboration, B. Abelev et al., *Multiplicity dependence of two-particle azimuthal correlations in pp collisions at the LHC*, JHEP **09** (2013) 049, arXiv:1307.1249 [nucl-ex].

[770] J. L. Albacete, H. Petersen, and A. Soto-Ontoso, *Symmetric cumulants as a probe of the proton substructure at LHC energies*, Phys. Lett. **B778** (2018) 128–136, arXiv:1707.05592 [hep-ph].

[771] J. Jia, *Event-shape fluctuations and flow correlations in ultra-relativistic heavy-ion collisions*, J. Phys. **G41** (2014) no. 12, 124003, arXiv:1407.6057 [nucl-ex].

[772] ALICE Collaboration, J. Adam et al., *Centrality dependence of particle production in p-Pb collisions at $\sqrt{s_{\rm NN}}$= 5.02 TeV*, Phys. Rev. **C91** (2015) no. 6, 064905, arXiv:1412.6828 [nucl-ex].

[773] M. L. Miller, K. Reygers, S. J. Sanders, and P. Steinberg, *Glauber modeling in high energy nuclear collisions*, Ann. Rev. Nucl. Part. Sci. **57** (2007) 205–243, arXiv:nucl-ex/0701025 [nucl-ex].

[774] J. S. Moreland, J. E. Bernhard, and S. A. Bass, *Alternative ansatz to wounded nucleon and binary collision scaling in high-energy nuclear collisions*, Phys. Rev. **C92** (2015) no. 1, 011901, arXiv:1412.4708 [nucl-th].

[775] ALICE Collaboration, S. Acharya et al., *Charged-particle pseudorapidity density at mid-rapidity in p-Pb collisions at $\sqrt{s_{\rm NN}}$ = 8.16 TeV*, Eur. Phys. J. **C79** (2019) no. 4, 307, arXiv:1812.01312 [nucl-ex].

[776] H.-J. Drescher, A. Dumitru, C. Gombeaud, and J.-Y. Ollitrault, *The Centrality dependence of elliptic flow, the hydrodynamic limit, and the viscosity of hot QCD*, Phys. Rev. **C76** (2007) 024905, arXiv:0704.3553 [nucl-th].

[777] ALICE Collaboration, S. Acharya et al., *Anisotropic flow in Xe-Xe collisions at $\sqrt{s_{\rm NN}} = 5.44$ TeV*, Phys. Lett. **B784** (2018) 82–95, arXiv:1805.01832 [nucl-ex].

[778] S. H. Lim, J. Carlson, C. Loizides, et al., *Exploring New Small System Geometries in Heavy Ion Collisions*, Phys. Rev. **C99** (2019) no. 4, 044904, arXiv:1812.08096 [nucl-th].

[779] Y. V. Kovchegov and E. Levin, *Quantum chromodynamics at high energy*, vol. 33. Cambridge University Press, 2012. ISBN 9780521112574, 9781139557689.

[780] L. V. Gribov, E. M. Levin, and M. G. Ryskin, *Semihard Processes in QCD*, Phys. Rept. **100** (1983) 1–150.

[781] A. H. Mueller and J.-w. Qiu, *Gluon Recombination and Shadowing at Small Values of x*, Nucl. Phys. **B268** (1986) 427–452.

[782] F. Gelis, E. Iancu, J. Jalilian-Marian, and R. Venugopalan, *The Color Glass Condensate*, Ann. Rev. Nucl. Part. Sci. **60** (2010) 463–489, arXiv:1002.0333 [hep-ph].

[783] J. Liu, C. Shen, and U. Heinz, *Pre-equilibrium evolution effects on heavy-ion collision observables*, Phys. Rev. **C91** (2015) no. 6, 064906, arXiv:1504.02160 [nucl-th]. [Erratum: Phys. Rev.C92,no.4,049904(2015)].

[784] H. Paukkunen, *Status of nuclear PDFs after the first LHC p-Pb run*, Nucl. Phys. **A967** (2017) 241–248, arXiv:1704.04036 [hep-ph].

[785] N. A. Perez, *Future of Nuclear parton densities*, PoS **DIS2018** (2018) 180.

[786] K. J. Eskola, P. Paakkinen, H. Paukkunen, and C. A. Salgado, *EPPS16: Nuclear parton distributions with LHC data*, Eur. Phys. J. **C77** (2017) no. 3, 163, arXiv:1612.05741 [hep-ph].

[787] K. Kovarik et al., *nCTEQ15 - Global analysis of nuclear parton distributions with uncertainties in the CTEQ framework*, Phys. Rev. **D93** (2016) no. 8, 085037, arXiv:1509.00792 [hep-ph].

[788] D. de Florian, R. Sassot, P. Zurita, and M. Stratmann, *Global Analysis of Nuclear Parton Distributions*, Phys. Rev. **D85** (2012) 074028, arXiv:1112.6324 [hep-ph].

[789] H. Khanpour and S. Atashbar Tehrani, *Global Analysis of Nuclear Parton Distribution Functions and Their Uncertainties at Next-to-Next-to-Leading Order*, Phys. Rev. **D93** (2016) no. 1, 014026, arXiv:1601.00939 [hep-ph].

[790] L. Frankfurt, V. Guzey, and M. Strikman, *Leading Twist Nuclear Shadowing Phenomena in Hard Processes with Nuclei*, Phys. Rept. **512** (2012) 255–393, arXiv:1106.2091 [hep-ph].

[791] N. Armesto, A. Capella, A. B. Kaidalov, J. Lopez-Albacete, and C. A. Salgado, *Nuclear structure functions at small x from inelastic shadowing and diffraction*, Eur. Phys. J. **C29** (2003) 531–540, arXiv:hep-ph/0304119 [hep-ph].

[792] R. D. Ball, V. Bertone, M. Bonvini, et al., *Parton distributions with small-x resummation: evidence for BFKL dynamics in HERA data*, Eur. Phys. J. **C78** (2018) no. 4, 321, arXiv:1710.05935 [hep-ph].

[793] xFitter Developers' Team Collaboration, H. Abdolmaleki et al., *Impact of low-x resummation on QCD analysis of HERA data*, Eur. Phys. J. **C78** (2018) no. 8, 621, arXiv:1802.00064 [hep-ph].

[794] ZEUS Collaboration, M. Przybycień, *Investigation of collective effects in DIS with the ZEUS detector*, Proceedings of **ICHEP2018** (2018) . https://indico.cern.ch/event/686555/contributions/2975347/attachments/1681772/2741853/ichep_2018_zeus.pdf.

[795] J. L. Albacete, A. Dumitru, and C. Marquet, *The initial state of heavy-ion collisions*, Int. J. Mod. Phys. **A28** (2013) 1340010, arXiv:1302.6433 [hep-ph].

[796] T. Lappi, *Initial state in heavy ion collisions*, in *Proceedings, 7th International Conference on Hard and Electromagnetic Probes of High-Energy Nuclear Collisions (Hard Probes 2015): Montréal, Québec, Canada, June 29-July 3, 2015*. 2016. arXiv:1509.04503 [hep-ph].

[797] LHeC Study Group Collaboration, J. L. Abelleira Fernandez et al., *A Large Hadron Electron Collider at CERN: Report on the Physics and Design Concepts for Machine and Detector*, J. Phys. **G39** (2012) 075001, arXiv:1206.2913 [physics.acc-ph].

[798] A. Accardi et al., *Electron Ion Collider: The Next QCD Frontier*, Eur. Phys. J. **A52** (2016) no. 9, 268, arXiv:1212.1701 [nucl-ex].

[799] LHCb Collaboration, R. Aaij et al., *Exclusive J/ψ and $\psi(2S)$ production in pp collisions at $\sqrt{s} = 7$ TeV*, J. Phys. **G40** (2013) 045001, arXiv:1301.7084 [hep-ex].

[800] LHCb Collaboration, R. Aaij et al., *Updated measurements of exclusive J/ψ and $\psi(2S)$ production cross-sections in pp collisions at $\sqrt{s} = 7$ TeV*, J. Phys. **G41** (2014) 055002, arXiv:1401.3288 [hep-ex].

[801] LHCb Collaboration, R. Aaij et al., *Measurement of the exclusive Υ production cross-section in pp collisions at $\sqrt{s} = 7$ TeV and 8 TeV*, JHEP **09** (2015) 084, arXiv:1505.08139 [hep-ex].

[802] LHCb Collaboration, R. Aaij et al., *Central exclusive production of J/ψ and $\psi(2S)$ mesons in pp collisions at $\sqrt{s} = 13$ TeV*, JHEP **10** (2018) 167, arXiv:1806.04079 [hep-ex].

[803] ALICE MFT Working Group Collaboration, A. Uras and f. t. A. M. W. Group, *Muon Physics in ALICE: The MFT Upgrade Project*, J. Phys. Conf. Ser. **446** (2013) 012054, arXiv:1212.6517 [hep-ex].

[804] A. Collaboration, *Technical Design Report for the Phase-II Upgrade of the ATLAS TDAQ System*, . https://cds.cern.ch/record/2285584.

[805] CMS Collaboration, *Technical proposal for a MIP timing detector in the CMS experiment Phase-2 upgrade*, CERN-LHCC-2017-027, 2017. https://cds.cern.ch/record/2296612.

[806] CMS Collaboration, *Expected performance of the physics objects with the upgraded CMS detector at the HL-LHC*, CMS-NOTE-2018-006, CERN, Geneva, Dec, 2018. https://cds.cern.ch/record/2650976.

[807] LHCb Collaboration, *Study of coherent J/ψ production in lead-lead collisions at $\sqrt{s_{\rm NN}} = 5$ TeV with the LHCb experiment*, LHCb-CONF-2018-003, CERN, Geneva, May, 2018. http://cds.cern.ch/record/2320135.

[808] LHCb Collaboration, *LHCb Trigger and Online Upgrade Technical Design Report*, CERN-LHCC-2014-016, LHCB-TDR-016, May, 2014. https://cds.cern.ch/record/1701361.

[809] ATLAS Collaboration, M. Aaboud et al., *Evidence for light-by-light scattering in heavy-ion collisions with the ATLAS detector at the LHC*, Nature Phys. **13** (2017) no. 9, 852–858, arXiv:1702.01625 [hep-ex].

[810] CMS Collaboration, *Measurement of light-by-light scattering in ultraperipheral PbPb collisions at $\sqrt{s_{\rm NN}}$ = 5.02 TeV*, CMS-PAS-FSQ-16-012 (2018) no. CMS-PAS-FSQ-16-012, . https://cds.cern.ch/record/2319158.

[811] ALICE Collaboration, J. Adam et al., *Coherent ρ^0 photoproduction in ultra-peripheral Pb-Pb collisions at $\sqrt{s_{\rm NN}} = 2.76$ TeV*, JHEP **09** (2015) 095, arXiv:1503.09177 [nucl-ex].

[812] STAR Collaboration, B. I. Abelev et al., *ρ^0 photoproduction in ultraperipheral relativistic heavy ion collisions at $\sqrt{s_{NN}}$ = 200 GeV*, Phys. Rev. **C77** (2008) 034910, arXiv:0712.3320 [nucl-ex].

[813] STAR Collaboration, B. I. Abelev et al., *Observation of pi+ pi- pi+ pi- Photoproduction in Ultra-Peripheral Heavy Ion Collisions at STAR*, Phys. Rev. **C81** (2010) 044901, arXiv:0912.0604 [nucl-ex].

[814] V. Guzey, E. Kryshen, and M. Zhalov, *Coherent photoproduction of vector mesons in ultraperipheral heavy ion collisions: Update for run 2 at the CERN Large Hadron Collider*, Phys. Rev. **C93** (2016) no. 5, 055206, arXiv:1602.01456 [nucl-th].

[815] S. Klein and J. Nystrand, *Exclusive vector meson production in relativistic heavy ion collisions*, Phys. Rev. **C60** (1999) 014903, arXiv:hep-ph/9902259 [hep-ph].

[816] V. Guzey, M. Strikman, and M. Zhalov, *Disentangling coherent and incoherent quasielastic J/ψ photoproduction on nuclei by neutron tagging in ultraperipheral ion collisions at the LHC*, Eur. Phys. J. **C74** (2014) no. 7, 2942, arXiv:1312.6486 [hep-ph].

[817] V. Guzey, E. Kryshen, M. Strikman, and M. Zhalov, *Evidence for nuclear gluon shadowing from the ALICE measurements of PbPb ultraperipheral exclusive J/ψ production*, Phys. Lett. **B726** (2013) 290–295, arXiv:1305.1724 [hep-ph].

[818] ALICE Collaboration, B. Abelev et al., *Coherent J/ψ photoproduction in ultra-peripheral Pb-Pb collisions at $\sqrt{s_{NN}} = 2.76$ TeV*, Phys. Lett. **B718** (2013) 1273–1283, arXiv:1209.3715 [nucl-ex].

[819] ALICE Collaboration, E. Abbas et al., *Charmonium and e^+e^- pair photoproduction at mid-rapidity in ultra-peripheral Pb-Pb collisions at $\sqrt{s_{\rm NN}}$=2.76 TeV*, Eur. Phys. J. **C73** (2013) no. 11, 2617, arXiv:1305.1467 [nucl-ex].

[820] ALICE Collaboration, J. Adam et al., *Coherent ψ(2S) photo-production in ultra-peripheral Pb Pb collisions at $\sqrt{s}_{\rm NN}$ = 2.76 TeV*, Phys. Lett. **B751** (2015) 358–370, arXiv:1508.05076 [nucl-ex].

[821] CMS Collaboration, V. Khachatryan et al., *Coherent J/ψ photoproduction in ultra-peripheral PbPb collisions at $\sqrt{s_{NN}} = 2.76$ TeV with the CMS experiment*, Phys. Lett. **B772** (2017) 489–511, arXiv:1605.06966 [nucl-ex].

[822] V. Rebyakova, M. Strikman, and M. Zhalov, *Coherent ρ and J/ψ photoproduction in ultraperipheral processes with electromagnetic dissociation of heavy ions at RHIC and LHC*, Phys. Lett. **B710** (2012) 647–653, arXiv:1109.0737 [hep-ph].

[823] A. Adeluyi and C. A. Bertulani, *Constraining Gluon Shadowing Using Photoproduction in Ultraperipheral pA and AA Collisions*, Phys. Rev. **C85** (2012) 044904, arXiv:1201.0146 [nucl-th].

[824] V. Guzey and M. Zhalov, *Exclusive J/ψ production in ultraperipheral collisions at the LHC: constrains on the gluon distributions in the proton and nuclei*, JHEP **10** (2013) 207, arXiv:1307.4526 [hep-ph].

[825] V. P. Goncalves and M. V. T. Machado, *Vector Meson Production in Coherent Hadronic Interactions: An update on predictions for RHIC and LHC*, Phys. Rev. **C84** (2011) 011902, arXiv:1106.3036 [hep-ph].

[826] T. Lappi and H. Mantysaari, *J/ψ production in ultraperipheral Pb+Pb and p+Pb collisions at energies available at the CERN Large Hadron Collider*, Phys. Rev. **C87** (2013) no. 3, 032201, arXiv:1301.4095 [hep-ph].

[827] A. Cisek, W. Schafer, and A. Szczurek, *Exclusive coherent production of heavy vector mesons in nucleus-nucleus collisions at LHC*, Phys. Rev. **C86** (2012) 014905, arXiv:1204.5381 [hep-ph].

[828] L. Frankfurt, V. Guzey, M. Strikman, and M. Zhalov, *Nuclear shadowing in photoproduction of ρ mesons in ultraperipheral nucleus collisions at RHIC and the LHC*, Phys. Lett. **B752** (2016) 51–58, arXiv:1506.07150 [hep-ph].

[829] ALICE Collaboration, M. Krivda et al., *The ALICE trigger system for LHC Run 3*, PoS **TWEPP-17** (2017) 149, arXiv:1711.01200 [physics.ins-det].

[830] A. J. Baltz, S. R. Klein, and J. Nystrand, *Coherent vector meson photoproduction with nuclear breakup in relativistic heavy ion collisions*, Phys. Rev. Lett. **89** (2002) 012301, arXiv:nucl-th/0205031 [nucl-th].

[831] G. Baur, K. Hencken, A. Aste, D. Trautmann, and S. R. Klein, *Multiphoton exchange processes in ultraperipheral relativistic heavy ion collisions*, Nucl. Phys. **A729** (2003) 787–808, arXiv:nucl-th/0307031 [nucl-th].

[832] STAR Collaboration, S. R. Klein, *Ultra-Peripheral Collisions with gold ions in STAR*, PoS **DIS2016** (2016) 188, arXiv:1606.02754 [nucl-ex].

[833] M. Diehl, *How well one needs to measure t for getting images in b space*, in *INT workshop on Gluons and the quark sea at high energies: distributions, polarization, tomography, 2010*. 1st Nov, 2010. http://www.int.washington.edu/talks/WorkShops/int_10_3/People/Diehl_M/Diehl1.pdf.

[834] T. Toll and T. Ullrich, *Exclusive diffractive processes in electron-ion collisions*, Phys. Rev. **C87** (2013) no. 2, 024913, arXiv:1211.3048 [hep-ph].

[835] STAR Collaboration, L. Adamczyk et al., *Coherent diffractive photoproduction of ρ^0 mesons on gold nuclei at 200 GeV/nucleon-pair at the Relativistic Heavy Ion Collider*, Phys. Rev. **C96** (2017) no. 5, 054904, arXiv:1702.07705 [nucl-ex].

[836] STAR Collaboration, S. R. Klein, *Dipion photoproduction and the Q^2 evolution of the shape of the gold nucleus*, in *26th International Workshop on Deep Inelastic Scattering and Related Subjects (DIS 2018) Port Island, Kobe, Japan, April 16-20, 2018*. 2018. arXiv:1807.00455 [nucl-ex].

[837] L. Frankfurt, M. Strikman, D. Treleani, and C. Weiss, *Evidence for color fluctuations in the nucleon in high-energy scattering*, Phys. Rev. Lett. **101** (2008) 202003, arXiv:0808.0182 [hep-ph].

[838] H. Mäntysaari and B. Schenke, *Evidence of strong proton shape fluctuations from incoherent diffraction*, Phys. Rev. Lett. **117** (2016) no. 5, 052301, arXiv:1603.04349 [hep-ph].

[839] H. Mäntysaari and B. Schenke, *Revealing proton shape fluctuations with incoherent diffraction at high energy*, Phys. Rev. **D94** (2016) no. 3, 034042, arXiv:1607.01711 [hep-ph].

[840] H. Mäntysaari and B. Schenke, *Probing subnucleon scale fluctuations in ultraperipheral heavy ion collisions*, Phys. Lett. **B772** (2017) 832–838, arXiv:1703.09256 [hep-ph].

[841] J. Cepila, J. G. Contreras, and J. D. Tapia Takaki, *Energy dependence of dissociative J/ψ photoproduction as a signature of gluon saturation at the LHC*, Phys. Lett. **B766** (2017) 186–191, arXiv:1608.07559 [hep-ph].

[842] J. Cepila, J. G. Contreras, and M. Krelina, *Coherent and incoherent J/ψ photonuclear production in an energy-dependent hot-spot model*, Phys. Rev. **C97** (2018) no. 2, 024901, arXiv:1711.01855 [hep-ph].

[843] V. Guzey, M. Strikman, and M. Zhalov, *Nucleon dissociation and incoherent J/ψ photoproduction on nuclei in ion ultraperipheral collisions at the Large Hadron Collider*, Phys. Rev. **C99** (2019) no. 1, 015201, arXiv:1808.00740 [hep-ph].

[844] L. Frankfurt, M. Strikman, and M. Zhalov, *Tracking fast small color dipoles through strong gluon fields at the LHC*, Phys. Rev. Lett. **102** (2009) 232001, arXiv:0811.0368 [hep-ph].

[845] L. Frankfurt, M. Strikman, and M. Zhalov, *Large t diffractive J/psi photoproduction with proton dissociation in ultraperipheral pA collisions at LHC*, Phys. Lett. **B670** (2008) 32–36, arXiv:0807.2208 [hep-ph].

[846] M. Strikman, R. Vogt, and S. N. White, *Probing small x parton densities in ultraperipheral AA and pA collisions at the LHC*, Phys. Rev. Lett. **96** (2006) 082001, arXiv:hep-ph/0508296 [hep-ph].

[847] I. Helenius, *Simulations of photo-nuclear dijets with Pythia 8 and their sensitivity to nuclear PDFs*, in *26th International Workshop on Deep Inelastic Scattering and Related Subjects (DIS 2018) Port Island, Kobe, Japan, April 16-20, 2018*. 2018. arXiv:1806.07326 [hep-ph].

[848] ATLAS Collaboration, *Photo-nuclear dijet production in ultra-peripheral Pb+Pb collisions*, ATLAS-CONF-2017-011, CERN, Geneva, Feb, 2017. http://cds.cern.ch/record/2244822.

[849] ZEUS Collaboration, M. Derrick et al., *Dijet angular distributions in direct and resolved photoproduction at HERA*, Phys. Lett. **B384** (1996) 401–413, arXiv:hep-ex/9605009 [hep-ex].

[850] H1 Collaboration, C. Adloff et al., *Measurement of dijet cross-sections in photoproduction and photon structure*, Phys. Lett. **B483** (2000) 36–48, arXiv:hep-ex/0003011 [hep-ex].

[851] R. D. Ball et al., *Parton distributions with LHC data*, Nucl. Phys. **B867** (2013) 244–289, arXiv:1207.1303 [hep-ph].

[852] I. Helenius, *Probing nuclear PDFs with dijets in ultra-peripheral Pb+Pb collisions*, in *9th International Conference on Hard and Electromagnetic Probes of High-Energy Nuclear Collisions: Hard Probes 2018 (HP2018) Aix-Les-Bains, Savoie, France, October 1-5, 2018*. 2018. arXiv:1811.10931 [hep-ph].

[853] F. Cornet, P. Jankowski, M. Krawczyk, and A. Lorca, *A New five flavor LO analysis and parametrization of parton distributions in the real photon*, Phys. Rev. **D68** (2003) 014010, arXiv:hep-ph/0212160 [hep-ph].

[854] M. Gluck, E. Reya, and A. Vogt, *Photonic parton distributions*, Phys. Rev. **D46** (1992) 1973–1979.

[855] G. A. Schuler and T. Sjöstrand, *Low and high mass components of the photon distribution functions*, Z. Phys. **C68** (1995) 607–624, arXiv:hep-ph/9503384 [hep-ph].

[856] V. Guzey and M. Klasen, *Inclusive dijet photoproduction in ultraperipheral heavy-ion collisions at the LHC in next-to-leading order QCD*, arXiv:1811.10236 [hep-ph].

[857] M. Klasen, *Theory of hard photoproduction*, Rev. Mod. Phys. **74** (2002) 1221–1282, arXiv:hep-ph/0206169 [hep-ph].

[858] V. Guzey and M. Klasen, *Diffractive dijet photoproduction in ultraperipheral collisions at the LHC in next-to-leading order QCD*, JHEP **04** (2016) 158, arXiv:1603.06055 [hep-ph].

[859] S. R. Klein, J. Nystrand, and R. Vogt, *Heavy quark photoproduction in ultraperipheral heavy ion collisions*, Phys. Rev. **C66** (2002) 044906, arXiv:hep-ph/0206220 [hep-ph].

[860] V. P. Gonçalves, G. Sampaio dos Santos, and C. R. Sena, *Inclusive heavy quark photoproduction in pp, pPb and $PbPb$ collisions at Run 2 LHC energies*, Nucl. Phys. **A976** (2018) 33–45, arXiv:1711.04497 [hep-ph].

[861] K. J. Eskola, V. J. Kolhinen, and P. V. Ruuskanen, *Scale evolution of nuclear parton distributions*, Nucl. Phys. **B535** (1998) 351–371, arXiv:hep-ph/9802350 [hep-ph].

[862] R. Bala, *Inclusive Open Charm Production in pp and Pb-Pb collisions with the ALICE Detector*, J. Phys. Conf. Ser. **381** (2012) 012034, arXiv:1201.0729 [nucl-ex].

[863] S. R. Klein, J. Nystrand, and R. Vogt, *Photoproduction of top in peripheral heavy ion collisions*, Eur. Phys. J. **C21** (2001) 563–566, arXiv:hep-ph/0005157 [hep-ph].

[864] V. P. Gonçalves, *Photoproduction of top quarks in coherent hadron-hadron interactions*, Phys. Rev. **D88** (2013) no. 5, 054025.

[865] ATLAS Collaboration, G. Aad et al., *Z boson production in p+Pb collisions at $\sqrt{s_{NN}} = 5.02$ TeV measured with the ATLAS detector*, Phys. Rev. **C92** (2015) no. 4, 044915, arXiv:1507.06232 [hep-ex].

[866] ATLAS Collaboration, *Measurement of $W \to \mu\nu$ production in p+Pb collision at $\sqrt{s_{_{NN}}} = 5.02$ TeV with ATLAS detector at the LHC*, ATLAS-CONF-2015-056, CERN, Geneva, Sep, 2015. https://cds.cern.ch/record/2055677.

[867] CMS Collaboration, V. Khachatryan et al., *Study of W boson production in pPb collisions at $\sqrt{s_{\rm NN}} = 5.02$ TeV*, Phys. Lett. **B750** (2015) 565–586, arXiv:1503.05825 [nucl-ex].

[868] CMS Collaboration, V. Khachatryan et al., *Study of Z boson production in pPb collisions at $\sqrt{s_{NN}} = 5.02$ TeV*, Phys. Lett. **B759** (2016) 36–57, arXiv:1512.06461 [hep-ex].

[869] CMS Collaboration, A. M. Sirunyan et al., *Constraining gluon distributions in nuclei using dijets in proton-proton and proton-lead collisions at $\sqrt{s_{\rm NN}} = 5.02$ TeV*, Phys. Rev. Lett. **121** (2018) no. 6, 062002, arXiv:1805.04736 [hep-ex].

[870] CMS Collaboration, A. M. Sirunyan et al., *Observation of top quark production in proton-nucleus collisions*, Phys. Rev. Lett. **119** (2017) no. 24, 242001, arXiv:1709.07411 [nucl-ex].

[871] CMS Collaboration, *Constraints on nuclear parton distributions from W boson production in pPb collisions at $\sqrt{s_{\rm NN}} = 8.16$ TeV*, CMS-PAS-HIN-17-007, CERN, Geneva, 2018. https://cds.cern.ch/record/2318138.

[872] S. Dulat, T.-J. Hou, J. Gao, et al., *New parton distribution functions from a global analysis of quantum chromodynamics*, Phys. Rev. **D93** (2016) no. 3, 033006, arXiv:1506.07443 [hep-ph].

[873] E. C. Aschenauer, S. Fazio, M. A. C. Lamont, H. Paukkunen, and P. Zurita, *Nuclear Structure Functions at a Future Electron-Ion Collider*, Phys. Rev. **D96** (2017) no. 11, 114005, arXiv:1708.05654 [nucl-ex].

[874] LHCb Collaboration, R. Aaij et al., *Study of prompt D^0 meson production in pPb collisions at $\sqrt{s_{\rm NN}} = 5$ TeV*, JHEP **10** (2017) 090, arXiv:1707.02750 [hep-ex].

[875] ALICE Collaboration, S. Acharya et al., *Production of muons from heavy-flavour hadron decays in p-Pb collisions at $\sqrt{s_{\rm NN}} = \mathbf{5.02}$ TeV*, Phys. Lett. **B770** (2017) 459–472, arXiv:1702.01479 [nucl-ex].

[876] I. Helenius and H. Paukkunen, *Revisiting the D-meson hadroproduction in general-mass variable flavour number scheme*, JHEP **05** (2018) 196, arXiv:1804.03557 [hep-ph].

[877] I. Helenius, K. J. Eskola, and H. Paukkunen, *Probing the small-x nuclear gluon distributions with isolated photons at forward rapidities in p+Pb collisions at the LHC*, JHEP **09** (2014) 138, arXiv:1406.1689 [hep-ph].

[878] D. Kharzeev, E. Levin, and L. McLerran, *Jet azimuthal correlations and parton saturation in the color glass condensate*, Nucl. Phys. **A748** (2005) 627–640, arXiv:hep-ph/0403271 [hep-ph].

[879] A. van Hameren, P. Kotko, K. Kutak, C. Marquet, and S. Sapeta, *Saturation effects in forward-forward dijet production in p+Pb collisions*, Phys. Rev. **D89** (2014) no. 9, 094014, arXiv:1402.5065 [hep-ph].

[880] F. Dominguez, C. Marquet, B.-W. Xiao, and F. Yuan, *Universality of Unintegrated Gluon Distributions at small x*, Phys. Rev. **D83** (2011) 105005, arXiv:1101.0715 [hep-ph].

[881] C. Marquet, E. Petreska, and C. Roiesnel, *Transverse-momentum-dependent gluon distributions from JIMWLK evolution*, JHEP **10** (2016) 065, arXiv:1608.02577 [hep-ph].

[882] J. L. Albacete, G. Giacalone, C. Marquet, and M. Matas, *Forward dihadron back-to-back correlations in pA collisions*, Phys. Rev. **D99** (2019) no. 1, 014002, arXiv:1805.05711 [hep-ph].

[883] E. Akcakaya, A. Schäfer, and J. Zhou, *Azimuthal asymmetries for quark pair production in pA collisions*, Phys. Rev. **D87** (2013) no. 5, 054010, arXiv:1208.4965 [hep-ph].

[884] C. Marquet, C. Roiesnel, and P. Taels, *Linearly polarized small-x gluons in forward heavy-quark pair production*, Phys. Rev. **D97** (2018) no. 1, 014004, arXiv:1710.05698 [hep-ph].

[885] C. Marquet, *Forward inclusive dijet production and azimuthal correlations in p(A) collisions*, Nucl. Phys. **A796** (2007) 41–60, arXiv:0708.0231 [hep-ph].

[886] P. J. Mulders and J. Rodrigues, *Transverse momentum dependence in gluon distribution and fragmentation functions*, Phys. Rev. **D63** (2001) 094021, arXiv:hep-ph/0009343 [hep-ph].

[887] D. Boer, P. J. Mulders, and C. Pisano, *Dijet imbalance in hadronic collisions*, Phys. Rev. **D80** (2009) 094017, arXiv:0909.4652 [hep-ph].

[888] D. Boer, S. J. Brodsky, P. J. Mulders, and C. Pisano, *Direct Probes of Linearly Polarized Gluons inside Unpolarized Hadrons*, Phys. Rev. Lett. **106** (2011) 132001, arXiv:1011.4225 [hep-ph].

[889] A. Metz and J. Zhou, *Distribution of linearly polarized gluons inside a large nucleus*, Phys. Rev. **D84** (2011) 051503, arXiv:1105.1991 [hep-ph].

[890] F. Dominguez, J.-W. Qiu, B.-W. Xiao, and F. Yuan, *On the linearly polarized gluon distributions in the color dipole model*, Phys. Rev. **D85** (2012) 045003, arXiv:1109.6293 [hep-ph].

[891] LHCb Collaboration, R. Aaij et al., *Observation of double charm production involving open charm in pp collisions at $\sqrt{s}$ = 7 TeV*, JHEP **06** (2012) 141, arXiv:1205.0975 [hep-ex]. [Addendum: JHEP03,108(2014)].

[892] S. Peigné and R. Kolevatov, *Medium-induced soft gluon radiation in forward dijet production in relativistic proton-nucleus collisions*, JHEP **01** (2015) 141, arXiv:1405.4241 [hep-ph].

[893] F. Arleo, R. Kolevatov, and S. Peigné, *Coherent medium-induced gluon radiation in hard forward $1 \to 1$ partonic processes*, Phys. Rev. **D93** (2016) 014006, arXiv:1402.1671 [hep-ph].

[894] F. Arleo and S. Peigné, *J/ψ suppression in pA collisions from parton energy loss in cold QCD matter*, Phys. Rev. Lett. **109** (2012) 122301, arXiv:1204.4609 [hep-ph].

[895] F. Arleo and S. Peigné, *Heavy-quarkonium suppression in pA collisions from parton energy loss in cold QCD matter*, JHEP **03** (2013) 122, arXiv:1212.0434 [hep-ph].

[896] F. Arleo, R. Kolevatov, S. Peigné, and M. Rustamova, *Centrality and $p_\perp$ dependence of J/ψ suppression in proton-nucleus collisions from parton energy loss*, JHEP **05** (2013) 155, arXiv:1304.0901 [hep-ph].

[897] T. Stavreva, I. Schienbein, F. Arleo, et al., *Probing gluon and heavy-quark nuclear PDFs with gamma + Q production in pA collisions*, JHEP **01** (2011) 152, arXiv:1012.1178 [hep-ph].

[898] LHCb Collaboration, R. Aaij et al., *Measurement of the B_c^+ meson lifetime using $B_c^+ \to J/\psi\mu^+\nu_\mu X$ decays*, Eur. Phys. J. **C74** (2014) no. 5, 2839, arXiv:1401.6932 [hep-ex].

[899] NNPDF Collaboration, R. D. Ball et al., *Parton distributions from high-precision collider data*, Eur. Phys. J. **C77** (2017) no. 10, 663, arXiv:1706.00428 [hep-ph].

[900] S. Alekhin, J. Blümlein, S. Moch, and R. Placakyte, *Parton distribution functions, α_s, and heavy-quark masses for LHC Run II*, Phys. Rev. **D96** (2017) no. 1, 014011, arXiv:1701.05838 [hep-ph].

[901] CHORUS Collaboration, G. Onengut et al., *Measurement of nucleon structure functions in neutrino scattering*, Phys. Lett. **B632** (2006) 65–75.

[902] NuTeV Collaboration, M. Goncharov et al., *Precise Measurement of Dimuon Production Cross-Sections in ν_μ Fe and $\bar{\nu}_\mu$ Fe Deep Inelastic Scattering at the Tevatron.*, Phys. Rev. **D64** (2001) 112006, arXiv:hep-ex/0102049 [hep-ex].

[903] D. A. Mason, *Measurement of the strange - antistrange asymmetry at NLO in QCD from NuTeV dimuon data*. PhD thesis, Oregon U., 2006. http://lss.fnal.gov/archive/thesis/2000/fermilab-thesis-2006-01.pdf.

[904] NOMAD Collaboration, O. Samoylov et al., *A Precision Measurement of Charm Dimuon Production in Neutrino Interactions from the NOMAD Experiment*, Nucl. Phys. **B876** (2013) 339–375, arXiv:1308.4750 [hep-ex].

[905] A. Kayis-Topaksu et al., *Measurement of charm production in neutrino charged-current interactions*, New J. Phys. **13** (2011) 093002, arXiv:1107.0613 [hep-ex].

[906] M. Hirai, S. Kumano, and T. H. Nagai, *Nuclear parton distribution functions and their uncertainties*, Phys. Rev. **C70** (2004) 044905, arXiv:hep-ph/0404093 [hep-ph].

[907] ATLAS Collaboration, M. Aaboud et al., *Precision measurement and interpretation of inclusive W^+ , W^- and Z/γ^* production cross sections with the ATLAS detector*, Eur. Phys. J. **C77** (2017) no. 6, 367, arXiv:1612.03016 [hep-ex].

[908] A. Kusina, F. Lyonnet, D. B. Clark, et al., *Vector boson production in pPb and PbPb collisions at the LHC and its impact on nCTEQ15 PDFs*, Eur. Phys. J. **C77** (2017) no. 7, 488, arXiv:1610.02925 [nucl-th].

[909] nCTEQ Collaboration, E. Godat et al., *PDF Flavor Determination and the nCTEQ PDFs: $W^\pm/Z$ vector boson production in heavy ion collisions*, PoS **DIS2018** (2018) 009, arXiv:1808.07514 [hep-ph].

[910] LHCb Collaboration, R. Aaij et al., *Observation of Z production in proton-lead collisions at LHCb*, JHEP **09** (2014) 030, arXiv:1406.2885 [hep-ex].

[911] ALICE Collaboration, J. Adam et al., *W and Z boson production in p-Pb collisions at $\sqrt{s_{\rm NN}}$ = 5.02 TeV*, JHEP **02** (2017) 077, arXiv:1611.03002 [nucl-ex].

[912] ATLAS Collaboration, G. Aad et al., *Determination of the strange quark density of the proton from ATLAS measurements of the $W \to \ell\nu$ and $Z \to \ell\ell$ cross sections*, Phys. Rev. Lett. **109** (2012) 012001, arXiv:1203.4051 [hep-ex].

[913] A. M. Cooper-Sarkar and K. Wichmann, *QCD analysis of the ATLAS and CMS $W^\pm$ and Z cross-section measurements and implications for the strange sea density*, Phys. Rev. **D98** (2018) no. 1, 014027, arXiv:1803.00968 [hep-ex].

[914] H. Paukkunen and C. A. Salgado, *Constraints for the nuclear parton distributions from Z and W production at the LHC*, JHEP **03** (2011) 071, arXiv:1010.5392 [hep-ph].

[915] H. Paukkunen and P. Zurita, *PDF reweighting in the Hessian matrix approach*, JHEP **12** (2014) 100, arXiv:1402.6623 [hep-ph].

[916] LHeC study Group Collaboration, H. Paukkunen, *An update on nuclear PDFs at the LHeC*, PoS **DIS2017** (2018) 109, arXiv:1709.08342 [hep-ph].

[917] A. Kusina, J. P. Lansberg, I. Schienbein, and H. S. Shao, *Impact of LHC Heavy-Flavour Data on Nuclear Gluon PDF*, Acta Phys. Polon. **B49** (2018) 1185.

[918] ALICE Collaboration, B. B. Abelev et al., *Measurement of prompt D-meson production in $p-Pb$ collisions at $\sqrt{s_{NN}}$ = 5.02 TeV*, Phys. Rev. Lett. **113** (2014) no. 23, 232301, arXiv:1405.3452 [nucl-ex].

[919] ALICE Collaboration, J. Adam et al., *D-meson production in p-Pb collisions at $\sqrt{s_{\rm NN}}$ =5.02 TeV and in pp collisions at $\sqrt{s}$ =7 TeV*, Phys. Rev. **C94** (2016) no. 5, 054908, arXiv:1605.07569 [nucl-ex].

[920] ALICE Collaboration, J. Adam et al., *Rapidity and transverse-momentum dependence of the inclusive J/ψ nuclear modification factor in p-Pb collisions at $\sqrt{s_{N\,N}} = 5.02$ TeV*, JHEP **06** (2015) 055, arXiv:1503.07179 [nucl-ex].

[921] ALICE Collaboration, B. B. Abelev et al., *J/ψ production and nuclear effects in p-Pb collisions at $\sqrt{S_{NN}}$ = 5.02 TeV*, JHEP **02** (2014) 073, arXiv:1308.6726 [nucl-ex].

[922] LHCb Collaboration, R. Aaij et al., *Study of J/ψ production and cold nuclear matter effects in pPb collisions at $\sqrt{s_{NN}} = 5$ TeV*, JHEP **02** (2014) 072, arXiv:1308.6729 [nucl-ex].

[923] LHCb Collaboration, *Measurement of B^+, B^0 and Λ_b^0 production and nuclear modification in pPb collisions at $\sqrt{s_{\rm NN}} = 8.16$ TeV*, LHCb-CONF-2018-004, CERN, Geneva, Oct, 2018. https://cds.cern.ch/record/2641671.

[924] ALICE Collaboration, B. B. Abelev et al., *Production of inclusive Υ(1S) and Υ(2S) in p-Pb collisions at $\sqrt{\mathbf{s}_{\rm NN}} = \mathbf{5.02}$ TeV*, Phys. Lett. **B740** (2015) 105–117, arXiv:1410.2234 [nucl-ex].

[925] LHCb Collaboration, R. Aaij et al., *Study of Υ production and cold nuclear matter effects in pPb collisions at $\sqrt{s_{NN}}$=5 TeV*, JHEP **07** (2014) 094, arXiv:1405.5152 [nucl-ex].

[926] ATLAS Collaboration, *D meson production and long-range azimuthal correlation in* 8.16 TeV *p+Pb collisions with ATLAS*, ATLAS-CONF-2017-073, CERN, Geneva, Sep, 2017. https://cds.cern.ch/record/2285811.

[927] CMS Collaboration, A. M. Sirunyan et al., *Measurement of exclusive Υ photoproduction from protons in pPb collisions at $\sqrt{s_{\rm NN}} = 5.02$ TeV*, Eur. Phys. J. **C79** (2019) no. 3, 277, arXiv:1809.11080 [hep-ex].

[928] CMS Collaboration, A. M. Sirunyan et al., *Measurement of prompt ψ(2S) production cross sections in proton-lead and proton-proton collisions at $\sqrt{s_{\rm NN}} = 5.02$ TeV*, Phys. Lett. **B790** (2019) 509–532, arXiv:1805.02248 [hep-ex].

[929] LHCb Collaboration, R. Aaij et al., *Prompt Λ_c^+ production in* pPb *collisions at $\sqrt{s_{NN}} = 5.02$ TeV*, JHEP **02** (2019) 102, arXiv:1809.01404 [hep-ex].

[930] B. A. Kniehl, G. Kramer, I. Schienbein, and H. Spiesberger, *Open charm hadroproduction and the charm content of the proton*, Phys. Rev. **D79** (2009) 094009, arXiv:0901.4130 [hep-ph].

[931] S. J. Brodsky, A. Kusina, F. Lyonnet, et al., *A review of the intrinsic heavy quark content of the nucleon*, Adv. High Energy Phys. **2015** (2015) 231547, arXiv:1504.06287 [hep-ph].

[932] F. Lyonnet, A. Kusina, T. Ježo, et al., *On the intrinsic bottom content of the nucleon and its impact on heavy new physics at the LHC*, JHEP **07** (2015) 141, arXiv:1504.05156 [hep-ph].

[933] ATLAS Collaboration, *Prompt photon production in $\sqrt{s_{\rm NN}} = 8.16$ TeV p+Pb collisions with ATLAS*, ATLAS-CONF-2017-072, CERN, Geneva, Sep, 2017. https://cds.cern.ch/record/2285810.

[934] S. Catani, L. Cieri, D. de Florian, G. Ferrera, and M. Grazzini, *Diphoton production at the LHC: a QCD study up to NNLO*, JHEP **04** (2018) 142, arXiv:1802.02095 [hep-ph].

[935] B. Boussaha, F. Iddir, and L. Semlala, *Predictions for the isolated diphoton production through NNLO in QCD and comparison to the 8 TeV ATLAS data*, Adv. High Energy Phys. **2018** (2018) 4174602, arXiv:1803.09176 [hep-ph].

[936] ATLAS, CDF, CMS, D0 Collaboration, M. Dunford, *W and Z production in association with light and heavy-flavour jets at the LHC and the Tevatron*, EPJ Web Conf. **49** (2013) 06004.

[937] ATLAS Collaboration, P. H. Beauchemin, *ATLAS measurements of jets and heavy flavor produced in association with W and Z bosons*, PoS **ICHEP2012** (2013) 263.

[938] ATLAS, CDF, CMS, D0 Collaboration, L. Di Ciaccio, *W and Z production in association with light and heavy-flavour jets at the LHC and the Tevatron*, EPJ Web Conf. **60** (2013) 05003.

[939] CMS Collaboration, V. Candelise, *Associated production of heavy flavors and W, Z bosons at CMS*, Nuovo Cim. **C38** (2015) no. 1, 6.

[940] CMS Collaboration, S. Chatrchyan et al., *Measurement of associated W + charm production in pp collisions at $\sqrt{s}$ = 7 TeV*, JHEP **02** (2014) 013, arXiv:1310.1138 [hep-ex].

[941] ATLAS Collaboration, G. Aad et al., *Measurement of the production of a W boson in association with a charm quark in pp collisions at $\sqrt{s} = 7$ TeV with the ATLAS detector*, JHEP **05** (2014) 068, arXiv:1402.6263 [hep-ex].

[942] D. d'Enterria, K. Krajczár, and H. Paukkunen, *Top-quark production in proton-nucleus and nucleus-nucleus collisions at LHC energies and beyond*, Phys. Lett. **B746** (2015) 64–72, arXiv:1501.05879 [hep-ph].

[943] J. M. Campbell, R. K. Ellis, and W. T. Giele, *A Multi-Threaded Version of MCFM*, Eur. Phys. J. **C75** (2015) no. 6, 246, arXiv:1503.06182 [physics.comp-ph].

[944] L. Apolinário, J. G. Milhano, G. P. Salam, and C. A. Salgado, *Probing the time structure of the quark-gluon plasma with top quarks*, Phys. Rev. Lett. **120** (2018) no. 23, 232301, arXiv:1711.03105 [hep-ph].

[945] H. Paukkunen, *Nuclear PDFs Today*, in *9th International Conference on Hard and Electromagnetic Probes of High-Energy Nuclear Collisions: Hard Probes 2018 (HP2018) Aix-Les-Bains, Savoie, France, October 1-5, 2018*. 2018. arXiv:1811.01976 [hep-ph].

[946] V. Emel'yanov, A. Khodinov, S. R. Klein, and R. Vogt, *Impact parameter dependence of J / psi and Drell-Yan production in heavy ion collisions at S**(1/2) (N N) = 17.3-GeV*, Phys. Rev. **C59** (1999) 1860–1863, arXiv:hep-ph/9809222 [hep-ph].

[947] E. G. Ferreiro, F. Fleuret, J. P. Lansberg, and A. Rakotozafindrabe, *Cold nuclear matter effects on J/psi production: Intrinsic and extrinsic transverse momentum effects*, Phys. Lett. **B680** (2009) 50–55, arXiv:0809.4684 [hep-ph].

[948] I. Helenius, K. J. Eskola, H. Honkanen, and C. A. Salgado, *Impact-Parameter Dependent Nuclear Parton Distribution Functions: EPS09s and EKS98s and Their Applications in Nuclear Hard Processes*, JHEP **07** (2012) 073, arXiv:1205.5359 [hep-ph].

[949] A. Kovner, T. Altinoluk, N. Armesto, G. Beuf, and M. Lublinsky, *Initial state correlations*, PoS **QCDEV2016** (2017) 010.

[950] CMS Collaboration, A. M. Sirunyan et al., *Charged-particle nuclear modification factors in XeXe collisions at $\sqrt{s_{\mathrm{NN}}} = 5.44$ TeV*, JHEP **10** (2018) 138, arXiv:1809.00201 [hep-ex].

[951] ATLAS Collaboration, *Charged hadron spectra and dijet p_{T} correlations measured in Xe+Xe collisions at $\sqrt{s_{_{NN}}} = 5.44$TeV with the ATLAS detector*, ATLAS-CONF-2018-007, CERN, Geneva, May, 2018. https://cds.cern.ch/record/2318588.

[952] K. Zapp, J. Stachel, and U. A. Wiedemann, *JEWEL - a Monte Carlo Model for Jet Quenching*, PoS **High-pT physics09** (2009) 022, arXiv:0904.4885 [hep-ph].

[953] R. Barrett and D. Jackson, *Nuclear Sizes and Structure*. The International Series of Monographs on Physics. Oxford University Press, Incorporated, 1977. ISBN 9780198512721. https://books.google.ch/books?id=-hxRAAAAMAAJ.

[954] Belle Collaboration, C.-C. Kuo et al., *Measurement of $\gamma\gamma \to p$ anti-p production at Belle*, Phys. Lett. **B621** (2005) 41–55, arXiv:hep-ex/0503006 [hep-ex].

[955] M. Kłusek-Gawenda, P. Lebiedowicz, O. Nachtmann, and A. Szczurek, *From the $\gamma\gamma \to p\bar{p}$ reaction to the production of $p\bar{p}$ pairs in ultraperipheral ultrarelativistic heavy-ion collisions at the LHC*, Phys. Rev. **D96** (2017) no. 9, 094029, arXiv:1708.09836 [hep-ph].

[956] M. Diehl, P. Kroll, and C. Vogt, *Two photon annihilation into baryon anti-baryon pairs*, Eur. Phys. J. **C26** (2003) 567–577, arXiv:hep-ph/0206288 [hep-ph].

[957] ALICE Collaboration, E. L. Kryshen, *Photoproduction of heavy vector mesons in ultra-peripheral Pb-Pb collisions*, Nucl. Phys. **A967** (2017) 273–276, arXiv:1705.06872 [nucl-ex].

[958] CMS Collaboration, A. M. Sirunyan et al., *Evidence for light-by-light scattering and searches for axion-like particles in ultraperipheral PbPb collisions at* $\sqrt{s_{\mathrm{NN}}} = 5.02$ *TeV*, arXiv:1810.04602 [hep-ex].

[959] ATLAS Collaboration, G. Aad et al., *Technical Design Report for the Phase-I Upgrade of the ATLAS TDAQ System*, CERN-LHCC-2013-018, ATLAS-TDR-023, 2013. https://cds.cern.ch/record/1602235.

[960] CMS Collaboration, A. Tapper and D. Acosta, *CMS Technical Design Report for the Level-1 Trigger Upgrade*, CERN-LHCC-2013-011. CMS-TDR-12, Jun, 2013. https://cds.cern.ch/record/1556311.

[961] L. A. Harland-Lang, V. A. Khoze, and M. G. Ryskin, *Exclusive LHC physics with heavy ions: SuperChic 3*, Eur. Phys. J. **C79** (2019) no. 1, 39, arXiv:1810.06567 [hep-ph].

[962] ALICE Collaboration, B. B. Abelev et al., *Neutral pion production at midrapidity in pp and Pb-Pb collisions at* $\sqrt{s_{\mathrm{NN}}} = 2.76$ TeV, Eur. Phys. J. **C74** (2014) no. 10, 3108, arXiv:1405.3794 [nucl-ex].

[963] M. Kłusek-Gawenda, *Importance of mesons in light-by-light scattering in ultraperipheral lead-lead collisions at the LHC*, EPJ Web Conf. **199** (2019) 05004, arXiv:1809.03823 [hep-ph].

[964] D. d'Enterria and G. G. da Silveira, *Observing light-by-light scattering at the Large Hadron Collider*, Phys. Rev. Lett. **111** (2013) 080405, arXiv:1305.7142 [hep-ph]. [Erratum: Phys. Rev. Lett.116,no.12,129901(2016)].

[965] M. Kłusek-Gawenda, P. Lebiedowicz, and A. Szczurek, *Light-by-light scattering in ultraperipheral Pb-Pb collisions at energies available at the CERN Large Hadron Collider*, Phys. Rev. **C93** (2016) no. 4, 044907, arXiv:1601.07001 [nucl-th].

[966] M. Kłusek-Gawenda, W. Schäfer, and A. Szczurek, *Two-gluon exchange contribution to elastic* $\gamma\gamma \to \gamma\gamma$ *scattering and production of two-photons in ultraperipheral ultrarelativistic heavy ion and proton-proton collisions*, Phys. Lett. **B761** (2016) 399–407, arXiv:1606.01058 [hep-ph].

[967] ALICE Collaboration, S. Acharya et al., *Neutral pion and* η *meson production at mid-rapidity in Pb-Pb collisions at* $\sqrt{s_{NN}} = 2.76$ *TeV*, Phys. Rev. (2018) , arXiv:1803.05490 [nucl-ex]. [Phys. Rev.C98,044901(2018)].

[968] E. Govorkova, *Study of* π^0/γ *efficiency using* B *meson decays in the LHCb experiment*, Phys. Atom. Nucl. **79** (2016) no. 11-12, 1474–1476, arXiv:1505.02960 [hep-ex].

[969] G. Jikia and A. Tkabladze, *Photon-photon scattering at the photon linear collider*, Phys. Lett. **B323** (1994) 453–458, arXiv:hep-ph/9312228 [hep-ph].

[970] Z. Bern, A. De Freitas, L. J. Dixon, A. Ghinculov, and H. L. Wong, *QCD and QED corrections to light by light scattering*, JHEP **11** (2001) 031, arXiv:hep-ph/0109079 [hep-ph].

[971] D. Bardin, L. Kalinovskaya, and E. Uglov, *Standard Model light-by-light scattering in SANC: analytic and numeric evaluation*, Phys. Atom. Nucl. **73** (2010) 1878–1888, arXiv:0911.5634 [hep-ph].

[972] Particle Data Group Collaboration, C. Patrignani et al., *Review of Particle Physics*, Chin. Phys. **C40** (2016) no. 10, 100001.

[973] S. R. Klein, *Comment on "η_c production in photon-induced interactions at the LHC"*, Phys. Rev. **D98** (2018) 118501, arXiv:1808.08253 [hep-ph].

[974] M. Kłusek-Gawenda and A. Szczurek, *$\pi^+\pi^-$ and $\pi^0\pi^0$ pair production in photon-photon and in ultraperipheral ultrarelativistic heavy ion collisions*, Phys. Rev. **C87** (2013) no. 5, 054908, arXiv:1302.4204 [nucl-th].

[975] R. D. Peccei and H. R. Quinn, *CP Conservation in the Presence of Instantons*, Phys. Rev. Lett. **38** (1977) 1440–1443.

[976] R. D. Peccei and H. R. Quinn, CP *Conservation in the Presence of Pseudoparticles*, Phys. Rev. Lett. **38** (Jun, 1977) 1440–1443. https://link.aps.org/doi/10.1103/PhysRevLett.38.1440.

[977] M. Bauer, M. Neubert, and A. Thamm, *Collider Probes of Axion-Like Particles*, JHEP **12** (2017) 044, arXiv:1708.00443 [hep-ph].

[978] K. Mimasu and V. Sanz, *ALPs at Colliders*, JHEP **06** (2015) 173, arXiv:1409.4792 [hep-ph].

[979] J. Jaeckel and M. Spannowsky, *Probing MeV to 90 GeV axion-like particles with LEP and LHC*, Phys. Lett. **B753** (2016) 482–487, arXiv:1509.00476 [hep-ph].

[980] S. Knapen, T. Lin, H. K. Lou, and T. Melia, *Searching for Axionlike Particles with Ultraperipheral Heavy-Ion Collisions*, Phys. Rev. Lett. **118** (2017) no. 17, 171801, arXiv:1607.06083 [hep-ph].

[981] I. Brivio, M. B. Gavela, L. Merlo, et al., *ALPs Effective Field Theory and Collider Signatures*, Eur. Phys. J. **C77** (2017) no. 8, 572, arXiv:1701.05379 [hep-ph].

[982] S. Knapen, T. Lin, H. K. Lou, and T. Melia, *LHC limits on axion-like particles from heavy-ion collisions*, in *Photon 2017: International Conference on the Structure and the Interactions of the Photon and 22th International Workshop on Photon-Photon Collisions and the International Workshop on High Energy Photon Colliders CERN, Geneva, Switzerland, May 22-26, 2017*. 2017. arXiv:1709.07110 [hep-ph].

[983] A. L. Read, *Presentation of search results: The CL(s) technique*, J. Phys. **G28** (2002) 2693–2704.

[984] C. Baldenegro, S. Fichet, G. Von Gersdorff, and C. Royon, *Searching for axion-like particles with proton tagging at the LHC*, JHEP **06** (2018) 131, arXiv:1803.10835 [hep-ph].

[985] K.-H. Kampert and M. Unger, *Measurements of the Cosmic Ray Composition with Air Shower Experiments*, Astropart. Phys. **35** (2012) 660–678, arXiv:1201.0018 [astro-ph.HE].

[986] Pierre Auger Collaboration, A. Aab et al., *Muons in air showers at the Pierre Auger Observatory: Mean number in highly inclined events*, Phys. Rev. **D91** (2015) no. 3, 032003, arXiv:1408.1421 [astro-ph.HE]. [Erratum: Phys. Rev.D91,no.5,059901(2015)].

[987] Liverpool Telescope, MAGIC, H.E.S.S., AGILE, Kiso, VLA/17B-403, INTEGRAL, Kapteyn, Subaru, HAWC, Fermi-LAT, ASAS-SN, VERITAS, Kanata, IceCube, Swift NuSTAR Collaboration, Liverpool Telescope, MAGIC, H.E.S.S., et al., *Multimessenger observations of a flaring blazar coincident with high-energy neutrino IceCube-170922A*, Science **361** (2018) no. 6398, eaat1378, arXiv:1807.08816 [astro-ph.HE].

[988] K. Werner, F.-M. Liu, and T. Pierog, *Parton ladder splitting and the rapidity dependence of transverse momentum spectra in deuteron-gold collisions at RHIC*, Phys. Rev. **C74** (2006) 044902, arXiv:hep-ph/0506232 [hep-ph].

[989] S. Ostapchenko, *Monte Carlo treatment of hadronic interactions in enhanced Pomeron scheme: I. QGSJET-II model*, Phys. Rev. **D83** (2011) 014018, arXiv:1010.1869 [hep-ph].

[990] F. Riehn, H. P. Dembinski, R. Engel, et al., *The hadronic interaction model SIBYLL 2.3c and Feynman scaling*, PoS **ICRC2017** (2018) 301, arXiv:1709.07227 [hep-ph]. [35,301(2017)].

[991] LHCb Collaboration, R. Aaij et al., *Measurement of the inelastic pp cross-section at a centre-of-mass energy of 13 TeV*, JHEP **06** (2018) 100, arXiv:1803.10974 [hep-ex].

[992] EAS-MSU, IceCube, KASCADE-Grande, NEVOD-DECOR, Pierre Auger, SUGAR, Telescope Array, Yakutsk EAS Array Collaboration, H. P. Dembinski et al., *Report on Tests and Measurements of Hadronic Interaction Properties with Air Showers*, in *Ultra High Energy Cosmic Rays (UHECR 2018) Paris, France, October 8-12, 2018*. 2019. arXiv:1902.08124 [astro-ph.HE].

[993] IceCube Collaboration, H. Dembinski, *Investigating cosmic rays and air shower physics with IceCube/IceTop*, in *Proceedings, 19th International Symposium on Very High Energy Cosmic Ray Interactions (ISVHECRI 2016): Moscow, Russia, August 22-27, 2016*, vol. 145, p. 01003. 2017.

[994] R. P. Kokoulin, A. G. Bogdanov, G. Mannocchi, et al., *Local muon density spectra at large zenith angles as a probe of high-energy hadronic interaction models*, Nucl. Phys. Proc. Suppl. **196** (2009) 106–109.

[995] Telescope Array Collaboration, R. U. Abbasi et al., *Study of muons from ultrahigh energy cosmic ray air showers measured with the Telescope Array experiment*, Phys. Rev. **D98** (2018) no. 2, 022002, arXiv:1804.03877 [astro-ph.HE].

[996] R. Ulrich, R. Engel, and M. Unger, *Hadronic Multiparticle Production at Ultra-High Energies and Extensive Air Showers*, Phys. Rev. **D83** (2011) 054026, arXiv:1010.4310 [hep-ph].

[997] T. Pierog and K. Werner, *Muon Production in Extended Air Shower Simulations*, Phys. Rev. Lett. **101** (2008) 171101, arXiv:astro-ph/0611311 [astro-ph].

[998] ALICE Collaboration, B. Kim, *ALICE results on system-size dependence of charged-particle multiplicity density in p–Pb, Pb–Pb and Xe–Xe collisions*, Nucl. Phys. **A982** (2019) 279–282, arXiv:1807.09061 [hep-ex].

[999] D. d'Enterria, T. Pierog, and G. Sun, *Impact of QCD jets and heavy-quark production in cosmic-ray proton atmospheric showers up to 10^{20} eV*, Astrophys. J. **874** (2019) 152, arXiv:1809.06406 [astro-ph.HE].

[1000] LHCf Collaboration, O. Adriani et al., *Measurements of longitudinal and transverse momentum distributions for neutral pions in the forward-rapidity region with the LHCf detector*, Phys. Rev. **D94** (2016) no. 3, 032007, arXiv:1507.08764 [hep-ex].

[1001] NA61/SHINE Collaboration, A. Aduszkiewicz, *Feasibility Study for the Measurement of Nuclear Fragmentation Cross Sections with NA61/SHINE at the CERN SPS*, CERN-SPSC-2017-035. SPSC-P-330-ADD-9, CERN, Geneva, Oct, 2017. https://cds.cern.ch/record/2287004.

[1002] NA61/SHINE Collaboration, A. Aduszkiewicz, *Study of Hadron-Nucleus and Nucleus-Nucleus Collisions at the CERN SPS: Early Post-LS2 Measurements and Future Plans*, CERN-SPSC-2018-008. SPSC-P-330-ADD-10, CERN, Geneva, Mar, 2018. https://cds.cern.ch/record/2309890.

[1003] Y. Genolini, D. Maurin, I. V. Moskalenko, and M. Unger, *Current status and desired precision of the isotopic production cross sections relevant to astrophysics of cosmic rays: Li, Be, B, C, and N*, Phys. Rev. **C98** (2018) no. 3, 034611, arXiv:1803.04686 [astro-ph.HE].

[1004] J. P. Lansberg, G. Cavoto, C. Hadjidakis, et al., *Physics at a Fixed-Target Experiment Using the LHC Beams,*, Adv. High. Energy Phys., Article ID 319654, 2015. https://doi.org/10.1155/2015/319654.

[1005] C. Barschel, *Precision luminosity measurement at LHCb with beam-gas imaging*. PhD thesis, RWTH Aachen U., 2014. CERN-THESIS-2013-301.

[1006] LHCb Collaboration, R. Aaij et al., *Measurement of Antiproton Production in* pHe *Collisions at* $\sqrt{s_{NN}} = 110$ *GeV*, Phys. Rev. Lett. **121** (2018) no. 22, 222001, arXiv:1808.06127 [hep-ex].

[1007] M. Anselmino, M. Guidal, and R. P. (eds.), *The 3-D Structure of the Nucleon*, Eur. Phys. J. **A52** (2016) no. 6, . https://epja.epj.org/component/toc/?task=topic&id=591.

[1008] S. J. Brodsky, P. Hoyer, C. Peterson, and N. Sakai, *The Intrinsic Charm of the Proton*, Phys. Lett. **93B** (1980) 451–455.

[1009] D. F. Geesaman, K. Saito, and A. W. Thomas, *The nuclear EMC effect*, Ann. Rev. Nucl. Part. Sci. **45** (1995) 337–390.

[1010] J. L. Albacete and C. Marquet, *Gluon saturation and initial conditions for relativistic heavy ion collisions*, Prog. Part. Nucl. Phys. **76** (2014) 1–42, arXiv:1401.4866 [hep-ph].

[1011] R. Vogt, *Are the* J/ψ *and chi(c) A dependencies the same?*, Nucl. Phys. **A700** (2002) 539–554, arXiv:hep-ph/0107045 [hep-ph].

[1012] H. Song and U. W. Heinz, *Causal viscous hydrodynamics in 2+1 dimensions for relativistic heavy-ion collisions*, Phys. Rev. **C77** (2008) 064901, arXiv:0712.3715 [nucl-th].

[1013] B. Schenke, S. Jeon, and C. Gale, *Elliptic and triangular flow in event-by-event (3+1)D viscous hydrodynamics*, Phys. Rev. Lett. **106** (2011) 042301, arXiv:1009.3244 [hep-ph].

[1014] I. A. Karpenko, P. Huovinen, H. Petersen, and M. Bleicher, *Estimation of the shear viscosity at finite net-baryon density from* $A + A$ *collision data at* $\sqrt{s_{\rm NN}} = 7.7 - 200$ *GeV*, Phys. Rev. **C91** (2015) no. 6, 064901, arXiv:1502.01978 [nucl-th].

[1015] C. Shen and B. Schenke, *Dynamical initial state model for relativistic heavy-ion collisions*, Phys. Rev. **C97** (2018) no. 2, 024907, arXiv:1710.00881 [nucl-th].

[1016] M. A. Stephanov, *QCD phase diagram and the critical point*, Prog. Theor. Phys. Suppl. **153** (2004) 139–156, arXiv:hep-ph/0402115 [hep-ph]. [Int. J. Mod. Phys.A20,4387(2005)].

[1017] PHENIX Collaboration, A. Adare et al., *Pseudorapidity Dependence of Particle Production and Elliptic Flow in Asymmetric Nuclear Collisions of* p+*Al,* p+*Au,* d+*Au, and* ^{3}*He*+*Au at* $\sqrt{s_{_{NN}}} = 200$ *GeV*, Phys. Rev. Lett. **121** (2018) no. 22, 222301, arXiv:1807.11928 [nucl-ex].

[1018] V. P. Goncalves and W. K. Sauter, η_c *production in photon-induced interactions at a fixed target experiment at LHC as a probe of the odderon*, Phys. Rev. **D91** (2015) no. 9, 094014, arXiv:1503.05112 [hep-ph].

[1019] V. P. Gonçalves and M. M. Jaime, *Exclusive vector meson photoproduction in fixed - target collisions at the LHC*, Eur. Phys. J. **C78** (2018) no. 9, 693, arXiv:1802.04713 [hep-ph].

[1020] PAMELA collaboration, V. Bonvicini et al., *The PAMELA experiment in space*, Nucl. Instrum. Meth. **A461** (2001) 262–268.

[1021] A. Kounine, *The Alpha Magnetic Spectrometer on the International Space Station*, Int. J. Mod. Phys. **E21** (2012) no. 08, 1230005.

[1022] A. Reinert and M. W. Winkler, *A Precision Search for WIMPs with Charged Cosmic Rays*, JCAP **1801** (2018) no. 01, 055, arXiv:1712.00002 [astro-ph.HE].

[1023] M. Korsmeier, F. Donato, and M. Di Mauro, *Production cross sections of cosmic antiprotons in the light of new data from the NA61 and LHCb experiments*, Phys. Rev. D **97** (May, 2018) 103019, arXiv:1802.03030 [astro-ph.HE]. https://link.aps.org/doi/10.1103/PhysRevD.97.103019.

[1024] IceCube collaboration, M. G. Aartsen et al., *Evidence for High-Energy Extraterrestrial Neutrinos at the IceCube Detector*, Science **342** (2013) 1242856, arXiv:1311.5238 [astro-ph.HE].

[1025] R. Laha and S. J. Brodsky, *IceCube can constrain the intrinsic charm of the proton*, Phys. Rev. **D96** (2017) no. 12, 123002, arXiv:1607.08240 [hep-ph].

[1026] HERMES collaboration, A. Airapetian et al., *The HERMES polarized hydrogen and deuterium gas target in the HERA electron storage ring*, Nucl. Instrum. Meth. **A540** (2005) 68–101, arXiv:physics/0408137 [physics].

[1027] D. Kikoła, M. G. Echevarria, C. Hadjidakis, et al., *Feasibility Studies for Single Transverse-Spin Asymmetry Measurements at a Fixed-Target Experiment Using the LHC Proton and Lead Beams (AFTER@LHC)*, Few Body Syst. **58** (2017) no. 4, 139, arXiv:1702.01546 [hep-ex].

[1028] G. Denicol, A. Monnai, and B. Schenke, *Moving forward to constrain the shear viscosity of QCD matter*, Phys. Rev. Lett. **116** (2016) no. 21, 212301, arXiv:1512.01538 [nucl-th].

[1029] F. Becattini and J. Cleymans, *Chemical Equilibrium in Heavy Ion Collisions: Rapidity Dependence*, J. Phys. **G34** (2007) S959–964, arXiv:hep-ph/0701029 [hep-ph].

[1030] I. Karpenko, *Rapidity scan in heavy ion collisions at* $\sqrt{s_{\rm NN}} = 72$ *GeV using a viscous hydro + cascade model*, Acta Phys. Polon. **B50** (2019) 141–148, arXiv:1805.11998 [nucl-th].

[1031] V. Begun, D. Kikoła, V. Vovchenko, and D. Wielanek, *Estimation of the freeze-out parameters reachable in a fixed-target experiment at the CERN Large Hadron Collider*, Phys. Rev. **C98** (2018) no. 3, 034905, arXiv:1806.01303 [nucl-th].

[1032] I. V. Moskalenko and A. W. Strong, *Production and propagation of cosmic ray positrons and electrons*, Astrophys. J. **493** (1998) 694–707, arXiv:astro-ph/9710124 [astro-ph].

[1033] A. E. Vladimirov, S. W. Digel, G. Johannesson, et al., *GALPROP WebRun: an internet-based service for calculating galactic cosmic ray propagation and associated photon emissions*, Comput. Phys. Commun. **182** (2011) 1156–1161, arXiv:1008.3642 [astro-ph.HE].

[1034] E. Orlando, G. Johannesson, I. V. Moskalenko, T. A. Porter, and A. Strong, *GALPROP cosmic-ray propagation code: recent results and updates*, Nucl. Part. Phys. Proc. **297-299** (2018) 129–134, arXiv:1712.09755 [astro-ph.HE].

[1035] STAR Collaboration, B. I. Abelev et al., *Longitudinal Spin Transfer to Lambda and anti-Lambda Hyperons in Polarized Proton-Proton Collisions at* $\sqrt{s}$ *= 200 GeV*, Phys. Rev. **D80** (2009) 111102, arXiv:0910.1428.

[1036] COMPASS Collaboration, M. Alekseev et al., *Measurement of the Longitudinal Spin Transfer to Lambda and Anti-Lambda Hyperons in Polarised Muon DIS*, Eur. Phys. J. **C64** (2009) 171–179, arXiv:0907.0388 [hep-ex].

[1037] D. Yu. Ivanov, A. Schafer, L. Szymanowski, and G. Krasnikov, *Exclusive photoproduction of a heavy vector meson in QCD*, Eur. Phys. J. **C34** (2004) no. 3, 297–316, arXiv:hep-ph/0401131 [hep-ph]. [Erratum: Eur. Phys. J.C75,no.2,75(2015)].

[1038] L. Massacrier, J. P. Lansberg, L. Szymanowski, and J. Wagner, *Quarkonium-photoproduction prospects at a fixed-target experiment at the LHC (AFTER@LHC)*, CERN Proc. **1** (2018) 163, arXiv:1709.09044 [nucl-ex].

[1039] J. Koempel, P. Kroll, A. Metz, and J. Zhou, *Exclusive production of quarkonia as a probe of the GPD E for gluons*, Phys. Rev. **D85** (2012) 051502, arXiv:1112.1334 [hep-ph].

[1040] Q. Wang, X.-H. Liu, and Q. Zhao, *Photoproduction of hidden charm pentaquark states* $P_c^+(4380)$ *and* $P_c^+(4450)$, Phys. Rev. **D92** (2015) 034022, arXiv:1508.00339 [hep-ph].

[1041] ALICE Collaboration, S. Acharya et al., *Energy dependence of exclusive J/ψ photoproduction off protons in ultra-peripheral p-Pb collisions at $\sqrt{s_{\rm NN}}$ = 5.02 TeV*, arXiv:1809.03235 [nucl-ex].

[1042] M. Mangano, P. Azzi, M. Benedikt, et al., *Future Circular Collider (FCC) Conceptual Design Report (CDR)*, CERN-ACC-2018-0056, CERN, Geneva, Dec, 2018. https://cds.cern.ch/record/2651294.

[1043] D. d'Enterria, *Top-quark and Higgs boson perspectives at heavy-ion colliders*, Nucl. Part. Phys. Proc. **289-290** (2017) 237–240, arXiv:1701.08047 [hep-ex].

[1044] ALICE Collaboration, K. Aamodt et al., *Charged-particle multiplicity density at mid-rapidity in central Pb-Pb collisions at $\sqrt{s_{NN}} = 2.76$ TeV*, Phys. Rev. Lett. **105** (2010) 252301, arXiv:1011.3916 [nucl-ex].

[1045] ALICE Collaboration, S. Acharya et al., *Centrality and pseudorapidity dependence of the charged-particle multiplicity density in Xe–Xe collisions at $\sqrt{s_{\rm NN}}$ =5.44TeV*, Phys. Lett. **B790** (2019) 35–48, arXiv:1805.04432 [nucl-ex].

[1046] J. M. Campbell and R. K. Ellis, *MCFM for the Tevatron and the LHC*, Nucl. Phys. Proc. Suppl. **205-206** (2010) 10–15, arXiv:1007.3492 [hep-ph].

[1047] A. V. Baskakov, E. E. Boos, L. V. Dudko, I. P. Lokhtin, and A. M. Snigirev, *Single top quark production in heavy ion collisions at energies available at the CERN Large Hadron Collider*, Phys. Rev. **C92** (2015) no. 4, 044901, arXiv:1502.04875 [hep-ph].

[1048] D. d'Enterria and C. Loizides, *Higgs boson suppression in quark-gluon matter*, arXiv:1809.06832 [hep-ph].

[1049] E. L. Berger, J. Gao, A. Jueid, and H. Zhang, *Production and hadronic decays of Higgs bosons in heavy ion collisions*, Phys. Rev. Lett. **122** (2019) no. 4, 041803, arXiv:1804.06858 [hep-ph].

[1050] J. Ghiglieri and U. A. Wiedemann, *Thermal width of the Higgs boson in hot QCD matter*, Phys. Rev. **D99** (2019) no. 5, 054002, arXiv:1901.04503 [hep-ph].

[1051] J. Casalderrey-Solana, Y. Mehtar-Tani, C. A. Salgado, and K. Tywoniuk, *New picture of jet quenching dictated by color coherence*, Phys. Lett. **B725** (2013) 357–360, arXiv:1210.7765 [hep-ph].

[1052] Y. Liu and C.-M. Ko, *Thermal production of charm quarks in heavy ion collisions at Future Circular Collider*, J. Phys. **G43** (2016) no. 12, 125108, arXiv:1604.01207 [nucl-th].

[1053] CMS Collaboration, S. Chatrchyan et al., *Suppression of non-prompt J/ψ, prompt J/ψ, and Y(1S) in PbPb collisions at $\sqrt{s_{NN}} = 2.76$ TeV*, JHEP **05** (2012) 063, arXiv:1201.5069 [nucl-ex].

[1054] Y.-p. Liu, Z. Qu, N. Xu, and P.-f. Zhuang, *J/psi Transverse Momentum Distribution in High Energy Nuclear Collisions at RHIC*, Phys. Lett. **B678** (2009) 72–76, arXiv:0901.2757 [nucl-th].

[1055] A. Andronic, P. Braun-Munzinger, K. Redlich, and J. Stachel, *The thermal model on the verge of the ultimate test: particle production in Pb-Pb collisions at the LHC*, J. Phys. **G38** (2011) 124081, arXiv:1106.6321 [nucl-th].

[1056] M. Arneodo, *Nuclear effects in structure functions*, Phys. Rept. **240** (1994) 301–393.

[1057] D. d'Enterria, M. Klasen, and K. Piotrzkowski, *High-Energy Photon Collisions at the LHC*, Nucl. Phys. Proc. Suppl. **179B** (2008) 1.

[1058] CMS Collaboration, S. Chatrchyan et al., *Search for exclusive or semi-exclusive photon pair production and observation of exclusive and semi-exclusive electron pair production in pp collisions at $\sqrt{s} = 7$ TeV*, JHEP **11** (2012) 080, arXiv:1209.1666 [hep-ex].

[1059] CMS Collaboration, S. Chatrchyan et al., *Study of exclusive two-photon production of W^+W^- in pp collisions at $\sqrt{s} = 7$ TeV and constraints on anomalous quartic gauge couplings*, JHEP **07** (2013) 116, arXiv:1305.5596 [hep-ex].

[1060] ATLAS Collaboration, G. Aad et al., *Measurement of exclusive $\gamma\gamma \to \ell^+\ell^-$ production in proton-proton collisions at $\sqrt{s} = 7$ TeV with the ATLAS detector*, Phys. Lett. **B749** (2015) 242–261, arXiv:1506.07098 [hep-ex].

[1061] G. J. Gounaris, P. I. Porfyriadis, and F. M. Renard, *The gamma gamma —> gamma gamma process in the standard and SUSY models at high-energies*, Eur. Phys. J. **C9** (1999) 673–686, arXiv:hep-ph/9902230 [hep-ph].

[1062] I. F. Ginzburg and A. Schiller, *Search for a heavy magnetic monopole at the Tevatron and CERN LHC*, Phys. Rev. **D57** (1998) 6599–6603, arXiv:hep-ph/9802310 [hep-ph].

[1063] D. Bernard, *On the potential of light by light scattering for invisible axion detection*, Nuovo Cim. **A110** (1997) 1339–1346.

[1064] T. Kikuchi, N. Okada, and M. Takeuchi, *Unparticle physics at the photon collider*, Phys. Rev. **D77** (2008) 094012, arXiv:0801.0018 [hep-ph].

[1065] K.-m. Cheung, *Diphoton signals for low scale gravity in extra dimensions*, Phys. Rev. **D61** (2000) 015005, arXiv:hep-ph/9904266 [hep-ph].

[1066] J. L. Hewett, F. J. Petriello, and T. G. Rizzo, *Signals for noncommutative interactions at linear colliders*, Phys. Rev. **D64** (2001) 075012, arXiv:hep-ph/0010354 [hep-ph].